13th International Conference on Fracture
June 16-21, 2013 Beijing, China

ICF13

Beijing (China)

2013

Vol. A

"Sir Alan gave but never broke

Like steel he studied and like oak,

He brought up science by his hand

The royal smith kept on the brand!"

The invariant integral: some news

Genady P. Cherepanov

Honorary Life Member, the New York Academy of Sciences, USA

(Elected on Dec. 8, 1976 together with Linus C. Pauling and George Polya)

genacherepanov@hotmail.com

Abstract. Earlier, this author introduced the invariant integral as a general mathematical tool for solving the physical problems based on conservation laws, without using partial differential equations, similarly to the calculus of variations. In this paper, the invariant integral was introduced for cosmic, gravitational, electromagnetic, and elastic fields combined. In a particular case of the united cosmic-gravitational field, from the corresponding invariant integral the force *F* acting upon point mass *m* from point mass *M* and from the cosmic field was derived : $F = GmMR^{-2} - (4\pi/3)\Lambda GmR$. Here: *G* is the gravitational constant, *Λ is* the cosmological constant, and *R* is the distance between the masses. The first term provides Newton's gravitation and the second term the cosmic repulsion. This force was used to build an elementary non-relativistic cosmological model of Universe and estimate the size of Universe as well as explain the accelerated expansion of Universe recently observed by astrophysicists. The orbital speed of stars in galaxies was found out to be constant and equal to about 250 *km/s.*

Keywords: invariant integral, cosmic and gravitational field, interaction force, expansion of Universe

1. Introduction

The integrals which are invariant with respect to the integration contour or surface provide a way to write down the laws of conservation of energy, mass, momentum and so on. From them, one can derive the differential equations as the local representation of the same conservation laws. However, the invariant integral approach is more powerful because it allows one to also deal with the field singularities where the differential equations have no meaning.

In 1967, using the energy conservation law, this author derived the main invariant integral for elastic and inelastic materials and introduced it into fracture science [1]. In this approach, the invariance of the integral with respect to any integration paths followed from the energy conservation law, so that this fact seemed to be trivial and was not discussed. Particularly, the characterizing index of power-law hardening materials and the similarity were found out, which constituted the basis of the later HRR approach. In 1968, while studying strain concentration by notches and cracks, Jim Rice

utilized this integral to prove its invariance using the divergence theorem. (For this famous work, Jim was awarded several medals and prizes). In 1972, John Landes and Jim Begley, not familiar with paper [1], re-introduced the invariant integral into fracture mechanics. At about that time this author discovered that in the case of elastic materials his integral coincided with that of Jock Eshelby introduced earlier into the theory of point defects in crystal lattices. Since 1968, Jock started on actively working in fracture mechanics, too.

I can't help but recall some events of that time related to paper [1]. Since 1959 my basic scientific interests have been connected with crack growth. However, up to 1964 when I became the youngest Doctor of Science in USSR, my most significant publications were done on the problems of mechanics with unknown boundaries, including the elastic-plastic, local buckling, and contact problems. It's on these problems I earned all my degrees, although fracture has always been my main subject. At that time in USSR, this area was monopolized by unscrupulous, powerful figures close to KGB who vetoed approaches different from their own. Still and all, in 1965 I decided to leave underground and submitted a Russian manuscript entitled "On crack propagation in continuous media" into the journal "Prikladnaia Matematika I Mekhanika" (PMM or Journal of Applied Mathematics and Mechanics, JAMM). However, the publication of the paper was blocked up by the authorities and it was kept in the portfolio of the journal for two years although my earlier, less significant papers used to come out within half a year. And yet, my luck was in because the Editor-in-Chief Leo Galin, even without knowledge of the paper subject, took over the responsibility and published my paper, much mutilated though by censors for two years. At last, it came out by May 1, 1967. Later, I and brave Professor Galin paid a heavy price for this sin. By the way, after the Soviets launched the first sputnik in 1957, the urgent airmail delivered fresh issues of PMM to the best US university libraries within several days.

Since that time, I tried to show that fracture mechanics is a legitimate branch of theoretical physics and my invariant integral can be used as an efficient mathematical tool for solving singular physical problems far beyond fracture mechanics (see my book [2] written in1969 but published in Russian only in 1974 and in English later, in 1978, by McGraw Hill).

However, these ideas were poorly understood. Hopefully, what follows below can make a difference.

2. General case

Let us consider stationary processes in elastic dielectrics, with taking account of cosmic-gravitational and electromagnetic forces. In this case, the main invariant integral can be written as follows [3 - 5]

$$\Gamma_k = \int_\Sigma \left[(8\pi G)^{-1}\left(\varphi_{,i}\varphi_{,i}n_k - 2\varphi_{,i}n_i\varphi_{,k}\right) + \Lambda\varphi n_k + W_0 n_k - D_i n_i E_k - B_i n_i H_k + U n_k - \sigma_{ij} n_j u_{i,k}\, d\Sigma \qquad i, j, k = 1, 2, 3 \tag{1}$$

$$(W_0 = W + E_i D_i + H_i B_i)$$

Here: Σ, any closed surface in the $Ox_1x_2x_3$ space of Cartesian coordinates; $G\ and\ \Lambda$, the gravitational and cosmological constants respectively; φ, the potential of united cosmic-gravitational field; E_i, D_i, H_i, B_i, the vector components of electromagnetic field; $W\ and\ U$, the potentials of electromagnetic and elastic fields respectively; $u_i\ and\ \sigma_{ij}$, elastic displacements and stresses; n_i, the orts of the outer normal to Σ.

Vector $(\Gamma_1, \Gamma_2, \Gamma_3)$ represents the driving force of field singularities inside Σ, which equals the work spent to move the singularities for unit length. If all $\Gamma_k = 0$, then there are no singularities inside Σ; in this case the basic differential equations inside Σ can be derived from the invariant integral (1), e.g. the Maxwell equations, the equations of elasticity theory and gravitation.

Moreover, Eq. (1) allows one to derive the interaction laws for any particular cases, e.g. Newton's law of gravitation, Coulomb's law for electric charges, Ampere's law for electric currents, Joukowski's equation for wing lift, Irwin's law for crack driving force, Peach-Koehler's law for dislocation driving force, Eshelby's law for point inclusion driving force, as well as many new ones [2-5]. For example, the interaction force F of two electric charges $q_1\ and\ q_2$ moving in a dielectric medium along the common symmetry axis at speed V was found to be equal to [3-5]

$$F = \frac{q_1 q_2}{\varepsilon R^2}\left(\frac{V^2}{a^2} - 1\right)\left(1 - \frac{V^2}{c^2}\right)^{-1} \qquad (2)$$

Here: R, the distance between the charges in the proper reference frame; ε, the dielectric constant; $c\ and\ a$, the speed of light in vacuum and medium respectively. For $V = 0$, Eq. (2) represents Coulomb's law. If $V > a$, the force applies only to the rear charge and the force's sign changes. Eq. (2) plays the main part in electron mode fracture [3, 5] by powerful electron beams.

Taking account only of two last terms in the right-hand part of Eq. (1) provides the original invariant integral which is the basis of modern fracture mechanics [1-5].

3. Cosmic-gravitational field

In what follows we consider the united cosmic-gravitational field defined by the invariant integral as follows

$$\Gamma_k = \int_\Sigma \left[(8\pi G)^{-1}\left(\varphi_{,i}\varphi_{,i}n_k - 2\varphi_{,i}n_i\varphi_{,k}\right) + \Lambda\varphi n_k\right]d\Sigma \qquad (i,k = 1,2,3) \qquad (3)$$

$$(G = 6.67 \cdot 10^{-11} m^3 kg^{-1} s^{-2},\ \Lambda = 10^{-26} kg/m^3)$$

In Eq. (3), the first term describes the flux of gravitational energy through the closed surface Σ, the second term the work of field tractions on Σ, and the third term the flux of cosmic energy through Σ. In the present non-relativistic approach, the cosmic energy can, probably, be

interpreted as "Dark Energy" , but we refrain from using this notion here. By ignoring the third term in Eq. (3) we arrive at the classical model of gravitational field [3-5]. Using physical dualisms the cosmological and gravitational constants can be written in other units.

Let us put $\Gamma_k = 0$ in Eq. (3). It means there are no field singularities inside Σ. In this case, by using the divergence theorem one can easily transform the surface integral in Eq. (3) into the volume integral and derive the following equation for φ which is valid at any point inside Σ :

$$\varphi_{,jj} = -4\pi G\Lambda \qquad (j = 1, 2, 3) \tag{4}$$

From Eq. (4), it follows that Λ represents the density of anti-gravitational matter (negative mass) which is uniformly distributed everywhere. As a matter of fact, this is the physical interpretation of the cosmic field in the present model. For example, in this model the space volume $10^{21}m^3$, which is equal to the volume of our Earth, contains $0.01gram$ of the anti-gravitational matter so that its density 10^{30} times less than the mean density of Earth.

Now, suppose there is a point mass m at a certain point *O* inside Σ. Using the invariance of the integral in Eq. (3) with respect to Σ , one can shrink Σ and turn it into a small sphere over point *O* . Then, applying the Γ-integration procedure provides the following equation for the force $\boldsymbol{F}(\Gamma_1, \Gamma_2, \Gamma_3)$ upon mass m [3]

$$\Gamma_k = -m\varphi_{,k} \qquad (k = 1, 2, 3) \tag{5}$$

Here, $\varphi_{,k}$ is the kth component of the field intensity vector at point *O,* when there is no mass at point *O.*

The physical nature of the cosmic force as well as gravity remains unclear despite the success of general relativity and numerous other theories.

4. Interaction force

Let us find the interaction law of two point masses in the cosmic-gravitational field. Let mass m_1 be concentrated at point $(0, 0, 0)$. Solving Eq. (4) provides the following field created by this mass

$$\varphi = -Gm_1r^{-1} - (2\pi/3)G\Lambda r^2 \qquad (r^2 = x_kx_k) \tag{6}$$

The intensity of this field at point $(R, 0, 0)$ is equal to

$$\varphi_{,1} = Gm_1R^{-2} - (4\pi/3)G\Lambda R, \qquad \varphi_{,2} = 0, \qquad \varphi_{,3} = 0\,. \tag{7}$$

From Eq. (5) and Eq. (7), it follows that force F_2 upon mass m_2 at point $(R, 0, 0)$ directed along the x_1 axis is equal to

$$F_2 = -Gm_1m_2R^{-2} + (4\pi/3)m_2G\Lambda R\,. \tag{8}$$

Also, by analogy force F_1 upon mass m_1 at point $(0, 0, 0)$ is equal to

$$F_1 = Gm_1m_2R^{-2} - (4\pi/3)m_1G\Lambda R. \quad (9)$$

Eqs (8) and (9) provide the interaction law of two point masses in this model. The first term describes Newton's gravitation/attraction, and the second term the cosmic repulsion. The latter does not depend on the opposite mass that plays the only role of a trigger and gauge; and so, the latter does not follow the Newton's law that action equals counteraction. When the distance increases, the gravitation tends to zero while the repulsion tends to infinity.

Let us study some problems for two point masses.

Two free masses in the cosmic-gravitational field. Let free masses m_1 *and* m_2 on the *x*-axis be acted upon by forces of Eq. (8) and Eq. (9) where $R = x_2 - x_1 \geq 0$ (x_1 *and* x_2 are the coordinates of corresponding masses movable along the x- axis). The distance between the masses satisfies the equation

$$\frac{dv}{dt} = -G\left(\frac{m_1+m_2}{R^2} - \frac{8\pi}{3}\Lambda R\right), \quad v = \frac{dR}{dt} \quad . \quad (10)$$

If $3(m_1 + m_2) > 8\pi\Lambda R^3$ at the initial moment of time when $v = 0$, then the masses move one towards the other until they collide. If $3(m_1 + m_2) < 8\pi\Lambda R^3$ at the initial moment of time when $v = 0$, then the masses move apart one from the other until they disconnect. The solution to Eq. (10) is as follows

$$v^2 = 2G\left(\frac{m_1+m_2}{R} + \frac{4\pi}{3}\Lambda R^2\right) + C\ , \quad \text{(where } C \text{ is defined by initial conditions).} \quad (11)$$

One mass is fixed and the other is free. Suppose mass m_1 is fixed at the coordinate origin and mass m_2 is free to move along the *x*-axis. In this case let us take into account the relativistic dependence of the latter mass on its velocity. (Yet, the introduced cosmic-gravitational field does not satisfy the special relativity). In this case the velocity of the free mass can be written as follows

$$ln\left(1 - \frac{v^2}{c^2}\right) = -2Gc^{-2}\left(\frac{m_1}{R} + \frac{2\pi}{3}\Lambda R^2\right) + C\ , \quad \text{(where } C \text{ is defined by initial conditions)} \quad (12)$$

Here *c* is the speed of light.

According to the present model, the cosmic field describes the intrinsic geometrical property of material space for accelerated self-expansion.

5. The cosmological system

Let us apply the introduced cosmic-gravitational field to cosmology.

First, consider a finite system of any number of point masses in a finite volume of the 3D Euclidian space. Designate by L the maximum distance between any two masses, and by M the total mass of the system. The cosmic field attached to this system is inside the sphere of diameter $2L$. According to Eqs (8) and (9) the dimensionless number $Ch = \Lambda L^3/M$

characterizes the ratio of repulsion force to that of attraction and, hence, this number characterizes also the global behavior of this system which depends on its scale. Evidently, when $Ch \ll 1$, we can ignore the cosmic energy and its repulsion effect, and when $Ch \gg 1$, we can ignore the gravitational energy and its attraction effect.

From Eq. (10), it follows that a system of two masses expands and disappears, when $Ch > 3/(8\pi)$, and the system exists, when $Ch < 3/(8\pi)$.

Let us estimate the value of Ch for some astronomical objects.

Our solar system: Sun, Mercury, Venus, Earth, Mars, Jupiter, Saturn, Uranus, Neptune, Pluto. The latter is $10^{13}m$ distant from Sun, so that we can take $L = 10^{13}m \;\; and \;\; M = 10^{30}kg$ (about the mass of Sun). From here, it follows that $Ch = 10^{-17}$ for our solar system. And so, there is no way to observe the cosmic field from any planetary observations, although the cosmic field makes the eccentricity of planetary orbits a little bit bigger by an undetectably small amount.

Milky Way. Our galaxy Milky Way consists of more than 200 billion stars which rotate around the galaxy center where there is a Black Hole. Milky Way has a shape of a flat pancake having thickness $10^{19}m$, radius $10^{21}m$, and mass about $M = 10^{42}kg$. From here, it follows that $Ch = 10^{-5}$ for Milky Way. And so, even in the scale of the galaxy it is, probably, impossible to measure the effect of the cosmic field.

Our Universe. Our Universe consists of more than 100 billion galaxies packed in clusters and super-clusters, each of many millions of galaxies. Our Universe's fractal dimension is about 2.2 so that it resembles a flat pancake, too. According to some recent estimates for our Universe, we have $M = 3 \cdot 10^{52}kg$, $L = 3 \cdot 10^{26}m$, and $Ch = 3$.
For typical super-clusters, we have $M = 10^{48}kg$, $L = 4.65 \cdot 10^{24}m$, and $Ch = 1$.

And so, it is evident that the effect of the cosmic field can be observed and estimated only from astronomical observations of very distant objects that are close to the edge of our Universe, i.e. to the time 13.7 billion years since the Bing Bang has happened.

Let us compare the gravitational force of attraction of Earth to Sun and the cosmic force of repulsion of Earth from Sun. The first one is equal to $3.56 \cdot 10^{22}N$ while the second $2.5N$.

Now, we present an elementary, non-relativistic model of our Universe and estimate its size as follows. Suppose our Universe of mass M is homogenous so that a gravitational probe mass m is acted upon by the gravitational force $GmML^{-2}$ of attraction to the center of Universe and by the cosmic force $(4\pi/3)G\Lambda mL$ of repulsion from the center of Universe where L is the distance of the mass from the center of Universe. We define our Universe as a closed community of gravitational masses in the unbounded cosmic field. From here, it follows that the probe mass goes away and leaves Universe if $L > L_\star$ where

$$L_\star = \frac{1}{2}\left(\frac{6}{\pi}\frac{M}{\Lambda}\right)^{1/3} \qquad \left(\; Ch = \frac{3}{4\pi} \; \right) \tag{13}$$

Hence, we can come up with the conclusion that $L_\star$ represents the radius of Universe in this model which for $M = 3 \cdot 10^{52} kg$ provides $L_* = 0.71 \cdot 10^{26} m$, i.e. comparatively close to the prediction of the Lambda-CDM model.

If the probe mass is inside the homogenous Universe (i.e. $L < L_*$) , then the total force upon the mass resulting from the gravitational and anti-gravitational matter is zero so that, in average, any domain inside Universe experiences no contraction and no expansion. Moreover, the total mass of Universe is equal to zero. The gravitational matter is concentrated in many moving clots inside Universe while the anti-gravitational matter of the cosmic field is uniformly distributed everywhere. From here, it may be assumed that Universe is a gigantic fluctuation created from nothing (i.e. something which energy-mass was zero).

However, the Universe is open so that, eventually, some gravitational masses on the edge move out and go away, that is they leave Universe forever. Their place in Universe is, then, taken by some insiders. This is the way how Universe expands and, evidently , this expansion is accelerated due to the arising and growing imbalance of gravitational and anti-gravitational forces inside Universe.

The incorporation of the introduced cosmic field into the framework of general relativity seems to be impossible but it is quite plausible for the field theories using non-metric theories of gravity.

6. Orbital speed of stars in spiral galaxies

The orbital speed V of a planet in our solar system determined by equilibrium of inertia force to that of gravitation equals $(GM/R)^{1/2}$ where M is the mass of Sun and R is the distance of the planet from Sun. And so, this speed decreases tending to zero when the distance grows. Because $Ch \ll 1$ in Milky Way and other galaxies, the orbital speed of stars rotating around the center of Milky Way has, seemingly, to be described by a similar law. However, it is not. The orbital speed of stars in galaxies appears to be independent of the distance to the center and equal to about $220 - 260 \; km/\text{sec}$ (for our Sun, $225 \, km/\text{sec}$).

This paradox produced some theories. For example, the well-known MOND theory accepts that the inertia force upon a star in a galaxy is directly proportional not to the acceleration (equal to V^2/R in the case of uniform circular motion) as follows from the Newton-Galileo mechanics, but to the square of acceleration. Certainly, this approach makes the orbital speed independent of R.

Another school of thought considers Dark Energy responsible for this paradox.

Meanwhile, the structure of Milky Way and other spiral galaxies provides a simple explanation of the paradox using the classical Newton-Galileo mechanics and Newton's law of gravitation which is the right approach because $Ch \ll 1$ in the scale of galaxies so that the cosmic field can be ignored. The gravitational matter of Milky Way is uniformly distributed along the logarithmic spirals having the common pole at the center of Milky Way. These spirals are well-documented. The length of an arc of a logarithmic spiral equals $(R_2 - R_1)/\cos\beta$ where β is the constant angle between the radius-vector of a point on the spiral and the tangent to the spiral at the point while R_1 and R_2 are the distances between the pole and the ends of the arc. The arc length is directly proportional to the distance R of a point from the center of the galaxy when $R = R_2 \gg R_1$. Mass M inside of the galactic disc of radius R is also directly proportional to R because such proportionality remains for any number of spirals. In other words, $M = kR$ where k is a certain structural constant of the galaxy.

The force of attraction of a star of mass m to the center of the galaxy is equal to $Gm \cdot kR/R^2$. This force is balanced by the inertia force of Galileo-Newton. From here, the orbital speed of stars is as follows

$$V = (kG)^{1/2} \tag{14}$$

For Milky Way $k = 10^{21}\ kg/m$ and $V = 250\ km/s$. This value is close to astrophysical data.

About the same value of the orbital speed of stars has been observed in all galaxies. It means that the density of gravitational matter in all galaxies obeys the following general law

$$\rho = k/(2\pi R) \qquad\qquad (k = 10^{21}\ kg/m) \tag{15}$$

Here, ρ is the mass of gravitational matter inside unit area of the galactic disc, R is the distance from the center of the galaxy, and k is the universal galactic constant. And so, the matter density is infinite at the center which is the galaxy's Black Hole.

The logarithmic spiral is the only spiral that corresponds to this general law, see Eq. (15).

7. The Einstein equivalence principle and no annihilation paradox

The general relativity is based on the equivalence principle which says that the gravity is the inertial force in the curved space-time. The cosmic-gravitational field does not obey this principle. We illustrate the difference using the following simple example.

Let a mass m, being fixed to a point by an inextensible string of length L, rotate at a constant speed V around the point. In absence of cosmic field, the inertia force mV^2/R is balanced by the extension force in the string. Replacing the action of this string by a gravitational mass M placed at the center of rotation, such that $GmML^{-2} = mV^2/L$, we come up with the equivalence principle. (It can be also formulated as the equity of inertial mass to gravitational one).

Now, imagine a slightly "pliant" string, which cross-section diameter being directly proportional to the square root of the distance from the rotation center and which strain inversely proportional to stress in the string, with a very small proportionality coefficient. In this case, substituting the increased value of L in the above balance equation provides

$$GmML^{-2} - \eta L = m\,V^2/L \qquad (\eta\ is\ a\ very\ small\ quantity) \tag{16}$$

Here, L is the undeformed string length which is different from the real one by a small value that cannot be detected in the scale of solar system. In presence of cosmic force, the term ηL imitates the cosmic force and Eq. (16) a modified equivalence principle.

The no annihilation paradox of the present model of cosmic-gravitational field can be understood only after we get known the physical nature of cosmic field. Such a remark is valid also for many non-metric theories of gravity.

References

[1] G. P. Cherepanov, Crack propagation in continuous media (in Russian), Prikl. Mat. I Mekh. (PMM), v. 31, n. 3, (1967), 476-488. The English translation in: FRACTURE: A Topical Encyclopedia of Current Knowledge (G. P. Cherepanov, Ed.), Krieger Publ., Melbourne, 1998, 41-53.

[2] G. P. Cherepanov, Mechanics of Brittle Fracture (in Russian), Nauka, Moscow, 1974. The English translation: McGraw Hill, New York, 1978.

[3] G. P. Cherepanov, Fracture Mechanics (in Russian), IKI publ., Izhevsk-Moscow, 2012.

[4] G. P. Cherepanov, Some new applications of the invariant integrals of mechanics (in Russian), Prikl. Mat. I Mekh. (PMM), v. 76, n. 5, (2012), 823-849. The English translation: in JAMM.

[5] G.P. Cherepanov, Methods of Fracture Mechanics: Solid Matter Physics, Kluwer, Dordrecht, 1997.

The Characterization of Dominating Region of Fracture (process region) around a Crack tip Based on the Concept of Mechanical Similarity and Atomic Mechanics

A. Toshimitsu Yokobori, Jr. [1,*], **Yoshiko Nagumo** [1], **Takahiro Yajima** [1]
Toshihito Ohmi [1]

[1] Department of Nanomechanics, Tohoku University, Sendai, 980-8579, Japan
* Corresponding author: yokobori@md.mech.tohoku.ac.jp

Abstract Brittle fracture at a crack tip is considered to be caused within a specified local region, that is, process region. However, the determination of this scale has not yet been theoretically clarified. The difficulty of this determination will be due to the wide range scale analysis from the range of nano scale (atomic scale) to macro scale (crack size scale). In this paper, on the basis of the atomic mechanics using super atom and hybrid method of the fractal concept which concerns self-similarity with the proposed analysis of scale projection from macro to nano scales, the disturbed region of atom arrangements around a crack tip were clarified under the local stress field by crack and dislocation. This disturbed region was related to fracture dominating region (process region) which is in good agreement with the scale obtained from experimental consideration by R. Ritchie.

Keywords Process region, Mechanical similarity, Atomic mechanics, Brittle fracture

1. Introduction

The fracture criterion of materials is considered to be a condition that fracture occurs when a specified mechanical condition is satisfied in the local damage region around a crack. As the criterion, the energy and the local stress conditions [1-3] in this region or the hybrid theory which is taken into account for both conditions [4] have been proposed. There are corresponding local damage regions in brittle fracture, fatigue fracture and creep fracture, respectively. Each scale of these local damage regions is different respectively. For example, each local damage region is considered to correspond with the plastic region [5] for fatigue fracture and creep damage region [6] for creep fracture. For brittle fracture, the end region or process region are considered to be the dominating region of fracture [7]. However, its physical meaning has not yet been clarified. Under this condition, determination of this local region using the experimental fracture toughness has been conducted and the scale of this region is considered to be that of several grains [8]. The process region is considered to be a disordered region of atomic arrangement [3] which concerns fracture of atomic bond. This analysis requires the effects of crack, dislocations and atoms of which scales are order of mm, μm and nm on local stress field around a crack or dislocation groups. Since it is necessary to construct two dimensional atomic arrangements to realize a modeled crack or dislocations, conduction of this analysis by atomic mechanics alone requires large scale and high accuracy numerical analyses.

Under this background, authors aim to show the possibility of conducting the analysis of determination of local dominating region of brittle fracture by convenient scale of numerical analysis such as PC level analysis to conduct various calculations conveniently.

The concept of this analysis is as follows.

(1) The macro and micro local stress fields such as a crack and a dislocation are introduced as mechanical boundary conditions of the region of analysis. It causes the elimination of the necessity of the establishment of two dimensional atomic models, which gives the validity of conducting one dimensional analysis.

(2) By utilizing property of potential system of atomic force, instead of using actual atoms array, super atoms array is considered since the mechanical similarity is valid between them. Super atom

has mechanical equivalence with several actual atoms. Under the boundary condition of (1), an array of these super atoms was considered and a convenient mechanical analysis which obtains mechanical equilibrium positions of super atoms was conducted.
(3) Furthermore, these super atoms were sequentially dispersed under the mechanically equivalent state. Consequentially, the number of these atoms was increased and at each stage of the corresponding scale of these atoms, the mechanical equilibrium positions of these atoms were numerically analyzed.
(4) The characteristic of self-similarity of atom arrays was investigated based on the fractal analysis through each stage of the scale of super atoms. Super atoms were sequentially dispersed and the mechanical equilibrium positions of these atoms were numerically analyzed.
(5) The numerical analyses were conducted up to the scale stage of the super atomic array which shows the characteristic of self-similarity. From this scale stage of super atoms, disordered region of atomic arrays around the crack tip or dislocation with the actual scale of atomic array was predictively calculated and this region was defined as the process region of fracture.
Using this theory, the characterization of disordered region in the macroscopic local stress field around the crack tip becomes possible conveniently and with high accuracy. It enables us to theoretical prediction of the process region which is the dominant region of brittle fracture without the aid of experimental results.

2. The Model and Method of Analysis

2.1. The Model of Analysis

The concept of super atoms and dislocations which represent mechanically equivalent several actual atoms and dislocations, that is, the concept of image atoms and dislocations were used. Since stress field around a dislocation and interactive force between atoms are conservative, mechanical similarity on scale will be valid. Therefore, similar equations of stress field and interactive forces of dislocation and atoms of which values of intensity are different are adopted for super atoms and dislocations. At each scale stage of super atoms, using equations of interactive forces which have corresponding intensity, the equilibrium positions of super atoms were numerically analyzed. The flow of analysis and the concept of mechanical equivalence between super and actual atoms were shown in Fig. 1. With increment increase in the number of atoms, interactive forces between these atoms were dispersed and the equilibrium positions of atoms in the array were numerically analyzed respectively. The fractal analyses were conducted for the morphology of distribution of atomic density in the array at each scale stage of super atoms and the existence of self-similarity of the atoms array was investigated through each scale stage. When the characteristic of the self-similarity appears through each scale, the projection method is applied to the sequential changing characteristics of the morphology of distribution of atomic density to predict the equilibrium distribution of actual atomic arrays by considering similarity of the changing characteristic being kept due to the existence of the self-similarity. The dominating local region of brittle fracture was predicted by this method and results obtained was compared with previous results [8].

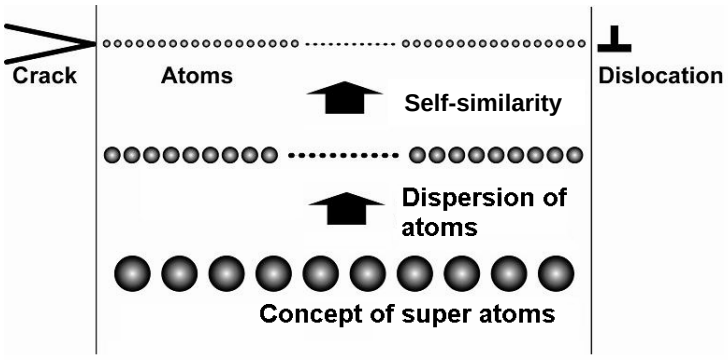

Figure 1. Dispersion method from super atoms to actual atoms under the mechanical equivalence (Scaling from macro to micro under the conservative mechanical system)

2.2. Basic Equation

In this analysis, the number of N of super atoms were placed between a crack and a super dislocation which represents dislocation groups. The equations of interaction forces exerted on super atoms were mechanically considered to be symmetry with those exerted on actual scale atoms [9]. The mechanical model used for this analysis was shown in Fig. 2. A crack tip exists at the site of $x = 0$ and shearing stress was exerted parallel to the crack that is mode II condition. The super dislocation exists at the site of $x = d$. The number of n of super atoms were placed the same scale interval. In this analysis, to avoid the jump out of atoms from this region during the process of analysis of obtaining the equilibrium positions of atoms between the crack and the super dislocation, fixed atoms were placed at the site of the crack tip and the super dislocation respectively. Local stress fields by the crack and super dislocation were given by boundary conditions in this analysis. The interaction forces between these local stress fields and fixed atoms were neglected.
The interaction force exerted on each super atoms due to the crack, super dislocation and other super atoms in the array was given by Eq. (1),

$$I_i^* = \sum_{\substack{j=0 \\ j\neq i}}^{N+1} \frac{4\varepsilon}{\sigma}\left\{12\left(\frac{\sigma}{x_i - x_j}\right)^{13} - 6\left(\frac{\sigma}{x_i - x_j}\right)^{7}\right\} + \frac{K_{II}}{\sqrt{2\pi x_i}} - \frac{nA^*}{(x_d - x_i)} \tag{1}$$

Where $i=1\sim(N-1)$, ε : constant with dimension of energy, σ : constant with dimension of length, K_{II}: stress intensity factor of mode II which concerns local stress of the crack tip, x_i: the position of the ith atom, n : intensity of the super dislocation, A^*: intensity of an isolated actual dislocation. The first and second terms of right hand side of Eq. (1) were interactive forces due to other super atoms exerted on the ith atoms. The third and the forth terms of right hand side of Eq. (1) were interactive forces due to local stress fields of the crack and super dislocation exerted on the ith super atom.

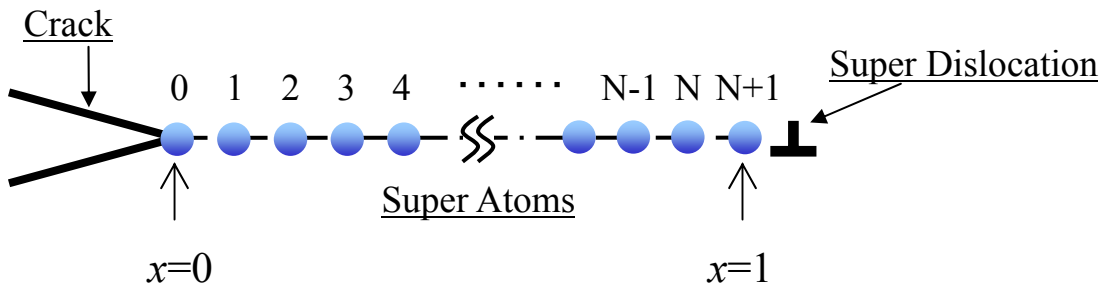

Figure 2. The mechanical equilibrium model of a crack, a super dislocation and super atoms

2.3. The algorithm of mechanical dispersion of atom groups

The value of $x^{+}_{i,n}$ is taken as the non-dimensional variable given by Eq. (2). σ is defined as l. Concerning the dispersion up to the scale of atom, $1/(\beta N)^{13}$ and $1/(\beta N)^{7}$ was exerted to the first and the second terms of Eq. (1) respectively to decrease and disperse interactive forces between super atoms with increase in the number of atoms. By converting Eq. (1) using Eq. (2), the non-dimensional representation of Eq. (1) was given by Eq. (3). That is, $1/(\beta N)$ is an adjusting parameter of the reasonable intensity of potential field corresponding with each scale of atoms.

$$x^{+}_{i,n} = \frac{x_{i,n}}{l} \quad , \quad \sigma = l \tag{2}$$

Where, x^{+} is non-dimensional position of atom, β is a dispersion coefficient of super atoms. l is a representative length and it equals to value of σ.

$$I_{i,n}{}^{*} = 4\varepsilon \sum_{\substack{j=1 \\ j\neq i}}^{N} \left\{ \frac{12}{(\beta N)^{13}} \frac{1}{\left(x^{+}_{i,n-1} - x^{+}_{j,n-1}\right)^{13}} - \frac{6}{(\beta N)^{7}} \frac{1}{\left(x^{+}_{i,n-1} - x^{+}_{j,n-1}\right)^{7}} \right\} + \frac{K_{II}\sqrt{l}}{\sqrt{2\pi x^{+}_{i,n-1}}} - \frac{nA^{*}}{\left(x_{d}{}^{+} - x^{+}_{i,n-1}\right)} \tag{3}$$

2.4. Method of analysis

On the basis of the basic equation, to obtain equilibrium positions of super atoms, following two methods were adopted.

2.4.1. Direct method

Equation (2) represents forces exerted on each super atom. When value of I_i^{*} is not zero, each super atom moves toward the corresponding equilibrium position dominated by Eq. (4).

$$M \frac{d^2 x_{i,n}}{dt^2} = I_{i,n}{}^{*} \tag{4}$$

Where n is the step number when corresponding atom moves step by step toward the equilibrium position under the Eq. (3).
By Eq. (4), velocity of each atom at the time incremental value, Δt is given by Eq. (5). Therefore, moving distance during the time incremental value, Δt is given by Eq. (6). Using Eq. (6), the position of each atom at the time of $(t+\Delta t)$ is given by Eq. (7). Where M is an imaginary mass and for convenience from the view point of calculation, M was taken as unity.

$$V_{i,n} = I^{*}_{i,n}\Delta t + V_{i,n-1} \tag{5}$$

$$\Delta x_{i,n} = V_{i,n}\Delta t \tag{6}$$

$$x_{i,n+1} = x_{i,n} + \Delta x_{i,n} \tag{7}$$

This method [9] can be applied to any cases of moving distance of atoms, however the calculation time of numerical analysis becomes longer as compared with Verlet method.

2.4.2. Verlet method

On the basis of Taylor expansion, Verlet method was proposed to obtain numerical solutions for the type of Eq. (4) with high accuracy and short calculation time. This method is mainly applied to molecular dynamics. This method is summarized as follows.
On the basis of Taylor expansion, finite difference representation of two order derivative was given by Eq. (8).

$$x(t+\Delta t)+x(t-\Delta t)=2x(t)+(\Delta t)^2\frac{d^2x}{dt^2} \tag{8}$$

Using Eq. (8), $x_{i,n+1}$ is given by Eq. (9).

$$x_{i,n+1} = 2x_{i,n}-x_{i,n-1}+(\Delta t)^2 I_{i,n}^{*} \tag{9}$$

In this paper, these two methods were adopted to conduct this numerical analysis and results obtained by these methods were compared from the view point of accuracy, the number of atoms which can be calculated and calculation time of numerical analysis.

The converged conditions on the equilibrium positions of atoms were given by Eqs. (10) and (11).

$$\left|\frac{x_{i,n+1}-x_{i,n}}{x_{i,n}}\right|<10^{-9} \tag{10}$$

$$\sum_{i=1}^{N}\left|I_{i,n}^{*}\right| \Big/ N<10^{-4} \tag{11}$$

The center position of atomic distance and atomic density and the changing rate of atomic density to the initial atomic density were given by Eqs. (12)-(14).

$$X_i=\frac{x_{i-1}+x_i}{2} \tag{12}$$

$$d_i=\frac{1}{x_i-x_{i-1}} \tag{13}$$

$$D_i=\frac{d_i-d_{i,0}}{d_{i,0}} \tag{14}$$

The center position of atomic density was shown in Fig. 3. The positive value of D means that the distance between neighboring atoms expands due to local stress field. The region with negative value of D was defined as the disordered region of atomic array and it is related to the process region which dominates brittle fracture [7, 8]. Conditions of analyses were shown in Table 1.

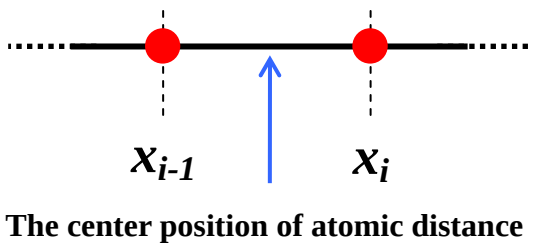

Figure 3. The definition of the center position of atomic distance

Table 1. Conditions of analyses

	Condition1	Condition2	Condition3
K_{II} (MPam$^{1/2}$)	20	40	20
nA^{*}(MPa)	0.049	0.049	0.1
N	10~1000 (Direct method) 10~3000 (Verlet method)		

Analyses were conducted for the following cases.

(1) The case of local stress by the crack and the super dislocation being equivalent at the center position of (0, 1). (Condition 1)
(2) The case of local stress by the crack being two times larger than that of super dislocation at the center position of (0, 1). (Condition 2)
(3) The case of local stress by the crack being half of that of super dislocation at the center position of (0, 1). (Condition 3)

Since the stress singularity of the crack against the distance from the crack tip ($r^{-1/2}$) is smaller than that of super dislocation (r^{-1}), the high stress region of the former is wider than that of the latter.

2.5. Fractal analysis based on Box counting method

In this paper, fractal analysis was adopted to estimate the self-similarity of the distributed characteristics of *D* based on Box counting method.

3. Results of Analysis

3.1. The comparison of two methods and the characteristics of changing rate of atomic density, *D*

The effects of atomic scale and number on the characteristics of *D* defined by Eq. (14) were shown in Figs. 4(a), (b) and (c) under three conditions.

Results obtained by both of the direct and Verlet methods showed the same characteristics of atomic distributions that atomic density increase at the center position of analysis region, (0, 1) and decrease at positions of both ends, that is the crack tip and the super dislocation. The direct method can be applicable for any case of the moving distance of atom, however the latter is based on the Taylor expansion and the small moving distance is required. Furthermore, the calculating time of the former is much longer than that of the latter as shown in Fig. 5.

In the region of *D* having a negative value as shown in Figs. 4 (a), (b) and (c), the breaking stress of atomic bond was applied. Therefore, this region is considered to be a dominating region of fracture. As shown in Figs. 4(a), (b) and (c), with increase in the effect of the crack or the super dislocation, correspondingly, the occurrence of the region of *D* having negative value near the crack or dislocation becomes typical.

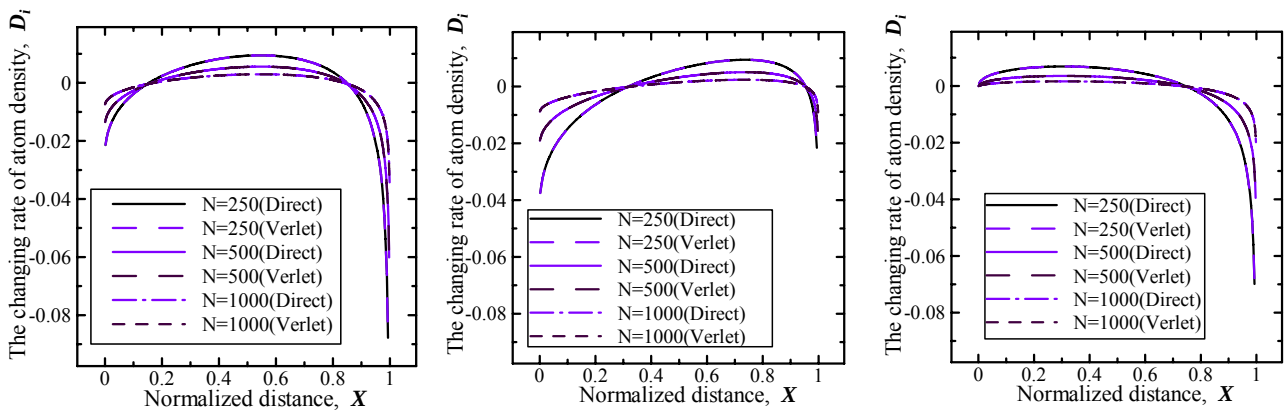

(a) Condition 1 (b) Condition 2 (c) Condition 3

Figure 4. Plots of changing rate of atomic density *D* vs. normalized distance on each condition

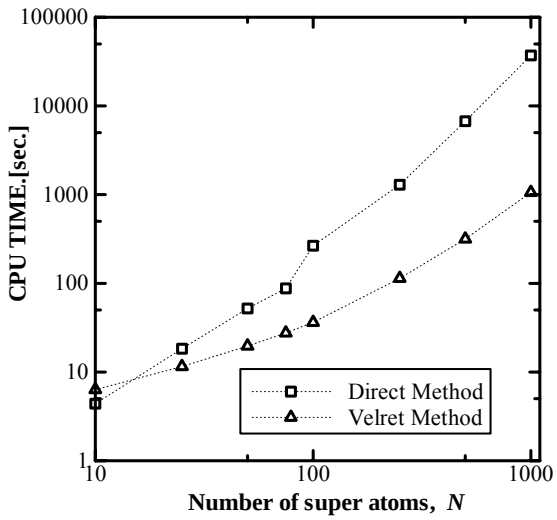

Figure 5. Plots of calculating time vs. number of super atoms on each method

3.2. Fractal analysis of the distribution of *D* values

On the basis of Box counting method, fractal dimensional values, *FD* were calculated and they were plotted against the number of super atoms as shown in Figs. 6 (a), (b) and (c). These results show that *FD* takes a specified saturated constant value when the number of super atoms is larger than N_c = 250.

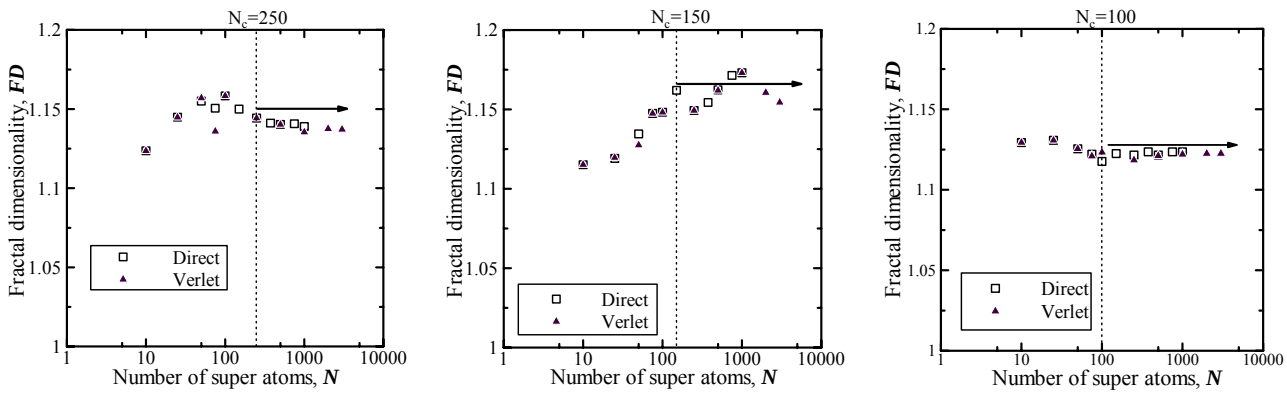

(a) Condition 1 (b) Condition 2 (c) Condition 3

Figure 6. Plots of fractal dimensional value vs. the number of super atoms on each condition

3.3. Determination of dominating region of fracture using projection method

To predict the dominating region of fracture, the region where a value of *D* takes negative value is defined as the disordered regions of super atoms. As shown in Fig. 7, they were characterized by *L* at the side of the crack and *G* at that of super dislocation. The changing characteristics of *L* and *G* were plotted against the number of super atoms as shown in Figs. 8 (a), (b) and (c). Both of characteristics of *L* and *G* were found to take constant values, respectively in the region where the distribution of *D* shows fractal characteristics.

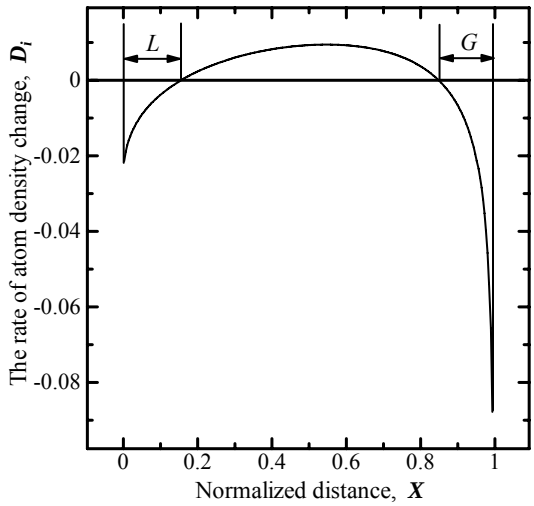

Figure 7. Definition of disordered regions of super atoms

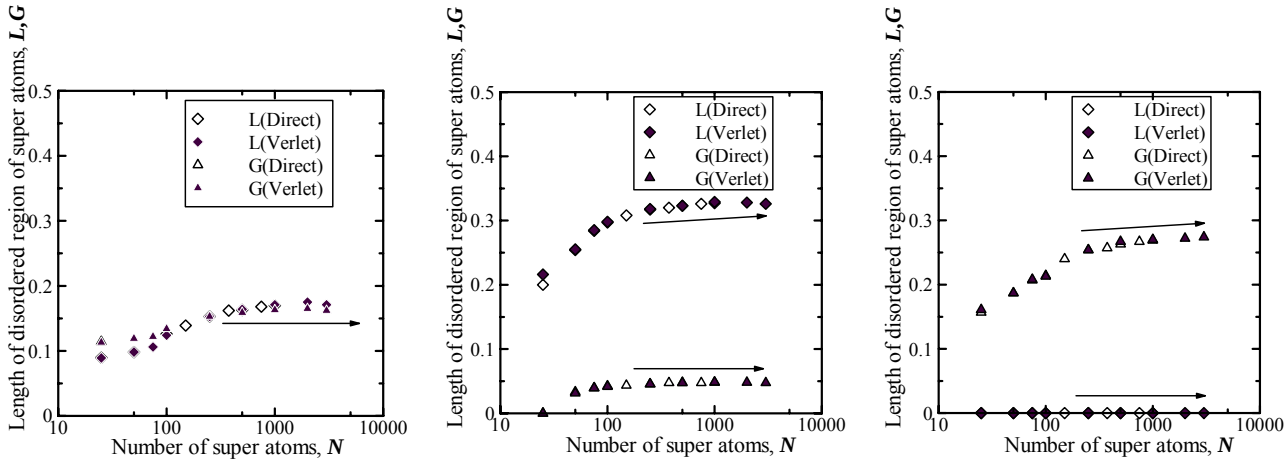

(a) Condition 1 (b) Condition 2 (c) Condition 3

Figure 8. Plots of the length of disordered regions of super atoms vs. the number of super atoms on each condition

4. Considerations

These fractal analyses show that self-similarity of the distribution of super atoms is considered to be held when N is larger than N_c (N_c = 250). Using this property and projection approach, it becomes possible to predict the actual arrangement of atoms. The region of analysis is assumed to be the average value of experimental values of trigger point for Ni-Cr-Mo-V steel, that is, 10 ~ 210 μm [10]. When actual distance between neighboring atoms is assumed to be 0.3 nm, the number of atom, N is considered to be 3×10^5. Based on Fig. 8, values of L and G at $N = 3\times10^5$ were predicted as shown in Table 2.

Table 2. Disordered region at $N = 3.0\times10^5$

	Direct method			Verlet method		
	Condition 1	Condition 2	Condition 3	Condition 1	Condition 2	Condition 3
L	0.238	0.384	0.0	0.211	0.359	0.0
G	0.203	0.062	0.398	0.183	0.055	0.420

These results show that the length of L and G are 20, 30 and 40 μm under three conditions, respectively. These values were almost equal to that of grain size for Ni-Cr-Mo-V steel and it is in good agreement with the dominating region of fracture obtained experimentally by Ritchie [8].
Therefore, our proposed method is found to well predict theoretically the dominating factor of fracture.

5. Conclusions

(1) On the basis of the analytical method using the concepts of super atoms, super dislocation and self-similarity, the atomic distribution from super atoms to those with small scale was found to show the self-similarity and the possibility of analyzing the behaviors of actual atoms using projection method was validated.
(2) The direct method and Verlet method were found to give the same results on the atomic distribution, however calculating time is different.
(3) Using our proposed method, the dominating region of fracture was shown to derive and it was in good agreement with that obtained experimentally by Ritchie.

References

[1] G.R. Irwin, Handbuch der Physik, Springer 6 (1958) 551.
[2] J.R. Rice, Int J Frac Mech, 2 (1966) 426.
[3] T. Yokobori, An Interdisciplinary Approach to Fracture and Strength of Solids, 1968, Wolters-Noordhoff Pub. The Netherlands, T. Yokobori, Zairyo kyoudogaku, The 2nd Edition (1974) Iwanami shoten, In Japanese.
[4] T. Yokobori, S. Sawaki, S. Nakanishi, Engng Fract Mech, 12 (1979) 125-141.
[5] T. Yokobori, A.T. Yokobori, Jr., J of the Japan Institute of Metals, 42 (1978) 88-95.
[6] A.T. Yokobori, Jr., T. Kuriyama, Y. Kaji, Advances in Fracture Research, Proc of ICF10, in the content of Special Lecture of CD-rom, Honolulu 2001, Elsevier Science (2001).
[7] K.B. Broberg, Cracks and Fracture, Academic Press, (1999).
[8] R.O. Ritchie, J.F. Knott, J.R. Rice, J Mech Phys Solids, 21 (1973) 395.
[9] A.T. Yokobori, Jr., T. Ohmi, Y. Nagumo, D. Yoshino, Proc. of the 50th Japan National Symposium Strength, Fracture and Fatigue (2006) 57-60.
[10] J. Watanabe, T. Iwadare, Y. Tanaka, T. Yokobori, Engineering Fracture Mechanics, 28, (1987) 589.

Numerical and analytical introduction to the prediction of grain boundary micro-crack initiation induced by slips bands impingement. Effect of material and microstructure parameters.

Mohamed Ould Moussa[1,*], **Maxime Sauzay**[1]

[1] CEA, DEN, DANS, DMN, SRMA, F-91191Gif-sur-Yvette, France

* Corresponding author: mohamed.ouldmoussa@cea.fr

Abstract

Micro-cracks are often observed at the intersections of thin slip bands (SB) and grain boundaries (GB) due to local stress concentration. Numerous models are based on the pile-up theory and the Griffith criterion, used since the pioneering work of Stroh. We have shown that the former underestimate strongly the macroscopic stress for GB micro crack nucleation. In fact, the key issue is that slip bands display finite thickness, observed to belong to [20nm 1000nm]. Therefore, one aims to account for the effect of SB thickness in crystalline finite element (FE) calculations performed using the Cast3M software. The simulations take into account the effects of isotropic elasticity parameters, cubic elasticity, GB orientation and crystallographic orientation of the considered grain. Following the theory of matching of asymptotic expansions, this leads to an analytical expression of the GB normal and shear stress, which show weaker stress singularities than the pile-up one.

Keywords Micro-cracks, slip bands, pile-up theory, linear fracture mechanics, FE method, crystalline plasticity

1. Introduction

Many issues are available dealing with the appearance and effects of either slip bands (SBs) or dislocation channels on the behavior of irradiated materials. Indeed, the intersection sites between SBs and grain boundaries (GBs) are prone to micro-crack nucleation because of strain localization. A series of papers [1 ; 2 ; 3 ; 4 ; 5 ; 6] highlight the presence of slip localization in Faced Centred Cubic (FCC) metals and alloys observed after post-irradiation tensile loading. Slip Bands were also observed in [7 ; 8 ; 9 ; 10 ; 11 ; 12 ; 13 ; 14] after cyclic loading. Such slip bands have been shown to be Persistent Slip Bands (PSBs) [9]. Some other works [15] have reported the formation of Slip Bands appearing during simple tensile loading. Whatever the loading conditions, such slip bands show a thickness lying between ten nanometers and a few micrometers, and a length about the grain size, usually varying from ten micrometers to a few hundred micrometers. Jiao *et al.* [5] have evidenced strong localization in austenitic stainless steels in post-irradiation tensile tests, using AFM measurements. Wejdemann and Pedersen [16] have applied the same techniques to observe such localization in the PSBs where plastic strain is shown to be fifty times larger than the macroscopic plastic strain. Sharp [1] and Edwards et al. [4] highlighted strain localization in single crystal and polycrystals of copper subjected to post-irradiation tensile loadings. Sauzay *et al.* [17] confirmed such localization in the case of irradiated austenitic stainless steels.

In addition, several works attempted to model the stress concentration at grain boundaries. Besides, it is proved that the anisotropy character of crystalline elasticity induces stress concentration at grain boundaries according to Neumann [18]. Margolin and co-workers [19 ; 20] have carried out optical observations of slip traces and conclude that stresses are more concentrated near grain boundaries. The stress gradients around GBs, induced by plastic deformation incompatibilities between neighbor grains, can be tracked thanks to large-scale finite element (FE) computations [21].

Such stress concentrations may allow to induce inter-granular crack initiation because they neglect plastic slip localization. Therefore, in the scope of the current contribution, one investigates the effect of localized slip on GB stress fields.

An analytical approach, based on the well-known Stroh model [22], has been largely applied in order to evaluate GB stress. One recurrent issue has indeed been, since decades, the using of discrete or continuous dislocation pile-ups. The stress singularity, due to an edge or screw pile-up of length $L^{\text{Pile-up}}$ has been shown to be the same as the one of a crack in the framework of linear elastic fracture mechanics (LEFM) [22 ; 23]. Therefore, an energy criterion has been proposed by [23], based on the Griffith criterion, for predicting micro-crack nucleation. The latter may be used for the case of a singularity exponent of 0.5 only and it fails when the exponent value is less than 0.5 because the energy release rate, G, becomes equal to zero [24 ; 25]. Cottrell [26] later suggested that the fracture process should be controlled by the critical crack growth stage under the applied tensile stress, which required higher stress than the crack nucleation itself as suggested by Stroh. Cottrell came with a modeling by supposing that slip occurs along two atomic planes which intersection shows pile-up dislocation.

However, Sauzay and Evrard [17] recently have outcame with the limitation of such basic pile-up theory to more accurately predict micro-crack initiation. Following their work, the pile-up theory leads to an underestimation of macroscopic stresses with comparison to experimental data. Indeed, the pile-up approach postulates that slip localization occurs on one atomic plane only, but, experiments carried out using various materials and loading conditions show slip occurring on many slip atomic planes [8], [27], [5 ; 16], [28]. Therefore, because of the distribution of plastic slip through the slip band thickness [2 nm, 1000 nm], accounting for the SB thickness in the models may improve the predictions.

The current contribution aims to validate an analytical model of GB stress fields in the case of SB impingement. Then, the first section presents the analytical modeling for close stress fields configuration which corresponds to points located near the intersection of the GB and the SB. The second section deals with finite element (FE) calculations in order to investigate numerically the effect of SB or GB geometry and material properties on GB stress fields. Besides, a final section is devoted, on one side, to adjust parameters and validate the analytical model and on the other side, to show the influence of GB and SB orientation on the adjusted model parameters and a conclusion will end the paper.

2. Analytical modeling

The subsequent problem is to be solved: an elastoplastic slip band is embedded at the free surface of an elastic matrix, subjected to a displacement controlled tensile loading (Fig. 1a).

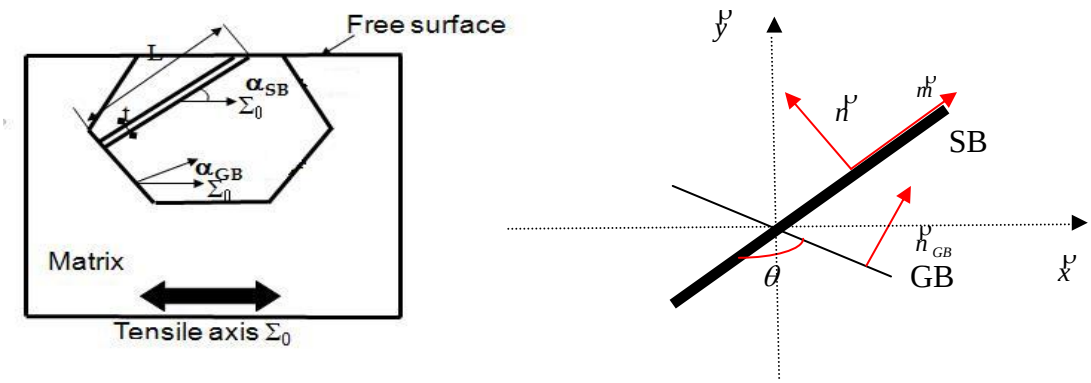

a) b)

Figure 1. a) Main grain, slip band and matrix b) SB-GB intersection and associated vectors

Fig. 1a and b show the following parameters:

- SB and GB orientation related ones:

  $\vec{m}\,(=\frac{1}{\sqrt{2}}(1,0,-1))$, $\vec{n}\,(=\frac{1}{\sqrt{3}}(1,1,1))$, $\vec{n}_{GB}, \alpha_{SB}, \alpha_{GB}$ and θ denote respectively slip direction vector, normal vector to slip plane, normal vector to the GB, angle between slip plane and loading direction ($\vec{m}, \vec{x}$), angle between the GB normal and loading direction ($\vec{n}_{GB}, \vec{x}$) and an angle between the SB and the GB, given by:

  $$\theta = 90^o - \alpha_{SB} + \alpha_{GB}. \qquad (1)$$

- SB size and loading parameters: t, L, Σ_0 and f are respectively SB thickness, SB length, macroscopic applied tensile stress and Schmid factor.

In addition, for further assumptions, let $\sigma_{nn}, \sigma_{nm}, \tau_0$ and r be respectively the GB normal stress, the GB shear stress, SB yield shear stress and the distance to the SB along the GB. It is worth to note that the developments involved in the current paper concern the close fields configuration which means that one focuses on stress evolution near the intersection of the SB and the GB (at a distance r such as 0 < r << t). The point located at the intersection of SB and GB corresponds to r = 0.

GB stresses singularity is the same as the crack one in the LEFM framework, leading to an exponent of 0.5 of the stress expansion. [22 ; 23], the GB normal stress field induced by one edge dislocation pile-up is given by:

$$\sigma_n^{pile\text{-}up}(r,\theta) = \frac{3}{2}\left(L^{pile\text{-}up}/r\right)^{1/2}(f\Sigma_0 - \tau_0)h(\theta) + \Sigma_n^{\infty}, \qquad (2)$$

where $h(\theta) = \sin\theta\cos(\theta/2), \Sigma_n^{\infty} = \Sigma_0\cos^2(\alpha_{GB})$ and $L^{pile-up} = L/2$.

The absence of any term accounting for the SB thickness, t, in Eq. 2 is noticeable. Indeed, slip is assumed to occur on one atomic plane only as mentioned earlier.

However, experimental observations have shown that slip may occur in many atomic plane and lead to the question of taking into account SB thickness. This implies the existence of two characteristic lengths: SB length and thickness, in the new problem of finite thickness. It is also proved [17] that the driving force ($f\Sigma_0 - \tau_0$) is proportional to the macroscopic shear stress. These two points make our problem be similar to the case of a crack with a V-noch tip in an elastic matrix even the stress singularity is induced by a slip localization in ours. That is why, following the theory of matching expansions [24 ; 29], we perform a modeling of the GB normal and shear stress close fields with respect to the SB length, L and the SB thickness, t:

$$\sigma_{nn}(r) = A_{nn}\left(L/t\right)^{0.5}\left(t/r\right)^{\alpha}(f\Sigma_0 - \tau_0), \qquad (3)$$

and

$$\sigma_{nm}(r) = A_{nm}\left(L/t\right)^{0.5}\left(t/r\right)^{\alpha}(f\Sigma_0 - \tau_0). \qquad (4)$$

α is the singularity exponent A_{nn} and A_{nm} are model parameters. The subscript “nn” corresponds to the GB normal stress and “nm” to the GB shear stress.

It is worth to highlight that this model assumes a linear dependence of GB stresses on the driving shear stress, T= $f\Sigma_0 - \tau_0$, and the same singularity exponent is valid for both shear and normal stress components and whatever L and t. The main difference between this model and the pile-up one is that the finite SB thickness, t, is taken into account. The stress singularity is assumed to be weaker in the proposed model than in the pile-up case, $\alpha < 0.5$ as it will be probably shown.

3. Finite Elements (FE) calculations

3.1. FE model and loading

A 2D matrix is considered, embedding a surface grain, main grain (MG), which contains a slip band. Constitutive laws in each material are:

- Both isotropic and cubic elasticity laws in SB. As shown in Fig. 2a, it is characterized by a quasi-perfect-plastic flow, indeed, a low hardening coefficient ($H_0 \sim$ 1MPa) is assumed for avoiding numerical convergence problems. Only, one slip system is activated in the SB, which slip plane is (111) and slip direction is $[10\bar{1}]$. A yield stress τ_0, equals to 60 MPa, is initial SB critical shear stress.
- Both isotropic and cubic elasticity laws in the MG.
- The matrix obeys isotropic elasticity, defined by a Young's modulus and Poisson ration values.

Crystalline FE elements are used in the mesh shown in Fig. 2b to allow FE calculations using Cast3M code. A tensile loading is imposed along $\vec{x}$ direction and plane strain is assumed. In addition, many FE computations proved that this model is insensitive to both the mesh size and the time stepping.

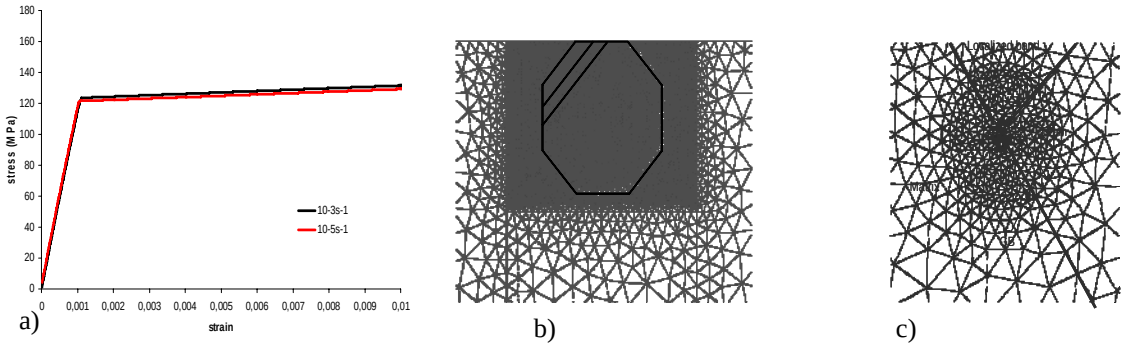

Figure 2.a) Perfect plasticity behavior of the slip band b) Zoom on the mesh: main grain (MG) and slip band (SB) c) Intersection of the SB and the GB.

The applied tensile stress Σ_0 is high enough to lead to slip band plastic flow and (Table 1) shows both isotropic and cubic elasticity parameters used in the calculations [30]. C_{11}, C_{12} and C_{44} are the crystalline elasticity parameters.

Table 1. Isotropic and cubic elasticity parameters

E (in matrix, MG and SB)		180 GPa
ν (in matrix, MG and SB)		0.33
	Isotropic elasticity (MG and SB)	Cubic elasticity (MG and SB)
C_{11}	267 GPa	267 GPa
C_{12}	131 GPa	131 GPa
C_{44}	68 GPa	224.4 GPa
a	1	3.3

The anisotropy coefficient is defined by $a = 2C_{44} / C_{11} - C_{12}$ and if it equals to one, crystalline elasticity is isotropic. In case of copper or austenitic stainless steel, the Young's modulus along the <111> directions is more than 3 times the one along the <100> directions. That is why it would be worth to numerically account for such anisotropy in our contribution.

3.2. Effect of the variation of GB and SB geometry

This part shows the effect of SB characteristic lengths on the GB normal and shear stresses. The length effect may be studied using Fig. 3 a) and b) and the thickness one using Fig. 4 a) and b). One assumes that crystalline elasticity is isotropic ($a = 1$).

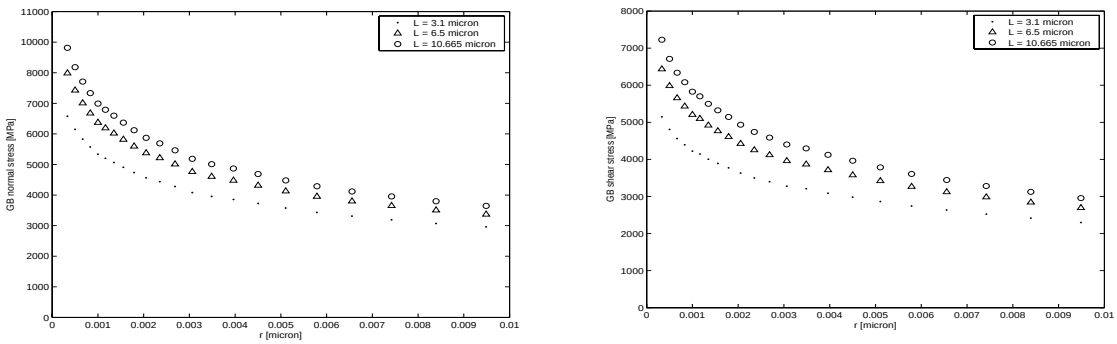

a) b)

Figure 3. a) GB normal stress b) GB shear stress, with respect to the distance to the GB-SB intersection in close field configuration for: austenitic stainless steel, t=0.09 μm, Σ_0 = 878 MPa, α_{GB} = 33°, α_{SB} = 45°, τ_0 = 60 MPa

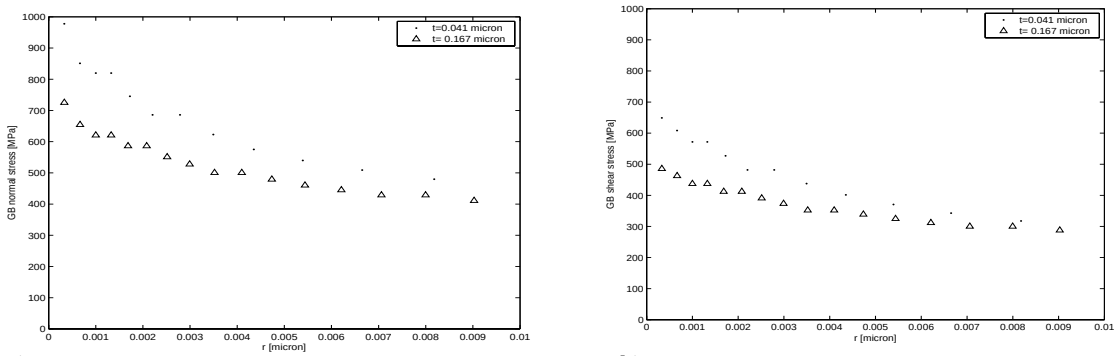

a) b)

Figure 4. a) GB normal stress b) GB shear stress, with respect to the distance to the GB-SB intersection in close field configuration for: austenitic stainless steel, L=10.71 μm, Σ_0 = 174 MPa, α_{GB} = 33°, α_{SB} = 45°, τ_0 = 60 MPa

Besides, one can observe: the higher the SB length the higher the GB normal and shear stresses, as also expected from the pile-up theory. However, the higher the SB thickness the lower the GB stresses. Physically, that highlights that very narrow SBs should lead to easier GB micro-crack nucleation than large ones.

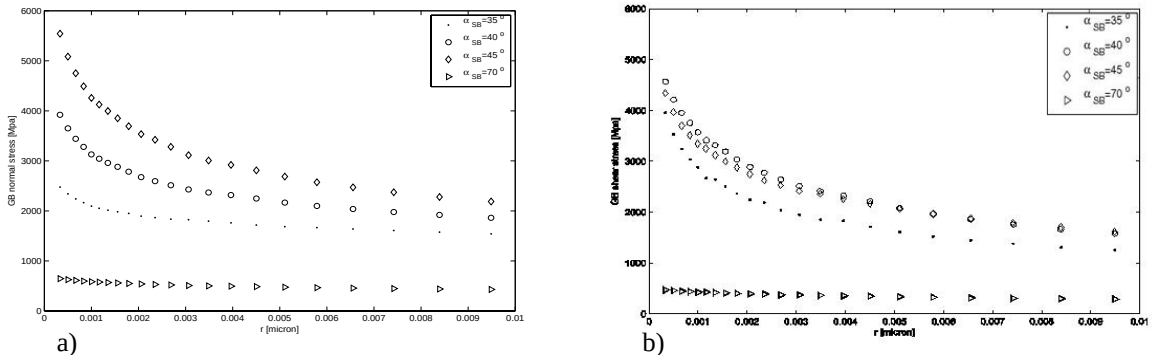

a) b)

Figure 5. a) GB normal stress b) GB shear stress, with respect to the distance to the GB-SB intersection in close field configuration for: Austenitic stainless steel, L=10.71 μm, t=0.09 μm, Σ_0 = 393 MPa, α_{GB} = 33°, τ_0 = 60 MPa

Moreover, GB and SB orientations are proved to induce strong change in GB stress fields. That is

why the normal and shear stress fields are computed for different values of α_{SB} and α_{GB}. The GB normal stress reaches a maximum peak for α_{SB} equal to 45° because of the corresponding highest Schmid factor value (f = 0.5). For lower or higher α_{SB} values, the normal stress is lower (Fig. 5 a)) and the same almost occurs to the shear stress (Fig. 5 b)). Indeed, a lower Schmid factor leads to delayed plastic flow and low plastic slip which induces the stress concentration.

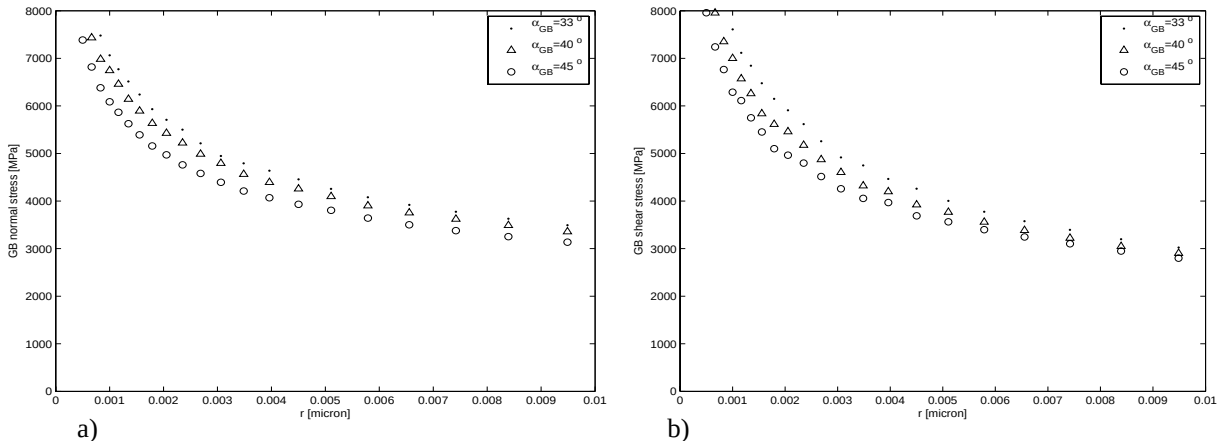

a) b)

Figure 6. a) GB normal stress b) GB shear stress, with respect to the distance to the GB-SB intersection in close field configuration for: Austenitic stainless steel, L=10.71 μm, t=0.09 μm, Σ_0 = 878 MPa, α_{SB} = 45°, τ_0 = 60 MPa

Concerning the GB orientation, the results show that GB stress fields slightly decrease with respect to α_{GB} (see Fig. 6 a) and b)).

3.3. Influence of elasticity parameters

One now aims to evaluate the influence of isotropic elasticity parameters. Fig. 7 a) and b) show GB stress fields computed for different materials, E_1 =68GPa (Aluminum), E_2 =110 GPa (Copper), E_3 = 180 GPa (Austenitic stainless steel), and corresponding Poisson ratios, ν_1 = 0.33 (Aluminum), ν_2 =

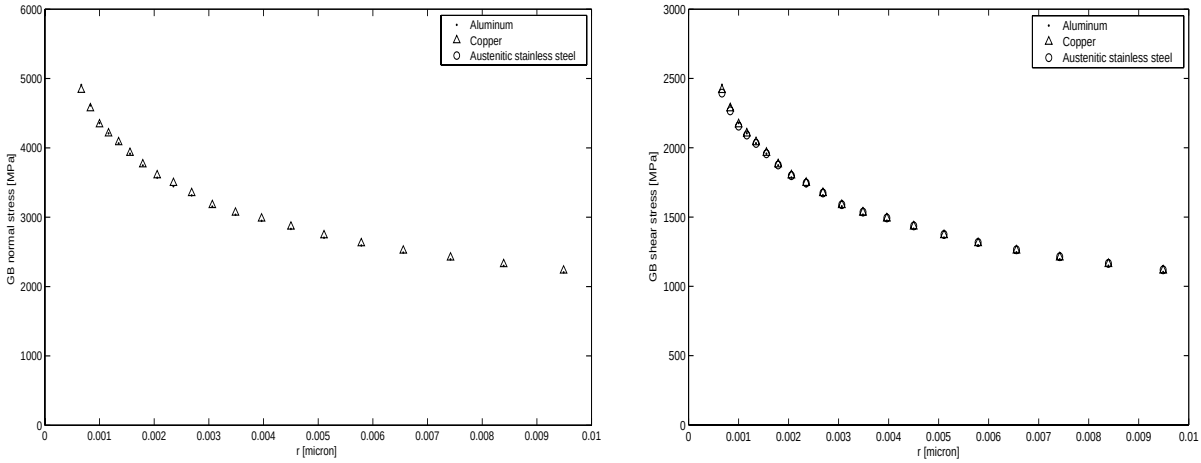

a) b)

Figure 7. a) GB normal stress b) GB shear stress, with respect to the distance to the GB-SB intersection in close field configuration for: L=10.71 μm, t=0.09 μm, Σ_0 = 393 MPa, α_{GB} = 33°, α_{SB} = 45°, τ_0 = 60 MPa

No difference with respect to these parameters is evidenced in the graphs. It has been checked that GB stresses are the same whatever the isotropic elastic parameters provided the remote tensile stress

is the same.
In copper and austenitic stainless steel, the anisotropy coefficient (Table 1) of cubic elasticity is high ($a = 3.3$), therefore, one should study the effect of such strongly anisotropic cubic elasticity on GB stress fields.

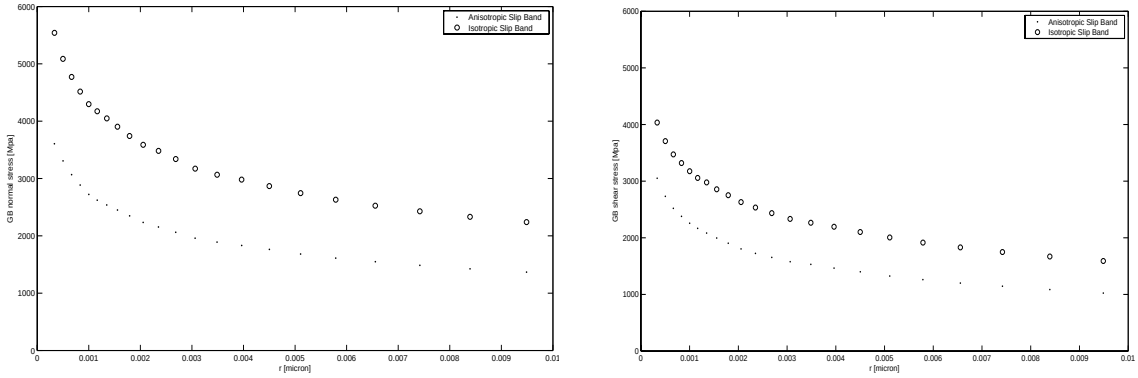

a) b)

Figure 8. a) GB normal stress b) GB shear stress, with respect to the distance to the GB-SB intersection in close field configuration for: The main grain and the SB obey either cubic elasticity or isotropic elasticity for: Austenitic stainless steel, L=10.71 μm, t=0.09 μm, Σ_0 = 393 MPa, α_{GB} = 33°, α_{SB} = 45°, τ_0 = 60 MPa

Fig. 8 a) and b) show that cubic elasticity may affect strongly GB stresses. The latter decrease and the micro-crack nucleation cannot occur so easily than for isotropic elasticity. Indeed, in the case of anisotropic cubic elasticity, local elasticity modulus become high and Schmid factor drops (about 0.43 in this case) [30] leading to lower values of GB stress fields.

3.4. Comparison to the pile-up based model

Fig. 9 gives a comparison between our model of GB normal stress for t=0.09 mm and the pile-up GB normal stress given by Eq. 2.

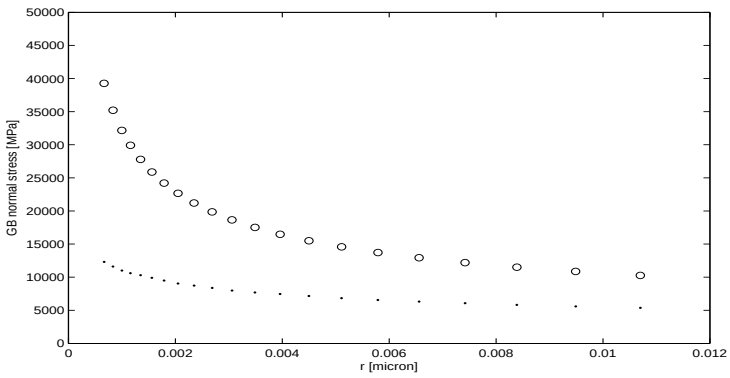

Figure 9. GB normal stress with respect to the distance to the GB-SB intersection in close field configuration for: Model (points) and Pile-up (circles) with L=10.665 μm, t=0.09 μm, Σ_0 = 878 MPa, α_{GB} = 33°, α_{SB} = 45°, τ_0 = 60 MPa

One can clearly observe that the pile-up theory based model overestimates the GB normal stress with comparison to ours which takes into account a finite SB thickness, t. Indeed, GB normal stress seems to be about three times higher in pile-up modeling than in our approach at the same distance from the intersection of the GB and the SB.

4. Model versus FE calculations

4.1 Parameters adjustment

It is worth to note that following the theory of matching expansions [Leguillon, 2002], a same singularity exponent, α, is valid for both GB normal and shear stresses. Therefore, the current section deals with the adjustment of analytical parameters A_{nn} , A_{nm} and α in order to fit FE curves.

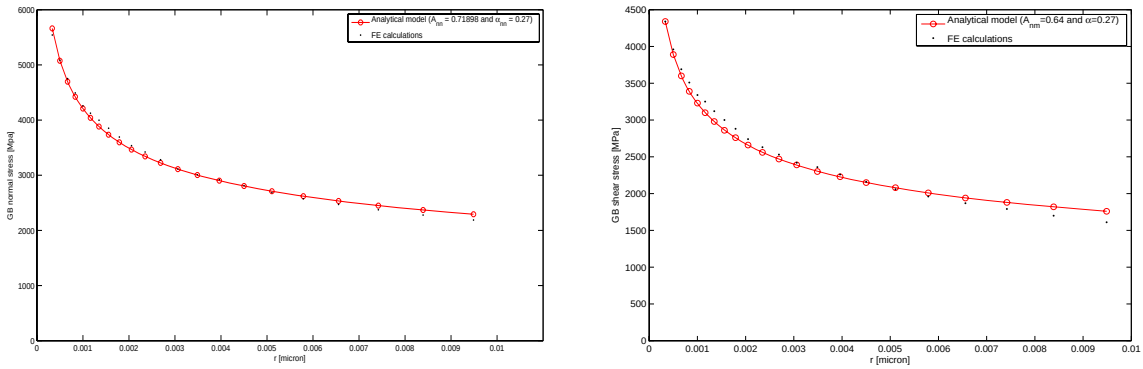

a) b)

Figure 10. a) GB normal stress (A_{nn} = 0.72) b) GB shear stress (A_{nm} = 0.64), with respect to the distance to the GB-SB intersection in close field configuration for: analytical model, Eq. 3 and 4, (red) with α = 0.27 and FE calculations (black) with L=10.71 μm, t=0.09 μm, Σ_0 = 393 MPa, α_{GB} = 33°, α_{SB} = 45°, τ_0 = 60 MPa

Fig. 10 a) and b) show a fair agreement between our optimized analytical model and the FE calculations: one suitable value of α (=0.27) is found for GB normal stress and GB shear one. As expected two different values of the factors are found depending on the chosen stress component. It takes 0.71 for the GB normal stress and 0.64 for the GB shear stress.

4.1 Validation

Let one now show the validity of our model with respect to the SB characteristic sizes (L and t). Indeed, the parameters adjustments are carried out for a new value of SB length (Fig. 11 a)) and a new one of SB thicknesses (Fig. 11 b)). For L=6.7 μm, for instance, the same parameters, A_{nn}=0.72 and α=0.27, are found and in the same manner, for t=0.04 mm, A_{nn}=0.72 and a=0.27. Therefore, we can conclude that our model is insensitive to the SB lengths for the GB normal stress.

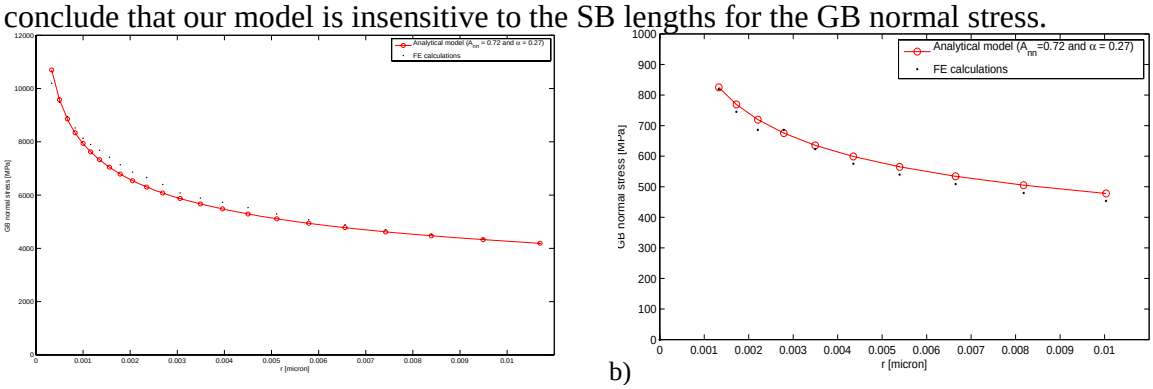

a) b)

Figure 11. a) GB normal stress (L = 6.7 μm, t = 0.09 μm, Σ_0 = 878 MPa, A_{nn}=0.72 and α = 0.27) b) GB normal stress (L = 10.665 μm, t = 0.04 μm, Σ_0 = 176 MPa, A_{nn}=0.72 and α = 0.27), with respect to the distance to the GB-SB intersection in close field configuration for: analytical model (red) and FE calculations (black) α_{GB} = 33°,α_{SB} = 45° and τ_0 = 60 MPa

4.1 Dependency on SB and GB orientation

We have performed some calculations for checking the validity of the analytical modeling with respect to GB and SB orientation (α_{GB} and α_{SB}). For the sake of simplicity, we have just carried out it for the normal corresponding parameter (A_{nn}) and it is shown in Fig. 12 a) and b) that A_{nn} and a equal respectively to 0.59 and 0.18 for $\alpha_{SB} = 35^o$ and 0.71 and 0.21 for $\alpha_{SB} = 40^o$.

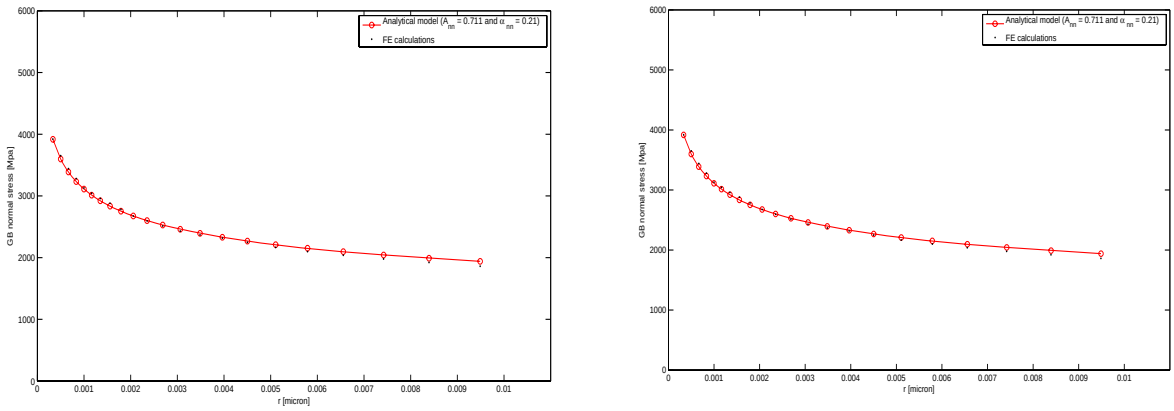

a) b)

Figure 12. a) GB normal stress ($\alpha_{SB} = 35^o$, $A_{nn}(\alpha_{GB}, \alpha_{SB})$=0.71 and $\alpha(\alpha_{GB}, \alpha_{SB})$= 0.21) b) GB shear stress ($\alpha_{SB} = 40^o$, $A_{nn}(\alpha_{GB}, \alpha_{SB})$=0.59 and $\alpha(\alpha_{GB}, \alpha_{SB})$= 0.18), with respect to the distance to the GB-SB intersection in close field configuration for: analytical model (red) and FE calculations (black) with L=10.665 µm, t=0.09 µm, Σ_0 = 393 MPa, α_{GB} = 33°, τ_0 = 60 MPa

Finally, we conclude that the model parameters slightly depend on the GB and SB orientation.

5. Conclusion

An analytical approach is adopted to perform a modeling of the GB stress fields with respect to the distance from the intersection of the grain boundary (GB) and the slip band (SB). It allowed tracking the stress singularity induced by the SB impingement on the GB. Afterwards, finite element calculations were computed in order to simulate the effect of the SB and GB characteristics on GB stress fields, such normal and shear components. In addition, model parameters were adjusted with respect to the involved length, thickness and angles in the problem. The model was then validated whatever the SB characteristic sizes. Finally, further works will deal with evaluating critical values (stress and crack length) in order to enhance a double criterion for the prediction of micro-crack initiation.

Acknowledgements

The current work is funded by the projects DEN/RSTB/RACOC-02-02 and DEN/RSTB/MASOL (CEA, FRANCE). Authors also acknowledge the project “FP7 Project Perform-60 Grant Agreement N° FP7-232612” for its support.

References

[1] J. V. Sharp. Phil. Mag., (1967) 16-77

[2] M. Victoria, N. Baluc, C. Bailat, Y. Dai, M. I. Luppo, R. Schäublin, B. N. Singh. J. Nucl. Mat., (2000) 276-114.

[3] E. H. Lee, M. H. Yoo, T. S. Byun, J. D. Hunn, K. Farrell, L. K. Mansur. Acta. Mater., (2001) 49-3277.

[4] D. J. Edwards, B. N. Singh, J. B. Bikde-Sorensen, Evolution of cleared channels in neutron-irradiated pure copper as a function of tensile strain. J. Nucl. Mat., 329-333(2004) 1072-1077.

[5] Z. Jiao, J. T. Busby, R. Obata, G. S. Was. Salt Lake City, Utah, 2008, pp. 379.
[6] T. S. Byun , N. Hashimoto, K. Farrell, . J. Nucl. Mat., (2006) 351-303
[7] P. Lukas, M. Knesnil, Krejci, . J. Phys. Stat. Sol., (1968) 27-545.

[8] J. M. Finney, C. Laird, Strain localization in cyclic deformation of copper single crystals. Phil. Mag., 31 (1975) 339-366.
[9] A. T. Winter, O. B. Pedersen, K. V. Rasmussen, Dislocation microstructures in fatigued copper polycrystals. Acta Metall., 29 (1981) 735-748.

[10] K. Mecke, C. Blochwitz, Saturation dislocation structures in cyclically deformed nickel single crystals of different orientations. Crystal Res. & Technol, 17 (1982) 743-758.
[11] L. C. Lim, R. Raj, . Acta Metall., (1984a) 32-1177.

[12] H. Mughrabi, R. Wang. Elsevier, 1988, pp.1.

[13] C. Blochwitz, J. Brechbühl , W. WTirschler, Analysis of activated slip systems in fatigued nickel polycrystals using the EBSD-technique in the scanning electron microscope. Mat. Sci. Eng., A 210 (1996) 42-47.

[14] J. Man, K. Obrtlik, C. Blochwitz, J. Polak, Atomic force microscopy of surface relief in individual grains of fatigued 316L austenitic stainless steel. Acta Mat., 50 (2002) 3767-3780.

[15] C. Perrin, S. Berbenni, H. Vehoff , M. Berveiller M, . Acta Mater., (2010) 58-4649.

[16] C. Wejdemann, O. B. Pedersen, . Mat. Sci. Eng. , A (2004) 387-556.
[17] P. Evrard, M. Sauzay. J. Nucl. Mat, 405 (2010) 83-94.
[18] P. Neumann. Scripta Met. Mater., (1992) 26-1535.

[19] Y. Chuang , H. Margolin. Metall. Trans., (1973) 4-1905.
[20] H. Margolin , M. S. Stanescu. Acta Met., (1975) 23-1411.

[21] O. Diard, S. Leclercq, G. Rousselier, G. Cailletaud. Int. J. Plast., 21 (2005) 691-722.
[22] A. N. Stroh. Adv. Phys., (1957) 6-418.

[23] E. Smith, J. T. Barnby. Metal Sci. J., (1967) 1-56.
[24] D. Leguillon. Eur. J. Mech, A/Solids (2002) 21- 61
[25] D. Taylor, P. Cornetti, N. Pugno . Eng. Fract. Mech., (2005) 72-1021.

[26] Cottrell, A.H., Theory of brittle fracture in steel and similar metals, 1958, Transactions of the metallurgical society of AIME, Vol. 212, p. 192-203.
[27] M. Sauzay, K. Bavard, W. Karlsen, TEM observations and finite element modeling of channel deformation in pre-irradiated austenitic stainless steels – interactions with free surfaces and grain boundaries. J. Nucl. Mater., 406 (2010) 152-65.

[28] T. Tabata, H. Fujita, M. A. Hiraoka, K. Onish. Phil. Mag., A (1983) 47-841.

[29] Leguillon D., Sanchez-Palencia E (1987). Computation of singular solutions in elliptic problems and elasticity. John Wiley & Sons / Masson.

[30] http://www.matweb.com/

Strain Concentrations in Tensile, Fatigue and Fracture Behaviour

Stephen D. Antolovich[1*], Ronald W. Armstrong[2]

[1] Schools of Materials Science and Mechanical Engineering, Georgia Tech, Atlanta, GA,30332-0245 USA & School of Mechanical and Materials Engineering, Washington State University, Pullman, WA 99164-2920 USA
[2] Center for Energetic Concepts Development, University of Maryland, College Park, MD 20742 USA
* Corresponding author: stevea@gatech.edu.

Abstract A critical survey has been made of tensile, fracture, shear banding and fatigue measurements and interpretations reported for different types of materials and test conditions. The mechanical properties of the materials are shown to be largely determined by microscopic plastic strain concentrations which depend on the inhomogeneity of the material microstructure, especially including importantly inhomogeneity of the dislocation substructure. Understanding this inhomogeneity is shown to provide a number of connections between seemingly disparate phenomena. The evolution of the dislocation substructure and its relationship to crystallography and various levels of microstructure are critically important. Professor Cottrell made seminal contributions to understanding the fundamental mechanisms involved in determining such strain concentrations. His work continues to provide clarity and guidance to current research accomplishments.

Keywords Pile-ups, Cleavage, PLC, ASB, PSB

1. Introduction

An article entitled "Plastic Strain Localizations in Metals: Origins and Consequences" has just been completed for the 2013 publication of the periodical: Progress in Materials Science [1]. The article has provided the basis for us to report in the ICF13 Cottrell Memorial Symposium on a number of important sub-topics on which Alan Cottrell has paved the way forward to modern developments. Four such sub-topics are:
(1) The Cottrell virtual work equation for a single-ended dislocation pile-up was first reported in Progress in Metal Physics [2] preceding Cottrell's seminal book on dislocations [3]; the equation is

$$\tau^* = n\tau_o \tag{1}$$

Where τ^* = stress at blocking obstacle, n = total number of dislocations in pile-up, τ_o = effective applied stress.
(2) The Cottrell-Bilby carbon locking of dislocations theory which provided a basis for understanding the Portevin-Le Chatelier (PLC) effect of serrated plastic flow;
(3) The Cottrell dislocation crack reaction for understanding cleavage in bcc metals and related materials; and
(4) The Cottrell-Hull analysis of slip band intrusions/extrusions for fatigue crack development associated with persistent slip band structures.

2. Deformation Behaviour – Dislocation Pile-ups

One of the most important parameters in a vast array of materials is grain size and the effects of grains on deformation, a topic to which Prof. Cottrell has made numerous contributions. His work was followed by the well-known Eshelby, Frank and Nabarro (EFN) analysis for the n – τ_0 relationship in the equilibrium equation for the pile-up dislocations spread over a length, L [4]:

$$\boldsymbol{\tau_o = \frac{Gnb}{2\pi kL}} \tag{2}$$

In Eq. (2), G is shear modulus, b is dislocation Burgers vector, and $1 \geq k \geq (1-\upsilon)$ for screw or edge dislocation character respectively with υ being Poisson's ratio. Substitution for n in Eq. (1) and taking $\tau_0 = \tau_{ys} - \tau_i$, leads to the Hall-Petch equation for yield stress, τ_{ys}:

$$\boldsymbol{\tau_{ys} = \left(\frac{Gb\tau^*}{2\pi k}\right)^{\frac{1}{2}} L^{\frac{-1}{2}} + \tau_i = \tau_i + k_y' L^{-\frac{1}{2}}} \tag{3}$$

In Eq. (3), τ_i is a "friction" stress and k'_y is now known as the microstructural shear stress intensity. Taking the pile-up length, L, to be equal to the average polycrystal grain diameter, ℓ, then Eq. (3) can be written in terms of tensile stresses:

$$\boldsymbol{\sigma_{ys} = \sigma_o + k_y \ell^{-\frac{1}{2}}} \tag{4}$$

One may view yielding as a process in which the local shear stress at the tip of a slip band builds up with each additional dislocation and eventually reaches a level at the boundary or nearby in the adjacent grain to trigger transmission of plastic deformation through the boundary. The microstructural stress intensity parameter, k_y, clearly controls this process and as such is, in principle, both temperature and strain rate dependent in addition to having sensitivity for other aspects of the materials microstructure.

The build-up to reach the critical stress is most rapid as the first few dislocations pile up against a boundary. The effect of adding one dislocation to the pile up, $\Delta n = 1$, in Cottrell's Eq. (1) gives:

$$\boldsymbol{\frac{\Delta\tau}{\tau} = -\frac{1}{n}} \tag{5}$$

Thus, the fractional decrease in stress necessary to reach the threshold for spreading plasticity decreases with each additional dislocation added to the pile-up. In essence, this describes the reduction in Hall-Petch stress provided by increasing the slip length (by increasing the grain size), so as to facilitate overcoming an obstacle to plastic flow. The model result is illustrated in Fig. 1.

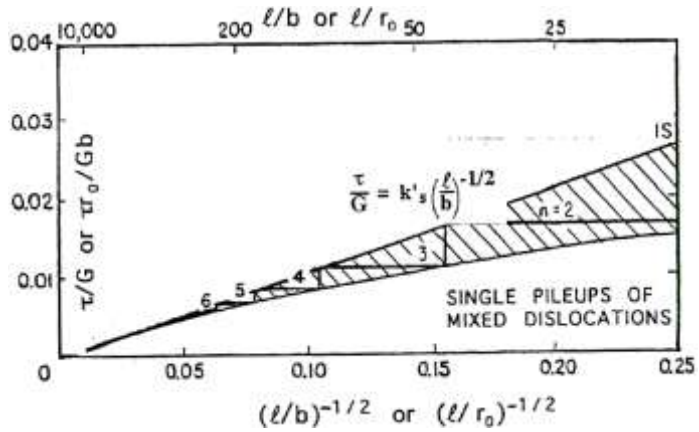

Figure 1. Normalized yield stress vs. reciprocal root of normalized grain size in metals. The core radius is r_o [5]. The integers represent the number of dislocations in the pile up.

Figure 1 also illustrates the lowered flow stress with an increased number of dislocations. It also illustrates the reason for "scatter" in the mechanical properties of ultra fine grained materials and nanocrystalline materials. Since slip bands cannot have fractional numbers of dislocations, a range

of grain size will contain, say, three dislocations. For two dislocations, say, to be in the pile-up the grain size must decrease to a pre-determined size. Joining the tips of the "steps" gives the envelope of possible values for the flow stress. Small grain sizes and low numbers of dislocations in them also relate to the improbability of cleavage in fine grained Fe as described by Armstrong and Antolovich [6] as discussed below.

3. Strain Concentration and Fracture

An updated model for plastically-induced cleavage fracturing of bcc and related metals and alloys is shown in Fig. 2. The basic model fracture had been developed originally by Cottrell [7].

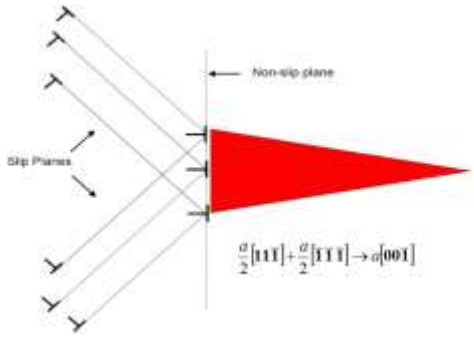

Figure 2. Cottrell model for fracture in BCC (α) Fe [7]

In this model, parallel dislocations on intersecting slip systems (i.e. {110}-type planes) react to form a sessile dislocation on a non-slip {100} plane thus providing a cleavage crack nucleus. Repetition of this reaction promotes growth of the microcrack until it is large enough to satisfy a Griffith-type criterion and spread by cleavage on a {100} type plane. The reaction shown in Fig. 2 is vectorily correct and energetically favourable. Furthermore, careful observations showed that *fracture occurred only after some plastic deformation* as would be required by this model. The model has been applied to explaining crystallographic aspects of cleavage fracture in other crystalline structures, for example, at indentations on MgO (001) crystal surfaces [8]. However, not all reactions such as that shown in Fig. 2 actually result in good predictions of cleavage. Antolovich and Kip [9] pointed out that not only must the reaction be energetically favourable but one must also consider the force barrier to be overcome. An analogy would be two parallel dislocations on parallel planes. Their lowest energy position is when they are lined up vertically forming a finite segment of a low angle tilt boundary. However, to bring the dislocations into the position shown, a force barrier must be overcome which is a maximum when a line joining the two dislocations is inclined at 22.5^{o} to the slip planes. Once aligned there is a restoring force directed against separation. Antolovich and Kip considered: (1) the effect of angular orientation of the two dislocations on the forces that must be overcome to form a crack nucleus and (2) the forces required to bring an additional dislocation to within a Burgers vector of the crack nucleus. The problem that they considered is illustrated in Fig. 3. The results were illuminating. First of all, with respect to BCC structures and α-Fe in particular, the calculations showed that for almost all angular orientations as defined above, glide dislocations are attracted to a common junction implying that overcoming the Peierls force would be sufficient to form a crack nucleus. This was in opposition to most other crystal structures (e.g. intermetallics, FCC crystals) in which such attractive ranges were rare. However, once formed, it becomes increasingly difficult to grow the crack since the back stress due to the nucleus requires additional force to move a dislocation into the vicinity of the nucleus (i.e. to grow the incipient crack). Based on these detailed calculations, one would expect

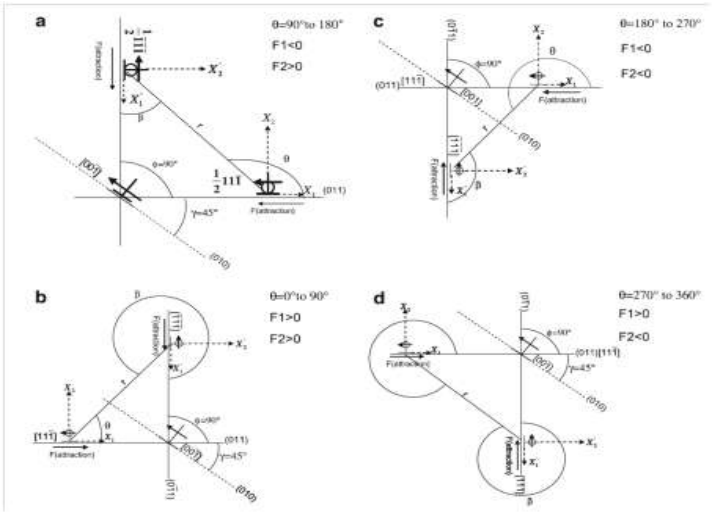

Figure 3. Two parallel reacting dislocations in BCC crystal structure. The axis system for each dislocation as well as angular variables are defined in (a). The signs of the forces on dislocations 1 and 2 that cause attraction to a common junction are shown in (a–d) for all possible angular orientations.

cleavage to be prevalent at low temperatures, which is observed in α-Fe, and some plasticity to precede cleavage, which is also observed.

The pile-up model is currently being used in to study near theoretical limiting stress levels reached for nanopolycrystals on a Hall-Petch basis. Antolovich and Armstrong considered possible modification of the Hall-Petch effect for cleavage of α-Fe if only a small number of dislocations were involved [6]. They computed the dimensional scale at which a stress concentration from the pile-up could duplicate that of a cleavage crack. As shown above, the pile-up approach can be applied at rather small dimensions and can also be used to explain "scatter" of strength data. Importantly they showed that for small numbers of dislocations the slip band generated stress computed directly for small numbers of dislocations can never reach the crack-like stress (computed using continuous distributions of dislocations) implying that at small grain sizes (and small numbers of dislocations) cleavage is improbable. The results of their calculations are shown in Fig. 4.

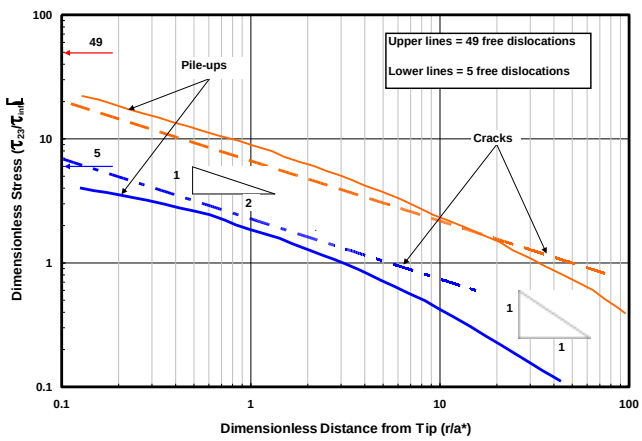

Figure 4. Dimensionless shear stress vs. dimensionless distance from crack or slip band tip (normalized to the crack length) [6]. For five free dislocations, the stress ahead of the slip band falls below that of a crack and cleavage is unlikely. Note further the crack like behaviour near the tip of the slip band (slope of -½) and the traditional slip band like behaviour (slope -1) for multiple Burgers vector representation.

The same result was obtained on incorporation of Griffith crack tip modification as prescribed with gradient elasticity theory (GET). Another related application of such pile-up model consideration, to be developed in Section 5, is to evaluate the breakthrough of a pile-up in providing a fundamental explanation of adiabatic shear banding behavior. In such case, the rapid avalanche-like dissipation of the stored energy in pile-up provides a ready energy source for appreciable thermal heating [1].

4. Strain Concentration in the Portevin-Le Chatelier Effect

The French researchers, A. Portevin and F. Le Chatelier discovered that for certain combinations of strain rates and temperatures the stress-strain curves of Al-Cu-Mn and Al-Cu-Mn-Mg alloys exhibited serrations in the stress strain curves and that fairly well-defined bands formed in the gage length of the specimens [10]. This discovery, now eponymously known as the PLC effect, has been of keen interest in the 90 years since it was first observed and to this day controversy exists in terms of the basic mechanisms and the effect on mechanical properties such as fatigue. It was not until the advent of dislocation theory that the outline of an understanding was developed and again Prof. Cottrell played a key role in clarifying, after his work with Bilby [11], the underlying physics of the process [12]. The model that evolved was based on the concept of thermal activation. For certain régimes of strain rate and temperature there is a dynamic interaction between solute atoms (e.g. C in Fe-C alloys, Mg in Al-Mg alloys) and dislocations such that there is a repeated locking and escape mechanism attributed to the mobile dislocation density.

During locking, the stress climbs for the dislocations held back by their “atmospheres” and when the dislocations escape, the stress drops. The process is repeated throughout the test. Thermal activation energies have been measured for this mechanism by numerous investigators and while one may object to some of the approaches used, it is clear that activation energies are on the order of that of diffusion of the solvent species [13,14]. Recent data for IN100, a Ni-base superalloy strengthened by the coherent $L1_2$ precipitate γ' is shown in Fig. 5 [15]. In Fig. 5 the temperature strain rate plane is divided into regions in which the PLC effect is observed and not observed. The boundary between the two regions marks the onset of the PLC effect and as such may be used to determine the activation energy which is 1.14 eV and comparing reasonably well to the activation energy for bulk diffusion of C in Ni of about 1.48 eV. However, there is an apparent contradiction in using the activation energy of an atom/dislocation pair and the large strains that are associated with the serrations and the corresponding large numbers of dislocations needed to carry that strain. In effect, currently-accepted theories describing this process appear to be incomplete. In broad outline, the deformation process is initiated by unpinning of the dislocations having the lowest effective unpinning stress. At this point, the free dislocation would encounter a more strongly pinned dislocation at a larger precipitate. However, the stress on the second dislocation would be essentially doubled since there would be a two dislocation pileup and the stress would drop. The group of two dislocations would next encounter a locked dislocation but the stress at the leading dislocation would now be three times the applied stress so, depending on the actual locking stress, the required stress to continue deformation would decrease. The process of increasing strain with decreasing stress would continue until all of the dislocations on a slip plane have been mobilized[1] [1]. We thus have a picture of a decreasing stress with increasing strain for the first slip plane. The next easiest dislocation to unlock would be activated elsewhere in the crystal and as it moves across

[1] This explanation is simplified and does not take into account the statistical distribution of the pinning points. This more realistic situation may be addressed through a detailed statistical analysis.

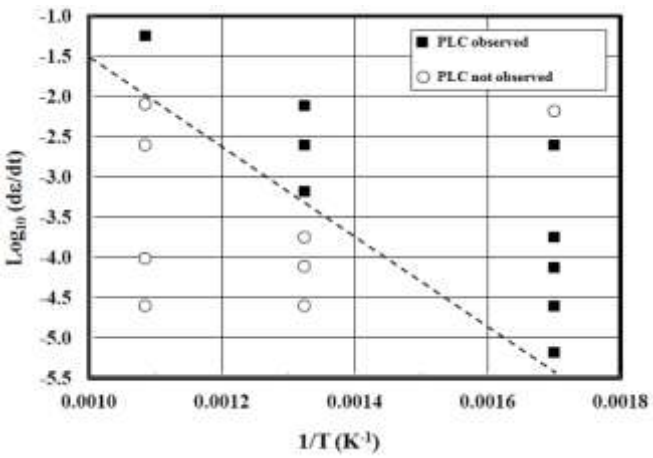

Figure 5. Arrhenius plot of deformation behaviour of IN 100 showing the boundary between PLC behaviour and non-PLC behaviour which gives an activation energy of 1.14 eV [5].

its slip plane the same process would operate. However, based on this model, the second slip plane to activate would do so at a higher stress because of the higher unlocking stress and the back stress due to the piled up dislocations in the first slip plane. Similarly the next source to operate would follow the same process but at an increased stress. Such a model would account for an accompanying Hall-Petch dependence that is known to apply for PLC behaviour. The pile-up mechanism implicitly accounts for ending the behaviour when all of the locked dislocations having relatively low unlocking stresses have been mobilized after which point deformation continues by normal flow processes. Thus this model description appears to account for:

- Temperature and strain rate effects through the initial unlocking of the initial dislocations on each slip plane.
- Macroscopic strain localization through local stress intensification at locked dislocations by the mobile dislocations.
- Exhaustion of the phenomenon through strain hardening due to the distribution of unlocking stresses, and activating normal flow processes at some stress level.
- An increasing mean stress (cyclically increasing flow stress) due to interactions from piled up dislocations and a generally increasing for each slip plane.

Extension of the Cottrell-Bilby model to the PLC effect has an interesting connection to the modern thermally activated strain rate analysis (TASRA) for dislocation plasticity. A positive or negative strain rate sensitivity (SRS) may occur according to whether one is on the upside or downside of the added PLC thermal activation curve [1]. Given that the PLC process is thermally activated, the following functional dependence is implied:

$$\tau_{th} = f\left(T, \ln \dot{\gamma}\right) \tag{6}$$

Here the symbols on the right have their usual meaning. However, some attention must be paid to the meaning of τ_{th} which is that component of the flow stress above long range internal stresses. There are examples in the literature in which it is mistakenly taken as the total stress which results in some errors in activation energies and over-all understanding. From calculus, Eq. (6) may be used to give the result:

$$\left(\frac{\partial \tau_{th}}{\partial T}\right)_{\ln \dot{\gamma}} \cdot \left(\frac{\partial T}{\partial \ln \dot{\gamma}}\right)_{\tau_{th}} \cdot \left(\frac{\partial \ln \dot{\gamma}}{\partial \tau_{th}}\right)_{T} = -1 \tag{7}$$

Equation (7) may be employed to provide insight into the PLC effect in terms of the separated factor dependencies. For normal dislocation velocity description with thermally activated shear stress, τ_{th}, the first factor in Eq. (7), is negative and the second two factors are positive. The same equation is usefully applied to the analysis of the incremental PLC effect for τ_{th}. Note that when the third term is negative (as seen for PLC), then each of the first two terms *must* be positive. Thus a negative strain rate sensitivity of the flow stress for dynamic strain aging (PLC) is associated *only* with the stress rising to the peak of strain aging and not for an "over the top" régime of decreasing stress. Misunderstanding of this feature has led to some controversy in the literature about the analysis of the PLC activation energy.

5. Strain Concentration and Adiabatic Shear Banding

Adiabatic shear banding refers in a formal sense to the case in which a localized shear band forms with no transfer of heat to or from the external environment (i.e. $\delta Q = 0$). The behaviour is favored in metals under conditions of low heat capacity and low thermal conductivity when deformed at high loading rates and/or low temperatures. The mechanical work associated with formation of the shear band is mainly transformed into heat and thereby manifested by an increase in temperature. *Unlike the PLC effect which is self-exhausting, the formation of adiabatic shear bands (ASBs) is self amplifying and leads to localized failure.* Recall that adiabatic shear banding was first observed by Tresca in a set of forging experiments on a Pt-Ir alloy [16]. When hammered just below the "red-hot" temperature, distinct X-type shear lines appeared on the longitudinal cross-section of the test specimen indicative of an exceptional temperature increase.

Eshelby and Pratt [17] used the mathematical solution for the temperature increase associated with a moving source of energy provided by Carslaw and Yaeger [18] and modified it to rows of equally spaced dislocations passing by a fixed lattice point. The main result of their calculation was:

$$\Delta T = \tau_o (nb) v / 2\pi K \left(\frac{\pi\Lambda}{2L}\right)^{\frac{1}{2}}, \ \Lambda \ll L \tag{8}$$

Where v is the dislocation velocity, K is the thermal conductivity, L is the length of the slip band and Λ is an effective thermal a length given by:

$$\boldsymbol{\Lambda = 2\alpha / v} \tag{9}$$

where α is the thermal diffusivity. Using reasonable values for Al, they showed that on the basis of this model, temperature increases of only 2° K was obtained from the model calculation. Furthermore, they examined other arrangements and concluded that no arrangement could be found which would give a large temperature increase. However, the very earliest work of Tresca proved that high temperature increases were occurring and thus the model of Eshelby and Pratt is a very useful step in developing a more complete understanding. This issue was re-examined by Coffey and Armstrong [19] on the basis of further accumulated evidence that appreciable temperature rises were being evidenced in shear banding experiments, A model favorable to shear banding was envisioned of isothermal stress build-up of stored energy in a dislocation pile-up, then leading to sudden obstacle collapse, and rapid dissipation of the stored energy by very localized plastic work in an earthquake-like dislocation avalanche. The model led, with employment of well-established slip band mechanics [20-21], to an expression for ΔT given by:

$$\Delta T < \frac{k_s L^{\frac{1}{2}} v(1-\upsilon)}{10\pi^2 K(1-2\upsilon)} ln\left(\frac{2K}{c^* v \Delta x_i}\right) \quad (10)$$

Where L is the grain size, k_s is the Hall-Petch microstructural stress intensity parameter, c* is the specific heat at constant volume, υ is Poisson's ratio, Δx_i is the spacing of dislocations in pile-up and v is the terminal dislocation velocity. Using an upper limit for the dislocation velocity of the shear wave speed and with other parameters for steel, a value of $\Delta T < 3.2 \times 10^3$ K was obtained. The over-estimated temperature rise for pile-up collapse was taken to give credence to the mechanism. Experimental results obtained on shear plugging of Ti-6Al-4V alloy material produced regions of sprayed molten metal onto the shear plug walls, consistent with prediction of the pile-up avalanche mechanism.

6. Strain Concentration in Fatigue-Persistent Slip Bands

It has long been known that fatigue loading results in roughening of the surface and that the bands in which deformation is carried are of a "persistent" nature [22]. Persistent slip bands (PSBs) have long been a subject intense research but it was not until the development of dislocation theory that some understanding of the fatigue process could be established on a physical basis. This too was a field in which Prof. Cottrell provided initial insight [23], particularly on the formation of slip band intrusions and extrusions. Considerable research has been carried to understand the details of this important phenomenon and a broad outline has emerged in which a unique structure is developed, at least in FCC single phase materials, of which Cu has received by far the most attention. A representative PSB is shown in Fig. 6. It consists of dislocation walls of primary edge character bounded by edge dislocations on the top and bottom surfaces with cyclic deformation being carried by screw dislocations. Controversy exists as to the signs of the dislocations at PSB boundary, the

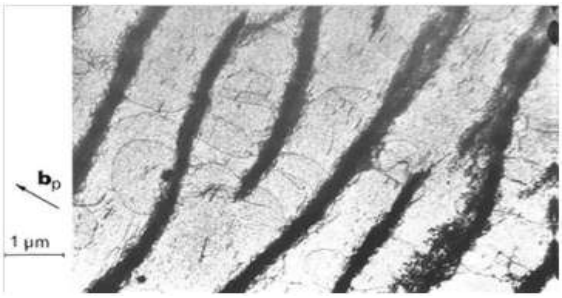

Figure 6. Walls in persistent slip bands (dark regions) and gliding screw segments in the channels between walls [24].

state-of-stress within the PSB's [25], the nature of intrusions, and the mechanism of crack formation [27]. Complex processes take place on the PSB walls which result in excess vacancy production. Evidence of this is found in the fact that a single PSB produced extrusions on both sides of a single crystal of Cu and also in the fact that at high temperatures the vacancies can migrate to sinks and the PSB's are actually thinner than at low temperature [28]. These ideas have been used with some success to numerically model crack nucleation at grain boundaries in Ni-base superalloys by accounting for the system energy including importantly the energy in the PSB and taking crack nucleation at an energy extremum. Of course application of the PSB morphology to precipitate systems may require some modification. An actual PSB taken from a fatigued René 95 LCF specimen in shown in Fig. 7 [30]. The morphology is very different from that shown in Fig. 6.

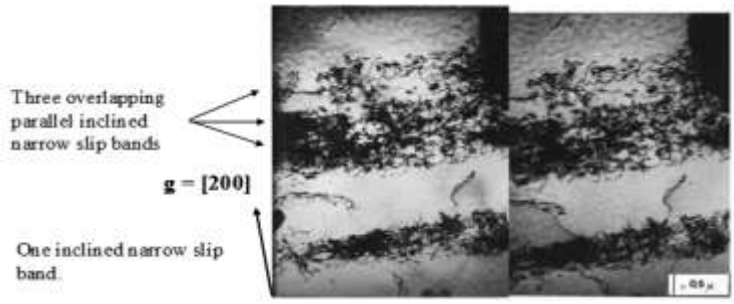

Figure 7. TEM Stereo pair of dislocations in fatigued René 95 [30] showing that there are four narrow slip bands, three of which are overlapping. Such information can serve to develop physically accurate models.

7. Summary

In this paper connecting the pioneering researches of Alan Cottrell and a current review of modern research results, we have demonstrated a critical role for localized strain concentrations in several deformation, fracture and fatigue processes. In all cases, the strain concentration arises from inhomogeneities in the microstructure including the dislocation substructure. The subject is not complete in that our understanding remains lacking in many important areas such as for PSB's in precipitate-bearing alloys. Accurate assessment of the true precipitate and dislocation structure will provide a sound basis for numerical modelling of industrially important materials and should also improve our ability to develop fatigue-resistant structures. In most of the literature, the effects of slip mode have been largely ignored and studies in which slip mode is varied (e.g. by controlling stacking fault energy) would be of great value.

Acknowledgements

The authors express thanks to colleagues and students for their contributions to our knowledge over the years. A particular note of thanks goes to Professor Ashok Saxena in this regards and for his presenting this paper for us at the ICF13 meeting.

References

[1] S.D. Antolovich and R.W. Armstrong, Plastic Strain Localizations in Metals: Origins and Consequences, accepted for publication in Prog. Mater. Sci., to appear in 2013.
[2] A.H. Cottrell, Theory of Dislocations, Prog. Met. Phys., 1, (1949), 77-126.
[3] A.H. Cottrell, Dislocations and Plastic Flow in Crystals, Oxford University Press, Oxford, UK, 1953.
[4] J.D. Eshelby, F.C. Frank and F.R.N. Nabarro, The Equilibrium of Linear Arrays of Dislocations, Philos. Mag., 42, (1951), 351-364.
[5] R.W. Armstrong and T.R. Smith: Dislocation Pile-up Predictions for the Strength Properties of Ultrafine Grain Size FCC Metals, in: *Processing and Properties of Nanocrystalline Materials* Eds, C. Suryanarayana, J. Singh and F. H. Froes, TMS, Warrendale, PA., (1996) 345-352.
[6] R.W. Armstrong and S.D. Antolovich: The Grain Size Dependence of Cleavage Cracking in α-Iron, 18th European Conference on Fracture, Dresden, Germany, August 30-September 3, 2010. Published in conference proceedings.
[7] A. H. Cottrell, Theory of Brittle Fracture in Steel and Similar Materials, Trans. TMS-AIME 212, (1958), 192-203.
[8] R.W. Armstrong, Dislocation Pile-ups: from {110} Cracking in MgO to Model Strength Evaluations, Mater. Sci. Eng. A, 409, (2005) 24-31.
[9] S.D. Antolovich and K.O. Findley, A New Look at Attractive/Repulsive Junctions and Cleavage Crack Formation in BCC Materials, Eng. Fract. Mech., 77, (2010), 201-216

[10] A. Portevin and F. Le Chatelier, Sur un Phénomène Observé lors de l'Essai de Traction d'Alliages en Cours de Transformation, Comptes Rendus de l'Académie des Sciences (CRAS), 176, (1923), 507-510.
[11] A.H. Cottrell and B.A. Bilby, Dislocation Theory of Yielding and Strain Ageing of Iron, Proc. Phys. Soc. London, A62, (1949), 49-62.
[12] A.H. Cottrell, A Note on the Portevin-Le Chatelier Effect, Philos. Mag., 44, (1953), 829-832.
[13] R. A. Mulford and U. F. Kocks, New Observations on the Mechanisms of Dynamic Strain Aging and Jerky Flow, Acta Metall., 27, (1979), 1125-1134.
[14] R.W. Hayes and C.W. Hayes, On the Mechanism of Delayed Discontinuous Plastic Flow in an Age-Hardened Nickel Alloy, Acta Metall., 30, (1982), 1295-1301.
[15] P. Frenandez-Zelalia, unpublished research, Mechanical Engineering, Georgia Tech, 2012.
[16] H. Tresca, On Further Applications of the Flow of Solids, Proc. Inst. Mech. Engrs., London, 30, (1878), 301-345.
[17] J.D. Eshelby and P.L. Pratt, Note on the Heating Effect of Moving Dislocations, Acta. Metall., 4, (1956), 560-562.
[18] H.S. Carslaw and J.C. Jaeger: *Conduction of Heat in Solids*, 2nd ed., Oxford University Press, 1947.
[19] C.S. Coffey and R.W. Armstrong, Description of 'Hot Spots' Associated with Localized Shear Zones in Impact Tests, in: *Shock Waves and High Strain Rate Phenomena in Metals: Concepts and Applications*, eds. M.A. Meyers and L.E. Murr, Plenum Press, N.Y., 1981, 313-324
[20] A.K. Head, Dislocation Group Dynamics, VI: The Release of a Pile- up, Philos. Mag., 27, (1973), 531-539.
[21] J.C.M. Li and Y.T. Chou, The Role of Dislocations in the Flow Stress Grain Size Relationship, Metall. Trans., 1, (1970), 1145-1159.
[22] J.A. Ewing and J.C.W. Humfrey, The Fracture of Metals under Repeated Alterations of Stress, Philos. Trans. Roy. Soc. London, 221A, (1903), 241-253.
[23] A.H. Cottrell and D. Hull, Extrusion and Intrusion by Cyclic Slip in Copper, Proc. Roy. Soc. London, 242A, (1957), 211-213.
[24] H. Mughrabi, F. Ackermann, and K. Herz, Persistent Slipbands in Fatigued Face-Centered and Body-Centered Cubic Metals, in: *Fatigue Mechanisms*, ed. J.T. Fong, ASTM STP 675, ASTM, Philadelphia, PA, (1979), 69-105.
[25] H. Mughrabi, Cyclic Slip Irreversibilities and the Evolution of Fatigue Damage, Metall. Mater. Trans., 40A, (2009), 1257-1279.
[26] L.M. Brown and S.L. Ogin, Role of Internal Stresses in the Nucleation of Fatigue Cracks, in: *Fundamentals of Deformation and Fracture*, eds. B.A. Bilby, K.J. Miller and J.R. Willis, Cambridge University Press, Cambridge, U.K., 1985, pp. 501-528.
[28] H. Mughrabi, M. Bayerlein and R. Wang, in: *Proc. 9th Int. Conf. on the Strength of Metals and Alloys (ICSMA 9)*, eds. D.G. Brandon, R. Chaim, and A. Rosen, Freund Publishing Company Ltd., London, 2, (1991), 879-886.
[29] M.D. Sangid, H.J. Maier, and H. Sehitoglu, The Role of Grain Boundaries on Fatigue Crack Initiation – an Energy Approach, Int. J. Plast., 27 (2011), 801-821.
[30] S.D. Antolovich, S. Bashir and Ph. Taupin, Low Cycle Fatigue of As-HIP and HIP + Forged René 95, Metall. Trans., 10A, (1979), 1481-1490.

The Cottrell Legacy: the Metamorphosis of ICF into the World Academy of Structural Integrity 2011-2021

Al Carpinteri[1], D M R Taplin[2]

1. ICF-WASI President

2. ICF-WASI Chief Executive Officer

Abstract

This paper is designed to address aspects of the immense contribution and enduring legacy of Sir Alan Cottrell FRS FREng FICF (1919-2012) - especially in the context of the creation and development of ICF - at the "ICF13 Memorial International Cottrell Symposium". One theme of this paper builds on the ICF0 paper of Cottrell in 1959, Cottrell's Opening Address at ICF2 in 1969 and Cottrell's ICF4 contribution "Fracture & Society" in 1977. A second theme of this paper is the BCS model of fracture and other models of fracture devised by Cottrell in the context of Cottrell's seminal 20thC contributions to the very creation of our disciplines of Structural Integrity and Materials Science: including archival research on the early work of Cottrell 1939-1941 on welding and cracking of low alloy steels at Birmingham. In particular, with the analytical BCS Model, Cottrell anticipated the numerical Cohesive Zone Models by at least two decades. This paper also addresses possible ways forward in this challenging 21stC for ICF-WASI following ICF13 in Beijing guided by the legacy of Cottrell's and Yokobori's ideas, inspiration & principles in establishing ICF during 1959-1969. At ICF13 the formal launch is arranged for the metamorphosis of ICF into "The World Academy of Structural Integrity". This is an ICF brand-development project explored at Sendai with Yokobori in 2010 and then initiated in 2011 at an ICF Interquadrennial Conference with ASTM in Anaheim, USA. This is much more than simply a name change but a comprehensive evolution in substance which like the original ten year creation process of ICF 1959-1969 is designed as a ten-year process 2011-2021. During the ICF13 Cottrell Forum in Beijing (as at the Sendai Interquadrennial in 2010) we seek full debate on the optimum ways forward for this metamorphosis.

1 Introduction

This paper is designed as an international tribute to Alan Cottrell at ICF13 and especially Cottrell's contribution to the creation of ICF. Following the "ICF0" MIT Swampscott Conference "Fracture" in 1959 (at which Cottrell was a principal speaker) work began on the creation of ICF. In 1961 at MIT the "Interim International Fracture Conference Committee" was established with Takeo Yokobori (Japan) as Chairman and as Committee Members, Alan Cottrell (UK), Ben Averbach (USA), Jacques Friedel (France), Max Williams (USA), Alan Head (Australia), Peter Haasen (Germany), Norman Petch (England), S N Zhurkov (Russia). Thereafter ICF1 was organised by the Japanese Society for Strength & Fracture of Materials at Tohoku University, Sendai, Japan in 1965 with over 300 delegates from 18 countries.

It is quite interesting to note that two of the key eleven references in the MSc thesis of Alan Howard Cottrell (Birmingham, October 1940 "The Arc Welding of High Tensile Alloy Steels") were Honda & Sekito 1928 and Honda & Nishiyama (1932) both from Tohoku Imperial University, Sendai, Japan. Indeed these were key references in Cottrell's PhD thesis as "Bowen Metallurgical Scholar" supervised by E C Rollason and D Hanson. So

that the fracture research at Sendai and Tohoku University was familiar to Cottrell from at least 1939.

This is all found in the “Cottrell Archive” in the Metallurgy & Materials Library at Cambridge which is also interesting in regard to a sheaf of letters to Cottrell in 1948-1949 when a Lecturer in Metallurgy at Birmingham University from Walter Boas (CSIRO

Australia and formerly Berlin, Germany), M B Bever (MIT, USA), Egon Orowan (MIT USA), W Hibbard (Yale, USA), R F Mehl (Carnegie, USA), Ulick Evans (Cambridge, England) indicating the strong thread of Cottrell’s international connections still in his twenties as a young researcher, including with MIT.

ICF2 was held in 1969 in England with 480 delegates from 25 countries. A major driving force in this second conference at which ICF was founded was to be sure Alan Cottrell who presented the Opening Address with Roy Nichols as Quadrennial Conference Chairman. ICF3 was held in Germany in 1973 with some 500 delegates from 26 countries and ICF4 was held in Canada in 1977 with over 750 delegates from 38 countries.

An earlier paper (Taplin & Saxena) outlines the historical development of ICF and this paper along with the full ICF-WASI Archive is available on www.icf-wasi.org now formally launched. This includes the Proceedings from “ICF0”, Swampscott 1959 through to ICF12, Ottawa 2009 and indeed ICF13, Beijing 2013 with plans forward regarding ICF14, Rhodes & ICF15, Vancouver, perhaps ICF15 Berlin 2025 we anticipate - plus various additional documents, papers and Interquadrennial Proceedings in a freely available internet library for the new “Academy”.

This present paper builds on a Cottrell Forum paper at ICF4 “Fracture & Society” based on interviews with Cottrell in 1977 coupled to a series of interviews with current researchers who are legatees of Cottrell’s enduring inspiration. A second part of the present paper focuses on the BCS model and related models devised by Cottrell. A third part of this paper addresses the future of ICF as a World Academy.

Metallurgy is arguably the oldest scientific and engineering profession perhaps seven thousand years old and the metallurgists who helped create the Parthenon attest to this with lead coated iron clamps for the epistyles. Some would argue that metallurgy was mainly a "black-art" until being transformed by such as Cottrell and others in the 1940's & 1950's to a modern science through for example Cottrell’s books on Structural Metallurgy & Dislocations.

Cottrell himself was brought-up in Birmingham in the inter-war years of industrial expansion and was trained in the older black-art traditions based on optical metallography and one can discern this old (more art than science) tradition in Cottrell's MSc/PhD theses of over seventy years ago. In particular there are just two equations in Cottrell’s PhD thesis on pages 38 and 83 which are simply stress calculation formulae. The thesis is based on simple tests and extensive optical metallography with an entirely qualitative approach consistent with the evolution of metallurgy as a discipline at that time.

Jim Charles was the first lecturer appointment Cottrell made at Cambridge as Goldsmiths’ Professor in 1960 who one could deduce continued the black-art intuitive approach also researching archeo-metallurgy creating a wider perspective for the more modernistic new lecturers such as John Knott appointed by Cottrell at Cambridge. Knott worked with

Cottrell from 1959 on his PhD on fracture of steels and therefrom until 1990 the Cottrell-inspired Knott Group was extremely active in our discipline. Indeed Knott is arguably Cottrell's foremost research student and co-worker who has made massive contributions (including as ICF President) and after over twenty years at Cambridge from 1990-present transferred his group back to Cottrell's alma mater Birmingham very successfully.

Arguably the most lasting contribution of Cottrell was through his years at Cambridge especially as Goldsmiths' Professor. Indeed a new "Cottrell Chair" is planned to be established at Cambridge in 2014 via especially contributions from former students of Cottrell. Probably the most prominent successor to Cottrell as Goldsmiths' Professor is Colin Humphreys who held this prestigious Chair from 1991-2008. Evidence suggests that the most significant research accomplishment (2000-2013) of Humphreys in the Cottrell tradition is on crack prevention/stress management in the manufacture of GaN for LED applications. Humphreys has also been Director of the Rolls-Royce Technology Centre at Cambridge since 1994 focussing on nickel-base superalloys with many outstanding achievements of this Rolls-Royce Centre. This is linked also to his appointment in the early 1990's of Julia King to replace John Knott when he left Cambridge for Birmingham and to be Deputy Director of the Rolls-Royce Centre, later joining Rolls-Royce as Director of Materials in Derby. King was a key appointment of Humphreys as Goldsmiths' Professor just as Knott was a key appointment of Cottrell himself when Goldsmiths's Professor.

A key Cottrell Legacy is also the many world-class and very influential series of textbooks and programmes of Mike Ashby on Materials Design.

In addition to ICF and the new World Academy the chief guardians ongoing of the Cottrell Legacy are Knott, Humphreys and Ashby and in a further paper we shall explore these legacy aspects of Cottrell.

There is an extensive oral interview of Cottrell in the archives of the British Library which covers his whole career anecdotally and since Cottrell's death there have been very many tributes and obituaries published including an extensive review by John Knott which is available now on the www.ICFWASI.org website. Accordingly there is no need to here delve in to the very many books and works by Cottrell, his great fount of ideas that inspired generations of researchers and transformed various realms of science and engineering. Our task is to examine the international inspirations and legacy of Cottrell especially in the discipline of our newly burgeoning World Academy of Structural Integrity and the contribution to Society. Documents from Trevor Churchman, Harold Paxton, Jacques Friedel & others have come to light via ICF and Ron Armstrong is assembling a parallel paper to our own to thereby create a debate in a Cottrell Forum at ICF13. So that this paper is simply one short introduction to this Forum which is additionally designed to address the further metamorphosis in comprehensive substance of the new "Academy" through ICF14 in Rhodes in June 2017 and to ICF15 in Vancouver in July 2021 as a ten year project.

Already noted is the new Academy Internet Library launched in Turin, Italy in August 2012. The Gold Medal prestigious awards in the names of the three most significant creators of ICF based on a micro-macro vision, Takeo Yokobori, Alan Cottrell and George Irwin were established at ICF12 in Ottawa in July 2009. Building on the original ICF Interquadrennial in Beijing in November 1983 we now have a comprehensive programme of several Interquadrennial Conferences each year. As well we now have a global network of MoU agreements with various societies and institutions. There are plans at ICF13 to establish a programme of "ICF-WASI Regional Directors" – perhaps as

many as a dozen to create a proactive Academy programme regionally for the common good. Many other significant ideas have been mooted for the new Academy and all these should be explored for the beneficial development of our Academy here in Beijing.

May 3 2013

Sir Alan Cottrell and the Dislocation Mechanics of Fracturing

R.W. Armstrong
Center for Energetic Concepts Development, Department of Mechanical Engineering, University of Maryland, College Park, MD 20742, U.S.A.

Abstract. Sir Alan Cottrell led the transformation of metallurgy from an observational science to analytical description. The following ditty, written for an analysis of the influence of polycrystal grain size on mechanical strength properties, could very well have been inspired by subliminal guidance from Cottrell:

The physically-weaker mortals are supported
With stronger materials, needfully, more so every day.
How so, you say – by brain power exhorted
To restrict the role that cracks and dislocations play!

The following account is an honoring contribution in recognition of the great man's leading researches on one of several materials-based topics that he led: the dislocation mechanics of fracturing.

1. Introduction

A previous festschrift for the 70th birthday celebration meeting in honor of Sir Alan Cottrell [1] may be compared with related recognitions given some years previously for Professors Egon Orowan [2], Norman Petch [3], and Takeo Yokobori [4], and a few years afterward, for Professor George Irwin [5]. The fracture-related research accomplishments of Cottrell were intimately connected with those of the persons who are referenced. Cottrell made quantitative use in a real sense of the dislocations figuratively invented by Orowan [6], and are also credited to Polanyi [7] and Taylor [8]. With Norman Petch, Cottrell developed the ductile-brittle transition theory for understanding the onset at lower temperatures or higher applied loading rates of brittleness in steel and related metals [9, 10]. Cottrell and Yokobori shared the vision of producing an understanding of fracturing on a combined microscopic and macroscopic level, this relating to encouragement from Cottrell for the founding by Yokobori of the International Congress on Fracture (ICF) [11]. Among Yokobori's earliest research articles is one on the Cottrell-Bilby theory of yielding of iron [12]. And, the later Bilby, Cottrell and Swinden [13] model of crack propagation with an attendant localized plastic zone at the crack tip provided a breakthrough example of fracturing at macroscopic dimensions, as pioneered also by George Irwin [14].

Four sub-topics among Cottrell's notable contributions to fracturing are to be covered: (1) the ductile-brittle transition temperature (dbtt); (2) the dislocation reaction mechanism for crack initiation; (3) the limiting theoretical strength of metals; and (4) the dislocation mechanisms of slip intrusions and extrusions involved in fatigue cracking. The following descriptions are intended to build onto the recent memorial articles honoring Cottrell by J.F. Knott [15], L.M. Brown [16] and D. Hull [17].

2. Dislocation mechanics of the ductile-brittle transition temperature

Both the Cottrell-Bilby theory of carbon-locking of dislocations for the yield point behavior in steel [18] and the Hall-Petch (H-P) dislocation pile-up model for a reciprocal square root of average grain diameter dependence of the yield and cleavage fracture stresses[19, 20] entered into Cottrell obtaining an implicit description of the dbtt in the relationship [9]

$$k_y(\sigma_{0y}\ell^{1/2} + k_y) = CG\gamma \tag{1}$$

In Eq. (1), k_y is the H-P microstructural stress intensity required for breaking-free Cottrell-locked dislocation sources so as to provide transmission of plastic flow across grain boundaries, ℓ is the polycrystal grain diameter, σ_{0y} is the friction stress resistance for individual dislocation movements in slip band pile-ups, G is the shear modulus, γ is the cleavage crack surface energy, and C is a numerical constant. Hull called attention in [17] to his measurements made with Mogford [21] showing an increase in σ_{0y} from neutron irradiation damage, thus raising the magnitude of the left-side of Eq. (1), and promoting brittleness. Petch obtained an explicit dependence of the dbtt on the temperature dependent component of the friction stress and on the ductile fracture stress dependent H-P determined value of k_f, as [10]

$$T_C = (1/\beta)[\mathbf{ln}B - \mathbf{ln}\{(CG\gamma/k_f) - k_f\} - \mathbf{ln}\ell^{-1/2}] \tag{2}$$

In Eq. (2), B is the limiting value of the temperature dependent component of the friction stress at T = 0 and β is the exponential temperature coefficient.

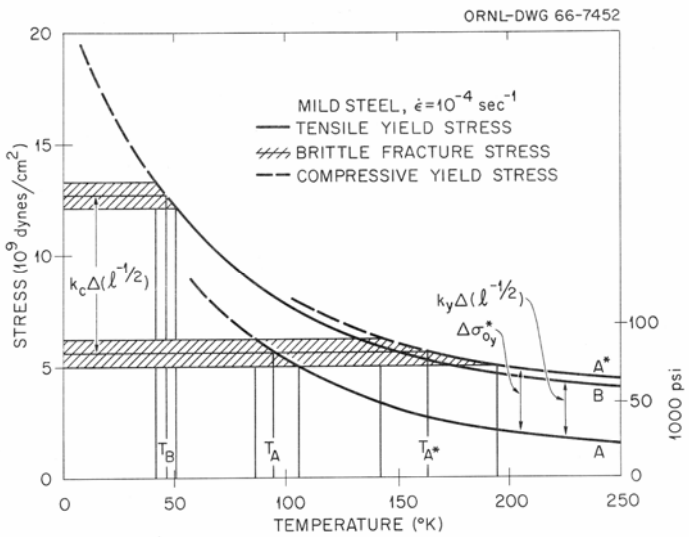

Fig. 1. Tensile ductile-brittle transition temperatures for two grain sizes, A of 100 μm and B of 5 μm; and, then of A altered by neutron irradiation to A* with raised value of $\Delta\sigma_{oy}$* [22].

Figure 1 provides an illustration produced at the U.S. Oak Ridge National Laboratory of the dbtt behavior as obtained on the basis of computed tensile test results applicable to grain size and neutron irradiation hardening [22]. In the figure, a comparison is made between the temperature dependences of the yield and cleavage fracture stresses of two annealed mild steel materials, "A" having a conventional grain size of ~100 μm and "B" having a grain size of ~5 μm. In addition, the yield stress is shown to be raised after neutron irradiation hardening of steel "A", now labeled "A*", but for which its cleavage stress is unchanged. As indicated in the figure, steel A has a lower dbtt because of the H-P inequality: $k_C > k_y$. And steel "A*" has an appreciably raised dbtt

due to addition of the athermal component $\Delta\sigma_{0y}$* to σ_{0y}, in the manner described by Hull and Mogford [21], thus raising the ambient temperature yield strength up to that of steel "B". The danger indicated in the figure, which was deemed important at the time, was that steels "B" and "A*" could have the same ambient yield strengths and temperature dependencies of them while exhibiting appreciably different values of the dbtt [23].

A historical note is that Orowan had drawn attention to the condition of the yield stress being raised to the level of the cleavage fracture stress as a criterion for the onset of brittleness in steel; and, this consideration, taken together with a plastic constraint factor for the notch in a Charpy impact test [24], provided for a quantitative description of the dbtt in the same vein as described by Cottrell and Petch [25]. Wessel reported at ICF1, in Sendai, on the correlation of changes in T_C associated with changes in σ_{0y} and k_y for a structural pressure vessel steel [26].

3. The Cottrell crack-forming dislocation reaction

In the seminal article by Cottrell on the dbtt [9], a breakthrough explanation was provided for the crystal structure dependent observation of cleavage occurring on cube-face {001} crystal planes in steel and related body-centered cubic (bcc) metals. On the basis of the bcc slip systems having lattice parameter, "a", focus was placed on the [uvw] direction- and (hkl) planar-dislocation reaction for two (mixed-type) dislocation lines mutually oriented along the [010] crystal axis as:

$$(a/2)[11\text{-}1]_{(101)} + (a/2)[\text{-}1\text{-}1\text{-}1]_{(\text{-}101)} = a[00\text{-}1]_{(001)} \qquad (3)$$

The (001) plane is not a slip plane in the bcc lattice and under an [001] directed tensile axis, the thus-formed [00-1] edge type dislocation with line direction along [010] would anyway be a sessile dislocation. Cottrell proposed that the reacted dislocation could form a cleavage crack nucleus. Chou, Garofalo and Whitmore, followed up Cottrell's model proposal with a quantitative analysis of arrested dislocation pile-ups which would be blocked at such intersection in alpha-iron [27]. And experimentally, Hahn *et al.* reported observations of initiated cleavage micro-cracks at temperatures centered on the dbtt for a number of polycrystalline iron and steel materials [28]. The observations relate to the Cottrell-Petch dbtt descriptions in that it had been proposed that break-out of cracking from within individual grains was required for material failure. Antolovich and Findley have reported on a re-examination of the Cottrell model [29].

Nevertheless, the importance of Cottrell's mechanism of crack initiation also took hold for other observations of cracking in single crystal experiments. Most notably, Keh, Li and Chou applied the Cottrell model to explaining the occurrence of cleavage cracking observed on otherwise unfavorable {110} type planes at aligned diamond pyramid hardness impressions put into rocksalt-type structure MgO (001) crystal surfaces [30]. Figure 2 shows a schematic view of the dislocations distributed among the indentation-activated {110}<1-10> slip systems [31]. For this crystal geometry, the Cottrell-type reaction is specified [32] as

$$(a/2)[10\text{-}1]_{(101)} + (a/2)[0\text{-}11]_{(011)} = (a/2)[1\text{-}10]_{(112)} \qquad (4)$$

The line direction of the reacted dislocation of Eq. (4) lies along the [11-1] direction. The square "picture frame" structure immediately encompassing the residual indentation is formed by volume accommodating slip on secondary <110>{1-10} slip systems. The sub-surface interaction of dislocation pile-ups at the intersection of conjugate slip systems, for example in the second quadrant of the (001) picture frame, produces the sessile Cottrell-type dislocation reaction described in Eq. (4).

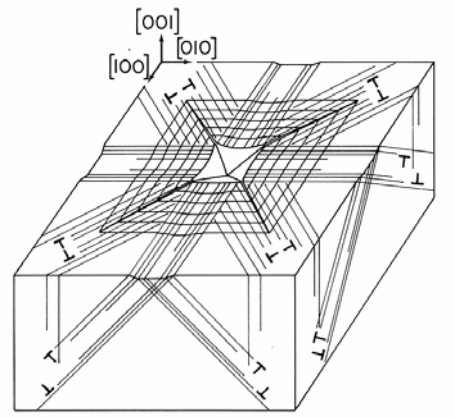

Fig. 2. The dislocation deformation pattern surrounding an aligned diamond pyramid microhardness indentation with indenter edges parallel to <100> put into an (001) MgO crystal surface [31].

The sub-surface dislocation structure leading to observation on the surface of diagonal <110> type cracking is illustrated in the cut-away diagram of Fig. 3. As mentioned, the cracking is on the unfavorable {110} planes compared to normally observed {010) cleavage planes.

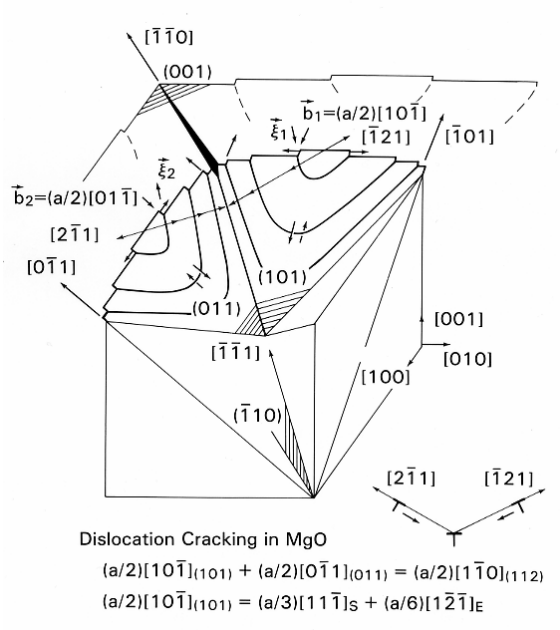

Fig. 3. Sub-surface dislocation reaction on intersecting <110>{1-10} slip planes in MgO [32].

The same type of crack-forming dislocation reaction mechanism was shown to occur at aligned microhardness impressions put into the (-210) crystal surfaces of body-centered tetragonal ammonium perchlorate (AP) crystals [33]. In this case, greater plastic anisotropy was reflected in the distorted shape of the residual diamond pyramid indentation such that cracking was only initiated in the adjacent top two indentation quadrants of the indented crystal surface in which a pair of intersecting slip systems had produced greater plastic deformation --- thus giving emphasis to the Cottrell mechanism of cleavage cracking being attributed to the local intersecting slip system blockages.

4. The theoretical strength and brittleness

The theoretical limiting strength of materials [34], including computations of the limiting strength to be obtained in cleaving perfect crystals [35], was of considerable research interest in the mid-1960's. The computations made in the latter reference built onto estimations of crystal strength that were described earlier in the pioneering article by Orowan [24]. Kitajima provided a report on the topic at ICF1 [36]. The situation was re-examined at the time in an important article by Kelly, Tyson and Cottrell [37] who looked in a fresh way into the stress required for separation of crystal lattice planes of potential cleavage systems. Such calculations provided a benchmark of local stress values needed at the tips of dislocation pile-ups in order to initiate cracking, for example, as described by Stroh [38]. Once such a smallest imaginable crack might be initiated, however, the question still obtains as to whether it would grow in the elastic manner described by Griffith [39] or its growth would be restricted because of initiation of plastic flow at the crack tip. As will be described subsequently, the larger scale consideration of crack growth with an associated plastic zone at the crack tip is another topic on which Cottrell and colleagues have provided an important analysis.

Figure 4 was developed based on the model consideration that the intrinsic brittleness of materials could be determined by whether a small crack would grow elastically by the (Griffith) mechanism or by initiation of plasticity at the crack tip [40]. Calculation of the ratio of the two stresses led to a suggested susceptibility factor of $(\gamma/Gb)^{1/2}$ to gage the intrinsic brittleness of metals. A tabulation of computed susceptibility factors for different metals and semi-metals demonstrated that low values of the ratio correlated reasonably well with the known propensities of the materials for cleavage. The model calculation was refined by Rice and Thomson [41] and then examined in further detail by Rice [42] who obtained the same type of agreement as originally proposed. Xu has produced a review of the subject, including further refinements of the model. In particular, Xu described a numerical evaluation of a single crystal type of dbtt controlled by the thermally-activated nucleation of dislocations at the crack tip [43].

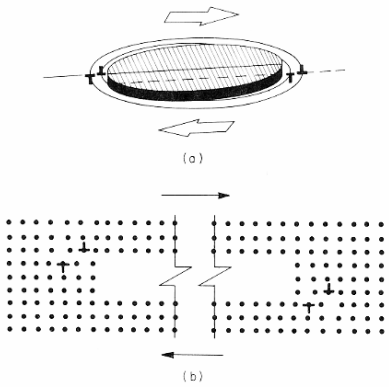

Fig. 4(a,b). Model for dislocation nucleation at the tip of a penny-shaped crack [40].

5. The Bilby-Cottrell-Swinden model of crack growth

Bilby, Cottrell and Swinden (BCS) had produced at micro- to macro-scopic dimensions, compared to the atomic-scale model illustration given in Fig. 4(a,b), the counterpart breakthrough description of critical crack growth with an attendant plastic zone at the crack tip [13]. Dugdale had also reported related results for a plane stress

description of cracking in thin sheet material [44]. The BCS analysis involved use of the method of continuous distributions of dislocations to model both the elastic stress state of the crack and extent of the plastic zone (as an inverted dislocation pile-up). Unstable growth of the crack was specified for a ratio of plastic zone size, s, to crack half-length, c, at fracture stress, σ_F, and yield stress, σ_y, in the transcendental equation

$$(s/c) = [\sec(\pi\sigma_F/2\sigma_y)] - 1 \tag{5}$$

In turn, Eq. (5) was shown to be well-approximated by the relationship [45]

$$\sigma_F \approx A\sigma_y\,[s/(c + s)]^{1/2} \tag{6}$$

The equation, with σ_y replaced by σ_C for crack-free material, was shown at ICF3 to describe the crack size dependence of the brittle fracture stress for several reference steel materials and for polymethylmethacrylate (PMMA) glass material. In Eq. (6), $A = (\pi/2)$ for $(s/c) < 1.0$ and $A = 1.0$ for $(s/c) \rightarrow 1.0$ [46].

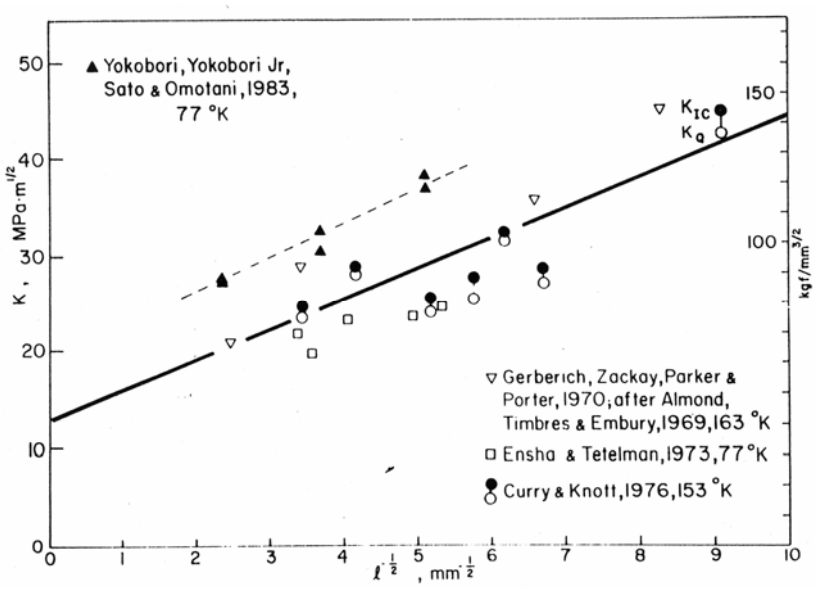

Fig. 5. Compilation of fracture mechanics stress intensity, K, values for mild steel [47].

The BCS description provided very importantly for specification of fracturing in terms of a critical crack tip opening criterion that has proved to be very useful in fracture mechanics testing [47]. But in either case of the critical stress criterion in Eq. (6) or in terms of the BCS-described crack tip opening, a same dependence on grain size and plastic zone size was obtained for the plane strain fracture mechanics stress intensity, K_{Ic} [48]. For yielding in plane strain on a von Mises basis, a value of K_{Ic} was given [49] as

$$K_{Ic} = (8/3\pi)^{1/2}[\sigma_{0C} + k_C\ell^{-1/2}]s^{1/2} \tag{7}$$

In Eq. (7), the quantity in square brackets is Petch's relationship for the cleavage fracture stress [20]. A compilation of cleavage fracture stress measurements was reported at ICF4 [50]. At constant plastic zone size, as appears to generally obtain in engineering fracture mechanics tests, a Hall-Petch type of dependence is obtained for K_{Ic}. Figure 5 shows a compilation of results reported for mild steel and related steel materials [51-55].
An unusual aspect of Fig. 5 is that an increase in fracture toughness is shown for materials obviously exhibiting an increase in yield stress (according to the corresponding H-P relationship for σ_y). In such a fracture mechanics test, however, yielding begins at the H-P determined σ_y at the root of the notch and the induced plastic zone strain hardens until a higher grain size dependent value of the cleavage stress, σ_C, is reached [56]. Knott provided an important review of the science and engineering aspects of fracture mechanics at ICF8 [57].

6. Slip band intrusions and extrusions

There is grain size dependence in the fatigue strength of metals also [25] but the situation is more complex, in no small part because of the occurrence of persistent slip bands (PSBs) and their increasingly pronounced behavior under cyclic loading [16, 17, 58].

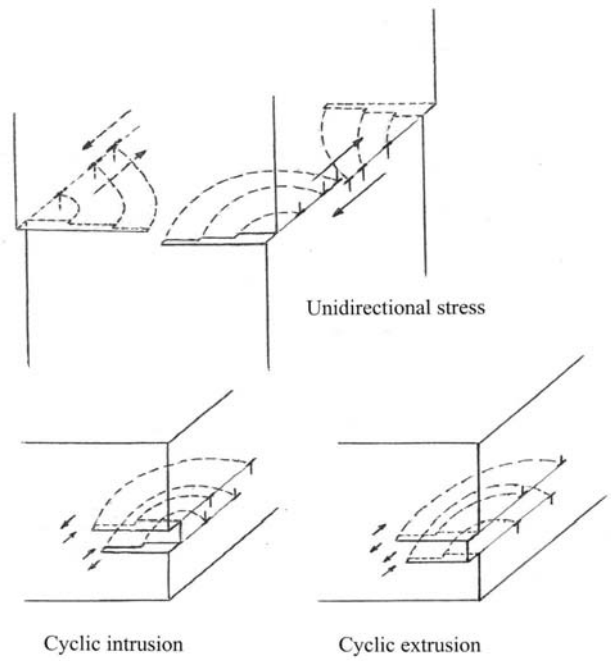

Fig. 6. Cyclically-induced slip intrusions/extrusions and internal dislocation structures.

Cottrell and Hull had produced a seminal description of surface intrusions/extrusions produced during fatigue testing [59]. Figure 6 provides a schematic illustration of the surface relief and internal dislocation structure accompanying cyclic loading [60]. Cottrell gave emphasis to the mechanical aspect of the nucleation and growth of cracking in a PSB as compared with the importance of mass transport by diffusion because of

results obtained by Hull on copper tested at temperatures as low as 4.2 K [17, 61]. More recently, Coupeau, Girard and Rabier have provided excellent observations via scanning probe microscopy of slip step heights at opposing dislocation pile-ups on parallel planes and evaluated the results in terms of mutually blocking dislocation pile-ups [62]. Head had reported the first numerical calculations of such opposing dislocation pile-ups [63]. A major result from the dislocation modeled behavior was that at sufficient applied shear stress and corresponding local stress concentration, the leading dislocations passed each other and formed dipoles. The behavior is in agreement with the associated slip band structure becoming more pronounced in PSBs in part because the self-stress associated with individual dislocation dipoles decreases more rapidly with distance, of the order of $\sim(\Delta r)^{-2}$ as compared with the normal $(1/\Delta r)$ individual dislocation behavior, and therefore leading to many more dislocations being fitted into a cyclically-defined slip band length. A sub-surface role of diffusion of atomic vacancies that has generated later research interest should be additive in the process [16].

7. Summary

A number of Sir Alan Cottrell's notable contributions, with colleagues too, on the dislocation mechanics of fracturing have been briefly described on four sub-topics. The listed contributions have been in the sequence of: (a) conditions for a ductile to brittle transition in steel and related metals; (b) evaluation of the theoretical limiting strength of crystals; (c) dislocation-modeled crack growth in relation to a fracture mechanics description; and, (d) geometrical aspects of the development of persistent slip band structures in fatigue. The purpose was to provide cogent examples, first, of the importance of original insights provided by Cottrell in producing a better understanding of relevant issues and, secondly, to show a positive connection with further developments already made or continuing to be made on the same subjects. In this regard, a note is added from the interview of Sir Alan at ICF4 in Waterloo, Canada, to the effect that more work needed to be done on multiple dislocation group dynamics, a topic that has been pursued in the interim time period and continues to be an important research activity [64].

Acknowledgments

It is a great pleasure for the author to thank colleagues, David Taplin and Stephen Antolovich, for encouragement to produce the present article. Involvement in the ductile to brittle transition topic began in 1958 during a post-doctoral appointment with Norman Petch, when at Leeds, and which appointment was suggested by Harold Paxton and assisted by Sir Alan. A grand remembrance was the joined recollection of the post-doctoral year and subsequent activities at morning tea with Sir Alan in 1984 at Jesus College, Cambridge. A much appreciated later sabbatical leave from the Westinghouse Research Laboratory during 1964 at the Commonwealth Scientific and Industrial Research Organization, Division of Tribophysics, spent with Walter Boas and Alan Head on a related fracturing topic [65], should also be mentioned.

References

[1]. J.A. Charles and G.C. Smith, editors, *Advances in Physical Metallurgy, Sir Alan Cottrell's 70th Birthday Meeting*, Institute of Metals, London, 1990.
[2]. A.S. Argon, editor, *Physics of Strength and Plasticity*, M.I.T. Press, Boston, MA, 1969.

[3]. T.N. Baker, editor, *The Yield, Flow and Fracture Strength of Metals*, Applied Science Publishers, London, 1983.
[4]. H. Liebowitz, editor, A Special Issue in Honor of Professor Takeo Yokobori On the Occasion of His 70th Birthday, *Engineering Fracture Mechanics*, **28**, [5-6], 481-816 (1987).
[5]. K.S. Chan, editor, *George R. Irwin Symposium on Cleavage Fracture*, Minerals, Metals, and Materials Society, Warrendale, PA, 1998.
[6]. E. Orowan, Zur Kristallplastizitaet, *Zeitschrift fur Physik*, **89**, 605-659 (1934)
[7]. M. Polanyi, Ueber ine Art von Gitterstoerung, die einemkristal plastich machen koennte, *Zeitschrift fur Physik*, **89**, 660-664 (1934).
[8]. G.I. Taylor, The Mechanism of Plastic Deformation of Crystals, *Proceedings of the Royal Society of London A*, **145**, 362-404 (1934).
[9]. A.H. Cottrell, Theory of brittle fracture in steel and similar metals, *Transactions of the American Institute of Mining and Metallurgical Engineers*, **212**, 192-203 (1958).
[10]. N.J. Petch, The ductile-brittle transition in the fracture of α-iron, *Philosophical Magazine*, **3**, 1089-1127 (1958).
[11]. D.M.R. Taplin and A. Saxena, ICF: The World Academy of Structural Integrity – retrospective and prospective, *Strength, Fracture and Complexity*, **7**, 109-121 (2011).
[12]. T. Yokobori, The Cottrell-Bilby theory of yielding of iron, *Physical Review*, 88, 1423 (1952).
[13]. B.A. Bilby, A.H. Cottrell and K.H. Swinden, The spread of plastic yield from a notch, *Proceedings of the Royal Society of London A*, **272**, 304-314 (1963).
[14]. G.R. Irwin, Plastic zone near a crack and fracture toughness, in: *Mechanical and Metallurgical Behavior of Sheet Materials, 7th Sagamore Ordnance Materials Research Conference*, Syracuse University Research Institute, NY, 1961, pp. 63-78.
[15]. J.F. Knott, Sir Alan Cottrell: Fracture and Structural Integrity, *The UK Forum for Engineering Structural Integrity (FESI) Bulletin*, **7**, [1], 5 pp. (2013).
[16]. L.M. Brown, Cracks and extrusions caused by persistent slip bands, *Philosophical Magazine,* in print (2013).
[17]. D. Hull, A.H. Cottrell at Harwell in the mid-1950s, *Philosophical Magazine*, DOI:10.1080/14786435.2013.765990 (2013).
[18] A.H. Cottrell and B.A. Bilby, Dislocation theory of yielding and strain ageing of iron, *Proceedings of the Physical Society of London*, **A62**, 49-62 (1949).
[19]. E.O. Hall, The deformation and ageing of mild steel; Discussion of results, *Proceedings of the Physical Society of London*, **B64**, 747-753 (1951).
[20]. N.J. Petch, The cleavage strength of polycrystals, *Journal of the Iron and Steel Institute*, **174**, 25-29 (1953).
[21]. D. Hull and I.L. Mogford, Ductile Brittle Transition in Steels Irradiated with Neutrons, *Philosophical Magazine*, **3**, 1213ff (1958).
[22]. R.W. Armstrong, Stress – Grain Size Analysis of the Ductile – Brittle Transition for Steel and Similar Metals, *Radiation Metallurgy Section, Solid State Division Progress Report, Oak Ridge National Laboratory*, ORNL-4020 (July 1966).
[23]. R.W. Armstrong, Influence of polycrystal grain size on several mechanical properties of materials, *Metallurgical Transactions*, **1**, 1169-1176 (1970).
[24]. E. Orowan, Notch Brittleness and the Strength of Materials, *Transactions of the Institute of Engineers and Shipbuilders of Scotland*, **89**, 165-215 (1946).
[25]. R.W. Armstrong, Dislocation Mechanics Description of Polycrystal Plastic Flow and Fracturing Behaviors, in: *Mechanics of Materials; Fundamentals and Linkages*, edited by M.A. Meyers, R.W. Armstrong and H.O.K. Kirchner, McGraw-Hill Publishers, N.Y., 1999, Chap. 10, pp. 363-398; see Fig. 10.19.
[26]. E.T. Wessel, Variations in the embrittlement of irradiated pressure vessel steels, in: *Fracture,* (ICF0), Technology Press of MIT, N.Y., 1959, pp. 147ff.

[27]. Y.T. Chou, F. Garofalo and R.W. Whitmore, Interactions between glide dislocations in a double pile-up in α-iron, *Acta Metallurgica*, **8**, 480-488 (1960).
[28]. G.T. Hahn, B.L. Averbach, W.S. Owen and M. Cohen, Initiation of cleavage microcracks in polycrystalline iron and steel, in: *Fracture*, (ICF0), Technology Press of MIT, N.Y., 1959, pp. 91ff.
[29] S.D. Antolovich and K.O. Findley, A new look at attractive/repulsive junctions and cleavage crack formation in bcc materials, *Engineering Fracture Mechanics*, **77**, 201-216 (2010).
[30]. A.S. Keh, J.C.M. Li and Y.T. Chou, Cracks due to the piling-up of dislocations on two intersecting slip planes in MgO single crystals, *Acta Metallurgica*, **7**, [10], 694-696 (1959).
[31]. R.W. Armstrong and C.Cm. Wu, Lattice Misorientation and Displaced Volume for Microhardness Indentations in MgO Crystals, *Journal of the American Ceramic Society*, **61**, [3-4], 102-106 (1978).
[32]. R.W. Armstrong and W.L. Elban, Dislocation Aspects of Plastic Flow and Cracking at Indentations in Magnesium Oxide and Cyclotrimethylenetrinitramine Explosive Crystals, in: *Microindentation Techniques in Materials Science and Engineering,* edited by P.J. Blau and B.R. Lawn, ASTM STP 889, American Society for Testing and Materials, 1986, pp. 109-126.
[33]. W.L. Elban and R.W. Armstrong, Plastic Anisotropy and Cracking at Hardness Impressions in Single Crystal Ammonium Perchlorate, *Acta Materialia*, **46**, [17], 6041-6052 (1998).
[34]. A. Kelly, *Strong Solids*, Clarendon Press, Oxford, U.K., 1966.
[35]. *Theoretical Strength of Materials*, U.S. National Academy of Science, Materials Advisory Board, Publication MAB-221-M (1966).
[36]. K. Kitajima, On the mechanism of cleavage of crystals. In: *International Conference on Fracture (ICF1)*, Sendai (1965).
[37]. A. Kelly, W.R. Tyson and A.H. Cottrell, Ductile and brittle crystals, *Philosophical. Mag*azine, **15**, 567-586 (1967).
[38]. A.N. Stroh, The Formation of Cracks as a Result of Plastic Flow, *Proceedings of the Royal Society of London A*, **223**, 404-414 (1954).
[39]. A.A. Griffith, The Phenomena of Rupture and Flow in Solids, *Philosophical Transactions of the Royal Society of London A*, **221**, 163-198 (1920-21).
[40]. R.W. Armstrong, Cleavage crack propagation within crystals by the Griffith mechanism versus a dislocation mechanism, *Materials Science and Engineering*, **1**, 250-254 (1966).
[41]. J.R. Rice and R. Thomson, Ductile versus Brittle Behaviour of Crystals, *Philosophical Magazine*, **29**, 73-97 (1974).
[42]. J.R. Rice, Dislocation nucleation from a crack tip: An analysis based on the Peierls concept, *Journal of the Mechanics and Physics of Solids*, **40**, 239-271 (1992).
[43]. G. Xu, Dislocation Nucleation from Crack Tips and Brittle to Ductile Transitions in Cleavage Fracture, in: *Dislocations in Solids*, edited by F.R.N. Nabarro and J.P. Hirth, Elsevier B.V., Oxford, 2004, **12**, Chap. 65, pp. 81-145.
[44]. D.S. Dugdale, Yielding of steel sheets containing slits, *Journal of the Mechanics and Physics of Solids*, **8**, 100ff (1960).
[45]. R.W. Armstrong, Crack size and grain size dependence of the brittle fracture stress, in: *Dritte Iinternationale Tagung uber den Bruch (ICF3)*, edited by A Kochendorfer, Verein Deutscher Eisenhuttenleute, Duesseldorf, 1973, Paper III-421, 6 pp.
[46]. R.W. Armstrong and O. Cazacu, Indentation fracture mechanics toughness dependence on grain size and crack size: Application to alumina and WC-Co, *International Journal of Refractory Metals and Hard Materials*, **24**, 129-134 (2006); see Fig. 1.
[47]. B.A. Bilby, Dislocations and Cracks, *Dritte Internationale Tagung den Bruch (ICF3)*, edited by A. Kochendorfer, Verein Deutscher Eisenhuttenleute, Duesseldorf, 1973, Paper PLI-III.
[48]. R.W. Armstrong, The (cleavage) strength of pre-cracked polycrystals, *Engineering Fracture Mechanics*, **28**, [5-6], 529-538 (1987).

[49]. R.W. Armstrong, Dislocation viscoplasticity aspects of material fracturing, *Engineering Fracture Mechanics*, **77**, 1348-1359 (2010).
[50]. R.W. Armstrong, Grain Size: The Fabric of Brittle Fracture of Polycrystals, in: *Fracture 1977, Fourth Internal Conference on Fracture (ICF4)*, edited by D.M.R. Taplin, University of Waterloo, Canada, 1977, **4**, pp. 83-96.
[51]. E.A. Almond, D.H. Timbres and J.D. Embury, The influence of second phase particles on brittle fracture, in: *Fracture 1969; The 2nd International Conference of Fracture (ICF2)*, Chapman and Hall Limited, London, 1969, pp. 253ff.
[52]. W.W. Gerberich, V.F. Zackay, E.R. Parker and D. Porter, The role of grain boundaries on crack growth, in: *Ultra-fine Grain Metals*, edited by J.J. Burke and V.V. Weiss, Syracuse University Press, NY, 1970, pp. 259-293.
[53]. S. Ensha and A.S. Tetelman, A quantitative model for the temperature, strain rate and grain size dependence of fracture toughness of low alloy steel, *Dritte Internationale Tagung uber den Bruch (ICF3)*, edited by A. Kochendorfer, Verein Deutscher Eisenhuttenleute, Duesseldorf, 1973, Paper I-331.
[54]. D.A. Curry and J.F. Knott, The relationship between fracture toughness and microstructure in the cleavage fracture of mild steel, *Metal Science*, **10**, 1ff (1976).
[55]. T. Yokobori, A.T. Yokobori, Jr., K. Sato and M. Omotani, The effects of ferrite grain size on fracture of low carbon steel under mixed modes I and II, *Engineering Fracture Mechanics*, **17**, 75-85 (1983).
[56]. N.J. Petch and R.W. Armstrong, Work hardening in cleavage fracture toughness, *Acta Metallurgica*, **37**, [8], 2279-2285 (1989).
[57] J.F. Knott, The Science and Engineering of Fracture, in: *Advances in Fracture Resistance and Structural Integrity (ICF8)*, Pergamon Press, Oxford, 1994, pp. 13-49.
[58]. H. Mughrabi, Cyclic slip irreversibilities and the evolution of fatigue damage, *Metallurgical and Materials Transactions A*, **40A**, 1257-1279 (2009).
[59]. A.H. Cottrell and D. Hull, Extrusion and intrusion by cyclic slip in copper, *Proceedings of the Royal Society of London A*, **242**, 211-213 (1957).
[60]. S.D. Antolovich and R.W. Armstrong, Plastic strain localizations in metals: Origins and Consequences, *Progress in Materials Science*, in print (2013).
[61]. D. Hull, Surface structure of slip bands in copper fatigued at 293 K, 90 K, and 4.2 K, *Journal of the Institute of Metals*, **86**, [9], 425-430 (1958).
[62]. C. Coupeau, J.-C. Girard and J. Rabier, Scanning Probe Microscopy and Dislocations, in: *Dislocations in Solids*, edited by F.R.N. Nabarro and J.P. Hirth, Elsevier B.V., Oxford, 2004, **12**, Chap. 67, pp. 273-338; see Figs. 46-48.
[63]. A.K. Head, The Position of Dislocations in Arrays, *Philosophical Magazine*, **4**, 295-302 (1959).
[64]. J.F. Knott and D.M.R. Taplin, Recorded Interview with Sir Alan Cottrell, *Fracture 1977*, Fourth International Conference on Fracture (ICF4), Waterloo, Canada, in: *Advances in Research on Strength and Fracture of Materials*, Pergamon Press, Oxford, 1977.
[65]. R.W. Armstrong and A.K. Head, Dislocation queueing and fracture in an elastically anisotropic material, *Acta Metallurgica*, **13**, 759-764 (1965).

A Pipeline Approach to Developing Virtual Tests for Composite Materials

Brian Cox[1,*], Hrishikesh Bale[2], Matthew Blacklock[3], Bao-Chan Do[4], Renaud Rinaldi[3], Robert Ritchie[2], Qingda Yang[4], Frank Zok[3], and David Marshall[1]

[1] Teledyne Scientific Co LLC, Thousand Oaks, CA 91360, USA
[2] University of California, Berkeley, CA 94720, USA
[3] University of California, Santa Barbara, CA 93106, USA
[4] University of Miami, Coral Gables, FL 33124, USA
* Corresponding author: bcox@teledyne.com

Abstract A multi-disciplinary project combines experiments and theory to build high-fidelity virtual tests of composite materials. The virtual test is assembled via a "pipeline" running through a number of collaborating institutions. Key experimental challenges are acquiring 3D data that reveal the random microstructure and damage events at high temperatures in the interior of the composite with very high resolution (~ 1 μm). Key theoretical challenges include representing the stochastic characteristics of the 3D microstructure, modeling the failure events that evolve within it, and developing efficient methods for executing large ensembles of stochastic virtual tests. To begin, 3D images of 3D woven ceramic composites are captured by x-ray μCT on a synchrotron beamline. The statistics of the shape and positioning of the fiber tows in the 3D architecture are used to calibrate a generator that creates virtual specimens that are individually distinct but share the statistical characteristics of measured specimens. Failure of the virtual specimens is simulated by advanced computational methods, revealing the complete failure sequence of multiple interacting crack types. Validation of the analytical methods is performed by comparing with data captured at 1500°C and above, using digital image correlation or μCT to track damage evolution.

Keywords virtual test, stochastic, high temperature, ceramic, textile

1. Introduction

One role of a virtual test, as its name suggests, is to replace a real engineering test by a computer simulation. Ideally, the simulation would predict engineering properties *ab initio* with sufficient fidelity that the real test becomes unnecessary. More realistically, a virtual test calibrated by a few real tests will reduce the matrix of real tests needed to ensure safe use of a material, perhaps by an order of magnitude or more [1].

Of equal interest is the possibility that a virtual test can function as a tool for optimizing material design [1-5]. Indeed, a virtual test can yield much richer information about the correlation between the microstructure of a material and its performance than is easily available from experiments: in the virtual test, we have full knowledge of the microstructure and its effect on the details of failure mechanisms, whereas in the real test, such effects are often concealed in the interior of the specimen.

Virtual tests are of special value for high temperature materials, e.g., the current generation of integral textile ceramic matrix composites [6] with potential use temperatures ranging up to 1500ºC. While mechanisms of failure in composites that act at room temperature can be determined quite readily either by modern 3D imaging or by destructive sectioning following interruption of tests, mechanisms acting at high temperatures are much more difficult to probe. The virtual test offers the possibility of probing details of damage mechanisms for different temperature and loading histories using simulations coupled to relatively simple surface observations on real specimens. Nevertheless, advancing test methods applicable to high temperatures remains critical: the proven fidelity of a virtual test can never exceed the ability to identify the mechanisms that must be

modeled by direct experimentation.

In the case of virtual tests for continuous-fiber composites, including composites reinforced by laminated unidirectional fiber plies and textile preforms, the high resolution now available in 3D imaging systems is yielding details of the stochastic variability of plies and fiber tows and even of the spatial distribution of the individual fibers that populate the plies and tows; certain characteristics of textile geometry and tow deformation have been measured [7-9], as well as porosity [10] and its changes during processing steps [10, 11]. These and other studies have also addressed achieving feature definition in ceramic composites [12], which is often made difficult by low x-ray absorption contrast between the constituent materials. In recent work, fiber tows are made to stand out by imaging composites with partially formed matrices [13]. This allows detailed analysis of the statistics of geometrical variability in the fiber reinforcement. The geometrical variability of fiber deployment is a source of scatter in composite performance [14-19].

In the remainder of this article, the sequential steps of constructing a virtual test are described. Interesting prior literature includes virtual tests for textile ceramic composites using models that directly reproduce a stochastic microstructure from micrographs [20] (rather than using a virtual specimen generator as described below).

2. The stochastic characteristics of textile composites

The details of fiber tow shape in textile composite specimens somewhat larger than but comparable in size to a single unit cell (several mm) can be determined most satisfactorily using micron-resolution X-ray computed tomography (μCT) in a high-flux synchrotron beamline. Avoiding the difficulty of reconstructing 3D domains from 2D images of serial sections in micro-toming techniques, μCT data reveal comprehensive geometrical information on the fiber tow scale. Information at even smaller scales, down to 1 μm, concerning matrix voids, individual fibers, and fiber coatings can also be extracted but image artefacts can compromise interpretation. Typical images of a 3D woven carbon/SiC composite are shown in Fig. 1. (This material was fabricated with only enough matrix to rigidify the structure, which simplified identifying tow domains [13].)

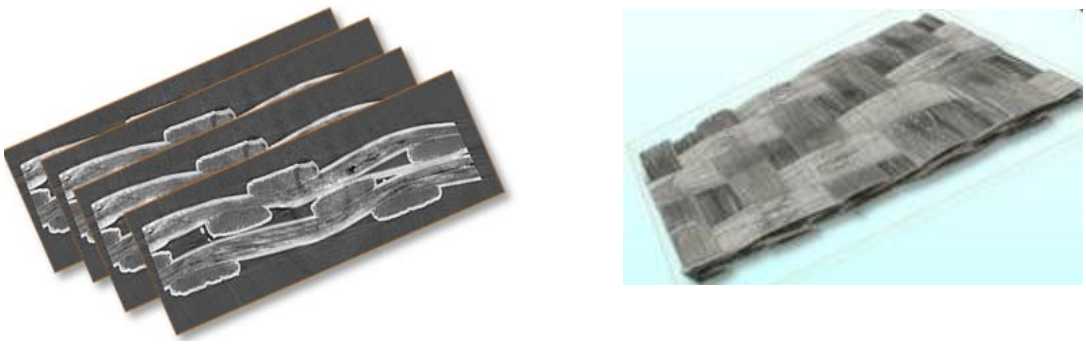

(a) (b)

Figure 1. μCT of a carbon/SiC woven composite, consisting of fiber tows coated by a thin layer of matrix material. (a) Image slices. (b) Re-constructed 3D image.

Fiber positioning variations can be decomposed into non-stochastic, periodic variations associated with the nominal periodicity in the textile architecture and stochastic deviations, which vary randomly though the fabric. A convenient and intuitively appealing treatment of the deviation divides it in turn into a superposition of “short-range” and “long-range” deviations. The

short-range deviations are those arising within a unit cell, referred to the center-of-mass of the unit cell, while the long-range deviations are the displacements of the centers-of-mass of unit cells over gauges much greater than the unit cell [13].

3. Virtual specimen generation

The art of formulating reconstruction algorithms or geometry generators for stochastic heterogeneous materials and related problems in statistical physics has a long history, mostly in the study of granular materials (e.g., [21, 22]. Textiles contrast with alloys in that they comprise long, continuous fiber bundles of essentially infinite aspect ratio, interlaced in complex but systematic patterns, a fact that calls for specialized algorithms in a virtual specimen generator, quite different in nature to those developed for statistically isotropic multi-phase materials (e.g., [23] and references therein).

The simplest geometry generator for a textile directly exploits the linear continuity of tows: a Markov Chain formulation generates fluctuations in any tow cross-sectional characteristic by marching systematically along the tow's length (Fig. 2) [24]. The key element of the Markov Chain is the Probability Transition Matrix (PTM), which determines the deviation and correlation length of any variable. The PTM is calibrated against measured statistical data, thus guaranteeing that the virtual specimens possess the same statistics as the real specimens that have been imaged. The Markov Chain formulation is very efficient and physically appropriate for the textile reconstruction problem, provided the dominant correlations are those along a tow, with correlations between tows relatively weak. It can be adapted to generate tows with 3D structure (Fig. 3) [25].

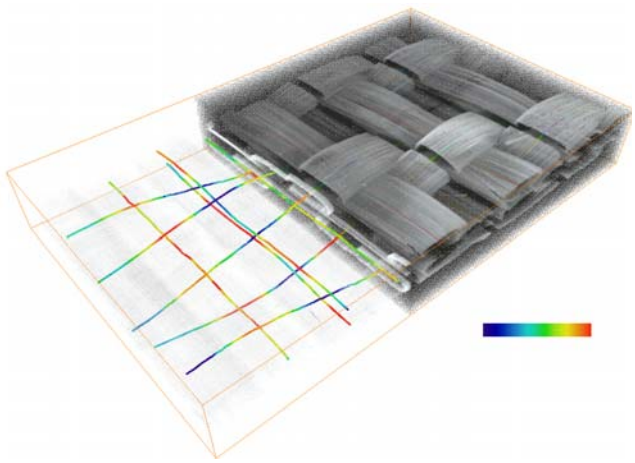

Figure 2. A μCT image yields statistics that are matched by generated virtual specimens. In this schematic, the generated tow structure at the left of the collage represents tows by 1D loci, suitable for use in the Binary Model [24, 26].

As it is described above, the Markov Chain formulation provides a purely empirical approach to virtual specimen generation: it simply matches statistical data from experiment. Models of the mechanics of fiber tow or preform deformation, which have been the basis for most other attempts to generate realistic geometric models of textiles, are not used. There is therefore no risk of errors flowing from uncertainty in the constitutive laws assumed to characterize such deformation, or in misrepresentation of the conditions during which preform fabrication or handling are carried out, including loading boundary conditions or the presence or absence of lubricating agents. The preform is analyzed as it is, in its final disposition.

However, an empirical approach has the disadvantage that the effects of changing processing conditions cannot be predicted. Such predictions are the province of mechanical models. An attractive future development will link mechanical modeling of preform deformation to empirical statistics, using the rich data content of detailed 3D measurements to calibrate and validate the mechanical model. The Markov Chain method may remain a useful tool within the linked super-model.

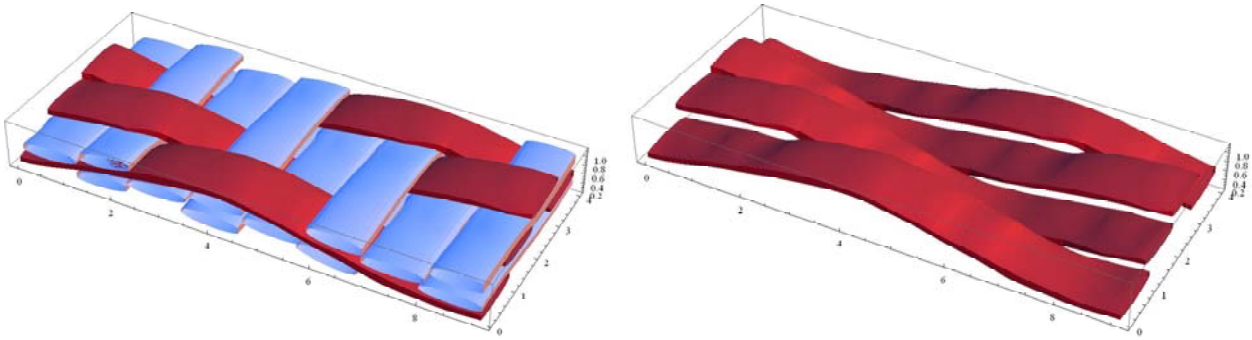

(a) (b)

Figure 3. The textile reinforcement of one virtual specimen generated with 3D tow representations using the Markov Chain method [25], showing (a) warp and weft tows together and (b) warp tows only. Tow shapes possess a combination of non-stochastic periodic variations (crimp features, etc.) and non-periodic stochastic deviations.

4. Observations of damage

The properties (strength, etc.) of a composite's constituent materials and their interfaces are generally unknown at high temperature. Phase properties cannot be calibrated by simple material tests, because the strength of different phases when they are juxtaposed at nm and μm scales is not represented by tests on large specimens of each phase isolated as a monolithic material. Tests are required on the composite materials themselves, executed at expected use conditions (i.e., temperatures of 1500ºC and higher), with sufficient resolution of mechanisms to enable the deduction of local material properties that control the mechanism. Direct observation of mechanisms is also critical to choosing correct formulations for simulations.

Measurements made at high temperature are the only faithful source of the details of failure. If a test specimen is cooled to an experimentally convenient 25°C for examination, the cooling itself introduces thermal strains of the order of at least 0.1–0.5% depending on composition and cooling rate, which can change the cracking patterns present before such cracks can be measured.

An apparatus was recently reported for acquiring 3D images via μCT of a specimen loaded in tension or compression at temperatures of 1500 – 1700°C in inert or oxidizing atmospheres (Fig. 4) [27]. Current maximum spatial resolution is 0.65 μm/voxel, yielding rich data on microstructure down to the fiber scale and μm-scale local failure mechanisms. Key data include variations of the opening displacements of fiber breaks and matrix microcracks as a function of load.

Data for a monotonic tension test of an angle interlock carbon-SiC woven composite specimens reveal different mechanisms of failure operating at 25°C and 1700°C (Fig. 5). At the lower resolution (1.3μm/voxel) used in these images, individual carbon fibers were not resolved. Nevertheless, the fiber tows are clearly distinguished from the matrix, which consists of a thin brighter layer of CVI SiC coating each tow and a polymer-derived SiC filling the remaining

occupied space. During initial loading at both temperatures, cracks formed in the matrix normal to the loading direction at positions where the matrix lay over a transverse fiber tow. With increasing load, the cracks grew through the transverse tows until they met an underlying axial tow (at loads in the range ~40 N to 70 N), where they were deflected. At 25°C this deflection involved formation of multiple splitting cracks (Fig. 5a), which progressed incrementally along the centers of the axial tows as the load was increased to the peak value of 150 N. Above 1600°C, the deflection of the crack at each tow involved a single crack that grew along the edge of the axial fiber tows as the load increased to 120 N (Fig. 5b), whereupon there was a large load drop. By influencing the access of ambient gas to the internal reinforcing fibers, differences in crack paths such as these could potentially have a large effect on subsequent high-temperature oxidation damage.

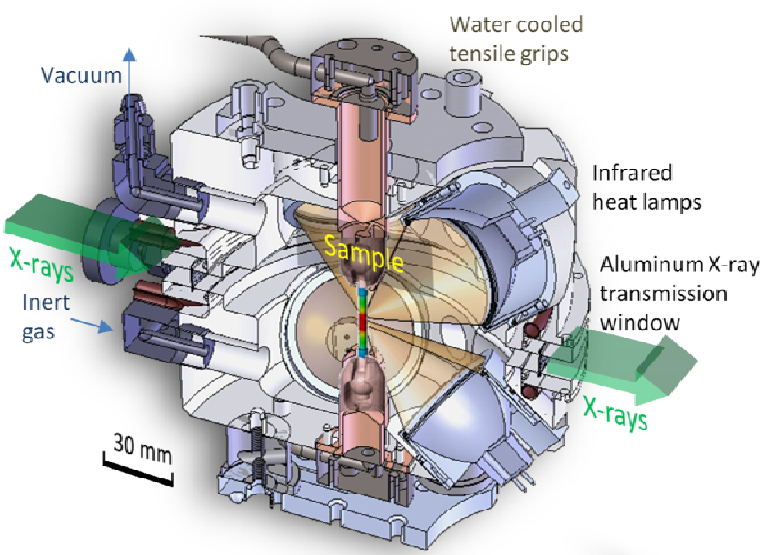

Figure 4. Sectional view of the heating chamber in a test rig designed to permit x-ray μCT imaging during testing at high temperature [27]. The x-ray beam passes through a load-supporting Al window, whose absorption is constant during rotations of the chamber and specimen and therefore does not impair image quality. The sample is held by water-cooled grips in the center of a sealed cell, which can be evacuated or filled with a selected gas. A hexapole arrangement of six 150 watt halogen lamps and reflectors gives a spherical hot zone of diameter ~5 mm.

5. Rapid computation of multiple discrete damage events

A critical element of high-fidelity simulations of failure is the ability to introduce new cracks during the execution of a simulation at locations and with orientation that are determined by the current local stress or strain fields. A major contribution to virtual test development has been the new formulation of finite elements (extended finite element method or X-FEM and others) that achieve this objective [28-32].

The augmented finite element method (A-FEM) [33, 34], similar in form to a conceptual element introduced earlier [29], has achieved detailed representations of generic multi-crack configurations and particularly high computational efficiency. Key attributes include: breakable elements that allow cracks to be introduced across which cohesive tractions exist, following a prescribed nonlinear fracture law; and breakable cohesive elements that allow the correct description of the local stress state around crack bifurcations or coalescence events (Fig. 6).

In addition to allowing correct description of key multiple crack configurations, the A-FEM incorporates a new iteration algorithm for searching for convergence in nonlinear problems, in which the global stiffness matrix is re-written in a piecewise linear form, allowing local convergence to be achieved in one or at most a few steps. The combination of A-FEM elements that use advanced quadrature algorithms and can be made somewhat larger than the length of the fracture process zone and the new iteration algorithm leads to gains in computational speed for typical nonlinear fracture problems of 2 – 3 orders of magnitude compared to standard methods such as X-FEM embedded in the ABAQUS commercial software [35]. As discussed further below, computational speed is essential in a virtual test strategy that seeks to address stochastic variability.

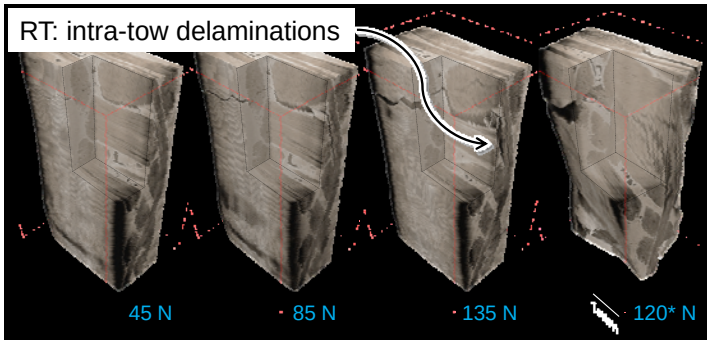

(a)

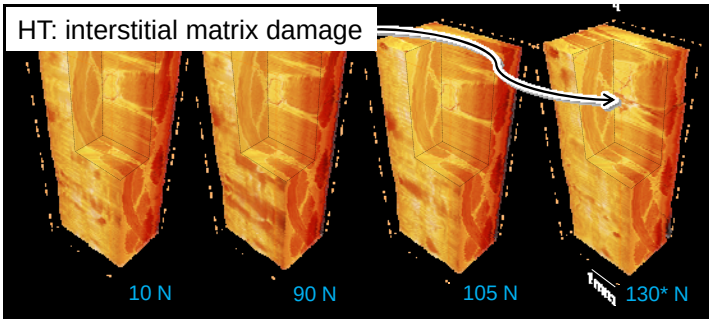

(b)

Figure 5. Internal damage in a C-SiC composite with textile-based carbon fiber reinforcements under tensile load at (a) 25°C and (b) 1600°C.

6. Monte Carlo methods vs. probabilistic theories

The Monte Carlo method using ensembles of stochastic virtual specimens provides the closest analogue of a real test matrix: a statistically significant number of virtual specimens are subjected to the same virtual test (or matrix of tests) and engineering predictions are deduced from the mean and scatter in the outcomes [36, 37]. Each specimen in the tested ensemble is one instance of a random microstructure that has been constructed by feeding pseudo-random numbers into calibrated distribution functions (a Monte Carlo procedure). The variance of the microstructure in the ensemble of virtual specimens is a major source of variance in predictions. With trivial modification, the load can also be made random, e.g., to simulate random overloads in a duty cycle.

Once a stochastic virtual specimen generator has been developed and constitutive laws have been calibrated, executing a Monte Carlo analysis is straightforward. Simulations are executed in sequence and predicted metrics (strength, strain to failure, etc.) are analyzed using the same statistical methods used to analyze real tests.

The computational expense of Monte Carlo analysis can be high. The uncertainty in a predicted mean property, such as the expected strength in a distribution of strengths, will fall as the number of computed cases N rises. If σ denotes the uncertainty in a predicted mean property normalized by the width of the distribution of the property, $\sigma \approx N^{-1/2}$. For example, if strength is predicted to have a deviance of 10%, then determining the mean strength to 1% accuracy requires 100 simulations.

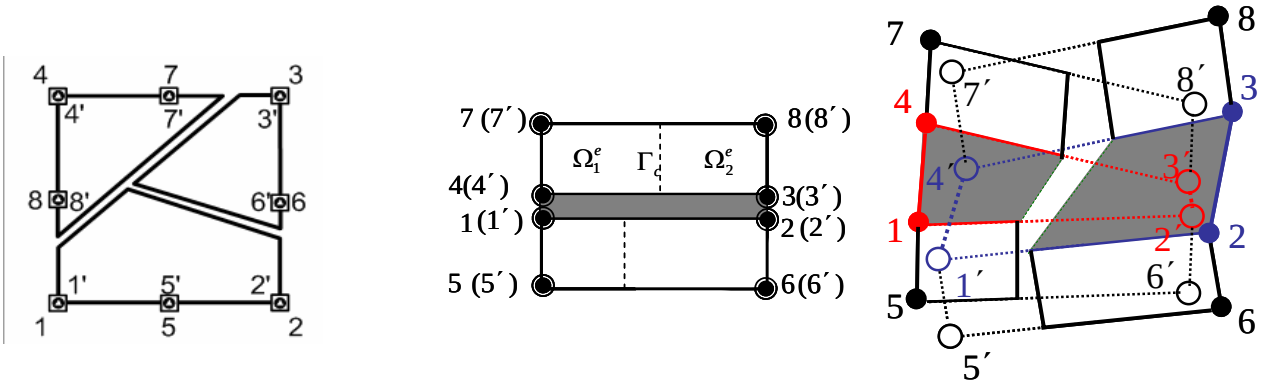

(a) (b)

Figure 6. (a) In the A-FEM formulation, a single element can split into several domains, accommodating a crack bifurcation event. (b) When a crack in a solid element impinges upon a material interface, the cohesive element governing fracture of the interface (grey domain, with width exaggerated for visibility) divides into two sub-elements, allowing the correct sign and magnitude of interfacial shear displacement to be computed on either side of the impinging crack.

If the virtual test is used in materials design, a design optimization study addressing the statistics of failure might require computing the effects of 10^2 – 10^4 different material or architectural parameters. To establish reasonably accurate trends in mean strength, 10^4 – 10^6 virtual tests must be executed. For the computational time to remain within one week (10^6 seconds) for a relatively wide search, a single virtual test should execute in 1 sec, to order of magnitude. Current execution times for multiple crack evolution leading to ultimate failure in a single virtual test are orders of magnitude higher than this.

Probabilistic models offer computational efficiency and the possibility of accurate predictions of rare events. In a probabilistic theory, instead of tracking damage evolution through a particular microstructure, one tracks the evolution of a probability distribution $P(X)$ for a damage variable X through time or elapsed fatigue cycles. Because $P(X)$ can be represented numerically with arbitrary precision over all values of X, accuracy in predicting the tails of the distribution is at least possible. However, is it not assured: accuracy also demands that the probabilistic theory incorporate a faithful representation of the details of the influence of the stochastic microstructure on the evolution of $P(X)$.

The first and simplest approach uses diffusion equations or discrete chain models to describe the evolution of a damage variable such as crack length, coupled to a simplified representation of the influence of some other factor, which could be a microstructural factor. However, such phenomenological models are limited in the degree of fidelity they can achieve in predicting the effects of microstructural variation within a single class of materials. They must use calibration data for the same materials as those for which predictions are to be made, with the same failure mechanisms and microstructural statistics being present. They cannot be used easily to make

predictions for materials with different microstructural statistics or different loading conditions. Improved fidelity requires incorporation of the details of how microstructure controls the evolution of local damage events.

A formulation that can improve fidelity in a probabilistic framework was presented by Pardee and colleagues [38, 39]. The Pardee formulation recognizes the discontinuous nature of crack growth by associating each of the three phases of damage development in the example of Fig. 7 with a distinct domain Ω_I, Ω_{II}, or Ω_{III} in the space in which probability density is defined. Thus, at a point in Ω_I one defines the probability density $P_I(X_I = a/D; t)da$ that a crack of length $X_I D \le a \le X_I D + da$ with $X_I < 1$ is propagating through the matrix at time t; at a point in Ω_{II} one defines the probability density $P_{II}(X_{II} = \beta; t)d\beta$ that an arrested crack has damage parameter $X_{II} \le \beta \le X_{II} + d\beta$ at time t; and at a point in Ω_{III} one defines the probability density $P_{III}(X_{III} = a; t)da$ that a crack of length $X_{III} \le a \le X_{III} + da$ with $X_I > 1$ is propagating into the fiber tow at time t.

With growth laws predicted by a small number of virtual tests and statistical distributions calibrated by experiments, the Pardee problem can be solved to generate rapid predictions of the full distribution function for engineering properties, such as the time to failure of the reinforcing tow in Fig. 7. Serving within such an efficient formulation, virtual tests can relate the statistics of rare failure events to microstructural variance with the least possible computational effort.

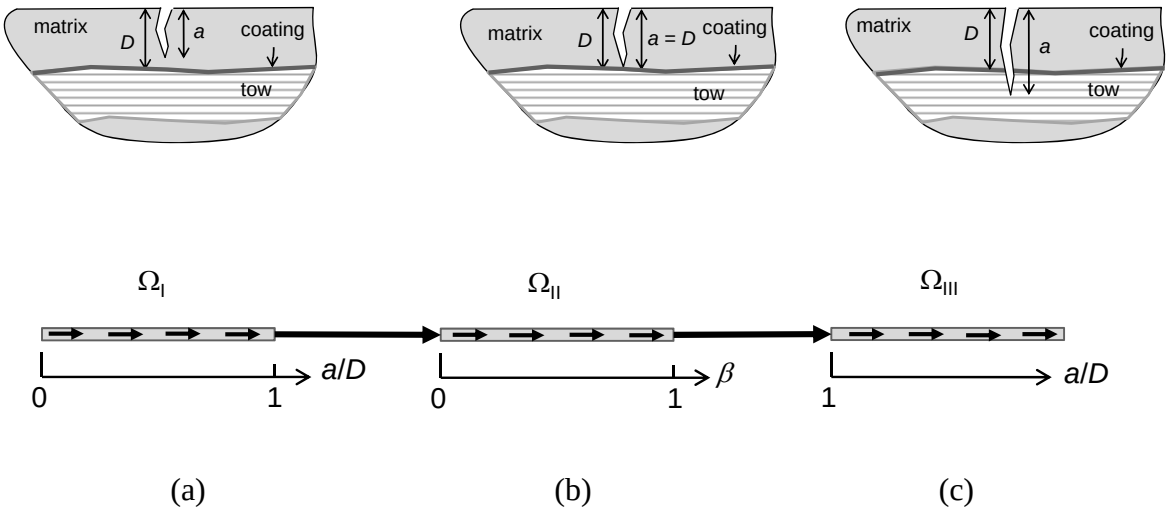

Figure 7. A microcrack (a) originating in a superficial matrix layer might (b) arrest temporarily at a fracture resistant coating that protects a tow before (c) propagating into the tow and exposing the fibers in the tow to the environment. In correspondence with the three stages of microcrack growth, there exist three domains Ω_I, Ω_{II}, and Ω_{III}, through which probability density flows in conservation equations describing their evolution; density flux is indicated by arrows. In domains I and III, the state variable is crack length a, while in domain II it is a damage parameter β that increases with time from 0 to unity.

References

1. Cox, B.N. and Q.D. Yang, *In quest of virtual tests for structural composites.* Science, 2006. **314**: p. 1102-1107.
2. Ashby, M.F., *Physical modelling of materials problems.* Materials Science and Technology, 1992. **8**: p. 102-111.
3. Llorca, J., et al., *Multiscale modeling of composite materials: a roadmap towards virtual testing.*

Advanced Materials, 2011. **23**: p. 5130-5147.
4. Pollock, T.M., et al., *Integrated computational materials engineering: A transformational discipline for improved competitiveness and national security.* 2008, National Research Council of the National Academies: Washington, D.C.
5. Evans, A.G., *Design and life prediction issues for high temperature engineering ceramic and their composites.* Acta Materialia, 1997. **45**: p. 23-40.
6. Marshall, D.B. and B.N. Cox, *Integral textile ceramic structures.* Annual Review of Materials Research, 2008. **38**: p. 425-443.
7. Badel, P., et al., *Simulation and tomography analysis of textile composite reinforcement deformation at the mesoscopic scale.* Composites Science and Technology, 2008. **68**: p. 2433-2440.
8. Desplentere, F., et al., *Micro-CT characterization of variability in 3D textile architecture.* Composite Science and Technology, 2005. **65**: p. 1920-1930.
9. Mahadik, Y., K.A. Robson Brown, and S.R. Hallett, *Characterisation of 3D woven composite internal architecture and effect of compaction.* Composites, Part A, 2010. **41**: p. 872-880.
10. Lee, S.-B., et al., *Pore geometry in woven fiber structures: 0/90 plain-weave cloth layup preform.* Journal of Materials Research, 1998. **13**(5): p. 1209-1217.
11. Kinney, J.H., et al., *X-ray tomographic study of chemical vapor infiltration processing of ceramic composites.* Science, 1993. **260**: p. 789-792.
12. Coindreau, O., G. Vignoles, and P. Cloetens, *Direct 3D microscale imaging of carbon-carbon composites with computed holotomography.* Nuclear Instruments and Methods in Physics Research B, 2003. **200**: p. 308-314.
13. Bale, H., et al., *Characterizing Three-Dimensional Textile Ceramic Composites using Synchrotron X-Ray Micro-Computed-Tomography.* Journal of the American Ceramic Society, 2011. **95**(1): p. 392-402.
14. Argon, A.S., *Fracture of composites*. Treatise of Materials Sciences and Technolgy. Vol. 1. 1972, New York: Academic Press.
15. Budiansky, B., *Micromechanics.* Composite Structures, 1983. **16**(1): p. 3-12.
16. Cox, B.N., et al., *Mechanisms of compressive failure in 3D composites.* Acta Metallurgica et Materialia, 1992. **40**: p. 3285-3298.
17. Fleck, N.A. and B. Budiansky, *Compressive failure of fibre composites due to microbuckling*, in *Inelastic Deformation of Composite Materials*, G.J. Dvorak, Editor. 1991, Springer-Verlag: New York. p. 235-274.
18. Fleck, N.A. and J.Y. Shu, *Microbuckle initiation in fibre composites: a finite element study.* Journal of the Mechanics and Physics of Solids, 1995. **43**(12): p. 1887-1918.
19. Marshall, D.B., et al., *Transverse strengths and failure mechanisms in Ti3Al matrix composites.* Acta Metallurgica et Materialia, 1994. **42**: p. 2657-2673.
20. Pineau, P., G. Couegnat, and J. Lamon, *Virtual testing applied to transverse multiple cracking of tows in woven ceramic composites.* Mechanics Research Communications, 2011. **38**(8): p. 7.
21. Cox, B.N. and W.L. Morris, *Monte Carlo simulations of the growth of small fatigue cracks.* Engineering Fracture Mechanics, 1988. **31**: p. 591-610.
22. Groeber, M., et al., *A framework for automated analysis and simulation of 3D polycrystalline microstructures. Part 2: Synthetic structure generation.* Acta Materialia, 2008. **56**: p. 1274-1287.
23. Jiao, Y., F.H. Stillinger, and S. Torquato, *A superior descriptor of random textures and its predictive capacity.* Proceedings of the National Academy of Science of the USA, 2009. **106**(42):

p. 17634-17639.
24. Blacklock, M., et al., *Generating virtual textile composite specimens using statistical data from micro-computed tomography: 1D tow representations for the Binary Model.* Journal of the Mechanics and Physics of Solids, 2012. **60**: p. 451-470.
25. Rinaldi, R., et al., *Generating virtual textile composite specimens using statistical data from micro-computed tomography: 3D tow representations.* Journal of the Mechanics and Physics of Solids, 2011. **in press**.
26. Cox, B.N., W.C. Carter, and N.A. Fleck, *A Binary Model of textile composites: I Formulation.* Acta Metallurgica et Materialia, 1994. **42**: p. 3463-3479.
27. Bale, H.A., et al., *Real-Time Quantitative Imaging of Failure Events in Ultrahigh-Temperature Materials under Load at Unprecedented Temperatures above 1700°C.* Nature Materials, 2012. **in press**.
28. Zi, G. and T. Belytschko, *New crack-tip elements for XFEM and applications to cohesive cracks.* International Journal for Numerical Methods in Engineering, 2003. **57**: p. 2221-2240.
29. Hansbo, A. and P. Hansbo, *A finite element method for the simulation of strong and weak discontinuities in solid mechanics.* Computational Methods in Applied Mechanics and Engineering, 2004. **193**: p. 3523-3540.
30. Andersson, T. and U. Stigh, *The stress–elongation relation for an adhesive layer loaded in peel using equilibrium of energetic forces.* International Journal of Solids and Structures, 2004. **41**(2): p. 413-434.
31. Moës, N., J. Dolbow, and T. Belytschko, *A finite element method for crack growth without remeshing.* International Journal for Numerical Methods in Engineering, 1999. **46**: p. 131-150.
32. Strouboulis, T., K. Copps, and I. Babuška, *The generalized finite element method.* Computational Mechanics Advances, 2001. **190**: p. 4801-4193.
33. Fang, X.J., et al., *An augmented cohesive zone element for arbitrary crack coalescence and bifurcation in heterogeneous materials.* International Journal of Numerical Methods in Engineering, 2011. **88**: p. 841-861.
34. Ling, D., Q. Yang, and B.N. Cox, *An augmented finite element method for modeling arbitrary discontinuities in composite materials.* International Journal of Fracture, 2009. **156**: p. 53-73.
35. Liu, W., et al., *An Accurate and Efficient Augmented Finite Element Method for Arbitrary Crack Interactions.* Journal of Applied Mechanics, 2012. **in press**.
36. Metropolis, N. and S. Ulam, *The Monte Carlo method.* Journal of the American Statistical Association, 1949. **44**: p. 335-341.
37. Cox, B.N., *Inductions from Monte Carlo simulations of small fatigue cracks.* Engineering Fracture Mechanics, 1989. **33**: p. 655-670.
38. Cox, B.N., W.J. Pardee, and W.L. Morris, *A statistical model of intermittent short fatigue crack growth.* Fatigue and Fracture of Engineering Materials and Structures, 1987. **9**(6): p. 435-455.
39. Pardee, W.J., et al., *Statistical Mechanics of Early Growth of Fatigue Cracks*, in *2nd Int. Symp. on Defects, Fracture and Fatigue*. 1982: Mont Gabriel, Canada. p. 99-111.

Acknowledgments

This work was supported by the Air Force Office of Scientific Research (Dr. Ali Sayir) and NASA (Dr. Anthony Calomino) under the National Hypersonic Science Center for Materials and Structures (AFOSR Contract No. FA9550-09-1-0477). We acknowledge the use of data from the x-ray synchrotron micro-tomography beam line (8.3.2) at the Advanced Light Source (ALS) at the Lawrence Berkeley National Laboratory (US Dept. of Energy, contract No. DE AC02 05CH11231).

A Vibration Energy Harvester with Internal Impact and Hybrid Transduction Mechanisms

Songmao Chen, Jing Sun, Junhui Hu*

State Key Lab of Mechanics and Control of Mechanical Structures,
Nanjing University of Aeronautics and Astronautics, 210016, Nanjing, P. R. China.
* Corresponding author: ejhhu@nuaa.edu.cn

Abstract To increase the power harvesting capability of an internal impact type vibration energy harvester (VEH), the authors have developed a novel hybrid VEH integrating both piezoelectric and electromagnetic (EM) modules for energy conversion. The proposed VEH transforms a low frequency external base vibration into an internal impact vibration of the tip of a cantilever beam, which is used to cause energy conversion by the piezoelectric effect and electromagnetic induction. A prototype is designed, fabricated and tested; the optimum load resistances are determined experimentally, and the power output performance and the total power density of the proposed VEH have been experimentally characterized with respect to the excitation amplitude and frequency. The dependence of the optimum excitation frequency for maximum total power output on the excitation amplitude has also been experimentally investigated. The total output power and power density are 0.8 mW and 15 μW/cm^3, respectively, when the excitation amplitude and frequency are 1 mm (rms) and 15 Hz, respectively.

Keywords Vibration Energy Harvesting, Impact, Piezoelectric, Electromagnetic, Hybrid

1. Introduction

With the evolution of low power electronics, harvesting the structural vibration energy, which is clean, ubiquitous and renewable, has gained increasingly extensive attentions from worldwide researchers in the recent decade [1-4] for its great potentials for applications in areas of wireless sensor networks (WSNs), autonomous low power microsystems, distributed computing and portable alternative power sources, remote sensing and actuation, etc., to replenish or even replace traditional power supply such as battery. A number of vibration energy harvesters (or vibration-powered generators) using the piezoelectric effect [5-9] and electromagnetic induction [10, 11] have been proposed and developed.

Generally, a typical piezoelectric VEH employs a cantilever beam structure with a proof mass at its tip and excitation at its base [6]; thus only d_{31} mode is used. To increase the vibration energy harvesting capability of such mechanism, a piezoelectric VEH combining the d_{31} mode caused by flexural vibration and the d_{33} mode caused by direct impact was proposed [7]. It was found that piezoelectric components operating in the d_{33} mode can significantly increase the power generation of the conventional cantilevered piezoelectric VEH. Similar work using impact method has also been carried out by other researchers [12-15]. Nevertheless, to widen the application range of VEHs, the output power still needs to be increased.

To further enhance the energy harvesting capability and more efficiently utilize the space of VEH structure, the authors have developed an evolutionary version based on their previous work [7]. In the evolutionary version, the VEH converts low frequency external vibration into its internal impact vibration and uses the piezoelectric effect and electromagnetic induction to convert the internal vibration energy into electric energy. The VEH topologically consists of three modules. The first one is a piezoelectric module harvesting the energy of internal impact directly; the second one is another piezoelectric module harvesting the impact induced vibration energy in the frames of the VEH; the third one is an electromagnetic module comprised of one hand-wound enameled copper coil and two pairs of anti-symmetrically placed bulk NdFeB permanent magnets, using the magnetic

flux change in the coil to generate AC voltage. A prototype has been designed, fabricated, tested and analyzed.

2. Structure and Principle

As shown in Fig. 1(a), the proposed VEH is generally comprised of three parts, i.e., the top and bottom frames, the middle cantilever beam, and the side frames. The frames are made of stainless steel, and the cantilever beam is made of phosphor bronze. Four piezoelectric modules (PZT-T-EX, PZT-T-IN, PZT-B-EX, and PZT-B-IN), each with five identical piezoelectric plates connected in parallel electrically, and two single piezoelectric plates (PZT-T-IMP and PZT-B-IMP) are bonded to the top and bottom frames. Two pairs of permanent magnets are anti-symmetrically bonded onto the side frames. A coil housing with a hand-wound enameled copper coil and impact body is attached to the tip of the middle cantilever beam, and acts as a proof mass. The coil housing is used to accommodate and fix the coil relative to the cantilever beam. The distance between the impact body and the impacted piezoelectric plates (PZT-T-IMP and PZT-B-IMP) is about 4.5 mm. The VEH could be mounted on a vibrating source for power generation. In our experiments, it is bolted on an electric shaker, as shown in Fig. 1(b).

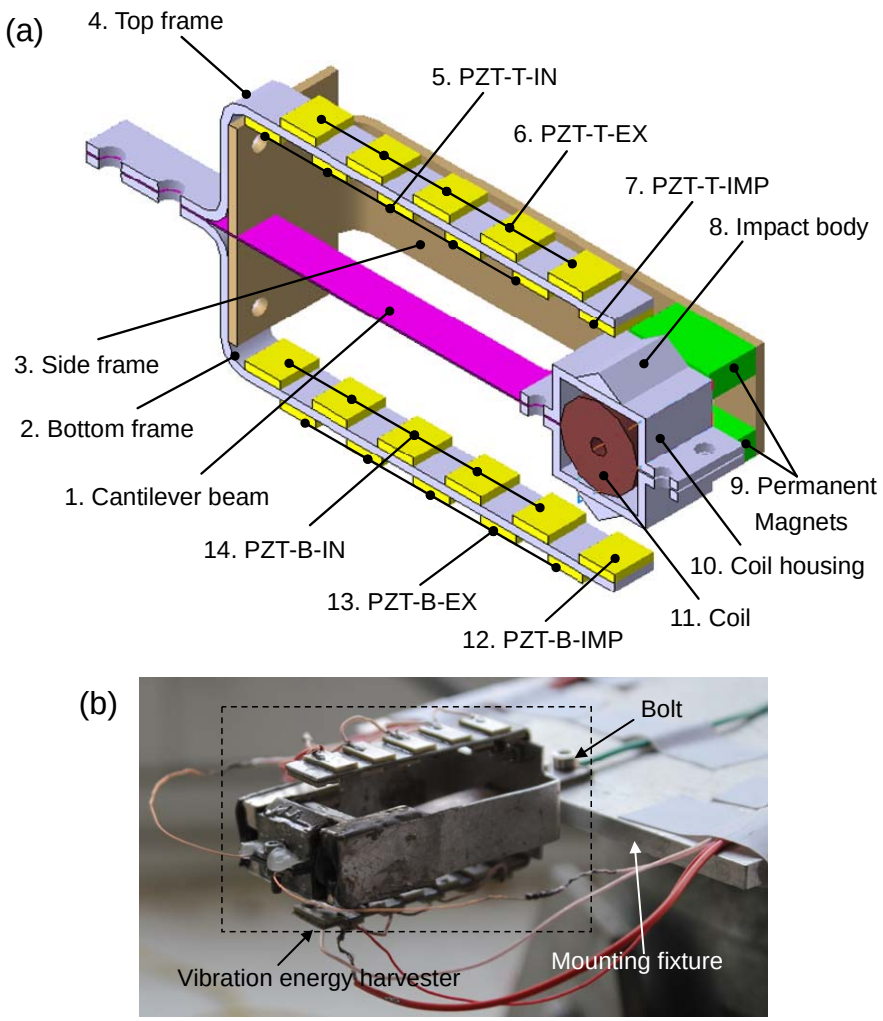

Figure 1. Harvester structure including (a) isometric section view of the proposed VEH structure and (b) photograph of the fabricated VEH prototype mounting on an electric shaker.

The detailed dimensions of structural components of the VEH prototype are listed in Table 1. The

piezoelectric material adopted here is Lead Zirconate Titanate (PZT) ceramics (HAIYING P-51), the major material parameters is shown in Table 2. The enameled copper coil with main parameters shown in Table 3, is wound by using a 40-μm-diameter copper wire (DAYANG WIRE & CABLE) with polyurethane coating. The magnets used here is the sintered rare earth Neodymium Iron Boron (NdFeB) N33 permanent magnet. Its property is listed in Table 4.

Table 1. Dimensions of structural components of the proposed vibration energy harvester

Component	Length (mm)	Width (mm)	Height (mm)	Thickness (mm)
1	60	10	-	0.2
2,4	65	10	14.9	1
3	52	30	24	1
5,6,7,12,13,14	10	5	1	-
8	17	6	2	-
9	10	6	3	-
10	20	17	6	1
11	-	-	15	-

Table 2. Material property parameters of the employed piezoelectric material

Electromechanical coupling factor	k_{31}	0.36
	k_{33}	0.70
Piezoelectric charge constant (10^{-12} C/N)	d_{31}	-185
	d_{33}	400
Relative dielectric constant	$\varepsilon_{11}^{T} / \varepsilon_0$	2400
	$\varepsilon_{33}^{T} / \varepsilon_0$	2100
Mechanical quality factor	Q_m	100
Dielectric dissipation factor (%)	$\tan\delta$	2.0

Table 3. Parameters of the wound copper coil

Number of turns	Internal resistance (R_o) (kΩ)	Inductance (L_o) (H)
~11000	~3.9	~0.3

Table 4. Properties of NdFeB permanent magnet

Residual Induction B_r (mT)	Maximum energy product $(BH)_{max}$ (KJ/m^3)	Coercive force H_{cb} (KA/m)
1.13~1.17	247~263	~836

The resonance frequency of the middle cantilever beam of our VEH prototype is $f_{cr} = \sqrt{k/m}/2\pi$ ≈ 11.0 Hz, where m and k, the effective mass and spring constant, are 1.04E-3 kg and 51.7 N/m, respectively. When subjected to external vibration excitation, bending vibration of the middle

cantilever beam would be excited. As seen in Fig. 2(a), while the beam vibrates, the impact body may hit PZT-T-IMP and PZT-B-IMP and induce resonant vibration mode in the top and bottom frames. Due to the piezoelectric effect, AC voltage is generated across all piezoelectric components. At the same time, the copper coil vibrates relatively to the permanent magnets, as shown in Fig. 2(b), causing a variation of magnetic flux through the coil. According to the Faraday's law, AC voltage will be generated in the coil. To generate voltage in the electromagnetic module efficiently, it is so designed that the net magnetic flux through the coil is zero when the middle cantilever remains static.

For low frequency (several to tens of Hertz) excitation, we only take into consideration the fundamental vibration mode of the middle cantilever beam, which can be simplified into an equivalent single-DOF spring-mass-damping system. As indicated in Fig. 2(a), the displacement of the vibration energy harvester and the tip of the cantilever beam are denoted by x_s and x, respectively, with respect to the inertial reference frame of the earth. Setting the relative displacement between the cantilever tip and VEH frame be $y = x - x_s$, and the source excitation of the shaker be harmonic, i.e. $x_s = A_s \sin\omega_s t$, the steady-state solution of the differential vibration equation of the cantilever beam is [16]

$$y = Y \sin(\omega_s t - \psi)\,, \tag{1}$$

$$Y = \frac{A_s \left(\dfrac{\omega_s}{\omega_{cn}}\right)^2}{\sqrt{\left[1-\left(\dfrac{\omega_s}{\omega_{cn}}\right)^2\right]^2 + \left(2\zeta\,\mathrm{g}\dfrac{\omega_s}{\omega_{cn}}\right)^2}}\,, \tag{2}$$

$$\psi = \tan^{-1}\left[\frac{2\zeta\,\mathrm{g}\dfrac{\omega_s}{\omega_{cn}}}{1-\left(\dfrac{\omega_s}{\omega_{cn}}\right)^2}\right]. \tag{3}$$

where ω_{cn} is the natural angular frequency of the cantilever beam, m, ζ and k are the equivalent mass, damping ratio and spring constant, respectively. Hence, the condition for impact is

$$Y \geq D\,. \tag{4}$$

For a given low excitation amplitude ($A_s < D$), there exists an excitation frequency range beyond which the impact cannot happen. Denoting ω_{sl} and ω_{su} as the lower and upper limits of the excitation frequency range, it is derived that

$$\omega_{sl} = \omega_s \sqrt{\frac{\left(1-2\zeta^2\right) - \sqrt{\left(1-2\zeta^2\right)^2 - \left(1-\dfrac{A_s^2}{D^2}\right)}}{1-\dfrac{A_s^2}{D^2}}}\,, \tag{5}$$

$$\omega_{su} = \omega_s \sqrt{\frac{\left(1-2\zeta^2\right)+\sqrt{\left(1-2\zeta^2\right)^2-\left(1-\frac{A_s^2}{D^2}\right)}}{1-\frac{A_s^2}{D^2}}} . \tag{6}$$

Since $\zeta = 1$, $\omega_{sl} = \omega_s \sqrt{1/\left(1+A_s/D\right)}$, $\omega_{su} = \omega_s \sqrt{1/\left(1-A_s/D\right)}$. Therefore,

$$f_{sl} = \frac{\omega_{sl}}{2\pi} = f_s \sqrt{\frac{1}{1+\frac{A_s}{D}}} , \tag{7}$$

$$f_{su} = \frac{\omega_{su}}{2\pi} = f_s \sqrt{\frac{1}{1-\frac{A_s}{D}}} . \tag{8}$$

When f_s = 11 Hz, A_s = 1.4 mm (0-peak) and D = 4.5 mm, f_{sl} and f_{su} are calculated to be about 9.6 Hz and 13.3 Hz, respectively.

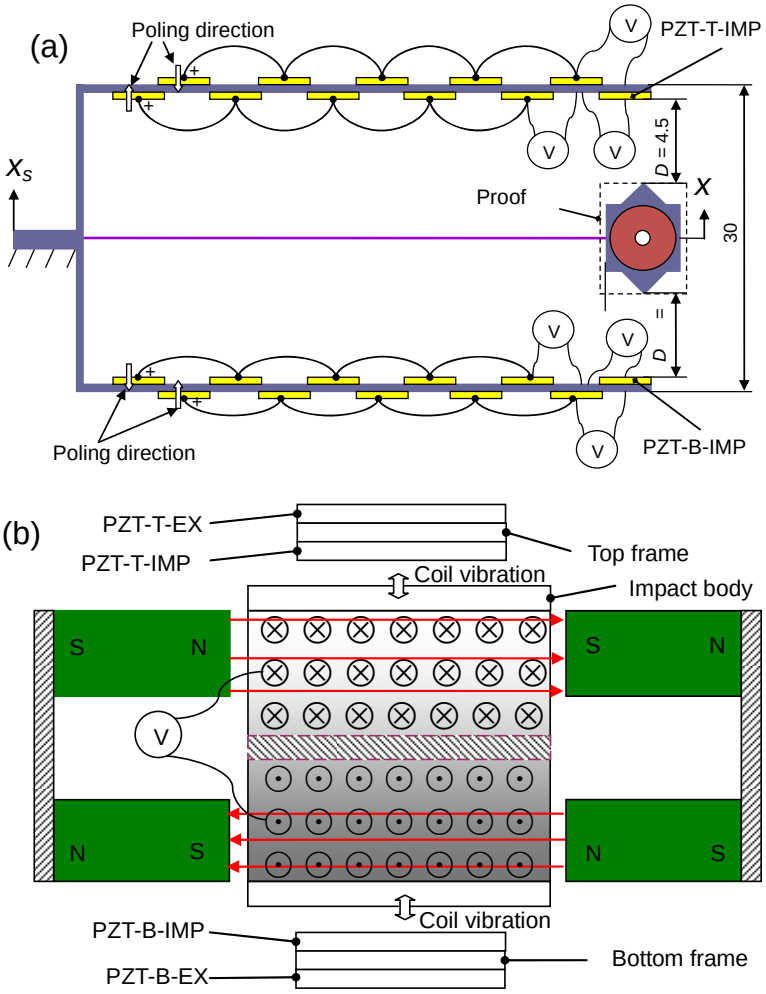

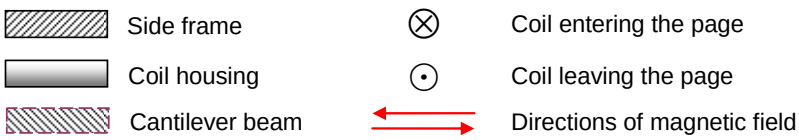

Figure 2 Schematics of (a) the piezoelectric energy harvesting modules and (b) the electromagnetic energy harvesting module.

According to Hayt et al.[17] and Fu et al.[9], the theoretical optimum load resistances of the electromagnetic and piezoelectric modules for maximum power output are

$$R_{LEO} = \sqrt{R_o^2 + \left(2\pi f_c L_o\right)^2}\ , \tag{9}$$

$$R_{LPO} = \frac{1}{10\pi f_{rf} C_p}\ . \tag{10}$$

where R_o and L_o are the internal resistance and inductance of the coil, respectively, f_c is the angular frequency of vibration of the cantilever beam, f_{rf} is the resonant frequency of the top or bottom frames, and C_p is the clamped capacitance of a piezoelectric plate.

3. Experimental Method

During the experiments, the VEH was firmly fixed on an electric shaker (HSB-01, HUASHEN) by bolting connection, as shown in Fig. 3. A function generator (AFG 3022B, TEKTRONIX) was used to supply sinusoidal excitation signal to a power amplifier, through which the signal was power amplified and transferred to the shaker to generate harmonic excitation for the test. Excitation frequency and amplitude can be controlled by adjusting the function generator and the power amplifier. The input signal to the shaker was monitored by digital oscilloscope (TDS 2014, TEKTRONIX). To measure the power generation capability, a resistive load R_L was directly connected to the VEH prototype; the root mean square (rms) voltage V_{rms} across the load was measured; the average power by R_L was calculated by $P_a = V_{rms}^2 / R_L$. In addition, the excitation acceleration of the electric shaker was measured by a strain gauge accelerometer (LC0801, LANCE) and the resonant frequency of first bending mode was measured by Polytec Scanning Vibrometer PSV-300.

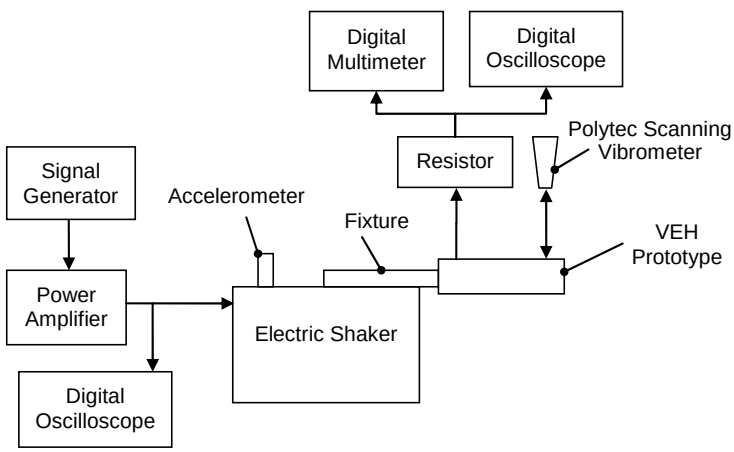

Figure 3 Schematic diagram of the experimental setup.

In our experiments, at first, the relationship between the cantilever vibration frequency and excitation frequency was investigated. Then different load resistances were connected to the prototype to determine the optimum load resistances for the electromagnetic and piezoelectric modules. After that, the experimentally determined optimum load resistances were used to obtain the quantitative effects of the excitation amplitude and frequency on the power output and the total power density. Finally, the optimum excitation frequency for maximum power output and the total output power at the optimum excitation frequency vs. the excitation amplitude were measured.

Since it was found that the power generation of the directly impacted piezoelectric plates (PZT-T-IMP and PZT-B-IMP) was much lower than that of the other four piezoelectric modules under the same excitation condition, this part of power extraction is neglected in the following study. All the following experiments were conducted only for the electromagnetic and piezoelectric modules at the excitation frequency around the resonance frequency of the middle cantilever beam ($f_{rc} \approx 11$ Hz).

4 Results and Discussion

Applying an excitation to the prototype and making the cantilever tip impact with the frames, the relationship between the vibration frequency of the cantilever beam f_c and the excitation frequency f_s has been measured firstly, and the result is shown in Fig. 4. It is manifested that either the cantilever tip vibrates freely or there is impact between the cantilever tip and frames, the cantilever vibration still has the same frequency as the external excitation.

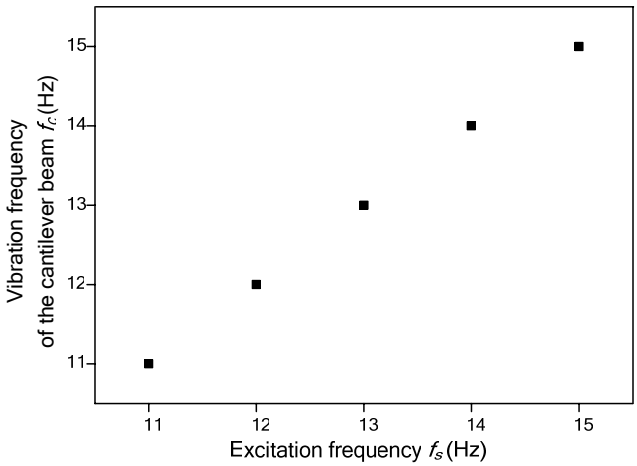

Figure 4. The vibration frequency of the cantilever beam f_c vs. the excitation frequency f_s.

According to Eqs. (9) and (10), the theoretical optimum load resistances can be obtained. In our VEH prototype, R_o =3.9 kΩ, L_o = 0.3 H, $C_p = \varepsilon_{33}^T \varepsilon_0 L_p W_p / H_p$ = 0.92925 nF, f_c=11 Hz and f_{rf} is measured to be 169.5 Hz using Polytec Scanning Vibrometer PSV-300, such that R_{LEO} and R_{LPO} are calculated to be 3.9 kΩ and 202 kΩ approximately. To acquire these values experimentally, the output power P_o vs. load resistance R_L was measured for the electromagnetic and piezoelectric modules under the excitation amplitude of 2 mm (rms) and excitation frequency of 11 Hz. As shown in Fig. 5(a), the optimum resistance for electromagnetic module R_{LEO} is found to be about 4 kΩ; from Fig. 5(b), it is found that the optimum resistance for each piezoelectric module R_{LPO} is almost the same and equals 200 kΩ approximately, which well agree with the theoretical values.

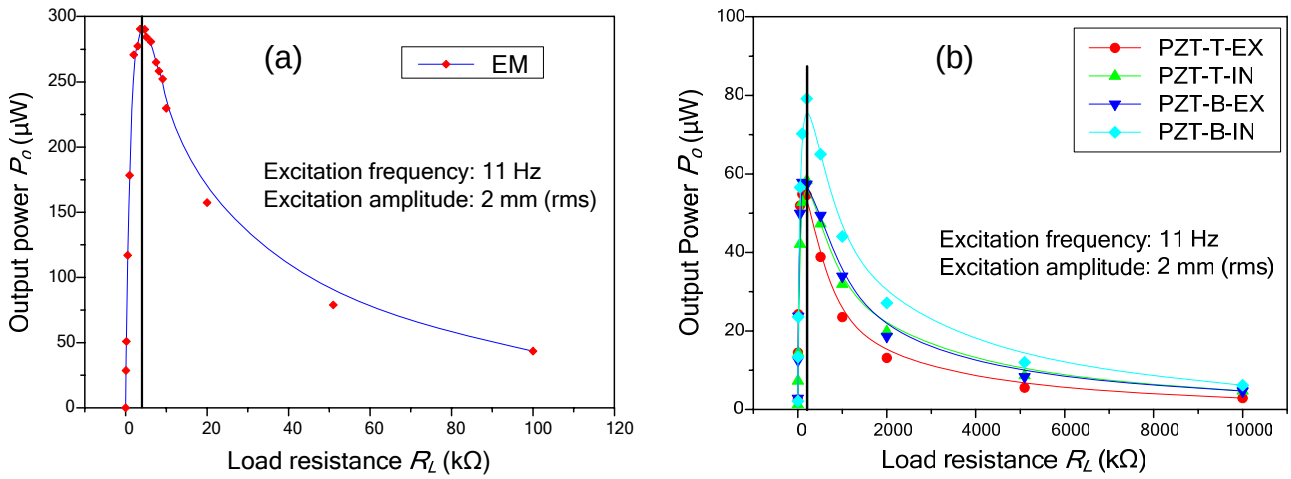

Figure 5. Output power P_o as a function of the load resistance R_L for (a) the electromagnetic module and (b) the piezoelectric modules when the excitation amplitude and frequency are 2 mm (rms) and 11 Hz, respectively.

Connecting resistors with the above experimentally determined optimum resistances to the VEH prototype individually, power consumed by the loads has been measured as a function of the excitation amplitude at the excitation frequency of 11 Hz. As shown in Fig. 6(a), the output power of the electromagnetic module and the total output power of the piezoelectric modules are at the same order. It is also seen that as the excitation amplitude increases, the change of the output power of electromagnetic and piezoelectric modules manifests in a similar way. At first, the output power of each energy harvesting module increases quickly as the excitation amplitude increases; with further increase of the excitation amplitude, the increasing speed of the output power slows down. With the increase of the excitation amplitude, the impact speed increases, resulting in the increase of harvested energy. However, when the excitation amplitude is larger than 1 mm (rms), the cantilever tip impacts the top and bottom frames, which limits the further increase of vibration velocity of the cantilever tip and the further increase of the output power. The total power density is calculated by the ratio of the total output power to the volume of VEH. As shown in Fig. 6(b), for the proposed VEH at the excitation frequency of 11 Hz, the total power density increases with the increase of the excitation amplitude.

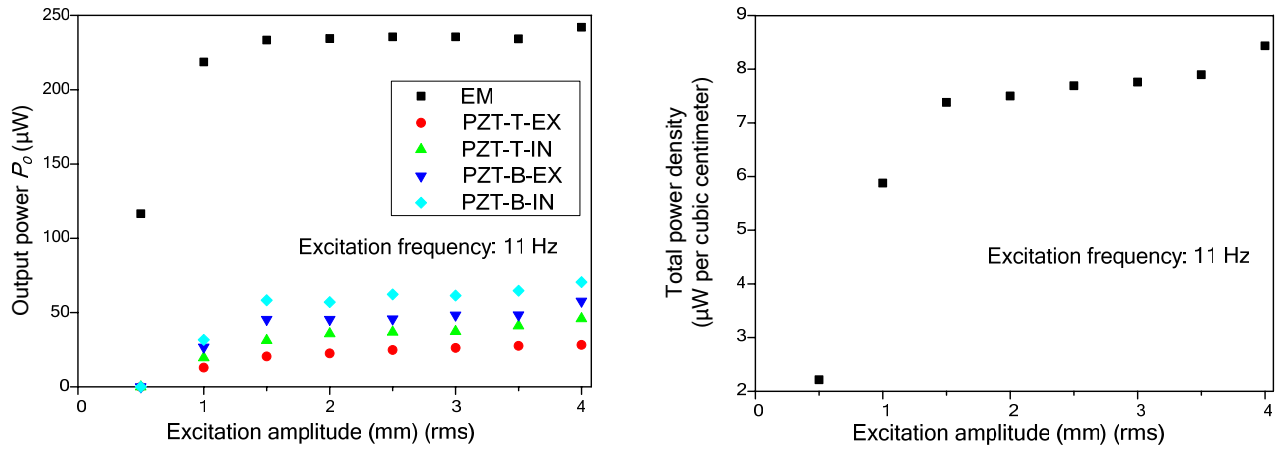

Figure 6. (a) Output power and (b) the total power density vs. the excitation amplitude at the excitation frequency of 11Hz.

The output power P_o vs. the excitation frequency f_s at the excitation amplitude of 1 mm (rms) has also been measured, and the result is shown in Fig. 7. For the electromagnetic module, with the

increase of f_s, P_o first increases and then reaches a summit at 15 Hz, passing which it begins to decrease. For the piezoelectric module, P_o is almost zero when f_s is less than 9 Hz; it increases as f_s increases from 9 Hz to 15 Hz; it reaches the maximum at 15 Hz and decreases as f_s increases further. From equations (7) and (8), the impact frequency range at the excitation amplitude of 1 mm (rms) is calculated to be from 9.6 to 13.3 Hz, which means a too small or too large excitation frequency may decrease the vibration of the cantilever tip and suppress the impact from happening, which qualitatively explains the phenomenon shown in Fig. 7. The maximum total output power and optimum excitation frequency f_s for the excitation amplitude of 1 mm (rms) are 0.8 mW and 15 Hz, respectively. In addition, comparing Figs. 6(a) and 7, it can be found that the energy harvesting of the proposed VEH is more sensitive to the excitation frequency than the excitation amplitude.

To further understand the energy harvesting characteristics of the VEH prototype, the optimum excitation frequency f_{so} for maximum total output power and the total output power at f_{so} (= the maximum total output power P_m) under different excitation amplitude have been measured, and the results are shown in Fig. 8. It is found that the maximum total output power P_m and optimum excitation frequency f_{so} increase with the increase of the excitation amplitude. From equation (8), it is seen that the upper limit of the impact frequency range increases as the excitation amplitude increases. It seems that the impact frequency range may increase the optimum excitation frequency.

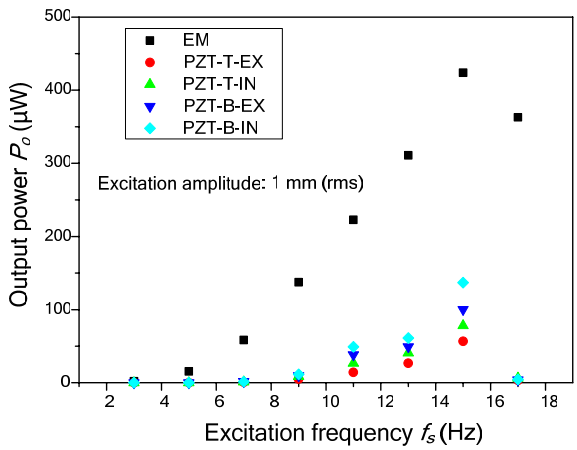

Figure 7. Output power P_o vs. the excitation frequency f_s at the excitation amplitude of 1 mm (rms).

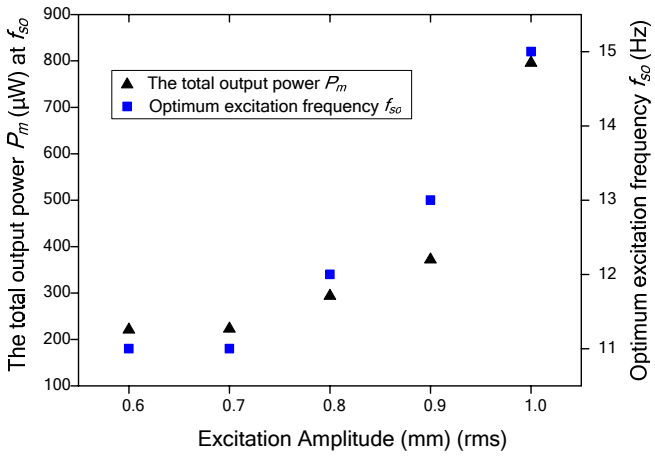

Figure 8. The optimum operating frequency f_{so} and the total output power at f_{so} vs. the excitation amplitude.

5. Conclusions

In this paper, a hybrid internal impact type vibration energy harvester that uses the piezoelectric effect and electromagnetic induction both has been investigated experimentally. It is found that, for a given excitation frequency, when the excitation amplitude increases, the total output power increases fast first and the increasing speed slows down when the excitation amplitude increases further; for a given excitation amplitude, there is a frequency range in which the total output power increases with the increase of the excitation frequency; the optimum excitation frequency and its corresponding total output power increases with the increase of the excitation amplitude. The total output power and power density are found to be 0.8 mW and 15 μW/cm^3, respectively, when the excitation amplitude and frequency are 1 mm (rms) and 15 Hz, respectively. The proposed vibration energy harvester may be used to harvest the vibration energy of low frequency vibration sources, which exist universally in nature, artificial structures, machines, vehicles, etc.

Acknowledgements

The authors would like to acknowledge the support of the Funding of Jiangsu Innovation Program for Graduate Education and the Fundamental Research Funds for the Central Universities (No.CXLX12_0140), NUAA Research Funds (No. S0896-013 and No. 56XZA12044), the Innovation and Entrepreneurship Program of Jiangsu and PAPD. In addition, the authors are also indebted to Miss Shiyang Hu for her kind help in winding the copper coil.

References

[1] C. B. Williams and R. B. Yates, Analysis of a micro-electric generator for microsystems. Sens. Actuators A, 52 (1996) 8-11.
[2] H. A. Sodano, D. J. Inman, G. Park, A review of power harvesting from vibration using piezoelectric materials. Shock Vib. Dig., 36 (2004) 197-205.
[3] S. Priya, Advances in energy harvesting using low profile piezoelectric transducers. J. Electroceram., 19 (2007) 165-182.
[4] J. J. McCoy, Harvesting mechanical energy via structural vibrations. J. Acoust. Soc. Am., 130 (2011) 1783-1786.
[5] P. G. Jones, S. P. Beeby, N. M. White, Towards a piezoelectric vibration-powered microgenerator. IEE Proc.-Sci. Meas. Technol., 148 (2001) 68-72.
[6] S. Roundy, P. K. Wright, A piezoelectric vibration based generator for wireless electronics. Smart Mater. Struct., 13 (2004) 1131-1142.
[7] J. Hu, J. Jong, C. Zhao, Vibration energy harvesting based on integrated piezoelectric components operating in different modes. IEEE Trans. Ultrason. Ferroelectr. Freq. Control, 57 (2010) 386-394.
[8] E. E. Aktakka, H. Kim, K. Najafi, Energy scavenging from insect flight. J. Micromech. Microeng., 21 (2011) 095016.
[9] F. Lu, H. P. Lee, S. P. Lim, Modeling and analysis of micro piezoelectric power generators for micro-electromechanical-systems applications. Smart Mater. Struct., 13 (2004) 57-63.
[10] M. El-hami, P. Glynne-Jones, N. M. White, M. Hill, S. Beeby, E. James, A. D. Brown, and J. N. Ross, Design and fabrication of a new vibration-based electromechanical power generator. Sens. Actuators A, 92 (2001) 335-342.
[11] B. Yang, C. Lee, W. Xiang, J. Xie, J. H. He, R. K. Kotlanka, S. P. Low, H. Feng, Electromagnetic energy harvesting from vibrations of multiple frequencies. J. Micromech. Microeng., 19 (2007) 035001.
[12] M. Umeda, K. Nakamura, S. Ueha, Analysis of the Transformation of Mechanical Impact Energy to Electric Energy Using Piezoelectric Vibrator. Jpn. J. Appl. Phys., 35 (1996) 3267-3273.
[13] M. Renaud, P. Fiorini, C. V. Hoof, Optimization of a piezoelectric unimorph for shock and impact energy harvesting. Smart Mater. Struct., 16 (2007) 1125-1135.
[14] S. Moss, A. Barry, V. Powlesland, S. Galea, G.P. Carman, A low profile vibro-impacting energy harvester with symmetrical stops. Appl. Phys. Lett., 97 (2010) 234101.
[15] L. Gu, C. Livermore, Impact-driven, frequency up-converting coupled vibration energy harvesting device for low frequency operation. Smart Mater. Struct., 20 (2011) 045004.
[16] W. T. Thomson, M. D. Dahleh, Theory of Vibration with Applications, 5th ed., Prentice-Hall, New York, 1998.
[17] W. H. Hayt, Jr., J. E. Kemmerly, S. M. Durbin, Engineering Circuit Analysis, 6th ed., McGraw-Hill, New York, 2002.

Effects of Electric Field and Poling on the Cyclic Bending Fatigue in Cracked Piezoceramics

Yasuhide Shindo[1,*], **Fumio Narita**[1], **Masayuki Sato**[1]

[1] Department of Materials Processing, Graduate School of Engineering, Tohoku University, Sendai 980-8579, Japan
* Corresponding author: shindo@material.tohoku.ac.jp

Abstract We investigates the fatigue behavior of cracked piezoelectric ceramics in cyclic bending under electric fields both theoretically and experimentally. Fatigue tests were carried out in three-point bending with the single-edge precracked-beam (SEPB) specimens. The crack was created normal to the poling direction. Number of cycles to failure was measured under electric fields. Plane strain finite element analysis was also performed, and the effect of polarization switching on the energy release rate was discussed under high negative electric field. In addition, mechanisms for crack growth were discussed by scanning electron microscope examination of the fracture surface of the piezoelectric ceramics.

Keywords Piezomechanics, Finite element method, Material testing, PZT ceramics, Fatigue

1. Introduction

Research on fracture and fatigue of the lead zirconate titanate (PZT) ceramics has increased during the past decade. In recent years, the dynamic fatigue of SEPB hard PZT ceramics was studied under direct current (DC) electric field [1]. In the case under cyclic mechanical loading, Narita et al. [2] studied the fatigue crack growth in SEPB hard PZT ceramics under sinusoidal mechanical load and DC electric field, and discussed the effect of electric field on the crack growth rate versus maximum energy release rate curves.

It is expected that the polarization switching under high negative electric field affects the crack behavior of piezoelectric ceramics [3]. In particular, the polarizations are easy to switch in soft PZT ceramics, whereas hard PZT ceramics are very difficult to switch. Literature studies of fatigue in the PZT ceramics under high negative electric field are sparse and inconclusive. The main aim of this work is to discuss the effects of the electric field and polarization switching on the fatigue of cracked soft PZT ceramics in cyclic bending.

2. Experimental Procedure

Commercially supplied soft PZT C-91 ceramics (Fuji Ceramics Co. Ltd., Japan) were used. The material properties are listed in Table 1, and the coercive electric field is about E_c = 0.35 MV/m. Fatigue tests under zero or negative electric fields were carried out using SEPB specimens. The specimen and testing set up are shown in Figure 1. PZT ceramics of 5 mm×5mm×5 mm were cut, and the specimen was produced by first poling a PZT and then bonding it between two unpoled PZTs. The size of the specimens was 5 mm thick, 5 mm wide, and 15 mm long. Vickers indents were introduced using the commercial microhardness testing machine. The specimens were compressed until a precrack was formed, and the crack has initial length of about 0.5 mm.

Three-point bending apparatus with 13 mm span was used, and load P with constant-amplitude sinusoidal variation was applied with 250 N load cell (resolution : 0.01 N) to the specimens at constant frequency f of 1 or 50 Hz. The load ratio, defined as the ratio of minimum load P_{min} to maximum load P_{max} of the fatigue cycle, was $R = P_{min}/P_{max} = 0.5$, and the maximum load P_{max} was 90, 100 or 110 N. Number of cycles to failure under constant applied load P_{max} and electric field was then measured. After the tests, scanning electron microscope (SEM) was used to examine

Table 1 Material properties of C-91

Elastic compliance (×10^{-12} m^2/N)					Piezoelectric constant (×10^{-12}m/V)			Dielectric permittivity (×10^{-10} C/Vm)	
s_{11}	s_{33}	s_{44}	s_{12}	s_{13}	d_{31}	d_{33}	d_{15}	$\in_{11}^{T}$	$\in_{33}^{T}$
17.1	18.6	41.4	-6.3	-7.3	-340	645	836	395	490

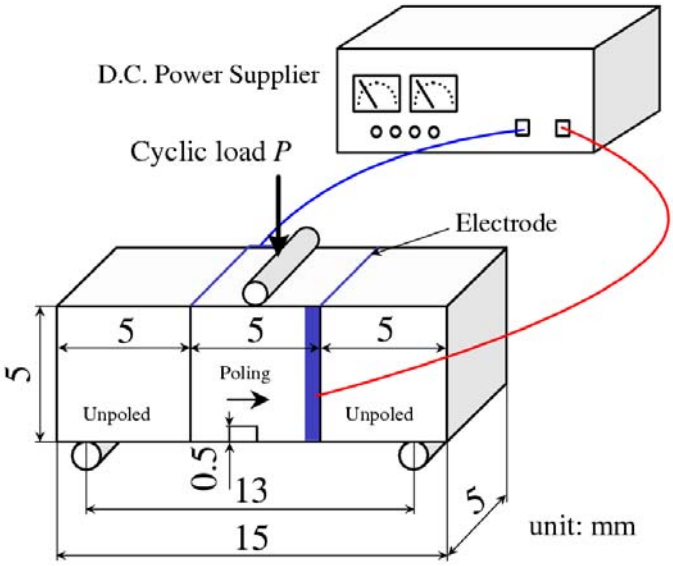

Figure 1. SEPB specimen and testing set up

fatigue fracture surfaces.

3. Analysis

Mechanical equilibrium and Gauss' law are given by

$$\sigma_{ji,j} = 0 \tag{1}$$

$$D_{i,i} = 0 \tag{2}$$

where σ_{ij} and D_i are the stress tensor and electric displacement vector, and a comma denotes partial differentiation with respect to the coordinates x_i (i = 1, 2, 3). We have employed Cartesian tensor notation and the summation convention for repeated tensor indices. In a ferroelectric material, domain switching leads to changes in remanent strain ε_{ij}^{r} and remanent polarization P_i^r. Constitutive relations are described by

$$\varepsilon_{ij} = s_{ijkl}\sigma_{kl} + d_{kij}E_k + \varepsilon_{ij}^{r} \tag{3}$$

$$D_i = d_{ikl}\sigma_{kl} + \in_{ik}^{T} E_k + P_i^r \tag{4}$$

where ε_{ij} and E_i are the strain tensor and electric field vector, and s_{ijkl}, d_{kij} and $\in_{ik}^{T}$ are the elastic compliance, direct piezoelectric constant and dielectric permittivity at constant stress, which satisfy the following symmetry relations:

$$s_{ijkl} = s_{jikl} = s_{ijlk} = s_{klij}\,, d_{kij} = d_{kji}\,, \in_{ij}^{T} = \in_{ji}^{T} \tag{5}$$

The strain and electric field may be expressed in terms of the displacement vector u_i and the electric potential ϕ by

$$\varepsilon_{ij} = \frac{1}{2}(u_{j,i} + u_{i,j}) \tag{6}$$

$$E_i = -\phi_{,i} \tag{7}$$

The constitutive equations (3) and (4) for PZT poled in the x_3-direction are found in Appendix A.

The enhanced electromechanical field level results in localized polarization switching. When the electromechanical work exceeds a critical value, polarization switching occurs [4]. Thus the switching criterion is defined as

$$\sigma_{ij}\Delta\varepsilon_{ij} + E_i\Delta P_i \geq 2P^s E_c \tag{8}$$

where P^s is spontaneous polarization, E_c is coercive electric field, and $\Delta\varepsilon_{ij}$ and ΔP_i are the changes in the spontaneous strain γ^s and spontaneous polarization during switching, respectively, and are given in Appendix B. The constitutive equations (3) and (4) after polarization switching are given by

$$\varepsilon_{ij} = s_{ijkl}\sigma_{kl} + d'_{kij}\,E_k + \varepsilon_{ij}^{r} \tag{9}$$

$$D_i = d'_{ikl}\,\sigma_{kl} + \in_{ik}^{T}\,E_k + P_i^{r} \tag{10}$$

where

$$d'_{ikl} = \{d_{33}n_i n_k n_l + d_{31}(n_i\delta_{kl} - n_i n_k n_l) + \frac{1}{2}d_{15}(\delta_{ik}n_l - 2n_i n_k n_l + \delta_{il}n_k)\} \tag{11}$$

In Eq. (11), n_i is the unit vector in the poling direction and δ_{ij} is the Kroneker delta.

In order to evaluate the energy release rate G of PZT, plane strain finite element analysis (FEA) was carried out for the cracked piezoelectric specimens under concentrated load P. The crack is assumed with faces normal (Case 1) or parallel (Case 2) to the polarization axis as shown in Fig.2. Let the coordinate axes $x = x_1$ and $z = x_3$ be chosen such that the $y = x_2$ axis coincides with the thickness direction. The z axis is the poling direction. The three-point flexure specimen with span S = 13 mm is the beam of width W = 5 mm and length L = 15 mm containing a crack of length a. The length between two electrodes is L_0 = 5 mm for Case 1 and W = 5 mm for Case 2. Because of symmetry, only the half of the model was used in the FEA.

We first consider the Case 1 as shown in Fig. 2(a). The permeable crack model is treated, and the boundary conditions at z = 0 can be expressed in the form

$$\begin{aligned} u_z(x,0) &= 0 \qquad (0 \leq x \leq W - a) \\ \sigma_{zz}(x,0) &= 0 \qquad (W - a < x \leq W) \end{aligned} \tag{12}$$

$$\sigma_{zx}(x,0) = 0 \qquad (0 \leq x \leq W) \tag{13}$$

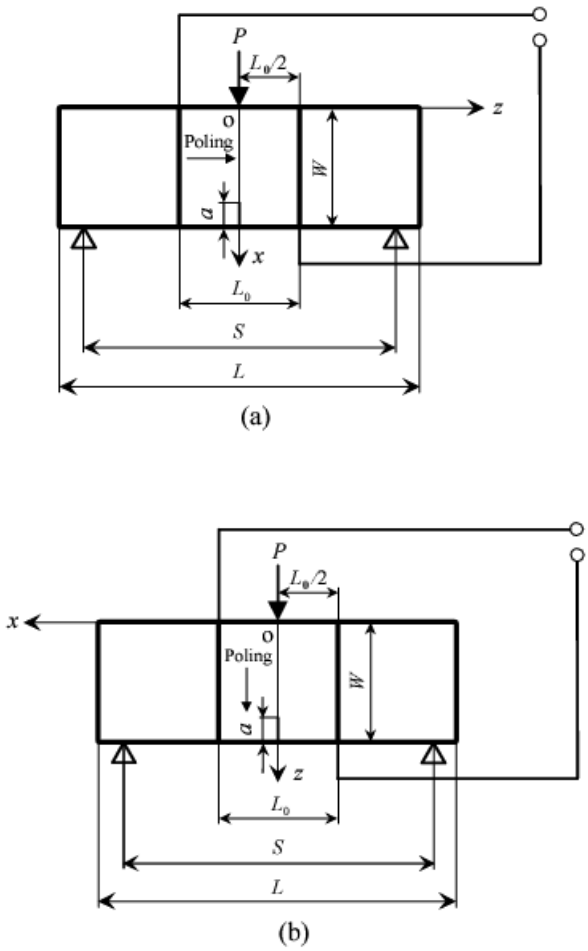

Figure 2. Schematic representation of the finite element model: (a) Case 1; (b) Case 2

$$\begin{aligned} &\phi(x,0) = 0 && (0 \le x \le W - a) \\ &E_x(x,0) = E_x^c(x,0) && (W - a < x \le W) \\ &D_z(x,0) = D_z^c(x,0) && (W - a < x \le W) \end{aligned} \tag{14}$$

where the superscript c stands for the electric quantity in the void inside the crack. The electric potential is all zero on the symmetry planes inside the crack and ahead of the crack, so the boundary conditions of Eqs. (14) reduce to $\phi(x, 0) = 0$ ($0 \le x \le W$). Eqs. (14) are the permeable boundary conditions, and appropriate for a slit crack in piezoelectric ceramics [5]. Note that the fracture mechanics parameters such as energy release rate predicted by the permeable and discharging crack models are not significantly different, using the standard air breakdown field for a critical discharge level within the crack gap. A mechanical load is produced by the application of the prescribed force P, corresponding to the appropriate experimental load, at $x = 0$, $z = 0$ along the x-direction. For an electrical load, the electric potential ($\phi_0/2$) is applied at the edge $0 \le x \le W$, $z = L_0/2$, so the condition is

$$\phi(x, L_0/2) = (\phi_0/2) \qquad (0 \le x \le W) \tag{15}$$

The magnitude of the electric field E_0 in the z-direction is $-\phi_0/L_0$. Other boundary conditions are

summarized below.
At $z = L/2$ (side surface)

$$\sigma_{zz}(x, L/2) = 0 \qquad (0 \le x \le W) \tag{16}$$

$$\sigma_{zx}(x, L/2) = 0 \qquad (0 \le x \le W) \tag{17}$$

$$D_z(x, L/2) = 0 \qquad (0 \le x \le W) \tag{18}$$

At $x = 0$ (top surface)

$$\sigma_{xx}(0, z) = -(P/2)\delta(z) \qquad (0 \le z \le L/2) \tag{19}$$

$$\sigma_{xz}(0, z) = 0 \qquad (0 \le z \le L/2) \tag{20}$$

$$D_x(0, z) = 0 \qquad (0 \le z \le L/2) \tag{21}$$

At $x = W$ (bottom surface)

$$\sigma_{xx}(W, z) = 0 \quad (0 \le z < S/2, S/2 < z \le L/2), \quad u_x(W, S/2) = 0 \tag{22}$$

$$\sigma_{xz}(W, z) = 0 \qquad (0 \le z \le L/2) \tag{23}$$

$$D_x(W, z) = 0 \qquad (0 \le z \le L/2) \tag{24}$$

In Eq. (19), $\delta(\ )$ is the Dirac-delta function.

Next, we consider the Case 2 (see Figure 2(b)). The boundary conditions at $x = 0$ are

$$\begin{aligned} u_x(0, z) &= 0 \quad (0 \le z \le W - a) \\ \sigma_{xx}(0, z) &= 0 \quad (W - a < z \le W) \end{aligned} \tag{25}$$

$$\sigma_{xz}(0, z) = 0 \quad (0 \le z \le W) \tag{26}$$

$$\begin{aligned} \phi_{,x}(0, z) &= 0 \qquad (0 \le z \le W - a) \\ E_z(0, z) &= E_z^c(0, z) \quad (W - a < z \le W) \\ D_x(0, z) &= D_x^c(0, z) \quad (W - a < z \le W) \end{aligned} \tag{27}$$

The partial derivative of the electric potential with respect to x is all zero on the symmetry planes inside the crack and ahead of the crack, so the boundary conditions of Eqs. (27) reduce to $\phi_{,x}(x, 0) = 0$ ($0 \le x \le W$). A mechanical load is produced by the application of the prescribed force P, at $x = 0$, $z = 0$ along the z-direction. For an electrical load, the electric potential ϕ_0 is applied at the surface $0 \le x < L_0/2$, $z = W$, and the surface $0 \le x < L_0/2$, $z = 0$ is grounded, so the conditions are

$$\phi(x,W)=\phi_0 \qquad (0\le x<L_0/2)$$
$$\phi(x,0)=0 \qquad (0\le x<L_0/2) \tag{28}$$

The magnitude of the electric field E_0 in the x-direction is $-\phi_0/W$. Other boundary conditions are summarized below.
At $x = L/2$ (side surface)

$$\sigma_{xx}(L/2,z)=0 \qquad (0\le z\le W) \tag{29}$$

$$\sigma_{xz}(L/2,z)=0 \qquad (0\le z\le W) \tag{30}$$

$$D_x(L/2,z)=0 \qquad (0\le z\le W) \tag{31}$$

At $z = 0$ (top surface)

$$\sigma_{zz}(x,0)=-(P/2)\delta(x) \qquad (0\le x\le L/2) \tag{32}$$

$$\sigma_{zx}(x,0)=0 \qquad (0\le x\le L/2) \tag{33}$$

$$D_z(x,0)=0 \qquad (L_0/2\le x\le L/2) \tag{34}$$

At $z = W$ (bottom surface)

$$\sigma_{zz}(x,W)=0 \qquad (0\le x<S/2, S/2<x\le L/2), \qquad u_z(S/2,W)=0 \tag{35}$$

$$\sigma_{zx}(x,W)=0 \qquad (0\le x\le L/2) \tag{36}$$

$$D_z(x,W)=0 \qquad (L_0/2\le x\le L/2) \tag{37}$$

In the FEA (ANSYS), the energy release rate was computed using the path-independent integral approach. The energy release rate G for Case 1 is given by

$$G=(\int_{\Gamma_0}-\int_{\Gamma_p})\{Hn_x-(\sigma_{xx}u_{x,x}+\sigma_{zx}u_{z,x})n_x-(\sigma_{zx}u_{x,x}+\sigma_{zz}u_{z,x})n_z+D_xE_xn_x+D_zE_xn_z\}d\Gamma \tag{38}$$

where Γ_0 is the contour closing the crack tip, Γ_p is the path embracing that part of phase boundary which in enclosed by Γ_0, H is the electrical enthalpy density, and n_x, n_z are the components of the outer unit normal vector. The energy release rate G for Case 2 is obtained by exchanging x and z in Eq. (38).

For the calculation of G, three contours were defined in the finite element mesh. The values of G for each of these contours are practically identical. Four-node element PLANE 13 was used in the model. The finite element mesh had 4400 elements and 4536 nodes.

4. Results and Discussion

Table 2 shows the results of average number of cycles to failure (from two data) for PZT ceramics

Table 2 Number of cycles to failure under electric fields

Electric field, E_0 (MV/m)	-0.2	-0.04	0
Number of cycles to failure, N	385	494645	38994

Table 3 Energy release rate under electric fields for Cases 1 and 2 without polarization switching effect

Electric field, E_0 (MV/m)		-0.2	-0.04	0
Energy release rate, G (J/m^2)	Case 1	5.5	5.5	5.5
	Case 2	4.3	4.3	4.3

C-91 under P_{max} = 110 N (R = 0.5, f = 50 Hz) and E_0 = 0, -0.04, -0.2 MV/m. The value of average number of cycles to failure increases by about 12 times due to the electric field of -0.04 MV/m, but decreases to less than about 0.01 times due to the electric field of -0.2 MV/m. Although the results are not shown here, the fracture surface of the PZT ceramics under E_0 = 0 V/m shows intergranular and transgranular regions, and the micrograph of the PZT ceramics under E_0 = -0.04 MV/m reveals a predominantly intergranular fracture. On the other hand, crack paths in the fracture for PZT ceramics under E_0 = -0.2 MV/m are predominantly transgrannular.

Table 3 lists the energy release rate G for SEPB C-91 ceramics with a crack of length a = 0.5 mm under load P_{max} = 110 N and E_0 = 0, -0.04, -0.2 MV/m for Cases 1 and 2 without polarization switching effect. The energy release rates for Cases 1 and 2 are independent of the electric field,

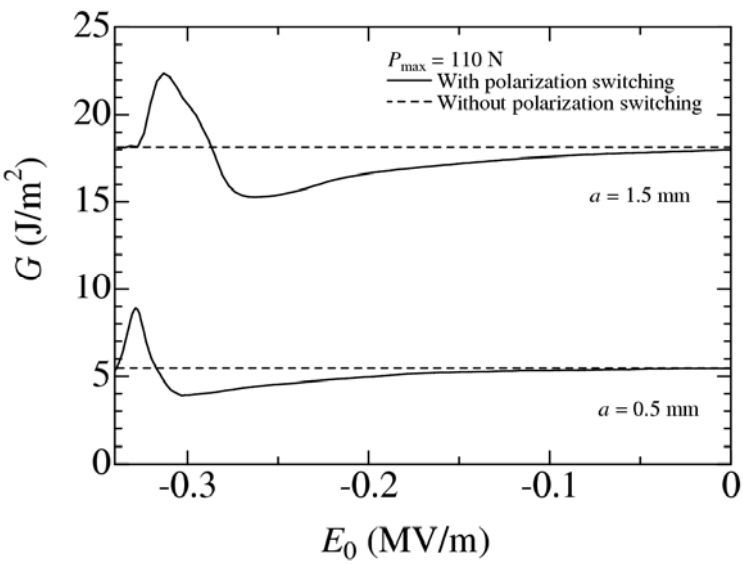

Figure 3. Energy release rate vs electric field for Case 1 with and without polarization switching effect

and the energy release rate for Case 1 is larger than that for Case 2. Figure 3 shows the energy release rate G versus electric field E_0 for SEPB C-91 ceramics with a = 0.5 and 1.5 mm under P_{max} = 110 N for Case 1. The dashed line represents the value of G without polarization switching effect, and the solid line represents the G with switching effect. The prediction with switching effect shows that localized polarization switching leads to a decrease in G and then an increase after E_0 reaches about -0.3 and -0.27 MV/m for a = 0.5 and 1.5 mm, respectively.

In concluding, numbers of cycles to failure under low and high negative electric fields were significantly larger and smaller than that under zero electric field, and correlated with the fracture surfaces. In addition, as the negative electric field increased, the localized polarization switching led to a decrease in the energy release rate, and the energy release rate increased when the negative electric field increased further.

References

[1] Y.Shindo, F.Narita, M.Hirama, Dynamic fatigue of cracked piezoelectric ceramics under electromechanical loading: Three-point bending test and finite element analysis. J Mech Mater Struct, 4 (2009) 719-729.
[2] F.Narita, Y.Shindo, F.Saito, Cyclic Fatigue Crack Growth in Three-Point Bending PZT Ceramics under Electromechanical Loading. J Am Ceram Soc, 90 (2007) 2517-2524.
[3] Y.Shindo, F.Narita, T.Matsuda, Electric field dependence of the mode I energy release rate in single-edge cracked piezoelectric ceramics: Effect due to polarization switching/dielectric breakdown. Acta Mech, 219 (2011) 129-143.
[4] S.C.Hwang, C.S.Lynch, R.M.McMeeking, Ferroelectric/ferroelastic interactions and a polarization switching model. Acta Metall Mater, 43 (1995) 2073-2084.
[5] Y.Shindo, F.Narita, M.Hirama, Effect of the electrical boundary condition at the crack face on the mode I energy release rate in piezoelectric ceramics. Appl Phys Lett, 94 (2009) 081902.
[6] Y.Shindo, M.Yoshida, F.Narita, K.Horiguchi, Electroelastic field concentrations ahead of electrodes in multilayer piezoelectric actuators: experiment and finite element simulation. J Mech Phys Solids, 52 (2004) 1109-1124.

Appendix A

For piezoelectric ceramics which exhibit symmetry of a hexagonal crystal of class 6 mm with respect to principal x_1, x_2 and x_3 axes, the constitutive relations can be written in the following form:

$$\begin{Bmatrix} \varepsilon_{11} \\ \varepsilon_{22} \\ \varepsilon_{33} \\ \varepsilon_{23} \\ \varepsilon_{31} \\ \varepsilon_{12} \end{Bmatrix} = \begin{bmatrix} s_{11} & s_{12} & s_{13} & 0 & 0 & 0 \\ s_{12} & s_{11} & s_{13} & 0 & 0 & 0 \\ s_{13} & s_{13} & s_{33} & 0 & 0 & 0 \\ 0 & 0 & 0 & s_{44}/2 & 0 & 0 \\ 0 & 0 & 0 & 0 & s_{44}/2 & 0 \\ 0 & 0 & 0 & 0 & 0 & s_{66}/2 \end{bmatrix} \begin{Bmatrix} \sigma_{11} \\ \sigma_{22} \\ \sigma_{33} \\ \sigma_{23} \\ \sigma_{31} \\ \sigma_{12} \end{Bmatrix} + \begin{bmatrix} 0 & 0 & d_{31} \\ 0 & 0 & d_{31} \\ 0 & 0 & d_{33} \\ 0 & d_{15}/2 & 0 \\ d_{15}/2 & 0 & 0 \\ 0 & 0 & 0 \end{bmatrix} \begin{Bmatrix} E_1 \\ E_2 \\ E_3 \end{Bmatrix} + \begin{Bmatrix} \varepsilon_{11}^r \\ \varepsilon_{22}^r \\ \varepsilon_{33}^r \\ \varepsilon_{23}^r \\ \varepsilon_{31}^r \\ \varepsilon_{12}^r \end{Bmatrix} \tag{A.1}$$

$$\begin{Bmatrix} D_1 \\ D_2 \\ D_3 \end{Bmatrix} = \begin{bmatrix} 0 & 0 & 0 & 0 & d_{15} & 0 \\ 0 & 0 & 0 & d_{15} & 0 & 0 \\ d_{31} & d_{31} & d_{33} & 0 & 0 & 0 \end{bmatrix} \begin{Bmatrix} \sigma_{11} \\ \sigma_{22} \\ \sigma_{33} \\ \sigma_{23} \\ \sigma_{31} \\ \sigma_{12} \end{Bmatrix} + \begin{bmatrix} \in_{11}^{\mathrm{T}} & 0 & 0 \\ 0 & \in_{11}^{\mathrm{T}} & 0 \\ 0 & 0 & \in_{33}^{\mathrm{T}} \end{bmatrix} \begin{Bmatrix} E_1 \\ E_2 \\ E_3 \end{Bmatrix} + \begin{Bmatrix} P_1^r \\ P_2^r \\ P_3^r \end{Bmatrix} \tag{A.2}$$

where

$$\sigma_{23} = \sigma_{32}, \quad \sigma_{31} = \sigma_{13}, \quad \sigma_{12} = \sigma_{21} \tag{A.3}$$

$$\varepsilon_{23} = \varepsilon_{32}, \quad \varepsilon_{31} = \varepsilon_{13}, \quad \varepsilon_{12} = \varepsilon_{21} \tag{A.4}$$

$$\varepsilon_{23}^r = \varepsilon_{32}^r, \quad \varepsilon_{31}^r = \varepsilon_{13}^r, \quad \varepsilon_{12}^r = \varepsilon_{21}^r \tag{A.5}$$

$$\begin{aligned} &s_{11} = s_{1111} = s_{2222}, \quad s_{12} = s_{1122}, \quad s_{13} = s_{1133} = s_{2233}, \quad s_{33} = s_{3333}, \\ &s_{44} = 4s_{2323} = 4s_{3131}, \quad s_{66} = 4s_{1212} = 2(s_{11} - s_{12}) \end{aligned} \tag{A.6}$$

$$d_{15} = 2d_{131} = 2d_{223}, \quad d_{31} = d_{311} = d_{322}, \quad d_{33} = d_{333} \tag{A.7}$$

Appendix B

The values of $\Delta\varepsilon_{ij} = \varepsilon_{ij}^r$ and $\Delta P_i = P_i^r$ for 180° switching can be expressed as

$$\Delta\varepsilon_{11} = 0, \quad \Delta\varepsilon_{22} = 0, \quad \Delta\varepsilon_{33} = 0, \quad \Delta\varepsilon_{12} = 0, \quad \Delta\varepsilon_{23} = 0, \quad \Delta\varepsilon_{31} = 0 \tag{B.1}$$

$$\Delta P_1 = 0, \quad \Delta P_2 = 0, \quad \Delta P_3 = -2P^s \tag{B.2}$$

For 90° switching in the x_3x_1 plane, the changes are

$$\Delta\varepsilon_{11} = \gamma^s, \quad \Delta\varepsilon_{22} = 0, \quad \Delta\varepsilon_{33} = -\gamma^s, \quad \Delta\varepsilon_{12} = 0, \quad \Delta\varepsilon_{23} = 0, \quad \Delta\varepsilon_{31} = 0 \tag{B.3}$$

$$\Delta P_1 = \pm P^s, \quad \Delta P_2 = 0, \quad \Delta P_3 = -P^s \tag{B.4}$$

For 90° switching in the x_2x_3 plane, we have

$$\Delta\varepsilon_{11} = 0, \quad \Delta\varepsilon_{22} = \gamma^s, \quad \Delta\varepsilon_{33} = -\gamma^s, \quad \Delta\varepsilon_{12} = 0, \quad \Delta\varepsilon_{23} = 0, \quad \Delta\varepsilon_{31} = 0 \tag{B.5}$$

$$\Delta P_1 = 0, \quad \Delta P_2 = \pm P^s, \quad \Delta P_3 = -P^s \tag{B.6}$$

Three-Phase Elliptical Inclusions with an Internal Stress Field of Linear Form

Xu Wang[1,*], **Weiqiu Chen**[2]

[1] School of Mechanical and Power Engineering, East China University of Science and Technology, 130 Meilong Road, Shanghai 200237, China

[2] Department of Engineering Mechanics, Zhejiang University, Hangzhou 310027, China

[*] Corresponding author: xuwang@ecust.edu.cn

Abstract This paper studies the internal stress field of a three-phase elliptical inclusion which is bonded to an infinite matrix through an interphase layer when the matrix is subjected to a linearly distributed in-plane stress field at infinity. Two conditions are found that ensure that the internal non-uniform stress field is simply a linear function of the two coordinates. For given material and geometric parameters of the composite, these conditions can be considered as two restrictions on the applied non-uniform loadings. When these two conditions are met, elementary-form expressions of the stresses in all the three phases are derived. In particular, it is found that the mean stress within the interphase layer is also a linear function of the coordinates. If the interphase layer and the matrix have the same elastic constants, the satisfaction of the two conditions will result in a harmonic inclusion under prescribed non-constant field.

Keywords Elliptical inclusion, Interphase layer, Non-uniform loading, Harmonic inclusion, Inverse problem

1. Introduction

Rigorous analysis of a composite system consisting of an internal inclusion, an intermediate interphase layer (or coating) and an outer matrix is challenging, especially when the inclusion is non-circular (see for example, [1–5] and the references cited therein). It has been found that the internal stress field within a three-phase confocal elliptical inclusion can be uniform and hydrostatic when the remotely applied uniform in-plane stresses satisfy a condition [2]. How about the stress field within a three-phase elliptical inclusion when the matrix is subjected to non-uniform in-plane stresses at infinity? Is there any elementary solution for the case of non-uniform loading?

In this paper two conditions are found that ensure that the internal stress field within a three-phase confocal elliptical inclusion is a linear function of the coordinates when the matrix is subjected to a linearly distributed (non-uniform) in-plane stress field at infinity. Elementary-form solution is derived when these two conditions are met. Some special examples are presented to demonstrate the solution. In particular, when the interphase layer and the matrix have identical elastic constants, the satisfaction of the two conditions will result in a harmonic elliptical inclusion under non-uniform loadings.

2. The Internal Stress Field of Linear Form

We study the stress-field of a three-phase elliptical inclusion with two confocal interfaces when the matrix is subjected to a linearly distributed stress field at infinity. Let S_1, S_2 and S_3 denote the inclusion, the interphase layer and the matrix, respectively, which are perfectly bonded across two confocal elliptical interfaces L_1 and L_2, as shown in Fig. 1. Throughout the paper, the subscripts 1, 2 and 3 are used to identify the respective quantities in S_1, S_2 and S_3.

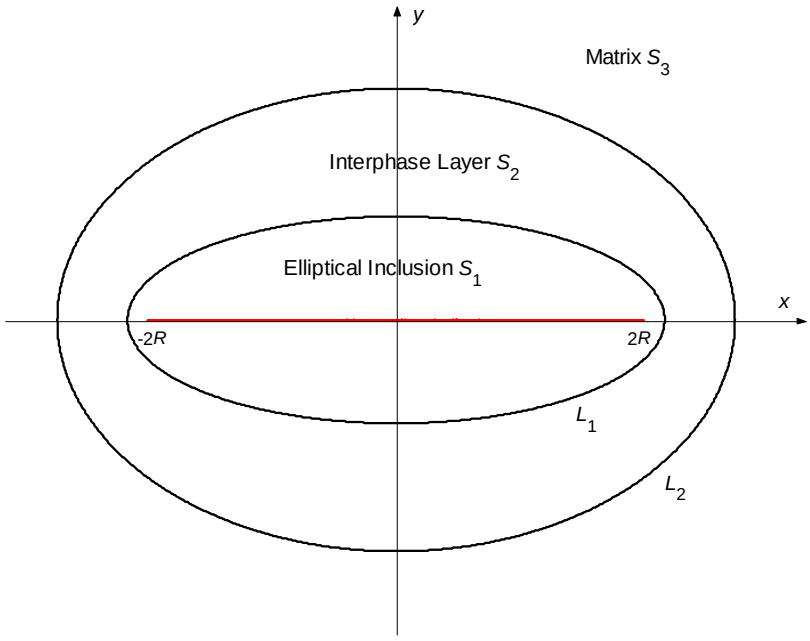

Figure 1 Three-phase elliptical inclusion with an internal stress field of linear form

For plane deformations of an isotropic elastic material, the in-plane displacements u and v, the two resultant forces f_x and f_y, and the in-plane stresses σ_{xx}, σ_{yy} and σ_{xy} can be expressed in terms of two analytic functions $\phi(z)$ and $\psi(z)$ of the complex variable $z=x+\mathrm{i}y$ as [6]

$$\begin{aligned} &2\mu(u+\mathrm{i}v)=\kappa\phi(z)-z\overline{\phi'(z)}-\overline{\psi(z)},\\ &f_x+\mathrm{i}f_y=-\mathrm{i}\left[\phi(z)+z\overline{\phi'(z)}+\overline{\psi(z)}\right], \end{aligned} \tag{1}$$

$$\begin{aligned} &\sigma_{xx}+\sigma_{yy}=2[\phi'(z)+\overline{\phi'(z)}],\\ &\sigma_{yy}-\sigma_{xx}+2\mathrm{i}\sigma_{xy}=2\left[\bar{z}\phi''(z)+\psi'(z)\right], \end{aligned} \tag{2}$$

where $\kappa=3-4\nu$ for plane strain, and $\kappa=(3-\nu)/(1+\nu)$ for plane stress; μ and ν, where $\mu>0$ and $0\le\nu\le 0.5$, are the shear modulus and Poisson's ratio, respectively.

In the physical z-plane, the boundary value problem for the three-phase elliptical inclusion takes the form:

$$\begin{aligned} &\phi_2(z)+z\overline{\phi_2'(z)}+\overline{\psi_2(z)}=\phi_1(z)+z\overline{\phi_1'(z)}+\overline{\psi_1(z)},\\ &\frac{1}{2\mu_2}\left[\kappa_2\phi_2(z)-z\overline{\phi_2'(z)}-\overline{\psi_2(z)}\right]=\frac{1}{2\mu_1}\left[\kappa_1\phi_1(z)-z\overline{\phi_1'(z)}-\overline{\psi_1(z)}\right],\quad z\in L_1; \end{aligned} \tag{3}$$

$$\begin{aligned} &\phi_2(z)+z\overline{\phi_2'(z)}+\overline{\psi_2(z)}=\phi_3(z)+z\overline{\phi_3'(z)}+\overline{\psi_3(z)},\\ &\frac{1}{2\mu_2}\left[\kappa_2\phi_2(z)-z\overline{\phi_2'(z)}-\overline{\psi_2(z)}\right]=\frac{1}{2\mu_3}\left[\kappa_3\phi_3(z)-z\overline{\phi_3'(z)}-\overline{\psi_3(z)}\right],\quad z\in L_2; \end{aligned} \tag{4}$$

$$\phi_3(z)\cong(A_1+\mathrm{i}A_2)z^2+O(1),\quad \psi_3(z)\cong(B_1+\mathrm{i}B_2)z^2+O(1),\qquad \text{as}\qquad |z|\to\infty \tag{5}$$

where A_1, A_2, B_1 and B_2 are real numbers related to the applied linearly distributed stress field at infinity.

Consider the following conformal mapping [2, 6]

$$z=\omega(\xi)=R\left(\xi+\frac{1}{\xi}\right),\quad \xi(z)=\frac{z}{2R}\left[1+\sqrt{1-\frac{4R^2}{z^2}}\right],\quad (|\xi|\geq 1) \tag{6}$$

which maps the segment [$-2R$ $2R$] onto the unit circle in the ξ-plane, and the two interfaces L_1 and L_2 are mapped onto two coaxial circles with radii R_1 and R_2, respectively. Thus the three regions S_1, S_2 and S_3 are mapped onto the annuli $1<|\xi|<R_1$, $R_1<|\xi|<R_2$ and $|\xi|>R_2$, respectively, as shown in Fig. 2. For convenience we will write $\phi_i(\xi)=\phi_i(\omega(\xi)),\ \psi_i(\xi)=\psi_i(\omega(\xi)),\ i=1,2,3$.

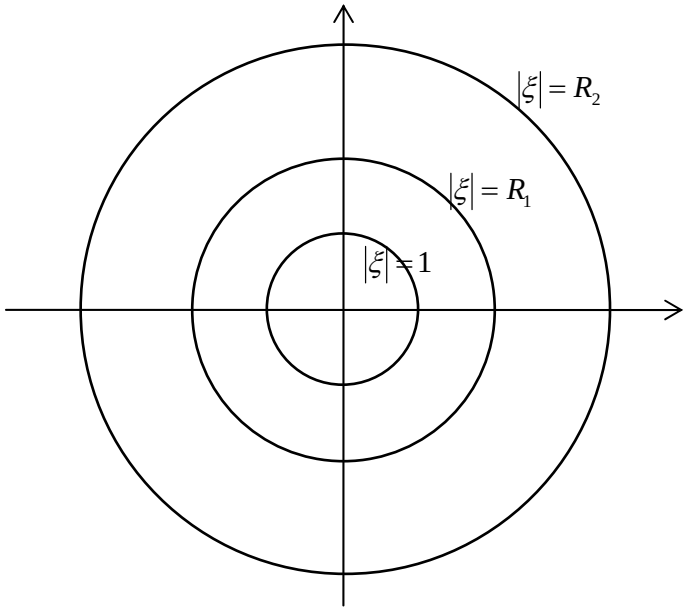

Figure 2 The mapped ξ-plane

In the mapped ξ-plane, the boundary value problem takes the form

$$\begin{aligned}
&\phi_2(\xi)+\omega(\xi)\frac{\overline{\phi_2'(\xi)}}{\overline{\omega'(\xi)}}+\overline{\psi_2(\xi)}=\phi_1(\xi)+\omega(\xi)\frac{\overline{\phi_1'(\xi)}}{\overline{\omega'(\xi)}}+\overline{\psi_1(\xi)},\\
&\kappa_2\phi_2(\xi)-\omega(\xi)\frac{\overline{\phi_2'(\xi)}}{\overline{\omega'(\xi)}}-\overline{\psi_2(\xi)}=\frac{\kappa_1}{\Gamma_1}\phi_1(\xi)-\frac{1}{\Gamma_1}\omega(\xi)\frac{\overline{\phi_1'(\xi)}}{\overline{\omega'(\xi)}}-\frac{1}{\Gamma_1}\overline{\psi_1(\xi)},
\end{aligned}\quad \text{on } |\xi|=R_1 \tag{7}$$

$$\begin{aligned}
&\phi_3(\xi)+\omega(\xi)\frac{\overline{\phi_3'(\xi)}}{\overline{\omega'(\xi)}}+\overline{\psi_3(\xi)}=\phi_2(\xi)+\omega(\xi)\frac{\overline{\phi_2'(\xi)}}{\overline{\omega'(\xi)}}+\overline{\psi_2(\xi)},\\
&\kappa_3\phi_3(\xi)-\omega(\xi)\frac{\overline{\phi_3'(\xi)}}{\overline{\omega'(\xi)}}-\overline{\psi_3(\xi)}=\Gamma_3\kappa_2\phi_2(\xi)-\Gamma_3\omega(\xi)\frac{\overline{\phi_2'(\xi)}}{\overline{\omega'(\xi)}}-\Gamma_3\overline{\psi_2(\xi)},
\end{aligned}\quad \text{on } |\xi|=R_2 \tag{8}$$

$$\phi_3(\xi)\cong R^2(A_1+\mathrm{i}A_2)\xi^2+O(1),\quad \psi_3(\xi)\cong R^2(B_1+\mathrm{i}B_2)\xi^2+O(1),\qquad \text{as}\qquad |\xi|\to\infty \tag{9}$$

where $\Gamma_1=\mu_1/\mu_2$ and $\Gamma_3=\mu_3/\mu_2$ are two stiffness ratios.

In order to ensure that the internal stress field is a linear function of the coordinates x and y, $\phi_1(\xi)$ and $\psi_1(\xi)$ must take the following forms

$$\phi_1(\xi) = X\left(\xi^2 + \frac{1}{\xi^2}\right), \quad \psi_1(\xi) = Y\left(\xi^2 + \frac{1}{\xi^2}\right), \qquad (1 \le |\xi| \le R_1) \tag{10}$$

where X and Y are complex constants to be determined.

Consequently it follows from Eqs. (7) and (10) that

$$(\kappa_2 + 1)\phi_2(\xi) = \frac{X(\Gamma_1 + \kappa_1)}{\Gamma_1}\left(\xi^2 + \frac{1}{\xi^2}\right) + \frac{2\overline{X}(\Gamma_1 - 1)}{\Gamma_1}\left(\frac{\xi^2}{R_1^2} + \frac{R_1^2}{\xi^2}\right) + \frac{\overline{Y}(\Gamma_1 - 1)}{\Gamma_1}\left(\frac{\xi^2}{R_1^4} + \frac{R_1^4}{\xi^2}\right),$$

$$(R_1 \le |\xi| \le R_2) \tag{11}$$

It is found that the necessary and sufficient condition for the validity of Eq. (10) for the internal stress field is that $\phi_2(\xi)$ should take the form of $\phi_2(\xi) = \lambda(\xi^2 + 1/\xi^2)$ with λ being a complex constant. This condition can be easily arrived at from Eq. (2.14) in [2]. The necessity is true only when $\rho = R_1^2/R_2^2 \ne 1$ and $\Gamma_3 \ne 1$. Consequently the following relationship between X and Y establishes

$$Y = -\frac{2X}{R_1^2 + R_1^{-2}}, \quad (\rho \ne 1, \Gamma_1 \ne 1, \Gamma_3 \ne 1) \tag{12}$$

Once the above relationship is satisfied, and all the interface conditions in Eqs. (7) are enforced, $\phi_2(\xi)$ and $\psi_2(\xi)$ are found to have the following expressions

$$\phi_2(\xi) = \frac{X(\Gamma_1 + \kappa_1)(R_1^2 + R_1^{-2}) + 2\overline{X}(\Gamma_1 - 1)}{\Gamma_1(\kappa_2 + 1)(R_1^2 + R_1^{-2})}\left(\xi^2 + \frac{1}{\xi^2}\right),$$

$$\psi_2(\xi) = \frac{2X\left[R_1^{-4}\left[\Gamma_1(\kappa_2 - 1) - (\kappa_1 - 1)\right] - \Gamma_1 - \kappa_1\right] + \overline{X}\left[R_1^{-2}\left[4 - \kappa_1 - \Gamma_1(4 - \kappa_2)\right] + R_1^{-6}(\Gamma_1\kappa_2 - \kappa_1)\right]}{\Gamma_1(\kappa_2 + 1)(R_1^2 + R_1^{-2})}\xi^2$$
$$+ \frac{2X\left[R_1^{4}\left[\Gamma_1(\kappa_2 - 1) - (\kappa_1 - 1)\right] - \Gamma_1 - \kappa_1\right] + \overline{X}\left[R_1^{2}\left[4 - \kappa_1 - \Gamma_1(4 - \kappa_2)\right] + R_1^{6}(\Gamma_1\kappa_2 - \kappa_1)\right]}{\Gamma_1(\kappa_2 + 1)(R_1^2 + R_1^{-2})}\frac{1}{\xi^2},$$

$$(R_1 \le |\xi| \le R_2) \tag{13}$$

Similarly by enforcing the interface conditions in Eq. (8), we arrive at the following expression of $\phi_3(\xi)$ and $\psi_3(\xi)$

$$\phi_3(\xi) = \frac{\left(\begin{array}{l}(\Gamma_3\kappa_2 + 1)\left[X(\Gamma_1 + \kappa_1)(R_1^2 + R_1^{-2}) + 2\overline{X}(\Gamma_1 - 1)\right]\left(\xi^2 + \frac{1}{\xi^2}\right) \\ + 2(1 - \Gamma_3)\left[\overline{X}(\Gamma_1 + \kappa_1)(R_1^2 + R_1^{-2}) + 2X(\Gamma_1 - 1)\right]\left(\frac{\xi^2}{R_2^2} + \frac{R_2^2}{\xi^2}\right) \\ + R_2^{-4}(1 - \Gamma_3)\left\{2\overline{X}\left[R_1^4\left[\Gamma_1(\kappa_2 - 1) - (\kappa_1 - 1)\right] - \Gamma_1 - \kappa_1\right] + X\left[R_1^2\left[4 - \kappa_1 - \Gamma_1(4 - \kappa_2)\right] + R_1^6(\Gamma_1\kappa_2 - \kappa_1)\right]\right\}\xi^2 \\ + R_2^4(1 - \Gamma_3)\left\{2\overline{X}\left[R_1^{-4}\left[\Gamma_1(\kappa_2 - 1) - (\kappa_1 - 1)\right] - \Gamma_1 - \kappa_1\right] + X\left[R_1^{-2}\left[4 - \kappa_1 - \Gamma_1(4 - \kappa_2)\right] + R_1^{-6}(\Gamma_1\kappa_2 - \kappa_1)\right]\right\}\frac{1}{\xi^2}\end{array}\right)}{\Gamma_1(\kappa_2 + 1)(\kappa_3 + 1)(R_1^2 + R_1^{-2})},$$

$$(|\xi| \ge R_2) \tag{14}$$

$$\psi_3(\xi)$$

$$= \frac{\left(\begin{array}{l}(\kappa_3-\Gamma_3\kappa_2)\left[\overline{X}(\Gamma_1+\kappa_1)(R_1^2+R_1^{-2})+2X(\Gamma_1-1)\right]\left(\frac{\xi^2}{R_2^4}+\frac{R_2^4}{\xi^2}\right)\\ +2(\kappa_3+\Gamma_3)\left[X(\Gamma_1+\kappa_1)(R_1^2+R_1^{-2})+2\overline{X}(\Gamma_1-1)\right]\left(\frac{\xi^2}{R_2^2}+\frac{R_2^2}{\xi^2}\right)\\ +(\Gamma_3+\kappa_3)\left\{2X\left[R_1^{-4}\left[\Gamma_1(\kappa_2-1)-(\kappa_1-1)\right]-\Gamma_1-\kappa_1\right]+\overline{X}\left[R_1^{-2}\left[4-\kappa_1-\Gamma_1(4-\kappa_2)\right]+R_1^{-6}(\Gamma_1\kappa_2-\kappa_1)\right]\right\}\xi^2\\ +(\Gamma_3+\kappa_3)\left\{2X\left[R_1^{4}\left[\Gamma_1(\kappa_2-1)-(\kappa_1-1)\right]-\Gamma_1-\kappa_1\right]+\overline{X}\left[R_1^{2}\left[4-\kappa_1-\Gamma_1(4-\kappa_2)\right]+R_1^{6}(\Gamma_1\kappa_2-\kappa_1)\right]\right\}\frac{1}{\xi^2}\end{array}\right)}{\Gamma_1(\kappa_2+1)(\kappa_3+1)(R_1^2+R_1^{-2})}$$

$$-\frac{2\left(\frac{\xi}{R_2^2}+\frac{R_2^2}{\xi}\right)}{\xi-\frac{1}{\xi}}$$

$$\times\frac{\left(\begin{array}{l}(\Gamma_3\kappa_2+1)\left[X(\Gamma_1+\kappa_1)(R_1^2+R_1^{-2})+2\overline{X}(\Gamma_1-1)\right]\left(\xi^2-\frac{1}{\xi^2}\right)\\ +2(1-\Gamma_3)\left[\overline{X}(\Gamma_1+\kappa_1)(R_1^2+R_1^{-2})+2X(\Gamma_1-1)\right]\left(\frac{\xi^2}{R_2^2}-\frac{R_2^2}{\xi^2}\right)\\ +R_2^{-4}(1-\Gamma_3)\left\{2\overline{X}\left[R_1^{4}\left[\Gamma_1(\kappa_2-1)-(\kappa_1-1)\right]-\Gamma_1-\kappa_1\right]+X\left[R_1^{2}\left[4-\kappa_1-\Gamma_1(4-\kappa_2)\right]+R_1^{6}(\Gamma_1\kappa_2-\kappa_1)\right]\right\}\xi^2\\ +R_2^{4}(\Gamma_3-1)\left\{2\overline{X}\left[R_1^{-4}\left[\Gamma_1(\kappa_2-1)-(\kappa_1-1)\right]-\Gamma_1-\kappa_1\right]+X\left[R_1^{-2}\left[4-\kappa_1-\Gamma_1(4-\kappa_2)\right]+R_1^{-6}(\Gamma_1\kappa_2-\kappa_1)\right]\right\}\frac{1}{\xi^2}\end{array}\right)}{\Gamma_1(\kappa_2+1)(\kappa_3+1)(R_1^2+R_1^{-2})},$$

$$(|\xi|\geq R_2) \quad (15)$$

In addition the satisfaction of the remote boundary condition in Eq. (9) will yield

$$R^2(A_1+\mathrm{i}A_2)$$

$$=\frac{\left(\begin{array}{l}(\Gamma_3\kappa_2+1)\left[X(\Gamma_1+\kappa_1)(R_1^2+R_1^{-2})+2\overline{X}(\Gamma_1-1)\right]+2R_2^{-2}(1-\Gamma_3)\left[\overline{X}(\Gamma_1+\kappa_1)(R_1^2+R_1^{-2})+2X(\Gamma_1-1)\right]\\ +R_2^{-4}(1-\Gamma_3)\left\{2\overline{X}\left[R_1^{4}\left[\Gamma_1(\kappa_2-1)-(\kappa_1-1)\right]-\Gamma_1-\kappa_1\right]+X\left[R_1^{2}\left[4-\kappa_1-\Gamma_1(4-\kappa_2)\right]+R_1^{6}(\Gamma_1\kappa_2-\kappa_1)\right]\right\}\end{array}\right)}{\Gamma_1(\kappa_2+1)(\kappa_3+1)(R_1^2+R_1^{-2})},$$

(16)

$$R^2(B_1+\mathrm{i}B_2)$$

$$=\frac{\left(\begin{array}{l}R_2^{-4}\left[\kappa_3-4+\Gamma_3(4-\kappa_2)\right]\left[\overline{X}(\Gamma_1+\kappa_1)(R_1^2+R_1^{-2})+2X(\Gamma_1-1)\right]\\ +2R_2^{-2}\left[\kappa_3-1+\Gamma_3(1-\kappa_2)\right]\left[X(\Gamma_1+\kappa_1)(R_1^2+R_1^{-2})+2\overline{X}(\Gamma_1-1)\right]\\ +(\Gamma_3+\kappa_3)\left\{2X\left[R_1^{-4}\left[\Gamma_1(\kappa_2-1)-(\kappa_1-1)\right]-\Gamma_1-\kappa_1\right]+\overline{X}\left[R_1^{-2}\left[4-\kappa_1-\Gamma_1(4-\kappa_2)\right]+R_1^{-6}(\Gamma_1\kappa_2-\kappa_1)\right]\right\}\\ +2R_2^{-6}(\Gamma_3-1)\left\{2\overline{X}\left[R_1^{4}\left[\Gamma_1(\kappa_2-1)-(\kappa_1-1)\right]-\Gamma_1-\kappa_1\right]+X\left[R_1^{2}\left[4-\kappa_1-\Gamma_1(4-\kappa_2)\right]+R_1^{6}(\Gamma_1\kappa_2-\kappa_1)\right]\right\}\end{array}\right)}{\Gamma_1(\kappa_2+1)(\kappa_3+1)(R_1^2+R_1^{-2})}.$$

(17)

It turns out that the necessary and sufficient condition for the existence of the complex coefficient X simultaneously satisfying Eqs. (16) and (17) is:

$$\frac{B_1}{A_1} = f(R_1, \rho), \qquad \frac{B_2}{A_2} = g(R_1, \rho), \tag{18}$$

where the two functions $f(R_1, \rho)$ and $g(R_1, \rho)$ are defined by

$$f(R_1, \rho) = \frac{\left(\begin{array}{l} \left\{\rho^2 R_1^{-4}\left[\kappa_3 - 4 + \Gamma_3(4-\kappa_2)\right] + 2\rho R_1^{-2}\left[\kappa_3 - 1 + \Gamma_3(1-\kappa_2)\right]\right\}\left[(\Gamma_1+\kappa_1)(R_1^2 + R_1^{-2}) + 2(\Gamma_1 - 1)\right] \\ + (\Gamma_3+\kappa_3)\left\{R_1^{-6}(\Gamma_1\kappa_2 - \kappa_1) + 2R_1^{-4}\left[\Gamma_1(\kappa_2-1) - (\kappa_1 - 1)\right] + R_1^{-2}\left[4 - \kappa_1 - \Gamma_1(4-\kappa_2)\right] - 2(\Gamma_1+\kappa_1)\right\} \\ + 2\rho^3(\Gamma_3 - 1)\left\{(\Gamma_1\kappa_2 - \kappa_1) + 2R_1^{-2}\left[\Gamma_1(\kappa_2-1) - (\kappa_1-1)\right] + R_1^{-4}\left[4-\kappa_1 - \Gamma_1(4-\kappa_2)\right] - 2R_1^{-6}(\Gamma_1+\kappa_1)\right\} \end{array}\right)}{\left(\begin{array}{l} \left[(\Gamma_3\kappa_2 + 1) + 2\rho R_1^{-2}(1-\Gamma_3)\right]\left[(\Gamma_1+\kappa_1)(R_1^2+R_1^{-2}) + 2(\Gamma_1-1)\right] \\ + \rho^2(1-\Gamma_3)\left\{R_1^2(\Gamma_1\kappa_2 - \kappa_1) + 2\left[\Gamma_1(\kappa_2-1) - (\kappa_1-1)\right] + R_1^{-2}\left[4-\kappa_1-\Gamma_1(4-\kappa_2)\right] - 2R_1^{-4}(\Gamma_1+\kappa_1)\right\} \end{array}\right)}, \tag{19}$$

$$g(R_1, \rho) = \frac{\left(\begin{array}{l} + \left\{2\rho R_1^{-2}\left[\kappa_3 - 1 + \Gamma_3(1-\kappa_2)\right] - \rho^2 R_1^{-4}\left[\kappa_3 - 4 + \Gamma_3(4-\kappa_2)\right]\right\}\left[(\Gamma_1+\kappa_1)(R_1^2 + R_1^{-2}) - 2(\Gamma_1 - 1)\right] \\ + (\Gamma_3+\kappa_3)\left\{R_1^{-6}(\kappa_1 - \Gamma_1\kappa_2) + 2R_1^{-4}\left[\Gamma_1(\kappa_2-1) - (\kappa_1 - 1)\right] + R_1^{-2}\left[\Gamma_1(4-\kappa_2) - (4-\kappa_1)\right] - 2(\Gamma_1+\kappa_1)\right\} \\ + 2\rho^3(\Gamma_3 - 1)\left\{(\Gamma_1\kappa_2 - \kappa_1) + 2R_1^{-2}\left[\kappa_1 - 1 - \Gamma_1(\kappa_2-1)\right] + R_1^{-4}\left[4-\kappa_1 - \Gamma_1(4-\kappa_2)\right] + 2R_1^{-6}(\Gamma_1+\kappa_1)\right\} \end{array}\right)}{\left(\begin{array}{l} \left[\Gamma_3\kappa_2 + 1 + 2\rho R_1^{-2}(\Gamma_3 - 1)\right]\left[(\Gamma_1+\kappa_1)(R_1^2+R_1^{-2}) - 2(\Gamma_1-1)\right] \\ + \rho^2(1-\Gamma_3)\left\{R_1^2(\Gamma_1\kappa_2 - \kappa_1) + 2\left[\kappa_1 - 1 - \Gamma_1(\kappa_2-1)\right] + R_1^{-2}\left[4-\kappa_1-\Gamma_1(4-\kappa_2)\right] + 2R_1^{-4}(\Gamma_1+\kappa_1)\right\} \end{array}\right)}. \tag{20}$$

If the two conditions in Eq. (18) are met, the internal stress field of linear form within the elliptical inclusion is given by

$$\begin{aligned} &\phi_1(z) = \frac{X}{R^2} z^2, \quad \psi_1(z) = -\frac{2X}{R^2(R_1^2 + R_1^{-2})} z^2, \\ &\sigma_{xx} = \frac{2(R_1 + R_1^{-1})^2 X_1 x - 2(3R_1^2 + 3R_1^{-2} + 2) X_2 y}{R^2(R_1^2 + R_1^{-2})}, \\ &\sigma_{yy} = \frac{2(3R_1^2 + 3R_1^{-2} - 2) X_1 x - 2(R_1 - R_1^{-1})^2 X_2 y}{R^2(R_1^2 + R_1^{-2})}, \\ &\sigma_{xy} = \frac{2(R_1 - R_1^{-1})^2 X_2 x - 2(R_1 + R_1^{-1})^2 X_1 y}{R^2(R_1^2 + R_1^{-2})}, \end{aligned} \qquad z \in S_1 \tag{21}$$

where X_1 and X_2 are the real and imaginary parts of the complex number X, which is determined by either Eq. (16) or Eq. (17). For example, it follows from Eq. (16) that

$$X_1 = \frac{R^2 A_1 \Gamma_1 (\kappa_2 + 1)(\kappa_3 + 1)(R_1^2 + R_1^{-2})}{\begin{pmatrix} (\Gamma_3\kappa_2 + 1)\left[(\Gamma_1 + \kappa_1)(R_1^2 + R_1^{-2}) + 2(\Gamma_1 - 1)\right] + 2R_2^{-2}(1 - \Gamma_3)\left[(\Gamma_1 + \kappa_1)(R_1^2 + R_1^{-2}) + 2(\Gamma_1 - 1)\right] \\ + R_2^{-4}(1 - \Gamma_3)\left\{R_1^6(\Gamma_1\kappa_2 - \kappa_1) + 2R_1^4\left[\Gamma_1(\kappa_2 - 1) - (\kappa_1 - 1)\right] + R_1^2\left[4 - \kappa_1 - \Gamma_1(4 - \kappa_2)\right] - 2(\Gamma_1 + \kappa_1)\right\} \end{pmatrix}},$$

$$X_2 = \frac{R^2 A_2 \Gamma_1 (\kappa_2 + 1)(\kappa_3 + 1)(R_1^2 + R_1^{-2})}{\begin{pmatrix} (\Gamma_3\kappa_2 + 1)\left[(\Gamma_1 + \kappa_1)(R_1^2 + R_1^{-2}) - 2(\Gamma_1 - 1)\right] + 2R_2^{-2}(\Gamma_3 - 1)\left[(\Gamma_1 + \kappa_1)(R_1^2 + R_1^{-2}) + 2(1 - \Gamma_1)\right] \\ + R_2^{-4}(1 - \Gamma_3)\left\{R_1^6(\Gamma_1\kappa_2 - \kappa_1) - 2R_1^4\left[\Gamma_1(\kappa_2 - 1) - (\kappa_1 - 1)\right] + R_1^2\left[4 - \kappa_1 - \Gamma_1(4 - \kappa_2)\right] + 2(\Gamma_1 + \kappa_1)\right\} \end{pmatrix}}. \tag{22}$$

Furthermore it is deduced from Eqs. (2) and $(13)_1$ that the mean stress is linearly distributed within the interphase layer as

$$\begin{aligned} \phi_2(z) &= \frac{X(\Gamma_1 + \kappa_1)(R_1^2 + R_1^{-2}) + 2\overline{X}(\Gamma_1 - 1)}{R^2\Gamma_1(\kappa_2 + 1)(R_1^2 + R_1^{-2})} z^2, \\ \sigma_{xx} + \sigma_{yy} &= \frac{8\left[(\Gamma_1 + \kappa_1)(R_1^2 + R_1^{-2}) + 2(\Gamma_1 - 1)\right]X_1 x - 8\left[(\Gamma_1 + \kappa_1)(R_1^2 + R_1^{-2}) - 2(\Gamma_1 - 1)\right]X_2 y}{R^2\Gamma_1(\kappa_2 + 1)(R_1^2 + R_1^{-2})}, \end{aligned} \qquad z \in S_2 \tag{23}$$

By making use of Eqs. (16) and (17), $\phi_3(\xi)$ and $\psi_3(\xi)$ in Eqs. (14) and (15) can be re-expressed into

$$\phi_3(\xi) = R^2(A_1 + \mathrm{i}A_2)\xi^2 + \frac{\begin{pmatrix} (\Gamma_3\kappa_2 + 1)\left[X(\Gamma_1 + \kappa_1)(R_1^2 + R_1^{-2}) + 2\overline{X}(\Gamma_1 - 1)\right] + 2R_2^2(1 - \Gamma_3)\left[\overline{X}(\Gamma_1 + \kappa_1)(R_1^2 + R_1^{-2}) + 2X(\Gamma_1 - 1)\right] \\ + R_2^4(1 - \Gamma_3)\left\{2\overline{X}\left[R_1^{-4}\left[\Gamma_1(\kappa_2 - 1) - (\kappa_1 - 1)\right] - \Gamma_1 - \kappa_1\right] + X\left[R_1^{-2}\left[4 - \kappa_1 - \Gamma_1(4 - \kappa_2)\right] + R_1^{-6}(\Gamma_1\kappa_2 - \kappa_1)\right]\right\} \end{pmatrix}}{\Gamma_1(\kappa_2 + 1)(\kappa_3 + 1)(R_1^2 + R_1^{-2})\xi^2}, \tag{24}$$

$$(|\xi| \geq R_2)$$

$$\psi_3(\xi) = R^2(B_1 + \mathrm{i}B_2)\xi^2 - \frac{2\left[\alpha(R_2^2 + R_2^{-2}) + \beta R_2^{-2}\right]\xi^2 + 2\beta R_2^2}{\Gamma_1(\kappa_2 + 1)(\kappa_3 + 1)(R_1^2 + R_1^{-2})\xi^2(\xi^2 - 1)} + \frac{\begin{pmatrix} R_2^4(\kappa_3 - \Gamma_3\kappa_2)\left[\overline{X}(\Gamma_1 + \kappa_1)(R_1^2 + R_1^{-2}) + 2X(\Gamma_1 - 1)\right] \\ + 2R_2^2(\kappa_3 + \Gamma_3)\left[X(\Gamma_1 + \kappa_1)(R_1^2 + R_1^{-2}) + 2\overline{X}(\Gamma_1 - 1)\right] \\ + (\Gamma_3 + \kappa_3)\left\{2X\left[R_1^4\left[\Gamma_1(\kappa_2 - 1) - (\kappa_1 - 1)\right] - \Gamma_1 - \kappa_1\right] + \overline{X}\left[R_1^2\left[4 - \kappa_1 - \Gamma_1(4 - \kappa_2)\right] + R_1^6(\Gamma_1\kappa_2 - \kappa_1)\right]\right\} \end{pmatrix}}{\Gamma_1(\kappa_2 + 1)(\kappa_3 + 1)(R_1^2 + R_1^{-2})\xi^2}, \tag{25}$$

$$(|\xi| \geq R_2)$$

where the two complex constants α and β are defined as

$$\begin{aligned} \alpha = {} & (\Gamma_3\kappa_2 + 1)\left[X(\Gamma_1 + \kappa_1)(R_1^2 + R_1^{-2}) + 2\overline{X}(\Gamma_1 - 1)\right] + 2R_2^{-2}(1 - \Gamma_3)\left[\overline{X}(\Gamma_1 + \kappa_1)(R_1^2 + R_1^{-2}) + 2X(\Gamma_1 - 1)\right] \\ & + R_2^{-4}(1 - \Gamma_3)\left\{2\overline{X}\left[R_1^4\left[\Gamma_1(\kappa_2 - 1) - (\kappa_1 - 1)\right] - \Gamma_1 - \kappa_1\right] + X\left[R_1^2\left[4 - \kappa_1 - \Gamma_1(4 - \kappa_2)\right] + R_1^6(\Gamma_1\kappa_2 - \kappa_1)\right]\right\}, \end{aligned}$$

$$\begin{aligned} \beta = {} & R_2^4(\Gamma_3 - 1)\left\{2\overline{X}\left[R_1^{-4}\left[\Gamma_1(\kappa_2 - 1) - (\kappa_1 - 1)\right] - \Gamma_1 - \kappa_1\right] + X\left[R_1^{-2}\left[4 - \kappa_1 - \Gamma_1(4 - \kappa_2)\right] + R_1^{-6}(\Gamma_1\kappa_2 - \kappa_1)\right]\right\} \\ & + 2R_2^2(\Gamma_3 - 1)\left[\overline{X}(\Gamma_1 + \kappa_1)(R_1^2 + R_1^{-2}) + 2X(\Gamma_1 - 1)\right] - (\Gamma_3\kappa_2 + 1)\left[X(\Gamma_1 + \kappa_1)(R_1^2 + R_1^{-2}) + 2\overline{X}(\Gamma_1 - 1)\right]. \end{aligned} \tag{26}$$

It is found that $\phi_3(\xi)$ and $\psi_3(\xi)$ given by Eqs. (24) and (25) are analytic outside the circle R_2 (in

view of the fact that $\xi^2 - 1 \neq 0$ for $|\xi| \geq R_2$) and meet the asymptotic condition in Eq. (9).

It can be easily proved that under a linearly distributed stress field at infinity, the internal stress field within an elliptical inclusion perfectly bonded to the surrounding matrix is always a linear function of the coordinates. The above obtained results demonstrate the interesting fact that the internal stress field within a three-phase elliptical inclusion can still keep a simple linear form if the remotely applied non-uniformly loadings satisfy the two conditions in Eq. (18).

3. Discussions

In this section several typical examples will be presented to illustrate the application of Eq. (18) to the design of three-phase elliptical inclusions when the matrix is subjected to a linearly distributed stress field at infinity.

3.1. The materials comprising the interphase layer and the matrix are identical ($\mu_2 = \mu_3$ and $\kappa_2 = \kappa_3$)

In this case, Eqs. (18) becomes

$$\frac{B_1}{A_1} = \frac{R_1^{-6}(\Gamma_1\kappa_2 - \kappa_1) + 2R_1^{-4}\left[\Gamma_1(\kappa_2 - 1) - (\kappa_1 - 1)\right] + R_1^{-2}\left[4 - \kappa_1 - \Gamma_1(4 - \kappa_2)\right] - 2(\Gamma_1 + \kappa_1)}{(\Gamma_1 + \kappa_1)(R_1^2 + R_1^{-2}) + 2(\Gamma_1 - 1)}, \tag{27}$$

$$\frac{B_2}{A_2} = \frac{R_1^{-6}(\kappa_1 - \Gamma_1\kappa_2) + 2R_1^{-4}\left[\Gamma_1(\kappa_2 - 1) - (\kappa_1 - 1)\right] + R_1^{-2}\left[\Gamma_1(4 - \kappa_2) - (4 - \kappa_1)\right] - 2(\Gamma_1 + \kappa_1)}{(\Gamma_1 + \kappa_1)(R_1^2 + R_1^{-2}) - 2(\Gamma_1 - 1)}. \tag{28}$$

In particular, if the inclusion is a hole ($\Gamma_1 << 1$), Eqs. (27) and (28) become

$$\frac{B_1}{A_1} = -\frac{1}{R_1^4} - \frac{2}{R_1^2}, \tag{29}$$

$$\frac{B_2}{A_2} = \frac{1}{R_1^4} - \frac{2}{R_1^2}. \tag{30}$$

On the other extreme end, if the inclusion is rigid ($\Gamma_1 >> 1$), Eqs. (27) and (28) become

$$\frac{B_1}{A_1} = \frac{\kappa_2}{R_1^4} - \frac{2}{R_1^2}, \tag{31}$$

$$\frac{B_2}{A_2} = -\frac{\kappa_2}{R_1^4} - \frac{2}{R_1^2}. \tag{32}$$

It is deduced from Eqs. (13) and (14) that

$$\phi_2(z) = \phi_3(z) = \frac{X(\Gamma_1 + \kappa_1)(R_1^2 + R_1^{-2}) + 2\overline{X}(\Gamma_1 - 1)}{R^2\Gamma_1(\kappa_2 + 1)(R_1^2 + R_1^{-2})} z^2, \tag{33}$$

which implies that the mean stress in S_2 and S_3 is not disturbed. Thus the elliptical inclusion is harmonic when the remote non-uniform loadings satisfy the two restrictions given by Eqs. (27) and (28). It seems that the discussion on harmonic elliptical inclusions under non-uniform loadings has not been recorded in the literature. Previously harmonic elliptical inclusions were found only for remote uniform stresses [2, 7, 8]; whereas only non-elliptical harmonic inclusions were found for non-uniform loadings [9, 10].

Results similar to those derived in this subsection can also be obtained from Eq. (18) by letting ρ=1, or by assuming that the materials comprising the inclusion and the interphase layer are identical ($\mu_1 = \mu_2$ and $\kappa_1 = \kappa_2$).

3.2. Extremely compliant interface layer ($\Gamma_1 >> 1$, $\Gamma_3 >> 1$ and $\rho \neq 1$)

In this case, Eq. (19) and (20) become

$$f(R_1,\rho) = -\frac{2\rho}{R_1^2} + \frac{\kappa_2(\rho+1) - 2R_1^2}{\rho R_1^2(\kappa_2 R_1^2 - 2) + \kappa_2 R_1^4}, \tag{34}$$

$$g(R_1,\rho) = -\frac{2\rho}{R_1^2} - \frac{\kappa_2(\rho+1) + 2R_1^2}{\rho R_1^2(\kappa_2 R_1^2 + 2) + \kappa_2 R_1^4}. \tag{35}$$

The above two equations together with Eq. (18) give us very simple formulas for determining the restrictions on the remote non-uniform loadings when the interphase layer is much more compliant than both the inclusion and the matrix.

3.3. Relatively rigid interphase layer ($\Gamma_1 << 1$, $\Gamma_3 << 1$ and $\rho \neq 1$)

In this case, Eqs. (19) and (20) become

$$f(R_1,\rho) = -\frac{2\rho}{R_1^2} - \frac{\kappa_3(\rho+1+2R_1^2)}{\rho R_1^2(R_1^2 + 2) + R_1^4}, \tag{36}$$

$$g(R_1,\rho) = -\frac{2\rho}{R_1^2} + \frac{\kappa_3(\rho+1-2R_1^2)}{\rho R_1^2(R_1^2 - 2) + R_1^4}. \tag{37}$$

The above two equations together with Eq. (18) also give us very simple formulas for determining the restrictions on the remote non-uniform loadings when the interphase layer is much stiffer than both the inclusion and the matrix.

3.4. A three-phase circular inclusion ($R_1 \to \infty$)

In this case, Eqs. (19) and (20) reduce to

$$R_1^2 f(R_1,\rho) = R_1^2 g(R_1,\rho) = -2\rho - \frac{2(1-\rho)(\Gamma_1+\kappa_1)(\Gamma_3+\kappa_3)}{\rho^2(1-\Gamma_3)(\Gamma_1\kappa_2 - \kappa_1) + (\Gamma_1+\kappa_1)(\Gamma_3\kappa_2 + 1)}. \tag{38}$$

4. Conclusions

Similar to the case of uniform loading [2], confocal elliptical interfaces are used in the present design to achieve an internal stress field of linear form under a linearly distributed stress field at

infinity. Two conditions given in Eq. (18) are derived that ensure that the internal field is a linear function of the two coordinates x and y. These two conditions can be considered as restrictions on the remote non-uniform stress field for given material and geometric parameters of the composite. The specific expressions of the two conditions, which are generally rather tedious, will become very concise for the four special cases: (i) the interphase and the matrix have the same elastic constants; (ii) the interphase layer is extremely compliant; (iii) the interphase layer is rather stiff; (iv) the three-phase inclusion is circular.

Acknowledgements

This work is supported by the National Natural Science Foundation of China (Grant No: 11272121), the Innovation Program of Shanghai Municipal Education Commission, China (Grant No: 12ZZ058), and the National Basic Research Program of China (Grant No. 2009CB623204).

References

[1] C.Q. Ru, Effect of interphase layers on thermal stresses within an elliptical inclusion. J Appl Phys, 84 (1998) 4872–4879.

[2] C.Q. Ru, Three-phase elliptical inclusions with internal uniform hydrostatic stresses. J Mech Phys Solids, 47 (1999) 259–273.

[3] J.C. Luo, C.F. Gao, Stress field of a coated arbitrary shaped inclusion. Meccanica, 46 (2011)1055–1071.

[4] X. Wang, X.L. Gao, On the uniform stress state inside an inclusion of arbitrary shape in a three-phase composite. Z Angew Math Phys, 62 (2011)1101–1116.

[5] X. Wang, P. Schiavone, Three-phase inclusions of arbitrary shape with internal uniform hydrostatic stresses in finite elasticity. ASME J Appl Mech, 79 (2012) art. no. 041012 (6 pages).

[6] N.I. Muskhelishvili, Some Basic Problems of the Mathematical Theory of Elasticity, Groningen, Noordhoff, 1953.

[7] G.S. Bjorkman, R. Richards, Harmonic holes–an inverse problem in elasticity. ASME J Appl Mech, 43 (1976) 414–418.

[8] L.T. Wheeler, The problem of minimizing stress concentrations at a rigid inclusion. ASME J Appl Mech, 52 (1985) 83–86.

[9] G.S. Bjorkman, R. Richards, Harmonic holes for nonconstant fields. ASME J Appl Mech, 46 (1979) 573–576.

[10] G.F. Wang, P. Schiavone, C.Q. Ru, Harmonic shapes in finite elasticity under nonuniform loading. ASME J Appl Mech, 72 (2005) 691–694.

Evaluation of Strength Recovery and Analysis of Damage Progression of Notched Unidirectional Carbon/Epoxy Composites Encompassing Self-Healing of Interfacial Debonding

Kazuaki Sanada[1,*], **Yuta Mizuno**[1], **Yasuhide Shindo**[2]

[1] Department of Mechanical Systems Engineering, Toyama Prefectural University, Toyama 939-0398, Japan
[2] Department of Materials Processing, Graduate School of Engineering, Tohoku University, Sendai 980-8597, Japan
* Corresponding author: sanada@pu-toyama.ac.jp

Abstract This study examines the interfacial debonding behavior of self-healing fiber reinforced polymers (FRPs) and the performance of repair of interfacial debonding. Self-healing is accomplished by incorporating a microencapsulated healing agent and a catalyst within a coating layer on the surface of the fiber strand. Single edge notched tensile (SENT) specimens of unidirectional FRPs with coated fiber strands were prepared and tested. The healing efficiency was evaluated by the critical fracture loads of virgin and healed specimens. To investigate the release of the healing agent from microcapsules during interfacial debonding, an ultra-violet (UV) fluorescent dye was added to the healing agent and post-fracture specimens were examined by an optical microscope under UV light. In addition to conducting experiments, finite element analyses were performed using a three-dimensional model to predict the damage progression in SENT specimens.

Keywords Interface mechanics, Composite materials, Notched tensile strength, Damage progression, Self-healing

1. Introduction

Interfacial debonding can cause a reduction in strength and stiffness of fiber-reinforced polymers (FRPs) and is extremely difficult to detect and repair by conventional methods. Thus, self-healing has the potential to mitigate the interfacial debonding. Although many studies have addressed the self-healing of internal damage in FRPs, there are few reports on the self-healing of interfacial debonding. Sanada et al. [1] proposed a methodology for self-healing of interfacial debonding in unidirectional FRPs by using fiber strands coated with the self-healing polymer developed by White et al. [2] and conducted transverse tensile tests to assess the self-healing efficiency. Also, Sanada et al. [3] investigated the effect of microstructure on the efficiency of transverse tensile strength recovery of self-healing FRPs. The maximum healing efficiency achieved with these specimens was about 20% and the low healing efficiency achieved was due to complete rupture of virgin specimens. Blaiszik et al. [4] performed a microbond test using a single fiber coated with DCPD-filled microcapsules and Grubbs catalyst, and assessed the recovery of interfacial shear strength.

The aim of this study is to investigate the interfacial debonding behavior of self-healing FRPs and to assess the performance of self-healing system for interfacial debonding. Tensile tests were carried out with single edge notched tensile (SENT) specimens of unidirectional FRPs containing fiber strands coated with DCPD-filled microcapsules and Grubbs catalyst, and healing efficiency was calculated using the critical fracture loads of virgin and healed specimens. Fluorescent labeling of damage in post-fracture specimens was performed to study the release of DCPD from microcapsules during interfacial debonding. Additionally, finite element analyses were employed to study the effect of specimen thickness and coating properties on the damage progression in SENT specimens.

2. Experimental procedures
2.1. Materials and specimen preparation

Self-healing FRP and reference FRP plates made of unidirectional carbon fiber-reinforced polymer were prepared. For self-healing FRP plates as shown in Fig. 1, Torayca T300B (Toray Industries, Inc.) carbon fiber strands were coated by manually dipping them into the Epikote 828 (Japan Epoxy Resins Co. Ltd)/Ancamine K54 (Air Products and Chemicals, Inc.) epoxy mixture containing 30wt% microcapsules and 2.5wt% Grubbs catalyst (Sigma-Aldrich Co.). Healing is triggered by crack propagation (interfacial debonding) through the microcapsules, which then release the healing agent into the crack plane. Subsequent exposure of the healing agent to the catalyst initiates polymerization and bonding of the crack faces. The number of filaments in the fiber strand was 6000. The healing agent used in this study was dicyclopentadiene (DCPD) monomer. DCPD was microencapsulated using the previously described procedure [1]. The microcapsules with mean diameter of around 300 μm were used. To aid inspection for the release of the healing agent from broken microcapsules, the microcapsules were also made from DCPD mixed with a UV fluorescent dye (Blenny Giken Ltd.). After coating, the coated fiber strands were held straight and cured for 24h at room temperature in order to obtain proper hardness. For reference FRP plates, coated carbon fiber strands without Grubbs catalyst were prepared using similar procedures.

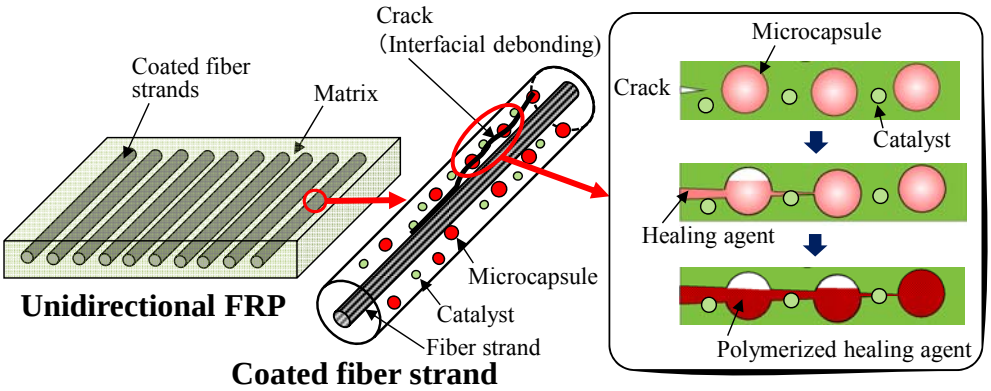

Figure 1 Self-healing system of interfacial debonding in unidirectional FRP

The semi-cured fiber strands were placed in a mold and impregnated with the Epikote 828/diethylenetriamine. The coated fiber strands were aligned parallel to the long direction. The mold was then closed and the samples were molded into the plate for 24h at room temperature, followed by 24h at 40 °C .

Once the plates were cured, they were machined using a water cooled diamond saw to produce SENT specimens as shown in Fig. 2. The SENT specimens had a nominal width W of 20mm, a nominal thickness t of 2 or 3mm, a gage length L of 40mm and an overall length of 70mm. A notch was cut using a diamond wafering saw and a sharp pre-crack was created by gently tapping a razor blade into the notch in the specimens. All specimens had an initial notch length to specimen width ratio a_0/W of approximately 0.25. Aluminum alloy gripping tabs (approximately 1mm thickness) were mounted to the specimens to prevent crushing due to the serrated rip faces. The specimens with t =2 and 3mm contained a fiber volume fraction of about 3.4 and 5.1%, respectively.

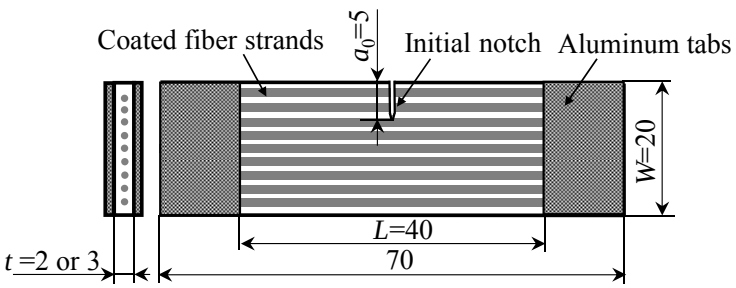

Figure 2 Specimen geometry (dimensions in mm)

2.2. Testing methods

The SENT specimens were tested using a tensile test machine in the displacement control at rate of 0.5mm/min. Load and crosshead displacement were recorded throughout the test. The self-healing FRP specimens were loaded until large load drops occurred, indicating damage progression. Before the specimens fractured completely, the specimens were unloaded and removed from the tensile test machine. Then, the specimens were clamped in a vise and allowed to heal for 10 days at room temperature. After healing, the specimens were tested again. For the reference FRP specimens, the specimens were immediately unloaded and reloaded to fracture after virgin tests, and the critical fracture load of the damaged specimen was evaluated. Healing efficiency η was defined as the ability of a healed specimen to recover critical fracture load

$$\eta = \frac{P_c^{\text{healed}} - P^{\text{residual}}}{P_c^{\text{virgin}} - P^{\text{residual}}} \tag{1}$$

where P_c^{virgin} is the critical fracture load of the virgin specimen, P_c^{healed} is the critical fracture load of the healed specimen and P^{residual} is the load value that was established at the end of the virgin test. To investigate the microstructure and damage behavior of the specimens, optical microscope observations were also performed.

2.3. Finite element analysis

The 3D finite element model was developed using ANSYS finite element code. A schematic diagram of the SENT specimen model is shown in Fig. 3. In this figure, R and h denote the radius of the fiber strand and the thickness of the coating layer, respectively. The geometric parameters of coated fiber strands as measured in the optical microscope were used. A rectangular Cartesian coordinate system (x_1, x_2, x_3) is used and x_1, x_2 and x_3 axes are assumed to lie along the longitudinal direction (fiber direction), transverse direction and thickness direction, respectively. Due to symmetry in both geometry and loading configurations, only one-quarter of the SENT specimens were modeled. Let the displacement and stress components be denoted by u_i^δ and σ_{ij}^δ $(i, j = 1,2,3, \delta = f, m, c)$, respectively. The subscripts 1, 2 and 3 are related to the three axes of the coordinate system and the superscripts f, m and c indicate the fiber strand, matrix and coating layer, respectively. The boundary conditions can be written as

$$\sigma_{11}^\delta(0, x_2, x_3) = 0 \quad (0 \le x_2 < a_0, 0 \le x_3 \le t/2) \tag{2}$$

$$u_1^\delta(0, x_2, x_3) = 0 \quad (a_0 \le x_2 \le W, 0 \le x_3 \le t/2) \tag{3}$$

$$\sigma_{12}^\delta(0, x_2, x_3) = 0 \quad (0 \le x_2 \le W, 0 \le x_3 \le t/2) \tag{4}$$

$$\sigma_{13}^{\delta}(0, x_2, x_3) = 0 \quad (0 \le x_2 \le W, 0 \le x_3 \le t/2) \tag{5}$$

$$u_1^{\delta}(L/2, x_2, x_3) = u_0 \quad (0 \le x_2 \le W, 0 \le x_3 \le t/2) \tag{6}$$

$$\sigma_{12}^{\delta}(L/2, x_2, x_3) = 0 \quad (0 \le x_2 \le W, 0 \le x_3 \le t/2) \tag{7}$$

$$\sigma_{13}^{\delta}(L/2, x_2, x_3) = 0 \quad (0 \le x_2 \le W, 0 \le x_3 \le t/2) \tag{8}$$

$$u_3^{\delta}(x_1, x_2, 0) = 0 \quad (0 \le x_1 \le L/2, 0 \le x_2 \le W) \tag{9}$$

$$\sigma_{23}^{\delta}(x_1, x_2, 0) = 0 \quad (0 \le x_1 \le L/2, 0 \le x_2 \le W) \tag{10}$$

$$\sigma_{13}^{\delta}(x_1, x_2, 0) = 0 \quad (0 \le x_1 \le L/2, 0 \le x_2 \le W) \tag{11}$$

$$(\delta = f, m, c)$$

where u_0 is the prescribed displacement in the direction of the loading axis. In addition to the symmetry conditions, one node was fixed in the x_2-direction to prevent rigid body motion.

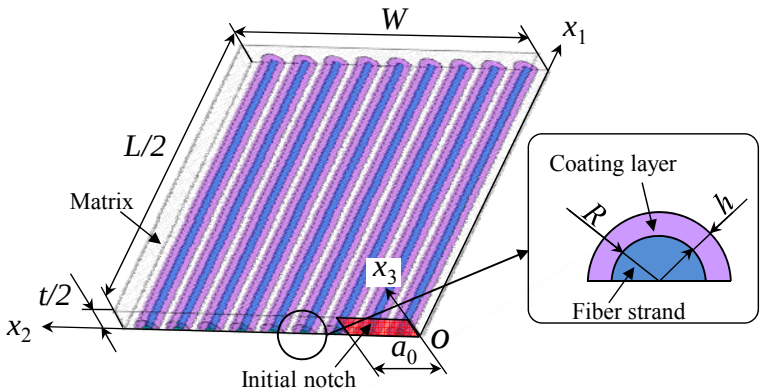

Figure 3 Finite element model of the SENT specimen

Under incrementally applied loading, stress analyses were carried out to identify the damage location according to a failure criterion. The von Mises criterion was selected as the criterion for microcracking of the matrix and the coating layer [5].

$$(\sigma_{22}^{\delta} - \sigma_{33}^{\delta})^2 + (\sigma_{33}^{\delta} - \sigma_{11}^{\delta})^2 + (\sigma_{11}^{\delta} - \sigma_{22}^{\delta})^2 + 6\{(\sigma_{23}^{\delta})^2 + (\sigma_{31}^{\delta})^2 + (\sigma_{12}^{\delta})^2\} \ge 2(\sigma_T^{\delta})^2 \quad (\delta = m, c) \tag{12}$$

where σ_T^{δ} is the tensile strength. The maximum stress criterion was also used to evaluate breaking of the fiber strand.

$$\sigma_{11}^{f} \ge \sigma_T^{f} \tag{13}$$

where σ_T^{f} is the tensile strength of fiber strand. Once the failure criterion is satisfied, all of the stiffness terms are reduced to 1×10^{-4} of the original value.

The epoxy matrix and coating layer are assumed to be elastic and isotropic. For the epoxy matrix, the Young's modulus and Poisson's ratio are taken to be 3.48GPa [6] and 0.35 [7], respectively, and the measured tensile strength is 70MPa. In previous work on this self-healing system [1], an investigation of tensile properties of epoxy specimens with the microcapsule and catalyst revealed that the Young's modulus and tensile strength of the specimen decreased with increasing the microcapsule concentration. Thus, the Young's modulus, Poisson's ratio and tensile strength of the coating layer are assumed to be 1.74GPa, 0.35 and 35MPa, respectively. The carbon fiber strand is modeled as an elastic and transversely isotropic composite (unidirectional carbon/epoxy composite) with properties as shown in Table 1 [8]. (E_1, E_2, E_3) are the Young's moduli, (G_{12}, G_{23}, G_{31}) are the shear moduli and (ν_{12}, ν_{23}, ν_{13}) are the Poisson's ratios, and the Poisson's ratio ν_{12} (ν_{23}, ν_{13})

reflects shrinkage (expansion) in the x_2 (x_3, x_3)-direction due to tensile (compressive) stress in the x_1 (x_2, x_1)-direction.

Table 1 Mechanical properties of the carbon fiber strand

Young's modulus (GPa)		Shear modulus (GPa)		Poisson's ratio		Tensile strength (MPa)
E_1	E_2, E_3	G_{12}, G_{31}	G_{23}	ν_{12}, ν_{13}	ν_{23}	σ_T^f
147	10.3	7.0	3.7	0.27	0.54	2280

3. Results and discussion

Fig. 4 shows typical virgin and damaged load-displacement curves for reference FRP specimens with t=2mm. It was found that the critical fracture load of the damaged specimen (P_c^{damaged}) was almost the same as the value of P_c^{residual}. Typical virgin and healed load-displacement curves for the self-healing FRP specimens with t=2mm are shown in Fig. 5. The slope is initially the same as the virgin test and this indicates that the damage has healed. The healing efficiency for the specimen with t=2mm shown in Fig. 5 is 45%. A healing efficiency of 98% was also achieved for the self-healing FRP specimen with t=3mm, but the healing probability for the specimen with t=3mm was slightly lower than that for the specimen with t=2mm (data not shown).

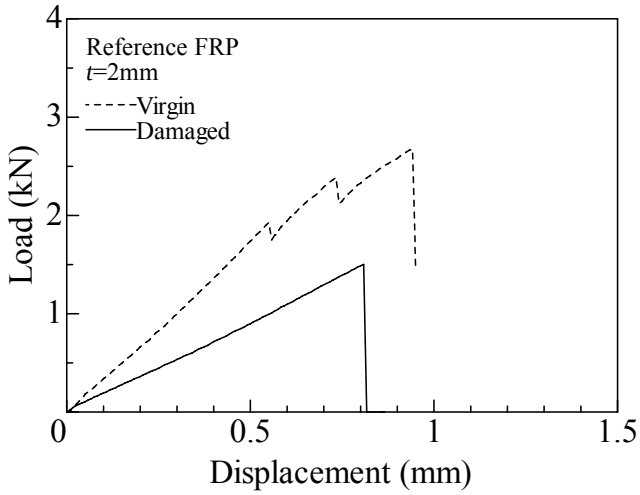

Figure 4 Measured load-displacement curves for reference FRP specimens with t=2mm

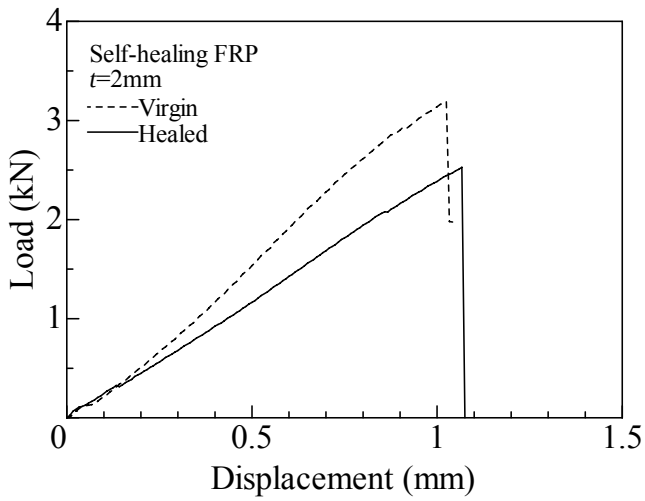

Figure 5 Measured load-displacement curves for self-healing FRP specimens with t=2mm

To investigate the damage progression behavior in the SENT specimen of the self-healing FRP, the finite element analysis coupled with damages was employed. In this analysis, the values of R=0.266mm and h=0.484mm were used. Fig. 6 shows the predicted damage progression in the SENT specimen with t=2mm at the applied displacement value of 0.4mm. The microcracking of the matrix initiated from the initial notch tip and propagated along the coated fiber strand. Moreover, the microcracking of the coating layer was followed by the microcracking of the matrix. This leads to the release of the healing agent from the microcapsules. The microcracking of the coating layer close to the fiber strand/coating layer interface also initiated and propagated, and could induce fiber strand/coating layer debonding. The corresponding result for the SENT specimen with t=3mm at applied displacement value of 0.5mm is shown in Fig. 7. The microcracking of the matrix initiated from the initial notch tip, and the microcracking of coating layer was followed by the

microcracking of the matrix. The microcracking of the matrix then propagated toward the edge of the specimen and induced final failure of the specimen. It is found that the prediction of the initiation and progression of the damage is in good agreement with experimental results.

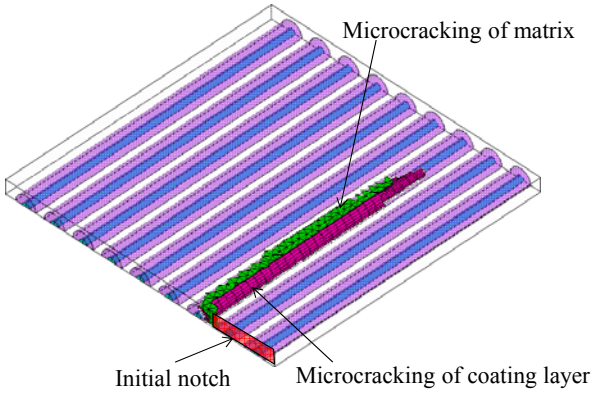

Figure 6 Predicted damage growth pattern in a SENT specimen with *t*=2mm at the applied displacement value of 0.4mm

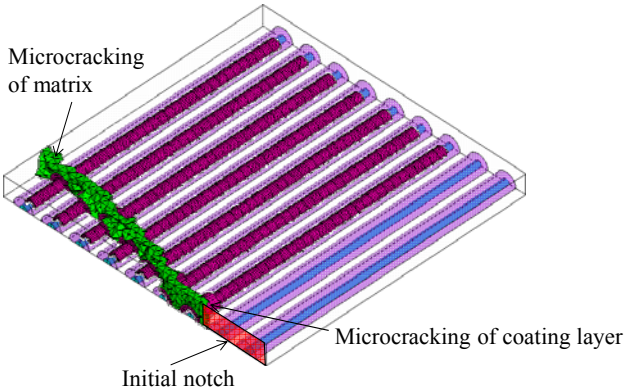

Figure 7 Predicted damage growth pattern in a SENT specimen with *t*=3mm at the applied displacement value of 0.5mm

In conclusion, we demonstrated that several SENT specimens of self-healing FRP exhibited damage progression along the coated fiber strands and achieved successful healing. Moreover, the numerical and experimental results showed similar trends.

References

[1] K. Sanada, I. Yasuda, Y. Shindo, Transverse tensile strength of unidirectional fibre-reinforced polymers and self-healing of interfacial debonding, Plast Rubber Compos, 35(2006)67-72.

[2] S.R. White, N.R. Sottos, P.H. Geubelle, J.S. Moore, M.R. Kessler, S.R. Sriram, E.N. Brown, S. Viswanathan, Autonomic healing of polymer composites, Nature, 409(2001)794-797.

[3] K. Sanada, N. Itaya, Y. Shindo, Self-healing of interfacial debonding in fiber-reinforced polymers and effect of microstructure on strength recovery, The Open Mech Engng J, 2(2008)97-103.

[4] B.J. Blaiszik, M. Baginska, S.R. White, N.R. Sottos, Autonomic recovery of fiber/matrix interfacial bond strength in a model composite, Adv Funct Mater, 20(2010)3547-3554.

[5] L.G. Zhao, N.A. Warrior, A.C. Long, Finite element modeling of damage progression in non-crimp fabric reinforced composites, Compos Sci Tech, 66(2006)36-50.

[6] K. Sanada, Y. Takada, S. Yamamoto, Y. Shindo, Analytical and experimental characterization of stiffness and damping in carbon nanocoil reinforced polymer composites, J Solid Mech Mater Engng, 2(2008)1517-1527.

[7] F.J.Guild, A.J. Kinloch, Predictive modeling of the mechanical properties of rubber-toughened epoxy, J Mater Sci Lett, 13(1994)629-632.

[8] I.M. Daniel, O. Ishai, Engineering Mechanics of Composite Materials, Oxford University Press, New York, 2006.

Anti-Plane Moving Polarization Saturation Crack in Ferroelectric Solids

Hao-sen Chen[2], Dai-ning Fang[1]

1 LTCS and College of Engineering, Peking University, Beijing, 100871, China
2Department of Engineering Mechanics, Tsinghua University, Beijing 100084, China
* Corresponding author: chenhs09@mails.tsinghua.edu.cn

Abstract
A moving polarization saturation (PS) model is proposed to study the anti-plane Yoffe-type crack with constant velocity in ferroelectric materials. Based on the extended Stroh formalism, the model is solved using complex function method. The closed-form expressions for the electroelastic fields are obtained in a concise way. Results are shown to converge to known solutions for static PS model and the moving linear piezoelectric model.
Keywords Moving polarization saturation model; Ferroelectric materials; anti-plane.

1 Introduction

Ferroelectric materials always endure dynamic loads, such as mechanical impact or pulse-like electric loading in application [1]. Since their instinct low fracture toughness, the reliability concerns and optimal design of smart devices using ferroelectrics call for a better understanding of the fracture behavior. Compared with the well developed static piezoelectric fracture mechanics, few investigations on the dynamic fracture mechanics of piezoelectric and ferroelectric materials have been reported.

The crack propagation problem is always the popular point of study among the theoretical dynamic fracture mechanics. Freund [2] classified the problems of crack propagation into three classes (1) The first type is the steady state crack growth. Chen and Yu [3] studied the anti-plane moving crack problem in piezoelectric materials. They found that the intensity factors are independent of the velocity of the crack. Soh et al. [4] researched the generalized plane problem of a finite Griffith crack moving with constant velocity in an anisotropic piezoelectric material. (2) The second type is self-similar crack growth. (3) The third type is the crack growth due to time-independent or time-dependent loading. In this case, Li and Mataga [5, 6] obtained the transient closed-form solutions for dynamic stress and electric displacement intensities and dynamic energy release rate of a propagating crack in homogeneous hexagonal piezoelectric materials dynamic anti-plane point loading. To et al. [7] studied propagation of a mode-III interfacial conductive crack along a conductive interface between two piezoelectric materials. Chen et al. [8] researched the problem of dynamic interfacial crack propagation in elastic–piezoelectric bi-materials subjected to uniformly distributed dynamic anti-plane loadings on crack faces.

All the aforementioned studies on the problems of crack propagation are mainly about the linear dynamic fracture mechanics. However, when the electrical load is not weak, ferroelectric materials exhibit strong electrical nonlinearity, Gao et al. [9] proposed a strip polar saturation (PS) model of electrical yielding. It is convenient to propose some simplified models or approximate analyses. Shen et al. [10] developed a strip electric saturation and mechanical yielding model for a mode III interfacial crack of Yoffe type between ferroelectric-plastic bi-materials.

In this paper, the static PS model is extended to the moving PS model for studying the anti-plane crack propagation problem of ferroelectric materials. The plan of the rest of the paper is

as follows. Section 2 introduces the governing equations and the boundary conditions. Section 3 proposes the moving PS model and solves the problem using the complex function method. And the explicit expressions of the electroelastic fields are obtained. Section 4 discusses the anti-plane case. Finally, Section 5 gives the conclusions.

2 Statement of the problem

Consider an infinite ferroelectric medium containing a Yoffe-type crack of fixed length 2*a*,which moves through an otherwise unbounded ferroelectric materials at speed *v*, with the crack opening at the leading crack tip and closing at the trailing crack speed. The ferroelectric solids are considered as a class of mechanically brittle and electrically ductile solids. The electrical polarization is assumed to be saturated only in a line segment in front of the crack. And the medium is subjected to remote uniform electro-mechanical loads as shown in Fig.1.

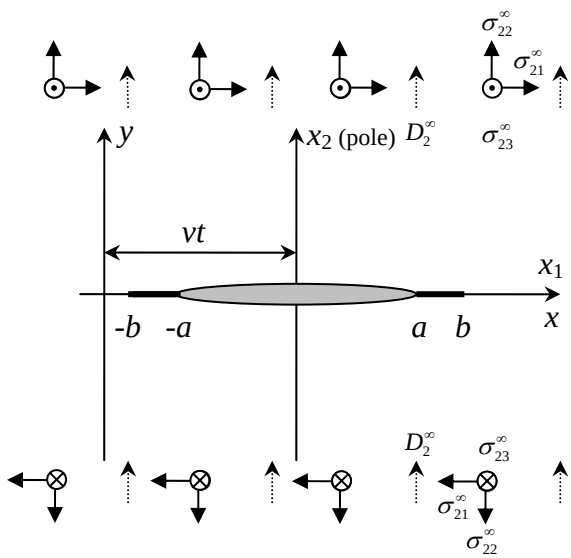

Fig.1. Schematic representation of the moving PS model

2.1 Basic equations

Our earlier work [4] has proposed the governing equations of the piezoelectric material and given the solutions using the Stroh formalism method in details. For the reason of a self-contained presentation, the basic equations and the solution method are also summarized as follows.

In a rectangular coordinate system x_i (i =1, 2, 3), the momentum balance equations and quasi static Maxwell equation for quasi-electrostatic piezoelectricity are as follows

$$\sigma_{ij,j} = \rho\, \partial^2 u_i / \partial t^2 , \quad D_{i,i} = 0 \tag{1}$$

where ρ is the density of the material, u_i, σ_{ij} and D_i are the elastic displacements, stresses, and electric displacements, respectively, and a subscript comma denotes partial differentiation with respect to one of the coordinates x_i. The constitutive relations are

$$\sigma_{ij} = c_{ijkl} u_{k,l} + e_{ijk}\phi_{,k} , D_i = e_{ikl} u_{k,l} - \varepsilon_{ik}\phi_{,k} \tag{2}$$

where ϕ is the electric potential, the electric fields E_i are related to ϕ as $E_i = -\phi_{,i}$, c_{ijkl}, e_{kij} and ε_{ij} are the elastic stiffness, piezoelectric and dielectric constants, respectively.

For a two-dimensional problem, all the variables are independent of x_3, Eqs. (1) and (2) can be expressed in the following compact form:

$$\boldsymbol{t}_{1,1} + \boldsymbol{t}_{2,2} = \rho \boldsymbol{g} \ddot{\boldsymbol{U}} \tag{3}$$

$$\boldsymbol{t}_1 = \boldsymbol{Q}\boldsymbol{U}_{,1} + \boldsymbol{R}\boldsymbol{U}_{,2}, \quad \boldsymbol{t}_2 = \boldsymbol{R}^{\mathrm{T}}\boldsymbol{U}_{,1} + \boldsymbol{T}\boldsymbol{U}_{,2} \tag{4}$$

where $\boldsymbol{U} = [u_1, u_2, u_3, \phi]^{\mathrm{T}}$, $\boldsymbol{t}_\beta = [\sigma_{\beta 1}, \sigma_{\beta 2}, \sigma_{\beta 3}, D_\beta]^{\mathrm{T}}$ (β =1,2), and $\boldsymbol{g} = \mathrm{diag}[1,\ 1,\ 1,\ 0]$. The matrices $\boldsymbol{Q}$, $\boldsymbol{R}$ and $\boldsymbol{T}$ are related to the material constants by

$$\boldsymbol{Q} = \begin{bmatrix} c_{i1k1} & e_{1i1} \\ e_{1k1}^{\mathrm{T}} & -\varepsilon_{11} \end{bmatrix}, \quad \boldsymbol{R} = \begin{bmatrix} c_{i1k2} & e_{1i2} \\ e_{2k1}^{\mathrm{T}} & -\varepsilon_{12} \end{bmatrix}, \quad \boldsymbol{T} = \begin{bmatrix} c_{i2k2} & e_{2i2} \\ e_{2k2}^{\mathrm{T}} & -\varepsilon_{22} \end{bmatrix} \tag{5}$$

Substituting Eq. (4) into Eq. (3) leads to

$$\boldsymbol{Q}\boldsymbol{U}_{,11} + \left(\boldsymbol{R} + \boldsymbol{R}^{\mathrm{T}}\right)\boldsymbol{U}_{,12} + \boldsymbol{T}\boldsymbol{U}_{,22} = \rho \boldsymbol{g} \partial^2 \boldsymbol{U} / \partial t^2 \tag{6}$$

2.2 Yoffe-type crack

As shown in Fig.1. (x, y, z) is a moving coordinate system fixed on the crack with the center as its origin. It has the relation with the fixed coordinate system (x_1, x_2, x_3) as follows

$$x = x_1 - vt, \quad y = x_2, \quad z = x_3 \tag{7}$$

Then

$$\frac{\partial}{\partial t} = -v \frac{\partial}{\partial x} \tag{8}$$

Thus, Eq. (6) can be written as

$$\left(\boldsymbol{Q} - \rho v^2 \boldsymbol{g}\right)\boldsymbol{U}_{,xx} + \left(\boldsymbol{R} + \boldsymbol{R}^{\mathrm{T}}\right)\boldsymbol{U}_{,xy} + \boldsymbol{T}\boldsymbol{U}_{,yy} = \boldsymbol{0} \tag{9}$$

Eq. (9) is the governing differential equation for the steady-state electroelastic fields. Note that the structure is identical to that of the static case when ($\boldsymbol{Q} - \rho v^2 \boldsymbol{g}$) is identified with $\boldsymbol{Q}$.

2.3 Boundary conditions

The medium is subjected to remote uniform electro-mechanical loads given by $\boldsymbol{t}_2^\infty = [\sigma_{21}^\infty, \sigma_{22}^\infty, \sigma_{23}^\infty, D_2^\infty]^{\mathrm{T}}$. The crack surfaces are traction-free and charge-free, with electrical yielding along strip $a \leqslant |x| \leqslant b$.

The full set of boundary conditions for the moving PS model considered in this paper can be summarized as

$$\boldsymbol{t}^+ = \boldsymbol{t}^- = -\boldsymbol{t}_2^\infty, \qquad \text{at} \quad |x| < a \tag{10a}$$

$$u_i^+ = u_i^-,\ i=1,\ 2,\ 3,\ \ D_2^+ = D_2^- = -D_2^\infty + D_s, \qquad \text{at} \quad a \le |x| \le b \tag{10b}$$

$$\boldsymbol{t} = 0 \qquad \text{at} \quad y \to \infty \tag{10c}$$

where D_s is the electrical saturation limit.

3 Solution of the problem

3.1 Full field solution

Adopting Stroh formalism for anisotropic elasticity, a general solution to Eq. (9) can be sought in the form

$$\boldsymbol{U} = \boldsymbol{a} f\left(z\right), \quad z = x + \mu y \tag{11}$$

where μ and $\boldsymbol{a}$ are a constant and a constant vector respectively; and $f(z)$ is an arbitrary function of variable z subject to the twice-differentiable requirement. Substitution of Eq. (11) into Eq. (9) results in

$$\left[\mathbf{Q} - \rho v^2 \mathbf{g} + \mu\left(\mathbf{R} + \mathbf{R}^{\mathrm{T}}\right) + \mu^2 \mathbf{T}\right]\boldsymbol{a} = 0 \tag{12}$$

This is a nonlinear eigenvalue problem. A nontrivial solution of $\boldsymbol{a}$ requires that the determinant of its coefficient matrix must be zero, i.e.,

$$\det\left[\mathbf{Q} - \rho v^2 \mathbf{g} + \mu\left(\mathbf{R} + \mathbf{R}^{\mathrm{T}}\right) + \mu^2 \mathbf{T}\right] = 0 \tag{13}$$

This is a polynomial of degree 8 for μ. If μ_α (α = 1, 2, 3, 4) are assumed to be the four distinct roots with positive imaginary parts, and $\boldsymbol{a}_\alpha$ are the associated eigenvectors, the general solution can then be expressed as

$$\boldsymbol{U} = 2\Re\sum_{\alpha=1}^{4} \boldsymbol{a}_\alpha f_\alpha\left(z_\alpha\right) \tag{14}$$

where $\Re$ denotes the real part and $z_\alpha = x + \mu_\alpha y$.

Substituting Eq. (14) into Eq. (4) and by using Eq. (3), the stress and electric displacement vectors can be expressed as

$$\boldsymbol{t}_1 = -\boldsymbol{\Phi}_{,y} + \rho v^2 \boldsymbol{g} \boldsymbol{U}_{,x}, \quad \boldsymbol{t}_2 = \boldsymbol{\Phi}_{,x} \tag{15}$$

in which

$$\boldsymbol{\Phi} = 2\Re\sum_{\alpha=1}^{4} \boldsymbol{b}_\alpha f_\alpha\left(z_\alpha\right) \tag{16}$$

where $\boldsymbol{\Phi} = [\phi_1, \phi_2, \phi_3, \phi_4]^{\mathrm{T}}$ is called the generalized stress function vector, and $\boldsymbol{b}_\alpha$ can be determined from $\boldsymbol{a}_\alpha$ by the following relation:

$$\boldsymbol{b}_\alpha = \left(\boldsymbol{R}^{\mathrm{T}} + \mu_\alpha \boldsymbol{T}\right)\boldsymbol{a}_\alpha = -\left[\left(\boldsymbol{Q} - \rho v^2 \boldsymbol{g}\right)\mu_\alpha^{-1} + \boldsymbol{R}\right]\boldsymbol{a}_\alpha \tag{17}$$

Introducing two 4×4 matrices, i.e.,

$$\boldsymbol{A} = \left[\boldsymbol{a}_1, \boldsymbol{a}_2, \boldsymbol{a}_3, \boldsymbol{a}_4\right], \quad \boldsymbol{B} = \left[\boldsymbol{b}_1, \boldsymbol{b}_2, \boldsymbol{b}_3, \boldsymbol{b}_4\right] \tag{18}$$

and a function vector, i.e.,

$$\boldsymbol{f}(z_\alpha)=\left[f_1(z_1),\, f_2(z_2),\, f_3(z_3),\, f_4(z_4)\right]^{\mathrm{T}} \tag{19}$$

Then Eqs. (14) and (16) can be rewritten as

$$\boldsymbol{U}=2\Re\left[\boldsymbol{A}\boldsymbol{f}\left(z_\alpha\right)\right],\quad \boldsymbol{\Phi}=2\Re\left[\boldsymbol{B}\boldsymbol{f}\left(z_\alpha\right)\right] \tag{20}$$

Eqs. (15) and (20) together with the relations given by Eq. (17) are the main results of this section. In these expressions, the only unknown is the function vector $\boldsymbol{f}(z_\alpha)$. The appropriate form of $\boldsymbol{f}(z_\alpha)$ depends on the boundary conditions.

In order to obtain the function vector $\boldsymbol{f}(z_\alpha)$, following the same procedure [11, 12], the continuity of $\boldsymbol{t}$(x) on the whole real axis is

$$\boldsymbol{B}\boldsymbol{f}^{'+}(x)+\overline{\boldsymbol{B}}\,\overline{\boldsymbol{f}}^{'-}(x)=\boldsymbol{B}\boldsymbol{f}^{'-}(x)+\overline{\boldsymbol{B}}\,\overline{\boldsymbol{f}}^{'+}(x),\qquad -\infty<x<+\infty \tag{21}$$

A new complex function vector $\boldsymbol{h}(z)$ is defined as

$$\boldsymbol{h}(z)=\boldsymbol{B}\boldsymbol{f}^{'}(z)=\overline{\boldsymbol{B}}\,\overline{\boldsymbol{f}}^{'}(z) \tag{22}$$

And it should satisfy the boundary conditions (10) along the crack faces

$$\boldsymbol{h}^{+}(x)+\boldsymbol{h}^{-}(x)=-\boldsymbol{t}_2^{\infty},\quad |x|<a \tag{23}$$

We also have

$$i\boldsymbol{\delta}^{'}(x)=\boldsymbol{H}\boldsymbol{B}\boldsymbol{f}^{'+}(x)-\boldsymbol{H}\boldsymbol{B}\boldsymbol{f}^{'-}(x) \tag{24}$$

where $\boldsymbol{\delta}^{'}(x)=\{u_1^{+}-u_1^{-},u_2^{+}-u_2^{-},u_3^{+}-u_3^{-},\phi^{+}-\phi^{-}\}$ is the generalized opening displacement, In addition, other two matrices are defined by

$$\boldsymbol{H}=2\Re[i\boldsymbol{A}\boldsymbol{B}^{-1}],\quad \boldsymbol{H}^{-1}=\boldsymbol{\Lambda} \tag{25}$$

Introduce a new complex function vector

$$\boldsymbol{g}(z)=\boldsymbol{H}\boldsymbol{B}\boldsymbol{f}^{'}(z) \tag{26a}$$

$$\boldsymbol{f}^{'}(z)=\boldsymbol{B}^{-1}\boldsymbol{H}^{-1}\boldsymbol{g}(z) \tag{26b}$$

And the next task is to determine the unknown complex function vector $\boldsymbol{g}(z)$. The $g_1(z)$, $g_2(z)$ and $g_3(z)$ are holomorphic functions in whole z plane with a cut ($-a$, a). $g_4(z)$ is holomorphic in whole z plane with a cut ($-c$, c).

Thus, using the Eqs. (23) and (10), we have the following equations

$$\Lambda_{1j}(g_j^{+}(x)+g_j^{-}(x))+\Lambda_{44}(g_4^{+}(x)+g_4^{-}(x))=-\sigma_{21}^{\infty},\qquad |x|<a \tag{27a}$$

$$\Lambda_{2j}(g_j^{+}(x)+g_j^{-}(x))+\Lambda_{44}(g_4^{+}(x)+g_4^{-}(x))=-\sigma_{22}^{\infty},\qquad |x|<a \tag{27b}$$

$$\Lambda_{3j}(g_j^{+}(x)+g_j^{-}(x))+\Lambda_{44}(g_4^{+}(x)+g_4^{-}(x))=-\sigma_{23}^{\infty},\qquad |x|<a \tag{27c}$$

$$\Lambda_{4j}(g_j^{+}(x)+g_j^{-}(x))+\Lambda_{44}(g_4^{+}(x)+g_4^{-}(x))=-D_2^{\infty},\qquad |x|<a \tag{27d}$$

$$\Lambda_{4j}(g_j^+(x)+g_j^-(x))+\Lambda_{44}(g_4^+(x)+g_4^-(x))=-D_2^\infty+D_s,\quad a\le|x|\le b \tag{27e}$$

where the Einstein summation convention for repeated indices is adopted, and j ranges from 1 to 3.

Solving the Eqs. (27a), (27b), (27c) and (27d) gives the following equation

$$\Lambda_{ij}^*(g_j^+(x)+g_j^-(x))=-t_{2i}^{\infty *},\quad |x|<a \tag{28}$$

where $\Lambda_{mj}^*=\Lambda_{mj}-\Lambda_{m4}\Lambda_{4j}/\Lambda_{44}$, $t_{2j}^{\infty *}=t_{2j}^\infty-t_{24}^\infty\Lambda_{j4}/\Lambda_{44}$, m, j=1, 2, 3.

Thus, we can obtain [12]

$$\Lambda^*\boldsymbol{g}^*(z)=\boldsymbol{t}_2^{\infty *}f_0'(z),\quad \boldsymbol{g}^*(z)=(\Lambda^*)^{-1}\boldsymbol{t}_2^{\infty *}f_0'(z),\qquad |x|<a \tag{29}$$

where

$$\boldsymbol{\Lambda}^*=[\Lambda_{mj}^*]_{3\times 3} \tag{30a}$$

$$\boldsymbol{g}^*=[g_1(z),g_2(z),g_3(z)]^T \tag{30b}$$

$$\boldsymbol{t}_2^{\infty *}=[t_{21}^{\infty *},t_{22}^{\infty *},t_{23}^{\infty *}]^T \tag{30c}$$

$$f_0'(z)=\frac{1}{2}\left(\frac{z}{\sqrt{z^2-a^2}}-1\right) \tag{30d}$$

Solving Eqs. (27d) and (27e), we have

$$g_4(z)=\{-\Lambda_{4j}g_j(z)+t_{24}^\infty f_b'(z)\}/\Lambda_{44}+D_s g_0(z)/\Lambda_{44} \tag{31}$$

where $g_0(z)$ has the same property as the function $g_4(z)$, which is holomorphic in whole z plane with a cut ($-c$, c).

$$f_b'(z)=\frac{1}{2}\left(\frac{z}{\sqrt{z^2-b^2}}-1\right) \tag{32a}$$

$$g_0(z)=\frac{1}{\pi}\left\{\frac{\pi}{2}-\frac{1}{2i}\log\frac{\frac{z}{a}\frac{\sqrt{b^2-a^2}}{\sqrt{z^2-b^2}}+i}{\frac{z}{a}\frac{\sqrt{b^2-a^2}}{\sqrt{z^2-b^2}}-i}-\frac{z}{\sqrt{z^2-b^2}}\arccos\left(\frac{a}{b}\right)\right\} \tag{32b}$$

Furthermore, $g_0(z)$ has the following property on the crack faces

$$g_0^+(x)+g_0^-(x)=0,\quad |x|<a \tag{33a}$$

$$g_0^+(x)+g_0^-(x)=1,\quad a\le|x|\le b \tag{33b}$$

Wang [12] gave the method to calculate the function $\log\frac{z+i}{z-i}$.

$$\log\frac{z+i}{z-i}=\log\frac{r_2}{r_1}+i(\theta_2-\theta_1) \tag{34}$$

where r_1 and r_2 are the modulus of the complex variables $z+i$ and $z-i$ respectively. θ_1 and θ_2 are the inclined angles of the complex variables $z+i$ and $z-i$ with respect to the negative imaginary axis. From Eqs. (29) and (31), the unknown complex function vector $\boldsymbol{g}(z)$ has been obtained. Then substituting the result into Eq.(26b), we can derive the unknown function vector $\boldsymbol{f}'(z)$, which provides the full-field solutions of the problem using Eq. (15).

3.2 Electric saturation zone size

From Eq. (15), we obtain the electric displacement ahead of the crack tip

$$\begin{aligned} D_2 &= \Lambda_{4j}(g_j^+(x)+g_j^-(x))+\Lambda_{44}(g_4^+(x)+g_4^-(x)) \\ &= 2T_4 f_b'(x)+D_s(g_0^+(x)+g_0^-(x)) \\ &= (D_2^\infty-\frac{2}{\pi}D_s\arccos(\frac{a}{b}))\frac{x}{\sqrt{x^2-b^2}}-D_2^\infty+D_s\frac{2}{\pi}\left\{\frac{\pi}{2}-\frac{1}{2i}\log\frac{\frac{x}{a}\frac{\sqrt{b^2-a^2}}{\sqrt{x^2-b^2}}+i}{\frac{x}{a}\frac{\sqrt{b^2-a^2}}{\sqrt{x^2-b^2}}-i}\right\} \end{aligned} \tag{35}$$

In order to ensure the non-singularity of the electric displacement at $|x|=b$, Eq. (35) only has a solution if the coefficient of the singular term $\frac{x}{\sqrt{x^2-b^2}}$ vanishes. The following equations must be satisfied

$$\frac{a}{b}=\cos(\frac{\pi}{2}\frac{D_2^\infty}{D_s}) \tag{36}$$

From the above equation, we can calculate the size of the electric saturation zone

$$r=b-a=a\sec(\frac{\pi}{2}\frac{D_2^\infty}{D_s})-a \tag{37}$$

Under small-scale yielding conditions, r<<a, Eq. (37) can be approximately reduced to $r=\frac{a}{2}(\frac{\pi}{2}\frac{D_2^\infty}{D_s})^2$.

3.3 Electroelastic fields near the crack tip

From Eqs. (15) and (20), the stresses and electric displacements can be obtained

$$\boldsymbol{t}_1 = 2\Re\left[\sum_{\alpha=1}^{4}(\rho v^2 \boldsymbol{g}_\alpha \boldsymbol{a}_\alpha f_\alpha^{'}(z_\alpha) - \mu_\alpha \boldsymbol{b}_\alpha f_\alpha^{'}(z_\alpha))\right] \tag{38}$$

$$\boldsymbol{t}_2 = 2\Re\left[\sum_{\alpha=1}^{4}\boldsymbol{b}_\alpha f_\alpha^{'}(z_\alpha)\right] \tag{39}$$

It is obvious that the distributions of the electroelastic fields near the crack tip are of great interest to us. By introducing a polar coordinate system (r, θ) with the origin at the crack right tip, we have

$$z_\alpha - a = r\left(\cos\theta + \mu_\alpha \sin\theta\right) \tag{40}$$

When r is small compared to the half-length a of the crack, $z_\alpha \approx a$. Eqs. (30d), (32d) and (34b) can be expressed as

$$f_0^{'}(z_\alpha) = \frac{1}{2}(\sqrt{\frac{a}{2r}}\frac{1}{\sqrt{\cos\theta + \mu_\alpha \sin\theta}} - 1) \tag{41a}$$

$$f_b^{'}(z) = \frac{1}{2}(\frac{1}{i}\frac{a}{\sqrt{b^2 - a^2}} - 1) \tag{41b}$$

$$\log\frac{z+i}{z-i} = i(\pi - 2\tan^{-1} a) \tag{41c}$$

From Eq. (39), the stress in front of the crack tip on the x-axis is calculated

$$\sigma_{2j} = t_{2j}^{\infty *}\frac{x}{\sqrt{x^2 - a^2}} + D_s\frac{\Lambda_{j4}}{\Lambda_{44}} \quad j=1,\ 2,\ 3 \tag{42}$$

By using the definition of dynamic intensity factor vector

$$\boldsymbol{K} = [K_{\mathrm{II}}, K_{\mathrm{I}}, K_{\mathrm{III}}, K_D]^T = \lim_{x\to a}\sqrt{2\pi(x-a)}\boldsymbol{t}_2 \tag{43}$$

4 Crack perpendicular to the poling axis, anti-plane problem

In this situation, the infinite plate only subjects to σ_{23}^{∞} and D_2^{∞} . The present authors have studied the anti-plane moving PS model using the continuous distribution dislocation method. In this article, some results will be verified using the complex function method.

From Eq. (**A**.13), we obtain

$$\boldsymbol{K} = [K_{\mathrm{III}}, K_D]^T = \sqrt{\pi a}[\sigma_{23}^{\infty} + \frac{e_{15}}{\varepsilon_{11}}D_2^{\infty}, 0]^T \tag{44}$$

where K_{III} is independent of the crack propagation velocity.

From Eqs. (15), (16) and (A.13), we have

$$\begin{aligned}\sigma_{23} &= \sqrt{\frac{a}{2r}}\Re\left[(\sigma_{23}^{\infty}+\frac{e_{15}}{\varepsilon_{11}}D_2^{\infty})(\cos\theta+\mu_1\sin\theta)^{-\frac{1}{2}}\right] \\ &= \sqrt{\frac{a}{2r}}(\sigma_{23}^{\infty}+\frac{e_{15}}{\varepsilon_{11}}D_2^{\infty})\cos\frac{\theta}{2}\end{aligned} \tag{45}$$

If the ferroelectric material is such that a crack propagates in a direction the maximum shear stress, it can be seen that the maximum shear stress σ_{23} occurs at $\theta=0$ for all the crack speeds. It means the crack remains in its straight line path for all the crack speeds.

5 Conclusions

The transient response of a anti-plane Yoffe-type crack moving with constant velocity in ferroelectric materials is investigated in this paper. The dynamic intensity factors of stress, electric displacement are obtained in explicit forms. When the velocity of the crack $v\to 0$, the moving PS model will reduce to the static PS model. When the size of the electric saturation zone $r\to 0$, the moving PS model is in agreement with the moving linear piezoelectric model. For the case of anti-plane problem, it is concluded that the crack remains in its straight line path for all the crack speeds.

Acknowledgements

The authors are grateful for the support by National Natural Science Foundation of China under Grants #11090330, #11090331, #11072003 and #G2010CB832701.

Appendix

The matrices ***Q***, ***R*** and ***T*** are

$$\boldsymbol{Q}=\begin{bmatrix} c_{44} & e_{15} \\ e_{15} & -\varepsilon_{11}\end{bmatrix},\ \boldsymbol{R}=\begin{bmatrix} 0 & 0 \\ 0 & 0\end{bmatrix},\quad \boldsymbol{T}=\begin{bmatrix} c_{44} & e_{15} \\ e_{15} & -\varepsilon_{11}\end{bmatrix} \tag{A.1}$$

The eigenproblem given by Eq. (12) becomes

$$\begin{bmatrix} c_{44}-\rho v^2+c_{44}\mu^2 & e_{15}(1+\mu^2) \\ e_{15}(1+\mu^2) & -\varepsilon_{11}(1+\mu^2)\end{bmatrix}\begin{bmatrix} a_1 \\ a_2\end{bmatrix}=0 \tag{A.2}$$

Similar to the static case, two characteristic roots are μ_1=i, . μ_2=i β.
in which

$$\beta=(1-v^2/c^2)^{1/2} \tag{A.3}$$

where $c=(\bar{c}_{44}/\rho)^{1/2}$ is the speed of the piezoelectric stiffened bulk shear wave, $\bar{c}_{44}=c_{44}+e_{15}^2/\varepsilon_{11}$ is the piezoelectric stiffened elastic constant.

The matrix ***H*** is then

$$\boldsymbol{H}=\frac{2}{\beta\bar{c}_{44}\varepsilon_{11}}\begin{bmatrix}\varepsilon_{11} & e_{15}\\ e_{15} & \dfrac{e_{15}^2}{\varepsilon_{11}}-\beta\bar{c}_{44}\end{bmatrix},\qquad \boldsymbol{\Lambda}=\boldsymbol{H}^{-1}=\frac{1}{2}\begin{bmatrix}\beta\bar{c}_{44}-\dfrac{e_{15}^2}{\varepsilon_{11}} & e_{15}\\ e_{15} & -\varepsilon_{11}\end{bmatrix} \tag{A.4}$$

As $\beta\to 1$ i.e. v=0, $\boldsymbol{H}$ will reduce to the static value [12].

References

[1] Kuna, M., Fracture mechanics of piezoelectric materials—Where are we right now? Eng. Fract. Mech. 77 (2010) 309–326.
[2] Freund, L.B.. Dynamic fracture mechanics. Cambridge: Cambridge Press, 1990.
[3] Chen, Z.T., Yu, S.W., Anti-plane Yoffe crack problem in piezoelectric materials. Int. J. Fracture. 84 (1997) L41-L45.
[4] Soh, A.K., Liu, J.X., Lee, K.L., Fang D.N., On a moving Griffith crack in anisotropic piezoelectric solids. Arch. Appl. Mech. 72 (2002) 458–469.
[5] Li, S., Mataga, P.A., Dynamic crack propagation in piezoelectric materials-part I. Electrode solution. J. Mech. Phys. Solids. 44 (1996a) 1799–1830.
[6] Li, S., Mataga, P.A., Dynamic crack propagation in piezoelectric materials-part II. Vacuum solution. J. Mech. Phys. Solids 44 (1996b) 1831–1866.
[7] To, A.C., Li, S., Glaser, S.D., Propagation of a mode-III interfacial conductive crack along a conductive interface between two piezoelectric materials. Wave Motion. 43 (2006) 368–386.
[8] Chen, X.H., Ma, C.C., Ing, Y.S., Tsai, C.H., Dynamic interfacial crack propagation in elastic–piezoelectric bi-materials subjected to uniformly distributed loading. Int. J. Solids. Struct. 45 (2008) 959–997.
[9] Gao, H., Zhang,T.Y. , Tong,P., Local and global energy release rates for an electrically yielded crack in a piezoelectric ceramic. J. Mech. Phys. Solids. 45 (1997) 491–510.
[10] Shen, S.P., Kuang, Z.B., Nishioka, T., Dynamic mode-III interfacial crack in ferroelectric materials. Int.J.Appl. Electrom. 11 (2000) 211–222.
[11] Suo, Z., Kuo C. M., Barnett, D. M., Willis, J. R., Fracture mechanics for piezoelectric ceramics. J .Mech. Phys. Solids. 40 (1992) 739-765.
[12] Wang, T.C., Analysis of strip electric saturation model of crack problem in piezoelectric materials. Int. J. Solids. Struct. 37 (2000) 6031–6049.
[13] Zhang, T.Y., Gao, C.F., Fracture behaviors of piezoelectric materials. Theor. Appl. Fract. Mec. 41 (2004) 339–379.

Fracture Criteria for Piezoelectric Ceramics

Leslie Banks-Sills

School of Mechanical Engineering, Tel Aviv University, Ramat Aviv, 69978, Israel
Division of Solid Mechanics, Lund University, Lund SE-221 00, Sweden
banks@eng.tau.ac.il

Abstract An analytical, numerical and experimental investigation was carried out to determine fracture criteria for piezoceramics with poling parallel and perpendicular to the crack faces. The asymptotic expressions of stress, strain, electric flux density and electric fields were derived. For a piezoelectric material, in addition to the usual three modes of fracture, there is a fourth mode associated with the electric field. The asymptotic expressions were used for determining the energy release rate and extending a conservative interaction energy or *M*-integral for calculating the intensity factors associated with piezoelectric material for energetically consistent boundary conditions on the crack faces. Tests were performed on four-point bend PZT-5H fracture specimens with the poling direction parallel to the crack faces. The specimens were analyzed numerically by means of the finite element method. Finally, a mixed mode fracture criterion for piezoelectric ceramics was developed. This criterion is based upon the energy release rate and two phase angles, determined from the ratio between the intensity factors K_{IV} and K_I, for the first, and K_{II} and K_I, for the second. This data and that taken from another source for poling perpendicular to the crack faces were used to produce failure criteria for each case.

Keywords Conservation integrals, Four-point bend tests, Mixed mode fracture, Piezoelectric ceramics

1. Introduction

Piezoelectric ceramics are in widespread use as sensors and actuators in smart structures, despite the absence of a fundamental understanding of their fracture behavior. Piezoceramics are brittle and susceptible to cracking. As a result of the importance of the reliability of these devices, there has been tremendous interest in studying the fracture and failure behavior of such materials. To understand failure mechanisms of piezoelectric materials and maintain the stability of cracked piezoelectric structures operating in an environment of combined electromechanical loading, analysis of the mechanical and electrical behavior is a prerequisite.

There have been many fracture tests carried out on piezoelectric material [1–12]. Fracture criteria have been presented in [10-17]. Each of these is based on the energy release rate. In fact, in [17] the energy was separated into its mechanical and electrical parts. Assuming impermeable crack face conditions, it was concluded in [17] that crack propagation of poled piezoelectric material is governed by the mechanical energy release rate. However, crack growth driven by purely electric fields in poled ferroelectrics has been observed in experiments [18,19]. A local energy release rate criterion was presented in [14] and [15] based on electric nonlinearity caused by a domain switching zone ahead of the crack tip. Impermeable crack face boundary conditions were also assumed there. The energy release rate obtained in [13] was used in [10] as a fracture criterion for analyzing results obtained with four-point bend specimens. This expression is based upon the load and electric current measured during the experiment. For an applied field of 0.5 MV/m, the energy release rate was zero or negative, which is not physically reasonable. Fracture curves of K_I versus K_{IV} were presented in [16] using impermeable and permeable assumptions. For both

conditions, there were discrepancies between the measured and calculated curves. A recent review article may be found in [20].

2. Fracture Criteria

A generalized fracture criterion for piezoelectric ceramics requires the development of a unified theory, which consists of mixed mode behavior, together with application of the energetically consistent crack face boundary conditions. In [11], the derivation for the energy release rate begins with the expression [21]

$$\mathcal{G} = \frac{1}{2}\boldsymbol{k}^T \boldsymbol{L}^{-1}\boldsymbol{k} \tag{1}$$

where $\boldsymbol{k}$ is the intensity factor vector given by

$$\boldsymbol{k}^T = \left[K_{II}, K_I, K_{III}, K_{IV}\right] \tag{2}$$

and the superscript T represents transpose. In Eq. (1), the 4×4 matrix $\boldsymbol{L}$ is one of the Barnett-Lothe tensors whose components are related to material properties.

For the numerical calculations, the intensity factors were normalized so that

$$\hat{\boldsymbol{k}} = \boldsymbol{V}^{-1}\boldsymbol{k} \tag{3}$$

where

$$\boldsymbol{V} = \begin{bmatrix} E_A\sqrt{L} & 0 & 0 & 0 \\ 0 & E_A\sqrt{L} & 0 & 0 \\ 0 & 0 & G_T\sqrt{L} & 0 \\ 0 & 0 & 0 & e_{26}\sqrt{L} \end{bmatrix} \tag{4}$$

E_A is Young's modulus in the poling direction, G_T is the shear modulus perpendicular to the poling direction, e_{26} is a contracted piezoelectric constant and L is a geometrical length parameter. The Barnett-Lothe tensor $\boldsymbol{L}^{-1}$ is normalized as

$$\hat{\boldsymbol{L}}^{-1} = \boldsymbol{V}\boldsymbol{L}^{-1}\boldsymbol{V}. \tag{5}$$

In this way, the diagonal and off-diagonal elements of $\boldsymbol{L}^{-1}$ are the same order of magnitude contributing to the accuracy of the intensity factor calculation [22]. Note that the units of $\boldsymbol{L}^{-1}$ are N/m.

The criterion presented in [11] with mode III deformation omitted is given by

$$\mathcal{G}_c = \mathcal{G}_{Ic}\left(1 + 2a_1\tan\psi + 2a_2\tan\phi + 2a_3\tan\psi\tan\phi + a_4\tan^2\psi + a_5\tan^2\phi\right) \tag{6}$$

where

$$a_1 = \frac{\hat{L}_{24}^{-1}}{\hat{L}_{22}^{-1}}, \quad a_2 = \frac{\hat{L}_{12}^{-1}}{\hat{L}_{22}^{-1}}, \quad a_3 = \frac{\hat{L}_{14}^{-1}}{\hat{L}_{22}^{-1}}, \quad a_4 = \frac{\hat{L}_{44}^{-1}}{\hat{L}_{22}^{-1}}, \quad a_5 = \frac{\hat{L}_{11}^{-1}}{\hat{L}_{22}^{-1}} \tag{7}$$

and

$$\mathcal{G}_{Ic} = \frac{1}{2}\hat{L}_{22}^{-1}\hat{K}_{Ic}^{2}. \tag{8}$$

To obtain $\mathcal{G}_{Ic}$, values of $\mathcal{G}_I$ given by

$$\mathcal{G}_I = \frac{1}{2}\hat{L}_{22}^{-1}\hat{K}_I^{2} \tag{9}$$

are obtained at failure for each test and averaged. In Eq. (7), the parameters $\hat{L}_{ij}^{-1}$ $(i, j = 1,...,4)$ are found from Eq. (5). The phase angles are defined as

$$\psi = \tan^{-1}\frac{\hat{K}_{IV}}{\hat{K}_I}, \qquad \phi = \tan^{-1}\frac{\hat{K}_{II}}{\hat{K}_I}. \tag{10}$$

Eq. (6) represents a three-dimensional failure surface for the case in which the crack faces are at an angle to the poling direction (which is in the plane) and in which the critical energy release rate $\mathcal{G}_c$ is a function of the phase angles ψ and ϕ. There is an assumption that the crack propagates in a self-similar manner.

Tests were carried out in [10] on four-point bend specimens fabricated from the piezoelectric ceramic PIC-151. This material is similar to PZT-5H. In these experiments, the crack faces were perpendicular to the poling direction and both mechanical loads and electric fields were applied. The electric field was perpendicular to the crack faces. Those experimental results were analyzed in [11]. In the analyses, $\hat{K}_{II}$ was found to be zero implying that ϕ in Eq. $(10)_2$ is zero. Hence, Eq. (6) may be rewritten as

$$\mathcal{G}_c = \mathcal{G}_{Ic}\left(1 + 2a_1 \tan\psi + a_4 \tan^2\psi\right). \tag{11}$$

The experimental results and the failure curve of Eq. (10), shown as the solid line, are presented in Fig. 1. Note that a is crack length. The value of $\mathcal{G}_{Ic}$ was found as 8.6 N/m. There is good agreement between the experimental data and the failure curve. To this end, the root mean square error (RMSE) given by

$$\text{RMSE} = \sqrt{\frac{\sum_{\text{N}}\left(\mathcal{G}_c^{\text{experiment}} - \mathcal{G}_c^{\text{theoretical}}\right)^2}{N}} \tag{12}$$

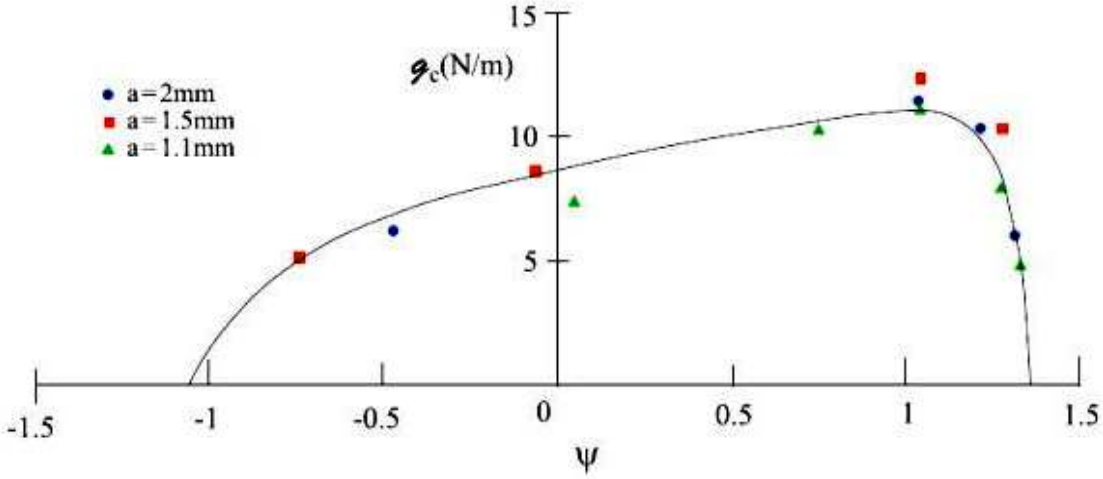

Figure 1. Failure curve and experimental results (PIC-151) [10] obtained in [11]. The crack is perpendicular to the poling direction.

was calculated to be 0.89 N/m. In Eq. (12), $\mathcal{G}_c^{\text{experiment}}$ is the experimental value or the point plotted in Fig. 1, $\mathcal{G}_c^{\text{theoretical}}$ is the value on the curve of $\mathcal{G}_c$ for the experimental value of ψ as calculated from Eq. (11) and N is the number of tests.

As a result of the coupling between the first and fourth modes of fracture, which is expressed by the second term in parentheses of the right hand side of Eq. (11), the fracture curve in Fig. 1 is not symmetric with respect to $\psi = 0$. Furthermore, it should be emphasized that the apparent fracture toughness $\mathcal{G}_{Ic}$ should not be used to predict catastrophic failure. Only the mixed mode fracture curve presented in Eq. (11) and Fig. 1 should be used to predict failure. To interpret the failure curve for a structure fabricated from the same material and containing a crack perpendicular to the poling direction, values of $\mathcal{G}_c$ below the curve are considered safe; for those above it, failure may be expected. Of course, a probabilistic analysis should be carried out.

Next, a fracture criterion for tests carried out in [12] on four-point bend specimens fabricated from PZT-5H (Morgan Electro Ceramics, Wrexham, UK) with poling parallel to the crack faces is presented. In that study, modes I, II and IV were present. Since poling is parallel to the crack faces, $a_1 = a_2 = 0$ in Eq. (7). Hence, the fracture criterion in Eq. (6) becomes

$$\mathcal{G}_c = \mathcal{G}_{Ic}\left(1 + 2a_3 \tan\psi \tan\phi + a_4 \tan^2\psi + a_5 \tan^2\phi\right). \tag{13}$$

Note that during the tests, the electric field was applied perpendicular to the crack faces. The value of $\mathcal{G}_{Ic}$ was found to be 20.3 N/m. In Fig. 2, the three-dimensional failure surface in Eq. (13) is plotted. The points shown are the experimental values obtained by analyzing the results from the four-point bend tests.

In order to have a better view of the scatter, the phase angle ϕ in the criterion of Eq. (13) was assumed zero resulting in

$$\mathcal{G}_c = \mathcal{G}_{Ic}\left(1 + a_4 \tan^2\psi\right). \tag{14}$$

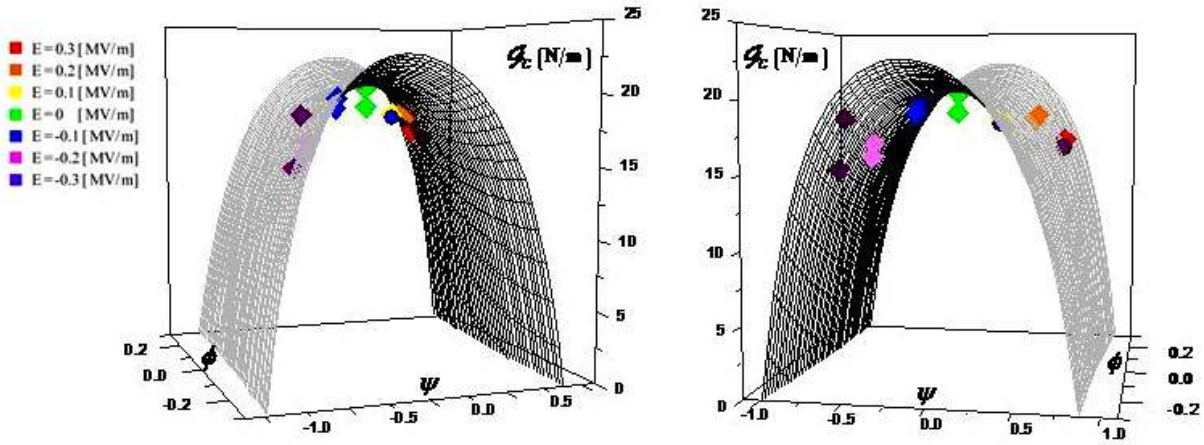

Figure 2. Two views of the three-dimensional failure surface from Eq. (13) with the test data shown. The crack is parallel to the poling direction.

This curve is plotted with $\mathcal{G}_{Ic} = 20.3$ N/m in Fig. 3. The test values $\mathcal{G}_c$, recalculated with $\hat{K}_{II} = 0$, together with the values of ψ are plotted as points in Fig. 3. This may be justified since the values of $\hat{K}_{II}$ are small with respect to $\hat{K}_I$ and $\hat{K}_{IV}$ except for one specimen. The root mean square error in Eq. (12) was calculated as 1.10 N/m for the three-dimensional surface and 1.05 N/m for the two-dimensional curve.

Finally, the crack propagation angle θ measured from a line extending ahead of the crack was obtained for each test. The angle varied between 1^0 and 10^0. Points for $9^0 \le \theta \le 10^0$ showed the greatest scatter from the theoretical curve, although even for 5^0 and 6.5^0 there was some scatter. Generally, smaller propagation angles led to less scatter in the test results as compared to the theoretical curve. There seemed to be no apparent correlation between large values of $\hat{K}_{II}$ or

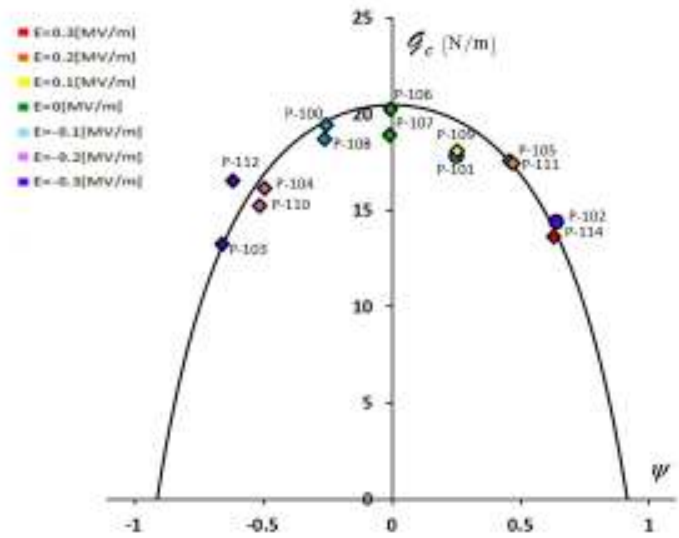

Figure 3. Two-dimensional failure curve from Eq. (14) with test data shown. The crack is parallel to the poling direction.

$\hat{K}_{IV}$ and θ. Theoretically, larger values of $\hat{K}_{II}$ imply larger values of θ. Recall that the fracture criteria were developed for self-similar crack propagation. For these small propagation angles, the results appear to be acceptable. But if one has a substantial value for θ, the criteria presented here may not be used.

Acknowledgements

I would like to acknowledge the contributions of Dr. Yael Motola, Ms. Liat Heller, Dr. Victor Fourman and Mr. Rami Eliasi in carrying out tests and analyses described here.

References

[1] A.G. Tobin, Y.E. Pak, Effect of electric fields on fracture behavior of PZT ceramics. SPIE, 1916 (1993) 78–86.
[2] S. Park, C.T. Sun, Fracture criteria for piezoelectric ceramics. J Am Cer Soc, 78 (1995) 1475–1480.
[3] H. Wang, R.N. Singh, Crack propagation in piezoelectric ceramics: effects of applied electric field. J Appl Phys, 81 (1997) 7471–7479.
[4] C.S. Lynch, Fracture of ferroelectric and relaxor electro-ceramics: influence of electric field. Acta Mater, 46 (1998) 599–608.
[5] R. Fu, T-Y. Zhang, Effects of an electric field on the fracture toughness of poled lead zirconate titanate ceramics. J Am Cer Soc, 83 (2000) 1215–1218.
[6] Y. Shindo, M. Oka, K. Horiguchi, Analysis and testing of indentation fracture behavior of piezoelectric ceramics under an electric field. J Engng Mater Techno, 123 (2001) 293–300.
[7] Y. Shindo, F. Narita, M. Mikami, Double torsion testing and finite element analysis for determining the electric fracture properties of piezoelectric ceramics. J Appl Phys, 97 (2005) 114109-1–114109-7.
[8] G.A. Schneider, F. Felten, R.M. McMeeking, The electrical potential difference across cracks in PZT measured by Kelvin Probe Microscopy and the implications for fracture. Acta Mater, 51 (2003) 2235–2241.
[9] X.P. Zhang, S. Galea, L. Ye, Y.W. Mai, Characterization of the effects of applied electric fields on fracture toughness and cyclic electric field induced fatigue crack growth for piezoceramic PIC 151. Smart Mater Struc, 13 (2004) 9–16.
[10] H. Jelitto, H. Kessler, G.A. Schneider, H. Balke, Fracture behavior of poled piezoelectric PZT under mechanical and electrical loads. J Euro Cer Soc, 25 (2005) 749–757.
[11] Y. Motola, L. Banks-Sills, V. Fourman, On fracture testing of piezoelectric ceramics. Int J Fract, 159 (2009) 167–190.
[12] L. Banks-Sills, L. Heller, V. Fourman, A supplementary study on fracture tests of piezoelectric material: cracks parallel to the poling direction. Int J Fract, 175 (2012) 109–125.
[13] Z. Suo, Mechanics concepts for failure in ferroelectric ceramics, in: A.V. Srinivasan (Ed.), Smart Structures and Materials, AMD 123, American Society of Mechanical Engineers, New York, 1991, pp. 1–6.
[14] H. Gao, T-Y. Zhang, P. Tong, Local and global energy release rates for an electrically yielded crack in a piezoelectric ceramic. J Mech Phys Solids, 45 (1997) 491–510.
[15] C.C. Fulton, H. Gao, Effect of local polarization switching on piezoelectric fracture. J Mech Phys Solids, 49 (2001) 927–952.
[16] H. Jellito, F. Felten, C. Hausler, H. Kessler, H. Balke, G.A. Schneider, Measurment of energy release rates for cracks in PZT under electromechanical loads. J Euro Cer Soc, 25 (2005) 2817–2820.
[17] S. Park, C.T. Sun, Effect of electric field on fracture of piezoelectric ceramics. Int J Fract, 70 (1995) 203–216.

[18] H. Cao, A.G. Evans, Electric-field-induced fatigue crack growth in piezoelectrics. J Am Cer Soc, 77 (1994) 1783–1786.
[19] J.K. Shang, X. Tan, A maximum strain criterion for electric-field-induced fatigue crack propagation in ferroelectric ceramics. Mater Sci Engng A, 301 (2001) 131–139.
[20] M. Kuna, Fracture mechanics of piezoelectric material–where are we right now? Eng Fract Mech, 77 (2010) 309–326.
[21] Z. Suo, C.M. Kuo, D.M. Barnett, J.R. Willis, Fracture mechanics for piezoelectric ceramics. J Mech Phys Solids, 40 (1992) 739–765.
[22] L. Banks-Sills, Y. Motola, L. Shemesh, The *M*-integral for calculating intensity factors of an impermeable crack in a piezoelectric material. Engng Fract Mech, 75 (2008) 901–925.

Experimental and analytical study of the effect of variable amplitude loadings in VHCF regime

T. Müller, M. Sander*

Institute of Structural Mechanics, University of Rostock, 18059 Rostock, Germany
* Corresponding author: manuela.sander@uni-rostock.de

Abstract

Components and structures (e.g. helicopter rotors, wind turbine components or wheelset axels) are commonly exposed a very high number of cycles with variable amplitudes. For the study of the influence of variable amplitude loadings in the very high cycle fatigue regime different load-time-histories up to 10^9 cycles are used, which have different amounts of small amplitudes beneath the fatigue strength of the investigated material. The experiments are performed with an ultrasonic fatigue testing system with frequencies up to 21 kHz. In order to avoid an excessive heat development of the specimen, pulsed loadings with adequate pause lengths are applied. Therefore, only block loadings can be realized. The used load-time-histories have been counted by the rainflow method and then divided into different number of classes providing that within every class a minimum number of cycles restricted by the experimental performance is given. The classes have been reconstructed to a load-time-history by varying the sequence of the classes. The influence of the different reconstructions as well as of the amount of the amplitudes beneath the fatigue strength is quantified by the fatigue lifetime. These experimental data are used to proof conventional analytical approaches (*Palmgren-Miner´*s rule) of structural durability in the VHCF regime.

Keywords very high cycle fatigue, variable amplitude loading, fatigue life prediction, load interaction effect, short crack growth

1. Introduction

In technical constructions of different application fields, components are very often subjected to cyclic stresses. Components like drive shafts, gear shafts, wheelset axles, helicopter rotors or highly stressed engine parts, such as blades, are often cyclically loaded with more than 10^7 cycles up to 10^9 and more cycles. The high number of load cycles can be attributed to a very long period of service up to 30 years or to high service frequencies. In present fatigue design standards the influence and effect of such high number of load cycles on the fatigue behavior are not sufficiently taken into account.

As *Bathias* [1] already showed in 1999, the determined fatigue strength, defined by the early investigations of *Wöhler*, does not exist. Thus, a decrease of the S-N curve is observable in the very high cycle fatigue regime, as numerous studies (e.g. [2-5]) have shown. The decrease in fatigue strength is caused by the transition from surface to subsurface crack initiation [5-7]. Moreover, microstructural features like cavities, non-metallic inclusions, grain boundaries, porosities or oxide layers at the surface and inside a component could lead to crack initiation.

Cracks, initiated at non-metallic inclusions, usually show the typical formation of a fish-eye. In the vicinity of inclusions within the fish-eye a distinctive area could be observed [8-10]. *Murakami* calls it an optical dark area (ODA) with a more rough fracture surface in comparison to the remaining fish-eye fracture surface. He assumed that the area occur due to hydrogen accumulation during cyclic loading. He also proposes a relationship between the size of the ODAs and non-metallic inclusions as well as the number of cycles to failure.

However, the influence of variable amplitude loading (VAL) on the fatigue behavior in the VHCF regime is, despite a few studies [11-18], poorly investigated. For instance *Mayer* [12] showed with two-step loading tests that low load amplitudes beneath the fatigue strength contribute to fatigue

damage depending on the height of the maximum load amplitudes.

2. Material and experimental procedure

2.1. Material

The experimental investigations are performed with specimens with a minimum diameter of 4 mm shown in Fig. 1. All specimens were machined from a 20 mm round bar of the quenched and tempered high-strength steel 34CrNiMo6. The chemical composition of the steel is summarized in Table 1 and the static material parameters are shown in Table 2.

Table 1. Chemical composition of the investigated high-strength steel (in wt %)

C	Si	Mn	Cr	Mo	Ni
0.34	0.3	0.5	1.5	0.2	1.5

Table 2. Mechanical Properties

UTS [MPa]	YS [MPa]	Young´s modulus [GPa]	Breaking elongation [%]
1200	1000	210	9

An average Vickers hardness of the material was 350 HV. The surface of the specimen has been emery-polished after machining.

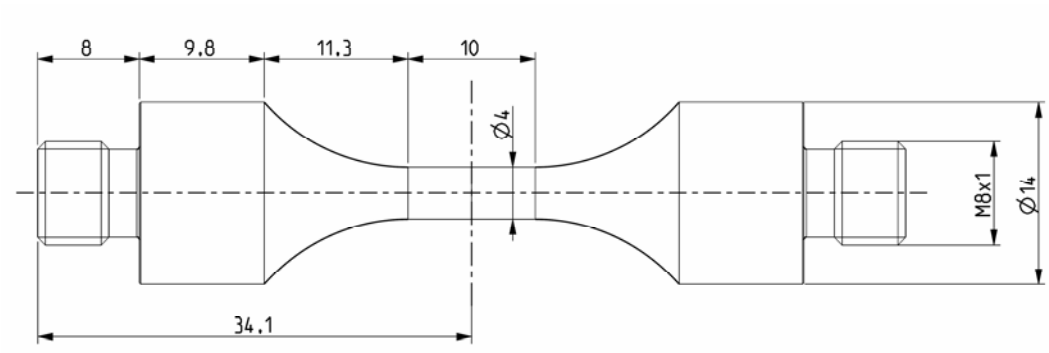

Figure 1. Specimen

2.2. Ultrasonic fatigue testing system

In service, components and structures are rather subjected to variable amplitude loadings (VAL) than to constant amplitude loadings (CAL). Fatigue tests with variable amplitude loadings or load time histories in the regime of 10^9 cycles or even higher are too time consuming and expensive using conventional testing systems. Therefore, an ultrasonic fatigue testing system of the BOKU

Vienna [19] is used. The system is stimulating the specimen in its resonance frequency and is with about 21 kHz many times higher than loading frequencies of conventional systems. Tests have been performed in pulse-pause-sequences to avoid excessive heating of the specimen. Thus, experiments with a fatigue life up to 10^9 cycles take between 0.6 and 6 days depending on the pulse- and pause-sequence. Using the ultrasonic fatigue testing technique no load time history could be subjected to the specimen. Because of increasing vibration amplitudes at the beginning and decreasing amplitudes at the end of a pulse, only block loading tests can be realized. Thus, for systematic studies firstly two block loading tests are performed with different block loading length. Furthermore, a reconstruction algorithm, generating adequate cumulative frequency distributions of load cycles, is used to perform fatigue tests on the basis of a load time history. Therefore, the software Ultrasonic Fatigue Testing Software for Variable Amplitude Loading (UFaTeS^{VAL}), which has been developed at the Institute of Structural Mechanics at the University of Rostock, is used for data acquisition and controlling of the VAL experiments.

2.3. Variable amplitude loading tests

A high demand is requested for investigating the influence of variable amplitude loadings, and load interaction effects in particular, on short crack growth and crack initiation in the VHCF.

2.3.1. Two-step loading tests

For systematic studies of the influence of load interaction effects on the fatigue life, particularly with regard to short crack growth, two-step loading tests have been performed (Fig. 2). The amount of numbers n_1 of the maximum load amplitude of the cumulative distribution is 10.000 cycles and constant for all experiments. Tests have been carried out with different maximum load amplitudes with 110% and 120% of the fatigue strength σ_D for each experiment. The low block load is 90% of the fatigue strength and the number of cycles n_2 was varied, characterized by the ratio $R_{bl} = n_2/n_1$. Three different ratios of 1, 10 and 100 have been investigated. However, the ratio was kept constant within one test. The two blocks are repeated until the specimen fails or the limit of 10^9 cycles is reached.

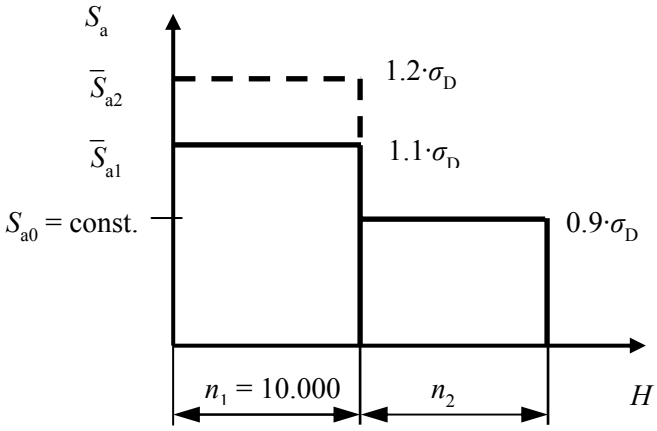

Figure 2. Schematic procedure of two-step loading tests

2.3.1. Tests with load-time history FELIX

For the investigation of realistic variable amplitude loadings, the standardized helicopter load spectrum FELIX [20] has been used. Therefore, the stress amplitudes of the FELIX spectrum have been transformed to a constant *R*-ratio of -1 using the equations accounting for the mean stress effect. After dividing the spectrum into different classes, they have been reconstructed to different load sequences (Fig. 3). The load sequence FELIX 10 was reconstructed with decreasing load amplitudes starting with the maximum amplitude and ending with the lowest amplitude. The load sequence FELIX 11 starts with the lowest amplitude and is step-wise increased up to the maximum load amplitude. The load amplitudes of the last reconstructed sequence FELIX 12 is randomly mixed. Each sequence is repeated until failure occurs or the limit of 10^9 cycles is reached.

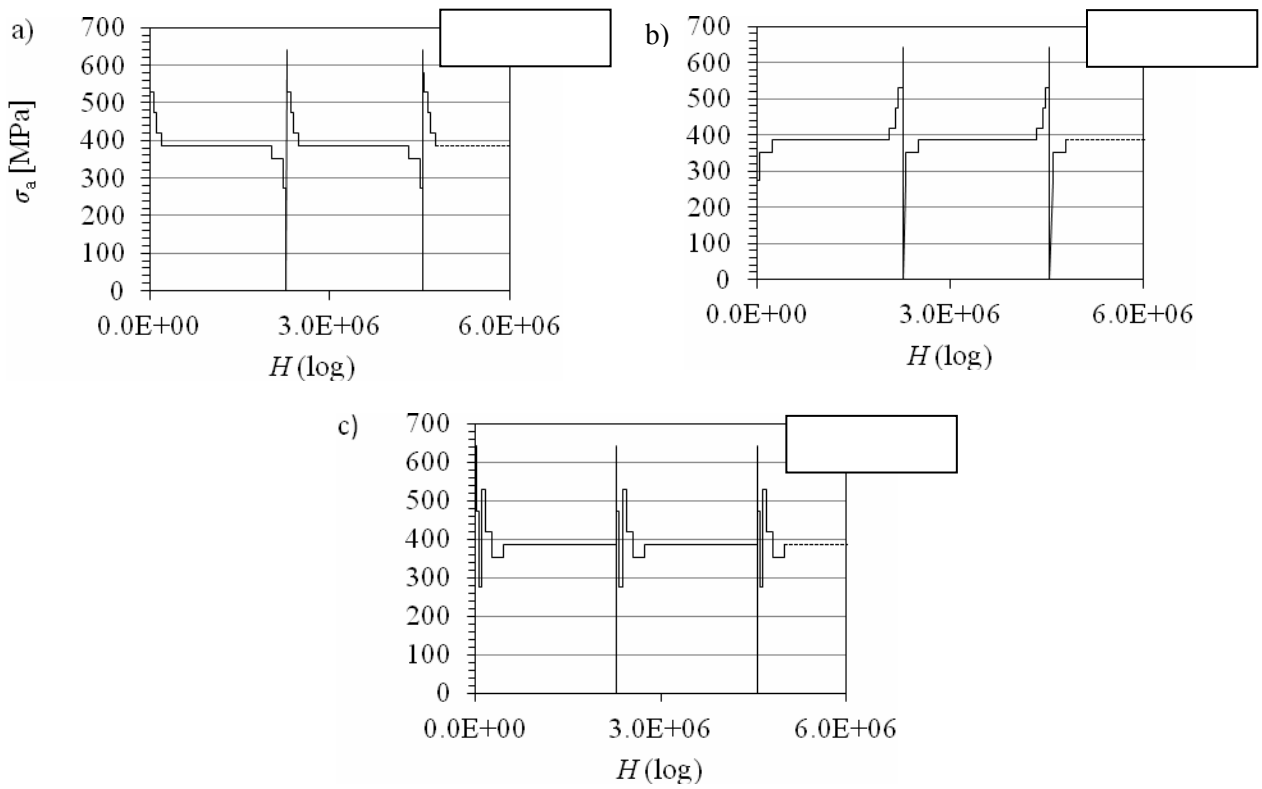

Figure 3. Reconstructed load time history FELIX with a) decreasing load amplitudes, b) increasing load amplitudes and c) mixed load amplitudes

3. Results

The influence of the size of non-metallic inclusions on the number of cycles to failure is shown in Figure 4, where $area_{inc}$ is the inclusion size projected on the plane perpendicular to the maximum principal stress. The data of constant amplitude (CA) loading tests show no significant influence of the inclusion size on the lifetime. In contrast, the size of inclusions tends to decrease with increasing lifetime for all variable amplitude (VA) loading tests.

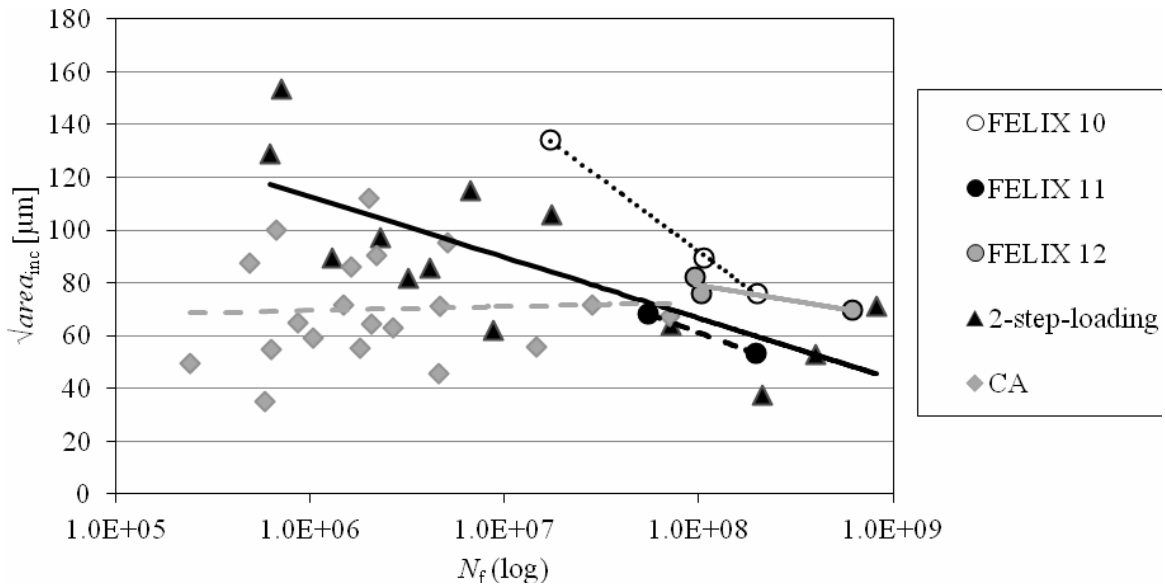

Figure 4. Influence of inclusion size on the fatigue life

Fig. 5 shows the results of the modified S-N curves of the VA-tests (FELIX) in comparison to the tests with constant amplitude loading using the approach by *Murakami* [8] with

$$\sigma_{\mathrm{w}} = \frac{1.43 \cdot (H_{\mathrm{V}} + 120)}{\left(\sqrt{area_{\mathrm{inc}}}\right)^{1/6}} \cdot \left[\frac{1-R}{2}\right]^{\alpha} \quad (1),$$

for inclusions near to the specimen's surface and

$$\sigma_{\mathrm{w}} = \frac{1.56 \cdot (H_{\mathrm{V}} + 120)}{\left(\sqrt{area_{\mathrm{inc}}}\right)^{1/6}} \cdot \left[\frac{1-R}{2}\right]^{\alpha} \quad (2)$$

for subsurface inclusions.

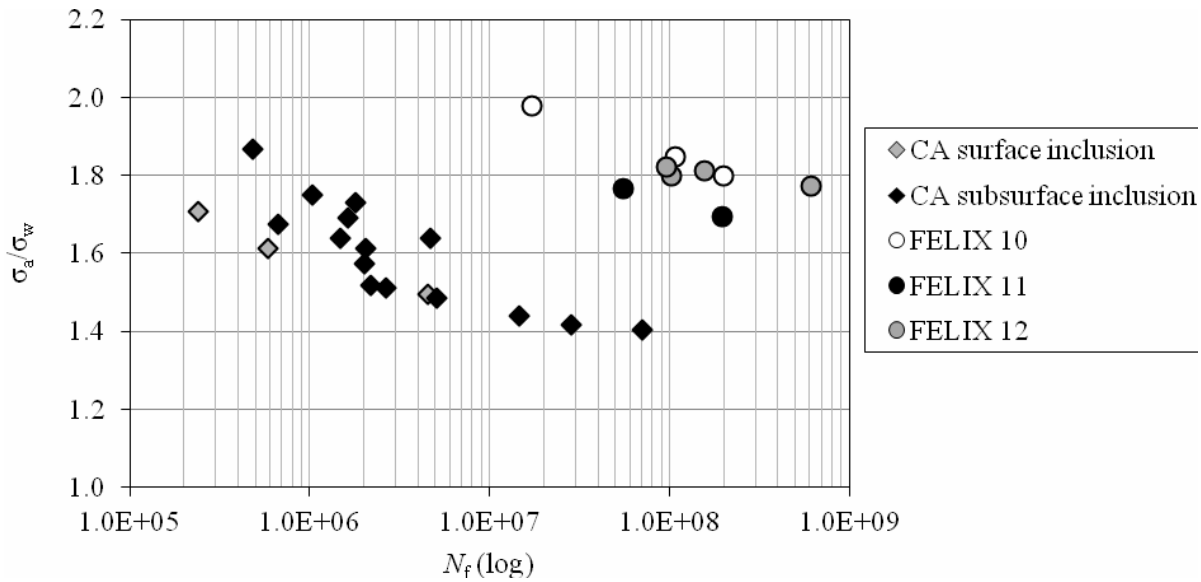

Figure 5. Reconstructed load-time history tests (FELIX) in comparison to constant amplitude tests

The S-N curves are shifted to higher lifetimes for variable amplitude loadings in comparison to constant amplitude loadings. However, the order of load amplitudes influences the lifetime. The reconstructed load time history FELIX 10 with decreasing load amplitudes and the load time history

FELIX 12 with mixed load amplitudes tend to equal lifetimes. Otherwise, the reconstructed load time history FELIX 11 with increasing load amplitudes tends to result in lower lifetimes than FELIX 10 and FELIX 12.

The analyses of the fracture surfaces show circular arrest marks formed around non-metallic inclusions within the fish-eye (Fig. 6b-d) for variable amplitude loading in contrast to the fracture surfaces of specimens subjected to constant amplitude loading (Fig. 6a). This could be an indicator for load interaction effects on the crack growth within the fish-eye, as it is well known in the regime for long crack growth. The arrest marks of FELIX 11 (Fig. 6c) are obviously more pronounced than in the case of FELIX 10 (Fig. 6b) and FELIX 12 (Fig. 6d). However, the sizes of the area, where arrest marks occur, as well as the spacings of the arrest marks are different for the investigated VAL.

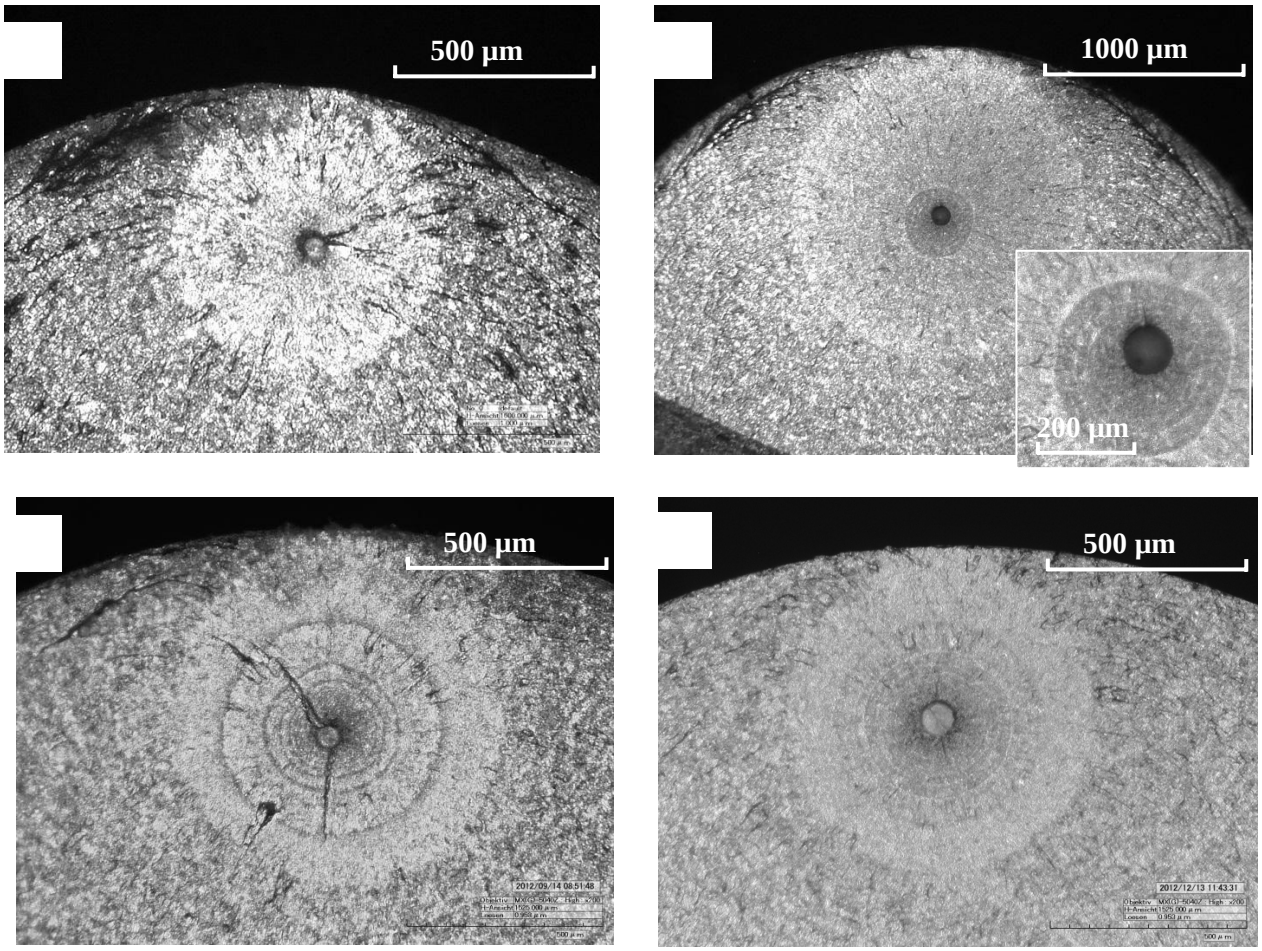

Figure 6. Fracture surfaces with typical fish-eye fracture around non-metallic inclusions: a) constant amplitude loading and FELIX-tests with arrest marks within fish-eye for b) FELIX 10, c) FELIX 11 and d) FELIX 12

By counting and measuring the arrest marks an average crack growth rate *da/dN* for the crack propagation within the fish-eye can be calculated, as plotted in Fig. 7. By using the √*area*-approach [8], the stress intensity factor ΔK was determined. Therefore, the stress amplitude of 386 MPa with the highest amount of cycles within the load sequence has been used. The load sequences of FELIX 10 and FELIX 12 lead to similar crack growth rates. In comparison, the crack growth rate of FELIX 11 is shifted to higher crack growth rates. Nevertheless, all three investigated load sequences lead to crack growth rates beneath the threshold value ΔK_{th} for long crack growth.

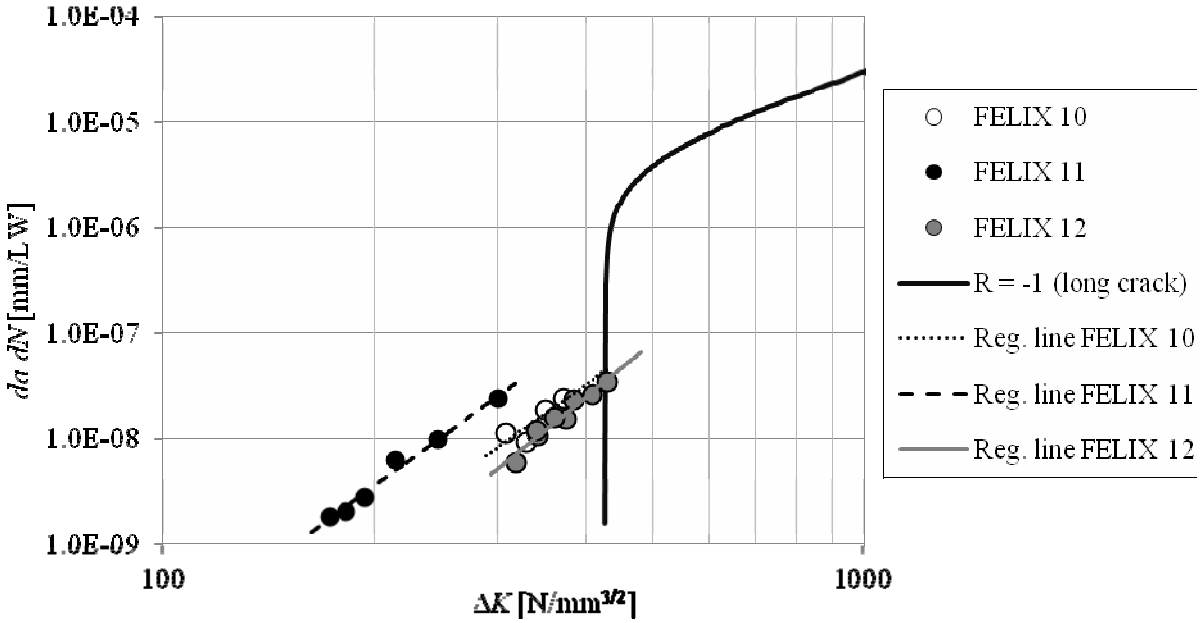

Figure 7. Crack growth curve in comparison to experimentally evaluated crack growth rates with variable amplitude loading tests (FELIX)

Using the *Palmgren-Miner's* rule a fatigue life $N_{f,calc}$ with an assumed damage sum of 1 can be calculated for the investigated variable amplitude loadings (see chap. 2.3). Beside the original *Palmgren-Miner* (PM) approach, the modified and elementary *Palmgren-Miner* approach as well as the approach by *Liu/Zenner* have been taken into account in order to consider amplitude levels beneath the fatigue strength. The calculated fatigue lifes $N_{f,calc}$ of the two-step loadings are compared with the appropriate experimental mean fatigue lifes $N_{f,exp}$ (Fig. 8). Moreover, in Fig. 8 the scatter bands $N_{f,calc}/N_{f,exp}$ for 10% and 90% probability of survival based on the CA tests are given.

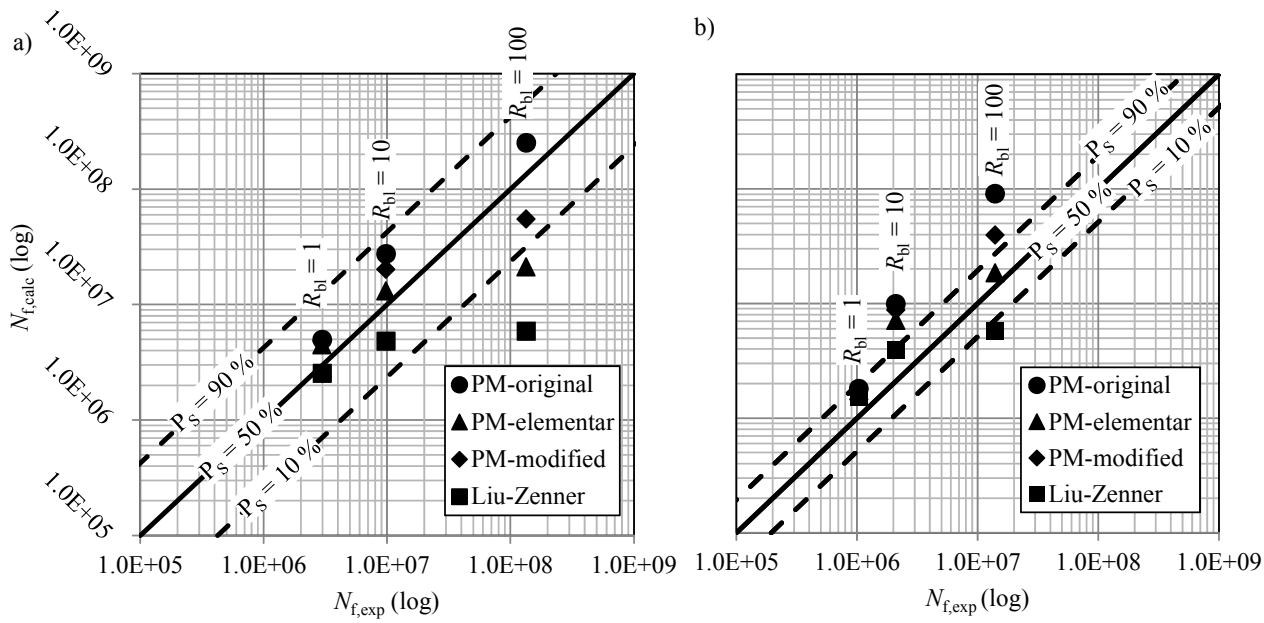

Figure 8. Comparison of two-step loading tests a) $\overline{S}_a$ = 584 MPa (1.1·σ_D) and b) $\overline{S}_a$ = 637 MPa (1.2·σ_D) with calculated lifetimes using *Palmgren-Miner*'s rule with a damage sum of 1

For $\overline{S}_a = 1.1 \cdot \sigma_D$ (Fig. 8a), the calculated lifetimes for the R_{bl} ratios 1 and 10 are within the scatter band. For $R_{bl} = 100$ only the results of the original and modified *Palmgren-Miner*'s rule are within the scatter band. The approach by *Liu/Zenner* always provides the most conservative results, which strongly increase with increasing R_{bl}-ratio.

In comparison, for $\overline{S}_a = 1.2 \cdot \sigma_D$ (Fig. 8b), all approaches provide approximately the same results for the lowest ratio $R_{bl} = 1$. The higher the R_{bl}-ratio is, the more the original PM approach overestimates the lifetime and the values are outside the scatter band. Thus, the low load amplitudes contribute to fatigue damage, if the high block loading is high enough with respect to the lower amplitudes and if the high blocks occur less frequently. The lifetimes obtained by *Liu/Zenner* for the R_{bl}-ratios of 1 and 10 provide good results. At a ratio of 100 it is again conservative. None of the approaches give suitable results for all three R_{bl}-ratios.

In Fig. 9 the calculated fatigue life $N_{f,calc}$ for the investigated load-time history FELIX is compared with the experimental mean fatigue life $N_{f,exp}$ of the three different reconstructed load sequences. For the investigated load sequences FELIX 11 and FELIX 12 the original *Palmgren-Miner*'s rule provides results within the scatter band. The approach slightly overestimates the fatigue life of FELIX 10. The elementary *Palmgren-Miner*'s rule as well as the approach by *Liu/Zenner* for FELIX 10 and FELIX 11 lead to conservative results, where again the approach by *Liu/Zenner* is the most conservative one. However, it is observable that each approach leads to the same calculated lifetimes $N_{f,calc}$ independent of the used reconstructed load sequence, while the experimental lifetimes $N_{f,exp}$ clearly differ.

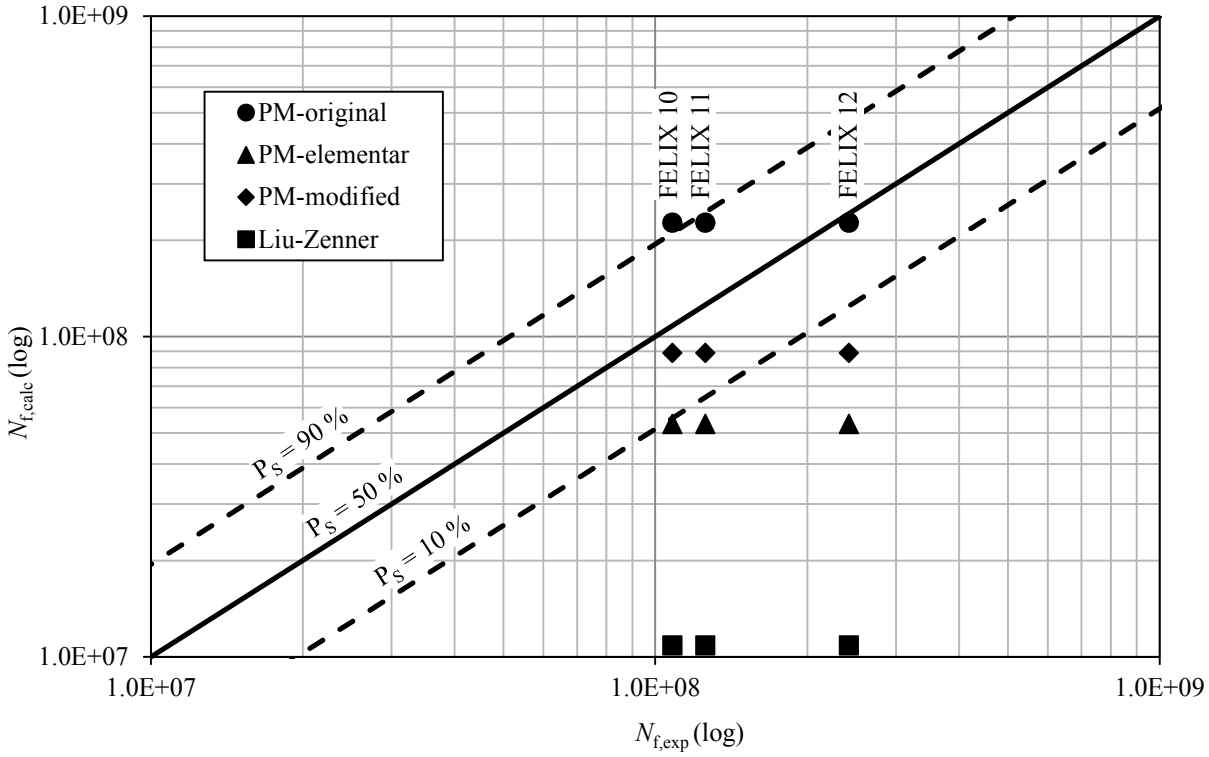

Figure 9. Comparison of different reconstructed load sequences (FELIX) with calculated fatigue life using *Palmgren-Miner*'s rule with a damage sum of 1

4. Conclusions

The high strength steel 34CrNiMo6 was investigated in the very high cycle fatigue regime under constant and variable amplitude loadings. An ultrasonic fatigue testing system has been used to perform fatigue tests in adequate testing time. An own developed software UFaTeS^{VAL} was used to realize variable amplitude loading tests. Two-step load amplitudes and reconstructed load time histories were investigated. The main conclusions are as follows:

(1) The fatigue life of variable amplitude tests is influenced by the size of non-metallic inclusions, in contrast to constant amplitude loadings.
(2) The two-step loading tests show that load amplitudes below the fatigue strength can contribute to damage depending on the height of the maximum load amplitude and the amount of maximum load amplitudes.
(3) Variable amplitude loading can provoke the occurrence of arrest marks around non-metallic inclusions within fish-eyes, which are used to calculate a mean fatigue crack growth rate in the fish-eye.
(4) As the FELIX investigations show, an influence of the kind of reconstruction of the load-time is observable.

Acknowledgements

The authors gratefully acknowledge the financial support by the 'Deutsche Forschungsgemeinschaft' (DFG) in the framework of SPP 1466.

References

[1] Bathias, C.: There is no infinite fatigue life in metallic materials. In: Fatigue Fract Engng Mat Struct 1999; 22(7): pp. 559-65

[2] Marines, I.; Dominguez, G.; Baudry, G.; Vittori, J.F.; Rathery, pp.; Doucet, J.P. et al.: Ultrasonic fatigue tests on bearing steel AISI-SAE 52100 at frequency of 20 and 30 kHz. In: Int. J. Fatigue 2003; 25: pp. 1037-1046.

[3] Pyttel, B.; Schwerdt, D.; Berger, C.: Very high cycle fatigue - Is there a fatigue limit? In: Int. J. Fatigue 2011; 33: pp. 49-58

[4] Sakai, T.: Review and prospects for current studies on very high cycle fatigue of metallic materials for machine structural use. In: J. Solid Mech Mater Eng 2009; 3(3): pp. 425-439.

[5] Shiozawa, K.; Lu, L.; Ishihara, S.: S-N curve characteristics and subsurface crack initiation behavior in ultra-long life fatigue of a high carbon-chromium bearing steel. Fatigue Fract Engng Mat Struct 2001; 24(12): pp. 781-90

[6] Tanaka, K.; Akinawa, Y.: Fatigue crack propagation behavior derived from S-N data in very high cycle regime. Fatigue Fract Engng Mat Struct 2002; 25: pp. 775-84

[7] Ochi, Y.; Matsumura, T.; Masaki, K.; Yoshida, S.: High-cycle rotating bending fatigue properties in

very long life regime of high-strength steel. Fatigue Fract Engng Mat Struct 2002; 25: pp. 823-30

[8] Murakami, Y.: Metal Fatigue: Effects of small defects and non-metallic inclusions. Elsevier, London, 2002

[9] Shiozawa, K.; Morii, Y.; Nishino, S.; Lu, L.: Subsurface crack initiation and propagation mechanism in high-strength steel in a very high cycle fatigue regime. In: Intern. J. Fatigue, Vol. 28, 2006, pp. 1521-1532

[10] Sakai, T.; Sato, Y.; Oguma, N.: Characteristic S-N properties for high-carbon-chromium-bearing steel under axial loading in long-life fatigue. In: FFEMS 25 (2002) pp. 765-773

[11] Mayer, H.: Fatigue damage of low amplitude cycle under variable amplitude loading condition. In: Proc VHCF 4. Ann Arbor; 2007. pp. 333-340

[12] Mayer, H.; Stojanovic, S.; Ede, C.; Zettl, B.: Beitrag niedriger Lastamplituden zur Ermüdungsschädigung von 0,15%C Stahl. Mat.-wiss. U. Werkstofftech. 2007; 38, No.8

[13] Mayer, H.; Fitzka, M.; Schuller, R.: Ultrasonic fatigue testing of 2024-T351 aluminium alloy at different load ratios under constant and variable amplitude. In: Proc. of VHCF5, Berlin, 2011, pp. 355-360

[14] Mayer, H.; Haydn, W.; Schuller, R.; Issler, S.; Bacher-Höchst, M.: Very high cycle fatigue properties of bainitic high carbon-chromium steel under variable amplitude conditions, Int. J. Fatigue 2009; 31: pp. 1300-1308

[15] Issler, S.; Bacher-Höchst, M.; Haydn, W.: Fatigue design for components under variable amplitude loading in the very high cycle fatigue area. In: Sonsino, C.M.; McKeighan, P.C. (eds.): 2nd Int. Conference on Material and Component Performance under Variable Amplitude Loading, DVM, Berlin, 2009, pp. 935-943

[16] Nakajima, M.; Kamiya, N.; Itoga, H.; Tokaji, K.; Ko, H.: Experimental estimation of crack initiation lives and fatigue limit in subsurface fracture of a high carbon chromium steel. In: Int. J. Fatigue, 2006, 28 (11), pp. 1540–1546.

[17] Lu, L.; Shiozawa, K.: Effect of two-step load variation on giga-cycle fatigue and internal crack growth behaviour of high carbon-chromium bearing steel. In: Sakai, T.; Ochi, Y. (eds.): Proc. of VHCF3. Japan, Society of Material Science, 2004, pp. 185-192

[18] Mayer, H.; Fitzka, M.; Schuller, R.: Ultrasonic fatigue testing of 2024-T351 aluminium alloy at different load ratios under constant and variable amplitude. In: Berger, C.; Christ, H.-J. (eds.): Proc. of VHCF5. DVM, Berlin, 2011, pp. 355-360

[19] Mayer, H.: Fatigue crack growth and threshold measurements at very high frequencies. In: International Materials Reviews, 1999, 44 (1), p. 1–34.

[20] Edwards, P.R.; Darts, J. (Eds.): Standardised Fatigue Loading Sequences for Helicopter rotors – Helix and Felix – Part 1: Background and fatigue evaluation and Part 2: Final Definition of Helix and Felix. NLR TR 84043 U, 1984

Is There a Threshold for PSB Formation in Iron

Chong Wang[1,*], Danièle Wagner, Claude Bathias

[1] LEME, University Paris Ouest Nanterre La Défense 50, rue de Sèvres, 92410 VILLE D'AVRAY, France
* Corresponding author: wangchongscu@163.com

ABSTRACT

Thin flat specimens (1mm thickness) have been tested on a piezoelectric fatigue machine in 20 KHz frequency on High cycle fatigue domain and beyond. The result shows that body centered cubic Armco iron (with 80ppm of carbon content) could fail after 10^9 cycles at a loading well below the yield stress. Observations under Scanning Electron Microscope on the specimen surface and the fracture surface indicated gigacycle fatigue failure originated in the specimen surface and related to the formation of Persistent Slip Bands (PSB). The microstructure evolution was observed by optical microscopy. It was found that PSB not only appear at the beginning of ultrasonic fatigue test but also increase with the number of cyclic loading.

Keywords Persistent Slip Band, irreversible deformation, localized plasticity, very high cycle fatigue

1. Introduction

For single phase materials without inclusions, testing in very high cycle fatigue regime, the first damage event of crack initiation is due to the occurrence of Slips Marks (SM) on the specimen surface [1, 2]. In f.c.c materials (which are the most studied materials), these SM are called Persistent Slips Bands (PSB), with a particular dislocation structure beneath the PSB [3]. When strain reached to cyclic stress-strain curve plateau, the deformation structure changes to the PSB instead of dislocation veins in matrix in order to accommodated the high value of plastic deformation [1]. Intrusions at PSB or PSB/matrix are interface preferential sites for the nucleation of microcracks[4]. In bcc materials, like Armco iron, the identification of these SM with PSB is matter of debate [3-9]. The reason lies in the very different temperature and strain rate dependent dislocation glide behavior in body centered cubic (b.c.c) metals, as compared to f.c.c metals. Moderate increase of temperature, low cyclic strain rates and alloying by substitution atoms (e.g. in Fe-Si) and interstitial atoms (e.g. C and N in α-iron) make the dislocation glide modes of bcc metals more similar to those of f.c.c metals and then, "PSBs" may be observed.

For a basic point of view, it is of interest to understand the initiation of a fatigue crack in the VHCF regime in pure alloys or metals without internal defects. Studies tested at different loading conditions given references for investigating fatigue features on iron. Dislocation arrangement in iron after fatigue bending test at low frequency are investigated by Mcgrath and Bratina[10]. They find that the average dislocation density for particular stress amplitude reaches a constant value after showing a rapid increase in the early portion of the fatigue life. When Wood et al [11] compare the fatigue mechanisms in bcc iron and fcc metals at low frequency in alternating

torsion, they noted that at amplitudes above the SN knee, slip markings appeared on a specimen after a few cycles. At amplitude below the knee they appeared after a million or so cycles. Wei and Baker found wall developed arrays of dislocation loops in iron specimen after only 10 cycles in push-pull fatigue [12]. Such observation at small number of cycles is difficult at high frequency in VHCF.

However, fatigue deformation features of iron at very high cycle fatigue regime are limited. PSBs formation at subsurface and at initiation area was not well discussed on literature. Current work intends to investigating the fatigue initiation and localized irreversibility of b.c.c. metals ARMCO iron (α-Fe) at very high cycle fatigue regime. In order to study this phenomenon a new flat specimen, easy for surface observation, was designed to be tested at 20 kHz up to 10^{10} cycles. Observations were performed on specimen surface during testing and fractographic after failure.

2. Experimental

The studied material is a polycrystalline α iron whose chemical composition is given in Table 1 and mechanical properties of corrected true stress-strain is given in Fig 1. The microstructure is ferrite with equiaxe grains. The ferrite grain size is included in 10 to 40 μm. No specifically orientation was observed by EBSD.

Table 1. Chemical compositions (wt.%)

C	P	Si	Mn	S	Cr	Ni	Mo	Cu	Sn	Fe
0.008	0.007	0.005	0.048	0.003	0.015	0.014	0.009	0.001	0.002	Balance

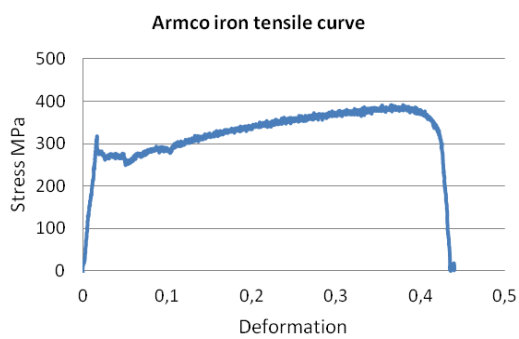

Fig 1. Stress-strain curve

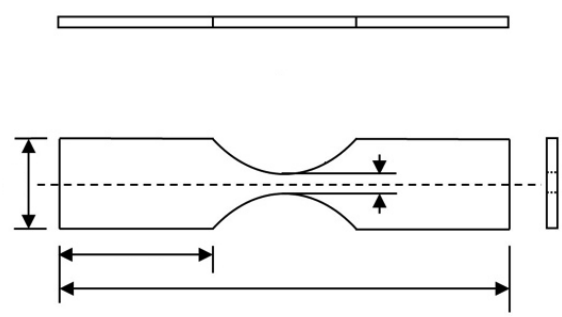

Fig 2. Sketch of flat ultrasonic specimen

For the reason of surface online observation condition by IR camera and optic microscope, a new design of 1 mm flat specimen (Fig. 2) was used to carry out fatigue tests. Specimen, special attachment and piezoelectric fatigue machine constituted the resonance system working at 20 kHz. The cyclic loading is tension-compression. The stress ratio is then R = -1. Before testing, both sides surface of the flat specimen were polished. One surface of the flat specimen was electrolytic etched.

According specimen designs, the specimen center has zero axial displacement theoretically during ultrasonic fatigue loading. The displacement rises continually at position both side away from the center. There is a small area on the surface which includes specimen center remains visible by optical microscope because the displacement maintained at very low level. Therefore a mobile optical microscope constructed for taking the online image. It has magnification 320X and recording image at frequency up to 1 Hz. With this mobile optical microscope, it is possible to observe general appearance when character deformation takes place in the specimen surface like enforced slip bands. The typical online observation system is shown at Fig. 3.

Fig. 3 Experimental system

3. Results and discussions

By the advantage of displacement node and stress distribution at center of gigacycle fatigue specimen, with online optical microscope observation, Fig. 4 shows the evolution of irreversible deformation in the specimen surface by increasing number of cycles. It is found that, irreversible slip bands formed at the beginning of fatigue loading. This slip bands are multiplied or grown in the same grain due to following cycle loading. At neighbor area, new irreversible slip bands formed independently in another grain where no deformation appears at previous $1.6x10^7$ cycles. Grain, either one already with slip band or one without slip band can has new slip band occurrence due to fatigue loading in same test condition. At the slip bands site where optical observation carried out, most of irreversible slip bands formed before $3x10^8$ cycles. Only slightly evolution occurs by cyclic loading during fatigue life between $3x10^8$ and 10^{10} cycles. Fig.4 suggests that new irreversible deformation (localized plastic strain) per each loading cycle $\Delta\varepsilon/N$ is decreasing with increasing number of cycle. $\Delta\varepsilon/N$ closing to zero after $3x10^8$ cycles in this case. In other words, crack initiation due to cumulating further new irreversible deformation after $3x10^8$ cycles is scattered dispersed. That may be the reason why the S-N curve is normally significantly dispersed at regime beyond 10^9 cycles.

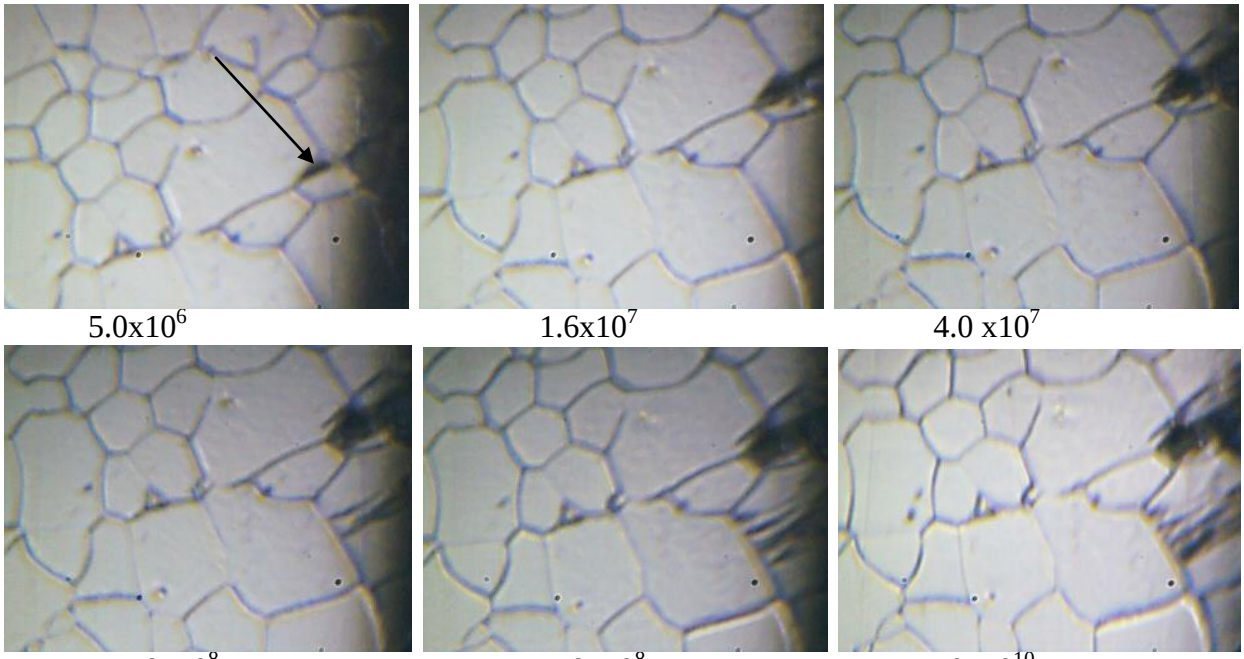

$5.0x10^6$ $1.6x10^7$ $4.0\ x10^7$

$1.0x10^8$ $2.9x10^8$ $1.0x10^{10}$

Fig. 4 Evolution of surface irreversible deformation under fatigue loading σ_a =174 MPa

Detail observations of surface irreversible slip bands or PSB under Scanning Electron Microscope (SEM) are given in Fig. 5. PSBs are found in 5 grains, where other grains remain undeformed at all. As described in f.c.c material, PSB formed by fatigue is localized irreversible plastic deformation. PSB is significantly changing the roughness of the original surface. At extrusion area, PSB lies to the mass of matrix out of the surface. At observation site, there are two main orientations of PSB at different grains whose PSB orientations have angle close to 90°. Even in similar orientation, the PSB have clear end at grain boundary. It suggests that PSB is anchored at grain boundary. PSB could active slip system in neighbor grain by enforce the stress concentration at inter boundary, but not go across the grain boundary. In the EBSD observation, same slip band direction always in the similar oriented grain (see slip band in red grain and orange grain). When neighbored grains have big difference in crystalline orientation, direction of slip band in different grain intents to be perpendicular (see slip band in red grain and blue grain). Unlike straight PSBs find in the f.c.c. crystalline, irreversible slip bands in b.c.c. are formed less individual.

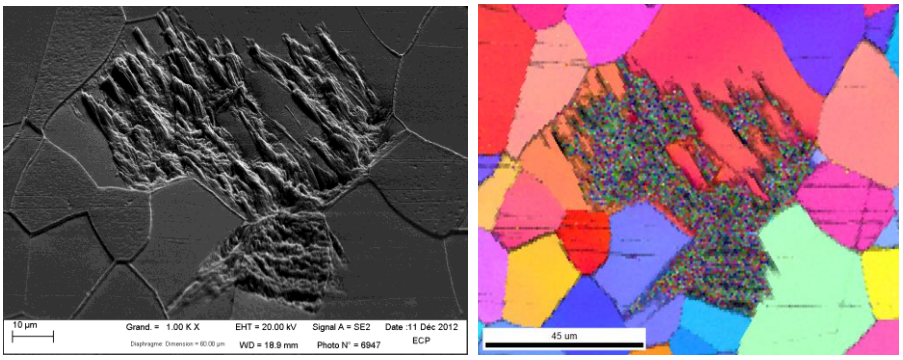

Fig. 5 PSB surface observation by SEM and EBSD

A specimen with pronounced PSBs was investigated in 3 perpendicular surfaces to have deeper understanding in 3 dimensions of PSB. The 3 surfaces are: original specimen surface, axial cutting surface and cross cutting surface as shown in Fig 6a. All 3 surfaces were prepared by carefully mechanical polish and 4% Nital etching. SEM observations at corner between axial cutting surface and original surface are presented in the Fig 6 b&c and cross section surface in the Fig 6d. Different oriented longitudinal slots were found pronouncedly at both side of corner on the axial cutting surface and original surface. Slots orientation changing takes place at grain boundary. It is reasonable to relate those slots to formation of PSB on the original specimen surface.

The figure 6c is the original surface observed with the inlens detector. It is easier to see, that the slots are not deep. It seems these slots are like cylinders. The width of each individual slot is around 0.5 μm, the distance between parallel slots varied from 1 μm to 3 μm and the length of slot is between 2 μm to 10 μm.

On the cross section (Fig. 6d), it appears equiaxe hollows separated or not by a thin wall of matrix (in nanoscale). Hollows are distributed linear in several lines as marked in the yellow square (Fig. 6d). Those lines with hollows are parallel. Equiaxe hollow has size in 0.5 μm. Hollow lines observed here have length about 3 μm to 5 μm. The distance between hollow lines is approximate 2 μm. Regarding this hollow deformation at cross section and longitudinal slots found in Fig 6c, it may be constructed a 3D schematic figure of the slots and hollows as Micron Abreast Pipes in Fig.6e

However in the fundamental material like ferrite, subsurface irreversible deformation is decreasing according plane stress condition function with distance to the surface

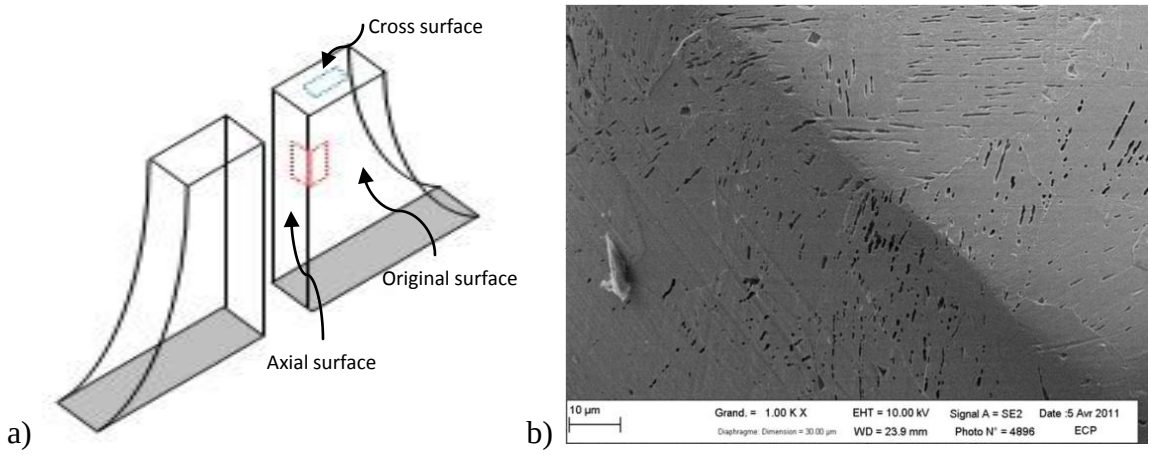

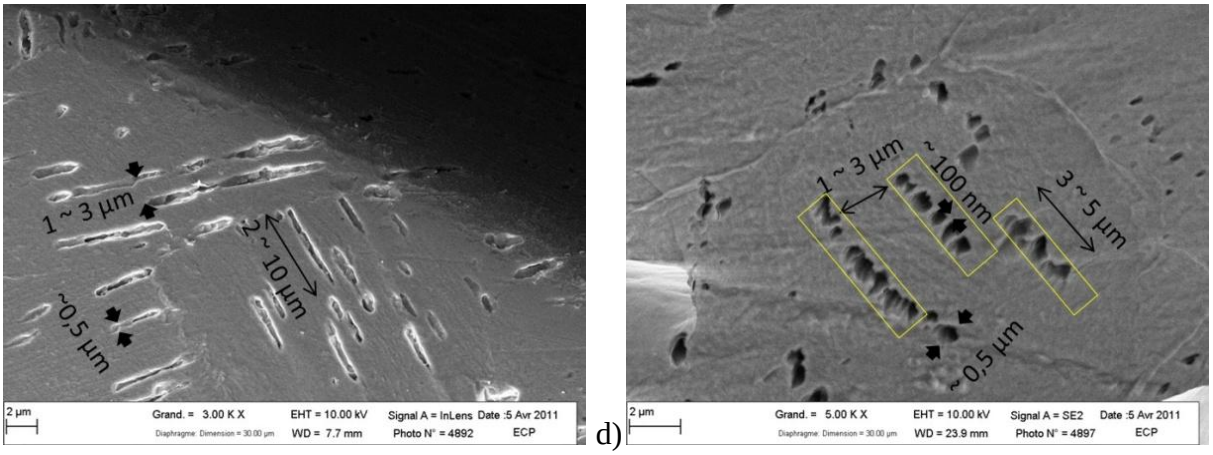

c) d)

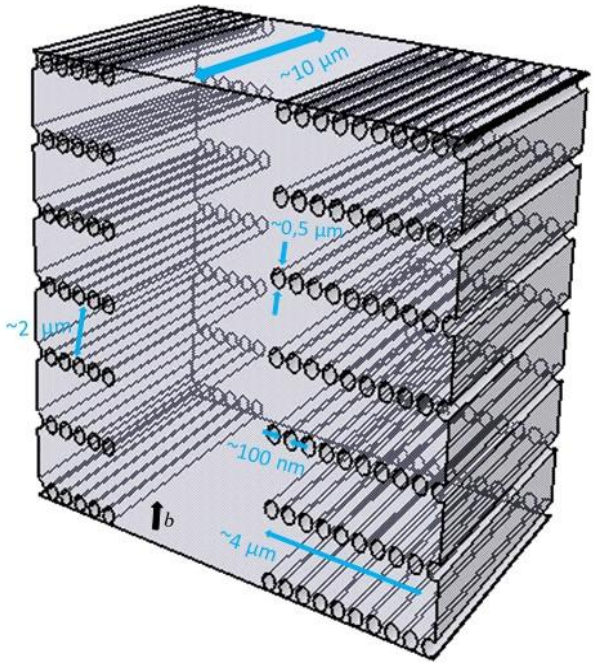

e)

Fig. 6 slots after polish and etching the PSB [13] and micron scale channel in matrix

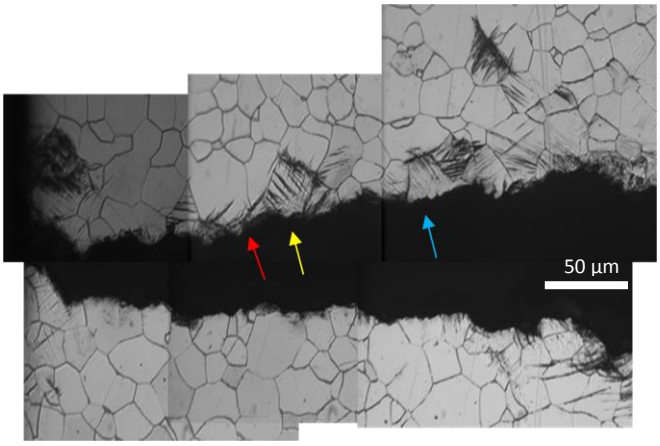

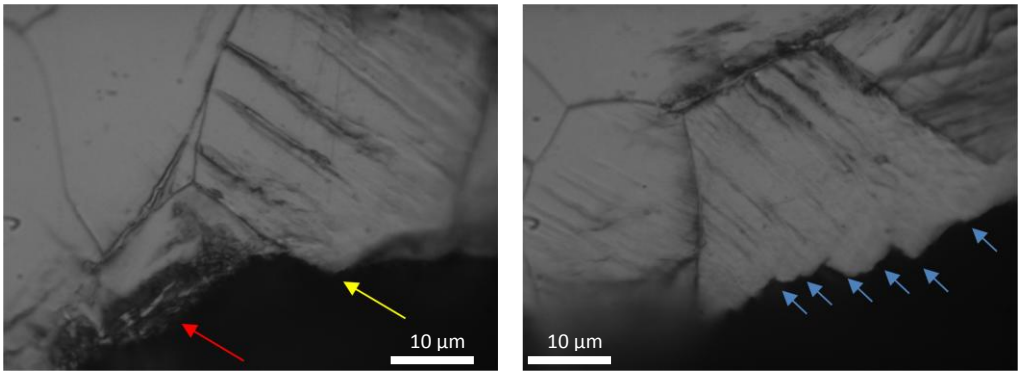

Fig. 7 Surface of cracked specimen

Surface microstructure observation after fracture shows as in Fig.7. Red arrow indicates a grain which has PSBs in it. In this PSB grain, crack opens along the PSBs which formed long time before crack occurs in this grain. Yellow arrow indicates the crack along a grain boundary. Intergranular crack takes place at grain boundary between two grains whose PSB are perpendicular to each other. Blue arrows denoted a transgranular crack. Crack stairs in the surface of this grain correspond to the appearance of slip bands below the fracture surface.

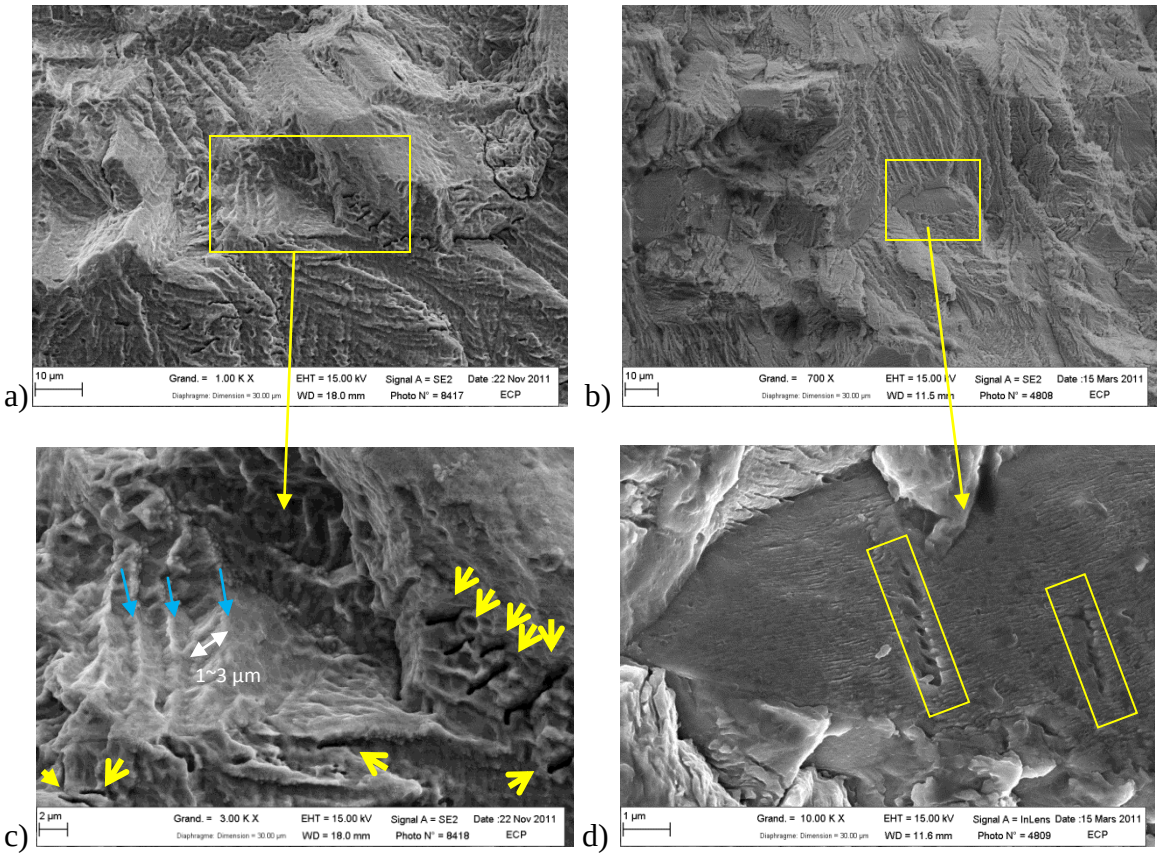

e) 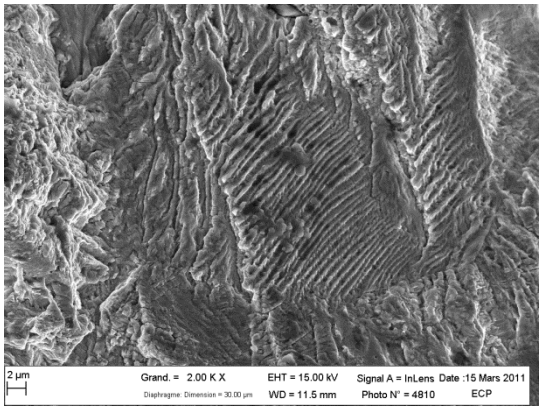

f) 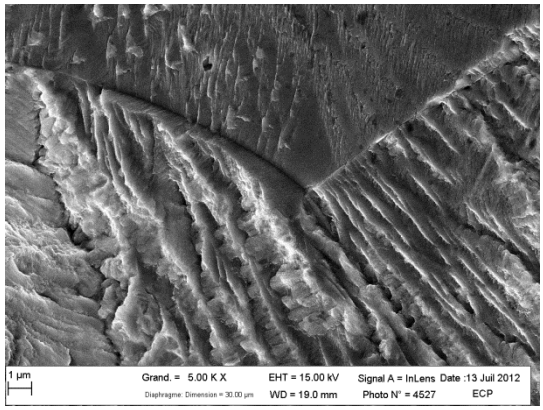

Fig.8 intergranular and transgranular crack at initiation area

Fracture surface gives more interesting results. In the initiation area, the grains trace is visible (Fig.8a and Fig.8b). Three types of pattern were found: one intergranular and two transgranulars. The intergranular pattern is seen in fig8b and 8d. This intergranular crack appears not smooth, but presents a very fine linear structure on the grain surface which believes related to the dislocation slips. Moreover, two lines of hollows separated by around 2 μm are visible (Fig. 8d). The first transgranular crack is shown in Fig. 8a and Fig.8c. The fracture surface through the grain is developed as a staircase. The distance between two stairs is about 2 μm. It suggests the same mechanism that those forming the stair structure in the surface as blue arrows in Fig.7. The second pattern of transgranular crack is shown Fig.8e or Fig.8f (where a transition from an intergranular crack to the second transgranular pattern is seen). In this transgranular case, the fracture surface is composed of longisectional pipes arranged side by side. The diameter of the pipes is 0.6μm in average. It may be correspond to PSB on the surface indicated by red arrows in Fig.7.

Now, it is interesting to relate the fracture surface pattern with the subscale damage produced by PSB as Micron Abreast Pipes seen in Fig.6. An illustration of this fracture mechanism is schematically reported on the Fig. 9. The staircase structure is probably a fracture occurring partially on abreast pipes, and crossing over to abreast pipe just below or above. The distance between two stairs is about 2 μm, in good agreement with the distance between two abreast pipes. In the case of second transgranular pattern, the crack path is entirely on abreast pipes in the same dislocation slip plane. The characteristic dimension of this pattern is pipe diameter about 0.5 μm. The line of hallows (separated in distance 2 μm) seen on the intergranular surface Fig 6d are probably the end of abreast pipes at grain boundary (in good agreement with the distance between two neighbored pipes). However, abreast pipes sometime may linked through the nanoscale wall between pipes to form subscale 2 dimensions planar default as small facets denoted by yellow arrows in Fig 8c.

As shown previously (Fig.6 and 8), irreversible slip band not only take place on the surface but also at subsurface (with a minor density). The internal irreversible plastic deformations will potentially facilitate the fatigue crack initiation. Then it can conclude here that very high cycle fatigue crack initiate not only by extrusion and intrusion, but also due to irreversible slip bands in the subsurface. It starts from the irreversible slip bands in the surface, which induces stress

concentration and produces the occurrence of PSB in subsurface [13]. Then irreversible slip bands in the subsurface makes easier the fatigue crack initiation stage. Fatigue crack at subsurface at initiation stage is form by connecting subscale defaults, such as Micron Abreast Pipes in same slip plane, inharmonious of deformation at grain boundary or links between small facets of irreversible slip bands.

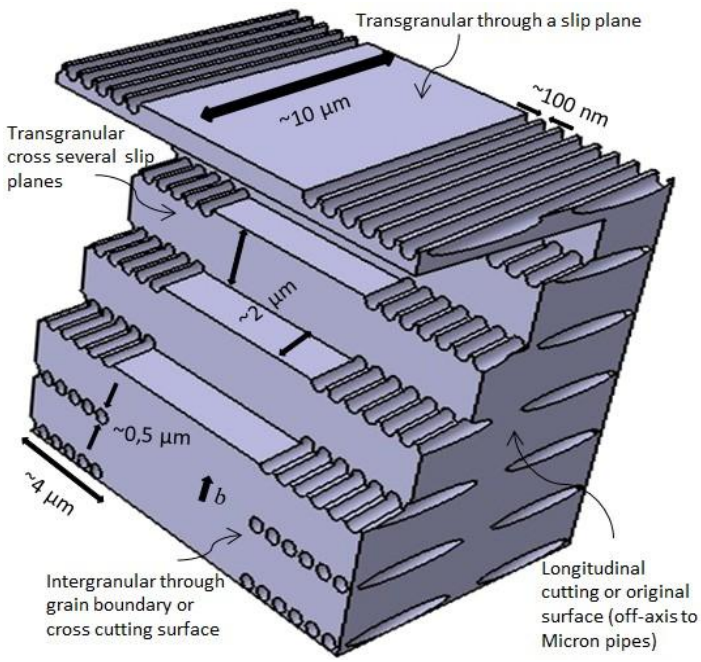

Fig. 9. Fatigue crack at initiation area relative to PSB in material

Regarding fatigue propagation threshold and temperature elevation [14,15], it may estimate following mechanism of fatigue initiation in ferrite at VHCF regime. PSB occurs on specimen surface at beginning stage of VHCF test. With following loading cycles, more PSBs formed in surface and subsurface, evidently at location of initiation area. In means material volume in a small initiation area is damaged by PSB but not opened by a crack. PSBs and other multiplied dislocation lines make more volume at initiation area extended and weak to undertake the long range stress. Therefore pronouncedly stress concentration takes place in front of area extended. Consequently extended area grown to the edge of initiation area which correspond to the fatigue stress intensity factor threshold $\Delta K_{th}=E\sqrt{b}$ (Herzberg-Paris-McClintock law) [16]. By sufficient stress concentration, the initiation area opened suddenly and remained some area in initiation cracked without plastic deformation. As blue arrows in Fig 7, between two slip planes, crack at stairs shows no plastic deformation on surface. The temperature recording [14] of VHCF test has shown that the crack initiation stage occurs at the end of VHCF test (less than 1% of the total life). More than 99% of the total life is takes up by the micro-damage due to forming PSBs in surface and subsurface, especially initiation area. The first fatigue crack appears on the specimen surface, the entire crack initiation zone appears supervening by connecting all defaults in the bulk material with in short time at end of VHCF.

4. Conclusions

According to the results described above, the following conclusions may draw for ferrite material failed in VHCF:

1) Irreversible deformation (PSB) forms on the surface specimen at the beginning stage of VHCF in plane stress condition
2) Irreversible deformation can growth or multiplies independently at neighbor grains. After 10^9 cycles new irreversible deformation (localized plastic strain) per each loading cycle $\Delta\varepsilon/N$ is decreasing by increasing number of cycle.
3) Irreversible deformation not only exists on the surface before crack but also in the subsurface volume.
4) Irreversible plastic deformations at subsurface makes easier the fatigue crack initiation.

Acknowledgements

This research was supported by the grant from the project of Microplasticity and energy dissipation in very high cycle Fatigue (DISFAT, project No. ANR-09-BLAN-0025-09), which funded by the National Agency of Research, France (ANR). Inner discussions of DISFAT project with Prof Mughrabi and other members are great appreciated here. The authors also thank F.Garnier for her participation of SEM observations.

References

[1] S. Suresh, Fatigue of materials (second edition), Cambridge university press, Cambridge, 1998
[2] Bathias,C.,Pineau, A. Fatigue des matériaux et des Structures, 2008, pp85-246
[3] Mughrabi, H. The Strength of Metals and Alloys, pp.1615-1639, Haasen,P., Gerold, V.,Kostorz, G., (Ed.), Pergamon Press, Oxford, 1980
[4] H. Mughrabi, Microscopic mechanisms of metal fatigue, Strength of Metals and Alloys, 3 (1979), pp. 1615-1638
[5] Mughrabi, H., Herz, K., Stark, X. (1976) Int Journal of Fracture 17,193-320
[6] Mughrabi, H., Wüthrich, Ch. (1976) Philosophical Magazine A33, 963-984
[7] Mughrabi, H., Ackermann, F., Herz, K. (1979) In: ASTM STP 675, pp 69-105
[8] Klesnil, M., Lukas, P. (1965) J. of the Iron and Steel Institute 203, 1043 – 1048
[9] Sommer, C., Mughrabi, H., Lockner, D. (1998) Acta Mater. 46, 1527-1536
[10] J.T.Mcgrath, W.J.bratina, Dislocation structures in fatigued iron-carbon alloys, The Philosophical Magazine, 12, 1293-1305,1965.
[11] Wood, W. A. ; Reimann, W. H. ; Sargant, K. R. Comparison of Fatigue Mechanisms in Bcc Iron and Fcc Metals, Transactions of the Metallurgical Society of AIM vol. 230, 511-518, 1964.
[12] R. P. Wei, A. J. Baker, Observation of dislocation loop arrays in fatigued polycrystalline pure iron, Philosophical Magazine, vol.12, 1087-1091,1965
[13] C. Wang, D. Wagner, Q.Y. Wang, C. Bathias. Gigacycle fatigue initiation mechanism in Armco iron, International Journal of Fatigue, Volume 45, December 2012, Pages 91-97
[14] Chong Wang, Danièle Wagner, Claude Bathias - Study of fatigue crack mechanism on an armco iron in the gigacycle fatigue by temperature recording and microstructural observations, Abstract paper accepted at ICF 13
[15] N. Ranc, D. Wagner, P.C. Paris – Study of thermal effects associated with crack propagation during very high cycle fatigue, Acta Materiala 56 (2008) 4012-4021.
[16] Claude Bathias, Paul C. Paris. Gigacycle fatigue of metallic aircraft components. International Journal of Fatigue, Volume 32, Issue 6, June 2010, Pages 894-897

Subsurface non defect fatigue crack origin and local plasticity exhaustion

Guocai Chai[1,2*]

[1] Strategy Research, Sandvik Materials Technology, 811 81 Sandviken, Sweden
[2] Engneering Materials, Linköping University, 581 83 Linköping, Sweden
* Corresponding author: guocai.chai@sandvik.com

Abstract Besides "fish eye", subsurface non-defect fatigue crack origin (SNDFCO) in the matrix is another fatigue crack origin observed during very high cycle fatigue (VHCF). This paper provides some discussion on the phenomena and damage mechanisms from the recent investigations using four metallic materials with different microstructures. The results show that the strains in these materials in the VHCF regime were highly localized, especially in the multi-phase materials, where the local maximum strain can be eight times higher than the average strain value in the specimen. This high strain localization can lead to a fatigue damage or fatigue crack initiation at grain boundaries or twin boundaries by impingement cracking. High strain localization causes dislocation accumulation of very small strain during each cyclic loading and consequently the formation of local "fine grain area" and also increases the local hardness of the material. This can cause quasi-cleavage crack origin, and finally the formation of SNDFCO. The results in this paper indicate that fatigue damage and crack initiation mechanisms in the VHCF regime can be different in different metals due to the mechanisms for local plasticity exhaustion.

Keywords Very high cycle fatigue, Local plasticity exhaustion, Fatigue crack initiation, stainless steels

1. Introduction

Fatigue behaviors of metals in very high cycle fatigue (VHCF) regime have been widely investigated during the last decade [1-5]. It has been found that fatigue crack initiation in metals can shift from surface defects, subsurface defects and subsurface matrix with decreasing applied stress or increasing fatigue life [1, 4, 6]. Subsurface fatigue crack initiation has been mostly reported to start at subsurface defects such as inclusions, pores and microstructure inhomogeneity [4]. The surface treatments like shot peening, case hardening and surface nitriding can prevent the surface fatigue crack initiation, and cause a shift to a subsurface fatigue crack initiation at relatively higher stress amplitudes, and therefore improve the fatigue life or fatigue strength of the material [7]. Recently, another type of subsurface crack initiation, namely subsurface non-defect fatigue crack origin (SNDFCO), has been reported [6-8]. These crack origins were observed in the material fatigue tested for a very high fatigue life, and start in some phase or matrix of the material and are not associated with pre-existing defects.

In very high cycle fatigue regime, the applied stresses or strains are sometime well below the bulk yield strength or in the elastic deformation regime. How a cyclic plastic deformation or damage can occur in such a situation is still not well known. Hydrogen has been considered as a source for the formation of fish eye of subsurface inclusion [9], but this cannot explain a subsurface matrix crack initiation or formation of SNDFCO. Other mechanism such as localized deformation by dislocation pileup or grain boundary imcompatibility has been proposed [6, 10]. These observations are however not enough to verify why SNDFCO has only been observed in some alloy systems. On the other hand, the mechanism for the shift of fatigue crack initiation from surface to subsurface is still not fully understood. Another phenomenon correlated to fatigue crack initiation in the VHCF regime is the formation of fine grains in the Fine Grain Area, FGA [11]. The reasons of the formation and the role of this FGA are not well explained either. In this investigation, fatigue crack initiation behavior and fatigue damage mechanism at a stress well below the bulk yield strength have been investigated in three metal materials with different microstructures using scanning electron microscopy, SEM, electron back scatter diffraction, EBSD and electron channel contrast

image, ECCI. The purposes are to get a better understanding of the mechanisms for sub-surface fatigue crack initiation in the matrix or formation of SNDFCO in the VHCF regime and the formation of FGA.

2. Materials and Experimental

2.1 Materials

Four metal materials: one nickel base alloy (Alloy 690), one martenistic–austenitic steel (MAS), one martensitic-ferritic (or bainite) steel (MFS), and one titanium alloy (Ti6Al4V), were used in this investigation. Table 1 and 2 show their nominal chemical compositions and mechanical properties.

Table 1: Chemical compositions (wt%) and conventional tensile properties of the materials used

Alloy	C	Si	Mn	Cr	Ni	Ti	Fe	N	Mo	σ_{YT} (MPa)	σ_{UT} (MPa)
Alloy 690	0.018	0.30	0.27	29.6	58.85	0.26	10.51	0.026		305	582
MAS	0.38	0.4	0.6	13.5					1.0	1468	1968
MFS	0.23	0.25	0.65	1.3	2.7				0.25	986	1200

Table 2: Chemical composition (wt%) and conventional tensile property of titanium alloy

Alloy	C	Al	V	N	O	H	σ_{YT} (MPa)	σ_{UT} (MPa)
Ti 6Al4V	0,008	5.6	4.1	130ppm	940ppm	6ppm	876	952

Fig. 1 shows the microstructures of these four materials. Alloy 690 is a single phase material. The others are two or multi-phase materials. For MAS and MFS materials, the microstructures are very fine as shown in the TEM images.

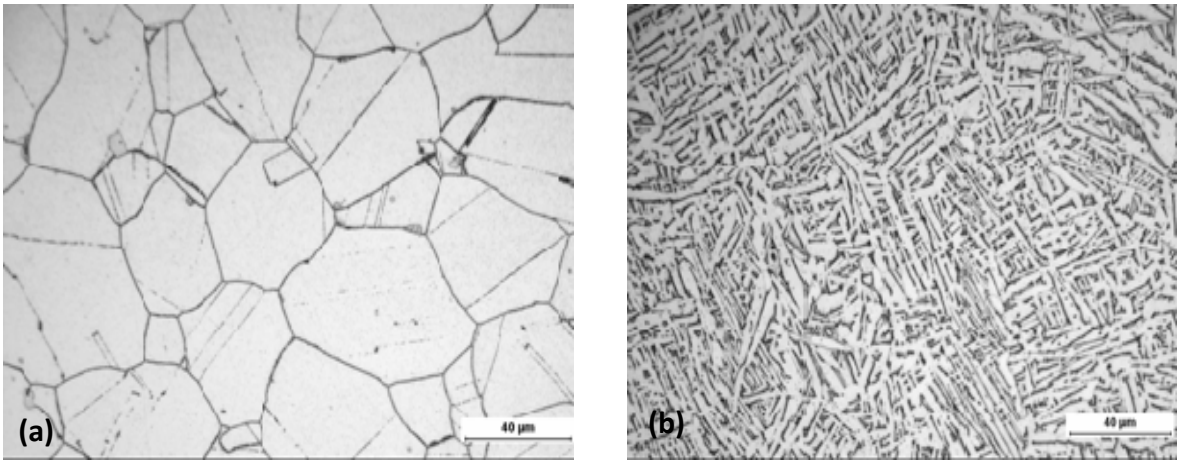

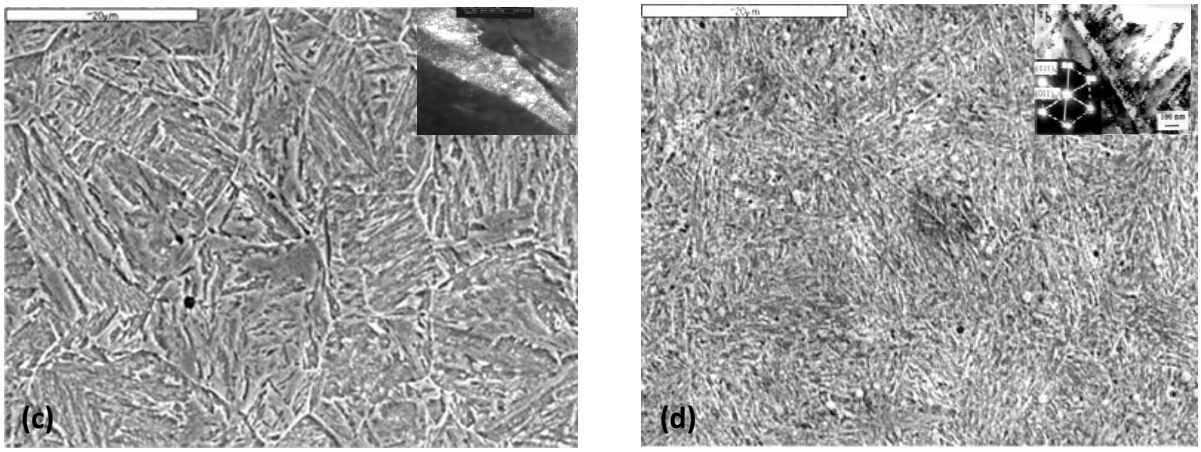

Fig. 1. Microstructures of the materials used for the fatigue tests. (a). Alloy 690, (b). Ti6Al4V, (c). Martensitic ferritic steel (MFS), (d). Martensitic austenitic steel (MAS).

2.2 Experimental

Two types of stress controlled fatigue tests have been carried out. One was performed using an Amsler machine with a frequency of about 140 Hz up to $5x10^8$ cycles. Another test was performed using an ultrasonic (Piezo) fatigue testing machine with a frequency of 20 kHz up to $5x10^9$ cycles. A round sample with a diameter up to 6mm was used. Pulsating tensile stresses with a stress ratio R=0.1 were applied for both tests.

The origins of fatigue crack initiation and fatigue pre-initiation damage (dislocation slip bands) were investigated using a JEOL 840 scanning electron microscope (SEM). In order to investigate the fatigue crack initiation mechanism and material damage process after the fatigue, the microstructures or damage in the samples after the VHCF testing were investigated using two scanning electron microscopy techniques: electron back scatter diffraction (EBSD) and electron channeling contrast image (ECCI). The EBSD technique was used to analyze the strain or stress localization or the influence of VHCF on the strain localization. Orientation maps were performed in a 6500 F JEOL field emission gun-scanning electron microscope (FEG-SEM) equipped with a TSL OIM EBSD system. EBSD maps were measured at 15 kV acceleration voltage and a working distance of 15mm. The ECCI technique has been recently proven as a powerful technique to image deformation damage and even dislocation structures steels by using a SEM [23]. ECCI observations were carried out in a Zeiss Crossbeam instrument (XB 1540, Carl Zeiss SMT AG, Germany) consisting of a Geminitype field emission gun (FEG) electron column and an focused ion beam (FIB) device (Orsay Physics). ECCI was performed at 10 kV acceleration voltage and a working distance of 5 mm, using a solid state 4-quadrant BSD detector. The microscope was run in the “high current” mode and an objective lens aperture of 120_m was used.

3. Results and discussion

3.1Fatigue life and crack initiation behavior

Fig. 2 shows the results of the fatigue tests for these four materials. The S-N curves use the applied stress amplitude versus number of cycles. Since these alloys have different strength, and therefore show different fatigue behaviors. Generally, the fatigue strength is related to the strength of the material.

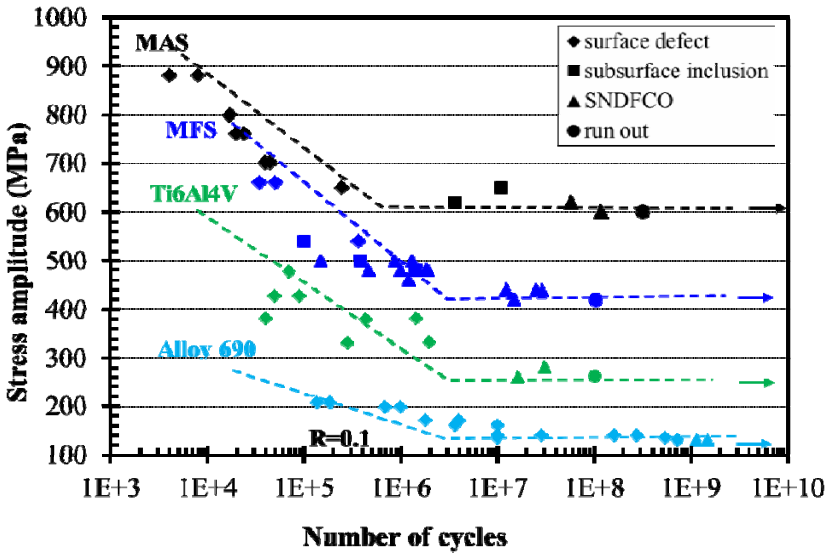

Fig. 2. S-N curves for four materials tested up to very high cycle fatigue regimes.

As expected, there is a shift of fatigue crack initiation from surface fatigue crack initiation (SFCO) to subsurface fatigue crack initiation (SDFCO) in all these four materials. With a further decease of stress or a longer fatigue life, however, fatigue crack initiation at subsurface matrix (SFDFCO) can be observed. Four types of SNDFCO can be observed, which are shown in Fig. 3. The first type is a quasi-cleavage type of origin. They appear near the edge or inner of the sample (Fig. 3a). The second is that fatigue crack initiation at grain boundary or phase boundary, which becomes a rather small crack origin (Fig. 3b). The third is a facet type of origin, but small deformation slips on the fracture surface can be observed with a large magnification (small picture in Fig. 3c). The fourth is a small origin with lath type of microstructure. Rough surface can be observed. Usually, different alloys show different type of crack origins.

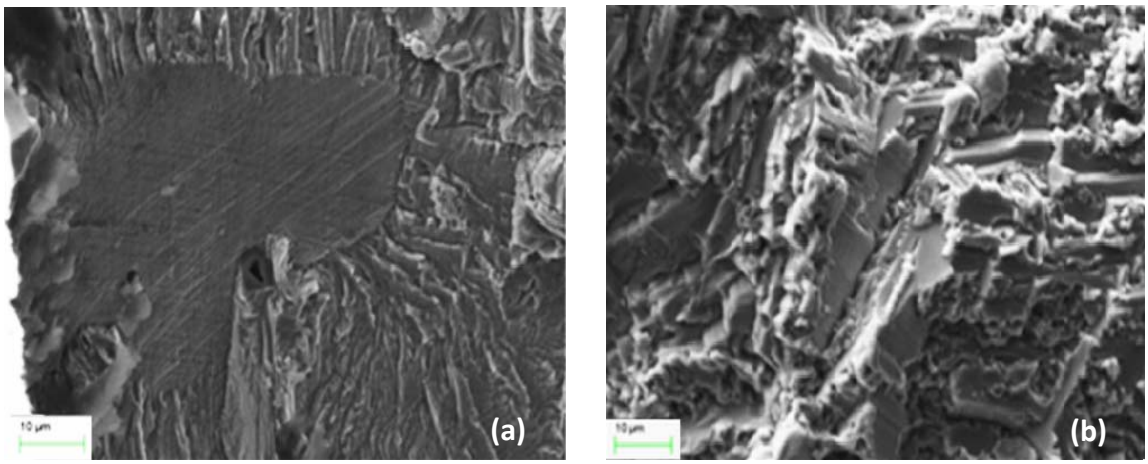

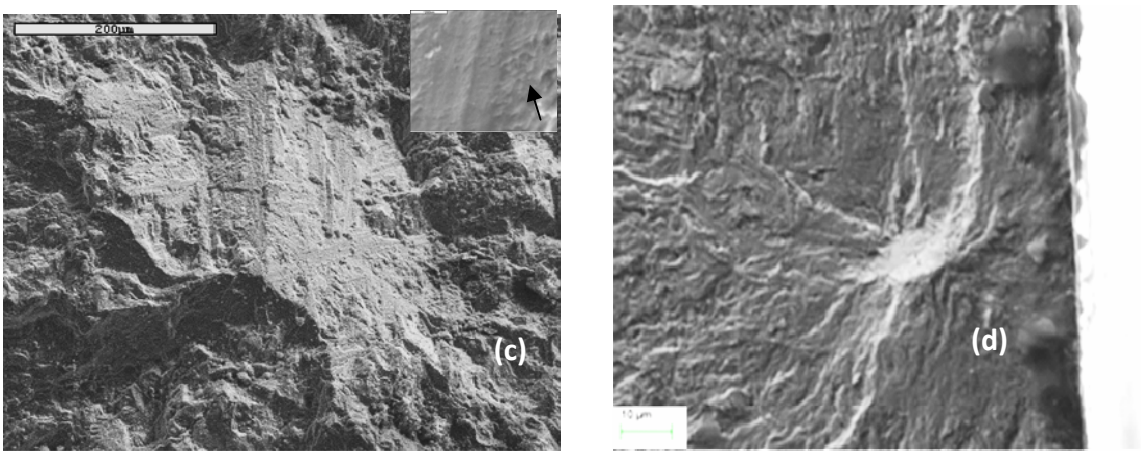

Fig. 3. Fatigue crack initiation in high cycle or very high cycle regime, (a). Alloy 690, quasi-cleavage, σ_a=140MPa, N_f=1.61x10^8, (b). Ti6Al4V, grain boundary, σ_a=280MPa, N_f=3.0x10^7, (c). Martensitic ferritic steel (MFS), facet, σ_a=460MPa, N_f=1.2x10^6, (d). Martensitic austenitic steel (MAS), lath, σ_a=600MPa, N_f=3,2x10^8.

3.2 Strain localization or plasticity exhaustion in very high cycle regime

In order to study the material damage mechanism in the VHCF regime, a special specimen was prepared by polishing the SNDFCO or fish eye. The local strains were then measured and evaluated using the EBSP technique. The local strain of each individual grain could be mapped through the image analysis of all the grains [12]. Fig. 4 shows the relative strains (strain contouring) for the specimens within SNDFCO or fish eye from Alloy 690, Ti6Al4V and MFS materials. A common character for these three specimens is that strain is very concentrated or localized (red color in the figures). Table 2 shows a comparison of the maximum strain and the average strain in SNDFCO or the views observed. The maximum strain is much higher than the average values. For MFS material, the maximum strain can be eight times higher than the average value. This indicates that the strain under SNDFCO is highly localized in this material.

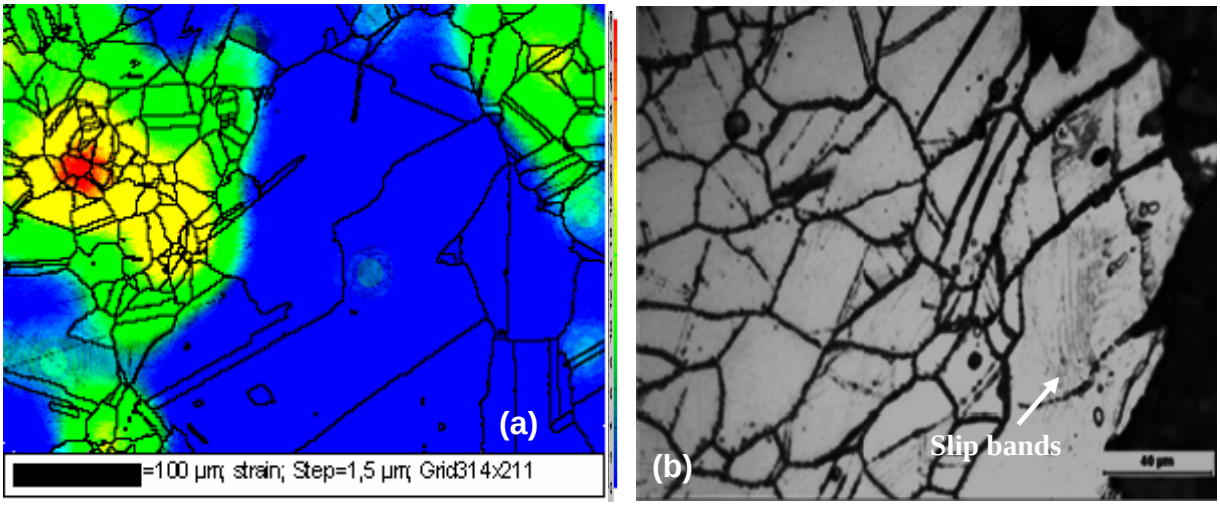

Figure 4. Strain contouring mappings obtained from EBSD analysis (a). Alloy 690 with Δσ=135 MPa, N=5.45x10^8 cycles, (b). Alloy 690 with Δσ=140 MPa, N= N=2.77x10^8 cycles.

Table 2. Maximum and average strain contouring from EBSD analysis of three materials

	MFS	Alloy 690	Ti6Al4V
Average	4,42	1,77	1,15
Maximum	36,46	9,35	3,76

MFS material, which has the highest strain localization (Table 2), has a hard martensitic phase and a soft ferritic phase. The soft phase could undertake cyclic plastic deformation at a stress even well below the bulk yield strength. This is because the applied stress can still be higher than the yield strength of the soft phase. The phase will thus undertake a cyclic plastic deformation, which can then cause a plasticity exhaustion and consequently formation of damage. SNDFCO is therefore formed for fatigue crack propagation. MAS material, which has a hard martensitic phase and a soft austenitic phase, has the similar situation. As known, strain localization can be related to accumulation of dislocations.

3.2 “Fine grains” in fatigue crack initiation area

Figure 5 shows the ECCI pictures under the fatigue crack initiation area (quasi-cleavage area) in Fig. 3a. Two types of microstructures can be identified. One is the “no or less deformation” area where is near the sample surface and center. Another is the area where “smaller or fine grains” can be observed (Fig. 5a). Actually, the area has high plastic deformation (Fig. 5b). “fine grains” have formed in some areas, but large plastic deformation can still be seen in other areas. This indicates that the formation of “fine grains” is a cyclic plastic deformation process, or formation of dislocation subcells. The size of “fine grains” depends on the stress concentration in the area and number of cycles. This phenomenon can explain the formation of FGA in the VHCF material reported earlier [11]. High stress concentration around the inclusion after giga numbers of cyclic loading can cause local dislocation initiation and movement, which cause the formation of dislocation subcells, and consequently the formation of fine grains.

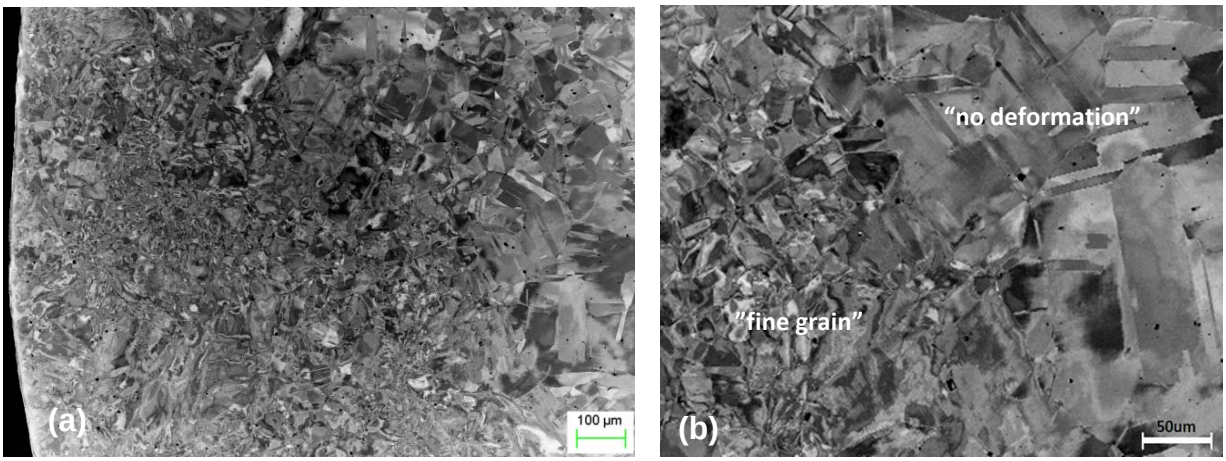

Figure 5. ECCI pictures show the microstructure under the fatigue crack initiation area in Fig. 3a, (a). Overview, (b). Enlarged (a).

In this "fine grain" area, high plastic deformation can be found (Fig. 6a). They are mainly appear near gran boundaries and twin boundaries. This may be attributed to dislocation pile-up as reported earlier [13]. Dislocation slip bands or eventually persistent slip bands (PSB) can be observed (Fig. 6b). They interact at grain boundaries and cause the formation of damage or micro crack due to impingement cracking. This observation shows that the fatigue crack initiation in the very high cycle fatigue regime can still compare with that in the low cycle fatigue regime [14].

Figure 6 ECCI pictures show the microstructure under the fatigue crack initiation area in Fig. 3a, (a). Plastic deformation in the "fine grain, (b). Slip bands or PSB, interaction between slip band and grain boundaries.

As known, grain boundary or twin boundary act always as barriers to stop the movement of dislocations carried by slip bands, which leads to the formation of dislocation piling-up. Figures 7 shows that the twin boundary has blocked the movement of dislocations carried by slip bands, which cause the formation of damage at twin boundary due to the stress concentration by the piling-up of dislocations.

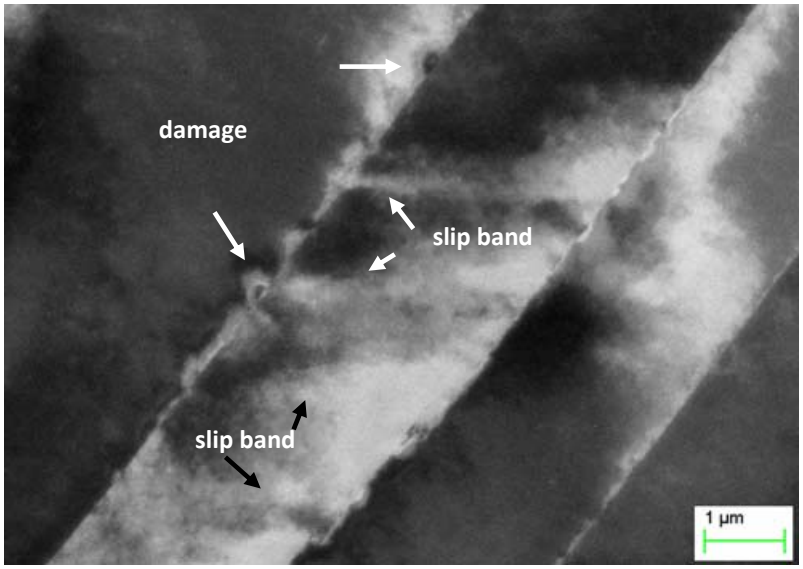

Figure 7 ECCI pictures show the microstructure under the fatigue crack initiation area in Fig. 3a, Formation of damage at twin boundary by dislocation slipping bands in the annealing twin.

The results discussed above are unexpected. High strain localization due to Schmid factor effect will cause an exhaustion of local plasticity of the material and dislocation slip band or persistent slip bands, and consequently formation of localized stress concentrations. This can lead to a fatigue damage or fatigue crack initiation at grain boundaries or twin boundaries by impingement cracking. High strain localization is the result of accumulation of very small strain during each cyclic loading in a much longer life or large number of cycles. This leads to the formation of local “fine grain area” and also increase the local hardness of the material, which can cause quasi-cleavage crack origin.

4. Size of SNDFCO

In this investigation, the formation of SNDFCO is treated as a crack propagation process. In the earlier work, the striations or ridges can be observed at the SNDFCO [6]. At small stress amplitudes, the striations can still be observed although the SNDFCO is facet (Fig. 3c). These striations are relatively small (50-100nm). The stress intensity factor ranges at the front of SNDFCO is evaluated using the following equation [15].

$$\Delta K = 0{,}5\sigma_{\max}\sqrt{\pi\sqrt{area}} \qquad (1)$$

In this study, area=L*b, where L is the maximum length of SNDFCO, and b is the shortest length of SNDFCO. This is a rather rough estimation since the actual SNDFCO is usually very irregular. Fig. 7 shows the stress intensity factor range at the front of SNDFCO in the martensitic-ferritic steel after the pulsating fatigue test. Although the size of SNDFCO is different, the stress intensity factor ranges at the front of SNDFCO are comparable, and vary from 2,8MPa√m to 4MPa√m, which is in the range of the fatigue threshold values. For the martensitic-austenitic steel, the stress intensity factor range at the front of SNDFCO is between 3.17 to 3.33MPa√m, which can compare with those of the

martensitic-ferritic phase alloy. These results show that the crack propagation within the SNDFCO is controlled by the microstructure mechanics, and the crack propagation outside the SNDFCO is controlled by elastic-plastic or linear mechanics. SNDFCO size depends on transition of crack propagation from stage I to stage II.

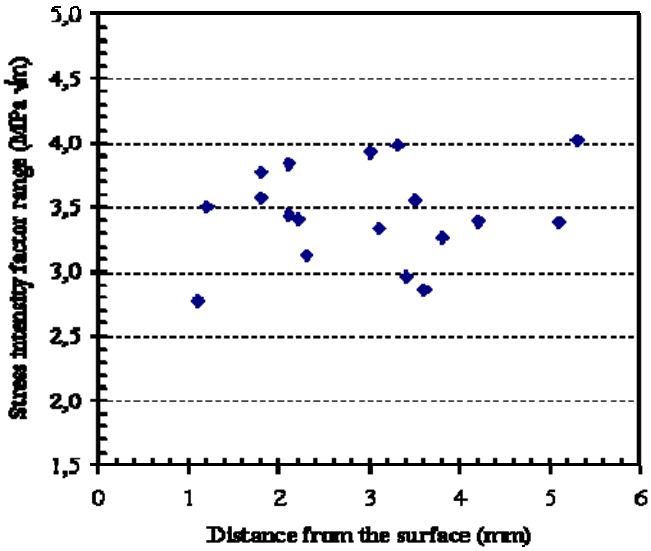

Figure 7. Stress intensity factor ranges at the front of SNDFCO in the martensite-ferritic steel.

5. Concluding remarks

In the VHCF regime, strain localization will occur in all these materials. This leads to local plasticity exhaustion the formation of local “fine grain area”. High strain localization causes dislocation accumulation of very small strain during each cyclic loading and consequently and also increases the local hardness of the material. This can cause quasi-cleavage crack origin, and finally the formation of SNDFCO.

The formation of SNDFCO is controlled by the microstructure mechanics. SNDFCO size depends on transition of crack propagation from stage I to stage II. The crack propagation outside the SNDFCO is controlled by elastic-plastic or linear mechanics.

Acknowledgements

This paper is published by permission of Sandvik Materials Technology. The author is also indebted to the co-authors in the reference list for their contribution and collaborations.

References

[1] H. Mughrabi, Fat. Fract. Eng. Mater Struct, 25 (2002) 755.
[2] P. Lukas and L. Kunz, Fat. Fract. Eng. Mater Struct, 25 (2002) 747.

[3] C. Bathias and P. C. Paris, Gigacycle fatigue in mechanical practice, editor: Marcel Dekker, Section 7, (2004) ISBN 0-8247-2313-9.
[4] Y. Murakami, Metal Fatigue: Effect of small defects and non-metallic inclusion, Elsevier Science Ltd, (2002).
[5] Y. Gu, X. Teng, C. Liu, Y. He, C. Tao, Acta Aeronautica et Astronautica Sinica, 33 (2012), pp. 2136.
[6] G. Chai, International Journal of Fatigue, 28 (2006) 1533.
[7] O. Umezawa, and K. Nagai, ISIJ International. 37 (1997), pp. 1170-1179.
[8] E. Notkina, G. Lütjering, and A. Gysler, Proc. Inter. Conf. on Fatigue in the very High Cycle Regime, University of Agriculture Science Press, (2001), Vienna, pp. 149-156.
[9] Y. Murakami, T. Nomoto and T. Ueda, Fat. Fract. Eng. Mater Struct, 22 (1999) 581.
[10] C. Stöcker, M. Zimmermann and H.-J. Christ, International Journal of Fatigue, 33 (2011) 2.
[11] T. Sakai, W. Li, B. Lian and N. Oguma, Review and new analysis on fatigue crack initiation mechanisms of interior inclusion – induced fracture of high strength steels in very high cycle regime, (2011), Proc. Of Conf. VHCF 5, eds: D berger, H. –J. Christ, pp. 19.
[12] N. Jia, R. Lin Peng, G. Chai, S. Johansson and Y. D. Wang, Mater. Sci. and Eng. A 491 (2008) 425.
[13] G. Chai, N. Zhou, S. Ciurea, M. Anderssona and R. Lin Peng, Scripta Materialia 66 (2012) p. 769.
[14] P. Zhang, S. Qu, Q.Q. Duan, S.D. Wu, S.X. Li, Z.G. Wang and Z.F. Zhang, Low-cycle fatigue-cracking mechanism in fcc crystalline materials, Philosophical Magazine, Vol. 91, No. 2, 11 January 2011, 229–249.
[15] Y. Murakami, Eng. Frac. Mech., 22 (1985), pp. 101-114.

Application of Dang Van criterion to rolling contact fatigue in wind turbine roller bearings

Michele Cerullo

Department of Mechanical Engineering ,Technical University of Denmark, Lyngby 2100, Denmark
mcer@mek.dtu.dk

Abstract A 2-D plane strain finite element simulation of rolling contact in wind turbine roller bearings is used to study very high cycle fatigue (VHCF). Focus is on fatigue in the inner ring, where the effect of residual stresses and hardness variation along the depth are accounted for. The purpose here is to ensure that VHCF failure does not initiate. For the purpose the Dang Van multiaxial fatigue criterion is applied, simulating the contact on the bearing raceway by substituting the roller with the Hertzian static pressure distribution. Contact without friction is assumed here and the material used for the simulation is taken to be an AISI 52100 bearing steel. Both an initially stress free bearing and different residual stress distributions are considered. An assumed residual stress distribution, equilibrated by an elastic step calculation, is subsequently subjected to the stresses caused by the contact with the roller. The effect of variable hardness along the depth is also studied, relating its values to the fatigue limit parameters for the material and it is found that its distribution can have a significant influence on the probability of failure for bearings subjected to VHCF loading.

Keywords High Cycle Fatigue, Wind turbine, Dang Van

1. Introduction

It has been seen [1,2] that one of the important reasons of corrective maintenance for a wind turbine is a failure due to rolling contact fatigue (RCF) in one of the bearings in the gear box [3]. Therefore, the interest on the reliability of gearboxes grew over the last years [4,5]. Though failure rates in electrical systems and other subassemblies in a wind turbine are in fact higher, or at least comparable with faults in the gearbox, recent studies [6–8] show that the downtime, in terms of hours lost per failure, is much higher for latter ones. This, rather than the failure rate, is therefore one of the main reasons for the industry's focus on these subsystems.

In the gearbox, the bearings used are mostly roller bearings, due to the high loads involved. Even if the lubricant is kept clean and the bearing is properly lubricated, roller bearings sometimes experience rolling contact fatigue that appears as a crack starting below the surface of the inner race [9]. Once nucleated, this crack quickly propagates to the surface, resulting in particles of material flaking and leading to the failure of the bearing. Roller bearings for wind turbine applications operate in the fully elastic range and are subjected to a very high number of load cycles, with an expected life of 20 years [10]. However, practical experience show a high life scatter in these machinery elements, with failures that sometimes occur after a few years. The failure of these elements is thought to be due mainly to inhomogeneities and nonmetallic inclusions, that act as sites for crack nucleation under rolling contact fatigue. The cracks usually nucleate around inclusions, where the material experiences high stress concentration and typical butterfly defects are observed.

The modelling in the present paper is focused on ensuring that the cyclic stress fields stay within limits so that very high cycle fatigue damage does not initiate. Several multiaxial fatigue models have been developed [11–15], and some of them have been applied to RCF problems. The Dang Van criterion [16] and its further modifications has been widely used, over the last decades, in automotive industry [17] and in rolling contact problems as railwails and bearings [18,19]. It seems that the Dang Van criterion is not sufficiently conservative for negative values of the hydrostatic stress, therefore a modified version has been recently proposed [20], predicting a less sensitive behavior with respect to this stress component. This paper also includes a study of the overall effect

of pre-existing residual stresses in the material, resulting from hardening process. Using the Dang Van criterion, different residual stresses and hardening distributions are studied, and results are compared.

2. Problem formulation

Part of the initial geometry of the inner ring of the roller bearing is illustrated in Fig. 1. The inner ring and the shaft have been considered as one body of external radius $R=R_s+t_k$, where R_s is the shaft radius and t_k is the thickness of the inner ring. This assumption is equivalent to neglecting contact stresses related to the mounting and any local stress concentrations at the interface between ring and the shaft.

In order to reduce the computational time, only an angular sector of the solid, with angular width $\alpha=10°$, has been modeled. Far away from the surface, the region analyzed is terminated by a circular arc boundary with radius r. Along the edges, the solid is free to slide in the radial direction, being constrained in the direction perpendicular to the edges. A cartesian coordinate system Oxyz is used, with the origin O in the center of curvature of R, the axis z pointing out of the paper, and the axes x and y, respectively, horizontally and vertically aligned. As a 2-D model is studied, no edge effects in the direction perpendicular to the plane of the model are accounted for. The pressure acting on the raceway and resulting from the contact with the roller, is evaluated according to classical Hertzian theory, and is considered identical in any plane parallel to xy:

$$p(x,y)=p_0\,[1-(\frac{x-x_p}{a})^2-(\frac{y-y_p}{a})^2]^{0.5} \tag{1}$$

In Eq.(1), p_0 is the maximum value of the pressure, x_p and y_p the coordinates of the center of the contact area, a the semi-width of the contact area under the roller and x and y the coordinates of a generic point on the surface in the contact area. The value of p_0 is related to the force acting on the roller by the relation

$$p_0=\sqrt{\frac{q}{\pi}\frac{\Delta}{\rho}} \tag{2}$$

where Δ is function of the Young moduli E_i and Poisson ratios ν_i of the roller and the inner race, here assumed of the same material. The constant ρ is a pure function of the curvature radii and q=F/L is the force per unit length acting on the roller.

A bearing with the inner ring thickness t_k=19 mm, mounted on a shaft of R_s=200 mm, has been used in the simulations. Furthermore values of 70 mm and 20 mm, respectively, are assumed for the length and the radius of the roller. A load of 37 KN is considered pushing the roller against the inner race, resulting in a static Hertzian maximum pressure p_0~1 GPa. The contact is assumed continuous without any vibrations effects. No friction or sliding are here accounted for.

The pressure distribution, that simulates the contact, is assumed to move along the surface, in a region where the mesh is uniform. Far away from the zone affected by the contact stresses, instead, the elements are stretched, both in the radial and in the tangential direction, close to the edges. The material is considered isotropic, with Young modulus E=210 GPa and Poisson ratio ν=0.3.

In terms of the displacement components u_i on the reference base vectors the strain tensor is given by

$$\varepsilon_{i,j}=\frac{1}{2}(u_{i,j}+u_{j,i}) \tag{3}$$

where $()_{,j}$ denotes partial differentiation. The equilibrium equations, written in terms of the stress tensor σ_{ij} and the strain tensor ε_{ij}, are obtained by the use of the principle of virtual work:

$$\int_V \sigma_{ij}\delta\varepsilon_{ij}\,dV=\int_S T_i u_i\,dS \tag{4}$$

where V and S are the volume and surface of the region analyzed, and T_i are the specified surface tractions.

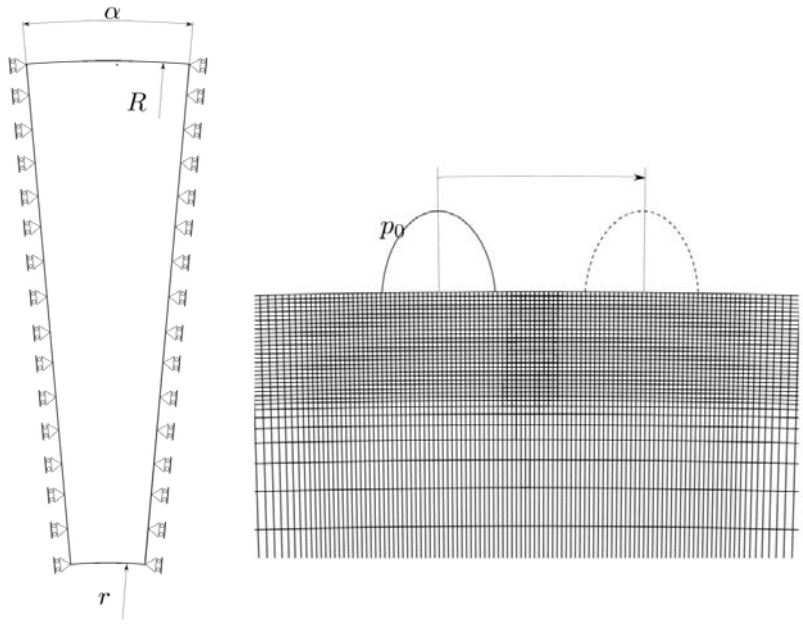

(a) (b)

Figure 1. (a) Geometry used to model the problem: r=100mm, R_s=200mm, t_k=19 mm, α=10°. (b) A detail of the mesh used.

2.1 The Dang Van criterion

A brief introduction to the basis of the fatigue criterion used will be given (see further details in [16]). The Dang Van criterion is a stress based multiaxial fatigue criterion. It relates the variation of the stress state in a material point to a critical parameter, that should not be reached:

$$f\,[\sigma_{ij}(t)] \leq \lambda \tag{5}$$

The critical value λ is usually function of the fatigue limits in pure torsion, τ_w, and the fatigue limit in pure bending, σ_w, and its choice is essential in a multiaxial criterion since it establishes which is the most important stress component that is assumed to have influence on the failure. The Dang Van criterion, in particular, can be formulated as:

$$\tau_{max}(t)+\alpha_{DV}\sigma_H(t) \leq \tau_w \tag{6}$$

where

$$\alpha_{DV}= 3\left(\frac{\tau_w}{\sigma_w}-\frac{1}{2}\right) \tag{7}$$

is a constant that depends on the material fatigue limits previously mentioned, $\sigma_H(t)$ is the instantaneous hydrostatic component of the stress tensor and $\tau_{max}(t)$ is the instantaneous value of the Tresca-like shear stress

$$\tau_{max}(t)= \frac{\widehat{\sigma_I}(t)-\widehat{\sigma_{III}}(t)}{2} \tag{8}$$

The stress deviator is obtained by the usual definition:

$$s_{ij}(t)=\sigma_{ij}(t)- \delta_{ij}\sigma_H(t) \tag{9}$$

Then a constant tensor, s_{ij}^m, is calculated by solving the minmax problem

$$s_{ij}^{m}=\min_{s_{ij}^{*}} \max_{t} [(s_{ij}(t)-s_{ij}^{*})(s_{ij}(t)-s_{ij}^{*})] \tag{10}$$

and the shifted deviator tensor is defined as

$$\widehat{s_{ij}}(t)=\sigma_{ij}(t)- s_{ij}^{m} \tag{11}$$

The principal values of the shifted tensor appear in Eq. (8).
The problem in Eq. (10) is solved iteratively using a move limit approach :

$$s_{ij}^{m}=\min_{s_{ij}^{*}} \max_{t} [(s_{ij}(t)-s_{ij}^{*})(s_{ij}(t)-s_{ij}^{*})] =\min_{s_{ij}^{*}} [\max_{t} \Phi] \tag{12}$$

with

$$\Phi=\Phi (t, s_{ij}(t), s_{ij}^{*}) \tag{13}$$

Choosing an arbitrarily starting value for s_{ij}^{*}, for example the average deviatoric stress tensor in the stress history for that material point, then for every iteration we identify the maximum value of Φ. Let t_m be the time step at which $\max \Phi$ happen, then the value of s_{ij}^{*} is updated

$$s_{ij}^{*}=s_{ij}^{*}+ ds_{ij}^{*} \tag{14}$$

with

$$ds_{ij}^{*}=\gamma (s_{ij}(t_m)-s_{ij}^{*}) \tag{15}$$

which can be interpreted as a modified steepest descend method. If at one step Φ increases, γ is reduced to 0.25 γ. The iteration is stopped if the norm of the difference between s_{ij}^{*} at the current iteration step k and at the previous step falls into a tolerance range:

$$\left\| s_{ij}^{*}]_{k}-s_{ij}^{*}]_{k-1} \right\| \leq \varepsilon_{toll} \tag{16}$$

Although a superimposed hydrostatic tension has an effect on the fatigue life in normal cyclic loading [21], several studies [11] have shown that a superimposed mean static torsion has no effect on the fatigue limit of metals subjected to cyclic torsion. The independency of the mean shear stress is correctly predicted through the minimization process in Eq. (10), see also [20]. The Dang Van criterion could also be used with $\tau_{max}(t)$ representing the maximum shear stress at every point of the stress history. Then, one would not account for the experimental observation that in cyclic torsion fatigue failure is independent of the mean shear stress, and this would usually result in lower permitted stress levels.
The Dang Van proposal is equivalent to request, in the $\sigma_H(t)-\tau_{max}(t)$ plane, that all the representative points of the stress state, fall below the line intersecting the $\tau_{max}(t)$ axis in τ_w with a negative slope of α: if all of the points fulfill this requirement, the criterion predicts a safe life for the component (see Fig. 2).
The original Dang Van safe locus predicts a detrimental effect of tensile hydrostatic stress while an over-optimistic positive effect is expected from compressive values. The negative effect of tensile mean stress is well known in literature from classic Haigh diagrams, that also show a flat response for negative stress ratios [22, 23]. For this reason it is not too conservative to choose a different safe locus in the Dang Van plane to be in agreement with this response, for example a bilinear limit curve, as proposed recently in [20]. The safe locus could be therefore identified in two segments, one with a null slope and the other one with a negative slope equal to α (Fig. 2). For $\sigma_H(t)\geq\sigma_A$ the safe region is identical to the original Dang Van region, while for smaller values of σ_A, the cut-off with the flat curve replaces the Dang Van limit curve by a curve more on the safe side. Values of $\sigma_A=\sigma_w/3$ and of $\tau_A=\sigma_w/2$ have been proposed in [20], on the basis of experimental results obtained on high-strength steel smooth specimens. However, it is possible to choose a different set of values for (σ_A, τ_A), though here the same choice has been made. If the ratio of the fatigue limits, σ_w/τ_w, was equal to 0.5, the value α_{DV} in Eq. (6) would be zero, which is far from reality, as steels usually

show ratios between 0.57 and 0.8 [21]. Anyway, it is always possible to assume different values of σ_A, more or less conservative than the cut off shown in Fig 2.
In the following sections, both the original safe locus and a new one with the mentioned cut-off will be used, and results will be compared. For τ_w a value of 360 MPa has been imposed [24] and a ratio $\sigma_w/\tau_w=\sqrt{3}$. With this assumption the value of the constant α_{DV} used in the calculations is approximately 0.23205.

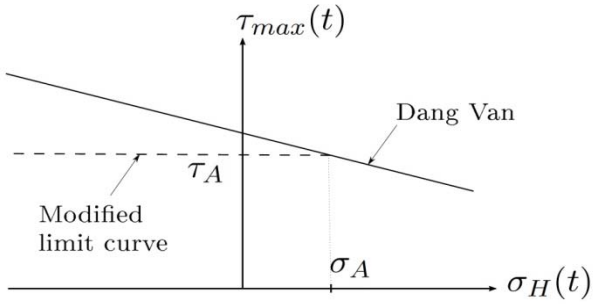

Figure 2. The Dang Van safe locus: the dashed line represents the alternative limit curve, for $\sigma_H(t)<\sigma_A$, here assumed equal to $\sigma_w/3$, as proposed in [20].

For a material point subjected, at time t, to $\sigma_H(t)$ and $\tau_{max}(t)$, the ratio between $\tau_{max}(t)$ and the corresponding limit value for that $\sigma_H(t)$ is here used to define the damage factor n(t). Points on the limit curve, then, result in a unit damage factor; points inside the safe region have damage factor smaller than one. As previously mentioned, two different safe loci are here used: one with a linear limit curve and another one with a bilinear limit curve. Consequently, a damage factor is here defined as

$$n(t)=\frac{\tau_{max}(t)}{\tau_w-\alpha_{DV}\,\sigma_H(t)} \tag{17}$$

if referred to the original Dang Van's safety region or

$$n(t)=\begin{cases}\dfrac{\tau_{max}(t)}{\tau_w-\alpha_{DV}\,\sigma_H(t)} & \text{if } \&\sigma_H>\sigma_A \\ \dfrac{\tau_{max}(t)}{\tau_A} & \&\text{if } \sigma_H\le\sigma_A\end{cases} \tag{18}$$

when the bilinear limit curve is used. As mentioned above, σ_A and τ_A are chosen equal to $\sigma_w/3$ and $\sigma_w/2$, respectively.

3. Results and discussion

The Dang Van criterion has been applied to the rolling contact problem and for the geometry described in section 2. The load history has been divided in an adequate number of steps and, for each time step, the value of the damage factor n(t) has been calculated, both with the original Dang Van limit curve and with the modified one. The maximum value in time

$$n=\max_t n(t) \tag{19}$$

is then chosen, as representative for that material point. If this $n<1$, the prediction is that initiation of fatigue failure will not occur in the material point. The representative points corresponding to the max value of the damage factor are plotted, in Fig. 3, in the Dang Van region, for all the integration points in the region analyzed.
In Fig. 4 the maximum values of this factor n are plotted against the distance from the surface. Both safe regions, as described before, are used. As we can see, n reaches the highest value in a sub-surface region, about 0.20 mm below the surface : this is consistent with literature, where a lot of sub-surface initiated failures in bearings for windmill applications are reported.

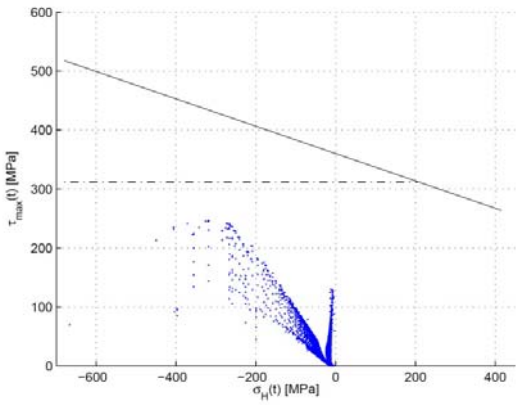

Figure 3. The Dang Van criterion: in order that the failure does not occur, all the representative points should be inside the safe region delimited by the limit curves. In this figure, and for the problem considered, only the representative points corresponding to max value of the damage factor are plotted for all the integration points in the region analyzed.

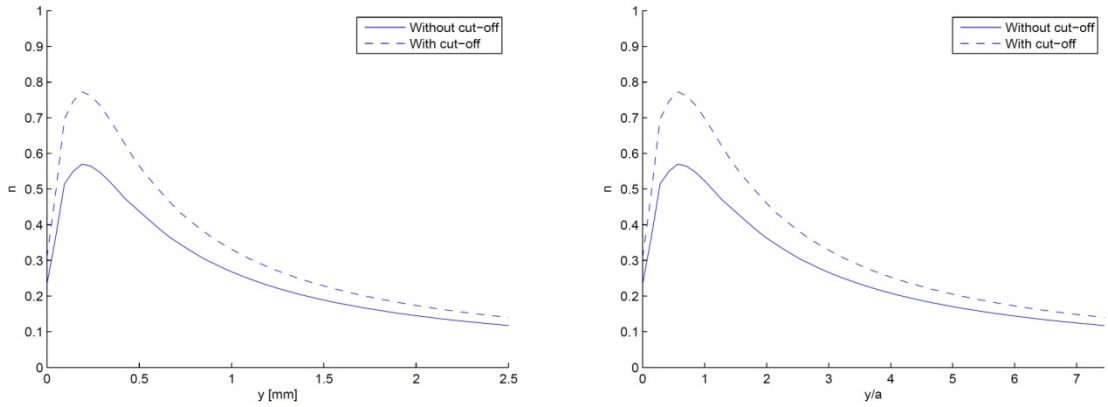

(a) (b)

Figure 4. Damage factor versus distance from surface (a) and versus distance from surface non dimensionalized by the half contact width (b).

3.1 Hardness variation

The relationships between fatigue strength, the hardness and the ultimate tensile strength are used, in this section, to study the influence of the hardness variation in the inner ring.
Since fatigue crack initiation is mainly caused by slip within grains, the yield stress, in the past, has been thought to have the strongest correlation with the fatigue limit. However Murakami [25] has found better correlations between tensile strength, hardness and fatigue limits.
In order to correlate the hardness to the fatigue limit, τ_w, this limit has first been related to σ_{UTS} through an approximate expression proposed in [26] for low-alloy steels:

$$\tau_w=\sigma_w/\sqrt{3}\approx 0.274\ \sigma_{UTS} \tag{20}$$

Denoting the Brinell hardness by HB and using an approximate relationship found in [27]

$$\sigma_{UTS}=0.0012\ HB^2+3.3\ HB \tag{21}$$

an approximate final relation between τ_w and HB can be written as

$$\tau_w=0.274\ (0.0012\ HB^2+3.3\ HB) \tag{22}$$

In the following we assume that the fatigue limit τ_w is given by the Eq. (22). If another expression $\tau_w(HB)$ applies for a material, this will not in principle change the procedure. In fact, all we need is

the value of τ_w in each material point of the solid analyzed.
Different hardness distributions along the depth have been studied here. Thus the value of τ_w corresponding to the value of the hardness at that depth has been imposed in the material for each Gauss integration point.
The different hardness distributions imposed in the subsurface region of inner ring and the correspondent τ_w distributions are shown in Fig. 5 (a)–(d). At distances greater than 1 mm from the surface, HB, for distributions (a) and (b), are taken to be constant, at a value such that the related fatigue limit, $\tau_w=\tau_w(HB)$, is approximately 360 MPa. This assumption is equivalent to considering how the effect of a surface hardening process would benefit the fatigue response of the bearing. Results show that the values of the damage factor n and the depth at which the maximum n is reached, are strongly dependent on the particular distribution of hardness imposed (Fig. 6).

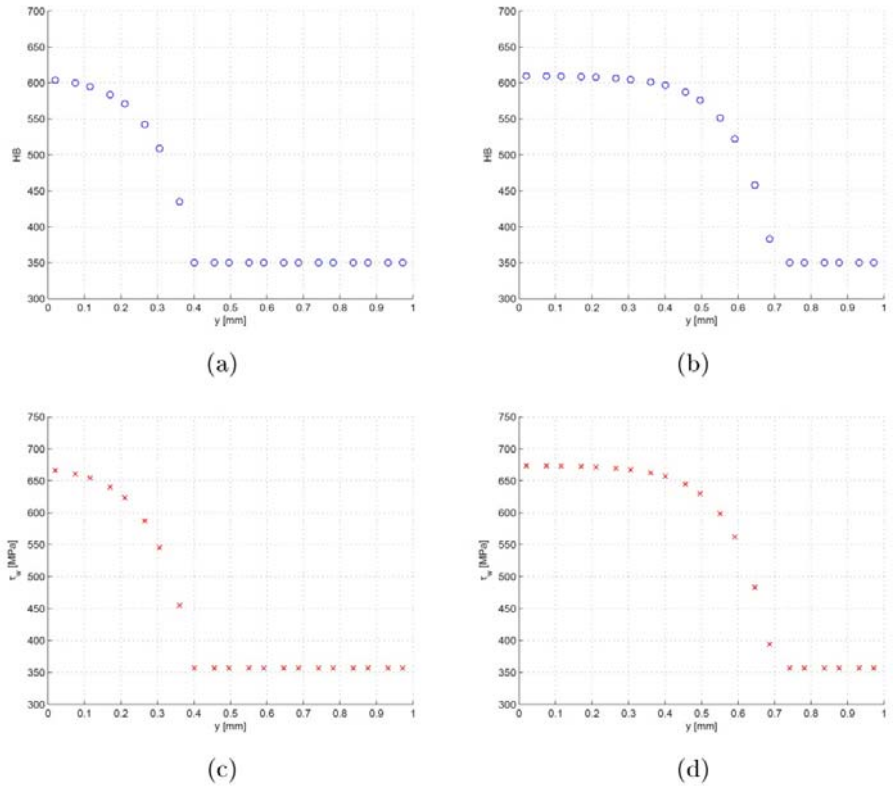

Figure 5. Hardness distributions ((a)-(b)) and correspondent values of τ_w ((c)-(d)) in the first millimeter of depth .

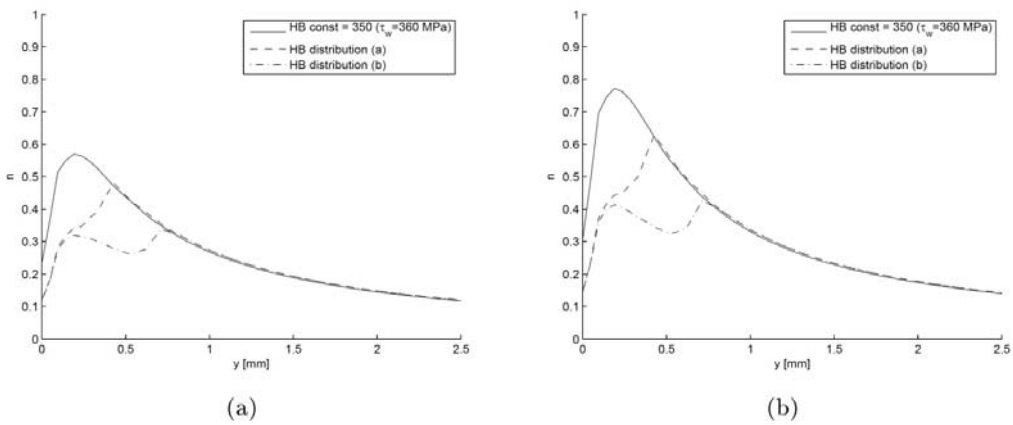

Figure 6. Damage factor versus distance from surface. In (a) the original Dang Vang safe locus has been used, while in (b) the bilinear limit curve, as described in section 2.1. The different distributions are referred to Fig. 5.

For all the cases analyzed, the peak of the n-curve shifts away from the surface of the inner ring and, for cases shown in Figs. 5a and 5b, the peak values of n are smaller than the correspondent peaks for a material with uniform hardness. In other words, the rings with extra surface hardening have higher safety against fatigue failure.

3.2 Residual stresses

In order to analyze the influence of pre-existing stresses in the bearing, two different residual stress distributions have been considered. The bearing with the assumed residual stress distribution, equilibrated by an elastic step calculation, is subsequently subjected to the stresses caused by the contact with the roller. The results obtained with the Dang Van criterion are then compared with the results obtained in the bearing free of residual stresses.

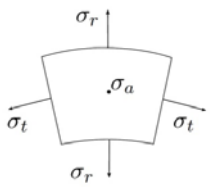

Figure 7. Convention used for the principal stresses in the polar coordinate system.

In Fig. 7 the convention used to name the residual stresses is clarified, while, in Figs. 8a and 8b, the residual stress distributions, in terms of principal stresses, are plotted versus the distance from the surface. Far away from the surface, the residual stresses are assumed to be constant and near zero.
The results for the two different safe loci (Fig. 2) are shown in Fig. 9. The pre-existing stress states in the inner ring, in the case of the modified safe locus, have little effect, neither positive nor negative (Fig. 9a). The residual stresses, in fact, result in a simple shift along the σ_H axis in the Dang Van region (Fig. 2) but this does not change the distance from the limit curve since all the most critical material points are subjected to values of σ_H smaller than σ_A and therefore they are in the region where the limit value for τ_{max} is constant and equal to τ_A. If the original limit curve is used, instead, the residual stress distribution (a) from Fig. 8 results in a reduction of the maximum damage factor for the compressive residual stresses, but an increase of the maximum damage factor for tensile residual stresses (Fig. 9b).

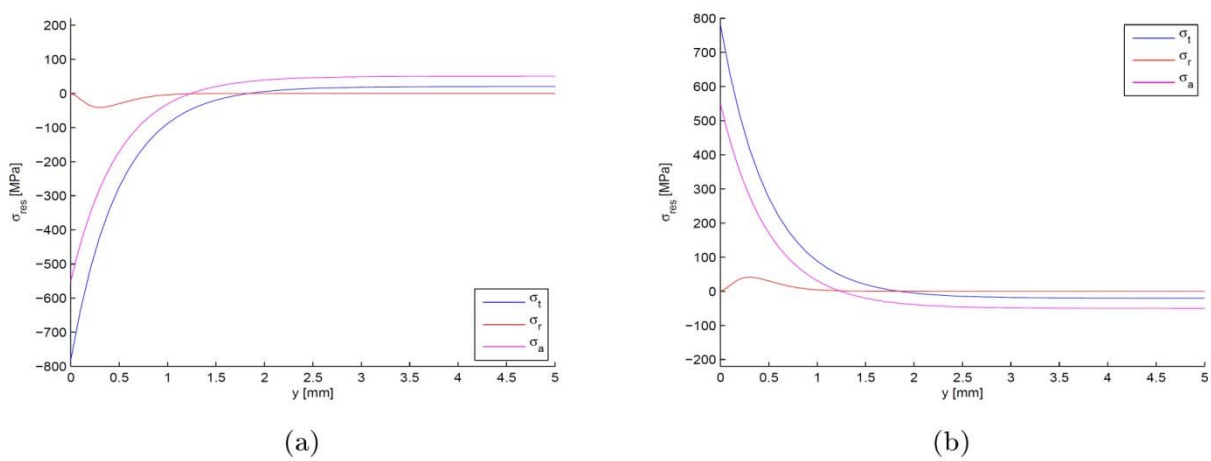

Figure 8. Residual stresses assumed in terms of principal stresses. Distribution (b) is obtained by multiplying (a) by -1.

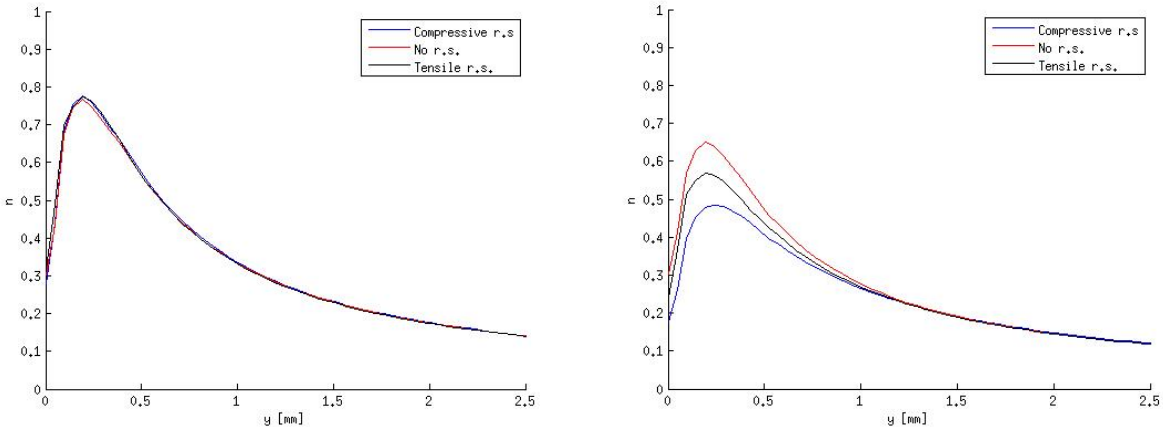

(a) (b)

Figure 9. Damage factor versus distance from surface for bilinear (a) and original limit curve (b).

4. Conclusions

The Dang Van criterion has been applied to a roller bearing for windmill applications and the influence of hardness variations and different residual stresses has been studied. Results have shown that, according to the Dang Van criterion, the highest damage factor is reached below the surface, regardless the safe locus used. This suggests that failure is most likely to initiate in the material a little below the surface, which is consistent with literature that reports subsurface failures of roller bearings for wind turbine applications.

The effect of increased hardness, in a thin layer close to the surface, has also been studied, relating the hardness to the fatigue strength of the material. The particular hardness distribution induced is seen to be important in evaluating the safety against fatigue for the bearing. Assuming that a higher fatigue strength corresponds to a higher Brinell hardness, the results indicate that a hardening surface treatment will be beneficial in terms of fatigue damage. However, surface hardening is not really possible for AISI 52100 bearing steel, though some recent work [28] seems to indicate an improvement of fatigue strength, for these steels, by induction heating and repeated quenching. It may be noted also that some steels show a maximum for the curve $\tau_w(\mathrm{HB})$, which would limit the applicability of Eq. (22). In fact, Eq.(22) is valid only for smaller values of hardness.

Bearings with different residual stress distributions have also been studied and calculations carried out show, for the Dang Van criterion, a positive effect of compressive residual stresses in the subsurface region according to the original safe locus. No influence of residual stresses has been found with the use of the modified safe locus and for the load case analyzed.

Acknowledgements

The author would like to thank Prof. Viggo Tvergaard and Associate Prof. Peder Kilt, Technical University of Denmark, for ideas, discussions and comments. This work is supported by the Danish Council for Strategic Research, in the DSF center REWIND.

References

[1] H. Arabian-Hoseynabadi, H. Oraee, P.J. Tavner, Failure Modes and Effects Analysis (FMEA) for wind turbines. Electrical Power and Energy Systems , 32 (2010) 817–824.

[2] Y. Amirat, M.E.H. Benbouzid, E. Al-Ahmar, B. Bensaker, S. Turri, Brief status on condition monitoring and fault diagnosis in wind energy conversion systems. Renew Sust Energ Rev, 13 (2009) 2629–2636.

[3] P.J. Blau, L.R. Walker, H. Xu, R.J. Parten, J. Qu, T. Geer, Wear analysis of wind turbine gearbox bearings - Final Report. Oak Ridge National Laboratory 2010.

[4] K. Smolders, Y. Feng, H. Long, P. Tavner Reliability Analysis and Prediction of Wind Turbine

Gearboxes. European Wind Energy Conference–EWEC 2010.
[5] C.Fernandes, R. C. Martins, Jorge H. O. Seabra, Friction torque of cylindrical roller thrust bearings lubricated with wind turbine gear oils. Tribology International (2012) (article in press).
[6] F. Spinato, P. J. Tavner, G. J. W. van Bussel, E. Koutoulakos, Reliability of Different Wind Turbine Concepts with Relevance to Offshore Application. European Wind Energy Conference 2008.
[7] F. Spinato, P. J. Tavner, G. J. W. van Bussel, E. Koutoulakos, Reliability of wind turbine subassemblies. IET Renewable Power Generation, 3 (2009) Issue 4, 387–401.
[8] Ma yang, He Chengbing, Feng Xinxin, Institutions Function and Failure Statistic and Analysis of Wind Turbine. Physics Procedia, 24 (2012), 25–30.
[9] F. Sadeghi, B. Jalalahmadi, T. S. Slack, N. Raje, N. K. Arakere, A Review of Rolling Contact Fatigue. Journal of Tribology, 131 (2009), Issue 4, 041403–1.
[10] A. Ragheb, M. Ragheb, Wind turbine gearboxes technologies. Proceedings of the 1st International Nuclear and Reneawble Energy Conference - INREC 2010.
[11] G. Sines, Behaviour of metals under complex static and alternating stresses, in: Metal Fatigue (eds. G. Sines and J.L. Waisman), McGraw-Hill, New York, 1959, pp. 145–169.
[12] W. N. Findley, Trans. ASME Ser B 81 (1959), 301.
[13] T. Matake, Bull. JSME 20 (1977), 257.
[14] D. L. McDiarmid, Fatigue Fract. Engng Mater. Struct. 17 (1994), 1475.
[15] I. V. Papadopoulos, Fatigue polycyclique des métaux: une nouvelle approche. Ph.d Thesis, spécialité: Mécanique, Ecole des Ponts et Chaussées, France, 1987.
[16] K. Dang Van, Sur la résistance à la fatigue des métaux. Sciences Technique Armement 47 (1973), 3.
[17] A.-S. Beranger, J.-V. Berard and J.-F. Vittori, A fatigue life assessment methodology for automotive components, in Fatigue Design of Components, in: ESIS Publication, 22, G. Marquis and J. Solind (eds.), Elsevier Science, 1997.
[18] A. Bernasconi, M. Filippini, S. Foletti, D. Vaudo, Multiaxial fatigue of a railwheel steel under non-proportional loading. International Journal of Fatigue, 28 (2006), 663–672.
[19] M. Ciavarella, F. Monno, G. Demelio. On the Dang Van fatigue limit in rolling contact fatigue. International Journal of Fatigue, 28 (2006), 852–863.
[20] H. Desimone, A. Bernasconi, S. Beretta, On the application of Dang Van criterion to rolling contact fatigue. Wear 260 (2006), 568–571.
[21] S. Suresh, Fatigue of materials, Cambridge University Press, New York, 2006.
[22] R.B. Heywood, Designining against fatigue, Chapman and Hall Ltd., London, 1962.
[23] T.J. Dalan, in: O.J. Horger (Ed.), ASME Handbook, Metal Engineering Design, New York.
[24] J. Lai, T. Lund, K. Rydén, A. Gabelli, I. Strandell, The fatigue limit of bearing steels – Part I: A pragmatic approach to predict very high cycle fatigue strength. Int. Journal of Fatigue 37 (2012), 166–167.
[25] Y. Murakami, Metal Fatigue: Effects of Small defects and Nonmetallic Inclusions, Elsevier, Oxford, 2002.
[26] B. Atzori, G. Meneghetti, L. Susmel, Material fatigue properties for assessing mechanical components weakened by notches and defects. Fatigue Eng Mater, 28 (2005), 83–97.
[27] M.L. Roessle, A. Fatemi, Strain-controlled fatigue properties of steels and some simple approximations. Int. Journal of Fatigue, 22 (2000), 495–511.
[28] E.C. Santos, K. Honda, H. Koike, J. Rozwadowska, Fatigue strength improvement of AISI 52100 bearing steel by induction heating and repeated quenching. Material Science, 47 (2011), No. 5, 677 –682.

Effects of microstructure on very-high-cycle fatigue crack initiation and life scatter for a high strength steel

Zhengqiang Lei, Jijia Xie, Sun Chengqi, Xiaolong Liu, Youshi Hong*

State Key Laboratory of Nonlinear Mechanics, Institute of Mechanics, Chinese Academy of Sciences, Beijing 100190, PR China
* Corresponding author: hongys@imech.ac.cn

Abstract A type of high strength steel was tempered at 150℃, 180℃, and 300℃ to form three groups of specimens, and rotating bending fatigue tests were performed to investigate the effects of microstructure on the behavior of very-high-cycle fatigue (VHCF) crack initiation. With the increase of tempering temperature, S-N curves for the three specimen groups show a tendency of increasing life scatter and the threshold value of VHCF crack initiation ΔK_{FGA} decreases. For 150℃ tempered specimens, grain boundary initiation is dominant for fatigue crack initiation while inclusion initiation is dominant for the other two groups. Effects of inclusion and retained austenite on fatigue crack initiation are discussed, and reliability analysis based on Tanaka-Mura model is carried out to characterize VHCF life scatter.

Keywords Very-high-cycle fatigue, FGA, life scatter, inclusion

1. Introduction

It is well known that S-N curve of ferrous materials tends to a limit between 106 and 10^7 cycles of loading. This fatigue limit was true until the fatigue failure beyond 10^7 cycles was first reported in 1980s [1]. Afterwards various types of materials [2] were confirmed to failure after 10^7 loading cycles which was named as very-high-cycle fatigue (VHCF) [3]. S-N curves for high strength steels including VHCF regime often presents a step-wise tendency (duplex S-N curves [4]), and it provides a challenge for safety design of industrial structures or components. Especially for aircrafts, automobiles, ship, railways which need to enduring long period of cyclic loading up to 10^{10} cycles, there is an urgent necessity to clarify the behavior and mechanism of VHCF failures.

In low cycle fatigue (LCF) and high cycle fatigue (HCF) regime, fatigue cracks often originate from defects at the specimen surface, and fatigue crack propagation is dominant in fatigue failure. When stress is below the conventional fatigue limit, these defects may become non-propagating cracks [5], and the interior defects such as non-metallic inclusions acting as stress raisers become fatigue crack origin in VHCF regime [6]. Sometimes the prior austenite grains boundary could also be a crack origin for high-carbon chromium steel under low tempering temperature [7]. Meanwhile fatigue crack initiation is dominated for HCF and VHCF, and first few microstructure barriers control fatigue limit and scatter of lifetime. However, fatigue cracks grow in elastic-plastic field with less microstructure influence for LCF [8]. Studies on VHCF mechanism have shown that the great role of microstructures influence on interior fatigue crack initiation as the fine granular area (FGA [4]) presents. The influencing factors include spherical carbide [9], hydrogen [10], inclusion size [11], chemical compositions of inclusion [12]. The portions of life attributed to subsurface crack initiation in FGA are beyond 90% [13], thus all these microstructures which can influence the formation of FGA are reasonable for life scatters of VHCF.

Primary inclusions are often dominant sites of fatigue crack formation and early growth in high

strength steels, powder metallurgy alloys, and casting alloys. Transition from surface-dominated fatigue processes to subsurface failure initiation is often observed in these systems in moving from the LCF to the VHCF regime. Competition between near surface and bulk inclusions is said to be key to this failure mode transition, and introduces the large scatter of S-N curves [8]. Many studies on fatigue crack propagation have shown that fatigue crack growth behavior near threshold differs with the change of tempering temperature [14; 15; 16], i.e. the threshold value of crack growth ΔK_{th} varied with different heat treatment conditions.

In this paper, a type of high strength steel was tempered at 150℃, 180℃, and 300℃, to obtain three groups of specimens, and rotary bending fatigue tests were performed with them to investigate the influence of tempering temperature on S-N curve scatter properties from LCF regime to VHCF regime. And effects of microstructure on fatigue crack initiation and growth are discussed.

2. Experimental procedure

The test material in the present investigation is a high carbon chromium bearing steels with main chemical compositions (wt. %) of: 1.06 C, 1.04 Cr, 0.88 Mn, 0.34 Si, 0.027 P, and 0.005 S (Fe balance). From the spheroidizing annealed material, specimens were machined into hourglass shape providing a certain amount of finishing allowance. The specimens were heated at 845℃ for 2 hours in vacuum, then oil-quenched and tempered for 2 hours in vacuum at 150℃, 180℃ and 300℃. Such heat-treated specimens are of the microstructure with tempered martensite, retained austenite, and carbides, and the volume fractions of retained austenite are about 15%, 8% and 0 for 150℃, 180℃, and 300℃ tempered specimens respectively by means of X-ray diffraction (Fig. 1). Mechanical properties of three groups of specimens are shown in Table 1.

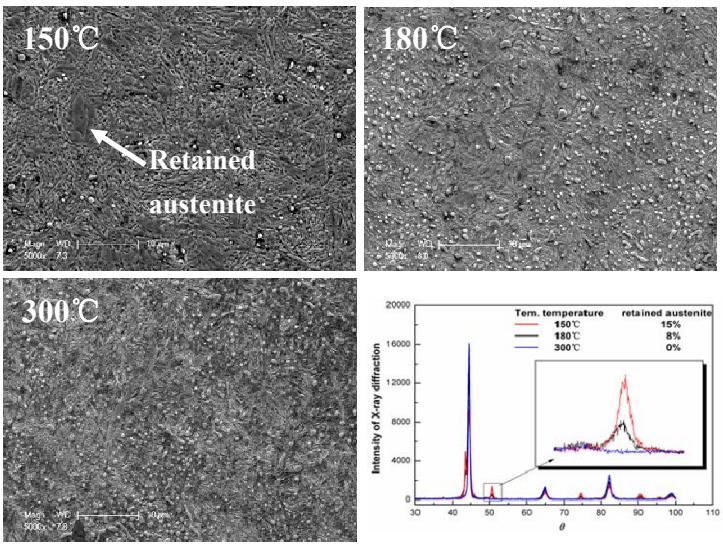

Fig. 1. The content of retained austenite for the specimens tempered at 150℃, 180℃ and 300℃ by means of X-ray diffraction.

The three specimen groups are denoted as RL150, RL180, and RL300 and their mechanical properties are shown in Table 1.

Table 1. Mechanical properties of three groups of specimens

Specimens group	Tempering Temp. (℃)	Micro-Hardness Hv (kgf/mm^2)	Tensile Stress σ_b
RL150	150	808	2163
RL180	180	753	1849
RL300	300	666	1690

Rotary bending tests were performed by using a "Giga-Quad" machine at room temperature with the frequency of 52.5 Hz and the stress ratio of -1. After the fatigue testing, the fracture surfaces of all fractured specimens were observed using a field-emission type scanning electron microscope (SEM). The geometries of specimens are shown in Fig. 2. The round notch surface was ground by the grade 400, 800, 1500 and 2000 abrasive papers and polished to a smooth finish.

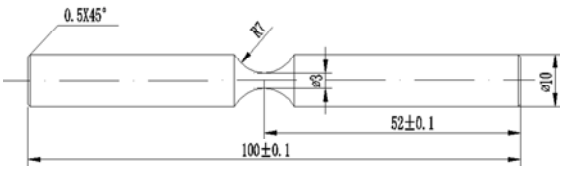

Fig. 2. Schematic drawing of the specimens (dimensions in mm).

3. S-N curves

Fig. 3 shows S-N curves of RL150, RL180, and RL300. It is seen that the shape of the S-N curve differed from each other for the three groups. For RL150, the S-N data almost locate at a straight line as the black line shows. The shape of S-N curves of RL180 presents a duplex stepwise tendency as one of the VHCF specific characteristics for metallic materials [4]. The S-N data scattered around two independent lines for RL300, resulting the uncertainty of fatigue life at a given stress level. For example, fatigue failures occurred at 10^4, 10^6, 10^7, 10^8 cycles when the maximum stress was about 700MPa. Meanwhile the increasing tendency of S-N curve as the decreasing of stress in VHCF regime is more obvious for RL300. The changes of the shape of S-N curves at different tempered temperature lead to a distinguishing scatter properties for the three groups of specimens. Comparing these S-N curves in Fig. 3, we can see an increasing tendency of life scatter as the tempering temperature increases from 150℃, 180℃ to 300℃.

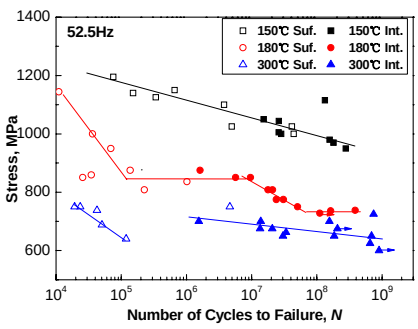

Fig. 3. S-N curves of 150℃, 180℃, and 300℃ tempered specimens under rotary bending loading. (Sur.: surface initiation, Int.: interior initiation)

4. Fracture surface observation

4.1 Characters of fracture surface

Fig. 4 shows the diminishing of the inter/trans granular zone in the fracture surface with the increase of the tempering temperature. The rough surface zone of region A outside of the fisheye (Fig. 4d) is considered as inter/trans granular zone by Zhao et al. [7]. Region A is clearly seen in the fracture surface of RL150 (Fig. 4a), while this zone diminishes gradually with the increase of the tempering temperature as Fig. 4b and Fig. 4c show. Under cyclic loading, materials with high brittleness is lack of sufficient number of independent slip systems to accommodate plastic deformation between contiguous grain leading to grain boundaries crack. Elevating of the tempering temperature can reduce its brittleness resulting the diminishing of inter granular fracture surface. This phenomenon also verifies the change of the microstructure with different heat treatments.

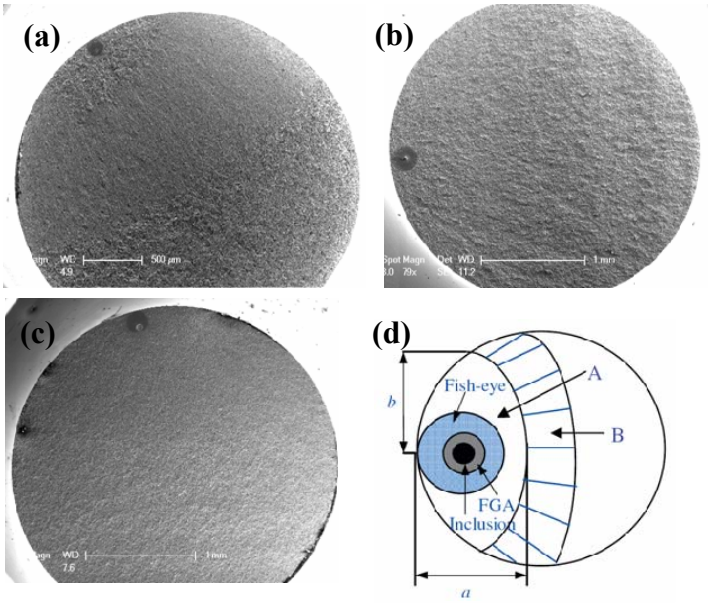

Fig. 4. Diminishing of the inter/trans granular zone with the increase of the tempering temperature: (a) RL150, (b) RL180, (c) RL300, and (d) Schematic drawing of the fracture surface (A denotes the inter/trans granular zone, and B denotes the fast growth zone).

4.2 Fatigue crack initiation

Fig. 5 shows the typical morphology of the fatigue crack origin for surface and interior initiation. For RL150, fatigue crack tends to initiate from the grains boundaries for VHCF as shown in Fig. 5a and Fig. 5b. Sometimes FGA was observed when the VHCF crack initiated from interior grains boundaries (Fig. 5b), and the proportion of grain boundary initiation is up to 88%. For RL180 and RL300, almost all VHCF failures originate from interior inclusions with a fisheye pattern as Fig. 5c shows. Fig. 5d shows an example of non-propagating cracks for surface inclusion. The size and the stress intensity factor (SIF) range are 29 μm and 3.65 MPa·m$^{1/2}$ for the subsurface inclusion, while they are 11 μm and 3.28 MPa·m$^{1/2}$ for the smaller one at the specimen surface. SIFs for both the two inclusion fall below the threshold value (5.0 MPa·m$^{1/2}$) for this heat treatment, and fatigue crack originates from the subsurface inclusion with higher SIF which indicates that SIF is an

key factor influencing fatigue crack initiation between surface inclusion and interior inclusion.

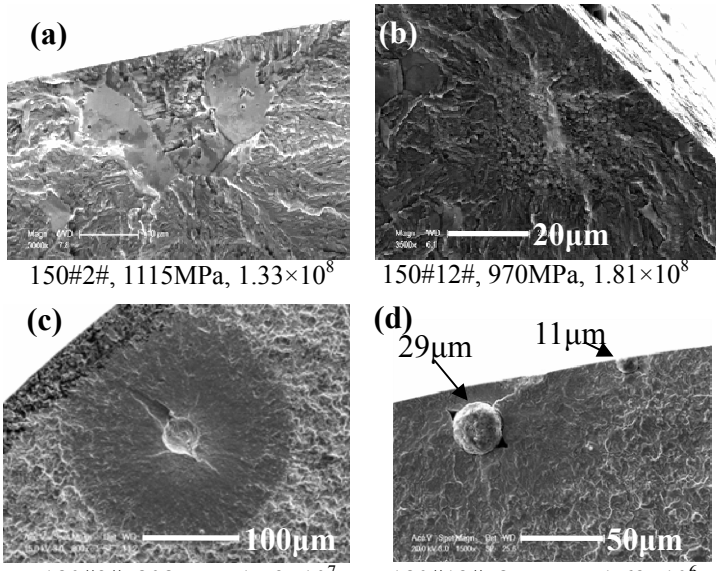

150#2#, 1115MPa, 1.33×10^8 150#12#, 970MPa, 1.81×10^8

180#3#, 808MPa, 1.79×10^7 180#12#, 875MPa, 1.62×10^6

Fig. 5. Typical examples of fracture surface morphology for fatigue crack initiation. (a) interior grains boundary initiation for RL150, (b) interior grains boundary initiation with FGA for VHCF of RL150, (c) fisheye pattern with FGA for VHCF of RL180, and (d) competition between surface inclusion initiation and interior inclusion initiation.

Effects of microstructures on VHCF crack initiation are shown in Table 2. On one hand, VHCF crack tends to originate from interior grain boundary at low tempering temperature for RL150, while interior inclusion is prone to be the crack origin when the tempering temperature is up to 180℃ and 300℃. On the other hand, values of stress intensity factor of FGA: ΔK_{FGA} fluctuate around a constant for each of specimen group. ΔK_{FGA} reaches its highest value for RL180, and the lowest value for RL300. Retained austenite content is responsible for the change of ΔK_{FGA}, for the threshold value of crack growth ΔK_{th} varies with the volume fraction of retained austenite[14].

Table 2. Statistical Comparison of VHCF crack initiation for the three specimen groups

	Inclusion	Grain boundary	ΔK_{FGA} (MPa*m$^{0.5}$)		ΔK_{Inc} (MPa*m$^{0.5}$)	
			Mean value	Standard deviation	Mean value	Standard deviation
RL150	11% (1/9)	89% (8/9)	5.29	0.1	2.54	0.28
RL180	100% (9/9)	0 (0/9)	5.52	0.58	4.27	0.39
RL300	73% (8/11)	27% (3/11)	4.31	0.36	3.83	0.51

5. Microstructure sensitivity analysis

As we know, FGA consumes more than 90 percent of VHCF life[13], thus it is reasonable to take the fatigue life of FGA formation as the whole fatigue life. Based on the conclusion that FGA is finished when the plastic zone size r_p of the microcrack exceeds the low boundary width l_m of the martensite[17], this paper considers that the martensite is the key factor for the FGA formation for

high strength steel. During the formation of FGA, localized and irreversible plastic flows are blocked within the twin martensite, and fatigue crack occur with the fracture of martensite when the accumulated energy reaches the critical value. We assume that the dislocations are piled up along the slip band in the martensite, and introduce the influence of the strength of the material and the law of FGA formation on the VHCF crack initiation life, thus we have the modified Tanaka-Mura model for life prediction of FGA:

$$N_{FGA} \cdot \pi(\tau-\kappa)^2 l_m^{\ 2} / G = C \cdot \sigma_b \cdot area_{FGA,net} \tag{1}$$

Where l_m is the width of martensite, σ_b is tensile strength of the material, $area_{FGA,net}$ is the area of FGA minus the area of inclusion, and C is a correction coefficient which shows the relationship between the strength of the martensite and tensile stress of material. Other parameters are same as Tanaka-Mura model[18]. With Von Misses yield criteria, Eq. [1] can be expressed as:

$$N_{FGA} = \frac{9CG\sigma_b}{2\pi l_m^{\ 2}(\sigma\text{-}\sigma_D)^2}\left(\frac{16\Delta K_{FGA}^2}{\pi^2\sigma^4} - area_{Inc}\right) \tag{2}$$

In Eq. [2], σ_D is the fatigue limit. With Eq. [2], sampling-based sensitivity measures are performed with direct Monte-Carlo simulation[19; 20]. The bulk shear modulus G, correction coefficient C, martensite width l_m and fatigue limit σ_D are assumed to be deterministic variables with values of 79 GPa, 1, 575 nm and 600MPa respectively. local stress σ, ΔK_{FGA}, and inclusion size $\sqrt{area_{Inc}}$ are assumed to be random variables. The stress is normally distributed with a mean value of 750 MPa and a COV of 0.03. ΔK_{FGA} is a normal distribution with a mean value of 5.5 MPam$^{0.5}$ and a COV of 0.03. Inclusion size is Gumbel distributed with a mean value of 30 μm and a COV of 0.4.

The calculated results of sensitivity measures are shown in Fig. 6. Both sensitivity of mean value S_μ and sensitivity of standard deviation S_σ are dimensionless and appropriate for variable ranking, and they are defined as[21]:

$$S_{\mu_i} = \frac{\partial P_f / P_f}{\partial \mu_i / \sigma_i}, \qquad S_{\sigma_i} = \frac{\partial P_f / P_f}{\partial \sigma_i / \sigma_i} \tag{3}$$

P_f , μ_i and σ_i are respectively the probability of failure, mean value and standard deviation of a variable X_i.

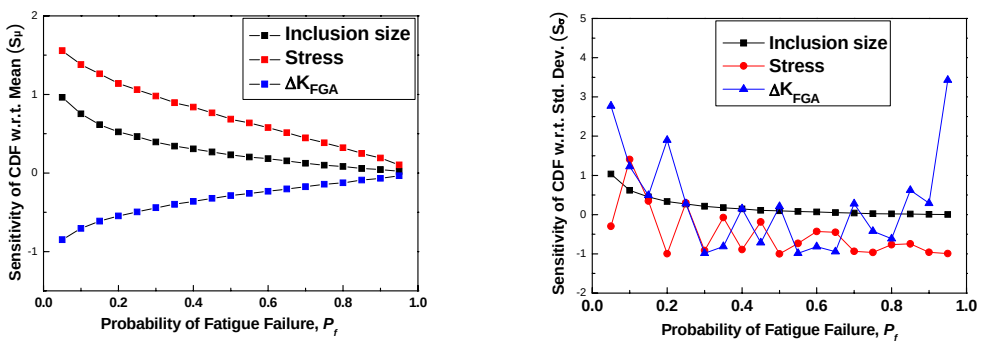

Fig. 6. (a) sensitivity of mean value (S_μ); (b) sensitivity of standard deviation (S_σ).

It is seen that fatigue failure being most sensitive to mean value of stress and standard deviation of ΔK_{FGA} by comparing the absolute value of S_μ and S_σ between these variables. Influence of mean value for the three variables does not appear to be much different from each other with the most sensitive variable of stress as shown in Fig. 6a. Mean value sensitivity of ΔK_{FGA} is close to that of inclusion size. Although inclusion size has an effect on life scatter by three orders when the stress is given[22], VHCF life with FGA has a much lower sensitivity of inclusion size under rotating bending as the stress gradient along the radius direction. Fig. 6b gives the sensitivity of standard deviation. As the probability of fatigue failure increased, standard deviation of stress and inclusion size have an decreasing influence on fatigue failure, while standard deviation sensitivity of ΔK_{FGA} is much higher than that of stress and inclusion size. For interior inclusion initiation, fatigue failure becomes more sensitive on ΔK_{FGA} deviation when the its mean value is obviously lower as the largest life scatter as RL300 shows.

6. Conclusions

A high carbon chrome steel was tempered at 150℃, 180℃, and 300℃, and VHCF test was performed with them. S-N curves show an increasing tendency of life scatter with the increasing of tempering temperature. In VHCF regime, interior inclusion initiation was dominant for RL180 and RL300 while interior grain boundary initiation was dominant for RL150 which has the highest volume fraction of retained austenite. FGA was observed in VHCF specimens, and ΔK_{FGA} is obviously lower for 300℃ with a large deviation of ΔK_{Inc}. A modified Tanaka-Mura model was proposed for the mechanism of FGA formation, and sensitivity measurements were carried out for microstructure variables ranking.

Acknowledgements

The authors gratefully acknowledge the support of the National Natural Science Foundation of China (Grant Nos. 11021262 and 11172304), and the National Basic Research Program of China (Grant No. 2012CB937500).

References

[1]T. Naito, H. Ueda, M. Kikuchi, Fatigue Behavior of Carburized Steel with Internal Oxides and Nonmartensitic Microstructure near the Surface. Metall Trans A, 15 (1984) 1431-1436.

[2]G.A. Qian, Y.S. Hong, Effects of Environmental Media on High Cycle and Very-High-Cycle Fatigue Behaviors of Structural Steel 40cr. Acta Metall Sin, 45 (2009) 1356-1363.

[3]G.A. Qian, C.E. Zhou, Y.S. Hong, Experimental and theoretical investigation of environmental media on very-high-cycle fatigue behavior for a structural steel. Acta Materialia, 59 (2011) 1321-1327.

[4]T. Sakai, B. Lian, M. Takeda, K. Shiozawa, N. Oguma, Y. Ochi, M. Nakajima, T. Nakamura, Statistical duplex S-N characteristics of high carbon chromium bearing steel in rotating bending in very high cycle regime. Int J Fatigue, 32 (2010) 497-504.

[5]J. Lai, T. Lund, K. Rydén, A. Gabelli, I. Strandell, The fatigue limit of bearing steels-Part I: A pragmatic approach to predict very high cycle fatigue strength. Int J Fatigue, 38 (2012) 155-168.

[6]M. Zimmermann, Diversity of damage evolution during cyclic loading at very high numbers of

cycles. Int Mater Reviews, 57 (2012) 73-91.
[7]A.G. Zhao, J.J. Xie, C.Q. Sun, Z.Q. Lei, Y.S. Hong, Effects of strength level and loading frequency on very-high-cycle fatigue behavior for a bearing steel. Int J Fatigue, 38 (2012) 46-56.
[8]D.L. McDowell, F.P.E. Dunne, Microstructure-sensitive computational modeling of fatigue crack formation. Int J Fatigue, 32 (2010) 1521-1542.
[9]K. Shiozawa, Y. Morii, S. Nishino, L. Lu, Subsurface crack initiation and propagation mechanism in high-strength steel in a very high cycle fatigue regime. Int J Fatigue, 28 (2006) 1521-1532.
[10]Y. Murakami, T. Nomoto, T. Ueda, Y. Murakami, On the mechanism of fatigue failure in the superlong life regime ($N>10^7$ cycles). Part I: influence of hydrogen trapped by inclusions. Fatigue Fract Eng Mater Struct, 23 (2000) 893-902.
[11]Y.B. Liu, Z.G. Yang, Y.D. Li, S.M. Chen, S.X. Li, W.J. Hui, Y.Q. Weng, Dependence of fatigue strength on inclusion size for high-strength steels in very high cycle fatigue regime. Mater Sci Eng A, 517 (2009) 180-184.
[12]S.X. Li, Effects of inclusions on very high cycle fatigue properties of high strength steels. Int Mater Reviews, 57 (2012) 92-114.
[13]Q.Y. Wang, C. Bathias, N. Kawagoishi, Q. Chen, Effect of inclusion on subsurface crack initiation and gigacycle fatigue strength. Int J Fatigue, 24 (2002) 1269-1274.
[14]R.O. Ritchie, V.A. Chang, N.E. Paton, Influence of Retained Austenite on Fatigue Crack-Propagation in Hp9-4-20 High-Strength Alloy-Steel. Fatigue Eng Mater Struct, 1 (1979) 107-121.
[15]D.Y. Wei, J.L. Gu, H.S. Fang, B.Z. Bai, Z.G. Yang, Fatigue behavior of 1500 MPa bainite/martensite duplex-phase high strength steel. Int J Fatigue, 26 (2004) 437-442.
[16]C.S. Lee, K.A. Lee, D.M. Li, S.J. Yoo, W.J. Nam, Microstructural influence on fatigue properties of a high-strength spring steel. Mater Sci Eng A, 241 (1998) 30-37.
[17]A.G. Zhao, J.J. Xie, C.Q. Sun, Z.Q. Lei, Y.S. Hong, Prediction of threshold value for FGA formation. Mat Sci Eng A, 528 (2011) 6872-6877.
[18]K. Tanaka, A Theory of Fatigue Crack Initiation at Inclusions. Metall Trans A, 13 (1982) 117-123.
[19]Y.T. Wu, S. Mohanty, Variable screening and ranking using sampling-based sensitivity measures. Reliab Eng Syst Saf, 91 (2006) 634-647.
[20]Z.Q. Lei, J.J. Xie, A.G. Zhao, Y.S. Hong, A simulation on microstructure sensitivity to very-high-cycle fatigue behavior of metallic materials. Procedia Eng, 4 (2010) 225-232.
[21]Y.T. Wu, S. Mohanty, Variable screening and ranking using sampling-based sensitivity measures. Reliab Eng Syst Saf, 91 (2006) 634-647.
[22]Z.Q. Lei, Y.S. Hong, J.J. Xie, C.Q. Sun, A.G. Zhao, Effects of inclusion size and location on very-high-cycle fatigue behavior for high strength steels. Mater Sci Eng A, 558 (2012) 234-241.

Very high cycle fatigue for single phase ductile materials: microplasticity and energy dissipation

Ngoc Lam Phung[1], Antoine Blanche[2], Nicolas Ranc[1], Véronique Favier[1*], André Chrysochoos[2], Nicolas Marti[1,3,5], Nicolas Saintier[3], Chong Wang[4], Danièle Wagner[4], Claude Bathias[4], Fabienne Grégori[5] , Brigitte Bacroix[5], Haël Mughrabi[6], Guillaume Thoquenne[7]

[1]Arts et Métiers ParisTech, PIMM UMR 8006, 75013 Paris, France
[2]Montpellier II University, LMGC UMR 5506, France
[3]Arts et Métiers ParisTech, I2M UMR 8006, 33607 Bordeaux, France
[4]Paris 10 University, LEME, France
[5]Paris 13 University LSPM UPR 3407, France
[6]Erlangen University, Germany
[7]Cetim, Senlis, France
* Corresponding author: veronique.favier@ensam.eu

Abstract

The DISFAT project is a ongoing French project financially supported by the French National Agency ANR. It aims at a deeper understanding of mechanisms leading to crack initiation in ductile metals in Very High Cycle Fatigue (VHCF). The VHCF regime is associated with stress amplitudes lower than the conventional fatigue limit and numbers of cycles higher than 10^9. Tests were conducted using an ultrasonic technique at loading frequency of 20 kHz. The mechanisms leading to crack initiation express via slip bands at the specimen surface and self-heating due to intrinsic dissipation. Thermal maps were used to estimate the mean dissipation and its change with number of cycles and stress amplitudes in case of pure copper polycrystals. At the same time, the surface relief changes due to plasticity were characterized using optical and scanning electronic microscopes. A good correlation was found between slip band initiation and dissipation. Dissipation and slip band amount always increased over the number of cycles. At very small stress amplitudes, no slip band appeared up to 10^8 cycles but the material was found to dissipate energy. These results reveal that the material never reached a steady state. Therefore it could break at higher number of cycles.

Keywords copper, self-heating, slip bands, IR thermography, ultrasonic fatigue

1. Introduction

Nowadays there is a growing demand for the development of fast and robust fatigue life prediction methods in the very high cycle fatigue (VHCF) domain. The VHCF regime is associated with stress amplitudes lower than the conventional fatigue limit and as a result, numbers of cycles higher than 10^9. Some mechanical components, such as pistons, rotating axes, have been designed previously using fatigue resistance data at lower numbers of cycles ($<10^7$ cycles ; the regime of High Cycle Fatigue, HCF) whereas they must endure oscillating loads for a number of cycles higher than $>10^9$ cycles and finally fail [1]. These requirements motivate the need to understand the fundamental mechanisms of fatigue in the VHCF regime, correspondingly, to explore novel methods for the characterization of fatigue behavior at these very long lifetimes. The DISFAT project is an ongoing French project financially supported by the French National Agency ANR. It aims at a deeper

understanding of mechanisms leading to crack initiation in metals and alloys in VHCF. Our strategy is first to analyze the response of metals and alloys having “simple” microstructure and deformation mechanisms but also controlled initial states, with special attention paid to the surfaces. From the existing knowledge of cyclic deformation mechanisms (High Cycle Fatigue range), we choose to study face-centered (fcc) and body centered (bcc) cubic metals and the role of two intrinsic properties of solid crystals: the tendency to wavy or planar slip and the lattice friction resistance. Second, the VHCF range is reached using ultrasonic fatigue machines. The working frequency is 20 kHz. The use of higher loading frequencies than conventional frequencies (~ 30 Hz) brings advantages (1) to reach the VHCF regime within a reasonable time and (2) to increase the dissipated power (energy per unit of time) and thus to generate temperature variations which can be detect with the current thermal measurement devices. Thus, the aim is to correlate surface dissipation field, surface relief changes due to the appearance of slip bands and plastic deformation mechanisms.

The project brings together four academic partners with complementary fields of expertise and equipments (PIMM – Arts et Métiers ParisTech, LEME - Université Paris X, LMGC - Université Montpellier II, LSPM – UPR CNRS). A technical center (CETIM Senlis) is also associated to transfer the results of this fundamental work to industrial applications. Most of participating researchers have worked in the HCF fatigue field and Professors Bathias and Mughrabi who contributed to the project provided pioneering and well-known works in the VHCF range. In this paper, we focus on results got for pure copper polycrystals. First, we explain our experimental procedure. Then, we introduce the calorimetric analysis. Finally, some results are presented in order to illustrate our methodology.

2. Experimental procedure

2.1. Materials and specimens

From the existing knowledge of cyclic deformation mechanisms [2-3], we choose to study the role of two intrinsic properties of solid crystals: the tendency to wavy or planar slip and the lattice friction resistance. In this project, we propose to study two classes of ductile single-phase metals with fcc and bcc structures. In both classes, we used a quasi-pure metal and alloys in order to change the ability to cross slip. Concerning bcc metals, low Fe-C, such as Armco iron, were used. Concerning fcc metals, pure copper and Cu-Zn (α-brass) alloys are good candidates. While pure Cu is known to deform with wavy slip, α-brass Cu-Zn displays planar slip [4-5]. Here, we only present results obtained on commercial polycrystalline copper CuOF 99.95% and α-brass Cu-15wt%Zn supplied by Griset Company.

In order to facilitate surface observation, a new hourglass shaped specimen with flat faces was designed (Fig. 1). The specimen dimensions were determined so that all the parts, such as transmission and amplification pieces, vibrate at a resonance frequency of 20 kHz in tension-compression [6-7]. After mechanical and electrolytic polishing, the specimen surfaces were mirror finished without any residual stresses. The stress distribution along the specimen axis

(calculated numerically) is presented in Fig. 1. The stress is concentrated in the middle of the gauge part of the specimen and reduced toward the specimen ends. This geometry allows to systematically study the material response at all desired stress amplitudes with one single specimen.

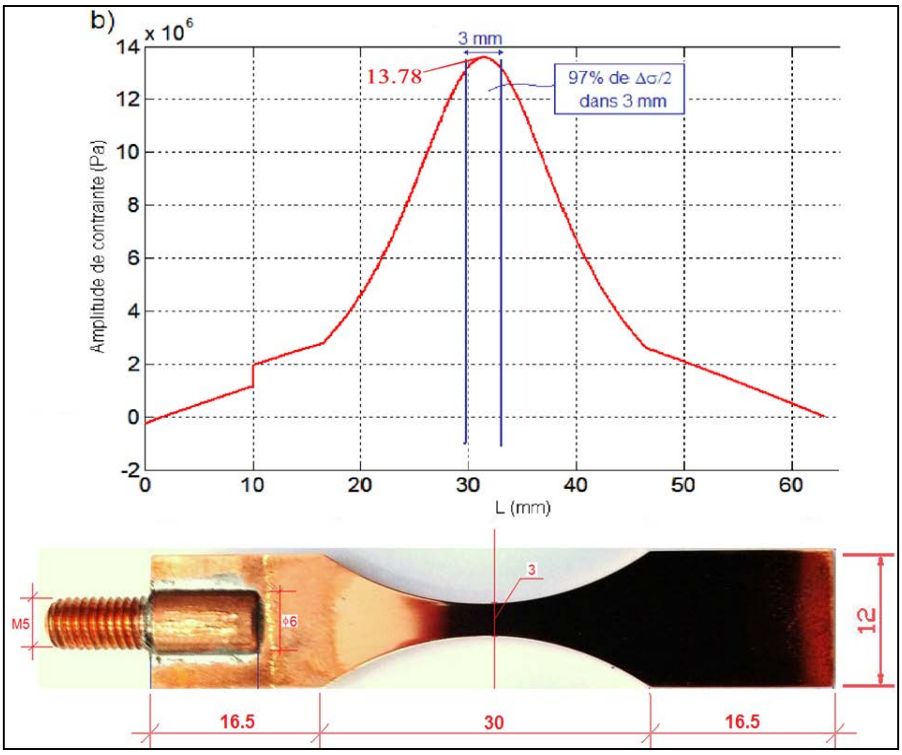

Figure 1. Ultrasonic fatigue plate specimen and distribution of stress along the specimen axis

2.2. Fatigue tests

The experimental setup involves the mechanical testing machine shown in Fig. 2. It essentially involves 3 components [1]:

- a piezoelectric system that transforms an electrical signal into a displacement
- an ultrasonic horn which amplifies this displacement (usually 3 to 9 times)
- a specimen screwed on the horn and free of stress at its bottom extremity.

This dynamic loading system is designed, assuming an elastic behaviour, in order to have a longitudinal vibration mode at a frequency of around 20 kHz. In order to obtain the relation between the displacement on the horn edge and the input electrical signal, the testing machine is calibrated with a laser extensometer.

During fatigue tests, an infrared camera (512x640 pixels) monitors the temperature field on the specimen surface. A pixel calibration is performed before each new test. The specimen surface is painted in matte black to have a uniform surface emissivity close to 1. Spatial resolution is about 0.1 mm/pixel. From the temperature measurements, the intrinsic dissipation was determined using a 1D heat diffusion model (see the following section).

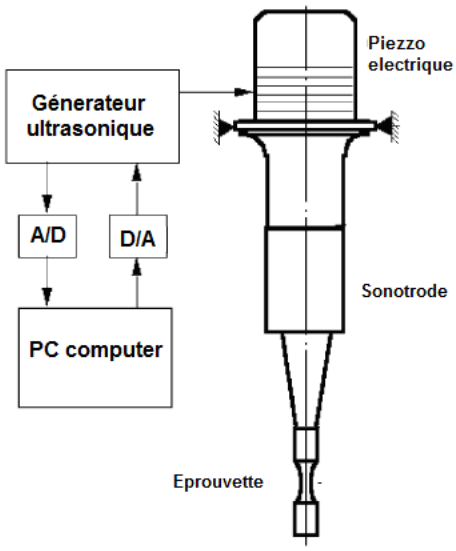

Figure 2. Scheme of the piezoelectric machine

3. Calorimetric analysis

3.1. Model of heat diffusion

A numerical model was built to estimate the evolution of intrinsic dissipation from temperature measurement fields during the fatigue test. We focused on the longitudinal distribution of heat sources within the specimen gauge part. A 1D calorimetric analysis has been justified assuming in a first approximation a uniaxial tension-compression stress state. From the heat equation:

$$\rho C \dot{T} - k\Delta T = s \tag{1}$$

where T is the temperature, ρ the mass density; C the heat capacity; k the thermal conduction coefficient. s(x,y,z,t) symbolizes the volume of heat source. Following Boulanger's hypotheses [8], the 1D diffusion equation for a non-constant cross-section can be written as [9]:

$$\frac{\partial\theta(x,t)}{\partial t} + \frac{\theta(x,t)}{\tau^{1D}(x)} - \frac{k}{\rho C}\left(\frac{\partial^2\theta(x,t)}{\partial x^2} + \frac{\partial\theta(x,t)}{\partial x}\frac{S'(x)}{S(x)}\right) = \frac{s(x,t)}{\rho C} \tag{2}$$

with $\theta = T - T°$ is the temperature change, $T°$ is the room temperature and τ^{1D} is a time constant term which characterizes the heat losses through lateral surfaces of the specimen:

$$\tau^{1D}(x) = \frac{\rho C \cdot S(x)}{2h(e + l(x))} \tag{3}$$

where e is the specimen thickness, $l(x)$ is its width with respect to x. We note by $S(x) = e \cdot l(x)$ the cross-section at this point. The mean dissipation over several thousand cycles was solely estimated

(the thermo elastic sources being not considered here regarding the test frequencies and the adiabatic character of the thermoelastic processes over a complete cycle duration (50 µs)). In the above equations, the unknown parameter is the heat transfer coefficient *h*. The method used to identify *h* is presented in the following section.

3.2. Heat loss time constant identification

The heat transfer coefficient is determined for each test, from thermal field measurements when the fatigue loading is stopped and the temperature of specimen returns to thermal equilibrium. More precisely, the initial temperature was considered as the temperature when the load was stopped. During the thermal return to equilibrium, no heat source occurs. Thermal measurements $\theta^{\exp}$ applied to each end of the specimen by Dirichlet method enabled us to know the boundary conditions. The unknown heat transfer coefficient *h* was well chosen to satisfy these conditions:

$$\begin{cases} \dfrac{\partial\theta(x,t)}{\partial t} + \dfrac{\theta(x,t)}{\tau^{1D}(x)} - \dfrac{k}{\rho C}\left(\dfrac{\partial^2\theta(x,t)}{\partial x^2} + \dfrac{\partial\theta(x,t)}{\partial x}\dfrac{S'(x)}{S(x)}\right) = 0 \\ \theta(x,t=0) = \theta^{\exp}(x,t=0) \\ \theta(\dfrac{-L}{2},t) = \theta^{\exp}(\dfrac{-L}{2},t) \end{cases} \tag{4}$$

As a result, *h* was found in ranges of 30 – 100 W/m^2/K. This result shows that the heat losses are caused by natural convection and also by an air flow above the specimen which aims at cooling the piezoelectric system.

4. Results for polycrystalline pure copper and discussions

Fig. 3a and 3b display the average temperature over the gauge length and several thousands of cycles and the corresponding intrinsic dissipation for various maximum stress amplitudes versus the number of cycles for CuOF 99.95%. The temperature rises over cycles and never reaches a constant value. In other words, the temperature does not stabilize, showing an evolution of the heat balance and consequently of the microstructure. Despite a slight raise of the temperature at $\Delta\sigma/2$= 44.1 MPa, the intrinsic dissipation increased very slowly with the number of cycles. It attained to 0.498 °C/s at 10^6 cycles and reached 0.505 °C/s at 10^8 cycles. It means that the heat sources were higher than the heat losses and remained active along the cycles. However, no slip bands were observed on specimen surface up to 10^8 cycles at this stress range. At $\Delta\sigma/2$ = 49.6 MPa, the intrinsic dissipation increased slowly up to 10^7 cycles. No slip bands were either observed between 10^6 and 10^7 cycles. At 10^8 cycles, a clear increase of the intrinsic dissipation was recorded and slip markings were observed on the specimen surface. The intrinsic dissipation was 1.322 °C/s (Fig. 4a). At higher stress amplitude, $\Delta\sigma/2$= 54.7 MPa, the intrinsic dissipation increases with the number of cycles more rapidly than in previous cases. First slip bands were observed at 10^7 cycles (Fig. 4b). They are more pronounced at 10^8 cycles (Fig. 4c). At $\Delta\sigma/2$ = 69.4 MPa, the intrinsic dissipation rises very fast with the number of cycles and reaches 7.477 °C/s at 10^6 cycles. First slip bands were observed

at 10^6 cycles (Fig. 4d). The roughness and the quantity of slip bands kept rising over the cycles as dissipation (Fig. 4e and 4f). At 10^7 cycles, the narrowest zone of the specimen was covered with slip bands and the specimen self-heating is about 70°C.

In addition to average values, the intrinsic dissipation distribution can be estimated along the specimen axis (Fig. 5a). The intrinsic dissipation is concentrated in the middle of the specimen and decreases toward the ends. As expected, it is related to the distribution of stress (Fig. 1). Optical micrographs revealed that this zone displays the highest quantity of slip markings (Fig. 5b). This result confirms that dissipation is related to microplasticity.

4. Conclusions

The DISFAT project is an ongoing French project financially supported by the French National Agency ANR. It aims at a deeper understanding of mechanisms leading to crack initiation in metals and alloys in Very High Cycle Fatigue (VHCF). Thermal maps were used to estimate the mean dissipation and its change with number of cycles and stress amplitudes in case of pure copper polycrystals. At the same time, the surface relief changes were characterized using optical and scanning electronic microscopes. A good correlation was found between slip band initiation and dissipation. Dissipation and slip band amount always increased over the number of cycles. They are higher with increasing stress amplitudes. The 1D dissipation distribution is in good agreement with the stress 1D profile. The strongest dissipation value was found at the place where the number of slip bands is the highest. At very small stress amplitudes, no slip band appeared up to 10^8 cycles but the material was found to dissipate energy. These results reveal that the material never reached a steady state. Therefore it could break at higher number of cycles.

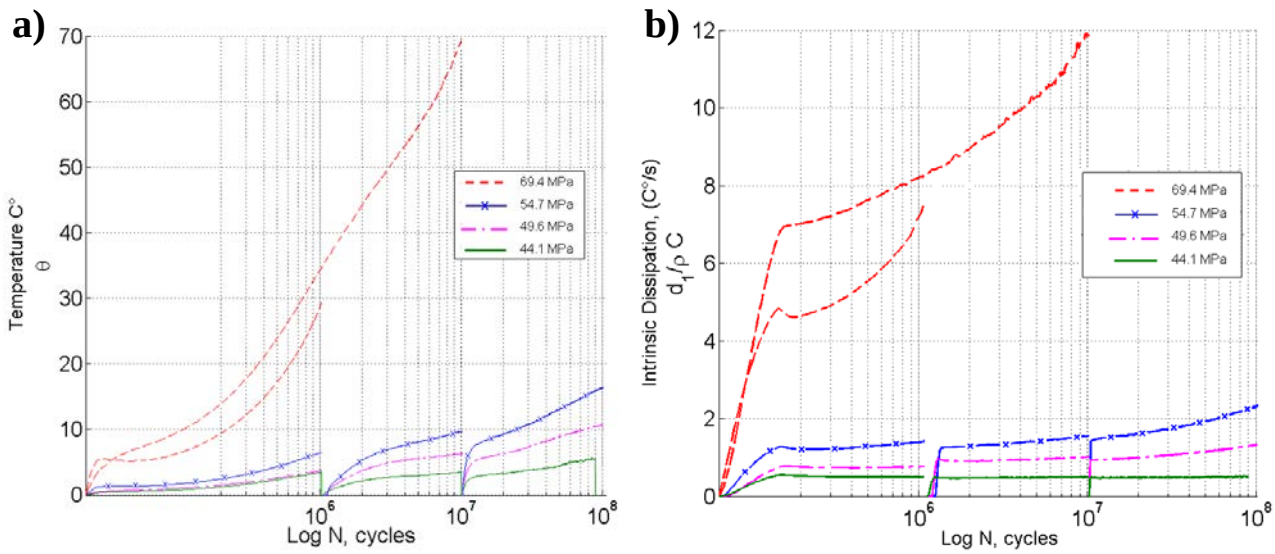

Figure 3. (a) Average temperature and (b) Average intrinsic dissipation during fatigue test at different constant stress amplitude fatigue test for CuOF 99.99%.

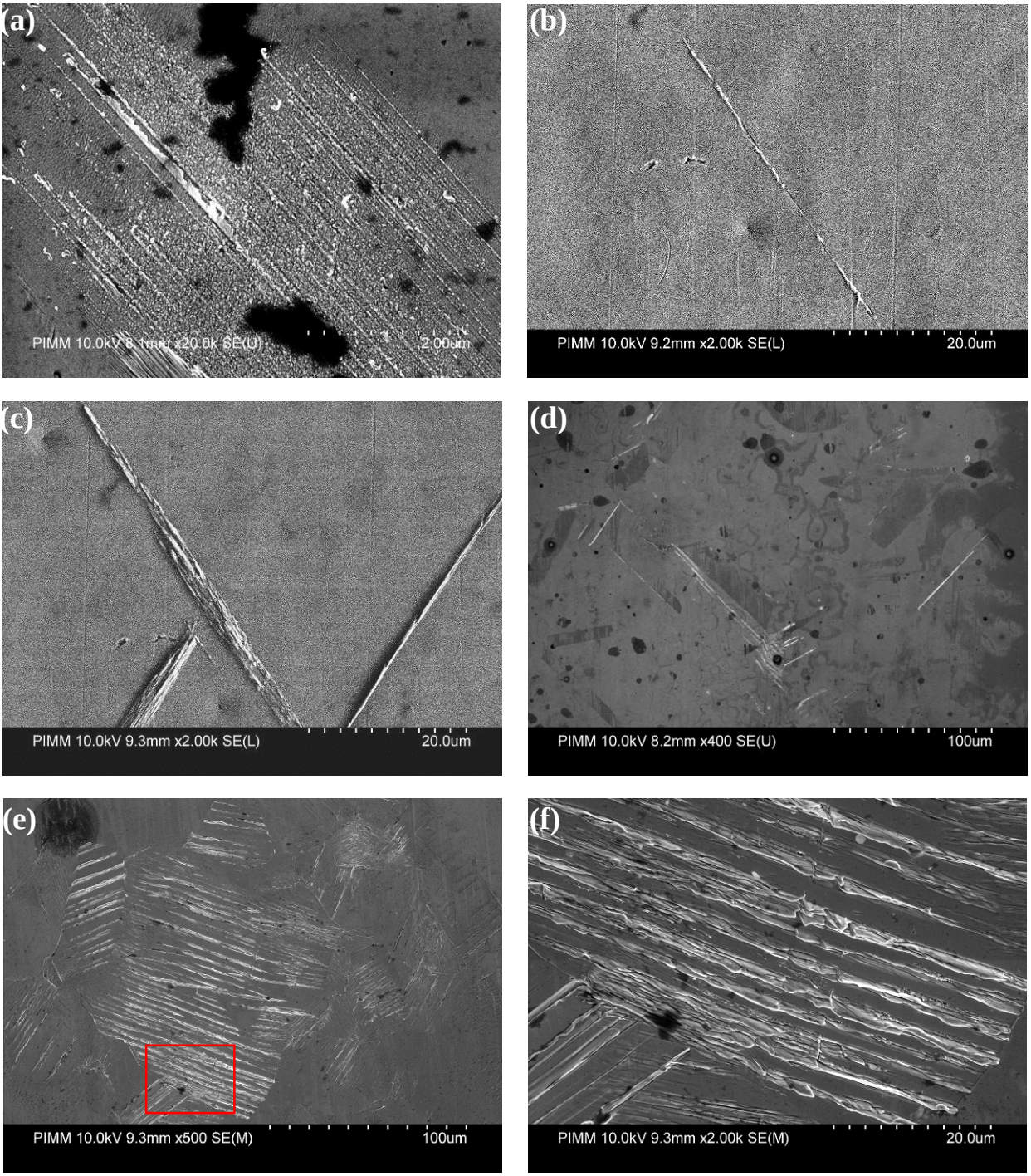

Figure 4. Scanning Electron Micrographs of the specimen surface - (a) $\Delta\sigma/2$ = 49.6 MPa - 10^8 cycles; (b) $\Delta\sigma/2$ = 54.7 MPa - 10^7 cycles and (c) at the same place after 10^8 cycles; (d) $\Delta\sigma/2$ = 69.4 MPa - 10^6 cycles; (e) $\Delta\sigma/2$ = 69.4 MPa - 10^7 cycles (f) zoom of (e)

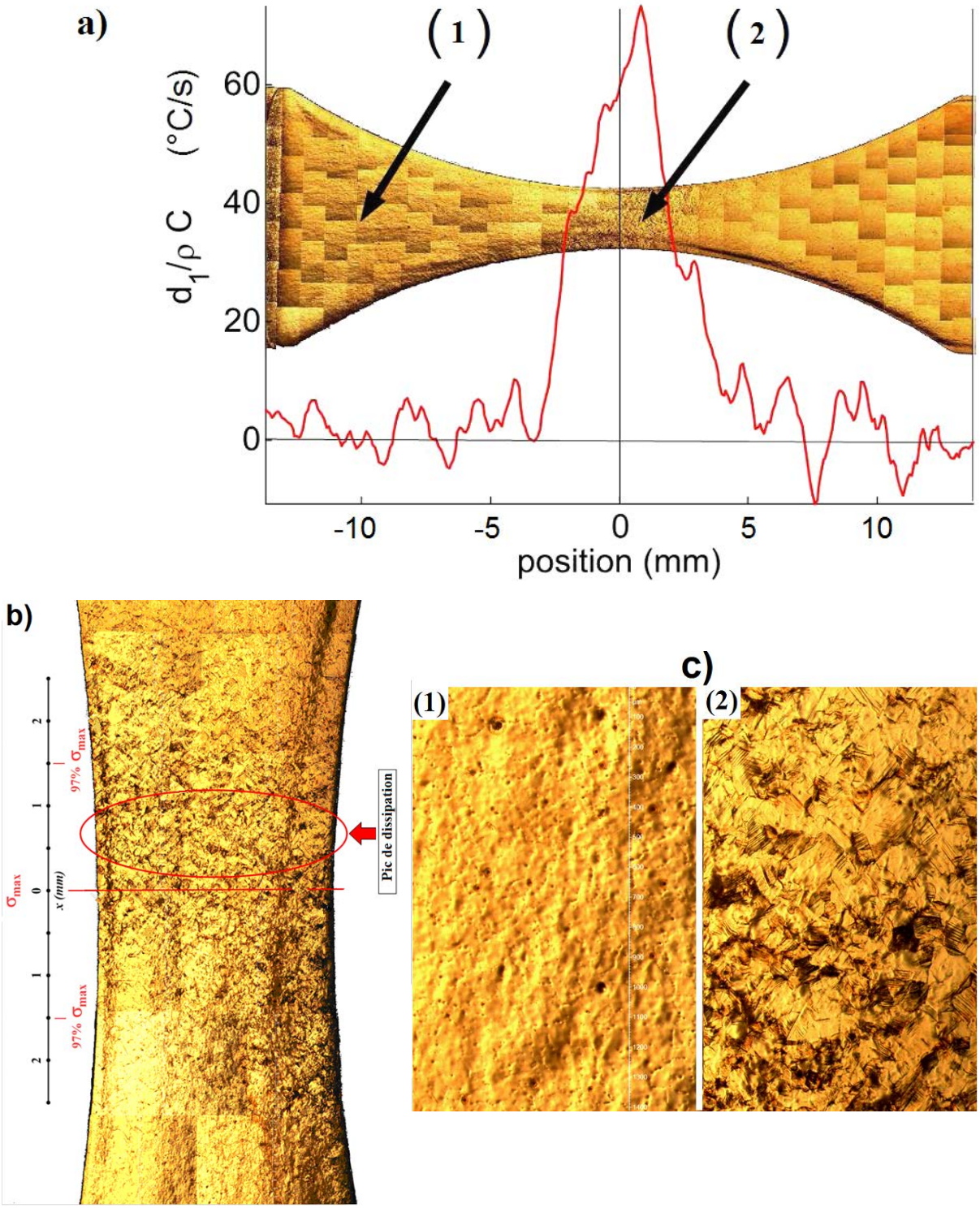

Figure 5. a) 1D distribution of the intrinsic dissipation along the specimen
b) Optical micrograph of the middle part of the specimen c) Optical micrographs at two places of the specimen surface (noted (1) and (2))
at $\Delta\sigma/2$ = 69.4 MPa - 10^7 cycles

Acknowledgements

We thank Agence Nationale de la Recherche France ANR-09-BLAN-0025-01 for their financial support and the company Griset for supplying copper.

References

[1] C. Bathias, P.C. Paris, Gigacycle fatigue in mechanical practice, editor: Marcel Dekker, ISBN 0-8247-2313-9, 2004.

[2] R. Wang, H. Mughrabi, Secondary Cyclic Hardening in Fatigue in Copper Monocrystals and Polycrystals Mater. Sci. Eng., 63 (1984) 147-163.

[3] C. Sommer, H. Mughrabi, D. Lochner, Influence of temperature and carbon content on the cyclic deformation and fatigue behavior of α-iron. Part II: crack initiation and fatigue life, Acta Mater., 46 (1998) 1537-1546.

[4] A.W. Thompson, W.A. Backofen, “The effect of grain size on fatigue,” Acta Metall., 19, 1971, 597-605.

[5] P. Lukas, L. Kunz, Cyclic slip localization and fatigue crack initiation in fcc single crystals, Mater. Sci. Eng. A 314 (2001) 75-80.

[6] N.L. Phung, A. Blanche, N. Ranc, A. Chrysochoos, V. Favier, Microplasticity evolution in polycrystalline pure copper subjected to very high cycle fatigue, Conference on Very High Cycle Fatigue 5, Berlin, 2011

[7] C. Wang, D. Wagner, C. Bathias, PSB Formation in Armco Iron loaded in the gigacycle fatigue, Conference Very High Cycle Fatigue 5, Berlin, 2011

[8] T. Boulanger, A. Chrysochoos, C. Mabru, A. Galtier, Calorimetric analysis of dissipative and thermoelastic effects associated with the fatigue behavior of steels', International Journal of Fatigue 26 (2004) 221 - 229.

[9] C. Doudard, S. Calloch, F. Hild, S. Roux, Identification of heat source fields from infra-red thermography: Determination of ‘self-heating' in a dual-phase steel by using a dog bone sample, Mechanics of Materials 42 (2010) 55 - 62.

Evaluation of an ultrasonic device to test fretting-fatigue in very high cycle regime

Pedro F. Filgueiras[1,*], Claude Bathias[2], Ernani S. Palma[1]

[1] Department of Mechanical Engineering, Universidade Federal de Minas Gerais, Belo Horizonte 31270-901, Brazil
[2] Laboratoire Energétique Mécanique Electromagnétisme, Université Paris Ouest, Ville d'Avray 92410, France
* Corresponding author: pedroffilgueiras@gmail.com

Abstract
Traditional fatigue tests are not suitable for very high cycle fatigue (VHCF) problems, because of the enormous time spent to reach this regime. Many mechanical components may, however, be subjected to VHCF. Fatigue strength beyond certain limit is usually estimated using statistical approaches or establishing a threshold for crack nucleation.
Fretting may take place whenever two fixed parts are under mechanical vibration and variable bulk load. It can have catastrophic effects for parts under fatigue, mainly in VHCF, virtually eliminating crack initiation period.
The objective of the present work was to evaluate an ultrasonic device to accelerate very high cycle fretting-fatigue tests. Axial load was imposed by a piezoelectric transducer to round cross-section specimens. Fretting was induced by forcing at right angle cylinder pads, which were replaceable and could be specified for each case. It was possible to choose, at the same time, both fretting amplitude and bulk load. Normal load was imposed by an adjustable spring.
Results confirmed that fatigue strength decreased significantly when specimens were subjected to fretting. Besides this, worn surfaces showed many characteristics evidencing the occurrence of fretting. Upgrades are necessary to decrease the influence of the apparatus on fretted amplitude and to facilitate surfaces alignment.

Keywords very high cycle fatigue, fretting-fatigue, ultrasonic fatigue testing

1. Introduction

The study of materials behaviour under Very High Cycle Fatigue (VHCF) is of real interest of researchers on different engineering fields and several industrial sectors. Many mechanical components can be subjected to VHCF once that their loading histories easily exceed the assumed high cycle fatigue limit, usually established between 10^6 and 10^8 cycles, depending basically on the material in analysis. For example, the crankshaft of a car equipped with 30in. diameter tires, considering an average 1:3 reducing factor, will attain 10^8 cycles after 80,000km in service. To reach the same number of cycles, a 1.02m diameter train wheel will take around 100,000km and a aircraft turbine running at 10,000rpm will take about 170h of service.

The transportation industry exemplified on the three cases above is perhaps where the study of VHCF is of importance. During their normal lives, vehicles', trains', and turbines' parts can run up to 10^9, 10^{10}, and 10^{11} cycles, respectively[1]. The time spent to reach such a high number of cycles using conventional fatigue testing machines is too long, making the study of VHCF in traditional ways prohibitive. The 100Hz testing line in Fig. 1 illustrates this problem: vertical layers delimit the span of cycles usually attained by each kind of craft's parts during their lives, while horizontal shadows divide the ordinate in subparts, giving the reader an idea of time length.

Beyond the usual limit of high cycle fatigue regime, fatigue properties are usually estimated based on statistical approaches, being a horizontal asymptote usually assumed for steels and other metals, while for aluminium alloys a steady decreasing in fatigue strength is supposed[2]. Nevertheless, the increasing necessity of full understanding of engineering phenomena made mandatory the

acceleration of fatigue testing. One of the evolutions that made possible the evaluation of VHCF was the ultrasonic fatigue testing device, frequency first reached by Mason[3] *apud* Bathias & Paris[1], in which fatigue experiments are carried out at 15kHz or more. The 20kHz testing line in Fig. 1 shows, in comparison with the 100Hz one, how greatly fatigue experiments carried out in such a high frequency can be achieved quicker, becoming feasible and affordable.

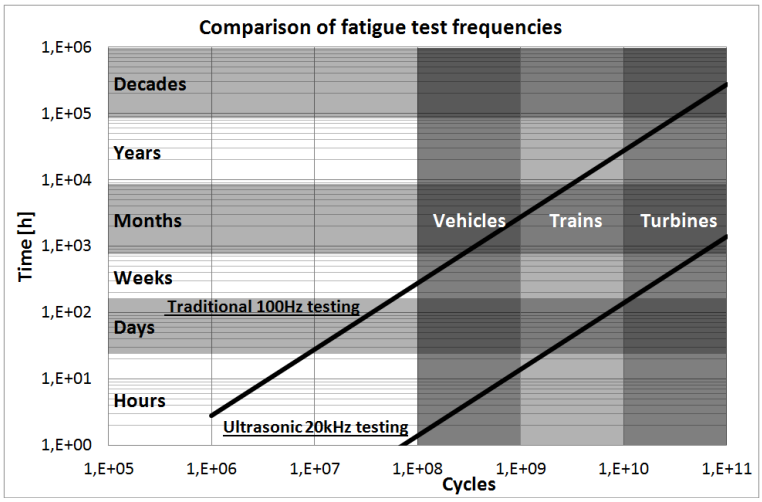

Figure 1 – Comparison of time spent to reach a certain number of cycles in 100Hz and 20kHz fatigue tests

As tests in the VHCF regime became more accessible and frequent, several studies [1,4-6] showed that the infinite fatigue life assumption for steels and other metals did not represent faithfully the reality of this phenomenon. On the contrary, fatigue strength of ferrous materials tends to decrease as the number of cycles increases. Moreover, it was proved that even crack nucleation mechanism in VHCF regime is different from low and high cycle ones. For the latter, cracks typically arise from the surface, while for the former, subsurface initiation preponderates [1,4-7].

Fatigue properties of a component can be deteriorated by many external reasons; a very common factor is the fretting phenomenon, which occurs whenever two surfaces subjected to mechanical vibration are fixed against each other, i.e., there is no nominal displacement between them. This vibration will result in minute displacement between both parts, mostly in regions of geometric or loading discontinuities. This random or cyclic movement will induce wear of surfaces in contact and, under specific conditions, will trig fretting cracks, which has been remarked in minute displacement as small as 0.1µm[8]. Many practical situations can be subjected to this phenomenon, like, for example, bolted connections, interference assemblies, flanges, keyways, cables, and ropes.

The effect of fretting can be catastrophic, once that it diminishes crack initiation period because of stress concentrations over the contact surfaces[9]. Virtually eliminating this span of life, fretting decreases a material's fatigue strength to very low levels, dropping it to values as low as $^1/_3$ of its original value[8]. This effect is still more remarkable when a steel body is subjected to VHCF, where crack initiation period accounts for the most of its fatigue life, such as in high cycle fatigue[10].

Unlike plain fatigue experiments, just a few works have been done using ultrasonic frequency to accelerate fretting tests[11-13]. These authors criticize the technique of increasing the oscillatory movement's amplitude in order to accelerate fretting experiments, inasmuch as it changes the contact conditions with simultaneous change in crack initiation and wear mechanisms. These studies conclude that many observed wear mechanisms exhibit the features described in some of the most accepted models for fretting. So ultrasonic testing seems to be a promising technique for

accelerated fretting wear experimenting. However, Söderberg *et al.*[11] and Bryggman *et al.*[13] recommend precaution to use it in low amplitude fretting, where fretting wear is less important than fretting corrosion and fretting fatigue. Moreover, it appears that the two latter phenomena rates improved by increasing the frequency of vibration. Although there is no apparent change in contact conditions, frequency influences both interfacial strain rate and temperature.

Finally, only one study was found in literature using ultrasonic frequency to accelerate fretting-fatigue tests[14]. These authors concluded that the developed ultrasonic fretting-fatigue testing machine worked well, reproducing the phenomenon rightly. Thus, the objective of the presented paper was to evaluate the same machine used by Sun *et al.*[14], presented in details in [15].

2. Materials and Methods

In order to evaluate the testing device first presented by Sun *et al.*[14], fretting-fatigue tests were run in ultrasonic frequency, i.e., around 20kHz, until specimens either fail or run out at the life of 10^9 cycles. Fretting was induced by a cylindrical pad in right angle with the specimen (crossed-cylinder configuration) with a normal load of 30N and constant fretting amplitude at 10µm. Axial bulk load was imposed by a piezoelectric transducer in ultrasonic frequency at one of the fundamental frequencies of the specimen. Plain ultrasonic fatigue results in VHCF region for the material in analysis is available from earlier experiments. All tests were made at the *Laboratoire Energétique Mécanique Electromagnétisme*'s facilities, at *Institut Universitaire de Technologie de Ville d'Avray*, France, directly linked to *Université Paris Ouest*.

The device in analysis can be split in two subsystems: the ultrasonic core, responsible to axially stress the specimen, and the fretting-apparatus, in charge of rubbing it. The ultrasonic core imposed full reverse axial stress cycles to specimens by vibrating in a frequency near to one of fundamental frequencies of the entire assembly. To achieve one these modes, a sinusoidal displacement was imposed by a piezoelectric transducer connected to a high frequency power source, which was piloted by a control unit. In general, displacements generated in a piezoelectric transducer are too small, so it was necessary to attach at one of its ends a horn (sonotrode), or mechanical amplifier, to reach desired displacements and consequently higher stress levels through specimens. A schema of core's main units can be seen in Fig. 2.

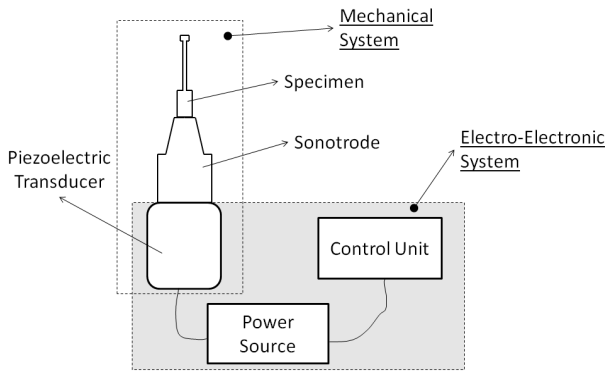

Figure 2 – Schema of the main units composing the ultrasonic core of the testing device

Once that specimen's fundamental modes and frequency and amplitude of imposed displacements at the specimen's bottom were known, it was easy to calculate displacement and stress fields through the piece and generate the iso-amplitude of displacement abacus. Using this powerful tool allowed the determination of the position where fretting pads were going to be placed in order to assure both desired fretting amplitude and bulk stress. An example of this kind of abacus is shown

in Fig. 3: if a X_i=10µm amplitude displacement is required with 300MPa bulk stress, it is only necessary to identify the intersection of the 10µm displacement line (dashed) with the 300MPa line coming from the vertical axis. This point, marked with a cross in the chart, shows where the fretting pads must be placed (around 45mm from the specimen's bottom – horizontal axis) and the displacement amplitude to be imposed at the specimen's bottom ($X_{(0)}$=14µm) – full line that intersects the cross.

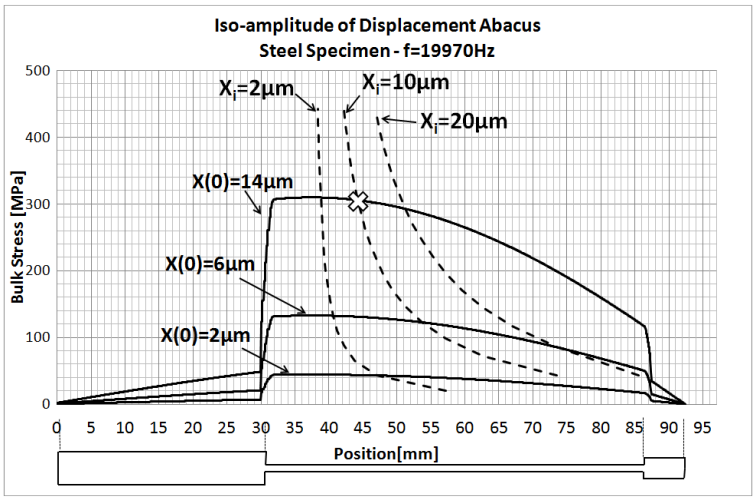

Figure 3 - Example of an iso-amplitude of displacement abacus.

The fretting-apparatus consisted of two 5-mm diameter cylindrical pads made of AFNOR XC48 steel, similar to ASTM510[16], soaked at 830°C for 30 minutes and quenched in water, carefully polished with 1000 CAMI graded sandpapers. Pads were diametrically opposed, pressing specimens with 30N normal load, imposed by two parallel springs, as shown in the schema of the mechanical assembly in Fig. 4. A rigid apparatus supported springs and pads, which were glued with Araldite®.

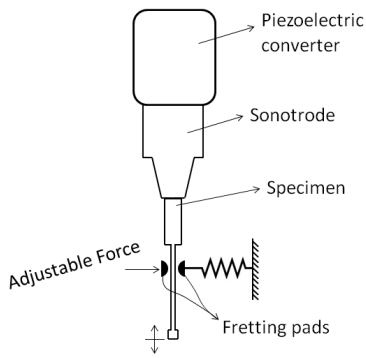

Figure 4 –Schema of mechanical assembly

At last, a cooling system using compressed air was necessary to keep specimens at room temperature, since that ultrasonic strain cycling and high fretting frequencies generate high heat rates.

2.1. Specimens

The material studied was a low alloy medium strength steel provided by an external supplier. All specimens were sequentially polished with 180, 320, 600, and 1000 CAMI-graded sandpapers in its axial direction. Their dimensions are shown in Fig. 5, and in Table 1.

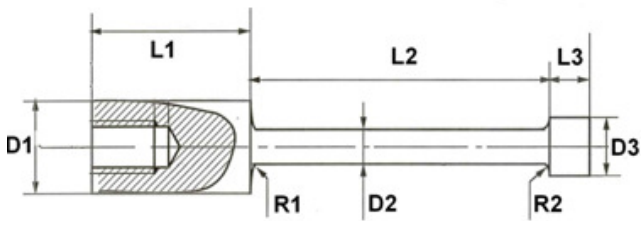

Figure 5 - Dimensions' codes

Table 1 – Nominal values and geometric tolerances

	D1	D2	D3	L1	L2	L3	R1	R2
Nominal value [mm]	10.00	4.00	7.00	30.00	57.40	5.00	2.00	1.00
Tolerance [mm]	0.05	0.02	0.05	0.10	0.05	0.05	0.1	0.1

3. Results and Discussion

3.1. Comparison between plain fatigue and fretting-fatigue

The fatigue curves are presented in Fig. 6. The fretting curve, calculated by using the least-squares method, showed good linearity (R^2=0.68). The data with triangular mark was excluded from linear regression calculations, because its value was completely out of general behaviour of the other tests. Further statistical analysis must be done to confirm this hypothesis. Despite the relatively low coefficient of determination of linear regression, it is a good result, taking into account the number of variables that influences fretting-fatigue. Moreover, it is necessary to remember that this phenomenon was investigated beyond the 10^7 cycle limit, which is historically hard to analyze, due to its complex stochastic behaviour. Finally, synergy between both phenomena when explored in ultrasonic regime was not deeply studied until the present time.

It also can be seen in Fig. 6 that fatigue strength in VHCF region decreased when specimens were subjected to fretting. With both linear regression data, a fatigue strength reduction factor (r) was defined. This factor represented the ratio of plain fatigue strength to fretting-fatigue strength at a given number of cycles. As shown in Fig. 6, this factor remained almost constant at around 1.5 in the whole VHCF region, decreasing less than 3% from 10^6 to 10^9 cycles.

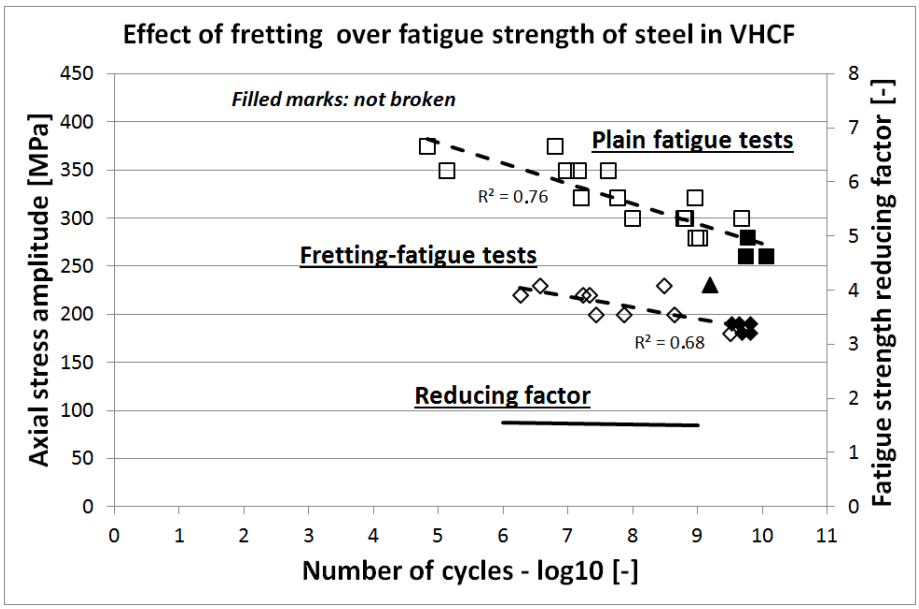

Figure 6 - Comparison between fatigue strength with and without fretting

3.2. Fretting evidences

A brief analysis of results can show some indirect clues of the reproduction of fretting in tests. It was observed that somehow superficial factors highly influenced fatigue life of component. First of all, as one can see in Fig. 6, the drop in fatigue strength of material in analysis was remarkable. Another indication was that cracks nucleated on surface, as exemplified in Fig. 7, unusual behaviour in VHCF regime, in which subsurface initiation preponderates.

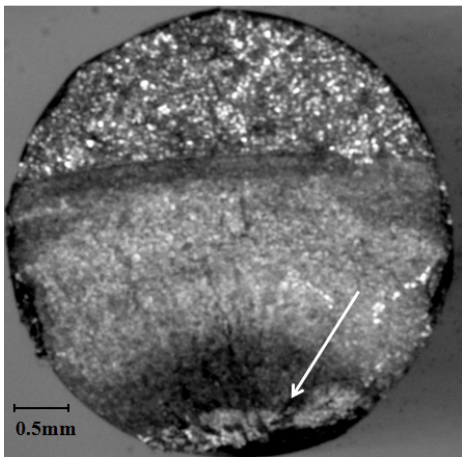

Figure 7 – Crack nucleation on surface

Fretted surfaces of tested specimens were analyzed and most of them showed fretting characteristics described by some of the most accepted fretting models in literature[8]. The presence of two clearly distinguishable areas can be seen in Fig. 8: smooth stick region and rough slip zone with scars in rubbing direction. Damaged surfaces were crossed vertically by a smooth and shinny section, which corresponds to stick zone, located about the centre of the contact ellipse. This stick zone is surrounded in its left and right sides by a rougher and deeper region, the slip zones.

The formation of oxidized regions and debris, mainly when excessive fretting occurs, is also very characteristic. Debris could be found in great quantity far from fretted surfaces, because they were really slender and were blown away by cooling apparatus. Red-brownish spots, characteristic of steel oxidization, were found in almost every worn surface, predominantly in regions subjected to heavy wear, as expected[8]. An example is illustrated in Fig. 8, where bright white spots represent the oxidized regions.

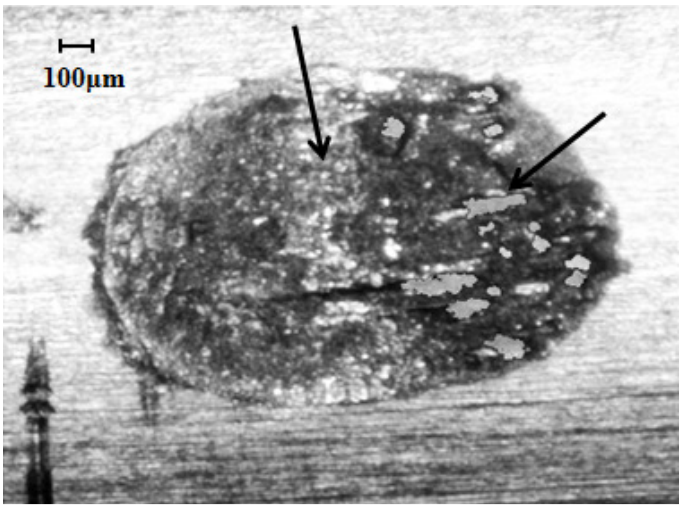

Figure 8 –Example of factors usually found in surfaces under fretting

Finally, the last aspect analyzed were the crack initiation sites. Fretting cracks are usually nucleated next to one of two existing bounds: stick-slip zones limit and the limit between slip zone and region out of contact surface[9,17]. Although it is very hard to determine which of these zones will predominate, authors linked crack nucleation site to contact pressure[17]. However, in the present work, crack nucleation site changed from test to test: in a few cases, crack nucleated near stick-slip zones bound (Fig. 9a), in specimens, cracks nucleated in the bound between region under contact and free region (Fig. 9b).

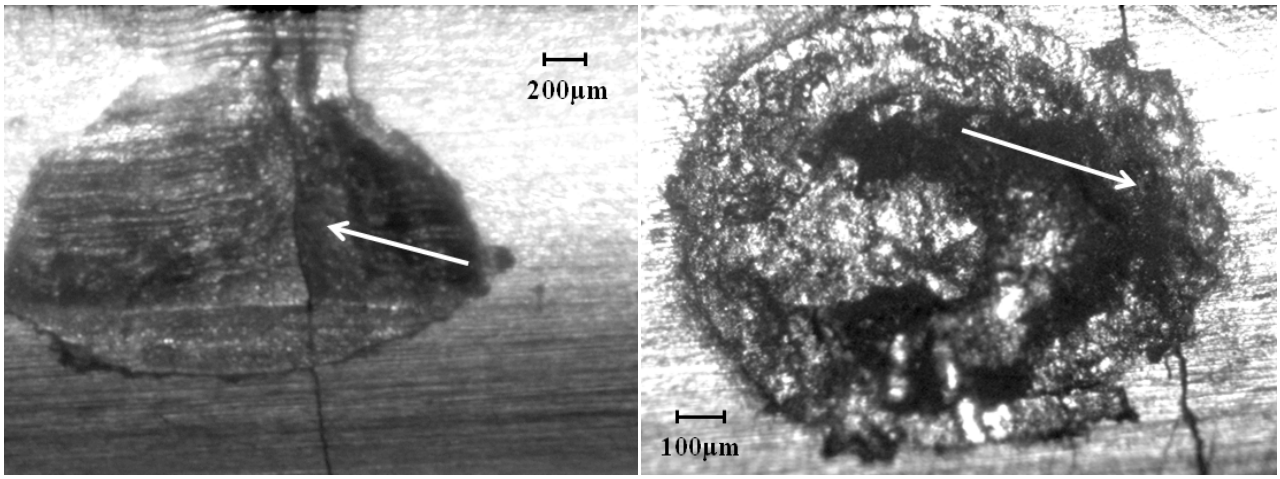

Figure 9 – Examples of crack nucleation sites: stick-slip zones limit (a) and bound between under contact and free region (b)

3.3. On the device

The most advantageous innovation of the ultrasonic device was clearly the possibility of accelerating enormously tests, as presented before. Some other benefits could be pointed out though. The mechanics of the machine is simple, resulting in easy maintenance and facilitating operators training. Also, setting-up and operating are easy, except for the alignment process. The components of the machine and instruments are light and inexpensive when compared to other axial fatigue machines. Finally, another great advantage is that, within certain limits, as discussed later in this paper, the choice of fretting amplitude and bulk stress is uncoupled. It used to be a problem in machines used in several studies[18-20] in which one factor was dependent on the other.

On the other hand, a few drawbacks were found linked to specimen manufacture costs and alignment problems. The necessity of extremely well polished specimens is inherent to the process, once that superficial problems can trig crack nucleation before reaching VHCF. Polishing this kind of geometry – cylinder 100mm long, 4mm diameter – can be very time and money consuming. Still more troubling is the necessity of very strict geometric tolerance in manufacture process. As one can see in Fig. 10, nonconformities can be very harmful to tests, once that small deviations in geometry can significantly change fretting displacement amplitude and bulk load at a given position (see Fig. 5 to dimensions' codes). In this chart, vertical axis represents the percentage of deviation in both properties per deviation percentage in geometry, e.g., 1% of deviation in diameter D1 provokes almost 2% of deviation in bulk load and around 0.3% in displacement amplitude.

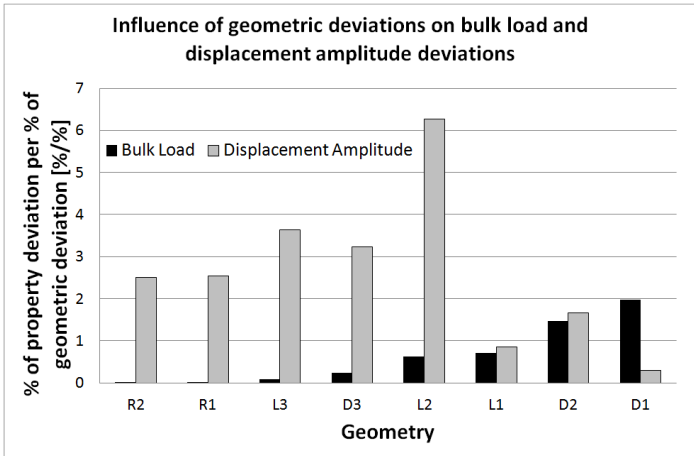

Figure 10 –Influence of geometry on bulk load and fretting amplitude deviations

Alignment was found to be another problem on the ultrasonic device. Position both pads such that their axis were parallel to each other and at the same height of the specimen, in order to avoid bending, was very difficult using the current fixture system. Complications came from the attachment process using Araldite® and from the loosing apparatus. It is advisable to revamp the support apparatus, aiming to facilitate the operation of the machine and to broaden its range of application, allowing the use of other types of contact configurations, e.g., line contacts as cylinder on flat or cylinder on cylinder, which are harder to align.

3.3.1 The overheating matter

Temperature rise in ultrasonic fretting-fatigue tests can be caused by two different methods. The first one is due to high strain cycling, which generates high heat rates. Specimen overheating must be avoided, because it modifies its mechanical properties and, beyond certain limit, changes fundamental frequency of specimen, killing the test. That is why the cooling apparatus is so necessary. The problem is that, as observed during tests, air coming out in high velocity from the apparatus blew away slender oxide debris formed in fretting contact. Nevertheless, the role of these debris in fretting is very important[8] and their forced expulsion from the area between surfaces clearly changes contact conditions. It is necessary to dedicate further efforts to understand its consequences to fretting-fatigue behaviour.

The second phenomenon is linked to wear caused by fretting, even more important at high frequencies. All other parameters being held constant, heat generated increases when wear volume per cycle raises. Superficial temperature, mainly at contact must remain in reasonable levels, in accordance with practical situations. Otherwise, high temperature tends to increase oxidation rates and to degenerate mechanical properties of materials in contact, affecting fretting conditions. In some tests, it was observed that superficial temperature raised when apparatus presented looseness and compliance, undergoing excessive vibration or when Araldite® softened because of high temperature. In both cases, it is probable that fretting pads were not properly fixed and was able to develop small displacements, increasing both surface and volume worn. It is recommended to rethink the apparatus that supports fretting pads, stiffening it, decreasing looseness, and principally changing how pads are attached to it, stop using gluing process.

3.3.2 Decoupling of fretting displacement amplitude and bulk stress

Decoupling fretting displacement amplitude and bulk stress at a given point without any additional equipment is a great advantage of the machine in study, so almost any combination of these

properties can be chosen. Nevertheless, as one can see in Fig. 3, given a bulk stress at the rubbing point, the higher the fretting amplitude (X_i) desired, the higher must be the amplitude imposed at specimen's bottom ($X_{(0)}$), therefore improving the maximum bulk stress over the specimen. As a result, a more elevated heat rate will be generated, rising specimen's temperature, leading to the implications discussed earlier. So, summarizing, maximum fretting amplitude is limited: the higher the desired amplitude at a place, the lower the bulk load that can be chosen at this same point.

4. Conclusions

The ultrasonic machine is a promising device to accelerate fretting-fatigue experiments, which can be carried out more than 200 times faster than in regular fatigue testing machines currently in use. Fretting could be reproduced, decreasing fatigue strength by a factor of 1.5 in the whole VHCF region. Surfaces under fretting presented many patterns characteristic of this phenomenon: presence of two distinguishable areas of stick and slip contact, formation of oxidized regions and debris in the slip zone, and crack initiation near the stick-slip regions bound or near the stick regions-region out of contact bound. Moreover, superficial factors brought crack nucleation to surface, unlike to happen in plain VHCF.

The mechanism of the machine is simple, of easy maintenance and operation. Its components are lighter and cheaper than usual axial fatigue machines. In contrast to other fretting-fatigue devices usually found in literature, choice of fretting displacement amplitude and bulk stress in specimen is decoupled within certain limits. On the other hand, the necessity of extremely well polished specimens with very strict geometric tolerances is inherent to the ultrasonic testing machine, making specimen manufacture expensive.

The use of a cooling system is mandatory in the ultrasonic machine device, especially on fretting-fatigue tests. The current system, using compressed air, was responsible for blowing away oxide debris out of the fretting contact. These debris play, nevertheless, a very important role in fretting and their forced expulsion changes contact conditions. Further work must be done to understand the consequences of this fact to fretting-fatigue phenomenon.

The main problems are, however, linked to the apparatus that supports fretting pads. Looseness and compliance caused excessive vibration, letting pads developed small displacements. Therefore, surface and volume worn as well as superficial temperature raised in some tests. Also, alignment was found to be very hard using the current fixture system. It is advisable to revamp the support apparatus, aiming to facilitate the operation, to allow the use of other types of contact configurations, and to decrease its influence on fretting amplitude.

Acknowledgments

The financial support of the Coordination of Improvement of Higher Level Personnel (CAPES) and National Council for Scientific and Technological Development – CNPq is greatly appreciated. The authors are grateful to Vallourec & Mannesmann do Brasil, for providing and manufacturing the specimens.

References

[1] C. Bathias and P. C. Paris, Gigacycle Fatigue in Mechanical Practice, New York: Marcel Dekker, 2005.

[2] J. Bannantine, J. Comer and J. Handrock, Fundamentals of Metal Fatigue Analysis, New Jersey: Prentice Hall, 1990.

[3] W. P. Mason, Piezoelectric Crystals and their Application in Ultrasonics, New York: Van Nostrand, 1956.

[4] Z. Duan, X. Ma, H. Shi, R. Murai and E. Yanagisawa, "Gigacycle fatigue behaviors of two SNCM439 steels with different tensile strengths," *Acta Mechanica Sinica,* vol. 27, p. 778–784, 2011.

[5] Y. Furuya, "Size effects in gigacycle fatigue of high-strength steel under ultrasonic fatigue testing," *Procedia Engineering,* vol. 2, p. 485–490, 2010.

[6] J. M. Zhang, S. X. Li, Z. G. Yang, G. Y. Li, W. Hui and Y. Weng, "Influence of inclusion size on fatigue behavior of high strength steels in the gigacycle fatigue regime," *International Journal of Fatigue,* vol. 29, p. 765–771, 2007.

[7] A. Atrens, W. Hoffelner, T. Duerig and J. Allison, "Subsurface crack initiation in high cycle fatigue in Ti6Al4V and in a typical martensitic stainless steel," *Scripta Metallurgica,* vol. 17, pp. 601-606, 1983.

[8] R. B. Waterhouse, Fretting Fatigue, Applied Science Publishers, 1981.

[9] H. Attia and R. B. Waterhouse, Standardization of fretting fatigue test methods and equipment, ASTM, 1992.

[10] Y. Lee, J. Pan, R. B. Hathaway and M. E. Barkey, Fatigue Testing and Analysis, Elsevier, 2005.

[11] S. Söderberg, U. Bryggman and T. McCullough, "Frequency Effects In Fretting Wear," *Wear,* vol. 110, pp. 19 - 34, 1986.

[12] S. Söderberg, S. Nikoonezhad, K. Salama and O. Vingsbo, "Accelerated fretting wear testing using ultrasonics," *Ultrasonics,* vol. 24, pp. 348-353, 1986.

[13] U. Bryggman and S. Söderberg, "Contact Conditions And Surface Degradation Mechanisms In Low Amplitude Fretting," *Wear,* vol. 125, pp. 39-52, 1988.

[14] Z. Sun, C. Bathias and G. Baudry, "Fretting fatigue of 42CrMo4 steel at ultrasonic frequency," *International Journal of Fatigue,* vol. 23, p. 449–453, 2001.

[15] C. Bathias, "Piezoelectric fatigue testing machines and devices," *International Journal of Fatigue,* vol. 28, p. 1438–1445, 2006.

[16] ASM International, Heat Treater's Guide: Practices and Procedures for Irons and Steels, 2nd Edition ed., 1995, p. 192.

[17] K. Nakazawa, N. Maruyama and T. Hanawa, "Effect of contact pressure on fretting fatigue of austenitic stainless steel," *Tribology International,* pp. 79-85, 2003.

[18] D. Nowell and D. Hills, "Mechanisms of Fretting Fatigue Tests," *International Journal of Mechanical Sciences,* vol. 29, pp. 355-365, 1987.

[19] S. Mall, H.-K. Kim, E. Saladin and W. Porter, "Effects of microstructure on fretting fatigue behavior of IN100," *Materials Science and Engineering A,* vol. 527, p. 1453–1460, 2010.

[20] O. Jin and S. Mall, "Effects of independent pad displacement on fretting fatigue behavior of Ti–6Al–4V," *Wear,* vol. 253, p. 585–596, 2002.

gigacycle fatigue behaviors in Fusion Zone and Heat Affected Zone of Q345 LA steel welded joints

He Chao, Liu yongjie, Tian Renhui, Wang qingyuan
Dept of Civil Eng & Mechanics, Sichuan University, Chengdu 610065, Sichuan

Abstract: The fatigue behavior in Fusion Zone (FZ) and Heat Affected Zone (HAZ) of widely used low alloy steel, Q345, in very high cycle fatigue regime was experimentally studied with ultrasonic fatigue testing system. It was found that the fatigue failure of HAZ specimen still occurred beyond 10^7 cycles, while a horizontal platform was obtained for FZ specimen in VHCF regime related to internal welding defects in fusing zone. A high-sensitivity infrared imaging system was used to measure the temperature changes during fatigue testing and the relationship of temperature variation and fatigue damage was discussed. The temperature of BM specimen would rise rapidly with the beginning of crack propagation. Fatigue crack propagation lives of HAZ and FZ were estimated by monitoring the natural frequency of specimen, which was varying with the crack size during the fatigue testing. Results showed that more than 99% of the total fatigue life was occupied by the crack initiation process for base metal (BM) and HAZ. However, this number was scattered for FZ specimen at relatively low stress amplitude owing to the crack propagation from welding defects directly, without crack initiate life.

Keywords: VHCF, Welded Joints, Fatigue Crack Propagation Life, Heat Affected Zone, Fusion Zone

1. Introduction

In the applications of aircrafts, automobiles, off-shore structures and railway equipment, many components would experience nominal vibratory stress conditions over a long period of time, running up to several hundred million cycles in their working service [1,2]. Conventional fatigue design specifications address the stress at 10^7 cycles as the fatigue strength limit, which was not applicative for mechanical equipment working in super long life. By the statistics, the fatigue failure at welded joints accounted for over 80% of the total and became the most dangerous failure mode for welded structure [3]. The study on the fatigue behavior of welded joints is of significant importance.

The research on very high cycle fatigue has been an important issue with the development of ultrasonic fatigue test system. In recent years, many researchers have studied VHCF properties. Bathias et al.[4,5] made great contribution to the development of bending and torsion ultrasonic fatigue test system. Murakami et al. [6] proposed a semi-empirical model for high strength steel to predict the fatigue strength in considering of hardness, inclusion size and stress ratio. Wang et al. [7] analyzed the fatigue failure mechanism and predict the fatigue strength and fatigue life for six ultra-high strength steels. Xue et al. [8] and Huang et al. [9] studied the heat dissipation of specimen in VHCF with the help of infrared video camera. Marines et al. [10,11] proposed a model of fatigue crack propagation for internal “fish-eye” and surface crack initiation, based on the fatigue crack propagation law proposed by Paris [12].

In the past twenty years, most of the studies were performed on base materials, while fatigue behaviors of welded joints were rarely studied, especially in very high cycle fatigue domain. He et

al. [13] studied the gigacycle fatigue behavior of titanium alloy Ti-6Al-4V using ultrasonic fatigue at 20 kHz. Yin et al. [14] analyzed the fatigue failure mechanism of welded joint by SEM observation, and discussed the effect of ultrasonic peening treatment on the fatigue performance. In this paper, a special designed specimen was fatigued in very high cycle fatigue regime to investigate the fatigue performance of base metal, heat affected zone and fusion zone for steel Q345. A high-precision infrared video camera was used to measure the variation of surface temperature. The natural frequency changes of specimen were monitored to discuss the fatigue crack propagation lives of FZ and HAZ.

2. Material and experimental method

Table 1 Chemical composition of the base metal and solder (wt.%)

Material	C	Si	Mn	S	Alu	P	Mo	Fe
Q345q(Base metal)	0.15	0.38	1.36	0.00003	---	0.00012	0.00002	Rest
E45(Solder)	---	0861	2.236	---	0.648	---	1.569	Rest

Table 2 Mechanical properties of Q345 steel

E /GPa	σ_y/MPa	UTS/MPa	ρ/g.cm^{-3}	A/%	HV30
201	420	570	7.85	13	136

The material used in this study was a widely used low alloy steel, Q345, with yield strength of 420MPa. It's chemical composition and mechanical properties are presented in Table 1 and Table 2 respectively. With good tensile strength, plasticity, weld ability and low temperature deformability, Q345 steel has a widespread application in automobile, watercraft, pressure vessel etc.

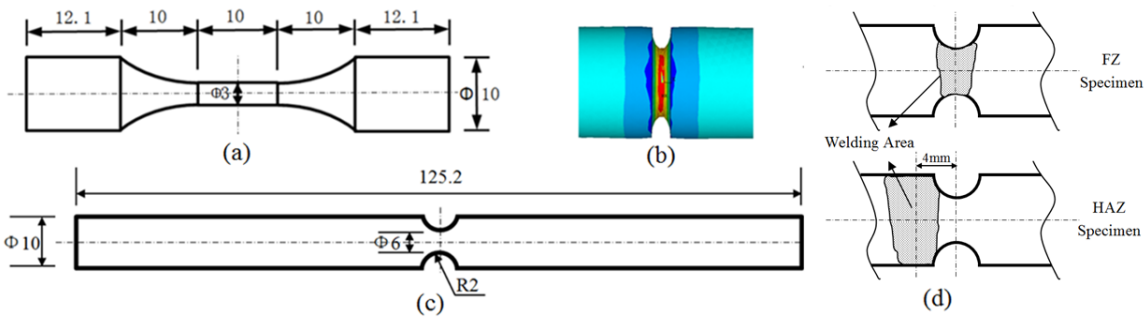

Fig.1 Specimens of ultrasonic fatigue test; (a) Parent specimen; (b) Stress field of welded joint specimen in mode analysis; (c) Dimensions of welded joint specimen; (d) schematic diagram of FZ and HAZ specimens

The dimensions of hourglass shape specimen for base metal are indicated in Fig2a.Welded joint specimen was machined from butt-welding plates with a thickness of 10mm. In ultrasonic fatigue test, the maximum stress always located in the middle of specimen. To ensure that the fracture section of HAZ and FZ specimen located in respective area, the center line of welding area

coincides with that of specimen length for FZ, while a distance of 4mm was designed between the center lines of welding area and HAZ specimen (Fig.1d). The radius of rounded roof for welded joint specimen was reduced to 2mm and other dimensions was determined by the method introduced in literature [15]. FEM results (shown in Fig.1b) showed that specially designed specimen was better to control the range of high stress area by restricting it at the root of arc during the test process. Fatigue test was performed on the USF-2000 ultrasonic fatigue test system (Fig.2) up to a limit of 10^9 load cycles under the conditions of stress ratio R=-1, at room temperature and compressed air cooling. The varying test resonance frequency of each specimen was measured by the computer control system. Moreover, an infrared thermometer was used to monitor the variations of temperature on the surface of specimen during test.

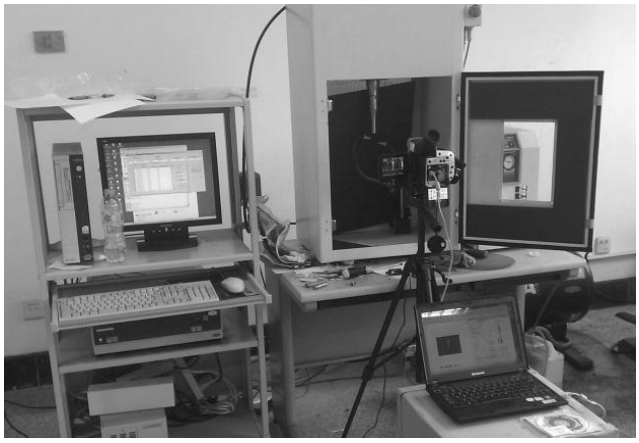

Fig.2 Ultrasonic fatigue test system with an infrared thermometer

3. Results and discussion

3.1 Summarizes of S-N curves

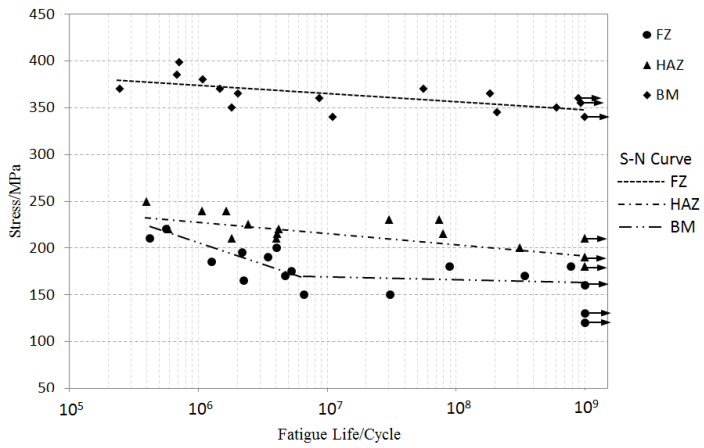

Fig.3 S-N fatigue curves of very high cycle fatigue test

Fig.3 presents the S-N curves for the three groups of specimens tested at room temperature in ultrasonic testing. Run out specimens over 10^9 cycles are represented by arrows. It was observed that that fatigue strength of HAZ and FZ was markedly lower than that of BM, with a percentage of 51.4% and 42.8% respectively at 10^9 cycles. Due to the local high temperature cycle in welding

process, unmatched mechanical properties and discontinuous microstructures between base metal and weld area were induced at the welded joint, which weakened the fatigue strength of welded structure significantly. It was confirmed from the observation of S-N curves of base metal and HAZ that failure continued to take place right up to gigacycle range (10^9 cycles) as mentioned in [3,8,16]. But for FZ specimen, a horizontal platform could be observed beyond 5.6×10^6 cycles. Because solder fill process caused welding defects such as micro cracks, pores and inclusions at fusing zone, fatigue crack propagated directly from thus defects without crack initiate life. If the loading stress is over the threshold of propagation, existing crack extent until final fracture rapidly in low cycle fatigue range In other case, the specimen would not fatigue to failure because of the insufficient for a new crack initiation at lower stress level. So the fatigue strength limit of FZ specimen existed, because no failure occurred below the stress of 150MPa.

3.2 Fractography analysis

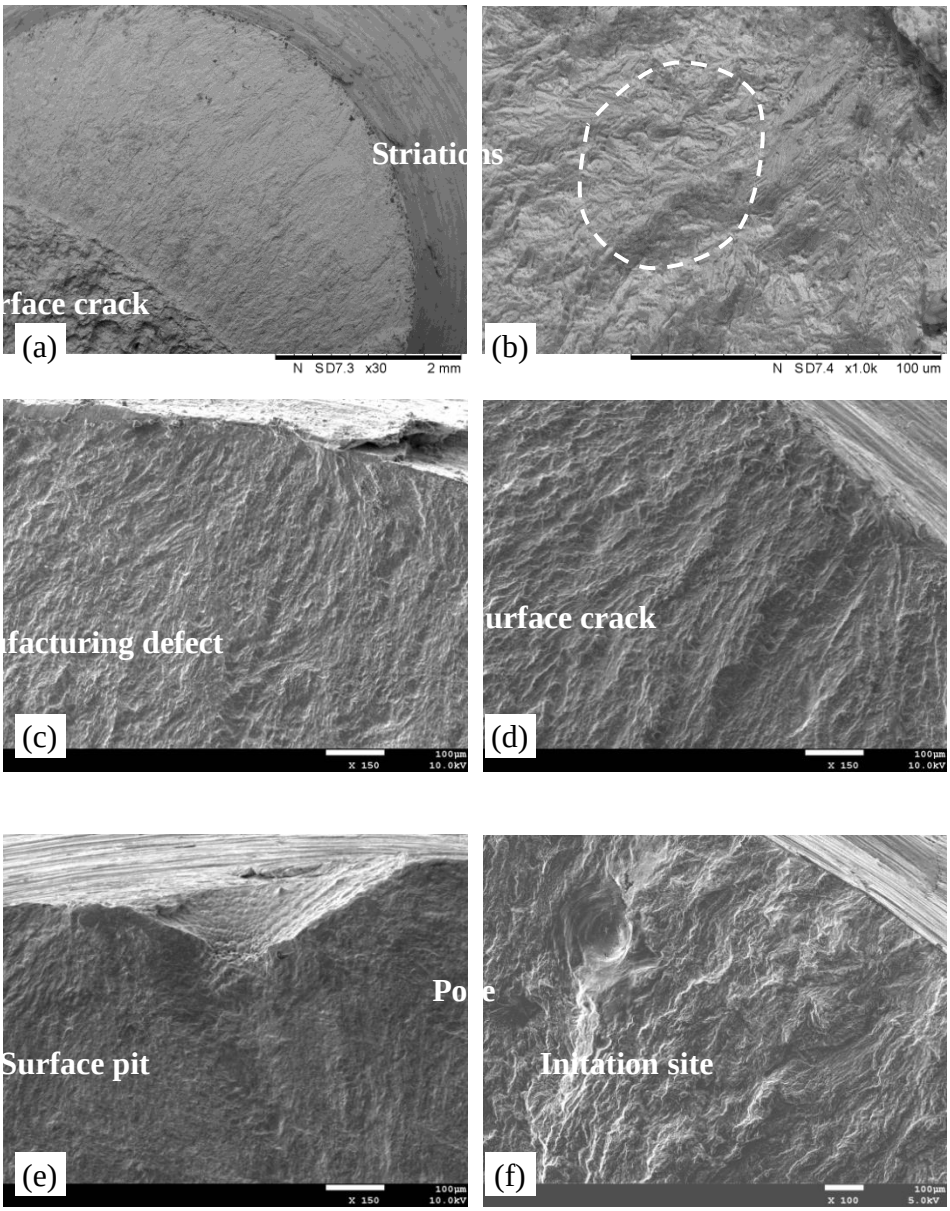

Fig.4 SEM fractographs of tested specimen; (a, b) Base metal specimen; (c, d) HAZ specimen; (e, f) FZ specimen

For high strength steel, it is known that the crack initiation and early propagation of interior-initiation fracture surface in VHCF range exhibit a pattern of “fish-eye” [17], a relatively rough region with fine granular morphology often presents surround the inclusion inside fish-eye. However, the fracture morphology of Q345 specimens in this test was different from high strength steel. Fig.5 illustrates the fatigue crack initiation modes based on SEM characterization. Due to the better plastic properties, the elongation of Q345 was much better than high strength steel. In addition, the stress at the surface was higher than internal, owing to the stress concentration effect caused by arc in the middle of the specimen. Local plastic deformation occurred more easily at the surface and fatigue cracks prone to start from surface of specimen for Q345 BM, which can be certified by the fatigue striations observed in Fig.4a and Fig.4b, around crack initiation site at the surface. The fatigue crack initiations of HAZ specimens were located at the surface (Fig.4c and d), which can be correlated to the local stress concentration at the retained surface defects caused by machining. For FZ specimens, cracks initiated from the welded defects such as pores and inclusions, as shown in Fig4 (e) and (f). Many researchers have reached an agreement that fatigue crack initiation process of base metal occupied over 99% of total fatigue life in very high cycle fatigue, but the fatigue cracks of FZ specimen begin to expand directly from existing welding defect, which reduced the crack initiation life. Therefore the fatigue strength of FZ specimen was much lower than that of base metal specimen and the crack propagation life in VHCF range will be discussed in the following sections.

3.3 The varying surface temperature of BM specimen

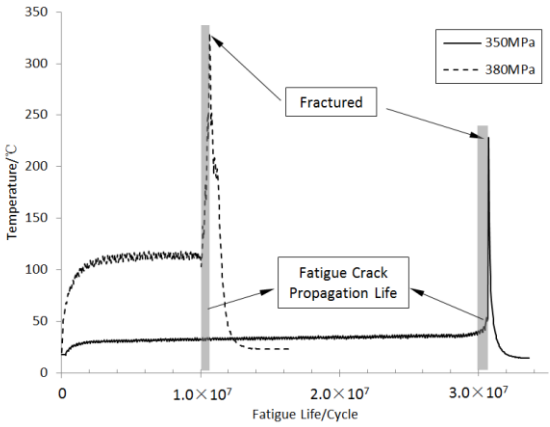

Fig.5 Temperature profiles of base metal specimen during testing.

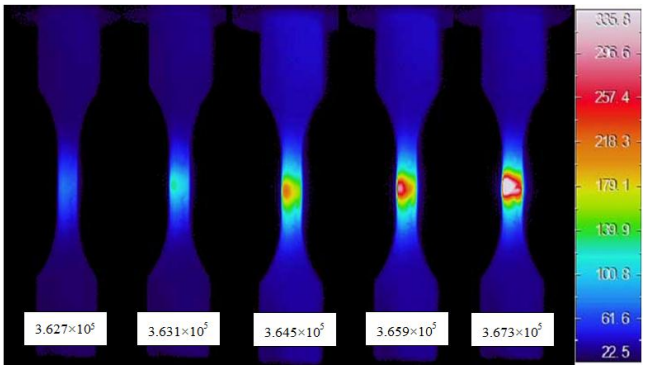

Fig.6 The rapidly increasing process of surface temperature for BM specimen

The surface temperature of specimen under high frequency is very complex including the effects of elastic strain energy, plastic strain energy, inelastic internal friction and heat dissipation [8,9,18]. An advanced infrared thermometer was used to monitor the variations of temperature on the surface of specimen during test. The temperature changes of weld specimen were not evident due to the low stress level and the larger waist diameter. But for BM specimens, it was found that the cyclic loading at an ultrasonic frequency generated a substantial amount of heat, and the temperature of BM specimen increased significantly at the center of the gage length of specimen as shown in Fig.6. The temperature distributions in the gage-length section of the specimen during ultrasonic testing were heterogeneous along the axis of the specimen, with the highest temperature occurring at the high strain location. Fig.5 illustrates the temperature variation at the center of the base metal specimen for two different stress levels without air cooling. The temperature increased evidently at the beginning of the test, which followed by a stable state. Thus stabilization could be explained by a balance between the mechanical energy dissipated into heat and the energy lost. The temperature was higher for higher stress loading. Fig.6 also shows that the temperature at the center of the specimen increased very sharply (3.627×10^6~3.673×10^6cycles) just before the fatigue failure occurred. Observation for fracture surface confirmed that the fatigue crack initiation site was located just on the point A plotted in Fig.6, which declared a close relation between the rise of temperature and crack propagation. XUE et al. [9] discussed that the dissipated energy came from internal material damping and the local plastic deformation at the microscopic scale, although the stress in the specimen is lower than the elastic limit. When the micro crack originated and started to propagate under cyclic loading, the plastic zone at the crack tip generated heat until the specimen fractured. Thus, the fatigue crack propagation life could be estimated by detecting the temperature variation of specimen and this will be discussed later.

3.4 The varying resonance frequency of welded joint specimen

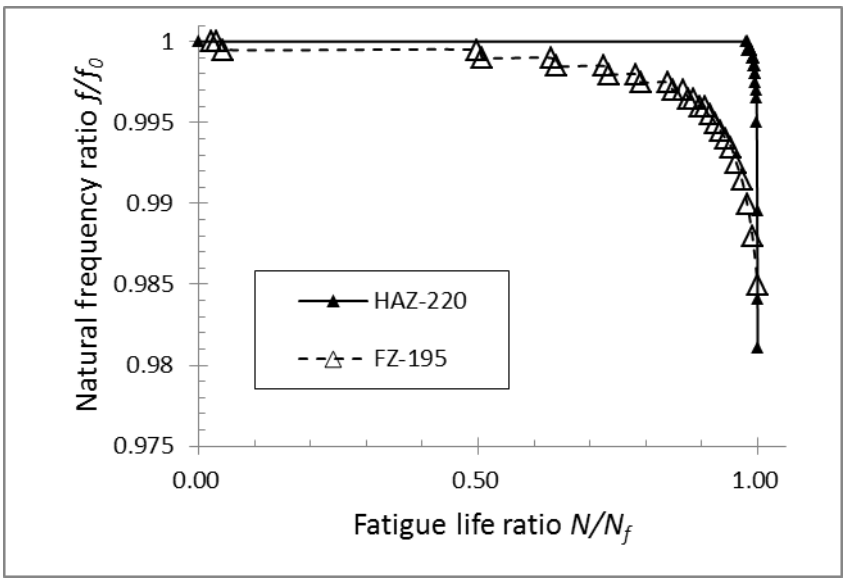

Fig.7 Natural frequency profiles of tested at different stress level.

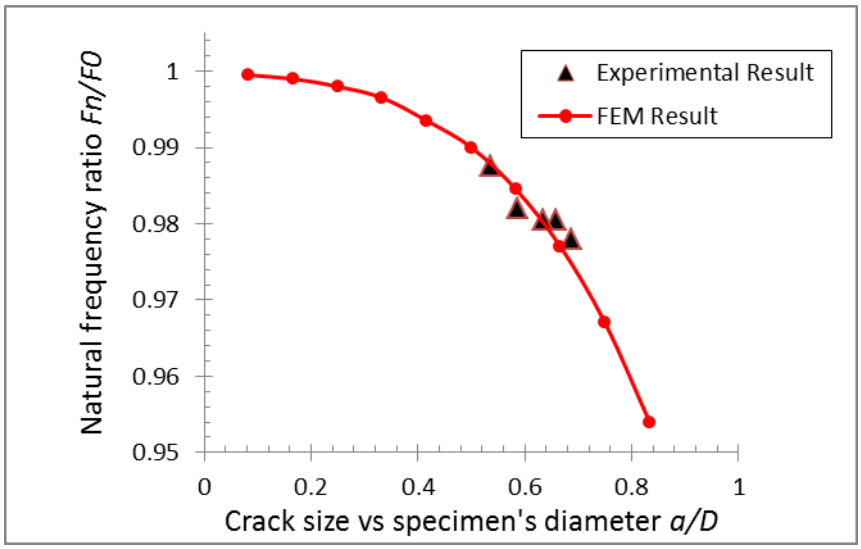

Fig.8 Comparison between the Finite element analysis values and the experimental results

It is interesting that a metallic noise could be heard just before the final fracture due to the decreasing of resonance frequency of welded joint specimen. The natural frequency of specimen was recorded per 20000 cycles in the course of the fatigue experiment and the changes of frequency in term of natural frequency ratio verse fatigue life ratio were shown in Fig.7, where N_f, f_0 were the final fatigue life and initial natural frequency, respectively. From the collected data of HAZ, a stable platform of natural frequency ratio could be observed, which occupied almost the whole fatigue life. Further, the fatigue life ratio was larger and the final stop frequency ratio for fracture was smaller with the higher loading stress. But for FZ specimen, the frequency ratio kept going down from the beginning of the test with no platform due to the fact that the frequency descent life was affected by the max size defect located in fusion zone. As mentioned previously, welded joint specimen fractured without obvious temperature-rise period, therefore, it could be due to the reason that fatigue propagation lead to the decreasing of natural frequency of welded joint. In order to verify, FEM model analysis method was employed to ascertain the relationship between natural frequency and fatigue crack size at the surface of specimen under the resonance condition. A half specimen model was established for computation time saving with a crack located in the middle section of the specimen. In the process of the resonance, the state of compression would result in crack surface contact, but any non-linear setting was not included in the analysis in ANSYS, which was neglected automatically, otherwise. To prevent the effect of crack surface compression on the analysis, an additional element layer with the thickness of 0.1mm was attached to the surface of fatigue crack. The modulus of elasticity for extra element is 1GPa, which was considerably less as compared to Q345.With the help of additional layer, the model of specimen remained linear without any penetrations of elements at the crack surface. After the model analysis of specimen with cracks in different sizes, the relation between fatigue crack size and natural frequency of welded joint specimen was obtained as presented in Fig.8. It could be found that with the increase in size of fatigue crack, the rate of natural frequency decreased. In this experiment, the final stop frequencies and max fatigue crack sizes from SEM observation were obtained on five HAZ specimens as plotted with solid triangle in Fig.9. It is noted that the experimental data just located near to the fitted curve of FEM, which confirmed that the decreasing of natural frequency was caused by the

fatigue crack propagation and fatigue crack propagation lives of HAZ and FZ could be estimated by monitoring the natural frequency of specimen.

3.5 The crack propagation lives of BM, HAZ and FZ specimens

Table 3 Fatigue crack propagation life of different specimens

Specimen	Stress/Mpa	Total life/cycle	Propagation Life/cycle	Ratio N_p/N_t
BM	350	6.08×10^8	1.72×10^6	0.28%
BM	365	1.83×10^8	7.27×10^5	0.40%
BM	370	5.60×10^7	1.66×10^5	0.29%
HAZ	200	3.12×10^8	8.8×10^5	0.28%
HAZ	220	7.42×10^7	5.8×10^5	0.78%
HAZ	230	3.02×10^7	3.0×10^5	0.99%
FZ	150	6.62×10^6	6.6×10^5	9.97%
FZ	185	1.26×10^6	9.6×10^5	76.2%
FZ	195	2.18×10^6	1.08×10^6	49.5%

The natural frequency of welded joint specimen was analysed in this section to clarify the fatigue crack propagation characteristic in VHCF range. It was believed that the fatigue crack start to grow at the moment that frequency of specimen decreased over 20Hz per 20000 cycles. For BM specimen, the period of temperature rise just before the fracture could be regarded as the crack propagation life, as discussed earlier. When the amplitude of temperature variation was larger than 5℃ per 700cycles, fatigue crack propagation was started for BM specimen. Finally, the fatigue crack propagation lives of BM, HAZ and FZ specimens were obtained in Table.3. Similar changes between BM and HAZ specimens were observed. It showed that with the increase in the loading stress, lower crack propagation life and ratio of propagation life to total fatigue life was obtained. The crack initiation process occupied over 99% of the total fatigue life for BM and HAZ in VHCF range. Therefore study on the mechanism of crack initiation was extremely important to clarify the fatigue properties in VHCF. In addition, the life ratio of FZ specimens were much larger than that of BM and HAZ, due to the fact that fatigue crack in FZ propagated directly from the welding defect with no apparent initiation process.

4. Conclusions

In this paper, ultrasonic fatigue test was performed on Q345 BM and welded joint to investigate the properties and failure mechanism in super long life fatigue range, the conclusions can be summarized as follows:

1.The fatigue strength of BM and HAZ continues to decline with the increase in fatigue live, and fatigue failure still occurred up to 10^9 cycles. Compared with BM specimen, the fatigue strength of FZ and HAZ decreased about 60% and 55% respectively.

2. The fatigue crack propagation process would lead to the temperature increment of BM and the decreasing of natural frequency descent in the test. Thus fatigue propagation life could be evaluated

by monitoring the changes of surface temperature and resonance frequency.

3. The crack initiation process occupied over 99% of the total fatigue life for BM and HAZ, but much larger for FZ specimens at relatively low stress amplitude. This was due to the reason that fatigue crack propagated directly from the welding defects for FZ specimen without apparent initiation process.

Acknowledgement

This work was financially supported by Chinese National Science Foundation (No.10925211). Thanks Prof. C. X. Huang for his guidance.

References

[1] Q.Y. Wang, C. Bathias, N. Kawagoishi, Q. Chen, Effect of inclusion on subsurface crack initiation and gigacycle fatigue strength, International Journal of Fatigue, Volume 24, Issue 12, December 2002, Pages 1269-1274

[2] Y Furuya, S Matsuoka, T Abe, K Yamaguchi, Gigacycle fatigue properties for high-strength low-alloy steel at 100 Hz, 600 Hz, and 20 kHz, Scripta Materialia, Volume 46, Issue 2, 18 January 2002, Pages 157-162, ISSN 1359-6462

[3] Lixing Huo, Dongpo Wang, Yufeng Zhang, Investigation of the fatigue behaviour of the welded joints treated by TIG dressing and ultrasonic peening under variable-amplitude load, International Journal of Fatigue, Volume 27, Issue 1, January 2005, Pages 95-101

[4] Claude Bathias, Piezoelectric fatigue testing machines and devices, International Journal of Fatigue, Volume 28, Issue 11, November 2006, Pages 1438-1445

[5] Z.D. Sun, C. Bathias, G. Baudry, Fretting fatigue of 42CrMo4 steel at ultrasonic frequency, International Journal of Fatigue, Volume 23, Issue 5, May 2001, Pages 449-453

[6] Yukitaka Murakami, Masayuki Takada, Toshiyuki Toriyama, Super-long life tension–compression fatigue properties of quenched and tempered 0.46% carbon steel, International Journal of Fatigue, Volume 20, Issue 9, October 1998, Pages 661-667

[7] Q.Y. Wang, M.R. Sriraman, N. Kawagoishi, Q. Chen, Fatigue crack growth of bonded composite repairs in gigacycle regime, International Journal of Fatigue, Volume 28, Issue 10, October 2006, Pages 1197-1201

[8] Zhi Yong Huang, Danièle Wagner, Qing Yuan Wang, Claude Bathias, Effect of carburizing treatment on the “fish eye” crack growth for a low alloyed chromium steel in very high cycle fatigue, Materials Science and Engineering: A, Volume 559, 1 January 2013, Pages 790-797

[9] H.Q. Xue, E. Bayraktar, C. Bathias, Damage mechanism of a nodular cast iron under the very high cycle fatigue regime, Journal of Materials Processing Technology, Volume 202, Issues 1–3, 20 June 2008, Pages 216-223

[10] Israel Marines-Garcia, Paul C. Paris, Hiroshi Tada, Claude Bathias, Fatigue crack growth from small to long cracks in very-high-cycle fatigue with surface and internal “fish-eye” failures for ferrite-perlitic low carbon steel SAE 8620, Materials Science and Engineering: A, Volumes 468–470, 15 November 2007, Pages 120-128

[11] Israel Marines-Garcia, Paul C. Paris, Hiroshi Tada, Claude Bathias, Fatigue crack growth from small to long cracks in VHCF with surface initiations, International Journal of Fatigue, Volume

29, Issues 9–11, September–November 2007, Pages 2072-2078

P.C. Paris, H. Tada, J.K. Donald.Service load fatigue damage – a historical perspective.Int. J. Fatigue, 21 (1999), pp. 35–46

[13] HE Chao, TIAN Ren-hui, WANG Qing-yuan, Study on ultra-long-life fatigue properties of welded joints under high-frequency loading, China Measurement & Test,Volume 38, Issues 3, May2012, Pages 20-26

[14] Danqing Yin, Dongpo Wang, Hongyang Jing, Lixing Huo, The effects of ultrasonic peening treatment on the ultra-long life fatigue behavior of welded joints, Materials & Design, Volume 31, Issue 7, August 2010, Pages 3299-3307

[15] Xue Hongqian. The design of specimen forfatigue test at ultrasonic frequency [J]. acta aeronautica ET Sstronautica Sinica, Volume 25, Issue 4, August 2004, Pages 425-428

[16] K. Shiozawa, Y. Morii, S. Nishino, L. Lu, Subsurface crack initiation and propagation mechanism in high-strength steel in a very high cycle fatigue regime, International Journal of Fatigue, Volume 28, Issue 11, November 2006, Pages 1521-1532

[17] Claude Bathias, Paul C. Paris, Gigacycle fatigue of metallic aircraft components, International Journal of Fatigue, Volume 32, Issue 6, June 2010, Pages 894-897, ISSN 0142-1123

[18] N. Ranc, D. Wagner, P.C. Paris, Study of thermal effects associated with crack propagation during very high cycle fatigue tests, Acta Materialia, Volume 56, Issue 15, September 2008, Pages 4012-4021

Very high cycle fatigue (VHCF) behavior of structured Al 2024 thin sheets

Sebastian Stille*, Tilmann Beck, Lorenz Singheiser

Institute of Energy and Climate Research (IEK-2), FZ Juelich, D-52425 Juelich, Germany
* Corresponding author: s.stille@fz-juelich.de

Abstract In the present study the VHCF behavior of Al 2024, a standard material in aerospace application, is investigated. The focus of the presented work is the influence of riblet-like surface structures on fatigue life and damage mechanisms. The cold-rolling process used for riblet forming results in slight work hardening and near-surface residual stresses. Furthermore the influence of pure Al-claddings on the VHCF behavior of Al 2024 sheets is examined. Fatigue tests are performed using an ultrasonic fatigue testing system at a frequency of around 20 kHz. The present work contributes to a deeper understanding of riblet structures and surface claddings on the VHCF behavior of Al 2024.

Keywords VHCF, Al 2024, surface structure

1. Introduction

An innovative approach for aerodynamic drag reduction, e.g. of airfoils, are surface riblet structures [1] combined with transversal surface waves with amplitudes of few 1/10 mm at frequencies of some 100 Hz [2]. The resulting very high cycle fatigue (VHCF) loading at cycle numbers beyond the value of $2x10^7$, taken as ultimate cycle number in most studies on fatigue of Al sheet alloys for aircraft application, has to be considered as a limiting factor for this approach.

Al 2024 is a standard material in aerospace applications. Its VHCF behavior has been evaluated in detail in different studies [3-7]. These contributions show that material failure takes place even beyond $2x10^7$ load cycles and that the S/N curve does not approach a horizontal fatigue limit. Fatigue experiments on cladded sheets have been performed in references [8-10]. Merati et al. [8] observed multiple crack initiation sites at the cladding layer in the regime up to $6x10^5$ cycles. Edwards et al. [9] report that the first crack in the cladding layer can be detected as early as 1 % of the total lifetime of the samples and that clad specimen are less sensitive to notching effects than bare Al 2024 sheets.

One intention of the present work is the investigation of the VHCF behavior of clad Al 2024 material up to cycle numbers distinctly beyond the existing data. Furthermore, the influence of riblet structures on the VHCF life of Al 2024 sheets needs to be determined for future application of active drag reduction. The experiments conducted in the frame of the present study cover nano-indentation, X-ray stress analysis, ultrasonic fatigue experiments and electron microscopy based fractography.

2. Material

The experiments were performed on the aluminium alloy Al 2024. The sheet material has been supplied by ALCOA Mill Products in the T-351 state (solutions heat treated at 493 °C and quenched in water, subsequently stress relieved by stretching to a controlled deformation and finally naturally aged for 8 days [11]). The sheets are supplied in two different thicknesses, 1.6 and 2 mm. Furthermore, sheets with a cladding layer of 64 µm of pure aluminium on one side were tested.

Table 1: Chemical composition of the investigated Al2024 material

Material	Cu	Fe	Mg	Mn	Si	Ti	Zn
Weight-%	4.58	0.21	1.48	0.47	0.073	0.016	0.098

Table 2: Key mechanical properties of Al2024 in the T-351 state

Young's modulus, E [12]	Yield strength, $R_{p0.2}$	Ultimate tensile strength	Elongation at break
73.1 GPa	321.5 MPa	446.5 MPa	18.5 %

Prior to testing the chemical composition of the material was analyzed by inductively coupled plasma optical emission spectroscopy (ICP-OES). The results are listed in Table 1. The key mechanical properties are listed in Table 2 (values determined by the supplier).

An important aspect of the present work is the influence of the surface state of the material on its VHCF behavior. As shown e.g. in reference [13], scratches significantly reduce the lifetime of clad Al 2024 sheets. To overcome this problem, fatigue samples are usually grinded and polished. This standard process to assure reproducible smooth surfaces is not applicable for clad material, since surface grinding and polishing would remove the thin cladding layer. A detailed analysis of the as-received specimen surface has thus been performed. Scratches on clad samples can be described as small notches with a diameter of a few µm in arbitrary orientation.

3. Experimental setup

For fatigue testing an ultrasonic fatigue testing machine, developed at BOKU Vienna, is employed. The testing system is described in references [14] and [15]. Modifications made on the system are described in detail in reference [16]. The sample geometry is presented in Fig. 1(b). Sheet samples are laser cut to their final geometry. The volume (surface) of the gage length is 64 mm^3 (105.6 mm^2) for 1.6 mm thick sheets and 80 mm^3 (112 mm^2) for 2 mm thick sheets, respectively.

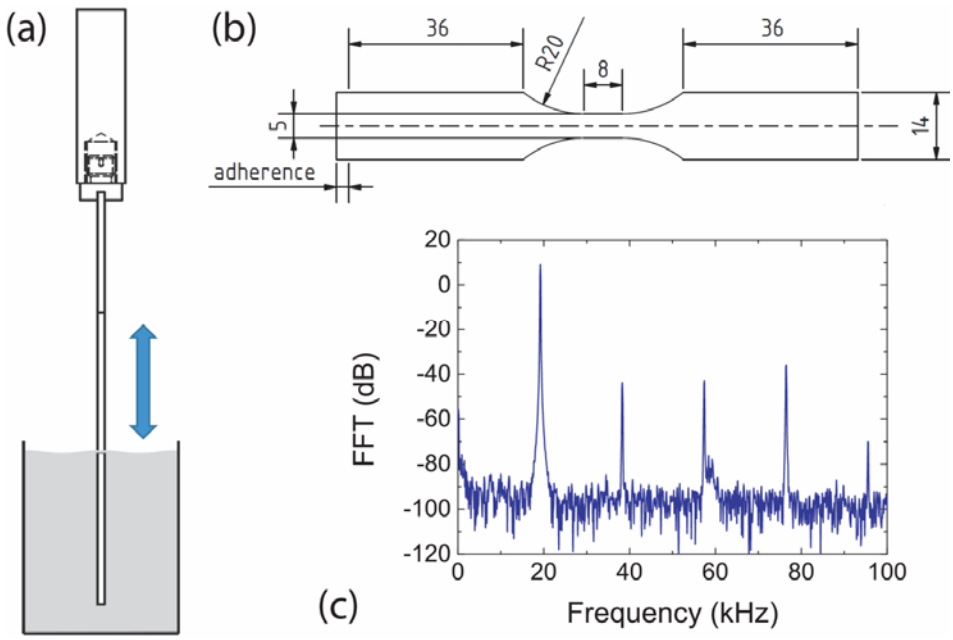

Figure 1. (a) Flat specimen connected to the load frame by an adapter and submerged in its lower part in glycerin. **(b)** Sample geometry. **(c)** Typical FFT spectrum of the vibration signal

The flat sheet samples are glued to an adapter which is connected via a thread to the testing machine. To avoid flexural vibrations, which have been observed in first experiments, samples are damped by submerging their lower part in glycerin during cyclic loading (cf. Fig 1(a)). In-situ monitoring of the sample vibration (Fig. 1(c)) shows a clean harmonic spectrum which is free of bending oscillations. All fatigue tests were performed at a frequency of around 20 kHz at room temperature and zero mean stress.

For further analysis, polished cross sections were prepared by embedding the samples in epoxy resin. The surface has been grinded with sand paper up to grade 1000 and subsequently polished with diamond paste. Indentation measurements were performed using a Berkovic type indenter. Fracture planes were analyzed in detail by scanning electron microscopy (SEM).

4. Results

4.1 Effects of riblet rolling

The cold working of the sheets during riblet forming lets expect the occurrence of work hardening as well as a surface-near stress. Therefore micro-indentation tests were performed on cross sections of flat as well as on riblet structured material. An indentation load of 5 mN was used.

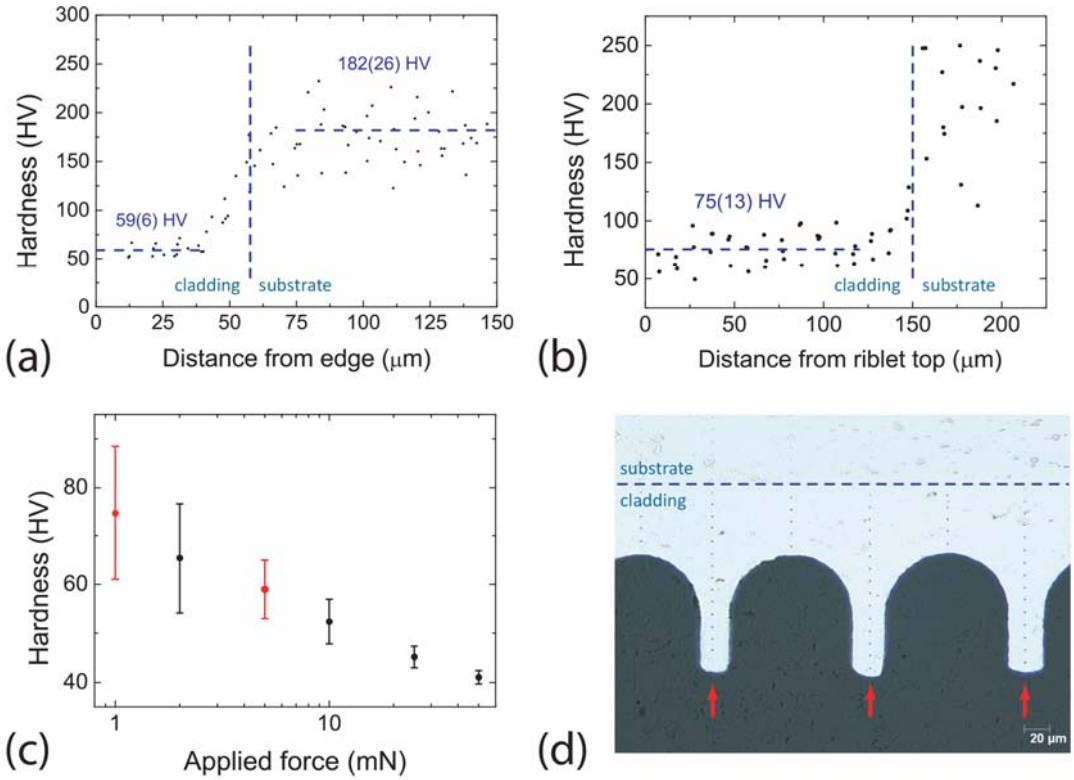

Figure 2. Microhardness measurements at clad material with and without riblet structure: **(a)** As-received (non-structured) material, $F = 5$ mN. The hardness is plotted against the distance from the cladding surface. **(b)** Structured material, $F = 1$ mN. The hardness is plotted against the distance from the riblet top. **(c)** Hardness of the cladding layer against the indentation load. **(d)** Polished cross-section of a structured sample. The measurements in Fig. 2(b) were performed in direction of the red arrows.

The results are presented in Fig. 2. Measurements on cladded sheets (Fig. 2(b)) show a hardness of (59 ± 6) HV0.005 for the cladding layer and of (182 ± 26) HV0.005 for the substrate. Measurements on structured samples were performed according to Fig. 2(d). The riblet structure is completely located in the cladding layer and does not affect the substrate. Since the riblets are quite narrow a smaller indentation load of 1 mN was applied to reduce the lateral size of the indentation. In spite of the strong local deformation during riblet forming, a nearly homogenous hardness of (75 ± 13) HV0.001 has been determined along the riblets and in the underlying part of the cladding. To investigate the influence of indentation load on the measured hardness, a series of indentation tests has been carried out in the cladding layer by performing 10 indentations at each of 6 forces in the range between 1 mN and 50 mN. The results are given in Fig. 2(c). A clear indentation-size effect is observed. Comparing the hardness values for 1 mN and 5 mN in Fig. 2(c) with cladding hardnesses in Figs. 2(a) and 2(b), it can concluded that the apparently increased hardness of the riblet structure can be completely attributed to the indentation size effect and the influence of work-hardening induced by the rolling process for riblet forming is negligible compared to the scatter of the indentation measurements.

The amount of surface residual stress, induced by the riblet rolling, was measured by X-ray diffraction using the $\sin^2(\Psi)$-method. Prior to riblet rolling, the residual stress was (-11 ± 8) MPa. Due to riblet rolling a change to (-29 ± 7) MPa was noticed.

4.2 Fatigue experiments

The results of the fatigue experiments are summarized in Fig. 3 and compared to literature values. Solid blue circles indicate results for bare Al2024 smoothened by grinding with sand paper (grit 600) prior to testing. The lifetime of these samples compares well with literature results taken from Refs [3,7] ensuring the reliability of the present measurements: Neither the adhesive connection of the samples to the testing machine, nor the thin sheet sample geometry that necessitate damping of flexural vibrations, have an influence of the sample lifetime.

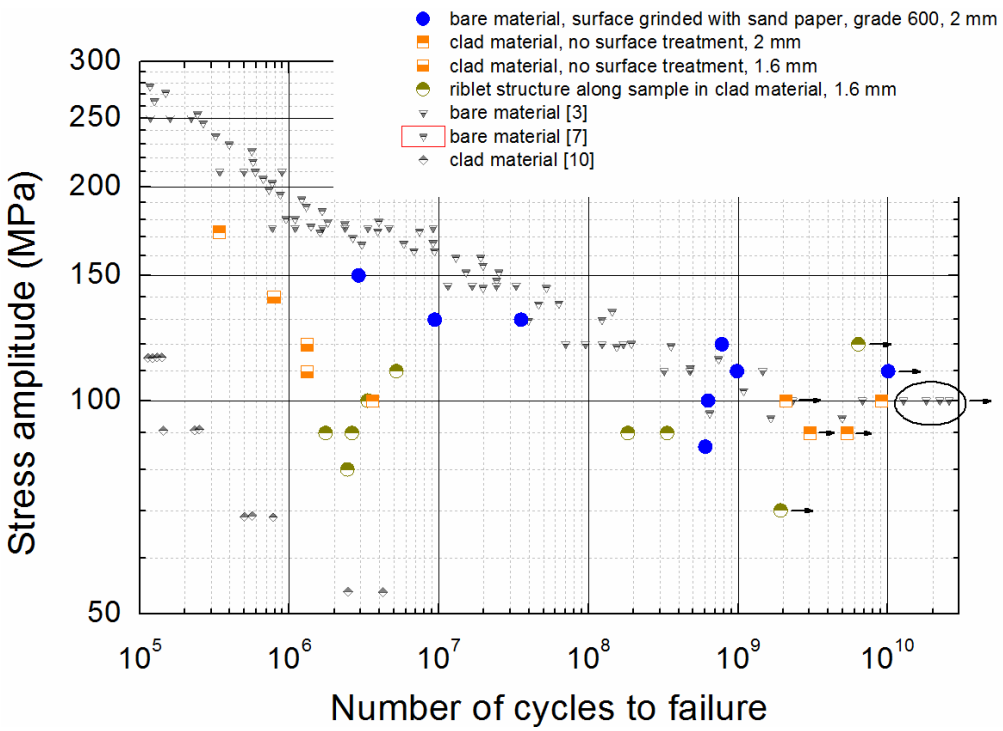

Figure 3. S/N graph of the fatigue lifetimes obtailed in the present work and from literature [3,7,10].

Just the scattering of our values seems to be slightly increased compared to the literature values.

For the clad material (orange half squares) surface smoothening is not possible without removing the cladding layer. The surface quality therefore seems to be the for lifetime reduction compared to bare Al 2024 by several orders of magnitude. Nevertheless, some samples, tested at 90 and 100 MPa, do not seem to be influenced by scratches and exhibit a much longer lifetime which lie in the same range as for the bare material. Furthermore, sample thickness in the tested range seems not to influence lifetime.

First measurements on structured samples with riblets along the sample direction (green half circles) show similar results as obtained for the unstructured clad material The fractures between 10^6 and 10^7 cycles at load amplitudes between 80 MPa and 110 MPa are is most induced by small scratches on the sample surface. Nevertheless, also run-outs above 10^8 cycles were observed in the same load regime.

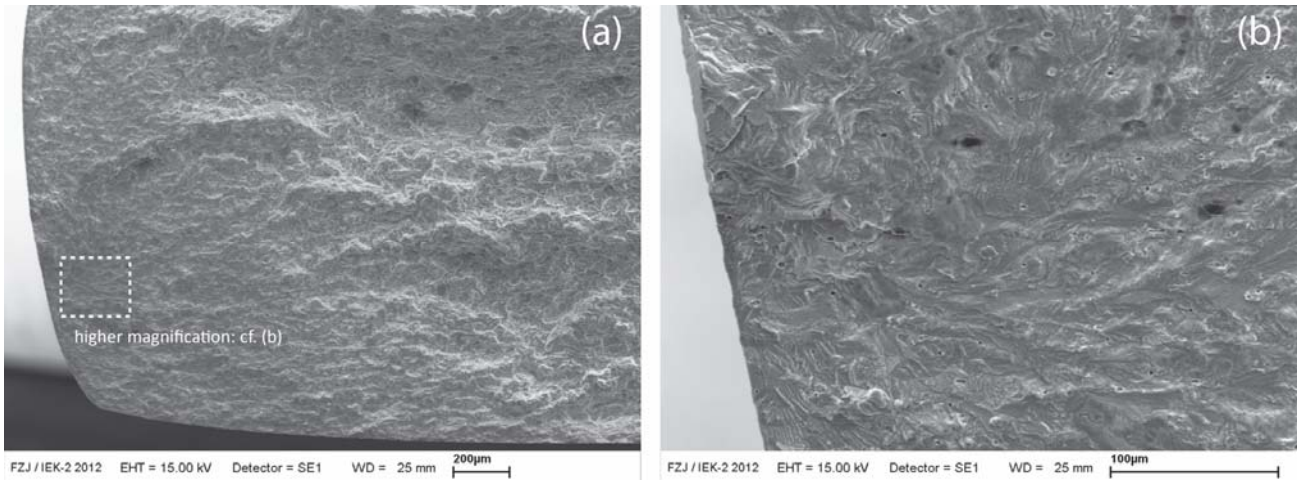

Figure 4. Fracture surface of a bare sample. $N = 9.8145\text{x}10^8$, $\sigma_{max} = 110$ MPa.
(a) Overview. **(b)** Higher magnification of the crack initiation site.

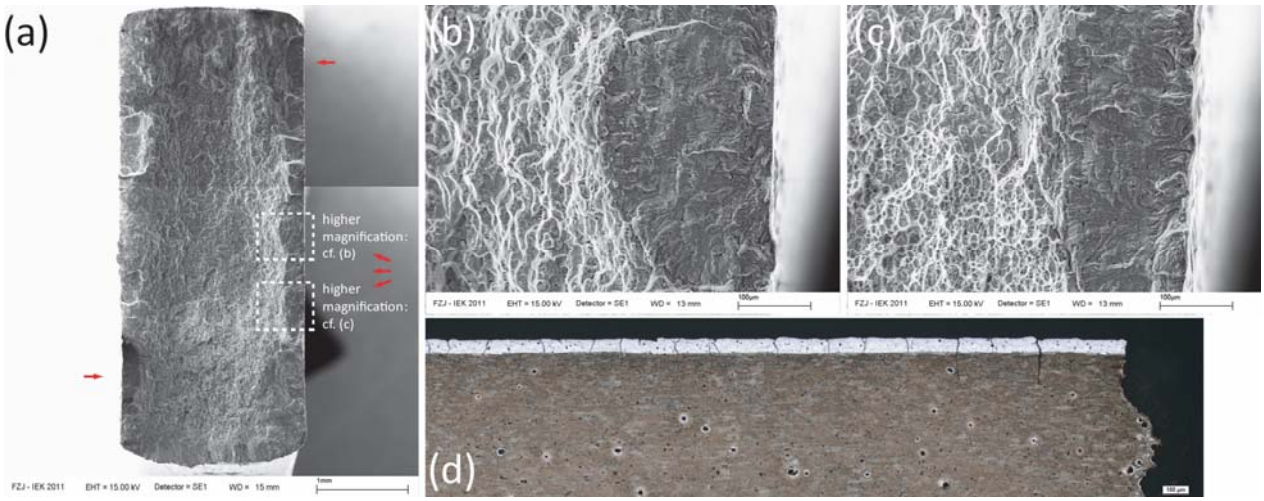

Figure 5. Fracture surface of a cladded specimen. $N = 3.38\text{x}10^5$, $\sigma_{max} = 173$ MPa. **(a)** Overview Crack initiation sites are indicated by red arrows. **(b)** and **(c)** Higher magnification of crack initiation sites. **(d)** Polished longitudinal section of the same sample. The fracture plane is located on the right.

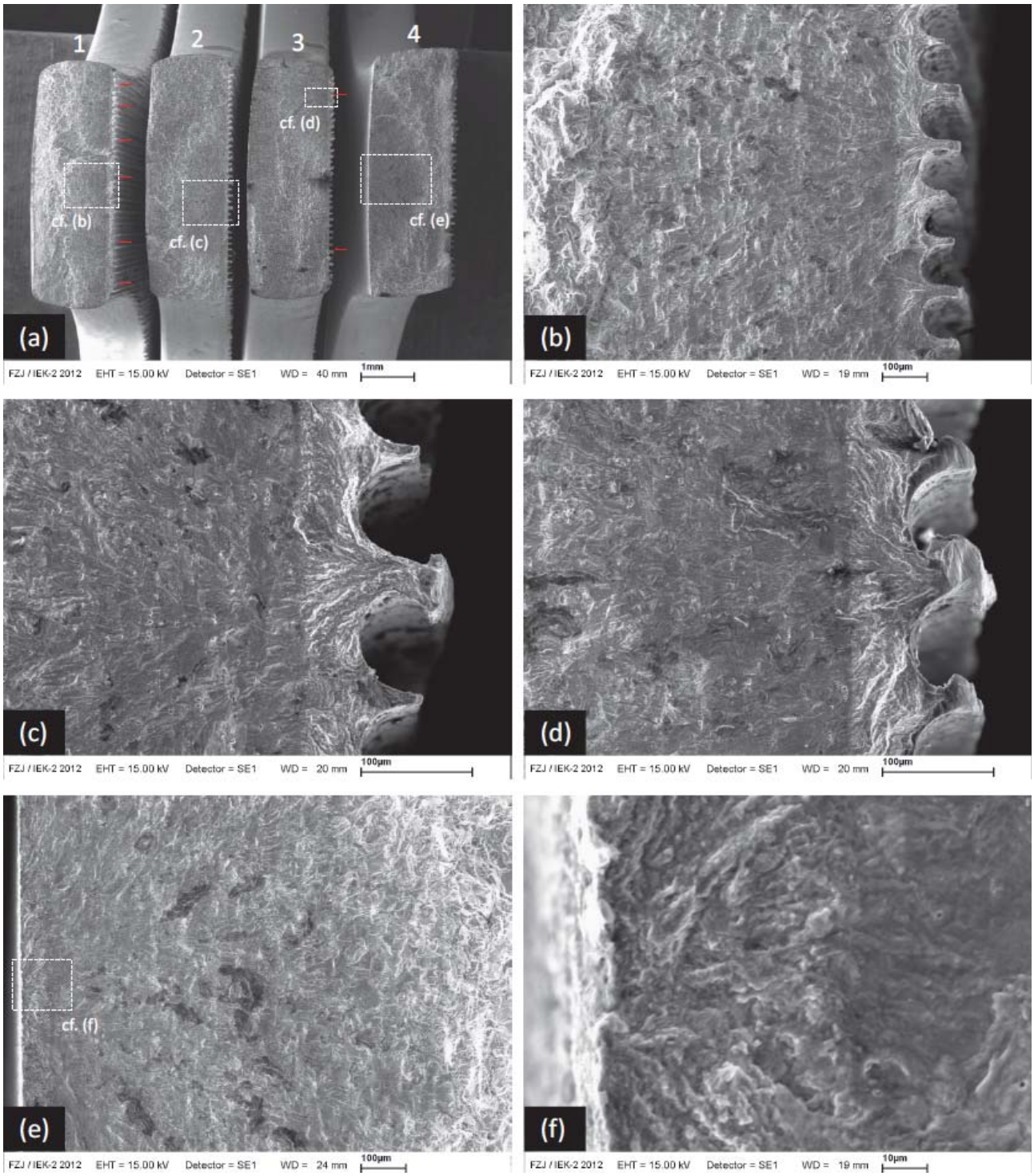

Figure 6. Fracture surfaces of structured samples. **(a)** Overview of four different specimen: (1) $N = 1.75\text{x}10^6$, $\sigma_{max} = 90$ MPa, (2) $N = 3.35\text{x}10^8$, $\sigma_{max} = 90$ MPa, (3) $N = 5.19\text{x}10^6$, $\sigma_{max} = 110$ MPa, (4) $N = 1.83\text{x}10^8$, $\sigma_{max} = 90$ MPa. Red arrows indicate crack initiation sites for samples with multiple crack initiation. **(b) – (f)** SEM images with higher magnification, showing crack initiation sites in detail.

5. Microscopy

Fig. 4 shows SEM images of a typical fatigue fracture of a bare sample at nearly 10^9 cycles. The fracture origin is located close to the surface inside the material. A magnified view of the crack initiation site is presented in Fig. 4(b). Bare samples typically show single crack initiation sites in

the VHCF-regime.
Fig. 5 shows the fracture surface of a clad sample after fatigue at relatively high load amplitude. Multiple crack initiation sites, both at the bare side and in the cladding (cf. red arrows in Fig. 5(a)) can be clearly seen. A detailed view on exemplary crack initiation sites are shown in Fig. 5(b) and (c). A polished longitudinal section of the same sample (Fig. 5(d)) illustrates multiple cracks starting at the surface of the cladding layer and crack growth into the substrate.
Failure of structured samples has been observed in two different lifetime regimes (cf. Fig. 3):(i) below 10^7 cycles and (ii) above 10^8 cycles. Fig. 6(a) gives an overview on typical fracture surfaces. Samples 1 and 3 represent the lifetime regime (i), whereas samples 2 and 4 are representative for the VHCF-regime (ii). Specimens with shorter lifetime show multiple crack initiation sites. In both cases the final fracture has its origin on the structured side close to the surface. For samples with longer lifetime, only one initiation site has been observed. In the case of sample 2 this is located on the structured side, for sample 4 on the backside, which does not have a cladding layer but a bare, smoothened surface. It is interesting to note that the lifetimes of both samples are similar to the lifetime of non-structured, bare sheets.

6. Conclusion

Fatigue experiments were performed on Al 2024 sheets with and without a pure Al cladding layer. Cold rolling of a riblet structure on the cladded side induces -if any- only slight work-hardening within the scatter of hardness measurements performed by microindentation, whereas a slight increase of compressive surface residual stress was observed after rolling. Fatigue lifetimes determined for the bare material match literature data quite well. For cladded material without riblet structure, a reduced lifetime is observed which is attributed to surface scratches which could not be removed from the thin cladding by grinding and polishing. Riblet structures produced by cold rolling do not significantly affect fatigue life of the clad material.

Bare sheets show crack initiation inside the material. Clad samples show crack initiation in the cladding layer surface and subsequent crack growth into the substrate. In general at $N < 10^7$ multiple crack initiation sites are observed, whereas in the VHCF regime only single crack initiation sites are found. Clad specimens show crack initiation both on their cladded and on their bare surface which complies well with the similar lifetimes observed for both specimen types.

Acknowledgements

The present work was funded by the Deutsche Forschungsgemeinschaft (DFG) in the framework of the DFG Research Unit 1779 “Active Drag Reduction”. The authors would like to thank H. Mayer and R. Schuller for helpful discussion on the experimental setup. Furthermore we thank T. Romans and J. Pöblau for the structuring of the sheets.

References

[1] D. W. Bechert, M. Bruse, W. Hage, J. G. T. Van Der Hoeven, and G. Hoppe, *Experiments on drag-reducing surfaces and their optimization with an adjustable geometry*, Journal of Fluid Mechanics **338**, 59 (1997).

[2] S. Klumpp, M. Meinke, and W. Schröder, *Friction Drag Variation via Spanwise Transversal Surface Waves*, Flow, Turbulence and Combustion **87**, 33 (2011).

[3] H. Mayer, M. Fitzka, and R. Schuller, *Ultrasonic fatigue testing of 2024-T351 aluminium alloy at different load ratios under constant and variable amplitude*, presented at the 5th Int. Conf. Very High Cycle Fatigue, Berlin (2011).

[4] Q. Y. Wang, T. Li, and X. G. Zeng, in *Fatigue 2010*, edited by P. Lukas (Elsevier Science Bv, Amsterdam, 2010), Vol. 2, pp. 65.

[5] T. Li, M. R. Sriraman, C. Wang, and Q. Y. Wang, *Gigacycle fatigue of precipitation hardening aluminium alloys*, presented at the Fourth international conference on very high cycle fatigue (VHCF-4), Ann Arbor, Michigan (2007).

[6] H. Mayer, *Ultrasonic torsion and tension–compression fatigue testing: Measuring principles and investigations on 2024-T351 aluminium alloy*, International Journal of Fatigue **28**, 1446 (2006).

[7] S. Stanzl-Tschegg, *Fracture mechanisms and fracture mechanics at ultrasonic frequencies*, Fatigue Fract Engng Mater Struct **22**, 1999).

[8] A. Merati, *A study of nucleation and fatigue behavior of an aerospace aluminum alloy 2024-T3*, International Journal of Fatigue **27**, 33 (2005).

[9] P. R. Edwards, M. G. Earl, and A. R. C. Britain, 1977.

[10] J. Schijve and F. A. Jacobs, *Fatigue Tests on Unnotched and Notched Specimens of 2024-T3 Alclad, 2048-T8 Alclad and 7178-T6 Extruded Material*. (Nationaal lucht- en ruimtevaartlaboratorium, 1968).

[11] G. Drossel, S. Friedrich, C. Kammer, and W. Lehnert, *Aluminium Taschenbuch: Band 2: Umformung von Aluminium-Werkstoffen, Gießen von Aluminium-Teilen, Oberflächenbehandlung von Aluminium, Recycling und Ökologie*, 15 ed. (Beuth, 2009).

[12] Alu-MATTER database, *aluminium.matter.org.uk*.

[13] M. Talia and J. E. Talia, *Crack propagation modeling for surface generated scratches in Al 2024-T3 clad alloy*, Journal of the Mechanical Behavior of Materials **8**, 117 (1997).

[14] S. E. Stanzl-Tschegg, *Ultrasonic fatigue* presented at the 6th Int. Fatigue Congress, Berlin (1996).

[15] H. Mayer, *Fatigue crack growth and threshold measurements at very high frequencies*, International Materials Reviews **44**, 1 (1999).

[16] S. Kovacs, S. Stille, D. Ernstes, and T. Beck, *Upgrading of an ultrasonic fatigue testing machine by means of early stage damage detection*, MP Materials Testing (submitted) (2012).

Effect of yttrium content on the ultra-high cycle fatigue behavior of Mg-Zn-Y-Zr alloys

D.K. Xu[1]*, E.H. Han[1]

[1] State Key Laboratory for Corrosion and Protection, Institute of Metal Research, Chinese Academy of Sciences, 62 Wencui Road, Shenyang 110016, China
* Corresponding author: dkxu@imr.ac.cn

Abstract In the super-long life regime, the fatigue behavior of as-extruded Mg-6wt%Zn-xY-0.8wt%Zr Mg alloys with Y content of 0, 1, 2 and 3 wt% have been investigated, respectively. The result indicates that for all measured S-N curves, a plateau exists in the regime of 5×10^6-10^8 cyc, and then the fatigue strength gradually decreases between 10^8 and 10^9 cyc. Therefore, only fatigue strength corresponding to 10^9 cyc can be determined. Compared with other alloys, the alloy with Y content of 2 wt% has the highest fatigue strength and its value is 105 MPa. SEM observations to fracture surfaces reveal that for all alloys, the fatigue crack mostly initiates at the surface or subsurface of samples failed within 10^6-10^9 cyc. Further observation indicates that the crack initiation is related with activated slip bands instead of phase particles and activated twins. Based on the measured results and Murakami equation, it demonstrates that the fatigue strength of alloys is more dependent on the hardness values.

Keywords Mg alloy, super-long fatigue, slip band, fatigue properties

1. Introduction

Magnesium alloys are currently used in cars for low stress applications such as covers and less frequently for the mechanically loaded structural components such as wheels, transmission housings and pedals [1]. Generally, car wheels need to be stressed at different amplitudes for several 10^8 cycles in service. For casting alloys, defects such as casting porosity and cavities are usually present and the fatigue properties are affected significantly by their shape and dimension [1-2]. Several material defects such as casting porosity, oxidation films and intermetallic inclusions, can act as crack initiation sites and reduce material's fatigue strength in the super-long fatigue life regime [1-2]. Therefore, the fatigue strength of as-cast Mg alloys corresponding to 10^9 cycles is generally about 40-50 MPa [1]. In contrast, wrought alloys are basically defect-free and have superior mechanical properties, thus the evaluation of their fatigue properties is of great interest for understanding the intrinsic fatigue mechanism of Mg alloys [3]. In early reported work, researchers mainly focused on the fatigue behavior of wrought Mg alloys with the fatigue lifetime less than 10^7 cyc [2, 4, 5]. However, as for the ultra-high cycle (10^7-10^9 cyc) fatigue behavior of wrought Mg alloys, only a few research papers can be referred [6-8]. Additionally, when compared with other system Mg alloys, Mg-Zn-Y-Zr alloys are much stronger [9-10], and their tensile strength can reach up to 380 MPa. Previous work demonstrated that Y content can remarkably influence the microstructure and tensile properties of Mg-Zn-Y-Zr system alloys [9-12]. Therefore, it can be predicted that the change of Y content should have some effect on the fatigue behaviour of Mg-Zn-Y-Zr system alloys. However, so far, no related literature can be referred. The aim of this work is to disclose the crack initiation mechanism and to establish the relationship between Y content and the fatigue strength in the gigacycle regime by investigating the fatigue behavior of Mg-5.65%Zn-xY-0.8%Zr alloys with Y content of 0, 1, 2 and 3 wt%, respectively.

2. Experimental procedure

The materials used in this study were the as-extruded Mg-Zn-Y-Zr alloys with different Y contents, which were prepared by special technology in magnesium alloy research department of

IMR, China. Through inductively coupled plasma atomic emission spectrum (ICP-AES) apparatus, the chemical compositions of alloys I-IV were determined, as listed in Table 1. The extrusion ratio was 10:1. Vickers hardness testing was performed with a load of 250g (HV).

Table 1 Chemical composition of the as-extruded Mg-Zn-Y-Zr alloys

Nominal alloy	Composition (wt %)					HV
	Mg	Zn	Y	Zr	Zn/Y	
Alloy I	Bulk	5.68	0	0.78	------	62 ± 5
Alloy II	Bulk	5.53	1.08	0.83	5.12	78 ± 4
Alloy III	Bulk	5.64	1.97	0.73	2.86	74 ± 4
Alloy IV	Bulk	5.49	3.08	0.82	1.78	68 ± 4

The specimens used for the super-long fatigue study were taken along extrusion direction (ED) of the plates. The dimensions of the specimens for fatigue test are shown in Fig. 1. Fatigue test was conducted on a Shimadazu USF-2000 ultrasonic fatigue testing machine at a resonance frequency of 20,000 Hz, with a resonance interval of 150 ms and a stress ratio of R = -1 in ambient air (temperature of 25-35 °C, relative humidity of 40-60 %). Specimens were cycled at constant amplitude until failure or until at least 10^9 cycles were reached. After test, fracture surfaces of failed samples were examined using Environmental Scanning Electron Microscope (XL30-FEG-ESEM).

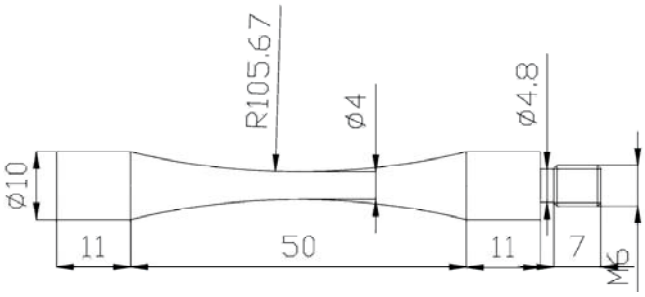

Fig. 1. Dimensions of the ultrasonic fatigue specimen.

3. Results and discussion

Fig. 2 shows the fatigue strength (S) versus lifetime (N) curves of four Mg-Zn-Y-Zr alloys. It can be seen that for all measured S-N curves, a plateau exists in the regime of 5×10^6-10^8 cyc, and then the fatigue strength gradually decreases between 10^8 and 10^9 cyc. Therefore, only fatigue strength corresponding to 10^9 cyc can be determined. Compared with other alloys, the alloy with Y content of 1 wt% has the highest fatigue strength and its value is 105 MPa.

To understand and compare the crack initiation mechanism of different alloys that failed in the super-long fatigue regime, four representative samples designated as S1, S2, S3 and S4 are chosen for analysis, as shown in Fig. 2. Fig. 3 shows the overall fracture surfaces of samples. It can be seen that for all samples, the fatigue crack preferentially initiates at the surface or subsurface.

Based on the backscattered electron image, the overall fracture surface can be divided into three regions, i.e. crack initiation region (Region 1), steady crack propagation region (Region 2) and tearing region (Region 3), as shown in Fig. 4. It is very interesting to find that basically no phase

particles exist in Region 1, whereas phase particles can be easily observed in Regions 2 and 3. Moreover, the number density of existing phase particles in Region 3 is obviously higher than that in Region 2. Therefore, it suggests that the existence of phase particles can not cause the fatigue crack initiation, but can act as the preferential route for crack propagation. Fig. 5 shows the optical microstructure of the areas just underneath the fracture surface of the sample S3. It reveals that only a few twins can be activated in the Region 1, whereas the activated twins can be easily observed in Regions 2 and 3. Additionally, density of the activated twins in Region 3 is remarkably higher than that in Region 2. In the same way, it indirectly demonstrates that the crack initiation is can not be caused by the activated twins under a stress amplitude far less than the yield stress. After crack initiation, the propagated crack will gradually increase the stress intensity factor near the crack tip, leading to the local plastic deformation and the activation of twins.

Previous work indicated that the micro cracks mainly initiate along the intense slip bands in the grain interior [12], as shown in Fig. 6. Therefore, it firmly demonstrates that the localized slip bands activated at elastic stress amplitude is the main reason for the crack initiation.

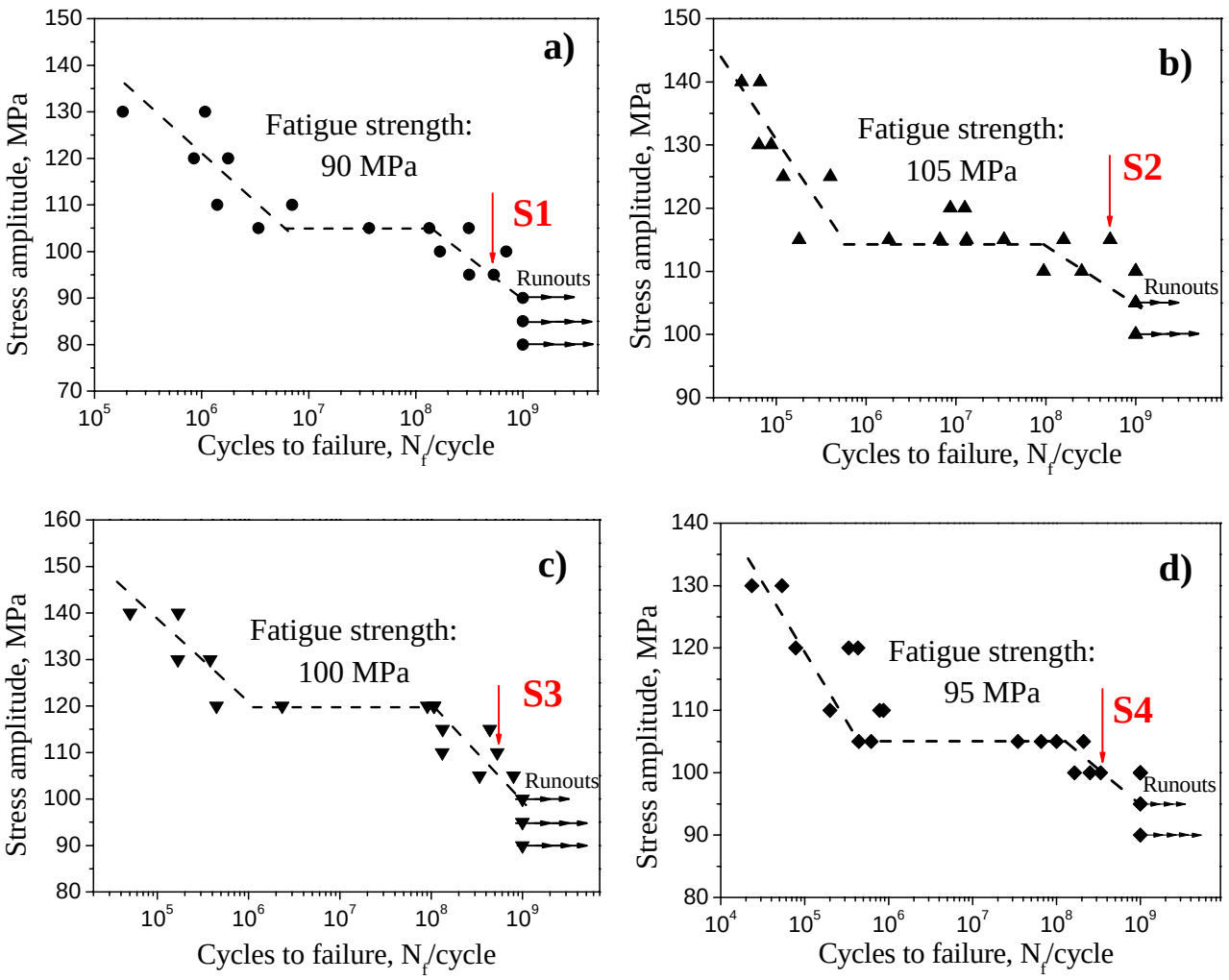

Fig. 2. S-N curves of the as-extruded Mg-Zn-Y-Zr alloys with Y content of: a) 0wt%, b) 1wt%, c) 2wt% and d) 3wt%.

Certainly, if the sample surface contains some scratches, it will further increase the occurrence possibility of crack initiation. Generally, the relationship between the "crack initiation area" size and fatigue strength or fatigue limit (σ_{-1}) proposed by Murakami can also be used for Mg alloys, which can be expressed as [13]:

$$\sigma_{-1} = \beta \frac{(\mathrm{HV}+120)}{(\sqrt{\mathrm{A}_{\mathrm{in}}})^{1/6}} \tag{1}$$

Where HV is the Vicks Hardness of Mg matrix, β is a coefficient and A_{in} is the crack initiation area.

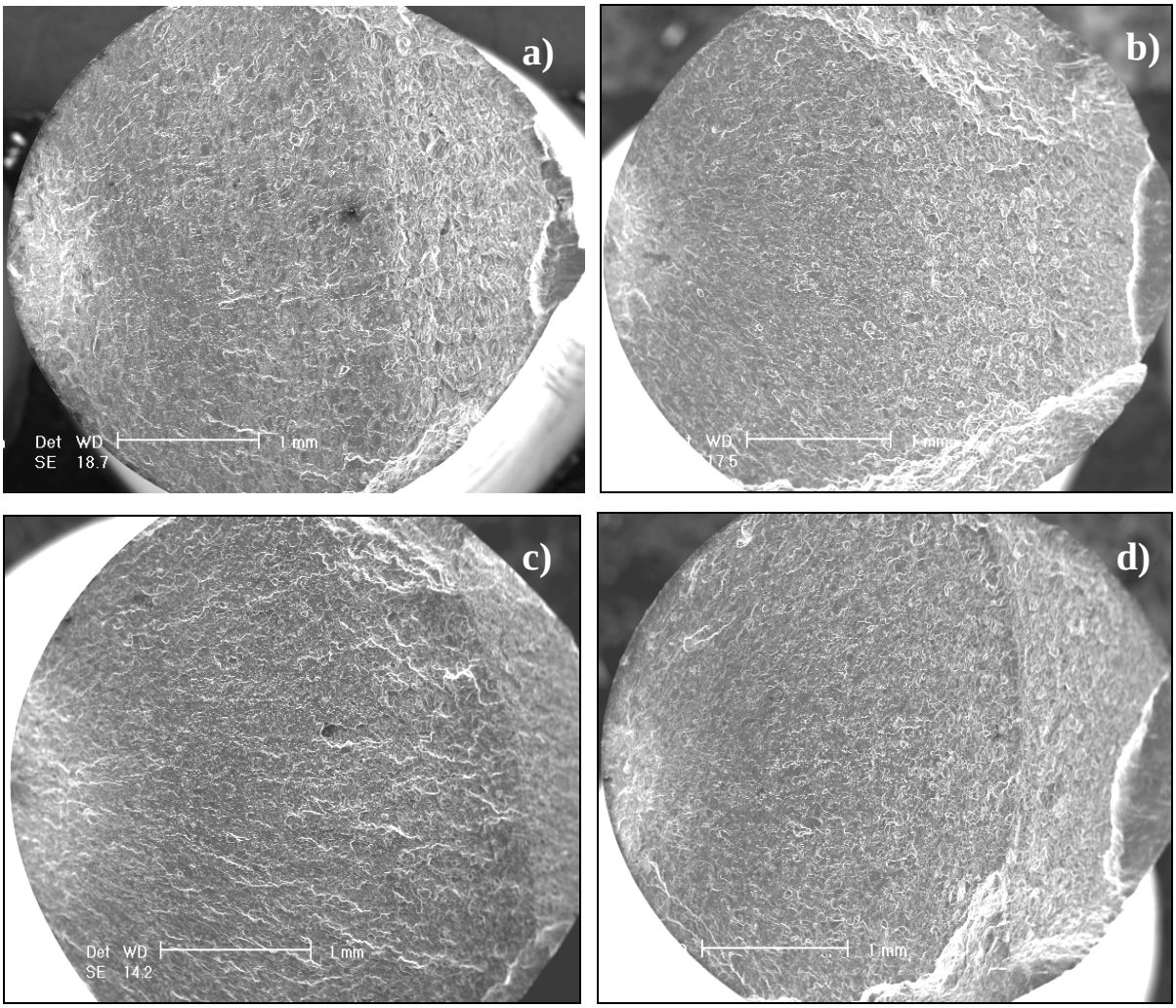

Fig. 3. Secondary electron images showing the overall fracture surfaces of samples: a) S1 (95MPa for 5E8 cyc), b) S2 (110MPa for 5.2E8 cyc), c) S3 (105MPa for 5.1E8 cyc) and d) S4 (100MPa for 5.3E8 cyc)

From Fig. 3, it can be seen that the crack initiation area for all failed samples is very similar. Then, the fatigue strength of alloys should be more dependent on the hardness values. Based on the results in Table 1, the hardness of the alloy with Y content of 1wt% is relatively higher. According to Equation (1), the calculated fatigue strength corresponding to 10^9 cycles should be higher than that of others, which is consistent with the measured results (Fig. 2).

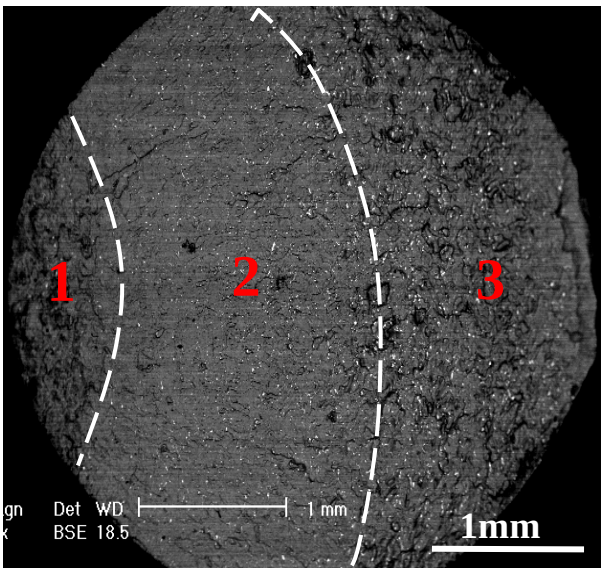

Fig. 4. Backscattered electron image showing the phase particle distribution on the fracture surface (S3).

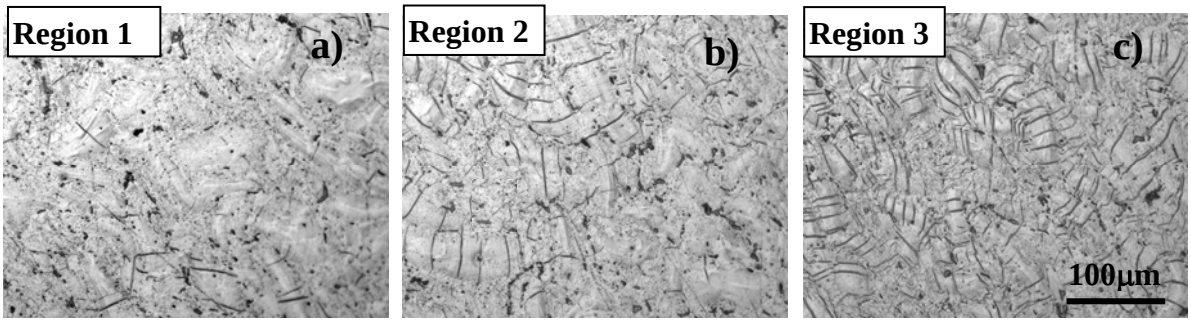

Fig. 5. Optical images of the as-polished fracture surface of sample S3 taken from regions 1-3 in Fig. 4.

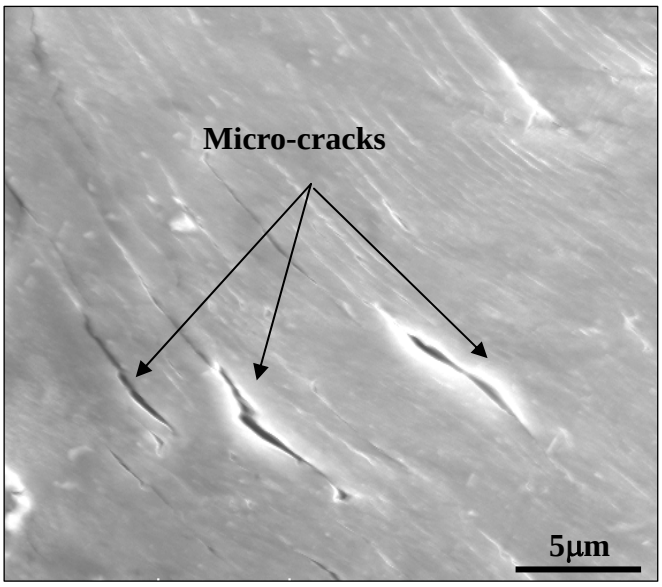

Fig. 6. Micro crack initiation at slip bands in the grain interior. [12]

4. Conclusions

For all measured S-N curves, a plateau exists in the regime of 5×10^6-10^8 cyc, and then the fatigue strength gradually decreases between 10^8 and 10^9 cyc. Therefore, only fatigue strength corresponding to 10^9 cyc can be determined. Compared with other alloys, the alloy with Y content of 2 wt% has the highest fatigue strength and its value is 105 MPa. Additionally, for all alloys, the fatigue crack mostly initiates at the surface or subsurface in the super-long fatigue lifetime regime.

Acknowledgements

This work was supported by National Natural Science Foundation of China projects under Grant No. 51171192 and No. 51271183, a National Basic Research Program of China (973 Program) project under Grant No. 2012CB067425 and an Innovation Fund of Institute of Metal Research (IMR), Chinese Academy of Sciences (CAS).

References:

[1] H. Mayer, M. Papakyriacou, Influence of porosity on the fatigue limit of die cast magnesium and aluminium alloys. Int. J. Fatigue, 25 (2003) 245-256.
[2] G. Eisenmeier, B. Holzwarth, H. Mughrabi, Cyclic deformation and fatigue behaviour of the magnesium alloy AZ91. Mater. Sci. Eng. A, 321 (2001) 578-582.
[3] K. Tokaji, M. Kamakura, Fatigue behaviour and fracture mechanism of a rolled AZ31 magnesium alloy Int. J. Fatigue, 26 (2004) 1217-1224.
[4] Z.B. Sajuri, Y. Miyashita, Y. Hosokai, Y.J. Mutoh, Effects of Mn content and texture on fatigue properties of as-cast and extruded AZ61 magnesium alloys. Int. J. Mech. Sci, 48 (2006) 198-209.
[5] T.S. Shih, W.S. Liu, Y.J. Chen, Fatigue of as-extruded AZ61A magnesium alloy. Mater. Sci. Eng. A, 325 (2002) 152-162.
[6] D.K. Xu, L. Liu, Y.B. Xu, E.H. Han, The crack initiation mechanism of the forged Mg-Zn-Y-Zr alloy in the super-long fatigue life regime. Scripta. Mater, 56 (2007) 1-4.
[7] D.K. Xu, L. Liu, Y.B. Xu, E.H. Han, The micro-mechanism of fatigue crack propagation for a forged Mg-Zn-Y-Zr alloy in the gigacycle fatigue regime. J. Alloys. Comps, 454 (2008) 123-128.
[8] F. Yang, S.M. Yin, S.X. Li, Z.F. Zhang, Crack initiation mechanism of extruded AZ31 magnesium alloy in the very high cycle fatigue regime. Mater. Sci. Eng. A, 491 (2008) 131-136.
[9] Z.P. Luo, D.Y. Song, S.Q. Zhang, Stengthening effects of rare-earths on wrought Mg-Zn-Zr-RE alloys. J. Alloy. Compd, 230 (1995) 109-114.
[10] Z.P. Luo, D.Y. Song, S.Q. Zhang, Effect of heat-treatment on the stability of the quasi-crystal in a Mg-Zn-Zr-Y alloy. Mater. Lett, 21 (1994) 85-88.
[11] D.K. Xu, L. Liu, Y.B. Xu, E.H. Han, Effect of microstructure and texture on the mechanical properties of the as-extruded Mg-Zn-Y-Zr alloys. Mater. Sci. Eng. A, 443 (2007) 248-256.
[12] D.K. Xu, L. Liu, Y.B. Xu, E.H. Han, The fatigue behavior of I-phase containing as-cast

Mg-Zn-Y-Zr alloy. Acta. Mater, 56 (2008) 985-994

[13] Y. Murakami, M. Endo, Proc. The Behavior of Short Fatigue Cracks, EGF, Mech Engng Pub, London, 1986.

Influence of high mean stresses on lifetime and damage of the martensitic steel X10CrNiMoV12-2-2 in the VHCF-regime

Tilmann Beck[1,*], **Stephan Kovacs**[1], **Lorenz Singheiser**[1]

[1] Institute of Energy and Climate Research (IEK-2), Forschungszentrum Jülich, Jülich 52425, Germany
* Corresponding author: t.beck@fz-juelich.de

Martensitic 9-12% Cr-steels are widely applied in steam turbines. In the low pressure rotor blades, fatigue loadings at several 100 Hz induced by the inhomogeneous flow field behind the vanes are superimposed by high mean stress due to centrifugal forces. Using an ultrasonic fatigue testing machine and in-depth microstructure analyses, the present study investigates the influence of mean stresses at load ratios up to R = 0.7 on the VHCF behavior with an ultimate cycle number of $2\cdot10^9$.
From R = -1 (no mean stress) up to R = 0.7 crack initiation changes consistently from the surface to internal inclusions at a cycle number around $4\cdot10^7$. Fractography indicates that fine grained areas around the inclusions only occur for R=-1. With increasing load ratio, fractures are observed at increasing cycle numbers. In spite of this fact and in spite of considerable cyclic creep at load ratios up from R = 0.5, the fracture mechanics approach proposed by Murakami consistently describes the lifetime behavior for load ratios up to R = 0.5 over 4 decades of lifetime. The contribution will give a comprehensive overview of these findings together with detailed microstructure studies of the fracture surfaces.

VHCF, Cr steel, turbine blade steel, mean stress, fatigue damage

1. Introduction

The research activities in the field of fatigue with very high cycle numbers (VHCF) were massively expanded in the past decade. Overviews of the basic mechanisms of VHCF are given in [1-4]. Generally, materials can be distinguished into two types according to their VHCF behavior. Type I materials are single-phase, inclusion-free materials like pure aluminum or copper. At very low stress amplitudes and high number of cycles, fatigue cracks in this type of materials usually originate at persistent slip bands (PSB), even at stress amplitudes below the PSB threshold, induced by local stress concentration at surface roughnesses. Type II materials on the other hand are multi-phase materials with a characteristic transition in the fracture mechanism between 10^7 and 10^8 cycles which commonly results in a multi-stage *S-N* curve as shown by Mughrabi in [5]. At high stress amplitudes, i.e. at low number of cycles to failure, fractures mainly occur at surface inclusions or at PSBs. At lower stress amplitudes in the VHCF-regime, subsurface cracks in the form of so-called "fish-eye fractures" occur, primarily originating from inclusions. Typically, subsurface fractures are reported in connection with the formation of a small zone around the inclusion called optical dark area (ODA), fine granular facets (FGA) or granular bright facets (GBF).
Such a multistage fatigue life behavior for type II metals has been found for rotating bending fatigue of Cr-Mo and high carbon bearing steels [4, 6] and also for a 42CrMo4 tempered steel and some aluminum alloys at axial fatigue loading [3, 4, 7, 8]. The stages are mainly influenced by inclusion size, surface roughness and notch factor. The critical inclusion size for internal fracture is not fixed and depends on many factors e.g. yield stress, and typically ranges from 5 µm to 500 µm. For high-strength steels, the critical inclusion size is in the range of 10 µm [2]. In this context, Murakami proposed a fracture mechanics approach, the $\sqrt{area}$-concept, to correlate the inclusion sizes with VHCF life [9]. He treated inclusions as preexisting short cracks and, based on this assumption, calculated fatigue strength, fatigue life and stress intensity factor of the crack taking into account the largest inclusion of the specimen.
However, especially the influence of superimposed mean stresses on the VHCF behavior of metallic materials is not yet sufficiently investigated. Shiozawa *et al.* [10] and Sakai *et al.* [11] investigated

the mean stress influence up to a load ratio of 0.5 on the HCF and VHCF behavior of a high-strength bearing steel (tensile strength: 2316 MPa, HV749) with high compressive residual surface stresses (-373 MPa). The VHCF tests were conducted up to an ultimate numbers of cycles of $2 \cdot 10^8$ and 10^9, respectively. Fatigue fracture is generally initiated at inclusions with an average size of 17 µm. With increasing *R* the slope of the *S-N* curves becomes extremely flat. For *R* = 0 and 0.5 the measured fatigue limits lie distinctly below the Goodman approximation.
To extend the relatively good knowledge of VHCF behavior of high strength fully martensitic steels to ferritic steels with intermediate strength and relatively high ductility typically used for steam turbine blades, the present study deals with the VHCF behavior of a typical representative of this type of materials up to $2 \cdot 10^9$ cycles. The investigated material is a martensitic 12% Cr steel frequently used for turbine blades in power plant applications. For this class of steels, the influence of mean stresses on the fatigue behavior is a main issue. Especially the last stages of low pressure steam turbine blades have to sustain fatigue loads with extremely high superimposed mean stresses due to a rotational speed of 50 Hz in combination with blade lengths of up to 1.5 m. High-frequency loading occurs due to inhomogeneous flow fields behind the vanes. With load frequencies above 2000 Hz and a component life up to 30 years, the number of cycles clearly reaches the very high cycle fatigue (VHCF) region above 10^9 cycles. Hence, VHCF loading must be considered in the design of low-pressure turbine blades. Currently, such turbine blades are designed with high safety coefficients based on S-N curves assumed to approach an asymptotic fatigue limit at $N > 10^7$ load cycles. Nevertheless, blade failures at high number of cycles still occur at corrosion pits or even at blade roots without environmental influence [12-16].

2. Materials and methods

The material tested in this study is a martensitic 12% Cr steel used for low pressure steam turbine blades in power generation. The chemical composition is shown in Table 1.

Table 1
Chemical composition of X10CrNiMoV12-2-2

element	C	Cr	Ni	Mo	Mn	V	Si
weight-%	0.117	11.4	2.70	1.64	0.70	0.31	0.23

To obtain a martensitic microstructure, the blades were hardened by annealing at 1040 °C for 60 min and subsequent compressed air cooling. For stress relief purposes, the blades were subsequently tempered at 660 °C for 3 h followed by annealing at 640 °C for 4 h and very slow furnace cooling. The resulting highly tempered martensitic microstructure has finely distributed Cr-carbides with diameters of around 100 nm along the martensite laths and the former austenite grain boundaries. Precipitation-hardening results in high ultimate tensile strength combined with a sufficient elongation at fracture (Table 2). Due to its heat treatment, the microstructure is stable up to temperatures as high as 600°C and ensures safe application of this steel for power plant applications.

Table 2
Mechanical properties of X10CrNiMoV12-2-2 at room temperature

Vickers hardness	334 HV
Yield strength	843 MPa
Ultimate tensile strength	1001 MPa
Elongation at fracture	17.7 %
Contraction at fracture	58 %
Young´s Modulus	213 GPa

Subsequently, cylindrical rods were eroded from the blade root by electro-discharge-machining and turned to the final specimen geometry with cylindrical gauge length and a diameter of 3 mm. Fig. 1shows the geometry for tests without mean stress (R = -1), Fig. 2 the specimen shape for tests with superimposed mean stresses (R > 0).

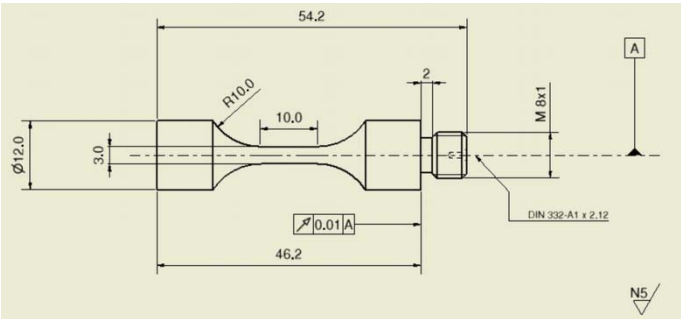

Figure 1. Specimen geometry for R = -1 fatigue tests.

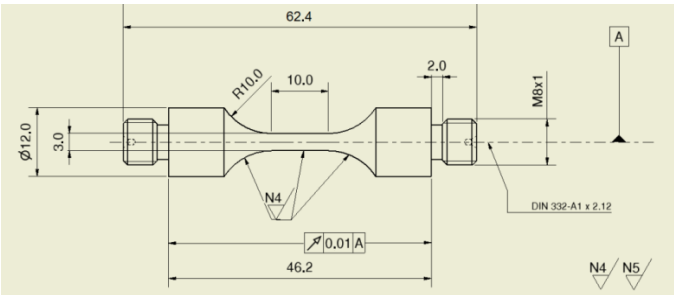

Figure 2. Specimen geometry for R > 0 fatigue tests.

Finally, the samples were ground with SiC abrasive paper and subsequently mechanically polished. The residual stresses in the polished state were determined to -34 ± 16 MPa by X-ray diffraction using the sin2ψ-method.

Testing system is the Ultrasonic Fatigue Testing Equipment (UFTE) developed and manufactured by Boku Wien attached to an Instron 5967 load frame for fatigue tests with superimposed mean stresses. The experimental setup is similar to that described in [17]. For tests at R = -1, the specimens are clamped at one end to allow free oscillation. The UFTE system develops a standing wave during oscillation. Ultrasonic fatigue tests were performed in displacement control at constant-amplitude tension-compression loading in laboratory air at room temperature. Assuming linear-elastic behavior in the VHCF regime, strain gauges can be utilized to calibrate the system prior to the experiments by using the linear correlation between displacement and stress in the gauge section [18]. To limit self-heating of the specimen during loading, a load pulse / pause ratio of 80-200 ms / 800-1200 ms was applied together with forced air cooling of the specimen. To analyze the influence of high mean stresses, load ratios ranging from -1 up to 0.7 were applied. Additionally, load controlled fatigue tests were conducted using an Instron 1603 electromagnetic resonance testing machine at frequencies of about 100 Hz to investigate the frequency influence on fatigue life. An ultimate number of cycles of $2 \cdot 10^9$ was chosen for the tests conducted with the ultrasonic device and of 10^8 for the electromagnetic fatigue testing machine, respectively.

After fatigue testing, fracture surfaces of failed specimens were observed by SEM, paying particular attention to classification of the fracture modes of surface and subsurface fracture at persistent slip bands and inclusions, respectively, and analyzing diameters as well as chemical composition of the inclusions.

3. Results and discussion

3.1 Fatigue life analysis and load ratio influence

The fatigue data of X10CrNiMo12-2-2 previously presented in [19] are shown in Fig. 3 with load ratios ranging between R = -1 and R = 0.7. In the *S-N* curves, no "two step" behavior indicating separate fatigue limits for surface and sub-surface cracks could be observed. Furthermore, for R = -1, there is a smooth transition in the curve from the literature data by Zhou et al. [20] for the LCF (grey symbols) to the HCF (blue symbols) data at approximately 10^5 load cycles. Considering all data plotted for R = -1, no significant frequency effect can be seen in a frequency range of over four orders of magnitude ranging from 1 Hz up to 20 kHz. Literature data of the investigated steel for load ratios higher than -1 is not available. Hence, the ultrasonic fatigue tests are considered to be representative for a wide frequency range allowing to reach high cycle numbers within appropriate time.

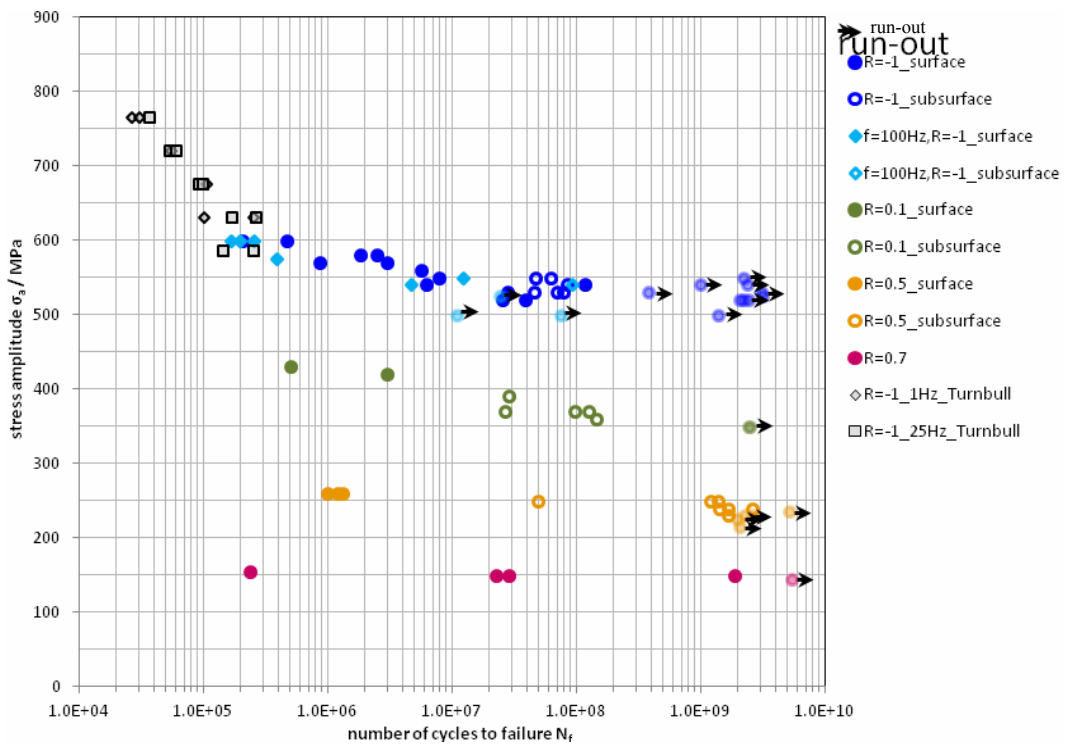

Figure 3. Stress amplitude vs. number of cycles to failure for load ratios R = -1. 0.1, 0.5 and 0.7 at RT.

In Fig. 3, filled symbols mark fractures originating from the surface (persistent slip bands or surface inclusions) and open symbols indicate volume fractures of subsurface inclusions. A quite narrow transition band from surface to internal fractures between approximately $2{\cdot}10^7$ and $4{\cdot}10^7$ load cycles exists independent of the load ratio. As expected, a quite large scatter in fatigue life was observed. Fatigue strength and the slope of the curves decrease with increasing load ratio. The huge scatter of the curves is mainly caused by the inclusion size distribution.

Another conspicuous feature of the *S-N* curves is the correlation between the load ratio and the highest numbers of cycles to failure: While for R = -1 failure only appears at less than 10^8 cycles (with one exception), there are fractures above 10^8 cycles for R = 0.1. For R = 0.5 and R = 0.7, failure even occurred above 10^9 cycles close to the defined run-out limit. Despite the small amount of data for higher load ratios, this trend is obvious and, at least for this material, has not been observed before and is subject of further research.

Furthermore, different approaches were applied to evaluate the fatigue strengths at the investigated load ratios: Because at load ratios $R > 0$ the database is insufficient for statistical evaluation of fatigue strength, a pragmatic approach is used. As the flat slope of the *S-N* curves (Fig. 3) is a convenient precondition for assessing the fatigue limit, the fatigue strength is defined as the highest stress amplitude where specimens still not failed. Hence, the following fatigue strengths were determined: 350 MPa for $R = 0.1$, 230 MPa for $R = 0.5$ and 145 MPa for $R = 0.7$. For $R = -1$, the arcsin$\sqrt{P}$-method [21] was applied for calculating the fatigue strength, taking all data points in the vicinity of the run-out specimens into account. The resulting fatigue limit for $R = -1$ is a stress amplitude σ_a of 495 MPa.

3.2 Fractographiy-based evaluation of fatigue life

In the next step, crack initiating defects were identified and analyzed using SEM and EDX. Up to about 10^7 cycles, most fractures initiated at persistent slip bands (PSBs) or at surface inclusions. Both HCF fracture types were observed for fatigue lives up to $4{\cdot}10^7$ cycles at all investigated load ratios. A more detailed investigation of the fracture surfaces is given in [19].

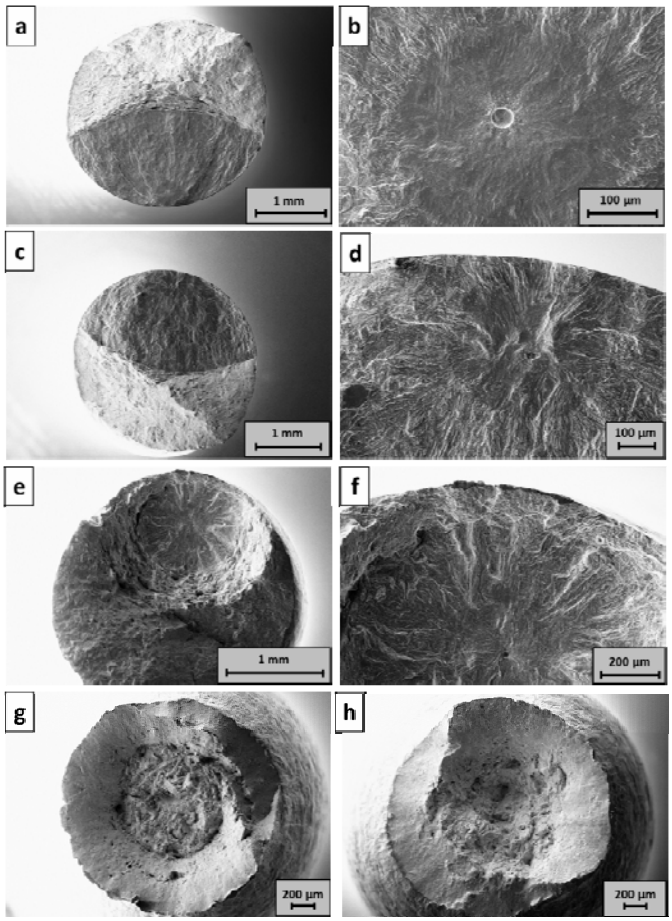

Figure 4. Fracture surfaces of typical fish-eye cracks: (a, b) $\sigma_a = 550$ MPa, $R = -1$, $N_f = 4.66{\cdot}10^7$; (c, d) $\sigma_a = 370$ MPa, $R = 0.1$, $N_f = 1.24{\cdot}10^8$; (e, f) $\sigma_a = 250$ MPa, $R = 0.5$, $N_f = 1.21{\cdot}10^9$; (g) $\sigma_a = 155$ MPa, $R = 0.7$, $N_f = 2.35{\cdot}10^5$; (h) $\sigma_a = 150$ MPa, $R = 0.7$, $N_f = 2.28{\cdot}10^7$.

In the VHCF-regime, i.e. at fatigue lives above approximately $4{\cdot}10^7$ cycles, fish-eye cracks, which are characteristic for VHCF failure of high strength steels [5], are found in all fracture surfaces (Fig. 4). The frequently observed “optical dark areas” (ODAs) [22-25] are difficult to identify in this steel.

In Fig. 4b) for R = -1, an ODA is visible in the region directly above the inclusion. Such structures could be observed in several specimens for R = -1, but were never found in samples fatigued at higher load ratios. Examples are given in Fig. 4d) and f).
Some uncertainty remains in this observation because ODAs are generally very difficult to detect in this steel. In [19], microstructural investigations were performed via focused ion beam technique (FIB) and SEM of cross-sections perpendicular to the fatigue crack surface close to the crack initiating inclusion. The results showed the presence of a nanocrystalline area around the inclusion only for R = -1. Based on this observation, a possible reason for the R-dependency of the highest observed number of cycles to failure is given in [19].

Furthermore, there is a change of the fracture surface profile with increasing load ratio. At higher load ratios, the fish-eyes become more distinguished and a step-like transition develops between the fish-eye and the residual fracture which indicates the occurrence of cyclic creep and plastic deformation. As shown by displacement measurements of the specimens during the fatigue tests in [19], increasing load ratio leads to higher total mean strains, i.e. plateau values of 0.4% and 4.5% for R = 0.1 and R = 0.5, respectively. At R = 0.7, steady cyclic creep occurs during the entire test. Additional fatigue tests at high stress amplitudes were performed showing weak cyclic softening of this steel in accordance with [26] for a similar kind of 12% Cr steel. The dominance of cyclic creep on deformation and failure at R = 0.7 corresponds to the fracture surface depicted in Fig. 4g) and h) showing a “tensile test like” cup-cone fracture without any distinct fatigue features. However, it should be noted that even at this high load ratio fatigue lives clearly above 10^7 have been reached.

For the fish-eye fractures at other load ratios, inclusion sizes and compositions as well as the area of the fish-eyes were determined by SEM and EDX. For all fractures, the crack initiated at oxide inclusions in the middle of the fish-eye with compositions either $CaO{\cdot}Al_2O_3$ or $MgO{\cdot}Al_2O_3$. However, the crucial factor for fatigue life is the diameter of crack inducing inclusions, following a normal distribution and ranging from 16 µm up to 45 µm in this test series. To consider the inclusion size dependency on fatigue life, the $\sqrt{area}$-concept of Murakami [9] was applied. The $\sqrt{area}$-parameter represents the inclusion size perpendicular to the applied maximum stress, which is treated equivalent to a fatigue crack of equal size. By means of fracture mechanics, this leads to Eq. (1) for the fatigue strength:

(1)

HV is the hardness of the material and α a material constant describing the influence of load ratio. C is 1.56 for internal defects and 1.43 for subsurface cracks, respectively. At first, the material constant α for the R-dependency of the fatigue limit needs to be determined from the slope of the fatigue strength vs. $(1-R)/2$ curve. In the present case, α is 0.546. In the next step, σ_a/σ_W can be plotted against the number of cycles to failure in a linear graph (Fig. 5). In this plot, the huge scatter of the S-N curves could be reduced to less than one order of magnitude, so the fatigue data of load ratios from -1 up to 0.5 can be described in a single curve in a fatigue life range of more than four orders of magnitude. The Murakami approach is convenient for describing the curve both in the HCF and the VHCF-regime and independent of load ratio. Thus, the α-parameter of 0.546 seems to be accurate for describing the dependency of fatigue strength on load ratio of the present material. An evaluation of the R = 0.7 data and a deeper analysis of the obtained α value is given in [19].

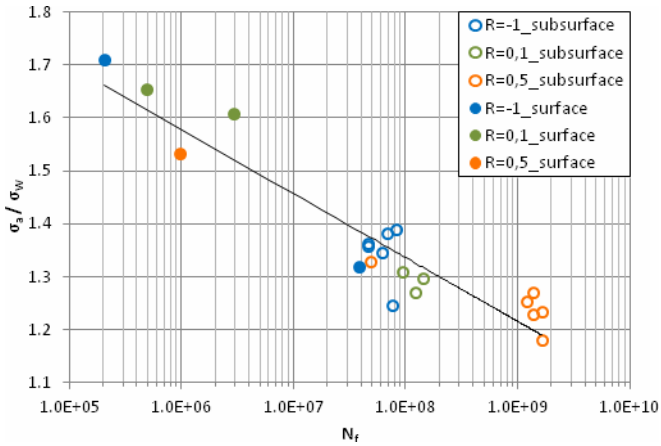

Figure 5. Modified *S-N* curve according to the $\sqrt{area}$-concept proposed by Murakami.

3.3 Crack growth threshold evaluation

Another appropriate data evaluation method is shown in [27, 28]. In the present work, this approach proposed by Döker is applied to small fatigue cracks assuming the fracture inducing inclusion sizes being identical with the initial crack length. Based on the linear elastic fracture mechanics, the threshold stress intensity factor ΔK_{th} can be plotted vs. the load ratio R. As mentioned in [27], only positive R can be used and given the fact that no fracture inducing inclusions were visible for fractured specimen at $R = 0.7$ (see Fig. 4g) and h)), this approach is only applied for fatigue data of $R = 0.1$ and 0.5. Initially, ΔK_{th} needs to be calculated. Assuming a circle shaped volume crack with the diameter of the crack initiating inclusion, Eq. (1) and Eq. (2) can be used as good approximations, where a_{incl} is the mean size of all measured inclusions and $\Delta\sigma_D$ and $\sigma_{D,max}$ are the corresponding fatigue strength values.

(2)

$$K_{max} = \frac{2}{\pi}\sigma_{D,max}\sqrt{\pi a_{incl}} \qquad (3)$$

According to [27], a ΔK_{th}–R curve can be derived from the above values (continuous line in Fig. 6). The curve is separated into multiple sections described by different equations (see Fig. 6). Here, the two curves nearly overlap at negative R. For $R < 0$, the green dotted line is valid and the threshold value asymptotically approaches ΔK_0. The red dotted line represents a downward oriented parabola which intersects with the positive R-axis at $R = -1$ and with the ΔK_{th} –axis at $\Delta K_{th} = K_{max,0}$. The different shape of the curves compared with [27] probably is due to the distinctly smaller crack length considered in the present study. Additionally, Fig. 6 shows the ΔK values calculated from the obtained fatigue test data using the stress amplitudes and the crack inducing inclusion sizes (blue diamonds). Note that for this evaluation only fractures close to the observed run-outs (see Fig. 3) were taken into account. Referring to the work of Grad et al. [29], ΔK was also calculated using the sizes of the ODAs found at $R = -1$ (green triangles).

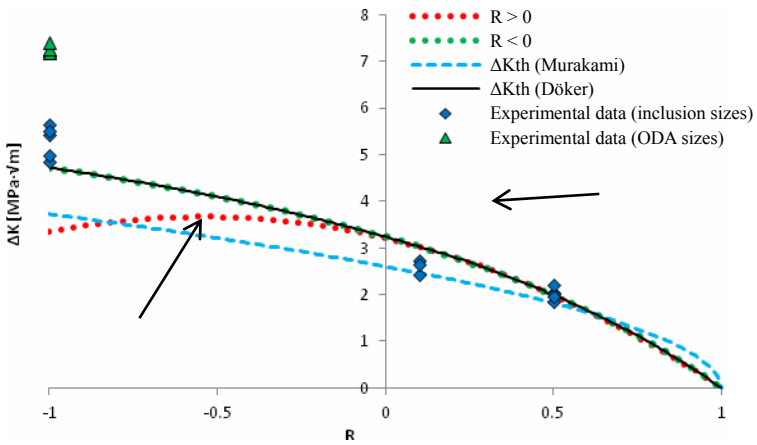

Figure 6. Threshold curves according to Döker and Murakami.

As expected, the data points for R = 0.1 and 0.5 lie close to the approximation curve. For R = -1, the data points calculated from the inclusion sizes are slightly above the calculated threshold value. The values considering the ODA sizes are around 7.3 MPa√m and with this lie well above the approximation curve. This difference indicates that, for R = -1, crack closure effects, which are not considered in the applied fracture mechanics approach, are an important issue.
Concerning the relatively high ductility of the investigated 12% Cr steel, crack closure effects due to residual stresses near the crack tip are probably much more pronounced than in the high-strength 100Cr6 examined in [29]. The same conclusions can be drawn from the comparison of the individually calculated ΔK values with the ΔK_{th}-R curve proposed by Murakami (blue dashed line in Fig. 6), which is determined according to Eq. (4) with the material hardness HV, the $\sqrt{area}$ parameter and the material constant α.

(4)

4. Summary

1. No frequency effect was found for fatigue tests with zero mean stress in a frequency range above four orders of magnitude.
2. In the LCF/HCF-regime, specimens either failed by cracks initiated at PSBs or surface inclusions. Above $2{\cdot}10^7$ - $4{\cdot}10^7$ load cycles, fish-eye cracks were found originating from oxide inclusions. The inclusion diameters ranged from 16 µm up to 45 µm and follow a normal extreme value distribution. The inclusion size has a decisive influence on fatigue life as shown by the modified S-N curve proposed by Murakami [9]. The α-parameter describing the load ratio dependency was determined to 0.546 and was in the vicinity of α values measured in recent investigations at other high-strength steels. Thus, the $\sqrt{area}$-concept is well applicable for this steel in a large range of load ratios ($-1 < R < 0.5$).
3. For R = 0.7, the fatigue fracture surfaces are similar to quasi-static tensile fractures with high deformation and sample elongation due to extremely pronounced cyclic creep.

4. ODAs were only found for fatigue tests at R = -1. A reason for this may be reduced crack closure at R > 0, which has to be proven by further investigations of fracture surfaces by means of an SEM after FIB preparation of sections perpendicular to the crack surface.
5. The evaluation of the threshold values according to Döker was applied to short cracks. The results also indicate that crack closure effects may play an important role in connection with the ODA formation.

Acknowledgements

The authors gratefully acknowledge funding of this study by the Deutsche Forschungsgemeinschaft (DFG).

References

[1] C. Berger, B. Pyttel, D. Schwerdt, Beyond HCF - Is there a fatigue limit?, Materialwissenschaften und Werkstofftechnik, 39 (2008) 769-776.
[2] S.X. Li, Effects of inclusions on very high cycle fatigue properties of high strength steels, Int. Mater. Rev., 57 (2012) 92-114.
[3] H. Mughrabi, Fatigue, an everlasting materials problem - still en vogue, Procedia Engineering, 2 (2010) 3-26.
[4] T. Sakai, Review and Prospects for Current Studies on Very High Cycle Fatigue of Metallic Materials for Machine Structural Use, International Journal of Fatigue, 3 (2009) 425-439.
[5] H. Mughrabi, Specific features and mechanisms of fatigue in the ultrahigh-cycle regime, International Journal of Fatigue, 28 (2006) 1501-1508.
[6] T. Sakai, M. Takeda, K. Shiozawa, Y. Ochi, M. Nakajima, T. Nakamura, N. Oguma, Experimental evidence of duplex S-N characteristic's in wide life region for high strength steels, China Higher Education Press Beijing, Beijing, 1999.
[7] H.W. Höppel, L. May, M. Prell, M. Göken, Influence of grain size and precipitation state on the fatigue lives and deformation mechanisms of CP aluminium and AA6082 in the VHCF-regime, International Journal of Fatigue, 33 (2011) 10-18.
[8] Q.Y. Wang, C. Bathias, N. Kawagoishi, Q. Chen, Effect of inclusion on subsurface crack initiation and gigacycle fatigue strength, International Journal of Fatigue, 24 (2002) 1269-1274.
[9] Y. Murakami, S. Kodama, S. Konuma, Quantitative evaluation of effects of non-metallic inclusions on fatigue strength of high strength steels. I: Basic fatigue mechanism and evaluation of correlation between the fatigue fracture stress and the size and location of non-metallic inclusions, International Journal of Fatigue, 11 (1989) 291-298.
[10] K. Shiozawa, T. Hasegawa, Y. Kashiwagi, L. Lu, Very high cycle fatigue properties of bearing steel under axial loading condition, International Journal of Fatigue, 31 (2009) 880-888.
[11] T. Sakai, Y. Sato, Y. Nagano, M. Takeda, N. Oguma, Effect of stress ratio on long life fatigue behavior of high carbon chromium bearing steel under axial loading, International Journal of Fatigue, 28 (2006) 1547-1554.
[12] Z. Mazur, A. Hernández-Rossette, R. García-Illescas, Investigation of the failure of the L-0 blades, Engineering Failure Analysis, 13 (2006) 1338-1350.
[13] W.-Z. Wang, F.-Z. Xuan, K.-L. Zhu, S.-T. Tu, Failure analysis of the final stage blade in steam turbine, Engineering Failure Analysis, 14 (2007) 632-641.
[14] Z. Mazur, R. Garcia-Illescas, J. Porcayo-Calderon, Last stage blades failure analysis of a 28 MW geothermal turbine, Engineering Failure Analysis, 16 (2009) 1020-1032.
[15] Z. Mazur, R. Garcia-Illescas, J. Aguirre-Romano, N. Perez-Rodriguez, Steam turbine blade failure analysis, Engineering Failure Analysis, 15 (2008) 129-141.

[16] R. Ebara, Long-term corrosion fatigue behaviour of structural materials, Fatigue Fract. Eng. Mater. Struct., 25 (2002) 855-859.
[17] C. Bathias, K. El Alami, T.Y. Wu, Influence of mean stress on ti6a14v fatigue crack growth at very high frequency, Engineering Fracture Mechanics, 56 (1997) 255-264.
[18] S. Stanzl-Tschegg, Ultrasonic Fatigue, in: K.H.J.B. Editors-in-Chief: , W.C. Robert, C.F. Merton, I. Bernard, J.K. Edward, M. Subhash, V. Patrick (Eds.) Encyclopedia of Materials: Science and Technology (Second Edition), Elsevier, Oxford, 2001, pp. 9444-9449.
[19] S. Kovacs, T. Beck, L. Singheiser, Influence of mean stresses on fatigue life and damage of a turbine blade steel in the VHCF-regime, International Journal of Fatigue (accepted for publication), (2012).
[20] Zhou, Turnbull, Influence of pitting on the fatigue life of a turbine blade steel, Fatigue Fract. Eng. Mater. Struct., 22 (1999) 1083-1093.
[21] D. Dengel, Die arc sin √P-Transformation — ein einfaches Verfahren zur grafischen und rechnerischen Auswertung geplanter Wöhlerversuche, Materialwissenschaft und Werkstofftechnik, 6 (1975) 253-261.
[22] Y. Murakami, T. Nomoto, T. Ueda, On the mechanism of fatigue failure in the superlong life regime (N>107 cycles). Part 1: influence of hydrogen trapped by inclusions, Fatigue Fract. Eng. Mater. Struct., 23 (2000) 893-902.
[23] Y. Murakami, T. Nomoto, T. Ueda, On the mechanism of fatigue failure in the superlong life regime (N>107 cycles). Part II: influence of hydrogen trapped by inclusions, Fatigue Fract. Eng. Mater. Struct., 23 (2000) 903-910.
[24] T. Nakamura, H. Oguma, Y. Shinohara, The effect of vacuum-like environment inside sub-surface fatigue crack on the formation of ODA fracture surface in high strength steel, Procedia Engineering, 2 (2010) 2121-2129.
[25] Z.G. Yang, S.X. Li, Y.D. Li, Y.B. Liu, W.J. Hui, Y.Q. Weng, Relationship among fatigue life, inclusion size and hydrogen concentration for high-strength steel in the VHCF regime, Materials Science and Engineering: A, 527 (2010) 559-564.
[26] T. Petersmeier, U. Martint, D. Eifler, H. Oettelt, Cyclic fatigue loading and characterization of dislocation evolution in the ferritic steel X22CrMoV121, International Journal of Fatigue, 20 (1998) 251-255.
[27] H. Döker, Fatigue crack growth threshold: implications, determination and data evaluation, International Journal of Fatigue, 19 (1997) 145-149.
[28] H. Döker, Schwellenwert für Ermüdungsrissausbreitung: Bestimmung und Anwendung, Fortschritte der Bruch- und Schädigungsmechanik, (2002) 9-18.
[29] P. Grad, B. Reuscher, A. Brodyanski, M. Kopnarski, E. Kerscher, Mechanism of fatigue crack initiation and propagation in the very high cycle fatigue regime of high-strength steels, Scripta Materialia, 67 (2012) 838-841.

Effect of Aging Condition on Fatigue Strength of Maraging Steel in Long Life Region

Qiang Chen[1,*], Qingyuan Wang[2], Norio Kawagoishi[3], Kohji Kariya[3], Yuzo Nakamura[4], Nu Yan[5]

[1] Center for Globalization, Kumamoto University, Kumamoto 860-8555, Japan
[2] Department of Civil Engineering & Mechanics, Sichuan University, Chengdu 610065, China
[3] Department of Mechanical System Engineering, Daiichi Institute of Technology, Kirishima 899-4395, Japan
[4] Department of Mechanical Engineering, Kagoshima University, Kagoshima 890-0065, Japan
[5] Department of Mechanical Engineering, China Three Gorges University, Hubei 443002, China
* Corresponding author: qchen@kumamoto-u.ac.jp

Abstract A novel aging treatment was proposed to improve the fatigue strength of maraging steel by taking the effects of aging condition and humidity into account. Rotating bending fatigue tests were carried out for a 350 grade of 18% Ni maraging steel in the long life region up to 10^8 cycles in the relative humidity of 25% and 85%. Aging conditions under investigation included a conventional aging or the so called single aging at 753K, and a two–step aging or double aging by ageing at lower temperature of 473K succeeded to the single aging. Through the double aging, the susceptibility of fatigue strength to humidity was significantly improved without any deleterious effects. The main reasons for the decrease in fatigue strength in high humidity are due to the promotion of crack initiation and the acceleration of small crack propagation. The improvement of fatigue property in high humidity by the double aging was explained from the roles of the additional precipitation of supersaturated Mo atoms during the second lower temperature aging.

Keywords Fatigue, Maraging steel, Aging, Humidity, Rotating bending

1. Introduction

Maraging steel has the highest tensile strength and high ductility among steels used in practice [1]. However, the fatigue strength of maraging steel is much lower than expected from its high static strength [2]. The reason for the lower fatigue strength is due to the high sensitivity of maraging steel to both notch [3] and humidity [4]. Since maraging steel is mainly hardened by the precipitation of intermetallic compounds such as Ni_3(Ti, Mo) and Fe_2Mo in martensite structure, the strength of the steel depends largely on the aging conditions. Many studies have been carried out on the precipitations in the steel. For example, it is well known that the in-coherent particle of Ni_3(Ti, Mo), which is one of the primary strengthening particles, precipitates at high aging temperature beyond 723K, while the particles of Fe_2Mo, ω phase and Mo cluster precipitate at low aging temperature below 723K [5]. Precipitation at high temperature is usually referred to as high temperature phase whilst that at low temperature as low temperature one. Considering the above-stated relation between aging temperature and precipitation, it is expected that additional precipitation and hardening may happen during a two-step aging or the conventional high temperature aging followed by a low temperature ageing, because the concentraion of Mo exceeds its solubility at low temperature. However, aging treatment of maraging steel is usually conducted under a constant high temperature only, and the study of the mechanical properties, especially the fatigue strength, of the two-step aged steel at high and low temperatures has not been reported.

In the present study, the effect of aging condition on the fatigue strength of 18%Ni maraging steel of grade 350 in long life region was investigated. A novel aging treatment was proposed for improving fatigue properties of the maraging steel. Fatigue tests up to 10^8 cycles were performed in relative humidity of 25% and 85% under rotating bending. Aging conditions examined were the conventional aging at 753K or the so called single aging, and a two–step aging or double aging at 473K subsequent to the conventional aging at 753K.

2. Experimental procedure

The material used was a commercial 350-grade maraging steel. The chemical composition was shown in Table 1. The steel was solution treated for 5.4ks at 1123K in vacuum followed by air cooling and age hardened in salt bath. The mean grain size of prior austenite was about 20 μm.
Figure 1 shows aging curves, in which hardness is increased by the two-step aging as stated in introduction. The reason for the increase in hardness by the two-step aging will be discussed later. Aging conditions investigated were a single peak-aging at the conventional aging temperature of 753K, which is denoted as SA-P, and a two-step or double aging by including an under-aging treatment at 473K after the conventional aging SA-P, which is denoted as DA-U, hereinafter. The two-step aging showed a definite hardening. These conditions were indicated by open marks in Fig.1 and were specified in Table 2. Further study on the variation of mechanical properties with different combination of two-step aging conditions can be found in the related presentation. [6]
Figure 2 shows the shape and dimensions of plain specimen. Specimens were machined after the solution treatment, and then age hardened as specified in Fig. 1. Prior to fatigue testing, specimens were sanded by emery paper followed by electro-polishing to remove work affected layer and secure surface state for easier observation. Fatigue tests were carried out using a Ono-type rotating bending fatigue machine with a capacity of 15 N·m, operating at about 50Hz in relative humidity (RH) of 25% and 85%, respectively. The humidity was moderated in a range of RH±5%.

Table 1. Chemical composition (mass%)

Grade	C	Si	Mn	Ni	Mo	Co	Ti	Al	Fe
350G	0.001	0.01	0.01	17.89	4.27	12.36	1.3	0.08	Bal.

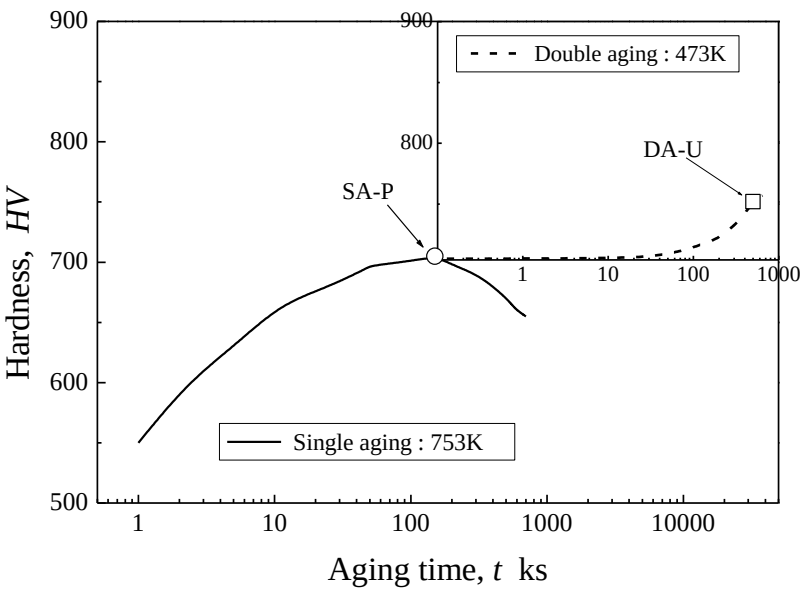

Figure 1. Aging curves of maraging steel

Table 2. Mechanical properties

Material	Aging condition	Vickers hardness *HV*	0.2% proof stress $\sigma_{0.2}$ (MPa)	Tensile strength σ_B (MPa)	Reduction of area ϕ (%)
SA-P	753K-150ks	705	2300	2370	54
DA-U	753K-150ks, 473K-500ks	750	2315	2378	55

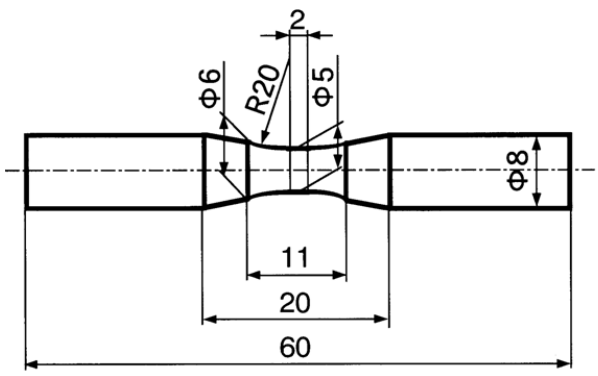

Figure 2. Shape and dimensions of plain specimen

The atmospheric temperature was not controlled and in the range of 295±3K. Surface cumulative damage observation and crack length measurement were carried out by plastic replication technique. Crack length, ℓ, was defined as a surficial length along the circumferential direction vertical to stress axis. Microstructure and fracture morphology were examined using both transmission electron microscope (TEM) and scanning electron microscope (SEM).

3. Results and discussion

Figure 3 shows *S-N* curves of the steels. Fracture occurred from specimen surfaces, irrespective of the age treatment and the humidity. Moreover, in case of low humidity, none of fatigue cracks were observed for specimens non-fractured after fatigued for 10^8 cycles, suggesting that fatigue limit defined as fatigue strength at 10^8 cycles was mainly controlled by the resistance to crack initiation. Fatigue limits in both steels are nearly the same in low humidity, meaning that the resistance to crack initiation was improved somewhat by the double aging, because the fatigue strength of a steel usually decreases with strengthening due to increasing notch sensitivity [7]. On the other hand, fatigue strength decreased in high humidity, and the extent of fatigue strength decrease was larger in SA-P steel than in DA-U steel.

To clarify the reason for the difference in high humidity susceptibility of fatigue limit between the SA-P and DA-U steels, successive observation of surface failure due to stress repetitions was conducted.

Figs. 4 and 5 show crack growth curves and relation between crack growth rate and stress intensity factor range in 25% and 85%, respectively. It can be seen that the initiation and early propagation of cracks short than a few grain sizes are definitely accelerated by high humidity and this trend is more remarked at lower stress levels, because the lower the stress level, the longer the crack initiation life and the stronger the influence of humidity. In other words, it is the acceleration of crack initiation and its early growth that caused the fatigue strength decrease in high humidity.

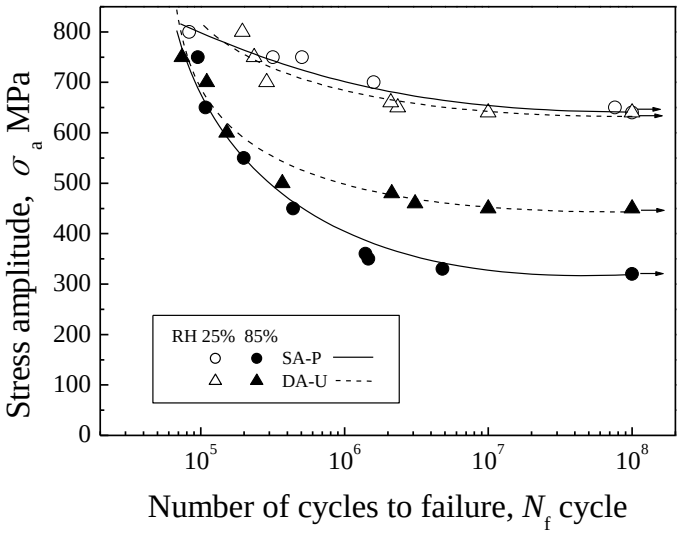

Figure. 3 *S-N* curves

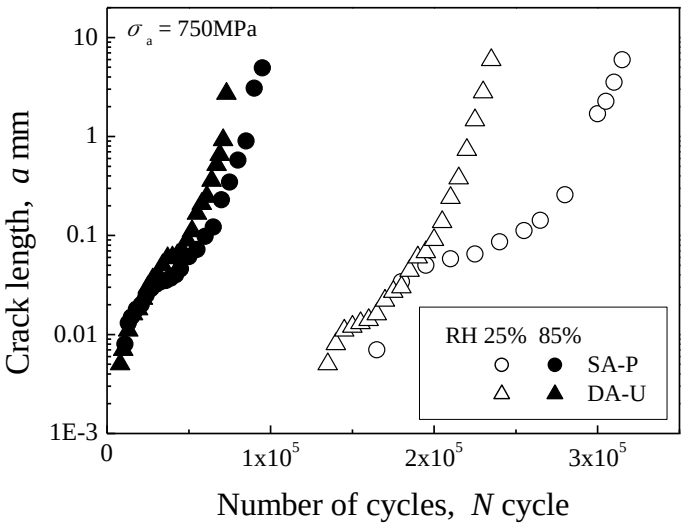

Figure 4. Crack growth curves

In case of SA-P steel subjected to fatigue in long life region in RH 85%, corrosion debris (Fig. 6a) and multi cracks initiated from a corroded pit (Fig. 6b) are confirmed on specimen surface, implying that crack initiation was promoted by anodic dissolution.

Figure 7 shows SEM morphology of SA-P steel fractured in both low and high humidity. In case of low humidity, slip steps appear on a facet in the vicinity of crack initiation site, as shown in Fig. 7a-1)), meaning that slip deformation or stage I cracking dominate crack nucleation [8]. On the other hand, in high humidity, crack initiation is characterized by many facets, especially river pattern-like facets (Fig. 7b-1), suggesting that hydrogen embrittlement assisted fracture occurred.

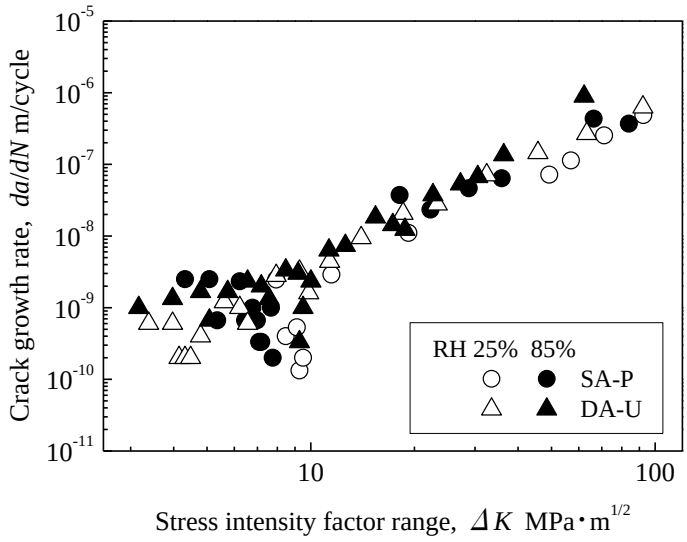

Figure 5. Crack growth rate vs. stress intensity factor range

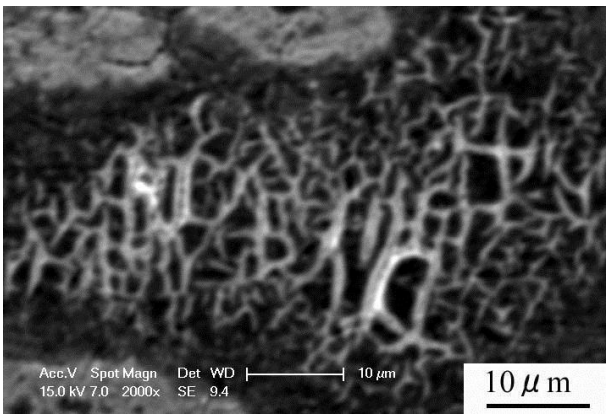

(a) Corroded area

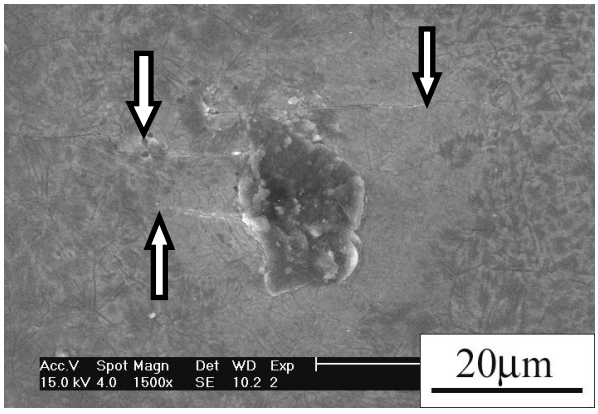

(b) Cracks initiated at corrosion pit

Figure 6. Surface state of SA-P specimens subjected to fatigue in long life region in RH 85% (Arrows indicate crack tips)

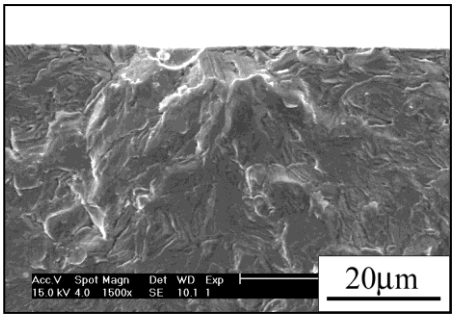

(a-1) Crack initiation site

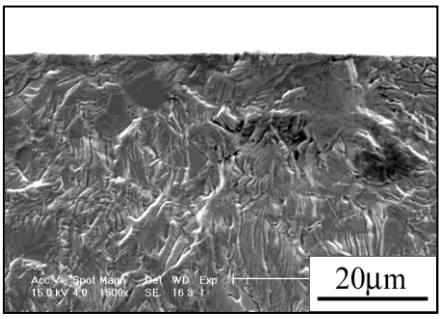

(b-1) Crack initiation site

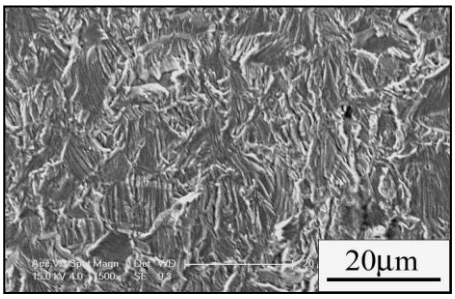

(a-2) Inner area (~200μm from surface)

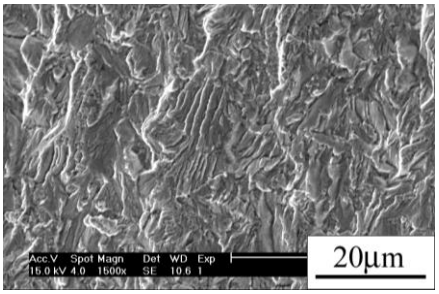

(b-2) Inner area (~200μm from surface)

Figure 7. Fracture surfaces of SA-P steel tested in (a) RH 25% and (b) RH 85%

Similar fatigue morphology can be found in DA-U steel tested in high humidity, as shown in Fig. 8. It is hard to distinguish any difference in fracture mechanism between the SA-P and the DA-U steels failed in high humidity, depending on the analysis of the results shown in Figs. 7 and 8. Therefore, it may be induced that the propagation of small cracks was accelerated by embrittlement due to hydrogen generated in cathode reaction. In addition, most of fracture surfaces in the region beyond crack initiation are occupied by martensite lath cracking regardless of humidity and aging condition, which may explains that little difference in growth rate of larger cracks is recognized between different aging conditions and humidity, as seen in Fig. 5.

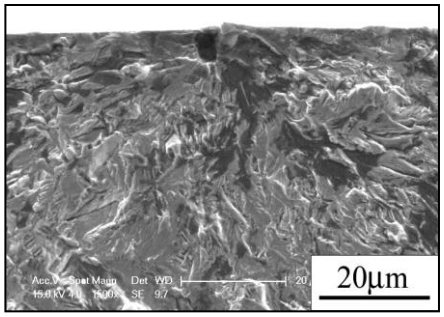

(a) Crack initiation site

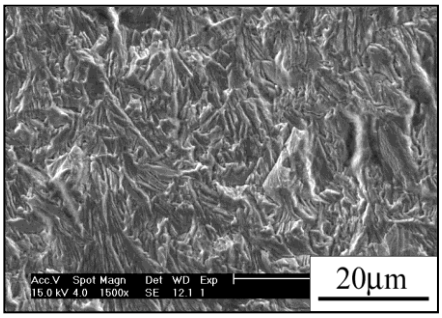

(b) Inner area (about 200μm from surface)

Figure 8. Fracture surfaces in DA-U steel at RH 85%

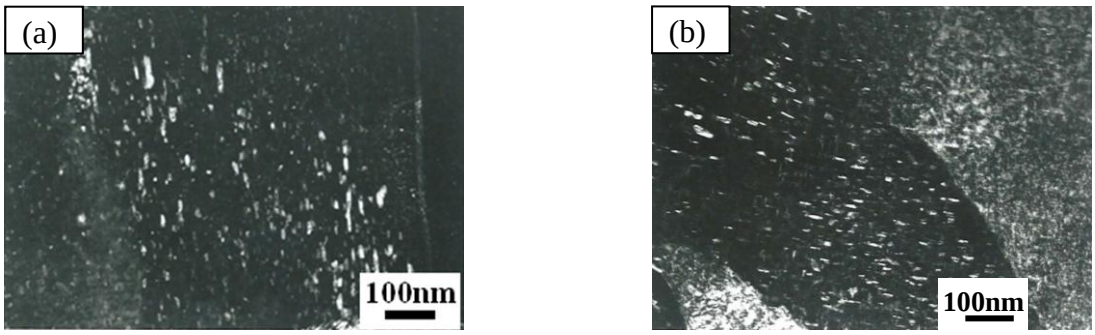

Figure 9. TEM micrographs showing microstructure of (a) SA-P and (b) DA-U

Figure 9 shows microstructures of SA-P and DA-U steels observed by TEM. Rod-shaped particles of ~10nm or less in length and spherical ones are observed in SA-P steel, which were identified as Ni3(Ti, Mo) and FeMo respectively by their diffraction patterns of TEM and the X-ray diffraction of electrolyte-extracted particles. In DA-U steel, it is difficult to confirm different particles by means of their microstructural features. Tewari et al. reported that fine particles of nano-sized ω-phase precipitated at low aging temperature in DA-U steel [5]. However, any other precipitates were difficult to distinguish, though it can be predicted from the phase diagram of Fe-Mo alloy that Mo atoms are supersaturated during the second aging at 473 K. Since a high density of dislocations are initially introduced by martensitic transformation, the supersaturated Mo atoms may migrate by the pipe diffusion along those dislocations so as to form the moderation of concentration or the clusters around the dislocations, which impede the motion of dislocations and cause the hardening at 473 K. DA-U steel is in such a way strengthened by the second aging at 473k.
On the other hand, in high humidity, hydrogen atoms generated in accompany with anodic reaction may diffuse into the matrix and concentrate at grain boundaries, inducing hydrogen embrittlement [9, 10]. It is concerned that the clusters of supersaturated Mo atoms around dislocations and the irregularity of concentration in the second aging may trap some hydrogen so as to suppress hydrogen embrittlement in high humidity.

4. Conclusions

The effect of aging condition on the fatigue strength of 18% Ni maraging steel of grade 350 in long life region in high humidity was investigated under rotating bending in relative humidity of 25% and 85%. Fatigue strength of both single aging and double aging hardened steels was markedly decreased in high humidity environment. However, the decrease of fatigue strength was suppressed by the double aging. Although most of fracture surface was characterized with lath boundary cracking regardless of the humidity and aging condition, a few brittle facets of prior austenite comparable to a grain size were observed at the origin of fracture in high humidity. The main reason for the decrease of fatigue strength in high humidity was the acceleration of both crack initiation and its early growth due to hydrogen embrittlement. The decrease in humidity susceptibility by the

double aging was explained by the precipitation of supersaturated Mo atoms as well as the fine particles of nano-sized ω-phase diffused in the matrix during the second aging of lower temperature.

Acknowledgements

Chen is grateful to the financial supports by JSPS KAKENHI through grant number 22560097 and by JKA through grant number JS23-99.

References

[1] R. F. Decker, C. J. Novak, T. W. Londig, Developments and projected trends in maraging steels, Journal of Metals, (1967) 60-66.

[2] G. W. Tuffnell, D. L. Pasquine, J. H. Olson, An investigation of fatigue behavior of 18% nickel maraging steel, Transactions of the ASM, 59(1966) 769-783.

[3] Y. Murakami , M. Shimizu, Effects of nonmetallic inclusions, small defects and small cracks on fatigue strength of metals, Transactions of the Japan Society of Mechanical Engineers, A, 54(1983) 413-425.

[4] K. Endo, K. Komai, T. Fujimoto and Y. Matsuda, "Fatigue crack growth under stress corrosion of a high strength steel", Transactions of the Japan Society of Mechanical Engineers, A, 45(1979) 1152-1159.

[5] R. Tewari, S. Mazumder, I.S. Batra, G.K. Dey and S. Banerjee, Precipitation in 18 wt% Ni maraging steel of grade 350, Acta Materials, 48(2000) 1187-1200.

[6] N. Kawagoishi, K. Kariya, T. Nagano, Y. Nakamura, Effect of second-stage-aging on the fatigue properties of maraging steel, Proceedings of 13th International Conference on Fracture, CD-ROM(2013) to be published.

[7] M.F. Garwood, H.H. Zurburg, M.A. Ericson, Interpretation of tests and correlation with service, "Correlation of laboratory tests and service performance", American Society for Metals, (1951) 1-77.

[8] H. Kobayashi, H. Nakazawa, A. Komine, Fatigue fracture toughness of maraging steel, Transactions of the Japan Society of Mechanical Engineers, 41(1975) 9-21.

[9] R.O. Ritchie, M.H. Cantro Cedemo, V.H. Zackey, E.R. Parker, Effects of Silicon additions and retained austenite on stress corrosion cracking in ultra strength steels, Metallurgical Transaction, 9A(1978) 35-40.

[10] N. Kawagoishi, T. Nagano, M. Moriyama, Y. Ohzono, T. Ura, Effect of humidity on fatigue strength of maraging steel, Transactions of the Japan Society of Mechanical Engineers, Series A, 71(2005) 600-606.

Influence of Deformation-Induced alpha prime Martensite on the Crack Initiation Mechanism in a Metastable Austenitic Steel in the HCF and VHCF Regime

Martina Zimmermann[1,*], A. Grigorescu[2], C. Müller-Bollenhagen[3], H.-J. Christ[2]

[1] Institut für Werkstoffwissenschaft, Technische Universität Dresden, Dresden 01062, Germany
[2] Institut für Werkstofftechnik, Universität Siegen, Siegen 57068, Germany
[3]Continental Teves AG & Co. oHG, Hannover 30419, Germany
* Corresponding author: martina.zimmermann@tu-dresden.de

Abstract
Fatigue failure in the VHCF regime of high strength steels is dominated by subsurface crack initiation around non-metallic inclusions with fisheye fracture morphology. However, this unique failure mechanism cannot be thoroughly confirmed for metastable austenitic steel 1.4301 (AISI 304), for its crack origin is heavily dependant on fatigue life and its amount of deformation-induced alpha prime martensite. In the HCF regime cracks originate at the specimen surface from inclusions exceeding 0.02 mm, irrespective of the volume fraction of deformation-induced alpha prime martensite. For a volume fraction beyond $V_M = 30\%$ the higher notch sensitivity of the martensite phase can lead to crack initiation at micro flaws at the surface. In the VHCF regime the influence of the martensite content is even more dominant, as for $V_M = 54\%$ the crack origin shifts to subsurface inclusions. While the formation of a fine granular area is observed for all cases with $V_M > 50\%$, the occurrence of a typical fisheye morphology depends on the inclusion's relative position to the specimen's surface. The diversity of crack initiation mechanisms can be explained by the interaction of the austenite and martensite phases and its different ductilities with the inclusions as shown by TEM micrographs and Murakami's model of hydrogen-induced VHCF failure.

Keywords
Very high cycle fatigue, metastable austenitic steel, deformation induced martensite, fisheye fracture

1. Introduction

In recent years, many investigations (e.g. [1,2]) focused on the diversity of damage mechanisms related to failure beyond the classical fatigue limit, i.e. at a number of loading cycles $N > 10^7$. At an early stage of research on the fatigue of materials in the very high cycle range, a distinction between single phase and defect free type I materials and multiphase type II materials with microstructural defects such as non-metallic inclusions or pores was proposed by Mughrabi [3,4]. The discussion about the fatigue behaviour of the two types of materials at very high number of cycles and the underlying damage mechanisms is often combined with hypotheses of the course of the S–N curve such as a duality of the curve related to the crack initiation position [5,6]. For type II materials a multistage S–N curve is defined by the change from surface crack initiation to a control of fatigue life by crack nucleation at internal defects. With regard to high strength steels, different models for damage mechanisms and the multistage S-N curve are currently under discussion.

Murakami et al. [7] related the formation of a so-called fisheye fracture surface, which is commonly observed in these types of materials in the VHCF range, to a hydrogen embrittlement due to a hydrogen concentration in the vicinity of inclusions. According to Murakami and Endo, the VHCF behavior can be correlated to the size and hardness of nonmetallic inclusions [8]. A different explanation was suggested by Sakai et al. [9] stating that the fisheye formation by means of the formation of a fine granular layer around the inclusion is a consequence of a nucleation and coalescence of microdebondings. The formation of fisheye fractures due to multiple microcracks initiated by the decohesion of spherical carbides from the matrix around the dominating inclusion is given as the major damage mechanism model by Shiozawa et al. [10]. This model was confirmed

by the findings of Sohar et al. for a high Cr alloyed cold worked tool steel, where internal as well as near surface fisheye fracture was observed in the VHCF regime and attributed to the formation and coalescence of microcracks around carbide clusters [11]. Despite these findings not all steels containing nonmetallic inclusions can be classified in one of the given models. Results for the HCF and VHCF behavior of a metastable austenitic stainless steel presented in this paper demonstrate that both the actual cyclic strength of a material, the course of the S–N curve and the underlying damage mechanisms are highly sensitive to microstructural changes.

2. Material and Experimental Methods

The material chosen for this study was a solution annealed metastable austenitic stainless steel sheet AISI304 (1.4301) with a thickness of 2 mm. Its chemical composition determined by means of spectral analysis is given in table 1. A relatively low stability of the austenite phase is caused by the low amount of nickel in the overall alloy composition. The deformation induced α' martensite content was regulated by a one-step predeformation carried out by means of a servohydraulic test system equipped with a liquid nitrogen-cooled chamber, allowing a deformation start temperature of -100°C. Before fatigue testing, all specimens were mechanically and subsequently electro-chemically polished but for several reference specimens with artificial micronotches at the surface. For the fatigue experiments two testing systems were used: a resonance pulsation test stand operating at ~ 90 Hz and an ultrasonic fatigue testing system working at a frequency of ~ 20 kHz. All fatigue experiments were executed in a fully reversed mode under load control. Specimens' heating was averted by cooling with compressed air and in addition by a pulse-pause testing mode for the ultrasonic system. The alpha prime martensite volume fraction was measured by means of a magneto-inductive testing device (Fischer feritscope).

The characterization of microstructure and the fractographic analysis of the fatigued samples were accomplished by means of a scanning electron microscope (FEI, Helios) equipped with an ion source which permits a selective removal of lamellae for transmission electron microscopy (Hitachi).

Table 1. Chemical composition of the alloying elements for AISI304 analysed by means of spectral analysis.

C	Si	Mn	P	S	Cu	Cr	Mo	Ni	V	N
0,024	0,43	1,43	0,021	0,007	0,14	18,3	0,038	8,11	0,1	0,067

3. Results

3.1 Fatigue behavior

Fatigue results are given in figure 1a, open symbols indicate samples that were solely tested with the resonance system up to 10^8 cycles while crossed symbols represent samples fatigued firstly with the resonance pulsation system up to cyclic saturation and subsequently with the ultrasonic system. In the fully austenitic condition the metastable austenitic steel studied exhibits a constant fatigue limit of 250 Pa in the HCF and the VHCF region. No failure happened even up to a number of loading cycles $N > 10^8$. A true durability for $N > 10^6$ cycles for AISI304 in the fully austenitic condition is confirmed by various authors [12-15] except for the work by Bathias [16], who observed failure in the VHCF regime for this steel type. In the fully austenitic condition the material's fatigue behavior is dominated by a strong transient behavior with a pronounced cyclic softening up to $N \sim 10^5$ followed by cyclic hardening up to 2×10^7 cycles. More details of the correlation between the cyclic deformation behavior of the material presented and its resonance behavior is given in [17]. The cyclic hardening can be explained by a martensite formation which

results in a decrease of the strain amplitude. Hence, the global loading situation declines well below a threshold value for irreversible slip activities so that the fatigue limit can be regarded as a true infinite durability for the fully austenitic condition. However, the martensite formation during cyclic loading in the VHCF regime is quite surprising as the plastic strain amplitude (3×10^{-4}) is well below the threshold value for martensite formation of 3×10^{-3} according to literature.

The fatigue behavior of specimens in the one-step predeformed condition displays a steady increase of cyclic strength in the HCF regime with increasing volume fraction of deformation induced martensite (Figure 1a). At the same time the disposition to a transient behavior during cyclic deformation fades. For the HCF regime the fatigue limit increases with increasing martensite volume fraction. However, this is only true for specimens with a well preserved surface without flaws and defects. In case of artificial micro notches (with a depth of 12 up to 40 µm) at the surface a peak cyclic strength could be identified for a volume fraction of α' martensite $\leq 30\%$. A comparison of actively cooled and uncooled fatigue tests demonstrate the influence of α' martensite formation on the cyclic strength during testing. The lack of active cooling prevents the formation of α' martensite and as a consequence lowers the cyclic strength drastically (figure 1b).

For the VHCF regime a change in the fatigue behavior can be observed with increasing volume fraction of alpha prime martensite. For a volume fraction of 54% failure occurs even beyond the classical fatigue limit resulting in a two-step S-N-curve with crack initiation up to a number of loading cycles $N > 10^8$. Therefore it stands to reason that a change in damage mechanism due to the degree of phase transformation is inherent for AISI304. This phenomenon can be explained by the metallographic analysis presented in the subsequent chapter.

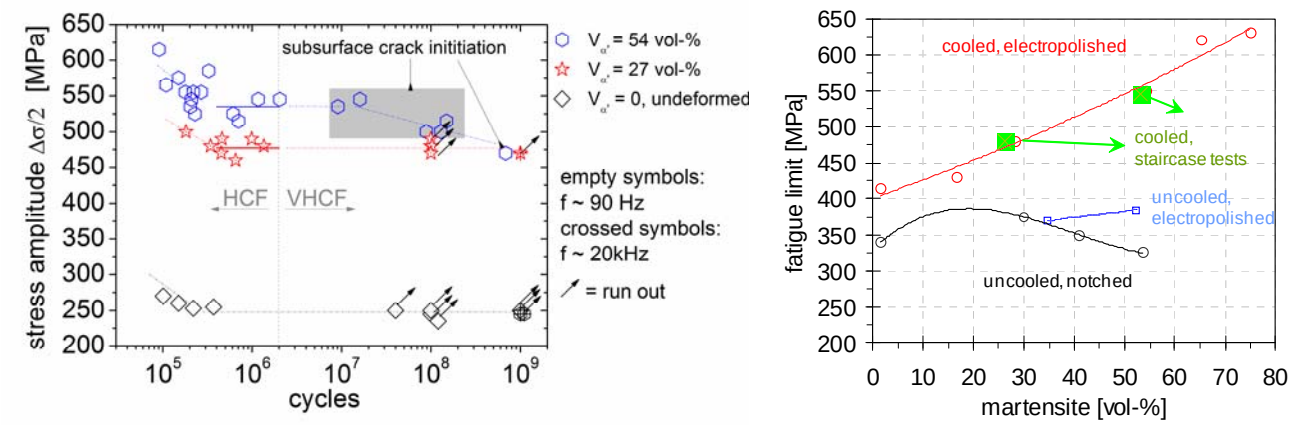

a) b)

Figure 1: Fatigue behavior in the HCF and VHCF regime (a) and comparison of fatigue limit for the HCF region related to different testing conditions and samples with artificial micro notches (b).

3.2 Damage mechanisms

The fatigue behavior of AISI304 in the fully austenitic condition is characterized by two major microstructural processes: inhomogeneously distributed strain localization in narrow slip bands and formation of α' martensite at intersections of slip bands as well as formation of martensite needles (figure 2). The phase transformation leads to a decrease of dislocation mobility and hence to an increase in cyclic strength and a true durability in the VHCF regime. Fractographic analysis of the specimens tested and failed in the HCF region (here: failure only for $N < 10^6$) reveal the importance of microstructural flaws and defects at or near the specimens surface. All failures in the HCF regime can be attributed to crack initiation at nonmetallic inclusions in the near-surface region (figure 3a).

However, inclusions with a size up to 20 μm did not result in HCF failure. In contrast, artificial micro notches at the surface are the reason for a decline of the fatigue strength in the HCF region for higher α' martensite volume fractions (figure 3b), which can be ascribed to the higher notch sensitivity of the martensite phase. According to Bowe et al. [18] the threshold value for fatigue crack growth for the fully austenitic condition of a FeNiAl-alloy is five times higher than that for the martensitic condition. It can therefore be assumed, that a higher amount of martensite phase enclosing a surface defect results in an earlier crack initiation and accelerated crack growth.

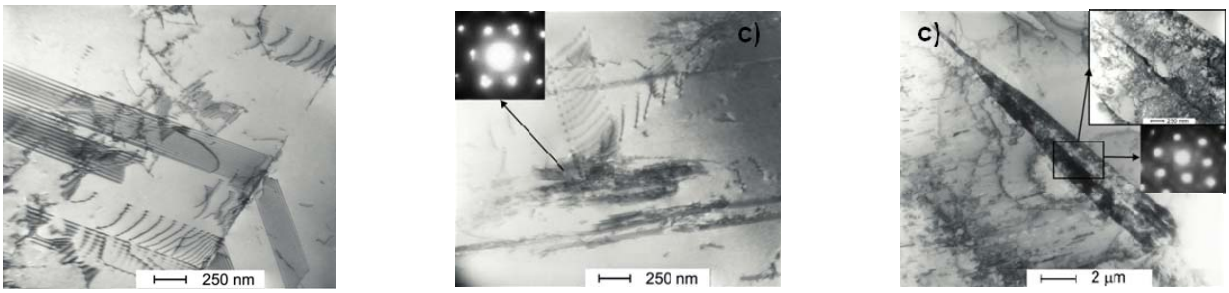

a) b) c)

Figure 2: Formation of slip bands (a), α' martensite in the bulk at slip band intersections (b) and a martensite needle (c) during cyclic loading at σ = 240 MPa and N = 10^7.

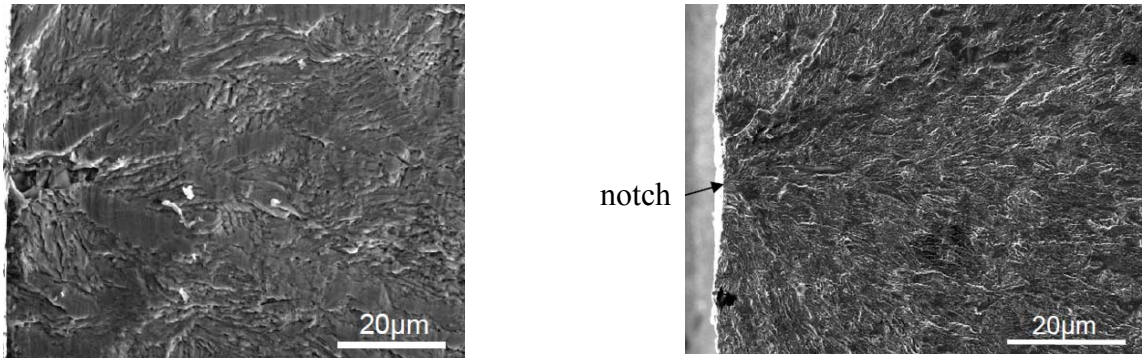

a) b)

Figure 3: Crack initiation in the HCF region at a surface inclusion for a specimen with 27% α' martensite volume fraction (a) and at an artificial micro notch for 30% α' martensite volume fraction (b).

A one-step predeformation leads to a pronounced increase of the cyclic strength for AIS304, but at the same time to failure even in the VHCF regime for an α' martensite volume fraction of 54%. This change in damage mechanism can be explained by comparing the microstructure of the fully austenitic with the predeformation condition. The major difference lies in the amount and distribution of α' martensite. For a volume fraction of 27% the α' martensite is loosely allocated at slip band intersections (figure 4a) and the local notch stress around an inclusion leads to a concentration of the deformation in the softer austenite phase (represented for a fully austenitic condition in figure 4c) and a formation of deformation induced martensite. The localized work hardening and the compression stresses due to phase transformation impede crack initiation at the inclusion. Interconnected clusters of α' martensite dominate the microstructure for a volume fraction of 56% (figure 4b). Due to the coherency of the martensite clusters, the deformation is no longer compensated by the softer austenite phase and the low ductility of the martensite phase results in crack initiation even at stress amplitudes in the VHCF range. Figure 5 depicts an example for crack initiation at an elongated inclusion for a sample with a volume fraction of martensite > 30%. The crack starts in the austenite phase leading to a brittle fracture of the inclusion before propagating into the notch-sensitive martensite phase. This example demonstrates that an inclusion does not necessarily have to be completely surrounded by the martensite phase. Elastic deformation in the martensitic phase might already be sufficient to have a crack initiating effect in the austenitic

phase in the vicinity of an inclusion.

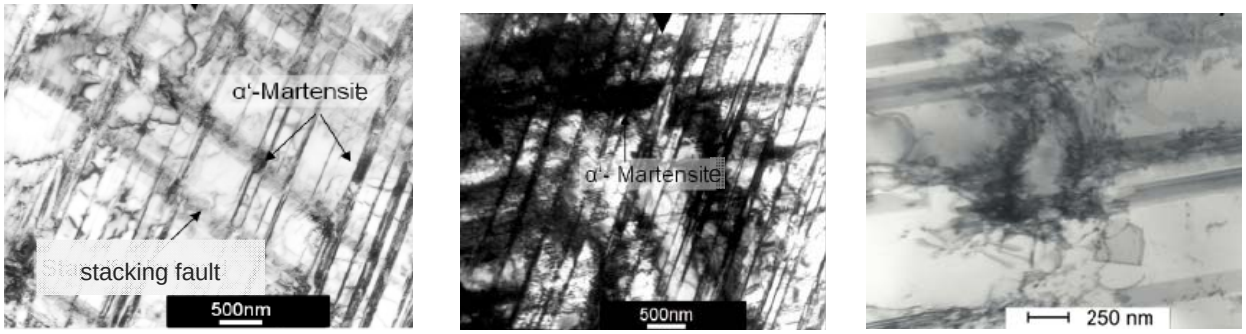

a) b) c)

Figure 4: Phase morphology after the formation of predeformation-induced α' martensite with a volume fraction of 27% (a) and of 54% (b) produced by different deformation start temperatures and dislocation coalescence around an inclusion (c).

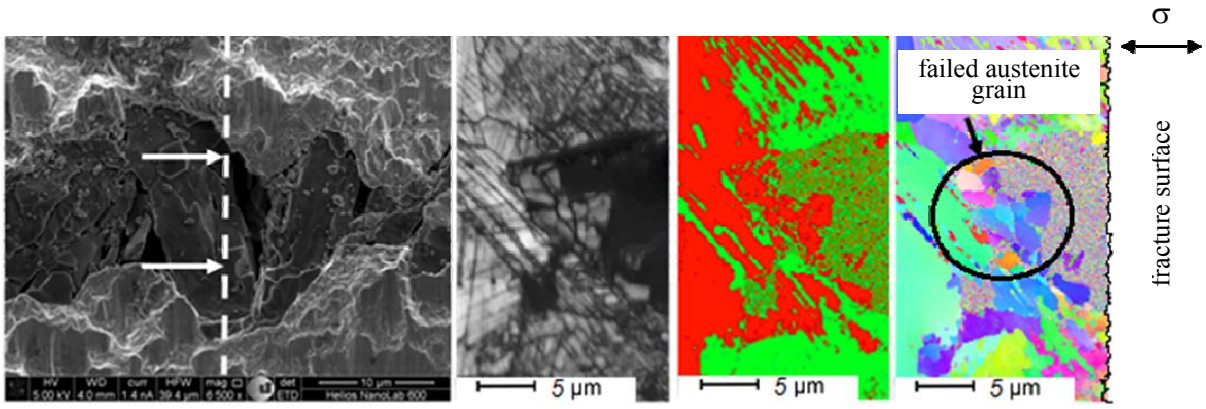

a) b) c) d)

Figure 5: Crack initiation at an inclusion (a), image quality of the inclusion in the direction perpendicular to the fracture surface (b), phase distribution around the inclusion (c) with red = austenite phase and green = martensite phase and inverse pole figure of the inclusion and its surrounding matrix (d).

The VHCF failure for AISI304 with a volume fraction of α' martensite > 30% is accompanied by a change of the crack initiation site from the surface to the specimen interior irrespective of the fact that inclusions encircled by clusters of martensite can also be found in the surface region. The fracture surface of the specimens failed in the VHCF region show a typical fisheye morphology. The crack initiation site is surrounded by a fine granular area (FGA), which according to Sakai [9] is characteristic for the VHCF failure of martensitic steels. The FGA for its part is encompassed by a smooth fracture surface which gives the typical fish-eye appearance. According to Murakami and Matsunaga [19] the cyclic stress intensity factor at the outer front of the FGA can be estimated by

$$\Delta K_{FGA} = 0.5\Delta\sigma\sqrt{\pi\sqrt{area_{FGA}}} \ .$$

An analysis of all specimens' FGAs, which failed in the VHCF regime (figure 1a), result in an average ΔK_{FGA} = 4 MPa√m beiing in good correlation with the threshold value for crack growth of the martensitic phase ΔK_{th} = 5 MPa√m as investigated by Bowe et al. [18]. Hence, the formation of FGA can be regarded as crack initiation phase provided one assumes that the ΔK-concept can be applied for the given VHCF failure mechanism. This phenomenon strongly depends on the number of loading cycles as depicted in figure 6a. There is a steady increase of FGA diameter with increasing number of loading cycles. After reaching a critical value (corresponding to ΔK_{FGA}) a

different crack growth mechanism emerges, developing a rather smooth fracture surface which together with the FGA forms the characteristic fisheye morphology. The cycle dependence of FGA formation explains the dual step S-N-curve (figure 1a). In the VHCF regime a minimum number of cycles is necessary before continuous crack growth in the form of the smooth fisheye fracture surface results in overall failure.

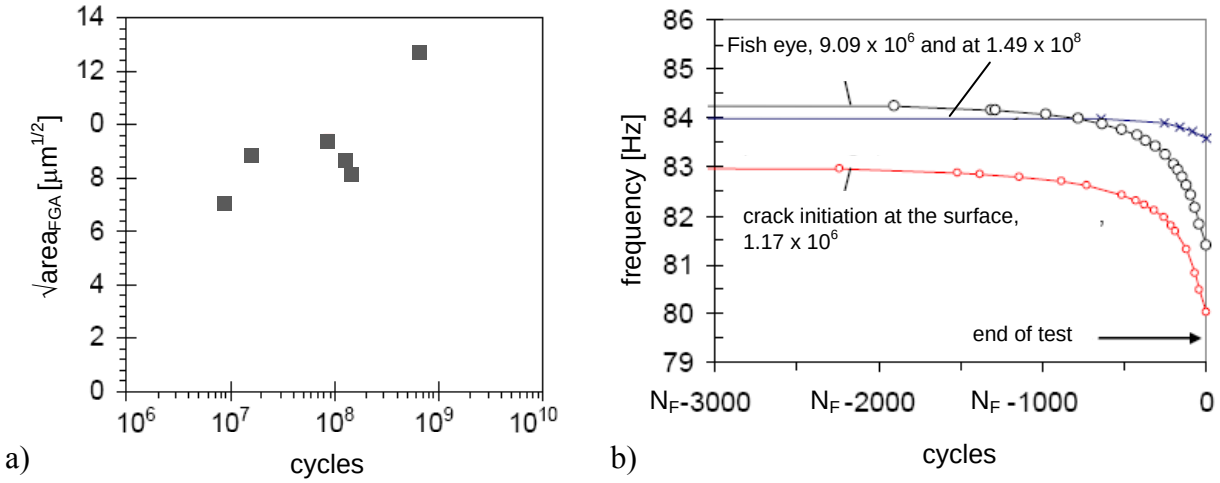

Fig. 6: Correlation between √area of the FGA and number of loading cycles (a) and correlation between fisheye formation and resonance frequency (b).

The smooth fracture surface of the fisheye develops as long as the crack growth is still within the interior of the specimen. Hence, the size of the fisheye fracture is directly correlated to the distance of the crack initiating inclusion to the specimen's surface as is depicted in figure 7 for several fracture surfaces. It is well known that crack growth under vacuum is retarded compared to crack growth in air for the material analyzed [20]. As a consequence, cracks will propagate very slowly since vacuum like conditions are still given while the crack front has not yet reached the surface, but will gain momentum the very moment the crack front touches the surface. A correlation between fisheye diameter (150 µm up to 1000 µm) and a predicted as well as measured change in resonance frequency during fatigue testing (figure 6b) revealed, that the formation of fisheye is limited to 2000-3000 cycles of the overall fatigue life. Hence, the major part of fatigue life in the VHCF regime is dominated by the formation of the FGA.

As the development of a FGA is the fatigue life dominating feature, its formation mechanism should be further discussed. Different assumptions as to the origin of the FGA were presented in the introducing chapter. According to Shiozawa et al. [10] the FGA is formed by a decohesion of finely dispersed carbides in the microstructure. This assumption is not plausible for AISI304 with its negligible carbon content (0.02 mass-%). Neither carbides nor microcracks at carbides could be detected in the FGA environment of the specimens (depicted in figure 7) by means of scanning electron microscopy and EDS-analysis. The suggestion made by Sakai [9], that FGA is formed due to a polygonization of very fine subgrains is yet to be discussed as no pronounced fine grained structure could be detected in the crack initiation region.

Murakami et al. [21] assumed that hydrogen trapped at the inclusion leads to the formation of FGAs due to the higher dislocation mobility in the presence of hydrogen. Hydrogen can lead to accelerated crack propagation in the martensitic phase of a metastable austenitic connected and moreover, the hydrogen diffusion coefficient in martensite is four orders of magnitude higher than that in the austenitic phase. Therefore, the model of hydrogen-assisted crack initiation at an

inclusion is assumed as most likely explanation for the formation of FGAs in AISI304 at VHCF-relevant numbers of cycles. Hence, crack initiation and FGA formation is the consequence of agglomerated hydrogen in the martensitic phase around the inclusion increasing the amount of localized plastic deformation in this particular microstructural region. However, this assumption has to be further discussed as in the study presented no final evidence for hydrogen assisted crack initiation was found. Fatigue crack growth tests simulating the microstructural and testing conditions discussed will be necessary for further clarification.

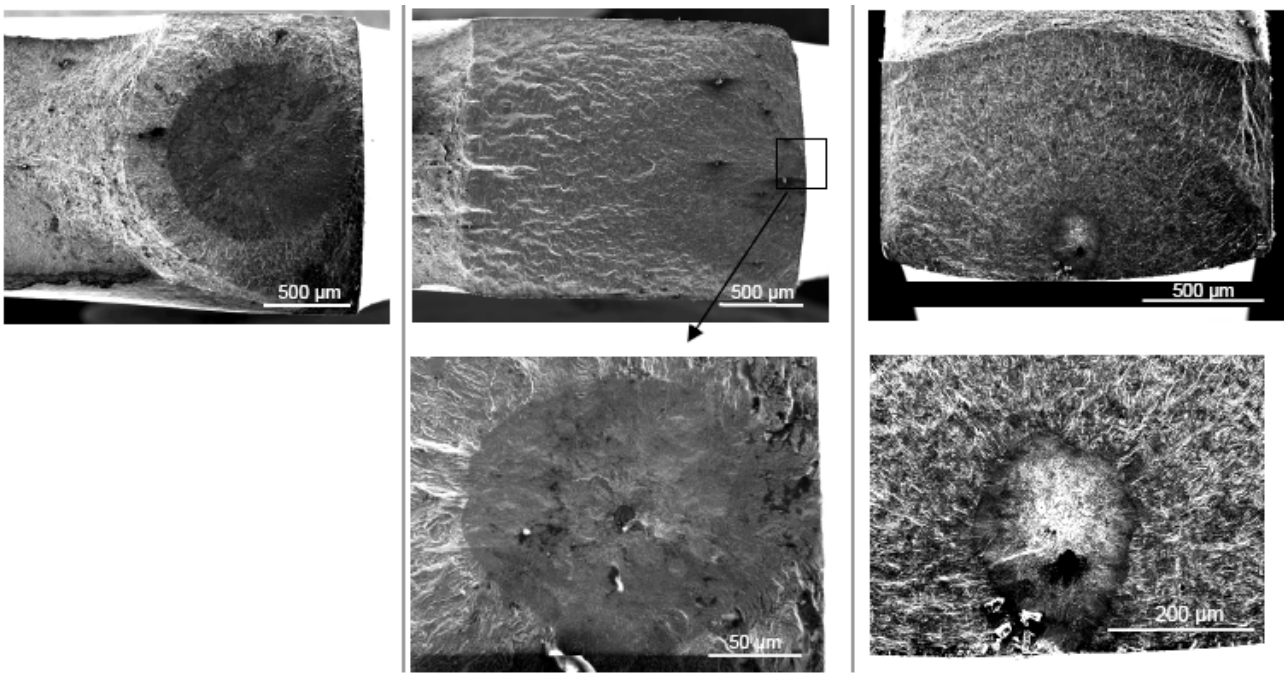

a) b) c)

Fig. 7: Examples for the formation of fisheye fracture morphology with different sizes (depending on the distance between inclusion and specimen surface) a) $\Delta\sigma/2$ = 515 MPa, N_F = 1.49 x 10^8, b) $\Delta\sigma/2$ = 535 MPa, N_F = 9.09 x 10^6 and c) $\Delta\sigma/2$ = 470 MPa, N_F = 6.84 x 10^8.

4. Conclusion

The study presented discusses the change in failure mechanisms of a metastable austenitic steel – an alloy that would typically be classified as material type II with respect to its VHCF behavior – as a function of its volume fraction of deformation-induced α' martensite. In the HCF region AISI304 always failed at inclusions at or very near to the surface, irrespective of its volume fraction of α' martensite. Only surface flaws of a certain size led to earlier failure for a martensite content > 30%. No failure was observed in the VHCF regime for the fully austenitic condition. The VHCF behavior can be explained by the local work hardening of the soft austenitic phase and a very localized phase transformation, both resulting in a decrease of strain amplitude. Hence, the load controlled fatigue tests no longer causes a strain amplitude exceeding a threshold value for crack initiation or microcrack propagation.

In case of an α' martensite volume fraction of 27% a true durability can still be confirmed together with an increase of cyclic strength from ~250 MPa to ~480 MPa compared to the fully austenitic condition. A surface roughening could be observed for the 27% specimens but did not result in crack initiation. However, failure mechanism changes completely with a higher amount of α' martensite volume fraction. A volume fraction of 54-56% leads to a formation of connected

martensite clusters. The localized plastic deformation can no longer be compensated by the softer austenite phase nor will the strain amplitude be reduced due to a local phase transformation. Moreover, it is assumed that hydrogen trapped in the vicinity of inclusions in the specimen's interior increases the dislocation mobility in this region and at the same time promotes the brittleness of the martensitic phase. Inclusions surrounded by such brittle martensite act as local stress raisers and lead to crack initiation in the form of a fine granular area. Fisheye morphology was observed for all specimens that failed in the VHCF regime and the typical smooth fracture surface surrounding the FGA can be explained by crack growth under vacuum-like conditions. A schematic summary of the different failure mechanisms of AISI304 determined for the VHCF behavior is presented in figure 8.

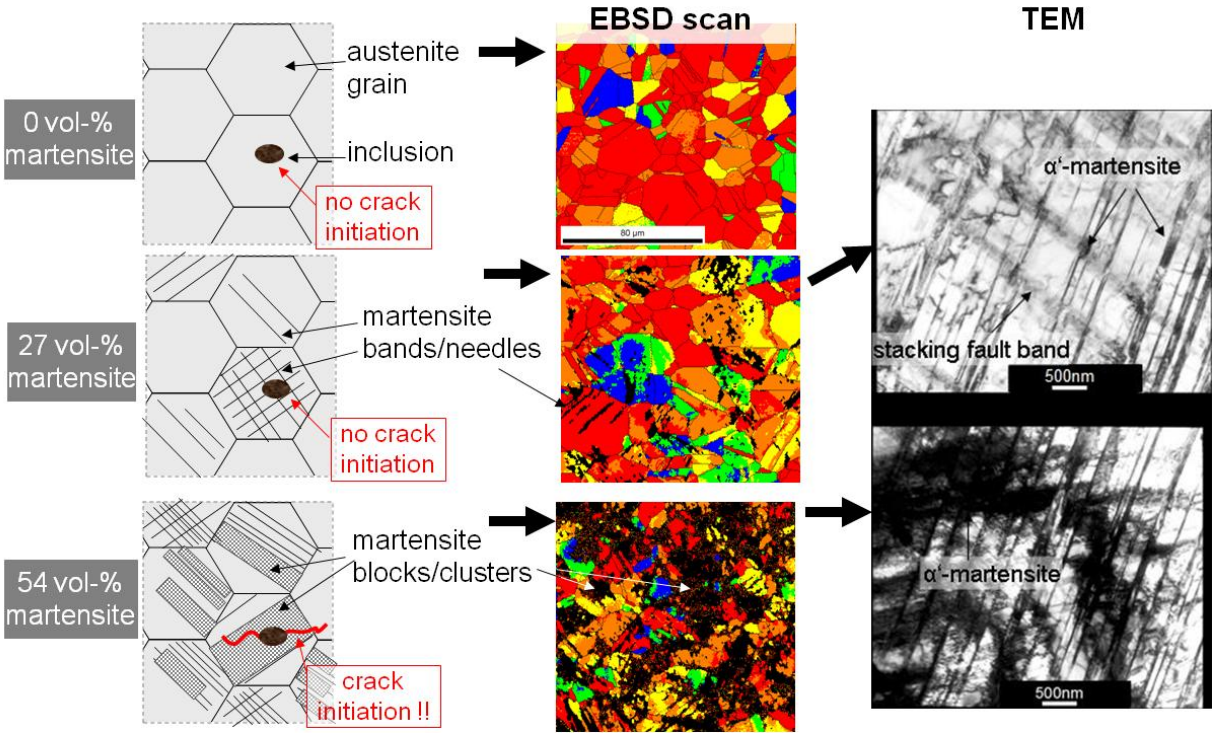

Fig. 8: Change in failure mechanism for VHCF crack initiation in correlation with the volume fraction of α' martensite.

Acknowledgements

The authors gratefully acknowledge the financial support of this study by Deutsche Forschungsgemeinschaft (DFG).

References

[1] M. Zimmermann, Diversity of damage evolution during cyclic loading at very high numbers of cycles – An overview, Int. Mater. Rev., 57 (2012) 73-91.

[2] S. X. Li, Effects of inclusions on very high cycle fatigue properties of high strength steels, Int. Mater. Rev., 57 (2012) 92-114.

[3] H. Mughrabi, Specific features and mechanisms of fatigue in the ultrahigh-cycle regime, Int. J. Fatigue, 28 (2006) 1501-1508.

[4] H. Mughrabi, On 'multi-stage' fatigue life diagrams and the relevant life-controlling mechanisms in ultrahigh-cycle fatigue, Fatigue Fract. Eng. Mater. Struct., 25 (2002)755-764.

[5] S. K. Jha, K. S. R. Chandran, An unusual fatigue phenomenon: duality of the S-N fatigue curve in the β-titanium alloy Ti-10V-2Fe-3Al, Scr. Mater., 48 (2003) 1207-1212.

[6] Y. Murakami, Mechanisms of fatigue failure in ultralong life regime in: S. Stanzl-Tschegg and H. Mayer (Eds), Proc. Int. Conf. on 'Fatigue in the very high cycle range', Vienna, Austria, University of Agricultural Sciences, 2001, pp. 11–22.
[7] Y. Murakami, T. Nomoto, T. Ueda, Factors influencing the mechanism of superlong fatigue failure in steels, Fatigue Fract. Eng. Mater. Struct., 22 (1999) 581–590.
[8] Y. Murakami, M. Endo, Effects of defects, inclusions and inhomogeneities on fatigue strength, Int. J. Fatigue, 16 (1994) 163–182.
[9] T. Sakai, Review and prospects for current studies on very high cycle fatigue of metallic materials for machine structural use, J. Soc. Mech. Eng. Int. J. Ser. A, 3A (2009) 425–439.
[10] K. Shiozawa, Y. Morii, S. Nishino, L. Lu, Subsurface crack initiation and propagation mechanism in high strength steel in a very high cycle fatigue regime, Int. J. Fatigue, 28 (2006) 1521–1532.
[11] C. R. Sohar, A. Betzwar-Kotas, C. Gierl, B. Weiss, H. Danninger, Gigacycle fatigue behavior of a high chromium alloyed cold work tool steel, Int. J. Fatigue, 30 (2008) 2191–2199.
[12] T. H. Myeong, Y. Yamabayashi, M. Shimojo, Y. Higo, A new life extension method for high cycle fatigue using micro martensitic transformation in austenitic stainless steel, Int. J. Fatigue, 19 (1997) 69-73.
[13] T. Nebel, Verformungsverhalten und Mikrostruktur zyklisch beanspruchter metastabiler austenitischer Stähle, Dissertation, 2002, Kaiserlautern.
[14] M. Hayashi, K. Enomoto, Effect of preliminary surface working on fatigue strength of type 304 stainless steel at ambient temperature and 288°C in air and pure water environment, Int. J. Fatigue, 28 (2006) 1626-1632.
[15] M. Nakajima, M. Akita, Y. Uematsu, K. Tokaji, Effect of strain-induced martensitic transformation on fatigue behavior of type 304 stainless steel, Proc. Eng., 2 (2010) 323-330.
[16] C. Bathias, Gigacycle fatigue in mechanical practice, Marcel Dekker, 2005, New York.
[17] P. M. Hilgendorff, A. Grigorescu, M. Zimmermann, C.-P. Fritzen, H.-J. Christ, The effect of damage accumulation in slip bands on the resonant behavior in the very high cycle fatigue (VHCF) regime, Proc. of the 13th Int. Conf. on Fracture, 2013, Beijing.
[18] K. H. Bowe, E. Hammerschmidt, E. Hornbogen, M. Hühner, Bruchmechanische Eigenschaften von metastabilen Austeniten, Materialwiss. Werkstofftech., 19 (1988) 193-201.
[19] Y. Murakami, H. Matsunaga, The effect of hydrogen on fatigue properties of steels used for fuel cell systems, Int. J. Fatigue, 28 (2006) 1509-1520.
[20] A. J. McEvily, J. L. Gonzalez Velazquez, Fatigue crack tip deformation processes influenced by the environment, Metall. Trans., 23A (1992) 2211-2221.
[21] Y. Murakami, T. Nomoto, T. Ueda, On the mechanism of fatigue failure in the superlong life regime ($N > 10^7$ cycles), Part 1: Influence of hydrogen trapped by inclusions, Fatigue Fract. Eng. Mater.Struct., 23 (2000) 893-902.

Very High Cycle Fatigue Strength of a High Strength Steel under Sea Water Corrosion

Thierry PALIN-LUC[1)*], Claude BATHIAS[2)]

[1)] Arts et Metiers ParisTech, I2M, UMR CNRS, Universite Bordeaux 1,
Esplanade des Arts et Metiers, 33405 Talence Cedex, France
[2)] Universite Paris X, LEME, 50 rue de Sevres, 92410 Ville d'Avray, France
*Corresponding author: thierry.palin-luc@ensam.eu

Abstract The effect of sea water corrosion on the gigacycle fatigue strength of a martensitic-bainitic hot rolled steel used for producing off-shore mooring chains for petroleum platforms was studied. Three different environments and conditions: (i) air; (ii) air after pre-corrosion, (iii) air under real time artificial sea water flow (in situ) were considered for testing smooth specimens under fully reversed tension between 10^6 and 10^{10} cycles. A drastic effect of corrosion was observed. For the fatigue life greater than 10^8 cycles, the fatigue strength is reduced by a factor more than 5 compared with non corroded specimens (virgin). Corrosion pits due to pre-corrosion, if any, or pits resulting from corrosion in real time during cyclic loading are the crack initiation sites. The calculation of the mode I stress intensity factor at hemispherical surface defects (pits) combined with the Paris-Hertzberg-Mc Clintock crack growth rate model showed that the fatigue crack initiation regime represents most of the fatigue life in the VHCF regime. Original additional experiments shew physical evidences that the fatigue strength in the gigacycle domain under sea water flow is mainly governed by the corrosion process with a strong coupling between cyclic loading and corrosion.

Keywords Gigacycle fatigue, corrosion, steel, crack initiation, crack growth

1. Introduction

Mooring chains for off-shore petroleum platforms are loaded in VHCF regime and in sea water environment. They are designed for 30 years that is around 10^9 cycles because of the ocean waves 24 hours a day. The aim of this study is to study the gigacycle fatigue strength of the low-alloy steel used for manufacturing such chains and the effects on this strength of both pre-corrosion and corrosion in sea water environment. Many studies carried out on steel and aluminum alloys in the gigacycle regime have demonstrated that there is not a fatigue limit for such metals beyond 10^7 cycles as was believed in the past [1, 2]. It has been shown that fatigue cracks initiate mainly at surface defects in the short fatigue life regime, but may shift to subsurface in the long life range [3]. Other studies have shown that defects like non-metallic inclusions, pores [4] or pits [5 - 7] are the key factors, which control the fatigue properties of metals in very high cycle fatigue (VHCF). Furthermore, in some works it has been proven that crack initiation dominates the total fatigue life of specimens in gigacycle fatigue [8, 9]. On the other hand, the influence of static deformation has been studied confirming that both passive and transpassive current densities on stainless steel reach a maximum in the course of growing plastic strain [10]. Other works have investigated the dissolution of chemical products in stainless steel with active, passive and intermediate potentials where it is presumed that dissolution is enhanced during cyclic loading [11]. But the effect of aqueous corrosion on the fatigue strength with regard to crack initiation in the VHCF regime is not very much studied in literature. In this regime the material is loaded in its elastic domain at the macroscopic scale. In this work the effect of sea water corrosion (under free potential) on the VHCF strength will be studied.

After presenting the investigated material and the experimental conditions both for crack initiation tests and crack propagation tests, experimental results are presented and discussed with regard to the SEM observation of the fracture surface. It is shown that a drastic effect of sea water corrosion decreases the fatigue strength of the steel under sea water flow. The assessment of the crack growth helps us to show that crack initiation dominates the total fatigue life in the gigacycle regime.

Furthermore, additional experiments allow the authors to show experimental evidences of coupling between corrosion and cyclic loading even under ultrasonic loading frequency.

2. Material and experimental conditions

The material studied hereafter is a non-standard hot rolled low alloy steel grade (named R5 according to the International Classification Societies of Off-shore Systems) with a typical fine grain microstructure composed by tempered martensite and bainite as illustrated in [12]. Its chemical composition is shown in Table 1. This steel is used after a double quenching in water at 920°C then 880°C and tempering at 650°C with water cooling. After this heat treatment its mechanical properties are: hardness 317 HB, yield strength 970 MPa, UTS=1018 MPa, Young modulus *E*=211 GPa. It has to be noticed that this steel is vacuum degassed with low hydrogen content (1 ppm maximum in the liquid steel after the vacuum treatment). Furthermore, very low non-metallic inclusions are present in this steel (see details in [12]).

Table 1: composition of R5 steel (% weight, Fe balance)

C	Mn	Si	P	S	Cr	Ni	Mo	V	O
0.22	1.22	0.3	0.009	0.003	1.07	1.07	0.5	0.09	12

2.1. Fatigue test conditions and specimen geometry

2.1.1. Testing machine and specimen geometry

All the fatigue tests (crack initiation and crack growth) presented hereafter were carried out with an ultrasonic fatigue testing machine [1] operating continuously at 20 kHz (no pulse loading) under fully reversed tension (R= -1) (see [1, 12] for details). Figure 1 shows the dimensions of the two types of specimens used for (i) VHCF crack initiation tests and (ii) fatigue crack growth (FCG) tests. The geometry of the FCG specimens was designed according to the works of Wu [13] and Sun [14]. The crack growth was measured with an optical binocular microscope with a maximum magnification ×200. The roughness of the tested area of the VHCF specimens was *Ra*=0.6 µm and a few additional specimens with a better roughness (*Ra*=0.1 µm) were tested too for investigating the effect of roughness. The VHCF specimens were tested under three different conditions: (i) without any corrosion (virgin state), (ii) after pre-corrosion and (iii) under real time artificial sea water flow.

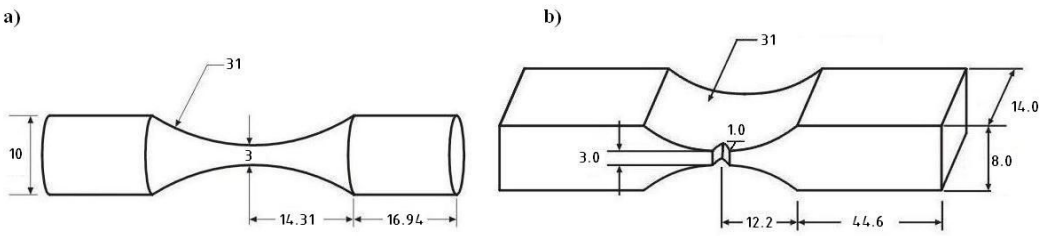

Figure 1: Specimen geometry for (a) VHCF tests, Kt=1.02 in tension, (b) crack growth tests (dimensions in mm).

All the VHCF tests were calibrated by using a wide band (0 to 100 kHz) strain gauge conditioner and a longitudinal strain gauge glued on the specimen surface. Such calibration allows the authors to be certain of the local strain (elastic stress) amplitude and mean value in the narrowest cross section of the specimen. These tests were carried out until a decrease of the resonance frequency of 0.5 kHz that indicates the presence of a macrocrack.

2.1.2. Corrosion of the specimens

The pre-corrosion of the specimens was done according to the ASTM G85 standard: 600 hours in a salt fog corrosion chamber under temperature and humidity control (35°C with 95% of humidity). The salt solution contained 5% of NaCl, its pH was 6.6 and it was applied in the chamber with a

flow rate of 1.52 ml/h. After the pre-corrosion process the specimens were first chemically cleaned and then cleaned with emery paper to remove the oxide layer. Many corrosion pits were created by the salt fog (Figure 2) their diameter is about 30 to 80 µm.

To carry out VHCF tests in sea water environment a special corrosion cell was designed (see [12] for details). To avoid any cavitation it was decided to test the specimens under sea water flow (without immersion). This is representative of the splash zone of the mooring chains. To do that a peristaltic pump creates a flow of sea water (100 ml/min) on two opposite sides of the specimen surface in the tested area (diameter 3 mm). The sea water used was the A3 standard synthetic sea water; its chemical composition in % weight is: 24.53% NaCl, 5.2% MgCl, 4.09% Na_2SO_4, 1.16% Ca_2Cl, 0.695% CaCl and 0.201% $NaHCO_3$. The pH of this solution is 6.6 and no electrical potential was applied between the corrosion solution and the specimens. The temperature of the sea water was 20 – 25°C (room temperature).

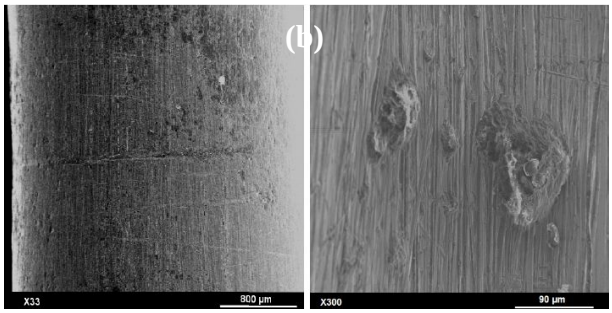

Figure 2: a) Surface of a specimen after pre-corrosion in the salt fog chamber, b) zoom on a corrosion pit.

2.1.3. Fatigue crack growth tests

Fatigue crack growth tests were carried out under fully reversed tension (R=-1) in mode I following a similar methodology than prescribed in ASTM E647 standard. Since with the ultrasonic fatigue testing device the specimen was loaded under displacement control, the range of the stress intensity factor ΔK was computed according to references [13, 14]:

$$\Delta K = U_o \left(\frac{E}{1-\nu^2} \right) \sqrt{\frac{\pi}{a}}\, Y(a/w) \tag{1}$$

with $Y(a/w) = 0.635(a/w) + 1.731(a/w)^2 - 3.979(a/w)^3 + 1.963(a/w)^4$. U_0 is the displacement amplitude imposed at the top of the specimen by the horn of the ultrasonic fatigue testing machine, E is the dynamic modulus and ν is the Poisson ratio of the material, $Y(a/w)$ is a function depending on the specimen geometry, a is the crack length and w is the width of the specimen:

3. Experimental results and discussion

3.1. Fatigue crack initiation tests

Figure 4 shows the S-N curves of the crack initiation tests. A decreasing of around 50 MPa of the fatigue strength for the specimens with pre-corrosion is observed compared to the specimens without any corrosion. The scatter of the fatigue strength of pre-corroded specimens is larger than for virgin ones. There is a drastic effect of sea water flow on the fatigue strength of the R5 steel in the VHCF fatigue regime. Indeed, for the specimens tested under sea water flow, the fatigue strength at 10^7 cycles is around 300 MPa, not far from the value for pre-corroded specimens (360 MPa), but for 3×10^8 cycles the fatigue strength is around 100 MPa only.

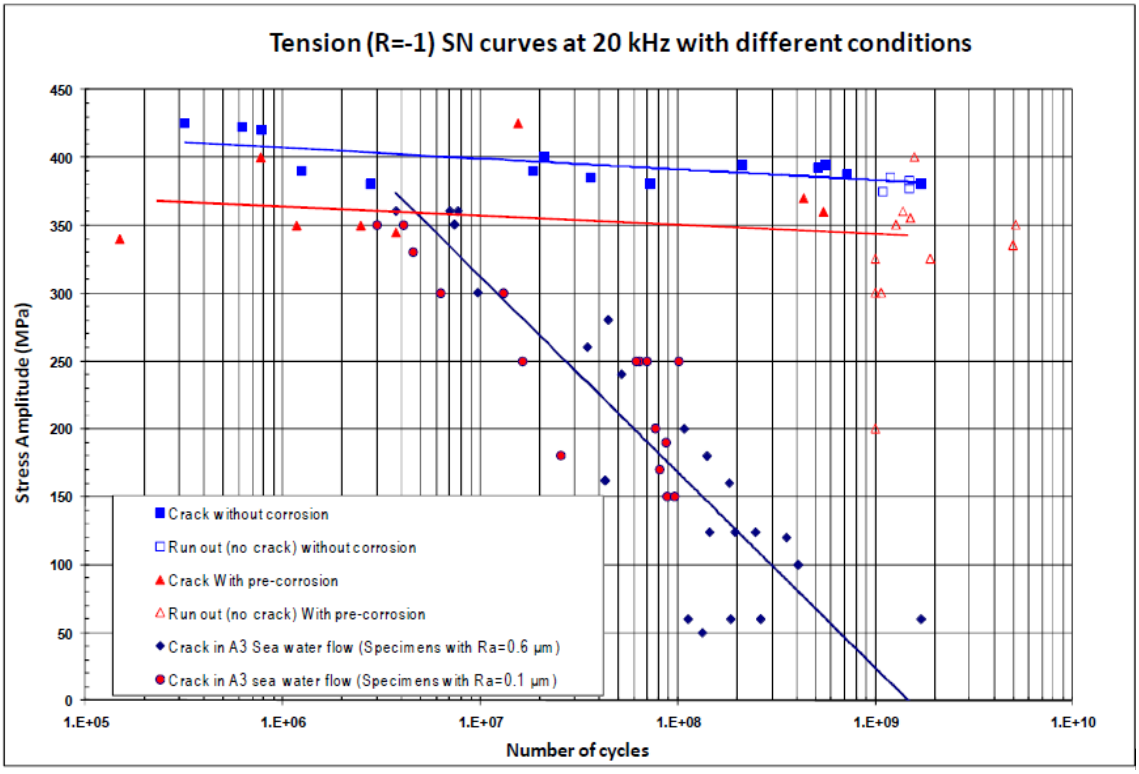

Figure 3: S-N curves of the R5 steel under fully reversed tension at 20 kHz.

The fatigue tests were carried out at 20 kHz under corrosive environment and may be seen first as non representative experiments because of the high loading frequency compared with the characteristic time of the corrosion process. However the results of our experimental data are not so far from the recommendations provided by the International Classification Societies of Off-shore Systems (for design purpose the fatigue strength at 10^8 cycles in sea water should be around 30 MPa). The competition between cyclic loading and corrosion is discussed later in this paper.

3.2. SEM observation of the fracture surfaces

On virgin specimens, even if some unusual internal crack initiations were observed (Figure 5), most of the fatigue cracks initiated at the specimen surface over the cycle range (10^6 – 10^9 cycles). Surface defects were the origin of the cracks for non-corroded specimens and corrosion pits for both pre-corroded specimens and specimens tested under sea water flow (Figures 6 and 7).

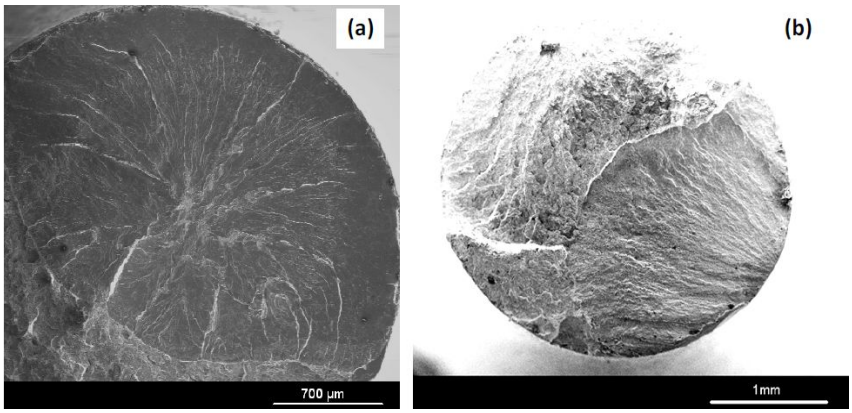

Figure 5: Fracture surface of R5 steel virgin specimens (a) Internal crack initiation σ_a= 380 MPa, N= 2.78×10^6 cycles, (b) surface crack initiation σ_a=395 MPa, N_f =5.61×10^8 cycles.

For the specimens tested under sea water flow the crack initiated all around the specimen surface due to several large corrosion pits. The size of the pits depends on the time (i.e. the number of cycles); their diameter is smaller on the pre-corroded specimens (30 to 80 µm) than under sea water flow (50 to 300 µm) (Figures 6 and 7). Furthermore, a lot of small cracks, perpendicular to the loading direction (mode I), were observed at the surface of the specimen tested under sea water flow (Figure 6C); whereas such small cracks were not observed on both virgin and pre-corroded specimens. This is characteristic of a corrosion/cyclic loading interaction. Since a significant decrease of the fatigue strength has been observed due to corrosion pits (seen as geometrical defects), it is important to determine if the crack propagation dominates or not the total fatigue life compared with the crack initiation phase.

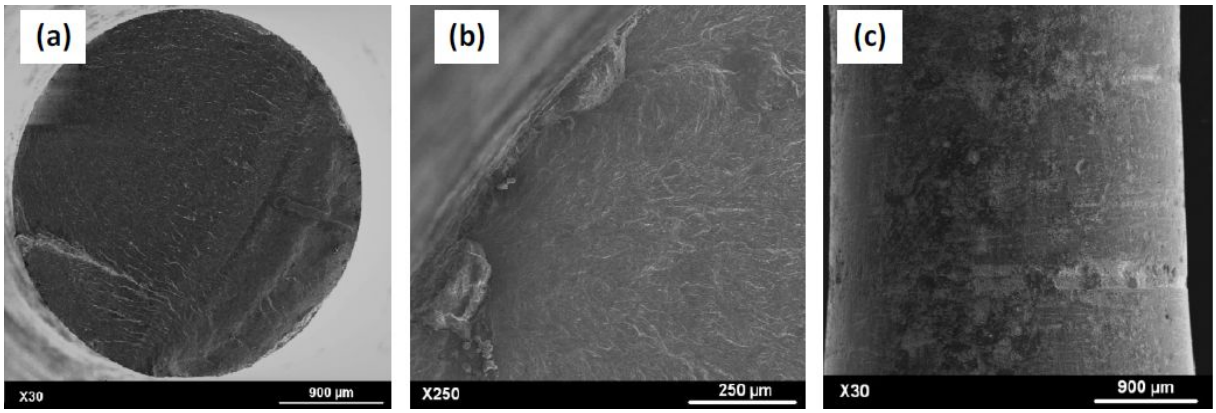

Figure 6: Specimen with pre-corrosion, σ_a=370 MPa, Nf=4.37×10^8 cycles

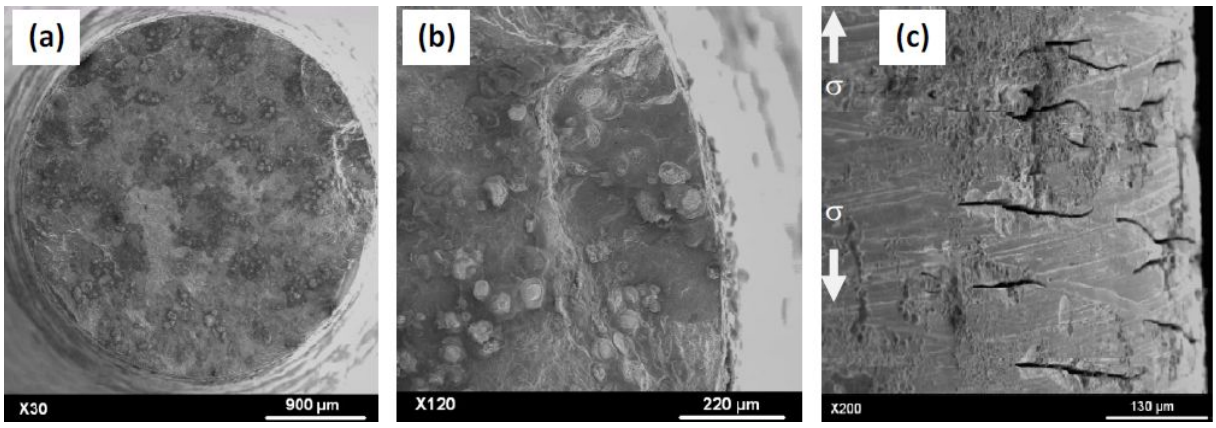

Figure 7: Specimen tested under sea water flow, σ_a=160 MPa, Nf=1.8×10^8 cycles.

4. Assessment of the crack initiation and propagation duration

The experimental $da/dN = f(\Delta K)$ curve for the investigated steel is shown in Figure 9. This shows that in air the mode I (R= –1) stress intensity threshold for R5 steel is around 3.3 MPa√m and as usual the crack growth rate is faster under sea water flow than in air [15]. The fatigue crack propagation duration was assessed according to the work of Paris et al. [8, 9], based on the Paris-Hertzberg-Mc Clintock crack growth model $\frac{da}{dN} = b\left(\frac{\Delta K_{eff}}{E\sqrt{b}}\right)^3$ and $\left(\frac{\Delta K_{eff}}{E\sqrt{b}}\right) = 1$ at the corner, where E is the elastic modulus and b is the Burger's vector. The good agreement of this equation with our experimental data and b=0.285 nm was shown in [12]. Since in our experiments at 20 kHz the measurement of K_{op} is not possible, in first approximation $\Delta K_{eff} \approx K_{max}$ was assumed and no water interaction with the stress intensity factor was considered.

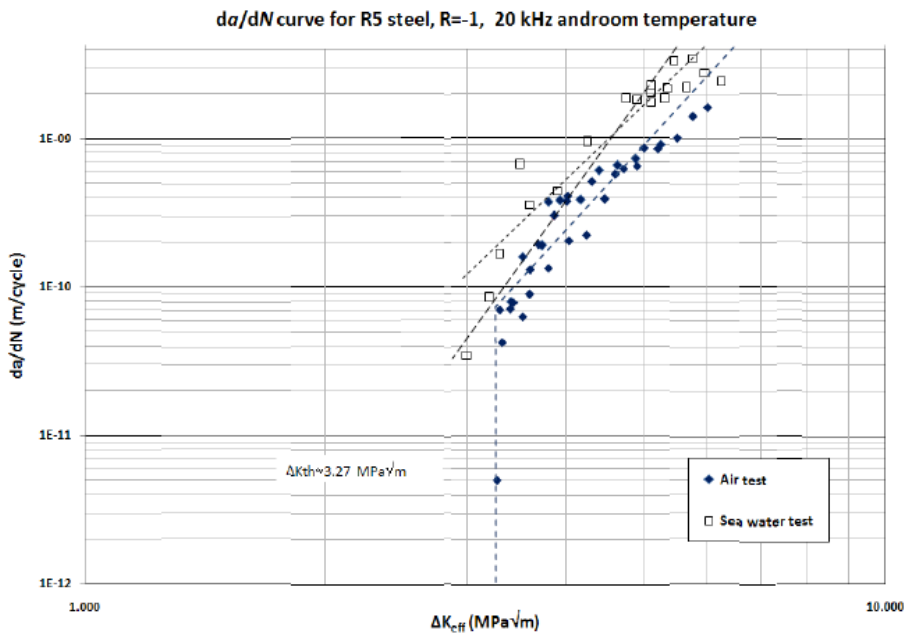

Figure 8: *da/dN =f(ΔK)* curve in mode I for the R5 steel (R= –1), in air and under sea water flow at room temperature.

To assess the duration of the crack propagation phase, a corrosion pit was modeled by a hemispherical surface defect with radius *R*. The existence of these hemispherical pits was observed by scanning electron microscopy on the surface of different specimens of R5 steel with pre-corrosion in salt fog chamber (Figure 3a) and with corrosion in A3 sea water flow (Figure 7). The longitudinal cross section of a pre-corroded specimen (after 4.37×10^8 cycles under a stress amplitude of 370 MPa) close to the fracture surface was observed as illustrated in Figure 9a. This shows a short crack initiated at a corrosion pit. Based on this observation, an initial fatigue crack of depth a_{int} emanating from the surface of the hemispherical pit and perpendicular to the loading direction due to intercristalline corrosion cracking was assumed. The length of the initial short crack emanating from hemispherical defects was assumed to be a_{int} =10 µm (close to the grain size).

According to the asymptotic approximation proposed by Paris et al [16] the crack tip stress intensity factor in mode I is: $K_I=\sigma Y(x,\nu)\sqrt{\pi a}$, where $x = a/R$, ν is the Poisson ratio, and a function $Y(x,\nu)$ for a penny shape crack emanating from hemispherical surface crack [16] :

$$Y(x/\nu)=1.015\left[A(\nu)+B(\nu)\left(\frac{x}{1+x}\right)+C(\nu)\left(\frac{x}{1+x}\right)^2+D(\nu)\left(\frac{x}{1+x}\right)^3\right](2) \qquad (2)$$

with:

$$A(\nu)=1.683+\frac{3.336}{7-5\nu},B(\nu)=-1.025-\frac{12.3}{7-5\nu},C(\nu)=-1.089+\frac{14.5}{7-5\nu},D(\nu)=1.068-\frac{5.568}{7-5\nu}\ .$$

It was assumed that the propagation of the fatigue crack is divided in three stages: (i) a short crack propagation during $N_{a_{\text{int}}-a_0}$ cycles, from initiation a_{int} to the crack size a_0, then (ii) a small crack propagation period $N_{a_0-a_i}$ cycles, from a_0 to the crack size a_i, and (iii) a long crack propagation N_{a_i-a} cycles, from a_i to the final crack size a: $N_{Total}=N_{a_{int}-a_0}+N_{a_0-a_i}+N_{a_i-a}$ .With these three different regimes the very quick propagation of short crack and the quick propagation of small crack compared to long crack were considered.

With these three different regimes [12] the very quick propagation of short crack and the quick propagation of small crack compared to long crack were considered. The detailed equations are given in [12], they were applied to our data assuming that the initial crack has a length, a_0, corresponding to the corner: $da/dN=b$.

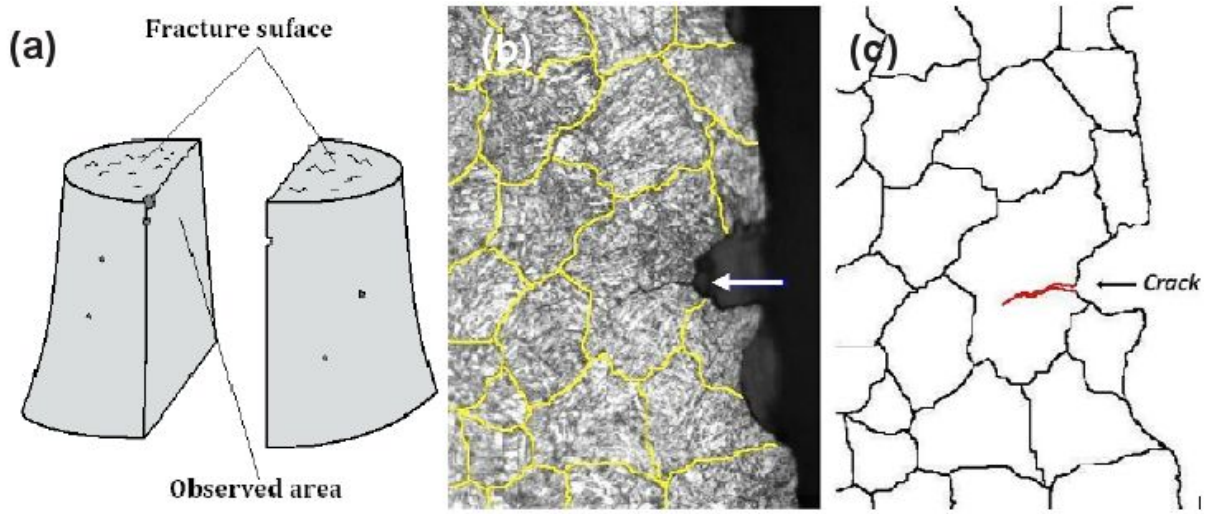

Figure 9: a) Longitudinal cross section of a specimen showing b) a fatigue crack initiation at a corrosion pit and the yellow highlighted old austenitic grains, c) illustration of the short fatigue crack and the grain boundaries.

Two cases are shown in Table 2 with two experimental total fatigue lives N_{exp}; several additional cases are detailed in [12]. In the first case 99.1% of the fatigue life is due to initiation. For the second case, 94% of the fatigue life was consumed by the initiation phase. Furthermore, it has been shown in [12] that with a high value of α and large a_{int}/a_0 one obtains similar N_{Total} results than with a low α and small a_{int}/a_0, that is because with a higher α the crack does not grow as far due to the slope of the da/dN curve in the threshold region, then a_{int}/a_0 must be larger, and with a lower α, a_{int}/a_0 must be smaller.

This calculations show that crack initiation dominates the fatigue life. Even if our calculations were carried out by using the crack growth curve in air, the conclusion is still valid because the crack growth rate for the R5 steel under sea water flow is higher than in air as shown Figure 8 and usually reported in literature [15]. Since the fatigue life is dominated by the crack initiation regime even in corrosive environment, additional experiments have been carried out to try to understand why this initiation period is significantly affected by sea water flow.

5. Additional experiments and discussion about the coupling between cyclic loading and corrosion

To complete these tests an ultrasonic fatigue test has been carried out on a cylindrical specimen. Since during an ultrasonic fatigue test a stationary wave is applied on the specimen, all along this cylinder different stress amplitudes are applied. Figure 9B shows the distribution of the stress amplitude along the cylindrical specimen loaded in its central part with a stress amplitude of 120 MPa (highest value along the specimen). This corresponds to a mean fatigue life of 2×10^8 cycles. For observation, the specimen surface was divided in 13 zones of around 1 cm long, each one was loaded to a specific stress amplitude interval. By testing such a cylinder under sea water flow (Figure 9a), observation of the damaged areas allowed us to investigate the link between the stress amplitude and the damage due to the in-situ fatigue – corrosion process. The specimen failed after 7.37×10^7 cycles.

Case 1: a_0=9.32 µm, σ_a=360 MPa, R=48 µm, a= 2.4 mm, N_{exp}=5.5×10^8 cycles on a pre-corroded specimen				
α	$a$int/a0	$N_{aint\text{-}a0}$	$N_{a0\text{-}ai}$	$N_{ai\text{-}a}$
100	0.9	115.801	44.151	4.507.080
	0.94	13.163		
	0.97	2.300		
Case 2: a_0=41.5 µm, σ_a =160 MPa, R=300 µm, a= 2.6 mm, N_{exp}=1.83×10^8 cycles on specimen tested under sea water flow				
α	$a$int/a0	$N_{aint\text{-}a0}$	$N_{a0\text{-}ai}$	$N_{ai\text{-}a}$
100	0.9	515.466	168.014	10.258.700
	0.94	58.593		
	0.97	10.237		

Table 2: Hemispherical surface crack growth vs. experimental fatigue life, for x=3, and different a_{int}/a_0 ratios.

Microscopic observations of the cylinder surface showed that R5 steel was damaged by fatigue – corrosion in the areas where the stress amplitude was higher than 56 MPa, a few corrosion traces only were observed where the stress amplitude was smaller (Figure 9d). The final fracture occurred where the stress amplitude was between 112 and 120 MPa. This shows an experimental evidence of the coupling between the corrosion process and cyclic loading, even at ultrasonic frequency (20 kHz), since below 56 MPa without any sea water flow there is no failure after 2×10^8 cycles (see the SN curves Figure 3).

Futhermore, three additional tests were carried out on VHCF specimens under the same conditions than all the other tests but, without any cyclic loading. Only the sea water flow was applied on the specimen surface with the same flow rate than for the tests with cyclic loading. The aim of these tests was to quantify the corrosion damage after the same duration than 10^7 cycles (8mn20s at 20 kHz), 10^8 cycles (1h23mn20s at 20 kHz) and 10^9 cycles (13h53mn20s at 20 kHz). No corrosion trace was observed by SEM after 8mn20s. After 1h23mn20s only a few traces of corrosion appear but not pits were observed. Corrosion pits were observed at the specimen surface after 13h53mn20s. The typical size of these pits was varying between 30 and 60 µm (Figure 11) this is significantly smaller than under simultaneous cyclic loading and sea water flow (Figure 8). The same pit size was observed under sea water flow with a stress amplitude of 240 MPa after 5×10^7 cycles. This corresponds to 42 mn only at 20 Khz! This proves that there is a coupling between corrosion and cyclic loading.

Because of such coupling, the question of the roughness effect occurred. Complementary fatigue tests were carried out under sea water flow at a stress amplitude of 250 MPa on the same VHCF specimens but with a polished surface (Ra=0.1 µm) to investigate a possible roughness effect. There was no evidence of the surface roughness effect under sea water flow (Figure 3): the fatigue life is in the scatter band of other experimental data (with Ra=0.6 µm).

This work shows experimental evidence of the coupling between corrosion and cyclic stress, even at 20 kHz while some authors think that fatigue corrosion interaction is not active when the loading frequency is high because of the long characteristic time of the corrosion process compared with the loading period. The observations of this study tend to show that the number of loading cycles (not the time) is a key factor in the fatigue crack initiation phenomenon under sea water flow. This has been recently confirmed by El May et al. [17] on a martensitic stainless steel in NaCl aqueous solution in HCF regime with in-situ fatigue test at around 100 Hz. These authors showed that PSB due to cyclic loading break the passive layer and then corrosion pits appears before crack initiation.

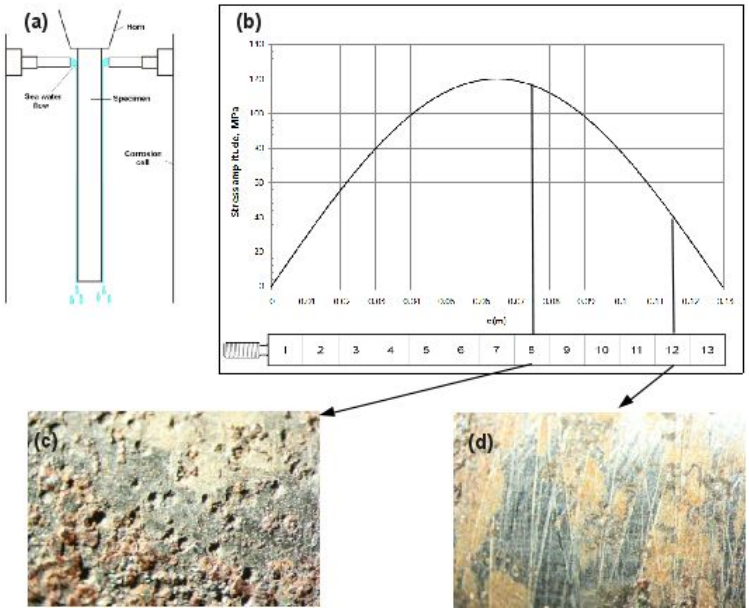

Figure 10: a) schematic illustration of the test principle of a cylindrical specimen with constant cross section under sea water flow, b) evolution of the stress amplitude along the longitudinal axis of the cylindrical specimen for a stress amplitude of 120 MPa in the central cross section, c) and d) optical picture of the specimen surface after 7.37×10^7 cycles in area 8 and area 12 loaded at different stress amplitudes.

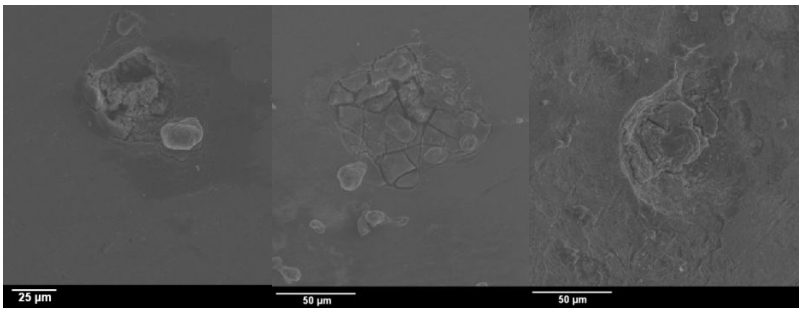

Figure 11: corrosion pits at the surface of a specimen under sea water flow during 13 h 53 min 20 s without any cyclic loading.

Further investigations should be carried out to understand the physical phenomenon involved in the VHCF damage process assisted by corrosion. One may imagine ultrasonic fatigue tests with potentiostatic measurements to monitor corrosion current and potential evolution during a fatigue test. However, not immerged experiments (to avoid cavitation) is a big experimental difficulty for carrying such tests. Investigation of the corrosion pitting kinetics under cyclic loading is probably a key factor for a better understanding of fatigue corrosion process. In situ micro-tomography under both ultrasonic cyclic loading and sea water corrosion may an interesting way for future researches.

6. Conclusion and prospects

Very high cycle fatigue tests were carried out up to 10^9 cycles on smooth specimens in hot rolled martensitic-bainitic steel under three different conditions (i) virgin specimens, (ii) pre-corroded specimens and (iii) under artificial sea water flow during the fatigue test. The fatigue strength at 10^8 cycles is significantly reduced by a factor of 74% compared to the virgin specimens and of 71% compared to the pre-corroded ones. The poor corrosion – fatigue strength is related to the size of the pits. The assessment of the crack growth shows that crack initiation dominates the total fatigue life when $N>10^7$ cycles. A strong coupling between environment and cyclic loading has been proven. Under cyclic loading, even at ultrasonic frequency, fatigue damage and corrosion pitting are interacting for creating crack initiation at very low stress amplitude where no fatigue crack initiates

under fatigue loading alone. This has to be more investigated for understanding the physical mechanisms involved in the corrosion fatigue. Anyway, it has been shown that ultrasonic fatigue test immersed in flowing sea water is a good experimental way to investigate very long life of steel under corrosion conditions with reasonable test time duration.

Acknowledgements

The authors acknowledge both Prof. P.C. Paris for the fruitful discussions about crack propagation modeling and Prof. J-L. Arana for allowing this work and for the financial support of the Vicinay Cadenas company that is thanks too.

References

[1] C. Bathias and P.C. Paris (2005) Gigacycle Fatigue in Mechanical Practice, Marcel Dekker Publisher Co., New York USA.
[2] I. Marines, X. Bin and C. Bathias (2003) An Understanding of very high cycle fatigue of metals, *Int J Fatigue* **25**, 1101-1107.
[3] J.H. Zuo, Z. Wang and H. Han (2008) Effect of microstructure on ultra-high cycle fatigue behavior of Ti-6Al-4V, *Mat Sci Eng* A **473**, 147-152.
[4] H.R. Ammar, A.M. Samuel and F.H. Samuel (2008) Effect of casting imperfections on the fatigue life of 319-F and A356-T6 Al-Si alloys, *Mat Sci Eng* A **473**, 65-75.
[5] H.T. Pang and P.A.S. Reed (2007) Microstructure effects on high temperature fatigue crack initiation and short crack growth in turbine disc nickel-base superalloy Udimet 720 Li, *Mater Sci Eng A* **448**, 67-69.
[6] R.A. Yeske and L.D. Roth (1982) Environmental effects on fatigue of stainless steel at very high frequencies, In: Wells (Westinghouse) J.M. Buck, Roth, Tien (Eds), Ultrasonic fatigue, The Metallurgical Society of AIME, New York, USA, pp. 365–385.
[7] R. Ebara and Y. Yamada (1982) Corrosion fatigue behaviour of 13Cr stainless steel and Ti-6Al-4V at ultrasonic frequency, In: Wells (Westinghouse) J.M. Buck, Roth, Tien (Eds), Ultrasonic fatigue, The Metallurgical Society of AIME, New York, USA, pp. 349–364.
[8] P.C. Paris (2004) The relationship of effective stress intensity, elastic modulus and Burgers-vector on fatigue crack growth as associated with “fish-eye” gigacycle fatigue phenomena, In : *Proceedings of VHCF-3*, Kyoto, Japan, 2004, pp. 1-13.
[9] I. Marines, P.C. Paris, H. Tada and C. Bathias, (2007) Fatigue crack growth from small to long cracks in VHCF with surface initiations, *Int J Fat* **29**, 2072-2078.
[10] E.M. Gutman and G. Soloviof (1996) The mechanochemical behavior of type 316L stainless steel, *Corrosion Science,* **38**, 1141–1145.
[11] T. Pyle, V. Rollins and D. Howard (1975) The influence of cyclic plastic strain on the transient dissolution behavior of 18/8 stainless steel in 3.7M H_2SO_4, *J. Electrochem. Soc.,* **122**, 1445–1453.
[12] T. Palin-Luc, R. Perez-Mora, C. Bathias, G. Dominguez, P.C. Paris and J.L. Arana (2010) Fatigue crack initiation and growth on a steel in the very high cycle fatigue regime with sea water corrosion, *Eng. Fract. Mech.*, **77**, 1953-1962.
[13] T.Y. Wu and C. Bathias (1994) Application of fracture mechanics concepts in ultrasonic fatigue, *Eng Fract Mech,* **47**, 683-690.
[14] Sun (2000) Etude du seuil de fissuration à haute fréquence en fatigue et en fretting fatigue. Ph.D. Thesis, CNAM, Paris France.
[15] C. Bathias and A. Pineau (2010) Fatigue of materials and structures, ISTE Ltd and John Wiley & Sons Inc., 512 p.
[16] P.C. Paris, T. Palin-Luc, H. Tada and N. Saintier (2009) Stresses and crack tip stress intensity factors around spherical and cylindrical voids and inclusions of different elastic properties and with misfit sizes, In Proceedings Int. Crack Path, 8 pages.
[17] M. El May, T. Palin-Luc, N. Saintier and O. Devos (2013) Effect of corrosion on the high cycle fatigue strength of a martensituc stainless steel X12CrNiMoV12-3, *Int. J Fatigue*, **47**, 330–339.

Study of fatigue crack mechanism on an armco iron in the gigacycle fatigue by temperature recording and microstructural observations

Chong WANG[1], Danièle WAGNER[1*], Claude BATHIAS[1]

[1] University Paris Ouest Nanterre La Défense – LEME Laboratory – 50, rue de Sèvres – 92410 VILLE D'AVRAY – France
[*]Corresponding author : daniele.wagner@u-paris10.fr ,

Abstract: Whatever the fatigue domain, the fatigue crack mechanism consists of an initiation crack stage (stage I) and a propagation stage (stage II). For materials without inclusions with a single phase, the first damage events in the stage I are due to the occurrence of Slips Marks (SM) on the specimen surface.
In this study, the fatigue crack mechanism was studied in the VHCF domain on a body centered cubic Armco iron (with 80ppm of carbon content).The tests were performed on a piezoelectric fatigue machine on plate specimens. During the tests, the microstructure evolution was observed by optical microscope, and the temperature recording on the specimen surface was achieved by an infrared camera. After the failure specimen, fractographic observations were performed under a Scanning Electron Microscope;
From the temperature recording on the specimen surface near the section where the fracture occurs, the spatio temporal localization of the point where the temperature was the highest was achieved. The highest temperature corresponds to the crack tip where the plastic zone takes place. This allows to follow the evolution of the crack tip during the test. The results are compared with the fractographic examinations on the fracture surface, and the number of cycles in each stage can be calculated.

Keywords: Very High Cycle Fatigue, fatigue crack mechanism, Armco iron, piezoelectric device, Slips Marks, infrared thermography

1. Introduction

Whatever the fatigue domain, the fatigue crack mechanism consists of an initiation crack stage (stage I) and a propagation stage (stage II). For materials without inclusions with a single phase, the first damage events in the stage I are due to the occurrence of Slips Marks (SM) on the specimen surface [1,2]. At the beginning of the long crack propagation stage, striations occur (stage II).
Previously, the temperature recording was performed on the surface of cylindrical specimens [4,5] on materials with inclusions which leads to subsurface crack initiations with "fish eyes" formations .
In this paper, flat specimens were used in order to improve the temperature recording on the surface specimen. The studied material is an Armco iron without inclusions which leads to a surface crack

initiation. With a flat surface, the spatiotemporal localization of the point where the temperature was the highest was possible. The highest temperature corresponds to the crack tip during the test. Then, the results are compared with the fractographic examinations for identification with each stage.

2. Material

The studied material is a polycrystalline α iron whose chemical composition is given in Table1. The carbon content is 80ppm. The microstructure is ferrite with equiaxe grains. The ferrite grain size is included in 10 to 40 μm. No specifically orientation was observed by EBSD. Yield Stress is 240 MPa.

Table 1: Chemical composition of studied material

C	P	Si	Mn	S	Cr	Ni	Mo	Cu	Sn	Fe
0.008	0.007	0.005	0.048	0.003	0.015	0.014	0.009	0.001	0.002	Balance

3. Experimental procedure

3.1. Mechanical and Thermal Procedure

Tests were performed on a piezoelectric fatigue machine designed by C. Bathias and co-workers [6].

For the reason of surface observation condition by IR camera, a new design of 1 mm flat specimen (Fig. 1) was used to carry out fatigue tests. Specimen, special attachment and piezoelectric fatigue machine constituted the resonance system working at 20kHz. The cyclic loading is tension-compression . The stress ratio is then R_σ = -1. For this test, the applied stress amplitude $\Delta\sigma$ was 175 MPa, and the number of cycles to failure 3.2155×10^7 cycles

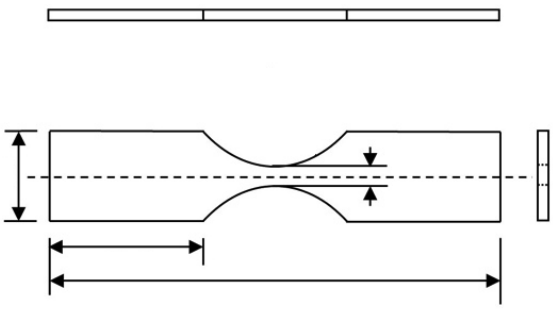

Fig. 1: Design of flat specimen

A CEDIP Orion infrared camera was used to record the temperature evolution during the test.The frequency of the camera was 50Hz and the aperture time was 100 μs.

Before testing, both side surface of the flat specimen were electrolytic polished. One side surface of the flat specimen was etched and another side painted in black color to have the surface emissivity close to 1.

4. Results

4.1. Thermal results

Figure 2 shows the entire temperature recording versus the number of cycles on the specimen surface during the test. As previously published [4], the temperature has a quick increase at the beginning of the test and tends progressively towards an asymptotic until the fatigue crack growth in mode II leading to the failure . Higher is the stress, higher is the temperature level.

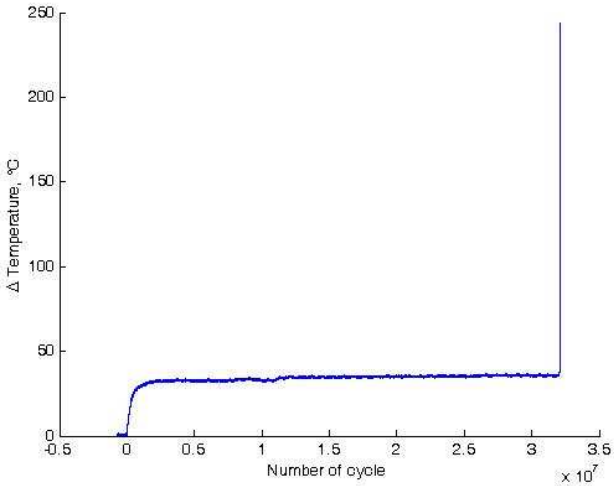

Figure 2: Temperature evolution versus number of cycles

From these data, the temperature profile (Figure 3) along the specimen width was extracted for the 168 latest pictures captured by the camera, that is to say from $3.2086.10^7$ cycles to $3.2153.10^7$ cycles (number of the cycles at the failure).

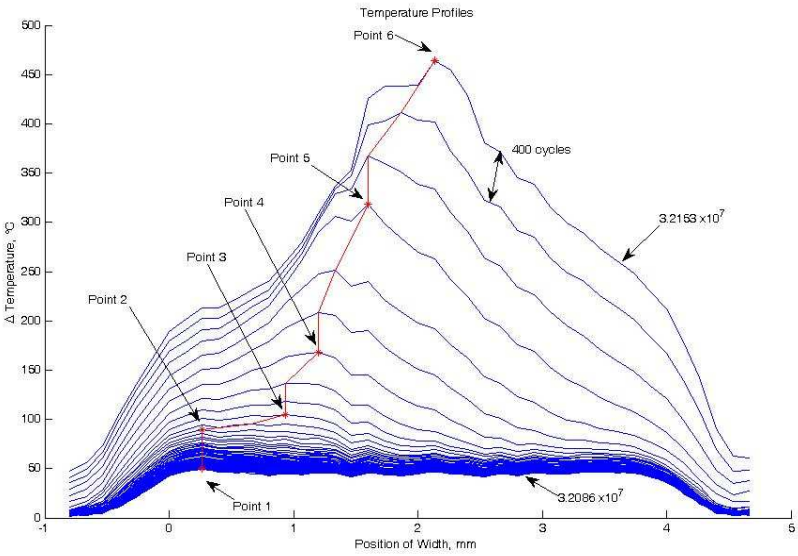

Figure 3 : Temperature profile along the specimen width

Between each profile, 400 cycles are performed. The red line on the figure 3 is the location where the temperature is maximum along the profile. Before 3.2086×10^7 cycles, it was not possible to determine a location where the temperature was maximum along the profile. For this test, the crack initiation site appeared on the left side of the specimen (on the left side of the figure 3). The locations of the points 1/2,3,4,5,6 where the maximum temperature rapidly increases were determined. From the specimen corner, the locations of the different points are : points 1 et 2 at 267 µm, point 3 at 933 µm, point 4 at 1200 µm, point 5 at 1600 µm, point 6 at 2000µm. The corresponding numbers of cycles are : N_1 (point 1) at 3.2086×10^7 cycles, N_2 (point 2) at 3.2148×10^7 cycles, N_3 (point 3) at 3.2149×10^7 cycles, N_4 (point 4) at 3.2151×10^7 cycles, N_5 (point 5) at 3.2152×10^7 cycles, N_2 (point 2) at 3.2153×10^7 cycles and the number of cycles at fracture N_f to 3.2155×10^7 cycles.

During the end of this test, the maximum temperature location moves from the left to the right of the specimen width in agreement with the increase of the fatigue crack length and the increase of the plastic zone ahead the fatigue crack tip.

4.2. Fractographic results

The fracture surface and the polished specimen surface (where the temperature was recorded) were observed under Scanning Electron Microscope (Figure 4a and b). Until the point 5, the fracture surface is flat and correspond to the plane strain fatigue crack. Between the point 5 and 6, the fracture surface presents shear lips.

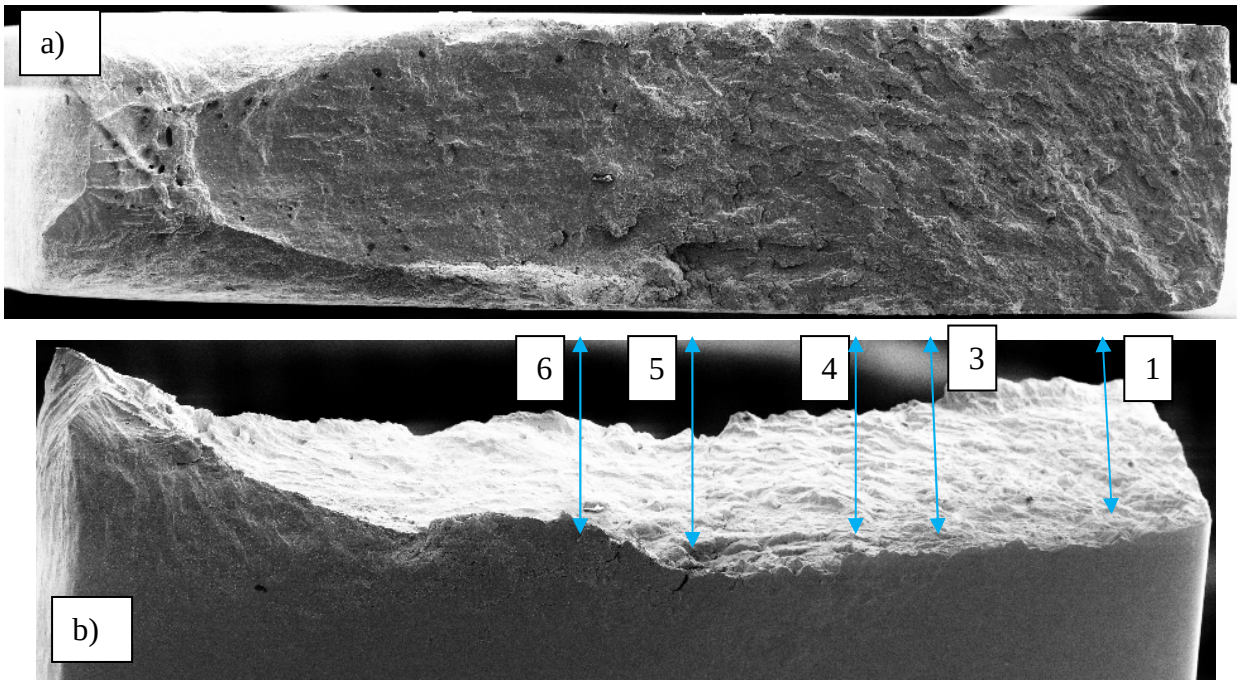

Figure 4a and b: SEM observations of the whole fracture and polished surface

The enlargement of the plane strain fatigue crack (Figure 5a) shows two main zones separated by the line at the point 3. The crack initiation site is located in the lower edge. In the stage I (Figure 5b), the trace of the grains in which Persistant Slips Bands (PSB) have appeared as previously shown [7] are visible. After the point 3, the stage II of long crack propagation begins with striations. At the beginning of this stage II, the striations are not well established (Figure 5c), whereas after the point 4 (and the corresponding line), the striations are well defined (Figure 5d).

The lower side of the specimen has been more particularly observed (Figure 6a,b,c). The figure 6c is the picture around the point 3 where a change in fracture surface can be observed. After the point 3, striations are present and correspond to the crack propagation as previously reported. Between the specimen corner and the point 3, another fracture surface change appears at the point 1. On the right side of the photo, the grain traces are clearly observed, whereas after the point 1 (Figure 6b), the fracture surface appearance change, change which is attributed to the transition from the crack initiation stage (stage I) to the short crack propagation.

From these observations, the locations of the different points can be measured. The results are: point 1 : ~ 294 μm, point 3 : ~ 882 μm, point 4 : ~ 1294 μm, point 4 : ~ 1629 μm.

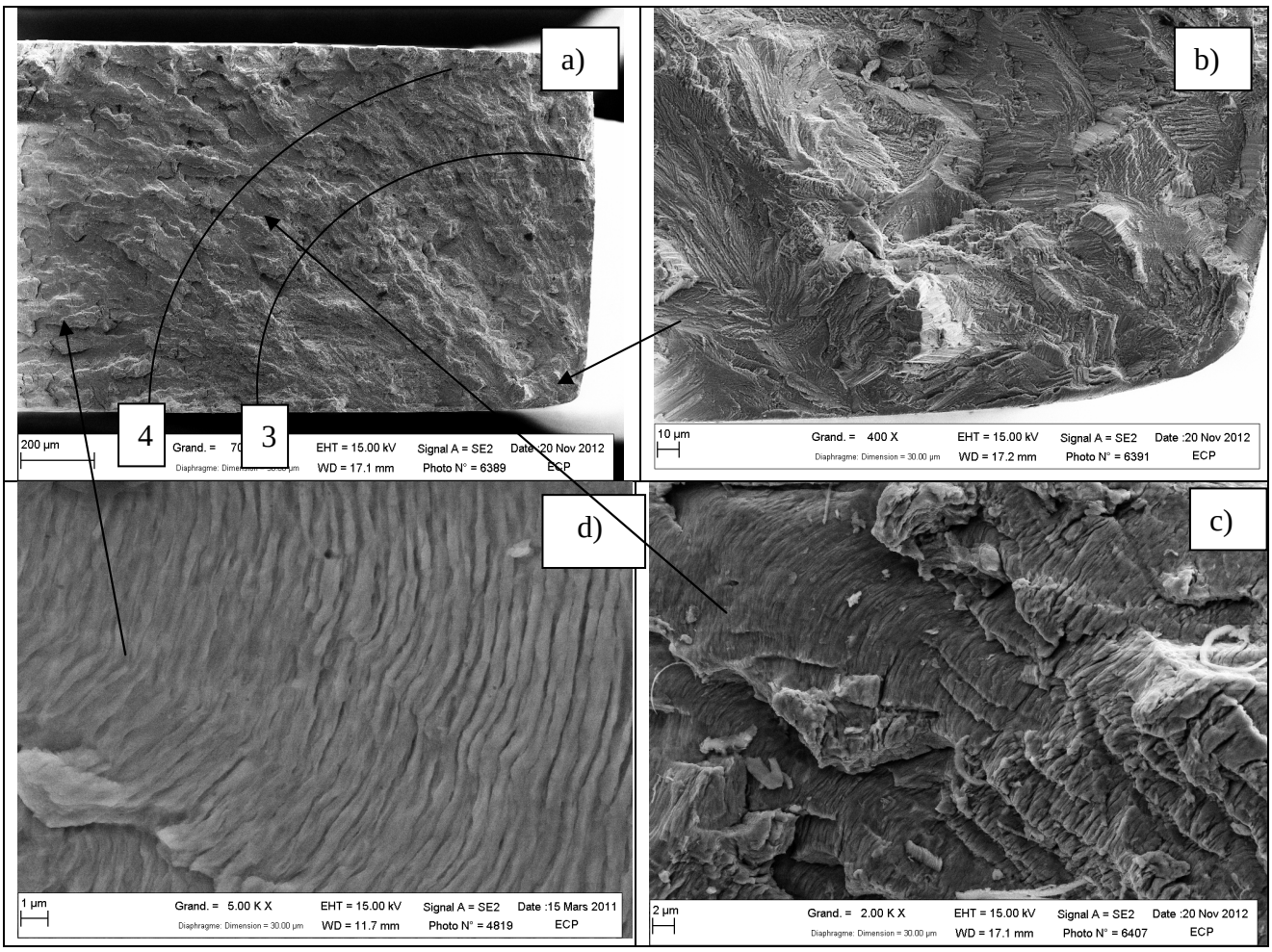

Figure 5 a)b)c)d) : SEM plane strain fatigue crack surface and details of each stage

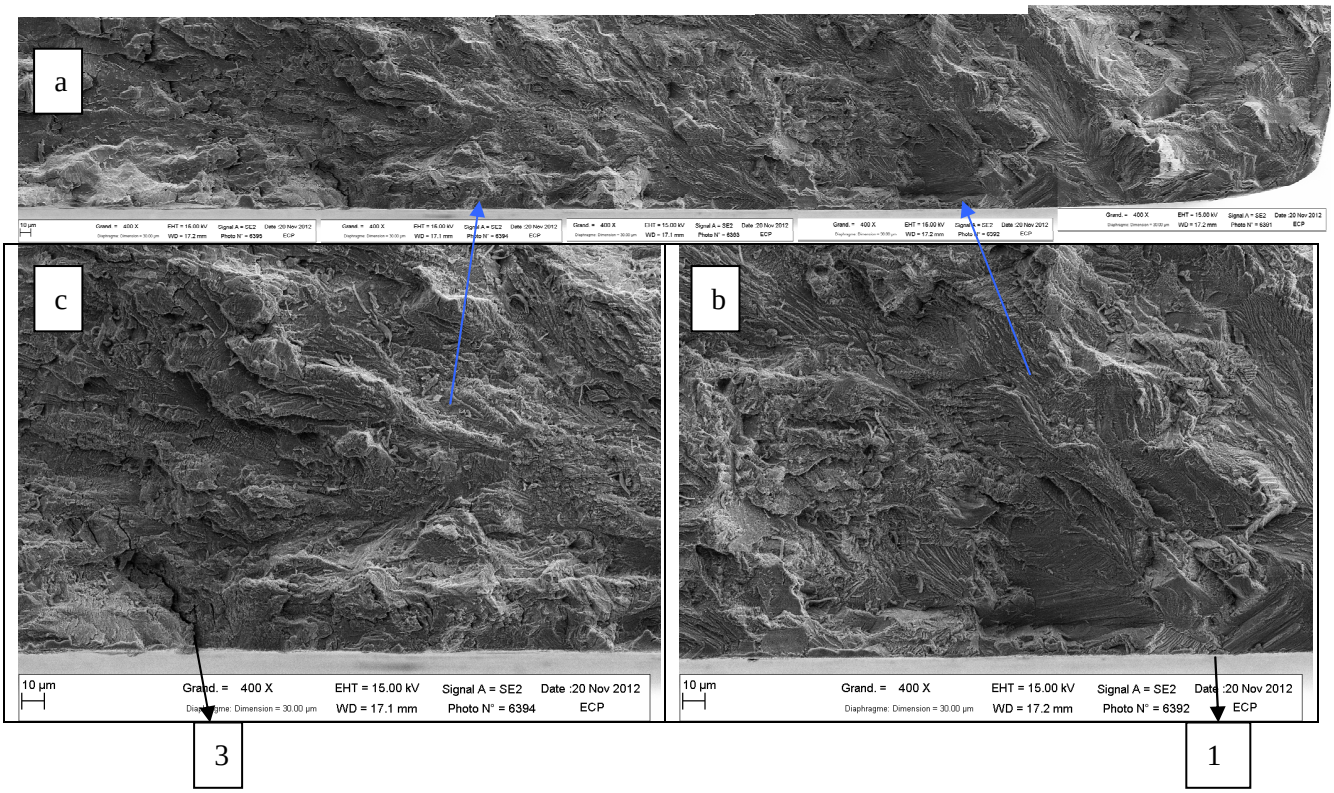

Figure 6 a)b)c: SEM observations of the fracture surface lower side (side where the temperature was achieved)

5. Discussion

The figure 7 a)b show the comparison between thermal results (yellow lines) and fracture surface observations. The agreement between the two data is very good.

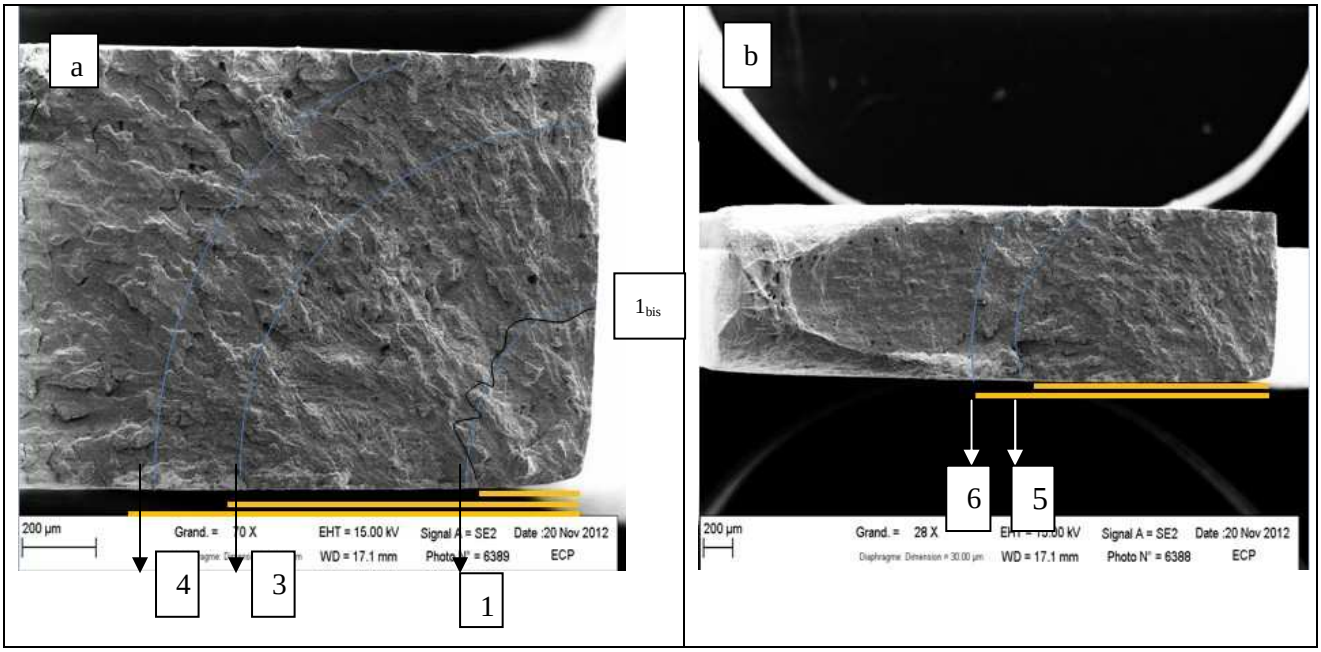

Figure 7a)b) :Comparison between thermal results (yellow lines) and fracture surface observations

(blue lines)

- When the number of cycles is below 3.2086×10^7 cycles, the temperature is the same on the overall width of the specimen. The PSB formation on specimen surface are scarce and located on both side of the middle section of the specimen [7,8]. The intrinsic dissipation d_1 (specific heat source due to PSB) measured from the temperature measurement on the specimen surface is about 5°C/s [8]. There is no crack on the specimen surface.
- At the number of cycles $N = 3.2086 \times 10^7$, the temperature profile on the specimen width shows a point (point 1, figure 3 and 7a) with a higher temperature. At this number of cycles, there is a rapid coalescence of PSB on specimen surface. Probably, the microcrack (due to the PSB) is also opened on the surface thickness of the specimen (point 1bis, figure 7a), and then, there is a coalescence between microcracks on the two surfaces (width and thickness). These points (1 and 1bis) correspond to the transition between crack initiation stage and short crack propagation stage (figure 6b).On the figure 7a, according to the all SEM observations (not presented here), this transition on the fracture surface has been reported. From the point 1, the temperature maximum increases, but this point does not move on the specimen width. This due to the formation of the crack initiation area between point 1 and 1bis When the crack spreads from point 1 to point 1bis, the ΔK threshold is reached. The calculation according to the blue line is 4.1 MPa√m, which correspond to a plastic zone size of ~ 47μm. The number of cycles $N = 3.2086 \times 10^7$ is the number of cycles at the crack initiation N_i. This allows to calculate the ratio N_i/N_f equal to 0.9978. So, 99.8% of the total life is devoted to the initiation of the crack. As previously reported for the subsurface crack initiation in the gigacycle fatigue domain [4-5, 9-11], the major part of the total life is devoted to the crack initiation.
- Between point 1 / 1bis and 3, it is the fast short crack propagation. The length crack on the surface goes from 294 to 882 μm. At the point 3, the ΔK is 10.7 MPa√m, which correspond to a plastic zone size of ~317 μm, and the d_1 about 20°C/s [8].
- From the point 3, the long crack propagation begins, with the occurrence of striations. From this point (figure 8), the crack length and the temperature increase favors related to the high dislocation density the formation of many PSB in the plastic zone ahead the crack tip (figure 8).
- Then, the fatigue crack propagation goes on to the point 5. At this point, the d_1, reachs around 400°C/s (unpublished results).

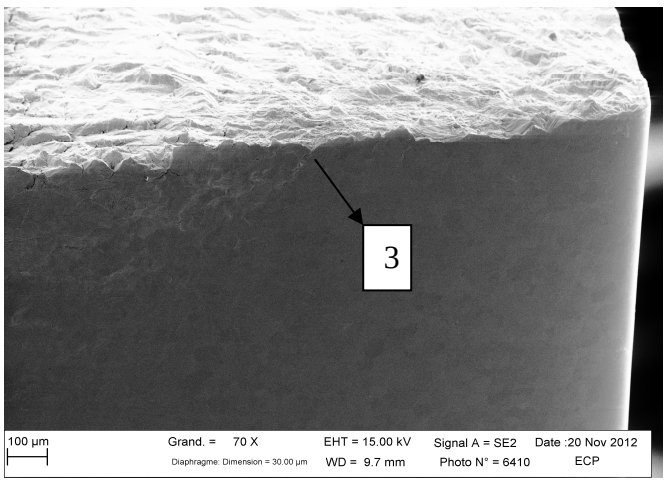

Figure 9: SEM observations of the high density PSB in the long crack propagation stage

From each point on the figure 3, the number of cycles can be calculated and reported on the curve

temperature versus number of cycles. Figure 9 is an enlargement of the end part of Figure 2, where the different points are reported. As previously published [5,9] for subsurface observations, the number of cycles of crack initiation N_i, corresponds to the weak temperature increase (point 1). The number of cycles between point 1 and 2 (Figure 9) corresponds to the crack initiation stage. Between point 2 and 3, the fast short crack propagation takes place. After the point 3, the plastic zone ahead the crack tip (figure 9) produces a great lot of PSB and then a great number of specific heat sources (PSB formation which are only visible on the specimen surface). The intrinsic dissipation d_1 and so the temperature grows rapidly until fracture.

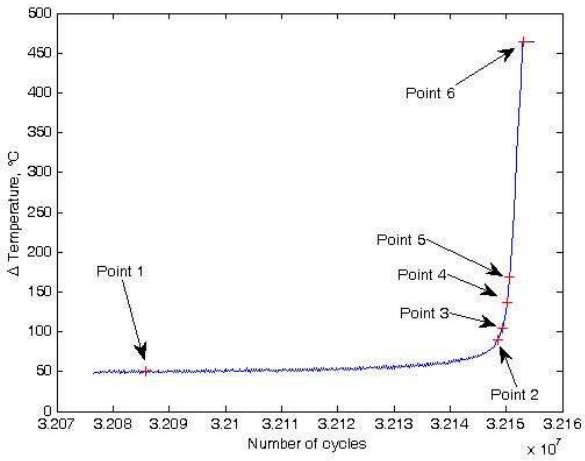

Figure 9: End of the temperature evolution versus number of cycles curve in relation with the number of cycles in each stage

6. Conclusion

In this paper, temperature follow-up on the surface of flat specimen for a ferrite Armco iron in the gigacycle fatigue domain is compared to the fracture surface observations made by SEM. The good agreement between thermal and SEM results allows to drawing the conclusions below:

- the crack initiation at the number of cycles N_i is due to a rapid coalescence of the PSB on the specimen surface (point 1 and 1bis). Then, the crack initiation spreads over the thickness of the specimen (coalescence of PSB between point 1 and 1bis in specimen volume) to achieve ΔK threshold (point 2) of about 4 MPa√m. In this test, more than 99% of the total life is devoted to the crack initiation.
- when the crack propagation (stage II) occurs, the temperature at the crack tip rapidly increases, firstly in short crack propagation regime (point 2→3), and then in a long crack propagation regime (point 3→5). In the long crack propagation regime, the number of PSB is very important, and so the specific heat sources and the temperature increase rapidly.

ACKNOWLEDGEMENTS

This research was supported by the grant from the project of Microplasticity and energy dissipation in very high cycle Fatigue (DISFAT, project No. ANR-09-BLAN-0025-09), which funded by the National Agency of Research, France (ANR). Aknowledgements are due to F. Garnier (Ecole Centrale de Paris) for the SEM observations.

REFERENCES

[1] S. Suresh, Fatigue of Materials, Cambridge University Press, Cambridge, UK, 2006

[2] C. Bathias, A. Pineau, Fatigue des matériaux et des Structures 1, Lavoisier, Paris, 2008

[3] H. Mughrabi, The Strength of Metals and Alloys, P. Haasen, V. Gerold, G. Kostorz, (Ed.), Pergamon Press, Oxford, 1980

[4] D. Wagner, N. Ranc, **C.** Bathias**,** P. Paris, Fatigue crack initiation detection by an infrared thermography method, Fat. Fract. Engng Mater Struct 33, (2009) 12-21

[5] N. Ranc, D**.**Wagner**,** P.C. Paris, Study of thermal effects associated with crack propagation during very high cycle fatigue, Acta Materiala **56,** (2008), 4012-4021

[6] C. Bathias, P. C. Paris, Gigacycle Fatigue in Mechanical Practice, Marcel Dekker, New York, 2004

[7] C. Wang, D. Wagner, Q.Y. Wang, C. Bathias – Gigacycle fatigue initiation mechanism in Armco iron, Int Jl Fatigue, Vol 45(2012)91-97

[8] C. Wang, A. Blanche, D. Wagner, A. Chrysochoos, C. Bathias – Study of Fatigue Crack initiation mechanism on an Armco Iron by dissipation assessments and microstructural observations, Crack Path 2012, Gaeta, Italie, septembre 2012

[9] Z. Huang, D. Wagner, C. Bathias – Effect of carburizing treatment on the “fish eye” crack growth for a low alloyed chromium steel in Very High Cycle Fatigue, Mat. Sc.& Eng.A, article sous presse

[10] Z. Huang, D. Wagner, C. Bathias, P. C. Paris - Subsurface Crack Initiation and Propagation Mechanism in the Gigacycle Fatigue, Acta Materiala, 58 (2010), 6046-6054

[11] Y. Hong, Z. Lei, C. Sun, A. Zhao – Characteristics of crack interior initiation and early growth originated from inclusion for very high cycle fatigue of high strength steels, Crack Path 2012, Gaeta, Italie, septembre 2012

Scaling invariance of fatigue crack growth in gigacycle regime

Vladimir Oborin[1,*], Mikhail Bannikov[1], Oleg Naimark[1], Thierry Palin-Luc[2]

[1] Institute of Continuous Media Mechanics of Ural branch of RAS, 614013, Perm, Russia
[2] I2M-DuMAS CNRS, Université de Bordeaux, Arts et Métiers-ParisTech, France
*oborin@icmm.ru

Abstract The role of the collective behavior of defect ensembles at the crack tip and the laws of fatigue crack propagation in R4 high-strength steel have been studied under conditions of symmetric tension–compression gigacycle loading at 20 kHz. At every stage of the fatigue crack growth, replicas from the sample side surface were taken and studied by the method of three-dimensional relief profilometry (using interferometer profilometer NewView 5010) so as to study the scaling-invariant laws of defect-related structure evolution.
Keywords gigacycle fatigue, scaling, crack, morphology.

1. Introduction

The task of assessing the working resource of important structures, in particular, those for aircraft engines, poses qualitatively new basic problem related to evaluation of the reliability of materials under conditions of cyclic loading in excess of 10^8–10^{10} cycles, which refer to the field of so-called gigacycle fatigue. This interest is related to the fact that the resource of loading for many important parts operating under conditions of cyclic loading exceeds the so-called multicycle range. The behavior of materials in the range of gigacycle fatigue reveals some qualitative changes in the laws governing both the nucleation of cracks (in the bulk of a sample) and their propagation, which are related to changes in the mechanisms of fatigue crack nucleation and propagation. In the range of gigacycle loading, the fatigue curve exhibits discontinuities and the behavior shows evidence of a significant increase in the role of environment, so that the problem acquires an interdisciplinary character.

The stages of material fracture in the range of gigacycle loading are classified based on the structural signs of damage related to a broad spectrum of spatial scales, including persistent slip bands (PSBs), fatigue striations, microcracks (formed as a result of PSB crossing), and grain-boundary defects. The main damage refers to the defect scales within 0.1 μm–1 mm, which are significantly smaller than those detected by the standard methods of nondestructive testing used for the conventional monitoring of reliability, in particular, during the exploitation of buildings.

An effective method for investigating the role of initial structural heterogeneity, monitoring the accumulation of defects on various scales (dislocation ensembles, micropores, microcracks), and determining critical conditions for the transition from dispersed to macroscopic fracture is offered by the quantitative fractography. This technique reveals the characteristic stages of fracture (crack nucleation and propagation), thus providing a base for evaluating the temporal resource of materials and structures under conditions of gigacycle loading.

The approach to characterization of the fracture surface morphology in terms of spatiotemporal invariants was originally proposed by Mandelbrot [1]. This method is based on an analysis of the relief of a fracture surface, which exhibits the property of self-affinity as manifested by the invariant characteristics of the surface relief (roughness) over a broad spectrum of spatial scales. On the other hand, these characteristics reflect a correlated behavior of defects on various scaling levels.

The universal character of kinetic laws establishing a relationship between the growth rate dl/dN of a fatigue cracks and a change in the stress intensity coefficient ΔK has been extensively studied both

experimentally and theoretically. The power laws originally established by Paris [2] (and presently referred to as the Paris law) reflect the automodel (self-similar) nature of development of fatigue cracks. This law is related to a nonlinear character of damage development in the vicinity of the crack tip (called the "process zone" [2]):

$$\frac{dl}{dN} = A(\Delta K)^m, \tag{1}$$

where A and m are the experimentally determined constants. For a broad class of materials and wide range of crack propagation velocities under multicycle fatigue conditions, the exponent is typically close to $m = 2$–4.

The universal nature of the Paris law was interpreted [3] based on the self-similar laws of damage development and fracture focus formation in the form of "dissipative structures" representing ensembles of defects localized on the spectrum of spatial scales. The formation of these structures reveals a critical character of the transition from dispersed to macroscopic fracture as manifested by the structural-scaling transitions [4]. According to these notions, the propagation of cracks is related to establishing a long-range correlation interaction in multiscale ensembles of dissipative structures. This interaction which can be characterized by a certain correlation scale, above which the interaction proceeds to a scale that determines the subsequent increment in the length of the propagating crack (size of the "process zone"). This assumption concerning the critical conditions for the aforementioned transition was used in interpretation of the experimental data so as to explain the self-similar scenario of fatigue crack propagation in a steel sample under conditions of gigacycle loading.

2. Experimental conditions and materials

The samples (Fig. 1) of R4 high-strength steel (with a room-temperature fatigue limit of 600 MPa for 10^6 cycles at 10 Hz) were tested under fatigue loading conditions with symmetric tension–compression cycling at 20 kHz (gigacycle loading regime) on an original setup [5]. The testing machine consisted of the following main parts: (i) generator, which converted 50 Hz oscillations into an ultrasonic electric sinusoidal signal with a frequency of 20 kHz; (ii) piezoelectric transducer, which generated longitudinal ultrasonic waves and produced mechanical action at a frequency of 20 kHz; and (iii) ultrasonic waveguide, which increased the amplitude of mechanical stresses in the (working) central part of the sample.

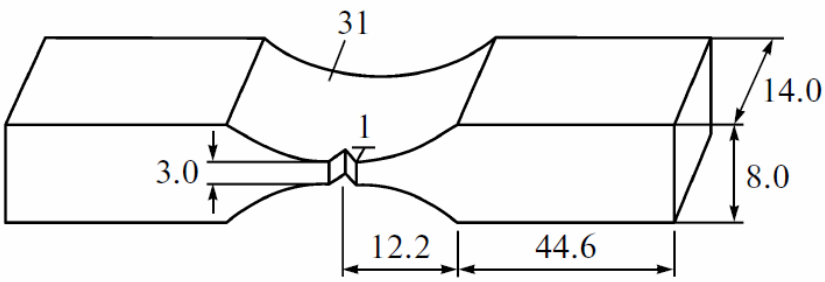

Figure 1. Schematic diagram and characteristic dimensions of the initial sample (in millimeters)

At the initial stage, a fatigue crack with a length of ~1.5 mm was nucleated, the subsequent growth

of which was controlled by varying the amplitude of oscillations. The corresponding stress intensity coefficient ΔK was calculated by the following formula:

$$\Delta K = \frac{E}{1-\nu^2}\sqrt{\frac{\pi}{l}}U_0 Y(l/w), \tag{2}$$

where E is the Young's modulus, ν is the Poisson ratio, U_0 is the amplitude of oscillations, Y is the polynomial factor, and w is the sample width. For a given sample geometry (Fig. 1) the polynomial factor was as follows:

$$Y(l/w) = 0.635(l/w) + 1.731(l/w)^2 - 3.979(l/w)^3 + 1.963(l/w)^4. \tag{3}$$

Figure 2 shows the typical surface relief observed on a sample, which was obtained using a high-resolution NewView interferometer. This profilometer ensured a vertical resolution of 0.1 nm and a lateral resolution of 0.5 μm. These patterns were analyzed using the methods of correlation analysis for determining the conditions of scaling invariance in the ensembles of structures, which were assumed to govern the subsequent stage of crack development.

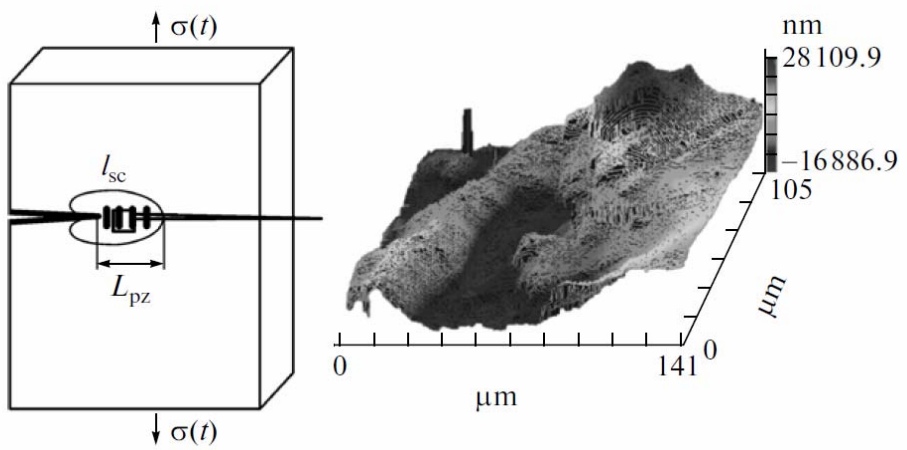

Figure 2. Schematic diagram showing a region at the crack tip and typical image of the surface relief

The structure scaling parameter of the measured surface profiles was determined based on the average difference $K(r)$ in relief heights z(x) on the fracture surface, which was defined and represented as follows:

$$K(r) = \left\langle \left(z(x+r) - z(x)\right)^2 \right\rangle_x^{1/2} \propto r^H, \tag{4}$$

where H is the index of surface roughness (Hurst exponent). By representing these data in logarithmic coordinates according to Eqs. (4), it is possible allows to evaluate the roughness index as a spatial invariant, which corresponds to a constant slope of the plot of $\ln K(r)$ versus $\ln(r)$ for a definite scale on which it is observed. The linearity of $\ln K(r)$ versus $\ln(r)$ plots allowed the roughness parameter to be evaluated as invariant in the given interval of scales r. The resolving power of the interferometer employed ensures determination of the upper and lower boundaries of scaling between K and r.

The minimal value of the scales r was assumed to determine the critical scale l_{sc} for establishing

long-range correlation interactions in the ensembles of defects formed in a process zone scale L_{pz} (Fig. 2). The values of the critical scale l_{sc} for various stages of crack propagation are presented in the Table 1.

Table 1. Values of parameters at various stages of fatigue crack development

ΔK, MPa$\sqrt{m}$	Δl, m	ΔN, cycle	dl/dN, m/cycle	l_{sc}, μm	H
6,200	$6{,}80\cdot10^{-4}$	$1{,}01\cdot10^{+6}$	$6{,}73\cdot10^{-10}$	2,6±0,2	0,57±0,02
5,890	$2{,}00\cdot10^{-4}$	$2{,}82\cdot10^{+5}$	$7{,}09\cdot10^{-10}$	2,5±0,1	0,56±0,03
5,596	$3{,}20\cdot10^{-4}$	$4{,}74\cdot10^{+5}$	$6{,}75\cdot10^{-10}$	3,4±0,1	0,54±0,03
5,316	$2{,}20\cdot10^{-4}$	$4{,}22\cdot10^{+5}$	$5{,}21\cdot10^{-10}$	1,7±0,3	0,52±0,02
5,050	$2{,}60\cdot10^{-4}$	$7{,}37\cdot10^{+5}$	$3{,}53\cdot10^{-10}$	3,7±0,2	0,49±0,03
4,797	$1{,}60\cdot10^{-4}$	$2{,}75\cdot10^{+5}$	$5{,}82\cdot10^{-10}$	2,2±0,2	0,47±0,05
4,558	$3{,}20\cdot10^{-4}$	$7{,}13\cdot10^{+5}$	$4{,}48\cdot10^{-10}$	4,1±0,3	0,59±0,03
4,330	$4{,}93\cdot10^{-4}$	$2{,}03\cdot10^{+6}$	$2{,}42\cdot10^{-10}$	3,6±0,2	0,49±0,03

Manifestations of the self-similar nature of the fatigue crack growth were studied using methods of the theory of similarity and dimensionality [6, 7]. The crack growth rate was defined as $a = dl/dN$ (where l is the crack length and N is the number of cycles) and studied as for correlation with the following parameters: $a_1 = \Delta K$, stress intensity coefficient; $a_2 = E$, Young's modulus; $a_3 = l_{sc}$, correlation scale in the ensemble of defects; $a_4 = L_{pz}$, the scale related to the process zone.

3D New View high resolution data of roughness in the crack process zone (Fig.1) revealed the existence of two characteristic scales: the scale of process zone L_{pz} and correlation length l_{sc} that is the scale when correlated behavior of defect induced roughness has started [1].

Using the Π-theorem and taking into account the dimensionality of variables $[dl/dN] = L$, $[\Delta K] = FL^{-3/2}$, $[l_{sc}] = [L_{pz}] = L$, and $[E] = FL^{-2}$, the kinetic equation for the crack growth:

$$dl/dN = \Phi(\Delta K, E, l_{sc}, L_{pz}), \tag{5}$$

can be rewritten as follows:

$$\frac{dl}{dN}\frac{1}{l_{sc}} = \bar{\Phi}\left(\frac{\Delta K}{E\sqrt{l_{sc}}}, \frac{L_{pz}}{l_{sc}}\right). \tag{6}$$

Estimation of the values $\Delta K/(E\sqrt{l_{sc}}) << 1$ and $L_{pz}/l_{sc} >> 1$ suggest an intermediate-asymptotic character of the crack growth kinetics for Eq. (6) in the following form:

$$\frac{d\bar{l}}{dN} = \left(\frac{\Delta K}{E\sqrt{l_{sc}}}\right)^{\alpha}\left(\frac{L_{pz}}{l_{sc}}\right)^{\beta}, \tag{7}$$

where $\bar{l} = l / l_{sc}$. Introducing the parameter $C = \left(L_{pz} / l_{sc}\right)^{\beta}$, we can reduce the scaling relation (7) to the following form analogous to the Paris law:

$$\frac{d\bar{l}}{dN} = \mathrm{C}\left(\frac{\Delta K}{E\sqrt{l_{sc}}}\right)^{\alpha}, \tag{8}$$

where α is a universal exponent. This form is similar to the equation proposed by Hertzberg for $l_{sc} \to b$, where b is the Burgers vector. In the limit of small scales $l_{sc} \approx b$ the application of stress intensity factor conception is problematic and corresponding scaling laws can be introduced [2].

Using relation (8), which constructed based on the results experimental investigation of the fatigue crack growth kinetics with allowance for the calculated l_{sc} values, it is possible to estimate the exponent as α ~2.3, which corresponds to the slope of the straight line in the rectifying coordinates (Fig. 3).

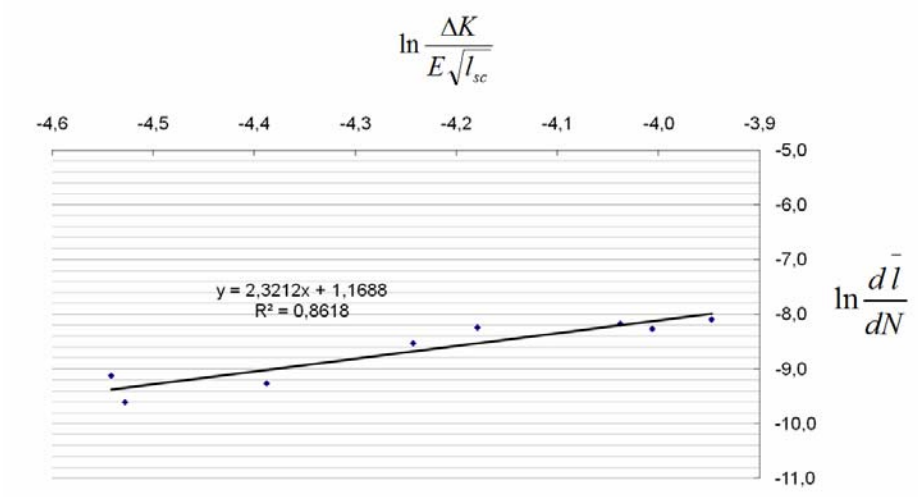

Figure 3. Rectified plot of relation (8)

A difference of the exponent α ~ 2.3 from values obtained in the regimes of multicycle fatigue testing suggests that there are certain specific features in the formation of fracture regions in the vicinity of crack tip under conditions of gigacycle loading.

3. Summary

The constancy of the scaling index (Hurst exponent) in a broad interval of spatial scales, which includes the scales of evolution of the typical defect substructures, leads to a conclusion that the kinetics of crack propagation can be considered within the framework of a broad class of critical phenomena, namely, structure–scaling transitions [3, 4] that describe the evolution of defects on various scaling levels. Determination of the scaling index of deformation induced defect structures can provide a physical explanation of the universality of this class of physical phenomena with respect to the scenarios of fracture in materials of various classes and the influence of structural states (including those formed by accidental dynamic impacts) on the “threshold” characteristics of

the transition of a loaded material from plastic deformation to fracture.

Acknowledgments

The study was supported by The Ministry of education and science of Russia, project № 8753.

References

[1] B.B. Mandelbrot, The fractal geometry of nature, W.H. Freeman, New York, 1983.
[2] P. Paris, D. Lados, H. Tad, Reflections on identifying the real $\Delta K_{effective}$ in the threshold region and beyond. Engineering Fracture Mechanics, 75 (2008) 299–305.
[3] J.L. Lataillade, O.B. Naimark, Mesoscopic and nonlinear aspects of dynamic and fatigue failure (experimental and theoretical results). Physical Mesomechanics, 7 (2004) 55–66.
[4] O.B. Naimark, Advances in Multifield Theories of Continua with Substructure, in: G. Capriz, P. Mariano (Eds.), Birkhauser, Boston, 2003, pp. 75–114.
[5] C. Bathias, Piezoelectric fatigue testing machines and devices. Int.J. of Fatigue, 28 (2006) 1438–1445.
[6] G.I. Barenblatt, Scaling phenomena in fatigue and fracture. Int.J. of Fracture, 138 (2006) 19–35.
[7] R.O. Ritchie, Incomplete self-similarity and fatigue-crack growth. Int.J. of Fracture, 132 (2005) 197–203.

The effect of damage accumulation in slip bands on the resonant behavior in the very high cycle fatigue (VHCF) regime

Philipp-Malte Hilgendorff[1,*], Andrei Grigorescu[2], Martina Zimmermann[3], Claus-Peter Fritzen[1], Hans-Jürgen Christ[2]

[1] Institut für Mechanik und Regelungstechnik - Mechatronik, Universität Siegen, Siegen 57068, Germany
[2] Institut für Werkstofftechnik, Universität Siegen, Siegen 57068, Germany
[3] Institut für Werkstoffwissenschaft, Technische Universität Dresden, Dresden 01062, Germany
* Corresponding author: philipp.hilgendorff@uni-siegen.de

Abstract
In many applications structural components are cyclically loaded up to a very high number of loading cycles due to high frequency or long product life. In this regime, particular attention is paid to the period of fatigue crack initiation and thus the localization of plastic deformation. The characterization of the damage accumulation in the VHCF regime is conducted by a new approach based on the resonant behavior of the specimen. The resonant behavior of a metastable austenitic stainless steel (AISI304) is studied experimentally in the VHCF regime and shows a distinct transient characteristic. To obtain a physically-based understanding of this characteristic, the underlying microstructural damage mechanisms and their influence on the resonant behavior are modeled. Microscopic examinations indicate that AISI304 executes localization of plastic deformation in planes/bands of intense slip. Therefore, a microstructural simulation model is proposed which accounts for the damage mechanisms of slip bands as documented by the experimental results. The model describes the behavior of slip bands taking the mechanisms of formation, sliding, slip irreversibility and cyclic hardening into account. In order to run simulations considering the real microstructure, the model is implemented into a numerical method. The two-dimensional (2-D) boundary element method is well suited for this purpose and is based on two integral equations: the displacement boundary integral equation applied to the external boundary and the stress boundary integral equation used in slip bands. Fundamental solutions within these integral equations represent anisotropic elastic behavior. By using this method, a 2-D microstructure can be reproduced that considers orientations as well as individual anisotropic elastic properties in each grain. The resonant behavior is characterized by evaluating the force-displacement hysteresis loop and using a hysteretic damping model. Results show that simulation of slip bands is in good agreement to microscopic examinations and that plastic deformation in slip bands influences the transient characteristic of the resonant behavior.

Keywords
simulation, damage accumulation, resonant behavior, boundary element method, very high cycle fatigue

1. Introduction

Observations in the regime of VHCF beyond 10 million cycles reveal that failure arises even at stress amplitudes below the conventional high cycle fatigue limit (as discussed in the series of VHCF conferences since 1998, e.g. Ref. [1]). For that reason the exploration of fatigue mechanisms in that regime and the characterization of fatigue life becomes more and more important. In the VHCF regime the period of fatigue crack initiation consumes the majority of the total fatigue life. The metastable austenitic stainless steel considered in this study conducts localization of cyclic plastic deformation by motion of dislocations which are arranged in slip bands. They are accepted as very important feature of cyclic straining in crystalline materials [2]. Slip bands are affected by cyclic slip irreversibility, which even in the VHCF regime leads to a sizeable irreversible accumulated plastic slip deformation [3].
The resonant behavior of a metastable austenitic stainless steel (AISI304) shows a distinct transient characteristic. In order to identify the microstructural damage mechanisms relevant for the transient characteristic, in the present study the damage accumulation in slip bands is modeled and its effect

on the resonant behavior is investigated. The slip band model adopted in this study is applied on a mesoscopic scale and accounts for the mechanisms of slip band formation, motion and multiplication of dislocations (expressed with the term sliding), its cyclic irreversibility and cyclic hardening.

To investigate the effect of the suggested slip band model on the resonant behavior it is adapted to the simulation of real microstructures. Several studies in the field of microstructural modeling and simulation of fatigue damage use the finite-element method (FEM) in conjunction with crystal plasticity models. Although the FE-method combined with crystal plasticity models has been devoted to a wide range of applications the implementation of the newly proposed slip band model of this study would present some difficulties: formation of new slip bands would require a remeshing algorithm and computation of sliding displacement in slip bands would necessitate special finite elements like cohesive-zone elements.

In this study a two-dimensional boundary element method (BEM) is applied, in which the proposed slip band model can be implemented very effectively. The most outstanding feature of this method is that it uses displacement differences or sliding displacements directly as unknowns on slip band layers and element discretization is confined to outer boundaries such as grain boundaries and on slip bands. The proposed BEM can simulate slip bands in a two-dimensional microstructure consisting of grains with individual anisotropic elastic properties.

In the following paragraphs at first the results of experimental examinations are given and then the simulation model with its slip band mechanisms is presented and the numerical method is specified. After presenting a procedure to determine the resonant behavior resulting from simulations, the effect of damage accumulation in slip bands on the resonant behavior is investigated in a model representing the morphology of a real microstructure.

2. Experimental Characterization

The resonant behavior of a metastable austenitic stainless steel (AISI304) is studied experimentally by means of a resonance-testing-machine, which readjusts the excitation resonant frequency during testing. The material shows a distinct transient characteristic, as shown in Fig. 1a. The lower curve in Fig. 1a indicates the test frequency at a stress amplitude of 240MPa, representing the damped resonant frequency f_{res} of the specimen-machine system. The upper curve in Fig. 1a indicates the testing frequency at low stress levels (50MPa) at distinct fatigue life stages (due to testing at 240MPa). It shows the resonance frequency f_0 of the sample without the damping effect of plastic deformation.

Fig. 1b shows a transmission electron microscopy (TEM) micrograph of the dislocation arrangement in metastable austenitic stainless steel in the fully austenitic condition fatigued under VHCF condition. The micrograph indicates that dislocations in slip bands are arranged in pile-ups at grain boundaries.

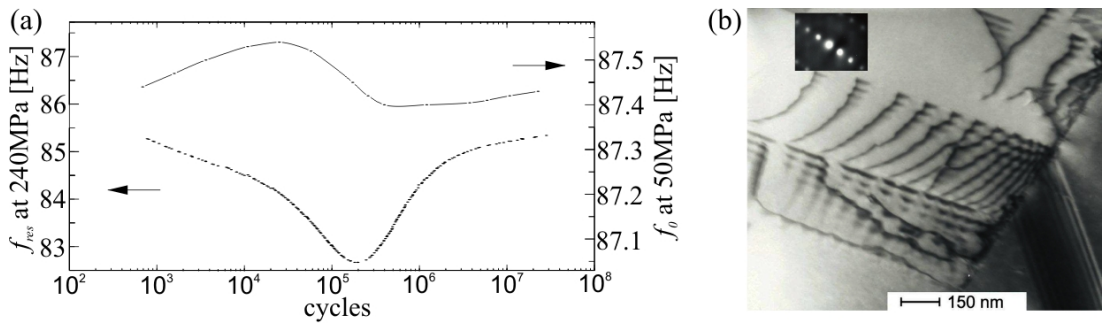

Figure 1. (a) Damped (f_{res}) and undamped (f_0) resonant frequency during cyclic loading of metastable austenitic stainless steel; (b) TEM micrograph of dislocation pile-ups at a grain boundary in metastable austenitic stainless steel (loading amplitude: 240MPa, number of cycles: 10^7)

3. Simulation Model

The plastic material behavior by localization of cyclic plastic deformation in slip bands will be considered by mechanisms which define the properties of formation, sliding, irreversibility and hardening of a slip band as follows.

Formation of a slip band is assumed to occur once a critical resolved shear stress is exceeded [4,5]. The critical resolved shear stress is defined as $\tau_{crit}^{0} = 80\text{MPa}$, which corresponds to the threshold for slip band formation observed in Ref. [6].

Motivated by the TEM micrograph in Fig. 1b the model used in this study is based on the theory of dislocation pile-ups at grain boundaries [7]. Due to the equilibrium of forces produced by external loading and repulsive forces between dislocations a characteristic dislocation distribution occurs. Taking into account the distortion of a dislocation, which is defined by the magnitude of the Burgers vector, a sliding distribution $\Delta u(\xi)$ can be determined:

$$\Delta u(\xi) = \frac{2\cdot(1-\nu)}{G}\sqrt{(l/2)^2 - \xi^2}\cdot(\tau - \tau_{crit}), \tag{1}$$

where ν and G are Poisson's ratio and shear modulus in the slip plane, respectively. l is the length of slip band and ξ is the coordinate along the slip band starting at the dislocation source. τ and τ_{crit} represent the shear stress existing in the dislocation source and the critical resolved shear stress.

It is concluded that the evolution of slip bands is related to cyclic slip irreversibility [3]. To be able to consider this mechanism in the simulation model, the slip band is approximated by two closely located layers, on which dislocation motion occurs separated in tensile and compressive loading (Fig. 2a), as Tanaka and Mura suggested in their model [8]. A special procedure was adopted to accumulate the irreversible fraction of cyclic slip. Fig. 2b shows exemplarily the variation of shear stress τ as a function of time in a slip band (in both layers) provoked by external loading and shows the resulting maximum sliding Δu^{I} in layer I and Δu^{II} in layer II.

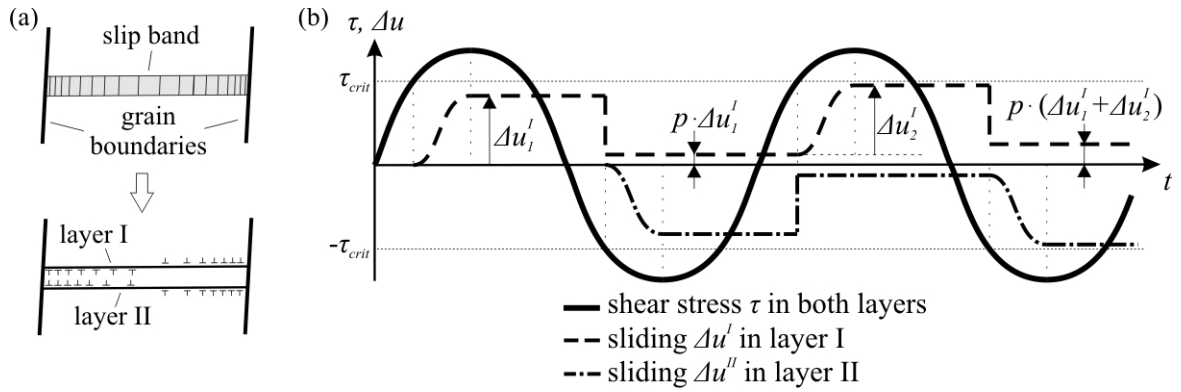

Figure 2. (a) Approximation of slip band by two closely located layers; (b) Exemplary variation of fatigue shear stress τ as a function of time in a slip band and resulting maximum sliding Δu^{I} in layer I and Δu^{II} in layer II

Once the critical resolved shear stress τ_{crit} in the first tensile loading is exceeded, layer I starts to slide by conducting the pile-up sliding model. As the shear stress decreases sliding is fixed at its maximum value Δu_1^{I}. During compressive loading layer II is activated as soon as the shear stress exceeds the critical resolved shear stress in opposite direction and concurrently in layer I, the fixed sliding Δu_1^{I} is reduced to an irreversible fraction $p\cdot\Delta u_1^{I}$. It is determined by the cyclic slip irreversibility p, which is defined as the fraction of plastic shear deformation that is irreversible in a microstructural sense [3]. One full cycle later the maximum sliding Δu_2^{I} is reduced again, but this time to an accumulated irreversible fraction denoted by the term $p\cdot(\Delta u_1^{I} + \Delta u_2^{I})$ taking the

irreversibility of the previous sliding into account. This procedure in combination with approximation of the slip band by two closely located layers is capable to account for irreversible fraction of sliding.

Hardening is assumed to result from a rising dislocation density. Therefore in the model the dislocation density is raised according to the plastic slip deformation in the slip band. After the slip band mechanisms are well defined in the simulation model in the following the numerical method is presented.

4. Numerical Method

The boundary element method used in this study combines the traditional displacement BEM as well as the displacement discontinuity BEM [9]. By doing so, sliding displacements can be directly evaluated in slip bands and element discretization is confined to outer boundaries such as grain boundaries and on slip bands.

The BEM used in this study is described by means of a problem statement, which consists of a two-dimensional homogeneous, anisotropic and linear elastic solid containing a finite slip line as shown in Fig. 3.

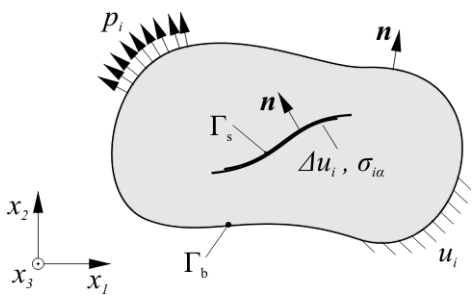

Figure 3. An anisotropic solid including a slip line

On the external boundary Γ_b displacements and tractions with components u_i and p_i are prescribed, while relative displacements Δu_i and stresses $\sigma_{i\alpha}$ are considered on one face Γ_s of the slip line. Here, relative displacements consist only of tangential relative displacements, because slip lines in contrast to cracks cannot perform opening - only sliding. Throughout the analysis the conventional summation rule over double indices is applied, Roman and Greek indices can only have the values 1 and 2. The procedure is based on two boundary integral equations: the displacement boundary integral equation, which is applied on the external boundary, and the stress boundary integral equation, which is used on the slip line face. The displacement boundary integral equation for a solid containing a slip line can be written as [9,10]:

$$c_{ij} \cdot u_i(\boldsymbol{x}) = \int_{\Gamma_b} \left[u_{ij}^*(\boldsymbol{x},\boldsymbol{y}) \cdot p_i(\boldsymbol{y}) - p_{ij}^*(\boldsymbol{x},\boldsymbol{y}) \cdot u_i(\boldsymbol{y}) \right] d\Gamma_y + \int_{\Gamma_s} p_{ij}^*(\boldsymbol{x},\boldsymbol{y}) \cdot \Delta u_i(\boldsymbol{y}) d\Gamma_y, \boldsymbol{x} \in \Gamma_b , \tag{4}$$

where c_{ij} equals 0.5 when Γ_b is smooth and $u_{ij}^*(\boldsymbol{x},\boldsymbol{y})$ and $p_{ij}^*(\boldsymbol{x},\boldsymbol{y})$ are the displacement and the traction fundamental solutions. Vector $\boldsymbol{x}$ denotes the positions, where displacements are determined, and $\boldsymbol{y}$ denotes the integration points on the boundaries Γ_b and Γ_s. The stress boundary integral equation is obtained by substituting equation (4) into Hooke's law:

$$\sigma_{j\gamma}(\boldsymbol{x}) = \int_{\Gamma_b} \left[d_{ij\gamma}^*(\boldsymbol{x},\boldsymbol{y}) \cdot p_i(\boldsymbol{y}) - s_{ij\gamma}^*(\boldsymbol{x},\boldsymbol{y}) \cdot u_i(\boldsymbol{y}) \right] d\Gamma_y + \int_{\Gamma_s} s_{ij\gamma}^*(\boldsymbol{x},\boldsymbol{y}) \cdot \Delta u_i(\boldsymbol{y}) d\Gamma_y, \boldsymbol{x} \in \Gamma_s , \tag{5}$$

where $d_{ij\gamma}^*(\boldsymbol{x},\boldsymbol{y})$ and $s_{ij\gamma}^*(\boldsymbol{x},\boldsymbol{y})$ are the stress and the higher-order stress fundamental solutions.

The displacement fundamental solution in equation (4) is given in Ref. [11] by Wang. He derived two-dimensional elastostatic fundamental solutions for general anisotropic solids by the use of Stroh's formalism [12]. The displacement fundamental solution in equation (4) can be given as an explicit expression:

$$u_{ij}^{*}(\boldsymbol{x},\boldsymbol{y}) = \frac{1}{\pi}\mathrm{Im}\sum_{m=1}^{M}\frac{A_{ij}(\eta_m)}{\partial_\eta D(\eta_m)}\log\left[\boldsymbol{d_m}\cdot(\boldsymbol{y}-\boldsymbol{x})\right] \tag{6}$$

with

$$A_{ij}(\eta_m) = adj\left[\Gamma_{ij}(1,\eta_m)\right], \tag{7}$$

$$D(\eta_m) = \det\left[\Gamma_{ij}(1,\eta_m)\right]. \tag{8}$$

$$\boldsymbol{d}_m = (1,\eta_m). \tag{9}$$

In equations (6)-(9) $\Gamma_{ij}(1,\eta_m)$ is defined by

$$\Gamma_{ij}(1,\eta_m) = C_{2ij2}\cdot\eta_m{}^2 + \left(C_{2ij1}+C_{2ji1}\right)\cdot\eta_m + C_{1ij1}, \tag{10}$$

where $C_{\alpha ij\beta}$ is the elasticity tensor. $D(\eta_m)$ in (6) and (8) is a polynomial function of order four and has M=2 complex roots η_m and two complex conjugates of η_m, which satisfy the following characteristic equation:

$$D(\eta_m) = 0. \tag{11}$$

The traction fundamental solution in equation (4) is defined by the following closed expression [10]:

$$p_{ij}^{*}(\boldsymbol{x},\boldsymbol{y}) = \frac{1}{\pi}\mathrm{Im}\sum_{m=1}^{M}\frac{B_{ij}(\eta_m)}{\partial_\eta D(\eta_m)}\frac{\boldsymbol{d_m}\cdot\boldsymbol{n}(\boldsymbol{y})}{\boldsymbol{d_m}\cdot(\boldsymbol{y}-\boldsymbol{x})} \tag{12}$$

with

$$B_{ij}(\eta_m) = \left(C_{2ip2}\cdot\eta_m + C_{2ip1}\right)\cdot A_{pj}(\eta_m), \tag{13}$$

and the outward unit normal vector $\boldsymbol{n}$. The stress and higher-order stress fundamental solutions in equation (5) are provided by:

$$d_{ij\gamma}^{*}(\boldsymbol{x},\boldsymbol{y}) = -\frac{1}{\pi}\mathrm{Im}\sum_{m=1}^{M}\frac{B_{ij\gamma}(\eta_m)}{\partial_\eta D(\eta_m)}\frac{\boldsymbol{d_m}}{\boldsymbol{d_m}\cdot(\boldsymbol{y}-\boldsymbol{x})}, \tag{14}$$

$$s_{ij\gamma}^{*}(\boldsymbol{x},\boldsymbol{y}) = -\frac{1}{\pi}\mathrm{Im}\sum_{m=1}^{M}\frac{C_{ij\gamma}(\eta_m)}{\partial_\eta D(\eta_m)}\frac{\boldsymbol{d_m}\cdot\boldsymbol{d_m}\cdot\boldsymbol{n}(\boldsymbol{y})}{\left[\boldsymbol{d_m}\cdot(\boldsymbol{y}-\boldsymbol{x})\right]^2}, \tag{15}$$

with

$$B_{ij\gamma}(\eta_m) = \left(C_{\gamma ip2}\cdot\eta_m + C_{\gamma ip1}\right)\cdot A_{pj}(\eta_m), \tag{16}$$

$$C_{ij\gamma}(\eta_m) = \left(C_{\gamma ip2}\cdot\eta_m + C_{\gamma ip1}\right)\cdot A_{pt}(\eta_m)\cdot\left(C_{2jt2}\cdot\eta_m + C_{2jt1}\right). \tag{17}$$

The integration of the fundamental solutions (6), (12), (14) and (15) are performed fully analytically. It should be noted that the solutions have a weak logarithmic singularity log[$\boldsymbol{y}$-$\boldsymbol{x}$] (6), a strong singularity 1/[$\boldsymbol{y}$-$\boldsymbol{x}$] (12,14), and a hypersingularity 1/[$\boldsymbol{y}$-$\boldsymbol{x}$]^2 in the higher-order stress fundamental solution (15). For spatial discretization of equation (4) and (5) a collocation method is utilized.

In Ref. [9] and [13] a substructure technique is presented, which enables coupling of individual homogeneous substructures by use of continuity condition. The implementation of this technique in the present method allows to represent each grain by a homogeneous, elastic anisotropic substructure which is combined with other grains to a continuous microstructure.

5. Resonant behavior

The characterization of the damage accumulation in slip bands based on the resonant behavior requires a procedure to describe the resonant behavior resulting from the microstructural simulations. With the use of both the viscous and the hysteretic damping model [14] an equivalent damping ratio D and finally the resonant frequency ratio η_{res} as a describing parameter for the resonant behavior can be identified. η_{res} is basically defined as the ratio of resonant frequency of the damped system (f_{res}) and that of the undamped system (f_0). By means of energy loss per cycle ΔW, stiffness k of the specimen and displacement amplitude $\hat{x}$ of the force displacement hysteresis loop the ratio η_{res} is given by:

$$\eta_{res} = \sqrt{1 - \frac{\Delta W^2}{2\pi^2 \cdot k^2 \cdot \hat{x}^4}} \tag{18}$$

ΔW, k and $\hat{x}$ can be taken from the hysteresis loop, which is calculated during simulation. η_{res} can also be evaluated by using the experimental results in Fig. 1a. Thus the ratio η_{res} is applicable to compare the results from experiments with those from simulations.
In the following, the effect of damage accumulation in slip bands on the resonant behavior is investigated.

6. Simulation of damage accumulation in slip bands

The implementation of the simulation model into the BEM allows to simulate damage accumulation in slip bands in a 2-D microstructure. The investigation was carried out on the basis of the real microstructure of a metastable austenitic stainless steel characterized by means of scanning electron microscopy (SEM) in combination with the electron backscattered diffraction (EBSD)-technique and the orientation imaging microscopy (OIM) analysis.
The SEM image and EBSD map of the observed zone are shown in Fig. 4a and 4b. In addition to grain boundaries, the SEM image also highlights markings of emerging slip bands at the surface after cyclic loading. The EBSD map in Fig. 4b with related stereographic triangle indicates the crystallographic orientation of each grain.

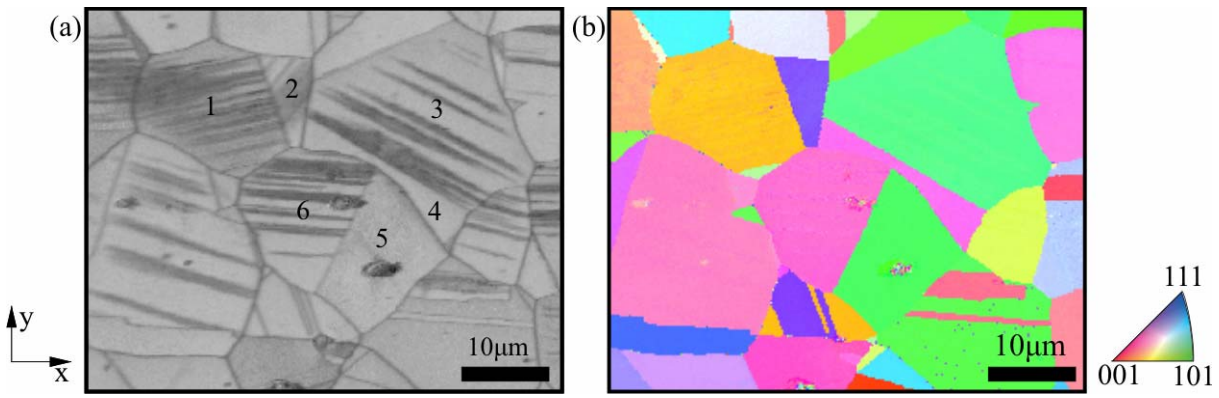

Figure 4. (a) SEM image and (b) EBSD map of the measured zone of surface grains (loading amplitude: 240MPa, number of cycles: 10^7)

In this study, primarily the contours of shear stresses in most critical slip systems are observed. For this purpose, shear stresses were computed in all of the 12 slip systems of each austenite grain and only the highest corresponding shear stresses were presented in the contours, regardless of highest Schmid factor. The elasticity tensor of the austenite phase is defined by the figures of the elastic

constants of the cubic material that are C_{11}=205 GPa, C_{12}=135 GPa and C_{44}=125 GPa in the present case. The 2-D BEM presupposes that exclusively in-plane sliding displacements in the x-y-plane are observed in simulations. Due to the fact, that surface roughening is strongly affected by out-of-plane sliding displacements, simulations in this study are not able to directly represent the surface roughening indicated in Fig. 4a.

Fig. 5 shows contours of simulated shear stresses in the microstructure when the simulation model is enabled. Due to the high computational effort, slip band modeling was confined to 6 grains labeled 1-6. Contours were chosen from the first, third and seventh simulated loading cycle and in each case at the maximum external loading of 240MPa. It should be noticed that one cycle in the simulation represents the microstructural damage evolution resulting from many cycles in the experiment. This was achieved by adapting the parameter of cyclic slip irreversibility p and by increasing the effect of cyclic hardening. In the simulation the cyclic slip irreversibility p is 0.2 that is much higher than usually observed for VHCF. For example in Ref. [3] a value of p=0.000034 for very high fatigued copper polycrystals was obtained. The effect of cyclic hardening was similarly increased in simulation.

The comparison between surface slip markings on the SEM image (Fig. 4a) and simulated slip band layers (Fig. 5) illustrates that slip bands are formed in correct slip systems. Sliding displacements in slip band layers lead to a decrease of shear stresses within grains, while at the end of slip bands significant stress peaks arise. This is particularly demonstrated in grain 4 (Fig. 5).

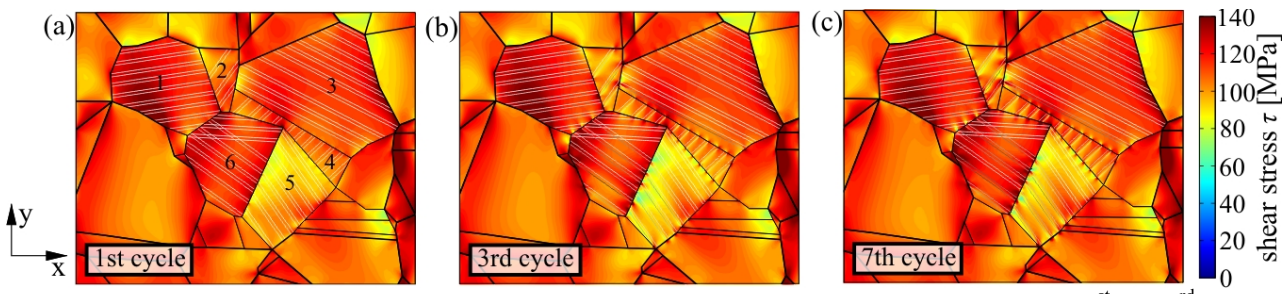

Figure 5. Contours of simulated maximum shear stresses in most critical slip systems in the 1st (a), 3rd (b) and 7th (c) loading cycle (loading amplitude: 240MPa, hypothetical cyclic slip irreversibility of p=0.2 (in order to represent many experimental cycles in one simulated cycle))

It is shown in Fig. 5 that slip bands deform differently depending on the specific polycrystalline boundary value problem. The comparison of contour plots in Fig. 5 in the first, third and seventh loading cycle shows that with increasing number of simulated cycles shear stresses at the end of slip bands and thus at grain boundaries increase. This is a result of the irreversible damage accumulation.

In order to investigate the effect of the microstructural damage accumulation on the resonant behavior, the force-displacement hysteresis loop is evaluated for each cycle of simulation and by using Eq. (18) the resonant frequency ratio η_{res} is determined. Fig. 6 shows the qualitative comparison of resonant frequency ratio η_{res} from simulation and experiment. Different assigning of scales for simulation (red) and experiment (black) demonstrate the qualitative manner of this comparison. A decrease of η_{res} relates to cyclic softening and an increase to cyclic strengthening.

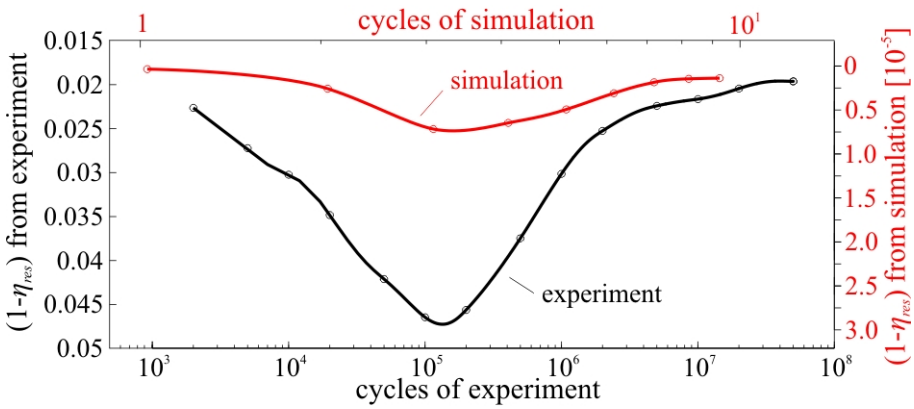

Figure 6. Qualitative comparison of resonant frequency ratio η_{res} from simulation and experiment

The results show that cyclic softening and subsequent strengthening arise from simulation of damage accumulation in slip bands. At first the mechanisms of formation and sliding cause a softening and later the mechanism of strengthening is dominating. However, by comparing the different scaling of both curves in Fig. 6 it gets obvious that the transient behavior of the experiment is much more pronounced than that of the simulation. Thus, the distinct transient characteristic of the metastable austenitic stainless steel cannot be completely reproduced by simulation of damage accumulation in slip bands. It has to be taken into account that the metastable austenitic stainless steel fulfills deformation induced martensite formation during fatigue, which might play an important role in the transient characteristic. But the mechanism of deformation induced martensite formation has not yet been considered in the model and, therefore, will be the subject of future investigations.

7. Conclusion

In this study, a simulation model is proposed that describes the damage mechanisms occurring in slip bands under VHCF condition. It is assumed that formation of a slip band occurs at sites of shear stress concentration and sliding distribution arises from the theory of dislocation pile-ups at grain boundaries. The irreversible slip character is observed as the slip band is approximated by two closely located layers and a special procedure was adopted. Hardening of the slip band results from an increasing dislocation density. The simulation model is implemented into a BEM, which is based on two boundary integral equations: the displacement boundary integral equation and the stress boundary integral equation. Fundamental solutions for general anisotropic elastic solids are used and by means of a substructure technique a 2D-microstructure with individual anisotropic elastic behavior in each grain is considered. The effect of damage accumulation in slip bands on the resonant behavior is investigated by conducting simulations in a real simulated 2-D microstructure. It turns out that slip planes of generated slip bands are in good agreement with SEM observation. The resonant behavior is characterized by the resonant frequency ratio η_{res} that can be determined from the simulated force-displacement hysteresis loop with the use of both the viscous and the hysteretic damping model. The qualitative comparison of η_{res} from simulation and experiment shows that cyclic softening and subsequent strengthening in the transient regime arise from simulation of damage accumulation in slip bands. But it becomes apparent that the variation of η_{res} from experiment is much more pronounced than that from simulation. Future work will concentrate on the effect of further microstructural inhomogeneities such as deformation induced martensite in combination with damage accumulation in slip bands.

Acknowledgements

We thank M. Wünsche for fruitful discussions regarding the boundary element method. The authors gratefully acknowledge financial support of this study by Deutsche Forschungsgemeinschaft (DFG) in the framework of the priority program Life∞ (SPP 1466).

References

[1] C. Berger, H.-J. Christ, Fifth international conference on very high cycle fatigue, DVM, Berlin, Germany, 2011.
[2] J. Man, K. Obrtlik, and J. Polak, Study of surface relief evolution in fatigued 316L austenitic stainless steel by AFM, Mat. Sci. Eng. A, 351, (2003) 123-132.
[3] H. Mughrabi, Cyclic slip irreversibilities and the evolution of fatigue damage, Metall. Mater. Trans. A, 40A, (2008) 1257-1279.
[4] J. Yang, Y.Li, Z. Cai, S. Li, C. Ma, E. Han, W. Ke, Evolution of persistent slip bands and simulation of its stress field in a fatigued copper single crystal, Mat. Sci. Eng. A, 345, (2003) 164-171.
[5] D. Zhou, J.C. Moosbrugger, D.J. Morrison, Finite element simulation of PSB macroband nucleation and propagation in single crystal nickel cycled at low plastic strain amplitudes, Int. J. Plasticity, 22, (2006) 1336-1366.
[6] C. Müller-Bollenhagen, M. Zimmermann, H.-J.Christ, Adjusting the very high cycle fatigue properties of a metastable austenitic stainless steel by means of the martensite content, Procedia Engineering, 2, (2010) 1663-1672.
[7] J.P. Hirth, J. Lothe, Theory of dislocations, 2nd ed., Krieger Publishing Company, 1992.
[8] K. Tanaka, T. Mura, A dislocation model for fatigue crack initiation, J. Appl. Mech., 48, (1981) 97-103.
[9] M. Kübbeler, I. Roth, U. Krupp, C.-P. Fritzen, H.-J.Christ, Simulation of stage I-crack growth using a hybrid boundary element technique, Eng. Fract. Mech., 78, (2011) 462-468.
[10] M. Wünsche, Ch. Zhang, M. Kuna, S. Hirose, J. Sladek, V. Sladek, A hypersingular time-domain BEM for 2D dynamic crack analysis in anisotropic solids, Int. J. Numer. Meth. Eng., 78, (2009) 127-150.
[11] C.-Y. Wang, Two-dimensional elastostatic Green's functions for general anisotropic solids and generalization of Stroh's formalism, Int. J. Solids Struct., 31, (1994) 2591-2597.
[12] A. Stroh, Dislocations and cracks in anisotropic elasticity, Philos. Mag., 3, (1958) 625-646.
[13] M.H. Aliabadi, The boundary element method, Vol. 2, John Wiley and Sons, 2002.
[14] L. Gaul, S. Bohlen, S. Kempfle, Transient and Forced Oscillations of Systems with Constant Hysteretic Damping, Mech. Res. Comm., 12, (1985) 187-201.

Very High Cycle Fatigue Behavior of Plasma Nitrided 316 Stainless Steel

Daisuke Yonekura[1,*], K. Ozaki[1], R. Shibahara[1], Insup Lee[2] and R. Murakami[1]

[1] Department of Mechanical Engineering, The University of Tokushima, Tokushima 770 8506, Japan
[2] Department of Advanced Material Engineering, Dongeui University, Busan 614 714, Korea
* Corresponding author: yonekura@tokushima-u.ac.jp

Abstract In this study, plasma nitriding was performed for 316 stainless steel under 2 different processing time, 15hours and 25hours. Cantilever type rotational bending fatigue tests were carried out using the nitrided and non-treated samples in high cycle and very high cycle fatigue life regime in order to examine the influence of the plasma nitriding on the fatigue properties in the both fatigue life regimes of 316 stainless steel. As a result, the fatigue strength was improved by the plasma nitriding and the shape of the S-N curves was a asymptote shape with a fatigue limit up to $N = 10^8$ cycles. The fatigue cracks initiated from specimen surface in all specimen. However, the improvement of fatigue strength by plasma nitriding and the influence of nitriding time on the fatigue strength was small because the nitriding layer was quite thin, especially in the diffusion layer. For this reason, it is believed that the nitrided layer could not affect significantly the fatigue strength.

Keywords Very high cycle fatigue, Plasma nitriding, Stainless steel, Cantilever-type rotary bending fatigue test.

1. Introduction

Surface treatment is widely used to improve fatigue, wear and corrosion resistance of various industrial products. There are many surface treatment methods, such as carburizing, induction hardening, shot peening and physical vapor deposition coating etc. These treatments form a hardened surface layer with compressive residual stress, and therefore, the fatigue properties are improved by the surface layer [1-9]. Nitriding is one of the surface treatment methods. Nitriding produces a nitrogen diffused surface layer with a compound layer which is formed by reaction between nitrogen and nitride-forming elements in a material such as aluminum, chromium, molybdenum and titanium. Good fatigue and wear resistance are obtained by the nitrided surface layer. However, it is well known that the nitriding treatment is difficult to apply to stainless steel because the stainless steel has a passivation film on the surface which hinders the diffusion of nitrogen into the material. Therefore, the removal of the passivation film is required when the nitriding treatment is applied to the stainless steel.

There are three major methods to perform the nitriding process; gas nitriding, salt-bath nitriding and plasma nitriding processes. In particular, plasma nitriding process is a very attractive method to improve the surface properties for various engineering materials due to its advantages, such as low emission of toxic gases, low maintenance cost and low pollution, compared with conventional gas or salt bath nitriding process [10]. Plasma nitriding process has many parameters: the nitriding temperature, the gas mixture and the time duration [11-12]. These parameters strongly affect the material properties of nitrided samples. Many researchers have reported the influence of the parameters on the fatigue properties using various steels and have also reported that the fatigue limit can be improved by the plasma nitriding. In particular, the fatigue limit increases with increasing the processing time under cyclic bending stress due to the thick hardened layer because the fatigue cracks initiate from internal defects such as inclusions or cavities or from the interface between substrate and nitriding layer [13-18].

Since the plasma nitriding process can use the hydrogen etching effect which can remove the surface oxide layer as well as surface contamination, the plasma nitriding process can form a nitrided and diffused surface layer for the stainless steel [19-22]. The plasma nitriding will improve the fatigue strength of the stainless steel but the plasma nitriding may cause the decrease of the fatigue strength in very high cycle fatigue life regime by an internal fracture because the plasma nitriding produces thin hardened layer and the fatigue failure of some surface hardened steel occurs at stress levels below the conventional fatigue limit in the life regime greater than 10^7 cycles [23]. However few studies on the fatigue life of plasma nitrided stainless steels have been carried out in the very high cycle regime.

In the present study, SUS316 austenitic stainless steel was treated by the plasma nitriding under two nitriding times. Rotating bending fatigue tests were carried out for these nitrided specimens in order to investigate the effect of the nitriding time on the fatigue behavior in the high cycle and very high cycle fatigue regime. Fracture morphologies were observed using a scanning electron microscope (SEM) and the influence of the plasma nitriding process on the fatigue behavior of austenitic stainless steel was discussed.

2. Experimental Procedure

The material used in this study was austenitic stain less steel, SUS316. The fatigue specimens were machined into the shape and dimensions as shown in Fig. 1. The round notch surface was polished with a grinder having a mesh size of #100. Notch radius was 7 mm and the stress concentration factor of the specimen was K_t=1.06.

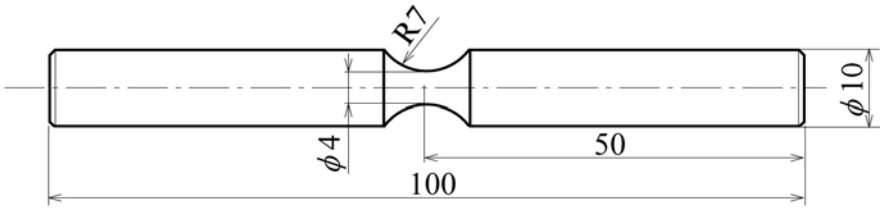

Figure 1. Shape and dimensions of specimen.

The surface of the specimen to be exposed to plasma was cleaned using an ultrasonic bath in acetone. A vacuum chamber was pumped down to 50 mTorr and then back-filled with a gas mixture of NH_3 and H_2 up to 3 Torr (NH_3:H_2 mixing ratio; 4:1). The plasma nitriding process was immediately carried out with a pulsed dc potential at the designed time in the glow discharge of the plasma. In the present study, plasma nitriding was performed at 703 K for 15 hours or 25 hours. These nitrided specimens will be called N15 and N25, respectively. After the plasma nitriding, the vacuum chamber was pumped down to 50 mTorr and the specimens were furnace cooled to room temperature.

Fatigue tests were carried out at room temperature by using a dual-spindle cantilever-type rotating bending fatigue-testing machine, which is the standard testing machine in the Research Group for Statistical Aspect of Materials Strength, Japan [24]. The stress frequency was 3150 rpm and the stress ratio $R = -1$. All of the fracture specimens were observed using SEM. The run-out number of cycles was $N = 1.0\times10^8$ cycles. The fracture surface of the specimen was observed using SEM. A Vickers microhardness tester was used to measure the microhardness of samples. The parameters used in the microhardness test were 100 gf and a duration 15 s. The microstructure was observed using a cross sectional surface etched by Marble's regent (4.0 g CuSO4, 20 ml HCl, and 20 ml H_2O).

3. Experimental Results and Discussions

3.1. Characterization of hardened layer

Figure 2 shows the cross sectional surfaces subjected to the two different nitriding processes, using Marble's regent as an etchant to reveal the microstructure. The unetched surface layers, which are well-known as "white layer", were formed at both specimen's surfaces. The white layer for the N25 was slightly thicker than that for the N15. However, the white layer was thin and the thickness were about 20 μm for the N15 specimen and 30 μm for the N25 specimen, respectively. In both cases, the microstructure and the grain size below the white layers were no difference from the as-received series and the diffusion layer could not be identified by etching. So, the difference between the as-received and nitrided series was only forming of the surface white layer.

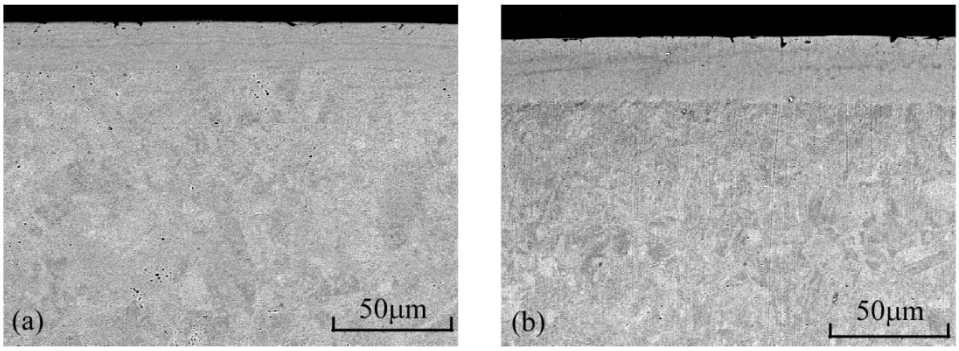

Figure 2. SEM images of plasma nitrided SUS316 stainless steel etched by Marble regent: (a) N15 and (b) N25 specimens.

Figure 3 shows the micro-Vickers hardness distribution of nitrided specimens on the cross sectional surface. The hardness of the as-received specimen was uniform from the surface to the core and the 30 points average value was about 331 HV. Compared with the virgin hardness, the hardness increased near the surface. The highest hardness values, 985 HV for the N15 specimen and 1041 HV for the N25 specimen, were measured at the surface, which is approximately three times of the virgin hardness of 331 HV. However, the hardness decreased steeply toward the center and the hardness at 50μm deep was almost same as virgin hardness for both nitrided specimens. Therefore, the thickness of the hardened layers, defined as a distance from the surface to the unhardened matrix, was less than 50 μm for both nitriding times. Since the thickness of white layer as shown in Fig.2 was about 20 - 30μm and the half size of indentation for 331 HV was about 12μm, the thickness of the diffusion layer was less than about 10μm.

In general, nitriding process produces a compound layer referred to as the white layer, and a diffusion layer below the compound layer. The former is a thin layer with high hardness but brittle [25]. As a result, the fatigue strength sometimes are degraded by the brittle layer. The latter is a relatively thick hardened layer. In the diffusion layer, the hardness gradually decreases gently toward the core. The depth of diffused zone is generally more than few hundred micrometers [13-18]. The depth of the diffused zone is important to improve the fatigue strength as well as the hardness [14]. In this study, however, no obvious diffusion layer was observed on the etched surface, and only the white layer was observed at the surface. Moreover, the hardened layer was quite shallow and the thickness was less than 50 μm which included the thickness of the compound

layer. These results suggest that the depth of diffusion layer is quite shallow for stainless steel. In our previous works, plasma nitriding was carried out using a same equipment using chromium molybdenum steel (JIS SCM435) [17]. The thickness of hardened layer was about 0.1 - 0.3 mm with ~10μm compound layer for each material. The hardened layer is obviously thicker than that of present study. The difference indicates that the passivation film reforms at the stainless surface during the plasma nitriding process though the passivation film is removed intermittently by hydrogen etching effect [26, 27]. The reformation of the passivation film hinders nitrogen diffusion, and this results in a thinner diffusion layer. The thickness of the hardened layer and the value of the hardness near the surface are important parameters that influence the site of fatigue crack initiation, as discussed in detail in the following sections.

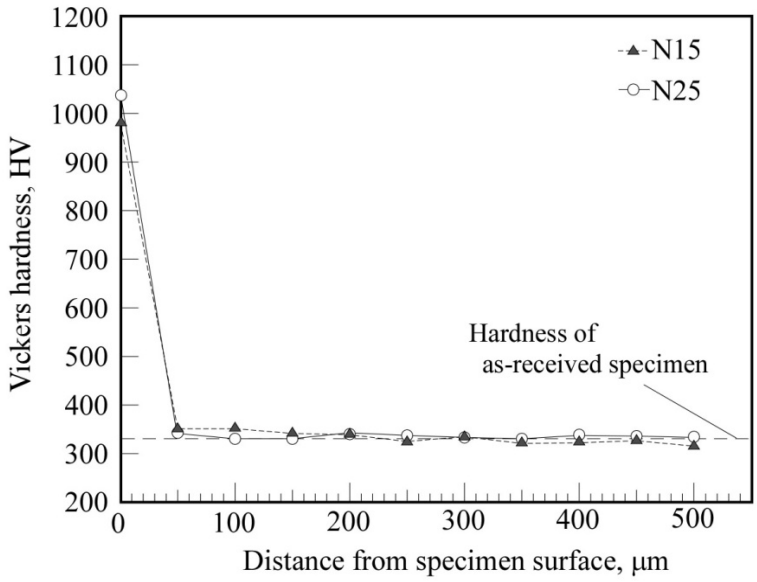

Figure 3. Distribution of Vickers-hardness in the nitrided specimens.

3.2. S-N curves

The fatigue tests to failure were carried out in air up to $N = 10^8$ cycles. Figure 4 shows the results of fatigue tests for as-received, N15 and N25 specimens. The *S-N* curve of the as-received specimens (represented by open square mark in Fig. 4) presented a horizontal asymptote shape, which is typical shape for low strength material [28, 29], with a fatigue limit up to $N = 10^8$ cycles. The fatigue limit σ_w defined as the horizontal line was about 500 MPa. The shape of two *S-N* curves of plasma nitrided specimens, represented by open triangle and circle marks in Fig. 4, showed also horizontal asymptote shape with a fatigue limit up to $N = 10^8$ cycles, that were similar to the *S-N* curve of the as-received specimens. The fatigue limit σ_w defined as the horizontal line was about 600 MPa for the N15 and 550 MPa for the N25 specimens, respectively. The fatigue limit of the N25 specimen with thicker hardened layer was slightly lower than that of the N15 specimen with relatively thin hardened layer as well as the fatigue strength in the life regime $N < 10^6$ cycles.

Increased fatigue strength after nitriding is a well-known phenomenon for various steels. The increase is caused by the increase of surface hardness and the formation of compressive residual stresses in the surface layer during the nitriding process. The high hardness layer hinders the fatigue crack initiation. The compressive residual stress is superimposed to the external load and leads to a reduction of the effective stress in tension. Since only a tensile stress produces fatigue cracks and contributes to crack propagation, a reduction of the effective stress in tension increases the fatigue

strength. In this study, the fatigue strength was improved by the plasma nitriding process, however, the fatigue limit was clearly smaller than that predicted by surface hardness using σ_w = 1.6 HV which is well-known equation between the hardness and upper bound for fatigue limit of low and medium strength materials. In addition, the specimen with thicker hardened layer showed lower fatigue limit. The small improvement and small influence of the thickness of hardened layer mean that the nitrided layer does not act on the fatigue strength efficiently.

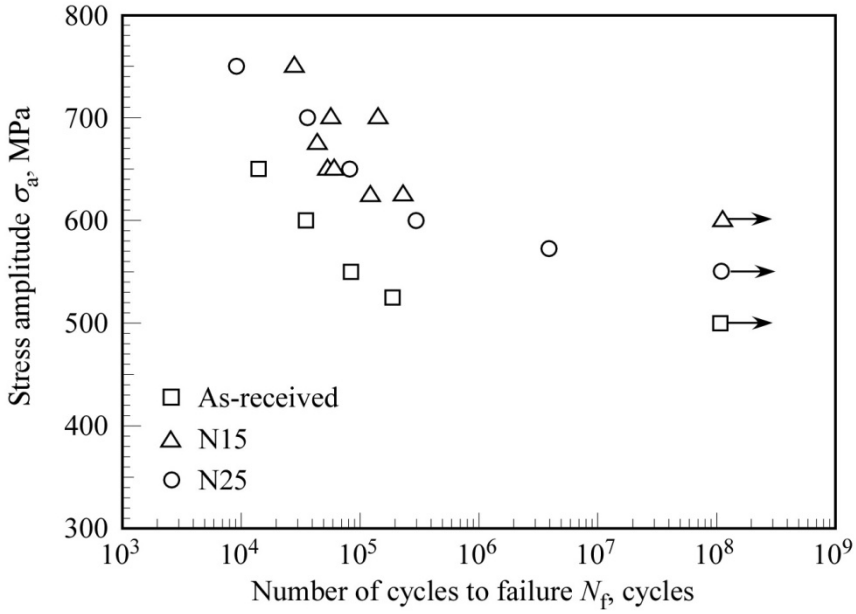

Figure 4. *S-N* curves.

3.3. Fracture surfaces

Fracture surfaces were observed using SEM. Figure 5 shows the typical SEM images of fracture surfaces for as-received and plasma nitrided specimens. Based on SEM observations of the fracture surfaces, only the surface fracture mode was observed though the hardened layer was formed on the surface of nitrided specimens. A subsurface fracture mode, fish-eye or fracture from substrate /nitriding layer interface, or cracking in the compound layer was not observed in all specimens.

The result means the nitrided layer increases the fatigue resistance on the specimen surface but the resistance is lower than the resistance for internal failure, and then the surface fracture occurs from the nitrided layer prior to internal fracture such as fish-eye failure. The nitrided layer at the stainless steel surface consists of the thin compound layer and quite thin diffusion layer as shown in Figs. 2 and 3. Since the influence of the diffusion layer on the fatigue strength can be ignored due to the small thickness, the compound layer is a dominant factor in the improvement of fatigue strength. However, the influence of compound layer is restricted because the thickness is only 20~30μm. In consequence, the small improvement of fatigue strength will be obtained for plasma nitrided specimens as shown in Fig.4. The small influence of the nitriding time will be also explained by the similar thickness of hardened layer.

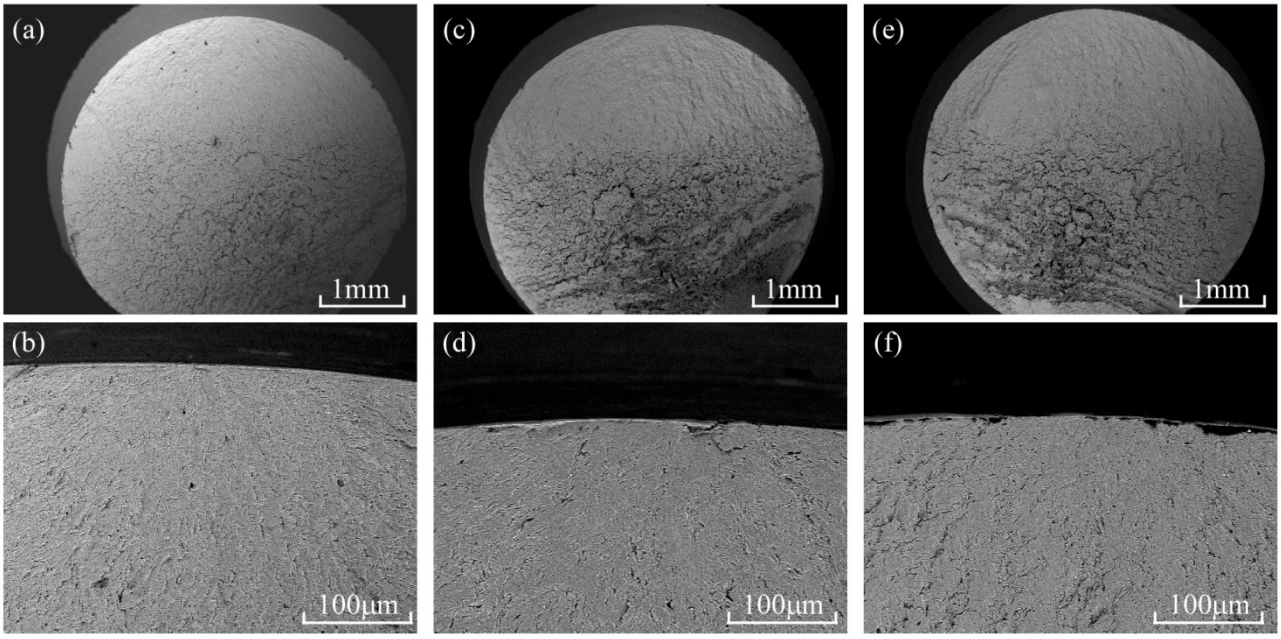

Figure 5. Typical SEM images of fracture surfaces; (a), (b) As-received, σ_a=525MPa, N_f = 1.88×10^5 cycles, (c), (d) N15, σ_a=625MPa, N_f=2.31×10^5 cycles and (e), (f) N25, σ_a=600MPa, N_f=2.96×10^5 cycles.

In conclusion, the degree of increase in the surface hardness and the thickness of the hardened layer are dominant factors determining the fatigue limit level of the plasma nitrided specimens. Therefore, the fatigue limit levels of the N15 and the N25 specimens were almost the same and thickness of the hardened layers had almost the same value. In addition, the improvement by plasma nitriding process is small because the nitrided layer, particularly diffusion layer, is quite thin. It is believed that the increase of the depth of diffused zone could improve the fatigue strength in plasma nitride stainless steels.

4. Conclusions

The following conclusion can be reached from the results of this study:

(1) A hardened surface layer was formed at the SUS316 stainless steel surface by plasma nitriding. However, the hardened layer was quite shallow. The thickness of the hardened layer was less than 50 μm for both nitriding time of 15 and 25 hours.

(2) The *S-N* curves represent a horizontal asymptote shape for all specimens.

(3) The fatigue strength was improved by plasma nitriding in all life regimes. However, the improvement of the fatigue strength was small due to the small thickness of the nitrided layer. The nitriding time also had a small influence on the fatigue strength because the thickness of the nitrided layer was similar for both nitriding times.

(4) Fatigue crack was initiated from specimen surface for all specimens.

(5) The degree of increase in the surface hardness and the depth of the hardened layer are dominant factors determining the fatigue limit level of the plasma nitrided specimens.

References

[1] A.D. Wilson, A. Leyland, A. Matthews, A comparative study of the influence of plasma treatments, PVD coatings and ion implantation on the tribological performance of Ti–6Al–4V, Surf. Coat. Technol., 114 (1999) 70–80.

[2] A. Wilson, A. Matthews, J. Housden, R. Turner and, B. Garside, A comparison of the wear and fatigue properties of plasma-assisted physical vapour deposition TiN, CrN and duplex coatings on Ti-6A1-4V, Surf. Coat. Technol., 62 (1993) 600–607.

[3] E.S. Puchi, M.H. Staia, H. Hintermann, A. Pertuz, J. Chitty, Influence of Ni-P electroless coating on the fatigue behavior of plain carbon steels, Thin Solid Films, 290–291 (1996), 370–375.
[4] J.A.M. Ferreria, J.D.M Costa, V. Lapa, Fatigue behaviour of 42Cr Mo4 steel with PVD coatings, Int. J. Fatigue, 19 (1997) 293–299.
[5] J.A. Berrios, D.G. Teer, E.S. Puchi-Cabrera, Fatigue properties of a 316L stainless steel coated with different TiNx deposits, Surf. Coat. Technol., 148 (2001), 179–190.
[6] D. Yonekura, H. Fukuda and R. Murakami, Influence of Deposition Bias Voltage on Fatigue Cracking Behavior of Chromium Nitride Film Deposited on Steel, Key Engineering Materials 353–358 (2007) 275–278.
[7] G.H. Majzoobi, A.R. Ahmadkhani, The effects of multiple re-shot peening on fretting fatigue behavior of Al7075-T6, Surf. Coat. Technol., 205 (2010), 102–109.
[8] S. Hotta, Y. Itou, K. Saruki, T. Arai, Fatigue strength at a number of cycles of thin hard coated steels with quench-hardenrd substrate. Surf. Coat. Technol., 73 (1995), 5–13.
[9] P. Schlund, P. Kindermann, R. Schulte, H.G. Sockel, U. Schleinkofer, K. Gorting, W. Heinrich, Mechanical behaviour of PVD/CVD-coated hard metals under cyclic loads, Int. J. Refract. Met. Hard Mater., 17 (1999) 179–185.
[10] T. Bell, Y. Sun1, A. Suhadi, Environmental and technical aspects of plasma nitrocarburising, Vacuum, 59 (2000) 14–23.
[11] M. Berg, C.V. Budtz-Jørgensen, H. Reitz, K.O. Schweitz, J. Chevallier, P. Kringhøj, J. Bøttiger, On plasma nitriding of steels, Surf. Coat. Technol., 124 (2000) 25–31.
[12] M. Keddam, Characterization of the nitrided layers of XC38 carbon steel obtained by R.F. plasma nitriding, Appl. Surf. Sci. 254 (2008) 2276–2280.
[13] T. BELL and N.L. LOH, The Fatigue Characteristics of Plasma Nitrided Three Pct Cr-Mo Steel, J. Heat Treating, 2 (1982) 232–237.
[14] Sule Yildiz Sirin, Kahraman Sirin, Erdinc Kaluc, Effect of the ion nitriding surface hardening process on fatigue behavior of AISI 4340 steel, Mater. Charact. 59 (2008) 351–358.
[15] X.J. Cao, F. Yang, R. Murakami, in: Auckland (New Zealand), International Conference on Structural Integrity and Failure, vol. 7, 2010.
[16] B. Golgeli, K. Genel, Fatigue strength improvement of a hard chromium plated AISI 4140 steel using a plasma nitriding pre-treatment, Fatigue Fract. Eng. Mater. Struct., 29 (2006) 105–111.
[17] N. Yan, R. Murakami, Insup Lee, Fatigue Behavior of Plasma Radical Nitrided SCM435 Steel in Super-Long Life Regime, Met. Mater. Int., 17 (2011) 577–581.
[18] B. Wu, P. Wang, Y.-S. Pyoun, J. Zhang, R. Murakami, Effect of ultrasonic nanocrystal surface modification on the fatigue behaviors of plasma-nitrided S45C steel, Surf. Coat. Technol., 213 (2012) 271–277.
[19] E. Menthe, K.-T. Rie, Further investigation of the structure and properties of austenitic stainless steel after plasma nitriding, Surf. Coat. Technol., 116–119 (1999) 199–204.
[20] B. Larisch, U. Brusky, H.-J. Spies, Plasma nitriding of stainless steels at low temperatures , Surf. Coat. Technol., 116–119 (1999) 205–211.
[21] G.P. Singh, J. Alphonsa, P.K. Barhai, P.A. Rayjada, P.M. Raole, S. Mukherjee, Effect of surface roughness on the properties of the layer formed on AISI 304 stainless steel after plasma nitriding, Surf. Coat. Technol., 200 (2006) 5807–5811.
[22] F. Borgioli, A. Fossati, E. Galvanetto, T. Bacci, G. Pradelli, Glow discharge nitriding of AISI 316L austenitic stainless steel: Influence of treatment pressure, Surf. Coat. Technol., 200 (2006) 5505–5513.
[23] J.W. Zhang,L.T. Lu, K. Shiozawa, W.N. Zhou, W.H. Zhang, Effect of nitrocarburizing and post-oxidation on fatigue behavior of 35CrMo alloy steel in very high cycle fatigue regime, Int. J. Fatigue 33 (2011) 880–886.
[24] T. Sakai, M. Takeda, K. Shiozawa, Y. Ochi, M. Nakajima, T. Nakamura and N. Oguma,

Experimental Reconfirmation of Characteristic S-N Property for High Carbon Chromium Bearing Steel in Wide Life Region in Rotating Bending, J. Soc. Mat. Sci. Jpn., Vol. 49, 779–785(2000).

[25] M.A. Terres, S. Ben Mohamed, H. Sidhom, Influence of ion nitriding on fatigue strength of low-alloy (42CrMo4) steel: Experimental characterization and predictive approach, International Journal of Fatigue, 32 (2010) 1795–1804.

[26] L.F. Zagonel, C.A. Figueroa, F. Alvarez, In situ photoemission electron spectroscopy study of nitrogen ion implanted AISI-H13 steel, Surf. Coat. Technol., 200 (2005) 2566–2570.

[27] C.A. Figueroa, F. Alvarez, On the hydrogen etching mechanism in plasma nitriding of metals, Appl. Surf. Sci., 253 (2006) 1806–1809.

[28] B. Pyttel, D. Schwerdt, C. Berger, Very high cycle fatigue – Is there a fatigue limit?, Int. J. Fatigue 33 (2011) 49–58.

[29] A. Zhao, J. Xie, C. Sun, Z. Lei, Y. Hong, Effects of strength level and loading frequency on very-high-cycle fatigue behavior for a bearing steel, Int. J. Fatigue 38 (2012) 46–56.

Experimental Investigation on Effects of Various Factors on Very High Cycle Fatigue Property for Spring Steels

Taku Miura[1] , Tatsuo Sakai[2*], Takayuki Sakakibara[3], Shingo Mimura[3] Takanori Kuno[3], Shoichi Kikuchi[2] and Akira Ueno[2]

[1]Graduate School of Science and Engineering, Ritsumeikan University, Kusatsu, Shiga, 525-8577 Japan
[2] College of Science and Engineering, Ritsumeikan University, Kusatsu, Shiga, 525-8577 Japan
[3] Research & Development Division, Chuo Spring Co., Ltd., Miyoshi, Nishikamo, Aichi, 470-0225 Japan
* Corresponding author: sakai@se.ritsumei.ac.jp

Abstract In order to investigate the effects of hardness, residual stress and loading type on the fatigue property for spring steel(SUP7), two kinds of tempering temperature, three kinds of surface finishing (grinding, electrolytic polishing and shot-peening) and two kinds of fatigue test (rotating bending and axial loading) were accepted. Specimens in harder (lower tempering temperature) series showed higher fatigue limit; however, those in shot-peened series showed approximately same fatigue limit as grinding finished series, although the former has compressive residual stress higher than that in the latter. In the case of same tempering temperature and surface finishing, specimens in rotating bending series showed higher fatigue limit comparing with the axial loading. This fact can be attributed to the difference of critical volume participating in the crack initiation. Fracture surfaces of all the failed specimens were carefully observed by a scanning electron microscope(SEM) in order to examine the fracture mode. Two types of interior initiated fracture, with and without inclusion, were found. The latter was found only in axial loading and had granular structure whose angle of slope to the loading direction was 60 degree. In the case of specimens with residual stress (grinding and shot-peening), the depth of interior fracture origin in rotating bending was shallower than that in axial loading. In both grinding and shot-peening series, the crack has initiated beneath the surface layer with compressive residual stress, and, the fatigue limits of these series were thus almost same to each other.

Keywords Spring steel, Very high cycle fatigue, High cleanliness steel, Duplex *S-N* property, Fish-eye

1. Introduction

During the long history of the study on *Fatigue of Metals*, a number of experimental data have been accumulated and a lot of fundamental aspects on the fatigue of metallic materials have been reported by many researchers[1-5]. Among them, one of the most important aspects is the fact that ferrous metals such as structural steels indicate the clear fatigue limit at the number of stress cycles less than 10^7 [1,6]. However, non-ferrous metals such as aluminum alloys have no fatigue limit such that the *S-N* curve tends to decrease continuously in the very long life regime longer than 10^7 cycles[4]. In recent years, practical structures such as railway wheels and rails, offshore structures, energy conversion and transportation systems have been used in a long term, sometimes, beyond their original design lives due to economic and environmental considerations. In such a circumstance, unexpected failures have been reported at stress levels lower than the fatigue limit even for structural components made of ferrous metals being assumed to have a distinct fatigue limit. The fatigue behavior of structural steels in the very high cycle regime longer than 10^7 cycles has become an important subject to ensure the long-term safety of the actual structures in the various areas of industries[4,5].

From this point of view, many researchers have carried out fatigue tests in the very high cycle regime for various kinds of metallic materials in the last decades[4]. Thus, it is known that the high strength steel indicates "duplex *S-N* characteristics" consisting of *S-N* curves for both the surface-initiated fracture and the interior-initiated fracture. According to the conventional works[4], the interior-initiated fracture is usually caused by non-metallic inclusions inside the material in very

high cycle regime. Therefore, if some high cleanliness steel without such inclusions is fabricated, it is supposed that the fatigue fracture caused by the inclusion can be depressed and the corresponding S-N curve is diminished.

From such a viewpoint, a conventional spring steel(SUP7) and a high cleanliness spring steel (SWOSC-V) were prepared mainly supposing the practical application as valve spring for automobile gasoline engine. For both kinds of steels, the rotating bending fatigue tests were performed in the very high cycle regime toward gigacycles. Thus, the fundamental S-N properties for the respective spring steels were experimentally clarified and the effect of the cleanliness on the fatigue property was discussed together with the fatigue fracture mechanism of this steel was also discussed from a view point of fractography.

2. Experimental Procedures

2.1. Material and specimen

Materials used in this study were two different kinds of spring steels; JIS Material Codes of SUP7 and SWOSC-V, respectively. The former is a spring steel for general use for wide variety of usual springs, and the latter is developed for special use as valve spring for automobile gasoline engine. Chemical compositions of these steels were shown in Teble1. In the case of SUP7 steel, the material was firstly oil-quenched at 1173K(900deg.C) /20min, after which it was tempered at each of 723K(450deg.C)/60min and 659K(386deg.C)/60min, respectively. The former is hereafter so-called as “T-450 series”, whereas the latter is as “T-386 series”. Some of T-386 specimens were electrochemically polished (named T-386EP series), and some of T-386EP specimens were further shot-peened(named T-386SP series). All the preparation process of the respective series for SUP7 steel is summarized as a flowchart in Fig.1.

Table 1. Chemical compositions of spring steels

Material	C	Si	Mn	P	S	Cu	Cr	Fe
SUP7	0.6	2.0	0.9	0.014	0.019	—	—	Bal.
SWOSC-V	0.58	1.45	0.69	0.01	0.01	0.02	0.68	Bal.

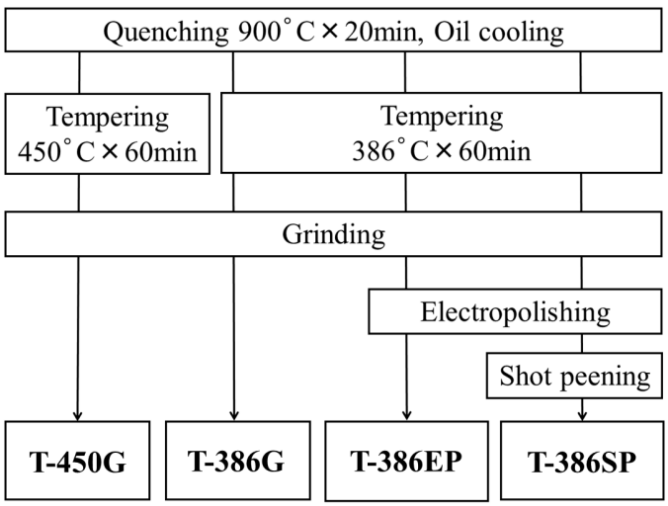

Figure 1. Flowchart of specimen preparation for SUP7 steel

In the case of SWOSC-V steel, the material was oil-quenched at 1123K(850deg.C)/20min and then it was tempered at each of 668K(395deg.C)/60min and 636K (363deg.C)/60min, respectively. Some of 363deg.C-tempered specimens were electrochemically polished, and some of them were shot-peened. In order to distinguish the respective series, notations such as “T-395G series”, “T-363G series”, “T-363EP series” and “T-363SP series”, were introduced similar to the case of SUP7 steel. Preparation process of the respective series for SWOSC-V steel is given in a flowchart in Fig.2.

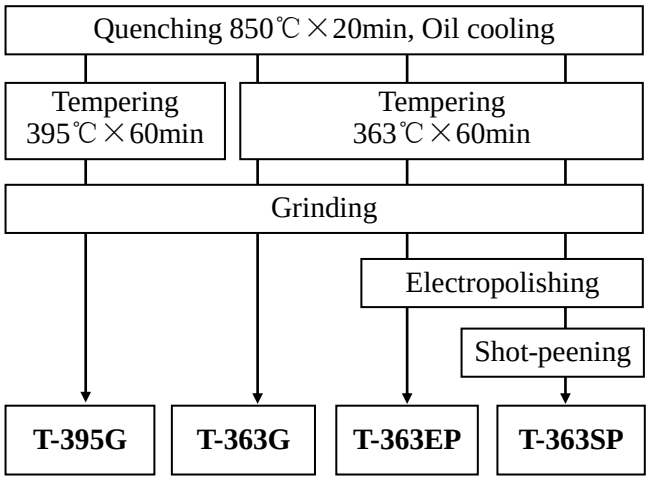

Figure 2. Flowchart of specimen preparation for SWOSC-V steel

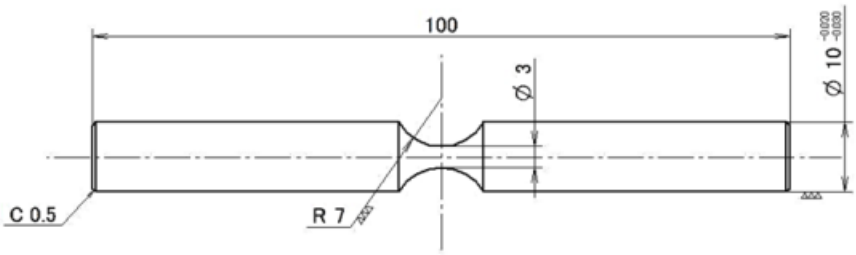

(a) Rotating bending (SUP7)

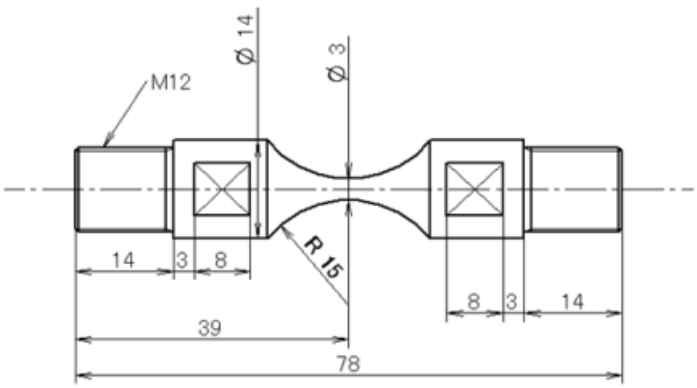

(b) Axial loading

Figure 3. Shape and dimensions of fatigue specimens

Specimens were machined into the shape and dimensions indicated in Fig.3. Figure 3(a) indicates the shape and dimensions of SUP7 specimen for rotating bending. Notch radius of the specimen was 7 mm and the diameter of the critical section was 3mm. The stress concentration factor of this specimen was K_t =1.06 as given by Peterson's handbook. The shape and dimensions of SWOSC-V specimen are quite same as SUP7 except for D=8mm. On the other hand, Fig.3(b) indicates the shape and dimensions of specimen for axial loading. Its notch radius was 15mm and the diameter of the critical section was designed to be 3mm similar to the rotating bending specimen. The stress concentration factor of this specimen was K_t =1.04 from the above handbook. Round notch surface of the specimen was finished by polishing with emery paper of #2000 after the grinding process. Of course, T-386EP series and T-386SP series were tested without such a polishing by emery paper.

In order to characterize the microstructure, the micro-Vickers hardness was measured and the microstructure was observed at cross-section using an optical microscope and a scanning electron microscope (SEM). The distribution of the residual stress was measured at the transverse section of the smallest diameter of the specimen using the X-ray diffraction (XRD). The residual stress distribution in the direction of inside was also measured after electrochemically removing the local surface area.

2.2. Fatigue tests

Photographs of the fatigue testing machines used in this study are shown in Fig.4. The left hand machine was used in rotating bending, whereas the right hand machine was in axial loading. Each of these machines can perform fatigue tests for four specimens simultaneously. The former machine has two spindles driven by an electric motor via a flat belt and each spindle has specimen grips at both ends [5]. The rotating speed of the spindles is 52.5 Hz (3150 rpm), and the stress ratio is given as $R=-1$. The latter machine has four actuators driven by hydraulic power, and the loading frequency is 80Hz. Fatigue tests were carried out at a definite stress ratio of $R=-1$. All the fatigue tests were performed in room atmosphere without any control of temperature and the moisture. After fatigue tests, fracture surfaces were observed by means of SEM and were analyzed by an energy dispersive X-ray spectrometer (EDS).

(a) Rotating bending

(b) Axial loading

Figure 4. Multi-type fatigue testing machines used in this study

3. Results and Discussions

3.1. Hardness and residual stress

Vickers hardness of the SUP7 specimens in the respective series was measured and the results are indicated in Fig.5. The hardness of T-386 series is higher than that of T-450 series due to the lower tempering temperature. It is found that the hardness is a little improved by performing the shot-peening. Residual stress distributions are plotted in Fig.6. The residual stress on the specimen surface caused by grinding is in a range of $-400 \approx -500$ MPa, and the residual stress is induced in surface layer within a thickness less than 20 μm. Another typical finding is that distinct compressive residual stress higher than 1000MPa was caused by shot-peening and the depth of the surface layer having such a distinct high residual stress is around 40 μm.

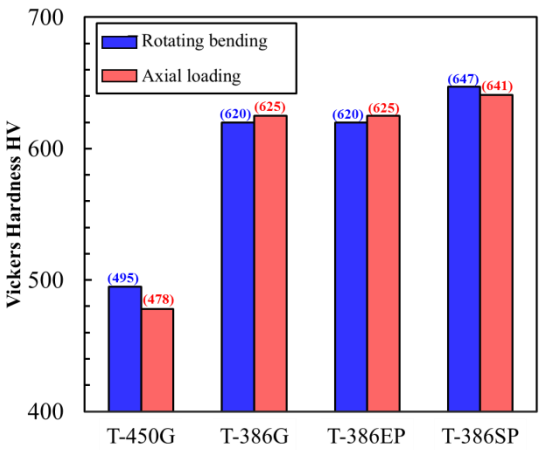

Figure 5. Vickers hardness of the respective series

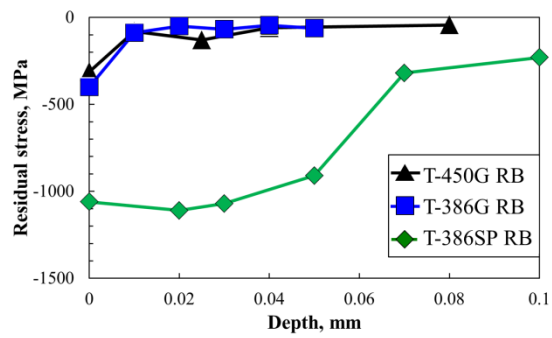

(a) Rotating bending

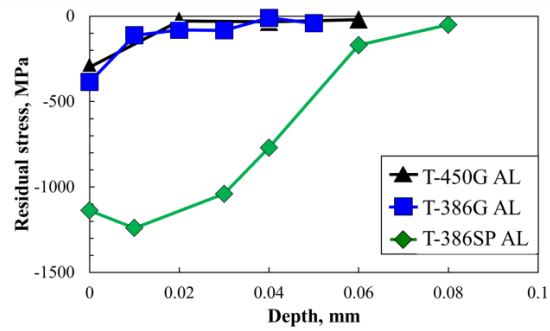

(b) Axial loading

Figure 6. Distributions of residual stress

Vickers hardness of the individual series for SWOSC-V steel is as follows; T-395G series: 584HV, T-363G series: 630HV, T-363EP series: 630HV and T-363SP series: 641HV, respectively. Resulting trend for tempering temperature and shot-peening is quite similar to the results for SUP7 steel. Residual stress for the respective series measured on the specimen surface is as follows; T-395G series: -376MPa, T-363G series: -378MPa, T-363EP series: -31MPa and T-363SP series: -1205MPa, respectively. Thus, residual stress caused by grinding is around 380MPa and this stress is almost entirely removed by electrochemical polishing. However, a distinct compressive residual stress of -1205MPa is produced by performing the shot-peening. This trend is corresponding to the results in Fig.6.

3.2. *S-N* characteristics

Fatigue test results of T-450G and T-386G series for SUP7 steel obtained in rotating bending are plotted as an S-N diagram in Fig.7(a). Every S-N curve was determined by accepting the bilinear

S-N model with fatigue limit in the JSMS standard (JSMS-SD-6-08)[6]. This procedure to determine the S-N curve is entirely common in this paper. It is found that the fatigue limit of T-386G specimen is clearly higher than that of T-450G specimen. This aspect can be attributed to the fact that the hardness of T-386G specimen is much higher than T-450G specimen. Another finding is that interior inclusion initiated fracture is caused only for T-386G specimen. Figure 7(b) indicates the S-N diagram obtained for T-386 specimens in the respective series. The fatigue limit of each series is given as follows; T-386G series: 1025MPa, T-386EP series: 775MPa and T-386SP series: 975MPa, respectively. The marked decrease of the fatigue limit for T-386EP series is caused due to removal of the surface layer having compressive residual stress. It is noted that this decrease of the fatigue limit was almost fully recovered by performing the shot-peening. Paying an attention to the fracture modes, one can find a trend that the interior-induced fracture are observed only for specimens in T-386G and T-386SP series. In the case of T-386EP specimen, the interior-induced fracture was observed for only one specimen.

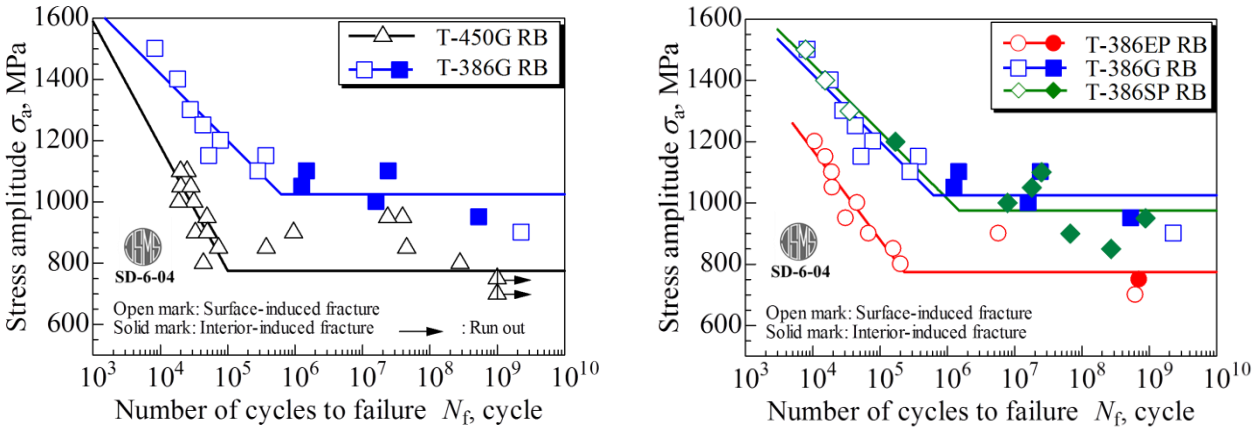

(a) T-450G series and T-386G series (b) Various series of T-386 specimens

Figure 7. S-N diagrams for SUP7 steel in rotating bending

In the next place, fatigue test results for SUP7 steel obtained in axial loading are plotted as S-N diagram in Fig.8. Figure 8(a) indicates the results for T-450G and T-386 specimens, in which the fatigue limit for T-386 specimen is higher comparing with the result for T-450G specimen. In addition, the interior-induced fracture is easily caused in T-386G specimen having higher hardness similar to the trend in the case of rotating bending. Figure 8(b) is S-N diagram obtained for T-386 specimens in the respective series. The fatigue limit of each series is given as follows; T-386G

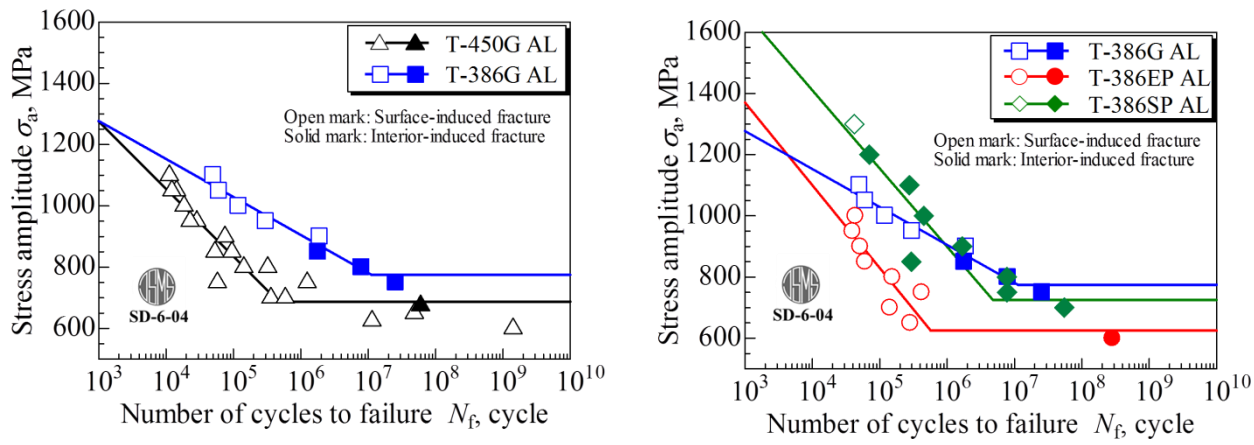

(a) T-450G series and T-386G series (b) Various series of T-386 specimens

Figure 8. S-N diagrams for SUP7 steel in axial loading

series: 775MPa, T-386EP series: 625MPa and T-386SP series: 725MPa, respectively. Variation of the fatigue limit and the fracture mode depending on the surface finishing is quite similar to the trend in the case of rotating bending.

Figure 9 indicates S-N diagram obtained for SWOSC-V steel in rotating bending. The fatigue limit for T-363G specimen is higher than that for T-395G specimen depending the hardness realized by the tempering at the respective temperatures. The interior-induced fracture was not observed even for the gigacycle regime in the case of low temperature tempering. The slope of the inclined portion in T-395G specimen is fairly steep comparing with that in T-363G specimen. Figure 10 is S-N diagram obtained for the respective series of T-386 specimens. The fatigue limit for T-363EP series is decreased due to the removal of the surface layer with the compressive residual stress. This trend is very common to the case of SUP7 steel as shown in Fig.7(b) and Fig.8(b).

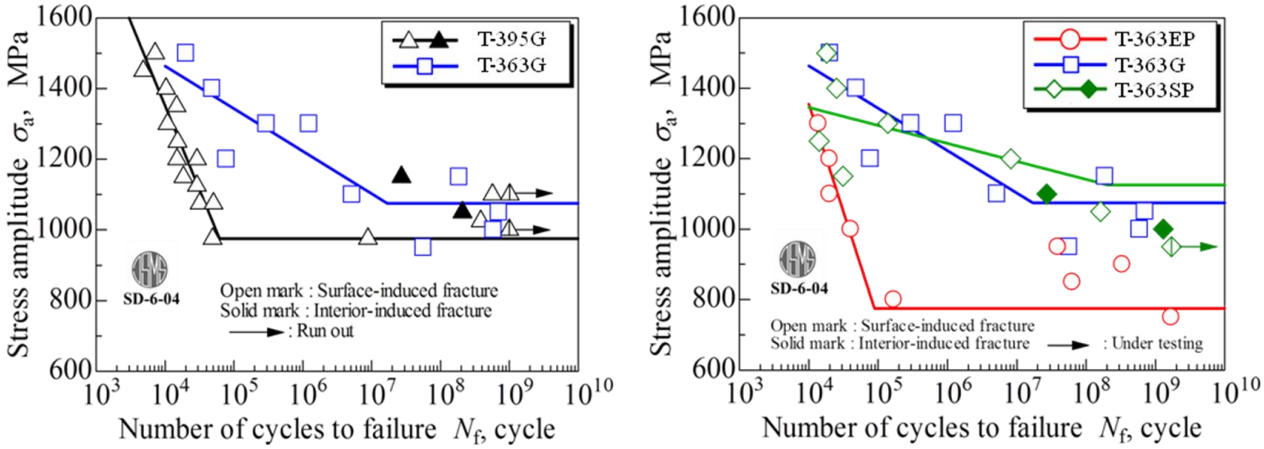

(a) T-395G series and T-363G series (b) Various series of T-363 specimens

Figure 9. S-N diagrams for SWOSC-V steel in rotating bending

3.3. SEM observations of fracture surface

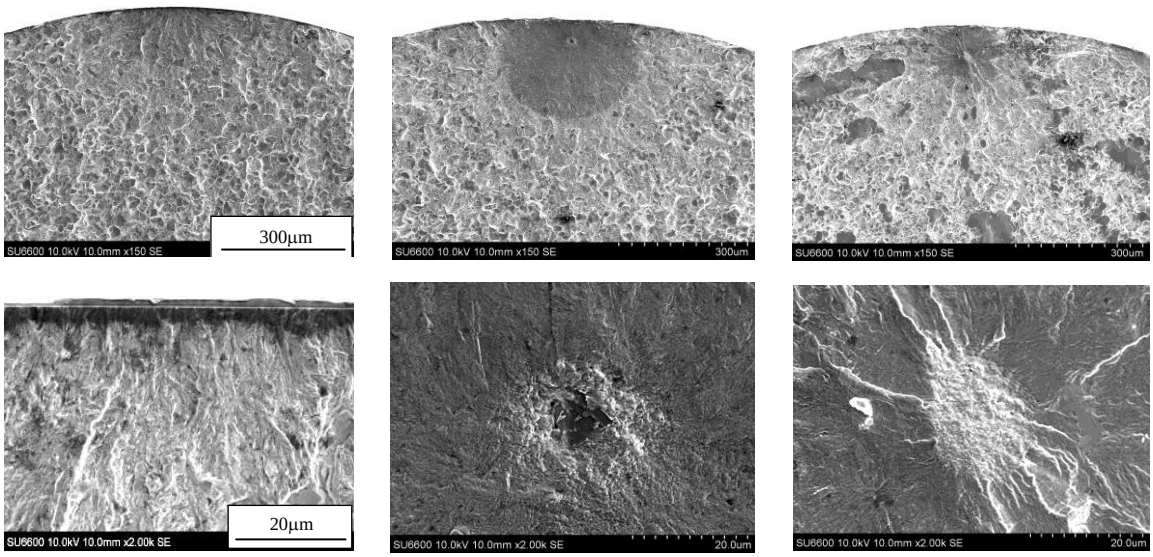

(a) Surface-induced fracture in rotating bending [$\sigma_a = 1400$ MPa, $N = 1.8\times10^4$]

(b) Interior-induced fracture in rotating bending [$\sigma_a = 950$ MPa, $N = 8.8\times10^8$]

(c) Interior-induced fracture in axial loading [$\sigma_a = 1200$ MPa, $N = 7.0\times10^4$]

Figure 11. Typical examples of fracture surfaces for SUP7 steel in both loading types

Fracture surface for T-386G specimen failed at $\sigma_a = 1400$ MPa with a short life of $N = 1.8 \times 10^4$ in rotating bending is shown in Fig.11(a), where the top is the result observed at low magnification and the bottom the result at high magnification. In this case, the fatigue crack took place on the specimen surface and it propagated inside the specimen. Figure 11(b) gives another example of the fracture surface at $\sigma_a = 950$ MPa with a life of $N = 8.8 \times 10^8$ in the interior-induced fracture modewith a clear fish-eye. In this case, the fatigue crack took place around the interior inclusion at the center of the fish-eye and the fine granular area[FGA] was found around the inclusion. These pairs of results give examples of the fracture surface in rotating bending. However, Fig. 11(c) gives other examples of the fracture surface at $\sigma_a = 700$ MPa with a life of $N = 7.7 \times 10^6$ in the interior-induced fracture mode in axial loading. No inclusion was found at the crack initiation site at the center of the fish-eye in this case, but the fine granular area[FGA] can be observed at the crack initiation site.

The fine granular area in Fig.11(c) was again carefully observed by inclining the sample ± 5deg., after which 3-D image of the fracture surface around the FGA was reconstructed by means of stereo-projection analysis[A Software of Mex supplied by Alicona Co. Ltd.]. Based on this analysis, it was found that a plane of the FGA inclined 60deg. against the macroscopic fracture surface and the gap of the local surface levels at both ends of the FGA is about 10 μm.

Several examples of fracture surfaces for SWOSC-V steel in rotating bending are indicated in Fig.12, in which the top is the result observed at low magnification and the bottom the result at high magnification. In the case of Fig.12(a), the fatigue crack took place at a shot-peened dimple on the specimen surface and it propagated inside the material resulting the final fracture. In Fig.12(b), the fine granular area[FGA] was formed at an interior site along a inclined plane. According to the stereo-projection analysis, this plane was inclined 60deg. against the macroscopic fracture surface similar to the previous result obtained for SUP7 steel. Figure 12(c) gives another example of the fracture surface in interior-induced fracture and a defect was found at the crack initiation site. However, any inclusion was not observed here regardless of careful EDS-analysis. Thus, no inclusion was found at the crack initiation site in every series of SWOSC-V steel. It is supposed that this fact comes from high cleanliness of the present steel.

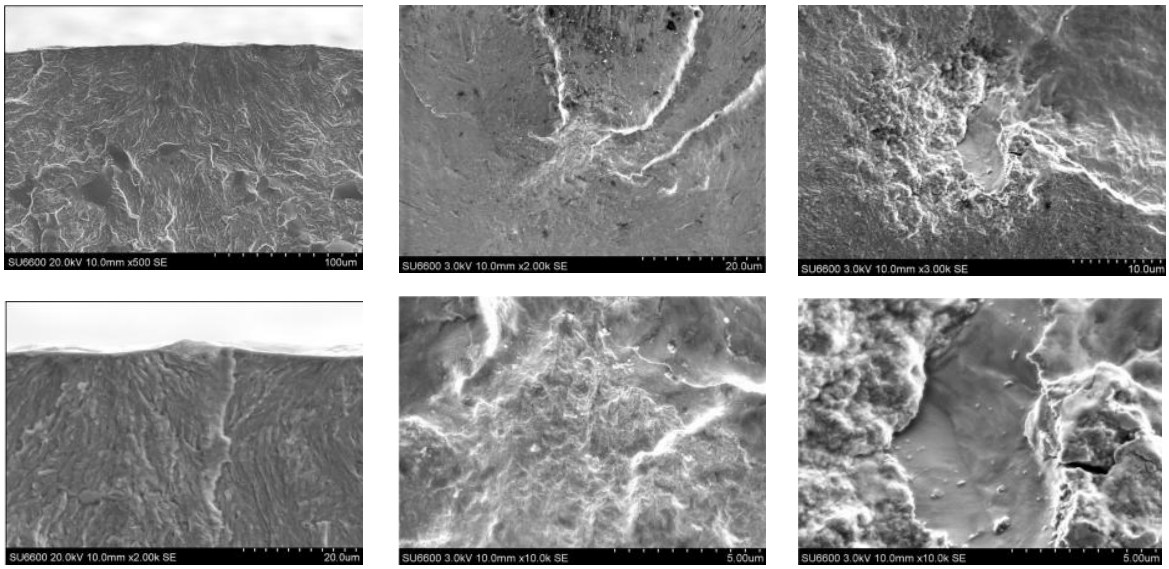

(a) Surface-induced fracture [$\sigma_a = 1050$ MPa, $N = 1.6 \times 10^8$]
(b) Interior-induced fracture [$\sigma_a = 1100$ MPa, $N = 2.7 \times 10^7$]
(c) Interior-induced fracture [$\sigma_a = 1050$ MPa, $N = 2.1 \times 10^8$]

Figure 12. Typical examples of fracture surfaces for SWOSC-V steel in rotating bending

3.4. Effects of loading type and residual stress on the fatigue property

Fatigue limits of the respective series of T-386 in both loading types are depicted in Fig.13, where values in the left hand side of each couple of the results are higher than the values in the right hand side. This aspect has been often reported for many kinds of metallic materials by many researchers. Thus, it was reconfirmed that the fatigue limit in rotating bending is a little higher than that in axial loading. It is another finding that the fatigue limit for T-386EP specimen is clearly lower than that for T-386G and T-386SP specimens. This can be attributed to the fact that the compressive residual stress is fully released by the electrochemical polishing. Figure 14 represents the difference of the crack initiation depth between both loading types for same fatigue test results as in Fig.13. The depth of crack initiation site for T-386EP specimen is almost same between both loading types, but the depth in axial loading is significantly deeper than that in rotating bending.

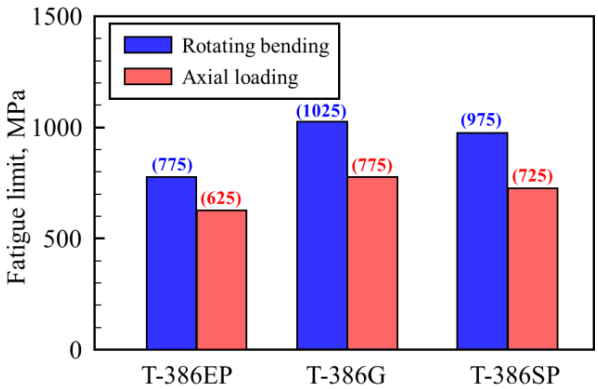

Figure 13. Difference of fatigue limits

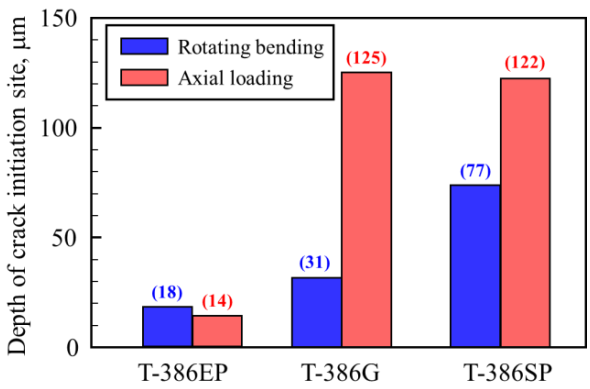

Figure 14. Difference of crack initiation depths

The fact that a significant difference of the crack initiation depth took place depending on the loading types can be well explained as follows; The stress distribution across the cross section in rotating bending has a significant gradient, while the stress distribution is uniform in axial loading as illustrated in Fig.15. In the case of rotating bending, the stress distribution has a steep slope and, therefore, the stress in the core portion is markedly lower than the outer layer. The crack is supposed to occur at higher stress region, but strength of the surface layer is improved by some kinds of surface treatments. In such a circumstance, the fatigue crack can occur at a definite

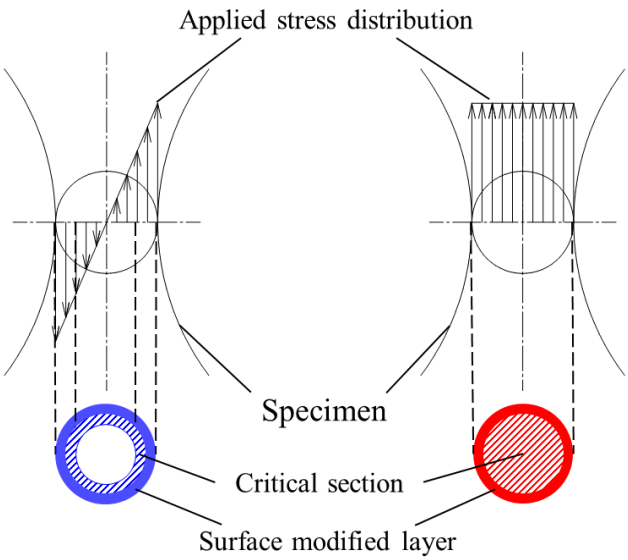

Figure 15. Schematics of stress distributions across the cross section in both loading types

ring-like area hatched in Fig.15. On the other hand, such an area occurring fatigue crack is the entire cross section without the modified surface layer having the improved strength in the case of axial loading. Thus, the critical volume participating in the fatigue crack initiation in axial loading is extremely larger than that in rotating bending. The fact that the crack initiation depth in axial loading is clearly higher than the results in rotating bending in Fig.14 can be well interpreted in this concept. In the case of high strength steels such as spring steel, material defects such as inclusion and machining flaws become sensitive to the crack initiation comparing with the usual structural steels with some moderate strength. Paying a particular attention to this aspect, the number of such defects in axial loading is much larger than the case in rotating bending. Therefore, the size of the most harmful defect in axial loading becomes larger than that in rotating bending. This is another reason why the fatigue limit in axial loading becomes a little lower than that in rotating bending.

4. Conclusions

In order to investigate the very high cycle fatigue properties of spring steels (SUP7 and SWOSC-V), fatigue tests were performed for specimens prepared by several different processes in both rotating bending and axial loading. Main conclusions obtained in this study are summarized as follows;

(1) In every series of the specimen preparation, fatigue fracture can occur in the very high cycle regime such as $10^7 - 10^9$ cycles regardless of the specimen's hardness, the surface roughness and the loading type.
(2) Fatigue limit in rotating bending is a little higher than that in axial loading for every series of specimens. This fact can be attributed to the difference of the stress distribution across the section, i.e. the critical volume participating in the crack initiation in axial loading is much larger than that in rotating bending.
(3) At higher stress levels with shorter life, the surface-induced fracture tends to occur instead of the interior-induced fracture, but the interior-induced fracture tends to occur at relatively higher stress levels in the case of shot-peened specimen due to suppression of crack initiation on the specimen surface by high value of the compressive residual stress.
(4) In the case of interior fracture mode for the conventional spring steel, an inclusion was usually found at the crack initiation site (Central portion of the fish-eye) and the FGA was observed around the inclusion. But, in the case of high cleanliness spring steel, such an inclusion was not found even in the interior fracture mode and a FGA-like facet inclined 60deg. against the macroscopic fracture surface was formed at the crack initiation site.

References

[1] A. Woehler, Uber die Festigkeits-Versuche mit Eisen und Stahl, Zeitschrift fur Bauwesen, 20, (1870), 74-106.
[2] K. Shiozawa, T. Sakai et al., Databook on Fatigue Strength of Metallic Materials, Vols. 1-3, Elsevier Science B. V. and JSMS, (1996).
[3] S. Mimura, T. Aoki, T. Sakakibara, M. Wakita, Development of High Fatigue-Proof Spring Using High Silicone Oil Tempered Wire, Transactions of the Japan Society of Spring Engineers, 46, (2001) , 1–6.
[4] T. Sakai, Review and Prospects for Current Studies on Very High Cycle Fatigue of Metallic Materials for Machine Structural Use, Journal of Solid Mechanics and Materials Engineering, 3(3), (2009), 425-439.
[5] T. Sakai, T. Furusawa, R. Takizawa, N. Oguma, H. Hohjo, H. Ikuno, Development of Multi-type High Efficiency Fatigue Testing Machines in Rotating Bending and Axial Loading, Proceedings of the Hael Mughrabi Honorary Symposium, TMS Annual Meeting, (2008), 69–73.
[6] T. Sakai et al., Standard Evaluation Method of Fatigue Reliability for Metallic Materials -Standard Regression Method of S-N Curves- [JSMS-SD-6-08], JSMS Committees on Fatigue and Reliability Engineering, (2008).

Surface Crack Initiation Phenomenon in Very High Cycle Fatigue

MuhammadKashif Khan[1,*], **QingYuan Wang**[1]

1 Department of Mechanics and Engineering Science, Sichuan University, Chengdu 610065, China.
* Corresponding author: email@address.aa.b.cc

Abstract Very High Cycle Fatigue behavior of Stainless Steel AISI 310 has been investigated through ultrasonic fatigue testing. In fatigue cycles, a horizontal asymptote of S-N curve was found without any step at 10^6 cycles. Surface crack initiation was found irrespective of the stress level. However, the fracture surfaces of the material showed different behavior of crack propagation for different stages of fatigue cycles. It was found that up to 10^6 cycles, cracks initiated from surface defects and carbide precipitates present on the grain boundaries. The mechanism of crack initiation changed at low stress levels and slip bands and deformation twins were found at the surface of the specimen which acted as fatigue crack initiation sites. At lower stress levels, at or below fatigue limit, PSBs were developed but the cracks were not initiated. The lower slope in S-N curve was attributed to the development of PSBs all over the surface of the specimen before crack initiation.

Keywords Very high cycle fatigue, Crack initiation , PSBs, Local plasticity

1. Introduction

The fatigue crack initiation and growth in metallic materials is now well-understood. Fatigue cracks initiate at stress concentrating features within a structure. An area of fatigue assessment is still under investigation, however, is how cracks are initiated from surface and subsurface regions at very low stress levels in the very high cycle fatigue (VHCF). It is believed that the fatigue life of numerous aerospace, locomotive, automotive and biomedical structures may go beyond 10^8 cycles [1]. Hence, better understanding of the long life fatigue behavior is extremely important for efficient design of the components and structures, especially between the 10^7-10^{10} cycles. Most engineering designs were based on the assumption that materials exhibit a fatigue limit and any cyclic stress below fatigue limit yield infinite life. Recent studies, however, point out the fact that most materials experience failure up to 10^{10} cycles or above at low stress levels, and concept of infinite fatigue life is not true [1-4].

The VHCF behaviour of metallic materials is generally divided in two types, based on the crack initiation region [1-4]. In first type, the cracks are initiated from the internal defects of the material and a fish-eye region is obtained at the crack initiation site. In second type, the cracks are initiated from the surface of the material. These surface cracks are attributed to the surface defects, heterogeneities, pores and absence of inclusions and microstructural defects in some other materials. In this type of materials, the S–N curve between 10^6 to 10^9 cycles show very little decreasing slope without any transition at 10^7 cycles and horizontal asymptote is obtained.

The VHCF behavior of some materials shows subsurface crack initiation from the internal defects and inclusions [4]. However, surface crack initiation is also obtained in structural alloys which show no inclusions and microstructural defects [5-7]. Plastic deformations at localized regions initiate the fatigue cracks during cyclic loading. During fatigue loading, the stress concentration due

to the induced microscale plasticity around surface defects and pores [5], planar slip bands [6] and grain boundaries [7], results in crack initiation. The crack initiation site for these materials remains at the surface of the specimens, even for higher fatigue cycles from 10^8 to 10^9 cycles. The most common plastic deformation in FCC materials is the development of Persistent Slip Bands (PSBs) which yields intrusions and extrusions on the surface of specimens. In this case, the S–N curve decreases linearly with very little slope without transition at 10^7 cycles [3].

One important structural material which show surface based crack initiation is high temperature grade stainless steel alloy AISI 310. The alloy is very commonly used in moist conditions owing to its excellent characteristic to resist against corrosion. It is used in heat exchangers, pipes, machinery parts etc. The alloy is subjected to pressure cycles, temperature cycles and many start up and shut down cycles during service life. Hence, it is expected to serve for large number of loading cycles. However, there is no such study for this material, to the best of authors' knowledge, which details the behavior of fatigue crack initiation phenomenon especially up to very high cycle fatigue domain. Hence, it is important to be able to assess the very high cycle fatigue behavior of the material.

The surface crack initiation phenomenon even at lower stress levels has been studied previously and different conclusions have been made. Tokaji et al. [8] and Yang et al. [9] in Mg alloys, Miura et al. [10] and Sakai et al. [11] in steels studied the surface based crack initiation. The surface cracks initiation has been attributed to micro-cracks [12], surface roughness [13] and, intrusions and extrusions [14]. In addition, few efforts have been made to characterize the nature of PSBs in range of materials. Man et al. [15] studied the difference in the topography of slip bands in FCC and BCC materials. Polak et al. [16-17] studied the different stainless steels and attributed the local plasticity due to the intrusions and extrusions and their interaction with nearby heterogeneities, for the fatigue crack initiation. The localized plastic deformation and surface roughness developed in fatigue loading, and their interaction with surface defects have been attributed for the surface based crack initiation. It has been concluded that any or combination of these parameters may initiate cracks from the surface of the specimens. However, the crystallographic orientations of the grains play major role in the surface crack initiation. Owing to the difference in basal slip and twining mechanism for FCC and HCP based crystal structure, difference in the topography of PSBs is obtained. Hence, case by case experimental investigation of the crack initiation region and slip and basal planes for different materials is considered inevitable.

Ultrasonic fatigue testing has been used in this study to investigate the VHCF behavior of Stainless Steel AISI 310. The S-N curve showed horizontal asymptote without any step at 10^6 cycles. Surface crack initiation was found irrespective of the stress level. However, the fracture surfaces of the material showed different behavior of the crack propagation for different stages of the fatigue cycles. It was found that up to 10^6 cycles, the cracks initiated from carbide precipitates present on the grain boundaries. The mechanism of crack initiation changed at low stress levels and PSBs were observed at the surface of the specimen which acted as the fatigue crack initiation sites.

The main aim of this study is to enhance the VHCF life of metallic materials though surface modification techniques like Ultrasonic Nanocrystal Surface Modification (UNSM). A precursor to this goal is better understanding of VHCF behaviour of the material. The surface crack initiation for AISI 310 makes it an ideal material for the application of UNSM. The materials which exhibit subsurface crack initiation, the application of compressive residual stresses may enhance the

subsurface crack initiation owing to the compensatory tension. Hence, it is anticipated that VHCF life of AISI 310 can be enhanced due to UNSM.

2. Materials and Experimental Methods

Cold rolled cylindrical rods of 12mm diameter of AISI 310 were used in this study. AISI 310 is a commonly used material in heat exchangers, pipes and machinery parts. The material exhibits excellent high temperature properties with good ductility and weldability. It resists oxidation at elevated temperature and corrosion in moist conditions and dry environments.

Metallographic sample were prepared up to 0.05 micron finish and etched with Aqua Regia Reagent (15 mL HCL + 5 mL HNO_3 + 100 mL H_20) for 120 sec. The grain size of the material was determined by quantitative metallography and was found to be ~10 um as shown in Fig. 1. The grains were equiaxed and showed a random orientation. Carbide particles were obtained on the grain boundaries of the material. Elastic–plastic properties of the material were obtained by tensile testing according to ASTM standard E8 and are given in Table 1. Vickers microhardness tester was used at 200g load. The average Vickers hardness of the material was found as 370HV.

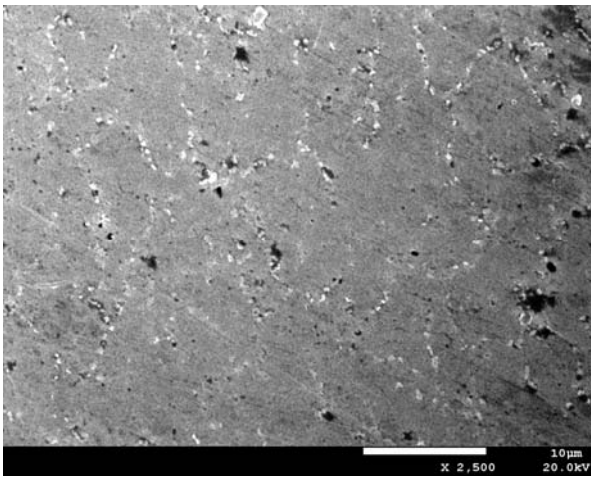

Figure 1. SEM Micrograph of the material. Carbide precipitates are prominent on the grain boundaries

Table 1. Mechanical property data for AISI 310

Material	E (GPa)	σ_y (MPa)	Gauge length (mm)	Hardness (HV)	E / σ_y
AISI 310	205	850	25	370	240

The chemical composition of the material is shown in Table 2. X-ray diffraction (XRD) was used to obtain the details of the diffracting planes and their preferred orientation. Diffraction planes (111), (200) and (220) were obtained for the material. The crystallographic orientations of diffracting planes were measured and it was found that the grains were randomly oriented without any preferred orientation. More details of the XRD and texture results can be found elsewhere [18].

Table 2. Composition of AISI 310 steel

Material	C%	Cr %	Ni %	Si %	Mn %	Cu %	Mo%	P%	Fe %
AISI 310	**0.04**	**23.3-23.4**	**18.9-**	**1.8 -**	**1.21 -**	**0.3**	**0.13-0.15**	**0.03**	**Bal**

			18.1	**1.9**	**1.27**				

The VHCF testing samples were designed to resonate longitudinally at 20kHz with the ultrasonic fatigue testing system. The detailed geometrical size of the specimens is shown in Fig. 2. The surface of the specimens was polished to surface roughness 0.2 um. Surface roughness of the material was determined with Atomic force microscope (AFM). Surface roughness Ra for different regions were measured and found up to 80nm.

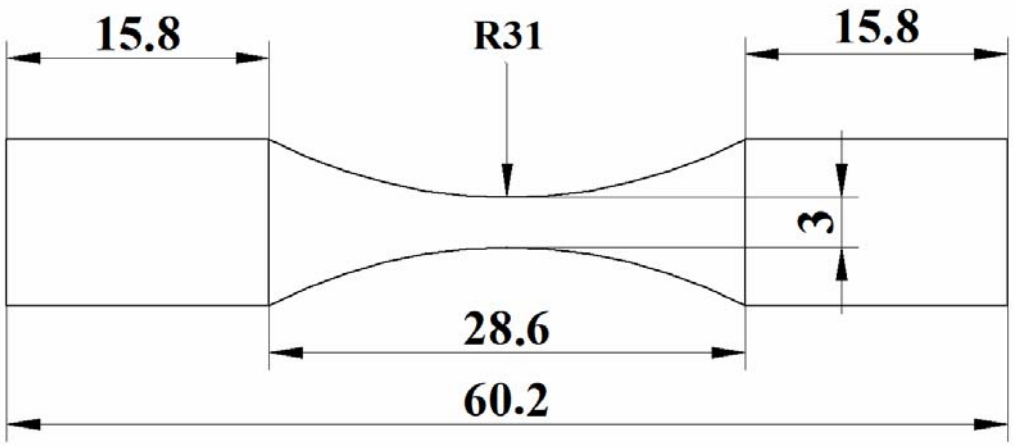

Figure 2. Schematic representation of fatigue specimen

3. Results and Discussion
3.1- S-N Curve

Fig. 3 shows the S-N curve for the material. The curve showed a higher decreasing slope at higher stress levels up to 10^6 cycles. This showed that at higher stress levels, the fatigue life was continuously decreasing. A semi-asymptote type curve was obtained and the curve became almost horizontal after 10^6 cycles. This was in agreement with earlier studies where a horizontal curve was reported for stainless steels [3, 10]. The material showed fatigue limit at around 500MPa and exhibited run out samples. It was found that the fatigue fracture for this material can occur beyond 10^7 cycles up to 10^9 cycles, though the difference in the fatigue strength was only around 50MPa.
The little difference in fatigue strength between 10^6 to 10^9 cycles and lower slope of S-N curve may be attributed to the relatively lower UTS of the material [3]. It was found that owing to the lower slope, little difference in stress levels changed the failure cycles significantly. This showed that fatigue crack initiation and propagation at relatively lower stress levels required considerable increase in the fatigue cycles to yield a failure. On the other hand, this showed that for a very small increase in stress level, the fatigue cycles would reduce significantly. The difference in stress levels for fatigue life between 10^6 to 10^8 cycles was almost 30MPa. For engineering applications, where materials are designed to serve 10^7 to 10^8 fatigue cycles, only increase in 30MPa may reduce the fatigue life from 10^6 to 10^8 cycles, which is significant.

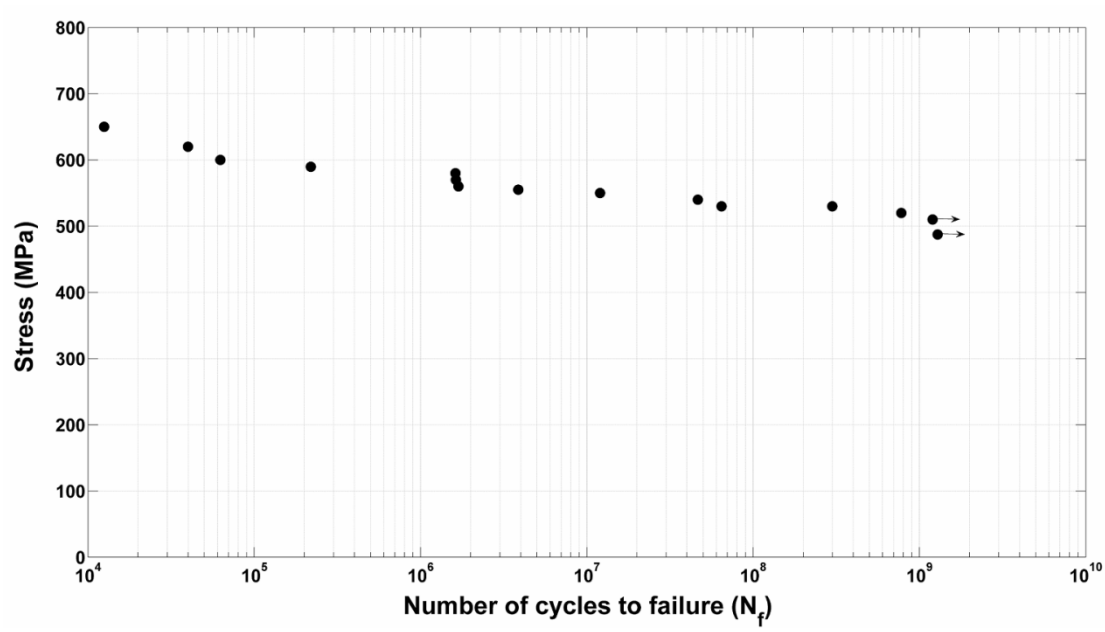

Figure 3. S-N curve for the material

3.2 Fractography

Scanning Electron Microscope (SEM) was used to observe the fatigue crack initiation sites and the fracture surfaces. It was observed that for all smooth and notched specimens, the cracks initiated from the surface of specimens, even at VHCF cycles.

Fig. 4 (a) shows the cross-section of the fracture surface of the specimen failed at 7.78×10^8 cycles when loaded at 520MPa. It can be seen that the appearance of fracture was different at different locations and based on the appearance, four different regions were visible. Radial patterns of striations were observed having 110 to 130um spacing between each other. The initiation site was a localized region on the surface of the specimen. Fig. 4 (b) shows the crack initiation region and crack propagation direction from the surface of specimen. The striations started from the crack initiation site and extended to more than three-quarter of the surface of specimens. The details about the regions are discussed elsewhere [18]. Cleavage fracture was observed with many secondary cracks and higher surface roughness.

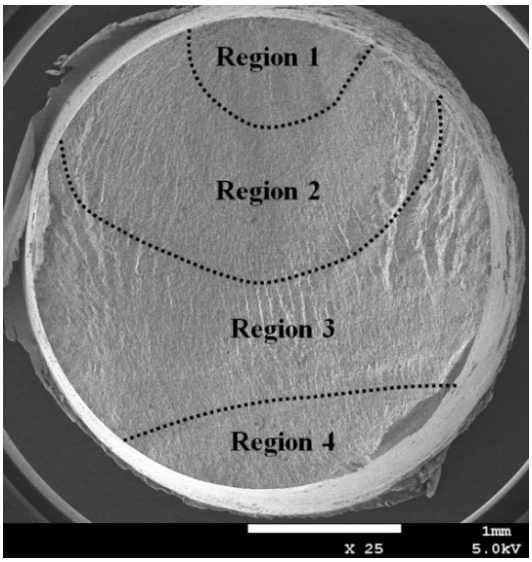

(a)

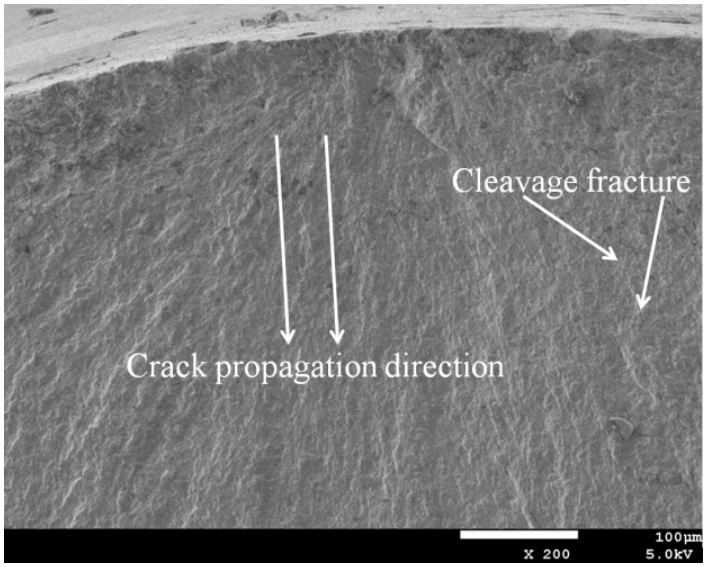

(b)

Figure 4. Fracture surface (a) sample failed at 7.78×10^8 cycles (b) Crack initiation from the surface

3.3 Fatigue Crack Initiation

It is well known that due to fatigue loading the cracks initiate from the localized plastic deformation [9]. For FCC materials, the local plasticity develops in the form of PSBs and twining and induces surface crack initiation. So far different conclusions have been made in the past for the surface based crack initiation phenomenon [8-11]. The changes in the microstructure, slip system, twin bands and surface defects have been attributed to the crack initiation in different materials. In this study, it was revealed that the mechanism of fatigue crack initiation at different fatigue loading cycles was different depending upon the stress levels. However, the initiation region was always found on the surface of the specimen.

The surfaces of the fractured specimens, parallel to the loading direction, were investigated through the SEM and AFM. The specimens failed at higher stress levels up to 10^6 cycles showed smooth surface without having any slip markings. No damage or sign of local plastic deformation was observed. The crack initiation site was very localized region at the surface of the material with no nearby damage. This showed that the carbide particles at the grain boundaries, as found in earlier studies, acted as stress concentration regions for crack initiation [15].

However, the specimens failed beyond 10^6 cycles showed high density PSBs and deformations on the surface. Fig. 5 shows SEM image of the surface of specimen failed at 3×10^8 cycles. It can be seen that high density slip bands were all over the periphery of the specimen. The near fracture surface showed more number of PSBs. The majority of the dislocations were parallel to the loading directions which were wider and broader as compared to the others. However, some dislocations were observed transverse to the loading directions as well.

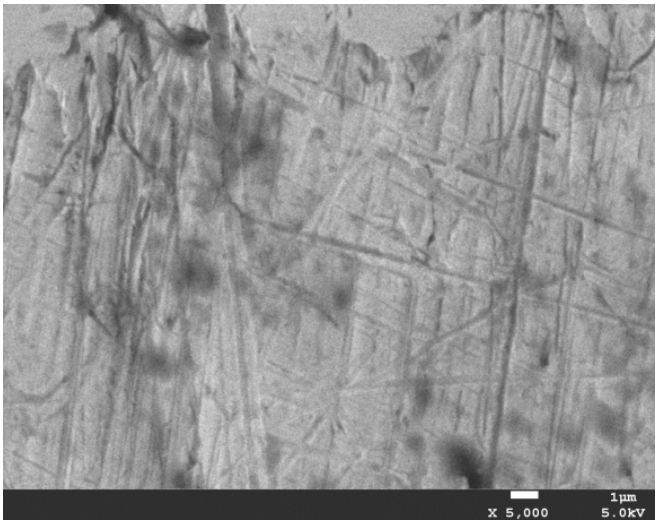

Figure 5. PSBs and dislocations on the surface of specimen failed at $3x10^8$ cycles (520MPa)

The surface parallel to the loading direction of other specimens were also investigate and it was found that the PSBs started to emerge out after 10^6 cycles on the surface of specimens. The density of PSBs continuously increased with further fatigue cycles [11]. With increase in the fatigue cycles, the topography of the PSBs enhanced. Longer, deeper and broader slip bands were obtained for higher fatigue cycles which increased the surface roughness of the specimen. The surface roughness of the specimens was measured as 178nm and 247nm for the specimen failed at $6.45x10^7$ and $7.78x10^8$ cycles respectively. This showed that the additional fatigue cycles after 10^6 cycles were utilized in the creation of PSBs at the surface of the specimen.

The topography of PSBs was investigated in detail through AFM. PSBs were present in the form of shallow intrusions and extrusions. Fig. 6 (a) shows 90um x 90um size AFM scanned image of a near fracture region in specimen failed at $3x10^8$ cycles. Fig. 6 (b) shows the 3D image of the area. The topography of intrusions and extrusions was like shallow scratches and waves, respectively [15-17]. Fig. 6 (c) shows the height profile data from the top corner of the area through the slip bands to the other corner of the area (shown by the red line in Fig. 6 (a)) showed many different crust and troughs. Several combinations of intrusions and extrusion, parallel to each other, were observed [16-17]. The distance between intrusions and extrusions was very small and maximum depth of the slip bands reached to around 250nm in some regions.

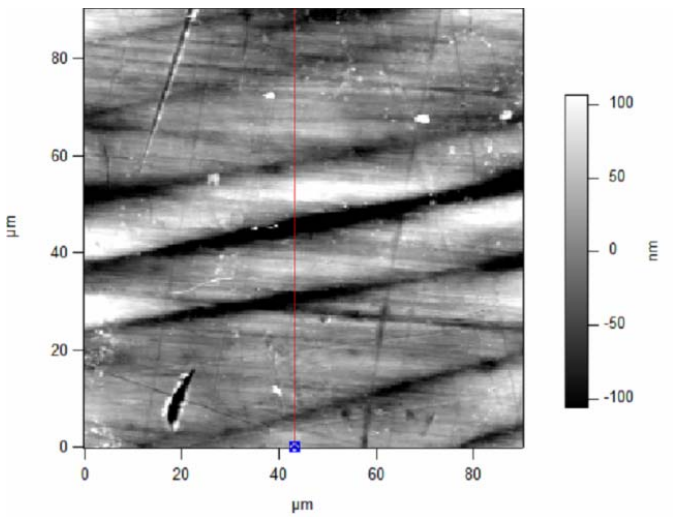

(a)

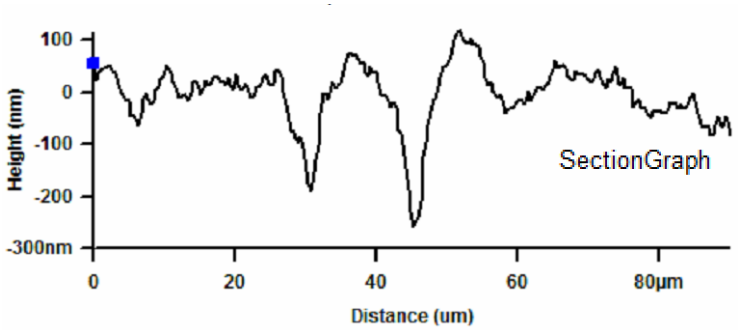

(b)

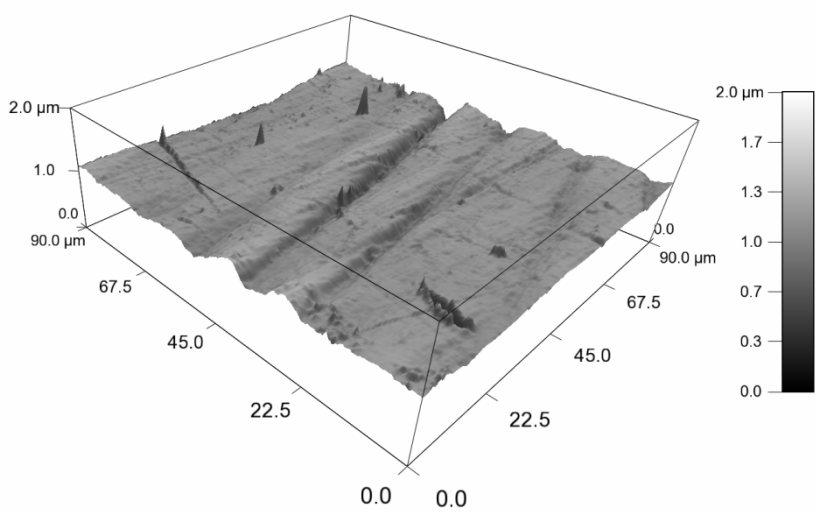

(c)

Figure 6 (a) AFM scanned image of an area near to crack initiation for the specimen failed at $3x10^8$ cycles (b) height profile through the area (from one corner to the other corner) showing significant PSBs and dislocations (c) 3D surface topography of the region

The process of utilization of additional fatigue cycles for the creation and enhancement of PSBs explains the large difference in fatigue failure cycles for very small decrease in the stress levels. At lower stress levels, development of PSBs and their subsequent enhancement required significantly higher fatigue cycles. However, for higher slope S-N curves, only small subsurface region is affected from the localized plasticity, hence relatively smaller difference in the fatigue cycles are usually required for any small decrease in the stress value.

FCC materials are known to show PSBs under loading [19]. The main slip system for the material was FCC structure (111) [18]. When the material was fatigue loaded, the crystal plane (111) with higher Schmid factor suffered from the higher degree of plastic deformation. The strains get localized due to the dislocation accumulation at grain boundaries of the material [11]. The interaction of precipitates at the grain boundaries of the material having higher Schmid factor with the dislocations started to occur [9, 15]. The partial surrounding of the grains at the leading surface of specimen [9] and this interaction in combination, not only generated the PSBs and local yielding

at the surface of the material, but also increased the surface roughness.
The local stress concentration created due to the sharp edges of PSBs act as the crack initiation and propagation [8, 14-15]. The slip markings developed due to the dislocation accumulation, transformed into the PSBs in the form of extrusions and intrusions. The deepest intrusion PSBs act as the potential fatigue crack initiation and propagation region [11, 15-17].
The fatigue failure with and without PSBs for specimens failed above and below 10^6 cycles showed that the fatigue crack initiation was highly dependent on the applied stress. At higher stresses, PSBs were not observed, yet the crack initiation took place from the surface of the specimen. The carbide precipitates were found as the crack initiation sites. However, when the stress levels were reduced, the PSBs played pivotal role in limiting the fatigue life of the material from 10^6 cycles and above. At further lower stress levels, at or below the fatigue limit, the PSBs were developed but found as non-damaging and the crack initiation was not observed. These PSBs were formed due to the large number of fatigue cycles and the stress concentration due to the lower stress was not sufficient to initiate the crack.

4. Conclusions

Fatigue behavior of AISI 310 was investigated up to very high cycles. S-N curve with very small decreasing slope was obtained without any step. It was found that the fatigue fracture can occur beyond 10^7 cycles in this material.
It was observed that all cracks were initiated from the surface of the specimen irrespective of the stress levels and the cycles before fatigue failure. No fish-eye or subsurface crack initiation was observed.
It was found that at higher stress levels, the specimen exhibited lower fatigue life and cracks initiated from carbide precipitates on the surface of specimen.
However, above 10^6 cycles at lower stress levels, PSBs were found at the surface of the specimen and acted as the fatigue crack initiation site. Arrays of intrusions and extrusions around the whole periphery of the specimen were observed. The sharp edges of PSBs served as the fatigue crack initiation and propagation.
The lower slope in S-N curve showed that little decrease in stress level increased the failure cycles significantly. The higher fatigue cycles were used in development of PSBs all over the surface of the specimen as compared to the materials exhibit fish-eye failure, which required localized plasticity in subsurface region for initiation of crack.

Acknowledgments

This work was supported by the National Natural Science Foundation of China (10925211 and 11150110139).

6. References

[1] C. Bathias and P. C. Paris. Gigacycle fatigue in mechanical practice. Taylor & Francis, 2004.
[2] I. Marines, X. Bin, C. Bathias. An understanding of very high cycle fatigue of metals. Int. J. Fat., 25 (2003), 1101–1107.
[3] C. Bathias, L. Drouillac, P. L. Francois. How and why the fatigue S–N curve does not approach a horizontal asymptote. Int. J. Fat., 23 (2001), S143–S151.
[4] H. Mughrabi. Specific Features and mechanisms of fatigue in the ultrahigh-cycle regime. Int. J. Fat., 28, 2006, 1501-1508.
[5] C. Stocker, M. Zimmermann, H. Christ. J. Effect of precipitation condition, prestrain and temperature on the fatigue behaviour of wrought nickel-based superalloys in the VHCF range. Acta Mater., 59 (2011), 5288-5304.
[6] S. T Stanzl, H. Mughrabi, B. Schoenbauer. Int. J. Fat., 29 (2007), 2050 – 2059.

[7] C. R. Sohar, A. Kotas, C. Gierl, B. Weiss. Gigacycle fatigue behavior of a high chromium alloyed cold work tool steel. Int. J. Fa.t, 30 (2008), 1137–1149.
[8] K. Tokaji, M. Kamakura, Y. Ishiizumi Y, N. Hasegawa. Fatigue behaviour and fracture mechanism of a rolled AZ31 magnesium alloy. Int. J. Fat., 26 (2004), 1217-1224.
[9] F. Yang , S. M. Yin, S. X. Li. Crack initiation mechanism of extruded AZ31 magnesium alloy in the very high cycle fatigue regime. Mat Sci. Eng A. 491 (2008), 131–136.
[10] N. Miura, Y. Takahashi. High-cycle fatigue behaviour of type 316 stainless steel at 288 C including mean stress effect. Int. J. Fat., 28 (2006), 1618-1625.
[11] T. Sakai, Y. Sato, N. Oguma. Fat. Fract. Engng. Mat. Struct., 25 (2001), pp 765-773.
[12] Chai G. Fatigue behaviour of duplex stainless steels in the very high cycle regime. Int. J. Fat., 28 (2006), 1611–1617.
[13] I. Marines, G. Dominguez, G. Baudry. Ultrasonic fatigue tests on bearing steel AISI-SAE 52100 at frequency of 20 and 30 kHz. Int. J. Fat., 25 (2003), 1037–1046.
[14] D. K. Xu, L. Liu,Y. B Xua. The crack initiation mechanism of the forged Mg－Zn－Y－Zr alloy in the super-long fatigue life regime. Scripta Mater., 56 (2007), 985-994.
[15] J. Man, M. Petrenec, K. Obrtlik and J. Polak. Acta Mater., 52 (2004), 5551－5561.
[16] J. Polak, T. Kruml, K. Obrtlik and J. Man. Proc. Engng., 2 (2010), 883–892.
[17] J. Polak, J. Man, K and Obrtlik K. Int. J. Fat. 25 (2003), 1027–1036.
[18] Khan M. K. Wang Q. Y. To be published.
[19] H. Mughrabi, K. Herz, X. Stark. Cyclic deformation and fatigue behaviour of alpha-iron mono- and polycrystals. Int. J. Fract. 17 (1981), 193-220.

Finite element modeling of the coupling between thermal dissipation and fish-eye crack growth in very high cycle fatigue regime

Laurent Gallimard*, **Hoang Quan Nguyen, Claude Bathias**

Laboratoire Energétique, Mécanique, Electromagnétisme,
Université Paris Ouest Nanterre-La Défense, 50 rue de Sèvres - 92410 Ville d'Avray – France.
* Corresponding author: laurent.gallimard@u-paris10.fr

Abstract The aim of the paper is to model the thermal dissipation associated to a fish-eye crack growth during an ultrasonic fatigue testing. We use a Paris-Hertzberg crack growth model to simulate the evolution of the crack and a perfectly elastic-plastic constitutive law to model the plastic dissipation per cycle. A finite element analysis is used to compute the evolution of the temperature field during the crack propagation. Numerical results are presented and they agree well with experimental results.

Keywords: very high fatigue cycle, ultrasonic testing, finite element modeling, crack growth, thermal dissipation

1. Introduction

The considerable attention given, in the past ten years, to fatigue fracture of metallic material in very high cycle regime, is mainly due to the increasing use of engineering materials in applications with service lives reaching up to 10^{10} load cycles. It has been shown that very high cycles fatigue (VHCF) failures of steels are characterized by a fracture which does not occurs on the surface but rather internally in the material, especially in high strength steels [1-3], and leads to the so-called fish-eye. Ultrasonic fatigue testing is a powerful tool for evaluating VHCF properties as 10^9 cycles can be completed in a day [4]. During an ultrasonic fatigue testing, the crack propagation in the tested specimen leads to an important cyclic plastic dissipation. One way of assessing this dissipated energy, and thus the crack propagation, is to use an infrared camera to measure the temperature increase during the test since part of this dissipation will occur as heat [5]. As far we know few studies have been devoted to the numerical computation of the temperature field associated with the propagation of a fatigue crack during VHCF failure [6,7].

In this presentation, we study numerically the temperature field associated with the propagation of a fatigue crack in a very high cycle fatigue regime during ultrasonic fatigue testing. The crack propagation is modeled by a classical Paris-Hertzberg crack growth law, and the plastic dissipation per cycle is determined by 3D-elastic plastic finite element modeling of stationary mode I crack under constant amplitude loading. A fraction of this plastic dissipation is converted heat and used as a mobile thermal source to compute the temperature field evolution. The first part of the presentation is devoted to the Finite Element modeling of the problem to be solved: The fatigue crack law is described, as well as the thermal dissipation model and the computation of the computation of the plastic energy dissipation. The second part of the presentation is devoted to the numerical results: The proposed model is compared with experimental results and the distribution of the plastic dissipation around the crack is computed.

2. Finite Element modeling

2.1. Fatigue crack growth law

Paris and co-workers [4] have developed estimation for crack growth life for internal initiation, termed *fish-eye* using the Paris-Hertzberg crack growth rate law [8]. In the present work we use this law to describe the growth of the fatigue crack

$$\frac{da}{dN} = b\left(\frac{\Delta K_{eff}}{E\sqrt{b}}\right)^3 \quad (1)$$

where b is the Burger's vector modulus, E the elastic modulus and ΔK_{eff} the effective stress intensity factor range.

2.2. Thermal dissipation model

We consider a problem of a fatigue crack in an elastic-plastic material. The temperature field in the cylinder is evaluated by solving the heat transfer equation

$$\rho\, C\, \frac{\partial T}{\partial t} = \lambda \Delta T + \beta \dot{W}^{irr} \quad (2)$$

where ρ is the mass density, C the specific heat, λ the heat conduction coefficient, and $\dot{W}^{irr}$ the plastic dissipation. The multiplicative factor β is the so-called Taylor-Quinney factor, which takes into account the energy storage.

2.3 Computation of the temperature field during the fish eye crack growth

The temperature field is computed in two steps, in a first step we perform an elastic plastic finite element analysis to compute the plastic energy dissipation as a function of the crack growth, and in a second step we perform a thermal finite element analysis to compute the evolution of the temperature field.

2.3.1 Computation of the plastic energy dissipation

The plastic energy dissipation is obtained by 3D elastic plastic finite element analysis. It was shown that in VHCF regime, the crack growth is not a significant portion of life in VHCF fatigue with *fish-eye* failure [9]. However, the number of cycles involved is still important ($\approx 10^5$ cycles) and a direct nonlinear computation will lead to prohibitive computational time. In this respect we choose to compute the energy dissipation per cycle dW^{irr}/dN during a single load cycle on a stationary crack for different radius a_i ($a_{in} = a_0 < a_1 < \ldots < a_n = a_{fi}$), as proposed by Klingbeil [10]. The mean energy dissipation per cycle is computed

$$\dot{W}^{irr} = \Omega\, \frac{dW^{irr}}{dN} = \int_{cycle} \sigma : d\epsilon^p \quad (3)$$

where Ω is the frequency of the loading. To simulate the plastic fatigue regime, and not a monotonic loading, two cycles are computed for each radius a_i and only the last cycle is used to

evaluate the plastic dissipation. Such an approach neglects the contribution of the actual crack extension during any given load cycle. However, for Paris-Regime crack growth, both the plastic work and the surface energy contributions associated with the actual crack extension in any given cycle are negligible compared to the total plastic dissipation. In VHCF regime the imposed load is small compared to the yield strength and the contribution of the plastic wake will be neglected in our work. Finally an elastic- perfectly plastic constitutive model is considered in this work.

2.3.1 Computation of the temperature field

In a second step, the plastic dissipation is used as a moving thermal source in a transient heat conduction problem. The thermal problem is solved with an implicit integration scheme. To define the time discretization ($t_0 < t_1 < \ldots < t_n$), we consider the following simplifications in the history of the crack propagation: the crack is supposed to remain circular during the crack growth process, the crack closure effect is neglected and we use the analytical formula for a circular crack in an infinite media

$$\Delta K_{eff} = \Delta K = \frac{2}{\Pi}\Delta\sigma\sqrt{\Pi a} \quad (4)$$

The loading is given by the energy dissipation per cycle computed in Equation (3). The meshes used are the meshes used during the mechanical computation to avoid errors due the data transfer on $\left(dW^{irr}/dN\right)(a_i)$ between different meshes.

3. Numerical results

The specimen is modeled by a cylinder *C* which has a circular cross-section of radius R_c and a height *2L*. A small circular crack perpendicular to the cylinder axis lies in the center of the cylinder, as shown in Fig. 1. The radius of the crack is denoted by *a(t)* and its eccentricity from the center of *C* is denoted by *e*. *C* is submitted to a cyclic loading: During each cycle the stress is varied linearly from an initial minimum value $\bar{\sigma}_{min}$ to a maximum value $\bar{\sigma}_{max}$ and back to the initial value $\bar{\sigma}_{min}$. An important parameter used to characterize the cyclic load is the so-called *load ratio*, defined as $R = \bar{\sigma}_{min}/\bar{\sigma}_{max}$. Because of symmetry conditions only one quarter of the cylinder is modeled.

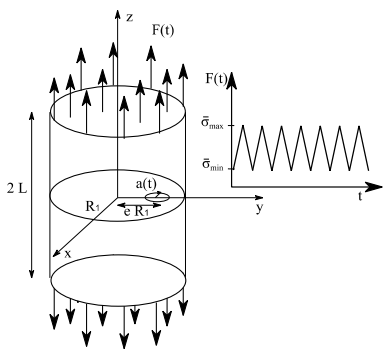

Figure 1. Specimen modeling

The tested material is a high-strength steel SAE 5120. Fatigue test are performed at ultrasonic fatigue frequency $\Omega = 20kHz$ with a stress ratio of $R = 0.1$ and stress amplitude $\Delta\sigma = 400Mpa$, using compressed air of 20^oC to cool the specimen. The material is approximated as elastic-perfectly plastic with thermomechanical properties $E = 200\,GPa$ (elastic modulus),

$\nu = 0.3$ (Poisson ratio), $\sigma_Y = 1067 Mpa$ (yield stress), $\rho = 7800 kg m^{-3}$ (mass density), $C = 460 J K^{-1} kg^{-1}$ (specific heat), $\lambda = 52 W K^{-1} m^{-2}$ (heat conduction coefficient). The Burger vector's modulus is taken such that $b = 1.8 \times 10^{-10} m$. The radius of the specimen is supposed to be $R_c = 1.5 mm$ and its height is defined by $L = 6 mm$. The finite element analysis is performed using Cast3M a general FE computer code developed by the CEA (French Alternative Energies and Atomic Energy Commission) with linear 3D elements.

3.1 Comparison with experimental data

The numerical results are compared with the experimental results obtained with two specimens. In Table 1 are given the number of cycles to failure N_f, the crack parameters measured after the failure a_{inc} and e, as well as the radius of the crack at $t = 0$ which is defined by $a_0 = a_{inc} / 0.94$ as proposed by Paris [20]

Table 1. Experimental parameters

Test	N_f (cycles)	a_{inc} (μm)	e	a_0 (μm)
1	$5,25 \times 10^7$	10.03	0.79	10.67
2	$4,24 \times 10^7$	13.80	0.83	14.68

The comparison between the measured and the computed temperature are plotted in Fig. 2 for test 1, and in Fig. 3 for test 2. These comparisons show a good agreement between the predicted and the measured values.

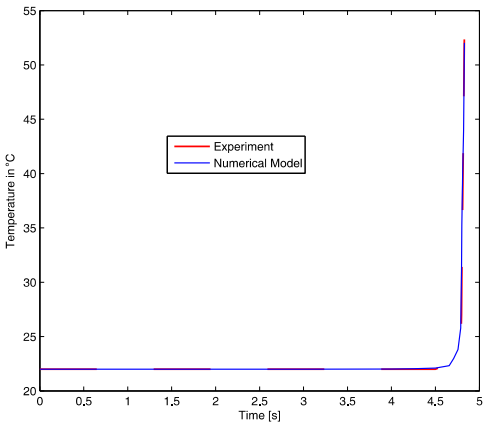

Figure 2. Test 1: Comparison between the modeled and the experimental temperature

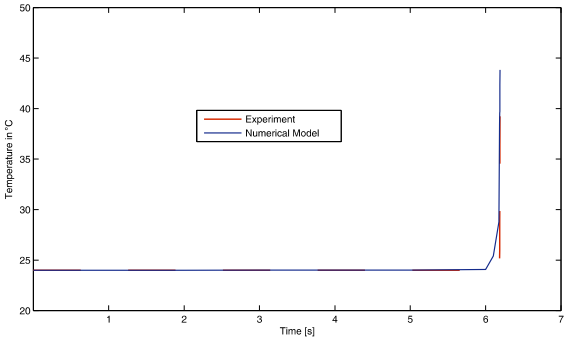

Figure 3. Test 2: Comparison between the modeled and the experimental temperature

3.2 Evolution of the plastic dissipation

The following results illustrate the evolution of the plastic dissipation per cycle, and of the temperature near the crack tip. The calculations are done with the geometric and materials values used for test 1. The crack tip line is divided in regular angular sections of 15°, and the evolution of the plastic dissipation evolution is computed in each section and shown in Fig 4. The plastic dissipation is not distributed regularly around the crack tip line as the crack progresses and is mainly concentrated in the two elementary volume which are the nearest to the surface.

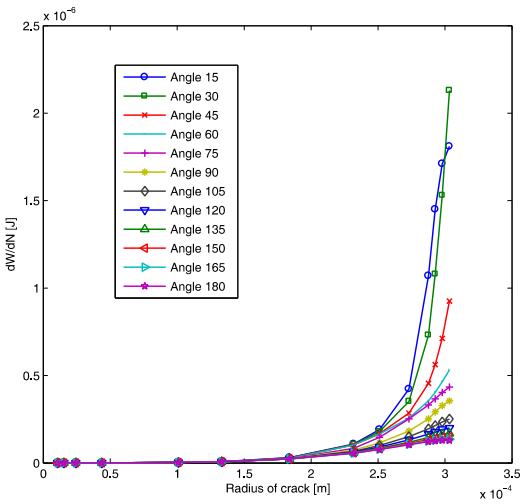

Fig 4. Evolution of the plastic dissipation as a function of the fish-eye radius

5. Conclusion

In this presentation, a weakly coupled thermo-mechanical finite element analysis of the propagation of a fatigue crack in VHCF fatigue regime has been proposed. The plastic dissipation per cycle has been computed from 3D finite element elastic perfectly plastic models of stationary crack in a cylinder under constant amplitude, mode I loading. The temperature rise during fatigue crack propagation is deduced from this plastic dissipation by the resolution of a transient heat conduction

problem with a moving source. The numerical results are in a good agreement with experimental test, and show that the plastic dissipation, and hence the thermal source, is concentrated near the surface of the specimen.

4. References

[1] Bathias C, Drouillac L, Lefrançois P (2001). How and why the fatigue sn curve does not approach a horizontal asymptote. *International Journal of Fatigue*;23:143-151.

[2] Sohar C, Betzwar-Kotas A, Gierl C, Weiss B, Dannineg H (2008). Gigacycle fatigue behavior of a high chromium alloyed cold work tool steel. *International Journal of Fatigue*;30:1137-1149.

[3] Li W, Sakai T, Li Q, Lu L, Wang P (2011). Effect of loading type on fatigue properties of high strength bearing steel in very high cycle regime. *Materials Science and Engineering: A*;528:5044-5052.

[4] Bathias C, Paris PC. *Gigacycle fatigue in mechanical practice*. New York: CRC Dekker; 2005.

[5] LaRosa G, Risitano A (2000). Thermographic methodology for rapid determination of the fatigue limit of materials and mechanical components. *International Journal of Fatigue*;22:65-73.

[6] Ranc N, Wagner D, Paris PC (2008). Study of thermal effects associated with crack propagation during very high cycle fatigue tests. *Acta Materialia*;56:4012-4021.

[7] Nguyen HQ, Gallimard L., C. Bathias, , Numerical simulation of the coupling between thermal dissipation and fish-eye crack growth in very high cycle fatigue regime, *Fatigue and Fracture of Engineering Materials and Structures*, pp 1-12, doi: 10.1111/ffe.12016, available online octobre 2012.

[8] Hertzberg RW. *Deformation and fracture mechanics of engineering materials*. 4th ed. New York; 1996.

[9] Marines-Garcia I, Paris PC, Tada H, Bathias C, Lados D (2008). Fatigue crack growth from small to large cracks on very high cycle fatigue with fish-eye failures. *Engineering Fracture Mechanics*;75:1657-1665.

[10] Klingbeil NW (2003). A total dissipated energy theory of fatigue crack growth in ductile solids. *International Journal of Fatigue*;25:117-128.

Investigations of Subcritical Crack Propagation under High Cycle Fatigue

Attilio Arcari[1], Nagaraja Iyyer[1], Madan Kittur[2], and Nam Phan[2]
[1]*Technical Data Analysis Inc., Falls Church, VA, USA*
[2]*Structures Division, Naval Air Systems Command, Patuxent River, MD, USA*

Abstract

Most of the fatigue life in high cycle fatigue (HCF) is expended in growing subcritical defects to a detectable damage size, followed by rapid growth to failure. This is a significant challenge in design as this leads to concerns with respect to the efficacy of planned inspections and routine repair operations. The variability of the damage phenomena in HCF can impact the characterization of the long fatigue life regimes, as the extent and severity of damage depends on the intensity of the operating loads, and on the intrinsic variations in material characteristics at different scales.

In this paper we propose a methodology to account for stochastic variability in HCF by using the framework of the Kitagawa-Takahashi diagram, and the El-Haddad formulation as the design curve for subcritical crack propagation in fatigue and in environmentally assisted cracking (EAC). Moment-based reliability, based on first order and second order reliability methods, as well as Monte Carlo simulation is used to handle stochastic variability in applied stress and defect size. The calculation of a probability of defect propagation at each instant of the subcritical growth process is the goal of the developed framework. Preliminarily validation with available data and an application of the framework to stochastic defect growth for block loading is presented.

1. Introduction

Designing against HCF can be challenging, particularly for dynamic components subjected to a large number of small amplitude or vibratory solicitations. While the growth of cracks from the subcritical level to a detectable size level has been extensively investigated in literature, current models show difficulties in estimating the fatigue life in HCF regimes and innovative solutions are sought [1-4].

The characterization of the fatigue behavior of materials in the long fatigue life regime is critical for fatigue life prediction models, but the investigation of damage phenomena in the proximity of the endurance stress can be experimentally intensive. Furthermore, crack growth under high R-ratios and near threshold is not well captured by currently employed frameworks [5, 6].

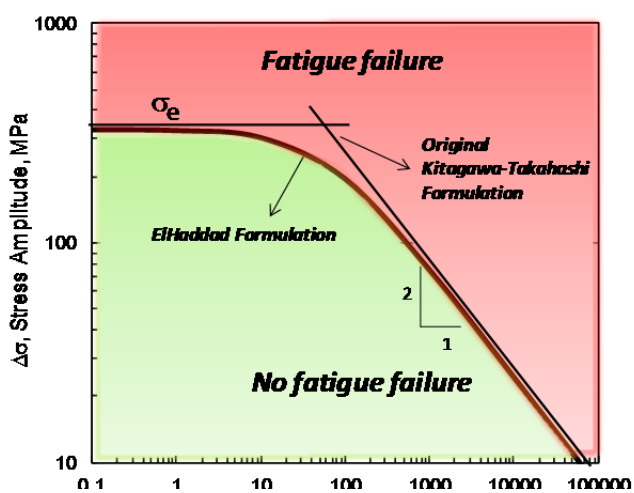

Figure 1: Kitagawa-Takahashi diagram for fatigue.

Therefore, certification becomes difficult for damage tolerance of components

predominantly subjected to HCF during the component lifetime and with limited or no possibilities of secondary load paths. The difficulty in characterizing the long life fatigue region interferes with the calculation of component retirement time, and the difficulties in crack growth predictions highly impacts the inspection intervals spacing [5].

The Kitagawa diagram, as modified by El Haddad to address crack growth threshold for short cracks (Figure 1), has been shown to be a powerful framework for the rationalization of initiation vs propagation of subcritical defects in metals and structural materials [7-10]. El Haddad introduced the correction factor a_0 into the Kitagawa diagram formulation, which can be interpreted as a subcritical defect size above which the long crack growth threshold holds. By dividing the stress-crack length space into two main areas, one where subcritical defects or crack are not expected to grow, and one where both fatigue and LEFM methodologies predict defects or cracks to grow in fatigue, the Kitagawa diagram can be used as a framework for the investigation of defect growth in HCF from the subcritical level to a detectable size level [3].

A statistical framework for the Kitagawa-Takahashi diagram in fatigue is here developed, with the goal of determining the likelihood that a nucleated defect propagates when subjected to a stress at a specific structure or component location, given a material behavior defined in terms of fatigue endurance, σ_e, and crack growth stress intensity threshold, ΔK_{th}. Additionally, a failure diagram in the form of a modified Kitagawa diagram for EAC is also developed by considering the corrosion fatigue (CF) and stress corrosion cracking (SCC) behavior of the material. The goal of this framework is to address whether a nucleated defect is likely to grow by CF by considering the concomitant SCC damage phenomena. The two frameworks are described in Section 2.

Probabilistic methods such as first order reliability method (FORM), second order reliability method (SORM) and the Monte Carlo simulation (MCS) can be employed in conjunction with fatigue and fracture mechanics to estimate the probability of the growth of a critical/propagating defect [11]. The reliability methods as used in the developed frameworks are described in Section 3.

The developed framework for fatigue is validated with available experimental data and finally an application example to HCF subcritical crack propagation is described.

2. Developed Framework in Fatigue and Environmentally Assisted Cracking

The Kitagawa diagram was introduced by Kitagawa and Takahashi [7] showing the transition as crack-size decreases from LEFM controlled growth (ΔK), to stress controlled behavior as the fatigue limit ($\Delta\sigma$) is approached. The Kitagawa diagram conveys two different thresholds: the minimum threshold stress intensity range for crack growth (ΔK_{th}) for a fracture mechanics specimen, and the endurance limit of a smooth specimen, that characterizes the minimum stress amplitude

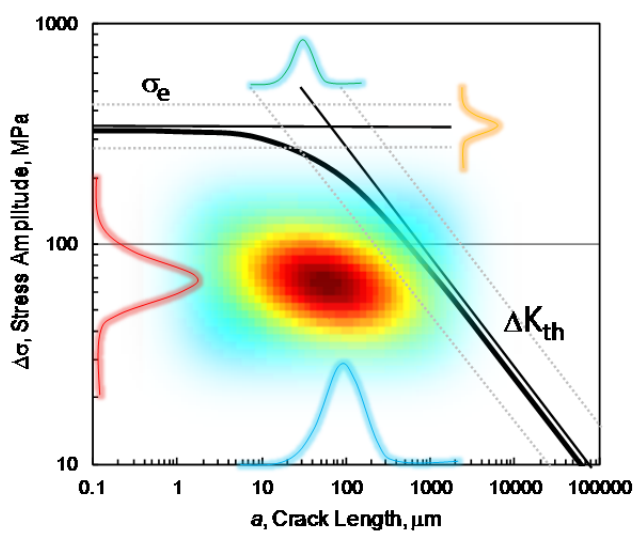

Figure 2: developed stochastic framework for the Kitagawa-Takahashi diagram.

(σ_e) to failure [8].

As mentioned above, in developing a statistical framework for the Kitagawa diagram, the limit state function used for reliability calculation is based on the mathematical formulation developed by El Haddad [8]. The limit state function defines the region in the stress-crack length space where the onset of crack propagation occurs for a nucleated defect, after which a flaw in HCF is expected to rapidly grow to a detectable length.

The El-Haddad formulation intrinsically considers the change in ΔK_{th} for cracks shorter than a_0, and elegantly describes this change in limiting condition by a simple mathematical formulation:

$$\Delta\sigma = \Delta K_{th}/(Y(a+a_0)\sqrt{\pi(a+a_0)}\,) \tag{1}$$

Although ΔK_{th} is nominally independent of crack length, at small crack sizes this function tends to a limit given by the fatigue endurance stress.

A statistical framework was initially developed for the Kitagawa diagram to consider statistical variability of stress and crack lengths; the extended framework allows including variability in any of the parameters (ΔK_{th}, a, $\Delta\sigma$,…), upon consideration of their relative interdependencies [11], as shown in Figure 2. The limit state is defined as the threshold of Kitagawa diagram in combination with El Haddad's correction which differentiates the non-propagating from propagating crack.

The limit state function for the fatigue framework developed can be written as follows:

$$g(X)_{Fatigue} = \Delta\sigma - \frac{\Delta K_{th}}{\sqrt{\pi(a+a_0{}^{Fatigue})}Y(a+a_0{}^{Fatigue})} \tag{2}$$

The criteria for crack propagation is defined as g(X)<0 with a probability of crack growth:

$$P_{c.p.} = \int_{g(x)\leq 0} f_X\,(x)dx \tag{3}$$

and reliability is expressed as $R=1-P_{c.p.}$

The failure diagram for corrosion is developed along the lines of the modified Kitagawa-Takahashi diagram for fatigue, as described elsewhere [3, 10, 12]. For SCC, by considering that in aggressive environment the material will be exposed to different concentrations of chemicals/ions involved in the corrosion damaging process, a limiting stress condition dependent upon the concentration level can be found. At concentration C, for example, the limiting threshold stress for crack propagation and failure of a smooth specimen, σ_{th}, forms a limiting condition in the SCC

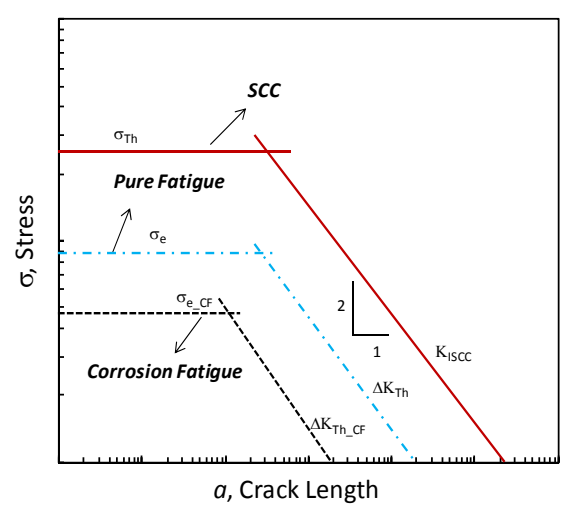

Figure 3: developed framework for EAC failure diagram.

diagram, as shown in Figure 3. For a fracture mechanics specimen the limiting threshold for crack propagation in SCC is K_{ISCC}, as calculated by EAC testing. Similarly to the original Kitagawa diagram, these two limiting conditions, σ_{th} and K_{ISCC}, can be used to develop an envelope diagram describing where crack propagation by SCC is expected to occur. By considering both stress related propagation and long crack condition, the diagram describes an SCC "safe" area and an SCC "unsafe" area.

The failure diagram for SCC can be described by the following equation:

$$\sigma_{Th} = K_{ISCC}/(Y(a + a_0{}^{SCC})\sqrt{\pi(a + a_0{}^{SCC})}\,) \tag{4}$$

Similarly, for corrosion fatigue, a Kitagawa like diagram can be envisioned, where the endurance stress in environmentally assisted fatigue, $\Delta\sigma_{e_CF}$, is combined with the stress intensity threshold in aggressive environment, ΔK_{th_CF}. The failure diagram will have the form:

$$\Delta\sigma_{CF} = \Delta K_{th_CF}/(Y(a + a_0{}^{CF})\sqrt{\pi(a + a_0{}^{CF})}\,) \tag{5}$$

Conceptually, a combined Kitagawa-like diagram with more than one mode of failure can be constructed for any material; it is the interest of this paper to ilustrate a failure diagram for CF, SCC and pure fatigue. The diagram can be pictured to look like Figure 3: the outermost Kitagawa-like diagram is expected to be the one representing SCC, with σ_{th} and K_{ISCC} as limiting values, the innermost Kitagawa-like diagram is expected to be the one representing CF, with $\Delta\sigma_{e_CF}$ and ΔK_{th_CF} as limiting values. The Kitagawa diagram for pure fatigue is pictured to lie between CF and SCC, with $\Delta\sigma_e$ and ΔK_{th} as limiting values. A failure diagram in aggressive environment can be constructed by considering only the outermost and innermost limiting conditions: CF and SCC.

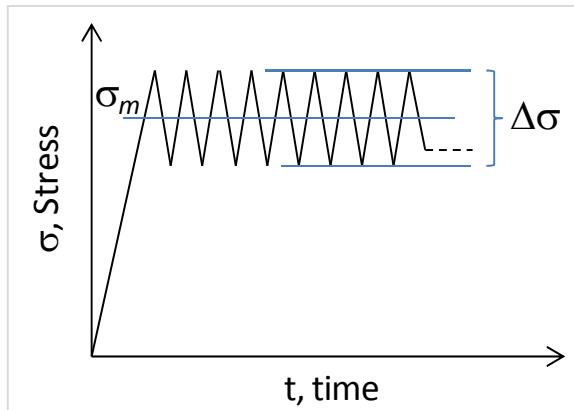

Figure 4: example loading in EAC.

Let's suppose that a component is subjected to fatigue loading in aggressive environment by cyclic stressing at a high R-ratio, as shown in Figure 4. In this situation we can infer that the component will be subjected to corrosion fatigue at a stress amplitude $\Delta\sigma$ and mean stress σ_m. Since the cyclic loading occurs at a high R-ratio, we can also infer that the component is subjected to stress corrosion cracking at a stress level σ_m. In this situation the Kitagawa-like diagram that can be applied are two: one for CF and one for SCC.

Two limit state functions need to be written for the failure diagram in EAC, one considering the CF and one the SCC damaging process; the limit states can be written as follows:

$$\begin{cases} g(X)_{CF} = \Delta\sigma - \dfrac{\Delta K_{th_CF}}{\sqrt{\pi(a+a_0{}^{CF})}Y(a+a_0{}^{CF})} \\ g(X)_{SCC} = \sigma_m - \dfrac{K_{ISCC}}{\sqrt{\pi(a+a_0{}^{SCC})}Y(a+a_0{}^{SCC})} \end{cases} \tag{6}$$

When considering both phenomena occurring simultaneously, it needs to be considered that the probability of a propagation event in CF or SCC is mutually influenced by both damaging phenomena. A possible approach to obtain probability bounds for a system subjected to both CF and SCC and the relative probability of each mode of propagation is the use of failure tree diagrams and common cause failure, as described by the authors elsewhere [1].

Note that all of the Kitagawa like diagrams shown correspond to a specific R-ratio level; multiple diagrams can be constructed for a single material at different R-ratios.

3. Reliability Methods

The modeling of the intrinsic variability of the controlling variables in a system is the foundation for the determination of a measure of reliability of a structure. The development of a statistical framework for a developed model is advantageous since it introduces mathematical and statistical concepts into the model and attempts to derive the statistical variability of the desired output directly computing the uncertainties associated with the parameters used in the model [13, 14].

First order and second order reliability methods are two analytical approaches that are used in this work to handle the variability of the stochastic inputs in the developed framework. The goal is the estimation of the probability of onset of HCF subcritical defect growth, in fatigue or CF and SCC, depending on the framework.

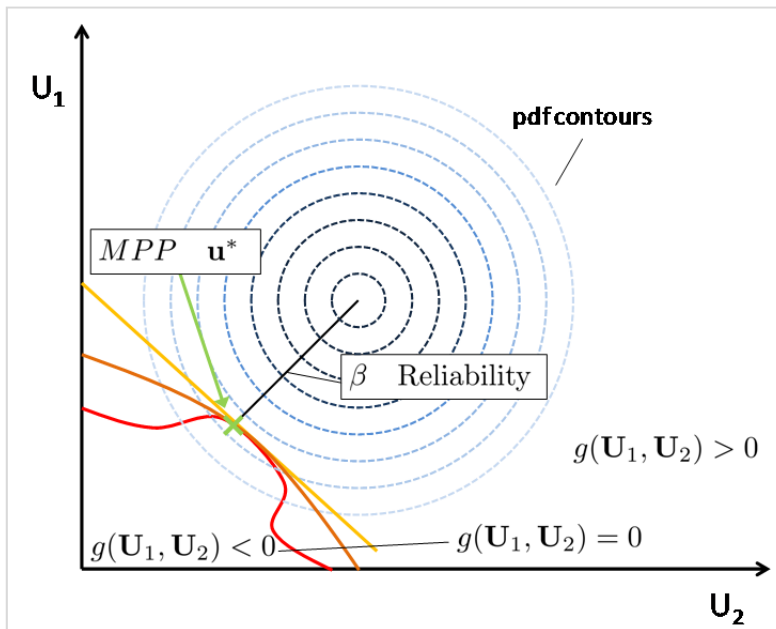

Figure 5: schematic of FORM and SORM calculation methods.

The name of First Order Reliability Method (FORM) comes from the fact that the performance function *g(X)* is approximated by the first order Taylor expansion (linearization), around the Most Probable Point (MPP). Two steps are involved in these approximation methods to make the probability integration easy to compute and to obtain the probability of exceeding a specified threshold**.**

The first step is to simplify the joint probability distribution, i.e. the function to be integrated, so that its contours become more regular and symmetric. The second step involves the approximation of the integration boundary on the limit state function *g(x)* at limit state *g(x) = 0*. After these two steps, an analytical solution to the probability integration can be obtained.

For ease of analytical development, all the variables are transformed into their standard forms. The transformation of the joint probability distribution is performed by mapping the

physical space to a standard space. Let $\boldsymbol{X}_i$ be the vector of stochastic variable under considerations, $\boldsymbol{U}_i$ is the vector of its transformed, as shown below.

$$\mathrm{F}_{\mathbf{X}_i}(\mathbf{x}_i) = \Phi(\mathrm{u}_i) \tag{7}$$

The transformation is performed on the premises that the cumulative density functions, c.d.f.s, of the random variables remain the same before and after the transformation.

$$\mathrm{U}_i = \Phi^{-1}\left[\mathrm{F}_{\mathbf{X}_i}(\mathbf{X}_i)\right] \tag{8}$$

The form of the limit state function consequently changes, and the calculation of the probability of failure remains the integration of the transformed limit state in the standard space domain where its value is less than 0:

$$p_f = P\{g(\boldsymbol{U}) < 0\} = \int_{g(\boldsymbol{U})<0} \phi_{\boldsymbol{U}}(\boldsymbol{u})d\boldsymbol{u} \tag{9}$$

FORM further approximate the integrand above by linearizing the limit state function $g(\mathbf{U})$ through Taylor series expansion around a point u*, called most probable point (MPP), as shown in Figure 5. SORM methods use a second order expansion around the MPP point to better approximate the limit state curvature. Reliability is then computed as the distance β from the center of the joint distribution to the MPP.

Another method that can be used and is here employed to handle the variability in the limit state function inputs is through numerical simulations, i.e. Monte Carlo methods. Although the application of direct simulations is more computationally intensive than the use of moment based methods FORM and SORM, Monte Carlo methods can be useful in many instances. As an example, the transformation of the distributions into the standard normal space can be challenging and simulations can be easily performed to calculate a measure of reliability, without the need of inverting $\mathrm{F}_{\mathrm{X}_i}(\mathrm{X}_i)$ to map the c.d.f.s to standard normal distributions. Additionally, by using Importance Sampling methods [15], results from FORM can be used to better target the Monte Carlo simulations and improve on the accuracy of the result.

In Monte Carlo simulations, typically uniformly distributed pseudo-random numbers are generated and then mapped into the proper distribution for each of the variables in the model. Finally, the pseudo-random values are used in the limit state function to obtain the limit state function output. Let n_f be the number of simulation cycles when $g(x)$ is less than zero and let N be the total number of simulation cycles, an estimate of the probability of crack propagation can be expressed as [16]:

$$P_{c.p.} = \int \dots \int I[g(x) < 0] f_x(x)dx \approx \frac{1}{N}\sum_{i=1}^{N} I[g(x_i) < 0] \approx \frac{n_f}{N} \tag{10}$$

The number of random variables in the problem does not affect the accuracy of Monte Carlo simulation, therefore the current framework allows to consider multiple input variability.

4. Verification and Validation of the Kitagawa Diagram for Fatigue

In this section, available experimental data are compiled and used for preliminary verification and validation of the developed stochastic framework for the Kitagawa diagram in fatigue.

A study on Type 403 (12% Cr) stainless steel focused on the development of pits in turbine blades developing into defects, eventually growing as fatigue cracks in service. An experimental data set is here compiled, and the stochastic Kitagawa diagram is used as the framework to determine whether the experimentally produced pits would cause a fatigue crack to grow during cyclic loading and possibly lead to failure.

The experimental study focused on fatigue testing pre-damaged smooth specimens by introducing a surface pit in their test section. The specimens are cycled in fatigue at different stress levels up to a very large number of cycles (10^7) or until failure occurs. The framework described in this paper was used to analyze the experimental data by calculating the probability of failure of each specimen cycled in fatigue, given the initial crack size defect (half pit width = a), and their statistical variation, including the statistical variation of threshold stress intensity factor ΔK_{th}.

Half pit width (a) and applied alternating stress ($\Delta\sigma$) are considered to be normally distributed, while stress intensity threshold distribution is lognormal, with mean and standard deviation as reported from experimental data. For each test a probability of crack propagation, calculated as a probability of failure using FORM is shown in the plot along with the experimental data point in the graph shown in Figure 6. Probability of failure calculated with Monte Carlo and SORM methods are within a 5% tolerance.

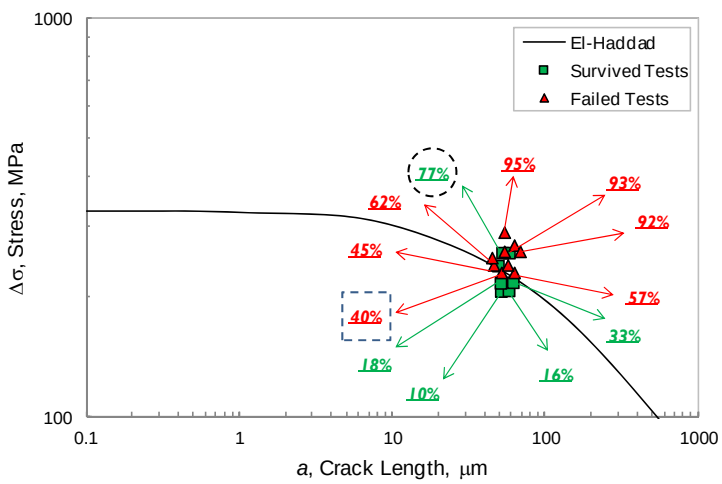

Figure 6: compiled data for framework validation.

The average probability of crack propagation for the tests shown, calculated from the experiments as the ratio between the number of tests where cracks grew to failure and the number of tests where cracks did not propagate is 0.57, and the average probability of crack propagation using the developed framework has been calculated as 0.569.

As observed from this experimental data set, on average the performance of the model reflects the results from experimental data. In some cases however, for tests with high probability of failure, experimental data showed no failure (circled results), or for others with low probability of failure (squared result), failures are observed. More data are needed in regions of

lower probability of failure or higher probability of failure to further validate this framework, and to test whether the populations described by the model are in agreement with experimentally observed populations. Additionally, sensitivity analysis studies are planned to understand the influence of the statistical distributions of the inputs with respect to the performance of the framework described.

5. Application to Fatigue Crack Growth in HCF

An example application of the developed framework is illustrated for fatigue; similar concepts and applications can be extended for the combined SCC, pure fatigue and CF framework. For simplicity it is supposed that all solicitations have R=0, therefore only one R-ratio is used for the Kitagawa diagram. Note that with appropriate material information and available data, this can be extended to any R-ratio level.

It is here assumed that a component subjected to fatigue loading has an initial crack length a_1. This component is subjected to HCF blocks of loading at constant R-ratio = 0. The blocks of loading are such that there is alternation of low amplitude stresses and higher amplitude ones. Within the framework of the Kitagawa diagram for fatigue the average point (σ, a), stress amplitude and crack length, will be moving from the safe zone into the fatigue crack propagation zone and vice versa frequently. This type of situation is illustrated in Figure 7, where the Kitagawa diagram for fatigue is shown with the failure diagram for static loading, whose bounds are the ultimate strength σ_U and the fracture toughness for the material K_{Ic}. The blocks of loading are shown in the top right corner of Figure 7.

As shown, the first block of cycles is well within the no-growth region of the Kitagawa diagram, therefore no crack propagation is expected. For the following block it is expected that fatigue crack propagation will occur, as the increase in stress level will bring the (σ, a) point outside the non-propagating area. The initial defect a_1 grows in fatigue to a dimension a_2 at the end of the block. In a similar way the third block will cause fatigue crack growth from a_2 to a_3. Note that at the time the defect has grown to a_3, the stress is reduced to the same level of the first loading block. Given the different crack length a_3, block 4 is near the limit condition described by the Kitagawa diagram. Nominally, no growth is expected for block 4 as well, but eventually the alternation of loading blocks of different stress amplitude will determine the (σ, a) point to lie outside the safe zone even for stress levels 1 and 4. Eventually the crack reaches the critical length for failure, i.e. when the (σ, a) point lies on the failure diagram for static loading.

It is here proposed to use the developed stochastic framework for fatigue to calculate for each loading block a probability of crack propagation, P_{CP}. Stress and crack length are taken as random variables within the current context, whose distribution needs to be estimated from available data. A probability of crack propagation can be calculated for each (σ, a) using the reliability methods described above and by considering for simplicity the correction factor Y constant and equal to unity. In the example described the P_{CP} will be very small for the first loading block, and it is expected to be much higher for the second and third block. When the crack has grown to a_3 however, even if the stress is decreased to a value equal to the one corresponding to the first block, the P_{CP} is expected to increase.

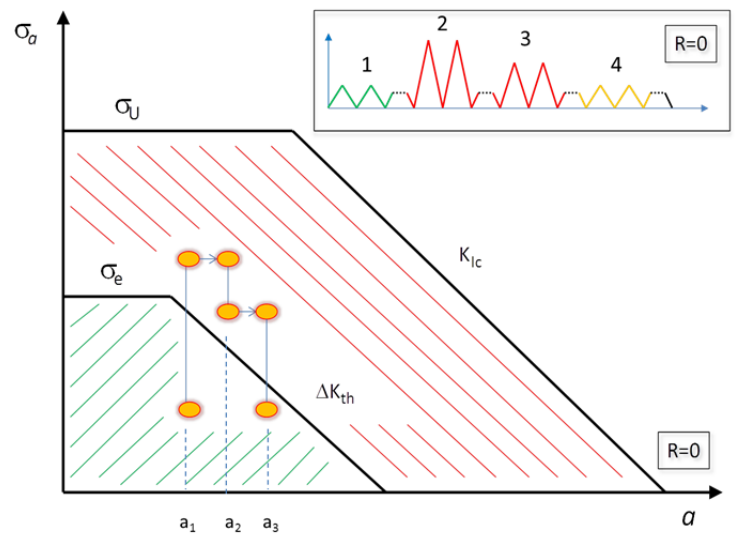

Figure 7: example of block loading and application of the developed framework for fatigue.

By considering that for every loading block the probability of crack propagation can be estimated using the framework developed in this paper, a probability tree can be constructed where each branch event (or block) has an associated probability of crack propagation. Cracks are assumed to grow following Paris' law at the ΔK corresponding to the stress $\Delta\sigma$. It is assumed that when (σ, a) lies within the "safe zone" of the Kitagawa diagram the crack will grow at the threshold level ΔK_{th}.

Each node of the tree will divide in two branches, one for a propagation event and one for a non-propagation event. By selecting consecutively at each node the branch with highest probability, a most probable crack growth path can be constructed. By selecting the branch that implies crack propagation at each node, no matter how probable the event is, a worst case scenario crack path can be constructed. Similarly a best case scenario can be constructed, by selecting the branch that implies no-propagation, creating an envelope for the most probable crack growth path.

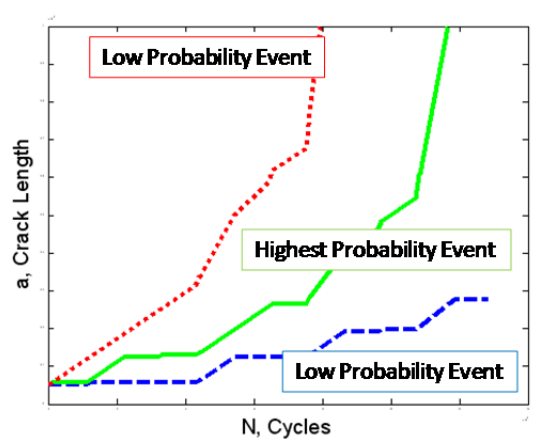

Figure 8: application example of the developed framework for subcritical crack growht in HCF block loading.

An example is shown in Figure 8 where different blocks at different stress levels are applied and crack propagation probabilities consecutively calculated for each loading block. Cracks are grown using Paris' law and three curves are calculated, a most probable path by choosing the highest probabilities, and a worst and best case scenarios.

6. Conclusions

In this paper subcritical crack propagation diagrams have been illustrated for fatigue and environmentally assisted cracking. The limit condition for subcritical crack propagation in the proposed framework is represented by Kitagawa-like diagrams combined with the El Haddad correction factor. Reliability methods for the estimation of probability of crack propagation for the diagrams shown have been proposed. Probability of crack propagation has been evaluated by using first and second order reliability methods (FORM/SORM) as well as Monte Carlo simulation.

Preliminary validation of the developed framework for fatigue has been shown, and more experimental data are currently being gathered for further validation of this diagram and for EAC diagrams. An example application of the developed framework to probabilistic subcritical crack growth has been illustrated. Further work is needed to apply the framework to multiple R-ratios data, and to extend to variable amplitude loading. Sensitivity analysis is planned to study the effects of selected stress and defect distributions on the reliability of the system.

References

1. A. Keshtgar, A. Arcari, N. Iyyer, M. Kittur, N. Phan, "A Reliability Approach for Subcritical Crack Propagation in High Cycle Fatigue", 15th Australian International Aerospace Congress, Melbourne Convention Centre, 25-28 February 2013
2. J. P. Gallagher, et al. "Demonstrating the effectiveness of an inspection system to detect cracks in safety of flight structures", Proceedings of a Workshop on Materials State Awareness National Research Council, Emily Ann Meyer Editor
3. Arcari A., Apetre N., Iyyer N., Nickerson W., "Probabilistic failure diagram for environmentally assisted cracking", International Committee on Aeronautical Fatigue and Structural Integrity, Jerusalem, Israel, June 3 – 7, 2013
4. Arcari, A., Apetre, N., Iyyer, N., Sarkar, S., Dowling, N.E., Stanzl-Tschegg, S., Phan, N., Rusk, D., Kang, P., Vasudevan, A.K.,, "Influence of superimposed VHCF loadings in cyclic fatigue and fracture of 7075-T6 aluminum alloy," 53rd AIAA/ASME/ASCE/AHS/ASC Structures, Structural Dynamics and Materials Conference, 23 - 26 Apr 2012, Honolulu, Hawaii
5. L. Lazzeri, U. Mariani, Application of Damage Tolerance principles to the design of helicopters, International Journal of Fatigue, Volume 31, Issue 6, June 2009, Pages 1039-1045, ISSN 0142-1123, 10.1016/j.ijfatigue.2008.05.010.
6. Noroozi, A. H., Glinka, G., Lambert, S., (2007), "A study of the stress ratio effects on fatigue crack growth using the unified two-parameters fatigue crack growth driving force", Int. J. Fatigue, vol. 29, n. 9-11, p. 1616-1633

7. H. Kitagawa, S. Takahashi, Applicability of fracture mechanics to very small cracks. In: ASM Proceedings of 2nd International Conference on Mechanical Behaviour of Materials, Metalspark, Ohio. 1976, pp. 627–631.
8. M. H. El Haddad, K. N. Smith, and T. H. Topper, Fatigue Crack Propagation of Short Cracks, J. Eng. Mater. Technol. 101, 42 (1979)
9. Theodore Nicholas, High Cycle Fatigue, A Mechanics of Materials Perspective, Copyright © 2006 Elsevier Ltd. , ISBN: 978-0-08-044691-2
10. K. Sadananda, A. Vasudevan, Failure Diagram for Chemically Assisted Crack Growth, Metallurgical and Materials Transactions A, V. 42-2. Pp. 296-303, 2011
11. P. Ramu, X. Qu, B. D. Youn, R. T. Haftka, Safety factor and inverse reliability measures, J. reliability and safety, 2006
12. Sadananda, K. and Vasudevan, A.K., (2011), "Review of environmentally assisted cracking", Met. Trans. A, vol. 42A, n. 2, p. 279–295
13. E. Thieulot-Laure, S. Pommier, S. Fréchinet, A multiaxial fatigue failure criterion considering the effects of the defects, International Journal of Fatigue, Volume 29, Issues 9–11, September–November 2007, Pages 1996-2004
14. D. S. Paolino, G. Chiandussi, M. Rossetto, A unified statistical model for S-N fatigue curves: probabilistic definition, Fatigue & Fracture of Engineering Materials & Structures, Blackwell Publishing Ltd, http://dx.doi.org/10.1111/j.1460-2695.2012.01711.x, 2012
15. C. N. Zeeb and P. J. Burns, A comparison of failure probability estimates by Monte Carlo sampling and latin hypercube sampling, Colorado State University, Department of Mech. Eng.
16. J. N. Siddall, Probabilistic Engineering Design: Principles and Applications, CRC Press, 1983 - 528 pages

The significance of two-phase plasticity for the crack initiation process during very high cycle fatigue of duplex steel

Alexander Giertler[1,*], Marcus Söker[1], Benjamin Dönges[2], Konstantin Istomin[2], Ullrich Pietsch[2], Claus Peter Fritzen[2], Wolfgang Ludwig[3], Hans-Jürgen Christ[2], Ulrich Krupp[1]

[1] Faculty of Engineering and Computer Science, University of Applied Sciences Osnabrück, 49009 Osnabrück, Germany
[2] Faculty IV: Science and Technology, University of Siegen, 57068 Siegen, Germany
[3] European Synchrotron Radiation Facility, 38000 Grenoble, France
* Corresponding author: a.giertler@hs-osnabrueck.de

Abstract The present paper reviews experimental results on the fatigue damage of grade 1.4462 austenitic-ferritic duplex steel in the very high cycle fatigue (VHCF) regime. Electrolytically polished miniature and bulk specimens have been fatigued in an ultrasonic fatigue testing machine while the surface is observed in-situ by an optical microscope. The pre-fatigued miniature specimens are investigated by synchrotron diffraction contrast tomography (DCT) to reveal three-dimensional crystallographic orientation data. These data are used for finite element modeling in combination with a material model accounting for elastic anisotropy and crystal plasticity to predict crack initiation sites. The bulk specimens are carefully analyzed by means of scanning electron microscopy (SEM) in combination with electron back-scatter diffraction (EBSD). Under VHCF loading conditions, slip band formation is limited to the softer austenite grains – in particular at twin boundaries. Once being formed, the bands generate high stress concentrations where they impinge the austenite-ferrite (γ–α) phase boundaries, eventually, leading to crack initiation. The results are discussed by means of a numerical modeling approach that is based on (i) the finite element method (FEM) mentioned above and (ii) a crack initiation model proposed by Tanaka and Mura [1] and Chan [2].

Keywords Duplex steel, VHCF, short fatigue cracks

1. Introduction

The fatigue life of metallic materials is determined by the plastic strain amplitude. The amplitude level determines the effective damage mechanism. For example, during LCF loading an early formation of slip bands can be observed, which leads to initiation and formation of long fatigue cracks [3]. In the HCF regime, the macroscopic strain amplitude is lower, but the microscopic strain amplitude can reach a critical value due to the elastic anisotropy of the microstructure, which results in the formation and propagation of microstructurally short fatigue cracks. In the VHCF range, the initiation and propagation of fatigue cracks is mainly influenced by the microstructure. Therefore, a large scatter can be observed in the fatigue life data. Life-determining factors are size, shape and distribution of non-metallic inclusions and the ability of grain and phase boundaries to block cyclic slip or microcracks. Duplex stainless steels exhibit a good combination of high strength, ductility and corrosion resistance [4]. Many applications imply cyclic loading, for instance the power transmission in off-shore boats. To ensure the reliability of such machines the knowledge about the fatigue behavior is essential. The assessment of the fatigue life is usually based on Wöhler data, but environmental effects, single overloads or the influences of varying microstructural impurities are often not taken into account, which leads to a non-conservative prediction. The present paper gives some evidences about the fatigue damage mechanism for ferritic austenitic duplex stainless steel in the VHCF regime and supports the hypothesis that phase boundaries act as effective barriers against fatigue crack initiation.

2. Experimental Procedure

The behavior of microstructurally short fatigue cracks were investigated in the VHCF regime on the austenitic ferritic duplex stainless steel DIN 1.4462. Duplex steel exhibit good strength and ductility values paired with excellent corrosion resistance [4]. The chemical composition of the material and the heat treatment pa-

rameters for the homogenizing and grain coarsening (required for 3D synchrotron tomography) is given in Table 1.

Table 1: Chemical composition of the duplex steel (wt. %) and heat treatment parameters.

C	Cr	Ni	Mo	Mn	N	P	S	Fe
0.02	21.9	5.6	3.1	1.8	0.19	0.023	0.002	bal.
grain coarsening	1250°C (4h); cooling down to 1050°C (1K/min); water quench							

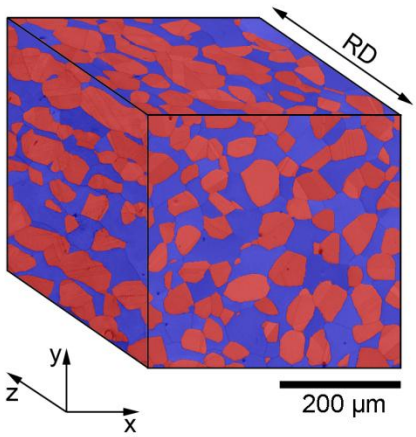

Figure 1: Microstructure of the investigated stainless duplex steel, austenite (red), ferrite (blue).

The grain coarsening heat treatment resulted in a microstructure consisting of 50 % austenite and 50 % ferrite, with a mean grain size of 33 µm for austenite and a mean grain size of 41 µm for ferrite. The geometries of the specimens are given in Figure 2; (a) shows the cylindrical bulk specimen, (b) shows the miniature specimen which has been developed for the synchrotron experiments at ESRF Grenoble. Both kinds of specimens are electro-polished in the gauge length; therefore, the surface of the specimens can be observed by means of light and electron microscopy in combination with automated electron back-scatter diffraction (EBSD).

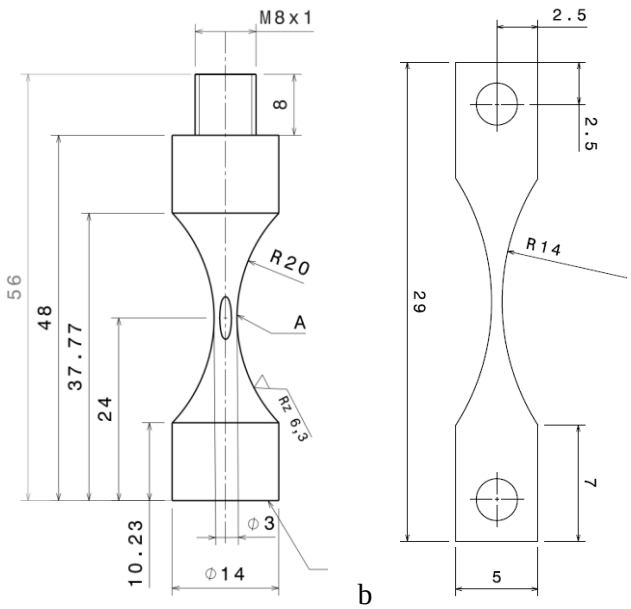

Figure 2: (a) shallow notched specimen for the VHCF tests, (b) flat bone shaped specimen for the VHCF tests.

For the cyclic loading of the samples an ultrasonic fatigue testing equipment designed and produced by BOKU Vienna was used, with an average frequency of f = 20 kHz and an load ratio of R = -1. To prevent heating of the specimens during cycling compressed air cooling is used. The observation of the fatigue dam-

age within the machine is done with an optical far field microscope Questar QM100. The microscope is focused on the shallow notched area in the middle of the gauge length of the specimen shown in Fig. 2 (a). The microscope is continuously taking pictures of the surface, thus a measurement of the crack growth is possible. The miniature specimens are used for phase contrast tomography (PCT) and the relatively new developed diffraction contrast tomography (DCT) to map the grain microstructure in the gauge length of the specimen. The digital reconstruction of the three-dimensional volume contains the grain shape and distribution and also the crystallographic orientation data of every individual grain. By using these data, it is possible to calculate the stress distribution within the two-phase microstructure by means of the finite element method (FEM) in combination with an elastic-anisotropic, crystal-plastic material model.

3. Results

The fatigue tests were carried out under uniaxial tension-compression (R=-1) at room temperature. As it was found in certain studies [5], a strong slip band formation in the austenite grains took place during the tests. The sample shown in Figure 3 was loaded with an stress amplitude of $\Delta\sigma/2$=400 MPa up to $1.6\cdot10^6$ cycles until the test was stopped. The crack initiation took place at a γ–α phase boundary between the grains 1 and 3. The crack initiation site has been analyzed by EBSD to calculate the corresponding slip systems and Schmid factors. For the austenite grain 1 a Schmid factor of M_s=0.46 was determined and the slip planes in grain 1 are oriented in the $(11\bar{1})$ direction; in comparison, the ferrite grain 3 has an corresponding Schmid factor of M_s=0.35. During the test, grain 1 shows a continuously increasing number of activated slip bands, thus it seems that the cracking of the phase boundary in this case is depending on the amount of accumulated micro strain caused by the local plastic deformation of grain 1.

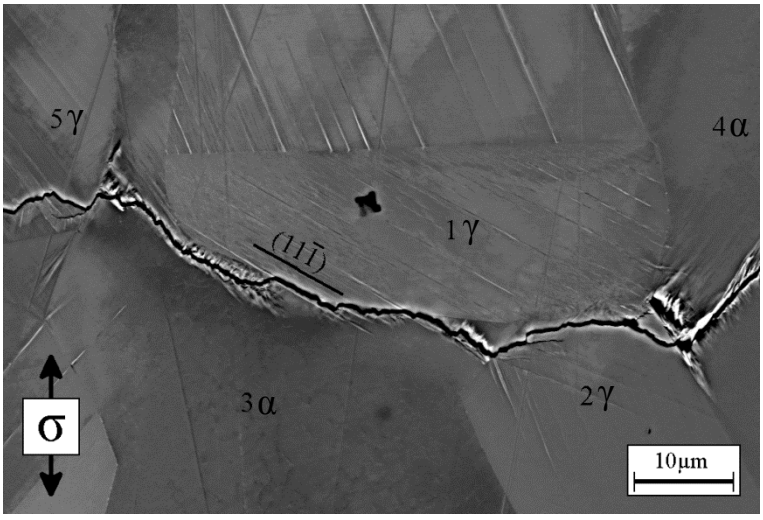

Figure 3: Crack initiation site of a fatigue sample loaded at $\Delta\sigma/2$=400MPa, $1.6\cdot10^6$ cycles.

Figure 4 shows the optically measured crack length vs. the number of cycles for the left and right crack front. The crack shown in Figure 3 corresponds only to the first 50 µm of the final crack length. The crack length is measured starting from its crack initiation site to the left and right direction, to show the varying crack propagation rates being visible at the surface. It was found that the propagating crack follows within the first $1.3\cdot10^6$ cycles the phase boundary in the left direction until it reaches grain 5. In the other direction it took the same number of cycles to overcome the grain boundary between grain 1 and grain 2 to reach grain number 4. The crack propagation starts to accelerate after the crack crosses the phase boundaries to the grains 4 and 5. The individual crack propagation rate was calculated for grains 4 and 5. For the ferrite grain 4 the rate was $1.1\cdot10^{-9}$ m/cycle, the rate for the austenite grain 5 was lower with $4.5\cdot10^{-10}$ m/cycle. This effect can be correlated to the different kinds of active slip mechanisms in austenite and ferrite. One possible explanation of this discrepancy between the different crack propagation rates in austenite and ferrite could be the splitting of the energy on multiple slip systems (= lower da/dN in austenite), which is necessary for local plastic deformation [5].

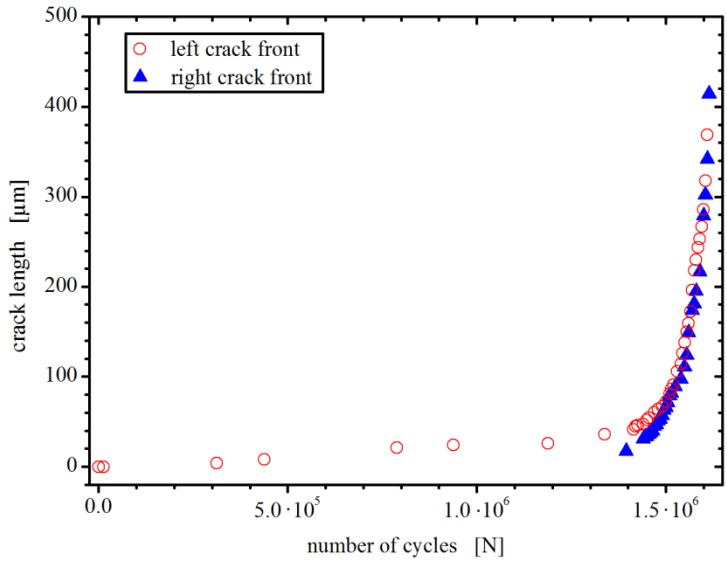

Figure 4: Crack length vs. the number of cycles for the left and right crack front.

The crack shown in Figure 5 initiated at the phase boundary between the austenite grain 3 and the ferrite grain 1. The specimen was loaded with a stress amplitude of $\Delta\sigma/2$=400 MPa up to $1.7\cdot10^6$ cycles until the test was stopped manually to prevent the breaking of the specimen.

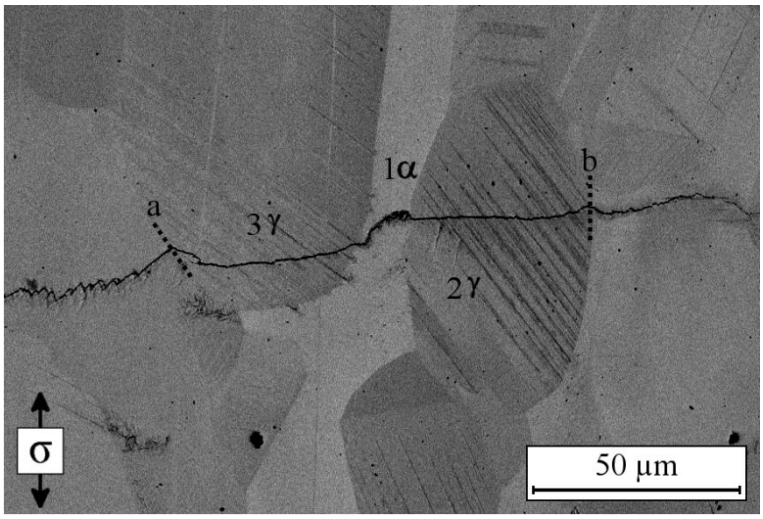

Figure 5: Crack path of a fatigue sample loaded at $\Delta\sigma/2$=400MPa, $1.7\cdot10^6$ cycles.

By analyzing the micrographs which have been taken every thousand cycles during the fatigue test, it was possible to reconstruct the crack propagation path. In this case, the crack spends about $1.3\cdot10^6$ cycles to cross the ferrite grain 1, starting from its initiation site and propagating in the direction of austenite grain 2 at an angle of about 45°with respect to the stress axis. This first part of the crack propagation process is quantified in Figure 6. After reaching the austenite grains 2 and 3, the crack is changing its propagation direction perpendicular to the stress axis by changing its slip mechanism into double slip.

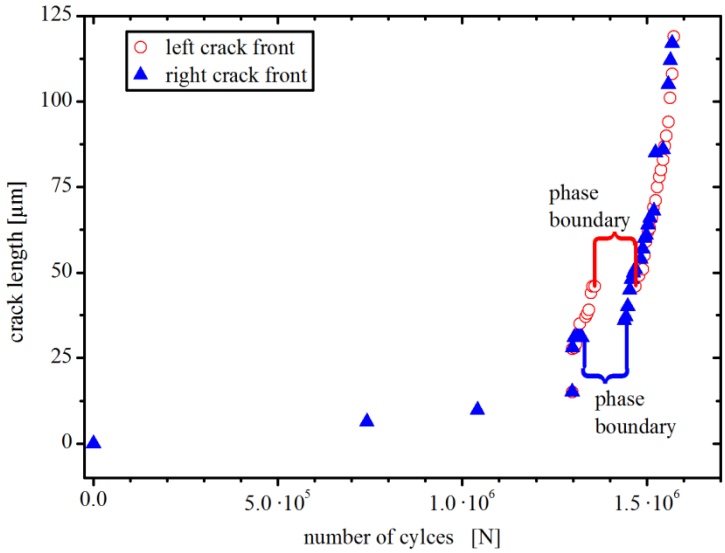

Figure 6: Crack length vs. the number of cycles for the left and right crack front

After crossing the austenite grains 2 and 3, the crack reaches the phase boundary marked with an "a" and "b" in Figure 5. Obviously, the phase boundary acts as an effective barrier against crack propagation, what is supported by the crack length data in Figure 6. This effect is caused by the incompatibility of the slip systems between neighboring grains [6]. The data from the crack length measurement was further analyzed to calculate the fatigue crack propagation rate of the left crack front as a function of the crack length, cf. Figure 7. The plotted data reveals that when approaching the phase boundary the crack propagation rate decreases down to da/dN≈0 and the crack arrests at the phase boundary. After crossing the phase boundary, the crack propagation rate increases again.

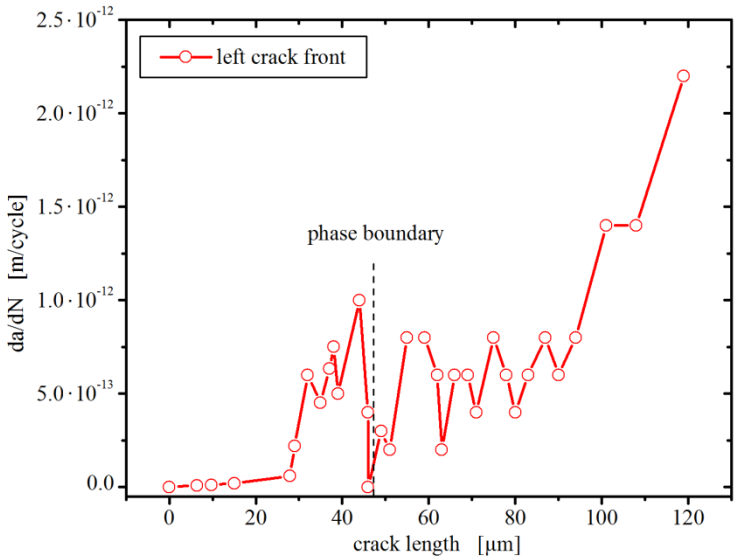

Figure 7: Crack propagation rate vs. the crack length for the left crack front in Fig. 5.

However, the observation by means of light microscopy can only reveal information about crack initiation and propagation processes that can be related to the surface grains of a specimen. In case of VHCF loading, the three-dimensional microstructure needs to be taken into account. Therefore, miniature specimens that can be attached to a titanium carrier for fatigue testing in an ultrasonic fatigue testing machine were developed to get three-dimensional information about the duplex microstructure by means of synchrotron tomography under cyclic loading. The experiments are done using the phase-contrast tomography (PCT) and the diffraction-contrast tomography (DCT). DCT is a new developed method which gives the possibility to image the 3D grain structure with its crystallographic orientation data, Figure 8 a. The specimen is placed in the beam

very close to the detector plane.

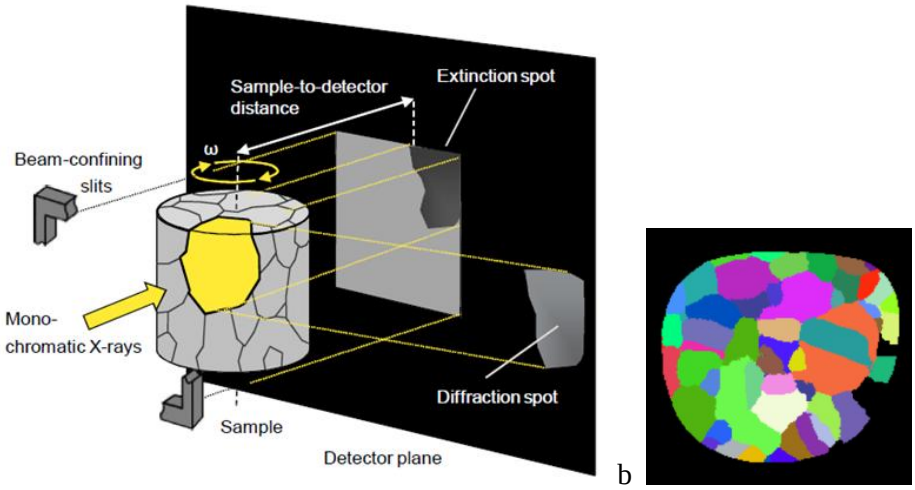

Figure 8: (a) Illustration of the working principle of the diffraction-contrast tomography (DCT) [7], (b) reconstructed slice of a duplex steel fatigue specimen mapped with DCT.

The beam is confined by slits to limit the number of penetrated grains. During the rotation of the sample, some of the grains fulfill the Bragg condition; therefore, the grains are producing diffraction spots on the detector plane. Afterwards, a semi-automated computer code reconstructs the individual grain shape and position in the volume from the pictures taken during the rotation of the sample, cf. Figure 8 b.
The data will be used for a more detailed prediction of local crack or slip band nucleation sites by means of the finite-element method (FEM). An example of the application of the FEM is given in Figure 9. The microcracks (see arrows in Figure 9 a) were initiated at a stress amplitude of $\Delta\sigma/2$=365 MPa. The emanation process of the slip bands within the austenite grain γ_1 leads to stress intensities at the phase boundaries and in the neighboring ferrite grain α_1.

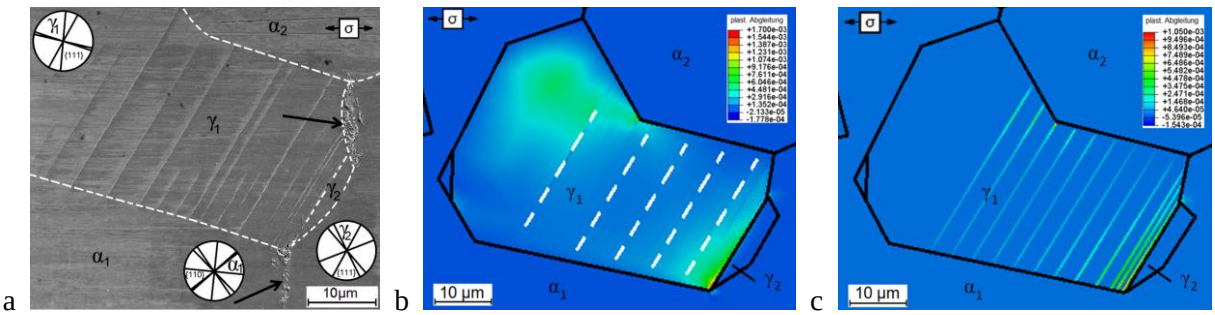

Figure 9: (a) intercrystalline und transcrystalline fatigue crack initiation (arrows) in the ferrite, introduced by local stress intensities caused by slip bands within the austenite, (b) plastic slip on the slip system with the highest stress, (c) plastic slip on discrete slip bands.

Eventually, the initiated dislocation motion in the ferrite leads to the crack initiation process described by Tanaka and Mura [1]. The transport of the plastic deformation was supported by the low twist and tilt angle between the austenite γ_1 and ferrite α_1 grains. With the help of a material model according for crystal plasticity, the slip on adjacent slip systems have been calculated by FEM [8]. The model is considering the elastic and plastic anisotropic deformation of the grains, which is leading to the inhomogeneous stress distribution. Figure 9 b shows the displacement on slip system in the austenite grain γ_1 with the highest stress, leading to pronounced slip band formation. To analyze the stress distribution at the phase boundaries, discrete slip bands have been integrated on the highly stressed austenite grain (cf. Figure 9 c), according to the results of Figure 9 b. These slip bands are activated when the local friction stress τ_{fr} is exceeded. Meanwhile, the other areas of the austenite grain are deforming only anisotropic-elastic. This approach allows to calculate a global stress value which is not sufficient to initiate any plastic deformation within the ferrite phase. Accordingly, the endurance limit for a certain area of the microstructure can be estimated.

4. Discussion

According to the results of the ultrasonic fatigue tests, it is shown that right at the beginning of fatigue loading local plastic deformation is concentrated in the austenite phase, caused by the elastic anisotropy of the duplex microstructure. Slip band formation within the austenite grains, produces strong dislocation pile ups at the phase boundaries. These local stress intensities are predominant sites for crack initiation (cf. Figure 3). The crack propagation process was observed by means of a far field microscope to correlate the crack path with its surrounding microstructure. The α/γ-phase boundary has been identified as an effective barrier against fatigue crack propagation, cf. Figure 7. By knowing the local phase and crystal orientation distribution, e.g., from EBSD measurements, it is possible to predict crack initiation sites in the microstructure by means of FEM. Here, a material model is required that accounts for elastic anisotropy and crystal plasticity. The calculated local shear stresses correlate with initiation sites for slip bands and cracks. As a subject of ongoing work, the 3D data from the diffraction-contrast-tomography experiments will be used for a more precise FEM prediction of slip band and crack initiation sites in the mapped volume. As described earlier, plastic deformation located in the slip band has been found also in the austenite grains even after 10^8 cycles due to the elastic anisotropy of the material. To model the fatigue crack initiation in the VHCF regime the focus has been placed on the evolution of slip bands, and in particular especially on the slip transmission in the neighboring grains and the crack initiation. The underlying model concept follows the work of Tanaka and Mura [1] on crack initiation along slip bands. It describes the fatigue-crack initiation by the accumulation of dislocation dipoles during strain cycling

$$N_i \approx \frac{4Gw_s}{\pi(1-\nu)} \frac{1}{d(\Delta\tau - 2\tau_{fr})^2}, \tag{1}$$

where N_i is the number of cycles for crack initiation, G the shear modulus, w_s the specific fracture energy per unit area along the slip band, ν the Poisson ratio, d the grain size, Δτ the shear-stress range and τ_{fr} the friction stress of dislocation motion. The model was modified for instances by Chan [2], who added the slip band height h and a factor for the cyclic slip irreversibility λ. For the HCF and VHCF regime, where low stress amplitudes are applied, cyclic slip consist of a reversible and irreversible fraction of dislocation movement. The number of cycles N_i for initiation of a crack of length c can be calculated as follows:

$$N_i \approx \frac{8G^2}{\lambda\pi(1-\nu)} \left(\frac{h}{d}\right)^2 \left(\frac{c}{d}\right) \frac{1}{(\Delta\tau - 2\tau_{fr})^2}. \tag{2}$$

Furthermore, it was shown that slip transmission from one grain to the neighboring grain plays an important role in crack initiation and propagation. This barrier and its effectiveness can be described by the twist and tilt angles of the adjacent slip planes [6, 9].

5. Conclusion

Under fatigue loading, plastic deformation is concentrated in the austenite phase by the emanation of intense slip bands. The formation of slip bands was observed already during the first thousand cycles, leading to local stress intensities at the phase austenite-ferrite boundaries. These areas have been identified experimentally by light microscopy and numerically by the finite element method as critical crack initiation sites. On the other hand, the results are showing that crack initiation is depending to a great extent on the configuration of the tilt and twist angles of the neighboring grains. They control the transport of the local plastic deformation concentrated on the slip bands in the austenite across the phase boundary into the ferrite phase. This effect supports the assumption that VHCF damage depends on the microstructure. Therefore, understanding of the fatigue mechanisms in the VHCF regime requires the knowledge about the microstructure. Anyhow, in case of crack initiation the cracking of the first grain is dominating the lifetime of the specimens. Furthermore, the experimental data from the fatigue experiments shows that phase boundaries play a major role in fatigue crack propagation. They exhibit the ability to slow down or to stop the crack propagation process. This effect is depending on the configuration of the tilt and twist angles of the slip systems of neighboring grains. A close look on the results show that crack initiation and propagation is a three-dimensional problem.

Hence, a set of miniature fatigue specimens have been fatigued with an ultrasonic fatigue testing machine and afterwards analyzed by means of synchrotron tomography. It is planed that these test data should assist in the near future the FE modeling.

Acknowledgements

The support of this work by the Deutsche Forschungsgemeinschaft (DFG) is gratefully acknowledged.

References

[1] K. Tanaka, T. Mura: A Dislocation Model for Fatigue Crack Initiation, J. Applied Mech., 48 (1981) 63.

[2] K.S. Chan: A Microstructure-Based Fatigue Crack Initiation Model, Met. Mat. Trans. A, 34A (2003) 43.

[3] M. C. Marinelli: Activated slip systems and microcrack path in LCF of a duplex stainless steel, Mat. Sci. Eng. A, 509, (2009), 81.

[4] B.I. Voronenko: Austenitic – Ferritic Stainless Steels: A State-Of-The-Art Review, Met. Sci. and Heat Treatm. 39 (1997) 428.

[5] O. Düber, Untersuchung zum Ausbreitungsverhalten mikrostrukturell kurzer Ermüdungsrisse in zweiphasigen metallischen Werkstoffen am Beispiel eines austenitisch-ferritischen Duplexstahls, PhD Thesis, University of Siegen 2007.

[6] T. Zhai: The grain boundary geometry for optimum resistance to growth of short fatigue cracks in high strength Al-alloys, Int. J. Fatigue, 27 (2005) 1202.

[7] M. Herbig: 3-D growth of a short fatigue crack within a polycrystalline microstructure studied using combined diffraction and phase-contrast X-ray tomography, Acta Mater. 59 (2011) 590.

[8] Y. Huang: A User-Material Subroutine Incorporating Single Crystal Plasticity in the ABAQUS Finite Element Program, Mech Report 178, Division of Engineering and Applied Sciences, Harvard University, Cambridge, 1991.

[9] W. Schaef: A 3-D view on the mechanisms of short fatigue cracks interacting with grain boundaries, Acta Mater., 59 (2011) 1849.

Microplasticity , Microdamage, Microcracking in Ultrasonic Fatigue

C Bathias [1], D Field[2], S Antolovich,[3] and PC Paris [4]

[1]University of Paris Ouest ,LEME, 50 rue de Sevres, Ville d'Avray ,92410 Fr, claude@bathias.com

[2]Washington State University, Pullman, WA 99164-2920 ,

[3] GeorgiaTech, Atlanta,Ga, 30332-0245

[4]Washington University, Saint Louis, Mo,63130

Abstract: Depending upon the fatigue domain, different types of crack initiation occur. In low cycle fatigue, the cyclic plastic deformation is critical at the surface but exists also in the bulk of the metal. In high cycle fatigue, the plastic deformation is limited to the surface in plane stress conditions. In very high cycle fatigue, the crack initiates from the interior, starting from a defect in plane strain conditions. This means that the initiation mechanisms in gigacycle fatigue depend not only on upon the stress field but also on the stability of the microstructure.

Keywords : Gigacycle fatigue, fish eye, plasticity, microstructure

1-Introduction

The initiation of fatigue cracks can be considered differently from physical or mechanical points of view. At the microscopic level, Mughrabi [1] shows that the initiation of fatigue crack in the gigacycle fatigue regime can be described in terms of a microstructurally irreversible portion of the cumulative cycle strain. This means that there is no basic difference between fatigue mechanisms in low, mega, and gigacycle fatigue except for the strain localization. However, specific mechanisms can occur depending on the fatigue life. The fatigue life seems to be a key parameter to determine correctly the fatigue initiation location. In low cycle fatigue, in megacycle fatigue and in gigacycle fatigue different mechanisms can operate at different scales of plasticity. In the low cycle fatigue regime, the cyclic plastic deformation is critical at the surface but exists also in the bulk of the metal. Typically, several cracks nucleate from the surface. When the fatigue life is below 10^5 cycles, general plastic deformation of the specimen bulk governs the initiation. When the fatigue life is between 10^6 and 10^7 cycles the plastic deformation depends on the plane stress surface effect and the presence of flaws which explain the critical location of fatigue initiation. Typically, the initiation starts with one crack only, from the surface. However approaching 10^9 cycles the plastic deformation in plane stress conditions vanishes; the macroscopic behaviour of the metal is elastic except around flaws, metallurgical defects or inclusions. In very high cycle fatigue, the plane stress conditions are not enough for a surface plastic deformation according the Von Mises criteria. The initiation may be located in an internal zone. When the crack initiation site is in the interior, this leads to the formation of one fish eye on the fracture surface, typical of gigacycle fatigue. In this case, the cyclic plastic deformation is related to the stress concentration around a defect: inclusion, porosity, super grain. Since the probability of occurrence of a flaw is greater within an internal volume than at a surface, the typical initiation in Gigacycle fatigue will ~~be~~ most often occur in the bulk of the metal.

To sum up the state of art, it is generally accepted that if the first damage in fatigue is located at the surface the typical feature is persistent slip band (PSB), intrusion or extrusion, all related to a strong planar shear deformation, in plane stress. ~~.~~ On the contrary, if the first

damage occurs around an internal defect, typically a cellular dislocation network in 3D is observed for plane strain. According to our own observations and those in the literature [2] [3] two main factors are operating in the Gigacycle regime:

- The stress concentration due to metallurgical microstructure misfit becomes an important parameter when the applied load is low. The inclusions in steels or in nickel base alloys or the porosity in cast aluminium or in powder metallurgy are among the most efficient stress concentrators.

- The stress concentration due to the anisotropy of metals is another parameter. At low deformation,- plasticity can appear only if the grain orientation and the grain size are in suitable for dislocation glide. A large grain can become a critical location for initiation in low carbon steel, austenitic steel or titanium alloy.

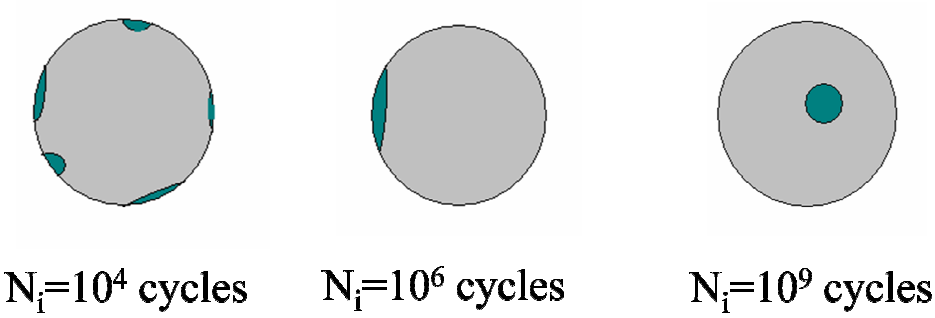

Figure 1 fatigue crack initiation sites

2-Fish eye growth

When the crack initiation site is in the interior, this leads to the formation of a “fish-eye” on the fracture surface, and the origin of the fatigue crack is an inclusion, a “super grain” (micro structural homogeneity), or porosity. At the macroscopic scale, under the optical microscope (or naked eye), the fish-eye area looks white, whereas the region outside of the fish-eye looks grey. In almost all cases, this fish-eye appears virtually circular, with a dark area in the centre, inside of which the crack initiation site is located. Controversies exist on the origin of this dark area, which some authors have variously named: “Optically Dark Area (ODA)” by Y.Murakami [4], “Fine Granular Area (FGA)” by T. Sakai [5], and “Granular Bright Facet (GBF) by Shiozawa [6]...). According to Y. Murakami et al., the mechanism of formation of ODAs is presumed to be micro-scale fatigue fracture caused by cyclic stress coupled with internal hydrogen trapped by non-metallic inclusions. It is presumed that when the size of an ODA exceeds the critical size for the intrinsic material fatigue limit in the absence of hydrogen, the crack grows without the assistance of hydrogen. According to T. Sakai et al., the mechanism of formation of FGAs is caused by intensive polygonisation induced around the inclusion, followed by micro-debondings which can coalesce leading to this fine granular area. By the way, no PSB has been reported for fish eye formation.

The fractographic observations show zones (figure 2) in agreement with a mechanical model:

- a dark area zone (so-called ODA) due to the initiation mechanisms. [4]
- a penny-shaped zone (short crack growth). Whatever the crack initiation site (spherical or elongated inclusion, super-grain, pore), the fracture surface becomes circular around the initiation site.
- A zone with small radial ridges corresponding to the short to long crack transition

- A zone with large radial ridges (long crack growth). In this zone, the fatigue crack propagation produces striations for which the mean distance between striations is a function of ΔK^2, in good agreement with the CTOD [7].

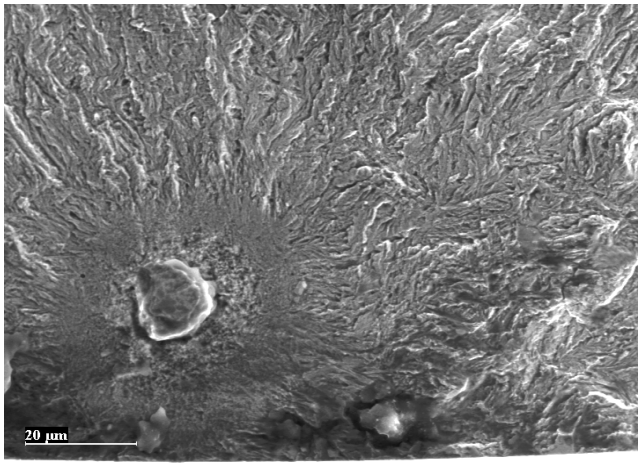

Figure 2 Typical fish eye with initiation and short crack growth.

3-Prediction of fish eye

In order to predict the fish eye propagation, one should refer to a general behaviour pattern of the crack growth rate curve as illustrated by the equations preceding. Estimating the life for a crack of this type beginning just above threshold it is then appropriate to consider the growth law as:

$$\frac{da}{dN} = b\left(\frac{\Delta K_{eff}}{E\sqrt{b}}\right)^3$$ Paris-Hertzberg Law

The figure 3 introduces the Paris-Herzberg model which is presented in detail in [2].At the beginning of the crack growth, a small crack a_o (with no crack closure and corresponding to $\Delta K_{eff} / E\sqrt{b} = 1$) starts from a defect of size a_{int}. This short crack becomes a long crack at a_i (figure 3). The growth rate is higher for small cracks than for long cracks. The transition point from a short crack to a long crack is located at a factor x in terms of the stress intensity factor from the threshold for short cracks (Fig. 2). The factor x has been observed at a maximum around 3 for low load ratios (R=0). The total crack growth lifetime for an internal failure can be estimated by the adding cycles associated with the following regimes:

- $N_{ao \to ai}$ small crack from an initial crack size a_o to a_i
- $N_{ai \to a}$ large crack from transition small to large crack point a_i to a (final crack)

The number of cycles related to initiation from an inclusion is:

- $N_{aint \to ao}$ below threshold from an initial crack size a_{int} to a_o

The time spent initiating from an inclusion or other defect itself must be close to the total life, perhaps much more than 99% of the life in many cases. This is made evident by integrating the fatigue crack growth rates for small cracks to estimate the possible extent of crack growth life. In order to do this one should refer to the general behaviour pattern of the crack growth rate curve. It is well-established that small cracks such as those growing from

small inclusions do not exhibit crack closure so these equations in terms of ΔK_{eff} apply fairly well with ΔK_{eff} being replaced by ΔK_{nom}. They form an upper bound on crack growth rates for the small cracks in the "fish eye" range for which crack closure is minimal, see figure 3.

The integration of the Paris Hertzberg law without transition, to determine the crack growth life will begin here with the crack growth rate corner which we shall denote as ΔK_0 corresponding to an initial circular crack of radius, a_0. In first approximation, we obtain [7]:

$$\boxed{N_f = \frac{\pi E^2}{2(\Delta\sigma)^2}}$$

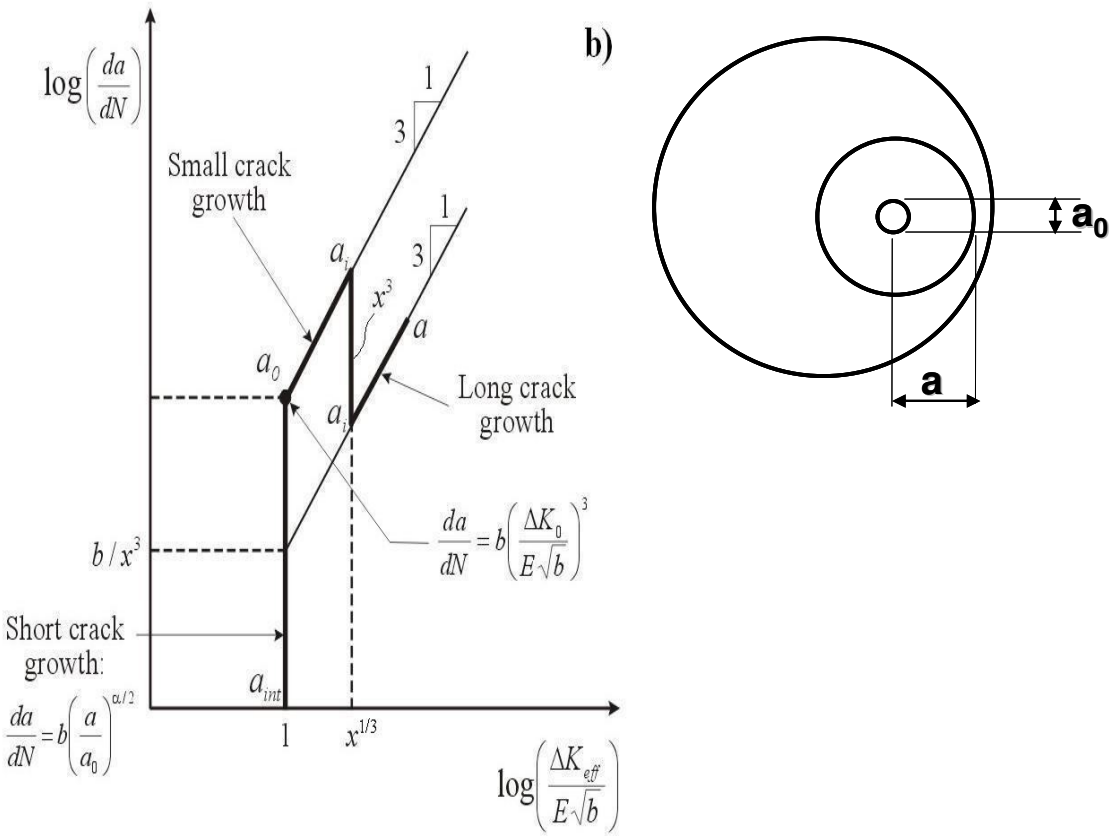

Figure 3 Fish eye scheme from the Paris Hertzberg relation.

This means that the number of cycles for the crack growth inside the fish eye is on the order of 10^5 cycles independent of the actual metal being considered. Initiation of the crack from a defect is the key problem in the gigacycle regime. Essentially we must determine the damage (or plasticity) to initiate a crack at about 10^9 cycles.

4-Micro Plasticity in the gigacycle fatigue

Generally ultrasonic tests are performed with round specimens. From a mechanical viewpoint, it is better to use cylindrical specimens which avoid edge effects.

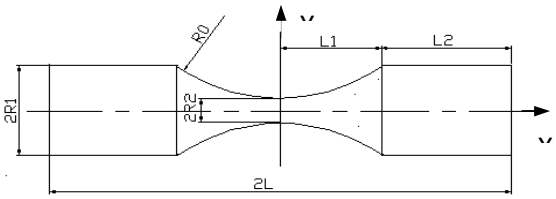

Figure 4 Typical round specimen for ultrasonic fatigue

However for microscopic observation, a flat specimen is more convenient (Fig 4). It must be pointed out that a plane stress field is favoured in a flat specimen of one millimeter thickness or less. In comparison, the plane stress effect is limited to the surface in a round specimen. In this respect, tests have been carried out with both specimens machined in Armco iron or high strength steel. Using flat specimens is more challenging than round specimens and proper testing requires some investigation. A flat specimen,figure 5, is used for ultrasonic frequency fatigue testing, with a special fitting attachment.

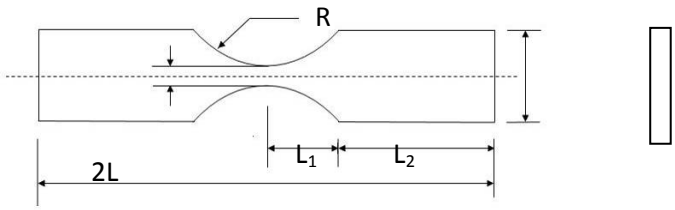

Figure 5. Flat specimen drawing

Working at resonance of 20 kHz frequency, the specimen was designed to have a natural frequency at 20kHz.. According to the longitudinal elastic wave equation on a one-dimensional elastic body and based on the given geometric and material properties, the resonance length and maximum stress in the middle of the specimen can be calculated using Equations 1 2.

$$L_1 = \frac{1}{k}\arctan\{\ \frac{1}{k}[\beta\coth(\ \beta L_2) - \alpha]\} \qquad (1)$$

$$\sigma_{\max} = E_d A_0 \beta \frac{\cos(\ kL_1)\exp(\ \alpha L_2)}{\sinh(\ \beta L_2)} \qquad (2)$$

Where:

$$C = \sqrt{E_d/\rho}, \quad k = \frac{2\pi f}{C}, \quad \alpha = \frac{1}{2L_2}\ln(\frac{T_2}{T_1}), \quad \beta = \sqrt{a^2 - k^2}$$

In order to observe the micro plasticity in the gigacycle regime, single phase (α) Armco iron was chosen, for which the UTS is 300 MPa and the yield strength 220 MPa. This is a reference metal with a simple microstructure of ferrite grains, without significant inclusions. This of course suggests comparison with very high strength martensitic steel using the same specimen geometry.

The iron is loaded below the yield point at 70, 85, and 120 MPa in push pull loading at 20kHz, for a failure beyond 10^8 cycles. Figures 6 and 8 show the initiation occurring at the surface of the flat specimen and of the round specimens in iron The damage is starting in stage 1 along more or less one millimetre depth before growing in stage 2. There is not any difference in mechanism between mega and giga cycle fatigue, in this case. During stage 1, it is clear that the microscopic mechanism is related to the formation of quasi-persistent slip bands (PSB). We use the term “quasi persistent slip bands” because they actually differ from what one traditionally

considers to be a PSB (i.e. hedge structure with strain being carried by screw dislocations).

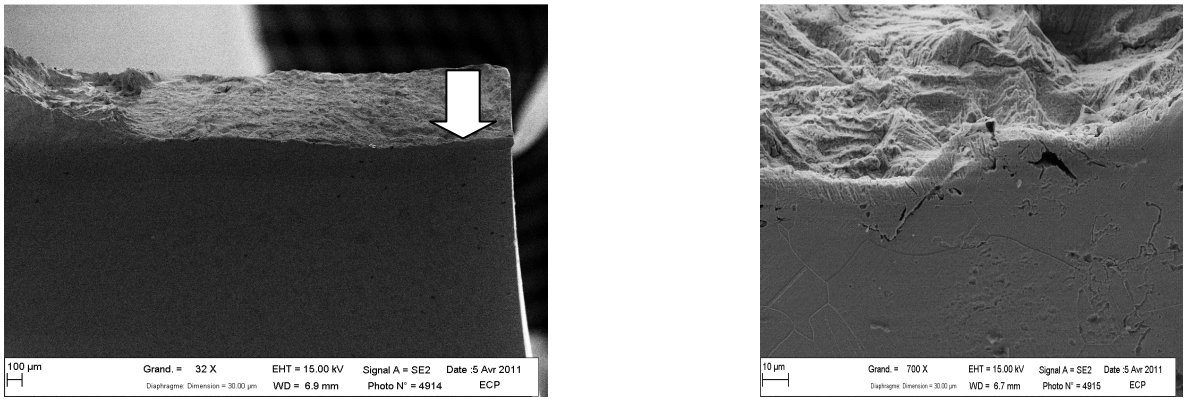

Figure 6 Initiation of a crack in a flat iron specimen. Quasi PSB starting at the surface

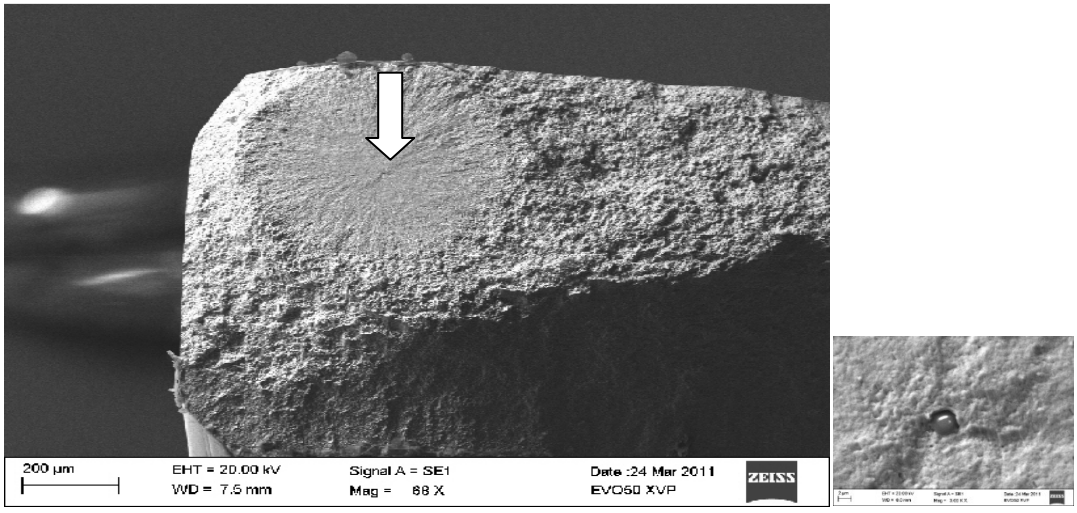

Figure 7 Initiation of a crack in a flat martensitic specimen. Fish eye at the interior.

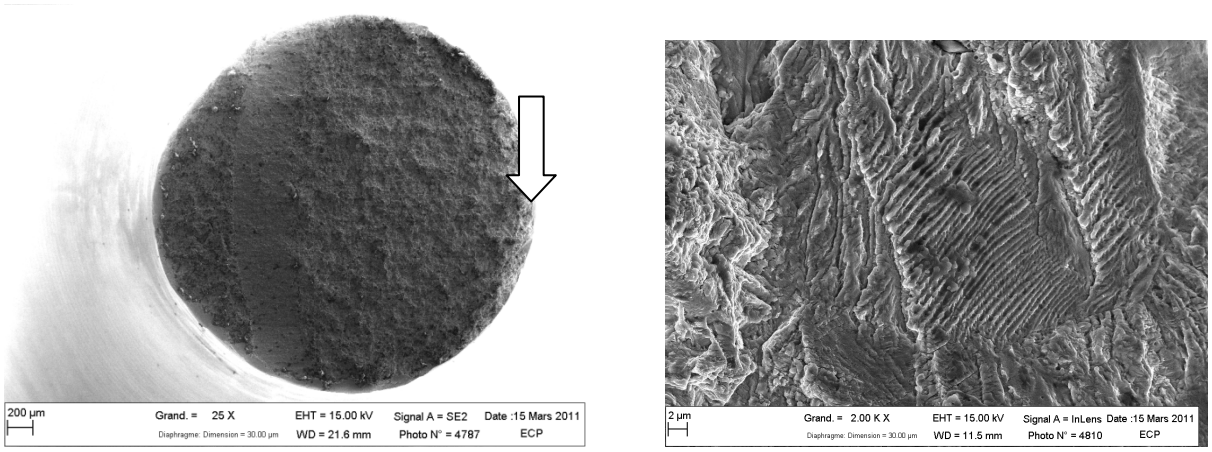

Figure 8 Initiation of a crack in a round iron specimen. Quasi-PSB starting from the surface in iron

Along these lines, Lukas [8] as shown that at least in Cu in the high cycle regime the "persistent slip bands" are composed of localized regions of very high vacancy concentration. It seems that a threshold exists, in iron, for the formation of the quasi-PSB. It is found that below 70 MPa no PSB occurs up to 10^9 cycles. However, the number of PSB increases with the number of cycles, but at present no experimental evidence is available to prove that some PSBs cannot form at 10^{10} cycles or more. No fish eye occurs in these conditions, probably due to the strong effect of the plane stress field and the very small size of the inclusions in a low yield stress Armco iron.

It is of interest to compare iron and martensitic steel, with the same flat specimen (1mm) and the same frequency, in push pull loading at 620 MPa, for a fatigue life beyond 10^8 cycles. Figure 7 shows that the initiation in martensitic steel starts from a fish eye and not from the surface. Reasons for this location must be addressed.

The fish eye occurs in the high strength steel from a small inclusion of oxide, in plane strain conditions, located inside a plastic zone around an inclusion. In this case, the plane stress effect at the surface is not efficient in causing plasticity due to a defect in steel where the UTS is close to 2000 MPa. There is a competition between plane strain plasticity and plane stress plasticity. In this case the micro plasticity is not governed by the Von Mises criteria but by the stress concentration effect. In plane strain plasticity the PSB or quasi PSB are not observed in the fish eye. The mechanism of plasticity seems relevant to polygonisation; grain refining or phase transformation, around the inclusion.

These results show that initiation in gigacycle fatigue is explained by a fish eye formation except when the effect of plane stress occurs in thin sheets or in thick bars when the yield point of the metal is low. In this condition the surface governs initiation. Otherwise in high strength alloys the initiation, in the gigacycle range, is sub-surface and always depends on defects: inclusions, pores, super grains. The surface effect is less important except if the residual stresses are important.

According to these observations more attention must be paid to the microplasticity (or damage accumulation) inside the fish eye in high strength alloys such as martensitic steels.

5-Instability of microstructure in VHCF

Our own results and those from the literature it is observed that the micro plasticity in gigacycle fatigue is more than simple dislocation slip. Sometimes phase transformation, refining of the grain, twinning, and instability of the yield point, occur even at low loads for a very high number of cycles. Several observations are enumerated up below:

-In austenitic stainless steels the austenite is not stable in the gigacycle fatigue regime even if the plastic deformation is theoretically very small. There is also a large thermal dissipation [9].

-When the amount of retained austenite approaches 10% in martensitic steels, a large thermal dissipation is observed at the beginning of the test followed by a high temperature rise when the fish eye propagates. [10]

-In low carbon steels the mobility of dislocations is affected by interstitial atoms, depending on the strain rate and the grain size. Several types of instability are observed in monotonic loading such as Luder's bands, Portevin-Le Chatelier bands or Neumann's bands, twinning, etc. It seems useful to consider similar effects in ultrasonic fatigue. [11]

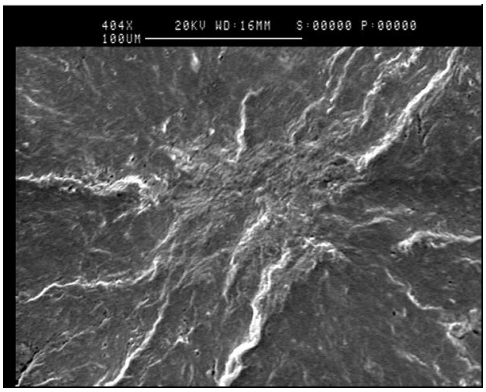

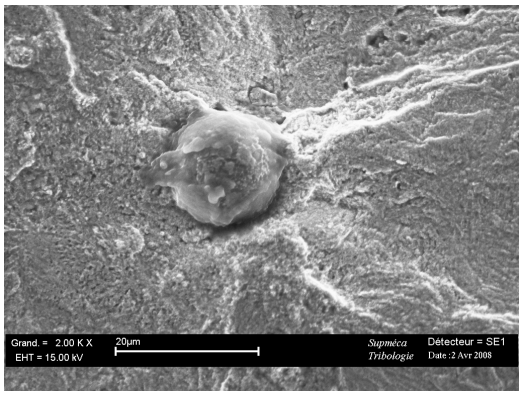

Figure 9 Initiation from a super grain (Pearlite)

Figure 10 Initiation from an oxide inclusion

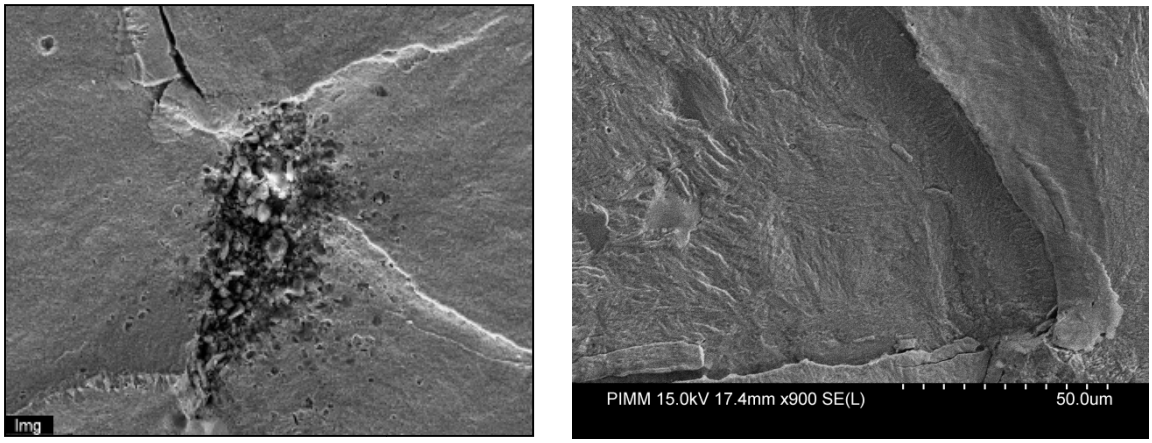

Figure 11 Initiation with phase transformation and grain boundary cracking starting from an oxide.

One of the most interesting behaviours is the instability of martensite or bainite in high strength steels. Depending on the chemical composition, heat treatments and processing, several types of microstructure are observed around the defect in the centre of the fish eye.

Figure 12 Comparison between wings in rolling contact fatigue and push pull gigacycle fatigue in a bearing steel

In a ferrite-pearlite steel (D38), the initiation starts in the centre of a fish eye, from a colony of pearlite, a so-called super-grain, but in a martensitic steel the initiation starts generally from an oxide inclusion, as shown in figures 9 and 10. This is typical of gigacycle plasticity. However, in high strength steel, that is to say when the UTS is higher than 900

MPa the initiation of the crack in the centre of the fish eye is sometimes more complicated as is shown in figure 11.

In high carbon and high strength steels, there is a transformation of the microstructure starting from the inclusion, in relation with the stress concentration and the stress field. It is difficult to understand this transformation which appears at the microscopic scale within a radius of 200 microns around an inclusion! Based on SEM observation, it can be said:

-Some wings (two to four) occur around the inclusion similar to the butterfly wings observed in rolling contact fatigue. Micro cracks are observed along the boundary between the wings and the matrix,Fig 11. In comparison with the rolling contact damage it seems that a phase transformation or grain refinement occurs. . In both cases, it is reasonable to assume that the microstructure of the wings should be a nano- ferrite phase. [11] Figure 12 compares the initiation of a fatigue crack in rolling fatigue and in push pull fatigue for a same bearing steel. Indeed the features are very similar.

-It is of interest to point out the relation between the wings, the oxide at the centre of the fish eye and the former austenitic grain boundaries, which is clear in figure 12. To prove this relation, a fish eye originating from a failure of high strength steel specimen was observed via electron backscatter diffraction (EBSD). To obtain a good EBSD map, the surface of the fractured specimen was polished slightly, with care taken to track the location of the particle at the center of the fish eye. The results are shown in figure 13. It is shown that the oxide inclusion, from which the initiation starts, is located at a triple point of former austenitic grains. The wings or the phase transformation appear along these grain boundaries producing internal stress and cracking along the wings for a length of about 200 microns. The orientations are colored according to the inverse pole figure color key shown in the figure. There is no indication of phase transformation from these images, but EBSD will not discern readily between bainite and martensite, so the nature of the microconstituent along the wings remains unknown.

This approach proves that the initiation of a fish eye in gigacycle fatigue is not only due to PSB or polygonisation, with or without the effect of hydrogen as mentioned by Murakami [4]. The grain boundary, the interaction between the defect and grain boundary, and sometimes the phase transformation or the refining of the microstructure are involved in a complex process leading up to the formation of a crack in stage 2.

6-Conclusions

When the cyclic stress is low, plasticity vanishes at the surface of the fatigue specimens, depending of the yield stress and the size of the defect. However, in low yield stress iron the initiation in VHCF is always at the surface in round and flat specimens. But, for high strength steels, the initiation around a defect occurs at the interior, even in flat specimens, due to the stress concentration in plane strain, in the gigacycle regime.

In high strength steels, the stability of the microstructure and the grain boundaries are involved in the plastic deformation to explain crack initiation in the fish eye. It seems that martensite or bainite could be transformed in nanoferrite inside butterfly wings, similar to what is observed in rolling contact fatigue. This mechanism is affected by the former austenite grain boundaries.

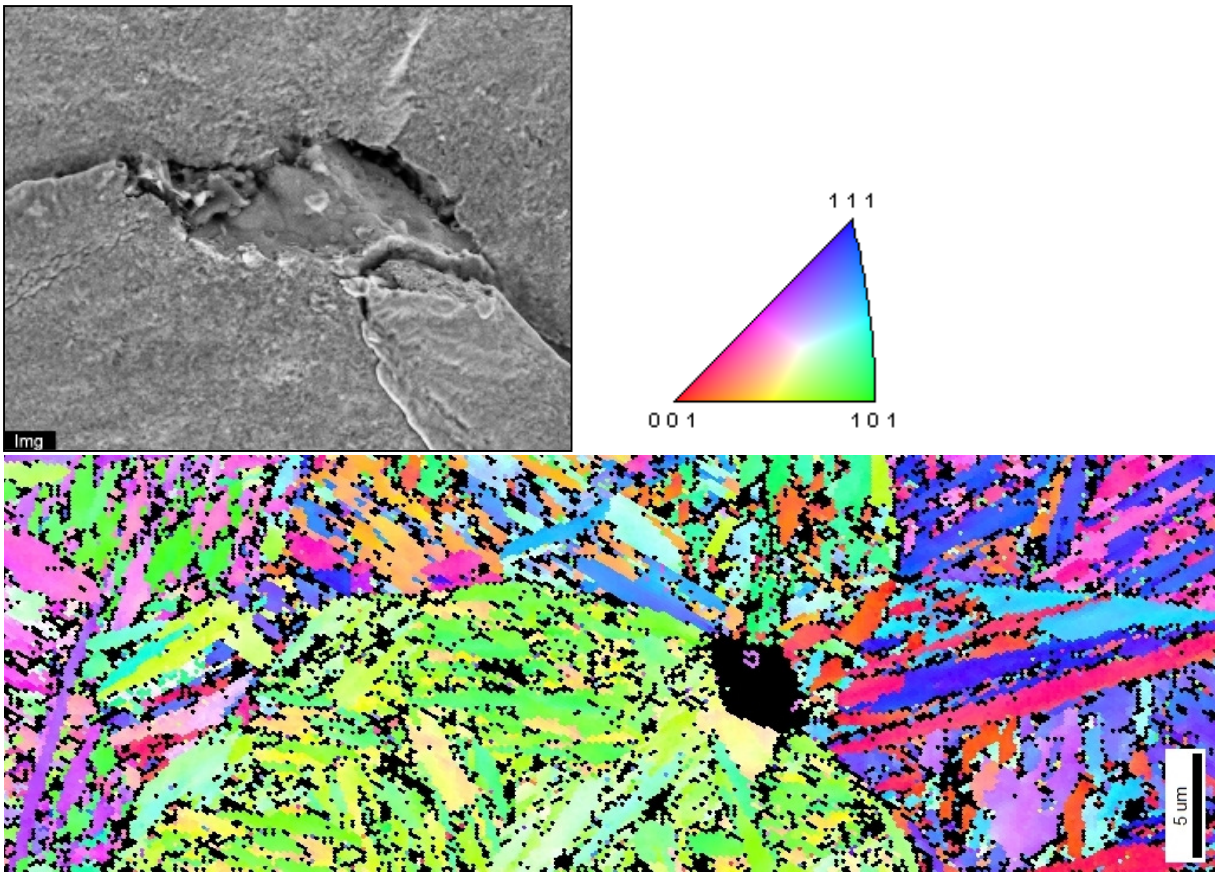

Figure 13 Relation between an oxide inclusion located at a triple point and three wings along the prior austenitic grain boundaries. Fish eye in a bearing steel failed in the gigacycle regime.

References

[1] Mughrabi H. Specific features and mechanisms of fatigue in the ultrahigh-cycle regime, *Int. Jl of fatigue* 28 (2006) 1501-1508

[2] Bathias C. and Paris P. C (2004). Gigacycle fatigue in mechanical practice, editor: Marcel Dekker, Section **7**, and ISBN 0-8247-2313-9

[3] Quian G., Zhou C. , Hong Y. Experimental and theoretical investigation of environment and theoretical investigation of environmental media on VHCF behavior for a structural steel. Acta Met. 59 (2011) 1321-132.

[4] Murakami Y. The Mechanisms of Fatigue Failure in the Ultra long Life Regime. *Metal Fatigue.* Elsevier. Oxford. 2002. UK

[5] Sakai T. Review and prospects for current studies on very high cycle fatigue of metallic materials for machine structural use, Fourth International Conference on Very High Cycle Fatigue (VHCF-4), *TMS* (The Minerals, Metals& materials Society),2007

[6]Shiozawa, K.Morii, Y. Nishino. Lu L. Subsurface crack initiation and propagation mechanisms in high strength steel in VHCF regime *IFJ* 2006, 28, 1521-1532

[7] Bathias C., Paris P.C. Initiation in the gigacycle fatigue regime, Fourth International Conference on Very High Cycle Fatigue (VHCF-4), *TMS* (The Minerals, Metals& materials Society),2007[

[8] P. Lukás, L. Kunz, L. Navrátilová, O. Bokuvka: Fatigue Damage of Ultrafine-Grain Copper in Very-High Cycle Fatigue Region, Materials Science and Engineering A, vol. 528, 2011, pp.7036– 7040]

[9] Muller-Bollengen C., Zimmermann M. , Christ H.J; VHCF behavior of austenitic steel and the effect of induced martensite

[10 C. Bathias. ASTM A01Symposium, Tampa, Nov 2011,Gigacycle fatigue: A new Tool For Exploring Bearing Steel; J.ASTM,2012

[11] Wang Chong, Wagner D., Bathias C.Gigacycle Fatigue Mechanisms in Armco Iron, IJF,June 2012

[12] Evans M. H. White Structure Flaking in Wind Turbine Gearbox bearings. Mat Sc. And tech. Aug 2011, 1-19.

An interaction integral method for 2D elastodynamic crack problems

Zhiyong Wang[1], Li Ma[1,*], Linzhi Wu[1], Hongjun Yu[2]

[1] Center for Composite Materials and Structures, Harbin Institute of Technology, Harbin 150001, PR China
[2] Institute of Applied Mathematics, Harbin Institute of Technology, Harbin 150001, PR China
* Corresponding author: mali@hit.edu.cn

Abstract In this paper, a domain formed interaction integral is derived for the evaluation of dynamic stress intensity factors (DSIFs) for arbitrary 2D cracks in non-homogeneous materials. The interaction integral is formulated by superimposing the actual and auxiliary fields on the path independent *J*-integral. By selecting the appropriate auxiliary fields, the derived interaction integral does not involve any derivatives of material properties compared to the available expressions in the literature. Moreover, it can be proved that the integrand is valid even when the integral domain contains material interfaces. Therefore, the integrand is simpler in form and it can be applied in more general situations. The numerical implementation of the new expression of interaction integral is then combined with the extended finite element method (XFEM) without tip enriched functions and a benchmark and test problem is presented. Finally, a non-homogeneous cracked body under dynamic loading is employed to investigate dynamic fracture behavior such as the variation of DSIFs for different material properties.

Keywords Interaction integral, dynamic stress intensity factors, XFEM without tip enriched functions

1. Introduction

Dynamic stress intensity factors (DSIFs) are crucial fracture parameters in understanding and predicting dynamic fracture behavior of a cracked body. To evaluate DSIFs for both homogeneous and non-homogeneous materials, numerous methods have been developed. Among these methods, the numerical techniques may be the most convenient and reliable ones to determine the fracture parameters for more complicated cases, as discussed below.

For homogeneous materials, Kishimoto et al. proposed a modified path-independent *J*-integral, which involves the inertial effects to determine DSIFs combined with the finite element method (FEM), and employed a decomposition procedure for mixed-mode problems [1]. Soon after, Nishioka et al. derived another dynamic *J*-integral to determine DSIFs for non-homogeneous materials [2]. However, the derived integrand is not well-suited for the finite element method. Kim et al. derived an equivalent domain form of the *J*-integral by using the divergence theorem and some additional assumptions [3]. As we known, it is difficult to extract mixed-mode DSIFs using *J*-integral. Instead, the interaction integral, which is known to be superior to both the displacement correlation technique (DCT) and *J*-integral, may be a suitable choice. Song et al. presented a domain formed interaction integral, namely *M*-integral, to investigate the DSIFs for homogeneous and smoothly non-homogenous materials [4]. In the formulation, the non-equilibrium formed auxiliary fields are employed, which have been discussed by Kim et al [5] and Dolbow et al. [6]. More recently, Réthoré et al. presented an interaction integral based on Lagrangian conservation for the estimation of DSIFs for arbitrary 2D moving cracks [7]. Most of the previous works are concerned with the materials with continuous and differentiable properties. If the above conditions are not met, the applications of the interaction integral method are impeded. Moreover, very few published papers have considered the cases that there are several material interfaces in the interaction integral domain. Actually, such phenomenon generally exists.

In this paper, the derivation of an interaction integral and its associated domain form without any derivatives of material properties is presented. We also present the mathematically rigorous proof that the proposed interaction integral method is still valid even when there are material interfaces in the integral domain. Several test problems and the comments are provided in the last section.

2. Numerical Strategy

The interaction integral utilizes two admissible fields: auxiliary and actual fields. Auxiliary fields are based on known fields such as Williams' solution, while actual fields utilize quantities such as displacements, strains and stresses obtained by means of XFEM without tip enriched functions. The choice of the auxiliary fields is discussed firstly. Then, the derivation of the interaction integral and the introduction of the numerical technique will be provided.

2.1. Interaction Integral

In this work, the asymptotic fields of Williams' solution are employed as the auxiliary fields for dynamic non-homogeneous materials, because the dynamic asymptotic fields of non-homogeneous materials show similar behavior to those of quasi-static homogeneous materials around the crack tip [8]. In addition, the incompatibility formulation, proposed by Dolbow et al. [6], is selected. In this formulation, the auxiliary displacements and stresses are obtained directly from Williams' solution and the auxiliary strains are evaluated from the non-homogeneous constitutive model. The auxiliary displacement is given by Eq. (1)

$$u_i^{aux} = \frac{K_I^{aux}}{2\mu_0}\sqrt{\frac{r}{2\pi}}u_i^I(\theta) + \frac{K_{II}^{aux}}{2\mu_0}\sqrt{\frac{r}{2\pi}}u_i^{II}(\theta) \tag{1}$$

The auxiliary stress is given by Eq. (2)

$$\sigma_{ij}^{aux} = \frac{K_I^{aux}}{\sqrt{2\pi r}}\sigma_{ij}^I(\theta) + \frac{K_{II}^{aux}}{\sqrt{2\pi r}}\sigma_{ij}^{II}(\theta) \tag{2}$$

Finally, the auxiliary strain is obtained from

$$\varepsilon_{ij}^{aux} = S_{ijkl}(x)\sigma_{kl}^{aux} \tag{3}$$

where $S_{ijkl}(x)$ is the compliance tensor of the non-homogeneous material.

Since the material property involved in the auxiliary displacement is the local value at the crack tip, the auxiliary strain fields are not compatible with the auxiliary displacement fields. Next, we will focus on the derivation of the interaction integral. The dynamic *J*-integral for cracked homogeneous linear elastic materials is [9]

$$J = \lim_{\Gamma\to 0}\int_\Gamma \left[(W+L)\delta_{1i} - \sigma_{ij}u_{j,1}\right]n_i d\Gamma \tag{4}$$

Superimposing the actual and auxiliary fields on Eq. (4) and one can obtain the interactional part

$$I = \lim_{\Gamma\to 0}\int_\Gamma \left[\frac{1}{2}(\sigma_{jk}^{aux}\varepsilon_{jk} + \sigma_{jk}\varepsilon_{jk}^{aux})\delta_{1i} + \rho\dot{u}_j\dot{u}_j^{aux} - (\sigma_{ij}^{aux}u_{j,1} + \sigma_{ij}u_{j,1}^{aux})\right]n_i d\Gamma \tag{5}$$

The related definitions of the interaction integral are illustrated in Fig. 1. Here, we call attention to an important assumption, namely, the auxiliary stress and strain fields are assumed to be related through the same elasticity tensor as the actual stress and strain fields

$$\sigma_{ij}\varepsilon_{ij}^{aux} = C_{ijkl}(x)\varepsilon_{kl}\varepsilon_{ij}^{aux} = \varepsilon_{kl}\sigma_{kl}^{aux} \tag{6}$$

Due to the way in which we have defined the auxiliary fields and the material property in-homogeneity, the associated terms do not vanish when we employ the divergence theorem. The contour integral is then converted into an equivalent domain integral which involves the term induced by the interface together

$$\begin{aligned} I = &\int_A \left[\sigma_{ij}(S_{ijkl}^{tip} - S_{ijkl}(x))\sigma_{kl,1}^{aux} + \rho\dot{u}_j\dot{u}_{j,1}^{aux} - \rho\dot{u}_{j,1}\dot{u}_j^{aux} - \rho\dot{u}_j\dot{u}_{j,1}^{aux}\right]q dA \\ &- \int_A \left[(\sigma_{jk}^{aux}u_{j,k} + \rho\dot{u}_j\dot{u}_j^{aux})\delta_{1i} - (\sigma_{ij}^{aux}u_{j,1} + \sigma_{ij}u_{j,1}^{aux})\right]q_{,i}dA + I_{interface}^* \end{aligned} \tag{7}$$

where q is the weight function varying from unity at the crack tip to zero on Γ_B, and

$$\Gamma_B = \Gamma_{11} + \Gamma_{12} + \Gamma_{13} \tag{8}$$

and S_{ijkl}^{tip} is the compliance tensor at the crack tip. As shown in Fig. 1, there is bi-material interface $\Gamma_{interface}$ in the domain and the interface is assumed to be perfectly bonded. Thus, the whole integral domain is divided by $\Gamma_{interface}$ into two parts, i.e., A_1 and A_2. In addition, $I^*_{interface}$ in Eq. (7) denotes the interface integral and will be discussed below.

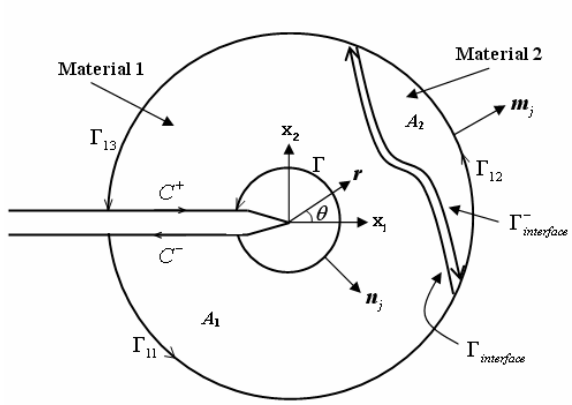

Fig. 1 Interaction integral domain cut by a material interface

The line integral corresponding to the interface can be written as

$$\begin{aligned} I^*_{interface} = \int_{\Gamma_{interface}} \Big[& \sigma_{jk}^{aux}(\varepsilon_{jk}^{(1)} - \varepsilon_{jk}^{(2)})\delta_{1i} - u_{j,1}^{aux}(\sigma_{ij}^{(1)} - \sigma_{ij}^{(2)}) - \sigma_{ij}^{aux}(u_{j,1}^{(1)} - u_{j,1}^{(2)}) \\ & + (\rho^{(1)} - \rho^{(2)})\dot{u}_j \dot{u}_j^{aux}\delta_{1i} \Big] m_i q d\Gamma \end{aligned} \tag{9}$$

To simplify the above equation, we firstly build a curvilinear coordinate system, as shown in Fig. 2.

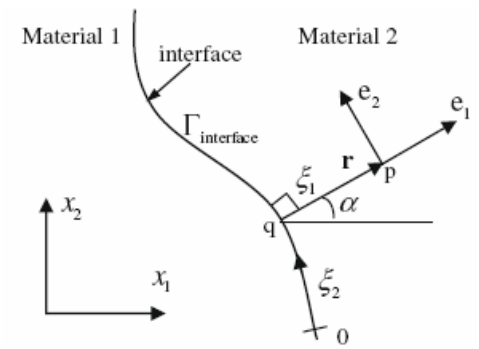

Fig. 2 A curvilinear coordinate system originating from the interface

Then, we have

$$\begin{aligned} \xi_1 &= \sqrt{(x_1 - x_{10})^2 + (x_2 - x_{20})^2} = r \\ \xi_2 &= \int_0^q dl \end{aligned} \tag{10}$$

$$\begin{aligned} \frac{\partial \xi_1}{\partial x_1} &= \cos\alpha = m_1 \\ \frac{\partial \xi_1}{\partial x_2} &= \sin\alpha = m_2 \end{aligned} \tag{11}$$

where (x_1, x_2) and (x_{10}, x_{20}) are the global coordinates of the point *p* and *q*, respectively. (ξ_1, ξ_2) are the curvilinear coordinates of the point *p*. m_1 and m_2 denotes the components of the outward

normal vector **m** to $\Gamma_{interface}$ at point *q*. According to the equilibrium condition on the bi-material interface, the tractions on both sides of the interface should be equal. We have

$$\mathbf{m}\cdot\boldsymbol{\sigma}^{(1)} = \mathbf{m}\cdot\boldsymbol{\sigma}^{(2)} \tag{12}$$

Since the interface is perfectly bonded, the derivatives of actual displacements with respect to the curvilinear coordinate ξ_2 are equal on both sides of the interface, as a result

$$\left(\frac{\partial \mathbf{u}}{\partial \xi_2}\right)^{(1)} = \left(\frac{\partial \mathbf{u}}{\partial \xi_2}\right)^{(2)} \tag{13}$$

According to the above assumptions, it can be found that the first term of the interface integral is equal to the third one, and the second term is zero. If the mass density of the materials on both sides of the interface is equal to each other, we can obtain

$$I^*_{interface} = 0 \tag{14}$$

In addition, we assign the values auxiliary velocity fields to zero. The interaction integral (*I*-integral) indicated in Eq. (7) can be simplified as

$$\begin{aligned} I = &\int_A \left[\sigma_{ij}(S^{tip}_{ijkl} - S_{ijkl}(x))\sigma^{aux}_{kl,1} + \rho \ddot{u}_j u^{aux}_{j,1}\right] q dA \\ &- \int_A \left[\sigma^{aux}_{jk} u_{j,k}\delta_{1i} - (\sigma^{aux}_{ij} u_{j,1} + \sigma_{ij} u^{aux}_{j,1})\right] q_{,i} dA \end{aligned} \tag{15}$$

In order to show the advantages of Eq. (15), we will compare it with the traditional *J*-integral and the *M*-integral given by Song et al. [4]. The *J*-integral in the form of the stiffness can be expressed as

$$J = \int_A (\sigma_{ij} u_{i,1} - W\delta_{1j}) q_{,j} dA + \int_A (\rho \ddot{u}_i u_{i,1} - \frac{1}{2} C_{ijkl,1}\varepsilon_{ij}\varepsilon_{kl}) q dA \tag{16}$$

The resulting *M*-integral is

$$\begin{aligned} M = &\int_A \left\{(\sigma^{aux}_{ij} u_{i,1} + \sigma_{ij} u^{aux}_{i,1}) - \sigma^{aux}_{ik}\varepsilon_{ik}\delta_{1j}\right\} q_{,j} dA \\ &+ \int_A \left\{\sigma^{aux}_{ij,j} u_{i,1} + \rho \ddot{u}_i u^{aux}_{i,1} - C_{ijkl,1}\varepsilon^{aux}_{kl}\varepsilon_{ij}\right\} q dA \end{aligned} \tag{17}$$

Through rigorous proof, we can conclude that the *M*-integral is totally equivalent to the *I*-integral. However, the expressions are quite different. It can be found that the derivatives of material properties exist unavoidably in both the above equations. Differently, the *I*-integral in Eq. (15) does not involve any derivatives of material properties. Moreover, in certain conditions, the *I*-integral is still valid even when the integral domain contains material interfaces. Therefore, the applicable range of the present interaction integral is wider than that of the two methods mentioned above for non-homogeneous materials.

2.2. Extended Finite Element Method without Tip Enriched Functions

By enriching the standard approximation with additional functions, the extended finite element method (XFEM) allows for the modeling of arbitrary geometric features independently of the finite element mesh. This advance has provided a convenient computational tool for modeling discontinuities and their evolvements. However, if both the strong discontinuities i.e., cracks and the weak discontinuities i.e., inclusions exist in the domain, especially when the crack tip approaches near the inclusions, it is difficult to obtain the accurate solutions i.e., stress intensity factors (SIFs) using the XFEM technique. In addition, in the XFEM modeling of cracked problems, the corresponding analytical results are pre-requisite. If the analytical solutions are difficult to obtain or are very complex themselves, the application is not convenient. Based on the above reasons, Wang et al. proposed a numerical method, named as extended finite element method without tip enriched functions, for modeling crack growth in particle reinforced composite materials [10]. We employ this numerical method to determine the basic solution of the boundary value

problems. Then, the mixed-mode SIFs can be easily extracted from the Irwins' relation after we get the values of the *I*-integral. The Newmark's method of direct integration schemes is used in dynamic analysis finally.

2.3. Numerical Examples

Young's modulus and mass density vary exponentially, such that $E/\rho \equiv constent$, as given by

$$E = E_0 \exp(\beta_1 x + \beta_2 y) \tag{18}$$

$$\rho = \rho_0 \exp(\beta_1 x + \beta_2 y) \tag{19}$$

where E_0 and ρ_0 are Young's modulus and mass density for initial values. β_1 and β_2 are the non-homogeneity parameters along the *x*- and *y*- directions, respectively. When β_1 and β_2 are equal to zero, the above two equations return to the case of homogeneous materials. A constant Poisson ratio of 0.3 is used during the whole simulation and the plane strain status is assumed. The geometry and the boundary conditions are illustrated in Fig. 3. The data used in the computation are: $L = 20mm$, $D = 40mm$, $2a = 4.8mm$, $E_0 = 199.992GPa$, $\rho_0 = 5000kg/m^3$, $C_d = 7.34mm/\mu s$. The time is normalized with respect to the dilatational wave speed (C_d), and the DSIFs are normalized with respect to

$$K_0 = \sigma_0 \sqrt{\pi a} \tag{20}$$

where the σ_0 is the magnitude of the applied stress and a is half of the total crack length. A time step is $\Delta t = 0.1\mu s$.

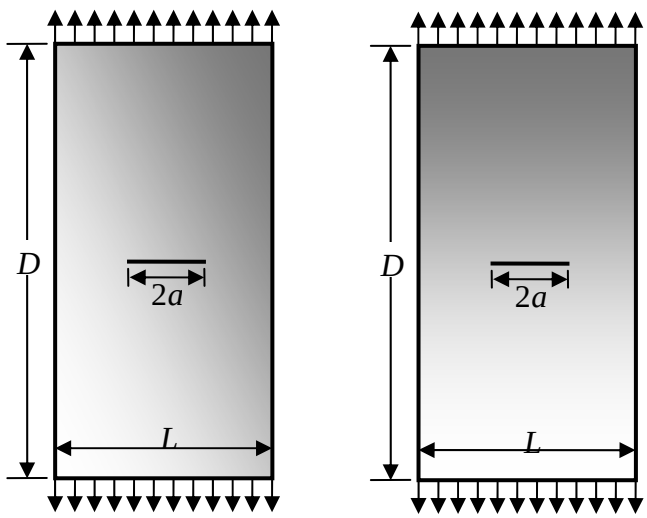

(*a*) (*b*)

Fig. 3 Center cracked tension specimen: (a) non-homogeneous materials (b) exponentially graded materials in the y-direction

In order to employ severe material gradations, relatively high β values are assigned: $\beta_1 = 0.1$ and $\beta_2 = 0.1$. Here, the units corresponding to the material gradation parameters are millimeters. Material properties vary simultaneously along both the *x*- and *y*-directions according to Fig. 3(a). Fig. 4 shows DSIFs at the right crack tip calculated by the present *I*-integral and *M*-integral and the reference ones in the paper written by Song et al. [4]. It can be found that there is an excellent agreement between the present numerical results and the reference ones. It demonstrates that the present method is valid for the fracture problems of such materials.

Next, we consider material properties that vary along the *y*-direction as shown in Fig. 3(b). The material gradation parameter β_1 is set to 0 and β_2 is set as 0, 0.05 and 0.1. Since material properties vary along the *y*-direction, the material properties are the same at both crack tips.

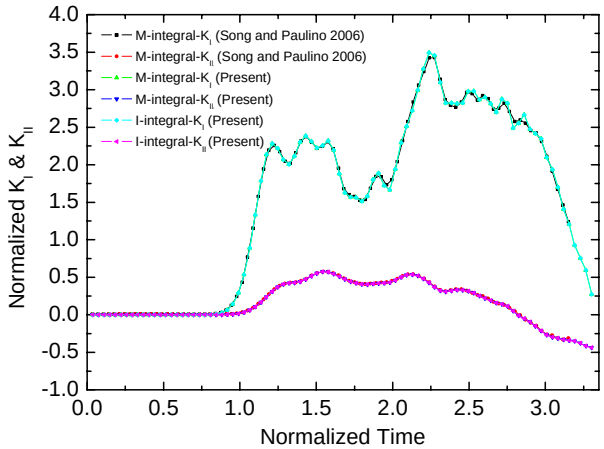

Fig. 4 Normalized DSIFs calculated by different methods

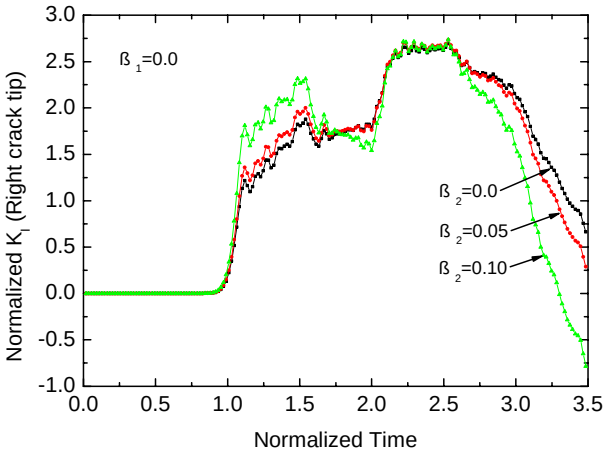

Fig. 5 Normalized mode *I* DSIFs for different material gradations along the *y*-direction

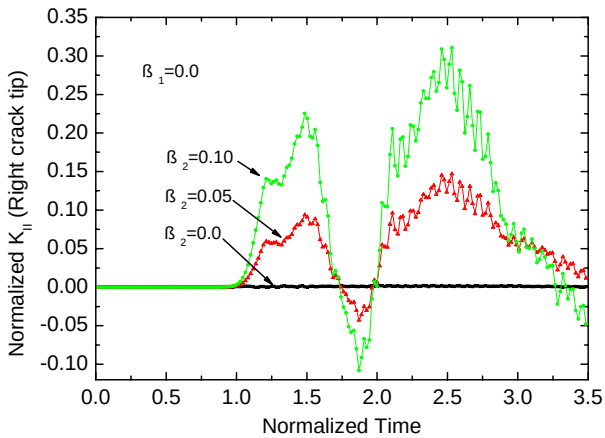

Fig. 6 Normalized mode *II* DSIFs for different material gradations along the *y*-direction

Fig. 5 and Fig. 6 show the mixed-mode DSIFs at the right crack tip. It is obvious that $K_I(t)$ is identical at both crack tips, while the magnitude of $K_{II}(t)$ at the left crack tip is equal in magnitude and opposite in sign to the value at the right crack tip. So we only list the results at the

right crack tip. The initiation time at both crack tips remains the same for all cases of material gradations because of the same definition of material properties. Values of $K_{II}(t)$, induced by material gradients, are more sensitive with increasing β, whereas the maximum magnitude of $K_I(t)$ is relatively insensitive to β. However, the magnitude of $K_{II}(t)$ is relatively small compared to that of $K_I(t)$.

Acknowledgements

This work is sponsored by the National Science Foundation of China under grant Nos. 11222216 and 11202058，the Fundamental Research Funds for the Central Universities under grant No. HIT. NSRIF. 2013082 and China Postdoctoral Science Foundation (20110491071)

References

[1] K. Kishimoto, S. Aoki, M. Sakata, Dynamic stress intensity factors using *J*-integral and finite element method. Eng Fract Mech, 13(1980) 387-394.
[2] T. Nishioka, S.N. Atluri, On the computation of mixed-mode *K*-factors for a dynamically propagating crack using path-independent integrals. Eng Fract Mech, 20(1984) 193-208.
[3] J.H. Kim, G.H. Paulino, The interaction integral for fracture of orthotropic functionally graded materials: evaluation of stress intensity factors. Int J Solids Struct, 40(2003) 3967-4001.
[4] S.H. Song, G.H. Paulino, Dynamic stress intensity factors for homogeneous and smoothly heterogeneous materials using the interaction integral method. Int J Solids Struct, 43(2006) 4830-4866.
[5] J.H. Kim, G.H. Paulino, T-stress, mixed-mode stress intensity factors, and crack initiation angles in functionally graded materials: a unified approach using the interaction integral method. Comput Method Appl M, 192(2003) 1463-1494.
[6] J.E. Dolbow, M. Gosz, On the computation of mixed-mode stress intensity factors in functionally graded materials. Int J Solids Struct, 39 (2002) 2557-2574.
[7] J. Réthoré, A. Gravouil, A. Combescure, An energy-conserving scheme for dynamic crack growth using the extended finite element method. Int J Numer Meth Engng, 63(2005) 631-659.
[8] J.W. Eischen, Fracture of non-homogeneous materials. Int J Fract, 34(1987) 3-22.
[9] B. Moran, F.C. Shih, Crack tip and associated domain integrals from momentum and energy balance. Eng Fract Mech, 27(1987) 615-642.
[10] Z.Y. Wang, L. Ma, L.Z. Wu, H.J. Yu, Numerical simulation of crack growth in brittle matrix of particle reinforced composites using the xfem technique. Acta Mech Solida Sin, 25(2012) 9-21.

The eXtended Finited Element Method for frictional contact problem

Zhiqiang Hu[1,*], **Guogang Fan**[1], **Gao Lin**[1]

[1] Faculty of Infrastructure Engineering, School of Hydraulic Engineering, Dalian University of Technology, No.2 Linggong Road, Ganjingzi District, Dalian, 116024, China
* Corresponding author: huzhq@dlut.edu.cn

Abstract Frictional contact is often observed in the problems with the presence of crack surface. In order to take effects of contact of crack surfaces on the structural response, in the framework of mesh-based approaches, e.g. Finite Element Method (FEM) or Boundary Element Method (BEM), usually the contact surfaces need to be discretized and nodes are placed on the contact surfaces, although the meshes for both contact surfaces are not necessary to be matched with each other. However, the crack surface will evolve under loading, so remeshing is needed to make the meshes consistent with the geometry of crack surfaces.

In this paper, we deal with the frictional contact problems resulting from presence of crack surfaces by combining the eXtended Finite Element Method (XFEM) and B-Differential Equation Method (BDEM). XFEM is used to model the discontinuities of displacement fields in the interior of the elements without the need for the remeshing of the domain. In BDEM, the normal and tangential contact conditions are formulated as B-differentiable equations and satisfied accurately. The B-differentiable Newton solution strategy with the good convergence performance is employed to solve with system equations. The Numerical examples including 2D and 3D frictional contact problems are given to demonstrate the effectiveness and accuracy of the presented approach.

Keywords Frictional contact, eXtended Finite Element Method, B-differential Equation

1. Introduction

Separation, stick and frictional sliding are often observed in the problems with the presence of crack surface or crack propagation. In order to take effects of contact on the behavior of cracks and structure, in the framework of mesh-based approaches, e.g. traditional Finite Element Method (FEM) or Boundary Element Method (BEM), remeshing is needed to trace the crack surfaces and make the meshes consistent with the geometry of crack surfaces. Although the meshes for contact surfaces in the framework of FEM and BEM are not necessary to be matched with each other, remeshing will result in the increase of the computational cost and additional mapping of the computational results from the original meshes to updated meshes. The invention of embedded discontinuity method, in which the discontinuity surfaces can be embedded in the element and traced effectively without remeshing, e.g., eXtended Finite Element Method[1], provides an alternative method to deal with contact problem, especially for the case in which contact surfaces evolve in the structure subjected to the complicated cyclic loads. The key feature of XFEM is that the discontinuity across crack surface can be resolved by additional enrichment functions and additional nodal degrees of freedom.

The contact problem which is solved in the content of XFEM is firstly proposed by J. Dolbow Möes et al. [2]. The contact condition were enforced by penalty method and the LArge Time INcrement method (LATIN) was employed to solve the system equations. Recently, FS. Liu and R.I. Borja [3] proposed the Petrov-Galerkin variational formation for the frictional contact problem, and the augmented Lagrangian technique was used for the enforcement of contact conditions. I. Nistor et al. [4] developed a hybrid X-FEM contact element for frictionless large sliding contact problem, in which the augmented Lagrangian method was also employed.
Due to the good performance and convergence property of B-differentiable Equations method to solve the frictional contact problem, so we extended this method to model the two and

three-dimensional elastic frictional contact problems between the crack surfaces in the framework of XFEM. The structure of the paper is given as follows. Firstly, the variational formulation for frictional contact problem and the contact conditions are reviewed in Section 2. Secondly, the details of computation of discontinuities across contact surfaces and the equivalent nodal force due to the contact force acting at the contact surface are described in the framework of XFEM in Section 3. In Section 4, after the B- differentiable equations method for frictional contact problem is introduced we give the formulation and solution procedure of the combined XFEM and BDEM for frictional contact problem. Two numerical examples are presented in Section 5 for demonstrate the feasibility and accuracy of the proposed method. The concluding remarks are given in the last section.

2. Problem formulation

2.1. General description of the problem

Consider a body $\Omega \in R^n$, (n=2,3) embedded with two crack surfaces Γ_c^1 and Γ_c^2 which are also taken as the contact surfaces. We denote by Γ the outside boundary of Ω. Γ is composed by Γ_u on which prescribed displacements are imposed, Γ_σ on which prescribed tractions are imposed and the crack surfaces, i.e. $\Gamma=\Gamma_u \cup \Gamma_\sigma \cup \Gamma_c^1 \cup \Gamma_c^2$. The crack surfaces may intersect the boundary Γ with points in 2D case or lines in 3D case. In the following sections, the variables with superscripts '1' and '2' indicate that they are related to Γ_c^1 and Γ_c^2 respectively. On the two crack surfaces, the displacements and tractions are denoted as $u_c^i, t_c^i (i=1,2)$ respectively. It should be noted that since the contact surfaces are embedded in the element, they are assumed to be coincident initially, i.e., no initial gap exists between the contact surfaces.

The quasi-static loading by a body force $\mathbf{b}_f$ and given traction $\bar{\mathbf{t}}$ on Γ_σ are assumed. The equilibrium equation and boundary conditions are described as follows.

$$\mathrm{div}(\boldsymbol{\sigma}) + \mathbf{b}_f = 0 \quad \text{in } \Omega \setminus \Gamma_c \tag{1}$$

$$\begin{aligned} &\boldsymbol{\sigma} \cdot \mathbf{n}_\sigma = \bar{\mathbf{t}} && \text{on } \Gamma_\sigma \\ &\mathbf{u} = \bar{\mathbf{u}} && \text{on } \Gamma_u \\ &\boldsymbol{\sigma} \cdot \mathbf{n}_c^1 = \mathbf{t}_c^1 && \text{on } \Gamma_c^1 \\ &\boldsymbol{\sigma} \cdot \mathbf{n}_c^2 = \mathbf{t}_c^2 && \text{on } \Gamma_c^2 \end{aligned} \tag{2}$$

Where, $\boldsymbol{\sigma}$ is the Cauchy stress tensor, $\bar{\mathbf{u}}$ is the prescribed displacement vector on boundary Γ_u. $\mathbf{n}_\sigma$ is the unit normal vector to the boundary Γ_σ. $\mathbf{n}_c^i$ and $\mathbf{t}_c^i$ (i=1,2) are the unit normal vectors to the contact surface Γ_c^i and contact stresses on Γ_c^i respectively.

2.2. Frictional contact constraint formulation by B-differentiable equation

According to the assumption of small displacement and small strain, a contact pair consists of the two points with the same coordinates on Γ_c^1 and Γ_c^2, which are denoted as $\mathbf{x}_c^1$ and $\mathbf{x}_c^2$ respectively. A local coordinate system **nab** is established on Γ_c^2 as shown in Figure 1. Therein, **n** is the normal vector and **a** and **b** are tangential vectors to the contact surface Γ_c^2.

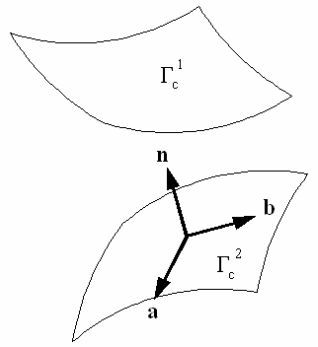

Figure 1. Local coordinate system on the contact surface Γ_c^2

Then the normal gap Δu_n between a contact pair can be defined as

$$\Delta u_n(\mathbf{x}_c) = \left(\mathbf{u}(\mathbf{x}_c^1) - \mathbf{u}(\mathbf{x}_c^2)\right)\cdot \mathbf{n} \tag{3}$$

Where, $\mathbf{u}(\mathbf{x}_c^1)$ and $\mathbf{u}(\mathbf{x}_c^2)$ are the displacements of contact points on Γ_c^1 and Γ_c^2 respectively.

Since part of the system energy will be dissipated due to the friction, the frictional contact problem is nonlinear and path-dependent and increment solution strategy is needed. So at every load step, when frictional sliding takes place between two contact surfaces, relative incremental sliding in tangential directions are defined as follows.

$$\Delta du_a = \left(\mathbf{du}(\mathbf{x}_c^1) - \mathbf{du}(\mathbf{x}_c^2)\right)\cdot \mathbf{a} \tag{4a}$$

$$\Delta du_b = \left(\mathbf{du}(\mathbf{x}_c^1) - \mathbf{du}(\mathbf{x}_c^2)\right)\cdot \mathbf{b} \tag{4b}$$

Where, **du** is the vector of incremental displacement at current load step.

The contact conditions in normal and tangential directions proposed by Christensen *et al*. [5] are expressed as a B-differentiable equation set. Due to the assumption of small displacement and small strain, the discrete point-to-point contact model is employed in the following, so that the contact conditions will be formulated by the quantities at these discrete contact pairs. For *i*-th contact pair, they are written as

$$\mathrm{H}_2^i\left(\mathbf{du}_c^i, \mathbf{dP}^i\right) = \min\left\{r\Delta u_n^i, P_n^i\right\} = 0 \tag{5a}$$

$$\mathrm{H}_3^i\left(\mathbf{du}_c^i, \mathbf{dP}^i\right) = P_a^i - \lambda P_a^i(r) = 0 \tag{5b}$$

$$\mathrm{H}_4^i\left(\mathbf{du}_c^i, \mathbf{dP}^i\right) = P_b^i - \lambda P_b^i(r) = 0 \tag{5c}$$

Where, $\mathbf{du}_c^i$ is the incremental displacement vector of two contact points consisting of the *i*-th contact pair. $\mathbf{dP}^i$ is the vector of increment contact force acting at the *i*-th contact pair. P_n^i, P_a^i and P_b^i are the total contact forces in the normal and two tangential directions. *r* is a positive scalar. Δu_n^i is the normal gap. Eq. (5a) corresponds to the normal contact condition, Eqs. (5b) and (5c) correspond to the tangential contact conditions in local *a* and *b* directions respectively. The

definitions of $P_a^i(r)$, $P_b^i(r)$ and λ are given as follows.

$$P_a^i(r) = P_a^i - r\Delta du_a^i \tag{6a}$$

$$P_b^i(r) = P_b^i - r\Delta du_b^i \tag{6b}$$

$$\lambda = \min\left\{\mu \min\{P_n^i, 0\} \Big/ \sqrt{\left(P_a^i(r)\right)^2 + \left(P_b^i(r)\right)^2}, 1\right\} \tag{7}$$

Where, Δdu_a^i and Δdu_b^i are tangential incremental relative displacements in local a and b directions respectively. The incremental relative displacements in global and local coordinate system for i-th contact pair at current load step are defined as

$$\Delta du_j^i = du_j^{i1} - du_j^{i2} \quad , \quad \left(j = n, a, b \quad or \quad x, y, z\right) \tag{8}$$

The normal relative displacement for i-th contact pair at current load step is defined as

$$\Delta u_n^i = \Delta \bar{u}_n^i + \left(du_n^{i1} - du_n^{i2}\right) \tag{9}$$

Where, $\Delta \bar{u}_n^i$ is the initial normal relative displacements at current load step.

3. Discretization by XFEM formulation

The XFEM is a promising method to simulate the existence and growth of the discontinuities, such as cracks, without the need to make the mesh conforming it. In order to characterize the discontinuous displacement field resulted from the embedded discontinuity, the Heaviside functions or asymptotic crack tip functions are often used to enrich standard continuous displacement fields of the elements cut entirely by the discontinuity surface or those including the crack tip in 2D or crack front in 3D case, respectively. The additional nodal degrees of freedom corresponding to these enrichment functions are needed.

3.1. The XFEM approximation

In XFEM, the displacement approximation at an arbitrary point **x** in the element with embeded discontinuity takes the form

$$\mathbf{u}(\mathbf{x}) = \bar{\mathbf{u}}(\mathbf{x}) + [\![\mathbf{u}(\mathbf{x})]\!] = \sum_{i=1}^{nd} N_i \bar{\mathbf{u}}_i + \sum_{j=1}^{nd} \mathbf{b}_{Hj} N_j \left(H(\mathbf{x}) - H(\mathbf{x}_j)\right) + \sum_{k=1}^{nd} N_k \sum_{l=1}^{4} \mathbf{c}_{kl} \left(g_l(r,\theta) - g_l(r_k,\theta_k)\right) \tag{10}$$

Where, nd is the number of nodes in one element, $\bar{\mathbf{u}}_i$ is the continuous displacement field at node i. The last two terms form the discontinuous part $[\![\mathbf{u}]\!]$. H(**x**) is generalized Heaviside function, and $\mathbf{b}_{Hj}$ is the vector of additional translational DOFs corresponding to generalized Heaviside function. g_l (l=1,2,3,4) are the tip enrichment functions, and $\mathbf{c}_{kl}$ is the vector of additional translational DOFs related to the l-th tip branch function for node k. The generalized Heaviside function is defined as

$$H(\mathbf{x})=\begin{cases} =1 & (\mathbf{x}-\mathbf{x}^*)\cdot\mathbf{n}\geq 0 \\ =-1 & (\mathbf{x}-\mathbf{x}^*)\cdot\mathbf{n}<0 \end{cases} \tag{11}$$

Where, $\mathbf{x}^*$ is the closest point on the crack surface for point **x**. The unit normal vector **n** is defined in Figure 1. The vector functions $\boldsymbol{g}(r,\theta)$ are defined as

$$\begin{aligned}\mathbf{g}(r,\theta)&=\mathbf{g}(\mathbf{x})=\{g_1(r,\theta),g_2(r,\theta),g_3(r,\theta),g_4(r,\theta)\}\\ &=\left\{\sqrt{r}\sin\frac{\theta}{2},\sqrt{r}\cos\frac{\theta}{2},\sqrt{r}\sin\frac{\theta}{2}\sin\theta,\sqrt{r}\cos\frac{\theta}{2}\sin\theta\right\}\end{aligned} \tag{12}$$

Where, (r,θ) are the local polar coordinates of point **x**. The local polar coordinate system is established at the crack tip in 2D case [1] or crack front in 3D case [7]. In (12), the first function is discontinuous across the discontinuity surface whereas the other three functions are continuous. So the displacement jump across the discontinuity surface comes from the generalized Heaviside function (11) and the first function in (12).

The equilibrium equations are obtained after the discretization of weak form of equilibrium equations and the implementation of the contact constrain by Lagrangian multiplier method.

$$\mathbf{Ku}=\mathbf{f}+\mathbf{F}_c(\mathbf{P}) \tag{13}$$

Where, **u** is the vector of nodal displacements including the conventional DOFs and additional nodal enrichment DOFs. **K** is the stiffness matrix. **f** is the nodal load vector resulted from body force and prescribed traction on Γ_σ. $\mathbf{F}_c$ is the equivalent nodal force vector resulted from the contact forces **P** acting on the contact surfaces which are equivalent to the contact stress acting on the crack surface. Note that the unknown vectors in Eq.(13) are **u** and **P**.

3.2. The derivation of equivalent nodal force resulted from the contact forces on the crack surfaces in the XFEM formulation

In the case that the contact surfaces are embedded in the interior of element, the contact pairs can be easily formed at the positions where the crack line/surface intersects the edges of the element. The two contact points in one contact pair have the same coordinates as the intersection point. Let $\mathbf{x}_c$ be the position of any contact pair. Then the displacement jump can be computed according to (10)~(12) and obtained as

$$[[\mathbf{u}(\mathbf{x}_c)]]=\mathbf{u}(\mathbf{x}_c^1)-\mathbf{u}(\mathbf{x}_c^2)=2\sum_{j=1}^{nd}\mathbf{b}_{Hj}N_j(\mathbf{x}_c)+2\sqrt{r}\sum_{k=1}^{nd}N_k(\mathbf{x}_c)\mathbf{c}_{k1} \tag{14}$$

Where, $\mathbf{x}_c^1$ and $\mathbf{x}_c^2$ are two contact points in the contact pair located on crack surface Γ_c^1 and Γ_c^2 respectively. Because no initial gap exists between the two contact surfaces, $\mathbf{x}_c^1=\mathbf{x}_c^1=\mathbf{x}_c$.

The equivalent nodal forces $\mathbf{F}_c$ can be obtained from virtual work done by the contact forces **P** acting at the contact points. It is assumed that the element is cut by contact surface into two pieces, as shown in Figure 2. In order to clarify the following procedure for more general cases, the nodes

are assumed to be enriched by both the generalized Heaviside and branch functions. In Figure 2, we focus on the contact pair i_1 on the edge "s", and the two contact points belonging to the Γ_c^1 and Γ_c^2 are denoted as i_1^1 and i_1^2 respectively. For every contact pair, the contact force acting at the point i_1^1 denoted by vector $\mathbf{P}^{i_1}$ is used to represent the pair of contact forces.

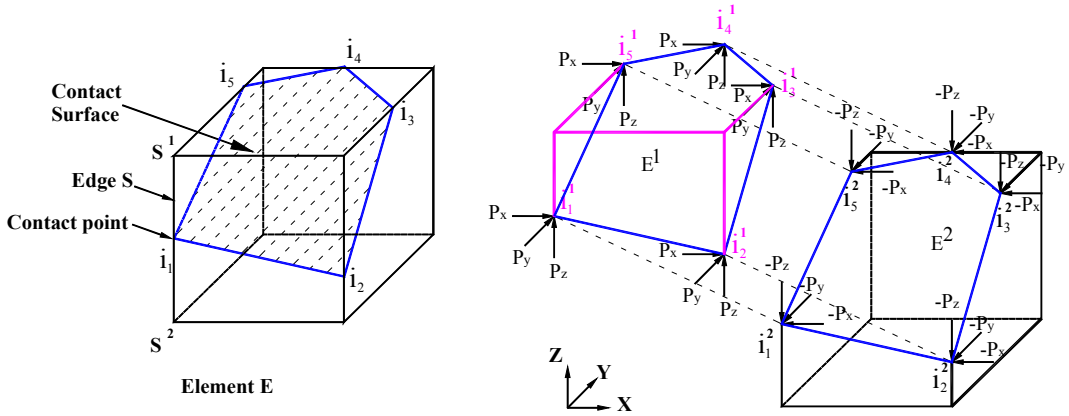

Figure 2 The element cut by contact surface and the contact forces

Then using (14), the virtual work done by the contact force at the contact pair i_1 is

$$W_{i_1} = \delta\mathbf{u}(\mathbf{x}_c^1)\cdot\mathbf{P}^{i_1} + \delta\mathbf{u}(\mathbf{x}_c^2)\cdot(-\mathbf{P}^{i_1}) = \delta[[\mathbf{u}(\mathbf{x}_c)]]\cdot\mathbf{P}^{i_1} = 2\left(\sum_{j=1}^{nd}\delta\mathbf{b}_j N_j(\mathbf{x}_c) + \sqrt{r}\sum_{k=1}^{nd} N_k(\mathbf{x}_c)\delta\mathbf{c}_{k1}\right)\cdot\mathbf{P}^{i_1} \quad (15)$$

As the contact pairs locate on the edges of element, so only the two shape functions related to nodes on the edge are nonzero. For example, in Figure 2, $\mathbf{x}_c$ locate on the edge "s", therefore only the shape function of nodes s^1 and s^2 may take nonzero values. The virtual work is then transformed into

$$\begin{aligned} W_{i_1} &= \left(2\left(\delta\mathbf{b}_{s^1}N_{s^1}(\mathbf{x}_c) + \delta\mathbf{b}_{s^2}N_{s^2}(\mathbf{x}_c)\right) + 2\sqrt{r}\left(N_{s^1}(\mathbf{x}_c)\delta\mathbf{c}_{s^1 1} + N_{s^2}(\mathbf{x}_c)\delta\mathbf{c}_{s^2 1}\right)\right)\cdot\mathbf{P}^{i_1} \\ &= \left\{\delta\mathbf{b}_{s^1}, \delta\mathbf{b}_{s^2}, \delta\mathbf{c}_{s^1}, \delta\mathbf{c}_{s^2}\right\}\cdot\left\{2N_{s^1}\mathbf{P}^{i_1}, 2N_{s^2}\mathbf{P}^{i_1}, 2\sqrt{r}N_{s^1}\mathbf{P}^{i_1}, 2\sqrt{r}N_{s^2}\mathbf{P}^{i_1}\right\}^T = \left(\delta\mathbf{u}^{add}\right)^T\cdot\mathbf{F}_c^{i_1} \end{aligned} \quad (16)$$

Where,

$$\begin{aligned} \delta\mathbf{u}^{add} &= \left\{\delta\mathbf{b}_{s^1}, \delta\mathbf{b}_{s^2}, \delta\mathbf{c}_{s^1}, \delta\mathbf{c}_{s^2}\right\}^T \\ \mathbf{F}_c^{i_1} &= \left\{2N_{s^1}(\mathbf{x}_c)\mathbf{P}^{i_1}, 2N_{s^2}(\mathbf{x}_c)\mathbf{P}^{i_1}, 2\sqrt{r}N_{s^1}(\mathbf{x}_c)\mathbf{P}^{i_1}, 2\sqrt{r}N_{s^2}(\mathbf{x}_c)\mathbf{P}^{i_1}\right\}^T \end{aligned} \quad (17)$$

$\mathbf{F}_c^{i_1}$ is the equivalent nodal loads resulted from the contact forces $\mathbf{P}^{i_1}$ acting at the contact pair i_1 on the embedded contact surfaces in one element. Thus the total nodal loads $\mathbf{F}_c$ resulted from the contact forces can be obtained by assembling $\mathbf{F}_c^{i_1}$ for every contact pair i_1.

4. Solution procedure

The equilibrium equation (13) and the contact equations (5) lead to the system equations which have the forms

$$
\begin{aligned}
\mathbf{H}_1 &= \mathbf{Ku} - \mathbf{f} - \mathbf{F}_c(\mathbf{P}) = \mathbf{0} \\
\mathbf{H}_2 &= \left\{\mathrm{H}_2^1, \mathrm{H}_2^2, \mathrm{K}, \mathrm{H}_2^{NC}\right\}^T = \mathbf{0} \\
\mathbf{H}_3 &= \left\{\mathrm{H}_3^1, \mathrm{H}_3^2, \mathrm{K}, \mathrm{H}_3^{NC}\right\}^T = \mathbf{0} \\
\mathbf{H}_4 &= \left\{\mathrm{H}_4^1, \mathrm{H}_4^2, \mathrm{K}, \mathrm{H}_4^{NC}\right\}^T = \mathbf{0}
\end{aligned}
\tag{18}
$$

Where, NC is the total number of contact pairs. The unknown vectors of displacement **du** and contact forces **dP** in the form of increment are grouped and denoted by vector **z**, i.e., **z**={**du**, **dP**}^{T}. The second to fourth equations in Eq. (18) are B-differentiable equations, because "min" operator in (5) is B-differentiable[5].

Because of the nonlinearity and non-smooth properties of (18), an iterative B-differentiable Newton method [6] which is an extension of classical Newton method, is employed for solving the system equations (18).

5. Numerical examples

5.1. 2D square plate with a crack

A square plate with 20 ×20m including a center crack oriented at 45° relative to the horizontal is considered. In order to examine the accuracy of the proposed method, two different discretizations by quadrilateral finite elements, which denoted as Model I and Model II respectively, are constructed as shown in Figure 3. In the Model I, the mesh is uniform and the crack intersects the elements at the two adjacent sides. In the Model II, the crack intersects the elements at the two opposite sides. The material is elastic with the properties: Young's Modulus 10GPa, Poisson's ratio 0.3. The bottom boundary of the plate is fixed. At the top boundary, uniform displacements with the value of -0.1m in vertical direction are prescribed. In this example, we assume that the crack surface can slide but the crack tip will not advance. The different friction coefficients with 0.1, 0.8 and 1.2 are used to test the convergence of the proposed method.

The results show that the convergent solutions can be obtained for the three frictional coefficients. The total reaction forces at the top boundary for different frictional coefficients are given in Table 1. And the contours of displacement in the case of frictional coefficient 0.1 for the two different discretizations are shown in Figure 4. Table 1 shows that for the two different discretizations, the resultant reaction forces agree well with each other for different frictional coefficients. The Figure 4 shows that the distribution and magnitude of displacements in x and y direction are almost the identical for both models.

Table 1 Resultant of reaction force on the top boundary (Unit: N)

Model	μ=0.1	μ=0.8	μ=1.2
Mesh I	973.3	1107.4	1137.5
Mesh II	973.7	1108.8	1141.6
Relative Error	4.11e-4	1.3e-3	3.6e-3

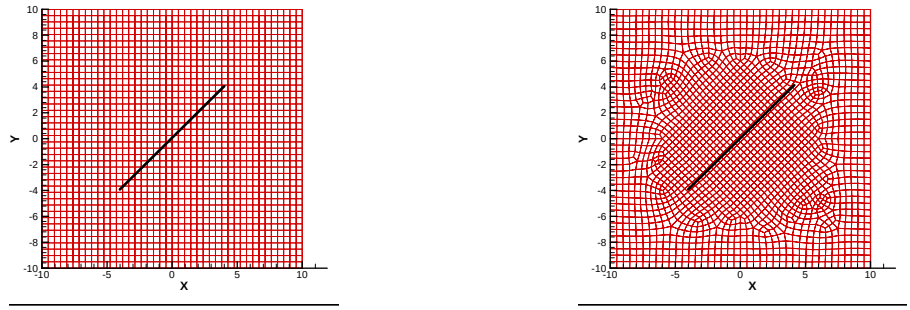

(a) Uniform mesh (Mesh I) (b) Non-uniform mesh (Mesh II)

Figure 3 Two finite element discretizations of the square plate

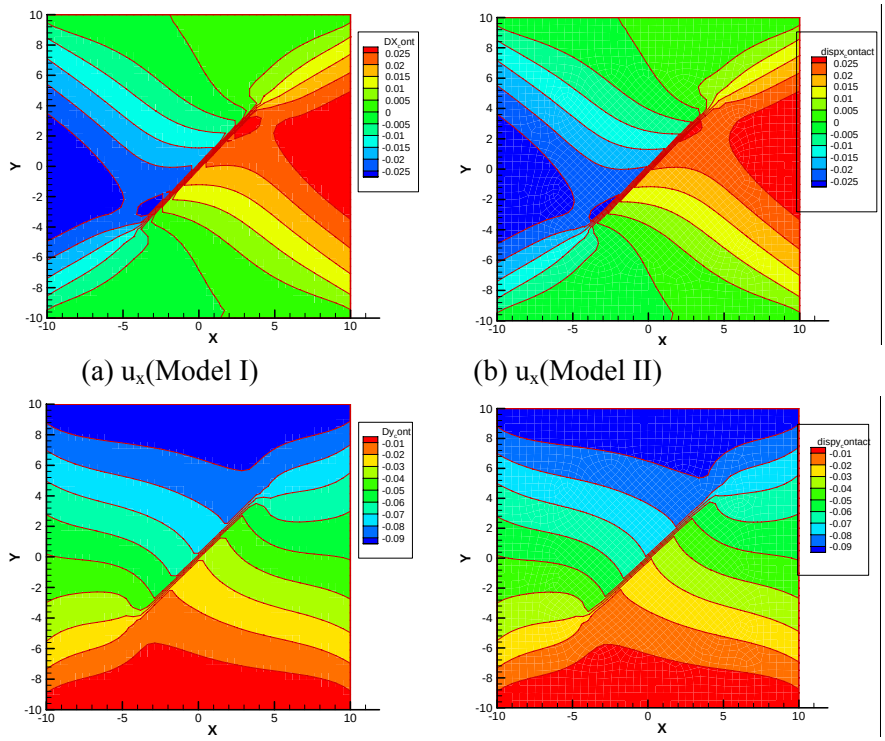

(a) u_x(Model I) (b) u_x(Model II)

(c) u_y (Model I) (d) u_y (Model II)

Figure 4 Distribution of displacement in the square plate for frictional coefficient 0.1(Unit: m)

5.2. Frictional contact of two parts of a 3D beam

In this example, a beam is divided into two identical parts by a contact surface shown in Figure 5. In order of comparison and validation, two finite element models denoted by Model I and Model II are constructed. In Model I the contact surfaces are embedded in the elements, while in Model II the contact surfaces coincide with the element boundaries. The finite element discretizations for the two models are given in Figure 6. The presented method in the framework of XFEM is used for solving Model I and the standard FEM with B-differential equation method for Model II. The material is elastic with the properties: Young's Modulus 1e10Pa, Poisson's ratio 0.3, frictional coefficient 0.1. At the left end of beams, part of the surface, i.e. the shadow area as shown in Figure 6, is fixed. So there are no constraints at the intersection line between contact surfaces and the boundary surfaces

of the cantilever beam. The distribution line load in negative X, Y and Z directions with the same density of 1e5N/m are applied at the top of free end as shown in Figure 6.

In the Model I and Model II, there are 7 nodes at the top of free end denoted by P_1 to P_7. The displacements at these nodes for the two models are listed in Table 2. It can be seen from this table that the displacements of selected points for both models agree well with each other.

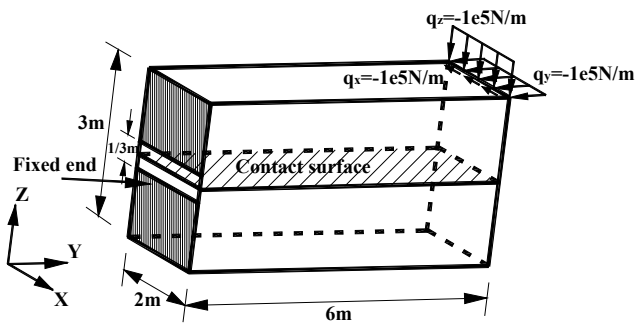

Figure 5 Cantilever beam with the planar crack surface

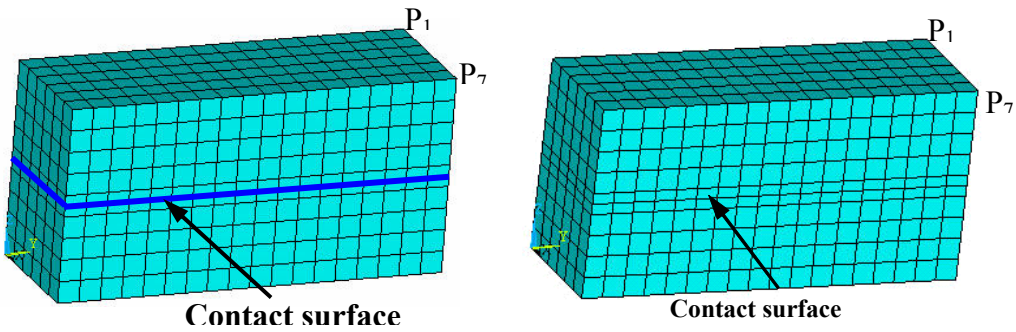

(a) Model I (b) Model II

Figure 6 Two finite element discretizations for the cantilever beam

Table 2 Displacements of nodes at the top of free end (Unit: cm)

Direction\Model		Points						
		P_1	P_2	P_3	P_4	P_5	P_6	P_7
X	Model I	-1.782853	-1.764749	-1.750595	-1.744385	-1.743544	-1.746958	-1.745677
	Model II	-1.782816	-1.764712	-1.750557	-1.744346	-1.743506	-1.746919	-1.745638
	Error	**2.1e-5**	**2.1e-5**	**2.17e-5**	**2.24e-5**	**2.18e-5**	**2.23e-5**	**2.23e-5**
Y	Model I	-0.2448591	-0.0981012	0.0265221	0.1475015	0.2680483	0.3910484	0.5294690
	Model II	-0.2450343	-0.0982756	0.0263494	0.1473310	0.2678800	0.3908819	0.5293037
	Error	**7.16e-4**	**1.78e-3**	**6.51e-3**	**1.16e-3**	**6.28e-4**	**4.26e-7**	**3.12e-4**
Z	Model I	-1.517652	-1.460974	-1.424242	-1.389137	-1.354119	-1.318229	-1.269198
	Model II	-1.516629	-1.459982	-1.423281	-1.388208	-1.353223	-1.317365	-1.268366
	Error	**6.74e-4**	**6.78e-4**	**6.75e-4**	**6.69e-4**	**6.62e-4**	**6.55e-4**	**6.56e-4**

6. Conclusions

In this paper, a combined eXtend Finite Element method and B-differentiable equations method for solving contact problems in which the contact surfaces are embedded in the elements. There are some salient features for the presented methods. Firstly, in the framework of XFEM, it is very convenient to construct the finite element meshes with minor consideration of the position of crack or contact surfaces. Due to the assumption of small deformation, the contact pairs are easily defined at the intersection points between the contact surfaces and the edges of elements. Secondly, the contact conditions are formulated as B-differentiable equations by the quantities at the contact pairs and satisfied exactly. Thirdly, the B-differential Newton method with guaranteed convergence property is utilized to solve the system equations consisting of equilibrium equations and contact conditions. The 2D and 3D frictional contact examples show the high accuracy and good convergence property of the presented method.

Acknowledgements

The first author greatly appreciates the financial support of State Scholarship fund provided by Chinese Scholarship Council and Professor Ted Belytschko to offer him a visiting scholarship position in Northwestern University. He also thanks postdoctors Qinglin Duan, Jeong-Hoon Song, Thomas Menouillard at Northwestern University, Dr. Fushen Liu at Stanford University for their kindly help in studying the XFEM and constructive discussion and suggestions. The support of the China National Science Foundation under grant 51178069 is gratefully acknowledged.

References

[1] N. Möes, J. Dolbow, T. Belytschko, A finite element method for crack growth without remeshing. International Journal for Numerical Methods in Engineering, 46 (1999) 131–150.

[2] J. Dolbow, N. Möes, T. Belytschko, An extended finite element method for modeling crack growth with frictional contact, Computer Methods in Applied Mechanics and Engineering, 190 (2001) 6825–6846.

[3] F.S. Liu, R. I. Borja, A contact algorithm for frictional crack propagation with the extended finite element method, International Journal for Numerical Methods in Engineering, 76 (2008) 1489–1512.

[4] I. Nistor, M. L. E. Guiton, P. Massin, N. Möes, S. Géniaut, An X-FEM approach for large sliding contact along discontinuities, International Journal for Numerical Methods in Engineering, 78 (2009) 1407–1431.

[5] P. Christensen, A. Klarbring, J.S. Pang, N. Stromberg, Formulation and comparison of algorithms for frictional contact problems, International Journal for Numerical Methods in Engineering, 42(1998), 145-173

[6] J.S. Pang, Newton's method for B-differentiable equations, Mathematics of Operations Research, (15) 1990 311-341 14.

[7] N. Sukumar, N. Möes, B. Moran, T. Belytschko, Extended finite element method for three-dimensional crack modeling, International Journal for Numerical Methods in Engineering, 48 (2000) 1549-1570

Implementation of the XFEM for Hydraulic Fracture Problems

Zuorong Chen*

CSIRO Earth Science & Resource Engineering, Melbourne, Australia
* Corresponding author: zuorong.chen@csiro.au

Abstract A new finite element has been implemented to incorporate the extended finite element method (XFEM) for the solution of hydraulic fracture problems. The proposed element includes the desired aspects of the XFEM so as to model crack propagation without explicit remeshing. In addition, the fluid pressure degrees of freedom have been defined on the element to describe the fluid flow within the crack and its contribution to the crack deformation. Thus the fluid flow within the crack and crack propagation are fully coupled in a natural way and are solved simultaneously. Verification of the proposed element has been conducted by comparing the finite element results with the analytical solutions available in the literature.

Keywords Hydraulic fracture, Extended finite element method, Internal pressure

1. Introduction

Hydraulic fracturing is a powerful technology for enhancing conventional petroleum production. It is playing a central role in fast growing development of unconventional gas and geothermal energy. The fully 3-D numerical simulation of the hydraulic fracturing process is of great importance to understand the complex, multiscale mechanics of hydraulic fracturing, to the efficient application of this technology, and to develop innovative, advanced hydraulic fracturing technologies for unconventional gas production. The accurate numerical simulation of hydraulic fracture growth remains a significant challenge because of the strong nonlinear coupling between the viscous flow of fluid inside the fracture and fracture propagation (a moving boundary), complicated by the need to consider interactions with existing natural fractures and with rock layers with different properties.

Great effort has been devoted to the numerical simulation of hydraulic fractures with the first 3-D modeling efforts starting in the late 1970s [1-2]. Significant progress has been made in developing 2-D and 3-D numerical hydraulic fracture models [3-15]. Boundary integral equation methods or displacement discontinuity techniques have generally been employed to investigate the propagation of simple hydraulic fractures such as penny-shaped or plane-strain fractures in a homogeneous, infinite or semi-infinite elastic medium where the appropriate fundamental solutions are available. The finite element method has been used and is particularly useful in modelling the hydraulic fracture propagation in inhomogeneous rocks which may include nonlinear mechanical properties and may be subject to complex boundary conditions. The finite element model is also able to investigate the propagation of hydraulic fractures in infinite or semi-infinite medium by using infinite elements or appropriate analytical solutions to efficiently approximate the far-field boundary [15]. However, the standard finite element model requires remeshing after every crack propagation step and the mesh has to conform exactly to the fracture geometry as the fracture propagates, and thus is computationally expensive.

By adding special enriched shape functions in conjunction with additional degrees of freedom to the standard finite element approximation within the framework of partition of unity, the extended finite element method [16-17] (XFEM) overcomes the inherent drawbacks associated with use of the conventional finite element methods and enables the crack to be represented without explicitly meshing crack surfaces, and so the crack geometry is completely independent of the mesh and remeshing is not required, allowing for the convenient simulation of the fracture propagation. The XFEM has been employed to investigate the hydraulic fracture problems [18-19].

In this paper, we explore the application of the extended finite element method to hydraulic fracture problems. By taking good advantage of the XFEM and the flexible functionality of user subroutines provided in ABAQUS [20], a user-defined 2-D quadrilateral plane strain element has been coded in Fortran to incorporate the extended finite element capabilities in 2-D hydraulic fracture problems. The user-defined element includes the desired aspects of the XFEM so as to model crack propagation without explicit remeshing. In addition, the extended fluid pressure degrees of freedom are assigned to the appropriate nodes of the proposed elements in order to describe the viscous flow of fluid inside the crack and its contribution to the coupled crack deformation.

2. Problem formulation

2.1. Problem definition

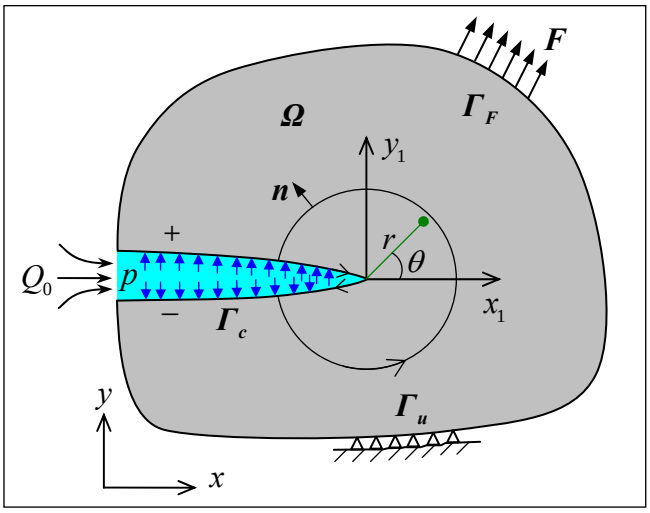

Figure 1. A two-dimensional domain containing a hydraulic fracture

Consider a two-dimensional hydraulically driven fracture $\boldsymbol{\Gamma}_c$ propagating in a homogeneous, isotropic, linear elastic, impermeable medium $\boldsymbol{\Omega}$ under plane strain conditions, see Figure 1. The boundary of the domain consists of $\boldsymbol{\Gamma}_F$ on which prescribed tractions $\boldsymbol{F}$, are imposed, $\boldsymbol{\Gamma}_u$ on which prescribed displacements (assumed to be zero for simplicity) are imposed, and crack faces $\boldsymbol{\Gamma}_c$ subject to fluid pressure. The fracture propagation is driven by injection of an incompressible Newtonian fluid at constant volumetric rate Q_0 at a fixed injection point. It is assumed that the fracture propagation is quasi-static, and that the fracture is completely filled with the injected fluid, i.e., there is no lag between the fluid front and the fracture tip. The solution of the problem consists of determining the evolution of the fracture length, as well as the fracture opening, the fluid pressure, and the deformations and stresses inside the domain as functions of both position and time.

2.2 Governing equations

The stress field inside the domain, $\boldsymbol{\sigma}$, is related to the external loading $\boldsymbol{F}$ and the fluid pressure p through the equilibrium equations:

$$\begin{aligned} &\nabla \cdot \boldsymbol{\sigma} = \boldsymbol{0}, \text{ on } \Omega \\ &\boldsymbol{\sigma} \cdot \boldsymbol{n} = \boldsymbol{F}, \text{ on } \Gamma_F \\ &\boldsymbol{\sigma} \cdot \boldsymbol{n}^- = -\boldsymbol{\sigma} \cdot \boldsymbol{n}^+ = -p\boldsymbol{n}^+ = p\boldsymbol{n}^-, \text{ on } \Gamma_c \end{aligned} \tag{1}$$

where $\boldsymbol{n}$ is the unit normal vector.

The kinematic equations include the strain-displacement relationship, the prescribed displacement boundary conditions and the definition of the separation between the two surfaces of the crack. Under the assumptions of small strains and displacements, the kinematic equations read

$$\begin{aligned} &\boldsymbol{\varepsilon} = \frac{1}{2}\left(\nabla \boldsymbol{u} + (\nabla \boldsymbol{u})^{\mathrm{T}}\right) \text{ on } \Omega \\ &\boldsymbol{u} = \boldsymbol{0} \text{ on } \Gamma_u \\ &\boldsymbol{w} = \boldsymbol{u}^+ - \boldsymbol{u}^- \text{ on } \Gamma_c \end{aligned} \tag{2}$$

where $\boldsymbol{u}$ is the displacement, $\boldsymbol{w}$ is the separation between the two faces of the crack, and $\boldsymbol{\varepsilon}$ is the strain.

The stress field insider the domain is expressed in terms of the isotropic, linear elastic constitutive law as:

$$\boldsymbol{\sigma} = \boldsymbol{D} : \boldsymbol{\varepsilon} \tag{3}$$

where $\boldsymbol{D}$ is Hooke's tensor.

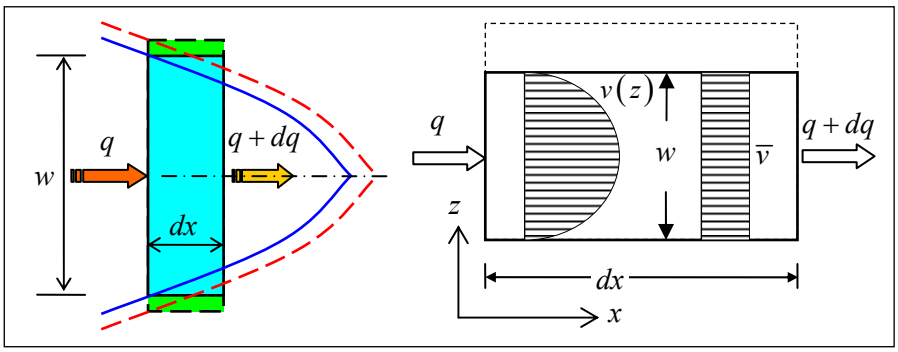

Figure 2. Fluid flow within crack

The fluid flow within the crack is modelled using lubrication theory, given by Poiseuille's law

$$q = -\frac{w^3}{12\mu}\frac{\partial p}{\partial x} \tag{4}$$

where μ is the dynamic viscosity of the fracturing fluid, q, the flow rate inside the crack per unit extend of the crack in the direction of x, is equal to the average velocity $\bar{v}$ times the crack opening w (see Figure 2), i.e.,

$$q(x) = \bar{v}(x)w(x) \tag{5}$$

The fracturing fluid is considered to be incompressible, so the mass conservation equation for the fluid may be expressed as

$$\frac{\partial w}{\partial t} + \frac{\partial q}{\partial x} + g = 0 \tag{6}$$

where the flux discontinuity $g(\boldsymbol{x})$ is taken as positive if fluid is leaving the fracture. It can be interpreted as a source density outside the fracture, which accounts for fluid exchange between the fracture and the surrounding medium (e.g. porous rock).

Substituting of Eq. (4) into Eq. (6) leads to the governing equation for the fluid flow within the fracture

$$\frac{\partial w}{\partial t}-\frac{\partial}{\partial x}\left(k\frac{\partial p}{\partial x}\right)+g=0 \tag{7}$$

where $k=w^3/12\mu$ is the permeability. The general form of the governing equation (Eq. (7)) may be expressed as

$$\dot{w}-\nabla^{\mathrm{T}}\left(\boldsymbol{k}\nabla p\right)+g=0 \tag{8}$$

where $\boldsymbol{k}$ is the permeability tensor.

According to linear elastic fracture mechanics, the criterion that the fracture propagates continuously in mobile equilibrium (quasi-static) takes the form

$$K_{\mathrm{I}}=K_{\mathrm{Ic}} \tag{9}$$

where K_{I} is the mode I stress intensity factor and K_{Ic} the material fracture toughness.

At the inlet, the fluid flux is equal to the injection rate, i.e.,

$$q\big|_{\mathrm{inlet}}=Q_0 \tag{10}$$

At the tip, the boundary conditions are given by the zero fracture opening and zero flow conditions,

$$w\big|_{\mathrm{tip}}=q\big|_{\mathrm{tip}}=0 \tag{11}$$

The above equations constitute the complete formulation that can be used to predict the evolution of the hydraulic fracture.

3. Weak form and FEM discretization

The weak form of the equilibrium equation is given by

$$\int_{\Omega}\delta\boldsymbol{\varepsilon}^{\mathrm{T}}\boldsymbol{\sigma}d\Omega-\int_{\Omega}\delta\boldsymbol{u}^{\mathrm{T}}\boldsymbol{b}d\Omega-\int_{\Gamma_t}\delta\boldsymbol{u}^{\mathrm{T}}\boldsymbol{t}d\Gamma-\left(\int_{\Gamma_c^+}\delta\boldsymbol{u}_c^{+\mathrm{T}}\boldsymbol{p}_c^{+}d\Gamma+\int_{\Gamma_c^-}\delta\boldsymbol{u}_c^{-\mathrm{T}}\boldsymbol{p}_c^{-}d\Gamma\right)=0 \tag{12}$$

where $\boldsymbol{b}$ is the body force, $\boldsymbol{t}$ is the applied traction on the boundary $\boldsymbol{\Gamma}_t$, $\delta\boldsymbol{u}$ is an arbitrary virtual displacement and $\delta\boldsymbol{\varepsilon}$ is the corresponding virtual strain, which is related to $\delta\boldsymbol{u}$ through the strain operator $\boldsymbol{S}$ as $\delta\boldsymbol{\varepsilon}=\boldsymbol{S}\delta\boldsymbol{u}$.

For the fluid pressure on the crack surfaces, we define

$$\boldsymbol{p}=\boldsymbol{p}_c^{+}=-\boldsymbol{p}_c^{-}=p\boldsymbol{n}_c=p\boldsymbol{n}_c^{-}=-p\boldsymbol{n}_c^{+}. \tag{13}$$

The crack opening displacement $\boldsymbol{w}$ is given by

$$w=\boldsymbol{n}_c^{\mathrm{T}}\cdot\left(\boldsymbol{u}_c^{+}-\boldsymbol{u}_c^{-}\right),\ \text{or}\ \ \boldsymbol{w}=\boldsymbol{n}_c\cdot\left(\boldsymbol{u}_c^{+}-\boldsymbol{u}_c^{-}\right)\cdot\boldsymbol{n}_c. \tag{14}$$

Then the weak from of the equilibrium equation can be expressed in a more compact form as

$$\int_{\Omega}\delta\boldsymbol{\varepsilon}^{\mathrm{T}}\boldsymbol{\sigma}d\Omega-\int_{\Omega}\delta\boldsymbol{u}^{\mathrm{T}}\boldsymbol{b}d\Omega-\int_{\Gamma_t}\delta\boldsymbol{u}^{\mathrm{T}}\boldsymbol{t}d\Gamma-\int_{\Gamma_c}\delta\boldsymbol{w}^{\mathrm{T}}\boldsymbol{p}d\Gamma=0. \tag{15}$$

The weak form of the governing equation for the fluid flow within the fracture can be written as

$$\int_{\Gamma_c}\delta p^{\mathrm{T}}\left(\partial\dot{w}-\nabla^{\mathrm{T}}\boldsymbol{k}\nabla p+g\right)d\Gamma=0 \tag{16}$$

which, after integration by parts and substitution of the boundary conditions describe above, yields

$$\int_{\Gamma_c}\delta p^{\mathrm{T}}\partial\dot{w}d\Gamma+\int_{\Gamma_c}\nabla^{\mathrm{T}}\left(\delta p\right)\boldsymbol{k}\nabla pd\Gamma+\int_{\Omega_c}\delta p^{\mathrm{T}}gd\Gamma=0 \tag{17}$$

Consider the coupled problem discretized in the standard (displacement) manner with the displacement vector $\boldsymbol{u}$ approximated as

$$\boldsymbol{u} \approx \hat{\boldsymbol{u}} = \sum_{i=1}^{n} \boldsymbol{N}_i^u \boldsymbol{u}_i = \boldsymbol{N}^u \tilde{\boldsymbol{u}}\,, \quad \delta \boldsymbol{u} \approx \boldsymbol{N}^u \delta \tilde{\boldsymbol{u}} \tag{18}$$

and the fluid pressure p similarly approximated by

$$p \approx \hat{p} = \sum_{i=1}^{n} N_i^p p_i = \boldsymbol{N}^p \tilde{\boldsymbol{p}}\,, \quad \delta p \approx \boldsymbol{N}^p \delta \tilde{\boldsymbol{p}} \tag{19}$$

where $\boldsymbol{u}_i$ and p_i are the nodal displacement and pressure, $\boldsymbol{N}_i^u$ and N_i^p are corresponding nodal displacement and fluid pressure shape functions.

The crack opening displacement $\boldsymbol{w}$ is approximated by

$$\boldsymbol{w} \approx \hat{\boldsymbol{w}} = \sum_{i=1}^{n} \boldsymbol{N}_i^w \boldsymbol{u}_i = \boldsymbol{N}^w \tilde{\boldsymbol{u}}\,, \quad \delta \boldsymbol{w} \approx \boldsymbol{N}^w \delta \tilde{\boldsymbol{u}} \tag{20}$$

where $\boldsymbol{N}_i^w$ are the appropriate crack opening displacement shape function. It will be shown later that the shape function $\boldsymbol{N}_i^w$ can be expressed in terms of the displacement shape functions $\boldsymbol{N}_i^u$ according to the relationship Eq. (14).

Substitution of the displacement and pressure approximations (Eqs. (18) - (20)) and the constitutive equation (Eq. (3)) into Eq. (15) yields a system of algebraic equations for the discrete structural problem

$$\boldsymbol{K}\tilde{\boldsymbol{u}} - \boldsymbol{Q}\tilde{\boldsymbol{p}} - \boldsymbol{f}^u = \boldsymbol{0} \tag{21}$$

where

$$\boldsymbol{K} = \int_\Omega \boldsymbol{B}^{\mathrm{T}} \boldsymbol{D} \boldsymbol{B} d\Omega\,, \quad \boldsymbol{f}^u = \int_\Omega \left(\boldsymbol{N}^u\right)^{\mathrm{T}} \boldsymbol{b} d\Omega + \int_{\Gamma_t} \left(\boldsymbol{N}^u\right)^{\mathrm{T}} \boldsymbol{t} d\Gamma\,, \quad \boldsymbol{Q} = \int_{\Gamma_c} \left(\boldsymbol{N}^w\right)^{\mathrm{T}} \boldsymbol{n} \boldsymbol{N}^p d\Gamma \tag{22}$$

By substituting Eqs. (19) and (20) into Eq. (17), the standard discretization applied to the weak form of the fluid flow equation leads to a system of algebraic equations for the discrete fluid flow problem

$$\boldsymbol{C}\dot{\tilde{\boldsymbol{u}}} + \boldsymbol{H}\tilde{\boldsymbol{p}} - \boldsymbol{f}^p = \boldsymbol{0} \tag{23}$$

where

$$\boldsymbol{C} = \boldsymbol{Q}^{\mathrm{T}} = \int_{\Gamma_c} \left(\boldsymbol{N}^p\right)^{\mathrm{T}} \boldsymbol{n}^{\mathrm{T}} \boldsymbol{N}^w d\Gamma\,, \quad \boldsymbol{H} = \int_{\Gamma_c} \left(\nabla \boldsymbol{N}^p\right)^{\mathrm{T}} \boldsymbol{k} \nabla \boldsymbol{N}^p d\Gamma\,, \quad \boldsymbol{f}^p = -\int_{\Gamma_c} \left(\boldsymbol{N}^p\right)^{\mathrm{T}} g d\Gamma \tag{24}$$

Then, the discrete governing equations for the coupled fluid-fracture problem can be expressed in matrix form as:

$$\begin{bmatrix} \boldsymbol{0} & \boldsymbol{0} \\ \boldsymbol{C} & \boldsymbol{0} \end{bmatrix} \begin{pmatrix} \dot{\tilde{\boldsymbol{u}}} \\ \dot{\tilde{\boldsymbol{p}}} \end{pmatrix} + \begin{bmatrix} \boldsymbol{K} & \boldsymbol{-Q} \\ \boldsymbol{0} & \boldsymbol{H} \end{bmatrix} \begin{pmatrix} \tilde{\boldsymbol{u}} \\ \tilde{\boldsymbol{p}} \end{pmatrix} = \begin{pmatrix} \boldsymbol{f}^u \\ \boldsymbol{f}^p \end{pmatrix} \tag{25}$$

The above equations form the basis for the construction of a finite element which couples the fluid flow within the crack and crack propagation.

4. The extended finite element method and element implementation

4.1 Extended finite element approximation

By adding special enriched shape functions in conjunction with additional degrees of freedom to the standard finite element approximation within the framework of partition of unity, the extended finite element method (XFEM) [16-17] overcomes the inherent drawbacks associated with use of the

conventional finite element methods and enables the crack to be represented without explicitly meshing crack surfaces, and so the crack geometry is completely independent of the mesh and remeshing is not required, allowing for the convenient simulation of the fracture propagation.

The XFEM approximation of the displacement field for the crack problem can be expressed as [17]

$$\mathbf{u}(\mathbf{x}) = \sum_{I\in N} \boldsymbol{N}_I(\mathbf{x})\mathbf{u}_I + \sum_{I\in N_{cr}} \tilde{\boldsymbol{N}}_I(\mathbf{x})\big(H(\mathbf{x}) - H(\mathbf{x}_I)\big)\mathbf{a}_I + \sum_{I\in N_{tip}} \tilde{\boldsymbol{N}}_I(\mathbf{x})\sum_{l=1}^{4}\Big(B^{(l)}(r,\theta) - B^{(l)}(r_I,\theta_I)\Big)\mathbf{b}_I^{(l)} \tag{26}$$

where N is the set of all nodes in the mesh, N_{cr} the set of nodes whose support are bisected by the crack surface Γ_c, N_{tip} the set of nodes whose support are partially cut by the crack surface, $\boldsymbol{N}_I(\mathbf{x})$ and $\tilde{\boldsymbol{N}}_I(\mathbf{x})$ are the standard finite element shape functions, $\mathbf{u}_I$ are displacement nodal degrees of freedom, $\mathbf{a}_I$ and $\mathbf{b}_I^{(l)}$ are additional degrees of freedom for the displacement, and $H(\mathbf{x})$ and $B^{(l)}(r,\theta)$ are the appropriate enrichment basis functions which are localized by $\tilde{\boldsymbol{N}}_I(\mathbf{x})$. The shape function $\tilde{\boldsymbol{N}}_I(\mathbf{x})$ can differ from $\boldsymbol{N}_I(\mathbf{x})$.

The discontinuity in the displacement field given by a crack Γ_c can be represented by the generalized Heaviside step function

$$H(\mathbf{x}) = H\big(d(\mathbf{x})\big) = sign\big(d(\mathbf{x})\big) = \begin{cases} 1 & d(\mathbf{x}) \ge 0 \\ -1 & d(\mathbf{x}) < 0 \end{cases} \tag{27}$$

where $d(\mathbf{x})$ is the signed distance of the point $\mathbf{x}$ to Γ_c.

The enrichment basis functions $B^{(l)}(r,\theta)$ are required to model the displacement around the crack tip, which are generally chosen as a basis that approximately spans the two-dimensional plane strain asymptotic crack tip fields in the linear elastic fracture mechanics:

$$\left\{B^{(l)}\right\}_{l=1}^{4} = \sqrt{r}\left\{\sin(\theta/2) \quad \cos(\theta/2) \quad \sin(\theta/2)\sin(\theta) \quad \cos(\theta/2)\sin(\theta)\right\} \tag{28}$$

where (r,θ) are the local polar coordinates at the crack tip. The first function in Eq. (28), $\sin(\theta/2)$, is discontinuous across the crack faces $(\theta = \pm\pi)$, so the Heaviside enrichment in Eq. (26) can be removed in the displacement field approximation of the elements which are partially cut by the crack surface.

According to Eq. (26), the displacement discontinuity between the two surfaces of the crack can be obtained as

$$\mathbf{w}(\mathbf{x}) = \mathbf{u}^{(+)}(\mathbf{x}) - \mathbf{u}^{(-)}(\mathbf{x}) = 2\sum_{I\in N_{cr}} \tilde{\boldsymbol{N}}_I(\mathbf{x})\mathbf{a}_I + 2\sum_{I\in N_{tip}} \tilde{\boldsymbol{N}}_I(\mathbf{x})B^{(1)}(r,\pi)\mathbf{b}_I^{(1)} \qquad \boldsymbol{x}\in\Gamma_c \tag{29}$$

Combination of Eqs. (29) and (20) enables determining the shape function $\boldsymbol{N}^w$.

The fluid pressure field within the crack is approximated by

$$p(\mathbf{x}) = \sum_{I\in N_{cr}} N_I^p(\mathbf{x})\,p_I \qquad \boldsymbol{x}\in\Gamma_c \tag{30}$$

where $N_I^p(\mathbf{x})$ are the standard finite element shape functions. In some cases, it can also be chosen as a special function so as to allow for the pressure singularity at the crack tip and the associated near-tip asymptotic fracture opening associated with a zero-lag viscosity dominated regime in a

hydraulic fracture [18].

4.2 Element implementation

As shown in Figure 3, the two-dimensional 4-node plane strain channel and tip elements have been constructed for the hydraulic fracture problem. Each node has the standard displacement degrees of freedom $\mathbf{u}_I$. The additional degree of freedom $\mathbf{a}_I$ and $\mathbf{b}_I^{(l)}$ are assigned to the four nodes of channel and tip elements, respectively. In addition, the virtual degree of freedom of fluid pressure has been assigned to nodes 3 and 4 so as to represent the internal fluid pressure within the crack. It should be pointed out that nodes 3 and 4 physically do not have fluid pressure degrees of freedom because here the fluid flow is confined within the crack. So the integral calculation of the related element matrixes and equivalent nodal forces (e.g. Eq. (24)) must be correctly carried out along the true crack path within the element.

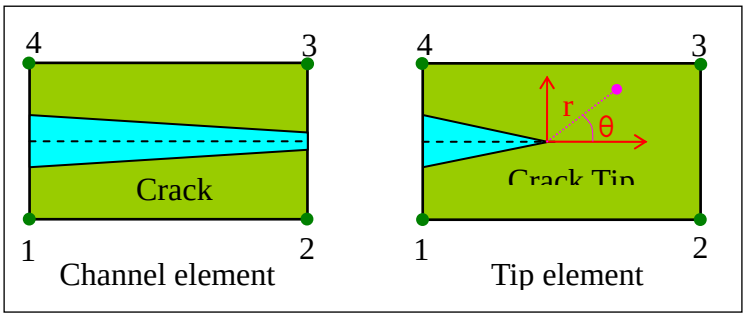

Figure 3. 2-D 4-node plane strain hydraulic fracture elements

So, the active degrees of freedom for the channel element are

$$\hat{\mathbf{u}}^{\mathbf{e}} = \{ \underbrace{u_1^x \quad u_1^y \quad u_2^x \quad u_2^y \quad u_3^x \quad u_3^y \quad u_4^x \quad u_4^y}_{\text{Standard}} \underbrace{a_1^x \quad a_1^y \quad a_2^x \quad a_2^y \quad a_3^x \quad a_3^y \quad a_4^x \quad a_4^y}_{\text{Heaviside Enriched}} \underbrace{p_3 \quad p_4}_{\text{Coupled}} \}_{18}^{\mathrm{T}} \tag{31}$$

and for the tip element the Heaviside enriched degrees of freedom $\mathbf{a}_I$ need to be replaced by the crack tip field enriched degrees of freedom $\mathbf{b}_I^{(l)}$.

According to the element connectivity and the arrangement of nodal degrees of freedom, the bilinear shape functions are used to approximate the displacement field, and the linear shaped functions are used to approximate the fluid pressure field.

Gauss quadrature is used to calculate the system matrix and equivalent nodal force. Since the discontinuous enrichment functions are introduced in approximating the displacement field, integration of discontinuous functions is needed when computing the element stiffness matrix and equivalent nodal force. In order to ensure the integral accuracy, it is necessary to modify the quadrature routine. Both the channel and tip elements are partitioned by the crack surface into two quadrature sub-cells where the integrands are continuous and differentiable. Then Gauss integration is carried out by a loop over the sub-cells to obtain an accurate integration result.

Due to the flexibility, the user subroutine of UEL provided in the finite element package ABAQUS [20] has been employed in implementing the proposed elements in Fortran code. The main purpose of UEL is to provide the element stiffness matrix as well as the right hand side residual vector, as need in a context of solving the discrete system of equations.

5. Numerical Examples

The proposed user element together with the structural elements provided in the ABAQUS element library are used to establish a finite element model to investigate a plane strain hydraulic fracture problem in an infinite impermeable elastic medium. The far-field boundary conditions are modelled by using infinite elements. The initial testing of this new element formulation involves using boundary value problems of an imposed fluid pressure and an imposed fracture opening. These problems are used to test for both of the two limiting cases of a toughness-dominated and viscosity-dominated plane-strain hydraulic fracture for which the analytical solutions are available in the literature [21].

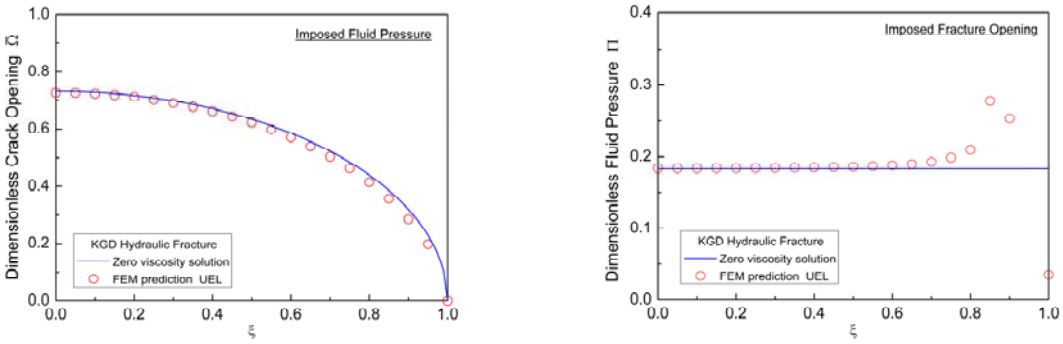

(a) (b)

Figure 4. Zero-viscosity case: (a) Imposed pressure; and (b) Imposed opening

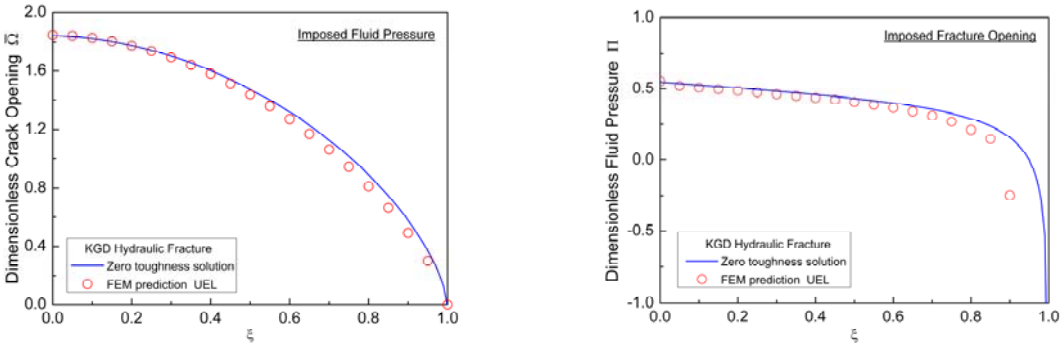

(a) (b)

Figure 5. Zero-toughness case: (a) Imposed pressure; and (b) Imposed opening

The simulation results for a plane strain toughness-dominated KGD hydraulic fracture are shown in Figure 4. The corresponding analytical solutions for the zero-viscosity case are also shown for comparison. The crack opening is obtained by imposing a given pressure calculated according to the analytical solution [21] on the crack surface of the finite element model. While the fluid pressure is obtained by applying an opening profile calculated from the analytical solution [21] to the crack surface of the finite element model. The results for the zero-toughness case are shown in Figure 5. Only twenty channel elements in total are meshed along the crack length in the finite element model.

It can be seen that the XFEM predictions generally compare well with the analytical solutions for crack openings, while for the fluid pressure the XFEM predictions differ from the analytical solutions at the region close to the crack tip. One main reason for the deviation of the predicted fluid pressure from the analytical solutions near the tip is likely to be because the user-defined element is assumed to be cut through by the crack and no tip element is included in the finite

element model. Another reason could be that a static fracture rather than a propagating fracture is simulated here. Improved prediction can be expected with including the crack tip element that captures the crack tip singularity correctly.

Figure 6 shows the stress field and crack opening profile of a center-cracked tension plate subjected to uniform tensile stress of 1.0 MPa. The width of the plate is 40 m and the half length of the crack is 5 m. The corrected stress intensity factor [22] is K_{I}=3.995 MPa$\sqrt{\mathrm{m}}$. The calculation of the stress intensity factors is performed with the domain form of interaction integral. The computed stress intensity factors are K_{I}=3.954 MPa$\sqrt{\mathrm{m}}$, and K_{II}=3.8×10^{-8} MPa$\sqrt{\mathrm{m}}$.

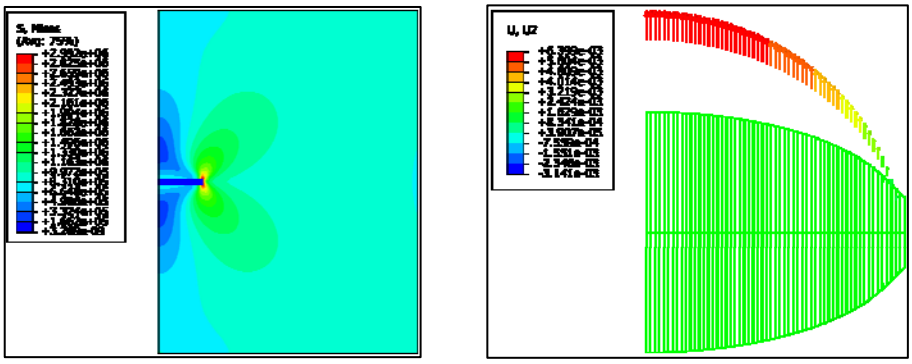

Figure 6. Stress and crack opening profile of a center-cracked tension plate

6. Summary

The application of the extended finite element method to the hydraulic fracture problems has been presented. The discrete governing equations for the coupled fluid-fracture problem have been derived. A user element based on the XFEM has been implemented in ABAQUS, which includes the desired aspects of the XFEM so as to model crack propagation without explicit remeshing. In addition, the fluid pressure degrees of freedom have been introduced and assigned to the appropriate nodes of the proposed element to describe the fluid flow within the crack and its contribution to the crack deformation. Verification of the user-defined element has been made by comparing the FEM predictions with the analytical solutions available in the literature. The preliminary result presented here is a first attempt to the promising application of the XFEM to the hydraulic fracture simulation.

Acknowledgements

The author would like to thank Dr. Rob Jeffrey for the support of this work. Furthermore, the author thanks CESRE for support and for granting permission to publish.

References

[1] R. J. Clifton, A. S. Abou-Sayed, On the computation of the 3-D geometry of hydraulic fractures, in Proceedings of the SPE Symposium on Low Permeability Gas Reservoir, Denver, Richardson, 1979, pp. 307-313.

[2] A. Settari, M. P. Cleary, 3-D simulation of hydraulic fracturing, Journal of Petroleum Technology, 36(1984) 1177-1190.

[3] L. Vandamme, J. H. Curran, A 3-D hydraulic fracturing simulator, International Journal for Numerical Methods in Engineering, 28(1989) 909-927.

[4] S. H. Advani, T. S. Lee, J. K. Lee, 3-D modeling of hydraulic fractures in layered media .1. Finite-element formulations, Journal of Energy Resources Technology-Transactions of the ASME, 112(1990) 1-9.

[5] P. Valko, M. J. Economides, Propagation of hydraulically induced fractures - a continuum damage mechanics approach, International Journal of Rock Mechanics and Mining Sciences & Geomechanics, 31(1994) 221-229.

[6] S. Ouyang, G. F. Carey, C. H. Yew, An adaptive finite element scheme for hydraulic fracturing with proppant transport, International Journal for Numerical Methods in Fluids, 24(1997) 645-670.

[7] P. Papanastasiou, An efficient algorithm for propagating fluid-driven fractures, Computational Mechanics, 24(1999) 258-267.

[8] X. Zhang, E. Detournay, R. Jeffrey, Propagation of a penny-shaped hydraulic fracture parallel to the free-surface of an elastic half-space, International Journal of Fracture, 115(2002) 125-158.

[9] J. Adachi, E. Siebrits, A. Peirce, J. Desroches, Computer simulation of hydraulic fractures, International Journal of Rock Mechanics and Mining Sciences, 44(2007) 739-757.

[10] B. Lecamplon, E. Detournay, An implicit algorithm for the propagation of a hydraulic fracture with a fluid lag, Computer Methods in Applied Mechanics and Engineering, 196(2007) 4863-4880.

[11] A. Peirce, E. Detournay, An implicit level set method for modeling hydraulically driven fractures, Computer Methods in Applied Mechanics and Engineering, 197(2008) 2858-2885.

[12] Z. R. Chen, A. P. Bunger, X. Zhang, R. G. Jeffrey, Cohesive zone finite element-based modeling of hydraulic fractures, Acta Mechanica Solida Sinica, 22(2009) 443-452.

[13] R. H. Dean, J. H. Schmidt, Hydraulic-fracture predictions with a fully coupled geomechanical reservoir simulator, SPE Journal, 14(2009) 707-714.

[14] B. Carrier, S. Granet, Numerical modeling of hydraulic fracture problem in permeable medium using cohesive zone model, Engineering Fracture Mechanics, 79(2012) 312-328.

[15] Z. R. Chen, Finite element modelling of viscosity-dominated hydraulic fractures, Journal of Petroleum Science and Engineering, 88-89(2012) 136-144.

[16] T. Belytschko, T. Black, Elastic crack growth in finite elements with minimal remeshing, International Journal for Numerical Methods in Engineering, 45(1999) 601-620.

[17] N. Moes, J. Dolbow, T. Belytschko, A finite element method for crack growth without remeshing, International Journal for Numerical Methods in Engineering, 46(1999) 131-150.

[18] B. Lecampion, An extended finite element method for hydraulic fracture problems, Communications in Numerical Methods in Engineering, 25(2009) 121-133.

[19] A. Dahi-Taleghani, J. E. Olson, Numerical modeling of multistranded-hydraulic-fracture propagation: Accounting for the interaction between induced and natural fractures, SPE Journal, 16(2011) 575-581.

[20] ABAQUS, Abaqus documentation version 6.11-1, 2011.

[21] E. Detournay, Propagation regimes of fluid-driven fractures in impermeable rocks, International Journal of Geomechanics, 4(2004) 35-45.

[22] H. L. Ewalds, R. J. H. Wanhill, Fracture mechanics. New York: Edward Arnold, 1989.

Thermal shock residual strength of ultra-high temperature ceramics with the consideration of temperature

Weiguo Li[1,*], **Dingyu Li**[1], **Ruzhuan Wang**[1], **Daining Fang**[2]

[1] College of Resource and Environment Science, Chongqing University, 400030, PR China
[2] LTCS and College of Engineering, Peking University, 100871, PR China
* Corresponding author: wgli@cqu.edu.cn

Abstract When suffered from severe thermal shock ultra-high temperature ceramics for high-temperature applications will present to strength reduction or fracture due to microcrack and macrocrack propagation induced by the shocks. And the thermal shock residual strength is one of the most important indexes that evaluate the ceramic material for further use after thermal shock. This paper established a temperature dependent thermo-fracture mechanics model to predict the residual strength of ultra-temperature ceramics after thermal shock. And the critical thermal shock temperature that causes the material strength drop is determined and show differences from the one without temperature-dependent material properties. Also these studies demonstrate the significance of incorporating temperature-dependent material properties on the prediction of thermal shock residual strength of ultra-high temperature ceramic materials.

Keywords Ultra-high temperature ceramics, Thermal shock, Fracture, Residual strength.

1. Introduction

Ultra-high temperature ceramics (UHTCs) are a family of ceramic based composites mainly consisted of transition metal compounds, particularly refractory borides and carbides composites of Zr, Hf and Ta, such as ZrB_2, TaC, HfN and HfB_2, which have melting points higher than 3000°C. Essentially, these UHTCs possess an excellent and unique set of bulk properties including unusually high melting points, high thermal conductivity, high elastic modulus and retain strength at high temperatures. And they can be potentially used at temperatures above 2000°C in an oxidizing environment [1-2]. This combination of properties make these materials potential candidates for a variety of high-temperature structural applications, including engines, thermal protection system such as leading edges and nose-cones for a new generation of hypersonic vehicles, plasma arc electrodes, furnace elements, and high temperature shielding [3-5]. In these applications, UHTCs usually experience severe thermal shock. And it is known that cracking and other forms of damages are induced in UHTCs or ceramic composites when subjected to severe thermal shocks. As a result, the strength of thermally shocked UHTCs can be significantly degraded. Therefore, it is necessary to investigate thermal shock fracture resistance behavior of UHTCs of these advanced materials.

Significant progress has been made in the understanding of thermal shock fracture behavior of ceramic materials with great efforts of theories and experiments done by many researchers. At present, the research of thermal shock resistance mostly focuses on the effects of surface defects, temperature, indentation crack length [7,8,9], particle reinforced [10,11] or whisker reinforced [12] on thermal shock resistance performance to explain the mechanisms of thermal shock failure in experimental way. Theoretical researches of the effect of surface heat transfer coefficient on thermal shock resistance had been made [13], and several evaluation theories of thermal shock resistance had been reported [6,14,15,16].

In many experiment research works of thermal shock fracture behavior, residual strength is usually used to evaluate thermal shock resistance behavior of UHTCs [5,8,9,15]. Because the microcracks exist in ceramics, when a ceramic specimen is subjected to sufficiently severe thermal shocks, some of the pre-existing micro-cracks will initiate and grow to form macrocracks. Crack propagation in thermally shocked ceramics may be arrested depending on the severity of thermal shock, thermal stress field characteristics and material properties. What is more, the thermal shock

residual strength is one of the most important properties that evaluate the ceramic materials for further use after thermal shock. However, few researchers do it in theoretical way [17] , and they didn't consider the effects of temperature on the thermo-physical properties. But in its actual operating condition the temperature range of the UHTCs is very large and the material properties are always function of temperature, the effects of temperature on the UHTCs material properties must been taken into consideration [7].

In this paper, thermal shock residual strength of UHTCs is studied. As basic research, firstly we only consider the strength degradation due to propagation of a single crack, which has proven reasonable in evaluating thermal shock residual strength of monolithic ceramics [18,19]. Effects of multiple crack propagation and particle-reinforced on strength degradation will be considered in the future study. And the material properties are function of temperature to take the effects of temperature on the UHTCs material properties into account. The critical thermal shock temperature that causes the material strength drop and thermal shock residual strength is determined by calculation and the results demonstrate the differences from the one without temperature-dependent material properties.

2. Temperature and thermal stress fields

2.1. Temperature fields of UHTC strip under cold shock

Consider a long UHTC strip with an edge crack as shown Fig. 1, where $2a$ is the thickness of the strip and c_0 is the crack length. The strip is initially at a constant temperature T_0, and its surfaces $x = 0$ are suddenly cooled by cooling media of temperatures T_∞ with the heat transfer coefficients h.

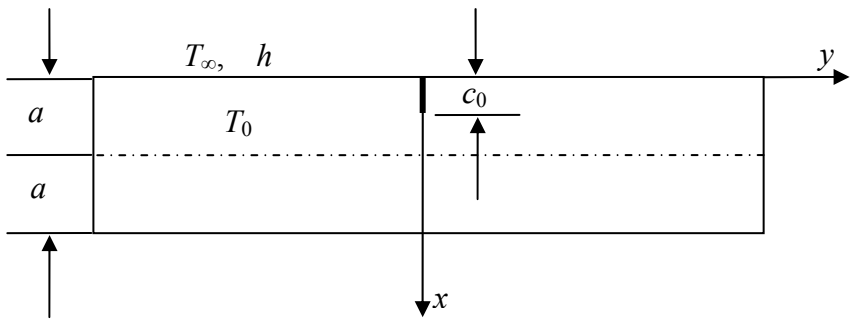

Figure 1. A UHTC strip with an edge cracks subjected to thermal shock

Assume that the crack whose plane is normal to the surface of the strip does not perturb the transient temperature distribution. Therefore, this is a one-dimensional heat conduction problem as the Fig. 1 shows. Taking the temperature-dependent material properties into account, the governing equation can be written in the form

$$\frac{\partial}{\partial x}\left(k(T)\frac{\partial T(x,t)}{\partial x}\right)=\rho(T)C_{\mathrm{p}}(T)\frac{\partial T(x,t)}{\partial t}, \qquad 0<x<2a,\ t>0 \tag{1}$$

The corresponding boundary and initial conditions are as follows

$$k(T)\frac{\partial T(x,t)}{\partial x}=h\left(T(x,t)-T_\infty\right), \qquad x=0,\ t>0 \tag{2}$$

$$\frac{\partial T(x,t)}{\partial x}=0\,,\qquad x=2a,\ t>0 \tag{3}$$

$$T(x,t)=T_0\,,\qquad t=0,0<x<2a \tag{4}$$

where $k(T)$, $\rho(T)$ and $C_p(T)$ are the temperature-dependent thermal conductivity, mass density and specific heat capacity, respectively. And t represents time.

Obviously this is a transient nonlinear heat conduction problem. In order to solve Eq. (1), we linearize this partial differential heat conduction equation using the Kirchhoff transformation [20], namely

$$\theta(T)=\frac{1}{k_0}\int_{T_0}^{T}k(T)dT \tag{5}$$

where k_0 is the thermal conductivity at reference temperature T_0. Under the transformation (5), equations (1), (2), (3) and (4) reformulate as

$$\frac{\partial^2\theta(x,t)}{\partial x^2}=\frac{1}{\kappa}\frac{\partial\theta(x,t)}{\partial t}\,,\qquad 0<x<2a,\ t>0 \tag{6}$$

$$k_0\frac{\partial\theta(x,t)}{\partial x}=h\left(\theta(x,t)-\theta_\infty\right),\qquad x=0,\ t>0 \tag{7}$$

$$\frac{\partial\theta(x,t)}{\partial x}=0\,,\qquad x=2a,\ t>0 \tag{8}$$

$$\theta(x,t)=\theta_{\mathrm{i}}\,,\qquad 0<x<2a,t=0 \tag{9}$$

However, in Eq. (6)

$$\kappa=\frac{k(T)}{\rho(T)C_{\mathrm{p}}(T)} \tag{10}$$

is still temperature-dependent. For the convenience of derivation and calculation, we determine a κ_0 with the use of Eq. (11) to replace in Eq. (6).Therefore, Eq.(6) becomes a total linear equation.

$$\kappa_0=\frac{1}{T_0-T_\infty}\int_{T_\infty}^{T_0}\frac{k(T)}{\rho(T)C_{\mathrm{p}}(T)}dT \tag{11}$$

Applying the variable separation approach, the expression of $\theta(x,t)$ is obtained.

$$\theta(x,t)=\theta_\infty+2\left(\theta_{\mathrm{i}}-\theta_\infty\right)\sum_{m=1}^{\infty}\frac{\left(\beta_m^2+H^2\right)\sin\beta_m L}{\beta_m\left(H+\left(\beta_m^2+H^2\right)L\right)}\cos\left(\beta_m\left(L-x\right)\right)e^{-\kappa_0\beta_m^2 t} \tag{12}$$

in which $h/k_0=H$, L=2a, and β_m is determined by the following Eq. (13). Therefore, the temperature fields $T(x,t)$ can be acquired from $\theta(x,t)$ in Eq. (12) making the use of their relationship in Eq. (5).

$$\beta_m \tan \beta_m L = H \tag{13}$$

2.2. Thermal Stress in UHTC strip under cold shock

After the temperature is obtained, the transient thermal stress in a fully free strip can be obtained from the classical beam analysis [21]. For plane-stress $\sigma_{yy}(x,t)$ has the form

$$\sigma_{yy}(x,t) = E(T(x,t))\left[Ax + B - \alpha(T(x,t))(T(x,t) - T_0)\right] \tag{14}$$

where E and α are the temperature-dependent elastic modulus and thermal expansion coefficient, respectively. Values for constants A and B are determined from:

$$\int_0^{2a} \sigma_{yy}(x,t)dx = 0 \quad \text{and} \quad \int_0^{2a} \sigma_{yy}(x,t)xdx = 0 \tag{15}$$

3. Thermal stress intensity factor and thermal shock cracking

The transient thermal stress intensity factor (TSIF) for an edge crack of quasi-static fracture problem can be obtained by using a non-dimensional weight function and the thermal stress.

$$K_{\mathrm{I}}(t) = \frac{\int_0^c \sigma_{yy}(x,t)dx}{c}\sqrt{\pi c}F\left(\frac{c}{2a}\right) \tag{16}$$

where c is the crack length, and F is the weight function[22], $K_{\mathrm{I}}(t)$ represents the TSIF at t.

It is obvious that the TSIF is proportional to thermal shock temperature difference ΔT, crack propagation will not occur if the thermal shock has no reached a critical value ΔT_{c}, at which the peak value of transient TSIF reaches the fracture toughness K_{IC}. At $\Delta T = \Delta T_{\mathrm{c}}$, the peak value $K_{\mathrm{I}}(t)$ reaches K_{IC} and crack propagation is initiated. Therefore, when $\Delta T \geqslant \Delta T_{\mathrm{c}}$, as the thermal shock proceeding, the crack propagation will occur when TSIF $K_{\mathrm{I}}(t) > K_{\mathrm{IC}}$ and results in severe damage in UHTC plate; And it will be arrested after extending when $K_{\mathrm{I}}(t) > K_{\mathrm{IC}}$ again, thus the crack will reach a final length c_{f} after thermal shock determined by Eq. (17).

$$K_{\mathrm{I}}(t) = \frac{\int_0^{c_{\mathrm{f}}} \sigma_{yy}(x,t)dx}{c_{\mathrm{f}}}\sqrt{\pi c_{\mathrm{f}}}F\left(\frac{c_{\mathrm{f}}}{2a}\right) = K_{\mathrm{IC}}, \quad \Delta T > \Delta T_{\mathrm{c}} \quad \text{and} \quad t > 0 \tag{17}$$

Therefore, the thermal shock residual strength can be determined by the final crack length as shown in Eq. (18).

$$\sigma_{\mathrm{R}} = \frac{K_{\mathrm{IC}}}{\sqrt{\pi c_{\mathrm{f}}}F\left(\frac{c_{\mathrm{f}}}{a}\right)} \tag{18}$$

4. Results and discussion

Refractory diborides of zirconium (ZrB_2) based ceramics are the most used UHTCs. Take it as an example, the temperature-dependent material properties of the diborides of zirconium based UHTCs are shown Table 1 [8, 16, 23]. And the thickness of UHTC strip $2a$ = 5mm.

Fig. 2 shows temperature has significant effect on crack resistance [5]. It shows that a higher temperature leads to a higher crack resistance. The highest crack resistances are about 5.5MPa·m$^{1/2}$ and 6MPa·m$^{1/2}$ for 20°C and 600°C respectively. Due to lack of temperature-dependent crack resistance data, while determining the thermal shock residual strength with temperature-dependent material properties, we consider that it is still the same as the crack resistance at 600°C when

thermal shock initial temperature is higher than 600°C. For without temperature-dependent material properties, it is considered to be the same as the crack resistance at 20°C.

Table1. Temperature-dependent material properties of the diborides of zirconium based UHTC

Material parameters	Values and expressions
E(GPa)	$E = E_0 - BTe^{-\frac{T_m}{T}} + B_1\left(T - B_2T_m + \lvert T - B_2T_m \rvert\right)\ e^{-\frac{T_m}{T}}$
E_0(GPa), B_0, B_1, B_2	500, 2.54, 1.9, 0.363
α (°C^{-1})	(2.01ln(T)-6.7652)×10^{-6}
k (W·(m·°C)$^{-1}$)	-16.79×ln(T)+178.2
v	0.16
$C_p(T)$ (cal/mol)	15.34+2.25×10^{-3}T-3.96×10$^{5}T^{-2}$
ρ(g.cm-3)	6.1

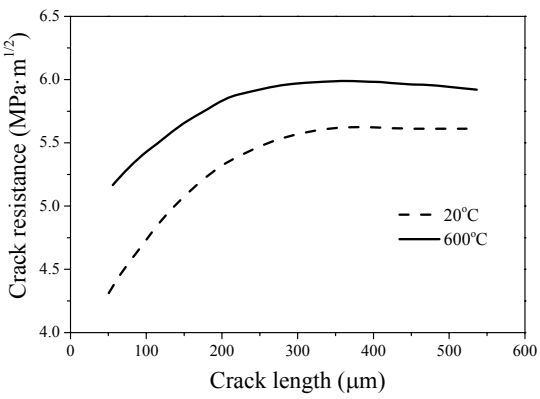

Figure 2. Crack resistance under different temperature

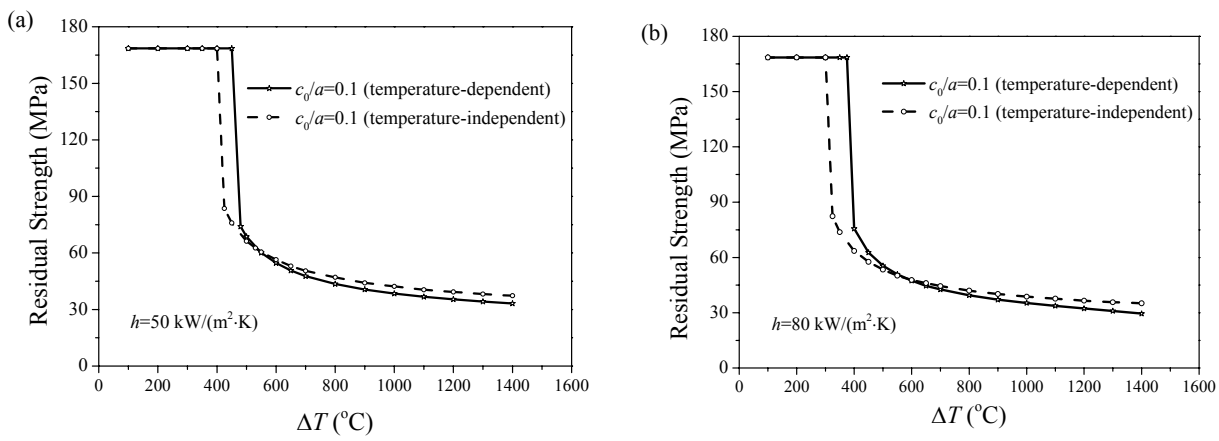

Figure 3. The relationship between thermal residual strength and thermal shock temperature difference ΔT ((a), h=50kW/(m^2·K), (b), h=80kW/(m^2·K))

As can be seen in Fig. 3, the curves of thermal shock residual strength have the same trends with the experiments results' trends which are common in literatures [5,9]. When the thermal shock temperature difference ΔT is less than the critical thermal shock temperature difference ΔT_c, crack propagation didn't occur and the strength remains unchanged. At $\Delta T = \Delta T_c$, the strength drops

precipitously, then decreases gradually and tends to be a constant as the increase of thermal shock temperature difference ΔT. Also the Fig. 3 shows that the critical thermal shock temperature difference ΔT_c with temperature-dependent material properties is higher than the one which does not take the effect of temperature on material properties into account. And, if the ΔT is less than a certain value the thermal shock residual strength with temperature-dependent material properties is higher than the one without the consideration of temperature-dependent material properties. However, the results are reversed as the ΔT becomes larger than the certain value. Therefore, if the temperature dependence of material is ignored, the critical thermal shock temperature difference ΔT_c will be underestimated, and the thermal shock residual strength will be wrong determined. Thus, consideration of temperature-dependent material properties is essential for correct evaluation of thermal shock resistance and thermal shock residual strength of a material, especially for UHTCs suffered high temperature thermal shock.

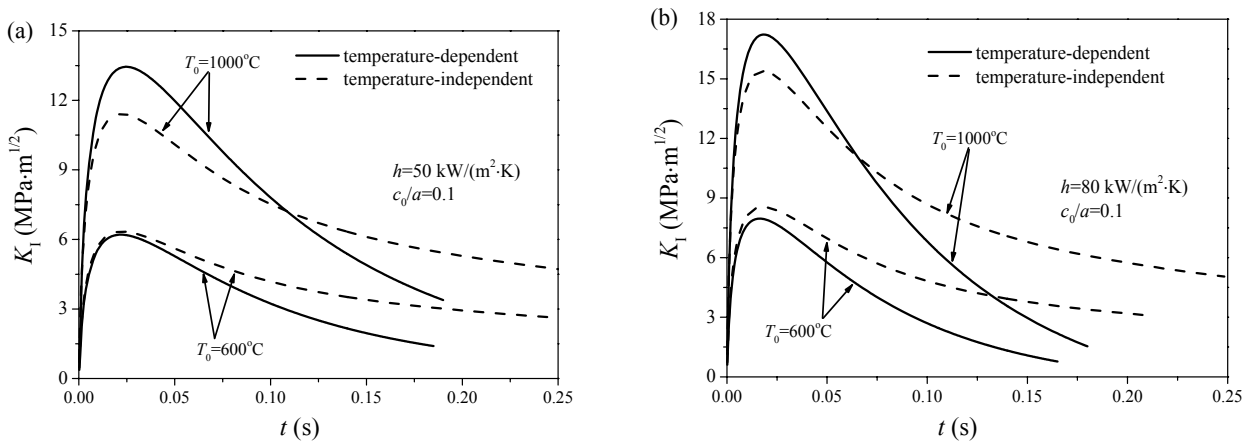

Figure 4. Thermal stress intensity factor as a function of time ((a), h=50kW/(m^2·K), (b), h=80kW/(m^2·K))

In Fig. 4, setting the crack to be the initial length during the thermal shock proceeding, the TSIF K_I is plotted as a function of thermal shock time for thermal shock initial temperature T0=600°C and 1000°C with surface heat transfer coefficient h=50kW/(m^2·K) in Fig. 4 (a) and h=80kW/(m^2·K) in Fig. 4 (b), respectively. The results show that the peak values TSIF K_I for 600°C with temperature-dependent material properties are lower than the one without temperature-dependent material properties, on the contrary, when thermal shock initial temperature is 1000°C, the peak values with temperature-dependent material properties is higher than the one which does not take the effect of temperature on material properties into account. Because the coefficient of thermal diffusion of high temperature without temperature-dependent material properties is larger than the one with temperature-dependent material properties, the serious temperature gradient will moderate sooner, which can result in relaxing of thermal stress induced by thermal shock. Therefore, the phenomenon, that if the ΔT is less than a certain value the thermal shock residual strength with temperature-dependent material properties is higher than the one without the consideration of temperature-dependent material properties but the results are reversed as the ΔT increase shown in Fig. 3, is explained. And it is obvious that the thermal shock residual strength is strongly affected by the dependence of temperature of material properties. Thus, when determining the thermal residual strength of UHTCs for high temperature used, the result of high temperature thermal shock, that thermal residual strength with the consideration of temperature-dependent material properties is higher than the one without temperature-dependent material properties, is not always right. It must fully consider the effect of temperature on the material properties.

5. Conclusions

In this paper, theoretical prediction thermal shock residual strength with the temperature-dependent material properties of UHTCs is presented. The theoretical model is capable of predicting qualitatively thermal shock residual strength behavior of UHTCs observed in experiments, i.e., when the thermal shock temperature difference ΔT is less than the critical thermal shock temperature difference ΔT_c, crack propagation didn't occur and the strength remains unchanged. At $\Delta T = \Delta T_c$, the strength drops precipitously, then decreases gradually and tends to be a constant as the increase of thermal shock temperature difference ΔT. The results of the theoretical model applying to the diborides of zirconium based UHTCs are compared to the results which haven't take the effect of temperature on material properties into consideration. It shows that the thermal shock residual strength and thermal shock resistance is very sensitive to their temperature-dependent material properties. If the temperature dependence of material is ignored, the critical thermal shock temperature difference ΔT_c will be underestimated. And the thermal shock residual strength with temperature-dependent material properties is higher than the one without the consideration of temperature-dependent material properties if the ΔT is less than a certain value, but the results are reversed as the ΔT is larger than the certain value. Therefore, when determined the thermal shock residual strength, it must take the temperature-dependent material properties into fully account.

Acknowledgements

This work was supported by the National Science Foundation of China (Project ID: 90916009 and 11172336).

References

[1] F. Monteverde, A. Bellosi, Microstruture and properties of an HfB_2-SiC composite for ultra high temperature applications. Advan Eng Mater, 6 (2004) 331–336.
[2] C. Wang, J. Yang, W.P. Hoffman, Thermal stability of refractory carbide/boride composites. Mater Chem Phys, 74 (2002) 272–281.
[3] M. Gasch, D. Ellerby, E. Irby, S. Beckman, M. Gusman, S. Johnson, Processing properties and arc jet oxidation of hafnium diboride-silicon carbide ultra high temperature ceramics. J Mater Sci, 39 (2004) 5925–5937.
[4] M.M. Opeka, I.G. Talmy, E.J. Wuchina, J.A. Zaykoski, S.J. Causey, Mechanical, Thermal, and oxidation properties of refractory hafnium and zirconium compounds. J Eur Ceram Soc, 19 (1999) 2405–2414.
[5] S.H. Meng, G.Q. Liu, S.L. Sun, Prediction of crack depth during quenching test for an ultra high temperature ceramic. Mater Des, 31 (2010) 556–559.
[6] W.D. Kingery, Factors affecting thermal stress resistance of ceramic materials. J Am Ceram Soc, 38 (1955) 3–15.
[7] J.C. Han, B.L. Wang, Thermal shock resistance of ceramics with temperature-dependent material properties at elevated temperature. Acta Mater, 59 (2011) 1373–1382.
[8] S.H. Meng, G.Q. Liu, Y. Guo, X.H. Xu, F. Song, Mechanisms of thermal shock failure for ultra-high temperature ceramic. Mater Des, 30 (2009) 2108–2112.
[9] S.H. Meng, H. Jin, J. An, G.H. Bai, W.H. Xie, Mechanism analysis of thermal shock properties for ZrB_2-20%SiC_p-10%AlN ultra-high temperature ceramic with the surface defects. Solid State Sci, 12 (2010) 1667–1671.
[10] J.C. Han, B.L. Wang, Thermal shock resistance enhancement of functionally graded material by multiple cracking. Acta Mater 54 (2006) 963–973.
[11] Z.H. Jin, R.C. Batra, Thermal shock cracking in a metal-particle-reinforced ceramic matrix composite. Eng Fract Mech, 62 (1999) 339–350.
[12] X.H. Zhang, L. Xu, S.Y. Du, W.B. Han, J.C. Han, C.Y. Liu, Thermal shock behavior of

SiC-whisker reinforced diboride ultra-high-temperature ceramics. Scr Mater, 59 (2008) 55–58.
[13] Q.N. Liu, S.H. Meng, C.P. Jiang, F. Song, Critical Biot's number for determination of the sensitivity of spherical ceramics to thermal shock. Chin Phys Lett, 27 (2010) 088104.
[14] D.P.H. Hasselman, Unified theory of thermal shock fracture initiation and crack propagation in brittle ceramics. J Am Ceram Soc, 52 (1969) 600–604.
[15] X.H. Zhang, Z. Wang, C.Q. Hong, P. Hu, W.B. Han, Modification and validation of the thermal shock parameter for ceramic matrix composites under water quenching condition. Mater Des, 30 (2009) 4552–4556.
[16] W.G. Li, F. Yang, D.N. Fang, Thermal shock modeling of ultra-high temperature ceramics under active cooling. Comp Math Applic, 58 (2002) 2373–2378.
[17] Z.H. Jin, W.J. Luo, Thermal shock residual strength of functionally graded ceramics, Mater Sci Eng A, 435-436 (2006) 71–77.
[18] Z.H. Jin, Y.W. Mai, Effects of damage on thermal shock strength behavior of ceramics. J Am Ceram Soc, 78 (1995) 1873–1881.
[19] B. Cotterell, S.W. Ong, C.D. Qin, Thermal shock and size effects in castable refractories. J Am Ceram Soc, 78 (1995) 2056–2064.
[20] S. Kim, A simple direct estimation of temperature-dependent thermal conductivity with Kirchoff transformation, Int Comm Heat Mass Transfer, 28 (2001) 537-544.
[21] F. Erdogan, B.H. Wu, Crack problems in FGM layers under thermal stresses. J Therm Stress, 19 (1996) 237–265.
[22] X.M. Zhang, L. Wan, B. Yan, P.Y. Zhang, Engineering Mechanics. Tsinghua University Press, Beijing, 2012.
[23] W.G. Fahrenholtz, G.E. Hilmas, I.G. Talmy, J.A. Zaykoski, Refractory diborides of zirconium and hafnium. J Am Ceram Soc, 90 (2007) 1347–1364.

UHPC Precast Product under Severe Freeze-Thaw Conditions

Ming-Gin Lee[1], Kun-Long Lee[1], Mang Tia[2]

[1] Department of Construction Engineering, Chaoyang University of Technology, Taichung 41349, Taiwan, ROC
[2] Department of Civil and Coastal Engineering, University of Florida, Gainesville, FL32611, USA
* Corresponding author: mglee@cyut.edu.tw

Abstract
In this study, ultra high performance concrete (UHPC) was used to investigate the effect of UHPC and its precast product by the severe freeze-thaw testing. The UHPC to be used as a precast product material contains a large amount of cement and cementitious materials, a large amount of superplasticizer, and a very small amount of water. The UHPC mixes with eight different volumes of steel fibres were tested and evaluated to find the optimum quality of precast production. The results show that the mechanical properties of UHPC possess high strength, ductility, and bond stress. The results also indicate that most of UHPC specimens presented a steady decrease in compressive and flexural strength after freeze-thaw testing. The 2.5, 3.0 and 3.5% steel fibres by volume were chosen and used in UHPC precast products, after UHPC specimens were tested and finished on their performance evaluations. The results show that the loading capacity of UHPC precast products increased significantly after 600 free-thaw cycles. As a result of freeze-thaw resistance, the appropriate mixes of UHPC applied in the precast products have been obtained; it would provide a reference manufacturing for the UHPC products.

Keywords: Ultra high performance concrete, UHPC, Freeze-thaw, Product

1. Introduction

Many severe circumstances are the result of extreme climate conditions such as low temperature, freeze–thaw action, fire attack, and exposure to deicing salts. Because of this, the environmental durability of both the construction materials and methods used in severe conditions and applications are of utmost importance. For example, a small fire can reach 250°C, while a common blaze can easily produce temperatures of around 800°C. In major conflagrations the temperature can even reach 1100°C. At this level, the heat affects most materials, provoking the spontaneous combustion of some of them and affecting the resistance of others. However, very little research has been performed in evaluating the environmental durability of construction materials for UHPC members. Very little work has been done on the effects of freeze–thaw cycling on UHPC materials and UHPC precast products too.

The process of degradation of concrete due to freeze-thaw cycling is known as occurring due to the expansion of pore water in the cement paste as it freezes to ice. The expansion of water into ice is approximately 9%. This results in the ice pushing water to take up the extra volume and in turn creates hydraulic pressure inside the concrete matrix when it has no more room to expand. Micro-crack or local crack is caused if the expansive forces exceed the tensile strength in the concrete during the freeze-thaw cycling. The effect of freeze-thaw cycling has a significant effect on cement concrete and it causes cracking and scaling and ultimately failure [1].

There are three categories of freezes: (1) dry freeze and hard dry freeze, (2) wet freeze, and (3) hard wet freeze. Freeze-thaw rresistance of concrete depends on the permeability, the degree of saturation, the amount of freezable water, the rate of freezing, and the average maximum distance from any point in the paste to a free surface where ice can form safely. If the pressure developed exceeds the tensile strength of the concrete, the cavity will expand and split. The accumulative effect of continuous freeze-thaw cycles and interruption of paste and aggregate can ultimately cause expansion and cracking, scaling, and collapsing of the concrete [1].

The UHPC was originally developed by Bouygues construction group and is currently being marketed by Lafarge Inc. This particular UHPC is the only one currently widely available in the United States; however, other companies also have similar materials available in other markets. A new class of concrete that exhibits greatly improved strength and durability properties has recently been developed. The Federal Highway Administration (FHWA) at its Turner-Fairbank Highway Research Center (TFHRC) is currently evaluating UHPC for use in the transportation industry [2-3].

Selecting new materials for concrete structures requires an understanding of how the material behaves in both the uncured and cured states, given the anticipated service and exposure conditions. One of the greatest challenges for the successful performance of new materials is to control their dimensional behavior relative to the substrate. Relative dimensional changes can cause internal stress within the material as well as within the substrate. High internal stress may result in tension cracking, which can lead to loss of load-carrying capability and deterioration. Particular attention must be paid to select materials that properly address relative dimensional behavior so as to minimize these stresses [4-5].

UHPC has remarkable flexural strength and very high ductility: the ductility is 250 times greater than that of conventional concrete [5-7]. The material's extremely low porosity gives its low permeability and high durability, making it potentially suitable for retrofitting reinforced concrete structures or for use as a new construction material and precast product [8].

The Atrium is setting a new stage for UHPC precast solutions. The Atrium is a unique, seven-story, mixed-use building located in the vibrant downtown core of Victoria, British Columbia. Aptly named for the large, free-form atrium space at its core, the building's exterior is clad with UHPC, a material at the cutting edge of innovation for new architectural applications. Thanks to its combination of superior properties, UHPC makes it possible to design and produce thin, complex shapes, curvatures and customized textures; concepts that were previously difficult or impossible to achieve with traditional reinforced precast concrete elements [9].

In recent times, a TechBrief was published by the Federal Highway Administration (FHWA) providing a final design for a full depth UHPC waffle deck system. This TechBrief highlights the results of a study aimed at evaluating the inelastic tensile response of UHPC subjected to simultaneous structural and environmental loading. Practical application of concrete in the highway infrastructure frequently subjects cracked sections to simultaneous mechanical and environmental stressors. This experimental investigation focused on the response of a UHPC beam subjected to

concurrent inelastic flexural loading and 15 percent sodium chloride (NaCl) solution application. The results provided insight into the sustained robustness of UHPC structural members loaded beyond their tensile cracking strength [10].

Test results from Lee et al. [11] revealed that UHPC specimen (5 cm × 10 cm cylinder) was still in good condition after 600 cycles of freezing and thawing in accordance with ASTM C 666-97. After freezing and thawing test, the non-shrinkage high strength mortar showed a reduction in compressive strength, slant shear strength, steel pull out strength, and dynamic modulus by 17, 21, 24, and 25 %, compared with the corresponding values of 6, 7, 5, and 10 %, respectively, for UHPC. Specimens of normal strength concrete were used as reference specimens. For the normal strength concrete, the average value of relative dynamic modulus of elasticity based on resonant frequencies after 600 freeze-thaw cycles was 55%, compared with the corresponding value of 92% for UHPC.

The goal of this paper is to describe the research done toward the realization of UHPC as an option for precast concrete products. Special concern will be given to the steel fibres by volume were chosen and used in UHPC precast products in severe freeze-thaw conditions. In addition to the above, this experimental study also focuses on evaluating the the optimum steel fibre of UHPC precast products.

2. Experiments

2.1. Materials and mix design

The cement used in this study was type II Portland cement conforming to ASTM C 150 which was manufactured by the Taiwan cement company. Table 1 displays its chemical composition and physical properties. The silica fume used was supplied by Sun-Li Trade Company in Taiwan. The specific gravity of the silica fume is 2.25. The physical and chemical properties of silica fume are displayed in Table 2. The UHPC to be used as a prospective material of precast product, contains type II Portland cement, silica fume, silica sand, quartz powder, steel fiber and a superplasticizer. The UHPC to be used as a precast product material contains a large amount of cement (type II Portland cement), silica fume, silica sand, quartz powder, steel fiber, superplasticizer, and a very small amount of water. The UHPC mixes with eight different volumes of steel fibres are shown in Table 3, were designed, tested and evaluated to find the optimum quality of precast production.

Table 1. Chemical composition and physical properties of Portland cement II .

Chemical composition (%)					Physical properties		
C_3S	C_2S	C_3A	C_4AF	CSH_2	1-day hydration heat	Blaine	1-day strength
50	24	4.9	12.2	5	250 J/G	250 cm^2/g	60 kgf/cm^2

CSH_2: gypsum

Table 2. Chemical composition and physical properties of silica fume

Chemical composition (%)					Physical properties		
SiO_2	Al_2O_3	K_2O	CaO	MgO	L.O.I	Blaine	SG
97.2	0.32	0.29	0.05	0.1	2.12 %	25.69 m^2/g	2.25

SG: Specific Gravity

Table 3. Mix design of UHPC concretes (kg/m^3)

Mix	Cement	Silica sand	Silica fume	Quartz	Steel fiber	SP	Water
UHPC0	720	900	256	252	0	7.1	133.7
UHPC0.5	720	860	256	252	40	7.1	133.7
UHPC1.0	720	820	256	252	80	7.1	133.7
UHPC1.5	720	780	256	252	120	7.1	133.7
UHPC2.0	720	740	256	252	160	7.1	133.7
UHPC2.5	720	700	256	252	200	7.1	133.7
UHPC3.0	720	660	256	252	240	7.1	133.7
UHPC3.5	720	620	256	252	280	7.1	133.7

Note: SP means Super-plasticizer.

2.2. Test Specimens

The UHPC precast specimens had dimensions of 600 mm × 350 mm ×40 mm with eight opening holes as shown in Figure 1. The fibers included in the UHPC were always Dramix steel fibers that were 13 mm long and had two 0.2-mm and 0.25-mm diameter. These fibers were included in the mix at a specific concentration of 0, 0.5, 1.0, 1.5, 2.0, 2.5, 3.0, and 3.5 percent by volume. The demolding of the UHPC precast specimens occurred approximately 48 hours after casting. The normal curing and heat curing treatments were used in this study. The heat curing treatment used heat water to cure the UHPC at 90 ºC for three days. In practice, this procedure included 2 hours of increasing temperature and 2 hours of decreasing temperature, leaving 68 total hours of constant heat water at 90 ºC. This treatment was initiated within 4 hours after demolding. This curing condition will henceforth be referred to as heat water treatment.

2.3. Freeze-thaw Tests

One accelerated deterioration environment, namely the freeze-thaw cycle test, was selected for the evaluation of UHPC precast products. Freeze-thaw cycling of all specimens was conducted using the cold climate testing facilities at Chaoyang University of Technology in Taiwan. Freeze-thaw cycles were applied to the blocks at a rate of one cycle/185 min, in accordance with ASTM C 666-97, Test Method for Resistance of Concrete to Rapid Freeze and Thawing, with 1.5 hours of freezing in cold air at – 18°C followed by 1.5 hours of thawing in cool air at + 4.4°C. Specimens that were not subjected to freeze-thaw cycling were stored in the material testing laboratory by immersing in saturated lime water for 24 hours prior to testing, for more detail see Lee et al [11]. The specimens were divided into groups of three, with groups subjected to 0, 200, 400, and 600 freeze-thaw cycles. Before and after freeze-thaw cycling, the samples were tested for their drop-off

test and loading test.

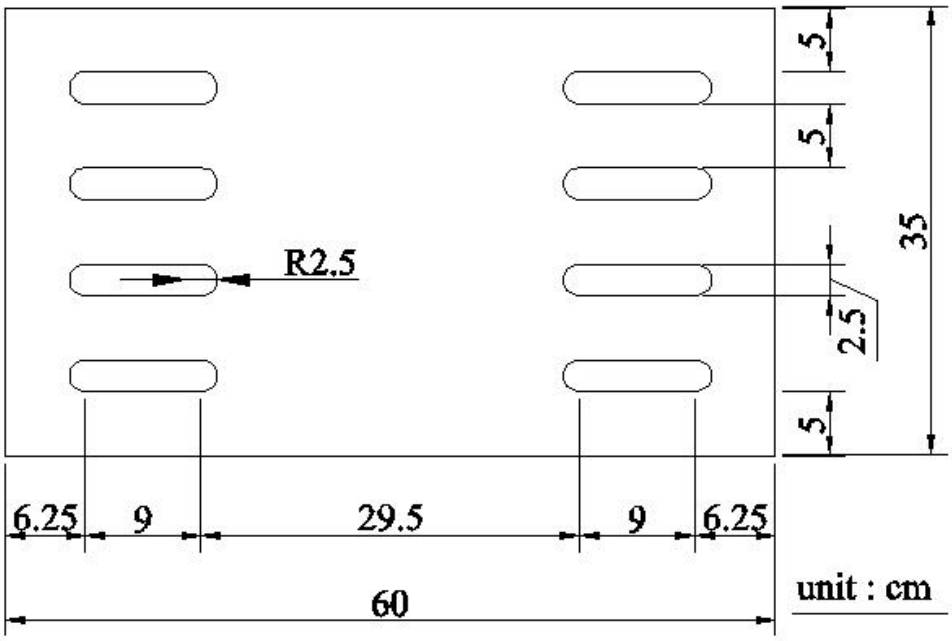

Figure 1. UHPC precast specimen with 8 opening holes

3. Results and Discussion

3.1. **Flexural Strength**

The ASTM C 1018 Standard Test Method for Flexural Toughness and First-Crack Strength of Fiber-Reinforced Concrete (Using a Beam with Third-Point Loading) was one test used to determine the flexural and tensile properties of UHPC at a specific steel fiber concentration of 0, 0.5, 1.0, 1.5, 2.0, 2.5, 3.0, and 3.5 percent by volume. The small-scale concrete prisms had dimensions of 160 mm × 40 mm ×40 mm were used in this test. During the test, the load on and the deflection of the prism are monitored. These data are then used to determine the cracking failure and flexural strength response of the UHPC concretes. The flexural strength test was performed on prisms from all two curing regimes. Table 4 shows flexural strength of UHPCs in comparison with different steel fiber concentration at normal curing and heat water curing. The result of the entire UHPC heat water curing treatment comparison is that UHPC exhibits significantly enhanced flexural strength compared with standard normal curing of UHPCs. The application of the heat water or steam treatment is clearly beneficial; however, this procedure is also not always necessary as long as the user is willing to accept its strength and durability in loss. Compared with the flexural strength of UHPCs in Table 4, the experimental result shows the UHPC containing up to 2.5% steel fiber content is reached the predetermined effect at particular load level of 30 kg/m^2 flexural strength. Final tensile failure of UHPC generally occurs when the steel fiber reinforcement begins to debond from and to pull out of the UHPC matrix. Steel fiber has a tremendous effect on flexural strength of UHPC concretes. Test results from Table 4 showed that the effect of steel fiber on the flexural strength was apparent. All the UHPC concretes with 2.5%, 3.0% and 3.5% by volume steel fiber replacement showed significantly higher flexural strength than those of the control one (UHPC0) with the same curing condition at all ages. Figure 2 displays the photo of prism UHPC2.5 with crack extension and failure after flexural test.

Table 4. Flexural strength of UHPCs in comparison with different steel fiber concentration (kg/m^2)

UHPC Mix	Normal curing		Heat water curing	
	14 day	28 day	14 day	28 day
UHPC0	18.83	20.54	18.81	21.53
UHPC0.5	19.44	21.31	23.35	23.52
UHPC1.0	21.65	24.15	24.65	25.09
UHPC1.5	22.89	24.51	24.76	29.17
UHPC2.0	22.94	24.82	25.15	31.68
UHPC2.5	23.82	31.21	29.7	34.66
UHPC3.0	26.47	32.48	33.56	34.83
UHPC3.5	28.95	32.73	34.88	38.44

Figure 2. Photo prism UHPC2.5 after flexural test of crack extension and failure

3.2. Free Falling Test

Figure 3 displays the photo of UHPC2.5 specimen in the free falling test setup for 6-meter high. After the 6-meter high free falling test, the UHPC2.5 specimen appeared three micro-cracks as shown in Figure 4. Table 5 indicates the surface cracks of UHPC2.5 specimen after the free falling test at three different heights. It was found from the free falling test result that UHPC2.5 specimen remains good condition on the surface at 2-meter height, but several micro-cracks appeared at 4-meter and 6-meter heights. It can be concluded that the surface micro-cracks of UHPC2.5 specimen increases substantially as height of the free falling test increases.

3.3. Loading Capacity Test

Table 6 shows ultimate loading strength of UHPC precast specimens in comparison with different steel fiber concentration at 90 °C water curing. The result of the diameter of steel fiber comparison is that UHPC exhibits non-significantly enhanced ultimate loading strength compared at 90 °C water curing. For the ranges of steel fiber contents investigated in the study, both flexural strength and ultimate loading strength of the UHPC specimens increase as the percent steel fiber increase. The 2.5, 3.0 and 3.5% steel fibres by volume were chosen and used in UHPC precast products, after UHPC specimens were tested and finished on their performance evaluations. Compared with the ultimate loading strength of UHPCs in Table 6, the experimental result shows the UHPC containing up to 2.5% steel fiber content reached the predetermined effect at particular load level of 12-ton ultimate loading strength. Table 7 displays ultimate loading strength of UHPC2.5 precast specimens

after freeze-thaw cycling test. The results show that the loading capacity of UHPC precast products increased significantly after 600 free-thaw cycles. As a result of freeze-thaw resistance, the appropriate mixes of UHPC applied in the precast products have been obtained; it would provide a reference manufacturing for the UHPC products.

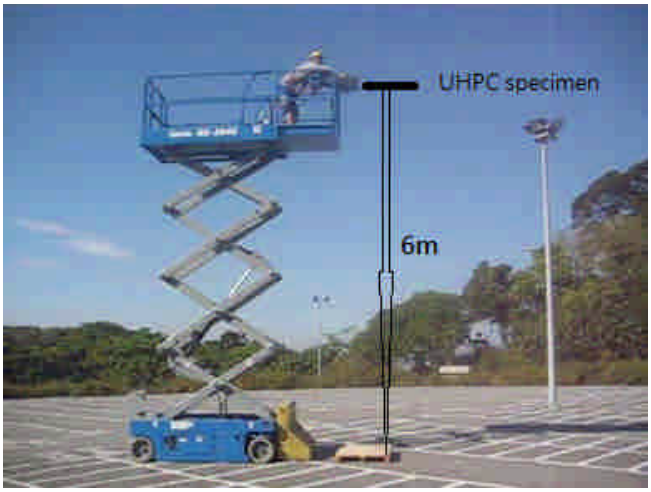

Figure 3. Photo UHPC2.5 specimen free falling test setup for 6-meter high

Figure 4. Photo UHPC2.5 specimen cracks after 6-meter high free falling test

Table 5. UHPC2.5 specimens cracks after free falling test at three different heights

Free falling height	2 meter	4 meter	6 meter
Surface crack	Non-crack	0.35 mm	1.40 mm

Table 6. Ultimate loading strength of UHPC precast specimens after loading capacity test

Specimen	Diameter of steel fiber	Ultimate loading strength
UHPC2.5	0.20 mm	13738 kg
UHPC2.5	0.25 mm	12293 kg
UHPC3.0	0.20 mm	13835 kg
UHPC3.0	0.25 mm	14369 kg
UHPC3.5	0.20 mm	13301 kg
UHPC3.5	0.25 mm	14733 kg

Table 7. Ultimate loading strength of UHPC2.5 precast specimens after freeze-thaw cycling test

Freeze-thaw cycling	0 cycle	200 cycles	400 cycles	600 cycles
Ultimate loading strength	12293 kg	12864 kg	13349 kg	14344 kg
Ratio of loading strength	0.0 %	4.4 %	8.1 %	15.8 %

4. Summary

1) For the ranges of steel fiber contents investigated in the study, both flexural strength and ultimate loading strength of the UHPC specimens increase as the percent steel fiber increase.
2) The application of the heat water curing or steam treatment is clearly beneficial to UHPC precast specimens.
3) The 2.5, 3.0 and 3.5% steel fibres by volume were chosen and used in UHPC precast products, after UHPC specimens were tested and finished on their performance evaluations.
4) Two diameters of steel fiber used in UHPC precast specimens exhibit non-significantly enhanced ultimate loading strength at 90 °C water curing.
5) UHPC precast specimens containing up to 2.5% steel fiber content reached the predetermined effect at particular load level of 12-ton ultimate loading strength.
6) The UHPC2.5 precast specimens displayed a continuous increase in ultimate loading capacity after 600 free-thaw cycles.

References

[1] A. M. Neville, *Properties of Concrete*, John Wiley &Sons, Inc., New York, 1995.
[2] J. Hartmann, and B. Graybeal, Testing of ultra-high-performance concrete girders. PCI Journal, 47-1 (2002) 148-149.
[3] B. Graybeal, and J. Hartmann, Ultra-high performance concrete material properties. Proceedings, Transportation Research Board Conference, January 2003.
[4] Yung-Chih Wang, and Ming-Gin Lee, Ultra-high strength steel fiber reinforced concrete for strengthening or new construction material of RC frames. Journal of Marine Science and Technology, 15-3 (2007) 972-976.
[5] Ming-Gin Lee, Yu-Cheng Kan, and Kuei-Ching Chen, A preliminary study of rpc for repair and retrofitting material. Journal of the Chinese Institute of Engineers, 29-6 (2006) 1099-1103.
[6] O. Bonneau, M. Lachemi, E. Dallaire, J. Dugat, and P. C. Aitcin, Mechanical properties and durability of two industrial reactive powder concretes. ACI Materials Journal, 94-4 (1997) 286-290.
[7] N. Roux, C. Andrade, and M. Sanjuan, Experimental study of durability of reactive powder concrete. Journal of Materials in Civil Engineering, 8-1 (1996) 12-20.
[8] F. J. Alaee, Retrofitting of concrete structures using high performance fiber reinforced cementitious composite (HPFRCC), Ph.D. Thesis, University of Wales, Cardiff , 2001.
[9] A. H. Kelly, M. Arch., and P. J. Seibert, Thin UHPC cladding exhibits green curves. Precast Magazines, 167 (2011). http://precast.org/precast-magazines/precast-solutions./2011-fall.
[10] TechBrief, Simultaneous structural and environmental loading of a UHPC component. FHWA Publication No: FHWA-HRT-10-055, 2010.
[11] Ming-Gin Lee, Chui-Te Chiu, and Yung-Chih Wang, The study for bond strength and bond durability of reactive powder concrete. ASTM STP 1463, Editor: Dennis Damico, West Conshohocken, PA, 2005, pp. 104-113.
[12] Ming-Gin Lee, Yi-Shuo Huang, Fire-damage or freeze-thaw of strengthening concrete using ultra high performance concrete. Advanced Materials Research, 79-82 (2009) 2047-2050.

Novel direct Method on the Life Prediction of Component under High Temperature–Creep Fatigue Conditions

Haofeng Chen[1,*], **Yevgen Gorash**[1]

[1] Department of Mechanical and Aerospace Engineering, University of Strathclyde, Glasgow G1 1XJ, UK
* Corresponding author: Haofeng.chen@strath.ac.uk

Abstract This paper presents a novel direct method, within the Linear Matching Method (LMM) framework, for the direct evaluation of steady state cyclic behaviour of structures subjected to high temperature – creep fatigue conditions. The LMM was originally developed for the evaluation of shakedown and ratchet limits. The latest extension of the LMM makes it capable of predicting the steady state stress strain solutions of component subjected to cyclic thermal and mechanical loads with creep effects. The proposed iterative method directly calculates the creep stress and cyclically enhanced creep strain during the dwell period for the assessment of the creep damage, and also creep enhanced total strain range for the assessment of fatigue damage of each load cycle. To demonstrate the efficiency and applicability of the method to assess the creep fatigue damage, two types of weldments subjected to reverse bending moment at elevated temperature of 550C are simulated by the proposed method considering a Ramberg-Osgood model for plastic strains under saturated cyclic conditions and a power-law model in "time hardening" form for creep strains during the dwell period. Further experimental validation shows that the proposed direct method provides a general purpose technique for the creep fatigue damage assessment with creep fatigue interaction.

Keywords Creep, Fatigue, Cyclically enhanced creep, Linear Matching Method, Weldment

1. Introduction

Engineering structures and components subjected to cyclic loading at elevated temperature means that the operating lifetime may be limited either by excessive plastic deformation, creep rupture, ratchetting, or cyclically enhanced creep deformation and total strain range enhanced by the creep-fatigue interaction. In order to assess the component lifetime associated with cyclic responses with creep fatigue interaction, construction of the hysteresis cycle (Fig. 1) is key to an R5 V2/3 assessment procedure [1] since it provides the strain range from which the fatigue damage is calculated, and the start-of-dwell stress σ_1 and creep strain ε^{cr}, from which the creep damage is assessed.

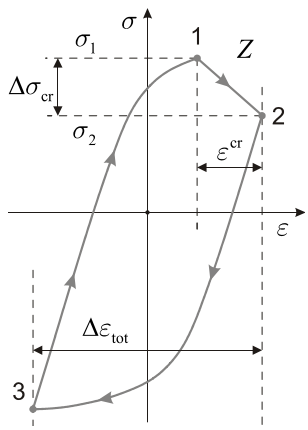

Figure 1. Typical saturated hysteresis loop with creep fatigue interaction

When a structural component is subjected to the cyclic load condition beyond the elastic shakedown limit, the introducing plastic strains will lead to the structure failure by either low cycle fatigue due to alternating plasticity or incremental plastic collapse due to ratchetting. In the presence of creep,

the response of the structure to cyclic loading changes significantly, due to the synergistic interaction of plasticity and creep. A structure subjected to cyclic loading with creep dwell period can present different asymptotic behaviours [2]: 1) no stress relaxation is taking place, as the accumulation of creep strain is determined by the steady-state primary load; 2) with a cyclically enhanced creep during dwell time, the stress relaxation process introduces an additional residual stresses field to enhance the total strain range, causing more significant creep and fatigue damages. In the asymptotic behaviour 2), a closed hysteresis loop could be generated if the creep dwell period is limited and the introducing creep strain could be recovered by the plastic strain during the unloading process.

In order to predict lifetime of component under high temperature and creep fatigue conditions, an evaluation of steady state cyclic behaviour of structures under such conditions would be necessary to construct a hysteresis loop. The simplified methods in R5 [1] assessment procedure for the high temperature response of structures are less restrictive than those based on elastic solutions, without requiring the complexity of full inelastic computation. These simplified approaches use reference stress and shakedown concepts and inevitably incorporate conservatism. Another method is to perform incremental step-by-step Finite Element Analysis (FEA). However, to achieving the steady state response of structures subject to cyclic loading, it requires a significantly large number of increments in full step-by-step analysis which becomes computationally expensive. Therefore, direct methods have been developed to assess the stabilised response of structures subject to cyclic loading. The Direct Cyclic Analysis (DCA) [3] has been recently incorporated into Abaqus [4] to evaluate the stabilized cyclic behaviour directly. This method uses a combination of Fourier series and time integration of the nonlinear material behaviour to obtain the stabilized cyclic response of the structure iteratively. Due to the characteristic of DCA and the inevitable numerical error due to the approximation and convergence problem, the DCA may not always be able to provide accurate solutions for complicated engineering problems.

In this paper, a novel direct method, the Linear Matching Method (LMM) [5, 6], is adopted for the direct evaluation of steady state cyclic behaviour of structures subjected to high temperature – creep fatigue conditions. The basis of the LMM is through the simple idea of representing histories of stress and inelastic strain as the solution of a linear problem where the linear moduli are allowed to vary both spatially and in time. In this way, the LMM combines both the convenience and efficiency of rule based methods [1] and the accuracy of simulation techniques. The LMM has been implemented into ABAQUS for all stages of life assessment code R5 [1] for the evaluation of high temperature responses of structures, based upon the same fundamental assumptions and materials database as R5 but with significantly greater accuracy. Typical of cyclic problems considered includes shakedown and limit analysis [7], ratchet limit analysis [8], creep rupture analysis [9], creep and fatigue interaction [5, 6]. The LMM ABAQUS user subroutines have been consolidated by the R5 research programme [10] of EDF energy to the commercial standard, and are counted to be the method most amenable to practical engineering applications involving complicated thermomechanical load history.

In this paper, the latest extension of the LMM [6] is summarised for directly predicting the steady state cyclic behaviour of component subjected to cyclic thermal and mechanical loads with creep effects. The efficiency and effectiveness of the method was validated in [6] through benchmark examples of Bree problem and a holed plate. In this paper, the developed method is further applied to more practical engineering applications, where two types of weldments subjected to different reverse bending moments with various creep dwell periods are simulated by the proposed method considering a Ramberg-Osgood model for plastic strains under saturated cyclic conditions and a power-law model in “time hardening” form for creep strains during the dwell period. The obtained

steady state cyclic stress strain solutions are then used to calculate the number of cycles to failure due to the creep fatigue damage, where the numerical lifetime results are validated by the existing experimental solutions [11, 12] for the Type 2 cruciform weldment.

2. Numerical Procedures

2.1. Asymptotic cyclic solution

We consider a structure subjected to a cyclic history of varying temperature $\lambda_\theta\theta(x_k,t)$ within the volume of the structure and varying surface loads $\lambda_p P(x_k,t)$ acting over part of the structure's surface S_T. The variation is considered over a typical cycle $0 \le t \le \Delta t$ in a cyclic state. Here λ_θ and λ_p denote the load parameters, allowing a whole class of loading histories to be considered. On the remainder of the surface S, denoted by S_u, the displacement u_k=0.

Corresponding to these loading histories there exists a linear elastic stress history:

$$\hat{\sigma}_{ij}^{e}(x_k,t) = \lambda_\theta \hat{\sigma}_{ij}^{\theta}(x_k,t) + \lambda_p \hat{\sigma}_{ij}^{p}(x_k,t) \tag{1}$$

where $\hat{\sigma}_{ij}^{\theta}$ and $\hat{\sigma}_{ij}^{p}$ denotes the varying elastic stresses due to $\theta(x_k,t)$ and $P(x_k,t)$, respectively. The asymptotic cyclic solution may be expressed in terms of three components, the elastic solution, a transient solution accumulated up to the beginning of the cycle and a residual solution that represents the remaining changes within the cycle. The general form of the stress solution for the cyclic problems involving changing and constant residual stress fields is given by

$$\sigma_{ij}(x_k,t) = \hat{\sigma}_{ij}^{e}(x_k,t) + \bar{\rho}_{ij}(x_i) + \rho_{ij}^{r}(x_k,t) \tag{2}$$

where $\bar{\rho}_{ij}$ denotes a constant residual stress field in equilibrium with zero surface traction on S_T and corresponds to the residual state of stress at the beginning and end of the cycle. The history ρ_{ij}^{r} is the change in the residual stress during the cycle and satisfies:

$$\rho_{ij}^{r}(x_k,0) = \rho_{ij}^{r}(x_k,\Delta t) = 0 \tag{3}$$

For the cyclic problem defined above, the stresses and strain rates will become asymptotic to a cyclic state where:

$$\sigma_{ij}(x_k,t) = \sigma_{ij}(x_k,t+\Delta t) \qquad \dot{\varepsilon}_{ij}(x_k,t) = \dot{\varepsilon}_{ij}(x_k,t+\Delta t) \tag{4}$$

It is worth noting that the above asymptotic cyclic solutions are common to all cyclic states associated with inelastic material behaviour including both the plasticity and creep.

2.2. Numerical procedure for the varying residual stress, creep strain and plastic strain range

Adopting the same minimum theorem for cyclic steady state solution and the same Linear Matching condition as described in [5, 6] for each iteration, we assume that plastic or creep strains occur at N instants, t_1, t_2.....t_N, where t_n corresponds to a sequence of points in the cyclic history. Hence the accumulation of inelastic strain over the cycle is $\Delta\varepsilon_{ij}^{T} = \sum_{n=1}^{N} \Delta\varepsilon_{ij}(t_n)$ where $\Delta\varepsilon_{ij}(t_n)$ is the increment of plastic or creep strain that occurs at time t_n. Define the shear modulus by linear matching

$$\sigma_0 = 2\bar{\mu}_n \bar{\varepsilon}(\Delta\varepsilon_{ij}(t_n)) \tag{5}$$

where σ_0 is the von Mises yield stress or creep flow stress and $\bar{\mu}_n$ is the iterative shear modulus. The von Mises yield stress σ_0 will be replaced by creep flow stress if the creep relaxation occurs at the load instance.

The Linear Matching Method procedure for the assessment of residual stress history and the

associated plastic or creep strain range due to the cyclic load history is described below. The entire iterative procedure includes a number of iteration cycles, where each cycle contains N iterations associated with N load instances. The first iteration is to evaluate the changing residual stress $\Delta\rho_{ij1}^{1}$ for the action of the elastic solution $\hat{\sigma}_{ij}^{e}(t_1)$ at the first load instance. We define $\Delta\rho_{ijm}^{n}$ as the evaluated changing residual stress for *nth* load instance at *mth* cycle of iterations, where $n = 1, 2, \ldots N$ and $m = 1, 2, \ldots M$. At each iteration, the above changing residual stress $\Delta\rho_{ijm}^{n}$ for *nth* load instance at *mth* cycle of iteration is calculated for the combined action of applied elastic stress at the *nth* load instance and previously calculated accumulation of residual stresses $\hat{\sigma}_{ij}^{e}(t_n)+\sum_{k=1}^{m-1}\sum_{l=1}^{N}\Delta\rho_{ij}{}_{k}^{l}+\sum_{l=1}^{n-1}\Delta\rho_{ij}{}_{m}^{l}$. When the convergence occurs at the *Mth* cycle of iterations, the summation of changing residual stresses at N time points must approach to zero ($\sum_{n=1}^{N}\Delta\rho_{ijM}^{n}=0$) according to the condition of the steady state cyclic response. Hence the constant element of the residual stress for the cyclic loading history must be determined by

$$\bar{\rho}_{ij} = \sum_{n=1}^{N}\Delta\rho_{ij1}^{n} + \sum_{n=1}^{N}\Delta\rho_{ij2}^{n} + \cdots + \sum_{n=1}^{N}\Delta\rho_{ijM-1}^{n} \tag{6}$$

The corresponding increment of plastic strain occurring at time t_n is calculated by

$$\Delta\varepsilon_{ij}^{p}(t_n) = \frac{1}{2\bar{\mu}_n}\left[\hat{\sigma}_{ij}^{e}(t_n)' + \rho_{ij}(t_n)'\right] \tag{7}$$

where notation (') refers to the deviator component of $\hat{\sigma}_{ij}^{e}$ and ρ_{ij}. $\rho_{ij}(t_n)$ is the converged accumulated residual stress at the time instant t_n, i.e.

$$\rho_{ij}(t_n) = \bar{\rho}_{ij} + \sum_{k=1}^{n}\Delta\rho_{ijM}^{k} \tag{8}$$

In this paper, the Ramberg-Osgood type is adopted for the cyclic stress and strain range relationship:

$$\frac{\Delta\bar{\varepsilon}}{2} = \frac{\Delta\bar{\sigma}}{2E} + \left(\frac{\Delta\bar{\sigma}}{2B}\right)^{\frac{1}{\beta}} \tag{9}$$

where $\Delta\bar{\sigma}$ is the true stress range, $\Delta\bar{\varepsilon}$ is the true strain range, E is the elastic modulus, B and β are the Ramberg-Osgood plastic hardening constants. The first term on the right-hand side of the above equation represents the elastic strain amplitude and the second term corresponds to the plastic strain amplitude. Then the plastic strain range from Eq. (9) can be written as:

$$\Delta\bar{\varepsilon}_p = 2\left(\frac{\Delta\bar{\sigma}}{2B}\right)^{\frac{1}{\beta}} \tag{10}$$

If we define yield stress σ_0 in Eq. (5) as half stress range:

$$\sigma_0 = \frac{\Delta\bar{\sigma}}{2} = B\left(\frac{\Delta\bar{\varepsilon}_p}{2}\right)^{\beta} \tag{11}$$

then the iterative von-Mises yield stress $\sigma_0(t_n)$ from Ramberg-Osgood material model can be obtained from Eq. (7) as:

$$\sigma_0(t_n) = B\left(\frac{\bar{\varepsilon}(\Delta\varepsilon_{ij}^{p}(t_n))}{2}\right)^{\beta} \tag{12}$$

For the calculation of creep strain and stress relaxation during a creep dwell period, the relevant numerical scheme and theoretical formulations are summarized below.

2.3. Numerical procedure for the creep strain and flow stress

When calculating the creep strain during the dwell period, σ_0 in equation (5) equals to creep flow stress $\sigma_0 = \sigma_c$, which is an implicit function of creep strain $\Delta\varepsilon^c$ and residual stress $\Delta\rho^c$ during the creep dwell period.

Adopting a time hardening creep constitutive relation:

$$\dot{\bar{\varepsilon}}^c = B\bar{\sigma}^n t^m \tag{13}$$

where $\dot{\bar{\varepsilon}}^c$ is the effective creep strain rate, $\bar{\sigma}$ is the effective von Mises stress, t is the dwell time, and B, m and n are the creep constants of the material. When m=0, the time hardening constitutive equation becomes the Norton's law. During the relaxation process there exists an elastic follow up factor Z, i.e.

$$\dot{\bar{\varepsilon}}^c = -\frac{Z}{\bar{E}}\dot{\bar{\sigma}} \tag{14}$$

where $\bar{E} = 3E/2(1+\nu)$, E is the Young's modulus and $\dot{\bar{\sigma}} = \dot{\bar{\sigma}}(\sigma_{ij})$.

Combining (13) and (14) and integrating over the dwell time, we have

$$\frac{B\bar{E}\Delta t^{m+1}}{Z(m+1)} = \frac{1}{n-1}\left\{\frac{1}{(\bar{\sigma}_c)^{n-1}} - \frac{1}{(\bar{\sigma}_s)^{n-1}}\right\} \tag{15}$$

where $\bar{\sigma}_s$ is the effective value of the start of dwell stress, $\bar{\sigma}_c$ is the effective value of the creep flow stress at dwell time Δt, and $\bar{\sigma}_c = \bar{\sigma}(\sigma_{sij} + \Delta\rho_{cij})$. Integrating (14) gives the effective creep strain during the dwell period Δt as,

$$\Delta\bar{\varepsilon} = -\frac{Z}{\bar{E}}(\bar{\sigma}_c - \bar{\sigma}_s) \tag{16}$$

Combining (15) and (16) and eliminating $Z/\bar{E}$ gives

$$\Delta\bar{\varepsilon}^c = \frac{B(n-1)\Delta t^{m+1}(\bar{\sigma}_s - \bar{\sigma}_c)}{\left(\frac{1}{\bar{\sigma}_c^{n-1}} - \frac{1}{\bar{\sigma}_s^{n-1}}\right)(m+1)} \tag{17}$$

For the pure creep where $\bar{\sigma}_s = \bar{\sigma}_c$, the creep strain becomes:

$$\Delta\bar{\varepsilon}^c = \frac{B\bar{\sigma}_s^n \Delta t^{m+1}}{m+1} \tag{18}$$

The creep strain rate $\dot{\bar{\varepsilon}}^F$ at the end of dwell time Δt is calculated by Eq. (15) and (17):

$$\dot{\bar{\varepsilon}}^F = B(\bar{\sigma}_c)^n \Delta t^m = \frac{\Delta\bar{\varepsilon}^c}{\Delta t}\frac{(m+1)}{(n-1)}\frac{\bar{\sigma}_c^n}{(\bar{\sigma}_s - \bar{\sigma}_c)}\left(\frac{1}{\bar{\sigma}_c^{n-1}} - \frac{1}{\bar{\sigma}_s^{n-1}}\right) \tag{19}$$

For the pure creep where $\bar{\sigma}_s = \bar{\sigma}_c$, the creep strain rate $\dot{\bar{\varepsilon}}^F$ becomes:

$$\dot{\bar{\varepsilon}}^F = B\left(\bar{\sigma}_s\right)^n \Delta t^m \tag{20}$$

Hence in the iterative process, we begin with current estimated $\bar{\sigma}_s^i$, $\bar{\sigma}_c^i$ and use Eq. (17), (19) or (20) to compute a new value of the creep stress $\bar{\sigma}_c$ from Eq. (21) to replace σ_0 in the linear matching condition (5):

$$\bar{\sigma}_c = \left(\frac{\bar{\dot{\varepsilon}}^F}{B\Delta t^m} \right)^{\frac{1}{n}} \tag{21}$$

To validate the efficiency and effectiveness of the numerical scheme, the proposed method was applied to benchmark examples of Bree problem and a holed plate [6]. In the next session of this paper, two types of weldments subjected to different reverse bending moments with various creep dwell periods are evaluated by the proposed method.

3. Numerical application: welded joints under high temperature–creep fatigue conditions

3.1. Problem Description

In this paper, the proposed LMM is applied to evaluate the creep fatigue lifetime of both Type 1 and Type 2 weldments [13] subjected to cyclic bending moment under creep condition. Fig. 2 shows the dimensions and configurations of the considered Type 1 and 2 welded joints, and the applied 2D symmetric FE model of the specimen assuming a plane strain condition with designation of different materials (parent, weld materials and heat-affected zone), boundary conditions and loading. A cyclic linear distribution of normal pressure P is applied to the end face of the parent material (Fig. 2) to simulate the reverse pure bending moment M, and a schematic bending moment loading history with a dwell period Δt considered for the creep-fatigue analysis is given in Fig.3. In addition to the pure fatigue case, one hour and 5 hours dwell periods are considered to investigate the effect of dwell period on the creep fatigue behavior. Five variants of reverse bending moment are analyzed, which correspond to 1.0%, 0.6%, 0.4%, 0.3% and 0.25% of total strain range at remote parent material.

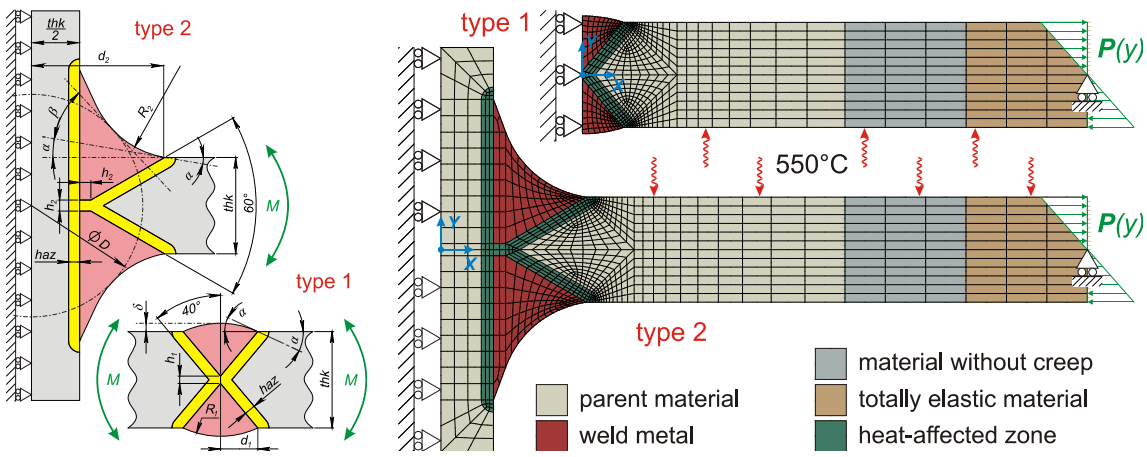

Figure 2. Dimensions and Finite Element models for Type 1 and Type 2 weldments, according to [13]

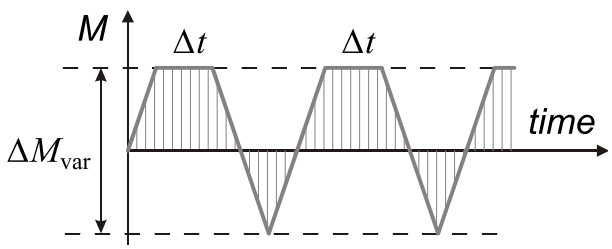

Figure 3. Schematic bending moment loading history for creep-fatigue analysis using the LMM

A Ramberg-Osgood formulation was adopted to simulate cyclic stress strain relationship, and a time hardening creep constitutive model was used to characterize creep behavior. The detailed material properties adopted are given in Table 1. In this creep fatigue damage assessment, the LMM was used to evaluate a steady-state cyclic behavior and to construct a saturated hysteresis loop. Then obtained total strain range during the cycle was used to assess fatigue damage combining R66 fatigue endurance curves [1]. The evaluated creep strain and stress relaxation data were adopted to evaluate creep damage considering time fraction rule and using the experimental creep rupture data. The final lifetime of the cruciform weldment was then obtained based on the calculated fatigue and creep damage under creep-fatigue interaction conditions.

Table 1. Material constants in Ramberg-Osgood model (Eq. 9) and creep time hardening model (Eq. 13)

Zone	E(MPa)	B(MPa)	β	σ_y(MPa)	A(MPa^{-n}/h)	n	m
Parent	160000	1741.96	0.2996	270.7	6.604e-19	5.769	-0.55
Weld	122000	578.99	0.1016	307.9	6.597e-23	7.596	-0.5
HAZ	154000	1632.31	0.2530	338.7	6.6e-21	6.683	-0.525

3.2. Numerical results and verifications

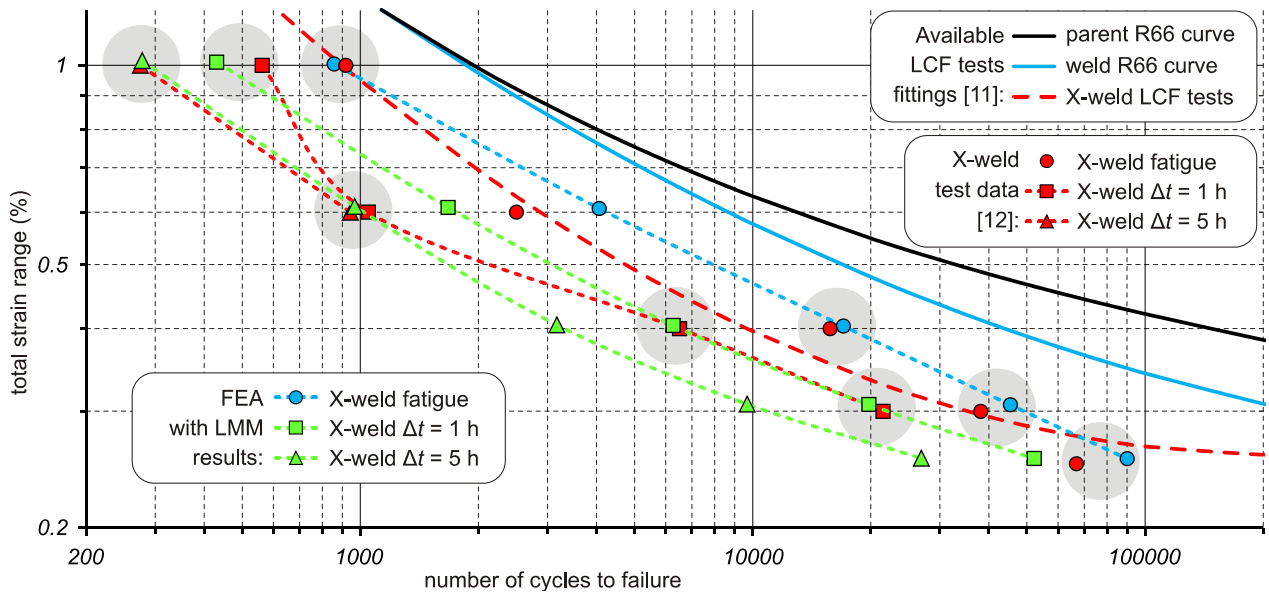

Figure 4. Results of creep-fatigue assessment in application to Type 2 cruciform weldment with experimental comparisons [11, 12]

The creep fatigue lifetime of Type 2 cruciform weldment assessed by the LMM and its experimental comparisons [11, 12] are presented in Fig. 4. Visual comparison of the observed and predicted number of cycles to failure in Fig. 4 for 3 variants of dwell period Δt (Δt=0 for pure fatigue) shows that 9 of the 11 simulations accurately predict the experimental results. Therefore, it can be used for the formulation of an analytic assessment model suitable for the fast estimation of lifetime for a variety of loading conditions. The low computational effort required by the LMM compared to other computational techniques makes it possible and relatively easy to extrapolate numerical predictions for loading conditions not captured by the available experiments.

The contour plots of LMM solutions including total strain range, creep strain, creep stresses at the beginning and end of dwell period, and the outputs of creep fatigue assessment procedure including

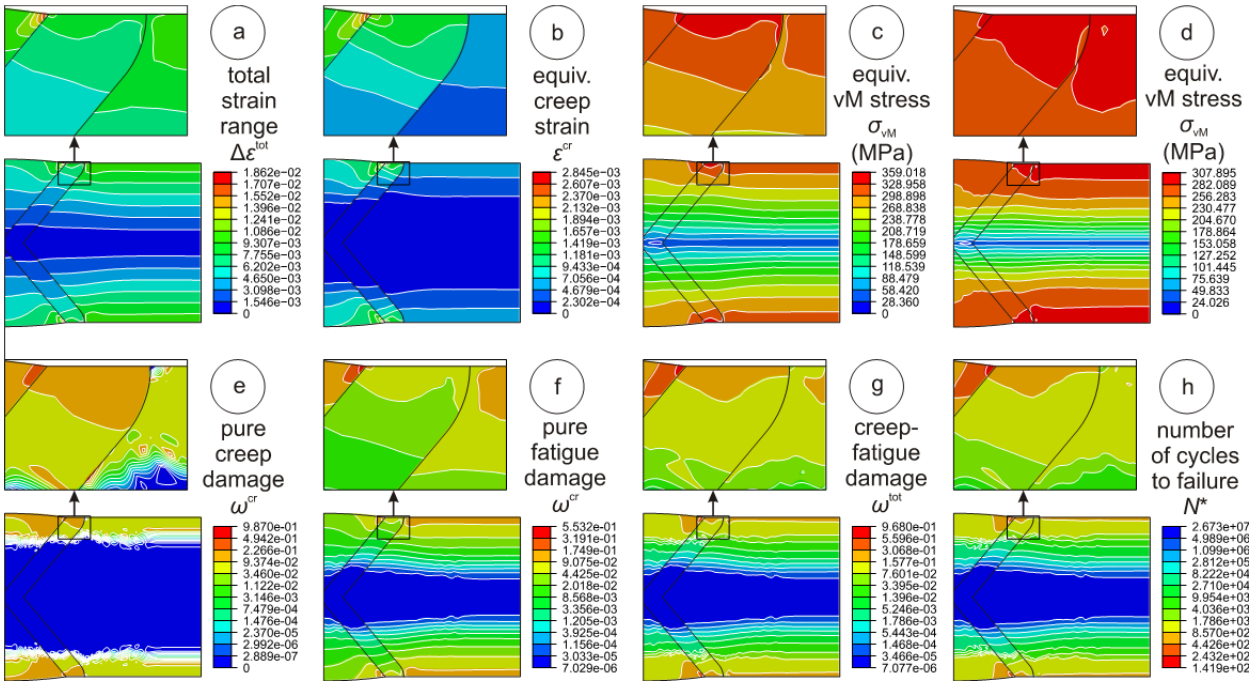

Figure 5. Contour plots of LMM results for type 1 weldment corresponding to $\Delta\varepsilon_{tot}$ = 1% on the outer fiber of plate and Δt = 5 hours of dwell period

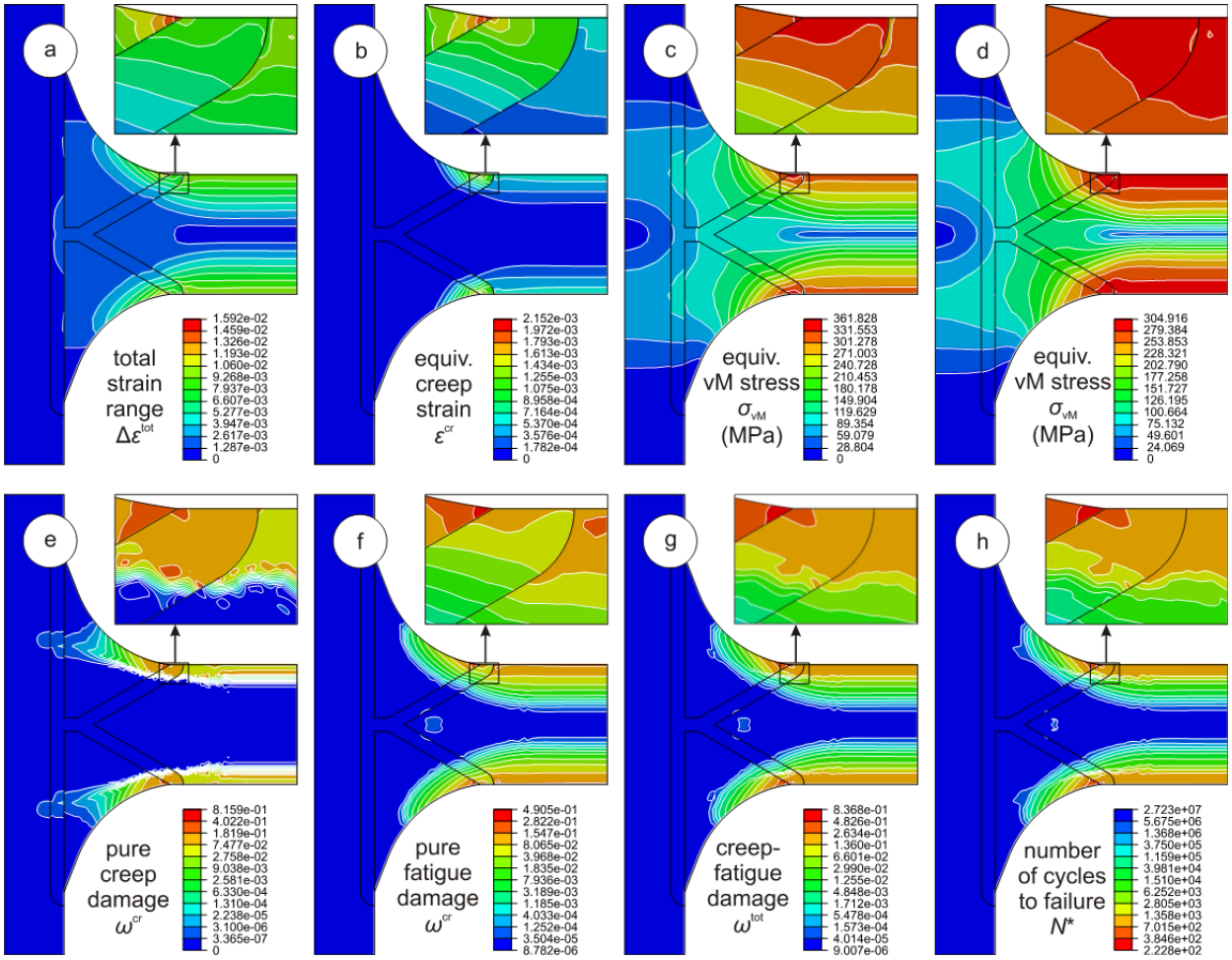

Figure 6. Contour plots of LMM results for type 2 weldment corresponding to $\Delta\varepsilon_{tot}$ = 1% on the outer fiber of plate and Δt = 5 hours of dwell period

pure creep damage, pure fatigue damage, creep-fatigue damage and number of cycles to failure are presented in Fig. 5 and 6 for Types 1 and 2 weldments corresponding to $\Delta\varepsilon_{tot}$ = 1% on the outer fiber of remote parent material and Δt = 5 hours of dwell period. It can be seen that both Types 1 and 2 weldments have the same critical location in the weld toe adjacent to HAZ. In terms of the accumulated total damage at failure, Type 1 weldment has less residual life (N* =142) than Type 2 weldment (N* =223) due to the increased values of parameters characterising hysteresis loop (e.g. total strain range and creep strain, see Figs. 5 and 6).

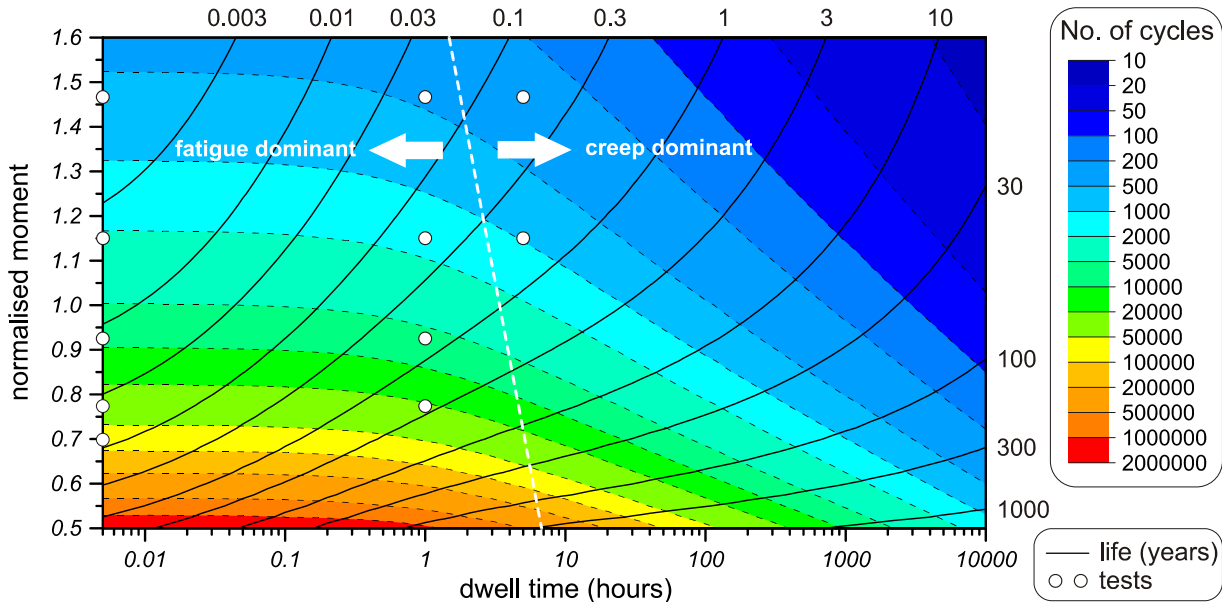

Figure 7. Design contour plot for creep-fatigue durability based on extrapolation of cycles to failure *N** and residual life *L**

The key engineering parameters including the numbers of cycle to failure N* and the residual life L* characterising creep-fatigue durability of the weldment have the principal importance for the design and assessment applications. For the purpose of usability, both parameters N* and L* obtained by LMM calculations and assessments can be represented in the form of design contour plot, shown in Fig. 7 for the Type 2 cruciform weldment. The contour lines (dashed for N* and solid for L*) allows a design engineer to define approximately and rapidly the level of reverse bending moment acceptable for the required service life and assumed average value of dwell period. For a given reverse bending moment and creep dwell period, the numbers of cycle to failure N* and the residual life L* of the cruciform weldment can be approximately estimated from Fig.7.

A full discussion of the solutions and further parametric studies are given by Gorash and Chen [14, 15], which demonstrate that, for such complex industrial problems, the LMM is capable of providing lifetime related solutions that are much more illuminating than conventional analysis.

4. Conclusions

This paper presents the latest development of the LMM on evaluation of the steady state behavior of an elastic plastic creep body subjected to cyclic loading under high temperature – creep fatigue conditions. The proposed LMM successfully calculates the plastic strain range, the creep stress and accumulated creep strain over a dwell period for a steady state load cycle by an iterative process using a general cyclic minimum theorem. Combining with the experimentally defined creep and fatigue damage data, the final lifetime of the component can then be obtained based on the

calculated fatigue and creep damage under creep-fatigue interaction conditions within the LMM framework.

By the application of the LMM to both Types 1 and 2 weldment subjected to reverse bending moment at creep fatigue condition with experimental comparisons, it confirms the efficiency and effectiveness of the proposed method for the creep fatigue damage assessment and demonstrates that LMM may be applied to complicated engineering applications with a much wider range of circumstances.

Acknowledgements

The authors deeply appreciate the Engineering and Physical Sciences Research Council (EPSRC) of the United Kingdom for the financial support (EP/G038880/1), the University of Strathclyde for hosting during the course of this work, and EDF Energy for the experimental data.

References

[1] R.A. Ainsworth, (Editor), R5: Assessment procedure for the high temperature response of structures, Issue 3, British Energy Generation Ltd, 2003.
[2] J. Bree, Elastic-plastic behaviour of thin tubes subjected to internal pressure and intermittent high-heat fluxes with application to fast-nuclear-reactor fuel elements. J strain anal, 2 (1967) 226–238.
[3] T. Nguyen, et al, Determination of the stabilized response of a structure undergoing cyclic thermal-mechanical loads by a direct cyclic method. ABAQUS Users' Conference Proceedings, 2003.
[4] ABAQUS, User's manual. Version 6.11, 2011.
[5] H.F. Chen, A.R.S. Ponter, Linear Matching Method on the evaluation of plastic and creep behaviours for bodies subjected to cyclic thermal and mechanical loading. International Journal for Numerical Methods in Engineering, 68 (2006) 13-32.
[6] H.F. Chen, W.H. Chen, J. Ure, A direct method on the evaluation of cyclic behavior with creep effect. ASME Pressure Vessels & Piping Division Conference, 2012.
[7] H.F. Chen, Lower and upper bound shakedown analysis of structures with temperature-dependent yield stress. Journal of Pressure Vessel Technology, 132 (2010) 1-8.
[8] H.F. Chen, A.R.S. Ponter, A direct method on the evaluation of ratchet limit, Journal of Pressure Vessel Technology, 132 (2010) 041202.
[9] H.F. Chen, M.J. Engelhardt, A.R.S. Ponter, Linear matching method for creep rupture assessment. International Journal of Pressure Vessels and Piping, 80 (2003) 213-220.
[10] D.J. Tipping, The Linear Matching Method: a guide to the ABAQUS user subroutines. E/REP/BBGB/0017/ GEN/07, British Energy Generation, 2007.
[11] S.K. Bate, J.P. Hayes, D.G. Hooton, N.G. Smith, Further analyses to validate the R5 volume 2/3 procedure for the assessment of austenitic weldments. SA/EIG/11890/R002, Serco Assurance, Warrington, UK, 2005.
[12] I. Bretherton, G. Knowles, J.P. Hayes, S.K. Bate, C.J. Austin, PC/AGR/5087: Final report on the fatigue and creep-fatigue behaviour of welded cruciform joints. RJCB/RD01186/R01, Serco Assurance, Warrington, UK, 2004.
[13] I. Bretherton, G. Knowles, I.J. Slater, S.F. Yellowlees, The fatigue and creep-fatigue behaviour of 26mm thick type 316L(N) welded cruciform joints at 550 C: An interim report. R/NE/432, AEA Technology plc, Warrington, UK, 1998.
[14] Y. Gorash, H.F. Chen, Creep fatigue life assessment of cruciform weldments using the linear matching method. Int J Press Vess Piping, (accepted) 2012.
[15] Y. Gorash, H.F. Chen, A parametric study on creep-fatigue strength of welded joints using the linear matching method. International Journal of Fatigue, (submitted) 2012.

Creep Crack Initiation and Growth Behavior in Weldments of high Cr steels

Ryuji Sugiura [1,*], **A. Toshimitsu Yokobori, Jr.** [1], **Kazuto Sato** [1], **Masaaki Tabuchi** [2] **Kenichi Kobayashi** [3], **Masataka Yatomi** [4], **Kamran Nikbin** [5]

[1] Graduate School of Engineering, Tohoku University, Japan
[2] NIMS, Japan
[3] Chiba University, Japan
[4] IHI Co., Ltd, Japan
[5] Imperial College, London, UK
* Corresponding author: sugiura@md.mech.tohoku.ac.jp

Abstract W added high Cr ferritic heat-resistant steels have been developed as a boiler material. Most of boiler component structures are mainly fabricated by welding which are likely to the regions of crack initiation and propagation. However, the method of predicting the life of creep crack initiation and growth have not been clearly established for weldments of high Cr ferritic heat resistant material due to many factors such as the variation in micro-structures and the residual stress caused by welding and thermal cycles. In the present study, the experiments of creep crack growth using a circular notched round bar specimen with variation of notch location in HAZ were conducted and the characteristics of creep crack growth rate and creep crack initiation life were summarized in terms of Q^* parameter, which has been proposed as fracture mechanics parameter to describe creep crack growth rate.

Keywords Creep crack initiation, Creep crack growth, Weldment, High Cr steel, C^* parameter, Q^* parameter.

1. Introduction

The W added high Cr ferritic heat-resistant steels have been developed as a boiler material. Most of boiler component structures are mainly fabricated by welding which are likely to the regions of crack initiation and propagation. However, the method of predicting the life of creep crack initiation and growth have not been clearly established for weldments of high Cr ferritic heat resistant material due to many factors such as the variation in micro-structures and the residual stresses caused by welding and thermal cycles.

In the previous work, we have reported that creep crack grows initially in the oblique direction to the direction of initial notch with 45 degree as it approaches the site of minimum hardness region near the boundary between base metal (BM) and heat affected zone (HAZ) [1-3], as shown in Fig. 1, by conducting the tests using a C(T) specimen for P92 weldment. Correspondingly, the site of maximum value of stress multiaxiality shifts to the site of minimum hardness. This process was defined as the incubation process of creep crack growth. Therefore, we suggested that in order to predict the fracture life for weldment, it is important to clarify the incubation process and path on a structural mechanical basis in order correctly determine the incubation time of creep crack growth.

In the present study, more detailed experiments of creep crack growth using a circular notched round bar specimen with variation of notch location in HAZ were conducted and the characteristics of creep crack growth rate and creep crack initiation life were summarized in terms of Q^* parameter, which has been proposed as fracture mechanics parameter to describe creep crack growth rate.

The present work is closely concerned with the Japanese result for the VAMAS Project and JSPS 129 Committee.

2. Creep crack growth test procedures

The material used is W-added 9%Cr ferritic heat-resistant steel (ASME Code Case 2179, ASTM A335 P92) and its plate of 31 mm thickness, which was subjected to normalizing at 1343K for 2hr

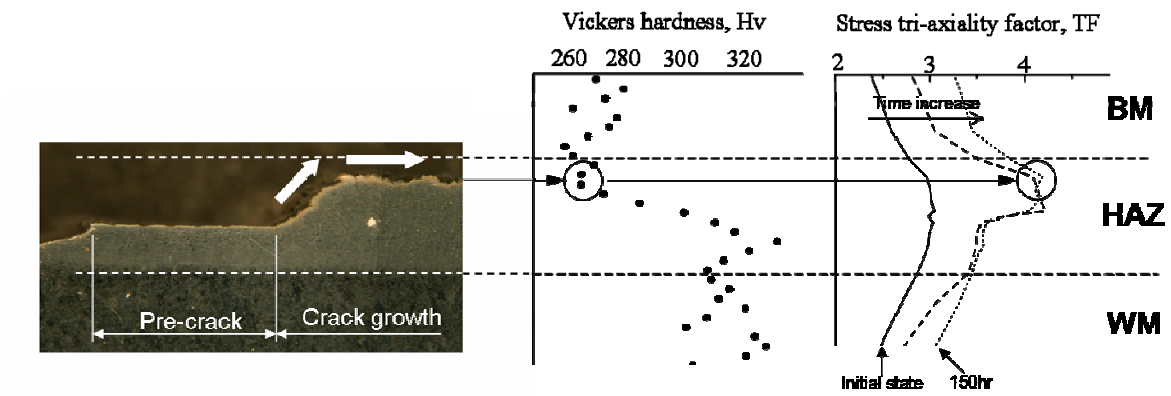

Figure 1. Comparison of creep crack growth path, Vickers hardness and stress tri-axiality for weldment of P92

and tempering for 2hr, was prepared as a base metal (BM). The chemical composition is shown in Table 1. The welded joint (WM) was fabricated using multi-layer gas tungsten arc (GTA) welding with single bevel of 20° [4]. Welding consumable used for GTA welding was matching filler wire developed recently for welding this class of steel [5]. Finally, the post weld heat treatment (PWHT) was carried out at 1013K for 4hr. The process parameters of multi-layer GTA welding are given in Table 2 [4].

The specimen used was manufactured into a circular notched round bar specimen, as shown in Fig. 2. For the welded joint specimen, two kinds of specimen with variation in the notch location such as one located in the middle part of HAZ and the other in the interface of fine-grained HAZ and base metal in the region of HAZ were prepared, as shown in Fig. 2.

Creep crack growth tests were performed using a lever arm creep testing machine of Type RT-30 manufactured by TOSHIN KOGYO. The test temperatures were kept at a specified temperature with the precision of ±2°C. The experimental conditions are shown in figures of experimental results. The crack length was measured by electrical potential method [6-8]. The creep crack growth tests were conducted based on ASTM E1457-07 [9] and JSPS standards [10].

3. Characteristics of creep crack length and deformation

The relationship between creep crack length Δa and non-dimensional time t/t_f of each specimen for weldment is shown in Fig. 3. The relationship between load line displacement $\Delta\delta$ and non-dimensional time t/t_f of them is shown in Fig. 4, where t and t_f are the current time of load application and the life of creep crack growth for each specimen.

From the creep crack initiation and growth tests, fracture lives for both specimens such as one located in the middle part of HAZ and the other in the interface of BM and fine-grained HAZ in the region of HAZ are the same and the characteristics of creep crack growth show the similar, as shown in Fig. 3. From these results mentioned above, even though notch was located in the lower hardness region, creep crack growth was found not to be immediately accelerated. This shows the possible presence of an incubation time of creep crack growth even if the notch was located in the interface between base metal and fine-grained HAZ in the region of HAZ, which corresponds to the region of minimum hardness.

However, specimen with the notch located in the interface between base metal and fine-grained HAZ in the region of HAZ shows the ability to deform.

Table 1. Chemical composition of P92 steel in wt. %

C	Si	Mn	P	S	Cr
0.09	0.16	0.47	0.01	0.001	8.72
Mo	W	V	Nb	B	N
0.45	1.87	0.21	0.06	0.002	0.05

Table 2. Process parameters of multi-layer GTA welding

groove	single bevel 20°
preheating	>373K
welding current	200～250A
arc voltage	10～10.5V
welding speed	1.2～1.5mm/s
multi-layer	33～37pass

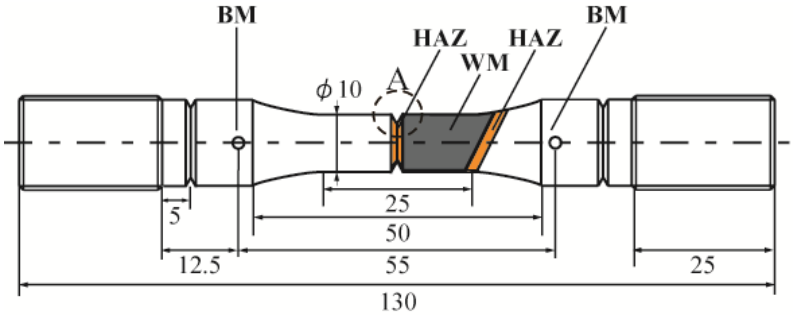

(a) The geometry and size of a circular notched specimen for weldment

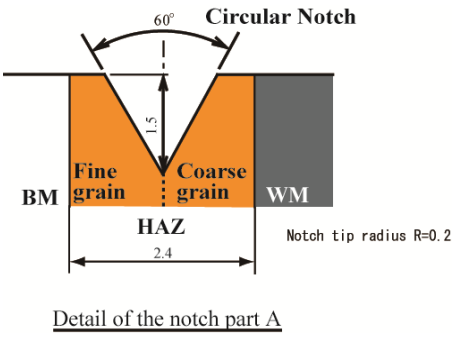

(b) Circular notch located in the middle part of HAZ

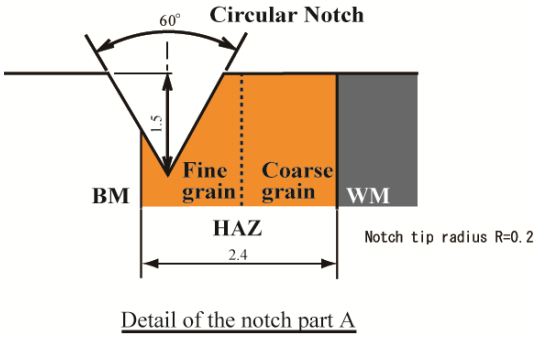

(c) Circular notch located in the interface between base metal and fine-grained HAZ

Figure 2. The geometry and size of a circular notched specimen for weldment and variation in the notch location in HAZ

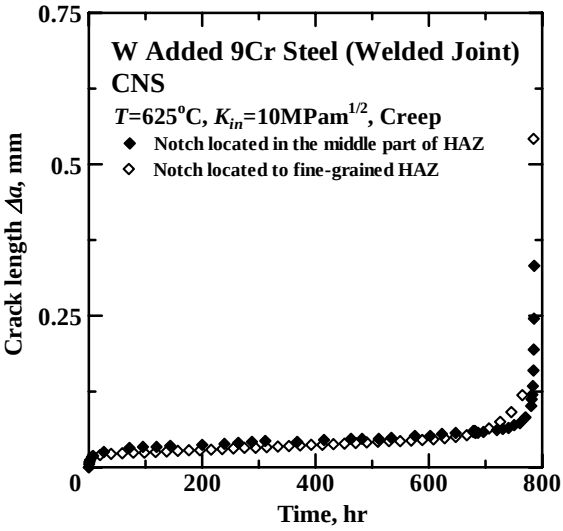

Figure 3. Characteristic of creep crack length

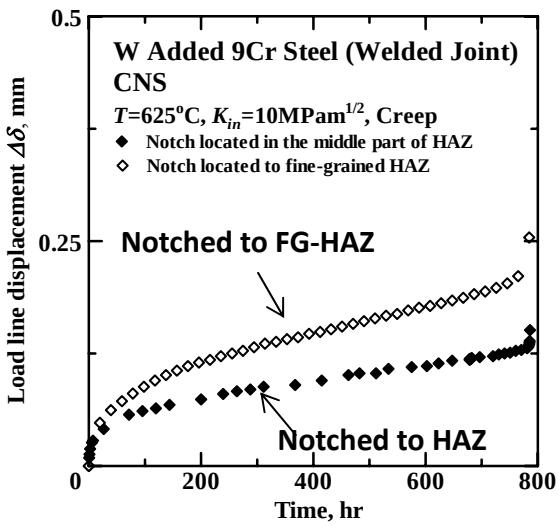

Figure 4. Characteristic of load line displacement

4. Creep crack growth rate characteristics

C^* [11-14], $d\delta/dt$ [15-17] and Q^* [18-19] have been proposed as the fracture mechanics parameter to describe the creep crack growth rate. The C^* parameter for a circular notched specimen is given by Eq. (1).

$$C^* = \frac{2n+1}{2n-1}\sigma_{net}\frac{d\delta}{dt}, \tag{1}$$

where n is creep exponent, σ_{net} is the net section stress (MPa).
The creep crack growth data for both base metals and weldmens (indication data are for the specimen with notch located in the middle part of HAZ) estimated by C^* and $d\delta/dt$ are shown in Figs. 5 and 6, respectively. The characteristics of creep crack growth rate estimated by C^* and $d\delta/dt$ show typical dual behavior which takes major portion of total crack growth life, approximately 60-70% of total life. An example of dual behavior on C^* is shown in Fig. 7.
By the way, Q^* concept enables crack growth in the steady state regions, which correspond to the circular region in Fig. 7, to be characterized uniquely [18-19].
The creep crack growth rate for creep-brittle materials is represented by the Q^* parameter as follow [19],

$$\frac{da}{dt} = A\exp\left(Q^*\right) = A^* K_{in}^n \exp\left(-\frac{\Delta H_g}{RT}\right), \tag{2}$$

where A and A^* are constant, K_{in} is the initial stress intensity factor (MPam$^{1/2}$), n is the exponent of initial stress intensity factor, ΔH_g is an activation energy (kJ/mol), R is the gas constant (=8.3145J/Kmol), T is the absolute temperature (K).
By taking logarithms of both sides of Eq. (2), Eq. (3) is obtained.

$$\log\frac{da}{dt} = \log A^* + \left[n\log K_{in} - \frac{\Delta H_g}{RT}\right]. \tag{3}$$

The bracket portion of Eq. (3) corresponds to the Q^* parameter which has been proposed as an estimation parameter of creep crack growth rate [18].
On the basis of Q^* concept, creep crack growth rate in this region is well predicted for base metals and weldments including the data for specimen with the notch located in the fine-grained HAZ, as shown in Fig. 8, regardless of the life of creep crack growth are different between them.

5. Characteristic of creep crack growth life

In the section 3, the possible presence of an incubation time of creep crack growth, regardless of variation in notch location, was shown and we suggested that in order to predict the fracture life for weldment, it is important to clarify the incubation process in order correctly determine the incubation time of creep crack growth. The comparison of creep crack growth behavior for weldment with that for base metal under the same condition (T=625°C, K_{in}=12MPam$^{1/2}$) is shown in Fig. 9. In Fig. 9, in spite of the fact that the creep crack growth rate in the constant region of creep crack growth both for weldment and base metal are the same, the life of creep crack growth for WM was shorter than that for BM. This will be due to the occurrence of the rapidly acceleration of creep crack growth for WM. In Fig. 9, the region of restrained creep crack growth rate due to the HAZ will correspond to the crack length of 100 μm. Therefore, this region is considered to be within an incubation region of creep crack growth which can be termed creep crack initiation for circular notched round bar specimen.

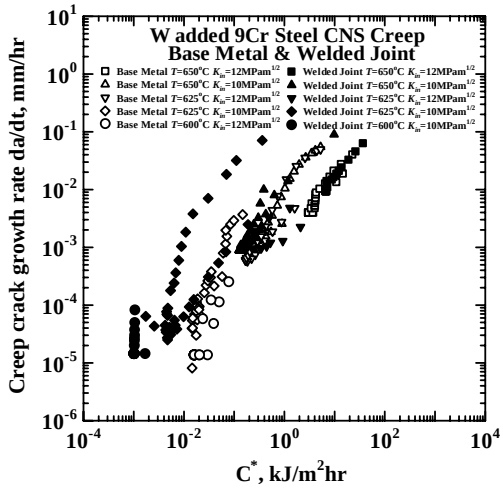

Figure 5. Characterization of creep crack growth rate estimated by C^* parameter

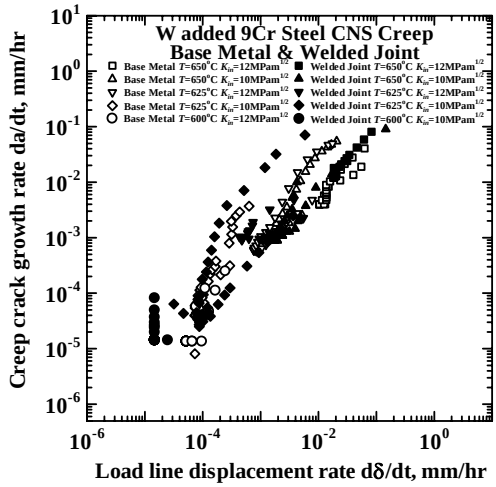

Figure 6. Characterization of creep crack growth rate estimated by $d\delta/dt$ parameter

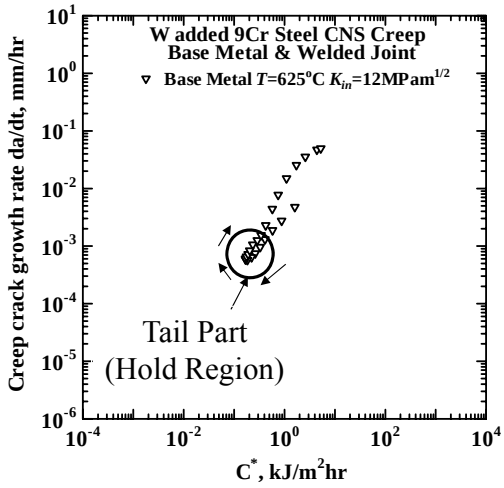

Figure 7. Example of creep crack growth data of base metal on C^* parameter

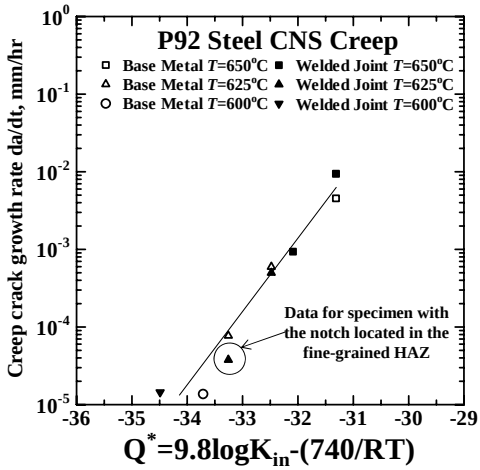

Figure 8. Characterization of creep crack growth rate estimated by Q^* parameter

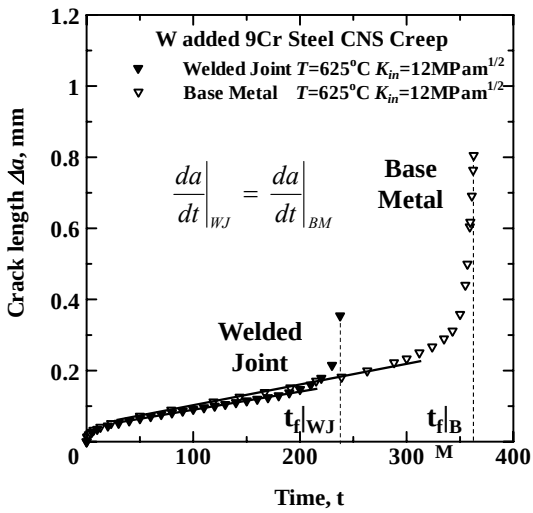

Figure 9. Comparison of creep crack growth behavior for base metal with that for weldment

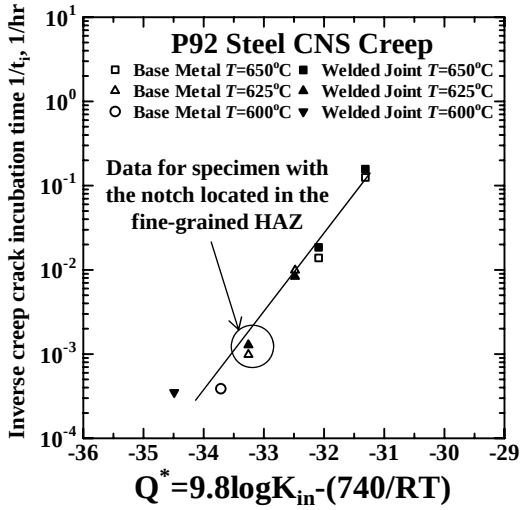

Figure 10. Creep crack initiation life estimated by Q^* parameter

The creep crack initiation times were estimated by Q^* parameter, as show in Fig. 10. In Fig. 10, Q^* was found to correlate uniquely creep crack initiation for weldment of P92 steel, including of the data for specimen with the notch located in the fine-grained HAZ.

6. Conclusions

By conducting more detailed experiments of creep crack growth using a circular notched round bar specimen with variation of notch location in HAZ, the possible presence of an incubation time of creep crack growth was shown, regardless of variation in notch location. We suggested that in order to predict the fracture life for weldment, it is important to clarify the incubation process in order correctly determine the incubation time of creep crack growth. Additionally, the characteristics of creep crack growth rate and creep crack initiation life were summarized in terms of Q^* parameter.

References

[1] R. Sugiura, A. T. Yokobori, Jr., K. Sato, M. Tabuchi, M. Yatomi, K. Kobayashi and K. Nikbin, Strength, Fracture and Complexity, An Int. J., 6 (2011) 177-189.
[2] R. Sugiura, A. T. Yokobori, Jr., K. Suzuki and M. Tabuchi, Eng. Frac. Mech., 77 (2010) 3053-3065.
[3] A.Toshimitsu Yokoboti. Jr., Ryuji Sugiura, Masaaki Tabuchi, Masataka Yatomi, Kenichi Kobayashi, Kamran Nikbin, Strength, Fracture and Complexity, An Int J., 7 (2011/2012) 315-320.
[4] M. Matsui, M. Tabuchi, T. Watanabe, K. Kubo, J. Kinugawa. Degradation of creep strength in welded joint of 9%Cr steel. ISIJ Int. 2001; 41 Supplement: S126-130.
[5] K. Ogawa, A. Iseda, Y. Sawaragi, S. Masumoto, F. Masuyama. Development of high strength 12%Cr steel pipe and tubes for boilers. Sumitomo Metals Japan. 1995;47:39-46.
[6] H.H. Johnson, “Calibrating the electric potential method for studying slow crack growth,” Materials Research and Standard, 5 (1965) 442-445.
[7] K.H. Schwalbe, and D. Hellman, “Application of the Electrical Potential Method to Crack Length Measurements Using Johnson’s Formula,” J. of Testing and Evaluation, 9, 4 (1980) 218-220.
[8] T. Adachi, A.T. Yokobori, Jr., M. Tabuchi, A. Fuji, T. Yokobori and K. Nikbin, “The Proposal of Q^* Parameter and Derivation of the Law of Creep Crack Growth Life for a Round Bar Specimen with a Circular Notch for Cr-Mo-V Steel,” Materials at High Temperatures, 21, 2, (2004) 95-100.
[9] ASTM E1457-07, 2007, “Standard Test Method for Measurement of Creep Crack Growth Times in Metals”.
[10] T. Yokobori, T. Iwadate, S. Konosu, M. Tabuchi, A. Fuji, A.T. Yokobori Jr., Strength of materials and fractology, 129 Committee of JSPS: Sasaki Press Japan, 1999, p.291.
[11] J.D. Landes, and J.A. Begley, “A Fracture Mechanics Approach to Creep Crack Growth,” ASTM STP., 590 (1976) 128.
[12] K. Ohji, K. Ogura and S. Kubo, Japan Soc. Mech. Engng., 44 (1975) 183. (in Japanese)
[13] S. Taira, R. Ohtani, and T. Kitamura, “Application of J-Integral to High-Temperature Crack Propagation”, Trans. ASME J. Engng. Mater. Technol., 101 (1979) 154-167.
[14] R. Koterazawa, and T. Mori, “Applicability of Fracture Mechanics Parameters to Crack Propagation Under Creep Condition”, Trans. ASME J. Engng. Mater. Technol., 99, (1977) 298-305.
[15] A. Fuji, and M. Kitagawa, “A comparison of creep crack growth behavior in Nickel based superalloy with low alloy steel”, Advances in Fracture and Structural Integrity., Prof. of ICF8, V. V. Panasyuk editor., (1994) 487.
[16] B. Dogan, and K.H. Schwalbe, “Creep Crack Growth Behavior of Ti-6242”, ASTM

Symposium *Proc. ASTM STP 1131*, H.A.Ernst et al., eds., Philadelphia, (1992) 284-296.

[17] A.T. Yokobori, Jr., T. Yokobori, T. Kuriyama, T. Kako, Y. Kaji, "Characterization of high temperature creep crack growth rate in terms of independent parameters", Proc. of the Int. Conf. on Creep, JSME, I Mech E, ASME., (1986) 135-140.

[18] A.T. Yokobori, Jr., T. Yokobori, "New concept to crack growth at high temperature creep and creep-fatigue," Advances in Fracture Research, Proc. ICF7, K. Salama et al., eds., Pergamon Press, 2, (1989) 1723-1735.

[19] A.T. Yokobori, Jr., T. Uesugi, T. Yokobori, A. Fuji, M. Kitagawa, I. Yamaya, M. Tabuchi, and K. Yagi, "Estimation of creep crack growth rate in IN-100 based on the Q^* parameter concept", J. of Materials Science, 33 (1998) 1555-1562.

Three-Dimensional Vacancy Diffusion Analysis Related to Micro Damage of C(T) Specimen for P92 Steel under Creep Condition

Haruhisa Shigeyama[1,*], **A. Toshimitsu Yokobori, Jr.**[1], **Ryuji Sugiura**[1], **Takashi Matsuzaki**[1]

[1] Department of Nanomechanics, Tohoku University, Sendai 980-8579, Japan
* Corresponding author: shigeyama@md.mech.tohoku.ac.jp

Abstract In this study, interrupted creep crack growth tests were conducted using C(T) specimens with side-grooves of P92 steel. After the interrupted tests, to investigate the creep crack growth behavior of P92 steel under the multi-axial stress field, the creep crack growth path of the center of the thickness direction and near the side-groove were observed. From observational results, it was indicated that the creep crack preferentially grew near the side-groove. Additionally, creep crack growth forms were different between the center of the thickness direction and near the side-groove. For the center of the thickness direction, the creep crack growth behavior showed the periodic convexo-concave manner. On the other hand, the creep crack grew in a linear manner near the side-groove. To mechanically clarify the difference of creep crack growth forms, three-dimensional diffusion analysis of vacancies which related to the void formation and crack growth was conducted. From analytical results, vacancies accumulated at the corner of the bottoms of notch and side-groove. This result is in good agreement with the experimental result.

Keywords P92 steel, C(T) specimen, Interrupted test, Creep crack growth, Three-dimensional stress induced vacancy diffusion analysis

1. Introduction

The W-strengthened 9%Cr ferritic heat-resistant steel (ASME code case 2179, ASTM A335 P92) has been developed as a boiler material for the ultra-supercritical power plant. When a component is used in the actual plant, the multi-axial stress field is caused due to the complicated three-dimensional structure. It is known that the ductility of materials decrease with increasing the multi-axial stress and this phenomenon is called “structural brittleness” [1, 2]. The reduction of ductility makes the lifetime-prediction difficult. Therefore, it is important to clarify the creep damage progression behavior of P92 steel under the multi-axial stress field.

It is reported that the initiation and growth of creep voids are accelerated due to the multi-axial stress field [3-6]. Additionally, the initiation and growth of creep voids were caused by the diffusion and accumulation of vacancies. Thus, it is necessary to clarify the diffusion behavior of vacancies under the multi-axial stress field. Actually, some authors proposed the numerical analytical method of two-dimensional stress induced vacancy diffusion [7-10].

In this study, interrupted creep crack growth (CCG) tests were conducted using C(T) specimens with side-grooves of P92 steel. After the interrupted tests, to investigate the CCG behavior of P92 steel under the multi-axial stress field, the CCG path of the center of the thickness direction and near the side-groove were observed. Then, three-dimensional stress induced vacancy diffusion analysis was conducted to clarify the diffusion behavior of vacancies for C(T) specimen with side-grooves.

2. Experimental Procedures

2.1. Material and Specimen

The material used is P92 steel. The chemical composition of P92 steel is shown in Table 1. The specimen used is a C(T) specimen with side-grooves of 25% of specimen thickness. The geometry and size of the C(T) specimen is shown in Fig. 1.

Table 1. Chemical composition of P92 steel in wt.%

C	Si	Mn	P	S	Cr	Mo	W	Nb	V	N	B
0.085	0.26	0.49	0.006	0.0012	8.85	0.50	1.80	0.06	0.20	0.0510	0.0030

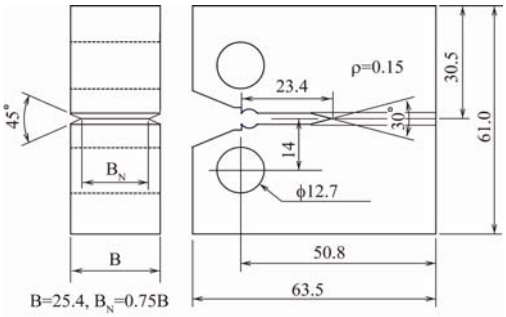

Figure 1. The geometry and size of a C(T) specimen (Unit: mm)

2.2. CCG Tests Procedures and Experimental Conditions

The interrupted CCG tests were conducted by lever-arm high temperature creep testing machine (Type RT-30) manufactured by TOSHIN KOGYO. The creep crack length was measured by direct current potential drop (DCPD) method [11, 12]. Load line displacement (LLD) was measured by displacement sensing bars and linear gauges. A schematic illustration of measurement methods of creep crack length and LLD is shown in Fig. 2. The interrupted CCG tests were carried out under the conditions of 600 °C and initial stress intensity factor K_{in} = 42 MPam$^{1/2}$. These tests were interrupted at different times, as shown in Table 2.

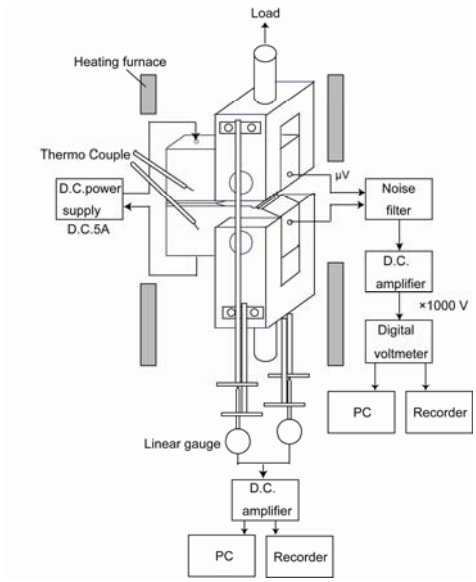

Figure 2. Measurement methods of creep crack length and LLD

Table 2. Experimental conditions of interrupted CCG tests

Temperature [°C]	Initial stress intensity factor K_{in} [MPam$^{1/2}$]	Interrupted time [hr]	Creep life fraction t/t_f
600	42	52.5	0.17
		150	0.50
		226	0.75
		301	0.99

3. Three-dimensional Vacancy Diffusion Analysis

The numerical analytical method of stress induced particle diffusion was proposed by Yokobori, *et al.* [13-15]. In this method, the stress distribution is calculated by finite element analysis (FEA) and stress induced particle migration is calculated by finite difference analysis (FDA). This analytical method was applied to the problems of hydrogen embrittlement [13, 14, 16], stressmigration and electromigration of LSI interconnect [8-10, 17] and high-temperature creep of heat-resistant steels [7]. All of these analyses were conducted in two dimensions. However, the actual plant has a complicated three-dimensional structure. Therefore, to apply this analytical method to the actual components, it is important to conduct the three-dimensional vacancy diffusion analysis. Thus, in this paper, the numerical analytical method of three-dimensional vacancy diffusion was developed and applied to the high-temperature creep of C(T) specimen.

3.1. Basic Equation of Vacancy Diffusion

Based on a multiplication concept [13-15], the basic equation of three-dimensional vacancy diffusion is given by Eq. (1).

$$\frac{\partial C}{\partial t} = \alpha_1 D\left(\frac{\partial^2 C}{\partial x^2} + \frac{\partial^2 C}{\partial y^2} + \frac{\partial^2 C}{\partial z^2}\right) - \alpha_2 D\frac{\Delta V}{RT}\left(\frac{\partial C}{\partial x}\frac{\partial \sigma_p}{\partial x} + \frac{\partial C}{\partial y}\frac{\partial \sigma_p}{\partial y} + \frac{\partial C}{\partial z}\frac{\partial \sigma_p}{\partial z}\right) - \alpha_3 D\frac{\Delta V}{RT}C\left(\frac{\partial^2 \sigma_p}{\partial x^2} + \frac{\partial^2 \sigma_p}{\partial y^2} + \frac{\partial^2 \sigma_p}{\partial z^2}\right) \tag{1}$$

where C is concentration of vacancies, t is time, D is the self diffusion coefficient of P92 steel, ΔV is a volume change due to accommodation of a vacancy, R is gas constant, T is absolute temperature, σ_p is hydrostatic stress, and α_i are the weight coefficients. The self diffusion coefficient D is given by Eq. (2).

$$D = D_0 \exp\left(-\frac{Q}{RT}\right) \tag{2}$$

where D_0 and Q are diffusion constant and activation energy of P92 steel, respectively.

3.2. Analytical Methods and Conditions

Distribution of hydrostatic stress for C(T) specimen was calculated by three-dimensional FEA. This analysis was performed by MSC Marc / MSC Marc Mentat ver. 2009 (Cyber Science Center, Tohoku University). A finite element model of C(T) specimen is shown in Fig. 3. Due to symmetry, only one quarter of the specimen is meshed. The material properties of P92 steel used in the FEA were shown in Table 3. Work hardening due to the plastic deformation is given by Eq. (3).

$$\bar{\sigma} = c\bar{\varepsilon}_p \tag{3}$$

where, $\bar{\sigma}$ is equivalent (Mises) stress, and $\bar{\varepsilon}_p$ is equivalent plastic strain.

The distributions of vacancy concentration were obtained by solving Eq. (1) using three -dimensional FDA. Figure 4 shows a model of three-dimensional vacancy diffusion analysis. To match the finite difference lattice and finite element mesh, unequally-spaced finite difference lattice was used in the FDA. Equation (1) was converted into the non-dimensional equation using the non-dimensional values given by Eq. (4).

$$x^+ = \frac{x}{a},\ y^+ = \frac{y}{a},\ z^+ = \frac{z}{a},\ C^+ = \frac{C}{C_0},\ t^+ = D_0\frac{t}{a^2},\ D^+ = \frac{D}{D_0} = \exp\left(-\frac{Q}{RT}\right) \tag{4}$$

The non-dimensional equation is discretized by the Crank−Nicolson implicit method and Eq. (5)

was obtained.

$$\begin{aligned}
&A(x,y,z)C^{+\,n+1}_{i+1,j,k} + (B(x,y,z)-1)C^{+\,n+1}_{i,j,k} + E(x,y,z)C^{+\,n+1}_{i-1,j,k} + F(x,y,z)C^{+\,n+1}_{i,j+1,k} \\
&+ G(x,y,z)C^{+\,n+1}_{i,j-1,k} + H(x,y,z)C^{+\,n+1}_{i,j,k+1} + I(x,y,z)C^{+\,n+1}_{i,j,k-1} \\
&= -A(x,y,z)C^{+\,n}_{i+1,j,k} - (B(x,y,z)+1)C^{+\,n}_{i,j,k} - E(x,y,z)C^{+\,n}_{i-1,j,k} - F(x,y,z)C^{+\,n}_{i,j+1,k} \\
&- G(x,y,z)C^{+\,n}_{i,j-1,k} - H(x,y,z)C^{+\,n}_{i,j,k+1} - I(x,y,z)C^{+\,n}_{i,j,k-1}
\end{aligned} \tag{5}$$

where,

$$\begin{aligned}
A(x,y,z) &= \frac{\Delta t^+}{\Delta x_i^+\left(\Delta x_{i-1}^+ + \Delta x_i^+\right)}\left(\alpha_1 D^+ - \frac{\alpha_2 D^+ \Delta V \Delta x_{i-1}^+}{2RT}\frac{\partial \sigma_p}{\partial x^+}\right) \\
B(x,y,z) &= -\alpha_1 D^+ \Delta t^+\left(\frac{1}{\Delta x_{i-1}^+ \Delta x_i^+} + \frac{1}{\Delta y_{j-1}^+ \Delta y_j^+} + \frac{1}{\Delta z_{k-1}^+ \Delta z_k^+}\right) \\
&\quad - \frac{\alpha_2 D^+ \Delta V \Delta t^+}{2RT}\left(\frac{\Delta x_i^+ - \Delta x_{i-1}^+}{\Delta x_{i-1}^+ \Delta x_i^+}\frac{\partial \sigma_p}{\partial x^+} + \frac{\Delta y_j^+ - \Delta y_{j-1}^+}{\Delta y_{j-1}^+ \Delta y_j^+}\frac{\partial \sigma_p}{\partial y^+} + \frac{\Delta z_k^+ - \Delta z_{k-1}^+}{\Delta z_{k-1}^+ \Delta z_k^+}\frac{\partial \sigma_p}{\partial z^+}\right) \\
&\quad - \frac{\alpha_3 D^+ \Delta V \Delta t^+}{2RT}\left(\frac{\partial^2 \sigma_p}{\partial x^{+\,2}} + \frac{\partial^2 \sigma_p}{\partial y^{+\,2}} + \frac{\partial^2 \sigma_p}{\partial z^{+\,2}}\right) \\
E(x,y,z) &= \frac{\Delta t^+}{\Delta x_{i-1}^+\left(\Delta x_{i-1}^+ + \Delta x_i^+\right)}\left(\alpha_1 D^+ + \frac{\alpha_2 D^+ \Delta V \Delta x_i^+}{2RT}\frac{\partial \sigma_p}{\partial x^+}\right) \\
F(x,y,z) &= \frac{\Delta t^+}{\Delta y_j^+\left(\Delta y_{j-1}^+ + \Delta y_j^+\right)}\left(\alpha_1 D^+ - \frac{\alpha_2 D^+ \Delta V \Delta y_{j-1}^+}{2RT}\frac{\partial \sigma_p}{\partial y^+}\right) \\
G(x,y,z) &= \frac{\Delta t^+}{\Delta y_{j-1}^+\left(\Delta y_{j-1}^+ + \Delta y_j^+\right)}\left(\alpha_1 D^+ + \frac{\alpha_2 D^+ \Delta V \Delta y_j^+}{2RT}\frac{\partial \sigma_p}{\partial y^+}\right) \\
H(x,y,z) &= \frac{\Delta t^+}{\Delta z_k^+\left(\Delta z_{k-1}^+ + \Delta z_k^+\right)}\left(\alpha_1 D^+ - \frac{\alpha_2 D^+ \Delta V \Delta z_{k-1}^+}{2RT}\frac{\partial \sigma_p}{\partial z^+}\right) \\
I(x,y,z) &= \frac{\Delta t^+}{\Delta z_{k-1}^+\left(\Delta z_{k-1}^+ + \Delta z_k^+\right)}\left(\alpha_1 D^+ + \frac{\alpha_2 D^+ \Delta V \Delta z_k^+}{2RT}\frac{\partial \sigma_p}{\partial z^+}\right) \\
x^+ &= \sum_{l=1}^{i-1}\Delta x_l^+, \quad y^+ = \sum_{m=1}^{j-1}\Delta y_m^+, \quad z^+ = \sum_{n=1}^{k-1}\Delta z_n^+
\end{aligned} \tag{6}$$

The obtained simultaneous equations were solved by the successive over relaxation (SOR) method. The material properties of P92 steel used in the FDA were shown in Table 4. It is known that vacancies were generated with the progress of the plastic deformation [18]. Therefore, distribution of initial vacancy concentration C_0 was set based on the distribution of equivalent plastic strain obtained by 3D-FEA as follows.

$$C_0 = 1.0 + b\bar{\varepsilon}_p \tag{7}$$

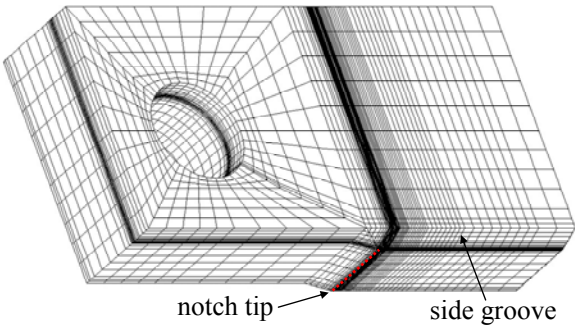

Figure 3. Three-dimensional finite element model (1/4 C(T) specimen)

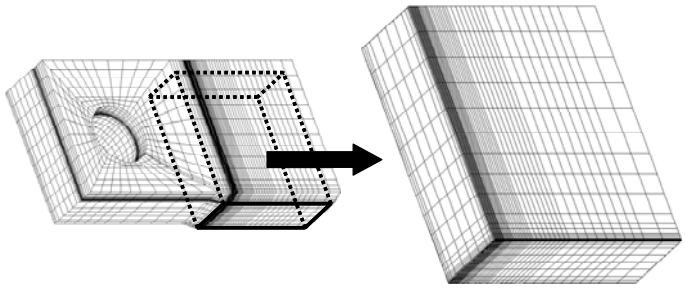

Figure 4. Three-dimensional finite difference model

Table 3. Material properties of P92 steel used in the FEA (600°C)

E [GPa]	ν	σ_{ys} [MPa]	c [MPa]
164	0.3	380	16400

Table 4. Material properties of P92 steel used in the FDA

R [J/Kmol]	ΔV [mm³/mol]	T [K]	Q [J/mol]	D_0 [mm²/sec]	C_0^e	b	α_1	α_2	α_3
8.31	2.00×10^3	873	2.00×10^5	3.72×10^1	1.00	50	10000	2000	10

4. Results and Discussions

4.1. Characteristics of CCG and LLD

The relationship between creep crack length Δa measured by DCPD method and creep life fraction t/t_f is shown in Fig. 5. The relationship between LLD $\Delta\delta$ and creep life fraction t/t_f is shown in Fig. 6. Where, t and t_f are the current time of load application and the life of CCG. From Fig. 5, creep crack was gradually accelerated from about 20% of CCG life. And the characteristic of CCG did not show the steady-state CCG rate region. On the other hand, the characteristic of LLD showed the steady-state creep deformation and it occupied approximately 50% of total life as shown in Fig. 6.

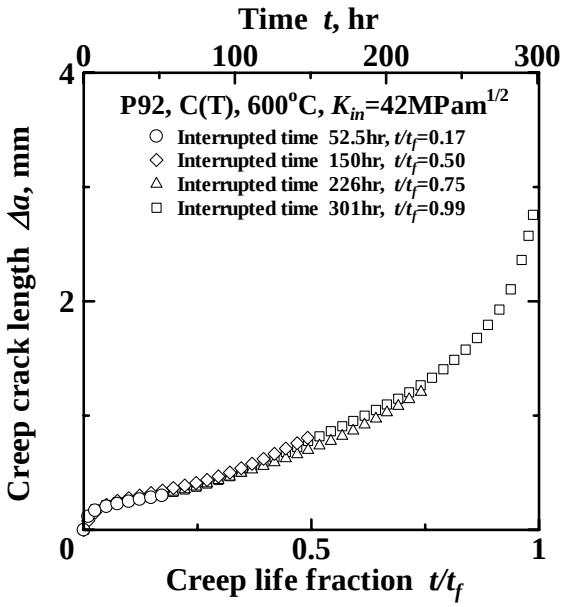

Figure 5. Characteristic of CCG

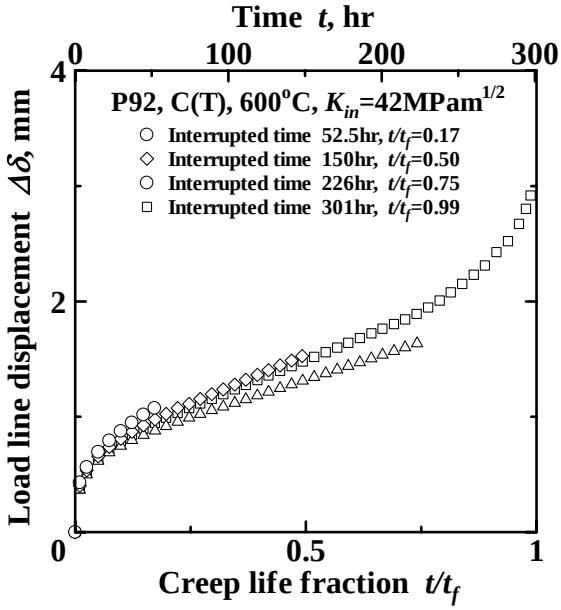

Figure 6. Characteristic of LLD

4.2. Observations of CCG Path

To investigate the three-dimensional CCG behavior for C(T) specimen of P92 steel, the CCG path at the center of the thickness direction (hereinafter referred to as "center") and near the side-groove (hereinafter referred to as "side") were observed using laser microscope. The observational results of the center and the side are shown in Fig. 7 and Fig. 8, respectively. From Fig. 7, the CCG behavior showed the periodic convexo-concave manner at the center. This crack path is called "fracture unit area (FA) cracking" [19-21]. On the other hand, the creep crack grew in a linear manner at the side as shown in Fig. 8.

Creep crack length of each interrupted times were measured. At 52.5h (t/t_f = 0.17), the creep crack did not initiate both at the center and at the side. After the middle of total life (t/t_f > 0.50), the creep crack has already initiated both at the center and at the side. And the creep crack length of the side was longer than that of the center. This tendency became marked at 226h (t/t_f = 0.75). This result indicates that the creep crack was preferential growth at the side from 50% to 75% of total life and accelerated at the center after 75% of total life. Therefore, it seems that the creep crack of C(T) specimen with side-grooves grew as shown in Fig. 9. The characteristic of CCG without the steady-state CCG rate region is thought to be due to the preferential CCG at the side.

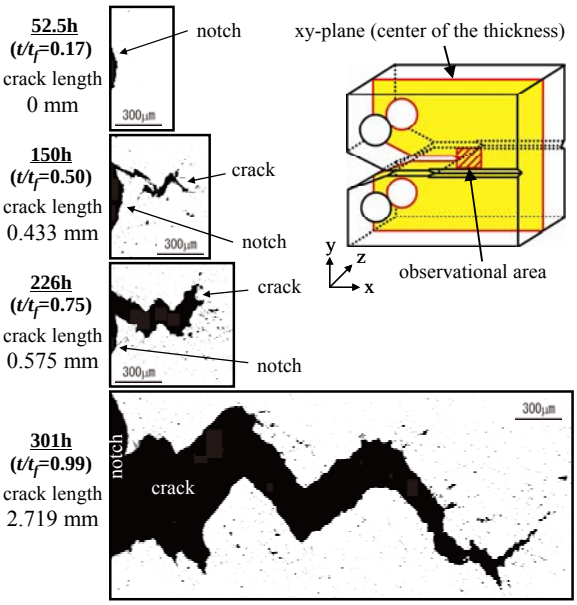

Figure 7. CCG path of center

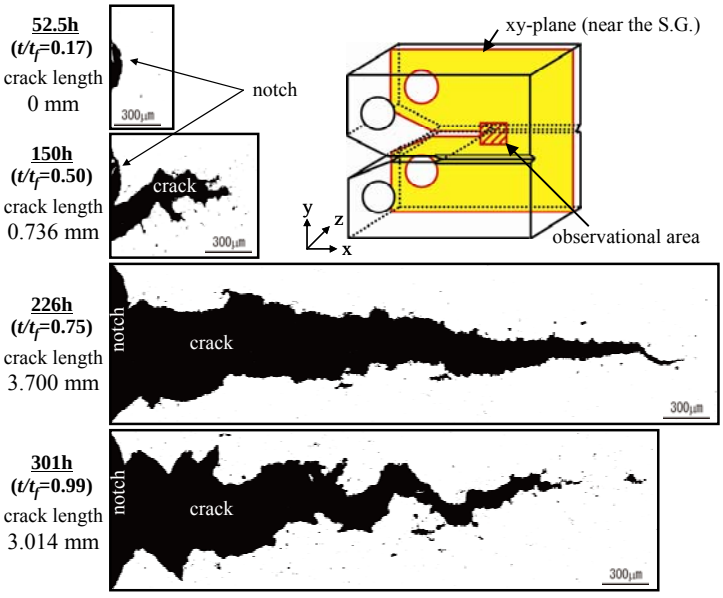

Figure 8. CCG path of side

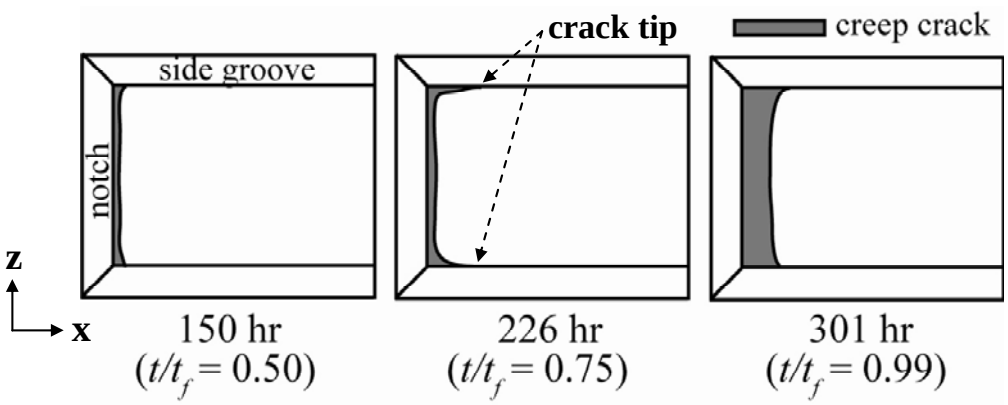

Figure 9. Schematic illustrations of CCG process on the xz-plane

4.3. Analytical Results

Figure 10 (a) and (b) represent the distributions of vacancy concentration at 0h (initial) and 100h in a shaded area shown in Fig. 11, respectively. From these figures, vacancies remarkably accumulated at the corner of the bottoms of notch and side-groove. And vacancies also accumulated at the bottom of side-groove near the notch tip. These results are in good agreement with the experimental result of the preferential CCG at the side. Figure 12 (a)-(c) show the distributions of vacancy concentration along line segment oa, bc and ob shown in Fig. 11, respectively. From Fig. 12 (b), the vacancy concentration at the bottom of side-groove increased within about 3 mm from the notch tip and this length correspond to the creep crack length of 226h and 301h at the side. These results indicate that the creep crack preferentially grows in the region of high vacancy concentration. Therefore, it seems that the three-dimensional vacancy diffusion analysis is useful to predict the behavior of creep damage such as creep voids and cracks.
From the experimental results, it was clarified that the creep crack of C(T) specimen with side-grooves of 25% of specimen thickness preferentially grew near the side-groove. On the other hand, the creep crack of C(T) specimen without side-grooves preferentially grows at the center and this is crack tunneling. Three-dimensional vacancy diffusion analysis enables us to predict the most appropriate depth of side-grooves which cause the uniform creep crack growth in the thickness direction.

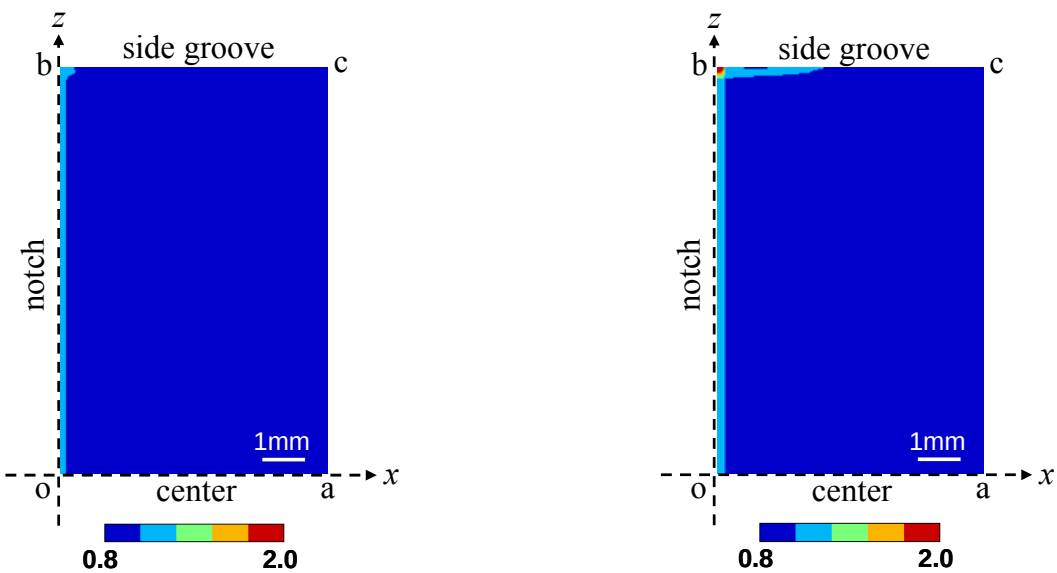

(a) 0h (initial) (b) 100h

Figure 10. Distributions of vacancy concentration at a shaded area shown in Fig. 10

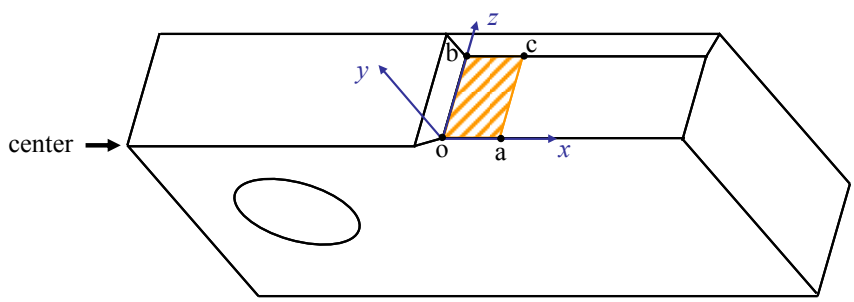

Figure 11. A Schematic illustration of 1/4 C(T) specimen

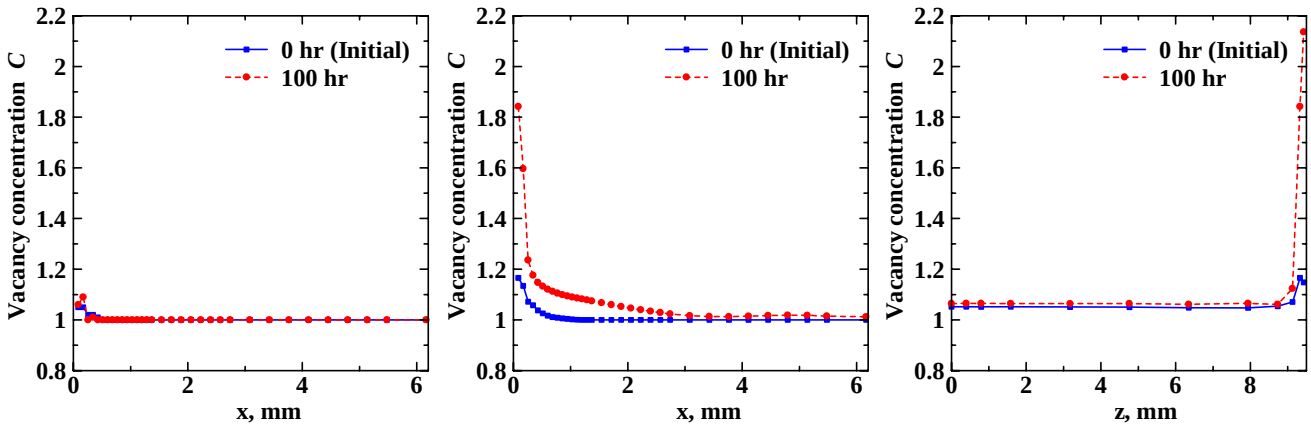

(a) Line segment oa (center) (b) Line segment bc (side) (c) Line segment ob (notch)

Figure 12. Distributions of vacancy concentration along each line segment

5. Conclusions

Interrupted CCG tests were conducted using C(T) specimens with side-grooves of P92 steel. Then, the creep crack growth path of each interrupted specimen was observed and the creep crack growth behavior of P92 steel was investigated. Furthermore, the three-dimensional vacancy diffusion analysis was conducted to clarify the three-dimensional diffusion behavior of vacancies which related to the void formation and crack growth. Following results were obtained:

(1) The creep crack growth forms were different between the center of the thickness direction and near the side-groove. For the center of the thickness direction, the creep crack growth behavior showed the periodic convexo-concave manner. On the other hand, the creep crack grew in a linear manner near the side-groove.

(2) The creep crack of C(T) specimen with side-grooves of 25% of specimen thickness preferentially grew near the side-groove.

(3) Vacancies remarkably accumulated at the corner of the bottoms of notch and side-groove. The vacancy concentration at the bottom of side-groove increased within about 3 mm from the notch tip and this length correspond to the creep crack length of 226h and 301h near the side-groove.

(4) The three-dimensional vacancy diffusion analysis is useful to predict the behavior of creep damage such as creep voids and cracks.

Acknowledgements

This work was partly supported by the Japan Society for the Promotion of Science Research Fellow 24.2235.

References

[1] A.T. Yokobori, Jr., R. Sugiura, M. Tabuchi, A. Fuji, T. Adachi, T. Yokobori, The effect of multi-axial stress component on creep crack growth rate concerning structural brittleness, Proc ICF 11 (2005) CD-ROM.

[2] R. Sugiura, A.T. Yokobori, Jr., M. Tabuchi, A. Fuji, T. Adachi, Characterization of structural embrittlement of creep crack growth for W-added 12%Cr ferritic heat-resistant steel related to the multi axial stress, Trans of ASME, J Eng Mater Technol, 131 (2009) 011004 1-9.

[3] K. Kimura, K. Fujiyama, R. Ishi, K. Saito, Estimation of Creep Damage for the Components of Mod. 9Cr-1Mo Steel: (2nd Report, Creep Damage Assessment for Welded Joint by Means of Void Observation), Trans Jpn Soc Mech Eng, A 66(647) (2000) 1411-1418 (in Japanese).

[4] T. Watanabe, M. Yamazaki, H. Hongo, M. Tabuchi, T. Tanabe, Relationship between Type IV

Fracture and Microstructure on 9Cr-1Mo-V-Nb Steel Welded Joint Creep-ruptured after Long Term, Tetsu-to-Hagane, 90(4) (2004) 206-212 (in Japanese).

[5] T. Ogata, T. Sakai, M. Yaguchi, Damage characterization of a P91 steel weldment under uniaxial and multiaxial creep, Mater Sci Eng A, 510−511 (2009) 238−243.

[6] H. Hongo, M. Tabuchi, T. Watanabe, Type IV Creep Damage Behavior in Gr.91 Steel Welded Joints, Metall Mater Trans A, 43A (2012) 1163-1173.

[7] A.T. Yokobori, Jr., K. Abe, H. Tsukidate, T. Ohmi, R. Sugiura, H. Ishikawa, Micro mechanics based on vacancy diffusion coupled with damage mechanics related to creep deformation and prediction of creep fracture life, Mater High Temp, 28(2) (2011) 126-136.

[8] S. Nakajima, T. Nemoto, A.T. Yokobori, Jr., Lifetime prediction of stress induced voiding failure by novel numerical analysis in Cu interconnects with an ultra low-k dielectric, Proc AMC, (2009) 751-755.

[9] H. Shigeyama, T. Nemoto, A.T. Yokobori, Jr., Prediction of stress induced voiding reliability in Cu damascene interconnect by computer aided vacancy migration analysis, Jpn J Appl Phys, 50 (2011) 05EA05 1-6.

[10] H. Shigeyama, A.T. Yokobori, Jr., T. Ohmi, T. Nemoto, Analysis of stress induced voiding using by finite element analysis coupled with finite difference analysis, Defect Diffus Forum, 326-328 (2012) 632-640.

[11] H.H. Johnson, Calibrating the electric potential method for studying slow crack growth, Mater Res Stand, 5 (1965) 442-445.

[12] K.H. Schwalbe, D. Hellmann, Application of the electrical potential method to crack length measurements using Johnson's formula, J Test Eval, 9(3) (1981) 218-221.

[13] A.T. Yokobori, Jr., T. Nemoto, K. Satoh, T. Yamada, Numerical analysis on hydrogen diffusion and concentration in solid with emission around the crack tip, Eng Fract Mech, 55(1) (1996) 47-60.

[14] A.T. Yokobori, Jr., Y. Chinda, T. Nemoto, K. Sato, T. Yamada, The characteristics of hydrogen diffusion and concentration around a crack tip concerned with hydrogen embrittlement, Corro Sci, 44(3) (2002) 407-424.

[15] A.T. Yokobori, Jr., T. Ohmi, T. Murakawa, T. Nemoto, T. Uesugi R. Sugiura, The application of the analysis of potential driven particle diffusion to the strength of materials, Strength, Fract Complex, 7 (2011) 215-233.

[16] A.T. Yokobori, Jr., T. Uesugi, M. Sendoh, M. Shibata, The effect of stress wave form on corrosion fatigue crack growth rate on the basis of hydrogen diffusion theory, Strength, Fract Complex, 1(4) (2003) 187-204.

[17] T. Nemoto, A.T. Yokobori, Jr., T. Murakawa, H. Miura, Numerical Analysis of Vacancy Transport by Residual Stress in Electromigration on LSI Interconnects, Jpn J Appl Phys, 49 (2010) 024301 1-7.

[18] T. Yokobori, Strength of Materials, Iwanami, Tokyo, 1964.

[19] A.T. Yokobori Jr., S. Takmori, T. Yokobori, Y. Hasegawa, K. Kubota, K. Hidaka, Mechanical Behavior and Strengthening Mechanism of W containing 9-12% Cr Steels under Creep Conditon for a Cracked Specimen, Key Eng Mater, 171-174 (2000) 131-138.

[20] R. Sugiura, A.T. Yokobori Jr., S. Takamori, M. Tabuchi, A. Fuji, M. Yoda, K. Kobayashi, T. Yokobori, Effects of Alloying Additions and Material Microstructure on the Accuracy of the Predictive Law of Creep Crack Growth for W-Strengthened 9-12%Cr Ferritic Heat-Resistant Steel, Mater Trans, 48(11) (2007) 2928-2936.

[21] Y. Nagumo, A.T. Yokobori, Jr., R. Sugiura, T. Matsuzaki, The occurrence mechanism of periodicity of creep crack path for P92, J ASTM Int, 8(8) (2011) 1-11.

Evaluation of Creep Damage and Fracture in High Cr Steel Welds

Masaaki Tabuchi[1,*]

[1] National Institute for Materials Science, Tsukuba Science City 305-0047, Japan
* Corresponding author: TABUCHI.Masaaki@nims.go.jp

Abstract Creep strength of high Cr ferritic steel welds decreases than base metals due to Type-IV creep damages formed in the heat affected zone (HAZ) during long-term use at elevated temperatures. In the present study, microstructural changes and damage evolution behaviors in HAZ during creep were investigated for the ASME Gr.91 and Gr.122 steel weld joints. Creep voids formed at an early stage of life and coalesced to form a macro crack at 0.8 of life for the Gr.91 steel weld. On the other hand, for the high strengthened Gr.122 steel weld, small amounts of Type-IV creep voids formed at 0.5 of life, increased slightly until 0.9 of life and rapid crack growth occurred after that. KAM and grain boundary length of fine-grained HAZ obtained by EBSD decreased and saturated till 0.2 of life in the Gr.91 steel weld, whereas they decreased after 0.5 of life in the Gr.122 steel weld. It was found that the recovery of dislocation structures in HAZ was completed at early stage of life for the Gr.91 steel weld, whereas it occurred after recrystallization at the later stage of life for the Gr.122 steel weld. These differences of microstructural changes was considered to relate to the differences of Type-IV creep damage behavior; early initiation of creep voids at 0.2 of life in the Gr.91 steel weld and later damage evolution after 0.5 of life in the Gr.122 steel weld. From these results the methods for remaining life assessment of high Cr steel welds were discussed.

Keywords High Cr ferritic steel, Welded joint, Creep, Type-IV creep damage, EBSD

1. Introduction

In order to improve the efficiency of power generation, the pressure and temperature conditions of steam in thermal plant have been continuously increased. In 1990s, the high Cr ferritic heat resisting steels were applied to the boiler components in 600 ˚C class ultra super critical (USC) thermal power plants in Japan. The base metals of these steels with tempered martensite structures have excellent high temperature strength; however, fine-grained structures without lath-martensite are formed in the heat-affected zone (HAZ) during weld thermal-cycle and the creep strength of welds decreases than the base metals. The Type-IV failure along the inter-critical and fine-grained HAZ of weld joints is caused through the nucleation and growth of creep voids and cracks during long-term services at high temperatures [1-8]. Recently, it was recommended to take the weld strength reduction factor (WSRF) into account for the high temperature design using high Cr steels [9, 10]. It is important to understand the microstructural changes and damage evolutions in HAZ during creep for the remaining life assessment of weld components.

In the present paper, aiming to elucidate the Type-IV failure mechanisms of Gr.91 and Gr.122 steel welds, we have evaluated the Type-IV creep damage evolutions and microstructural degradations through interrupting creep tests of the large-scale welded joint specimens. Remaining life assessment methods of high Cr steel welds were discussed based on the experimental results.

2. Experimental procedure

The materials investigated are the Gr.91 steel (9Cr-1Mo-VNb steel) plate with a thickness of 25mm and the Gr.122 steel (11Cr-0.4Mo-2W-CuVNb steel) plate with a thickness of 30mm. The plates were welded by gas tungsten arc (GTA) welding using a double U groove. After welding, a post-weld heat treatment (PWHT) was conducted at 745 ˚C for 60 min for the Gr.91 steel weld and for 75 min for the Gr.122 steel weld.

The simulated fine-grained HAZ (f-HAZ) specimens were produced using a weld simulator (a Gleeble testing machine) by rapid heating to a peak temperature of 900 ˚C for the Gr.91 steel and 950 ˚C for the Gr.122 steel, respectively. Creep tests of the base metal and simulated f-HAZ were conducted using smooth bar specimens and those of the welded joints were conducted using smooth plate type specimens of 17.5 × 5 mm^2 in cross-section and 100 mm in gauge length (S-welded joint) at 550, 600 and 650 ˚C [7].

Creep interruption tests were conducted using a large-scale thick plate type specimen (L-welded joint) of 21 × 21 mm^2 in cross-section and 100 mm in gauge length for the Gr.91 steel weld and of 24.5 × 24.5 mm^2 in cross-section and 120 mm in gauge length for the Gr.122 steel weld, which included the full original plate thickness close to the structural components [7, 8]. Creep tests were conducted using several L-welded joint specimens at 600 ˚C and interrupted at several time steps. Because creep voids formed inside the specimen, we cut the specimens in the center of width after interruption of creep tests, and observed the creep voids in HAZ using SEM or laser-microscope. The area and number of creep voids were measured using the image processing software. Changes of microstructures in fine-grained HAZ were investigated by measuring KAM (Kernel average misorientation) and grain boundary length using EBSD (Electron backscatter diffraction).

3. Results and discussion

3.1. Creep strength of welded joints

Figure 1 and 2 show the creep test results for the base metal, simulated f-HAZ and welded joints of the Gr.91 steel and Gr.122 steel, respectively. The failure locations of the welded joint specimens are indicated with the subscripts attached to the plots, where BM means failure in base metal and HAZ means Type-IV failure in the fine-grained HAZ. In the Gr.91 steel weld, the Type-IV failure occurred after 10,000h at 550 ˚C and 1,000h at 600 ˚C. The differences in creep rupture times between welded joint and base metal tended to widen with decreasing stress. The creep rupture times of the simulated f-HAZ were more than one order shorter than those of the base metal for the same stresses at all temperatures. The creep rupture times of the welded joint approached those of the simulated f-HAZ for low stresses at all temperatures.

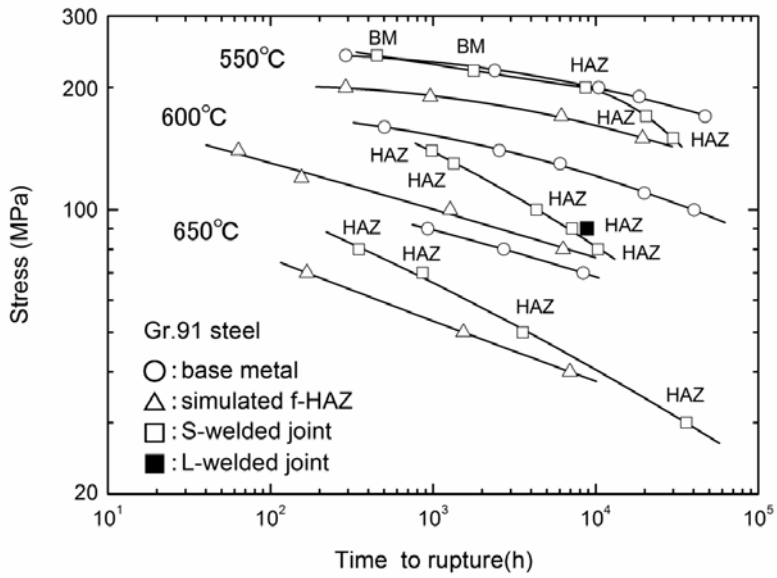

Figure 1. Creep rupture times of the base metal, simulated f-HAZ and welded joints of the Gr.91 steel.

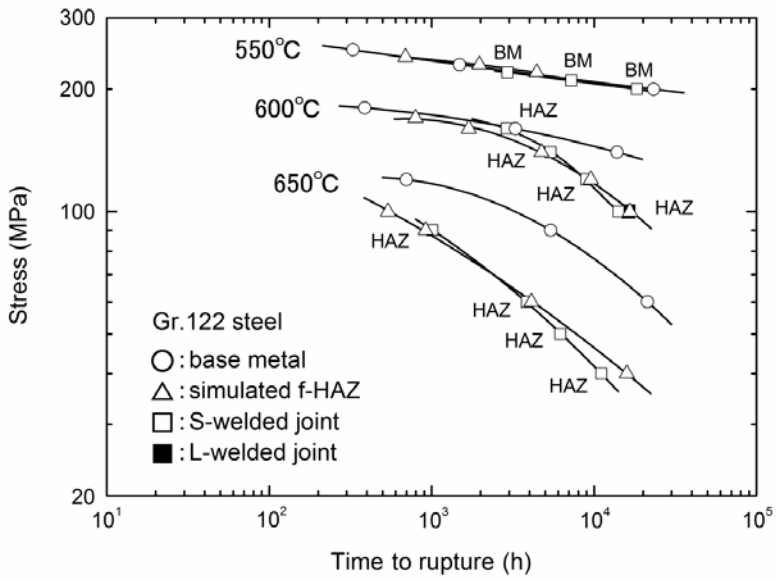

Figure 2. Creep rupture times of the base metal, simulated f-HAZ and welded joints of the Gr.122 steel.

For the Gr.122 steel welds, Type-IV failure did not occur at 550 ˚C within this test stress. It was observed after 5,000 h at 600 ˚C. The creep rupture times of the simulated f-HAZ were nearly the same as the base metal at 550 ˚C; they decreased than the base metal after 5,000 h at 600 ˚C. The differences in creep rupture times between base metal and simulated f-HAZ were more than one order at all test conditions for the Gr.91 steel, whereas they appeared at lower stresses than 140 MPa at 600 ˚C for the Gr.122 steel. At these test conditions, the simulated f-HAZ of the Gr.122 steel revealed void- type inter-granular failure and its creep ductility decreased.

3.2. Evolution of Type-IV creep damage

Creep rupture times of the L-welded joints were 8,853 h at 600 ˚C and 90 MPa for the Gr.91 steel and 16,340 h at 600 ˚C and 100 MPa for the Gr.122 steel; they also showed the Type-IV failure and their rupture times were slightly longer than the S-welded joints as shown in Figs. 1 and 2. We have conducted the creep interruption tests using the L-welded joints for both steels at these test conditions and investigated the processes of Type-IV damage and fracture. Figure 3 shows the binary images of creep voids and cracks observed in HAZ of the central cross-section of the L-welded joints of the Gr.91 steel creep-interrupted at 600 ˚C and 90 MPa. It was found that a small number of creep voids formed at about 0.2 of creep rupture life, and the number of voids increased with time, and then coalesced to form a crack at 0.8 of life. Creep voids and cracks were mostly observed in the area about 20% below the plate surfaces.

The area fraction of creep voids in the HAZ of the Gr.91 and Gr.122 steel welds are plotted against the life ratio (t/t_r) in Fig. 4. In this figure, the area fraction of creep voids in the area about 20% below the plate surfaces where it shows the highest value is plotted. It was found that the Type-IV damage behavior and amounts of creep voids were considerably different for both steel welds. In the Gr.91 steel weld, Type-IV creep voids formed at the early stage 0.2 of creep life and increased gradually with elapse of time. On the other hand, in the Gr.122 steel weld, only a small amount of creep voids formed at 0.5 of creep life and slightly increased till 0.9 of life. Type-IV crack was not observed till 0.92 of life; it was observed in the specimen interrupted at 0.98 of life as shown in Fig. 4. The formation and growth of creep voids were suppressed during steady-state condition;

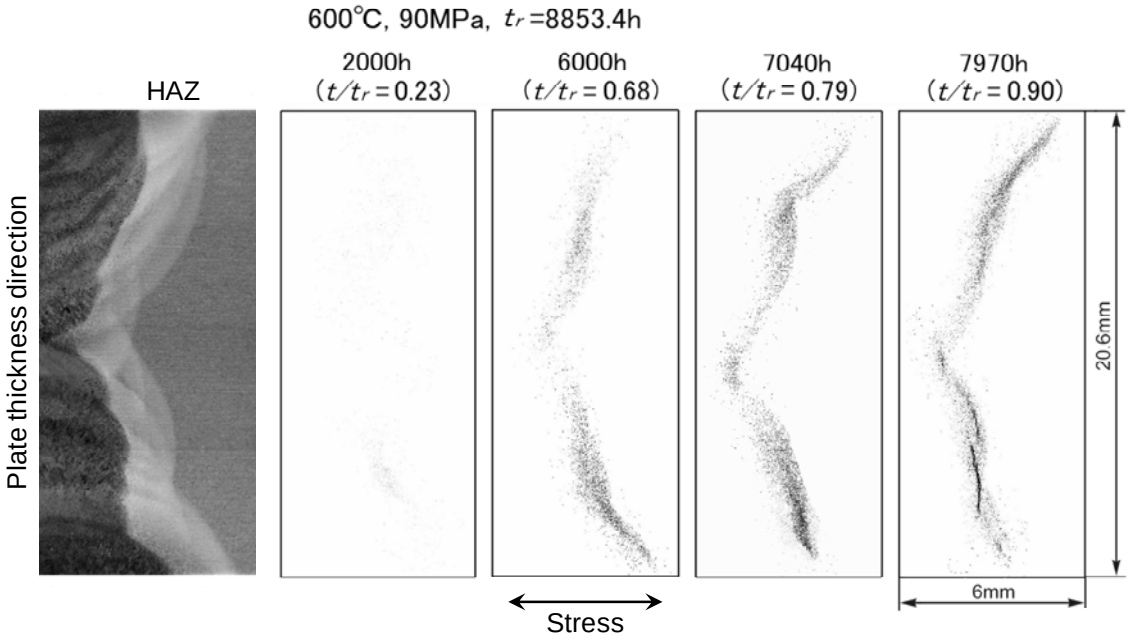

Figure 3. Binary images of creep voids and cracks observed in the HAZ of a central cross-section of the L-welded joints for the Gr.91 steel crept at 600 ˚C and 90 MPa.

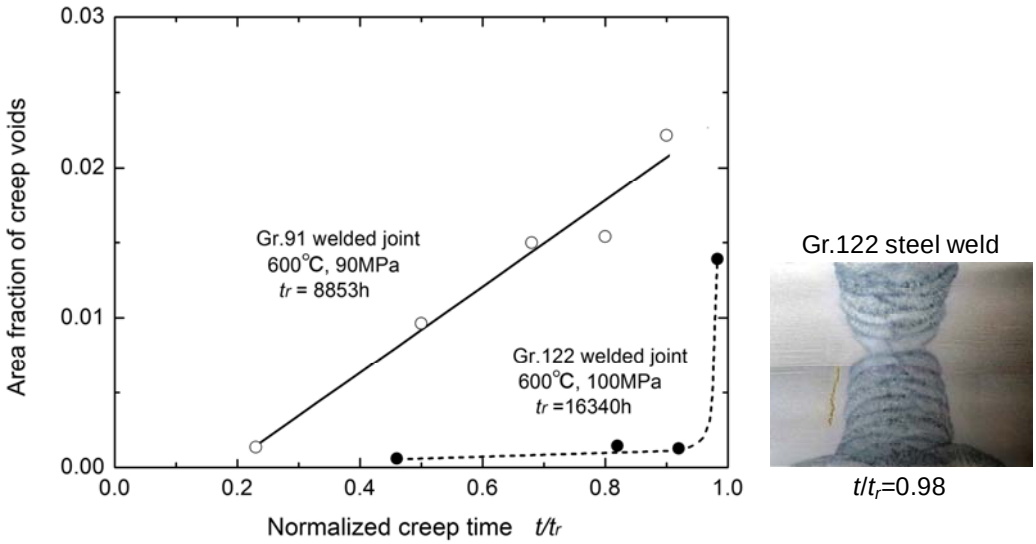

Figure 4. Changes of the area fraction of creep voids in HAZ during creep of the Gr.91 and Gr.122 steel welds at 600 ˚C.

however, the crack growth rate in the accelerated stage was high for the high strengthened Gr.122 steel. The lower creep ductility of the Gr.122 steel is related to these damage behavior.

3.3. Micro-structural changes in HAZ

Changes of microstructures of HAZ in the creep-interrupted L-welded joints was observed and KAM and grain boundary length were measured using EBSD. Figure 5 shows the changes in the grain boundary length in the fine-grained HAZ during creep for both steel welds. Here, length of grain boundaries with misorientation from 5˚ to 65˚ is plotted as prior austenitic boundaries. For the

f-HAZ in the Gr.91 steel weld, the grain boundary length decreased till 0.2 of life and saturated after that. On the other hand, for the f-HAZ in the Gr.122 steel weld, the grain boundary length increased till 0.5 of life, and then decreased after that. The decrease of grain boundary length occurs due to the recovery of microstructures during creep.

Figure 6 shows the changes in the micro-hardness and KAM of fine-grained HAZ during creep for both steel welds. Here, average value of KAM is plotted excluding the points whose misorientation is larger than 5˚ in order to investigate the changes of dislocation structures. For the f-HAZ in the Gr.91 steel weld, hardness and KAM decreased till 0.2 of life and saturated to constant value, whereas they did not change till 0.5 of life and then decreased after that for the Gr.122 steel weld. The decrease of KAM and hardness occurs due to the recovery of dislocation structures. Because the grain boundary length increased without changing KAM and hardness till 0.5 of life, dynamic recrystallization was considered to be occurred in the fine-grained HAZ of the Gr.122 steel.

These differences of microstructural changes are considered to relate to the differences of creep damage behavior between two steels. In the Gr.91 steel weld, the recovery of dislocation structures of f-HAZ occurs at early stage of life, and then early initiation and evolution of Type-IV creep voids occur. In the Gr.122 steel weld, the recovery of dislocation structures occurs after the recrystallization of f-HAZ, and then damage evolution occurs at later stage of life.

From these experimental results, we consider about the methods for the residual life assessment of weld components as follows. For the Gr.91 steel weld, ultrasonic nondestructive testing is available for residual life assessment because creep voids and cracks increase gradually inside the plate thickness. Hardness measurement and microstructural observation are not available because their changes saturate in the early stage of life. Local necking on the specimen surface in HAZ is also available because the creep ductility is high for the Gr.91 steel. For the Gr.122 steel weld, ultrasonic testing may be difficult to detect Type-IV creep damages because the amount of voids are small and crack grows rapidly after 0.9 of life. Evaluation of hardness and dislocation structures (KAM) are available because they change largely in the latter half of life. Local necking on the specimen surface was scarcely observed for the Gr.122 steel weld with low creep ductility.

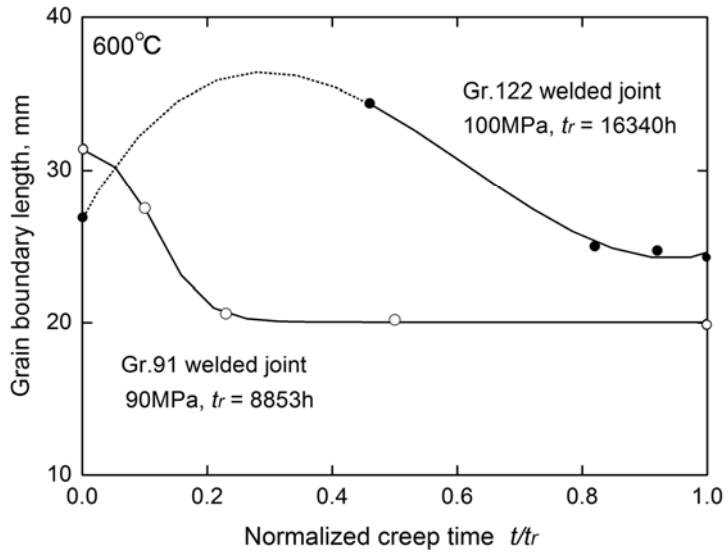

Figure 5. Changes in the grain boundary length in the fine-grained HAZ during creep for the Gr.91 and Gr.122 steel welds measured by EBSD.

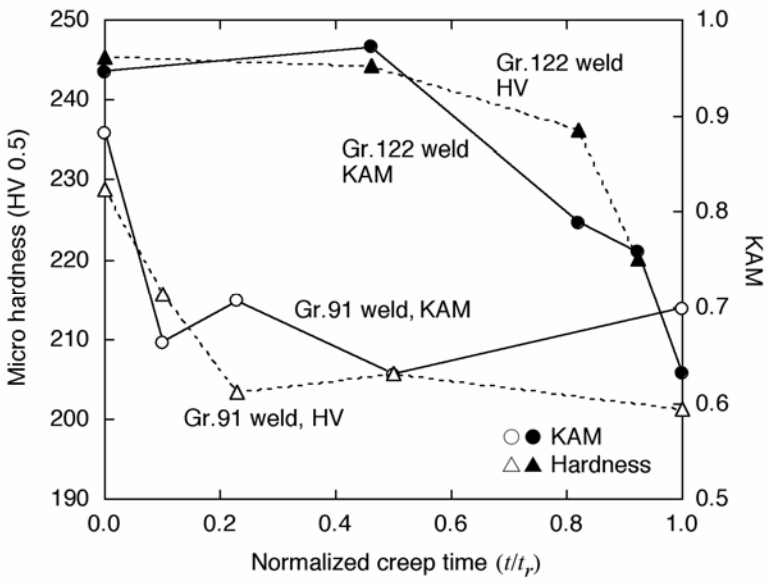

Figure 6. Changes in the micro hardness and KAM in the fine-grained HAZ during creep for the Gr.91 and Gr.122 steel welds measured by EBSD.

4. Conclusions

In the present paper, creep strength, Type-IV damage evolution and microstructural change during creep in the Gr.91 and Gr.122 steel welds were investigated quantitatively using the large-scale welded joint specimens. The results are summarized as follows:

(1) In the Gr.91 steel weld, the Type-IV failure occurred after 10,000h at 550 ˚C and 1,000h at 600 ˚C. In the Gr.122 steel weld, Type-IV failure did not occur at 550 ˚C; it occurred after 5,000 h at 600 ˚C.

(2) Type-IV creep voids in the Gr.91 steel weld formed at the early stage 0.2 of creep life, increased with elapse of time, and then coalesced to form a macro crack after 0.8 of life.

(3) In the Gr.122 steel weld, a small number of Type-IV creep voids formed at 0.5 of life, increased slightly until 0.9 of life, and then rapid crack growth occurred after that. The area fraction of creep voids in the Gr.122 steel weld was much smaller than that in the Gr.91 steel weld.

(4) In the Gr.91 steel weld, the recovery of dislocation structures of fine-grained HAZ occurred at early stage 0.2 of life, and was followed by early initiation and evolution of Type-IV creep voids. In the Gr.122 steel weld, the recovery of dislocation structures occurred after recrystallization of fine-grained HAZ, and then damage evolution occurred at later stage of life.

(5) Form the above experimental results, for the Gr.91 steel weld; it is considered that ultrasonic nondestructive testing etc. is available for the residual life assessment because creep voids and cracks increase gradually inside the plate thickness. Hardness measurement and microstructural observation of fine-grained HAZ are not available because their changes saturate in the early stage of life.

(6) For the Gr.122 steel weld, ultrasonic testing is considered to be difficult to detect Type-IV creep damages because the amount of voids are small and crack grows rapidly after 0.9 of life. Evaluation of hardness and dislocation structures (KAM) are available for the residual life assessment because they change largely after 0.5 of life.

References

[1] G. Eggeler, A. Ramteke, M. Coleman, B. Chew, G. Peter, A. Burblies, J. Hald, C. Jefferey, J. Rantala, M. deWitte, R. Mohrmann, Analysis of creep in a welded P91 pressure vessel. International Journal of Pressure Vessels and Piping, 60 (1994) 237-257.

[2] J.A. Francis, W. Mazur, H.K.D.H. Bhadeshia, Review-Type IV cracking in ferritic power plant steels. Materials Science and Technology, 22 (2006) 1387-1395.

[3] F. Masuyama, Creep degradation in welds of Mod.9Cr-1Mo steel. International Journal of Pressure Vessels and Piping, 83 (2006) 819-825.

[4] Y. Hasegawa, T. Muraki, M. Ohgami, Identification and formation mechanism of a deformation process determining microstructure of Type-IV creep damage of the advanced high Cr containing ferritic heat resistant Steel. Tetsu-to Hagane, 92 (2006) 609-617.

[5] K. Kubushiro, S. Takahashi, K. Morishima, Degradation of microstructures during creep in high Cr steel weldment. Journal of the Society of Materials Science, Japan, 59 (2010) 840-845.

[6] T. Ogata, T. Sakai, M. Yaguchi, Damage assessment method of P91 steel welded tube under internal pressure creep based on void growth simulation. International Journal of Pressure Vessels and Piping, 87 (2010) 611-616.

[7] H. Hongo, M. Tabuchi, T. Watanabe, Type IV creep damage behavior in Gr.91 steel welded joints. Metallurgical and Materials Transactions A, 43A (2012) 1163-1173.

[8] M. Tabuchi, H. Hongo, Evaluation of long-term creep damage in high Cr ferritic steel welds. Materials at High Temperatures, 28 (2011) 172-180.

[9] M. Tabuchi, Y. Takahashi, Evaluation of creep strength reduction factors for welded joints of modified 9Cr-1Mo steel. Transactions of the ASME, Journal of Pressure Vessel Technology, 134 (2012) 031401-1-6.

[10] Y. Takahashi, M. Tabuchi, Evaluation of creep strength reduction factors for welded joints of Grade 122 steel. Transactions of the ASME, Journal of Pressure Vessel Technology, 133 (2011) 021401-1-5.

Fracture Based Testing and Modelling, and Component Life Assessment of Welds

Kamran Nikbin

Mechanical Engineering Department, Imperial College, London, SW7 2AZ, UK
Corresponding author: k.nikbin@imperial.ac.uk

Abstract Fracture mechanics based methodologies are an important area of research that benefit life assessment techniques in components operating at elevated temperatures. There are many factors which determine a successful methodology for remaining life assessment of engineering components. Important elements are good testing techniques, the development of appropriate and accurate correlating parameters to treat the results in a the unified and verifiable manner in order to produce 'benchmark' material crack growth properties and developing accurate modelling procedures for life assessment methods. This presentation considers the first two aspects and identifies future trends and improvements in the developments of standardisations in creep and creep/fatigue crack growth testing of weldments containing residual stress. The paper highlights the important points in these pre-standardisation collaborative efforts by presenting the methods of analyses and example of their application to feature type components.
.

Keywords Creep Damage; Damage Mechanics; Life Assessment; crack growth; fatigue

1. Introduction

The power generation industry is striving to meet criteria for clean and sustainable energy production by increasing efficiency while simultaneously decreasing levels of chemical emissions and pollutants. The efficiency of conventional steam and gas turbine power plant can be significantly improved by increasing the operating temperature, leading to reduced fuel consumption and lower levels of harmful emissions. With the trend towards higher operating temperatures and the competing need to extend the life of existing power plant, more accurate and reliable experimental data for use in improved predictions of component lifetimes at elevated temperatures are needed.

In recent years a number of European and International collaborative programmes [1-78] have developed the testing and analysis methodologies as well as a number of databases of laboratory crack growth data base on homogenous parent material. More recently work on crack growth of weldments has been initiated under the auspices of VAMAS TWA31 to address the problems relating to specimens containing welds.

The main objective is to establish accurate and reliable testing methods and a unified procedure for assessing creep crack growth at elevated temperatures in industrial specimens, which contain defects. Determination of procedures for analysing the test data using fracture mechanics concepts is important and therefore the validated correlating parameters are made available in the Code of Practice (CoP) [1]. Validation of results against measurements on standard Compact Tension C(T) laboratory specimens using ASTM E1457 has been also been carried out as it indicates the effects of constraint on specimen geometry and size. There are a number of parameters such as K, linear elastic fracture mechanics, Q^* based on the thermally activated process and K_{cmat} based on creep toughness properties that are included in the CoP [1]. However recommendations are only made

on the basis that they are validated with experimental data. In this paper an outline of geometries that have been tested in a number of EU programmes are identified and the differences in method of analysis using the fracture mechanics parameter C^* in laboratory and components will be highlighted and compared for a pipe and plate component.

1.1 Background to life assessment codes

Components in the power generation and petrochemical industry operating at high temperatures are almost invariably submitted to static and/or combined cycle loading. The alloys used can vary between low carbon steels to high chrome superalloys with various alloying contents. In addition these components have welded parts which will have different alloying and microstructural properties. The failures can be due to large deformations, creep rupture and/or crack growth. The development of codes in different countries has moved in very similar direction and in many cases the methodology has been borrowed from a previously available code in another country. Early approaches to high temperature life assessment have used methodologies based on defect-free assessment codes. For example ASME Code Case N-47 [9] and the French RCC-MR [10], which have many similarities, are based on lifetime assessment of un-cracked structures. More recent methods make life assessments based on the presence of defects in the component. The more advanced codes dealing with defects over the range of creep and creep/fatigue interaction in initiation and growth of defects are the BS 7910 [11], British R5/R6 [12,13], the API RP 579 [14] and the French A16 [15] which have clear similarities in terms of methodology. It is also obvious from these assessment methods that the correct evaluation of the relevant fracture mechanics parameters, for which the lifetime prediction times are dependent upon, are extremely important.

It is also evident therefore that the detailed calculation steps, which are proposed in these documents alone, do not improve the accuracy of the life prediction results. In any event as these procedures have been validated for limited sets of geometries and ‘Benchmark’ material data, their use in other operating conditions will need careful judgment. These aspects have been considered in this paper in order to produce validated fracture mechanics parameters form different geometries for this purpose. The paper highlights recommendations for improved test methods so that verifiable material properties are collected. This allows the modelling methods using standard laboratory and feature component data to be used with increased confidence in life estimation codes. This pre-standardisation work is of relevance to ASTM, ISO, ASME, API (American Petroleum Institute) and PVRC (Pressure Vessels Research Council (USA)) as well as to allow further improvements to life assessment CoP such as R5, BS7910 and A16. Clearly the recommendations resulting from this CoP will be useful for increasing confidence in defect assessment codes.

2 Parameters for Analysing High Temperature Cracking

Typically, fracture mechanics concepts are used to characterise crack initiation and growth at high temperatures. Usually at short times the stress intensity factor K, or the elastic-plastic parameter J, is employed to describe the stress and strain distributions at a crack tip whereas at long times, when

steady state conditions have been reached, the creep fracture mechanics term C^* is used [8,16-20]. During the intervening stage damage formation and stress redistribution is occurring at the crack tip. The parameters are validated by the right usage of parameters to describe creep brittle and creep ductile crack growth [8].

2.1. Steady state CCG analysis

Creep crack growth rate under steady state for a creep ductile material is usually analysed using the fracture mechanics parameter C^* [16-20]. The derivation for C^* which is analogous to J is well documented [16,17] and will not be detailed in this paper. Once a steady-state distribution of stress and creep damage has been developed ahead of a crack tip, it is usually found that creep crack growth rate $\dot{a}$ can be described by an expression of form [16-20]:

$$\dot{a} = D \cdot C^{*\phi} \tag{1}$$

where D and ϕ are material constants.

Where creep dominates most often the constants in Eqn. (1) are obtained from tests that are carried out on compact tension (C(T)) specimens based on the recommendations of ASTM E1457 [8] standard and hence, C^* is estimated experimentally from measurements of creep load-line displacement according to the experimentally determined value of C^* given by

$$C^* = \frac{P\dot{\Delta}^c}{B_n(W-a)}\frac{n}{n+1}\eta \tag{2}$$

where $\dot{\Delta}^c$ is the load line displacement rate due to creep alone, B_n, W and a are the specimen net thickness (accounting for side-grooves), width and crack length, respectively, n is the creep stress exponent. The geometry function η from [16,21-22] is given as

$$\eta = -\frac{1}{m}\frac{dm}{d(a/W)}. \tag{3}$$

Where m is a function of collapse load of the cracked body [22]. Solutions for the η functions, in different geometries, based on analytical solutions (limit load analyses) and finite element calculations are available [22]. From Eqn. (2) therefore providing that the displacement rates can be measured it is possible to simply derive C^* experimentally [23,24] for subsequent use in Eqn. (1).

2.2. Reference stress method of estimating C^*

The data obtained from C(T) specimens using Eqn. (1) is considered as ‘benchmark’ material data

for creep crack growth properties of the materials in the same way as creep strain rate and rupture for uniaxial creep tests. These data can be employed directly in crack initiation and growth models described in the different codes [11-15] to estimate residual lives in components. For components such as pipes and plates, on the other hand, C^* must be determined from finite element analysis or reference stress methods. For this the reference stress procedure is adopted in line with that used in the defect assessment codes [11-15]. With this approach C^* is expressed approximately as [16]:

$$C^*_{ref} = \sigma_{ref} \cdot \dot{\varepsilon}_{ref} \cdot \left(\frac{K}{\sigma_{ref}} \right)^2 \tag{4}$$

where $\dot{\varepsilon}_{ref}$ is the creep strain rate at the appropriate σ_{ref} for the component and K is the stress intensity factor corresponding to the applied loading. When the creep strain rate $\dot{\varepsilon}$ at an applied stress σ can be described in terms of the Norton creep law [16]:

$$\dot{\varepsilon} = A \cdot \sigma^n \tag{5}$$

where A and n are material constants at constant temperature. Thus, Eqn. (4) can be rewritten as:

$$C^*_{ref} = A \cdot \sigma_{ref}^{n-1} \cdot K^2 \tag{6}$$

The typical value for n is between 5 and 12 for most metals. In addition, the concept of the average creep rate, $\dot{\varepsilon}_{Ave}$, obtained directly from rupture data, has been used to account for all three stages of creep as an approximate method for estimating the average creep rate $\dot{\varepsilon}_{Ave}$ as shown and defined by

$$\dot{\varepsilon}_{Ave} = \frac{\varepsilon_f}{t_R} = \dot{\varepsilon}_o \cdot \left(\frac{\sigma}{\sigma_0} \right)^{n_{Ave}} = A_{Ave} \cdot \sigma^{n_{Ave}} \tag{7}$$

where σ is the applied stress, ε_f is the uniaxial failure strain, t_R is the time-to-rupture and A_{Ave}, n_{Ave}, σ_o and $\dot{\varepsilon}_0$ are material constants.

2.3. Creep Crack Initiation (CCI) analysis

When a structure containing a defect is first loaded the stress distribution is given by the elastic K-field or the elastic-plastic J-field. Therefore, time is required for the stresses to redistribute to the steady-state creep stress distribution controlled by C^*. During this period, transient conditions exist which are not uniquely defined by C^*. In addition, a period of time is needed for creep damage to develop around the crack tip [16]. Furthermore due to the practical limitations of crack detection equipment, the initiation of crack growth is difficult to determine precisely. Typically, this ranges between an extension Δa of between about 0.1 and 0.5 mm depending on component and crack

dimensions. For laboratory specimen such as CT, ASTM E1457 [8] identifies an extension of 0.2 mm to cover the entire transition time to steady state conditions and this distance also takes into account the resolution of crack monitoring equipment. However, in order to increase the confidence in the crack measurement of the different components, it has been determined, in this present work, that Δa = 0.5 mm was the best value to choose to compare both the CT data and the semi-elliptical defects in the pipes and plates.

From Eqn. (1) it may be expected that the time, t_i, to initiate a crack extension of Δa can be expressed by:

$$t_i = D_i \cdot C*^{\phi_i} \tag{8}$$

where D_i and ϕ_i are material constants. For steady-state cracking D_i is expected to be given approximately by $\Delta a / D$ with $\phi_i = -\phi$ and hence Eqn. (8) can be re-written as follows [23,24]:

$$t_i = \frac{\Delta a}{D} \cdot C*^{-\phi_i} \tag{9}$$

This equation assumes that the entire initiation period is governed by steady-state C*. This cannot be expected to be true during at least part of the initiation period t_i. The applicability of the equation has been examined for the pipes and plates [1] in the same as has been done for crack growth.

2.4. Fatigue crack growth (FCG) rates

For fatigue crack growth it is assumed that the mechanism is time and temperature independent and K or J dominates at the crack tip. At room temperature under cyclic loading conditions, crack propagation usually occurs by a fatigue mechanism where the Paris Law can describe crack growth/cycle $(da/dN)_f$ in terms of stress intensity factor range ΔK by

$$(da/dN)_f = C' \Delta K^{m'} \tag{10}$$

Where da/dN is fatigue crack growth rate per cycle, C' and m' are material dependent parameters, which may be sensitive to the minimum to maximum load ratio R of the cycle. The procedure for fatigue crack growth testing is well known [25]. However for low frequency dwell periods where creep dominates the parameter of choice would be the same as for static creep testing such as C*[16,26].

2.5. Analysis of creep/fatigue crack growth (CFCG) rates

At elevated temperatures combined creep and fatigue crack growth may take place. However in most cases fatigue dominates at higher frequencies (f>1Hz) and creep dominates at lower

frequencies and dwell periods (f<0.1Hz) [26]. In most cases the total crack growth crack growth calculations under cyclic loading can be described as

$$(da/dN) = (da/dN)_c + (da/dN)_f \tag{11}$$

Where this linear summation combines creep and fatigue components. This can be refined using the method given in the British Energy's R5 Procedure [12].

Total crack growth per cycle, (*da/dN*), can be described by Eqns. (1,(10). It can be shown that a simple cumulative damage law can be applied to describe creep/fatigue interactions [26]. Fatigue analysis is usually conducted by using the linear elastic *K* parameter [1,8] and the creep portion can be described by *C** [26].

1. GEOMETRIES USED IN CRACK GROWTH TESTS

The VAMAS procedure covers a range of geometries for testing at high temperatures. These are placed in two categories. The first are the recommended standard fracture mechanics specimens and the second are the 'feature specimens' which cover all non-standard test specimens which could resemble components. These are described in brief in the following sections.

Table 1: Specimen names and abbreviations

C(T)	Compact Tension
CS(T)	C-Shaped Tension
SEN(T)	Single Edge Notched Tension geometry
SEN(B)	Single Edged Notched Bending geometry
DEN(T)	Double Edge Notched Tension geometry
M(T) or CC(T)	Middle Tension or Centre (through) Cracked Panel in Tension

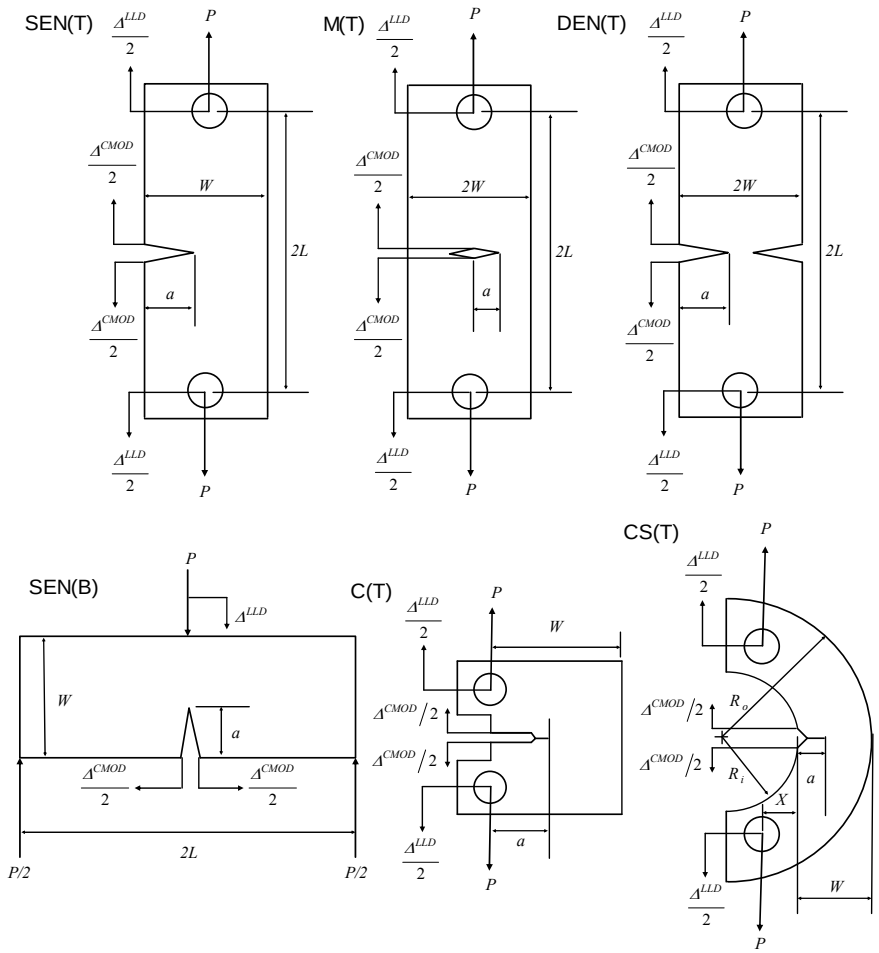

Figure 1: Schematic drawings for the fracture mechanics geometries showing the loading directions, and the load-line Δ^{LLD} and crack Mouth opening Δ^{CMOD} measuring positions.

2.6. Fracture mechanics specimens

As a result of EU collaborative programmes [2-7] especially in HIDA [3], LICON [4] and CRETE [5] tests were performed on a number of fracture mechanics geometries. The VAMAS procedure [1] uses the information provided by these programmes to identify and catalogue six specimen geometries, as given in Table 1, that have been verified for the purpose of creep and creep/fatigue crack growth and initiation testing and are comparable to C(T) test data [23]. Abbreviations denoting the specimen geometries are also given in Table 1. The choice of specific specimens does not mean that other geometries should not be used for testing but that they would need validation before their inclusion in the procedure. Detailed dimensions, machining instructions methods of setting up and limits of testing accuracies are described in the procedure. Figure 1 shows the schematic drawings of the six fracture mechanics geometries showing the loading directions, and the load-line Δ^{LLD} and crack Mouth opening Δ^{CMOD} measuring positions.

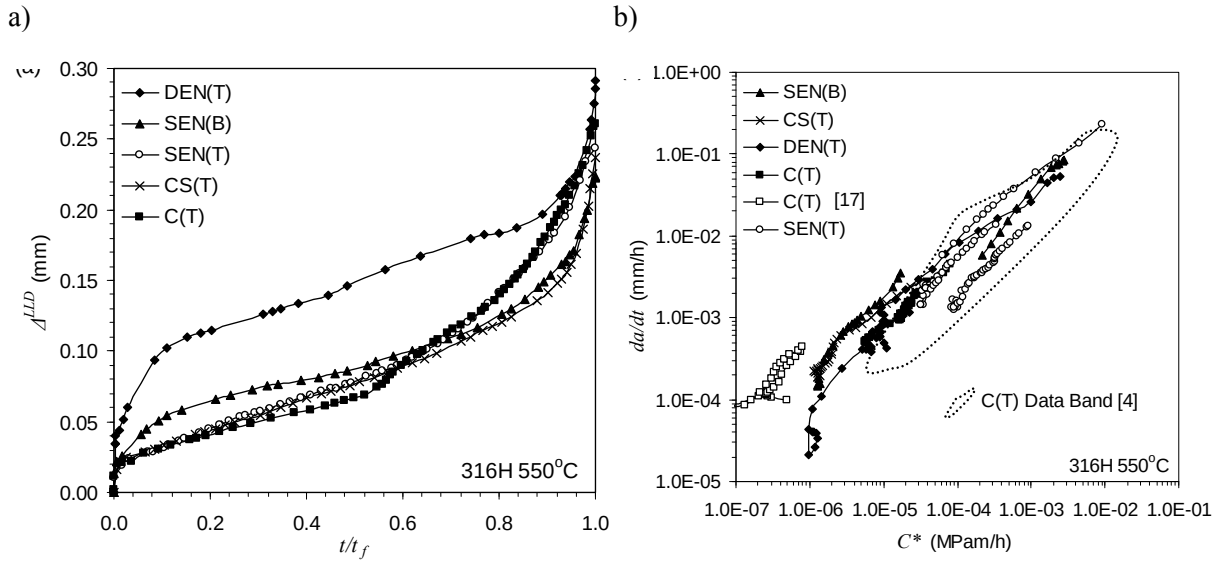

Figure 2: a)Example of normalised crack length versus time data and b) Comparison of the creep crack growth rates with C^* for different geometries with the C(T) databand, for $\Delta a \geq 0.2$ mm, in 316H stainless steel at 550 °C.

An example of data obtained and analysed from these specimens are shown in Fig. 2. Fig. 2a shows the normalised crack length versus time for the different geometries and Fig. 3b shows the correlation of the data when compared to a C(T) databand of the same 316 type stainless steel material. This suggests that for the range of sizes and geometries used the crack growth data obtained is comparable to within the inherent scatter of data.

2.7. Feature Specimens

Feature type specimens, which can represent component related geometries, were also tested for verification and validation in different collaborative programme [3]. These consist of pipes, plates and notched bar cracked specimens. The testing of such specimens is costly and difficult and is not recommended as a routine procedure for deriving data but they can be used to validate the laboratory data in comparison to components.

Analysis of component or feature component testing was an important part of VAMAS TWA25 procedure [1]. It has been shown previously that although different codes employ Eqns. (5-7), often different formulae are used to evaluate K and σ_{ref}. Greater sensitivity of C^* and cracking rate to reference stress than to K is expected from Eqn. (5) since ϕ in Eqn. (1) is close to one, and typically n>>1 and evidence of this has been demonstrated previously [28]. It has also been previously demonstrated that 'global' collapse solution represent best the cracking behaviour in pipe components [1]. Some examples of the comparisons of data for the plate and pipe with C(T) specimens are given in the next section to highlight the analysis and the difficulties that exist in producing and treating the data from feature test. Furthermore since it has been shown [28] that there is no absolute correct solution for reference stress in components and that in order to get an overall agreed definition compromises have to be made. It may be possible by using detailed FE

analysis of the geometry in 3D and the right boundary conditions and material properties to improve the solutions in the future.

For plates there exist several reference stress solutions [11-15] which use Eqns. (4),(6) to derive C^*. However in the VAMAS procedure [1] one reference stress solution is chosen. It has been shown that for small partially penetrating defects in plates subjected to combined tension and bending loading, these reference stresses can significantly over-estimate creep crack growth rates. Therefore a recommended reference stress, which is based on a global collapse mechanism is expressed as follows:

$$\sigma_{ref\ Plate} = \frac{(\sigma_b + 3\cdot\gamma\cdot\sigma_m) + \left\{(\sigma_b + 3\cdot\gamma\cdot\sigma_m) + 9\cdot\sigma_m^2\cdot\left[(1-\gamma)^2 + 2\cdot\gamma\cdot(\alpha-\gamma)\right]\right\}^{1/2}}{3\cdot\left\{(1-\gamma)^2 + 2\cdot\gamma\cdot(\alpha-\gamma)\right\}} \qquad (12)$$

where $\gamma = (a\cdot c) / (W\cdot l)$ and $\alpha = a / W$. In these equations, a is crack depth, c is half crack length at the surface, W is the thickness of the plate and l is the half-width of the plate, respectively.

a) b)

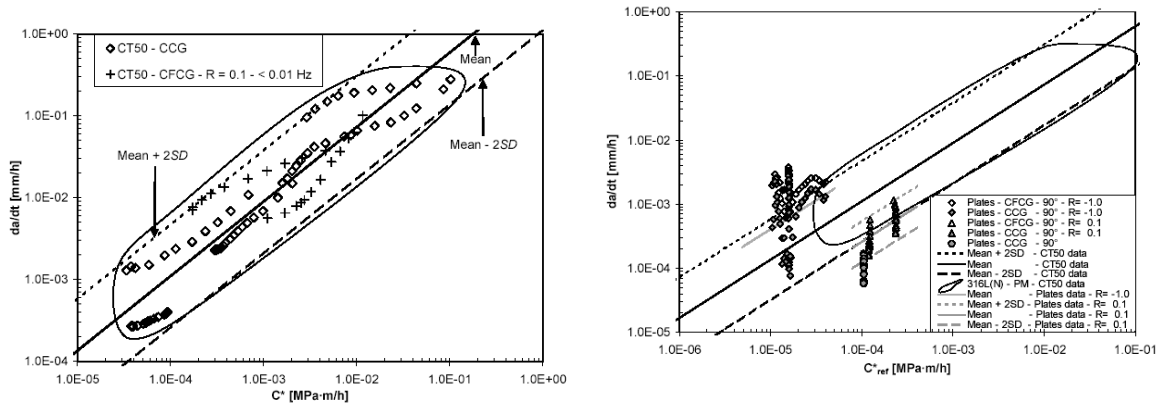

Figure 3: Effect of static and cyclic loading on crack growth rate, for 316LN at 650°C for a) C(T) specimens [3] showing the range of data scatter and b) comparison of plate crack growth data at different frequencies with the same C(T) databand as in Fig. 5(a)

Fig. 4 gives an example of comparing the effects of frequency and the plate geometry for a 316LN type stainless steel tested at 650 ^{o}C [3]. Fig. 5a highlights that for low frequencies the crack growth data for this steels lies within the scatter of the static load data, suggesting that the cracking is time dependent and due to creep at low frequencies. Fig. 5b compared the same databand with data from plate tests. In this case there is a clear difference between negative R ratios and the rest of the cyclic test data of the plate lying at the upper and lower bounds of the C(T) databand respectively. This suggests that caution would be needed in using standard laboratory tests to predict component behaviour where negative R-ratios are present.

2.8. Geometry definitions for pipe components

In the same way as the plates Eqns. (4),(6) are used to derive C^* for pipe geometries. Equations For a range of pipes also exist to derive K and reference stress. It has been shown that solutions for K

due to Raju and Newman [27] and the 'global' collapse solution for the reference stress are best to estimate C^* in the analysis for pipes. 'Global' solutions of reference stress are based on the collapse of the entire cross-section at the site of a defect. For a semi-elliptical axial defect in a pipe subjected to an internal pressure p, R6 [13] gives the reference stress as:

$$\sigma_{ref\ Pipe} = \frac{p}{\frac{1}{R_e - a} \cdot bate(a,c) + \ln\left(\frac{R_e - a}{R_i}\right)} \tag{13}$$

where *bate(a, c)* is given by : $$bate(a,c) = \frac{a}{\sqrt{1 + 1.61 \cdot \frac{c^2}{[(R_e - a) \cdot a]}}} \tag{14}$$

where *bate*(*a, c*) function of dimensions, a is crack depth, c is half crack length at the surface and R_i and R_e are the internal and external radii of the pipe, respectively.

Figure 5 gives an example of comparison of crack growth analysis of the C(T) and pipes geometries in both parent and weld P22 steel tested at 565 ^{o}C. Fig. 6a shows little difference between parent and heat affected zone (HAZ) region tests for the C(T) P22 specimens. On the other hand Fig. 6b, for the pipe test whilst not showing a noticeable difference between parent and HAZ cracking it does show an effect due to geometry when compared with the databand of Fig. 6a. This could be due to constraint as well as the fact that derivation of data from pipe test are much more difficult than for standard C(T) specimen [8,28]. This highlights the fact that more tests would be needed to improve the validation of laboratory data with component data.

a) b)

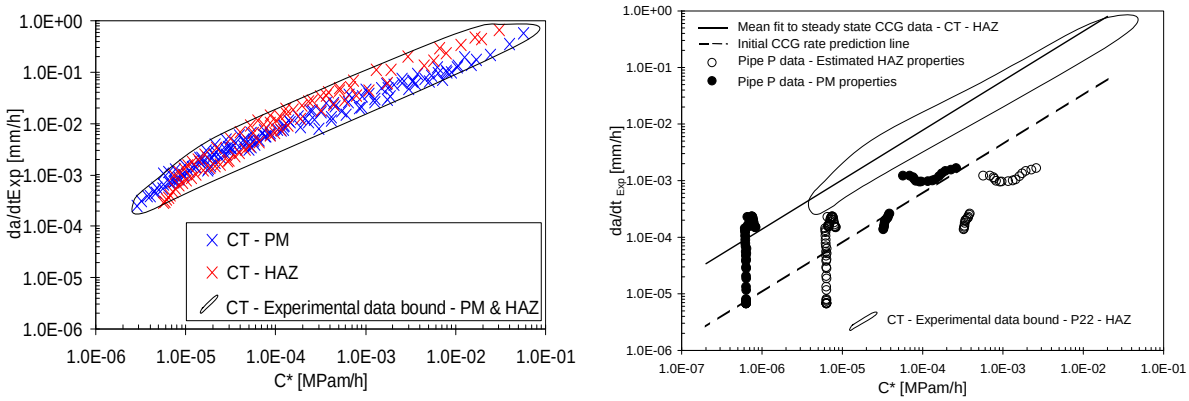

Figure 4: a) Comparison of welded and parent crack growth rate for P22 steel tested at 565 ^{o}C, and b) Comparison of crack growth versus C^* for P22 CT and pipe specimens with C(T) data band (Fig. 6a) showing the effects of geometry constraint on crack growth [3].

2. CONCLUSIONS

Creep and fatigue crack growth models as well as residual defect assessment codes need reliable

and verifiable material properties data and validated fracture mechanics parameters for use in their predictive methodologies. The paper has incorporated the results from the research in a number of EU collaborative projects [2-6] to develop an overall methodology for deriving acceptable data and validated parameters for life assessment analysis. The results are also compatible with ASTM E1457 [8] standard for testing C(T) specimens. In addition the newly developed ASTM E2670 [29] on creep/fatigue crack growth testing identifies the problems associated with creep/fatigue interaction and presents an analysis method for a range of frequencies.

In addition the similarities of the approaches in the various codes do not necessarily imply that calculations by the different methods will give the same predictions. It may be possible that under certain controlled and validated circumstance the predictions can be optimised. It is clear that a critical comparison is only possible when the same method is used on another material and condition or the same test cases are examined by the different codes.

3. ACKNOWLEDGEMENT

The author acknowledges the collaboration of partner institutions in HIDA, LICON and CRETE (European Collaborative programmes (1996-2004) in addition to the partners in VAMAS TWA25, VAMAS TWA31 and ASTM E08 Committees.

4. REFERENCES

1. VAMAS TWA25, Code of Practice, ISO/TTA draft, ' Creep/fatigue Crack Growth in Components', VAMAS document, Ed. K. Nikbin, May 2005.
2. ‘CCG in C-Mn’, ‘CCG in Carbon-Manganese at 320-400’, Brite/Euram project, 1993-1997
3. ‘HIDA’, ‘High Temperature Defect Assessment’ Brite/Euram project, 1996-2000,
4. ‘LICON‘, ‘Accelerated Test Methods for Advanced Steels’ Brite/Euram project, 1997-2001
5. ‘CRETE’, ‘Creep Crack Growth Testing for an EU CoP’ , Brite/Euram project 2001-2004
6. FITNET, ‘Fitness for service analysis of structures using the FITNET procedure; An Overview’, 24th Int. Conf. on Offshore Mechanics and Artic Eng., Greece 12-17 June 2005.
7. 'SINTAP', ‘Structural integrity assessment procedures for European Industry’, Brite/Euram project no. BE 95-1426, contract no BRPR-CT95-0024, Final Report Nov. 1999.
8. ASTM E 1457-10, 2010, “Standard Test Method for Measurement of Creep Crack Growth Rates in Metals”, ASTM Standards 03.01.
9. ASME Boiler and Pressure Vessel Code (1991), Case N-47 (29), Class 1 components in elevated temperature service, Section III, Division I, ASME, New York.
10. RCC-MR (1985) Technical Appendix A3, Section 1, Subsection Z, Materials design and construction rules for mechanical components of FBR nuclear test islands, AFCEN, Paris.
11. BS7910,”Guide on methods for assessing the acceptability of flaws in fusion welded structures,” London, BSI, 2000.
12. R5-British Energy, “Defect assessment code of practice for High temperature metallic components,” British Energy Generation Ltd. 2000

13. R6, Assessment of the integrity of structures containing defects, Revision 3, British Energy Generation, 2000.
14. API RP 579, ‘Standardized fitness-for-service assessment techniques for pressurized equipment used in the petroleum industry’, API, 2004.
15. AFCEN, “Design and construction rules for mechanical components of FBR nuclear islands,” RCC-MR, Appendix A16, AFCEN, Paris.,1985
16. Webster, G.A. and Ainsworth R.A., ‘High temperature components life assessment’ Chapman and Hall, London, 1994.
17. Saxena, A. ‘Non-linear fracture mechanics for engineers’ CRC Press, Boca Raton, USA, 1998.
18. Nikbin, K.M., Smith, D.J. and Webster, G.A., 'Prediction of creep crack growth from uni-axial creep data', Proc. Roy. Soc. A.396, 1984, 183-197.
19. Nikbin, K.M., Smith, D.J. and Webster, G.A., 'An engineering approach to the prediction of creep crack growth', J. Eng. Mat. and Tech., Trans ASME, 108, 1986, 186-191.
20. Nikbin, K., ‘A unified European approach to high temperature defect assessment code and its incorporation in a knowledge base system’, Int. J. PVP, (2001) pp. 929-935.
21. Webster, G. A, Nikbin, K. M., Chorlton, M. R., Célard, N. J. C. and Ober, M. ‘Comparison of High Temperature Defect Assessments Methods’; Material at High Temperature; Vol. 15: pp. 337-346, 1998.
22. Davies, C. M., Kourmpetis, M., O'Dowd, N. P. and Nikbin, K. M., ‘Experimental Evaluation of the J or C* Parameter for a Range of Cracked Geometries’ published in ASTM STP 1480, 2006.
23. Davies, C. M., Mueller, F., Nikbin, K. M., O'Dowd, N. P. and Webster, G. A., ‘Analysis of Creep Crack Initiation and Growth in Different Geometries for 316H and Carbon Manganese Steels’, to be published in ASTM STP 1480, 2006.
24. Tan, M., Célard, N. J. C., Nikbin, K. M and Webster, G. A., ‘Comparison of Creep Crack Initiation and Growth in Four Steels Tested in HIDA’, International Journal of Pressure Vessels and Piping, 2001, 78(12), pp. 737-747.
25. ASTM E647-99, ‘Standard test method for measurement of fatigue crack growth rates’, ASTM 2000, 03-01, 591-630.
26. Winstone, M.R., Nikbin, K.M. and Webster, G.A., ‘Modes of failure under creep/fatigue loading of a nickel-based superalloy’, J. Mat. Sci., 20, 1985, 2471-2476.
27. Raju, I. S. and Newman, J. C. ‘Stress-Intensity Factors for Internal and External Surface Cracks in Cylindrical Vessels’; Journal of Pressure Vessel Technology; Vol. 104: pp. 293-298, 1982.
28. Wasmer, K., Nikbin, K. M., Webster, G. A., “Sensitivity of Creep Crack Initiation and Growth in Plates to Material Properties Variations”, Fatigue and Fracture Mechanics, ASTM STP 1461, Vol: 34, S. R. Daniewicz, J. C. Newman and K.-H. Schwalbe, Eds., ASTM International, West Conshohocken, PA, 2004.
29. ASTM E 2670-10, 20110 “Standard Test Method for Measurement of Creep/fatigue Crack Growth Rates in Metals”, ASTM Standards 03.01.

Integrity increasing of damaged steel pipelines using external and internal reinforcing

János Lukács[1,*], Gyula Nagy[1], Imre Török[1]

[1] Department of Mechanical Engineering, University of Miskolc, H-3535 Miskolc-Egyetemváros, Hungary
* Corresponding author: janos.lukacs@uni-miskolc.hu

Abstract The integrity management and the lifetime assessment of different engineering structures and structural elements is one of the important technical-economic problems nowadays. The aim of the paper is to present the role of the external and internal reinforcing on the structural integrity of transporting steel pipelines, based on own experimental investigations. On the one hand, external and internal reinforcement technologies were developed using carbon fibre reinforced polymer matrix composite (CFR PMC) and glass fibre reinforced polymer matrix composite (GFR PMC), respectively. On the other hand, known external technology was used for the reinforcing of girth welds. Fatigue and burst tests were performed on large pipeline sections containing natural and artificial metal loss defects, and girth welds including weld defects (passed and not passed quality). Burst tests were executed after fatigue tests, using 20.000 or 100.000 cycles. Different corrosion defects were tested as natural defects, and longitudinal and circumferential gouges as well as holes and through holes were investigated as artificial defects. Both unreinforced and reinforced pipeline sections were examined. The applicability of the hybrid structures (steel + polymer matrix composites) were demonstrated by means of the experimental results and defined safety factor.

Keywords pipeline, reinforcing, structural integrity, PMC, burst test

1. Introduction

The treatment of the degradation and failure of different engineering structures, structural elements and equipment, the management of their lifetime is one of the important technical and economic problems of nowadays [1]. The cause of it is unambiguous: on the one hand, significant part of the structures have already reached or exceeded their originally planned lifetime [2], accordingly their following operation is a general interest; on the other hand, the safe and economic operation of the new structures is a key-question. The experiences of the operation [3], the frequency data of fractures, and the different failure statistics [4-6] of the engineering structures having great importance show, that the significance of cyclic loadings, fatigue and fatigue crack propagation is emphasized in general.

Among the engineering structures, hydro-carbon transporting pipelines fill an important part. Approximately, the half of the total length of the Hungarian gas transporting system is over 30 years. In the technical requirements for the pipelines, the estimated lifetime was 30 years in the 1970's [7]. However, as the pipeline age is over 30 years, a sharp increase can be experienced in the probability of failures, according to the "bath tub" failure curve [8]. Therefore, the first global aim of our research work is to improving the integrity of the Hungarian natural gas transmission system.

Material databases play important role both on the integrity management and on the Engineering Critical Assessment (*ECA*) of the pipeline systems. Therefore, the second global aim of our research work is to establish a Pipeline Integrity Management System (*PIMS*) with different data, frequently with experimental data. Material databases collected for general or special purposes and the synergy among the databases can be used to increase the efficiency of the user decisions and the reliability of the lifetime estimation. Different databases were developed for managing different pipeline systems. Data found in standards, in rules, in prescriptions and measured values were integrated in the databases. Additional databases were developed for design calculations and numerical analysis, including physical and plasticity constants of steels, polymers and Polymer Matrix Composites

(*PMCs*), such as potential reinforcing materials. Accordingly, material databases contain data of steel pipe materials, mechanical properties, geometrical dimensions; polymer matrix composite materials, mechanical properties; physical properties of steels and *PMCs* [6].

The most frequently joining technology in the field of steel pipes is the welding, numerous girth welds can be found on the pipelines. The girth welds, as separated parts of the pipeline, have own integrity [9] and the girth weld integrity has influence on the pipeline integrity. The girth weld integrity depends on many factors – *Y/T* ratio, weld metal yield strength (*YS*) mismatch, continuous or discontinuous yielding, elastic or non-elastic design, inspection level (x-ray or ultrasonic), failure mode (brittle vs. ductile) – interacting with each other [6, 9, 10].

Based on the above mentioned facts, the direct purpose of the paper is to present the role of the external and internal reinforcing on the fatigue and burst behaviour of transporting steel pipelines, reviewing our full-scale examinations. External and internal reinforcement was developed using carbon fibre (*CF*) and glass fibre (*GF*) polymer matrix composites (*PMC*), respectively [6, 11]. Known external reinforcing technology (*Clock Spring*) was used, too [12]. Fatigue and burst tests were performed on full scale pipeline sections containing natural and artificial metal loss defects, and girth welds including weld defects. Both unreinforced and reinforced pipeline sections were examined. Safety factor, burst pressure divided by Maximum Allowable Operating Pressure (*MAOP*), was defined and their calculated values demonstrate both the reserves of steel pipes and the usefulness of the reinforcing materials and technologies.

2. Testing circumstances

Full-scale, seamless (*SMLS*), seam welded (*SW* and *SW/HFW*) and spiral welded (*SPW*) steel pipeline sections were examined. Pipeline sections with and without girth welds were investigated, too, in order to study the influence of the girth weld quality and integrity on the pipeline integrity. Manual metal arc welding (*111*) and tungsten inert gas welding combined with manual metal arc welding (*141/111*) technologies were used for the making of the girth welds. The main characteristics of the investigated pipeline sections are summarized in Table 1, where *DN* is the diameter nominal of the steel pipe, d_k is the external/outside diameter of the steel pipe (*OD*) and t_a is the wall thickness of the steel pipe.

Table 1. The main characteristics of the investigated pipeline sections

Mark	DN	d_k, mm	t_a, mm	Pipe Material	Pipe Type	Girth Weld
A_e	100	108,0	4,5	L360NB	SMLS	111
B_a	200	219,1	5,0	L360MB	SW/HFW	no or 111 or 141/111
B_b	200	219,1	5,0	L360MB	SW/HFW	no or 111 or 141/111
C_d	300	323,9	7,1	L360MB	SW/HFW	no
CS_a	400	410,4	7,2-8,0	A35K	SMLS	111
CS_b	400	405-412	7,7-8,3	DX42	SPW	111
D_c	600	609,0	7,92	DX52	SW	no
E_o	200	219,1	5,0	L360MB	SW/HFW	no

The investigated pipeline sections are divided into testing sections, as follows:

- burst test of base (unwelded) pipeline;
- fatigue test (10^5 *cycles*) + burst test of base (unwelded) pipeline;
- burst test of operated (fatigued and replaced) pipeline containing girth weld with „NOT PASSED" quality;
- fatigue test ($2*10^4$ *cycles*) + burst test of pipeline containing girth weld with „PASSED" quality;

- fatigue test (*2*10*^{4} or *10*^{5} *cycles*) + burst test of pipeline containing girth weld or seam weld or artificial discontinuity with „NOT PASSED" quality;
- burst test of operated (fatigued and replaced), externally reinforced pipeline containing girth weld with „NOT PASSED" quality;
- fatigue test (*10*^{5} *cycles*) + burst test of externally or internally reinforced pipeline containing girth weld or artificial discontinuity with „NOT PASSED" quality.

Clock Spring glass fibre reinforced *PMC* (*CS*), and own developed carbon fibre reinforced *PMC* (*CFRPMC*) were used for external reinforcing. The application of the *Clock Spring* composite sleeve reinforcing system can be found in the literature [13]. The installation of the own developed external reinforcing consists of five steps: cleaning and drying of the pipe; preparation of the reinforced area with resin; reinforcing with carbon fibre (tape); covering with polymer film; hardening using heat treatment. Own developed glass fibre reinforced *PMC* (*GFRPMC*) was used for internal reinforcing. The applied reinforcing technology was as follows: cleaning and drying of the pipe; proofing of the shell material; reeling up of the proofed shell onto packet; setting of the packet into the pipe; reinforcing using internal pressure; hardening.

One pipeline section was prepared for strain-gage measurements in order to investigate the behaviour of artificial failures under internal pressure and to establish basic data for finite element (*FEM*) calculations. Fig. 1 shows the detail of this pipeline section (*B_b8*) with artificial longitudinal gouge, strain-gages and an extensometer (see Table 2 and Table 3, too).

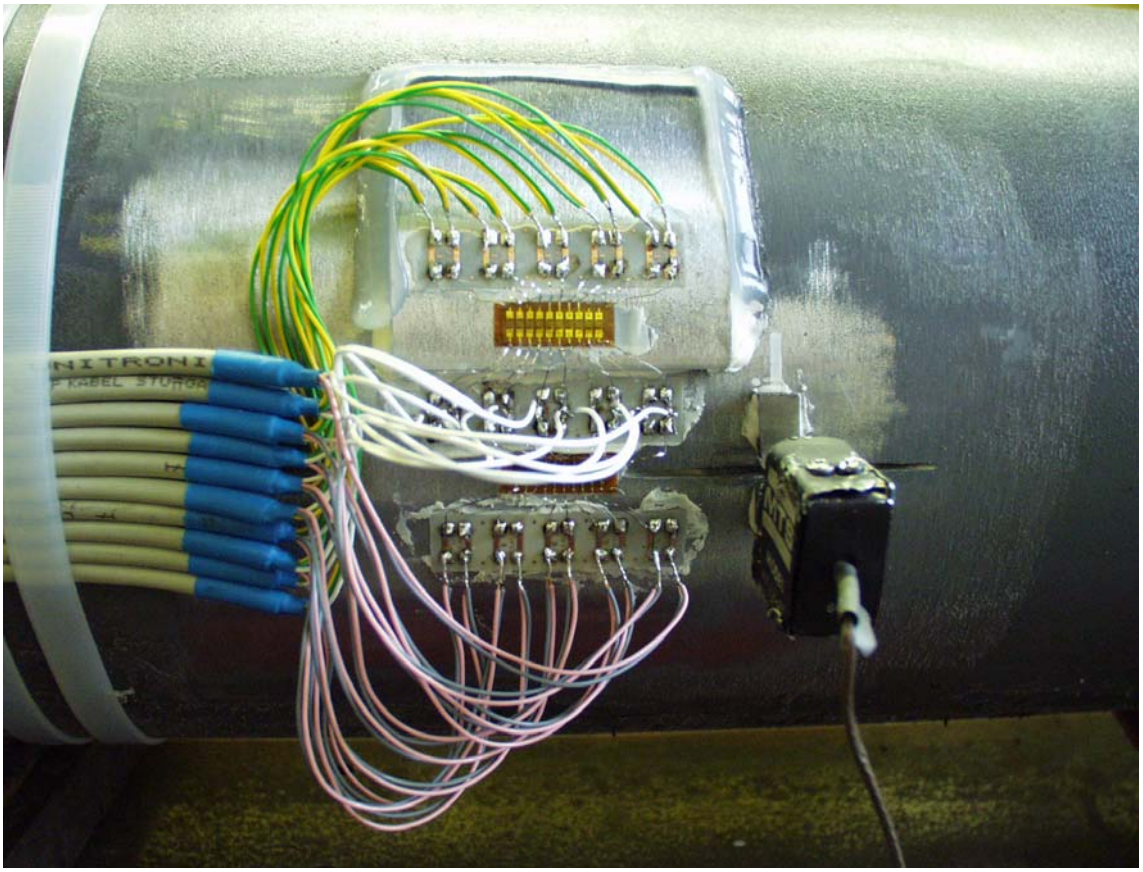

Figure 1. Pipeline section (*B_b8*) with artificial longitudinal gouge, strain-gages and an extensometer

The important characteristics (girth or seam welds and the quality of the welding, types and measurements of the failures, reinforcing) of the investigated pipeline sections are summarized in

Table 2; where h_k and h_b are the longitudinal dimension, m_k and m_b are the depth of the external and internal failures (gouges and holes), respectively, furthermore *d* is the diameter of the artificial holes (holes and through holes).

Table 2. The important characteristics of the investigated pipeline sections

Mark	Details of Pipeline Section	Reinforcing
	Groups of externally reinforced pipeline sections	
A_e1	111 girth weld, „NOT PASSED" quality	–
A_e2	111 girth weld, „NOT PASSED" quality	CFRPMC
B_a1	base (unwelded) pipe	–
B_a3	141/111 and 111 girth welds, „PASSED" quality	–
B_a4	111 girth weld, „NOT PASSED" quality	–
B_b1	base (unwelded) pipe	–
B_b2	141/111 girth weld, "NOT PASSED" quality	–
B_b3	114/111 girth weld, "NOT PASSED" quality	CFRPMC
B_b4	114/111 girth weld, "NOT PASSED" quality	CFRPMC
B_b5	114/111 girth weld, "NOT PASSED" quality	CFRPMC
B_b6	artificial longitudinal gouge (h_k = 75 mm, m_k = 2 mm), circumferential gouge (h_k = 85 mm, m_k = 4,1 mm and interacting circumferential gouges (h_k = 2*75 mm, m_k = 3,2 mm)	–
B_b7	artificial longitudinal gouge (h_k = 75 mm, m_k = 2 mm), circumferential gouge (h_k = 100 mm, m_k = 2,9 mm and interacting circumferential gouges (h_k = 2*75 mm, m_k = 3,2 mm)	CFRPMC
B_b8	artificial failure: longitudinal gouge (h_k = 70 mm, m_k = 2 mm)	–
C_d1	artificial longitudinal gouge (h_k = 100 mm, m_k = 3 mm), circumferential gouge (h_k = 150 mm, m_k = 4,7 mm and interacting circumferential gouges (h_k = 2*130 mm, m_k = 4 mm)	–
	artificial longitudinal gouge (h_k = 100 mm, m_k = 3 mm)	–
	new artificial longitudinal gouge (h_k = 100 mm, m_k = 3,1 mm)	–
C_d2	artificial longitudinal gouge (h_k = 100 mm, m_k = 3 mm), circumferential gouge (h_k = 150 mm, m_k = 4,7 mm and interacting circumferential gouges (h_k = 2*130 mm, m_k = 4 mm)	CFRPMC
	artificial longitudinal gouge (h_k = 100 mm, m_k = 3 mm)	CFRPMC
CS_a1	111 girth weld, „NOT PASSED" quality	CS
CS_b1	111 girth weld, „NOT PASSED" quality	–
CS_b2	111 girth weld, „NOT PASSED" quality	CS
CS_b3	111 girth weld, „NOT PASSED" quality	CS
CS_b4	111 girth weld, „NOT PASSED" quality	CS
D_c1	seam weld, "NOT PASSED" quality	–
	Group of internally reinforced pipeline sections	
E_o4	artificial holes (d = 4, 8, 10, 12, 16 and 20 mm, m_b = 4 mm)	–
E_o1	artificial longitudinal gouge (h_b = 70 mm, m_b = 3,2 mm)	GFRPMC
E_o2	artificial through holes (d = 4, 8, 10, 12, 16 and 20 mm)	GFRPMC
E_o3	artificial holes (d = 4, 8, 10, 12, 16 and 20 mm, m_b = 4 mm)	GFRPMC

3. Results of the full-scale investigations

Fig. 1 demonstrates the internal pressure vs. time diagrams of the investigated *DN 200* pipeline sections in the *B_a* and *B_bi* testing groups (see Table 1 and Table 2) during their burst tests. Fig.1

displays the average pressure growth rate range (*0,15 – 0,52 MPa/s*) at the initial stage of the burst tests, which can be evaluated as quasi-static value range.

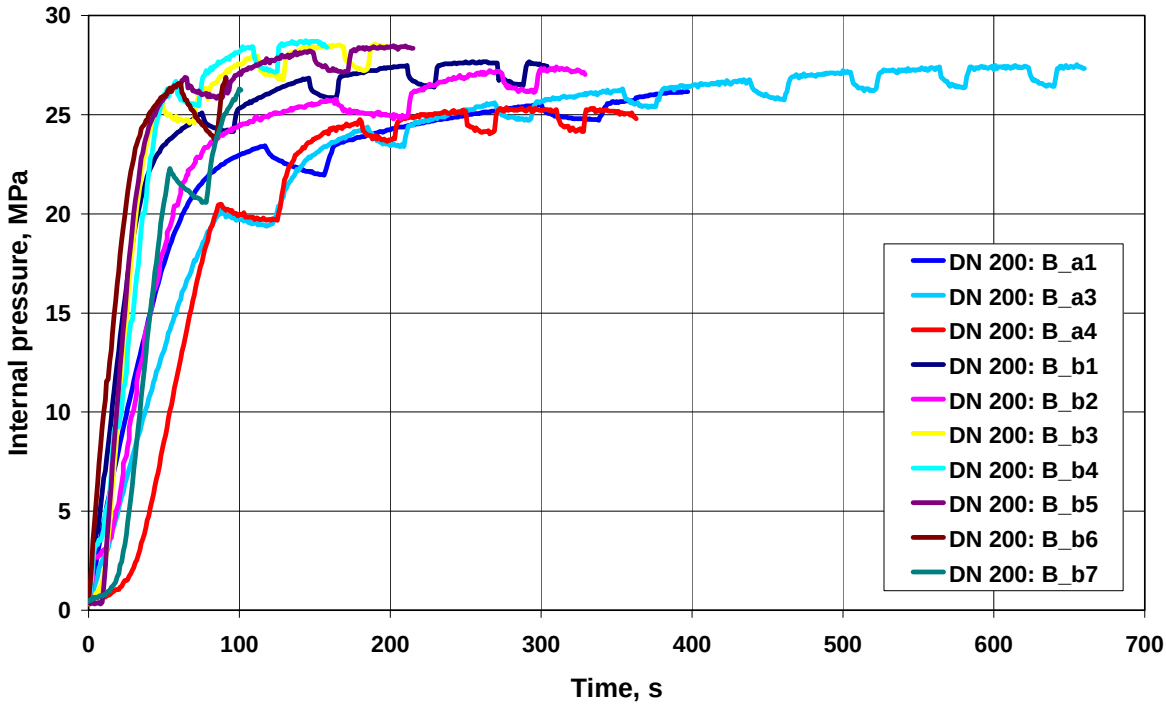

Figure 2. Internal pressure vs. time diagrams during the burst tests of the pipeline sections in the *B_a* and the *B_b* testing groups

Fig. 2 demonstrates the internal pressure vs. time diagrams of the investigated *DN 400* pipeline sections in the *CS_b* testing group (see also Table 1 and Table 2) during their burst tests.

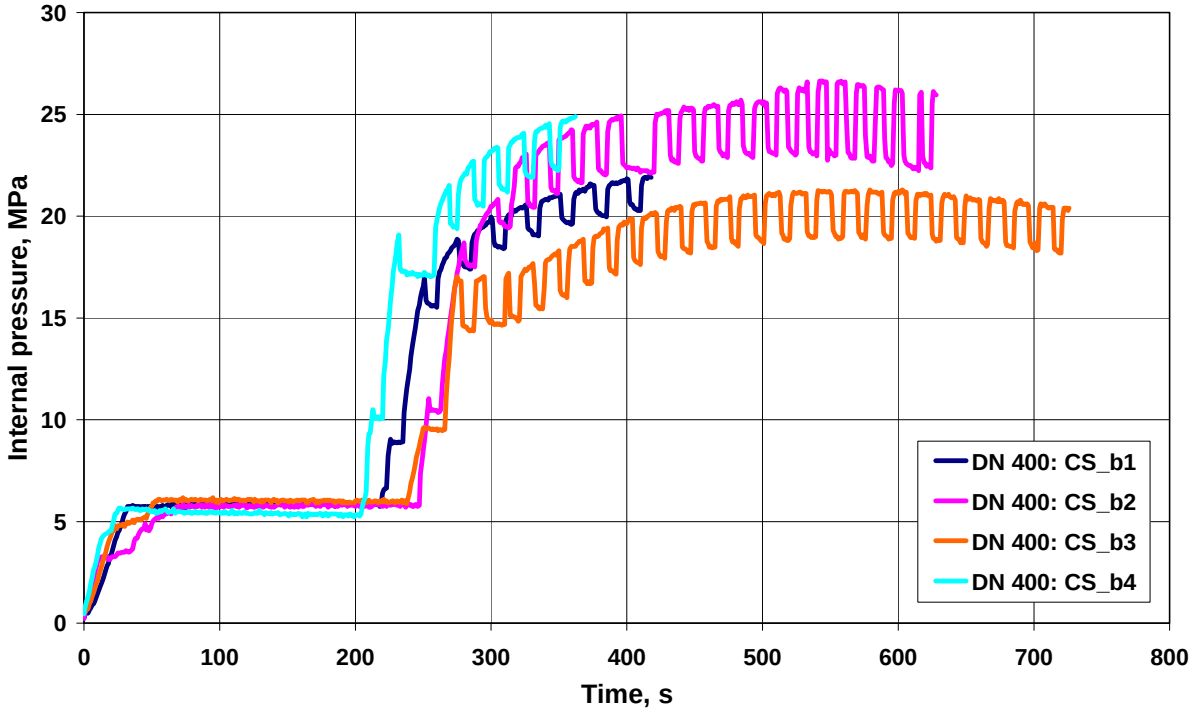

Figure 2. Internal pressure vs. time diagrams during the burst tests of the pipeline sections in the *CS_b* testing group

Fig. 2 shows the loading history of the pipeline sections, which consists of three parts: rising the pressure up to the operating pressure (*6,4 MPa*), holding the pressure (*3 min = 180 sec*), and rising the pressure up to the final damage. Fig. 1 and Fig 2 show the volume growth of the pipeline sections through the pressure growth, too.

Fig. 3 and Fig 4 show the externally reinforced pipeline section *CS_a1* (reinforced girth weld) using *Clock Spring* repair system before and after the burst test, respectively.

Figure 3. Externally reinforced pipeline section (girth weld) *CS_a1* before the burst test

Figure 4. Externally reinforced pipeline section (girth weld) *CS_a1* after the burst test

Fig. 5 and Fig. 6 show the externally reinforced pipeline section *CS_b3* (reinforced girth weld) using *Clock Spring* repair system and the failured area after the burst test, respectively.

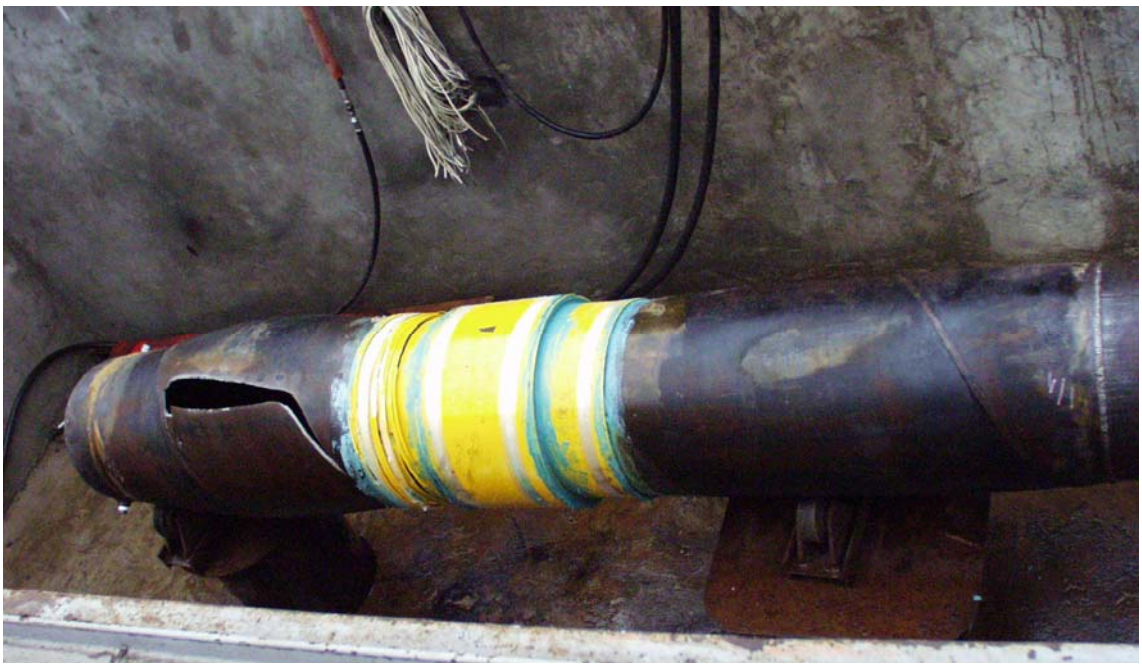

Figure 5. Externally reinforced pipeline section (girth weld) *CS_b3* after the burst test

Figure 6. The failured area of the externally reinforced pipeline section (girth weld) *CS_b3* after the burst test

Fig. 4 and Fig. 6 demonstrate that in these cases, the failed area located far from the girth weld area, and the reinforcing material has riven through the deformation of the unreinforced pipe body.

The results of the investigations executed on the unreinforced and externally or internally reinforced pipeline sections, furthermore the calculated safety factors are summarized in Table 3.

Table 3. Results of the executed full-scale investigations

Mark	Examination	Cycles	Failure location	Burst pressure, bar	Safety factor, –
Groups of externally reinforced pipeline sections					
A_e1	fatigue + burst	10^5	pipe body	464,6	7,26
A_e2	fatigue + burst	10^5	pipe body	472,3	7,38
B_a1	burst	–	pipe-end seam	> 261,7	> 4,09
B_a3	fatigue + burst	$2*10^4$	pipe body	275,3	4,30
B_a4	fatigue + burst	$2*10^4$	pipe body	253,5	3,96
B_b1	fatigue + burst	10^5	pipe body	276,6	4,32
B_b2	fatigue + burst	10^5	pipe body	274,0	4,28
B_b3	fatigue + burst	10^5	pipe body	285,6	4,46
B_b4	fatigue + burst	10^5	pipe body	287,2	4,49
B_b5	fatigue + burst	10^5	pipe body	284,7	4,45
B_b6	fatigue + burst	10^5	pipe body	268,1	4,19
B_b7	fatigue + burst	10^5	pipe body	262,9	4,11
B_b8	strain-gage measurements	–	pipe body	not relevant	not relevant
C_d1	fatigue	$0,795*10^5$	circumferential gouge	not relevant	not relevant
	fatigue	$0,936*10^5$	longitudinal gouge	not relevant	not relevant
	burst	–	new longitudinal gouge	233,5	3,65
C_d2	fatigue + burst	10^5	circumferential gouge	264,6	4,13
	fatigue + burst	10^5	longitudinal gouge	273,2	4,27
CS_a1	burst	operated	pipe body	245,0	3,83
CS_b1	burst	operated	girth weld	220,0	3,44
CS_b2	burst	operated	pipe body	270,0	4,22
CS_b3	burst	operated	pipe body	220,0	3,44
CS_b4	burst	operated	pipe body	250,0	3,91
D_c1	fatigue	10^5	–	–	–
Group of internally reinforced pipeline sections					
E_o4	fatigue + burst	10^5	hole (d = 12 mm)	255,7	4,00
E_o1	fatigue + burst	10^5	longitudinal gouge	241,6	3,78
E_o2	fatigue + burst	$0,447*10^5$	through hole (d = 20 mm)	242,9	3,80
E_o3	fatigue + burst	10^5	hole (d = 20 mm)	268,5	4,20

4. Conclusions

Based on the results of our full-scale examinations and the calculated safety factors, the following conclusions can be drawn.

The reinforcing materials (carbon fibre reinforced *PMC* and glass fibre reinforced *PMC*) and the own developed external and internal reinforcing technology can be used

– for transporting and industrial steel pipelines;

- for wide variety of pipe diameters and length (e.g. for casings);
- for both quasi-static and cyclic loaded pipeline sections or pipelines;
- for both workshop-work and field-work.

Beside the *Clock Spring* (*CS*) repair system, the developed external technology is suitable for the reinforcing of girth welds, frequently "NOT PASSED" quality girth welds, too.

The usability of the own developed external reinforcing technology and the effectiveness of the external reinforcing for "NOT PASSED" quality seam welds (*D_c* pipe section) require further investigations.

The defined safety factor and their calculated values demonstrate both the reserves of the steel pipes and the usefulness of the reinforcing materials and technologies.

Results of full-scale tests correspond with results of numerical investigations [14-17] in case of externally and internally reinforced damaged pipelines.

Databases and especially experimental data have a determinant role in the integrity assurance of different structures, like pipeline systems [18]. With the help of these databases and frequently with the using of the experimental data, integrity management tasks can be solved [1].

Acknowledgements

This research was carried out and will be continued as part of the TAMOP-4.2.1.B-10/2/KONV-2010-0001 project with support by the European Union, co-financed by the European Social Fund.

References

[1] J. Lukács, Dimensions of lifetime management. Materials Science Forum, 473-474 (2005) 361-368.
[2] H. Jakubczak, W. Sobczykiewicz, D. Dudek, Probabilistic fatigue life prediction of degraded structures, in: V. Bicego, A. Nitta, R. Viswanathan (Eds.), Materials Ageing and Component Life Extension, EMAS, Warley, 1995, Vol. II, pp. 1231-1240.
[3] I. Vehofsits, Diagnostic examinations of hydro-carbon transporting pipelines. Gépgyártás-technológia, 38/6 (1998) 49-53. (In Hungarian: Szénhidrogén-szállító távvezetékek diagnosztikai vizsgálata.)
[4] Á. Zsáry, Fatigue design in mechanical engineering, Műszaki Könyvkiadó, Budapest, 1965. (In Hungarian: Méretezés kifáradásra a gépészetben.)
[5] S. J. Findlay, N. D. Harrison, Why aircraft fail. Materials Today, 5/11 (2002) 18-25.
[6] J. Lukács, Gy. Nagy, I. Török, Selected topics in lifetime management, J. Lukács (Ed.), Miskolci Egyetem, Miskolc, 2009. (In Hungarian: Szemelvények az élettartam gazdálkodás témaköréből.)
[7] M. Vida, Handbook of Gas Technology, Műszaki Könyvkiadó, Budapest, 1991. (In Hungarian: Gáztechnikai Kézikönyv.)
[8] P. Hopkins, Pipeline Internal Inspection – What a Pipeline Operator Needs to Know. http://www.penspenintegrity.com /virtual-library, 2012.
[9] R. M. Denys, Weld-defect acceptance models need more validated inputs. Part 2: Using good mechanical, toughness and defect-size data could reduced unneeded repairs. Pipe Line and Gas Industry, 82/10 (1999) 59-64.
[10] R. M. Denys, Consensus on judging multi-level weld defects would benefit all. Part 4: Economics may eventually be the lever to bring a change from current assessment methods.

Pipe Line and Gas Industry, 82/12 (1999/2) 60-65.
[11] G. Czél, J. Csordás, Á. Door, J. Égert, J. Farkas, G.. Fekete, K. Jármai, J. Kiss, Gy. Kovács, Gy. Kónya, J. Lukács, Gy. Nagy, B. Pere, I. Török, L. Varga, Integrity of hybrid pipes reinforced by polymer matrix composite. J. Lukács (Ed.) Miskolci Egyetem, Miskolc, 2008. (In Hungarian: Polimer mátrixú kompozittal erősített hibrid csövek integritása.)
[12] CLOCK SPRING Composite Sleeve Reinforcement System. http://www.clockspring.com/products/clock-spring/, 2012.
[13] Field Report – Pipeline Girth Weld Repair. http://www.clockspring.com/field-report-pipeline-girth-weld-repair/, 2012.
[14] B. Pere, J. Égert, T. Szabó, Reinforcement of inner and outer circular failures of pipes by textile composite layers. Journal of Computational and Applied Mechanics, 10/1 (2009) 1-15.
[15] J. Égert, B. Pere, Repair of Internal and External Longitudinal Failures of Pipes by Fabric Composite Reinforcement. Acta Technica Jaurinensis, 2/1 (2009) 3-17.
[16] J. Lukács, Gy. Nagy, I. Török, J. Égert, B. Pere, Experimental and Numerical Investigations of External Reinforced Damaged Pipelines. Procedia Engineering, 2/1 (2010) 1191–1200.
[17] J. Lukács, Gy. Nagy, I. Török, J. Égert, B. Pere, Experimental and Numerical Investigations of Internally Reinforced Damaged Pipelines, in: Proceedings of the 18th European Conference on Fracture (ECF18) – Fracture of Materials and Structures from Micro to Macro Scale, CD ROM (2010) 126-133.
[18] J. Lukács, Gy. Nagy, I. Török, The Role of Process Models, Flow Charts and Material Databases on the Structural Integrity of High Strength Steel Pipeline Systems, in: Proceedings of the International Conference on New Developments on Metallurgy and Applications of High Strength Steels, CD-ROM (2008) 1-12.

Based on cycle strain damage prediction of the crack growth behavior of elliptic surface crack

LONG CHEN[1,*], LIXUN CAI[1], KAIKAI SHI[1]

[1] School of Mechanics and Engineering, Southwest Jiaotong University, Chengdu, Sichuan 610031, China
* Corresponding author: lix_cai@263.net

Abstract According to the low cycle fatigue strain damage, a unit average damage parameter over the cyclic plastic zone along the crack extending direction is defined, and a new fatigue crack growth rate prediction model (LCF-FCGM) is established. Then combined with Newman-Raju formula, simulation of the fatigue crack growth problem of a half elliptic surface crack in tension plate under cyclic loading is fulfilled. The fatigue crack growth rate curve of Al 7075-T6 alloy predicted by LCF-FCGM agrees well with that obtained from the corresponding test. Assuming that the shape of the surface crack front keeps elliptic and is controlled by two critical points: the deepest point and the surface point, a numerical approach based on material's low cycle fatigue properties is developed to analyze the configuration evolution of surface cracks during fatigue crack growth. The new approach is well applied to Al 7075-T6 alloy surface cracked plate, and six different initiate crack shapes are discussed and all reflect the same phenomenon of round first to oval again, which are consistent with the test results.

Keywords fatigue crack propagation; low-cycle fatigue damage; Newman-Raju formula; elliptic surface crack; Al 7075-T6 alloy

1. Introduction

In engineering the crack is always in three-dimensional stress status, especially for the surface crack in pressure vessel pipe. So study on the surface crack growth problem has great importance. Because of the uncertainty of the crack front shape, it brings much difficulty on solving these nonpenetrating crack problems. Nowadays, there are three methods have been proposed: conservative estimate method, shape assuming method and crack shape tracking method. ASME X1(1997) assumed the crack shape parameter α=a/c is constant. And BSI PD6493（1980）assumed that the crack width c keeps still until the shape changes to round and the round shape kept till the end. Known as the representative of crack shape assuming method, Newman-Raju formula[1] (Newman and Raju, 1981) has been wildly used in solving the surface crack problem, in which the crack shape parameter α is assumed to be changeable. By using the crack shape tracking method, the simulation of nonpenetrating crack is fulfilled with 3D finite element method[2] (Smith and Copper, 1989), the 3D crack propagation problem is studied by boundary element method[3] (Deng Jiangang et al., 2003). Based on the continuum damage mechanics method the fatigue crack growth behavior of surface crack is discussed[4] (Feng Xiqiao and He Shuyan, 1997), and by using S-version FEM the process of surface crack growth under mixed mode cyclic loading condition is simulated[5] (Masanori et al., 2011). What's more, many researchers have proposed different approaches in mathematic way to predict the growth behavior of surface crack. Take energy approach for example, Song, Sheu and Shieh[6] (2002) have well applied it to predict the surface crack growth in 2024-T4 aluminium alloy. And, an approach with data obtained from the testing of through-thickness cracks was established to predict surface crack growth, in which the effects of crack closure[7] was considered (Liu Yanping et al., 2010). Therefore, the study on surface crack growth behavior is still hot to solve the fatigue fracture problem in engineering like the pressure vessels and pipes. However, the past researches on the crack growth behavior of surface crack are all based on the Paris formula[8] (Paris and Erdogan, 1963). As we know, the fatigue crack growth rate behavior and the low cycle fatigue behavior are just different way to describe material's fatigue properties, so there should be a connection to each other[9] (Cui Weicheng, 2002). And many theoretical models have been proposed based on material's fatigue properties[10-12] (Castro J.T.P.,

2005 & Li D.M, et al., 1998 & Ramsamooj D.V., 2003), but they are still involved with some human debugs. Therefore, combined Newman-Raju formula, a fatigue crack growth prediction model based on the material's low cyclic fatigue properties (LCF-FCGM) is proposed to predict the extending process of the surface crack. The proposed LCF-FCGM has been well discussed in author's previous studies[13-14] (Chen Long et al., 2012). Notice that the influence of the extending direction on the fatigue crack growth properties is ignored.

2. Analysis Theory of Elliptic Surface Crack Growth

2.1. The Proposed LCF-FCGM Theory

Based on the HRR field, the stress-strain field near the crack tip was modified to describe the cyclic crack tip stress-strain field[15] (Schwalbe, 1974),

$$\begin{cases} \Delta\varepsilon_{\mathrm{P}}(r) = \dfrac{2\sigma_{yc}}{E}\left(\dfrac{\mathrm{PZ}c}{r}\right)^{1/(1+n)} \\ \Delta\sigma(r) = 2k\left(\dfrac{\Delta\varepsilon_{\mathrm{P}}(r)}{2}\right)^{n} \end{cases} \tag{1}$$

in which E is Young's modulus, σ_{yc} is cyclic yield stress, k is cyclic hardening coefficient, n is cyclic hardening exponent, r is the distance to the crack tip, and PZc is the cyclic plastic zone size that can be calculated as follows.

$$\mathrm{PZ}c = \frac{1}{4\pi\kappa^2(1+n)}\left(\frac{\Delta K}{\sigma_{yc}}\right)^2 \tag{2}$$

Where, $\kappa = \begin{cases} 1 & plane-stress \\ \dfrac{1}{1-2v} & plane-strain \end{cases}$, v is poison ratio and ΔK is stress intensity factor amplitude.

In fact, according to amount of FEA analyses, the curvature of the crack tip is non-zero, and the plastic strain of the crack tip is finite. So, a fatigue blunting factor x_1 is introduced into (1), and the cyclic plastic strain amplitude can be further described as follows.

$$\Delta\varepsilon_{\mathrm{P}}(r+x_1) = \frac{2\sigma_{yc}}{E}\left(\frac{\mathrm{PZ}c}{r+x_1}\right)^{1/(1+n)} \tag{3}$$

Informed researches show that material near the crack tip can be considered as a serial of fatigue elements under cyclic loading[15] (Schwalbe, 1974). According to the fatigue theory, the relationship between fatigue life Nf and the cyclic plastic strain amplitude $\Delta\varepsilon_{\mathrm{p}}$ can be described as follows.

$$\frac{\Delta\varepsilon_{\mathrm{P}}}{2} = \varepsilon'_f\left(2N_f\right)^c \tag{4}$$

Where, ε'_f and c are plastic hardening coefficient and plastic hardening exponent, respectively.

According to the Miner accumulative damage theory, combined (3) and (4), the damage D of the material per one cycle is defined as $1/N_{\mathrm{f}}$, where N_{f} is associated with the plastic strain amplitude. Therefore the distribution of the plastic strain damage along the crack growth direction in the cyclic plastic zone can be described as follows.

$$D(r+x_1) = 2\left(\frac{\sigma_{yc}}{E\varepsilon'_f}\right)^{-1/c}\left(\frac{\mathrm{PZ}c}{r+x_1}\right)^{-1/(1+n)c}, 0 < r \le \mathrm{PZ}c - x_1 \tag{5}$$

According to the fatigue striations phenomenon of the fatigue fracture image, assuming that each step of the crack advancement size equals to the cyclic plastic zone size (PZc-x_1) along the growth

direction. The plastic strain amplitude is much bigger than the elastic strain amplitude in the cyclic plastic zone, so the damage of elastic strain can be ignored. Then, a unit average damage parameter over the cyclic plastic zone along the crack extending direction is defined as $\overline{D}=\frac{\int_0^{\mathrm{PZ}c-x_1} D(r+x_1)\mathrm{d}r}{\mathrm{PZ}c-x_1}$.

According to the Miner accumulative damage theory, when $\overline{D}=1$ the crack will grow forward one step. Therefore, the life and the rate of each step can be calculated as follows.

$$\begin{cases} N_{fi}=\dfrac{1}{\overline{Di}}=\dfrac{\mathrm{PZ}c-x_1}{\int_0^{\mathrm{PZ}c-x_1} D(r+x_1)\mathrm{d}r} \\ \left(\dfrac{\mathrm{d}a}{\mathrm{d}N}\right)_i=\dfrac{\mathrm{PZ}ci-x_1}{N_{fi}}=\int_0^{\mathrm{PZ}c-x_1} D_i(r+x_1)\mathrm{d}r \end{cases} \tag{6}$$

From (6), it is found that the fatigue crack growth equals to the sum of the nodes' damages in the cyclic plastic zone. Combined (5) and (6), a new FCG prediction model based on the mean plastic strain in the cyclic plastic zone can be given as (7).

$$\left(\frac{\mathrm{d}a}{\mathrm{d}N}\right)_i=2\left(\frac{E\varepsilon'_f}{\sigma_{yc}}\right)^{1/c}\cdot\mathrm{PZ}ci\cdot\frac{c+cn}{c+cn+1}\cdot\left[1-\left(\frac{x_1}{\mathrm{PZ}ci}\right)^{1+1/(c+cn)}\right] \tag{7}$$

As known to all, in the initiation stage of the FCG curve, where the stress intensity factor amplitude $\Delta K=\Delta K_{\mathrm{th}}$, no crack growth occurs approximately. So, the fatigue blunting factor x_1 can be calculated through (8).

$$x_1=\mathrm{PZ}c\mathrm{th}=\frac{1}{4\pi\kappa^2(1+n)}\left(\frac{\Delta K_{\mathrm{th}}}{\sigma_{yc}}\right)^2 \tag{8}$$

From (8), the fatigue blunting factor equals the cyclic plastic zone size corresponding to ΔK_{th}. Then a zero range of cyclic plastic strain damage is obtained from (8) and (5) nearby the crack initiation, which means there is no damage accumulated under this condition. Then the LCF-FCGM can be further developed as (9),

$$\begin{aligned}\left(\frac{\mathrm{d}a}{\mathrm{d}N}\right)&=\frac{\mathrm{PZ}ci-x_i}{N_{fi}} \qquad i=1,2,3\ldots\ldots \\ &=\frac{c}{2\pi\kappa^2(1+c+cn)}\bullet\left(\frac{E\varepsilon'_f}{\sigma_{yc}}\right)^{1/c}\bullet\left(\frac{\Delta K_i}{\sigma_{yc}}\right)^2\bullet\left[1-\left(\frac{\Delta K_{\mathrm{th}}}{\Delta K_i}\right)^{2+2/(c+cn)}\right]\end{aligned} \tag{9}$$

where i is the serial number.

2.2. Simulation of Surface Crack Growth Theory

As for the surface crack front, the crack growth behavior can not be described as one point, which must be considered as a whole curve, two controller points are defined: the crack deepest point B and the crack surface point A, shown in Fig. 1. Follow the assumption on surface crack by Newman and Raju, during the extending process, the crack front shape always can be described with ellipse function. Therefore, the prediction of the surface crack front shape can be achieved by applying the LCF-FCGM at the two controller points A and B. The maximum average plastic strain damage $\{\overline{D}_{\mathrm{A}},\overline{D}_{\mathrm{B}}\}$max decides the main controller point, and the corresponding minimum growth life $\{N_{\mathrm{fA}}$,

N_{fB} }min is chose as the crack growth life. What's over, the corresponding extending steps of the two controller points A and B have the following relationship.

$$\frac{(\mathrm{d}c)_{\mathrm{A}}}{(\mathrm{d}a)_{\mathrm{B}}}=\frac{\mathrm{PZ}c_{\mathrm{A}}-x_1}{\mathrm{PZ}c_{\mathrm{B}}-x_1}\bullet\frac{N_{f\mathrm{B}}}{N_{f\mathrm{A}}}$$
$$=\left(\frac{\Delta K_{\mathrm{A}}}{\Delta K_{\mathrm{B}}}\right)^2\bullet\left[1-\left(\frac{\Delta K_{\mathrm{th}}}{\Delta K_{\mathrm{A}}}\right)^{2+2/(c+cn)}\right]\Big/\left[1-\left(\frac{\Delta K_{\mathrm{th}}}{\Delta K_{\mathrm{B}}}\right)^{2+2/(c+cn)}\right] \tag{10}$$

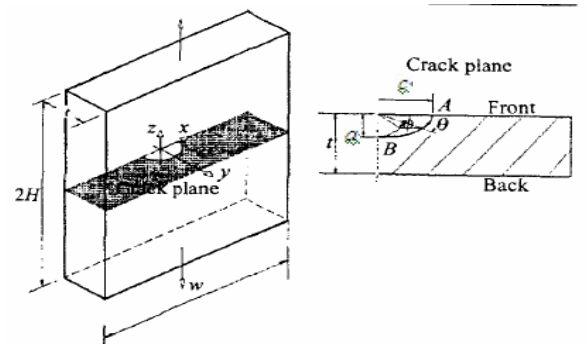

Fig. 1. scheme of flat surface crack under tension loading

The famous Newman-Raju formula[1] (Newman and Raju, 1981) is applied to obtain the stress intensity amplitude along the surface crack front, as Eq..11,

$$K=\left[(\sigma_t+H\sigma_b)\sqrt{\pi a}/E(\kappa)\right]F_s(a/c,a/t,c/W,\varphi) \tag{11}$$

where $E(\kappa)$ can be approximated by

$$E(\kappa)=\begin{cases}\left[1+1.464(a/c)^{1.65}\right]^2, a/c\le 1\\ \left[1+1.464(c/a)^{1.65}\right]^2, a/c>1\end{cases} \tag{12}$$

and the load combination factor H can be calculated through

$$\begin{aligned}&H=H_1+(H_2+H_3)\sin^p\varphi, p=0.2+a/c+0.6a/t\\&H_1=1-0.34(a/t)-0.11(a/c)*(a/t)\\&H_2=1+G_1(a/t)+G_2(a/t)^2\\&G_1=-1.22-0.12(a/c)\\&G_2=0.55-1.05(a/c)^{0.75}+0.47(a/c)^{1.5}\end{aligned} \tag{13}$$

The geometry modifying factor F_s is obtained by FEA as

$$F_s=\left[M_1+M_2(a/t)^2+M_3(a/t)^4\right]gf_\varphi f_W \tag{14}$$

in which

$$M_1=\begin{cases}1.13-0.09(a/c) & ,a/c\le 1\\ \sqrt{c/a}\left[1+0.04(c/a)\right], & a/c>1\end{cases} \tag{15}$$

$$M_2=\begin{cases}-0.54+0.89/\left[0.2+(a/c)\right] & ,a/c\le 1\\ 0.2(c/a)^4 & ,a/c>1\end{cases} \tag{16}$$

$$M_3 = \begin{cases} 0.5 - [1/(0.65 + (a/c))] + 14(1 - a/c)^{24} & , a/c \le 1 \\ -0.11(c/a)^4 & , a/c > 1 \end{cases} \tag{17}$$

$$g = \begin{cases} 1 + [0.1 + 0.35(a/t)^2](1 + \sin\varphi)^2 & , a/c \le 1 \\ 1 + [0.1 + 0.35(c/a)(a/t)^2](1 + \sin\varphi)^2 & , a/c > 1 \end{cases} \tag{18}$$

The function f_φ, an angular function from the embedded elliptical-crack solution[16] (Green and John, 1965), is

$$f_\varphi = [(a/c)^2 \sin^2\varphi + \cos^2\varphi]^{0.25} \tag{19}$$

The function f_W, a finite-width correction from reference[17] (Newman, 1976), is

$$f_W = [\sec(\pi c/(2W)\sqrt{a/t})]^{0.5} \tag{20}$$

so, the corresponding stress intensity amplitude can described as $\triangle K=(1-R)K$. The specific prediction approach is given in Fig. 2.

3 Results and Discussion

3.1 Comparable Analysis of The Proposed Model

The crack growth behavior of the Al 7075-T6 alloy elliptic surface crack in tension plate was tested[18] (Putra and Schijve, 1992), and the shape change of the crack front had been obtained, shown in Fig. 4. A literature [19] (Noroozi, 2005) had studied the fatigue properties of Al 7075-T6 alloy, and the specific fatigue data are shown in Table. 1, and the feasibility of LCF-FCGM is tested as shown in Fig. 3. It is found that the prediction result by LCG-FACGM is consistent with the reference result [19](Noroozi et al., 2005).

Based on the proposed prediction theory, the shape change of the elliptic crack front with different initiate crack shape is predicted by following the prediction process, which has been compared with the reference paper in Fig. 4. The geometry scale and the material properties are the same as the reference paper, in which the initiate crack depth a_0 is fixed as 0.2 mm. Seen from Fig. 4, the prediction results for different initiate crack shape are consistent with the test results, especially for the initiate shape parameter α_0 equals 0.8,0.4 and 0.2.

Table. 1. Geometry size and low cycle fatigue properties

Material	E /GPa	σ_{yc} /MPa	n	ε_f'	c	R	$\triangle K_{th}$ /MPa.m$^{1/2}$
Al 7075-T6	71	469	0.0865	0.19	-0.52	0.1	1.45
	H /mm		α_0		W /mm		t /mm
	65		2.5,1,0.8 ,0.6,0.4,0.2		20		10

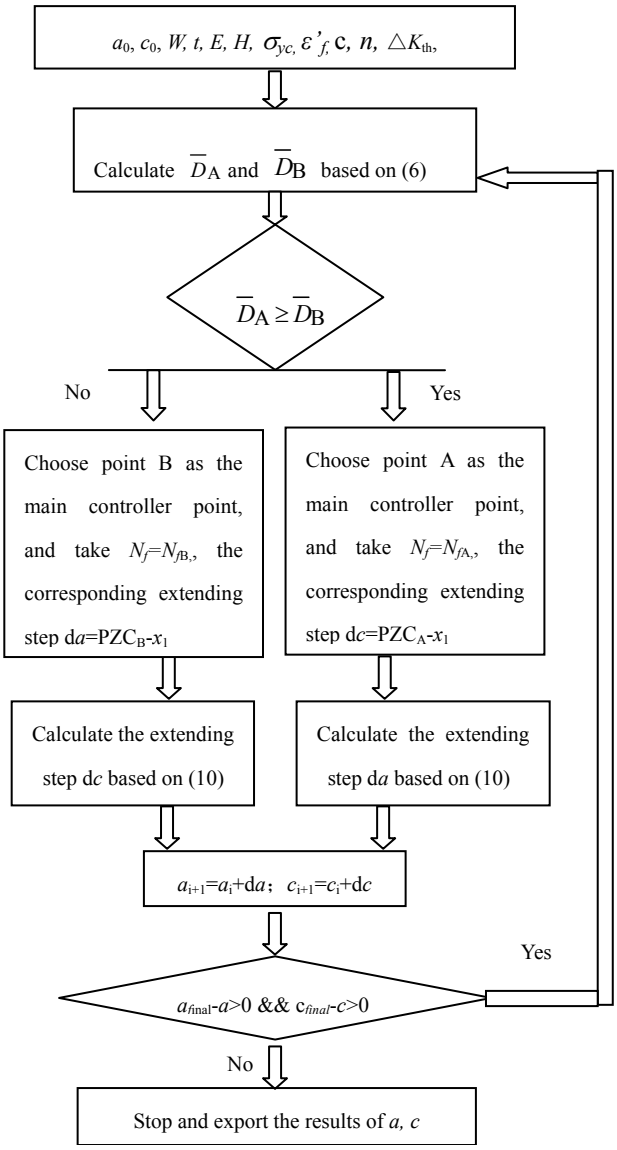

Fig. 2. the specific simulation approach of surface crack

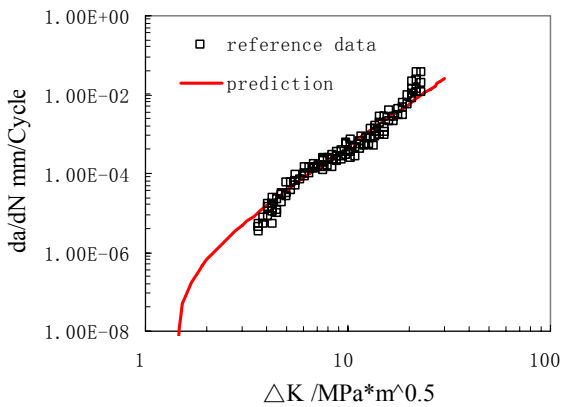

Fig. 3. Comparison of FCG result of Al 7075-T6 alloy

3.2 Prediction Results of Different Initiate Crack Shape

Taking the Al 7075-T6 alloy for example, the crack front change of the elliptic surface crack with different shape parameters is simulated. The initiate geometry parameters are: thickness d equals 10 mm, width W equals 20 mm, and the shape parameters α0 are 2.5, 1, 0.8, 0.6, 0.4 and 0.2 respectively. The prediction results of shape change of the crack front during the extending process are shown in Fig. 5. Meanwhile, the relationship curves between the shape parameter α and the depth ratio $\beta=a/t$ are also shown in Fig. 6. Seen from Fig. 6, when initiate shape parameter $\alpha_0<1$, the maximum damage is found in the controller point A, which defines the corresponding crack growth life of the whole surface crack. Otherwise, the maximum damage turns to the deepest point B. Combined with Fig. 4, it shows that the same crack growing trend is found with different initiate crack shape parameter, the crack front shape all become oval after getting round, which is consistent with results in some recent reports[20-21] (Wu zhixue, 2007; Brennan *et al*., 2008). What's more, every two parameters of the three initiate factors: shape parameter α_0, crack depth a_0 and crack width c_0 control the change of the surface crack front.

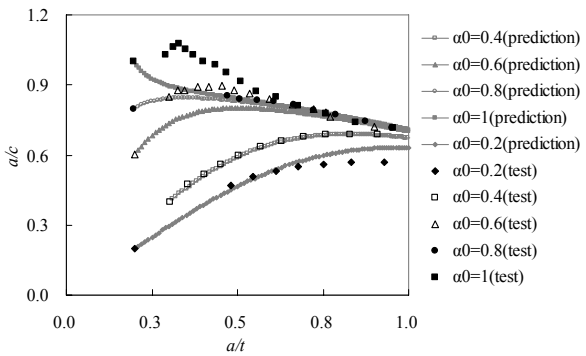

Fig. 4. Comparison of the shape change of the elliptic crack front

4 Conclusions

From the point of low cycle fatigue strain damage, this paper proposed a new fatigue crack growth rate prediction model. It has been well testified with Al 7075-T6 alloy. Meanwhile, combined with the famous Newman-Raju formula used to solve the stress intensity along the surface crack front, a numerical approach is obtained to predict the fatigue crack growth behavior of elliptic surface crack. The prediction results of different initiate crack shape are all consistent with the reference test, and they all present a conversion process of rounding first to oval again. And every two parameters of the three initiate factors: shape parameter α_0, crack depth a_0 and crack width c_0 control the change of the surface crack front.

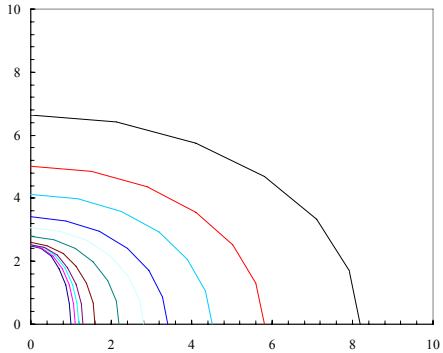

a) $\alpha_0=a/c=2.5$

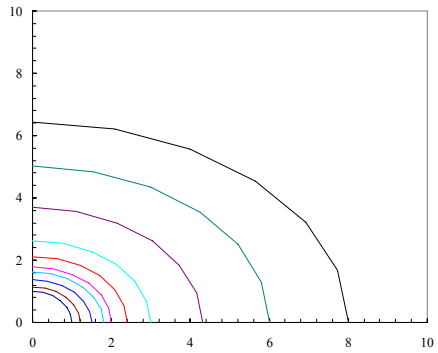

b) $\alpha_0=a/c=1$

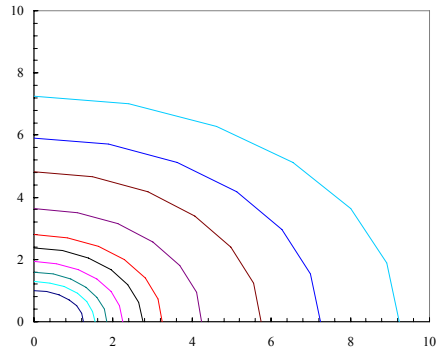

c) $\alpha_0=a/c=0.8$

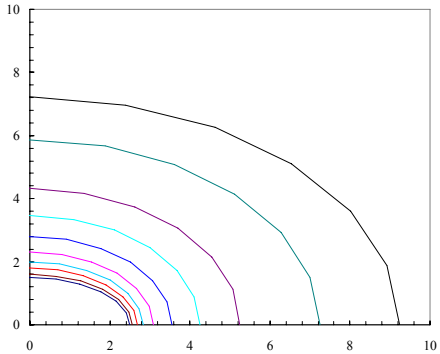

d) $\alpha_0=a/c=0.6$

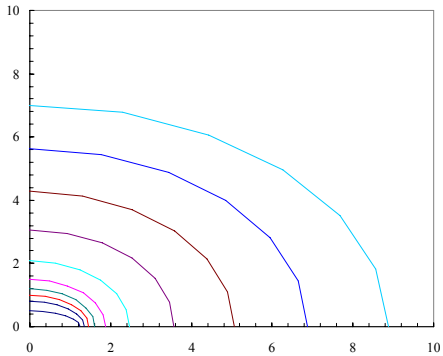

e) $\alpha_0=a/c=0.4$

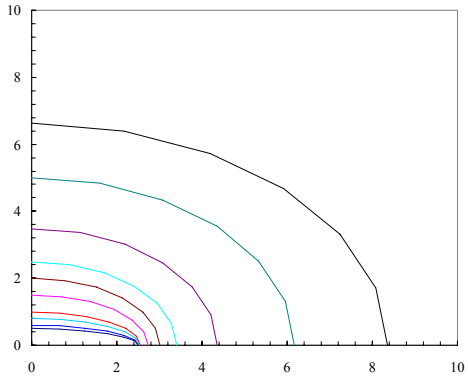

f) $\alpha_0=a/c=0.2$

Fig. 5. the prediction shape change of crack front

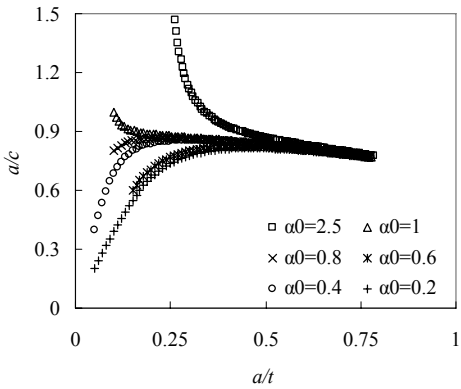

Fig. 6. α~β curve during the crack growth process

Acknowledgements

The financial support of the National Nature Science Foundation of China, Grant NO.11072205, is gratefully acknowledged. We are also grateful for the valuable assistance of Key Laboratory of Strength and Vibration, the SWJTU Laboratory.

References

[1] Newman, Jr J.C., Raju, I.S., 1981. An empirical stress intensity factor equation for the surface crack. Journal of Engineering Fracture Mechanics, 15(1-2):185-192.

[2] Smith, R.A., Cooper, J.F., 1989.A finite element model for the shape development of irregular planar cracks. .International Journal of Pressure Vessel and Piping. 36(04):315-326.

[3] Den Jiangang, Jiang Heyang, Li Zailiang, 2003. Boundary Element Numerical Simulation of Three-Dimensional Crack-Growth Trajectory. Chinese Journal of Applied Mechanics. 20(02):49-53.(in Chinese)

[4] Feng Xiqiao, He Shuyan, 1997. Continuum damage mechanics method for fatigue growth of surface cracks. Journal of Tsinghua University(Sci & Tech). 37(05):78-82.(in Chinese)

[5] Masanori Kikuch, Yoshitaka Wada, Kazuhiro Suga, 2011. Surface crack growth simulation under mixed mode cyclic loading condition. Journal of Procedia Engineering. 10:427-432.

[6] Song P.S., Sheu B.C., Shieh Y.L., 2002. Prediction of semi-elliptical surface crack growth in 2024-T4 aluminium alloy. International Journal of Pressure Vessels and Piping. 79(4):273-278.

[7] Liu Yanping, Chen Chuanyao, Li Guoqing, Li Jianbing, 2010. Fatigue life prediction of semi-elliptical surface crack in 14MnNbq bridge steel. Journal of Engineering Failure Analysis. 17(6):1413-1423.

[8] Paris, P.C., Erdogan, F., 1963. A critical analysis of crack propagation laws. Trans. ASME, Journal of Basic Engineering, 85D: 528-34.

[9] Cui Weicheng, 2002. Relation between crack growth rate curve and S-N curve for metal fatigue. Journal of ship mechanics. 6(6):93-105.

[10] Castro J.T.P., 2005. Singluar and non-singular approaches for predicting fatigue crack growth behavior. International Journal of Fatigue. 27(10-12): 1366-1388.

[11] Li D.M., Nam W.J,, Lee C.S., 1998. An improvement on prediction of fatigue crack growth from low cycle fatigue properties. Journal of Engineering Fracture Mechanics. 60(4): 397-406.

[12] Ramsamooj D.V., 2003. Analytical prediction of fatigue crack propagation in metals. Journal of Engineering Propagation Mechanics. 129(6): 672-682.

[13] Chen Long, Cai Lixun, Yao Di, 2012. Study on the FCG prediction model based on material's LCF damage. Journal of Applied Mechanics and Materials. 117-119:38-42.

[14] Chen Long, Cai Lixun, Yao Di, 2012. A new method to predict fatigue crack growth rate of materials based on average cyclic plasticity strain damage accumulation. Chinese Journal of Aeronautic. (in press)

[15] Schwalbe, K.H., 1974. Comparison of several fatigue crack propagation laws with experimental results. Engineering Fracture Mechanics. 6(2): 325-341.

[16] Green, A.,.E., John, E., Srawley, 1965. Stress-intensity factors for single-edge-notch specimens in bending or combined bending and tension by boundary collocation of a stress function. NASA TN D-2603.

[17] Newman,J.C. Jr., 1976. Predicting failure of specimens with either surface cracks or corner cracks at holes. NASA TN D-8244.

[18] Putra, I.S,, Schijve, J., 1992. Crack opening stress measurements of surface cracks in 7075-T6 aluminum alloy plate specimen through electron fractography. Fatigue Fract Engng Mater Struct, 15(4):323-338.

[19] Noroozi A.H., Glinka, G.., Lambert, S., 2005. A two parameter driving force for fatigue crack growth analysis. International Journal of Fatigue. 27(10-12): 1277-1296.

[20] Wu Zhixue, 2007. Numerical simulation to surface crack fatigue growth（II）[J]. Chinese Journal of Applied Mechanics. 24(1):42-47.(in Chinese) .

[21] Brennan, F.P., Ngiam, S.S., Lee, C.W., 2008. An experimental and analytical study of fatigue crack shape control by cold working. Journal of Engineering Fracture Mechanics. 75(3-4):355-363.

Effect of Pitch Difference on Anti-loosening Performance and Fatigue Strength for High Strength Bolts and Nuts

Xin Chen[1,*], Nao-Aki NODA[1], Yu-Ichiro AKAISHI[1]
Yoshikazu SANO[1] and Yasushi TAKASE[1]

[1] Department of Mechanical Engineering, Kyushu Institute of Technology, Fukuoka 804-8550, Japan
* Corresponding author: xin96995@126.com

Abstract A slight pitch difference is considered between the bolt and nut in this study. Here, the pitch of nut is α μm larger than the pitch of bolt. In the first place, the distance δ, of nut screwed onto bolt without any prevailing torque, is experimentally and analytically obtained for each level of α. Then, the relationship between axial force and prevailing torque during tightening process is tested. According to the obtained torque-axial force relationship, for four different levels of α, the loosening experiment based on NAS3350 (National Aerospace Standard) is performed, and the loosening and dropping status of the nuts are investigated. Considering both the anti-loosening ability and the clamping ability of the nut, the desirable range of α is discussed. After that, according to the loosening experiment results, three levels of α are selected to make a further study about the effect of the pitch difference on the fatigue life of bolt. The fatigue experiment is performed and the S-N curves are obtained. Finally, the finite element method is used to make a simulation of the fatigue experiment and the mean stress and stress amplitude at each thread bottom of bolt are analyzed.

Keywords Bolted Joint, Pitch Difference, Anti-loosening Performance, Fatigue Life

1. Introduction

The bolts and nuts are important joining elements disassembled easily for maintenance and widely used because of low cost. To ensure the structure safety, the anti-loosening performance and high fatigue strength have been always requested, and therefore, several special nuts were invented in order to prevent self-loosening [1-3]. The previous experimental results showed that the fatigue strength may be improved under suitable pitch error existing between bolt and nut [4]. The tapered bolt named CD bolt proposed by Nishida, indicated higher fatigue strength experimentally and being widely used in structures [5].

The authors previously analyzed the anti-loosening effect and stress reduction effect for the bolt and nut having slightly pitch difference by applying the finite element method [6-7]. However, the previous studies are limited to theoretical investigations. Therefore, the effect of pitch difference on anti-loosening performance has not been experimentally verified yet, and an experimental analysis for the effect of pitch difference on the fatigue life is also necessary.

In this paper, the M16 (JIS) bolt and nuts are employed and designed with a slight pitch difference. The standard M16 bolt and nut usually have the same pitch of 2000μm. Here, we assume that the nut pitch is equal or slightly larger than the bolt pitch, and we will consider four types of pitch difference, that is, $\alpha=0$, $\alpha=\alpha_{small}$, $\alpha=\alpha_{middle}$ and $\alpha=\alpha_{large}$. The clearance between bolt and nut is assumed as a common dimension of 125μm. At the first place, the position where the prevailing torque appears will be discussed towards four different levels of pitch difference. Then, the relationship between axial force and prevailing torque will be experimentally obtained. To investigate the effect of pitch difference on the anti-loosening performance, the loosening experiment will be performed by using the four groups of bolt joint specimens. Considering the clamping force and loosening status of bolts and nuts during the loosening experiment, the desirable pitch difference will be discussed. Next, according to the loosening experiment results, then the

fatigue experiment will be performed to obtain the S-N curves. After that, the finite element method will be applied to simulate the fatigue experiment, and then the endurance limit diagrams will be discussed.

2. Relationship between prevailing torque and axial force

For the normal bolt and nut, the nut can be screwed onto the bolt without torque until touching the clamped member. When a slightly pitch difference α is introduced on each nut pitch, the height of the nut increases accordingly, and therefore, during the screwing process, the contact status will also changes between the bolt threads and nut threads. It can be imagined that the nut threads may get stuck in the bolt threads if the pitch difference α is large enough, and in that case, a prevailing torque is necessary to continue screwing the nut to the requested position. Figure 1 shows a schematic illustration of a screwing status appeared until which the nut becomes immovable without any prevailing torque. Actually, as the nut is screwed onto the bolt, the pitch difference will be accumulated between the bolt threads. Finally, the two ends threads of nut contact with the bolt threads at the same time as shown in Figure 1. Theoretically, when a pitch difference is added on each nut pitch, the distance δ which nut be screwed onto bolt without any torque, can be obtained by formula (1).

$$\frac{\delta\alpha}{P} = \frac{nC_y}{2tan\theta} \quad , \quad C_x = \frac{C_y}{tan\theta} \tag{1}$$

where δ is the distance where the prevailing torque appears, α is the pitch difference, n is the thread number of nut, θ is the thread angle, P is the pitch of bolt, C_x and C_y are the clearance between bolt and nut (see Figure 1). To clarify the mechanism, four sets specimens of bolts and nuts with different levels of α are investigated. The four levels of α has a relationship of $\alpha=0<\alpha_{small}<\alpha_{middle}<\alpha_{large}$, where α=0 represents the normal bolt and nut. As seen in Figure 2 (a), the thread length of bolt is of 42mm and the height of nut is 16mm. The clamped plate, shown in Figure 2 (b), has a width of 34.5mm. It is known that without clamped plate, the normal nut (α=0) can be screwed onto the blot until δ equals 42mm. However, with increasing the pitch difference, the fitting distance δ without any prevailing torque will decrease. The relationship between δ and the pitch difference are investigated. Table 1 shows the measured value of fitting distance δ for four levels of α.

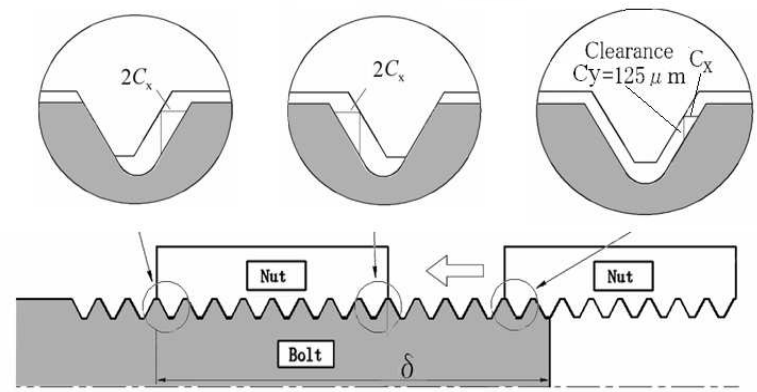

Figure 1. Schematic illustration for bolt and nut which have slight pitch difference

Table 1. Fitting distance δ without any prevailing torque

Pitch difference α (μm)	δ (mm)
0	42
α_{small}	25.5<δ<42
α_{middle}	16<δ<25.5
α_{large}	δ<16

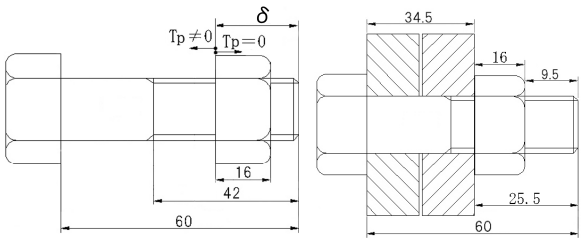

(a) Without clamped plate (b) With clamped plate

Figure 2. Fitting status [mm]

When $\alpha=\alpha_{small}$, the nut can be screwed to the requested position for clamped plate (δ=25.5mm) without any prevailing torque. For the cases of $\alpha=\alpha_{middle}$ and $\alpha=\alpha_{large}$, a prevailing torque is necessary to carry the nut touching the clamped plate.

Next, we will focus on the relationship between axial force and prevailing torque of the bolt in the tightening process. Figure 3 shows the experimentally obtained torque-axial relationship of the bolt during the tightening process until the nut reaches the position in Figure 2(b). Whether the prevailing torque is needed or not, for all the nuts, the final tightening torque is set as the same value of 70 N·m. For the normal bolt and nut, the axial force produces just after the torque is applied on the nut. At the point of torque equals 70 N·m, the axial force, in other words, the clamping force of the bolt, reaches 24 kN. The case of $\alpha=\alpha_{small}$ has the same torque-axial force relationship with α=0. When α increases to α_{middle}, a prevailing torque of 40 N·m is needed before the nut becomes contacting with the clamped plate. Under the same tightening torque of 70 N·m, the axial force of bolt is reduced by 4 kN compared with the normal case. When $\alpha=\alpha_{large}$, the prevailing torque increases accordingly, on the other hand, the axial force decreased significantly to 8 kN.

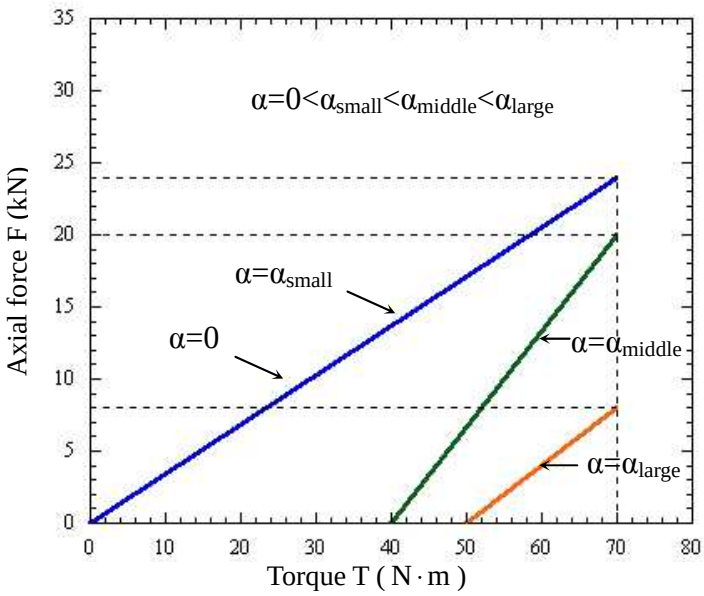

Figure 3. Relationship between torque and axial force

3. Effect of pitch difference on anti-loosening performance

Based on the torque-axial force relationship obtained above, the loosening experiment is performed to investigate pitch difference effect on the anti-loosening performance. The same specimens are used in the torque-axial force and loosening experiments for $\alpha=0$, $\alpha=\alpha_{small}$, $\alpha=\alpha_{middle}$ and $\alpha=\alpha_{large}$. Two specimens are investigated together for the loosening experiment. The experimental device is impact-vibration testing machine based on NAS3350 (National Aerospace Standard) whose vibration frequency is 1,800 cycles per minute, and vibration acceleration is 20G. If the vibration cycles are over 30000, we may judge the anti-loosening performance is enough. The specimens are fixed on the experimental device under the same torque of 70 N·m before the vibration starts. The experiment device is shown in Figure 4. When the device starts vibrating, a counter connected with the experiment device shows the cycles of vibrations. Table 2 shows the cycles of vibrations when dropping happens and when loosening happens.

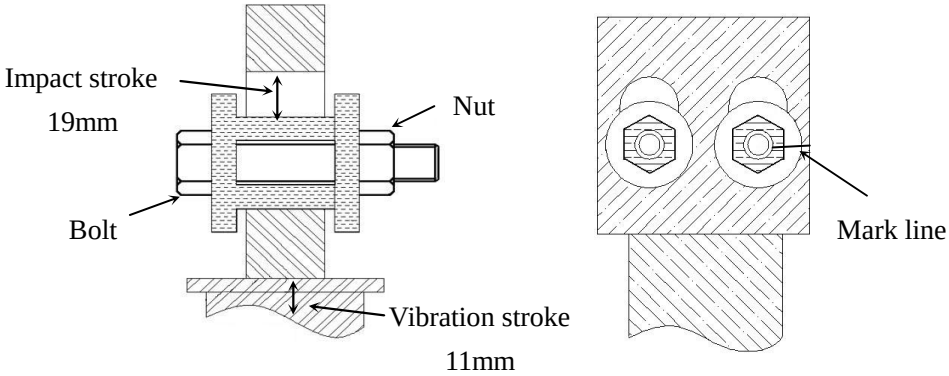

Figure 4. Loosening experimental device based on NAS3350

For $\alpha=0$ and $\alpha=\alpha_{small}$, the nuts drops when the vibration number is nearly 1000 cycles. For $\alpha=\alpha_{middle}$, the nuts does not drop before 30,000 cycles of vibration, but the loosening is observed for one specimen. Moreover, the axial force decreases to 20 kN in this case. For $\alpha=\alpha_{large}$, neither dropping nor loosening happens, however, the clamping ability of the bolt and nut decreases significantly to F=8 kN, which is not acceptable for actual application. It is found that, on the one hand, when α is

Table 2. Experimental result for anti-loosening performance

Pitch difference α	Sample	Nut drop	Cycles for dropping	Cycles for start loosening	Prevailing torque (N·m)	Axial force (kN)
0	No.1	Yes	751	-	0	24
	No.2		876	-		
α_{small}	No.3		813	-	0	24
	No.4		1528	-		
α_{middle}	No.5	No	30000	21000	30	20
	No.6		30000	30000		
α_{large}	No.7		30000	30000	67	8
	No.8		30000	30000	57	

too small, the expected anti-loosening performance cannot be realized. On the other hand, when α is too large, the clamping ability will decrease significantly because large deformation takes place on the bolt thread. Therefore, considering both the anti-loosening ability and the clamping ability, $\alpha=\alpha_{middle}$ can be selected as the most suitable pitch difference.

From the loosening experiment results we can see that, a proper pitch difference has a positive effect on the anti-loosening performance of bolt and nut. Next, we will focus on the effect of pitch difference on fatigue strength of bolt, considering three types of pitch difference of α=0, $\alpha=\alpha_{small}$ and $\alpha=\alpha_{middle}$.

4. Effect of pitch difference on fatigue strength of bolt

4.1. Fatigue experiment

The M16 (JIS) blots and nuts, strength grade 8.8, are employed in the fatigue experiment. The specimens are subjected to a mean force of 30 kN. Since the cross sectional area A_R of the bolt is 141 mm^2, the corresponding mean stress of the specimens is 213 MPa. For normal M16 bolt, it is known that the fatigue strength is about 50 MPa. Here, the stress amplitude is ranged from 50 MPa to 160 MPa in this experiment. The 392kN (40tonf) Servo Fatigue Testing Machine is used with cycling frequency 8Hz. The assembly drawing is illustrated in Figure 5 and the experimental device is shown in Figure 6. Three groups of bolt joint specimens of α=0, $\alpha=\alpha_{small}$ and $\alpha=\alpha_{middle}$ are investigated.

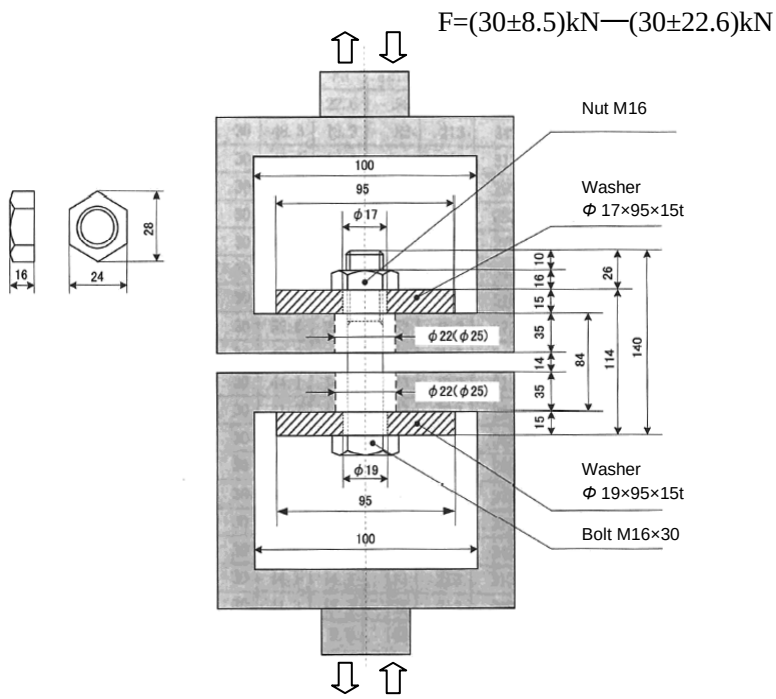

Figure 5. Schematic illustration of fatigue experiment [mm]

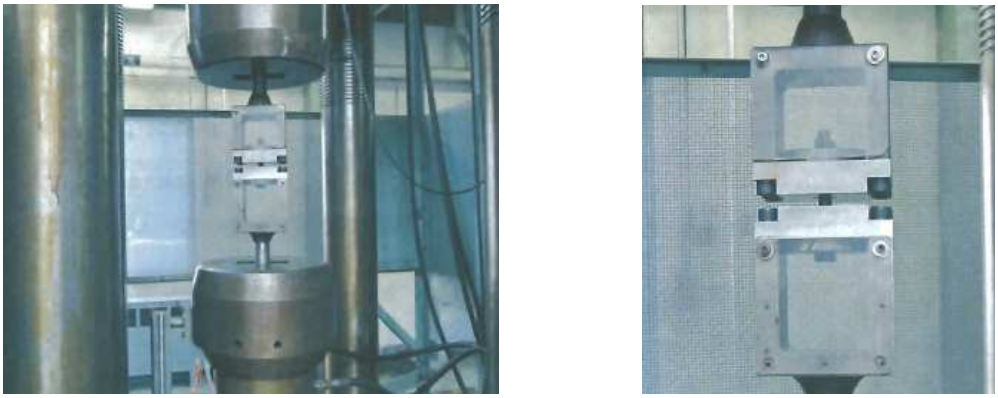

Figure 6. Fatigue experimental device

4.2. S-N curves

The S-N curves with fatigue limit at $N=2\times10^6$ are obtained as shown in Figure 7. It is found that the fatigue lives are different clearly depending on the three levels of pitch difference. Table 3 shows the comparison between the fatigue life normalized by the results of α=0. When the stress amplitude is above 80 MPa, the fatigue life for $\alpha=\alpha_{small}$ is about 1.4 times larger and the fatigue life for $\alpha=\alpha_{middle}$ is about 1.2 times larger than the one of the normal bolt and nut of α=0.

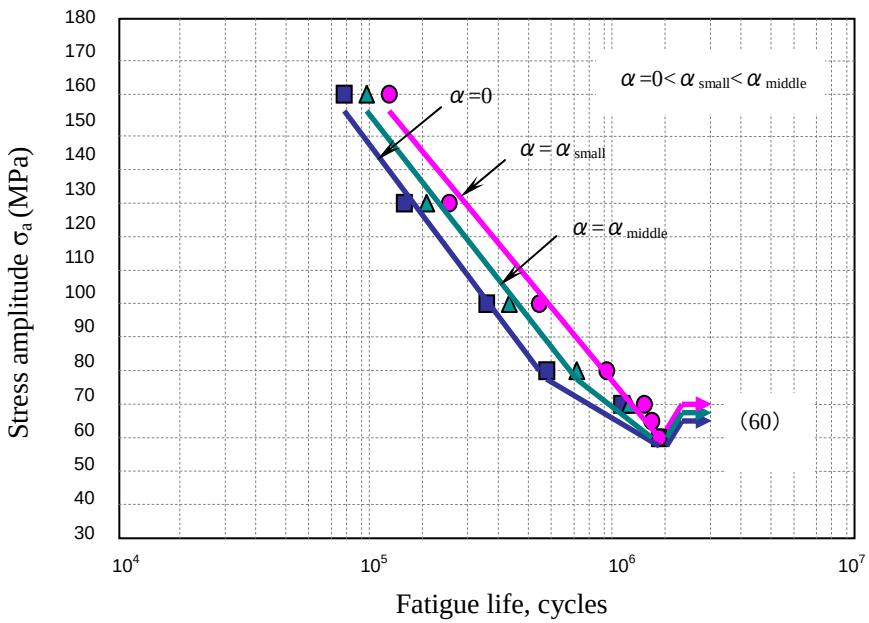

Figure 7. S-N curves

Table 3. Comparison between the fatigue life for α=0, $\alpha=\alpha_{small}$ and $\alpha=\alpha_{middle}$ (Mean stress σ_m=213MPa)

Pitch difference α	Stress amplitude σ_a (MPa)				
	160	130	100	80	70
0	1	1	1	1	1
α_{small}	1.49	1.60	1.53	1.61	1.21
α_{middle}	1.26	1.22	1.20	1.21	1.02

However, near the fatigue limit, the fatigue life of three group specimens is not very different, and the fatigue limit remains the same value of 60 MPa for three cases of pitch difference.

4.3. Investigation of the fractured specimens

Figure 8 shows the examples of fractured specimens (σ_a=130MPa). For the normal bolts and nuts, it is confirmed that the fracture is always happened at the first thread bottom as shown in Figure 8(a). For the specimens of $\alpha=\alpha_{small}$, the fracture position is between the No.1 thread and No.3 thread of bolt. It should be noted that the fracture surfaces have the different characteristic compared with the

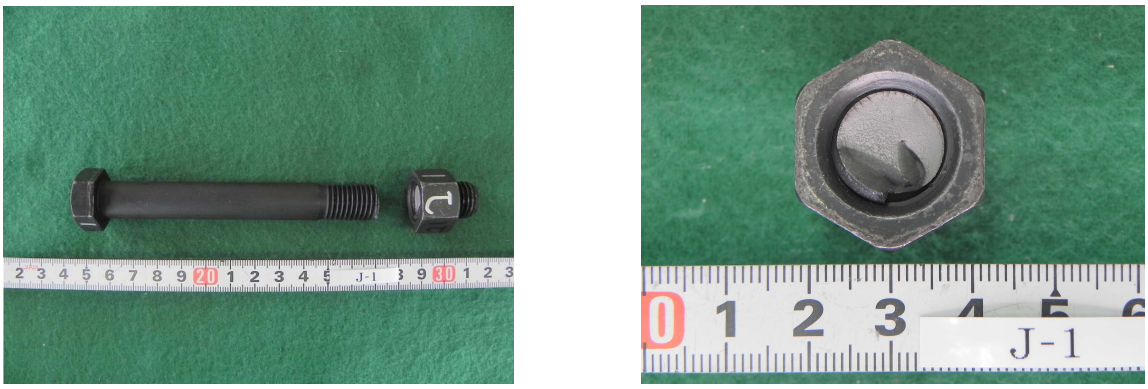

(a) α=0 (fatigue life 151,860 cycles)

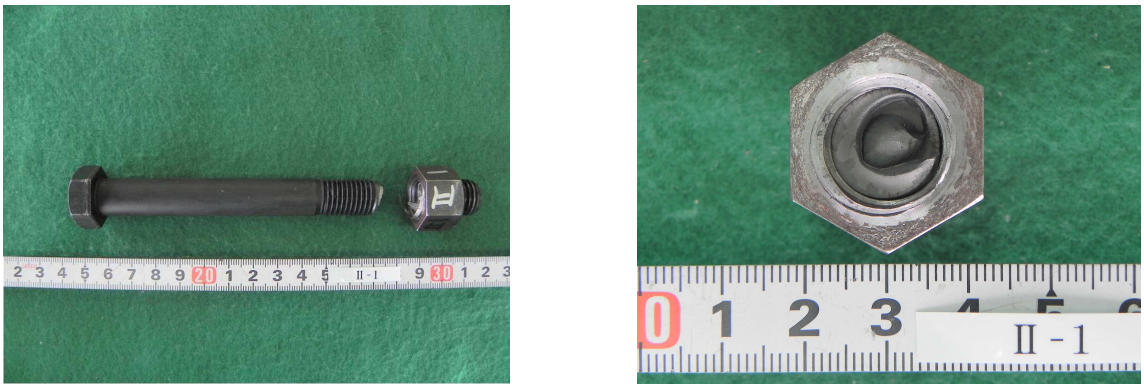

(b) $\alpha=\alpha_{small}$ (fatigue life 242,810 cycles)

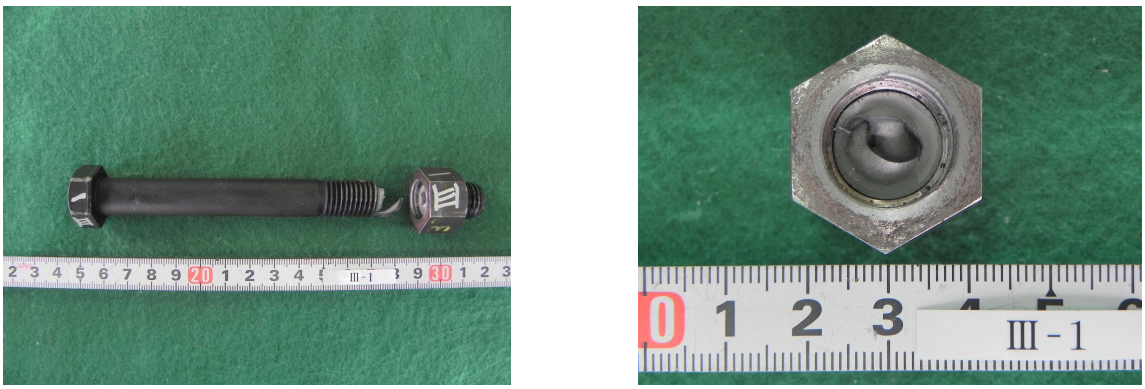

(c) $\alpha=\alpha_{middle}$ (fatigue life 184,770 cycles)

Figure 8. Fractured specimens (σ_a=130MPa)

case of α=0. For the specimens of $\alpha=\alpha_{middle}$, the fracture position of bolt and the fracture surface are nearly same with the case of $\alpha=\alpha_{small}$.

4.4. FEM analysis

For the normal bolt and nut, it is known that the largest stress concentration appears at the No.1 thread of bolt. However, when α is introduced, the contact status between bolt and nut is changed, and therefore, the stress distribution along the bolt threads should be reconsidered. To analyze the stress status of the bolt threads, the finite element models are created by using FEM code MSC.Marc/Mentat 2007. Three models have the different pitch difference of α=0, $\alpha=\alpha_{small}$ and $\alpha=\alpha_{middle}$ in according with the experiment. As shown in Figure 9, the axisymmetric model of bolt and nut is created. The fixed component is assumed as a cylindrical clamped plate with an inner diameter 17.5mm, outer diameter 50mm and thickness 35mm. The Young's modulus is 206GPa and the Poisson's ratio is 0.3 for all the materials for bolt, nut and clamped plate. In the experiment, the bolt axial force F=(30±8.5)kN—(30±22.6)kN was studied. In the analysis, the bolt axial force F=30 ±14.1kN is considered as an example. The assumed amplitude Fa=14.1kN is corresponding to the stress amplitude σ_a=100 MPa at the minimum section of the bolt. The elastic calculation is performed as the first step, but the results show that the stress is over the yield stress σ_s=800 MPa of the material SCM435 for the wide region. Then, the elastic-plastic calculation is performed again. Based on the mean stress and the stress amplitude at each root of bolt thread, the endurance limit diagrams are obtained as shown in Figure 10 to Figure12. The fatigue limit σ_N of the material SCM435 is 420 MPa. The mean stress σ_m and stress amplitude σ_a are explained as following:

$$\sigma_m=\frac{\sigma_{max}+\sigma_{min}}{2}, \quad \sigma_a=\frac{\sigma_{max}-\sigma_{min}}{2} \tag{2}$$

where σ_{max} is the maximum stress of each thread bottom under the maximum load of F=30+14.1KN and σ_{min} is the maximum stress of each thread bottom under the minimum load of F=30-14.1KN. The endurance limit diagrams show the dangerous level of each bolt thread. From Figure 10, we can see that the No.1 thread bottom has the high stress amplitude and mean stress, which is corresponding to the fracture position in the experiment as shown in the section 4.3. In Figure 11, when a pitch difference of α_{small} is introduced, the stress amplitude decreases at the No.1 thread bottom. On the other hand, plastic deformation happens mainly at the bottoms of No.7 and No.8 threads. However, the difference among the stress status at each thread is not very large compared

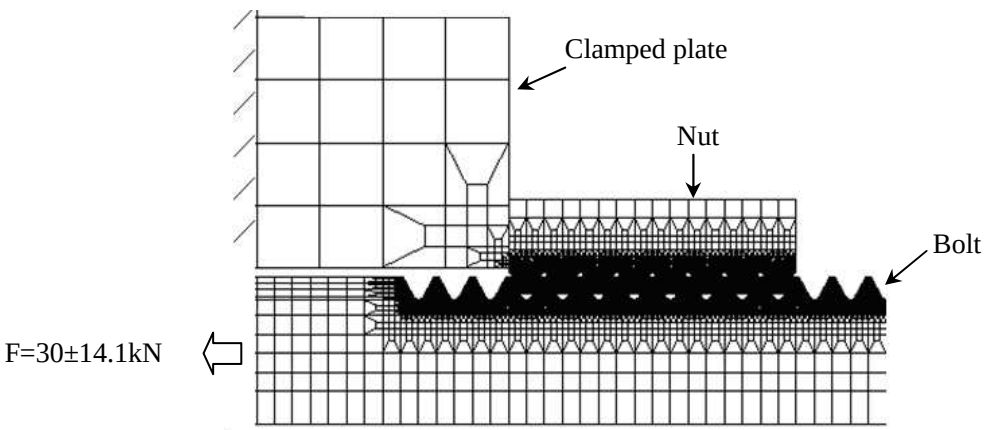

Figure 9. Axisymmetric finite element model

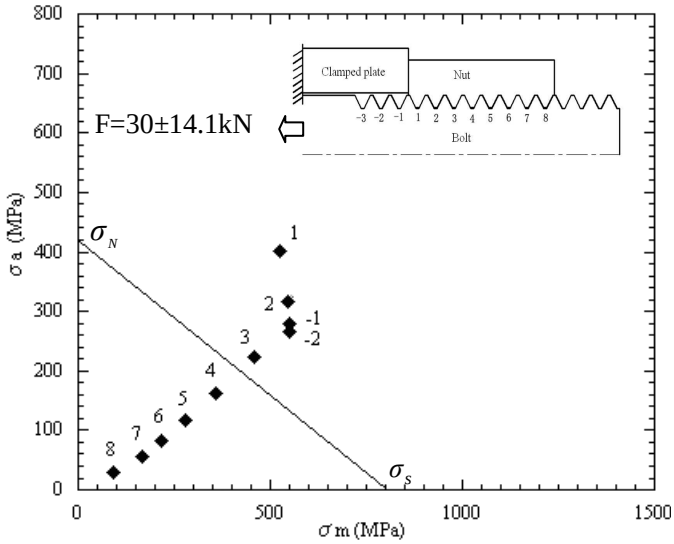

Figure 10. Endurance limit diagram for α=0

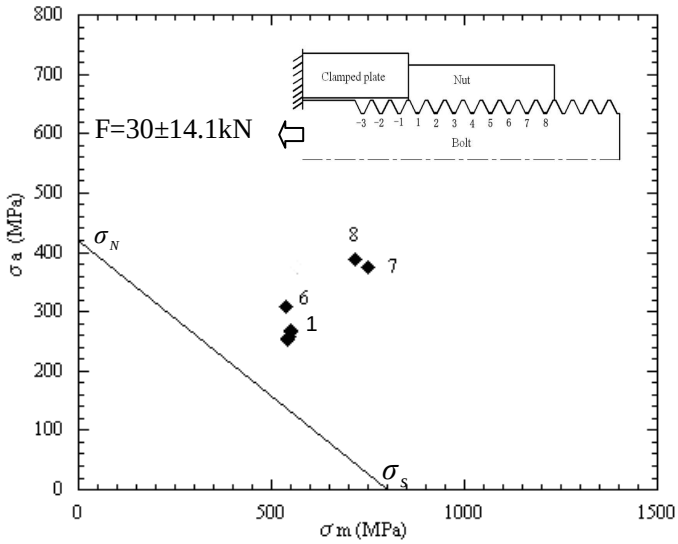

Figure11. Endurance limit diagram for $\alpha=\alpha_{small}$

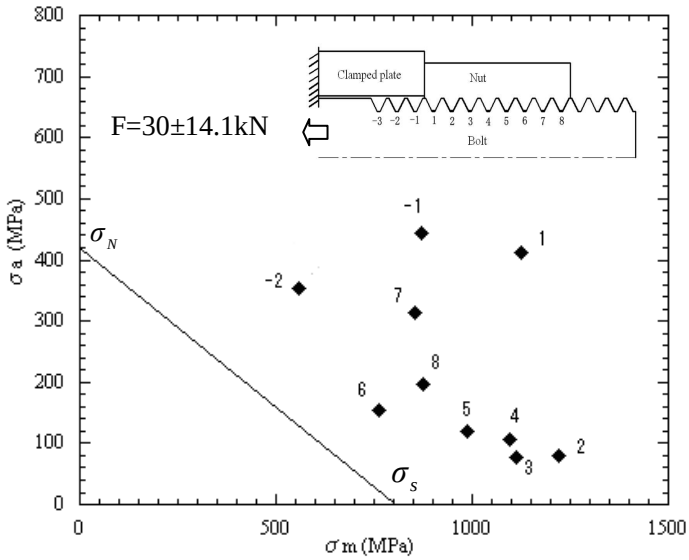

Figure 12. Endurance limit diagram for $\alpha=\alpha_{middle}$

to the normal bolt. For the case of $\alpha=\alpha_{middle}$, as Figure 12 shows, because of the large pitch difference, it is seen that the mean stress values for most threads is over the yield stress the material.

Conclusions

In this study, a slightly pitch difference is designed between bolt and nut. Four different levels of pitch difference $\alpha=0$, $\alpha=\alpha_{small}$, $\alpha=\alpha_{middle}$ and $\alpha=\alpha_{large}$ are experimentally considered. The relationship between prevailing torque and axial force for each case of α has been analyzed as the first step. Next, the loosening experiment and the fatigue experiment have been performed successively to study the anti-loosening performance and the fatigue strength of bolt. Finally, by using the finite element method, the effect of pitch difference on the stress status of the bolt thread bottom has been numerically analyzed. The conclusions can be summarized as follows:

(1) It is found that $\alpha=\alpha_{middle}$ is the most desirable pitch difference to realize both the anti-loosening and clamping abilities.

(2) It is found that $\alpha=\alpha_{small}$ is the most desirable pitch difference to extend the fatigue life of the bolt and nut. Compared with the normal bolt and nut, the fatigue life for $\alpha=\alpha_{small}$ can be extended by about 1.4 times and the fatigue life for $\alpha=\alpha_{middle}$ can be extend ed by about 1.2 times.

(3) According to the FEM analysis, it is found that the stress amplitude at the No.1 thread bottom decreases significantly for $\alpha=\alpha_{small}$, and due to the large plastic deformation at No.7 and No.8 thread bottoms, the stress amplitude here is almost the same as other thread bottoms.

Acknowledgements

This study is supported by Hidetoshi TAMASAKI, in KHI corporation, Moji-ku Kitakyushu, Japan. We also show great gratitude to Yang Yu, who provided much valuable work during the writing of this paper.

References

[1] Daiki Kogyo KK., 2004, Super Slit Nut, Japan Patent (in Japanese) 2004–218674.
[2] Hard Lock Kogyo KK., 2002, Hard Lock Nut, Japan Patent (in Japanese) 2002–195236.
[3] Minamida KK., 1999, Anti-loosening Nut, Japan Patent (in Japanese) H11–177902.
[4] Kazuo, M., Stress Analysis of a Bolt-Nut Joint by the Finite Element Method and the Copper-Electroplating Method. The Japanese Society of Mechanical Engineers, 19(1976) 360–368
[5] Nishida, S., et al, 1980, Screw Connection Having Improved Fatigue Strength, United States Patent 4,189,975.
[6] Noda, N.-A., Kuhara, M., Xiao, Y., Piao, Q C, Takase, Y. and Nishida, S.-I., Anti-loosening performance of bolts and nuts which have slightly different pitches. The Japan Society of Mechanical Engineers, 46 (2008) 71–72
[7] Xiao, Y., Noda, N.-A., Morita, M., Nishida, S.-I., Stress reduction effect of bolts and nuts which have slightly different pitches. The Japan Society of Mechanical Engineers, 62 (2009) 29–30

Research on the New Low Temperature Self-Protective Paste Boronizing Processes of Thermal Power Plant Economizer Pipe

Jianjun HE, Jian CHEN, Yanjie REN, Wei QIU, Beier LUO

School of energy and power engineering, Changsha University of Science and Technology, Changsha, 410114, China
* Corresponding author: hejianjun329@126.com

Abstract: Power plant boiler economizer pipe tend to crack rapidly due to the erosion of high temperature flue gas. In this paper, the power plant boiler economizer pipe (annealing 20 steel) was chosen as the research materials, three new formulations of self-protective paste in which quartz powder, fly ash and coal gangue were as the main ingredients were investigated,what's more,the low temperature self-protective paste boronizing technology with the rare earth added was studied. The experimental results show that the quartz powder, fly ash and coal gangue protective layer sintered at the boride temperature have the virtues of high strength, good sealing and easier peeling off, and these protective layers also brought good boronizing effect. 9wt% rare earth addition can bring good boronizing effect, when the boronizing temperature down to 700 ℃, the rare earth added self-protection paste boronizing process can still achieve boronizing layer. The wear-resisting and corrosion resistant performance of the economizer pipe after boronizing process obviously improved.

Keywords Self-protective paste boronizing, Protective coating, rare earth, economizer pipe, low temperature

1 Introduction

Economizer is an important heat-absorbing surface in the power plant boiler. It is usually equipped in the flue and absorbs the quantity of heat of flue gas in order to heat the boiler. But the existence of the large number of solid particles and corrosive gases in flue gas will cause the high temperature erosion wear and hot corrosion to the economizer tube and even leads to abnormal tube wall thinning and premature failure, frequent detonation tube leakage thus become serious threat to the safe and economic operation of boilers [1]. In coal-fired power plants, boiler accidents accounted for more than half of the power plant accident, while economizer of boiler tube blasting accidents accounted for 45% ~ 50%, among those economizer abrasions leakage is a main reason [2, 3]. So the improvement on the operational process of economizer pipe outer surface erosion and hot corrosion resistance is of great significance to improve the service life of the power plant boiler economizer, boost the reliability of boiler and prolong average trouble-free operation time of the boiler.

Boronizing is a kind of important chemical heat treatment technology. Take steel material for an example, after dealing with boron, its wear resistance, corrosion resistance, and the rigid and high oxidation resistance can be improved. Paste boronizing is a technological method in which the boron agent, activator, and filler are mixed through the use of the binder paste to be applied to the clean metal surface, and then sealed, packed, heated and preserved heat to achieve the boronizing layer [4,5]. Self-protection paste boron which overcomes the shortcomings that the traditional medicinal extract boron needs seal packing or the protection of the atmosphere, adapts the paste outer take cover [6,7],then in boronizing temperature a glaze shell generates on the paste coating surface to achieve self protection in the process of boronizing. The technology has the characteristics of simple process, fast boron permeability speed, good effect and low cost [8-10], which is suitable various shapes of the workpiece. It is a promising surface treatment technology [8]. The paste boronizing temperature of boron treatment is commonly in 800 ~ 1000 ℃, in such a high temperature, the traditional boronizing agent generates active boron atom which is essential to the boronizing process. But generally such a high temperature may reach to the austenitic temperature of steel tube. what's more, considerable changes in the organization of the original material took place, affected the performance of the matrix, then restricted the development and application of

self-protection paste boronizing technology. Therefore, the research and development of new low-temperature self-protection paste boronizing technology is of important engineering application value.

2 Experimental details

Thermal power plant boiler economizer tube blasting operation pipe (20 steel annealing states) was used as boron material. B_4C 、KBF_4、 the activated carbon,、SiC 、Al_2O_3 (filler), sodium silicate solution (adhesive) and a certain amount of lanthanum rare earth were prepared for boron paste, then the prepared cream boron paste was evenly coated on the surface of the sample, thickness is 3 ~ 5 mm, as is shown in Fig.1. The coated boron sample was dried in the drying oven at 160℃, and then moved into carbon silicon rod furnace to be heated for boronizing. The boronizing experiments were made in a series of set temperature. After a certain period of boron heat preservation time, electric power supply were turned off. When the samples in the furnace were cooled to 100 ~ 200 ℃, they were removed to cool in the air. Then the protective layer and paste layer were removed to prepare metallographic specimen which was to be corroded with nitric acid of 5% alcohol. Then the 200 MAT inverted metallographic microscopes was used to observe the microstructure of the boron samples, and the HBRV 187.5 hardness tester was used to test the hardness of the boron samples.

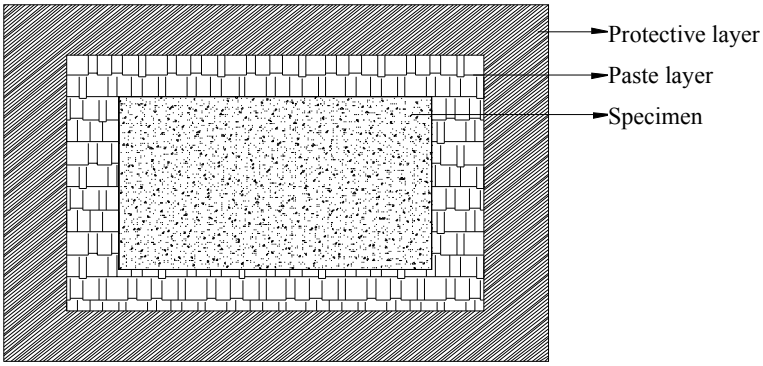

Fig.1 Schematic diagram of the specimen surface coating

3 Results and discussion

3.1 Temperature's influence on the boron effect without the rare earth

With no rare earth added, the microstructures of the self-protective paste boron sample are shown in Fig.2.

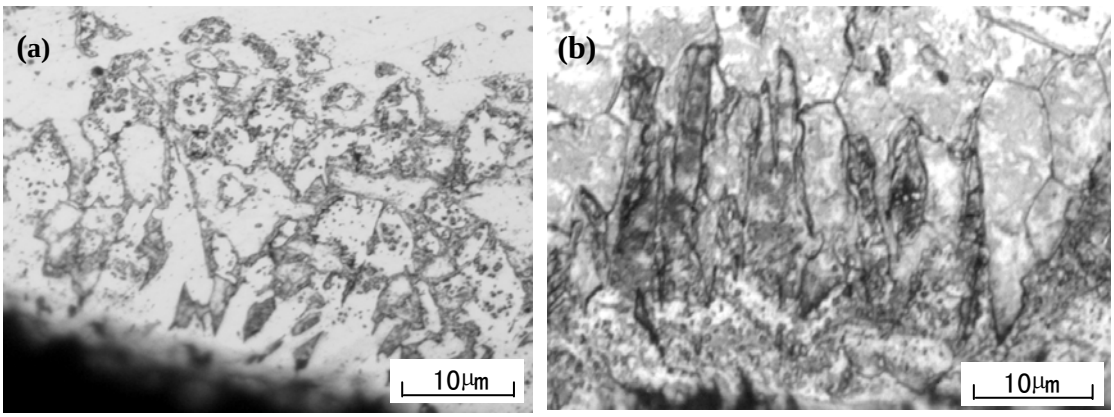

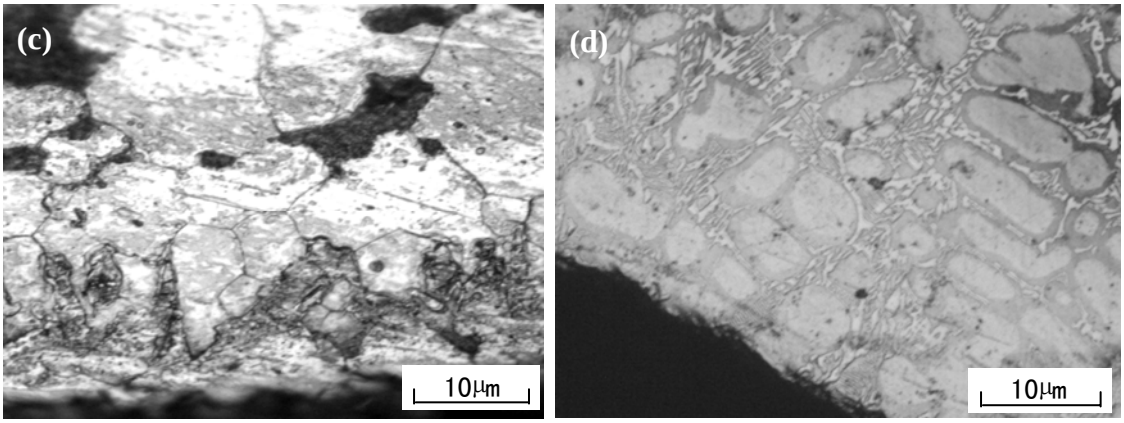

Fig.2 Microstructures of self-protective paste boronizing specimens at different boronizing temperature with no rare earth added (a) 960℃, (b) 900℃, (c) 850℃,(d) 800℃

It can be seen from Fig.2 that with the increase of boronizing temperature, boronizing layer thickness has a trend of increase. When the temperature is at 850℃, the boronizing layer of the sample is very thin, and discontinuous, the leading end of the sample has the trend of expansion along the steel matrix grain boundary; when the temperature is at 900℃, the ideal boronizing layer which was closely integrated like fingers and continuous on the surface of the whole sample can be obtained; when the temperature is at 960℃, the hardness of the boron sample increased, the appearance also changed, and fragmentation occurred in the boronizing layer which was in block or granular form. The main reason is related to boron carbide of nucleation characteristics and the obstacles that boron carbide suffered in the process of growing up. When the crystal nucleus formed on the surface grain boundary grew up, the distortion of the crystal nucleus formed in the crystal lattice lead to the increase of local stress which may cause the slight deviation of the growth of boride. 20G steel has the characteristics of small austenitic grain size, multi-grain boundary, multi-crystal nucleus formed on the surface grain boundary, all sorts of oblique nucleation. As for the economizer, the steel pipe carbon content is low and diffusion resistance is not big, which results in the irregular tooth structure.

When the temperature is decreased to 850 ℃, the boronizing layer was very shallow and boron effect was not obvious; when the temperature is at 800℃, no boron boronizing layer was found (as shown in Fig.2 (d)). Therefore, in the experiment, self-protective paste boronizing process can only be achieved when the temperature is over 800℃.

3.2 The influence of adding rare earth on the boron temperature

For the study of the influence of the addition of rare earth on the boron temperature in low temperature, protective paste in which fly ash and coal gangue are the main components was adopted. 7wt% rare earth was added into the original Boronizing agent formula, and then the same self-protective paste boronizing was employed. Heat preservation boron were adopted at 850℃、800℃、750℃、700℃ and 680℃ respectively, then it could be seen that the protective layer showed brick-red and on the surface there was a thin enamel layer, boron paste and sample were bonded but easy to clean up. Parts of boron sample microstructures at boronizing temperature are shown in Fig.3. The experiment results showed that when the temperature was over 700℃, boronizing layer could be achieved effectively; when the temperature was decreased to 680℃, no boron boronizing layer was found(as shown in Fig.3(c)).With higher boron temperature, the boronizing layer was deeper and the boron effects were better(as shown in Fig.3(a)).

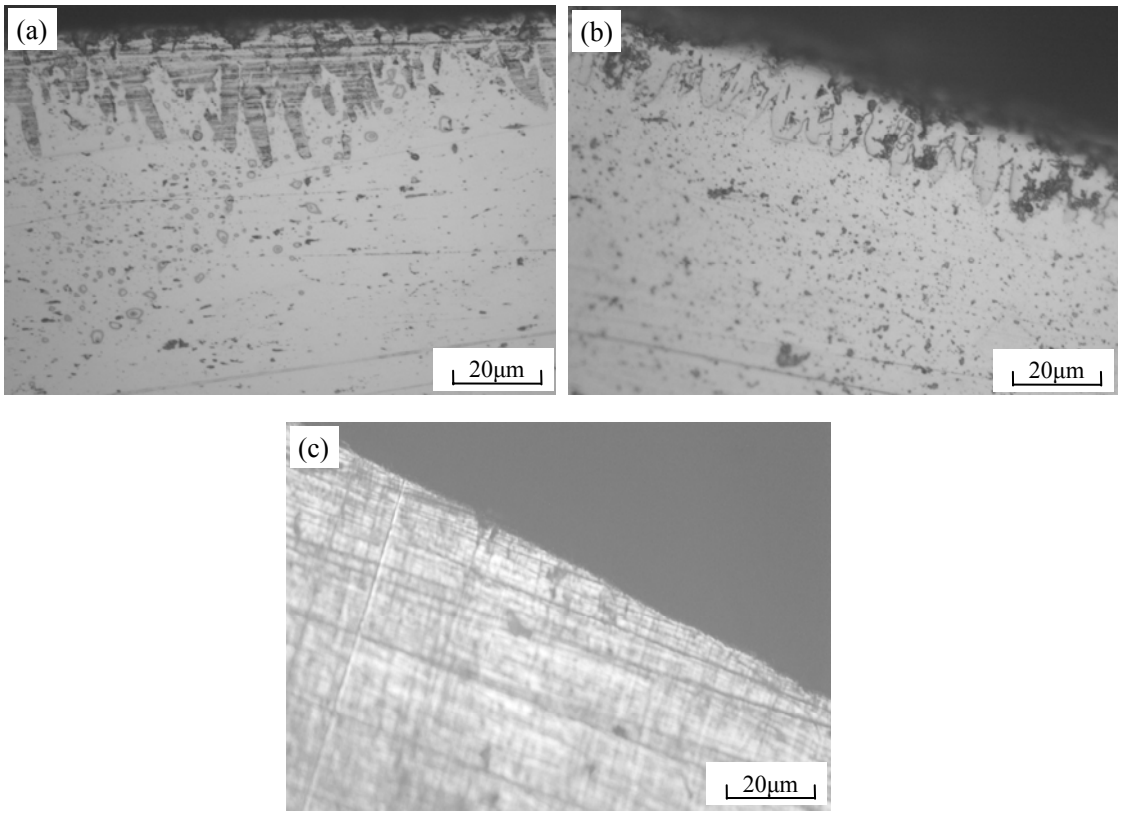

Fig.3 Microstructures of self-protective paste boronizing specimens at different boronizing temperature with rare earth added （a）850℃,（b）700℃,（c）680℃

3.3 The influence of the amount of rare earth added on the boron effect

To study the influence of the amount of rare earth added on the boron effect, 7wt%、8wt%、9wt% and 10wt% rare earth were chosen to add into the boron paste respectively, the addition of the amount of KBF4 and that of B4C were the same in each boron experiment, the same self-protective paste and the same boronizing processes were adopted, when the boron temperature was at 800℃, the microstructures of the self-protective paste boron samples with different amount of rare earth added were shown in Fig.4.

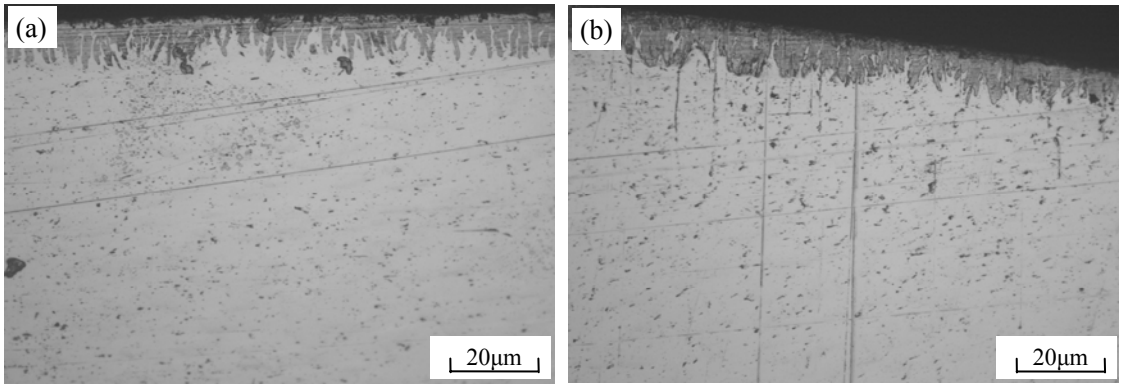

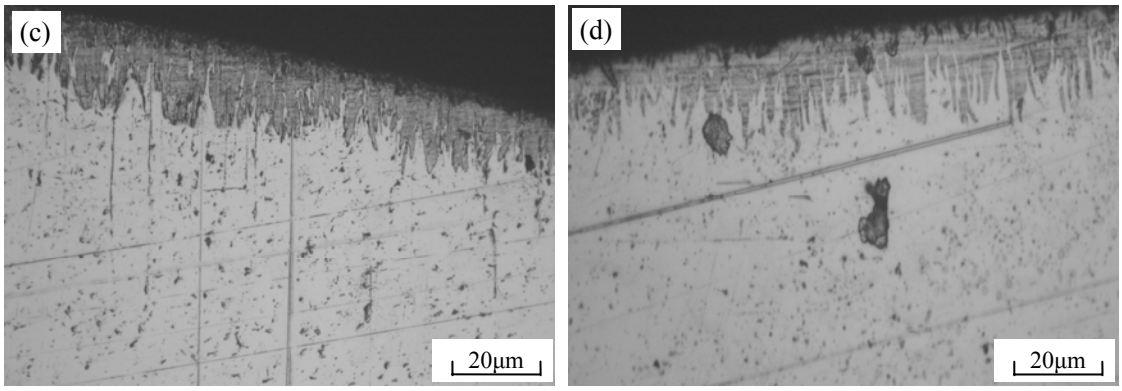

Fig.4 Microstructures of self-protective paste boronizing specimens with different rare earth addition
(a) 7wt%, (a) 7wt%, (b) 8wt%, (c) 9wt%, (d) 10wt%

It can be seen from Fig.4 that on the surface of the self-protective paste boron samples with rare earth added, a certain boronizing layer occurred. Under the circumstances of 8% rare earth addition and 9wt% rare earth respectively, boronizing layer was regular and closely integrated, which brought good boron effect. However, with the increase of the amount of rare earth added (as shown in Fig.4(d)), boronizing layer expanded further towards the sample, and the structure of which was irregular and its uniformity fell. From the hardness data of the boron samples (as shown in Fig.5), it can be seen that the hardness achieved the maxi value when the rare earth addition was 9wt%. Therefore, it can be drawn that in the current boronizing conditions and in the process of low-temperature boronisation, the optimum amount of rare earth added is 9wt%.

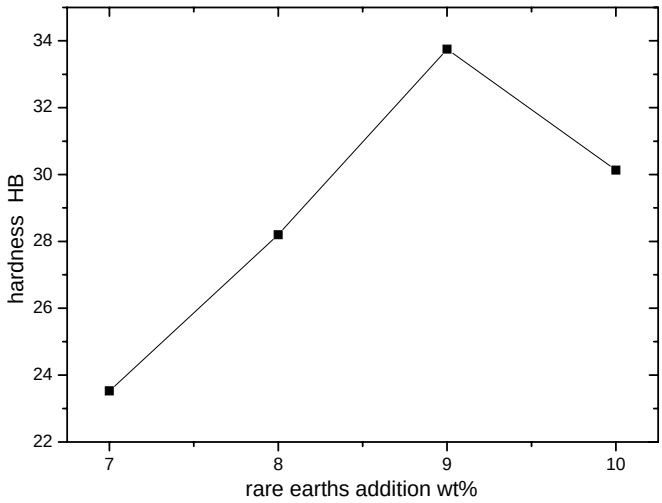

Fig.5 Hardness of self-protective paste boronizing specimens at different rare earth addition

3.4 Discussion

In the process of boronisation, the boron agent supplier in the paste had reaction and generated activate B atoms which had been absorbed by the iron and steel sample surface and were segregated and enriched on crystal defects such as grain boundary and the surface phase boundary and space [11], Then had a short-range diffusion in the direction of the internal lattice and matrix. With the continuous migration of B atoms, in the lattice when the conditions of concentration and fluctuation of energy were ready, Fe2B crystal nucleus formed. Then with the crystal grain's growing up, Fe2B-γ phase boundary propeled toward the inner matrix [12]. The protective paste in which quartz powder, the covering layer of fly ash and coal gangue were as the main ingredients, has the characteristics of high strength, good sealing and easy peeling in boronizing temperature, could achieve good boron effect.

Due to the intro protection layer, in the process of the self-protective paste boronizing,parts local boronisation can be achieved. When the boron temperature decreased effectively, the economizer steel pipe's online instant boronisation could be achieved and this technology can be applied to the strengthening treatment of the surface of other boiler heat pipes and other high- temperature resistant and corrosion resistant parts.

4 conclusion

With no rare earth added, self-protective paste boronizing can only be carried out when the temperature was over 800℃. Within a certain range, rare earth could speed up the boronisation and make the boronizing layer be well-distributed and closely integrated. Therefore, the binding force between the boronizing layer and matrix was increased and the performance of the steel pipe was improved. Rare earth was used to assist boron, when the boriding technology was properly handled, the temperature of the economizer self-protective paste borinisation can be decreased to 700℃, the addition of 9wt％ rare earth could achieve good boron effect. The protective paste in which quartz powder, the covering layer of fly ash and coal gangue were as the main ingredients, has the characteristics of high strength, good sealing and easy peeling in boronizing temperature, could also achieve good boron effect.

Acknowledgements

This research supported by national natural science foundation of China(51275058) and Hunan provincial natural science foundation of China（09JJ3097）.

References

[1] W.L. Cheng, Y. Zhou, A Model to be Used for Monitoring the Wear of Boiler Economers, Power Engineering, 26（2006）646–649.

[2] J.M. Ye, Power plant boilers principle and equipment, China Electric Power Press, Beijing, 2004.

[3] W.P. Yan, Y.Z. Liu, Y.H. Gao, Comparing Study on Styles of Exetended Heating Surfaces of Economizers in Utility Boilers, Boiler Technology, 37(2006) 26-30

[4] X.H. Yi, F.H. Li, Z.G. Fan, Technology for Solid- State Pack Boronizing of Q235 Steel and Kinetic Study of Boron Diffusion in Steel, MATERIALS PROTECTION,42（2009）13-16.

[5] J.S. Hu, Z.Y. Li, J.M. Hao et al., Development and applications of self-protective boronising paste based on thermodynamic analysis, Ordnance Material Science and Engineering, 25（2002）38-40.

[6] S.Roumiana, Petrova, S. Naruemon., S. Veljko, The Effect of Boronizing on Metallic Alloys for Automotive Applications, Journal of Materials Engineering and Performance, 17(2008) 340-345.

[7] D.C. Loua, J.K. Solbergb, O.M. Akselsena, N. Dahlc, Microstructure and Property Investigation of Paste Boronized Pure Nickel and Nimonic 90 Superalloy, Materials Chemistry and Physics, 115 (2009) 239-244.

[8] X.M. Ou, Z.Y. Ni, Study and Analysis on Process of Paste Boronization Without Boxing, Journal of China University of Mining & Technology, 27(1998)200-203.

[9] Y.Z Gong, L.D. Zhang Research on Self-protective Rare Earth-Boronizing Pasty Agent[J]. ELECTRONICS PROCESS TECHNOLOGY, 7(2001) 161-165.

[10] J.S. Hu, Z.Y. LI, J.M. Hao, et al. Application and Thermodynamic Analysis on Self-Shield Boronizing Pasty, HEAT TREATMENT OF METALS, 27(2007) 26-28.

[11] Z.S. Ji, Multivariate Boronizing Technology and Applications, Metallurgical Industry Press, Beijing,2004.

[12] I. Campos, M. Islas, E. González, et al.. Use of fuzzy logic for modeling the growth of Fe_2B boride layers during boronizing, Surface & Coatings Technology, 201(2006)2717-2723.

LCF behavior and life modeling of DZ125 under complicated load condition at high temperature

Yang Xiaoguang*, Huang Jia, Shi Duoqi, Hu Xiaoan, Dong Chengli

School of Energy and Power Engineering, Beihang University, Beijing 100191, China

* Corresponding author: yxg@buaa.edu.cn

Abstract Based on the author and co-worker's systemically experimental investigation on low cycle fatigue (LCF) of directionally solidified (DS) Ni-based superalloy DZ125 at 850 and 980℃, LCF behavior analysis and life modeling are carried out here, where the influence of temperature, strain ratio, stress concentration, dwell types and dwell times on fatigue resistance is considered. (1) The steady cyclic stress/strain response is captured based on the transversely isotropic continuum elastic-viscoplasticity model. (2) For the coherent face centered cubic (FCC) structure of DS Ni-based superalloy DZ125, it is physically motivated to consider slip planes as critical plane under fatigue load, the mean stress modified Smith-Watson-Topper (SWTM) parameter $\Delta\gamma_{max}\cdot(\tau_{max}+\tau_m)/2$ on the discrete crystallographic slip planes is evaluated. The combination of the theory of critical distance and critical plane method exhibits acceptable predicted LCF life affected by stress concentration. (3) Based on SWTM parameter, Miner's linear cumulative damage theory and Larson-Miller plots, accurate life prediction on smooth LCF with complicated dwell forms is gotten. However, to predict the LCF life affected by dwells and stress concentration, the critical distance concept and the average processed creep stress is introduced, which shows acceptable accuracy of predicted LCF life.

Keywords Low cycle fatigue, Dwell times, Stress concentration, Theory of critical distance, Critical plane method

1 Introduction

Ni-based DS superalloy is increasingly being applied for turbine blades in high performance aircraft engines for superior creep and fatigue strength at high temperatures [1]. Turbine components work in harsh and vibration environments, such as increased operating temperatures, existed cooling holes on blades and vanes; dwell effects is also introduced by start-up, operation, and shut-down sequences. So life modeling of hot sections components of gas turbines is complicated by the presence of stress concentration, dwell times, elevated temperature. However, much more interest has been still precipitated in developing models to obtain accurate predicted service life for costly inspecting, servicing, and replacing of damaged components [2].

According to the literature survey, critical plane based life models and theory of critical distance are typical methods developed for predicting continuous smooth and notched LCF life of DS superalloy. Critical plane methods are originally developed for multi-axial fatigue; this method could predict not only the fatigue life but also the

location and direction of the crack. With well-defined crystallographic slip planes of DS superalloy, the plastic flow takes place along the slip planes and eventually persistent slip bands start to appear, which might act as fatigue crack initiation location. So it is physical based to consider crystallographic slip planes as critical planes. Up to now, lots of critical plane approaches, such as stress based, strain based or energy based models, have been proposed [3]. Arakere and Swanson [4], Naik [5] considered the octahedral and cube slip planes as critical planes, and then correlated damage parameters on these planes with LCF behavior of PW1480/1493 and HCF behavior of PW1484. The results showed that damage parameters on critical plane were partly promising. Moreover, life prediction using the maximum peak stress or strain is often conservative for characterizing the fatigue life affected by stress concentration. The theory of critical distance is proposed by Neuber [6] and Peterson [7], who assumes that fatigue damage cannot be correctly estimated except the entire stress or strain field damaging the fatigue fracture process zone is taken into account, this method has been successfully applied to predict the fatigue life with different load conditions from the LCF to HCF region. However, lots of work still needs to be done on evaluating the accuracy and reliability of more materials systematically. For the FCC structure of DS and single crystal (SC) superalloy, when the notched component is subjected to cyclic load condition, the combination of critical plane and critical distance method is an interesting attempt. Up to now, lots of work following this combined theory has been carried out. Based on the elastic-plastic finite element analysis (FEA), Zhang Li et al [8] obtained the stress/strain condition at notch root, but just the critical plane method and isotropic material is evaluated; Zhufeng Yue et al [9] considered the slip planes as critical planes and assumed the mean stress modified resolved shear stress range as fatigue damage parameter, this method shows good prediction ability of SC superalloy DD3, but critical distance concept was not evaluated. Especially, Leidermark et al [10] carried out notch fatigue investigation on SC superalloy MD2, they found that conservative predicted life will be obtained if only the slip systems based critical plane method was adopted, but obvious improvement could be seen when the critical distance concept is introduced.

Meanwhile, when considering the influence of dwell times, not only the individual effects of fatigue and creep damages, but also effect of their interaction should be considered. Continuum damage mechanics (CDM) method [11] is a traditional one for fatigue life prediction affected by dwells. However, a simply and efficient approach is Miner's linear cumulative damage theory [12], where the creep damage could be determined by the classic Larson-Miller plots [13].

DZ125 is DS superalloy exhibits excellent high temperature thermo-mechanical properties. For the typical load condition of turbine blades, much more interest of our research group on DZ125 has been precipitated on experimental investigation, constitutive modeling and life prediction, which mainly consider the influence of temperature, strain ratio, stress concentration, dwell types and dwell times. Although lots of research of DZ125 has been carried out [14, 15], life modeling of LCF on

smooth and notch components with and without dwells are still needed. Therefore, based on the experimental investigation of DZ125 [16-18] at high temperatures, one purpose of this study is focused on LCF behavior analysis. The other purpose seeks to develop acceptable approaches for predicting the LCF life under complicated load condition. The slip systems based critical plane method, combined with critical distance concept and Miner's linear cumulative damage theory are adopted to evaluate their feasibility on those complicate load condition.

2 LCF behavior of DZ125 at elevated temperatures

The chemical compositions (wt %) of DZ125 are 0.07-0.12C, 8.4-9.4Cr, 9.5-10.5Co, 6.5-7.5W, 1.5-2.5Mo, 4.8-5.4Al, 0.7-1.2Ti, 3.5-4.1Ta, 0.01-0.02B, 1.2-1.8Hf and balanced Ni. The alloy roughcast is melted in vacuum induction furnace, the solution and aging heat treatment procedure is as follows: 1180℃/2h +1230℃/3h/AC +1100℃/4h/AC +879℃/20h/AC (AC means air cooling). As shown in Fig. 1, the microstructure of DZ125 superalloy mainly contains γ-matrix and γ' -reinforced phase. Up to now, the author and co-worker have carried out systemically experimental investigation work on low cycle fatigue (LCF) tests of DZ125 at high temperatures. As is shown in Table 1, the experimental work is focused on exhibiting the influence of temperature, strain ratio, stress concentration, dwell types and dwell times on fatigue resistance. It is worth notice that the expression of dwell forms, such as T_t/T_c, means holding T_t seconds at tensile peak and T_c seconds at compressive peak. Smooth round bar, U-type and O-type notched plate specimens were adopted, their geometries are shown in Fig. 2. Corresponding experimental results is shown as follows.

2.0 Cyclic stress response

Cyclic stress response at 850 and 980℃ at longitudinal (L) orientation is shown in Fig. 3, the cyclic stress range changes obviously at the early cycles for each strain range, and then tends to be stable soon. The strain range related cyclic hardening behavior is observed at 850℃, the larger the strain range is, the more obvious cyclic hardening phenomenon happened. However, this material also seems to be strain range independent slight cyclic softening at 980℃. Those cyclic behaviors observed above are similar to that of Ni-based superalloy CM247LC [2].

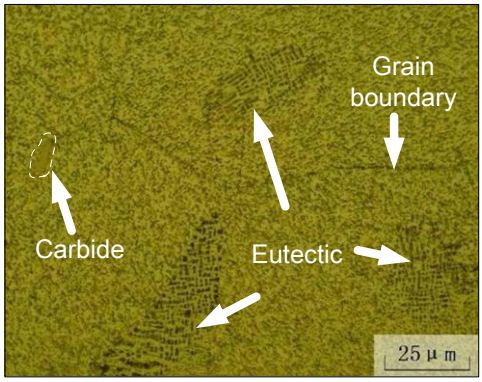

Fig. 1 Microstructure of DZ125 after heat treatment

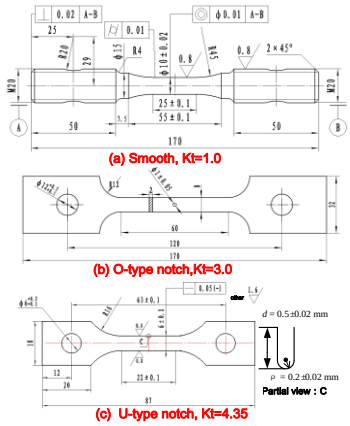

Fig. 2 Geometries and dimensions of specimens

Table 1 LCF test matrix of DZ125 at high temperature

Affected factors of LCF		Specimen type	Temperature	Load ratio	Load direction	Strain or stress range(MPa)	Hold times
Temperature		Round	850	-1	L	±0.5%, ±0.55%, ±0.6%, ±0.7%, ±0.8%	0/0
					T	±0.8%	0/0
					45	±0.8%	0/0
			980	-1	L	±0.3%, ±0.35%, ±0.4%, ±0.6%, ±0.8%, ±1.0%, ±1.5%	0/0
Strain ratio		Round	980	0	L	0.6%, 0.8%, 1.0%, 1.2%, 1.4%, 1.6%	0/0
Strain hold	Tensile hold	Round	850	-1	L	±0.8%	60/0,120/0,300/0
			850	0		1.60%	60/0,120/0,300/0
			980	-1		±0.35%, ±0.4%, ±0.6%, ±0.8%, ±1.0%	60/0
						±0.6%	120/0,300/0
			980	0		1.20%	60/0,120/0,300/0
	Compression hold	Round	980	-1		±0.35%, ±0.4%, ±0.6%, ±0.8%, ±1.0%	0/60
	Balanced hold	Round	980	-1		±0.35%, ±0.4%, ±0.6%, ±0.8%, ±1.0%	30/30
Stress hold	Tensile hold	Round	850	0	L	0-560	0/0,1/0,60/0,120/0,240/0
			980	0		0-260	0/0,1/0,60/0,120/0,240/0
Stress concentration		U-type notch plate	850	0.1	L	40-400,50-500,60-600,70-700	0/0
		O-type notch plate		0.05-0.1		42-500,21-489,21-411,16-372,17-320	0/0
Both stress concentration and stress hold		O-type notch plate	850	0.05-0.1	L	25-412,25-375,25-322	120/0

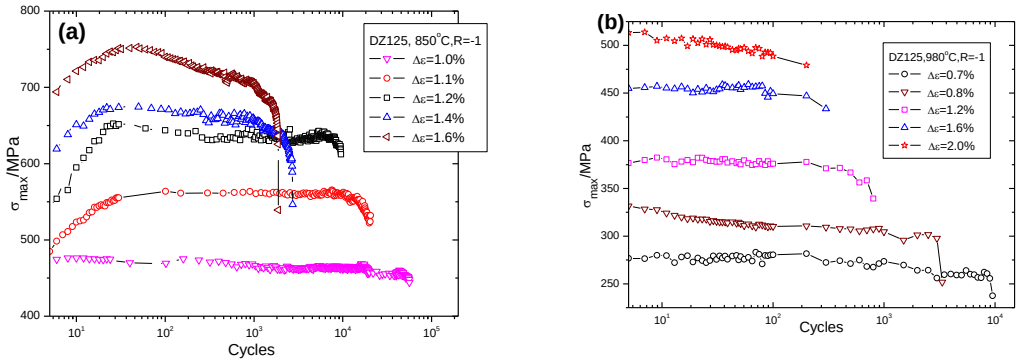

Fig. 3 The cyclic stress response curves, (a) 850°C, (b) 980°C

2.1 Effect of temperature and stress ratio on LCF

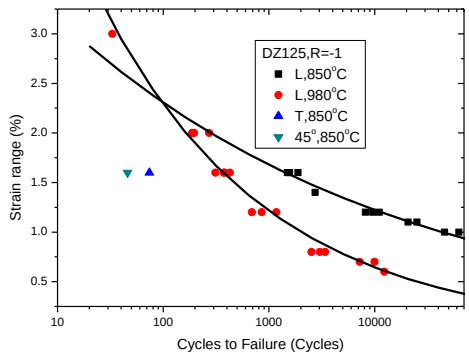

Fig. 4 The influence of temperature and load orientation on LCF

LCF results at 850 and 980°C are shown in Fig. 4. Generally, fatigue life at 850°C is larger than that at 980°C, the fatigue resistance at transverse and 45° orientation is much lower than longitudinal orientation. However, there existing an obvious transition life at short life region, the potential reason may be due to the different cyclic stress response at 850 and 980°C. Although slight cyclic softening phenomenon is happened at 980°C, obvious cyclic hardening phenomenon is happened at 850°C, especially at high strain range (short life region), so maybe the competition between the cyclic hardening induced increased stress and temperature leads to the transition

life. All the solid lines in figures are fitted by a power fitting function, $f(N)=aN^b$.

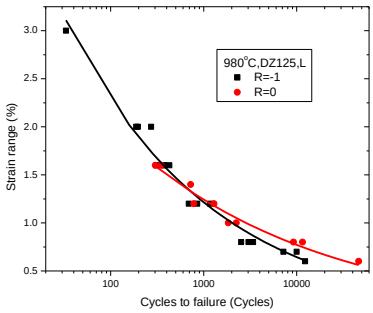

Fig. 5 The effect of stress ratio on LCF

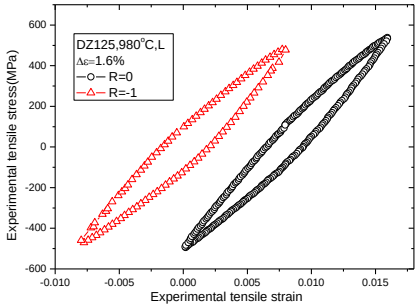

Fig. 6 The strain-stress curves

LCF results at 980°C with different strain ratio are shown in Fig. 5. It is interesting to found that little difference could be found at short life region, on the contrary, better fatigue life are obtained with strain ratio R_ε=0 at long life region where obvious mean stress existed. The potential reason for the slight difference may be due to the similar area of steady-state hysteresis loop at 980°C shown in Fig. 6, which also exhibits similar mean stress.

2.2 Effect of dwell types and dwell times on LCF

2.2.1 Dwell types

LCF life with and without dwell times at 980°C are shown in Fig. 7. Compared with continuous fatigue, all the three dwell types with the same dwell times lead to obvious life degradation. Roughly, no obvious difference of these three dwell types could be found except that the balanced dwell type gets the entirely shortest life, the bigger area of simulated hysteresis loop of balanced dwell type 30/30 in second paragraph is much more big than the other ones, which maybe the potential reasons; the tensile dwell type with reduced mean stress shows predominant fatigue property at low strain range but bad fatigue resistance at high strain range, the possible reason is the competition between mean stress related fatigue damage and creep damage.

2.2.2 Dwell times

Fig. 8 shows the evolution curves of cyclic peak stress with different dwell times at 850°C. As the mentioned cyclic stress response before, cyclic hardening behavior could be observed with no dwell times, but it turns to be cyclic softening behavior with dwell times. Especially the relaxation of cyclic peak stress is also associated with dwell times. Firstly, with the increased dwell times from 0s to 60s, increased stress relaxation is obtained. However, with the increased dwell times reach up to 120s and 300s, similar relaxation curves are exhibited.

Compared with the fatigue life with no dwell times, the introduction of increased dwell times leads to an obvious gradually life degradation with strain ratio equals to -1 at both 850 and 980°C shown in Fig. 9, except for the abnormal fatigue life with 300s dwells at 980°C; however, when R_ε=0, no obvious fatigue life degradation could be distinguished at 850°C but not for 980°C. The observed dwell-times-related cyclic

peak stress relaxation behavior in Fig. 3 maybe could explain the similar fatigue life with 120s and 300s dwell times at 850°C. The potential reason for the influence of strain dwell times may be due to the competition between fatigue and creep damage, where the fatigue damage is decreased with the relaxed peak stress but creep damage increases with added dwell times.

Meanwhile, based on the similar fatigue life between R_ε=0 and -1 with no dwell times at both 850 and 980°C shown in Fig. 9, we can conclude that, compared with zero strain ratio, the continuous fatigue with R_ε=-1 is more sensitive to dwell times and exhibits low fatigue life, this difference is more visible at 980°C.

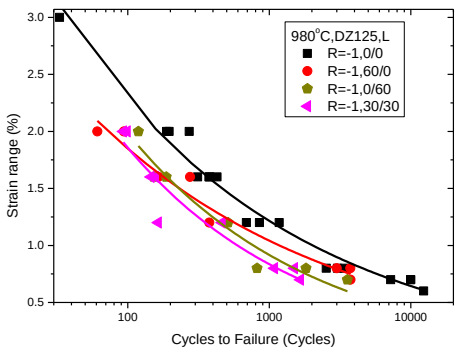

Fig. 7 The influence of dwell types on LCF

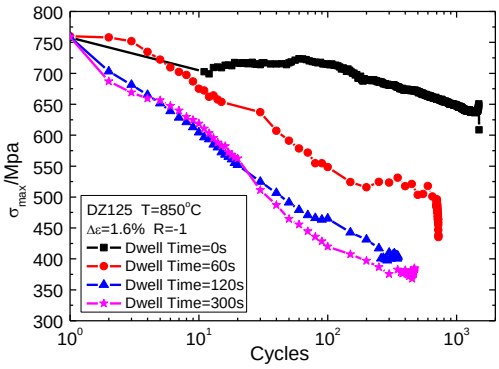

Fig. 8 The stress relaxation with dwells

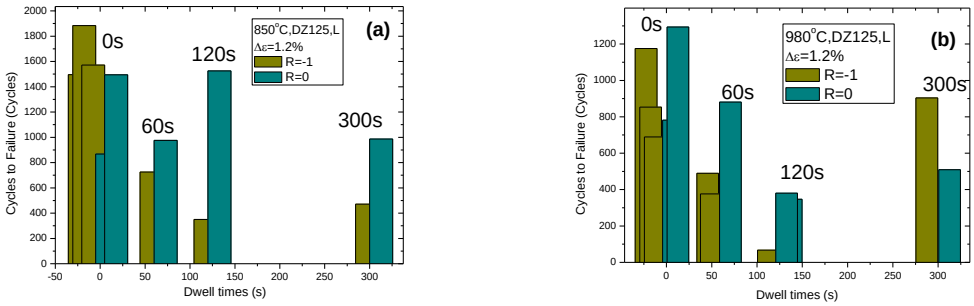

Fig. 9 The influence of strain dwells at different strain ratio on LCF, (a) 850°C; (b) 980°C

LCF results under different stress tensile dwell times at 850 and 980°C are shown in Fig. 10, all the introduced dwells lead to a degradation of fatigue life; persistent degradation is obtained under the increased dwells, which is more obvious at 980°C.

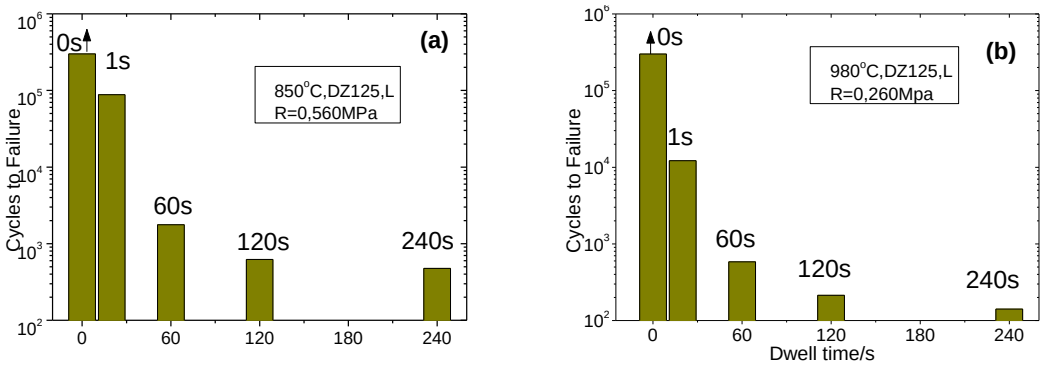

Fig. 10 The influence of stress dwell times on LCF life, (a) 850°C; (b) 980°C

Except for the above mentioned influence of dwell times on fatigue life, a contrary attempt is considering the influence of cyclic load on creep life. As is shown in Fig. 11, at the first stage, the total fracture time is decreased with increased dwell times, but the minimum fracture time is obtained with dwell times equals to 120s at both 850 and 980°C. Then the fracture time is gradually increased as the increased dwell times, at last the static creep life is obtained.

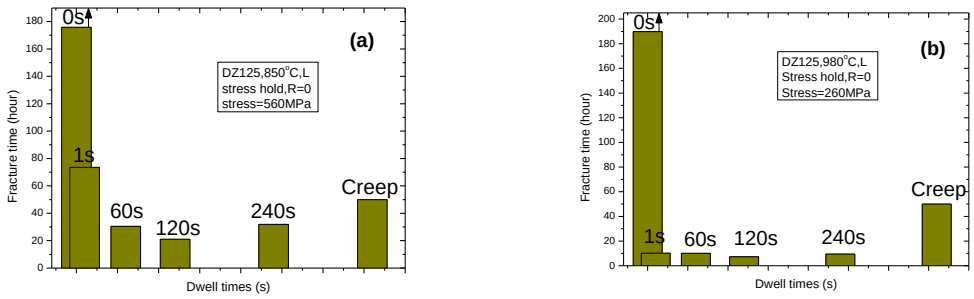

Fig. 11 The influence of stress dwell times on fracture time, (a) 850°C; (b) 980°C

2.3 Effect of dwell times and stress concentration on LCF

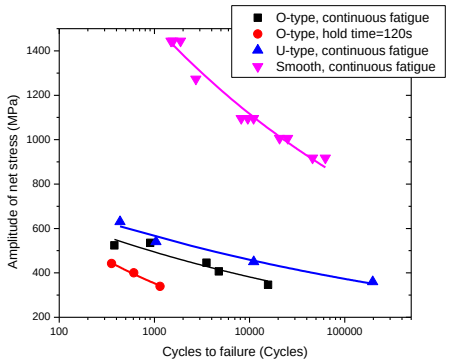

Fig. 12 The relationship between amplitude of net stress and fatigue life

Compared with the continuous fatigue life of smooth round bar specimens at 850°C shown in Fig. 12, obvious life degradation is induced by stress concentration of notched U-type and O-type plates. Furthermore life degradation is still happened for the stress dwell times at peak tensile stress.

2.4 Cyclic stress/strain response

In this paper, the cyclic stress/strain response of smooth and notched DZ125 components affected by dwell times at high temperatures, based on the modified Chaboche constitutive model [19], is carried out. This constitutive model is implemented as an ABAQUS user material (UMAT) subroutine. Totally 22 material parameters existed in this model, the Levenberg-Marquardt optimization method is employed and the material parameters are fitted by experimental curves of isothermal tension and creep load at high temperature. Moreover, it is necessary to note that the 11-22 plane of symmetry and 33 normal are represented by transverse and longitudinal orientations.

Compared with the experiment curves, this elastic-viscoplastic constitutive model shows acceptable accuracy on predicting stress/strain response of continuous fatigue, which is shown in Fig. 13. The simulated strain/stress response with three strain dwell types is shown in Fig. 14, obvious dwell-time-induced mean stress could be found, the hysteresis loop area of the dwell type 30/30 is bigger than the other two, and this is the potential reason for shorter fatigue life of dwell type 30/30 shown in Fig. 7. As shown in Fig. 15, the strain/stress response with stress dwells, which could reveals dwell time's effect on deformation, the hysteresis loop area is also increased with the increased dwell times, which is the possible reasons for gradually life degradation with increased stress dwells shown in Fig. 10.

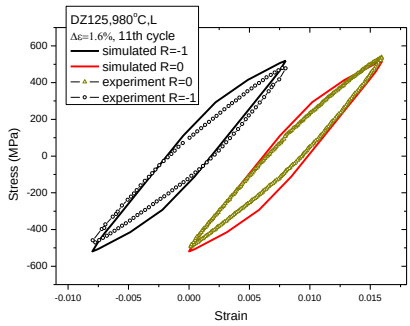

Fig. 13 Simulated hysteresis loop of continuous fatigue

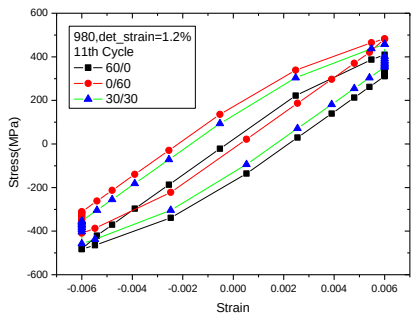

Fig. 14 The strain/stress response with strain dwells

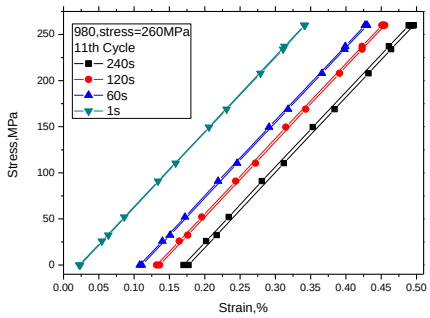

Fig. 15 The strain/stress response with stress dwells

The evolution of tensile stress and deformation at notch tip with 120s dwell time is shown in Figs. 16 and 17, where we can see obvious stress relaxation with the peak stress decreased from 850 to 725 MPa, especially the location of the maximum tensile stress is changed from notch surface to inner surface, and obvious creep deformation is happened near the notch tip.

4 Life modeling

A physical based method considering crystallographic slip planes as critical planes and corresponding damage parameters is evaluated here on LCF life prediction; The critical distance concept is introduced for the load condition with stress concentration. Furthermore, the Larson-Miller plots and Miner's linear accumulative damage accumulative theory are adopted for life prediction affect by dwell times; The life prediction affected by stress concentration and dwell times is also carried out here.

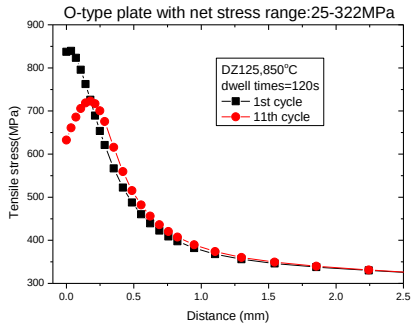

Fig. 16 The evolution of tensile stress with dwell times at notch tip

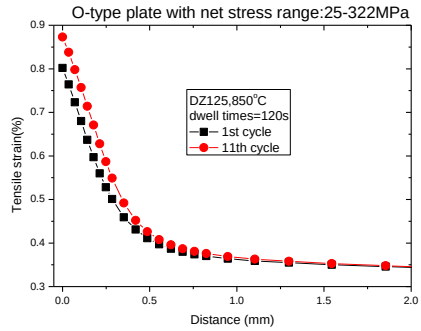

Fig. 17 The evolution of tensile strain with dwell times on notch tip

4.1 SWTM Parameters

Critical plane based methods are originally developed for multi-axial fatigue, with well defined crystallographic slip planes and corresponding plastic flow mechanism of DS superalloy, a physical based method is considering crystallographic slip planes as critical planes. The mean stress modified SWT parameter $\Delta\gamma_{max}\cdot(\tau_{max}+\tau_m)/2$ on the discrete crystallographic slip planes are evaluated, which could consider the influence of anisotropic properties and mean stress. In this paper, the slip systems both on the octahedral and cube planes including totally 30 slip systems are utilized, i.e. 12 primary and 12 secondary slip systems come from the octahedral planes, the rest 6 slip systems are located on cube planes. The analytical procedure of obtaining the resolved shear stress/strain on these slip systems is referenced to Arakere and Swanson's literature [4]. The life model is shown in Eq. 1:

$$\Delta\gamma_{\max} \bullet \frac{\tau_{\max}+\tau_m}{2} = a(2N_f)^b \qquad (1)$$

$$\begin{aligned} 850℃: \Delta\gamma_{\max} \bullet \frac{\tau_{\max}+\tau_m}{2} &= 11.08252(2N_f)^{-0.16864}, R^2 = 0.92947 \\ 980℃: \Delta\gamma_{\max} \bullet \frac{\tau_{\max}+\tau_m}{2} &= 29.86975(2N_f)^{-0.36556}, R^2 = 0.92348 \end{aligned} \qquad (2)$$

Where a and b are model parameters fitted by experimental data from smooth specimens, N_f is fatigue failure life. Although few experimental data is carried out at T and 45 °orientations, the model parameter at 850 and 980℃ is well fitted shown in Fig. 18, the influence of anisotropic properties and mean stress are well considered and Eq. 2 is obtained.

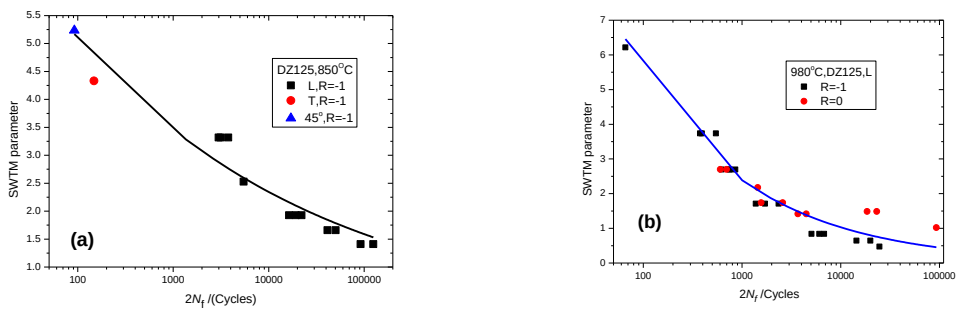

Fig. 18 The SWTM parameter versus LCF lives, (a) 850℃; (b) 980℃

4.2 Life prediction

4.2.1 Life prediction under stress and strain dwelsl

LCF life prediction with strain and stress dwells is carried out based on Miner's linear cumulative damage theory shown in Eq. 3, where the pure fatigue life N_f is determined by the above-mentioned SWTM parameter. The static creep fracture time is determined by traditional Larson-Miller plots shown in Eq. 4, where θ is temperature with units ℃, σ is the tensile stress, b_0, b_1, b_2, b_3, b_4 are four material parameters confirmed by materials engineering manual [20].

$$\sum_{i=1}^{n}\frac{N_i}{N_f}+\sum_{j=1}^{m}\frac{t_j}{t_c}=1 \qquad (3)$$

$$\begin{aligned} \lg t &= b_0 + b_1/T + b_2 X/T + b_3 X^2/T + b_4 X^3/T \\ T &= (9\theta/5+32)+640 \\ X &= \lg\sigma \end{aligned} \qquad (4)$$

As is shown in Fig. 19(a), the LCF life at 850℃ with tensile strain dwell and tensile stress dwell at different strain and stress ratio is predicted, a factor of three is still obtained in spite of the complicated tensile dwell forms. Moreover, life prediction with tensile, compressive and balanced strain dwells at 980℃ are further investigated, a factor of three is also obtained shown in Fig. 19(b). So we can conclude that, based on SWTM parameter, Miner's linear cumulative damage theory and Larson-Miller plots, acceptable predicting accuracy of fatigue life affected by dwell times is obtained.

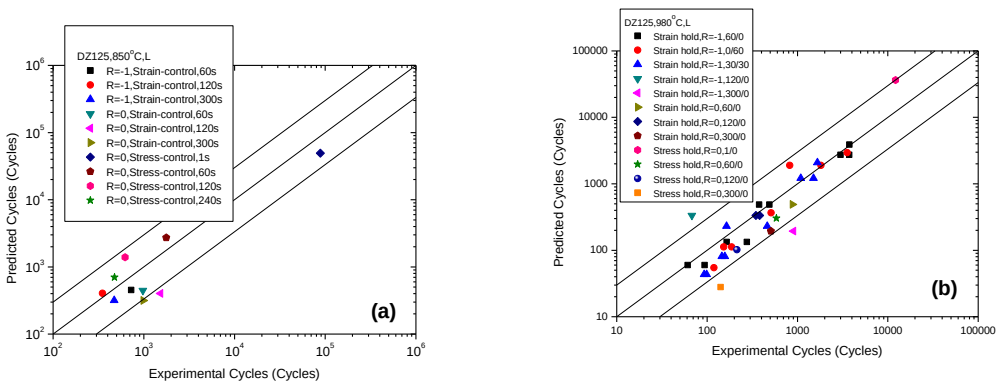

Fig. 19 Experimental life under dwell times versus predicted life, (a) 850℃; (b) 980℃

4.2.2 Life prediction under stress concentration

To predict a more appropriate fatigue behavior, combined with the slip systems based SWTM parameter, the critical distances concept is used; concretely the Point Method (PM) is used here. The critical distance is determined as following: the experimental fatigue life should be inserted into Eq. 2 to obtain the SWTM parameter, and then based on the resolved shear strain/stress at the middle line of notched plate, the experimental critical distance could be determined with the solved SWTM parameter. The experimental critical distance is shown in Fig. 20.

A method for determining the critical distance is proposed by Susmel and Taylor [21],

who assumes that the critical distance is dependent on the number of cycles to failure, which is successfully applied to LCF issues. The relationship between critical distance $D_{PM}(N_f)$ and failure life N_f is shown in Eq. 5， the fitted curve is shown in Fig. 20 and Fig. 21 shows a factor of two in life prediction.

$$D_{PM}(N_f) = 0.31133 \bullet N_f^{-0.08153} \quad (5)$$

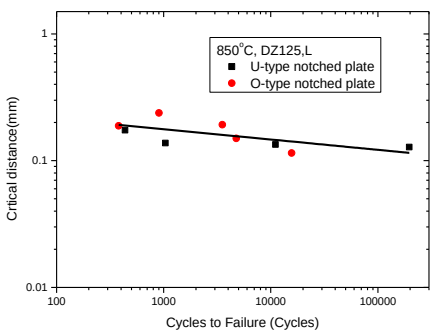

Fig. 20 The experimental critical distances for each test specimen

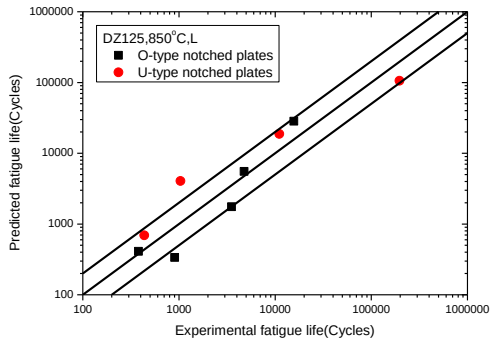

Fig. 21 Experimental life with stress concentration versus predicted life

4.2.3 Life prediction under both stress concentration and dwells

Based on SWTM parameter, Miner's linear cumulative damage theory and Larson-Miller plots, acceptable life prediction on LCF with dwell times could be gotten. However, to predict LCF life affected by both stress concentration and dwell times, firstly the fatigue damage is calculated based on the critical distance concept in obtained Eq. 5, then the concentrated stress should be average processed for determining creep damage; the equivalent stress is confirmed by the tensile strain weighted correction shown in Eq. 6, where the integration interval is on the middle line of notched plate. As is shown in Table 2, this method shows acceptable accuracy for LCF life affected by both dwell times and stress concentration.

$$\sigma_{creep,eq} = \int \sigma_{33} d\varepsilon_{33} / \int d\varepsilon_{33} \quad (6)$$

Table 2 Experimental life with concentrated stress and dwells at 850°C versus predicted life

$\Delta\sigma_{net}$/ MPa	Predicted D_{PM}/mm	Predicted pure fatigue life/Cycles	Equivalent stress/MPa	Predicted creep life/hour	Hold time/s	Predicted life/Cycles	Experimental life/Cycles
25-321	0.1235	83964.85	560.825	46.6051	120	1375.3	1150
25-375	0.1348	28696.96	636.728	14.5199	120	429.1	609
25-412	0.1431	13822.23	689.174	6.8279	120	201.8	355

5 Conclusion

Based on the author and co-worker's systemically experimental investigation work on smooth and notch fatigue behavior of DZ125 at high temperatures with and without dwell times, LCF behavior analysis and life modeling considering the influence of temperature, dwells and stress concentration is carried out. The main conclusions are summarized as follows:

(1) The influence of temperature, strain ratio, stress concentration, dwell types and

dwell times on fatigue resistance is obvious. ① The cyclic stress response of DZ125 is temperature dependent. At 850℃ it is cyclic hardening, but it seems to be slight cyclic softening at 980℃. ② The fatigue resistance at 850℃ is better than 980℃ in long life region, but worse fatigue strength is obtained at 850℃ in short life regime. ③ Roughly, the introduction of compressive, tensile and balanced strain dwell times can all lead to obvious fatigue life degradation, but the balanced dwell type gets the entirely shortest life, the tensile dwell type with reduced mean stress shows predominant fatigue property at low strain range but bad fatigue resistance at high strain range. ④ The cyclic hardening behavior could be observed with no strain dwell times, but it turns to be cyclic softening behavior with dwell times. Especially the relaxation of cyclic peak stress is also closely associated with dwell times. ⑤ Based on the similar fatigue life between R_ε=0 and -1 with no dwell times at both 850 and 980℃, the continuous fatigue with strain ratio equals to -1 is more sensitive to dwell times. Compared with smooth fatigue life at 850℃, obvious life degradation is induced by stress concentration. Furthermore life degradation is happened with added stress dwell times.

(2) The critical method is used and damage parameters on critical plane is the modified SWT parameter; Moreover, the failure cycles related critical distance concept is combined for predicting fatigue life affected by stress concentration where a factor of two is obtained. Based on SWTM parameter, Miner's linear cumulative damage theory and Larson-Miller plots, a factor of three is obtained in spite of the complicated dwell forms on smooth specimens. Furthermore, with added critical distance concept and confirmed creep equivalent stress, the prediction LCF life affected by both dwell times and stress concentration is successfully carried out.

6 References

[1] R. Mucke, O.E. Bernhardi, A constitutive model for anisotropic materials based on Neuber's rule. Comput Method Appl M, 192 (2003) 37-38.

[2] ZJ. Moore, Life modeling of notched CM247LC DS Nickel-base superalloy. Atlanta: Georgia Institute of Technology, 2008.

[3] A. Karolczuk, E. Macha, A review of critical plane orientations in multiaxial fatigue failure criteria of metallic materials. Int J Fracture, 134 (2005) 267-304.

[4] N.K. Arakere, G. Swanson, Effect of crystal orientation on fatigue failure of single crystal nickel base turbine blade superalloys. J Eng Gas Turb Power, 124 (2002) 161-76.

[5] RA. Naik, DP. Deluca, Critical plane fatigue modeling and characterization of single crystal nickel superalloys. J Eng Gas Turb Power, 126 (2004) 391-400.

[6] H. Neuber, Theory of notch stresses: principles for exact calculation of strength with reference to structural form and material. 2rd ed. Berlin: Springer Verlag; 1958.

[7] RE. Peterson, Notch sensitivity. In: G. Sines, JL. Waisman, editors. Metal fatigue, New York: McGraw Hill (1959) 293-306.

[8] ZHANG Li, CHENG Jin, LI Xinggang. The fatigue life prediction method of notched specimen based on the critical plane. Journal of Astronautics, 28 (2007)

824-826. (in Chinese)

[9] JS. Wan, ZF. Yue, A low-cycle fatigue life model of nickel-based single crystal superalloys under multiaxial stress state. Mat Sci Eng A-Struct, 392 (2005) 145-149.

[10] D. Leidermark, et al, A combined critical plane and critical distance approach for predicting fatigue crack initiation in notched single-crystal superalloy components. Int J Fat, 33 (2011) 1351-59.

[11] TW. Kim, DH. Kang, Continuum damage mechanics based creep-fatigue-interacted life prediction of nickel based superalloy at high temperature. Scripta Mater, 57 (2007) 1149-52.

[12] M.A. Miner, Cumulative damage in fatigue. J Appl Mech, 12 (1945) A159-A164.

[13] F.R. Larson, J. Miller, A time-temperature relationship for rupture and creep stresses. Trans. ASME, 74 (1952) 765-771.

[14] LIU Jinlong, SHI Duoqi, YANG Xiaoguang, Study on influence of strain ratio on low cycle fatigue behavior of directionally solidified superalloy DZ125. Materials engineering, 12 (2010) 47-51. (in Chinese)

[15] ZHOU Tianpeng, YANG Xiaoguang, HOU Guichang, Experimental analysis of low cycle and creep fatigue for directionally solidified DZ125 with a hole. Journal of Aerospace Power, 22 (2007) 1526-1531. (in Chinese)

[16] Zhou Tianpeng. Research of advanced stress-strain analysis and low cycle fatigue life for directionally solidified turbine blade. Beijing: Beihang University, 2007: 67-93. (in Chinese)

[17] LIU Jinlong. Investigation on cast simulation and low cycle fatigue behavior of Ni-based single crystal and directionally solidified turbine blade. Beijing: Beihang University, 2011: 57-83. (in Chinese)

[18] WANG Jingke. Investigation on notch fatigue of Ni-based superalloy and Ti-alloys. Beijing: Beihang University, 2011: 79-103. (in Chinese)

[19] SHI Duoqi, DONG Chengli, YANG Xiaoguang, Constitutive modeling and failure mechanisms of anisotropic tensile and creep behaviors of nickel-base directionally solidified superalloy. Mater Design, 45 (2013) 663-673.

[20] China aeronautic material handbook (Internal Publication). Beijing (China): Institute of Aeronautical Materials; 2004.

[21] L. Susmel L, D. Taylor, On the use of the theory of critical distances to estimate fatigue strength of notched components in the medium-cycle fatigue regime. Proceedings of fatigue 2006. Altanta, USA: 2006.

Effect of SiC particles on fatigue crack growth behavior of spray-formed SiC particulate-reinforced Al-Si alloy composites

Li Wei*, Chen Jian, Qiu Wei, Ren Yanjie

School of Energy and Power Engineering, Changsha University of Science and Technology, 410004, China

* Corresponding author: lwzzgjajie@126.com

Abstract

Fatigue crack growth (FCG) and closure mechanisms in spray-formed Al-7Si alloy matrix composites reinforced with two different sizes of SiC particles has been studied. The experimental dates demonstrate that the composite containing 4.5μm SiC particles exhibits lower FCG rate and higher threshold stress intensity factor range ΔK_{th} (3.878 $MPa \bullet \sqrt{m}$) than the 20μm SiC particles composite(3.630 $MPa \bullet \sqrt{m}$) and the unreinforced alloy (3.605 $MPa \bullet \sqrt{m}$). The SEM crack path observations show that the extent of micoracking inside in the 4.5μm SiC particles induces higher level of fatigue crack closure, which effectively reduces the crack growth driving force to slow down fatigue crack growth. Crack deflection caused by the SiC particles attributes the lower FCG rate in the 20μm SiC composite to the high levels of roughness-induced crack closure at the low ΔK, then the propensity for the fracture of large SiC particles increased with increasing ΔK resulted in a higher FCG rate in the fast fracture state.

Keywords Fatigue crack growth, spray-formed, SiC particulate-reinforced Al-Si alloy composites, closure mechanism, size

1. Introduction

The outstanding mechanical, physical, and casting properties of Al-Si–Mg alloys, on the other hand, make them attractive for use in cheaper and lighter engineering components[1]. These composites are produced by several processing methods, such as stir casting, squeeze casting [2], powder metallurgy [3] and spray forming, etc. Amongst these methods, spray forming technique has drawn considerable research interest due to its scope of forming near-net shape product with a reduced number of process steps compared to the powder metallurgy. Apart from this, the process offers advantage of rapid solidification, such as refined equiaxed structure with negligible segregation, extension of the solid solubility limit [4], and wider compositional flexibility. With the engineering application of metal matrix composites (MMCs), the fatigue crack growth behavior will become critical in design, life-prediction and reliability analysis of the components made of these materials.

The fatigue crack growth behavior in particle MMCs is very much dependent on a variety of factors, including reinforcement particle volume fraction, particle size, matrix and interfacial microstructure, the presence of inclusions and testing

environment [5-7]. Of these variables, particle size is one of microstructural parameters influencing the fatigue crack growth behavior [8, 9]. Sugimura et al. [10] have reported that increasing the volume fraction of SiC particulates in cast Al-Si alloy promotes higher FCG rate. The effects of SiC volume fraction and particle size on the fatigue behavior of powder metallurgy 2080 Al alloy have been investigated by Chawla et al. [11]. They find that increasing volume fraction (from 10% to 30%) and decreasing particle size (from 23μm down to 5 μm) result in an increase in fatigue resistance. Xu et al. [12] have pointed out that the retardation of FCG was found when crack propagated from low volume fraction of SiC to high volume fraction of SiC. The crack deflection and branching decreased FCG rates.

Although a number of studies on fatigue resistance and fatigue crack growth (FCG) in SiC_p/Al composites and Al-Si-Mg alloys have been done , the effect of particle size on fatigue crack growth behavior of this kind of composites produced by spray deposition has been limited. Thus it is necessary to carry out a fundamental research work in this respect. The purpose of the present study is to understand the effect of particle size on fatigue crack growth behavior and closure mechanism of spray-deposited SiC_p/Al composites.

2. Experimental

2.1 Material and microstructure

Al-7Si-Mg alloy fabricated by spray deposition was used in the unreinforced condition and with 15 vol.% SiCp reinforcement. The chemical composition (mass. %) is Si 7, Mg 0.3, Mn 0.01, Cu 0.01, balance Al. Extrusion at 450℃ was used to produce plates with dimensions of $10\times120mm^2$.

Fig. 1 shows the microstructures of the sections parallel (L-plane) to the extrusion direction in the unreinforced alloy and the composites. It can be seen that SiC particles tend to be partially aligned along the extrusion direction. Some clustering tendency observed in the 4.5μm SiC_p/Al-7Si composite decreases as the size of the particulates increases.

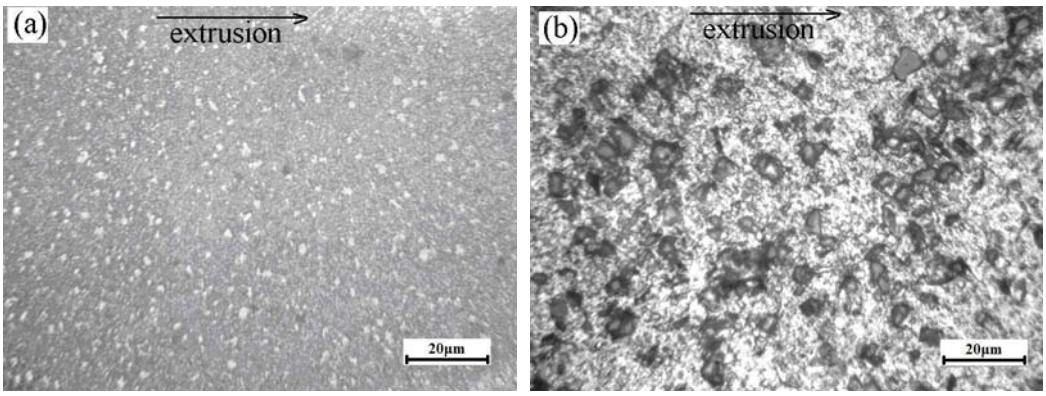

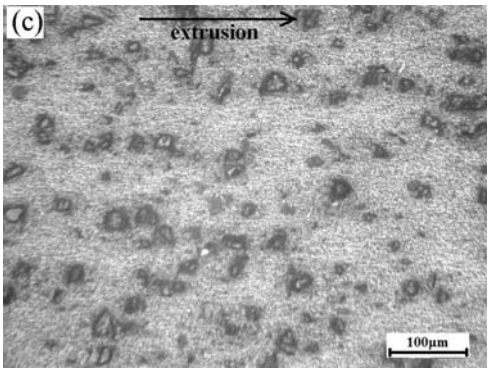

Figure 1. Optical micrographs of longitudinal planes of the (a) 4.5μm SiC_p/Al-7Si composite (b) 20μm Al-7Si/ SiC_p composite

2.2 Specimen preparation

All specimens were solution treated at 535℃for 2.5h, quenched in eater and then aged at 160℃ to achieve peak-aged condition. The aging time was 7h for the Al-7Si alloy and 4.5μm SiC_p/Al-7Si composite, 11h for 20μm SiC_p/Al-7Si composite. Compact tension (CT) specimens, of width W=48mm, height H=57.6mm, thickness B=10mm, were machined from the extruded plates of the materials with the loading axis parallel to the extrusion direction and with the plane of the notch perpendicular to the loading axis.

2.3 Mechanical properties

The room temperature tensile properties of the two kinds of the composites and the Al-7Si alloy are listed in Table 1. Incorporation of the reinforcing particles promotes the elastic modulus 15.84~18.94%. The composite containing large reinforcing particles is higher in yield strength, defined as the stress corresponding to a plastic strain of 0.2%, but lower in elastic modulus than that containing small particles. The composites display a slight decrease of the ultimate tensile strength and elongation with respect to the matrix alloy.

Table 1. Mechanical properties of the Al-7Si alloy and composite at room temperature

SiC content (vol. %)	SiC Size （μm）	Elastic modulus, E (GPa)	0.2% proof strength, $\sigma_{0.2}$ (MPa)	Ultimate tensile strength, σ_b (MPa)	Elongation, A (%)
0	0	72.3	242.5	336.2	11.2
15	4.5	86.0	240.5	328.8	9.0
15	20.0	83.7	270.9	321.3	8.6

2.4 Procedure

The tests according to ASTM E647 were conducted in laboratory air at room temperature (298K) and relative humidity 40-50% at constant stress ratio of 0.1, using a sinusoidal waveform signal at 25Hz.Region Ⅰ data were obtained following the guidelines for near-threshold testing. A computer controlled load shedding technique

(normalized K gradient set at -0.10mm^{-1}) was used to gradually decrease crack growth rates to the near-threshold level. The fatigue threshold stress-intensity range (ΔK_{th}) was defined at a maximum growth rate of 10^{-10} m/cycle. For determine the Paris' constants *c* and *m* in Paris' equation ($da/dN=m\Delta K^c$). Constant amplitude technique (ΔK-decreasing) had been used. Data recorded during the tests were analyzed to obtain da/dN- ΔK curves.

3. Results

3.1 Fatigue crack growth

Fig. 2 shows the variation of the fatigue crack growth rates, da/dN, as a function of the stress intensity factor range, ΔK, for the unreinforced alloy and the two composites. It is obvious that the curve for the 4.5μm SiC reinforcement composite is below the other two curves for the 20μm and the Al-7Si alloy. Therefore, the 4.5μm SiC/Al-7Si composite has the best fatigue crack growth resistance. The threshold stress intensity factor range ΔK_{th} of 3.878 $MPa \bullet \sqrt{m}$ for the 4.5μm SiC reinforcement composite is larger than the 20μm(3.630 $MPa \bullet \sqrt{m}$) and the Al-7Si alloy (3.605 $MPa \bullet \sqrt{m}$). The 20μm SiC particulates reinforced composite shows lower FCG rate than the unreinforced alloy at ΔK < 14.88 $MPa \bullet \sqrt{m}$, but exhibits lower fatigue crack growth rate at ΔK > 14.88 $MPa \bullet \sqrt{m}$. This is to say, the values of the FCG rate for the 20μm are lower than the matrix alloy in the near-threshold regime and Paris regime, however, it become higher than those of Al-7Si alloy at the fast fracture state.

Comparison of the FCG curve of the 4.5μm SiC with 20μm gives a clear indication that the increase in particle size results in an obvious higher FCG rate in the near-threshold regime and the fast fracture state. However, in the Paris regime, i.e. between 10^{-6} and 10^{-4} mm/cycle, the composite reinforced with 20μm SiC particulates exhibits a slighter smaller slope than the 4.5μm SiC. The results depicted in Fig.2 for the particulate-reinforced spray-formed aluminum-matrix composite are similar to that reported of composite [10], where reinforcements cause marker improvements in resistance to fatigue fracture, especially in the near-threshold regime. In general, in the Paris region, there is almost no effect of SiC particle size on fatigue crack growth, while in the near-threshold regime and fast fracture state, the SiC particle size has great influence. This is possibly attributed to the different failure mechanism of crack growth caused by the actions of SiC size, shape and distribution.

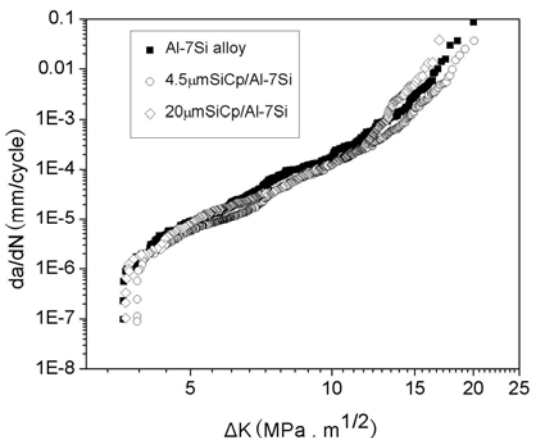

Figure 2. Fatigue crack growth rate as a function of ΔK in the Al-7Si-Mg alloy reinforced with 4.5μm and 20μm SiC particles

The extent of crack closure that developed in the three materials during tension fatigue crack growth is plotted in Fig. 3. This figure shows the variation of the experimentally measured closure stress intensity factor K_{cl}, normalized with maximum stress intensity factor K_{max}, as a function of the stress intensity range, ΔK. It can be seen that the small particulates-reinforced composite exhibits a significantly higher level of crack closure than the two materials over the entire range of fatigue crack growth. The 20 μm SiC reinforcement exhibits higher closure level than the matrix alloy in the $\Delta K < 7.4\,\mathrm{MPa} \bullet \sqrt{m}$ region, but shows lower closure level than the matrix alloy in the $\Delta K > 7.4\,\mathrm{MPa} \bullet \sqrt{m}$ region.

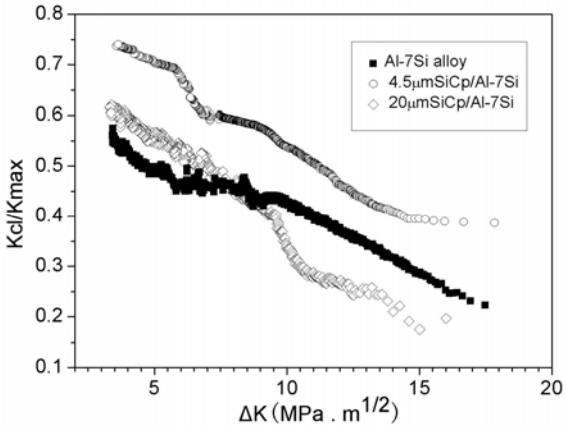

Figure 3. Variation of stress intensity factor at crack closure, K_{cl}/K_{max}, as a function of ΔK in the unreinforced alloy and the reinforced alloys

3.2 Crack path analysis

The relationship between fatigue crack propagation and SiC particle morphology is followed by carefully observing the propagation of the crack tip on well-polished surfaces of CT specimens processing different microstructures and tested at different values of ΔK. Figures 4 through 6 are SEM micrographs of fatigue surface cracks formed in CT specimens of the three materials, tested at various ΔK values,

respectively. The direction of crack propagation for all surface cracks is from left to right in the micrographs.

For the unreinforced alloy, crack propagating around Si particles is observed in the near-threshold regime (Fig.4 (a)). It can be seen that the fatigue crack mainly propagate through the α-Al matrix. Crack deflection caused by Si phase, gives rise to a higher degree of roughness of crack surface, and then results in the occurrence of crack closure effect. Little of the Si breakage is observed in Fig 4(a). It means that Si particle is not easy to break and the crack path had predisposition to avoid Si particles in the near threshold. This is probably attributed to the spherical Si particle with small size (1~3 μm), whereas it is difficult to break at the low level ΔK because of the large fracture energy to break, according to the Griffith theory. Nevertheless, the occurrence of Si particle/matrix bebonding is increasing to the factor of the crack propagating due to the increase of the K value around the crack zone, which can be indicated by the arrows in Fig.4 (b). The crack profile is smoother in the matrix alloy than in the composite.

In the composite with 4.5μm and 20μm SiC particles, crack deflection caused by Si phase is observed just as in the case of the unreinforced alloy. Light microscopy also demonstrated that the fatigue crack in the composite follows a tortuous crack path and that crack branching occurs (Fig. 5 and Fig. 6). Significant differences were observed in the crack propagating characteristics of the two composites in the three regions.

As seen in the 4.5μm SiC composite (Fig 5(a) and (b)), crack deflection caused by the SiC particles and extensive microcracking inside SiC particles are observed through the whole fatigue crack growth region. And these microcracks remained open after they were unloaded behind the crack tip. Similar microcracks were also noted in fatigue crack growth of TiC/Ti-6Al-4V[13]. Reinforcing particles apparently serve as effective barriers to fatigue crack growth in 4.5μm SiC/Al-7Si composite.

For the composite with 20μm SiC particle, it can be seen that the fatigue crack avoid SiC particles, consequently the direction of propagation of fatigue crack is changed at the low ΔK(see as Fig. 6(a)). They attributed the lower crack growth in the composite to the high levels of roughness-induced crack closure. With the increase of ΔK level, it was apparent that the crack with an inclination angle to the SiC particles < 45° or >135°had a tendency to progress around SiC particles, while crack with angles between 45° and 135° was expected to advance through SiC particles (see as Fig. 6(b)). Fatigue crack makes function on SiC particles in two ways: SiC particle/matrix debonding and particle breakage. Then, the propensity for the fracture of SiC particles increased with increasing ΔK in the 20μm SiC. A higher FCG rate in the fast fracture state is considered to be a reflection of the strong tendency toward particle fracture in the 20μm SiC material.

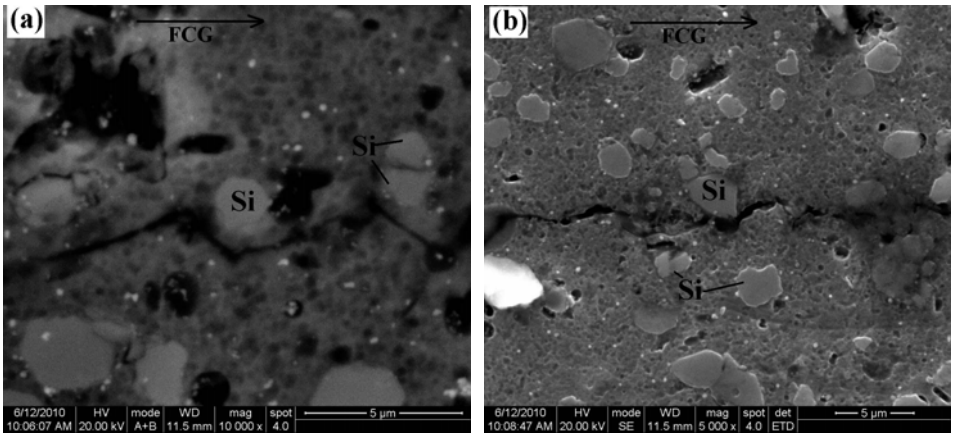

Figure 4. Fatigue crack extension observed on the polished surface of Al-7Si alloy sample, tested at R-0.1 for (a) ΔK_{th}=3.605 MPa•m$^{1/2}$ and (b) ΔK=5.0 MPa•m$^{1/2}$

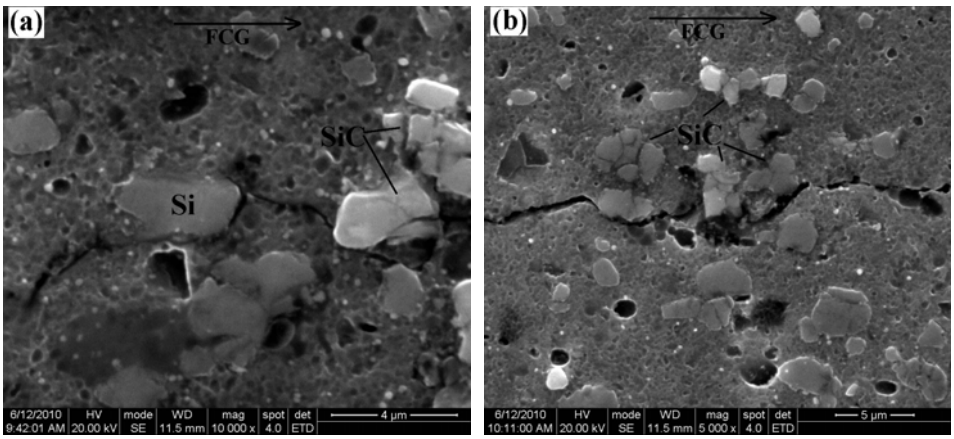

Figure 5. Fatigue crack extension observed on the polished surface of 4.5μm/Al-7Si alloy sample, tested at R-0.1 for (a) ΔK_{th}=3.878 MPa•m$^{1/2}$ and (b) ΔK=7.0 MPa•m$^{1/2}$

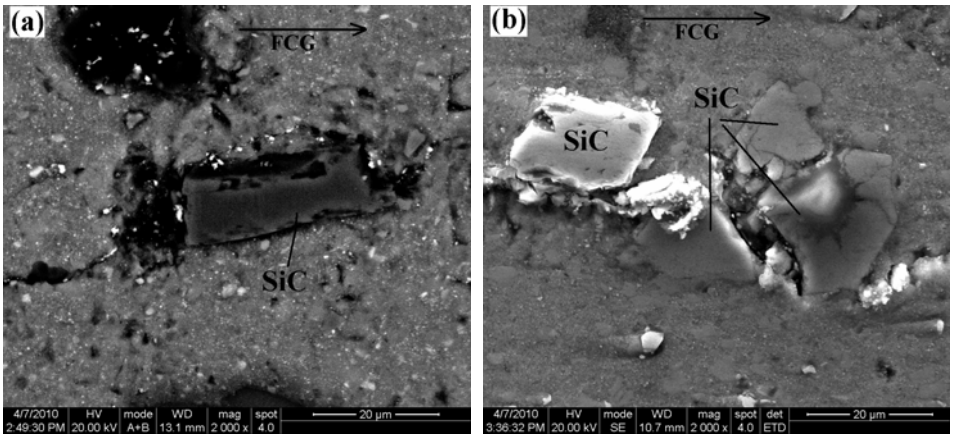

Figure 6. Fatigue crack extension observed on the polished surface of 20μm/Al-7Si alloy sample, tested at R-0.1 for (a) ΔK_{th}=3.630 MPa•m$^{1/2}$ and (b) ΔK=7 MPa•m$^{1/2}$

4. Discussion

In Al-7Si alloy, where fatigue cracks avoid Si particles, enhanced crack closure has been observed through roughness-induced crack closure. Crack deflection around

Si particles is the main fracture mechanism.

Corresponding crack path profiles are shown in Fig.5 and Fig. 6. At low ΔK, fatigue surfaces in the SiC/ Al-7Si composite exhibit a zig-zag crack propagation path, with crack deflection around the particles microcacking inside in the 4.5μm SiC along the side of the crack(Fig.5(a)), whereas in the 20μm SiC composite they exhibit only crack deflection around the large particles. The results has shown that in comparison with the composite with 20μm SiC, the FCG rate at 4.5μm SiC was significantly decreased by the development of a higher level of crack closure. The increased crack closure was accompanied by extensive small particle cracking evident. The opening of a microcrack formed from particle cracking under the combined action of the crack-tip stress can result in a local volume expansion around the microscrack, referred to as microcrack-induced crack closure. The effect of the closure force is similar to the reduction of crack-tip stress intensity by transformation toughening.

For the composite with 20μm SiC, the major effect of the large SiC reinforcement is to alter the fracture path, which enhanced crack closure through roughness-induced crack closure. However, roughness-induced crack closure diminishes at high stress intensities. The fatigue cracks do not avoid but run through the SiC particles. Therefore, the effectiveness of particles in crack deflection should be much smaller than the matrix alloy and 4.5μm SiC composite and would be further reduced because of the higher tendency of the large SiC fracture.

5. Conclusions

(1) The 4.5μm SiC/Al-7Si composite has the best fatigue crack growth resistance, i.e. lower fatigue crack growth rate and higher threshold stress intensity factor range ΔK_{th}. The ΔK_{th} is 3.878 $\mathrm{MPa}\bullet\sqrt{m}$ for the 4.5μm SiC reinforcement composite, 3.630 $\mathrm{MPa}\bullet\sqrt{m}$ fore the 20μm, and 3.605 $\mathrm{MPa}\bullet\sqrt{m}$ for the Al-7Si alloy, respectively. The values of the fatigue crack growth rate for the 20μm are lower than the matrix alloy in the near threshold region and Paris regime, however, it become higher than those of Al-7Si alloy at the fast fracture state.

(2) For the unreinforced alloy, crack propagating around Si particles is observed in the near-threshold regime. Crack deflection caused by Si phase, gives rise to a higher degree of roughness of crack surface, and then results in the occurrence of crack closure effect.

(3) For the 4.5μm SiC reinforcement composite, crack deflections around SiC and microcracking inside SiC particles are the principle mechanisms of interaction between SiC particles and crack tip. Crack path analyses indicates that the extent of microcracking inside SiC particles induces a high level of fatigue crack closure ,which effectively reduces the crack growth driving force to slow down fatigue crack growth.

(4) For the composite with 20μm SiC particle, crack deflection caused by the SiC particles attributes the lower crack growth due to the high levels of roughness-induced crack closure at the low ΔK, then the propensity for the fracture of large SiC particles

increased with increasing ΔK resulted in a higher crack growth rate in the fast fracture state.

Acknowledgements

This work was supported by the National Natural Science Foundation of China under Contract No.51205030, Energy efficient and clean use of open fund of Key Laboratory of Colleges and Universities in Hunan Province (2010NGQ007, and Key Project of Chinese Ministry of Education (No. 211136).

References

[1] S. Suresh, A. Mortensen, Functionally graded metals and metal-ceramic composites: Part 2. Thermo-mechanical behavior. Int. Mater. Rev. 42(1997) 85-116.

[2] Y. Sahin, Preparation and some properties of SiC particle reinforced aluminum alloy composites. Mater. Des. 24(2003) 671-679.

[3] F. Wang, B. Yang, X.J. Duan, B.Q. Xiong, J.S. Zhang, The microstructure and mechanical properties of spray-deposited hypereutectic Al-Si-Fe alloy. J. Mater. Proc. Technol.137(2007) 191-194.

[4] E.J. Lavernia, Spray atomization and deposition processing of particulate reinforced metal matrix composites. Key. Eng. Mater. 53-55(1991) 153-159.

[5] N. Chawla, V.V.Ganesh, B.Wunsh, Thress-dimensional (3D) microstructure visualization and finite element modeling of the mechanical behavior of SiC particle reinforced aluminum composites. Script. Mater. 51(2004) 161-165.

[6] J. Huang, J. E. Spowart, J. W. Jones, The role of microstructural variability on the very high-cycle fatigue behavior of discontinuously-reinforced aluminum metal matrix composites using ultrasonic fatigue. Int. J. Fat. 32(2010) 1243-1254.

[7] N. Chawla, C. Andres, L. C. Davis, J. W. Jones, J. E. Allison, The interactive role of inclusion and SiC reinforcement on the high-cycle fatigue resistance of particle reinforced metal matrix composites. Metall. Mater. Trans. A. 31(2000) 951-957.

[8] J. Llorca, J. Ruiz, J. C. Healy, M. Elices, C. J. Beevers, Fatigue crack propagation in salt water, air and high vacuum in a spray-formed particulate-reinforced metal matrix composite. Mater. Sci. Eng. A. 185(1994) 1-15.

[9] J. N. Hall, J. W. Jones, A. K.Sachdev, Particle size, volume fraction and matrix strength effects on fatigue behavior and particle fracture in 2124 aluminum-SiC_p composites. Mater. Sci. Eng. A. 183(1994) 69-80.

[10] Y.Sugimura, S Suresh. Effects of SiC contents on fatigue crack growth in aluminum alloys reinforced with SiC particles. Metall. Trans. A, 1992, 23(1992) 2231-2242.

[11] N.Chawla, C. Andres, J.W. Jones, J.E. Allison, Effect of SiC volume fraction and particle size on the fatigue resistance of a 2080 Al/SiC_p composite, Metall. Mater. Trans. 29(1998) 2843-2854.

[12] F M Xu, S J Zhu, J Zhao, M Qi, F G Wang, S X Li, Z G Wang, Fatigue crack growth in SiC particulates reinforced Al matrix graded composite. Mater. Sci. Eng. A. 360(2003) 191-496.

[13] G Liu, D Zhu, J K Shang, Enhanced fatigue Crack growth resistance at elevated

temperature in TiC/Ti-6Al-4Vcomposite: microcrack-induced crack closure. Metall. Mater. Trans. A. 26(1995) 159-166.

Interlaminar Shear Strength for Three Kinds of Ceramic Matrix Composites at 1173K

Jianjie GOU, Chengyu ZHANG, Shengru QIAO, Xuanwei WANG

National key Laboratory of Thermostructure Composite Materials, Northwestern Polytechnical University, Xi'an 710072, P. R. China

blao@nwpu.edu.cn

Abstract: Interlaminar shear strength (ILSS) of a two-dimensional carbon fiber reinforced silicon carbide (2D-C/SiC) composite, two-and-a-half-dimensional carbon fiber-reinforced silicon carbide (2.5D-C/SiC) composite along the warp and weft directions and two-dimensional silicon carbide fiber reinforced silicon carbide (2D-SiC/SiC) composite were investigated by the double-notch shear (DNS) test at 1173K in air. The microstructure and fracture morphologies of the DNS specimens were observed by a scanning electron microscope (SEM) and an optical microscope. Experimental data shows that ILSS of 2.5D-C/SiC along the warp direction is not only lower than that of the weft direction, but also lower than 2D-C/SiC. Besides, ILSS for 2D-SiC/SiC is higher than that of the 2D-C/SiC. The possible reasons are analyzed through SEM images, optical micrographs and results of ILSS at 1173K in air. Finally the fracture mechanism is discussed.

Key words：Ceramic matrix composites; ILSS; Fracture morphology

1. Introduction

Successful development of Continuous Fiber-reinforced Ceramic Matrix Composites (CFCCs) has led to great improvements to the intrinsic problems of brittleness, low fracture toughness and catastrophic failure of the monolithic ceramic. CFCCs are now used in various high-temperature applications, such as structural materials for aerospace industry, aircraft brakes, burner nozzles and rocket thrusters [1-3]. However, even though CFCCs have shown significant increase of damage tolerance and the ability of resistance to fracture in in-plane area, inherent processing defects or cracks in the matrix-rich interlaminar regions of the CFCCs can cause delamination under shear stress, resulting in some kind of structural failure [4-6].

A number of studies with respect to the shear properties for CFCCs have been reported. In-plane and interlaminar shear strength of a unidirectional SiC fiber-reinforced $(BaSr)Al_2Si_2O_8$ celsian composite were measured by the double-notch shear (DNS) test method between room temperature and 1473K, the difference in layer architecture and alignment of fiber-rich layers with the shear plane in the interlaminar specimens appeared to be the reason for the lower strength of this composite [7]. Choi et al investigated the interlaminar mechanical properties determined for six

different CFCCs at ambient temperature and observed the degradation of interlaminar shear strength (ILSS) with decreasing shear stress rate, containing SiC fiber-reinforced SiC matrix composites, SiC fiber-reinforced glass ceramic composites and carbon fiber-reinforced SiC matrix composites [8,9]. Investigation of the life limiting behavior of the melt-infiltrated Hi-Nic SiC/SiC subjected to interlaminar shear was made at 1589K in air under stress rupture loading [10]. M.B. Ruggles-Wrenn and P.D. Laffey investigated the creep behavior of the Nextel™720/alumina (N720/A) composite in interlaminar shear loading at 1473K in air environments [11]. In our previous work, ILSS of 2D-C/SiC at elevated temperature was investigated in air [12]. Nevertheless, a comparison of several kinds of ceramic matrix composites on ILSS in the same condition is still very limited up to now, especially at elevated temperature. Since 2D-C/SiC, 2.5D-C/SiC and 2D-SiC/SiC are commonly used at high temperature, so a detailed investigation and comparison of the shear properties of these composites at elevated temperature appears to be necessary.

The objective of this work was to compare the shear behaviors of 2D-C/SiC, 2.5D-C/SiC and 2D-SiC/SiC. Double-notch shear (DNS) test method was specified to determine ILSS of ceramic matrix composites at elevated temperature by American Society for Testing and Materials (ASTM) standard (C-1425-05) [13]. ILSS of the mentioned ceramic matrix composites was determined by DNS at 1173K in air. An analysis of material damage and the failure characteristics with respect to different fibers and woven structures was discussed in the text.

2. Experimental

2.1 Materials and Specimens

The 2D-C/SiC,2.5D-C/SiC and 2D-SiC/SiC composites used in this study were fabricated by chemical vapor infiltration (CVI) of SiC into preforms. Fibrous preforms for 2D-C/SiC and 2D-SiC/SiC are plain weaving structure, while fibrous preform for 2.5D-C/SiC is shown in Fig.1. The fibers were coated with pyrocarbon (PyC) with thickness of 200 nm before infiltration of SiC matrix. Residual porosity is sealed by depositing on the external surface of the specimens a suitable coating at the end of the process. The parameters of tested composites are listed in table 1.

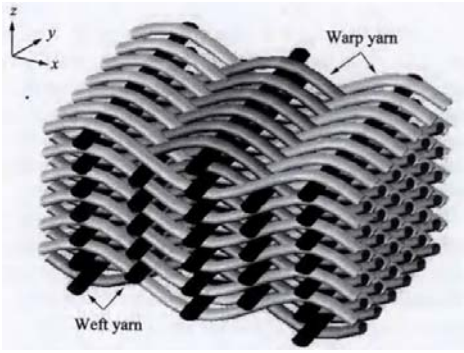

Figure 1. Schematic diagram of fiber perform for 2.5D-C/SiC composite

Table 1. The parameters of tested composites

materials	reinforcement	preforms	fiber volume fractions (%)	Bulk density (g/cm^3)	residual porosity(%)
2D-C/SiC	3K-PAN carbon fibers	2D	40	1.99	15
2.5D-C/SiC	3K-PAN carbon fibers	2.5D	45	2.05	15
2D-SiC/SiC	0.25K silicon carbide fibers	2D	40	2.61	11.5 (open porosity)

Interlaminar shear failure was conducted in a region between two notches that were asymmetrically located on opposite sides of the specimens at an equal distance from the mid-plane, as shown in Fig.2. A layer of SiC coating was deposited on the specimens after the machining of notches, and the thickness of coating was added to specimen dimension. It's worth noting that both the warp loading direction and weft loading direction of the specimens for 2.5D-C/SiC were fabricated respectively.

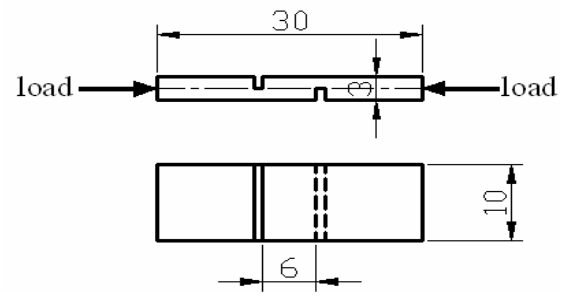

Figure 2.Geometry and dimensions of the DNS specimen

2.2 Mechanical property measurement

All tests were performed at 1173K in air. The specimens were heated at a rate of 40–50K/min, followed by a soaking period of 10 min after reaching the test temperature. Then the DNS specimens were applied to a compression load along the specimen axis, as shown in Fig. 2. Monotonic loading was carried out in displacement control at a rate of 0.595 mm/min. Five specimens were tested for each kind of ceramic matrix composites. The ILSS is calculated as Eq. 1:

$$ILSS=P_{max}/WL \quad (1)$$

Where P_{max} is the ultimate compressive load, W is the specimen width and L is the notch spacing between the inner franks of the notches.

The morphologies of fracture surfaces were examined by a scanning electron microscope (SEM, HITACHI S-4700) and an optical microscope.

3. Results and discussion

3.1 Shear load versus cross-head displacement curves

Fig. 3 displays the shear load versus cross-head displacement curves obtained at 1173K in air. In the initial loading stage, nonlinearity exists for all curves. Except the curve of 2.5D-C/SiC along the warp direction, the slopes of curves keep increasing until to peak load followed by a sudden load drop when the specimens failed, although the test was conducted under a constant rate of 0.595 mm/min. It suggests that the process containing a stable propagation of cracks in the interlaminar region is impossible, and that shear failure occurs whenever the inherent ILSS is reached partly anywhere in the shear plane.

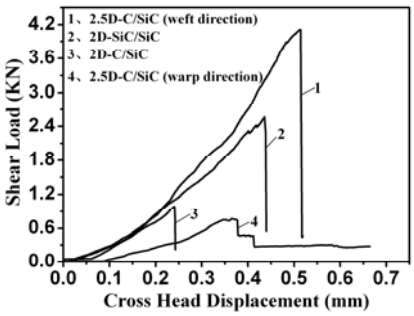

Figure 3. Interlaminar shear load versus cross-head displacement curves from the compression of DNS specimens for the three kinds of ceramic matrix

It can be found for the curve of 2.5D-C/SiC along the warp direction that the stage prior to failure is similar to those mentioned above, while several steps occur after reaching the peak load, which is related to the special weaving structure.

3.2 ILSS at 1173K

ILSS of the tested specimens at 1173K in air are shown in Fig. 4. It clearly shows that ILSS of 2D-C/SiC is higher than that of 2.5D-C/SiC along the warp direction，but considerably lower compared with that of the weft direction for 2.5D-C/SiC. The great shear anisotropy between the warp and weft direction for 2.5D-C/SiC can be understood by the characteristics of the fiber preform architecture, shown in Fig.1. When the specimens were subjected to a shear load along the

weft direction, the load was mainly carried by weft yarns and then by the weft and contacted warp yarns. What's more, being interlocked by tightly contacted warp yarns, the lateral movements of the weft yarns were well restricted. Conversely, in the warp direction, the fewer distributed weft yarns couldn't perfectly limit the lateral movements of warp yarns, and the sinusoidal warp yarns may weaken the ability of resistance to failure.

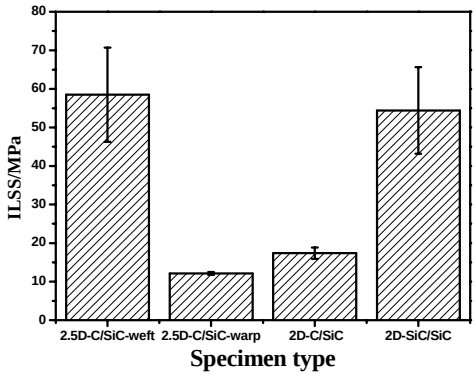

Figure 4. ILSS of the three kinds of composites at 1173K in air

ILSS for 2D-SiC/SiC is considerably higher than that of the 2D-C/SiC. The poor ILSS for 2D-C/SiC is mainly associated with the oxidation of fibers. This will be discussed further from the SEM observations.

3.3 Fracture morphology

Fig. 5 presents typical optical micrographs of fracture surface for the three kinds of composites.

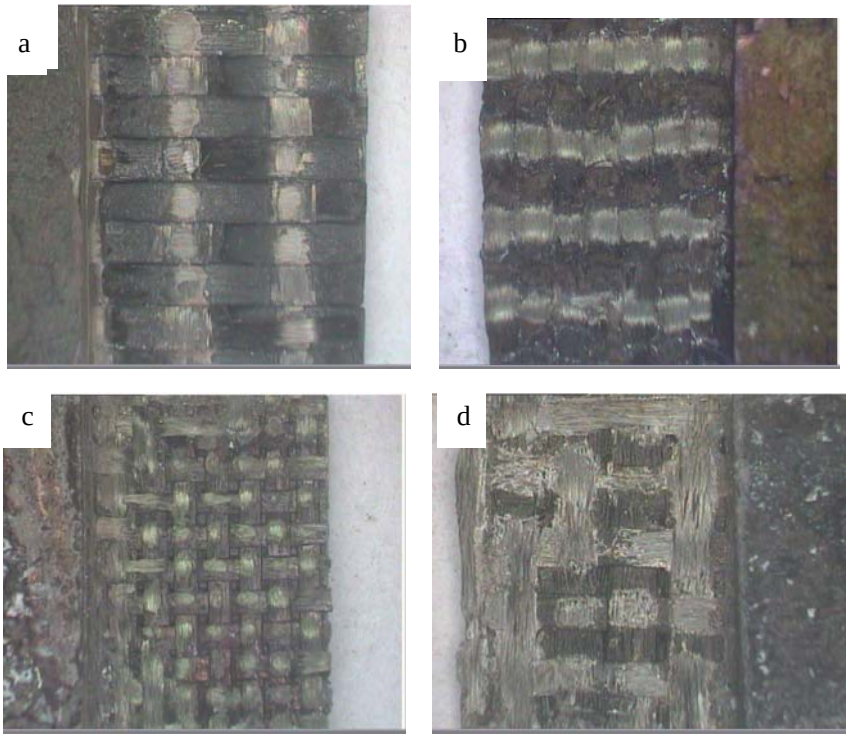

Figure 5. Optical micrographs of the failed 2.5D-C/SiC along the warp (a) and weft (b) direction, 2D-C/SiC (c)and 2D-SiC/SiC (d) specimens.

All the specimens failed in a typical shear mode along their respective interlaminar shear planes. As shown in Fig. 5(a) and (b) for 2.5D-C/SiC, it can also prove that only the fewer weft interlocked yarns played a resisting role in the process of shear failure along the warp direction，while the more interlocked yarns resist to fracture and fracture surface is rough in the weft direction.

As presented in Fig. 5(c) and (d), for 2D-C/SiC and 2D-SiC/SiC, the fracture surfaces are both somewhat smooth and clean, and the fiber bundle are clearly observed.

Owing to a mismatch of the thermal expansion coefficients of the fibers and matrix, a certain mount of microcracks already exist in the SiC coating as well as in the SiC matrix upon cooling from the processing temperature for the three kinds of composites. And microcracks are formed in the coating that favor the in-depth diffusion of oxygen. When shear test is carried out at 1173K, the oxygen can diffuse through these microcracks and reach to the carbon interface and fibers. The oxidation kinetics is controlled by the gas-phase diffusion through the microcracks in the SiC coating, resulting in a nonuniform degradation of the carbon phases [15]. The oxidation of carbon interface and fiber causes degradation of bond between the fiber and matrix, so the fiber is easier pulling out owing to the weak interface, as illustrated in Fig. 6(a). Due to the inhomogeneous SiC coating and stress concentration in the vicinity of notches, failure of the specimens usually generates from the notches, resulting in severe oxidation at this site (Fig. 6(b)). Carbon fibers are rapidly oxidized at temperatures above 400°C, while the silicon carbide fiber possesses relatively high anti-oxidation temperature, as shown in Fig. 6(c) and (d), consequently, ILSS of 2D-SiC/SiC is higher than that of 2D-C/SiC.

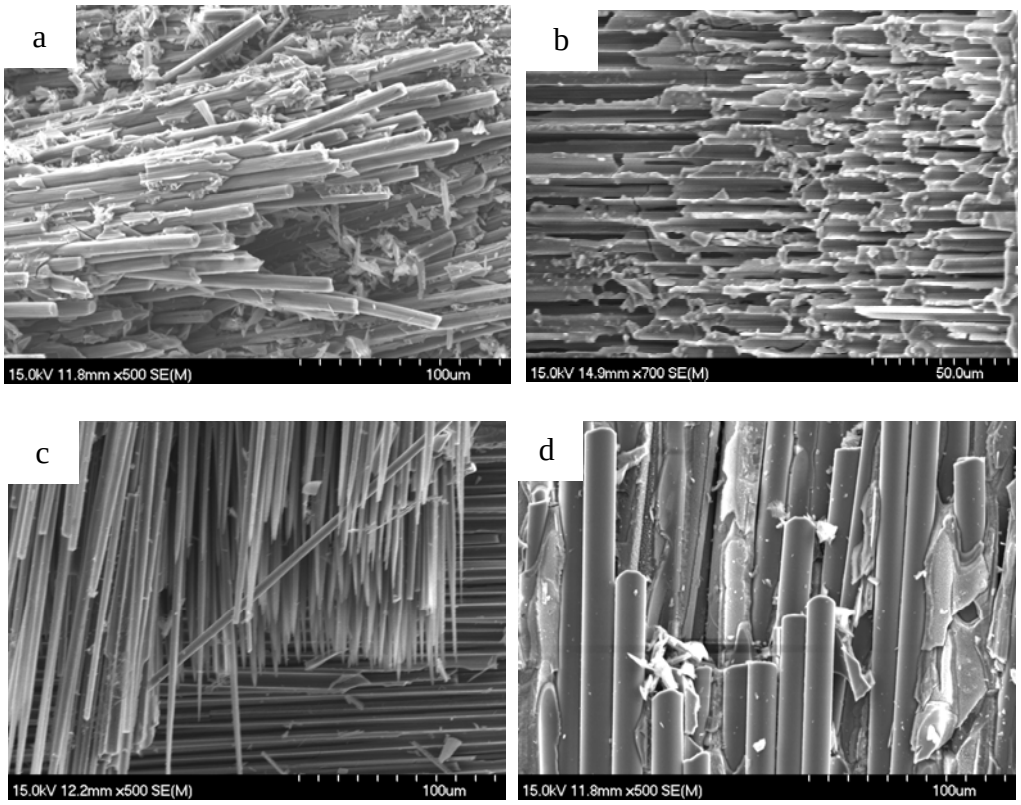

Figure 6. SEM images of 2.5D-C/SiC at fracture surface (a) and near notch (b), 2D-C/SiC (c) and 2D-SiC/SiC (d) failed by interlaminar shear load

4. Conclusions

(1)At 1173K in air, ILSS of 2D-C/SiC is higher than that of 2.5D-C/SiC along the warp direction, but considerably lower compared with that of the weft direction for 2.5D-C/SiC. ILSS for 2D-SiC/SiC is considerably higher than that of 2D-C/SiC.

(2) The great shear anisotropy between the warp and weft direction for 2.5D-C/SiC is associated with the characteristics of fiber preform architectures. For 2D-SiC/SiC and 2D-C/SiC composites, the difference of ILSS is mainly attributed to the kinds of fiber and oxidation of carbon fibers in the latter at 1173K in air.

Acknowledgements

This work has been supported by National Science Foundation of China (Grant No. 51172182), Basic Research Foundation of NWPU (Grant No. JC20100227), and the Program for New Century Excellent Talents in University (NCET-08-0460).

References

[1] R.R. Naslain, António Pereira Nascimento Filho, Processing of ceramic matrix composites. Key Eng Mater, 164–165(1998) 3-8.
[2] K.G. Dassios, D.G. Aggelis, E.Z. Kordatos, T.E. Matikas, Cyclic Loading of a SiC-fiber Reinforced Ceramic Matrix Composite Reveals Damage Mechanisms and Thermal Residual Stress State. Composites Part A: Applied Science and Manufacturing, 44(2013) 105-113.
[3] L. Daniel and G. Ramusat, ‘‘Prospective and Economic Impact of Composites in Reusable Launch Vehicle,’’ AIAA, 2005-6618.
[4] Yan KF, Zhang CY, Qiao SR, Li M, Han D, Failure and strength of 2D-C/SiC composite under in-plane shear loading at elevated temperatures. Mater Des, 32(2011) 3504–8.
[5] Camus G, Guillaumat L, Baste S, Development of damage in a 2D woven C/SiC composite under mechanical loading. Compos Sci Technol, 56(1996) 1363-72.
[6] Dalmaz A, Reynaud P, Rouby D, Fantozzi G, Abbe F, Mechanical behavior and damage development during cyclic fatigue at high-temperature of a 2.5D carbon/SiC composite. Compos Sci Technol, 58(1998) 693–9.
[7] Ö. Ünal, Narottam P, Bansal, In-plane and interlaminar shear strength of a unidirectional Hi-Nicalon fiber-reinforced celsian matrix composite. Ceramics International, 28(2002) 527–540.
[8] Choi SR, Bansal NP, Interlaminar tension/shear properties and stress rupture in shear of various continuous fiber-reinforced ceramic matrix composites. Ceram Trans, 175(2006) 119-34.
[9] Choi SR, Bansal NP, Shear strength as a function of test rate for SiC_f/BSAS ceramic matrix

composite at elevated temperature. J Am Ceram Soc, 87(2004) 1912–8.

[10] Sung R. Choia, Robert W. Kowalik, Donald J. Alexandera, Narottam P. Bansal, Elevated-temperature stress rupture in interlaminar shear of a Hi-Nic SiC/SiC ceramic matrix composite. Composites Science and Technology, 69(2009) 890-897.

[11] M.B. Ruggles-Wrenn, P.D. Laffey, Creep behavior in interlaminar shear of Nextel^{TM}720/alumina ceramic composite at elevated temperature in air and in steam. Composites Science and Technology, 68 (2008) 2260-6

[12**]** Wang HL, Zhang CY, Liu YS, Han D, Li M, Qiao SR, Temperature dependency of interlaminar shear strength of 2D-C/SiC composite. Mater Des, 36(2012) 172–176.

[13] ASTM Designation C-1425-05. Standard test method for interlaminar shear strength of 1-D and 2-D continuous fiber-reinforced advanced ceramics at ambient temperatures. ASTM Designation, 2005.

[14]Cheng LF, Xu YD, Zhang LT, Yin XW, Oxidation behavior of three dimensional C/SiC composites in air and combustion conditions [J]. Carbon, 38(2000) 2103-2108

[15] Franck Lamouroux and Gérald Camus, Kinetics and Mechanisms of Oxidation of 2D Woven C/SiC Composites: I, Experimental Approach. J. Am. Ceram. Soc, 77(1994) 2049-57.

Atomistic simulation of fatigue crack growth in α-Fe under high temperature

Tong Liu[1,*], **Minshan Liu**[1]

[1] Thermal energy engineering research center of Zhengzhou University, Zhengzhou 450002, China
* Corresponding author: liutung@zzu.edu.cn

Abstract The crack growth behaviors loaded in mode I under strain and stress control at different temperatures were presented in α-Fe by atomistic simulations using LAMMPS code. The interatomic bonds of atoms were characterized using the embedded atom method interatomic potential. The simulation models were built with initial edge crack subjecting to cyclic uniaxial constant strain rate and constant stress. A temperature range from 100 K to 1200 K was considered to probe the influence of the temperature on crack growth. The crack growth mechanism and the radial distrinution function (RDF) during crack growth were investigated. The results indicated that the crack propagation mechanisms were sensitive to temperature and the boundary conditions. By proposed image adjusting technology the dislocation slip bands can be more clearly displayed on screen. In order to include the effect of temperature on crack growth, a temperature factor defined as a function of temperature in exponential form was introduced to modify the theoretical expressions based on thermal activation theory. Its coefficent and index can be determined by the RDF peak value obtained from atomistic simulations. For cyclic loading the crack growth process was dependent on both temperature and cyclic loading period in terms of simulations.

Keywords Molecular simulation; Fatigue crack growth; High temperature; Iron; Thermal activation.

1. Introduction

Ferritic steels are widely used in process industry, modern nuclear power plants, military industry and others. The main crystal structure of steels is body-centered cubic (bcc) lattice of iron and it is comonly called α-Fe[1]. It is unavoidable for steels with defects so safety assessment on strucure integrity with defects is essential for engineering application. While in critical components of nuclear facilities, the radiation, high temperature and presssure, start and stop operations influence behavior of steels significantly and imply high potential failure risks for the integrity of reactor components with crack-like defects. The detail understanding of the processes occurring near the crack tip during the crack nucleation and growth can largely help in the material development and safety assessment under service in particular high temperature environments[2].

As the fatigue fracture is the primary cause of failure for almost all engineering structures subjecting to repeated cyclic loading, so many people have been do much research efforts on this scope. Most investigations on fatigue fracture have been performed at the macroscale and the theory on analysis methods and experimental approaches related to fatigue strength and fracture mechanics has been well established based on mechanics of continua and test at the macroscale with the crack lengths ranging from a few decades of microns to centimeters. However, on the kernel mechanism of fatigue crack initiation and growth are maily determined by interatomic bond rupture,crystal plastic deformation and the associated material defects in the vicinity of the crack tip. Recent developed atomistic simulations provide a high efficient approach to investigate fatigue fracture behavior at the nanoscale. With the knowledge of nanoscale fatigue, more accurate macroscale predictive tools can be got, mechanism understanding of grain boundary effects, crystal orientation effects, and driving force versus material resistance effects can be clearly obtained.

The material deformation and fracture mechanism of a structure with cracks have been paid close attention in worldwide. The fracture response of a material under mechanical load and temperature is a multiscale problem. It is the result of dislocation slip, grain boundary motion, plastic deformation and interplanar cleavage. The literature indicates that the atomistics of the crack

growth in metals is considerablt complicated than current model postulation. The fracture mode of steels appears as ideal cleavage under low temperatures condition. The currently most widespread model for brittle crack growth in metals proposed by Rice and Thomson is that the high stress concentrations at the crack tip causes bond breaking in the cleavage plane and promotes dislocation emission from the crack tip. A successfully emitted dislocation will slightly blunts the crack tip. At very low temperatures the nucleation and/or removal of dislocations near the crack tip is suppressed, while at higher temperatures this constraint is relieved as a result of the thermally activated nucleation of dislocations. All these phenomena initiate at the atomic scale and form macroscopic consequences. As continuous advances on microscopic physics science and high speed development of computer technology, the molecular dynamics method is widely applied to analyze crack propagation mechanisms[3-14]. Utilizing molecular dynamics method not only a great deal of valuable micro-behaviors can be got but also the macro-properties of a material can be reproduced[15]. The behavior of crack growth in metals depends strongly on the structure evolution of the crack tip, load type and temperature. But at present it is still a lack of research on the influence of temperature on crack growth. The aim of our research was focus on the effect of temperature on crack growth in α-Fe by using numerical simulations. For this purpose large scale molecular dynamics was applied to study the mechanisms of a crack growth under different temperature. Molecular simulations can reveal some crack propagation behavior in atomistic scale and offer a better understanding about crack growth. It even enhances an accurate evaluation method on crack growth and fracture behaviors at extreme temperature.

In present paper a model with constant rate of straining load in tension mode I and free surfaces was considered. Symetrical strain proportional to an atomic position in some dimension is imposed to all atoms. Periodicity along the thickness dimension z was applied. Here atomistic simulations were applied to model the process of crack growth in steels under different temperature. The embedded atom method (EAM) potentials belonging to many-body interatomic potentials[1], which provide an essentially better description of the inter-atomic interactions and free surfaces, were employed to get accuracy results. The simulation parameters such as box geometry, timestep, loading rate were determined after performing parameter sensitivity analysis. The computation is implemented by utilizing large-scale atomic/ molecular massively parallel simulator (LAMMPS)[16], Visual Molecular Dynamics (VMD) [17] and developped programs in Python.

The simulation results demonstrated that with a crack growing the phenomena involving crack tip passivation, crack opening distance increment, dislocation emission, dislocation slip, plasticity deformation, voids formation and voids coalescence have been appeared and can be observed. Slip bands formation at the crack tips and ligament region and their development with incremental strain and temperature were demonstrated during crack growth. The crack growing with same initial state behaves differently under different temperature. It means that the crack growth trace and fracture configuration are realted with temperature. The dynamic radial distribution function and corresponding number density integral for variable time and temperature were calculated to explorer the relationship between the crack growth and temperature.

In this paper, the profile evolution of the crack tip for crack propagation system (0 0 1)[010] in α-Fe at low and high temperatures was investigated. It is expected to probe whether crack growth properties have relationship with some parameters referring to radial distribution function in α-Fe during crack propagation at different temperatures. Some phenomenological descriptions on temperature-dependent relations allowing to predicting crack growth were proposed. The crack growth process, radial distribution function, atomic stresses in a bcc iron single crystal were analyzed utilizing molecular simulations with LAMMPS. Edge crack specimens under tentional strain loading were selected as simulation models. Limited by volume of the paper, here we only provide some key results. Other contents will be reported elsewhere.

2. Crack growth and temperatrue

2.1. The effect of crystal plasticity on crack growth

It has been known that the strength of metallic materials of various structures at extreme temperatures has a strong relationship with crystal plasticity generated by thermally activated microscopic mechanisms, which is usually controlled by elementary dislocation mechanisms. In order to understand and predict the crack growth and fracture behaviors of materials, it is extremely important to know what determine dislocation mobility and how it changes under the influence of stress and temperature. Based on thermal activation theory the derivation expression of the strain rate can be written by[18]

$$\dot{\gamma} = \dot{\gamma}_0 \exp(-\Delta G / kT) \quad \text{with} \quad \dot{\gamma}_0 = A\rho_m b(A'/l)\nu_{id}, \tag{1}$$

where A is a geometrical coefficient, ρ_m is the mobile dislocation density, b is the Burger' s vector, A' is the area swept by segment l between two successive obstacles, l is the wavelength of the vibration scales depending on the conditions, v_{id} is the vibration frequency of the dislocation segment, k is the Boltzmann constant and T the absolute temperature. Here ΔG is the change of Gibbs free energy of the sample as the dislocation moves along dislocation coordinate. ΔG is used to characterize the energy barrier opposing dislocation motion.

In terms of fracture mechanics the crack growth is related with strain rate. Considering the above and from the point of view in engineering it prompts us to introduce a factor C_m(T) referring to thermally activated energy to take the effect of temperature on crack growth into account. Factor C_m(T) is defined as a function in form of

$$C_m(T) \propto e^{-\mathrm{m}/kT} . \tag{2}$$

where m is a constant which can be determined by molecular simulation.

2.2. Radial distribution function (RDF)

In statistical mechanics, the radial distribution function or pair correlation function $g(r)$ in a system of particles describes how the density varies as a function of the distance from a reference particle. It can also be determined experimentally, by radiation scattering techniques or by direct visualization for large enough particles via traditional or confocal microscopy. The radial distribution function is of fundamental importance in thermodynamics because the macroscopic thermodynamic quantities can usually be determined from $g(r)$. It is a primary reference for theory verification by experiments and also a fundamental function characterizing non-sequential system. For an ideal crystal structure the value and location of peaks at different near neighbour position indicates effect of temperature. Therfore it gives us an idea about whether it has realtionship with crack growth by means of thermal activation energy in different temperature. Based on the simulation results the atomic radial distribution function g(r) and the corresponding number integral are calculated and over a given trajectory.

3. Molecular simulaton modeling

3.1. Interatomic potential

An appropriate description of potential functions is essential in a molecular dynamics simulation. It concerns the accuracy and reliability of simulation results. Lots of potentials have been proposed to approximate the interactions of atoms, such as Lennard – Jones, Tersoff, embedded atom method (EAM) and etc. The steels studied for the crack growth simulation belong to amorphous metal model and is assumed to be made from Fe. The EAM potential for describing interatomic interaction in a semi-empirical form is used to study the crack growth of steels. It is suitable for characterizing metals and alloys with FCC, BCC and HCP structures. In a simulation, the EAM

potential energy of an atom i is expressed by

$$u(\{\mathbf{r}_i\}) = \sum_{i<j} \phi(|\mathbf{r}_i - \mathbf{r}_j|) + \sum_i F(\rho_i), \quad \rho_i = \sum_{j \neq i} f(r_{ij}) \tag{3}$$

Where$|r_i - r_j|$is the distance between atoms i and j, Φ is a pair-wise potential function, $f(r)$ is the contribution to the electron charge density ρi from atom of j at the location of atom i, and $F(\rho_i)$ is an embedding function that represents the energy required to place atom i into the electron cloud. Since the electron cloud density is a summation over many atoms, usually limited by a cutoff radius, the EAM potential is a multibody potential. The EAM of alpha iron used in present study comes from 'Interatomic Potentials Repository Project' which is included in potentials base of LAMMPS.

3.2. Simulation models and methods

The initial α–Fe planes were assumed to be perfect single crystal lattice having bcc structures. The simulations were performed on major slip plane of bcc iron. Edge crack model was chosen to analyze the crack growth characteristics in an infinite domain under plane strain condition acquired by perform periodic boundary condition in z dimension. The x-direction was defined forward in the crack plane, and the z-direction in the thickness direction. The schematic of the molecular dynamics simulation is shown in Figure 1. Three-dimensional model with a small thickness in order to reduce the calculation and to avoid the difficulty of the data analysis is constructed. The sizes of the simulation box were 858×297×5.7 (Å). It consisted of over 120000 atoms. There were two layers of transitional regions around the simulation domain. These layers were used to alleviate the effect of the boundaries and were not included in final results processing. The maximum positive and minimum negative strain loads were applied on the top and bottom boundaries at a certain strain rate to keep the crack faces apart (Figure 3). In all simulations, the initial crack was placed at the midpoint of the left side of the simulation lattice. And all related data including time step, coordinates, velocities, displacements, stresses, strains, temperatures etc. were saved.

The initial α–Fe planes are perfect single crystal lattice having bcc structures was assumed in present paper. The simulations were performed on slip plane of bcc iron. The edge crack specimen geometry model adopted for the present simulation is illustrated in Figure 1. The initial crack was introduced by shutting off pairwise interactions between two slabs of atoms in perfect crystal to effectively create a sharp crack. The ratio of the initial crack length to the width of the specimen was a_0/w = 0.067. The crystal orientation of the initial cracks in crack propagation system (0 0 1)[010] was concerned and illustrated in Figure 2. Crack growth simulation was implemented by moving the atoms with the linearly varied velocity along y dimension in accordance with a given constant deformation rate, which is shown in Figure 3. The strain rate used in simulation was 0.005. A typical simulation cell with a pre-crack is drawn in Figure 4.

Surfaces on two transitional layers located at bottom and top constructed to alleviate the boundary effects were set free. The deformation loading was applied along y-direction perpendicular to the crack plane and varies linearly with y coordinate. The constant strain rate loading was applied in such a way that the velocity is linearly distributed along the y-direction in core region. The velocity in transitional layer at the bottom and the top were set to the maximum positive and minimum negative value, respectively. The used loading method can effectively eliminate the stress oscillation and impact effect produced by acting sudden load. In the z-direction the periodic boundary condition was assigned to keep an expected plane strain state.

Another loading type used in simulation was to act forces directly on atoms in loading layers. External forces were applied in the way distributed in top and bottom surface boundary layers. The sizes of the simulation box are 578×458×2.86 (Å) which contains about 65000 atoms. Time step 0.002 ps was utilized in simulations. The cyclic loading and unloading timesteps was 20000. The initial crack length corresponds to 17.2,57.2 Å.

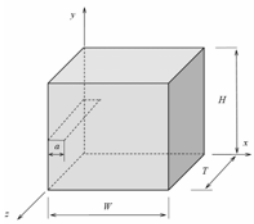

Figure 1. Schematic representation of the model to study the behavior of a crack growth

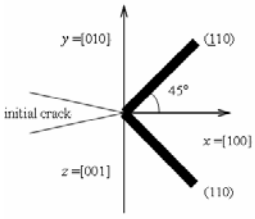

Figure 2. Crystallographic orientation of the studied initial crack

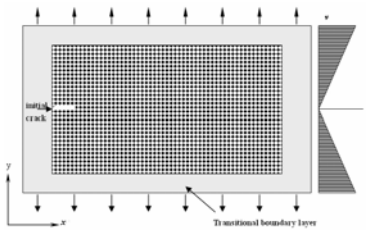

Figure 3. Edge crack specimen used for the simulation

Figure 4. A typical simulation cell with a pre-crack

The temperatures in performed all simulations varies in the range of temperature keeping the iron in body-centered cubic crystal structure. The purpose of our research was to probe the influence of temperature on the crack growth behavior, thus the temperature of atoms in simulation was controlled to given value. The temperature of a group of atoms was reset by explicitly rescaling their velocities without performing time integration, unlike the NVT ensemble which performs Nose/Hoover thermostatting and time integration. It only modifies velocities that effect thermostatting. Therefor NVE ensemble using a separate time integration fix was utilized to actually update the positions of atoms using the modified velocities.

4. Results and discussions

4.1. Direct observations of dislocation slip bands

The dislocation as a result of atomic movement simualtion results can be shown in graphic mode through developped postprocessing code and VMD. In a general standard display style the dislocation and slip band stripes are not very clear and it is not easy to distinguish them. In terms of Moire interferometry method, an appproach to obtain clearer image of slip band patterns generated by deformed material crystals was put out in this paper by means of adjusting the drawing method, lattice node scale, plot size and screen grid resolution. This approach was called stripe image adjusting technique here. Figure 5 and 6 are two examples after applying proposed stripe image adjusting technique. By utilizing this new method the emission of slip bands from pre-crack tips can be observed clearly and picturesquely with the response of cracks propagating under congstant

deformation rate control in the considered temperature range. However it needs more detail investigation to do quantitatively analysis because Moire patterns are sensitive to crystal lattice parameter, sphere scale and simulation cell sizes, as well as the screen grid intervals. The simulations demonstrate that slip bands started from the atomistically sharp crack tip. Simulations show that a slight blunting of pre-crack tips does not preclude slip band formation.

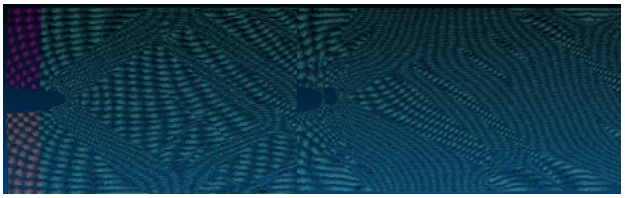

(a) (b)

Figure 5. Dislocation slip bands for edge crack specimen at 300 K. (a) t=3 ns, (b) t=5 ns.

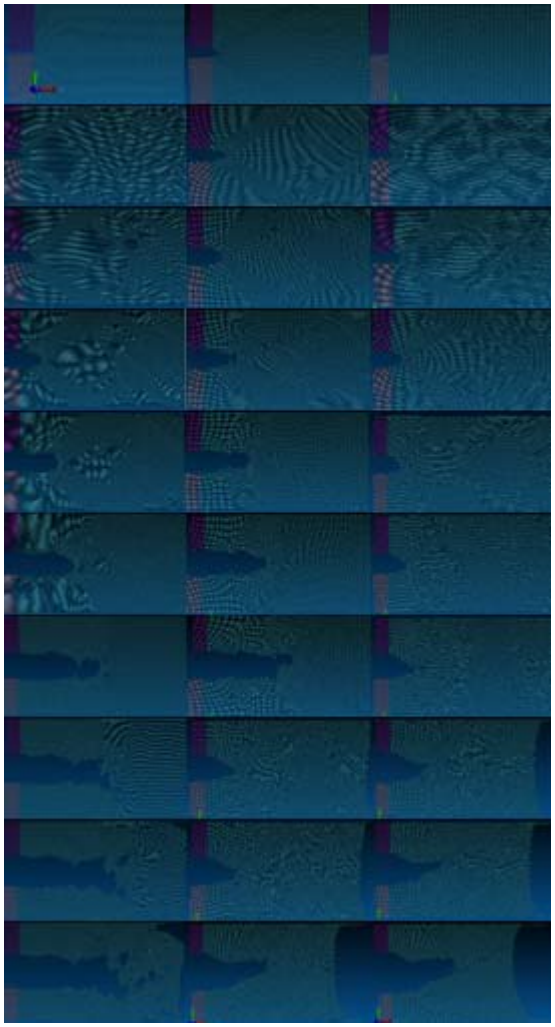

Figure 6. Intense dislocation slip bands at the crack tips.

A series of snapshots showing the crack growth at different time and temperatures were obtained in terms of performed molecular simulation results. The simulation time was measured in nanoseconds. Intense dislocation emssion and slip twin bands at the crack tip under different temperature (T=200 K, 300 K, 600 K) are illustrated in Figure 6. The slip bands evolving via time for present crack propagation system can be observed distinctly. The snapshots demonstrate the shapes and internal structure of slip bands near the tips of propagating crack. The slip band expansion paths were basically similar for simulation cases for given particular crack propagation system. The simulation

results indicate that the crack growth modes under low and high temperature are different for their different brittleness and ductility. In a wide range of temperature the localized viscous flow, cavity formation and coalescence in ligament can be observed.

4.2. Crack propagation processes

Snapshots of propagating cracks under continuous strain loading at temperatures of 200 K, 300 K and 700 K are illustrated in Figure 7. All the phenomena involving dislocation, voids formation and merge were visually demonstrated. Figure 8 shows the crack growth difference for different temperatures at a given loading time. It is easy to see the crack propagating process and find that with same loading time duration the crack propagation rate reduces with an incremental temperature. The snapshots of dynamic crack growth also show that the ligament size and back boundary constraint condition influence the crack process and fracture profile considerably.

4.3. Fatigue crack growth

The cyclic loading was applied with a maximum stress σ= 50 MPa and a stress ratio of r = 0. External forces in the tensional direction were distributed in each atom located in top and bottom surface layers. The upper, lower and right boundaries were ensured constant displacement conditions in y and x direction respectively. The simulations were performed at a constant temperature of 300 K and 900 K. In the case of initial crack length a_0=17.2 Å with 300 K and 900 K temperature cyclic simulations were performed and the crack propagation behavior is shown in Figure 9 and 10. The cracktip shape change and its moving process as well as dislocations can be observed. During the first ten cycles the crack grew slowly and then started to speed up. At sixteen cycles the crack penetrated the full section and specimen fracture occured. Based on the simulation results it is found that the crack growth rate were related to cyclic loading periods. Some more detail analysis should be done in future.

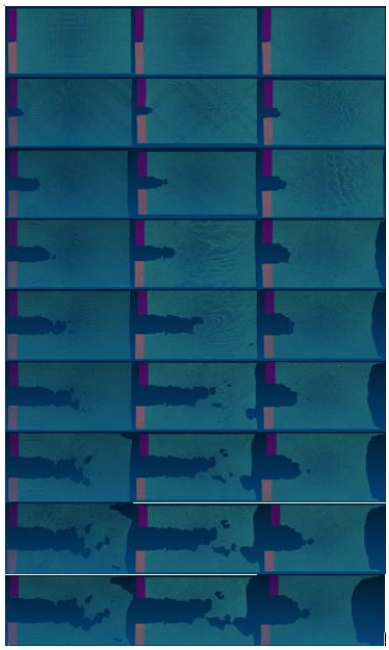

Figure 7. Crack propagation processes: Time t=1~15ns, Temperature T= 200 K, 300 K, 700 K

4.4. RDF via crack growth

Composing all the number density RDF integration curves under changing temperature and time

cases and we obtained a plot as Figure 11. It is obvious that the variation or fluctuation is rather slight and implies that the simulation resutls have a good consistency. On the other hand it also supplys the used simulation model and parameters are appropriate. In addition, it illustrates that temperature has a weaker influence on RDF curve fluctuation than the crack growth process.

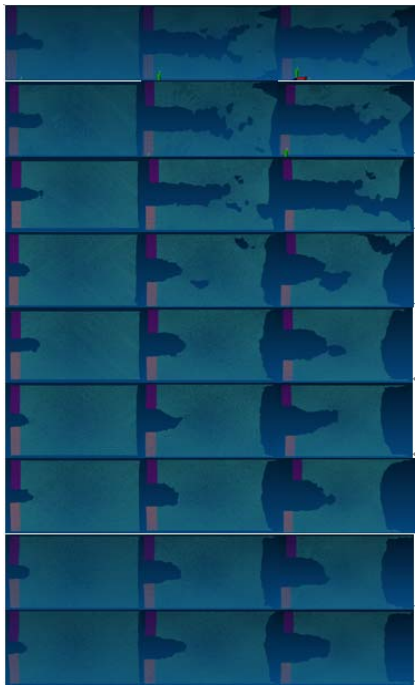

Figure 8. Crack propagation processes for Time t=5,10 and 15 ns,Temperature T= 100 ~1200 K

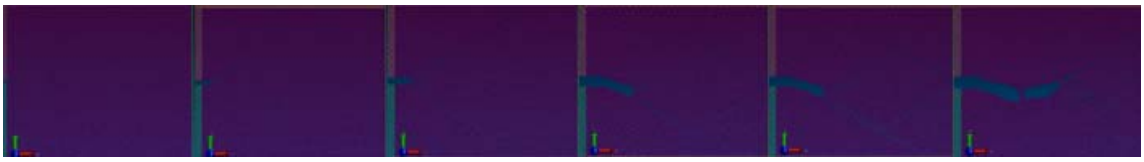

Figure 9. Crack growth process at 300 K with incremental load cycles N=10~16

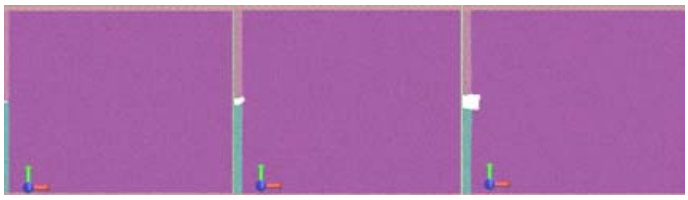

Figure 10. Crack growth process at 900 K with incremental load cycles N=10,15,20

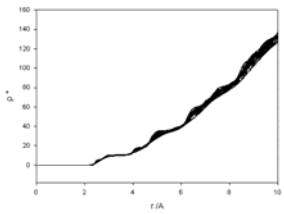

Figure 11. Number density integration curves

The RDF curves correspond to crack growth at 200 K,300 K,500 K,700 K,900 K and 1100K are illustrated in Figure 12. It shows that the RDF curve reduces with increasing temperature. The changing patterns of maximum value or peak of RDF are plotted in Figure 13. All the curves have the same fixed oscillating modes but with different amplitude peak values. Only during the later stage of crack growth, there are a little phase shift. It is the results of large material plastic

deformation.flow accompanying an increasing crack tip opening displacement. During fatigue cycles increase not only the crack size became largebut also the peak values of corresponding RDF curves reduced continuously.

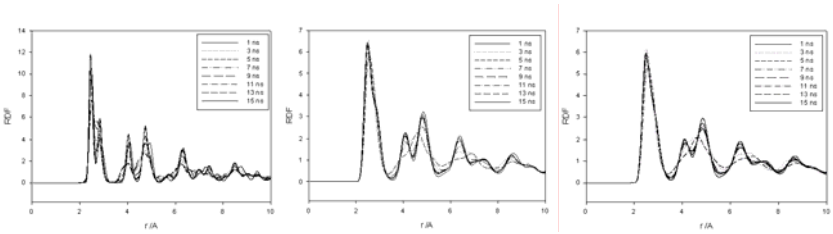

Figure 12. The RDF curves at 300 K, 900 K and 1100 K

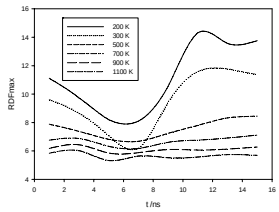

Figure 13. Relationship between the ultimate values of RDF and time

Figure 14 shows the RDF curves via temperature change at 5, 10 and 15 ns respectively. The ultimate values of RDF at different temperatures are plotted in Figure 15. Based on thermal activation theory and simulation results, the effect of temperature on crack growth can be taken into account by an expression in an exponential function form similar to expressions (1) and (2) which describes crystal plasticity. The coefficent and index values in expression are determined by the RDF peak value obtained from atomistic simulations. Here are some data processing results.

For time 5 ns: $C_m(T) = 5.2191e^{-\frac{99.53}{T}}$, with correlation coefficient R=0.91.

For time 10 ns: $C_m(T) = 4.6203e^{-\frac{234.89}{T}}$, with correlation coefficient R=0.99.

For time 15 ns: $C_m(T) = 4.9712e^{-\frac{225.61}{T}}$, with correlation coefficient R=0.97.

High regression correlation coefficients imply that the explanation and the used function form for considering the temperature influence on crack growth are appropriate.

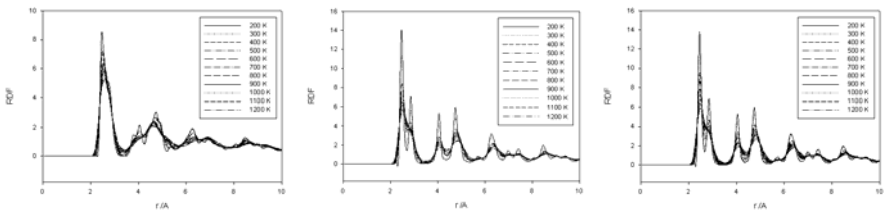

Figure 14. RDF curves via temperature change at 5 ns, 10ns and 15 ns

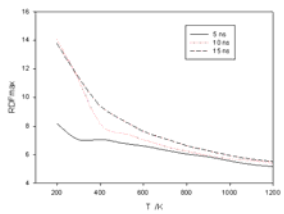

Figure 15. Relationship between the ultimate values of RDF and temperatures

5. Conclusive remarks

In this paper crack growth behaviors and fracture in α-Fe under different temperatures through molecular simulations have been investigated using Large-scale Atomic Molecular Massively Parallel Simulator code.

The mode I crack growth behaviors of an edge crack specimen under constant strain rate control at different temperatures have been investigated. A new image enhancement technique has been proposed to multiply the stripes of dislocation slip bands. It has been found that the temperature significantly affects the crack growth rate. As the temperature increases, the crack growth decreases. The results show that the mechanisms at the crack tip are sensitive to temperature and the boundary conditions.

The simulation results show that the crack growth behavior under cyclic loading was related to temperature, loading mode and cyclic loading period.

We performed atomistic simulations to study the relationship between RDF and crack growth behavior under a wide range of temperatures. Based on thermal activation theory and simulation results, the effect of temperature on crack growth can be taken into account by an expression in an exponential function form which describes crystal plasticity. The coefficent and index values in expression were determined by the RDF peak value obtained from atomistic simulations. The simulation results show that the crack growth process is highly dependent on the temperature.

References

[1] Wiki - Wikipedia, the free encyclopedia:en.wikipedia.org/wiki/Wiki

[2] J. L. Rempe and D. L. Knudson. High Temperature Thermal and Structural Material Properties for Metals used in LWR Vessels. Proceedings of ICAPP 2008. Anaheim, CA USA, June.2008.

[3] Ryosuke Matsumoto, Michihiko Nakagaki, Akihiro Nakatani and Hiroshi Kitagawa. MOLECULAR-DYNAMICS SIMULATION OF CRACK GROWTH WITH CRYSTAL NUCLEATION IN AMORPHOUS METAL. European Congress on Computational Methods in Applied Sciences and Engineering, ECCOMAS 2004.

[4] Yuan Gao, Cheng Lu, Guillaume Michal, Anh Kiet Tieu. A Study of Crack Propagation in BCC Iron by Molecular Dynamics Method. Key Engineering Materials, 385-387, 2008,453.

[5] Inga Ringdalen Vatne, etc..Quasicontinuum simulation of crack propagation in bcc-Fe. Materials Science and Engineering A 528 (2011) 5122–5134.

[6] V.A. Borodin, P.V. Vladimirov. Molecular dynamics simulations of quasi-brittle crack development in iron. Journal of Nuclear Materials 415 (2011) 320–328

[7] Ya-Fang Guo, Dong-Liang Zhao. Atomistic simulation of structure evolution at a crack tip in bcc-iron. Materials Science and Engineering A 448 (2007) 281–286.

[8] M.F. Horstemeyer, D. Farkas, S. Kim, T. Tang, G. Potirniche. Nanostructurally small cracks (NSC): A review on atomistic modeling of fatigue. International Journal of Fatigue 32 (2010) 1473–1502

[9] Tian Tang, Sungho Kim, J.B. Jordon, M.F. Horstemeyer , Paul T. Wang. Atomistic simulations of fatigue crack growth and the associated fatigue crack tip stress evolution in magnesium single crystals. Computational Materials Science 50 (2011) 2977–2986.

[10] Tian Tang, Sungho Kim, M.F. Horstemeyer. Fatigue crack growth in magnesium single crystals under cyclic loading: Molecular dynamics simulation. Computational Materials Science 48 (2010) 426–439.

[11] D. Terentyev, E.E. Zhurkin, G. Bonny.Emission of full and partial dislocations from a crack in BCC and FCC metals:An atomistic study. Computational Materials Science 55 (2012) 313–321.

[12] Yue Fan, Akihiro Kushima, Sidney Yip, and Bilge Yildiz. Mechanism of Void Nucleation and Growth in bcc Fe: Atomistic Simulations at Experimental Time Scales. PRL 106, 125501 (2011) PHYSICAL REVIEW LETTERS.

[13] Gao, Y, Lu, C, Tieu, AK Zhu. Molecular Dynamics Simulation of Crack Propagation on Different Slip Planes of BCC Iron. International Conference on Nanoscience and Nanotechnology, ICONN 2008,Melbourne, 25-29.
[14] Alena Uhnakova,Ann Machova,Petr Hora. 3D atomostic simulation of fatigue behavior of a ductile crack in bcc iron. International Journal of Fatigue. 33(2011) 1182-1188.
[15] Frenkel & Smit. Understanding Molecular Simulation-From Algorithms to Applications. Academic Press. 1996.
[16] LAMMPS Molecular Dynamics Simulator: lammps.sandia.gov.
[17] VMD - Visual Molecular Dynamics, www.ks.uiuc.edu/Research/vmd/
[18] D. Caillard and J.L. Martin. Thermally Activated Mechanisms in Crystal Plasticity. London: PERGAMON, An Imprint of Elsevier,2003.

Comparing Crack Growth Testing and Simulation Results Under Thermo-Mechanical Fatigue Conditions

Chris Timbrell[1], Ramesh Chandwani[1,*], Steve Jacques[2], Lee Waterhouse[2], Andrew Wisbey[2], Steve Williams[3]

[1] Zentech International Limited, 590b Finchley Road, London, NW11 7RX, UK
[2] Amec Technical Services (was Serco), Walton House, Birchwood Park, Risley, Warrington, Cheshire. WA3 6GA, UK
[3] Rolls-Royce plc, PO Box 31, Derby. DE24 8BJ. UK
* Corresponding author: ramesh@zentech.co.uk

Abstract As the need for improved prediction of component life and development of new materials for use at high temperatures becomes more demanding, there is increasing requirement for a detailed understanding of thermo-mechanical fatigue (TMF) behaviour including the combined effects of fatigue and dwell on the overall crack growth rates under such conditions.
To generate experimental TMF crack growth test data, a conventional servo-electric load frame, used in combination with a radiant lamp furnace, has been employed. The method for the measurement of crack growth under the TMF load cycle is also described. The performance of the experimental method is demonstrated with trials on an advanced nickel-based superalloy, RR1000.
To reduce future testing requirements, simulation via the finite element method provides a means for crack growth prediction. This clearly requires validation with real test data at the outset. A method is described whereby separate fatigue and time dependent growth data can be combined and applied to TMF load cycles ranging from simple test cycles to full flight cycles. Results of this method used in conjunction with finite element based crack growth simulation are compared with experimental data, using the test method described above, from several TMF load cycles for RR1000 specimens.

Keywords thermo-mechanical fatigue, crack growth rates, finite element analysis, crack growth simulation

1. Introduction

The ultimate objective of simulating thermo-mechanical testing by analysis is to develop a method which can be applied to crack growth prediction during complex loading cycles. One particular application is for aerospace engine flight cycles. Such flight cycles consist of out-of-phase stress and temperature time histories having duration of order of several hours. An example is shown in Figure 1.

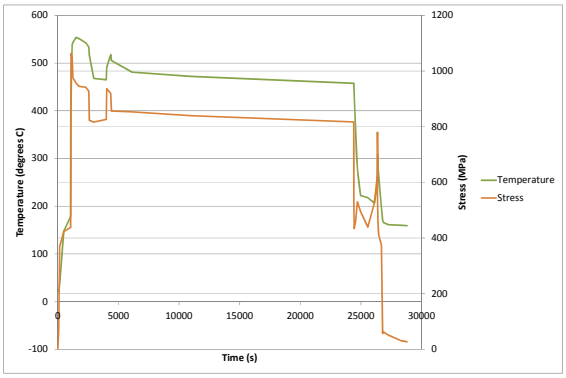

Figure 1. Typical stress and temperature time histories

For a crack located within a component experiencing such flight cycles, each point along the crack front will experience a slightly different stress and temperature time history. The salient features are:

- Peak temperature and stress occur at the end of the climb phase with the temperature

reaching a maximum at a different time to the stress.
- The cruise condition has a relatively uniform stress and temperature.
- Additional local fluctuations in stress and temperature may occur depending upon manoeuvres carried out during the flight

2. Development of the Test Facility

In the work presented here a new fatigue crack growth test facility has been developed and this is briefly described. There are three essential elements in the provision of thermo-mechanical fatigue crack growth testing:

1. an adaptable and stable mechanical load application system
2. a responsive heating system
3. a suitable crack monitoring system

A standard servo-electric test frame was used for the load application system, because of the long term load stability and previous experience with this equipment. Appropriate calibration of the load cell [1] was undertaken, along with checking the load-train alignment [2].

Figure 2. The general test piece arrangement within the radiant lamp furnace

A radiant lamp furnace was decided to be the most appropriate heating system for this application (rather than induction/RF heating) because of the need to obtain a uniform temperature profile around the cracked test piece. Thus a 12kW furnace, with 12 lamps (~250 mm long) vertically aligned around the test piece (Figure 2), was installed on the test frame.

A reasonably conventional crack length monitoring approach was used - applying electrical DC potential difference measurements and then cross-calibrated against the physical crack length. The relatively simple thermal cycles required initially (Figure 3) were consistent with this method. A constant current (DC – 20A) source was used.

3. Test Technique Development

There is currently no standard methodology for the measurement of fatigue crack growth rates under TMF conditions. However, a proprietary test method [3], based upon an ASTM standard [4], but using a square section corner crack test piece; has formed the basis of the new test technique. The second part of the test technique that is required here is the application of the desired thermal cycle (and mechanical load). A related code-of-practice [5] for strain controlled TMF testing has been used to standardise the method of calibrating the thermal cycle applied to the test piece.

Bespoke control software was also developed to perform and record these tests.

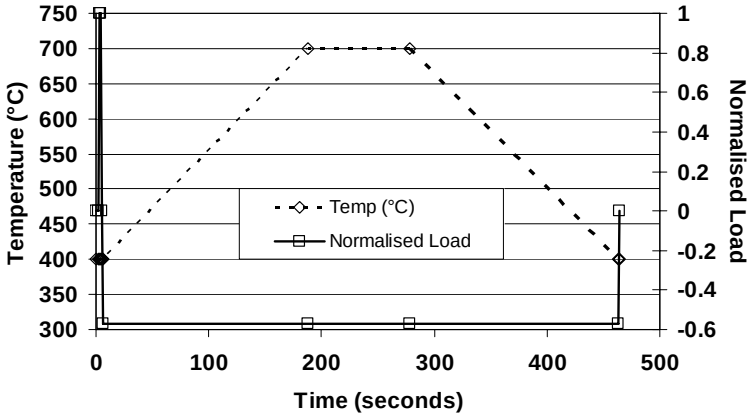

Figure 3. The desired load (normalised) and temperature cycle for the measurement of crack growth rate

3.1 Temperature Measurement

Dynamic temperature measurement during TMF, when using radiant lamp furnaces, requires a reliable experimental method and standard mineral insulated N type thermocouples have been used but these require careful control of shielding from direct radiant light on the thermocouple tip.

Spot-welded N type thermocouples (i.e. thermocouple wires spot-welded onto the specimen surface ~1 mm apart, as recommended in [5] and location shown in Figure 4) have been used to calibrate the thermal behaviour of the test. These are thought to provide the most accurate test piece temperature but cannot be used during the test because of the risk of inducing cracks.

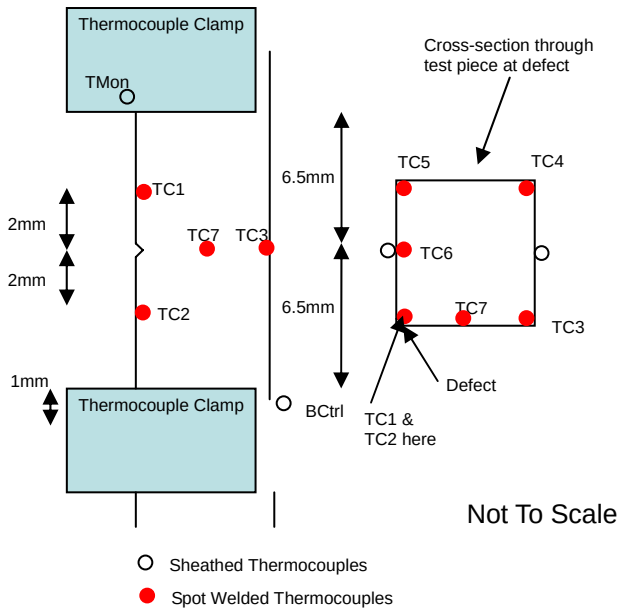

Figure 4. Schematic of the placement of the thermocouples for the TMF thermal trials

3.2 Thermal Cycle Calibration

Prior to TMF testing, there were two calibration trials required:

- to demonstrate that the temperature variation (gradient) was less than 10°C throughout the desired thermal cycle, using the spot welded thermocouples located as shown in Figure 4.

- to cross-correlate the test piece temperature, measured by a spot-welded thermocouple (e.g. TC7 in Figure 4) with the controlling sheathed thermocouples and ensure that the thermal and load cycles were correctly applied and synchronised.

3.3 Test Set-Up

The test piece had a square section (7 x 7 mm), with a corner notch introduced into the centre of a 20 mm parallel gauge length. The sheathed thermocouples were attached as shown before and ~63µm diameter Pt wires were then spot-welded to the test piece surface to monitor the PD across the crack. The sample was pre-cracked with load shedding to reduce the stress intensity factor below that of the desired starting stress intensity factor. Once the thermal performance on the two sheathed thermocouples matched that previously observed during the calibration, then it was possible to commence the test.

4. Crack Growth Rate Measurements and Facility Demonstration

To calculate the crack lengths and growth rates it was found that fitting a polynomial to the PD measurements provided the best way to generate reasonable data. A simple linear relationship between the crack length and the PD measurement is assumed for this procedure. The stress intensity factors were calculated using proprietary fits for the "geometry dependent compliance factor" (Y_n) within the basic equation:

$$\Delta K = \Delta\sigma . Y_n . (\pi . a)^{1/2} \quad (1)$$

- where ΔK = change in stress intensity factor, $\Delta\sigma$ = the change in applied stress, Y_n= a geometry dependent compliance factor and a = crack length. Only the tensile portion of the loading was used in the stress intensity factor calculation and hence a maximum stress intensity factor is shown in the plot against the normalised da/dN (Figure 5).

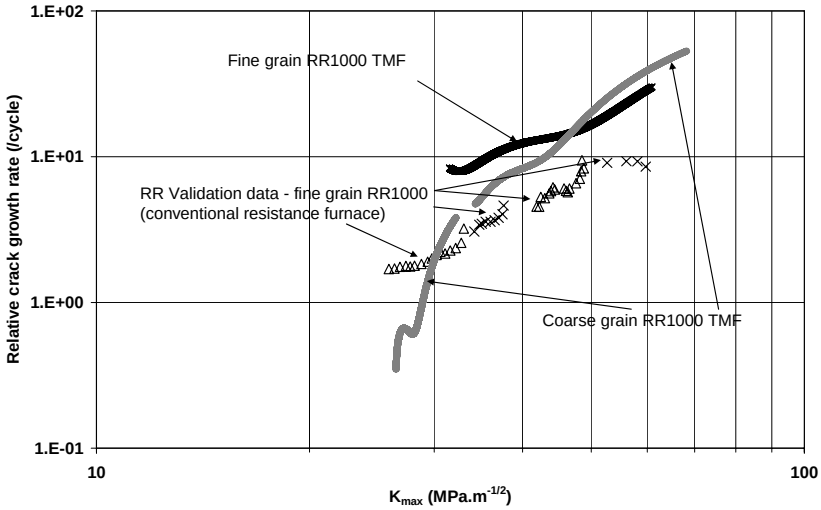

Figure 5. Plot of relative crack growth rate again the maximum stress intensity factor for two microstructural variants of RR1000

The final stage of the facility development was to demonstrate its operation and compare it with existing data obtained using a conventional resistance furnace. This demonstration was undertaken using an advanced nickel base superalloy known as RR1000, used for gas turbine disc applications and manufactured using a powder metallurgy and forging process. These initial trial tests showed reasonable agreement with existing data, although somewhat higher rates were measured with the

new facility. Following the initial demonstration, the RR10000 material in a coarse grained condition was also tested and this data is also shown on Figure 5, highlighting the potential benefit from this material, compared with the fine grained variant. All of the crack growth modelling was based upon the coarse grained variant of RR1000 and a range of additional thermal/load cycles were evaluated experimentally and compared with the modelled behaviour below.

5. TMF Crack Growth Simulation Procedure

The approach often used for calculating the combined effect of fatigue and time dependent crack growth is a linear summation through the load cycle of the separate fatigue and time contributions to the overall growth [6-8] to give the effective overall growth rate for a single load cycle:

$$\left(\frac{da}{dN}\right)_{total} = \left(\frac{da}{dN}\right)_{fatigue} + \left(\frac{da}{dN}\right)_{time} \tag{2}$$

The way in which this expression is used in the literature often relates to simple repeated loading waveforms with a single cyclic event e.g. ramp-up, hold time, and ramp-down. [9] presents a summary of approaches used by several authors. However, for a general and complex loading cycle such as the one in Figure 1, the load history and resulting stress intensity factors are defined by a series of data points which do not conform to a simple waveform. It is then necessary to generalize Eq. (2) to account for major and minor fatigue cycle effects within the overall load cycle as well as the time history of load variation. This generalization can be written as:

$$\left(\frac{da}{dN}\right)_{total} = \sum_{1}^{fatigue\ cycles}\left(\frac{da}{dn}\right) + \int_{load\ cycle}\left(\frac{da}{dt}\right)dt \tag{3}$$

where *da/dn* is the growth rate due to an individual fatigue cycle within the total load cycle and *da/dt* is the instantaneous time dependent growth rate at some time t within the total load cycle. Summation of Eq. (3) over multiple load cycles provides the accumulated crack growth history:

$$da = \sum_{1}^{load\ cycles}\left[\left(\frac{da}{dN}\right)_{total}\right] \tag{4}$$

In order to carry out this summation, two sets of data must be provided to an appropriate integration scheme: (1) the time history of stress intensity factor and temperature for points on the crack front; (2) the crack growth laws for calculating instantaneous da/dn and da/dt values.

5.1 Integration scheme

For simple 2D geometries where a handbook K solution is available, it is possible to obtain K vs t with a combination of a spreadsheet and results from finite element analyses of an uncracked component. This procedure is used in-house at Rolls-Royce and has been used to validate the finite element based implementation described below [10]. For general cases with an arbitrary 3D crack front, the finite element method can be used to provide the K solution as a function of time. In using this approach, a finite element model containing a particular crack size is analysed through a full load cycle. The results of the analysis can be used to provide a K vs time history for each crack front node. The time histories can then be cycle counted to extract discrete cyclic events. A typical (normalized) K time history and the cyclic events associated with it are shown in Figure 6.

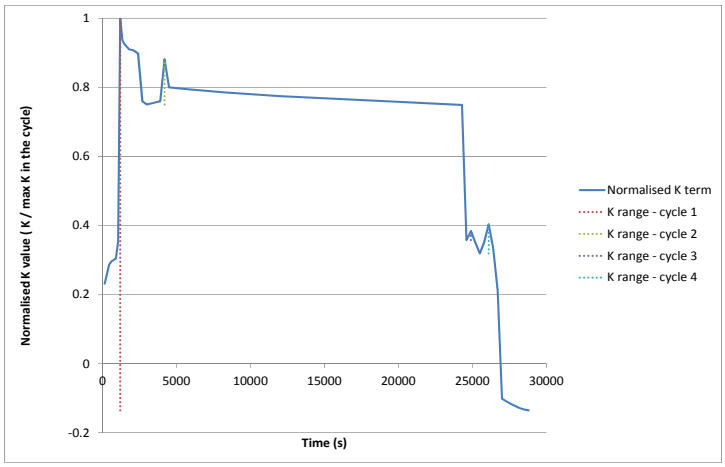

Figure 6. Normalised K time history and cyclic events

The calculation of crack growth for a single crack front position through one load cycles using Eqn. 2 and Eqn. 3 then proceeds by integrating the sequence of K vs t segments with discrete da/dn effects added as the fatigue cycles occur. The procedure of extracting a full K vs t time history from a finite element analysis and carrying out a combined fatigue and time integration has been implemented for a general 3D crack in version 7.8 of Zencrack [11]. A number of aspects of the integration process cannot be described fully here but are mentioned briefly:

- The finite element analysis provides K vs t data for one crack size and one load cycle. The integration scheme modifies the basic K vs t history to account for changes due to the increased crack size as the crack grows. When the mesh is updated to a new crack position and submitted for a new finite element analysis, a new baseline K vs t solution is generated.
- The definition of cyclic events as a result of the cycle counting process will, in general, lead to different temperatures at minimum and maximum conditions for a fatigue cycle. When calculating da/dn for the cycle, an appropriate temperature assumption must be made.
- Mode mixity and local changes of growth direction through the load cycle are possible.

Two examples of integration output from this process are shown in Figure 7. The da/dt contributions are only non-zero when the temperature is above the threshold temperature defined for the da/dt growth law. The first (and largest) cyclic event produces a visible instantaneous (vertical segment) on the da plot. Cyclic events 2, 3 and 4 have much lower da/dn values and the vertical segment da contributions from them are too small to be seen on the scale of this figure.

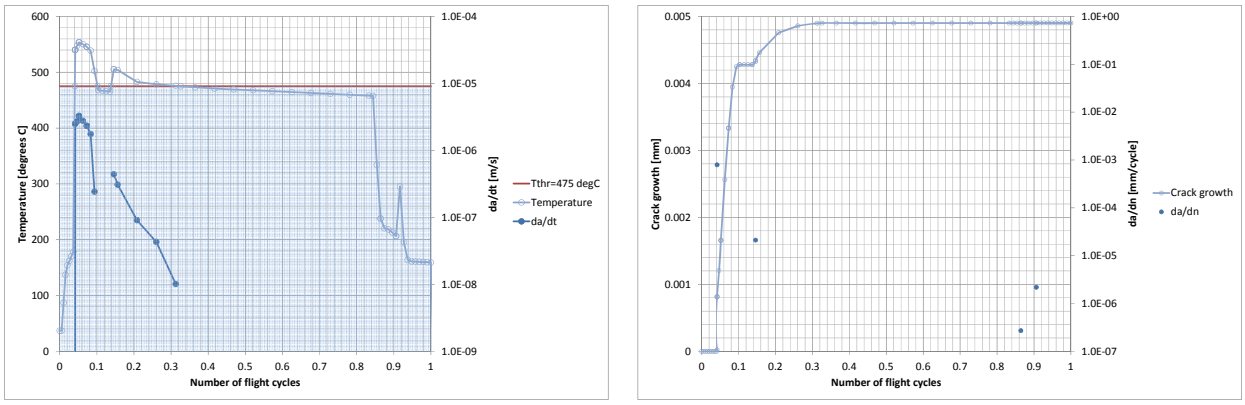

Figure 7. T, da/dt, da/dn and da through integration of a load cycle

5.2 Crack Growth Laws

The practical implementation of a combined fatigue and time dependent crack growth integration scheme using a linear summation model requires use of meaningful crack growth data. Baseline fatigue crack growth data is available in many forms but the combined use with time dependent data is more challenging. The approach used here is the use of isothermal testing to derive temperature dependent growth laws which can be applied for non-isothermal cases. Results for the simulation of the non-isothermal tests using this isothermally derived data can then be compared to the actual non-isothermal TMF test results.

A number of authors have reported the use of a rate dependent Arrhenius law for addressing temperature dependency in time dependent crack growth data [12,13]. This type of law has been implemented in Zencrack as a "COMET" crack growth law [10]. This equation (Eq. (5)) takes account of the synergetic interaction of **C**reep, **O**xidation, **M**icrostructure, **E**nvironment and **T**emperature through the definition of the D coefficient. A and B are temperature independent material constants, n is a temperature dependent material parameter and T_C is the temperature in °C. A full description of the law and a process for determining A and B is given in [10].

$$\frac{da}{dt} = D\left(K\right)^n \quad , \quad D = Ae^{\left(\frac{-B}{Tc+273.15}\right)} \tag{5}$$

6. Application of Simulation Procedure to TMF Test Specimens

The geometry for the test specimen is shown in Figure 8. This figure also shows an initial cracked mesh and a typical mesh with an advanced crack position. The specimen contains a central 7mm square cross-section into which the starter crack is located (at the mid-length position). The finite element model is a half symmetry model with the crack introduced at the symmetry plane. An uncracked Abaqus model containing C3D20 elements is created and the crack is introduced by Zencrack. The crack tip is modelled with collapsed crack front elements having quarter point nodes. The load is applied at a single point and distributed onto the cylindrical outer surface of the end of the model using a distributed coupling constraint. The load and temperature time histories are defined using *AMPLITUDE definitions. For these analyses the temperature changes are deemed to be instantaneous throughout the body (i.e. the temperature is uniform through the model at any time instant). The Abaqus *CONTOUR INTEGRAL option is used to calculate energy release rates along the crack front through the time history. The analysis uses temperature dependent Young's modulus and Poisson ratio for coarse grained RR1000. Temperature dependent Walker coefficients are used for the fatigue law and a COMET law is used for the time dependent growth law. The cracked model is analysed using Abaqus and the full time history results are extracted and processed by Zencrack using the procedure described in section 5. The crack growth is calculated and the mesh updated. This process repeats to simulate crack growth in the specimen.

Several TMF load cycles were defined for testing and simulation. The temperature and normalized load variations for the cycles designated 1, 3, 4a, 4b, 4c and 4d are shown in Figure 9. Due to project time constraints not all tests were completed. Simulation results in section 7 are presented for all load cycles with test results available for cycle 1, 3 and 4d. A 400°C isothermal load cycle using the load variation of cycle 3 is also presented in the results.

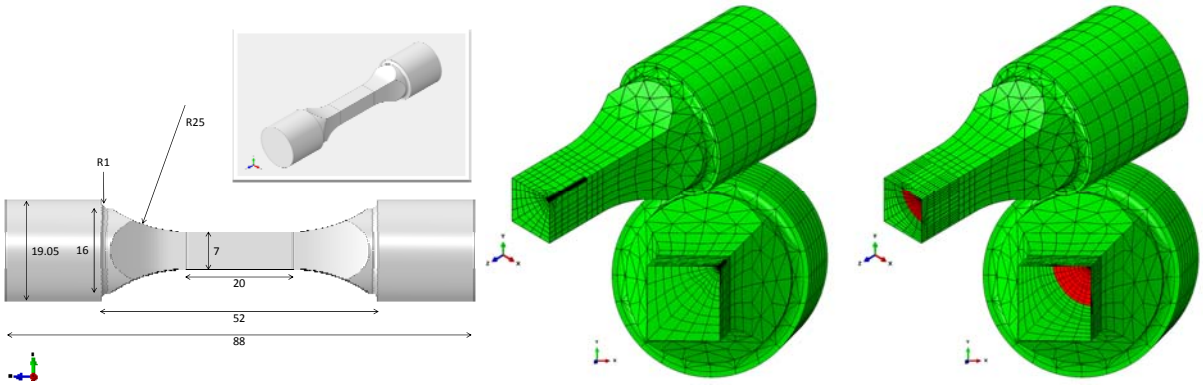

Figure 8. Geometry and typical meshes for initial (left) and advanced (right) crack positions

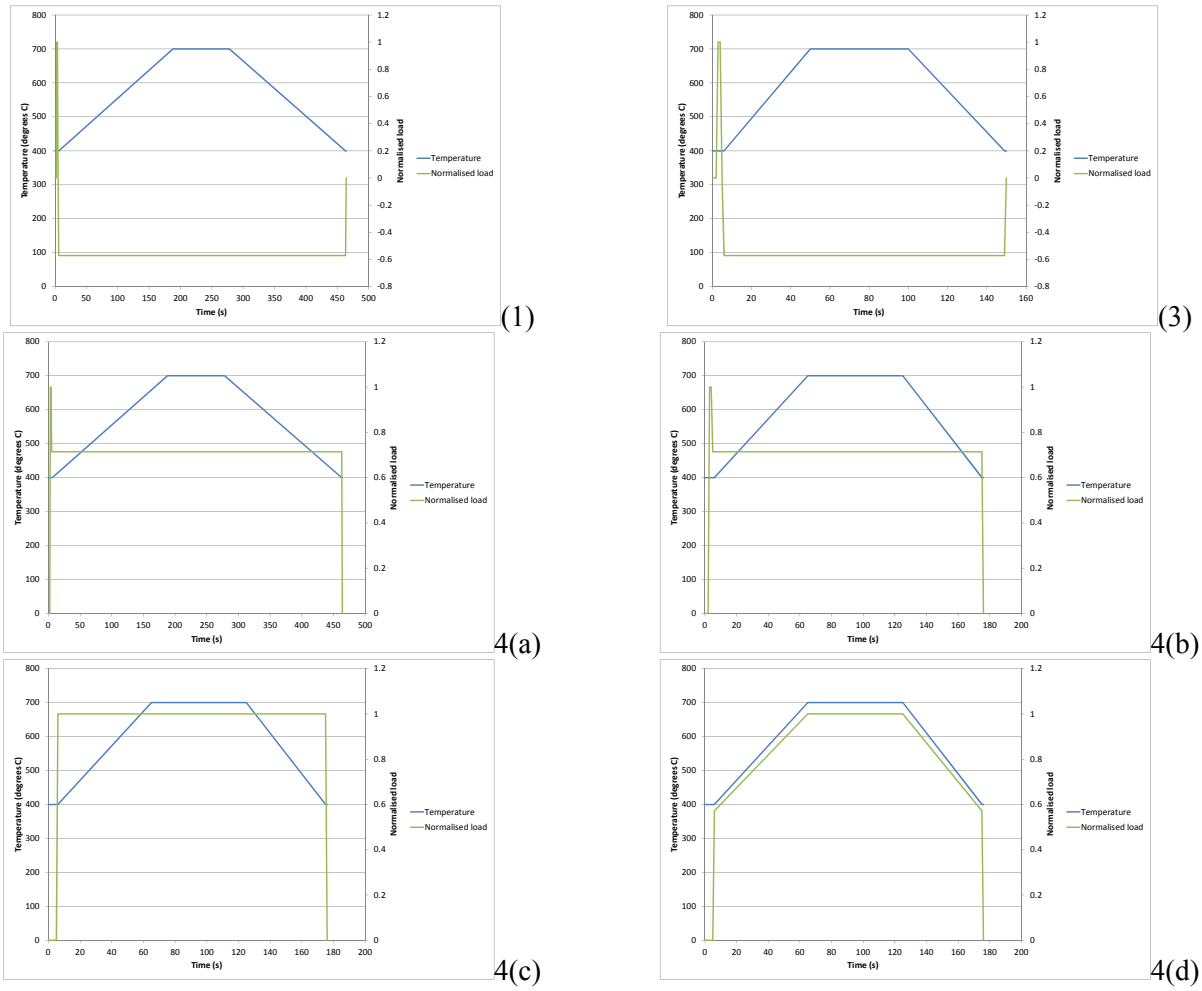

Figure 9. Definition of TMF cycle 1, 3, 4a, 4b, 4c and 4d

7. Simulation Results Compared With Test Results

The test and simulation results are presented as relative da/dN against K_{max} in Figure 10 and Figure 11. The da/dN value is total effective da/dN per TMF cycle. The K_{max} value is the maximum K for the TMF load cycle.

The load and temperature variations in cycles 1 and 3 are the same – the difference being that cycle 1 has duration of 464s compared to 300s for cycle 3. For both these load cycles, the applied load is

compressive when the temperature is above the threshold for time dependent crack growth to become active i.e. the value of da/dt is always zero in the simulation. Therefore, simulation results for cycles 1 and 3 are effectively dependent only upon the fatigue cycle which occurs during the load cycle. This fatigue cycle is the same for cycles 1 and 3 and so the simulation results for cycles 1 and 3 are identical in Figure 10. The test results for these two cycles are also similar and show good agreement with the simulation. Cycle 4d presents a more interesting case as the temperature is above the threshold for time dependent growth for about 80% of the cycle duration and during this time the load is either increasing, at maximum hold value or decreasing. Therefore time dependent growth can be expected.

Simulation results for all cycles are shown in Figure 11. On this scale, cycle 4c appears to have the same result as cycle 4d. However, the cycle 4c result is slightly higher. This is the expected outcome since, although the temperature histories for the cycles are the same, cycle 4c has a longer period at maximum load than cycle 4d and hence more time dependent growth is expected. The additional time dependent growth is however relatively small as the extra time at maximum load is in the region close to the temperature threshold for time dependent growth (i.e. da/dt will be small even if K is high). The result for cycle 4a falls above cycle 4b. Again this is not an unexpected result: cycle 4a has a longer period than 4b with extra time spent accruing time dependent growth at high temperature. Cycle 4a falls below 4c. The maximum load level for 4a is lower than for cycle 4c but the period is greater. The trade-off between high load and longer duration in this case has the result that the high load short duration of cycle 4c produces a higher overall growth rate (i.e. higher da/dt values).

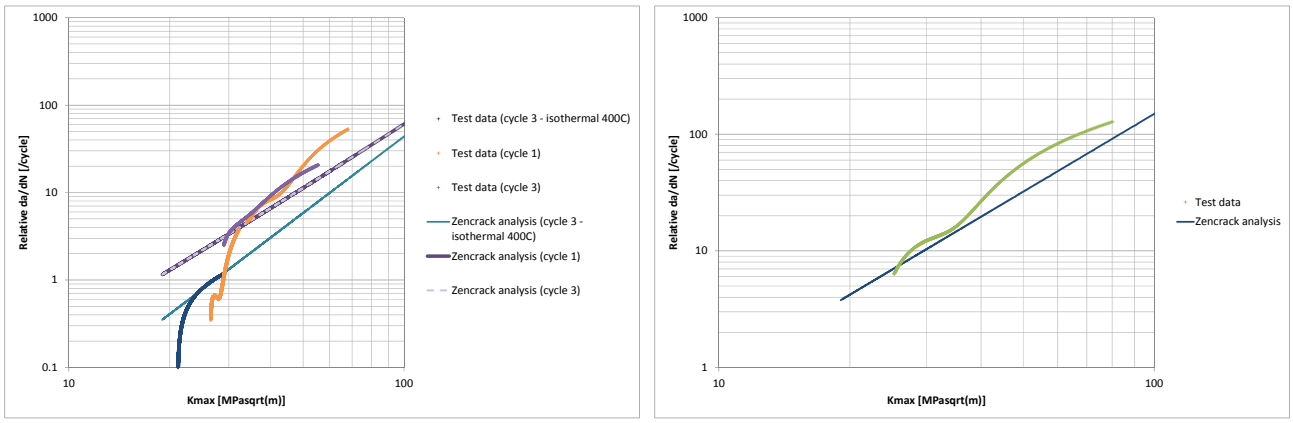

Figure 10. Test and simulation results for cycles 1 and 3 (left) and 4d (right)

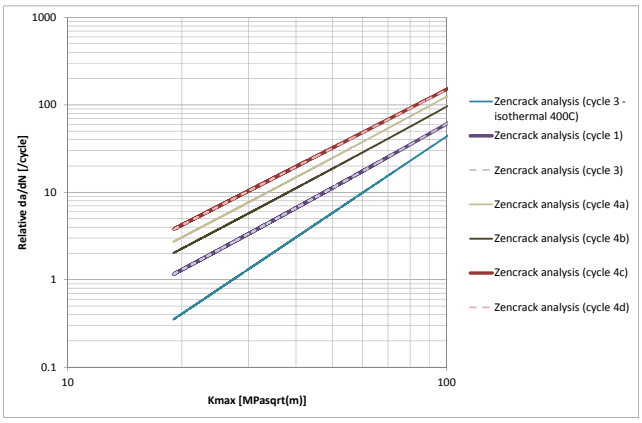

Figure 11. Simulation results for cycles 1, 3, 4a, 4b, 4c and 4d

8. Summary

Development of a TMF test facility has been demonstrated and a simulation technique has been developed to predict TMF crack growth in test specimens based on growth laws determined from isothermal tests. The simulation technique is a general one which can be applied to complex loading scenarios applied to real components. Only a small number of TMF test results are so far available but initial comparisons between test and simulation are encouraging. Additional test results and simulation comparisons are required to further verify the simulation approach.

Acknowledgements

The authors would like to acknowledge the financial support of the UK Technology Strategy Board (TSB) and the Ministry of Defence (MoD) project called "Developing Improved Service Propagation Lives in Arduous Cyclic Environments (TP/8/MAT/6/I/Q1525K)" and Rolls-Royce plc.

References

[1] British Standards Institution, "Metallic materials – verification of static uniaxial testing machines. Part 1: Tension/compression testing machines – Verification and calibration of the force-measuring system", BS EN ISO 7500-1:2004.
[2] "A procedure for the measurement of machine alignment in axial testing", VAMAS Report No. 42, ISSN 1016-2186, February 2003.
[3] F.J. Horton, "Crack propagation in corner-crack test pieces – test procedure", Rolls-Royce plc Materials and Mechanical Methods MMM31002, Issue 1, 15 May 1995.
[4] ASTM E647-08e1, "Standard test method for measurement of fatigue crack growth rates".
[5] European Commission Directorate-General Joint Research Centre – Institute for Energy, "Validated Code-of-Practice for Strain Controlled Thermo-mechanical Fatigue Testing", EUR 22281 EN.
[6] J. Gayda, T.P. Gabb, R.V. Miner, Fatigue crack propagation of nickel-base superalloys at 650°C, NASA Technical Memorandum 87150, 1985.
[7] T. Nicholas, T. Weerasooriya, Hold-time effects in elevated temperature fatigue crack propagation, in: Fracture Mechanics: Seventeenth Volume, ASTM STP 905, J. H. Underwood, et al, Eds., American Society for Testing and Materials, Philadelphia, 1986, p. 155
[8] T. Nicholas, M.L. Heil, G.K. Haritos, Predicting crack growth under thermo-mechanical cycling, Int. J. Fracture, 41 (1989) 157-176.
[9] C. Moura Branco, A. Sousa e Brito, J. Byrne, Life extension methodology based on creep-fatigue models, RTO AVT Workshop, Corfu, Greece, Oct 5-6 1998, in: "Qualification of Life Extension Schemes for Engine Components", ISBN 92-837-1012-6.
[10] C. Timbrell, R. Chandwani, D. MacLachlan, S. Williams, A time dependent crack growth law for high temperature conditions, NAFEMS European Conference: Multiphysics Simulation, Frankfurt, Germany, Oct 16-17 2012.
[11] Zencrack 7.8-1, Zentech International Limited, UK.
[12] D.A. Jablonski, J.V. Carisella, R.M. Pelloux, Fatigue crack propagation at elevated temperatures in solid solution strengthened superalloys, Metallurgical Transactions A, 8A (1977) 1893-1900.
[13] K. Makhlouf, J.W. Jones, Effects of temperature and frequency on fatigue crack growth in 18% Cr ferritic stainless steel, Int. J. Fatigue, 15 No. 3 (1993) 163–171.

Reliability of micro/macro- fatigue crack growth behavior in the wires of cable-stayed bridge

Keke Tang[1,2,*]

[1] Key Laboratory of Pressure Systems and Safety, Ministry of Education, School of Mechanical Engineering and Power Equipment, East China University of Science and Technology, Shanghai 200237, China
[2] Department of Engineering Mechanics, Southeast University, No.2 Si Pai Lou, Nanjing 210096, China
* Corresponding author: kktang@ecust.edu.cn

Abstract

The principle of least variance is applied to evaluate the reliability of fatigue crack growth behavior in the steel wires of Runyang cable-stayed bridge. Micro/macro- crack growth model is proposed in that both micro- and macro scale effects can be included. These features are best exhibited by the normalized generic parameters that reflect the effects of material, loading and geometry. Attention is paid to the 5mm diameter wire in cables under traffic that is reflected by the additional applied tension force. Combination of theory of least variance and the dual scale model offers a new perspective for the reliability analyses of structural systems. The aim is to demonstrate there exists a time range of high reliability for the crack length history that correspond to the least variance of the time dependent R-integrals. The results coincide with the scale range established empirically by in-service health monitoring for micro-macro cracking. Such agreements are encouraging with regard to the potential application of principle of least variance in multiscale reliability assessment for multi-component and multi-function systems.

Keywords Reliability, Least variance, Micro/macro- crack growth model, Cable-stayed bridge, Fatigue

1. Introduction

Bridges, particularly cable-stayed bridges, are the superstar of engineering world. Aesthetically, they allow for creative freedom by varying the shape of towers and arrangement of the cables. Technically speaking, the critical components in a cable-stayed bridge are clearly the cables that behave differently and act as a structure in itself. Each of the cables consists of bundles of high strength steel wires. The structural integrity is inevitably affected by the degradation of the individual cables and wires, making replacement of cables necessary and crucial events during the life span of cable-stayed bridges. For this reason alone, rational assessment of the reliability of in-service cables in structural health monitoring can be of a big concern. However, multiple factors such as material degradation, changing environment and operating conditions, in many cases, have made structural reliability hard to predict.

Fatigue crack growth behavior in wires of cables plays a substantial role in the degradation of the individual wires and cables, which stands out in the reliability analyses. Specifically for the 5mm diameter steel wires included in cables, the crack initiation and propagation are intimately related under traffic load, such that they should be treated as the same process. Fatigue damage accumulation occurs at distinctive scales. The conventional crack growth approach [1] is no longer applicable and a dual scale crack growth model in which both micro- and macro- effects are involved, should be mandated. Demonstrated in [2] are earlier researches on dual scaling. Studied in [3] was the loosening and tightening effects on the fatigue crack growth behavior of cables and wires for the cable-stayed portion of Runyang Bridge. However, emphasized here are the reliability analyses of fatigue crack growth behavior in wires. In spite of unpredictable difficulties, it is, however, desirable to let the service time span be coincident with the reliable portion. The attainment of such a goal is not straightforward because of the interactive effects of material, load and geometry. They can compensate the trade off with one another. Their delineation has been problematic. Recent works on the principle of least variance [4, 5] has shown that ‘trade-off effect’ can be made more transparent by exploring the variables including length [6-8], velocity, mass and

energy. Under extreme conditions they are expressed as large versus small; fast versus slow; thick versus thin; high versus low. The extreme conditions are those that deviate more appreciably from the mean or the average. They are regarded as being ‘least’ reliable, while the opposite being ‘most’ reliable.

Application of the least variance approach will be made to investigate the reliability aspects of the fatigue crack growth behavior in the wires of Runyang cable-stayed bridge. Dual scale fatigue crack growth model is employed. Only cable that undergoes the most severe tension under traffic will be singled out to be explored for the purpose of reliability analyses.

2. Problem statement of cable-stayed portion of Runyang bridge

The Runyang Bridge [9] consists of two major bridges that link the south bank and the north bank. The south bridge is a suspension bridge with a main span of 1,490 meters. The north bridge is a cable-stayed bridge with a main span of 406 meters. Keep in mind that current research is focused on the cable-stayed portion, compare Fig.1. The cables are mounted onto the two towers and anchored at the girders of the bridge. Due to the load variations, tightening and loosening of the cables is expected. Only tightening case for reliability analyses will be discussed in the current work.

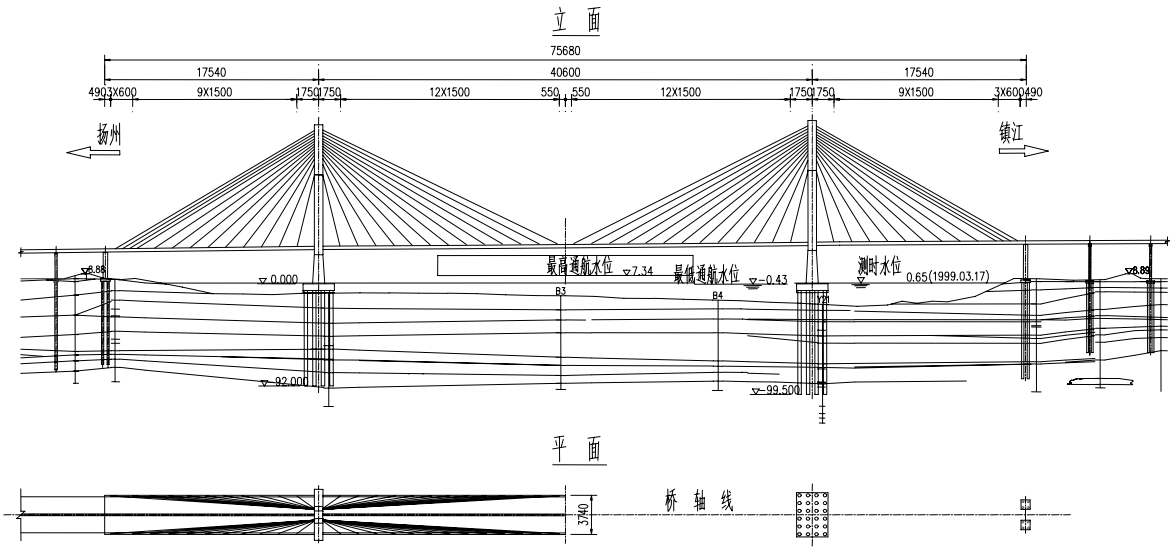

Fig.1 Cable-stayed portion of Runyang Bridge

2.1. Cable forces with and without traffic

There are 104 cables used to support the deck with the help of towers. Due to the symmetry, only a total of 52 cables on each side need to be shown here. The position of each cable is shown and numbered from left to right in Fig.2. Note the largest forces prevail in cable no.3 and no.50. Therefore only cable no.3 will be chosen to demonstrate the reliability of fatigue crack growth behavior.

A detailed description of cable construction can be referred to Fig.3. The cable consists of multiple high strength steel strands arranged in a bundle and encased in a polyethylene pipe filled with cement grout. Since the polymer carries little load and their resistance can be neglected. Each cable consists of 37 stranded steel ropes and each of the ropes contains 7 galvanized steel wires. Hence, a total of 259 galvanized steel wires construct one cable. With the diameter of steel wire being 5mm, the stress calculation thus is executed based on the effective section areas as follows

$$\sigma = \frac{F}{A_c} \tag{1}$$

in which F is the cable force and A_c being the effective cross section of each cable.

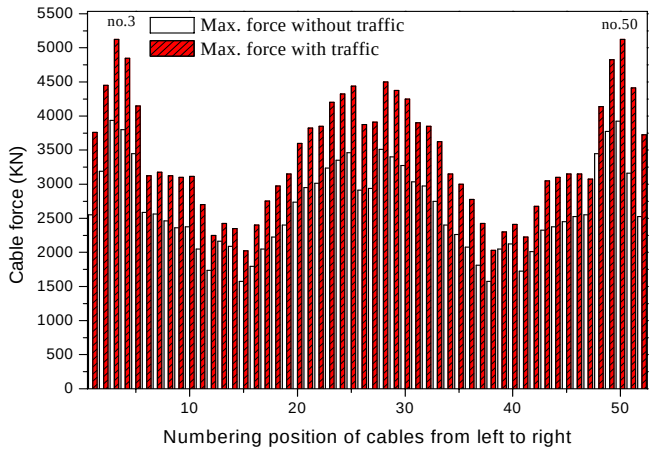

Fig.2 Maximum and minimum loads in cables with/without traffic

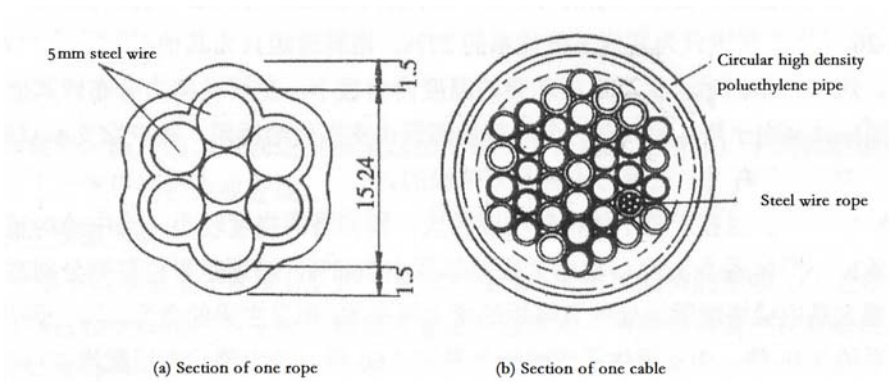

Fig.3 A typical section of the bridge cable

2.2. Tightening and loosening of cables and wires

Variations of the tension in the cable and wire, a set of $\sigma_a \sigma_m$ for the cable and wire will be defined. They are referred to be Cases I and II.

Case I $\quad \sigma_a = \eta\sigma_{\max}^{\eta} - \sigma_{\max}^{0}, \quad \sigma_m = \dfrac{\eta\sigma_{\max}^{\eta} + \sigma_{\max}^{0}}{2}$ (2)

Case II $\quad \sigma_a = \sigma_{\max}^{\eta} - \eta\sigma_{\max}^{0}, \quad \sigma_m = \dfrac{\sigma_{\max}^{\eta} + \eta\sigma_{\max}^{0}}{2}$ (3)

σ_a and σ_m respectively denote stress amplitude and mean stress. $\sigma_{\max}^{\eta}$ and $\sigma_{\max}^{0}$ in Eqs. (2) and (3) represent the maximum stress with and without traffic. Note the parameter α greater than 1 reflect the degree of cable tightening, while η less than 1 reflect the degree of cable loosening. Bear in mind that $\eta = 1.0$ stands for normal tension. Fig. 4 displays a plot of the product $\sigma_a \sigma_m$ for the cables as a function of the cable position from left to right numbered as 1 to 52. The product

$\sigma_a\sigma_m$ fluctuates according to the variations of the tension in the cables with traffic load. Notice the peaks of the curves correspond to cable no.3 and no.50 in which maximum cable forces occur.

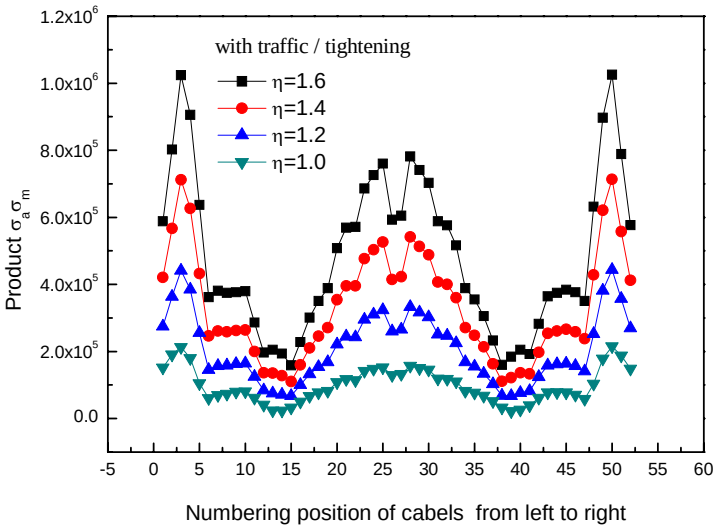

Fig.4 Product $\sigma_a\sigma_m$ of cables versus position of cables for tightening case under varying traffic

3. Multiscale micro/macro- fatigue crack growth model

3.1. Fatigue crack growth of steel wire

There are three normalized physical parameters $\sigma^*(=\sigma_o/\sigma_\infty)$, μ^* $(=\mu_{micro}/\mu_{macro})$ and d^* $(=d/d_o)$ defined in the micro/macro- fatigue crack growth model. They, respectively, reflect the influences of load, material and geometry.

$$\mu^* = \frac{\mu_{\text{micro}}}{\mu_{\text{macro}}}, \qquad d^* = \frac{d}{d_0}, \qquad \sigma^* = \frac{\sigma_0}{\sigma_\infty} \tag{4}$$

When it comes to structural applications, incidental material parameters can be absorbed by the macro empirical parameters which will be confined to two. Thus further being incorporated into the current fracture control approach expressed as follows:

$$\frac{\mathrm{d}a}{\mathrm{d}N} = B(\Delta S_{\text{micro}}^{\text{macro}})^m \tag{5}$$

where floating parameters B and m can be found by test data in a regular fatigue test. Here, B is the y-intercept and m being the slope of the curve for the straight line portion of the log-log plot of Eq. (5). The crack length can be computed by integrating Eq. (5). $\Delta S_{\text{micro}}^{\text{macro}}$ has the following expression:

$$\Delta S_{\text{micro}}^{\text{macro}} = \frac{2(1-2\nu_{\text{micro}})(1-\nu_{\text{macro}})^2\sigma_a\sigma_m a}{\mu_{\text{macro}}}\mu^*\sqrt{d^*}\sqrt{\frac{d_0}{r}}(1-\sigma^*)^2 \tag{6}$$

in which σ^* is the ratio of material restraining stress σ_0 to the applied stress σ_∞. σ^* must always be less than one. This corresponds to the threshold for the onset of crack growth. d^* is the normalized characteristic dimension compared to the microscopic length d_0. r is the radial distance from the crack tip. μ^* is the ratio of microscopic modulus μ_{micro} to the macroscopic modulus μ_{macro}. ν_{micro} and ν_{macro} respectively stand for the Poison's ratio at micro- and macro-scales.

3.2. Fatigue properties of steel wire

Macroscopic material properties such as steel can be achieved from experimental test. Refer to Table 1 for the mechanical properties of bridge steel wire.

Table 1. Mechanical properties of bridge steel wire [9]

Elastic modulus E_{macro}	Shear modulus μ_{macro}	Poisson's ratio ν_{macro}
199.81GPa	76.85GPa	0.3

Without going into the details, the floating parameters B and m are given by [10,11]

$$m = 1, \quad B = 2.15 \times 10^{-6} \tag{7}$$

Microscopic material properties cannot be achieved through specimen test as macroscopic properties do. They prevail, more specifically, at local place comparing to the big bulk of macroscopic specimen and are location dependent. The following assumptions are made:

$$\mu^* = \frac{\mu_{\text{micro}}}{\mu_{\text{macro}}} = 2, \qquad d^* = \frac{d}{d_0} = 1, \qquad \sigma^* = \frac{\sigma_0}{\sigma_\infty} = 0.3,$$

$$d_0 = 10^{-3}\,\text{mm}, \qquad \nu_{\text{micro}} = 0.4, \qquad \frac{d_0}{r} = 1 \tag{8}$$

This completes all the parameters in the micro/macro fatigue crack growth model. Crack length and velocity history thus can be explicitly illustrated.

4. Theory of least variance for reliability

Reliability is associated with the failure of a component or system to satisfy the intended function for a specified period of time. Uncertainties can have a major effect on the cause of failure. They can be attributed to degradation of material properties, variance of loading and change of environmental conditions. These changes can affect the reliability of long run predictions. Hindsight is not a solution here. It is unrealistic to overemphasize the deterministic and probabilistic aspects of life prediction. However, there is still the need to understand the physical applications of the monitored data. Crack initiation and propagation should be treated as multiscale transition process. Time increment effects also affect reliability differently for the different scale ranges such as micro to macro scale, which can be reflected by the weighted functions proposed in the theory of least variance.

4.1. R-integrals

Let n denotes the number of R-integral $R_1, R_2 \ldots, R_n$ which correspond, respectively, to

$$\int_0^{t_1} \alpha_1(t)\, p_1^{a_1}(t)dt, \int_0^{t_2} \alpha_2(t)\, p_2^{a_2}(t)dt, \ldots, \int_0^{t_1 n} \alpha_n(t)\, p_n^{a_n}(t)dt \tag{9}$$

When $a^1, a^2, \ldots, a^n$ are given, then $p_1(t), p_2(t), \ldots, p_n(t)$ are treated as ordinary functions. If $a^1 = a^2 = a^3 = a^4 = 1$, then $p_1(t), p_2(t), p_3(t)$ and $p_4(t)$ stand for the four root functions defined in the CTM/IDM theory [12,13]. They correspond, respectively, to the length, velocity, mass density and energy density. The weighted functions $\alpha_1(t), \alpha_2(t), \ldots, \alpha_n(t)$ interconnect the space-time effects at the different scale ranges. Depending on the number of time segments chosen by normalizing

$$p_1(t) = a_1(t)/a_1(0), \;\; p_2(t) = a_2(t)/a_2(0), \;\; \ldots, \;\; p_n(t) = a_n(t)/a_n(0) \tag{10}$$

Note that the initial values of $a_1(t), a_2(t), ..., a_n(t)$ at $t = 0$ are given by $a_1(0), a_2(0), ..., a_n(0)$.

4.2. Principle of least variance

As a rule, reliability counts on the continuous operation of systems in time. Since physical systems are inherently non-homogeneous, ranking the different degree of variability would be of potential solution. Identifying the least reliable space-time segment of the system operation will be made by invoking the ‘ principle of least variance’ which can be stated as:

The segment with the least variance ΔR_i *is assumed to be most reliable up to the time* t_f *of potential failure.*

The variance ΔR_i is obtained by the linear sum average (LS) of the R-integrals

$$R_{ave}^{ls} = \frac{1}{n}\sum_{i=1}^{n} R_i \tag{11}$$

Other approaches including root mean square average (RMS) or inverse linear sum average (ILS) are also the options. However, they are outside the scope of this work.

The absolute value of the deviation of each of the R_i from the average will be referred to as the variance ΔR_i. The expression for LS variance is

$$\Delta R_i^{LS} = \left| R_i^{LS} - R_{ave}^{LS} \right| \tag{12}$$

Minimizing the oscillation of $R_1, R_2, ..., R_n$ with reference to their average has been assumed to be a possible measure of system reliability. The principle of least variance identifies the time span to which ΔR_i takes the smallest values. Hence, range of reliability will be decided on the basis of linear sum average.

5. Reliability of micro/macro- fatigue crack growth history in steel wire

Conventionally three regions are divided along the sigmoidal curve for the plot of log da/dN versus log ΔK. They are referred to, respectively, as crack initiation, stable crack growth and fast fracture. Crack locally initiates from a very small length and extends slowly in a relatively stable fashion. It finally enters into the stage of fast fracture. In practical engineering, non-destructive testing measurements of the crack length are made for establishing the period of maintenance before the curve turns around the corner into the region of rapid crack propagation. The point to be made here is, there exists a region where crack grows slowly and stably is most reliable for detection, refer to Fig.5 for the range of reliability in practice.

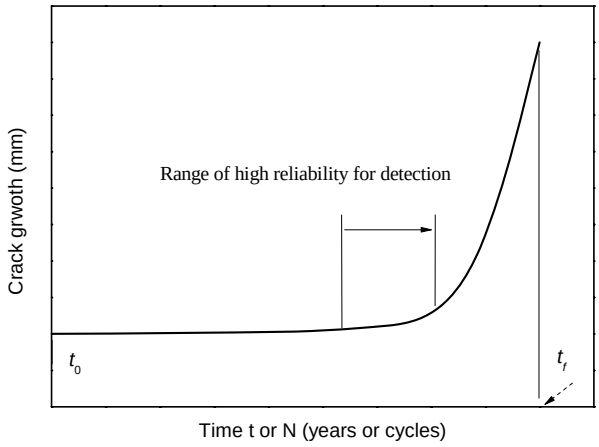

Fig. 5 Range of high reliability for fatigue crack growth

5.1. Micro/macro- fatigue crack growth in steel wire

An initial crack length of 0.2mm is taken compared to the 5mm diameter of steel wire. Keep in mind that the cables of bridges are usually replaced every 10 years. The situation also varies with the positions of the cables since they bear tremendously different cable forces under traffic. Breakage of steel wires cause the cable failure, although multiple factors such as corrosion also come into play during the operating period of bridges. Assumption of 10-year in-service of cable is made here for simplification. This gives steel wire roughly 10 years of fatigue life. Conversion of the crack length fatigue cycle history to the corresponding time history requires the specification of load frequency. The following load frequency is proposed:

$$dN / dt = 80,000 \; cycles / year \tag{12}$$

Combining Eqs (7), (8) and (12), Eq. (6) can be put into Eq. (5) for finding $a(t)$ by integration from 0 to t with an initial crack length of 0.2mm. Depicted in Fig. 6 is the graphical presentation of crack length growth history of steel wires in cables. Recall only cable no.3 is selected since it bears the biggest cable force among 52 cables listed.

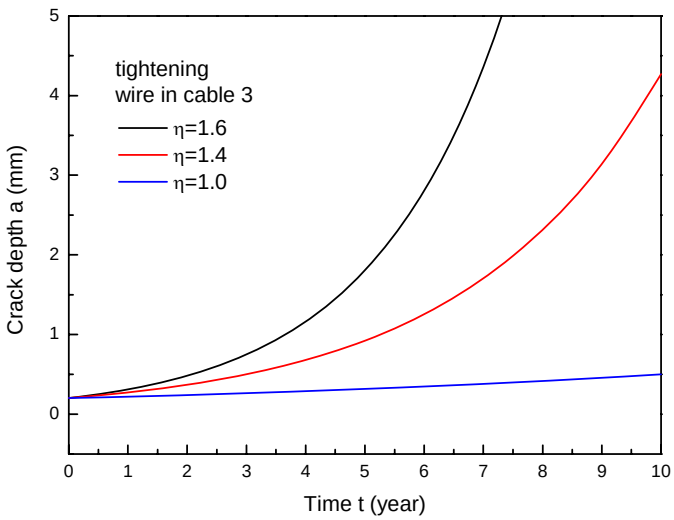

Fig.6 Crack depth a versus time t (years) for cable no.3 with tightening effects under traffic

The reference crack growth curve is given by $\eta = 1.0$ as shown in the bottom of Fig.6. It remained nearly constant for the range of 10 years. As the cable is tightened gradually with the perturbation parameter $\eta = 1.4$ and 1.6. The curves deviate from the reference with increasing crack length. The crack depth reaches 5mm approximately at 7 years for tightening coefficient $\eta = 1.6$. Even for $\eta = 1.4$, the crack depth is over 4mm after 10 years. Thus conclusion can be made that increase of cable tension tends to enhance crack growth.

5.2. Reliability of micro/macro fatigue crack growth history of steel wires

The reliability of fatigue crack growth vary during the life span. Determination of the reliable portion of fatigue crack growth will be studied by applying the principle of least variance. This will be done based on the crack growth history obtained in Fig.6.

5.2.1. Weighted functions

Notice that the fatigue life for steel wire varies with different tightening coefficients. For $\eta = 1.4$, fatigue life is approximately 10 years while it is reduced to 7 years after the increase of η

from 1.4 to 1.6. Thus different life time ranges of 0-7 years and 0-10 years should be employed.

With attention placed on seven years, seven time segments from 0-1, 1-2, 2-3, 3-4, 4-5, 5-6 and 6-7 year will be chosen for integration. In Eq. (10), $n=7$ such that the condition $a^1=a^2=...=a^7=1$ is used in Eq. (9). And same can be done to the range of 0-10 years. Ten time segments from 0-1, 1-2, …, 9-10 year will be chosen for integration. In Eq. (10), $n=10$ such that the condition $a^1=a^2=...=a^{10}=1$ is made. These conditions together with the weighted function $\alpha(t)$ in Fig.7 are needed for determining the R-integrals and variances.

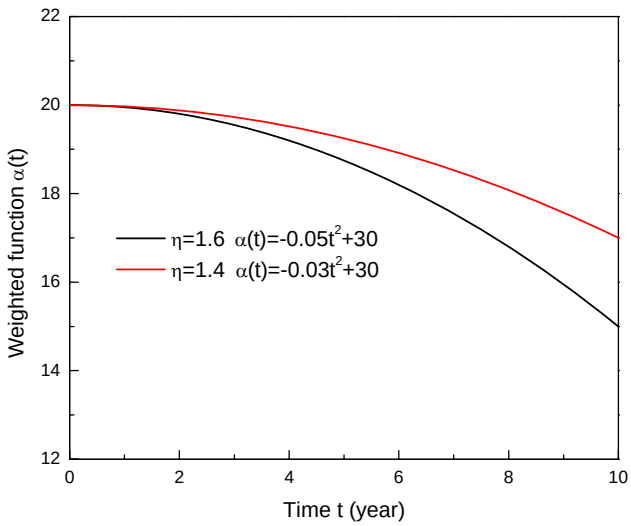

Fig.7 Weighted functions

Choice of weighted function $\alpha(t)$ depends on several factors, It is applied to adjust the time degradation effect of the root function $p(t)$. The decay function can also be seen as a description of material degradation.

5.2.2. R-integrals and variances of crack length

Application of Eqs. (9) and (10) together with the weighted functions in Fig.7, the R-integrals and the corresponding variances for the micro/macro fatigue crack growth of wire in cable no.3 are evaluated. The numerical values can be found in Tables 2-5 inclusive.

Table 2 R-integrals for fatigue crack growth with $\eta=1.4$

R_1	R_2	R_3	R_4	R_5	R_6	R_7	R_8	R_9	R_{10}	R_{ave}
23.4	31.7	42.7	57.5	77.1	103.1	137.4	182.4	241.2	317.6	121.4

Table 3 Variances for fatigue crack growth with $\eta=1.4$

ΔR_1	ΔR_2	ΔR_3	ΔR_4	ΔR_5	ΔR_6	ΔR_7	ΔR_8	ΔR_9	ΔR_{10}
98.0	89.8	78.7	63.9	44.3	18.3	16.0	61.0	119.8	196.2

Table 4 R-integrals for fatigue crack growth with $\eta=1.6$

R_1	R_2	R_3	R_4	R_5	R_6	R_7	R_{ave}
25.1	38.8	59.6	91.1	138.6	209.5	314.7	125.3

Table 5 Variances for fatigue crack growth with $\eta = 1.6$

ΔR_1	ΔR_2	ΔR_3	ΔR_4	ΔR_5	ΔR_6	ΔR_7
100.2	86.6	65.7	34.2	13.2	84.2	189.4

Depicted in Figs. 8 and 9 are the plots of non-monotonic variations of the data that can be found in Tables 2-5 for crack length. The minima are shown for both of the curves. The curves display the feature of decreasing and then increasing. Distinctive minimum are found to be around 6 years and 4.5 years, respectively. According to the principle of least variance, compare Fig.6 for the reliable portions of the fatigue crack growth. With $\eta = 1.4$, the time range before fast fracture is approximately between 5 and 7 years. Increase of tightening coefficients from 1.4 to 1.6 reduces the reliable portion to be around between 4 and 5 years. It is noticeable that variance for the range of fast fracture deviates tremendously from the average. This means that it is least reliable. The initial stage of crack initiation also possesses substantial deviation from the average. It is, however, relatively difficult for detection at such an early stage. The region of high reliability for the fatigue crack growth can be identified with the span of 5-7 years and 4-5 years, respectively. It should be pointed out that time rates and time intervals also affect the variances in a modest manner. Nevertheless, similar conclusions can be made based on the theory of least variance.

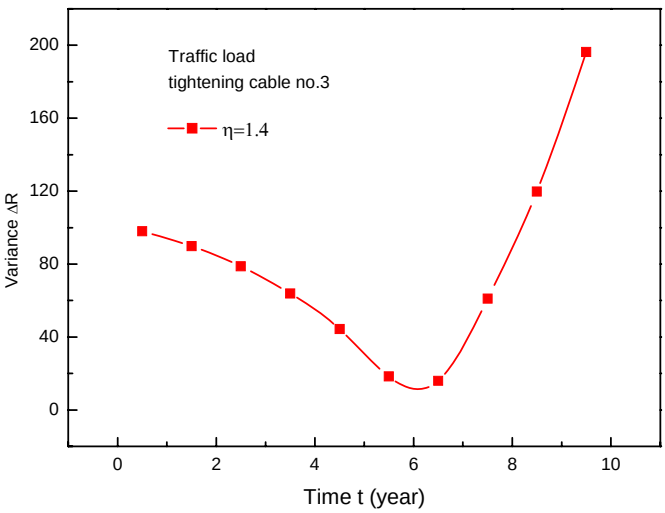

Fig. 8 Variance for crack depth with $\eta = 1.4$

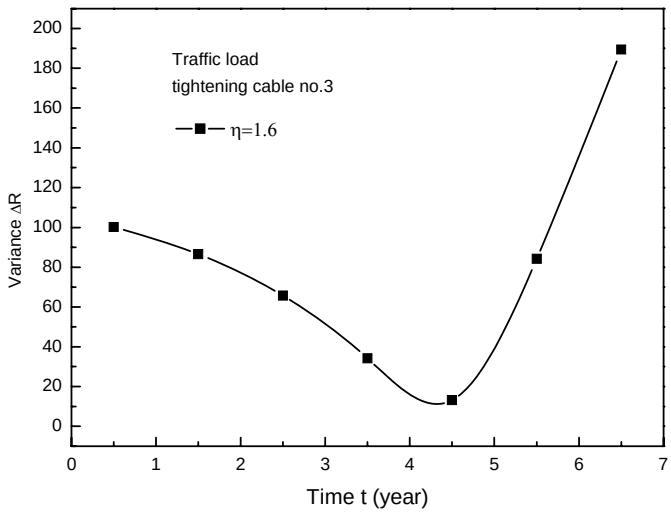

Fig. 9 Variance for crack depth with $\eta = 1.6$

6. Concluding remarks

Long-span bridge cables usually consist of thousands of high strength steel wires that are measured in millimeters. Wire breakages cause the eventual failure of cables. Fatigue degrades the life of wires and cables as well as material aging and stress corrosion. It has become one of the biggest concerns in the maintenances of bridges. Clearly, uncertainty of cable force variation in the operating period can greatly affect the fatigue crack growth behavior. One problem emerges with regard to the inspection of cables. That is, each of the cables is unique on the aspects of loads and configuration. During the operating time, some of the cables may need replacement at a time when other cables of the same bridge may still possess ample remaining life. This poses great challenge for the assessment of reliability of wires and cables.

The theory of least variance offers one of the possible solutions by proposing significant variables including length, velocity, mass and energy. Minimizing the oscillation of $R_1, R_2 \ldots, R_n$ has been assumed to be a measure of system reliability. The principle of least variance identifies the

time span to which ΔR_i takes the smallest values. By application of principle of least variance, identification of the most reliable time range to detect micro/macro- fatigue crack growth in the wires of cable has been made possible. The results coincided with the empirical practice in engineering. Over the past decades, the scale of range research interest has been extended to micro, nano and even pico effects. Scale interactive effects for the most part have not been made transparent until the space-time scale rages were extended to the extremes. These problems have been tentatively explored in the framework of principle of least variance.

With the advent of defect-detecting techniques of 21st century, structural health monitoring system (SHMS) [14] is increasingly installed in the bridges that are newly put on. Collected data are astronomical and interpretation of the field data can be more challenging, since the modern sensors are so accurate that both micro- and macro-effects are often mingled. Theory of least variance together with dual scale modern provides a potential solution for defect detection in SHM. Further applications of theory of least variance to multiscale system and structures are expected. This will be left for future studies.

Acknowledgements

Project supported by SPSFC (the Shanghai Postdoctoral Sustentation Fund, China, Grant No. G200-2R-1238) is appreciated. The author is indebted to Professor George C. Sih for his guidance.

References

[1] P. C. Paris, The growth of cracks due to variations in load. Ph. D. Dissertation, Department of Mechanics, Lehigh University, 1962.

[2] G. C. Sih, Simultaneous occurrence of double micro/macro stress singularities for multiscale crack model. J. Theoret. Appl. Fract. Mech. 46 (2006) 87-104.

[3] G. C. Sih, X. S. Tang, Z. X. Li, A. Q. Li, K. K. Tang, Fatigue crack growth behavior of cables and steel wires for the cable-stayed portion of Runyang bridge: Disproportionate loosening and/or tightening of cables. J. Theoret. Appl. Fract. Mech. 49(1) (2008) 1-25.

[4] G. C. Sih, Principle of least variance for dual scale reliability of structural systems. J. Theoret. Appl. Fract. Mech. 54 (2010) 137-140.

[5] G. C. Sih, K. K. Tang, Assurance of reliable time limits in fatigue depending on choice of failure simulation: Energy density versus stress intensity. J. Theoret. Appl. Fract. Mech. 64(2) (2010) 117-126.

[6] G. C. Sih, K. K. Tang, On-off switching of theta-delta brain waves related to falling asleep and awakening. J. Theoret. Appl. Fract. Mech. (2013) http://dx.doi.org/10.1016/j.tafmec.2013.03.001

[7] G. C. Sih, K. K. Tang, Sustainable time and stability of hippocampal and cortical EEG theta waves. J. Theoret. Appl. Fract. Mech. (2013), dx.doi.org/10.1016/j.tafmec.2013.01.001

[8] G. C. Sih, K. K. Tang, Sustainable reliability of brain rhythms modeled as sinusoidal waves with frequency-amplitude trade-off. J. Theoret. Appl. Fract. Mech. 61 (2012) 21-32.

[9] Q. B. Ou, Construction of Runyang Bridge: Cable-stayed Portion. China Communications Press, Beijing, 2005.

[10] S. Y. Wang, Z. J. Dang. Research on heavy-load high fatigue stress amplitude cable and anchorage of cable-stayed bridge. J. of Bridge Construction, 3(2002) 14-16.(in Chinese)

[11] Editorial Board, Practical Handbook of Engineering Materials. Chinese Standard Press, Beijing, 2002.

[12] G. C. Sih, Crack tip mechanics based on progressive damage of arrow: hierarchy of singularities and multiscale segments. J. Theoret. Appl. Fract. Mech. 51(1) (2009) 11-32.

[13] G. C. Sih, Ideomechancis of transitory and dissipative systems associated with length, velocity, mass and energy. J. Theoret. Appl. Fract. Mech. 51(3) (2009) 149-160.

[14] J. P. Ou, H, Li, Structural health monitoring in mainland China: review and future trends. Struct. Health Monit. 9(3)(2010) 219-231.

Development of classical boundary element analysis of fracture mechanics in gradient materials

Zhong-qi QuentinYue[1,*], Hongtian Xiao[2]

[1] Department of Civil Engineering, The University of Hong Kong, Hong Kong, China
[2] College of Civil Engineering and Architecture, Shandong University of Science and Technology, Qingdao, 266590, China
* Corresponding author: yueqzq@hku.hk

Abstract Over the last decade, the authors have extended the classical boundary element methods (BEM) for analysis of the fracture mechanics in functionally gradient materials. This paper introduces the dual boundary element method associated with the generalized Kelvin fundamental solutions of multilayered elastic solids (or Yue's solution). This dual BEM uses a pair of the displacement and traction boundary integral equations. The former is collocated exclusively on the uncracked boundary, and the latter is collocated only on one side of the crack surface. All the singular integrals in dual boundary integral equations have been solved by numerical and rigid-body motion methods. This paper then introduces two applications of the dual BEM to fracture mechanics. These research results include the stress intensity factor values of different cracks in the materials, some fracture mechanics properties of layered rocks in rock engineering.

Keywords boundary element method, generalized Kelvin solution, FGMs, fracture mechanics, singular integrals

1. Introduction

The functionally gradient materials (FGMs) are applicable to many engineering fields. In FGMs, the composite medium is processed in such a way that the material properties are continuous functions of the depth or thickness coordinate. The knowledge of fracture mechanics in FGMs is important in order to evaluate their integrity. Crack problems in FGMs have become one of the hottest topics of active investigation in fracture mechanics [1].

The boundary element method (BEM), also known as the boundary integral equation method, has firmly established in many engineering disciplines and is increasingly manifested to be an effective numerical approach. The attraction of BEM can be largely attributed to the reduction in the dimensionality of the problem and to the efficient modeling of the stress concentration. Thus, BEM can overcome the limitations associated with FEM or other numerical methods in accurately and efficiently analyzing the crack problems. Aliabadi [2] pointed out that fracture mechanics has been the most active specialized area of using BEM and probably the one mostly exploited by industry.

If the material properties of FGMs vary in a complicated form along a given direction, it would be difficult to obtain their fundamental solutions. This limits the application of the BEM to analyze fracture mechanics of FGMs. Yue [3] obtained the fundamental solutions for the generalized Kelvin problems of a multilayered elastic medium of infinite extent subjected to concentrated body force vectors, which is referred to as Yue's solution. The potential application of the solutions is to formulate the BEM suitable for the multilayered media and graded materials encountered in science and engineering.

Over the last decade, the authors have extended the classical boundary element methods (BEM) for analysis of the fracture mechanics in FGMs. The new BEM method incorporates Yue's solution into the classical BEM methods. The BEM developed by the authors can be classified into two types: multi-region BEM and single region BEM (i.e., dual BEM). In this paper, we introduce mainly the some developments of the Yue's solution based dual BEM and their applications in the fracture mechanics of the layered and graded materials.

2 A brief introduction of the multi-region BEM based on Yue's solution

Mathematical formulation and computational procedures of the multi-domain BEM have been published by Yue et al. [4,5]. The BEM discretizes a FGM layer as a system of *n* number of fully bonded dissimilar sub-layers. The Yue's solution is used as the fundamental solution to replace the classical Kelvin point load solution in conventional three-dimensional boundary element methods. As a result, any FGMs with arbitrary property gradient in depth can be examined using this BEM.

Since Yue's solution satisfies the continuous conditions at any interface, there is no need to consider any sub-layer interfaces as boundary surfaces or sub-domain interfaces in the numerical formulation of BEM. In other words, the crack problem can be straightforwardly carried out using the similar BEM procedure for the same crack in a homogeneous elastic solid of infinite extent. It is only need to generate the BEM meshes for the crack interfaces and their associated auxiliary surfaces. The auxiliary surfaces are needed since the conventional multi-region method is used in the BEM. In the computational formulation, the eight-node isoparametric elements are usually employed to discretize the boundary surfaces. The so-called traction-singular elements are used to model the singular fields around the crack tip.

Authors [5,6] used the multi-region BEM to analyze the stress intensity factors of a penny crack *parallel or perpendicular to* the interfacial layer of FGMs and the growth of the penny crack under remote inclined loads. Besides, authors [7,8] further analyzed the stress intensity factors of an elliptical crack *parallel or perpendicular to* the interfacial layer of FGMs and the growth of the penny crack under remote inclined loads.

3. Yue's solution based dual boundary element method

3.1 General

As mentioned in Section 2, the multi-region BEM based on Yue's solution has been applied for the analysis of penny and elliptical cracks in a FGM system. It can be found that the proposed method has the following drawbacks: (1) The introduction of artificial boundaries is not unique and thus cannot be implemented into an automatic procedure. (2) The method generates a larger system of algebraic equations than strictly required. (3) If artificial boundaries are located in FGMs, the unknown quantities of linear equations increase greatly because of the variations of material properties. Dual BEM can overcome the above drawbacks. Dual boundary element formulation is based on a pair of boundary integral equations (BIE), namely, the displacement and traction BIEs. The method is a single-region based, thus it can model the solids with multiple interacting cracks or damage. Although dual BEMs have been widely applied, few of the crack problems in

non-homogeneous media may be not involved. In the following, we will present a numerical implementation of the dual boundary integral equations based on Yue's solution [9].

3.2. Yue's solution based Dual BIEs

Fig. 1 shows a three-dimensional crack in a multilayered solid. By collocating the source point on the uncracked boundary, the conventional displacement BIE can be written as

$$c_{ij}(P_S)u_j(P_S)+\int_{S+\Gamma^++\Gamma^-} t_{ij}^Y(P_S,Q)u_j(Q)dS(Q)=\int_{S+\Gamma^++\Gamma^-} u_{ij}^Y(P_S,Q)t_j(Q)dS(Q), \qquad i,j=x,y,z \quad (1)$$

where P_s and Q are the source and field points, respectively; $t_{ij}^Y(P_S,Q)$ and $u_{ij}^Y(P_S,Q)$ are the tractions and displacements of Yue's solution, respectively; $t_j(Q)$ and $u_j(Q)$ are the tractions and displacements of the field point Q on the boundaries; S is the uncracked boundary of the cracked body; Γ^+ and Γ^- are two crack surfaces; $c_{ij}(P_S)$ is a coefficient dependent on the local boundary geometry at the source point P_s.

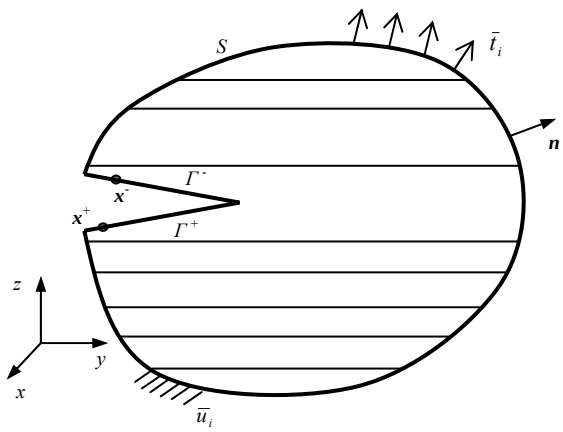

Fig. 1 A three-dimensional crack in a multilayered solid

Before loading, the points Q_{Γ^-} and Q_{Γ^+} on two crack surfaces are completely coincident and there are opposite outward normal directions on the two points. Thus, there exist the following relationships of kernel functions of the points on two crack surfaces

$$t_{ij}^Y(P_S,Q_{\Gamma^+})=-t_{ij}^Y(P_S,Q_{\Gamma^-}), \quad u_{ij}^Y(P_S,Q_{\Gamma^+})=u_{ij}^Y(P_S,Q_{\Gamma^-}) \quad (2)$$

Assume that there is a balanced relationship of tractions: $t_j(Q_{\Gamma^+})=-t_j(Q_{\Gamma^-})$. The relative crack opening displacement (COD) can be described as

$$\Delta u_j(\mathrm{Q}_{\Gamma^+})=u_j(\mathrm{Q}_{\Gamma^+})-u_j(\mathrm{Q}_{\Gamma^-}), j=x,y,z \quad (3)$$

Using the above relationships, the two integrals in equation (1) can be written as

$$\int_{S+\Gamma^++\Gamma^-} t_{ij}^Y(P_S,Q)u_j(Q)dS(Q)=\int_S t_{ij}^Y(P_S,Q)u_j(Q)dS(Q)+\int_{\Gamma^+} t_{ij}^Y(P_S,Q)\Delta u_j(Q)dS(Q) \quad (4a)$$

$$\int_{S+\Gamma^++\Gamma^-} u_{ij}^Y(P_S,Q)t_j(Q)dS(Q)=\int_S u_{ij}^Y(P_S,Q)t_j(Q)dS(Q) \quad (4b)$$

Thus, equation (1) can be rewritten as

$$c_{ij}(P_S)u_j(P_S)+\int_S t_{ij}^Y(P_S,Q)u_j(Q)dS(Q)+\int_{\Gamma^+} t_{ij}^Y(P_S,Q)\Delta u_j(Q)dS(Q)=\int_S u_{ij}^Y(P_S,Q)t_j(Q)dS(Q) \quad (5)$$

The integral equation (5) is a general form of the displacement boundary integral equation based on Yue's solution.

By collocating the stress boundary integral equation on the source point P_{Γ^+} on the crack surface Γ^+ shown in Fig. 1, the conventional stress BIE can be written as

$$\frac{1}{2}\sigma_{ij}\left(P_{\Gamma^+}\right)+\frac{1}{2}\sigma_{ij}\left(P_{\Gamma^-}\right)+\int_{S+\Gamma^++\Gamma^-}T_{ijk}^{Y}\left(P_{\Gamma^+},Q\right)u_k(Q)dS(Q)=\int_{S+\Gamma^++\Gamma^-}T_{ijk}^{Y}\left(P_{\Gamma^+},Q\right)t_k(Q)dS(Q). \tag{6}$$

where T_{ijk}^{Y} and U_{ijk}^{Y} are the new kernel functions obtained by using the numerical difference of the derivatives of Yue's tractions and displacements.

Multiplying equation (6) by the outward unit normal $n_i\left(P_{\Gamma^+}\right)$ and noticing that $n_i\left(P_{\Gamma^+}\right)=-n_i\left(P_{\Gamma^-}\right)$, the traction boundary integral equation on the crack surface results in

$$\frac{1}{2}t_j\left(P_{\Gamma^+}\right)-\frac{1}{2}t_j\left(P_{\Gamma^-}\right)+n_i\left(P_{\Gamma^+}\right)\int_{S+\Gamma^++\Gamma^-}T_{ijk}^{Y}\left(P_{\Gamma^+},Q\right)u_k(Q)dS(Q)=n_i\left(P_{\Gamma^+}\right)\int_{S+\Gamma^++\Gamma^-}U_{ijk}^{Y}\left(P_{\Gamma^+},Q\right)t_k(Q)dS(Q) \tag{7}$$

The points Q_{Γ^-} and Q_{Γ^+} on two crack surfaces are completely coincident and there are opposite outward normal directions on the two points. Thus, there exist the following relationships of kernel functions of the points on two crack surfaces

$$T_{ijk}^{Y}\left(P_S,Q_{\Gamma^+}\right)=-T_{ijk}^{Y}\left(P_S,Q_{\Gamma^-}\right),\quad U_{ijk}^{Y}\left(P_S,Q_{\Gamma^+}\right)=U_{ijk}^{Y}\left(P_S,Q_{\Gamma^-}\right). \tag{8}$$

Applying expressions (8), the two integrals in equation (7) can be written as

$$\int_{S+\Gamma^++\Gamma^-}T_{ijk}^{Y}\left(P_{\Gamma^+},Q\right)u_k(Q)dS(Q)=\int_{S}T_{ijk}^{Y}\left(P_{\Gamma^+},Q\right)u_k(Q)dS(Q)+\int_{\Gamma^+}T_{ijk}^{Y}\left(P_{\Gamma^+},Q\right)\Delta u_k(Q)dS(Q) \tag{9a}$$

$$\int_{S+\Gamma^++\Gamma^-}U_{ijk}^{Y}\left(P_{\Gamma^+},Q\right)t_k(Q)dS(Q)=\int_{S}U_{ijk}^{Y}\left(P_{\Gamma^+},Q\right)t_k(Q)dS(Q) \tag{9b}$$

Using expressions (8) and (9), equation (7) can be further written as

$$\begin{aligned}t_j\left(P_{\Gamma^+}\right)+n_i\left(P_{\Gamma^+}\right)\int_{S}T_{ijk}^{Y}\left(P_{\Gamma^+},Q\right)u_k(Q)dS(Q)+n_i\left(P_{\Gamma^+}\right)\int_{\Gamma^+}T_{ijk}^{Y}\left(P_{\Gamma^+},Q\right)\Delta u_k(Q)dS(Q)\\ =n_i\left(P_{\Gamma^+}\right)\int_{S}U_{ijk}^{Y}\left(P_{\Gamma^+},Q\right)t_k(Q)dS(Q)\end{aligned} \tag{10}$$

The integral equation (10) is a general form of the traction boundary integral equation based on Yue's solution.

Equations (5) and (10) give explicit expressions of the dual boundary integral equations based on Yue's solution. These two integral equations do not contain the integrations on the interfaces of multilayered media because Yue's solution strictly satisfies the interface conditions. Collocating equation (5) on the uncracked boundary S and equation (10) on Γ^+ constitutes the dual boundary integral equations for crack problems. In these equations, the unknown quantities are the tractions and displacements on the uncracked boundary and the discontinuous displacements on the crack surfaces. When the dual BIEs are applied for the study of the crack problems in a multilayered medium of infinite extent, the displacement boundary integral equation is not required and then dual BEM degenerates into the discontinuous displacement method (DDM) [10,11].

3.3 Numerical implementation of the dual BIEs

In the context of the dual boundary integral equations, we apply four- to eight-node isoparametric elements to discretize the uncracked boundary and three types of nine-node quadralateral curved elements to discretize the crack surface. Once these quantities are determined, the displacements, tractions and CODs on boundary are known everywhere. Thus, we can now rewrite the dual boundary integral equations in a discretized form in terms of these parameters to be determined using the shape functions. According to the nature of the kernel and the relative position of the source point with respect to the element on which the integration is carried out, the integrals in the discretized dual BIEs are regular or non-regular. All these integrals have been calculated carefully [9].

Based on the numerical method, computer programs have been written in Fortran to calculate displacements, tractions and the CODs of a multilayered dissimilar elastic solid of finite or infinite extent containing cracks. The stress intensity factors (SIFs) can be calculated by using the CODs on the crack surface. We have examined the accuracy of the proposed DBEM in [9].

4 A square crack in the FGM interlayer

In Fig. 2, a square crack is located in the FGM interlayer bonded to the two homogeneous half-spaces and parallel to the interfaces between a homogeneous half-space and the FGM interlayer. The square crack has the side length 2*c*. The crack surfaces are subjected to uniform compressive stress *p*. Among three materials, materials 1 and 3 are homogeneous media and material 2 is a gradient medium. The elastic modulus of the materials is approximated by

$$E_2(z) = E_1 e^{\alpha z} \quad \text{and} \quad \alpha = 1/h \ln(E_3/E_1) \tag{11}$$

where *h* is the thickness of the interfacial layer, the constant α can be positive or negative, and E_1, E_2 and E_3 are the elastic moduli of three layers.

Let $\alpha c = 2$, $h/c = 0.5$ and $\nu_1=\nu_2=\nu_3=0.3$. The five cases, $d/c = 0.05, 0.15, 0.25, 0.35, 0.45$, are analyzed. The crack surface is discretized into 100 nine-node elements. For the FGM described in expression (11), the FGM is closely approximated by *n* bonded layers of elastic homogeneous media. Each layer has the thickness equal to *h*/*n* and shear modulus equal to $E_2(z)$ at the top depth of the layer, i.e. for the *i*-th layer, $z=H_i$, where $H_i=ih/n$, ($i = 1, 2, \Lambda, n$). Two homogeneous materials bonded through the FGM are considered as semi-infinite domains for the layers H_0 and H_{n+1} respectively. For all the layers, the Poisson's ratios are the same and equal to 0.3. It can be observed that a close approximation of the elastic modulus variation can be obtained using a large number of *n* [5].

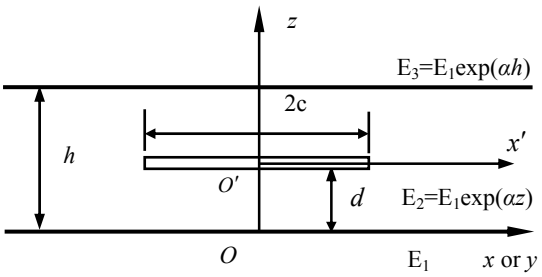

Fig. 2 A square crack in the FGM interlayer

Figs. 3 and 4 illustrate the variations of the SIF values with the crack distance *d* to the FGM interlayer. In these figures, K_I and K_{II} are symmetrical to the x'-axis. It can be found that the crack distance *d* increasing, the K_I and K_{II} values increase. From $d = 0$ to $d = h$, the elastic modulus on

the crack position becomes large and the constraint of the crack opening becomes strong so that the K_I values decrease. At the same time, the relative sliding of the crack surfaces along the x and y directions occurs so that the K_{II} values are not equal to zero and increase with the crack distance d increasing. Referring to the results of the case $\alpha c = 2$ and $h/c = 0.5$, the variations of the SIF values for the case $\alpha c = -2$ and $h/c = 0.5$ can be obtained easily from Figs. 3 and 4. For the case $\alpha c = -2$ and $h/c = 0.5$, the crack position d should be calculated from the plane $z/c = 0.5$, the K_I values are positive and the K_{II} values are negative, and the K_I values and the absolute values of K_{II} are the same as the case $\alpha c = 2$ and $h/c = 0.5$.

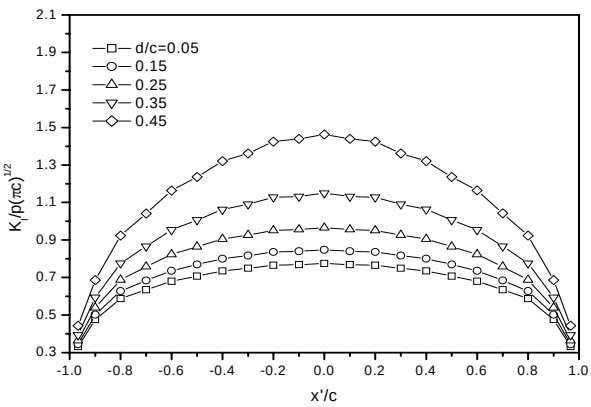

Fig.3 Variation of K_I with the crack distance

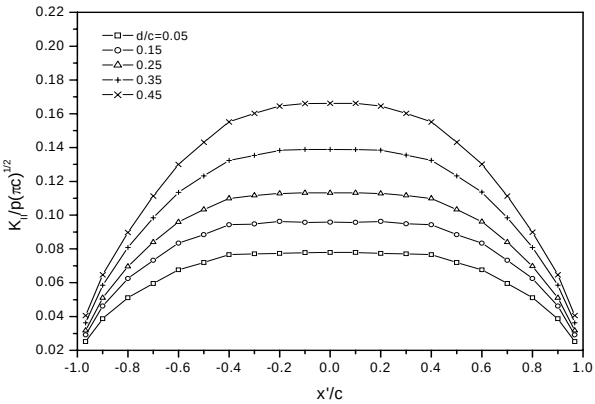

Fig. 4 Variation of K_{II} with the crack distance

5 A rectangular crack in layered rocks

As shown in Fig. 5, an elastic layer is bonded to two semi-infinite domains and contains a rectangular crack parallel to its surfaces. The two elastic half-spaces are assumed to have the same elastic properties. Two types of rock, i.e., fine-grained sandstone and mudstone, are selected. The elastic parameters of fine-grained sandstone E_1=56GPa and ν_1=0.3, and the ones of mudstone E_2=20GP and ν_2=0.25. Thus, there are four types of layered rocks shown in Table 1. The thickness of the mid-layer h=2m. The side lengths of the square crack are 2m and 4m and the crack surface is parallel to the interface of the layered rocks. The crack surfaces are smooth and are subjected to a linear load shown in Fig. 6. The crack surface is discretized into 100 nine-node elements.

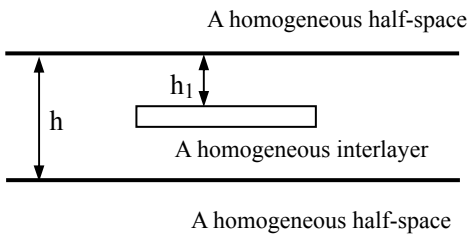

Fig.5 A rectangular crack in the interlayer of infinite domain

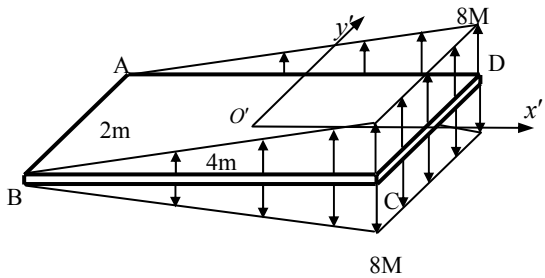

Fig. 6 A rectangular crack subject to linear load

In order to plot the values of the SIFs along crack front lines, a line coordinate L is used to measure the crack front lines from AB, BC to CD, shown in Fig. 6. The line coordinate L starts at the corner point A of the square crack (i.e. L=0). It increases along the line AB, BC to CD. Correspondingly, L increases from 0-2, from 2-6, and from 6-8, respectively.

Table 1 Cases of layered rocks containing a rectangular crack

Case no.	Layered rocks of infinite extent
1	The homogeneous solid of infinite extent consists of fine-grained sandstone.
2	The sandwich solid consists of two semi-infinite extents of mudstone and the mid-layer of fine-grained sandstone.
3	The homogeneous solid of infinite extent consists of mudstone.
4	The sandwich solid consists of two semi-infinite extents of fine-grained sandstone and the mid-layer of mudstone.

(1) Case 1 and case 2

For case 1, there are no relative sliding displacements along the crack surfaces because of symmetry of geometry and loads. Due to the same reasons, there are no relative sliding displacements for case 2 (h_1=1m). For case 2, the COD values increase and the K_I values also increase in comparison with case 1. This is because the elastic module of mudstone in semi-infinite domain is less than the one of fine-grained sandstone.

For case 2 ($h_1 \neq$ 1m), the absolute values of displacements along the upper surface increase and the ones along the lower surface decrease. This leads to the appearance of the sliding discontinuous displacements along the crack surface. Due to the non-uniform load on the crack surfaces, there are different SIF values at the crack fronts $x' = \pm 2m$ whilst there are the same SIF values at the crack fronts $y' = \pm 1m$. In the following, the SIF values at the crack fronts $x' = \pm 2m$ and $y' = -1m$ are discussed.

Fig. 7 shows the variation of the SIF values at the crack fronts $x' = \pm 2m$ and $y' = -1m$. The K_I values are positive and the K_{II} values are negative. Obviously, these phenomena are related to the load on the crack surfaces and the relative position of the crack in this medium. Along the crack front $y' = -1m$, the larger the load, the larger the absolute values of K_I and K_{II}. As the crack surface approaches to the interface, the absolute values of K_I and K_{II} increase.

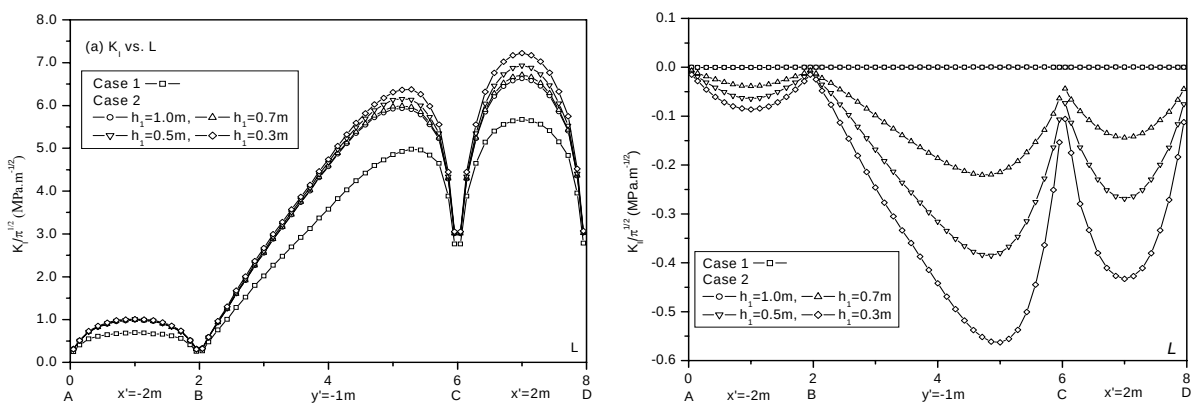

Fig. 7 SIF values of rectangular crack subjected to linear loads (Cases 1 and 2)

(2) Case 3 and case 4

Fig. 8 shows the variation of the SIF values at the crack fronts $x' = \pm 2m$ and $y' = -1m$. Herein, the K_{I} and K_{II} values are positive. Along the crack front $y' = -1m$, the K_{I} and K_{II} values become larger near the side $x' = 2m$. As the crack surface approaches to the interface, the absolute values of K_{I} and K_{II} decrease.

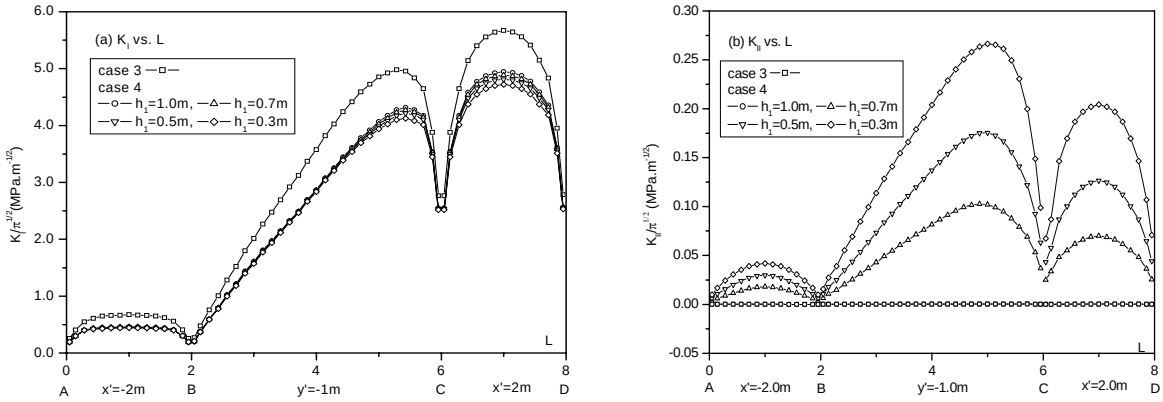

Fig. 8 SIF values of rectangular crack subjected to linear loads (Cases 3 and 4)

5 Concluding remarks

This paper introduces a novel dual boundary element method associated with Yue's solution. In analyzing the crack problems in FGMs and layered materials, the advantages of this approach are: (1) it is not necessary to introduce elements at the interface, (2) the method is applicable for multilayered solids with any layer number and (3) the high accuracy can be obtained for the crack in multilayered solids. Only the results of crack problems in infinite domains are presented in this paper and the numerical examples of crack problems in finite domains can be found in [9].

In 1995, Yue [12] developed the fundamental solution of a transversely isotropic bi-material. The authors also used this fundamental solution to develop the BEMs of the bi-material similar to the ones of Yue's solution. The proposed BEM includes the multi-domain BEM and the single domain BEM (i.e., dual BEM). The application of the BEMs to analyze a penny crack, an elliptical crack and a square crack in bi-materials has been presented [13-15].

In the book [16], the authors introduced the research results by using the fundamental solutions [3, 12] systematacially. The proposed BEMs and the results can be a powerful numerical tool, which can apply to various complex three-dimensional geometries of layered or gradient materials with cracks under mixed-mode loading.

Acknowledgements

The authors would like to thank the financial supports from the Committee on Research and Conference Grants of The University of Hong Kong and the National Natural Science Foundation of China (Grant No. 51079081).

References

[1] V. Birman, L.W. Byrd, Modeling and analysis of functionally graded materials and structures. ASME Applied Mechanics Reviews, 60(2007):195-216.
[2] M.H. Aliabadi, Boundary element formulations in fracture mechanics. ASME Applied

Mechanics Reviews, 50(1997):83-96.
[3] Z.Q. Yue, On generalized Kelvin solutions in a multilayered elastic medium. J. Elasticity, 40(2005):1-43.
[4] Z.Q. Yue, H.T. Xiao, Generalized Kelvin solution based boundary element method for crack problems in multilayered solids. Eng. Anal. Bound. Elements, 26(2002): 691-705.
[5] Z.Q. Yue, H.T. Xiao, G.L. Tham, Boundary element analysis of crack problems in functionally graded materials. Int. J. Solids Structures, 40(2003):3273-91.
[6] H.T. Xiao, Z.Q. Yue, G.L. Tham, Analysis of elliptical crack parallel to graded interface of bimaterials under inclined tension. Mech. Mater., 37(2005):785-799.
[7] H.T. Xiao, Z.Q. Yue, et al, Stress intensity factors for penny-shaped cracks perpendicular to graded interfacial zone of bonded bi-materials. Eng. Fract. Mech., 72(2005):121-143.
[8] Z.Q. Yue, H.T. Xiao, G.L. Tham, Analysis of elliptical crack perpendicular to functionally graded interface of bonded solids under tension or shear. Theoret. Appl. Fract. Mech., 42(2004):227-248.
[9] H.T. Xiao, Z.Q. Yue, Dual boundary element analysis of rectangular-shaped cracks in graded materials (in Chinese). Chinese Journal of Theoretical and Applied Mechanics. 40(2008): 840-848.
[10] S.L. Crouch, A. M. Starfield. Boundary element methods in solid mechanics. London: George Allen and Unwin Publishers, 1983.
[11] H.T. Xiao, Z.Q. Yue, A three-dimensional displacement discontinuity method for crack problems in layered rocks. Int. J. Rock Mech. Min. Sci., 2011, 48:412-420.
[12] Z.Q. Yue, Elastic fields in two joined transversely isotropic due to concentrated forces. Int. J. Engng Sci. 33(1995): 351-369.
[13] H.T. Xiao, Z.Q. Yue, G.L. Tham, Analysis of elliptical cracks perpendicular to the interface of two joined transversely isotropic solids. Int. J. Fracture, 133(2005):329-354.
[14] Z.Q. Yue ZQ, H.T. Xiao, G.L. Tham. Boundary element analysis of 3D crack problems in two joined transversely isotropic solids. Computational Mechanics, 2005, 36:459-474.
[15] Z.Q. Yue, H.T. Xiao, E. Pan. Stress intensity factors of square crack inclined to interface of transversely isotropic bi-material. Eng. Anal. Bound. Elements, 2007, 31:50-65.
[16] H.T. Xiao, Z.Q. Yue, New boundary element analysis of fracture mechanics in functionally graded materials (in Chinese). Higher Education Press, Beijing, 2011.

A BEM for transient coupled thermoelastic crack analysis of homogeneous/functionally graded bimaterials

Alexander Ekhlakov[1,2*], **Oksana Khay**[1,3], **Chuanzeng Zhang**[1]

[1] Department of Civil Engineering, University of Siegen, Paul-Bonatz-Str. 9-11, D-57076 Siegen, Germany
[2] Faculty of Architecture and Civil Engineering, RheinMain University of Applied Sciences, Kurt-Schumacher-Ring 18, D-65197 Wiesbaden, Germany
[3] Pidstryhach Institute for Applied Problems of Mechanics and Mathematics NASU, 3b Naukova Str., 79060 L'viv, Ukraine
* Corresponding author: alexander.ekhlakov@hs-rm.de

Abstract A transient coupled thermoelastic analysis of two-dimensional, isotropic and linear elastic bimaterials, which are composed of a functionally graded (FG) layer attached to a homogeneous substrate, subjected to thermal shock is investigated. For this purpose, a boundary element method (BEM) for linear coupled thermoelasticity is developed. The material properties of the FG layer are assumed to be continuous functions of the spatial coordinates. The boundary-domain integral equations are derived by using the fundamental solutions of linear coupled thermoelasticity for the corresponding isotropic, homogeneous and linear thermoelastic solids in the Laplace-transformed domain. For the numerical solution, a collocation method with piecewise quadratic approximation is implemented. Numerical results for the dynamic stress intensity factors are presented and discussed.

Keywords Functionally graded materials, Homogeneous/functionally graded bimaterials, Transient linear coupled thermoelasticity, Boundary element method, Dynamic stress intensity factors

1. Introduction

Functionally graded materials (FGMs) represent a new generation of high-performance composite materials formed by continuously variable composition of the constituents over volume [1]. They possess many superior mechanical, thermal, corrosion-resistant and wear-resistant properties in comparison to the conventional composite materials. Therefore, in recent years FGMs have received an increasing research interest in materials and engineering sciences. An important application area of FGMs is in the thermal barrier coating technology, where a functionally graded (FG) layer is deposited on a homogeneous substrate. Thermoelastic fracture analysis of FG coated materials and structures is of particular importance to their thermal and mechanical integrity, reliability and durability in novel engineering applications. Such analysis may provide a fundamental understanding of and a deep insight into the failure mechanisms of FG coated materials and structures, which may aid in their design, optimization and applications. Due to the high mathematical complexity of the corresponding dynamic thermoelastic problems for non-homogeneous FGMs, analytical methods can be obtained only for very simple geometry and loading conditions. In general cases, numerical and experimental methods have to be applied to fracture and fatigue analysis in FG coated materials and structures subjected to thermal shock loading conditions.

In this paper, a boundary element method (BEM) for transient thermoelastic crack analysis in two-dimensional (2-D), isotropic and linear thermoelastic bimaterials consisting of an FG coating layer attached to a homogeneous substrate under thermal shock is developed. The FG/homogeneous bimaterials are modeled by using a sub-domain technique [2]. The bimaterial system is divided into a homogeneous and a non-homogeneous sub-domain along the interface. The equations of motion and the thermal balance equation constitute the governing equations of the transient linear coupled thermoelasticity. The Laplace-transform technique is applied to eliminate the time-dependence in the governing equations. A boundary-domain integral equation representation is derived from the generalized Betti's reciprocal theorem for FGMs in conjunction with the fundamental solutions for

homogeneous and linear thermoelastic solids. The boundary-domain integral equations (BDIEs) are obtained for the unknown mechanical and thermal fields and then applied to each sub-domain and the continuity conditions are employed on the interface boundary. The BDIEs for the FG layer contain domain integrals, which describe the material's non-homogeneity. A crucial point of the numerical solution procedure is how to evaluate the domain integrals without discretization of the non-homogeneous sub-domain into internal cells. In this analysis, the domain integrals are transformed into boundary integrals over the global boundary by using the radial integration method (RIM) [3, 4]. For the homogeneous and linear elastic substrate, only boundary integrals need to be considered in the boundary integral equations. A collocation method is implemented for the spatial discretization. The final time-dependent solutions are obtained by using the Stehfest's algorithm [5] for the inverse Laplace-transform. Numerical results are presented and discussed to demonstrate the accuracy and efficiency of the proposed BEM as well as the effects of the material gradation and thermo-mechanical coupling on the dynamic stress intensity factors (SIFs).

2. Problem statement

Let us consider isotropic and linear thermoelastic bimaterials in a 2-D domain, which are composed of an FG layer attached to a homogeneous substrate. The FG/homogeneous bimaterials are modeled by using a sub-domain technique [2]. The bimaterial system is divided into a homogeneous $\Omega^{(0)}$ and a non-homogeneous sub-domain $\Omega^{(1)}$ along the interface. The material properties of the FG layer such as the mass density $\tilde{\rho}_1(\mathbf{x})$, the Young's modulus $E_1(\mathbf{x})$, the thermal conductivity $k_1(\mathbf{x})$, the specific heat $c_1(\mathbf{x})$ and the linear expansion coefficient $\alpha_1(\mathbf{x})$ are assumed to be continuous functions of the Cartesian coordinates, while the Poisson's ratio ν_1 and the material parameters of the homogeneous substrate, which are denoted by a subscript zero, are taken as constant. In this case, the elasticity tensor can be written as

$$c_{ijkl}^{(0)} = \mu_0 c_{ijkl}^{(0)0}, \qquad c_{ijkl}^{(1)}(\mathbf{x}) = \mu_1(\mathbf{x}) c_{ijkl}^{(1)0} \tag{1}$$

with

$$\mu_0 = \frac{E_0}{2(1+\nu_0)}, \qquad \mu_1(\mathbf{x}) = \frac{E_1(\mathbf{x})}{2(1+\nu_1)}, \qquad c_{ijkl}^{(n)0} = \frac{2\nu_n}{1-2\nu_n}\delta_{ij}\delta_{kl} + \delta_{ki}\delta_{lj} + \delta_{kj}\delta_{li}, \qquad n = 0,1,$$

where μ_n is the shear modulus and δ_{ij} is the Kronecker delta symbol. The relation between the stresses $\sigma_{ij}^{(n)}(\mathbf{x},t)$ and the displacements $u_{k,l}^{(n)}(\mathbf{x},t)$ with the consideration of the temperature changes $\theta^{(n)}(\mathbf{x},t)$ is defined by the Duhamel-Neumann constitutive equations

$$\sigma_{ij}^{(n)}(\mathbf{x},t) = c_{ijkl}^{(n)}(\mathbf{x}) u_{k,l}^{(n)}(\mathbf{x},t) - \gamma_n(\mathbf{x})\theta^{(n)}(\mathbf{x},t)\delta_{ij}, \qquad n = 0,1, \tag{2}$$

where the stress-temperature modulus is given by $\gamma_n = E_n \alpha_n / (1-2\nu_n)$. In the absence of body forces and heat sources, the governing equations in transient linear coupled thermoelasticity are given by the equations of motion and the thermal balance equations [6]

$$\sigma_{ij,j}^{(n)}(\mathbf{x},t) - \tilde{\rho}_n(\mathbf{x})\ddot{u}_i^{(n)}(\mathbf{x},t) = 0, \tag{3}$$

$$\left(k_n(\mathbf{x})\theta_{,i}^{(n)}(\mathbf{x},t)\right)_{,i} - \tilde{\rho}_n(\mathbf{x}) c_n(\mathbf{x})\dot{\theta}^{(n)}(\mathbf{x},t) - k_n(\mathbf{x})\eta_n(\mathbf{x})\dot{u}_{k,k}^{(n)}(\mathbf{x},t) = 0, \tag{4}$$

where $\eta_n = \gamma_n T_0 / k$ and T_0 is the reference temperature. Unless otherwise stated, the conventional summation rule over double indices is implied, $n = 0,1$ and other Latin indices take the values of 1

and 2. From the mathematical point of view, the governing equations are the coupled partial differential equations with variable coefficients for the FG sub-domain $\Omega^{(1)}$. A measure of the thermo-mechanical coupling due to the dilatational term $\eta_n \dot{u}_{k,k}^{(n)}$ in Eq. (4) is defined by a dimensionless coupling parameter [6, 7]

$$\delta_n = \frac{(1+\nu_n)}{(1-\nu_n)(1-2\nu_n)} \frac{E_n \alpha_n^2 T_0}{\tilde{\rho}_n c_n}, \tag{5}$$

that equals zero for an uncoupled problem.

The following essential and natural boundary conditions for the mechanical and thermal quantities are prescribed as

$$\begin{aligned} u_i^{(n)}(\mathbf{x},t) &= \tilde{u}_i^{(n)}(\mathbf{x},t), \quad \mathbf{x} \in \Gamma_u^{(n)}, & \theta^{(n)}(\mathbf{x},t) &= \tilde{\theta}^{(n)}(\mathbf{x},t), \quad \mathbf{x} \in \Gamma_\theta^{(n)}, \\ t_i^{(n)}(\mathbf{x},t) &= \tilde{t}_i^{(n)}(\mathbf{x},t), \quad \mathbf{x} \in \Gamma_t^{(n)}, & q^{(n)}(\mathbf{x},t) &= \tilde{q}^{(n)}(\mathbf{x},t), \quad \mathbf{x} \in \Gamma_q^{(n)}, \end{aligned} \tag{6}$$

where $t_i^{(n)}$ and $q^{(n)}$ represent the traction vector and the heat flux defined by

$$t_i^{(n)}(\mathbf{x},t) = \sigma_{ij}^{(n)}(\mathbf{x},t) n_j(\mathbf{x}), \qquad q^{(n)}(\mathbf{x},t) = -k_n(\mathbf{x}) \theta_{,i}^{(n)}(\mathbf{x},t) n_i(\mathbf{x}).$$

Here, $n_i(\mathbf{x})$ denotes the components of the outward unit normal vector, $\Gamma_u^{(n)}$ and $\Gamma_t^{(n)}$ are the parts of the external boundary $\Gamma^{(n)} = \Gamma_u^{(n)} \cup \Gamma_t^{(n)}$, $\Gamma_u^{(n)} \cap \Gamma_t^{(n)} = \varnothing$, in which the displacements $\tilde{u}_i^{(n)}$ and the tractions $\tilde{t}_i^{(n)}$ are given, respectively; $\Gamma_\theta^{(n)}$ and $\Gamma_q^{(n)}$ are the parts of the boundary $\Gamma^{(n)} = \Gamma_\theta^{(n)} \cup \Gamma_q^{(n)}$, $\Gamma_\theta^{(n)} \cap \Gamma_q^{(n)} = \varnothing$ with the specified temperature $\tilde{\theta}^{(n)}$ and the heat flux $\tilde{q}^{(n)}$, respectively. The crack-faces are assumed to be free of mechanical and thermal loadings

$$t_i^{(n)}(\mathbf{x},t) = 0, \quad \mathbf{x} \in \Gamma_c, \qquad q^{(n)}(\mathbf{x},t) = 0, \quad \mathbf{x} \in \Gamma_c, \tag{7}$$

where $\Gamma_c = \Gamma_c^+ \cup \Gamma_c^-$ represents the upper and lower crack-faces. The continuity conditions on the interface are prescribed as

$$\begin{aligned} u_i^{(0)}(\mathbf{x},t) &= u_i^{(1)}(\mathbf{x},t), & \theta^{(0)}(\mathbf{x},t) &= \theta^{(1)}(\mathbf{x},t), \quad \mathbf{x} \in \Gamma^{(01)}, \\ t_i^{(0)}(\mathbf{x},t) &= -t_i^{(1)}(\mathbf{x},t), & q^{(0)}(\mathbf{x},t) &= -q^{(1)}(\mathbf{x},t), \quad \mathbf{x} \in \Gamma^{(01)}. \end{aligned} \tag{8}$$

The initial conditions are given by

$$u_i(\mathbf{x},t) = \dot{u}_i(\mathbf{x},t) = 0, \quad \theta(\mathbf{x},t) = 0 \qquad \text{for} \quad t \le 0. \tag{9}$$

Applying the Laplace-transform to Eqs. (3) and (4) and substituting Eqs. (1) and (2) yield

$$\begin{aligned} & c_{ijkl}^{(n)0} \left(\mu_n \bar{u}_{k,lj}^{(n)} + \mu_{,j}^{(n)} \bar{u}_{k,l}^{(n)} \right) - \left(\gamma_n \bar{\theta}_{,i}^{(n)} + \gamma_{n,i} \bar{\theta}^{(n)} \right) - \tilde{\rho}^{(n)} p^2 \bar{u}_i^{(n)} = 0, \\ & \bar{\theta}_{,ii}^{(n)} + \frac{k_{n,i}}{k_n} \bar{\theta}_{,i}^{(n)} - \beta_n^2 \bar{\theta}^{(n)} - \eta_n p \bar{u}_{k,k}^{(n)} = 0, \end{aligned} \tag{10}$$

where a superimposed bar over a quantity denotes the Laplace-transformed quantity, p is the Laplace-transform parameter, $\kappa_n = k_n / \tilde{\rho}_n c_n$ is the thermal conductivity and $\beta_n^2 = p / \kappa_n$.

Integral representations of the displacements and the temperature at an arbitrary point of the domain are derived from the generalized Betti's reciprocal theorem in conjunction with the fundamental solutions of the Laplace-transformed linear coupled thermoelasticity for a homogeneous solid [6, 8, 9]. By moving the observation point to the boundary $\mathbf{x} \in \Gamma^{(n)}$ or keeping it in the domain $\mathbf{x} \in \Omega^{(n)}$ the

following system of boundary-domain integral equations (BDIEs) for the mechanical and thermal fields at the boundary and interior points is obtained as

$$\begin{aligned}
&\bar{u}_j^{(n)}(\mathbf{x},p)+\int_\Gamma\left[\bar{T}_{ij}(\mathbf{x},\mathbf{y},p)\bar{u}_i^{(n)}(\mathbf{y},p)-\frac{1}{\tilde{E}(\mathbf{y})\tilde{\alpha}(\mathbf{y})}\bar{U}_{ij}(\mathbf{x},\mathbf{y},p)\bar{t}_i^{(n)}(\mathbf{y},p)\right]d\Gamma\\
&\quad-\kappa_0\int_\Gamma\left[\bar{Z}_j(\mathbf{x},\mathbf{y},p)\bar{\theta}^{(n)}(\mathbf{y},p)-\frac{\tilde{k}(\mathbf{y})}{\tilde{E}(\mathbf{y})\tilde{\alpha}(\mathbf{y})}\bar{U}_j(\mathbf{x},\mathbf{y},p)\bar{q}^{(n)}(\mathbf{y},p)\right]d\Gamma-\bar{F}_j^{(n)(u)}(\mathbf{x},p)=0,\\
&\bar{\theta}^{(n)}(\mathbf{x},p)-\frac{\kappa_0\eta_0 p}{\gamma_0}\int_\Gamma\left[\bar{T}_i(\mathbf{x},\mathbf{y},p)\bar{u}_i^{(n)}(\mathbf{y},p)-\frac{1}{\tilde{E}(\mathbf{y})\tilde{\alpha}(\mathbf{y})}\bar{U}_i(\mathbf{x},\mathbf{y},p)\bar{t}_i^{(n)}(\mathbf{y},p)\right]d\Gamma\\
&\quad+\kappa_0\int_\Gamma\left[\bar{F}(\mathbf{x},\mathbf{y},p)\bar{\theta}^{(n)}(\mathbf{y},p)-\frac{\tilde{k}(\mathbf{y})}{\tilde{E}(\mathbf{y})\tilde{\alpha}(\mathbf{y})}\bar{T}(\mathbf{x},\mathbf{y},p)\bar{q}^{(n)}(\mathbf{y},p)\right]d\Gamma-\bar{F}^{(n)(\theta)}(\mathbf{x},p)=0,
\end{aligned}\tag{11}$$

where $\mathbf{x}$ and $\mathbf{y}$ represent the source and observation points, $\bar{U}_{ij}(\mathbf{x},\mathbf{y},p)$, $\bar{U}_i(\mathbf{x},\mathbf{y},p)$, $\bar{T}(\mathbf{x},\mathbf{y},p)$, $\bar{T}_{ij}(\mathbf{x},\mathbf{y},p)$, $\bar{T}_i(\mathbf{x},\mathbf{y},p)$, $\bar{Z}_i(\mathbf{x},\mathbf{y},p)$ and $\bar{F}(\mathbf{x},\mathbf{y},p)$ are the fundamental solutions [6, 8, 9]. Here, a tilde denotes the ratio of the non-homogeneous quantity to the corresponding homogeneous quantity. The functions $\bar{F}_j^{(1)(u)}$ and $\bar{F}^{(1)(\theta)}$ describe the non-homogeneity of the FG layer. They vanish completely for the homogeneous substrate $\Omega^{(0)}$. The functions $\bar{F}_j^{(1)(u)}$ and $\bar{F}^{(1)(\theta)}$ are defined as [8, 9]

$$\begin{aligned}
\bar{F}_j^{(1)(u)}(\mathbf{x},p)=&-p^2\int_\Omega\gamma^{(1)}(\mathbf{y})\bar{U}_{ij}(\mathbf{x},\mathbf{y},p)\bar{u}_i^{(1)}(\mathbf{y},p)d\Omega_y\\
&+\int_\Omega\left[\gamma_k^{(2)}(\mathbf{y})\bar{U}_{ij}(\mathbf{x},\mathbf{y},p)-\alpha^{(1)}(\mathbf{y})\bar{V}_{ijk}(\mathbf{x},\mathbf{y},p)\right]\bar{u}_{i,k}^{(1)}(\mathbf{y},p)d\Omega_y\\
&+\int_\Omega\left[p\eta^{(1)}(\mathbf{y})\bar{U}_j(\mathbf{x},\mathbf{y},p)-\gamma_j^{(3)}(\mathbf{y})\bar{U}_{kk}(\mathbf{x},\mathbf{y},p)\right]\bar{\theta}^{(1)}(\mathbf{y},p)d\Omega_y\\
&+\int_\Omega\left[\eta^{(2)}(\mathbf{y})\bar{E}_{ji}(\mathbf{x},\mathbf{y},p)-\gamma_i^{(4)}(\mathbf{y})\bar{U}_j(\mathbf{x},\mathbf{y},p)\right]\bar{\theta}_{,i}^{(1)}(\mathbf{y},p)d\Omega_y,
\end{aligned}\tag{12}$$

$$\begin{aligned}
\bar{F}^{(1)(\theta)}(\mathbf{x},p)=&\frac{\kappa_0\eta_0 p}{\gamma_0}\left\{p^2\int_\Omega\gamma^{(1)}(\mathbf{y})\bar{U}_i(\mathbf{x},\mathbf{y},p)\bar{u}_i^{(1)}(\mathbf{y},p)d\Omega_y\right.\\
&\left.-\int_\Omega\left[\gamma_k^{(2)}(\mathbf{y})\bar{U}_i(\mathbf{x},\mathbf{y},p)-\alpha^{(1)}(\mathbf{y})\bar{W}_{ik}(\mathbf{x},\mathbf{y},p)\right]\bar{u}_{i,k}^{(1)}(\mathbf{y},p)d\Omega_y\right\}\\
&-\int_\Omega\left[p\eta^{(1)}(\mathbf{y})\bar{T}(\mathbf{x},\mathbf{y},p)-\frac{\kappa_0\eta_0 p}{\gamma_0}\gamma_j^{(3)}(\mathbf{y})\bar{U}_j(\mathbf{x},\mathbf{y},p)\right]\bar{\theta}^{(1)}(\mathbf{y},p)d\Omega_y\\
&-\int_\Omega\left[\eta^{(2)}(\mathbf{y})\bar{G}_i(\mathbf{x},\mathbf{y},p)-\gamma_i^{(4)}(\mathbf{y})\bar{T}(\mathbf{x},\mathbf{y},p)\right]\bar{\theta}_{,i}^{(1)}(\mathbf{y},p)d\Omega_y,
\end{aligned}\tag{13}$$

where the fundamental solutions $\bar{E}_{ij}(\mathbf{x},\mathbf{y},p)$, $\bar{G}_i(\mathbf{x},\mathbf{y},p)$, $\bar{V}_{ijk}(\mathbf{x},\mathbf{y},p)$ and $\bar{W}_{ik}(\mathbf{x},\mathbf{y},p)$ are given in [8]. It should be noted that Eqs. (11) are no longer pure boundary integral formulations in the non-homogeneous sub-domain $\Omega^{(1)}$ because they involve domain integrals containing unknown fields. The BDIEs (11) contain boundary and domain integrals with singular kernels. The strongly singular integrals are interpreted in the sense of the Cauchy principal value. Making use of the

singularity subtraction technique and the variable transformation technique the strong and weak singularities in Eqs. (11) can be removed [2, 8, 9].

3. Numerical solution procedure

In order to avoid the domain discretization into internal cells for evaluating the domain integrals in Eqs. (12) and (13) the radial integration method (RIM) developed by Gao is applied [3, 4]. The functions (12) and (13) can be rewritten in matrix form [8] as

$$\bar{\mathbf{F}}(\mathbf{x}, p) = \int_{\Gamma} \bar{\mathbf{F}}(\mathbf{x}, \mathbf{y}, p)\bar{\mathbf{u}}(\mathbf{y}, p)d\Gamma + \int_{\Omega} \mathbf{G}(\mathbf{x}, \mathbf{y}, p)\bar{\mathbf{u}}(\mathbf{y}, p)d\Omega, \tag{14}$$

where $\bar{\mathbf{F}}$ is the vector of functions $\bar{F}_i^{(1)(u)}$ and $\bar{F}^{(1)(\theta)}$, $\bar{\mathbf{u}}$ is the vector containing the displacements $\bar{u}_i$ and the temperature $\bar{\theta}$, and the 3×3 matrices $\bar{\mathbf{F}}$ and $\bar{\mathbf{G}}$ are given in [8]. The unknown fields $\bar{u}_i$ or $\bar{\theta}$ are approximated by a series of prescribed basis functions and the linear polynomials

$$\bar{u}_i(\mathbf{x}, p) = \sum_A \bar{\alpha}_i^A(p)\phi^A(R) + \bar{a}_i^j(p)x_j + \bar{a}_i^0(p), \quad \sum_{A=1} \bar{\alpha}_i^A(p) = \sum_{A=1} \bar{\alpha}_i^A(p)x_j^A = 0, \tag{15}$$

where $R = \| \mathbf{x} - \mathbf{x}^A \|$ is the distance from the application point A to the field point $\mathbf{x}$, $\bar{\alpha}_i^A$ and $\bar{a}_i^j$ are the unknown expansion coefficients to be determined and x_j^A denotes the coordinates at the application point A, which consist of all boundary nodes and some selected internal nodes. The fourth order spline-type radial basis function [3, 4] is used

$$\phi^A(R) = 1 - 6R^2 + 8R^3 - 3R^4. \tag{16}$$

The unknown coefficients $\bar{\alpha}_i^A$ and $\bar{a}_i^j$ can be determined by applying the application point A in Eq. (16) to every node. Then, a system of linear algebraic equations can be obtained in matrix form as

$$\{\bar{u}\} = [\Phi]\{\bar{\alpha}\}, \tag{17}$$

where $\{\bar{\alpha}\}$ is the vector consisting of the coefficients $\bar{\alpha}_i^A$ for all points and $\bar{a}_i^j$. If two application points do not coincide, the matrix $[\Phi]$ is invertible and thereby

$$\{\bar{\alpha}\} = [\Phi]^{-1}\{\bar{u}\}. \tag{18}$$

Substitution of Eqs. (15) into the domain integrals of Eq. (14) yields

$$\int_{\Omega} \bar{G}_{ij}\bar{u}_j d\Omega = \bar{\alpha}_j^a \int_{\Omega} \bar{G}_{ij}\phi^a d\Omega + \bar{a}_j^k \int_{\Omega} \bar{G}_{ij} y_k d\Omega + \bar{a}_j^0 \int_{\Omega} \bar{G}_{ij} d\Omega. \tag{19}$$

Applying the RIM [3, 4, 8] to the domain integrals in Eq. (19) results in

$$\int_{\Omega} \bar{G}_{ij}\bar{u}_j d\Omega = \bar{\alpha}_j^a \int_{\Gamma} \frac{1}{r}\frac{\partial r}{\partial n}\bar{F}_{ij}^a d\Gamma + \bar{a}_j^k \int_{\Gamma} \frac{r_{,k}}{r}\frac{\partial r}{\partial n}\bar{F}_{ij}^1 d\Gamma + (\bar{a}_j^k x_k + \bar{a}_j^0)\int_{\Gamma} \frac{1}{r}\frac{\partial r}{\partial n}\bar{F}_{ij}^0 d\Gamma \tag{20}$$

with the radial integrals

$$\bar{F}_{ij}^a = \int_0^r r\bar{G}_{ij}\phi^a dr, \qquad \bar{F}_{ij}^1 = \int_0^r r^2\bar{G}_{ij} dr, \qquad \bar{F}_{ij}^0 = \int_0^r r\bar{G}_{ij} dr. \tag{21}$$

It is important to note here that the term $r_{,i}$ appearing in the radial integrals is constant [4] and the relation $y_k = x_k + r_{,k} r$ is used for the transformation from $\mathbf{y}$ to $\mathbf{r}$. The radial integrals (21) are regular and can be evaluated numerically by using standard Gaussian quadrature for every field point.

The BDIEs (11) can be solved numerically by applying a collocation method. The usual discretization procedure applied in BEM is utilized for the boundary discretization of the BDIEs in the Laplace-transformed domain [2, 6]. After numerical integrations, applying the prescribed boundary conditions and a rearrangement of the equations, a system of linear algebraic equations can be obtained as

$$\begin{array}{llll} \mathbf{A}_0^b \mathbf{x}_0^b & = \mathbf{y}_0^b, & \text{for boundary nodes,} & \\ \mathbf{A}_0^i \mathbf{x}_0^b + \mathbf{u}_0^i & = \mathbf{y}_0^i, & \text{for internal nodes,} & \text{for } \Omega_0, \\ \mathbf{A}_1^b \mathbf{x}_1^b & = \mathbf{y}_0^b + \mathbf{D}_1^b \mathbf{u}_1, & \text{for boundary nodes,} & \\ \mathbf{A}_1^i \mathbf{x}_1^b + \mathbf{u}_1^i & = \mathbf{y}_0^i + \mathbf{D}_1^i \mathbf{u}_1, & \text{for internal nodes,} & \text{for } \Omega_1. \end{array} \tag{22}$$

Here, $\mathbf{x}_n^b$ is the $3N^b$ vector of the unknown values of the displacements $\bar{u}_i^{(n)}$, the tractions $\bar{t}_i^{(n)}$, the temperature $\bar{\theta}^{(n)}$ and the heat flux $\bar{q}^{(n)}$ at the boundary collocation points, $\mathbf{u}_n^i$ is the $3N^d$ vector of the unknown displacements $\bar{u}_i^{(n)}$ and temperature $\bar{\theta}^{(n)}$ at the internal nodes, $\mathbf{y}_n^b$ and $\mathbf{y}_n^i$ denote the $3N^b$ and $3N^d$ vectors composed of the prescribed boundary conditions. The sizes of the matrices $\mathbf{A}_n^b$, $\mathbf{A}_n^i$, $\mathbf{D}_1^b$ and $\mathbf{D}_1^i$ are $3N^b \times 3N^b$, $3N^d \times 3N^b$, $3N^b \times 3N$ and $3N^d \times 3N$, respectively, N^b and N^d are the numbers of boundary and internal nodes and $\mathbf{I}$ is the identity matrix. The system of linear algebraic equations (22) with the continuity conditions on the interface nodes (8) is solved numerically for discrete values of the Laplace-transform parameter p to obtain the boundary unknowns $\mathbf{x}_n^b$, the interior primary field quantities $\mathbf{u}_n^i$ and the unknown fields at the interface nodes [2]. The final time-dependent solutions can be calculated by using the Stehfest's algorithm [5] for the inverse Laplace-transform.

Different methods can be used for the evaluation of the SIFs. In this analysis, the extrapolation technique following directly from the asymptotic expansion of the displacements in the vicinity of the crack-tip is employed [2, 10]. For a crack located on the x_1-axis, the dynamic mode-I and mode-II SIFs are related to the crack-opening-displacements $\Delta u_i(\mathbf{x}, t)$ by

$$\begin{Bmatrix} K_{\mathrm{I}}(t) \\ K_{\mathrm{II}}(t) \end{Bmatrix} = \frac{\sqrt{2\pi}}{\kappa + 1} \mu^{\mathrm{tip}} \lim_{\varepsilon \to a} \frac{1}{\sqrt{a - \varepsilon}} \begin{Bmatrix} \Delta u_2(\varepsilon, t) \\ \Delta u_1(\varepsilon, t) \end{Bmatrix}, \tag{23}$$

where $\kappa = 3 - 4\nu_0$ or $\kappa = (3 - \nu_0)/(1 + \nu_0)$ for plane-strain or plane-stress conditions, respectively, μ^{tip} is the shear modulus at the crack-tip, and ε is a small distance from the crack-tip to the considered node on the crack-faces.

4. Numerical results

As a numerical example we consider an edge crack in a rectangular, isotropic and linear thermoelastic FG/homogeneous bimaterial plate, which is subjected to a cooling thermal shock $\theta(\mathbf{x}, t) = -\theta_0 H(t)$ as shown in Fig. 1a. Here, θ_0 is the constant loading amplitude and $H(t)$ is the Heaviside step function. The geometry of the cracked plate is determined by the width $w = 1$,

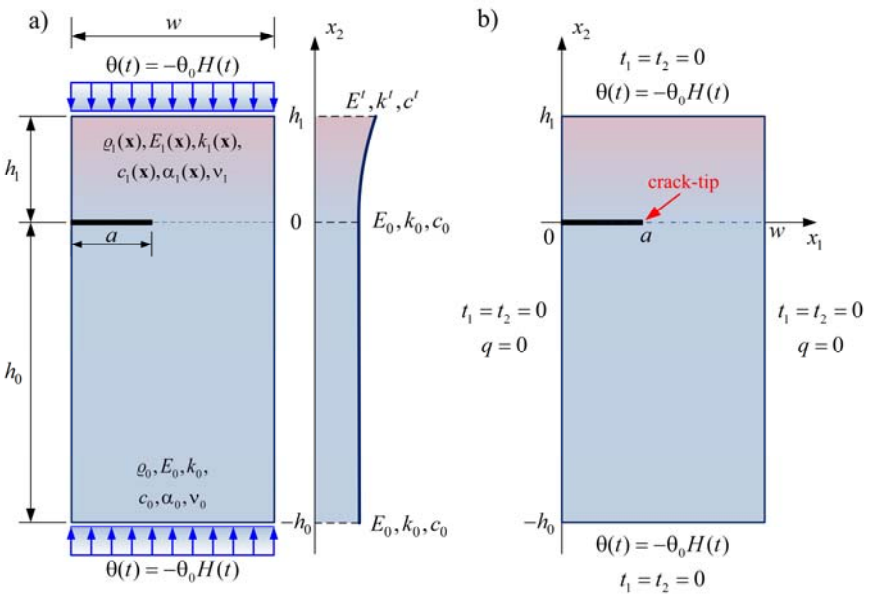

Figure 1. An edge crack in a FG/homogeneous bimaterial plate

height $h_0 + h_1 = 3w$ and crack-length $a = 0.4w$. An exponential material gradation with the gradient parameter α_g in the x_2-direction perpendicular to the crack-line of the FG coated structure is assumed as [8]

$$E = E_0 \exp(\alpha_g x_2), \qquad k = k_0 \exp(\alpha_g x_2), \qquad c = c_0 \exp(\alpha_g x_2). \tag{24}$$

The mass density, the Poisson's ratio and the linear thermal expansion coefficient are taken as $\tilde{\rho}(\mathbf{x}) = 1$, $\alpha(\mathbf{x}) = 0.02$ and $\nu = 0.25$, respectively. Plane-strain condition is assumed in the numerical calculations. The non-homogeneity of the FG layer induces a mixed mode crack-tip loading even though the cracked plate is subjected to a pure thermal loading on the top and the bottom side symmetric to the crack-faces, i.e., the mode-II dynamic SIF is also present along with the mode-I dynamic SIF. For convenience, the dynamic SIFs and the time are normalized as $\bar{K}_{I,II}(t) = K_{I,II}(t) / (\alpha_0 E_0 \theta_0 \sqrt{\pi a})$ and $\bar{t} = t\, k_0 / (a^2 \tilde{\rho}_0 c_0)$.

To test the accuracy of the proposed BEM, the numerical results are compared with those obtained by the FEM analysis, which show a good agreement [8, 9, 11]. The time variations of the normalized mode-I and mode-II SIFs for the three selected combinations of the gradient parameters $\alpha_g h_1 = \ln(2),\ \ln(3),\ \ln(5)$ and $\alpha_g h_1 = \ln(0.5),\ \ln(0.333),\ \ln(0.2)$ are presented in Figs. 2 and 3. The negative gradient parameters (Fig. 3) result in a reduction of the peak dynamic SIFs in comparison to that for positive gradient parameters (Fig. 2). The wave velocity in this case is also decreasing. Hence, the peak values of the dynamic SIFs are reached at larger time instants. The opposite tendency is observed in Fig. 2 with the increasing gradient parameters. Thus, the present results show that the gradient parameters may have significant influences on the dynamic SIFs. To investigate the influence of the thickness of the FG coating on the dynamic SIFs, four relative thickness values $h_0 / h_1 = 5,\ 10,\ 15,\ 20$ are selected for the gradient parameters $\alpha_g h_1 = \ln(2)$ and $\alpha_g h_1 = \ln(0.5)$ in the numerical analysis. The time variations of the normalized mode-I and mode-II dynamic SIFs for the selected thickness ratios are shown in Figs. 4 and 5. The peak of the SIFs decreases with decreasing thickness of the FG layer for both values of the material gradient parameter.

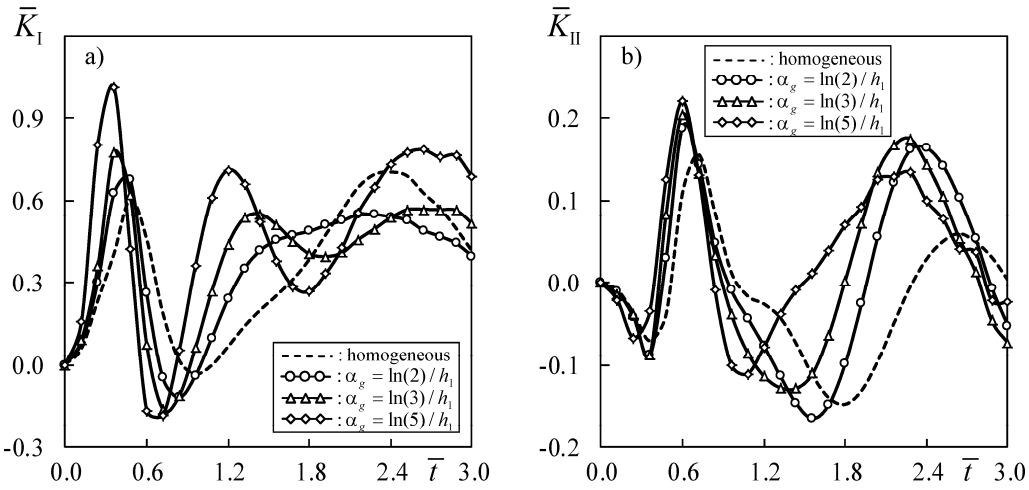

Figure 2. Normalized dynamic a) mode-I and b) mode-II SIFs for $\alpha_g h_1 = \ln(2), \ln(3), \ln(5)$

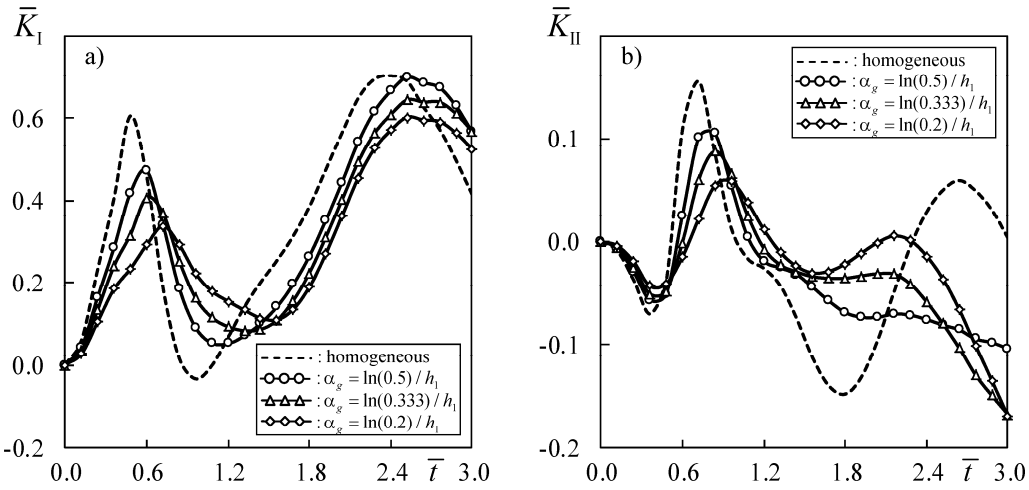

Figure 3. Normalized dynamic a) mode-I and b) mode-II SIFs for $\alpha_g h_1 = \ln(0.5), \ln(0.333), \ln(0.2)$

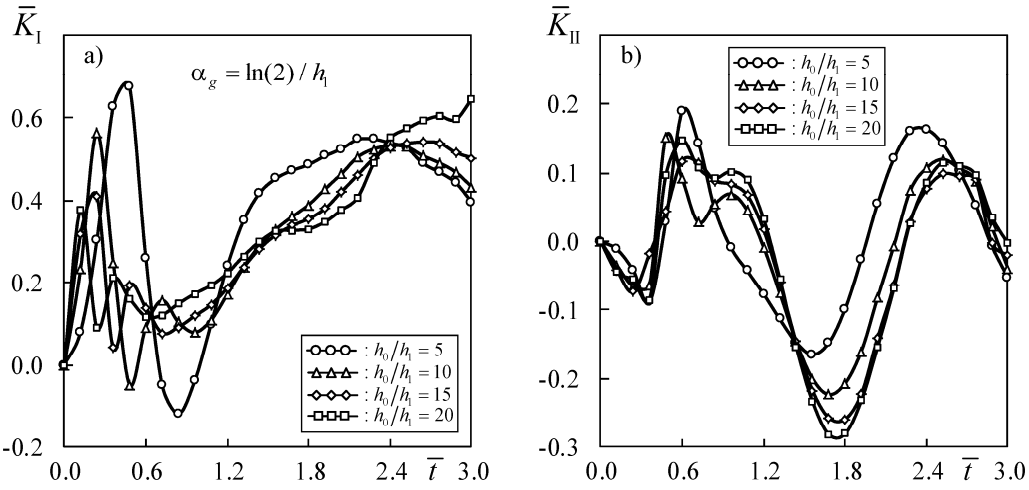

Figure 4. Normalized dynamic a) mode-I and b) mode-II SIFs for $h_0 / h_1 = 5,10,15,20$ and $\alpha_g h_1 = \ln(2)$

The effects of the thermo-mechanical coupling on the normalized dynamic mode-I and mode-II SIFs can be observed in Figs. 6 and 7. In this case, the thermo-mechanical coupling parameter (5) is taken as $\delta = 0.133$ and $\delta = 0.3$, which correspond to the previously used material parameters with the reference temperatures $T_0 = 100$ and $T_0 = 225$, respectively. With the increase of the coupling

parameter, the peak values of the normalized dynamic SIFs are reduced. The numerical results imply that the maximum amplitudes of the normalized dynamic SIFs and the time instants, at which they occur, depend significantly on the values of the gradient parameters, the ratios of the thicknesses and the thermo-mechanical coupling.

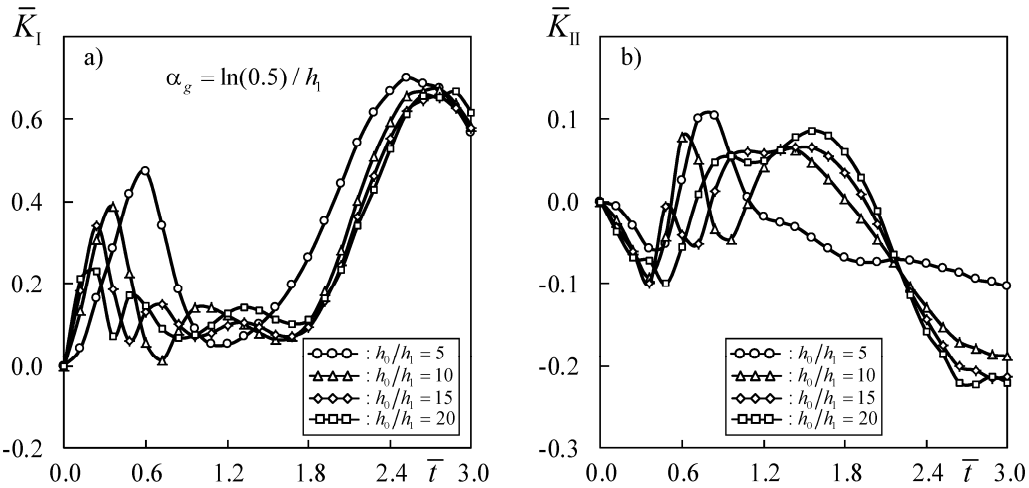

Figure 5. Normalized dynamic a) mode-I and b) mode-II SIFs for $h_0 / h_1 = 5,10,15,20$ and $\alpha_g h_1 = \ln(0.5)$

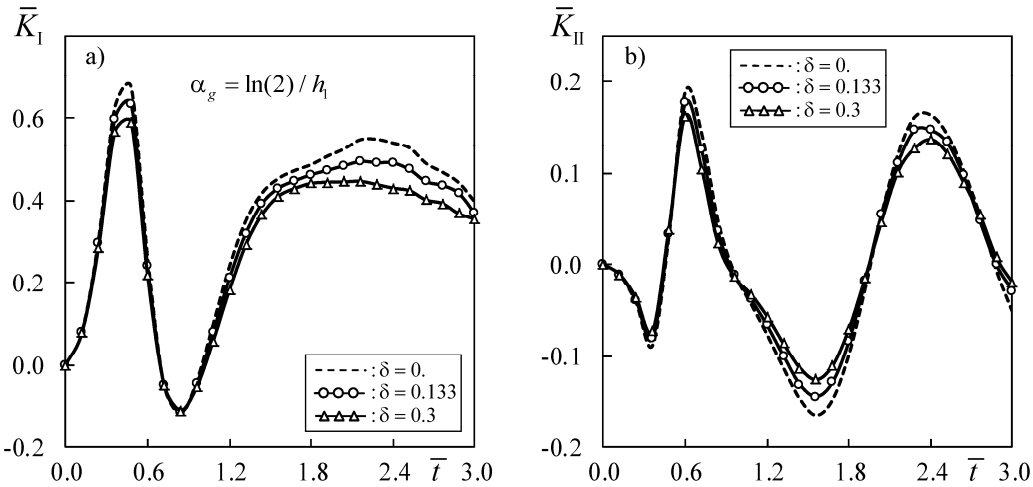

Figure 6. Normalized dynamic a) mode-I and b) mode-II SIFs for $\delta = 0, 0.133, 0.3$

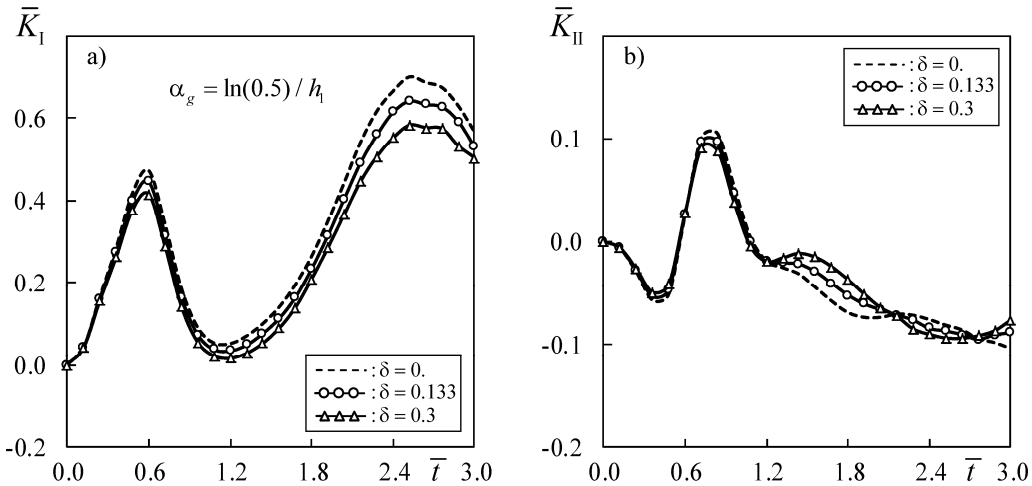

Figure 7. Normalized dynamic a) mode-I and b) mode-II SIFs for $\delta = 0, 0.133, 0.3$

5. Summary

A BEM for 2-D transient coupled thermoelastic crack analysis in FG/homogeneous bimaterials under thermal shock is presented in this paper. The sub-domain technique is applied to model the FG/homogeneous bimaterials. Fundamental solutions of linear coupled thermoelasticity for homogeneous, isotropic and linear thermoelastic solids are used to derive the boundary-domain integral equations. The material non-homogeneity of the FG layer is described by domain integrals, which are evaluated by using the RIM. A collocation-based BEM is developed in the Laplace-transformed domain. The numerical inversion of the Laplace-transform is performed by Stehfest's algorithm. The dynamic SIFs are evaluated by using displacement extrapolation technique. The temporal variations of the dynamic SIFs for an edge crack in a 2-D FG/homogeneous bimaterial plate are presented. The effects of the material gradation, the FG coating thickness and the thermo-mechanical coupling on the dynamic SIFs are analyzed.

Acknowledgement

This work is supported by the German Research Foundation (DFG, Project-No.: ZH 15/10-2), which is gratefully acknowledged.

References

[1] S. Suresh and A. Mortensen, Fundamentals of functionally graded materials: Processing and thermomechanical behaviour of graded metals and metal-ceramic composites. IOM Communications Ltd, London, 1998.

[2] L. C. Wrobel and M. H. Aliabadi, The boundary element method. J. Wiley, Chichester, New York, 2002.

[3] X. W. Gao, The radial integration method for evaluation of domain integrals with boundary-only discretization. Eng Anal Boundary Elem, 26 (2002) 905-916.

[4] X. W. Gao, A boundary element method without internal cells for two-dimensional and three-dimensional elastoplastic problems. J Appl Mech, 69 (2002) 154-160.

[5] H. Stehfest, Numerical Inversion of Laplace Transforms. Commun ACM, 13 (1970) 47-49.

[6] J. Balaš, J. Sládek and V. Sládek, Stress analysis by boundary element methods. Elsevier, Amsterdam, New York, 1989.

[7] J. Sladek, V. Sladek, C. Zhang and C. L. Tan, Meshless local Petrov-Galerkin method for linear coupled thermoelastic analysis. Comp Model Eng Sci, 16 (2006) 57-68.

[8] A. Ekhlakov, O. Khay, C. Zhang, J. Sladek, V. Sladek and X. W. Gao, Thermoelastic crack analysis in functionally graded materials and structures by a BEM. Fatigue & Fract of Eng Mater & Struct, 35 (2012) 742-766.

[9] A. V. Ekhlakov, O. M. Khay, C. Zhang, J. Sladek and V. Sladek, A BDEM for transient thermoelastic crack problems in functionally graded materials under thermal shock. Comput Mater Sci, 57 (2012) 30-37.

[10] J. Sladek, V. Sladek and C. Z. Zhang, An advanced numerical method for computing elastodynamic fracture parameters in functionally graded materials. Comput Mater Sci, 32 (2005) 532-543.

[11] A. V. Ekhlakov, O. M. Khay, C. Zhang, J. Sladek and V. Sladek, Transient coupled thermoelastic crack analysis in functionally graded materials. Struct Durab Health Monitor, 6 (2010) 329-350.

Crack Growth-based Fatigue Life Prediction Using Spline Fictitious Boundary Element Method

Cheng Su[1,2,*], Chun Zheng[1]

[1] School of Civil Engineering and Transportation, South China University of Technology, Guangzhou 510640, PR China
[2] State Key Laboratory of Subtropical Building Science, South China University of Technology, Guangzhou 510640, PR China
* Corresponding author: cvchsu@scut.edu.cn (C. Su)

Abstract Fatigue life prediction is of great importance to the design and maintenance of structural components. A boundary element method (BEM)-based approach is proposed in this paper for fatigue life prediction using crack growth analysis. The proposed methodology is based on the well-known Paris equation for fatigue crack growth rate, which is related to the amplitude of the stress intensity factor (SIF) as a crack grows. The SIF is determined by the fracture spline fictitious boundary element method (SFBEM) based on the Erdogan fundamental solutions for plane cracked problems. The fusion of SFBEM and the Erdogan fundamental solutions is computationally efficient and provides a powerful tool for crack growth-based fatigue life prediction. A numerical example based on the mode-I crack problem is presented to validate the present method. The results show that the predicted fatigue life obtained by the present approach is accurate in comparison with the analytic solution.

Keywords Fatigue crack growth, life prediction, fracture mechanics, spline fictitious boundary element method

1. Introduction

According to a survey conducted by the ASCE Committee on Fatigue and Fracture Reliability [1], fatigue is the main reason that causes the failure in steel structures. Therefore, fatigue life prediction is an important task for the design and maintenance planning of structures. In general, there are two major types of approaches to predict the fatigue life [2]. The first is based on *S-N* curves combined with a damage accumulation rule. The second is based on the fracture mechanics and crack growth analysis. Generally, these two approaches are used sequentially. The one with *S-N* curves is used at the 'design' stage, and the one with fracture mechanics is used at the 'assessment' stage for existing structures [3]. From the point of view that initial flaws inevitably exist in engineering materials, the crack growth analysis based on fracture mechanics may be more suitable for refined fatigue life prediction of structural components.

Crack growth theories have formed the bridge that links fatigue and fracture mechanics concepts [4]. The most important contribution is the establishment of the relationships between the crack growth rate $\mathrm{d}a/\mathrm{d}N$ and the stress intensity factor (SIF). The most widely used fatigue crack growth model, commonly known as Paris law, was proposed by Paris and Erdogan [5]. The Paris law connects the crack growth rate with the amplitude of SIF through a simple power function, which makes the engineering application more easily. After that, various modifications and extensions to Paris law have emerged, and different forms of modified crack growth equations have been offered by Forman [6], Elber [7] and Walker [8], et al.

Another important task in the crack growth-based fatigue life prediction is the fracture analysis. Since few analytical solutions to SIFs are available, especially for engineering structures, numerical

methods are widely employed. The boundary element method (BEM) is one of the most frequently used numerical methods. Its high precision and efficiency make it particularly suitable for fracture analysis.

In this paper, the Paris law is used to predict the crack growth-based fatigue life. To calculate the SIF, an efficient indirect boundary element method (IBEM), the spline fictitious boundary element method (SFBEM) [9-16], is adopted to perform the fracture analysis. Numerical examples are presented to illustrate the application of the proposed method.

2. Fracture analysis by SFBEM

As a modified IBEM, in SFBEM, nonsingular integral equations are derived rather than singular ones; spline functions with excellent performance are adopted as the trial functions to the unknown fictitious loads; and the boundary-segment-least-square technique is employed for eliminating the boundary residues. Because of these modifications, SFBEM is of high accuracy and efficiency in general. SFBEM was first applied to the solution of static plane elasticity problems [9], and so far it has been extended to multi-domain plane problems [10], orthotropic plane problems [11], plate bending problems [12], elastic fracture problems [13], stochastic elastostatic problems [14, 15] and probabilistic fracture mechanics [16].

In this study, a SFBEM based on the Erdogan fundamental solutions for infinite cracked plates [13, 16] is employed to conduct fracture analysis of linear-elastic cracked structures. As the Erdogan fundamental solutions [17, 18] are derived from an infinite plate containing a crack, when they are used in the formulation of BEM, the stress boundary conditions on the crack surface are automatically satisfied, and the singular behavior at the crack tip can be naturally captured. Therefore, no boundary elements are required to place along the crack surface. In addition, the SIF of the crack problem can be calculated directly from the corresponding fundamental solution of SIF, with no need of transformation from the displacement field around the crack tip, as is normally required in SIF analysis by the other numerical methods. The SFBEM in combination with the Erdogan fundamental solutions has been shown to be more computationally accurate and efficient and thus provides a powerful tool for fracture analysis.

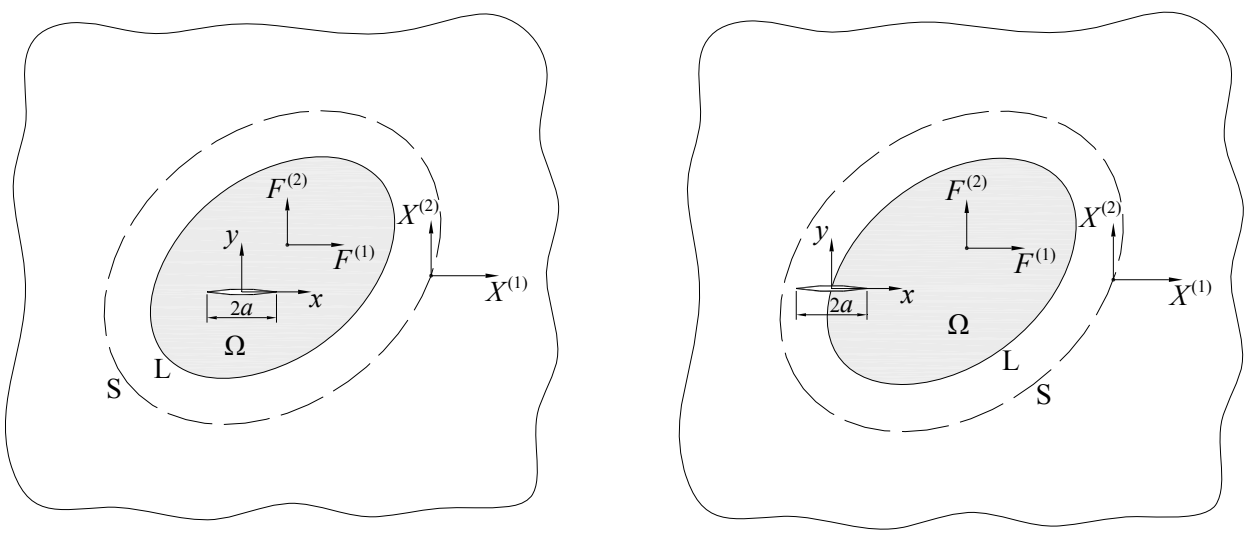

(a) Inner crack (b) Edge crack

Figure 1. Plane domain embedded in an infinite plane with a crack

Consider an elastic plane domain with a crack, as shown in Fig.1. Let the domain studied be Ω, and assume the configuration boundary of the domain to be L, not including the crack surface. The body forces within the domain are assumed to be $F^{(l)}$ (l=1, 2), and the lengths of the inner crack and the edge crack are taken to be 2a and a, as shown in Fig.1(a) and Fig.1(b), respectively. Embed Ω into an infinite plane domain with a crack, the crack length being 2a, and apply unknown fictitious loads $X^{(l)}$ (l=1, 2) along a fictitious boundary S outside Ω, whose shape is similar to that of the real boundary L, as also shown in Fig.1.

Due to the use of the Erdogan fundamental solutions [18], not only the governing differential equations within Ω but also the stress boundary conditions on the crack surface are satisfied automatically. Therefore, only the boundary conditions along the contour of Ω need to be considered. Under the combined action of the body force $F^{(l)}$ and the fictitious loads $X^{(l)}$ (l=1, 2), the boundary conditions along L can be expressed as

$$\sum_{l=1}^{2}\int_{\mathrm{S}} G_k^{(l)}\left(z_{\mathrm{L}};z_{\mathrm{S}}\right)X^{(l)}\left(z_{\mathrm{S}}\right)\mathrm{d}s+\sum_{l=1}^{2}\iint_{\Omega} G_k^{(l)}\left(z_{\mathrm{L}};z_{\Omega}\right)F^{(l)}\left(z_{\Omega}\right)\mathrm{d}V=H_k\left(z_{\mathrm{L}}\right)\qquad\left(k=1,2\right),\tag{1}$$

where $z_{\mathrm{L}}\in\mathrm{L}$, $z_{\mathrm{S}}\in\mathrm{S}$, $z_{\Omega}\in\Omega$; k=1,2 denotes that two boundary conditions exist along L for plane problems; H_k are the known boundary functions along L; and $G_k^{(l)}$ are the kernel functions consisting of the Erdogan fundamental solutions.

Eq. (1) are nonsingular fictitious boundary integral equations because the source points will never coincide with the field points in the kernel functions. However, analytic solutions to Eq. (1) are normally not available, and the integral equations should be solved on a numerical baisis. For this purpose, the unknown fictitious loads $X^{(l)}$ are expressed in terms of a set of B-spline functions, and the boundary-segment technique is used to eliminate the resulting boundary residues [10]. Then Eq. (1) turns into the following numerical equation as

$$\left[A\right]\left\{X\right\}+\left\{B\right\}=\left\{C\right\},\tag{2}$$

where $\left\{X\right\}$ is the column matrix consisting of the unknown spline node parameters of the fictitious loads along S; $\left[A\right]$ is influence matrix of $\left\{X\right\}$; and $\left\{B\right\}$ and $\left\{C\right\}$ are the known column matrices depending on the body forces $F^{(l)}$ within Ω and the boundary condition functions H_k along L, respectively. Usually Eq. (2) needs to be solved on a least-squares basis as generally overdeterminate collocation is conducted to achieve a better solution with more boundary segments while keeping the number of fictitious boundary elements to be at a lower level.

Once the spline node parameter $\left\{X\right\}$ is determined, the mode-I and II SIFs of the cracked problem can be obtained from the discrete forms of the following equations:

$$K_j=\sum_{l=1}^{2}\int_{\mathrm{S}} K_j^{(l)}\left(z_{\mathrm{S}}\right)X^{(l)}\left(z_{\mathrm{S}}\right)\mathrm{d}s+\sum_{l=1}^{2}\iint_{\Omega} K_j^{(l)}\left(z_{\Omega}\right)F^{(l)}\left(z_{\Omega}\right)\mathrm{d}V\qquad\left(j=\mathrm{I},\mathrm{II}\right),\tag{3}$$

where $K_j^{(l)}$ (j=I,II; l=1,2) are the Erdogan fundamental solutions of SIFs [18].

3. Crack growth-based fatigue life prediction

3.1. Paris law

Crack growth can occur under cyclic loading. Using Paris equation, the crack growth rate can be expressed as the function of the SIF range, and can be written as

$$\frac{\mathrm{d}a}{\mathrm{d}N} = C\left(\Delta K\right)^m \qquad \left(\Delta K > \Delta K_{\mathrm{th}}\right), \tag{4}$$

where a is the crack size; N is the number of cycles of the alternating stress; $\Delta K = K(\sigma_{\max}) - K(\sigma_{\min})$ is the SIF range; ΔK_{th} is the fatigue threshold, which means if $\Delta K \le \Delta K_{\mathrm{th}}$, the crack is assumed to be non-propagating; C and m are the material constants obtained from experiments.

By integrating Eq. (4), the crack growth-based fatigue life can be obtained as

$$N_{\mathrm{p}} = \int_{a_0}^{a_{\mathrm{c}}} \frac{\mathrm{d}a}{C\left(\Delta K\right)^m}, \tag{5}$$

where a_0 is the initial crack size; a_{c} is the critical crack size at fatigue failure and can be determined using the fracture toughness K_{Ic}.

Generally, the explicit solutions to SIFs for most engineering problems are not available. Therefore, numerical approaches are required for fatigue life prediction when using Eq. (5).

3.2. Fatigue life prediction using SFBEM

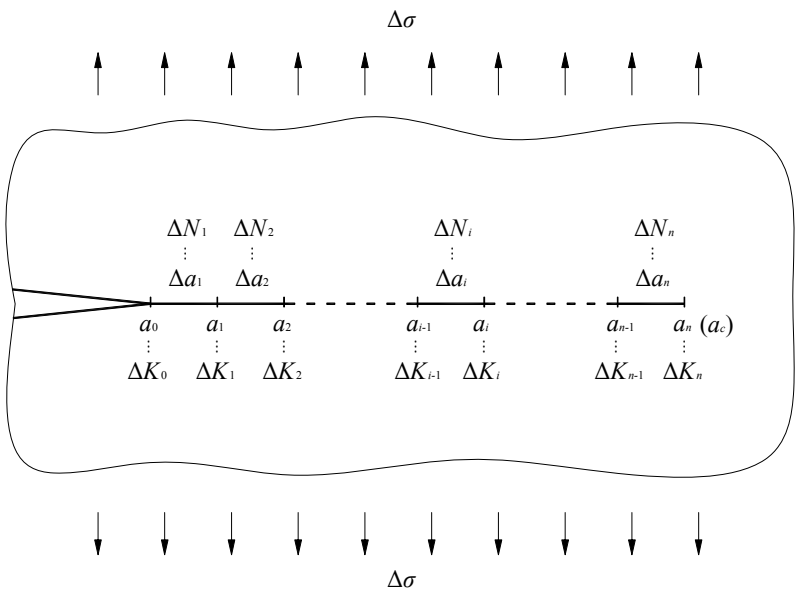

Figure 2. Propagation of a crack

The propagation of a crack from the initial crack size a_0 to the critical crack size a_{c} can be illustrated in Fig.2. The number of cycles of the alternating stress corresponding to the ith step of the crack growth can be approximately expressed as

$$\Delta N_i = \frac{\Delta a_i}{\overline{\left(\frac{\mathrm{d}a}{\mathrm{d}N}\right)_i}}, \tag{6}$$

where Δa_i is the crack growth size of the ith step; $\overline{\left(\frac{\mathrm{d}a}{\mathrm{d}N}\right)_i}$ is the average crack growth rate during the current step and can be determined using the Paris equation, that is

$$\overline{\left(\frac{\mathrm{d}a}{\mathrm{d}N}\right)_i} = C\left(\overline{\Delta K_i}\right)^m. \tag{7}$$

In the above equation, $\overline{\Delta K_i}$ is the average SIF range of the ith step and can be defined as

$$\overline{\Delta K_i} = \left(\Delta K_{i-1} + \Delta K_i\right)/2\,, \tag{8}$$

where $\Delta K_{i\text{-}1}$ and ΔK_i are the amplitudes of SIF corresponding to $a_{i\text{-}1}$ and a_i, respectively, and can be determined using the SFBEM presented in section 2.

The procedure for fatigue life prediction based on SFBEM is as follows:

1. Determine the initial SIF range ΔK_0 corresponding to the given initial crack size a_0 using the SFBEM in conjunction with the Erdogan fundamental solutions.

2. Check if $\Delta K_0 > \Delta K_{\text{th}}$. If yes, the propagation of the crack will occur.

3. Assume the crack growth size of the ith step to be $\Delta a_i = \eta a_{i\text{-}1}$ (i=1,2,…), in which η=0.1~0.01. Then the crack size of the ith step is $a_i = a_0 + \sum_{j=1}^{i} \Delta a_j$.

4. Determine the SIF range ΔK_i corresponding to a_i using SFBEM.

5. Calculate the average SIF range of the ith step $\overline{\Delta K_i}$ using Eq. (8).

6. Calculate the number of cycles of the alternating stress of the ith step ΔN_i using Eqs. (6) and (7).

7. Check if $K_i(\sigma_{\max}) < K_{\text{Ic}}$. If yes, go to step 3. If no, then stop. Assume the final step number is n. Then the fatigue life can be obtained as

$$N_{\text{p}} = \sum_{i=1}^{n} \Delta N_i\,. \tag{9}$$

4. Numerical examples

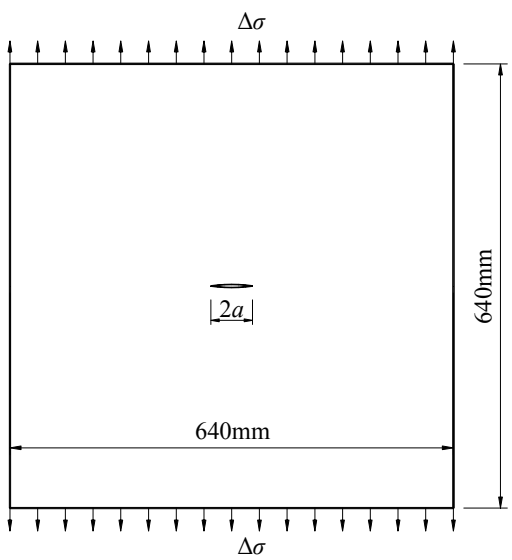

Figure 3. A square plate with a center crack

Fig.3 shows a square plate with a center crack subjected to a cyclic loading with $\Delta\sigma$=200MPa ($\sigma_{\max}$=200MPa, $\sigma_{\min}$=0). The fatigue threshold and the fracture toughness of the material are taken to

be ΔK_{th}=5.5MPa·m$^{1/2}$ and K_{Ic}=104MPa·m$^{1/2}$, respectively. The material constants C and m in the Paris equation are assumed to be C=6.9×10^{-12} m/cycle/(MPa·m$^{1/2}$)^3 and m=3, respectively. The initial crack size is taken to be a_0=0.5mm.

4.1. Analytic solution

Since the crack size is much smaller than the size of the plate, the SIF in this case can be approximately determined using the analytic solution for an infinite plate with a crack, that is

$$K = \sigma\sqrt{\pi a}\ . \tag{10}$$

It can be deduced from the above equation that

$$\Delta K_0 = \Delta\sigma\sqrt{\pi a_0} = 7.927\,\mathrm{MPa}\cdot\mathrm{m}^{\frac{1}{2}} > \Delta K_{\mathrm{th}} = 5.5\,\mathrm{MPa}\cdot\mathrm{m}^{\frac{1}{2}}, \tag{11}$$

and thus the crack propagation will occur.

From Eq. (10), we also have

$$a_{\mathrm{c}} = \frac{1}{\pi}\left(\frac{K_{\mathrm{Ic}}}{\sigma_{\max}}\right)^2 = 86.07\,\mathrm{mm}\ . \tag{12}$$

Therefore, the fatigue life can be obtained using Eq. (5) as follows:

$$N = \int_{a_0}^{a_{\mathrm{c}}} \frac{\mathrm{d}a}{C(\Delta K)^m} = \frac{1}{C(m/2-1)\left(\Delta\sigma\sqrt{\pi}\right)^m}\left(\frac{1}{a_0^{m/2-1}} - \frac{1}{a_{\mathrm{c}}^{m/2-1}}\right) = 2.688\times10^5\ \mathrm{cycle}\ . \tag{13}$$

4.2. Numerical solution

When using SFBEM to calculate the SIF of the plate, 16 fictitious boundary elements and 40 boundary segments are adopted, and the distance between the fictitious boundary and the real boundary is taken to be d=40mm. The value of the coefficient η in step 3 of section 3.2 is assumed to be 0.1. In the calculation, 53 steps of crack propagation have been involved in total. The results obtained by the present method are listed in Table 1. For the purpose of comparison, the results of the analytic solution are also presented in the table.

Table 1. Results of fatigue life prediction

Method	ΔK_0 (MPa·m$^{1/2}$)	a_{c} (mm)	N_{p} (cycle)
Present method	7.928	74.57	2.652×10^5
Analytic method	7.927	86.07	2.688×10^5

It can be seen from Table 1 that, for the fatigue life of the plate, the results obtained by both methods are in good agreement, while for the critical crack size, certain discrepancy occurs. Actually, as the crack size increases with propagation, the error of Eq. (10) corresponding to the case of infinite plate becomes larger, leading to the error of the critical crack size in the analytic solution, as shown in Fig.4. But as the crack size approaches the critical size, the number of cycles at this stage contributes much less to the fatigue life. Therefore, good agreement is still observed for the prediction of the fatigue life between the two methods, as can be seen from Fig.5.

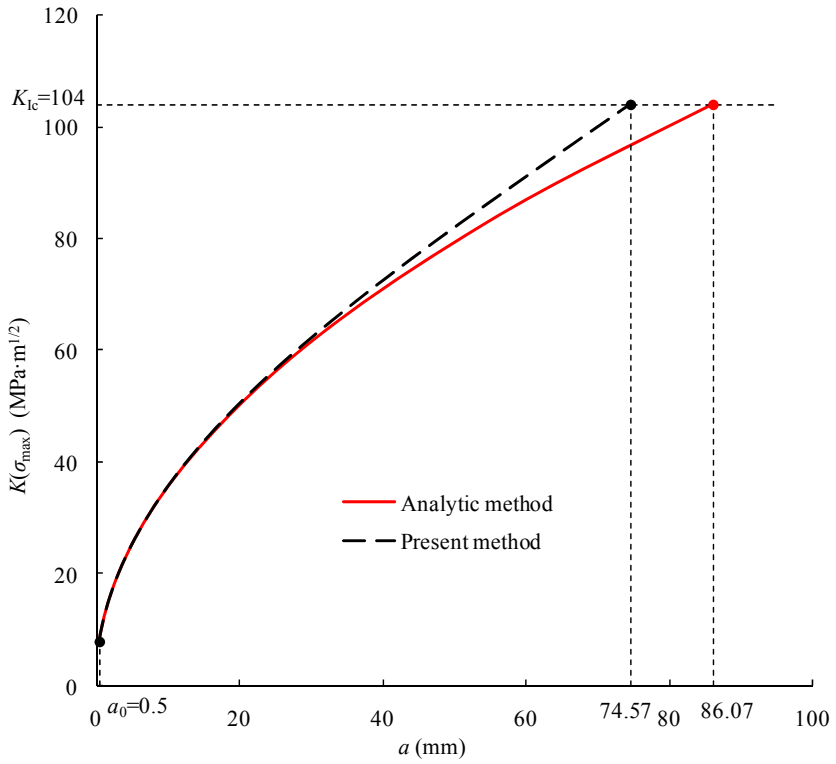

Figure 4. SIF versus the crack size

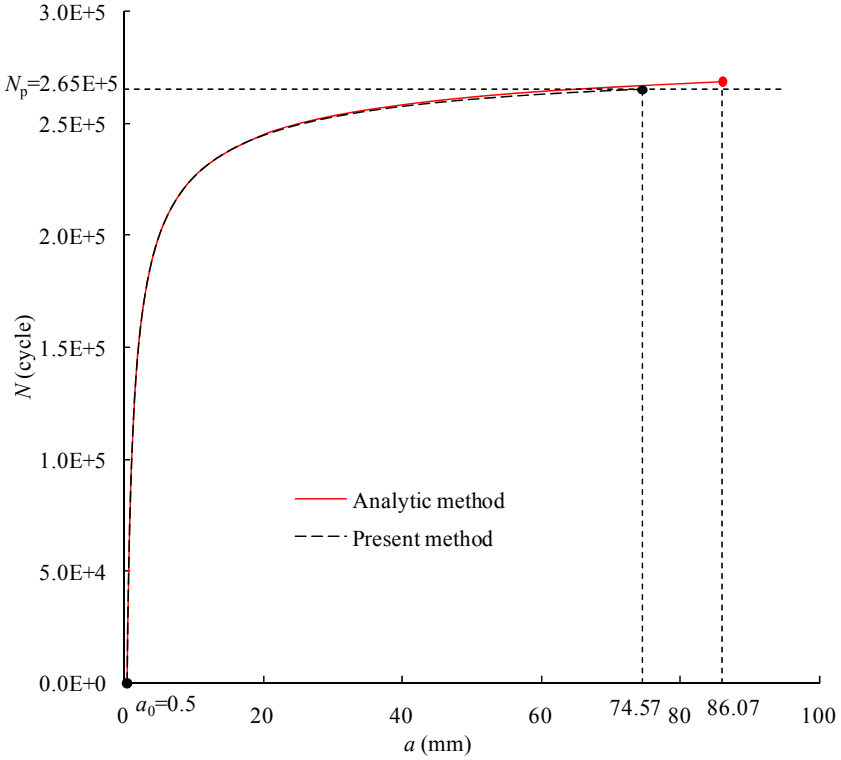

Figure 5. Number of cycles versus the crack size

5. Conclusions

The SFBEM based on the Erdogan fundamental solutions has high accuracy and efficiency for SIF analysis of linear-elastic cracked structures, and therefore can serve as an effective approach for

crack growth-based fatigue life prediction using the Paris equation. A numerical example is presented to demonstrate the validity of the present method. The results show that the predicted fatigue life obtained by the present method agrees well with the analytic solution.

Acknowledgements

This research was supported by the National Natural Science Foundation of China (51078150) and the State Key Laboratory of Subtropical Building Science, South China University of Technology (2013ZA01).

References

[1] ASCE, Committee on Fatigue and Fracture Reliability of the Committee on Structural Safety and Reliability of the Structural Division. Fatigue reliability 1-4. J. Struct. Engrg., ASCE, 108 (1982) 3-88.
[2] Y.B. Xiang, Z.Z. Lu, Y.M. Liu. Crack growth-based fatigue life prediction using an equivalent initial flaw model. Part I Uniaxial loading. International Journal of Fatigue, 32 (2010) 341-349.
[3] M.K. Chryssanthopoulos, T.D. Righiniotis. Fatigue reliability of welded steel structures. Journal of Constructional Steel Research, 62 (2006) 1199-1209.
[4] J.C. Newman Jr. The merging of fatigue and fracture mechanics concepts a historical perspective. Progress in Aerospace Sciences, 34 (1998) 347-390.
[5] P.C. Paris, F. Erdogan. A critical analysis of crack propagation laws. ASME J Basic Eng, 85 (1963) 528-534.
[6] R.G. Forman, V.E. Kearney, R.M. Engle. Numerical analysis of crack propagation in cyclic-loaded structures. Journal of Basic Engineering, 89 (1967) 459-464.
[7] W. Elber. Fatigue crack closure under cyclic tension. Engng Fract Mech 2 (1970) 37-45.
[8] K. Walker. The effect of stress ratio during crack propagation and fatigue for 2024-T3 and 7075-T6 aluminum. ASTM STP 462, 1970, 1-14.
[9] C. Su, D.J. Han. Analysis of elastic plane problems by the spline fictitious boundary element method. Computational Method in Engineering and Science-Theory and Practice, South China University of Technology Press, Guangzhou, PR China, 1997, 538-542.
[10] C. Su, D.J. Han. Multi-domain SFBEM and its application in elastic plane problems. Journal of Engineering Mechanics, ASCE, 126 (2000) 1057-1063.
[11] C. Su, D.J. Han. Elastic analysis of orthotropic plane problems by the spline fictitious boundary element method. Applied Mathematics and Mechanics, 23 (2002) 446-453.
[12] C. Su, D.J. Han. Analysis of raft foundation by spline fictitious boundary element method. Journal of China Civil Engineering, 34(2001) 61-66 (in Chinese).
[13] C. Su, C. Zheng. Calculation of stress intensity factors by boundary element method based on Erdogan fundamental solutions. Chinese Joumal of Theoretical and Applied Mechanics, 39 (2007) 93-99 (in Chinese).
[14] C. Su, S.W. Zhao, H.T. Ma. Reliability analysis of plane elasticity problems by stochastic spline fictitious boundary element method. Engineering Analysis with Boundary Elements, 36 (2012) 118-124.
[15] C. Su, S.W. Zhao, Stochastic spline fictitious boundary element method in elastostatic problems with random fields, Engineering Analysis with Boundary Elements, 36 (2012) 759-77.
[16] C. Su, C. Zheng, Probabilistic fracture mechanics analysis of linear-elastic cracked structures by spline fictitious boundary element method, Engineering Analysis with Boundary Elements，36 (2012) 1828－1837.
[17] F. Erdogan. On the stress distribution in a plate with collinear cuts under arbitrary loads. Proc. 4th U. S. National Congress of Applied Mechanics, 1962, 547-553.

[18] P.W. Tan, I.S. Raju, J.C. Newman Jr. Boundary force method for analyzing two-dimensional cracked bodies. NASA Langley Research Center, Hampton, Virginia, 1986.

Null-field integral approach for the piezoelectricity problems with arbitrary elliptical inhomogeneities

Ying-Te Lee[1], Jeng-Tzong Chen[1*], Shyh-Rong Kuo[1]

[1] Department of Harbor and River Engineering, National Taiwan Ocean University, Keelung 20224, Taiwan
* Corresponding author: jtchen@mail.ntou.edu.tw

Abstract Based on the successful experience of solving anti-plane problems containing arbitrary elliptical inclusions, we extend to deal with the piezoelectricity problems containing arbitrary elliptical inhomogeneities. In order to fully capture the elliptical geometry, the keypoint of the addition theorem in terms of the elliptical coordinates is utilized to expand the fundamental solution to the degenerate kernel and boundary densities are simulated by the eigenfunction expansion. Only boundary nodes are required instead of boundary elements. Therefore, the proposed approach belongs to one kind of meshless and semi-analytical methods. Besides, the error stems from the number of truncation terms of the eigenfuntion expansion and the convergence rate of exponential order is better than the linear order of the conventional boundary element method. It is worth noting that there are Jacobian terms in the degenerate kernel, boundary density and contour integral. However, they would cancel each other out in the process of the boundary contour integral. As the result, the orthogonal property of eigenfunction is preserved and the boundary integral can be easily calculated. Finally, the problem of two elliptical inhomogeneities in an infinite piezoelectric material subject to anti-plane remote shear and in-plane electric field is considered to demonstrate the validity of the present method. Besides, two circular inhomegenieties can be seen as a special case to compare with the available data by approximating the major and minor axes.

Keywords Piezoelectricity, Elliptical inhomogeneity, In-plane electric field, Anti-plane shear

1. Introduction

In recent years, more and more investigators paid their attention to study the actuators and sensors because they were widely used in smart materials or structures technology. Therefore, the study of electromechanical behavior of piezoelectric material becomes an important issue. It is well-known that it results in the stress concentration when the inhomogeneities or defects exist in the materials. In this article, we extend the previous works [1] on the piezoelectricity problems with “circular” inclusions to deal with the problem containing “elliptical” inhomogeneities.

For an elliptical shape, it may be more general than a circular geometry in the practical applications. Based on the concept of complex potential, Gong and Meguid [2] used the conformal mapping and Laurent series expansion to solve an infinite medium containing an elliptical inhomogeneity under anti-plane shear. Explicit form of the stress function in the inhomogeneity as well as in the matrix was derived in their work. Then, a generalized and unified treatment was developed by Gong [3] for the elliptical inclusion embedded in an infinite matrix not only under the remote shear but also interacting by the screw dislocation. Besides, Shen *et al*. [4] developed a semi-analytical solution for the problem of an elliptical inclusion not perfectly bonded in an infinite matrix under anti-plane shear. Under the assumption of continuous tractions and discontinuous displacements across the interface, they used a model of a spring layer with thickness to simulate the interface. They found the non-uniform stress field and the average stresses in the inclusion is highly related to the aspect ratio of the inclusion and the parameter of interface simulation. For arbitrary distributed elliptical inclusions under remote shears, few works were found in literature.

To the authors' knowledge, Noda and Matsuo [5] have used the Cauchy-type singular integral equations to solve an interaction problem of elliptical inclusions distributed in an infinite medium under a longitudinal shear loading. They discussed different outlet of two elliptical inclusions as well as different ratios of shear moduli. Later, Lee and Kim [6] also revisited the problem of Noda and Matsuo by using the volume integral equation method. Lee and Chen [7] also successfully used the null-field boundary integral equation in conjunction with degenerate kernels to solve the problem. Besides, we don't find other works to discuss on this issue containing more than two inclusions.

For the piezoelectricity problems with circular inclusions, many researchers [8-12] made much contribution on this issue. However, for containing elliptical inhomogenieties, Meguid and Zhong [13] used the complex-variable method to study the problem of a piezoelectric elliptical inhomogeneity. They derived the analytical solution in their works. Pak [14] used the conformal mapping technique to obtain a closed-form solution. The previous works were very similar. The main difference is that Meguid and Zhong provided a general series solution, but Pak derived an explicit closed-form solution. Besides, numerous researchers have successfully solved similar problems with an elliptical inclusion. However, to the authors' best knowledge, we don't find any work on dealing with anti-plane piezoelectric problems containing two or more than two elliptical inclusions in the literature. This is our main concern.

In this paper, we extend the successful experience of solving piezoelectricity with circular inclusions to deal with the problem containing elliptical holes and/or inclusions. By fully employing the elliptical geometry, fundamental solutions were expanded into the degenerate kernel by using an addition theorem in terms of the elliptical coordinates, and boundary densities are approximated by the eigenfunction expansion. The proposed approach can be seen as one kind of meshless and semi-analytical methods because only collocation points on the real boundary are required and the error purely attributes to the number of truncation terms. In order to verify the accuracy for solving two or more than two elliptical inclusions, the available result of two circular-inclusion case is used to compare with the solution of present approach by numerically approaching the length of the major axis to be equal to the minor axis.

2. Problem statement and formulation

2.1. Problem statement

The problem to be considered here is an infinite piezoelectric medium with multiple elliptical inclusions under the remote anti-plane shears (σ_{zx}^{∞} and σ_{zy}^{∞}) and the in-plane far-field electric field

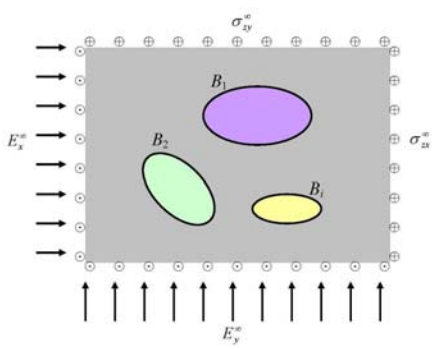

Figure 1 Sketch of the problem

(E_x^∞ and E_y^∞) as shown in Fig. 1. Bleustein [12] has pointed out that if one takes the plane normal to the poling direction as the plane of interest, only the anti-plane displacement (w) couples with the in-plane electric fields (E_x and E_y). Therefore, only the anti-plane displacement and in-plane electric field are considered in this article such as u, v and E_z are the vanishing components. In the absence of the body forces and body charges, the governing equations coupled by the displacement and electric potential can be obtained as follows:

$$c_{44}\nabla^2 w + e_{15}\nabla^2\Phi = 0\,,\quad e_{15}\nabla^2 w - \varepsilon_{11}\nabla^2\Phi = 0\,, \tag{1}$$

where ∇^2 is the two-dimensional Laplacian operator, c_{44} is the elastic modulus, e_{15} is the piezoelectric constant, ε_{11} is the dielectric constant, w is the anti-plane displacement and Φ is the in-plane electric potential. From Eq.(1), we can simplify the equaitons as

$$\nabla^2 w = 0 \quad \text{and} \quad \nabla^2\Phi = 0\,. \tag{2}$$

The constitutive equations coupled between the elastic filed and electric field are

$$\sigma_{zx} = c_{44}\gamma_{zx} - e_{15}E_x\,,\quad \sigma_{zy} = c_{44}\gamma_{zy} - e_{15}E_y\,, \tag{3}$$

$$D_x = e_{15}\gamma_{zx} + \varepsilon_{11}E_x\,,\quad D_y = e_{15}\gamma_{zy} + \varepsilon_{11}E_y\,, \tag{4}$$

where γ_{zx} and γ_{zy} are the anti-plane shear strains, and D_x and D_y are the in-plane electric displacements. By taking free body technique, the problem can be decomposed into two parts. One is an infinite piezoelectric medium with N elliptical holes (Fig.2(a)) and the other is only N-inclusions problem (Fig.2(b)). For the problem in Fig.2(a), it can be superimposed by two parts as shown in Fig.3(a) and Fig.3(b). Both the two parts in Figs. 2(b) and 3(b) satisfy the Lapalce

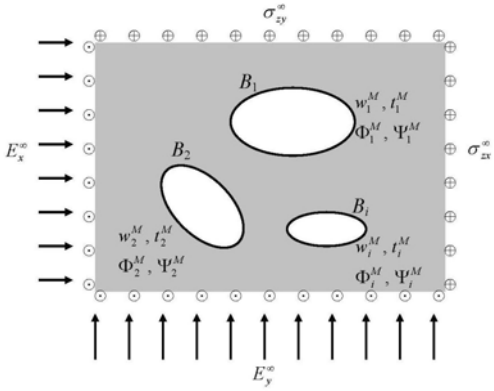

Figure 2(a) An infinite plane containing elliptical holes subject to remote shears and far-field in-plane electric fields

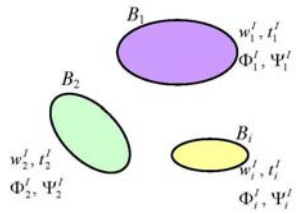

Figure 2(b) Multiple elliptical inclusions

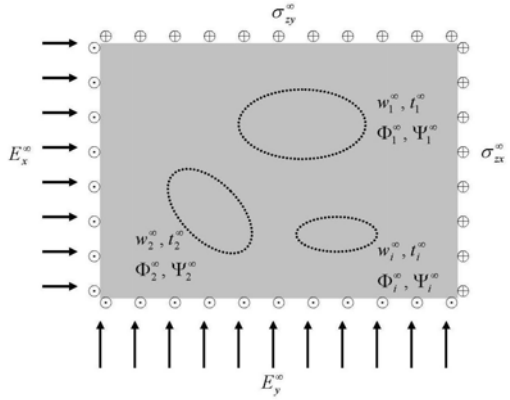

Figure 3(a) An infinite medium subject to remote shears and far-field in-plane electric fields

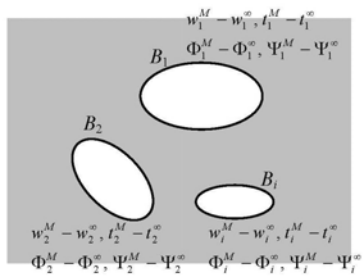

Figure 3(b) An infinite medium containing elliptical holes

equations as shown in Eq.(2). Besides, the interface between the matrix and inclusion is assumed perfectly bonded and it satisfies the following interface condition for stress fields and electric fields

$$w^M = w^I \quad \text{and} \quad \sigma_{z\xi}^M = \sigma_{z\xi}^I \quad \text{on} \quad B_k\,, \tag{5}$$

$$\Phi^M = \Phi^I \quad \text{and} \quad D_\xi^M = D_\xi^I \quad \text{on} \quad B_k\,. \tag{6}$$

2.2. Dual null-field boundary integral formulation

2.2.1 Conventional version

The integral equation for the domain point can be derived from the third Green's identity, we have

$$w(\mathbf{x}) = \int_B T(\mathbf{s},\mathbf{x})\, w(\mathbf{s})\, dB(\mathbf{s}) - \int_B U(\mathbf{s},\mathbf{x})\, t(\mathbf{s})\, dB(\mathbf{s}),\ \mathbf{x} \in D\,, \tag{7}$$

$$t(\mathbf{x}) = \int_B M(\mathbf{s},\mathbf{x})\, w(\mathbf{s})\, dB(\mathbf{s}) - \int_B L(\mathbf{s},\mathbf{x})\, t(\mathbf{s})\, dB(\mathbf{s}),\ \mathbf{x} \in D\,, \tag{8}$$

where B is the boundary, $\mathbf{s}$ and $\mathbf{x}$ are the source and field points, respectively, $t(\mathbf{x}) = \partial w(\mathbf{x})/\partial \mathbf{n}_\mathbf{x}$, $t(\mathbf{s}) = \partial w(\mathbf{s})/\partial \mathbf{n}_\mathbf{s}$, $\mathbf{n}_\mathbf{s}$ and $\mathbf{n}_\mathbf{x}$ denote the outward normal vectors at the source point $\mathbf{s}$ and field point $\mathbf{x}$, respectively, D is the domain of interest and the kernel function, $U(\mathbf{s},\mathbf{x}) = \dfrac{1}{2\pi}\ln r$ ($r \equiv |\mathbf{x}-\mathbf{s}|$), is the fundamental solution which satisfies

$$\nabla^2 U(\mathbf{x},\mathbf{s}) = \delta(\mathbf{x}-\mathbf{s})\,, \tag{9}$$

in which $\delta(\mathbf{x}-\mathbf{s})$ denotes the Dirac-delta function. The other kernel functions, $T(\mathbf{s},\mathbf{x})$, $L(\mathbf{s},\mathbf{x})$, and $M(\mathbf{s},\mathbf{x})$, are defined by

$$T(\mathbf{s},\mathbf{x}) = \frac{\partial U(\mathbf{s},\mathbf{x})}{\partial \mathbf{n}_\mathbf{s}}\,,\quad L(\mathbf{s},\mathbf{x}) = \frac{\partial U(\mathbf{s},\mathbf{x})}{\partial \mathbf{n}_\mathbf{x}}\,,\quad M(\mathbf{s},\mathbf{x}) = \frac{\partial^2 U(\mathbf{s},\mathbf{x})}{\partial \mathbf{n}_\mathbf{s}\partial \mathbf{n}_\mathbf{x}}\,. \tag{10}$$

By moving the field point $\mathbf{x}$ to the boundary, the dual boundary integral equations for the boundary point can be obtained as follows:

$$\frac{1}{2}w(\mathbf{x}) = C.P.V.\int_B T(\mathbf{s},\mathbf{x})\, w(\mathbf{s})\, dB(\mathbf{s}) - \int_B U(\mathbf{s},\mathbf{x})\, t(\mathbf{s})\, dB(\mathbf{s}),\mathbf{x} \in B\,, \tag{11}$$

$$\frac{1}{2}t(\mathbf{x}) = H.P.V.\int_B M(\mathbf{s},\mathbf{x})\, w(\mathbf{s})\, dB(\mathbf{s}) - C.P.V.\int_B L(\mathbf{s},\mathbf{x})\, t(\mathbf{s})\, dB(\mathbf{s}),\mathbf{x} \in B\,, \tag{12}$$

where *C.P.V.* and *H.P.V.* denote the Cauchy principal value and Hadamard (or called Mangler) principal value, respectively. Besides, once the field point $\mathbf{x}$ locates outside the domain ($\mathbf{x} \in D^c$), we obtain the dual null-field integral equations as shown below

$$0 = \int_B T(\mathbf{s},\mathbf{x})\, w(\mathbf{s})\, dB(\mathbf{s}) - \int_B U(\mathbf{s},\mathbf{x})\, t(\mathbf{s})\, dB(\mathbf{s}),\ \mathbf{x} \in D^c\,, \tag{13}$$

$$0 = \int_B M(\mathbf{s},\mathbf{x})\, w(\mathbf{s})\, dB(\mathbf{s}) - \int_B L(\mathbf{s},\mathbf{x})\, t(\mathbf{s})\, dB(\mathbf{s}),\ \mathbf{x} \in D^c\,, \tag{14}$$

where D^c is the complementary domain. Equations (7), (8), (13) and (14) are conventional formulations where the point is not located on the real boundary. Singularity occurs and concept of principal values is required once Eqs.(11) and (12) are considered. The traction $t(\mathbf{s})$ is the directional derivative of $w(\mathbf{s})$ along the outer normal direction at $\mathbf{s}$. In order to satisfy the interface condition, the collocation points are located on the boundary. For calculating the stress in the domain, the normal vector of an interior point is artificially given, *e.g.* $t(\mathbf{x}) = \partial w(\mathbf{x})/\partial x$, if $\mathbf{n}_\mathbf{x} = (1,0)$ and $t(\mathbf{x}) = \partial w(\mathbf{x})/\partial y$, if $\mathbf{n}_\mathbf{x} = (0,1)$. In other words, the selection of $\mathbf{n}$ depends on the stress under consideration.

2.2.2 Present version

By introducing the degenerate kernels, the collocation point can be located on the real

boundary free of calculating principal value using a small circular bump. Therefore, the representations of integral equations including the boundary point for the interior problem can be written as

$$w(\mathbf{x}) = \int_B T^i(\mathbf{s},\mathbf{x}) w(\mathbf{s})\, dB(\mathbf{s}) - \int_B U^i(\mathbf{s},\mathbf{x}) t(\mathbf{s})\, dB(\mathbf{s}), \mathbf{x} \in D \cup B, \tag{15}$$

$$t(\mathbf{x}) = \int_B M^i(\mathbf{s},\mathbf{x}) w(\mathbf{s})\, dB(\mathbf{s}) - \int_B L^i(\mathbf{s},\mathbf{x}) t(\mathbf{s})\, dB(\mathbf{s}), \mathbf{x} \in D \cup B, \tag{16}$$

and

$$0 = \int_B T^e(\mathbf{s},\mathbf{x}) w(\mathbf{s})\, dB(\mathbf{s}) - \int_B U^e(\mathbf{s},\mathbf{x}) t(\mathbf{s})\, dB(\mathbf{s}), \mathbf{x} \in D^c \cup B, \tag{17}$$

$$0 = \int_B M^e(\mathbf{s},\mathbf{x}) w(\mathbf{s})\, dB(\mathbf{s}) - \int_B L^e(\mathbf{s},\mathbf{x}) t(\mathbf{s})\, dB(\mathbf{s}), \mathbf{x} \in D^c \cup B, \tag{18}$$

once the kernels are expressed in terms of an appropriate degenerate forms (denoted by subscripts *i* and *e*) instead of the closed-form fundamental solution. It is noted that **x** in Eqs.(15)-(18) can be exactly located on the real boundary.

For the exterior problem, the domain of interest (D) is in the external region of the elliptical boundary and the complementary domain (D^c) is in the internal region of the ellipse. Therefore, the null-field boundary integral equations are represented as

$$w(\mathbf{x}) = \int_B T^e(\mathbf{s},\mathbf{x}) w(\mathbf{s})\, dB(\mathbf{s}) - \int_B U^e(\mathbf{s},\mathbf{x}) t(\mathbf{s})\, dB(\mathbf{s}), \mathbf{x} \in D \cup B, \tag{19}$$

$$t(\mathbf{x}) = \int_B M^e(\mathbf{s},\mathbf{x}) w(\mathbf{s})\, dB(\mathbf{s}) - \int_B L^e(\mathbf{s},\mathbf{x}) t(\mathbf{s})\, dB(\mathbf{s}), \mathbf{x} \in D \cup B, \tag{20}$$

and

$$0 = \int_B T^i(\mathbf{s},\mathbf{x}) w(\mathbf{s})\, dB(\mathbf{s}) - \int_B U^i(\mathbf{s},\mathbf{x}) t(\mathbf{s})\, dB(\mathbf{s}), \mathbf{x} \in D^c \cup B, \tag{21}$$

$$0 = \int_B M^i(\mathbf{s},\mathbf{x}) w(\mathbf{s})\, dB(\mathbf{s}) - \int_B L^i(\mathbf{s},\mathbf{x}) t(\mathbf{s})\, dB(\mathbf{s}), \mathbf{x} \in D^c \cup B, \tag{22}$$

Also, the observation point **x** in Eqs.(19)-(22) can be exactly located on the real boundary. For various problems (interior or exterior), we used different kernel functions (denoted by superscripts "*i*" and "*e*") so that the jump behavior across boundary can be captured. Therefore, different expressions of the kernels for the interior and exterior observer points are used and they will be elaborated on later.

2.2.3 Expansions of the fundamental solution and the boundary density

Based on the separable property, the kernel function $U(\mathbf{s},\mathbf{x})$ can be expanded into degenerate form by employing the separating technique for source point and field point under the elliptical coordinates. The fundamental solution, $U(\mathbf{s},\mathbf{x})$, in terms of degenerate (separable) kernel is shown below:

$$U(\mathbf{s},\mathbf{x}) = \begin{cases} U^i(\bar{\xi},\bar{\eta};\xi,\eta) = \dfrac{1}{2\pi}\left(\bar{\xi} + \ln\dfrac{c}{2} - \displaystyle\sum_{m=1}^{\infty}\dfrac{2}{m}e^{-m\bar{\xi}}\cosh m\xi\cos m\eta\cos m\bar{\eta}\right. \\ \qquad\qquad \left. - \displaystyle\sum_{m=1}^{\infty}\dfrac{2}{m}e^{-m\bar{\xi}}\sinh m\xi\sin m\eta\sin m\bar{\eta}\right), \quad \bar{\xi} \ge \xi, \\ U^e(\bar{\xi},\bar{\eta};\xi,\eta) = \dfrac{1}{2\pi}\left(\xi + \ln\dfrac{c}{2} - \displaystyle\sum_{m=1}^{\infty}\dfrac{2}{m}e^{-m\xi}\cosh m\bar{\xi}\cos m\eta\cos m\bar{\eta}\right. \\ \qquad\qquad \left. - \displaystyle\sum_{m=1}^{\infty}\dfrac{2}{m}e^{-m\xi}\sinh m\bar{\xi}\sin m\eta\sin m\bar{\eta}\right), \quad \bar{\xi} < \xi, \end{cases} \tag{23}$$

where the position of the source point is $\mathbf{s} = (\bar{\xi},\bar{\eta})$ and the field point is $\mathbf{x} = (\xi,\eta)$, the superscripts "*i*" and "*e*" denote the interior ($\bar{\xi} \ge \xi$) and exterior ($\bar{\xi} < \xi$) cases, respectively. The other kernels in the boundary integral equation can be obtained by utilizing the operators of Eq.(10) with respect to the kernel $U(\mathbf{s},\mathbf{x})$. In the real computation, the degenerate kernel can be expressed as finite sums of products of functions of **s** alone and functions of **x** alone.

For the kth boundary densities, we apply the eigenfunction expansions to approximate the potential $w(\mathbf{s})$ and its normal derivative $t(\mathbf{s})$ on the boundary

$$w(\mathbf{s}) = a_0 + \sum_{n=1}^{\infty} a_n \cos n\overline{\eta} + \sum_{n=1}^{\infty} b_n \sin n\overline{\eta}\,, \tag{24}$$

$$t(\mathbf{s}) = \frac{1}{J_s}(p_0 + \sum_{n=1}^{\infty} p_n \cos n\overline{\eta} + \sum_{n=1}^{\infty} q_n \sin n\overline{\eta})\,, \tag{25}$$

where a_0, a_n, b_n, p_0, p_n and q_n are the coefficients of the Fourier series, $\overline{\eta}$ is the angle ($0 \le \overline{\eta} < 2\pi$) and $J_{\mathbf{s}}$ is the Jocobian with respect to the source point and the definition is

$$J_{\mathbf{s}}(\overline{\xi}, \overline{\eta}) = c\sqrt{(\sinh\overline{\xi}\cos\overline{\eta})^2 + (\cosh\overline{\xi}\sin\overline{\eta})^2}\,. \tag{26}$$

Here, it can be observed that the terms of J_s which may exist in the degenerate kernel, boundary density and boundary integral are cancelled out each other naturally in the boundary integration. Therefore, the elliptic integral is not required to deal with. In the real computation, only the finite M number of terms is used in the summation. The present method belongs to one kind of semi-analytical methods since error only attributes to the truncation of eigenfunction expansions.

2.2.4 Linear algebraic system

In order to calculate the Fourier coefficients, N_p (N_p=2M+1) boundary nodes for each elliptical boundary are needed and they are uniformly collocated on each elliptical boundary. After locating the null-field point $\mathbf{x}_k$ exactly on the kth elliptical boundary in Eq.(17), we have

$$0 = \sum_{j=1}^{N} \int_{B_j} T(\mathbf{s},\mathbf{x})\, w(\mathbf{s})\, dB_j(\mathbf{s}) - \sum_{j=1}^{N} \int_{B_j} U(\mathbf{s},\mathbf{x})\, t(\mathbf{s})\, dB_j(\mathbf{s}),\ \mathbf{x} \in D^c \cup B\,, \tag{27}$$

where N is the number of boundary elements. Since the boundary integral equations are frame indifferent, *i.e.* objectivity rule is satisfied. The origin of observer system is adaptively chosen at the center of elliptical boundary under integration. For the B_j integral of the jth elliptical boundary, the kernels of $U(\mathbf{s},\mathbf{x})$ and $T(\mathbf{s},\mathbf{x})$ are expressed in terms of degenerate kernels, and $w(\mathbf{s})$ and $t(\mathbf{s})$ are substituted by using the Fourier series. For simplicity, a linear algebraic system is obtained

$$[\mathbf{U}]\{\mathbf{t}\} = [\mathbf{T}]\{\mathbf{w}\}\,, \tag{28}$$

where [**U**] and [**T**] are the influence matrices with a dimension of $N \times (2M+1)$ by $N \times (2M+1)$, $\{\mathbf{u}\}$ and $\{\mathbf{t}\}$ denote the column vectors of Fourier coefficients with a dimension of $N \times (2M+1)$ by 1 in which $[\mathbf{U}], [\mathbf{T}], \{\mathbf{u}\}$ and $\{\mathbf{t}\}$ can be defined as follows:

$$[\mathbf{U}] = \begin{bmatrix} \mathbf{U}_{11} & \mathbf{U}_{12} & \cdots & \mathbf{U}_{1N} \\ \mathbf{U}_{21} & \mathbf{U}_{22} & \cdots & \mathbf{U}_{2N} \\ \vdots & \vdots & \ddots & \vdots \\ \mathbf{U}_{N1} & \mathbf{U}_{N2} & \cdots & \mathbf{U}_{NN} \end{bmatrix},\ [\mathbf{T}] = \begin{bmatrix} \mathbf{T}_{11} & \mathbf{T}_{12} & \cdots & \mathbf{T}_{1N} \\ \mathbf{T}_{21} & \mathbf{T}_{22} & \cdots & \mathbf{T}_{2N} \\ \vdots & \vdots & \ddots & \vdots \\ \mathbf{T}_{N1} & \mathbf{T}_{N2} & \cdots & \mathbf{T}_{NN} \end{bmatrix},\ \{\mathbf{w}\} = \begin{Bmatrix} \mathbf{w}_1 \\ \mathbf{w}_2 \\ \vdots \\ \mathbf{w}_N \end{Bmatrix},\ \{\mathbf{t}\} = \begin{Bmatrix} \mathbf{t}_1 \\ \mathbf{t}_2 \\ \vdots \\ \mathbf{t}_N \end{Bmatrix}, \tag{29}$$

where the vectors $\{\mathbf{w}_k\}$ and $\{\mathbf{t}_k\}$ are in the forms of $\{a_0^k\ a_1^k\ b_1^k \cdots a_M^k\ b_M^k\}^T$ and $\{p_0^k\ p_1^k\ q_1^k \cdots p_M^k\ q_M^k\}^T$, respectively; the first subscript "j" ($j = 1, 2, \cdots, N$) in [$\mathbf{U}_{jk}$] and [$\mathbf{T}_{jk}$] denotes the index of the jth ellipse where the collocation point is located and the second subscript "k" ($k = 1, 2, \cdots, N$) denotes the index of the kth ellipse where the boundary data $\{\mathbf{w}_k\}$ and $\{\mathbf{t}_k\}$ are specified and M indicates the truncated terms of eigenfunction expansions.

2.2.5 Solution procedures and interface conditions

In the real computation, two problems in Figure 2(b) and Figure 3(b) are solved by using the present formulation. For the exterior problem of the matrix in Figure 3(b), we have

$$[\mathbf{T}^M]\{\mathbf{w}^M - \mathbf{w}^\infty\} - [\mathbf{U}^M]\{\mathbf{t}^M - \mathbf{t}^\infty\} = \{\mathbf{0}\}, \tag{30}$$

$$[\mathbf{T}^M]\{\mathbf{\Phi}^M - \mathbf{\Phi}^\infty\} - [\mathbf{U}^M]\{\mathbf{\Psi}^M - \mathbf{\Psi}^\infty\} = \{\mathbf{0}\}, \tag{31}$$

from Eq.(22). For the interior problem of each inclusion in Figure 2(b), we have

$$[\mathbf{T}^I]\{\mathbf{w}^I\} - [\mathbf{U}^I]\{\mathbf{t}^I\} = \{\mathbf{0}\}, \tag{32}$$

$$[\mathbf{T}^I]\{\mathbf{\Phi}^I\} - [\mathbf{U}^I]\{\mathbf{\Psi}^I\} = \{\mathbf{0}\}, \tag{33}$$

from Eq.(18), where the subscripts "*M*" and "*I*" denote the matrix and inclusion, respectively. The four influence matrices, $[\mathbf{U}^M]$, $[\mathbf{T}^M]$, $[\mathbf{U}^I]$ and $[\mathbf{T}^I]$, are obtained from the degenerate kernels, while $\{\mathbf{w}^M\}$, $\{\mathbf{t}^M\}$, $\{\mathbf{w}^I\}$, $\{\mathbf{t}^I\}$, $\{\mathbf{\Phi}^M\}$, $\{\mathbf{\Psi}^M\}$, $\{\mathbf{\Phi}^I\}$, $\{\mathbf{\Psi}^I\}$ represent the coefficient vectors of eigenfunction expansions. Based on the continuity of displacement and equilibrium of traction between the interface of matrix and the *k*th inclusion as shown in Eqs.(6) and (7), we have

$$\{\mathbf{w}^M\} - \{\mathbf{w}^I\} = \{\mathbf{0}\}, \tag{34}$$

$$[\mathbf{c}_{44}^M]\{\mathbf{t}^M\} + [\mathbf{c}_{44}^I]\{\mathbf{t}^I\} + [\mathbf{e}_{15}^M]\{\mathbf{\Psi}^M\} + [\mathbf{e}_{15}^I]\{\mathbf{\Psi}^I\} = \{\mathbf{0}\}, \tag{35}$$

$$\{\mathbf{\Phi}^M\} - \{\mathbf{\Phi}^I\} = \{\mathbf{0}\}, \tag{36}$$

$$[\mathbf{e}_{15}^M]\{\mathbf{t}^M\} + [\mathbf{e}_{15}^I]\{\mathbf{t}^I\} - [\mathbf{\varepsilon}_{11}^M]\{\mathbf{\Psi}^M\} - [\mathbf{\varepsilon}_{11}^I]\{\mathbf{\Psi}^I\} = \{\mathbf{0}\}, \tag{37}$$

where $[\mathbf{c}_{44}^M]$, $[\mathbf{e}_{15}^M]$, $[\mathbf{\varepsilon}_{11}^M]$, $[\mathbf{c}_{44}^I]$, $[\mathbf{e}_{15}^I]$ and $[\mathbf{\varepsilon}_{11}^I]$ are the diagonal matrices to the material parameters. According to Eqs.(30)-(37), we have a linear system as follows:

$$\begin{bmatrix} \mathbf{T}^M & -\mathbf{U}^M & \mathbf{0} & \mathbf{0} & \mathbf{0} & \mathbf{0} & \mathbf{0} & \mathbf{0} \\ \mathbf{0} & \mathbf{0} & \mathbf{T}^I & -\mathbf{U}^I & \mathbf{0} & \mathbf{0} & \mathbf{0} & \mathbf{0} \\ \mathbf{0} & \mathbf{0} & \mathbf{0} & \mathbf{0} & \mathbf{T}^M & -\mathbf{U}^M & \mathbf{0} & \mathbf{0} \\ \mathbf{0} & \mathbf{0} & \mathbf{0} & \mathbf{0} & \mathbf{0} & \mathbf{0} & \mathbf{T}^I & -\mathbf{U}^I \\ \mathbf{I} & \mathbf{0} & -\mathbf{I} & \mathbf{0} & \mathbf{0} & \mathbf{0} & \mathbf{0} & \mathbf{0} \\ \mathbf{0} & \mathbf{c}_{44}^M & \mathbf{0} & \mathbf{c}_{44}^I & \mathbf{0} & \mathbf{e}_{15}^M & \mathbf{0} & \mathbf{e}_{15}^I \\ \mathbf{0} & \mathbf{0} & \mathbf{0} & \mathbf{0} & \mathbf{I} & \mathbf{0} & -\mathbf{I} & \mathbf{0} \\ \mathbf{0} & \mathbf{e}_{15}^M & \mathbf{0} & \mathbf{e}_{15}^I & \mathbf{0} & -\mathbf{\varepsilon}_{11}^M & \mathbf{0} & -\mathbf{\varepsilon}_{11}^I \end{bmatrix} \begin{Bmatrix} \mathbf{w}^M \\ \mathbf{t}^M \\ \mathbf{w}^I \\ \mathbf{t}^I \\ \mathbf{\Phi}^M \\ \mathbf{\Psi}^M \\ \mathbf{\Phi}^I \\ \mathbf{\Psi}^I \end{Bmatrix} = \begin{Bmatrix} \mathbf{a} \\ \mathbf{0} \\ \mathbf{b} \\ \mathbf{0} \\ \mathbf{0} \\ \mathbf{0} \\ \mathbf{0} \\ \mathbf{0} \end{Bmatrix}, \tag{38}$$

where $[\mathbf{I}]$ is the identity matrix and $\{\mathbf{a}\}$ and $\{\mathbf{b}\}$ are the forcing terms due to the remote shear stress as shown below

$$\{\mathbf{a}\} = [\mathbf{T}^M]\{\mathbf{w}^\infty\} - [\mathbf{U}^M]\{\mathbf{t}^\infty\}, \tag{39}$$

$$\{\mathbf{b}\} = [\mathbf{T}^M]\{\mathbf{\Phi}^\infty\} - [\mathbf{U}^M]\{\mathbf{\Psi}^\infty\}. \tag{40}$$

From Eq. (38), the unknown Fourier coefficients can be easily determined.

3. Numerical examples and discussions

To the authors' knowledge, we don't find any paper to discuss on the piezoelectricity with two or more than two elliptical inhomogeneities. Therefore, we consider the available case containing two circular inhomogeneities to demonstrate the validity of present approach for dealing with a problem containing two elliptical inhomogeneities. Besides, we also provide a numerical example for the case containing two elliptical inhomogeneities.

Case1: An infinite medium with two circular inhomogeneities

The first example considered here is an infinite medium with two elliptical inhomogeneities. Here, we used the limiting concept by numerically setting the semi-major and semi-minor axes to be near the same by using 1.000000 and 0.999999 for the first inclusion and 2.000000 and 1.999999 for the second inclusion to compare with the available results of two circular inclusions subject to remote shears and electric fields. The mechanical and electric parameters of medium and inhomogeneities are

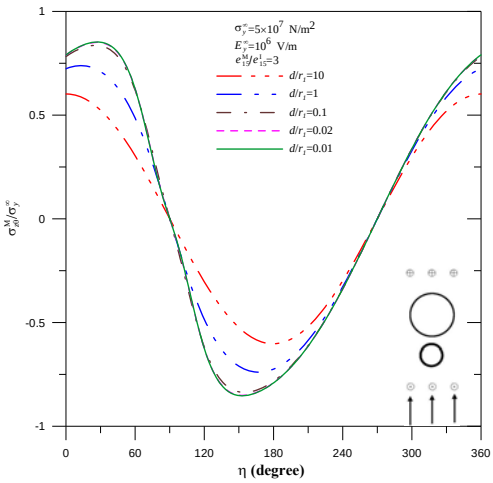

Figure 4(a) Tangential stress distribution for different ratios d/r_1 with $e_{15}^M/e_{15}^I=3$

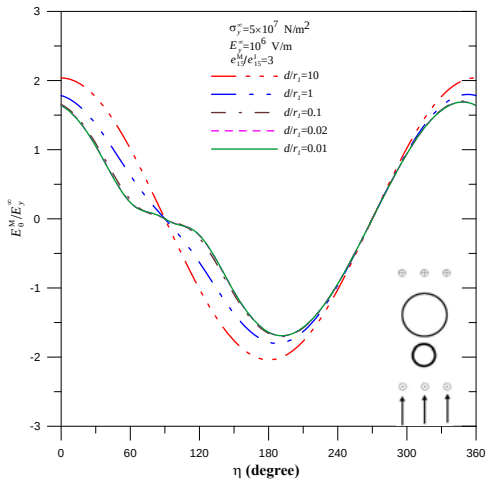

Figure 4(b) Tangential electric field distribution for different ratios d/r_1 with $e_{15}^M/e_{15}^I=3$

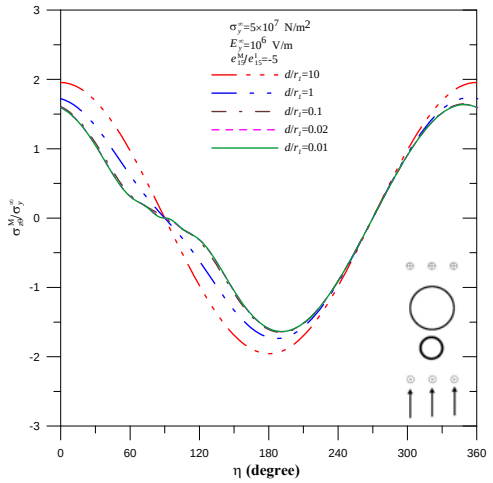

Figure 5(a) Tangential stress distribution for different ratios d/r_1 with $e_{15}^M/e_{15}^I=-5$

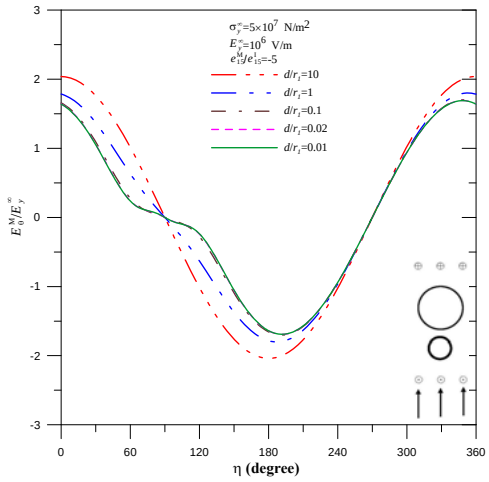

Figure 5(b) Tangential electric field distribution for different ratios d/r_1 with $e_{15}^M/e_{15}^I=-5$

given as $c_{44}^M=c_{44}^I=3.53\times10^{10}\ N/m^2$, $\varepsilon_{44}^M=\varepsilon_{44}^I=1.51\times10^{-8}\ C/Vm$, $e_{15}^I=10\,C/m^2$. The remote shears are $\sigma_{zx}^\infty=0$, $\sigma_{zy}^\infty=5\times10^7\ N/m^2$ and far-field electric fields are given as $E_x^\infty=0$ and $E_y^\infty=10^6\ V/m$. All the numerical results are given below by using the 30 terms of eigenfunction (M). In order to examine the generality of the present formulation for the problem containing two elliptical inclusions, the case of an infinite medium with the two circular inclusions ($r_2=2r_1$) paralleled to the applied loadings ($\beta=90°$) is used to verify the present approach. Figures 4(a) and 4(b), respectively, show the tangential shear stress and tangential electric field distribution in the matrix along the boundary of the smaller inhomogeneity for the ratio of $e_{15}^M/e_{15}^I=3$. After comparing with the results of Chao and Chang [10] and Chen and Wu [1], it can be found that good agreement is made. By changing the ratio of the piezoelectric constant, Figures 5(a) and 5(b), respectively, show the tangential stress and tangential electric field distribution corresponding to $e_{15}^M/e_{15}^I=-5$. The two figures also show the consistency between the present data and those of Chen and Wu [1].

However,

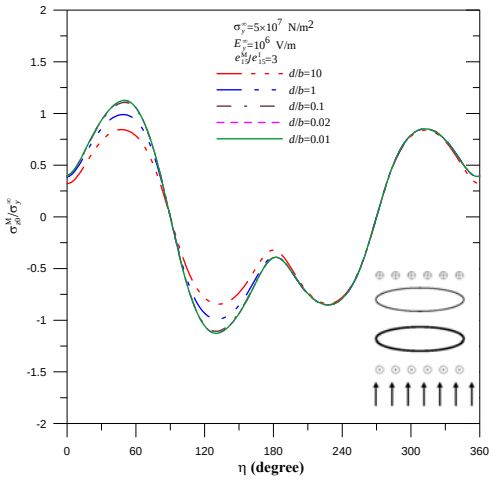

Figure 6(a) Tangential stress distribution for different ratios d/b with $e_{15}^M/e_{15}^I=3$

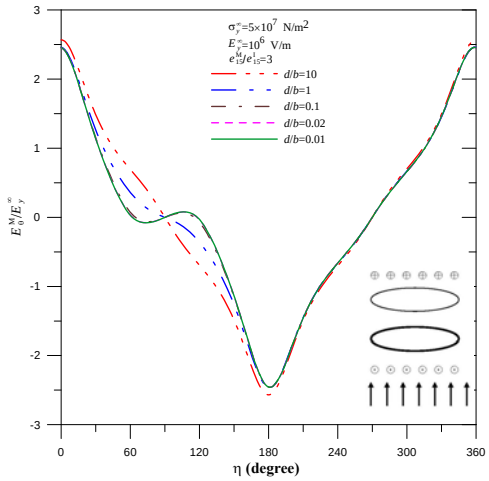

Figure 6(b) Tangential electric field distribution for different ratios d/b with $e_{15}^M/e_{15}^I=3$

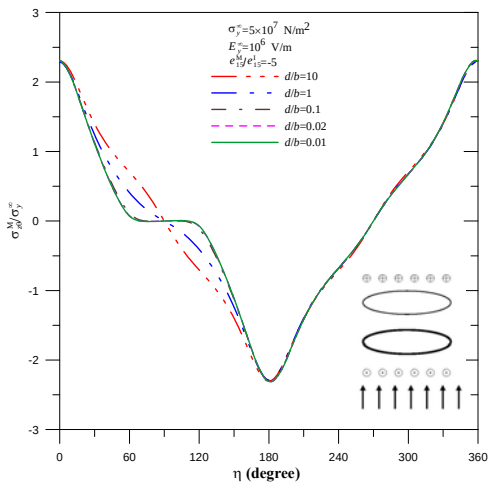

Figure 7(a) Tangential stress distribution for different ratios d/b with $e_{15}^M/e_{15}^I=-5$

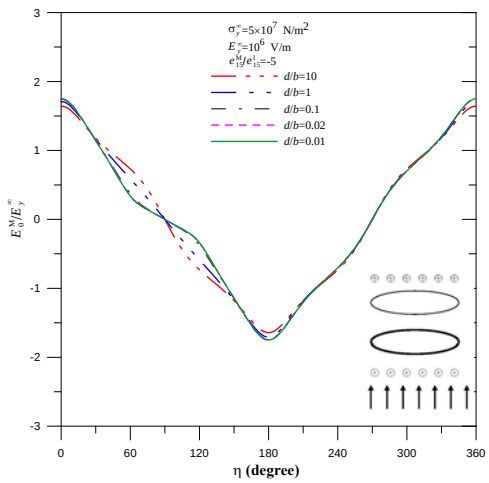

Figure 7(b) Tangential electric field distribution for different ratios d/b with $e_{15}^M/e_{15}^I=-5$

in the Chao and Chang's paper [10], it changes very sharply near $\theta=90°$ and is not consistent with our results when two inclusions are very close to each other (d/r_1 =0.01 and 0.02). It is open for discussions why our results are different from those of Chao and Chang near $\theta=90°$.

Case2: An infinite medium with two elliptical inhomogeneities

In this case, the two elliptical inhomogeneities arrayed paralleled to the applied loadings ($\beta=90°$) are considered. The semi-major (a) and semi-minor (b) axes are 2 and 1 for two inhomogeneities. The tangential stress and tangential electric field in the matrix along the boundary of the lower inhomogeneity for different ratios of d/b are plotted in Figures 6(a) and 6(b), respectively. For the different ratio of the piezoelectric constant ($e_{15}^M/e_{15}^I=-5$), the tangential stress and tangential electric field in the matrix along the lower inhomogeniety are given in Figures 7(a) and 7(b), respectively. It can be found that the stress concentration in the case of containing the elliptical inhomogeneities is greater than the case of containing circular ones. Since there are few literatures for discussions on the piezoelectricity containing two elliptical inhomogenieties, we used the limiting case as given in Case 1 to verify the validity of our program. Further, we provided a

case containing two identical elliptical inhomogenieties and it can be a benchmark for comparison when other numerical method is developed.

4. Conclusion

We have successfully proposed a systematic method to solve an infinite plane containing elliptical inclusions under remote anti-plane shears and in-plane electric fields. Although a Jacobian term may appear in the degenerate kernel, boundary density and boundary contour integral by using the elliptical coordinates, it can be cancelled out in our formulation to preserve the orthogonal condition. Although the work containing two elliptical inhomogenieties is not available in the literature, the piezoelectricity with two circular inclusions is used as a limiting case to demonstrate the validity of present approach. Besides, the case containing two identical elliptical inhomogenieties was provided as a benchmark example. The developed program can be generally used for piezoelectricity problems containing elliptical inhomogenieties of arbitrary number, position, size and inclination angle.

Acknowledgements

This research was partially supported by the National Science Council in Taiwan through Grant NSC 101-2811-E-019-002.

References

[1] J.T. Chen, A.C. Wu, Null-field approach for piezoelectricity problems with arbitrary circular inclusions," Eng Anal Bound Elem, 30 (2006) 971-993.
[2] S.X. Gong, S.A. Meguid, A general treatment of the elastic field of an elliptical inhomogeneity under antiplane shear. J Appl Mech-ASME, 59 (1992) 131-135.
[3] S.X. Gong, A unified treatment of the elastic elliptical inhomogeneity under antiplane shear, Arch Appl Mech, 65 (1995) 55-64.
[4] H. Shen, P. Schiavone, C.Q. Ru, A. Mioduchowski, An elliptic inclusion with imperfect interface in anti-plane shear," Int J Solids Struct, 37 (2000) 4557-4575.
[5] N.A. Noda, T. Matsuo, Stress analysis of arbitrarily distributed elliptical inclusions under longitudinal shear loading. Int J Fract, 106 (2000) 81-93.
[6] J. Lee, H.R. Kim, Volume integral equation method for multiple circular and elliptical inclusion problems in antiplane elastostatics. Composites Part: B, 43 (2012) 1224-1243.
[7] Y.T. Lee, J.T. Chen, Null-field approach for the antiplane problem with elliptical holes and/or inclusions. Composites Part: B, 44 (2013) 283-294.
[8] Y.E. Pak, Circular inclusion problem in antiplane piezoelectricity. Int J Solids Struct, 29 (1996) 2403-2419.
[9] T. Honein, B.V. Honein, E. Honein, G. Herrmann, On the interaction of two piezoelectric fibers embedded in an intelligent material. J Intell Mater Syst Struct, 6 (1995) 229-236.
[10] C.K. Chao, K.J. Chang, Interacting circular inclusions in antiplane piezoelectricy. Int J Solids Struct, 36 (1999) 3349-3373.
[11] X. Wang, Y.P. Shen, On double circular inclusion problem in antiplane piezoelectricity. Int J Solids Struct, 38 (2001) 4439-4461.
[12] J.L. Bleustein, New surface wave in piezoelectric materials, Appl Phys Lett, 46 (1968) 412-413.
[13] S.A. Meguid, Z. Zhong, Electroelastic analysis of a piezoelectric elliptical inhomogeneity. Int J Solids Struct, 34, pp. 3401-3414, 1997.
[14] Y.E. Pak, Elliptical inclusion problem in antiplane piezoelectricity: implications for fracture mechanics. Int. J. Solids Struct., Vol. 48 pp. 209-222, 2010.

Modeling the Effect of Residual Stress on the Ductile Fracture Behavior of an Aluminum Alloy 5083-H116

Xiaosheng Gao[1,*], Jun Zhou[1], Matthew Hayden[2]

[1] Department of Mechanical Engineering, The University of Akron, Akron, OH 44325, USA
[2] Alloy Development and Mechanics Branch, Naval Surface Warfare Center, West Bethesda, MD 20817, USA
* Corresponding author: xgao@uakron.edu

Abstract The influence of residual stress on the ductile fracture behavior of an aluminum alloy 5083-H116 is investigated in this study through a series of experiments and finite element analyses. A recently developed stress state dependent I_1-J_2-J_3 plasticity model, is implemented to describe the plastic response of this material. A ductile failure criterion based on the damage parameter defined in terms of the accumulative plastic strain as a function of the stress triaxiality and Lode angle is established. The calibrated I_1-J_2-J_3 plasticity model and ductile failure model are utilized to study the residual stress effect on ductile fracture resistance. A local out-of-plane compression approach is employed to generate residual stress fields in the compact tension specimens. Fracture tests of C(T) specimens having zero, positive and negative residual stresses are conducted. The numerical results, such as load-displacement curves and crack front profiles, are compared with experimental measurements and good agreements are observed. Both experimental and finite element results show significant effect of residual stress on ductile fracture resistance.

Keywords Ductile fracture, Plasticity, Damage accumulation, Stress triaxiality, Lode angle

1. Introduction

Residual stresses in the engineering structures are generated from forming, welding, assembling, heat treatment etc., which play an important role in either increasing or decreasing the fracture resistance. The compressive residual stress generally improves the fracture toughness, while the tensile residual stress can detrimentally reduce the loading capacity of the structure. This is usually attribute to the additional crack driving force and change of the crack front constraint [1]. To quantify the effect of residual stress on fracture toughness, it is necessary to introduce well characterized and reproducible residual stress fields into fracture specimens. There are plenty of literatures on residual stress generation techniques, which can either be mechanical or thermal process. Almer et al. [2] deformed large tensile specimens and cut the gauge sections to produce C(T) specimens. Meith et al. [3] applied local compression to the sides of fracture specimens. Because of the strain incompatibility between elastic and plastic region caused by the permanent plastic deformation, the residual stress field can be generated in the specimen. This local out-of-plane compression (LOPC) approach is further explored by Mahmoudi et al. [4], who ran a series experiments and finite element analyses to examine how the position of compression tools influences the residual stress distribution in the specimen.

In this study, we employ the LOPC approach and use two pairs of compression punches to generate various residual stress fields in C(T) specimens. To model these specimens, a recently developed I_1-J_2-J_3 dependent plasticity model is used to describe the plastic response of the material, an aluminum alloy 5083-H116. The residual stress field is quantified by conducting finite element simulation of the out-of-plane compression process. After the residual stress field is generated, fracture tests of C(T) specimens having positive and negative residual stresses are conducted and simulated numerically. A damage parameter is defined as a weighted integral with respect to the effective strain, where the integrand is the reciprocal of the effective failure strain as a function of the stress triaxiality and the Lode angle. Fracture is assumed to have initiated at a material point once the failure criterion is reached. A mesh-independent, post-initiation material degradation model based on an effective plastic displacement is adopted before the element is removed. The

numerical results, such as load-displacement curves and crack front profile, are compared with the experimental measurements and good agreements are observed.

2. Plasticity and Fracture Models

Gao et al. [5] and Zhou et al. [6] have demonstrated that the plastic response of the aluminum alloy 5083-H116 considered in this study can be described by an I_1-J_2-J_3 dependent plasticity model with the yield function and flow potential given by

$$F = c_1(a_1 I_1^6 + 27J_2^3 + b_1 J_3^2)^{1/6}; \qquad G = c_2(a_2 I_1^6 + 27J_2^3 + b_2 J_3^2)^{1/6} \tag{1}$$

where a_i and b_i are material constants, $c_i = 1/(a_i+4b_i/729+1)^{-1/6}$, I_1 is the first invariant of the stress tensor, and J_2 and J_3 are the second and third invariants of the stress deviator tensor respectively. The equivalent stress-strain relation (true stress vs. logarithm strain) is obtained by the uniaxial tension test, which can be described by a power-law hardening relation

$$\begin{aligned} \varepsilon &= \frac{\sigma}{E} && \text{when } \sigma \le \sigma_0 \\ \varepsilon &= \frac{\sigma_0}{E}\left(\frac{\sigma}{\sigma_0}\right)^{1/N} && \text{when } \sigma > \sigma_0 \end{aligned} \tag{2}$$

with E = 68.4 GPa, σ_0 = 198.6 MPa, ν = 0.3, and N = 0.155. Other material constants are calibrated using experimental data obtained from uniaxial tension, compression, pure torsion and combined torsion-tension tests. The calibrated values are $a_1 = a_2 = 0$, b_1 = -60.75 and b_2 = -50.

The cumulative strain damage models assume damage toward eventual fracture is due to the plastic deformation history and the equivalent fracture strain depends on the stress state subjected by the material. Here a damage parameter, D, is introduced and given by

$$D = \int_0^{\bar{\varepsilon}^p} \frac{d\bar{\varepsilon}^p}{\varepsilon_f(T^*, \xi)} \tag{3}$$

with ε_f being the failure strain depending on the stress triaxiality ratio and the Lode parameter ξ defined as

$$T^* = \frac{\sigma_h}{\sigma_e}, \qquad \xi = \frac{27J_3}{2\sigma_e^{\,3}} \tag{4}$$

where ξ is related to the Lode angle, θ, through $\xi = \cos(3\theta+\pi/2)$. Under proportional loading and if T^* and ξ remain unchanged during the loading history, when the equivalent plastic strain, $\bar{\varepsilon}^p$, reaches the critical value ε_f, D will equal to unit. For general cases, when the cumulative damage according to Eq. (3) reaches one, ductile failure is said to have happened.

When ξ is a constant, ε_f becomes a function of T^* only. It is well documented that the ductility of metals increases when the material is subjected to hydrostatic pressure. Here an exponentially

decaying function having the same form as the Johnson-Cook fracture model [7] is used to describe the dependency of ε_f on T^*

$$\varepsilon_f^{\xi=const.} = [A + B\exp(C \cdot T^*)] \tag{5}$$

where A, B and C are material constants to be calibrated using experimental data.

The Lode angle distinguishes the deviatoric stress state and it is mathematically convenient to use the parameter ξ defined in Eq. (4), whose range is from -1 to 1, to quantify the Lode angle. Wilkins et al. [8] was first to introduce the effect of Lode angle on ductile fracture, where the function $\varepsilon_f(T^*, \xi)$ was taken to be symmetric with respect to ξ. Here we follow Xue and Wierzbicki [9] and assume $\varepsilon_f(T^*, \xi)$ take the following form

$$\varepsilon_f(T^*, \xi) = \varepsilon_f^{\xi=1}(T^*) - (\varepsilon_f^{\xi=1}(T^*) - \varepsilon_f^{\xi=0}(T^*))[1-(1-|\xi|^n)^{1/n}] \tag{6}$$

where a symmetric function of ξ is used to interpolate the value of ε_f between two bounding values $\varepsilon_f^{\xi=1}$ and $\varepsilon_f^{\xi=0}$. The two bounding curves, $\varepsilon_f^{\xi=1}(T^*)$ and $\varepsilon_f^{\xi=0}(T^*)$ given by Eq. (7), can be calibrated by conducting simple mechanical tests: ξ =1 for notched, round tensile specimens and ξ =0 for flat-grooved plates under tension and the thin-walled torsion specimen. Calibration of parameter n requires performing additional tests using specimens having ξ values between zero and one, which can be done by conducting combined torsion-tension tests of thin-walled cylindrical specimens.

$$\varepsilon_f^{\xi=1} = [A_1 + B_1\exp(C_1 \cdot T^*)]; \quad \varepsilon_f^{\xi=0} = [A_2 + B_2\exp(C_2 \cdot T^*)] \tag{7}$$

The calibrated material parameters are A_1 =0, B_1=0.85, C_1=-1.9, A_2 =0, B_2=0.64, C_2=-1.9, and n = 1.31. The 3D failure locus expressed in terms of ε_f as a function of ξ and T^* is shown in Figure 1.

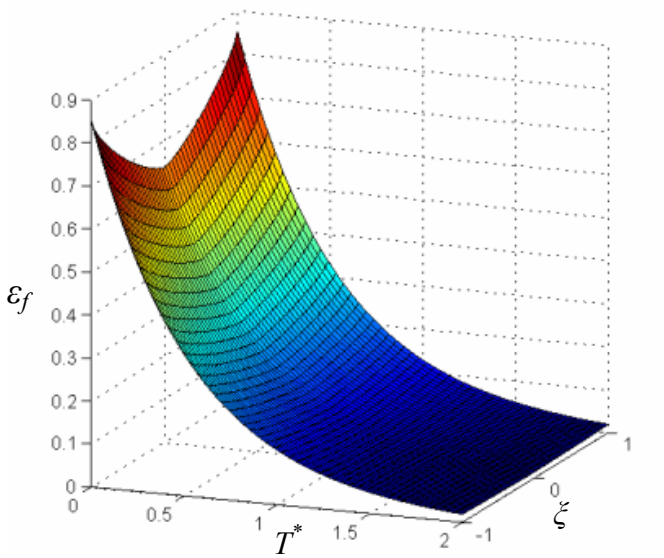

Figure 1. 3D plot of the failure locus

Fracture is assumed to have initiated at a material point once the failure criterion is reached. The post-initiation softening process needs to be considered in order to model crack propagation. As illustrated by Li et al. [10], because the finite element has a finite size, additional work is needed to

propagate the crack through the element, i.e., the element gradually loses its strength as crack grows through it. A mesh-independent, post-initiation material degradation model based on an effective plastic displacement (u_f) is available in ABAQUS [11] and is adopted in this study. The element is removed when it is fully degraded (stresses being reduced to zero).

3. Fracture Specimen and Residual Stress Generation

The 1/2T C(T) specimens (thickness: 12.7 mm) are used in the fracture tests. The specific design utilized in this study is modified from the standard design specified by ASTM-E1820 as a means of applying controlled residual stresses. The aim is to introduce residual stresses into the C(T) specimen by compressing the two faces with cylindrical punches to a specified displacement to produce a pair of permanent depressions on both faces of the specimen. From the analyses performed by Mahmoudi et al. [4], the size and position of the punching tools have strong influence on the magnitude and distribution of the residual stress field. Thus one can tailor the residual stress field at the crack tip by varying the position of the set of depressions relative to the crack tip.

A series finite element analyses are conducted first to determine the diameter, applied displacement, and locations of each depression, in order to obtain larger residual stress influenced region. From these analyses, the 8.89 mm punch radius is selected and the punch position is chosen to be $\delta_x / R = 1$ and -1, $\delta_y / R = 1.2$, where δ_x and δ_y are the distances from the punch center to the crack tip parallel and normal to the crack growth direction respectively and R is the radius of the punch.

With the aid of the above analyses, fixtures were designed for use in side compression. The specimen is sandwiched between two guide plates. The guide plates are aligned with the specimen by threading two pins through one guide plate, the pin loading holes of the specimen, and through the other guide plate. These guide pins ensure consistency in locating the side compression indentations between specimens. Two side compression punches (one on either side of the crack plane) are placed in the top guide plate and two mating punches are placed in the bottom guide plate. Once assembled, the compression force is applied to the top punches while the bottom punches remain fixed. Sets of fixtures were designed and machined for both the δ_x/R = 1 and δ_x/R = -1 configurations (δ_y/R = 1.2). Figure 2 illustrate the schematic of side compression fixture.

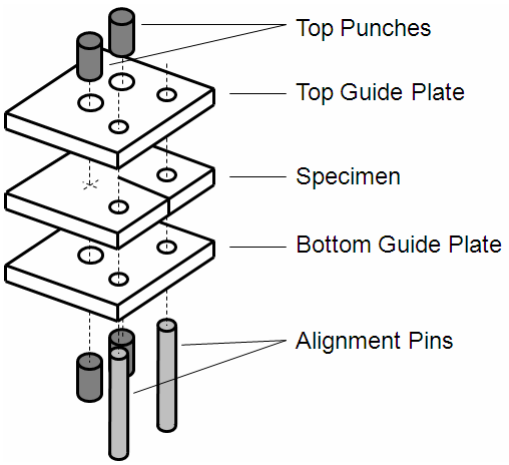

Figure 2. Schematic of side compression fixture

4. Experimental and Numerical Results

4.1. C(T) specimens without residual stress

The plane-sided C(T) specimen is considered first. Due to symmetry of the geometry and the boundary conditions, only a quarter of the specimen is meshed. The element size along the crack path is 0.254 mm in all three directions. The eight-node, isoparametric, brick elements with reduced integration are used in the analysis. Figure 3 compares the predicted crack profile with the fracture surface of the broken specimen and the agreement is very good. A “V” shape crack profile, seen in both test and simulation results, shows strong crack tunneling effect. This is due to the variation of the constraint in the thickness direction, where the plane stress prevails at the free surface and the plane strain condition prevails in the center. Figure 3 (b) displays the stress triaxiality contour on the crack plane, showing the stress triaxiality decreases from the mid-plane to the free surface. The computed and measured load vs. load line displacement curves of the plane-sided C(T) specimen are compared in Figure 4. Good agreement is observed before fracture initiation and at the early stage of crack growth.

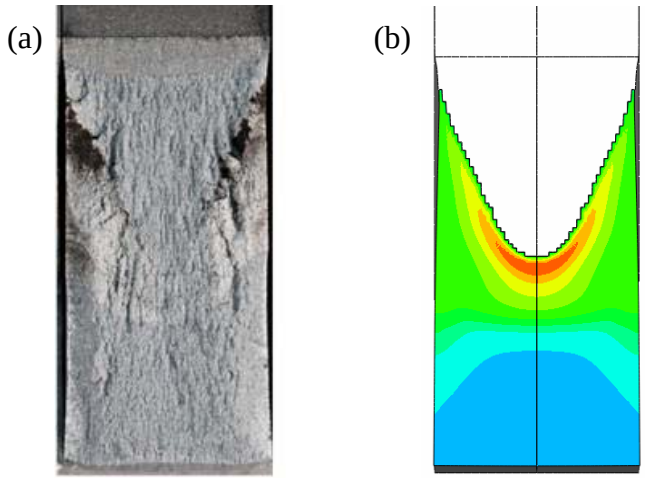

Figure 3. Fracture surface and stress triaxiality distribution in the plane-sided C(T) specimen

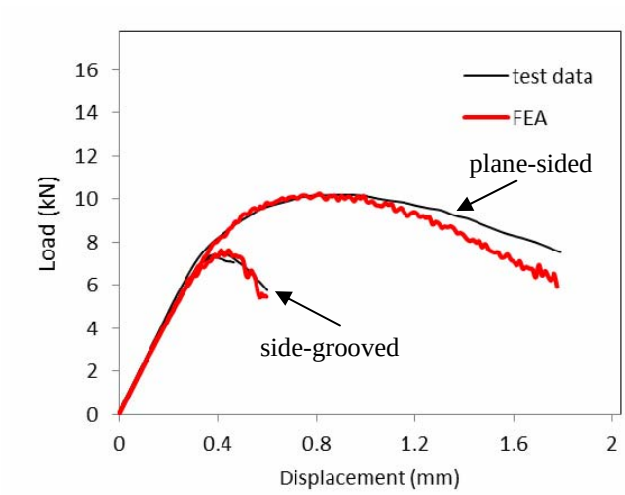

Figure 4. Comparison of the load-displacement curves for plane-sided and side-grooved specimens

In order to promote plane strain constraint along the crack front and obtain more uniform though thickness crack growth, the C(T) specimens are side-grooved by 20% of the thickness (10% each side). Consequently, a quarter-symmetric finite element model is generated for the side-grooved specimen, in which the same element type and size are used as those for the plane-sided specimen. With the side grooves, the constraint level is significantly raised close to specimen edges and as a result, more uniform crack growth (less tunneling) is observed. Figure 5(a) compares the predicted crack profile with the crack surface of the broken specimen. Figure 5(b) shows stress triaxiality becomes almost uniform through specimen thickness due to the side grooves. Because the constraint level is raised by the side grooves, fracture becomes easier, resulting in a lower load carrying capacity by the specimen. As shown in Figure 4 the load carrying capacity of the C(T) specimen is significantly reduced by the side grooves.

In conducting the experiments, the test was stopped after some amount of crack extension and the specimen was broken by fatigue loading. The post fatigue marks were used to determine the amount of crack growth. Due to the non-uniform crack growth through the specimen thickness, a nine-point

average was used to determine the crack length. We compare the model predicted crack growth with experimental measurements at the same applied load levels and find very good agreements between the two. For examples, C(T)-17 has crack extensions of 6.81 mm (measured from post fatigue marks) when the test was stopped. The finite element analyses predict the amount of crack extension of 7.11 mm at the same load level.

(a) (b)

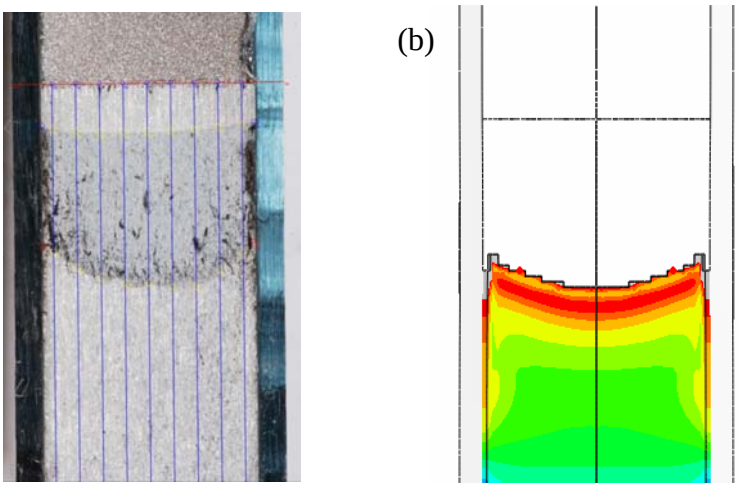

Figure 5. Fracture surface and stress triaxiality distribution in the side-grooved C(T) specimen.

4.2. Fracture tests with tensile residual stress

The C(T) specimens considered hereafter are all side-grooved. Two levels of compression forces, 182 kN and 220 kN, were used in the experiments to generate tensile residual stresses. The average total indentation depths (after the punches were removed) are 0.083 mm and 0.244 mm for 182 kN and 220 kN respectively. The finite element analyses results in 0.089 mm and 0.259 mm total indentation depths for these two cases.

Since the LOPC method creates residual stress field by introducing plastic strain into structure, too much side compression may results in the crack extension. Several methods, such as dye injection and SEM observation of the fracture surface, are used to verify if this has happened. From result of the dye and also SEM observations, the tensile residual side compression does result in crack initiation and growth when 220 kN load was applied. SEM observations also showed clear damage, i.e., inclusions broken and pulled loose from the matrix. However, this was not observed for the 182 kN case.

The simulation results for both cases confirm the experimental observations. Figure 6 shows the crack front region after side compression, suggesting crack does extend about 1.5 mm when 220 kN of compression force is employed, whereas crack extension does not happen when 182 kN compression force is applied. The contours of residual stresses normal to the crack plane for both cases are shown in Figure 6. The high positive residual stress is confined in a small region close to the crack tip, within about 1.3 mm from the crack tip, and the residual stress distribution is fairly uniform along the crack front except in the region close to the free surface.

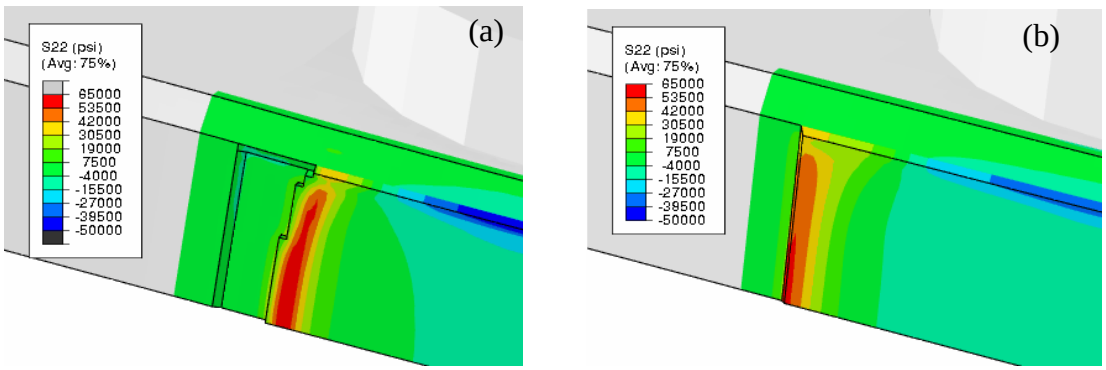

Figure 6. Contour plots of the residual stress normal to the crack plane: (a) 220 kN side-compression, (b) 182 kN side-compression (stress unit in contour plots: psi)

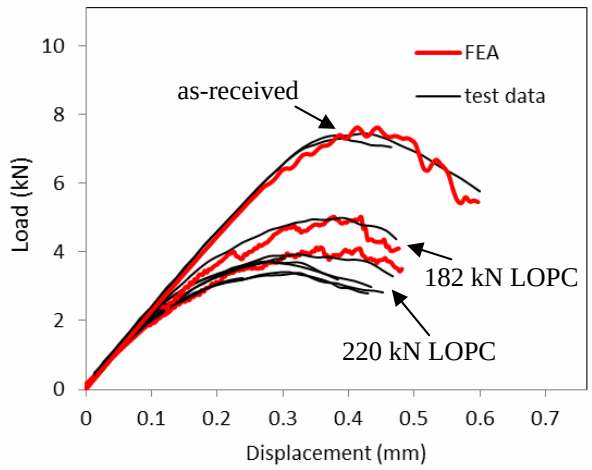

Figure 7. Comparisons of the computed and measured load-displacement curves for C(T) specimen without residual stress and with tensile residual stress

After the residual stress fields have been generated in the specimens, finite element analyses of the compact tension tests of these specimens are carried out. Figure 7 compares the model predicted load-displacement curves with experimental records for the as-received specimen as well as the specimens with tensile residual stress field. The numerical model captures the effect of the tensile residual stress on the fracture resistance. The existence of tensile residual stress drastically reduces the fracture resistance and lowers the specimen's load carrying capacity. After crack grows away from the residual stress influence area, the features of crack growth become similar to those exhibited by the virgin specimen.

4.3. Fracture tests with compressive residual stress

When side-compression is applied behind the crack tip, crack will close and the crack surfaces will contact each other. In finite element analysis, to prevent crack surface penetration, a rigid surface is added to the symmetric plane behind the crack tip. The finite element analysis results show that the high compressive residual stress region is at the initial EDM notch (behind the fatigue pre-crack front) and the residual stress distribution is not as uniform as tensile residual stress case, Figure 8(a). Figure 8(b) shows the variation of the residual stress (σ_{22}) with the distance in the crack growth

direction at the mid-plane respectively.

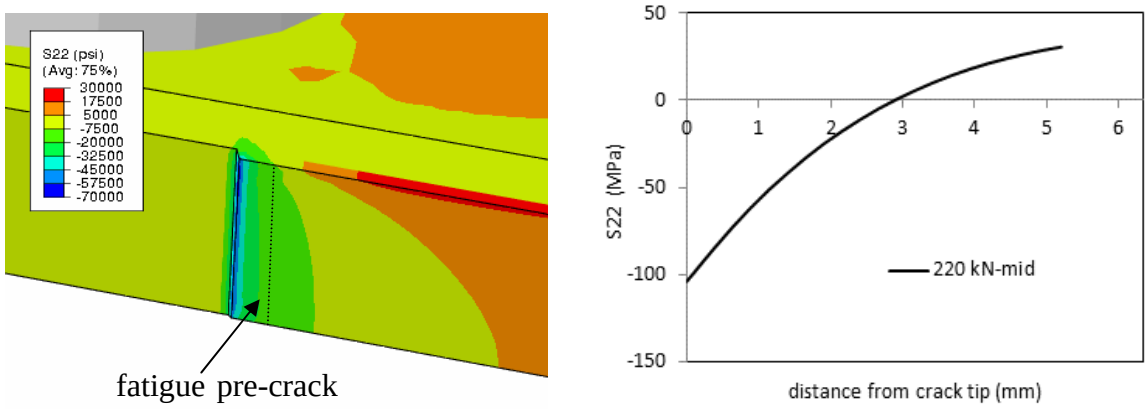

(a) (b)

Figure 8. (a) Contour plot of the residual stress normal to the crack plane, (b) variation of the residual stress (σ_{22}) with the distance in the crack growth direction

Compressive residual stresses reduce the constraint level at the crack front region and tend to close the crack, and consequently, increase the fracture resistance. Figure 9 compares the load-displacement curves of the specimen with compressive residual stress field generated by 220 kN side compression with the as received specimen. Included in the figure are also comparisons between the model predictions and the experimental measurements. Again, good agreement is observed.

3. Concluding Remarks

In this study, the residual stress effects on the ductile fracture behavior of the aluminum alloy 5083-H116 are investigated through a series of experiments and finite element analyses. An I_1-J_2-J_3 dependent plasticity model is used to describe the plastic response of the materials and a damage parameter is defined as a weighted integral with respect to the effective strain, where the integrand is the reciprocal of the effective failure strain as a function of the stress triaxiality and the Lode angle. The model parameters are calibrated and validated by comparing the numerical predictions with experimental measurements. To generate residual stress fields in fracture specimens, a local out-of-plane compression approach is adopted and an experimental fixture is designed. The analysis results show that tensile residual stress not only increases the crack driving force but also raises the constraint level in crack tip region, which results in a lower fracture resistance. Compressive residual stress has the opposite effect. The numerical results, such as load-displacement curves and crack front profiles, are compared with experimental measurements and good agreements are observed, suggesting that the numerical model is capable of capturing the residual stress effect on ductile fracture resistance.

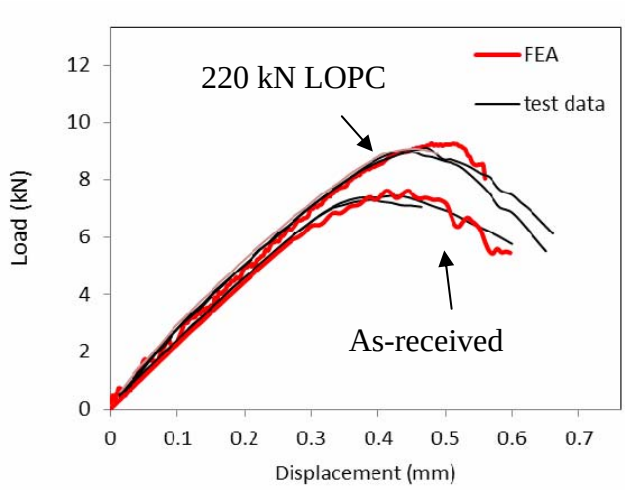

Figure 9. Comparisons of the computed and measured load-displacement curves for C(T) specimen without residual stress and with compressive residual stress.

Acknowledgements

This research is supported by the Ship Structures Committee and the Naval Surface Warfare Center, Carderock Division.

References

[1] T. Panontin, M. Hill, The effect of residual stresses on brittle and ductile fracture initiation predicted by micromechanical models. Int J Fract 82(1996) 317-333.

[2] J. Almer, J. Cohen, R. Winholtz, The effects of residual macrostresses and microstresses on fatigue crack propagation. Metall Mater Trans A 29(1998) 2127-2136.

[3] W. Meith, M. Hill, T. Panontin, Analytical & Experimental Study of Fracture in Bend Specimens Subjected to Local Compression, in: W.G. Reuter, R.S. Piascik (Eds), Fatigue and Fracture Mechanics: 33rd Volume, ASTM STP 1417, Philadelphia, PA, 2003, pp. 426-444.

[4] A. Mahmoudi, C. Truman, D. Smith, Using local out-of-plane compression (LOPC) to study the effects of residual stress on apparent fracture toughness. Eng Fract Mech 75(2008) 1516-1534.

[5] X. Gao, T. Zhang, J. Zhou, S.M. Graham, M. Hayden, C. Roe, On stress-state dependent plasticity modeling: Significance of the hydrostatic stress, the third invariant of stress deviator and the non-associated flow rule. Int J Plas 27(2011) 217-231.

[6] J. Zhou, X. Gao, M. Hayden, J.A. Joyce, Modeling the ductile fracture behavior of an aluminum alloy 5083-H116. Eng Fract Mech 85(2012) 103-116.

[7] G.R. Johnson, W.H. Cook, Fracture characteristics of three metals subjected to various strains, strain rates, temperatures and pressures. Eng Fract Mech 21(1985) 31-48.

[8] M. Wilkins, R. Streit, J. Reaugh, Cumulative-strain-damage model of ductile fracture: simulation and prediction of engineering fracture tests. Technical Report UCRL-53058, Lawrence Livermore National Lab., CA , 1980.

[9] L. Xue, T. Wierzbicki, Ductile Fracture Characterization of Aluminum Alloy 2024-T351 Using Damage Plasticity Theory. Int J Appl Mech 1(2009) 267-304.

[10] Y. Li, T. Wierzbicki, M.A. Sutton, J. Yan, X. Deng, Mixed mode stable tearing of thin sheet AI 6061-T6 specimens: experimental measurements and finite element simulations using a modified Mohr-Coulomb fracture criterion. Int J Fract 168(2011) 53-71.

[11] SIMULIA, ABAQUS User's Manual (version 6.9), Providence, RI, 2008.

Mechanisms for cleavage fracture in duplex stainless steels

Guocai Chai[1,2*] and Peter Stenvall[1]

[1]Strategic Research, Sandvik Materials Technology, 811 81 Sandviken, Sweden
[2]Engneering Materials, Linköping University, 581 83 Linköping, Sweden
* Corresponding author: guocai.chai@sandvik.com

Abstract Duplex stainless steels that have two phases with different mechanical and physical properties exhibit micro deformation heterogeneity and localized cracking or fracture in nature. In this study, the cleavage fracture behaviors in two super duplex stainless steels have been investigated in the following three conditions: at low temperatures, the material with spinodal decomposition and that with other precipitates and defects. By both impact toughness and fracture toughness tests, the ductile to brittle transition and cleavage behaviors have been investigated. The fracture is analyzed using a SEM with EBSD. The fracture mechanisms are focused; mainly the parameters or factors that cause the occurrence of cleavage in the materials. Since the austenitic phase in the material in these conditions is still tough, a coupling effect will be discussed to explain the cleavage in the austenitic phase observed. Local approach to fracture is used to assess or discuss the influence of local hardness, precipitates and stress concentration on the formation of cleavage fracture in the materials in different conditions.

Keywords Duplex stainless steel, cleavage, local approach method, spinodal decomposition, fracture

1. Introduction

Multiphase materials due to their microstructures and excellent properties are becoming more attractive for both engineering applications and academic interests. Duplex stainless steels (DSS) are a group of steels that consist of approximately equal volume of austenite and ferrite. Due to a good combination of excellent corrosion resistance and high mechanical properties, they are increasingly employed in various industries [1-4].

Duplex stainless steels have two phases with different mechanical and physical properties such as modulus of elasticity, yield strength and deformation hardening rate, and therefore exhibit micro deformation heterogeneity [5-13]. As a result, both stress and strain are not uniformly distributed at the phases and the actual load sharing on the microscopic scale is dependent on the property mismatch and microstructural features. It is believed that the difference in the elasto-plastic properties between the phases and the coupling effect, i.e., the load and strain sharing between the phases, is largely responsible for the varying elasto-plastic deformation mechanisms with varying plastic strain ranges in DSSs [8]. The phase-specific stresses, i.e., the total stresses that the constituent phases are subjected to is the sum of macrostresses, corresponding directly to the applied stresses, and microstresses due to micromechanical responses. The importance of micromechanical interactions under mechanical load has been recognized [8, 9]. Recently, the micro yielding and damage behavior of the austenitic and ferritic phases in duplex stainless steels have been studied by in-situ X-ray and neutron diffraction and multiscale modelling [8-13]. Fracture in duplex stainless steel is a local process in nature. Several works on local approach to fracture have been done to discuss the fracture in duplex stainless steels [14-17]. However, less

investigation has been done on the factors that affect the ductile to brittle transition behavior. In this paper, the influences of the factors such as temperature, ferrite content, cold deformation, phase size and different precipitates on the ductile to brittle transition and cleavage behaviors of a super duplex stainless steel are discussed with the purpose to increase the understanding on the micro fracture behaviors in duplex stainless steels and provide the information for the reliability and integrity to use the material.

2. Material and experimental

The material used is super duplex stainless steel (SDSS): UNS S32750 (Sandvik SAF 2507) with a nominal chemical composition as shown in Table 1:

Table 1 Nominal chemical compositions and information of DSS used

Materials	C_{max}	Si	Mn	Cr	Ni	Mo	N	Dimension	Rp0.2
								(mm)	(MPa)
SAF 2507	0.03	0.8	1.2	25	7	4	0.3	ϕ260x14	595
Filler 25.10.4.L	0.02	0.3	0.4	25	9.5	4	0.24	ϕ2.4	537

Two types of materials were used. One was a tube with an outer diameter of 260 mm and a wall thickness of 14mm. The other type of material was all-weld metal produced with TIG-welding using super duplex filler Sandvik 25.10.4.L. The welding was carried out in a V-groove using 13mm plates in SAF 2507 with 10° beveling and a back strip 6 mm in thickness in SAF 2507. Distance between the plates was 14 mm. Arc energy varied between 0.69 and 0.82 kJ/mm and the shielding gas consisted of Ar + 2%N_2. Totally 32 runs were used to build up the all-weld metal. Interpass temperature was below 150°C. Figure 1 shows the typical microstructure of the base material (Fig. 1a) and the weld metal (Fig. 1b).

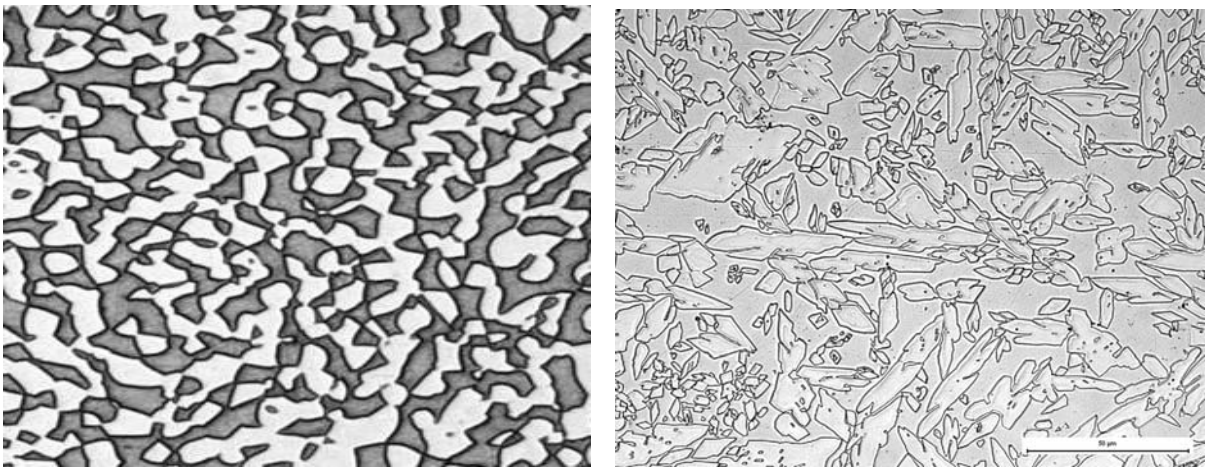

Figure 1 Typical microstructure of SAF 2507; (a). Base material, X200, (b). Weld metal.

Two types of toughness tests (impact toughness and CTOD) have been performed in a temperature range from -196°C up to room temperature (RT). Two to three samples/temperature were tested and

an average value was used in the toughness versus temperature or DBT curves. For impact toughness testing, standard sample with a dimension of 50x10x10mm (SS-EN 10045-1) was used. For CTOD sample, SENT type of sample with a dimension of 90x20x10mm was used and tested according to BS 7448, 1991.

In this paper, two methods have been used to determine a ductile to brittle transition temperature (DBTT). One is to determine the transition temperature, T_{50}, by Eq. 1 with 50% probability from a ductile to brittle transition curve [18, 19].

$$KV = \frac{\left(KV_{\max} - KV_{\min}\right) \times \exp\left(\frac{2 \times \left(T - T_{50}\right)}{C}\right)}{1 + \exp\left(\frac{2 \times \left(T - T_{50}\right)}{C}\right)} + KV_{\min} \tag{1}$$

Where KV is the toughness at temperature T, KV_{max} is the maximum toughness, KV_{min} is the minimum toughness, and T_{50} is the temperature with 50% probability of brittle fracture, C is a constant.

Another is though fracture analysis using a scanning electron microscopy (SEM). DBTT is the temperature where no cleavage could be observed on the fracture of an impact sample. In this investigation, no cleavage could be observed on the fracture of the sample with impact toughness higher than 90 joules. Therefore, T_{90J} is another definition of DBTT for this material.

In order to study the influence of factors on cleavage behaviors in DSS, some special tests were arranged. One is the effect of spinodal decomposition. The samples were aged at 450°C for up to 300 hours. The second is the effect of intermetallic phase, mainly sigma phase. The samples were tempered at 850°C for up to 10 minutes. The third is the effect of hydrogen or hydrogen induced stress cracking, HISC. The experimental details are described in reference [21]. The effect of other defects such as inclusion and Al nitride were also investigated.

3. Results and discussion

3.1 Influence of temperature on DBT behavior

Figure 2 shows the DBT curves from the CTOD and the impact toughness tests. As expected, both CTOD and impact toughness decrease with decreasing temperature. The modeling curves using Eq. 1 with C=35 were used to determine T_{50} and T_{90J}. Table 2 shows a summary of the influences of the factors such as amount of ferrite, cold deformation and phase size on the DBTT. The influence of phase size on the DBTT is relatively small. This result is quite different from that of the weld material where the DBTT (T_{27J}) increases significantly with increasing grain size [20]. An increase in ferrite content will raise the DBTT. This is due to the fact that it is the ferrite that causes a DBT. Cold deformation that introduces dislocations in the material can cause a decrease of impact toughness and consequently increase the DBTT since cold deformation increases both the strength of the material and the density of dislocation, which will promote the tendency for cleavage [21].

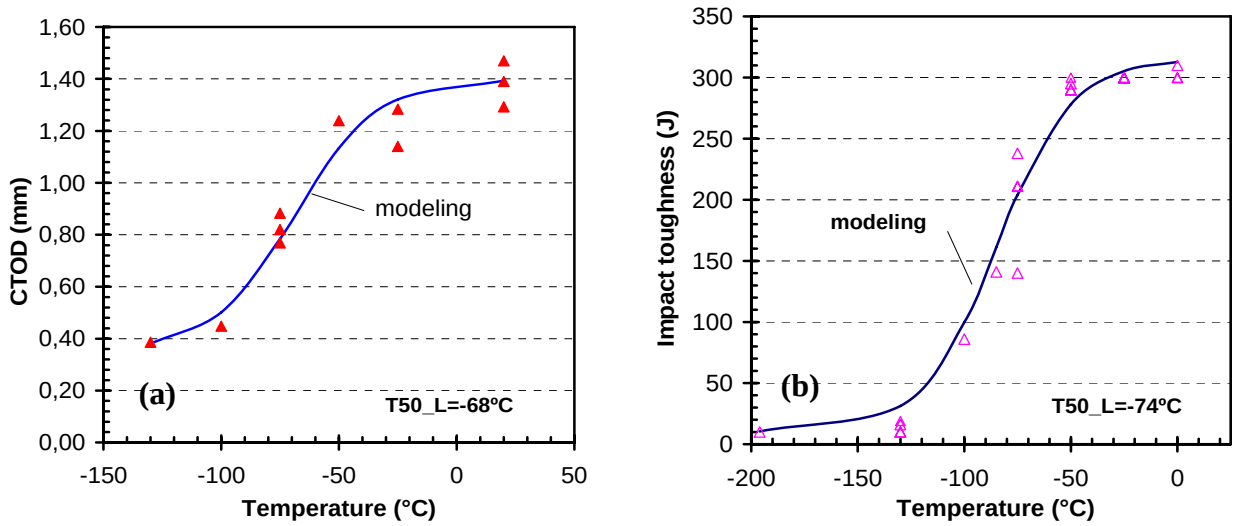

Figure 2 DBT behavior of UNS S32750 SDSS, (a). CTOD (b). Impact toughness.

Table 2 Influences of the different factors on DBTT

DBTT (°C)	Reference	Ferrite content (%)			Cold deformation (%)				Austenite spacing (μm)		
		45	61	68	0	5	10	15	18	23	32
T_{50}	-86	-74	-58	-41					-74	-76	-72
T_{90J}	-100	-92	-74	-54	-85	-76	-58	-52	-92	-94	-90

As known, the tendency for cleavage in the ferritic phase can increase when temperature decrease [22]. At -75°C, isolated cleavage fracture can be observed (Fig. 3a). It is in the transition regime as shown in Fig. 2. At -130°C, cleavage fracture is now dominant (Fig. 3b). It seems that brittle fracture could have also occurred in the austenitic phase. As discussed in [15, 16], the ferrite that has a BCC structure obeys the weakest link theory and shows a brittle fracture. For the austenitic phase, the weakest link theory can not be applied, but it follows the coupling effect. The effect of crack front length on fracture toughness is now practically absent when the hardness of austenitic phase is high enough. A sharp cleavage crack in the ferrite can lead to a stress concentration that can be higher than the critical shear stress for a cleavage fracture in the austenitic phase. In this investigation, quasi-cleavage or cleavage fracture can be observed in the austenitic phase. The cleavage in the ferrite shows multiple lines, not converge but are vertical to single big line like a “river” (Fig. 3c). The cleavage in the “river” may nucleate at some nuclei (Fig. 3c). A small cracking inclusion can be one of them (Fig. 3d).

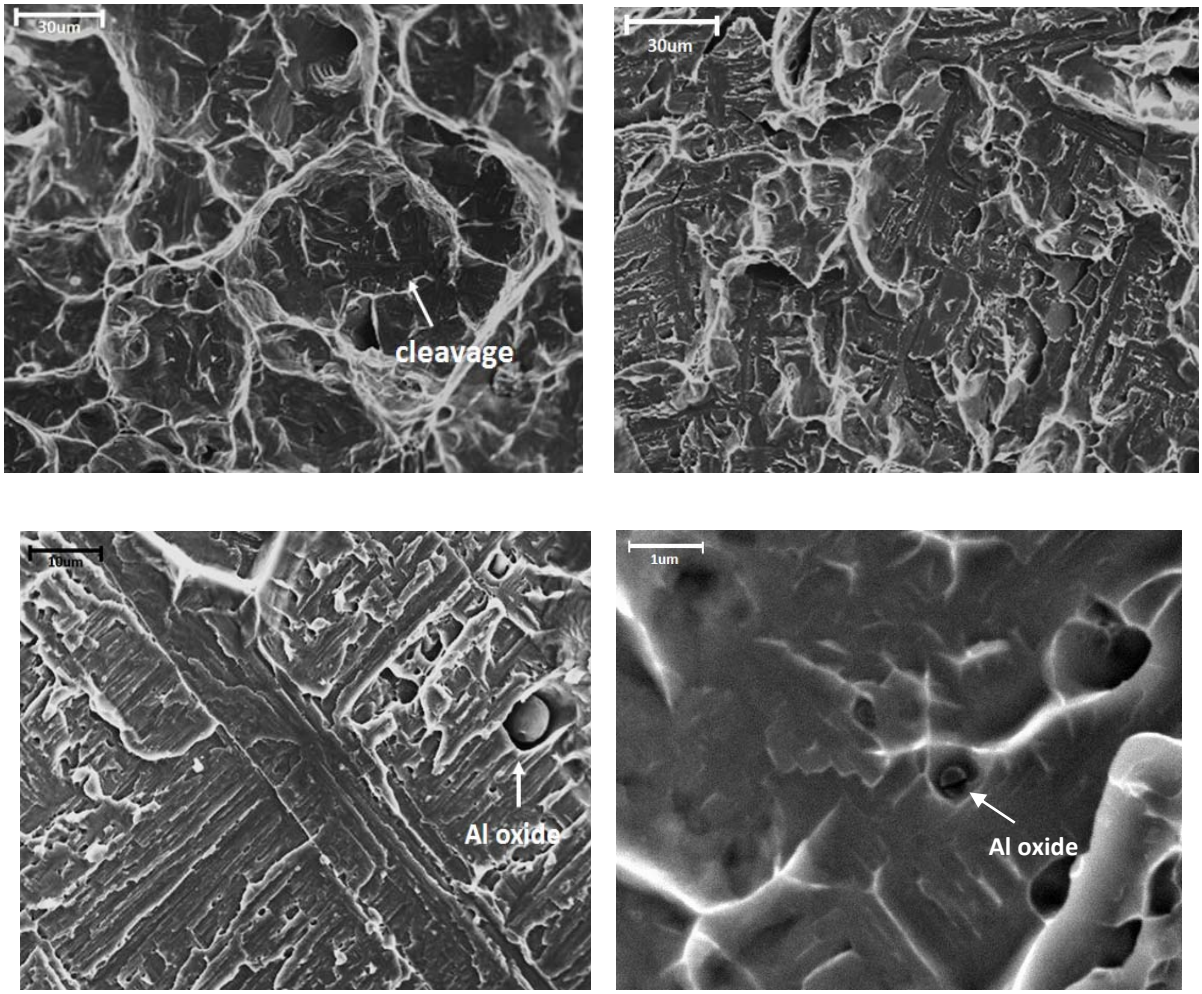

Figure 3 Influence of temperature on fracture in duplex stainless steel, (a). At -75°C, impact toughness 46J, (a). At -130°C, impact toughness 14J, (c). Enlarged cleavage fracture at -75°C, (d). Enlarged cleavage in weld metal at -100 °C, a cracking inclusion is a Griffith crack.

3.2 Influence of cluster on DBT behavior

Duplex stainless steel can suffer from a spinodal decomposition at temperatures between 300-500°C where the ferritic phase undertakes a miscibility gap that gives rise concentration variations with Fe-rich (α) and Cr-rich (α') regions (Fig. 4a), which leads to the formation of Fe-rich and Cr-rich clusters or phases [1, 2, 5]. Spinodal decomposition leads to an increase in the hardness of the ferritic phase, but not the austenitic phase (Fig. 4b). It was found that an increase in hardness of the ferritic phase promotes the occurrence of cleavage or DBT (Fig. 4c). Using Eq. 1, the hardness at T_{50} can also be determined as shown in Fig. 4d. This type of curve provides useful information for a quick evaluation of the influence of spinodal decomposition on the brittleness of the material.

The fracture structure in Fig. 4c is different from that in Fig. 3b. In Fig. 4c, the ferritic phase has a cleavage fracture, but not the austenitic phase. The austenitic phase is still ductile, and dimples can be observed. This indicates that the stress concentration at the cleavage crack in the ferritic phase is not high enough to initiate a quasi-brittle fracture as that in Fig. 3b since the fracture toughness in the austenitic phase in this case is still high enough. The above discussion shows that local approach to

fracture should be considered when a fracture in duplex stainless steel is involved, but the mechanical behaviors of both phases in the considered environment should be considered.

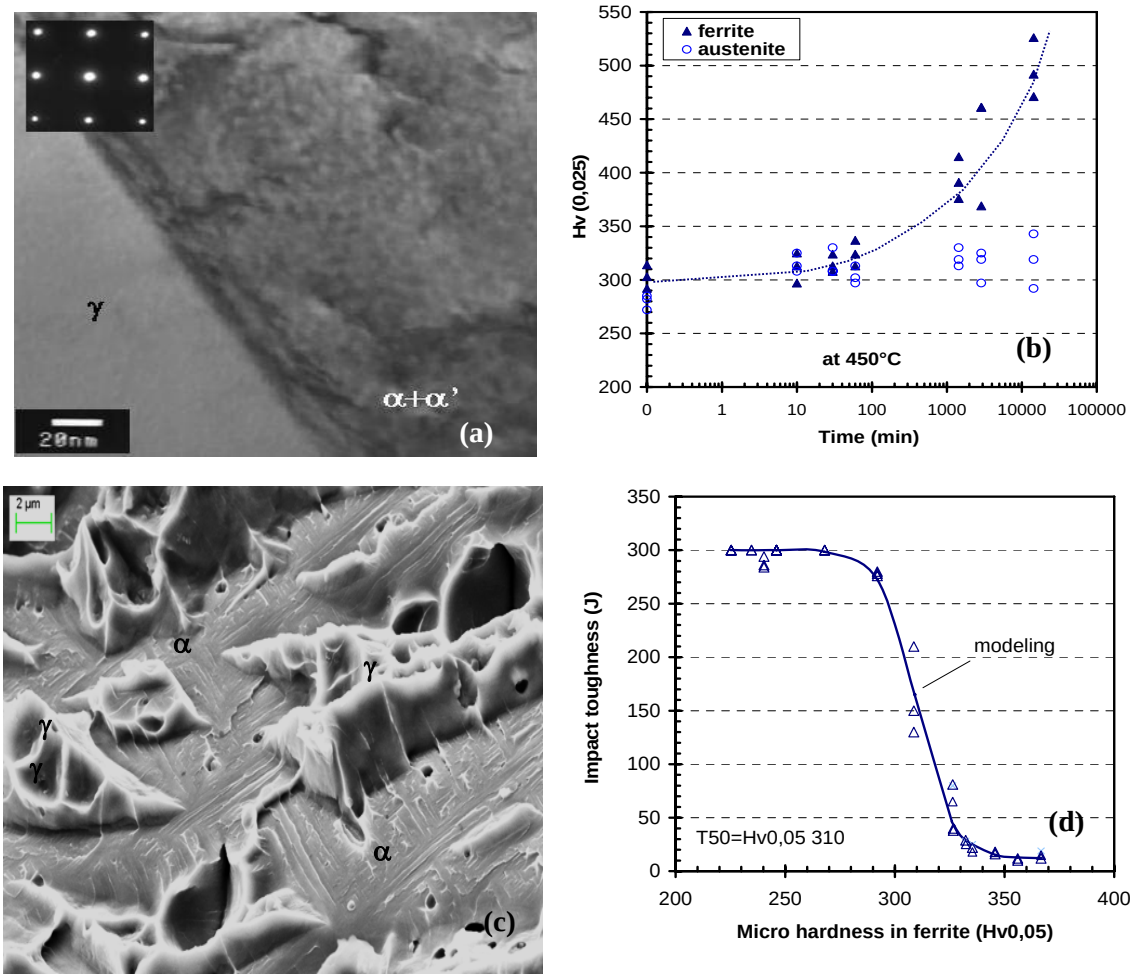

Figure 4 Influence of spinodal decomposition on DBT of DSS, (a). Formation of cluster, (b). Influence of spinodal decomposition on the hardness of individual phases, (c). Fracture, (d). Correlation between hardness and impact toughness; α is the ferritic phase or Fe rich cluster, γ is the austenhitic phase, α´ is the Cr rich cluster or phase.

3.3 Influence of precipitates and other defects on DBT behavior

Classically, a second phase particle induced cleavage is treaded as the formation of cracks or Griffith cracks in the particle because of plastic strain in the surrounding matrix. If the stress ahead of the crack is sufficient, it will propagate into the matrix, causing failure by cleavage [21]. For duplex stainless steels, the following cases can be considered. It was found that the influences of different precipitates on the DBT or cleavage behaviors are different. Figure 5 shows the force versus time curves from an instrumental impact toughness testing for SAF 2507 material with different conditions. For the as received material and the weld joint, both the crack initiation and propagation energies are high, which lead to high impact toughness. For the material containing small amount of Al nitrides, the crack initiation energy is high, the propagation energy is also high, but lower than that the as received and welded material. This indicates that crack propagation rate in this case can be higher.

For the material containing sigma phase, both the crack initiation and propagation energies are low, which lead to a low impact toughness.

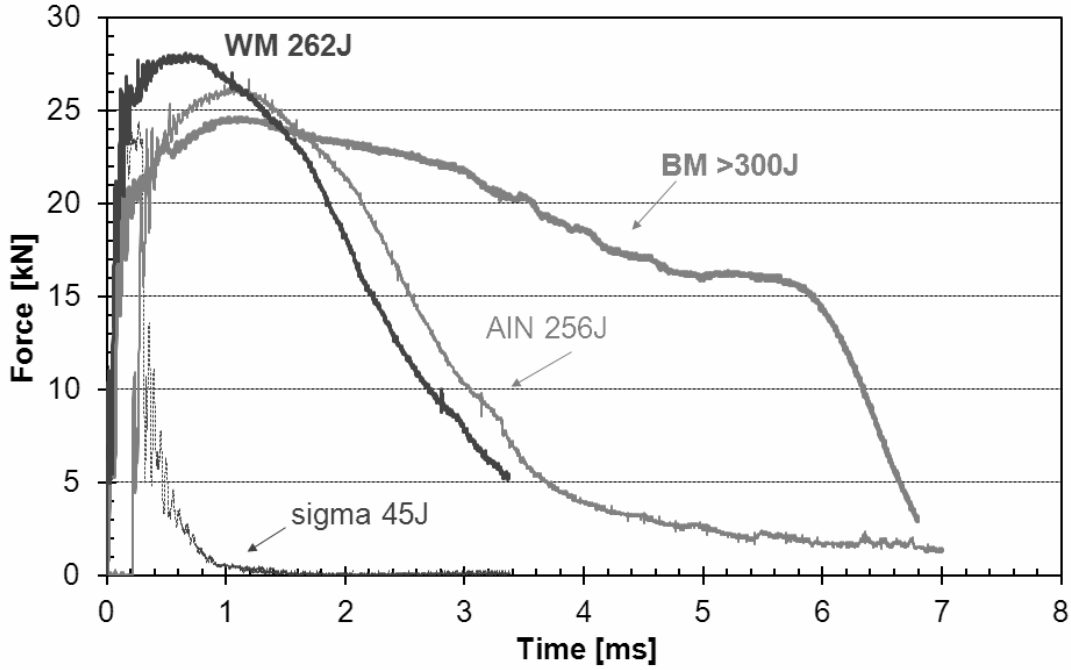

Figure 5 Force versus time curves from the instrumental impact toughness testing for SAF 2507 material with different conditions

The different cleavage behavior from different precipitates depends on the nature of precipitates and fracture mechanisms. Sigma phase has a $P4_2/mnm$ structure and is brittle. They precipitate mainly along grain or phase boundaries. These particles become easily cracking during plastic deformation. The cracking usually occurs usually through the particle (Fig. 6a). These sharp microcracks become then stress raisers or Griffith cracks that provide a local stress concentration that initiate cleavage fracture in the ferritic phase (Fig. 6b). High amounts of sigma phase will increase number of microcracks or Griffith cracks formed during plastic deformation, the hardness of the ferritic phase is also increased. This leads to an easier cleavage fracture with smaller cleavage plans (Fig. 6c).

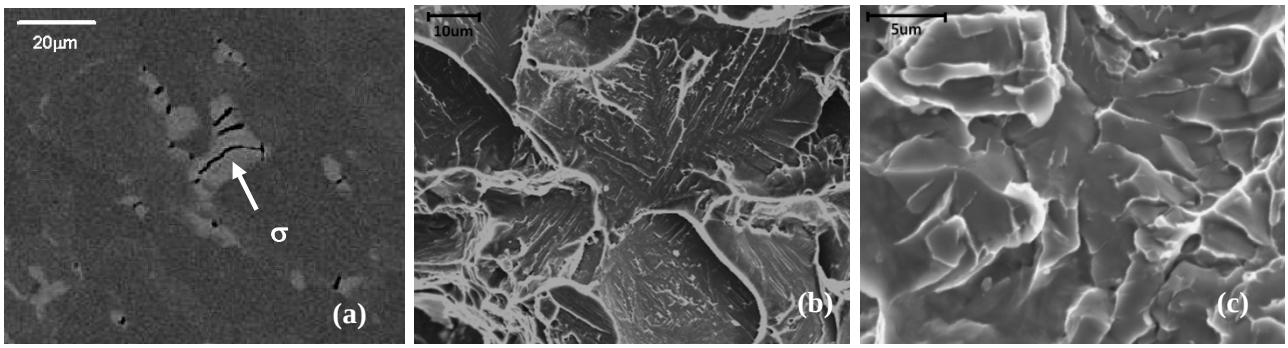

Figure 6 Influence of sigma phase on cleavage in duplex stainless steel at RT. (a). Cracking of sigma phase, (b). Cleavage fracture in the material with about 1% sigma phase, (c). Cleavage fracture in the material with about 10% sigma phase.

As shown in Fig. 5, the presence of small amount of Al nitrides has a small effect on the impact toughness comparing with sigma phase. However, at low temperature, Al nitride can also initiate cleavage fracture as shown in Fig. 7a. This does not happen for an Al oxide that is round and has a larger size (Fig. 7b). The results show that needle type of Al nitride can create a stress concentration that is higher than the critical stress for cleavage fracture in the ferritic phase. The morphology of the second particle can also play an important role to cleavage fracture.

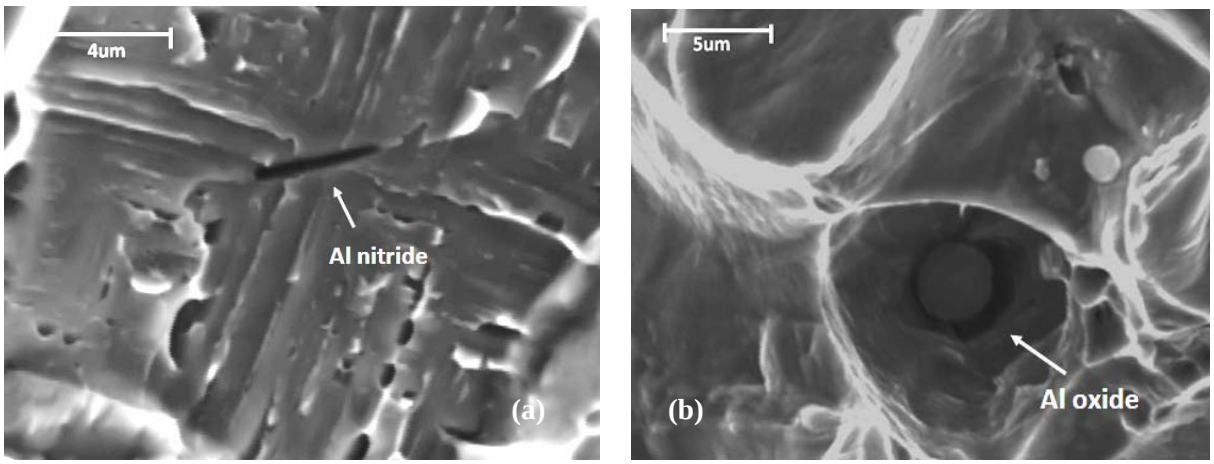

Figure 7 Influence of precipitate and defect on cleavage in duplex stainless steel. (a). Al nitride, (b). Al oxide at -130°C.

Recently, hydrogen induced stress cracking (HISC) in duplex stainless steel is concerned [22]. Diffusion of hydrogen into the material can lead to an increase in hardness, and on the other hand hydrogen can accumulate at phase and grain boundaries, which causes the formation of hydrogen pore or voids [22], and consequently the formation of stress concentration. When the hydrostatic pressure in the void reaches a critical value or a critical shear stress, the void can develop into a small crack or Griffith crack, and eventually cleavage initiation (Fig. 8a). Cleavage fracture propagates discontinuously due to the austenitic phase that acts as a hinder for crack propagation, which creates an unusual top-valley fracture (Fig. 8b). The cracks in the ferritic phase are mainly classical brittle cleavage. The herringbone pattern of fracture with the cleavage plane of {100} and two growth directions from <110> is the most common one (Fig. 8c). The situation here is similar to that due to the spinodal decomposition as discussed above.

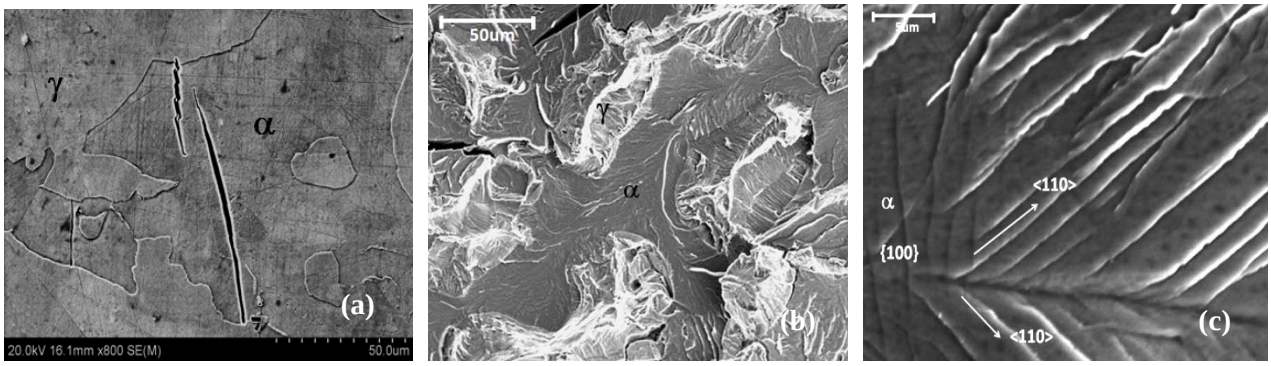

Figure 8 Cleavage initiation and propagation in hydrogen enriched duplex stainless steel, γ –austenite, α-ferrite.

The results and discussion above indicate that fracture initiation and propagation in duplex stainless steel are local processes but also have coupling effects. They can behave very differently in different environments. Local approach to fracture should be applied by considering the heterogeneous mechanical behaviors in these two phases.

4. Concluding remarks

Duplex stainless steels have heterogeneous mechanical and fracture behaviors in the ferrtic and austenitic phases. The cleavage behavior of the material depends strongly on the microstructure and environments. Influences of small variations of the microstructure such as phase size, ferrite content and cold deformation on the DBTT are small. Spinodal decomposition and precipitates can significantly raise the DBTT. The cleavage propagation in duplex stainless steel can be discontinuous since the austenitic phase behaves as a stopper.

Acknowledgments

This paper is published by permission of Sandvik Materials Technology.

References

[1] J. O. Nilsson: Mater. Sci. Technol. No. 8 (1992), p. 685
[2] J. Charles, Proc. Conference on DSS ’91, Les Ulis, France, Les Editions de Physique, 3 (1991)
[3] J. O. Nilsson and G. Chai: Physical metallurgy of duplex stainless steels, (2010), Proc. Of Conf. DSS 2010, pp. 35.
[4] G. Chai and P. Kangas, Hyper duplex stainless steels, (2010), Proc. Of Conf. DSS 2010, pp. 125.
[5] M. Hättestrand, P. Larsson, G. Chai, J-O Nilsson and J. Odqvist, Materials Science and Engineering A, A 499 (2009) 489–492.
[6] J.J. Moverare: in *Microstresses and anisotropic mechanical behaviour of duplex stainless steels*, Ph D thesis, (2001), Linköping University, Sweden.
[7] R. Lin Peng, G. Chai, N. Jia, Y. D. Wang and S. Johansson: Fat. & Fract. of Engng. Mat. &

Struct., 31(10): (2008), p. 892

[8] N. Jia, R. Lin Peng, Y. D. Wang, G. C. Chai, S. Johansson, G. Wang and P. K. Liaw: ACTA Materialia, 54 (2006) p. 3907

[9] R. Lin Peng, J. Gibmeier, S. Eulert, S. Johansson and G. C. Chai: Materials Science Forum, 524-525 (2006), p. 847

[10] R. Lillbacka: in *On the multiscale modelling of duplex stainless steel*, Ph D thesis, (2007), Chalmers university of technology.

[11] G. Chai, R. Lillbacka and P. Liu: *Damage and crack initiation behaviour of a duplex stainless steel during cyclic loading*, MRS fall meeting, (2005), .Boston.

[12] R. Lillbacka, G. Chai, M. Ekh, P. Liu, E. Johnson and K. Runesson: Acta Materialia, 55 (2007), p. 5359

[13] G. Chai, and R. Lillbacka: Key Engineering Materials, 324-325 (2006), p. 1117

[14] A. Hazarrabedian, P. Forget and B. Marini, Materials Research, (2002). vol. 5, No. 2, pp. 131

[15] B. Z. Margolon, V. A. Shvetsova and V. I. Kostylev, Modeling of fracture for austenitic materials with ferritic phase on the basis of local approach, (2002), Proc. IFC 11.

[16] B. Z. Margolon and V. A. Shvetsova, Journal de Physique IV, (1996), vol. 6, C6-255.

[17] A. Pineau, nales de la Mecanica de fracture, (2007), vol. 1, pp. 9.

[18] ASME VIII: *Rules for construction of pressure vessels*, ASME 1989.

[19] EN 13445: *Unfired pressure vessels Part 2 -Materials*, European Standard 2002

[20] B. E. S. Lindblom, B. Lundqvist and N-E. Hannerz: Duplex stainless steels 91, Vol. 1, (1991), p. 373-381.

[21] T. L. Anderson: *Fracture Mechanisms in Metals*, CRC, (1995), p. 285-299.

[22] G. Chai1, S. Ronneteg, U. Kivisäkk, R. Lin Peng and S. Johansson, Steel Research Int. 80 (2009) No. 72, pp484.

Cleavage modelling with experimental particle size distribution and novel particle failure criterion

Andrey P Jivkov[1,*], **Peter James**[2]

[1] School of Mechanical, Aerospace and Civil Engineering, The University of Manchester, Manchester M13 9PL, UK.
[2] AMEC, Walton House, Birchwood, Warrington WA3 6GN, UK.
* Corresponding author: andrey.jivkov@manchester.ac.uk

Abstract Most of the existing local approaches for cleavage fracture derive from the assumptions that global failure is a weakest-link event and that only the tail of the size distribution of micro-crack initiating features is significant. This appears to be sufficient in predicting lower shelf toughness under high constraint conditions, but may fail when attempting to predict toughness in the transition region or for low constraint conditions when using the same parameters. While coupled ductile damage models with Beremin-like failure probability could be useful in the transition region, uncoupled models with "a posteriori" probability calculations are advantageous to the engineering community. Cleavage toughness predictions in the transition regime, which can be extended to low constraint conditions, are here made with improved criterion for particle failure and experimentally based size distribution of initiators for specific RPV steel. The model is shown to predict experimentally measured locations of cleavage initiators. Further, the model predicts the fracture toughness in a large part of the transition region and accurately predicts a measured shift with irradiation. All results are obtained without changes in model parameters. This suggests that the model can be used for assessing toughness changes due to constraint- and temperature-driven plasticity changes.

Keywords RPV steel; local failure criterion; global failure probability; transition temperature regime

1. Introduction

Safety assessment and life extension decisions in nuclear plant require reliable methodologies for predicting changes in cleavage fracture toughness behaviour of ferritic RPV steels due to irradiation and defect geometry effects. Local approaches (LA) to cleavage fracture are promising as these could account for the micro-mechanisms involved in the cleavage failure phenomenon, such as the nucleation of micro-cracks at second-phase brittle particles, the propagation of such micro-cracks within grains and the propagation of a critical micro-crack leading to component failure [1]. The pioneering LA to cleavage, proposed by the Beremin group [2], is based on two main assumptions: that the global failure probability is a weakest-link event and that the individual failure probabilities are dictated by local mechanical fields and specific microstructure data such as the size distribution and number density of cleavage-initiating particles. Assuming that the tail of the size distribution can be approximated by a power-law, the weakest-link statistics leads to a global failure probability expressed as a Weibull-type function of a generalised stress, the Weibull stress σ_w [2, 3]:

$$P_f(V) = 1 - \exp\left[-\left(\frac{\sigma_w}{\sigma_u}\right)^m\right] \tag{1}$$

The shape, m, and scale, σ_u, of the Weibull function can be calibrated using fracture toughness data obtained with particular crack geometry at a given temperature and corresponding FE analysis [4]. For calibrations performed with high-constraint crack geometries at or below the ductile-to-brittle transition temperature, T_0, the shape and scale obtained can be used with sufficiently good accuracy to predict cleavage fracture toughness of other high-constraint geometries at temperatures below T_0 [2-4]. However, an attempt to use the same parameters to calculate cleavage toughness under lower constraint conditions or higher temperatures leads to predictions that do not match experimental values. For cleavage fracture toughness data obtained at a given temperature with low- and high-constraint geometries, independent calibrations would typically show that the low-constraint m

is smaller than the high-constraint m (assuming that σ_u is not dependent on constraint), see e.g. [5]. This suggests that the excess of plastic deformations introduced by the lower constraint require reduction of m to make reliable predictions. The methodology proposed in [5] for cross-calibration of m between high and low constraint geometries has shown promise [5, 6], but remains limited to temperatures well below T_0, where the lower constraint conditions do not introduce substantial increase in plastic deformations relative to the high constraint case. This may prove problematic when used to predict cleavage fracture toughness for short cracks in irradiated material, where the reference temperature is shifted to higher values. To predict the irradiation effects on cleavage one needs a reliable model for the ductile-to-brittle transition (DBT) regime. Here, however, the Weibull parameters need to be varied to match experimental data. One possibility is to keep the shape parameter constant, which leads to temperature dependence of the scale, σ_u [7, 8]. Another possibility is to keep the scale parameter constant, which leads to temperature dependence of the shape, m [9, 10]. As for the low-constraint situation, m needs to be reduced with increasing temperature, i.e. with enhanced plasticity.

Considering the physical basis for the Beremin LA [2, 3], the current state of affairs is not satisfactory, because the Weibull parameters must depend exclusively on the material microstructure. If the model for individual failure probability accounted adequately for the local fields and microstructure effects on particle failure, and the global failure were a weakest-link event, then the changes in plasticity due to constraint reduction or temperature increase should be already accounted for, leaving the Weibull parameters constants. In particular, m should be linked to the shape of size distribution of cleavage initiation particles, while σ_u should depend on the elastic properties and surface energy of the material as well as on the scale of the particle size distribution. Since these parameters do not change noticeably with constraint or temperature, the need to vary m and σ_u at increasing plastic deformations suggests that the link between physics and mechanics breaks. One possibility is that the individual failure probability model does not account adequately for the mechanical and particle size effects. A second possibility is that with the increase of plastic deformations the population of micro-cracks that needs to be accounted for in the weakest-link statistics becomes larger than the tail of the distribution, approximated by power-law in the Weibull-stress models. A third possibility is that the weakest-link assumption becomes increasingly invalid with increasing plasticity and micro-crack interaction effects need to be accounted for.

To improve the individual failure probability, the effect of the plastic strain has been introduced in modifications of the Beremin model [11, 12] as well as in incremental formulations [13]. Recently, in addition to plastic strains the effect of stress triaxiality has also been introduced [14]. In a previous work [15], we have compared these models with the original Beremin and demonstrated that they provide improvements in the predicted failure probability profiles ahead of cracks with different constraints. This comparison has been done against a large set of experimental data for the locations of cleavage initiation sites reported in [16]. However, the prediction of the cleavage fracture toughness temperature dependence with these models remained unsatisfactory when performed with single set of Weibull parameters calibrated at T_0. The effect of particle size on local failure probability was first proposed in [17]. The model now known as WST, however, remained as a microstructure-informed local model and to our knowledge had not been applied for global failure predictions. A different direction of work considers ductile damage prior to cleavage in the DBT regime, employing damage models for the material behaviour coupled with subsequent calculation of failure probability following Beremin [18, 19]. This approach has the potential to capture better the fracture behaviour in the DBT, but the models are presently too simplified with no interaction of void growth and micro-cracking at microstructure level [20]. Until advanced coupled models are developed and tested, the wider engineering community would benefit from a simpler uncoupled cleavage fracture model for the DBT region.

In [15] we have proposed a model incorporating mechanical and particle size effects and demonstrated that it provides excellent predictions for failure probability profiles. In this work we report on application of the model to predict cleavage fracture toughness in DBT regime. We focus on the first two possibilities mentioned above: to improve individual probability of failure and to account directly for the real particle size distribution rather than approximating the tail. The validity of the weakest-link assumption for the calculation of global probability is maintained. The model is applied to specific RPV steel, Euro Material A, for which fracture toughness data is available in [21] and particle size distribution, obtained via metallographic analyses, is given in [22].

2. Theory and model

LA methods share a common philosophy based on two distinct components. Firstly, the local mechanical fields provide a local or 'individual' probability of failure when linked to the size distribution of the micro-crack initiators. The individual probability of failure at location i is

$$p_{f,i} = \int_{r_{c,i}}^{\infty} p_{c,i}\ f(r)\, dr\,, \tag{2}$$

where $f(r)$ is the probability density of initiators' sizes, $p_{c,i}$ is the probability of micro-crack nucleation, and $r_{c,i}$ is a critical micro-crack size at location i. Note, that $p_c\, f(r)$ is the probability density of nucleated micro-crack sizes. Existing LAs can be recast into Eq. (2) albeit with different definitions of p_c and r_c. For example in [2-4] $p_c = 0$ or 1 for zero and non-zero plastic strains. In [11, 12] p_c scales with the equivalent plastic strain, while in [14] p_c scales with the equivalent plastic strain and exponent of the stress triaxiality. In [13] p_c is a more complex function of stress and plastic strain increments. In all cases r_c is defined via Griffith or plasticity-modified Griffith criterion. Common feature of [2-4, 11-14] is that p_c is independent of particle size.

Secondly, it is assumed that the individual failure events are independent. This allows the weakest-link argument to be invoked for calculating the global failure probability, so that

$$P_f(V) = 1 - \prod_{i=1}^{N} \left(1 - p_{f,i}\right), \tag{3}$$

where N is the number of possible weakest-links, i.e. active micro-cracks, in volume V. In practice, LAs are applied to FE solutions of cracked components, where the mechanical fields are constant within an integration point volume, V_i. The failure probability of such a volume is thus

$$P_f(V_i) = 1 - \left(1 - p_{f,i}\right)^{N_i} = 1 - \left(1 - p_{f,i}\right)^{\rho_i V_i}\,, \tag{4}$$

where $N_i = \rho_i V_i$ is the number of micro-cracks in V_i, and ρ_i is the density of the micro-cracks. Strictly speaking $\rho_i = \rho\, p_{c,i}$, where ρ is the density of initiating particles in the material. The component probability of failure is then calculated by repeated application of (3) to get

$$P_f(V) = 1 - \prod_{i=1}^{IP} \left(1 - p_{f,i}\right)^{\rho_i V_i}\,, \tag{5}$$

where the product is taken over all integration points. When p_c is independent of particle size, Eq. (2) can have a closed-form solution in terms of critical micro-crack sizes, r_c. With a power law approximation for particle sizes and assuming small individual failure probabilities, Eq. (5) yields the Weibull-stress function in Eq. (1). We use Eq. (5) directly for global failure probability, because the experimental particle size distribution, Section 2.1, and our expression for individual failure probability, Section 2.3, do not allow for closed form solution of Eq. (2).

2.1. Experimental data

The material analysed is an RPV 22NiMoCr37 ferritic steel, known as Euro Material A, for which we have the mechanical and fracture toughness properties at a number of temperatures and irradiation states within the lower shelf and in DBT from the Euratom FP6 project PERFECT [21] and FP7 project PERFORM60. The temperature dependence of Young's modulus E, proportionality stress σ_0, and ultimate tensile strength σ_u under un-irradiated conditions are

$$E = -90T + 206000, \tag{6}$$

$$\sigma_0 = 421.2 + 63.9\exp(-T/91), \quad \sigma_u = 564.1 + 70.2\exp(-T/108), \tag{7}$$

where T is in ^{o}C and E, σ_0, and σ_u are in MPa. Poisson's ratio is $\nu = 0.3$ independent of temperature. For the irradiated state considered here, fluence of 4.3 x 10^{19} n cm^{-2}, En > 1 MeV at 285°C, E is given by Eq. (6) while σ_0 and σ_u are given by

$$\sigma_0 = 490.4 + 62.1\exp(-T/95.2), \quad \sigma_u = 524.2 + 155.1\exp(-T/188.2). \tag{8}$$

The fracture toughness properties of Material A were determined according to the ASTM standard [23] using SEN(B) specimens in three-point bending [21]. This standard is based on the Master Curve formalism, which defines the temperature dependence of a reference toughness, K_0, relative to a reference temperature, T_0, at which K_0 = 108 MPa√m, for high-constraint cracked geometries with reference crack front length B_0 = 25.4 mm

$$K_0 = 31 + 77\exp[0.019(T - T_0)]. \tag{9}$$

The scatter in measured cleavage fracture toughness values is described as a function of the probability of failure, p, and the actual crack front length, B, with

$$K_p = K_{\min} + (K_0 - K_{\min})\left(\frac{B_0}{B}\right)^{1/4}\left(\ln\frac{1}{1-p}\right)^{1/4}, \tag{10}$$

where $K_{\min}$ is a temperature independent threshold toughness, $K_{\min}$ = 20 MPa√m in [23]. Eqns. (9) and (10) define the cleavage fracture toughness behaviour of a material with known T_0. The reference temperatures for deep-notch (a_0/W = 0.5) specimens reported in [21] are T_0 = -104ºC for un-irradiated and T_0 = -78ºC for irradiated state. In the present work, we assume that Eqns. (9) and (10) provide a relevant representation of experimental data and assess our model against it.

The density and size distribution of cleavage initiating particles in Material A have been reported in [22]. The nature of the initiators has been determined by fractography revealing that cleavage in this material initiated predominantly at metal carbides, specifically M_3C and $M_{23}C_6$, and occasionally at carbide-sulphate composites. Comprehensive metallographic examination of carbides provided number density $\rho = 7.6\times10^{17}$ m^{-3} and a probability density of particle sizes which was fit by

$$f(r) = \frac{\beta}{r_0}\left(\frac{r}{r_0}\right)^{-\beta-1}\exp\left[-\left(\frac{r}{r_0}\right)^{-\beta}\right], \tag{11}$$

with shape $\beta = 2.7$ and scale r_0 = 0.036 μm.

2.2. Micro-mechanically informed model

The expression for the probability of particle failure is based on experimental observations that this probability depends not only on the mechanical fields but also on the particle size, similarly to the

WST model [17]. The rationale is that larger particles have higher probability of failure than smaller particles under identical mechanical conditions. The particles are assumed to be elastic-brittle with elastic constants equal to those of the matrix as a first approximation. The principle stresses, Σ_α, in a particle can be given in terms of the principal stresses, σ_α, and plastic strains, ε^p_α, in the matrix with

$$\Sigma_\alpha = \sigma_\alpha + \frac{E}{1+\nu}\,\varepsilon^p_\alpha, \qquad \alpha = 1,2,3\,. \tag{12}$$

The criterion of particle failure is based on a critical value of the strain energy density in a particle associated with failure normal to the maximum principal stress. This is given by

$$\psi_c = \frac{1+\nu}{E}\,\Sigma_I^2 - \frac{\nu}{E}\,\Sigma_I \Sigma_h\,. \tag{13}$$

where Σ_I and Σ_h ($=\sigma_h$) are the maximum principal and the hydrostatic stress in the particle, respectively. If a particle of size r ruptures normally to the maximum principal stress upon achieving some critical condition, the energy lost (or the work of rupture) will be proportional to $\Psi_c = r^3 \cdot \psi_c$. The survival probability, p_s, of the particle must decrease with increasing work of rupture, which can be written in the form

$$\frac{dp_s}{p_s} = -\frac{d\Psi_c}{\Psi_0}\,, \tag{14}$$

where Ψ_0 is a scaling energy. The survival probability at a given Ψ_c can be determined by integrating Eq. (14) from the initial value of the work of rupture, which is zero, to the current value. The probability of particle rupture, p_c, is one minus the survival probability

$$p_c = 1 - \exp\left(-\frac{\Psi_c}{\Psi_0}\right) = 1 - \exp\left[-\left(\frac{r}{r_0}\right)^3 \frac{\psi_c}{\psi_0}\right], \tag{15}$$

where the rupture energy density scale $\psi_0 = \Psi_0 / r_0^3$ is introduced for convenience. Note, that Eq. (15) incorporates the effects of plastic strain and stress triaxiality. Increased plastic strains will result in increased ψ_c and hence probability of micro-crack formation. Inversely, increased hydrostatic stress, which could lead to micro-crack blunting, will result in reduced ψ_c and hence probability of micro-crack formation under equal other conditions, see Eqns. (12) and (13).

We use Eq. (15) and Eq. (11) into Eq. (2) to calculate individual probabilities of failure at the integration points by numerical integration. The lower limit of the integral, i.e. the critical micro-crack size, is defined with a heuristic argument leading to a new modification of the Griffith criterion. We assume that the behaviour of a micro-crack of radius r formed in the plastic matrix corresponds to a fictitious micro-crack with $r_f > r$ in an elastic matrix. The crack opening displacement of a penny-shaped crack of radius r_f in an elastic material subject to normal stress σ_I is

$$u(x) = \frac{4\left(1-\nu^2\right)\sigma_I}{\pi\, E}\sqrt{r_f^2 - x^2}\,, \qquad 0 < x < r_f\,. \tag{16}$$

The blunting of the physical micro-crack formed after particle rupture can be approximated by $r\varepsilon^p_I$. The fictitious micro-crack size is then defined in such a way that the opening at $x = r$ equals the blunting of the physical micro-crack, i.e. $u(r) = r\varepsilon^p_I$. Solving Eq. (16) with this constraint leads to the following expression for the fictitious micro-crack size

$$r_f = r\sqrt{1 + \left[\frac{\pi\, E\, \varepsilon_I^p}{4\left(1-\nu^2\right)\sigma_I}\right]^2}\,. \tag{17}$$

Used in conjunction with the Griffith criterion an effective critical micro-crack size can be defined

$$r_c = \frac{\pi E \gamma_s}{2\left(1-\nu^2\right)\sigma_I^2}\sqrt{1+\left[\frac{\pi E \varepsilon_I^p}{4\left(1-\nu^2\right)\sigma_I}\right]^2} \quad . \tag{18}$$

The square-root factor in Eq. (18) replaces the exponent of plastic strain in the modified Griffith criterion used previously [2-14]. As before, it is intended to account for the reduction in crack driving force due to plastic dissipation in the matrix. The difference is that in the case of Eq. (18) the effect is not only dependent on the plastic strain but also on stress triaxiality via the ratio between the maximum plastic strain and the maximum stress.

2.4. FE model

The developed LA has been applied to an FE model of Pre-Cracked Charpy-V (PCCV) specimens used in the tests [21]. These were 30 mm thick, 200 mm long and 25.4 mm deep. Here, this is modelled in 2D under plane strain conditions. Crack depth was 12.7 mm representing high constraint conditions. Rigid loading rollers were positioned with a total span of 180 mm (i.e. 10 mm from the specimen edge) and at the crack back-face. The FE model, with account for symmetry, was created and analysed with ABAQUS 6.11 [24]. The crack tip region was modelled as a fine blunt notch with a radius of 25 μm for use in large strain analyses. The crack tip elements were 5 μm long and 0.6 μm wide. In total 34,000 CPE8R elements were used. Model illustration is given in Fig. 1.

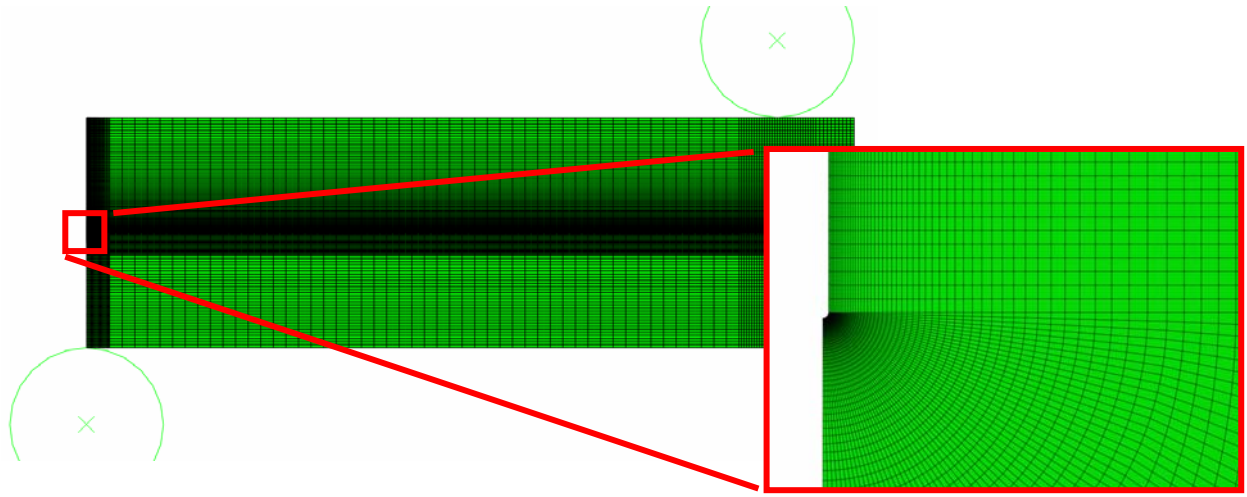

Figure 1. FE Model of 3PB specimen

We considered a range of temperatures in un-irradiated and irradiated states, spaced between approximately ±60°C of the un-irradiated T_0 in a maximum of 10°C increments. Power-law stress-strain relation was used to describe material behaviour at each temperature, such that $\varepsilon = \sigma/E$ for $\sigma < \sigma_0$, and $\varepsilon = (\sigma_0/E)(\sigma/\sigma_0)^n$ for $\sigma > \sigma_0$, where E was determined from Eq. (6) and σ_0 was determined from Eqns. (7) or (8). The power law exponent, n, was found using the Considère's rule describing the stress-strain condition at the point of loss of stability, represented by σ_u.

Loading was applied by displacing the bottom loading pin into the specimen whilst preventing the top pin from moving. It was also necessary to apply boundary conditions to the loading pins to prevent free rotation and unwanted displacement. Standard contact was used with a small adjustment of 0.015 mm to the mesh around the rigid surface of the loading pins to ensure correct transference of the load. The contact was also modelled as having no separation, ensuring contact throughout the analyses. Large strain analyses were performed in all cases.

In each analysis the J-contour integral, calculated by Abaqus, was used to determine the stress intensity factor for comparisons with Master Curve. The validity of J for this purpose can be questioned as the applied load caused the plastic zone to reach the back face and interact with the loading pin, preventing the contour zone from fully encompassing the plastic zone. To try and encompass as much of the plastic zone as possible up to 80 contours were taken away from the crack tip node set. Thus, the estimate of J covered as much of the plastic zone as possible whilst remaining contained in the model. Validation of the model was performed that provided confidence in the model, loading and extracted values of J.

3. Results and discussion

For known carbide distribution parameters, β and r_0, in principle the model requires a single calibration of the rupture energy density scale, ψ_0, in Eq. (15). This can be performed by comparing experimentally measured positions of cleavage initiation sites with the profile of the individual failure probability ahead of the crack, calculated using Eq. (2) with Eqns. (15) and (18). For surface energy γ_s = 2.4 Jm^{-2} available for typical ferritic steels in the literature [25] and β=2.7 we have previously calibrated ψ_0 using experimental data for Material A at several constraints and temperatures taken from [16] and found a value $\psi_0 = 10^5$ that was fairly insensitive to such changes [15]. Here, we used this value for all cases analysed. However, to investigate the sensitivity of the results to variations in carbide size distribution we considered two shapes: the experimental β=2.7 and a higher β=4. To accommodate for this, keeping $\psi_0 = 10^5$, we calibrated γ_s at a single temperature, T_0 for the un-irradiated material, so that at applied K = 100.3 MPa√m the model predicted 50% probability of cleavage. The calibrated values for γ_s were 2 Jm^{-2} for β=2.7 and 8 Jm^{-2} for β=4. Note that the calibrated γ_s for β=2.7 is within 20% to the literature value.

Fig. 2 shows two failure probability profiles as functions of normalised distance ahead of the crack obtained with β=2.7 and β=4 and the calibrated ψ_0 and γ_s. For both profiles r_0 = 0.036 μm is used. The green stars show experimentally measured locations of cleavage initiation sites reported in [16] for SEN(B) specimens with deep cracks tested to fracture at several temperatures. The results are normalised so that the maximum individual failure probability is at unity. Note that the predicted profiles do not change significantly with the shape β, suggesting a small dependence of the calibration results on particle size distribution. Clearly, the model captures the peak location of initiating particles accurately and approximates the overall shape sufficiently well. The experimental β=2.7 appears to give a slightly better fit.

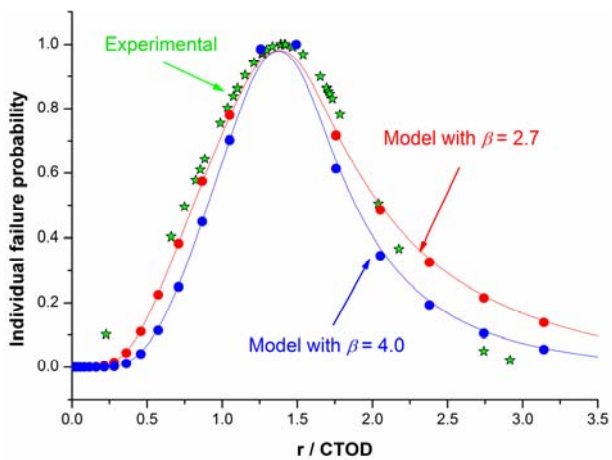

Figure 2. Individual failure probability predicted by proposed model with β = 2.7 and β = 4.

The predictive bounds from the model compared to both experimental data and the Master Curve are given in Fig. 3 for the un-irradiated material for both the β =2.7 (left) and β =4 (right) carbide size distributions. It can be seen that our model provides a good fit of the experimental data for both values of β with only a couple of points slightly outside the lower bound prediction. This, however, is also observed for the Master Curve. The comparison to the Master Curve is very good over the lower transition region before becoming slightly wider at higher temperatures. This provides confidence in the finite element analyses and developed local approach model. That the results widen at higher temperatures is likely to be an effect of plasticity which could manifest in both the accuracy of the finite element analyses and of the assumptions in the local approach model. The effect of changing β is only slight over the lower DBT transition region, where the higher value of β provides a narrower probability bound, as reflected in Fig. 2.

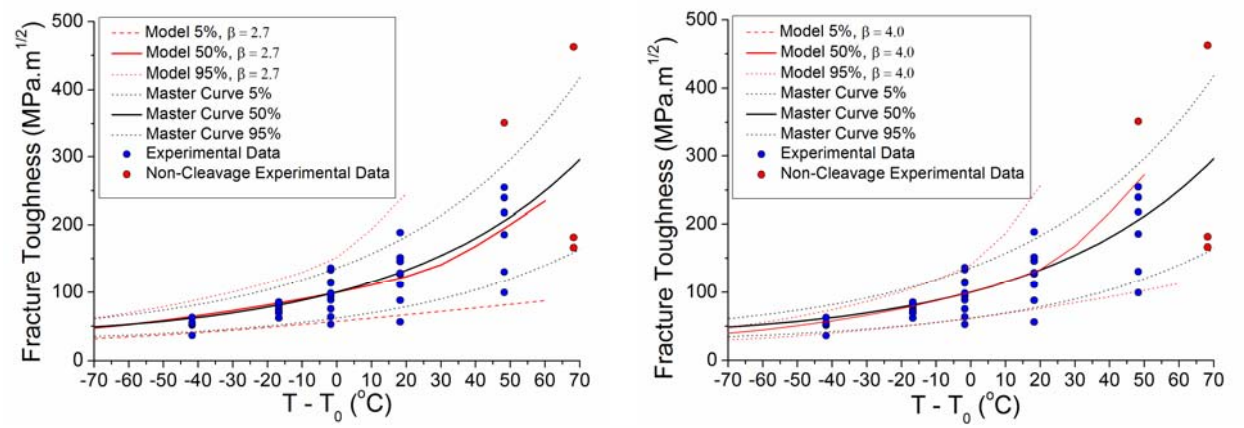

Figure 3. Temperature dependence predicted by proposed model with β = 2.7 (left) and β = 4.0 (right) for the un-irradiated material. Experimental data and Master Curve predictions shown for comparison.

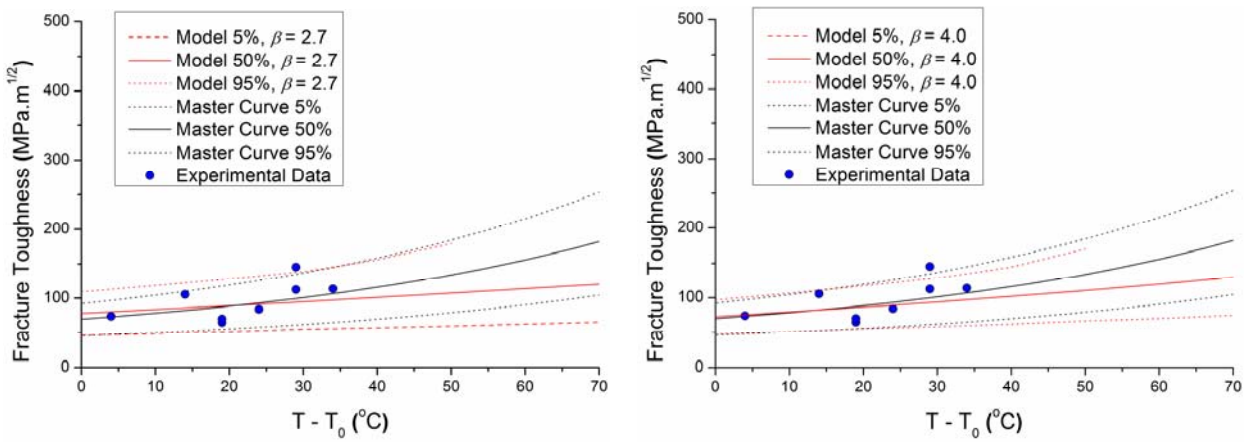

Figure 4. Temperature dependence predicted by proposed model with β = 2.7 (left) and β = 4.0 (right) for the irradiated material (4.3 x 10^{19} n cm^{-2}, En > 1 MeV at 285°C).

The predictive bounds from the model for the irradiated material are given in Fig. 4, again with β =2.7 (left) and β =4 (right) carbide size distributions. It can be seen that both the developed model and the Master Curve profiles provide a good fit to the experimental data. It must be emphasised that our model's predictions are based only on the changes in the tensile properties from the un-irradiated analyses while the calibrated model parameters were the same. At the same time the position of the Master Curve is dictated by the experimentally determined T_0 for the irradiated state.

If assessed in terms of a shift in the Master Curve T_0 value the proposed model provides a +33°C reference temperature shift, whereas the Master Curve assessment provides a +29°C shift. This means that the model has, for this case, accurately predicted the shift in toughness with irradiation with some additional safety margin.

The strong side of the proposed model is that it offers a microstructure-property relation that remains as true to the physics as presently possible within the constraints of the uncoupled material behaviour and the weakest-link assumption. The model takes directly microstructure data: the density of initiators and the probability distribution of their sizes, which can be determined by metallography. It basically requires the calibration of a single parameter: the rupture energy density scale, for which the additional information for positions of cleavage initiators can be determined by fractography. In the particular case reported here, the surface energy was also calibrated. This however was necessary to study a distribution with a higher than the experimental shape, while the scale parameter and density of initiators remained the same. It should be noted that the shape, scale and density are intrinsically related for a given material, so that the need to calibrate the surface energy could be eliminated for accurate experimental data. We have shown, at least in principle, that by advancing the local failure probability expression and accounting for a "real" size distribution data, one can achieve improved predictions for cleavage fracture toughness, certainly in the lower transition region. The outcome at higher temperatures is not yet satisfactory, but the reason for this could be the third possibility described in the introduction: interactions between micro-cracks, the density of which increases with plasticity, may become strong enough to invalidate the weakest-link assumption behind the current model. This will be a subject of future investigations.

4. Conclusions

- The proposal offers a microstructure-informed strategy for calculating the probability of failure in a large part of the DBT region.
- The calibration provides an estimate of surface energy that is close to values available in the literature, indicating that if all available parameters were well defined, the model would provide meaningful predictions of fracture toughness.
- The predicted initiation sites (individual probability profiles) correspond very well with experimentally determined initiation sites for this material.
- Cleavage toughness predictions in the DBT regime correlate well with both experimental data and Master Curve fits in the un-irradiated state.
- On changing the tensile properties to consider irradiation, the shift in fracture toughness and spread of experimental results are well predicted. This is achieved with a single calibration at one temperature in the unirradiated state.

Acknowledgements

The support from BNFL to Jivkov is gratefully acknowledged. James would also like to acknowledge assistance from colleagues at AMEC in the FEA and to PERFORM60 for data.

References

[1] A. Pineau, Development of the local approach to fracture over the past 25 years: theory and applications. Int J Fract 138 (2006) 139–166.
[2] F.M. Beremin, A local criterion for cleavage fracture of a nuclear pressure vessel steel. Metal Trans 14A (1983) 2277-2287.
[3] F. Mudry, A local approach to cleavage fracture. Nucl Eng Design 105 (1987) 65-76.

[4] F. Minami, A. Bruckner-Foit, D. Munz, B. Trolldenier, Estimation procedure for the Weibuli parameters used in the local approach. Int J Fract 54 (1992) 197-210.
[5] C. Ruggieri, R.H. Dodds Jr., A transferability model for brittle fracture including constraint and ductile tearing effects: a probabilistic approach. Int J Fract 79 (1996) 309-340.
[6] X. Gao, R.H. Dodds Jr., Constraint effects on the ductile-to-brittle transition temperature of ferritic steels: a Weibull stress model. Int J Fract 102 (2000) 43–69.
[7] J.P. Petti, R.H. Dodds Jr., Calibration of the Weibull stress scale parameter, σ_u, using the Master Curve. Eng Fract Mech 72 (2005) 91–120.
[8] B. Wasiluk, J.P. Petti, R.H. Dodds Jr., Temperature dependence of Weibull stress parameters: Studies using the Euro-material. Eng Fract Mech 73 (2006) 1046–1069.
[9] P. Akbarzadeh, S. Hadidi-Moud, A.M. Goudarzi, Global equations for Weibull parameters in a ductile-to-brittle transition regime. Nucl Eng Design 239 (2009) 1186–1192.
[10] Y. Cao, H. Hui, G. Wang, F.-Z. Xuan, Inferring the temperature dependence of Beremin cleavage model parameters from the Master Curve. Nucl Eng Design 241 (2011) 39-45.
[11] G. Xiaosheng, G. Zhang, T.S. Srivatsan, A probabilities model for prediction of cleavage fracture in the ductile-to-brittle transition region and the effect of temperature on model parameters. Mater Sci Eng 415A (2006) 264-272.
[12] M. Kroon, J. Faleskog, H. Oberg, A probabilistic model for cleavage fracture with a length scale – Parameter estimation and predictions of growing crack experiments. Eng Fract Mech 75 (2008) 2398-2417.
[13] S.R. Bordet, A.D. Karstensen, D.M. Knowles, C.S. Wiesner, A new statistical local criterion for cleavage fracture of steel. Part I: model presentation. Eng Fract Mech 72 (2005) 435-452.
[14] J. Hohe, V. Hardenacke, S. Luckow, D. Siegele, An enhanced probabilistic model for cleavage fracture assessment accounting for local constraint effects. Eng Fract Mech 77 (2010) 3573-3591.
[15] A.P. Jivkov, D.P.G. Lidbury, P. James, Assessment of local approach methods for predicting end-of-life toughness of RPV steels. In Proc PVP2011 (2011) paper 57546, Baltimore, USA.
[16] J. Hohe, V. Friedmann, J. Wenck, D. Siegele, Assessment of the role of micro defect nucleation in probabilistic modeling of cleavage fracture, Eng Fract Mech 75 (2008) 3306–3327.
[17] K. Wallin, T. Saario, K. Torronen, Statistical model for carbide induced brittle fracture in steel. Metals Sci 18 (1984) 13-16.
[18] L.C.A. Folch, F.M. Burdekin, Application of coupled brittle-ductile model to study correlation between Charpy energy and fracture toughness values. Eng Fract Mech 63 (1999) 57-80.
[19] G. Bernauer, W. Brocks, W. Schmitt, Modifications of the Beremin model for cleavage fracture in the transition region of a ferritic steel. Eng Fract Mech 64 (1999) 305-325.
[20] A. Pineau, Modeling ductile to brittle fracture transition in steels - micromechanical and physical challenges. Int J Fract 150 (2008) 129–156.
[21] E. Keim, Summary of material data for 22NiMoCr37. Areva ANP GmbH, Technical Report, 2005.
[22] S.R. Ortner, J. Duff, Characterisation of Euro 'A' reference steel for application of EOH model of brittle fracture. Nexia Solutions, Technical Report, 2005.
[23] ASTM E 1921-05, Standard Test Method for Determination of Reference Temperature T_0 for Ferritic Steels in the Transition Range. ASTM, 2005.
[24] ABAQUS 6.11, DS Simulia Corp, 2011.
[25] A. Hung, I. Yarovsky, J. Muscat, S. Russo, I. Snook, R.O. Watts, First-principles study of metallic iron interfaces. Surface Sci 501 (2002) 261-269.

Load history effects on fracture toughness of RPV steel

Jérémy Hure*, **Benoît Tanguy**

CEA, DEN, Service d'Etudes des Matériaux Irradiés, 91191 Gif-sur-Yvette, France
* Corresponding author: Jeremy.hure@cea.fr

Abstract Fracture toughness is required for assessing structural integrity of reactor pressure vessels (RPV). However, it has been long recognized that load history effects can increase the apparent toughness, which is not considered in practical rules assessment. This could lead to over pessimistic assessment in case of thermomechanical transient. The so-called warm prestress (WPS) effect corresponds to the absence of crack propagation after prestressing if the load is held constant or decreased as the temperature is decreased. This study investigates the WPS effect on A508 Cl3 RPV steel, focusing on transient loadings in which the load is increased during cooling, with a twofold aim. Firstly to investigate experimentally to which extent it is possible to go beyond the WPS effect by progressively increasing the slope of the transient. Secondly, to assess numerically the ability of local approach to fracture (LAF) models to quantitatively predict the experimental results. The evolution of local quantities such as opening stress, cumulated plastic strain, triaxiality close to the crack tip are finally described in details.

Keywords Warm prestress effect, Cleavage fracture, RPV steel, Local approach to fracture

1. Introduction

The warm prestress (WPS) effect describes the fact that, when a crack is loaded at a temperature T_1 to a stress intensity factor K_1, no fracture will occur if the stress intensity factor decreases or is held constant between T_1 and $T_2 < T_1$, even if the fracture toughness of the virgin material (*i.e* without prior loading) is exceeded [1, 2]. The WPS effect has been the object of several experimental studies on ferritic steels (see e.g. [3]) as security assessment of nuclear reactor pressure vessels (RPV) requires to consider the case of a loss of coolant accident (LOCA) in which the vessel is subjected to a mechanical loading associated with a variation of the temperature. In this particular case, the embrittlement due to neutron irradiation has to be considered and, in the perspective of prolongation of nuclear power plant lifetime, the WPS effect has to be well understood in order to justify security margins. In this paper, we study the WPS effect on French RPV 16MND5 (similar to A508 Cl3) steel, focusing on transient loadings in which the load is increased while cooling the specimen (Fig. 1). Our aim is first, from an engineering point of view, to quantify how much it is possible to go beyond the conservative principle of WPS effect, *i.e.* no propagation if the load is held constant or decreased during cooling. Secondly, we use these WPS cycles to compare the numerical predictions of local approach to fracture (LAF) models, the differences being discussed by looking in details at the evolution of the crack tip stress/strain fields.

2. Experimental results

2.1 Mechanical tests

The material studied is a 16MND5 steel (similar to A508 Cl3 steel) that originates from a forged nozzle shell of a pressurized water reactor of 220 mm thickness [4]. CT specimens precracked at a ratio $a_0/W \sim 0.56$ (where a_0 is the fatigue precrack length and W the width) are tested using ASTM E1921 standard recommendations [5]. Isothermal fracture toughness tests were performed using specimens of two different thicknesses (B=12.5 and 25 mm), leading to a reference temperature, T_0, equal to -104.7°C [4].

WPS experiments presented in this study were performed using standard CT specimens with a 25 mm thickness. Four different types of WPS cycles were conducted: LCF (Load-Cool-Fracture), LCDKF (Load-Cool-Decreasing K-Fracture), LCIKF (Load-Cool-Increasing K-Fracture) and LCOIKF (Load-Cool-Oscillating Increasing K-Fracture) (Fig. 1). For all the WPS cycles, the loading sequence was: (i) Loading up to 500 N under displacement control with a crosshead speed of 0.25 mm/min, (ii) loading up to K_{WPS} under extensometer control at 0.1 mm/min, (iii) Cooling from T_{WPS} down to T_{frac} under load control with a temperature rate of -1.5°C/min, (iv) Reloading up to fracture under extensometer control at 0.1 mm/min if the specimen survived the transient. All values of K presented here, at WPS loading and fracture levels, are elastic values, thereafter noted K_{el}, calculated according to ASTM E 1921 [5].

2.1 Synthesis of the experimental data

The whole set of WPS experiments that were performed in this study are presented in Table 1. The first four cycles give us a reference base which will be useful for comparison to the main object of the study, LCIKF cycles. All specimens survived to the transient and failed during reloading phase. From all the WPS tests performed, the following observations can be made:

- LCF and LCDKF cycles performed on the 16MND5 RPV steel confirmed the numerous experimental results on ferritic steels published in the literature, *i.e.* no propagation if the load is held constant or decreased during cooling ;

- LCIKF cycles performed in this study confirm and extend the previous results [6, 7] that a critical slope has to be exceeded to induce cleavage during cooling.

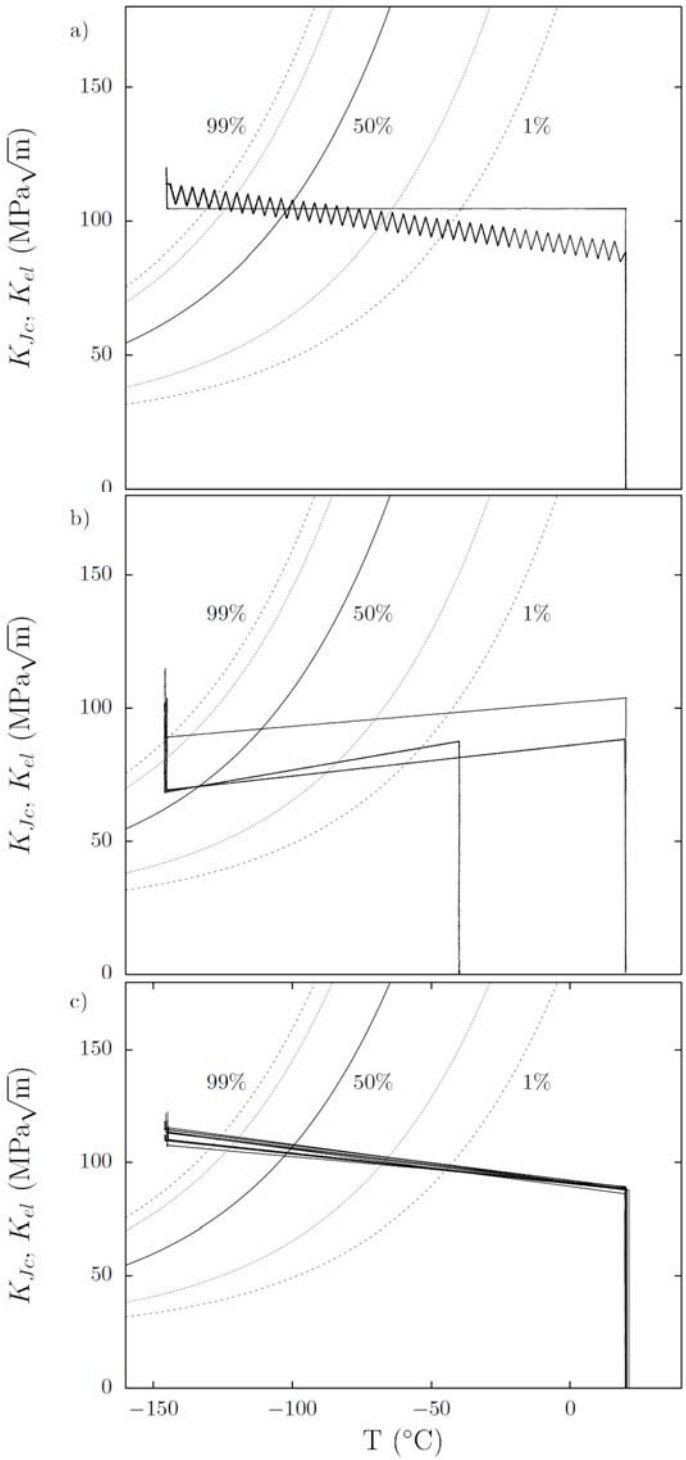

Figure 1 : Overview of all the transient loadings studied (LCF/LCOIKF (a), LCDKF (b), LCIKF (c)). Note that Master Curve confidence bounds are obtained considering elasto-plastic fracture toughness values, K_{Jc}, so that comparison with elastic values of stress intensity factors are not strictly valid.

No.	Cycle type	T_{WPS} (°C)	T_{frac} (°C)	K_{el}^{WPS} (MPa$\sqrt{m}$)	Targeted K_{el} (MPa$\sqrt{m}$)	$-\frac{\Delta K}{\Delta T}$ (MPa$\sqrt{m}$/°C)	K_{el}^{frac} (MPa$\sqrt{m}$)	$\frac{K^{frac}}{K^{WPS}}$	$\frac{K^{frac}}{K_{95\%}}$
H1ACT1	LCF	20.0	-145.2	104.6	-	-	114.3	1.09	1.40
H1ACT2	LCDKF1	20.0	-145.7	103.9	89.2	-0.089	114.8	1.10	1.41
H1ACT11	LCDKF2	19.6	-145.1	88.4	69.4	-0.115	103.8	1.17	1.27
H1ACT22	LCDKF3	-40.0	-145.9	87.5	68.5	-0.179	102.1	1.17	1.25
H1ACT16	LCIKF1	19.8	-144.9	89.2	107.6	0.112	114.7	1.29	1.41
H1ACT14	LCIKF2	20.0	-144.6	88.3	110.2	0.133	115.6	1.31	1.42
H1ACT5	LCIKF2	20.0	-145.0	87.9	109.7	0.132	112.1	1.28	1.37
H1ACT20	LCIKF3	20.0	-145.7	89.0	114.8	0.156	118.1	1.33	1.45
H1ACT41	LCIKF3	20.4	-145.0	88.2	113.6	0.154	119.0	1.35	1.44
H1ACT40	LCIKF3	19.9	-145.6	87.8	113.2	0.153	120.9	1.39	1.49
H1ACT27	LCIKF4	20.3	-145.1	86.0	113.3	0.165	117.9	1.37	1.44
H1ACT26	LCIKF4	21.1	-144.9	87.8	115.5	0.167	122.6	1.40	1.50
H1ACT15	LCOIKF*	20.0	-145.2	88.3	113.8	0.133	119.8	1.36	1.47

Table 1 : Experimental results on CT specimens are given for the various WPS cycles. * For LCOIKF cycle, the mean slope ΔK/ ΔT is given.

3. Numerical modeling

3.1 Local approach to fracture

As the local approach to fracture needs an accurate description of the stress/strain fields at the crack tip, the mechanical behavior of the material has to be modeled as precisely as possible, as well as the evolution of the characteristics with temperature. Large plastic deformations occur during the pre-loading at the crack tip, producing work-hardening so that finite strain formalism was used. Thus, elasto-visco-plastic constitutive equations were used in order to describe accurately the behavior of the material [8]:

$$\frac{1}{\dot{p}} = \frac{1}{\dot{p}_1} + \frac{1}{\dot{p}_2} \qquad \dot{p}_i = \left\langle \frac{f(\sigma,p)}{k_i} \right\rangle^{n_i}$$

$$f(\sigma,p) = \sqrt{\frac{3}{2}\underline{\underline{s}} : \underline{\underline{s}}} - R(p) \qquad R(p) = R_0 + Q_1(1-e^{-b_1 p}) + Q_2(1-e^{-b_2 p})$$

where p is the cumulated plastic strain, s the stress deviator and f(σ,p) the yield surface. The parameters determined in previous studies [4,9] are given in Table 2 and allow reproducing accurately both smooth tensile and notched tensile tests up to plastic strains of about 40% (Fig. 3).

	20°C	-50°C	-100°C	-150°C
E (MPa)	195224	203540	209480	215420
R_0 (MPa)	430.7	463.5	522.2	650.8
Q_1 (MPa)	167.9	203.1	228.3	253.5
b_1	26.8	19.1	13.6	10.1
k_1 (MPa s^{1/n_1})	31.25	62.05	84.05	84.05
n_1	5.18	6.24	6.99	6.99
Q_2 (MPa)		295.8		
b_2		3.5		
k_2 (MPa s^{1/n_2})		0.185		
n_2		1.15		
ν		0.3		

Table 2 : Young's modulus, Poisson's ratio and visco-plastic coefficients for 16MND5 steel

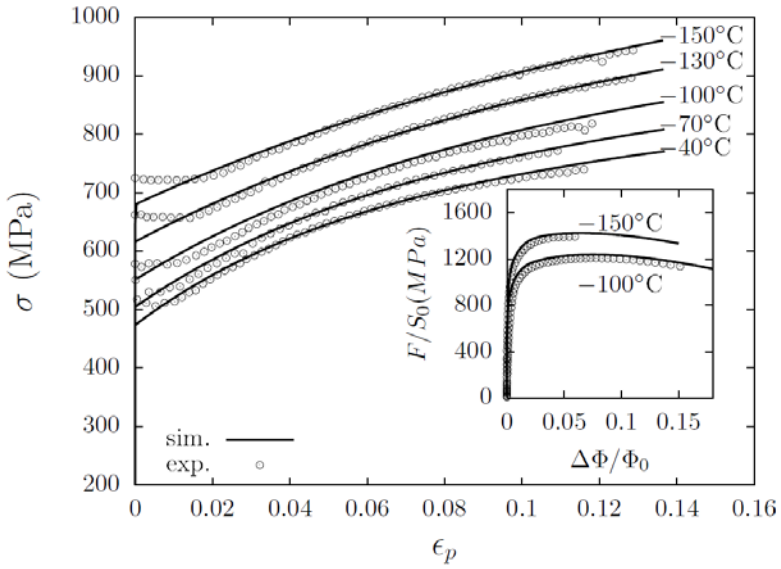

Figure 2 : Tensile curves at different temperature for 16MND5 steel. Open symbols correspond to the experimental data, solid lines to the modeling. Inset: Applied force vs. diameter reduction for AE notched specimens (notch radius 0.6mm, initial diameter φ_0=6mm). All the mechanical tests correspond to a strain rate of $\varepsilon = 5.10^{-4}s^{-1}$.

All the analysis were performed using the finite element software Cast3m [10] using the elasto-visco-plastic constitutive equations described above. CT specimens are modeled with 2D plane strain, quadratic, full integration elements.

Two different LAF models were used to predict the probabilities of cleavage fracture. The first one is the seminal Beremin model [11] modified to account for non-monotonic loadings [12]. The second is a simplified version of the model proposed by Bordet [6,13] which has the particularity to account explicitly for the necessity of active plasticity to trigger cleavage. The fracture probability for both models can be written as:

$$P_f = 1 - \exp\left(-\int_V \max_{t' \leq t, \dot{p}(t')>0, \sigma_I(t')>0} \left(\frac{\sigma_I(t')}{\sigma_u(t')}\right)^m \frac{dV}{V_0}\right)$$

$$P_f = 1 - \exp\left(-\left\{\int_V \left(\int_0^{\epsilon_p(t)} \frac{\sigma_Y}{\sigma_{Y,0}} \max\left(\frac{\sigma_I^m}{\sigma_u^m}, 0\right) d\epsilon_p\right) \frac{dV}{V_0}\right\}\right)$$

where σ_I is the largest principal stress and σ_Y the yield stress. In both models, the normalization volume V_0 is taken to be 0.001mm^3, and in the Bordet model, the reference yield stress $\sigma_{Y,0}$ = 650MPa. The parameters σ_u and m have to be determined independently for each model to reproduce the experimental results of fracture toughness without prestressing. A F.E. simulation of a CT specimen was performed at -150°C, and the Beremin and Bordet models parameters were fitted so as to reproduce the fracture probability given by the Master Curve approach (with a reference temperature T_0 = -104.7°C). The parameters obtained are given below:

$$\sigma_{u,\mathrm{Beremin}} = 2575\mathrm{MPa} \qquad m_{\mathrm{Beremin}} = 25$$
$$\sigma_{u,\mathrm{Bordet}} = 2065\mathrm{MPa} \qquad m_{\mathrm{Bordet}} = 21$$

As shown in [8,14], for this steel a constant value of σ_u can be used only on a typical range [-150:-50°C], higher values being needed at higher temperatures. However, for the LCIKF cycles where cleavage is potentially expected, the loading path is under the Master Curve for T>-50°C (see Fig. 1), so that no cleavage fracture is expected. The temperature dependence of σ_u is thus not considered here. For practical reasons, when post-processing the simulations, the value of σ_u is taken as constant in the range [-150:-50°C], and to a very high value above. The results from LAF models - corresponding to probability of failure of 5%, 50% and 95% - and their comparisons with experimental data are shown in Fig. 3.

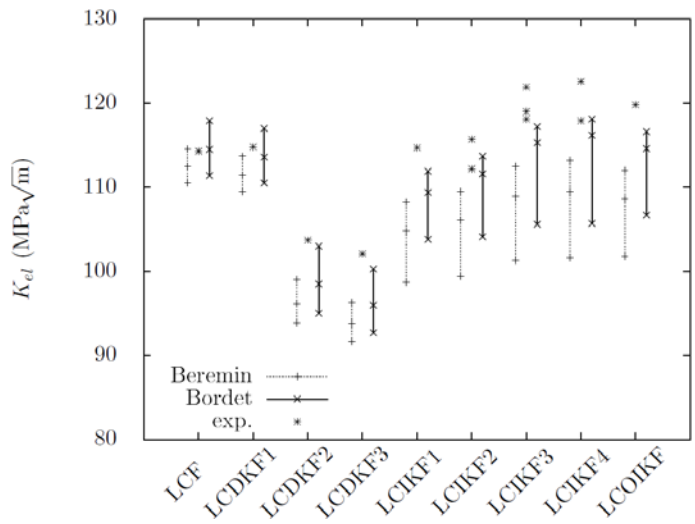

Figure 3 : Elastic stress intensity factor K_{el} at fracture for the different WPS cycles. Dots correspond to the experimental data, dashed and solid lines to the fracture probability of 5%, 50% and 95% for Beremin and Bordet models, respectively.

Several observations can be made from the comparison in Fig. 3:

- For the LCF and LCDKF cycles, both models give predictions in good agreement with experimental data, Bordet model being less conservative than the Beremin model.

- For LCIKF cycles, both models underestimate the toughness after warm prestressing, but predictions from Bordet model are closer to the experimental data.

- For all transient loadings, the scatter after warm prestressing is larger for Bordet model than for Beremin model.

These results tend to indicate that, after warm prestressing, the simplified version of the model proposed by Bordet gives more accurate predictions than the Beremin model which is more conservative. To better understand and assess the physical hypothesis used in the models – and thus why do they lead to slightly different results - the evolution of mechanical quantities such as plastic zone size and stress/strain fields during the WPS cycles are investigated in more details in the following section.

3.2 Evolution of local parameters

The basic assumption for the WPS effect to happen is that the size of the plastic zone at reloading is much smaller than the one at preloading. In other words, this means that the material keeps the memory of the prestressing at high temperature. Conversely, if the size of the plastic zone when reloading is much larger than the one at preloading, no WPS effect is expected. The evolution of the size of the active plastic zone as a function of the temperature is shown in Fig. 4 for LCIKF cycles. The size is normalized by the square of the thickness B^2, which confirms the plane strain assumption. For all the transient, the size is roughly constant up to a temperature of about -75°C, and then decreases drastically. In the temperature range where the size of the plastic zone is large, the path is under the Master Curve, thus no cleavage is expected. When the paths goes through the Master Curve and above, plasticity is almost not active - except on a very small area close to the crack tip - which explains roughly why cleavage fracture was not observed for the LCIKF cycles. Note that the evolution of the active plastic zone size could have been guessed without F.E. simulations: under small scale yielding assumption plastic zone extent scales as $(K/\sigma_Y)^2$ and K increases linearly with temperature in LCIKF experiments, while σ_Y increases exponentially.

Beremin and Bordet models both account for active plasticity, by integrating Weibull stress on the active plastic zone for the former, by considering nucleation of microcracks that depends on plastic strain for the latter so that the models will not predict cleavage fracture during the studied transients.

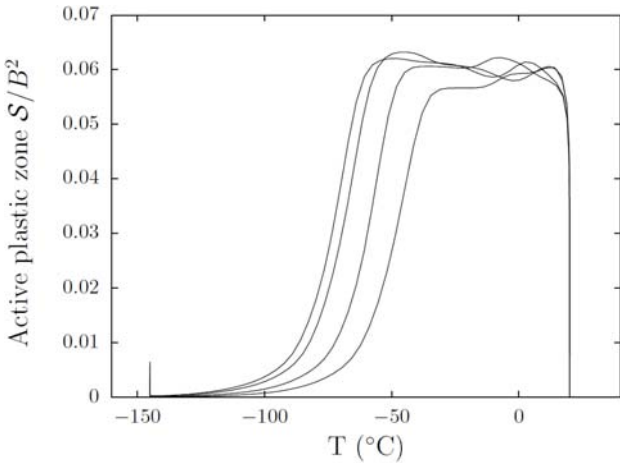

Figure 4 : Evolution of the active plastic zone for LCIKF cycles.

The history of local mechanical parameters - principal stress σ_I, cumulated plastic strain p and triaxiality τ - at the physical point where cleavage is triggered (identified by SEM investigations) were computed for each specimen. The results corresponding to the different experiments are shown in Fig. 5 where circles indicate cleavage fracture. The case of an isothermal test was added in Fig. 5 for comparison.

For all the experiments, the maximum principal stress and the cumulated plastic strain are increasing at cleavage triggering. This is consistent with the hypotheses of Beremin type models that consider the necessity of plastic flow to initiate microcracks and a stress-controlled propagation. Moreover, we note that the value of principal stress at which the cleavage fracture is triggered is almost the same for all the experiments (with or without warm prestressing), about 2250MPa, whatever the level of plastic strain, reinforcing the idea of a critical stress needed to propagate cracks. Note that this value of critical stress is higher than the one found in [4], as our modeling slightly overestimates stresses at large strains (see inset fig. 3). Compared to the isothermal test, the plastic strain at fracture - and its evolution with stress - is larger for WPS tests. The evolution of the triaxiality *vs.* stress is also different for WPS tests than for isothermal tests, which suggests that LAF models should include the effect of triaxiality.

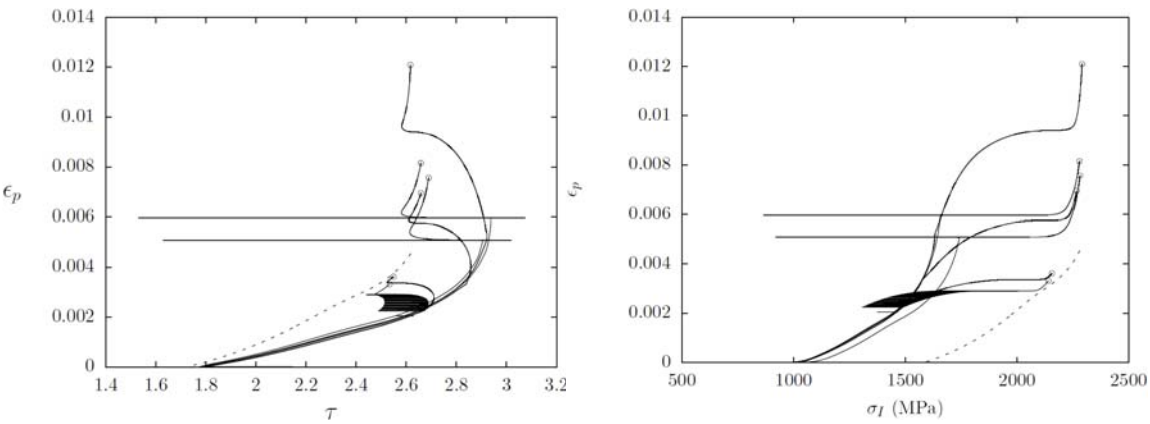

Figure 5: Evolution of plastic strain as a function of the principal stress (b) and triaxiality (b) at the location where cleavage was found to be triggered from microstructural investigations. Solid lines correspond to WPS experiments, dashed lines to isothermal test at -150°C.

Results from Fig. 5, and especially the different levels of plastic strains for a given stress that can be achieved in WPS experiments compared to isothermal tests, suggest that integrating over the active plastic zone may not be enough to account for the necessity of plastic strains. This may explain why considering strain-controlled germination of microcracks as in the Bordet model leads to better estimate of fracture toughness after prestressing.

4. Conclusion

In this study, the warm prestress effect on 16MND5 RPV steel was studied, focusing on transient loadings in which the load increases during cooling. The existence of a critical slope under which no propagation occurred is confirmed for this steel. Looking at the evolution of the active plastic zone gives some insights into the physical explanation of this critical slope: in the last part of the transient where the loading path is above the Master Curve, plasticity is confined to the vicinity of the crack tip and is much smaller than the size of the plastic zone at prestressing. Local approach to fracture models give predictions in good agreement with experimental data, a simplified version of the model proposed by Bordet *et. al.* leading to more accurate predictions The difference between the two models investigated is explained by looking at the evolution of stress, strain and triaxiality close to the crack tip: compared to an isothermal test, cumulated plastic strain can be larger for a given stress for WPS tests, suggesting that accounting explicitly for the necessity of plastic strain – as in the Bordet model – is required.

Acknowledgements

Financial and technical supports from CEA program RSTB and project MASOL is acknowledged. B. T. would like to thank P. Wident from SRMA/LC2M and his Master students N. Mozzani and J. Li who have been involved in this research project.

References

[1] B. Pickles, A. Cowan, A review of warm pre-stressing studies. Int. J. Pres. Ves. And Piping, 14 (1983) 95-131
[2] D. Smith, S. Garwood, The significance of prior overload on fracture resistance: A critical review. Int. J. Pres. Ves. And Piping, 41 (1990) 225-296
[3] K. Wallin, Master Curve implementation of the warm pre-stress effect. Eng. Fract. Mech. 70 (2003) 2587-2602
[4] B. Tanguy, C. Bouchet, S.R. Bordet, J. Besson, A. Pineau, Toward a better understanding of the cleavage in RPV steels: Local mechanical conditions and evaluation of a nucleation enriched Weibull model and of the Beremin model over a large temperature range. In 9th European Mechanics of Materials Conference, Local approach to fracture, Moret-sur-Loing (2006)
[5] ASTM E 1921- Standard test method for determination of reference temperature T_0 for ferritic steels in the transition range
[6] S. Bordet, B. Tanguy, J. Besson, S. Bugat, D. Moinereau, A. Pineau, Cleavage fracture of RPV steel following warm-prestressing: micromechanical analysis and interpretation through a new model. Fatigue Fract. Engng. Mater. Struct. 29 (2006) 799-816
[7] T. Yuritzinn, L. Ferry, S. Chapuliot, P. Mongabure, D. Moinereau, A. Dahl, Illustration of the WPS benefit through batman test series: Tests on large specimens under WPS loading

configurations. Eng. Fract. Mech 75 (2008) 2191-2207
[8] B. Tanguy, J. Besson, R. Piques, A. Pineau, Ductile to brittle transition of A508 steel characterized by Charpy impact test: Part II: modeling of the Charpy transition curve. Eng. Fract. Mech, 72 (2005) 413-434
[9] C. Bouchet, B. Tanguy, J. Besson, A. Pineau and S. Bugat, "Transferability of cleavage fracture parameters between notched and cracked geometries", The 16th European conference of fracture, Failure analysis of Nano and Engineering Materials and Structures, Alexandroupolis, July, 3-7, (2006)
[10] Cast3m DEN/DANS/DM2S
[11] F.M. Beremin, A local criterion for cleavage fracture of a nuclear pressure vessel steel. J. Metall. Trans. A 14A (1983) 2277-2287
[12] W. Lefevre, G. Barbier, R. Masson, G. Rousselier, A modified beremin model to simulate the warm pre-stress effect. Nucl. Eng. Design 216 (2002) 27-42
[13] S. Bordet, A. Karstensen, D. Knowles, C. Wiesner, A new statistical local criterion for cleavage fracture in steel Part I: Model presentation. Eng. Fract. Mech 72 (2005) 435-452
[14] B. Tanguy, C. Bouchet, S. Bugat, J. Besson , Local approach to fracture based prediction of the ΔT_{56J} and $\Delta T_{Kic,100}$ shifts due to irradiation for an A508 pressure vessel steel, Eng. Fract. Mech., 73, (2006), 191-206

Fracture Toughness Predictions Using the Weibull Stress Model with Implications for Estimations of the T_0 Reference Temperature

Claudio Ruggieri[1,*], **Rafael G. Savioli**[1], **Robert H. Dodds Jr.**[2]

[1] Department of Naval Architecture and Ocean Engineering, University of São Paulo, 05508-030, Brazil
[2]Dept. Of Civil Engineering, University of Illinois at Urbana-Champaign, Urbana, IL 61801, USA
* Corresponding author: claudio.ruggieri@poli.usp.br

Abstract This work presents a numerical and experimental investigation into the applicability of precracked Charpy specimens to determine the T_0 reference temperature for pressure vessel steels. A central objective is evaluate the effectiveness of the Weibull stress model to correct effects of constraint loss in PCVN specimens which serves to determine the indexing temperature T_0 based on the Master Curve methodology. Fracture toughness testing conducted on an A285 Grade C pressure vessel steel provides the cleavage fracture toughness data needed to estimate T_0. For the tested material, the Weibull stress methodology yields estimates for the reference temperature from small fracture specimens which are in good agreement with the corresponding estimates derived from testing of much larger crack configurations.

Keywords Cleavage Fracture, Constraint Effects, Weibull Stress, Master Curve, PCVN Specimen

1. Introduction

Standard compact tension and three-point bend specimens containing deep, through cracks ($a/W \geq 0.5$) are commonly employed in fracture toughness testing of ferritic steels in the ductile-to-brittle transition (DBT) region. The primary motivation to use deeply cracked specimens is to guarantee SSY conditions leading to high crack-tip constraint with limited-scale plasticity. Under these conditions, fracture toughness values (such as the *J*-integral at cleavage instability, J_c, or the elastic-plastic stress intensity factor, K_{Jc}) prove effective to characterize the essentially stress-controlled failure by a transgranular cleavage mechanism.

Current structural integrity assessment procedures for reactor pressure vessels (RPVs) focus on the utilization of small fracture specimens to facilitate experimental measurements of fracture toughness data. In particular, three-point bend testing of precracked Charpy (PCVN) specimens become necessary when severe limitations exist on material availability, for example, in nuclear irradiation embrittlement studies, as this specimen configuration is predominant within surveillance capsule programs. However, the measuring capacity of these specimens for fracture toughness prior to constraint loss may be insufficient for moderate strength pressure vessel and structural steels. Once constraint loss occurs, measured values of cleavage fracture toughness (J_c, K_{Jc}) increase markedly as the global plastic deformation interacts with the local crack front fields (governed by *J*) thereby relaxing the level of stress triaxiality. Moreover, cleavage fracture is a highly localized phenomenon which exhibits strong sensitivity to material characteristics at the microlevel. In particular, the random inhomogeneity in local features of the material causes large scatter in measured values of cleavage fracture toughness. The coupled effects of constraint loss and inherent scatter of toughness values in the DBT region greatly complicate the development of fracture mechanics assessments based on small specimen data.

Motivated by these observations, this work explores application of a micromechanics model to determine the T_0 reference temperature for pressure vessel steels from precracked Charpy (PCVN) specimens. A central objective is evaluate the effectiveness of the Weibull stress model to correct effects of constraint loss in PCVN specimens which serves to determine the indexing temperature T_0 based on the Master Curve methodology. Fracture toughness testing conducted on an A285

Grade C pressure vessel steel provides the cleavage fracture toughness data needed to estimate T_0. For the tested material, the Weibull stress methodology yields estimates for the reference temperature, T_0, from small fracture specimens which are in good agreement with the corresponding estimates derived from testing of much larger crack configurations.

2. Overview of the Weibull Stress Model for Cleavage Fracture

2.1. Weakest Link Modeling of Cleavage Fracture

Extensive work on cleavage fracture in ferritic steels demonstrates that cracking of grain boundary carbides in the course of plastic deformation and subsequent extension of these cracks into the surrounding matrix governs failure. The inherent random nature of failure micromechanism causes large scatter in the measured values of cleavage fracture toughness for ferritic steels tested in the DBT region thereby complicating quantitative assessments of fracture behavior in terms of meaningful toughness values. A continuous probability function derived from weakest link statistics conveniently characterizes the distribution of toughness values, described by J_c-values, as [1]

$$F(J_c) = 1 - \exp\left[-\left(\frac{J_c - J_{th}}{J_0 - J_{th}} \right)^{\alpha} \right] \tag{1}$$

which is a three-parameter Weibull distribution with parameters (α, J_0, J_{th}). Here, α denotes the Weibull modulus (shape parameter), J_0 defines the characteristic toughness (scale parameter) and J_{th} is the threshold fracture toughness. Often, the threshold fracture toughness is set equal to zero so that the Weibull function given by Eq. (1) assumes its more familiar two-parameter form. The above limiting distribution remains applicable for other measures of fracture toughness, such as K_{Jc} or δ (CTOD). Under SSY conditions, the scatter in cleavage fracture toughness data is characterized by $\alpha = 2$ for J_c-distributions or $\alpha = 4$ for K_{Jc}-distributions [2].

A number of micromechanics models to describe transgranular cleavage, most derived from the *local approach* philosophy, have focused on probabilistic methodologies which couple the micromechanical features of the fracture process with the inhomogeneous character of the near-tip stress fields. By adopting weakest link arguments to describe the failure event, the overall fracture resistance is assumed to be driven by the largest fracture-triggering particle that is sampled in the fracture process zone ahead of crack front. This approach enables defining a probability distribution for the fracture stress of a cracked solid with increased loading (represented by the *J*-integral) in terms of a two-parameter Weibull distribution [3-5] in the form

$$P(\sigma_w) = 1 - \exp\left[-\frac{1}{\Omega_0} \int_{\Omega} \left(\frac{\sigma_1}{\sigma_u} \right)^m d\Omega \right] = 1 - \exp\left[-\left(\frac{\sigma_w}{\sigma_u} \right)^m \right] \quad , \quad \sigma_1 \geq 0 \tag{2}$$

where Ω denotes the volume of the (near-tip) fracture process zone, Ω_0 represents a (unit) reference volume and σ_1 is the maximum principal stress acting on material points inside the fracture process zone. In the present work, the active fracture process zone is defined as the loci where $\sigma_1 \geq \lambda \sigma_{ys}$, with $\lambda \approx 2 \sim 2.5$ and σ_{ys} represents the material's yield stress. Parameters *m* and σ_u appearing in Eq. (2) denote the Weibull modulus and the scale parameter of the Weibull

distribution. The stress integral appearing in Eq. (2) defines the Weibull stress, σ_w, a term coined by the Beremin group [3], in the form

$$\sigma_w = \left[\frac{1}{\Omega_0} \int_{\Omega} \sigma_1^m d\Omega \right]^{1/m} \quad , \quad \sigma_1 \geq 0 \tag{3}$$

A central feature of this methodology involves the interpretation of σ_w as a macroscopic crack driving force [4-5]. Consequently, it follows that unstable crack propagation (cleavage) occurs at a critical value of the Weibull stress; under increased remote loading (as measured by *J*), differences in evolution of the Weibull stress reflect the potentially strong variations of near-tip stress fields

2.2. Effects of Plastic Strain on the Probabilistic Crack Driving Force

The previous approach can be further extended to include the strong effects of near-tip plastic strain on cleavage microcracking thereby altering the microcrack distribution entering into the local criterion for fracture. Based upon direct observations of cleavage microcracking by plastic strain made in ferritic steels at varying temperatures [6-8], a *generalized* form of the Weibull stress can be defined as

$$\sigma_w = \left[\frac{1}{\Omega_0} \int_{\Omega} \varepsilon_p^{\gamma(1+\beta)} \sigma_1^m d\Omega \right]^{1/m} \quad , \quad \sigma_1 \geq 0 \tag{4}$$

Here, $\varepsilon_p = f(J)$ is the near-tip effective plastic strain, and γ and β are parameters defining the contribution of the plastic strain on cleavage fracture probability; for example, setting $\gamma = 0$ recovers the conventional description for the probability distribution of fracture stress. The above plastic term correction simply reflects the increase in cleavage fracture probability that results from the growth in microcrack density with increased levels of near-tip plastic strain. Ruggieri [5] provides further details on the character of the previous definition for the generalized Weibull stress.

Early work of the Beremin group [3] also recognized the potential strong effects of plastic deformation on cleavage fracture. Based on experimental analyses of the failure strain for notched specimens made of an ASTM A508 steel, they proposed a modified form of previous Eq. (3) as

$$\sigma_w = \left[\frac{1}{\Omega_0} \int_{\Omega} \exp\left(-\frac{m\varepsilon_p}{2} \right) \sigma_1^m d\Omega \right]^{1/m} \quad , \quad \sigma_1 \geq 0 \tag{5}$$

which indicates that σ_w increases approximately with $\exp(\varepsilon_p/2)$.

3. Summary of the Master Curve Approach

Wallin [9] has developed a relatively straightforward procedure to characterize fracture toughness data over the DBT region, widely known as the *master curve approach*, which relies on the concept of a normalized curve of median fracture toughness *vs.* temperature applicable to hold experimentally for a wide range of ferritic pressure vessel and structural steels. The approach begins by adopting a three-parameter Weibull distribution to describe the distribution of toughness values in the form

$$F(K_{Jc}) = 1 - \exp\left[-\left(\frac{K_{Jc} - K_{\min}}{K_0 - K_{\min}} \right)^{\alpha} \right] \tag{6}$$

where the Weibull modulus, α, takes the value of 4.

Now, following a standard maximum likelihood estimate, the scale parameter, K_0, corresponding to the 63.2% cumulative failure probability, is given by

$$K_0 = \left[\sum_{i=1}^{N} \frac{\left(K_{Jc(i)} - 20\right)^4}{\left(r - 0.3068\right)} \right]^{1/4} + 20 \qquad \text{MPa}\sqrt{\text{m}} \tag{7}$$

where N denotes the total number of specimens tested and r represents the number of valid tests (uncensored data). The median toughness at the tested temperature follows simply as

$$K_{Jc(med)} = 0.9124\left(K_0 – 20\right) + 20 \qquad \text{MPa}\sqrt{\text{m}} \tag{8}$$

The *master curve* of median toughness, $K_{Jc(med)}$, for 1-T specimens over the transition range for the material has the final form

$$K_{Jc(med)} = 20 + 70\exp\left[0.019\left(T - T_0\right)\right] \qquad {}^{\circ}\text{C, MPa}\sqrt{\text{m}} \tag{9}$$

where T is the test temperature and T_0 is the reference (indexing) temperature The above expression for the median toughness applies throughout the lower part of the DBT range prior to the occurrence of significant ductile tearing. ASTM E1921 [10] test standard outlines procedures to construct various tolerance bounds based on the above representation for the toughness distribution.

4. Computational Procedures and Finite Element Models

Calibration of the Weibull modulus for the tested pressure vessel steel is conducted by performing detailed finite element analyses on 3-D models for the SE(B) and precracked Charpy specimens. described in Section 5.1. The analysis matrix includes conventional, plane-sided SE(B) specimens with $a/W = 0.2$ and 0.5, and precracked Charpy (PCVN) specimens with $a/W = 0.5$.

Figure 1 shows a typical finite element model constructed for the 3-D analyses of the SE(B) specimen with $a/W =$ 0.5. A conventional mesh configuration having a focused ring of elements surrounding the crack front is used with a small key-hole at the crack tip where the radius of the key-hole, ρ_0, is 0.0025 mm. Symmetry conditions permit modeling of only one-quarter of the specimen with appropriate constraints imposed on the remaining ligament and symmetry planes. A typical quarter-symmetric, 3-D model has 22 variable thickness layers with ~27000 8-node, 3-D elements (~31000 nodes) defined over the half-thickness $B/2$; the thickest layer is defined at $Z = 0$ with thinner layers defined near the free surface ($Z = B/2$) to accommodate strong Z variations in the stress distribution. The finite element models are loaded by displacement increments imposed on the loading points to enhance numerical convergence with increased levels of deformation.

The next section addresses cleavage fracture predictions using the Weibull stress model based on toughness data measured at different lower-shelf temperatures. The numerical computations for the cracked configurations at the test temperature reported here are generated using the research code WARP3D [11]. The analyses utilize an elastic-plastic constitutive model with J_2 flow theory and conventional Mises plasticity in large geometry change (LGC) setting. The plastic stress-strain

response for the tested material follows a power hardening law given by $\varepsilon/\varepsilon_{ys} \propto (\sigma/\sigma_{ys})^n$ where n denotes the strain hardening exponent, σ_{ys} and ε_{ys} are the (reference) yield stress and strain. Using the tensile properties provided in Savioli and Ruggieri [12] and an improved estimate for the hardening exponent given by API 579 [13], the strain hardening exponents yield $n = 6.3$ at $T = -80°\text{C}$ and $n = 5.2$ at $T = -60°\text{C}$.

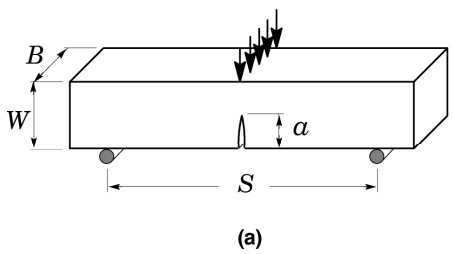

Specimen	B	W	a	a/W	S
SE(B) 1-T $a/W = 0.2$	25	50	10	0.2	200
SE(B) 1-T $a/W = 0.5$	25	50	25	0.5	200
PCVN	10	10	5	0.5	40

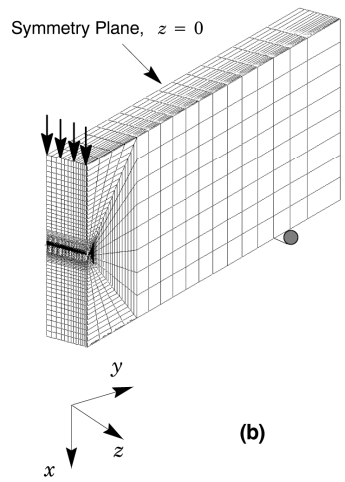

Figure 1. Fracture specimens utilized in the analyses (all dimensions in mm).

5. Cleavage Fracture Predictions

5.1. Mechanical Properties and Experimental Toughness Data for Tested Material

A series of toughness tests was conducted on bend fracture specimens made of a C-Mn low alloy pressure vessel steel in the T-L orientation. The fracture mechanics tests include: (1) conventional, plane sided SE(B) specimens with $a/W = 0.2$ and 0.5, $B = 25$ mm, $W = 50$ mm and $S = 4W$ and (2) a precracked Charpy specimen with $a/W = 0.5$, $B = 10$ mm, $W = 10$ mm and $S = 4W$. Testing of these configurations was performed at $T = -80°\text{C}$ for the deeply-cracked SE(B) specimen and PCVN specimens and $T = -60°\text{C}$ for the shallow-cracked SE(B) specimen; these temperatures correspond to the lower-shelf, ductile-to-brittle transition behavior for the tested steel. Figure 2(a) shows the measured toughness-temperature properties for the material in terms of conventional Charpy-V impact energy (T-L orientation).

The material is an ASTM A285 Grade C pressure vessel steel with 230 MPa yield stress at room temperature (20°C) and high hardening properties ($\sigma_{uts}/\sigma_{ys} \approx 2.36$). Figure 2(b) shows the engineering stress-strain response at room temperature. Additional tensile tests were conducted at $T = -60°\text{C}$ and $-80°\text{C}$ to measure the flow properties utilized in the finite element analyses of the fracture specimens described previously. Savioli and Ruggieri [12] provide the measured

mechanical properties at different temperatures.

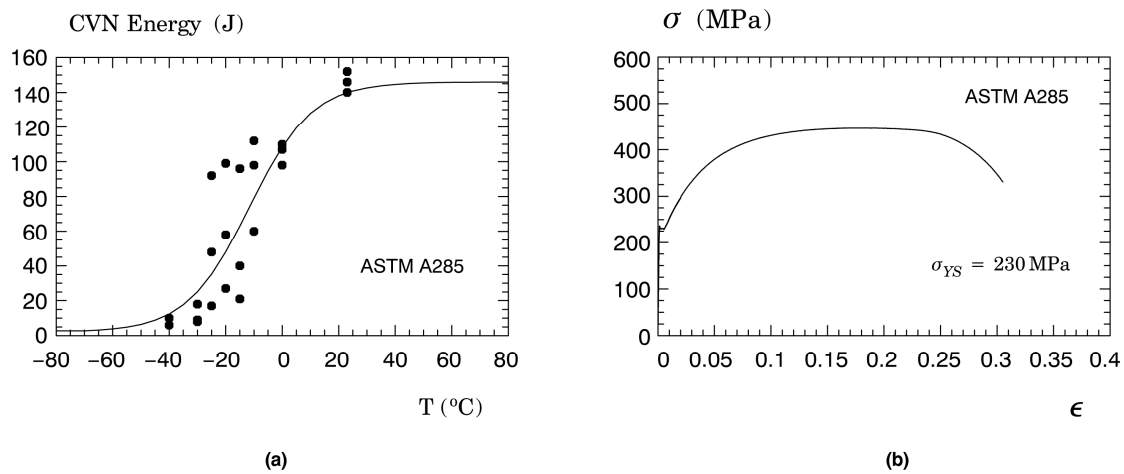

Figure 2. Mechanical properties of the tested A285 Gr C steel: (a) Charpy-V impact energy (T-L orientation) versus temperature; (b) Engineering stress-strain response at room temperature.

Figure 3 provides a Weibull diagram of the measured toughness values for both test temperatures. These J_c-values were determined using revised η-factors based on crack mouth opening displacement (CMOD) recently developed by Ruggieri [14] using full 3-D finite element analyses of 1-T SE(B) specimens and PCVN configurations with varying crack sizes (as characterized by a/W) and different hardening properties. The solid symbols in the plots indicate the experimental fracture toughness data for the specimens. Values of cumulative probability, $F(J_c)$, are obtained by ordering the J_c-values and using $F(J_c^k) = (k-0.3)/(N+0.4)$, where k denotes the rank number and N defines the total number of experimental toughness values. The curves displayed in this plot indicate the two-parameter Weibull distribution, Eq. (1), obtained by a maximum likelihood analysis of the data set with $\alpha = 2$. Here, the maximum likelihood estimates of the Weibull parameters, $(\hat{\alpha}, \hat{J}_0)$, are $(2.0, 72.6\,\mathrm{kJ/m^2})$ for the SE(B) specimen with $a/W = 0.5$, $(2.0, 215.2\,\mathrm{kJ/m^2})$ for the SE(B) specimen with $a/W = 0.2$ and $(2.0, 217.8\,\mathrm{kJ/m^2})$ for the PCVN configuration. In particular, the experimental toughness distribution for the deep crack SE(B) specimen agrees very well with the theoretical Weibull distribution.

5.2. Determination of T_0 and Master Curve Analysis

The master curve analysis described here followed the procedures of ASTM 1921 [10] summarized previously. The reference temperature was estimated from the toughness distribution of J_c-values at $T = -80°\mathrm{C}$ converted to K_{Jc}-values using $K_{Jc} = \sqrt{EJ_c/(1-\nu^2)}$, where plane-strain conditions are assumed. For the tested pressure vessel steel, the indexing (reference) temperature has the value of $T_0 = -93.5\,^\circ\mathrm{C}$.

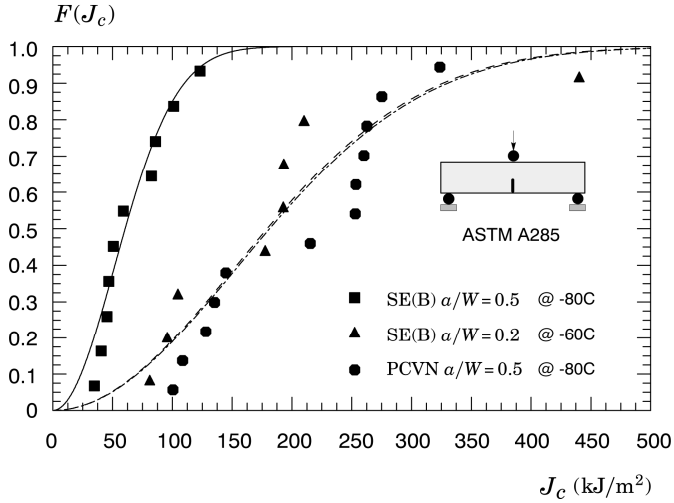

Figure 3. Two-parameter Weibull distribution of experimentally measured J_c-values.

5.3. Calibration of Weibull Stress Modulus

The parameter calibration scheme described in Gao et al. [15] and Ruggieri [5] is applied to determine the Weibull stress parameters for the tested pressure vessel steel. The Weibull modulus, *m*, is calibrated using the SE(B) specimens. Because these specimens were not tested at the same temperature, the present methodology adopts a simple procedure to correct the measured toughness values for temperature in which the J_c-values for the deep crack SE(B) specimens ($a/W = 0.5$) at $T = -80$°C are scaled to corresponding J_c-values at $T = -60$°C using the Master Curve fitting obtained previously. The characteristic toughness values for the deep notch and shallow notch SE(B) specimens are then given as: $J_0 =$ 116.5 KJ/m^2 and 215.2 KJ/m^2.

With the toughness values for the deep and shallow crack SE(B) specimens set at the same temperature ($T = -60$°C) and using σ_w *vs.* J curves constructed from the 3-D finite element analyses for both crack configurations, the calibration procedure is then applied to determine the *m*-value that yields the best correction $J_0^{SE(B)_{a/W=0.5}} \rightarrow J_0^{SE(B)_{a/W=0.2}}$. Table 1 provides the calibrated Weibull stress modulus, *m*, for the tested material based on different definitions for σ_w: 1) $\gamma = 0$ (no plastic strain correction); 2) $\gamma = 1$ and $\beta = 0$ (linear plastic strain correction); 3) $\gamma = 1/2$ and $\beta = 0$ (square root plastic strain correction) and 4) Beremin plastic strain correction.

Table 1. Calibrated Weibull parameter, *m*, for different forms of σ_w

Weibull Stress Model	***m***
Standard Beremin ($\gamma = 0$ with no plastic strain correction)	10.4
Generalized Weibull Stress with $\gamma = 1$ and $\beta = 0$ (linear correction)	28.5
Generalized Weibull Stress with $\gamma = 1/2$ and $\beta = 0$ (square root correction)	28.0
Plastic Strain Modified Beremin Model	29.0

5.4. Cleavage Fracture Predictions Using the Weibull Stress Model

The procedure used here to predict the effects of constraint loss for the experimental cleavage fracture toughness data follows the toughness scaling model introduced by Ruggieri and Dodds [4]. Based upon micromechanics considerations, the scaling model requires the attainment of a specified value for the Weibull stress to trigger cleavage fracture in different specimens even though *J*-values may differ markedly. Here, we predict the distribution of cleavage fracture values for the deep crack SE(B) specimens ($a/W = 0.5$) using the distribution of measured fracture toughness for the precracked Charpy (PCVN) configuration.

Figures 4(a-b) show the computed evolution of σ_w with increased levels of loading, as characterized by *J*, for the deep crack SE(B) specimen and PCVN configuration using the calibrated *m*-values displayed previously in Table 1. Here, we direct attention to the evolution of σ_w *vs. J* derived from using $\gamma = 0$ (no plastic strain correction) and the plastic strain modified Beremin model (Eq. (5) previously described). In each plot, the correction $J_0^{PCVN_{a/W=0.5}} \rightarrow J_0^{SE(B)_{a/W=0.5}}$ defines the *predicted* J_0-value for the deep crack SE(B) specimen at $T = -80°\text{C}$ which then enables estimating the reference temperature, T_0, for the tested pressure vessel steel. Table 2 summarizes the *predicted* J_0-values and the estimated T_0 for all different forms of σ_w adopted in the present work.

The sensitivity of J_0-predictions on the adopted formulation for σ_w is evident in these results which also strongly impacts estimates of T_0. The standard definition of σ_w described by previous Eq. (3), which is essentially the original Beremin model, provides a conservative estimate of T_0. In contrast, adoption of the linear plastic correction overpredicts the J_0-value for the deep crack SE(B) specimen and, consequently, the reference temperature. However, use of the plastic strain modified Beremin models yields a T_0 estimate which is in very good agreement with the corresponding estimate derived from the master curve analysis based on toughness values for the 1-T, deep crack SE(B) specimen with $a/W = 0.5$.

6. Concluding Remarks

This study describes a probabilistic framework based on the Weibull stress model to predict the effects of constraint loss on macroscopic measures of cleavage fracture toughness in the ductile-to-brittle transition region. A central objective is to determine the indexing temperature T_0 based on the Master Curve methodology from PCVN specimens. An additional feature of the proposed approach also includes the effect of near-tip plastic strain on cleavage microcracking which impacts directly the magnitude of the Weibull stress and, consequently, the toughness scaling curves. While the correction term included into the Weibull stress assumes an *ad-hoc* linear dependence of microcrack density on plastic strain, our exploratory analyses demonstrate the effectiveness of the Weibull stress model to provide estimates for the reference temperature, T_0, from small fracture specimens which are in good agreement with the corresponding estimates derived from testing of much larger crack configurations.

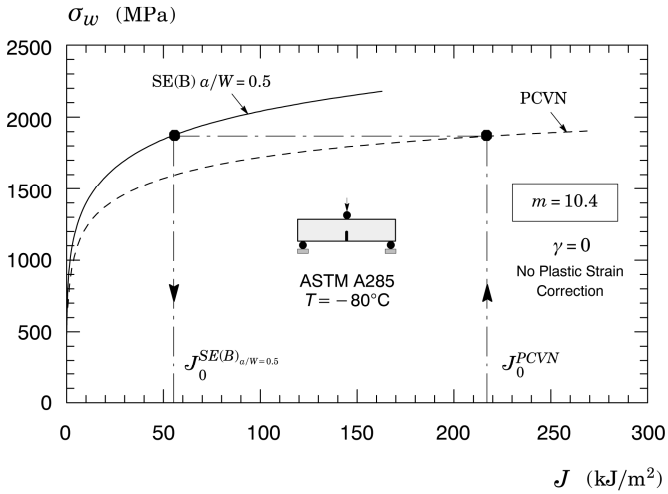

(a)

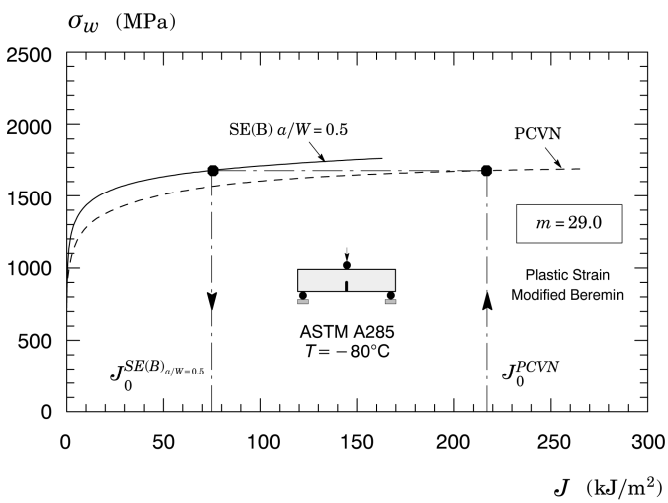

(b)

Figure 4. Weibull stress trajectories with increased levels of J for the deep crack SE(B) and PCVN specimens: (a) Standard Beremin model; (b) Plastic strain modified Beremin model.

Table 2. Estimates of J_0 and T_0 derived from different forms of the Weibull stress model

Weibull Stress Model	$\boldsymbol{J_0}$ (kJ/m^2)	$\boldsymbol{T_0}$ (◦C)
Standard Beremin ($\gamma = 0$ with no plastic strain correction)	54.1	-82.0
Generalized Weibull Stress with $\gamma = 1$ and $\beta = 0$ (linear correction)	100.8	-103.6
Generalized Weibull Stress with $\gamma = 1/2$ and $\beta = 0$ (square root correction)	137.6	-113.7
Plastic Strain Modified Beremin Model	74.1	-93.2

Acknowledgements

This investigation is supported by Fundação de Amparo à Pesquisa do Estado de São Paulo (FAPESP) through Grant 2012/13053-2 and by the Brazilian Council for Scientific and Technological Development (CNPq) through Grant 304132/2009-8.

References

[1] Mann, N. R., Schafer, R. E. and Singpurwalla, N. D., Methods for Statistical Analysis of Reliability and Life Data, Jonh Wiley & Sons, New York, 1974.

[2] Wallin, K. The Scatter in K_{Ic} Results, Engineering Fracture Mechanics, 19 (1984), 1085-1093.

[3] Beremin, F.M, A Local Criterion for Cleavage Fracture of a Nuclear Pressure Vessel Steel, Metallurgical Transactions, 14A (1983), 2277-2287.

[4] Ruggieri, C. and Dodds, R. H., A Transferability Model for Brittle Fracture Including Constraint and Ductile Tearing Effects: A Probabilistic Approach, International Journal of Fracture, 79 (1996), 309-340.

[5] Ruggieri, C., An Engineering Methodology to Assess Effects of Weld Strength Mismatch on Cleavage Fracture Toughness Using the Weibull Stress Approach, International Journal of Fracture, 164 (2010), 231-252.

[6] Brindley, B. J., The Effect of Dynamic Strain-Aging on the Ductile Fracture Process in Mild Steel, Acta Metallurgica, 18 (1970), 325-329.

[7] Lindley, T. C., Oates, G. and Richards, C. E., A Critical Appraisal of Carbide Cracking Mechanism in Ferride/Carbide Aggregates, Acta Metallurgica, 18 (1970), 1127-1136.

[8] Gurland, J., Observations on the Fracture of Cementite Particles in a Spheroidized 1.05% C Steel Deformed at Room Temperature, Acta Metallurgica, 20 (1972), 735-741.

[9] Wallin, K., Master Curve Analysis of the Euro Fracture Toughness Dataset, Engineering Fracture Mechanics, 69 (2002), 451-481.

[10] American Society for Testing and Materials, Standard Test Methods for Determination of Reference Temperature, T_0, for Ferritic Steels in the Transition Range, ASTM E-1921, Philadelphia, 2008.

[11] Gullerud, A., Koppenhoefer, K., Roy, A., RoyChowdhury, S., Walters, M., Bichon, B., Cochran, K. and Dodds, R., WARP3D: Dynamic Nonlinear Fracture Analysis of Solids Using a Parallel Computers and Workstations. Structural Research Series (SRS) 607. UILU-ENG-95-2012. University of Illinois at Urbana-Champaign. 2004.

[12] Savioli, R. G. and Ruggieri, C., T_0 Reference Temperature Estimates from Precracked Charpy Specimens Using the Weibull Stress Model, Manuscript in Preparation.

[13] American Petroleum Institute. Fitness-for-Service, API RP-579-1 / ASME FFS-1, 2007.

[14] Ruggieri, C., FRACTUS2D: Numerical Computation of Fracture Mechanics Parameters for 2-D Cracked Solids, EPUSP, University of São Paulo, 2011.

[15] Gao,X., Ruggieri, C. and Dodds, R. H., Calibration of Weibull Stress Parameters Using Fracture Toughness Data. International Journal of Fracture, 92 (1998), 175-200.

A Local Approach to Creep-Fatigue -Oxidation Interactions in Inco 718 Alloy

André Pineau[1], Raul De Moura Pinho[2], Stéphane Pierret[2], Caroline Mary[2],

[1] Mines ParisTech, Centre des Matériaux, UMR CNRS 7633, BP 97, 91003 Evry Cedex, France
[2] Snecma-SAFRAN, Villaroche, 77550 Moissy-Cramayel, France
* Corresponding author: stephane.pierret@snecma.fr

Abstract . Understanding and modeling hold time effects on fatigue crack growth rate (FCGR) above 500 °C in Inco 718DA is a great challenge. Fatigue tests with a trapezoidal wave shape signal including hold times from 90 s to 3600 s were carried out on Inco 718DA with a small grain size (5-15 µm) over a wide range of temperatures (500 °C-650 °C). FCGRs were measured using potential drop technique. SEM observations were carried out to correlate the measured FCGRs with the trans- or inter-granular aspect of the fatigue fracture surfaces. Two regimes must be distinguished. The first regime associated with relatively short hold times can be represented by a power law, where da/dN is proportional to t^{α}, $\alpha \simeq 0.25$. This first regime corresponds to the situation where the fatigue crack does not propagate during the hold time but its propagation takes place during the cyclic part of the loading over a damaged zone ahead of the crack tip. The second regime associated with longer hold times corresponds to the case where crack propagation during hold time (creep crack growth) is predominant. This regime is purely time dependent. Simple models are introduced to describe both regimes.

Keywords: Inco 718, High temperature fatigue, hold time effect, fatigue crack growth

1. Introduction

Inco 718 alloy is a Ni- base superalloy which is widely used in the fabrication of a number of gas turbine components, especially turbine disks, operating at high temperatures (up to 650 °C). Both the low cycle fatigue properties and the fatigue crack growth rate (FCGR) behavior of this material have been investigated in some detail by a number of investigators (see e.g. [1-12]). The creep crack growth resistance of this alloy has also been examined (see e.g. [13-15]). It is also well established that this alloy, like other Ni-base superalloys, is sensitive to oxidation. This oxidation effect depends on the microstructure, in particular the grain size [5]. These studies constitute the basis for the application of a defect tolerance approach. However most of these studies have been limited to relatively short hold times ($\leq$ 300 s) which are clearly too small compared to in-service conditions. The recent work by Gustafsson et al. [10-12] constitutes one exception. The first aim of the present study is an extension of the effect of hold time, t_m, on FCGR over longer times (up to 1 hour). It is also well established that this alloy, like other Ni-base superalloys, is sensitive to oxidation. This oxidation effect depends on microstructure, in particular the grain size [5].

In gas turbine design, the main load cycle is typically defined by the start-up and shut-down of the engine. The loading varies from component to component but often is a combination of both temperature variations and mechanical loads. These two events defining the main load cycle are separated by few hours in the case of an aero engine, and weeks or months in turbines for power generation. When searching for a model for predicting the interaction between pure cyclic damage (PF), creep (C), oxidation (Ox) the following requirements will appear [10] : (i) the interactions between the time dependent and cyclic load need to be separated, (ii) a damage accumulation between the time dependent damage and the cyclic damage must be considered. This is the second aim of the present study.

The methodology developed in this work is, to some extent, similar to the "local approach to fracture" (LAF) which is now widely used for predicting the variation of fracture toughness of ferritic steels with temperature (see e.g. [16]). However the LAF approach has been much less developed for high temperature applications and for Ni base superalloys. This is the reason why the present study should be considered as a preliminary attempt in this field.

2. Material and experimental procedures

The chemical composition of the material is, in weight%: $Ni_{54,18}Cr_{17,97}Fe_{17,31}(Nb+Ta)_{5,4}Mo_{2,97}Ti_1Al_{0,56}Co_{0,14}Mn_{0,08}Cu_{0,03}C_{0,023}B_{0,0041}$. This heat of Inconel 718 alloy was received as a forged disk. It was given a conventional heat-treatment (720 °C – 8 h + 620 °C – 8 h) directly after forging (DA). This resulted in a small grain size (5 - 15 µm) with particles of the stable phase δ (Ni_3Nb), precipitated along the grain boundaries (Fig. 1a) with small strengthening γ' (Ni_3TiAl) and γ'' (Ni_3Nb) precipitates (Fig. 1b).

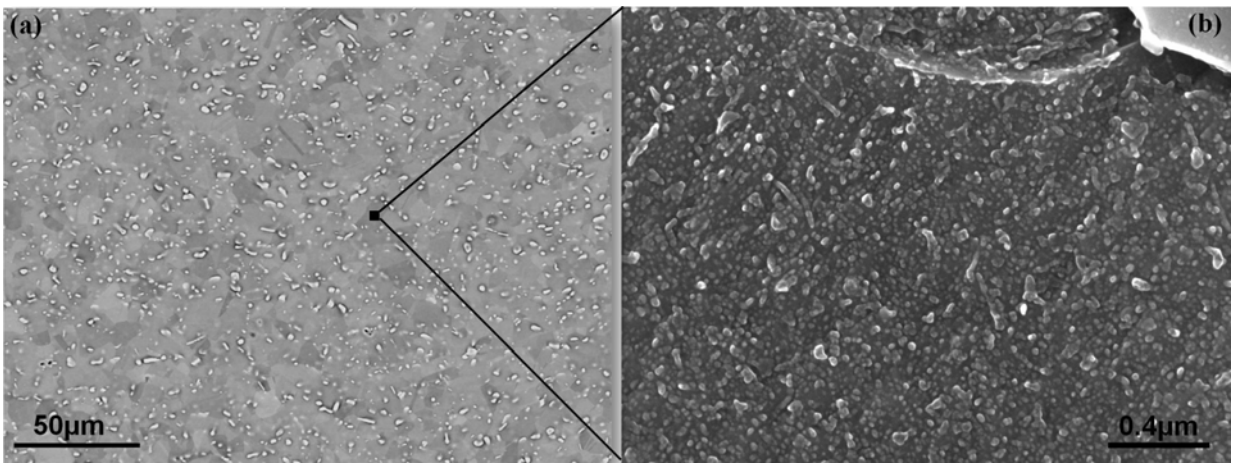

Figure 1. a) Optical micrograph showing the crystalline structure of the material and δ phase particles located at the grain boundaries (in white); (b) SEM observations showing γ' and γ'' precipitates within a grain.

FCGR tests were performed between 500°C and 650°C under an air environment using KBr specimens shown in Figure 2. A small EDM semi-circular notch (depth 0.3mm) was introduced and the specimens were fatigue-precracked at room temperature (RT) and at a frequency of 2 Hz in order to extend the notch over a distance by about 0.3mm (Fig. 2b).

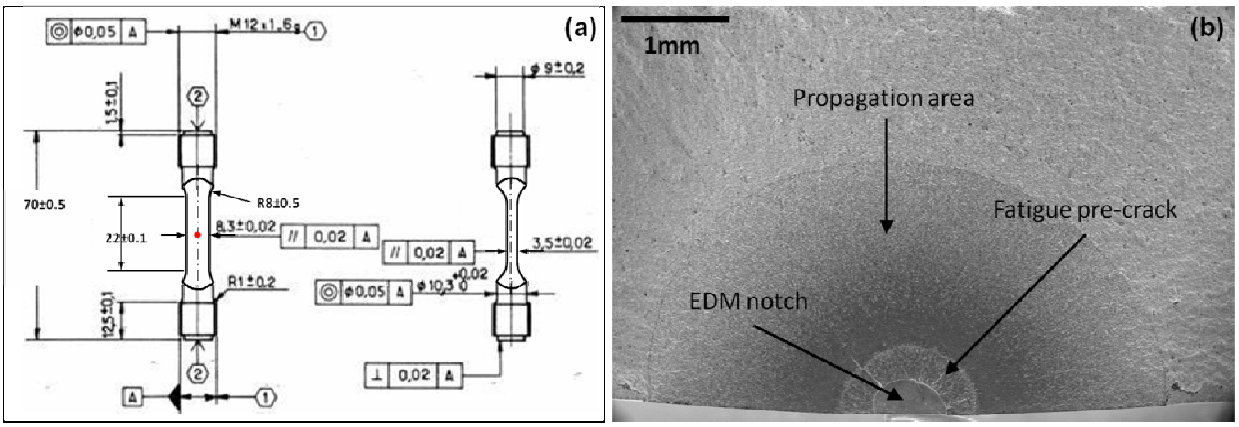

Figure 2. KBr specimens used for fatigue crack growth rate measurements. a) Schematic diagram showing the dimensions (mm) and the position of the EDM notch (red dot); b) Fracture surface of a specimen where the EDM notch (0.3mm), the fatigue pre-crack (0.6mm) and the propagation area can be distinguished.

Then the specimens were heated up and tested at R ratio of 0.05 where $R = K_{min}/K_{max}$. These tests were performed either under continuous pure fatigue (PF) at 2 Hz or with a trapezoidal shape signal 10/X/10 where 10 is the time (in s) to reach the maximum load and to unload the specimen while X designates the hold time at K_{max} in seconds. A potential drop technique which was previously calibrated was used to measure the crack growth rate expressed in terms of da/dN or da/dt, where N is the number of cycles and t is the total time (rising time + hold time + unloading time). The stress intensity factor (SIF) K was calculated using an expression which was calibrated previously. The measurement of the fatigue crack growth rate was performed following the standard ASTM E647-08.

Scanning electron microscopy (SEM) was used to observe the fracture surfaces of the specimens. A special attention was paid to the fracture surface character, i.e. transgranular with fatigue striations or intergranular.

3. Results

The results of FCGR measurements, da/dN expressed as normalized values, are shown in Figure 3 $(da/dN)_{tm}$ / $(da/dN)_{2Hz}$ for a given value of ΔK equal to 25 MPa.m$^{1/2}$. The results reported by Pédron and Pineau [5] and by Gustafsson et al. [10-12] for a similar ΔK are also included in figure 3.

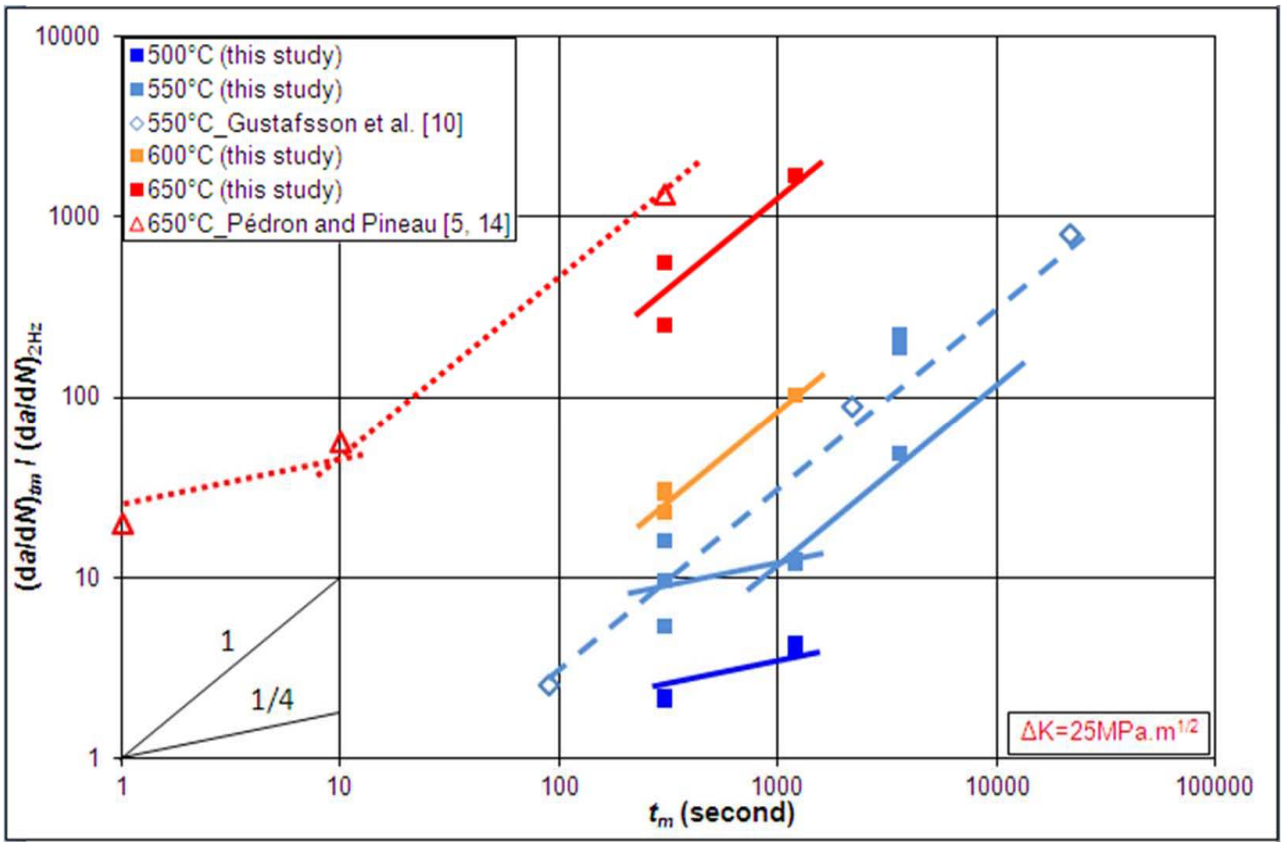

Figure 3. Normalized fatigue crack growth rate $(da/dN)_{tm}$ / $(da/dN)_{2Hz}$ as a function of hold time, t_m. Test conditions are given in the insert. Squares and full lines indicate data from this study whereas diamonds/dashed line and triangle/dot line represent data from Gustafsson's [10] and Pédron's and Pineau's [5, 14] work. Results obtained for ΔK = 25 MPa.m$^{1/2}$.

A close examination to this figure shows that, in all cases, the introduction of a hold time into the fatigue cycle produces an acceleration of the fatigue crack growth rate which can reach up to three orders of magnitude for long hold times and for elevated temperature (650 °C). Two regimes are distinguished in this acceleration of $(da/dN)_{tm}$. For short hold times (typically 1200 s at 550 °C and 10 s at 650 °C), the slope of the normalized FCGR versus hold times, t_m is of the order of 0.20 - 0.40. In this regime (named A), the slope of $(da/dN)_{tm}$ versus t_m is assumed to value 0.25 for the reasons detailed in the following. This regime A extends over hold times lower than a transition time named t_i hereafter (~ 1200 s at 550 °C and ~ 10 s at 650 °C). This transition time is thus dependent on temperature. It is also dependent on ΔK but this load dependence is not introduced here because it is out of the scope of the present work.

Figure 3 shows also that when $t_m > t_i$, the slope of the $(da/dN)_{tm} - t_m$ curves is close to 1, which means that in this regime, called hereafter regime B, the crack growth rate is purely time dependent. The *a*-*N* records reported by Gustafsson et al. [10] showed that in regime B, the crack propagated during the hold time (see their figures 7 and 8).

A comparison of our results at 550 °C with those reported previously by Gustafsson et al. [10] shows that both materials exhibit similar properties although they experienced different heat treatments. The same comparison at 650 °C with the results reported by Pédron and Pineau [5] indicates that, for the same testing conditions: $\Delta K = 25$ MPa.m$^{1/2}$, same temperature, same hold time, our material tends to exhibit better fatigue crack propagation properties. These variations in FCGR in the presence of a hold time are related to differences in the microstructure of the materials. In particular our material has a much smaller grain size as compared to those investigated by Pédron and Pineau (d $\simeq$ 50 µm) [5].

SEM observations showed significant differences in the fracture modes depending on test conditions (Figure 4). At low temperature and for small hold times the fracture mode is purely transgranular with the presence of fatigue striations (Fig. 4a). At increasing temperature and for longer t_m, i.e. in the regime B, the fracture mode is purely intergranular, as shown in figures 4c. In the intermediate regime A, i.e. close to the transition with regime B, the fracture surface is also predominantly intergranular, although less brittle than that observed in regime B. In this particular condition as shown in figure 4b, the fracture mode is mixed, with areas showing features of intergranular and transgranular fracture.

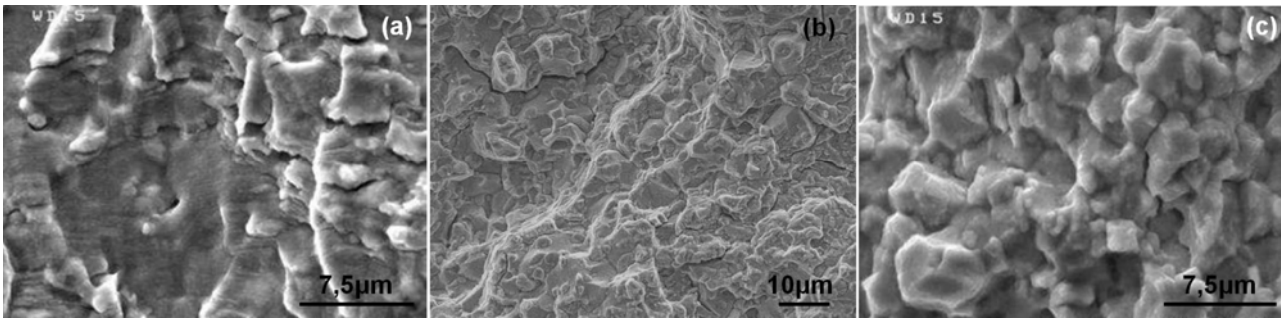

Figure 4. SEM observations of fracture surfaces. a) 450 °C, 2 Hz; b) 550 °C, 10/300/10; c) 600 °C, 10/1200/10.

4. A tentative model in the frame of the local approach to fracture

A simple model based on a linear summation of three components is proposed to account for the effect of hold time on FCGR, i.e.:

(1)

Most terms in Eq. 1 have already been defined. The remaining ones are defined in the following. The three components in Eq. 1 are successively analyzed in more detail.

The first term $(da/dN)_{PF}$ represents the pure fatigue (PF) component. This contribution to FCGR which is temperature dependent but not environment dependent has already been modeled by Clavel and Pineau [2]. It is enough to say that at low FCGR ($\leq 10^{-8}$m/cycle), the crack propagation rate was modeled as successive discontinuous crack jumps according to the first LAF model introduced by McClintock [17] for fatigue. At higher FCGR ($\simeq 10^{-6}$ m/cycle) the fatigue damage is associated with the formation of striations. The corresponding crack propagation rate can be described by the crack tip opening displacement (*CTOD*) first introduced by Pelloux [18]. It is well to remember that, in this regime of FCGR, one observes that the distance between fatigue striations, *i*, can simply be expressed as:

(2)

where E is the Young's modulus and σ_Y the yield strength of the material.

The second term in Eq. 1 represents the oxidation component. It is assumed that no crack propagation takes place during the hold time provided that $t_m < t_i$. However stress assisted grain boundary oxidation occurs at the crack tip and produces a damaged zone. This might correspond to the "damaged zone" evidenced by Gustafsson et al. [12]. These authors showed that the extent, *x*, of this damaged zone could be written as:

$$x = (t_m)^{\alpha} \text{ with } \alpha = 0.25 \quad (3)$$

Several mechanisms have been proposed to account for this oxidation-assisted regime (see e.g. [5, 19-22]). It is out of the scope of the present study to discuss these mechanisms. The results of Gustafsson et al. [10, 12] strongly suggest that the time dependence in this regime can be described by a power law with an exponent of 0.25 (see Eq. 3).

Theoretical results giving the diffusion distance, z, along a grain boundary and the concentration in oxygen along this grain boundary, C_b, in equilibrium with a concentration C_o at the free surface, which is itself in equilibrium with the oxides covering the grain boundary and the matrix surface [21] is given by [23]:

(4)

where D is the diffusion coefficient of oxygen through the grain matrix and D_b is the grain boundary diffusion coefficient of oxygen along the grain boundary of thickness, δ. Assuming that fracture occurs during the cyclic part of the loading over a critical distance, z, when C_b reaches a critical value at that position, Eq. 4 predicts that the crack growth rate will be proportional to $t^{1/4}$, i.e.:

(5)

The $t^{1/4}$ time dependence is thus in good agreement with the experiments, especially those reported by Gustafsson et al. [12]. Moreover Eq. 5 predicts that the temperature dependence will be given by an exponential law with activation energy of ($Q_b/2 - Q_m/4$) where Q_b and Q_m are the activation energies of oxygen along the grain boundaries and through the matrix, respectively. The value of Q_b in nickel is close to 275 KJ/mole [19]. Unfortunately nothing is known about the value of D and Q_m. This shows that further studies are necessary for a better understanding of the damage mechanisms prevailing in the regime A of FCGR.

The transition between regime A and B requires the evaluation of the initiation time t_i. It is well to remember that Riedel and Rice [24] have shown that the viscoplastic strain in creeping solids with a Norton type law can be expressed as:

$$\varepsilon = F\, t^{\frac{1}{n+1}} \left(K / \sqrt{r} \right)^{\frac{2n}{n+1}} \tag{6}$$

In this expression, F is a numerical factor which is an increasing function of temperature and which is equal to 8.34 10^{-9} at 650°C for plane strain conditions [25] (time in h, K in MPa $m^{1/2}$, r in m), n is the exponent of the stationary creep law and was found to be around 10 in Inco 718 at 650°C [25].

Assuming that crack initiation takes place during the hold time, when a critical strain ε_c, is reached over a characteristic distance X_c, Eq. 6 predicts that:

$$K^{2n} t_i = \beta (\varepsilon_c)^{n+1} (X_c)^n = C \tag{7}$$

where β is a constant. In Eq. 7, ε_c may be strongly dependent on oxidation as underlined by Diboine and Pineau [25] (see their figure 9). The parameter C can be evaluated from the tests performed by Pédron and Pineau [5, 14] at 650°C. These tests suggest that $t_i \approx 10$ s for $K = 25$ MPa.m$^{1/2}$ leading to $C \approx 9.10^9$ (t in s, K in MPa.m$^{1/2}$). Moreover the critical distance X_c, must be lower than the calculated creep zone size, R_{vp} given by [24]:

(8)

with $G = 10^{-8}$ for R_{vp} (m), t (h) and K (MPa m$^{1/2}$) [25]. The parameter G increases with temperature. This leads to $R_{vp} \approx 10$ µm at 650°C, which is close to the grain size of our material.

These calculations indicate that, within a first approximation, t_i could be calculated from Eq. 7 with X_c equal approximately to the grain size or from Eq. 8 written as Eq. 9:

(9)

The transition time t_i in Eq. 1 can thus be evaluated with two expressions (Eqs 7 and 9). However it appears to be difficult to establish a definite model for the FCGR behavior in regime A in the absence of more detailed measurements of t_i and variations of ε_c with time.

The third term in Eq. 1 can be determined using the FCGR behavior in regime B which is purely time dependent (Figure 3). The creep crack growth (CCG) regime ($t_m >> t_i$) has been investigated by a number of authors (see e.g. [5, 15, 25]). However, the test procedure used by these authors is completely different from ours. They start from a fatigue precrack and then maintain the load constant. This procedure does not allow investigating the initiation and the propagation of a crack in a continuously creep-oxidation damaged material. Our test procedure allows us avoiding the tail of the curves observed in most CCG rate measurements reported in the literature. An attempt was made to model these transient curves observed in stainless steel [26]. These tails lead to an apparent threshold in K which is load and time dependent, as clearly shown elsewhere [25]. In our tests the CCG rate component is simply obtained by noting that for long t_m the third term in Eq. 1 is much larger than the two other ones. This means that the CCG rate, $(da/dt)_{cr}$ at a given temperature, can simply be obtained using Eq. 1 with long hold times only (3600 s at 550 °C, 1200 s at 600 °C and 650 °C). The results are shown in figure 5 where test results by Gustafsson et al. [10] obtained with long hold times (2160 s) have also been included. A good agreement between both sets of results is observed which suggests that crack propagation in regime B is not too much dependent on microstructural details. The results obtained by Sadananda and Shahinian [15] are also included in figure 5 but, as these authors have investigated the propagation of a fatigue precrack under constant

load, the results obtained by Sadananda and Shahinian and corresponding to the "steady" state regime are included in figure 5 to avoid the transient regime. Their results are also close to ours and to those of Gustafsson et al. [10], reinforcing our conclusion on the moderate effect of microstructure in this regime of crack propagation.

The slope of the $(da/dt)_{cr}$ curves drawn in figure 5 is between 2 and 4. The temperature dependence is indicated in figure 6 where an apparent activation energy of the order of 300 KJ/mole is observed from our tests and Gustafsson et al. experiments [10]. This energy is close to the activation energy for oxygen grain boundary diffusion (274 KJ/mole) in nickel, as noted earlier. It is clear that the CCG rate behavior is also affected by oxidation and can be described as successive crack jumps over a critical distance ($\approx R_{vp}$) with lasting times of the order of the transition time t_i defined earlier by Eq. 7. This simple approach leads to a predicted slope of the $(da/dt)_{cr} - K$ curves of $2(2n^2 - n\text{-}1) / (n\text{-}1)$, i.e. to a slope close to $4n$ for sufficiently large values of the exponent n. This predicted slope is much higher than the slope indicated in figure 6 which was found to be between 2 and 4. However this simplified approach is valid only when it can be assumed that the critical creep strain, ε_c (Eq. 7) is constant. This assumption is not valid when the tests are carried out under air environment. Results of CCG rate measurements under vacuum [27] showed that the slope of the $(da/dt)_{cr} - K$ curves was much higher (> 20) compared to those determined in air environment. These large values of the slope under vacuum are thus in better agreement with the predicted value of ~ $4n$. This indicates that it is necessary to develop more sophisticated models when the material is tested under air environment. These models must include a variation of the critical creep strain ahead of the crack tip with oxygen grain boundary diffusion given by Eq. 4.

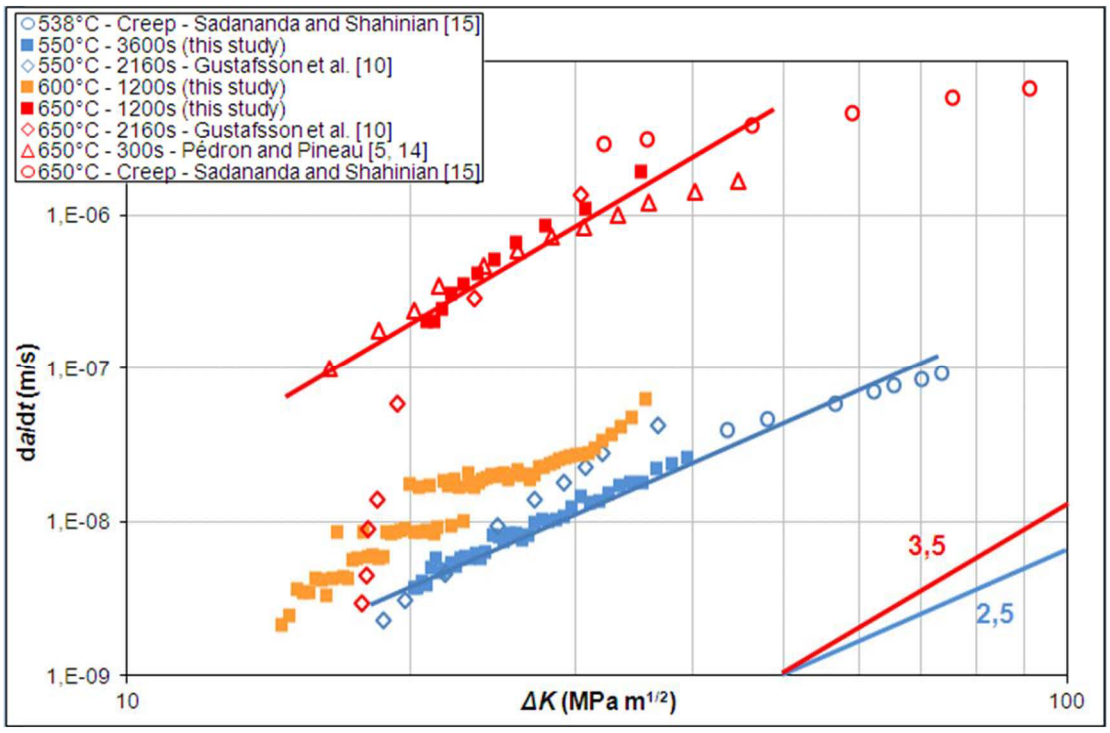

Figure 5. Creep crack growth rate versus ΔK curves corresponding to regime B (see text). The results by Gustafsson et al. (diamonds) [10] and Pédron and Pineau (triangles) [5, 14] obtained under similar conditions and those reported by Sadananda and Shahinian (circles) [15] using fatigue precracked specimens are shown.

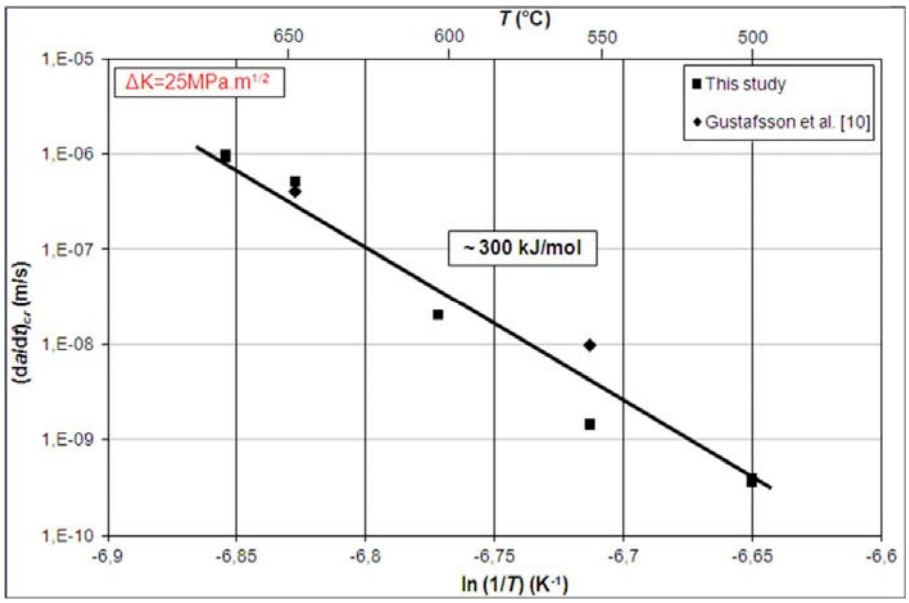

Figure 6. Creep crack growth rate as a function of 1/T (log scale). The slope giving the activation energy is indicated.

5. Conclusions

1. This study has confirmed that Inco 718 alloy exhibits a strong dependence to hold time, t_m , effect when tested at elevated temperature (500 °C – 650 °C) in air environment with fatigue cycles including long hold times (< 1 h). These results are in good agreement with other results published in the literature. The t_m dependence is related to a combination of creep strain accumulation ahead of the crack tip and detrimental effect of oxidation.

2. A simple linear damage accumulation law has been proposed to account for this hold time effect. This law includes three terms: (i) a pure fatigue component, (ii) an oxidation component (Regime A), and (iii) a pure creep component (Regime B).

3. The oxidation component $(da/dN)_{ox}$ leads to an acceleration in fatigue crack growth rate proportional to $(t_m)^{\alpha}$, where α is close to 0.25. This component prevails for hold times, t_m lower than a critical transition time, t_i , which is a decreasing function of temperature.

4. The pure creep component $(da/dt)_{cr}$ gives rise to a crack growth rate proportional to hold time, t_m. It is better to determine this component using cyclic tests with hold times, similar to those of the present study, than using fatigue precracked specimens submitted to a steady load.

5. An attempt has been made to model the time dependent regimes A and B. It has been shown that Regime A can be interpreted as resulting either from the kinetics of oxygen diffusion or from creep damage accumulation. Both explanations are more complementary than contradictory. An estimate of the transition time t_i between regimes A and B has been given. Regime B which occurs for very long hold times has been interpreted as a pure creep crack growth. It has been shown that the crack growth rate in regime B is an increasing function of hold time with apparent

activation energy close to the activation energy for oxygen diffusion along the grain boundaries.

References

[1] D. Fournier, A. Pineau, Low cycle fatigue behavior of Inconel 718 at 298K and 823K, Met. Trans. 8A, 1977, pp. 1095-1105.
[2] M. Clavel, A. Pineau, Frequency and waveform effects on the fatigue crack growth behavior of alloy 718 at 298K and 823K, Met. Trans. 9A, 1978, pp. 471-480.
[3] M. Clavel, A. Pineau, Fatigue behaviour of two nickel-base alloys I: Experimental results on low cycle fatigue, fatigue crack propagation and substructure, Mat. Sci. Eng. 25, 1982, pp. 157-171; II: Physical modeling of the fatigue crack propagation process, Mat. Sci. Eng. 25, 1982, pp. 173-180.
[4] L.A. James, W.J. Mills, Effect of heat treatment and heat-to-heat variations in the fatigue crack growth response of alloy 718, Engng. Fract. Mech. 22, 1985, pp. 797-817.
[5] J.P. Pédron, A. Pineau, The effect of microstructure and environment on the crack growth behaviour of Inconel 718 alloy at 650°C under fatigue, creep and combined loading, Mat. Sci. Eng. 56, 1982, pp. 143-156.
[6] J.E. King, Fatigue crack propagation in nickel-base superalloys – Effects of microstructure, load ratio and temperature, Mat. Sci. Eng. 3, 1987, pp. 750-764.
[7] H.H. Smith, D.J. Michel, Effect of environment on fatigue crack propagation behavior of alloy 718 at elevated temperature, Met. Trans. 17A, 1986, pp. 370-374.
[8] M.R. Bache, W.J. Evans, M.C. Hardy, The effects of environment and loading waveform on fatigue crack growth in Inconel 718, Int. J. Fatigue, 21, 1999, pp. S69-S77.
[9] G.A. Osinkulu, G. Onofrio, M. Marchionni, Fatigue crack growth in polycrystalline IN 718 superalloy, Mat. Sci. Eng., A 356, 2003, pp. 425-433.
[10] D. Gustafsson, J.J. Moverare, S. Johansson, K. Simonsson, M. Hörnqvist, T. Månsson, S. Sjöström, Influence of high temperature hold times on the fatigue crack propagation in Inconel 718, Int. J. Fatigue, 33, 2011, pp. 1461-1469.
[11] M. Hörnqvist, T. Månsson, D. Gustafsson, High temperature fatigue crack growth in Alloy 718 – Effect of tensile hold times, Proc. Eng., 10, 2011, pp. 147-152.
[12] D. Gustafsson, J. Moverare, K. Simonsson, S. Johansson, M. Hörnqvist, T. Månsson, S. Sjöström, Fatigue crack growth behaviour of Inconel 718 – The concept of a damaged zone caused by high temperature hold times, Proc. Eng., 10, 2011, pp. 2821-2826.
[13] S. Floreen, The creep fracture of wrought nickel-base alloys by a fracture mechanics approach, Met. Trans. 6A, 1975, pp. 1741-1749.
[14] J.P. Pédron, A. Pineau, Influence de l'oxydation sur la propagation des fissures à haute température dans l'alliage Inconel 718, Mémoires et Etudes Scientifiques Revue de Métallurgie, 1983, pp. 665-674.
[15] K. Sadananda, P. Shahinian, Creep crack growth in Alloy 718, Met. Trans. 8A, 1977, pp. 439-449.
[16] A. Pineau, Development of the local approach to fracture over the past 25 years: Theory and applications, Int. J. Fracture, 138, 2006, pp. 139-166.
[17] F.A. McClintock, On the plasticity of the growth of fatigue cracks, in D.C. Drucker, J.J. Gilman, Fracture of solids, Interscience Publishers, John Wiley & Sons, New York, London, 1962, pp. 65-102.
[18] R.M. Pelloux, Mechanisms of formation of ductile striations, ASM Trans., 62, 1969, pp. 221-285.
[19] D.A. Woodford, Gas phase embrittlement and time dependent cracking of nickel based superalloys, Energy Materials 1, 2006, pp. 59-79.

[20] A. Pineau, Fatigue and creep-fatigue behaviour of Ni-base superalloys: Microstructural and environmental effects in M. Branco, R. Ritchie, V. Sklenicka, Mechanical behaviour of materials at high temperature, NATO ASI Series, Kluwer Academic Publishers, Dordrecht, Boston, London, 1995, pp. 135-167.
[21] R. Molins, G. Hochstetter, J.C. Chassaigne, E. Andrieu, Oxidation effects on the fatigue crack growth behaviour of Alloy 718 at high temperature, Acta Mater., 45, 1997, pp. 663-674.
[22] H. Ghonem, D. Zheng, Depth of intergranular oxygen diffusion during environment-dependent fatigue crack growth in alloy 718, Mater. Sci. Eng., A150, 1992, pp. 151-160.
[23] I. Kaur, Y. Mishin, W. Gust, Fundamentals of grain and interphase boundary diffusion, John Wiley & Sons, New York, 1995.
[24] H. Riedel, Fracture at high temperatures, MRE, Springer-Verlag, Berlin, Heidelberg, New York, 1987.
[25] A. Diboine, A. Pineau, Creep crack initiation and growth in Inconel 718 alloy at 650°C, Fatigue Fract. Engng. Mater. Struct., 10, 1987, pp. 141-151.
[26] E. Maas, A. Pineau, Creep crack growth behaviour of type 316L steel, Eng. Fracture Mechanics, 22, 1985, pp. 305-325.
[27] J. Charpigny, Fissuration sous fluage dans l'Inconel 718, PhD thesis, Ecole des Mines de Paris, 1981.

On Modeling of Thermal Embrittlement in PWR Steels using the Local Approach to Fracture

Antoine Andrieu[1], André Pineau[1*], Pierre Joly[2], François Roch[2]

[1] Centre des Matériaux, Mines ParisTech, UMR CNRS 7633, BP 87, 91003 Evry Cedex, France
[2] AREVA, Tour Areva, 1 Place Jean Millier, 92084 Paris La Défense
* Corresponding author: andre.pineau@ensmp.fr

Abstract Experiments on Charpy and CT specimens were carried out on one heat of A533B steel under two conditions: (i) as received, and (ii) thermally aged (450°C – 5000h). A shift of the ductile to brittle transition temperature (DBTT) was measured after aging. In both cases SEM observations showed that fracture occurred both by intergranular and transgranular cleavage fracture modes when the materials were tested at sufficiently low temperature. Detailed examinations revealed that intergranular fracture was associated with micro-segregated zones, enriched in carbon and phosphorus. A recent model developed by the authors for predicting the fracture toughness of inhomogeneous materials was applied to describe the large scatter related to the bimodal failure modes observed in both conditions and the DBTT shift after aging. It is shown that thermal aging produces a slight decrease of the critical cleavage stress (due to the crossing of grain boundaries embrittled by phosphorus segregation) and a larger decrease of the critical intergranular fracture stress. The McLean-Guttmann- Militzer model is used to predict the kinetics of segregation during aging. An attempt is made to show how these results can be used to model DBBT variations under in-service conditions.

Keywords Ductile to brittle transition, intergranular, phosphorus segregation

1. Introduction

It is often noticed the presence of segregated zones (S.Z) in large components used for the fabrication of pressurized water reactors (PWR) (see e.g. [1, 2]. These SZs are linked to the solidification process of large ingots. They are enriched in the alloying elements (Mn, Ni, Mo, C, etc.) present in the steel. They are also enriched in impurities, such as P which may segregate at grain boundaries during aging. These local microstructural modifications can generate a bimodal fracture process (cleavage and intergranular fracture), as shown elsewhere [2].

Brittle (cleavage and intergranular) fracture in homogeneous ferritic (or bainitic) steels has been investigated by many authors, for a review see e.g. [3]. The seminal work by Beremin [4] has shown that in a homogeneous material the fracture toughness, K_{IC} obeys a size effect given by $K_{IC}^4 B =$ constant, where B is the thickness of the specimen, while the scatter in test results can be described by a Weibull law. The probability of failure can be expressed as:

$$P_r = 1 - \exp\left[-\frac{K_{IC}^4 B \sigma_o^{m-4} C_{m,n}}{V_o \sigma_u^m} \right] \tag{1}$$

Where σ_o is the yield strength of the material, m is the Weibull shape factor, $C_{m,n}$ is a parameter depending both on material work-hardening exponent, n, and the Weibull shape factor, m (see [5] for detailed values of C_{mn}.) V_o is a representative volume and σ_u is the Weibull scale factor. Recently it has been shown how Eq.1 must be modified in the presence of inhomogeneities leading to local intergranular fracture [2].

The main aim of the present study is the application of these recent modifications of the original

Beremin model to predict the variation of fracture toughness with temperature. One heat of 18 MND5 grade steel (type A533B) was used for this purpose. The material (a 100mm thick hot-rolled plate) was tested in the as-received condition and after aging at 450°C for 5000 hours. This aging heat treatment was introduced to reinforce the segregation of phosphorus at grain boundaries and to decrease the grain boundary fracture resistance. The McLean [6]–Guttmann [7] theories for impurity intergranular segregation was used to calculate the grain boundary enrichment in phosphorus and in carbon under isothermal conditions. These theoretical values were compared to experimental values determined by Auger spectrometry. The interaction between C and P atoms was adjusted from this comparison. Therefore the approach developed in the present study contributes to an improvement in the prediction of the shift in DBTT with thermal aging.

2. Material and experimental procedures

The composition of the investigated steel is (in weight %): C = 0.192, Mn = 1.44, Ni = 0.683, Mo = 0.473, Cr = 0.194, Si = 0.249, S = 0.0053, P = 0.010. It was received as a thick plate (100 mm) produced for simulating welding operations. This material was used in the past for the manufacturing of steam generator secondary pressure vessel, and is very close to plates used in the past for pressurizer vessels. The material was given the conventional heat-treatments applied to PWR components, including the final stress-relieving heat-treatment (615°C-Air cooling at ~ 30°C /hour). The prior austenite grain size was between 20 and 30 µm. The yield strength determined at RT was 490 MPa.

The microstructure of the material is shown in Fig.1. Segregated zones (SZ) aligned along the rolling direction (L) and distant of about 0.2 mm in the short-transverse (ST) directions are observed in Fig.1a. This is the consequence of micro-segregations of alloying elements during solidification, deformed by the rolling process. The dark zones are much harder than the matrix (~ 300 HV instead of ~ 210 HV) (Fig.1b). They are enriched in all alloying elements (C, Mn, Mo, Si) and in P as revealed by microprobe analysis (Fig.1b). The surface fraction covered by these segregated zones is about 10%. SEM and Auger spectrometry were used to examine the fracture surfaces and to determine the amount of phosphorus segregated along the grain boundaries.

a)

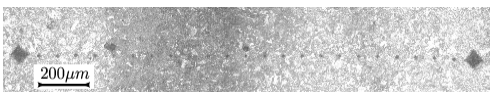

b)

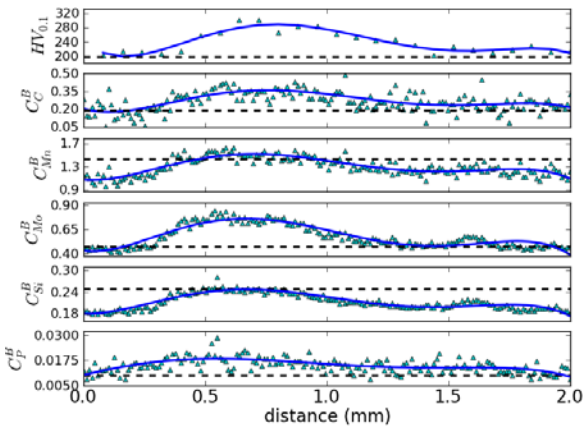

Figure 1. a) Optical micrograph showing two segregated zones aligned along the rolling direction; b) Microprobe analysis across one segregated zone showing the bulk concentration C^B in carbon, manganese, molybdenum, silicon and phosphorus. The variations of micro-hardness (100g) are also shown.

3. Results – Mechanical tests and fractography

The results obtained on Charpy specimens and on CT specimens, tested along the T (transverse) – L orientation are reported in Fig. 2. A shift of the ductile to brittle transition temperature (DBTT) measured at 41J appears in Fig. 2a when comparing the as-received and the aged conditions. This shift is of about 39°C. Similarly the fracture toughness determined on CT_{20} specimens is lowered by aging (Fig. 2b and c). In these figures we have also reported the probabilities to fracture for 5%, 63% and 95% determined from the master curve (MC) analysis [8, 9]. The temperature T_o at which K_{JC} = 100MPa $m^{1/2}$ is shifted from – 124°C in the as-received condition to – 91°C in the aged condition. The scatter in the aged material is much wider than in the as-received material. In particular it is noticed that the MC analysis is unable to describe this large scatter.

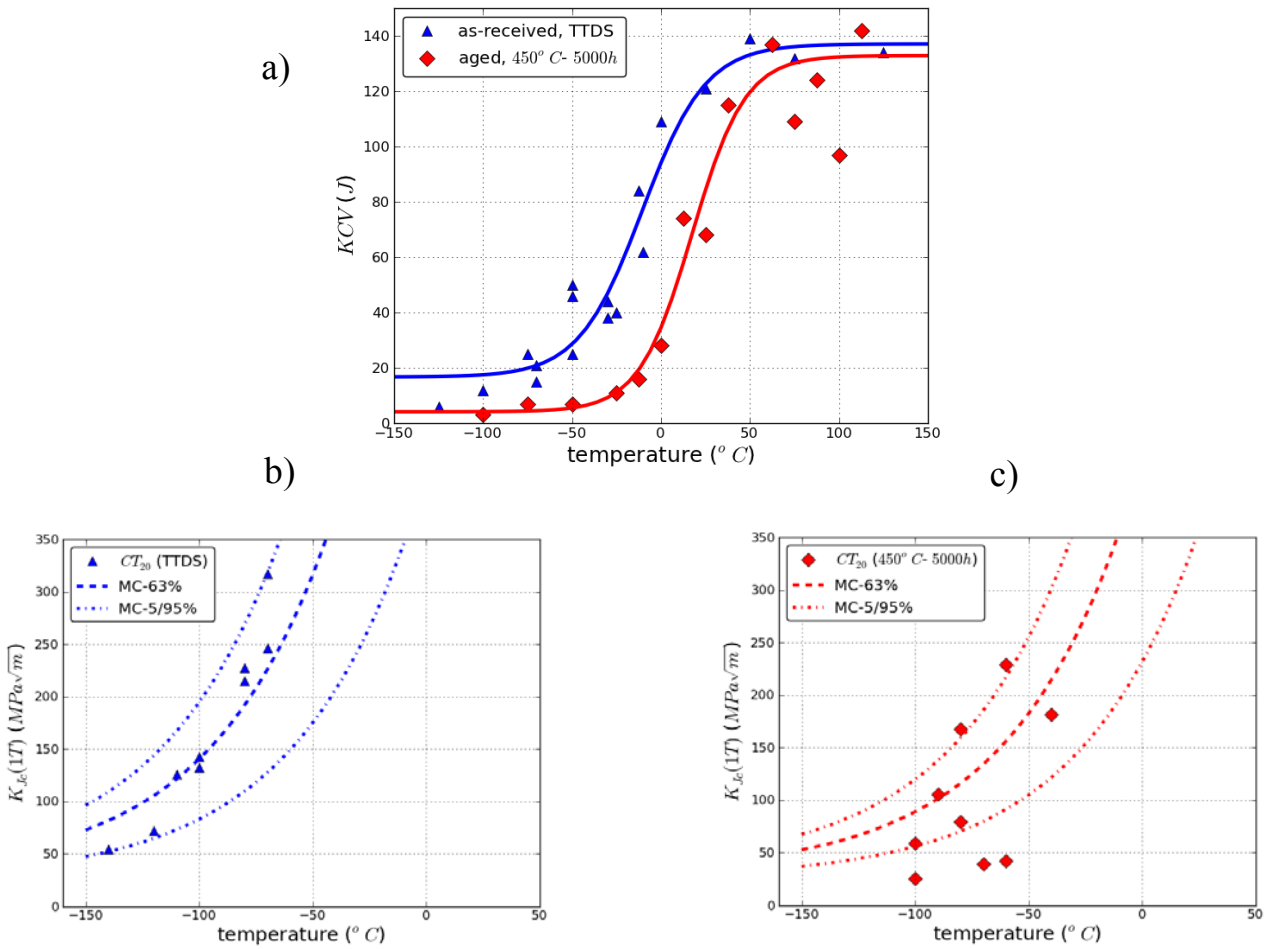

Figure 2. a) Charpy tests in as-received and aged (450°C – 5000 h) conditions; b) Fracture toughness, K_{JC} (thickness) determined on CT 20 mm thick specimens as a function of temperature in the as-received material; c) Fracture toughness K_{JC} on CT20 mm thick specimens in the aged (450°C – 5000 h) condition. The probabilities P_r = 5%, 63%, 95% determined from the Master Curve (MC) are also drawn.

Fracture surface examination of Charpy and CT specimens tested at relatively low temperature showed the presence of elongated zones aligned along the L direction (Fig. 3a) in which the fracture

mode was intergranular (Fig. 3c). This local intergranular fracture mode was observed in both conditions. These zones correspond to the SZ evidenced in Fig. 1a. They contained very often MnS inclusions (Fig. 3b) and were surrounded by cleavage facets as observed in Fig. 3b. This observation is thus similar to previous examinations on a segregated PWR material (see Fig. 1 in [2]). The ratio of intergranular/transgranular cleavage fracture was similar in both conditions.

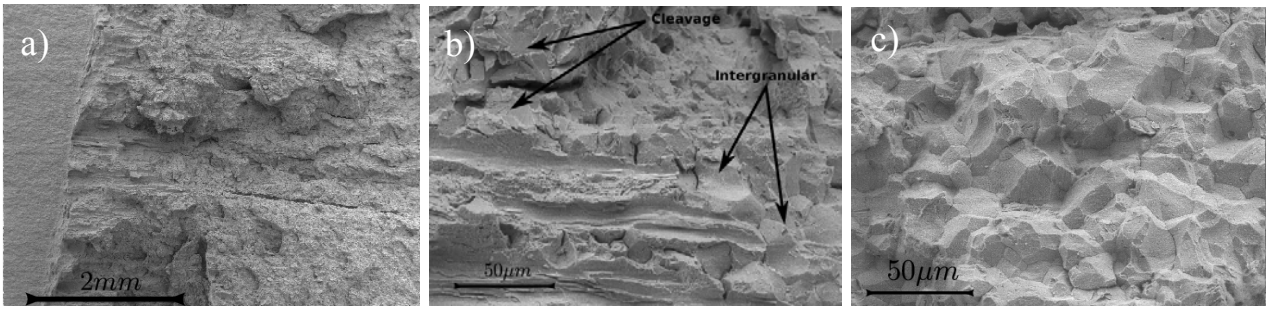

Figure 3. SEM observations: a) and b) As received material; c) Aged (450°C – 5000 h) condition.

4. Intergranular segregation – Results and theoretical considerations

Auger spectrometry measurements showed that the phosphorus concentration (atomic %) at grain boundaries increased significantly between the as-received condition $\left(C_p^{gb} = 12.5 \pm 6\%\right)$ and the aged condition $\left(C_p^{gb} = 23 \pm 9\%\right)$. The grain boundary concentration in carbon tended to decrease with aging ($C_c^{gb} = 37 \pm 14\%$ in the as-received condition compared to $C_c^{gb} = 28 \pm 10\%$ in the aged condition). Full details about these measurements can be found elsewhere [10]. Intergranular P phosphorus segregation was shown to occur during cooling after the stress-relieving heat treatment. The relatively low cooling rate (~ 30°C/h below 615°C) thus produces temper-embrittlement effect in the segregated zones enriched in phosphorus.

The theory of isothermal intergranular segregation has been developed by McLean [6] in his pioneering work. This theory was extended by Guttmann [7] to account for the interaction of an impurity element (here P) with other elements, in particular carbon atoms. A comprehensive review of these theories can found in the recent book of Lejcek [11]. The grain boundary concentration at equilibrium, $C^{gb,eq}$ in a system containing N elements in solid solution C^B can be written as:

$$\frac{C_i^{gb,eq}}{1-\Sigma_{j=o}^{N} C_j^{gb,eq}} = \frac{C_i^B}{1-\Sigma_{j=o}^{N} C_j^B} \exp\left[-\frac{\Delta G^{seg}}{\mathrm{R}T}\right] \tag{1}$$

The segregation energy ΔG_i^{seg} is expressed as:

$$\Delta G^{seg} = \Delta G_i^o + \Delta G_i^E = \Delta H_i^o - T\Delta S_i^o + \Delta G_i^E \tag{2}$$

where ΔG_i^E represents the deviation from an ideal system due to the presence of elements other than the impurity, i.

In a binary system, such as Fe-C or Fe-P, the kinetics of segregation $C^{gb}(t)$ is given by [6]:

$$C^{gb}(t) = C^{gb,eq}(T_2) - C_o(\alpha_2 - \alpha_1)\exp\left[\frac{4Dt}{\alpha_2^2\delta^2}\right] erfc\left[\frac{2\sqrt{Dt}}{\alpha_2\delta}\right] \quad (3)$$

where $C^{gb,eq}$ is the concentration at equilibrium of the impurity, at temperature T_2, given by Eq. 1, $Co = C^B$ (t = 0) is the impurity concentration in the matrix which is assumed to be constant, $\alpha_1 = C^{gb,eq}(T_1) / C_o$ with T_1 the temperature from which the material is cooled down, $\alpha_2 = C^{gb,eq}(T_2) / C_o$, D the coefficient of diffusion of the impurity at T_2, t the time and δ, the thickness of the grain boundary.

In a ternary system, Guttmann [7] assumed that ΔG_i^{seg} can be expressed as:

$$\Delta G_i^{seg} = \Delta G_i^o - 2\alpha_{ii} C_i^{gb} + \alpha_{ij} C_j^{gb} \quad (4)$$

where the coefficients α_{ii} and α_{ij} describe the interaction between the elements segregating at grain boundaries (α_{ii} > O or α_{ij} < O correspond to a repulsive interaction which is the situation met with C and P).

The solution for the kinetics of segregation for non-isothermal conditions can be derived from Militzer's work [12].

All terms in Eqs. 1-4 have been determined in the literature:

$d = 810^{-10}$ m

$$D_p = 0.25\exp\left(-\frac{200\,000}{RT}\right) \quad \left(\mathrm{cm^2 s^{-1}}\right) \quad [13, 14] \quad (5)$$

$$D_C = 0.003\exp\left(\frac{76000}{RT}\right) \quad \left(cm^2 s^{-1}\right) \quad [15] \quad (6)$$

$$\Delta G_p^o = 64273 - 23.7T \left(\mathrm{J\,mol^{-1}}\right) \quad [13] \quad (7)$$

$$\Delta G_c^o = 16752 + 40.9T \left(\mathrm{J\,mol^{-1}}\right) \quad [13] \quad (8)$$

$$\alpha_{cc} = 4000\,\mathrm{J\,mole^{-1}}; \quad \alpha_{pp} = 1500\,\mathrm{J\,mole^{-1}}; \quad \alpha_{cp} = -4500\,\mathrm{J\,mole^{-1}} \quad [10, 16] \quad (9)$$

The McLean-Guttmann-Militzer model has been applied to our steel with T_1= 888 K, C_C^B= 80 ppm (Wt %) and C_P^B = 150 ppm (Wt %) for predicting the C and P grain boundary concentration in the

as-received condition (t = 0) and during aging at 450°C. Full details can be found elsewhere [10]. The results are compared to experimental measurements in Fig. 4 where it is observed that in the as-received condition (t = 0), phosphorus and carbon atoms are already segregated. Carbon atoms desegregate during aging while phosphorus concentration is increasing. This results from the repulsive interaction between C and P atoms (Eq. 9). The calculated values are in good agreement with the experimental values.

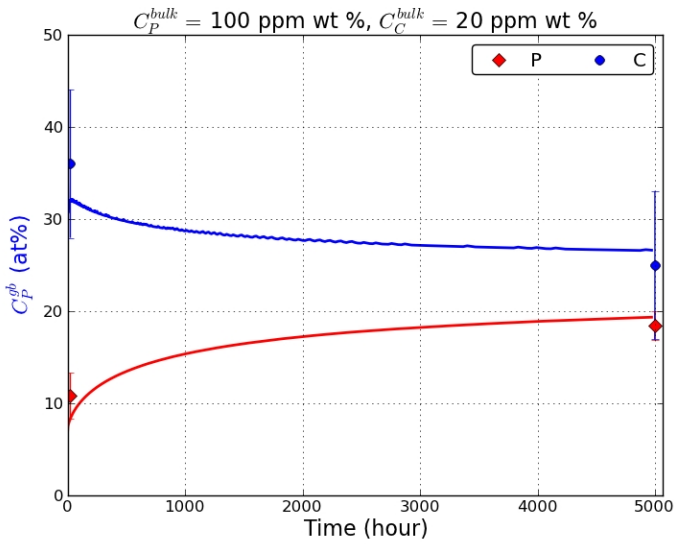

Figure 4. Phosphorus (P) and carbon (C) concentration at grain boundaries (expressed in atomic %) a function of aging time at 450°C. Experimental results and calculated curves.

5. Prediction of fracture toughness – Influence of impurity segregation

It has been shown that the fracture mode of our material in the DBTT regime was bimodal: transgranular cleavage and intergranular. A recent model has been proposed for this situation [2]. However this model includes a number of parameters (Weibull shape factors, critical cleavage and intergranular fracture stress, σ_u) which have to be discussed first. This is related to the fact that aging produces a variation in the concentration of impurities (C and P) segregated along the grain boundaries. It is well to remember that C atoms produce a strengthening effect of the grain boundaries while P atoms have an opposite effect [17].

It has been shown previously that the intergranular fracture stress decreases linearly with C_p^{gb} [18, 19] as soon as the grain boundary concentration in P is larger than about 10 at %. These results can be used to predict the variation of the fracture toughness with aging using the kinetics models developed in the preceding section.

The cleavage fracture stress is also dependent on the grain boundary composition as explained below. This effect is related to the crossing of grain boundaries by cleavage cracks, which has already been studied in some detail by Qiao [20, 21]. This crossing depends on the misorientation between two adjacent grains, as depictured in Fig. 5 where the tilt, ϕ, and the twist, ψ, components

between two grains are defined. The tilt component produces only a deviation of the crack front. The twist component produces a segmentation of the crack front and the formation of ridges, as observed in Fig. 6a and as schematically depictured in Fig. 6b. Complete crossing of the grain boundary by the cleavage crack in grain 1 necessitates in these conditions that the intergranular "triangles" are also broken. The = global? cleavage stress is thus also dependent on the local composition of the grain boundaries.

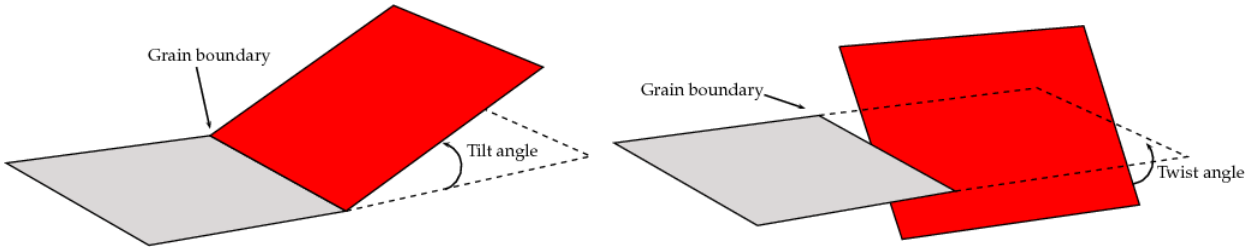

Figure 5. Notations for tilt and twist grain boundaries.

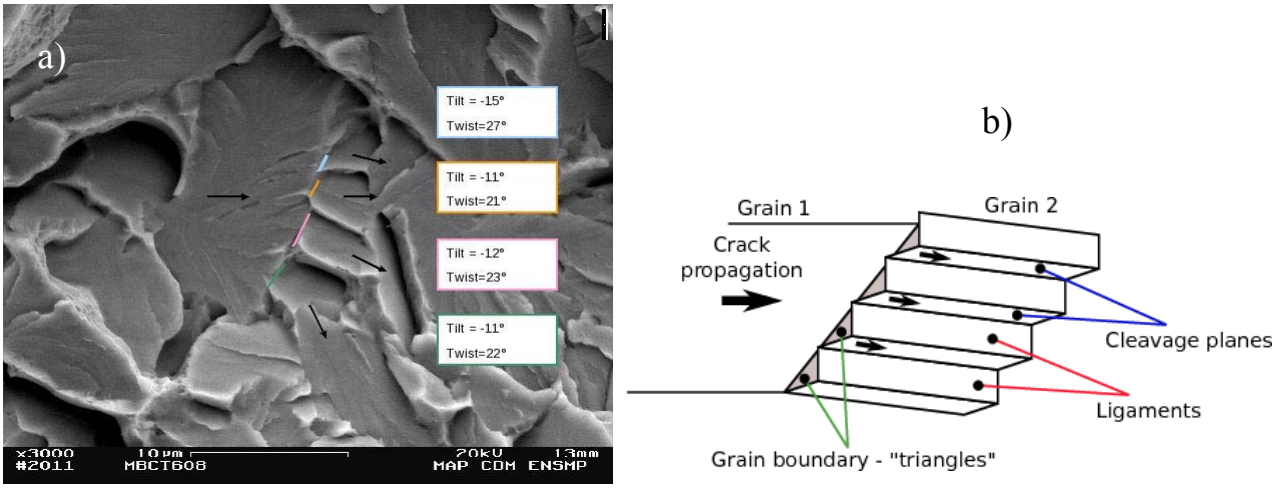

Figure 6. a) SEM observations showing the formation of bifurcations when a cleavage crack crosses a grain boundary. Four ridges are formed. The values of the tilt and twist angles determined by quantitative stereoscopy are given; b) Sketch.

A model was developed to analyze this phenomenon of crossing of twisted grain boundary cleavage cracks. It is out of the scope of the present paper to describe in detail this model which is schematically shown in Fig. 7. The grain boundary crossing process includes four steps. The cleavage crack in grain 1 is approaching the grain boundary in step 1. Cleavage microcracks are assumed to nucleate on (001) planes in grain 2 (step 2). These microcracks propagate in the second grain and break the "triangles" remaining along the grain boundary and which belong to the grain boundary itself (step 3). This generates a perturbed crack front which is still attached to the grain boundary by remaining ligaments. In step 4 the perturbed crack front propagates and leads to final fracture. The model is based on an energy balance between the driving energy corresponding to the strain energy release rate of the perturbed crack and the dissipated energy. This energy includes

three contributions: (i) the cleavage surface energy on the facets of the second grain, (ii) the intergranular energy of the "triangles", and (iii) the energy spent in breaking the remaining ligaments. This model predicts that the number of segmentations along a given grain boundary is an increasing function of ψ, as observed experimentally [10] and that the = global? cleavage stress is also increasing with ψ.

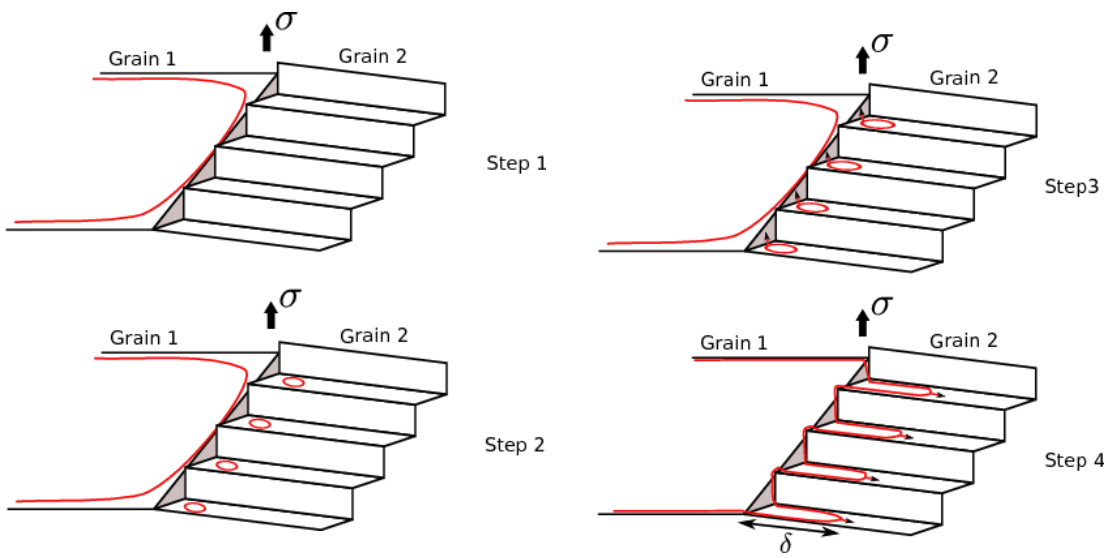

Figure 7. The four steps for a cleavage crack to cross a twisted grain boundary.

This model of grain boundary crossing has been used to identify the parameters introduced in the Beremin-type model for predicting the fracture toughness of inhomogeneous materials [2] in which two modes of failure (intergranular and cleavage) are competing. The results shown in Fig. 8 were obtained using V_o = (50 μm)^3, m_B = m_{SZ} = 30 (Weibull shape factors for base metal (B) and segregated zones (SZ)) in the as-received and aged conditions), f = 10 % (volume fraction of segregated zones). The critical stresses were taken as:

$$\sigma_u^B = 3300\,MPa\,(as-received),\ \sigma_u^B = 3230\,MPa\,(aged),$$
$$\sigma_u^{SZ} = 3250\,MPa\,(as-received),\ \sigma_u^{SZ} = 2750\,MPa\,(aged)$$

It is thus observed that aging produces a small decrease of the cleavage stress (by about 2%), due to the mechanism for cleavage described in Figs. 6 & 7, and a larger decrease of the intergranular fracture stress in the segregated zones (by about 15%)due to phosphorus intergranular segregation after aging. This value is in good agreement with the measurements carried out on homogeneous material representing the composition of the segregated zones [18].

Fig. 8 shows that the bimodal model for fracture is able to reproduce the observed variations in fracture toughness with temperature in both conditions (as-received and aged). This model accounts also reasonably well for the shift in DBTT with aging (~ 30°C at $K = 100\,MPa\sqrt{m}$ and P_r = 63 %). It accounts also for the increased scatter observed in test results on aged material. This model can also be used for predicting the variation of fracture toughness with longer aging times and lower

temperatures typical of those of in-service conditions.

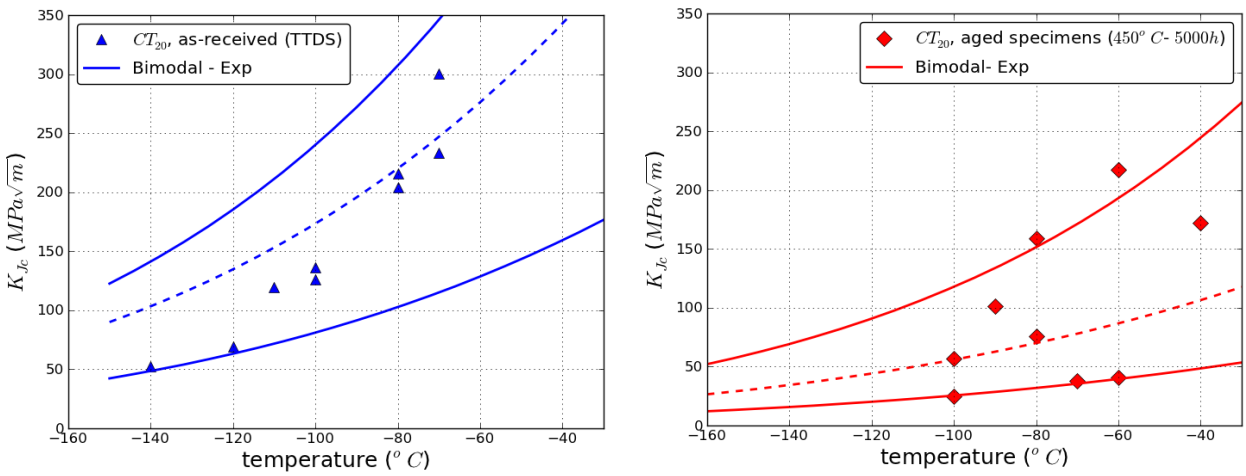

Figure 8. Variation of the fracture toughness with temperature. Experiments and predictions from Beremin-type bimodal model [2]. The calculated values corresponding to failure probabilities of 5%, 63% and 95% are shown.

6. Conclusions

1. Thermal aging of a 18MND5 plate (type A533B) at 450°C for 5000 hours produces a shift of the ductile-to-brittle transition temperature (DBTT) of about 39°C. This shift is not accompanied by a drastic change in fracture modes which remain partly intergranular in the segregated zones and transgranular cleavage in the matrix. The fracture toughness of aged material is much more scattered than that of the as-received material.
2. The slow cooling rate applied during cooling after the stress-relieving heat treatment (~ 30°C/h) generates intergranular phosphorus segregation which is sufficient to provoke intergranular fracture in the segregated zones, even in the as-received conditions.
3. Auger spectrometry measurements showed that during aging at 450°C, phosphorus continues to segregate along the grain boundaries, while carbon concentration at grain boundaries decreases. Both phenomena produce an embrittlement effect of the grain boundaries.
4. A model of intergranular segregation including the interaction between C and P atoms and non-isothermal conditions was identified. The results of this model were used as inputs for the prediction of bimodal fracture toughness of an inhomogeneous material representing the banded structure of the micro-segregated steel. The kinetics is represented using the McLean – Guttmann – Militzer theories.
5. The variations in DBTT and in the scatter of fracture toughness test results induced by aging are correctly predicted using these models of segregation and of fracture toughness.

Acknowledgments

This work has been made in the frame of the Areva - Ecole des Mines industrial professorship. Support from Areva is acknowledged. The authors would like to acknowledge also D. Loizon, S.

Cremel and O. Bouaziz from ArcelorMittal Research for Auger spectrometry measurements.

References

[1] C. Naudin, A. Pineau, J.- M. Frund, Numerical modeling of fracture toughness in RPV steel containing segregated zones in PVP 443-1, Fatigue, Fracture and Damage Analysis, ASME PVP 2002-1333, 2002, pp. 69-75.

[2] A. Andrieu, A. Pineau, J. Besson, D. Ryckelynck, O. Bouaziz, Bimodal Beremin-type model for brittle fracture of inhomogeneous ferritic steels: Theory and applications, Eng. Fract. Mech. 95, 2002, pp. 84-101.

[3] A. Pineau, Development of the local approach to fracture over the past 25 years: Theory and applications, Int. J. Fract. 138, 2006, pp. 139-166.

[4] F. M. Beremin, A local criterion for cleavage fracture of a nuclear pressure vessel steel, Metall. Mater. Trans. A14, 1983, pp. 2277-2287.

[5] A. Andrieu, A. Pineau, J. Besson, D. Ryckelynck, O. Bouaziz, Beremin model : Methodology and application to the prediction of the Euro toughness data set, Eng. Fract. Mech. 95, 2002, pp. 102-117.

[6] D. McLean, Grain boundaries in metals, Oxford University Press, London, 1957.

[7] M. Guttmann, Ph. Dumoulin, M. Wayman, The thermodynamics of interactive cosegregation of phosphorus and alloying elements in iron and temper-brittle steels, Met. Trans. 13A, 1982, pp. 1693-1711.

[8] K. Wallin, Fracture toughness of engineering materials, EMAS Publishing, Warrington, U.K., 2011.

[9] ASTM standards E1921-97, Standard test method for determination of reference temperature, T_o, for ferritic steels in the transition range, 1997, pp. 1068-1084.

[10] A. Andrieu, PhD thesis Ecole des Mines de Paris, 2013.

[11] P. Lejcek, Grain boundary segregation in metals, Springer Heidelberg, Dordrecht, London, New York, 2010.

[12] M. Militzer, J. Wieting, Theory of segregation kinetics in ternary systems, Acta Metall. 34, 1986, pp. 1229-1236.

[13] S. G. Druce, G. Gage, G. Jordan, Effect of ageing on properties of pressure vessel steels, Acta Metall. 34, 1986, pp. 641-652.

[14] C. A. Hippsley, S. G. Druce, The influence of phosphorus segregation to particle/matrix interfaces on ductile fracture in a high strength steel, Acta Metall. 31, 1983, pp. 1861-1872.

[15] K.H.D.H. Badeshia, R.W.K . Honeycombe, Steels – Microstructure and properties, 3rd edition, Butterworth-Hennemann, Oxford,UK, 2006.

[16] H. Erhart, H. J. Grabke, Equilibrium segregation of phosphorus at grain boundaries of Fe-P, Fe-C-P, Fe-Cr-P and Fe-Cr-C-P alloys, Metal Science 15, 1981, pp. 401-408.

[17] J. R. Rice, J.- S. Wang, Embrittlement of interfaces by solute segregation, Mater. Sci. Engng A107, 1989, pp. 23-40.

[18] C. Naudin, J.- M. Frund, A. Pineau, Intergranular fracture stress and phosphorous grain boundary segregation of a Mn-Ni-Mo steel, Scripta Mater. 40, 1999, pp. 1013-1019.

[19] R. Ding, A. Islam, S. Wu, J. Knott, Effect of phosphorus segregation on fracture properties of two quenched and tempered structural steels, Mater. Sci. and Tech. 21, 2005, pp. 467-475.

[20] Y. Qiao, A. S. Argon, Cleavage crack-growth resistance of grain boundaries in polycrystalline Fe-2% Si alloy: experiment and modeling, Mech. Materials 35, 2003, pp. 129-154.

[21] W. Lu, J. Chen, X. Kong, S. S. Chakravarthula, Y. Qiao, Non uniform cleavage across persistent grain boundary, Mech. Materials 43, 2011, pp. 567-573.

Hierarchical Damage Simulation to Correlate Micro-structural Characteristics of Steel with Ductile Crack Growth Resistance of Component

Mitsuru Ohata[1,*], Hiroto Shoji[1], Fumiyoshi Minami[1]

[1] Division of Materials and Manufacturing Science, Graduate School of Engineering,
Osaka University, 2-1 Yamada-Oka, Suita, Osaka 565-0871, JAPAN
* Corresponding author: ohata@mapse.eng.osaka-u.ac.jp

Abstract The final goal of this study is to develop a method for estimating the effect of micro-structural characteristics of steel (especially two-phase steel) on ductile crack growth resistance of a structural component. For this purpose, hierarchical approach to link the micro-structural characteristics of steel and ductile crack growth resistance curve of a component is proposed. First attention is paid to reveal mechanical properties that control ductile crack growth resistance curve (CTOD-R curve), so that the R-curve could be numerically predicted only from those properties. It is shown from the observation of a mechanism for ductile crack growth that two types of "ductile properties" of steel associated with ductile damage can mainly influence CTOD-R curve; one is a resistance of ductile crack initiation estimated with critical local strain for ductile cracking from the surface of notch root, and the other one is a stress triaxiality dependent ductility obtained with circumferentially notched round-bar specimens. The damage model for numerically simulating the R-curve is proposed taking these two "ductile properties" into account, where ductile crack initiation from crack-tip is in accordance with local strain criterion, and subsequent crack growth triaxiality dependent damage criterion. This macroscopic simulation can correlate the mechanical properties of steel with CTOD-R curve of a component. The second approach is to develop a simulation method to predict the effect of micro-structural characteristics of two-phase steel on the two types of ductile properties that were found to be ductile crack growth controlling mechanical properties. To simulate meso-scale ductile damage behaviors, 3D micro-structural FE-model is developed for analyzing the stress/strain localization behaviors by micro-structural strength mismatch and ductile damage model for reproducing damage evolution up to micro-void/micro-crack formation. This meso-scopic simulation can correlate micro-structural characteristics with mechanical properties of two-phase steel. Through the proposed hierarchical approaches, micro-structural morphology of two-phase steel to improve ductile crack growth resistance of a component can be discussed.

Keywords Damage model, 3D-simulation, Microstructure, Ductile crack growth resistance

1. Introduction

It is necessary to estimate ductile crack growth property of a steel structure for rational assessment of unstable fracture associated with ductile crack initiation and subsequent crack growth. Furthermore, from steel developing side, it should be required to provide a guideline for improving ductile crack growth resistance from *material properties* point of view. On the other hand, it is expected to improve resistance of ductile crack initiation and extension by controlling heterogeneous micro-structure of steel. However, no effective guideline in terms of material properties for improving resistance of ductile crack growth resistance of a cracked structural component has been necessarily established.

For this purpose, the target was focused on proposing a hierarchical approach to link the micro-structural characteristics of multi-phase steel and ductile crack growth resistance of a structural component, which consists of macroscopic approach and mesoscopic approach. Figure 1 describes this concept. The final goal of this study is to develop a numerical simulation method for estimating the effect of micro-structural characteristics of multi-phase steel on ductile crack growth resistance of a structural component.

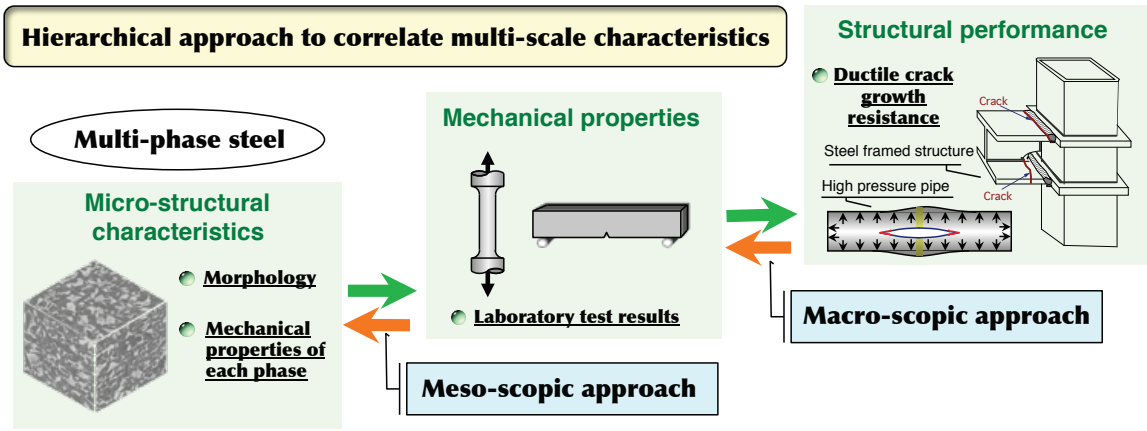

Figure 1. Concept for developing simulation method.

2. Simulation method for correlating ductile crack growth resistance with mechanical properties (Macroscopic approach)

First attention in this study, that is macroscopic approach, was paid to developing a simulation method for correlating ductile crack initiation and extension properties (CTOD-R curve) with mechanical properties that could be obtained by laboratory tests. One of the authors has already proposed the numerical simulation model [1]. The ductile crack initiation from crack-tip is in accordance with *local strain criterion* [1-4], and the subsequent crack extension *triaxiality dependent damage criterion* [1]. This model can predict a CTOD-R-curve only from two types of ductile properties and stress-strain curve of steel; one is a resistance of ductile crack initiation estimated with *critical local strain* for ductile cracking from the surface of notch root obtained with notched bend specimen, and the other one is a *stress triaxiality dependent ductility* obtained with circumferentially notched round-bar specimens. In this chapter, the applicability of this model to prediction of CTOD-R curve of a cracked component of high strength steel is demonstrated.

2.1. Mechanical properties controlling ductile crack growth resistance

The steels used in this study are steels A, B and C. The steels A and B have almost the same yield stress and work hardening, whereas the steel C has higher strength and lower work hardening as shown in Figure 1. Table 1 summarizes the strength properties of all the steels used.

Two types of the ductile properties, which are critical local strain and stress triaxiality dependent ductility, of all the steels that would control ductile crack growth resistance of cracked components were measured.

To measure a critical local strain $(\bar{\varepsilon}_p^{tip})_{cr}$, static 3-point bending tests were conducted using V-notched Charpy specimen. Typical shear mode ductile cracking was observed, which implies that the local strain criterion can be applicable to the steels used. By means of FE-analysis, a critical equivalent plastic strain $(\bar{\varepsilon}_p^{tip})_{cr}$ at crack-tip element was estimated. Another ductile property of the steels, that is stress triaxiality dependent critical local strain $(\bar{\varepsilon}_p)_{cr}$, was examined by conducting tensile test as well as FE-analysis for round-bar specimens with circumferential notch. $(\bar{\varepsilon}_p)_{cr}$ as a function of stress triaxiality were estimated on the middle of the notch-root section where ductile cracking occurred in experiments. The details of the method of experiments and FE-analysis are described in the literature [1]. Figure 2 summarizes the obtained two types of the *ductile properties*. The $(\bar{\varepsilon}_p^{tip})_{cr}$ and tress triaxiality dependent critical local strain $(\bar{\varepsilon}_p)_{cr}$ for the steel C are lower than those for steels A and B. From these results, ductile crack growth resistance for the steel C can be supposed to be the lowest.

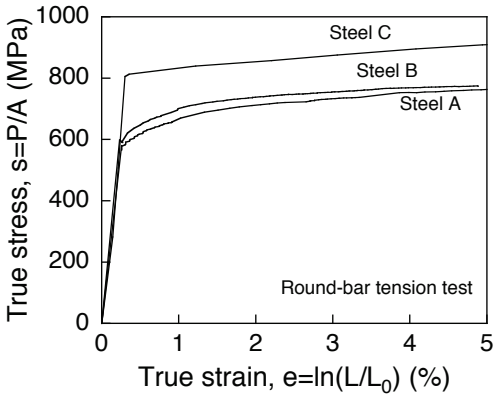

Figure 2. True stress-true strain curves for steels used.

Table 1. Mechanical properties of steels used.

	$\sigma_{0.2}$ (MPa)	σ_T (MPa)	YR	ε_T (%)
Steel A	620	721	0.86	8.5
Steel B	650	735	0.88	5.1
Steel C	829	879	0.94	5.8

$\sigma_{0.2}$: 0.2%proof stress, σ_T : Tensile strength,
ε_T : Uniform elongation (G.L.=32mm),
YR : Yield to tensile ratio (=$\sigma_{0.2}/\sigma_T$)

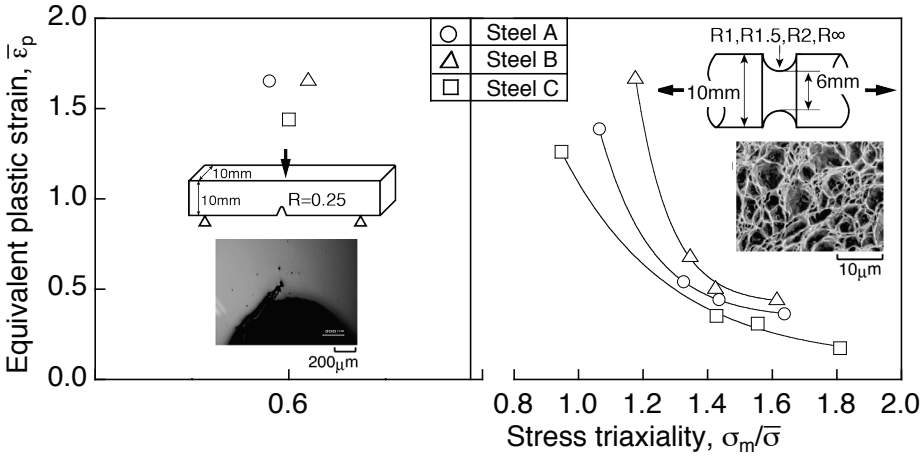

Figure 3. Ductile properties controlling ductile crack growth resistance for steels A, B and C.

2.2. Simulation based prediction of ductile crack growth resistance

2.2.1. Simulation model for ductile crack growth behavior [1]

The damage model for numerically simulating a ductile crack growth resistance, that is R-curve, has been proposed taking the two *ductile properties* of steel into account, where the ductile crack initiation from crack-tip is in accordance with *local strain criterion*, and the subsequent crack growth *triaxiality dependent damage criterion*. The details of the criteria are described in the literature [1]

The *local strain criterion* is applied only for predicting ductile crack initiation from tip of a crack-like defect. In the FE-model, a first element ahead of crack-tip losses a stiffness when an equivalent plastic strain at this element $\bar{\varepsilon}_p^{tip}$ attains to a critical local strain $(\bar{\varepsilon}_p^{tip})_{cr}$ of steel of interest.

The *triaxiality dependent damage criterion* is applied for simulating subsequent ductile crack extension. The proposed yield function, that is the plastic potential, as a function of the damage variable D^* is expressed in Eq. (1),

$$\Phi = \left(\frac{\bar{\Sigma}}{\bar{\sigma}}\right)^2 + a_1 D^* \exp\left(a_2 \frac{\Sigma_m}{\bar{\sigma}}\right) - 1 = 0 \tag{1}$$

where $\bar{\Sigma}$ and Σ_m are macroscopic equivalent stress and hydrostatic stress of the unit cell, respectively, and $\bar{\sigma}$ is flow stress of a matrix material. This yield function, which is based on a

void growth model that was originally proposed by Gurson [6], was derived so that the relation between the critical strain $(\bar{E}_{\mathrm{p}})_{\mathrm{i}}$ for micro-voids formation and the stress triaxiality can be in accordance with an exponential function as expressed in Eq. (2).

$$(\bar{E}_{\mathrm{p}})_{\mathrm{i}} = A\exp\left(B\frac{\Sigma_m}{\bar{\Sigma}}\bigg|_{\mathrm{const.}}\right), \quad \begin{cases} A = \dfrac{2}{a_1 a_2}\ln\dfrac{(1-D_0)D_{\mathrm{c}}}{(1-D_{\mathrm{c}})D_0} \\ B = -a_2 \end{cases} \tag{2}$$

Therefore, the material parameters a_1 and a_2 can be identified only from the stress triaxiality dependent ductility of steel. The $(\bar{E}_{\mathrm{p}})_{\mathrm{i}}$ is generally set to be 80% of ductile cracking strain $(\bar{\varepsilon}_{\mathrm{p}})_{\mathrm{cr}}$ for the steel which exhibits mico-voids nucleation controlled ductile failure behavior.

2.2.2. Simulation of ductile crack growth resistance of a cracked component.

In the light of two types of ductility of each steel presented in Fig. 3, critical local strain $(\bar{\varepsilon}_{\mathrm{p}}^{\mathrm{tip}})_{\mathrm{cr}}$ and damage parameters a_1 and a_2 were identified. Table 2 summarizes these parameters for all the steels used: D_0, D_{c} and K are fixed as 0.0001, 0.001 and 4, respectively.

Table 2. Materials parameters used for simulation.

	Initiation	Extension				
	Critical local strain	Damage process based variables			Ductility based variables	
		D_0	D_c	K	a_1	a_2
Steel A	1.6	0.0001	0.001	4	1.54	1.28
Steel B	1.6				0.66	1.59
Steel C	1.4				0.72	1.78

Figure 4 exhibits a FE-model of 3-point bend specimen with a deep crack (a_0/W=0.5) used for simulation, which has the same configuration and size as used in experiments. The simulated ductile crack growth resistance curves, that are CTOD-R curve, were compared with experimental results. As shown in Fig. 5, it was demonstrated that the proposed simulation method could predict CTOD-R curve of the cracked 3PB specimen with high accuracy even for the high strength steel C.

Consequently, by means of the proposed simulation method, a ductile crack growth resistance of a cracked component can be quantitatively correlated with the mechanical properties obtained by laboratory tests.

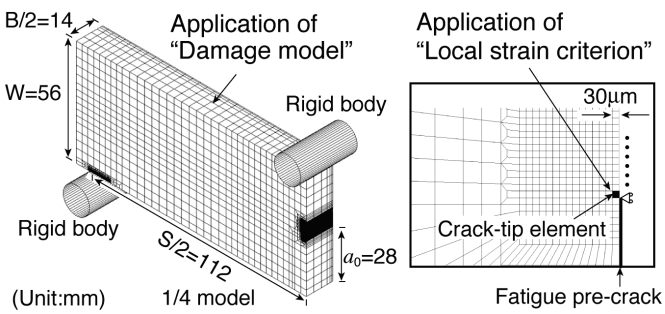

Figure 4. FE-mesh division and simulation model.

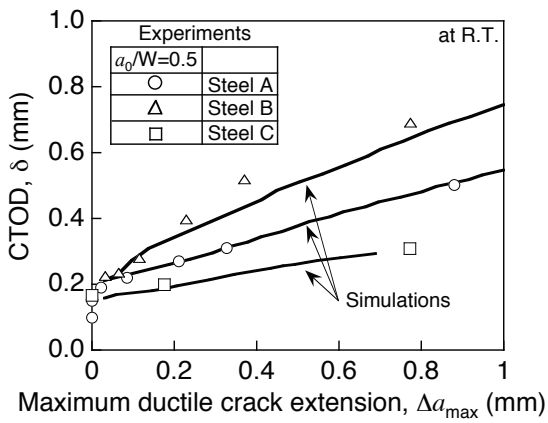

Figure 5. Comparison between CTOD-R curves obtained by experiment and simulation for steels A, B and C.

3. Simulation method for correlating micro-structural characteristics with mechanical properties of two-phase steel (Mesoscopic approach)

Second effort is to develop the mesoscopic method for correlating micro-structural characteristics with mechanical properties of two-phase steel, for instances Ferrite-Pearlite, Ferrite-Bainite, Ferrite-Martensite steel and so on. The authors have proposed a simulation method for predicting the effect of micro-structural morphology on ductile cracking for two-phase structural steel on the basis of micro-mechanism for ductile cracking through the following developments [3-5]: one is a meso-scale 3D micro-structural FE-model that enables the analysis of stress/strain localization behaviors dependent on the morphology of two phases with strength heterogeneity in real steel, another is a damage evolution and subsequent micro-void nucleation model. This model is expected to be able to predict the two ductile properties, which was found in the macroscopic approach to be the mechanical properties controlling CTOD-R curve, as well as stress-strain curves. In this chapter, it is demonstrated that the proposed model could simulate ductile cracking behaviors associated with heterogeneous micro-structure of two-phase, Ferrite-Pearlite, steel. Then, the effect of morphology of micro-structure of two-phase steel on two ductile properties, which are the *critical local strain* and the *stress triaxiality dependent ductility*, is analyzed.

3.1. Ductile cracking behaviors of two-phase steel with heterogeneous micro-structure

The structural steel JIS SM490YB with Ferrite-Pearlite two phases (F-P steel) was used. The hardness of Pearlite phase is about 1.4 times larger than Ferrite phase. Volume fraction of Pearlite phase is about 30 %, the average grain size is about 25 μm.

Table 2. Mechanical properties of SM490YB steel used.

σ_Y (MPa)	σ_T (MPa)	YR (%)	ε_T (%)	El. (%)	Hv	
					Ferrite	Pearlite
344	540	64	17.6	31	198	276

σ_Y : Lower yield stress, σ_T : Tensile strength, YR : Yield to tensile ratio $=\sigma_Y/\sigma_T$, ε_T : Uniform elongation
El. : Elongation(G.L. = 36 mm, Dia. = 6 mm), Hv : Average Vickers hardness (Load : 25 gf)

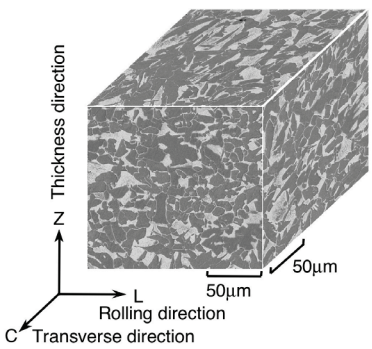

Figure 6. Microstructures of SM490YB steel used.

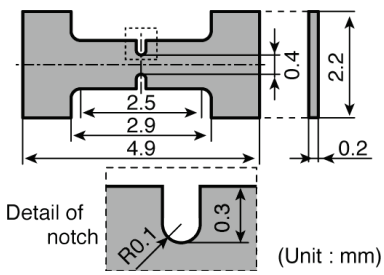

Figure 7. Configuration of notched micro-tensile specimen used.

The specimen for observing ductile cracking behaviors is flat micro-tensile specimen with side notches, as shown in Fig. 7. Figure 8 presents load *P* and displacement *u* curves obtained by tensile testing for three specimens. The specimens were unloaded at levels 1 and 2, and observed damage evolution up to failure. The ductile cracks generated from not only notch-root surface but also middle of net section, that is inside of the specimen, were observed at loading level 2, as shown in Fig. 9. These micro-cracks seem to mainly nucleate at Ferrite side with lower hardness near Ferrite-Pearlite boundary. This implied ductile damage was localized by stress/strain

concentration that would be due to micro-structural strength mimatch. The other important point to be notice is that no large voids associated with non-metallic inclusions were found after large amount of plastic straining, as is observed in the cross section at loading level 1.

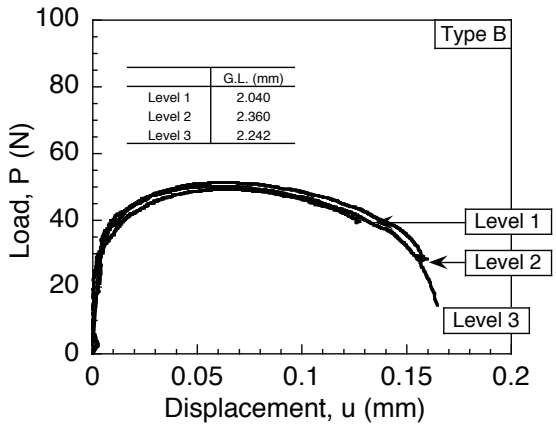

Figure 8. Load - displacement curves obtained by tensile tests for micro-tensile specimen with side notches.

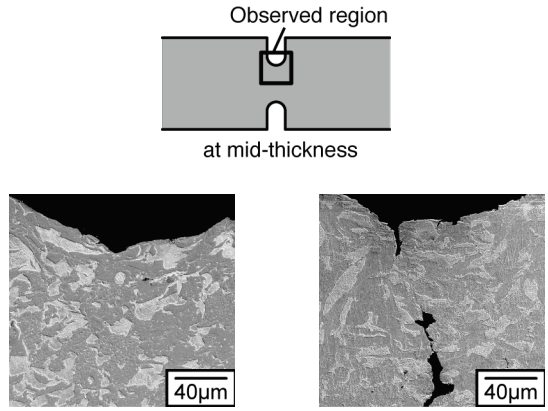

(a) Level 1 (b) Level 2

Figure 9. Ductile damage evolution in notched micro-tensile specimen.

3.2. Simulation method of ductile cracking behavior associated with heterogeneous micro-structure

In order to simulate ductile cracking behaviors associated with heterogeneous micro-structure of two-phase steel, ductile damage simulation method was proposed [5]. Figure 10 shows the conceptual illustration of this method. According to this method, ductile cracking behaviors of two-phase steel can be predicted from the following characteristics of constituent phase by using 3D micro-structural model; one is two kinds of mechanical properties i.e., strength property and damage property. The former is stress-strain curve, and the later is stress triaxiality dependent ductility. Another one is morphology of micro-structure of steel, for instances size and aspect ratio of grain size, volume fraction of second phase, connectivity of matrix phase and so on. In this method, the same numerical damage model as that used in the macroscopic approach is applied.

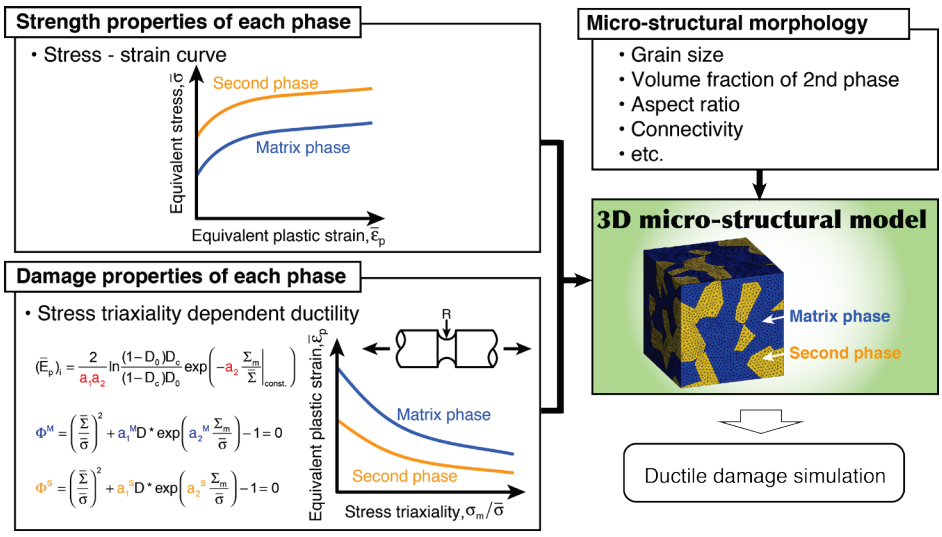

Figure 10. Conceptual illustration of the mesoscopic simulation method.

A simulation model of the micro-tensile specimen that has the same configuration of that used in the experiment is shown in Fig. 11. 3D micro-structural model is employed only around the net

section. The two-phase polycrystalline model has totally 187 grains and volume fraction of hard Pearlite phase of about 30%. Average grain size is about 25μm, and element size 5μm.

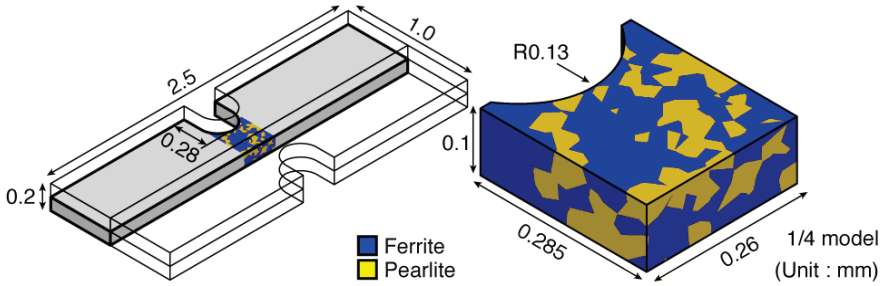

Figure 11. Meso-scale 3D FE-model of flat micro-tensile specimen with side notches.

The mechanical properties needed for the proposed simulation can be identified from testing for full Ferrite and full Pearlite steels having the same morphological and metallurgical properties as those of each phase in F-P steel used. However, in this work, some assumptions were employed for identifying those properties. As for the stress-strain curves of Ferrite and Pearlite phases, they were estimated in accordance with a rule of mixture from stress-strain curve of two-phase steel used [5]. Figure 12(a) shows the equivalent stress $\bar{\sigma}$ – equivalent plastic strain $\bar{\varepsilon}_p$ curves for the Ferrite and Pearlite phase along with that obtained by tension test for F-P steel used. The damage parameters for the each phase can be obtained by conducting tension tests for round-bar specimens with/without circumferential notches in accordance with the proposed procedure (section 2.2). However, these parameters were determined based on the stress triaxiality dependent ductility for the F-P steel as presented in Fig. 12(b). The properties for the Ferrite phase were identified by reverse analysis so that the stress triaxiality dependent ductility for the F-P steel might be reproduced by simulation using a 3D micro-structural model (see Fig. 15(b)). As for the Pearlite phase, the same properties as those for F-P steel were used, because no significant effect of those parameters on simulated result was found in this case.

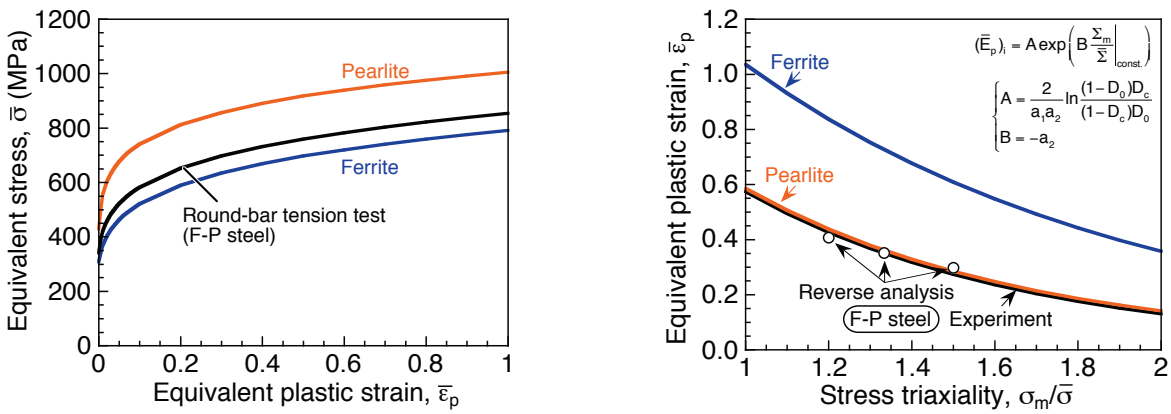

(a) Stress-strain curve (b) Stress triaxiality dependent ductility

Figure 12. Mechanical properties of constituent phases of F-P steel needed for damage simulation.

Figure 13 shows *P–u* curves obtained by experiment and simulation. The simulation reproduces critical tensile displacement where load drop due to ductile cracking occurred. Ductile damage evolution behaviors from notch root surface and middle of the specimen obtained by simulation are well consistent with experimental results, and damage localization in Ferrite phase near Ferrite/Pearlite boundary is well simulated as shown in Fig. 14.

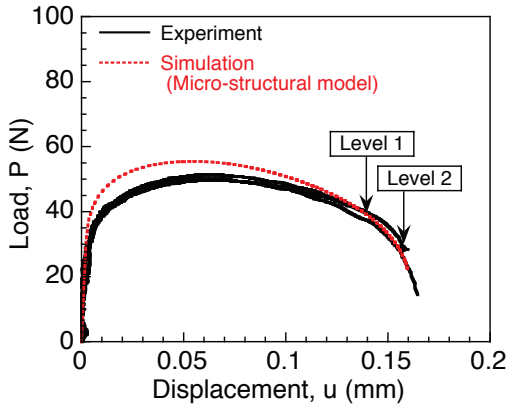

Figure 13. Load - displacement curves obtained by experiment and simulation for notched micro-tensile specimen.

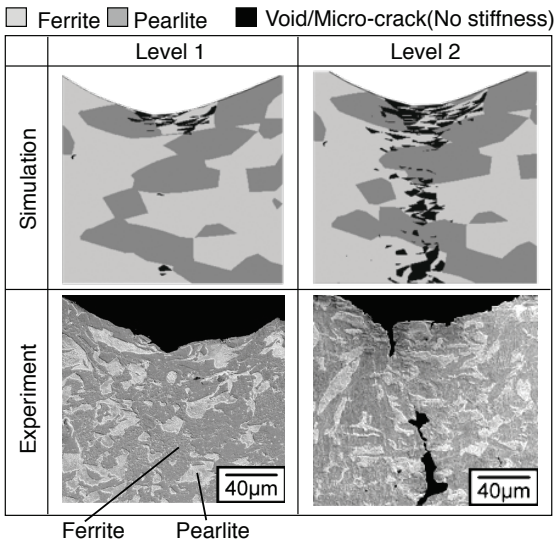

Figure 14. Comparison between simulated and observed ductile damage evolution for notched micro-tensile specimen.

3.3 Effect of micro-structural morphology on mechanical properties

It is demonstrated that the developed simulation model can well simulate ductile cracking behaviors regardless of surface or inside of a specimen, namely regardless of global triaxial stress conditions. Therefore, effect of micro-structural characteristics of two-phase steel on the macro-scopic ductile properties i.e., critical local strain and stress triaxiality dependent ductility which were found to control ductile crack growth resistance of a cracked component could be expected to be able to predict on the basis of the meso-scopic simulation method.

Simulation model to estimate those macro-scopic ductility are proposed as given in Figure 15; (a) is 3-point bend specimen with sharp crack for critical local strain and (b) is tensile RVE (Representative Volume Element) under constant stress triaxiality for stress triaxiality dependent ductility, which controls macro-scopic ductile crack initiation and extension, respectively.

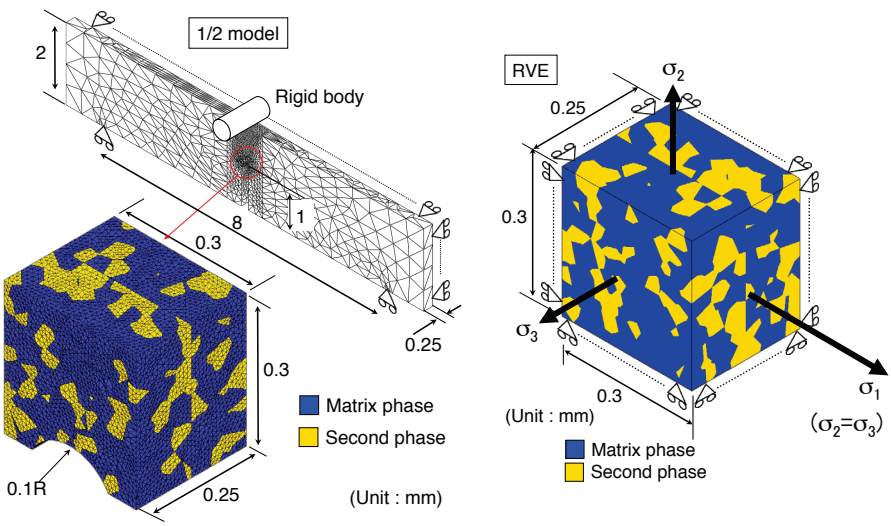

(a) For critical local strain

(b) For stress triaxiality dependent ductility

Figure 15. Models for simulating the effect of micro-structural characteristics of two-phase steel on ductility.

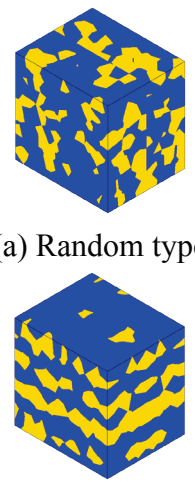

(a) Random type

(b) Layered type

Figure 16. Type of morphology of micro-structure

As a case study, effect of second phase (harder phase) distribution of two-phase steel is estimated using a random type and layered type morphology as presented in Fig. 16. Both types have the same volume fraction of the second phase of 30%, and the same average grain size of 25μm. The matrix and second phases are assumed to be Ferrite and Pearlite, respectively, and the mechanical properties given in Fig. 12 are used for damage simulation.

Results of simulated damage evolution are presented in Fig. 17. Critical global deformation for ductile cracking from notch root surface, which is defined as Vg where ductile crack growth Δa reaches 50μm, can be obtained from the 3-point bending simulation (Fig. 17(a)). Then, in contrast to the FE-analytical results for homogeneous material model of the 3PB specimen, macro-scopic critical local strain $(\bar{\varepsilon}_p^{tip})_{cr}$ can be estimated. Figure 17(b) gives evolution of damage fraction D of RVE as a function of macro-scopic equivalent plastic strain $\bar{E}_p$. The stress triaxiality dependent ductility that is defined as $\bar{E}_p$ where D reaches 0.001 ($=D_c$) can be estimated.

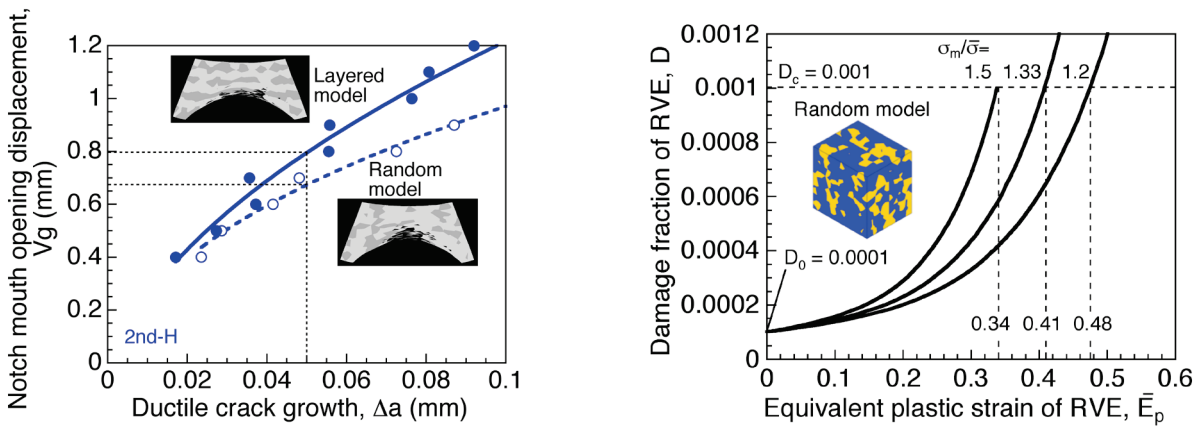

(a) For critical local strain (b) For stress triaxiality dependent ductility

Figure 17. Damage simulation to estimate the effect of micro-structural morphology of two-phase steel on macro-scopic ductility.

Figure 18 summarizes the estimated macro-scopic critical local strain $(\bar{\varepsilon}_p^{tip})_{cr}$ and stress triaxiality dependent ductility for the random and layered type morphology of F-P steel. It was predicted that the layered type morphology provided larger macro-scopic ductility than the random type morphology as long as a volume fraction of second phase were the same. Therefore, the layered type morphology could enlarge ductile crack growth resistance of a cracked structural component.

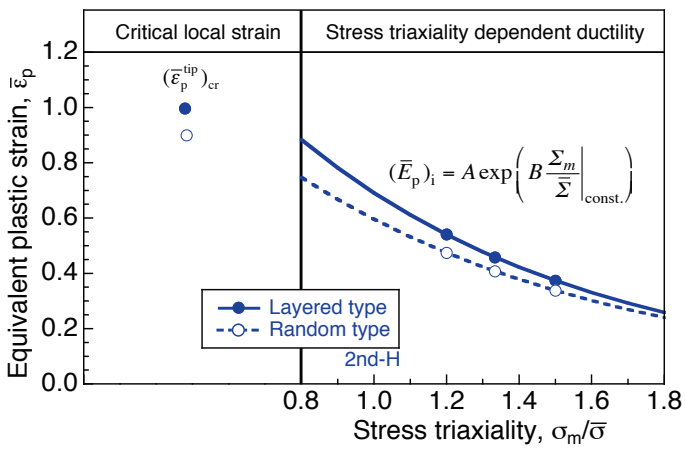

Figure 18. Effect of micro-structural morphology of two-phase steel on macro-scopic ductility simulated on the basis of the proposed meso-scopic approach.

4. Conclusions

In this work, hierarchical approach to link the micro-structural characteristics of multi-phase steel and ductile crack growth resistance of a structural component was proposed (see. Fig. 19). This approach consists of *macro-scopic approach* and *meso-scopic approach*. The macro-scopic approach can provide a guideline to control mechanical properties for improving ductile crack growth resistance of a cracked structural component. And the meso-scopic approach can correlate micro-structural characteristics with mechanical properties of two-phase steel. Through the proposed hierarchical approach, micro-structural characteristics of two-phase steel to improve ductile crack growth resistance of a structural component can be discussed, however further verification works should be conducted.

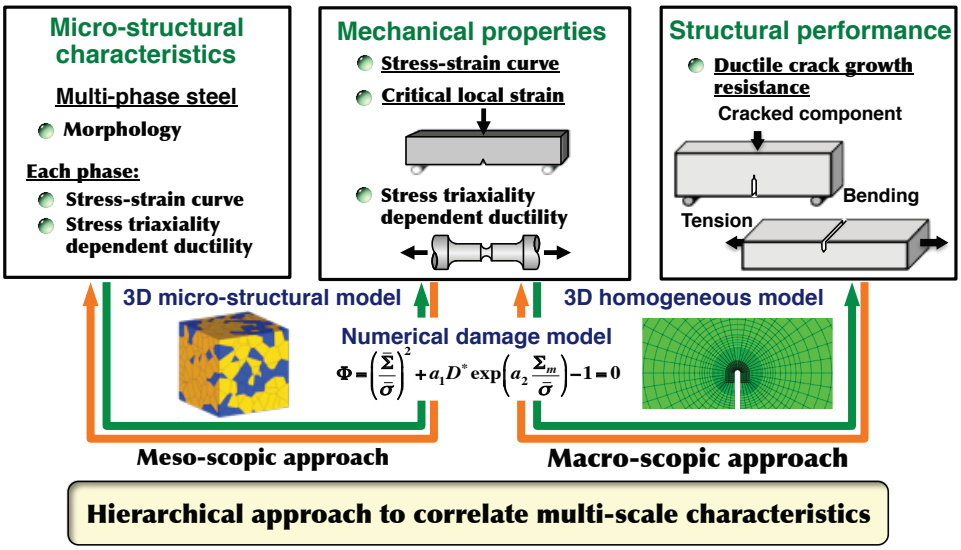

Figure 19. Hierarchical approach to correlate multi-scale characteristics i.e., micro-structural characteristics, mechanical properties and structural performance.

References

[1] M. Ohata, T. Fukahori and F. Minami, Damage Model for Predicting the Effect of Steel Properties on Ductile Crack Growth Resistance, International Journal of Damage Mechanics, 19 (2010) 441-459.

[2] M. Ohata, M. Toyoda and G-B, An, Effect of Strength Mismatch on Ductile Crack Initiation Behavior from Notch Root, Welding in the World, 48, N°11/12 (2004) 9-13.

[3] M. Ohata and M. Toyoda, Damage Concept for Evaluating Ductile Cracking of Steel Structure Subjected to Large-Scale Cyclic Straining, Science and Technology of Advanced Materials, 5 (2004) 241-249.

[4] M. Ohata and M. Toyoda, Damage Mechanism for Controlling Ductile Cracking of Structural Steel with Heterogeneous Microstructure, Materials Science Forum, 512 (2006) 31-36.

[5] M. Ohata, M. Suzuki, A. Ui and F. Minami, 3D-Simulation of Ductile Cracking in Two-Phase Structural Steel with Heterogeneous Microstructure, Engineering Fracture Mechanics, 77, 2 (2010) 277-284.

[6] A.L. Gurson, Continuum Theory of Ductile Rupture by Void Nucleation and Growth: Part I - Yield Criteria and Flow Rules for Porous Ductile Media, Journal of Engineering Materials and Technology, 99 (1977) 2-15.

Integrated Damage Mechanics Approach to Brittle and Ductile Crack Propagation

Geralf Hütter[1,*], **Thomas Linse**[2], **Uwe Mühlich**[1], **Meinhard Kuna**[1]

[1] Institute of Mechanics and Fluid Dynamics, TU Bergakademie Freiberg, 09596 Freiberg, Germany
[2] Institute of Solid Mechanics, TU Dresden, 01062 Dresden, Germany
* Corresponding author: Geralf.Huetter@imfd.tu-freiberg.de

Abstract With decreasing temperature the failure of typical engineering metals changes from ductile fracture to cleavage. A possible cleavage initiation in the brittle-ductile transition region is typically evaluated by stress-based criteria like those after Ritchie-Knott-Rice or of Weibull-type. Such models describe the experimental results adequately in the lower brittle-ductile transition region but problems arise in the upper part of the transition region.
In the present study cleavage is modeled by a cohesive zone and ductile damage is described by a non-local Gurson-model. With this modeling of both failure mechanisms the fracture initiation and propagation can be simulated in the whole brittle transition region. The results show that the crack tip constraint has a considerable influence on the stability of the crack propagation.
Keywords fracture mechanics, brittle-ductile transition, non-local Gurson model, FEM simulation

1. Introduction

In the range of room temperature typical engineering metals fail by a ductile mechanism. Thereby, the voids nucleated at non-metallic inclusions grow and coalesce finally to a macroscopic crack. Due to the plastic deformations much energy is dissipated with this mechanism leading to a high macroscopic fracture toughness. In contrast, at low temperatures fracture by cleavage occurs at favorably oriented crystallographic planes in the particular grains. With this mechanism considerably less energy is dissipated compared to the ductile mechanism which is why the macroscopic material behavior is termed as brittle. In the ductile-brittle transition region both mechanisms are observed, see Fig. 1. In this regime a large scatter of the fracture toughness values is observed for specimens of nominally identical material. This behavior is caused by the strong sensitivity to local material imperfections.

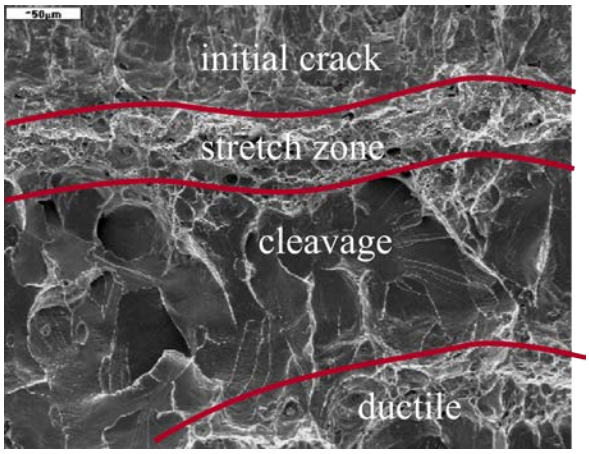

Fig. 1: Ductile-brittle fracture surface [1]

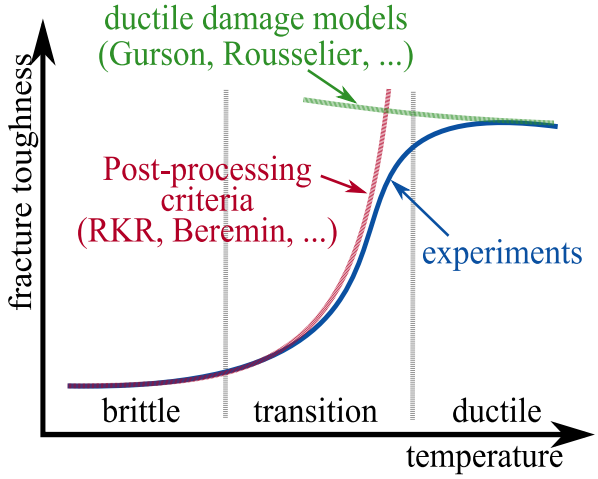

Fig. 2: Models for brittle-ductile transition

Due to the relevance in engineering applications numerous approaches were developed to describe the behavior in the ductile-brittle transition region. Mostly, the ductile mechanism is incorporated

by damage models like those after Gurson or Rousselier or modifications thereof. With such models all stages of crack initiation and propagation can be simulated. In contrast, cleavage is typically associated with unstable crack propagation. For this reason a possible cleavage initiation is usually evaluated by stress-based criteria like those after Ritchie-Knott-Rice (RKR) [2] or Beremin [3]. Especially the Beremin model and its numerous modifications enjoy great popularity as those models are probabilistic and the prediction of failure probabilities corresponds to the experimentally observed large scatter of measured fracture toughness values. The failure probabilities rely on the so-called weakest-link theory where the failure of an element is assumed to coincide with the failure of the complete structure.
Comparisons with experiments show that models of Beremin-type allow realistic predictions in the lower ductile-brittle transition region. However, problems arise in the upper ductile-brittle transition region even if the ductile crack propagation is incorporated as sketched in Fig. 2. Furthermore, the weakest-link theory predicts a vanishing survival probability of very large specimens at arbitrary small loadings. Anderson, Stienstra and Dodds [4] argue that this prediction is physically questionable since some work is always necessary to separate the crystallographic planes. Experiments confirm the existence of a corresponding lower-bound fracture toughness, see e.g. [5]. The problem of models of Beremin-type is the identification of cleavage initiation with immediate unstable crack propagation since the stability of crack propagation is in general a matter of the interaction of material properties, specimen type, specimen size and loading.
In the present study cleavage is modeled by a cohesive zone and ductile damage is described by a non-local Gurson-model. With this modeling of both failure mechanisms the fracture initiation and propagation can be simulated in the whole brittle transition region. The stability is an outcome of the simulations.

2. Model

Concretely, cleavage is modeled by a so-called cohesive zone. In a model of this kind it is assumed that the normal stress $\sigma(x)$ transmitted at each point x in the process zone depends on the local separation $\delta(x)$ of the crack edges as sketched in Fig. 3. The particular relation between σ and δ is described by the cohesive law. In the present study the exponential law after Xu and Needleman [6] is employed. The maximum transmittable stress σ_c is termed as cohesive strength. The area Γ_0 is the work of separation and corresponds to the work which is necessary for the formation of new surfaces. Correspondingly, Γ_0 has the unit of work per area.

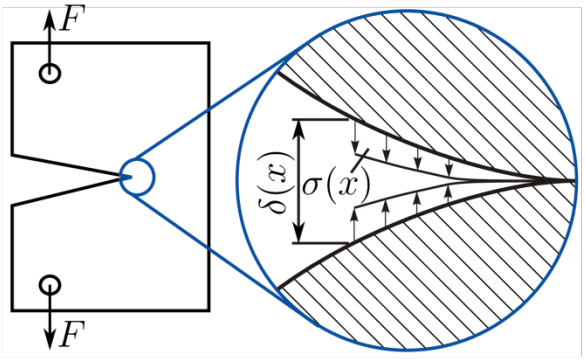

Fig. 3: Cohesive zone at the crack tip

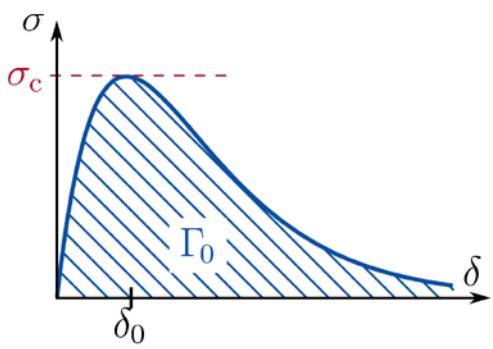

Fig. 4: Exponential cohesive law

Modeling cleavage by means of a cohesive zone captures phenomenologically two essential

experimentally observed issues. Firstly, the softening initiates (in the considered case of mode-I loading) if the maximum principal stress in the ligament reaches the value σ_c. Secondly, Γ_0 is the minimum work necessary for the formation of free surface in absence of plastic deformations and corresponds thus to the lower-bound fracture toughness. In finite-element models implementing a cohesive zone, the results are expected to converge with an increasing mesh resolution.

In the bulk material embedding the cohesive zone the ductile damage mechanism is described by the Gurson-model [7] in the established modification by Tvergaard und Needleman [8] (GTN-model). However, from this approach (and all other classical damage models) it is known that the results depend strongly on the element size and orientation. But for a consistent numerical implementation of the cohesive zone the stresses around the crack tip need to be resolved very fine. In order to overcome this problem the non-local extension of the GTN-model by Linse et al. [9] is employed for the following simulations. In classical constitutive theories the softening at a material point depends only on the internal state variables at this point. Within a non-local approach a region of finite size around the particular material point is incorporated for the softening. The dimension of this region is associated with a relevant microstructural length of the damage mechanism, for the ductile mechanism thus to the mean distance of the voids.

Concretely, in the non-local modification by Linse et al. the flow potential

$$\Phi = \frac{\sigma_{\mathrm{eq}}^2}{\sigma_{\mathrm{M}}^2} + 2q_1 f^* \cosh\left(\frac{3q_2}{2}\cdot\frac{\sigma_{\mathrm{h}}}{\sigma_{\mathrm{M}}}\right) - 1 - \left(q_1 f^*\right)^2 \tag{1}$$

of the original GTN-model is retained. Therein, σ_{eq} and σ_{h} denote the Mises stress and the hydrostatic stress, σ_{M} is the equivalent yield stress of the matrix material and q_1 and q_2 are the fitting parameters after Tvergaard und Needleman. In the following the established values q_1=1.5 and q_2=1 are assigned. In the initial stage the effective void volume fraction f^* corresponds to the actual value f. In the stage of void coalescence which initiates at $f = f_c$, the effective value f^* increases faster than f by the factor K:

$$f^* = \begin{cases} f & f \le f_{\mathrm{c}} \\ f_{\mathrm{c}} + (f - f_{\mathrm{c}})K & f_{\mathrm{c}} < f \le f_{\mathrm{f}} \end{cases} \quad \text{with} \quad K = \frac{f_{\mathrm{u}} - f_{\mathrm{c}}}{f_{\mathrm{f}} - f_{\mathrm{c}}}, \quad f_{\mathrm{u}} = \frac{1}{q_1} \tag{2}$$

At $f = f_f$ (corresponding to $f^*=f_u$) the material has lost its load carrying capacity completely. The non-local modification concerns the evolution law of f. In contrast to the classical GTN-model the non-local plastic volumetric strain $\varepsilon_{\mathrm{nl}}$ is used in this law:

$$\dot{f} = (1 - f)\dot{\varepsilon}_{\mathrm{nl}} + \dot{f}_{\mathrm{N}} \tag{3}$$

The nucleation term f_N is not considered in the following for simplicity, but all voids are assumed to be initially present and are thus captured with the initial void volume fraction f_0. The non-local plastic volumetric strain $\varepsilon_{\mathrm{nl}}$ is defined in a so-called implicit-gradient formulation by an additional partial differential equation of Helmholtz-type

$$\varepsilon_{\mathrm{nl}} + l_{\mathrm{nl}}^2 \Delta\varepsilon_{\mathrm{nl}} = \varepsilon_v \tag{4}$$

wherein the local volumetric plastic strain ε_v forms the source term. A region around the current material point is incorporated through the Laplace-operator Δ. The intrinsic length scale l_{nl} enters as

the weighting prefactor of the Laplace-operator. Regarding the boundary conditions necessary in addition to the Helmholtz-equation the reader is referred to [9,10]. A one-parametric power-law is implemented for the matrix yield stress σ_M in such a way that in a uniaxial tension test with the compact material f=0 a relation

$$\sigma = \sigma_y \left(\frac{E\varepsilon}{\sigma_y} \right)^N \tag{5}$$

between true stress σ and logarithmic strain ε is obtained. Therein, E denotes Young's modulus and σ_y and N are the initial yield stress and the hardening exponent, respectively. The following simulations are performed with σ_y/E=0.003 and N=0.1 and a Poisson ratio of ν=0.3 corresponding to typical medium strength engineering alloys (e.g. E=210 GPa, σ_y=500…700 MPa). The initial void volume fraction is assumed to be f_0=0.01. The work of separation is taken as Γ_0=1/3 $\sigma_y l_{nl}$ which is realistic for the material which will be considered finally for a comparison between simulations and experiments.

Due to the non-local formulation the boundary-value problem is well-posed also in the case of ductile softening. Thus, the combined model of cohesive zone and non-local GTN-model leads to a mesh-independent solution in the complete temperature range. Correspondingly, the local field quantities in the process zone are determined only through the material parameters and the loading. In particular, the size of the process zone is defined by the material parameters of unit length. For ductile failure this is the non-local length l_{nl} whereas for cleavage the size of the process zone is related to the characteristic cohesive separation δ_0 which is necessary to reach the cohesive strength σ_c. For the employed cohesive law this value amounts to $\delta_0=\Gamma_0/(\sigma_c \exp(1))$, compare Fig. 4. For the simulation of the crack propagation by means of the finite element method (FEM) the fields in the process zone need to be resolved sufficiently fine. For realistic values, δ_0 is always smaller than l_{nl} so that the maximum feasible element size is determined by δ_0. According to a performed convergence study elements of edge length b_e=1.2 δ_0…1.8 δ_0 are placed at the ligament. A typical mesh at the crack tip is depicted in Fig. 5. Only a half-model needs to be meshed for symmetry reasons. The cohesive elements do not have a geometric thickness and are thus only sketched in the figure.

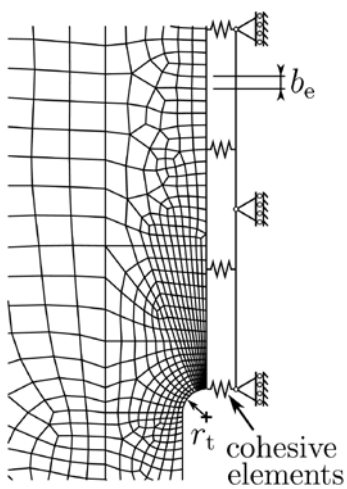

Fig. 5: FE-mesh at the crack tip

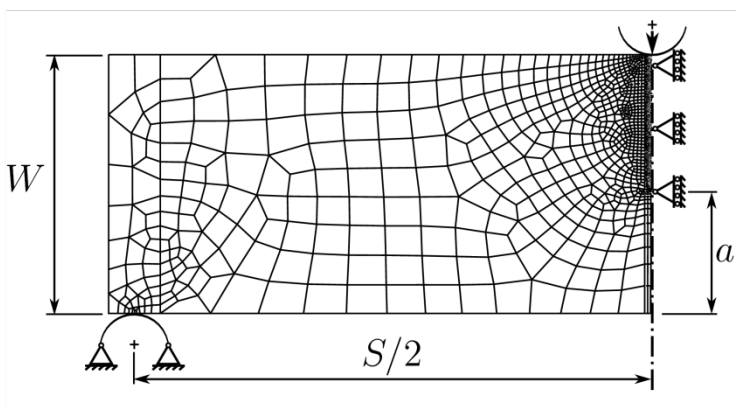

Fig. 6: FE-mesh for 3PB specimen

Realistically, an initial stage of crack tip blunting is expected to occur with the non-local GTN-model before the fracture initiation [9,10]. In order to handle the associated strain singularity an initial radius r_t is introduced in the FE-model. The radius r_t has to be small compared to l_{nl} preventing an inadmissible perturbance of the solution. The mesh in Fig. 5 fulfills this requirement.
For the computations the commercial FE-code Abaqus/standard is employed. Dynamic simulations are performed with implicit time integration under plane-strain conditions. The loading is applied quasi-statically. The elements for non-local GTN-model and the cohesive elements are both implemented with quadratic shape functions as user-defined elements via the UEL-interface. The crack propagation is simulated in the following for a three-point bending specimen (Fig. 6) or under a K_I-dominated far-field (boundary-layer model, see [10]).

3. Results

First, the influence of the cohesive strength σ_c is investigated. In order to exclude possible effects of the geometry of a particular specimen, the limit case of a K_I-dominated far-field is considered. A dimensional analysis shows that under these conditions the ratio of σ_c and initial yield stress σ_y is the only relevant parameter. In metals σ_y increases with decreasing temperature. If σ_c is assumed to be independent of the temperature, σ_c/σ_y increases with increasing temperature.
Computed crack growth resistance curves (R-curves) are shown in Fig. 7 for several values of σ_c/σ_y. In addition, the active damage mechanism is marked. It has to be noticed that the crack growth resistance J_R is normalized with respect to the yield stress σ_y and the non-local length l_{nl}. The amount of crack growth Δa is normalized by l_{nl} as well. The results show that the crack growth resistance increases with the ratio σ_c/σ_y, i.e. with increasing temperature. For σ_c/σ_y=2.6 the crack growth resistance is determined by the work of separations Γ_0. In the lower ductile-brittle transition

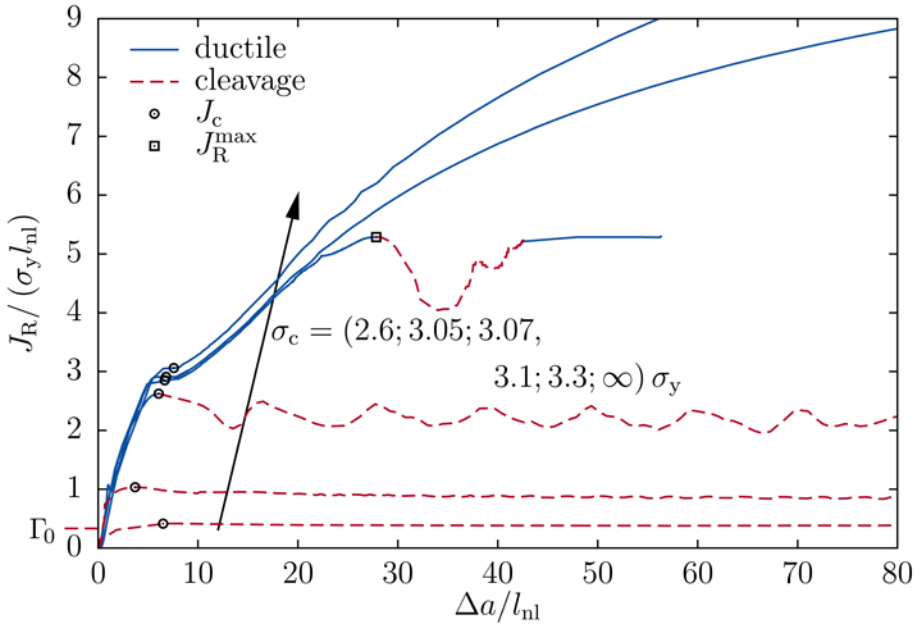

Fig. 7: Crack growth resistance curves

region at σ_c/σ_y=3.05 there is still pure cleavage but already a considerably higher crack growth resistance J_R. The difference between J_R and Γ_0 is caused by the dissipation due to the plastic

deformations during the blunting of the crack tip. After the fracture initiation at $J_R=J_c$ the plastic dissipation decreases leading to a decaying R-curve. For a prescribed loading $J=J_c$ this point is unstable so that a dynamic crack propagation initiates. For σ_c/σ_y=3.07 and σ_c/σ_y=3.10 the crack begins to propagate with the ductile mechanism until cleavage initiates and the propagation becomes dynamic, too. The distribution of the void growth behind the current crack tip is depicted in Fig. 8 showing a so-called stretch zone. Whilst the crack propagates only by cleavage for σ_c/σ_y=3.07, the crack arrests again for σ_c/σ_y=3.10 followed by ductile propagation. Such a behavior accords to experimental results, compare Fig. 1.

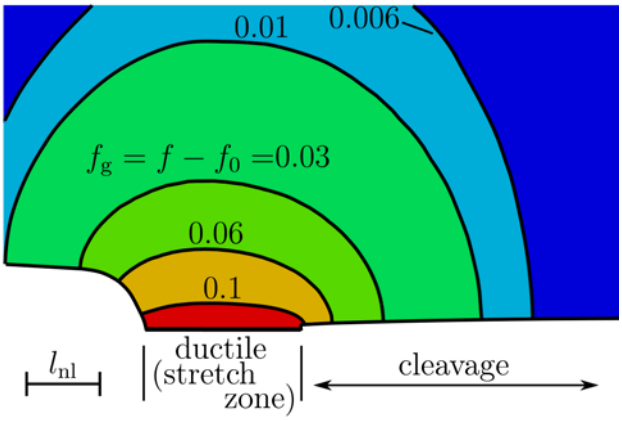

Fig. 8: Stretch zone at initial crack tip (σ_c/σ_y=3.07)

In order to investigate the effect of the crack tip constraint, now the crack propagation in a shallow-crack three-point bending specimen of width W=100 l_{nl} is simulated with a FE-mesh like that in Fig. 6. The relative crack depth amounts to a/W=0.15, a value corresponding to the experimental data which will be used below for a comparison. The computed R-curves are depicted in Fig. 9 for the lower ductile-brittle transition region.

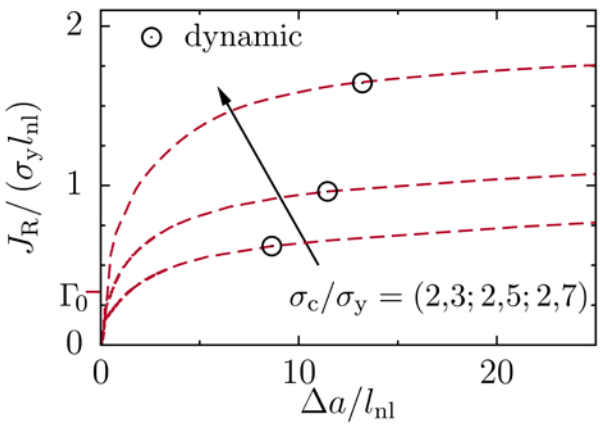

Fig. 9: R-curves for shallow-cracked specimen (a/W=0.15)

The results show that initially the crack grows by cleavage but nevertheless stably until the crack propagation becomes dynamic at the unstable point. Typically, in the context of brittle damage this point is used for the definition of the fracture toughness J_c. However, because of the initially stable crack propagation a J_c defined this way does not depend only on the crack tip constraint at the initial crack tip. Merely, it is also significantly influenced by the evolution of the crack tip constraint with ongoing crack growth.

In order to verify the presented model the simulation results are compared to the experimental data of Sorem, Dodds und Rolfe [11] in the following. These authors investigated the fracture behavior of an A36 steel in the ductile-brittle transition region. They focused on the effect of the crack-tip constraint which is why specimens of different crack depth were employed having all a width of W=34 mm. Since the predictive capabilities of the presented model shall be checked the model parameters are determined only from the deep-cracked standard specimen with a/W=0.50. Finally, the behavior of the shallow-cracked specimen with a/W=0.15 is simulated.

According to the procedure proposed in [10] the intrinsic length of the non-local GTN-model is determined to be l_{nl}=0.34 mm corresponding to a size ratio of W/l_{nl} = 93.5. The yield stress is given in [11] for the complete temperature range. The work of separation corresponds to the lower-bound fracture toughness as discussed above and is assumed to be temperature-independent for simplicity leading to a value Γ_0=0.028 MPam. The cohesive strength is now determined via the ductile-brittle transition temperature which gives σ_c=780 MPa.

The fracture toughness values extracted from the simulations of the shallow-cracked specimens (a/W=0.15) are compared to the corresponding experimental data in Fig. 10. It has to be noted that the simulation results from above with W/l_{nl} = 100 are used for convenience. Fig. 10 shows that the shift of the ductile-brittle transition temperature is predicted adequately. Furthermore, it is predicted correctly that even at a high level of fracture toughness of about J_c=0.15 MPam there is pure cleavage. This high fracture toughness is attributed to the initially stable crack propagation by cleavage as found above.

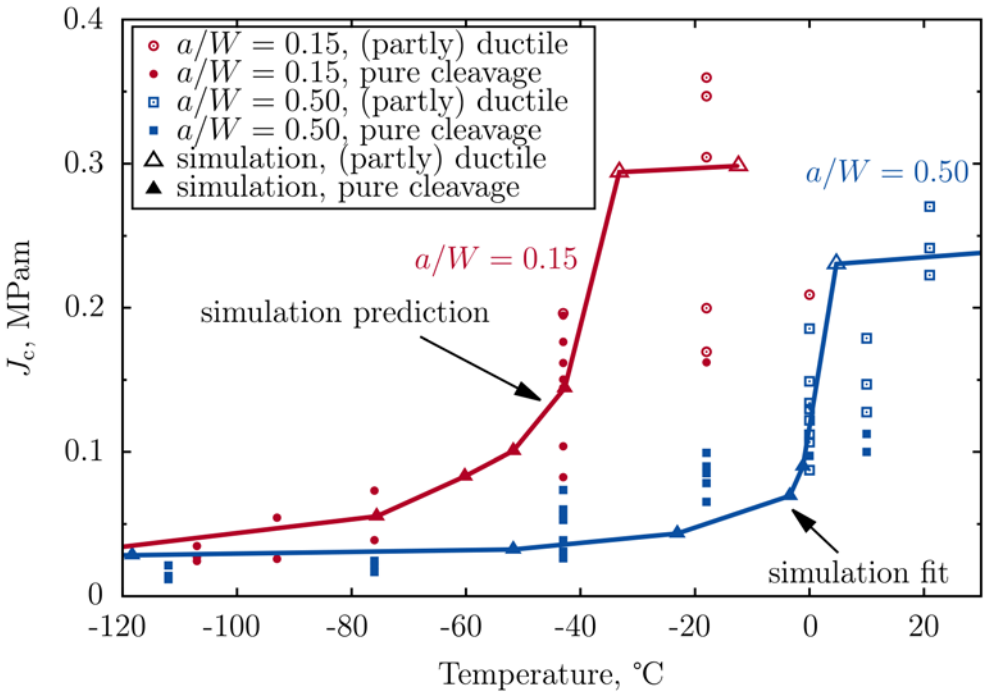

Fig. 10: Fracture toughness of an A36-steel [11] in comparison to simulation results

The employed model is deterministic. Thus, in the current state only mean properties can be considered. It remains open to investigate whether information about the scatter of the fracture toughness values can be gained if local imperfections are considered in the model.

The present contribution is a translation of [13] and outlines the results of [12]. Details of the model, numerical methods, the procedure for the determination of the parameters and the comparison with experimental data can be found in the latter reference.

Acknowledgement

The financial support by the Deutsche Forschungsgemeinschaft (German Research Foundation) under contracts KU 919-14 (Hütter) and INST 267/81-1 FUGG (computing facilities) and by the German Federal Ministry of Economics and Technology under contracts 1501298 and 1501343 (Linse) is gratefully acknowledged. The authors thank Stephan Roth for providing the implementation of the cohesive element for Abaqus.

References

[1] A. Neimitz, J. Galkiewicz and I. Dzioba, The ductile-to-cleavage transition in ferritic Cr-Mo-V steel: A detailed microscopic and numerical analysis, Eng. Fract. Mech., 77(2010), 2504-2526.
[2] R. Ritchie, J. Knott and J. Rice, On the relationship between critical tensile stress and fracture toughness in mild steel, J. Mech. Phys. Solids, 21(1973), 395-410.
[3] F. M. Beremin, A Local Criterion for Cleavage Fracture of a Nuclear Pressure Vessel Steel, Metall. Mater. Trans. A., 14(1983), 2277-2287.
[4] T. Anderson, D. Stienstra and R. Dodds Jr, A Theoretical Framework for Addressing Fracture in the Ductile-Brittle Transition Region, ASTM STP 1207 (1994), 186-214.
[5] J. Heerens and D. Hellmann, Development of the Euro fracture toughness dataset, Eng. Fract. Mech., 69(2002), 421-449.
[6] X. P. Xu and A. Needleman, Void nucleation by inclusion debonding in a crystal matrix, Model. Simul. Mater. Sc., 1 (1993), 111-132.
[7] A. L. Gurson, Continuum Theory of Ductile Rupture by Void Nucleation and Growth, J. Eng. Mater-T. ASME, 99(1977), 2-15.
[8] V. Tvergaard, Influence of voids on shear band instabilities under plane strain conditions, Int. J. Fracture, 17(1981), 389-407.
[9] T. Linse, G. Hütter and M. Kuna, Simulation of crack propagation using a gradient-enriched ductile damage model based on dilatational strain, Eng. Fract. Mech., 95(2012), 13-28.
[10] G. Hütter, T. Linse, U. Mühlich and M. Kuna, Simulation of Ductile Crack Initiation and Propagation by means of a Non-local GTN-model under Small-Scale Yielding, Int. J. Solids. Struct., 50(2013), 662-671.
[11] W. A. Sorem, R. H. Dodds and S. T. Rolfe, Effects of crack depth on elastic-plastic fracture toughness, Int. J. Fracture, 47(1991), 105-126.
[12] G. Hütter, Multi-Scale Simulation of Crack Propagation in the Ductile-Brittle Transition Region, TU Bergakademie Freiberg, dissertation, in preparation.
[13] G. Hütter, T. Linse, U. Mühlich, T. Linse, Simulation der Rissausbreitung im gesamten spröd-duktilen Übergangsbereich, in: P. Hübner (Ed.), DVM-Bericht 245, 2013, 49-58

Application of damage models to the ductile-brittle transition region of Reactor steels

Thomas Linse[1,*], Meinhard Kuna[2,*]

[1] TU Dresden, Institute for Solid Mechanics, 01062 Dresden, Germany
[2] TU Bergakademie Freiberg, Institute of Mechanics and Fluid Dynamics, 09596 Freiberg, Germany
* Corresponding author: meinhard.kuna@imfd.tu-freiberg.de

Abstract Two German ferritic pressure vessel steels (JFL, JQR) are examined in the brittle to ductile transition regime as function of temperature and irradiation. The experiments are done by a miniaturized Small-Punch-Test (SPT) in hot cells within the temperature range of -185°C up to 70°C.
From the load-displacement curve of the SPT, the yield curves and parameters of both a non-local GURSON-TVERGAARD-NEEDLEMAN ductile damage model and the BEREMIN-model are identified. The influence of temperature and irradiation on the determined model parameters is analyzed. All parameters are verified by comparison with results from standard test methods.
The parameters, identified from SPT, are used to simulate the failure behaviour in standard fracture mechanics specimens. In the upper shelf, the non-local GTN-model is applied to simulate J-Δa-resistance curves, from where the fracture toughness data J_{Ic} could be successfully predicted. In the lower shelf, the WEIBULL-stress of the specimens was computed to find out the statistics of K_{Ic} - values. Finally, a modified BEREMIN-model and the non-local GTN-model were combined to evaluate the failure of fracture specimens in the brittle-ductile transition region. This way, an acceptable agreement with Master-curve data for non-irradiated steels could be achieved over the whole temperature range.

Keywords non-local GTN-model, Beremin-Model, small-punch-test, brittle-ductile transition

1. Introduction

The quantification of irradiation effects on ferritic steels is an essential task to warrant the safety of existing nuclear power plants. While a large number of tests is needed for the description of the brittle and transition region, the available volume of irradiated material for testing is very limited.
Damage mechanics can be used to assess the integrity of mechanical structures with micro-defects through the evaluation of local criteria. In contrast to the methods of linear-elastic and elastic-plastic fracture mechanics, this approach, the concept of the Local Approach [1], can in principle be applaied to any structure. The application of the Local Approach to determine fracture mechanical properties requires the exact knowledge of the hardening and softening behavior of the material.
A promising method for the description of the failure behavior of ferritic steels in the brittle, transition and ductile region consists in minimal invasive sampling and testing of miniaturized specimens followed by the numerical simulation of standard fracture mechanical tests to predict fracture mechanical properties.
The small punch test (SPT, [2]-[6]) is a miniaturized deep drawing process that requires only tiny volumes of material. Its load displacement curve contains information about the elastic, hardening and softening properties of the tested material.
Cleavage fracture is the typical failure mechanism observed when testing in the brittle and transition region. The probability of cleavage fracture depends on the distribution of microcracks resulting from microplastic deformation, which causes a large scatter of the fracture mechanical properties. Therefore, a probabilistic model such as the Beremin local approach model [7][8], is required to

describe the failure in the brittle or transition region. It quantifies the probability of cleavage fracture based on the weakest link theory and the Griffith criterion.

Due to the absence of an initial macroscopic crack and a rather small stress triaxiality compared to fracture mechanic specimens, large parts of the SPT specimen undergo high plastic deformations even if brittle fracture is finally observed. In any case, the evolution of ductile damage precedes failure. Therefore, it is necessary to account for the influence of ductile damage when identifying material properties from the measured load displacement curves of the SPT.

In this paper, fracture toughness values are predicted solely by numerical simulation of fracture mechanics tests using material parameters identified from the SPT. A non-local formulation of a ductile damage model is used in combination with a modified Beremin model to characterize the fracture behavior of pressure vessel steels in the transition region.

2. Damage models

2.1. Non-local ductile damage model

When standard continuum damage models are implemented numerically using the finite element method, they exhibit a high sensitivity of the results to the spatial discretization size [9][10]. Material softening due to the evolution of damage localizes in a small portion of the model that is controlled by the finite element mesh, i.e. the finite element size becomes an additional model parameter. As a consequence, it is generally not possible to use the same damage model parameters in dissimilar FE models with very different element sizes.

A common idea of different methods to reduce the mesh sensitivity of damage models is to account for the influence of the surrounding material at a given material point in the constitutive equations. This results in a formulation that introduces a characteristic length scale into the model. Non-local formulations [11][12] of damage models may be divided in to three main types: formulations of the integral type, explicit gradient formulations and implicit gradient models.

The continuum damage model established by Gurson and modified by Tvergaard and Needleman (GTN, [13]-[15]) provides the basis for the constitutive equations applied in the present work. It was developed to describe the growth and coalescence of initially present or later nucleating voids in isotropic ductile materials. The GTN model accounts for the growth, nucleation and coalescence of voids. It consists of the yield condition and evolution equation for the two relevant internal variables. The change of the void volume fraction is determined by the growth of existing voids and the nucleation of voids in the matrix.

Motivated by the approach of generalized continua, the GTN continuum damage model is modified by replacing the dilatational part of the plastic strain rate by its non-local spatial average in the evolution equation for the growth of existing voids.

$$\dot{f}_G^{nl} = (1 - f)\,\dot{\bar{\varepsilon}}_p$$

All other equations of the GTN model remain untouched. For the considered case of elastic strains being small compared to plastic strains, the change of the micro-volume becomes an additional degree of freedom. The local behavior is sustained for the elastic case. The non-local dilatational part of the plastic strain rate is treated as an additional independent field quantity that is governed by the partial differential equation of the Helmholtz type

$$\overline{\varepsilon}_p - c\nabla^2\overline{\varepsilon}_p = \varepsilon_p \ ,$$

where the local hydrostatic part of the plastic strain rate ε_p acts as a source term. The constant c can be regarded as an internal length parameter that controls the influence of the surrounding material. To complete the implicit gradient formulation, homogeneous Neumann boundary conditions are chosen at all boundaries to solve the averaging equation. Details of the non-local damage model and its numerical implementation into the commercial FEM software ABAQUS can be found in [16].

2.2. Modified Beremin-Model

In the transition region both ductile damage and brittle fracture occur. Therefore, material models are needed that represent both micromechanical processes independently. The combined use of a non-local GTN-model together with the Beremin model for the calculation of the probability of cleavage fracture is conceivable in principle. However, the problems that accompany the original Beremin are getting worse when ductile damage is considered, i.e. dependence of the Weibull parameters with regard to sample shape, temperature and strain rate, difficulties in the iterative determination of the Weibull parameters, and large variations in the calculated probabilities of cleavage fracture.

Bordet et al [17] discussed that the above problems are a result of a oversimplified description of local cleavage in the Beremin model. Already in [7], a proposal for the consideration of the influence of plastic strain is made. Further modifications of the Beremin model, mainly concerning the calculation of the Weibull stress can be found in [18]-[23].

In this paper, we apply a modification proposed by Bernauer et al [24]. This modification takes into account that the nucleation of voids is promoted by the presence of carbide particles, either by the detaching of the surrounding matrix or the breaking of the particles. Both lead to the formation of cavities, whereby the initiation of cleavage fracture is no longer possible at this point. Therefore, the number of active micro-cracks is variable in the modification proposed by Bernauer. The modified Weibull stress is calculated numerically as

$$\sigma_W^B(t) = \sqrt[m]{\sum_{i=1}^{N_{pl}} \frac{V_i}{V_0} \cdot \max_{\tau \le t} \left\{ \sigma_{B_1} + \sigma_{B_2} \right\}}$$

with

$$\sigma_{B_1} = \left(\sigma_I^i(\tau)\right)^m \cdot \left(1 - \frac{c_n}{f_n} \sum_{t_j \le \tau} f_N^i\left(\Delta t_j\right)\right)$$

$$\sigma_{B_2} = \sum_{t_j \le \tau} \left(\left(\sigma_I^i\left(t_j - 1\right)\right)^m \cdot \frac{c_n}{f_n} f_N^i\left(\Delta t_j\right) \right) \ .$$

As in the original model, the probability of cleavage fracture is determined according to

$$P_f(L) = 1 - \exp\left\{ -\left(\frac{\sigma_W(L)}{\sigma_u} \right)^m \right\} \ .$$

In conjunction with the non-local ductile damage model, the nucleation of voids and the associated reduction of cleavage initiation points can be considered.

3. Identification of material properties

For a small initial void volume fraction of the investigated material ductile damage affects the behavior of the SPT specimen in a deformation state, where large equivalent plastic strains occur. Accordingly, the parameter identification is performed in two phases: First, the yield curve parameters are determined neglecting ductile damage. Here, the material is modeled as elastic-plastic with the von Mises yield condition and the associated flow rule with isotropic hardening. Subsequently, the identification of the ductile damage parameter is carried out together with the adoption of a reduced number of yield curve parameters.

3.1. Identification of yield curves

For the determination of yield curves from measured load-displacement curves of the SPT, a method was used, which does not require FEM calculations during the identification process. Instead, previously trained Neural Networks are used. The parameter determination is done by minimizing the difference between measured load-displacement curves and those approximated by the Neural Networks. The optimization algorithm simulated annealing (SA, [25]) was used. Details of the identification of yield curves can be found in [4].

3.2. Identification of the parameters of the non-local ductile damage model

The identification of damage parameters is done after the determination of the yield curve parameters, now with ductile damage taken into account. Here, the parallel optimization algorithms Appspack and Hopspack are used [26]-[28] . Both algorithms are based on Generating Set Search Methods (GSS, [29][30]), a class of derivative-free optimization methods. The asynchronous parallel implementations Appspack and Hopspack start FE-simulations on different processors; the algorithms are not waiting for the results of simultaneous calculations.

3.3. Identification of Weibull-parameters

For the determination of the Weibull parameters load-displacement curves of experiments in which the specimens failed brittle are simulated by FEM and the stress state at the time of failure is analyzed. The calculated probabilities of cleavage fracture are adapted to the experimental distribution using the maximum likelihood method (ML, [31]-[33]).

3.4. Prediction of fracture mechanical properties

Tests with fracture mechanics specimens are simulated to determine fracture toughness values. Here, the material behavior is described by the parameters of the implemented damage models that were previously identified from the SPT. The evaluation of the stress state in the fracture mechanics specimen provides the relation between Weibull stress and fracture toughness values in the brittle and the transition region, which allows the comparison with the Master Curve [34]. The determination of fracture mechanical parameters by numerical simulations of conventional fracture mechanics tests is based on the hypothesis that the crack initiation both in SPT specimens as well as in fracture mechanics specimens is accurately described by the same material models. In the brittle and transition region, critical fracture toughness values K_{Ic} are calculated from J-integral values if the Weibull stress reaches 5%, 50% and 95% probability of cleavage fracture.

4. Application and results

4.1. Identified Hardening Parameters

The explained identification strategy was applied to determine yield curve parameters from load-displacement curves of SPTs carried out for the two materials, both in non-irradiated and irradiated state, at different temperatures.

The influences of test temperature and irradiation level on the hardening characteristics of the reactor steels are clearly visible in the measured load-displacement curves of SPT [4][5]. They are also found in the identified yield curves. Lower temperatures and higher irradiation levels lead to a significant increase in yield stresses in the entire strain range. Figure 1 shows the identified initial flow stresses for the material JFL. The results for the material JRQ are not shown here as they are comparable in quality; however JRQ shows a much higher sensitivity to radiation than the steel JFL. The identified values agree well with data measured with standard tensile test.

4.2. Determined Weibull Parameters

Weibull parameters were determined for those temperatures and irradiation levels, respectively, for which the tested specimens failed in a brittle manner. Using the maximum likelihood method, unreasonable high Weibull modules were obtained for some test series. Therefore, it was decided to set the Weibull module to a constant value of m=30. The parameters of the original Beremin model were identified for reference purpose. Figure 2 represents the determined Weibull reference stresses for the material JFL.

Both the parameters of the original and the modified Beremin model show dependencies on irradiation level and test temperature. The influence of temperature on the Weibull reference stress is best visible for the non-irradiated materials: Within the same irradiation level, the specific Weibull reference stresses decrease for higher test temperatures.

4.3. Critical Fracture Toughness values

Subsequent to the identification of the yield curves and the damage parameters critical fracture toughness values were indirectly quantified by numerical simulation of fracture mechanics tests. The developed non-local ductile damage model was used in combination with the original Beremin model or the modified version after Bernauer to calculate the probability of cleavage fracture.

The fracture toughness values from FEM calculations of CT specimens using the identified parameters are shown in Figure 3 for the non-irradiated material JFL. In the brittle region and the ductile region, the calculated values agree well with experimental results. For the transition region, the calculated fracture toughness values and their scatter are clearly too small.

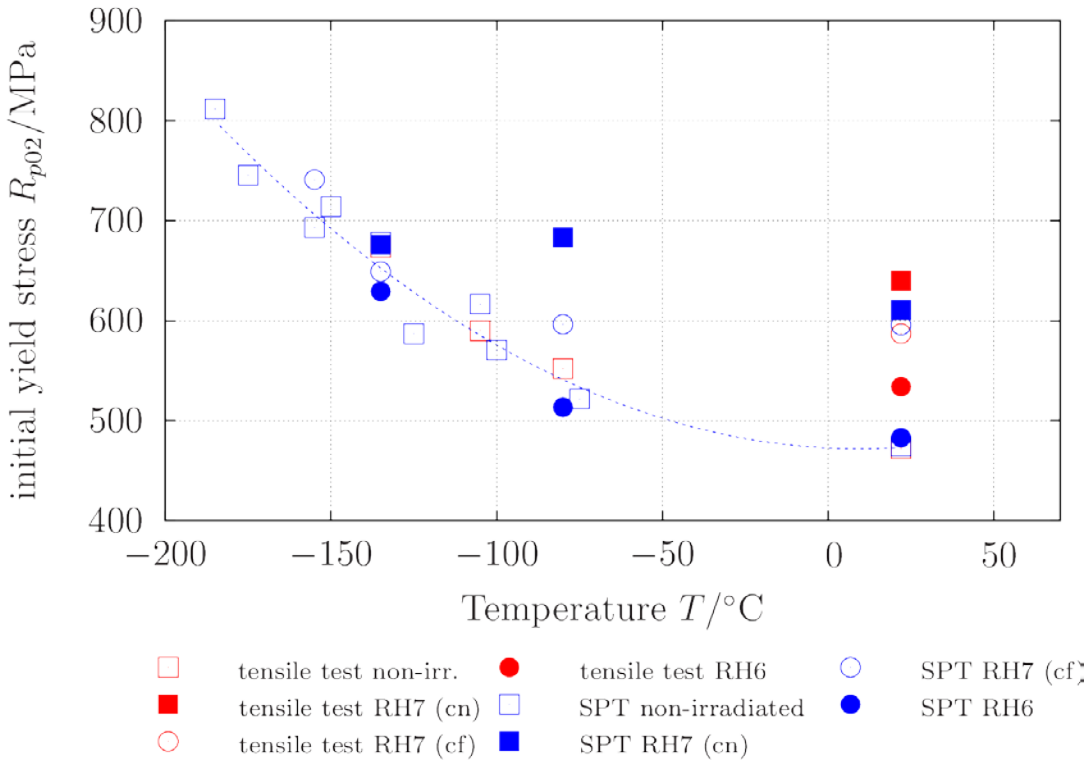

Figure 1: Initial yield stresses identified from the SPT (material JFL; irradiation levels: non-irradiated, RH6, RH7cf/cn)

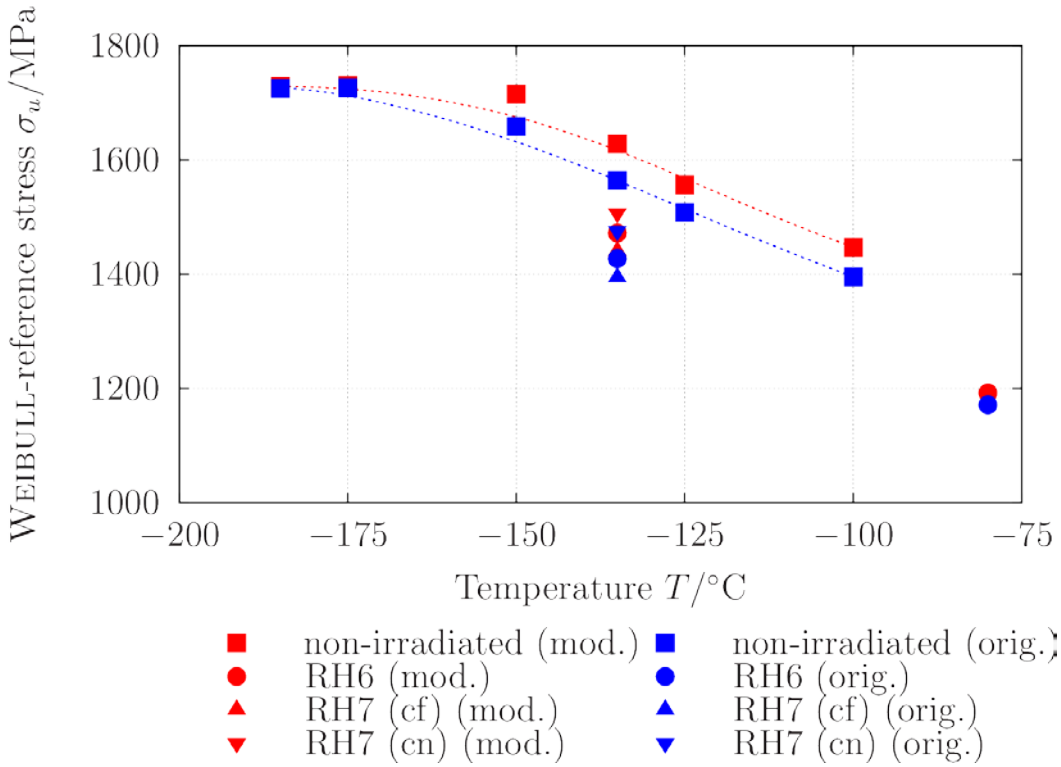

Figure 2: Weibull reference stresses identified from the SPT (material JFL; irradiation levels: non-irradiated, RH6, RH7cf/cn)

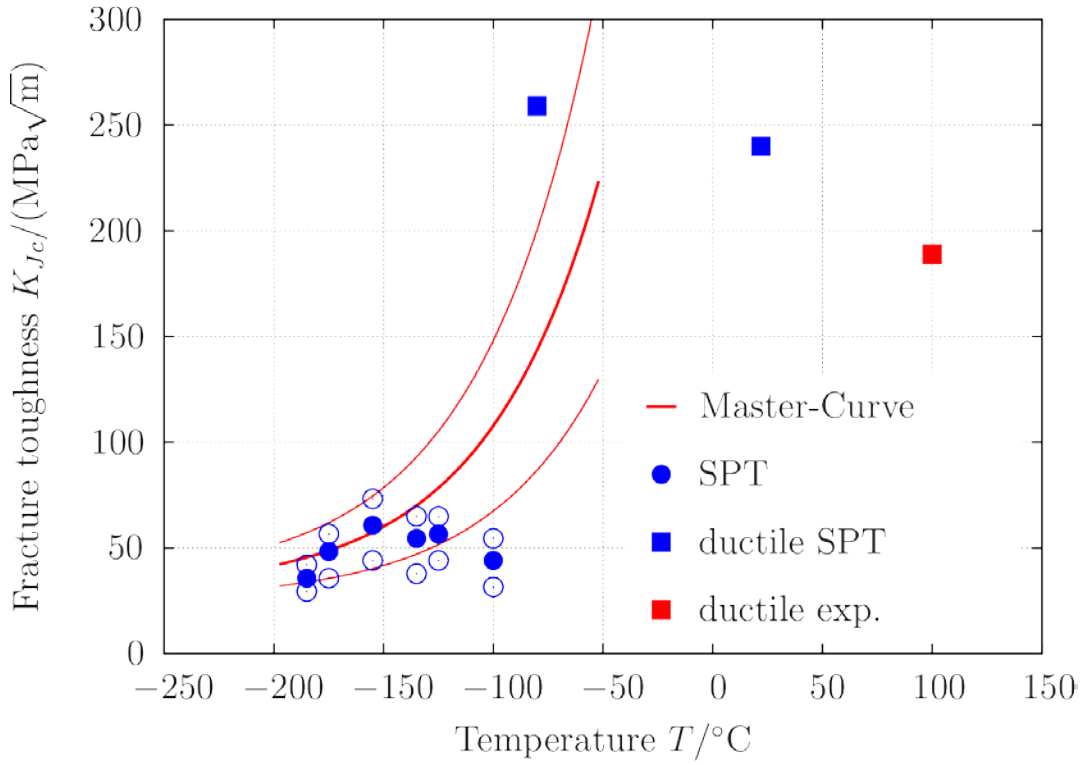

Figure 3: Fracture toughness values for the non-irradiated material JFL

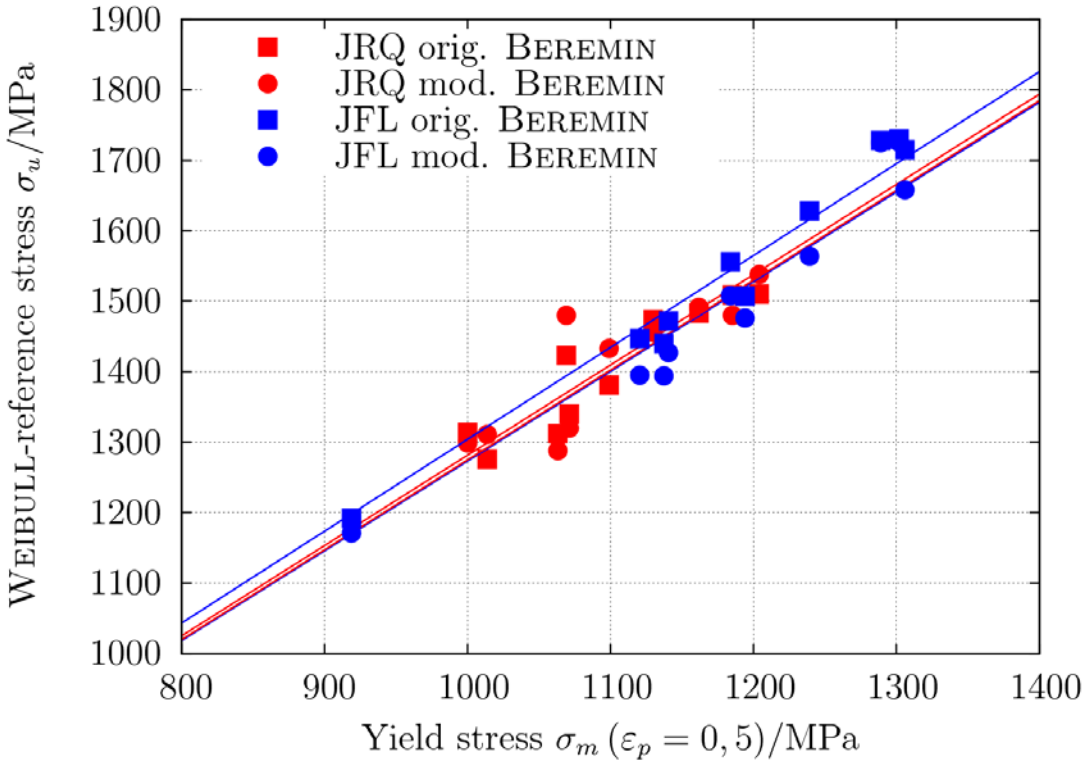

Figure 4: Relation between identified yield stresses and Weibull reference stresses

5. Discussion and conclusions

The parameters of both Beremin models clearly show dependencies on irradiation level and test temperature. In the relevant range of the load-displacement curve of the SPT, large parts of the specimen are subjected to a biaxial stress state which is characterized by approximately equal first and second principal stresses. Accordingly, the maximum principal stresses at the onset of void coalescence and consequently the determined Weibull reference stresses are mainly determined by the current yield stress of the material. Figure 4 shows the almost linear relationship between calculated Weibull reference stresses and identified yield stresses. The strong influence of the test temperature and irradiation level on the hardening properties of the matrix material thus transfers to the particular Weibull reference stresses: for higher temperatures, the Weibull reference stresses decrease. This result is consistent with the temperature dependence of principal stresses leading to cleavage fracture that were experimentally determined on notched tensile specimens [35]. Note that there are several temperature-dependent modifications of the Beremin model, e.g. [36]-[38]. However, in these modifications the Weibull reference stress must be increased with higher temperatures to get reasonable results, which lacks a micromechanical motivation [39] and contradicts with our results.

The predicted fracture toughness values agree well with experimental results in the brittle region and in the ductile region. In the brittle-ductile transition region, the values determined from the SPT cannot be transferred to the fracture mechanics specimen. The calculated fracture toughness values are much smaller than the experimentally determined values. It is therefore questionable whether the assumptions made in the Beremin model are sufficient to capture size effect and influence of stress triaxiality. Particular in the transition region, the assumption of the failure of the whole structure by the unstable crack growth of a micro-crack (weakest link assumption) seems to be not justified for the fracture mechanics specimen.

Acknowledgements

The financial support by the German Federal Ministry of Economics and Technology (BMWi) is gratefully acknowledged (projects 1501298 and 1501343).

References

[1] Pineau, A.: Development of the local approach to fracture over the past 25 years: theory and applications. In: International Journal of Fracture 138 (2006), 139–166.

[2] Abendroth, M.; Kuna, M.: Determination of deformation and failure properties of ductile materials by means of the small punch test and neural networks. In: Computational Materials Science 28 (2003), Nr. 3-4, 633-644

[3] Abendroth, M.; Kuna, M.: Identification of ductile damage and fracture parameters from the small punch test using neural networks. In: Engineering Fracture Mechanics 73 (2006), 710-725

[4] Linse, T.; Kuna, M.; Schuhknecht, J.; Viehrig, H.-W.: Usage of the small-punch-test for the characterisation of reactor vessel steels in the brittle-ductile transition region. In: Engineering

Fracture Mechanics 75/11 (2008), 3520-3533

[5] Linse, T.; Kuna, M.; Schuhknecht, J.; Viehrig, H.-W. : Application of the small-punch-test to irradiated reactor vessel steels in the brittle-ductile transition region, Journal of ASTM International, Vol. 5, No. 4, (2008)

[6] Bicego, V.; Cerutti, P.; Foulds, J.; Hurst, R.; Matocha, K.; Abendroth, M.: CEN - European Committee for Standardization Workshop 21: Small Punch Test Method for Metallic Materials Part B: A Code of Practice for Small Punch Testing for Tensile and Fracture Behaviour, final Draft12/2006

[7] Beremin, F.M.: A local criterion for cleavage fracture of a nuclear pressure vessel steel. In: Metallurgical Transactions A 14A (1983), 2277-2287

[8] Mudry, F.: A local approach to cleavage fracture. In: Nuclear Engineering and Design 105 (1987), 65-76

[9] Pijaudier-Cabot, P., Z. P. Baant, M. Tabbara: Comparison of various models for strain-softening, Engineering Computations 5 (2) (1988), 141 – 150.

[10] R. de Borst, L. Sluys, H.-B. Mühlhaus, J. Pamin: Fundamental issues in finite element analyses of localization of deformation, Engineering Computations 10 (2) (1993), 99–121.

[11] Jirasek, M. Nonlocal models for damage and fracture: Comparison of approaches. International Journal of Solids and Structures, (35) 31-32:4133-4145, 1998

[12] Peerlings, R.H.J.; Geers, M.G.D.; de Borst, R.; Brekelmans, W.A.M. A critical comparison of nonlocal and gradient-enhanced softening continua. International Journal of Solids and Structures, (38) 44-45: 7723-7746, 2001

[13] Gurson A.L. Continuum theory of ductile rupture by void nucleation and growth: part I - Yield criteria and flow rules for porous ductile media. J Eng Mater Technol 99:2–5, 1977

[14] Tvergaard,V. Influence of voids on shear band instabilities under plane strain conditions. Int J Fracture 17:389–407, 1981

[15] Tvergaard, V., A. Needleman. Analysis of the cup-cone fracture in a rod tensile bar. Acta Metallurgica, 32:157–169, 1984.

[16] Linse, T. et al.: Simulation of crack propagation using a gradient-enriched ductile damage model based on dilatational strain. In: Engineering Fracture Mechanics (2012).

[17] Bordet et al.: A new statistical local criterion for cleavage fracture in steel. Part I: model presentation. In: Engineering Fracture Mechanics 72 (2005), 435–452.

[18] Gao, X. et al: Calibration of Weibull stress parameters using fracture toughness data. In: International Journal of Fracture 92 (1998), 175–200.

[19] Gao, X. et al: A Weibull stress model to predict cleavage fracture in plates containing surface cracks. In: Fatigue and Fracture of Engineering Materials and Structures 22 (1999), 481–493.

[20] Gao, X. et al: Weibull stress model for cleavage fracture under high-rate loadingWeibull stress model for cleavage fracture under high-rate loading. In: Fatigue and Fracture of Engineering Materials and Structures 22 (1999), 481–493.

[21] Gao, X. et al: Prediction of cleavage fracture in ferritic steels: a modified Weibull stress model. In: Materials Science and Engineering A.394 (Okt. 2005), 210–219.

[22] Gao, X. et al: A probabilistic model for prediction of cleavage fracture in the ductile-to-brittle transition region and the effect of temperature on model parameters. In: Materials Science and Engineering A.415 (Okt. 2006), 264–272.

[23] Kroon, M., J. Faleskog. A probabilistic model for cleavage fracture with a length scale-influence of material parameters and constraint. In: International Journal of Fracture 118 (2002), 99–118.

[24] Bernauer, G. et al: Modifications of the Beremin model for cleavage fracture in the transition region of a ferritic steel. In: Engineering Fracture Mechanics 64 (1999), 305–325

[25] Corana, A.; Marchesi, M. ; Martini, C. ; Ridella, : Minimizing Multimodal Functions of Continuous Variables with the Simulated Annealing Algorithm. In: ACM Transactions on Mathematical Software 13 (1987), Nr. 9, 262-280

[26] Gray, G. A., T. G. Kolda. Algorithm 856: APPSPACK 4.0: Asynchronous Parallel Pattern Search for Derivative-Free Optimization. In: ACM Transactions on Mathematical Software 32.3 (2006), 485–507.

[27] Plantenga, T. D. HOPSPACK 2.0 User Manual. Techn. Ber. SAND2009-6265. Sandia National Laboratories, Albuquerque, NM and Livermore, CA, 2009.

[28] Griffin, J. D. et al: Asynchronous Parallel Generating Set Search For Linearly-Constrained Optimization. Techn. Ber. Sandia National Laboratories, Albuquerque, NM and Livermore, CA, 2006.

[29] Kolda, T. et al: Optimization by Direct Search: New Perspectives on Some Classical and Modern Methods. In: SIAM Review 45.3 (2003), 385–482.

[30] Kolda, T. et al: Stationarity results for generating set search for linearly constrained optimization. In: SIAM Journal on Optimization 17.4 (2006), 943– 968.

[31] A. Khalili, A., K. Kromp. Statistical properties of Weibull estimators. In: Journal of Materials Science 26 (24 1991), 6741–6752.

[32] Minami, F. et al: Estimation procedure for the Weibull parameters used in the local approach. In: International Journal of Fracture 54 (1992), 197–210.

[33] Riesch-Oppermann, H., A Brückner-Foit. WEISTRABA: A code for the numerical analysis of Weibull stress parameters from ABAQUS finite element stress analysis - procedural background and code description. Techn. Ber. FZKA 6155. Forschungszentrum Karlsruhe, Institut für Materialforschung, 1998.

[34] Wallin, K. et al: Applicability of miniature size bend specimens to determine the master curve reference temperature T0. In: Engineering Fracture Mechanics 68.11 (2001), 1265 –1296.

[35] Grimpe, F. et al: Influence of temperature, strain rate and specimen geometry on the microscopic cleavage fracture stress. In: Nuclear Engineering and Design 188.2 (1999), 155 – 160.

[36] J. P. Petti, J. P., R. H. Dodds. Calibration of the Weibull stress scale parameter σu using the Master Curve. In: Engineering Fracture Mechanics 72.1 (2005), 91 –120.

[37] Seebich, H.-P. Mikromechanisch basierte Schädigungsmodelle zur Beschreibung des Versagensablaufs ferritischer Bauteile. Dissertation. Universität Stuttgart, 2007.

[38] Wasiluk, B. et al: Temperature dependence of Weibull stress parameters: Studies using the Euro-material. In: Engineering Fracture Mechanics 73 (2006), 1046–1069.

[39] Tanguy, B. et al: Ductile to brittle transition of an A508 steel characterized by Charpy impact test Part II: modeling of the Charpy transition curve. In: Engineering Fracture Mechanics 72 (2005), 413–434

Application of the Local Approach for Prediction of Ductile Fracture of Highly Irradiated Austenitic Steels

Boris Margolin[1,*], **Alexander Sorokin**[1], **Victor Kostylev**[1]

[1] Central Research Institute of Structural Materials "Prometey", Saint-Petersburg, Russia
* Corresponding author: margolin@prometey2.spb.su

Abstract The physical-and-mechanical model of ductile fracture has been developed to predict fracture toughness and fracture strain of irradiated austenitic steels taking into account stress-state triaxiality and irradiation swelling. Comparison of experimental data on fracture strain of irradiated austenitic weld metal with predicted results by the model has been performed. The model also allows to describe sharp decrease of ultimate strength on the basis of the proposed mechanism called as "the running collapse mechanism".

Keywords Ductile fracture model, Fracture toughness, Swelling, Irradiated austenitic steels, Vacancy voids

1. Introduction

Ductile fracture of unirradiated austenitic and ferritic steels may be sufficiently successfully described on the basis of well known model – The Gurson-Tvergaard-Needleman model (GTN-model) [1, 2], and also on the basis less known model – Margolin-Karzov-Shvetsova-Kostylev model (MKSK-model) [3].

Ductile fracture of irradiated austenitic steels has many features. Some of them are the following.

(1) Ductile fracture is controlled by not only evolution of voids, nucleating by deformation (deformation voids), but also by vacancy voids (resulting in swelling) arising under irradiation before deformation.
(2) Deformation voids nucleation rate is higher for irradiated steel than for unirradiated steel.
(3) Neutron irradiation reduces fracture toughness stronger than fracture strain of tensile smooth specimens. It means that stress state triaxiality (SST) enhances the effect of neutron irradiation on fracture strain.
(4) For some value of radiation swelling a fracture of smooth specimens occurs when stress less than yield strength, but fracture surface contains dimples. It means that fracture mechanism is ductile due to evolution of voids.

The aim of this paper is development of MKSK-model for prediction the fracture strain on neutron dose for different stress states, prediction the influence of neutron irradiation and radiation swelling on material fracture toughness and also prediction fracture at high level of swelling when stress less than yield strength.

2. The main considerations of the physical-mechanical ductile fracture model

The main considerations of the proposed model are following:

(a) Fracture proceeds by the mechanism of nucleation, growth and coalescence of voids. Two void populations are considered: vacancy voids and deformation voids, i.e. voids nucleating during the process of material deformation.

(b) Polycrystalline material is presented as an aggregate of unit cells in the form of cubes with homogeneous properties of a material.

(c) The rate of change of void volume concentration $\frac{d\rho_v^{def}}{d\sigma_{nuc}}$ is presented in the form

$$\frac{d\rho_v^{def}}{d\sigma_{nuc}} = \frac{\rho_v^{max} - \rho_v^{def}}{\sigma_d}, \tag{1}$$

where ρ_v^{def} is the concentration of deformation voids in a unit of volume of a material matrix, ρ_v^{max} is the maximum volume concentration of void nucleation sites.

In (Eq. 1) σ_{nuc} is stress which controls nucleation of discontinuity near some barriers [4, 5]. In case of void nucleation the following barriers are considered: inclusions of second phase or coarse carbides and others. According to papers [4, 5] σ_{nuc} can written in the form

$$\sigma_{nuc} = \sigma_1 + m_{T\varepsilon} \cdot \sigma_{eff}, \tag{2}$$

where the parameter $m_{T\varepsilon}$ is concentration coefficient of local stress near dislocation pile-up; σ_1 is maximum principal stresses; $\sigma_{eff} = \sigma_{eq} - \sigma_Y$ is effective stress; σ_{eq} is equivalent stress; σ_d is a local strength of matrix-inclusion interface.

In general case σ_d depends on neutron dose and does not depend on test temperature [4, 5]. It is necessary to note that equation for σ_{nuc} is similar to equation proposed in paper [6].

From (Eq. 2) it follows that as a neutron dose D increases, σ_{nuc} will increase at the expense of an increase of σ_Y and, correspondingly, σ_1. According to papers [4, 5], as a dose D increases, σ_d decreases. Then from (Eq. 1) it follows that irradiation results in an increase of void concentration. This conclusion following from the considered equations is confirmed by the experimental data. It is shown in paper [7] that dimple concentration on a specimen surface in an irradiated condition is higher than that in the initial one.

(d) When analysing the growth of vacancy and deformation voids the Huang's equation [8] is used. To describe a void growth under conditions of their interaction an additional factor was introduced into Huang's equation in the form $\frac{1}{1-f}$

$$\frac{dV_{void}}{V_{void}} = \frac{3 \cdot \alpha}{1-f} \cdot d\text{æ}, \tag{3}$$

where

$$\alpha = 0.427\left(\frac{\sigma_m}{\sigma_{eq}}\right)^k \cdot \exp\left(\frac{3}{2}\frac{\sigma_m}{\sigma_{eq}}\right); \; k = \begin{cases} 0{,}25, \text{ for } \frac{\sigma_m}{\sigma_{eq}} \le 1 \\ 0, \text{ for } \frac{\sigma_m}{\sigma_{eq}} > 1 \end{cases}; \tag{4}$$

$\text{æ} = \int d\varepsilon_{eq}^p$ is the Odquist's parameter; $d\varepsilon_{eq}^p$ is equivalent of a plastic strain increment, f is material void volume fraction

$$f = \frac{V_\Sigma}{V + V_\Sigma}, \tag{5}$$

In (Eq. 5) V_Σ is the total volume of vacancy and deformation voids in a material matrix of the volume V.

(e) The criterion of a unit cell plastic collapse or, in other words, the criterion of plastic instability is used as fracture criterion [3, 9]

$$\frac{dF_{eq}}{d æ} = 0, \tag{6}$$

where $F_{eq}=\sigma_{eq}\cdot(1-\overline{A}_{\Sigma})$, σ_{eq} is equivalent stresses related to a material matrix (without voids), $\overline{A}_{\Sigma}$ is a relative void area, i.e. void cross-section area related to the cross-section area unit of a unit cell with voids. It should be noted that when analysing conditions in (Eq. 6) stress state triaxiality is taken to be constant [3].

The parameter $\overline{A}_{\Sigma}$ is calculated on the basis of following considerations. In the general case α in (Eq. 4) depends on æ and does not depend on a void volume. Then an increase in the volume of vacancy and deformation voids taking into account (Eq. 1) and (Eq. 3) may be calculated by the equation:

$$d\overline{V}_{\Sigma} = \frac{3\cdot\alpha}{1-f}\cdot\overline{V}_{\Sigma}\cdot d æ + V_{nuc}^{def}\cdot\left[\rho_v^{def}(æ + d æ) - \rho_v^{def}(æ)\right], \tag{7}$$

where V_{nuc}^{def} is the volume of a nucleus deformation void.

When integrating (Eq. 7) the initial condition is formulated in the form:

$$\left(\overline{V}_{\Sigma}\right)_0 = S_w + V_{nuc}^{def}\cdot\left[\rho_v^{def}(æ = 0)\right], \tag{8}$$

where $\left(\overline{V}_{\Sigma}\right)_0$ is the value of a relative void volume with æ=0, S_w is material swelling.

The parameter $\overline{A}_{\Sigma}$ is connected with volume of voids by the following manner

$$\overline{A}_{\Sigma} = \left(\frac{\overline{V}_{\Sigma}}{1+\overline{V}_{\Sigma}}\right)^{2/3}. \tag{9}$$

It is necessary to note that for prediction of material behavior in ductile fracture regime GTN-model [1, 2] is widely used. According to this model the plastic potential introduced by Gurson [1] is presented in the form

$$\Phi = \frac{\sigma_{eq}^{\ 2}}{\sigma_2^{\ 2}} + 2f^* q_1\cdot\cosh\left(\frac{3}{2}q_2\frac{\sigma_m}{\sigma_S}\right) - [1-(q_1 f^*)^2 = 0, \tag{10}$$

where σ_S is the function describing the yield surface for material without voids, q_1, q_2,f_c and k_a are material constants;

$$f^* = \begin{cases} f & \text{for } f \le f_c \\ f_c + k_a(f - f_c) & \text{for } f > f_c \end{cases}. \tag{11}$$

The increase of void volume fraction is written

$$df = df_{nucl} + df_{growth}, \tag{12}$$

where

$$df_{growth} = (1-f)d\varepsilon_{ii}^p, \tag{13}$$

In (Eq. 13) $d\varepsilon_{ii}^p$ is the sum of normal plastic strain. Value of $\frac{df_{nucl}}{d æ}$ may be calculated by formula [10]

$$\frac{df_{nucl}}{d æ} = \frac{f_N}{S_N\sqrt{2N}}\exp\left[-\frac{1}{2}\left(\frac{æ - \varepsilon_N}{S_N}\right)\right], \tag{14}$$

where S_N, f_N and ε_N are material constant.

As you can see for use of GTN-model it is necessary to identify seven parameters or six parameters if ε_N is assumed to be equal zero. Moreover in common case f_c depends on stress triaxiality. It is increase number of constants. If the criterion (Eq. 6) is used we need to identify three constant, namely ρ_v^{max}, σ_d and V_{nuc}^{def} (initial volume of deformation void).

Of course, as for both criterion (Eq.6) and GTN-model function $\sigma_S(æ)$ should be known. So it is clear that the use of criterion (Eq. 6) is much simpler than GTN-model.

3. Simulation of material fracture under different conditions of irradiation and testing

The weld metal of 18Cr-10Ni-Ti steel in the initial and irradiated conditions was chosen as an object for the use of the model. Welding was performed with the use of 19Cr-11Ni-3Mo welding wire without subsequent heat treatment. Weld metal specimens were irradiated in the BOR-60 reactor by neutron doses in the range from 6-7 to 46 dpa at a temperature T_{irr}=320-340°C [11].

As the criterion of fracture of a smooth cylindrical specimen the fracture of the central fibre of a specimen neck was taken. To describe the dependences characterizing SST in the central fibre of a specimen neck, $q_m(æ) \equiv \frac{\sigma_m}{\sigma_{eq}}$ and $q_1(æ) \equiv \frac{\sigma_1}{\sigma_{eq}}$ the Bridgman's formulas [12] were used. Over the range of T_{test}=80-495°C the values of fracture strain ε_f^{calc} were calculated on the basis of the condition (Eq. 6). Model parameters are assumed as temperature independent. Fig. 1a shows the experimental data and the dependence $\varepsilon_f^{calc}(T_{test})$. As input data generalized stress-strain curves (SSCs), calculated by equations presented in [11] were used. Values of model parameters are presented in [13, 14].

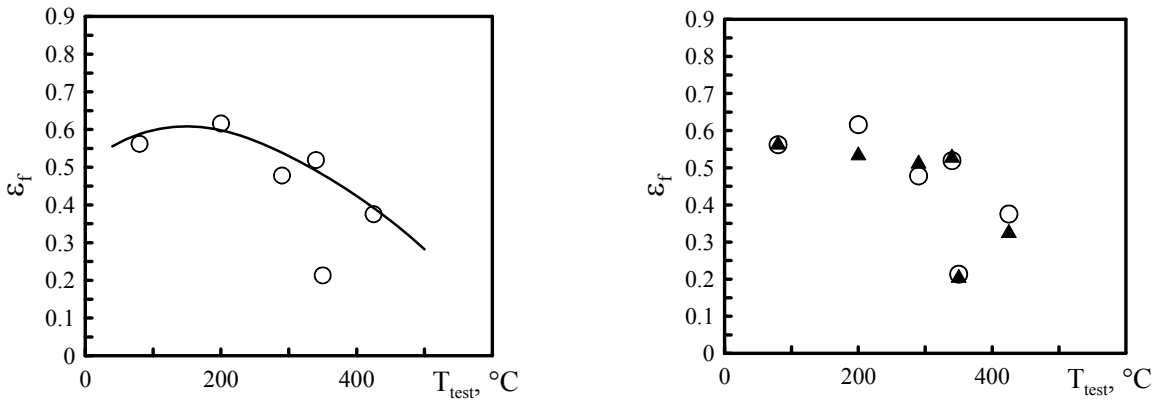

a) b)

Figure 1. Temperature dependence of the fracture strain of material irradiated by the dose D=46 dpa at T_{irr}=330-340°C: ○ - experimental data, (a) curve - calculated by the model with regard for generalized stress-strain curves [11]; (b) ▲ - points calculated by the model on the basis of individual SSC

Additional calculations ε_f^{calc} were performed for each temperature taking into accounts individual SSCs, obtained from test of each specimen. Results of performed calculations for each test temperature presented on the Fig. 1b. As is seen from Fig. 1, a good agreement between the experimental data and results calculated by the model is observed. The presented data shows that with invariant values of σ_d and ρ_v^{max} the model makes correct predictions of the value ε_f^{exp} at different T_{test} especial with taking into account the peculiarities of individual stress-strain curves for

each T_{test}. Thus the effect of T_{test} on ε_f is basically determined by the influence of strain hardening on the realization condition of a plastic collapse of a unit cell.

For analysis of swelling effect and verification of model the weld metal specimens irradiated by a dose of 49 dpa at T_{irr}=400-450°C [15] were used. Swelling of these specimens varies from 3 up to 7%.

Numerical simulation of the influence of vacancy void volume fraction on fracture strain is based on the following propositions:

(1) the SSC for a material matrix, i.e. material without vacancy and deformation voids is invariant to swelling and irradiation temperature and depends only on a neutron dose and test temperature;
(2) when calculating fracture strain for each temperature the individual values of swelling for each specimen [15] were used;
(3) values of the parameters σ_d and ρ_v^{max} are determined from the equality condition $\varepsilon_f^{exp} = \varepsilon_f^{calc}$ at T_{irr}=320-340°C (i.e. without swelling [11, 15]) and T_{test}=80°C, i.e. the same way as described for analyzing of test temperature effect.

The results of the calculation of fracture strain in the absence and existence of swelling are shown in Fig. 2. It is seen from the figure that there is a close coincidence of the experimental and calculated data for specimens without and with swelling (for specimens without swelling comparison of ε_f^{exp} and ε_f^{calc} was shown above in Fig. 1). The obtained results suggest that a decrease of ε_f at T_{irr}=400-450°C compared with ε_f at T_{irr}=320-340°C is connected exclusively with vacancy void volume fraction that determines material radiation swelling. It should be noted that nonmonotonic of the dependence $\varepsilon_f^{exp}(T_{test})$ at T_{irr} =400-450°C is evidently determined by the inhomogeneity of specimens swelling. At the same time the average value of fracture strain $\bar{\varepsilon}_f$ over a temperature range of 80-425°C obtained experimentally approaches the calculated value: $\bar{\varepsilon}_f^{exp}$=0.26, $\bar{\varepsilon}_f^{calc}$=0.25.

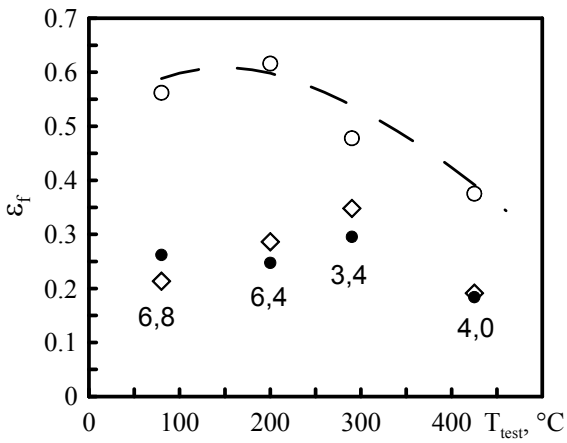

Figure 2. Temperature dependences ε_f^{exp} and ε_f^{calc} for weld metal with and without swelling; the digitals denote swelling of specimens as a percentage: ○ - fracture strain of weld metal without swelling (experiment); ◇ - fracture strain of weld metal with swelling (experiment); ● - calculated value of fracture strain of weld metal with swelling; — — — - calculated temperature dependence of fracture strain of weld metal without swelling.

4. Analysis of an irradiation effect on fracture toughness

To estimate the influence of SST in the dependence $\varepsilon_f(D)$ let us compare the dependence $\frac{\varepsilon_f}{\varepsilon_f^0}(D)$

obtained on the basis of test data processing of smooth cylindrical tensile specimens and the dependence $\frac{\varepsilon_{f_crack}}{\varepsilon^0_{f_crack}}(D)$ calculated by the model. For ε_{f_crack} let us take ε_f^{calc} calculated for the stress state typical for a material near a crack tip on the line of its extension. The ε_f^0 and $\varepsilon^0_{f_crack}$ is fracture strain of material in initial condition with regard to corresponding SST.

Calculation of $q_m(æ)$ and $q_1(æ)$ for tensile specimens was made according to Bridgeman's formulas [12], while calculation for a material near a crack tip was made by the dependences proposed in [16]. The calculation by the model $\frac{\varepsilon_{f_crack}}{\varepsilon^0_{f_crack}}(D)$ was made for T_{test}=290°C. The choice of such temperature is connected with the available representative data on $J_c(D)$ for T_{test} = 290-350°C [17]. Table 1 presents the calculation results of $\frac{\varepsilon_f}{\varepsilon_f^0}$ by equation presented in [11] and $\frac{\varepsilon_{f_crack}}{\varepsilon^0_{f_crack}}$ calculated by the model.

Table 1. The values $\frac{\varepsilon_f}{\varepsilon_f^0}$, $\frac{\varepsilon_{f_crack}}{\varepsilon^0_{f_crack}}$ and $\frac{J_c}{J_c^0}$ at different doses and for the same T_{test}=290°C.

D, dpa	Stress state			σ_{flow}, MPa	$\frac{J_c}{J_c^0}$ (calc)	$\frac{J_c}{J_c^0}$ (exp)
	in the centre of a tensile specimen neck	near the crack tip				
	$\frac{\varepsilon_f}{\varepsilon_f^0}$	ε_{f_crack}	$\frac{\varepsilon_{f_crack}}{\varepsilon^0_{f_crack}}$			
0	1	0.0671	1	413	1	1
27	0.480	0.0055	0.082	883	0.175	0.169
46	0.480	0.0056	0.083	883	0.177	0.164

On the basis of above calculations it is possible to estimate a fall of J_c with an increasing dose.

Taking into account the approximate dependences $\delta \sim \frac{J}{\sigma_{flow}}$ where δ is a crack opening and $\varepsilon^p \sim \frac{\delta}{r}$ where r is the distance from a crack tip the value J_c under ductile fracture may be presented in the form similar to the proposed in [9]:

$$J_c = \eta \cdot \sigma_{flow} \cdot r_f \cdot \varepsilon_{f_crack}, \tag{15}$$

where J_c is the critical value of J-integral, r_f is a process zone size, ε_{f_crack} is a fracture strain near the crack tip determined with regard to SST typical for a crack, η is some numerical coefficient, σ_{flow} is the flow strength

$$\sigma_{flow} = \frac{\sigma_Y + \sigma_{ul}}{2}, \tag{16}$$

where σ_Y is yield strength, σ_{ul} is ultimate tensile strength.

Assuming that process zone size r_f is invariant to material condition calculation of a relative decrease of J_c may be determined on the basis of the following expression

$$\frac{J_c}{J_c^0} = \frac{\varepsilon_{f_crack}}{\varepsilon_{f_crack}^0} \cdot \frac{\sigma_{flow}}{\sigma_{flow}^0}, \tag{17}$$

where J_c is a critical value of the J-integral for irradiated material, J_c^0 is the critical value of the J-integral for material in the initial condition, σ_{flow} is calculated on the basis of dependencies presented in [11].

The calculation performed by the model at T_{test}=290°C was compared with the experimental data presented in [17] (See Table 1).

As it seen from the presented results, a decrease of ε_f with an increasing dose is considerably enhanced with increasing stress state triaxiality. Thus, for the triaxiality typical for a tensile specimen with D=46 dpa ε_f decreases by half compared to an unirradiated condition, while for the triaxiality typical for material near a crack tip a decrease of ε_f reaches 12 times. In other words, the influence of SST increases with a growth of a neutron dose. Calculation of ε_f with regard to the influence of SST on dependence $\varepsilon_f(D)$ makes possible to describe adequately the change of material fracture toughness under irradiation.

In order to investigate the influence of radiation swelling on J_c we determined the dependences $\varepsilon_{f_crack}(S_w)$ for different neutron doses from 6 to 46 dpa.

The value of a relative decrease of $\bar{J}_c$ resulted from the value S_w was calculated by the formula

$$\bar{J}_c = \frac{J_c(S_w)}{J_c(S_w = 0)} = \frac{\varepsilon_{f_crack}(S_w)}{\varepsilon_{f_crack}(S_w = 0)} \cdot \frac{\sigma_{flow}(S_w)}{\sigma_{flow}(S_w = 0)}, \tag{18}$$

According to [11], $\sigma_{flow}(S_w)$ can be calculated by the formula

$$\sigma_{flow}(S_w) = \sigma_{flow}(S_w = 0) \cdot \left(1 - \left(\frac{S_w}{1 + S_w}\right)^{2/3}\right), \tag{19}$$

Fig. 3 shows the dependence $\bar{J}_c(S_w)$ for different neutron doses. It is seen from the figure that the value $\bar{J}_c$ practically does not depend on a neutron dose, but depends only on the value of swelling S_w.

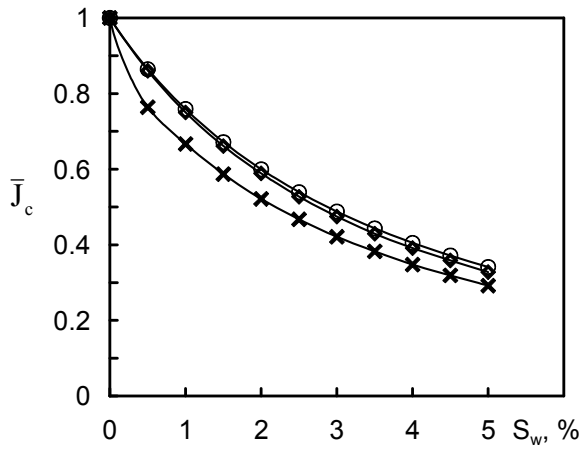

Figure 3. Calculative dependence of relative fracture toughness on radiation swelling for different neutron doses: ○, ———— - D=6 dpa, ◇, — — — - D= 27 dpa, ×, — · — · — - D =46 dpa

At present very few data on swelling effect on fracture toughness are available. That's why prediction by the model needs experimental verification.

5. The swelling effect on ultimate strength of austenitic steel

There are some papers in which the effect of swelling on ultimate strength of irradiated austenitic steels is investigated. According to these papers when swelling reaches some critical value the sharp embrittlement of austenitic steels is observed so that smooth tensile specimens rupture at $\sigma < \sigma_{0.2}$. For example, ultimate strength of irradiated 18Cr-10Ni-Ti steel decreases by 5 times when swelling of steel increases from 17 to 25% [18] (See Fig. 4). It is necessary to note that fracture mode for the considered cases is ductile due to vacancy voids coalescence.

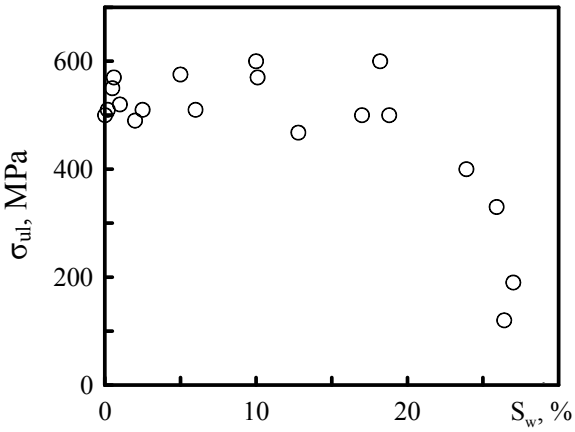

Figure 4. Ultimate strength of irradiated 18Cr-10Ni-Ti steel depending on swelling (T_{test}= 400–500°C) [18]

The widespread explanation of such behavior of material is reduction of specimen net-section due to vacancy voids. But in this case minimal value of ultimate strength of material with swelling σ_{ul} may be calculated by

$$\sigma_{ul} = \left(1 - \overline{A}_v\right) \cdot \sigma_{ul}^{m}, \tag{20}$$

where $\overline{A}_v = \left(\frac{S_w}{1+S_w}\right)^{2/3}$ – average area of vacancy voids; σ_{ul}^{m} – ultimate strength of material without swelling.

Estimation with (Eq. 20) shows that minimum value of σ_{ul} at S_w=30% is equal to 315 MPa. It is clear that this value much higher than experimental values, so the above explanation is insufficient.

According to model proposed by us the embrittlement of a material is caused by two processes. The necessary process is formation of inhomogeneous of vacancy voids distribution that is a result of voids coalescence at some level of swelling. This process may lead to local fracture at low stress, i.e. to microcrack initiation under low stress. Unstable growth of this microcrack up to macro-fracture (fracture of specimen) without increase of stress is considered as sufficient condition for sharp embrittlement. This unstable growth is caused by nano-size of vacation voids and void ligaments when material is loaded in "process zone" Z with very small sizes (~80÷400 nm) being more less than grain size. We have called such mechanism as "running collapse mechanism" (RCM).

According to papers [19, 20] for some value of swelling $S_w = (S_w)_{inh}$ vacation voids begin to

coalesce. Void coalescence results in significant inhomogeneity of voids distribution over a material. Voids distribution inhomogeneity is described by the following formula [21]

$$\frac{S_w^{max}}{\widetilde{S}_w} = \begin{cases} 1 \quad \text{for} \quad \widetilde{S}_w < (S_w)_{inh} \\ \exp\left(\alpha \cdot \left[\widetilde{S}_w - (S_w)_{inh}\right]^2\right) \quad \text{for} \quad \widetilde{S}_w \geq (S_w)_{inh} \end{cases} . \tag{21}$$

where S_w^{max} is maximal local swelling (in volume of grain); $\widetilde{S}_w$ is average swelling of specimen; α is material constant.

In a region with swelling about S_w^{max}, fracture occurs at stress $\sigma_N^{collaps} < \sigma_Y$ and disk-shaped microcrack initiates with size equal to grain size. Fracture stress $\sigma_N^{collaps}$ is calculated by the collapse criterion (See (Eq. 6). This microcrack begins to grow due to ductile fracture of moving "process zone" without increasing stresses. It is possible as the fracture strain of material with vacancy voids is very small and level of local stress and strain in very small "process zone' is sufficiently high.

Figure 5 shows the calculation of ultimate strength of material as a function of radiation swelling.

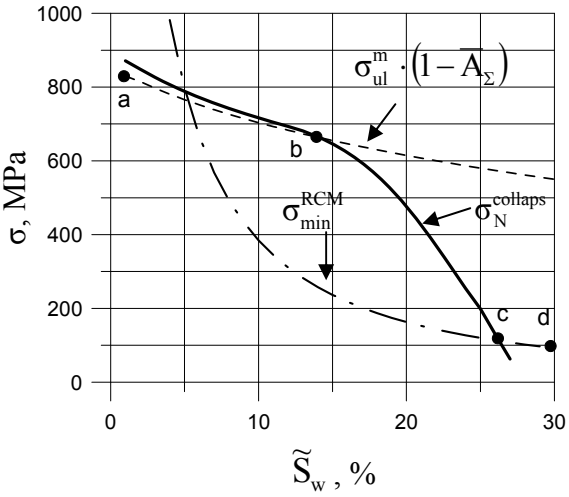

Figure 5. Calculation of ultimate strength of material as a function of swelling $\widetilde{S}_w$ (a-b-c-d line):

σ_{ul}^{m} – ultimate strength of material without swelling;

$\sigma_N^{collaps}$ – stress corresponds to fracture of grain with swelling S_w^{max} (disk-shaped crack nucletion);

σ_{min}^{RCM} - minimal stress for running collapse mechanism;

$\sigma_{ul}^{m} \cdot \left(1 - \overline{A}_{\Sigma}\right)$ – ultimate strength decrease due to net-section decrease.

6. Conclusions

(1) The model of ductile fracture was developed, which makes it possible to describe the influence of stress state triaxiality, neutron irradiation and radiation swelling on the critical parameters controlling fracture: fracture strain ε_f and the critical value of J-integral J_c.

(2) Predictions were made on the influence of a neutron dose on ε_f and fracture toughness J_c. It was shown that as stress state triaxiality increases the irradiation influence on ε_f increases. The calculation results of J_c showed that this parameter for D ≥6 dpa decreases by ~6 times.

This prediction is in complete agreement with the experimental data.

(3) The model predicts a severe decrease of J_c with a growth of swelling in relation to J_c of a material irradiated under the condition when radiation swelling is absent.

(4) It is shown that the root causes of ductile fracture of highly irradiated austenitic steels at low stresses (less than yield strength) and sharp reduction of ultimate strength are the following:
- formation of inhomogeneous distribution of vacancy voids at some critical level of swelling $(S_w)_{inh}$;
- fracture in "process zone" which has nano sizes (80-400 nm) considerably less than grain size.

(5) Initiation of fracture in a grain with high level of swelling and unstable microcrack propagation result in fracture of specimen at stress less than yield strength. Unstable microcrack propagation occurs due to local ductile fracture of moving "process zone" (this mechanism is named as "running collapse mechanism").

(6) The proposed model allows one to predict the swelling effect on sharp reduction of ultimate strength.

References

[1] A.L. Gurson, Continuum theory of ductile rupture by void nucleation and growth: Part 1-yeild criteria and flow rules for porous ductile media. J. Engng Mater Techn, 99 (1977) 2-13.

[2] V. Tvergaard and A. Needleman, Analysis of the cupcone fracture in a round tensile bar. Acta Met, 32 (1984) 157-169.

[3] B.Z. Margolin, G.P. Karzov, V.I. Kostylev, V.A. Shvetsova, Modelling for transcrystalline and intercrystalline fracture by void nucleation and growth. Fatigue Fract. Eng. Mater. Struct. 21 (1998) 123-137.

[4] B.Z. Margolin, V.A. Shvetsova, A.G. Gulenko, V.I. Kostylev, Prometey local approach to brittle fracture: development and application. Eng. Fract. Mech. 75 (2008) 3483 – 3498.

[5] B.Z. Margolin, V.A. Shvetsova, A.G. Gulenko, E.V. Nesterova, Brittle fracture local criterion and radiation embrittlement of reactor pressure vessel steels. Strength of Materials. 42 (2010) 506-527

[6] F.M. Beremin, Cavity formation from inclusions in ductile fracture of A508 Steel, Met. Trans. 12A (1981) 723-731.

[7] E.A. Little, Fracture mechanics evaluation of neutron irradiated type 321 austenitic steel. J. of Nuc. mat. 139 (1986) 261-276.

[8] Y. Huang, Accurate dilatation rates for spherical voids in triaxial stress fields. Transaction of the ASME, Ser. E, Journal of Applied Mechanics. 58 (1991) 1084-1086.

[9] B.Z. Margolin, V.I. Kostylev, A.V. Il'in, A.I. Minkin, Simulation of J_R-curves for reactor pressure vessels steels on the basis of a ductile fracture model. Int. J. Pres. Ves.& Piping. Vol. 78, Issue 10 (2001) 715-725.

[10] C.C. Chu and A. Needleman. Void nucleation effects in biaxially stretched sheets. J Engng Mater, 102 (1980) 249-256

[11] A.A. Sorokin, B.Z. Margolin, I.P. Kursevich, A.I. Minkin, V.S. Neustroev, S.V. Belozerov, Effect of neutron irradiation on mechanical properties of the WWWER-type reactor internals. Voprosy Materialovedenia (Problems of Material Science). 66 (2011) 131-152 (in Russian).

[12] Bridgman PW. Studies in large plastic flow and fracture. New York: McGraw-Hill, 1952.

[13] B. Margolin, A. Sorokin, Physical and mechanical modeling of fracture and prediction of fracture strain and fracture toughness. Proceedings of ECF19 “Fracture mechanics for durability, reliability and safety” (2012) 448.

[14] B.Z. Margolin, A.A. Sorokin, Prediction the Effect of neutron irradiation on the ductile fracture of austenitic steels. Voprosy Materialovedenia (Problems of Material Science). 69 (2012) 126-147 (in Russian).

[15] B.Z. Margolin, I.P. Kursevich, A.A. Sorokin, A.N. Lapin, V.I. Kokhonov, V.S. Neustroev, Embrittlement and fracture toughness of highly irradiated austenitic steels for vessel internals of WWER type reactors. Part 1. Relation between irradiation swelling and irradiation embrittlement. Experimental results. Strength of Materials. 41 (2009) 593-602.

[16] Margolin B.Z., Gulenko A.G., Shvetsova V.A. Improved probabilistic model for fracture toughness prediction based for nuclear pressure vessel steels// Int J Pres Ves Piping. – 1998, Vol. 75, pp. 843-855.

[17] V.I. Smirnov, B.Z. Margolin, A.N. Lapin, V.I. Kohonov, A.A. Sorokin, Investigation of neutron irradiation effect on fracture toughness 18Cr-10Ni-Ti steel and its weld. Voprosy Materialovedenia (Problems of Material Science). 65 (2011) 167-183 (in Russian).

[18] V.S. Neustroev, F.A. Garner, Very high swelling and Embrittlement observed in a Fe–18Cr–10Ni–Ti hexagonal fuel wrapper irradiated in the BOR-60 fast reactor. Fusion Materials. V. 43. Semiannual Progress Report for Period Ending December 31, (2007) 109–122.

[19] A.V. Kozlov, I.A. Portnykh, Dependence of steady- state radiation swelling rate of l 0.1C-16Cr-15Ni-2Mo-2Mn-Ti-Si austenitic steel on dpa rate and irradiation temperature. J. Nucl. Mater. 386-388 (2009) 147-151.

[20] A.V. Kozlov, I.A. Portnykh. Connection between swelling rate and growth and coalescence of radiation voids. Voprosy atomnoy nauki I tehniki, seriya materialovedenie i novye materially (Problems of nuclear science and technique , material science and new materials). 71 (2008) 3-13.

[21] B.Z. Margolin, A.A. Sorokin, On the effect of irradiation swelling on ultimate strength of irradiated austenitic steels. Voprosy Materialovedenia (Problems of Material Science). 69 (2012) 148-162 (in Russian).

Stress-Controlled and Stress-and-Strain Controlled Criteria of Brittle Fracture in Local Approach

Victoria Shvetsova[1,*], **Boris Margolin**[1], **Alexander Gulenko**[1]

[1] Central Research Institute of Structural Materials "Prometey", 191015 Saint-Petersburg, Russia
* victoria.shvetsova@prometey2.spb.su

Abstract Stress-controlled and stress-and-strain controlled criteria are compared in light of prediction of brittle fracture on a macro-scale and in light of adequate description of microstructural features of brittle fracture of irradiated RPV steels.

Keywords brittle fracture, local criterion, radiation defects, modelling, RPV steel

1. Introduction

At present, several brittle fracture models based on local criteria are developed. The local approach models differ from each other just in the formulation of local criteria. Basically, two types of local criteria may be defined: stress-controlled and stress-and-strain controlled criteria.

According to stress-controlled criterion proposed by Ludwik [1] and Yoffe [2] brittle fracture occurs when the maximum principal stress reaches some critical fracture stress S_C independent of temperature. Later Davidenkov [3] and Knott [4] added necessary condition to initiate brittle fracture - a requirement of active plastic deformation. This stress-controlled criterion was initially used for low-strength steels. Application of this criterion for middle and high strength steels, in particular, for reactor pressure vessel (RPV) steels, showed that S_C varies for specimens with various geometries. It means that stress-controlled criterion does not work, at least, in deterministic statement.

The Beremin model [5] based on stress-controlled criterion takes into account a stochastic nature of brittle fracture using the Weibull approach. This model allows one to describe the scale effect and provide the agreement of test results from notched and cracked specimens from RPV steel over narrow temperature range. However to predict the temperature dependence of fracture toughness with the Beremin model for RPV steels the introduction of additional a priori assumption is required. More difficulties arise when using stress-controlled criterion for irradiated RPV steels.

To overcome these difficulties, stress-and-strain controlled criterion was proposed near 20 years ago [6]. Application of this criterion allows one not only to provide the transferability of test results from specimens with various geometries, but also to predict known properties of brittle fracture.

The application of fracture modelling with a local cleavage fracture criterion (local approach) in principle allows the prediction of the fracture properties on a macro-scale without any additional assumptions. Local approach models may be enlarged to include in the consideration microstructural characteristics, in particular, irradiation-induced defects. Thus, fracture modelling with local fracture criterion unites various scales from irradiation-induced defects on a nano-scale to cleavage microcrack on micro-scale and to fracture on a meso- and macro-scales. This approach may provide reliable (both from mechanical and physical viewpoints) underpinning for engineering methods that are required for RPV integrity assessment. The predictable possibilities of fracture models appear to be substantially determined by local criterion used.

The present report compares stress-controlled and stress-and-strain controlled criteria in light of prediction of brittle fracture on a macro-scale and discusses which local criterion provides adequate

description of microstructural features of brittle fracture of irradiated RPV steels.

2. Local brittle fracture criteria

Currently two local cleavage fracture criteria are mainly used in brittle fracture modelling. Traditional formulation is written as [4]

$$\sigma_{eq} \geq \sigma_Y \tag{1a}$$

$$\sigma_1 \geq S_C, \tag{1b}$$

where σ_{eq} is the equivalent stress, σ_Y, the yield stress, σ_1, the maximum principal stress and S_C, the critical brittle fracture stress, which is independent of temperature, strain rate and stress triaxiality.

Another local criterion of cleavage fracture was formulated and verified in the papers [6-10]. This formulation is written in the form

$$\sigma_{nuc} \equiv \sigma_1 + m_{T\varepsilon} \cdot \sigma_{eff} \geq \sigma_d, \tag{2a}$$

$$\sigma_1 \geq S_C(æ), \tag{2b}$$

where the effective stress is $\sigma_{eff} = \sigma_{eq}-\sigma_Y$, $æ = \int d\varepsilon_{eq}^p$ is the accumulated plastic strain, $d\varepsilon_{eq}^p$ is the equivalent plastic strain increment, σ_d is the critical stress for microcrack nucleation and $m_{T\varepsilon}$ is the concentration coefficient for the local stress near the microcrack-nucleating particles. This coefficient depends on temperature T and plastic strain and may be written as $m_{T\varepsilon}=m_T(T)\cdot m_\varepsilon(æ)$. From the physical viewpoint the parameter σ_d is the strength of carbides or carbide-matrix interfaces or other particles on which cleavage microcracks are nucleated. The functions $S_C(æ)$, $m_T(T)$ and $m_\varepsilon(æ)$ are calculated as [6-10]

$$S_C(æ) = \left[C_1 + C_2 \exp(-A_d æ)\right]^{-1/2}, \tag{3}$$

$$m_\varepsilon(æ) = S_0/S_C(æ), \tag{4}$$

$$m_T(T) = m_0 \cdot \sigma_{Ys}(T), \tag{5}$$

where C_1, C_2, A_d are material constants, $S_0 \equiv S_C(æ=0)$ is the stress of start for the nucleus microcrack, m_0 is a constant which may be experimentally determined and σ_{Ys} is the temperature-dependent component of the yield stress.

From the physical viewpoint, Eqs. (1a) and (2a) are the conditions for cleavage microcracks nucleation, and Eqs. (1b) and (2b) are the conditions of their propagation. In criterion (1) the condition (1a) is the simplest requirement to reach a minimum plastic strain corresponding to yield stress that is usually equal to 0.2%. As distinct from condition (1a), cleavage microcrack nucleation according to condition (2a) depends on the maximum principal stress, plastic strain and temperature and is characterized by the critical stress σ_d. It is important that the plastic strain when microcrack is nucleated may exceed 0.2% and increases with the temperature growth [8, 10].

It may be noted that the connection of cleavage microcrack nucleation with plastic deformation seems to be quite clear from the physical point of view. Nevertheless, when formulating the local cleavage fracture criterion this connection was explicitly used only near twenty years ago [6, 11]. Now this consideration is widely used in other models, for example, [12]).

The important consequences follow from this difference between (1a) and (2a). In criterion (2) two critical parameters - S_C and σ_d may control cleavage fracture and this depends on material properties and loading conditions, mainly, on the ratio S_C/σ_Y, stress triaxiality and temperature. For example, the brittle fracture of smooth specimens is controlled by (2b) and, by contrast, the brittle fracture of

notched or cracked specimens from RPV steels by (2a) [9, 10]. For smooth tensile specimens for that stress triaxiality is low, condition (2a) is satisfied earlier than condition (2b). Therefore condition (2b) controls the brittle fracture of smooth tensile specimens. When stress triaxiality is high that is typical for notched and cracked specimens, condition (2b) is satisfied for medium and high strength steels already at very small plastic strain when cleavage microcracks are still not nucleated (condition (2a) is not fulfilled). That's why brittle fracture occurs just after satisfaction of condition (2a). By other worlds, condition (2a) controls brittle fracture for this case.

According to criterion (1) the brittle fracture on a macro-scale is controlled practically by the only process – microcrack propagation, i.e. by condition (1b) as the microcrack nucleation condition (1a) is practically always satisfied earlier than condition (1b). In terms of mechanical parameters it means that criterion (1) is stress-controlled fracture criterion and criterion (2) is stress-and-strain controlled fracture criterion.

Prediction of brittle fracture on a macro-scale in a stochastic manner may be performed with the Beremin model [5] that uses criterion (1) and stochastic parameter S_C, and with the Prometey model [9, 13] that uses criterion (2) and one (σ_d) or two (σ_d and S_C) stochastic parameters. Both models use the Weibull statistics for stochastic parameters and the weakest link model to predict the brittle fracture on a macro-scale.

3. Local criteria and microstructural features of brittle fracture of RPV steels

3.1 Microcrack nucleation sites for cracked specimens

The first interesting consequence from local brittle fracture criteria concerns localization of cleavage fracture initiation sites (i.e. sites where microcrack is nucleated and propagates) for cracked specimens. It follows from criterion (1) that cleavage fracture near the crack tip is always initiated where the peak stress is located as the probability of microcrack propagation is maximum at the peak stress, and the microcrack nucleation condition is satisfied over the whole plastic zone.

Brittle fracture of cracked specimens according to criterion (2) is mainly controlled by condition of cleavage microcrack nucleation (2a) as condition (2b) is satisfied practically over the whole plastic zone (excepting regions close to the crack tip and plastic zone boundary). As a result, both stress and plastic strain determine the cleavage fracture initiation sites.

Criterion (2) predicts that, firstly, site of the maximum probability of nucleation of propagating microcrack is located between the crack tip and the peak stress. This trend predicted with the model with one stochastic parameter σ_d [9] is schematically shown in Figure 1. (The model with two stochastic parameters σ_d and S_C [13] predicts some strip for sites of the maximum probability of nucleation of propagating microcrack.) Criterion (2) shows also that this site moves to the peak stress as degree of embrittlement of a material increases. The latter follows from increasing the contribution of stress as compared with plastic strain in condition (2a) for the embrittled material. These results are confirmed to a larger degree by fractographic examination of fracture surfaces [12]. Criterion (2) and the developed models of the prestrain effect on cleavage microcrack nucleation [14] allows also an analysis of the WPS effect on localization of initiation sites for cracked specimens. WPS results in a shift of initiation sites from the crack tip as plastic prestrain decreases a number of possible initiators especially near the crack tip. This trend was observed in [15].

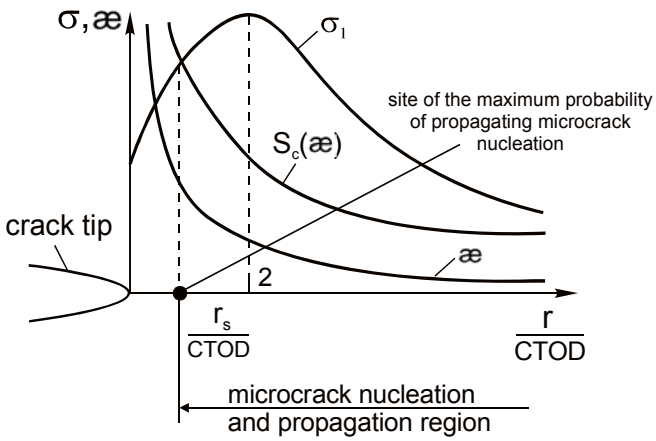

Figure 1. Microcrack nucleation sites near the crack tip according to criterion (2) for initial and not highly embrittled conditions of a material [10].

3.2. A link of local criterion with irradiation-induced defects

Local fracture criteria (1) and (2) contain internal parameters that, in principle, may be linked with the physical mechanisms of fracture and material microstructure. From viewpoint of fracture modeling for irradiated RPV materials, first of all, it is important to find how internal parameters in local criterion are linked with irradiation-induced defects.

For RPV steels three types of irradiation-induced damage are found: *matrix damage* caused by irradiation-induced lattice defects, such as clusters of point defects and dislocation loops, *precipitation* of various elements, namely, copper, nickel, manganese and other, and *segregation* of impurities, mainly phosphorus [16-18]. These radiation damages and mechanical properties of irradiated RPV materials are linked as follows. The matrix damage and precipitates result in an increase of σ_Y as they affect the dislocation mobility. An increase of σ_Y is caused by an increase of the athermal component σ_{YG} of the yield stress. Segregation of impurities, as a rule, is not associated with changes in σ_Y due to irradiation, at the same time these segregations may result in increase of the ductile-to-brittle transition temperature (DBTT), T_{tr}. [18]. Thus, segregation of impurities, in particular, phosphorus, results in so-called non-hardening mechanism of embrittlement.

When analysing the link of the above criteria with irradiation-induced defects it should be taken into account that the critical stress S_C does not practically depend on neutron fluence (at least, for transcrystalline fracture) [10, 17, 18]. This follows from experimental and theoretical results. From a physical viewpoint, irradiation-induced lattice defects and precipitates result in not decreasing the critical stress S_C. It follows from the model [8] of propagation of Griffith's crack on cleavage plane through the microstress fields which are considered as barriers for microcracks. Then criterion (1) contains the only parameter σ_Y that depends on fluence. Hence, criterion (1) describes radiation embrittlement as a result of the material hardening only and cannot describe non-hardening mechanisms of embrittlement, for example, caused by P segregation. Thus, criterion (1) describes radiation embrittlement through the mechanical factor only - increase of σ_1 due to increase of σ_Y.

Criterion (2) contains two parameters - σ_d and σ_Y that depend on fluence. It means that criterion (2) takes into account not only the material hardening but also a possible weakening of microcrack initiators that is described by decreasing σ_d. This process may be considered as the physical factor of embrittlement. It is clear that impurity segregation resulting in embrittlement without hardening may be explained with criterion (2). Indeed, as known the P segregation may occur on ferrite-carbide

interfaces [16] and result in decreasing the interface strength (i.e. in decreasing σ_d). This means that the nucleation of cleavage microcracks becomes easier compared with unirradiated steel.

The mechanisms of the effect of radiation defects on cleavage microcrack nucleation were proposed in [13, 14]. It should be noted that for RPV steels in unirradiated condition the cleavage microcrack initiators are mainly globular carbides [19] and additional initiators do not arise under irradiation as practically all radiation defects are very small to nucleate a sharp cleavage microcrack. (For example, sizes of dislocation loops are near 5÷20 nm and the nucleus microcrack size estimated from the Griffith's condition is 100÷400 nm.) The proposed mechanisms explain how radiation defects affect cleavage microcrack nucleation on carbides. The proposed mechanisms allow the determination of the dependence of critical parameter σ_d on neutron fluence [13, 14].

These mechanisms are divided into two groups. The first group includes the mechanisms [13, 14] connected with decreasing the strength of carbide-matrix interface. One mechanism of decreasing σ_d is the impurity (P) *segregation* on ferrite-carbide interfaces caused by the P diffusion accelerated by irradiation. Another mechanism for decreasing σ_d is *the arising of internal stresses* caused by irradiation-induced dislocation loops and precipitates on carbide-matrix interface. These internal stresses result in rupture of the interface at stress σ_{nuc} being less than σ_{nuc} for unirradiated material.

The second group includes the mechanism connected with easier formation of dislocation pile-ups near initial microcrack initiators (for example, globular carbides) due to increasing the concentration of radiation defects [13, 14]. This process may be described by increasing the probability of dislocation pile-up formation in material with high concentration of barriers for dislocations. The detailed consideration is given in [13, 14] where the probability of pile-up formation is described with the Weibull function and the Orovan stress used as a characteristic parameter for concentration of various barriers.

3.3. On the intergranular fracture mode

Brittle fracture of unirradiated RPV steels occurs, as a rule, by transcrystalline cleavage and microcleavage. Neutron irradiation and post-irradiation annealing may result in appearance of intercrystalline fracture mode. It is interesting that a fraction of intercrystalline fracture is not always correlated with mechanical properties. For irradiated steels the mechanical parameters (DBTT and σ_Y) speak about significant embrittlement, however a fraction of intercrystalline fracture is usually small (near 20% of fracture surface). After annealing, significant recovery of mechanical properties is observed, at the same time, a fraction of intercrystalline fracture may increase.

These findings may be explained with criterion (2) and the proposed mechanisms of the effect of radiation defects on the critical stress σ_d [13, 14]. In deterministic statement, value of σ_d is determined by minimum value of the critical stresses for nucleation of transcrystalline σ_d^{tr} and intercrystalline σ_d^{int} microcracks. The fracture mode may be trans- or intercrystalline that depends on which value is less if the critical stress S_C is the same for both types of microcracks. In probabilistic statement, mixed fracture is expected if the difference of σ_d^{tr} and σ_d^{int} is not large.

The interpretation for variation of the parameters σ_d^{tr} and σ_d^{int} is schematically shown in Figure 2, for RPV steels in various conditions (unirradiated, irradiated and after post-irradiation annealing). Two steels are considered: 2.5Cr-Mo-V and 2Cr-Ni-Mo-V (steels for WWER-440 and WWER-1000 RPV respectively). For unirradiated steels (Fig. 2a) brittle fracture occurs mainly by the

transcrystalline mechanism that means that $\sigma_d^{tr} < \sigma_d^{int}$ and $S_C^{tr} < S_C^{int}$, where S_C^{tr} and S_C^{int} are the critical stresses for propagation of transcrystalline and intercrystalline microcracks. The difference of σ_d^{tr} and σ_d^{int} is less for 2Cr-Ni-Mo-V steel for which some fraction of intercrystalline fracture is observed.

For irradiated steels (Fig. 2b) σ_d^{tr} and σ_d^{int} decrease. For carbides located on grain boundary, segregation of impurities and arising of internal stresses caused by dislocation loops occur more intensively. Intercrystalline phosphorus segregation caused by irradiation decreases also S_C^{int} as sharp microcrack nucleation and propagation on phosphorus monolayer weakening atomic bonds, require less energy. Nevertheless, for irradiated 2.5Cr-Mo-V steel the conditions $\sigma_d^{tr} < \sigma_d^{int}$ and $S_C^{tr} \approx S_C^{int}$ are more possible, so that transcrystalline brittle fracture is more typical. For irradiated 2Cr-Ni-Mo-V steel the situation is possible when $\sigma_d^{tr} \approx \sigma_d^{int}$ (this steel is more sensitive to the P segregation) and $S_C^{tr} \approx S_C^{int}$ as so that mixed trans- and intercrystalline brittle fracture is observed.

After post-irradiation annealing at T_{ann}=475°C (Fig. 2c) phosphorus segregations dissociate in a grain only, and do not dissociate on grain boundary [16, 17]. Radiation-induced dislocation loops and precipitates may be dissociated practically completely both in a grain and on grain boundary. Therefore the σ_d^{tr} value increases up to the value for the unirradiated condition but the σ_d^{int} and S_C^{int} values remain less than for the unirradiated condition. As a result, for 2.5Cr-Mo-V steel a fraction of intercrystalline fracture may increase as compared with irradiated specimens as the values of σ_d^{tr} and σ_d^{int} become close, although this annealing results in full recovery of the mechanical properties (T_{tr} and σ_Y). For 2Cr-Ni-Mo-V steel the situation is possible when intergranular carbides become "weakest link" and intercrystalline fracture predominates, and although σ_Y may recover fully, T_{tr} recovers not fully so that $(T_{tr})^{unirr} < (T_{tr})^{ann} < (T_{tr})^{irr}$. The reason is clear: for this case the brittle fracture resistance is controlled by σ_d^{int} that does not recover fully.

Annealing at T_{ann}≈600°C (Fig. 2d) results in full recovery of σ_d^{int} as dissociation of grain boundary P segregations occurs at this temperature [16] and the situation become close to the unirradiated condition (Fig. 2a). Full recovery of the mechanical properties and the fracture modes is observed.

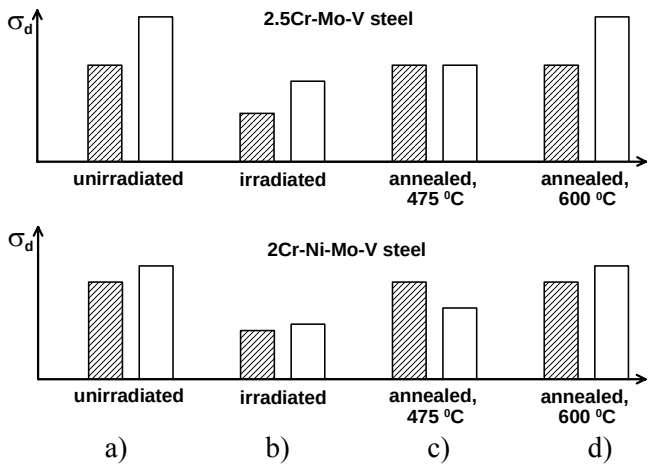

Figure 2. Variation of σ_d^{tr} (shaded bar) and σ_d^{int} (open bar) for RPV steels in various conditions: unirradiated (a), irradiated (b), after post-irradiation annealing (c) and (d) [14].

Let us analyze the above experimental findings from viewpoint of criterion (1). It is clear that criterion (1) may explain an appearance of intercrystalline fracture for irradiated steel but does not

explain an increase of fraction of intercrystalline fracture after post-irradiation annealing. Indeed, brittle fracture according to criterion (1) is controlled by minimum value of the two values S_C^{tr} and S_C^{int}. For unirradiated steels brittle fracture occurs mainly by the transcrystalline mechanism so that it follows from criterion (1) that $S_C^{tr} < S_C^{int}$ and S_C^{tr} is the controlling parameter. Intercrystalline phosphorus segregation caused by neutron irradiation decreases the critical stress S_C^{int}. (The critical stress S_C^{tr} does not decrease for irradiated RPV steels [18].) For irradiated RPV steels the relation $S_C^{tr} \approx S_C^{int}$ or $S_C^{tr} > S_C^{int}$ become possible and, hence, either both stresses S_C^{tr} and S_C^{int} or S_C^{int} control brittle fracture according to criterion (1). As a result, intercrystalline fracture is predicted for irradiated steel. However post-irradiation annealing can not result in additional S_C^{int} decrease (on the contrary, annealing may increase S_C^{int}) so that an increase of fraction of intercrystalline fracture after post-irradiation annealing can not be expected from viewpoint of criterion (1).

4. Comparison of local criteria in light of prediction of brittle fracture on a macro-scale

4.1 Prediction of $K_{JC}(T)$ curve and its transformation for irradiated RPV materials

Application of the Beremin model [5] for prediction of $K_{JC}(T)$ for various materials may be found in [20], application of the Prometey model for RPV steels in various conditions (initial, irradiated and highly embrittled) – in [9, 10, 13]. It was found that there are difficulties with the use of the Beremin model for medium and high strength steels, in particular, for RPV steel [6-10]. It was shown that the prediction of fracture toughness of irradiated RPV materials with this model is not correct. The reason consists in the fact that according to this model the dependence $K_{JC}(T)$ is determined practically by the dependence $\sigma_Y(T)$ as S_C does not depend on temperature. The fact of the matter is that according to criterion (1) the rate of growth of K_{JC} with temperature T is controlled by the parameter $\frac{1}{\sigma_Y} \cdot \frac{d\sigma_Y}{dT}$.

For highly embrittled material the variation of K_{JC} with temperature T occurs over the temperature range where this parameter $\rightarrow 0$. As a result, K_{JC} does not practically depend on temperature that is in contradiction with test results.

Some attempts (for example, [21]) were undertaken to reform the Beremin model by introduction of the temperature dependence for the parameter S_C (or the parameter σ_u in the terms of the Beremin model). The parameter S_C becomes not invariant relative to stress triaxiality and temperature. From physical viewpoint such "reformation" cannot be considered as reasonable. It has been found in [6-9] that difficulties with the use of the Beremin model for medium and high strength steels are connected with the use of microcrack nucleation condition in the form (1a).

When using the Prometey model there is no problem with prediction of $K_{JC}(T)$ for embrittled RPV steels as the parameter $\sigma_{Ys}(T)$ is used in criterion (2) as temperature dependent parameter (see Eq. (5)). As a result, over the temperature range where $\frac{1}{\sigma_Y} \cdot \frac{d\sigma_Y}{dT} \rightarrow 0$, the ratio $\frac{1}{\sigma_{Ys}} \cdot \frac{d\sigma_{Ys}}{dT} \neq 0$. That' why criterion (2) allows one to describe $K_{JC}(T)$ adequately even for highly embrittled material.

Transformation of $K_{JC}(T)$ curve for irradiated RPV steels as the test results [22, 23] show may be approximately described as a lateral shift to higher temperature range for small degree of embrittlement, and as a variation in the $K_{JC}(T)$ curve shape for high degree of embrittlement [22]. Criterion (2) and the Prometey model provide a possibility to predict this transformation of the $K_{JC}(T)$

curve as illustrated in Figure 3a where the decrease in σ_d models increasing neutron fluence.

At the same time criterion (2) and the Prometey model may also predict a pure lateral shift of $K_{JC}(T)$ curve to higher temperature range [14]. It may be achieved by an increase of the parameter m_0 with increasing neutron fluence F, i.e. an increase of "driving force" $\sigma_{nuc} \equiv \sigma_1 + m_{T\varepsilon} \cdot \sigma_{eff}$ in condition (2a) (without the decrease in σ_d). For this case the calculated $K_{JC}(T)$ curves are shown in Figure 4b. It should be noted that the parameter m_0, being to some degree sensitive to material microstructure, may depend on the particularities of plastic deformation in steels with radiation defects. It is clear that as a common case, irradiation-induced dislocation loops and precipitates may affect the geometry of dislocation pile-ups arrested by carbides and, hence, the coefficient m_0. However, at present, the experimental data are too few to allow an analysis of this effect. Possible trends of this effect have been considered in [14]. In principle, the coefficient m_0 may increase as F increases due to decrease of the width and blunting of dislocation pile-up near microcrack initiator that is a result of an increase of the density of radiation defects.

Thus, criterion (2) provides a possibility to predict not only a change in $K_{JC}(T)$ curve shape but also pure lateral shift of $K_{JC}(T)$ curve to higher temperature range. It should be emphasize that any models based on the stress controlled criterion (1) predict a variation in the $K_{JC}(T)$ curve shape for any degree of embrittlement. This is because the $K_{JC}(T)$ dependence is determined according to criterion (1) by the $\sigma_Y(T)$ dependence. These models may predict lateral shift of $K_{JC}(T)$ only if the dependence of S_C (or σ_u in terms of the Beremin model) on temperature and neutron fluence is a priori introduced, for example, as it is made in [21]. Thus, it should be concluded that at present the Prometey model based on criterion (2) is the only model that allows the prediction of lateral shift of $K_{JC}(T)$ curves without additional assumptions.

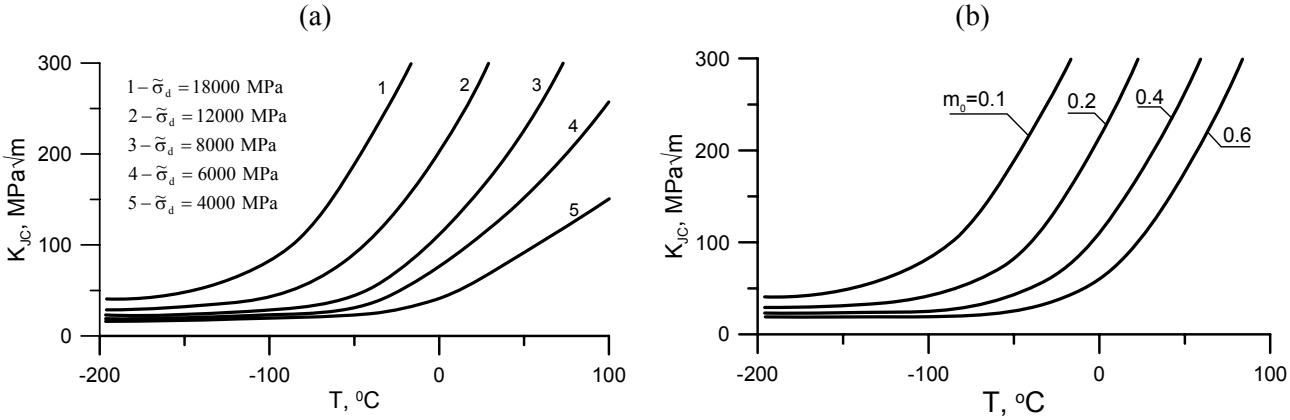

Figure 3. The $K_{JC}(T)$ curves calculated with the Prometey model for decreasing parameter σ_d and m_0 = const (a) and for increasing function $m_0(F)$ and σ_d =const (b). (Specimen thickness is 25 mm and P_f = 0.5.) [14]

4.2. On minimum value of fracture toughness for RPV materials

The Master Curve [24]] and Unified Curve [22] methods use the Weibull statistics to describe the scatter in K_{JC} results and the effect of specimen thickness on $K_{JC}(T)$ curve. The fracture probability P_f and K_{JC} is connected by the Weibull distribution function [24]

$$P_f = 1 - \exp\left[-\left(\frac{K_{JC} - K_{min}}{K_0 - K_{min}}\right)^4\right], \tag{6}$$

where K_0 is a scale parameter depending on the test temperature and specimen thickness; deterministic parameter K_{min} is the minimum value of fracture toughness.

As a common case, K_{min} may depend on the test temperature. In [24] it was accepted that $K_{min}(T)$ = const and on the basis of large number of experimental data sets for RPV steels over low temperature range (on the lower shelf of $K_{JC}(T)$ curve) it was determined that K_{min}= 20 MPa√m.

In the present section the results are represented on calculation of K_{min} as a function of temperature, $K_{min}(T)$, for RPV steels on the basis of local criteria (1) and (2). These results are calculated with the Beremin and Prometey models based on criteria (1) and (2) respectively.

To obtain $K_{min}(T)$ the following considerations are used. (1) When calculating with the Beremin model the value of K_{min} is taken as stress intensity factor K_I when conditions (1a) and (1b) are satisfied for the unit cell nearest to the crack tip.

(2) When calculating with the Prometey model the value of K_{min} is taken as K_I when condition (2a) is satisfied for the unit cell nearest to the crack tip. (For cracked specimens from RPV steels brittle fracture is controlled by microcrack nucleation condition (2a).)

(3) For both models the unit cell size ρ_{uc} is taken to be equal to 50 μm. The dependence $\sigma_Y(T)$ was taken as obtained in [9] for RPV steel in initial conditions. For the Beremin model two values of the parameter S_0 are taken as more typical for RPV steels [9, 10]: S_0= 1300 and 1500 MPa. For the Prometey model three values of the controlling parameter σ_{d0} are taken as σ_{d0} = 1300, 1500 and 2000 MPa that corresponds to various estimations of σ_{d0} in [9, 10]. It is important to note that when calculating $K_{min}(T)$ the critical parameters are taken as calibrating from specimens without cracks, i.e. from smooth tensile specimens.

(4) Stress-and-strain fields near the crack tip are calculated by approximated solution of elastic-plastic problem represented in [9].

The calculation results are shown in Figure 4 for cracked specimens with 50 mm in thickness from RPV steel in initial condition. (Here maximum temperature is restricted by T=100°C as for higher temperatures brittle-to-ductile transition occurs for this steel.) As seen from Figure 4a $K_{min}(T)$ decreases over low temperature range and becomes constant at T>0°C for curve 1 and T>-75°C for curve 2. This behavior is caused by different controlling conditions in (1) for these temperature ranges: Eq. (1a) gives decreasing part and Eq. (2) gives const part. As seen from Figure 4b according to the Prometey model $K_{min}(T)$ is practically constant or slightly increasing (from 18 to 25 MPa√m for curve 3).

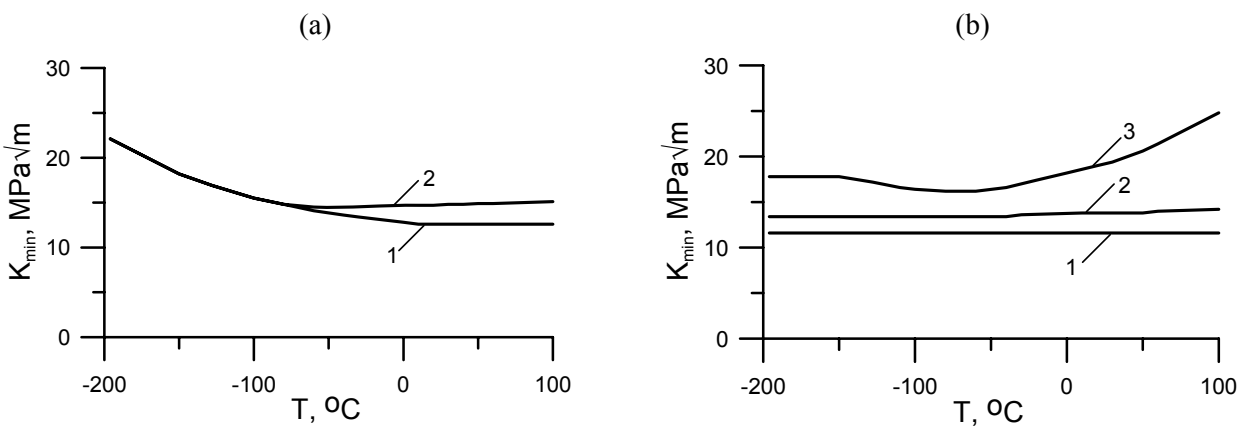

Figure 4 The $K_{min}(T)$ curves calculated with the Beremin (a) and Prometey (b) models model for RPV steel: (a): 1 - S_0=1300; 2 - S_0=1500 MPa; (b): 1 - σ_{d0} = 1300; 2 - σ_{d0} =1500; 3 - σ_{d0} =2000 MPa.

Acknowledgements

The part of this work has been carried out within the framework of the EC-sponsored ISTC project 3973 performed in collaboration with the Integrated Project PERFORM 60.

References

[1] R. Ludwik, Elemente der technologischen Mechanik, Berlin, 1909.

[2] A. Yoffe, M. Kirpicheva, M. Levitskay, Deformation and strength of crystals. Zhurnal Rus. Phys.Chim. Obz, 56 (1924) 489-504. (in Russian)

[3] N. Davidenkov, Dynamic Testing of Materials, ONTI, Moscow, 1936 (in Russian)

[4] J.F. Knott, Fundamentals of Fracture Mechanics, Butterworths, London, 1973.

[5] F.M. Beremin, A local criterion for cleavage fracture of a nuclear pressure vessel steel. Met.Trans, 14A (1983) 2277-2287.

[6] B.Z. Margolin, V.A.Shvetsova, Brittle fracture criterion: physical and mechanical approach. Problemy Prochnosti, (1992) N2 3-16. (in Russian)

[7] B.Z.Margolin, V.A. Shvetsova, Local criterion for cleavage fracture: structural and mechanical approach. J. de Physique IV, 6 (1996) C6-225-C6-234.

[8] B.Z. Margolin,V.A. Shvetsova, G.P. Karzov, Brittle fracture of nuclear pressure vessel steels. Part I. Local criterion for cleavage fracture. Int. J. Pres. Ves. Piping, 72 (1997) 73-87.

[9] B.Z. Margolin, A.G. Gulenko, V.A. Shvetsova, Improved probabilistic model for fracture toughness prediction for nuclear pressure vessel steels. Int. J. Pres. Ves. Piping, 75 (1998) 843-855.

[10] B.Z. Margolin, V.A. Shvetsova, A.G. Gulenko, V.I. Kostylev, Application of a new cleavage fracture criterion for fracture toughness prediction for RPV steels. Fatigue Fract. Engng. Mater. Struct, 29(9) (2006) 697-713.

[11] J.H. Chen, C. Yan, J. Sun, Further study on the mechanism of cleavage fracture at low temperatures. Acta Metall. Mater, 42 (1994) 251-261.

[12] S. Bordet, A. Karstensen, D. Knowles, C. Wiesner, A new statistical local criterion for cleavage fracture in steel. Eng. Fracture Mech, 72 (2005) 453-474.

[13] B.Z. Margolin V.A. Shvetsova, A.G. Gulenko, V.I. Kostylev, Prometey local approach to brittle fracture: development and application. Eng. Fracture Mech, 75 (2008) 3483-3498.

[14] B. Margolin, V. Shvetsova, A. Gulenko, Radiation embrittlement modeling in multi-scale approach to brittle fracture of RPV steels. Int.J. Fracture, 179 (2012) 87-108.

[15] S. Bordet, B. Tanguy, J. Besson et al, Cleavage fracture of RPV steel following warm pre-stressing: micromechanical analysis and interpretation through a new model. Fatigue Fract. Eng. Mater. Struct, 29(9) (2006) 799-816.

[16] B.A Gurovich, E.A Kuleshova, Y.A. Nikolaev, Y.I. Shtrombakh, Assessment of relative contributions from different mechanisms to radiation embrittlement of reactor pressure vessel steels. J. Nucl. Mater., 246 (1997) 91-120.

[17] V. Nikolaev, V. Rybin, Mechanisms controlling the composition influence on radiation hardening and embrittlement of iron-base alloys. in: *Effect of radiation on materials*: ASTM STP 1270, 1996, 3-24.

[18] N.N. Alekseenko, A.D.Amaev, I.V. Gorynin, V.A. Nikolaev, Radiation damage of nuclear power plant pressure vessel steels. La Grange Park, Illinois USA, 1997.

[19] S.R. Ortner, The ductile-to-brittle transition in steels controlled by particle cracking. Fatigue Fract. Eng. Mater. Struct, 29(9) (2006) 752-769.

[20] EUROMECH-MECAMAT'96: Local Approach to Fracture. (Edited by A. Pineau and G. Rosselier) J. de Physique IV, 1996, vol.6, C6.

[21] B. Tanguy, C. Bouchet, S. Bugat, J. Besson, Local approach to fracture based prediction of the ΔT_{56J} and $\Delta T_{Ic,100}$ shifts due to irradiation for an A508 pressure vessel steel. Engng. Fract. Mech, 73 (2006) 191-206.

[22] B. Margolin, A. Gulenko, V. Nikolaev, L. Ryadkov, A new engineering method for prediction of the fracture toughness temperature dependence for RPV steels. Int. J. Pres. Ves. & Piping, 80 (2003) 817-829.

[23] B. Margolin, B.Gurovich, V. Fomenko et al, Fracture toughness prediction for highly irradiated RPV materials: from test results to RPV integrity assessment. J. Nuclear Materials, 432 (2013) 313-322.

[24] K.Wallin. The scatter in K_{IC} results. Eng. Fract. Mech, 19 (1984) 1085-1093.

Scatter of measured K_{IC} related to the scatters of local parameters X_f, σ_f and ε_{pc}

Jian Hong Chen* **and Rui Cao**

Department of Material Science and Engineering and State Key laboratory of Non-ferrous Metals of Lanzhou University of Technology, Lanzhou, China
* Corresponding author: zchen@lut.cn

Abstract 42 values of K_{IC} measured at -100°C are related to the measured values of local fracture stress σ_f and the fracture distance X_f by the formula: $K_{IC}= \beta^{-(N+1)/2}X_f^{1/2}[\sigma_f^{(1+N)/2N}/ \sigma_y^{(1-N)/2N}]$. The scatters of K_{IC} caused by σ_f or X_f are assessed separately at constant values of X_f or σ_f. It is found that at a constant X_f the scatter of K_{IC} induced by the scatter of σ_f accounts for only 20% of the total scatter, while at a nearly constant σ_f the scatter of K_{IC} caused by the scatter of X_f can reach almost 100% of the total scatter of K_{IC}. It means that the effect of the scatter of X_f on the scatter of K_{IC} is much larger than that of σ_f. This idea is opposite to the assumption widely accepted in local approach that the distribution of various sizes of the carbide particles which present various values of σ_f is the main event in the statistical calculation. Instead, the random distribution of (X_f) of weakest particles with the lowest values of σ_f should be considered as the determining factor in statistical assessment for the cleavage fracture.

Keywords Scatter of K_{IC}, Local fracture stress σ_f, Fracture distance X_f, Fracture strain ε_{pc}

1. Introduction

The relationships between global toughness, such as the critical stress intensity factor K_{IC} and the critical values of parameters specified in the micromechanism of cleavage fracture, such as local fracture stress σ_f, fracture distance X_f and fracture strain ε_{pc}, are of great significance. These relationships offer the bases for establishing the statistical model (such as the local approach) which uses the micro-parameters to predict the global failure probability.

For pre-cracked specimens of a normalized C-Mn steel the relations between the global toughness measured in cleavage-fractured specimens and the critical values of local parameters ε_{pc}, σ_f and X_f had been discussed in a previous paper[1], where the discussion started from the Eq. (1) [2]

$$K_{IC} = \beta^{-(N+1)/2} X_K^{1/2} \left[\sigma_f^{(1+N)/2N} / \sigma_y^{(1-N)/2N}\right], \qquad (1)$$

β is the amplitude of HRR crack tip stress singularity [3,4]

Here this equation is modified to Eq. (2) by substituting X_f for X_k.

$$K_{IC} = \beta^{-(N+1)/2} X_f^{1/2} \left[\sigma_f^{(1+N)/2N} / \sigma_y^{(1-N)/2N}\right], \qquad (2)$$

In Eq. (1) X_k is the 'characteristic distance' [5], In Eq. (2) X_f is the fracture distance i.e. the measured distance from the cleavage initiation site to the blunted precrack tip. In Eq. (2) the factor

$$F = X_f^{1/2} \left[\sigma_f^{(1+N)/2N} / \sigma_y^{(1-N)/2N}\right], \qquad (3)$$

correlates the global fracture toughness K_{IC} to the local parameters σ_f and X_f.

In following, the relations will be analyzed using the data of Table 1 which were measured in 42 specimens at -100°C. The C-Mn steel specimens were normalized, austenized at 900°C for 2 hours then air cooled. The uniform microstructure is composed of the ferrite grains of 9.3μm in average size and 22μm for the largest grains and the pearlite colonies around 3.2μm in the average size and 20μm for the largest.

Table 1 fracture toughness-associated parameters measured in COD tests of a normalized C-Mn steel

T=100°C σ_y=470MPa σ_{max}=1880MPa Qmax=4.0 DMS/δ_c=1.25 N=0.21

Test No.	P_{Gy} (N)	P_f (N)	δ_c (μm)	X_f (μm)	$X_f^{1/2}$ ($mm^{1/2}$)	X_f/δ_c	σ_f (MPa)	ε_{pc}	σ_m/σ_e	F (MPa $m^{-1/2}$)	K_{IC}	d (μm)	Mark
Y02	8036	9016	114	102	0.32	0.89	1852	0.0458	2.41	241.9	131.0	4.0	L
Y40	8330	8673	74	158	0.4	2.14	1795	0.0058	2.81	276.3	105.5	3.0	R
Y41	7840	8820	121	131	0.36	1.08	1861	0.0369	2.62	276.0	134.9	3.0	L
Y05	7644	8036	72	60	0.24	0.83	1852	0.0678	2.10	181.4	104.1	11.3	L
Y26	7448	8232	100	120	0.35	1.2	1861	0.0311	2.73	268.3	122.7	4.5	L
Y31	7644	7840	53	75	0.27	1.41	1847	0.0140	3.10	202.5	89.3	3.8	R
Y36	8036	8330	64	139	0.37	2.17	1791	0.0052	2.85	254.0	98.1	4.4	R
Y25	7644	8526	111	90	0.3	0.81	1852	0.0673	2.12	226.8	129.2	3.2	L
Y35	7350	8330	128	175	0.42	1.37	1852	0.0180	3.05	317.5	138.8	7.5	R
Y11	8428	9212	117	119	0.34	1.02	1800	0.0241	2.57	232.6	132.7	7.5	L
Y47	8036	8232	55	86	0.29	1.56	1842	0.0184	3.06	215.8	91.0	5.4	R
Y13	—	7350	20	63	0.25	3.15	1617	0.0050	2.65	127.9	54.9	8.6	R
Y21	—	7840	22	62	0.25	2.82	1678	0.0052	2.72	142.2	57.5	3.8	R
Y44	7448	7644	52	112	0.33	2.15	1790	0.0075	2.96	226.2	88.4	7.5	R
Y43	7840	7840	26	78	0.28	3	1645	0.0063	2.64	153.6	62.5	6.6	R
Y15	—	6468	10	69	0.26	6.9	1391	0.0036	2.27	58.1	38.8	5.4	R
Y22	6860	7448	131	169	0.41	1.29	1861	0.0219	2.90	314.3	140.4	6.1	L
Y42	7840	8134	81	75	0.27	0.93	1861	0.0458	2.84	188.4	110.4	4.8	L
Y19	7546	7840	80	131	0.36	1.64	1842	0.0133	3.03	267.9	109.7	8.3	R
Y12	8036	8232	73	113	0.34	1.55	1833	0.0184	3.08	249.5	104.8	6.5	R
Y27	7350	7350	42	16	0.13	0.38	1810	0.1829	1.62	92.0	82.3	3.0	L
Y23	6953	7252	56	66	0.26	1.18	1861	0.0233	2.71	199.3	91.8	3.8	L
Y14	7546	7546	33	69	0.26	2.09	1860	0.098	2.94	199.0	70.5	6.3	R
Y16	7840	8036	72	169	0.41	2.35	1758	0.0040	2.81	266.8	104.1	3.0	R
Y30	7644	8330	82	96	0.31	1.17	1861	0.0240	2.70	237.6	111.1	8.1	L
Y04	—	8036	29	138	0.37	4.75	1490	0.0035	2.44	149.5	66.1	3.5	R
Y37	8428	8624	77	124	0.35	1.61	1833	0.0183	3.08	256.8	107.6	6.5	R
Y38	8722	8918	47	10	0.32	2.13	1795	0.0080	2.90	221.1	84.1	2.7	R
Y33	8330	8526	36	93	0.3	2.58	1840	0.0057	2.66	222.6	73.6	3.8	R
Y10	8036	8036	30	67	0.26	1.68	1763	0.0052	2.93	170.5	67.2	3.2	R
Y17	—	7546	14	60	0.24	4.29	1513	00042	2.51	101.3	45.9	2.9	R
Y03	—	7350	12	30	0.17	2.5	1767	0.0046	2.83	112.2	42.5	3.8	R
Y1	—	5330	10	20	0.14	2	1734	0.0059	2.80	87.5	38.8	*	R
Y2	—	6270	12	17	0.13	1.42	1838	0.0186	2.80	96.1	42.5	*	R
Y3	—	7500	17	85	0.29	5	1466	0.0035	2.45	111.8	50.6	*	R
Y4	—	7690	22	50	0.22	2.27	1706	0.0051	2.92	134.4	57.5	*	R
Y5	8560	8670	35	43	0.21	1.23	1875	0.0254	2.69	164.5	72.6	*	L
Y6	8570	8670	36	44	0.21	1.22	1875	0.0245	2.72	164.5	73.6	*	L
N01	6370	7640	132	25	0.16	0.19	1800	0.4257	2.57	111.4	140.9	6.0	L
N23	8430	8430	34	20	0.14	0.59	1828	0.1166	1.71	101.9	71.5	3.7	L
N06	5684	6080	54	51	0.23	0.94	1852	0.0443	2.84	173.9	90.2	4.3	L
N21	8530	8530	30	0	0	0	1743	0.9727	0.60	0.0	67.2	2.3	L

No: specimen number ; T: test temperature; Py: yield load; Pf: fracture load; σ_y: yield stress; δ_c: critical value of COD; X_f: distance from cleavage initiation site to blunted precrack tip ; σ_f: local fracture stress; ε_{pc}: critical plastic strain; σ_m/σ_e: critical stress triaxiality; $F=X_f^{1/2}\{\sigma_f^{(1+N)/2N}/\sigma_y^{(1-N)/2N}\}$, K_{IC}: critical stress intention factor, d: diameter of particle triggering cleavage; Mark: denoting the distance of cleavage initiation site relative to that of peak stress; L: distance shorter than that of peak stress position DMS, X_f ＜DMS; R: distance longer than that of peak stress position DMS, X_f ＞DMS;

2. Relationship between K_{1c} and factor $F=X_f^{1/2}[\sigma_f^{(1+N)/2N}/\sigma_y^{(1-N)/2N}]$

Fig.1 depicts the relationship between the measured values of K_{1c} and the factor (3) $F=X_f^{1/2}[\sigma_f^{(1+N)/2N}/\sigma_y^{(1-N)/2N}]$. As seen in Fig.1 in a general trend K_{1C} increases with F in a linear pattern, however the variation of K_{1C} values measured at -100°C is quite large. The highest value of K_{1C} of 140.9MPam$^{-1/2}$ is as large as 363% of the lowest value of 38.8MPam$^{-1/2}$. The absolute difference (scatter) reaches 102MPam$^{-1/2}$. The scatter of measured values of K_{IC} at an identical value of F accounts for 55.8 MPam$^{-1/2}$ which implies that besides the X_f and σ_f a factor has significant effect on the values of K_{IC}.

Three parallel lines divide the K_{IC}-distributing zone to two areas: in the upper area all points ● represent the crack initiation site (X_f) locating on the left side of the peak stress position DMS, X_f ＜DMS(shown in Fig.4). In the lower area, all points ○ represent the crack initiation site (X_f) locating on the right side of DMS, X_f ＞DMS (Fig.4). As discussed in authors' previous work [1] the higher ε_{pc} makes the crack initiation site to the left side of DMS, where the plastic strain is higher, As seen in Fig.1, at same F values, all specimens marked by ● present values of K_{IC} higher than that of specimens marked by ○. That is, the measured values of K_{IC} are higher for points (marked by ●) which represent the crack initiation site (X_f) located at the left side of DMS due to the higher ε_{pc}. This observation demonstrated the effects of higher ε_{pc} on the increments of the scatter of K_{IC}. In addition in the upper area, the scatter of measured values of K_{IC} (the vertical distance between the upper and the median lines) accounts for about 34. 1MPam$^{-1/2}$ which is considered to be caused by variation of ε_{pc} at fixed F. The scatter of measured values of K_{IC} in the lower area accounts for about 21.7MPam$^{-1/2}$ which is considered to be caused by some intrinsic factors, such as the errors made in measurements and also by variations of ε_{pc} which varies in a range with values lower than that to cause the crack initiation site locating on the left side. The scatter in the lower area is appreciably lower than the scatter in the upper area.

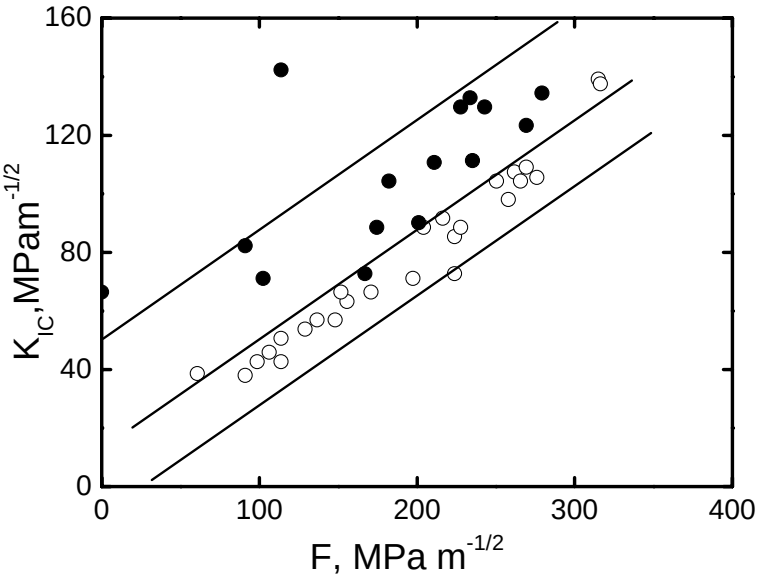

Figure 1. K_{IC} plotted against $F=X_f^{1/2}[\sigma_f^{(1+N)/2N}/\sigma_y^{(1-N)/2N}]$for a normalized C-Mn steel,
● for X_f on the left side of DMS, ○ for X_f on the right side of DMS

In following sub-sections, relationships between global toughness and critical values of microscopic parameters of the normalized C-Mn steel are analyzed in the order of σ_f, X_f and ε_{pc}.

3 Effects of σ_f

For investigating the effect of σ_f on the scatter of measured values of K_{IC}, Fig.2 is drawn, which shows the plots of K_{IC} against the square root of the fracture distance, $X_f^{1/2}$, using the data of Table 1. Then Fig.2 is compared with Fig.1 where the K_{IC} is plotted against $F= X_f^{1/2}[\sigma_f^{(1+N)/2N}/ \sigma_y^{(1-N)/2N}]$. Because in Fig.1, the product of $X_f^{1/2}$ and σ_f (in the term of $[\sigma_f^{(1+N)/2N}/ \sigma_y^{(1-N)/2N}]$) is fixed at an abscissa value, the effects of the variations of $X_f^{1/2}$ and σ_f on the K_{IC} values offset to each other, the effect of the variation of σ_f alone is minor. While in Fig.2 at a fixed $X_f^{1/2}$, only the σ_f is varied, thus the difference of scatters presented between Fig.1 and Fig.2 at a fixed abscissa is attributed to the scatters of the σ_f. The scatter of K_{IC} at a fixed $X_f^{1/2}$ reaches 77. 5MPam$^{-1/2}$ in Fig.2. Comparing this value with the scatter of 55.8MPam$^{-1/2}$ at a fixed F in Fig.1, the total scatter of σ_f from 1391MPa to 1875MPa (demonstrated in the Table 1) causes about 21.7MPam$^{-1/2}$ in the scatter of K_{IC}, which accounts for about 28% of the scatter of 77. 5MPa m$^{-1/2}$ at a fixed $X_f^{1/2}$ and only 21% in whole scatter of 102MPam$^{-1/2}$ measured at -100°C for the 42 specimens of the normalized C-Mn steel.

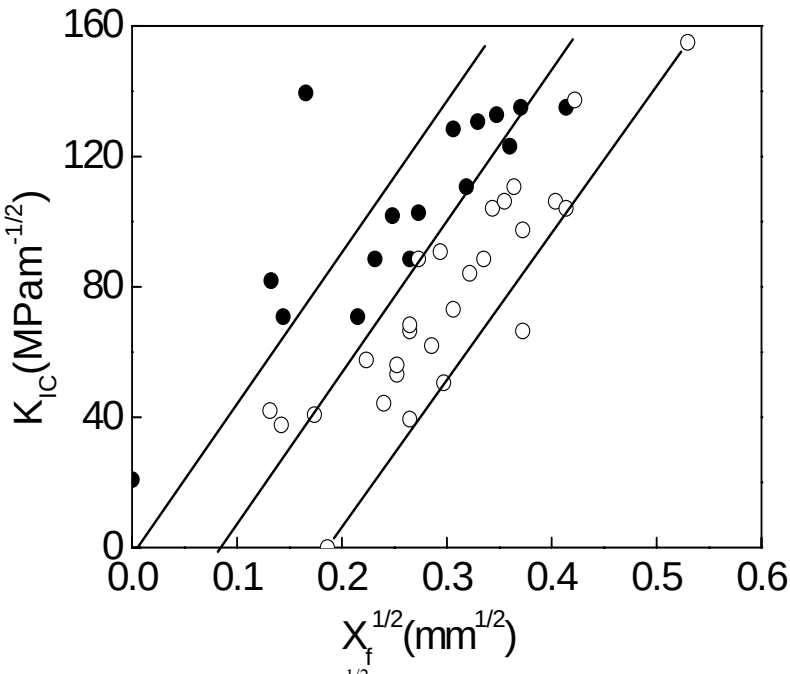

Figure 2. K_{IC} plotted against $X_f^{1/2}$for a normalized C-Mn steel
● for X_f on left side of DMS ○ for X_f on right side of DMS, (Chen, 1998)

For further analyses, in Fig.2 one median line is also drawn, which divides the K_{IC}-distributing zone to two areas: in the upper area all points ● represent the crack initiation site (X_f) locating at the left side of DMS and have higher $K_{IC.}$ The scatter in this area (the vertical distance between the upper and median lines) of measured values of K_{IC} reaches about 34.1MPam$^{-1/2}$ at a fixed X_f which is almost the same in Fig.1. It means that the scatter of σ_f has little influence on the scatter of K_{IC} in the upper area. In the lower area, all points ○ represent the crack initiation site (X_f) locating at right side of DMS and have lower K_{IC}. The scatter in this lower area (the vertical distance between the lower and median lines) of measured values of K_{IC} accounts for about 43.4MPam$^{-1/2}$ which is 21.7 MPam$^{-1/2}$ larger than that in Fig.1 and the difference is considered to be caused by variation of the σ_f in term of $[\sigma_f^{(1+N)/2N}/ \sigma_y^{(1-N)/2N}]$at a fixed X_f.

In summary, the effects of the variation of σ_f from 1391MPa to 1875MPa at a fixed X_f induce 21.7 MPam$^{-1/2}$ i.e. only 20% increase in scatter of K_{IC} and manifests itself in the lower area where the normal stress predominates the cleavage fracture process. Therefore it is not reasonable for a statistical model to be based on the statistical distribution of the local fracture stress σ_f i.e. on the

microcrack size distribution.

4 Effects of X_f

In Fig.2 K_{IC} measured at -100°C is plotted against $X_f^{1/2}$ for the normalized C-Mn steel. It is seen that with increasing X_f, the K_{IC} values increase remarkably. The K_{IC} increases from 38.7MPam$^{-1/2}$ to 140.7 MPam$^{-1/2}$ (along one parallel line) at the variation of X_f from 16μm to 175μm. For further analyses of the effect of X_f, Fig.3 is drawn with the plots of measured values of K_{IC} against the factor

$$F' = \left[\sigma_f^{(1+N)/2N} / \sigma_y^{(1-N)/2N}\right] \quad (4)$$

so that at a fixed abscissa the σ_f is fixed while the X_f is able to vary and to show its effect on the K_{IC}.

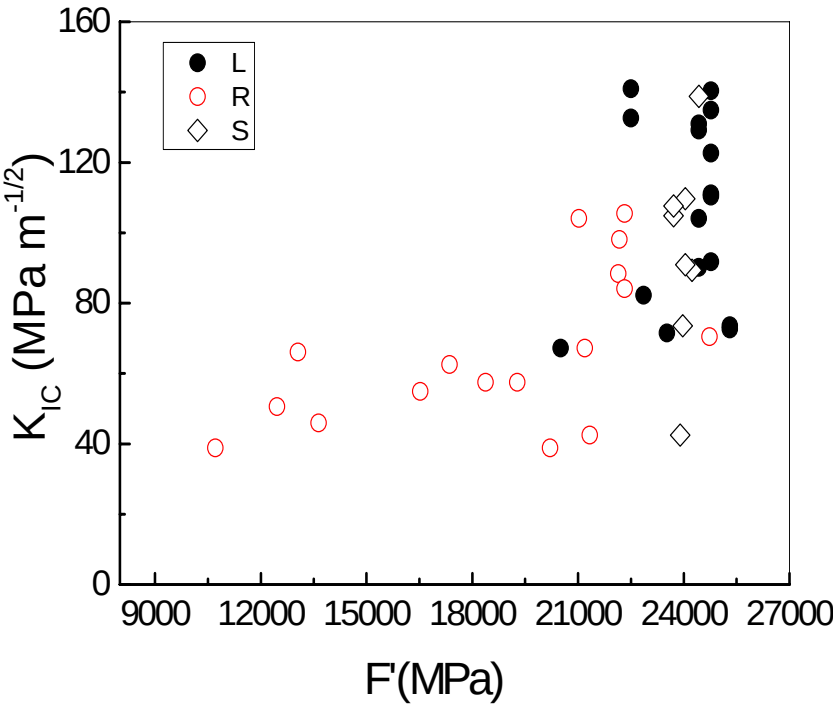

Figure 3. K_{IC} plotted against F'=[$\sigma_f^{(1+N)/2N}$/ $\sigma_y^{(1-N)/2N}$] for a normalized C-Mn steel
● for X_f on left side of DMS ○ for X_f on right side of DMS

Fig.3 shows a unique shape distinct from Fig.1 and Fig.2. Unlike Fig. 1 and Fig.2, the distribution of scatter cannot be delimited between two parallel lines. In the region of F' less than 20000 MPa the scatter of K_{IC} is low and can be neglected. In the region of F' higher than 20000 MPa the scatter of measured values of K_{IC} is large and shows a uniform pattern. The points ● representing the crack initiation site (X_f) locating on the left side of DMS mix uniformly with points ○ and ◇ representing the crack initiation site (X_f) locating on the right side of DMS. It means that at a fixed abscissa of F' the effects of ε_{pc} on the scatter of K_{IC} are incorporated into the effects of X_f. It is worth noticing that at a near constant abscissa (marked by ◇) the scatter covers almost the whole scale in measurement. Table 2 lists the values of K_{IC} for specimens with F' distributed in a narrow region (from 23709MPa to 24424MPa). The corresponding points are marked by ◇ in Fig.3. All points represent the crack initiation site (X_f) locating on the right side of DMS.

Table 2. Data of K_{IC}, X_f and correlated parameters

T=100°C σ_y=470MPa σ_{max}=1880MPa, Q_{max}=4.0 N=0.21							
No	F (MPa $m^{-1/2}$)	F' (MPa)	σ_f (MPa)	X_f (μm)	$X_f^{1/2}$ ($mm^{1/2}$)	K_{IC} ($MPam^{-1/2}$)	Mark
Y35	317.5	24424.7	1852	175	0.42	138.8	R
Y19	267.9	24046.7	1842	131	0.36	109.7	R
Y37	256.8	23709.7	1833	124	0.35	107.6	R
Y12	249.5	23709.7	1833	113	0.34	104.8	R
Y47	215.8	24046.7	1842	86	0.29	91.0	R
Y31	202.5	24235.2	1847	75	0.27	89.2	R
Y33	222.6	23971.5	1840	93	0.30	73.6	R
Y2	96.1	23896.5	1838	17	0.13	42.5	R

NO: specimen number ; T: test temperature; N: work hardening exponent, σ_y: yield stress; $F=X_f^{1/2}[\sigma_f^{(1+N)/2N}/\sigma_y^{(1-N)/2N}]$, $F'=[\sigma_f^{(1+N)/2N}/\sigma_y^{(1-N)/2N}]$, σ_f: local fracture stress; X_f: distance from cleavage initiation site to blunted precrack tip ; K_{IC}: critical stress intention factor, Mark: denoting the distance of peak stress position site relative to that of peak stress; L: distance shorter than that of peak stress position; R: distance longer than that of peak stress position;

As revealed by Fig.3 and Table 2, in a very narrow range of variation of F' (from 23896kgmm^{-2} to 24424 kgmm^{-2}) the increase of K_{IC} from 42.5 MPam$^{-1/2}$ to 138.8 MPam$^{-1/2}$ reaches 96.3MPam$^{-1/2}$ which almost covers total scatter of measured values of K_{IC}. Because in this narrow range of F' the σ_f almost keeps constant (varies from 1833MPa to 1852MPa) and the effect of ε_{pc} on the scatter of K_{IC} is incorporated into the effect of X_f, the increase of K_{IC} can only be attributed to the increases with X_f. The small variation of X_f from 17μm to 175μm causes the increase of K_{IC} from 42.5 MPam$^{-1/2}$ to 138.8MPam$^{-1/2}$ almost covering total scatter of measured values of K_{IC}. Thus, the effect of X_f on the scatter of K_{IC} is of major significant. This phenomenon also indicates that the macro-index of the fracture toughness, $K_{IC,}$ can not represent a true material's property, instead it is a parameter dependent on the location of the precrack. The same argument has been held by Pineau and Tanguy[6].The K_{IC} has not a unique value but has a minimum value which is determined by the minimum fracture distance X_f.

5. **Effects of ε_{pc}**

As discussed in section 2 the major effects of high $\boldsymbol{\varepsilon_{pc}}$ manifest their selves in making the cleavage crack initiation site closer to the pre-crack tip (move to left side of DMS) and then increasing K_{IC}. In previous work [1] for revealing the effect of ε_{pc} the X_f in the factor F for points locating on the left side is replaced by X_o the distance of a corresponding point on the right branch of the normal stress distribution curve with the same local fracture stress σ_f (as shown in Fig.4).

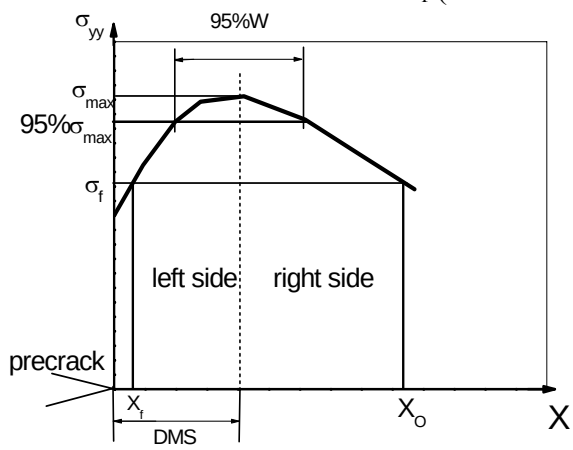

Figure 4. Schematics showing replacing X_o for X_f [1]

Fig.5 plots K_{IC} against F in which the $X_o^{1/2}$(marked by o), is substituted for $X_f^{1/2}$ (marked by ●) i.e. $F=X_o^{1/2}[\sigma_f^{(1+N)/2N}/\sigma_y^{(1-N)/2N}]$ and the major effect of ε_{pc} is evaded. Comparing Fig.1 with Fig.5 it is apparent that when the major effect of ε_{pc} is evaded the relation between K_{IC} and F is more stringed. The scatter in K_{IC} at an identical F is reduced to about 21.7MPam$^{-1/2}$ in Fig.5 from 55.8MPam$^{-1/2}$ in Fig.1. It means that through moving the cleavage site from the right side to the left side the scatter in ε_{pc} (0.0035 to 0.1829) could have caused about 34.1MPam$^{-1/2}$ in scatter of K_{IC}.

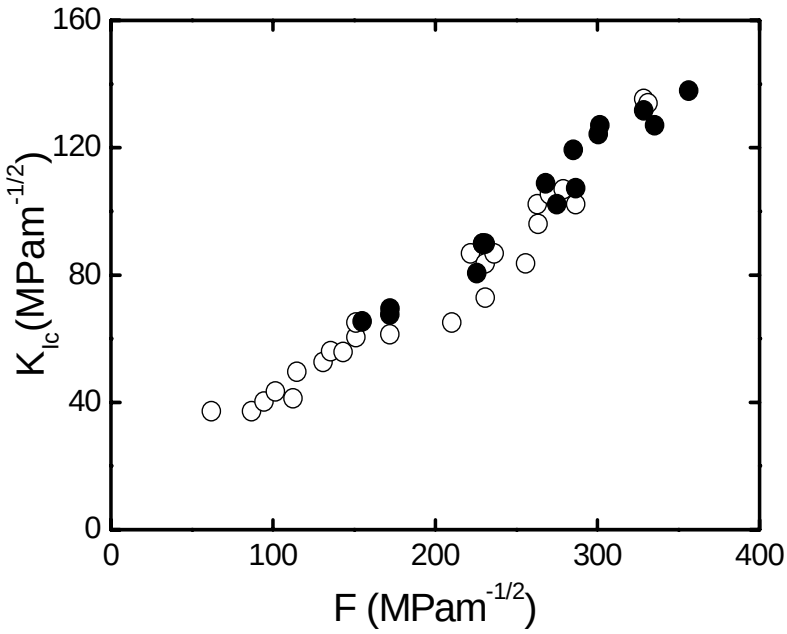

Figure 5. K_{IC} plotted against $F=X_o^{1/2}[\sigma_f^{(1+N)/2N}/\sigma_y^{(1-N)/2N}]$ for a normalized C-Mn steel ● for X_f originally on left side of DMS ○ for X_o originally on right side of DMS

Fig.6 plots K_{IC} against $X_o^{1/2}$, where X_o is modified from X_f and the major effect of variation of ε_{pc} is evaded. Comparing it with Fig.2, it also shown that the scatter at same $X_o^{1/2}$ could be much reduced from 77.5 MPam$^{-1/2}$ to about 43.4 MPam$^{-1/2}$, part of which(about 21.7 MPam$^{-1/2}$) is caused by the variation of σ_f. Thus both Fig.5 and Fig.6 show the effects of the variation of ε_{pc} (0.0035 to 0.1829) on the scatter of K_{IC} account for about 34.1 MPam$^{-1/2}$.

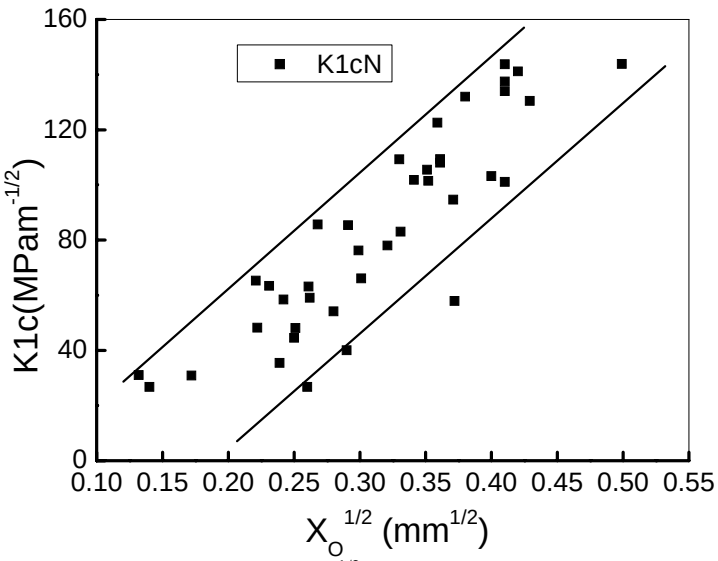

Figure 6. K_{IC} plotted against $X_o^{1/2}$ for a normalized C-Mn steel [1]

In summary, the relationship between fracture toughness K_{IC} and parameters of micromechanism of cleavage fracture X_f, σ_f, and σ_y of a C-Mn normalized steel can be generally described by the formula

$$K_{IC} = \beta^{-(N+1)/2} X_f^{1/2} \left[\sigma_f^{(1+N)/2N} / \sigma_y^{(1-N)/2N} \right], \tag{2}$$

Here the work hardening exponent N is taken as 0.21, and the amplitude of HRR crack tip stress singularity β is about 6.14.

As shown in Fig.1, the measured values of K_{IC} exhibit a linear pattern of distribution against the term $F=X_f^{1/2}[\sigma_f^{(1+N)/2N}/\sigma_y^{(1-N)/2N}]$ with a slope content of 1/3. The total scatter of K_{IC} reaches 102MPam$^{-1/2}$ and at a fixed F value it reaches 55.8 MPam$^{-1/2}$.

The scatters in K_{IC} caused by the micro-parameters in micromechanism of cleavage fracture are summarized as follows:

X_f, variation from 17μm to 175μm at fixed σ_f produce scatter of 96.3 MPam$^{-1/2}$ accounting for 95% in total scatter of 102MPam$^{-1/2}$

σ_f, variation from 1391MPa to 1875MPa at fixed X_f produce scatter 21.7 MPam$^{-1/2}$ accounting for 21% in total scatter of 102MPam$^{-1/2}$

ε_{pc}, variation from 0.0035 to 0.1829 at fixed σ_f produce scatter 34.1 MPam$^{-1/2}$ accounting for 34% in total scatter of 102MPam$^{-1/2}$

Among these three main micro-parameters, the X_f is the major significant factor in production of scatter in measured values of K_{IC}. Thus, in a statistical model, the variation of X_f should be taken into account as the main factor firstly. The effect of ε_{pc} present in moving the X_f. In case the variation of X_f, (including on both left and right sides) has been taken as the main factor, the effect of ε_{pc} is diminished. In common cases, the σ_f is a stable parameter and its scatter is within ±10%, which causes about 20% of the scatter of K_{IC} so its effect is minor. Therefore, it is unreasonable to take the distribution of σ_f as the main event in a statistic model.

Acknowledgements

This work was financially supported by National Nature Science Foundation of China (No. 51035004 and 51265028).

References

[1] J. H. Chen, G. Z. Wang, On scattering of measured values of fracture toughness parameters. Inter. J. Fract, 94(1998)33-49.

[2] D. A. Curry, Cleavage micromechanisms of crack extension in steels. Metal. Sci, 14(1980)319-326.

[3] J. W. Hutchinson, Plastic stress and strain field at a crack tip. J. Mech. Phys. Solids, 16(1968)13-31.

[4] J. R. Rice, G. R. Rosengren, Plain strain deformation near a crack tip in a power-law hardening material. J. Mech.Phys. Solids, 16(1968)1-12.

[5] R.O. Ritchie, J. F. Knott, J. R. Rice, On the relationship between critical tensile stress and fracture toughness in mild steel. J. Mech. Phys. Solids, 21(1973) 395-410.

[6] A. Pineau and B. Tanguy, Advances in cleavage fracture modeling in steels:Micromechanical, numerical and multiscale aspects, Comptes Rendus Physique, 11, (2010) 316-325

The Elusive Temperature Dependence of the Master Curve

Kim Wallin

VTT Materials and Built Environment, P.O. Box 1000, FI-02044 VTT, Espoo, Finland
Kim.Wallin@vtt.fi

Abstract The Master Curve methodology for describing cleavage fracture toughness, scatter, size-effects and temperature dependence has been standardized in ASTM E1921. The scatter and size-effects predicted by the method are based on theory, whereas the temperature dependence is the result of empirical observations. The reason for the seemingly nearly invariant temperature dependence of the cleavage fracture toughness of different steels has until now eluded theoretical explanations. The standard fracture toughness temperature dependence is expressed in terms of the normalization fracture toughness K_0. However, K_0 is really the product of three separate parameters, K_{min}, K_{0i} and $P(K_\infty)$, all of which are temperature dependent. K_{min} is related to the steepness of the stress distribution in front of the crack, K_{0i} is connected to the likelihood of initiation and $P(K_\infty)$ describes the likelihood of cleavage crack propagation in a unified stress field. This presentation gives some more insight into the factors that lead to the experimentally observed temperature dependence. Finally, a new more material specific temperature dependence usable instead of the standard expression is given.

Keywords Master Curve, Cleavage fracture, Temperature dependence

1. Introduction

The Master Curve (MC) method is a statistical, theoretical, micromechanism based, analysis method for fracture toughness in the ductile to brittle transition region. The method, originally developed at VTT simultaneously account for the scatter, size effects and temperature dependence of fracture toughness.

The method has been successfully applied to a very large number of different ferritic steels and it forms the basis of the ASTM testing standard for fracture toughness testing in the transition region (ASTM E1921-12).

1.1. The basic Master Curve

The MC approach is based on a statistical brittle fracture model, which gives for the scatter of fracture toughness in the form of Eq. (1) [1].

$$P\left[K_{IC} \le K_I\right] = 1 - \exp\left(-\left[\frac{K_I - K_{min}}{K_0 - K_{min}}\right]^4\right), \tag{1}$$

In Eq. (1), $P[K_{IC} \le K_I]$ is the cumulative failure probability, K_I is the stress intensity factor, K_{min} is the theoretical lower bound of fracture toughness and K_0 is a temperature and specimen size dependent normalization fracture toughness, that corresponds to a 63.2% cumulative failure probability being approximately $1.1 \cdot \overline{K}_{IC}$ (mean fracture toughness). The special form of Eq. 1 with $(K_I - K_{min})^4$, instead of $K_I^4 - K_{min}^4$, comes from a conditional crack propagation criterion, which makes the MC to deviate from a simple weakest link model of the weakest link. The model predicts a statistical size effect of the form of Eq. (2) [1].

$$K_{B_2} = K_{min} + \left[K_{B_1} - K_{min} \right] \cdot \left(\frac{B_1}{B_2} \right)^{1/4}, \tag{2}$$

The parameters B_1 and B_2 correspond to respective specimen thickness (length of crack front).

On the lower shelf of fracture toughness (K_{IC} << 50 MPa√m) the equations may be inaccurate. The model is based upon the assumption that brittle fracture is primarily initiation controlled, even though it contains the conditional crack propagation criterion. On the lower shelf, the initiation criterion is no longer dominant, but the fracture is completely propagation controlled. In this case there is no statistical size effect (Eq. 2) and also the toughness distribution differs (not very much) from Eq. (1). In the transition region, where the use of small specimens becomes valuable, Eqs. (1) and (2) are valid.

For structural steels, a "Master Curve" describing the temperature dependence of fracture toughness is assumed in the form of Eq. (3).

$$K_0 = 31 + 77 \cdot \exp\left(0.019 \cdot \left[T - T_0\right]\right), \tag{3}$$

T_0 is the transition temperature (°C) where at which the mean fracture toughness, corresponding to a 25 mm thick specimen, is 100 MPa√m and K_0 is 108 MPa√m.

The original data used to define Eq. (3) are shown in Fig. 1. It should be pointed out that the temperature dependence is purely empirical, even though it has been found to provide a rather good description of a large number of structural steel. The assumption is that the dislocation mobility in the ferrite matrix controls the temperature dependence. So far, attempts to provide a theoretical derivation of the temperature dependence have not been successful. One reason for this may be that most theoretical models only deal with cleavage fracture initiation. However, it is not only the probability of initiation that is affected by temperature. The theoretical temperature dependence is considered next.

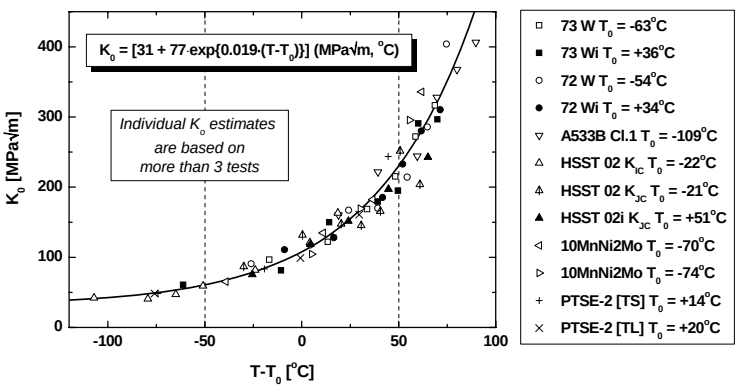

Figure 1. Original data used to define the temperature dependence of the MC. Each point denotes a K_0 estimate based on more than three tests [1].

1.2. Basis for the temperature dependence

The different possible mechanisms of cleavage fracture are qualitatively rather well known. Primarily the initiation is a critical stress controlled process, where stresses and strains acting on the

material produce a local failure, which develops into a dynamically propagating cleavage crack. The local "initiators" may be precipitates, inclusions or grain boundaries, acting alone or in combination. An example of a typical cleavage fracture initiation process is presented schematically in Fig. 2. The first step involves the cracking of a precipitate or inclusion (sometimes, it may also be a grain boundary or grain triple point). The second step consists of the carbide size micro-crack propagating into the surrounding matrix and the third step consists of the grain-size crack propagating into neighboring grains. The two first steps are mainly affected by the particle size and the local stress and strain at the initiation site. The third step, however, is also affected by the stress gradients in the vicinity of the initiation site, since the third step covers a larger material volume.

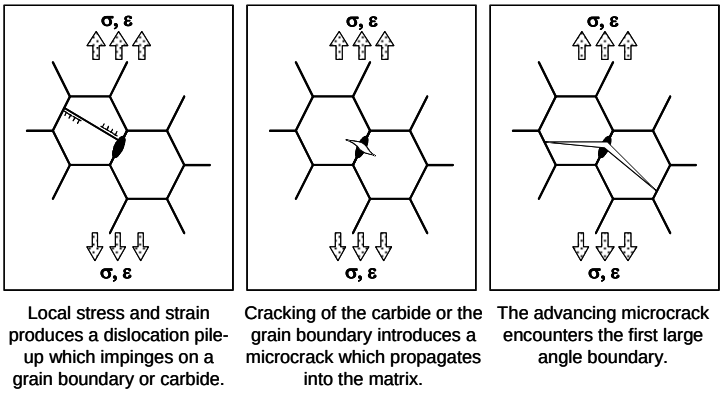

Figure 2. Schematic presentation of the necessary steps for cleavage fracture initiation [1].

Depending on loading geometry, temperature, loading rate and material, different steps are more likely to be most critical. For structural steels at lower shelf temperatures and ceramics, in the case of cracks where the stress distribution is very steep, steps II and III are more difficult than initiation and they tend to control the fracture toughness. At higher temperatures, where the steepness of the stress distribution is smaller, propagation becomes easier in relation to initiation and step I becomes more and more dominant for the fracture process. The temperature region where step I dominates is usually referred to as the transition region.

On the fracture surface of a specimen with a fatigue crack this is usually seen as a difference in the number of initiation sites visible on the fracture surface (Fig. 3). At lower shelf temperatures, numerous initiation sites are visible, whereas at higher temperatures, corresponding to the transition region, only one or two initiation sites are seen. In the case of notched or plain specimens, only a few initiation sites are seen even on the lower shelf. This is due to that, for cracks, the peak stresses are very high virtually from the beginning of loading, whereas for notched and plain specimens, the peak stresses increase gradually during loading. The fracture surface appearance is an effective tool in the decision if the material is on the lower shelf or in the transition region. The region has an implication on the macroscopic statistical behavior of cleavage fracture and is therefore also affecting the application of the fracture toughness test results.

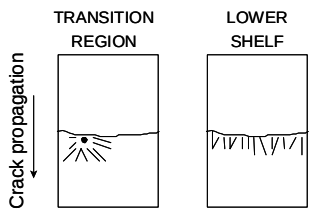

Figure 3. Typical cleavage fracture surfaces for fatigue pre-cracked specimens indicating differences in transition region and lower shelf behavior [1].

Due to the complexity of the cleavage process, a statistical model is needed to understand the effect of the different steps on the temperature dependence.

2. Statistical modeling of cleavage fracture initiation

The basis of a general statistical model is the following. It is assumed that the material in front of the crack contains a distribution of possible cleavage fracture initiation sites i.e. cleavage initiators. The cumulative probability distribution for a single initiator being critical can be expressed as Pr{I} and it is a complex function of the initiator size distribution, stress, strain, grain size, temperature, stress and strain rate etc. The shape and origin of the initiator distribution is not important in the case of a "sharp" crack. The only necessary assumption is that no global interaction between initiators exists. This means that interactions on a local scale are permitted. Thus a cluster of cleavage initiations may be required for macroscopic initiation. As long as the cluster is local in nature, it can be interpreted as being a single initiator. All the above factors can be implemented into the initiator distribution and they are not significant as long as no attempt is made to determine the shape and specific nature of the distribution. A quantitative description of the initiator distribution is also hindered by the statistical variation in stress and strain between grains and laths. Further, also the local orientations would need to be known. This is one reason why all present cleavage fracture models have had difficulties in connecting the models to real microstructural variables.

If a particle (or grain boundary) fails, but the broken particle is not capable of initiating cleavage fracture in the matrix, the particle sized microcrack will blunt and a void will form. Such a void is not considered able to initiate cleavage fracture. Thus, the cleavage fracture initiator distribution is affected by the void formation, leading to a conditional probability for cleavage initiation (Pr{I/O}).The condition being that the cleavage initiator must not have become a void. The cleavage fracture process contains also another conditional event, i.e. that of propagation. An initiated cleavage crack must be able to propagate through the matrix in order to produce failure. Thus the conditional probability will be that of propagation after initiation (Pr{P/I}). The cleavage fracture initiation process can be expressed in the form of a probability tree (Fig. 4).

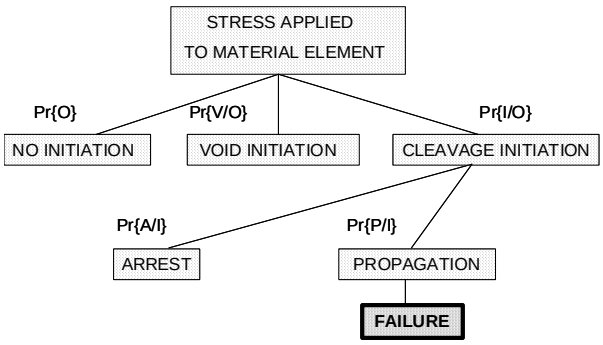

Figure 4. Probability tree for cleavage fracture [1].

2.1. Probability of initiation

For a "sharp" crack in small scale yielding the stresses and strains are described by the HRR field. One property of the HRR field is that the stress and strain distribution is self-similar and another that the stresses and strains have an angular dependence. The term “small scale yielding” is in this derivation used to describe the loading situation where the self-similarity of the stress field remains unaffected by loading. For such a situation, it has been shown, by weakest link statistics, that the probability of initiation alone can be expressed in the form of Eq. (4) [1].

$$P_f = \Pr\{I/O\} = 1 - \exp\left\{-\frac{B}{B_0}\cdot\left(\frac{K_I}{K_{0i}}\right)^4\right\}, \tag{4}$$

B_0 is a freely definable normalization crack front length and K_{0i} corresponds to a cumulative initiation probability of 63.2%.

2.2. Conditional cleavage propagation

Eq. (4) would imply that an infinitesimal K_I value might lead to a finite failure probability. This is not true in reality. For very small K_I values the stress gradient becomes so steep that even if cleavage fracture can initiate, it cannot propagate into the surrounding and other adjacent grains, thus only causing a zone of microcracks in front of the main crack. If propagation in relation to initiation is very difficult, a stable type of fracture may evolve. This is an effect often seen with ceramics. The need for propagation leads to a conditional crack propagation criterion, which causes a lower limiting K_{min} value below which cleavage fracture is impossible. For structural steels in the lower shelf temperature range, the fracture toughness is likely to be the controlled by the inability of propagation (Fig. 3).

The question regarding propagation alters the above pure weakest link type argument somewhat. It means that initiation is not the only requirement for cleavage fracture, but additionally a conditional propagation requirement must be fulfilled. Thus one must examine the probability of cleavage initiation during a very small load increment, assuming that no initiation has occurred before. Such a probability constitutes a conditional event and the resulting function is known as the hazard function. When the hazard function for initiation is multiplied by the conditional probability of propagation (Pr{P/I}), the cumulative failure probability including propagation becomes thus as Eq. (5) [1].

$$P_f = 1 - \exp - \int_{K_{min}}^{K_I} \Pr\{P/I\}\cdot\frac{B}{B_0}\cdot\frac{4\cdot K_I^3}{K_{0i}^4}\cdot dK_I, \tag{5}$$

There are two requirements for Pr{P/I}. It must be an increasing function starting from K_{min} and for large K_I values it must saturate towards a constant probability corresponding to a uniform stress denoted by an infinite stress intensity factor K_∞. One possible form of Pr{P/I} is given by Eq. (6). Other possible forms have also been discussed in e.g. [1].

$$\Pr\{P/I\} = P(K_\infty)\cdot\left(1 - \frac{K_{min}}{K_I}\right)^3, \tag{6}$$

All the possible equations are functions growing from 0 to $P(K_\infty)$, where $P(K_\infty)$ is a number smaller than 1. The constant $P(K_\infty)$ reflects the finite probability of crack propagation even in a uniform stress field, being due to a possible miss-orientation between the micro-crack and the possible cleavage crack planes and the need to cross a grain boundary. $P(K_\infty)$ will increase with increasing stress and decrease with increasing temperature.

Insertion of Eq. (6) into Eq. (5) leads to the equation for the cumulative cleavage fracture probability including the conditional propagation criteria, (Eq. 7).

$$P_f = 1 - \exp\left\{ -\frac{B}{B_0} \cdot \frac{P(K_\infty)}{K_{0i}^4} \cdot \left(K_I - K_{min} \right)^4 \right\}, \tag{7}$$

Eq. (7) is equivalent to the basic MC expression given by Eqs. (1) and (2). Eq. (7) shows that the basic MC K_0 parameter is actually a complex parameter having the detailed form of Eq. (8).

$$K_0 = \frac{K_{0i}}{P\left(K_\infty\right)^{1/4}} + K_{min}, \tag{8}$$

K_0 is really the product of three separate parameters, all of which are temperature dependent. The parameter K_{min} is usually only weakly temperature dependent, since it is mainly a result of the steepness of the crack stress distribution and the effective surface energy. The increase in K_{min} usually occurs at temperatures where K_0 already is close to upper shelf. The temperature dependence of K_{0i}, is a function of the changes in initiator distribution with temperature and the materials yield stress. The temperature dependence connected to K_{0i} should mostly be controlling at low temperatures, where the yield stress sensitivity to temperature is large. This leaves the probability of cleavage crack propagation in a unified stress field, $P(K_\infty)$, as the likely parameter describing most of the temperature dependence in the transition region. This is also in line with the fact that the crack arrest toughness has very similar temperature dependence as K_0 [1].

3. Discussion

Considering the complicity of K_0, one should not assume that all ferritic steels have exactly the same temperature dependence. This is especially the case for such steels, where the chemistry affects the dislocation mobility in the ferrite matrix. E.g. high nickel steels, even though ferritic, are likely to show different temperature dependencies, since nickel is known to affect the materials crack arrest properties favorably. To study the possible variation in the fracture toughness temperature dependence between different structural steels, 82 data sets each with at least 20 significant samples have been fitted with the MC, with K_0 in the form of Eq. (3), where the parameter C (normally 0.0019°C^{-1}) is a variable. The median fracture toughness curves are shown in Fig. 5. The figure shows also the theoretical statistical uncertainty related to a sample size of 20, if the parameter corresponds to C = 0.019°C^{-1}. Even though nearly 80% of the estimates fall within this region, there are materials that clearly deviate from the standard MC.

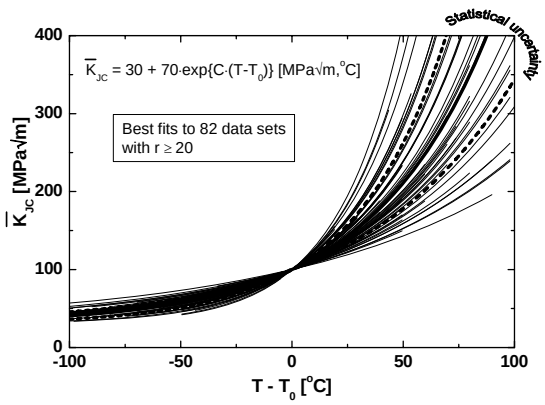

Figure 5. Compilation of median fracture toughness temperature dependence estimates for a large variety of structural steels having more than 20 significant samples. The thick full line indicates the standard MC and the dashed lines indicates the statistical 5% and95% uncertainty limits related to a sample size of 20. [1].

A three-dimensional fit of the temperature dependence can be expressed in the form of Eq. (9) [1], even though other similar forms provide practically the same accuracy. Regardless of the exact choice of function, the trend is clear. Yield stress has a rather insignificant effect on the temperature dependence whereas the transition temperature has a more significant effect.

$$C\left[°C^{-1}\right] \approx 0.008 + \left(\frac{20.9\ \text{MPa}}{\sigma_Y}\right)^{2.24} + \left(\frac{0.6°C}{T_0 + 273°C}\right)^{0.77}, \tag{9}$$

The reasons for the effect of T_0 on the shape of the transition curve, may partly be due to fact that the difference between initiation toughness and crack arrest toughness are affected by T_0 (See [1]) or it can be partly related to a rough connection between upper shelf toughness and T_0. The difference in initiation toughness and crack arrest toughness would affect K_0 by affecting K_{min} and $P(K_\infty)$, in relation to K_{0i}, whereas the upper shelf toughness would control the amount of ductile tearing prior to cleavage fracture and would thus affect K_{0i}.

Overall, the analysis indicates that the use of the standard MC with a fixed C = 0.019°C-1 is well applicable for steels with T_0 in the range -100°C…+50°C. Since the MC is fitted to the data in the temperature range T_0-50°C to T_0+50°C, it will provide a satisfactory description of the fracture toughness in this temperature region. Any deviations in transition curve steepness will be adjusted for by shifts in T_0 and the overall description of the data in that region is adequate. However, if the materials T_0 value or the application temperature is outside these limits, it is recommended to make tests at or near to the application temperature. Due to the considerable statistical uncertainty connected to parameter C, it is not recommended to experimentally estimate it for a single application. As long as there are test results not too far from the application temperature, the standard MC can well be used. As a sensitivity analysis, the standard MC analysis can be complemented with an analysis using Eq. (9). In this case, a first estimate of T_0 is obtained with a standard analysis, which is then repeated using the C value obtained from Eq. (9). This way, it is not necessary to increase the number of tests from a standard analysis. An experimental estimation of C requires 20 to 40 specimens. A bigger source of uncertainty in the MC analysis, than the transition curve shape, is the possible material in-homogeneity.

Most cleavage fracture local approach models have adopted the basic MC temperature dependence as a calibrator for the models, since they only consider K_{0i} and do not thus account for the effect of the conditional propagation criterion. Only one model claims to be able to theoretically correctly describe the material-to-material variation of the temperature dependence. This model is known as the Unified Curve method based on the Prometey probabilistic model for cleavage fracture [2]. The model, like most others, only predicts K_{0i}, even though the Unified Curve has adopted the MC form with a constant K_{min} parameter. The Prometey model does not, however, predict a K_{min}. The temperature dependence of the Prometey model comes mainly from two parameters: 1)the thermal part of the yield strength's temperature dependence and 2)the characteristic strength of initiating carbides (σ_u). The effect of σ_u is shown in Fig. 6 [2] where the other parameters have been calibrated to a Russian pressure vessel steel (2Cr-Ni-Mo-V), and kept constant. The difference between the figures a) and b) is the athermal part of the materials yield strength which in a) is 510 MPa and in b) 710 MPa and the Weibull modululs η which is 6 in a) and 12 in b). Even these very simple changes in the parameter are seen to produce a large difference in the predicted fracture toughness.

Any changes in the thermal part of the materials yield strength should, according to the model, have even a larger effect on the sensitivity of the model to used parameters. On top of this, the strongest

sensitivity to temperature is, as seen in Fig. 6, above 0°C, where the thermal part of the yield strength becomes very small. The model is thus strongly dependent on the correct estimate of the thermal yield strength component in this temperature region. Considering this, it is surprising that this single material calibration has been applied to develop the so called Unified Curve method and claimed to be correct for all kinds of steels. Scientifically, the claim is clearly invalid. The model is incomplete, and since it does not account for the conditional propagation criterion it cannot be used to predict the temperature dependence of fracture toughness. The temperature dependence has been calibrated only for one material and therefore, similar to other local approach models considering only K_{0i}, the model cannot be used to predict a quantitative fracture toughness temperature dependence.

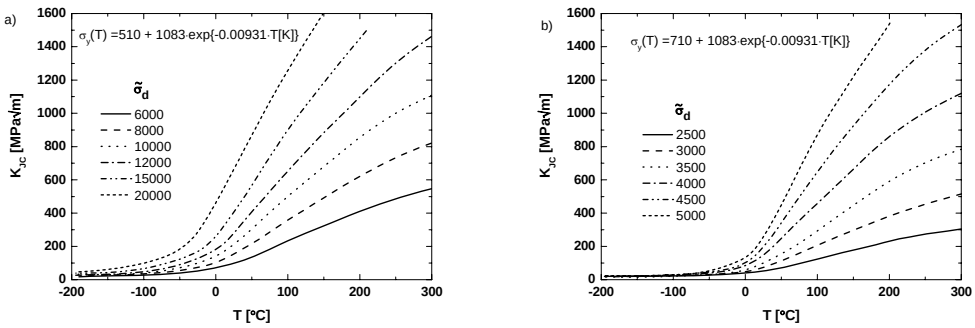

Figure 6. Two examples of the predictions based on the Prometey model [2]. The difference in the figures is the athermal part of the materials yield strength and the Weibull modululs (η = 6 vs. 12). Changing the thermal part of the materials yield strength would greatly enhance the differences.

4. Summary and Conclusions

The Master Curve methodology for describing cleavage fracture toughness, scatter, size-effects and temperature dependence has been standardised in ASTM E1921. The scatter and size-effects predicted by the method are based on theory, whereas the temperature dependence is the result of empirical observations. The reason for the seemingly nearly invariant temperature dependence of the cleavage fracture toughness of different steels has until now eluded theoretical explanations.
The standard fracture toughness temperature dependence is expressed in terms of the normalization fracture toughness K_0. However, K_0 is really the product of three separate parameters, K_{min}, K_{0i} and $P(K_\infty)$, all of which are temperature dependent.

K_{min} is related to the steepness of the stress distribution in front of the crack, K_{0i} is connected to the likelihood of initiation and $P(K_\infty)$ describes the likelihood of cleavage crack propagation in a unified stress field.

K_{min}, despite its temperature dependence, does not explain the temperature dependence of K_0, since the increase in K_{min} usually occurs at temperatures where K_0 already is close to upper shelf.

The same is the case for the initiation toughness K_{0i}, which mainly should be a function of the initiator distribution and the materials yield stress. The temperature dependence connected to K_{0i} should mostly be effective at low temperatures, where the yield stress sensitivity to temperature is large.

This leaves the probability of cleavage crack propagation in a unified stress field, $P(K_\infty)$, as the likely parameter describing most of the temperature dependence. This is also in line with the fact

that, the crack arrest toughness has very similar temperature dependence as K_0.

This presentation gave some more insight into the factors that lead to the experimentally observed temperature dependence. Finally, a new more material specific temperature dependence usable instead of the standard expression has been given.

Finally it has been shown that the so called Unified Curve method, based on the Prometey cleavage fracture model is scientifically invalid and should not be used to predict a quantitative fracture toughness temperature dependence.

Acknowledgements

This work has been part of the FAR project belonging to the SAFIR 2014 research program funded by VTT and by the State Nuclear Waste Management Fund (VYR), as well as other key organizations. The present work is connected to the quantification of constraint effects in brittle and quasi-brittle materials.

References

[1] K.R.W. Wallin, Fracture toughness of engineering materials - estimation and application, EMAS Publishing, Warrington UK, 2011.
[2] B.Z. Margolin, A.G. Gulenko, V.A. Nikolaev, L.N. Ryadkov, A new engineering method for prediction of the fracture toughness temperature dependence for RPV steels, International Journal of Pressure Vessels and Piping, 80, (2003), 817–829.

Local Approach Applied to the Fracture Toughness of Resistance Spot Welds

Florent Krajcarz[1,2], Anne-Françoise Gourgues-Lorenzon[1,*], Emmanuel Lucas[2], Matthieu Mazière[1], André Pineau[1]

[1] MINES ParisTech, Centre des Matériaux, UMR CNRS 7633, BP 87, 91003 Evry cedex, France
[2] ArcelorMittal Global R&D, BP 30320, 57283 Maizières-lès-Metz cedex, France
* Corresponding author: anne-francoise.gourgues@ensmp.fr

Abstract A recently developed methodology for measuring the nugget fracture toughness in mode I was applied to three high-strength steel resistance spot welds, exhibiting either mixed cleavage/ductile or ductile fracture at room temperature. Fracture toughness tests revealed a difference in ductile-to-brittle transition temperature between the welds. Constitutive equations of weld nuggets were determined and implemented in a finite element model of the fracture toughness test, revealing both in-plane bending and in-plane stretching in front of the crack tip. Brittle cleavage fracture of the nuggets is not conveniently described using a simple Ritchie-Knott-Rice approach but the Rice-Tracey model allowed quantitatively relating the high number density of small particles to the nugget fracture toughness in the ductile regime.

Keywords Local approach, Brittle to ductile transition, High strength steels, Resistance spot welds

1. Introduction

The need for car-lightening has led to the development of Advanced High Strength Steels containing more alloying elements than standard steels. Resistance spot welding issues become of major concern for these steels. Due to the severe cooling conditions, the weld may exhibit an unusual microstructure that could be sensitive to unstable cracking in opening mode, inducing interfacial failure of the weld. In the opening mode, several tests are available to determine the strength of resistance spot welds (RSWs) [1]. The transition between crack propagation across the heat-affected zone and interfacial failure strongly depends on the molten zone (nugget) fracture toughness [2]. A new methodology (referenced hereafter as UXT tests) has recently been developed [3] to determine the nugget fracture toughness, using cross-tensile tests on double U-shaped specimens (Fig. 1), together with crack extension monitoring using a potential drop method. The purpose of the present study is to determine, if any, the ductile-to-brittle transition of the weld nugget for different steel compositions (and thus, nugget microstructures), by using the UXT test. A mechanical analysis of the test is then performed using a finite element modelling approach to determine the loading conditions ahead of the tip of the precrack. For this purpose, constitutive equations of the nugget are estimated from heat-treated microstructures, as already reported in literature [1]. A simple initiation criterion for both brittle cleavage and ductile dimple fracture is then tentatively derived as a function of the material microstructure and fracture mechanisms.

2. Experimental details

2.1. Materials and welding conditions

Three high strength steels were provided as 2-mm-thick bare sheets. Their chemical composition and room temperature properties are reported in Table 1. Resistance spot welds were fabricated using a Sciaky pedestal welding machine, following ISO 18278-2 (2004) standard parameters, without cold times. A low welding current (Table 2) was applied (i) to ensure the presence of a weak Diffusion Bonded Zone (DBZ), which serves as an circular precrack, and (ii) to facilitate interfacial failure under UXT tests [2]. The corresponding weld diameter, *d* was measured from fracture surfaces after interfacial failure (Table 2). Conventional cross-tensile strength, *CTS*

(averaged over four tensile tests on cross-welded 125x38 mm² coupons), hardness (average of 30 measurements at room temperature with a dwell time of 10s) and nugget microstructure (observed in cross-section after Béchet-Beaujard + Nital etching) are reported in Table 2.

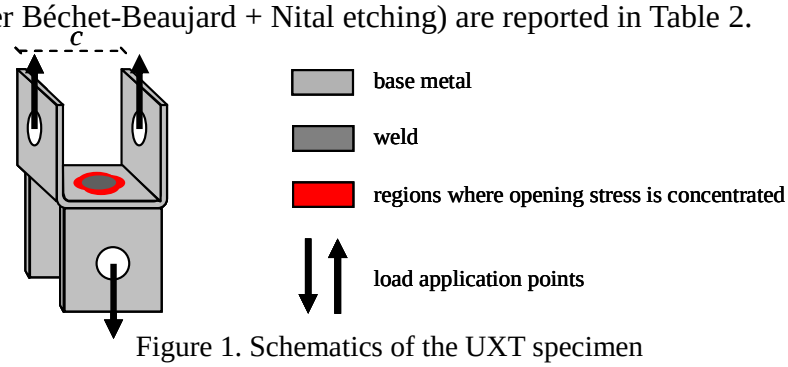

Figure 1. Schematics of the UXT specimen

Table 1. Chemical composition and mechanical properties of the three base material sheets

Material	C [wt%]	Mn [wt%]	Si [wt%]	0.2% proof stress [MPa]	Tensile strength [MPa]	Uniform elongation [%]
Steel F	0.15	0.68	0.01	380	505	14
Steel D	0.15	1.90	0.21	510	780	14
Steel T	0.19	1.71	1.68	540	820	22

Table 2. Welding conditions, room temperature properties and microstructure of the welds

Base metal	Welding current (kA)	*d* (mm)	CTS (kN)	$HV_{0.5}$ (base metal)	$HV_{0.5}$ (nugget)	Nugget microstructure
Steel F	7.6	6.2 ± 0.1	6.3 ± 0.1	160 ± 6	373 ± 30	martensite + lower bainite
Steel D	6.8	5.9 ± 0.1	7.2 ± 0.6	243 ± 3	420 ± 11	martensite
Steel T	7.0	6.4 ± 0.2	7.5 ± 0.1	243 ± 9	500 ± 10	martensite

2.2. Ductile to brittle transition curves of the weld nuggets

Specimen halves (full thickness 30x95 mm² coupons) were press-brake bent into U shapes with a bending radius of 2 mm, leaving a 30x30 mm^2 central region, and then welded perpendicularly to each other (Fig. 1). The specimen was attached to grips by bolts, with spacers inserted between specimen and bolts. The weld was thus loaded normally to the sheet plane. This setup was fitted to an Instron servohydraulic tensile machine, with a 250 kN load cell and a climatic chamber. Temperature was recorded using a thermocouple spot-welded on the UXT specimen. The tensile load and load line displacement curves were recorded, together with the increase in potential drop. The stress intensity factor was estimated using the analytical formula developed by Lin and Pan for square-cup specimens [4] (Eq. 1) over the first 2 mm of crack propagation:

$$K_I = \frac{\sqrt{3}T}{2\pi t^{3/2}} \left\{ \frac{f_c c^2 \left[d^2 - c^2 + 2d^2 \ln(c/d)\right]}{Y(d^2 - c^2)} - \frac{(d^2 - c^2)(-1+\nu) + 2c^2(1+\nu)\ln(c/d)}{d^2(-1+\nu) - c^2(1+\nu)} \right\} \quad (1)$$

In Eq. (1), c is the cup diameter (taken as equal to c', the equivalent diameter of the U tensile specimen), t the sheet thickness, d the weld diameter and T the tensile load. $Y = d^2(\nu - 1) - c^2(\nu + 1)$, $\nu = 0.3$ (Poisson ratio) and f_c is a geometrical parameter set to 1. Ductile-to-brittle transition (DBT) curves were determined using the fracture toughness at crack initiation, K_{Ic} (in fact, crack propagation leading to a reduction of the bearing area by 2%). Ductile and brittle temperature ranges were estimated from fracture surface examinations by scanning electron microscopy in a secondary electron imaging mode. Energy dispersive spectrometry (EDS) was used to analyse particles on fracture surfaces.

2.3. Plastic yield and fracture properties of the weld nugget

Two approaches have been reported in literature to estimate the constitutive behaviour of the nugget: using miniature specimens machined from "actual" nuggets (e.g. [5]), or simulating the coarse-grained heat-affected zone by heat treatment (e.g. [1]). The second approach was chosen here. Using a Gleeble 3500 simulator under a vacuum, full-thickness 12x100 mm² blanks were heated at 1500°C.s^{-1} up to 1290°C (maximum heating rate and temperature that ensured homogeneous heating without local melting), and then cooled using helium gas blowing or water spraying (the actual spot welding cooling rate lying in between). From temperature monitoring with spot-welded thermocouples and microhardness measurements, a homogeneous heat treatment was applied over a length of at least 20 mm. Flat uniaxial tensile specimens (15x4 mm² in gauge dimensions) were spark erosion machined from heat-treated blanks and pulled in tension using the same Instron equipment at various temperatures, with an elongation rate of 1.1 10^{-3} s^{-1}, as measured from an *in situ* extensometer (initial gauge length: 8.7 mm). The criterion for small scale yielding (SSY) conditions in the UXT test was derived from these tensile properties. Double edge U-notched tensile (DENT) specimens were machined from heat-treated blanks of Steel D with a ligament width of 6 mm, a notch radius of 1 mm, and then pulled in tension using the same machine. Notch opening was recorded by averaging measurements of two extensometers placed at either edge.

3. Experimental results and discussion

3.1. Ductile to brittle transition curves of the weld nuggets

3.1.1. Steel T

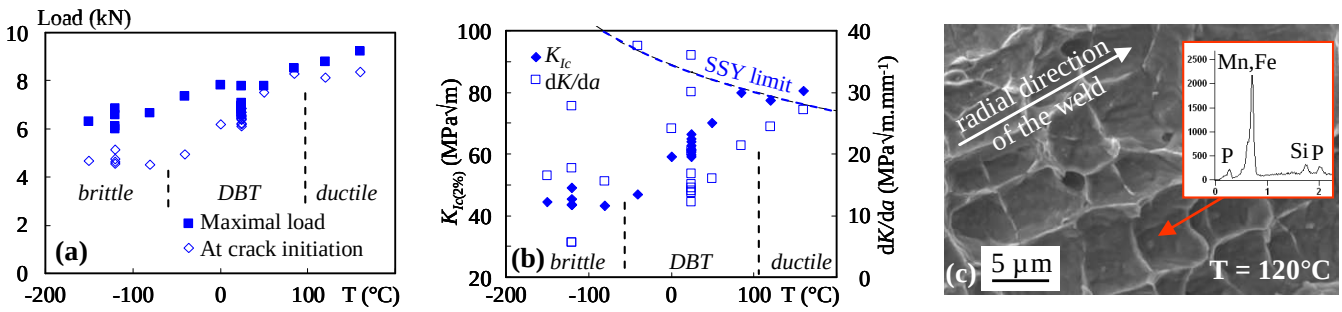

Figure 2. DBT curves for Steel T nuggets: (a) load at crack initiation and weld strength (i.e. maximal load); (b) fracture toughness at crack initiation and crack-extension resistance d*K*/d*a*. c) Detailed view of ductile fracture and EDS analysis of precipitates located within dimples (red arrow)

Only interfacial failure (FIF) was observed. While the weld strength only slightly increases with temperature, a transition is observed in the load at crack initiation vs. temperature curve (Fig. 2). Above room temperature, the load only slightly increases between crack initiation and fracture. The fracture toughness transition curve showed a marked transition from 40-50 MPa√m up to 70-80 MPa√m. In the brittle temperature range, pure cleavage fracture initiated from multiple sites all around the weld. The microstructural feature at the origin of crack initiation could not be determined. Many crack deviations led to a rough fracture surface and to serrations in the load vs. displacement curves. In the ductile domain, smooth interfacial cracking occurred. Small dimples (~5 µm in size) aligned along the radial direction of the weld initiated from tiny particles of 0.4 µm in average size (Fig. 2c) that were mainly phosphides and sometimes aluminium oxides. The dimple size was consistent with the secondary dendrite arm spacing of the weld estimated from metallographic observations [6]. In the DBT range, cracks propagated in a mixed cleavage + ductile

manner. The roughness of the fracture surface decreased with increasing test temperature.

3.1.2. Steel D

Although some welds failed in a partial interfacial mode, FIF was observed in the vast majority of tests. The transition in crack initiation and fracture load is less obvious and more scattered than for Steel T but, again, the DBT range encompasses room temperature (Fig. 3). The fracture toughness in the brittle domain is similar to that of Steel T but in the ductile domain, it is lower. Cleavage and dimple ductile fracture exhibit similar macroscopic (crack deviation) and microscopic features as for Steel T. No particle was found at cleavage initiation sites. The average size of dimples and tiny particles (mainly MnS particles together with some phosphides) was 4.5 and 0.3 µm, respectively.

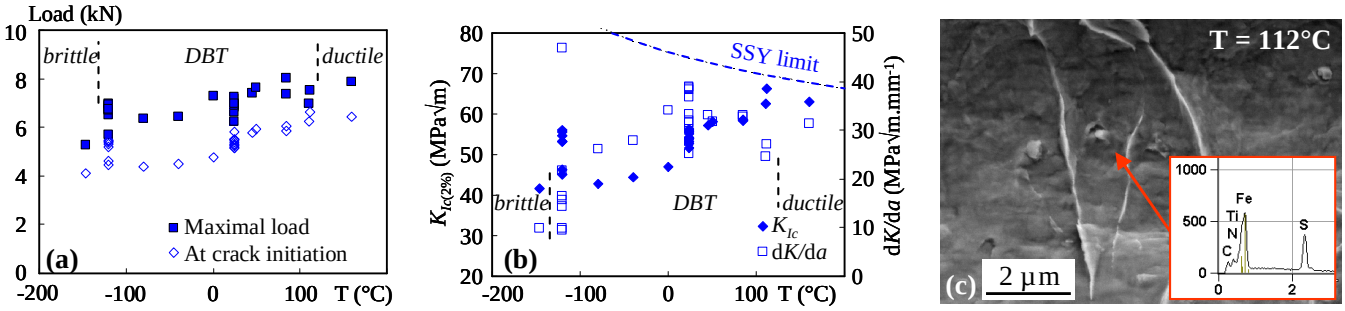

Figure 3. DBT curves for Steel D nugget: (a) load at crack initiation and weld strength; (b) fracture toughness at crack initiation and crack-extension resistance. (c) Ductile dimples nucleated at sulphides

3.1.3. Steel F

Only FIF was observed for Steel F. The load at crack initiation and the ultimate load increase with temperature up to 0°C and -100°C respectively, and then decrease (Fig. 4). The fracture toughness varies in the same way as the load at crack initiation. In contrast to Steels T and D, only ductile fracture was observed at room temperature, yet with limited fracture toughness (~55 MPa√m). The fracture mechanisms were similar to those of Steels T and D, with a dimple size of ~4 µm and a fine precipitation of MnS particles of ~0.5 µm in size together with a few aluminium oxides. Only a few cleavage facets were found at 0°C but cleavage facets linked by torn ligaments dominated fracture surfaces at -40°C. Combined with transition curves, it suggests that cleavage and ductile fracture toughness could be very close to each other in this particular case.

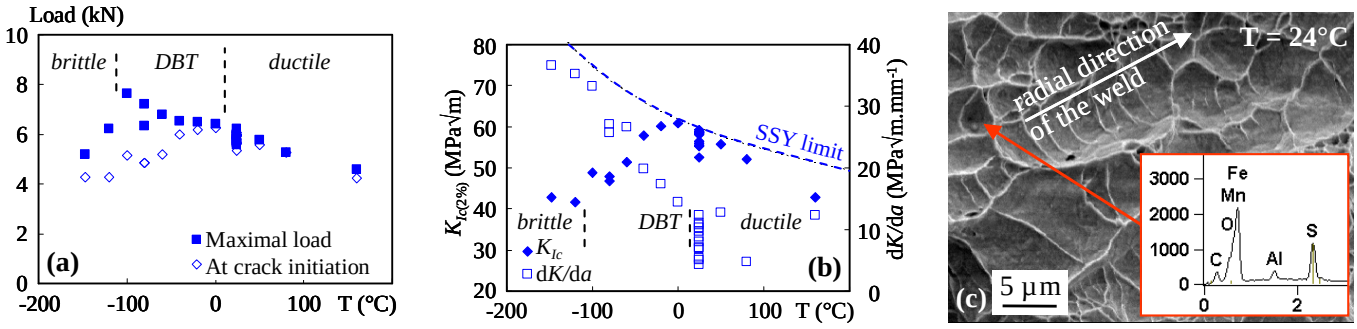

Figure 4. DBT curves for Steel F nugget: (a) load at crack initiation and maximal load; (b) fracture toughness at crack initiation and crack-extension resistance. (c) Ductile dimples nucleated at sulphides

3.1.4. Comparison between Steels T, D, and F

Despite their difference in fracture mechanisms, Steels F and D exhibit similar weld fracture

toughness at room temperature. The main difference between these steels seems to be the fracture toughness in the ductile domain, which increases with nugget hardness. This is consistent with the similar fracture mechanisms, dimple and particle size for the three steel nuggets: for the investigated welding conditions and sheet thickness, only the yield strength, controlled by their microstructure after cooling, seems to influence their fracture toughness in the ductile regime. Strong fracture deviation was associated with cleavage dominated fracture. Crack initiation occurred perpendicular to the applied load, where Mode I dominates. Cleavage initiation sites found all around the weld suggest a rather uniform value of Mode I stress intensity factor for this test. As cleavage cracks have to deviate to propagate across high-angle boundaries, the influence of Mode II loading, which is not uniform around the weld, may increase during cleavage crack propagation. No correlation appears between crack extension resistance and fracture mechanism (Figs 2b, 3b, 4b).

3.2. Tensile properties of simulated nugget microstructures

3.2.1. Tensile properties of smooth specimens

The dependence of yield strength, *YS*, on temperature was satisfactorily modelled (Fig. 5) using a Zener-Hollomon equation (Eq. 2), with T the absolute temperature and $\dot{\varepsilon}$ the elongation rate:

$$YS = 10^{a}\left[T\log_{10}\left(\frac{10^{8}}{\dot{\varepsilon}}\right)\right]^{b}. \tag{2}$$

For Steels D and T, tensile properties are not very sensitive to cooling conditions (Table 3) due to the higher hardenability of these steels leading to auto-tempered martensite. The mechanical properties of the nugget were assumed to be similar to those of the helium-blown samples. Since the hardness and microstructure of Steel F nugget are intermediate between those of the martensitic water-sprayed and bainitic helium-blown samples, a “fictitious” material was considered in order to represent Steel F nugget: its mechanical properties and constitutive parameters were thus estimated from those of water-sprayed and helium-blown materials balanced by their respective hardness.

Table 3. Mechanical properties of heat-treated microstructure, nugget (edge) and “fictitious” material used to represent steel F nugget. *Z* is the reduction of area at fracture; *a* and *b* refer to Eq. 2

Steel	Cooling	Hardness (HV0.5)	0.2% proof stress (MPa)	Tensile strength (MPa)	Fracture elongation (%)	*Z* (%)	*a*	*b*
T	Helium-blown	511 ± 9	1061	1547	19	45	4.19	-0.33
	Water-sprayed	548 ± 12	1086	1666	18	46	4.21	-0.33
D	Helium-blown	436 ± 11	932	1345	17	48	3.77	-0.23
	Water-sprayed	478 ± 8	1008	1443	17	49	4.26	-0.37
F	Helium-blown	296 ± 8	678	978	15	40	4.23	-0.41
	Water-sprayed	451 ± 9	862	1351	7	47	4.39	-0.41
	“Fictitious”						4.31	-0.41

3.2.2. Tensile properties of notched Steel D specimens

As ductile fracture of the nugget is influenced by fine particles inherited from rapid solidification, heat-treated specimens were not representative of the nugget microstructure concerning ductile fracture. They were only used to derive an estimate of the critical stress necessary to initiate cleavage cracking. Five specimens were tested at -100°C, close to the brittle domain of Steel D nugget. Load vs. notch opening displacement curves presented a small serration around 18 kN, (Point B in Fig. 6a), well before final fracture. This could indicate brittle fracture initiation; no interrupted tensile test was available to prove this. Fracture surfaces (Fig. 6c) exhibited cleavage facets surrounded by ductile shear lips. Close to notch roots, cleavage facets are about 100-200 µm in size, similar to the prior austenite grain size of both helium-blown and nugget edge materials.

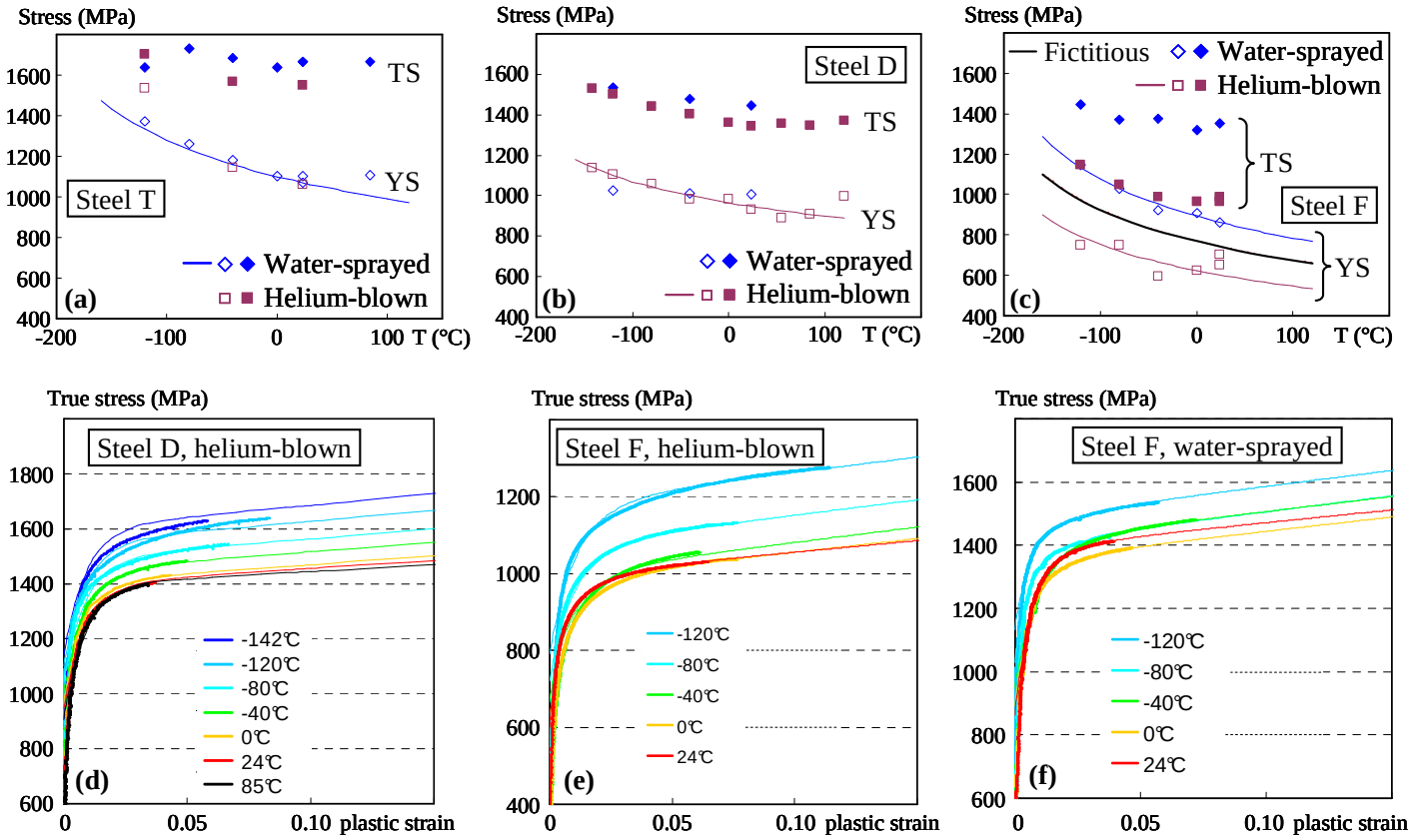

Figure 5. (a-c) Yield strength (YS), Zener-Hollomon fit (lines), and tensile strength (TS) of heat-treated steels. (d-f): Tensile curves: experiments (up to necking, thick lines) and model predictions (thin lines)

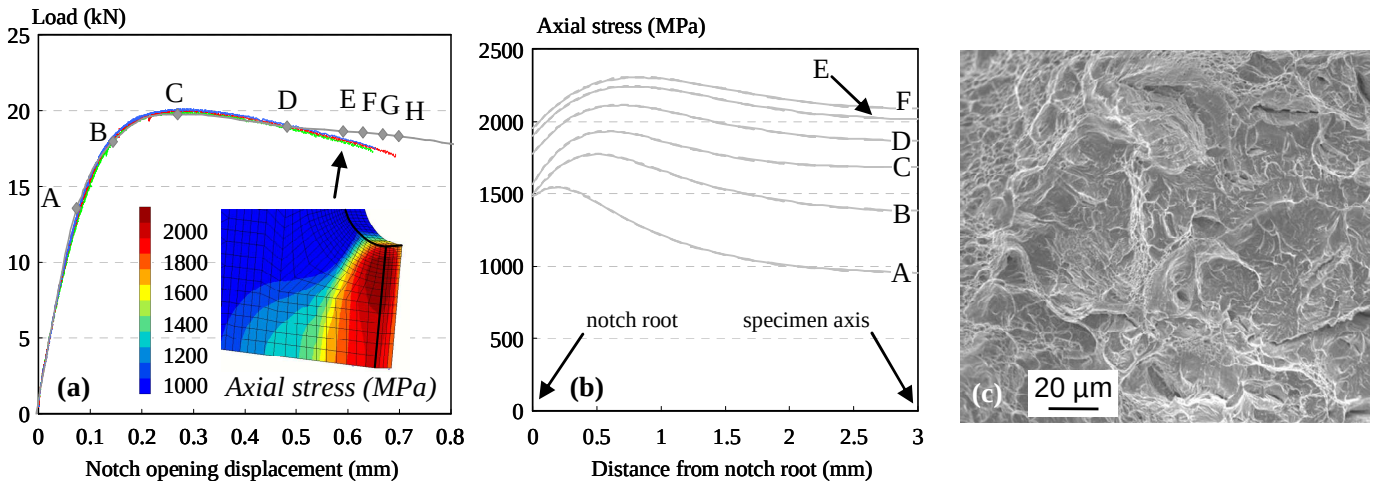

Figure 6. (a) Load vs. notch opening curves, (b) calculated axial stress along the ligament, and (c) fracture surface close to notch root of DENT specimens of helium-blown Steel D tested at -100°C

4. Mechanical analysis and derivation of a fracture criterion

4.1. Constitutive equations

Constitutive equations were determined from uniaxial tensile tests. The material were considered as elastic-plastic, homogeneous and isotropic, with Young's modulus E = 210,000 MPa, and Poisson ratio ν = 0.3. A von Mises yield criterion was used with a combined linear + Voce-like isotropic strain hardening equation, which reads as follows in the particular case of uniaxial tension:

$$\sigma_{eq} = \sigma_y + H\varepsilon_p + \sigma_y Q_1\left(1-\exp^{-b_1\varepsilon_p}\right) + \sigma_y Q_2\left(1-\exp^{-b_2\varepsilon_p}\right) \tag{3}$$

with σ_{eq} the von Mises equivalent stress, σ_y the yield strength, H a linear strain-hardening parameter mainly used for large amounts of strain, Q_1, Q_2, b_1 and b_2 being material parameters. According to the shape of experimental tensile curves, the values of Q_1 and b_1 were kept independent of temperature. The values of σ_y, H, Q_2 and b_2 were fitted for each temperature. Parameter H was determined from the constitutive equation [5] of a material similar to Steel D. This yields a value of e.g. 600 MPa at 24°C. The fitted sets of constitutive parameters very satisfactorily described tensile curves (Fig. 5d-f).

4.2. Cleavage crack initiation criterion from mechanical analysis of the DENT specimens

The mechanical analysis of the test was performed in three dimensions thanks to the in-house Z-set finite element software. One-eighth of the specimen was meshed with quadratic bricks with reduced integration. The specimen head and the region close to the notch were respectively attributed constitutive parameters of base metal and of the helium-blown material. Displacement of the specimen head was prescribed as in experiments. The simulated load vs. notch opening curve fits well with experimental results up to a notch opening of ~0.5 mm (Fig. 6a). The axial stress reaches its maximum ($\sigma_{c,p}$ = 1790 ± 40 MPa) at 0.5 mm from the notch root at the onset of experimentally observed serrations, and ($\sigma_{c,f}$ = 2270 ± 20 MPa) at 0.8 mm from the notch root for notch opening corresponding to experimental fracture (Points E-H in Figs 6a and 6b).

4.3. Simplified finite element modelling of the U-shape cross-tensile test

4.3.1. Modelling the UXT test

Only the upper part of the specimen was modelled, with usual symmetry conditions. Instead of a U-shaped cross tensile specimen, involving full 3D modelling, a circular-cup geometry was selected and represented by an axisymmetrical model (Fig. 7a). Consequently, the crack is only loaded in Mode I, which can induce dissimilarities with UXT tests especially during crack propagation but here, only crack initiation was considered. The finite element analysis software Abaqus/Implicit Standard was used with CAX4R elements (4-node bilinear axisymmetrical quadrangles with reduced integration and hourglass control). The following simplifying assumptions were made:

- Indentations caused by the electrodes, located far from the notch tip were not taken into account. The spacer inserted in the U specimen was not meshed but taken into account by allowing no displacement along the horizontal axis of the inner side of the flange.
- The ligament was only composed of the nugget section, i.e. the initial crack included both the non-welded interface and the DBZ. The nugget and harder part of the heat-affected zone was assimilated to the nugget material, the softer part of the heat-affected zone being assimilated to the base metal. The boundary between these two regions was taken perpendicular to the interface and located at 0.8 mm from the crack tip.
- Prescribed displacement was applied to a spring on the specimen flange which represents the stiffness of the load line [1]. The load is the resultant force on the spring. The stiffness of the spring (25 kN.mm^{-1}) was fitted to the linear part of the load vs. displacement curves. To this aim, the shift in displacement observed at low loads, probably due to some clearance compensations at the beginning of the tests, were ignored (Fig. 7b).
- To ensure an accurate description of the stress and strain fields around the crack tip, an initial semi-circular blunting was modelled. Taking typical values of K_I (60 MPa√m) and σ_y (1000 MPa) leads to a crack tip opening displacement of about 17 µm under a plane strain assumption.

Consequently, the initial crack tip radius was set to 2 µm together with a mesh size close to 0.5 µm. Although the weld strength is overestimated by the model (Fig. 7b) (presumably because of neglecting work-hardening in folded regions and/or of the axisymmetry hypothesis), modelling results have been used to estimate stress and strain fields in front of the crack tip.

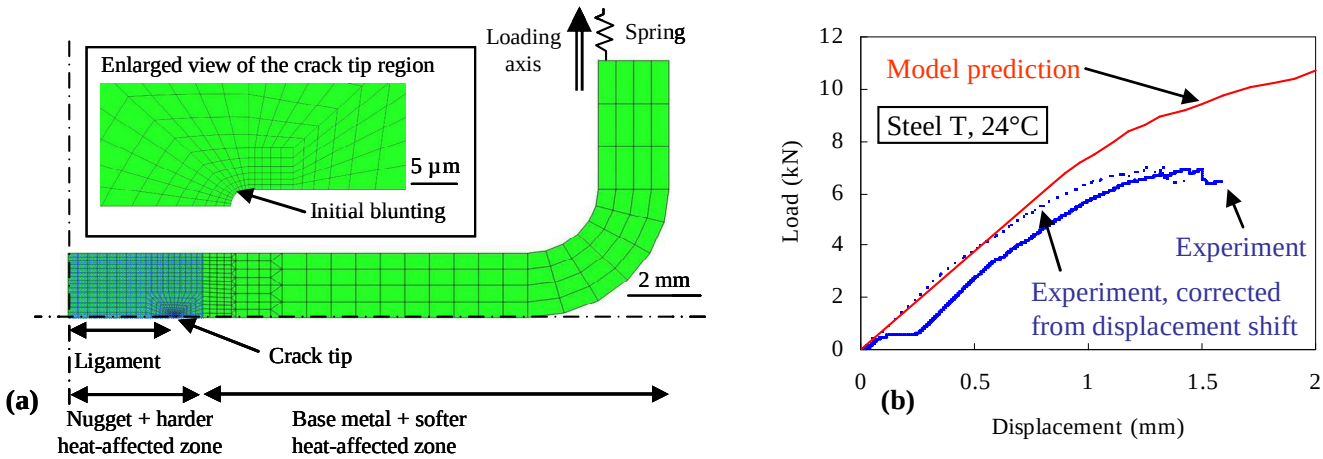

Figure 7. (a) Simplified finite element model and (b) experimental and simulated UXT load vs. displacement curves of Steel T

4.3.2. Derivation of the stress intensity factor and energy release rate

The finite element model was validated by considering a fully elastic specimen. The difference between the predicted value of K_I and that derived from the Lin & Pan formula is only 3 MPa√m for K_I = 60 MPa√m. As a consequence of the elastic-plastic behaviour of the material, the crack tip singularity was then described by the energy release rate, assimilated to the J-integral. The independence of calculated J with respect to the contour (chosen within the weld material, at least 0.5 mm from the crack tip) was verified in the case of Steel T welds tested at room temperature.

4.4. Assessment of a cleavage crack initiation criterion using the UXT test

The stress state in the nugget during the UXT test is described here by considering Steel D tested at room temperature (Fig. 8a-b). The central part of the nugget (up to 2mm from the weld centre) is loaded in compression. Positive values of opening stress are concentrated within a narrow region (0.6-0.8 mm in width) in front of the crack tip, leading to high values (up to 4000 MPa). The high radial stress, which can reach 2500 MPa, was attributed to constraints induced by spacers: the base material is not only bent but also stretched along the sheet plane. The high resulting stress triaxiality limits plastic yielding in front of the crack tip. The opening stress ahead of the crack is represented in Fig. 8c for J = 9.9 kJ.m^{-2} (close to the fracture toughness at 0°C.) The opening stress depends on test temperature over 50 µm ahead of the crack tip, i.e. in the plastically deformed region. For a given value of J, decreasing the test temperature tends to increase the maximal opening stress. The distance (~15 µm) at which the stress is highest is almost independent of test temperature.

The Ritchie-Knott-Rice (RKR) model [7] was tentatively applied (Fig. 8c). The region where the opening stress is higher than $\sigma_{c,f}$ ($\sigma_{c,f}$ = 2270 MPa) is about 70 µm in size for J~10 kJ.m^{-2} whatever the test temperature. This is larger than the plastic zone size (about 50 µm). As plastic deformation is required to initiate cleavage cracking, crack initiation could be controlled by the extent of the plastic zone rather than by that of the region where the maximum principal stress exceeds its critical value. Cleavage fracture is thus not well described using such a simple approach. A statistical model based on the weakest link like that of Beremin [8] would probably be more appropriate.

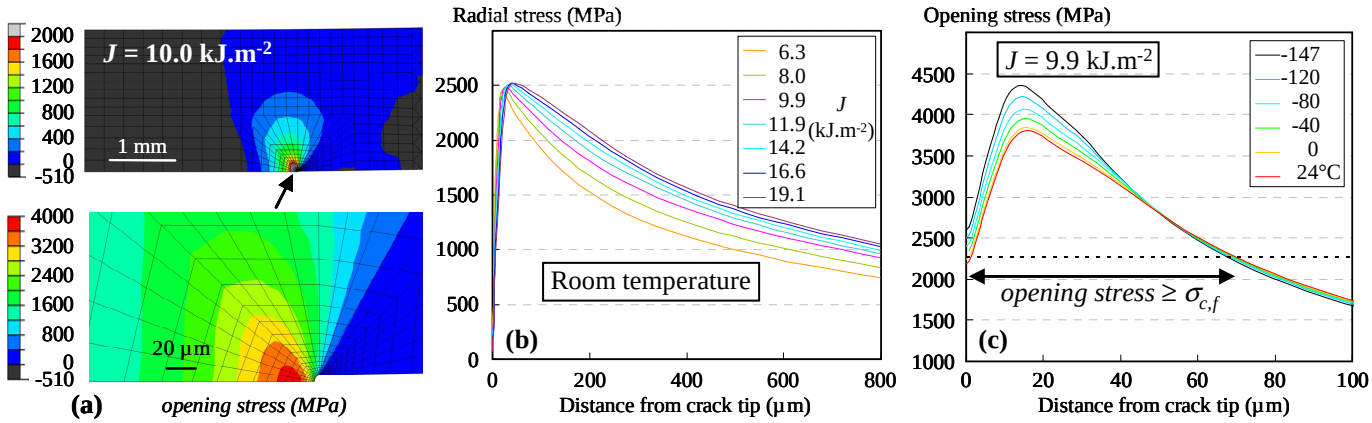

Figure 8. Model predictions of (a) opening stress field at room temperature in the weld, (b) radial stress along the interface as a function of J and (c) opening stress profile as a function of temperature for Steel D

4.5. Assessment of a ductile fracture criterion using the UXT test

By using the Rice & Tracey model [9], the instantaneous void growth rate can be written as:

$$\frac{dR}{R} = \alpha \exp\left(\frac{3}{2}\tau\right) dp \text{, leading to } \ln\frac{R}{R_0} = \int_{p_0}^{p} \alpha \exp\left(\frac{3}{2}\tau\right) dp \qquad (4)$$

In Eq. 4, R is the void radius (R_0 is its initial value), $\alpha = 0.283$, τ is the stress triaxiality ratio, p is the equivalent plastic strain and p_0 is the equivalent plastic strain at void nucleation. In the absence of interrupted UXT tests, the value of p_0 was set to zero. Determination of the critical value $(R/R_0)_c$ of R/R_0 requires a microstructure representative of the fine particle-containing nugget and could thus only be fitted from the UXT tests. Macroscopic fracture, characterized by $J = J_c$, occurs as soon as the local criterion $R/R_0 = (R/R_0)_c$ is satisfied over a critical distance d_c ahead of the crack tip. This critical distance is usually close to a typical distance involved in the fracture process: the initial void spacing for instance. It was arbitrarily set to d_c = 8µm, i.e., two times the void spacing observed in fracture surfaces (Fig. 3c).

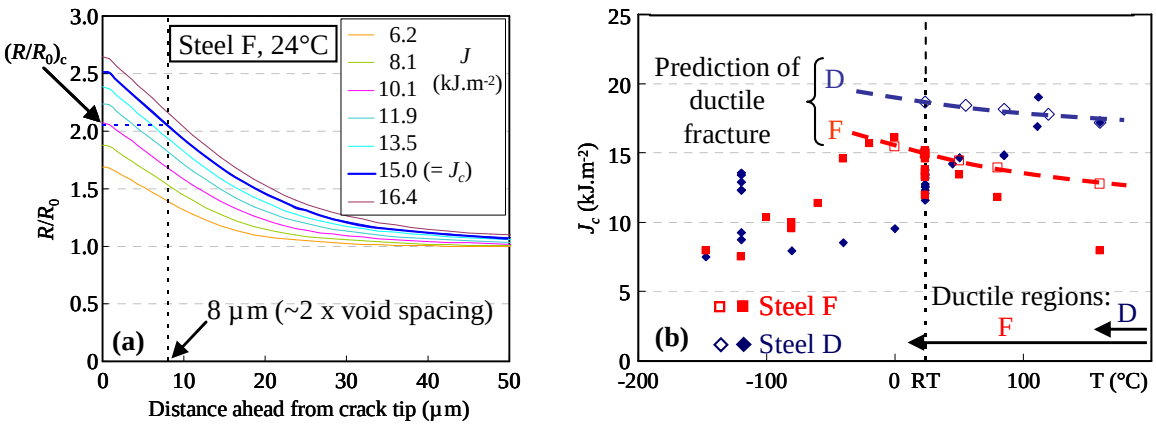

Figure 9. (a) Predicted void radius at room temperature and (b) comparison between experimental (full symbols) and predicted J_c (open symbols interpolated with lines) as a function of temperature

The Rice & Tracey model was first applied to ductile fracture of Steel F nugget at room temperature. The experimental fracture toughness of 58 MPa√m corresponds to J_c~15 kJ.m^{-2}, under a plane strain assumption. This value is reached when R/R_0 exceeds 2.05 over d_c (Fig. 9a). The value of $(R/R_0)_c$ is thus estimated to around 2.05. The void growth model was then applied to describe the evolution of

the fracture toughness in the ductile temperature range of Steel F and Steel D nuggets (Fig. 9b). The values of d_c were set to two times the initial void spacing and $(R/R_0)_c = 2.05$ for the two materials. Void growth occurs much more rapidly with J when the temperature increases, due to the decrease in yield strength and strain hardening. Consequently, the values of the J-integral for which $R/R_0 > (R/R_0)_c$ over distance d_c decrease with increasing temperature. The values of J_c calculated from the void growth model were compared to those experimentally determined thanks to the UXT tensile tests with a plane strain approximation to estimate J_c from K_{Ic} (Fig. 9b). For Steel F, the decrease in J_c in the ductile region is qualitatively predicted but the predicted fall of J_c at higher temperatures is underestimated. A possible source of discrepancy is the extrapolation of constitutive parameters for temperatures above 24°C. Model predictions are satisfactory for Steel D nugget at 120°C where ductile fracture prevails.

5. Conclusions

The U-shape cross-tensile (UXT) test was applied to the local approach of fracture of high strength steel resistance spot welds. A ductile-to-brittle transition curve was obtained for the three steels. For two of them, the transition encompasses room temperature.

- Brittle fracture occurred by cleavage cracking. The critical cleavage initiation stress was estimated to around 2270 MPa. The lower the temperature, the higher the tendency to crack deviation in the UXT test, leading to macroscopic fracture toughness that could reach that obtained in ductile fracture (~60 MPa√m). The complex stress state in the UXT test combines in-plane tension and bending ahead of the crack tip. This reduces the size of the plastic zone; a simple approach such as the RKR model is not applicable.
- Ductile voids initiate from a dense distribution of fine sulphide or phosphide precipitates that result from rapid solidification of the weld. The high stress triaxiality and the small distance between voids lead to rapid interfacial crack propagation without crack deviation. This behaviour was quantitatively related to microstructural features using a Rice and Tracey approach.

References

[1] S. Dancette, D. Fabrègue, V. Massardier, J. Merlin, T. Dupuy, M. Bouzekri, Experimental and modelling investigation of the failure resistance of Advanced High Strength Steels spot welds. Eng Fract Mech, 78 (2011) 2259-2272.

[2] Y.J. Chao, Failure mode of spot welds: interfacial versus pullout. Sci. Technol. Welding Joining, 8 (2003) 133-137.

[3] F. Krajcarz, A.F. Gourgues-Lorenzon, E. Lucas, A. Pineau, Fracture toughness of the molten zone of resistance spot welds, submitted to Int J Fract (January, 2013)

[4] P.C. Lin, J. Pan, Closed-form structural stress and stress intensity factor solutions for spot welds in commonly used specimens. Eng Fract Mech, 75 (2008) 5187-5206.

[5] R. Lacroix, A. Lens, G. Kermouche, J.M. Bergheau, H. Klöcker, Local mechanical characterisation of a resistance spot weld of advanced high strength steel, in: Proc. 19th French Congress of Mechanics, AFM, Courbevoie, 2011 (in French) http://hdl.handle.net/2042/37135.

[6] F. Krajcarz, A. F. Gourgues, V. Bochard, E. Lucas, M. Bobadilla, Development and solidification of the molten zone of resistance spot welds : influence of welding parameters, in : Matériaux 2010, paper 1211 (2010) (in French) http://hal-ensmp.archives-ouvertes.fr/hal-00570567.

[7] R.O. Ritchie, J. Knott, J.R. Rice, On the relationship between critical tensile stress and fracture toughness in mild steel, J Mech Phys Solids, 21 (1973) 395-410.

[8] F.M. Beremin, A local criterion for cleavage fracture of a nuclear pressure vessel steel. Metall Trans A, 14 (1983) 2277-2287.

[9] J.R. Rice, D.M. Tracey, On the ductile enlargement of voids in triaxial stress fields, J Mech Phys Solids, 17 (1969) 201-217.

Analysis of a singular stress field near the edge of joint using molecular dynamics

Hideo Koguchi[1,*], **Nobuyasu Suzuki**[1]

[1] Department of Mechanical Engineering, Nagaoka University of Technology, 940-2188, Japan
[2] Graduate School of Nagaoka University of Technology, 940-2188, Japan
* Corresponding author: koguchi@mech.nagaokaut.ac.jp

Abstract Recently, thin films with a nanometer thickness been used in electronic parts. When the size of material reduces to a nanometer, the area to volume ratio increases, then the mechanical property of surface or interface influences on mechanical behavior of bulk. Hence, it is very important to investigate the mechanical properties of interface and surface for the stress analysis in nano-scale materials. In the present paper, stress distribution near a wedge composed of several different materials is investigated using molecular dynamics (MD). The model used in the present analysis is a bonded joint of copper and gold, which is used in electronic parts. In the analysis, temperature of the model increases up to 5K for relaxation of the structure. A tensile load is applied in a radial direction along the outer surface of the model. The atomic stress distributions near the wedge tip in the joints and the angular function for the stress, which is derived from the theory of anisotropic elasticity, are compared. It can be found from the comparison that interface stress influences on the distribution of singular stress in the bulk and the intensity of singularity at the wedge tip.

Keywords Molecular dynamics, Singular stress, Interface, Joint, Stroh formalism

1. Introduction

Recently, thin films of nanometer thickness have been used in numerous electronic components in highly integrated devices, such as semiconductor devices. As the area-to-volume ratio increases in nanoscale structures, the physical properties of the surface or the interface affect the mechanical behavior near surface in bulk. Therefore, it is important to investigate the mechanical properties of the interface and the surface in the stress analysis of nanoscale materials. The molecular dynamics (MD) method can be used to evaluate the physical properties of materials in a nanometer scale by tracing individual atoms. Recently, Horiike et al.[1] investigated singular stress fields at the interfacial corner between dissimilar crystals using molecular statics (MS). In their analysis, a restricted displacement was applied to the outer surface in the joint model.
In the present paper, singular stress fields in joints composed of materials used in electronic devices are analyzed using MD. The atomic stress distribution near the edge of the joints is investigated under tensile loading in the radial direction. Incoherent interface and coherent interface models are used in the analysis. Through a comparison of the stress distributions in both models, the usefulness of the coherent interface model is demonstrated. It will be shown that if the atomic stress distribution before loading is subtracted from the stress distribution after loading, the stress distribution near the edge can be approximated by an equation based on the theory of anisotropic elasticity considering interface mechanical properties. Furthermore, the effect of wedge angles on the stress distribution will be investigated.

2. Singular stress analysis

From a standpoint in continuum mechanics, the stress distribution within singular stress fields near the edge of the interface in anisotropic joints can be expressed as

$$\sigma_{ij} = \sum_{m=1}^{n} K_{ij}^{m} f_{ij}^{m}(\theta) r^{-\lambda_m} \tag{1}$$

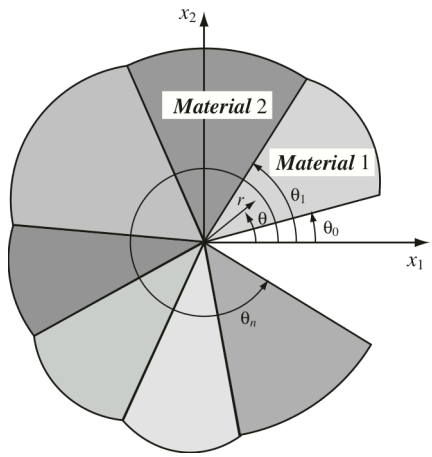

Figure 1. Multi-wedge model

where K_{ij}^{m} is the intensity of the singularity corresponding to the mth-order stress singularity, λ_m, r is the distance from a singular point [1], and $f_{ij}^{m}(\theta)$ is an angular function of stress σ_{ij}.

Koguchi derived an eigenequation with interface mechanics [2]. The eigenequation, **K,** is a 6×6 matrix composed of material properties and wedge angles and is expressed as follows:

$$\mathbf{K}=\begin{bmatrix}\mathbf{K}_1 & \mathbf{K}_2\\ \mathbf{K}_3 & \mathbf{K}_4\end{bmatrix}\begin{Bmatrix}\mathbf{p}^*\\ \mathbf{0}\end{Bmatrix}=\Big[\mathbf{G}_{1(1)}\ \mathbf{G}_{1(0)}^{-1}\begin{bmatrix}\left\langle \hat{p}_{*1}^{1-\boldsymbol{\lambda}}(\boldsymbol{\theta}_1)\hat{p}_{*1}^{-1+\boldsymbol{\lambda}}(\boldsymbol{\theta}_0)\right\rangle & 0\\ 0 & \left\langle \hat{\bar{p}}_{*1}^{1-\boldsymbol{\lambda}}(\boldsymbol{\theta}_1)\hat{\bar{p}}_{*1}^{-1+\boldsymbol{\lambda}}(\boldsymbol{\theta}_0)\right\rangle\end{bmatrix}$$
$$-\begin{bmatrix}\mathbf{A}_2 & \bar{\mathbf{A}}_2\\ \mathbf{B}_2 & \bar{\mathbf{B}}_2\end{bmatrix}\mathbf{G}_{2(2)}^{-1}\begin{bmatrix}\left\langle \hat{p}_{*2}^{1-\boldsymbol{\lambda}}(\boldsymbol{\theta}_1)\hat{p}_{*2}^{-1+\boldsymbol{\lambda}}(\boldsymbol{\theta}_2)\right\rangle & 0\\ 0 & \left\langle \hat{\bar{p}}_{*2}^{1-\boldsymbol{\lambda}}(\boldsymbol{\theta}_1)\hat{\bar{p}}_{*2}^{-1+\boldsymbol{\lambda}}(\boldsymbol{\theta}_2)\right\rangle\end{bmatrix}\Bigg]\begin{Bmatrix}\mathbf{p}^*\\ \mathbf{0}\end{Bmatrix}=\begin{Bmatrix}\mathbf{0}\\ \mathbf{0}\end{Bmatrix} \tag{2}$$

where $\mathbf{K}_i$ are 3×3 sub-matrices, **p*** represents the eigenvector of displacement, the angular brackets < > indicate a 3×3 diagonal matrix in which each component is changed according to its subscript, $\hat{p}_j(\theta)=\cos\theta+p_j\sin\theta$, λ is the singular order to be determined from the boundary conditions. Moreover, $\mathbf{A}_k$ and $\mathbf{B}_k$ are the matrices for material k given by the Stroh eigenvector, p_j is Stroh's eigenvalue, and $\bar{}$ denotes a complex conjugate [3], θ_i are the angles shown in Fig. 1., and $\mathbf{G}_{k(s)}$ is a 6×6 matrix that is defined as follows:

$$\mathbf{G}_{k(s)}=\Omega_k\begin{bmatrix}\mathbf{A}_k & \bar{\mathbf{A}}_k\\ \mathbf{B}_k & \bar{\mathbf{B}}_k\end{bmatrix}-\left(\mathbf{H}_{10s}-\frac{\mathbf{H}_{21s}}{\ell}\lambda\right)\Omega_k\begin{bmatrix}0 & 0\\ \mathbf{A}_k & \bar{\mathbf{A}}_k\end{bmatrix} \tag{3}$$

where

$$\Omega_k=\begin{bmatrix}\cos\theta & \sin\theta & 0\\ -\sin\theta & \cos\theta & 0\\ 0 & 0 & 1\end{bmatrix},\mathbf{H}_{10k}=\frac{1}{\ell}\begin{bmatrix}d_{1111i}^{k(a)} & 0 & d_{1131i}^{k(a)}\\ 0 & 0 & 0\\ d_{3111i}^{k(a)} & 0 & d_{3131i}^{k(a)}\end{bmatrix},\mathbf{H}_{21k}=\begin{bmatrix}d_{a1111i}^{k(a)} & 0 & d_{a1131i}^{k(a)}\\ 0 & \tau_{a11i}^{k(a)} & 0\\ d_{a1131i}^{k(a)} & 0 & d_{a3131i}^{k(a)}\end{bmatrix} \tag{4}$$

where ℓ is a representative length of stress field, $d_{\alpha\beta\gamma\delta i}$ are interface elastic constants, and $\tau_{\alpha\beta i}$ is interface stress.

The order of the singularity can be then obtained by setting to be zero the determinant of the coefficient matrix:

$$\left|\mathbf{K}_3\right|=0 \tag{5}$$

The eigenvalue, λ, obtained from Eq. (5) exists infinitely. However, the stress field at the tip in an anisotropic elastic composite wedge is expressed primarily in terms of the stress singularity. Displacements in the singular stress field are definite. Hence, $0 < \mathrm{Re}(\lambda) < 1$.

If the angular function for the displacement is expressed by $m_k^j(\theta)$, the angular function $f_k^j(\theta)$ for

stress is given by

$$\begin{Bmatrix} \mathbf{m}_k \\ \mathbf{f}_k \end{Bmatrix} = \begin{bmatrix} \mathbf{A}_k & \bar{\mathbf{A}}_k \\ \mathbf{B}_k & \bar{\mathbf{B}}_k \end{bmatrix} \mathbf{G}_{k(j)} \begin{bmatrix} \left\langle \hat{p}_{*k}^{1-\lambda}(\theta)\hat{p}_{*k}^{-1+\lambda}(\theta_2) \right\rangle & 0 \\ 0 & \left\langle \hat{\bar{p}}_{*k}^{1-\lambda}(\theta)\hat{\bar{p}}_{*k}^{-1+\lambda}(\theta_2) \right\rangle \end{bmatrix} \begin{Bmatrix} \mathbf{p}^* \\ \mathbf{0} \end{Bmatrix} \tag{6}$$

where j=0 for k=1 and j=2 for k=2.Here, the stress function is expressed as $\boldsymbol{\phi}^{(k)} = K_m r^{\lambda_m} \mathbf{f}^k(\theta)$.

3. Molecular dynamics

3.1. GEAM potensial

The molecular dynamics method is used for rearranging atomic structures near surfaces and interfaces, and the distribution of atomic stress near the tip of the wedge is calculated using the GEAM potential, which can be used to adequately express the potential for joint structures composed of anisotropic materials. The GEAM potential is composed of many-body and two-body potentials, which covers multi-component systems [4, 5].
The GEAM potential E is defined as

$$E_{tot} = \sum_{\alpha} \left\{ F_\alpha\left(\rho^\alpha\right) + \frac{1}{2} \sum_{\beta(\neq\alpha)} V_{\alpha\beta}\left(r^{\alpha\beta}\right) \right\} \tag{7}$$

where the embedding function F_α, which gives the potential energy arising from embedding a particular atom having electron density ρ^α at the site α, and $V_{\alpha\beta}$ is the pair interaction between atoms α and β, the separation of which is given by $r^{\alpha\beta}$. In the present analysis, Cu and Au are used for a joint model. The two-body cross potential $V^{\text{Cu-Au}}(r)$ between Au and Cu is constructed as

$$V^{Cu-Au}(r) = \frac{1}{2}\left[\frac{g^{Cu}(r)}{g^{Au}(r)} V^{Au-Au}(r) + \frac{g^{Au}(r)}{g^{Cu}(r)} V^{Cu-Cu}(r) \right] \tag{8}$$

where $g^A(r)$ and $V^{A\text{-}A}(r)$ are the functions of $g(r)$ and $V(r)$ for material A, respectively
The atomic stress is given by

$$\sigma_{ij}^{\alpha} = \frac{1}{\Omega^\alpha} \frac{\partial E_\alpha}{\partial \varepsilon_{ij}} \tag{9}$$

where Ω^α is Voronoi volume of atom α, and ε_{ij} is the bulk strain.

3.2. Models in MD analysis

The material combination of (Material 1, Material 2) = (Cu, Au) is employed. In modeling the joint, a prior calculation for determining the gap at the interface between Cu and Au was carried out. In the calculation, a bicrystalline model with a constant thickness was used. Coherent and incoherent bicrystalline interface models composing of fcc crystal cells with dimensions $10c \times 10c \times 14c$ (the lower region) and $10c \times 10c \times 10c$ (the upper region) along the cubic axes of the conventional unit cell [100], [010] and [001], respectively are considered. c is the lattice constant of the crystal. Here, the coherent interface model has an average lattice parameter of material 1 and material 2. The potential parameter in both materials is modified due to the change of the lattice parameter. Bicrystal (100) plane is the interface plane. Periodic boundary conditions are imposed along the [100] and [010] directions, and the top and bottom planes normal to [001] direction are free. The lattice constant c is 0.3615nm for Cu and 0.4086nm for Au. The gap between Cu and Au is determined for minimizing the interface energy. In the analysis, temperature in the model is varied for achieving the relaxation of atomic structures, i.e., temperature is increased up to 5K until 1000

steps, is kept at 5K until 7000 steps, is decreased down to 0K until 9000 steps, and is kept at 0K until 10000 steps. Time step in the MD calculation is 50fs.
Figure 2 shows a wedge model consisting of two different materials. In the model, radius a is 7 nm, and the thickness is 2 nm. The total number of atoms is from 13,000 to 15,000. Boundaries Γ_1 and Γ_2 are free surfaces, and the periodic boundary condition is applied in the z-direction. An external traction F of 100 MPa is applied in the normal direction of the outer surface Γ_o. The crystal plane on the interface is (001). The wedge angle ω is varied from 90º to 170°, and a precise analysis of the result obtained at ω= 170º using models with coherent and incoherent interfaces is performed. A joint model of ω=170º with the incoherent interface is shown in Fig.3.

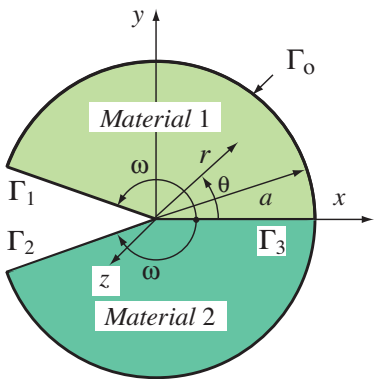

Figure 2. Wedge model for analysis

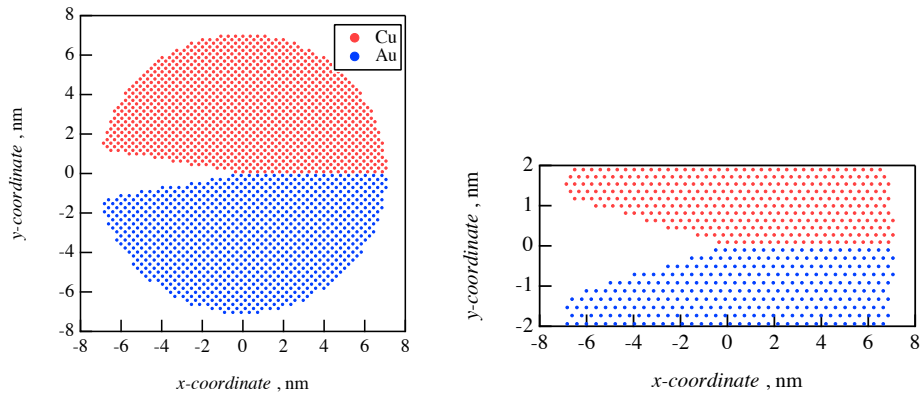

(a) A joint model with ω=170º in MD (b) Enlargement along the interface

Figure 3. MD model for the joint (red symbol : Cu, blue symbol : Au)

4. Results of anaysis

4.1. Results for an incoherent interface

A model with an incoherent interface is firstly analyzed. A distribution map of the stress σ_{yy} in the x-y plane is shown in Fig. 4. The plane is selected so that the misfit of the z-direction is the smallest. The stress is calculated using eq.(8) in which the Voronoi volume is involved. Moreover, the distribution of stress σ_{yy} along the interface is shown in Fig. 5. The stress distribution fluctuates along the interface since the Voronoi volume may be vary. The stress near the interface varies periodically, as shown in Fig. 4. This is attributed to the influence of lattice misfit. The period of the

stress variation is approximately 3 nm and agrees with the distance between the smallest lattice misfit in the x-direction. This stress variation does not exist in the model with a coherent interface.
In order to investigate the influence of interface and surface stresses on the stress distribution near the wedge, an initial stress before loading is subtracted from the distribution shown in Fig. 5. The stress distribution along the interface is shown in Fig. 6. It is found that the difference in stress between Au and Cu becomes small, and the stress near the wedge subsequently becomes large.

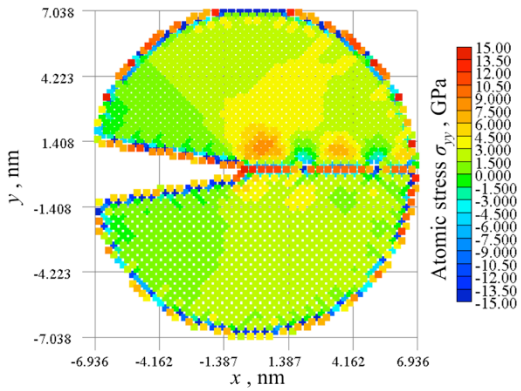

Figure 4. Stress distribution, σ_{yy}, in incoherent model

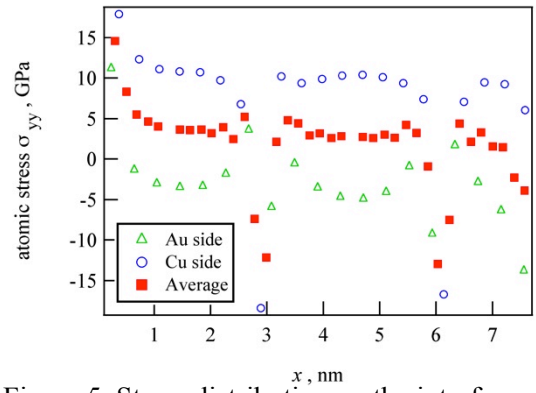

Figure 5. Stress distribution on the interface, σ_{yy} (incoherent interface model)

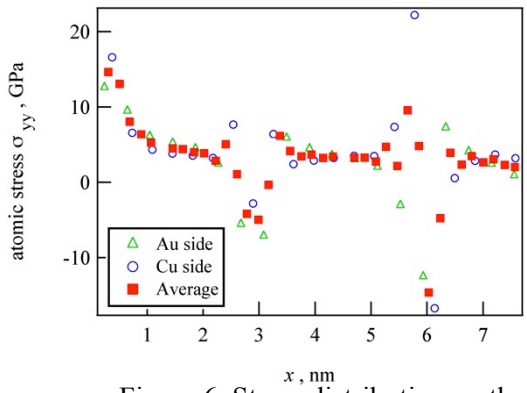

Figure 6. Stress distribution on the interface, σ_{yy}, after subtracting initial stress (incoherent interface model)

4.2. Results for a coherent interface

Next, the model with a coherent interface is analyzed. The lattice length in the model is the average of the lattice lengths of Au and Cu. The potential parameters r_e of Au and Cu in the model are changed due to the change in the lattice length. A distribution map of the stress σ_{yy} in the x-y plane is shown in Fig. 7. The distributions of stress σ_{yy} for incoherent and coherent interfaces along the interface are shown in Fig. 8. The stress in the coherent model distributes smoothly, except near the edge of the interface.
As shown in Fig. 7, the stress in the direction of about 45° from the interface is larger, and the contour of the stress distribution is a fan shape. The stress in Cu (the upper material) is larger than that in Au. The atomic stress along the interface is slightly larger than that in other locations. The stresses on Γ_1, Γ_2, and Γ_0 in the model are large due to the influence of the surface or the interface. In Fig. 8, the stress (blue open circle) decreases slightly at x = 0.5 nm. The same tendency can be seen in the results of the surface stress analysis [6]. This is due to the influence of surface effect.

In order to investigate the influence of interface and surface stresses on the stress distribution near the wedge, the initial stress before loading is subtracted from the distribution shown in Fig. 8. The results for the stress distribution are shown in Fig. 10. The difference in stress between the Au and Cu regions decreases, and the stress near the wedge becomes large. The distribution of stress σ_{yy} on $r = 4$ nm is shown in Fig. 9. The stress distribution is disturbed near the interface. This is due to the interface stress effect. A comparison of the results for the coherent interface and the incoherent interface is shown in Fig. 10. Figure 10 shows the stress distribution obtained after subtracting the initial stress from the distribution shown in Fig. 8. When the initial stress is subtracted, the stress distribution on the incoherent interface approaches to that on the coherent interface.

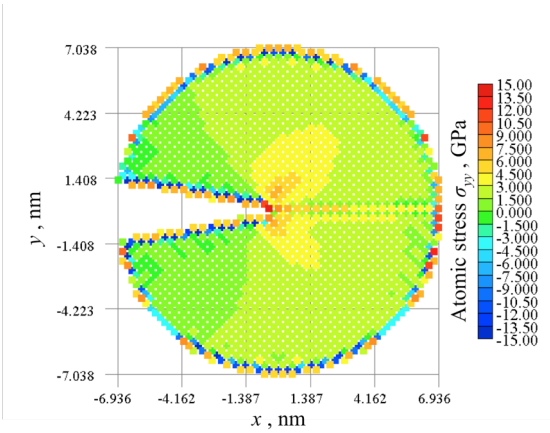

Figure 7. Stress distribution, σ_{yy}, in coherent model

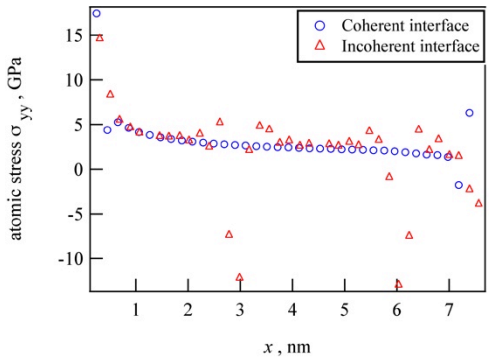

Figure 8. Stress distribution on the interface, σ_{yy}, including the initial stress

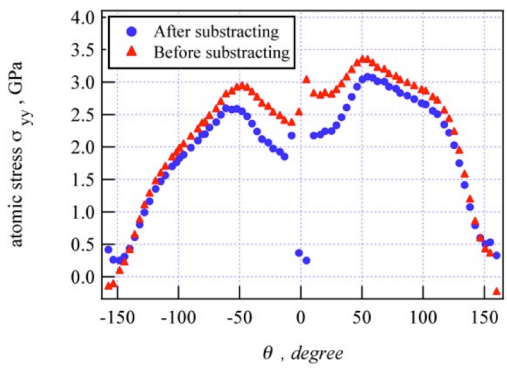

Figure 9. Stress distribution on a circle of radius 4 nm

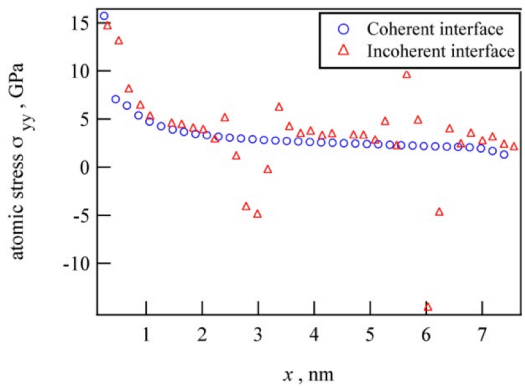

Figure 10. Stress distribution on the interface, σ_{yy}, after subtracting the initial stress

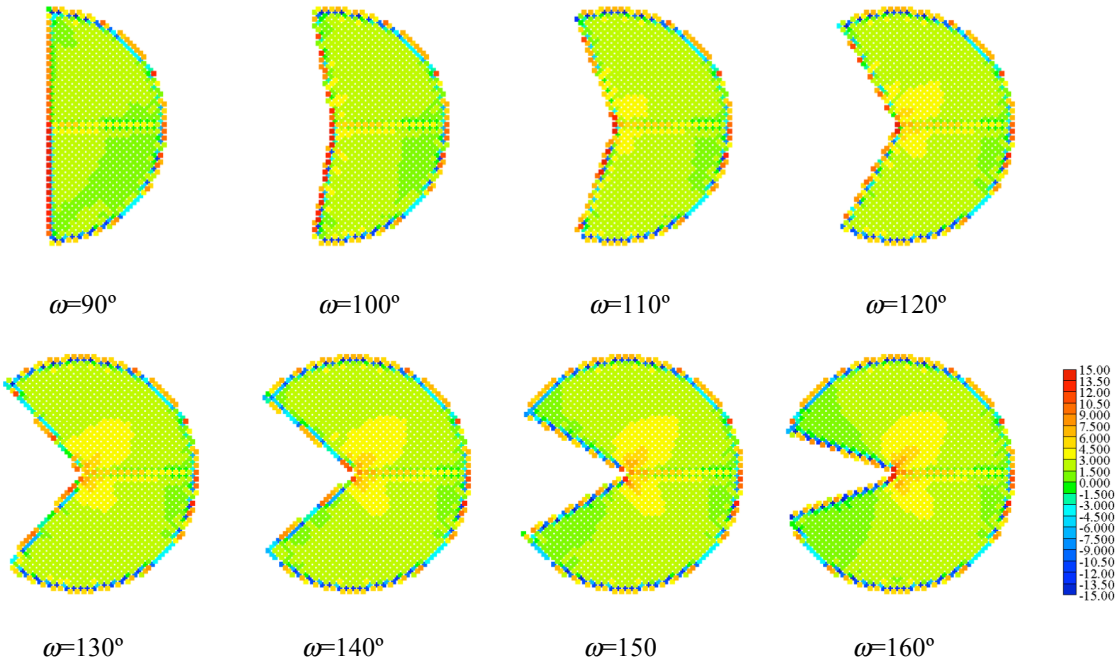

Figure 11. Contour map of stress, σ_{yy}, in coherent interface model with various wedge angles (Before subtracting the initial stress)

4.3. Influence of wedge angle on the stress distribution

Here, the influence of the wedge angle, ω, on the stress distribution σ_{yy} is investigated. The angle ω is varied from 90° to 170° at 10° intervals. A surface traction of 100 MPa is applied to the outer surface Γ_o. A coherent interface model is used for the analysis. The results of the analysis are shown in Fig. 11. A small stress concentration appears in the model with ω= 90°. As the wedge angle ω increases, the stress concentration increases. In particular, as shown in these figures, the region of large stress extends in the directions of θ= 65° and -70°. The distributions of atomic stress σ_{yy} for various wedge angles ω along the interface are shown in Fig. 12. Figures 12(a) and 12(b) show the stress distributions including the initial stress and subtracting the initial stress, respectively. These stresses are the average values for the nearest atom in both regions. The stress σ_{yy} increases with the wedge angle ω.

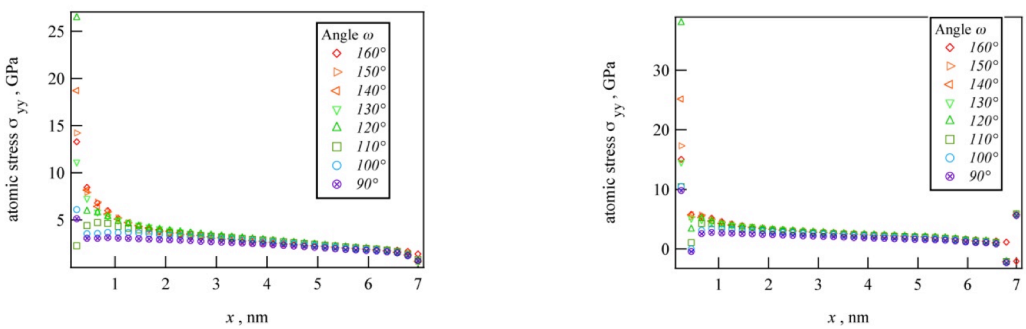

(a) Before subtraction (b) After subtraction

Figure 12. Distribution of atomic stress σ_{yy} along the interface

4.4. Comparison of the MD results for stress singularity and angular function

The order of stress singularity λ is obtained for various angle ω using Eq. (5). The angle ω is varied from 90° to 180°. The value of λ is shown in Fig. 13. A complex value of λ appears in the range 174° < $\omega \leq$ 180°. In the case of ω= 180°, λ is 0.5±iε (where ε is a constant that depends on the material combination: 0.0042(Cu-Au)). This case corresponds to a notch.
Figure 14 shows both log plots of the data shown in Fig. 12. Figures 14(a) and 14(b) are stress distributions including and subtracting the initial stress, respectively. As shown in these figures, the stress distribution after subtracting the initial stress is straighter than that before subtracting the initial stress. Next, the results for ω= 170° are precisely investigated. Figure 13 shows that the imaginary part of λ for ω= 170° does not exist and that three roots exist corresponding to λ_{I} = 0.499, λ_{II} = 0.462, and λ_{III} = 0.461. The angular functions are continuous at the interface, and f^{I} and f^{III} are approximately 0 around θ= 0° and at the free surface (θ= ±170°). Hence, the stress distribution along the interface may be expressed by a power-law with an index of -0.499. The stress distributions shown in Figs. 8 and 10 are then compared with the stress distributions approximated using $\sigma_{yy} = K_{yy} r^{-0.499}$. Here, r is used in place of x.

Both log plots for σ_{yy} in the incoherent model are shown in Fig. 15. Figure 15(a) represents the stress distribution before subtracting the initial stress due to surface stress. Figure 15(b) demonstrates the stress distribution after subtracting the initial stress. The blue line in these figures indicates the approximated stress distribution using Eq. (9). As shown in Fig. 15(b), the atomic stress σ_{yy} with the initial stress subtracted agrees fairly well with the approximated line in 0.6 nm < r < 2 nm. However, the atomic stress increases near the tip and is larger than the approximated line given by the power-law that is derived from the theory of anisotropic elasticity. This might be due to a variation in surface stress near the tip. Log plots of atomic stress σ_{yy} in the coherent model are shown in Fig. 16. Figure 16(a) shows the distribution of atomic stress σ_{yy} corresponding to Fig. 15(a). The blue line indicates the plot of the same line shown in Fig. 15. The blue line does not agree with the atomic stress shown in Fig. 16(a). The stress distribution with the initial stress subtracted agrees fairly well with the blue line, as shown in Fig. 16(b). However, the atomic stress σ_{yy} becomes larger than the value estimated from the theory of anisotropic elasticity near the tip. Here, the order of stress singularity is determined as a function of distance along the interface using eqs.(2)-(5). The interface stress and interface elastic moduli are obtained as functions of the distance of the wedge tip along the interface. These relationships are used for solving eq.(5). The order of stress singularity is plotted against the distance as shown in Fig. 17. The plotted values are approximated using the power law function of the distance r as $\lambda_{\mathrm{I}}(r) = 0.496 + 0.00114(r/\ell)^{-4.45}$. Here, ℓ=1nm. Then, the distribution of atomic stress along the interface is presented in Fig. 18. It is found that the atomic stress can be expressed by the equation of $4.8r^{-\lambda_{\mathrm{I}}(r)}$ considering the interface stress and elasticity.

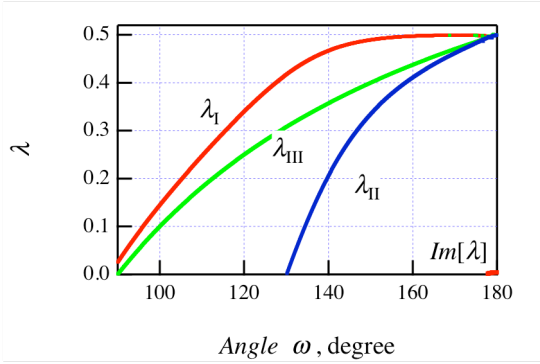

Figure 13. Order of stress singularity λ against the angle ω

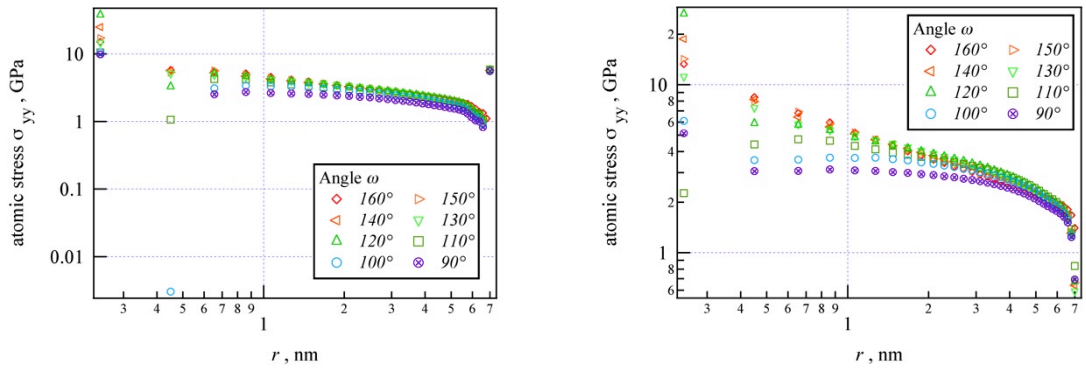

(a) Before subtraction (b) After subtraction

Figure 14. Both log plots of the atomic stress σ_{yy} along the interface

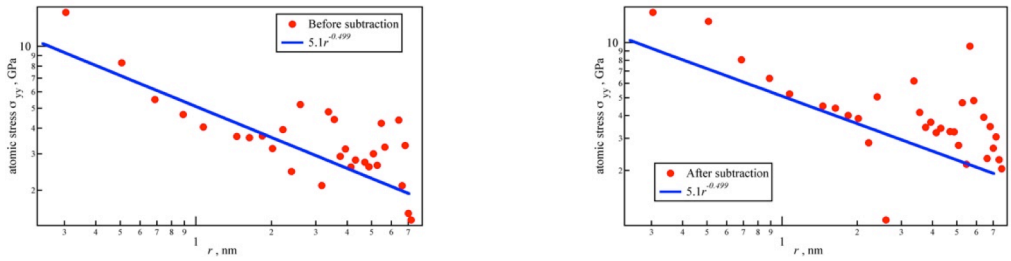

(a) Before subtracting the initial stress (b) After subtracting the initial stress

Figure 15. Stress distribution along the interface in the incoherent model

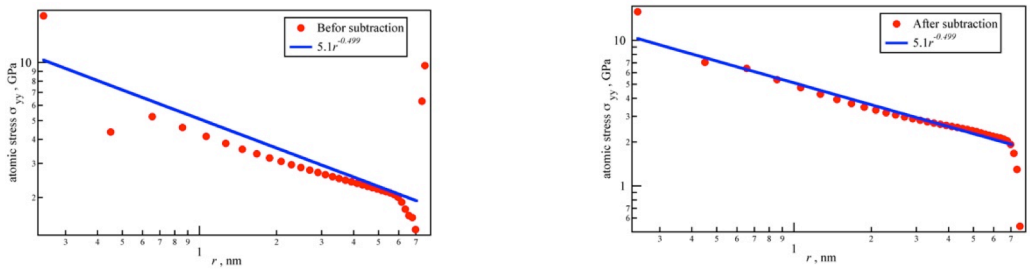

(a) Before subtracting the initial stress (b) After subtracting the initial stress

Figure 16. Distribution of stress, σ_{yy}, on the interface in the coherent interface model

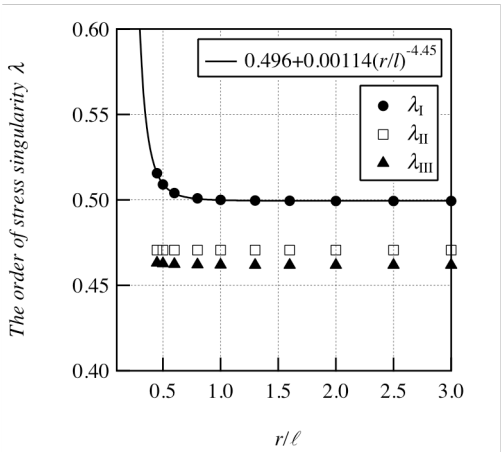

Figure 17. A variation of the order of stress the singularity

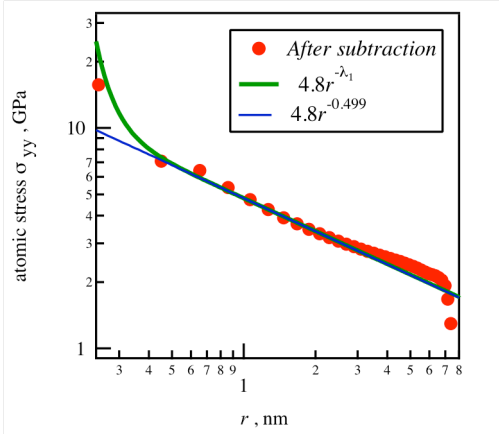

Figure 18. Distribution of stress σ_{yy} along interface

5. Conclusions

In the present paper, the stress distributions in incoherent and coherent wedge models were analyzed using MD, in which the GEAM potential was used. The stress distributions in both models were compared, and the usefulness of coherent model was demonstrated. The coherent model is applicable for analyzing the stress singular field by subtracting the initial stress from the stress distribution after loading. The stress distribution near the edge tip of the interface in MD can be expressed using the anisotropic theory of elasticity considering the interface properties.

Acknowledgements

The present research was supported in part by a Grant-in-Aid for Scientific Research (B) (No. 2136051) from the Japan Society for the Promotion of Science.

References

[1] Horike K., Ikeda T., Matumoto R. and Noriyuki N., Stress Singularity Analysis at an Interfacial Corner between Dissimilar Crystals and Evaluation of Mixed Modes Fracture Criteria Using Molecular Statics, *Journal of the Society of Materials Science*, Vol. 59, No. 12, (2010), pp.908-915.

[2] Koguchi H., Analysis for Stress Singular Fields near a Wedge Corner in 2D Joints Considering Interface Elasticity, ASME 2012 International Mechanical Engineering Congress & Exposition, 2012.

[3] Ting T. C. T., Anisotropic Elasticity: Theory and Applications, Oxford University Press, (1996), pp.134-263.

[4] Wadley H.N.G., Zhou X., Johnson R.A. and Neurock M., Mechanisms, models and methods of vapor deposition, *Progress in Materials Science,* 46, Issue 3-4(2001), pp.329-377.

[5] Zhou X. W, Wadley H. N. G. and Johnson R. A, Atomic Scale Structure of Sputtered Metal Multilayer, *Acta Materialia*, 49, (2001), pp.4005-4015.

Appendix

The embedding function is defined as

$$F(\rho)=\begin{cases}\sum_{i=0}^{3}F_{ni}\left(\frac{\rho}{\rho_n}-1\right)^i & (\rho<\rho_n,\rho_n=0.85\rho)\\ \sum_{i=0}^{3}F_{i}\left(\frac{\rho}{\rho_e}-1\right)^i & (\rho<\rho_e,\rho_e=1.15\rho)\\ F_e\left[1-\ln\left(\frac{\rho}{\rho_e}\right)^n\right]\left(\frac{\rho}{\rho_e}\right)^n & \end{cases} \tag{10}$$

$$V(r)=\frac{A\exp\left[-\alpha\left(\frac{r}{r_e}-1\right)\right]}{1+\left(\frac{r}{r_e}-\kappa\right)^{20}}+\frac{B\exp\left[-\beta\left(\frac{r}{r_e}-1\right)\right]}{1+\left(\frac{r}{r_e}-\lambda\right)^{20}} \tag{11}$$

$$\rho=\sum_{\beta(\neq\alpha)}g(r) \tag{12}$$

$$g(r)=\frac{g_e\exp\left[-\beta\left(\frac{r}{r_e}-1\right)\right]}{1+\left(\frac{r}{r_e}-\lambda\right)^{20}} \tag{13}$$

The two-body cross potential $V^{\text{Cu-Au}}(r)$ between Au and Cu is constructed as

$$V^{Cu-Au}(r)=\frac{1}{2}\left[\frac{g^{Cu}(r)}{g^{Au}(r)}V^{Au-Au}(r)+\frac{g^{Au}(r)}{g^{Cu}(r)}V^{Cu-Cu}(r)\right] \tag{14}$$

where $g^A(r)$ and $V^{A\text{-}A}(r)$ are the functions of $g(r)$ and $V(r)$ for material A, respectively, g_ε, r_ε, ρ_ε, α, β, A, B, κ, λ, F_{ni}, F_i, η, and F_ε are potential parameters[(4),(5)].

Table 1 Values of potential functions

	Au	Cu		Au	Cu
r_e	2.88503	2.556162	F_{n0}	−2.937772	−2.170269
g_e	1.529021	1.554485	F_{n1}	−0.500288	−0.263788
ρ_e	19.991632	21.175871	F_{n2}	1.601954	1.088878
ρ_n	19.991509	21.175395	F_{n3}	−0.83553	−0.817603
ι	9.516052	8.12762	F_0	−2.98	−2.19
χ	5.075228	4.334731	F_1	0	0
B	0.229762	0.39662	F_2	1.706587	0.56183
κ	0.356666	0.548085	F_3	−1.134778	−2.100595
λ	0.35657	0.308782	η	1.021095	0.31049
λ_n	0.748798	0.756515	F_e	−2.978815	−2.186568

Chirality and Size Dependent Elastic Properties of Silicene Nanoribbons under Uniaxial Tension

Yuhang Jing[1,2,*], **Yi Sun**[1], **Hongwei Niu**[1], **Jun Shen**[2]

[1] Department of Astronautical Science and Mechanics, Harbin Institute of Technology, Harbin 150001, China
[2] School of Materials Science and Engineering, Harbin Institute of Technology, Harbin 150001, China
* Corresponding author: jingyh@hit.edu.cn

Abstract The mechanical properties of silicene are investigated using *ab initio* calculation and molecular dynamics simulations with different empirical potentials. The simulation results show that the calculated Young's modulus of bulk silicene with EDIP model is consistent with the *ab initio* calculations. The chirality has a significant effect on the critical strain and stress of bulk silicene under uniaxial tension. In addition, the Young's modulus depends strongly on the chirality and size of the silicene nanoribbon. The fracture process of a silicene nanoribbon is also studied.
Keywords Silicene, Young's modulus, Chirality and Size effects

1. Introduction

Graphene, which is a two-dimensional (2D) atomic layer of graphite, forms the basis of both 3D graphite and 1D carbon nanotubes. Since the discovery of graphene, graphene has attracted a worldwide attraction due to its extraordinary mechanical and electronic properties and potential applications [1-5]. The silicon analogue of graphene, the so called silicene, also attracts considerable scientific interest [6-8]. Recently, the possible growth of silicene nanoribbons on Ag (100), Ag (110), and Ag (111) substrates has been reported [9-11]. The electronic properties of silicene have also been investigated theoretically [12-14], some of which have been shown to be similar to those of graphene [12]. Thus, it can be expected that silicene can have the remarkable characters as graphene. Similar to graphene nanoribbons, the electronic properties of silicene nanoribbons are dependent of the structural size and chirality. Armchair silicene nanoribbons are semiconducting while the zigzag silicene nanoribbons are metallic when the width of the ribbons is broader [15]. However, compared with graphene, silicene have more potential applications in future nanoscale devices due to its compatibility with conventional Si-based electronic technology. Mechanical properties of nanoscale structures need to be understood in detail to enable design of high-performance and reliable micro/nanoelectromechanical systems (MEMS/NEMS) [16]. From a theoretical viewpoint, many correlative theoretical predictions have been performed in recent years and the attentions are mainly paid on the microstructural and electronic properties of the silicene [12-15]. The theoretical investigation of the mechanical properties of the silicene is also necessary and timely. However, the mechanical properties of silicene have not been reported so far. Therefore, in this work, *ab initio* calculations are performed to obtain robust predictions of the mechanical properties of the silicene, and then we investigate the chirality and size effects on the elastic properties of silicene nanoribbons using molecular dynamics (MD) simulations.

2. Simulation details

We employ *ab initio* calculations in order to obtain robust predictions of the mechanical properties of silicene using SIESTA code [17] and check different empirical potentials' accuracy. By means of extensive optimization, a user-defined double zeta plus polarization (DZP) basis set is constructed for the silicene. The Perdew-Burke-Ernzerhof (PBE) formulation of the generalized gradient approximation (GGA) for the exchange and correlation functional is used in the calculation to account for the electron-electron interactions. The k-grid sampling of 16×16×1 for the silicene, together with a meshcutoff of 200 Ry for the system are used in the calculation. Small stress is applied along zigzag or armchair direction of silicene and then relax the geometry until the forces on each atom are less than 0.01 eV $Å^{-1}$.

In order to study the chirality and size effects on the elastic properties of silicene nanoribbons, MD simulations are performed using LAMMPS [18]. Several inter-atomic potentials have been used in the MD simulations, including EDIP [19,20], Stillinger-Weber (SW) [21], Erhart-Albe [22], MEAM [23]. Isothermal-Isobaric (NPT) simulations are performed at a given temperature for 100 ps with a time step of 0.1 fs to let the system reach its equilibrium configuration. The strain is then applied along the uniaxial direction to perform uniaxial tensile tests. The applied strain rate is 0.005/ps. The pressure component vertical to the loading direction is controlled to maintain the uniaxial tensile condition. The strain increment is applied to the structure after every 10000 time steps with the step size of 0.1 fs. All the MD simulations are carried out at 300K and the temperature is controlled by employing the Nosé-Hoover thermostat [24]. The Velocity-Verlet algorithm is employed to integrate the equations of motion.

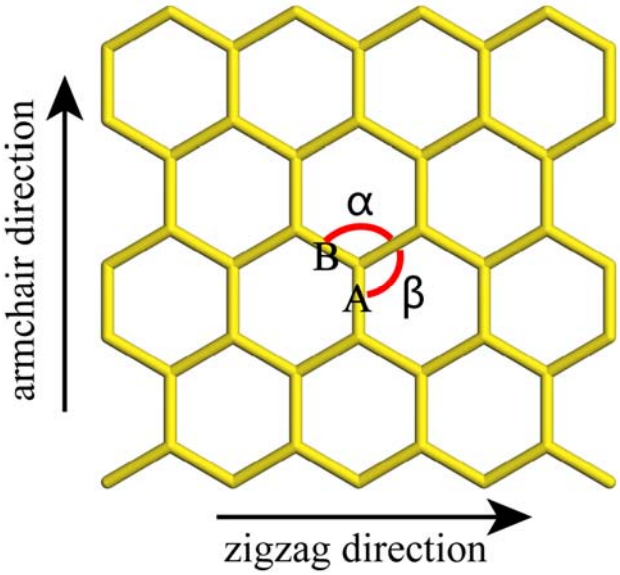

Figure 1 A silicene nanoribbon, along with the definitions of zigzag and armchair directions, bond types, and bond angles.

3. Results and discussion

As shown in Figure 1, we investigate the mechanical properties of rectangular bulk silicene in both the zigzag direction and armchair direction. The silicene thickness is assumed to 0.42 nm which is twice size of van der waals radius of silicon [25]. In *ab initio* calculations, the Young's modulus in both zigzag and armchair directions of bulk silicene with 60 atoms (1.94 nm × 2.01 nm) is calculated from $Y = \frac{1}{V_0}\frac{\partial^2 E}{\partial \varepsilon^2}$ with a low strain ($\leq 2\%$), where $\frac{\partial^2 E}{\partial \varepsilon^2}$ is the second derivative of the total energy with respect to the strain of the silicene and V_0 is the minimum total energy volume. The calculated results are 148.5 and 140.7 GPa along zigzag direction and armchair direction, respectively. In MD simulations, in order to investigate the effect of chirality on the mechanical properties of bulk silicene, we perform displacement-control uniaxial tensile tests in both zigzag and armchair directions of bulk silicene with 7168 atoms (around 21 nm × 21 nm) with periodic boundary conditions in the in-plane two directions. Figure 2 shows the strain-stress relations for uniaxial tensile tests in both zigzag and armchair directions from MD simulations. The Young's modulus is evaluated using the expression, $Y = \sigma / \varepsilon$ in the elastic region, where σ and ε are the stress and strain, respectively. Table I displays the Young's modulus of bulk silicene for different potentials, and a comparison with *ab initio* calculations is also shown. As we can see from Table I, the calculated Young's modulus of bulk silicene using EDIP model is a little bigger than the *ab initio* calculations because the EDIP model is a short ranged potential, which will lead to an increased stiffness [26]. The results from Erhart-Albe are a little smaller than the *ab initio* calculations. However, the stress increases dramatically when the strain reaches certain value (see

Figure 2). This awkward phenomenon results form the cut-off function in the Erhart-Albe (Tersoff-like) potential [27]. The results from SW and MEAM potentials are much lower than the *ab initio* calculations. Therefore, we select the EDIP model for the following calculations.

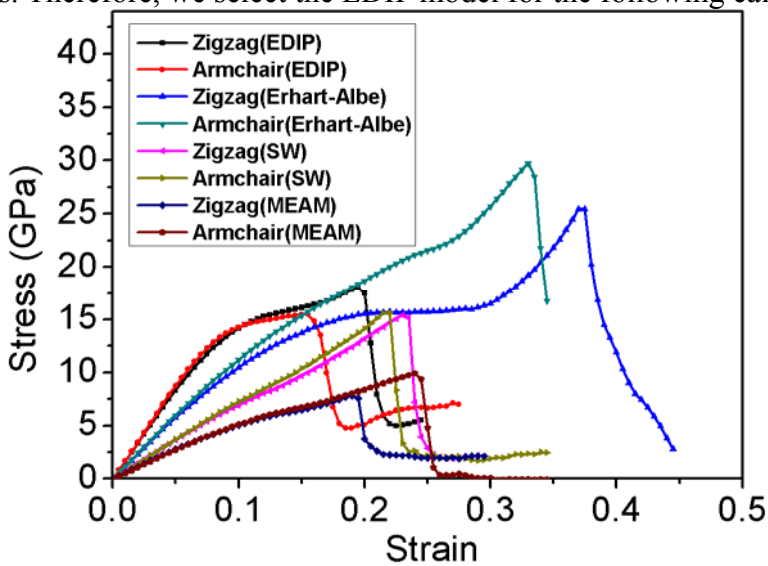

Figure 2 Strain-Stress relations of bulk silicene under tensile tests in the zigzag and armchair directions with different potential.

Table 1 Young's moduli for bulk silicene from *ab initio* calculations and different potential models. All values are in units of GPa.

Direction of tension	*Ab initio* results	EDIP	Erhart-ALbe	SW	MEAM
Zigzag direction	148.5	166.7	120.7	73.3	57.2
Armchair direction	140.7	170.8	121.2	67.0	56.1

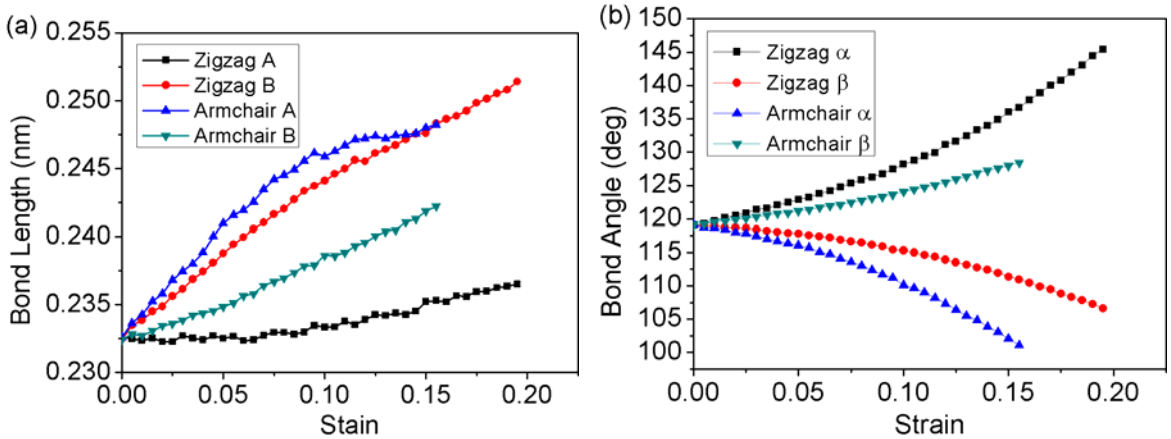

Figure 3 Evolutions of bond length (a) and bond angle (b) with a function of strain when uniaxial tension is applied on bulk silicene along zigzag and armchair directions.

As the strain increases, the chirality dependence becomes obvious for all potentials. As for EDIP model, the critical strain is 15.5% and 19.5% in the armchair and zigzag direction, respectively. The calculated critical stress of bulk silicene is 15.5 and 18.1 GPa in the armchair and zigzag direction, respectively. The critical strain and stress are different for zigzag and armchair load tests. To give more insight into this phenomenon, the variation of the bond length and bong angle with the strain in the tensile direction for zigzag and armchair cases are shown in Figure 3. One can see that in the zigzag loading case, the main bond elongation is experienced by bond B. In the armchair loading case, the main bond elongation is experienced by bond A. When the strain is smaller, the elongation ratio of amchair A is larger than that of zigzag B (see Figure 3(a)). However, the elongation ratio of amchair A become smaller and is lower than that of zigzag B when the strain is larger than 0.1. Moreover, the magnitude of the bond angle variation in the amchair direction tension test is larger

than that in the zigzag direction tension test when the strain is larger than 0.1. Smaller angle α can release stress which results in slower stress increase, which will enlarge the critical strain. Hence, the larger critical strain in zigzag direction tension than that in armchair direction tension can be understood.

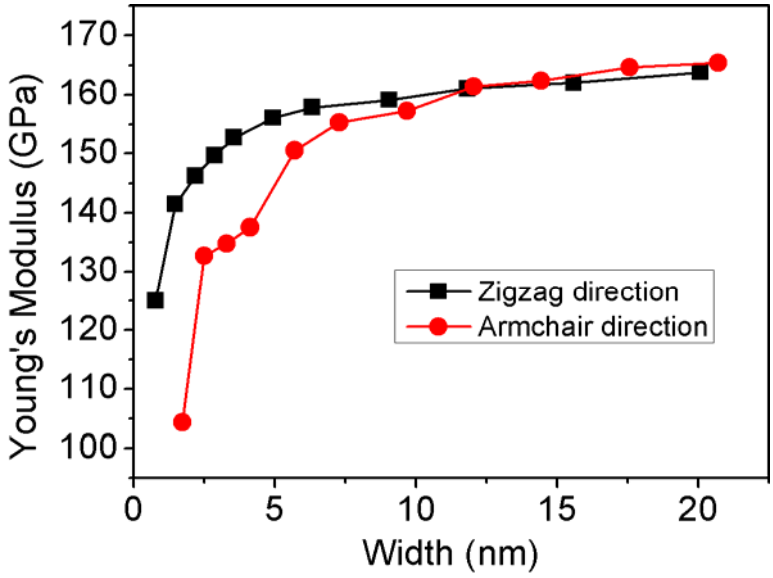

Figure 4 Young's modulus as a function of the silicene nanoribbon's width for uniaxial tension along the armchair and zigzag directions.

To study the size and chirality effects on the mechanical properties of silicene nanoribbons, deformation-control uniaxial tensile tests are performed. The width of square-shaped silicene nanoribbons in armchair and zigzag directions varies from 0.8 to 20.7 nm. An NVT ensemble is used with 10.0 nm vacuum space on each side of the nanoribbon. The Yong's modulus is calculated for armchair and zigzag directions using the above expression, $Y = \sigma / \varepsilon$ in the elastic region. In Figure 4 we plot the variation of Young's modulus as a function of the size of the silicene nanoribbon. It can be seen that Young's modulus along zigzag and armchair directions increases with the width of the nanoribbon. This variation is similar to the size-dependent Young's modulus of graphene nanoribbon [28]. For example, the size effect on Young's modulus is negligible when the width of the silicene nanoribbon is over 15.0 nm. Furthermore, significant chirality effects are found in the Figure 4. For the nanoribbons with the same size, Young's modulus is larger along the zigzag direction than along the armchair direction when the width of nanoribbon is smaller than 10.0 nm, which is consistent with the results for the graphene nanoribbon [28].

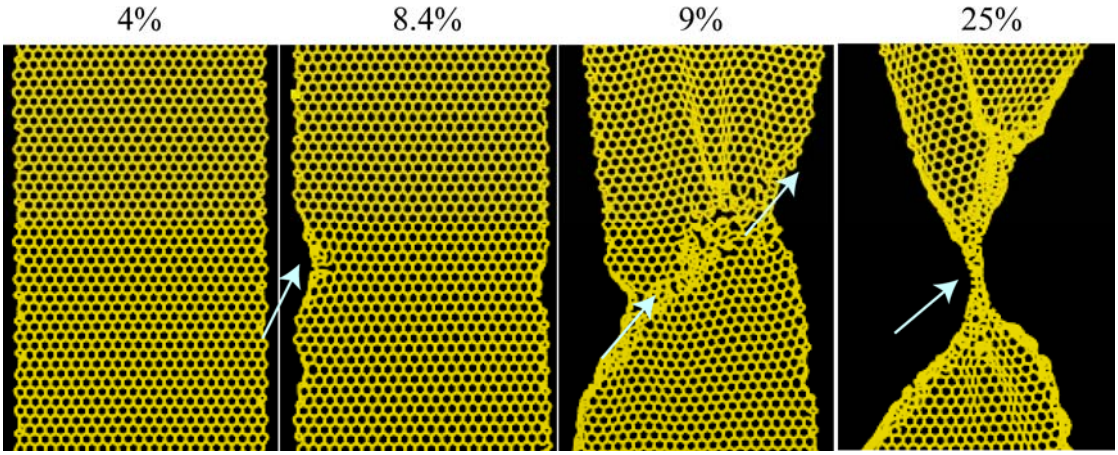

Figure 5 Snapshots of atomix configurations at various strains.

As shown in Figure 2, as the strain increase to certain value, the bulk silicene starts to fracture, which is same for silicene nanoribbon under uniaxial tension. Figure 5 presents the fracture process of an armchair silicene nanoribbon with the width of 9.7 nm. The applied strain rate is 0.0005/ps.

For small strains, both sides of nanoribbon shrink to release the deformation energy, and no structural defects appear at this stage. For larger strains, bond breakage in the edge is observed and spreads toward the center as the strain increases. With the strain increasing further more, we find that sliding happens, and many atoms rearrange in the neck region. The deformation mechanism of a shearing action is similar to that of silicon nanowire [29]. After the formation of the neck, the plastic deformations have been carried mainly through the reconstruction and rearrangement of the neck reion. Beyond this region, the nanoribbon keeps ordered structure and have no significant change. Despite that the EDIP model gives a considerably accurate Young's modulus of bulk silicene, a detailed analysis of the fracture behavior of silicene nanoribbons is still needed with different empirical potentials or *ab initio* calculations.

4. Conclusions

In this paper, the chirality and size effects on the mechanical properties of silicene nanoribbons are investigated based on atomistic simulation. Compared with the *ab initio* calculations, EDIP model of bulk silicene gives a more accurate Young's modulus than other empirical potentials. As for bulk silicene, uniaxial tensile test along the zigzag direction has a larger critical strain and stress compared to the armchair direction. The Young's modulus increases as the size of silicene nanoribbons increases. Significant slip activities are observed in MD simulations with EDIP model. Further theoretical and experimental studies are needed to study the mechanical properties of this new 2D silicon nanomaterial.

Acknowledgements

The work is supported by China Postdoctoral Science Foundation, and Fundamental Research Funds for the Central Universities under Grant No.HIT.NSRIF.2013031.

References

[1] C. Lee, X. Wei, J. W. Kysar, and J. Hone, Measurement of the Elastic Properties and Intrinsic Strength of Monolayer Graphene. Science 321 (2008) 385.
[2] C. A. Marianetti and H. G. Yevick, Failure Mechanisms of Graphene under Tension. Phys. Rev. Lett. 105 (2010) 245502.
[3] K. S. Novoselov, A. K. Geim, S. V. Morozov, et al., Thin Carbon Films. Science 306 (2004) 666.
[4] A. H. Castro Neto, F. Guinea, N. M. R. Peres, K. S. Novoselov, and A. K. Geim, The electronic properties of graphene. Reviews of Modern Physics 81 (2009) 109.
[5] C. Soldano, A. Mahmood, and E. Dujardin, Production, properties and potential of graphene. Carbon 48 (2010) 2127-2150.
[6] J. Kang, F. Wu, J. Li, Symmetry-dependent transport properties and magnetoresistance in zigzag silicene nanoribbons. Appl. Phys. Lett. 100 (2012) 233122.
[7] S. Lebegue, O. Topsakal, Electronic structure of two-dimensional crystals from *ab initio* theory. Phys. Rev. B 79 (2009) 115409.
[8] R. Qin, C. Wang, W. Zhu, Y. Zhang, First-principles calculations of mechanical and electronic properties of silicene under strain. AIP ADVANCES, 2 (2012) 022159.
[9] C. Leandri, H. Saifi, O. Guillermet, B. Aufray, Silicon thin films deposited on Ag(001): growth and temperature behavior. App. Surf. Sci. 177 (2001) 303.
[10] P. D. Padova, C. Quaresima, C. Ottaviani, et al., Evidence of graphene-like electronic signature in silicene nanoribbons. Appl. Phys. Lett. 96 (2010) 261905.
[11] C. Lin, R. Arafune, K. Kawahara, et al., Structure of Silicene Grown on Ag(111). Applied Physics Express 5 (2012) 045802.
[12] S. Cahangirov, M. Topsakal, E. Akturk, H. Sahin, S. Ciraci, Two- and One-Dimensional Honeycomb Structures of Silicon and Germanium. Phys. Rev. Lett. 102 (2009) 236804.
[13] Z. Ni, Q. Liu, K. Tang, et al., Tunable Bandgap in Silicene and Germanene. Nano lett. 12 (2012) 113.
[14] N. D. Drummond, V. Zolyomi, V. I. Fal'ko, Electrically tunable band gap in silicene. Phys. Rev. B 85 (2012) 075423.

[15] Y. Song, Y. Zhang, J. Zhang, D. Lu, Effects of the edge shape and the width on the structural and electronic properties of silicene nanoribbons. Appl. Surf. Sci. 256 (2010) 6313-6317.
[16] X. Li, B. Bhushan, K. Takashima, C. Baek, Y. Kim, Mechanical characterization of micro/nanoscale structures for MEMS/NEMS applications using nanoindentation techniques. Ultramicroscopy 97 (2003) 481-494.
[17] Soler JM, Artacho E, Gale JD, Garcia A, Junquera J, Ordejon P, et al. The SIESTA Method for *ab Initio* Order-N Materials Simulation. J Phys: Condens Matter 2002;14:2745-79.
[18] S. Plimpton. Fast Parallel Algorithms for Short-Range Molecular Dynamics. J. Comput. Phys. 117 (1995) 1.
[19] M.Z. Bazant, E. Kaxiras, J.F. Justo, Environment-dependent interatomic potential for bulk silicon. Phys. Rev. B 56 (1997) 8542.
[20] J.F. Justo, M.Z. Bazant, E. Kaxiras, V.V. Bulatov, S. Yip, Interatomic potential for silicon defects and disordered phases. Phys. Rev. B 58 (1998) 2539.
[21] F.H. Stillinger, T.A. Weber, Computer simulation of local order in condensed phases of silicon. Phys. Rev. B 31 (1985) 5262.
[22] P. Erhart and K. Albe, Analytical potential for atomistic simulations of silicon, carbon, and silicon carbide. Phys. Rev. B 71 (2005) 035211.
[23] M. I. Baskes. Modified embedded-atom potentials for cubic materials and impurities. Phys. Rev. B 46 (1992) 2727.
[24] W. G. Hoover, Canonical dynamics: Equilibrium phase-space distribututions. Phys. Rev. A 31 (1985) 1695-1697.
[25] A. Bondi, van der Waals Volumes and Radii. J. Phys. Chem., 68 (1964) 441-451.
[26] Y. Jing, Q. Meng, Molecular dynamics simulations of the mechanical properties of crystalline/amorphous silicon core/shell nanowires. Physica B 405 (2010) 2413-2417.
[27] O. A. Shenderova, D. W. Brenner, A. omeltchenko, X. Su, Atomistic modelling of the fracture of polycrystalline diamond. Phys. Rev. B 61 (2000) 3877-3888.
[28] H. Zhao, K. Min, N. R. Aluru, Size and Chirality Dependent Elastic Properties of Graphene Nanoribbons under Uniaxial Tension. Nano Lett. 9 (2009) 3012-3015.
[29] Y. Jing, Q. Meng, W. Zhao, Molecular dynamics simulations of the tensile and melting behaviours of silicon nanowires. Physica E 41 (2009) 685-689.

Dislocation dynamics analysis of hydrogen embrittlement in alpha iron based on atomistic investigations

Shinya Taketomi[1,*], Honami Imanishi[2], Ryosuke Matsumoto[2], Noriyuki Miyazaki[2]

[1] Department of Mechanical Engineering, Saga University, 840-8502, Japan
[2] Department of Mechanical Engineering and Science, Kyoto University, 606-8501, Japan
* Corresponding author: taketomi@me.saga-u.ac.jp

Abstract Hydrogen embrittlement is well known phenomenon in which hydrogen lowers the strength of materials. Hydrogen atoms show unique characteristics such as high diffusivity and low concentration in metals, so the direct observations of hydrogen effects on mechanical properties are still difficult. Nevertheless, experimental studies have been revealed many valuable results; HEDE (Hydrogen Enhanced Decohesion), HELP (Hydrogen Enhanced Localized Plasticity), HESIV (Hydrogen Enhanced Strain Induced Vacancy) and others have been proposed as a fracture mechanism of hydrogen embrittlement so far. However, the overview of the hydrogen embrittlement under various conditions is still unclear. In this study, we focus on the edge dislocation motion in the presence of hydrogen atom as one of the elementary process of hydrogen embrittlement in alpha iron. Our previous studies showed that the dislocation velocity increace (softening) occurs at lower hydrogen concentration and lower applied stress conditions. In contrast, dislocation velocity decrease (hardening) occurs at higher hydrogen concentration or higher applied stress conditions. Therefore, we performed the dislocation dynamics calculation around a crack tip based on the results obtained by our atomistic calculations. The results indicate that the hydrogen embrittlement mechanisms possibly change depending on boundary conditions (hydrogen concentration and applied stress intensity factor rate).

Keywords Hydrogen embrittlement, Dislocation dynamics, Atomistic simulation, Alpha iron

1. Introduction

Hydrogen embrittlement is well known phenomenon in which hydrogen lowers the strength of materials. Hydrogen atoms show unique characteristics such as high diffusivity and low concentration in metals, so the direct observations of hydrogen effects on mechanical properties are still difficult. Nevertheless, experimental studies have been revealed many valuable results; e.g. macroscopic hydrogen embrittlement fracture process, stress-strain relation and so on. HEDE (Hydrogen Enhanced Decohesion [1]), HELP (Hydrogen Enhanced Localized Plasticity [2]), HESIV (Hydrogen Enhanced Strain Induced Vacancy [3]) and others have been proposed as a fracture mechanism of hydrogen embrittlement so far. However, the overview of the hydrogen embrittlement under various conditions is still unclear. Here, we believe the evaluation of the elementary process can lead the understanding of whole image of hydrogen embrittlement, and we also believe the atomistic simulations can contribute the understanding of the hydrogen embrittlement, since the atomistic simulations show information in high resolution, and can easily exchange the boundary conditions (i.e. stress, temperature, hydrogen concentration). In this study, we focus on the edge dislocation motion in the presence of hydrogen atom as one of the elementary process of hydrogen embrittlement in alpha iron. Our previous studies [4-5] showed that the dislocation velocity increase (softening) occurs at lower hydrogen concentration and lower applied stress conditions. In contrast, dislocation velocity decrease (hardening) occurs at higher hydrogen concentration or higher applied stress conditions. These contradictive behaviors attribute the applied stress dependent competition between dislocation motion and hydrogen diffusion [4-5]. These atomistic studies, however, evaluated the individual dislocation motion due to the limitation of calculation cost. Therefore, in this study, we perform the dislocation dynamics calculations around a

crack tip based on the results obtained by our atomistic calculations for alpha iron, to evaluate the many-body effects of dislocations around a stress singularity field of a crack tip.

2. Methods of Dislocation Dynamics Analysis

In this study, we employ the analysis model as shown in Figure 1. In this model, one-dimensional edge dislocations are emitted from a mode II crack tip. The crack length is set as $2a$ and the dislocation source S is located at some finite distance of x_S from a crack tip. In this model, x_S is taken as 10^{-9} m, which corresponds to the order of the dislocation core, thus this dislocation source is regarded to be located at the crack tip from the viewpoint of continuum mechanics.

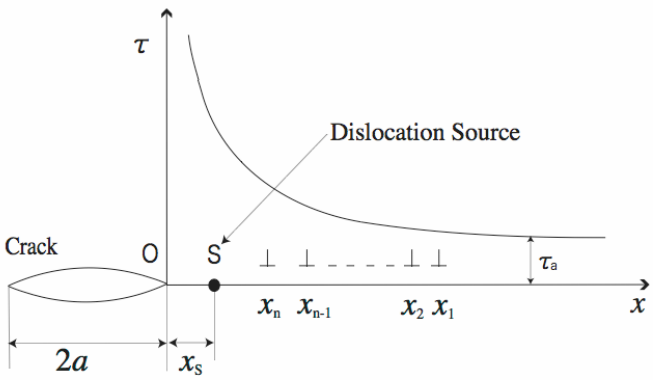

Figure 1. The model of dislocation emission and motion under the local stress field around crack tip

In this study, dislocation dynamics method which has been performed by A. T. Yokobori, Jr. et al. is adopted. Since the detailed analysis methods were reported in the previous papers [6-7], here we show the outline of the analysis method. As the stress distribution near a crack tip $\tau_a(x, t)$, the stress singularity near a crack tip was taken into account under a constant rate of stress application as follows:

$$\tau_a(x,t) = \dot{\tau}\sqrt{\frac{a}{x}} \quad , \tag{1}$$

where $\dot{\tau}$ is the increasing rate of stress application, t is time and x is the distance from the crack tip. The relationship between effective stress exerted on each dislocations moving along x direction and dislocation velocity are written for each individual dislocation in a coplanar array by the following equation:

$$v_i = \frac{\mathrm{d}x_i}{\mathrm{d}t} = Q\left(\Delta E_{\mathrm{dis}}\left(\tau_{\mathrm{eff},i}\right)\right)b \quad , \tag{2}$$

where, $Q(\Delta E_{\mathrm{dis}})$ is the frequency of dislocation motion with $1b$, ΔE_{dis} is the free energy barrier for dislocation motion and is a function of effective stress $\tau_{\mathrm{eff},i}$ and temperature T. b is the length of Burger's vector. The frequency of dislocation motion is determined by atomistic simulation as described later. Here, the effective stress exerted on the i th dislocation is written as follows:

$$\tau_{\mathrm{eff},i} = \dot{\tau}\sqrt{\frac{a}{x_i}} - A^*\left\{\frac{1}{2x_i} + \sum_{\substack{j=1\\ i\neq j}}^{n}\left(\frac{1}{x_i + \sqrt{x_i x_j}} + \frac{1}{x_j - x_i}\right)\right\} \quad , \tag{3}$$

where, $A^* = \mu b / 2\pi(1-\nu)$, μ is the shear modulus, ν is the Poisson's ratio, x_i is the distance of the i th dislocation from the crack tip. The first term is the macroscopic stress field around a crack tip by applied stress, the second and third terms are the image force of dislocations by the free boundary of

crack surface, and the fourth term is the interaction between other dislocations in the same dislocation array. Therefore the effective stress exerted on a dislocation source is written as follows:

$$\tau_{\mathrm{eff,s}} = \tau_{\mathrm{s}} \sqrt{\frac{a}{x_{\mathrm{s}}}} - A^{*}\left\{\frac{1}{2x_{\mathrm{s}}} + \sum_{j=1}^{n}\left(\frac{1}{x_{\mathrm{s}} + \sqrt{x_{\mathrm{s}} x_j}} + \frac{1}{x_j - x_{\mathrm{s}}}\right)\right\} \quad , \tag{4}$$

In this analysis, when the effective stress on dislocation source equals to the activation stress τ_{s}, then a new dislocation is introduced at the source.

3. Material Properties Obtained by Atomistic Simulations

3.1. Equilibrium Hydrogen Concentration

In order to evaluate the material properties (critical stress intensity factor for dislocation emission from mode II crack tip, dislocation velocity) in the presence of hydrogen, the realistic hydrogen concentration should be adopted. According to Sievert's law, the equilibrium concentration of hydrogen is proportional to $p^{1/2}$ and $\exp(-\Delta H/k_{\mathrm{B}}\,T)$, where p is the hydrogen gas pressure, ΔH is the heat of the solution, k_{B} is the Boltzman's constant and T is the temperature. Hirth [8] has reported the hydrogen concentration (atom fraction of hydrogen) for alpha iron under the gaseous hydrogen condition based on Sievert's law. The hydrogen atom stably exists at the tetrahedral site (T-site) within the non-deformed bcc structured alpha iron [9]. Therefore, the hydrogen occupancy at the T-site under thermal equilibrium conditions is given by equation (5) as a function of hydrogen gas pressure p (Pa) and temperature T (K).

$$\theta_{\mathrm{T-site}} = 0.9686 \times 10^{-6} \sqrt{p} \exp\left(-\frac{3440}{T}\right) \quad , \tag{5}$$

A close relation was also obtained by our evaluation using first-principles calculations [10]. Using the hydrogen occupancy at T-site, $\theta_{\mathrm{T\text{-}site}}$, the hydrogen occupancy at a specific trap site θ_i with hydrogen-trap energy $E^{\mathrm{Trap}}{}_i$ under thermal equilibrium condition is given by the following equation:

$$\frac{\theta_i}{1-\theta_i} = \frac{\theta_{\mathrm{T\text{-}site}}}{1-\theta_{\mathrm{T\text{-}site}}} \exp\left(\frac{E^{\mathrm{Trap}}{}_i}{k_{\mathrm{B}}T}\right) \quad , \tag{6}$$

where, the hydrogen-trap energy corresponds to the energy difference between the system with a hydrogen atom trapped at the specific trap site and the system with a hydrogen atom at a T-site within the non-deformed perfect lattice; this definition is the same as in our previous study [11]. To estimate the number of hydrogen atoms exist around the crack/dislocation at a thermal equilibrium conditions, these hydrogen occupancies are employed as same as our previous study[4,12].Using the equations (5) and (6), the hydrogen concentration around a {112}<111> edge dislocation (number of hydrogen atoms per unit length of dislocation line); C_{H} = 0.49 /nm under thermal equilibrium conditions can be realized at 300 K and 0.01 MPa hydrogen gaseous conditions. And C_{H} = 1.24 /nm can be realized at 300 K and 0.32MPa hydrogen gas.

3.2. Dislocation velocity

Dislocation motion is considered as stress-dependent thermal activation process. Our previous studies [4-5] showed that {112}<111> edge dislocation velocity as a function of applied shear stress via the estimation of energy barrier for dislocation motion. The dislocation velocity especially for the case of hydrogen free condition is written as following equation:

$$v = \nu_{\mathrm{d}} \exp\left(-\frac{\Delta E_{\mathrm{w/oH}} l^{*}}{k_{\mathrm{B}}T}\right) b \quad , \tag{7}$$

where, $\Delta E_{\mathrm{w/oH}}$ is the energy barrier for dislocation motion without hydrogen as a function of shear

stress, l^* is the length of edge dislocation line at the energy saddle point of the dislocation motion which are required to surmount for dislocation motion. k_B is the Boltzman's constant, T is the absolute temperature, ν_d is the attempt frequency of dislocation motion. On the other hand, in the presence of hydrogen, energy barrier landscape becomes complex depending on the correlation between the positions of dislocation and hydrogen atoms. According to the case analyses of the competition between dislocation motion and hydrogen atom diffusion, dislocation velocity vary from softening to hardening depends on applied shear stress [4] under the lower hydrogen concentration (C_H = 0.49 /nm). These results indicated that the softening attribute the decrease of energy barrier from 0b to 1b from the position of hydrogen atom, and hardening attribute the increase of energy barrier from 1b to 2b[4]. Moreover, the softening does not occur under high hydrogen concentration (C_H = 1.24 /nm) due to the increment of energy barrier from 0b to 2b[5]. These results of dislocation velocity obtained by atomistic simulations are employed as material properties for dislocation dynamics analyses. Here, the energy barrier is approximated as following function[13]:

$$\Delta E = A \cdot \left(1 - \tau / \tau_{ath}\right)^n \quad , \tag{8}$$

where, τ_{ath} is the athermal stress for dislocation motion, A and n are the fitting parameters. The parameters used in this study are shown in Table 1. Here, the dislocation velocity at higher hydrogen concentration condition (C_H = 1.24 /nm) is approximated as shown in Table 1. The energy barrier obtained in these results, however, neglected the contribution of the enthalpy effects. The effect of enthalpy is approximately considered as following equation[14], therefore the activation free energy for dislocation motion is written as:

$$\Delta E^{\text{act-free}} = A\left(1 - T / T_m\right)\left(1 - \tau / \tau_{ath}\right)^n \quad , \tag{9}$$

where, T_m is the surface disordering temperature, and half of the melting temperature (T_m= 904 K) is adopted. In this study, the activation free energy as shown in equation (9) is employed as an energy barrier of dislocation motion, the obtained relationship between dislocation velocity and applied shear stress at 300 K are shown in Figure 2. At the low hydrogen concentration, dislocation velocity increase (compared with that in the absence of hydrogen) occurs when the applied stress is lower than 29 MPa, and decrease occur when the stress takes higher than 29 MPa. Moreover, applied stress takes over 81 MPa, dislocation velocity does not show the effect of hydrogen.

Table 1. Fitting parameters of the energy barrier for dislocation motion

	n	τ_{ath}	A
Hygrogen free	1.48	660	0.0821
C_H=0.49 /nm ($\tau \leqq$ 28MPa)	1.41	680	0.0795
C_H=0.49 /nm ($\tau \geqq$ 81MPa)	1.48	660	0.0821
C_H=1.24 /nm	1.41	680	0.0795

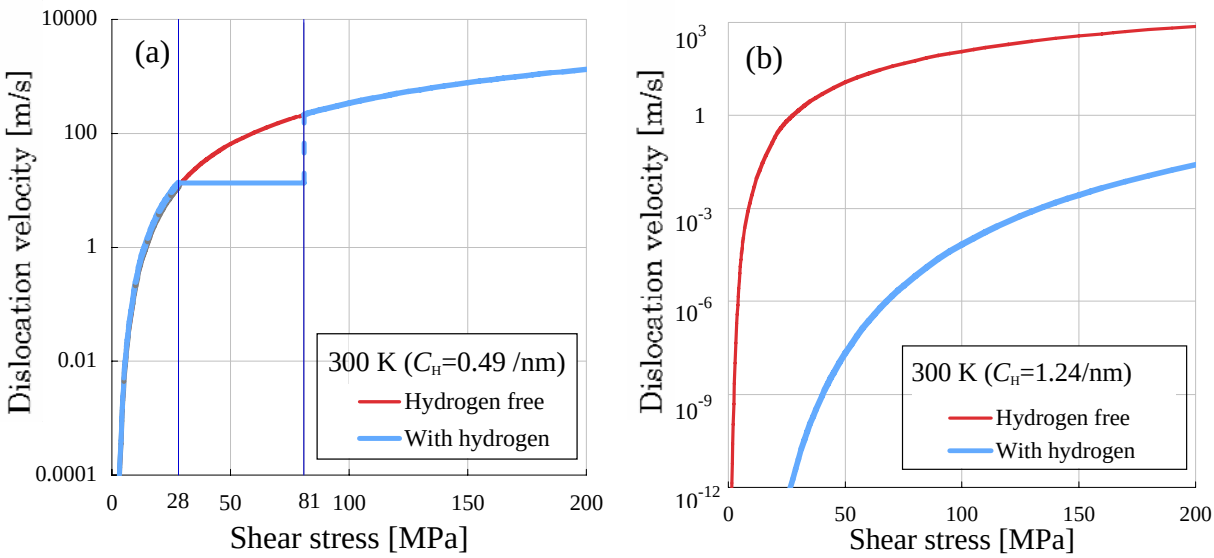

Figure 2. Relationship between dislocation velocity and shear stress at 300 K; (a) low hydrogen concentration condition(C_H = 0.49 /nm), (b) high hydrogen concentration condition(C_H = 1.24 /nm)

3.3. Dislocation Emission from Crack Tip

The activation stress of dislocation source to emit a new dislocation is determined as follows:

$$\tau_s = \frac{K_{IIC}}{\sqrt{\pi x_s}} \quad , \tag{10}$$

where, K_{IIC} is the critical stress intensity factor for edge dislocation emission from a mode II crack tip. The atomistic analyses showed that increasing the hydrogen concentration, the K_{IIC} value decrease in alpha iron[12]. We employ these relationships and the critical stress intensity factors used in this study are shown in Table 2. It clearly shows that the dislocation emission is enhanced in the presence of hydrogen.

Table 2. Critical stress intensity factor for dislocation emission

	Hydrogen free	C_H = 0.49 [/nm]	C_H = 1.24 [/nm]
K_{IIC} [MPam$^{1/2}$]	0.443	0.440	0.430

4. Analysis Results of Dislocation Dynamics

4.1. Low Hydrogen Concentration (C_H = 0.49 /nm)

The correlation between applied stress intensity factor rate ($\dot{K} = \dot{\tau}\sqrt{\pi a}$ MPam$^{1/2}$/s) and the distance of leading dislocation (first emitted dislocation) from a crack tip (i.e. the size of the plastic zone) at the specific stress intensity factor (K = 0.589 MPam$^{1/2}$) is shown in Figure 3 (a). It reveals that the size of the plastic zone becomes large in the presence of hydrogen, which is considered to attributes the increase of dislocation velocity (τ < 29 MPa in Figure 2), and the enhancement of dislocation emission (in Table 2). On the other hand, at the high applied stress intensity factor rate conditions, the size of plastic zone becomes small compared with that in the presence of hydrogen. It is considered to attributes the increase of effective stress exerted on each dislocation near the crack tip (τ > 29 MPa in Figure 2). Figure 3 (b) shows the number of emitted dislocations. This figure shows

the increase of the number of emitted dislocations at lower applied stress intensity factor rate, however, it also decrease at high stress intensity factor rate conditions. The distributions of dislocations at several applied stress intensity factor rate (A) $\dot{K}$=0.56 MPam$^{1/2}$/s, (B) $\dot{K}$=56 MPam$^{1/2}$/s are shown in Figure4. In this figure, we considered that dislocation motion is softened when the exerted effective stress at each dislocation takes below 29 MPa. And the hardening is also considered to occur when the effective stress takes between 29 to 81 MPa. At this hydrogen concentration, both the size of plastic deformation zone and the number of emitted dislocations increase due to the softening effect at lower applied stress intensity factor rate conditions. However the hardening becomes dominant at higher applied stress intensity factor rate. This result indicate that the local hardening near the crack tip can occur even the macroscopic softening conditions, and thus the plastic deformation is supposed to be complex in these conditions.

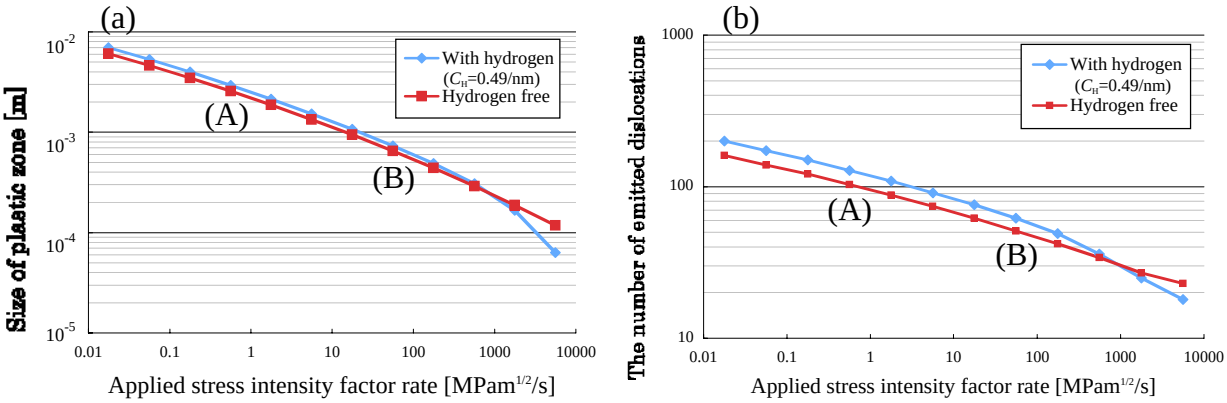

Figure 3. Correlation between the applied stress intensity factor rate and;
(a): distance of first emitted dislocation, (b): the number of emitted dislocations

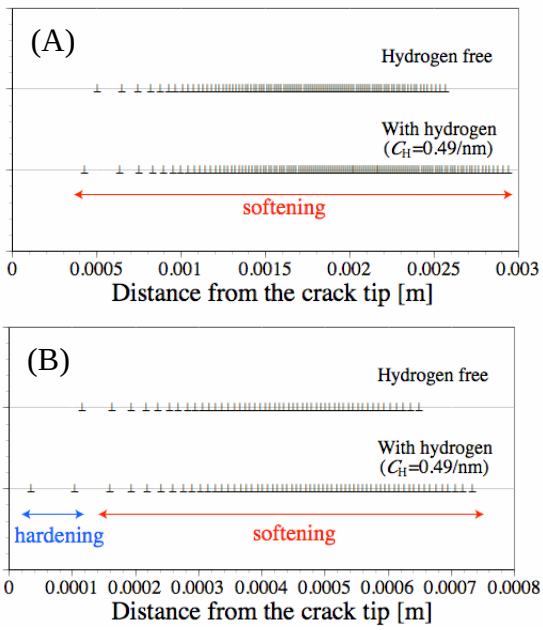

Figure 4. Dislocation distribution around a crack tip at the stress intensity factor rate of
(A): 0.56 MPam$^{1/2}$/s, (B): 56 MPam$^{1/2}$/s

4.2. High Hydrogen Concentration (C_H = 1.24 /nm)

The correlation between applied stress intensity factor rate and the distance of leading dislocation from a crack tip (i.e. the size of the plastic zone) at the specific stress intensity factor (K = 0.589 MPam$^{1/2}$) at high hydrogen concentration is shown in Figure 5(a). The size of plastic zone at this hydrogen concentration becomes typically small. The correlation between applied stress intensity factor rate and the number of emitted dislocation is shown in Figure 5(b). Although, the dislocation emission is enhanced at this hydrogen concentration, the number of emitted dislocations typically decreases. The dislocation distributions are also shown in Figure 6. These results indicate that only hardening can occur at this high hydrogen concentration conditions.

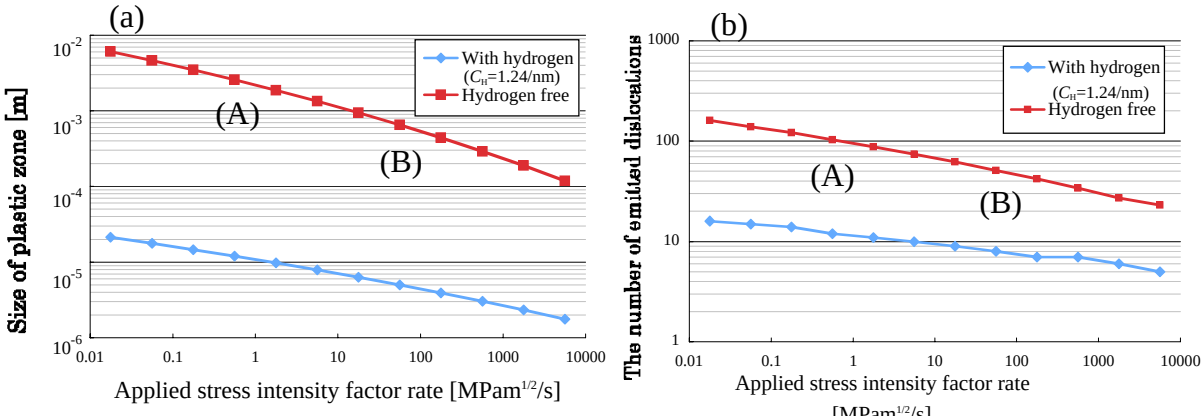

Figure 5. Correlation between the applied stress intensity factor rate and;
(a): distance of first emitted dislocation, (b): the number of emitted dislocations

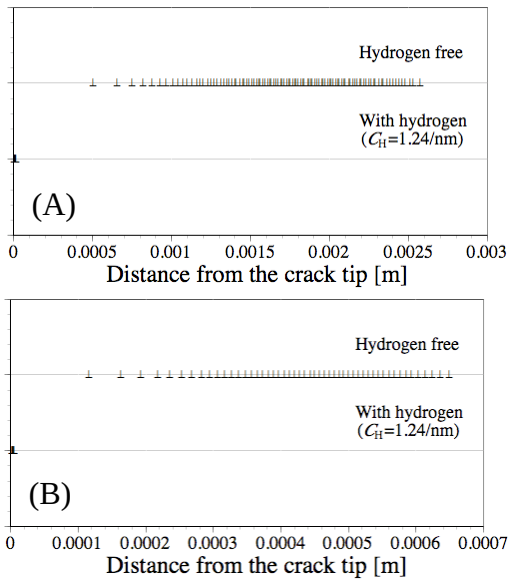

Figure 6. Dislocation distribution around a crack tip at the stress intensity factor rate of
(A): 0.56 MPam$^{1/2}$/s, (B): 56 MPam$^{1/2}$/s

4.3. Hydrogen Effects on Fracture Mechanisms

Dislocation slip behavior around a crack tip is enhanced at low hydrogen concentration and low stress intensity factor rate conditions, which result in softening. At the high hydrogen concentration

conditions, on the other hand, only hardening occur independent of applied stress intensity factor rate conditions. Based on these analyses results mentioned above, softening around a crack tip occur at the low hydrogen concentration and the low applied stress intensity factor rate conditions. Therefore, the amount of plastic deformation around a crack tip is supposed to increase and yield in the fracture mechanism of HELP and/or HESIV so far. However, at the high hydrogen concentration or the high applied stress rate conditions, hardening around a crack tip lead the brittle type fracture, HEDE so far. The schematic illustration of these relationships of hydrogen embrittlement mechanisms depending on environmental and mechanical conditions are shown in Figure 7.

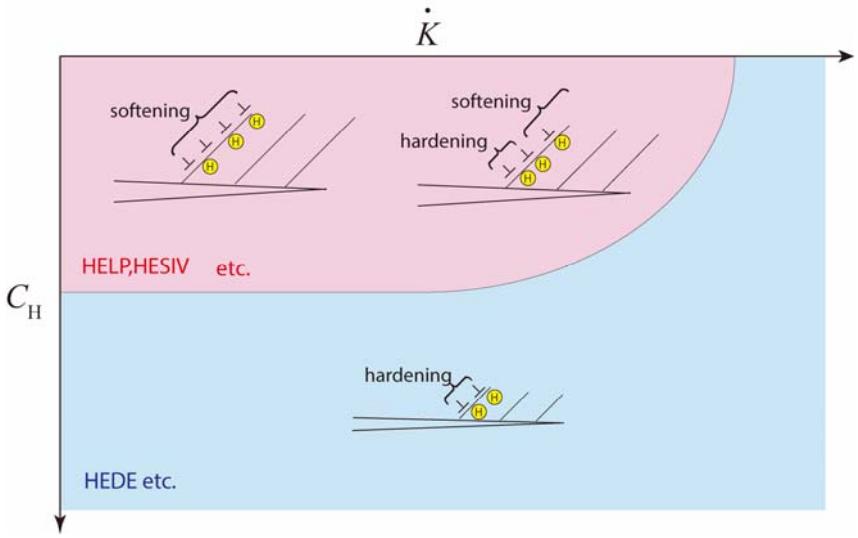

Figure 7. Hydrogen embrittlement fracture mechanisms for different hydrogen concentration and applied stress intensity factor rate conditions

5. Conclusion

In this study, we performed the dislocation dynamics calculation around a crack tip based on the results obtained by atomistic calculations. The results indicate that the hydrogen embrittlement mechanisms possibly change depending on boundary conditions (hydrogen concentration and applied stress intensity rate).

Acknowledgements

The author would like to acknowledge Prof. A.T. Yokobori,Jr.(Tohoku Univ.) for useful discussions and suggestions.

References

[1] R.A. Oriani, H.Josephic, Acta Metallurgica, 22 (1974) 1065–1074.
[2] C.D. Beachem, Metall. Trans. 3 (1972) 437–451.
[3] M. Nagumo, Mater. Sci. Tech. 20 (2004) 940–950.
[4] S. Taketomi, R. Matsumoto, N. Miyazaki, J. of Mat. Res., 26, 10 (2011) 1269–1278.
[5] S. Taketomi, R. Matsumoto, N.Miyazaki, Proc. of 2012 Hydrogen Conference, (2012) (submitted).
[6] A.T. Yokobori, Jr., T. Iwadate, T. Isogai, Acta Metall. Mater., 41 (1993) 1405–1411.
[7] A.T. Yokobori, Jr., T. Iwadate, T. Isogai, ASTM STP1207 (1994) 464–477.
[8] J.P. Hirth, Metall. Trans. A. 11A (1980) 861–890.

[9] R. Matsumoto, Y. Inoue, S. Taketomi, N. Miyazaki, Scripta Materialia, 60 (2009) 555–558.
[10] Y. Sakagami, R. Matsumoto, D. Alfè, S. Taketomi, T. Enomoto and N. Miyazaki, Transactions of the Materials Research Society of Japan ,37 (2012) 1–6.
[11] S. Taketomi, R. Matsumoto, N. Miyazaki, Acta Materialia, 56 (2008) 3761–3769.
[12] S. Taketomi, R. Matsumoto, N. Miyazaki, Journal of Mechanical Science, 52 (2010) 334–338.
[13] S. Izumi, S. Yip, Proc. of MD sympo. (2008) 1–4. (in Japanese)
[14] D.H. Warner, W.A. Curtin, Acta Materialia, 57 (2009) 4267–4277.

Finite Element Simulation of Crack Propagation for α-Ti Based on Cohesive Zone Law Deriving from Molecular Dynamics

Yi Liao[1], Xiangguo Zeng[1], Jun Chen[2], Rongpeng Xu[1,3]*, Huayan Chen[1]

[1] College of Architecture and Environment, Sichuan University, Chengdu, 610065, PR China
[2] Institute of Applied Physics and Computational Mathematics, Beijing, 100094, PR China
[3] School of Engineering, Alfred University, Alfred, NY, USA 14802
Corresponding author: xuyun14567@163.com

Abstract In order to parameterize and obtain a traction-separation (T-S) law, molecular dynamics (MD) simulations via Large-Scale Atomic/Molecular Massively Parallel Simulator (LAMMPS) are used at atomic scale for the deformation and fracture for models with dimension of 200Å×204Å×8.82Å with crack for alpha titanium (α-Ti) with HCP crystal structure under tensile loadings at different loading directions. Visualization of the atomistic configurations during deformation is realized by use of ATOMEYE. It can be concluded that crack extension are correlate with the α-Ti crystal structure and crystal orientation intrinsically. We also found that HCP→BCC phase transition and twin deformation occur in the vicinity of the crack tip for HCP α-Ti under different loading directions via the common neighbor analysis (CNA). The complex mechanisms of deformation, i.e., phase transition, twin deformation, and failure, i.e., crack blunting and extension, were contained in the traction-separation (T-S) law. Then, the generated parameterized traction-separation law is implemented in the finite element model with the behavior of the CZM governed by traction-separation (T-S) law. Finally, the ABAQUS finite element commercial software is employed to simulate the crack propagation behavior for α-Ti CT specimen.

Keywords Alpha Titanium, Molecular dynamics, Cohesive zone model, Crack propagation, Finite element

1. Introduction

Titanium has two kinds of superior properties: high specific strength and corrosion resistant. Titanium has long had appeal to metal designers and material scientists[1]. Commercially, pure titanium is, of course, alpha titanium (α-Ti). Its elemental crystal structure is closed-packed hexagonal, as illustrated in Fig.1[2]. Alpha titanium is anisotropic material. The mechanical properties in its different crystal orientations have significant difference. In this paper, the micro-deformed mechanisms of α-Ti on different conditions of loading are obtained by means of open source MD code LAMMPS[3] developed by Sandia. Visualization of the atomistic configurations during deformation is realized via ATOMEYE software[4].

Xu and Needleman[5,6] first related the cohesive zone model (CZM) with finite element analysis, and they successfully applied it to simulate crack propagation problems. Cohesive elements that possess zero volume in an undeformed state are inserted between bulk elements. They are particularly appropriate when the crack propagation path can be determined. Cohesive zone law defines the relation between traction and crack opening displacement. Because it is difficult to direct experimentally quantify the relation, construction of such a law has been a challenging task in the past decade[7,8]. The traction-separation (T-S) relationship in a CZM is generally parameterized through empirical data.

Our approach to studying crack propagation has included the use of MD simulation for obtaining the functional form of parameterized T-S relations in cohesive elements[9,10]. This paper simulated a compact tension fracture mechanics specimen through cohesive elements whose T-S relation was derived from MD simulations. These results enable us to make several recommendations to improve the methodology to obtain cohesive laws and better comprehend the crack propagation behavior of

α-Ti.

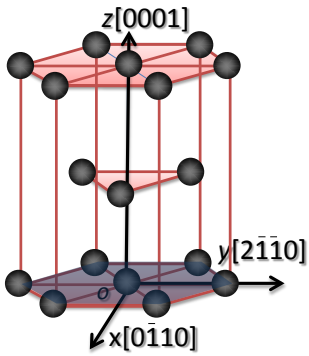

Figure 1. The elemental crystal structure of α-Ti

2 EAM/alloy potential function

Zhou[11]have developed a procedure to generalize the conventional EAM potentials and their cut-off distance. These potentials are well fitted to basic material properties such as lattice constants, elastic constants, modulus of bulk.

In the generalized EAM (EAM/alloy) potential, the total energy E of the crystal can be expressed as:

$$E = \frac{1}{2}\sum_{i,j,i\neq j}\phi_{ij}\left(r_{ij}\right) + \sum_{i}F_i\left(\rho_i\right) \tag{1}$$

Where ϕ_{ij} represents the pair energy between atoms i and j separated by r_{ij}, and F_i stands for the embedding energy to embed an atom i into a local site with electron density ρ_i. ρ_i can be calculated using:

$$\rho_i = \sum_{j,j\neq i} f_j\left(r_{ij}\right) \tag{2}$$

With $f_j(r_{ij})$ the electron density at the site of atom i arising from atom j at a distance r_{ij} away. Alloy EAM potentials can be constructed from elemental EAM potentials if the potentials are normalized and unified cutoff functions are used. To fit such an EAM potential set, the generalized pair potentials were chosen to have the form:

$$\phi(r) = \frac{A\exp\left[-\alpha\left(\frac{r}{r_e}-1\right)\right]}{1+\left(\frac{r}{r_e}-\kappa\right)} - \frac{B\exp\left(-\beta\left(\frac{r}{r_e}-1\right)\right)}{1+\left(\frac{r}{r_e}-\mu\right)^{20}} \tag{3}$$

Where r_e is the equilibrium spacing between nearest neighbors, A, B, α, β are four adjustable parameters, and κ, μ are two additional parameters for the cut off[12].

The electron density function is taken with the same form as the attractive term in the pair potential with the same values of β, and μ, i.e.,

$$f(r) = \frac{f_e\exp\left[-\beta\left(\frac{r}{r_e}-1\right)\right]}{1+\left(\frac{r}{r_e}-\mu\right)^{20}} \tag{4}$$

Table1. EAM potential parameters of titanium

R_e(Å)	f_e	ρ_e	α	β	A	B	μ	κ
2.933872	1.863200	25.56513	8.775431	4.680230	0.373601	0.570968	1.0	0.5

The potential function usually is empirical, and it is also controversial in MD simulation. The melting point of α-Ti was obtained by LAMMPS in order to verify the EAM/alloy potential. The atomic structure of α-Ti is shown in Fig.1. The initial configuration of the simulated system was composed of 8×8×5 HCP-Ti cellular, a total of 1280 atoms, the time step was 0.01*ps*, using three-dimensional periodic boundary conditions, let the system in the 2.5*K* relaxation 500000 steps, and then use the Nose-Hover method to keep the pressure around zero, and then elevated system temperature from T=2.5*K* to 2500*K*. During the simulation, the thermodynamic results were output every 1000 steps, as shown in Fig.2 and Fig.3 respectively. The average atomic volume almost linear increases with the temperature and simulation time in the heating process. But it suddenly jumps when the temperature reaches a certain value. This phenomenon indicated that the system had undergone some kind of phase transition. The melting point of α- T_i is about 1951*K*, and simulation value is 1943*K* near a phase transition. The error between them is about 0.41%. Such deviation derived from the melting point between the MD simulation and the actual sample were relatively consistent, which was related with using three-dimensional periodic boundary conditions in simulation system, the limited number of particles and the accuracy of interaction potential.
The EAM/alloy potential function parameters, which were evaluated by melting point test were shown in Table1.

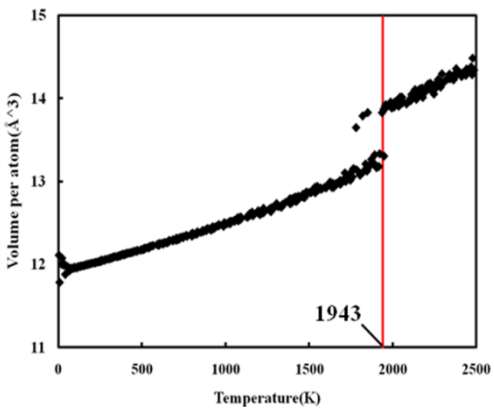

Figure 2. The mean volume of single atom changing with temperature during heating process.

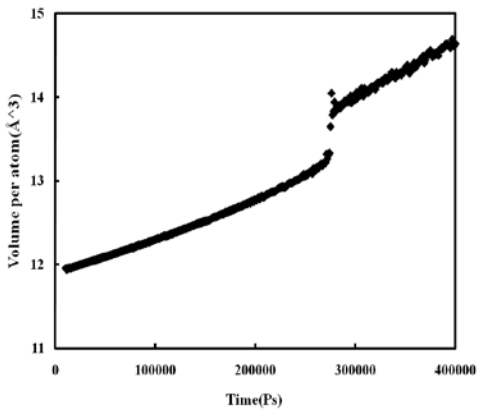

Figure 3. The mean volume of single atom changing with modeling time during heating process.

3 Specimen setup

Due to anisotropic characteristic of α-Ti, it is very meaningful for comprehending failure mechanism of material on different conditions of loading.
The MD models with different loading directions used for conducting fracture studies were shown in Fig.4 and 5. The MD model in Fig.4 showed that the loading direction was $[0\bar{1}10]$, while it was $[0001]$ in Fig.5. The dimensions in the x-y plane are 200*Å*×204*Å* with thickness in the z-direction

equaling 9.64*Å*. The length of crack is 70*Å* in the two models. Non-periodic and shrink-wrapped boundary conditions were used in the x and y directions, while it was periodic boundary in the z-direction. Before loading, the whole system was made relax freely till the valley of energy status. During MD simulations of tensile crack propagation, the boundaries were stretched by moving different distance increment on different regions of boundaries in the Y-direction at each time step. Molecular dynamics simulation time step was given with t=0.005*ps*.

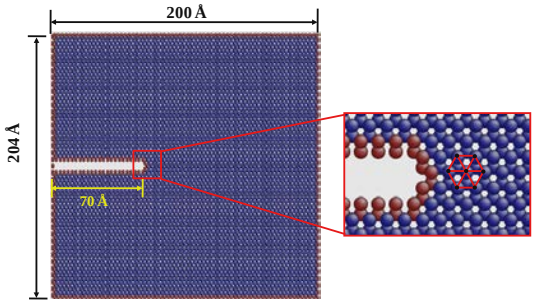

Figure 4. MD model with loading direction $[0\bar{1}10]$

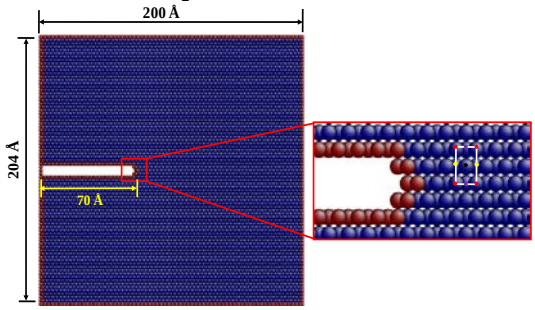

Figure 5. MD model with loading direction [0001]

For the loading condition shown in Fig.4, the phenomenon observed in model by means of CNA was shown in Fig.6. Step=0 indicated that the relaxation was finished. The energy of the system reached minimal. With the increment of loading, crack constantly opened. When the loading increased to Step=3600，it was obvious that crack tip successively emitted dislocations along crystal orientation $[2\bar{1}\bar{1}0]$ and $[\bar{2}110]$ respectively[13]. The phenomenon continued in the whole process of loading. With the emission of dislocation, crack tip moved forward slowly and the crack blunting phenomenon is obvious at crack tip. When Step=8400, we also found that HCP→BCC phase transformation in the vicinity of the crack tip for *α*-Ti via CNA. The values of CNA corresponding to different atomic structure were displayed in Fig.6.

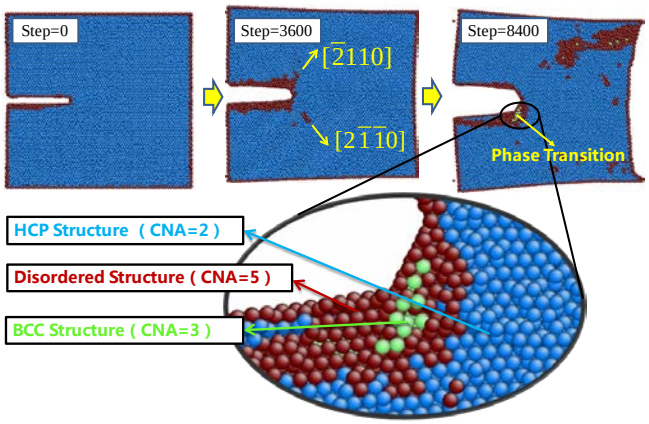

Figure 6. Deformed mechanisms of α-Ti on the condition of loading direction $[0\bar{1}10]$

When Step=2200, there was region where atoms arranged disorderedly near the crack tip. With the increment of loading, the deformed region expanded in the vicinity of the crack tip. When Step=3000, it was obvious that some red atoms (CNA=5) surrounded a lump of blue atoms (CNA=2) in Fig.7. The structure of atoms is identical in the inside and outside of the region that the

red atoms surrounded, but their orientations were different. The orientations of lattice deflected to form twin deformation. The area of twin band increased following the crack propagation. From the crack propagation deformation in Fig.6 and Fig.7, it was shown that twin crystal easily occurred for α-Ti under loading direction$[0001]$, while phase transition and dislocation easily happened under loading direction$[0\bar{1}10]$. Dislocation and twin are two kinds of principal mechanisms for α-Ti.

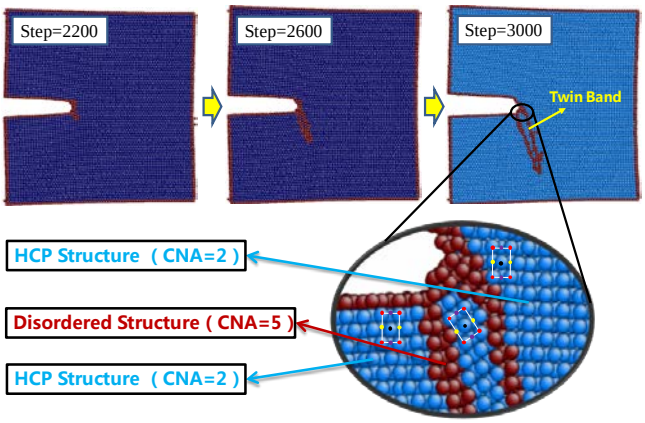

Figure 7. Deformed mechanisms of α-Ti on the condition of loading direction$[0001]$

4 Traction-separation response

To quantify the cohesive zone law, stresses and displacements at local positions are analyzed in detail. MD simulation is conducted for loading direction $[0\bar{1}10]$ at temperature of 300K to develop traction-separation relationships for the CZM.

Tensile (σ_{yy}) traction is calculated as the average atomic stress at a distance of ± 20 Å adjacent to the crack. The region is called T-S region, as illustrated in Fig.8. As this stress is calculated locally near the crack surface it therefore relates to the traction in the traction-separation law[8,9,13,14]. The crack opening displacement (separation) was also calculated from the average displacement of the atoms in T-S region. The opening displacements in normal direction therefore are defined and measured as the average atom displacement in Up Region with respect to Down Region. The average traction and opening displacement associated with region were calculated using all the atoms in T-S region. This effectively reduces the scatter of the data.

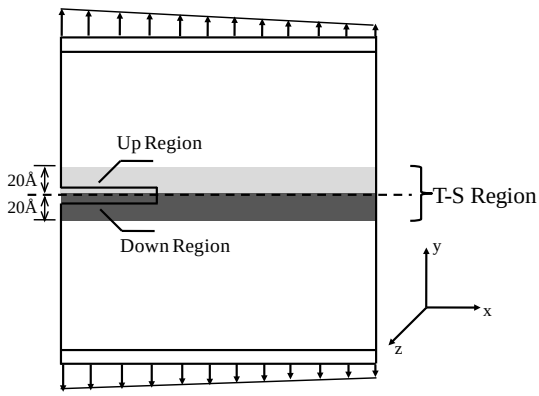

Figure 8. T-S region selected and loading form

The simulation process applying *NVE* system tracking and in every time step, maintain the

temperature of 300*K*, constantly through re-calibration of the speed of atoms. Ladder-shaped loading is applied on the boundary, as shown in Fig.8.

From Fig.9, the traction initially increases as the crack opening distance was increased until they reached a peak value, then decreased as the crack opening was further increased. To represent the CZM, a model that includes an exponential term is suggested to approximate the traction-separation response for tensile mode failure. The complex mechanisms of deformation, i.e., phase transition, dislocation, and crack blunting, were contained in the traction-separation (T-S) law. *A* in the T-S curve indicated damage occurred, which was shown by the typically non-linear decreasing of the curve. It corresponded to remarkable dislocations emission in the crack tip. *B* in the curve corresponds with the moment at which phase transition occurs in the MD model. The curve shows a wide scatter band in the region beyond the elastic deformations, since the data contain traction and separation in all stages of atoms along the crack path. During initial crack growth the scatter band in the cohesive law is very large. This behavior implies that the initial crack starts to grow at different maximum tractions and is not in a steady-state. With crack propagation, the scatter band becomes narrow, which indicates that crack growth becomes steady[15].

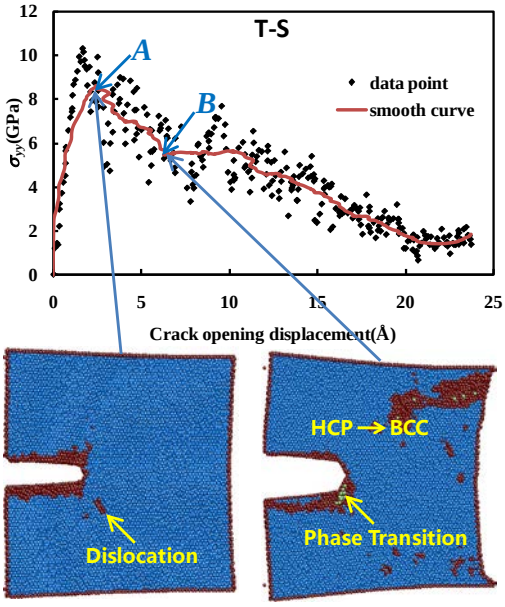

Figure 9. Traction-Separation relationship for α-Ti under tensile loading

A relationship between the traction and the crack opening displacement must be obtained when we use cohesive element. In the CZM, the fracture process zone is simplified as being an initially zero-thickness zone, composed of two coinciding surfaces. Under loading, the two surfaces separate and the traction between them varies in accordance with a specified T-S law. In our study a parameterized exponential T-S law is proposed based on the MD simulations. The traction-separation law ($F(\lambda)$) is then implemented through Eq.(5). The non-dimensional parameter (λ) in Eq. (5) relates the normal (u_n) separation to the maximum allowable normal (δ_n) separation of the cohesive element[14]. In Eq.(5) the maximum cohesive strength (σ_{max}) is simulated at room temperature. The constants in Eq.(5) are obtained in table 2. According to Eq.(5) and table 2, the fitting curve of traction-separation relationship has been illustrated in Fig.10.

$$F(\lambda) = A\sigma_{\max}\lambda^{c}\exp(-B\lambda)(1-0.001T)$$
$$\lambda = u_n / \delta_n \tag{5}$$

Table 2 The constants in Eq.(12)

Simulated temperature (K)	$\sigma_{max}(GPa)$	A	B	C
300	8.61	3.75	2.73	0.37

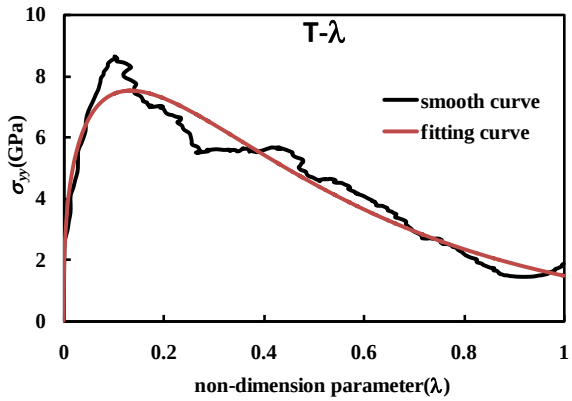

Figure 10. T-λ relationship

5. Simulation of the T-S fracture test

In order to model stable crack growth under static loading and analyze cohesive behavior derived from MD towards greater length scales, we perform a simulation of crack growth for a CT specimen subject to displacement loading via prescribed motion of loading pins. Fracture of a CT specimen can verify whether the cohesive law derived from MD simulations displays behavior consistent with linear elastic fracture mechanics. The geometry and mesh of our CT specimen is shown in Fig.11. The specimen is 384 *nm* wide by H = 369 *nm* tall, with an effective width (the distance between the pin holes and the uncracked edge) of W = 307 nm, an initial crack length of a = 155 *nm* ($a/W \approx 0.5$), and pin holes of radius 38.4 *nm*. Cohesive elements are placed along the predefined crack path, and are 1*Å* wide. The displacement loadings are applied on reference points, i.e. PR-1 and PR-2. The parameterized T-S law given was implemented in ABAQUS to simulate the behavior of the CZM.

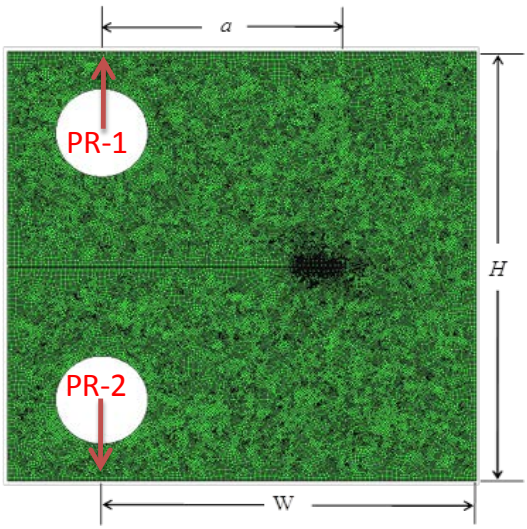

Figure 11. FEA mesh of CT specimen. The specimen's height H =369nm, its effective width W=307nm, and its initial crack length a =155nm

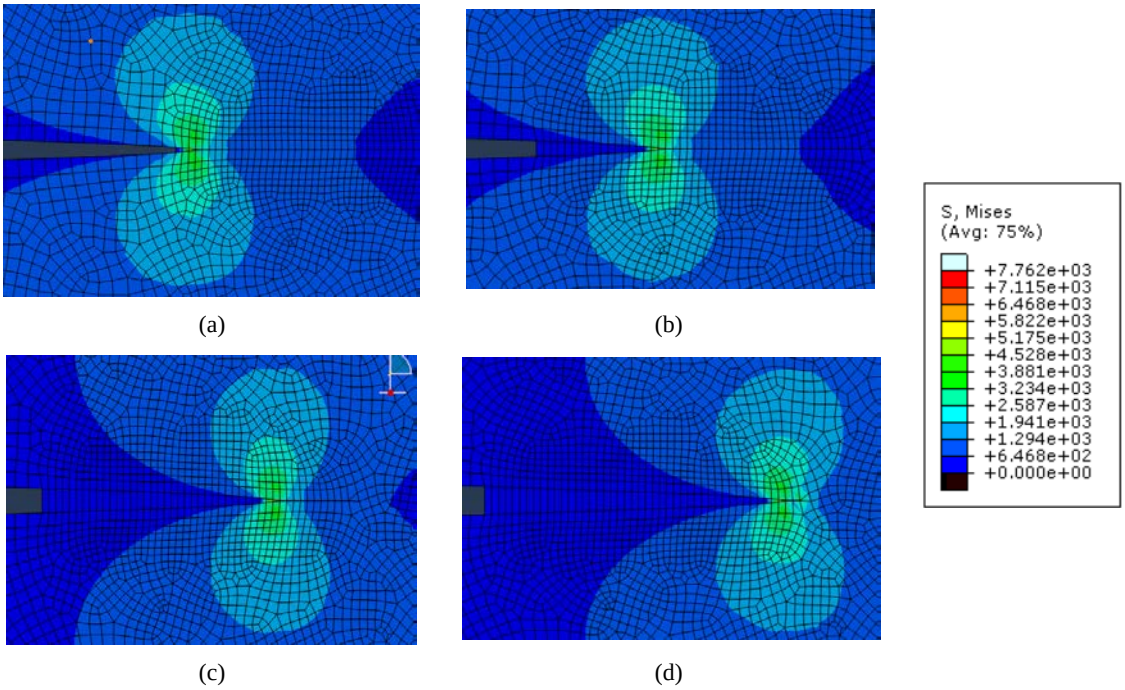

Figure 12. Static crack growth in the CT geometry, plots are colored according to element values of σ_{yy} in units of *GPa* as shown in the legend

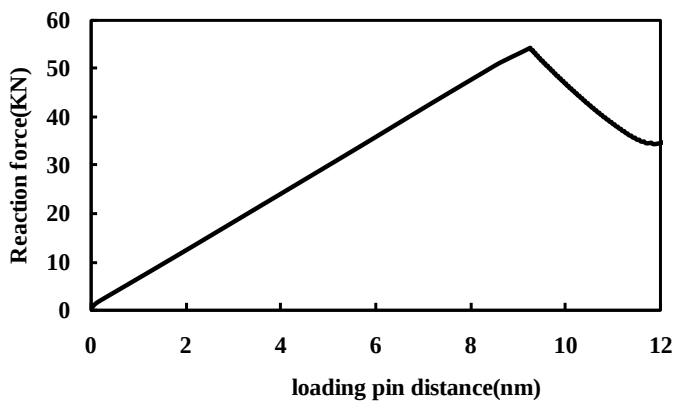

Figure 13. Reaction force versus loading-pin displacement for CT specimen

The crack opening behavior due to displacement of the top and bottom pins is observed in Fig.12. Before crack propagation begins to occur, the cohesive zone begins to form, as shown in Fig.12(a) and (b). Once a critical displacement is reached, crack propagation is seen in Fig.12(c) and (d).
It shows the expected linear relationship between loading-pin displacement and reaction force in Fig.13. More complex fracture mechanics problems can be analyzed through combining the cohesive law derived from MD simulations and finite element method.

6. Conclusion

(1) Molecular dynamics simulations under a special configuration have been performed to study the mechanism of α-Ti under tensile loading condition, and the EAM/alloy potential used in LAMMPS is certified by melting point verification.
(2) Crack tip successively emitted dislocations along crystal orientation $[2\bar{1}\bar{1}0]$ and $[\bar{2}110]$ respectively for loading direction $[0\bar{1}10]$. The phenomenon continued in the whole process of loading. With the emission of dislocation, crack tip moved forward slowly and the crack blunting phenomenon is obvious at crack tip. In the process, we also find that HCP→BCC phase transformation near the crack tip for α-Ti via CNA. It is obvious that twin occurred for α-Ti under loading direction $[0001]$. Dislocation and twin are two kinds of principal mechanisms for α-Ti. The deformation mechanisms of α-Ti are included in the T-S curve derived from MD simulations.
(3) The traction-separation relation of α-Ti with crack is characterized via MD simulations. The parameterized cohesive traction-separation relation under tensile loading condition at room temperature to simulate the crack propagation behavior of *CT* specimen composed of α-Ti in a FEA. The curve obtained through our simulation is agreement with predictions from linear elastic fracture mechanics, showing the expected linear relationship between loading-pin displacement and reaction force. It shows our methodology is feasible. Our study may provide several novel ideas for simulating complex fracture problems based cohesive laws used in FEA.

Acknowledgements

This work was supported by the National Defense Basic Scientific Research Program of China through the contract of B1520132013 and the Fundamental Research Funds for the Central Universities through the contract of 2010SCU21014 and NSAF through the contract of 10776023.

References

[1] J.D.Matthew, Jr. Titanium-A Technical Guide. ASM INTERNATIONAL™ Metal Park, 1988.
[2] C Leyens, M Peters. Titanium and Titanium Alloys. WILEY-VCH GmbH & Co. KGaA. Weinheim, 2003.
[3] S J Plimpton. Fast parallel algorithms for short-range molecular dynamics. J Comput Phys 1995;117:1–19. <http://lammps.sandia.gov/>.
[4] J Li. AtomEye: an efficient atomistic configuration viewer. Modell Simul Mater Sci Eng 11 (2003) 173.

[5] X.P. Xu , A. Needleman, Numerical simulations of fast crack growth in brittle solids, J. Mech. Phys. Solids 42 (1994) 1397-1434.

[6] X.W.Zeng, Shaofan Li, A multiscale cohesive zone model and simulations of fractures. Comput. Methods Appl. Mech. Engrg. 199 (2010) 547–556.

[7] X.W. Zhou, J.A. Zimmerman et al, Molecular dynamics simulation based cohesive surface representation of mixed mode fracture, Mechanics of Materials 40 (2008) 832-845.

[8] X.W. Zhou, N.R. Moody, R.E. Jonesa, J.A. Zimmermana, E.D. Reedyc, Molecular-dynamics-based cohesive zone law for brittle interfacial fracture under mixed loading conditions: Effects of elastic constant mismatch. Acta Materialia, 57 (2009) 4671–4686.

[9] V.Yamakov, E.Saether, D.R.Phillipsc, E.H. Glaessgen. Molecular-dynamics simulation-based cohesive zone representation of intergranular fracture processes in aluminum. Journal of the Mechanics and Physics of Solids. 54 (2006) 1899–1928.

[10] J.T. Lloyd, J.A. Zimmerman, R.E. Jones, X.W. Zhou, D.L. McDowell, Finite element analysis of an atomistically derived cohesive model for brittle fracture. Modelling Simul. Mater. Sci. Eng., 19 (2011) 065007.

[11] X.W. Zhou, H.N.G.Wandley, R.A.Johnson, D.J.Larson. Atomic scale structure of sputtered metal multilayers[J]. Acta materialia. 49 (2001) 4005～4015.

[12] H.N.G.Wadley, X.Zhou, R.A.Johnson, M.Neurock. Mechanisms, Models and Methods of Vapor deposition. Progress in Materials Science. 46 (2001) 329-377.

[13] D. Farkasa, M. Durandurua, W. A. Curtinb , C. Ribbensc. Multiple-dislocation emission from the crack tip in the ductile fracture of Al 81(2001)1241-1255.

[14] K. Gall, M.F. Hostemeyer, M.V. Schilfgaarde, M.I. Baskes, Atomistic simulations on the tensile debonding of an aluminum–silicon interface. J Mech Phys Solids, 48 (2000) 2183–212.

[15] C.R.Dandekar, Yung C. Shin, Molecular dynamics based cohesive zone law for describing Al-SiC interface mechanics. Composites: Part A 42 (2011) 355–363.

[16] H. Krull, Huang Yuan. Suggestions to the cohesive traction-separation law from atomistic simulations. Engineering Fracture Mechanics. 78 (2011) 525-533.

Finite Element Simulation of Interfacial Fracture between Fe_3C and α-Fe Based on Cohesive Zone Law Deriving from Molecular Dynamics

Taolong Xu[1], Xiangguo Zeng[1], Anlin Yao[2,*], Yi Liao[1], Rongpeng Xu[1,3]

[1] College of Architecture and Environment, Sichuan University, Chengdu 610065, PR China
[2] School of Petroleum Engineering, Southwest Petroleum University, Chengdu 610500, PR China
[3] School of Engineering, Alfred University, Alfred, NY, USA 14802
* Corresponding author: yaoalt@sina.com

Abstract Once the cohesive zone model (CZM) is used to describe material behavior near crack front zone, it was convenient to simulate crack propagation by using finite element. Actually, the cohesive zone model is depicted by means of the traction-separation relation. But, It is very difficult to determinate such a relation, i. e, the traction-separation relation, through experiment, respectively. The traction-separation laws of most previous work are often assumed rather than predicted. First of all, in order to parameterize and obtain a traction-separation (T-S) law, Molecular dynamics (MD) simulations via Large-Scale Atomic/Molecular Massively Parallel Simulator (LAMMPS) are carried out at atomic scale for the deformation and fracture of *Fe_3C-α-Fe* interface in tensile loadings at different temperatures in our study. Then, the generated parameterized traction-separation law is implemented in the finite element model with the behavior of the CZM described by traction-separation (T-S) law. Finally, the ABAQUS finite element commercial software is employed to simulate the crack propagation behavior for *X70* pipeline steel CT specimen.

Keywords Crack propagation, Cohesive zone model, Molecular dynamics, Parameterized traction-separation law

1. Introduction

After more than ten years of construction and development, the length of high pressure gas pipeline made of *X70* steel has over 8,000 kilometers in China. As a structure material, *X70* pipeline has high excellent strength and toughness. The research of mechanical properties, deformation and fracture mechanism of *X70* steel become more and more important. Metallographic analysis show that *X70* steel mainly consists of ferrite and a small amount of pearlite[1]. Physics-based modeling of fracture begins at nanometer length scales in which atomic simulation is used to predict the formation, propagation and interaction of fundamental damage mechanisms[2,3]. In recent years, in this research field, great attentions have been paid to use the cohesive zone model (CZM) to set up the leaking between atomic-scale and macro-scale near crack front zone. The theory of cohesive zone model may be traced back to the early works by Dugdale[4] and Barrenblatt[5], in which both concepts of atomistic de-cohesion and the defect process zone are established. Xu and Needleman[6,7] first related the cohesive zone model (CZM) with finite element analysis, and they developed the cohesive finite element method and successfully applied it to simulate crack propagation problems. Cohesive elements that possess zero volume in an undeformed state are inserted between bulk elements. They are particularly appropriate when the crack propagation path can be well-reasoned. Cohesive zone law defines the relation between traction and crack opening displacement. Because it is difficult to direct experimentally quantify the relation, construction of such a law has been a challenging task in the past decade[8,9]. The traction-separation (T-S) relationship in a CZM is generally parameterized through empirical data, such as by using the macroscopic fracture toughness of the material or by conducting nanocrystalline experiments to obtain the stress-strain data[10]. The problem with inputting macroscopic/empirical values of fracture toughness is that these are aggregate responses of hundreds of thousands of grains applied to the location where fracture occurs[11].

This paper simulated a compact tension fracture mechanics specimen through cohesive elements whose T-S relation between *Fe_3C* and *α-Fe* was derived from MD simulations. These results enable

us to make several recommendations to improve the methodology used to derive cohesive laws from MD simulations. Furthermore the numerical analysis presented here helps to better understand the crack propagation behavior of *X70* pipeline steel.

2. MD model and simulation procedure

2.1. EAM/FS potential function

Molecular dynamics method, which considers the atomic movement is governed by Newton equations under the experience potential field which was determined by all other atoms in multi-body system, can be used to calculate system dynamic problems consisting of a large number of atoms. The interaction between the atoms can be reflected through potential function. Proper selection of the potential function types as well as the potential function parameters plays the key roles in the simulation results.

As a representative of the multi-body potential, the basic idea of Embedded Atom Method (EAM) is to divide the total potential energy into pair potential among the interaction of atomic crystal and the embedded potential of nucleus, which are embedded in the electron cloud and representing the interaction of multi-body.

In 1984, based on EAM potential, Finnis and Sinclair[12] developed a kind of multi-body potential with embedded energy function, hereinafter referred to as the FS-EAM potential. Like the majority of the potential functions based on EAM potential, the FS-EAM potential can be used to simulate the atomic-scale mechanisms of deformation and failure in metal materials, and the i_{th} atom potential energy can be expressed by the equation:

$$E_i = F_\alpha \sum_{j\neq i} \rho_{\alpha\beta}\left(r_{ij}\right) + \frac{1}{2}\sum_{j\neq i} \phi_{\alpha\beta}\left(r_{ij}\right) \tag{1}$$

The form of EAM potential and FS-EAM potential is consistent, but the ρ is the function of the type of atom i and j, which means the contribution of different elements on the same position of the atoms of the total electron density is not equal, and it can be given by the following expression:

$$\rho_i = \sum_{j\neq i} \rho_j\left(r_{ij}\right) \tag{2}$$

In expression (2),

$$\rho_j\left(r_{ij}\right) = \sum_{k=1}^{2} A_k\left(R_k - r_{ij}\right)^3 H\left(R_k - r_{ij}\right) \tag{3}$$

$$\phi_{ij}\left(r_{ij}\right) = \sum_{k=1}^{6} a_k\left(r_k - r_{ij}\right)^3 H\left(r_k - r_{ij}\right) \tag{4}$$

Thereinto,

$$H\left(x\right) = \begin{cases} 0 & \left(x > 0\right) \\ 1 & \left(x < 0\right) \end{cases} \tag{5}$$

In which, A_k, R_k, a_k, r_k for constants, and $R_1>R_2$, $r_1>r_2>\ldots>r_6$.

The melting point of *α-Fe* was obtained by LAMMPS in order to verify the FS-EAM potential. The initial configuration of the simulated system was composed of 8×8×5 *bcc-Fe* cellular, a total of 640 atoms, the time step was 0.005*ps*, using three-dimensional periodic boundary conditions, let the system in the 2.5*K* relaxation 100000 steps, and then use the Nose-Hover method to keep the pressure around zero, and then elevated system temperature from T=2.5*K* to 2500*K* the rate of 4.1625×1011*K/s*. During the simulation, the thermodynamic results were output every 1000 steps, as shown in Fig.1 and Fig.2, respectively. The average atomic volume almost linear increase with

the temperature and simulation time in the heating process, which turn upsuddenly increases when the temperature reaches a certain value. This phenomenon indicated that the system had undergone some kind of phase transition. The melting point of *α-Fe* is about 1873*K*, and simulations in the 1990*K* near a phase transition, increased by 6.2% than its equilibrium melting point. Such deviation derived from the melting point between the MD simulation and the actual sample were relatively common, which was related with using three-dimensional periodic boundary conditions in simulation system, the limited number of particles and the accuracy of interaction potential.

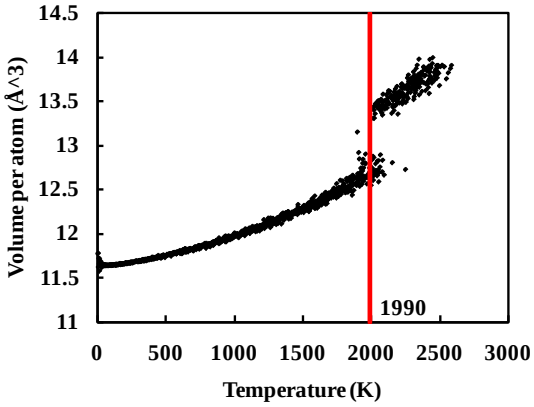

Figure 1. The mean volume of single atom changing with temperature during heating process

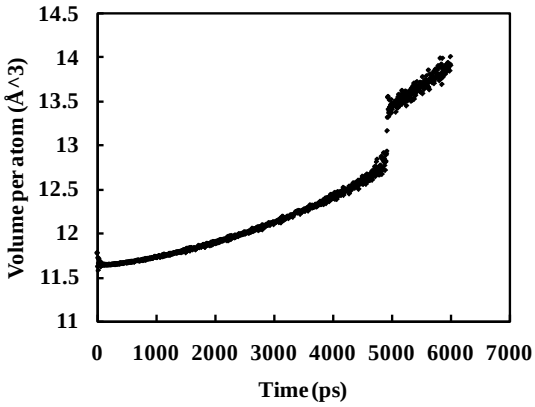

Figure 2. The mean volume of single atom changing with modeling time during heating process

In the simulation, the system contains two elements, i.e., *Fe* and *C* .The *Fe*/*C* alloy EAM/FS potential function parameters[13], which were evaluated by melting point testing were adopted in this work.

2.2. Specimen setup

The MD model used for conducting fracture studies is shown in Fig. 3. The dimensions in the x-y plane are 200*Å*×192*Å* with thickness in the z-direction equaling 8.82*Å*.The total atoms of the model were 31978. The x y z coordinate system represents the lattice directions [0 1 0], [1 0 0] and [0 0 1] respectively. In the model free boundary conditions were used in the x- and y-directions, while it was periodic boundary in the z-direction. As shown in Fig. 3, the simulation domain is divided into three regions. Atoms that are in regions 1 and 3 are boundary atoms through which tensile load are applied. A crack of length 100*Å* was generated at the interface of Fe_3C and *α-Fe*. During MD simulations of tensile crack propagation, the system is uniformly stretched (by moving each atom a distance corresponding to a uniform normal strain increment) in the Y-direction at each time step[2]. And the duration was less than 0.001*ps*, which made it relax freely till the valley of energy status. Molecular dynamics simulation time step was given with t=0.001*ps*. Integral calculation on system movement equation through Verlet techniques was applied during simulation. The simulation process: applying *NVE* system tracking and in every time step, maintain the temperature (300*K*, 473*K* and 673*K*) constantly through re-calibration of the speed of atoms. Firstly perform static relaxation to bring the system to the minimum energy status, and applying 3.128*Å*/*ps* strain rate in *y* direction. A systematic analysis on the effect of strain rate was not conducted in this study.

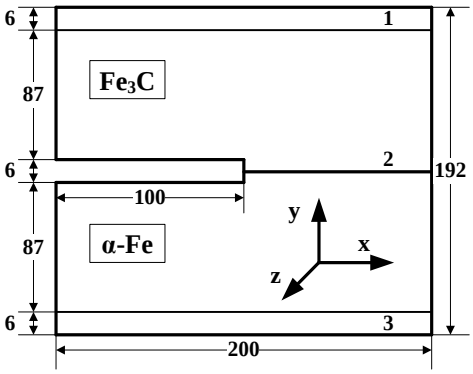

Figure 3. The molecular dynamics models with pre-existing crack along the interface, all dimensions are in *Å*

Due to the complex crystal structure of Fe_3C, in this paper, only [110] orientation faces were simulated, as shown in Fig.4. In Fig.4(a), for cementite (Fe_3C) with complex trapezius crystal structure, every single cell contains 4 carbon atoms (gray ball) and 12 Fe atoms (blue ball)[14], while Fig.4(b) shows that the interface structure combined with body-centered cubic iron and cementite.

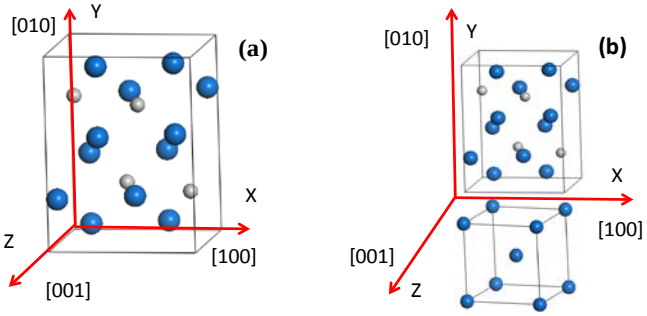

Figure 4. Fe_3C unit cell and interface structure schematic drawing

3. Simulation results

3.1. Stress-strain response

Fig.5 shows the atomic snapshots of tensile mode failure at temperature of 473*K* in different strains. The simulation model starts with elastic deformation from its initial state (Fig. 5(a)) to the yield stress at a strain ε= 0.0303. On yielding there is large scale debonding along the Fe_3C-*Fe* interface (Fig. 5(b)). After this the Fe_3C-*Fe* interface progressively degrades (Fig. 5(c)) and carries virtually no load at strain values above 0.1106.

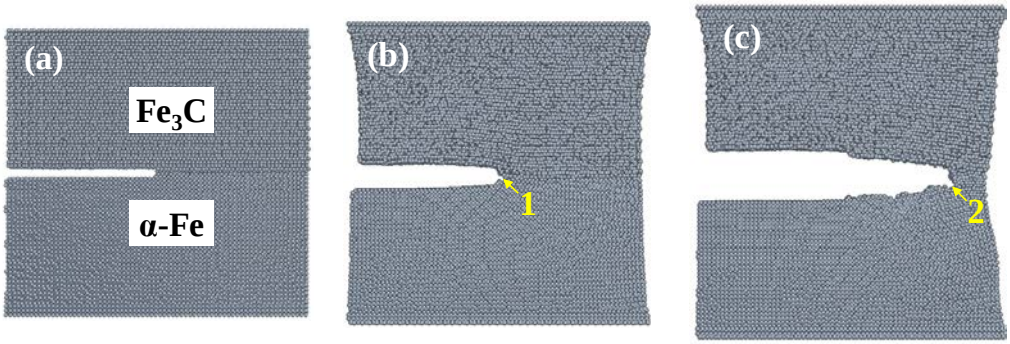

Figure 5. MD snapshots of tensile mode failure of a cracked interface at 473*K* at strains (ε) of (a) ε= 0.00, (b) ε=0.0397 and (c) ε= 0.0960. Areas of interest are (1) crack initiation and (2) crack progression

Selected examples were examined to characterize stress-strain curves dynamics. Average atomic

stresses based on the Virial theorem[16] were used to estimate global normal (*yy*) stresses applied to the system, which could be defined as the volume average of potential for all of the atoms in the system:

$$\sigma_{ij} = \frac{1}{V_i}\left[\frac{1}{2}\sum_{j\neq i}^{N} r_{ij} \otimes f_{ij}\right] \tag{6}$$

Zhou[15] has presented the specific formula for calculation:

$$\sigma_{ij} = \frac{1}{V}\left[\frac{1}{2}\sum_{\alpha,\beta}^{N}\left(-\frac{1}{r}\frac{\partial\phi}{\partial r}\right) r_i r_j \,\middle|\, r = r_{\alpha\beta}\right] \tag{7}$$

The strain used here is the nominal strain actually. The results were used to map the stress-strain curves. To reduce thermal oscillation, values of stress and strain were averaged over 10 time steps (each time step is 0.001*ps*). A short averaging time of 0.01*ps* was used to retain the time dependence of the properties. While this averaging time is small, it still helps mitigate thermal noises as the averaging is performed over many atoms. The normal stress-normal strain curve obtained from the tensile mode simulation is shown in Fig. 6. It indicates that during the tensile test, the normal stress initially linearly increases as the normal strain is increased, corresponding to an elastic deformation of the system. To examine the effect of the presence of the crack, a similar normal stress-normal strain curve obtained from the tensile mode loading of with a crack sample is included in Fig.7, the maximum normal stress at same temperature is significantly reduced and only about half value of the no crack model.

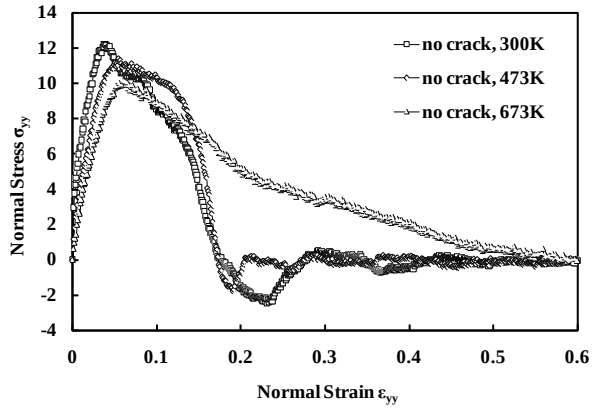

Figure 6. The normal stress-normal strain curve of models without crack at different temperatures

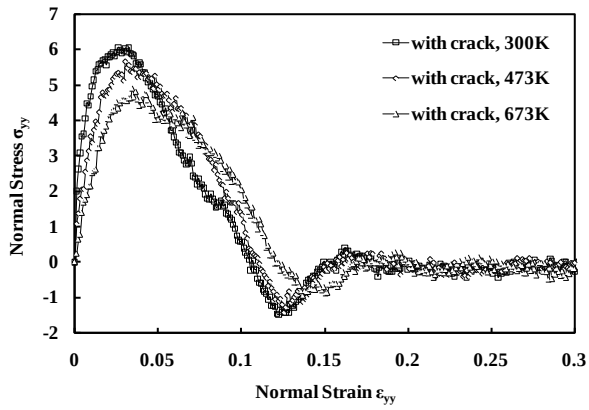

Figure 7. The normal stress-normal strain curve of models with cracks at different temperatures

The simulation results for the elastic modulus and maximum stress as a function of the simulated temperature for both with and without crack models are summarized in Table 1. They have the same changing regularity for both perfect interface and imperfect interface, which is found the elastic modulus and maximum stress are reduced by the increase of simulated temperature, and the maximum values of modulus and maximum stress for no crack model at roomtemperature are seen to be 332.67*GPa* and 12.17*GPa*, respectively. Presence of a crack reduces the maximum load carrying capacity and additionally reduces the stiffness of the composite system.

Table 1. simulation results of model failure.

Crack	Simulated temperature (*K*)	Modulus (*GPa*)	Maximum stress (*GPa*)
No	300	332.67	12.17
	473	210.11	11.40
	673	193.18	9.88
Yes	300	186.94	6.04

473	187.41	5.67
673	142.42	4.90

3.2. Traction-separation response

To quantify the cohesive zone law, stresses and displacements at local positions are analyzed in detail. MD simulations are conducted for temperatures of 300*K*, 473K and 673*K* for tensile mode failure to develop traction-separation relationships for the CZM. Tensile (σ_{yy}) tractions are calculated as the average atomic stresses at a region of 20*Å*×10*Å*×8.82*Å* adjacent to the crack. As these stresses are calculated locally near the crack surface they therefore relate to the traction in the traction–separation law [17].The average traction and opening displacement associated with region were calculated using all the points in the region adjacent to the crack. This effectively reduces the scatter of the data [9].

Regardless of the temperature of the system or the mode of failure, the traction always initially increases as the crack opening distance was increased until they reached a peak value. The traction then decreased as the crack opening was further increased. To represent the CZM, a model that includes an exponential term is suggested to approximate the traction-separation responses shown in Fig. 8 for tensile mode failure. It indicates that the stresses initially increased as the crack opening distance was increased until they reached a peak value. The result for the maximum stress as a function of the simulated temperature is summarized in Table 2.

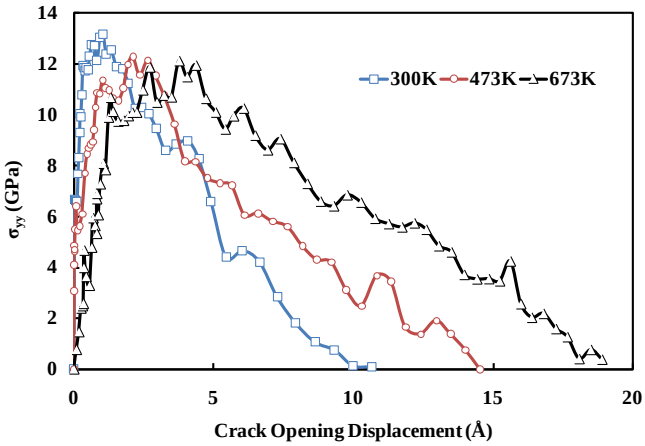

Figure 8. Traction-Separation relationship for tensile mode failure in a Fe_3C-*Fe* interface

Table 2. Simulation results to gage the effect of temperature CZM

Case	Simulated temperature (*K*)	Maximum stress (*GPa*)
1	300	13.15
2	473	12.29
3	673	12.11

4. Parameterization of the T-S law

Researches constructed cohesive models as that: tractions increase until reach a maximum, and then approach zero when the separation displacement increases. The thickness of the interface in the unloaded state is considered as zero. Tvergaard and Hutchinson (1993) [18] introduced traction-separation relation: let δ_n^c and δ_t^c be the maximum allowable normal and tangential components of the cohesive element. δ_n and δ_t denote the normal and tangential components of the relative displacement of the crack faces across the interface in the zone where the fracture

processes are occurring (as shown in Fig.9). The non-dimensional parameter λ is expressed by Eq.(8).

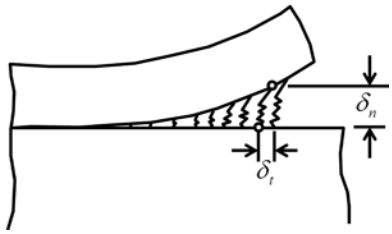

Figure 9. Traction-separation relation

$$\lambda = \left\{ \left(\delta_n / \delta_n^c \right)^2 + \left(\delta_t / \delta_t^c \right)^2 \right\}^{1/2} \tag{8}$$

Failure is attained in the cohesive element when λ=1.
The potential is:

$$\Pi\left(\delta_n, \delta_t\right) = \delta_n^c \int_0^{\lambda} \sigma\left(\lambda'\right) d\lambda' \tag{9}$$

The normal and tangential components of the traction are given by:

$$\begin{aligned} T_n &= \frac{\partial \Pi}{\partial \delta_n} = \frac{\sigma(\lambda)}{\lambda} \frac{\delta_n}{\delta_n^c} \\ T_t &= \frac{\partial \Pi}{\partial \delta_t} = \frac{\sigma(\lambda)}{\lambda} \frac{\delta_t}{\delta_t^c} \frac{\delta_n^c}{\delta_t^c} \end{aligned} \tag{10}$$

If the tangential component of the traction is zero, the traction-separation law is a purely normal separation. The peak normal traction under purely normal separation is termed the interface strength. Generally, for Mode I cohesive zone model it only contains opening mode fracture, the relationship between the cohesive traction and the separation displacement could be expressed as:

$$F(\lambda) = \sigma = \sigma_c f\left(\lambda\right) \tag{11}$$

In this equation, σ_c is the peak traction, f is a dimensionless function which relate to the shape of the cohesive traction-separation displacement curve.
A relationship between the traction and the crack opening displacement must be obtained when we use cohesive element. In the CZM, the fracture process zone is simplified as being an initially zero-thickness zone, composed of two coinciding surfaces. Under loading, the two surfaces separate and the traction between them varies in accordance with a specified T-S law. In our study a parameterized exponential T-S law is proposed based on the MD simulations. According to Eq.(11), the traction-separation law ($F(\lambda)$) is then implemented through Eq.(12). In Eq.(12) the maximum cohesive strength (σ_c) is simulated at room temperature. The constants parameterized from the MD results of Mode I are obtained in table 3. According to Eq.(12) and table 3, the curve of traction-separation relationships under different simulate temperatures has shown in Fig.10.

$$F\left(\lambda\right) = \sigma_c f\left(\lambda\right) = A\sigma_c \lambda \exp(-B\lambda) \times (1 - 0.001T) \tag{12}$$

Table 3The constants parameterized from the MD results of Mode I.

Simulated temperature (K)	Maximum stress (GPa)	A	B
300	13.15	2.6338	0.8142
473	12.29	1.6951	0.4712
673	12.11	1.1905	0.2643

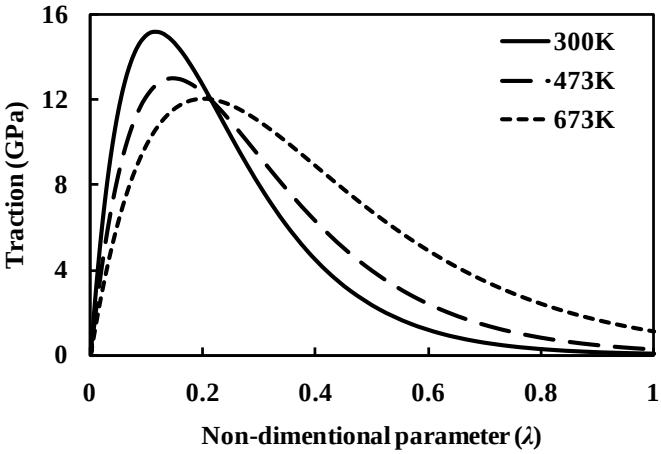

Figure 10. Traction-separation relationships under different simulate temperatures

5. Simulation of the T-S fracture test

In order to model stable crack growth under static loading and analyze cohesive behavior derived from MD towards greater length scales, it is necessary to examine a scenario in which the effective stress intensity factor in the process of crack growth. Thus, we perform a simulation of crack growth for a CT specimen subject to displacement loading via prescribed motion of loading pins. Fracture of a CT specimen can verify whether the cohesive law derived from MD simulations displays behavior consistent with linear elastic fracture mechanics. The geometry and mesh of our CT specimen is shown in Fig.11. The specimen is 384 *nm* wide by H = 369 *nm* tall, with an effective width (the distance between the pin holes and the uncracked edge) of W = 307 *nm*, an initial crack length of a = 155 *nm* ($a/W \approx 0.5$), and pin holes of radius 38.4 *nm*. Our initial geometry contains a zero-width crack rather than the finite-width crack. Cohesive elements are placed along the predefined crack path, and are 1*Å* wide. This element size enables the cohesive zone to be resolved over a length of approximately 45*Å* (45 elements).The parameterized T-S law given was implemented in ABAQUS to simulate the behavior of the CZM. For the FE model of outside of the CZM, two-dimensional continuum plane strain incompatible elements (CPEI4) were used with isotropic material properties to represent the bulk elastic behavior while two-dimensional cohesive elements (COH2D4) were used for the CZM.

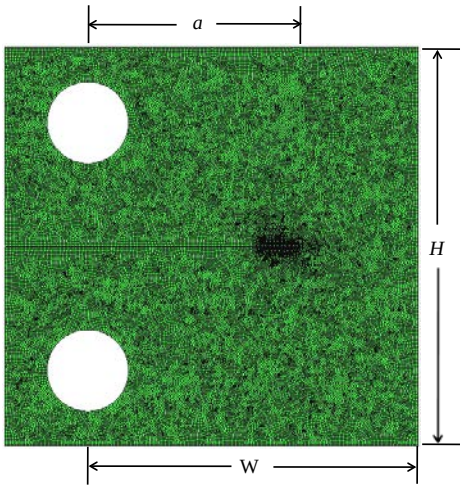

Figure 11. FEA mesh of CT specimen. The specimen's height H=369 *nm*, its effective width W=307 *nm*, and its initial crack length a=155 *nm*

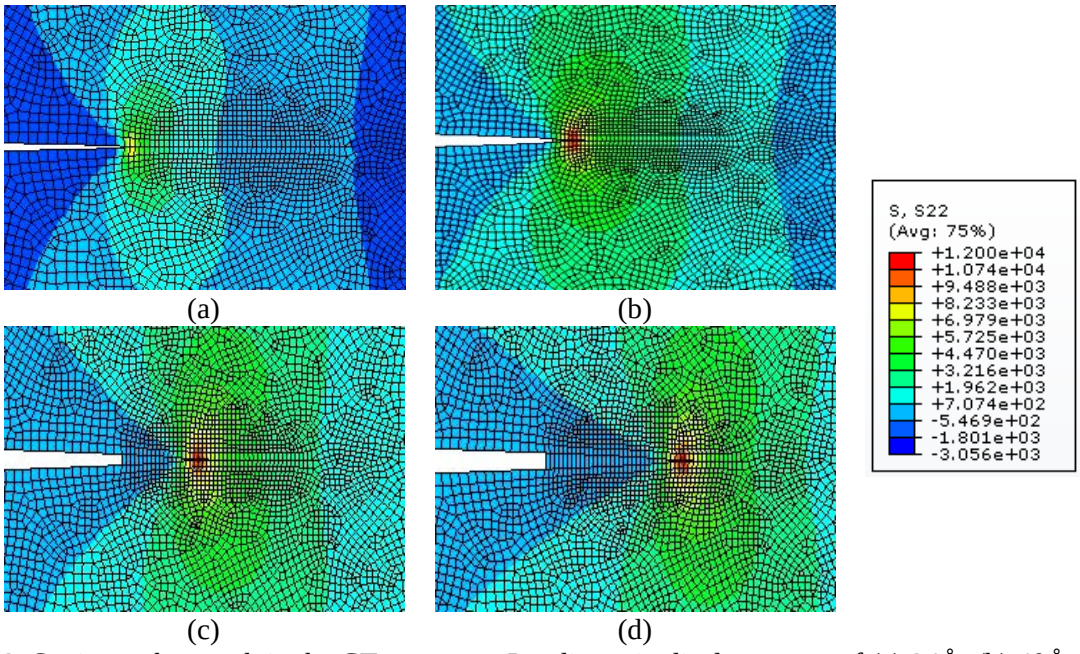

Figure 12. Static crack growth in the CT geometry. Loading–pin displacements of (a) 24Å, (b) 40Å, (c) 60Å, and (d) 70Å are shown. Plots are colored according to element values of σ_{yy} in units of *GPa* as shown in the legend

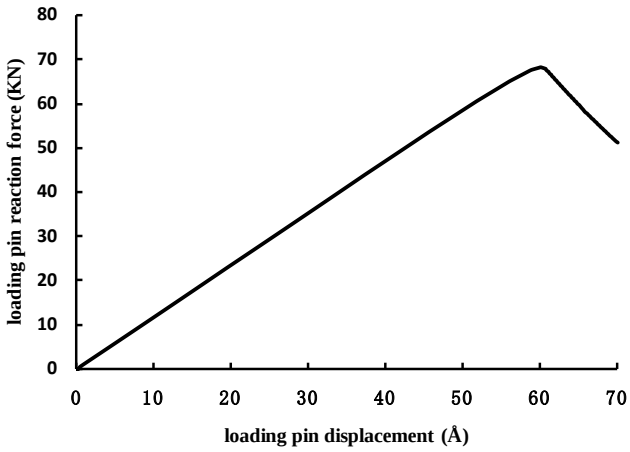

Figure 13. Reaction force versus loading-pin displacement for CT specimen

The crack opening behavior due to displacement of the top and bottom pins is observed in Fig.12. Before crack propagation begins to occur, the cohesive zone begins to form, as seen in Fig.12(a) and (b). Once a critical displacement is reached, crack propagation is seen in Fig.12(c) and (d).

We can further verify our analysis by taking the value of peak load in Fig.13, 68.06 *kN*, and combining it with geometric dimensions of the system to obtain the stress intensity factor. We obtain a value for fracture toughness of J_c=0.42 *MPa·m*. This value lies close to experimental result in literature [19].

Our study shows that the estimated fracture toughness coincides with test value from experiment. It shows the expected linear relationship between loading-pin displacement and reaction force. More complex fracture mechanics problems can be analyzed through combining the cohesive law derived from MD simulations and finite element method.

6. Conclusion

(1) Molecular dynamics simulations under a special configuration have been performed to study the mechanism of Fe_3C-Fe interface under Mode I loading condition at different temperatures, and the FS-EAM potential used in LAMMPS is certified by melting point verification.
(2) The elastic modulus and maximum stress as a function of the simulated temperature for both with and without crack models, and the maximum values of modulus and maximum stress for no crack model at roomtemperature are seen to be 332.67*GPa*, 12.17*GPa*, 86.94*GPa* and 6.04GPa for crack model. The traction-separation relation of *X70* pipeline steel with crack is characterized by MD simulations, the peak traction value of 13.15*GPa* for tensile model at room temperature.
(3) The parameterized cohesive traction-separation relation for Mode I failure at room temperature to simulate the crack propagation behavior of *X70* pipeline steel in a FEA. The curve obtained through our simulation is agreement with predictions from linear elastic fracture mechanics, showing the expected linear relationship between loading-pin displacement and reaction force.
(4) The fracture toughness gained from our simulations is close to the experimental result. It shows our methodology is feasible. Our study may provide several novel ideas for simulating complex fracture problems based cohesive laws used in FE analysis.

Acknowledgements

Project supported by the Fundamental Research Funds for the Central Universities (Grant No. 2010SCU21014) and the Project of West-East Gas Pipeline Company at PetroChina Company Limited (Grant No. XQSGL01423).

References

[1] Yu. Ivanisenko, I. MacLaren, X. Sauvage, R.Z. Valiev,. H.J. Fecht, Shear-induced transformation in nanoscale Fe–C composite. Acta Mater., 54 (2006) 1659–1669.
[2] C.R. Dandekar, Y.C. Shin, Molecular dynamics based cohesive zone law for describing Al-SiC interface mechanics. Composites: Part A, 42 (2011) 355–363.
[3] V.Yamakova, E. Saether, D.R. Phillipsc, E.H. Glaessgen, Molecular-dynamics simulation-based cohesive zone representation of intergranular fracture processes in aluminum. Journal of the Mechanics and Physics of Solids, 54 (2006) 1899–1928.
[4] D.S. Dugdale, Yielding of steel sheets containing slits. J. Mech. Phys. Solids, 8 (1960) 100–104.
[5] G.I. Barrenblatt, The mathematical theory of equilibrium of cracks in brittle fracture. Adv. Appl. Mech., 7 (1962) 55–129.
[6] X.P. Xu, A. Needleman, Numerical simulations of fast crack growth in brittle solids. J. Mech. Phys. Solids, 42 (1994) 1397–1434.
[7] X.W. Zeng, S.F. Li, A multiscale cohesive zone model and simulations of fractures. Comput. Methods Appl. Mech. Engrg., 199 (2010) 547–556.
[8] X.W. Zhou, J.A. Zimmerman, E.D. Reedy, N.R. Moody, Molecular dynamics simulation based cohesive surface representation of mixed mode fracture. Mechanics of Materials, 40 (2008) 832–845.
[9] X.W. Zhou, N.R. Moody, R.E. Jonesa, J.A. Zimmermana, E.D. Reedyc, Molecular-dynamics-based cohesive zone law for brittle interfacial fracture under mixed loading conditions: Effects of elastic constant mismatch. Acta Materialia, 57 (2009) 4671–4686.
[10] Y.J. Wei, L. Anand, Grain-boundary sliding and separation in polycrystalline metals:application to nanocrystalline fcc metals. J Mech Phys Solids, 52 (2004) 2587–616.
[11] J.T. Lloyd, J.A. Zimmerman, R.E. Jones, X.W. Zhou, D.L. McDowell, Finite element analysis of an atomistically derived cohesive model for brittle fracture. Modelling Simul. Mater. Sci. Eng., 19 (2011) 065007.
[12] M.W. Finnis，J.E. Sinclair, A simple empirical N-body potential for transition metals. Phil.

Mag. A, 50 (1984) 45–55.
[13] D.J. Hepburn, G.J. Ackland, Metallic-covalent interatomic potential for carbon in iron, Phys. Rev. B, 78 (2008) 165115.
[14] C.W. Chiou, Jr., E.A. Carter, Structure and stability of Fe_3C-cementite surfaces from first principles. Surface Science, 530 (2003) 87–95.
[15] J.A. Zimmerman, E.B. Webb III, J.J. Hoyt, R.E. Jones, P.A. Klein, D.J. Bammann, Evaluation of continuum stress in atomistic simulation. Computational Fluid and Solid Mechanics, (2003) 804–807.
[16] M. Zhou, A new look at the atomic level virial stress: on continuum-molecular system equivalence. Proc. R. Soc. Lond. A, 459 (2003) 2347–2392.
[17] K. Gall, M.F. Hostemeyer, M.V. Schilfgaarde, M.I. Baskes, Atomistic simulations on the tensile debonding of an aluminum–silicon interface. J Mech Phys Solids, 48 (2000) 2183–212.
[18] V. Tvergaard, J.W. Hutchinson. The influence of plasticity on mixed mode interface toughness, J. Mech. Phys. Solids, 41 (1993) 1119–1135.
[19] Y.R. Feng, Y.N. Liu. Dynamic fracture of pipeline steel X70, The papers of West-East Gas Pipeline and the steel pipe application infrastructure and research technical, Petroleum Industry Press, Beijing, 2004, pp. 140–151.

Tunable Negative Poisson's Ratio of 3D Spanned-Fullerene Nanotube Nanotruss

Jianyang Wu[1], Jianying He[1], Zhiliang Zhang[1,*]

[1]Department of Structural Engineering, NTNU Nanomechanical Lab, Norwegian University of Science and Technology (NTNU), Trondheim N–7491, Norway
* Corresponding author: zhiliang.zhang@ntnu.no

Abstract CNT-based network, as an emerging class of material, attracts extensive research interest in recent years from both the scientific community and industry. In this study we proposed novel covalently bonded bcc-lattice like 3D nanotruss made up of fullerenes spanned by CNTs. The mechanical properties of such architecture are systematically investigated via full atomistic simulation. Our simulations reveal that the CNTs length of the 3D nanotruss plays a significant role on the mechanical properties. This nanotruss network displays orientation dependent deformation behaviour. Under <100> direction tension, negative Poisson's ratio is observed exclusively for the case of $N = 0$, while a "flipping" behaviour of Poisson's ratio with "Negative → Positive → Negative" appears when the tension is applied along <110> direction. The findings in our work would provide guidance to optimal design of CNT-fullerene based structures towards tailor-made properties.

Keywords Single-walled carbon nanotubes, Fullerene, Nanotruss, Negative Poisson's ratio, Atomistic simulation

1. Introduction

Since their discovery [1, 2], the properties of fullerenes and nanotubes have been extensively studied both by experiment and by simulation. It is found that they, as unique zero-/one-dimensional carbon materials, possess predominant physical, chemical, and mechanical properties combined with a very little weight. To fully exploit their unique properties and explore additional properties, various types of carbon architectures made up of fullerenes and carbon nanotubes (CNTs) have been successfully fabricated and investigated. A hybrid carbon nanostructure termed "nanopeapod" □ fullerenes are encapsulated in CNTs, has been fabricated, and the nanopeapod exhibits a variety of intriguing physical and chemical properties [3-6]. Another nanostructure based on fullerenes and CNTs called "nanobuds" holds exceptional field emission properties [7]. A Y-shaped CNT junction displays rectifying and electrical switching properties, such that it can serve as a switching device [8]. Moreover, organized 2D and 3D CNT architectures can be fabricated to realize specific functional properties for a variety of meso- and macro-scale engineering applications. Hall et al. [9] revealed that the CNT networks can exhibit unusual mechanical properties such as negative Poisson's ratio. By infiltrating a polymer into a reticulate CNT (RCNT) architecture, CNT-network-based reinforced composites are formed to achieve superior mechanical properties [10], originating from strong molecular-level coupling between reticulate CNTs and polymer chains. The RCNTs/polydimethylsioxane with high transparency, high conductivity, and excellent stretchability in addition to the facile fabrication, is a promising candidate as interconnects and electrodes for stretchable intelligent and functional devices [11]. Covalently bonded 3D CNT networks have also been produced at large scale [12], in which an effective stress distribution in the network improves the mechanical strength of the materials. Computer-aided design and simulation of 2D and 3D nanostructures consisting of fragments of CNTs-junctions also helps to exploit their potentials [13-20]. For example, Romo-Herrera et al. [14] showed that 2D and 3D systems can be utilized for complex integrated nanoelectronic circuits due to specific paths of charges flowing through the nodes of the systems, and the 3D super-cubic and super-diamond architectures have the ability of supporting extremely high unidirectional stress. Despite the increasing interest in CNT architectures,

nano-joining and assembly conforming 3D networks are still in very early stages.
Accordingly, in the present work we invoke concept of hierarchical nano-joining to propose new architectures comprised of fullerenes and SWCNTs. We present a systematical atomistic simulation study on the mechanical properties of the novel 3D spanned-fullerene nanotruss architecture.

2. Model and Methodology

We adopt a CNT (6,6) and a giant fullerene C_{372} with D_{2d} molecular symmetry as parent bricks for constructing novel covalent bonded 3D nano-truss systems. As illustrated in Figure 1, 3D nanostructures are built from a fullerene C_{372}. Three atomic pairs are added as patches (red atoms in Figure 1b) in the face of fullerene (green atoms in Figure 1a and 1b) to create an open-cage cluster with a terminal. This terminal is able to coaxially dock a (6,6) CNT segment (purple atoms in Figure 1c), forming three octagon rings dispersed at the junction. The truss-like 3D network with an all-sided coalescence of fullerenes with (6,6) CNTs is finally created as shown in Figure 1d, resembling a body center cubic (bcc) lattice. The mechanical responses of as-generated 3D nano-truss under tension are systematically investigated with respect to the connection CNT length *N* varying from 0 to 10.

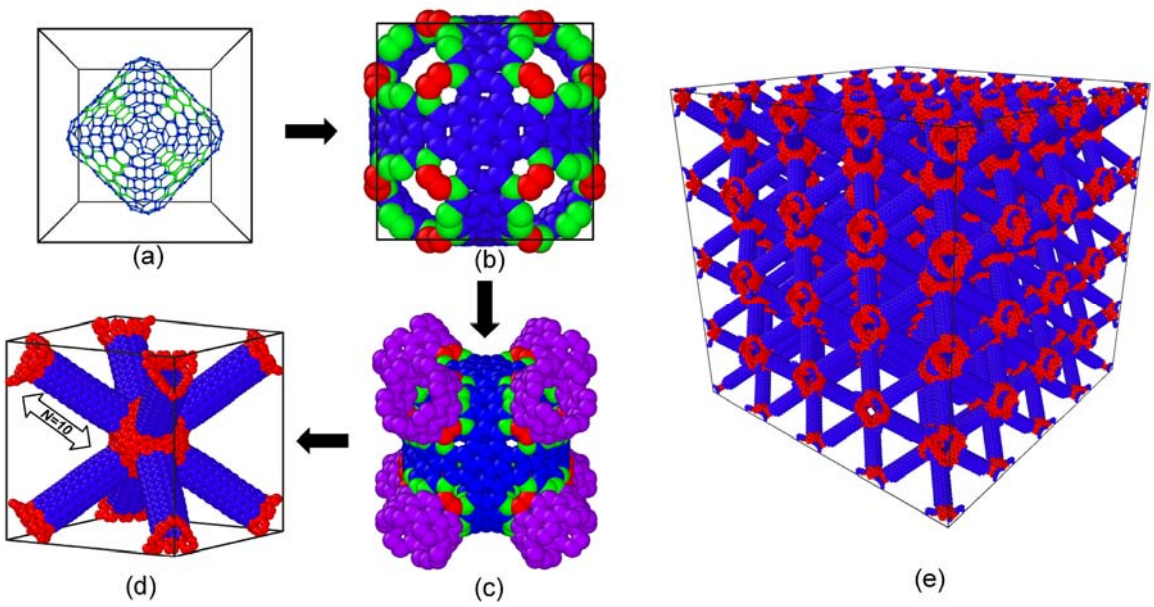

Figure 1 (a)□(d) Schematic illustration for constructing the unit of 3D spanned-fullerene nanotube nanotruss. (e) Perspective of 3D architecture models with 3×3×3 unit cells.

The full atomistic simulations are carried out using LAMMPS software package capable of running on large computing clusters. The adaptive intermolecular reactive empirical bond-order (AIREBO) potential [21] is used for carbon atomic interactions in the simulations. The cutoff parameter for the REBO part of the potential is set to be 2.0 Å as described by Shenderova [22] in order to avoid the spuriously high bond forces and nonphysical phenomenon during the fracture process. As-constructed architecture models with 3×3×3 unit cells (Figure 1e) are first quasi-statically relaxed by minimizing the total potential energy through a conjugate gradient method. The mechanical loads of uniaxial tension under deformation-control as our previous study [23], are performed on 3D equilibrated structures until complete rupture of each specimen. The samples are deformed with a reasonable strain rate 0.0001/ps based on Nosé-Hoover thermostat. Stresses and strain are calculated every 1000 steps.

The nominal strain parallel to the direction of deformation is defined as

$$\varepsilon = \frac{L - L_0}{L_0} = \frac{\Delta L}{L_0}, \tag{1}$$

where L_0 and L are the equilibrium and the current length of the entire systems in the direction of loading.

Under uniaxial tension, the transverse repositioning of nanostructures perpendicular to the load axis gives a measure of the strain from which the Poisson's ratio can be calculated

$$\nu = -\frac{d\varepsilon_{\mathrm{T}}}{d\varepsilon_{\mathrm{L}}}, \tag{2}$$

where ε_{T} and ε_{L} are the transverse and longitudinal strains, respectively.

3. Results and Discussions

A uniaxial tension test has been carried out to study the mechanical properties of fullerene 3D foam-like nanostructures formed by CNTs and fullerene. The basic 3D bcc-lattice nano-truss unit is displayed in Figure 1d. Figure 2 shows the stress-strain evolutions of 3D nanotruss with CNT length N varying from 0 to 10. Except for small N where linear elasticity was observed, the 3D nanostructures exhibits nonlinear elasticity and the CNT length plays a key role on the mechanical properties. The dense 3D network (small N) has more constraints that limit the realignment and bending of CNTs, and results in a linear behavior. A nonlinear up-swing behavior appears in the sparse network due to the increase of CNTs length, as in Figure 2. Such nonlinear stiffening behavior results from the different deformation mechanisms at different strain level, such as realignment and bending dominated deformation at smaller strain, and the stretching dominated deformation at larger strain. Subsequent sharp stress load drop reveals a permanent failure due to bond-breaking at the junction for all tests.

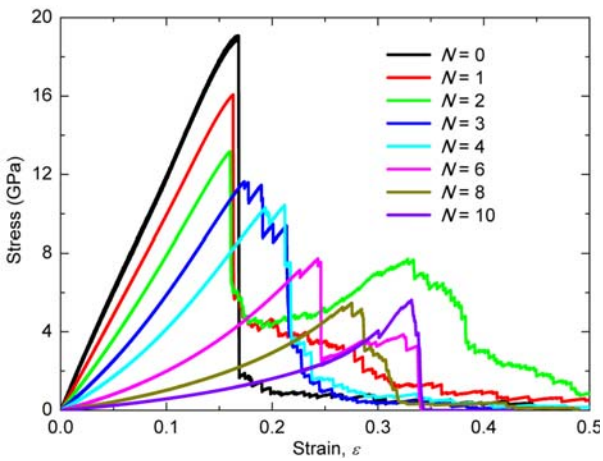

Figure 2 Stress–strain curves of 3D nano-truss networks with N varying from 0 to 10 under uniaxial tension.

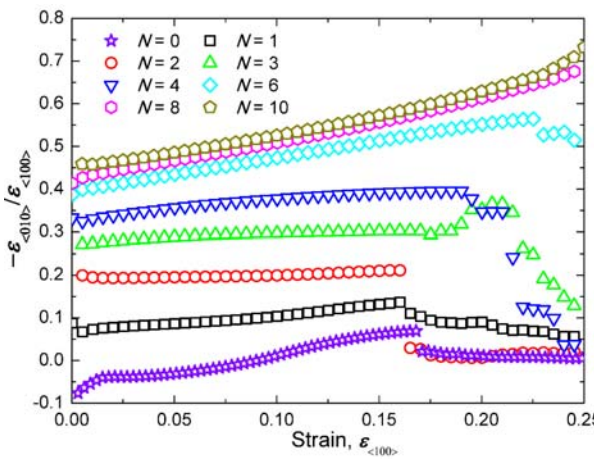

Figure 3 Deformation dependence of the ratio of the transverse and longitudinal strains for the 3D networks under uniaxial tension.

An in-depth investigation on the Poisson's ratio is then performed. Figure 3 presents the calculated strain-dependent Poisson's ratio of the 3D networks. It can be seen that the CNTs length dominates the Poisson's ratio of the 3D networks. With N = 0, the 3D covalent pack of fullerenes exhibits a negative Poisson's ratio. The negative Poisson's ratio of 3D network is attributed to a reduction of absolute curvature in fullerene hub due to high constraint from direct covalent connection between fullerenes without participation of CNTs. The linkage of CNTs would actively involve the bending and stretching dominated deformation, and causes a different stress concentration on the fullerene

hub. The Poisson's ratio is strikingly strain-dependent, sign change from negative to positive when an extensional strain reach around 0.09, which suggests that the transverse strain begins to act in an opposite sense to the longitudinal strain.

Many cubic metals when stretched along the specific 110 off-axis direction become auxetic [24]. Accordingly, we conduct tension tests on the bcc-lattice 3D nano-truss network along the <110> orientation and the resulting stress–strain relations with *N* varying from 0 to 10 are shown in Figure 4. We again see clearly that the CNT length dominates the mechanical properties. The tensile stress, tensile stain and stiffness all decreases with the increase of the segment length *N* for the case under tension along the <110> direction. Compared with the Figure 3 we observe that both the tensile strain and tensile stress are smaller than those under <100> direction, resulting from a pure stretching of octagon rings in the fullerene hub. For large CNT segment length of nanotruss, the fracture strain, however, is significantly larger than those under <100> direction.

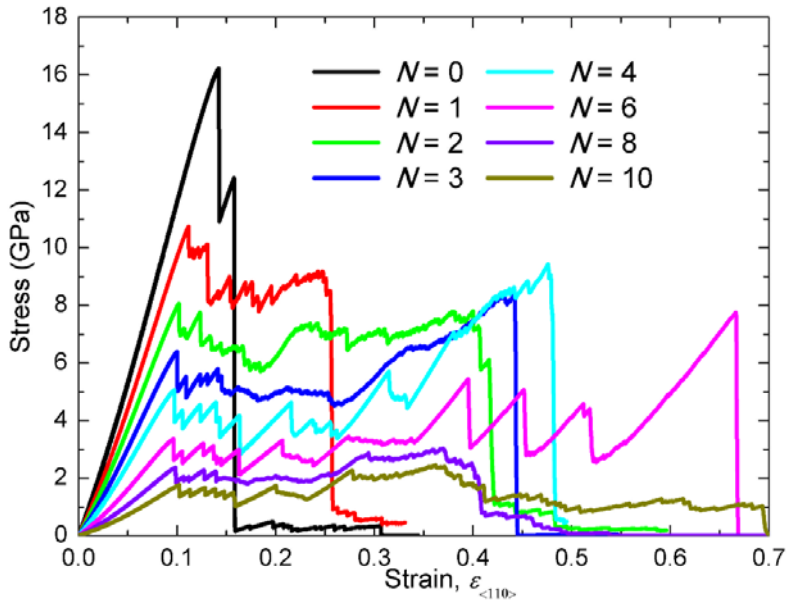

Figure 4 Stress–strain curves of 3D nano-truss networks with *N* varying from 0 to 10 under uniaxial tension.

The corresponding Poisson's ratio is determined and plotted in Figure 5. It can be seen that this bcc-latticed 3D network also exhibits a negative Poisson's ratio when tension is applied along the <110> direction. Figure 5c and 5d compare the value of $-\varepsilon_{<-110>}/\varepsilon_{<110>}$ and $-\varepsilon_{<001>}/\varepsilon_{<110>}$ as a function of CNTs length at a specific small strain $\varepsilon_{<110>}$ = 0.01. It must be noted that this 3D network yields a very wide range of Poisson's ratios that are both controlled and tunable by virtue of the microstructural parameter — the length of CNTs. The magnitude of $-\varepsilon_{<-110>}/\varepsilon_{<110>}$ and $-\varepsilon_{<001>}/\varepsilon_{<110>}$ roughly covers a wide range from □0.4 to 0.3, and from 0.1 to 1.2, respectively. The spectacular change of $-\varepsilon_{<001>}/\varepsilon_{<110>}$ appears in this 3D network exceeds 0.5, which is the threshold value for isotropic materials in the theory of elasticity. Interestingly, a dramatic "flip" behaviour of the Poisson's ratio from negative → positive → negative with increase of CNTs length appears (Figure 5c). The findings can be utilized on tailor-making auxetic CNT-fullerene networked nanostructures with the wanted properties. Two different mechanisms, involving curvature flattening and rigid mechanical model, are identified to be responsible for the "flipping" of Poisson's ratio.

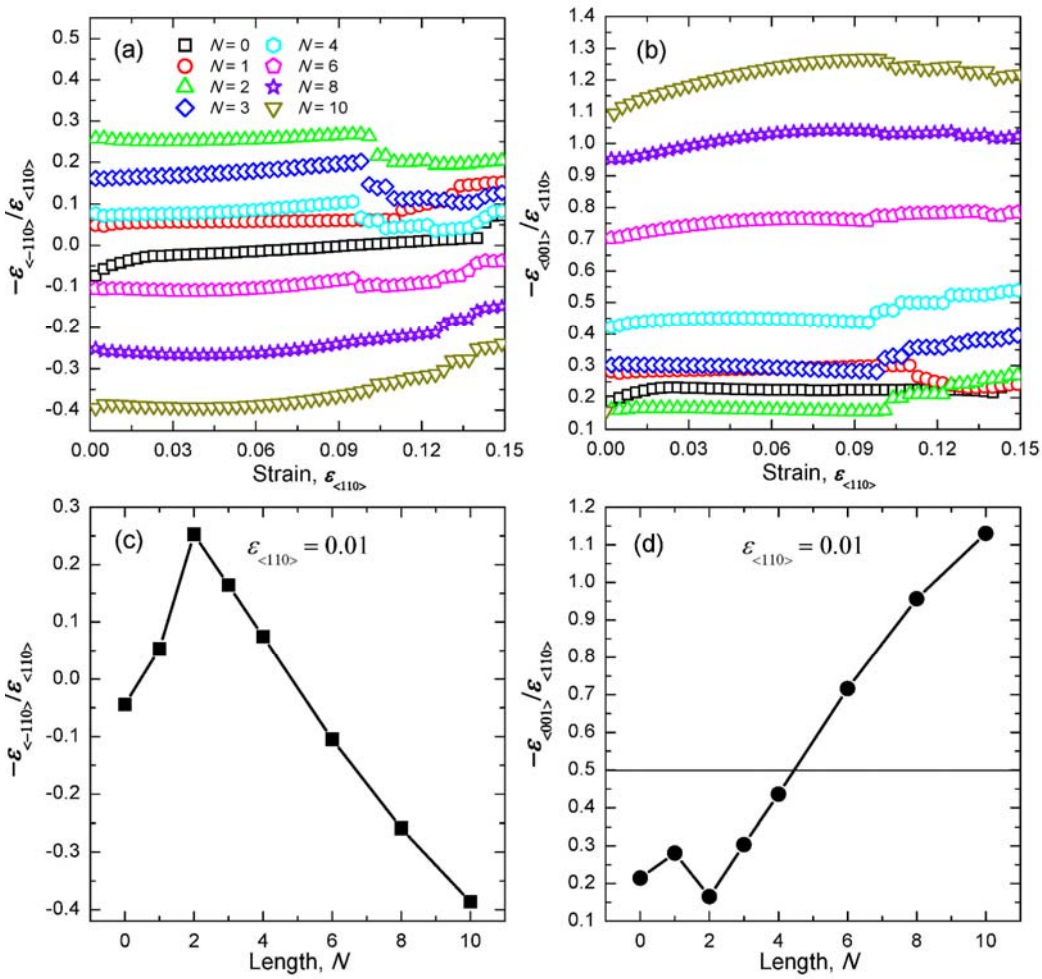

Figure 5 (a) and (b) Deformation dependence of the ratio of the transverse and longitudinal strains, $-\varepsilon_{<-110>}/\varepsilon_{<110>}$ and $-\varepsilon_{<001>}/\varepsilon_{<110>}$ for the 3D networks under uniaxial tension, respectively. (c) and (d) Ratio of transverse and longitudinal strains as a function of CNT segment length N at $\varepsilon_{<110>} = 0.01$.

Visualizing the detailed structural evolutions of this 3D nano-truss provides insights on the structural and mechanical properties, such as the deformation mechanism, the negative Poisson's ratio and fracture modes. Figure 6 displays straining direction dependence of the representative atomic structural development of the 3D nano-truss. For N = 0, the initial side-view shows the porosity of the 3D nanostructures, analogous to the zeolite structure [25], offering a possibility for molecular storage and filters. During the deformation, three stages can be identified: firstly, there is a curvature flattening process with the increase of the strain, as presented in the zoomed-in local structures of Figure 6a and 6c, which results in a negative Poisson's ratio. In this stage, the curvature-flattening dominates the deformation with no irreversible structural changes, triggering an expansion of pore between fullerenes as well as the fullerene cages. Secondly, the subsequent graphitic structure with negative curvature ultimately causes a contraction when the strain approaches a critical value. This is confirmed by the change of Poisson's ratio from negative to positive as shown in Figure 3. Finally, an additional strain increment leads to a fracture at the weak octagon rings at the junction. The fracture propagates in the plane perpendicular to the strain direction towards complete rupture, in which a number of monoatomic carbon chains formed, similar to what is widely observed in the stretching of pure CNTs. A longer CNT for spanning the fullerenes is exploited to tune the properties of this 3D networks. Particularly, sequential deformation configurations of the 3D network with N = 10 are displayed in Figure 6b and 6d. It can be noticed that the long length of CNTs brings a sparse 3D network, and orientation dependence of

deformation mechanism on the 3D network with long CNTs length is also clearly observed. In addition, a different deformation mechanism is revealed by comparing with that of $N = 0$.

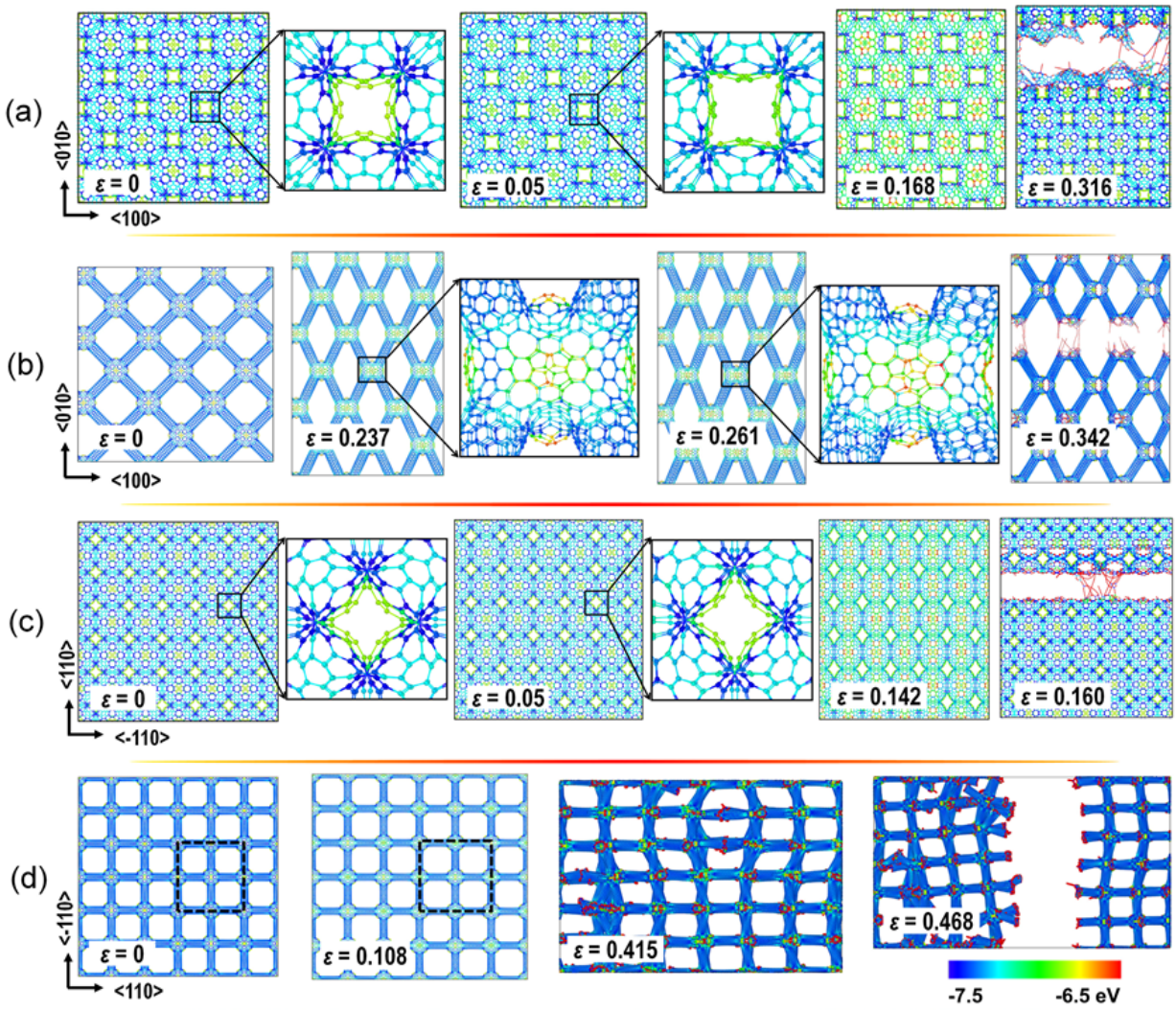

Figure 6 Size- and orientation- dependence on the atomic structural development of 3D networks under uniaxial straining. (a) Sequential deformation snapshots of 3D networks with $N = 0$ under <100> directional tension. The zoomed-in local atomic structures clearly illustrate the mechanism of negative Poisson's ratio. (b) Sequential deformation snapshots of 3D networks with $N = 10$ under <100> directional tension. The zoomed-in local atomic structures distinctly display the buckling of fullerene in the node of 3D network prior to the fracture. (c) Sequential deformation snapshots of 3D networks when $N = 0$ under <110> directional tension. The negative Poisson's ratio is explained by the zoomed-in local atomic structures. (d) Sequential deformation snapshots of 3D networks when $N = 10$ under <110> directional tension. The local potential energy shows how the high amount of stress during uniaxial tension resides on the fullerene nodes.

Three deformation stages are also observed from the overall tension processes for both loading directions. Straining along the <100> direction involves direct stretching of all the CNTs in the network, whereas half of CNTs in the network when deformed along <110> undergo direct tension because the axis of other CNTs is perpendicular to the tension direction. For the former case, straining along <100>, an initial tension of the system induces the angles change between CNTs, accompanying with the structural transformation of fullerene hub where the negative curvature structures become either flattening or more curved as in the zoomed-in local structure of Figure 6b. As clearly shown in the second zoomed-in local motif of Figure 6b, an excessive straining induces a striking inversion of a two-pentagon without bond breaking, which is similar to the inversion of a

two-pentagon nanocone via an indenter compression [26]. Finally, one octagon ring initially develops to a clean cleavage followed by rest fracturing, and the formation of monoatomic carbon chains. For the latter case of straining along <110>, an incipient straining also induces the change of angles as well as the structural change of the fullerene hubs. As expected, the zoomed-in top-viewed snapshots covered by dash square in Figure 6d show that the tension in <110> direction increases the view-plane-distance between fullerene hubs as a result of rigid mechanical models, indicating a negative Poisson's ratio. The mechanism of this negative Poisson's ratio differs with the case of N = 0 in the absence of CNT segments. Beyond the tensile limit, excess angle change and the octagon rings damage occurs, generating morphology as displayed in third snapshot of Figure 6d, similar to a metallic plastic deformation. Further straining results in compete rupture with a clean cleavage. As a whole, the strong correlation between deformation mechanism and organizational parameters demonstrates a close structure–property relationship in this 3D nano-truss network.

4. Conclusions

Carbon-based nanomaterials have attracted significant attention due to their unique optical, electrical, thermal and mechanical properties. In our study, 3D nanotruss architecture is constructed by spanning fullerenes with single-walled carbon nanotube (SWCNT) super-bonds. The mechanical properties of this novel architecture are systematically investigated by full atomistic simulation. The deformation and fracture behavior of 3D periodic graphitic nanostructures are largely dictated by the inter-fullerene distance and loading orientation. Surprising negative Poisson's ratio observed in this 3D network is revealed to originate as a result of curvature-flattening or rigid mechanical model. The magnitude of Poisson's ratio is strongly dependent on the level of strain and CNT length. The insight on the deformation mechanism of these periodic graphitic nanostructures will facilitate the integration of low-dimensional materials towards high-dimensional organized structures to realize targeted multi-functional properties.

Acknowledgements

This work is supported by the Research Council of Norway (RCN) under NANOMAT KMB Project (MS2MP) No. 187269 and the computational resources provided by NOTUR – the Norwegian Metacenter for Computational Science.

References

[1] H. W. Kroto, J. R. Heath, S. C. O'Brien, R. F. Curl, R. E. Smalley, C_{60}: Buckminsterfullerene, Nature 318 (1985)162-163.

[2] S. Iijima, Helical microtubules of graphitic carbon, Nature 354 (1991)56 – 58.

[3] B. W. Smith, M. Monthioux, D. E. Luzzi, Encapsulated C_{60} in carbon nanotubes, Nature 396(1998)323-324.

[4] R. Kitaura, H. Shinohara, Carbon-Nanotube-Based Hybrid Materials: Nanopeapods, Chem-Asia. J. 1(2006)646-655.

[5] F. Simon, M. Monthioux, 5b. Fullerenes inside Carbon Nanotubes: The Peapods, in: Carbon Meta-Nanotubes: Synthesis, Properties and Applications, John Wiley & Sons, Ltd, 2011, pp. 273-321

[6] E. Hernández, V. Meunier, B. W. Smith, R. Rurali, H. Terrones, M. Buongiorno Nardelli, M. Terrones, D. E. Luzzi, J. C. Charlier, Fullerene Coalescence in Nanopeapods: A Path to Novel Tubular Carbon, Nano Lett. 3(2003)1037-1042.

[7] A. G. Nasibulin, P. V. Pikhitsa, H. Jiang, D. P. Brown, A. V. Krasheninnikov, A. S. Anisimov, P. Queipo, A. Moisala, D. Gonzalez, G. Lientschnig, A. Hassanien, S. D. Shandakov, G. Lolli, D. E. Resasco, M. Choi, D. Tomanek, E. I. Kauppinen, A novel hybrid carbon material, Nat. Nanotech. 2(2007)156-161.

[8] L. J. Hall, V. R. Coluci, D. S. Galvão, M. E. Kozlov, M. Zhang, S. O. Dantas, R. H. Baughman, Sign Change of Poisson's Ratio for Carbon Nanotube Sheets, Science 320 (2008)504-507.

[9] W. Ma, L. Q. Liu, Z. Zhang, R. Yang, G. Liu, T. H. Zhang, X .F. An, X. S. Yi, Y. Ren, Z. Q. Niu, J. Z. Li, H. B. Dong, W. Y. Zhou, P. M. Ajayan, S. S. Xie, High-Strength Composite Fibers: Realizing True Potential of Carbon Nanotubes in Polymer Matrix through Continuous Reticulate Architecture and Molecular Level Couplings, Nano Lett. 9(2009)2855-2861.

[10] L. Cai, J. Z. Li, P. S Luan, H. B. Dong, D. Zhao, Q. Zhang, X. Zhang, M. Tu, Q. S. Zeng, W. Y. Zhou, S. S Xie, Highly Transparent and Conductive Stretchable Conductors Based on Hierarchical Reticulate Single-Walled Carbon Nanotube Architecture, Adv. Funct. Mater. 22(2012)5238-5244.

[11] Y. F. Fu, B. Carlberg, N. Lindahl, N. Lindvall, J. Bielecki, A. Matic, Y. X. Song, Z. L. Hu, Z. H. Lai, L. L. Ye, J. Sun, Y. H. Zhang, Y. Zhang, J. Liu, Templated Growth of Covalently Bonded Three–Dimensional Carbon Nanotube Networks Originated from Graphene, Adv. Mater. 24(2012)1576-1581.

[12] V. R. Coluci, D. S. Galvão, A. Jorio, Geometric and electronic structure of carbon nanotube networks: 'super'-carbon nanotubes, Nanotechnology 17(2006)617-621.

[13] Y.Lin, W. Cai, X. Shao, Fullerenes connected nanotubes: An approach to build multidimensional carbon nanocomposites, Chem. Phys. 331(2006)85-91.

[14] J. M. Romo-Herrera, M. Terrones, H. Terrones, S. Dag, V. Meunier, Covalent 2D and 3D Networks from 1D Nanostructures: Designing New Materials, Nano Lett. 7(2006)570-576.

[15] M.Wang, X. Qiu, X. Zhang, Mechanical properties of super honeycomb structures based on carbon nanotubes, Nanotechnology 18(2007)075711-075716.

[16] Y. Li, X. Qiu, F. Yang, Y. Yin, Q. Fan, Stretching-dominated deformation mechanism in a super square carbon nanotube network, Carbon 47(2009)812-819.

[17] I. Zsoldos, I. Laszlo, Computation of the loading diagram and the tensile strength of carbon nanotube networks, Carbon 47(2009)1327-1334.

[18] Y. Li, X. Qiu, Y. Yin, F. Yang, Q. Fan, The elastic buckling of super–graphene and super–square carbon nanotube networks, Phys. Lett. A 374(2010)1773-1778.

[19] X. Liu, Q.-S. Yang, X.-Q. He, Y.-W. Mai, Molecular mechanics modeling of deformation and failure of super carbon nanotube networks, Nanotechnology 22(2011)475701-475711.

[20] I. Zsoldos, Planar trivalent polygonal networks constructed from carbon nanotube Y–junctions, J. Geom. Phys. 61(2011)37-45.

[21] S. J. Stuart, A. B. Tutein, J. A. Harrison, A reactive potential for hydrocarbons with intermolecular interactions, J. Chem. Phys. 112(2000) 6472-6486.

[22] O. A. Shenderova, D. W. Brenner, A. Omeltchenko, X. Su, and L. H. Yang, Atomistic modeling of the fracture of polycrystalline diamond, Phys. Rev. B 61(2000)3877-3888.

[23] J. Y. Wu, S. Nagao, J. Y. He, Z. L. Zhang, Role of Five-fold Twin Boundary on the Enhanced Mechanical Properties of fcc Fe Nanowires, Nano Lett. 11(2011)5264-5271.

[24] R. H. Baughman, J. M. Shacklette, A. A. Zakhidov, S. Stafstrom, Negative Poisson's ratios as a common feature of cubic metals, Nature 392(1998)362-365.

[25] J. Y. Wu , Q. L. Liu, Y. Xiong, A. M. Zhu, Y. Chen, Molecular Simulation of Water/Alcohol Mixtures' Adsorption and Diffusion in Zeolite 4A Membranes, J. Phys. Chem. B 113(2009)4267–4274.

[26] S. P. Jordan, V. H.Crespi, Theory of Carbon Nanocones: Mechanical Chiral Inversion of a Micron-Scale Three-Dimensional Object, Phys. Rev. Lett. 93(2004)255504-255507.

Influence of Interfacial Mechanical Properties on Elongation of Multilayered Composite Metals

Tomotsugu Shimokawa[1,*]

[1] School of Mechanical Engineering, Kanazawa University, Kakuma-machi, Kanazawa, Ishikawa 920-1192, Japan
* Corresponding author: simokawa@t.kanazawa-u.ac.jp

Abstract Multilayered composite metals (e.g., pearlitic steels) composed of alternating layers of cementite and ferrite show unique and excellent mechanical properties, such as coexistence of strength and ductility. In this study, we investigate the influence of interfacial mechanical properties on the elongation of multilayered composite metals through molecular dynamics simulations. When the interface has weak interatomic bonding, it is difficult for mobile dislocations to transmit through the interface. Thus, the multilayered model shows small elongation due to the cleavage of the brittle phase under large tensile stress by stress partitioning between the brittle and ductile phases. On the other hand, when the interface has strong interatomic bonding, dislocations can easily transmit through the interface and thus the multilayered model displays larger elongation.

Keywords Interface, Dislocation, Crack, Atomic Simulation, Mechanical Property

1. Introduction

Generally, the strength and ductility of pearlitic steel containing lamella structures with random orientations can be improved by a line drawing process. However, when drawing strain becomes greater than 1 and the lamella structures are oriented parallel to the drawing direction, the strength effectively increases but the ductility begins to decrease. For example, cold-drawn, hypereutectoid pearlitic steel wires with lamellar spacing of less than 10 nm that exhibit cementite decomposition have maximum tensile strength of greater than 6 GPa but have very limited elongation properties [1]. On the other hand, cold-drawn pearlitic steel aged at 698 K and still containing oriented lamella structures exhibit significant uniform elongation [2]. In this case, the cementite decomposition was recovered. It is still unclear how elongation can be improved by this type of annealing process.

In this study, we hypothesized that the interfacial structure is changed by cementite decomposition. We investigated the influence of interfacial mechanical properties on the elongation of multilayered composite metals through molecular dynamics simulations.

2. Virtual Materials with Ductile and Brittle Properties

2.1. Material Design

To model virtual materials with either ductile or brittle properties, we used a two-dimensional triangular lattice system. The interatomic potential of the system is expressed in terms of the Morse potential as follows:

$$\phi(r)=D\{\exp[-2\alpha(r-r_0)]-2\exp[-\alpha(r-r_0)]\} \quad (1)$$

Here, r is the distance between two atoms; D, α, and r_0 are controllable parameters and are closely related to the cohesive energy, elastic moduli, and lattice constant, respectively. Moreover, to introduce the cut-off distance, r_c, $\phi(r)$ is modified into the shifted-force potential $\phi_s(r)$ as follows:

$$\phi_s(r)=\begin{cases}\phi(r)-\phi(r_c)-[r-r_c]\left(\dfrac{d\phi}{dr}\right)_{r_c}, & r\le r_c\\ 0, & r>r_c\end{cases} \tag{2}$$

Here, we set r_c to 0.6 nm.

It has been shown that the dimensionless value of $\mu b/\gamma_s$ can roughly determine the inherent mechanical properties of single-phase materials, i.e., ductile or brittle properties [3]. Here, μ, b, and γ_s are the shear modulus, Burgers vector, and surface energy, respectively. If $\mu b/\gamma_s$ is greater than 10, the material generally exhibits brittle properties. On the other hand, if $\mu b/\gamma_s$ is smaller than 10, the material shows ductile deformation. There are two physical descriptions for the threshold value of $\mu b/\gamma_s$. One is the relationship between the ideal tensile strength and ideal shear strength, and the other is the relationship between the stress intensity factors for brittle cleavage and dislocation nucleation from the crack tip.

Table 1 shows the material parameters for two designed virtual materials. The dimensionless values of $\mu b/\gamma_s$ are 6.5 for the virtual material "M-D" and 17.7 for "M-B." Therefore, we can consider the M-D material as a ductile phase and the M-B material as a brittle phase. To simplify the mechanical phenomena around the interface between the brittle and ductile phases, we set the same value for the lattice constant of each model; it is not necessary to consider the lattice mismatch influence.

Table 1. Parameters of designed virtual materials with ductile and brittle properties.

	lattice constant a_0 (nm)	cohesive energy E_c (eV)	elastic constant C_{11} (GPa)	elastic constant C_{12}=C_{44} (GPa)	Young's modulus E (GPa) (Voigt average)	shear modulus μ (GPa) (Voigt agerage)	surface energy γ_s (mJ/m^2)	$\frac{\mu b}{\gamma_s}$	
M-D	0.2493	-2.488	206.6	68.9	172.2	68.9	2645	**6.5**	**ductile**
M-B	0.2493	-1.579	308.7	102.9	257.3	102.9	1452	**17.7**	**brittle**

2.2. Mechanical Properties of Virtual Materials

To confirm the mechanical properties of the single-phase material described by the designed Morse potential, tensile deformation tests were performed at a strain rate of 4×10^8 1/s and 10 K. Figure 1(a) shows stress–strain curves of the two designed virtual materials, M-B and M-D. Defects in the form of micro-cracks are initially introduced into each material by removing three atoms from the perfect structure. The number of micro-cracks is 1 for M-B and 12 for M-D. After relaxation before tensile loading, all initial cracks of M-D changed into dislocation dipoles. This transition should be closely related to the large value of the surface energy of M-D. In the case of M-B, the micro-crack begins to propagate at the peak stress and M-B shows the brittle fracture mode with small elongation. On the other hand, in the case of M-D, yielding occurs by dislocations moving from the dislocation dipoles, and then, M-D displays ductile properties with large elongation. Therefore, it

can be confirmed that the $\mu b/\gamma_s$ value can determine the mechanical properties of the simple two-dimensional single-phase materials on the atomic scale. In the following section, we investigate the influence of interfacial mechanical properties on the elongation properties of multilayered composite materials by combining these two virtual materials.

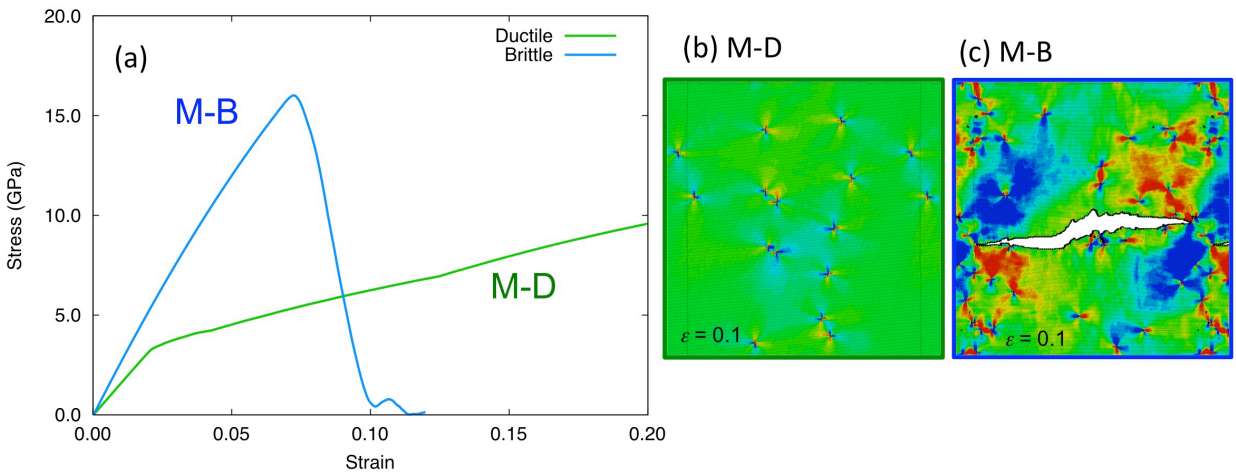

Figure 1. Stress–strain curves of virtual materials with ductile (M-D) and brittle (M-B) properties. (b) and (c) show the shear stress distributions of the single-phase models under tensile loading.

3. Mechanical Properties of Multilayered Composites

3.1. Multilayered Composite Models

Figure 2 shows the analysis model of the multilayered composite consisting of M-B and M-D. The crystal orientation of M-D is rotated 30 degrees from M-B, and thus, the interface has the misalignment angle. Initial micro-cracks are introduced into each phase, and all initial cracks in M-D change their structures into dislocation dipoles after relaxation. Periodic boundary conditions are adopted in all directions and the tensile deformation in the y-direction occurs at a strain rate of 4×10^8 1/s and 10 K.

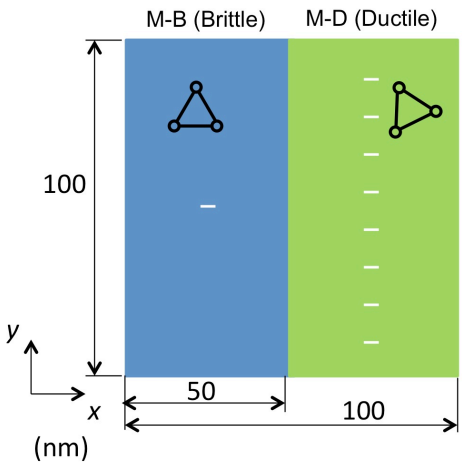

Figure 2. Schematic of the multilayered composite model.

To investigate the influence of interfacial region's mechanical properties on the elongation of multilayered composites, we consider three different types of interatomic bonding strengths between the M-D and M-B phases. The interaction between the M-D and M-B phases $\phi_{BD}(r)$ is calculated by $(\phi_B(r) + \phi_D(r))/A$, where A = 1 (strong bonding strength), A = 2 (normal bonding strength), or A = 5 (weak bonding strength).

3.2. Influence of Interfacial Mechanical Properties on Mechanical Properties of Multilayered Composites

Figure 3 shows the stress–strain curves for single-phase materials and multilayered composite materials with different interfacial bonding strengths. The multilayered composites demonstrate a better combination of strength and elongation than the single-phase materials. It is also apparent that the stronger the interfacial bonding, the larger the peak stress on the multilayered composite model. However, for the elongation, we can see the opposite tendency.

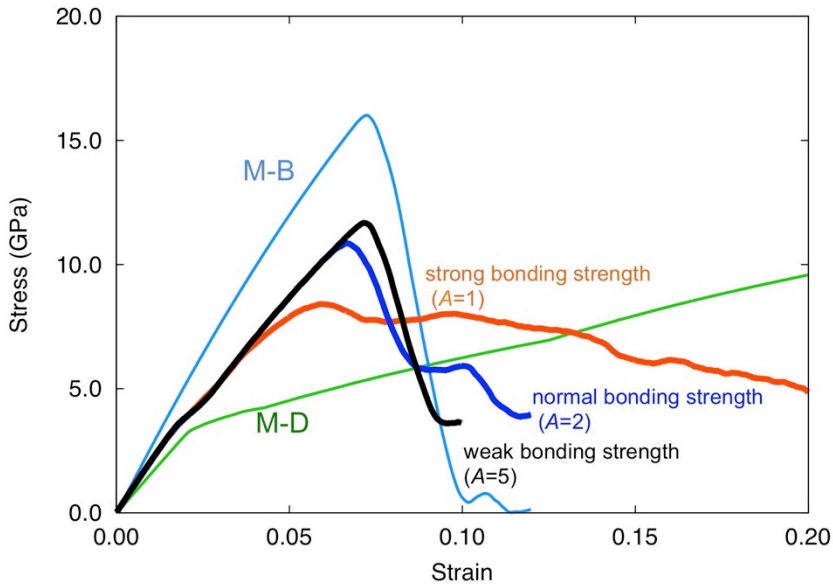

Figure 3. Stress–strain curves of multilayered composites with different interface strengths.

Figure 4 shows the plastic deformation phenomena around the interfacial region with different mechanical properties. Atomic color represents the shear stress component. First, dislocations in the ductile phase move toward the interface in cases of both A = 1 and 5 when ε=0.02. In the case of the weak bonding strength of A = 5, the dislocations are impinged into the interface and further plastic deformation does not occur from the interface. Therefore, initiation of plastic deformation in the brittle phase is delayed. These results show that it is difficult for dislocations from the ductile phase to transmit through the interface when the interfacial region has a weak bonding strength. Consequently, the multilayered model with A = 5 shows high peak stress but small elongation owing to the cleavage of the brittle phase under large tensile stress by stress partitioning between the brittle and ductile phases (see Fig. 4(a)). On the other hand, in the case of a strong bonding strength of A = 1, dislocation emissions can easily propagate from the interface, and thus, plastic deformation propagation occurs from the ductile to brittle phases across the interface. The stored

elastic energy in the brittle phases can be released by the plastic deformation. Therefore, it is not easy to reach the critical stress for the cleavage fracture in the brittle phase (see Fig. 4(b)). As a result, the multilayered model with a strong interfacial bonding strength, namely with the interface having the role of the dislocation source, shows much better ductility than the model with a weak interfacial bonding strength. These results imply that it is important to control the interfacial structure to design the multilayered composite metals with coexistence of strength and ductility.

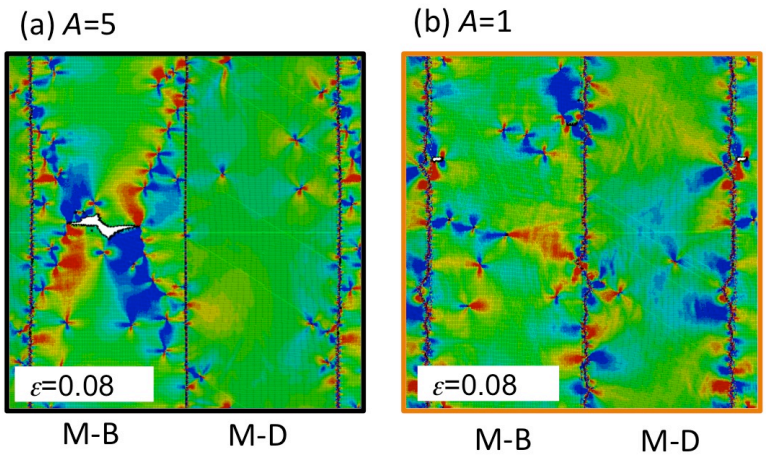

Figure 4. Plastic deformation phenomena around the interface with different mechanical properties.

3.3. Discussion

Heavily drawn pearlitic steel wires having high tensile strength but small elongation exhibit cementite decomposition at the vicinity of the interfacial region. On the other hand, cold-drawn pearlitic steel aged at 698 K exhibits large uniform elongation [2] and the cementite decomposition recovers. This suggests that the interfacial structures between cementite and ferrite phases change by cementite decomposition due to the equilibrium interfacial structure having the maximum solubility of carbon in both phases. In particular, the role of the interface in plastic phenomena in heavily drawn pearlitic steel wires could change from that in aged pearlitic steel.

In our atomic simulations, the multilayered composite model, having a small dislocation source ability of the interface, showed a smaller elongation property than the model having a high dislocation source ability of the interface. This result implies the possibility that the interface structure after cementite decomposition also has a smaller dislocation source ability than that of aged pearlitic steels.

4. Conclusion

We investigated the influence of interfacial mechanical properties on the elongation of multilayered composite metals through molecular dynamics simulations. We designed two-dimensional virtual materials having brittle or ductile properties by controlling the parameters of the Morse interatomic potential. We demonstrated that multilayered composite models with ductile and brittle phases have a superior strength–ductility relationship than single-layered models and that this relationship is closely related to interfacial mechanical properties. These results imply that it is important to

control interfacial properties when designing multilayered composite metals with coexistence of strength and ductility.

Acknowledgments

This research was supported by Japan Science and Technology Agency (JST) under Collaborative Research Based on Industrial Demand "Heterogeneous Structure Control: Towards Innovative Development of Metallic Structural Materials."

References

[1] Y. J. Li, P. Choi, S. Goto, C. Borchers, D. Raabe, R. Kirchheim, Acta Materialia, 60 (2012) 4005-4016.
[2] Y. Tomota, P. Lukas, D. Neov, S. Harjo, Y. R. Abe, Acta Materialia, 51 (2003) 805-817.
[3] I. –H. Lin, Journal of Materials Science Letter, 2 (1983) 295.

Failure mode transition of Zr-based bulk metallic glass

Fan Zeng[1], LanHong Dai[1,*]
[1]State Key Laboratory of Nonlinear Mechanics, Institute of Mechanics,
Chinese Academy of Sciences, Beijing 100190, PR China
* Corresponding author: lhdai@lnm.imech.ac.cn

Abstract

$Zr_{41.2}Ti_{13.8}Cu_{10}Ni_{12.5}Be_{22.5}$ (Vit 1) bulk metallic glass (BMGs) exhibits different failure modes under low strain rate ($10^{-4}s^{-1}$) and high strain rate ($10^{3}s^{-1}$) uniaxial compression at room temperature. Quasistatically deformed samples often fail along one dominant shear band and fracture into two large millimeter-scale blocks, whereas at impulsive loading, the samples usually break into many small scale fragments with rough fracture surfaces, such as non-uniformly distributed vein patterns and micro multiple shear bands (network-like shear bands). A theoretical model that takes into account the balance between the energy dissipation within shear band and the stored energy released in the vicinity of the shear band to fuel shear localization is developed. Furthermore, the underlying mechanisms of one dominant shear band and network-like multiple shear bands controlling the failure mode transition are revealed.

Keywords: Compression test; Bulk metallic glass; Failure mode; Shear bands.

1. Introduction

Because of their unique properties such as high room-temperature(RT) strength and large elastic limit, bulk metallic glasses (BMGs) as a potential engineering and structural material have triggered extensive scientific interest over the years [1-5].However, the poor macroscopic plastic deformation ability of BMGs limits their application. Therefore, the need for a more fundamental understanding of the deformation and failure mechanisms in BMGs has motivated numerous experimental investigations, especially under high strain rate. It has been found that some tough amorphous metals, such as Zr- and Pd-based metallic glasses, often fail along a narrow shear band both under quasi-static and dynamics compressive loading[6-10]. But some authors reported that the dynamically BMG samples fractured into several fragment similar to the failure behavior of some brittle Mg-,Fe-,and Co-based metallic glasses subjected to quasi-static loading[11, 12]. In this paper, we find that the failure mode of $Zr_{41.2}Ti_{13.8}Cu_{10}Ni_{12.5}Be_{22.5}$ (Vit1) bulk metallic glass (BMGs) was dependent of the strain rate in compression at room temperature. And, we develop local evolution model of the shear band, as to why Zr-based metallic glass exhibit the different failure modes.

2. Experimental

The $Zr_{41.2}Ti_{13.8}Cu_{10}Ni_{12.5}Be_{22.5}$ bulk metallic glass was prepared by arc melting high purity composition elements together in a Ti-gettered purified argon atmosphere. Each ingot was re-melted several times to ensure homogeneity and then prepared by suction-casting the molten alloy into a copper mold to form rods (Φ5×100mm). Quasi-static and dynamic compression tests were performed on a MTS-810 material testing machine and SHPB using cylinders 5 mm in diameter and 7.5 mm height. In quasi-static compressive test, the strain rate was fixed at $1.0\times10^{-4}s^{-1}$. In dynamic compression, the strain rate ranged from $1.0\times10^{3}s^{-1}$ to $2.5\times10^{3}s^{-1}$. After testing, the scanning electron microscopy (SEM) was used to characterize the fracture morphology of all specimens.

3. Results

The material exhibits the maximum fracture strength~1.9GPa and less macroscopic plastic strain at a quasi-static strain rate. It is of interest to note that the fracture strength markedly decreases at high strain rates, which agree well with the previous observations for other Zr-based [8, 13] BMGs. Another interesting observation is that quasistatically deformed samples fractured into two large millimeter-scale blocks, whereas at impulsive loading, the samples broke into many small scale fragments. Fractured samples were examined to understand the failure behavior by SEM. The samples fracture along a single plane at low strain rates, indicating a major shear band dominates the final fracture process. And vein-like pattern spreads over the whole fracture surface and extends in a uniform direction, corresponding to the propagation direction of the primary shear band. On the other hand, the considerable randomly distributed vein-like patterns, corresponding to the different propagation directions of shear bands on surface of fragments formed in dynamic loaded case show that multiple shear bands occur and dominate failure process. The network-like multiple shear bands are observed in the surface of the small fragments. Therefore, the transition from one dominant shear band to network-like multiple shear bands results in the different failure modes. But the mechanisms of transition are unknown.

4. Discussion

4.1 Local evolution model for shear band

Room-temperature plastic deformation of metallic glasses has been known to be accomplished through shear bands in which plastic flow driven mainly by shear stresses is localized within a nanoscale zone [14, 15]. As is known, the shear-banding process is a dissipation system [7, 16-20].There are three types of diffusion, i.e. conventional momentum/viscous, thermal/energy and special free-volume dissipation within the propagation shear band. In our previous work, the coupled effect of free-volume softening and thermal softening upon shear-banding evolution in metallic glasses was discussed [6, 9, 21, 22]. Nanometer-scale defects[23], a density fluctuation[24] and then a viscosity fall[9, 10, 18, 25] usually are results of the shear band propagation, suggesting the coalescence of free volume in the band. When the shear stress τ at the shear band vanishes (or the shear displacement ψ reaches a critical ψ_c), the shear band is regarded as being fully mature, and a finite amount of energy is expended. Zhang *et al* [18] proposed a micromechanical model based on momentum diffusion controlling shear band spacing. Additionally, Lewandowski and Greer[26, 27] have experimentally shown a significant temperature rise within and around the shear bands using tin-coated specimens, and some authors [27-29] observed the heat-affected zone (HAZ) around the shear band due to heat conduction which may play an important role in shear-band propagation. As discussed above, momentum and thermal derived from shear band spread to the neighboring elastic medium. Thus shear stress release also occurs in the undisturbed medium and stored energy is released. Based on these analyzes, a theoretical model that takes into account the balance between the energy dissipation within shear band and the stored energy released in the vicinity of the shear band to fuel shear localization is developed.

4.2 Shear-band dissipation energy

It has been demonstrated that the following equations properly govern the shear banding in BMGs [1, 9, 30]:

$$\rho \frac{\partial \dot{\gamma}_b}{\partial t} = \frac{\partial^2 \tau_b}{\partial y^2} \tag{1}$$

$$\tau_b \frac{\partial \gamma_b}{\partial t} = \rho c \frac{\partial \theta_b}{\partial t} - \lambda \frac{\partial^2 \theta_b}{\partial y^2} \tag{2}$$

$$G = \frac{\partial \xi_b}{\partial t} - D \frac{\partial^2 \xi_b}{\partial y^2} \tag{3}$$

where γ_b is the shear strain , $\dot{\gamma}_b = \partial\gamma/\partial t$ is the strain rate, θ_b the temperature, ξ_b the concentration of free volume and G the net generation rate of free volume.

In order to capture free-volume and thermal softening nature, the elementary constitutive relation,

$$\tau_b = \tau_y (1 - \alpha\upsilon - \beta\theta) \tag{4}$$

in terms of flow stress τ_y ,free-volume softening coefficient α , thermal softening coefficient β , free-volume concentration increment $\upsilon = \xi - \xi_0$ from initial value ξ_0 and temperature rise $\theta = T - T_0$ with an initial temperature T_0 .

The critical dissipated energy Γ_c within shear band as the deformation proceeds to a critical displacement ψ_c , is introduced as:

$$\Gamma_c = \left(\tau_y \psi_c\right)/2 \tag{5}$$

Consistent with concepts of fracture mechanics, Γ_c is the energy per unit area within one-half of the shear band.

Combining Eqs. (1)—(5) results in an specific expression of the critical dissipation energy Γ_c omitted here.

4.3 Stored energy in the heat-affected zone and momentum diffusion zone

As we mentioned above, during the propagation process of the shear band, thermal diffusion and momentum diffusion out of the band and into neighboring medium both lead to stress relaxation and then energy residing in the material release to fuel the shear-band process [31]. Energy near the shear band resides as both kinetic energy and elastic strain energy. The cumulative energies of each contribution as a function of width of thermal or momentum diffusion region. The shear-banding event in BMGs is different from ASBs in crystalline alloys. Both low and high strain rate process can produce significant localization of plastic flow. And heat would not be trapped in the shear band. Now the question is in what situation, the shear-band is fueled predominantly by the momentum diffusion or the thermal diffusion region. As a result of thermal diffusion, energy residing in the material near the shear-band would be release. We discover that stored energy almost all releases due to the momentum diffusion at high strain rates; nevertheless, it doesn't reduce at low strain rates, considering the momentum equation (1) of the material near the shear band. Some investigators have attributed shear bands spacing to the momentum diffusion [18, 32-34]. Since the momentum diffusion is much faster than thermal diffusion, momentum diffusion region is much wider than thermal diffusion region. For the high strain rate process, the shear-band is fueled predominantly by the energy E_v of the momentum diffusion region. On the other hand, energy E_h within thermal diffusion region would be the principle energy fueling growth of the shear-band respect to the low strain rate process.

At quasi-static compression loading, the supplied energy, only from elastic strain energy residing in thermal diffusion region, is so smaller than the critical dissipated energy, i.e., $\Gamma_{sc} > \mathrm{E}_h$, that a single nucleated and propagated shear band would dominate and cause a catastrophic shear fracture of the material.

But under the dynamics loading, the strain and kinetic energy together drive the process of the shear-band evolution. Similarly, when one shear band is not sufficient to dissipate the supplied

energy, i.e., $\Gamma_{dc}<E_v$, so that additional shear bands form and subsequently formation of a network of shear-bands induces the fragmentation failure mode of the material.

4.4 Fracture strength

Considering the intrinsic heterogeneity and preexisting flaw resulted from casting, the shear band generates via the cascade of a number of individual atomic jumps around free-volume sites[15] or shear transformation zones[14, 35] under the action of a stress smaller than macro yielding stress [2, 36]. Under dynamic compression, the formation and accumulation of damage resulted from network-like multiple shear bands events, causes the materials would loose bearing load earlier, however, the materials could not bear load until the stress level achieves macroscopic yield situation under quasistatic compression.

5 Conclusion

The mechanical properties of the $Zr_{41.2}Ti_{13.8}Cu_{10}Ni_{12.5}Be_{22.5}$ bulk metallic glass were investigated under uniaxial compression at strain rates from $10^{-4}s^{-1}$ to $10^{3}s^{-1}$. The compressive failure process consists of typical shear fracture and fragmentation fracture, depending on the loading strain rate. The failure mode changes dramatically as loading strain rate is increased into high strain rate range. The different modes indicate that different mechanisms control fracture. Considering the balance between the energy dissipation within shear band and the energy residing within the vicinity of the shear band released to fuel shear localization, one dominant shear band controls the failure process at low strain rate, however, that is controlled by network-like multiple shear bands at high strain rate. The relationship between the failure mode and fracture strength is briefly discussed.

Acknowledgments

Financial support is from National Key Basic Research Program of China (Grant No. 2012CB937500), the NSFC (Grants Nos. 11202221, 11132011, 11002144 and 11021262), and the National Natural Science Foundation of China-NSAF (Grant No: 109761010).

References

[1] L.H. Dai, Shear Banding in Bulk Metallic Glasses. in: Y.L. Bai, B.Dodd (2nd Eds.) Adiabatic Shear Localization : Frontiers and Advances. Elsevier, 2012, pp. 311—361
[2] T. Mukai, T.G. Nieh, Y. Kawamura, A. Inoue, K. Higashi, Effect of strain rate on compressive behavior of a Pd40Ni40P20 bulk metallic glass. Intermetallics, 10 (2002) 11-121071-1077.
[3] Y. Yang, J.C. Ye, J. Lu, Y.F. Gao, P.K. Liaw, Metallic Glasses: Gaining Plasticity for Microsystems. Jom, 62 (2010) 293-98.
[4] M. Ashby, A. Greer, Metallic glasses as structural materials. Scripta Mater, 54 (2006) 3321-326.
[5] C. Schuh, T. Hufnagel, U. Ramamurty, Mechanical behavior of amorphous alloys. Acta Mater, 55 (2007) 124067-4109.
[6] L. Liu, L. Dai, Y. Bai, B. Wei, Initiation and propagation of shear bands in Zr-based bulk metallic glass under quasi-static and dynamic shear loadings. J Non-Cryst Solids, 351 (2005) 40-423259-3270.
[7] L.H. Dai, Y.L. Bai, Basic mechanical behaviors and mechanics of shear banding in BMGs. Int J Impact Eng, 35 (2008) 8704-716.
[8] Y. Xue, H. Cai, L. Wang, F. Wang, H. Zhang, Effect of loading rate on failure in Zr-based bulk

metallic glass. Mater Sci Eng A, 473 (2008) 1-2105-110.
[9] M.Q. Jiang, L.H. Dai, On the origin of shear banding instability in metallic glasses. J Mech Phys Solids, 57 (2009) 81267-1292.
[10] S.X. Song, T.G. Nieh, Direct measurements of shear band propagation in metallic glasses – An overview. Intermetallics, 19 (2011) 121968-1977.
[11] P. Wesseling, T.G. Nieh, W.H. Wang, J.J. Lewandowski, Preliminary assessment of flow, notch toughness, and high temperature behavior of CU60Zr20Hf10Ti10 bulk metallic glass. Scripta Materialia, 51 (2004) 2151-154.
[12] D.H. Xu, G. Duan, W.L. Johnson, C. Garland, Formation and properties of new Ni-based amorphous alloys with critical casting thickness up to 5 mm. Acta Materialia, 52 (2004) 123493-3497.
[13] X. Gu, T. Jiao, L.J. Kecskes, R.H. Woodman, C. Fan, K.T. Ramesh, T.C. Hufnagel, Crystallization and mechanical behavior of (Hf, Zr)–Ti–Cu–Ni－Al metallic glasses. J Non-Cryst Solids, 317 (2003) 1-2112-117.
[14] A.S. Argon, PLASTIC-DEFORMATION IN METALLIC GLASSES. Acta Metall, 27 (1979) 147-58.
[15] F.Spaepen, A microscopic mechanism for steady state inhomogeneous flow in metallic glasses. Acta Mater, 23:615 (1977).
[16] R.D. Conner, W.L. Johnson, N.E. Paton, W.D. Nix, Shear bands and cracking of metallic glass plates in bending. J Appl Phys, 94 (2003) 2904.
[17] R.D. Conner, Y. Li, W.D. Nix, W.L. Johnson, Shear band spacing under bending of Zr-based metallic glass plates. Acta Mater, 52 (2004) 82429-2434.
[18] H. Zhang, S. Maiti, G. Subhash, Evolution of shear bands in bulk metallic glasses under dynamic loading. J Mech Phys Solids, 56 (2008) 62171-2187.
[19] M.Q. Jiang, L.H. Dai, Formation mechanism of lamellar chips during machining of bulk metallic glass. Acta Mater, 57 (2009) 92730-2738.
[20] A. Molinari, Collective behavior and spacing of adiabatic shear bands. J Mech Phys Solids, 45 (1997) 91551-1575.
[21] X.Gu, K.J.T.Livi, T.C.Hufnagel, Mater.Res.Soc.Proc.754:CC7.9.1, (2003).
[22] M.Q. Jiang, L.H. Dai, Shear-band toughness of bulk metallic glasses. Acta Mater, 59 (2011) 114525-4537.
[23] J. Li, F. Spaepen, T.C. Hufnagel, Nanometre-scale defects in shear bands in a metallic glass. Philos Mag, 82 (2002) 132623-2630.
[24] A. Furukawa, H. Tanaka, Inhomogeneous flow and fracture of glassy materials. Nature Materials, 8 (2009) 7601-609.
[25] S.X. Song, T.G. Nieh, Flow serration and shear-band viscosity during inhomogeneous deformation of a Zr-based bulk metallic glass. Intermetallics, 17 (2009) 9762-767.
[26] J.J. Lewandowski, A.L. Greer, Temperature rise at shear bands in metallic glasses. Nature Materials, 5 (2006) 115-18.
[27] D.B. Miracle, A. Concustell, Y. Zhang, A.R. Yavari, A.L. Greer, Shear bands in metallic glasses: Size effects on thermal profiles. Acta Mater, 59 (2011) 72831-2840.
[28] B. Yang, C.T. Liu, T.G. Nieh, M.L. Morrison, P.K. Liaw, R.A. Buchanan, Localized heating and fracture criterion for bulk metallic glasses. J Mater Res, 21 (2006) 04915-922.
[29] H. Guo, J. Wen, N.M. Xiao, Z.F. Zhang, M.L. Sui, The more shearing, the thicker shear band and heat-affected zone in bulk metallic glass. J Mater Res, 23 (2008) 082133-2138.
[30] L.F. Liu, L.H. Dai, Y.L. Bai, B.C. Wei, G.S. Yu, Strain rate-dependent compressive deformation behavior of Nd-based bulk metallic glass. Intermetallics, 13 (2005) 8827-832.
[31] D.E. Grady, Adiabatic shear failure in brittle solids. Int J Impact Eng, 38 (2011) 7661-667.
[32] Y.L.Bai, B.Dodd. Vol. Adiabatic Shear Localization.Pergamon Press,Oxford. 1992.
[33] D.E. Grady, M.E. Kipp, THE GROWTH OF UNSTABLE THERMOPLASTIC SHEAR

WITH APPLICATION TO STEADY-WAVE SHOCK COMPRESSION IN SOLIDS. J Mech Phys Solids, 35 (1987) 195-118.

[34] D.E. Grady, PROPERTIES OF AN ADIABATIC SHEAR-BAND PROCESS ZONE. J Mech Phys Solids, 40 (1992) 61197-1215.

[35] M.L. Falk, J.S. Langer, Dynamics of viscoplastic deformation in amorphous solids. Phys Rev E, 57 (1998) 67192-7205.

[36] W.D. Liu, K.X. Liu, Notable internal thermal effect on the yielding of metallic glasses. Appl Phys Lett, 100 (2012) 14141904.

On bifurcation of homogenous deformation in metallic glasses

Yan Chen & Lanhong Dai*

State Key Laboratory of Nonlinear Mechanics, Institute of Mechanics,
Chinese Academy of Science, Beijing, 100190, China
* Corresponding author: lhdai@lnm.imech.ac.cn

Abstract At temperatures well below the glass transition and at high stresses, the homogenous deformation in metallic glasses (MGs) usually develops to a critical point, at which the discontinuity in deformation rate is incipient across nano-scale shear bands. However, such a bifurcation condition of homogeneous deformation concerning the unique properties of MGs is still lacking for general stress state. In this paper, a new constitutive is introduced for MGs accounting for the pressure-sensitivity, dilatancy and structural evolution; the shear banding is regarded as the appearance of instability in the constitutive description of inelastic deformation. Tying the bifurcation theory to the new model, the general condition of deformation localization is derived. The shear band initiation and failure orientation are then precisely predicted for MGs by constructing a bridge between the microscopic origin and the loss-of-ellipticity instability in the constitutive law in continuum mechanics.

Keywords Metallic glasses, Bifurcation, Shear band

1. Introduction

Metallic glass (MG) represents a relatively young class of structural materials with a combination of excellent properties. Due to their random atomic structure, plastic deformation in MGs is usually accommodated by localized shear bands. These nanoscale shear bands as a precursor of crack lead to a fast fracture of material, which presents little plasticity at room temperature. Being a key process to understand the underlying plasticity of MGs, shear banding, including its origin and propagation, has attracted lots of attention for last decades[1-5].

Although the precise physical picture of how it originates from the internal structure remains elusive, it is well accepted that the shear banding of MGs occurs as a consequence of formations and self-organizations of shear plastic flow events [3, 6-8]. Those flow events are essentially local arrangements of atoms around free volume sites, termed shear transformation zones (STZs) or flow defects [9-12]. The transition from local plastic events to macroscopic shear-band instability is dominated by the stress-driven free volume softening and assisted by thermal softening [1, 2, 13-15]. Regardless of micro-mechanisms, at the continuum level, the shear banding, a physically material unstable event, can be regarded as the appearance of instability in the macroscopic constitutive description of inelastic deformation [16-19]. It is accepted that the homogenous deformation in MGs develops to a critical point, at which the discontinuity in deformation rate is incipient across nano-scale shear bands, at temperatures well below the glass transition and at high stresses. Tying the bifurcation theory to a pressure-sensitive dilatant constitutive model, Rudnicki and Rice [17] derived both the general conditions for shear localization and the orientation of shear band in the stress space. Based on this, the shear band direction as an important feature in shear band formation was predicted for MGs by Gao et al. [20], which closely depends on the pressure coefficient, the dilatancy factor, and etc. In nature, shear banding as a material instability is greatly correlated to atomic structural change. Such a picture is also realized by Ruan et al. [21] who embody the atomic structural change by the plastic strain and the associated dilatation for MGs. On the other hand, through perturbation analysis of constitutive instability, the conditions for the shear instability for a given stress state (usually simple shear) can be also obtained for MGs [1, 2, 13]. These analyses confirm the important role of free volume, as a state variable, in the constitutive instability. However, such a bifurcation condition of homogeneous deformation concerning the unique

properties of MGs is still lacking for general stress state. In this paper, we attempt to derive the critical condition of the shear band initiation and direction for MGs by constructing a bridge between the microscopic origin and the loss-of-ellipticity instability in the constitutive law in continuum mechanics.

2. Theoretical model

For initial homogeneously deformed material, the loss of constitutive stability will cause strain localization into a shear band [16-19]. Therein, the homogeneous deformation develops to a bifurcation point, at which the discontinuity in deformation rate is incipient across a band. As to MGs, two internal factors are critical for the shear instability, namely, free volume and thermo [1, 2, 13-15]. The onset of shear banding in MGs can be reasonably described as a result of constitutive instability induced by dramatic change of internal state variables.

2.1 Constitutive model

For the instability analysis, a proper constitutive is required for MGs. In this section, a new constitutive model is developed for MGs due to the following considerations. At macroscopic scale, MGs exhibit inherent pressure sensitivity and shear-dilatancy during plastic deformation, which usually renders a non-associated flow. Microscopically, the nucleation and coalescence of free volume decreases the flow stress of MGs and further leads to shear localization. This is actually quite similar to the void evolution mechanism in the continuum damage mechanics. One of the best known micro-mechanical models is that of Gurson [22], who studied the plastic flow of a void-containing material and established a yielding function reflecting the softening effect due to the presence of voids. Here, by introducing the free volume evolution into the framework of continuum mechanics, we can establish a new constitutive model to comprehensively and satisfactorily describe the deformation in MGs. “Free volume” as the topological disorder in MGs, can be simply considered as randomly distributed atomic voids in material. Treating those voids to be spherical, the yield function of Gurson is reasonably extended to MGs by taking into the pressure sensitivity of the matrix. The free volume evolution is assumed to obey the self-consistent dynamic free volume model proposed by Johnson et al.[23]. The thermal effect is neglected since the structural disorder induced softening precedes thermal softening at the origin of the shear banding [13], especially for the present quasi-static loading case.

For a pressure-independent material containing spherical voids, Gurson model gives the following yield function [22]:

$$F = \left(\frac{\sigma_e}{\sigma_y}\right)^2 + 2\upsilon_f \cosh\left(\frac{3\sigma_m}{2\sigma_y}\right) - \upsilon_f^{\,2} - 1 = 0\,, \tag{1}$$

where $\sigma_e = \sqrt{3s_{ij}s_{ij}/2} = \sqrt{3J_2}$ ($s_{ij} = \sigma_{ij} - \sigma_m\delta_{ij}$) is the effective stress, $\sigma_m = \sigma_{ii}/3$ is the mean stress, υ_f is the current fraction of voids, equivalent to free volume concentration, and σ_y is the yield stress of the matrix. Numerous studies have demonstrated clearly that pressure affects the yield behavior of MGs [24-27]. This is easily reflected by the tension-compression asymmetry of failure [28]. Since the Gurson model considers the von Mises matrix, an additional pressure-dependent term i.e. $\alpha\sigma_m$, should be taken into account (analogous to the Drucker-Prager criterion) for a proper description of MGs. For simplicity, one can modify the above criterion as below by neglecting the minor term $(1-\cosh^2(3\sigma_m/2\sigma_y))\upsilon_f^{\,2}$. We define the initial free volume in

MGs to be υ_0 . The corresponding shear strength σ_0 satisfies $\sigma_0 = \sigma_y\left(1-\upsilon_0 \cosh\left(3\sigma_m/2\sigma_y\right)\right)/\sqrt{3}$ .Therefore, the new yield criterion can be obtained from Eq.(1) as

$$\Phi = \sqrt{J_2} + \alpha\sigma_m - \sigma_0\left(1-\frac{\Lambda}{\operatorname{sech}\left(3\sigma_m/2\sigma_y\right)-\upsilon_0}\right), \tag{2}$$

where $\Lambda = \upsilon_f - \upsilon_0$ is the free volume increment. It is obvious that the shear strength is softening with increasing free volume concentration.

Following the self-consistent dynamic free volume model [23], the local time rate of change of the free-volume concentration is

$$\dot{\upsilon}_f = \chi\left(R\dot{\varepsilon}_e^p - \frac{\Lambda}{\sigma_e/\left(G\dot{\varepsilon}_e^p\right)}\right), \tag{3}$$

where χ is a material parameter of order unity, R is a free-volume creation function defining the free volume produced by a unit shear strain and is given by $G\Lambda/\sigma_{ss}$ (σ_{ss} is the effective stress at steady state) [29], $\dot{\varepsilon}_e^p = \sqrt{2\dot{e}_{ij}^p\dot{e}_{ij}^p/3}$ ($\dot{e}_{ij}^p = \dot{\varepsilon}_{ij}^p - \dot{\varepsilon}_{kk}^p\delta_{ij}/3$) is the effective plastic shear strain rate, σ_e is the effective stress, and G is the shear modulus at room temperature.
Considering the shear dilatancy inherent in the deformation of MGs, we introduce the dilatancy factor β and invoke Q as the plastic potential as below

$$Q = \sqrt{J_2} + \beta\sigma_m - \sigma_0\left(1-\frac{\Lambda}{\operatorname{sech}\left(3\sigma_m/2\sigma_y\right)-\upsilon_0}\right). \tag{4}$$

When $\beta \neq \alpha$, the deformation is non-associative. The deviatoric components of the plastic deformation strain tensor are obtained as

$$\dot{e}_{ij}^p = \frac{1}{H}\frac{\partial Q}{\partial\sigma_{ij}}\frac{\partial\Phi}{\partial\sigma_{kl}}\dot{\sigma}_{kl}, \tag{5}$$

where H is the plastic hardening modulus.

If we adopt the spineless strain rate, the generalized constitutive relation is recast as

$$D_{ij} = \frac{\overset{\nabla}{s}_{ij}}{2G} + \frac{s_{ij}}{2H\sqrt{J_2}}\left(\frac{s_{kl}}{2\sqrt{J_2}}\overset{\nabla}{\sigma}_{kl} + \frac{\alpha'}{3}\overset{\nabla}{\sigma}_{kk}\right) + \frac{\beta'}{3H}\left(\frac{s_{kl}}{2\sqrt{J_2}}\overset{\nabla}{\sigma}_{kl} + \frac{\alpha'}{3}\overset{\nabla}{\sigma}_{kk}\right)\delta_{ij} + \frac{\overset{\nabla}{\sigma}_{kk}}{9K}\delta_{ij}, \tag{6}$$

where $\overset{\nabla}{\sigma}_{ij} = \dot{\sigma}_{ij} + \Omega_{ik}\sigma_{kj} + \Omega_{ki}\sigma_{jk}$ is the Jaumann rate of the true stress σ_{ij} , $\alpha' = \alpha + \sqrt{3}\upsilon_f \sinh\left(3\sigma_m/2\sigma_y\right)/2$, $\beta' = \beta + \sqrt{3}\upsilon_f \sinh\left(3\sigma_m/2\sigma_y\right)/2$, and $H = \frac{\sigma_0\chi G\Lambda}{\sqrt{3}\left(\operatorname{sech}\left(3\sigma_m/2\sigma_y\right)-\upsilon_0\right)}\left(\frac{1}{\sqrt{3J_2}} - \frac{1}{\sigma_{ss}}\right)$.
The instantaneous rate of the deformation and the spin tensor are respectively $D_{ij} = \left(\partial v_i/\partial x_j + \partial v_j/\partial x_i\right)/2$, and $\Omega_{ij} = \left(\partial v_i/\partial x_j - \partial v_j/\partial x_i\right)/2$ .The stress rate and deformation rate are related by

$$\overset{\nabla}{\sigma}_{ij} = L_{ijkl}D_{kl}, \tag{7}$$

where L_{ijkl} is the elasto-plastic modulus tensor.

2.2 Constitutive instability analysis

We ascribe the initiation of shear band in MGs to bifurcation arisen from the constitutive description of the homogeneous deformation. The shear bands inclination is obtained at the onset of instability. An initially uniform deformation field of a homogeneous MG plate is considered, see Fig. 1. The constitutive instability is viewed as a formation of a narrow localized band of deformation within the plate under external load [17]. Use rectangular Cartesian coordinates (x_1, x_2, x_3), such that the x_2-direction is normal to the planes bounding the band. Outside the band the velocity field remains uniform and within it varies only in the direction normal to the band. Thus, the non-uniformities in the rate of deformation field are expressed as

$$\Delta\left(\partial v_i / \partial x_j\right) = g_i\left(x_2\right)\delta_{j2}, \ (i, j) = 1, 2, 3 \quad , \tag{8}$$

where v_i is a velocity component, Δ denotes the difference between the local field inside the band and the uniform field outside, and the functions g_i of x_2 are nonzero only within the band.

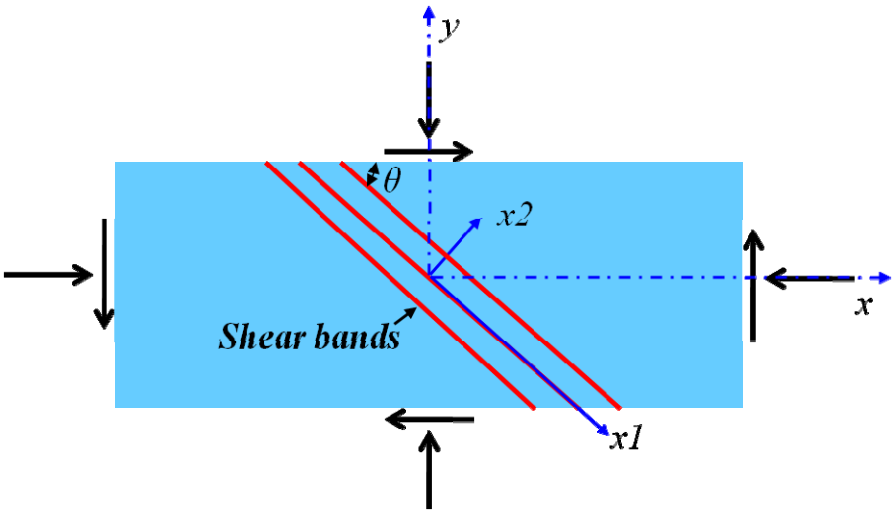

Fig.1 Illustration of shear band localization.

The condition $\partial\sigma_{ij}/\partial x_i = 0$ and $\partial\left(\partial\sigma_{ij}/\partial t\right)/\partial x_i = 0$ make sure that the stress equilibrium continues to be satisfied at the inception of bifurcation. The stress rates at incipient localization from the original uniform field is thus following

$$\partial\dot{\sigma}_{ij}/\partial x_i = 0, \tag{9}$$

where the superposed dot denotes its material time rate. The condition of the continuity of the stress rate at the band interfaces can be expressed as

$$\Delta\dot{\sigma}_{2j} = 0, \quad j = 1, 2, 3. \tag{10}$$

Since $\dot{\sigma}_{ij}$ is not invariant under rigid rotations, by introducing the Jaumann (co-rotational) stress rate $\overset{\nabla}{\sigma}_{ij} = \dot{\sigma}_{ij} - \sigma_{ip}\Omega_{pj} - \sigma_{jp}\Omega_{pi}$. Eq. (10) can be regarded as a set of three quasi-homogeneous equations in g_1, g_2, g_3 and the conditions for bifurcation are merely those for which solutions other than $g_1 = g_2 = g_3 = 0$ exist.

If at the bifurcation of deformation-rates, the values L_{ijkl} remain the same inside and outside the band, the following difference can be formed based on Eq. (7):

$$\Delta\overset{\nabla}{\sigma}_{ij} = L_{ijkl}\Delta D_{kl} = L_{ijk2}g_k. \tag{11}$$

Combining Eqs. (10) and (11) yields a set of linear, homogeneous equations in g' s ,

$$L_{2jk2}g_k = R_{jk}g_k, \quad j = 1, 2, 3, \tag{12}$$

The above equation have nontrivial solution when

$$\det\left|L_{2jk2} - R_{jk}\right| = 0 . \tag{13}$$

Eq. (13) represents the condition for the deformation bifurcation when a non-uniform ($g_i \neq 0$) continuation of deformation is possible. The bifurcation condition relates the free volume concentration at localization Λ_c to the parameters *G*, *K*, *α*, *β* and to the prevailing stress state. Since the stress to modulus ratio is significantly small, R_{jk} introduced by the co-rotational stress rate are neglected in Eq. (13). We can then obtain the instability condition as below

$$\Lambda_c = \left(-\sqrt{B^2 - 4C_1^2 D} - B\right) \Big/ 2C_1^2 , \tag{14}$$

where $B = \sqrt{3}C_1\left(\frac{2(\alpha+\beta)}{3} - \frac{s_{22}}{\sqrt{J_2}}\right) - \frac{\chi\sigma_0 C_2}{\sqrt{3}}\left(\frac{4G}{3K}+1\right)\left(\frac{1}{\sigma_{ss}} - \frac{1}{\sqrt{3J_2}}\right) + 2\upsilon_0 C_1^2$,

$D = \left(\frac{4G}{3K}+1\right)\left(1 - \frac{s_{21}^2 + s_{23}^2}{J_2}\right) - \frac{G}{K}\frac{s_{22}^2}{J_2} + (\alpha+\beta)\left(\frac{2\upsilon_0 C_1}{\sqrt{3}} - \frac{s_{22}}{\sqrt{J_2}}\right) + \frac{4\alpha\beta}{3} - \sqrt{3}\upsilon_0 C_1 \frac{s_{22}}{\sqrt{J_2}} + \upsilon_0^2 C_1^2$ and

$C_1 = \sinh(3\sigma_m / 2\sigma_y)$, $C_2 = 1\big/\left(\cosh^{-1}(3\sigma_m/2\sigma_y) - \upsilon_0\right)$.

It means that, shear localization starts when the free volume increment Λ reaches a critical value Λ_c given by Eq. (14). Λ_c is a function of the orientation of the potential plane of localization, indicating it would vary from place to place. At a fixed stress state, the shear instability will first occur at the location or along the direction where the minimum of Λ_c is required. For the stress state as illustrated in Fig. 1, the preferential direction for shear banding should exist, which satisfies $\partial\Lambda_c / \partial\theta = 0$ and the corresponding θ denotes the shear band angle. The hardening modulus *H* is a function of Λ. The increase of free volume causes a gradual loss of load-carrying capacity of MGs, corresponding to a decreasing *H*. The minimal Λ_c for preferential shear localization is actually consistent with the maximum *H* first meeting the instability condition as proposed by Rudnicki and Rice [17].

3. Discussion

According to the theoretical model above, the constitutive instability occurs in MGs when the free volume increment Λ satisfies the condition as described by Eq. (14), which gives birth to shear band in original homogenous materials. The onset of condition and the incipience direction for MGs under pure bending will be specifically discussed next, where both tension and compression cases can be included. The related material properties of Vit-1 MGs and parameters used in the subsequent analysis have been adopted from elsewhere [23, 29, 30]: Shear strength $\sigma_0 = 1GPa$, Young's modulus $E = 96GPa$, Poison ratio $\nu = 0.36$, pressure sensitive factor $\alpha = 0.1$, density $\rho = 6120 Kg/m^3$, $\chi = 1.5$, $d_1 = 46981$, $d_2 = 162$, $T_{ref} = 672\text{K}$, $T = 300\text{K}$, and $\sigma_{ss} = 0.36GPa$.

The critical free volume increment Λ_c versus θ for α=0.1 and different β can be plotted by Fig. 2. Under both tension and compression, the critical Λ_c is found to reach a minimum at the directions around $\theta = 45^\circ$ (within the green circle), indicating that the free volume required to cause a shear instability is smallest along these directions and thus shear band will preferentially initiate. With a gradual deviation from these angles, the Λ_c for shear banding increases, denoting a smaller

possibility of shear band formation. As is known, $\theta = 45^{\circ}$ corresponds to the direction of the maximum shear stress, which is usually the shear direction of crystalline alloys. However, shear bands for MGs are predicted to form at the angles normally >45° in tension while <45° in compression (see Fig. 2), consistent with the experimental observations in MGs [28]. This deviation of shear direction from the maximum shear stress can be partly attributed to the pressure effect which usually cannot be ignored in MGs [24-27]. In addition, the Λ_c also shows an obvious dependence on dilatancy factor β. With increasing β, the minimum value of Λ_c decreases in tensile case while increases in compressive case. It means that shear dilatancy promotes the shear banding in tension while impedes that in compression. In Fig. 2, the minimum point of Λ_c in tension is relatively lower than that in compression. Due to this asymmetry, strain localization in tensile part is usually easier than that in compressive part.

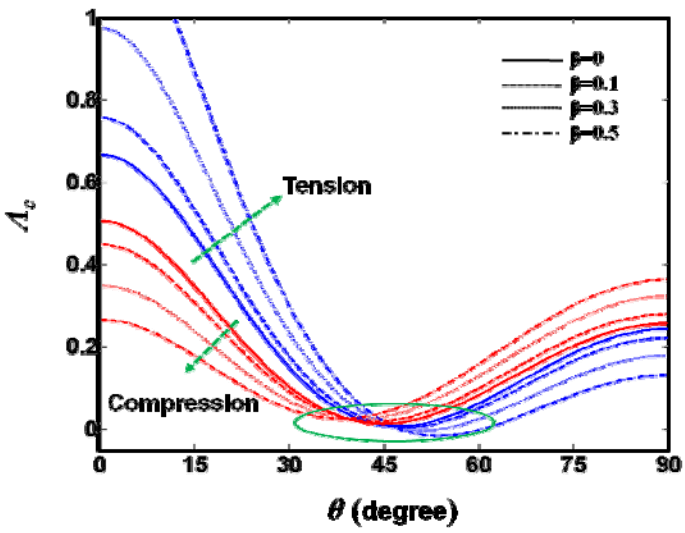

Fig. 2 Dependence of Λ_c on θ for α=0.1 and different β both on tensile side (the blue curves) and on compressive side (the red curves).

The inclination angle of shear banding θ versus the dilatancy factor β for different α is plotted by Fig.3. We interestingly find that θ is a little bigger than 45° for both tension and compression even excluding the pressure sensitivity and dilatancy ($\alpha \to 0$ and $\beta \to 0$). This is attributed to the specific stress state and depends on the Poisson ratio [20]. Increasing β or α, the inclination angle increases in tensile part while decreases in compressive part, showing a asymmetrical deviation from 45°. This prediction is similar to those results of uniaxial loading (tension and compression) from continuum and molecular simulations [31, 32]. For Vit-1, the pressure sensitive factor is around 0.1 [33]. Ranging β from 0 to 0.5, the shear band angles are predicted to be 47° ~54° and 38° ~44°, respectively in tension and compression. Actually, the shear band angles observed in the experiment are 55° on tensile side and 40° on compressive side. In the above discussion, the Poisson ratio ν is set to be a constant 0.36 for Vit-1.

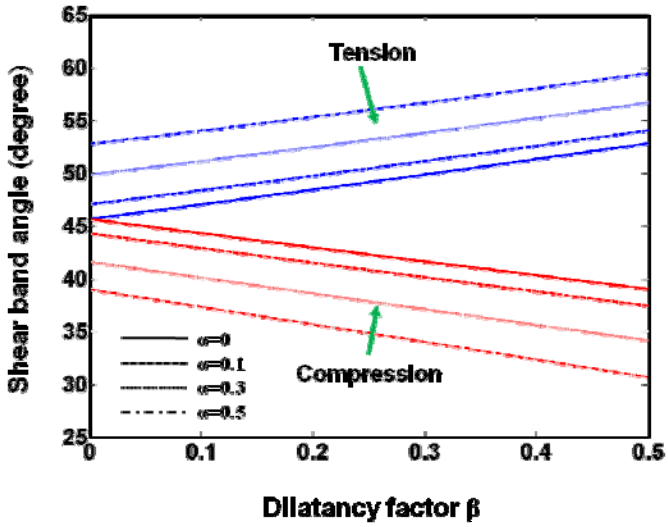

Fig. 3 Dependence of Shear band angle on β for different α both on tensile side (the blue curves) and on compressive side (the red curves).

4. Conclusions

The critical condition for bifurcation of homogenous deformation in MGs has been derived in terms of free volume. It has been found that pressure sensitivity and shear dilatancy exert important effects on the initiation and direction of shear banding. Pressure sensitivity and dilatancy, which are usually coupled together, have the similar trends of influence on the shear band birth and propagation direction. With the enhancement of these two properties, the tension-compression asymmetry of shear banding would be intensified. The instability of constitutive occurs with a smaller Λ_c in tension, and the plastic flow is therefore easier to localize into shear bands. This highly localization may lead to a poor tensile ductility at room temperature. The asymmetrical deviation of shear band angle from 45° has been revealed to be mainly ascribed to these two properties.

Acknowledgements

Financial support is from the National Key Basic Research Program of China (Grant No. 2012CB937500), the NSFC (Grants Nos. 11202221，11132011, 11002144 and 11021262), and the National Natural Science Foundation of China-NSAF (Grant No: 10976100).

References

[1] R. Huang, Z. Suo, J. H. Prevost,W. D. Nix, Inhomogeneous deformation in metallic glasses. J Mech Phys Solids, 50 (2002) 1011-1027.

[2] L. H. Dai, M. Yang, L. F. Liu,Y. L. Bai, Adiabatic shear banding instability in bulk metallic glasses. Appl Phys Lett, 87 (2005) 141916.

[3] L. Wang, Z. P. Lu,T. G. Nieh, Onset of yielding and shear band nucleation in an Au-based bulk metallic glass. Scripta Mater, 65 (2011) 759-762.

[4] S. X. Song,T. G. Nieh, Direct measurements of shear band propagation in metallic glasses – An overview. Intermetallics, 19 (2011) 1968-1977.

[5] H. M. Chen, J. C. Huang, S. X. Song, T. G. Nieh,J. S. C. Jang, Flow serration and shear-band propagation in bulk metallic glasses. Appl Phys Lett, 94 (2009) 141914.

[6] W. H. Wang, Correlation between relaxations and plastic deformation, and elastic model of flow in metallic glasses and glass-forming liquids. J Appl Phys, 110 (2011) 053521.

[7] C. Schuh, T. Hufnagel,U. Ramamurty, Mechanical behavior of amorphous alloys. Acta Mater, 55 (2007) 4067-4109.

[8] M. W. Chen, Mechanical Behavior of Metallic Glasses: Microscopic Understanding of Strength and Ductility. Annu Rev Mater Res, 38 (2008) 445-469.

[9] A. S. Argon, Plastic deformation in metallic glasses. Acta Metall, 27 (1979) 47-58.

[10] F. Spaepen, *Defects in amorphous metals*. 1981, Les Houches Lectures XXXV on Physics of Defects edited by R. Balian et al. (North-Holland, Amsterdam). p. 133-174.

[11] W. Johnson,K. Samwer, A Universal Criterion for Plastic Yielding of Metallic Glasses with a (T/Tg)2/3 Temperature Dependence. Phys Rev Lett, 95 (2005) 195501.

[12] M. L. Falk,J. S. Langer, Dynamics of viscoplastic deformation in amorphous solids. Phys Rev E, 57 (1998) 7192-7205.

[13] M. Q. Jiang,L. H. Dai, On the origin of shear banding instability in metallic glasses. J Mech Phys Solids, 57 (2009) 1267-1292.

[14] P. Thamburaja,R. Ekambaram, Coupled thermo-mechanical modelling of bulk-metallic glasses: Theory, finite-element simulations and experimental verification. J Mech Phys Solids, 55 (2007) 1236-1273.

[15] H. Zhang, S. Maiti,G. Subhash, Evolution of shear bands in bulk metallic glasses under dynamic loading. J Mech Phys Solids, 56 (2008) 2171-2187.

[16] R. Hill, Acceleration waves in solids. J Mech Phys Solids, 10 (1962) 1-16.

[17] J. W. Rudnicki,J. R. Rice, Conditions for the localization of deformation in pressue-sensitive dilatant materials. J Mech Phys Solids, 23 (1975) 371-394.

[18] R. Hill,J. W. Hutchinson, Bifurcation phenomena in the plane tension test. J Mech Phys Solids, 23 (1975) 239-264.

[19] J. R. Rice, ed. *The localization of plastic deformation*. ed. Theoretical and Applied Mechanics e W T K p-P t I, North-Holland, Amsterdam. 1977.

[20] Y. F. Gao, L. Wang, H. Bei,T. G. Nieh, On the shear-band direction in metallic glasses. Acta Mater, 59 (2011) 4159-4167.

[21] H. H. Ruan, L. C. Zhang,J. Lu, A new constitutive model for shear banding instability in metallic glass. Inter J Solids Struct, 48 (2011) 3112-3127.

[22] A. L. Gurson, Continuum theory of ductile rupture by void nucleation and growth: part I- yield criteria and flow rules for porous ductile media. Transactions of the ASME, 99 (1977) 2-15.

[23] W. L. Johnson, J. Lu,M. D. Demetriou, Deformation and flow in bulk metallic glasses and deeply undercooled glass forming liquids-a self consistent dynamic free volume model. Intermetallics, 10 (2002) 1039-1046.

[24] K. M. Flores,R. H. Dauskardt, mean stress effects on flow localization and failure in a bulk metallic glass. Acta Mater, 49 (2001) 2527-2537.

[25] C. A. Schuh,A. C. Lund, Atomistic basis for the plastic yield criterion of metallic glass. Nat Mater, 2 (2003) 449-452.

[26] C. H. Hsueh, H. Bei, C. T. Liu, P. F. Becher,E. P. George, Shear fracture of bulk metallic glasses with controlled applied normal stresses. Scripta Mater, 59 (2008) 111-114.

[27] J. Fornell, A. Concustell, S. Suriñach, W. H. Li, N. Cuadrado, A. Gebert, M. D. Baró,J. Sort,

Yielding and intrinsic plasticity of Ti–Zr–Ni–Cu–Be bulk metallic glass. Inter J Plasticity, 25 (2009) 1540-1559.

[28] Y. Chen, M. Q. Jiang, Y. J. Wei,L. H. Dai, Failure criterion for metallic glasses. Phil Mag, 91 (2011) 4536-4554.

[29] Q. Yang, A. Mota,M. Ortiz, A Finite-Deformation Constitutive Model of Bulk Metallic Glass Plasticity. Comput Mech, 37 (2006) 194-204.

[30] Y. F. Gao, An implicit finite element method for simulating inhomogeneous deformation and shear bands of amorphous alloys based on the free-volume model. Modelling Simul Mater Sci Eng, 14 (2006) 1329-1345.

[31] L. Anand,C. Su, A theory for amorphous viscoplastic materials undergoing finite deformations, with application to metallic glasses. J Mech Phys Solids, 53 (2005) 1362-1396.

[32] M. Zhao,M. Li, Interpreting the change in shear band inclination angle in metallic glasses. Appl Phys Lett, 93 (2008) 241906.

[33] C. E. Packard,C. A. Schuh, Initiation of shear bands near a stress concentration in metallic glass. Acta Mater, 55 (2007) 5348-5358.

Mesh Dependence of Transverse Cracking in Laminated Stainless Steel with both High Strength and High Ductility

Xiang Guo[1, 2], Wenjun Zhang[3], Jian Lu[4,*]

[1] School of Mechanical Engineering, Tianjin University, Tianjin 300072, China
[2] Tianjin Key Laboratory of Nonlinear Dynamics and Chaos Control, Tianjin 300072, China
[3] School of Civil Engineering, Tianjin University, Tianjin 300072, China
[4] Department of Mechanical and Biomedical Engineering, City University of Hong Kong, Hong Kong
* Corresponding author: jianlu@cityu.edu.hk

Abstract A combination of surface mechanical attrition treatment (SMAT) and co-rolling can produce large-scale laminated nanostructured stainless steel (SS) with both high strength and high ductility. Recent numerical results based on the cohesive finite element method have revealed that brittle nanograined interface layer can enhance the ductility of the co-rolled SMATed SS. Here, numerical investigation focuses on effects of both shape of the bilinear cohesive law and mesh size and shows that the larger thickness of the phases in uniform state allows the use of coarser meshes.

Keywords Laminated nanostructured metals, cohesive finite element method, bilinear cohesive law, mesh dependence

1. Introduction

Surface mechanical attrition treatment (SMAT) and co-rolling can be combined to produce large-scale laminated nanostructured metals with both high strength and high ductility [1]. Therefore, it is believed to have a good future to be applied in structural engineering. Through the SMAT, a nano-crystalline surface can be generated for various metals to enhance their yield stress and fatigue life. The co-rolled SMATed metals with nanograined interface layers (NGILs) can be produced. This approach can generate laminated nanostructured 304 stainless steel (SS) with tensile yield stress 878 MPa and failure strain 48% [1].

A computational framework for fracture analysis is in need to investigate the toughening mechanism. The main concern is on the nucleation and the propagation of non-localized microcracks into coarse-grained layer (CGL). Therefore, the cohesive finite element method (CFEM) is appealing to investigate the cracking. The CFEM can model damage initiation/evolution and fracture processes explicitly and has been used to investigate brittle and ductile fracture extensively. The intrinsic CFEM embeds cohesive elements along boundaries of all volumetric elements as part of the physical model [2]. It was adopted in our former studies [3,4]. Our studies have shown that both the critical energy release rate and the thickness of the NGIL play critical roles in determining the overall ductility of the co-rolled SMATed 304SS. However, the dependences of the results on both shape of the cohesive law and the mesh have not been addressed.

2. Mesh dependence issue and numerical framework

Many cohesive laws have been developed [5]. The bilinear cohesive law was used in [3,4], as shown in Fig. 1. $T_{\max}$, cohesive strength, is the stress at which the damage initiates and the

separation is δ_m^0. G_{coh}, critical energy release rate, is given by $G_{\text{coh}} = \int_0^{\delta_m^f} T(\delta)\,\mathrm{d}\delta = 0.5 T_{\max}\delta_m^f$, where T is an effective traction, δ an effective separation, and δ_m^f a critical crack opening. The damage associated with the cohesive surface separation can be defined [6]. Many researchers assumed that $T_{\max}$ and G_{coh} played key roles while the shape of the cohesive law was relatively unimportant. Series of studies indicated that it could lead to unreasonable results [5,7]. Therefore, the shape of the cohesive law should be considered. Dependence of the results on the shape of the cohesive law is closely relevant to the dependence of the results on the mesh. Stress distribution in the cohesive zones must be resolved accurately. Therefore, a minimum number of elements are needed in each cohesive zone and the minimum number has attracted much attention [8]. On the other hand, insertion of cohesive elements introduces fictitious compliance [9]. To alleviate it, Geubelle and Baylor [9] used an adjustable initial slope in the bilinear cohesive law.

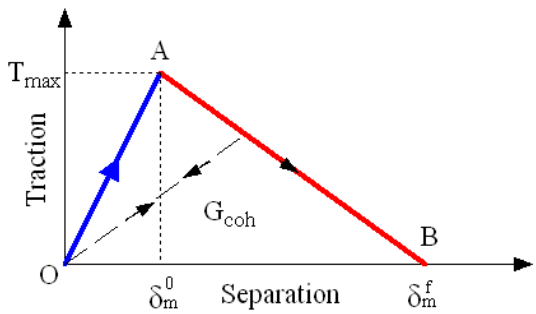

Figure 1. Bilinear cohesive law

The co-rolled SMATed 304SS contains the CGL and the NGIL. A computational configuration with a length 1 mm and a width 0.9 mm is illustrated in Fig. 2. The thickness of the NGIL is taken as 40 μm. Two levels of structured cross-triangular mesh size, namely, 10 by 10 μm and 5 by 5 μm, are used. The cross-triangular meshes with uniform size 10 by 10 μm are illustrated in Fig. 2.

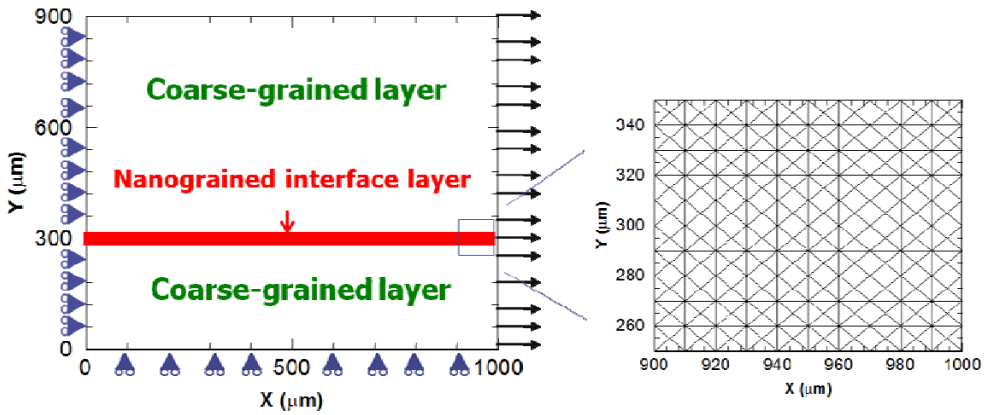

Figure 2. Computational configuration and cross-triangular meshes

Constitutive parameters for the bulk and cohesive elements are listed in Table 1. Both phases are treated as isotropic, elasto-plastic metals. The density, Young's modulus E, Poisson's ratio ν, and flow stress for the two phases are the same as those in [3,4]. The critical energy release rate of the CGL, G_{Ic}, is obtained in terms of its fracture toughness K_{Ic}, which is taken as 100 $\mathrm{MPa}\sqrt{\mathrm{m}}$. The cohesive strength of the NGIL can be calibrated at different critical energy release rate and failure strain [3,4]. Two types of boundaries between the CGL and the NGIL are considered: i) a tough boundary implying that its cohesive parameters are the same as those of the CGL and ii) a brittle boundary implying that its cohesive parameters are the same as those of the NGIL. NGIL's failure strain was estimated to be 3.26% [3]. Here, the critical energy release rate of the NGIL is taken as 60 Jm^{-2} and its cohesive strength is calibrated as 1.89 GPa [3,4]. With the calibrated results, simulations are carried out at two levels of the cohesive strength of the CGL (T_{m}=1.87σ_0 and 1.94σ_0) and for two types of boundaries.

Table 1. Constitutive parameters for bulk and cohesive elements of the co-rolled SMATed 304SS

Phase	Density $(\mathrm{kg/m^3})$	Yield stress	E (GPa)	ν	$T_{\max}$	G_{coh}
CGL	8000	σ_0	200	0.29	T_{m}	G_{Ic}
NGIL	8000	σ_0'	200	0.29	T_{m}'	G_{Ic}'

3. Numerical results

3.1 Effect of the shape of bilinear cohesive law

δ_m^0 is taken as 10^{-2} μm and 10^{-3} μm. When the mesh size is taken as 10 and 5 μm, the simulated results for the co-rolled SMATed 304SS are shown in Figs. 3(a-b) and 4(a-b), respectively. With δ_m^0 decreasing, the computational burden increases obviously, consistent with the finding in [10], and the overall fluctuation in the stress-strain curve also decreases. As δ_m^0 decreases, simulations show that the peak stress around the microcrack nucleation decreases in Figs. 5 and 6, which is in agreement with [7].

3.2 Effect of the mesh size

For refined mesh, the incipient microcrack occurs relatively earlier, more minor branches occur and then arrest after running one or a few elements length, similar with the experimental study [11]. On comparing Figs. 3 with 4, it can be observed that the stress history when the mesh size is 5 μm is more detailed than that when the mesh size is 10 μm. Meanwhile, at each level of δ_m^0, both the

peak stress before the microcrack nucleation and that after the microcrack nucleation have negligible dependence on the mesh size.

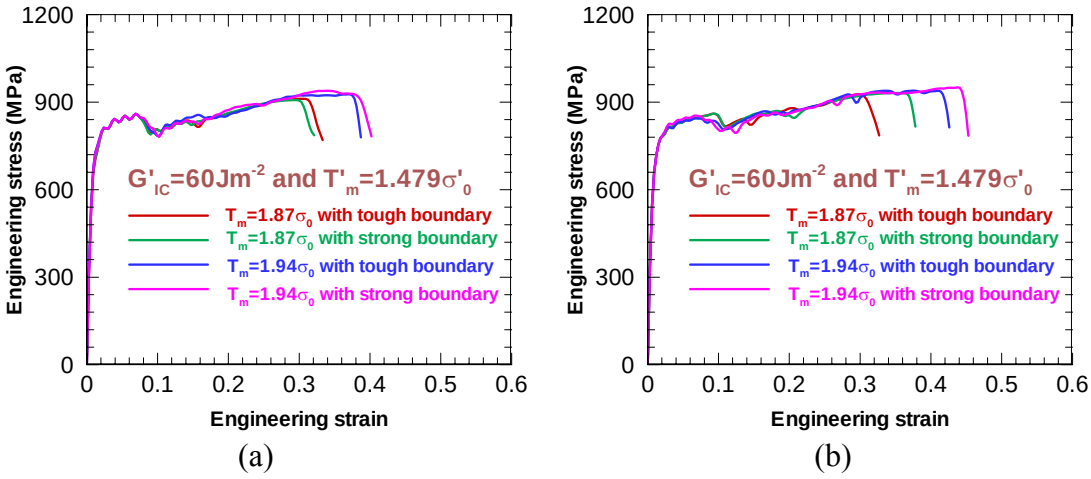

Figure 3. The results with mesh size 10 μm when δ_m^0 is (a) 10^{-2} and (b) 10^{-3} μm

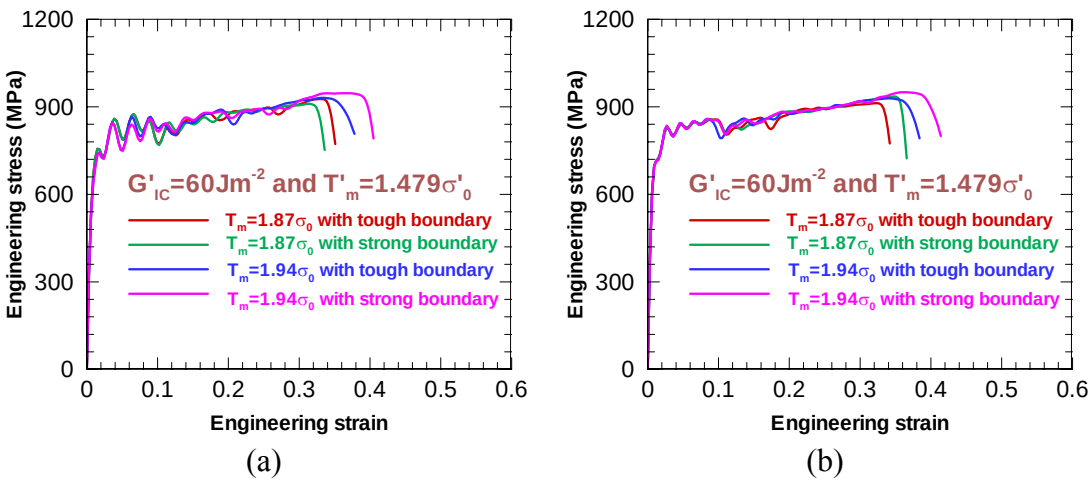

Figure 4. The results with mesh size 5 μm when δ_m^0 is (a) 10^{-2} and (b) 10^{-3} μm

The cohesive zone size has been studied extensively. The widely-used estimate in plane strain condition is Rice's model [12], which gives the cohesive zone size to be $\frac{9\pi}{32}\left(\frac{K_{IC}}{\tau_{max}}\right)^2$. For the CGL, the estimated cohesive zone sizes are 7690 and 7190 μm. The mesh sizes, 10 and 5 μm, are much smaller than them. For the NGIL, the estimated cohesive zone size is 3.24 μm, smaller than the mesh sizes. Due to its brittle nature, the size of cohesive zones in the NGILs is relatively easy to reach the level of the NGIL thickness. The cohesive zones in the NGILs contain 4 and 8 cohesive elements when the mesh size is 10 and 5 μm, respectively. Therefore, there is no need to further refine the mesh in the NGILs. The above justifies using two levels of mesh size. Note that in Figs. 3 and 4, at each level of δ_m^0, the main results are fairly consistent despite the fact that the mesh sizes are not apparently smaller than the estimated cohesive zone size for the NGILs. Previous

investigation has also suggested that the mesh size requirement can be relaxed under certain conditions [8,9]. Our simulation shows that the larger thickness of the brittle phase in uniform state allows the use of coarser meshes.

4. Conclusions

The simulations show that the shape of the bilinear cohesive law can obviously change the stress response, including the overall numerical fluctuation and peak stress. For crack initiation and propagation in a laminated composite structure, overall stress response has weak dependence on the mesh size. Simulation results show that the comparatively larger thickness of the phases in uniform state relaxes the requirement on the mesh size.

Acknowledgements

Dr. X. Guo acknowledges the support from National Natural Science Foundation of China (Project No. 11102128). Professor J. Lu acknowledges the support from the Research Grants Council of the Hong Kong Special Administrative Region of China under grants CityU8/CRF/08 and GRF/CityU519110, and the Croucher Foundation under grant CityU9500006.

References

[1] A.Y. Chen, D.F. Li, J.B. Zhang, H.W. Song, J. Lu, Make nanostructured metal exceptionally tough by introducing non-localized fracture behaviors. Scripta Mater, 59 (2008) 579–582.

[2] A. Needleman, A continuum model for void nucleation by inclusion debonding. ASME J Appl Mech, 54 (1987) 525–531.

[3] X. Guo, A. Y.T. Leung, A.Y. Chen, H. H. Ruan, J. Lu, Investigation of non-local cracking in layered stainless steel with nanostructured interface. Scripta Mater, 63 (2010) 403–406.

[4] X. Guo, G.J. Weng, A.K. Soh, Ductility enhancement of layered stainless steel with nanograined interface layers. Comp Mater Sci, 55 (2012) 350–355.

[5] N. Chandra, H. Li, C. Shet, H. Ghonem, Some issues in the application of cohesive zone models for metal-ceramic interfaces. Int J Solids Struct, 39 (2002) 2827–2855.

[6] ABAQUS, ABAQUS theory manual and user's manual, version 6.10, Dassault (2012).

[7] H. Li, N. Chandra, Analysis of crack growth and crack-tip plasticity in ductile materials using cohesive zone models, Int J Plast 19 (2003) 849–882.

[8] Z. Zhang, G.H. Paulino, Cohesive zone modeling of dynamic failure in homogeneous and functionally graded materials. Int J Plast, 21 (2005) 1195–1254.

[9] P.H. Geubelle, J.S. Baylor, Impact-induced delamination of composites: a 2D simulation. Compos Part B, 29 (1998) 589–602.

[10] D.V. Kubair, P.H. Geubelle, Comparative analysis of extrinsic and intrinsic cohesive models of dynamic fracture. Int J Solids Struct, 40 (2003) 3853–3868.

[11] E. Sharon, J. Fineberg, Microbranching instability and the dynamic fracture of brittle materials. Phys Rev B, 54 (1996) 7128–7139.

[12] J.R. Rice, The mechanics of earthquake rupture. Physics of the Earth's interior. Italian Physical Society, Italy, North-Holland Publ. Co.: Amsterdam (1980) 555–649.

Hamiltonian analysis applied to the dynamic crack growth and arrest in a Double Cantilever Beam.

Gilles DEBRUYNE[1,*], **Radhi ABDELMOULA**[2]

[1] LaMSID-EDF-CEA, *1 avenue du Gal de Gaulle 92141 Clamart, France*
[2] Paris XIII University, LSPM *,Avenue J.B. Clément 93430 Villetaneuse, France*
* Corresponding author: *gilles.debruyne@edf.fr*

Abstract

The paper deals with the dynamic crack growth and arrest in an elastic DCB specimen, idealized by a Bernoulli-Euler beam. The surface energy of the material is $2\Gamma_1$ and the initial crack is blunted with the energy $2\Gamma_0 > 2\Gamma_1$. The crack is then pushed ahead while the loading is frozen, the crack velocity and arrest length depending on the ratio $R = \Gamma_0 / \Gamma_1$. The analytical approach used to investigate the beam behaviour and the crack growth, is based on the Hamilton's principle of stationary action, considering an approximate equation of motion, based on a N modes decomposition of the beam deflection . This process leads to a set of N second order differential equations where the unknowns are the mode amplitudes and their derivatives, coupled to a single equation exhibiting the current crack length $l(t)$, velocity $\dot{l}(t)$ and acceleration $\ddot{l}(t)$.

The results concerning the crack kinematics, particularly the arrest length, are in good accordance with those obtained by a Finite Element Model associated to a cohesive zone model.

The method is then applied to a material with heterogeneous fracture properties, in particular with a distribution of small brittle flaws perturbating the crack kinematics. This method allows a large range of configurations with a low computational time.

Keywords Crack arrest, Hamiltonian, Lagrange equations, Double Cantilever Beam, pops-in

1. Introduction

The double cantilever beam (DCB) specimen is widely used for crack arrest investigations, and its geometry is suitable for one-dimensional analysis models. For dynamic crack growth in a finite solid, analytical solutions are uncommon. The first quantitative prediction for the kinematics of a fast propagating crack, using an energy balance, is due to Mott [1]. Whereas crack propagation problems with transient motion are often achieved only with Finite Element Models, some analytical procedures are available for one dimensional models as DCB specimens. We focus here on a bimaterial DCB specimen, with a high toughness part where the initial crack is blunted, welded to a low toughness section where the crack enters with a high velocity. Transient kinetic analyses may be also achieved with some analytical methods, such hyperbolic equations solved by a finite difference scheme applied to characteristic lines [2,3]. An original analytical way, based on solving Lagrange's equation of a DCB specimen motion, considered as a Bernoulli-Euler beam, has been initiated by Burns and Webb [4], assuming a special form of the kinetic energy corresponding to a specific constant loading rate. Freund [5] has extended this approach for a general loading,

suggesting a modal decomposition, but limiting his work to the mode $N = 0$. It is suggested here to extend the modal analysis to higher vibration modes to investigate the dynamic crack growth and arrest in a DCB specimen.

2. The Bernoulli beam model applied to a duplex DCB.

An elastic Double Cantilever Beam specimen is illustrated in the figure 1. The specimen arms are slowly prescribed to a monotonic opening displacement $W^0(t)$ which gives rise to a quasi-static mode I crack growth (denoted by the current value $l_0 \le l < l_c$) in a first part of the beam, made up of a $2\Gamma_0$ surface energy material. A second material with a lower toughness, denoted the test section, is welded to the first one (the corresponding surface energy is $2\Gamma_1 < 2\Gamma_0$). When the crack tip reaches the critical point corresponding to the sections interface ($x = l_c$) where the toughness jump occurs, its rapidly runs throughout the test section, while the loading is frozen. The crack velocity $\dot{l}$ (and the arrest length l_A) in this test section, is governed by the surface energy ratio of the two sections ($R = \Gamma_0 / \Gamma_1, R > 1$). We investigate here the crack kinematics during this stage, including the crack arrest $l_c \le x \le l_A$, with the assumption of a straight crack path, without any branching or kinking.

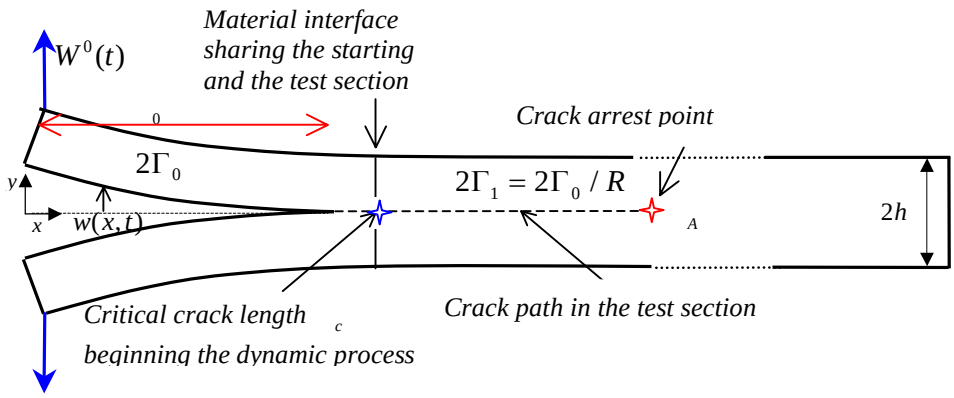

Figure 1 Crack growth and arrest in a bimaterial DCB specimen.

Only half of the specimen, and then half of the surface energy (Γ_0, Γ_1) are considered here. A Bernoulli-Euler model is assumed to model the beam (the ratio h / l_c is considered small enough

to bear out a classical beam theory). Therefore, the motion only exhibits the scalar beam deflection $w(x,t)$. The general differential motion equation, associated with the boundary conditions may be written as follows, $\forall l\ ,l_0 \le l\ \le l_a$:

$$\begin{cases} EI\dfrac{\partial^4 w}{\partial x^4}+\rho A\dfrac{\partial^2 w}{\partial t^2}=0, \quad \forall x\in[0,l],\forall t \\ w(0,t)=W^0(t),\ \dfrac{\partial^2 w}{\partial x^2}(0,t)=0, \\ w(l,t)=0,\ \dfrac{\partial\ w}{\partial x}(l,t)=0, \end{cases} \tag{1}$$

where E, I, A, ρ are respectively the elastic modulus, the area moment of inertia of the beam cross section, the area of this section, and the mass density of the material.
As the dynamic stage is the only one which matters, the initial conditions will refer to the crack running onset time when $l(t=0)=l_c$, so that the quasi-static growth stage ($t<0\ x\in[0,l_c]$) is disregarded here.

3. Approximate equation of the DCB motion by modal decomposition

3.1. Approximate equation of motion.

It is supposed, as already suggested by Freund [5], that the deflection of the beam is given by the following approximation :

$$w\left(X(t),t\right)=w^{stat}\left(X\right)+\hat{w}\left(X,t\right)=w^{stat}\left(X\right)+a_i\left(t\right)\phi_i\left(X\right),\quad i=1,N \tag{2}$$

where the Einstein summation convention is henceforth adopted, from now on. The new variable $X=x/l,\ X\in[0,1]$ is the normalized beam coordinate, useful in the case of a growing crack, such that the moving integration domain $[0,l(t)]$ is replaced by the stationary reference domain $[0,1],\forall l(t)$. $w^{stat}(X)$ is the quasi-static deflection solution, $\hat{w}\left(X,t\right)$ the perturbation around the equilibrium solution, ϕ_i the ith normal mode shape for free vibration of the beam, and a_i the unknown deflection amplitude associated to ϕ_i.

The homogeneous boundary conditions associated to the free vibration of the beam are derived from (1) :

$$\begin{cases} \phi_i(1) = \phi_i'(1) = 0, \\ \phi_i''(0) = \phi_i(0) = 0, \quad \forall\, i = 1, N \end{cases} \quad (3)$$

3.2. Free vibration mode shape.

An harmonic motion for the free vibration mode is assumed :

$$\hat{w}(X,t) = \phi_i(X)\sin(\omega_i t + \theta), \quad i = 1, N \quad (4),$$

where ω_i is the angular frequency associated to the mode ϕ_i, θ the phase angle.

The motion equation may be written as :

$$\phi_i^{(4)}(X) = \mu_i^4 \phi_i(X), \quad \forall i, i = 1, N, \quad \forall\, X \in [0,1], \mu_i^4 = \frac{\rho A l^4 \omega_i^2}{EI} \quad (5)$$

The general solution of (10) is :

$$\phi_i(X) = \left[sin(\mu_i X) - \frac{cos(\mu_i)}{sh(\mu_i)} sh(\mu_i X) \right] \quad (6)$$

and each angular frequency is given by the following equation:

$$tg(\mu_i) = th(\mu_i), \forall i, i = 1, N \quad (7)$$

4. Hamilton's principle applied to a domain with a moving crack.

Hamilton's principle of stationary action is widely used in classical mechanics [6]. It postulates that the dynamics of a system is governed by a variational problem for a functional integrating the Lagrangian function, which contains some information about the energy of the system and the forces acting on it. It is the weak form of the differential equations of motion of the system.

4.1. General Hamilton's principle applied to a system described by a discrete set of degrees of freedom.

Let us recall the outlines of the principle for a system described by the generalized coordinates $(q_i), i = 1, N$, in a formal way. Hamilton's principle states that the true evolution of (q_i) along a path γ between two mechanical states at time t_0 and t_1 is a stationary point of the action functional : $\varphi(\gamma) = \int_{t_0}^{t_1} L(q_i, \dot{q}_i, t)\, dt$ (8), where $L(q_i, \dot{q}_i, t)$ is the Lagrangian function of the system. This principle involves the following system of N Euler-Lagrange equations [6] :

$$\frac{\partial L}{\partial q_i} - \frac{d}{dt}\frac{\partial L}{\partial \dot{q}_i} = 0, \quad \forall i, i = 1, N \ (9)$$

Let us introduce the Hamiltonian function as the Legendre transform of the Lagrangian function :

$$H\ (q_i, p_i, t) = p_i \dot{q}_i \ - L\ (q_i, \dot{q}_i, t), \quad 1 \le i \le N \ (10)$$

with $p_i = \dfrac{\partial L}{\partial \dot{q}_i}$. The following relations :

$$\dot{p}_i = \ -\frac{\partial H}{\partial q_i}, \quad \dot{q}_i = \frac{\partial H}{\partial p_i} \ (11)$$

are called Hamilton's equations. The system of Euler-Lagrange's equations (14) is equivalent to the Hamilton's equations (16) (under some assumptions).

4.2. Application to the DCB specimen.

These previous considerations are very formal and general. They can be applied to an elastodynamic system such our model, considering that $q_i = a_{i,}\ \ i = 1, N, q_{N+1} = \mathrm{l}$. Therefore, the Lagrangian is :

$$\mathcal{L}\left(a_i, \dot{a}_i, \mathrm{l}, \dot{\mathrm{l}}\right) = K\left(a_i, \dot{a}_i, \mathrm{l}, \dot{\mathrm{l}}\right) - U\left(a_i, \mathrm{l}\right) - \int_0^{\mathrm{l}} \Gamma\ (x)dx, \quad i = 1, N \qquad (12)$$

and the Euler-Lagrange equations become :

$$\frac{d}{dt}\left(\frac{\partial\left(K - U\right)}{\partial \dot{a}_i}\right) - \frac{\partial\left(K - U\right)}{\partial a_i} = 0, \quad \forall i, 1 \le i \le N \quad (13)$$

$$\frac{d}{dt}\left(\frac{\partial\left(K - U\right)}{\partial \dot{\mathrm{l}}}\right) - \frac{\partial\left(K - U\right)}{\partial \mathrm{l}} + \Gamma(\mathrm{l}) = 0, \quad (14)$$

which are respectively the local motion equations similar to equ. (1) for each eigenmode and the expression of the energy release rate. Using the Legendre transform of L , the following relation holds :

$$\mathcal{H}\left(a_i, \dot{a}_i, \mathrm{l}, \dot{\mathrm{l}}\right) = K\left(a_i, \dot{a}_i, \mathrm{l}, \dot{\mathrm{l}}\right) + U\left(a_i, \mathrm{l}\right) + \int_0^{\mathrm{l}} \Gamma(x)dx, \quad i = 1, N \quad (15)$$

Thus, the Hamiltonian is the total energy of the beam. Furthermore, since the Lagrangian equations are fulfilled, the energy balance is fulfilled. Starting from now, the complete solution of the dynamic crack growth problem in the DCB is restricted to the determination of the time dependent variables $a_i(t), \mathrm{l}(t)$

5. Setting up the equations system, starting from the Hamilton's principle.

The relations (13) associated to the modal decomposition lead to the following second order ordinary differential system of N equations, describing the beam motion :

$$\ddot{a}_i = \frac{\ddot{\Gamma}}{l}\left(C_3^i + a_j C_4^{ij}\right) + \frac{2\dot{\Gamma}}{l}\dot{a}_j C_4^{ij} + \frac{\dot{\Gamma}^2}{l^2}\left(C_2^i + a_j C_1^{ij}\right) - \frac{1}{l^4}\frac{EI}{\rho A} a_i \mu_i^4, \ \forall i = 1, N \quad (16)$$

where ($a_i, \dot{a}_i, \ddot{a}_i$, $i = 1, N$) are the unknowns and ($l, \dot{\Gamma}, \ddot{\Gamma}$) the equation parameters. The coefficients $\left(C_1^{ij}, C_2^i, C_3^i, C_4^{ij}\right)$ depend on the mode shape of the beam, and μ_i corresponds to the angular frequency computed with the relation (7). The relation (14) leads to the single equation, describing the crack kinematics (where the summation convention holds) :

$$\ddot{\Gamma} = \frac{\dot{\Gamma}^2}{2l} + \frac{\dot{\Gamma}}{\Delta}\left(-2\dot{a}_j C_2^j - 2\dot{a}_j a_i C_1^{ij}\right) + \frac{3EI}{2l^3 \Delta \rho A}\left(3(w^c)^2 + a^2{}_i \mu^4{}_i\right) + \frac{l}{\Delta}\left(\ddot{a}_i C_3^i + \ddot{a}_i a_j C_4^{ij} - \frac{\Gamma_1}{2\rho A}\right) \quad (17)$$

with $\Delta = \frac{6(w^c)^2}{35} + a_i a_j C_1^{ij} + 2a_i C_2^i$ and ($l, \dot{\Gamma}, \ddot{\Gamma}$) are the unknowns and ($a_i, \dot{a}_i, \ddot{a}_i$, $i = 1, N$) the equation parameters. It is important to point out that the above coupled system does not take into account two features : the irreversibility of the crack growth ($\dot{\Gamma} \geq 0$) and the non overlap of the crack lips ($w(x,t) \geq 0$), involving constraints on the amplitudes a_i, are not considered. This lack in the model will not affect the results in most of the cases as we will see in the next sections.

6. Application to an homogeneous test material

6.1. Number of modes influence.

The surface energy ratio is $R = 3$. From $N = 3$, the crack growth solution convergence may be considered as correct (with some oscillations, related to the propagation reversibility, see fig. 2).

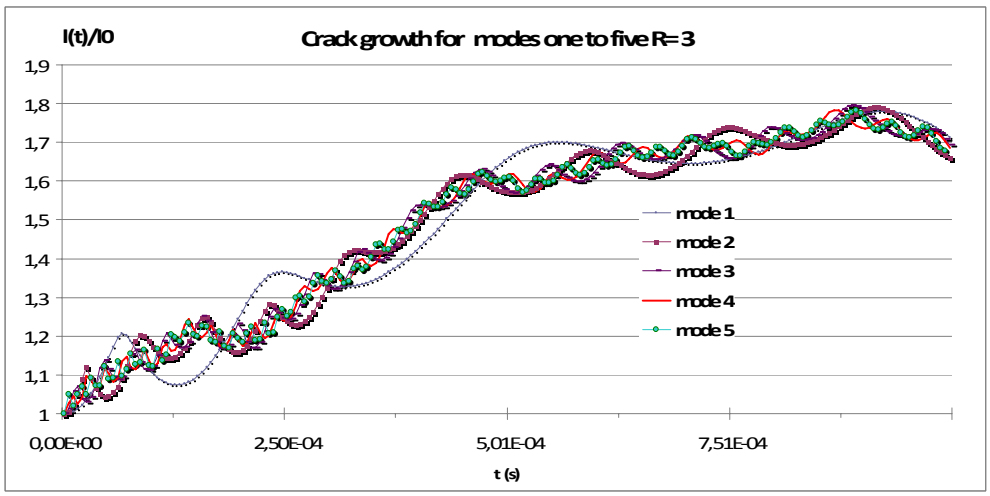

Fig. 2. Crack kinematics for a modal decomposition up to 5 modes (R=3).

The crack arrest point arises as soon as the solution globally decreases.

6.2. Comparison with a cohesive zone model.

Our method has been compared with a cohesive zone model with a sufficiently small cohesive zone, to be close to the Griffith model [7] . Furthermore, this cohesive model is applied to a plane strain behavior while the present method uses a beam model. The comparative results from the present model and the cohesive model for $R = 3$ are illustrated on the figures 3 and 4. The results (for N=4) are in a good accordance. The crack arrest takes place when the kinetic energy reaches its minimum, before a second bounce, which corresponds to the beam vibration at the end of the crack propagation.

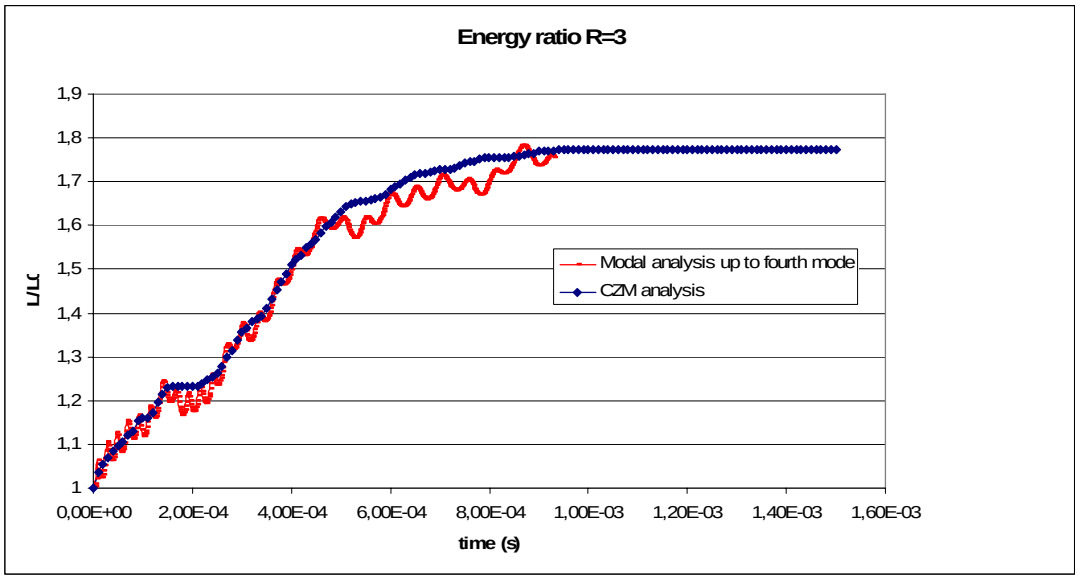

Fig. 3. Comparative analysis with a cohesive zone model :Crack kinematics versus time for R=3.

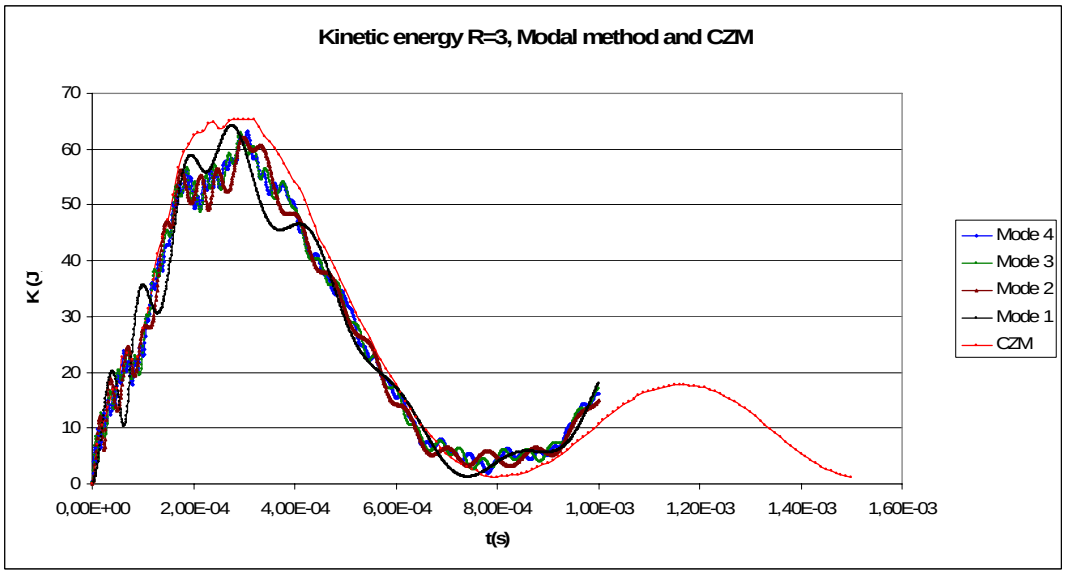

Fig. 4. Comparative analysis with a cohesive zone model :Kinetic energy versus time for R=3.

7. Application to materials with heterogeneous toughness .

The case of heterogeneous fracture properties is investigated, in particular when one single flaw may upset the crack kinematics. If the flaw is weaker than the safe material, the crack may jump over it. This phenomenon, called “pop-in” [8] is investigated here with the following parameters : the flaw position, and its toughness. Conversely, tougher inclusions inside the test material may slow down or stop the crack, or reduce the crack arrest length.

7.1. One single weak flaw ahead the initial crack tip.

In a first case, a e length single flaw, located just ahead the initial crack tip, is considered (see fig. 5). The flaw toughness value is $\Gamma_1 = \Gamma_0 / R$ and the material recovers its original toughness Γ_0 beyond the flaw. The aim is to check if the crack will stop just after the flaw or deeper in the original material, and in this latter case, which is the arrest length, depending of e and R.

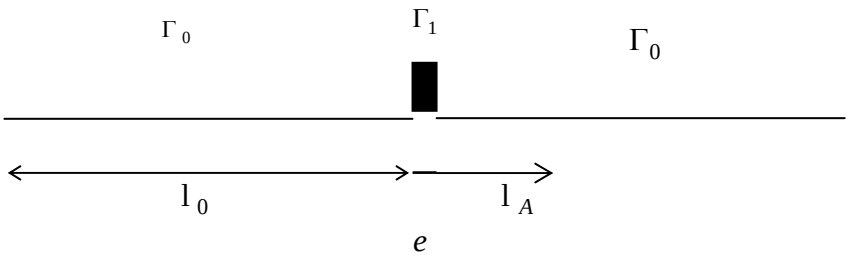

Fig. 5. One single weak inclusion ahead the initial crack tip in the test material.

The figure 6 displays the ratio crack arrest length over flaw length, versus the ratio flaw length over initial crack length, for a range of $1.5 < R < 4$. It is noteworthy that for $0.2 \le e / L_0 \le 0.4$ (this range of e / L_0 and R is usual for industrial components, the crack arrest occurs around the flaw tip, and the crack does not deeply penetrate inside the safe material.

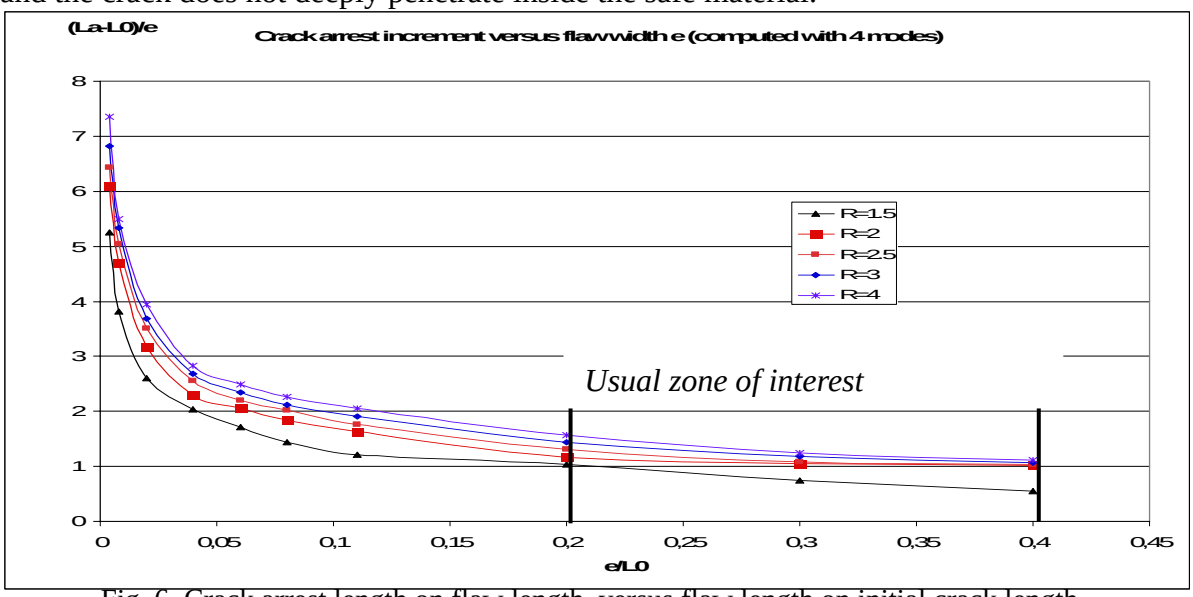

Fig. 6. Crack arrest length on flaw length, versus flaw length on initial crack length.

7.2. One single tough flaw ahead the initial crack tip.

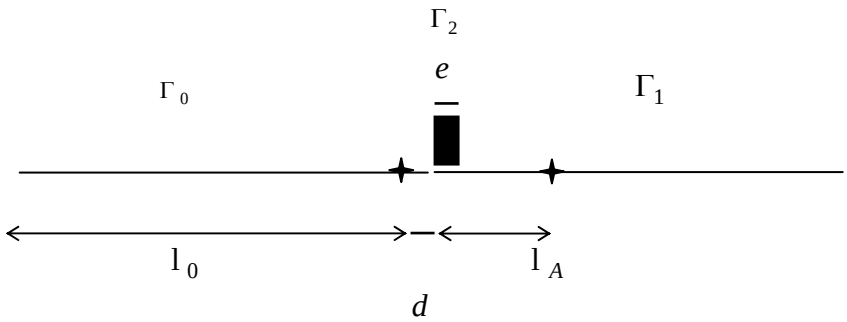

Fig. 7. One single tough inclusion in the test material.

On the contrary, a tough e length flaw ($\Gamma_2 \geq \Gamma_0$) is embedded in the regular test material ($\Gamma_1 = \Gamma_0 / R$, with the fixed value $R = 3$), at a distance d ahead the initial crack tip (fig. 7). The influence of the flaw features d, e and Γ_2 on the crack kinematics is investigated. If the flaw is sufficiently long (in our specific case $e / l_0 > 6\%$, see fig.8), the crack is immediately stopped inside the flaw. In the other hand where $e / l_0 < 1\%$ the crack kinematics is very close to that without flaw. In the intermediate situations, a transient crack arrest takes place in the flaw (the longer the flaw, the longer the transient arrest time), followed by a crack restart with either a reduced final crack arrest (for $e / l_0 = 5\%$) or a regular one (for $e / l_0 = 3\%$).

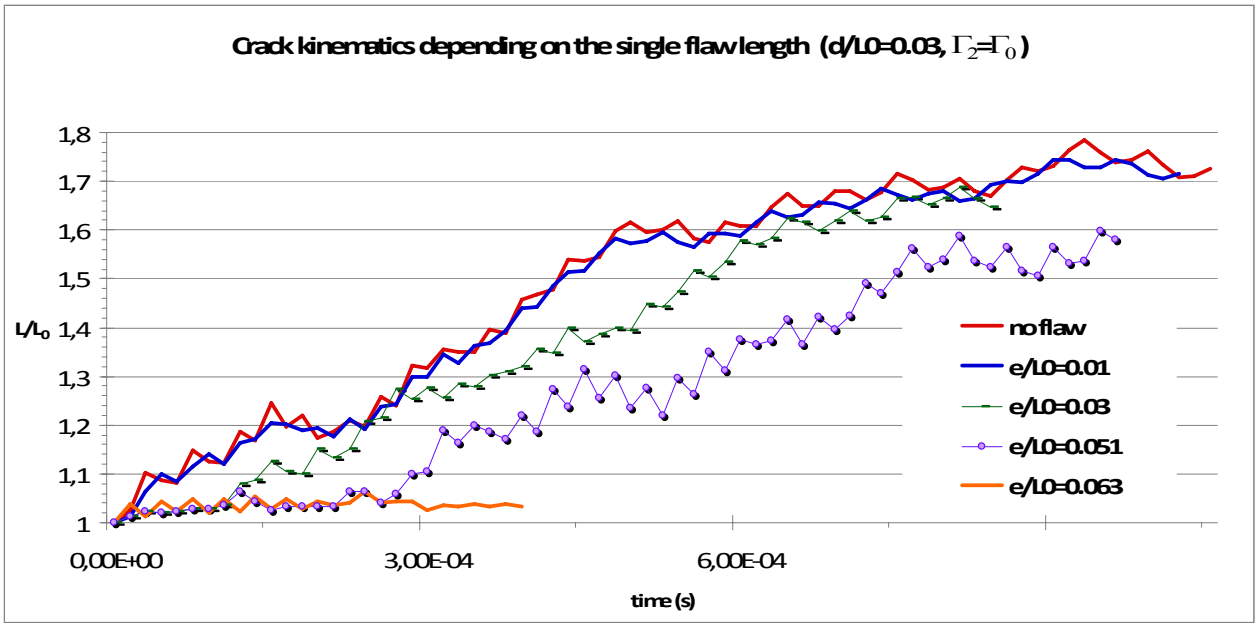

Fig. 8. Influence of the flaw length.

8. Conclusions and outlines.

The complete dynamic crack kinematics is described from the Hamiltonian variational formulation associated to a modal decomposition. It is correctly described in a swift time, compared to the prediction of more heavy FE methods, even for a small number of modes (in many cases, three modes are sufficient, for a few seconds of computational time). The method has been also applied to a material, embedding some flaws with heterogeneous fracture properties. The crack kinematics, including the crack arrest, is very sensitive to the flaw position and toughness. The main drawback of our method is the non account of the crack growth irreversibility, which leads to small stages with negative crack velocities instead transient crack arrest, but without significant consequence on the results fairness. This disadvantage may be circumvented, adding the constraint inequality $\dot{\Gamma} \geq 0$ in the motion equations, but with probably an increase in the computational cost. An extension of this method to a beam with variable section geometry (tapered DCB), a complex toughness distribution, is straightforward. On the other hand, some developments concerning the material behaviour such as the viscosity or plasticity, or the application to bidimensionnal geometries are possible but more ticklish.

References

1. N.F. Mott, Brittle fracture in mild steel plates, Engineering 165, pp. 16-18, 1948.
2. L.B. Freund, A simple model of the double cantilever beam crack propagation specimen, J. Mech. Phys. Solids, Vol. 25, pp. 69-79, 1977.
3. K. Hellan, An alternative one-dimensional study of dynamic crack growth in DCB test specimens, Int. J. of Fracture, Vol.17, n°3, pp. 311-319, June 1981.
4. S.J. Burns, W.W. Webb, Fracture Surface Energies and Dislocation Processes during Dynamical Cleavage of LiF. I. Theory, J. of Applied Physics, Vol. 41, n° 5, pp. 2078-2085, April 1970.
5. L.B. Freund, Dynamic Fracture Mechanics, Cambridge University Press, ISBN 0-521-30330-3, 1998 (first edition 1989).
6. V.I. Arnold, Mathematical Methods of Classical Mechanics, Springer Verlag, 2nd edition, pp. 59-68, 1989.
7. G. Debruyne, P.E. Dumouchel, J. Laverne, Dynamic crack growth : Analytical and numerical Cohesive zone models approaches from basic tests to industrial structures , Eng. Fr. Mech., 2012.
8. A.A Willoughby, Significance of Pop-in fracture toughness testing, in Int. J. of Fract. 30, R3-R6, 1986

The concepts and properties of nanoskin materials and components created by ultrasonic nanocrystal surface modification

Young Shik Pyoun[1], Qingyuan Wang[2], Muhammad Kashif Khan[3], Ravil Kayumov[4, *], Junhyong Kim[4]

[1]Dept. of Mechanical Engineering, Sun Moon University, Asan, 336-708, South Korea
[2]Dept. of Civil Engineering and Mechanics, Sichuan University, Chengdu, 610065, China
[3]Dept. of Mechanics and Engineering Science, Sichuan University, Chengdu, 610065, China
[4]Dept. of Mechanical Engineering, Graduate School, Sun Moon University, Asan, 336-708, South Korea
*ravilkayumov@yahoo.com

Abstract
Material surface and immediate subsurface layers can be called "skin". A novel Ultrasonic Nanocrystal Surface Modification (UNSM) technology produces uniformed micro dimples on the top surface and nanometer grain in the subsurface, increases surface hardness and induces compressive residual stress. This way mechanical characteristics related to fatigue, wear, friction, etc. can be improved. The concepts and properties of nanoskin materials and components are proposed with their potential application.

Keywords: Nano grain materials; Nano skin materials; Ultrasonic Nanocrystal Surface Modification.

1. Introduction.
Concept of Nanoskin Materals and Components

Friction and wear, low, high and very high cycle fatigue, rolling contact fatigue and some other characteristics of machine components are influenced by the surface characteristics of material. The top surface and immediate subsurface layers can be called "skin". When subsurface grain dimensions reach nanometer range and top surface acquire micro or nano scale roughness and texture, these properties are much different from those of the ordinary structure. The hardness, compressive residual stress and grain size of subsurface are major factors that determine fatigue, friction, wear and fatigue characteristics. Therefore, nanoskin materials and components can be defined as *top surface of material consisting of nano scale roughness and nano and/or micro scale texture, and subsurface nanoscale grain size with improved hardness and compressive residual stress*.
Lowest roughness of 10 - 200 nm is usually achieved through various forms of abrasive surface finish [1]. However, manufacturing costs rise exponentially with decreasing of the surface roughness. Surface texturing can reduce friction and wear characteristics, but there is no general rule yet to explain its effects on wear and friction. Besides, the size of the pattern is usually bigger than several dozen micro millimeters [2, 3, 4].
Grain size refinement is usually achieved through conventional heat treatment and deformation processes like forging, rolling, drawing and extrusion. However, 1μm (for steels) is a limit for the grain size refinement [5]. The severe plastic deformation process such as ECAP (Equal Channel Angular Process) is a novel technology which refines the grain size of bulk rod into nano scale [6]. But from the view point of nano skin of materials and components, there is still a lot more research to do.

2. The UNSM Technology

Ultrasonic Nanocrystal Surface Modification (UNSM) stands out for ability to generate specifically nanoskin on the surface of material. The main concept and mechanism of UNSM shown in Figure 1 are as following [7, 8, 9]. A tungsten carbide ball attached to an ultrasonic device strikes the surface of a work piece 1.2 ~2.4 x 10^6 times per minute with 1,000 to 100,000 shots per mm^2 and under contact pressure range from 3 to 100 GPa. These strikes bring severe plastic-elastic deformation to surface and subsurface. Thus *uniformed micro dimple pattern* on the surface and *nanocrystalline structure* and *compressive residual* stress in subsurface layer are induced. This change has potential to simultaneously improve static and fatigue strength, as well as surface hardness and surface roughness of the work piece.

Figure 1. UNSM Mechanism and UNSM Device with CNC Lathe for Hub Bearings

2.1 Top surface properties: roughness and micro dimples texture

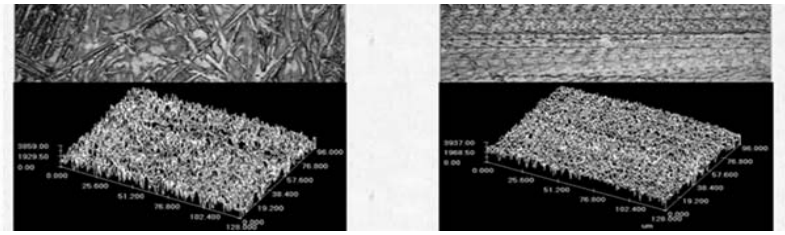

Figure 2. Micrograph images and 3-D topology of AISI52100

The uniform micro dimple pattern of the surface is the *signature mark* of the UNSM treatment. Figure 2 shows modification of the surface pattern of SAE52100 bearing steel ground specimen treated with UNSM. Ra roughness is improved from 0.19 µm to 0.11 µm and uniform micro dimple structure improved entrapped oil volume [9, 10, 11]. Table 1 shows that dimensions of micro-dimples measured by AFM are rather in nano order.

Table 1. Micro dimple size for AISI52100 treated with UNSM

Conditions	Feedrate, mm/rev	Amplitude, µm	Lathe Spindle Speed, rpm	Static Load, N	Tip diameter, mm	Micro dimple diameter/depth, µm
UNSM I	0.07	30	50	60	2.38	0.8/0.07
UNSM II			100			0.56/0.05
UNSM III			150			0.42/0.04

2.2 Subsurface properties

2.2.1. Nano crystallization

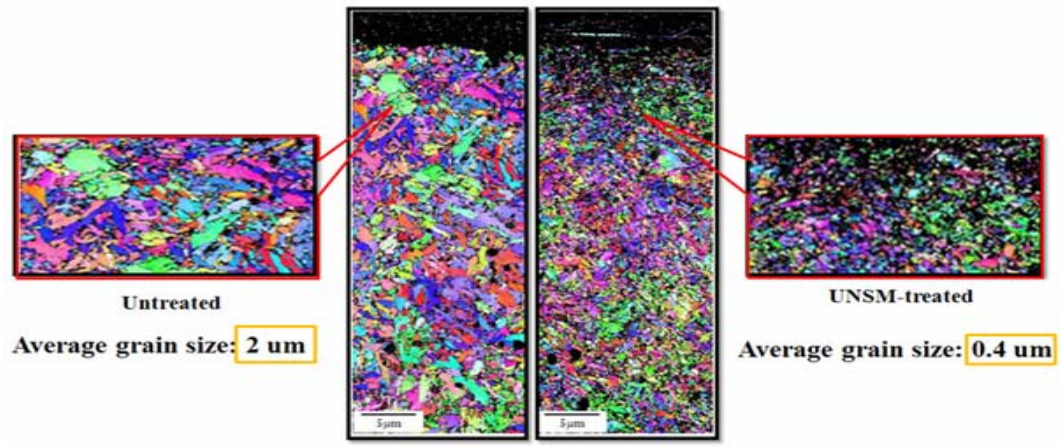

Figure 3. Comparison of grain size before and after UNSM treatment for SAE52100 bearing steel specimen.

Figure 3 shows modification of the grain structure in the subsurface of specimen made of SAE52100 bearing steel. It can be seen that strikes induced grain size refinement from 2 µm to 0.4 µm. Figure 4 shows grain size in the subsurface of UNSM generated nanoskin of SUS 304 steel. The grain was refined almost 1/1000 [8, 13].

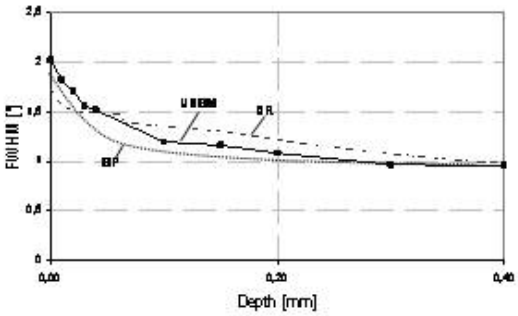

Depth, µm	Grain size, nm
5	30
10	36
20	42
30	45

Figure 4. TEM and XRD analysis and calculation of SUS 304 steel grain size of after UNSM

2.2.2. Increase of top surface and subsurface hardness

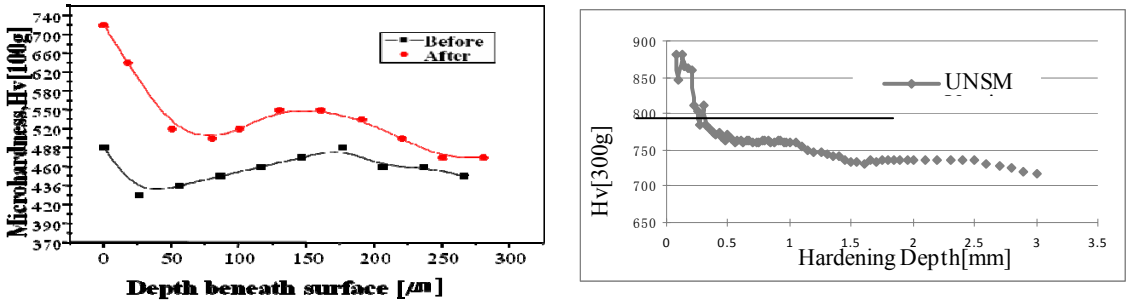

SKD61 SAE52110

Figure 5. Microhardness depth profile of SKD61 and SAE52110 steels treated with UNSM

Table 2. Top surface hardness

	Ti–6Al-4V	Inconel738	Inconel690	Cu-Zn alloy	Al6061-T6
Untreated/UNSM Hardness(HV)	380/424	405/448	164/280	130/210	100/141

Hardness at the top surface increased by 33% and 17% for SKD61 and SAE52110, respectively. Table 2 shows improvement of top surface hardness of some other materials nanoskin-treated by UNSM technology.

2.2.3. Increase of compressive residual stress

A:SKD61 (H13) B: Ti-6Al-4V

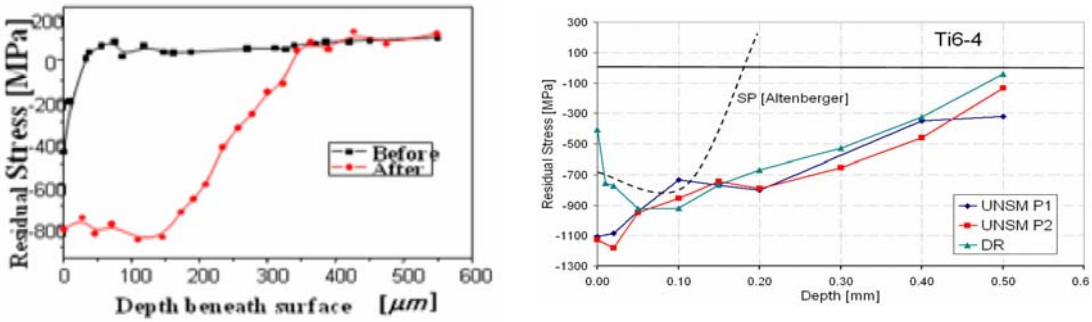

Figure 6. Compressive residual stress treated by UNSM technology

Compressive residual stress within a nanoskin created by UNSM of SKD61 (equivalent of H13) is shown in Figure 6A, and of a Ti-6Al-4V for medical and aircraft application is shown in Figure 6B. Comparison between deep rolling (DR) and UNSM is also shown in Figure 6B [9, 12, 14].

2.3. Mechanical performance of nanoskin: fatigue, wear, friction and rolling contact fatigue

2.3.1. Improvement of HCF and VHCF strength

In order to evaluate the effects of UNSM generated nanoskin on fatigue performance of some automotive, aircraft and medical alloys, ultrasonic fatigue tests (UFT) were carried out on Al6061-T6, Ti-6Al-4V (TC4) and Ti-3Al-2Mo-2Zr (TAMZ) specimens. Using UFT device reduced test time and better simulated extremely high frequency loading and influence of strain rate on fatigue behavior of tested material. The test frequency was 20 kHz and stress ratio R=-1. The specimens were hourglass shape with neck diameter 6 mm and notch radius 60 mm for Al-alloy and 3 mm/31 mm for Ti-alloys. Figure 7 shows S-N curves acquired through UFT for UNSM treated and untreated specimens.

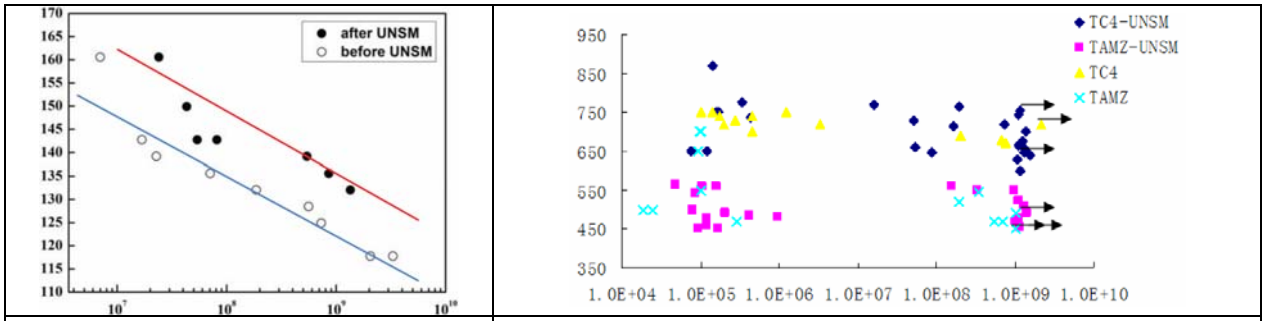

a b

Figure 7. S-N curves for UNSM treated and untreated Al6061-T6 specimens (a) and TC4 and TAMZ (b)

It is shown that UNSM induced nanoskin prolongs fatigue life of all three alloys. In many instances UNSM treated specimens lasted well beyond 10^9 cycles or run out. S-N curve of UNSM treated Al6061-T6 is shifted approximately 25 – 30 % towards higher stress level compared with untreated specimens. Meanwhile, UNSM induced nanoskin improved fatigue strength of TC4 and TAMZ by 11 % and 13 % respectively.

Untreated Al6061-T6 specimens show various fracture surfaces. At high stresses (Figure 8a) cracks are initiated at inclusions or other defects and rapidly spread, forming a "canyon" shaped damage. At medium stresses (Figure 8b) fatigue failure occurs at the surface followed by propagation into the interior, as indicated by cross-section lines. At lower stresses (Figure 8c) slip bands occur at crack starting point.

Figure 8d shows a typical high cycle fatigue fracture of UNSM treated specimens.

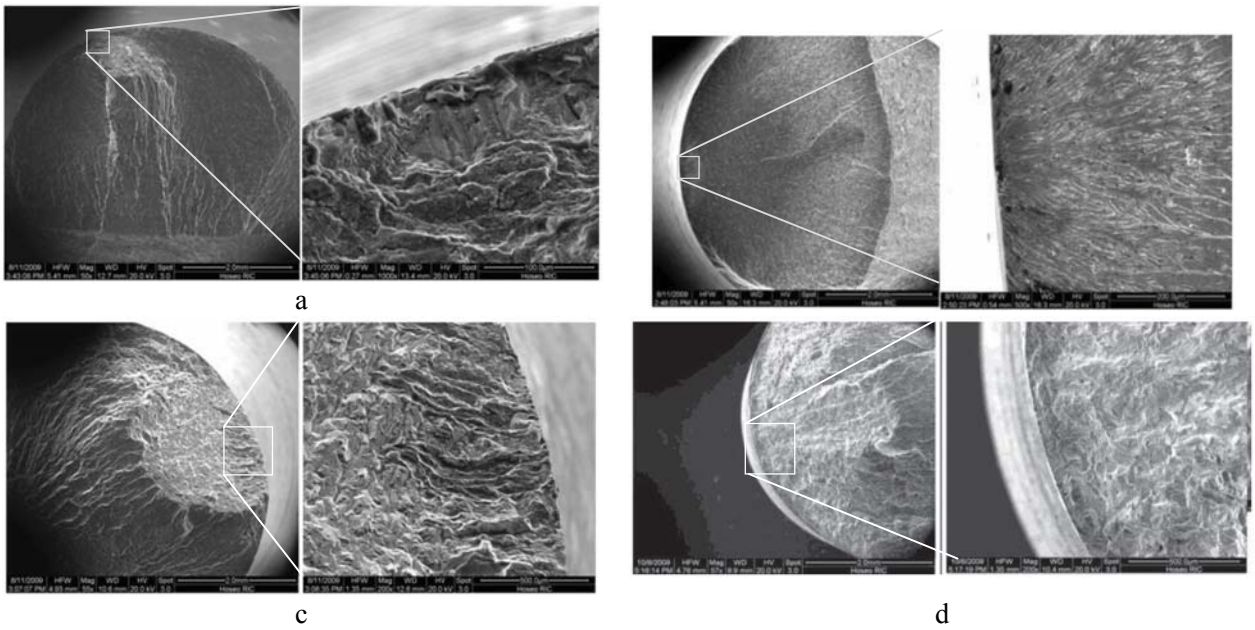

Figure 8. Untreated (a-c) and UNSM treated (d) Al6061-T6 specimens fracture surfaces

Although fatigue strength of TC4 is higher than that of TAMZ alloy, their fracture behavior is very similar. Fractographic analysis of typical untreated Ti-alloy gigacycle (> 10^8 cycles) specimens displays that cracks always initiate at the surface, as shown on Figure 9. The fracture surface can be divided in to four areas: (I) an initial relatively flat area; (II) a distinctly rough area with propagation traces like radiate wave lines; (III) a wider fracture surface with radial streaks along propagation direction and (IV) overload fracture area.

For specimens with UNSM induced nanoskin, the fracture surface can be divided in four areas, much the same way as untreated specimens. The important difference, however, is that the crack initiation always occurs in the subsurface, about 50 μm below, at the internal inclusion and form a fish-eye, as shown on Figure 10.

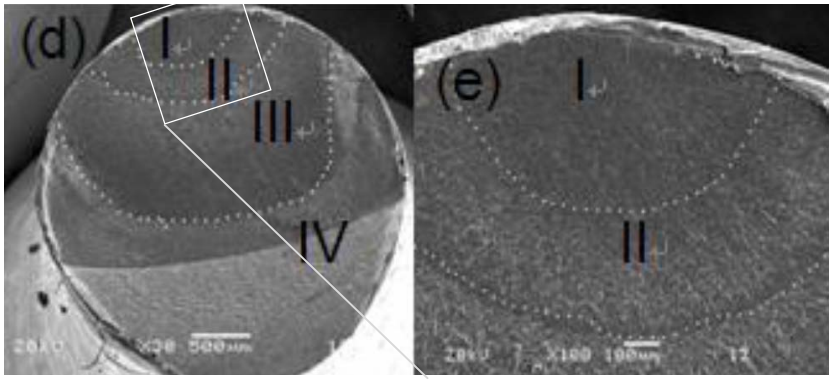

Figure 9. Fracture surface of untreated Ti-alloys, gigacycles

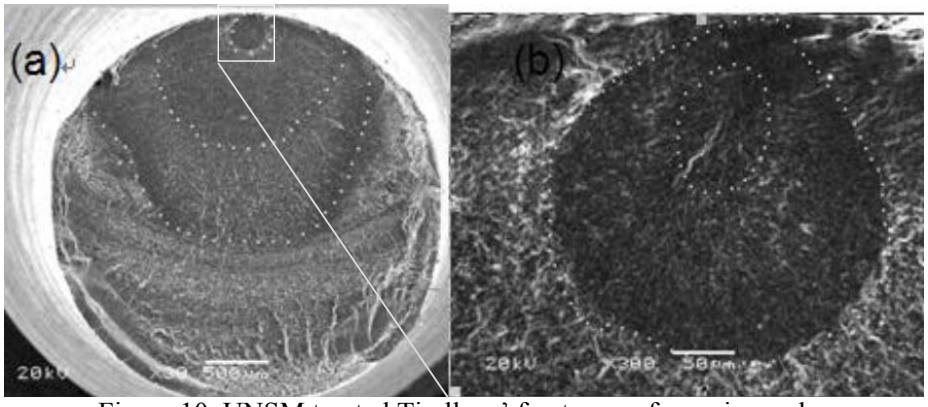

Figure 10. UNSM treated Ti-alloys' fracture surface, gigacycles

The crack initiation area appears as a white dot in the middle of dark spot (also known as "optically dark area", or ODA). This dark zone is relatively flat and circular, and relates to short crack propagation, where no crack closure is present. Typically, specimen with larger ODA has longer fatigue life [15, 16]. Outside of ODA there is wide fracture surface with large radial patter. There are some ridge patterns and striation.

2.3.2. Improvement of RCF strength and reduction of friction torque

In order to evaluate the effects of nanoskin on rolling contact fatigue strength of bearings steel SAE52100 (SUJ2), two kinds of tests were carried out: 6 balls test and roller test. The life cycle in 6 balls test is increased from 6.3 x 10^6 to 25.7 x 10^6 and in roller test increased from 4.9 x 10^6 to 10.2 x 10^6. Friction torque is 20~30% lower than that of untreated specimens as shown in Figure 8 [9, 10].

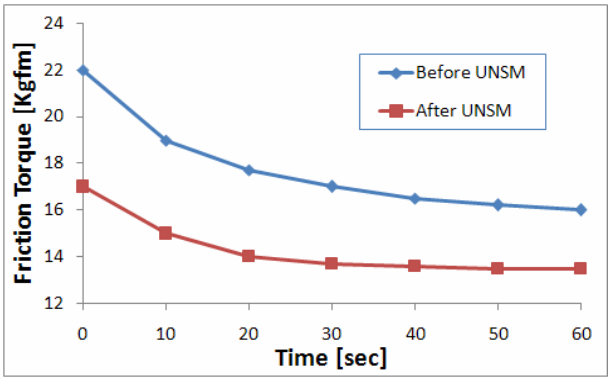

Figure 8. Friction Torque of 6 Balls Test Specimens Before and After UNSM (500rpm, 8000N)

2.3.3. Reduction of friction coefficient and wear rate

In order to evaluate the effects of nanoskin on tribological properties of SKD61 specimens, a dry pin-on-disc test was carried out. The friction coefficient and wear rate of UNSM treated specimens are reduced by 48% and 96%, respectively. Industrial tests of UNSM trimming knives for hot and cold rolling mills of high strength steel manufacturing had been carried out for several years. Results showed that UNSM generated nanoskin doubled production intervals between knives replacements, therefore increasing productivity and reducing production cost [9, 12, 14].

3. Conclusions

Due to effects of surface nano and/or micro scale roughness and texture, and subsurface nanoscale grain size with improved hardness and compressive residual stress of UNSM created nanoskin the limits of fatigue strength and rolling contact fatigue strength of conventional materials can be extended by nanoskin materials and components. Coincidental size and weight reduction of mechanical components can be obtained also by nano skin components as well. High cycle and very high cycle fatigue improvements are supported by changes in fracture mechanism as illustrated by fractographic analysis.

References

[1] Erik Oberg, Franklin D. Jones, Holbrook L. Norton and Henry H. Ryffel, Relation of Surface Texture to Tolerances, Machinery Handbook, 25th edn. (Industrial Press, New York, 1996)

[2] C. Chouqueta, J. Gavilleta, C. Ducrosa and F. Sanchette, Effect of DLC surface texturing on friction and wear during lubricated sliding, Materials Chemistry and Physics, Volume 123, 1 October 2010, Issues 2-3, pp. 367-371

[3] X. Wang, W. Liu, F. Zhou, D. Zhu, Preliminary investigation of the effect of dimple size on friction in line contacts, Trib. Int., Vol. 42(7), pp. 1118-1123.

[4] G.C. Buscaglia, I. Ciuperca, M. Jai, The effect of periodic textures on the static characteristics of thrust bearings, Journal of Tribology, Vol. 127, (2005) pp. 899–902.

[5] An Introduction to Iron and Steel Processing, JFE 21st Century Foundation, http://www.jfe-21st-cf.or.jp/chapter_1/1a_4.html

[6] G. Yanga, C.X. Huangb, C. Wanga, L.Y. Zhanga, C. Hua, Z.F. Zhangb and S.D. Wu, Enhancement of mechanical properties of heat-resistant martensitic steel processed by equal channel angular pressing, Materials Science and Engineering: A, Volume 515, Issues 1-2, 25 July 2009, pp. 199-206
[7] C.H. Han, Y.S. Pyoun and C.S. Kim, Ultrasonic Micro-Burnishing in View of Eco-Materials Processing Advances in Technology of Materials and Materials Processing, Vol.3, 2001, pp. 89-92.
[8] Cho I. H, Song G. H, Kim C. S, Nobuhide A, Suh C. M, Park J. H, Combs A, Park J, Pyoun Y. S. Nano structured surface modification of tool steel and its beneficial effects in mechanical properties, Journal of Mechanical Science and Technology, Vol.19, 2005, pp. 2151-2156.
[9] Inho Cho, Y.S. Pyoun, Nano surface modification of hub bearing race ways for increasing the dynamic load rating and decreasing the friction loss, 07APAC-280, 2007.
[10] Y. S. Pyoun, I.H. Cho, C. S Kim, J. H. Park, C.S. Lee, I. G Park, I. S Cho, J. Park, Tribological and RCF effects of UNSM treatment on the bearings 2nd International Conference on Advanced Tribology, Paper No. iCAT-124, Singapore, 2008.
[11] Y. S. Pyoun, J. H. Park, I.H. Cho., C.M. Suh, A. Amanov, A. Gafurov, J. Park. Tribological characteristics of radial journal bearings by ultrasonic nanocrystal surface modification technology, AMDP-2008, 13-15 October, Beijing, China, 2008.
[12] C.M. Suh, G.H. Song, M.S. Suh, Y.S. Pyoun, Fatigue and mechanical characteristics of nano-structured tool steel by ultrasonic cold forging technology, Materials Science and Engineering A, Vol.443, 2007, pp. 101-106.
[13] K.S. Shin, J.L. Dong, K. Shin, D.H. Yoo, J.S. Jung, S. J.Kim, J.H.Kim, Microstructure evolution and mechanical properties of SUS304 by ultrasonic and air blast shot peening, Proceeding of ICSP-10, pp. 523-528, Tokyo, Japan
[14] C.S. Suh, G.H. Song, H.D. Park, Y.S. Pyoun A Study of the Mechanical Characteristics of Ultrasonic Cold Forged SKD 61 International Journal of Modern Physics B, vol.20, 2006, pp. 4541-4546
[15] Wang QY, Accelerated Fatigue Testing by Ultrasonic Loading, Sichuan University (Engineering Science Edition), 2002, Vol.34, pp.6-11
[16] Zhiyong Huang, Daniele Wagner, Claude Bathias, Paul C. Paris, Subsurface crack initiation and propagation mechanisms in gigacycle fatigue, Acta Materialia 58 (2010), pp. 6046-6054

Efficient simulation of crack growth in multiple-crack systems considering internal boundaries and interfaces

Paul Judt[1,*], **Andreas Ricoeur**[1]

[1] Department of Engineering Mechanics, University of Kassel, 34125 Kassel, Germany
[*]Corresponding author: judt@uni-kassel.de

Abstract The paper presents numerical methods used for predicting crack paths in technical structures based on the theory of linear elastic fracture mechanics. To simulate crack growth, the FE-method is used in combination with a smart re-meshing algorithm. Different methods providing accurate crack loading parameters particularly for curved cracks such as the J-integral or stress intensity factors (SIF) are presented. Path-independent contour integrals [12] are used to avoid special requirements concerning crack tip meshing and to enable efficient calculations for domains including interfaces and internal boundaries. The integration paths being finite and far from the crack tip, special attention has to be directed to the treatment of the crack face integral since the calculation of the coordinate J_2 is challenging [5]. The same holds for the coordinate M_2^{II} of the interaction integral related to a mode-II auxiliary loading. In particular, the interaction of multiple cracks and internal boundaries and interfaces is investigated. Calculating the global J-integral, including all crack tips existing in a structure, leads to the necessity of a separation procedure to determine the parts of J related to each single crack tip.

Keywords J-integral, M-integral, mixed-mode fracture, curved crack faces, fictitious crack faces

1. Introduction

Path-independent integrals are widely applied to calculate loading quantities such as stress intensity factors, the energy release rate or the J-integral. The J-integral is based on Eshelby's [6] general theory of forces acting at singularities. Rice [12] and Cherepanov [4] applied the formulation of this path-independent integral to strain concentration problems like notches and cracks. Herrmann and Herrmann [10] extended Rices' approach of J, which was limited to straight cracks, by a formulation of the two-dimensional J_k-integral vector which is composed of the coordinate $J_1 = J$ and J_2. Bergez [2] presented a relation between J_k-integral and SIF. It is well-known that the calculation of the J_2-integral is challenging since the numerical treatment of the singular stresses at the crack tip is going along with problems finally leading to inaccurate results. A semi-analytical approach for the calculation of J_2 considering straight cracks was presented by Eischen [5].
The M-integral is a conservation integral based on the superposition of two loading scenarios [13, 14], i.e. the actual and an auxiliary loading. In general, the near tip solution is employed to obtain auxiliary fields limiting this method to straight cracks in homogeneous materials without interfaces. Gosz et. al. [7, 8] applied the M-integral to three-dimensional crack problems considering interfaces and curved crack fronts, however still maintaining straight crack faces.
This paper presents two new methods for calculating accurate values of J_2 which are valid for straight and curved cracks. Further, the M_k-interaction integral vector is calculated for arbitrary curved crack faces.
Crack path predictions for multiple crack systems are carried out classically by applying crack tip elements [3] or the M-integral associated with small integration contours [16]. Additionally, a separation procedure is introduced, to calculate accurate loading quantities from a global J_k-integral calculation, representing the sum of all $J_k^{(i)}$-integral vectors, related to the i-th crack tip. Resulting crack paths of a crack propagation simulation considering two cracks are presented.

2. Path-independent contour integrals

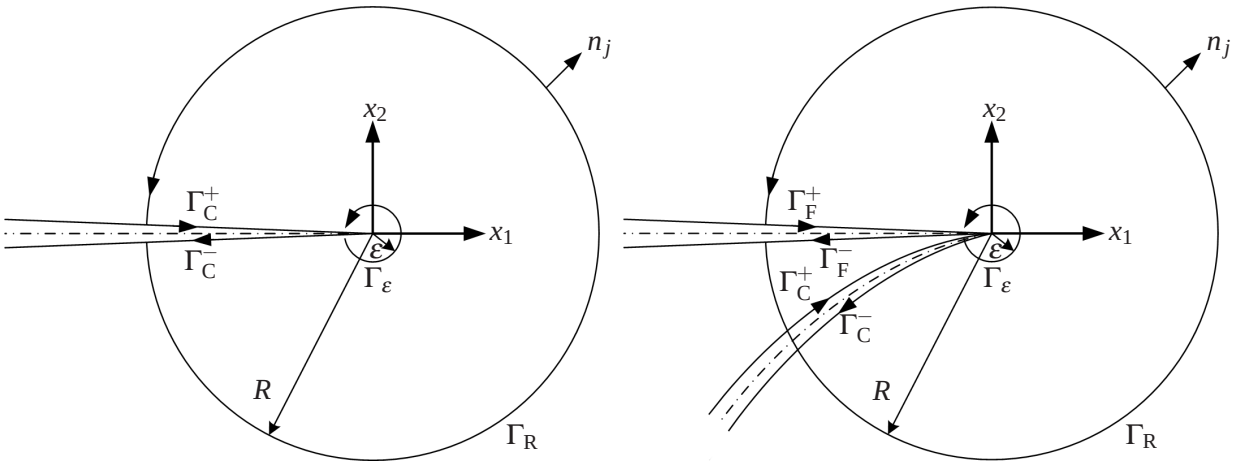

(a) (b)

Figure 1. Integration contours, actual and fictitious crack faces Γ_C and Γ_F for path-independent J_k and M_k-integrals.

Within the theory of Linear Elastic Fracture Mechanics (LEFM) the J_k-integral vector is a path-independent energy conservation integral. With an integration contour Γ_ε in the vicinity of the crack tip at a distance ε, the J_k-integral is defined as

$$J_k = \lim_{\varepsilon \to 0} \int_{\Gamma_\varepsilon} Q_{kj} n_j \mathrm{d}s \tag{1}$$

with Eshelby's tensor Q_{kj}, including the stress tensor σ_{mn}, the strain tensor ε_{mn} and the displacement derivatives $u_{i,k}$:

$$Q_{kj} = \frac{1}{2}\sigma_{mn}\varepsilon_{mn}\delta_{kj} - \sigma_{ij}u_{i,k} \tag{2}$$

The Kronecker identity tensor is denoted as δ_{kj}. In LEFM the coordinates of Eq. (1) are related directly to the stress intensity factors [2]:

$$J_1 = \frac{K_\mathrm{I}^2 + K_\mathrm{II}^2}{E'}, \qquad J_2 = -2\frac{K_\mathrm{I} K_\mathrm{II}}{E'} \tag{3}$$

For plain stress $E' = E$ and for plain strain $E' = E/\left(1-\nu^2\right)$. The energy release rate G is the projection of J_k onto the unit vector of crack propagation direction z_k:

$$G = J_k z_k \tag{4}$$

If the J_k-integral is calculated, assuming two different superimposed loading scenarios $^{(1)}$ and $^{(2)}$ for an arbitrary crack configuration, one obtains the following expression:

$$J_k^{(1)+(2)} = \lim_{\varepsilon \to 0} \int_{\Gamma_\varepsilon} Q_{kj}^{(1)+(2)} n_j \mathrm{d}s = \lim_{\varepsilon \to 0} \int_{\Gamma_\varepsilon} \left(Q_{kj}^{(1)} + Q_{kj}^{(2)} + Q_{kj}^{(1/2)}\right) n_j \mathrm{d}s = J_k^{(1)} + J_k^{(2)} + J_k^{(1/2)} \tag{5}$$

The third term of Eq. (5) is the interaction integral vector $J_k^{(1/2)}$ and will be denoted from now on as M_k,

$$M_k = \lim_{\varepsilon \to 0} \int_{\Gamma_\varepsilon} Q_{kj}^{(1/2)} n_j \mathrm{d}s \tag{6}$$

with Eshelby's tensor related to the interaction integral

$$Q_{kj}^{(1/2)} = \frac{1}{2}\left(\sigma_{mn}^{(1)}\varepsilon_{mn}^{(2)} + \sigma_{mn}^{(2)}\varepsilon_{mn}^{(1)}\right)\delta_{kj} - \left(\sigma_{ij}^{(1)}u_{i,k}^{(2)} + \sigma_{ij}^{(2)}u_{i,k}^{(1)}\right) \tag{7}$$

For straight crack faces, the near-tip solution yields valid fields ε_{mn}, σ_{mn}, $u_{i,k}$ associated to an auxiliary loading configuration and is therefore usually applied as auxiliary field. The relation between the coordinates of Eq. (6) and stress intensity factors is as follows:

$$M_1^{\mathrm{I}} = 2\frac{K_{\mathrm{I}}}{E'}, \qquad M_2^{\mathrm{I}} = -2\frac{K_{\mathrm{II}}}{E'}, \qquad M_1^{\mathrm{II}} = 2\frac{K_{\mathrm{II}}}{E'}, \qquad M_2^{\mathrm{II}} = -2\frac{K_{\mathrm{I}}}{E'} \tag{8}$$

The superscripts I and II denote a single mode-I or single mode-II auxiliary loading. If finite integration contours Γ_{R} are considered, the coordinates of J_k and M_k in general become path-dependent. If crack faces are straight, see Fig. 1(a), the path-dependence is restricted to J_2 and M_2^{II} in the case of mixed-mode loading. If curved crack faces are considered, see Γ_{C} in Fig. 1(b), both coordinates of J_k and M_k are depending on the chosen integration contour Γ_R. To hold path-independence, crack face integrals with $\mathrm{d}\Gamma_{\mathrm{C}} = \mathrm{d}\Gamma_{\mathrm{C}}^{+} = -\mathrm{d}\Gamma_{\mathrm{C}}^{-}$ have to be introduced, describing the jump of Eshelby's tensor across the crack faces:

$$J_k = \int_{\Gamma_{\mathrm{R}}} Q_{kj} n_j \mathrm{d}s + \int_{\Gamma_{\mathrm{C}}} \left[\!\left[Q_{kj} \right]\!\right]_{-}^{+} n_j \mathrm{d}s \tag{9a}$$

$$M_k = \int_{\Gamma_{\mathrm{R}}} Q_{kj}^{(1/2)} n_j \mathrm{d}s + \int_{\Gamma_{\mathrm{C}}} \left[\!\left[Q_{kj}^{(1/2)} \right]\!\right]_{-}^{+} n_j \mathrm{d}s \tag{9b}$$

In contrast to the J_k-integral according to Eq. (9a), the M_k-integral according to Eq. (9b) is still not path-independent, if curved crack faces are considered. Path-independence is finally achieved including an integration along the fictitious crack surfaces $\mathrm{d}\Gamma_{\mathrm{F}} = \mathrm{d}\Gamma_{\mathrm{F}}^{+} = -\mathrm{d}\Gamma_{\mathrm{F}}^{-}$, see Fig. 1(b):

$$M_k = \int_{\Gamma_{\mathrm{R}}} Q_{kj}^{(1/2)} n_j \mathrm{d}s + \int_{\Gamma_{\mathrm{C}}} \left[\!\left[Q_{kj}^{(1/2)} \right]\!\right]_{-}^{+} n_j \mathrm{d}s + \int_{\Gamma_{\mathrm{F}}} \left[\!\left[Q_{kj}^{(1/2)} \right]\!\right]_{-}^{+} n_j \mathrm{d}s \tag{10}$$

These are corresponding to the auxiliary fields which are taken from the asymptotic crack tip solutions. Thus, the fictitious crack faces Γ_{F} and the actual ones Γ_{C} always coincide at the crack tip. The integration in the vicinity of the crack tip based on numerical values provided from the FE-calculation is challenging. As the numerical representation of the singularity in stresses and strains deviates strongly from analytic solutions, the calculation of crack face integrals needs a special treatment.

3. Extended crack face integration

In this section, two methods are presented producing sufficiently accurate results for the crack face integration. Both are applied to the J_k- and M_k- integral calculation, however only the first one is

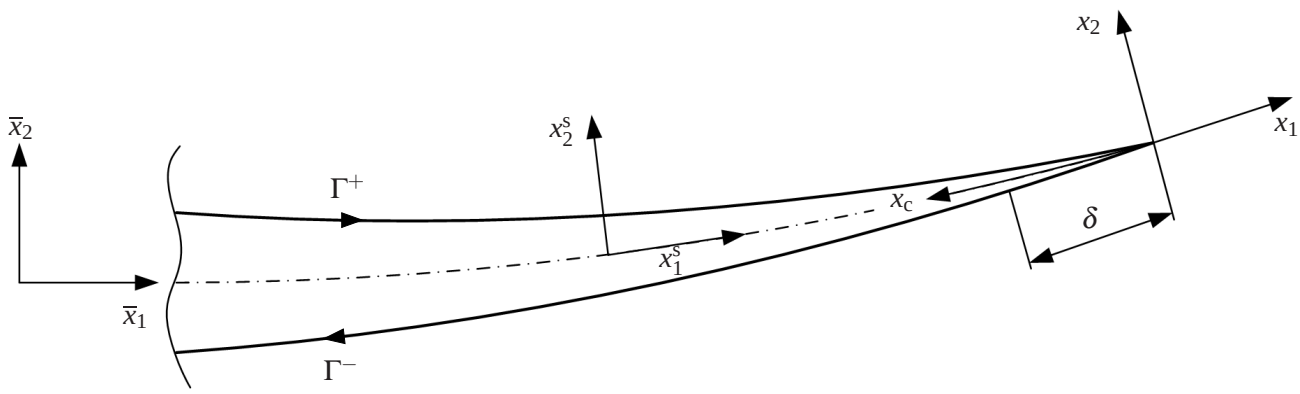

Figure 2. Curved crack faces Γ^+, Γ^-, crack tip coordinate system x_i, global coordinate system $\bar{x}_i$, local crack face coordinate system x_i^s depending on the position, arc length x_c along the crack faces with its origin at the crack tip, region δ where numerically calculated values for crack face integrals deviate strongly from the analytic ones.

presented here.
When calculating J_k by integrating along a circular contour Γ_R with the radius R and considering curved cracks as shown in Fig. 1(b), the crack face integral needs to be taken into account. Is the crack face integral calculated conventionally, this leads to a considerable error in the second coordinate J_2, and therefore in the SIF calculated from J_k with Eqs. (3):

$$K_{\mathrm{I}} = \pm\sqrt{\frac{E' J_1}{2}\left[1 \pm \sqrt{1-\left(\frac{J_2}{J_1}\right)^2}\right]}, \qquad K_{\mathrm{II}} = \pm\sqrt{\frac{E' J_1}{2}\left[1 \mp \sqrt{1-\left(\frac{J_2}{J_1}\right)^2}\right]} \tag{11}$$

3.1. Method 1: Analytic extension method

In the vicinity of the crack tip, the integrand can be formulated analytically. Therefore, the crack face integral of Eq. (9a) is divided into one part calculated numerically and the other part calculated analytically:

$$J_k = \int_{\Gamma_{\mathrm{R}}} Q_{kj} n_j \mathrm{d}s + \int_R^{\delta} \left[\!\left[Q_{kj} \right]\!\right]_-^+ n_j \mathrm{d}s + \int_{\delta}^{0} \left[\!\left[Q_{kj} \right]\!\right]_-^+ n_j \mathrm{d}s \tag{12}$$

The parameter δ separates both parts, see Fig. 2. The crack is assumed to be straight in the vicinity of the crack tip, as the curvature can be neglected for small δ. For such a crack, the dominant terms are the first terms of the series expansions $\sigma_{ij}^{(n)}$ and $u_i^{(n)}$ found by Williams [15], representing an infinite sum of eigenfunctions, completely describing the stress and displacement fields in a cracked body

$$\sigma_{ij}^{(n)}(r,\varphi) = \sum_{n=1}^{\infty} r^{\frac{n}{2}-1}\left[a_n M_{ij}^{(n)}(\varphi) + b_n N_{ij}^{(n)}(\varphi)\right] \tag{13a}$$

$$u_i^{(n)}(r,\varphi) = \frac{1}{2\mu}\sum_{n=1}^{\infty} r^{\frac{n}{2}}\left[a_n F_i^{(n)}(\varphi) + b_n G_i^{(n)}(\varphi)\right] \tag{13b}$$

with a_n and b_n being constant coefficients and $M_{ij}^{(n)}(\varphi)$, $N_{ij}^{(n)}(\varphi)$, $F_i^{(n)}(\varphi)$ and $G_i^{(n)}(\varphi)$ trigonometric angular functions. The coefficients a_1 and b_1 of the first eigenfunction are related to the SIF K_{I} and K_{II} and the coefficient a_2 of the second eigenfunction is related to the T-stress T_{11}:

$$K_{\mathrm{I}} - \mathrm{i}K_{\mathrm{II}} = \sqrt{2\pi}\,(a_1 + \mathrm{i}b_1)\,, \qquad T_{11} = 4a_2 \tag{14}$$

Substituting Eqs. (13) into Eq. (2), calculating the jump of Eshelby's tensor across the crack faces according to the third term on the right hand side of Eq. (12) and considering Eq. (14), the analytical part of the crack face integral is obtained:

$$J_2^{\mathrm{ana}} = \int_{\delta}^{0} \left[\!\left[Q_{kj} \right]\!\right]_{-}^{+} \mathrm{d}s = 8\,\frac{K_{\mathrm{II}} T_{11} \sqrt{\delta}}{E' \sqrt{2\pi}} \tag{15}$$

As $n_j = (0, \pm 1)$ all along the crack faces, the integral of Eq. (15) contributes to J_2 only. The remaining two terms of Eq. (12) are calculated numerically, excluding the small region δ at the crack tip from the integration, now reading J_k^{num} [11]. An iterative procedure is necessary to calculate the analytical part J_2^{ana}, see Fig. 3.

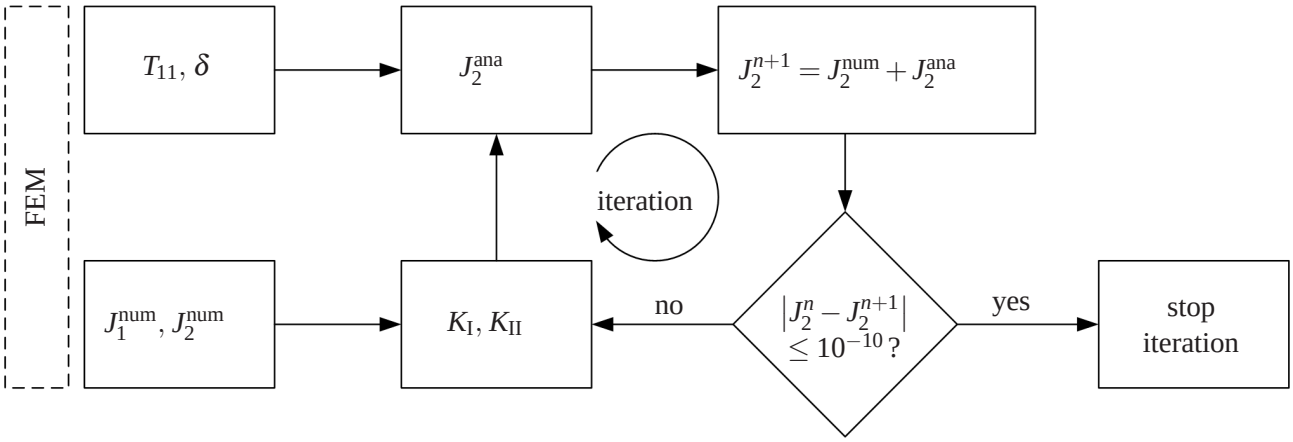

Figure 3. Flow chart of the iterative scheme for the calculation of the analytical part of the J_k-integral.

The constant T-stress on the crack faces is therefore determined at the position $r = \delta$ from the series expansion Eq. (13a):

$$T_{11} = \frac{1}{2}\left(\sigma_{11}^{\mathrm{s}}(\delta, +\pi) + \sigma_{11}^{\mathrm{s}}(\delta, -\pi)\right) \tag{16}$$

The stresses on the positive and negative crack faces $\sigma_{11}^{\mathrm{s}}(\delta, \pm\pi)$ are extracted from the FE calculation and substituted into Eq (16). As a first approach, K_{II} is calculated by substituting J_1^{num} and $J_2^{\mathrm{num}} = J_2^n$ into Eq. (11). J_2^{ana} is calculated by substituting T_{11}, K_{II} and δ into Eq. (15). The value J_2^{n+1} of the present step is the sum of J_2^{num} and J_2^{ana}. If the absolute difference between J_2^{n+1} of the present and J_2^n of the previous step is below a critical value, the iterative procedure is stopped and the final value is $J_2 = J_2^{n+1}$. If the stop criterion is not fulfilled, K_{II} of the next step is now calculated by substituting J_1^{num} and J_2^{n+1} into Eq. (11) and so on.

3.2. Method 2: Extrapolation method

The research revealed, that the incorrect calculation of J_2 is an outcome of non-symmetric numerical errors within the region δ at the crack tip, which are related to a mixed-mode loading configuration

[11]. A mixed-mode loading is a superposition of a single mode-I and single mode-II loading. Thus, the values of stresses and strains are split into parts related to mode-I and mode-II loading as follows. The stresses and displacement gradients related to the symmetric crack tip opening are calculated according to:

$$\sigma_{11}^{\mathrm{I}}(x_{\mathrm{c}}) = \frac{1}{2}\left(\sigma_{11}^{\mathrm{s}}(x_{\mathrm{c}},+\pi) + \sigma_{11}^{\mathrm{s}}(x_{\mathrm{c}},-\pi)\right) \tag{17a}$$

$$u_{1,1}^{\mathrm{I}}(x_{\mathrm{c}}) = \frac{1}{2}\left(u_{1,1}^{\mathrm{s}}(x_{\mathrm{c}},+\pi) + u_{1,1}^{\mathrm{s}}(x_{\mathrm{c}},-\pi)\right) \tag{17b}$$

The stress and displacement gradient related to the antimetric crack tip opening are determined by subtracting the symmetric parts from the total values, i.e.

$$\sigma_{11}^{\mathrm{II}}(x_{\mathrm{c}},\pm\pi) = \sigma_{11}^{\mathrm{s}}(x_{\mathrm{c}},\pm\pi) - \sigma_{11}^{\mathrm{I}}(x_{\mathrm{c}}) \tag{18a}$$

$$u_{1,1}^{\mathrm{II}}(x_{\mathrm{c}},\pm\pi) = u_{1,1}^{\mathrm{s}}(x_{\mathrm{c}},\pm\pi) - u_{1,1}^{\mathrm{I}}(x_{\mathrm{c}}) \tag{18b}$$

As the mode-I stresses and strains according to Eqs. (17) exhibit a non-singular behavior on the crack faces, extrapolating σ_{11}^{I} and $u_{1,1}^{\mathrm{I}}$ towards the crack tip is feasible. From Fig. 4(a) is becomes obvious, that particularly σ_{11}^{I} exhibits large numerical errors and thus an extrapolation is reasonable [11]. The mode-I values within $[0,\delta]$ are replaced by those, calculated from a linear regression. Rearranging Eqs. (18), the mode-I and mode-II stresses and strains are recombined and the crack face integral is calculated as usual following Eq. (9a), considering the new values. Substituting the resulting values J_k into Eq. (11), this provides accurate SIF for curved cracks under mixed-mode conditions.

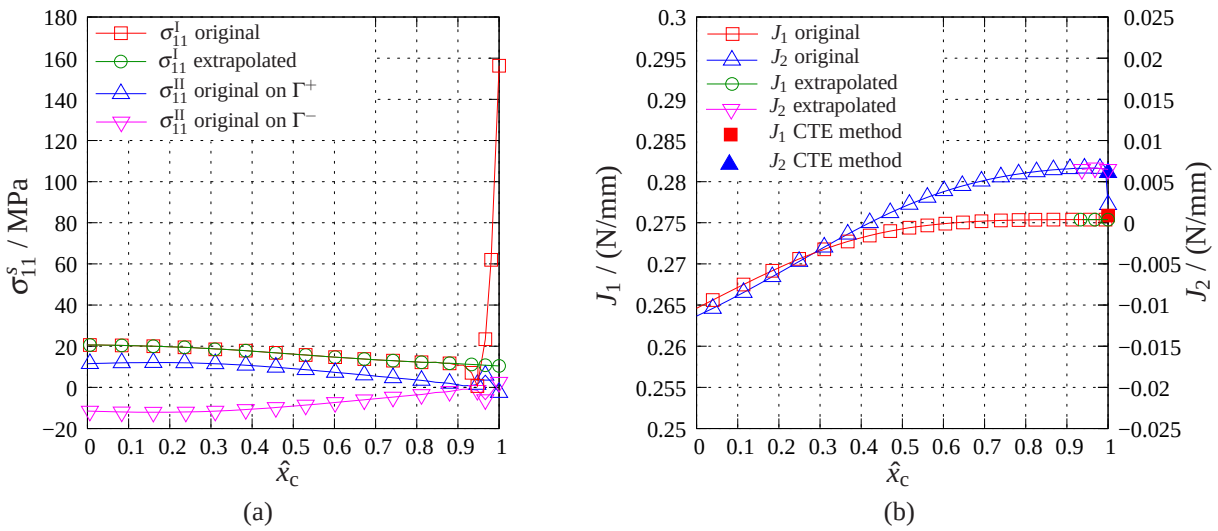

Figure 4. (a) Decomposed mode-I and mode-II stress distributions σ_{11}^{I} and $\sigma_{11}^{\mathrm{II}}$, original and extrapolated. (b) Numerically calculated J_k-integral, crack face integral calculated within the range $[0,\hat{x}_{\mathrm{c}}]$, comparison of different methods.

In Fig. 4(a) the tangential stress σ_{11}^{s} on the crack faces is plotted vs. a normalized crack face coordinate $\hat{x}_{\mathrm{c}} = (R - x_{\mathrm{c}})/R$, with $\hat{x}_{\mathrm{c}} = 1$ at the crack tip and $\hat{x}_{\mathrm{c}} = 0$ for $x_{\mathrm{c}} = R$. The considered boundary value problem is that one of a Double Cantilever Bream with dissimilar forces $F_1 = 100\mathrm{N}$ and $F_2 = 99\mathrm{N}$

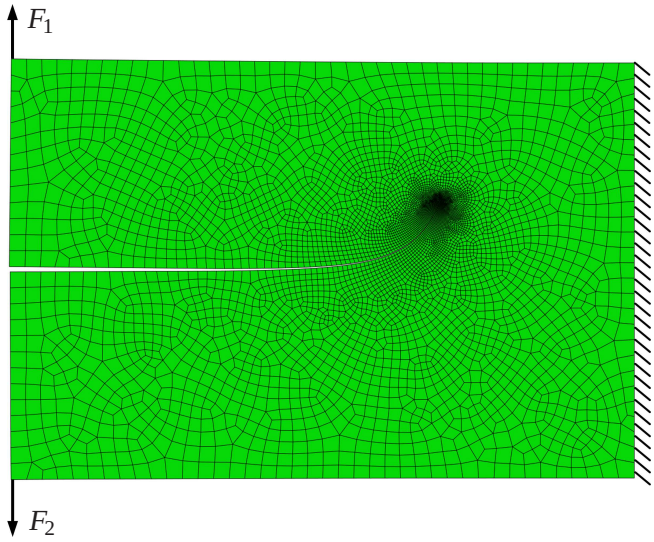

Figure 5. FE-mesh of the grown curved crack shown in a deformed configuration.

acting at the front end leading to a curved crack path, see Fig. 5. The corresponding J_k-integral calculated within the range $[0, \hat{x}_c]$ is shown in Fig. 4(b). The function $J_k(\hat{x}_c)$ has got nothing to do with path-dependence but enables to localize the incorrect contribution to the crack face integral. The value that J_k reaches approaching the crack tip $\hat{x}_1 = 1$ is the relevant loading quantity according to Eqs. (12) and (1). For the sake of comparison, results from the Crack Tip Element (CTE) method [9, 1] have been included in the figure.
The choice of the parameter δ has an influence on the results. For $\delta < \delta_c$, not all inaccurate values are excluded from the numerical integration and therefore the resulting values of J_k are inaccurate. For $\delta > \delta_c$, the values of J_k obtained by the extrapolation method (Method 2) show little influence. On the other hand, the values of J_k calculated by the analytic extension method (Method 1) show increasing deviation for increasing δ. The research revealed that the best choice of δ_c includes the region of the first three element rings around the crack tip. Both methods are suitable for the accurate calculation of the coordinate M_2^{II} as well.

Table 1. Comparison of stress intensity factors calculated from the CTE-method and the M_k-integral considering the actual crack face integral (ACFI) and the fictitious crack face integral (FCFI), neglecting FCFI only or neglecting both FCFI and ACFI.

	CTE	M_k	M_k without FCFI	M_k without FCFI and ACFI
$K_{\mathrm{I}}/(\mathrm{MPa}\sqrt{\mathrm{mm}})$	240.39	240.31	276.77	261.72
$K_{\mathrm{II}}/(\mathrm{MPa}\sqrt{\mathrm{mm}})$	-2.86	-2.95	-38.38	7.26

Results of SIF calculated from the CTE-method [9, 1] and the M_k-integral are presented in Tab. 1. It is obvious, that neglecting the integration along the fictitious crack faces of the auxiliary fields produces considerable errors. The same holds, when neglecting both the fictitious crack face integral (FCFI) and the actual crack face integral (ACFI), as shown in the last column of Tab. 1.

4. Systems of multiple interacting cracks

The loading quantities of multiple crack systems, related to every single crack tip, are calculated by path independent integrals. With regard to crack tips approaching interfaces such as material

interfaces, internal boundaries or crack surfaces, it is beneficial to evaluate the integrals along large contours containing all N tips of a multiple crack system, see Fig. 6(a). For comparison, the crack paths are simulated by calculating the integral along small contours in the vicinity of the crack tip, as shown in Fig. 6(b). The resulting value of the J_k-integral along a large contour Γ_0 equals the sum of

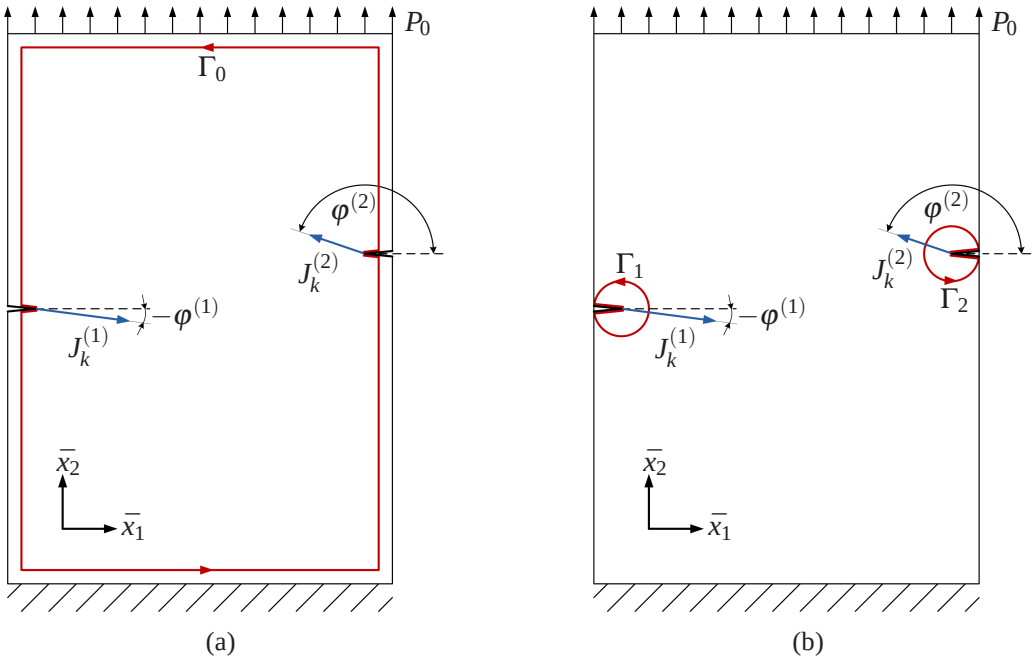

Figure 6. Integration contours Γ_0, Γ_1, Γ_2 for path-independent J_k and M_k-integral and J_k-integral vectors $J_k^{(i)}$.

the loading quantities of all N crack tips.

$$J_1 = \sum_{i=1}^{N} \cos\varphi^{(i)} \left| J_k^{(i)} \right| \tag{19a}$$

$$J_2 = \sum_{i=1}^{N} \sin\varphi^{(i)} \left| J_k^{(i)} \right| \tag{19b}$$

The angle $\varphi^{(i)}$ is related to the global coordinate system $\bar{x}_i$. The applied crack deflection criterion is that of the *maximum energy release rate*, i.e. the J_k-vector points into the direction of the crack propagation z_k, see Eq. (4). This and the principle of minimum potential energy lead to the auxiliary condition, that the sum of the absolute values of the J_k-integrals related to every single crack tip, reaches a global maximum. Further, each absolute value $J_k^{(i)}$ must be smaller or equal to the value of the critical energy release rate G_c. If another condition is required, in order to reduce the solution space it can be postulated that the crack deflection angle must be smaller or equal to a maximum value $\mathrm{d}\varphi_{\max}$. The latter criterion is motivated by the fact that cracks usually show a smooth curvature whereas sharp kinks are only observed if the loading regime is subjected to a sudden and fundamental change.

$$\sum_{i=1}^{N} \left| J_k^{(i)} \right| \stackrel{!}{=} \max \tag{20a}$$

$$\left| J_k^{(i)} \right| \leq G_c \tag{20b}$$

$$\mathrm{d}\varphi \leq \mathrm{d}\varphi_{\max} \tag{20c}$$

Developing a separation procedure to determine $J_k^{(i)}$ based on Eqs. (19), this method has to satisfy the conditions according to Eqs. (20). A numerical validation is achieved by calculating the J_k-integral along small contours around the crack tip, see Fig. 6(b). The loading quantities calculated by small contours Γ_i must be equal to the values that are calculated by the separation procedure. Here it must be taken into account that numerical errors dominate, if Γ_i is chosen too small, whereas large contours must not intersect other crack faces or boundaries. In Fig. 7(b) results of a simulation with two cracks are presented. The plate specimen is exposed to a uniform load $P_0 = 100$MPa and exhibits two non-symmetric incipient cracks of the length $a_1 = a_2 = 5$mm. All geometric dimensions are shown in Fig. 7(a). A crack growth simulation with fatigue crack growth rates assumed to be constant and equal for both cracks, leads to the crack paths as shown in Fig. 7(b).

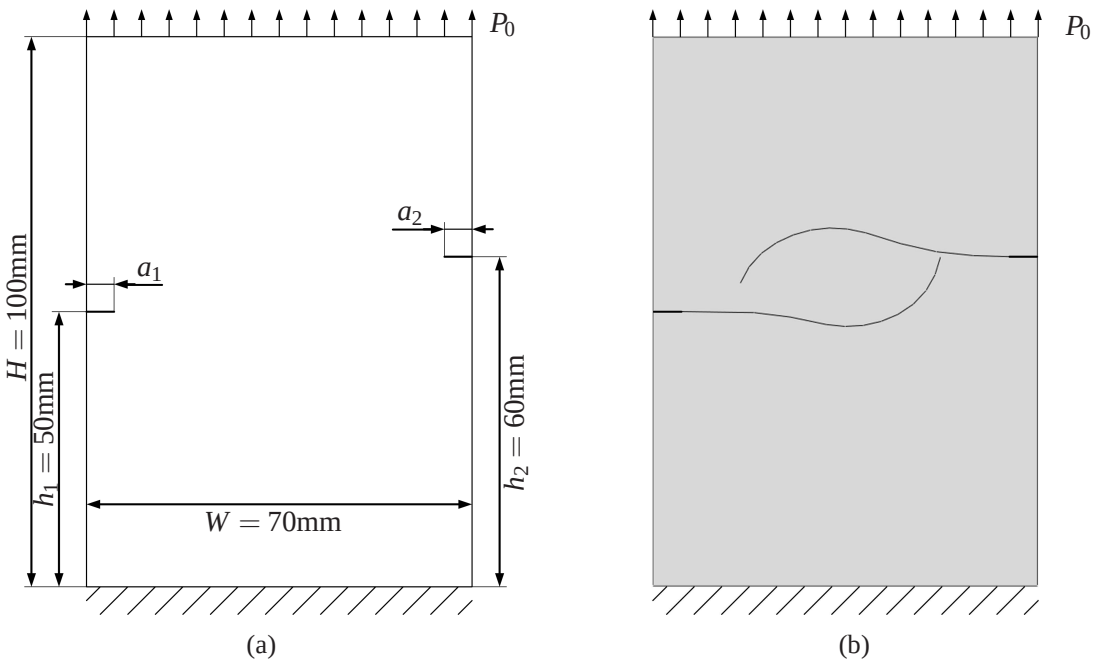

Figure 7. (a) Geometric dimensions of plate specimen exhibiting two non-symmetric incipient cracks. (b) Crack paths resulting from a crack growth simulation exposing the specimen to a uniform load $P_0 = 100$MPa.

5. Closure

Introducing path-independent integrals J_k and M_k, the necessity of the calculation of crack face integrals is outlined. Considering interfaces, internal boundaries or crack surfaces, it is beneficial to apply large contours including crack face integrals for the calculation of J_k or M_k. To achieve path-independence for the M_k-integral considering curved crack faces, an integration along the fictitious crack faces of the corresponding auxiliary fields is nessecary. When calculating the stress intensity factors or the energy release rate from path independent integrals, it is inevitable to calculate these integrals accurately. The challenging calculation of the crack face integrals is explained and two new

methods to calculate accurate values are presented. An analytical extension method and the extrapolation of singular stresses and strains on the crack faces provide very good results for straight and curved cracks.

The J_k-integral is applied to multiple crack systems, calculating a global value of J_k, being the sum of all local values related to every single crack tip. Auxiliary conditions are introduced to solve a global minimization problem. A separation procedure enables to calculate loading quantities related to each crack tip. Based on the specimen in Fig. 7, experiments are about to be carried out, in order to verify the theoretically predicted crack patterns.

References

[1] R. S. Barsoum, On the use of isoparametric finite elements in linear fracture mechanics. Int J Numer Methods Eng, 10 (1976) 25-37.

[2] D. Bergez, Determination of stress intensity factors by use of path-independent integrals. Mech Res Commun, 1 (1974) 179-180.

[3] P. O. Bouchard, F. Bay, Y. Chastel, I. Tovena, Crack propagation modelling using an advanced remeshing technique. Comput Methods Appl Mech Eng, 189 (2000) 723-742.

[4] G. P. Cherepanov, Mechanics of brittle fracture, McGraw-Hill, New York, 1979.

[5] J. W. Eischen, An improved method for computing the J_2 integral. Eng Fract Mech, 26 (1987) 691-700.

[6] J. D. Eshelby, The force on an elastic singularity. Solid State Phys, 3 (1956) 79-144.

[7] M. Gosz, J. Dolbow, B. Moran, Domain integral formulation for stress intensity factor computation along curved three-dimensional interface cracks. Int J Solids and Struct, 35 (1998) 1763-1783.

[8] M. Gosz, B. Moran, An interaction energy integral method for computation of mixed-mode stress intensity factors along non-planar crack fronts in three dimensions. Eng Fract Mech, 66 (2002) 299-319.

[9] R. D. Henshell and K. G. Shaw, Crack tip finite elements are unnecessary. Int J Numer Methods Eng, 9 (1975) 495-507.

[10] A. G. Herrmann, G. Herrmann, On energy release rates for a plane crack. J Appl Mech, 48 (1981) 525-528.

[11] P. O. Judt, A. Ricoeur, Accurate loading analyses of curved cracks under mixed-mode conditions applying the J-integral. Submitted to Int J Fract.

[12] J. R. Rice, A path independent integral and the approximate analysis of strain concentration by notches and cracks. J Appl Mech, 35 (1968) 379-386.

[13] M. Stern, E. B. Becker, R. S. Dunham, A contour integral computation of mixed-mode stress intensity factors. Int J Fract, 12 (1976) 359-368.

[14] S. S. Wang, J. F. Yau, H. T. Corten, A mixed-mode crack analysis of rectilinear anisotropic solids using conservation laws of elasticity. Int J Fract, 16 (1980) 247-259.

[15] M. L. Williams, On the stress distribution at the base of a stationary crack. J Appl Mech, 24 (1957) 109-114.

[16] G. Zi, J.-H. Song, E. Budyn, S.-H. Lee, T. Belytschko, A method for growing multiple cracks without remeshing and its application to fatigue crack growth. Model Simul Mater Sci Eng, 12 (2004) 901-915.

Crack Growth Life Assessment on Turbine Component under Combined Fatigue Loading

Dianyin Hu[1,*], **Rongiqao Wang**[1], **Huawei Liu**[1], **Jiaming Wei**[1]

[1] School of Energy and Power Engineering, BeiHang University, Beijing 100191, China
* Corresponding author: hdy@buaa.edu.cn

Abstract This paper focuses on a crack growth life assessment method for a turbine component under high-low combined cycle fatigue (HLCCF) loading through experimental and numerical methods. Crack growth tests under HLCCF loading on five full scale turbine components, attached to actual turbine discs, were conducted at elevated temperature by using a Ferris wheel combined fatigue system to simulate the stress under HLCCF loading and temperature distributions. Then, the fracture mechanics (FM) analysis was utilized to simulate crack growth of the turbine component to implement crack growth. The experimental life data agrees well with the crack growth life prediction for the turbine component. In summary, this paper provides a new way to estimate the crack growth lifetime criterion of the turbine components under HLCCF loading through experimental and numerical investigations.

Keywords High-low combined cycle fatigue, Crack growth life, Turbine component, Elevated temperature

1. Introduction

The turbine blades of an aero-engine are generally attached to the disc by means of a fir-tree design, a typical multiple load path structure, to allow for different rates of expansion between the disc and the blade while still holding the blade firmly against centrifugal loads. During operation, the fir-tree attachments are subjected to significant tensile stresses due to centrifugal loading and during the flight cycle may experience aerodynamically induced vibrations, leading to additional stresses. The amplitude of the vibrational loading is typically much smaller than that due to centrifugal loading and hence vibration is generally thought to give rise to high cycle fatigue (HCF). In contrast, the effect of centrifugal loading is frequently considered to be low cycle fatigue (LCF). Under the overall high-low combined cycle fatigue (HLCCF) loading, the fatigue damage of the turbine attachments is largely increased[1,2,3,4]. These effects may be responsible for the unscheduled crack failures in service of the mortise on a certain aeroengine second turbine disc.

Conventional life assessment methods of blade-disc connections of gas turbines are almost based on finite element analysis [5] and the experimental data of specimens and component-like specimens instead of actual components so as to reduce experimental costs [6,7,8]. However, the actual crack growth and fracture failure of the mortise teeth are not only determined by the characteristics of the material, but are also affected by the structure, dimension, and the teeth space of the mortise. Furthermore, the differences in crack growth lives between laboratory specimens and full scale components can arise from some characteristics, such as geometry, volume and manufacture process, and therefore influences the accuracy of life assessment. To overcome the above shortcomings, the crack growth life prediction method of the blade-disc connection based on experimental life data of a full scale turbine blade attached to actual turbine disc in conjunction with the fracture mechanics (FM) analysis, is more accurate, since the components own the same manufacture process with real flight turbine components.

The only way to accurately predict the life of a fir-tree contact is to perform fatigue test on a full scale turbine blade attached to an actual turbine disc. For this study, the most challenge work is how to simulate operating conditions of actual turbine attachments in laboratory, especially under

HLCCF loading at elevated temperature.

This paper focuses on a crack growth life assessment method for a turbine component under HLCCF loading through experimental and numerical methods, as shown in Figure 1. Crack growth tests on five groups of full scale turbine components, attached to an actual turbine disc, were conducted under HLCCF loading at elevated temperature. In this study, we have developed a new Ferris wheel combined fatigue system to simulate the stress under HLCCF loads and temperature distributions of a full scale turbine blade attached to a part of actual turbine disk instead of simulated blades at elevated temperature based on our previous test system [9], and the details can be referred to [4]. Then the fracture mechanics (FM) analysis was utilized to simulate crack growth of the turbine component to implement crack growth. The lifetime criterion for withdrawal from service of turbine component was established based on experimental life data and predicted crack growth life.

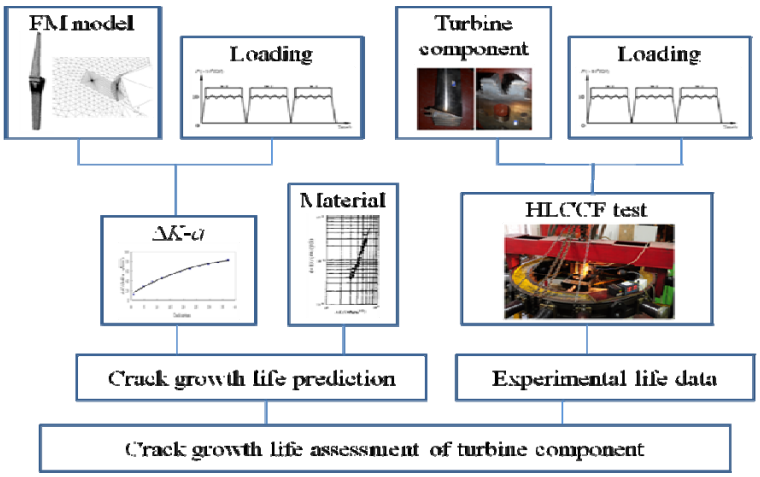

Figure 1. Strategy for crack growth life assessment of turbine component under HLCCF loading

2. Crack growth tests on turbine components

2.1. Experimental system for actual turbine attachment under HLCCF loading

The loading scheme is the key technique of this experiment to achieve failure rendition of the mortise teeth in the laboratory. The diagrammatic sketch of the actual loading is shown in Figure 2. Where, F is the low cycle loading due mainly to the centrifugal force of the blade, and M is the vibration bending moment.

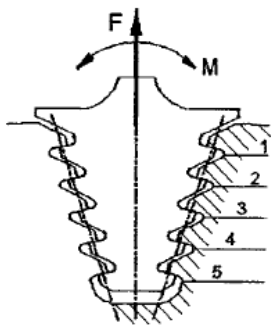

Figure 2. A sketch of an attachment structure and loading

To achieve a rational and noninterfering treatment of the HLCCF loading, a low and high cycle noninterference loading method for a full scale turbine blade attached to a part of the actual turbine disk is presented referred to [4] using a Ferris Wheel (a LCF tester). The sketch is shown in Figure

3. For performing a life test on an actual turbine attachment under HLCCF loading, there are two key techniques including a high and low cycle nointerference loading method and a blade clamp for a full scale turbine blade.

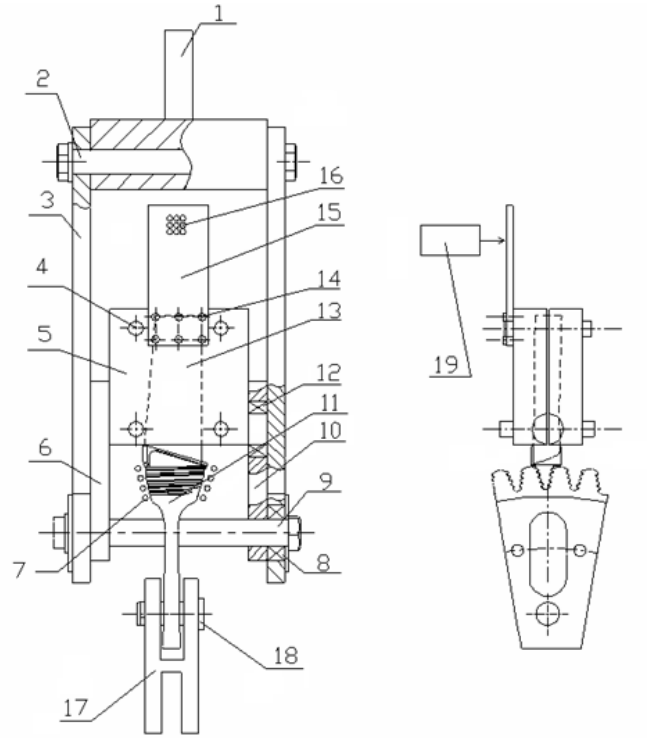

1.Upper jointer for LCF loading 2.Upper load-transmission pin 3.Drawplate 4.Hold-down bolt 1 5.Blade clamp 6.Left load-transmission plate 7.Heating coil 8.Rolling bearing 1 9.Load-bearing bar 10.Right load-transmission plate 11.Part of actual turbine disc 12.Rolling bearing 2 13.Actual turbine blade 14.Hold-down bolt 2 15.HCF loading transmission plate 16.Vibration point 17.Lower jointer for LCF loading 18.Lower load-transmission pin 19.Electromagnetic vibrator

Figure 3. A sketch of the HLCCF loading method

The HLCCF loading method places the LCF load exerting point from load-transmission pin (see (2) in Figure 3) to the back of the mortise through the drawplate (see (3) in Figure 3), then transmitting the loading using a load-bearing bar (see (9) in Figure 3) and a pair of load-transmitting plates (see (6), (10) in Figure 3) to the bearing ear welded to the blade clamp (see (5) in Figure 3). Meanwhile, there is a pair of rolling bearing (see (12) in Figure 3) between the loading-transmission plates and the bearing ear so as to reduce the friction of vibration transmission. Thus the high cycle vibrating center point moves backward and lengthens the arm of the high cycle vibration. Another pair of rolling bearings (see (8) in Figure 3) is placed between the drawplate and the load-bearing bar to further reduce the friction of vibration transmission. Therefore, the vibrating force can be transmitted to the mortise teeth with no loss.

A clamp to apply LCF loading on the full scale turbine blade (see (13) in Figure 3) to simulate the stress distribution of the fir-tree attachment is designed. The most distinctive characteristic of the clamp is that the load from the hydraulic-servo through the friction force between the clamp and the blade, which causes no damage to the blade. Two interior sides of the blade clamp are CNC(Computerized Numerical Control)-machined into complicated surface shapes just as contrary to the concave surface and convex surface of the turbine blade. The LCF loading is transferred to the turbine blade by means of friction force cause by the normal pressure of four hold-down bolts (see (4) in Figure 3). The full scale turbine blade is attached to a part of actual turbine disc (see (11) in Figure 3) cut from a full size disc.

An electromagnetic vibrator (see (19) in Figure 3) is used to exert the sinusoidal vibration force through HCF loading-transmission plate (see (15) in Figure 3) to the blade clamp, and last to the fir-tree attachment. Through measuring the vibration amplitude on the vibrating point (see (16) in Figure 3) using a BSZ605 vibrating amplitude measure apparatus, the dynamic stress on the turbine attachment can be well controlled.

2.2. Tests and results

2.2.1. Test conditions

HLCCF tests on actual turbine attachment were conducted using a 140KN hydraulic-servo system Ferris Wheel to simulate the centrifugal force of the blade during operation and an electromagnetic vibrator SIMOVERT MM220/3 produced by Siemens company to act the vibration force. Using high frequency induction local heating, the temperature of the experimental turbine attachment can be controlled about 500˚C±5˚C, measured by an electric thermocouple. In this study, a uniform temperature distribution near the turbine attachment was simulated. The load spectrum is shown in Figure 4, with the centrifugal force 100KN, vibration frequency 23.8Hz and vibration amplitude 3.5mm, and duration time 98s at the peak load. Then crack growth tests on five turbine components with pre-cracked size of 0.5×0.5mm in the second teeth (see Figure 5) were conducted under HLCCF loading at elevated temperature. All the tests were not stopped until the turbine components fractured.

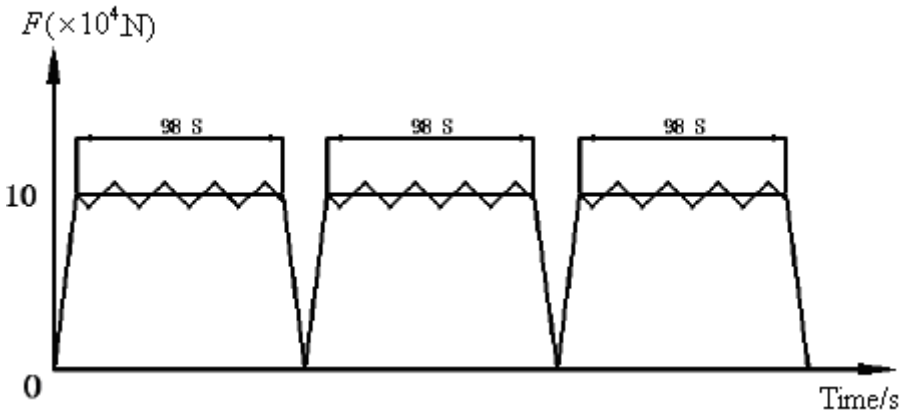

Figure 4. Load spectrum of HLCCF tests

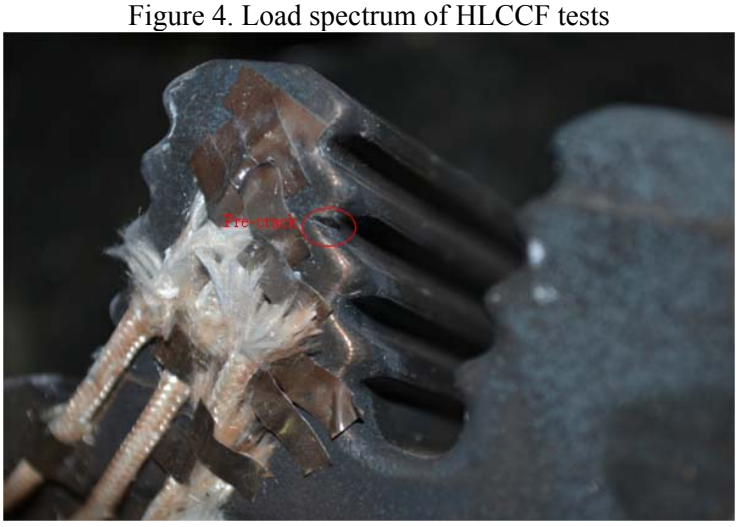

Figure 5. Pre-crack at the second tooth of the turbine disc

2.2.2. Results and discussions

The macro morphology of the turbine component is shown in Figure 6. It can be seen that crack propagates at the second mortise tooth of the leading edge of the disc. The SEM observations provide further information for understanding the interaction of HCF and LCF. The examination of fracture surfaces shows that fatigue cracks initiate from many positions in Figure 7(a), and there are obvious wide fatigue striations in the crack initiated region (see Figure 7(b), which indicates that stress resulting in crack initiation is large due to LCF loading. The crack propagation area of the fracture surface is dominated by transgranular mode and many thin fatigue striations emerged in Figure 7(c). This implies that HCF loading controls the crack growth. At the same time, oxidation features can be observed at the crack propagation region, as shown in Figure 7(d). The SEM observations reveal that high frequency vibration stress greatly affects the crack growth under HLCCF loading. Thus the effect of HCF damage on LCF damage should be considered for turbine attachments.

Figure 6. Macro morphology of the turbine component

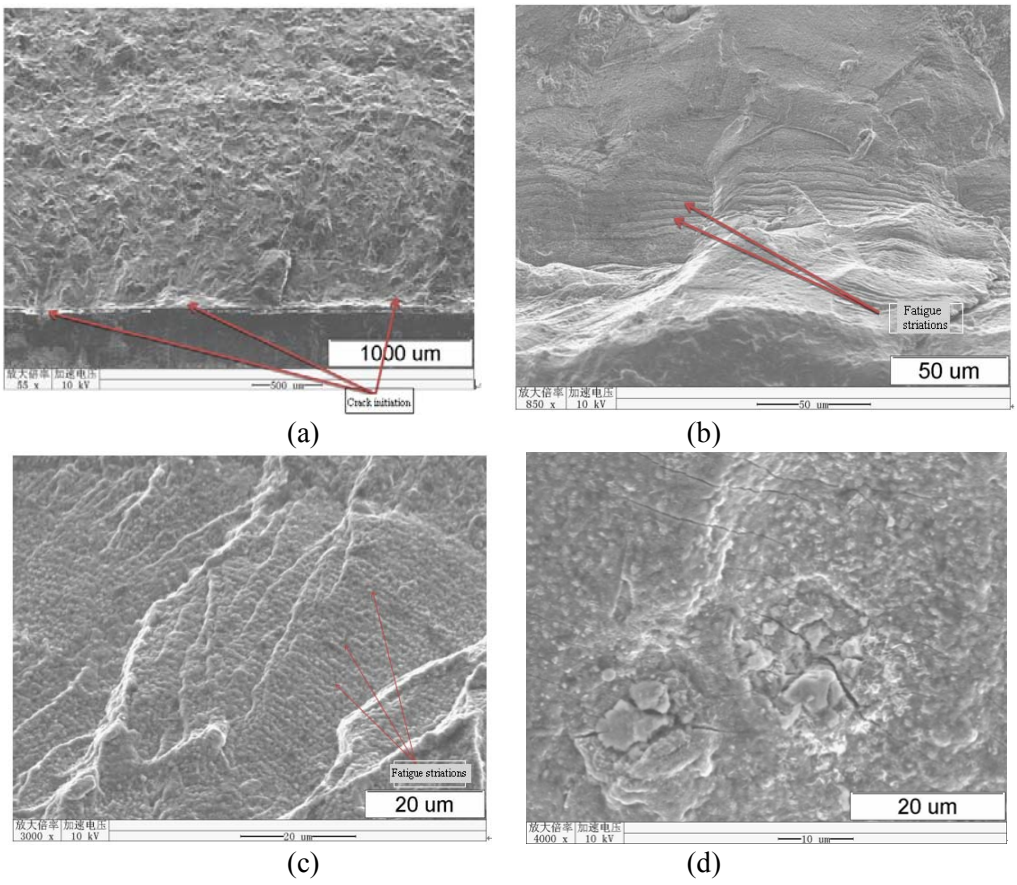

Figure 7. SEM micrographs. (a)Crack initiation. Arrows indicate the crack initiation zones. (b) Crack initiation. Arrows indicate the fatigue striations. (c)Crack growth at the position 2249μm away from main crack origin. Arrows indicate the fatigue striations. (d)Oxidation features.

Experimental life data of the five turbine components is shown in Table 1. It is shown that crack growth rate increases with flight time at early stage of crack propagation. Then crack growth rate decreases with flight time. The reason is that the fir-tree mortise, a typical multiple load path structure. When the crack propagated at the second tooth, the loading in the fir-tree attachment will be reallocated, which caused the crack growth rates decreased. Based on experimental life data, the relation between flight life and the crack length is shown in Figure 8. According to material's fracture toughness referred to [10], the critical crack growth life *N*c is 1017.1hours. If the overhaul period is 300hours and 500hours, the critical crack size are 23.5mm and 17mm respectively. Considering twice overhaul period, we can obtain critical crack size 14.5mm for 300hour-overhaul period and 7.7mm for 500hour-overhaul period.

Table 1. Experimental results

Sample No.	Crack growth life *N*/hours	Crack size *a*/mm	$\Delta a/\Delta N$(mm/hours)
1	331.0	13.5	—
2	582.8	16	0.0098
3	762.2	25	0.0510
4	771.8	26	0.1042
5	886.8	31	0.0435

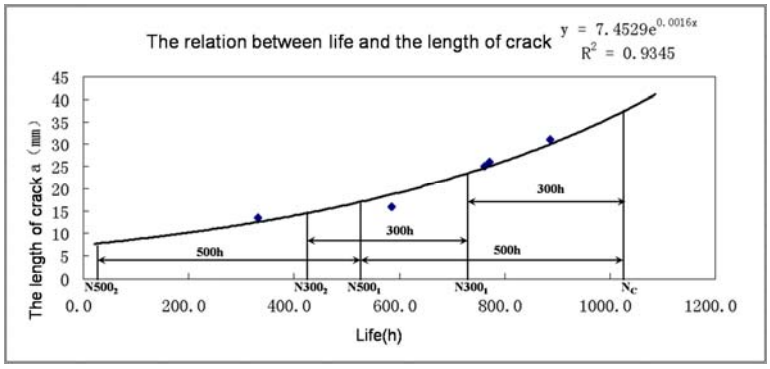

Figure 8. The relation between crack growth life and crack size

3. Crack growth life prediction

A 3-D finite element model of a turbine component including a blade and a sector of the disc was created, as shown in Figure 9. Most of the significant geometric features were modeled and a relatively finer mesh was used for the region of the blade-disc connection. The turbine blade is made of GH4033, a ferrum-base wrought superalloy and the turbine disc is made of GH2036, a nickel-based wrought superalloy. FM analysis was conducted using the commercial code MARC. The singular finite elements at the crack tip are shown in Figure 10. The HLCCF loading spectrum and the temperature distribution are similar to experimental loads.

The stress intensity factor range (SIF) ΔK_{block} under HLCCF loading can be expressed as [11]

$$\Delta K_{block} = \Delta K_{LCF} + n \cdot \Delta K_{HCF} \tag{1}$$

where ΔK_{LCF} is the SIF range under LCF loading, ΔK_{HCF} is the SIF range under HCF loading, n is the number of HCF cycles at a period.

With varying the crack size, the corresponding ΔK_{block} can be obtained by the use of *J*-integral method[12], as shown in Table 2. The ΔK_{block} is fitted by a least square method as follow：

$$\Delta K_{block} = -0.0724a^2 + 4.131a + 26.198 \tag{2}$$

where the correlation coefficient R^2=0.9934.

The crack growth life prediction under HLCCF loading is based on Paris crack growth law which gives the expression between the crack growth rate *da*/*dN* and the stress intensity factor range ΔK:

$$da/dN = C(\Delta K)^m \tag{3}$$

where the two parameters of *C* and *m* can be obtained experimentally. Referred to [10], the values of *C* and *m* in equation (3) are 1.0527×10^{-8}, 3.1826 respectively. Then crack growth life is derived by integrating Paris equation (3) over the crack length. Substituting equation (2), we can get

$$N = \int_{a_0}^{a} \frac{1}{1.0527\times10^{-8}(\Delta K_{block}(a))^{3.1826}} da \tag{4}$$

The crack growth life for the turbine component is 7691cycles, which is equal to flight life 2673.8 hours . If the safety factor is set as 2.0 referred to [13], then the life prediction is 1336.9hours which agrees well with the experimental result.

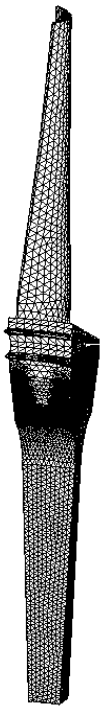

Figure 9. Mesh of turbine component

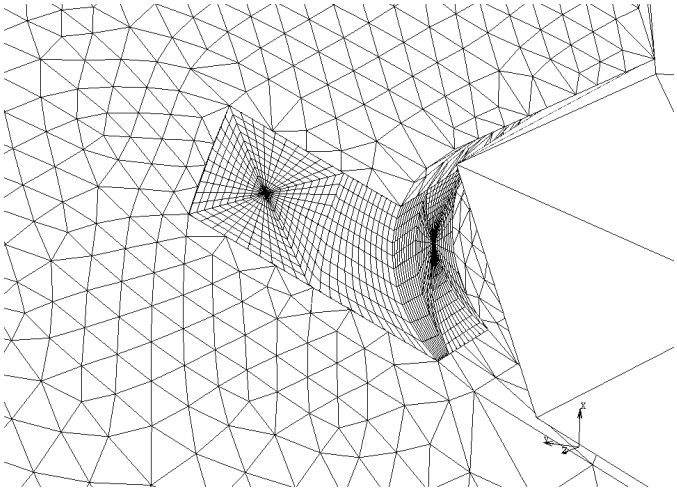

Figure 10. Singular finite elements at the crack tip

Table 2. Stress intensity factor value through FM analysis

Crack size *a*/mm	Stress intensity factor range ΔK/(MPa√m)
0.8	24.04
4.5	45.61
8.2	59.00
11.9	67.99
15.6	74.31
19.3	78.71
23	81.63

26.7	81.01
30.4	81.50
34.1	82.66
37.8	82.95

Therefore, based on experimental and numerical investigations, a new criterion for withdrawal from service of this type of turbine component to assure the structural integrity of this aeroengine is established by the industrial corporation, that is, if the overhaul period is 300hours and 500hours, the critical crack size are 23.5mm and 17mm respectively. And considering twice overhaul period, we can obtain critical crack size 14.5mm for 300hour-overhaul period and 7.7mm for 500hour-overhaul period.

4. Conclusions

This paper studied the crack growth life of a full scale turbine component at elevated temperature under HLCCF loading through experimental and numerical methods. The experimental system achieves HLCCF loading of the full scale turbine component, and a special design of the blade clamp successfully simulates the stress field of the turbine blade.

A new reliable crack growth life assessment strategy for turbine component is developed based on experimental and numerical investigations under HLCCF loading. In summary, this paper provides a new way to establish a lifetime criterion for withdrawal from service of turbine components.

Acknowledgements

This work is supported by Aviation Science Fund of China (2011ZB51015) and Doctoral Fund of Ministry of Education of China (20111102120011). The writers are grateful.

References

[1]R.Q. Wang, C.D. Cho, J.X. Nie. Combined fatigue life test and extrapolation of turbine disk mortise at elevated temperature. Journal of Engineering for Gas Turbine and Power, Transactions of the ASME, 127 (2005) 863-868.

[2]N.X. Hou, Z.X. Wen, Q.M. Yu, et al. Application of a combined high and low cycle fatigue life model on life prediction of SC blade. International Journal of Fatigue, 31(2009) 616-619.

[3]C. Schweizer, T. Seifert, B. Nieweg, et al. Mechanisms and modeling of fatigue crack growth under combined low and high cycle fatigue loading. International Journal of Fatigue, 33(2011) 194-202.

[4]D.Y. Hu, R.Q. Wang, G. C. Hou, Combined Fatigue Experiments on Full Scale Turbine Components", Aircraft Engineering and Aerospace Technology, 2013, 85(2013) (on line).

[5]S.A. Meguid, P.S. Kanth, A. Czekanski. Finite element analysis of fir-tree region in turbine discs. Finite Elements in Analysis and Design, 35(2000) 305-317.

[6]A. Pineau, S.D. Antolovich. High temperature fatigue of nickel-base superalloys-a review with special emphasis on deformation models and oxidation. Engineering Failure Analysis, 16(2009) 2668-2697.

[7]P. J. Golden, T. Nicholas. The effect of angle on dovetail fretting experiments in Ti-6Al-4V. Fatigue & Fracture of Engineering Materials & Structures, 28(2005) 1169-1175.

[8]S. Issler, E. Roos. Numerical and experimental investigations into life assessment of blade-disc connections of gas turbines. Nuclear Engineering and Design, 226(2003) 155-164.

[9]R.Q. Wang, J.X. Nie. A new experimental method to study combined fatigue of actual turbine disk mortise teeth at elevated temperature. Journal of Engineering for Gas Turbines and Power, Transaction of the ASME, 119(1997) 969-972.

[10]Editorial Committee of Handbook of Chinese Aviation Material Handbook. Chinese Aviation Material Handbook, China Standard Press, Beijing, 2002.
[11]J.Byrne. Fatigue crack growth from foreign object damage under combined low and high cycle loading part Ⅱ: A two-parameter predictive approach. International Journal of Fatigue, 29(2007) 1350-1358.
[12]Rice JR. A path independent integral and the approximate analysis of strain concentrations by notches and cracks. Journal of Applied Mechanics, 35(1968) 376-386.
[13]International Aviation Editorial Department. Spey MK202 engine stress criteria (EGD-3). International Aviation Editorial Department, Beijing, 1979.

Numerical Investigation of the Fracture Behavior of Tungsten at the Micro Scale

Christoph Bohnert[1,2*], **Sabine M. Weygand**[1], **Nicola J. Schmitt**[2], **Ruth Schwaiger**[2], **Oliver Kraft**[2]

[1] Faculty of Mechanical Engineering and Mechatronics (MMT), Karlsruhe University of Applied Sciences, Moltkestr. 30, 76133 Karlsruhe (Germany)
[2] Institute for Applied Materials (IAM), Karlsruhe Institute of Technology (KIT), Hermann-von-Helmholtz-Platz 1, 76344 Eggenstein-Leopoldshafen (Germany)
* Corresponding author: christoph.bohnert2@hs-karlsruhe.de

Abstract Due to its high melting point tungsten has the potential to be used as a structural material in future energy applications. However, one of the challenges is to deal with the brittleness of tungsten at room temperature, where the fracture behavior of polycrystalline tungsten is strongly influenced by the grain structure and texture as well as sample dimensions. The aim of the present work is to numerically analyze the stress field at a notch in a single crystal tungsten micro cantilever. A three dimensional finite element model is presented representing the microstructure of the cantilever which is deflected by a nanoindentation device.
The study addresses experimental shortcomings as, for instance, in the experimental setup pure mode I cannot be realized. Due to friction between indenter and microbeam, lateral forces arise and have an impact directly on the stress field at the notch. The FE model is used to study the influence of the friction coefficient on the lateral forces and on the stress intensity factor. The simulations reveal that with rising friction coefficient the lateral force increasing linearly and the stress intensity factor decreases.

Keywords Micro Cantilever, Single Tungsten Crystal, Fracture Toughness, FE Model, Crystal Plasticity

1. Introduction

Tungsten – a material with many outstanding advantages and features – has been mainly used in the light engineering industry as a functional material. Owing to its high melting point, tungsten may be used in the future as a significant structural-material in energy applications. Improvement of the fracture toughness represents one of the challenges due to the brittle-to-ductile transition of tungsten above the room temperature.
Several fracture studies have been already performed on macro specimens. Rupp et al. [1] as well as Gludovatz et al. [2] found a strong influence of the microstructure on the fracture morphology and toughness as well as on the brittle-to-ductile transition temperature in polycrystalline tungsten. The grain structure and texture has namely a decisive influence on the dominating failure mechanisms and on the resulting fracture toughness. In order to consider ways of increasing the fracture toughness, it is therefore necessary to understand the entire complexness of the mechanisms. Gumbsch et al. [3] investigated the fracture toughness of tungsten single crystals with different crystal orientation. They identified fracture toughness values varying from 6.2 to 20.2 MPa $m^{1/2}$ for the {100} and {110} cleavage planes at different crack front directions. However, fracture studies using micro specimens are very rare. Wurster et. al. [4-5] performed fracture experiments on tungsten single crystal notched micrometer-sized cantilevers.
In the present work the fracture behavior of single tungsten crystals is numerically analyzed for micro scale samples. This is related to an ongoing experimental study on single crystal tungsten microbeams with the focus on crack initiation and crack growth performed by N. Schmitt [6]. In the experimental work notched cantilevers with a height of 55 μm and a width of 28 μm are manufactured and bend by a nanoindenter. Experimental shortcomings are for instance the deviation from ASTM standard geometry and the deviation from the pure mode I. To support and complement the experiments a finite element model of the microbending test is presented in the present paper. It is applied to compute the stress intensity factor K for the present nonstandard specimen geometry. Furthermore, it is used to analyze the influence of lateral forces (due to friction between indenter and microbeam) on the stress intensity factor and to evaluate different nanoindenter geometries.

2. Modelling

2.1 Geometry

To determine the fracture toughness standardized test geometries are mainly used in accordance with ASTM standards, such as the three-point bending test (3PB) or the compact tensile specimen (CT). However, it should be noted that the stress intensity factor K depends on the specimen geometry as well as the respective crack opening mode. Mode I, the opening mode, represent the most important type of crack opening which is characterized by a tensile stress normal to the crack plane. By considering the critical case under mode I and plane strain conditions, the fracture toughness K_{Ic} can be determined at the beginning of the crack extension according to ASTM standard E399-90 [7]. As in the present work fracture is studied at the micro scale, the rules of the ASTM standard do not hold anymore. Therefore a new geometry had to be developed.

To ensure efficient and rapid manufacturing of the tungsten micro cantilevers, a geometry based on the specifications of the standard ASTM sample is chosen. This geometry is shown in Fig. 1. Its width W is 55 µm with a thickness B of 28 µm and a crack length a of 15 µm. The proportions between width W, thickness B and crack length a are identical to the ones of the standard ASTM samples. This is to ensure the relationship between macro and micro scale. The developed sample geometry allows the analysis of micro-specific effects of notches and multiaxial load conditions. Due to the miniaturized geometry size-effects occur, which is caused by proportions of the plastic zone in front of the crack tip as well as the changed sample ratio of surface to volume. Therefore it is not possible to transfer known macroscopic material properties into the micro scale. Based on this fact an experimental programme is carried out (N. J. Schmitt) and combined with a numerical analysis to determine the necessary characteristics at the micro scale (100 to 300 µm).

2.2 Finite element model

The notched micro cantilever is represented by a three dimensional finite element (FE) model shown in Fig. 2. Due to the symmetry only one half of the specimen is modeled and meshed with 8-node brick elements with linear function (C3D8). Besides the symmetry conditions fixed boundary conditions are applied at the right end (see Fig. 2). The indenter is modeled as rigid body. Its movement in z-direction is prescribed while the indenter cannot move in x-direction (lateral direction) and in y-direction. The developed model is implemented in the finite element code ABAQUS [8]. In the first simulations purely linear elasticity is applied as constitutive law. In later simulations crystal plasticity is added.

2.3 Crystal plasticity as constitutive law

As plastic behavior can be observed at the crack tip, crystal plasticity is implemented in the FE model as a plastic constitutive law as it allows specifying the crystal orientation of the tungsten single crystal. The theory of crystal plasticity is based on the assumption that plastic deformation (crystalline slip) results as the sum of all activated slip systems. Schmid (1931) [9] found, that the resolved shear stress onto a crystallographic plane leads to plastic slip, if stress reaches a critical value. This resolved stress on a slip system, which is also called the Schmid stress is assumed for this constitutive law as the only driving force for slip. The exact theory was formulated by Hill and Rice (1972) [10]. First FE studies of single crystals have been carried by Peirce, Asaro and Needleman (1982) [11].

The rate dependent plastic constitutive law was formulated by Asaro [12] and written by Huang [13] as a user-material subroutine UMAT. This UMAT is used in the presented simulations. It allows investigating the influence of the crystal orientation on the stress intensity factor. Two slip system families are taken into account, namely the {110}<111> and the {112}<111>.

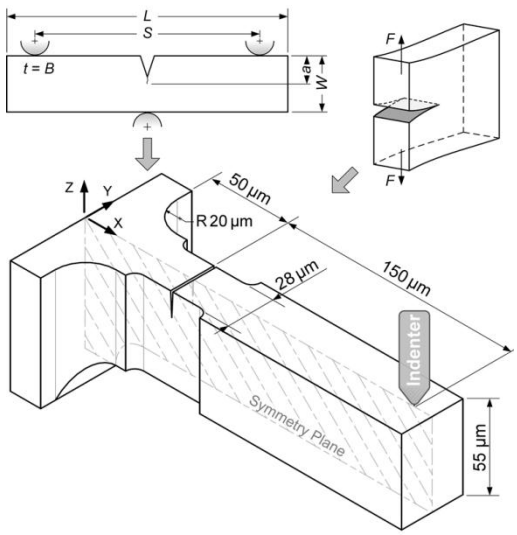

Figure 1. Specimen geometry of the micro cantilever based on single edge notch bending mimicking crack opening mode I.

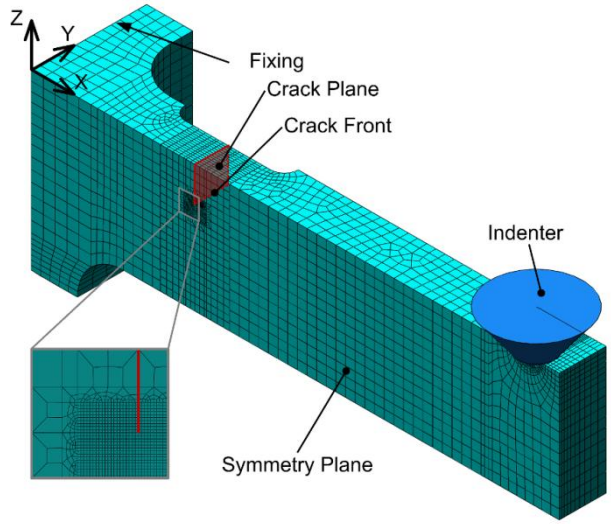

Figure 2. Three-dimensional finite element model of the micro cantilever showing the used mesh and the applied boundary conditions.

The material parameters are fitted to experimental results of Argon and Maloof (1966) [14]. They investigated the mechanical behavior of single tungsten crystals via tensile tests at different orientations. The material parameters were fitted to the {112}-tensile orientation. Table 1 summarizes the found material parameters initial hardening modulus h_0, initial yield stress τ_0 and stage 1 stress τ_s for each slip system family.

Table 1. Estimated material parameters of the two system families

slip system	{110}<111>	{112}<111>
h_0 [MPa]	3700	3800
τ_0 [MPa]	140	145
τ_s [MPa]	385	400

3. Results and Discussion

Elastic study of the bending of the micro cantilever

In the fracture experiment an indenter moves with a speed of 20 nm per second in negative z-direction (see Fig. 2). Its reaction force (named *RF3*) is measured together with the prescribed displacement u in z-direction. As the crack opens during bending, the cantilever moves relative to the indenter and friction occurs resulting in a lateral force called *RF1* and in a deviation from pure mode I. Its size and effect on the stress field around the crack tip are unknown and experimentally hardly accessible. To clarify the influence of the lateral forces, the purely elastic model presented in section 2 was applied to simulate displacement controlled bending of the micro cantilever. As the friction coefficients μ are not available, it was varied between 0 and 0.4. Additionally, different geometries of the indenter tip were applied in the FE simulations:

1. Indenter R2 (0.2 µm)
2. Indenter R10 (0.2 and 0.5 µm)
3. Wedge R10 (0.5 µm)
4. Concentrated Force
5. Pressure

Indenter R2 and indenter R10 are simplified axisymmetric simplifications of the common Berkovich tip; contrary to the common tip radius of a Berkovich tip of less than 20 nm, the elected tip radiuses are 2 and 10 µm. The values in parentheses correspond to the mesh size at the contact. To demonstrate the effect of an increased contact surface a wedge tip was chosen resulting in line loading instead of point loading.
Beside these displacement controlled simulations load controlled bending simulations are also performed where concentrated point loads (in z- and y-direction) are applied on a surface in place of contact conditions (referred as concentrated force). The advantage of this load condition is that normal (*RF3*) and lateral force (*RF1*) can be chosen independently. The concentrated point load has also been replaced with a surface pressure normal to beam surface (referred as pressure).

As expected the indenter penetration strongly depends on the indenter tip geometry. Fig. 3 shows the computed displacement of the material beneath and near the indenter in the z-direction for the three different indenter tip geometries (Indenter R2, Indenter R10 and Wedge R10) and the force controlled loading (Concentrated Force / Pressure) at the same indenter tip depth of 11.1 µm with a friction coefficient of $\mu = 0.2$. It becomes apparent that tips with a small radius lead to a more localized deformation beneath the indenter tip. On the one hand, the difference between the displacement of the indenter tip (experimentally easy measurable) and the displacement at the beam surface is relative large. This causes an indenter dependent error in the displacement measurement. On the other hand the indentation with a small tip radius ($R = 2$ µm) results in a larger lateral force *RF1* in relation to the normal force *RF3*. With a wedge indentation the deformation is more homogeneous. Thus, in the experimental setup with the wedge tip the measured displacement is more accurate.

Several simulations were performed to evaluate the influence of the lateral forces on the stress field at the crack tip. In linear elastic fracture mechanics (LEFM) the stress intensity factor K characterizes this stress field. The critical stress intensity factor K_{Ic}, which leads to crack growth is also called fracture toughness.

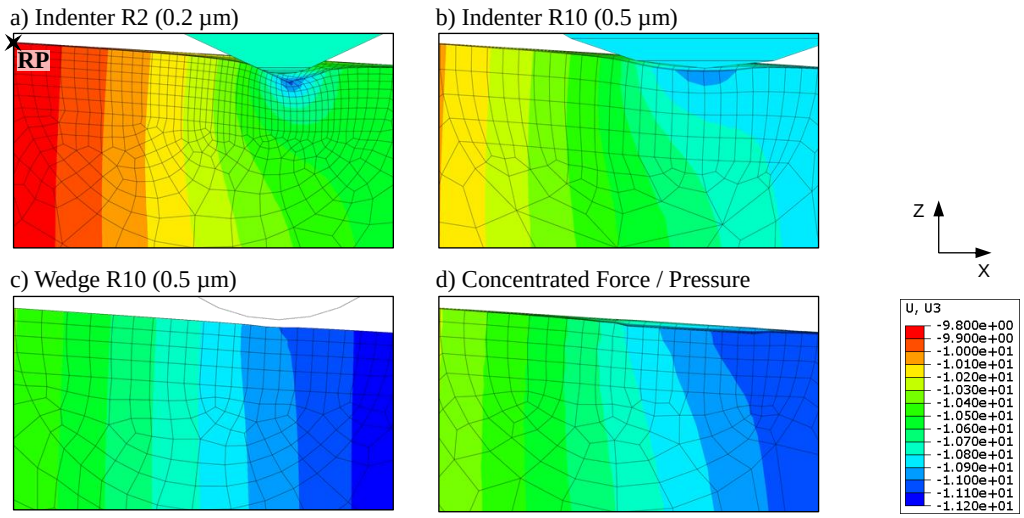

Figure 3. Displacement in z-direction of the material in the symmetry plane in the vicinity of the indenter for different indenter tip geometries at the same indenter tip displacement. The indenter with R = 2 µm shows in a) a substantially greater penetration compared to R = 10 µm in b), to the wedge tip in c) and the concentrated force and pressure in d).

Another fracture parameter is the *J*-integral which characterizes the strain energy release rate and which can be calculated in the linear elastic range for mode I with

$$J_{\mathrm{Ic}} = G_{\mathrm{Ic}} = K_{\mathrm{Ic}}{}^{2}\left(\frac{1-\nu^{2}}{E}\right) \tag{1}$$

from the fracture toughness K_{Ic}. G_{Ic} corresponds to the critical strain energy release rate, ν is the Poisson's ratio of 0.28 and E is the elastic modulus of tungsten with 410 GPa.
Applying the purely elastic FE model the stress intensity factor for each mode (I, II or III) as well as the *J*-integral was calculated along the crack front for various indenter tip geometries. Additionally a parameter study with a friction coefficient varying from 0 to 0.4 was performed. The results are shown in Fig. 4. The *J*-integral (at an indenter tip displacement of 11.1 µm) is plotted as a function of the ratio of the lateral force to the normal force (*RF1*/*RF3*).
First it shows that independently of the indenter tip geometry the *J*-integral decreases linearly with increasing lateral force *RF1*. Furthermore, it is apparent that even without friction ($\mu = 0$) a lateral force occurs where the *RF1*/*RF3* values vary from 0.25 to 0.44. The lateral force itself increases with increasing friction coefficient. The diagram also reveals the influence of the indenter tip geometry: the more localized the penetration of the indenter, the smaller is the overall bending of the cantilever leading to smaller *J* values (see Indenter R2 and R10).
Instead of using the indenter tip as reference point for the displacement a different reference point (RP) outside the process zone of the indenter has been selected at the sample surface of the beam with the coordinates of 10 µm in negative x-direction at the crack tip. This time the *J*-integrals are compared at 10 µm displacement of this newly selected reference point (Fig. 3 a)). Fig. 5 shows the computed *J*-integrals as a function of the lateral to normal load for various indenters. In this way the dependence of the *J*-integral on the indenter geometry is eliminated and the j-integral is only determined by the ratio of the lateral to normal force. The deviation of the *J* values for the same indenter tip displacement can reach up to 12%.

In a mesh study the local mesh refinement at the contact surfaces from 0.5 to 0.2 µm indicates no effect on the *J*-integral.

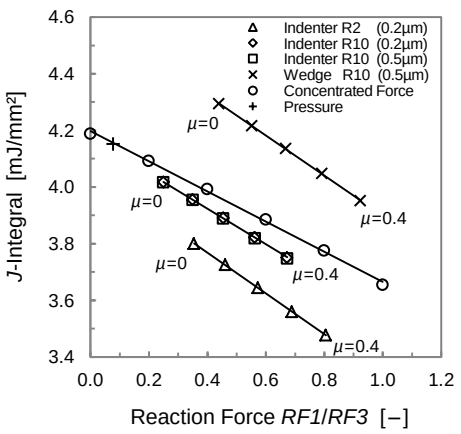

Figure 4. *J*-integral as a function of the ratio of lateral to normal load at 11.1 µm indenter tip displacement revealing an influence of the indenter geometry.

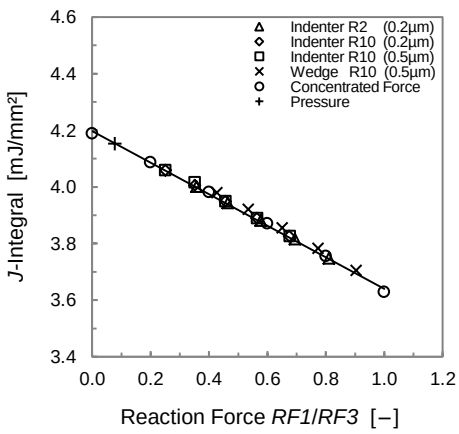

Figure 5. *J*-integral as a function of the ratio of lateral to normal load at 10 µm displacement of a chosen reference point (RP).

As already mentioned a lateral force always occurs during bending. Therefore, we analyze the mixed mode.
On the basis of the LEFM, stress intensity factors of the respective modes with K_I, K_{II} and K_{III} can be calculated and evaluated. Mathematically, the K factors can be calculated numerically very well within the finite element code. Fig. 6 shows the resulting three K factors for different indenter tip geometries and varying friction. It becomes clear that mode I is the dominant mode. However, its value slightly decreases with increasing lateral force. The K_{II} value is about 6% of K_I and its value slightly rises with increasing lateral force. Mode III is not present. Based on the large differences between the values of K_I to K_{II} we can assume pure mode I.

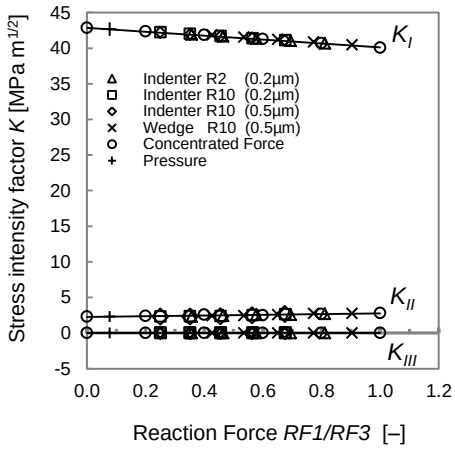

Figure 6. Stress intensity factors for mode I, II and III as a function of the ratio of lateral to normal load at 10 µm reference point displacement.

Simulation of the bending of the micro cantilever with crystal plasticity

As described in Section 2 the elastic FE model was extended by crystal plasticity. This allows to take into account the orientation of the single crystal and to evaluate the plastic deformation ahead of the crack front. The crystal plasticity model was applied to simulate the bending of a beam without (CF0.0) and with a ratio of the lateral force to the normal force of 0.4 (CF0.4). Instead of modeling the contact between indenter and beam explicitly the simulation is performed load controlled as concentrated force in normal and lateral load (see concentrated force).
The simulated beams are aligned in such a way that the $\{110\}\langle 0\bar{1}1\rangle$-crack system lies in the loading direction.
Results of the simulations are, besides stress and strain fields, the force-displacement curve, the evolution of the J-integral at the crack front and the slip activities. Fig. 7 illustrates the resulting force-displacement curves for the two cases with and without lateral force. Is a lateral force *RF1* present, the normal force *RF3* is increased. The difference in force results from the interplay of material deformation and material accumulation in front of the indenter (during bending).

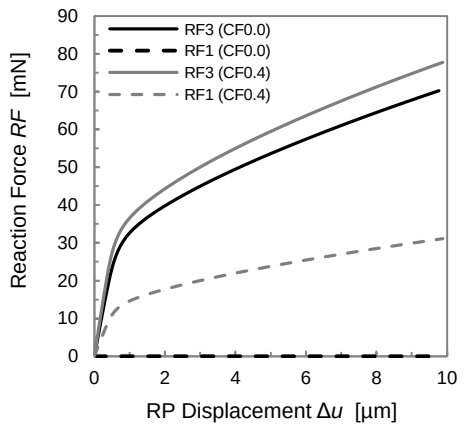

Figure 7. Characteristic force-displacement curve of the normal (*RF3*) and the lateral force (*RF1*) under load of a single tungsten crystal with {011}<0$\bar{1}$1> -crack system, exemplary for the ratio *RF1*/*RF3* = 0 (CF0.0) and *RF1*/*RF3* = 0.4 (CF0.4).

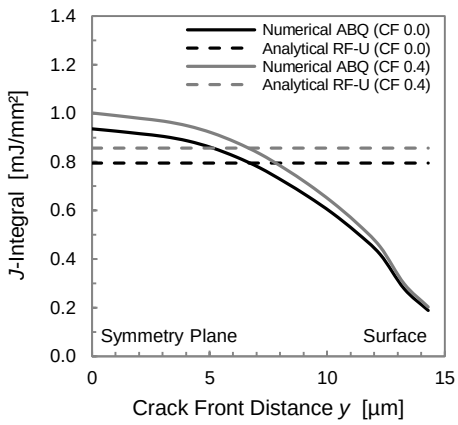

Figure 8. Course of the J-integral along the crack front, from the symmetry plane up to surface., exemplary for the ratio *RF1*/*RF3* = 0 (CF0.0) and *RF1*/*RF3* = 0.4 (CF0.4) at 10 µm reference point displacement.

We obtained the *J*-integral in two ways: first with the analytical relations of the standard ASTM E1820 [15] using the force-displacement curve (commonly applied in fracture experiments) and secondly numerically.
J consists of an elastic J_{el} and plastic J_{pl} contribution. According to [15] the *J*-integral is calculated with:

$$J = J_{el} + J_{pl} = \frac{K^2(1-\nu^2)}{E} + \frac{\eta A_{pl}}{B\, b_o}, \tag{2}$$

where A_{pl} defines the plastic work of the applied load, *B* the specimen thickness and b_o is defined by the difference between the width *W* and the initial crack length a_o. The non-dimensional η describes the effect of plastic work normalized by the ligament area. For deep notch specimens, standard [7] and [15] prescribe η by the following definition:

$$\eta = 2 \qquad \text{,when } 0.45 \le a/W \le 0.55 \tag{3}$$

With an investigated *a*/*W*-relation of 0.27, the standard approach of η is just an approximation. Based on a numerical fit to a number of different FEM solutions, Nevalainen and Wallin [16] obtained a crack length dependent correlation of η:

$$\begin{aligned} \eta &= 13.818 \cdot a/W - 25.124 \cdot \left(a/W\right)^2 && \text{, when } 0 < a/W \le 0.274 \\ \eta &= 1.859 + \frac{0.03}{1 - a/W} && \text{, when } 0.274 < a/W \le 0.9 \end{aligned} \tag{4}$$

According to [16] and with a geometry relation of *a*/*W* = 0.27, η can be determined from Eq. (4) to be 1.9 leading to a *J* of 0.80 mJ/mm^2 at an reference point displacement of 10 µm when no lateral force is present. In case of *RF1*/*RF3* = 0.4 the *J* increases to 0.86 mJ/mm^2.

In the numerical approach the *J*-integral can be determined along the crack front. Its course is given in Fig. 8. As expected, the maximum *J* value occurs at the symmetry plane in the state of plane strain, the so-called critical condition. Here, it is also expected that crack initiation starts with subsequent crack propagations.

Fig. 8 shows furthermore, that the numerical J values in the center of the specimen (symmetry plane) are larger and at the surface smaller than the analytical values. A comparison of the analytical solution with $J_{an} = 0.71$ mJ/mm^2 and the average numerical solution with $J_{num} = 0.80$ mJ/mm^2 shows a good and plausible approximation.

Thanks to crystal plasticity the activities on various slip systems can be revealed. To get an idea of the size of the zone with slip activities the accumulated shear strain is shown in Fig. 9 in front of the crack tip and at the surface for an indenter displacement of 0.5 µm. As known from the fracture mechanics, the plastic zone is in the symmetry plane due to plane strain smaller than at the surface. The influence of the asymmetric specimen geometry can be also seen. The fixing is located on the left side and the loading takes place on the right side. Here, the load results to $RF3 = 25$ N and to $RF1 = 10$ N.

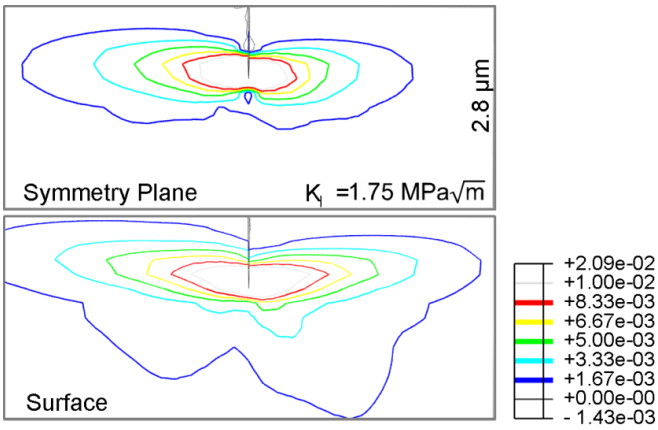

Figure 9. Accumulated shear strain ahead of the crack tip at a indenter displacement of 0.5 µm for an orientation $\{011\}\langle 0\bar{1}1\rangle$ of the crack system, exemplary details were chosen in the symmetry plane and at the surface.

5. Conclusion

In this paper we presented a three dimensional finite element model of a notched single crystalline tungsten micro cantilever which is deflected in the bending test by a nanoindentation device. The model was applied to study the influence of friction and indenter geometry on the stress field around the crack (notch) characterized by the stress intensity factor K or the J-integral. The results show that with increasing friction coefficient μ the lateral force increases linearly and with it the J-integral decreases linearly. Furthermore, the indenter tip geometry plays an important role. Based on these numerical results following recommendations can be made regarding the experimental setup. To exclude the influence of the indenter tip geometry, the displacement should not be measured at the indenter tip but at a point slightly ahead of the indenter (outside the penetration area). The simulations show that otherwise the error of the J-integral can reach up to 12% (e.g. in case of an axisymmetric Berkovich tip like indenter with a tip radius of 2 µm). If only the displacement of the indenter tip is experimentally accessible, an indenter with a large contact area (e.g. a wedge indenter) is recommended as localized penetration is prevented and the error in J is minimized.

Acknowledgements

The authors would like to thank the Karlsruhe University of Applied Sciences and Karlsruhe Institute of Technology (KIT) for providing the necessary equipment.
The research was financial supported by a fellowship of the "Kooperatives Promotionskolleg: Gefügestrukturanalyse und Prozessbewertung" funded by the Postgraduate Research Grants Programme of Baden-Württemberg (Germany).

References

[1] D. Rupp, S. M. Weygand, Anisotropic fracture behaviour and brittle-to-ductile transition of polycrystalline tungsten, Philosophical Magazine, vol. 90, pp. 4055–4069, 2010.
[2] B. Gludovatz, S. Wurster, A. Hoffmann, R. Pippan, Fracture toughness of polycrystalline tungsten alloys, Int. J. of Refrac. Met. and Hard Mat., vol. 28, pp. 674–678, 2010.
[3] P. Gumbsch, Brittle fracture and the brittle-to-ductile transition of tungsten, J. of Nuclear Materials, vol. 323, pp. 304–312, 2003.
[4] S. Wurster, C. Motz, M. Jenko, R. Pippan, Micrometer-Sized Specimen Preparation Based on Ion Slicing Technique, Advanced Engineering Materials, vol. 12, pp. 61–64, 2010.
[5] S. Wurster, C. Motz, R. Pippan, Characterization of the fracture toughness of micro-sized tungsten single crystal notched specimens, Phil. Mag., vol. 92, pp. 1803–1825, 2012.
[6] N. J. Schmitt, C. Bohnert, C. Eberl, R. Schwaiger, S. M. Weygand, O. Kraft, Investigation of the fracture behavior of tungsten at the micro scale, ICF13th International Conf. on Fracture, Beijing, 2013.
[7] ASTM E399 - 90: Standard test method for plane-strain fracture toughness of metallic materials, Annual Book of the ASTM Standards.
[8] Simulia Dassault Systemes GmbH, Abaqus CAE (Version 6.11), www.3ds.com.
[9] E. Schmid, Beiträge zur Physik und Metallographie des Magnesiums, Zeitschr. Elektrochem., vol. 37, pp. 447–459, 1931.
[10] R. Hill, J. R. Rice, Constitutive analysis of elastic-plastic crystals at arbitrary strain, Journal of the Mechanics and Physics of Solids, vol. 20, pp. 401–413, 1972.
[11] D. Peirce, R. J. Asaro, A. Needleman, An analysis of nonuniform and localized deformation in ductile single crystals, Acta Metallurgica, vol. 30, pp. 1087–1119, 1982.
[12] R. J. Asaro, Micromechanics of Crystals and Polycrystals, Advances in Applied Mechanics, vol. 23, pp. 1–115, 1983.
[13] Y. Huang, A user-material subroutine incorporating single crystal plasticity in the ABAQUS finite element program, Mech Report, 1991.
[14] A. S. Argon, S. R. Maloof, Plastic deformation of tungsten single crystals at low temperatures, Acta Metallurgica, vol. 14, pp. 1449–1462, 1966.
[15] ASTM E1820 - 01: Standard Test Method for Measurement of Fracture Toughnes, Annual Book of the ASTM Standards.
[16] M. Nevalainen, K. Wallin, The effect of crack depth and absolute thickness on fracture toughness of 3 PB specimens, Proc. ECF10th European Conf. on Fracture, pp. 997–1006, 1994.

Mechanics Mechanism of Re-fracturing in Inclusion Reservoirs

Xue Shifeng[1,*], Chen Xinmin[1], Han Zhongying[1], Zhang Weidong[2]

[1] College of Pipeline and Civil Engineering, China University of Petroleum, Qingdao, Shandong, 266580, China
[2] School of Petroleum Engineering, China University of Petroleum, Qingdao, Shandong, 266580, China
* Corresponding author: xuesf@126.com

Abstract Hydraulic fracturing is an important EOR technology of low permeability reservoirs which occupy a considerable proportion in China's oil reserves. If hydraulic fracturing fails, re-fracturing will be used in most oil-water wells. However, there are often a large number of inclusions in low-permeability reservoirs. Due to the complexity of the re-fracturing mechanism in inclusion reservoirs, the theoretical researches are far behind the field practices. Theoretical and experimental studies on the mechanical mechanism of re-fracturing are significant for the development of inclusion reservoirs.
Ground stress distribution is one of the major factors which affect fracture propagation after re-fracturing. In this paper line inclusion is seen as a thin bar, and the basic solution of elastic mechanics for line inclusion in infinite plane is used to solve the stress field. Stress field around artificial fracture which is influenced by single line inclusion is deduced. The interference problem of single line inclusion and artificial fracture under internal pressure is reduced to a set of Cauchy singular integral equations. In addition, a validation test with a large size (500mm×500mm×500mm) true tri-axial test equipment is carried out. The results show that, the inclusions reduce rock intensity, and induce reservoir to generate more complex fractures.

Keywords Mechanical mechanism of re-fracturing, Inclusion reservoir, Evolution of stress, Fracturing physical simulation

1. Introduction

The re-fracturing technology, as an enhanced recovery technique, was first developed in the 1950s, and it has become one of the important means to improve the recovery of oil and gas fields. The initiation and propagation of new fracture are greatly influenced by the reservoir structural characteristics during re-fracturing. Present studies mainly focus on the interference problems between artificial fracture and natural ones in natural fractured reservoirs. Many experiments have shown that fracture may present different state by the influence of various factors after the interference of artificial and natural fractures in natural reservoirs [1-6]. Zhou and Xue analyzed the impact of pre-existing fracture conductivity, stress state and injection rate on fracture path complexity [7]. On the basis of laboratory and field evidence, it is conceivable that several events may occur during the time period of the hydraulic fracture propagating toward the natural fracture [8]. However, there are numerous kinds of complex isolated inclusions in the reservoirs. The stress singularity may exist at the tip of the flake inclusions, and under certain conditions, it may also lead to the generation of micro-cracks [9]. Jin Yan et al. [10] analyzed the effects of salutatory barrier on hydraulic fracture propagation, but they have no further theoretical analysis.

At present, the inclusion theory is mainly used for composite materials. In this paper, inclusion theory was introduced for the inclusion reservoir. Stress intensity factor is derived at the tip of artificial fractures and inclusions. The direction of fracture propagation after re-fracturing can be judged by the maximum tensile stress criterion in defect reservoirs. In addition, the effects of

isolated defects on the fracture shape after re-fracturing are verified by large size true tri-axial experiments.

2. Basic model

The basic model of stress distribution before re-fracturing in inclusion reservoir is shown as figure 1. The length of the inclusion is assumed far greater than its width, and the inclusion is seen as a line inclusion. For an elastic inclusion body, to better reflect the discontinuity of normal stress and tangential stress between the inclusion and rock matrix, the line inclusion is treaded as a thin bar. The Eshelby equivalent inclusion theory [11, 12] is used to solve the problem, only considering rock skeleton stress.

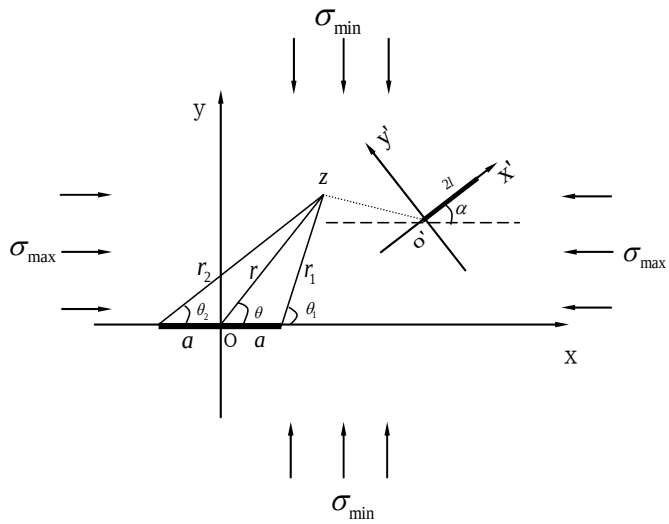

Figure 1. The stress distribution before re-fracturing in inclusion reservoir

The stress field in the inclusion reservoir is composed of the following three parts:

(1) The stress field induced by the artificial fracture;

(2) The stress field induced by the line inclusion;

(3) Far-field stress.

The total stress state of elastic plane can be expressed as

$$\sigma_{ij}(x,y)=\sigma_{\mathrm{a},ij}(x,y)+\sigma_{\mathrm{d},ij}(x,y)+\sigma_{\mathrm{w},ij}(x,y) \qquad (i,j)=(x,y) \tag{1}$$

where, $\sigma_{ij}(x,y)$ is the total stress field, MPa; $\sigma_{\mathrm{a},ij}(x,y)$ is the stress field induced by artificial fracture, MPa; $\sigma_{\mathrm{d},ij}(x,y)$ is the stress field induced by the line inclusion, MPa; $\sigma_{\mathrm{w},ij}(x,y)$ is the far-field stress, MPa.

The boundary conditions are as follows,

(1) Total stress at the edge of the line inclusions needs to meet the displacement compatibility relations. That can be written in the local coordinate $x'o'y'$ as follows,

$$\begin{aligned}
&\frac{\partial u_{\mathrm{a}}'(x',+0)}{\partial x'}+\frac{\partial u_{\mathrm{d}}'(x',+0)}{\partial x'}+\frac{\partial u_{\mathrm{w}}'(x',+0)}{\partial x'}=\frac{\partial u_{\mathrm{d}}^{*}(x')}{\partial x'} \qquad (0<=x'<=2l)\\
&\frac{\partial v_{\mathrm{a}}'(x',+0)}{\partial x'}+\frac{\partial v_{\mathrm{d}}'(x',+0)}{\partial x'}+\frac{\partial v_{\mathrm{w}}'(x',+0)}{\partial x'}=\frac{\partial v_{\mathrm{d}}^{*}(x')}{\partial x'} \qquad (0<=x'<=2l)
\end{aligned} \tag{2}$$

where, u_i' and v_i' are displacement components.

(2) The inner stress p is exerted at the edge of artificial fracture. The direction is perpendicular to the fracture surface.

$$\begin{aligned}
&\sigma_{\mathrm{a},yy}(x,0)+\sigma_{\mathrm{d},yy}(x,0)+\sigma_{\mathrm{w},yy}(x,0)=p, \quad (-a=<x<=a)\\
&\sigma_{\mathrm{a},xy}(x,0)+\sigma_{\mathrm{d},xy}(x,0)+\sigma_{\mathrm{w},xy}(x,0)=0, \quad (-a=<x<=a)
\end{aligned} \tag{3}$$

Based on inclusion theory, combined with the equations (2) and (3), we can obtain four Cauchy singular integral equations. After solving, the stress field at any point of the inclusion reservoirs can be expressed after a series of coordinate conversion. At the same time, we can deduce the stress intensity factor at the tip of artificial fracture and inclusions.

When the artificial fracture and line inclusions are disjoint, the stress intensity factor at the tip of the artificial fracture can be obtained by the following equations.

$$\begin{aligned}
K_{\mathrm{I}}(-a)&=\frac{2\mu}{\kappa+1}\lim_{x\to -a}\sqrt{2(a+x)}g(x)\\
K_{\mathrm{I}}(a)&=-\frac{2\mu}{1+\kappa}\lim_{x\to a}\sqrt{2(a-x)}g(x)
\end{aligned} \tag{4}$$

where, a is the half-length of artificial fracture, m; K_{I} is the stress intensity factor of model I crack, $\mathrm{MPa}\cdot\sqrt{\mathrm{m}}$; κ is the elastic constant of rock matrix, and for plane strain problem, $\kappa=3-4\upsilon$, where, υ is Poisson ratio; $g(x)$ is the dislocation density function of the artificial fracture at $x=-a\sim+a,\ y=0$,

$$g(x)=\frac{\partial}{\partial x}\left[u_y(x,+0)-u_y(x,-0)\right] \qquad (-a<x<a) \tag{5}$$

In the local coordinate system, the stress intensity factor at the tip of line inclusions can be expressed as follows.

$$\begin{aligned}
K_{\mathrm{I}}'(0)&=-\frac{\kappa-1}{2(\kappa+1)}\lim_{x'\to 0}\sqrt{2x'}q(x')\\
K_{\mathrm{I}}'(2l)&=\frac{\kappa-1}{2(\kappa+1)}\lim_{x'\to 2l}\sqrt{2(2l-x')}q(x')
\end{aligned} \tag{6}$$

where, $2l$ is the length of the inclusion, m; $q(x')$ is the tangential constraint physical stress of the inclusion on rock matrix,

$$q(x')=\sigma_{xy}(x',-0)-\sigma_{xy}(x',+0) \tag{7}$$

Therefore, when we compare the above results with the critical stress intensity factor K_{IC}, we can judge the extension of the fractures in the inclusion reservoir. From equation (6) and (7), we can

conclude that the stress intensity factor of the inclusion tip is affected by the local stress field around the inclusion. In the whole model, the local disturbance of the inclusion is controlled by the far field stress and the inner boundary pressure. Therefore, when the load changes, K_I' may be greater than K_{IC}. And the new fracture may produce along the defect. The experiment will be done to prove it.

3. Experimental verification

3.1 Experimental equipments

The experiments were performed in an improved large true tri-axial rock mechanics experiment system. Cubic model blocks of 500mm on a side were positioned in the high-pressure cylinder for simulating in-situ stress conditions. The random defects were added in the samples, and the initial artificial fracture was simulated by a thin plastic sheet. The appearance of the high-pressure cylinder, which is one of the main equipments, is shown in figure 2.

Figure 2 The appearance of the high-pressure cylinder

3.2 The experiment process and results

In fact, the critical stress intensity factor of the line inclusion is greatly difficult to measure. However, we can make a perceptual knowledge for the fracture propagation mechanism after re-fracturing in defect reservoirs by changing the size of the ground stress directly.

There are six samples designed for the experiments. The stresses of three samples is applied as shown in table 1, where σ_x and initial artificial fracture are in the same direction. Before re-fracturing experiment, we measured the rock mechanics parameters of the sample through a group of small samples. Elastic modulus of sample matrix is 2.4GPa, Poisson ratio is 0.23.

Table 1 Experimental stress data

Sample number	The first fracturing			The second fracturing		
	σ_x	σ_y	σ_z	σ_x	σ_y	σ_z
$2^{\#}$	3	3	3	3	4	5
$4^{\#}$	4	4	4	1	2	3
$6^{\#}$	3	4	5			

For example, when the confining pressure was 3MPa for $2^{\#}$ sample, a horizontal main fracture formed after the first fracturing. The highest pump pressure was 6.5MPa. The second fracturing was carried out after changing the size of stress. A vertical main crack was created along the maximum horizontal principal stress direction. The highest pump pressure was 2.4MPa affected by the defects.

The strength of the rock is dispersed for defects of various scales in the rock, and the ability of resisting external force is weakened [13]. Under external loads, the defects of the sample will be activated. The activation defects extend under the load, and finally lead to mutual merger and samples are destructed. Therefore, when the loads are up to a certain threshold, random defects are activated in the defect reservoirs during the experiments. And more complex fractures may produce.

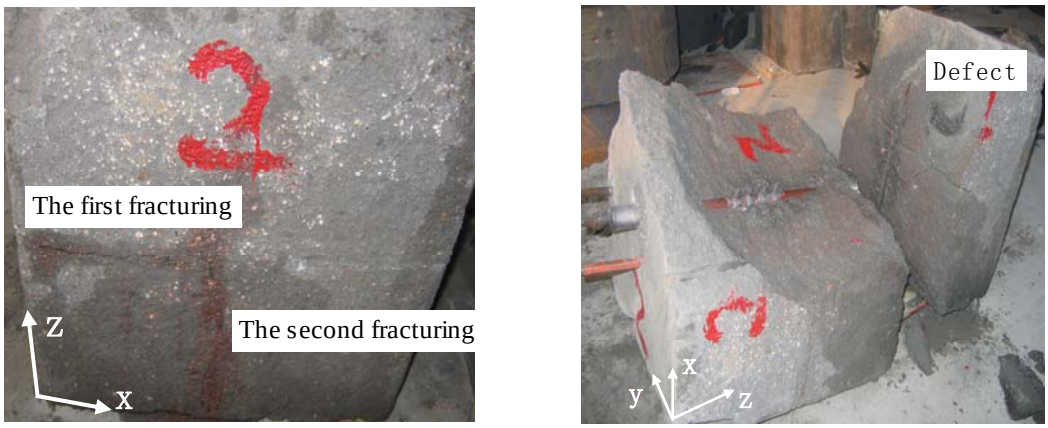

Figure 3 Experimental image of $2^{\#}$ sample after hydraulic fracturing

For $4^{\#}$ sample, under the higher uniform confining pressure, the artificial fracture closed. And a new fracture produced along the direction perpendicular to the preset fracture which affected by the defects. The highest pump pressure was 6.2MPa. When the size and orientation of the stresses were changed, the direction of the new fracture would not change, which still followed the direction of the maximum horizontal principal stress.

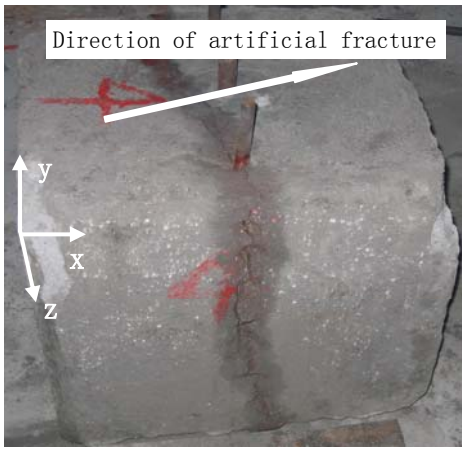

Figure 4 Experimental image of 4# sample after hydraulic fracturing

From the above experiments, we can conclude that the defect is one of the most important factors for the fracture morphology after re-fracturing in heterogeneous reservoir. However, whether the direction of the fracture propagation will be changed by the defect is finally directed by the stress distribution state in the reservoir, which meets the maximum tensile stress criterion. At the same time, we found that, under the higher uniform pressure stress, the direction of the new fracture may have no relation with the preset fracture in the defect reservoirs.

Conclusion

Theoretical research and indoor experiments have shown that the defect is one of the most important factors affecting the fracture distribution state after re-fracturing in the reservoir. From this paper, we can conclude as follows.

(1) Theory research shows that, in a certain stress condition, a new fracture may produce along the tip of the inclusion.

(2) The strength of the rock is dispersed for defects of various scales in the rock.

(3) Whether the presence of defects will cause the new fracture, to a great extent, is controlled by the far field stress.

(4) From the experiments, under some higher confining pressure, the defect may be the dominant factor of fracture propagation in the reservoirs.

References

[1] Beugelsdijk L J L, Pater C J, Sato K. Experimental hydraulic fracture propagation in a multi-fractured medium. SPE 59419, 2000.
[2] Peacock D C P, Mann A. Controls on fracturing in carbonate rocks. SPE 92980, 2005.
[3] Warpinski N R, Lorenz J C, Branagan P T, Myal F R and Gall B L. Examination of a cored hydraulic fracture in a deep gas well. SPE 22876, 1993.

[4] Olson J E, Bahorich B, Holder J. Examining hydraulic fracture-natural fracture interaction in hydrostone block experiments. SPE 152618, 2012.

[5] Meng Chunfang. Hydraulic fracture propagation in pre-fractured natural rocks. SPE 140429, 2011.

[6] ZHOU Jian, CHEN Mian, JIN Yan, ZHANG Guang-qing. Experimental study on propagation mechanism of hydraulic fracture in naturally fractured reservoir. Acta Petrolei Sinica, 2007, 28(5): 109-113. (in Chinese)

[7] Zhou and Xue, Experimental investigation of fracture interaction between natural fractures and hydraulic fracture in naturally fractured reservoirs. SPE 142890, 2011.

[8] H.Gu, X.Weng, J.Lund, et al. Hydraulic fracture crossing natural fracture at nonorthogonal angles: a criterion and its validation. SPE 139984, 2012

[9] ZHANG Hong-tu, ZHE Xiao-li. Theory of inclusion and applications in the study of fracture. Acta Physica Sinica, 1981, 30(6): 761-773. (in Chinese)

[10] JIN Yan, CHEN Mian, ZHOU Jian, GENG Yu-di. Experimental study on the effects of salutatory barrier on hydraulic fracture propagation of cement blocks. Acta Petrolei Sinica, 2008, 29(2): 300-303. (in Chinese)

[11] HUANG Chun-ping, LI Zhong-hua. An approximate solution for the interaction forces between model I crack and an inclusion of arbitrary shape. Journal of Shanghai Jiaotong University, 2005, 39(1): 142-146. (in Chinese)

[12] ZHANG Ming-huan, TANG Ren-ji. Interaction between crack and elastic inclusion. Applied Mathematics and Mechanics, 1995, 16(4): 289-300. (in Chinese)

[13] DENG Yue-hong. Dimension stone strength and fractal characteristics of inner fault distribution. MINING R & D. 2001, 21(6): 13-15.

On propagation of interface cracks parallel to free boundaries in relation to delamination of multilayered coatings

Konstantin B. Ustinov*, Robert Goldstein

IPMech RAS, 119526, Russia
* Corresponding author: ustinov@ipmnet.ru

Abstract. The problem of a crack propagation in multilayered coating either between the individual layers, or between the whole package forming the coating and substrate (possibly also non-uniform) is considered. According to the model the delaminated part of the coating is treated as a plate with a special attention given to the boundary conditions, which are supposed to be of the elastic clamping type, which means that the angle of rotation at the clamping point is related to the acting bending moment at that point. The generalized model of elastic clamping is also considered in the frame of which it is supposed that components of displacements and angle of rotation at the clamping point are related to the acting total force and total moment by means of 3x3 matrix of elastic coefficients. Several variants of analytical models to determine the coefficients of this 3x3 matrix were considered and discussed. The case of non-uniform (multi-layered) coating is considered with a special attention paid to analysis of the influence of the relative dimensions involved, such as the individual layer and the multilayer coating thicknesses, distance from the crack to the free surface, crack length.
Using the obtained solution the problem on buckling of the delaminated coatings is addressed. It has been shown that for a wide range of parameters even for anisotropic and multilayered structures the ratio of the obtained critical stress and the critical stress of a rigidly clamped plate is determined by a single nondimensional parameter, which is a combination of the elastic constants of the coating and substrate, and the ratio of the delamination length to the coating thickness. The analytical results correlate well with the results obtained using the numerical calculations.

Keywords. Interface crack, Multilayered coatings, Delamination, Elastic clamping, Buckling

1. Introduction

Problems related to propagation of interface cracks have been investigated widely due to importance for industry. Lately they appealed additional interest owing to applications in micro- and nano-electronics, biology, medicine. The problems were addressed by many authors by using both analytical and numerical approaches e.g. [1-10]. In [2], [3], in particular, the problem of stability loss of coating delaminated from rectilinear rigid substrate was solved. The critical stress, magnitude of deflection [2], [3], and energy release rates along and across the delamination front were found. The delaminated part of coating was considered as a clamped plate, which corresponds to rigid substrates. However, detailed studies yield that, from the one hand, the condition of rigid clamping are not satisfied exactly even for absolutely rigid substrates [5], and, from the other hand, on the base of numerical calculations it is said [6], [7] that even for substrates tree times softer then coating the condition of rigid clamping yields acceptable errors. In our opinion the last statement has to be accepted with cautions, because the influence of delamination size, importance of which being confirmed by other studies [5], [8], was not investigated in [6].

Influence of the substrate rigidity was studied by [4-6], however without paying attention to the influence of the delamination width to the critical stress. The analysis of influence of both substrate compliance and delamination width on the critical stress was performed in [5]. The delamination was modeled by a plate, with boundary condition corresponding to generalized elastic clamping, i.e. magnitudes of tangential displacements and gradient of deflection of the clamped edges were supposed to be proportional to tangential force and bending moment acting at the points of clamping. The coefficients of elastic clamping depending on two mentioned parameters were

calculated by solving numerically a system of integral equations [9].

Here, as well as in [9-12] the attempts were made to estimate the coefficients of elastic clamping analytically, and semi-analytically.

2. Problem formulation

Consider elastic half-plane (substrate) with adjusted layer (coating) of thickness h having elastic properties, different from the properties of substrate. The layer is perfectly glued to the half-plane everywhere except a section of length, $2b$, along which it is delaminated. The Cartesian coordinate system is chosen with x-axis being parallel the half-plane boundary, and y-axis coinciding with its external normal, the origin of the coordinate frame coinciding with the delamination centre. Thus the half-plane occupies area $y < -h/2$, the layer does $-h/2 < y < h/2$, the delamination does $-b < x < b,\ y = -h/2$. The Young moduli and Poisson ratios of the coating and substrate are E, ν, E_s, ν_s, respectively. The layer is assumed to be subjected to the tensile eigenstrain causing compressive stresses, σ_0, acting along the boundary. Such a situation takes place while heating the system in question if thermal extension of the layer is higher than the one of the half-plane. On reaching by the compressive stress some particular level of σ_{cr}, the system loses stability and the layer bends (Figure 1). The problem is to find the value of stress, $\sigma_0 = \sigma_{cr}$, corresponding to the loss of stability

.

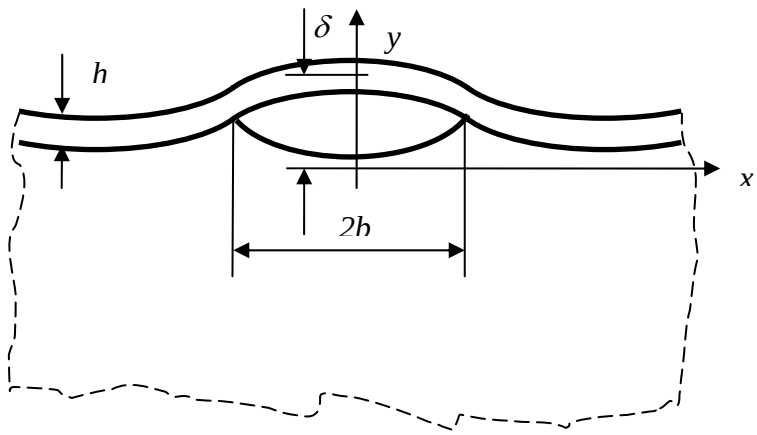

Fig. 1. Geometrical configuration.

The problem was solved in [6] numerically, using FEM, the value of σ_{cr} being presented as products of corresponding values, calculated for the clamped plane σ_0^{cr} and a coefficient γ_σ

$$\sigma^{cr} = \sigma_0^{cr} \gamma_\sigma \tag{1}$$

Magnitude of σ_0^{cr} may be calculated using elementary methods. Thus for the clamped plate of length $2b_0$ the critical stress is [13]:

$$\sigma_0^{cr} = \frac{\pi^2 h^2 E^*}{12 b_0^2} \quad E^* = \frac{E}{1-\nu^2} \tag{2}$$

In [9-10] and here estimations for coefficient γ_σ are obtained with the help of the theory of plates.

3. Model of simple elastic clamping

In the framework of von Karman theory the plate deflection is

$$E^* \frac{h^3}{12} v^{IV}(x) + \sigma(x) h v''(x) = 0 \tag{3}$$

Here $\sigma(x)$ is the compressive stress within the cross-section of the coating. It should be noted that this stress is generally differ from σ_0 due to relaxation caused by curving of the delaminated part of the coating. For $-b < y < b$, $\sigma(x) = \sigma^{cr} = const$ the general solution of Eq. (3) is

$$v(x) = A_1 \cos kx + A_2, \ |x| < b \tag{4}$$

$$k = \sqrt{\frac{12\sigma^{cr}}{E^* h^2}} \tag{5}$$

Here constants A_i need to be determined from the boundary conditions. As a variant of the solution it may be suggested that the delaminated section of coating could be treated as a plate with elastically clamped ends. Condition of elastic clamping at points $x = \pm b$ is

$$v'(x)\big|_{x=b} = hd\, v''(x)\big|_{x=b} \tag{6}$$

Here hd is the coefficient of proportionality between the angle of the plate at clamping and the second derivative of the displacement (proportional, in turn, to the bending moment, acting at this point); d is a dimensionless coefficient that can be not determined in the frame of elementary theory. The presence of plate thickness h is due to necessity of adjusting dimensions: this parameter is the only one of the dimension of length in the model, because the clamping stiffness may not depend on the plate size b (for more information see [9-10]). Substitution of Eq. (4) into Eq. (6) yields

$$\tan kb + khd = 0 \tag{7}$$

The expression for coefficient d were obtained in [11] on the base of the model where the coating was considered as a plate and the substrate as half-plane. The solution was found with the help of Fourier transform and Wiener-Hopf technique. By neglecting the action of shear stress it was found

$$d = d_0 \sqrt[3]{E^*/E_s^*}, \ d_0 = 2^{2/3} 3^{-5/6} \approx 0,636 \tag{8}$$

Here

$$E^* = E/\left(1-\nu^2\right) \tag{9}$$

For rigid clamping

$$k_0 = \frac{\pi}{b} \tag{10}$$

Substituting Eq. (1), Eq. (5), Eq. (8), Eq. (10) into Eq. (7) gives

$$\tan \pi \sqrt{\gamma_\sigma} + d_0 \pi \beta \sqrt{\gamma_\sigma} = 0 \tag{11}$$

Here

$$\beta = (h/b) \sqrt[3]{E^* / E_s^*} \tag{12}$$

Dependence of γ_σ on β according to this model is also presented on Figure 2. The most probable reason for the slight systematical divergence seems to be in underestimation of the critical stresses in numerical calculations.

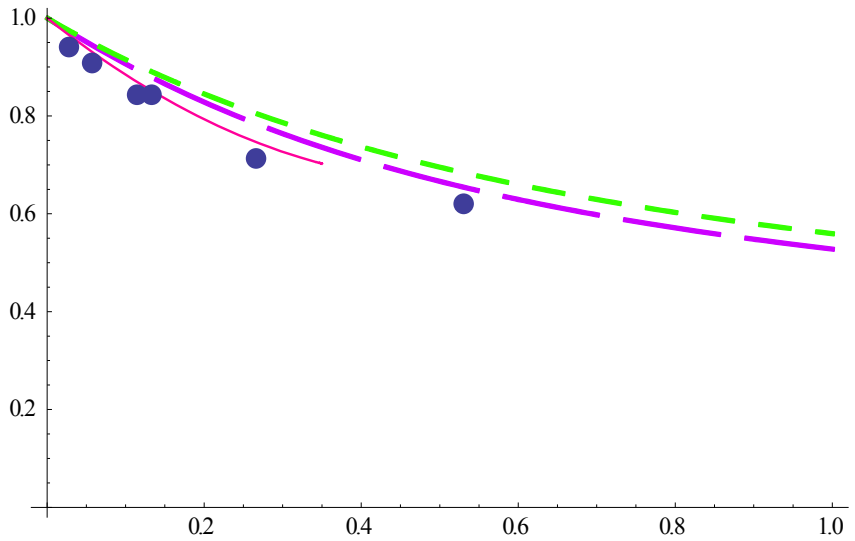

Figure 2. Dependence of relative critical stress on geometrical and elastic parameters: purple dashed line – solution Eq. (11); green dashed line (short dashes) – Eq. (18); solid red thin line – Eq. (26); dots – numerical solution [9]

4. Generalization for the case of multilayered coating and substrate

The above model is easily generalized for the case of anisotropic (orthotropic) and multilayered coating and substrate. For anisotropic phases all the above formulae remain valid with replacing the values of effective moduli Eq. (9) of coating and substrate by the values corresponding to anisotropic media. Thus for substrate instead of the second formula of Eq. (9) we have

$$E_s^* = 2\left\{\beta_{22}\left[\beta_{66} + 2\left(\beta_{11} + \sqrt{\beta_{11}\beta_{22}}\right)\right]\right\}^{-1/2} \tag{13}$$

Here β_{ij} are components of compliance tensor written in matrix form (eg [14]), axis x_1 is

directed along layering, axis x_2 is directed along the normal.

For anisotropic (orthotropic) coating modulus E^* should simply be replaced with the longitudinal modulus: $E^* = E_{22}$.

For multilayered structures, if the thickness of individual layers are much less than the characteristic size of delaminated part of coating, the layered structure may be described as an effective homogeneous anisotropic media [15]. The value of effective longitudinal modulus of coating may be calculated as an averaged over the individual layers forming its delaminated part

$$E^* = \frac{\sum E_i^* h_i}{\sum h_i} \tag{14}$$

Here E_i^*, h_i are elastic moduli and thicknesses of the individual layers.

Similarly, for the multilayered substrate the effective elastic constants may be expressed as follows

$$c_{11}^* = \frac{\sum c_i^{11} h_i}{\sum h_i} \qquad c_{12}^* = \frac{\sum c_i^{12} h_i}{\sum h_i} \qquad c_{22}^* = \frac{\sum h_i / c_i^{22}}{\sum h_i} \qquad c_{66}^* = \frac{\sum h_i / c_i^{66}}{\sum h_i} \tag{15}$$

Coefficients of matrix of elastic compliance β_{ij} to be substituted to (13) are obtained from here by inversing the matrix of elastic constants.

$$\beta_{11} = \frac{c_{22}^*}{c_{11}^* c_{22}^* - c_{12}^{*\,2}} \qquad \beta_{22} = \frac{c_{11}^*}{c_{11}^* c_{22}^* - c_{12}^{*\,2}} \qquad \beta_{66} = c_{66}^{*\,-1} \tag{16}$$

It is worth to note, that the above formulae describe the crack propagation in multilayered coating both between the individual layers and between the whole package forming the coating and substrate. The difference consists in accounting the particular number of layers while calculating the effective properties Eq. (14), Eq. (15).

5. Model of generalized elastic clamping

The model of elastic clamping may be generalized in order to account the influence of longitudinal force on the boundary conditions. Such a model was used by [5] for finding the critical stress of buckling of the delaminated coating. In the frame of that model it is supposed that longitudinal displacement u and angle of rotation are linear function of longitudinal force F and bending moment M acting at the point of clamping

$$\begin{aligned} EU_0 &= a_{11} F + a_{12} h^{-1} M \\ E\frac{dV_0}{dx} &= a_{21} h^{-1} F + a_{22} h^{-2} M \end{aligned} \tag{17}$$

Although condition of elastic clamping Eq. (6) was proven to be asymptotically correct [16], and other terms might be beyond the accuracy of beam (plate) theory, accounting for additional terms in Eq. (17) may be useful in numerical calculations.

The direct application of boundary condition Eq. (17) to Eq. (4) is impossible due to presence of unknown parameter F, which, however, may be found by solving the equation for longitudinal

displacement u , simultaneously with Eq. (3). That was done in [5] with the final result for the critical stress after writing it in the form convenient for our purposes being:

$$\frac{12b}{\pi h\sqrt{\gamma_\sigma}}\tan\pi\sqrt{\gamma_\sigma}+a_{22}-\frac{a_{12}^2}{1+a_{11}}=0 \tag{18}$$

The coefficient of symmetric matrix a_{ij} of elastic clamping were calculated in [5] by numerical solving of a system of integral equations as functions of ratio of moduli of coating and substrate and ratio of coating thickness to the delamination length.

Taking into account that according to Eq. (12)

$$a_{22}=12d_0\sqrt[3]{E^*/E_S^*} \tag{19}$$

expression Eq. (18) differ from Eq. (11) only by its last term, which is usually not large; nevertheless its accounting leads to (slight, but systematic) deviation of the results from the master curve, obtained by using more simple Eq. (11).

Dependence of γ_σ on β according to this model is also presented on Fig. 2, coefficient a_{11} was calculated with the help of the first formula of Eq. (20) for $E^*/E_S^*=1$. If the initial surface is curved, then in addition to longitudinal force and bending moment, transverse force N appears at the clamping point. Hence, condition Eq. (17) may be generalized:

$$\begin{aligned}
&EU_0=a_{11}F+a_{12}h^{-1}M+a_{13}N\\
&E\frac{dV_0}{dx}=a_{21}h^{-1}F+a_{22}h^{-2}M+a_{23}h^{-1}M\\
&EV_0=a_{13}F+a_{23}h^{-1}M+a_{33}N
\end{aligned} \tag{20}$$

Here 3x3 matrix a_{ij} may be called the extended matrix of coefficient of elastic clamping. Calculating coefficients of the extended matrix a_{ij} may become useful for studying delamination and buckling of initially curved coatings.

6. Calculating coefficients of matrix of elastic clamping

Coefficients of matrix (20) were calculated in [4] for a particular geometric parameters numerically, and in [5] by numerical solving a system of integral equations for various ratios geometric parameters and moduli. However it is desirable to have an asymptotical, or at least, approximating formulae.

Formulae for a_{22} were obtained in [11] on the base of the model where the coating was considered as a plate and the substrate as half-plane by using Fourier transformation and Wiener-Hopf technique. The value is given by Eq. (8), Eq. (19). The value of a_{23} were found (ibid.) to be

$$a_{23}=2^{7/3}3^{-2/3}\left(E/E_S\right)^{2/3}=2.52\left(E/E_S\right)^{2/3} \tag{21}$$

Coefficients a_{11}, a_{12} (as well as some coefficients of the extended matrix Eq. (16)) for the case of

coating and substrate being of the same material were obtained in [12]. The results were obtained on the base of solution of the matrix Wiener-Hopf problem [17], which was extended to describe displacements. The extraction of the coefficient a_{22} for this case was made before [18], [19]. 3-D case was considered in [20].

It follows from the results of [5] that the value for a_{12} does not effectively depend on the ratio elastic moduli, unless very soft substrates. For this case value

$$a_{12} = \sqrt{3} \tag{22}$$

was obtained [12]. It was also obtained (ibid.) the value for a_{13} for the case of the same moduli of coating and substrate

$$a_{13} = 1 + \sqrt{3} \tag{23}$$

The obtained formula for a_{11} appeared rather awkward to be represented here.

An intent look at the results for a_{11} reveals that all points may be represented as a single master curve (Fig 3) with rather good accuracy.

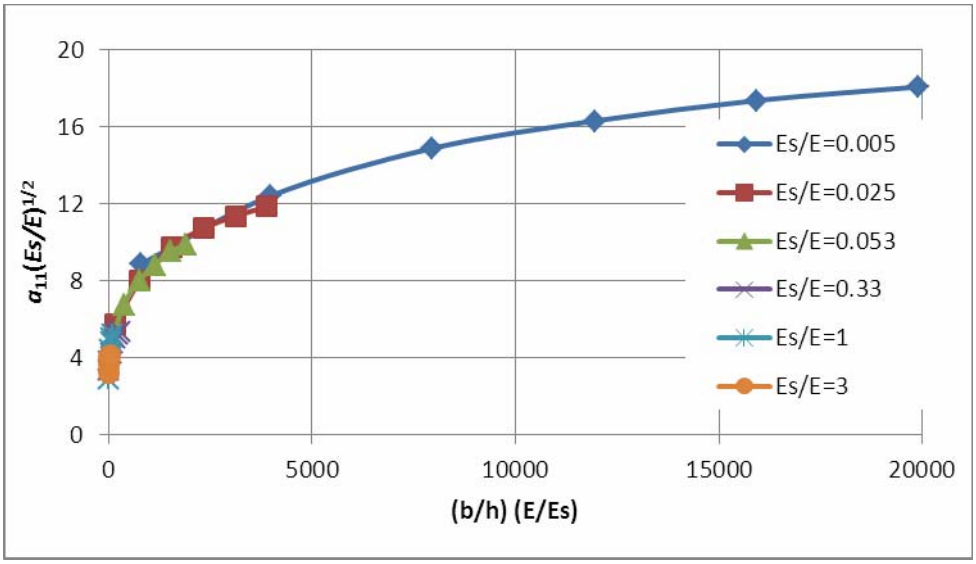

Fig. 3. Numerically obtained master curve for a_{11} on the base of results [5].

The curve may be fitted by one of the following (purely approximating) formulae

$$a_{11} = \frac{1}{2}\sqrt{\frac{E}{E_S}} + \frac{3}{2}\left[\frac{b}{h}\left(\frac{E}{E_S}\right)^3\right]^{1/4} \qquad a_{11} = \frac{3}{2}\left[\frac{b}{h}\left(\frac{E}{E_S}\right)^3\right]^{1/4}$$
$$a_{11} = \sqrt[3]{\frac{E}{E_S}}\left[\left(\frac{b}{h}\frac{E}{E_S}\right)^{1/5} - 1\right] \qquad a_{11} = \sqrt{\frac{E}{E_S}}\left[4\left(\frac{b}{h}\frac{E}{E_S}\right)^{1/6} - 3\right] \tag{24}$$

7. Some asymptotic estimations for critical stress

For γ_σ. slightly diverging from unity, which corresponds to small β, asymptotic solution of Eq. (11) may be obtained by the following substitution

$$\sqrt{\gamma_\sigma} = 1 + a_1\beta^m + a_2\beta^n + \ldots \tag{25}$$

On expanding Eq. (25) into series for small β, the coefficients a_1, a_2, as well as exponents m, n for which the solution exists are found. The corresponding solution is

$$\sigma^{cr} = \frac{\pi^2 h^2 E^*}{12b^2}\left(1 - 2d_0\beta + 3d_0^2\beta^2 + \ldots\right) \tag{26}$$

Dependence of γ_σ on β. according to this model is also presented on Fig. 2.

The carried FE analysis [9], the results of which are presented on Figure 2 (dots), confirms the analytically obtained dependence of the critical stress on the elastic and geometric parameters according to the suggested models.

Summary

The problem of a crack propagation in multilayered coating either between the individual layers, or between the whole package forming the coating and substrate (possibly also non-uniform) is considered. According to the model the delaminated part of the coating is treated as a plate with a special attention given to the boundary conditions, which are supposed to be of the elastic clamping type, which means that the angle of rotation at the clamping point is related to the acting bending moment at that point. The generalized model of elastic clamping is also considered in the frame of which it is supposed that components of displacements and angle of rotation at the clamping point are related to the acting total force and total moment by means of 3x3 matrix of elastic coefficients. Several variants of analytical models to determine the coefficients of this 3x3 matrix were considered and discussed. The case of non-uniform (multi-layered) coating is considered with a special attention paid to analysis of the influence of the relative dimensions involved, such as the individual layer and the multilayer coating thicknesses, distance from the crack to the free surface, crack length.

Using the obtained solution the problem on buckling of the delaminated coatings is addressed. It has been shown that the difference between the obtained critical stress and the critical stress of a rigidly clamped plate can be significant. It has also been shown that for a wide range of parameters even for anisotropic and multilayered structures the ratio of the obtained critical stress and the critical stress of a rigidly clamped plate is determined by a single nondimensional parameter, which is a combination of the elastic constants of the coating and substrate, and the ratio of the delamination length to the coating thickness. The analytical results correlate well with the results obtained using the numerical calculations.

References

[1] J.W. Obreimoff, Splitting Strength of Mica. Proc Roy Soc London A 127 (1930) 290-297.

[2] L.M. Kachanov, Delamination Buckling of Composite Materials. Kluwer, Boston (1988).

[3] J.W.Hutchinson, Z. Suo, Mixed Mode Cracking in Layered Materials, in: J. W. Hutchinson and T. Y. Wu (eds.), Advances in Applied Mechanics, 29 (1992) 63-191.

[4] B. Cotterell, Z. Chen, Buckling and cracking of thin film on compliant substrates under compression, Int J Fract 104 (2000) 169-179.
[5] H.H. Yu, J.W. Hutchinson, Influence of substrate compliance on buckling delamination of thin films, Int J Fract 113 (2002) 39-55.
[6] G. Parry, J. Colin, C. Coupeau, F. Foucher, A. Cimetière, J. Grilhé, Effect of substrate compliance on the global unilateral post-buckling of coatings: AFM observation and finite element calculations, Acta Mater 53 (2005) 441-447.
[7] S. Faulhaber, C. Mercera, M.-W. Moon, J.W. Hutchinson, A.G. Evans, Buckling delamination in compressed multilayers on curved substrates with accompanying ridge cracks, J Mech Phys Solids, 54 (2006) 1004-1028.
[8] H.H. Yu, M.Y. He, J.W. Hutchinson, Edge effects in thin film delamination, Acta Mater 49 (2001) 93-107.
[9] R.V. Goldstein, K.B. Ustinov, A.V. Chentsov, Influence of substrate compliance on stresses generating stability loss of a delaminated coating, Computational continuum mechanics, 4 (2011) N3 48-57.
[10] K.B. Ustinov, On influence of substrate compliance on delamination and buckling of coatings. Books of Abstracts 19-th European conference on fracture. Fracture Mechanics for Durability, Reliability and Safety. ESIS19 August 26-31 2012, Kazan. CD-PROCEEDINGS ISBN 978-5-905576-18-8
[11] R.L. Salganik, K.B. Ustinov, Deformation Problem for an Elastically Fixed Plate Modeling a Coating Partially Delaminated from the Substrate (Plane Strain), Mech Solids N4 (2012) 415-425.
[12] K.B. Ustinov. Once more on a problem of a half plane, weakened by semi-infinite crack parallel to its boundary. Preprint IPM RAS (2013) in print
[13] S.P. Timoshenko, Strength of materials. Vol. 2 Nauka Moscow (1965).
[14] S.G. Lekhnitsky, The Theory of Elasticity of an Anisotropic Body, Holden and Day, San Fransisco (1963).
[15] I.M. Lifshiz, L.N. Rosenzweig, On the theory of elastic properties of polycrystals, JETP 16 N11 (1946) 967-978.
[16] K.B. Ustinov, On the refinement of boundary conditions for the beam model of the cantilever of the atomic force microscope and their influence on the interpretation of the measurement results, Mech Solids N3 (2008) 470-476.
[17] A.N. Zlanin, A.A. Khrapkov, A semi-infinite crack parallel to the boundary of the elastic half-plane, DAN SSSR 31 N3 (1986) 1009-1010.
[18] Ustinov, K.B., A.V. Dyskin, L.N. Germanovich, Asymptotic analysis of extensive crack growth parallel to free boundary, in: Aliabadi et al (eds.), 3rd Int Conf Localized Damage 94 (1994) 623-630.
[19] Dyskin, A.V., L.N. Germanovich, K.B. Ustinov, Asymptotic analysis of crack interaction with free boundary, Int J Sol Struct 37 (2000) 857-886.
[20] R.V. Golstein, A.B. Konovalov, Asymptotic analysis of 3-D problem on crack-delamination in two layered plate. Preprint IPMech RAS N 565 (1996).

On the Formation of Regular Crack Networks around a Circular Hole under Uniform Compression

Ilya Nickolaevich Dashevskiy

A. Ishlinsky Institute for Problems in Mechanics, Russian Academy of Sciences, 119526, Russia
dash@ipmnet.ru

Abstract The energy approach is used to propose a model of arising of regular systems of cracks, emerging the surface of a circular cavity, being observed, for example, around oil and gas wells under uniform compression. The cracks are supposed to arise due to the accumulation of elastic compression energy in the system. The limit compression (the exhaustion of strength) being achieved, a network of cracks is formed in the most stressed layer adjacent to the interior of the body, thus utilizing the accumulated elastic energy of this layer. In this case, of all the possible grids the least energy-consuming one is formed, that is, the system with such a number n and length L of the cracks, that the energy needed for its creation is minimal. In the simplest scheme the number n of "petals"-wedges arising from the cracking turns out to be equal to 5 (which corresponds to $2n = 10$ cracks) and (contrary to limit compression pressure magnitude) be independent on geometrical and physical-mechanical parameters of the problem.

Keywords Crack Systems, Oil and Gas Wells

1. Introduction

Around oil and gas wells under hydrostatic pressure [1, 2] (Fig. 1, 2) a pattern of regular cracks grids, emerging the surface of a circular cavity, is frequently observed. In the so-called «geoloosening» (directed layer unloading) method such systems are produced specially for increasing the rock fracturing and stimulation of oil input to the well [1, 2]. That is why it is important studying the structure of this crack networks, in particular, their number, length, etc.

Regular systems of cracks are found in many structures and natural objects (examples and references see, eg, [3]). They may be initially due to both non-mechanical factors, such as thermal stress, the effect of aggressive media, phase transforms (drying, freezing [4]), etc., as well as have purely mechanical nature. Note that the problem of regular cracking of bark in technically elementary but quite substantial statement was considered in [5] already in 1952. Point also the paper [6], in which the formation of regular ordered crack systems was used to illustrate the capabilities of the variational principle of cracks mechanics there proposed. In [3] for the near-surface thermal cracks the formation of "nested doll" systems was studied, where a regular system of equal cracks turns into two analogous crack systems, each with its own size but double period with respect to the original system. Moreover, it was shown that, in some cases, the crack may develop by jumps, and in others, for subsurface cracks it turns out more profitable not to extend into the material, but curl and form spalling. In [7] issues of arising of ordered crack systems and/or crack-like defects under compression were briefly touched upon. In [8] development of regular systems of surface cracks under the thermal shock, and in [9] – multiple cracking of brittle coatings upon loaded solids was studied. In [10-12] an experimental study was performed, and a model was proposed on formation and evolution of cracks echelon in the vicinity of a main longitudinal shear elastic-brittle crack. In [13-16] distribution of fragments of glass after break by size and time was experimentally studied and theoretically treated using methods of the theory of fractals.

Fig. 1 [4, p. 33]

Fig. 2 [4, p. 33]

2. Statement of the problem on regular cracks grid around oil and gas wells

In [17-20] the energy approach was used to propose a model of symmetric brittle crack formation in a thin plate (and a wedge) under bending by a point indenter. The main purpose of that idealized minimal model was to quantify the study of some possible mechanisms determining the number of the cracks arising. In this paper, similar approach is used to model the formation of a regular grid of cracks around a circular cavity under hydrostatic pressure [21-22]. The basic idea is that cracks are formed due to the accumulation in the system of elastic energy of compression (or rather, the shear energy). As the material strength is exhausted, in the most stressed layer, adjacent to the interior of the body, a regular network of cracks appears, which formation takes all the elastic energy of that layer. In this case, of all the possible grids the minimum-energy-consuming fracture scheme occurs, that is, a system with such a number n and length L of the cracks, that the energy needed for its creation, is minimal.

Unlike the case of plate bending here cracks go from the surface of the hole not perpendicular to it, but at an acute angle (though not necessarily at 45^0, ie in the direction of slip lines). In other words, they are not tensile cracks, though perhaps not quite shear ones. More precisely, in [2, p. 21, 37-38] "usual for rocks Coulomb-Mohr type criterion, according to which the failure on these planes occurs when the shear stress achieves some limit value $[\tau] = k - \sigma_n \mathrm{tg}\, \rho$, where k and ρ are cohesion modulus and internal friction angle of rock respectively, which are the strength characteristics of the rock" is taken as a failure criterion. Aimed to clarify the fundamental possibility of constructing a simple model of cracks ordered systems of such type and calculation of cracks number, as well as

maximum simplification of the problem and using the features of its stress-strain state, we assume that the cracks propagate along the slip lines, and their formation is due to stored elastic energy, but not all, but only the shear energy, the energy of hydrostatic compression being not taken into account

So, the model is based on the following provisions:

I. Suppose we have an infinite plane with a circular cavity in a uniform compression, stress-strain state is plane.

II. As the material strength is exhausted, fracture occurs instantaneously with the formation of a symmetric system of shear cracks.

III. Cracks occur along the slip lines, forming a regular pattern like Fig. 1-3.

IV. One can neglect the irreversible (inelastic, heat, etc.) losses (plate behaves quasi-brittle), and possible dynamics (waves).

V. Energy balance equation expresses the equality of the energy of formation of new surfaces (cracks) to the elastic energy of shear, released from the ring (layer), which was cut through with those cracks.

VI. The minimum-energy-consuming fracture scheme occurs, i.e., the scheme with such a number n and length L of the cracks, that the energy needed for its creation, is minimal.

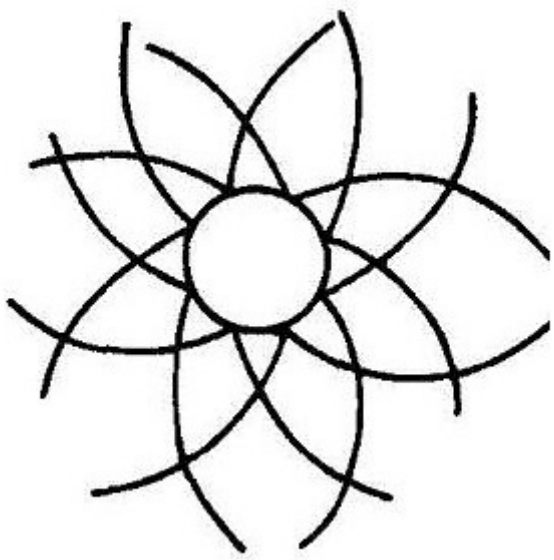

Fig. 3 [24, p. 326]

The proposed scheme can essentially be considered as a version of that classical approach by Griffith [23], adopted for cases where the problem symmetry requires the hypothesis on occurrence of one crack to be replaced with the assumption of arising a symmetrical system with n cracks.

3. Crack creation energy

To formalize the above speculations we write according to the condition «V» the basic equation of energy balance

$$W = W_e \tag{1}$$

where W, W_e are the energy of formation of new surfaces (shear cracks) and elastic energy gone to it of the layer, weakened (destroyed) by the cracks net arised, respectively.
Somewhat roughenning the real situation, we assume that the fracture pattern is axially periodic

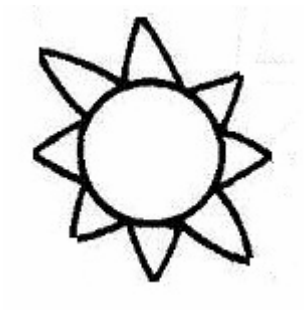

Fig. 4

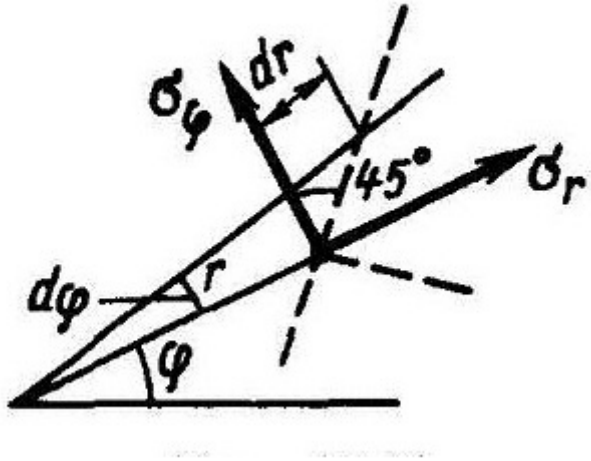

Fig. 5 [24, p. 326]

(Fig. 4) and is built of n «petals", each seen from the center of the cavity at an angle $2\varphi_n$ and formed by a couple of cracks emanating from the surface of the cavity at an angle of 45^0 and directed to each other

$$2\varphi_n = 2\pi/n,\ \varphi_n = \pi/n \tag{2}$$

The energy of formation of new surfaces (shear cracks)

$$W = \gamma L = \gamma \cdot 2n\Lambda \tag{3}$$

where γ is corresponding effective (specific) surface fracture energy (or more precisely, the specific energy of cracking, since there are two surfaces but one crack), L – total length of all the cracks, n – number of petals-sectors formed ($2n$ cracks), Λ – the length of a crack.
Taking that fracture occurs along the slip lines and the cracks grid forms a regular pattern like Fig. 4, calculate the total length of cracks

$$L = 2n\Lambda = n \cdot 2 \cdot \int_{\varphi=0}^{\varphi=\frac{\pi}{n}} dS \tag{4}$$

where n is the number of pieces (wedges), cut out by the cracks, φ – polar coordinate, dS – differential of arc length along the crack.
As is known, the direction of the maximum shear stresses divides the angles between the principal axes of the stress tensor in two [25, p. 265]. Circular cavity considered is a special case of a tube with an infinite outer radius. The principal stresses in the cross section of the tube are directed radially and circumferentially, the slip lines being inclined to these directions at an angle 45^0 (Fig.

5). From this figure we see that

$$dR = \pm R d\varphi \tag{5}$$

where R and φ are polar coordinates. This equation gives two orthogonal families of slip lines

$$R(\varphi) = Ce^{\pm\varphi}; \qquad R|_{\varphi=0} = R^* = C, \qquad R(\varphi) = R^* e^{\pm\varphi} \tag{6}$$

where C is the integration constant, R^* – the radius of the hole. Taking R^* and

$$W^* = 2\sqrt{2}\,\pi\gamma R^*, \tag{7}$$

as the length and energy reference scales, respectively, pass on to dimensionless variables r, λ, l, w by the formulas

$$r = \frac{R}{R^*}, \quad \lambda = \frac{\Lambda}{R^*}, \quad l = \frac{L}{R^*}, \quad w = \frac{W}{W^*} = \frac{W}{2\sqrt{2}\pi\gamma R^*} \tag{8}$$

$$R = R^* r, \qquad \Lambda = R^*\lambda, \qquad L = R^* l, \qquad W = W^* w \tag{9}$$

Then (6) takes the form $r(\varphi) = e^{\pm\varphi}$, and choosing to be definite one of the branches (families) with the sign +, we obtain the dimensionless radial coordinate of the "petal"-wedge end r_n

$$r_n = r(\varphi_n) = |(2)| = r(\pi/n) = e^{\pi/n}, \qquad n = \pi/\ln r_n \tag{10}$$

Writing now the expression for the differential of arc length in polar coordinates, expressing φ in R using (5) and integrating over the entire crack length, we find the length of one crack Λ, λ and the total dimensionless length of all the cracks l

$$\Lambda = \int_{\varphi=0}^{\varphi=\frac{\pi}{n}} dS = \int_{\varphi=0}^{\varphi=\frac{\pi}{n}} \sqrt{(Rd\varphi)^2 + (dR)^2} = |(5)| = \int_{R^*}^{R_n} \sqrt{2}dR = R^* \int_1^{r_n} \sqrt{2}dr = \sqrt{2}R^*(r_n - 1) \tag{11}$$

$$\lambda = \sqrt{2}(r_n - 1)$$

$$l = 2n\lambda = 2\sqrt{2}n(r_n - 1) = |(10)| = 2\sqrt{2}\pi\frac{r_n - 1}{\ln r_n} \tag{12}$$

For the dimensionless cracking energy with (8), (3), (11) we have

$$w = \frac{W}{W^*} = |(3),(8)| = \frac{2n\gamma\Lambda}{2\sqrt{2}\pi\gamma R^*} = |(11)| = \frac{2n\gamma\sqrt{2}R^*(r_n - 1)}{2\sqrt{2}\pi\gamma R^*} = |(10)| = \frac{r_n - 1}{\ln r_n} \qquad 13)$$

A plot of the dimensionless cracking energy w on r_n is represented by the upper curve (almost straight) in Fig. 6. It is the function defined for $r_n \geq 1$, monotonically increasing, concave upwards and equal to 1 for $r_n = 1$.

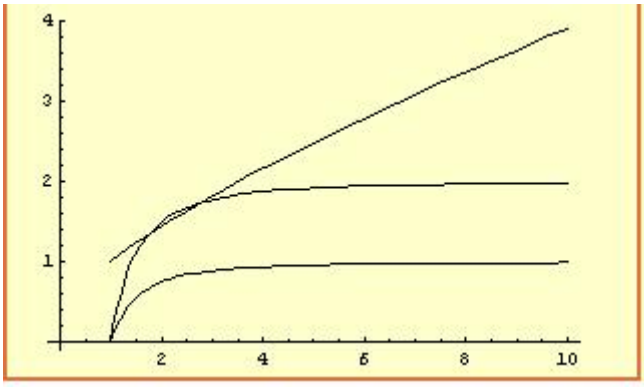

Fig. 6.

4. The elastic energy

Now we write the expression for the right hand side of (1) – elastic energy W_e, stored in the near-well layer, cut through with the cracks, which goes to the formation of cracks

$$W_e = W_f = \int_1^{R_n} W_{fs} 2\pi R dR$$

where W_f is shear energy, W_{fs} (s = specific) – specific shear energy, and the integration is over the ring $R \in [1, R_n]$. According to [25, p. 284, formula (7.28)], the expression for the specific shear energy can be written as

$$\begin{aligned} W_{fs} &= \frac{(1+\mu)}{6E}\left[(\sigma_1-\sigma_2)^2+(\sigma_2-\sigma_3)^2+(\sigma_3-\sigma_1)^2\right]= \\ &= \frac{(1+\mu)}{6E}\left[(\sigma_1-\sigma_2)^2+\sigma_2{}^2+\sigma_1{}^2\right] \end{aligned} \tag{14}$$

where μ is Poisson's ratio, E – Young's modulus, $\sigma_{1,2,3}$ – principal stresses.
Substituting for the right side of (14) the well-known Lame solution for the very thick cylinder with inner radius R^*, being under internal pressure P [25, p. 338-339, formula (9.21)]

$$\sigma_{1,2} = \pm P\left(\frac{R^*}{R}\right)^2 = \pm\frac{P}{r^2} \tag{15}$$

we obtain for the specific W_{fs} and entire W_f shear energy in the ring (layer) $r \in [1, r_n]$

$$\begin{aligned} W_{fs} &= \frac{(1+\mu)}{6E}\left(2^2+1+1\right)\frac{P^2}{r^4} = \frac{(1+\mu)}{E}\frac{P^2}{r^4} \\ W_f(r) &= \int_1^{R_n}\frac{(1+\mu)}{E}\frac{P^2}{r^4}2\pi R dR = \left|R = R^* r\right| = \pi(1+\mu)ER^{*2}\left(\frac{P}{E}\right)^2\left(1-\frac{1}{r_n^2}\right) \end{aligned} \tag{16}$$

Going from P and W_f with the aid of scales of pressure E and energy

$$W^{**} \equiv \pi(1+\mu)ER^{*2} \tag{17}$$

respectively, to dimensionless p and w_f by formulas

$$p = \frac{P}{E}, \quad w_f = \frac{W_f}{W^{**}}, \quad P = pE, \quad W_f = W^{**}w_f \tag{18}$$

we obtain for the dimensionless energy w_f

$$w_f(p, r_n) = p^2\left(1 - \frac{1}{r_n^2}\right) \tag{19}$$

The formula (19) determines for $r_n \geq 1$ monotonically increasing function, concave upwards, equal to 0 for $r_n = 1$ and getting onto a horizontal asymptote at $r_n \to \infty$. The graphs of this function for two values of p are shown in Fig. 6 by two lower curves

.

5. Calculation of the index *n*

For small internal pressures p shear energy plot $w_f(r_n)$ lies below the cracking energy plot $w(r_n)$. The pressure arising, the in-tube stored elastic energy increases monotonically, the plot $w_f(r_n)$ goes higher and at some moment it touches the graph $w(r_n)$ for some r_n. The moment of contact will be the first moment when the elastic energy be equal to the energy required for the formation of an appropriate system of cracks (see similar arguments in Mohr theory [25, § 61, p. 300-306]). Touching specifies two conditions (equality of functions and equality of their derivatives) to determine two unknowns: the pressure and the thickness of the elastic layer, which gives its elastic energy for cracking.

From the condition of equality of functions, by substituting into (1) the expressions (7), (13), (17), (19), we obtain

$$W = W^*w = W_f = W^{**}w_f \tag{20}$$

$$2\sqrt{2}\pi\gamma R^* \frac{r_n - 1}{\ln r_n} = \pi(1+\mu)Ep^2R^{*2}\left(1 - \frac{1}{r_n^2}\right),$$

$$\frac{r_n - 1}{\ln r_n} = \frac{(1+\mu)ER^*}{2\sqrt{2}\gamma} p^2\left(1 - \frac{1}{r_n^2}\right) \tag{21}$$

or, setting the dimensionless constant

$$A = \frac{(1+\mu)ER^*}{2\sqrt{2}\gamma} \tag{22}$$

$$W = W_e: \quad \frac{r_n - 1}{\ln r_n} = Ap^2\left(1 - \frac{1}{r_n^2}\right), \qquad Ap^2(r_n + 1)\ln r_n = r_n^{\ 2} \tag{23}$$

Tangency condition we obtain by differentiating (23)

$$\frac{dW}{dr} = \frac{dW_e}{dr}: \quad \frac{\ln r_n - \dfrac{r_n - 1}{r_n}}{\ln^2 r_n} = Ap^2 \frac{2}{r_n^{\ 3}}, \quad Ap^2\left(\ln r_n + \frac{r_n + 1}{r_n}\right) = 2r_n \tag{24}$$

Dividing (23_1) to (24_1), we obtain governing equations for r_n

$$\frac{\dfrac{r_n - 1}{\ln r_n}}{\dfrac{\ln r_n - \dfrac{r_n - 1}{r_n}}{\ln^2 r_n}} = \frac{\left(1 - \dfrac{1}{r_n^{\ 2}}\right)}{\dfrac{2}{r_n^{\ 3}}} \tag{25}$$

$$\ln r_n = \frac{r_n + 1}{r_n + 2} = 1 - \frac{1}{r_n + 2} \tag{26}$$

Equation (26) for r_n is transcendental and needs numerical solution, but it can be seen that its root is close to e, therefore, representing r_n in (26) as $r_n = e(1 + \varepsilon)$, expanding in powers of ε and holding the first order, one can obtain simple approximate estimates for ε, r_n and n

$$\varepsilon \approx -0.25,$$

$$n = \frac{\pi}{\ln r_n} = \left|r_n = e(1+\varepsilon)\right| = \frac{\pi}{\ln[e(1+\varepsilon)]} \approx \frac{\pi}{1+\varepsilon} \approx \frac{3.14}{0.75} \approx 4.2$$

It is seen, that the value for n obtained is a fractional number. For the model assumed it means that the solution will be one of the two integers closest to the fractional value found (ie, either 4 or 5), which gives a lower value for the elastic energy. Those integer solutions n appear with changing $W_e(p)$ on increasing p, which, as is clear from Fig. 6, leads to the splitting of the solution found above into two solutions (corresponding to one and the same p), one of which, as can be seen from the graphs in Fig. 6, crawls down ($r_{n1} \downarrow$), and the other – up ($r_{n2} \uparrow$). By (13) $w(r_n) = (r_n - 1)/\ln r_n$ is a monotonically increasing function ($\uparrow$), ie $r_{n1} < r_{n2} \Rightarrow w(r_{n1}) < w(r_{n2})$; vice versa, $n(r_n)$ decreases monotonically (by (10): $n = \pi / \ln r_n \downarrow$). The lower elastic energy corresponds to the lower value of r_n and, accordingly, to the larger value of n. Consequently, $n_{\min} = 5$. Here, with the growth of p the total stored elastic energy in the body increases, but cracking consumes less energy due to the fact that though the number n of cracks increases, but because of the reduction in r_n their total length l in (12) becomes less.

6. CONCLUSIONS

The energy approach is used to propose a model of arising of regular systems of cracks, emerging the surface of a circular cavity, being observed, for example, around oil and gas wells under uniform compression. The cracks are supposed to arise due to the accumulation of elastic compression energy in the system. The limit compression (the exhaustion of strength) being achieved, a network of cracks is formed in the most stressed layer adjacent to the interior of the body, thus utilizing the accumulated elastic energy of this layer. In this case, of all the possible grids the least energy-consuming one is formed, that is, the system with such a number n and length L of the cracks, that the energy needed for its creation is minimal. In the simplest scheme the number n of "petals"-wedges arising from the cracking turns out to be equal to 5 (which corresponds to 2n = 10 cracks) and (contrary to limit compression pressure magnitude) be independent on geometrical and physical-mechanical parameters of the problem. The approach presented can be obviously formalized in the form of a corresponding variational principle of E.M. Morozov type [5, p. 11-24], provided that the core of the functional there introduced, would be modified appropriately and will be proportional not to the maximum normal stress or the maximum linear strain (similar to the first and second strength theories [5, p. 12]), but to the value, corresponding to the failure criterion here adopted.

Acknowledgements

The author is grateful to N.M. Osipenko for useful and stimulating discussions, and A.O. Chernyavsky for literary references and interesting indications.

This work was partially supported by the Russian Foundation for Basic Research (grant № 11-08-01243-a).

References

1. V.I.Karev, The influence of the stress-strain state of the rocks to the filtration process, and well production. Dr. Sc. Thesis, SPb., 2010 [in Russian].
2. Y.F. Kovalenko, Geomechanics of oil and gas wells. Dr. Sc. Thesis, M., 2012 [in Russian].
3. A.O. Cherniavsky, Crack grids in structures and natural objects, Mashinostroenie, M, 2010 [in Russian].
4. J. Walker, Cracks in a Surface / / Sci. Amer. - 1986. - Vol. 255, N4. - P. 158-164.
5. A.V. Dumansky A.Y. Ishlinskii On the patterns of tree bark cracking Dokl. USSR Academy of Sciences, 1952, Vol 84, № 1, p. 161-164 [in Russian].
6. S.S. Solntsev, E.M. Morozov, Glass fracture. Mashinostroenie, M, 1978 [in Russian].
8. R.V. Goldstein, Compression failure / / Adv. in Mech, 2003. Vol. 2. Number 2. P. 3-20 [in Russian].
7. R.V. Goldstein, N.M. Osipenko, Modeling delamination of coatings under thermomechanical loading in beam approximation / / Mechanics of Solids. 2007. Number 5. Pp. 75-90.
9. V.E. Panin, S.V. Panin., R.V. Goldstein, Mesomechanics of multiple cracking of brittle coatings in a loaded solid, International Journal of Fracture. 2008. Vol. 150. № 1-2. Pp. 37-53.
10. R.V. Goldstein, N.M. Osipenko, The gradual development of the fracture structure in the neighborhood of a longitudinal shear crack front. DAN. 2012. Vol. 445. Number 2. Pp. 164-167.

11. R.V. Goldstein, N.M. Osipenko, Fracture structures in the vicinity of microscopic longitudinal shear / / Mechanics of Solids. 2012. Number 5. Pp. 22-34.
12. R.V. Goldstein, N.M. Osipenko, Structures of fracture near a longitudinal shear main crack. In: Proc. 19th European Conference on Fracture (ECF19), August 26-31, 2012, Kazan, Russia. CD Proceedings ID400.
13. O.B. Naimark, M.M. Davydova, O.A. Plekhov, S. Uvarov, Experimental and theoretical study of dynamic stochasticity and scaling at crack propagation / / Phys. Mesomech. - 1999. - Vol. 2. - № 3. - P. 47-58
14. M.M. Davydova, Experimental study of glass fragmentation statistical regularities Physical mesomechanics. 2008. V. 11. Number 5. Pp. 77-82.
15. M. Davydova, S. Uvarov, Fractal Laws for Spatial and Temporal Variables of Brittle Fragmentation / / In: 19th European Conference on Fracture "Fracture Mechanics for Durability, Reliability and Safety", Kazan, Russia, 26-31 August, 2012. Book of Abstracts. Kazan: Foliant, 2012 . P. 123. ISBN 978-5-905576-18-8.
16. M. Davydova, S. Uvarov, Fractal laws for spatial and temporal variables of brittle fragmentation / / In: 19th European Conference on Fracture "Fracture Mechanics for Durability, Reliability and Safety", Kazan, Russia, 26-31 August, 2012. ECF19 Proceedings. (CD) N. 119 [8 pp.]. ISBN 978-5-905576-18-8.
17. I.N. Dashevsky, Crack modeling in a plate under the action of a point indenter / / IX All-Russian Congress of Theoretical and Applied Mechanics. Abstracts. Vol. III. (Nizhny Novgorod, 22-28 August 2006). Nizhny Novgorod: Publishing House of the Nizhny Novgorod State University named after N.I. Lobachevsky, 2006. - P. 81 [in Russian].
18. I.N. Dashevsky, How many parts the plate will break to? Moscow, 2008. - 25 pp. - (Preprint / RAS. Institute of Problems in Mechanics; № 865) [in Russian].
19. I.N. Dashevsky, Cracking model in a plate and a wedge under bending by a point indenter. - In. "Problems in Mechanics: Mechanics of Solids." Moscow: Nauka, 2009. Pp. 115-135. ISBN 978-5-02-036961-0 [in Russian].
20. I.N. Dashevsky, Model of symmetric crack formation in a plate and a wedge under bending by a point indenter / / Mechanics of Solids. 2011. Number 3. Pp. 112-121.
21. I.N. Dashevsky, On the formation of regular cracks systems around a circular hole under uniform compression / / In.: Proceedings of the International Conference "Survivability and Structural Material Science" Zhivkom 2012 (22-24 October 2012). Volume 1. - Moscow, 2012. P. 73-80 [in Russian].
22. I.N. Dashevsky, On the formation of polar-periodic fracture structures at the boundary of round cavity under hydrostatic pressure. M., 2012. – 20 pp. - (Preprint / RAS. Institute of Problems in Mechanics; № 1027) [in Russian].
23. A.A. Griffith, The phenomenon of rupture and flow in solids, Phil. Trans. Roy. Soc. A221, 1920, pp. 163-198.
24. A.V. Alexandrov, V.D. Potapov, Fundamentals of the theory of elasticity and plasticity. Vysshaya. shk., Moscow: 1990. 400 pp [in Russian].
25. V.I. Feodosyev, Strength of Materials. Moscow: Nauka, 1986. 512 p. [in Russian].

Fatigue Crack Growth Modelling in Welded Stiffened Panels under Cyclic Tension

Željko Božić[1,*], **Siegfried Schmauder**[2], **Marijo Mlikota**[2], **Martin Hummel**[2]

[1] University of Zagreb, Faculty of Mech. Eng. And Nav. Arch., I. Lucica 5, 10000 Zagreb, Croatia
[2] University of Stuttgart, IMWF, Pfaffenwaldring 32, D-70569 Stuttgart
* Corresponding author: zeljko.bozic@fsb.hr

Abstract The influence of welding residual stresses in stiffened panels on effective stress intensity factor values and fatigue crack growth rate was studied in this paper. Interpretation of relevant effects on different length scales such as dislocation appearance and microstructural crack nucleation and propagation are taken into account using Molecular Dynamics (MD) simulations as well as a Tanaka-Mura approach for the analysis of the problem. Mode I stress intensity factors (SIF), K_I, were calculated by the ANSYS program using shell elements and assuming plane stress conditions. The SIFs were calculated from FE results using the crack tip displacement extrapolation method. A total SIF value, K_{tot}, is contributed by the part due to the applied load K_{app}, and by the part due to weld residual stresses, K_{res}. In the FE software package ANSYS the command INISTATE is used for defining the initial stress conditions. The FE analysis for the stiffened panel specimens showed that high tensile residual stresses in the vicinity of a stiffener significantly increase K_{res} and K_{tot}. Correspondingly, the simulated crack growth rate was higher in this region, which is in good agreement with experimental results. Compressive weld residual stresses between two stiffeners decreased the effective SIF value, K_{eff}, which was considered as a crack growth driving force in a power law model.

Keywords Fatigue crack growth rate, Welding residual stresses, Stiffened panel, Dislocation, Microstructural crack

1. Introduction

In stiffened panels of a ship deck structure, fatigue cracks may initiate under cyclic loading at sites of stress concentration and further propagate, which can eventually result in unstable fracture and structural failure. The crack growth rate in welded stiffened panels can be significantly affected by the residual stresses which are introduced by the welding process. The high heat input from the welding process causes tensile residual stresses in the vicinity of a stiffener. These tensile stresses are equilibrated by compressive stresses in the region between the stiffeners. Welding residual stresses should be taken into account for a proper fatigue life assessment of welded stiffened panels under cyclic tension loading.

The complete process of fatigue failure of mechanical components may be divided into the following stages: (1) micro-crack nucleation; (2) small crack growth; (3) long crack growth; and (4) occurrence of final failure. In engineering applications, the first two stages are usually termed as the "crack initiation or small crack formation period" while long crack growth is termed as the "crack propagation period". Dislocation development can be simulated by using the molecular dynamics (MD) simulation code IMD [1]. To analyze dislocation development atomistic scale simulation methods are implemented, [2, 3, 4, 5].

The crack initiation period generally accounts for most of the service life, especially in high-cycle and very high cycle fatigue [6]. In pure metals and some alloys without pores or inclusions, irreversible dislocations glide under cyclic loading. This leads to the development of persistent slip bands, extrusions and intrusions in surface grains that are optimally oriented for slip. With continued strain cycling, a fatigue crack can be nucleated at an extrusion or intrusion within a

persistent slip band. [7, 8, 9, 10, 11, 12, 13].
Non-metallic inclusions, which are present in commercial materials as a result of the production process, can also act as potential sites for fatigue crack nucleation. In the high cycle regime fatigue cracks initiate from inclusions and defects on the surface of a specimen or component. For very high cycle fatigue, fatigue cracks initiate from defects located under the surface of the specimen [14,15]. Micro-crack nucleation can be analyzed by using the Tanaka-Mura model or some of its modifications [16, 17, 18].
Fatigue crack growth prediction models based on fracture mechanics have been developed to support the damage tolerance concepts in metallic structures, [19]. A well known method for predicting fatigue crack propagation under constant stress range is a power law described by Paris and Erdogan [20]. Dexter et al. [21, 22] analysed the growth of long fatigue cracks in stiffened panels and simulated the crack propagation in box girders with welded stiffeners. He conducted cyclic tension fatigue tests on approximately half-scale welded stiffened panels to study propagation of large cracks as they interact with the stiffeners. Measured welding residual stresses were introduced in the finite element model and crack propagation life was simulated. Sumi at al. [23] studied the fatigue growth of long cracks in stiffened panels of a ship deck structure under cyclic tension loading. For that purpose fatigue tests were carried out on welded stiffened panel specimens damaged with a single crack or an array of collinear cracks.
This paper presents a study of the influence of welding residual stresses in stiffened panels on effective stress intensity factor values and fatigue crack growth rate. Mode I SIF values, K_I, were calculated by the FE software package ANSYS using shell elements and the crack tip displacement extrapolation method in an automatic post processing procedure. A total SIF value, K_{tot}, was obtained by a linear superposition of the SIF values due to the applied load, K_{app}, and due to weld residual stresses, K_{res}. The effective SIF value, K_{eff}, as defined by Elber [24], was considered as a crack growth driving force in a power law model. Simulated fatigue crack propagation life was compared with the experimental results as obtained by Sumi at al. [23]. The molecular dynamics (MD) simulation was implemented to analyze dislocation development in an iron cuboid model with a triangular notch tip. Numerical simulations of the fatigue crack initiation and growth for martensitic steel, based on modified Tanaka-Mura, were carried out.

2. Molecular dynamics (MD) simulation of dislocation development in iron

2.1. Methods and model

Taking a close look on dislocation development leads to the necessity of atomistic scale simulation methods. Therefore, we used for the present work the molecular dynamics (MD) simulation code IMD [1]. It was developed at the Institute of Theoretical and Applied Physics (ITAP) belonging to the University of Stuttgart. In MD the atoms are seen as mass m points at the position $\vec{r}$ for which Newton´s equations of motion:

$$F(\vec{r},t) = m * \frac{\partial^2 \vec{r}}{\partial^2 t} \tag{1}$$

are solved in every time step. The force $F(\vec{r},t)$ is given by the derivative of the interatomic embedded atom method (EAM) [2] pair potential $U(\vec{r}\ ,t)$ (Eq. 2):

$$F(\vec{r},t) = -\nabla U(\vec{r},t) \tag{2}$$

The system we investigated contains about half a million iron atoms. They form a cuboid of the size

286 x 143 x 143 Å³ where a notch (dimensions 15 x 90 Å²) with a triangular notch tip was inserted along the (110) plane.

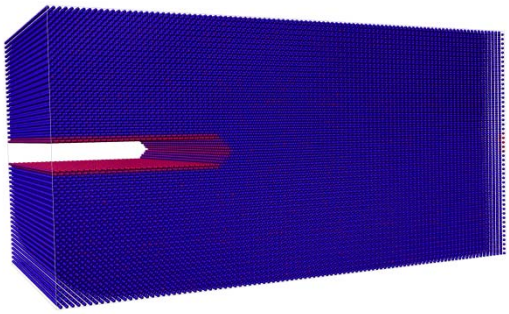

Figure 1. Bcc iron cuboid 286 x 143 x 143 Å³ with a 15 x 90 Å² notch on a (110) plane. The 486000 atoms are color coded via von Mises stress (red ≙ high stress, blue ≙ low stress). Image by MegaMol™ [3].

Cyclic deformation of the simulation box was applied in the [001]-direction. Therefore, the z-component of the simulation cell was elongated with a constant rate of 5x10^-7 at each time step. After reaching a strain of seven percent we applied pressure at the same rate until we reach seven percent of strain in compression. This procedure was repeated continuously. Periodic boundary conditions were used in every direction.

2.2. Results and discussion

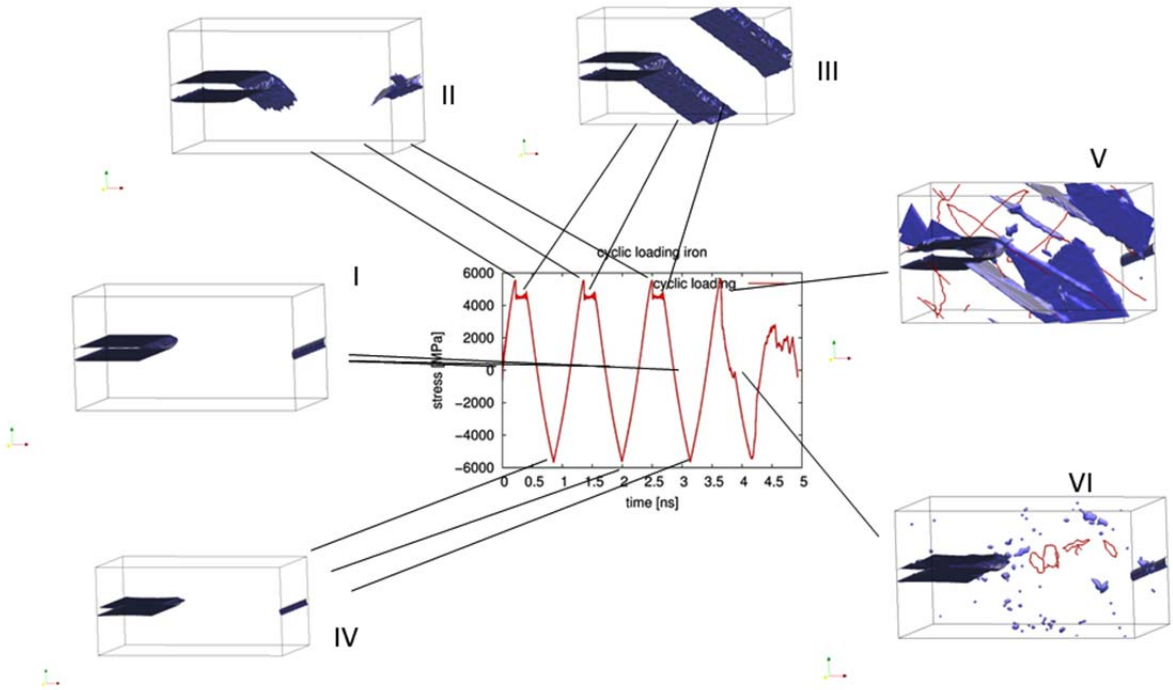

Figure 2. Stress [MPa] in z-direction in terms of the time [ns] during cyclic loading of a nanostructure of a notched iron cuboid. System configurations at different times are depicted: blue are according to DXA [4] “defect surfaces”, red represent dislocations. The view is from lower left.

During the continuous cyclic change from elongation to compression different stages of the system appeared (see Figure 2).

- Stage I: Configuration under no pressure.
- Stage II: Initiation of reversible local restructuring under tensile loading.
- Stage III: Formation of one continuous plane with hcp structure.
- Stage IV: Compression leads to a resolution of the deformation introduced in the previous steps into the structure and to bending of the middle of the notch surfaces towards each other up to a minimum distance of 6.8 Å.
- Stage V: During the fourth loading cycle dislocations are initiated. The Dislocation Extraction Algorithm (DXA) [4] detects "defect surfaces". "The defect surface consists of those parts of the interface mesh, which have not been swept by elastic Burgers circuits." [5]
- Stage VI: Dislocations still remain in the structure even though no pressure remains in the system.

3. Microstructural crack nucleation and propagation

To solve problems of micro-crack nucleation the Tanaka-Mura model [16] is frequently used. The number of stress cycles N_c required for micro-crack nucleation can be determined as follows:

$$N_c = \frac{8GW_s}{\pi(1-\nu)d(\Delta\bar{\tau}-2k)^2} \tag{3}$$

Eq. (3) presumes that micro-cracks form along slip bands within grains, depending on slip band length d and average shear stress range $\Delta\bar{\tau}$ on the slip band. Other material constants (shear modulus G, specific fracture energy per unit area W_s, Poisson's ratio ν and frictional stress of dislocations on the slip plane can be found in the specialized literature [17]. Jezernik et al. [18] used the Tanaka-Mura model to numerically simulate the small crack formation process. Three improvements were added to this model: (a) multiple slip bands inside each crystal grain as potential sites for crack nucleation, (b) micro-crack coalescence between two grains and (c) segmented micro-crack generation inside one grain. A numerical model was directed at simulating fatigue properties of thermally cut steel. The authors took into account accompanying residual stresses in order to simulate the properties of the thermally cut edge as faithfully as possible.

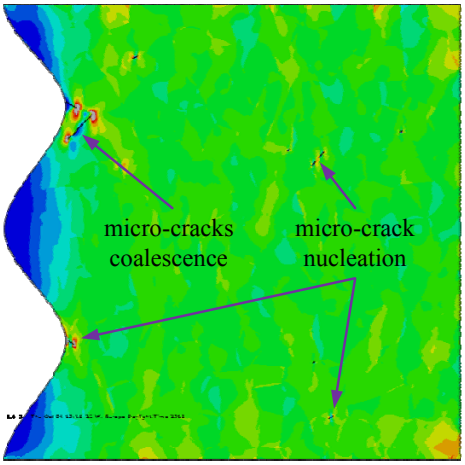

Figure 3. Micro-crack nucleation and subsequent coalescence [18]

As residual stresses are not considered in the Tanaka-Mura model according to Eq. (3), they are imposed as additional external loading. Therefore, the residual stresses are in the Tanaka-Mura equation implicitly evaluated through the average shear stress range on the slip band $\Delta\bar{\tau}$. Figure 3 shows the shear stress distribution and nucleated micro-cracks for a typical high cycle fatigue regime load level (450 MPa). In the beginning, micro-cracks tended to occur scattered in the model and form in larger grains that are favorably oriented and show higher shear stresses. But after a while, existing micro-cracks started coalescing, causing local stress concentrations and amplifying the likelihood of new micro-cracks forming near already coalesced cracks.

4. Modeling and analysis of crack propagation in welded stiffened panels

It is well-known that the residual stress in a welded stiffened panel is tensile along a welded stiffener and compressive in between the stiffeners. Residual stresses may significantly influence the stress intensity factor (SIF) values and fatigue crack growth rate. A total SIF value, K_{tot}, is contributed by the part due to the applied load, K_{app}, and by the part due to weld residual stresses, K_{res}, as given by equation (4):

$$K_{tot} = K_{appl} + K_{res} \tag{4}$$

The so-called residual stress intensity factor, K_{res}, is required in the prediction of fatigue crack growth rates. The considered analysis method is based on the superposition rule of linear elastic fracture mechanics (LEFM). The finite element method (FEM) has been widely employed for calculating SIFs. For evaluating K_{res}, it is important to input correct initial stress conditions to numerical models in order to characterize residual stresses [22, 25]. In the FE software package ANSYS [26] the command INISTATE is used for defining the initial stress conditions.

4.1. Specimen's geometry and loading conditions

Fatigue tests with constant stress range and frequency were carried out on a stiffened panel specimen with a central crack, [23]. The specimen geometry is shown in Figure 4. The material properties of the used mild steel for welding are given in Table 1. Table 2 shows the fatigue test conditions applied in the experiment. The cross sectional area of the intact section, and the average stress range away from the notch, are denoted as, A_o and $\Delta\sigma_o$, respectively. The force range, and the stress ratio are denoted by $\Delta F = F_{max} - F_{min}$, and $R = F_{min}/F_{max}$, respectively. The average applied stress range was $\Delta\sigma_o$ = 80MPa. The initial notch length was $2a$ = 8mm and the loading frequency was 3 Hz.

Table 1. Material properties

E – Young's modulus	206 000 MPa
ν - Poisson's coefficient	0.3
σ_o – Yield strength	235 MPa

Table 2. Fatigue test conditions

A_o [mm^2]	ΔF [N]	$\Delta\sigma_o$ [MPa]	R
1200	96000	80	0,0204

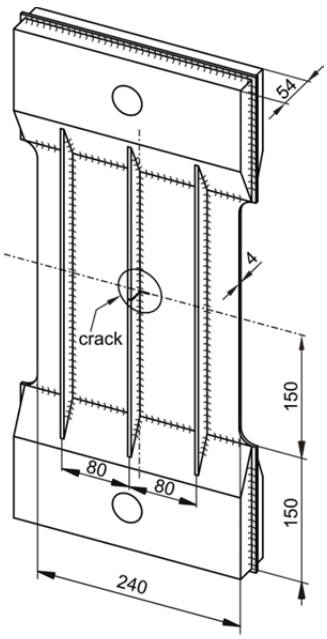

Figure 4. Stiffened panel specimen

4.2. Modeling of welding residual stresses in a stiffened panel by using FEM

In this study the distribution of welding residual stresses in a stiffened panel is taken into account in a similar manner as in the model developed by Dexter at. al. [22], and is shown in Figure 5. Dexter suggested the implementation of a rectangular shape of the residual stresses, which proved to give good results for the simulated fatigue life for such a type of welded stiffened panels.

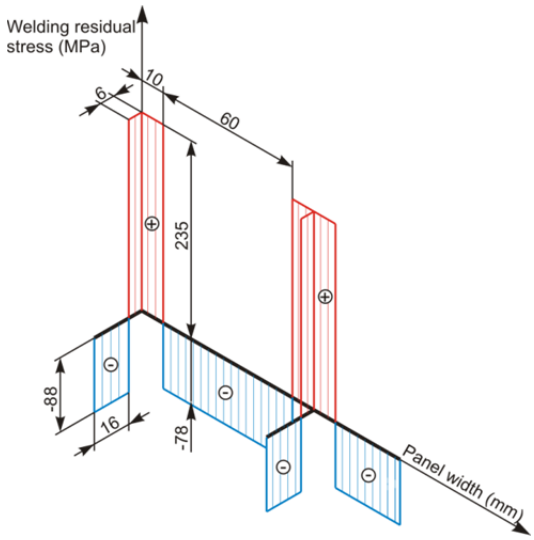

Figure 5. Welding residual stress distribution

To evaluate the SIF value contributed by the residual stresses, K_{res}, it is important to input correct initial stress conditions in the numerical model. In ANSYS software package the command INISTATE can be used to define initial stress conditions [26]. These initial stresses are equilibrated in the first analysis step. Due to the symmetry of specimen's geometry and loading conditions it was sufficient to model only one quarter of the specimen. Figure 6 shows welding residual stresses in the stiffened panel specimen obtained for the implemented stress distribution as given in Figure 5.

Figure 7 shows the σ_y stress component along a selected path in the crack line for the crack length a=4.7 mm, where in the model both, residual stresses and the loading stress range, $\Delta\sigma_o$ = 80MPa, are implemented. A higher stress concentration is observed in the crack tip region.

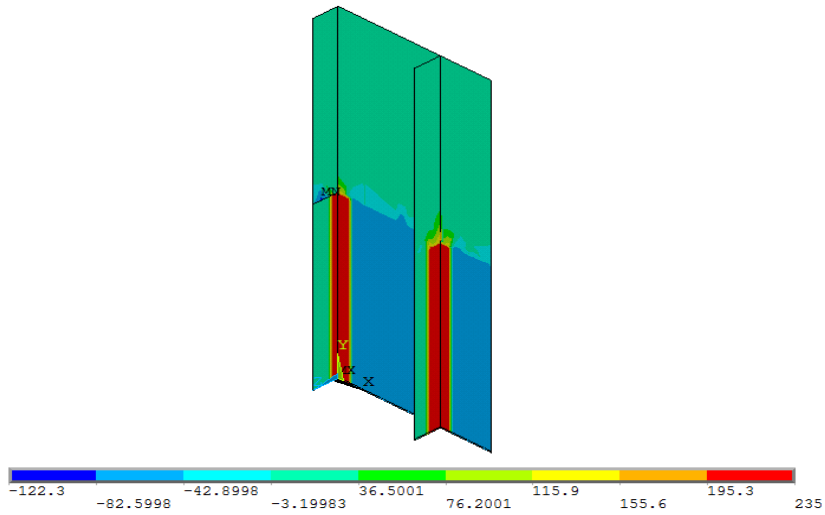

Figure 6. Welding residual stresses in the stiffened panel specimen

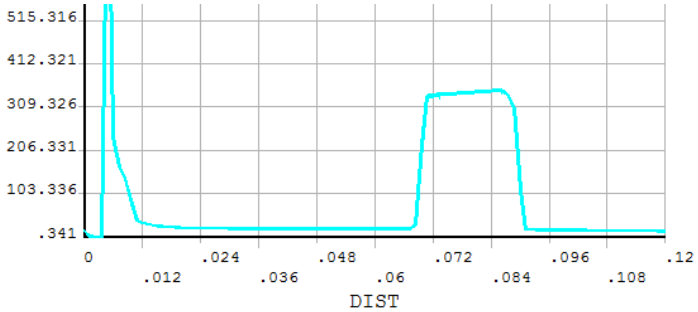

Figure 7. σ_y stress component along a selected path in the crack line

4.3. Stress intensity factors and fatigue crack growth rate

For evaluating SIFs by FEM, the crack tip displacements extrapolation method was implemented [26]. In the general post processing procedure, the "KCALC" command was used to calculate SIFs. The Mode I SIF values, K_I, are determined for a stiffened panel specimen for a loading stress range $\Delta\sigma_o$ = 80MPa, assuming the presence of residual stresses as described above. SIF values with respect to crack length a are given in Fig. 8. K_{app} represents the SIF values due to the applied stress range only, without residual stresses. K_{tot} represents the SIF values for the case when the residual stresses are taken into account along with the external loading stress range. It can be seen that residual stresses significantly increase K_{tot} values for shorter crack lengths, where tensile residual stresses prevail. Between the stiffeners residual stresses reduce the K_{tot} values.
Assuming material constants of a power law equation, C=5.05*10^{-11} and m=2.75 [27], fatigue life was simulated by integrating the power law equation as given by equation (5) (The units for ΔK and $\Delta a/\Delta N$ are [MPa ·m$^{1/2}$] and [m], respectively):

$$\frac{da}{dN} = C\left(\Delta K_{eff}\right)^m \tag{5}$$

The effective stress intensity range, ΔK_{eff}, was defined by Elber as $\Delta K_{eff} = K_{max} - K_{th}$, where K_{th} is a SIF threshold value below which no crack propagation occurs and K_{max} is the maximal SIF value in a loading cycle [24]. Assuming the stress ratio, $R = 0$, as applied in the experiment, the threshold SIF value for a mild steel, as used in the experiment, is taken as $K_{th} = 6.8$MPa, [28, 29]. For the two cases considered crack propagation life was obtained as shown in Figures 9 a) and b).

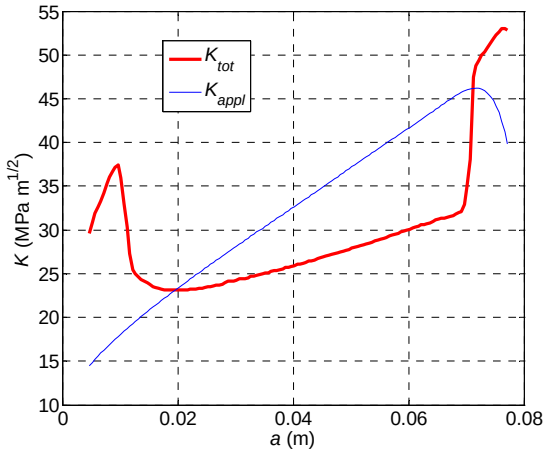

Figure 8. K_{tot} and K_{appl} values

The FE analysis for the stiffened panel specimens showed that high tensile residual stresses in the vicinity of a stiffener significantly increase K_{res} and K_{tot}, as shown in Figure 8. Correspondingly, the simulated crack growth rate was higher in this region, which is in good agreement with experimental results, as can be seen in Figure 9b. Compressive weld residual stresses decreased the total SIF value K_{tot}. The model which does not take account of welding residual stresses could not simulate high crack growth rates in the vicinity of the stiffener, as can be seen in Figure 9a.

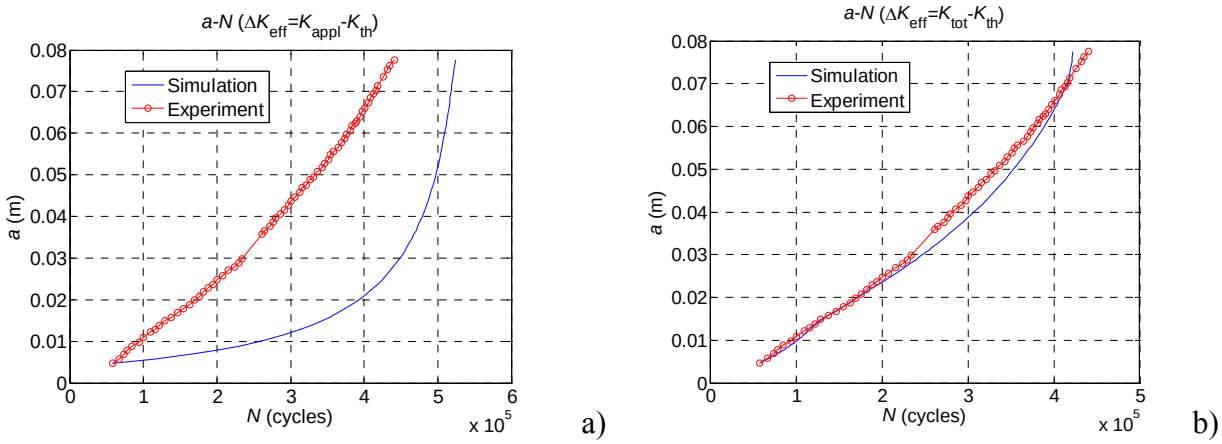

Figure 9. Fatigue crack growth life for the applied stress range $\Delta\sigma_o = 80$MPa : a) without residual stresses, b) including residual stresses

Fatigue crack growth simulation which takes into account the welding residual stresses provides thus better agreement with experimental results in terms of crack growth rate and total number of cycles. In conclusion, residual stresses in welded stiffened panels should be taken into account for a proper evaluation of SIFs and fatigue crack growth rates.

5. Conclusions

Simulation of cyclic loading to model fatigue is possible in MD. Already after very few cycles, essential changes in the system behavior were observed. Contrary to the first cycles, where reversible changes were dominant, not dissolving restructuring occurs in the sense of dislocations and remaining lattice defects or in other words, plasticity.
Numerical simulations of the fatigue crack initiation and growth of martensitic steel, based on modified Tanaka-Mura, was presented. A simulation model related to the micro-crack nucleation along slip bands was presented. Results obtained by using the proposed simulation model were compared to high cycle fatigue tests and showed reasonably good agreement.
Crack propagation simulation based on numerical integration of a power law equation, taking account of welding residual stresses, was implemented to welded stiffened panel specimens. The FE analysis of the stiffened panel specimens showed that high tensile residual stresses in the vicinity of a stiffener significantly increase K_{res} and K_{tot}. The simulated crack growth rate was higher in this region, which is in good agreement with experimental results. Compressive welding residual stresses decreased the total SIF value K_{tot}, and the crack growth rate between the two stiffeners. Residual stresses should thus be taken into account for a proper evaluation of SIFs and fatigue crack growth rates in welded stiffened panels.

Acknowledgements

This work was supported by the Deutsche Forschungsgemeinschaft (DFG) under Grant No. Schm 746/132-1. The support is gratefully acknowledged.

References

[1] J. Stadler, R. Mikulla, H.-R. Trebin, IMD: A software package for molecular dynamics studies on parallel computers, Int. J. Mod. Phys., 8 (1997) 1131.
[2] G. Bonny, R.C. Pasianot, N. Castin, L. Malerba, Ternary Fe-Cu-Ni many-body potential to model reactor pressure vessel steels: First validation by simulated thermal annealing, Phil. Mag., 89 (2009) 3531–3546.
[3] S. Grottel, G. Reina, C. Dachsbacher, T. Ertl, Coherent Culling and Shading for Large Molecular Dynamics Visualization, Computer Graphics Forum (Proceedings of EUROVIS 2010), 29(3) (2010) 953 – 962.
[4] A. Stukowski, V.V. Bulatov, A. Arsenlis, Automated identification and indexing of dislocations in crystal interfaces, Modelling Simul. Mater. Sci. Eng., 20 (2012) 085007.
[5] A. Stukowski, DXA user manual Version 1.3.4, (2010), http://dxa.ovito.org/README.txt
[6] S. Glodez, N. Jezernik, J. Kramberger and T. Lassen, Numerical modelling of fatigue crack initiation of martensitic steel, Advances in Engineering Software, 41(5) (2010) 823-829.
[7] WA. Wood, Fatigue in aircraft structures, Academic Press, New York, 1956.
[8] M.E. Fine, R.O. Ritchie, Fatigue-crack initiation and near-threshold crack growth. In: M. Meshii (Eds.), Fatigue and microstructure, Metals Park (OH): ASM, 1978, pp. 245–278.
[9] C. Laird, Mechanisms and theories of fatigue. In: M. Meshii (Eds.), Fatigue and microstructure. Metals Park (OH): ASM, 1978, pp. 149–203.
[10] M. Klesnil, P. Lukas, Fatigue of metallic materials, Elsevier, New York, 1980, pp. 57–80.
[11] H. Mughrabi, Rev Phys Appl, 23 (1988) 367–379.
[12] H. Mughrabi, In: K.S. Chan, P.K. Liaw, R.S. Bellows, T. Zogas, W.O. Soboyejo (Eds.), Fatigue: David L. Davidson symposium, Warrendale (PA): TMS, 2002, pp. 3–15.
[13] D.L. Davidson, K.S. Chan, Crystallography of fatigue crack initiation in Astrology at ambient

temperature. Acta Metall, 37(4) (1989) 1089–1097.
[14] Q. Y. Wang, C. Bathias, N. Kawagoishi, Q. Chen, Effect of inclusion on subsurface crack initiation and gigacycle fatigue strength. International Journal of Fatigue, 24(12) (2002) 1269-1274.
[15] Y. Murakami, T. Nomoto, T. Ueda, On the mechanism of fatigue failure in the superlong life regime ($N>10^7$ cycles). Part 1: influence of hydrogen trapped by inclusions. Fatigue Fract. Engng. Mater. Struct., 23(11) (2000) 893-902.
[16] K. Tanaka, T. Mura, A dislocation model for fatigue crack initiation. J. Appl. Mech., 48 (1981) 97–103.
[17] A. Brückner-Foit, X. Huang, Numerical simulation of micro-crack initiation of martensitic steel under fatigue loading. International Journal of Fatigue, 28(9) (2006) 963-971.
[18] N. Jezernik, J. Kramberger, T. Lassen, S. Glodez, Numerical modelling of fatigue crack initiation and growth of martensitic steels. Fatigue & Fracture of Engineering Materials & Structures, 33 (2010) 714–723.
[19] D. Broek, The Practical Use of Fracture Mechanics. Kluwer Academic Publishers, Dordrecht, The Netherlands, 1989.
[20] P. Paris, F. Erdogan, A critical analysis of crack propagation laws. Journal of Basic Engineering, 85 (1963) 528–534.
[21] R.J. Dexter, P.J. Pilarski, H.N. Mahmoud, Analysis of crack propagation in welded stiffened panels. International Journal of Fatigue, 25 (2003) 1169-1174.
[22] H.N. Mahmoud, R.J. Dexter, Propagation rate of large cracks in stiffened panels under tension loading. Marine Structures 18 (2005) 265-288.
[23] Y. Sumi, Ž. Božić, H. Iyama, Y. Kawamura, Multiple Fatigue Cracks Propagating in a Stiffened Panel. Journal of the Society of Naval Architects of Japan, 179 (1996) 407-412.
[24] W. Elber, The significance of fatigue crack closure. Damage tolerance in aircraft structures. ASTM STP 486. American Society for Testing & Materials; (1971) 230–242.
[25] R. Bao, X. Zhang, N. A. Yahaya, Evaluating stress intensity factors due to weld residual stresses by the weight function and finite element methods. Engineering Fracture Mechanics, 77 (2010) 2550–2566.
[26] Swanson Analysis System, Inc. ANSYS User's Manual Revision 11.0, 2009.
[27] Ž. Božić, H. Wolf, D. Semenski, Fatigue Growth of Multiple Cracks in Plates under Cyclic Tension. Transactions of FAMENA, 34(1) (2010) 1 – 12.
[28] Ž. Božić, S. Schmauder and M. Mlikota, Fatigue growth models for multiple long cracks in plates under cyclic tension based on ΔK_I, ΔJ-integral and $\Delta CTOD$ parameter. Key Engineering Materials, 488-489 (2012) 525-528.
[29] Y. Liu, S. Mahadevan, Threshold stress intensity factor and crack growth rate prediction under mixed-mode loading. Engineering Fracture Mechanics, 74, 2007, 332–345.

Numerical study of the fracture behavior of an electron beam welded steel joint by cohesive zone modeling

Haoyun Tu*, **Siegfried Schmauder, Ulrich Weber**

Institute for Materials Testing, Materials Science and Strength of Materials (IMWF) University of Stuttgart, Pfaffenwaldring 32, D-70569 Stuttgart, Germany
* Corresponding author: haoyun.tu@imwf.uni-stuttgart.de

Abstract The cohesive model has been used studying the ductile and brittle fracture mechanisms of homogenous and inhomogeneous structures in recent years. The traction-separation law which is described by the cohesive strength T_0, critical separation δ_0 and cohesive energy Γ_0 is used to study the damage of materials. In this paper, the cohesive model is adopted to study the fracture behavior of an electron beam welded steel joint. The dimensions of different weld regions can be obtained from hardness tests across the welded joint. Local stress-strain curves are derived from the tensile test results of flat specimens which are obtained from the respective weld regions. Based on the axial stress versus diameter reduction curve of notched round specimens, the cohesive strength can be fixed. For pure mode I loading, the Γ_0 value is set equal to the J_i value which is the J-integral value at fracture initiation. The cohesive parameters obtained from the base material (BM), the fusion zone (FZ) and the heat affected zone (HAZ), respectively, are used to predict the fracture behavior of compact tension (C(T)) specimens with the initial crack located at different positions in the weld region. Good comparison is obtained between the numerical and the experimental results in terms of force vs. Crack Opening Displacement (COD) curves as well as fracture resistance (J_R) curves.

Keywords Cohesive zone model, electron beam welded joints, crack propagation, finite element modeling

1. Introduction

Compared to the traditional arc welding technique, advanced welding technique, such as electron beam welding (EBW) has found wide applications in industry fields as a narrow heat affected zone and small residual stresses are obtained after the welding process. The failure of the weldments always draws attentions as the fracture behavior of the welded joints influences the crack growth of structures, which affects the lifetime and safety of components. With the development of the finite element method, attention has been focused on the fracture behavior of welded joints in a numerical way. The Gurson-Tvergaard-Needlemann (GTN) model [1-3] has been used in studies of the fracture behavior of conventional fusion welded joints [4-6] and laser welded joints [7-9]. Later, the GTN model and the Rousselier model [10] were used successfully to study the ductile fracture of electron beam welded steel joints at IMWF [11-13].

Compared to the previous two damage models, the cohesive model possesses less model parameters, which make the model easy to use. The material separation is usually described by interface elements - the cohesive element, continuous elements remain undamaged in the cohesive model. The damage of the cohesive zone is depicted by a traction-separation law which is described by cohesive strength T_0, critical separation δ_0 and cohesive energy Γ_0. The concept of a cohesive model was first introduced by Dugdale [14] and Barenblatt [15]. They assume that the crack consists of two parts: the stress-free part and the parts loaded by cohesive stresses. Following this assumption, different traction-separation laws were proposed in the past to investigate the ductile or brittle

fracture behavior of a number of materials. Some typical traction-separation laws are shown in the following. The linear decreasing traction-separation law shown in Fig. 1(a) was introduced by Hillerborg [16] to describe the brittle fracture behavior of a concrete beam. The polynomial and the exponential traction-separation laws shown in Fig. 1(b-c) were provided by Needleman [17, 18] to describe the decohesion behavior. Tvergaard and Hutchinson [19] invented a trapezoid shape to study the ductile fracture of solid, this traction-separation law was later modified by Scheider [20] for the investigation of a laser welded joint. In this paper, the cohesive zone model is adopted to study fracture of S355 EBW joints.

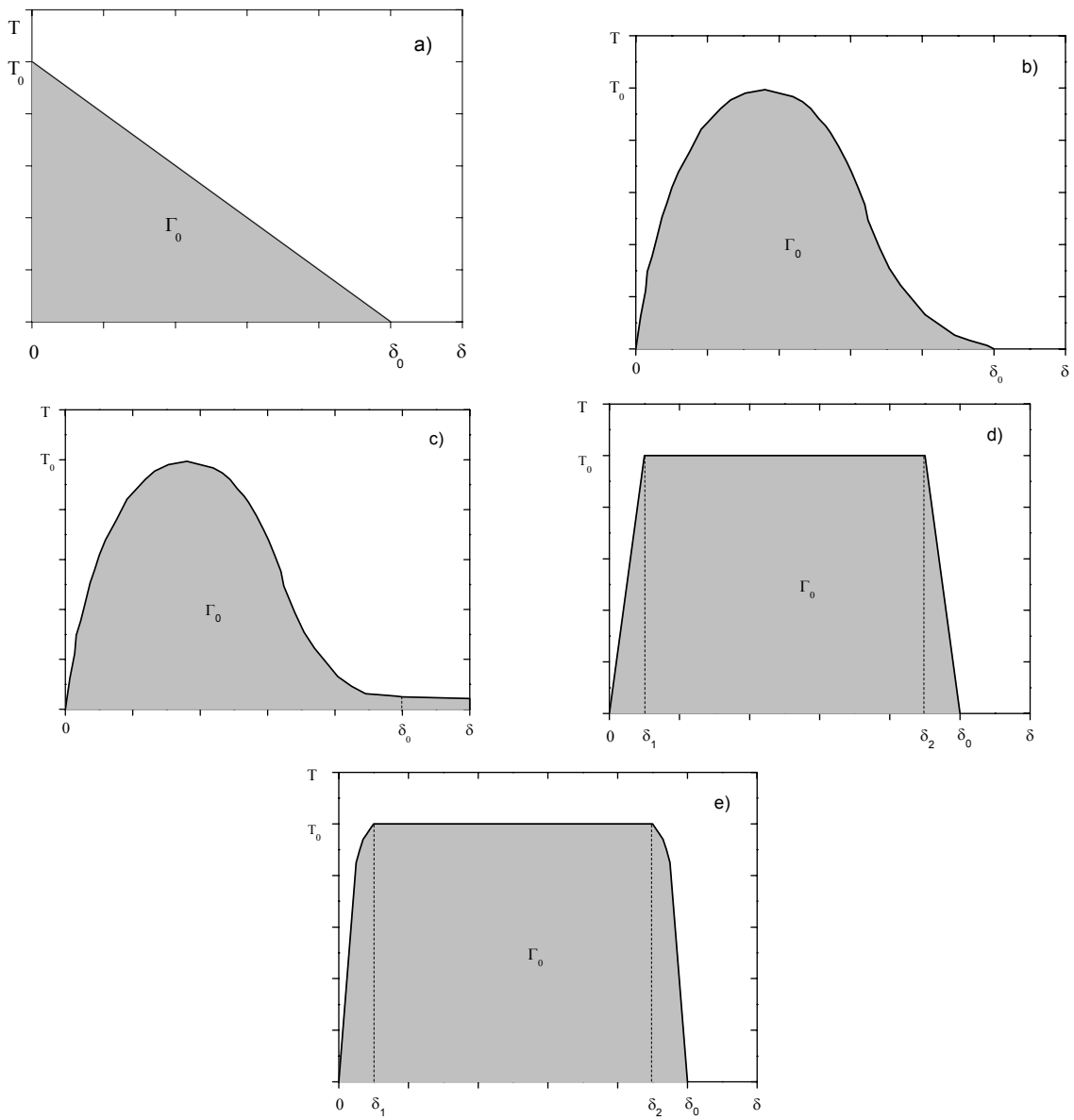

Fig. 1: Shape of traction separation laws: a) from Hillerborg [16], b)+c) from Needleman [17, 18], d) from Tvergaard and Hutchinson [19] and e) from Scheider [20] where T_0 is cohesive strength, δ_0 is critical separation and Γ_0 is cohesive energy.

2. Experimental investigations

In this paper, a low-alloyed structural steel S355NL was adopted as the base material (BM) for producing the weldments. After the electron beam welding process, a butt joint is obtained from two S355NL plates with the thickness of 60 mm. The chemical components of S355NL are shown in Table 1, which is obtained from spectrometric analysis.

Table 1: Chemical composition of the steel S355NL, mass contents in %

Steel	C	Si	Mn	P	S	Cr	Mo	Ni	Al	Co
S355NL	0.198	0.260	1.386	0.026	0.013	0.020	<0.005	<0.005	0.013	0.006

After the hardness test, the dimensions of the fusion zone (FZ) and the heat affected zone (HAZ) are found to be 2.8 mm and 3.1 mm, respectively. The mechanical properties of different weld regions of S355 EBW joints are obtained from flat specimens along the weld line of which the gauge length is 50 mm. These stress-strain curves [12] are used as finite element model input data. Table 2 shows the mechanical properties of base material (BM) and fusion zone (FZ) of the welded joints containing yield strength R_e, tensile strength R_m, uniform elongation A_g and strain at rupture A.

Table 2: Mechanical properties of different weld regions of S355NL EBW joint

R_e^{BM} (MPa)	R_e^{FZ} (MPa)	R_m^{BM} (MPa)	R_m^{FZ} (MPa)	A_g^{BM}	A_g^{FZ}	A^{BM}	A^{FZ}
348	513	533	687	0.151	0.037	0.246	0.052

Fracture toughness tests of S355 electron beam welded joints were performed using compact tension (C(T)) specimens. The specimens were manufactured and tensile tested according to ASTM standard [21] which have a thickness of B=25 mm, a net thickness of B_n=20 mm due to 20% side grooves, the width of specimen is W=50 mm. After the C(T) test, the experimental results are shown in terms of force vs. Crack Opening Displacement (COD) as well as fracture resistance J_R curves. The F-COD curves of compact tension (C(T)) specimens with initial crack located in the BM (C(T)-BM), in the center of FZ (C(T)-FZ) and at the interface between the FZ and HAZ (C(T)-HAZ) can be found in Fig. 2(a). For a C(T) specimen with the crack in the FZ, the specimen suddenly ruptures, showing a rather brittle fracture behavior. The C(T)-FZ specimen broke suddenly without stable crack propagation, no fracture resistance (J_R) curves were obtained during the test process. The J_R curves for a C(T)-BM and a C(T)-HAZ specimen can be found in Fig. 2(b).

3. Numerical calculation

Before the application, the cohesive parameters must be fixed first. According to the discussion of Cornec and Scheider [22], for mode I situation, the cohesive parameter T_0 is equal to the projection of the applied force on a plane perpendicular to the specimen cross section. The notched round specimen extracted from the BM is used for the determination of T_0. For the notched round specimen, as the geometry and loading are axisymmetric and symmetric to the cross section, only one quarter of the structure is used for the modeling. The finite element (FE) mesh of the notched round specimen and the detailed mesh can be found in Fig. 3. The comparison of axial stress versus the diameter reduction curve from the FE simulation and the experiment as well as the maximum true axial stress in the center of the specimen can be found in Fig. 4. The simulated axial stress

versus the diameter reduction curve coincides with the experimental one until crack initiation, where the experimental curve drops suddenly. At this point, the maximum value of stress distribution over the cross section of the specimen is determined from the simulation and set equal to the cohesive stress T_0. After the comparison of simulation and experiment for the BM, T_0=1180 MPa was found. The exponential and trapezoid traction-separation laws are used to study the fracture behavior of the C(T)-BM specimen. Because the structure shows symmetry with respect to the crack plane, only half of the C(T)-BM specimen is modeled, loading is defined on the loading point (Red point) by the displacement, the finite element mesh and boundary conditions are shown in Fig. 5. Fig. 6 shows the detailed mesh around the initial crack tip.

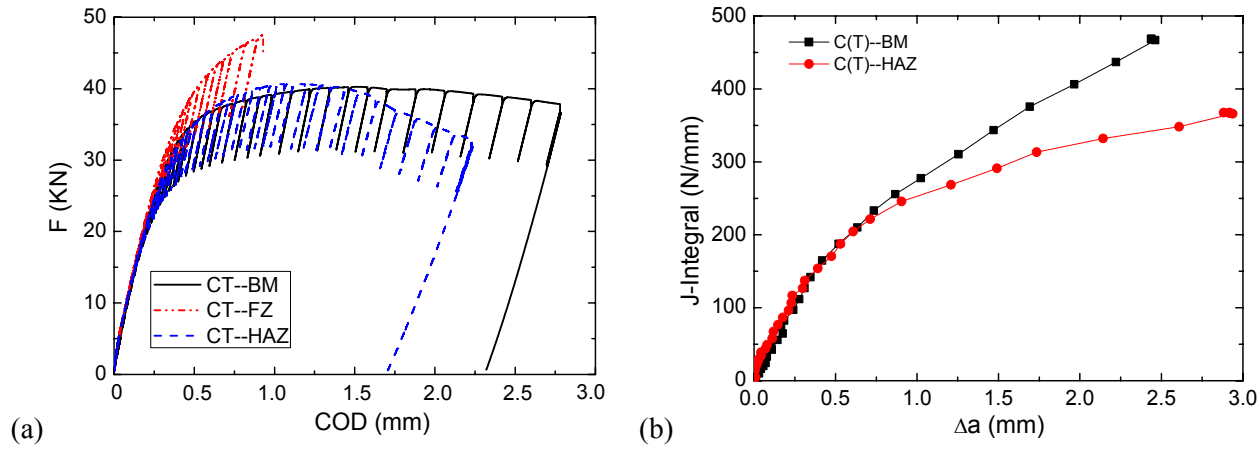

Fig. 2: Experimental (a) Force vs. Crack Opening Displacement (COD) and (b) fracture resistance J_R curves of compact tension (C(T)) specimens with the initial crack located in the BM, in the middle of the FZ and at the interface between the FZ and the HAZ, respectively.

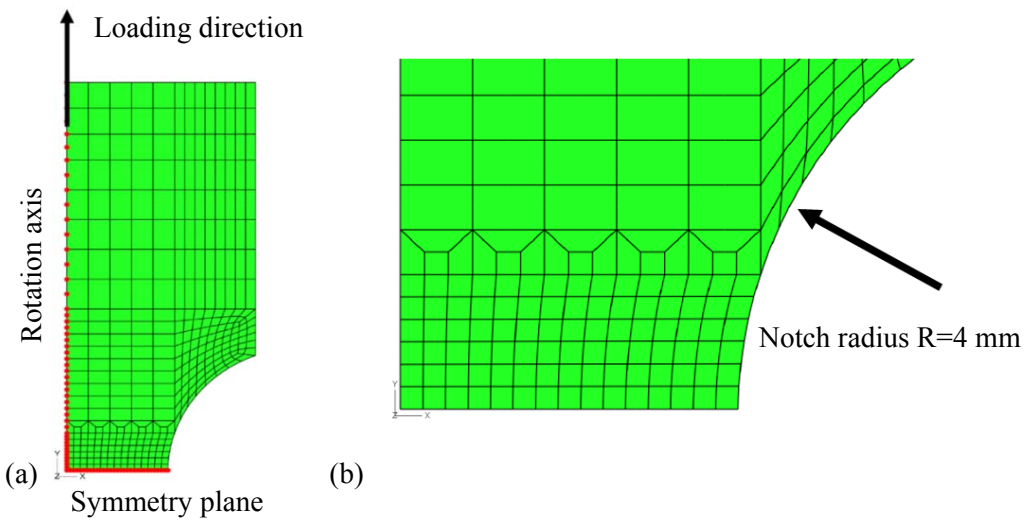

Fig. 3: (a) Axisymmetric finite element mesh and boundary conditions of the notched round specimen and (b) detailed mesh.

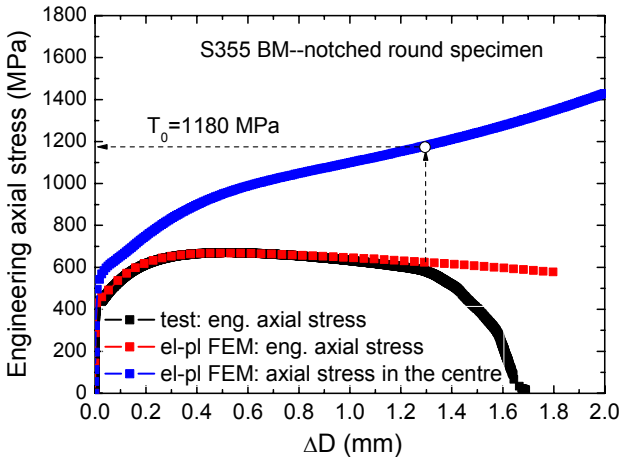

Fig. 4: Determination of the cohesive stress T_0: comparison of axial stress versus the diameter reduction curve from FE simulation and the experiments and the maximum true axial stress in the center of the specimen.

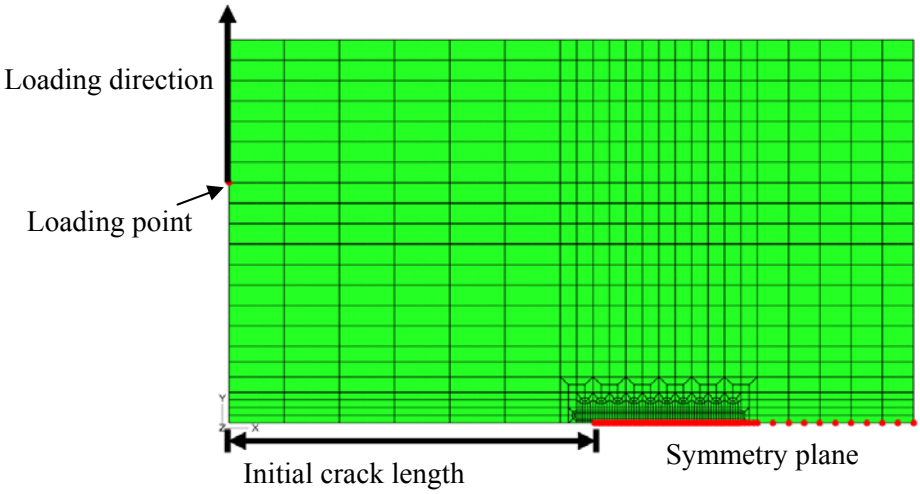

Fig. 5: Finite element mesh and boundary conditions of the C(T) specimen.

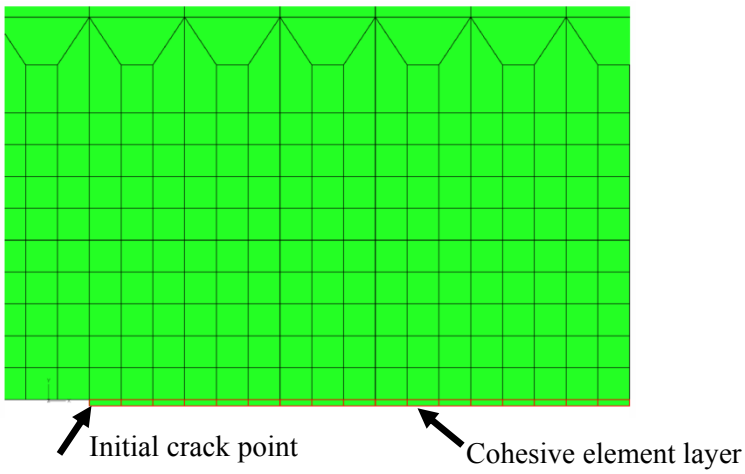

Fig. 6: Detailed finite element mesh around the initial crack position.

For the C(T)-BM specimen, when an exponential shape traction separation law is adopted, good agreement between the numerical and experimental results can be obtained in terms of FCOD and J_R curves when T_0=1180 MPa and Γ_0=18.5 N/mm are applied (Fig. 7). The trapezoid shape traction-separation law is also adopted to study the fracture behavior of the C(T)-BM specimen. As can be found in Fig. 8, good agreement between the numerical and experimental results can be obtained in terms of FCOD and J_R curves when T_0=1180 MPa and Γ_0=23.6 N/mm is used. This means that both exponential and trapezoid shape traction separation law can predict the crack propagation of C(T) specimens obtained from the BM well when different parameter sets are chosen.

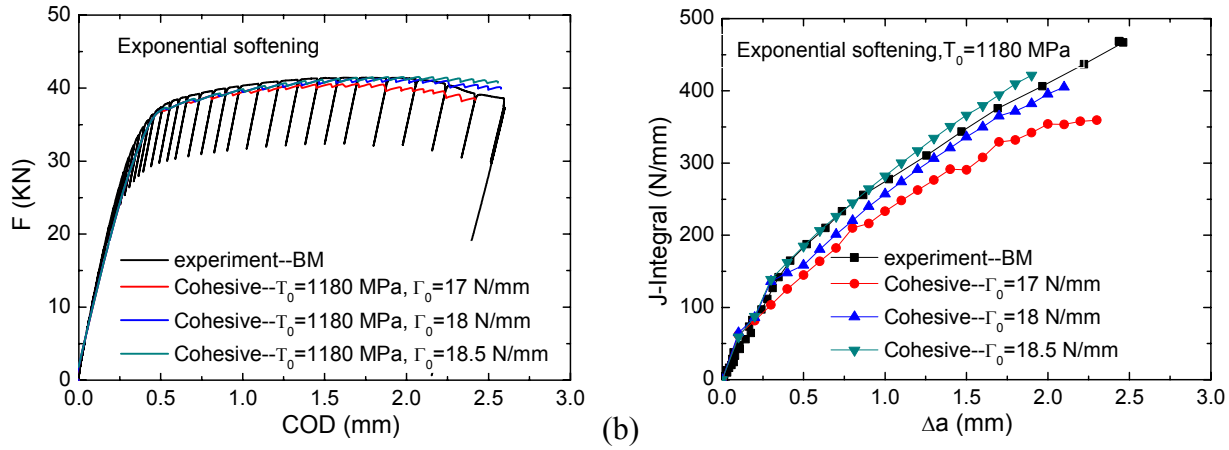

Fig. 7: Comparison of experimental and numerical (a) force vs. Crack Opening Displacement (COD) curves, and (b) fracture resistance curves for C(T) specimens with initial crack located in the BM when an exponential shape of the traction-separation law is adopted.

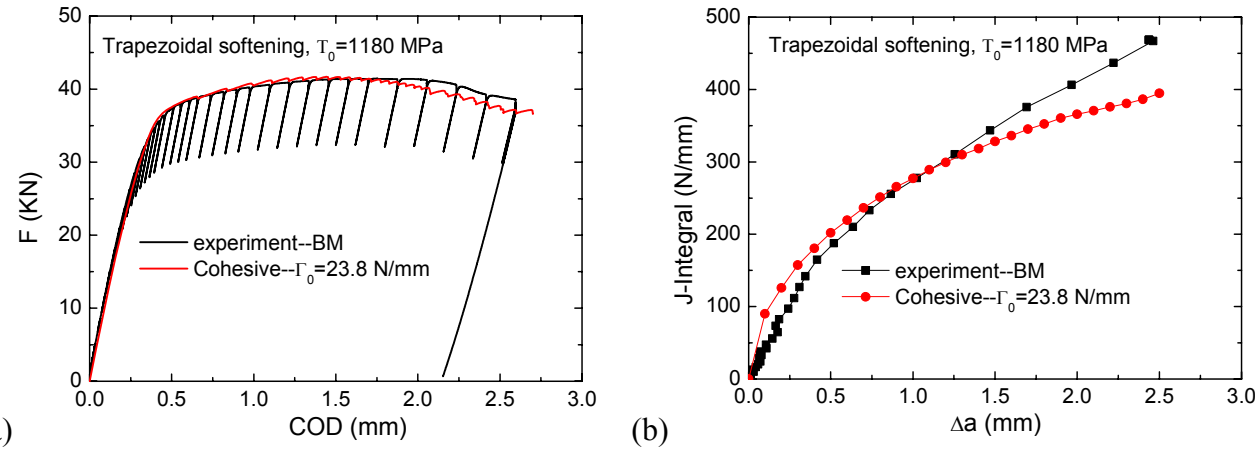

Fig. 8: Comparison of experimental and numerical (a) force vs. Crack Opening Displacement (COD) curves, and (b) fracture resistance curves for C(T) specimens with initial crack located in the BM when trapezoid shape traction separation law is adopted.

For the C(T)-FZ, as what has been observed in Fig. 2, the FZ showing more brittle behavior, a linear decreasing traction-separation law is required for the cohesive model. The numerical FCOD curve matches the experimental one well before the sudden rupture, showing the cohesive model

can predict the FCOD curve of the C(T)-FZ specimen well, as can be seen in Fig. 9. For the C(T)-HAZ specimen, an exponential traction-separation law is chosen for the cohesive model. Good agreement between the numerical and experimental results can be obtained in terms of FCOD and J_R curves when T_0=1350 MPa and Γ_0=16.5 N/mm is used, as can be found in Fig. 10.

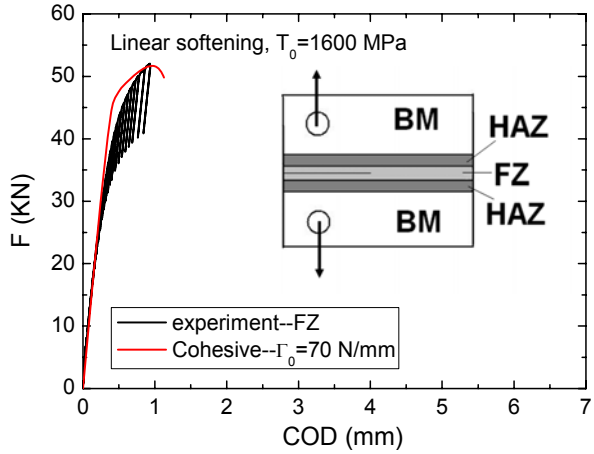

Fig. 9: Comparison of experimental and numerical force vs. Crack Opening Displacement (COD) curves for C(T) specimen with the initial crack located in the center of the FZ.

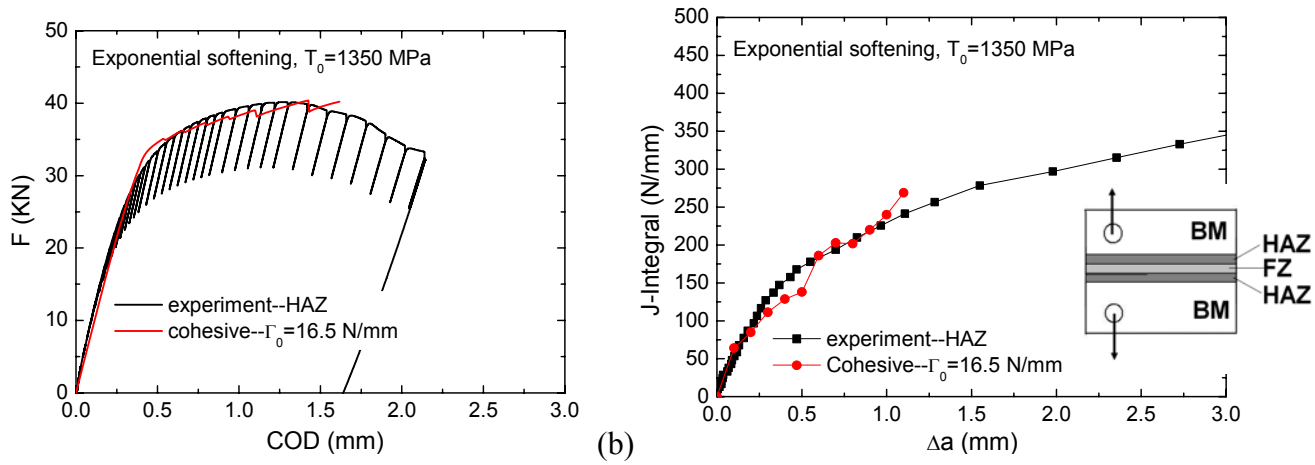

Fig. 10: Comparison of experimental and numerical (a) force vs. Crack Opening Displacement (COD) curves, and (b) fracture resistance curves for C(T) specimens with the initial crack located at the interface between the FZ and the HAZ when an exponential traction separation law is adopted.

4. Conclusions

Crack propagation was studied on S355 EBW joints using the cohesive model. Stress-strain curves of respective weld regions are derived from the tensile test results of flat specimens which are obtained from these regions. Three different C(T) specimens, i.e., the C(T)-BM, the C(T)-FZ and the C(T)-HAZ are investigated. Based on the axial stress versus diameter reduction curve of notched round specimens, the cohesive strength T_0 is fixed. When choosing different parameter sets for different traction separation laws, the cohesive model can predict the FCOD and J_R curve of C(T)

specimens from the BM well. This shows, both, exponential and trapezoid shaped traction-separation laws are able to predict the crack propagation in BM specimens. The cohesive model can also predict FCOD curves of C(T)-FZ specimens before the sudden rupture. When choosing the exponential traction-separation law, the cohesive model can predict good FCOD and J_R curve for the C(T)-HAZ specimens. All in all, the investigations of the fracture behavior of S355 EBW joints with the cohesive model confirm that the cohesive model is able to predict the crack propagation of the homogenous BM and the inhomogeneous welded joints well.

Acknowledgements

The research has been financially supported by China Scholarship Council (CSC) and SFB 716. This financial support is gratefully acknowledged. The authors would like to thank Prof. V. Ploshikhin and Dr. Y. Rudnik from Neue Materialien Bayreuth GmbH, for providing some of the experimental results.

Reference

[1] A. L. Gurson. Continuum theory of ductile rupture by void nucleation and growth: Part I-Yield criteria and flow rules for porous ductile media. J Eng Mater Techno-Trans. ASME 99 (1977), pp. 2-15.

[2] V. Tvergaard. Influence of void nucleation on ductile shear fracture at a free surface. J Mech Phys Solids 30 (1982), pp. 399-425.

[3] V. Tvergaard, A. Needleman. Analysis of the cup-cone fracture in a round tensile bar. Acta Metall 32 (1984), pp. 157-169.

[4] A. Needleman, V. Tvergaard. A micromechanical analysis of ductile-brittle transition at a weld. Engng Frac Mech 62 (1999), pp. 317-338.

[5] V. Tvergaard, A. Needleman. Analysis of the Charpy V-notch test for welds. Engng Frac Mech 65 (2000), pp. 627-643.

[6] V. Tvergaard, A. Needleman. 3D analyses of the effect of weld orientation in Charpy specimens. Engng Frac Mech 71 (2004), pp. 2179-2195.

[7] P. Nègre, D. Steglich, W. Brocks. Crack extension in aluminium welds: a numerical approach using the Gurson-Tvergaard-Needleman model. Engng Fract Mech 71 (2004), pp. 2365-2383.

[8] P. Nègre et al.. Numerical simulation of crack extension in aluminium welds. Comp Mater Sci 28 (2003), pp. 723-731.

[9] A. Nonn, W. Dahl, W. Bleck. Numerical modelling of damage behaviour of laser-hybrid welds. Engng Fract Mech 75 (2008), pp. 3251-3263.

[10] G. Rousselier. Ductile fracture models and their potential in local approach of fracture. Nucl Eng Design 105 (1987), pp. 97-111.

[11] H. Y. Tu, S. Schmauder, U. Weber, Y. Rudnik, V. Ploshikhin. Numerical simulation and experimental investigation of the damage behavior on electron beam welded joints. Proc Engng 10 (2011), pp. 875-880.

[12] H. Y. Tu, S. Schmauder, U. Weber, Y. Rudnik, V. Ploshikhin. Simulation of the damage behavior of electron beam welded joints with the Rousselier model. Engng Fract Mech (2012),

in press.

[13] H. Tu, S. Schmauder, U. Weber. Numerical study of electron beam welded butt joints with the GTN model. Comput Mech 50 (2012), pp. 245-255.

[14] D. S. Dugdale, Yielding of steel sheets containing slits. J Mech Phys Solids 8 (1960), pp. 100-104.

[15] G. I. Barenblatt. The mathematical theory of equilibrium cracks in brittle fracture. Adv Appl Mechanics 7 (1962), pp. 55-129.

[16] A. Hillerborg et al.. Analysis of crack formation and crack growth in concrete by means of fracture mechanics and finite elements. Cem Conc Research 6 (1976), pp. 773–782.

[17] A. Needleman. A continuum model for void nucleation by inclusion debonding. J Appl Mech ASME 54 (1987), pp. 525–531.

[18] A. Needleman. An analysis of decohesion along an imperfect interface. I J Frac 42 (1990), pp. 21-40.

[19] V. Tvergaard, J. W. Hutchinson. The relation between crack growth resistance and fracture process parameters in elastic-plastic solids. J Mech Phys Solids 40 (1992), pp. 1377–1397.

[20] I. Scheider. Bruchmechanische Bewertung von Laserschweissverbindungen durch numerische Rissfortschrittsimulation mit dem Kohäsivzonenmodell. PhD thesis, TU Hamburg-Harburg, Geesthacht, 2001.

[21] ASTM E 1820-96. Standard test method for measurement of fracture toughness. In: Annual Book of ASTM Standards, Vol. 03.01. American Society for Testing and Materials, Philadelphia, PA, USA.

[22] A. Cornec et al.. On the practical application of the cohesive model. Engng Fract Mech 70 (2003), pp. 1963-1987.

Solidification Cracking of IN 718 TIG Welds

Myriam Brochu[1,*], **Alexis Chiocca**[1], **Rafael Navalon-Cabanes**[1], **Jean Fournier**[2]

[1] Department of Mechanical Engineering, École Polytechnique de Montréal, Montréal H3T 4A6, Canada
[2] Special Process Development Group, Pratt & Whitney Canada, Longueil J4G 1A1, Canada
* Corresponding author: myriam.brochu@polymtl.ca

Abstract Solidification cracking was observed during a tungsten–inert gas (TIG) welding process used to join two thin sheets of nickel-based superalloy IN718. Microstructural analysis of cracked specimens showed a centerline grain boundary (CLGB) susceptible to limit the hot ductility of the welds. Different welding parameters were modified to avoid the formation of the CLGB; such as the current waveform, the heat input and the welding speed. Results show that it is possible to obtain a microstructure free of a straight CLGB when using a heat input below 135 J/mm. However, to achieve full penetration, the heat input cannot be decreased below 112 J/mm. The experimental results are presented in the form of a weldability map as proposed by Dye et al. and they can be used to predict the range of process parameters favorable to successfully TIG weld IN718 sheet metal.

Keywords Fusion welding, solidification cracking, nickel superalloy, microstructure, process

1. Introduction

1.1. Context

Nickel superalloy IN718 is used to manufacture gas turbine engine components such as disks, cases, shafts, blades, stators, seals, supports, tubes and fasteners [1]. This alloy is selected for its high temperature mechanical properties but also for its weldability, especially its resistance to strain age cracking [2, 3]. Nevertheless, a recurrent weld cracking problem was observed while TIG welding sheets of IN718. Furthermore, in all cracked welds, microstructural observation revealed the existence of a centerline grain boundary. Based on the hypothesis that the CLGB reduces the alloy resistance to solidification cracking [4], the objective of the research project is to identify process conditions that will produce a weld free of CLGB. Our research efforts were oriented toward the improvement of the welding parameters since the weld geometry and the materials chemistry are restricted. To reach our objective, several welding experiments were conducted as reported in section 1. The microstructure of the welds produced was examined and is reported in section 3. In section 4, the effects of the welding speed and of the welding power on the microstructure are discussed. Finally, the practical limitations of the proposed welding conditions are exposed and future work is planned.

1.2. Background: Solidification cracking

Even though alloy 718 is nearly immune to strain age cracking, it is susceptible to other cracking mechanisms such as solidification cracking, heat affected zone liquation cracking, and ductility dip cracking [3]. Solidification cracking happens within the weld, when the deformations induced by the liquid-solid phase transformation and the thermal contraction are higher than the ductility of the mushy zone. This type of cracking occurs more specifically in the last stage of solidification, when the fraction of liquid is less than 10%. The remaining liquid forms a film between the grains and

between dendrites, and the deformations and stresses due to shrinkage of the material grow gradually as solidification is ending, tearing the joint apart.

The amount of minor addition elements such as B, Zr and Nb, have a significant influence on the weldability of nickel alloy IN718. During solidification, segregation of Nb leads to the formation NbC and Lave phases which are widening the solidification range increasing the size of the crack susceptible mushy zone. Moreover, NbC and Lave phases are brittle and deleterious to the weld ductility even after solidification is completed [5].

Since B, Zr and Nb are added intentionally in superalloy IN718 for strengthening purposes, it is important to promote the formation of a homogeneous solidification structure. If the last liquid to be solidified (rich in alloying elements) is concentrated in one region, the weld ductility can be reduced significantly [6, 7]. This is the case when a centerline grain boundary (CLGB) forms. Weld microstructures with a CLGB are susceptible to crack propagation along the length of the weld just behind the melt. Welding can be successful (no cracking) for welds having a CLGB. However, the unevenly distributed fragile phases will create a weak plane that can compromise the weld mechanical properties [8]. For these reasons, a straight centerline grain boundary is an unwanted feature often related to solidification cracking [4].

2. Methodology

2.1. Nominal welding conditions and microstructure

The TIG welds for which cracking occurred are but-welded IN718 sheet rings having an average thickness of 1.33 mm. The nominal chemical composition of the sheet material and the nominal welding parameters are reported in Table 1 and 2 respectively.

Table 1. Chemical composition of nickel superalloy IN718 (weight %)[1,2]

	Ni	Cr	Nb	Mo	Ti	Al	Co	Mn	Si	Cu	Ta	C	B
Min.	50.00	17.00	4.75	2.80	0.65	0.20							
Max.	55.00	21.00	5.50	3.30	1.15	0.80	1.00	0.35	0.35	0.30	0.05	0.08	0.006

[1]Remaining is iron [2] Phosphorus and sulfur content must be below 0.015

Table 2. Welding parameters

DC Current I (A)	Voltage U (V)	Welding Speed WS (mm/s)	Filler wire speed (mm/s)	Diameter of filler wire (mm)	Electrode angle (°)	Linear Heat input HI (J/mm)[1]
86	8	5.27	5.72	0.889	45	140

[1]Calculated by $\boldsymbol{HI = \frac{U*I}{WS}}$

Visual and optical microscopy observations were performed on cracked specimens to identify the failure mechanism. The longitudinal aspect of the crack, its position at the center of the fusion zone, and its interdendritic path led to the identification of a solidification cracking problem. The same features were observed by Kerrouault [9] and Shinozaki et al. [10] while monitoring solidification cracking in austenitic stainless steels. Moreover, the microstructure of all specimens observed contained a centerline grain boundary (CLGB) as shown in Fig. 1.

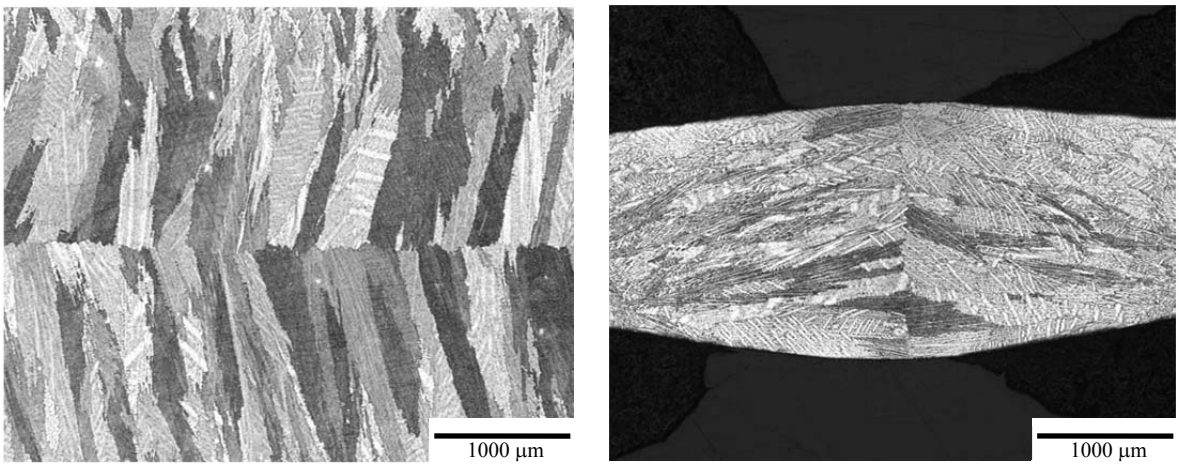

a) Longitudinal section b) Cross section

Figure 1. Typical microstructure of a cracked specimen revealed with etchant composed of 5% H_20_2 (30%), 47.5% HCl (40%) and 47.5% methanol

2.2 Welding experiments

Experiments were performed to identify a range of welding parameters that creates a weld free of CLGB. The ideal microstructure would be fully or partly equiaxe and fine. If it is impossible to form equiaxe grains, a more tortuous central grain boundary would be an improvement of the actual microstructure. To reach the objective, theoretical considerations were reviewed and the following approaches were tested:

2.2.1 Current pulsing,
2.2.2 Constitutional supercooling,
2.2.3 Weld pool shape control.

Tests were done on rectangular sheet coupons having a thickness of 1.27 mm. Two coupons were firmly clamped together and a semi-automated TIG machine was used to produce a straight 10 cm long weld. Longitudinal and cross sections of the welds were prepared for metallographic observations.

2.2.1. Current pulsing

According to the results of Ram and Reddy [8], current pulsing can produce a weld with a fine and homogeneous microstructure which considerably improve the weld ductility at 650°C. Their study was performed for autogeneous welding of 2 mm thick sheets of IN718. In another paper from the same research team, it was explained that current pulsing increases the cooling rate resulting in significant refinement of the fusion zone structure [11].

In our study, current pulsation was attempted at a frequency of 3.3 hertz using four different current ratios (low current/high current) as reported in Table 3. The welding speed and the filler wire speed were kept constant at values of 3.39 mm/s and 4.66 mm/s respectively. This welding speed is lower than the nominal welding speed for which the cracking problem was initially observed. It was decided to reduce the welding speed following unsuccessful current pulsation welding tests

performed at a welding speed of 5.2 mm/s. In the experiments of Sivaprasad et al. [11] the beneficial effect of current pulsation was observed for a welding speed of 1.11 mm/s. Overall, 4 specimens were welded (Pulse 1 to 4 in Table 3) and the fusion zone microstructure was observed as will be presented in section 3.1.

Table 3. Welding parameters for the current pulsing experiments

		Pulse 1	**Pulse 2**	**Pulse 3**	**Pulse 4**
Voltage, U (V)		8.0	8.0	8.0	8.0
Current parameters	Current ratio	0.66	0.42	0.35	0.21
	Low Current, LC (A)	54.0	40.0	30.0	20.0
	Low time, LT (s)	0.15	0.15	0.15	0.15
	High Current, HC (A)	82.0	96.0	86.0	96.0
	High time, HT (s)	0.15	0.15	0.15	0.15
Welding speed, WS (mm/s)		3.39	3.39	3.39	3.39
Filler wire speed (mm/s)		4.66	4.66	4.66	4.66
Heat Input[1], HI (J/mm)		160.6	160.6	137.0	137.0
Welding Power[2], W (Watt)		544	544	464	464

[1]Calculated by $\mathbf{HI} = \frac{\mathbf{U*(LC*LT+HC*HT)}}{\mathbf{(LT+HT)*WS}}$ [2] Calculated by $\mathbf{W} = \frac{\mathbf{U*(LC*LT+HC*HT)}}{\mathbf{(LT+HT)}}$

2.2.2. Constitutional supercooling

Theoretically, equiaxe grains can form spontaneously in supercooling conditions. This should be achieved by welding in conditions of high solidification rate (R) but low temperature gradient (G) as proposed by Kou et al. [12]. To produce such conditions within the weld pool, the welding speed and the welding power were increased as presented in Table 4. Three trials (SC1 to SC3) were conducted at a high welding speed (8.47 mm/s) and with an increasing welding power as reported in Table 4. The filler wire speed was also increased in order to reproduce comparable weld geometries. According to the theoretical solidification map of Gaümann et al. [13] obtained for nickel superalloy CMSX-4, these welding conditions should result in the formation of equiaxe dendrites. The resulting microstructures will be presented in section 3.2.

Table 4. Welding parameters for constitutional supercooling

	SC 1	**SC 2**	**SC 3**
Voltage, U (V)	7.8	7.8	7.8
Current (A)	121.9	137.5	147.5
Welding speed, WS (mm/s)	8.47	8.47	8.47
Filler wire speed (mm/s)	9.53	9.53	9.53
Heat Input[1], HI (J/mm)	112.2	124.0	135.8
Welding power[2], W (Watt)	951	1072	1150

[1]Calculated by $\mathbf{HI} = \frac{\mathbf{U*A}}{\mathbf{WS}}$ [2] Calculated by W = U*A

2.2.3. Weld pool shape control

According to the work of Savage [14] an elliptical weld pool shape promotes the formation of a microstructure composed of columnar dendrites but free of CLGB. CLGB forms when columnar grains growing perpendicular to the solid walls meet at the center of the weld. This type of microstructure is typically observed at high welding speed when a tear drop shape weld pool forms. Welding conditions can be modified to favor grain curvature and avoid the formation of a CLGB. Reducing the welding speed favors the formation of an elliptical weld pool and the curvature of grains within the longitudinal plane as experimented by Kou and Le [12]. Moreover, reducing the heat input reduces the depth to width ratio of a weld which favors the formation of a radial grain structure [3] which is also beneficial to the microstructure. It was attempted to produce a weld with an elliptical pool shape and with a low depth to with ratio by decreasing the weld speed (WS) and the heat input (HI) as proposed in Table 5. The filler wire speed was also decreased in order to reproduce comparable weld geometries. Overall, 5 specimens were welded (a combination of 3 WS and 3 HI) and their microstructures were observed as will be presented in section 3.3.

Table 5. Welding parameters for the elliptical weld

	WS 1, HI 1	**WS 1, HI 2**	**WS 1, HI 3**	**WS 2, HI 1**	**WS 3, HI 1**
Voltage, U (V)	8.0	8.0	8.0	8.0	8.0
Current (A)	94.0	85.0	74.0	60.0	44.6
Welding speed (mm/s)	5.27	5.27	5.27	3.39	2.54
Filler wire speed (mm/s)	5.72	5.72	5.72	4.66	2.79
Heat Input[1] (J/mm)	142.7	129.0	112.3	141.6	140.5
Welding power[2], W (Watt)	752	544	592	480	357

[1]Calculated by $\mathbf{HI} = \frac{\mathbf{U*A}}{\mathbf{WS}}$ [2] Calculated by W = U*A

3. Results

3.1. Current pulsing

All welds produced with pulsed current have a similar microstructure which is shown in Fig. 2. Current pulsing did not have the expected effect on the microstructure and changing the current ratio had no significant influence. The most noticeable feature observed by comparing Fig. 2 to Fig. 1, is the existence of a longitudinal grain at the centerline of the welds produced with pulsed current. This was possibly caused by the reduction in welding speed rather than by the current pulsing as will be shown in section 3.3. The formation of a longitudinal grain is not beneficial to the weld microstructure. The grain is coarse and it is bounded by two weak planes oriented perpendicularly to the transversal stresses.

According to the work of Sivaprasad and al. [11], current pulsing is more effective for welds performed at low heat input. Their experiments were done on 3 mm thick sheets at a heat input of 180 J/mm. The experiments presented in this document were performed on 1.2 mm thick sheets using a heat input as low as 137.0 J/mm. The heat input range is comparable considering that our

weld thickness is about 2 mm when considering the addition of the filler material.

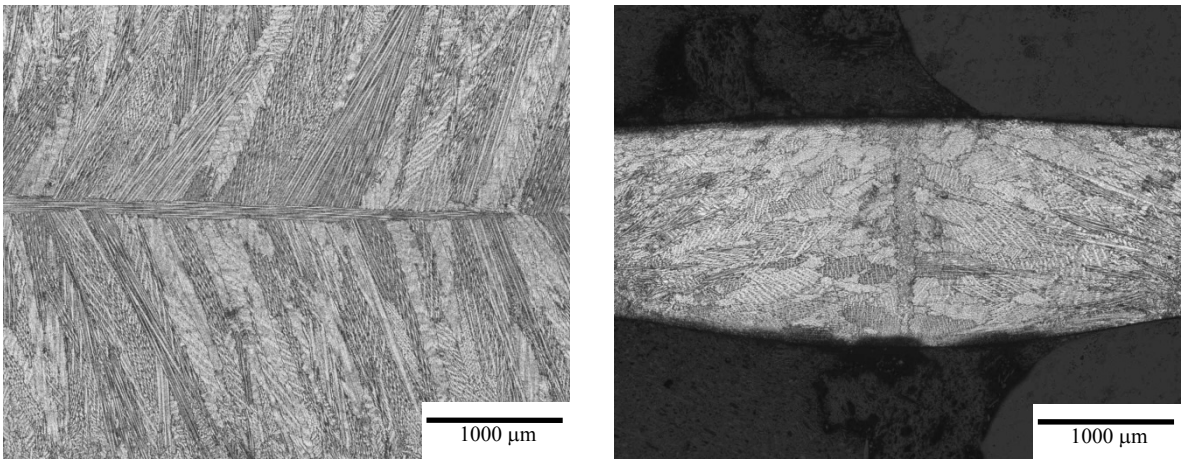

a) Longitudinal section b) Cross section

Figure 2. Typical microstructure of the specimens welded with pulsed current, welding speed of 3.39 mm/s (Pulse 1)

3.2. Supercooling

Within the conditions tested to produce equiaxe dendrites in supercooling conditions, the microstructure obtained with the highest welding power (SC3) is presented in Fig. 3. On Fig.3a showing a top view of the weld, it is clear that the centerline is not as marked as on Fig. 1. However, few equiaxe and fine dendritic grains were formed. Four grains having an equiaxe shape are circled on Fig. 3a. On the cross section of the weld, it is more difficult to evaluate the grain geometry because of the orientation of the cutting plane. If columnar grains are cut on a plane that is not parallel to the grains, it could look equiaxe. Nevertheless, from Fig 3b it can be noticed that the centerline junction is more tortuous than in Fig. 1. This should have a beneficial effect on the resistance to hot cracking and on the mechanical properties of the weld. The microstructures of the welds produced in the two other “supercooling conditions” are comparable to Fig. 3 but with less equiaxe grains. This is an indication that further increasing the speed and the welding power could lead to the desired microstructure.

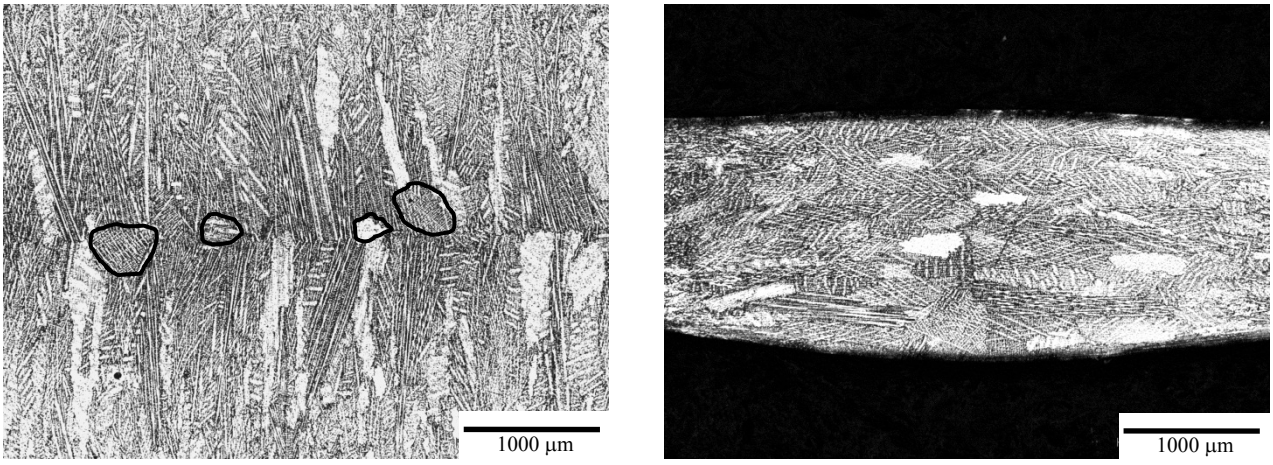

a) Longitudinal section b) Cross section

Figure 3. Microstructure of the weld performed at a welding speed of 8.47 mm/s and with the highest welding power (SC3)

3.3. Weld pool shape

The pictures reported on Fig. 4 show that it was possible to obtain an elliptical pool shape by a reduction of the welding speed. However, the reduction of the welding speed did not cause a significant grain curvature as shown on Fig. 5a. On the other hand, a longitudinal grain formed at the center of the weld. At the lowest welding speed (2.54 mm/s), a thicker longitudinal grain was observed and there was still no evidence of grain curvature.

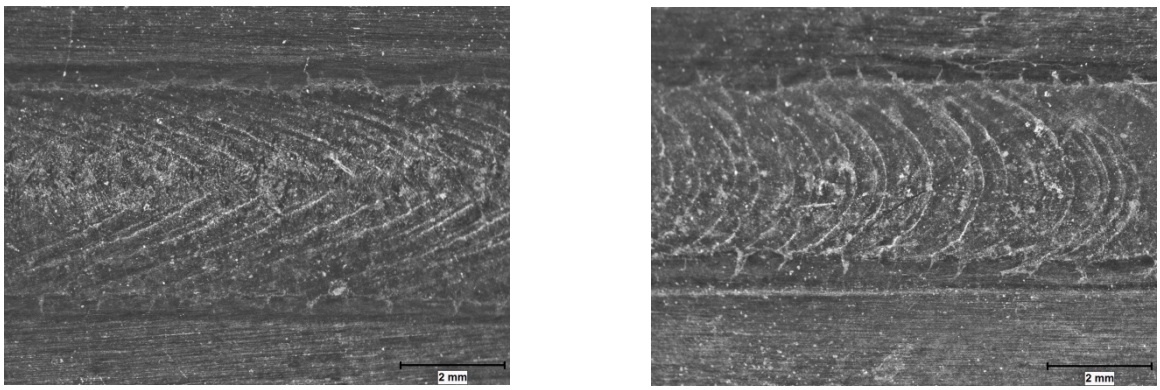

a) Welding speed of 5.27 mm/sec (WS 1, HI 1) b) Welding speed of 2.54 mm/sec (WS 3, HI 1)

Figure 4. Weld pool shape at two different speed, for the same heat input (142 J/mm)

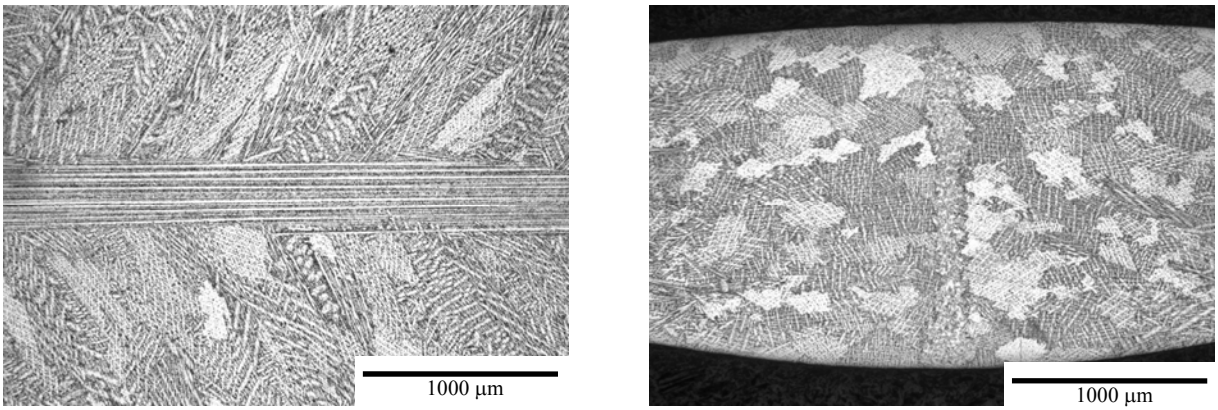

a) Longitudinal section b) Cross section

Figure 5. Microstructure of the specimen produced at 3.39 mm/sec (WS 2, HI 1)

The effect of a reduction in heat input is shown on Fig. 6. The microstructure observed was produced at the same speed as the ones shown in Fig. 1 (5.27 mm/s) but at a heat input of 129.0 J/mm rather than 140.0 J/mm. Reducing the heat input had the expected effect on grain growth. The grain growing direction tilted toward the top of the weld (radial grain growth). This is beneficial to the weld microstructure as it avoids the formation of a sharp centerline. On Fig. 6a and b, the grains nearly seem equiaxe but this could be an optical illusion caused by the fact that the growing directions of the grain are not parallel to the cross section and the longitudinal plane. To produce radial grain growth, it is necessary to promote the formation of a V shape weld. Such a weld is however more susceptible to incomplete penetration. In fact, the weld produced at a heat input of 112.3 J/mm was not fully penetrated.

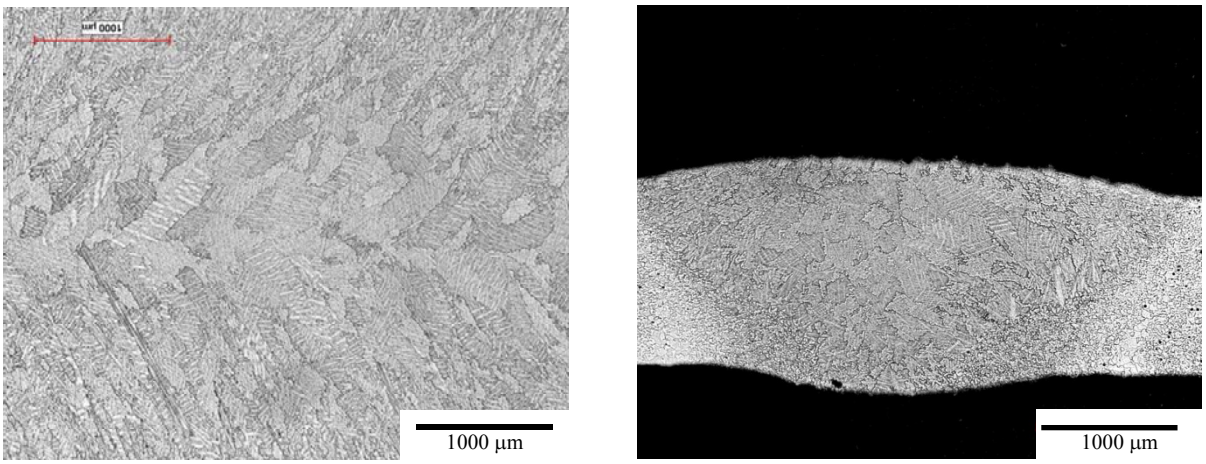

a) Longitudinal section b) Cross section

Figure 6. Typical microstructure of the weld produced at 129 J/mm and 5.27 mm/s(WS 1, HI 2)

4. Discussion

To analyze the microstructural observations, all the test conditions described in section 3 were reported in a graph of the effective welding power (efficiency × current × voltage) versus the welding speed (Fig. 7a). Such a graph was used by Dye et al. to study the effect of the welding parameters on the microstructure of autogeneous TIG welds in IN718 [15]. For the purpose of result presentation, we used a power efficiency factor of 75% as proposed by Dye et al. In Fig. 7a, the microstructural features of the welds are represented by different symbols. Empty circles indicate that the weld is not fully penetrated. Welds without a straight centerline grain boundary, such as the ones shown in Fig. 3 and 6, are presented by full circles. Welds showing a straight centerline grain boundary (CLGB) are presented by full rectangles. Finally, welds with a longitudinal grain (LG) are reported using empty rectangles. To complete the map, we performed additional tests at different welding speed and welding power. In the map of Fig. 7a, the "weldable area" is defined by combinations of welding speed and welding power leading to a fully penetrated weld, free of CLGB and of LG. The "weldable area" was circumscribe using three straight lines. Two lines of constant heat input represented the frontier for the formation of a centerline grain boundary (HI = 134 J/mm) and for incomplete penetration (HI = 112 J/mm). The boundary for the formation of a longitudinal grain was fixed to a constant weld speed of 3.39 mm/sec (vertical line). According to these boundaries, the weldability area identified is very narrow.

Dye et al. predicted theoretically a weldabilty diagram for the autogeneous TIG welding of 2 mm thick IN718 sheets. In Fig. 7b, we adapted their predictions to our sheet thickness. To fit our experimental results at a welding speed of 4.23 mm/sec, the ratio $\Delta x/\rho$ characterizing the CLGB criterion was adjusted to 0.75. Other material and process related constants were considered identical to Dye et al. A comparison of our experimental map (Fig.7a) with the theoretical map of Dye et al., reveals three significant observations. First, the incomplete penetration criterion of Dye et al. is adapted to our weld configuration. Secondly, the criterion proposed for the formation of a centerline grain boundary is not well adapted. According to Dye et al., as the welding speed decreases, a microstructure free of centerline grain boundary could be obtained for a wider range of

welding power. Our results are following an opposite trend. Our experimental criterion for the formation of a CLGB is nearly parallel to the incomplete penetration criterion. The third and final observation concerns the weld speed. In all welds done at a welding speed below 3.39 mm/s, a longitudinal grain formed. This weld microstructure was not reported by Dye et al. and is not acceptable for our application. A lower speed limit criterion was thus added to the map of Fig. 7a.

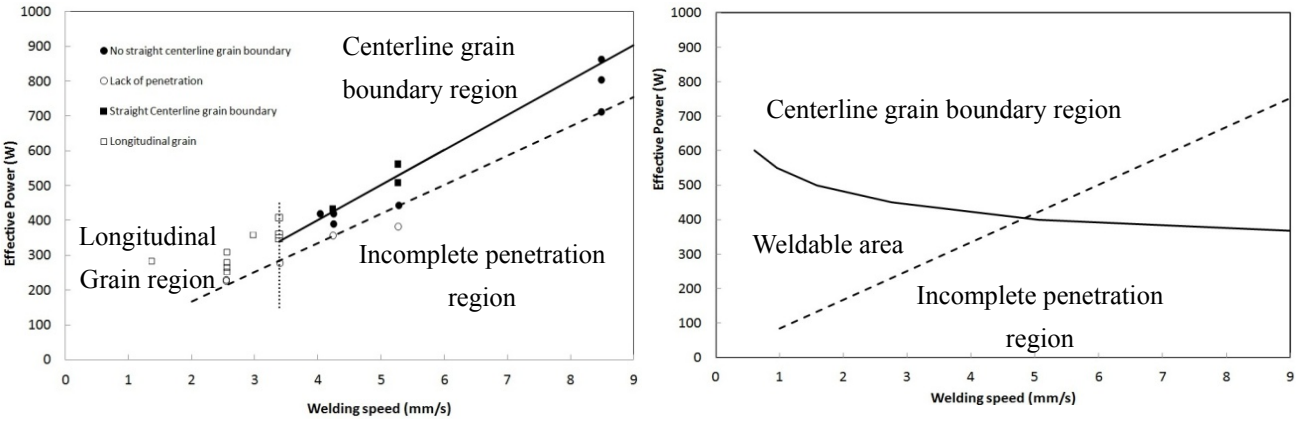

a) Experimental b) Predicted by Dye et al. model

Figure 7. Weldability map

5. Conclusion

The TIG weldability of IN718 sheets was studied in order to reduce the occurrence of solidification cracking. The objective of the experimental work was to identify welding parameters that would prevent the formation of a centerline grain boundary within the weld microstructure. Three welding strategies were tested and the results are summarized below:

Current pulsation

Current pulsation did not improve our weld microstructure and modifying the current ratio had no significant effect on the weld microstructure.

Constitutional supercooling

Welding at high speed and power did not produce the expected fine and equiaxe microstructure. However, the formation of few equiaxe grains suggests that nucleation of grains from the weld pool could happen.

Weld pool shape control

By controlling the depth to width ratio, an improvement of the microstructure was observed. Grain growth inclination resulted in a microstructure free of centerline grain boundary, but partially penetrated welds were produced at heat input below 112 J/mm. Decreasing the welding speed had a detrimental effect since a longitudinal grain formed within the welds performed at welding speed below 3.39 mm/s.

Results reported in a weldability diagram revealed that the weldable area of our IN718 TIG weld is very narrow, for the range of welding conditions tested. This is caused by the fact that the centerline grain boundary criterion is nearly parallel and very close to the incomplete penetration criterion. In practice, restricting the welding power in such a narrow band is limiting. Adjustments of the current intensity are often necessary to better control the dimensions of the assembly and the penetration of

the welds. Further studies should be done in order to identify other welding conditions susceptible to produce a metallurgically sound weld. According to our results, the supercooling strategy should be investigated further. Usage of a current pulsation or cooling shielding gas could favor the germination of equiaxe dendrites in the weld pool.

Acknowledgements

The authors wish to acknowledge Pratt & Whitney Canada for their support.

References

[1] D. F. Paulonis and J. J. Schirra, "Alloy 718 at Pratt and Whitney - Historical perspective and future challenges," in *Superalloys 718, 625, 706 and Various Derivatives, Jun 17 - 20 2001*, Pittsburgh, PA, United states, 2001, pp. 13-23.
[2] B. T. Alexandrov, J. C. Lippold, and N. E. Nissley, "Evaluation of Weld Solidification Cracking in Ni-Base Superalloys Using the Cast Pin Tear Test," in Th. Böllinghaus, H. Herold, C.E. Cross, C. Lippold (Eds.), Hot Cracking Phenomena in Welds II, Berlin, 2008, pp. 193-213.
[3] J. N. Dupont, J. C. Lippold, and S. D. Kiser, Welding metallurgy and weldability of nickel-base alloys, Hoboken, New Jersey: John Wiley & Sons, 2009.
[4] O. Hunziker, D. Dye, and R. C. Reed, "On the formation of a centreline grain boundary during fusion welding," *Acta Mater,* vol. 48, pp. 4191-4201, 2000.
[5] G. Sjoberg, T. Antonsson, S. Azadian, R. Warren, and H. Fredriksson, "Effect of -phase on the weldability and the hot ductility of alloy 718," in *6th International Symposium on Superalloys 718, 625, 706 and Derivatives, October 2, 2005 - October 5, 2005*, Pittsburgh, PA, United states, 2005, pp. 351-362.
[6] W. F. Savage and B. M. Krantz, "Investigation of hot cracking in hastelloy X," *Welding J,* vol. 44, pp. 13--25, 1966.
[7] G. D. J. Ram, A. V. Reddy, K. P. Rao, and G. M. Reddy, "Control of Laves phase in Inconel 718 GTA welds with current pulsing," *Sci Technol Weld Joi,* vol. 9, pp. 390-398, 2004.
[8] G. D. Janaki Ram, A. V. Reddy, K. P. Rao, and G. M. Reddy, "Improvement in stress rupture properties of inconel 718 gas tungsten arc welds using current pulsing," in *J Mater Sci*, 2005, pp. 1497-1500.
[9] N. Kerrouault, "Fissuration à chaud en soudage d'un acier inoxydable austénitique," Ph.D. Ph.D., Mécanique et Matériaux, Ecole Centrale des Arts et Manufactures, Châtenay-Malabry Cedex, 2000.
[10] K. Shinozaki, Y. Motomichi, P. Wen, and T. Tomoko, "Prediction of occurrence of solidification cracking in weld metal," *Weld Inter,* vol. 24, pp. 942-8, 2010.
[11] K. Sivaprasad, S. Ganesh Sundara Raman, P. Mastanaiah, and G. Madhusudhan Reddy, "Influence of magnetic arc oscillation and current pulsing on microstructure and high temperature tensile strength of alloy 718 TIG weldments," *Mat Sci Eng A,* vol. 428, pp. 327-331, 2006.
[12] S. Kou and Y. Le, "Welding parameters and the grain strudture of weld metal - A thermodynamic consideration," *Metall Trans A, Physical metallurgy and materials science,* vol. 19 A, pp. 1075-1082, 1988.
[13] M. Gaumann, C. Bezencon, P. Canalis, and W. Kurz, "Single-crystal laser deposition of superalloys: processing-microstructure maps," *Acta Mater,* vol. 49, pp. 1051-62, 2001.
[14] W. F. Savage, "1980 Houdremont lecture - Solidification, segregation and weld imperfections," *Welding in the World, Le Soudage Dans Le Monde,* vol. 18, pp. 89-114, 1980.
[15] D. Dye, O. Hunziker, and R. C. Reed, "Numerical analysis of the weldability of superalloys," *Acta Mater,* vol. 49, pp. 683-697, 2001.

Mechanical properties of lattice truss structures made of a selective laser melted superalloy

Håkan Brodin[1,2 *] **and Jonas Saarimäki**[2]

[1] Siemens Industrial Turbomachinery AB, 612 31 Finspång, Sweden
[2] Linköping University, Department of Management and Engineering, Division of Engineering Materials, 581 83 Linköping, Sweden
* Corresponding author: hakan.brodin@liu.se

Abstract
Selective laser melting is a free-form manufacturing process, where components are built up layer by layer using metal powder. Complicated geometries can be manufactured and the exact dimensional tolerances allow direct manufacturing with a minimum of post-processing. Many materials are available in powder form today, e.g. aluminium, titanium, stainless steels, tool steels and superalloys. The current work is performed on a nickel based superalloy, conforming in principle to Hastelloy X.

Different lattice truss structures were manufactured with the selective laser melting process. In parallel, solid bars were produced with the same manufacturing process. Hollow rectangular tubes and composites of tubes with an interior of lattice truss structures were also manufactured. Hot rolled material of Hastelloy X was included for reference. Mechanical testing was performed in tension.

Mechanical testing shows that the selective laser produced material is highly anisotropic and that the material has many advantages compared to the traditionally manufactured Hastelloy X alloy. Tests also show that fracture is promoted along certain planes in the lattice truss structure

Keywords
free form fabrication, selective laser melting, superalloys, tensile testing, lattice

1. Introduction

Free form fabrication, rapid prototyping and 3D-printing are different designations for processes where material can be built to finished or near-finished shape without machining a block of material or casting material in a mould [1-3]. The processes were initially developed for very simple materials, such as thermoset plastics and plaster. Early-on laser was used to melt materials with a low melting point [4, 5], for instance brass. With some free-form manufacturing processes the material with a low melting point was mixed with a material of a high melting point (for instance brass and steel powders). A laser would be able to melt the brass, but steel would not melt, or only partially melt. This method for manufacturing materials would not be sufficient in cases where high stress or elevated temperature use will come into play. With improved process control and higher laser power, the range of materials was expanded. With a higher heat input, more difficult materials are possible to melt and it will be possible to create a microstructure with low amount of porosity and a material without internal defects such as solidification cracks or poor bonding [6].

Free-form fabrication of superalloys is gaining increased interest from the industry, since the available alloys range is growing. Today alloys for selective laser melting include aluminium, titanium, tool steel, stainless steel and heat resistant materials of cobalt- and nickel base [7-13]. In the case of melting of metal powders, the dominating manufacturing process is laser melting, often denoted selective laser melting (SLM) [6], direct laser metal sintering (DMLS) or LaserCusing. All of these names are trade marks for different companies manufacturing equipment for laser melting.
The laser melting manufacturing process can briefly be described as a layer-by layer process, where powder is distributed on a powder bed, Figure 1. After powder distribution, the powder is melted

and a metal slice is formed on the powder bed.

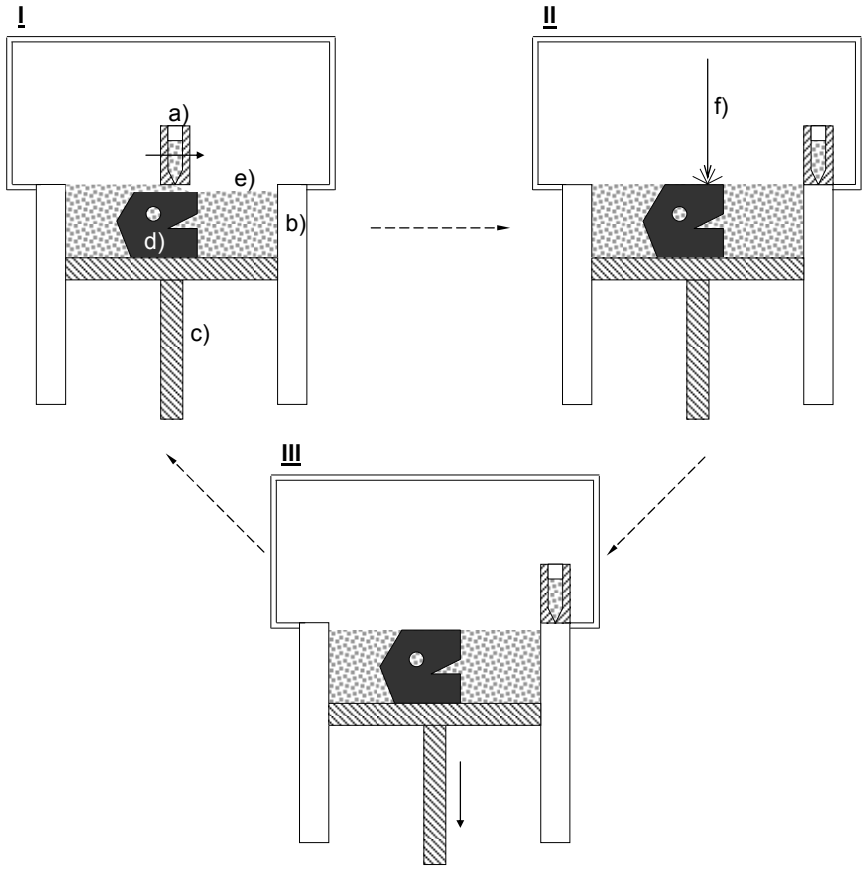

Figure 1. Schematic description of the SLM process. a) Powder is distributed on a powder bed, the build platform. b) The powder is melted by a laser beam and a slice of solid metal is formed. c) The powder bed is lowered and the process is repeated until a finished component is formed.

I: A powder distributer travels over the powder bed cavity contained by the build chamber walls b) and build plate c). Molten and solidified powder constitutes the component d) surrounded by unmolten powder e). II: A laser beam f) melts the powder layer and creates a new slice of solid material in the component d). III: A ram lowers the build platform c) and the process is repeated until a finished geometry is formed. After finalization, the remaining loose powder is removed and the component is cut off from the build platform.

2. Experimental details

2.1. Material

In the current work, material in principle conforming to AMS 5754 / UNS N06002 (i.e. Hastelloy X from Haynes International) has been used. In literature the material is sometimes identified as “Alloy X” when not available from the original supplier. The powder material is gas atomized and sieved to a fraction suitable for the SLM process, Figure 2. Solid test bars, hollow specimens and lattice truss structures with diamond geometry, Figure 3, were produced in an Eosint M270 DM machine. After manufacturing no heat treatment was adopted. In Table 1, the nominal composition of Hastelloy X is shown. The typical microstructure of the SLM material after manufacturing is shown below, Figure 4.

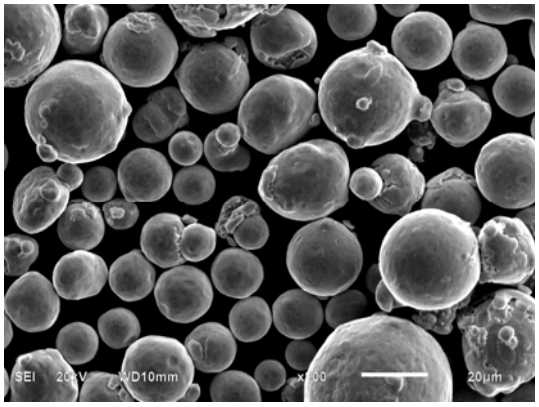

Figure 2. Morphology of the gas atomized powder used for SLM manufacturing in the current work.

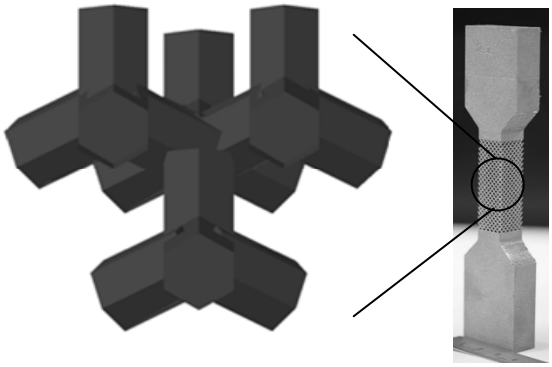

Figure 3. Least repetitive unit in diamond cell as used in the current work, here aligned in the 90° direction.

Table 1. Nominal composition of Hastelloy X as per standard for hot rolled material.

Ni	Cr	Fe	Mo	Co	Si	Mn	W
Bal.	22	18	9	1.5	<1	<1	0.6

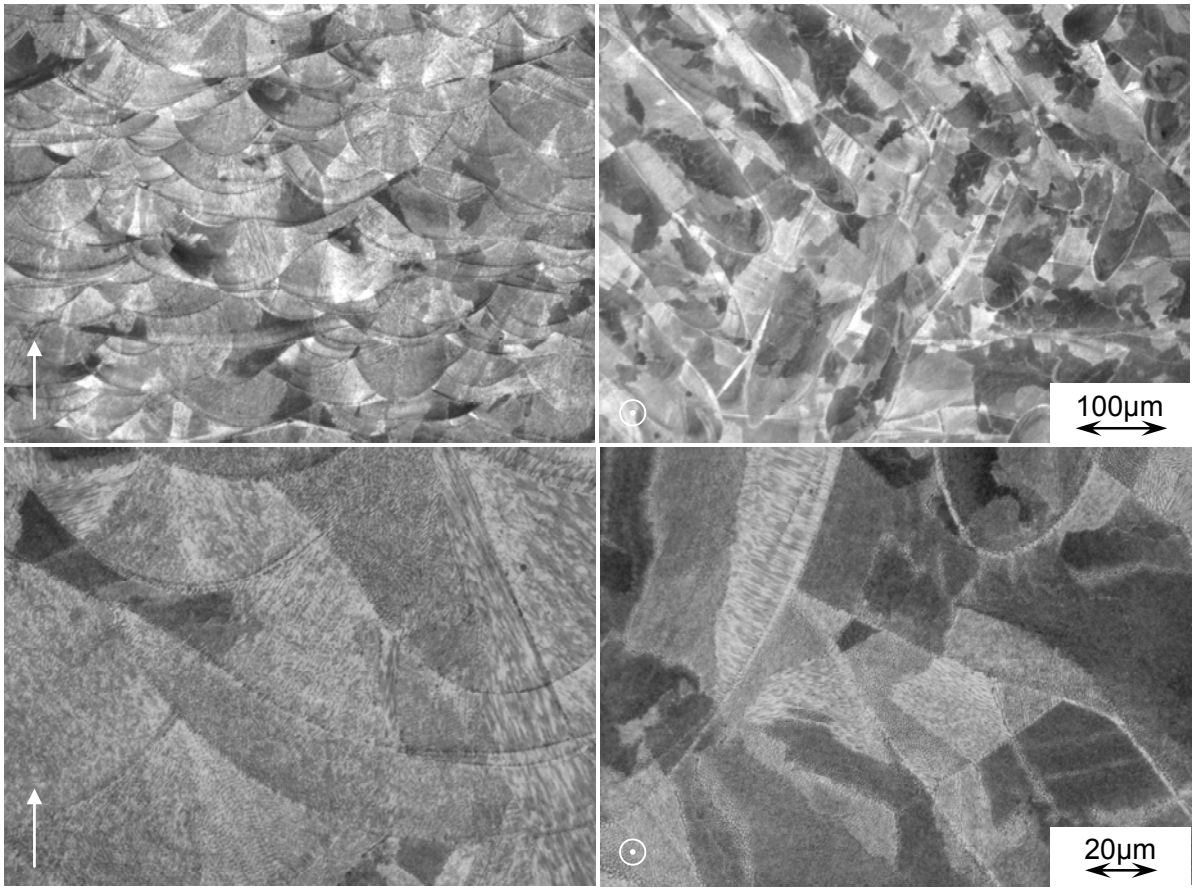

Figure 4. SLM bulk material in the as-manufactured condition. Top left (a) view parallel to build direction. Top right (b), view perpendicular to build direction. Bottom (c and d), close-up of weld-like structure after manufacturing. Build direction indicated by arrows.

2.2. Geometry

Different structures with and without lattices have been evaluated in the current work. Cross sections of the tubular shell, lattice and hybrid structures included are shown below, Figure 5. The lattice structure is designed to have a comparable density throughout the range of available dimensions. The measure d/l was kept constant throughout manufacturing of all test bars. As mentioned above, tensile testing was done using a "diamond" structure on the three different types of specimens a hollow tubular, an open lattice truss structure and a hybrid consisting of a tube containing a lattice truss structure as shown in Figure 5 containing the three different types of lattice truss structures. The structure sizes are called 2,2, 2,6 and 3,0 because of the dimensions that are calculated with the formula $w/s=v$ where w = cell size, s = lattice diameter and v is value that needs to be less than three for the structure to be manufactureable. The specimen sizes were chosen to be (LxWxD), Lx15x15mm and Lx13x13mm for the open lattice truss structure.

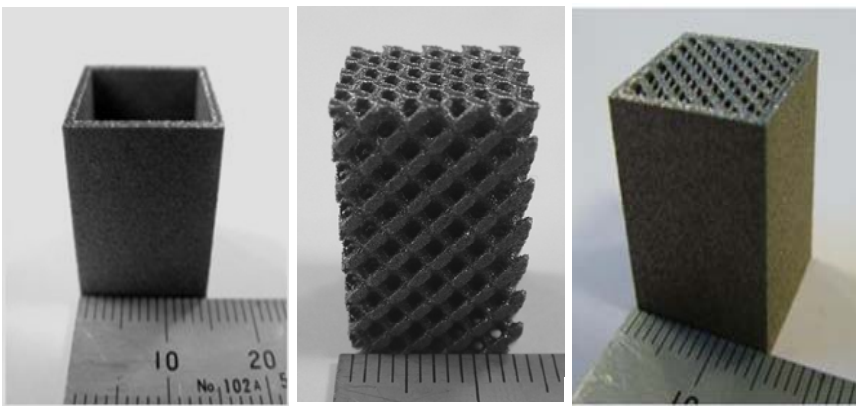

Figure 5. Cross-section of the three geometries for mechanical testing and evaluation of lattice truss structure testing: hollow shell (left), lattice truss structure (middle) and hybrid (right).

Tensile strength tests were done on laser sintered Alloy X at build angles of 0° and 90°. The results show that the mechanical properties vary considerably depending on the build angle. Build angle is defined with the specimen compared to the build platform and shown below, Figure 6.

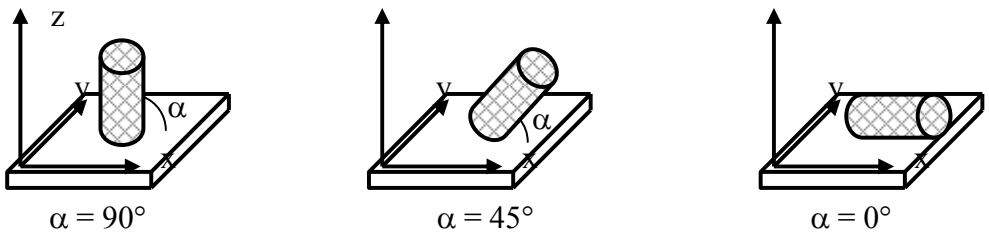

Figure 6. Definition of specimen build and loading direction relative to the build platform plane. A specimen "0°" would be a specimen in any direction in the build plane and a specimen "α°" (0° < α < 90°) would be a specimen built out of the build platform. An angle α = 90° would indicate a specimen being built parallel to the SLM equipment build direction.

3. Results
3.1. Solid test bars

Tensile testing was conducted on solid material manufactured by selective laser melting and material produced by hot-rolling. Figure 7 shows typical tensile stress-strain data. The SLM material was tested in the as-manufactured state, whilst the hot-rolled material is tested in a solution heat treated material condition. In Figure 8 and Figure 9 more detailed tensile test results are shown for ambient and elevated temperature testing. Data are normalized to average values for hot-rolled Hastelloy X material.

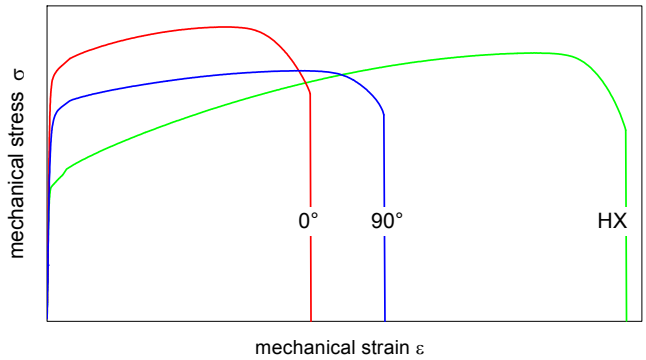

Figure 7. Generalized results from tensile testing of solid bars, stress-strain curves for standard Hastelloy X (HX), SLM Alloy X (0° and 90°).

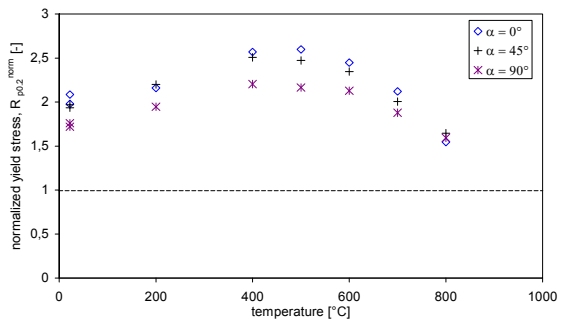

Figure 8. Normalized yield stress. Dashed line $R_{p0.2}$ =1 equals hot-rolled material.

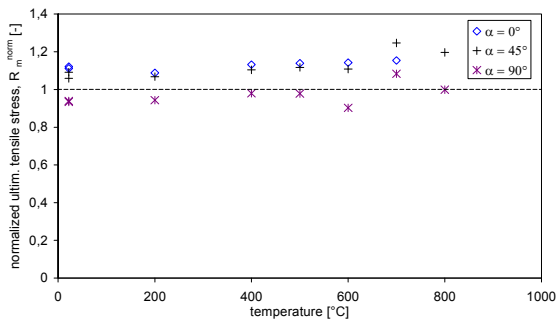

Figure 9. Normalized ultimate tensile stress. Dashed line R_m =1 equals hot-rolled material.

Due to the weld-like manufacturing process, the material is highly anisotropic. This is clearly shown above in material data (Figure 7 to Figure 9) together with microstructural observations in Figure 4.

3.2. Lattice truss structures

Tensile testing has been performed on geometries as shown above, Figure 5. Results are presented and discussed below. From tensile tests, data for hollow, open lattice and hybrid structures are presented in Figure 10. The data set is a typical response from testing and represents all geometry variations 2.2 – 3.0 included in the test series.

The component stiffness can be calculated as the slope of the force-displacement curve for hollow,

open lattice and composite structures, since the tests here are performed on geometries where the hybrid specimen shell and the tubular specimens have identical shell measures. The open lattice truss structure was designed to fit inside the tube and, accordingly, the hybrid specimen interior hence matches the open truss structure.

In practical design work, the aim is often to use a light-weight material and data are often presented as a correlation between, for instance, density and stiffness. Plotting the material stiffness relative to measured density for open lattice, tubes and hybrid material yields Figure 11 below. For comparative purposes, the apparent density (the weight per unit volume of a material including internal cavities inherent in the material as tested) is used instead of density for a solid material.

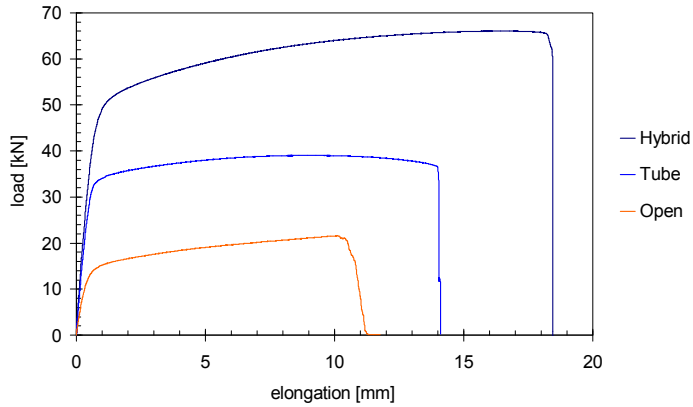

Figure 10. Tensile test results for the investigated geometries (tube, open lattice and hybrid test bar).

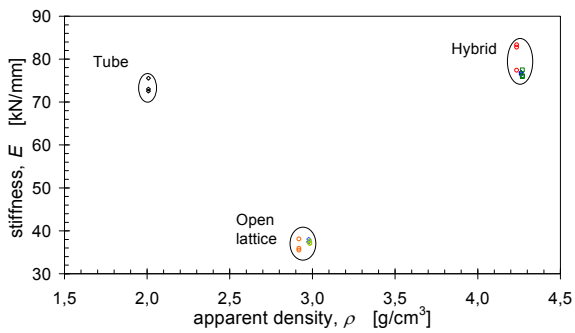

Figure 11. Design curves for measured stiffness *E* as a function of apparent density *ρ*.

Data have been further processed in order to compare stiffness, force at yield and peak force for the geometries in the test series. Comparisons are made of how an open truss structure and a tube interact in a hybrid material. Figure 12 shows a comparison between the measured behaviour (E, F_m and $F_{p0.2}$) of a hybrid test bar to the superpositioning of data for corresponding open lattice and tube specimen as shown below, Equation (1).

$$\begin{cases} E_s = E_t + E_{ol} \\ F_{p0.2,\,s} = F_{p0.2,\,t} + F_{p0.2,\,ol} \\ F_{m,\,s} = F_{m,\,t} + F_{m,\,ol} \end{cases} \qquad (1)$$

where index *"s"* indicates superpositioned. *"t"* is tube and *"ol"* stands for open lattice. E is the stiffness (force/length) and $F_{p0.2}$ *and* F_m are force at yield and ultimate force. Due to the geometrical nature of the specimens, comparisons using these quantities are more convenient than quantities based on stress.

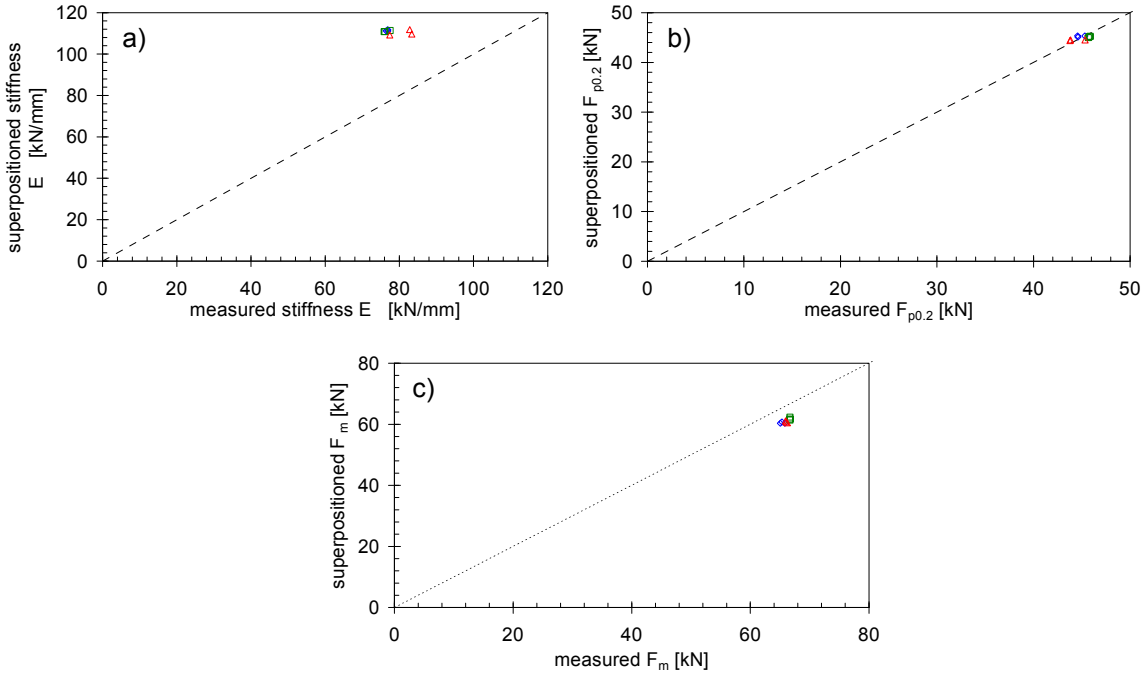

Figure 12. Comparison of superpositioned and measured stiffness *E*, load at yield $F_{p0.2}$ and maximum load before failure F_m for the hybrid geometry investigated in the current work.

3.3. Fracture surfaces

Fractographic observations from solid test bars and lattice trusses are shown below, Figure 13 to Figure 16. Figure 13 show the ductile fracture surface of an SLM manufactured solid test bar. In Figure 14 the failure of an open lattice truss structure is shown. In Figure 15 and Figure 16 bulk and surface regions of a lattice specimen can be viewed.

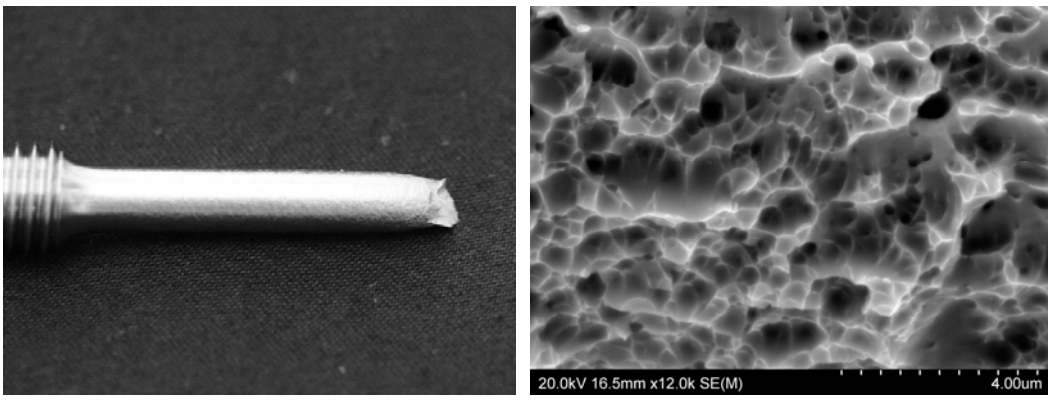

Figure 13. Typical cup and cone dimple fracture in solid as-manufactured alloy X manufactured by SLM (build and load direction perpendicular to build platform.

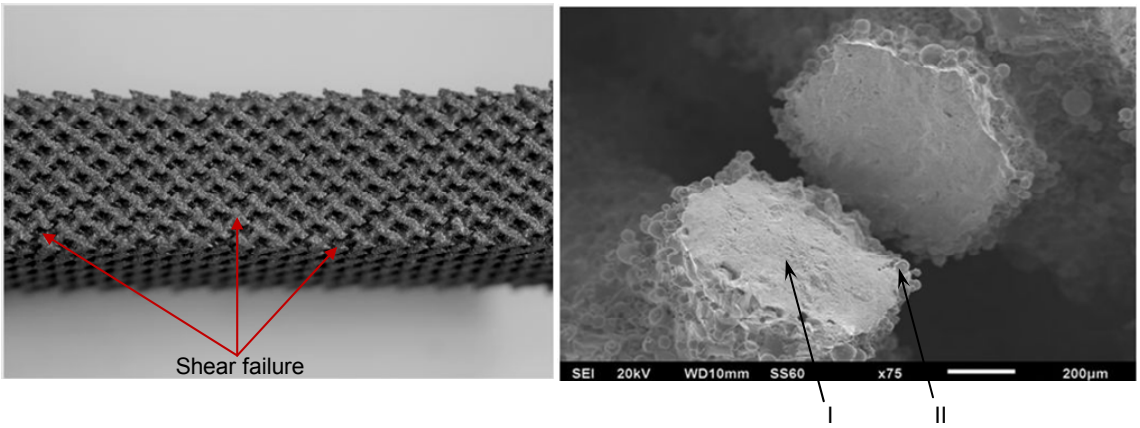

Figure 14. Typical shear damage of lattice struts due to axial tensile loading. Left: Shearing of the struts after tensile testing. Right: Shear fracture of a single strut after tensile testing. Note that the interior (I) and the exterior (II) exhibit differences in fracture appearance.

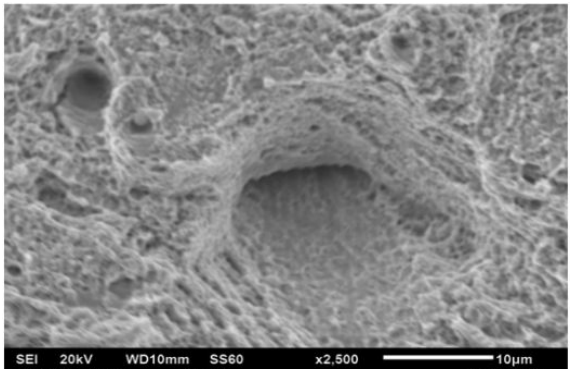

Figure 15. Strut failure of hybrid specimen.

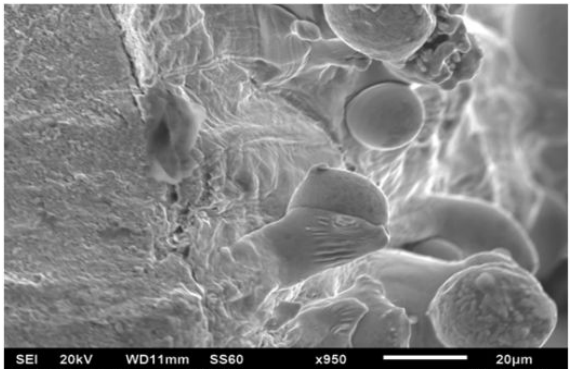

Figure 16. Fracture of as-manufactured surface. A skin of partly molten material is obvious.

4. Discussion

By comparison of data in Figure 11 and Figure 12 it is obvious that a superpositioning of stiffness for a tube and an open lattice structure does not equal the stiffness of a hybrid specimen. A conclusion must be that in tension the stiffness of a hybrid specimen is mainly influenced by the stiffness of the tube. I.e., for the tube the relation is according to Equation 2.

$$E_{hm} < E_t + E_{ol} \tag{2}$$

Regarding strength, in Figure 12 it is shown that for the geometry investigated here, the load is shared between the lattice structure and the tube so that the load applied to cause yield in the hybrid specimen equals the load applied to a tube and an open lattice as indicated by Equation 3.

$$F_{p0.2,\,hm} = F_{p0.2,\,t} + F_{p0.2,\,ol} \tag{3}$$

The same analysis for maximum load before failure yields that the maximum load in the hybrid specimen is slightly higher compared to the load in a tube and the open lattice superpositioned as described by Equation 4.

$$F_{m,hm} > F_{m,t} + F_{m,ol} \quad (4)$$

The reason for a stronger hybrid material can be attributed to change of constraint during loading. Figure 10 shows information on the material ductility. Not only does the hybrid material exhibit an increased strength compared to the tube plus open lattice but also a larger strain to failure (here plotted as elongation, which, in this case with equal initial lengths of the different geometries, yields comparable results).

The fractographic examination shows that the bulk SLM material is ductile with the expected cup and cone appearance and dimples on the tensile test specimen fracture surface. Open lattice truss structures and lattices in a hybrid specimen tend to fail due to a shear mechanism between struts along preferred planes. The typical fracture appearance is shown above in Figure 14. Tensile testing of components with as-manufactured surfaces reveals that the SLM material has a significant different fracture surface appearance in bulk and surface-near material. During manufacturing, SLM material will have a dense, completely remelted internal bulk. Externally, a thin layer of partly molten material will be present as observed in Figure 16.

5. Conclusions

The current paper shows how a selective laser melted material behaves in tensile testing. It is shown that the material is not as ductile as a normal hot-rolled material. However the material strength is good and the yield stress is superior to the hot-rolled material. Ultimate tensile strength is comparable between a selective laser melted material and the corresponding hot-rolled material. The selective laser melted material is highly anisotropic with respect to strength.

In light-weight designs, hybrid materials can easily be manufactured with the selective laser melting manufacturing method. It is shown that the yield strength of a hybrid material can be superpositioned by the yield strength of the individual shell and lattice structures. At failure the hybrid material will act stronger compared to the tubular shell and open lattice truss structure components in the hybrid part. The stiffness of the hybrid structure investigated here will mainly be influenced by the tubular shell.

6. References

[1] Chu J., Engelbrecht S., Graf G., and Rosen D.W., 2010. “A comparison of synthesis methods for cellular structures with application to additive manufacturing”. Rapid Prototyping Journal, 16, pp. 275-283.

[2] Rosen D.W., 2007. “Computer-aided design for additive manufacturing of cellular structures”. Computer-Aided Design and Applications, 4, pp. 585-594.

[3] Marchelli G., Prabhakar R., Storti D., and Ganter M., 2011. “The guide to glass 3D printing: developments, methods, diagnostics and results”. Rapid Prototyping Journal, 17(3), pp. 187 – 194.

[4] Das S., Beama J.J., Wohlert M., and Bourell D.L., 1998. "Direct laser freeform fabrication of high performance metal components". Rapid Prototyping Journal, 4(3), pp. 112 – 117.

[5] Kruth J.P., Froyen L., Van Vaerenberg J., Mercelis P., Rombouts M., and Lauwers B., 2004. “Selective laser melting of iron-based powder”. Journal of Materials Processing Technology, 149, pp. 616-622.

[6] Agarwala M., Bourell D., Beaman J, Marcus H., and Barlow J., 1995. "Direct selective laser sintering of metals". Rapid Prototyping Journal, 1(1), pp. 26 – 36.
[7] Abd-Elghany K., and Bourell D.L., 2012. "Property evaluation of 304L stainless steel fabricated by selective laser melting". Rapid Prototyping Journal, 18(5), pp. 420 – 428.
[8] Li R., Liu J., Shi Y., Du M., and Xie Z., 2010. “316L Stainless Steel with Gradient Porosity Fabricated by Selective Laser Melting”. Journal of Materials Engineering and Performance, 19(5), pp. 666-671.
[9] Li R., Shi Y., Wang L., Liu J. and Wang Z., 2011. “Theory and technology of sintering, thermal and chemothermal treatment. The key metallurgical features of selective laser melting of stainless steel powder for building metallic part”. Powder Metallurgy and Metal Ceramics, 50(3-4), pp. 141-151.
[10] Buchbinder D., Schleifenbaum H., Heidrich S., Meiners W., and Bültmann J., 2011. “ High Power Selective Laser Melting (HP SLM) of Aluminum Parts“ Physics Procedia, 12, pp. 271–278.
[11] Wang Z., Guan K., Gao M., Li X., Chen X., and Zeng X., 2012. “The microstructure and mechanical properties of deposited-In718 by selective laser melting“., Journal of Alloys and Compounds, 513(5), pp. 518-523.
[12] Vilaro T., Colin C., Bartout J.D., Nazé L., and Sennour M., 2012. “Microstructural and mechanical approaches of the selective laser melting process applied to a nickel-base superalloy” Materials Science and Engineering A, 534, pp. 446-451.
[13] Wang F., 2012. “Mechanical property study on rapid additive layer manufacture Hastelloy® X alloy by selective laser melting technology”. International Journal of Advanced Manufacturing Technology, 58, pp. 545-551.

Evaluation of Optimal Condition in Laser Shock Peening Process by AE Method

Tomoki Takata[1,*], **Manabu Enoki**[1], **Akinori Matsui**[2], **Yuji Kobayashi**[2]

[1] Department of Materials Engineering, School of Engineering, The University of Tokyo,
7-3-1 Hongo, Bunkyo-ku, Tokyo 113-8656, Japan
[2] Shintokogio, Ltd., 1-1-1 Nishiki, Naka-ku, Nagoya city, Aichi 460-0003, Japan
[*] Corresponding author's e-mail address: takata@rme.mm.t.u-tokyo.ac.jp

Abstract
Laser shock peening (LSP) is now recognized as an efficient surface treatment to improve the fatigue life of metal components. To evaluate the process conditions, Almen strip is used as well as shot peening. As this is limited to specific material and size, we cannot apply to a wide variety of substrates. Acoustic emission (AE) method is expected to be useful for understanding LSP process because an elastic wave generates when laser is radiated on a target. The water layer on a target confines the shock wave due to laser irradiations during LSP process. In this study, laser irradiations during LSP process were monitored by AE method with varying the temperature and the thickness of the water layer on a target, respectively. Impact forces during LSP process were obtained from detected AE waveforms by deconvolution technique. In addition, laser irradiations were observed by high speed camera, and the image was compared with the detected AE signal. This result shows that shock wave was emitted by not only laser ablation but also collapse of a bubble which was generated after laser irradiation and a bubble was affected by the water layer.

Keywords Laser shock peening, Acoustic emission, Cavitation bubble

1. Introduction

Peening is one of surface treatment method to improve the fatigue strength of metals by inducing compressive stresses generated from mechanical means such as hammer blows or by blasting with shot (shot peening). Laser shock peening technique, which use laser to generate the reaction force near material surface by laser ablation, can impact a layer of compressive stress four times deeper than that attainable from conventional shot peening. However, the effect of laser irradiation on materials and phenomenon near radiation point are not well understood yet. The residual stress in depth direction is generally used to evaluate the degree of laser peening. A sample for residual stress measurement has to be cut and electrochemically polished, which is a destructive method. Although there are several in-situ methods to evaluate residual stress during laser peening process such as probe beam polarization and VISAR method, these are some limitations such as an exact adjustment required for fiber position and applicability for only thin samples for the first and latter methods respectively.

Acoustic emission (AE) method is one of the nondestructive evaluation methods to evaluate the size, location and generation time of deformation and damage in real-time. AE method has been successfully applied to shot peening method to analyze impact behavior of particles and evaluate the impact force by inverse analysis [1]. In this paper, AE method was applied to laser peening process. A high speed camera was also used to observe the laser radiation behavior. The impact pressure due to laser ablation was evaluated from the detected AE signals and simulated waveforms. The laser radiation phenomenon was discussed with results of AE and high speed camera observations.

Cavitation is phenomenon that a bubble generates by pressure difference in stream and collapses with emitting shock wave after the short time. In our present group, a cavitation bubble was observed during laser shock peening process [2].

2. Experimental Procedure

2.1 Laser shock peening

Two experimental set-ups to evaluate the effects of water temperature and water thickness layer are shown in Fig. 1(a) and 1(b), respectively. A target sample was A7075 aluminum alloy with demensions of 50 × 50 × 10 mm.A Q-switched Nd:YAG laser with a wavelength of 532 nm and a pulse width of 3 – 5 ns was used for both experiments. A laser beam was focused to the center of sample using lens. The laser was irradiated at least two times for each test. In set-up of Fig. 1(a), experiment was conducted with varying laser energy and water temperature. In set-up of Fig. 1(b), experiment was conducted with varying the thickness of water layer on a target sample. The detail of experomental conditions are shown in Table 1.

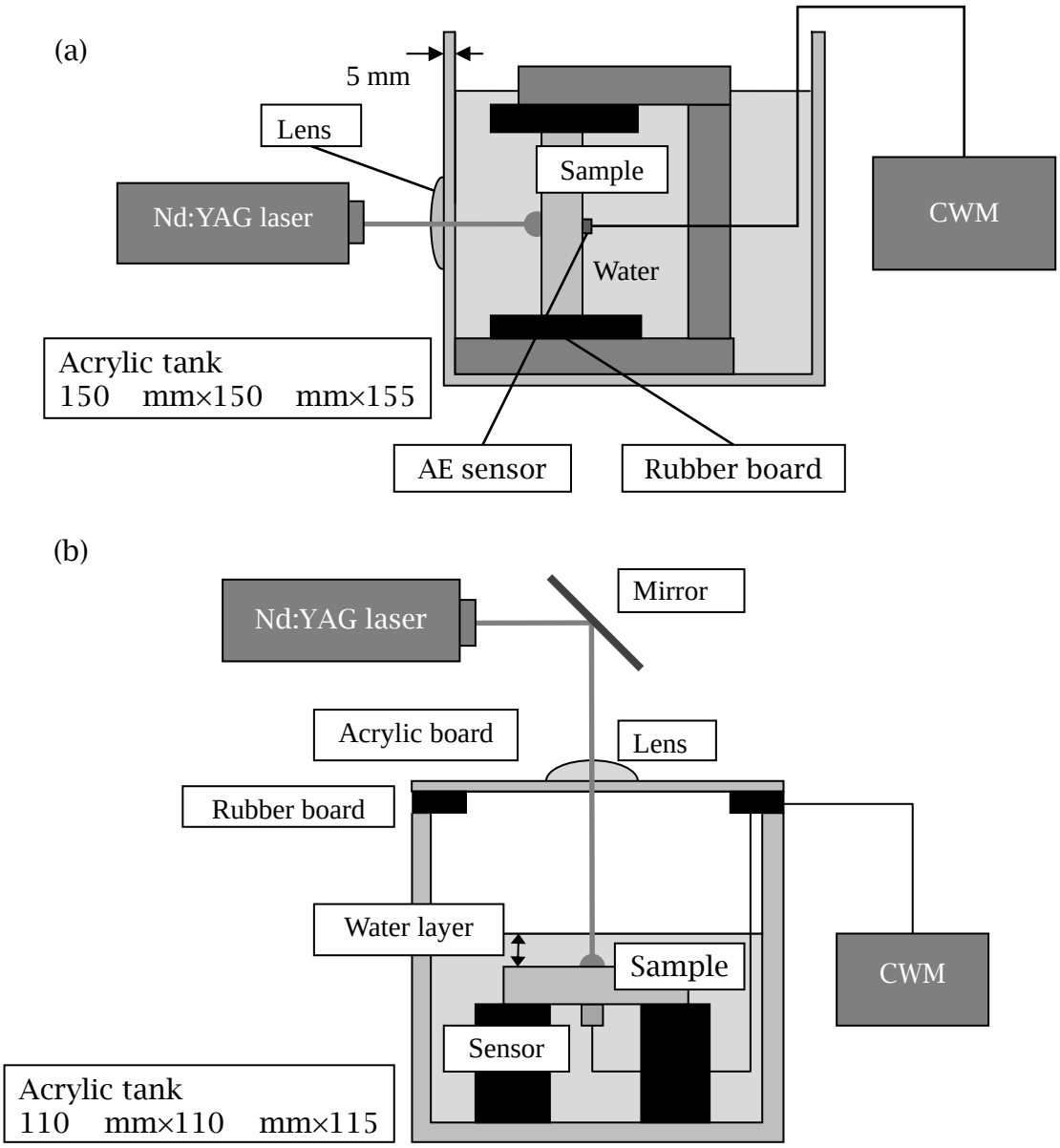

Figure 1. Schematic of experimental set-ups for studying effects of
(a) water temperature and (b) water layer thickness

Table 1. — Experimental conditions

	Laser energy	Water temperature	Water layer thickness
(a)-1	10 – 100 mJ	20 °C	-
(a)-2	100 mJ	15 - 50 °C	-
(b)	60 mJ	20 °C	1 – 10 mm

2.2 Optical observation by high speed camera

High speed cameras (Phantom Miro LC310 producted by Vision Research® Inc. and HyperVision HPV-2A producted by SHIMADZU CORPORATION) were used to observe the phenomenon during laser shock peening in experiment set-up as shown in Fig.2. The camera was set to observe the sample from an oblique direction. The phenomenon was recorded using lighting from opposite side of high speed camera. At the same time, fluctuation in water near sample surface was mainly also recorded by Phantom Miro LC310 with the sampling rate of 120,000 fps and pixels of 128 × 128.

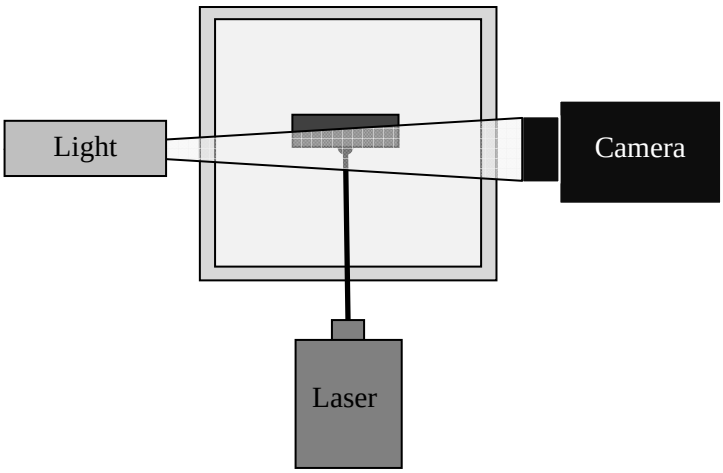

Figure 2. Top view of camera setting in Fig. 1(a)

2.3 AE measurement

An AE sensor (Pico, Physical Acoustics Corp.) was attached on the back side of the sample as shown in Fig. 1(a). Elastic waves associated with laser irradiation were recorded by Continuous Wave Memory (CWM) system, which is developed by our research group [3]. This system provides a capability to memorize all waveforms continuously at the sampling rate of 10 MHz. Waterproof paste was used to cover cables.

2.4 AE inverse analysis

Impact forces generated from laser irradiation were evaluated by an inverse analysis of AE waveform [1]. Detected AE waveform can be represented by $V(t)=S(t)*G(t)*I(t)$ where $V(t)$, $S(t)$, $G(t)$ and $I(t)$ are detected waveform, response function of sensor, Green's function of media and source function of impact force, respectively. $S(t)$ and $G(t)$ could be obtained from a simulation of AE waveform by finite element method and experimental of sharp pencil lead breaking and then $I(t)$

was estimated by the deconvolution technique. All AE waveforms were analyzed by this inverse method and obtained impact force values were discussed.

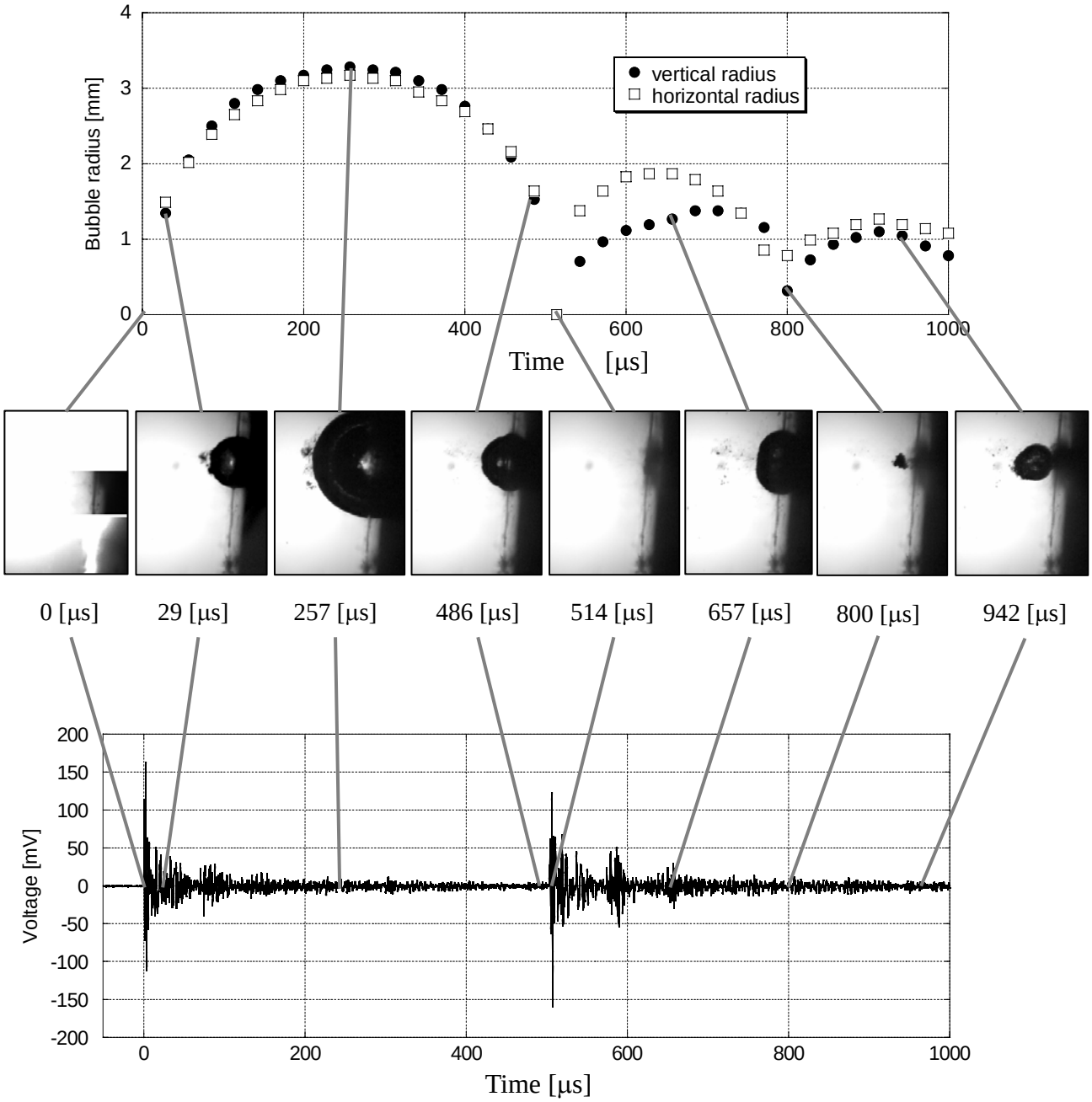

Figure 3. Transition of bubble radius and detected AE waveform in set-up (a)-2 (laser energy: 100mJ, water temperature: 25.1°C)

3. Results and discussion

3.1 Detected AE waveform compared with photos by high speed camera

During laser shock peening process, a bubble was generated after laser irradiation. Fig. 3 shows typical AE waveforms detected during laser peening process coupling with photos recorded by the high speed camera and a graph demonstrated a change of radius of a bubble on sample surface. Two AE events were generated with time duration of several hundred microseconds for each laser irradiation. The results of high speed camera showed that after laser irradiation a bubble generated and expanded its size up to the maximum radius. Then it became smaller and finally collapsed. According to this observation, the first and latter AE events were considered to correspond to laser irradiation and bubble collapse, respectively. Let t_1 and t_2 are times for the first and second AE events, respectively while t_c and R_{max} are time for bubble collapse and maximum bubble radius obtained from the high speed camera results, respectively. A time interval between two events, Δt, is defined as $t_2 - t_1$. A plot of Δt vs. t_c and R_{max} vs. t_c for experiment condition (a)-1 is shown in Fig. 3 and 4, respectively. A linear relationship of these parameters supported that the first and latter AE events were generated from impacts due to laser irradiation and bubble collapse, respectively. Fig. 4 shows a plot of in room temperature. It is clear that larger bubble required longer collapse time at constant temperature.

3.2 A cavitation bubble

A cavitation bubble was generated by laser irradiation, expanded, shrank and collapsed. A bubble was almost hemisphere, but after bubble collapse a bubble became ellipsoid, repeated expanding and shrinking, and finally became some smaller bubbles (Fig. 3). In the case of laser irradiation from horizontal direction (Fig. 1(a)), a bubble comes off the sample after second collapse, so AE event was not detected. In case of laser irradiation from vertical direction (Fig. 1(b)), they are sometimes detected more AE event than three when a bubble does not come off. Time detected third and fourth AE event is equal to second and third bubble collapse time respectively (Fig. 5).
By using HyperVision HPV-2A, collapse of a cavitation bubble was observed in detail with the sampling rate of 1,000,000 fps and pixels of 312 × 256 (Fig. 6). Immediately after bubble collapse,

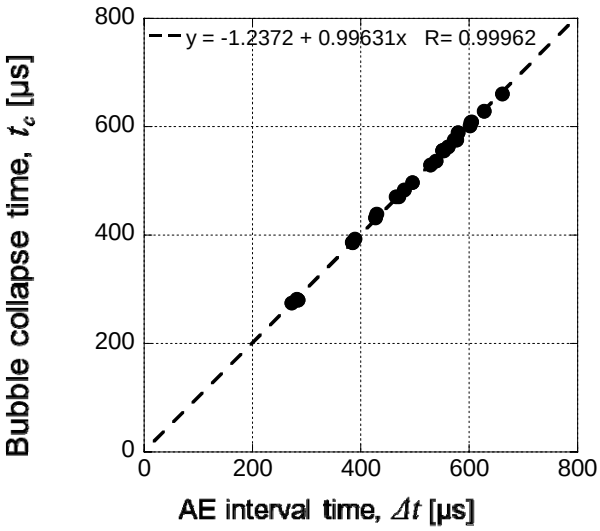

Figure 4. Relationship between bubble collapse time, t_c and AE interval time, Δt in room temperature

it was emitted a hemisphere tremor from the center of a bubble before collapse. The speed of propagation of the tremor is about 1,500 m/s, so the tremor was caused by shock wave due to bubble collapse.

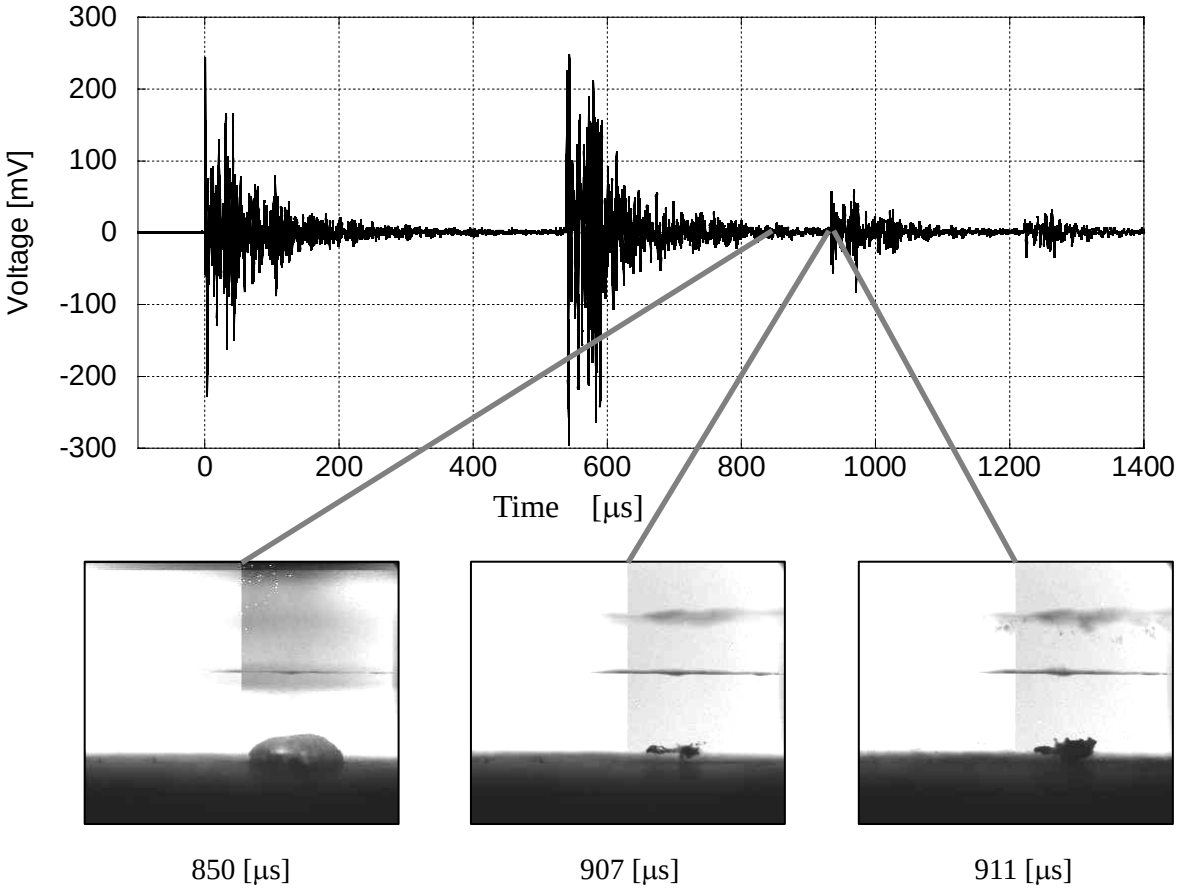

Figure 5. Detected AE waveform in set-up (b), (laser energy: 100mJ, water thickness: 5mm)

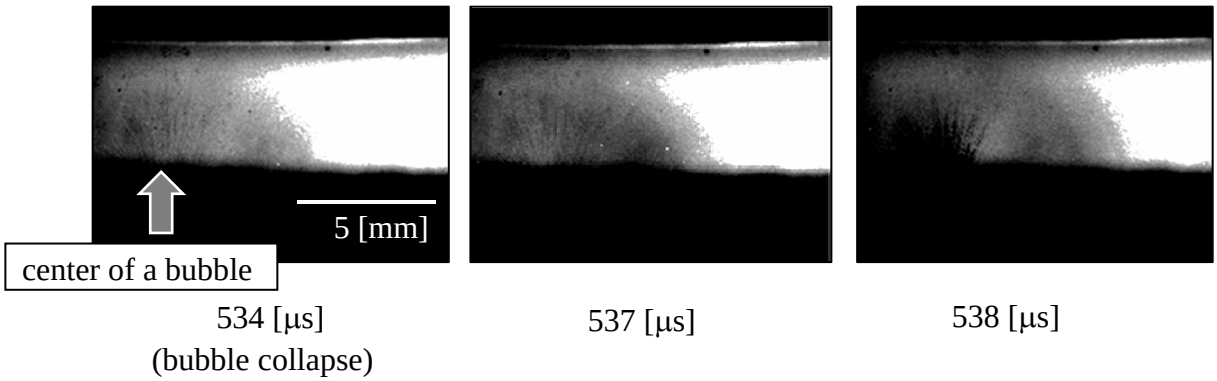

Figure 6. Optical observation of propagation of shock wave by bubble

3.3 Effect of water temperature

In Fig. 7, maximum radius of a cavitation bubble, R_{max} is plotted with AE interval time, Δt. A relationship between maximum radius of a cavitation bubble and bubble collapse time is linear in room temperature. On the other hand, the relationship in experiment with varying water temperature is not linear as shown in Fig. 8. In Fig.9, maximum bubble radius, R_{max} is plotted for water temperature, T_w. The maximum radius of a cavitation bubble increases with water temperature. These results suggested that temperature affects the maximum radius and shape of a bubble.
The graph in Fig. 10 shows a plot of impact forces of laser irradiation, I_L and these of bubble collapse, I_B with water temperature. Impact force from laser ablation became smaller than that from laser irradiation with increasing water temperature. Fig. 11 shows a plot of a ratio of impact forces due to laser irradiation and bubble collapse, I_B /I_F with water temperature. Impact forces from laser irradiation are not affected by water temperature. On the other hand, impact force from bubble collapse became smaller than that from laser irradiation with increasing water temperature and the ratio of I_B /I_F decrease clearly in Fig. 11.

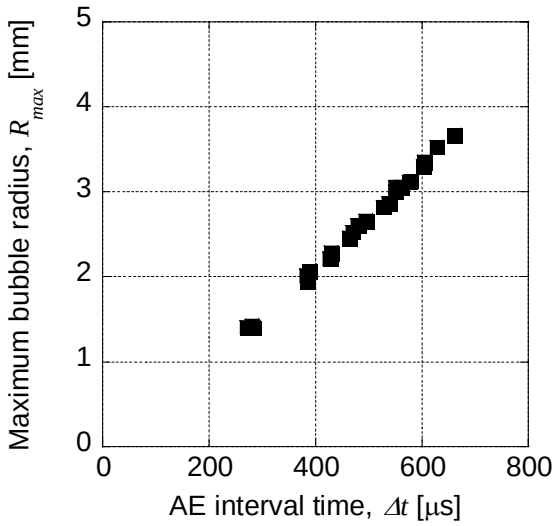

Figure 7. Relationship between maximum bubble radius, R_{max} and AE interval time, Δt in room temperature

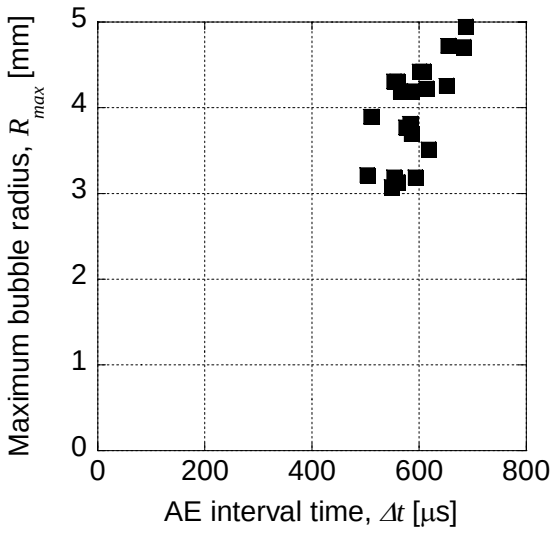

Figure 8. Relationship between maximum bubble radius, R_{max} and AE interval time, Δt with varying water temperature

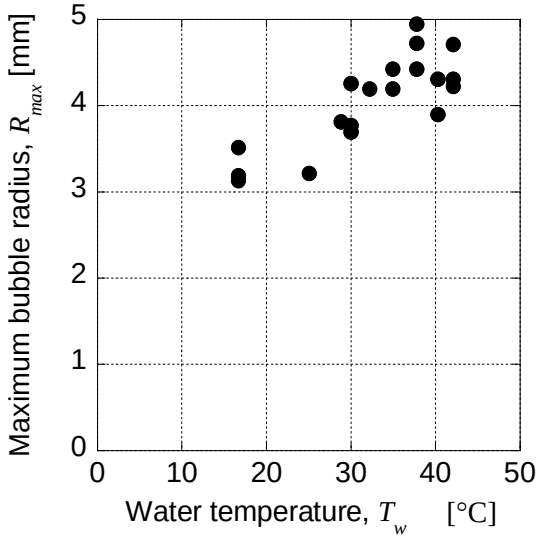

Figure 9. Relationship between water temperature, T_W and AE event interval, Δt

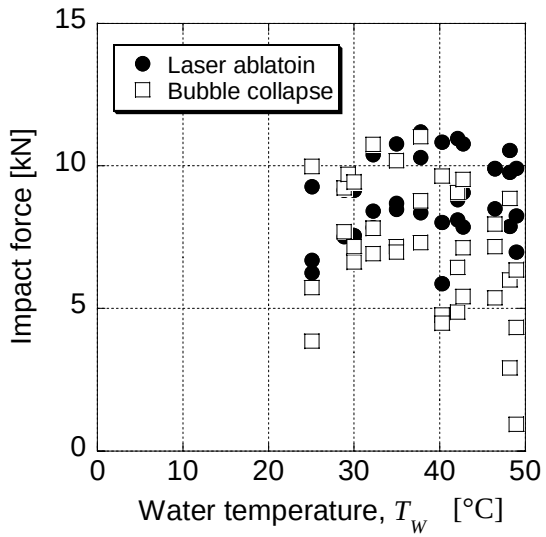

Figure 10. Relationship between water temperature, T_W and impact force, I_L and I_B

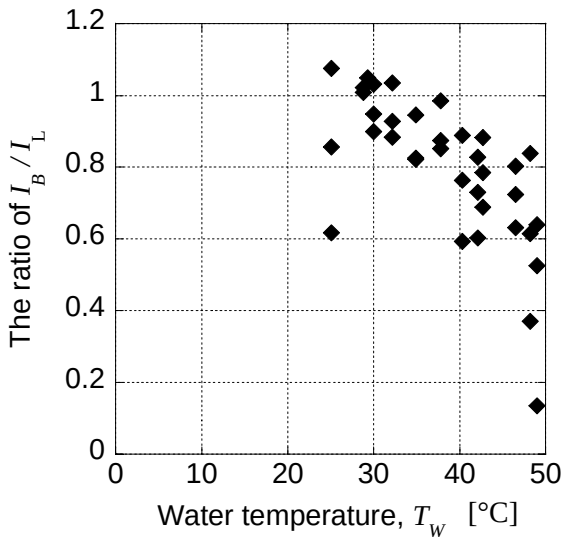

Figure 11. Relationship between water temperature, T_W and the ratio of I_B / I_L

3.4 Effect of thickness of water layer

In experimental set-up (b), impact forces during laser shock peening process were obtained from detected AE waveforms by deconvolution technique, which is plotted in Fig. 12 as a function of water layer thickness. When the water layer was thinner than 2 mm, impact forces of laser irradiation and a bubble collapse were very small. Impact force by a bubble collapse showed the maximum value when thickness of water layer was 3-5 mm, while impact force by laser irradiation was a certain value.

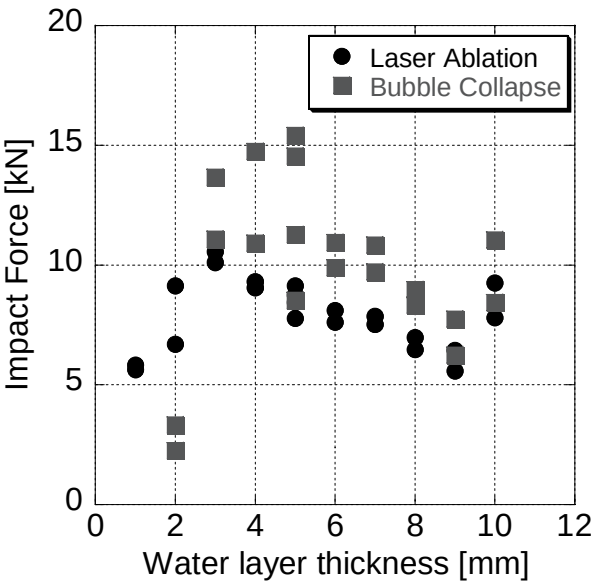

Figure 12. Relationship between water layer thickness and impact

4. Conclusions

In the present study, the effect of water layer and temperature in laser shock peening was evaluated by AE method and high speed camera, and following conclusions were drawn;

(1)Impacts were emitted by not only laser irradiation but also bubble collapsed.
(2)Maximum radius of a cavitation bubble increases with temperature of water layer and has a linear relationship with AE event interval time in constant temperature.
(3)Impact forces of laser irradiation are not affected by water temperature. Impact forces of bubble collapse decrease with increasing water temperature. The ratio of two impact forces due to laser ablation and bubble collapse decreases with increasing water temperature.
(4)Impact forces by laser irradiation and bubble collapse have the maximum value at the of water layer thickness around 4 mm.

Acknowledgement

This work was partially supported by JSPS KAKENHI Grant Number 23246124.

References

[1] D.J.Buttle, C.B.Scruby, Characterization of particle impact by quantitative acoustic emission, Wear, 137(1990) 63-90
[2] M. Enoki, K. Kobayashi, T. Tomoki, M. Matsui, Y. Kobayashi, Quantitative Acoustic Emission Measurement of Laser Peening in EWGAE 2012
[3] K.Ito, M.Enoki, Acquisition and Analysis of Continuous Acoustic Emission Waveform for Classification of Damage Sources in Ceramic Fiber Mat, Mater. Trans., 48 (2007) 1221-1226.

Low Frequency Laser Ultrasonics for Evaluation of Internal Cracks in Multi-layered Steels

Sho Ikeda[1], Kaita Ito[1], Shoichi Nambu[1] and Manabu Enoki[1]
enoki@rme.mm.t.u-tokyo.ac.jp

[1]Department of Materials Engineering, The University of Tokyo,
7-3-1 Hongo, Bunkyo-ku, Tokyo 113-8656, Japan

Keywords: *laser induced ultrasonic, multi layered steels, finite element method*

A novel, non-contact, non-destructive evaluation technique for plate-like specimens which may have internal cracks is now drawing attention. In this technique, pulsed lasers generate ultrasonic waves on the specimen surface [1]. And an interferometer was used to measure the waves of the specimen surface. Investigation about correlation between laser induced ultrasonic waves and size of internal cracks was tried. Resin specimens with various size and location of internal cracks were prepared and ultrasonic waves generated by YAG pulsed laser were measured by laser interferometer. FEM analysis was used to compare with the results of experiments [2]. As a result, this method could detect location of cracks by using correlation coefficient and FFT peak frequency and there were quantitative correlations between induced ultrasonic waves and size of internal cracks, and this method also could evaluate the specimens of multi-layered steels with interlayer cracks which are generated during manufacturing (Figure 1).

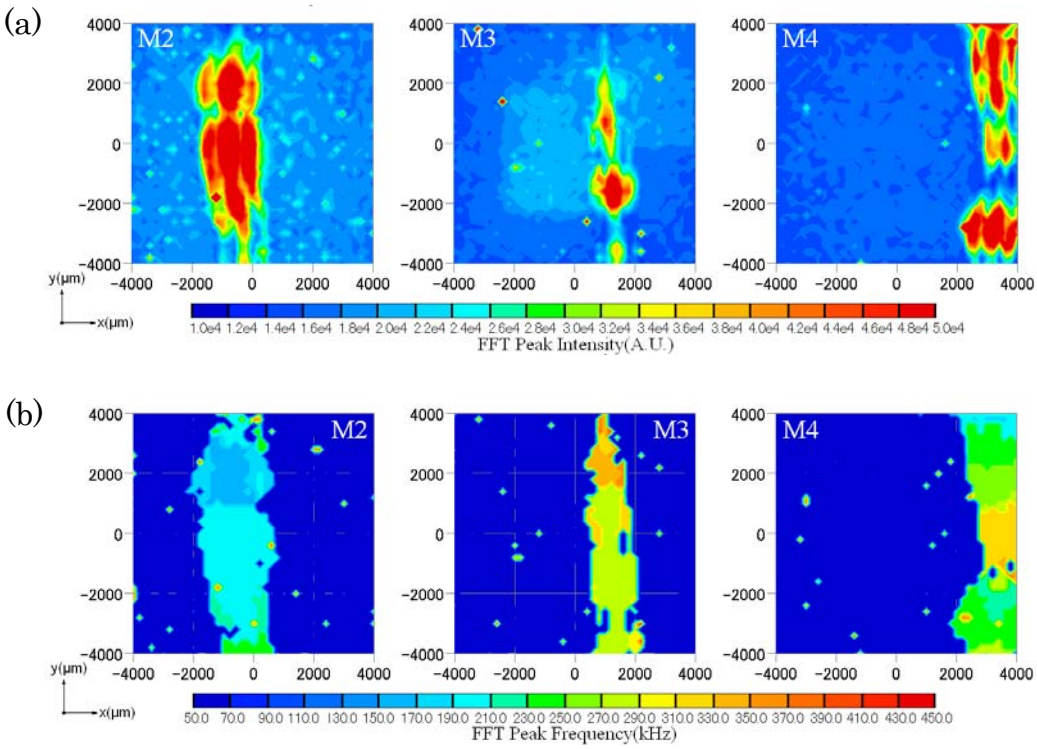

Figure 1 Evaluation of internal cracks using (a) FFT peak intensity and (b) FFT peak frequency.

References:
[1] J. P. Monchalin, IEEE Trans. Components and Packaging Tech. 33(1986) 485-499.
[2] K. Mori et al, NDT&E International 35 (2202) 399-406.

Mode I Fatigue Crack Growth Behaviour in a Welded Cruciform Joint under Biaxial Stresses

Xiang Zhang[1,*], Haiying Zhang[2], Rui Bao[3]

[1] Department of Aerospace Engineering, School of Engineering, Cranfield University, Bedford, MK43 0AL, UK
[2] Aircraft Strength Research Institute, Xi'an, 710065, P.R. China
[3] Institute of Solid Mechanics, School of Aeronautic Science & Engineering, Beihang University, Beijing, 100191, P.R. China

* Corresponding author: xiang.zhang@cranfield.ac.uk

Abstract Biaxial load fatigue crack growth tests were performed for a cruciform joint made of aluminium-lithium alloy 2198-T8 containing a butt weld joint fabricated by the friction stir welding process. In all tests crack propagated in parallel with the weld joint. Two material rolling directions were studied in relation to the welding and crack growth direction, showing that the material rolling direction affects the crack growth path. Specimens welded orthogonally to the rolling direction exhibit shorter fatigue life than specimens welded parallel to the rolling direction. A simple method is then developed for predicting crack growth rate. FEM is used to calculate the stress intensity factors and *T* stress, which are subsequently used to predict the crack propagation rates and trajectory. Influence of applied stress biaxiality on stress intensity factors, *T* stress, crack trajectory and growth rates have been analysed. Out-of-plane bending caused by the specimen geometry is also modelled. Predicted and test measured crack growth lives are in reasonably good agreement. Reasons for discrepancy are discussed.

Keywords: Biaxial stresses, weld joint, crack propagation, fatigue, finite element method, aluminium alloy

1. Introduction

Trend in aircraft structural design and manufacture has been moving towards more integral structures by extrusion, machining and welding rather than the traditional mechanical fastening. Fatigue crack growth behaviour under biaxial stresses is complex even without weld joints. Welding will add additional challenge in the analysis due to the process induced residual stress and changes in weld metal microstructure and mechanical properties.

Fatigue crack growth behaviour in aluminium welded joints has been investigated by experiments [e.g. 1-2], analysis [3], or modelling [4-7]. These research efforts were carried out under the uniaxial load cases. Current state-of-the-art in predicting crack growth rates is to use empirical crack growth laws and incorporate the effective stress intensity factor ratio.

Biaxial load fatigue crack growth behaviour (without weld) has been investigated [8-16] for various applied biaxial load ratios ($k = \sigma_y/\sigma_x$). In summary, qualitatively similar results have been reported for a number of steel and aluminium alloys that crack growth rate is higher at k=-1 (pure shear), than k=0 (uniaxial) followed by k=1. Difference in the growth rates in different biaxial stress ratios depends also on the magnitude of applied stress. In terms of crack growth trajectory, crack was kept straight at $k \leqslant 1$ [10-11]. Crack growth deviation was found to be dependent on the K_I/T ratio [13-15]. The maximum tangential stress criterion (function of K_I and K_{II}) is widely used for crack turning analysis [17]. The criterion is implemented in some FE codes, e.g. ABAQUS and FRANC2D/3D.

The influence of weld joint (in terms of welding residual stress and microstructure change) on crack

growth behaviour and their interaction with the applied biaxial loads should be investigated. With this motivation, experimental test was conducted on a cruciform specimen made of aluminium alloy 2198-T8 containing a butt weld joint and subject to biaxial loads [18], which is briefly summarised in Section 2. This paper focuses on the modelling of crack growth behaviour.

2. Summary of fatigue tests

Four cruciform specimens were manufactured and tested under biaxial stresses [18]. Geometry and dimensions are shown in Fig. 1. The specimens were made of aluminium-lithium alloy 2198-T8 and joined by the friction stir weld (FSW) process. The panel skin has nominal thickness of 1.6 mm and the weld area has a nominal thickness of 3.1 mm. The top side of the thicker pad-up area measures 50 mm wide and the bottom side (specimen flat surface) is about 62 mm wide, making the average width of the pad-up 56 mm. Specimen COI-BIAX1 and COI-BIAX3 had weld seam orthogonal to the material rolling direction, whereas the weld path in COI-BIAX2 and COI-BIAX4 was parallel to the rolling direction. Initial crack was introduced parallel to the weld seam orientation and located at the specimen geometric centre. It is in the thermal-mechanical affected zone (TMAZ) on the so-called weld retreating side, about 5 mm from the weld nugget centre. The weld centre is not placed in the specimen geometric centre. Details are in Table 1. All tests were performed at applied biaxial stress ratio k = 1 and maximum nominal stress 100 MPa acting on the 250-mm-wide loading arm area with the thickness of 1.6 mm. The cyclic stress ratio was 0.1 in both load directions. Details of test measured crack growth lives and growth path can be found in [18]. Test results are presented in Section 4 in comparison with predicted crack growth behaviour. Further studies were undertaken by performing numerical modelling on various k ratios (k=0-2) to investigate the influence of biaxial stress ratio on crack growth rate and trajectory.

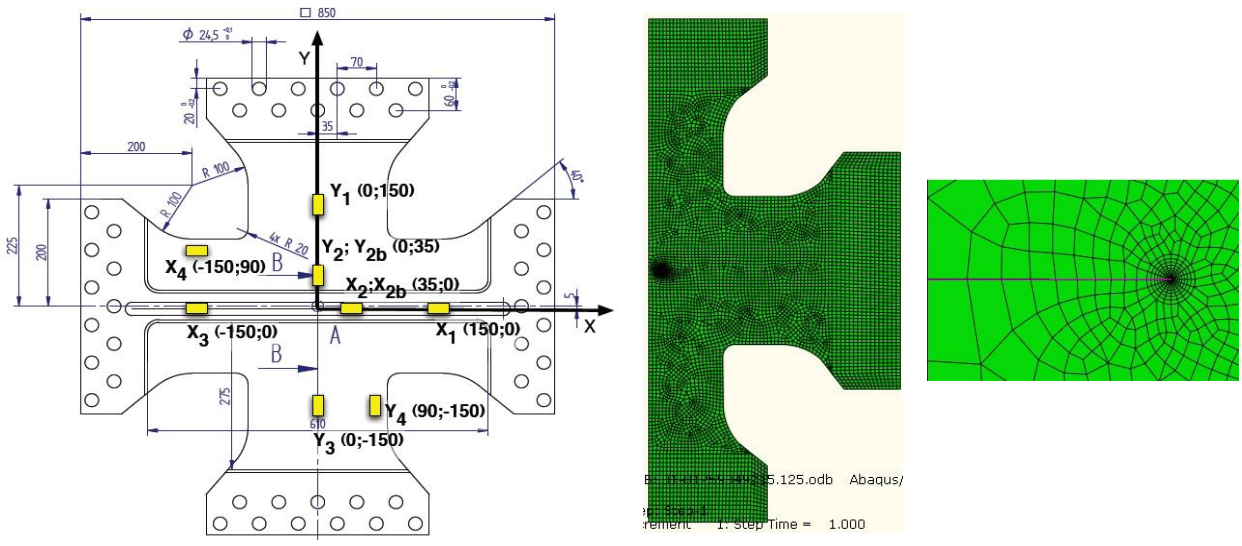

Fig 1. a) Test specimen and strain gauge locations (thickness of pad-up and griping area is 2.8 mm; skin pocket thickness is 1.6 mm); b) FE model of ½ specimen and local model of the crack tip.

Table 1 Test specimens and loading condition (applied stress σ_y = 40 kN)

Specimen No.	Weld orientation	Applied load ratio (k)
COI-BIAX1	Weld orthogonal to rolling direction	1
COI-BIAX2	Weld parallel to rolling direction	1
COI-BIAX3	Weld orthogonal to rolling direction	1
COI-BIAX4	Weld parallel to rolling direction	1

3. Computational analysis

3.1. FE model

Commercial code ABAQUS [19] was used. One half of the specimen was modelled using the second-order 8-node quadrilateral shell element. All elements are offset to the back surface (flat surface) to model the thickness variation in the pad-up and clamping areas. Due to the thickness change in the pad-up and four load-end clamping areas, there is considerable out-of-plane bending deformation even the panel is subjected to in-plane tensile load. This secondary bending can cause variation in the stress intensity factors (SIF). Therefore, prior to performing the fracture mechanics analysis, crack-free specimen was modelled first to verify the FE model against the strain gauge measurement at locations indicated in Fig. 1a. To model the secondary bending more accurately, 3D solid elements were used to provide a benchmark solution to the subsequent shell element models. In order to capture the bending deformation more accurately four elements are used through the 1.6 mm thickness. Out-of-plane deformation and strains were also calculated by the shell element model. Calculated strains and deformation agree with the 3D model output. Model geometry detail is given in Table 2.

Table 2 Configurations in FE models (unit: mm)

Configuration	a_o	h	t_1	t_2
1	10	30	2.80	1.60
2	20	56	3.11	1.55

Note: Configuration 1 is for numerical model only; Configuration 2 has the same dimension as the test specimen; a_o is half initial crack length, h is the pad-up width; t_1, t_2 are the pad-up and skin pocket thickness, respectively.

3.2. Fracture mechanics analysis

SIF is calculated using the interaction integral method available in the ABAQUS, which is similar to the *J*-integral method. FE model with an initial crack is shown in Fig. 1b. The middle nodes of the rosette elements around the crack tip are moved to the quarter-point position in order to model the crack tip stress singularity more accurately. User can instruct the ABAQUS code to extract the K_I, K_{II} and *T*-stress for each given crack length using the integration integral technique and then predict the crack propagation trajectory using the maximum tangential stress criterion. Subsequent crack configuration will be implemented by the user to manually extend the crack tip in the predicted direction by a specified crack extension increment. Subsequently, the area around the crack path will be re-meshed and the calculation of the SIF and crack growth angle repeated until a user-defined or critical crack length is reached. Calculated SIF (K_I) is normalised by the crack length and applied stress perpendicular to the crack plane, σ_y, to find the β factor:

$$\beta = \frac{K_I}{\sigma_y \sqrt{\pi a}} \qquad (1)$$

The β vs. a relation is then used in conjunction with the measured weld metal da/dN vs. ΔK data for life prediction. For variable amplitude loading with the same biaxial load ratio (k), ΔK for a specific load cycle can be found by multiply β by the applied stress range perpendicular to the crack growth path ($\Delta\sigma_y$). Weld metal crack growth rate (da/dN vs. ΔK) was measured under uniaxial-load [20] using “middle crack tension” geometry specimen, M(T), made of the same alloy and same welding

process. The weld was perpendicular to the applied load direction. Hence, the weld metal microstructure should be the same as that of the cruciform. Crack growth rates in the M(T) were obtained from constant amplitude load tests at R = 0.1.

4. Results and Discussion

4.1 Deformation, strain and stress

Due to the secondary bending effect the panel exhibits out-of-plane deformation even the load is in-plane. Calculated stress contours show a double curvature shaped deformation Fig 2. Positive deformation on the face of the pad-up side means bending towards the pad-up side. The maximum out-of-plane displacement is just outside the pad-up area with a value of 2.5 mm (k = 0) and 2.2 mm (k = 1). The panel centre (where the crack growth path is) is also bending towards the pad-up side with smaller displacement of 1.8 mm (k = 0) and 1.5 mm (k = 1). The bending deformation shown in Fig 2 is under the applied load of 40 kN (equal to a stress of 100 MPa in the loading arm of 1.6 mm thickness). The FE model shows that bending magnitude depends on the applied stress as well as the biaxial stress ratio. Under the same y-axis applied load, uniaxial loading results in more out-of-plane deformation (k = 0, Fig. 2a) than that by equal-biaxial case (k = 1, Fig. 2b), but the bending pattern is the same and the difference in bending magnitude is small. The out-of-plane deformation and in-plane strains were calculated using both 3D solid elements and 2D shell element; calculated values agree with each other. Therefore the thin-shell elements are employed in the crack growth models to reduce the computational cost. Computed strains agree well with the measured at most of the strain gauge positions, and the computed deformation pattern agrees with that described by the distributions of the strain gauges.

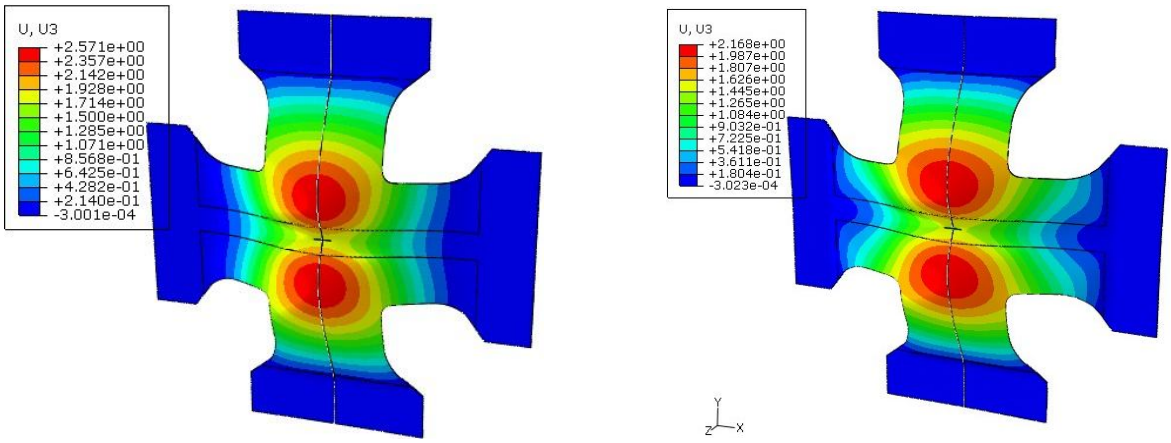

Fig. 2 Calculated out-of-plane deformation by 3D FE model under applied stress 100 MPa (figure showing the pad-up face): a) uniaxial load (k = 0); b) biaxial load (k = 1)

4.2 Stress intensity factors

Four biaxial load ratios (k = 0, 0.5, 1, 2) were modelled at the applied stress σ_y=100 MPa acting on the loading arm of the cross section of 250 mm width x 1.6 mm thickness. This stress level is reduced in the wider section and will be further reduced at the thicker pad-up area where the crack propagates. Calculated σ_y in the pad-up area is about 50 MPa [21]. Cases were also modelled for k = 1, 2 at applied stress σ_y = 50 MPa. Calculated mode I stress intensity factors (K_I) at the different k

are presented in Fig. 3a. As the k increases, K_I will decrease. Since crack growth rate is an exponential function of ΔK and the Paris law exponent is usually 2-4 for aluminium alloys, crack growth rate will be significantly reduced as the biaxial load ratio increases. This is reported in test measured crack growth rates [11-12]. Fig. 3b shows the non-dimensional K, i.e. the β factor by eq. (1), which is independent of the y-axis applied stress σ_y.

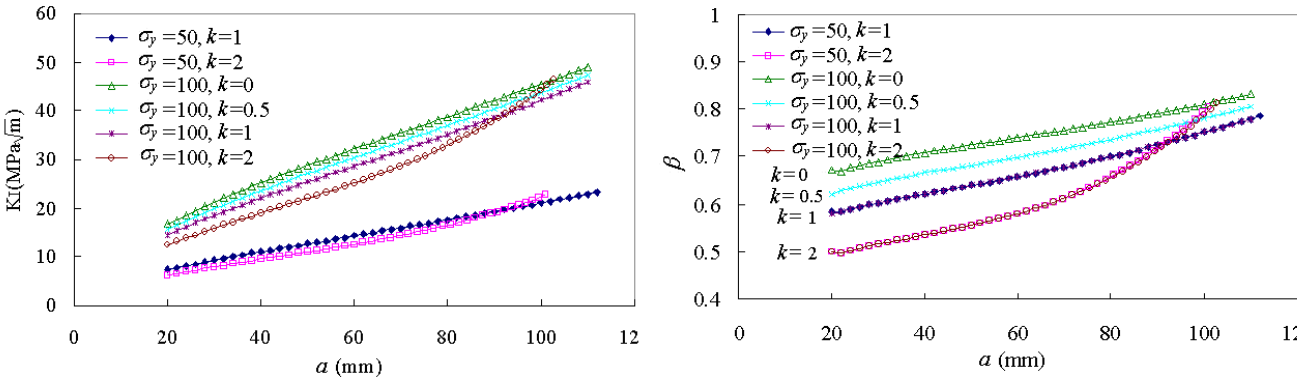

Fig. 3 FE calculated stress intensity factors under various biaxial load ratios: a) K_I; b) β factor.

4.3 Prediction of crack growth life and trajectory

Fig 4 shows comparison of predicted and test measured crack growth lives. There are three possible reasons for underestimating the crack growth life. 1) Residual stress effect was accounted for by using the measured *da*/*dN* data of an M(T) specimen fabricated by the same welding process with crack growing parallel in weld (perpendicular to the load direction) [20]. The magnitude of residual stresses are not exactly the same due to different geometry and size between the M(T) and cruciform specimens. However, since the welds were parallel to the crack growth path in both specimens, the transverse residual stress, which is perpendicular to the crack plane, is low in magnitude compared to the longitudinal residual stress parallel to the crack plane. Therefore the effect of transverse residual stress on crack growth is considered to be small. 2) Influence of weld metal microstructure change on crack growth rates is also contained in the measured *da/dN* data from the M(T). However, crack in the M(T) had was in the weld nugget centre, but the cruciform specimens had weld in the weld TMAZ zone about 5 mm from the weld nugget centre. Microstructures in these two zones are different, and this difference in microstructure is not modelled in this work. 3) FE calculated y-axis strains are found to be higher than the test measurement, leading to higher SIF values and, consequently, shorter predicted crack growth life.

Fig. 4b shows the measured and predicted crack growth trajectories. Calculated crack trajectory is modelled by crack extension under static loading rather than cyclic loading. Crack turning is predicted by the maximum tangential stress criterion in the Abaqus code. Calculated maximum crack deviation for “Configure 1” is about 3 mm, which is larger than that of “Configuration 2 (test specimen geometry)”. The difference is caused by the width of the pad-up, which is 30 mm and 56 mm, respectively. Narrower pad-up (30 mm) encourages crack deviation into the thinner skin. Although crack turning is predicted by the FE modelling, calculated crack deviation magnitude is smaller than the test measured Fig. 4b. Predicted deviation also started at longer crack length (120

mm) comparing to the test results [18].

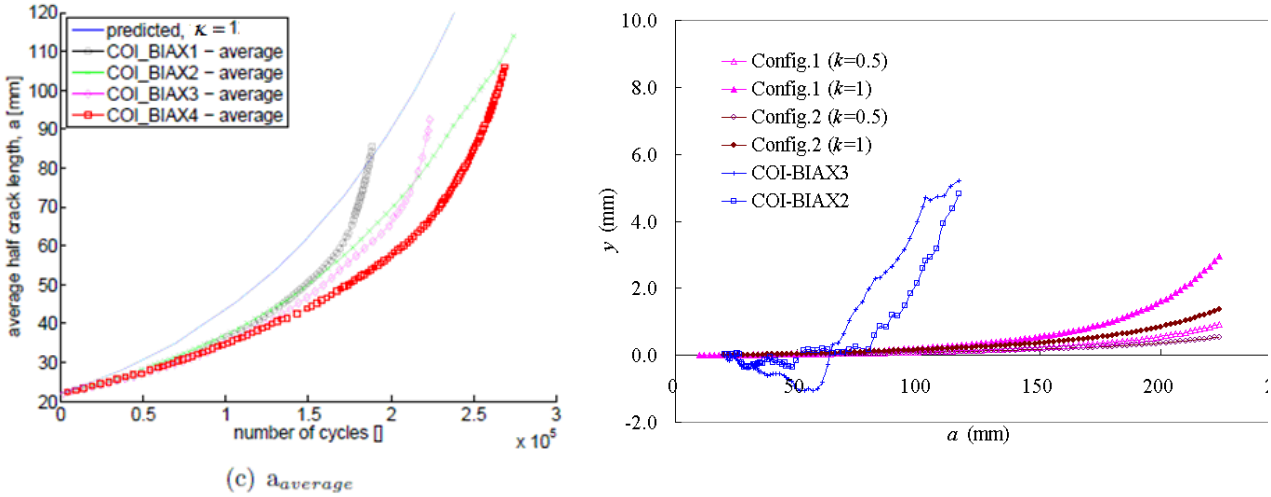

Figure 4 a) predicted crack growth life and b) trajectory, and comparison with test measurement.

4.4 Discussion based on further FE analysis

4.4.1. Influence of biaxial stress ration on crack growth rate

Mode II SIF (K_{II}) was calculated using the Abaqus interactive integration method [19]. Model shows that K_{II} is virtually zero for k = 0, 0.5 & 1. For k = 2 and at longer crack lengths (a > 60 mm), K_{II} has very low values of 0.3-0.6 MPa√m [21]. Since all specimens were tested at k = 1, K_{II} influence can be neglected. According to the literature, influence of lateral stress σ_x on crack growth rates is negligible in aluminium sheets [10] and steel alloys [11] under constant amplitude loading, if biaxial load ratio (k) is within the range of -1.5 to 1.75. Note work reported in [10-11] was for plain metals (no welds). In the test measured crack growth and life prediction analysis presented in Fig. 4, changes in weld metal properties and weld residual stresses are accounted for by using the weld metal property of da/dN vs. ΔK data.

4.4.2. Influence of biaxial stress on crack trajectory

It has been shown that applied mixed mode loading is the main cause of a major loss of directional stability [14]. Apart from K_{II}, the elastic T-stress (a stress quantity parallel to the crack face) is also a useful quantity for assessing the crack stability and kinking for linear elastic materials. T-stress is directly proportional to the load applied to the cracked part and also depends on its geometry. It has been shown that for small amount of crack growth under the mode I loading, a straight crack path will be stable when T < 0, whereas the path will be unstable when T > 0 [22]. In this paper T-stress is calculated by the Abaqus code. Fig 5 shows calculated T-stress normalised by the applied stress; positive values indicate the likelihood of crack deviation. For the test case of k = 1, T-stress is about the same magnitude of the applied stress when half crack length is beyond 40 mm. However, it is also reported that some cracks are directionally stable when T > 0 [15].

To explain the observed crack turning (Fig. 4b), we use the T_R parameter as defined in Eq. (2) [23]:

$$T_R = \frac{T}{\sigma_x} \qquad (2)$$

where $\sigma_x = K_I/\sqrt{(2\pi r)}$ is the crack tip *local* stress component parallel to the crack plane and r is the distance to the crack tip. Pook [23] recommends that T_R is evaluated at a characteristic distance $r = r_{ch}$, which is the same order of a microstructural feature size. Taking r_{ch} = 0.0159 mm [23], using Eq. (2) and the MN-m units, find:

$$T_R = 0.01\frac{T}{K_I} \qquad (3)$$

According to [15, 23], when T_R exceeds its critical value T_{RC}, crack will deviate from its original path. In [15] Pook stated a typical T_{RC} value suitable for many metals as at least 0.021 (unit: $m^{-1/2}$).

Calculated T_R values for various k ratios are presented in Fig. 6. For the test case of k =1, at half crack length a = 50 mm, calculated T_R according to Eq. (3) is 0.038 $m^{-1/2}$, which is greater than the suggested T_{RC} value. Therefore, under *tension* biaxial loading at ratio k=1, calculated crack deviation was expected, however the magnitude of deviation is small, just 3 mm away from the original crack path (Fig. 4b), which is not a major loss of directional stability. Measured crack deviation was nearly doubled at 5 mm, and crack deviation started at much earlier in shorter crack length (Fig. 4b). This discrepancy could be due to the changes in weld metal microstructure and the anisotropy property of the 2198-T8 alloy as reported in [24-25]. Material microstructure change and anisotropy properties were not modelled in this study.

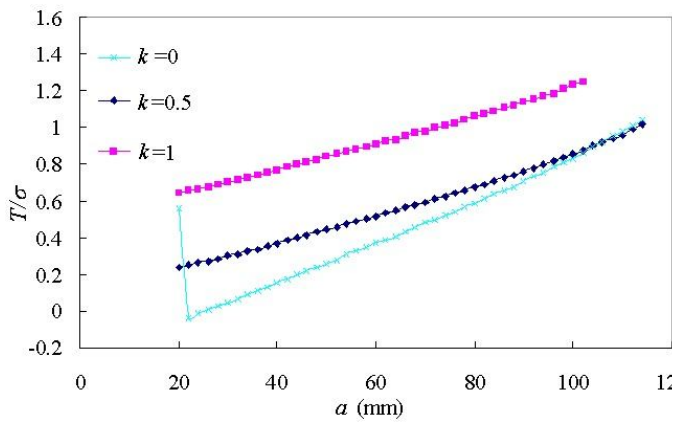

Fig. 5 T-stress (normalised by applied stress σ_y).

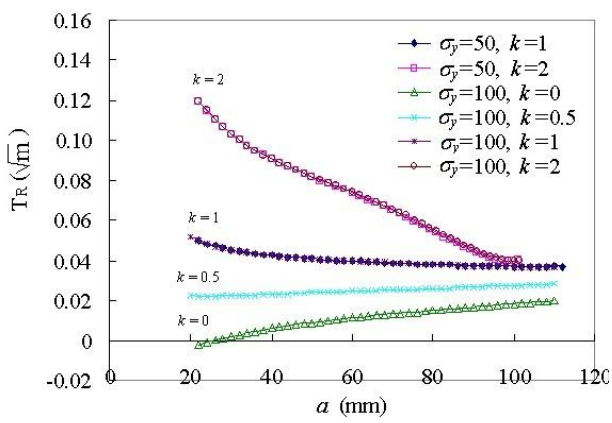

Fig. 6 Calculated T_R distribution.

4.4.3. Influence of weld-induced residual stress

Test measured crack turning is more pronounced than FEA predicted, Fig. 4b. One possible reason could be that the longitudinal residual stresses were present in the test specimen making the *actual* biaxial load ratio much higher than 1, but this residual stress was not considered in the prediction model. In this work, K_I, K_{II} and T are calculated for biaxial load ratio k = 1 without considering the welding-induced residual stresses. If the longitudinal residual stress (e.g. 150 MPa maximum magnitude according literature) is added to the applied lateral stress σ_x, then the biaxial stress ratio k

is about 2.5. According to the literature, no crack turning was observed at k = 0, 0.5 and 1 [11], but crack will turn when k > 2 [10]. Therefore there is more crack deviation in the test than predicted.

We have used the weld metal *da/dN* data for the life prediction presented in Fig. 4a, in which residual stress effect is included in the coupon tests to acquire the *da*/*dN* data. However, we have not used the combined lateral stresses ($\sigma_{x_applied} + \sigma_{x_residual}$) in the calculation of the crack growth driving forces (K_I, K_{II}, and T-stress); this could affect the magnitude of crack turning. Further, although residual stress effect is reflected in the measured crack growth data of welded M(T) sample with a same transverse weld, because the cruciform specimen has different geometry and dimension, welding induced residual stresses in the cruciform specimen could be different from those in the M(T).

4.4.4. Effect of weld metal microstructure and anisotropic material property

Although mixed mode loading is believed as the primary cause of loss of directional stability by many researchers, microstructure changes in the weld metal also contribute to the crack directional instability. In the test specimens, initial crack plane was 5 mm from the weld nugget centre meaning that material properties are different for each side of the crack plane, i.e. weld nugget property on one side of the crack and TMAZ/HAZ on the other side.

Furthermore, alloy 2198-T8 has highly anisotropic microstructures [24-25]. According to Yates et al. [14], highly anisotropic microstructures can also lead to significant changes in crack orientation, but more often in a zigzag pattern maintaining the overall mode-I trajectory. Crack path deviation triggered by material property irregularity can be enhanced by the applied biaxial loads as demonstrated by the test results in Fig. 4b. Test measured crack growth route shows a zigzag path when a < 70 mm [18]. However, predicted crack deviation is in one direction. Crack turning angle is determined by the sign of K_{II}, which is function of applied stress and geometry but not the material property. It is worth noting that crack deviation was not observed in M(T) under uniaxial loading with weld perpendicular to the loading direction, but observed in the cruciform specimen under biaxial loads; this is due to the influence of K_{II} and T-stress.

4.4.5. Other influential factors

Welding-induced distortion was significant in magnitude [18]. In the tests initial distortion was corrected by applying clamping forces at the specimen's four loading ends. This will affect the initial stress condition in the specimen. The initial distortion was not completely illuminated by clamping. However, the initial out-of-plane deformation and clamping force induced initial stresses were not modelled. This could affect the accuracy in the predicted crack growth rates and trajectory. Test specimens involved two material rolling directions in relation to the welding and crack growth direction, showing that the material rolling direction affects the crack growth path. This is caused by material anisotropy [24-25], weld microstructure change, and residual stresses in both material directions. However, these effects are not modelled. Research also shows that crack location within weld, e.g. in the nugget centre or the HAZ, will also influence the crack growth rates considerably [26].

5. Summary and Conclusions

Finite element analysis was performed for a cruciform specimen containing weld joint and being subjected to biaxial cyclic loads. First, stress distribution and out-of-plane deformation are determined to assess the effect of secondary bending on fracture mechanics parameters. Second, influence of biaxial stress on crack growth behaviour is modelled, and fatigue crack growth life is predicted using calculated stress intensity factors and weld metal crack growth rates measured from M(T) specimens made of the same material and same welding process. Main conclusions are:

1. Mode-I stress intensity factor (SIF) decreases as the biaxial load ratio k increases. Comparing to the uniaxial load case ($k = 0$), reduction in SIF is 12% ($k = 1$) and 24% ($k = 2$).
2. For $k \leq 1$, no crack path deviation is predicted by the analysis; models show very small deviation when a crack is longer than half of the panel width. For $k = 2$, small deviation is predicted. The model solution is in agreement with the fracture mechanics theory based on the mode II SIF and elastic T stress.
3. Test observed crack turning is larger than model prediction. This could be due to a few complex factors that are not considered in the present FE model, such as weld metal microstructure, anisotropic material properties, and residual stress in the weld longitudinal direction.

Acknowledgement

The authors are grateful for the financial support from the European Union through its Sixth Framework Programme under the “cost effective integral metallic structures” project. They also thank Drs. Richter-Trummer and Dos Santos at Helmholtz-Zentrum Geesthacht Germany for providing test data. The modelling work was conducted at Cranfield University.

References

1. Bussu G, Irving PE. The role of residual stress and heat affected zone properties on fatigue crack propagation in friction stir welded 2024-T351 aluminium joints, Int J Fatigue, 25(2003): 77-88.
2. Pouget G, Reynolds AP. Residual stress and microstructure effects on fatigue crack growth in AA2025 friction stir welds, Int J Fatigue, 30(2008): 463-472.
3. Glinka G. Effect of residual stresses on fatigue crack growth in steel weldments under constant and variable amplitude load. In: Fract. Mech., ASTM STP 677, American Society for Testing and Materials, 1979, pp. 198-214.
4. Beghini M, Bertini L, Vitale E. Fatigue crack growth in residual stress fields: experimental results and modelling. Fatigue Fract Engng Mater Struct 1994; 17: 1433-1444.
5. Ghidini T, Dalle Donne C. Fatigue crack propagation assessment based on residual stresses obtained through cut-compliance technique, Fatigue & Fracture of Eng Mater & Struct, 30(2006): 214-222.
6. Fratini L, Pasta S, Reynolds AP, Fatigue crack growth in 2024-T351 friction stir welded joints: longitudinal residual stress and microstructural effects. Int J Fatigue 2009; 31: 495-500.
7. Servetti G, Zhang X. Predicting fatigue crack growth rate in a welded butt joint: the role of effective R ratio in accounting for residual stress effect. Eng Fract Mech 76 (2009) 1589-1602.
8. Cotterell B. International J of Fracture Mechanics, 2 (1966): 526-533.

9. Leevers PS, Radon JC, Culver LE. J of mechanics and Physics of Solids, 24 (1976), 381-395.
10. Liu AF, Allison JE, Dittmer DF, Yamane JR. Effect of biaxial stresses on crack growth, Fracture Mechanics, ASTM STP 677, CW Smith ed., ASTM, 1979, pp. 5-22.
11. Brown MW, Miller KJ. Mode I fatigue crack growth under biaxial stress at room and elevated temperature, ASTM STP 853, 1985, 135-152.
12. Eftis J, Jones D L, Liebowitz H. Load biaxiality and fracture: synthesis and summary. Engineering Fracture Mechanics, 36 (1990): 537-574.
13. Llopart L, et al. Investigation of fatigue crack growth and crack turning on integral stiffened structures under mode I loading, Engineering Fracture mechanics, 73 (2006):2139-2152.
14. Yates JR, et al. Crack paths under mixed mode loading, Engineering Fracture mechanics, 75 (2008): 319-330.
15. Pook LP, Five decades of crack path research, Engineering Fracture mechanics, 77 (2010):1619-1630.
16. Huang W-L, Zhu W, Zhao J-P. Effect of lateral load on fatigue growth rate of surface cracks in welded joints, Int J Pres Ves & Piping, 69 (1996): 59-64.
17. Erdogan F, Sih G. On the crack extension in plates under plane loading and transverse shear, J of Basic Engineering, 85(1963): 519-527.
18. Richter-Trummer V, Dos Santos J. Biaxial fatigue crack propagation testing, Technical Report, 2010, Helmholtz-Zentrum Geesthacht, Institute of Materials Research, Geesthacht, Germany.
19. Anonymous. ABAQUS/Standard User's Manual, V6.5. Hibbitt, Karlsson & Sorensen, 2005
20. Ma Y-E, Irving PE, Zhang X, Servetti G, Effects of residual stresses on fatigue crack propagation in friction stir welded 2198-T8 and 2195-T8 Al-Li alloy joints, Proc 12th Int Conf. in Fracture (ICF12), July 2009, Ottawa.
21. Zhang H. Numerical Modelling of Crack Propagation in a Friction Stir Welded Cruciform Specimen. MSc Thesis, Cranfield University, 2009.
22. Cotterell B, Rice JR. Slightly curved or kinked cracks, Int J of Fracture, 16 (1980): 155-169
23. Pook, LP. Crack Paths. WIT Press, Southampton. 2002 (Eq. 4.4).
24. Cavaliere P, De Santisa A, Panellaa F, Squillaceet A. Effect of anisotropy on fatigue properties of 2198 Al–Li plates joined by friction stir welding, Engineering Failure Analysis, 2008.
25. Cavaliere P, Cabibboc M, Panellaa F, Squillace A. 2198 Al–Li plates joined by friction stir welding: mechanical and microstructural behavior, Materials and Design 30 (2009): 3622–3631
26. Pacchione M, Werner S, Ohrloff N. Design principles for damage tolerant butt weld joints for application in the pressurized fuselage, Proceedings 24th Symposium of International Committee on Aeronautical Fatigue (ICAF 2007), Naples, May 16-18, 2007

Ultrasonic Spot Welding of Lightweight Alloys

V.K. Patel[1], S.D. Bhole[1], D.L. Chen[1,*]

[1]Department of Mechanical and Industrial Engineering, Ryerson University, M5B 2K3, Canada
*Corresponding author: dchen@ryerson.ca

Abstract The structural applications of lightweight alloys in the automotive and aerospace industries inevitably involve welding and joining of challenging dissimilar Mg-to-Al and Mg-to-steel while guaranteeing safety and structural integrity. Sound dissimilar lap joints were achieved via ultrasonic spot welding (USW) – an environment-friendly solid-state joining technique. The addition of Sn interlayer during USW effectively blocked the formation of brittle $Al_{12}Mg_{17}$ intermetallic compound in the Mg-to-Al dissimilar joints without interlayer, and led to the presence of a distinctive composite-like Sn and Mg_2Sn eutectic structure in both Mg-to-Al and Mg-to-HSLA (high strength low alloy) steel joints. The lap shear strength of both types of dissimilar joints with a Sn interlayer was significantly higher than that of the corresponding dissimilar joints without interlayer. Failure during the tensile lap shear tests occurred mainly in the mode of cohesive failure in the Mg-to-Al dissimilar joints and in the mode of partial nugget pull-out in the Mg-to-HSLA steel dissimilar joints. In particular, the addition of Sn interlayer resulted in energy saving since the welding energy required to achieve the maximum strength decreased from 1250 J to 1000 J in the Mg-to-Al joints and from 1750 J to 1500 J in the Mg-to-HSLA steel joints.

Keywords Magnesium alloy; Ultrasonic spot welding; Intermetallic compounds; Tin interlayer

1. Introduction

Various industries, especially automotive and aerospace sectors, have a pressing need for structural components that are lighter and stronger, aiming to improve energy efficiencies and reduce anthropogenic environment-damaging emissions and pollution while guaranteeing safety and reliability. Aluminum (Al) and steel have already a wide variety of structural applications in the transportation industry due to their excellent properties, such as good ductility, formability and thermal conductivity. To reduce pollution and save energy [1], ultra-lightweight magnesium (Mg) alloy has increasingly been used in the vehicle fabrication due to its lower density, higher specific strength and stiffness, excellent size stability and acceptable process ability [2]. The structural application of Mg alloys inevitably involves welding and joining of similar Mg-to-Mg alloys and dissimilar Mg-to-Al and Mg-to-steel. In the auto body manufacturing resistance spot welding (RSW) has been a predominant process [3,4]. Since the differences in properties among these metals are large, like melting point, electric conductivity and thermal physical properties, etc., it is fairly challenging to join Mg-to-Al and Mg-to-steel [5,6]. Also, the high-energy consumption and the requirement for frequent electrode maintenance have limited its prevalent application to the Mg-to-Al alloys. Furthermore, in the welding of dissimilar metals a rapid formation of brittle intermetallic compounds (IMCs) occurs, which can seriously degrade the mechanical properties of welded joints [3].

Recently attention has been paid to two solid-state welding processes, namely friction stir spot welding (FSSW) and ultrasonic spot welding (USW), because the liquid phase reaction in the fusion zone during RSW can be avoided. Although FSSW has the potential to produce effective welds between dissimilar materials, the relatively long welding cycle (or time) would be a limiting factor for its widespread adoption in automotive manufacturing [4]. Another solid-state welding technology of USW is able to produce coalescence via a simultaneous application of localized high-frequency vibratory energy and moderate clamping forces [7,8]. In comparison with FSSW, USW has been shown to have a shorter weld cycle (typically <0.4 s) and produce high quality joints that are stronger than FSSW when compared on basis of the same nugget area [9,10]. Besides, the

normal FSSW leaves an exit hole after welding [11]. From the point of view of energy consumption, USW is far more advantageous. For example, welding of aluminum alloys using a USW process consumes only about 0.3 kWh per 1000 joints [4,12], compared to 20 kWh with RSW, and 2 kWh with FSSW [4].

Our previous studies [13] and other investigations [14-17] showed that in the joining of dissimilar Mg-to-Al alloys, the formation of IMCs of $Al_{12}Mg_{17}$ and Al_3Mg_2 seems to be unavoidable. Since the mechanical properties of the welded joints are closely related to the formation of the brittle intermetallic layer [18], it is difficult to obtain a strong joint between Mg and Al alloys. In the study of dissimilar Mg-to-steel joint, Santella *et al*. [19] and Schneider *et al*. [20] reported that Mg and steel do not react with each other and the joint could be easily broken by hand. To improve the mechanical properties of the Mg-to-Al and Mg-to-HSLA steel joints, Chowdhury *et al*. [21] (FSSW) and Xu *et al*. [22] (RSW) have tried to weld Mg-to-Al and Mg-to-HSLA steel joint, respectively, using adhesive placed in-between the faying surface. However, the application of adhesive is a time consuming process. Some researchers have used Zn as an interlayer between Mg and Al alloys [23,24] and Mg and HSLA steel [19,25] for improving the mechanical properties of the dissimilar joints. Others, e.g., Liu *et al*. [26] and Qi and Liu [27] in the tungsten inert gas (TIG) and hybrid laser-TIG welding of Mg-to-Al alloys, respectively, and Liu *et al*. [28] in the hybrid laser-TIG welding of Mg-to-steel, have used Sn as an interlayer and also showed the improvement of the mechanical properties. However, it is unclear how Sn interlayer would affect the microstructure of USWed Mg-to-Al and Mg-to-HSLA steel joints, and if the intermetallic layer would form, and whether Sn interlayer would improve the mechanical properties of the joints. This study was, therefore, aimed to identify the effect of the Sn interlayer on the microstructure and lap shear tensile properties of USWed AZ31B-H24-to-Al5754-O and to-HSLA steel. The selection of Sn in the present study was also based on Mg-Sn, Al-Sn and Fe-Sn binary phase diagrams [29-31], which showed that Sn may interact with Mg and generated IMCs, while Sn might be dissolved into Al and Fe to form solid solution of Sn-Al and Sn-Fe. Furthermore, it was selected on the basis of the findings that Sn improved the wettability of Mg, Al and Fe during the welding process [26,28] and also refined the grain size in the Mg alloy [28,32].

2. Material and Experimental Procedure

In the present study, commercial 2 mm thick sheet of AZ31B-H24 Mg alloy (composition in wt.%: 3Al, 1Zn, 0.6Mn, 0.005Ni, 0.005Fe and balance Mg), 1.5 mm thick sheet of Al5754-O Al alloy (3.42Mg, 0.63Mn, 0.23Sc, 0.22Zr, and balance Al), and 0.8 mm thick sheet of high strength low alloy (HSLA) steel (0.06C, 0.227Si, 0.624Mn, 0.006P, 0.004S, 0.013Ni, 0.041Cr, 0.005Mo, 0.044Cu, 0.039Al, 0.003Ti, 0.021Nb and balance Fe) were selected for the USW. The specimens of 80 mm long and 15 mm wide were sheared, with the faying surfaces ground using 120 emery papers, and then washed using acetone followed by the ethanol and dried before welding. During welding a 50 μm thick pure Sn interlayer was placed in-between the work pieces of Mg/Al and Mg/HSLA steel samples. The welding was conducted with a dual wedge-reed Sonobond-MH2016 HP-USW system. The samples were welded at an energy input ranging from 500 to 2500 J at a constant power setting of 2000 W, an impedance setting of 8 on the machine, and a pressure of 0.414 MPa. Four samples were welded in each welding condition. Two of them were used for microstructural examination and microhardness tests, and the other two were used for the lap shear tensile tests. Cross-sectional samples for scanning electron microscopy (SEM) were polished using diamond paste and MasterPrep. A computerized Buehler microhardness testing machine was used for the micro-indentation hardness tests diagonally across the welded joints using a load of 100 g for 15 s except for the thin IMC interlayer, where a load of 10 g was used for 15 s. The mean value of three indentations along the IMC interlayer was taken for a better accuracy with the low

indentation load of 10 g. To evaluate the mechanical strength of the welded joints and establish the optimal welding conditions, tensile shear tests of the welds were conducted to measure the lap-shear failure load using a fully computerized United testing machine at a constant crosshead speed of 1 mm/min at room temperature in air. In the tensile lap shear testing, restraining shims or spacers were used to minimize the rotation of the joints and maintain the shear loading as long as possible. X-ray diffraction (XRD) was carried out on both matching fracture surfaces of Mg-Al and Mg-HSLA steel sides after tensile shear tests, using CuKα radiation at 45 kV and 40 mA. The diffraction angle (2θ) at which the X-rays hit the samples varied from 20° to 100° with a step size of 0.05° and 2 s in each step.

3. Results and Discussion

3.1 Microstructural evaluation

Microstructural characterization was conducted across the weld line of the samples. Fig. 1(a) and (b) show microstructures at the center of weld nugget of USWed Mg/Al and Mg/HSLA steel joints without a Sn interlayer, respectively. Sound joints were obtained since no large defects were present, such as crack or tunnel type of defects. It is seen from Fig. 1(a) that there was a heterogeneously distributed IMC layer between the Mg and Al alloy sheets. In our previous study [6] of USW of Mg/Al alloys without Sn interlayer, the non-uniform IMC layer had a solidified microstructure containing the brittle phase through the eutectic reaction, liquid→$Al_{12}Mg_{17}$+Mg. In the USWed Mg/HSLA steel joint, as there was no interaction between Mg and Fe, the interface of AZ31B-H24 and HSLA steel was clear without transitional zone, as shown in Fig. 1(b). Due to a large difference of hardness, the sections of Mg alloy and steel were not in the same level in the process of metallographic sample preparation, indicating by white arrows where some hydroxides produced, which will be confirmed by EDS analysis later. Fig. 1(c) and (d) show the welded joints of Mg/Al and Mg/HSLA steel with a Sn interlayer, which could be clearly seen. However, this interlayer was no longer pure Sn interlayer after USW. It became a layer of Sn-Mg_2Sn eutectic structure, which will be identified in the following sections.

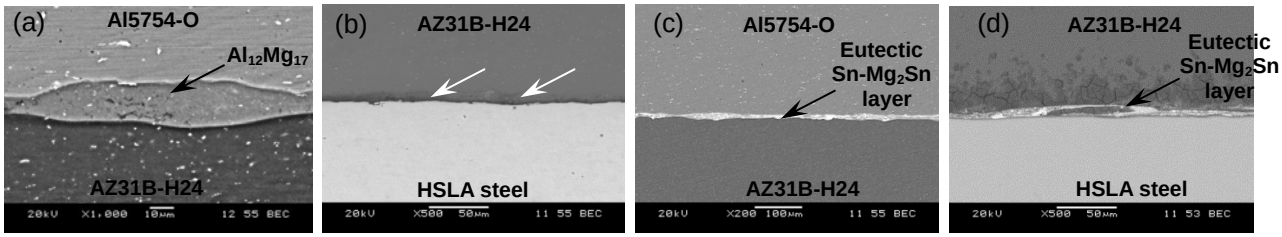

Figure 1. Microstructure of the dissimilar USWed joints made with a welding energy of 1000 J, (a) Mg/Al and (b) Mg/HSLA steel without a Sn interlayer, and (c) Mg/Al and (d) Mg/HSLA steel with a Sn interlayer.

3.2 Energy-dispersive X-ray spectroscopy (EDS) analysis

Fig. 2(a) and (b) show the SEM image at the center of the nugget zone (NZ) of USWed Mg/Al with a Sn interlayer, and its EDS line scan, respectively. The chemical composition (in at.%) at points A and B was 64.4% Mg - 36.4% Al - 1.2% Sn and 63.5% Mg - 21.8% Al - 14.7% Sn, respectively, which suggests that the dark area (A) had less Sn than the white area (B). Fig. 2(c) and (d) show the SEM image at the center of the NZ of USWed Mg/HSLA steel with a Sn interlayer, and its EDS line scan, respectively. The chemical compositions (in at.%) at points C (Fig. 2(c)) was 70.3% Mg-29.7% Sn, suggesting that only Mg and Sn elements were present in the interlayer. The

chemical composition (in at.%) at point D was 62.3% Mg-37.7% O, which suggested the presence of galvanic corrosion product by forming magnesium hydroxide of $Mg(OH)_2$ during the metallographic sample preparation [33,34]. The occurrence of galvanic corrosion was attributed to the large difference between Mg and Fe positioned in the galvanic series. In both Fig. 2(a) and (c), the IMC layer displayed a composite-like eutectic structure at the center of the weld nugget, where the Sn-containing fine white particles were distributed homogeneously or as a network in the interlayer. EDS line scan revealed that the intensity of Al was lower than that of Mg in the NZ of the USWed Mg/Al joint (Fig. 2(b)), and little or no Fe present in the NZ of USWed Mg/HSLA steel (Fig. 2(d)). This was due to the higher solubility of Sn in Mg than Sn in Al and Sn in Fe. Therefore, these results (Fig. 2(d)) in conjunction with the Mg-Sn phase diagram [29] suggested the presence of Mg_2Sn phase, where the eutectic structure consisting of β-Sn (or Mg-Sn solid solution) and Mg_2Sn, which would occur at a temperature of as low as 203°C [29].

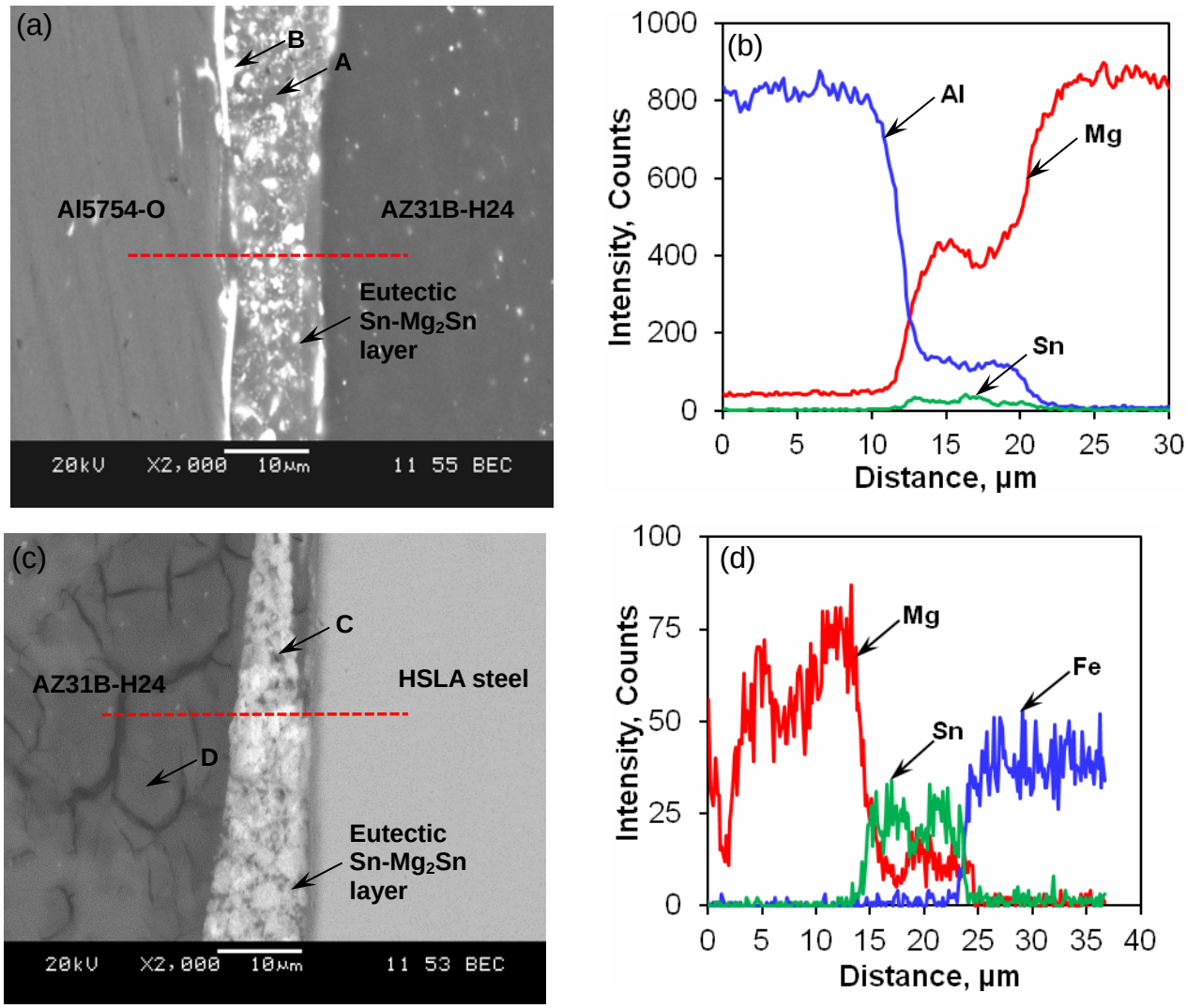

Figure 2. (a) SEM micrograph at the center of NZ of USWed Mg/Al joint and (b) EDS line scan across the interlayer in (a), (c) SEM micrograph at the center of NZ of USWed Mg/HSLA steel joint and (d) EDS line scan across the interlayer in (c) made at a welding energy of 1000 J.

In the USW, the simultaneous application of localized high-frequency vibratory energy and moderate clamping force leads to a fast relative motion and rubbing/friction heat at the interfaces [7,8] between Al-Sn (Mg/Al joint) or Fe-Sn (Mg/HSLA steel joint) and Mg-Sn (in both types of

joints), which would cause a potential melting and coalescence of Sn. In the presence of the Sn interlayer in the USW, Al and Sn in the Mg/Al joint, and Fe and Sn in the Mg/HSLA steel joint combine to form solid solutions, while Mg and Sn combine to form β-Sn and Mg_2Sn IMCs. The Mg_2Sn phase has an antifluorite-type (CaF_2) AB_2 crystal structure with a moderately high melting temperature of 770°C and a lattice parameter of a = 0.676 nm [35]. It is apparent that the large Mg_2Sn particles resulted from the eutectic reaction (L $\rightarrow$ β Sn + Mg_2Sn) when the temperature reached the eutectic temperature during USW. The addition of Sn to the lap joint was observed to refine the grain size in the fusion zone and the base Mg alloy [28,32] due to the presence of a eutectic Mg_2Sn particles, which restricts the growth of the Mg grains via the Zener pinning pressure (or pinning role). Furthermore, it also improves the wetability of Mg with Al and Fe during the welding process [26,28]. Thus, the surface tension of the liquid was reduced so that more liquid spreads evenly over the surface of the base metal.

3.3 X-ray diffraction analysis

To further verify the above microstructural observations, XRD patterns obtained on both matching fracture surfaces of Mg/Al and Mg/HSLA steel joints after tensile shear tests are shown in Fig. 3(a) and (b), respectively. It is clear that apart from strong peaks of Al on the Al side, Mg on the Mg side and Fe on Fe side, both Sn and Mg_2Sn appeared on both sides of welded joints. It is of interest to note that there was no single peak of $Al_{12}Mg_{17}$ IMCs in the USWed Mg/Al joint. On the other hand, in the Mg/HSLA steel joint Sn worked as an intermediate medium and reacted with both Mg and Fe. Thus, the addition of a Sn interlayer in-between the Mg/Al and Mg/HSLA steel sheets during USW led to the formation of solid solutions of Sn-Al (in the Mg/Al joint), Sn-Fe (in the Mg/HSLA steel joint) and Sn-Mg (in both Mg/Al and Mg/HSLA steel joints), as well as the Sn + Mg_2Sn eutectic structure (in both Mg/Al and Mg/HSLA steel joints). This is in agreement with the SEM observations shown Fig. 2(a) and (c), and EDS analysis shown in Fig. 2(b) and (d).

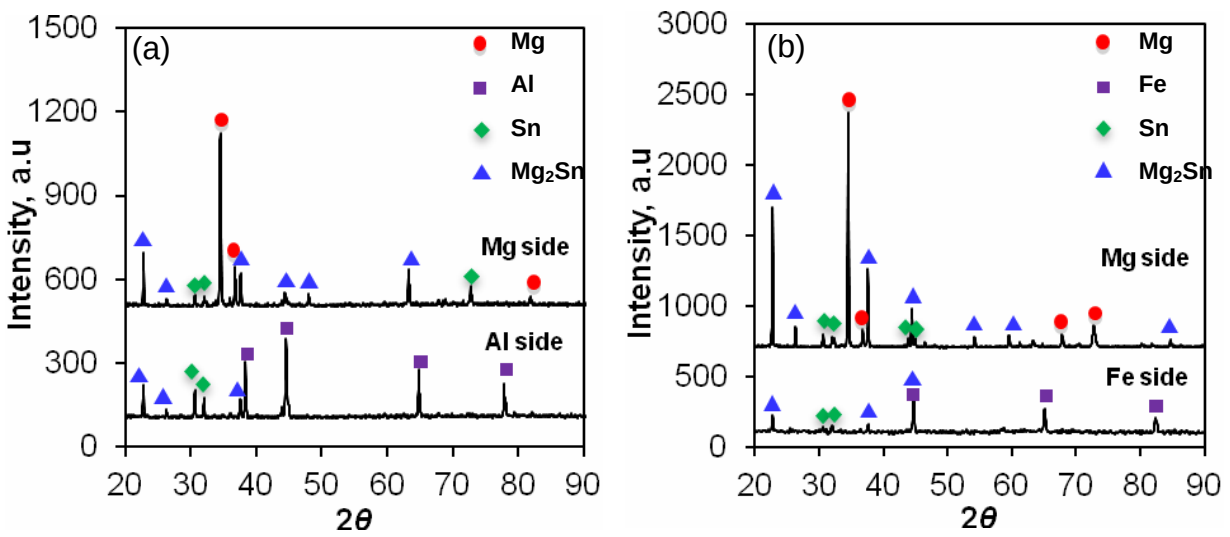

Figure 3. XRD patterns obtained from the matching fracture surfaces of USWed (a) Mg/Al and (b) Mg/HSLA steel joints made at a welding energy of 1000 J.

Furthermore, from our previous studies of USWed Mg/Al joint without any interlayer, lap shear failure occurred predominantly in-between the IMCs of $Al_{12}Mg_{17}$ and Al side [6], i.e., in the mode of "adhesive failure" [36]. However, the presence of Mg_2Sn and Sn eutectic structure on the both sides of the fracture surfaces indicated that the failure occurred mainly through the interlayer. This type of failure is called as the "cohesive failure" which is a desirable failure mode as it assures the use of more strain energy via the weaker part of the joint [36]. Indeed, failure in the USWed

Mg/HSLA steel joint with a Sn interlayer occurred even in the mode of partial nugget pull-out and partial "cohesive failure", giving rise to a higher tensile shear strength which will be seen in the following section.

3.4 Mechanical properties

3.4.1 Microhardness

The hardness profile across the welded joint diagonally is shown in Fig. 4. It is seen that a characteristic hardness profile across the USWed Mg/Al joint was obtained with an average hardness value of about 66 HV on the AZ31B-H24 side and 64 HV on the Al5754-O side, which was basically symmetrical. However, an asymmetrical hardness profile was obtained for the USWed Mg/HSLA steel joint with approximately 61 HV on the AZ31B-H24 side and 145 HV on the HSLA steel side. Interestingly, the hardness value of Mg in the USWed Mg/HSLA steel joint was slightly lower than that of in the USWed Mg/Al joint. This would be associated with the lower thermal conductivity of HSLA steel than Al alloy, which would give rise to a slower cooling rate and higher peak temperature in the welding of Mg/HSLA steel during USW. There were no significant hardness changes in the HAZ in both USWed Mg/Al and Mg/HSLA steel joints, which was in agreement those reported in the literature that USW did not produce a severe HAZ [7,8]. This was related to the relatively low welding temperature that was below the melting points of the welded materials. However, a high hardness value of about 200 HV was detected in the interlayer of both Mg/Al and Mg/HSLA steel joints, as shown in Fig. 4. This was obviously due to the presence of composite-like Mg_2Sn and Sn eutectic structure (Figs 2 and 3), since the hardness value of Mg_2Sn IMCs was higher. This was in agreement with the results reported by other researchers [37,38].

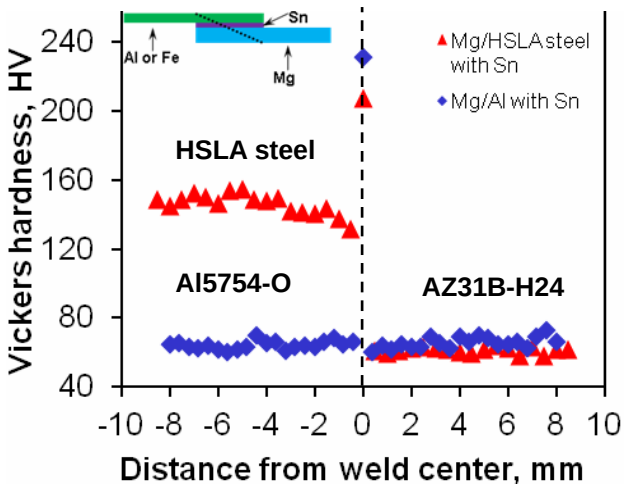

Figure 4. Microhardness profiles across the USWed Mg/Al and Mg/steel joints with a Sn interlayer at a welding energy of 1000 J.

3.4.2 Lap shear tensile strength

As shown in Fig. 5(a), the addition of a Sn interlayer led to an increase in the lap shear strength of both USWed Mg/Al and Mg/HSLA steel dissimilar joints. For example, at a welding energy of 1000 J (Fig. 5(b)), the lap shear strength of USWed Mg/Al and Mg/HSLA steel joints was ~29 MPa and ~45 MPa, respectively, without the addition of a Sn interlayer, and became ~41 MPa and ~54 MPa, respectively, with the addition of a Sn interlayer. This represented an increase of ~55% and ~32% in the lap shear strength for USWed Mg/Al and Mg/HSLA steel joints after a Sn interlayer was added

during USW. Such a significant increase in the lap shear strength was attributed to the formation of solid solutions of Sn-Al, Sn-Fe, Mg-Fe and Mg-Sn, and especially the composite-like eutectic structure of Sn and Mg_2Sn (Figs 2 and 3), instead of the brittle IMCs of $Al_{12}Mg_{17}$ in Mg/Al direct joint [6] and without the interaction of Mg and Fe in Mg/HSLA steel direct joint [28]. In addition, it can be seen from Fig. 5(a) that in the absence of Sn interlayer in the USWed Mg/Al joint, the lap shear strength increased with increasing energy input and reached its maximum at an energy input of 1250 J and then decreased. This was due to the competition between the increasing diffusion bonding arising from higher temperatures at the higher energy inputs and the deteriorating effect of the brittle intermetallic $Al_{12}Mg_{17}$ layer of increasing thicknesses. In the USWed Mg/HSLA steel joint, the lap shear strength increased with increasing energy up to a welding energy of ~1750 J, after which joining was not possible since the tip started to penetrate through the sheets, supposing that it also had the same trend of lap shear strength as that of the USWed Mg/Al joint without Sn interlayer.

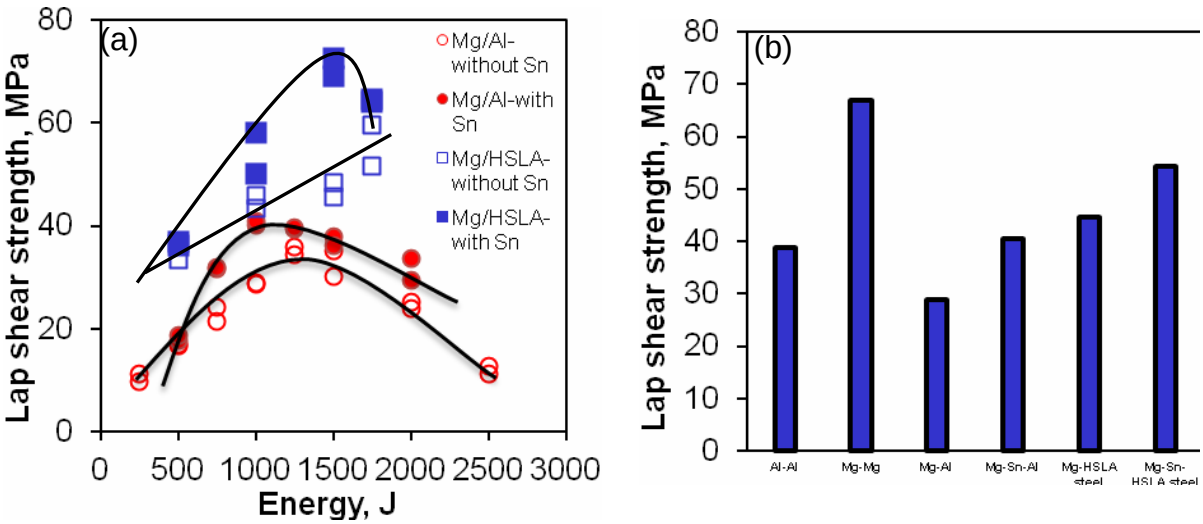

Figure 5. (a) Lap shear strength with and without a Sn interlayer as a function of energy input, (b) comparison of lap shear strength among different welded joints at a welding energy of 1000 J.

In the presence of Sn interlayer, the lap shear strength of both USWed Mg/Al and Mg/HSLA steel dissimilar joints increased initially with increasing welding energy, reached its peak values, followed by a decrease with further increasing welding energy. Such a change occurred due to the fact that at lower energy inputs the temperature was not high enough to soften or melt the Sn interlayer. On the other hand, at higher energy inputs, the specimen was subjected to higher temperatures at larger vibration amplitudes for a longer time, resulting in more Sn interlayer being squeezed out. As summarized in Fig. 5(b), it is seen that the USW of similar joints were fairly effective especially for the Mg/Mg joints with a lap shear strength of 67 MPa. However, the lap shear strength of Al/Al joints made at a welding energy of 1000 J was lower (~39 MPa). The lap shear strength of the USWed Mg/Al dissimilar joint without a Sn interlayer was approximately 25% lower than that of the USWed Al/Al joint and 57% lower than that of the USWed Mg/Mg joint. However, the USWed Mg/Al dissimilar joint with a Sn interlayer had a lap shear strength approximately 5% exceeding that of USWed Al/Al similar joint. The lap shear strength of USWed Mg/HSLA steel dissimilar joint without a Sn interlayer was approximately 33% lower than that of the USWed Mg/Mg similar joint, while with the addition of a Sn interlayer it was about only 19% lower than that of the USWed Mg/Mg similar joint. It is of particular interest to observe that, in addition to enhancing the optimum/maximum lap shear strength in both dissimilar joints, the addition of Sn interlayer also led to an energy saving since the optimal welding energy required to achieve the highest strength decreased from ~1250 J to ~1000 J in the Mg/Al dissimilar joint and

from ~1750 J to ~1500 J in the Mg/HSLA steel dissimilar joint.

4. Conclusions and Remarks

1. The ultrasonic spot welding of AZ31B-H24 Mg alloy to Al5754-O Al alloy and AZ31B-H24 Mg alloy to HSLA steel sheet with a Sn interlayer was successfully performed, with a characteristic composite-like Sn and Mg_2Sn eutectic structure present in the interlayer of both dissimilar joints.
2. The lap shear strength of Mg/Al dissimilar joints with a Sn interlayer was achieved to be significantly higher than that of Mg/Al dissimilar joints without interlayer. This improvement was mainly attributed to the formation of solid solutions of Sn with Mg and Al as well as the composite-like Sn and Mg_2Sn eutectic structure in the interlayer, which effectively prevented the occurrence of brittle $Al_{12}Mg_{17}$ intermetallic compound present in the Mg/Al dissimilar joints without interlayer. The fact that Sn and Mg_2Sn were located on both Al and Mg sides of matching fracture surfaces indicated that the tensile shear failure occurred through the interior of the interlayer in the mode of "cohesive failure".
3. The lap shear strength of Mg/HSLA dissimilar joints with a Sn interlayer was observed to be much higher than that of Mg/HSLA dissimilar joints without interlayer. Sn interlayer actively worked as an intermediate medium to join Mg to Fe by the formation of solid solutions of Sn with Mg and Fe as well as the composite-like Sn and Mg_2Sn eutectic structure in the interlayer.
4. In addition to the beneficial role of enhancing the lap shear strength in both Mg/Al and Mg/HSLA steel dissimilar joints, the addition of Sn interlayer further led to energy saving since the welding energy required to achieve the maximum lap shear strength decreased from 1250 J to 1000 J in the Mg/Al dissimilar joint and from 1750 J to 1500 J in the Mg/HSLA steel dissimilar joint.
5. Further studies are needed to (1) explore other potential interlayers, such as, Zn, Ni, Cu, etc., for further improving the strength of the USWed Mg/Al and Mg/HSLA steel dissimilar joints and (2) evaluate the fatigue and dynamic (or impact) resistance of the dissimilar joints for the safe and reliable applications of the welded lightweight components.

Acknowledgements

The authors would like to thank the Natural Sciences and Engineering Research Council of Canada (NSERC) and AUTO21 Network of Centers of Excellence for providing financial support. This investigation involves part of Canada-China-USA Collaborative Research Project on the Magnesium Front End Research and Development (MFERD). The authors thank Dr. A.A. Luo, General Motors Research and Development Center for the supply of test materials. One of the authors (D.L. Chen) is grateful for the financial support by the Premier's Research Excellence Award (PREA), NSERC-Discovery Accelerator Supplement (DAS) Award, Canada Foundation for Innovation (CFI), and Ryerson Research Chair (RRC) program. The assistance of Q. Li, A. Machin, J. Amankrah, and R. Churaman in performing the experiments is gratefully acknowledged.

References

[1] J. Murray, D. King, Oil's tipping point has passed. Nature, 481 (2012) 433−435.
[2] T.M. Pollock, Weight loss with magnesium alloys. Science, 328 (2010) 986−987.
[3] R. Qiu, C. Iwamoto, S. Satonaka, Interfacial microstructure and strength of steel/aluminum alloy joints welded by resistance spot welding with cover plate. J Mater Proc Technol, 209 (2009) 4186−4193.

[4] P.B. Prangnell, F. Haddadi, Y.C. Chen, Ultrasonic spot welding aluminum to steel for automotive applications-microstructure and optimization. Mater Sci Technol, 27 (2011) 617−624.
[5] X. Qi, G. Song, Interfacial structure of the joints between magnesium alloy and mild steel with nickel as interlayer by hybrid laser-TIG welding. Mater Des, 31 (2010) 605–609.
[6] V.K. Patel, S.D. Bhole, D.L. Chen, Microstructure and mechanical properties of dissimilar welded Mg-Al joints by ultrasonic spot welding technique. Sci Technol Weld Join, 17 (2012) 202−206.
[7] R. Jahn, R. Cooper, D. Wilkosz, The effect of anvil geometry and welding energy of microstructures in ultrasonic spot welds of AA6111-T4. Metall Mater Trans A, 38 (2007) 570−583.
[8] E. Hetrick, R. Jahn, L. Reatherford, J. Skogsmo, S. Ward, D. Wilkosz, J. Devine, K. Graff, R. Gehrin, Ultrasonic spot welding: A new tool for aluminum joining. Weld J, 84 (2005) 26−30.
[9] P.B. Prangnell, D. Bakavos, Novel approaches to friction spot welding thin aluminium automotive sheet. Mater Sci Forum, 638-642 (2010) 1237−1242.
[10] V.K. Patel, S.D. Bhole, D.L. Chen, Influence of ultrasonic spot welding on microstructure in a magnesium alloy. Scripta Mater, 65 (2011) 911–914.
[11] S.H. Chowdhury, D.L. Chen, S.D. Bhole, X. Cao and P. Wanjara, Lap shear strength and fatigue life of friction stir spot welded AZ31 magnesium and 5754 aluminum alloys. Mater Sci Eng A, 556 (2012) 500–509
[12] D. Bakavos and P.B Prangnell, Mechanisms of joint and microstructure formation in high power ultrasonic spot welding 6111 aluminum automotive sheet. Mater Sci Eng A, 527 (2010) 6320−6334.
[13] V.K. Patel, S.D. Bhole, D.L. Chen, Improving weld strength of magnesium to aluminum dissimilar joints via tin interlayer during ultrasonic spot welding. Sci Technol Weld Join, 17 (2012) 342–347.
[14] D. Choi , B. Ahn ,C. Lee , Y. Yeon, K. Song, S. Jung, Formation of intermetallic compounds in Al and Mg alloy interface during friction stir spot welding. Intermetallics, 19 (2011) 125–130.
[15] Y.C. Chen and K. Nakata, Friction stir lap joining aluminum and magnesium alloys. Scripta Mater, 58 (2008) 433–436.
[16] Y.S. Sato, A. Shiota, H. Kokawa, K. Okamoto, Q. Yang, C. Kim, Effect of interfacial microstructure on lap shear strength of friction stir spot weld of aluminum alloy to magnesium alloy, Sci Tech Weld Join, 15 (2010) 319–324.
[17] A. Panteli, Y. Chen, D. Strong, X. Zhang, P. Prangnell, Optimization of aluminum to magnesium ultrasonic spot welding. JOM, 64 (2012) 414–420.
[18] L. Liu, X. Qi, Strengthening effect of nickel and copper interlayers on hybrid laser-TIG welded joints between magnesium alloy and mild steel. Mater Des, 31 (2010) 3960–3963.
[19] M. Santella, T. Franklin, J. Pan, T.Y. Pan, E. Brown, Ultrasonic spot welding of AZ31B to galvanized mild steel. SAE Inter, 3 (2010) 652–657.
[20] C. Schneider, T. Weinberger, J. Inoue, T. Koseki, N. Enzinger, Characterization of interface of steel/magnesium FSW. Sci Tech Weld Join, 16 (2011) 100–106.
[21] S.H. Chowdhury, D.L. Chen, S.D. Bhole, X. Cao and P. Wanjara, Lap shear strength and fatigue behavior of friction stir spot welded dissimilar magnesium-to-aluminum joints with adhesive. Mater Sci Eng A, 562 (2013) 53–60.
[22] W. Xu, D.L. Chen, L. Liu, H. Mori, Y. Zhou, Microstructure and mechanical properties of weld-bonded and resistance spot welded magnesium-to-steel dissimilar joints. Mater Sci Eng A, 537 (2012) 11–24.
[23] L.M. Zhao, Z.D. Zhang, Effect of Zn interlayer on interface microstructure and strength of diffusion-bonded Mg-Al joints. Scripta Mater, 58 (2008) 283–286.

[24] H.T. Zhang, J.Q. Song, Microstructural evolution of aluminum/magnesium lap joints welded using MIG process with zinc foil as an interlayer. Mater Lett, 65 (2011) 3292–3294.
[25] S. Jana, Y. Hovanski, G.J Grant, Friction stir lap welding of Magnesium alloys to steel: A preliminary investigation. Metall Mater Trans A, 41 (2010) 3173–3182.
[26] X.J. Liu, R.S. Huang, H.Y. Wang, S.H. Liu, Improvement of TIG lap weldability of dissimilar metals of Al and Mg. Sci Tech Weld Join, 12 (2007) 258–260.
[27] X.D. Qi, L. Liu, Fusion welding of Fe-added lap joints between AZ31B magnesium alloy and 6061 aluminum alloy by hybrid laser-tungsten inert gas welding technique. Mater Des, 33 (2012) 436–443
[28] L. Liu, X. Qi, Z. Wu, Microstructural characteristics of lap joint between magnesium alloy and mild steel with and without the addition of Sn element, Mater Lett 64 (2010) 89–92.
[29] A.A Nayeb-Hashemi, J.B. Clark, The Mg-Sn (magnesium-tin) system. Bulletin of alloy phase diagram, 5 (1984) 466–475.
[30] A.J. McAlister, D.J Kahan, Binary alloy phase diagrams, in: T. B. Massalski (Eds.) Al–Sn (Aluminum–Tin), 2nd Eds, Vol. 1, ASM International, Materials Park, OH, 1990, pp. 215–216.
[31] M. Singh, S. Bhan, Contribution to the Fe-Sn system. J Mater Sci Lett, 5 (1986) 733–735.
[32] A.A. Luo, P. Fu, L. Peng, X. Kang, Z. Li and T. Zhu, Solidification microstructure and mechanical properties of cast magnesium-aluminum-tin alloys. Metall Mater Trans A, 43 (2012) 360–368.
[33] C. Liu, D.L. Chen, S. Bhole, X. Cao and M. Jahazi, Polishing-assisted galvanic corrosion in the dissimilar friction stir welded joint of AZ31 magnesium alloy to 2024 aluminum alloy. Mater Charact, 60 (2009) 370–376.
[34] G.L. Song, B. Johannesson, S. Hapugoda, D. StJohn, Galvanic corrosion of magnesium alloy AZ91D in contact with an aluminum alloy, steel and zinc. Corr Sci, 46 (2004) 955–977.
[35] E. Doernberg, A. Kozlov, R. Schmid-Fetzer, Experimental investigation and thermodynamic calculation of Mg-Al-Sn phase equilibria and solidification microstructures. J Phase Equilib Diffu, 28 (2007) 523–535.
[36] W. Xu, L. Liu, Y. Zhou, H. Mori, D.L. Chen, Tensile and fatigue properties of weld-bonded and adhesive-bonded magnesium alloy joints, Mater Sci Eng A, 563 (2013) 125–132.
[37] B.H. Kim, J.J. Jeon, K.C. Park, B.G. Park, Y.H. Park, I.M. Park, Microstructural characterization and mechanical properties of Mg-xSn-Al-Zn alloys. Arch Mater Sci Eng, 30 (2008) 93–96.
[38] V. Kevorkijan, S.D Skapin, Studies of Mg_2Sn based composite. MJoM, 16 (2010) 47–61.

Analysis and residual strength prediction for multiple site damage in aircraft structures by using weight function method

X.R. Wu[*1,2], **W. Xu**[2,3], **H. Wang**[2]

[1] AVIC Beijing Institute of Aeronautical Materials, Beijing 100095, China
[2] School of Aeronautics and Astronautics, Shanghai Jiao Tong University, Shanghai 200240, China
[3] School of Naval Architecture, Ocean and Civil Engineering, Shanghai Jiao Tong University, Shanghai 200240, China
* Corresponding author: xueren.wu@gmail.com

Abstract

This paper presents a review of recent progress of the development of weight function method for analyzing multiple site damage in aircraft structural panels. An analytical method, the Weight Function Method (WFM), has been proposed and further developed to analyze the MSD problems and to determine the related various fracture mechanics parameters. The plastic zone sizes and crack opening displacements were extensively verified and validated by excellent agreement with available analytical and finite element method results. Combined with Crack Tip Opening Angle criterion (CTOA), the present WFM is employed to predict the stable crack growth and residual strength of aircraft aluminum sheets containing MSD. The predicted results compared very well with the corresponding experimental data. Thereby a novel analytical approach with high efficiency and reliability has been devised for MSD analyses in aircraft structures.

Keywords: Multiple site damage, Weight function method, Plastic zone size, Crack opening displacement, Residual strength.

1. Introduction

Multiple Site Damage (MSD) has been a serious threat to modern transport airplane structure safety, and therefore has become a great concern in aircraft damage tolerance design and airworthiness certification. A historical milestone case of this type of failure was the in-flight disintegration of a 5.5m long piece of the pressure cabin skin of upper fuselage of Aloha Airlines Boeing 737-200 over Hawaii in 1988 [1]. After the Aloha accident, all the major commercial airplane manufacturers were required to evaluate their aircraft for MSD in the critical areas of the wing, empennage and pressure fuselage [2].

Various models and methods [3-5] have been developed to determine the stress intensity factors, plastic zone sizes and crack opening displacements for the prediction of the fatigue life and residual strength for structures with MSD. Most current approaches rely mainly on advanced numerical techniques, especially the Finite Element Method (FEM). Despite its powerfulness, reliable FEM solutions for MSD require great efforts, time and experience in modeling and computation. Classical analytical method, e.g. the complex variable method, is limited to idealized MSD configurations.

Recently, the Weight Function Method (WFM) has been proposed and further developed by the authors to analyze various fracture mechanics parameters and stable crack growth of sheets with MSD[6-10]. It is shown to be versatile and cost-effective for tackling sheets with MSD problems. The approach is outlined in this paper.

2. Weight function method for fracture parameters analysis for collinear cracks

2.1. Basic principle

According to the weight function theory, for a crack subjected to an arbitrary pressure $\sigma(x)$ distributed at the crack faces, the non-dimensional stress intensity factor f can be determined by a simple quadrature [11,12].

$$f = \int_0^a \frac{\sigma(x)}{\sigma} \cdot \frac{m(a,x)}{\sqrt{\pi a}} \mathrm{d}x \qquad m(a,x) = \frac{E'}{f_r(a)\sigma\sqrt{\pi a}} \frac{\partial u_r(a,x)}{\partial a} \tag{1}$$

where $m(a, x)$ is the weight function for the crack body, $E'=E$ for plane stress, $E'=E/(1-\nu^2)$ for plane strain，σ is a reference stress, a and x are the non-dimensional crack length and coordinate along the crack normalized by the characteristic length W (often taken as unity), here W refers to half plate width for the finite width panel containing a center crack. f_r(a) and $u_r(a, x)$ are the stress intensity factor and crack opening displacement, respectively, for a reference load case.

The corresponding crack opening displacements can also be easily determined when the relevant weight function, $m(a, x)$, is available. From Eq. (1), we have

$$u(a,x) = \frac{\sigma}{E'} \int_{a_0}^{a} [f(s)\sqrt{\pi a}] \cdot m(s,x) \mathrm{d}s \tag{2}$$

where the non-dimensional stress intensity factor $f(s)$ is obtained using Eq. (1).

It should be emphasized that, the $\sigma(x)$ in Eq. (1) refers to the stress distribution at the prospective crack line, and is determined from stress analysis for the same configuration but without crack. This implies that once the weight function is known for a given crack geometry and $\sigma(x)$ is determined, the stress intensity factors and crack opening displacements for any crack length can be obtained by simple integration through Eqs.(1) and (2). The advantages are especially useful for stress intensity factor and strip yield model analysis of multiple site damage.

2.2. Weight function method for special collinear cracks

The weight function method for single crack is applied for a special multiple site damage case[7]: one large center crack formed by coalescing three un-equal length center cracks in a panel of finite width, with compressive yield stress σ_s uniformly acting along the un-cracked ligament and in the crack tip region, Fig.1a.

The analysis for this case is conducted by assuming the coalesced three un-equal length cracks as one single fictitious crack subjected to segment pressure distribution in plastic zones, in addition to the applied external load, Fig.1b. Essentially, the Dugdale[13] strip yield model is the superposition of two linear elastic solutions. One is for remote uniform tension stress, which is available in Ref. [14]. Another is for segment uniform compressive yield stress acting in the plastic zones. The stress intensity factor and crack opening displacement for this load case can be determined by using WFM, equations (1) and (2). The weight functions for a center crack in a finite sheet were given in Ref.[12].

For the three coalesced cracks, the critical stress and the fictitious crack length are determined based on two conditions [4]: i) Vanishing of the stress singularity at the fictitious crack tips shown in Fig.1b; and ii) Zero of the minimum crack opening displacement at the ligament [a_1, a_1+d].

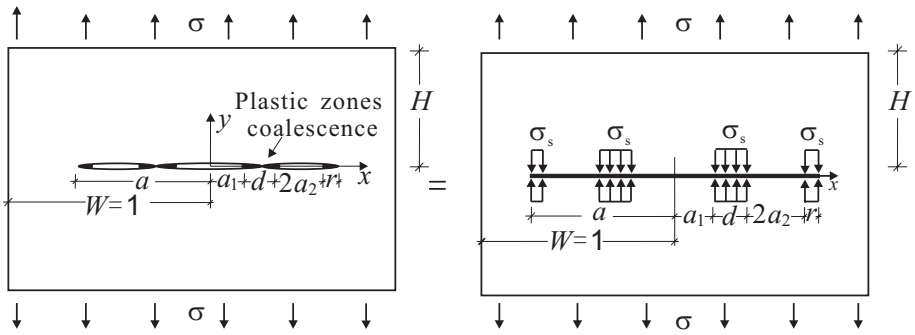

Fig.1 A coalesced center crack in a finite width panel containing three un-equal cracks, the total length of the fictitious crack includes all the strip yield zones

2.3. Weight function method for general collinear cracks

In this section, the weight functions for general collinear cracks are presented. The derivation of the weight function method for general collinear cracks was based on the reciprocity theorem and the superposition principle [8]. It was found that the weight functions for general collinear cracks are quite different from that for a single crack configuration.

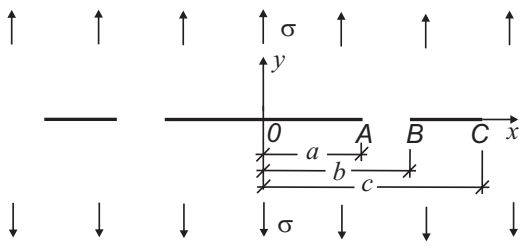

Fig.2. Three symmetric collinear cracks in an infinite sheet subjected to remote uniform stress

Take a typical MSD configuration, three collinear cracks in an infinite sheet, Fig.2, as an example. The weight functions for the crack tips A, B and C are given in Eqs.(3-5), respectively [8].

$$m_a(a,b,c,x)=\frac{E'}{f_{rA}(a,b,c)\cdot\sigma\sqrt{\pi a}}\cdot\begin{cases}\partial u_1^r(a,b,c,x)/\partial a;\ x\in[0,a]\\ \partial u_2^r(a,b,c,x)/\partial a\ ;\ x\in[b,c]\end{cases} \tag{3}$$

$$m_b(a,b,c,x)=\frac{-E'}{f_{rB}(a,b,c)\cdot\sigma\sqrt{\pi(c-b)/2}}\cdot\begin{cases}\partial u_1^r(a,b,c,x)/\partial b\ ;\ x\in[0,a]\\ \partial u_2^r(a,b,c,x)/\partial b\ ;\ x\in[b,c]\end{cases} \tag{4}$$

$$m_c(a,b,c,x)=\frac{E'}{f_{rC}(a,b,c)\cdot\sigma\sqrt{\pi(c-b)/2}}\cdot\begin{cases}\partial u_1^r(a,b,c,x)/\partial c;\ x\in[0,a]\\ \partial u_2^r(a,b,c,x)/\partial c;\ x\in[b,c]\end{cases} \tag{5}$$

where the non-dimensional stress intensity factors f_{rA} (a,b,c), f_{rB} (a,b,c) and f_{rC} (a,b,c) for remote uniform tension stress were given in Ref.[14]. The corresponding crack opening displacements for center and side crack $u_1^r(a,b,c,x)$ and $u_2^r(a,b,c,x)$ are:

$$u_1^r(a,b,c,x)=\frac{2\sigma}{E'}\int_{-a}^{x}\frac{x\left\{x^2-\left[\left(c^2-a^2\right)E(k)/K(k)+a^2\right]\right\}}{\sqrt{\left(a^2-x^2\right)\left(b^2-x^2\right)\left(c^2-x^2\right)}}\cdot\mathrm{d}x\ ;\ -a\le x\le a \tag{6a}$$

$$u_2^r(a,b,c,x)=\frac{2\sigma}{E'}\int_b^x \frac{x\left\{x^2-\left[\left(c^2-a^2\right)E(k)/K(k)+a^2\right]\right\}}{\sqrt{\left(x^2-a^2\right)\left(x^2-b^2\right)\left(c^2-x^2\right)}}\mathrm{d}x\ ;\ b\le x\le c \tag{6b}$$

Having obtained the weight functions for this crack configuration, the stress intensity factors, crack opening displacements and plastic zone size of its strip yield model can be determined [8].

2.4. A unified method for strip yield collinear cracks

It is observed that the weight function method is accurate and efficient to obtain the stress intensity factor and crack opening displacement. However it is hard to obtain the weight functions for cracks in finite sheet. In this section, a simple and efficient unified method [9] is proposed to solve the strip yield model for collinear cracks in infinite and finite sheets. The key idea of this method is to treat all the cracks, the plastic zones and the remaining elastic ligament between the cracks as a single crack, which is solved using the weight function method. For example, the strip yield model for two collinear cracks in an infinite sheet shown in Fig.3a is modeled by an equivalent single center crack shown in Fig.3b. The center crack of length $2l=(4a+2b+2r_B)$ is subjected to (i) remote uniform stress σ; (ii) segments uniform compression yield stress $-\sigma_s$ over the plastic zones r_A and r_B; and (iii) continuous compression stress $-\sigma(x)$ distributed along the remaining elastic ligament $x\in[-(b-r_A), (b-r_A)]$, respectively. The $\sigma(x)$ is further discretized by a set of uniform segment stress, as shown in Fig.3c. The requirements for the equivalent single crack are: 1) No stress singularity at the fictitious crack tip, 2) Zero crack opening displacements along the elastic ligament between the fictitious crack tips, $x\in[-(b-r_A), (b-r_A)]$.

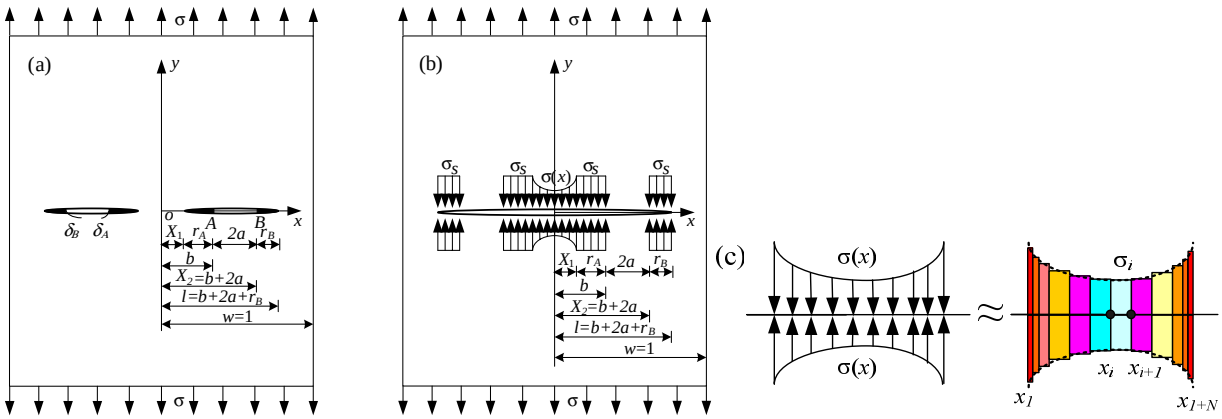

Fig.3. The concept of the unified method: (a) a strip yield model for two collinear cracks in an infinite sheet, (b) an equivalent single crack for modeling problem (a), (c) discretized stress distribution.

The stress intensity factor F and crack opening displacement $U(l, x)$ for the equivalent crack subjected to such complex loading are determined by the superposition of three component elastic solutions. Closed form solutions for the first two load cases are available in Ref.[12]. For the equivalent crack, the following equations are established to obtain the unknown variables.

$$\begin{cases} F=0\,; \\ U(l,x)=0\,;\, x=\left(x_i+x_{i+1}\right)/2, b-r_A, -\left(b-r_A\right); i=1,2,3...N \end{cases} \tag{10}$$

Having established the equations, the plastic zone sizes and stress distribution along the elastic ligament $\sigma(x)$ can be determined by solving the above equation using the weight function method and Newton-iteration. Then, the corresponding crack opening profile for the strip yield model can be obtained by superposition.

2.5. Examples and validations

In this section, two and three collinear cracks in finite and infinite sheets are solved using the above methods. Some existing results and FEM results are also presented for comparison.

2.5.1 Three collinear cracks with plastic zones coalesced in a finite sheet

For a given three crack configuration a_1=0.3, a_2=0.1 and d=0.2 in a finite sheet shown in Fig.1, the critical applied stress σ_c/σ_s and fictitious crack length a are obtained based on the method described in section 2.2, which are 0.3777 and 0.7417 respectively. Figure 4 shows the corresponding CODs determined by WFM and FEM, and very good agreement is observed.

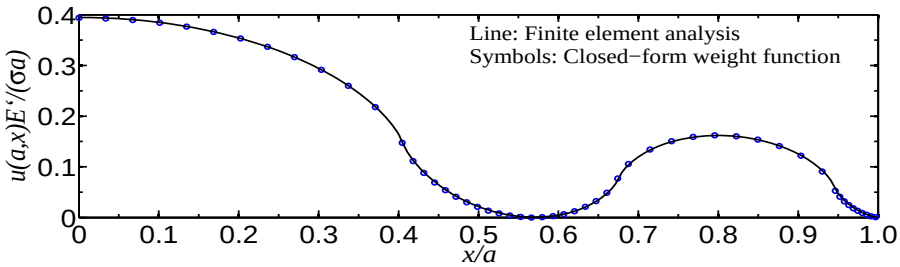

Fig.4. Crack opening profile for the fictitious crack of three un-equal length cracks with coalesced plastic zones. (In Fig.1, a_1 = 0.3, d = 0.2, $2a_2$ = 0.2, the half-length of fictitious crack a = 0.7417) [7].

2.5.2 Two equal-length collinear cracks in finite and infinite sheets

The strip yield models for two equal-length collinear cracks infinite sheets can be obtained by using the WFM and the unified method. However, for the cracks in finite sheet, the unified method is applied. Figure 5 shows some typical results of the inner plastic zone sizes and CTOD as a function of the applied stress. These results are normalized by the plastic zone size r_0 of a single Dugdale crack of the same length, $r_0=a[\sec(0.5\pi\sigma/\sigma_s)-1]$, $a=(c-b)/2$. Also shown in these figures are the results for the plastic zones critical coalescence. To verify the solution accuracy of the present weight function approach, the results are compared to those given by Collins and Cartwright [5] by using complex stress function method. It is observed that the results for two collinear cracks in an infinite sheet obtained from the weight function method, complex stress function method and unified method agree very well. Fig.6 shows the CODs for the strip yield model of the two cracks in finite sheet subjected various applied loads. Also shown in this figure are the FEM results, very good agreement is observed. However, the unified method (UM) is much more efficient than FEM for solving the strip yield model.

2.5.3 Three collinear cracks in an infinite sheet

Figure 5 and 6 show the strip yield model for three symmetric collinear cracks in an infinite sheet. The plastic zone sizes and CODs were obtained by using the WFM and unified method.

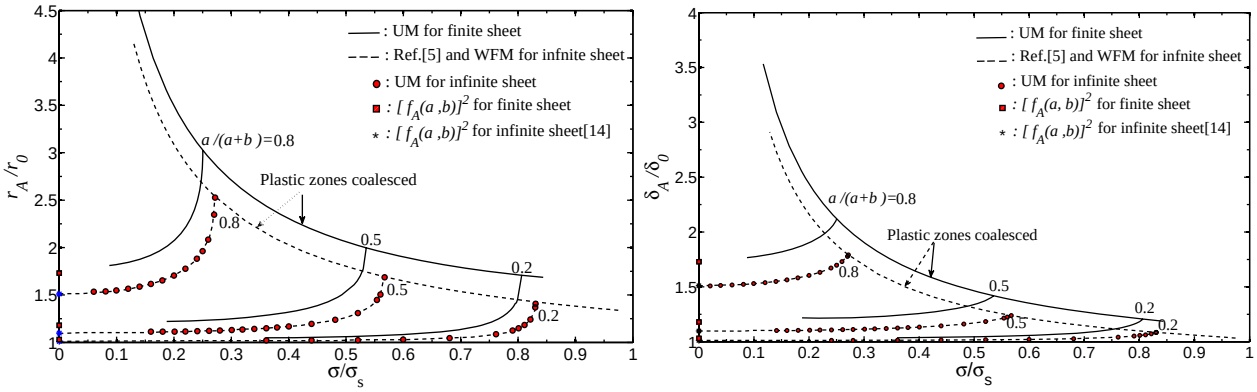

(a) Plastic zone size r_A (b) Crack tip opening displacement δ_A

Fig.5 Plastic zone sizes and crack tip opening displacement for two collinear cracks in finite and infinite sheets[9].

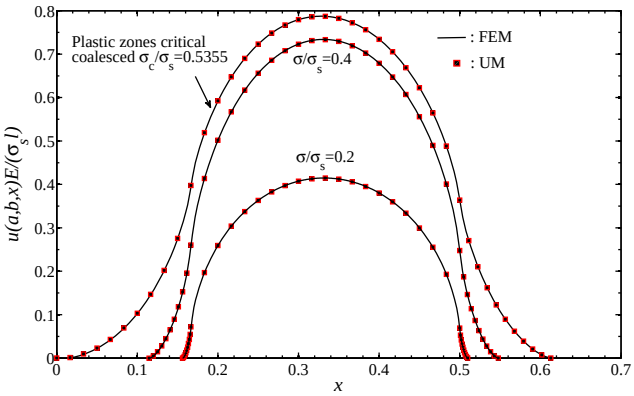

Fig.6 Crack opening profiles for the strip yield model for two equal-length collinear cracks in a finite sheet shown in Fig.4a with a=b=1/6[9].

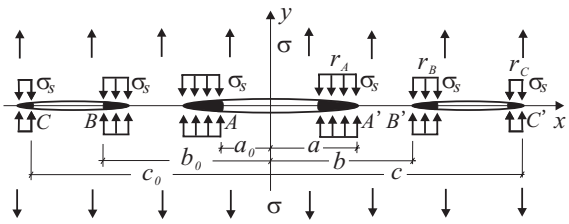

Fig.7. Strip-yield model for three collinear cracks, with separated plastic zones.

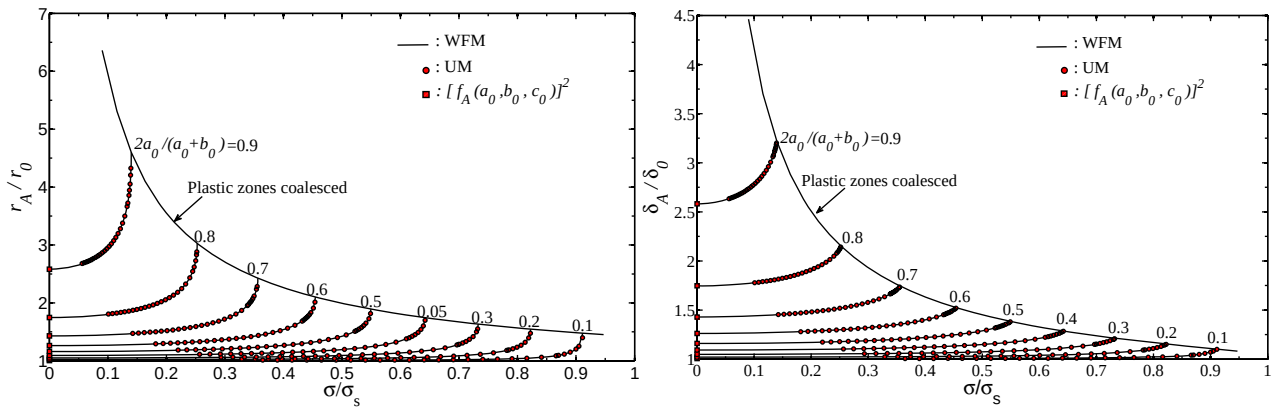

(a) Plastic zone size r_A (b) Crack tip opening displacement δ_A

Fig.8. Plastic zone sizes and CTOD for three equal-length collinear cracks in infinite sheets [9]

Some results for the inner crack tip A of three collinear cracks are given in Fig.8. It is observed that the results obtained from the unified method agree well with those from weight function method. It is also found that for $\sigma/\sigma_s \to 0$, the crack tip plastic zone size and opening displacement for the crack tip A approach the non-dimensional stress intensity factor squares $[f_A(a_0,b_0,c_0)]^2 \cdot r_0$ and $[f_A(a_0,b_0,c_0)]^2 \cdot \delta_0$ shown in Figs.8a and b, respectively. The variables r_0 and δ_0 are the crack tip plastic zone size and opening displacement for a center crack in an infinite sheet.

3. Residual strength prediction and validation for sheets with MSD

3.1 CTOA criterion based on strip yield model

The crack tip opening displacement in combination with the strip yield model had been used by several researchers to predict the stable crack growth behavior [10,15]. In the method, the crack growth was controlled by two parameters. One is critical crack opening displacement δ_0 which is used to describe the crack initiation, Fig.9a; the other is used to characterize the stable crack growth by a constant critical CTOA α, Fig.9b. The crack growth equation for the whole process is

$$\begin{cases} \delta(a_0, a_0) = \delta_0; \text{crack initiation} \\ \delta(a, a-d) = 2d\tan(\alpha_c/2) + \delta_c(a-d, a-d); \text{crack propagation} \end{cases} \tag{8}$$

where, $\delta(a, a\text{-}d)$ is the crack opening displacement at a distance d behind the crack tip, the first variable in the bracket is the crack length, and the second is the x location. $\delta_c(a\text{-}d, a\text{-}d)$ is the plastic wake height, which is equal to the crack tip opening displacement. α_c is the critical CTOA.

In practice, a pair of 'optimal' δ_0 and α_c is selected as the critical values. Using the 'optimal' values, the predicted crack growth behaviors of coupon specimens agree very well with the corresponding experiment observations. Here, the C(T) specimen is used to determine these critical values. The weight function method is adopted here to determine the COD for crack growth analysis. Figure 10 shows the predicted load-crack extension curves obtained by three different pairs of parameters. Also in the figure are the results measured from experiment [10]. It is observed that the predicted result obtained by the parameters δ_0=0.10mm and α_c=4° agrees well with test data. It is assumed that the criterion for single crack is also applicable to sheets with MSD. And these critical values will be used as material properties to predict crack growth for MSD specimens.

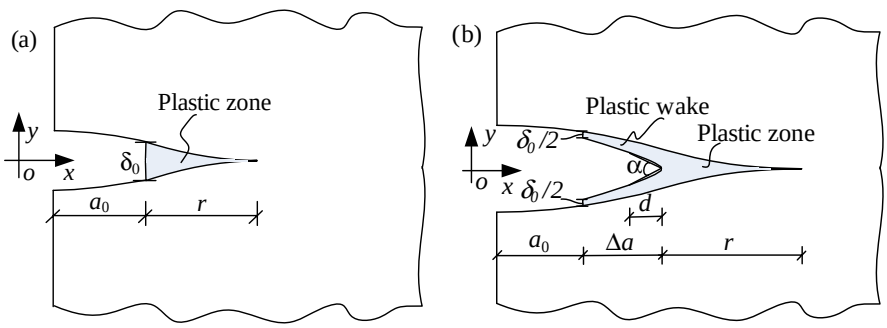

Fig.9. Crack opening profile of modified Dugdale strip yield model at (a) initiation and (b) at propagation with definition of crack growth parameters α and δ_0

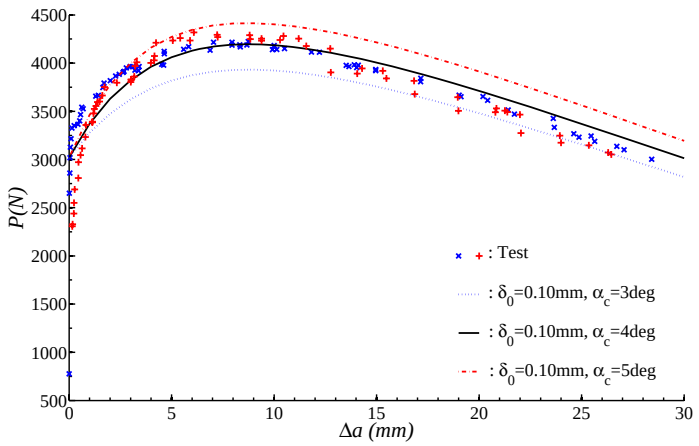

Fig.10 Crack extension against load of C(T) specimen (Δa-P curve)[10]

3.2 Experimental and predicted stable crack growth

With the critical δ_0 and α_c values determined, the main task for stable crack growth analysis of sheets with MSD is to solve the strip yield model to obtain the crack opening displacement for cracked panels. As a result, the efficiency and accuracy of the stable crack growth prediction are much dependent on the method for solving the strip yield model.

The unified method was applied to determine the COD for stable crack growth analysis. Here, the results for sheets (600mm×1140mm) with five different cracks shown in Fig.11a are presented as examples. Figure 11b and c shows the predicted and experimental crack growth behaviors for two sheets with five different cracks. In both cases, the length of the side cracks is 15mm. The length of the center lead crack and ligaments between cracks are different. In Fig.11b, the experimental and predicted maximum residual strengths occurred after the fracture of all the ligaments. In Fig.11c, the sheet failed immediately at the fracture of ligament l_2 shown. Due to the quick fracture of this specimen, the crack growth information for the outside crack tip was not recorded. However, the predicted result was able to describe the entire crack growth process, see the solid lines in Fig.11. When the applied load reached at the maximum residual strength 99.0KN, all the crack tips started to grow, resulting in the fracture of the whole sheet. More detailed information about the experiment and prediction on various MSD configurations was given in Ref.[10].

The elastic-plastic FEM is widely used to predict the residual strength for cracked structures. Using the "plane strain core" model [16] and CTOD criterion embedded in ABAQUS software, the ligament fracture loads and residual strengths for some of the MSD configurations were given in Ref.[10]. It is found that the accuracy of both methods is comparable. However, the computational and modeling demands are quite different. For a given MSD configuration, it takes at least *two hours* (a computer with a Pentium® Dual-Core CPU E5300@2.60GHz and 3.00GB RAM) to complete a residual strength prediction by using FEM. Yet, it does not include the time for creating the finite element model. In order to model the crack growth, the "debond" technique in ABAQUS was used. The FEM involves material and contact non-linear analysis [10]. Rich experiences on finite element modeling and analysis are required. However, for most of the MSD configuration

given in Ref.[10], *two minutes* is enough to complete a residual strength analysis by using the present method. Furthermore, once the crack growth analysis program for a given crack configuration is available, there is no modeling time. These advantages are very useful for parametric analysis.

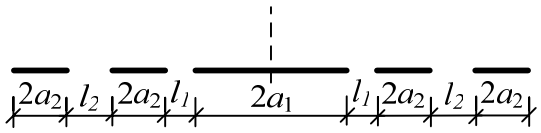

(a) Schematic geometrical dimensions for five collinear cracks

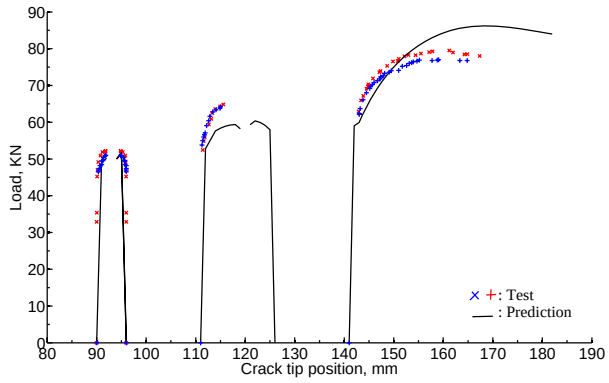

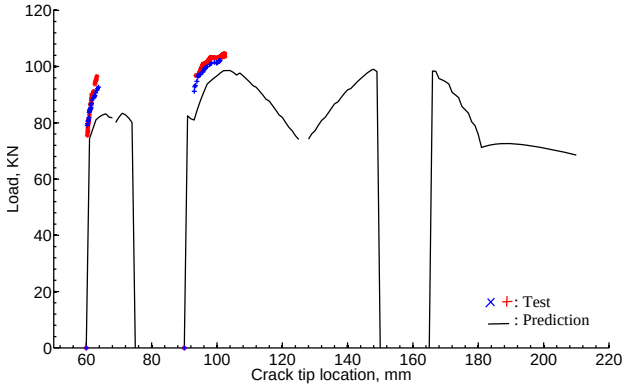

(b) a_1=90mm, l_1=6mm, l_2=15mm; (c) a_1=60mm, l_1=15mm, l_2=60mm;

Fig.11 Experimental and predicted Δa-P curves for sheet with five collinear cracks

4 Conclusions

An analytical approach, the weight function method for dealing with the MSD problems is presented in this paper. The study leads to the following conclusions:

1. For special collinear crack configurations which can be treated as a single crack problem, such as three collinear cracks with strip yield plastic zones critical coalescence in a finite sheet, the strip yield model solutions can be easily solved by the weight functions for a single crack. The results are in perfect agreement with FEM results.

2. Weight function formulas for more general collinear cracks have been derived, which are markedly different from those for the single crack cases. With the derived weight functions, the key fracture mechanics parameters, stress intensity factors and crack opening displacements for the three collinear cracks under arbitrary load conditions are easily computed by a simple quadrature.

3. A unified method based on the weight function for a single crack is proposed to solve the strip yield models for collinear cracks in infinite and finite sheet. The method is used to solve the strip yield models for two and three symmetrical collinear cracks in infinite and finite sheets to obtain plastic zones, crack opening displacements and stress distributions along the elastic ligaments between cracks. These results are widely compared with exact solutions and FEM results, perfect agreements are observed. This method is simple, efficient, reliable, and versatile.

4. Combined with CTOD criterion, the WFM is used to predict the stable crack growth behaviors and residual strengths of MSD configurations in finite-width sheets subjected to monotonic loading. The solution efficiency is significantly better than the FEM.

In summary, the present WFM for MSD provides a powerful analytical approach for fracture mechanics analyses and residual strength assessment for MSD-contained aircraft structures.

References

[1] R.J.H.Wanhill. Milestone case histories in aircraft structural integrity. In: Milne I, Ritchie RO, Karihaloo B, editors. Comprehensive Structural Integrity, Oxford: Elsevier Ltd; 2003, 61-72.

[2] FAA. Aging Airplane Program: Widespread Fatigue Damage. Federal Register Rules and Regulations 2010; 75(219): 69746-69789.

[3] X.Y.Deng, J.W.Hutchinson. Approximate methods for analyzing the growth of large cracks in fatigue damaged aircraft sheet material and lap joints. Finite Elem Anal Des 1996; 23: 101-114.

[4] T. Nishimura. Strip yield analysis of two collinear unequal cracks in an infinite sheet. Engng Frac Mech 2002; 69: 1173-91.

[5] R.A.Collins, D.J.Cartwright. An analytical solution for two equal-length collinear strip yield cracks. Engng Frac Mech 2001; 68: 915-24.

[6] W.Xu, X.R.Wu, H.Wang. Weight functions and strip yield solution for two equal-length collinear cracks in an infinite sheet. Engng Fract Mech 2011; 78(11): 2356-2368.

[7] X.R.Wu, W.Xu. Strip yield crack analysis for multiple site damage in infinite and finite panels – A weight function approach. Engng Fract Mech 2011; 78(14): 2585-2596.

[8] W.Xu, X.R.Wu. Weight functions and strip-yield model analysis for three collinear cracks. Engng Fract Mech 2012; 85(1):73-87.

[9] W.Xu, X.R.Wu, H.Wang. A unified method for strip yield model solution of multiple collinear cracks. Engng Fract Mech 2012. (under review).

[10] W.Xu. Weight function method for aircraft structure multiple site damage analyses and residual strength prediction[PHD thesis]. Shanghai Jiao Tong University.2012. (in chinese).

[11] H.F.Bueckner A novel principle for computation of the stress intensity factors. Z Angew Math Mech 1970; 50(9): 529-546.

[12] X.R.Wu, A.J.Carlsson. Weight functions and stress intensity factor solutions. Oxford: Pergamon Press; 1991.

[13] D.S.Dugdale. Yielding of steel sheets containing slits. J. Mech. Phys. Solids 1960; 8:100-104.

[14] H.Tada, P.C.Paris, G.R.Irwin. The stress analysis of cracks handbook.3rd ed. New York:ASME Press; 2000.

[15] R.Galatolo, KF.Nilsson. An experimental and numerical analysis of residual strength of butt-joints panels with multiple site damage. Engng Fract Mech 2001; 68(13):1437-1461.

[16] J.C.Newman Jr, M.A.James,U.Zerbst. A review of the CTOA/CTOD fracture criterion. Engng Fract Mech 2003;70(3-4): 371-385.

Effect of welding defects on plastic behaviour and fatigue lifetime of friction stir welded Al-Cu-Li alloy

Thomas Le Jolu[1,2], Thilo F. Morgeneyer[1,*], Anne Denquin[3], Anne-Françoise Gourgues-Lorenzon[1]

[1] MINES ParisTech, Centre des Matériaux, UMR CNRS 7633, BP 87, 91003 Evry cedex, France
[2] Now at CEA Saclay, 91191 Gif-sur-Yvette cedex, France
[3] Onera BP 72-29 Avenue de la Division Leclerc 92322 CHATILLON cedex, France
* Corresponding author: thilo.morgeneyer@mines-paristech.fr

Abstract The effects of joint line remnant (JLR), kissing bond (KB), and clearance between the sheets (Gap) on tensile and fatigue properties of 2198-T851 friction stir welds have been quantitatively evaluated with respect to a reference weld made using one single sheet. The JLR has no significant influence in the investigated conditions. KB and Gap-induced defects do not significantly influence plastic yield but may induce premature crack initiation by ductile tearing and intergranular decohesions respectively. A critical value for KB opening (280 MPa), a threshold value for fatigue crack propagation from the KB (1 MPa√m) and crack growth rates consistent with literature data have been determined.

Keywords Friction stir welds, Welding defects, Tensile properties, Fatigue resistance

1. Introduction

Friction stir welding (FSW) of so-called “non-weldable” Al-Cu alloys has been developed to substitute riveting in lightweight structures [1]. It allows avoiding hot cracking and limiting component distortion. Internal flaws that are difficult to detect by using non-destructive evaluation (NDE) may appear under certain processing conditions. After welding, the natural oxide layer at butt surfaces may yield a defect [2-6] sometimes called “joint line remnant” (JLR). If the JLR is connected to the weld root and induces fracture after severe bending of the weld (e.g. [3, 7-8]), it is often referred to as a “kissing bond” (KB). In butt-welding conditions, a “Gap” might be left between the two sheets, leading to poor mixing of matter during FSW. The impact of such defects on tensile and fatigue properties has only been scarcely investigated [9-10]. The purpose of the present study is to compare the effects of JLR, KB and Gap-induced features on the tensile behaviour and fatigue lifetime of FSW joints of an Al-Cu-Li alloy dedicated to aircraft applications.

2. Experimental details

2.1. Materials and welding conditions

A 3.1-mm-thick sheet of AA2198-T851 with chemical composition Al-3.20 Cu - 0.98 Li - 0.31 Ag - 0.31 Mg - 0.11 Zr - 0.04 Fe - 0.03 Si (wt %) was considered. The sheet had been aged at 155°C for 16h. Pancake-shaped grains (10 - 20 µm in thickness) were observed in this material (Fig. 1). The hardness of this material was around 150±5 $HV_{0.1}$, except at mid-thickness (137±5 $HV_{0.1}$).

FSW butt joints were realised along the rolling direction using 500 mm (RD) x 150 mm (TD) coupons. Optimised welding parameters allowed minimising external defects such as flashes. Except for Gap bearing welds, the welding machine was displacement-controlled with a travelling speed of 480 $mm.min^{-1}$, a rotational speed of 1200 rpm, a conventional retractable tool with 13 mm in shoulder diameter and 4.2 mm in pin diameter. “Sound” welds were made by moving the tool into a single sheet, to avoid any native oxides at edges before welding. “JLR bearing” welds resulted from natural oxidation of the coupons before welding. “KB bearing” welds were fabricated

as for JLR but with retracting the pin by 80 µm to modify mixing conditions within the weld. “Gap bearing” welds were realised under load control with a constant clearance between the sheets, of either 0.3 mm (“Gap3”: 10% of the parent sheet thickness) or 0.7 mm (“Gap7”: 23% of the parent sheet thickness). Only KB bearing welds cracked under severe bending conditions (width 10 mm, bending angle 90°, bending radius 7 mm, and bottom part of the weld outside).

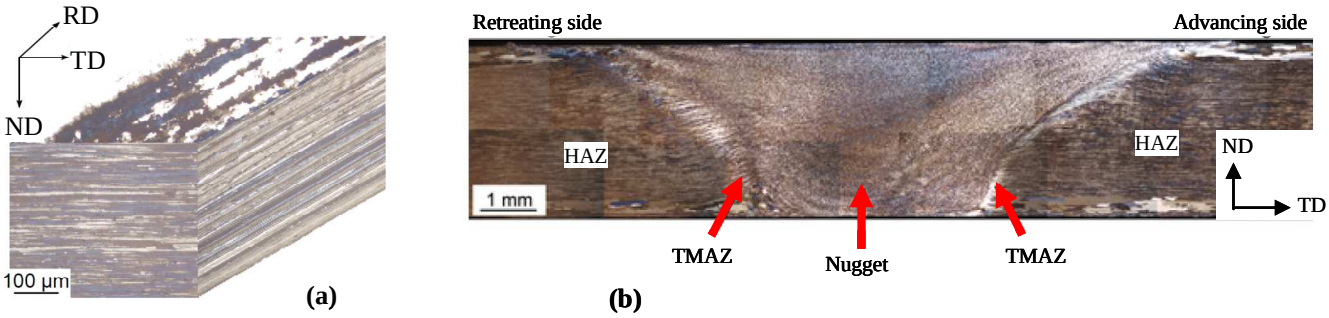

Figure 1. General view (a) of the grain structure of the studied sheet and (b) of a FSW joint (TMAZ: thermo-mechanically affected zone; HAZ: heat-affected zone)

The JLR appears as a dark line across the nugget (Fig. 2a). The KB has the same appearance as the JLR (Fig. 2b). Detailed observations revealed that this defect is intergranular [11]. In the Gap bearing samples, small regions with deeply etched grain boundaries (“sensitive GBs” hereafter) were observed from place to place in the nugget, at the bottom surface (Fig. 2c). The hardness profile (Fig. 3a) is identical for all welds. A minimum in hardness was detected at TMAZs, as already reported e.g. in a 2098-T8 friction stir weld [12].

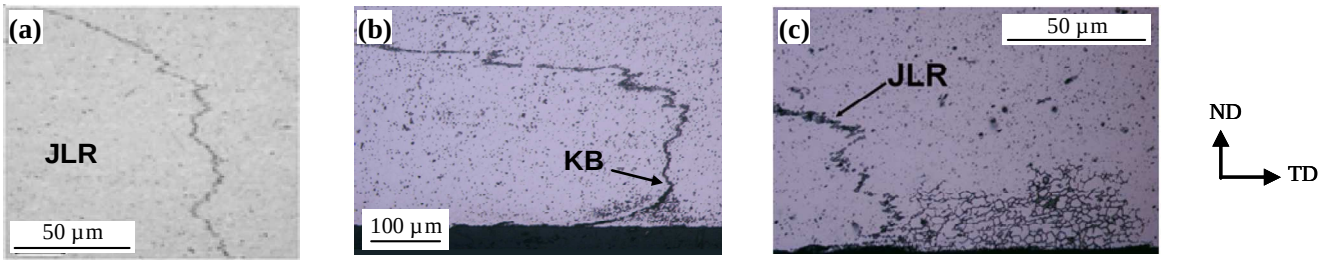

Figure 2. Cross-section observations of weld defects: (a) JLR; (b) KB (bottom) and JLR (upper, nearly horizontal part); (c) etched grain boundaries (bottom) and JLR in a Gap3 bearing weld

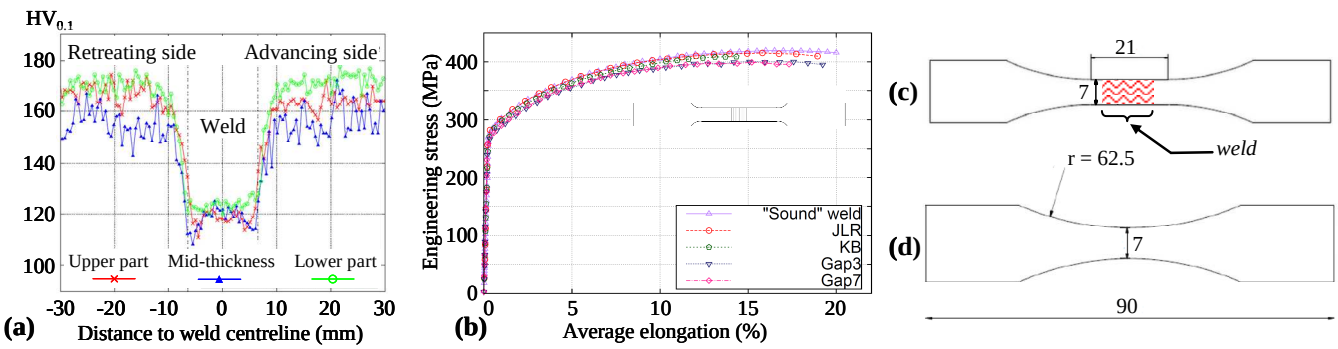

Figure 3. (a) Hardness profiles across a sound weld. (b) Tensile curves of the various kinds of welds. Drawings of full-thickness (c) cross-weld and (d) base metal fatigue specimens (dimensions in mm)

2.2. Mechanical testing

2.2.1. Uniaxial tensile tests

At least two full-thickness smooth tensile specimens (64x12 mm² in gauge dimensions) were cut across each welded joint and pulled in tension, in room temperature laboratory air, using a 250 kN servohydraulic testing machine under displacement control (elongation rate: 2.10^{-4} s^{-1} based on a gauge length of 14 mm). Local strains were monitored thanks to a random black-and-white speckle deposited onto the specimen and to conventional strain field monitoring techniques. Incremental calculation of displacements and strains was selected. To determine the onset of KB opening, an in situ tensile test on a miniature dogbone specimen (full thickness, 3×13 mm² in gauge dimensions) was carried out in the SEM, while observing the slightly polished bottom surface of the nugget.

2.2.2. Uniaxial fatigue tests

Uniaxial fatigue tests were performed on full-thickness specimens along TD (Fig. 3c,d). A straight gauge part was chosen for the cross-weld specimen, in order to study the fatigue crack initiation site under a homogeneous nominal stress (i.e., load divided by the initial area of the bearing section). All specimen corners and edges were slightly ground using 1200-grit SiC paper, except otherwise stated, to limit the influence of surface irregularities on fatigue crack initiation. Fatigue specimens were tested in room temperature laboratory air, under load control, with a load ratio of 0.1 and a frequency of 20 Hz. Most of the tests were carried out up to fracture.

A few tests were started at a lower frequency (0.5 Hz) for the first 10 cycles together with strain field monitoring on one edge thanks to the digital image correlation as described previously. Then, the frequency was changed to 20Hz. After a given fraction of the estimated lifetime at that load level, these tests were interrupted and the specimens were fractured under uniaxial tension.

2.3. Microstructural observations

Metallographic samples were polished in cross-section with diamond paste and first etched by anodic oxidation (3% aqueous solution of tetrafluoroboric acid in water, under 30 V with respect to pure Al, for 2-3 min) and then further chemically etched with the Dix-Keller reagent (2 mL HF, 3 mL HCl, 20 mL HNO_3, and 175 mL distilled water) and observed using optical microscopy under white light. Fracture surfaces were observed using a Leo 1540VP or a Zeiss DSM 982 Gemini scanning electron microscope (SEM) in secondary electron imaging. After each test, one specimen half was cut along the TD-ND plane at the crack initiation site, polished and etched using the above procedure to determine the influence of welding defects on crack initiation and propagation.

3. Experimental results and discussion

3.1. Tensile properties

No significant effect of the welding conditions was detected on tensile properties of JLR and KB bearing welds, with respect to sound welds (Fig. 3b). The yield strength and tensile strength of the welds were lower than those of the base metal (along the same loading direction) by about 40 and 20%, respectively (Table 1). Strain field measurements yielded identical results for all welds, except for a slight strain localisation at the bottom surface of the Gap7 bearing nugget [11].

All cross-weld specimens failed by strain localization, followed by ductile fracture. Sound welds fractured from close to the TMAZ-HAZ boundary with mixed dimpled / “fibrous” fracture surfaces (Fig. 4a). No obvious effect of the JLR was evidenced, as already reported by [1, 5, 13-14].

Table 1. Yield strength, tensile strength and ratio of weld tensile strength to that of base metal (along TD)

Weld	Yield strength (MPa)	Tensile strength (MPa)	Ratio of weld strength to base metal strength
Sound	282-302	412-429	0.80-0.83
JLR bearing	285-296	413-416	0.80
KB bearing	265-287	398-410	0.77-0.80
Gap3 bearing	282-284	401-404	0.78
Gap7 bearing	277-281	398-399	0.77

In KB bearing specimens, fracture initiated as a striated, locally ductile region whose location and geometry closely matched those of the KB itself (Fig. 4b), as in [7]. The crack then left the KB to propagate across the nugget. From in situ tensile tests, opening of the KB (Fig. 4c) occurred for an engineering stress higher than about 280 MPa (more details are reported in [11]). Multiple crack initiation sites were found in that case.

No effect of “sensitive GBs” was detected for the Gap3 bearing welds, whereas intergranular cracking triggered fracture of Gap7 welds (Fig. 4d). As already reported in [9], a clearance of 10% of the parent sheet thickness may be high enough to induce a decrease in strength. A clearance of 23% of the parent sheet thickness is high enough, in the investigated conditions, to trigger intergranular crack initiation and propagation from the nugget root.

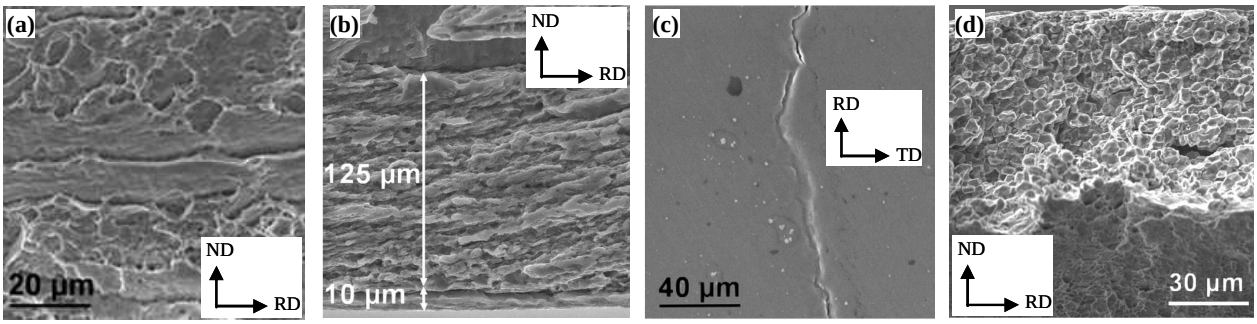

Figure 4. (a,b,d) fracture surfaces (a) in the TMAZ (sound and JLR bearing welds), (b) of a KB bearing weld (the striated zone corresponding to the KB defect itself) and (d) close to the root of a Gap7 weld. (c) Onset of cracking at the lower surface of a KB bearing specimen, slightly polished and then pulled in tension in the SEM (loading axis horizontal)

3.2. Fatigue properties

Fatigue properties of base metal and welds are summarized in Fig. 5 and Table 2. Despite of the high experimental scatter, the cross-weld specimens can be ranged as follows, with respect to their fatigue strength (Fig. 5 and Table 2):

Sound > JLR bearing > KB bearing (as-welded) > KB bearing (ground) > Gap3, Gap7 (1)

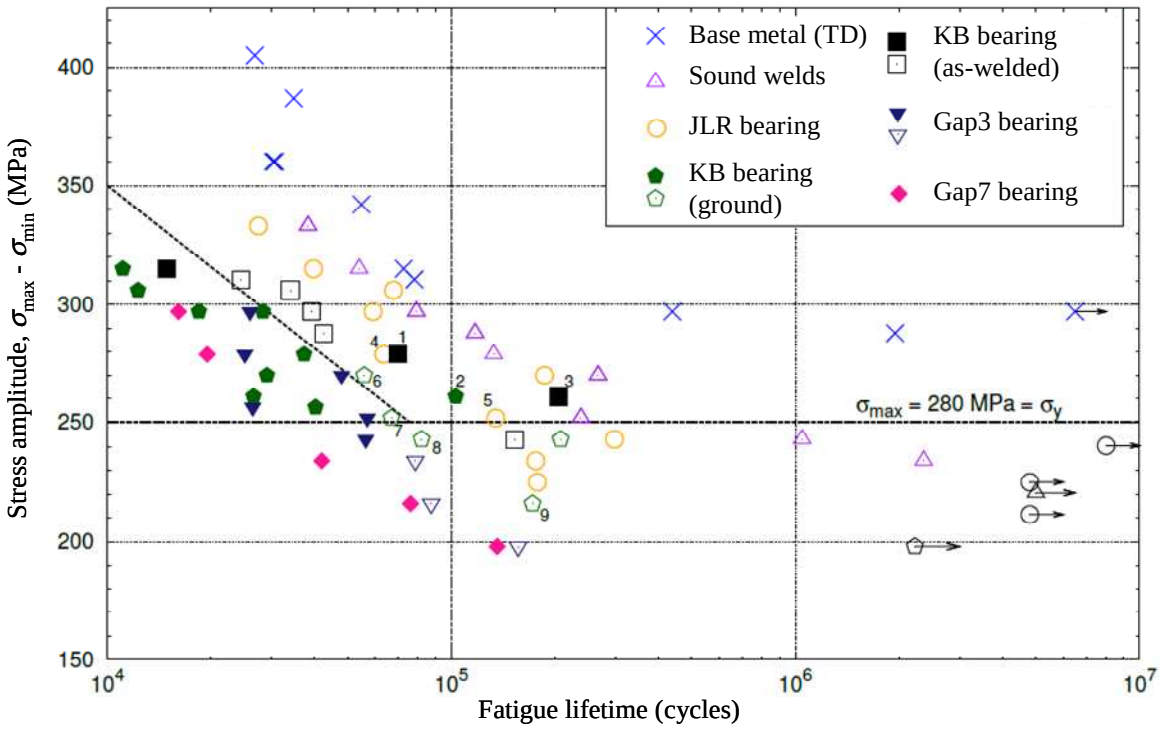

Figure 5. Fatigue lifetime of base metal, sound and defect bearing welds. Full symbols indicate that fracture initiated from the investigated weld defect. For all tests above the horizontal line, large scale yielding occurred during the first cycle. Comments on the numbered symbols: see text

Table 2. Fatigue strength, estimates of the number of cycles at crack initiation and crack initiation sites

Specimens	$\Delta\sigma$ at 10^5 cycles (MPa)	Relative difference with respect to sound welds (%)	Number of cycles at crack initiation (ratio to lifetime)	Crack initiation locus (number of specimens)
Base metal (TD)	315	+7%	-	-
Sound welds	280	-	> 50%	nugget (3) TMAZ / HAZ (6)
JLR bearing welds	270	-7%	≈ 50%	nugget far from JLR (6) HAZ (4)
KB bearing welds, ground	240	-17%	≈ 0 (0.25 cycle)	nugget far from KB (1) HAZ (4) KB (9)
KB bearing welds, as-welded	270	-7%	≈ 0 (0.25 cycle)	nugget far from KB (2) TMAZ/HAZ (3) KB (3)
Gap3 bearing welds, as-welded	210	-28%	≈ 0 (0.25 cycle)?	HAZ (3) sensitized GBs (6)
Gap7 bearing welds, as-welded	210	-28%	≈ 0 (0.25 cycle)?	sensitized GBs (5)

3.2.1. Fatigue properties of sound welds

The fatigue lifetime of sound welds is close to that of the base metal for higher loads, despite of their lower strength. From strain field monitoring, plastic yielding occurred during the first cycle and from the second cycle, only elastic strains were detected. The loss in fatigue strength (about 10%) of sound welds with respect to base metal, for lifetimes higher than ~10^5 cycles is lower than that reported by Cavaliere et al. [15] for a load ratio of 0.33 and a lifetime of 3.10^5 cycles (about 22%). This might be due to the difference in specimen surface preparation (Cavaliere et al. used polished surfaces) or in welding parameters.

Fatigue cracks in sound welds initiated either at the TMAZ/HAZ or within the nugget. Typical fracture surfaces observed in the nugget are shown in Fig. 6. Typical striations are observed in the Stage II crack propagation regime. No fatigue crack was detected either in the fracture surface or in a longitudinal cross-section after interrupted testing ($\Delta\sigma$ = 270 MPa, test interrupted after 50,000 cycles ~ 50% of fatigue lifetime). Consequently, the lifetime at crack initiation was higher than 50% of total lifetime in the considered case.

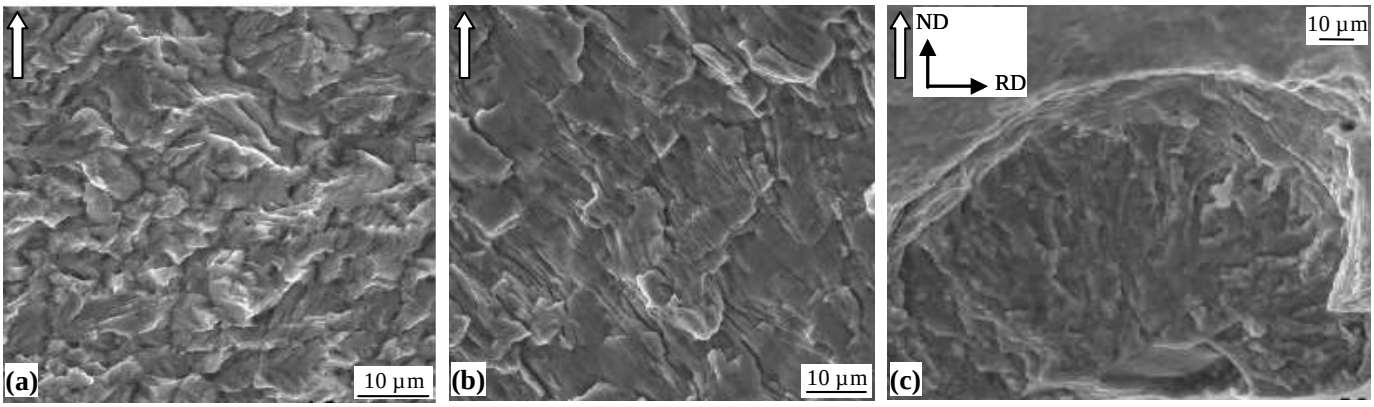

Figure 6. (a,b) Fracture surface of a sound weld ($\Delta\sigma$ = 270 MPa, lifetime ~ 133,000 cycles): (a) onset of crack propagation in the nugget; (b) Stage II crack propagation in the nugget. (c) Fatigue crack initiation and propagation in a JLR bearing specimen, $\Delta\sigma$ = 270 MPa, test interrupted after 50,000 cycles (~ 50% of fatigue lifetime). Average crack propagation indicated with a white arrow; same specimen orientation in (a,b,c)

3.2.2. Fatigue properties of JLR bearing welds

The fatigue strength of JLR bearing specimens is close to that of sound weld specimens. For data points 4 and 5 in Fig. 5, fracture initiated from the TMAZ at the top surface, so that any possible influence of a small flash could not be discarded. The slight difference evidenced from Table 2 and Fig. 5 is much lower than that reported in literature [3, 16-18] for 5083, 2024 and 7075 alloys. However, in the present study only, JLR bearing welds were quantitatively compared with sound welds realized with the *same* base metal and welding conditions. From the two interrupted tests, only one specimen showed indications of fatigue crack initiation and propagation from the bottom surface of the nugget, yet over limited distance (Fig. 6c). This suggests that for the investigated load level, the crack initiation lifetime could be close to 50% of the total fatigue lifetime.

3.2.2. Fatigue properties of KB bearing welds

As the KB is tilted by only about 20° with respect to the loading axis over a depth of about 20 µm (Fig. 1b), two preparation procedures were used for the bottom surface of KB bearing fatigue specimens. The first set of specimens was tested with as-welded bottom surface. The lower surface of the second set of specimens was ground over about 20 µm as for sound and JLR bearing welds. Only in the latter case did the part of KB that was nearly perpendicular to the loading axis intersect the bottom free surface of the specimens.

A significant difference in lifetime was observed between both sets of specimens (Fig. 5). Crack initiation in ground KB bearing specimens occurred at the KB for $\Delta\sigma$ > 255 MPa, i.e., for a maximum stress higher than the value of 280 MPa that was also required to open the KB under uniaxial tension. The fracture surface of the KB (Fig. 7) was similar to that observed after uniaxial tension and to that reported in [8]. After 7,000 (respectively, 15,000) cycles, the fracture surface

evidenced local opening of the KB over 60-80 µm (respectively, ~50 µm) followed by fatigue crack propagation over 30-40 µm (respectively, 30-55 µm) (Fig. 7c). Thus, even after only 20% of the fatigue lifetime, crack initiation and propagation was observed from place to place all along the KB as in [7, 8]. This confirms that at high stresses, early crack initiation occurs due to opening of the KB, most probably during the first cycle. At lower stresses, crack initiation occurred away from the KB but the lifetime was still significantly lower than that of sound or JLR bearing welds (data points 6 to 9 in Fig. 5). In KB specimens with an as-welded lower surface, the crack initiation site (either at the KB, or from surface defects far from the KB) did not significantly depend on the load level. This suggests that the effect of the as-welded KB on the fatigue lifetime could be of the same order as that of surface defects after welding.

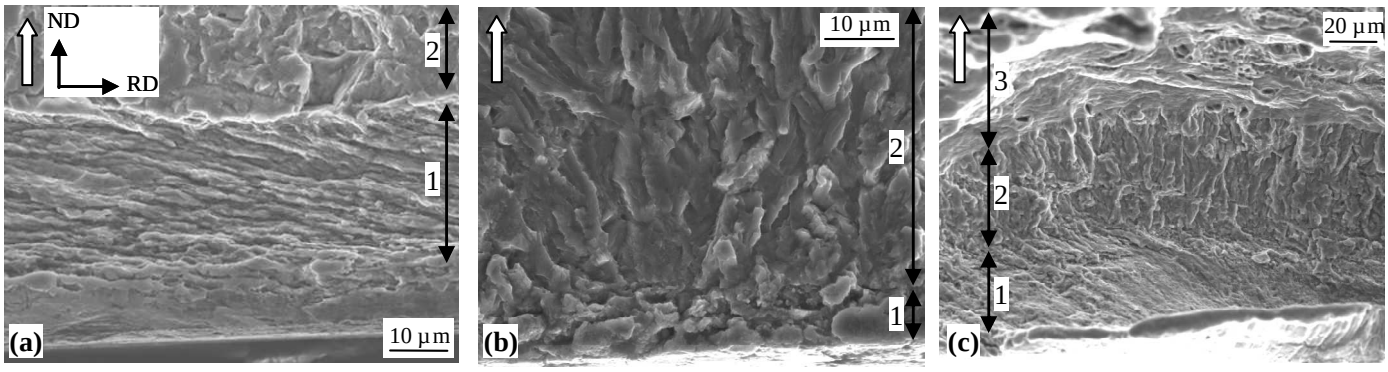

Figure 7. Fracture surface of KB bearing specimens (a) with a ground bottom surface, $\Delta\sigma$ = 306 MPa, lifetime ~13,000 cycles with the crack propagating in mode I along the exposed KB, (b) with an as-welded bottom surface; initiation at, and propagation away from the KB, $\Delta\sigma$ = 279 MPa, lifetime ~70,000 cycles; (c) with a ground bottom surface, $\Delta\sigma$ = 279 MPa, interrupted after 15,000 cycles. (1), (2), and (3) respectively denote cracking along the KB, away from the KB and under uniaxial tension. Average crack propagation indicated with a white arrow; same specimen orientation in (a,b,c)

3.2.3. Fatigue properties of Gap3 and Gap7 bearing welds

The lifetime of Gap bearing welds was significantly lower than that of the other cross-weld specimens (Fig. 5 and Table 2). In all Gap7 specimens and in Gap3 specimens tested at higher stresses, fracture initiated from small regions close to the bottom surface and showing intergranular decohesions (Fig. 8), similar to those found after uniaxial tension (Fig. 4d). This suggests that in these conditions, the Gap-induced defects strongly affect the lifetime at crack initiation. Even when the fatigue crack did not initiate from such regions, the lifetime was low, as already found for KB bearing welds.

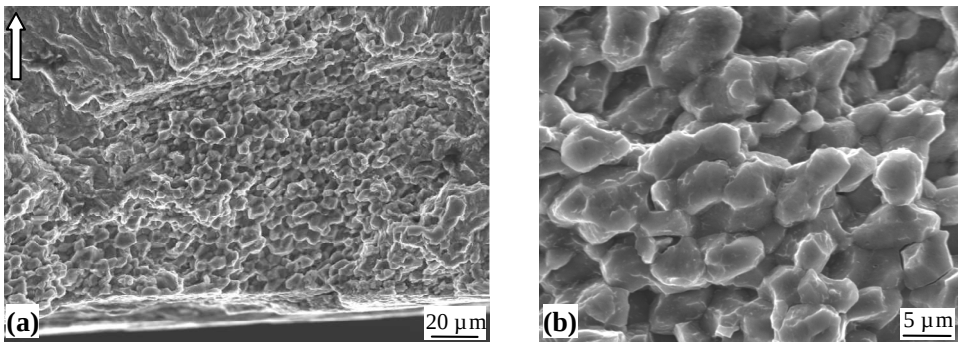

Figure 8. (a) Fatigue crack initiation from “sensitive” GBs of a Gap3 bearing specimen, $\Delta\sigma$ = 256 MPa, lifetime ~26,500 cycles. The average crack propagation is indicated with a white arrow and the specimen orientation is the same as in Fig. 7a. (b) Detailed view of intergranular fracture of “sensitive” GBs

4. Discussion

4.1. Estimation of the crack propagation threshold

To tentatively derive a crack propagation rate from experimental data, ground KB bearing specimens tested at higher stresses were selected because (i) crack initiation was thought to occur during the first cycle, so that the number of cycles corresponding to crack propagation could be easily estimated, and (ii) because crack initiation occurred all along the KB, so that to a first approximation, the crack could be considered to affect the whole width of the specimens. Under these assumptions, a very simple estimate of the stress intensity factor was made by considering a crack of length *a*, propagating in pure Mode I from one side of an infinite plate, leading to the following equation [19]:

$$K_I = \sigma\sqrt{\pi a}\, Y\left(\frac{a}{W}\right) = \sigma\sqrt{\pi a}\left[1.12 - 0.231\left(\frac{a}{W}\right) + 10.55\left(\frac{a}{W}\right)^2 - 21.72\left(\frac{a}{W}\right)^3 + 30.39\left(\frac{a}{W}\right)^4\right] \quad (2)$$

In Eq. (2), *W* is the length of the ligament, here nearly equal to the plate thickness (3 mm). Eq. (2) was applied to all KB bearing specimens showing crack initiation from the KB, by using the minimum length over which KB opening was observed. This yielded a lower bound value for the stress intensity factor after opening of the KB defect. Fig. 9a shows a threshold for crack propagation in KB bearing welds of about 1 MPa√m, close to that reported for 2198-T8 base metal with the same load ratio (Fig. 9b). As-welded specimens exhibited only slight opening of the (tilted) KB, leading to Mode I stress intensity factors close to the threshold value (data points 1 to 3 in Fig. 5). This could explain why their fatigue lifetime was not correlated with the fracture initiation locus.

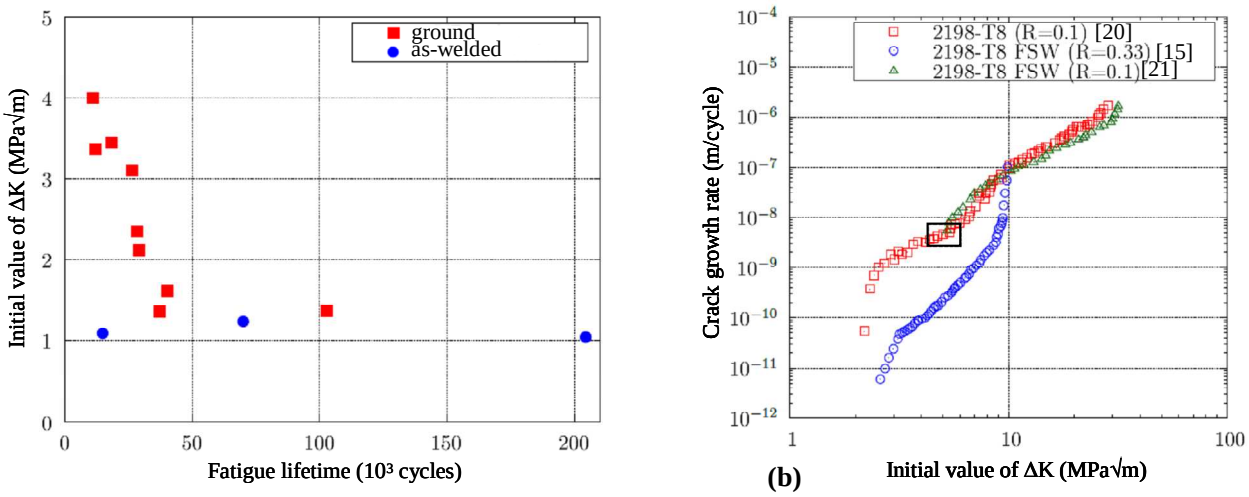

Figure 9. (a) Initial value of ΔK_I for KB bearing welds with either ground or as-welded lower surfaces, showing an apparent threshold value of about 1 MPa√m. (b) Comparison of estimated crack propagation rates during interrupted tests on KB bearing specimens (black box) with literature data

4.2. Estimation of the crack propagation rate in ground KB bearing specimens

To tentatively derive a value of the average crack propagation rate over a small distance, Eq. (2) was used (i) after opening of the KB, and (ii) after interrupted crack propagation. As the length of the fatigue crack varied from place to place, minimum and maximum values were used, leading to upper and lower bounds listed in Table 3. These values are consistent with literature data obtained using the same load ratio (Fig. 9b).

Table 3. Determination of average crack propagation rate from interrupted tests on KB bearing welds

Δσ = 279 MPa, ground bottom surface	After 7,000 cycles (≈ 20% of lifetime)	After 15,000 cycles (≈ 40% of lifetime)
Δ*K* after opening of KB (MPa√m)	4.3	4.3
Δ*K* after fatigue crack propagation (MPa√m)	5.2 - 5.8	5.5 - 6.1
Average value of crack growth (10^{-9} m/cycle)	4.3 - 7.1	2.6 - 4.0

4.3. Effect of welding conditions on fatigue crack initiation and propagation

In KB and Gap bearing specimens, the defect clearly affects crack initiation mechanisms, leading to a strong reduction in fatigue lifetime at high stresses. The fatigue lifetime at low stresses cannot be related to an obvious effect of defects on crack initiation, hardness or tensile strength, while it is significantly affected by the change in welding conditions. Thus, changing the welding conditions not only produced "visible" defects, but also influenced the sensitivity of the welds to fatigue crack initiation even away from those defects. Consequently, the effect of such changes on the fatigue strength cannot be inferred from using only tensile test results and metallographic inspection of the welds. For a maximal stress lower than the yield strength of the nugget (horizontal line in Fig. 5), residual stresses cannot be relieved during the fatigue test and have to be taken into account to further interpret data from e.g. Gap3 and Gap7 bearing specimens. The estimated crack propagation rate in KB bearing specimens seems to be close to that reported in literature (Fig. 9b), indicating that crack propagation could be less affected than crack initiation by the change in welding conditions. More experimental data points are needed to confirm this result.

5. Conclusions

Tension-tension fatigue tests on 2198-T851 butt friction stir welds led to the following conclusions.

- The effect of the joint line remnant is negligible in the investigated conditions.
- The kissing bond opens during tension or during the first fatigue cycle if the maximum stress is higher than about 280 MPa. The crack growth rate (4-7.10^{-9} m/cycle) is consistent with literature data. The threshold stress intensity factor amplitude, Δ*K*, for crack propagation is close to 1 MPa√m.
- A clearance of 10% of the sheet thickness is large enough to trigger local intergranular decohesions close to the lower surface of the nugget, for sufficiently high values of stresses. A clearance of 23% of the sheet thickness systematically leads to premature crack initiation by intergranular decohesions both in uniaxial tension and fatigue tests. The resulting low fatigue strength could be affected by residual stresses because no large scale plastic strain develops in that particular case.
- The change in welding conditions seems to lower the fatigue strength even far away from the visible defects, while keeping hardness and tensile properties almost unaffected. The appearance of defects is not the only consequence of this change that influences fatigue properties.

Acknowledgements
This study was supported by the FNRAE (National Aerospace Foundation) under "MASAE" grant.

References

[1] P. L. Threadgill, A. J. Leonard, H. R. Shercliff, P. J. Withers, Friction stir welding of aluminium alloys. Int. Mater. Rev., 54 (2009) 49-93.

[2] Y. S. Sato, H. Takauchi, S. H. C. Park, H. Kokawa, Characteristics of the kissing-bond in friction stir welded Al alloy 1050. Mater. Sci. Eng., A405 (2005) 333-338.
[3] S. Di, X. Yang, G. Luan, B. Jian, Comparative study on fatigue properties between AA2024-T4 friction stir welds and base materials. Mater. Sci. Eng., A435-436 (2006) 389-395.
[4] H. B. Chen, K. Yan, T. Lin, S. B. Chen, C. Y. Jiang, Y. Zhao, The investigation of typical welding defects for 5456 aluminum alloy friction stir welds. Mater. Sci. Eng., A433 (2006) 64-69.
[5] Y. Uematsu, K. Tokaji, H. Shibata, Y. Tozaki, T. Ohmune, Fatigue behaviour of friction stir welds without neither welding flash nor flaw in several aluminium alloys, Int. J. Fatigue, 31 (2009) 1443-1453.
[6] L. Cui, X. Yang, G. Zhou, X. Xu, Z. Shen, Characteristics of defects and tensile behaviors on friction stir welded AA6061-T4 T-joints. Mater. Sci. Eng., A543 (2012) 58-68.
[7] T. L. Dickerson, J. Przydatek, Fatigue of friction stir welds in aluminium alloys that contain root flaws. Int. J. Fatigue, 25 (2003) 1399-1409.
[8] C. Zhou, X. Yang, G. Luan, Effect of root flaws on the fatigue property of friction stir welds in 2024-T3 aluminum alloys. Mater. Sci. Eng., A418 (2006) 155-160.
[9] J. E. Barnes, J. Mc Michael, A. Reynolds, Effects of friction stir welding defects on 7075 joint strength and fatigue life, in: Proc. 6th Int. Symp. on Friction Stir Welding, Curran Associates, Inc., New York, 2006 (CD-ROM).
[10] B. K. Christner, G. D. Sylva, Friction stir welding development for aerospace application, in: Int. Conf. on Advances in Welding Technology, Joining of High Performance Materials, Columbus, OH, 1996.
[11] T. Le Jolu, T. F. Morgeneyer, A. Denquin, J. Besson, A. F. Gourgues-Lorenzon, Characterisation of internal welding defects and effect on the plastic behaviour of FSW joints of AA2198 Al-Cu-Li alloy, to be submitted to Mater. Sci. Eng. A (2013).
[12] A. Denquin, D. Allehaux, G. Lapasset, H. Ostersehlte, Microstructural phenomena of FSW joints; friction stir welding behaviour of 2098 type alloys and resulting weld properties, in: G. Gottstein, J. Hirsch, B. Skrotzki (Eds.), 11th Int. Conf. on aluminium alloys, Wiley, 2008, pp. 1939-1944.
[13] H. J. Liu, H. Fujii, M. Maeda, and K. Nogi, Tensile properties and fracture locations of friction-stir-welded joints of 2017-T351 aluminum alloy. J. Mater. Proc. Technol., 142 (2006) 692-696.
[14] K. Kumar and S. V. Kailas, Positional dependence of material flow in friction stir welding: analysis of joint line remnant and its relevance to dissimilar metal welding. Sci. Technol. Welding Joining, 15 (2010) 305-311.
[15] P. Cavaliere, A. De Santis, F. Panella, A. Squillace, Effect of anisotropy on fatigue properties of 2198 Al-Li plates joined by friction stir welding. Eng. Failure Analysis, 16, (2009) 1856-1865.
[16] C. Z. Zhou, X. Q. Yang, G. H. Luan, Effect of kissing bond on fatigue behavior of friction stir welds on Al 5083 alloy. J. Mater. Sci., 41 (2006) 2771-2777.
[17] C.Z. Zhou, X. Q. Yang, G. H. Luan, Effect of oxide array on the fatigue property of friction stir welds. Scr. Mater., 54 (2006) 1515-1520.
[18] S. Di, X. Yang, D. Fang, G. Luan, The influence of zigzag-curve defect on the fatigue properties of friction stir welds in 7075-T6 Al alloy. Mater. Chem. Phys., 104 (2007) 244-248.
[19] H. Tada, P. C. Paris, G. R. Irwin, The stress analysis of cracks handbook. Del Research Corp. Saint Louis, 1973.
[20] S. Richard, Fatigue cracking of third generation aluminium-lithium alloys, PhD dissertation, http://tel.archives-ouvertes.fr/docs/00/60/54/26/PDF/ThA_se_SA_bastien_RICHARD_2011.pdf, ENSMA, Poitiers, France (in French).
[21] Y. E. Ma, P. E. Irving, T. Fisher, X. Zhang, G. Servetti, Effects of residual stresses on fatigue crack propagation in friction stir welded 2198-T8 and 2195-T8 Al-Li alloy joints, in: 12th International Conference on Fracture, Curran Associates, Inc., New York 2010, 1797-1806.

Fibre Bridging and Crack Tip Shielding in Glare: Numerical and Experimental Validation

Sunil Bhat[1]

[1] School of Mechanical and Building Sciences, VIT Univeristy, Vellore, 632014, Tamil Nadu, India
* Corresponding author: ss_bht @rediffmail.com

Abstract The paper validates the phenomenon of fibre bridging and crack tip shielding in Fibre Metal Laminate (Glare) with the help of numerical and experimental procedures. Laminates, with Mode I cracks of different sizes in all their aluminum layers, are subjected to load-extension test to obtain critical loads for estimation of their fracture toughness. Similarly cracked, plain aerospace aluminum alloy specimens are also tested for fracture. Fracture toughness of Glare laminates is found to be higher than those of plain aluminum alloy specimens. Cracked laminates are finally modeled under critical loads by finite element method for quantification of fibre bridging in them. Crack tip shielding is demonstrated.

Keywords Fibre metal laminate, Fibre bridging, Glare, Crack tip shielding

1. Introduction

Fibre metal laminate (FML) is an advanced hybrid structure that consists of layers of thin and light metallic sheets which are alternately bonded and cured with composite prepregs by heat and pressure, each prepreg built up of several resin impregnated fibre cloth layers laid in similar or different orientations. Besides offering gain in specific strength, FML exhibits properties like excellent fatigue and fracture resistance, good impact strength and high fire resistance that makes it a good substitute for monolithic metallic structure especially in aerospace and aircraft applications. FML (Glare), comprising several aerospace aluminum alloy layers and glass fibre based composite prepregs, is considered for investigation in the present work.

Cracks can nucleate in soft aluminum layers, across the interfaces of prepregs, when Glare is pressed into service. The cracks are however shielded due to fibre bridging. Bridging diverts load towards stronger fibres in prepregs that in turn diminishes the intensity of stress fields around crack tips thereby augmenting fracture toughness of Glare vis-à-vis plain aerospace aluminum alloy. Published work, notably by Guo *et al*. [1], Alderliesten *et al*. [2] etc., confirms superior fatigue and fracture properties of FML's. This paper presents an explicit validation of the phenomenon of fibre bridging in Glare with the help of numerical and experimental procedures. Glare laminates, with Mode I cracks of different sizes in all their aluminum layers, are subjected to load-extension test to obtain break or critical loads for estimation of their fracture toughness. Similarly cracked, plain aerospace aluminum alloy specimens are also tested for fracture. Toughness values of laminates are found to be higher than that of plain aluminum alloy specimens. The laminates are finally modeled under critical loads by finite element method. Crack tip shielding in them is demonstrated and convincingly verified.

2. Construction of Glare

Refer Figure 1. Glare laminate consists of three, 0.4 mm thick, 2014-T6 aerospace aluminum alloy sheets, bonded alternately with two prepregs at curing temperature of 160 deg. C, each prepreg built up of three composite layers in the sequence, c0-c90-c0. A composite layer consists of 4 mil or 0.1mm thick unidirectional E-glass fibre cloth that is coated on both the sides with a thin layer of epoxy resin. Composite, c0, has fibres laid in *y* direction i.e. along the direction of the applied load

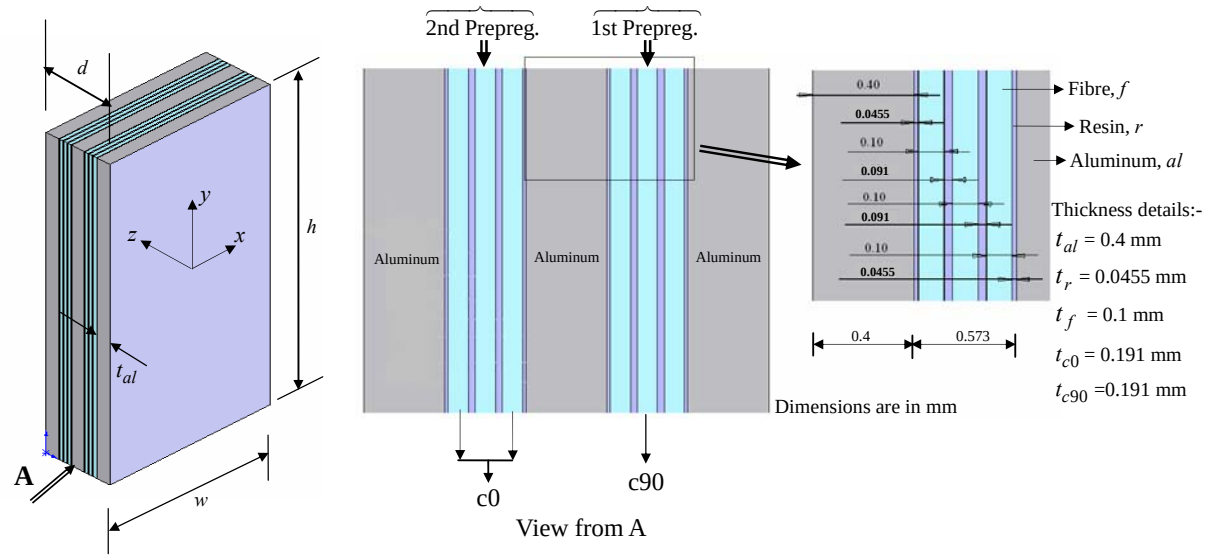

Figure 1. Glare laminate

whereas composite, c90, has fibres laid in x direction i.e. perpendicular to the direction of the applied load. Volume fractions of fibre and resin in each composite layer are 0.522 and 0.478 respectively. The coefficients of thermal expansion of the laminate in longitudinal (y) direction, α_{ll}, and in transverse (x) direction, α_{tl}, are found to be 19.4×10^{-6} C^{-1} and 19.77×10^{-6} C^{-1} respectively. Expected dimensions of the laminate were 200 mm (h), 50 mm (w) and 2.346 mm (d). However, minor deviations could not be avoided during fabrication. Important material data are available in Table 1.

Table 1. Material properties

Property	Aluminum 2014-T6 alloy, *al* (Isotropic)	E-Glass fibre, *f* (Amorphous)	Epoxy resin, *r* (Isotropic)
Modulus of elasticity, E (MPa) Shear modulus, μ (MPa)	72000.0 27060.0	71000.0 29710.0	3500.0 1250.0
Poisson's ratio (υ), % elongation	0.33, 8.0	0.22, 4.8	0.33, 4.0
Yield strength, Y (MPa) Ultimate tensile strength (MPa)	372.0 415.0	--- 3450.0	--- 60.0
Coeff. of thermal expansion (α), C^{-1}	23×10^{-6}	5.0×10^{-6}	57.5×10^{-6}
Plane strain fracture toughness (K_{IC}), MPa$\sqrt{\text{m}}$	14.0-20.0	4.0-5.0	0.5-0.7

3. Theoretical aspects

Stress that develops in un-identical material layers of un-cracked Glare subjected to load differs from the applied stress due to load redistribution caused by elasticity mismatch between the layers. Also, the presence of residual stress, generated in materials during laminate curing due to their varying stiffness and coefficients of thermal expansions, further changes the stress state. The stress-strain constitutive equations and stiffness matrices of the materials in plane stress case (x-y plane) are given as follows:-

i) Aluminum, *al*

$$\sigma_x = \frac{E_{al}}{(1-\upsilon_{al}^2)}\{\varepsilon_x + \upsilon_{al}\varepsilon_y\}$$
$$\sigma_y = \frac{E_{al}}{(1-\upsilon_{al}^2)}\{\upsilon_{al}\varepsilon_x + \varepsilon_y\} \quad ; \quad \text{Stiffness matrix, } \{\mathrm{M}\}_{al} = \begin{bmatrix} \frac{E_{al}}{1-\upsilon_{al}^2} & \frac{E_{al}}{1-\upsilon_{al}^2}\upsilon_{al} & 0 \\ \frac{E_{al}}{1-\upsilon_{al}^2}\upsilon_{al} & \frac{E_{al}}{1-\upsilon_{al}^2} & 0 \\ 0 & 0 & \mu_{al} \end{bmatrix}$$
$$\tau_{xy} = \mu_{al}\gamma_{xy}$$

ii) Resin, *r*

$$\sigma_x = \frac{E_r}{(1-\upsilon_r^2)}\{\varepsilon_x + \upsilon_r\varepsilon_y\}$$
$$\sigma_y = \frac{E_r}{(1-\upsilon_r^2)}\{\upsilon_r\varepsilon_x + \varepsilon_y\} \quad ; \quad \text{Stiffness matrix, } \{\mathrm{M}\}_r = \begin{bmatrix} \frac{E_r}{1-\upsilon_r^2} & \frac{E_r}{1-\upsilon_r^2}\upsilon_r & 0 \\ \frac{E_r}{1-\upsilon_r^2}\upsilon_r & \frac{E_r}{1-\upsilon_r^2} & 0 \\ 0 & 0 & \mu_r \end{bmatrix}$$
$$\tau_{xy} = \mu_r\gamma_{xy}$$

iii) Fibre, *f*

$$\sigma_x = \frac{E_f}{(1-\upsilon_f^2)}\{\varepsilon_x + \upsilon_f\varepsilon_y\}$$
$$\sigma_y = \frac{E_f}{(1-\upsilon_f^2)}\{\upsilon_f\varepsilon_x + \varepsilon_y\} \quad ; \quad \text{Stiffness matrix, } \{\mathrm{M}\}_f = \begin{bmatrix} \frac{E_f}{1-\upsilon_f^2} & \frac{E_f}{1-\upsilon_f^2}\upsilon_f & 0 \\ \frac{E_f}{1-\upsilon_f^2}\upsilon_f & \frac{E_f}{1-\upsilon_f^2} & 0 \\ 0 & 0 & \mu_f \end{bmatrix}$$
$$\tau_{xy} = \mu_f\gamma_{xy}$$

Stiffness matrix of the laminate is obtained from classical theory as follows:-

$$\{\mathrm{M}\}_{lam} = \{\mathrm{M}\}_{al} \times \frac{t_{al} \times 3}{d} + \{\mathrm{M}\}_r \times \frac{t_r \times 12}{d} + \{\mathrm{M}\}_f \times \frac{t_f \times 6}{d}$$

For applied stress state over the laminate, $\{\sigma\}_{applied} = \begin{Bmatrix} \sigma_x \\ \sigma_y \\ \tau_{xy} \end{Bmatrix}_{applied}$,

Strain in the laminate, $\varepsilon_{lam} = \begin{Bmatrix} \varepsilon_x \\ \varepsilon_y \\ \gamma_{xy} \end{Bmatrix}_{lam} = \{\mathrm{M}\}_{lam}^{-1}\sigma_{applied}$

Residual strain (*rs*) in material layers is written as:-

Aluminum, $\{\varepsilon\}_{al,rs} = \left[\begin{Bmatrix} \alpha_x \\ \alpha_y \\ 0 \end{Bmatrix}_{al} - \begin{Bmatrix} \alpha_{tl} \\ \alpha_{ll} \\ 0 \end{Bmatrix}\right] \times \left(T_{cuiring} - T_{ambient}\right)$

Resin, $\{\varepsilon\}_{r,rs} = \left[\begin{Bmatrix} \alpha_x \\ \alpha_y \\ 0 \end{Bmatrix}_{r} - \begin{Bmatrix} \alpha_{tl} \\ \alpha_{ll} \\ 0 \end{Bmatrix}\right] \times \left(T_{cuiring} - T_{ambient}\right)$

Fibre, $\{\varepsilon\}_{f,rs} = \left[\begin{Bmatrix} \alpha_x \\ \alpha_y \\ 0 \end{Bmatrix}_{f} - \begin{Bmatrix} \alpha_{tl} \\ \alpha_{ll} \\ 0 \end{Bmatrix}\right] \times \left(T_{cuiring} - T_{ambient}\right)$

Residual stress in aluminum = $\{\mathrm{M}\}_{al} \times \left[\{\varepsilon\}_{al,rs}\right]$; Residual stress in resin = $\{\mathrm{M}\}_r \times \left[\{\varepsilon\}_{r,rs}\right]$; Residual stress in

fibre = $\{\mathrm{M}\}_f \times \left[\{\varepsilon\}_{f,rs}\right]$

Stress developing in material layers (Induced stress), $\{\sigma\}_{induced} = \begin{Bmatrix} \sigma_x \\ \sigma_y \\ \tau_{xy} \end{Bmatrix}_{induced}$, is determined as follows:-

$\{\sigma\}_{induced,al} = \{\mathrm{M}\}_{al} \times \left[\varepsilon_{lam} + \{\varepsilon\}_{al,rs}\right]$; $\{\sigma\}_{induced,r} = \{\mathrm{M}\}_r \times \left[\varepsilon_{lam} + \{\varepsilon\}_{r,rs}\right]$; $\{\sigma\}_{induced,f} = \{\mathrm{M}\}_f \times \left[\varepsilon_{lam} + \{\varepsilon\}_{f,rs}\right]$

In the case of cracked Glare, stress state around cracked aluminum and affected fibre zone differs from the induced stress due to the presence of crack and onset of the process of fibre bridging. These effects are assessed numerically in Section 5.

Plane stress fracture toughness or induced stress intensity parameter of Glare, at fracture (*fr*), containing cracks of length, *c*, in aluminum layers is obtained from the following expression pertaining to Linear Elastic Fracture Mechanics (LEFM)

$$K_{C,lam} = (\sigma_{y,induced,al})_{fr} \times \sqrt{\pi c} \times CF \tag{1}$$

where configuration factor, *CF*, for an edge crack is empirically given by $CF = \left[1.12 - 0.23\frac{c}{w} + 10.55\left(\frac{c}{w}\right)^2 - 21.72\left(\frac{c}{w}\right)^3 + 30.39\left(\frac{c}{w}\right)^4\right]$ and , *w*, is the width of the laminate. For cracked plain aluminum alloy specimen, the expression takes the form, $K_{C,al} = (\sigma_{y,applied})_{fr} \times \sqrt{\pi c} \times CF$, term $(\sigma_{y,induced,al})_{fr}$ used in the laminate being replaced by $(\sigma_{y,applied})_{fr}$ since load redistribution does not take place in plain specimen. In the case of a thin plain specimen, plane strain fracture toughness, $K_{IC,al}$, is estimated from plane stress toughness value, $K_{C,al}$, by the following expression [3]

$$K_{C,al} = K_{IC,al}\left[1 + \frac{1.4}{p^2}\left(\frac{K_{IC,al}}{Y_{al}}\right)^4\right]^{1/2} \tag{2}$$

where *p* is the thickness of the specimen. Knowing $K_{IC,al}$, plane stress toughness of hypothetical plain aluminum alloy specimen, $K_{C,al}{}^d$, with higher thickness, *d*, equal to that of Glare laminate, is again obtained from Eq. (2). The following condition holds good in Glare at fracture

$$K_{C,lam} = K_{tip} + K_{br} \text{ or } K_{C,lam} = K_{C,al}{}^d + K_{br} \text{ since } K_{tip} = K_{C,al}{}^d \tag{3}$$

where K_{tip} is the crack tip stress intensity parameter and K_{br} is the bridging stress intensity parameter. Fulfillment of the conditions, $t_{al} < 2.5\left(\frac{K_{IC,al}}{Y_{al}}\right)^2$ and $p < 2.5\left(\frac{K_{IC,al}}{Y_{al}}\right)^2$, supports plane stress conditions in cracked aluminum of Glare and of plain specimen respectively.

4. Experimental work

Starter notches were machined across the interfaces of all material layers at the edges of Glare laminates. Mode I cracks, nucleated at notch tips by fatigue cycles, were made to grow up to

lengths, c, of 5 mm, 7 mm, 9.5 mm, 14 mm and 20 mm in laminates numbered 1 to 5 respectively. Refer Figure 2a). As expected, the cracks developed in all soft aluminum layers and not in stronger fibres of prepregs. No interfacial crack growth (Delamination) was observed at aluminum fibre interfaces. Each cracked laminate was then subjected to load-extension test in a hydraulic test rig to measure the load line stress applied over it at fracture, $(\sigma_{y,applied})_{fr}$. Refer Figure 3 for the test arrangement. At fracture, aluminum layers failed first by critical crack growth followed by stretching of fibre layers till the laminate separated. $(\sigma_{y,applied})_{fr}$ values varied in the laminates due to different crack sizes in them. As explained in Section 3, induced stress in aluminum layers at fracture, $(\sigma_{y,induced,al})_{fr}$, was different from $(\sigma_{y,applied})_{fr}$. The values are provided in Table 2. Refer Figure 2b). Five cracked specimens of plain aerospace aluminum 2014-T6 alloy, also numbered 1 to 5, with small thickness, p, but same crack sizes and other dimensions similar to the laminates, were also tested for fracture. For same crack length, $(\sigma_{y,applied})_{fr}$ values of plain aluminum alloy specimens were found to be greater than that of the laminates due to smaller thickness of the former. Thickness effects were however nullified by obtaining $K_{C,al}{}^{d}$. Sample load-extension curves of laminate and of plain aluminum specimen at 20 mm crack length are displayed in Figure 4. All the curves, including those at other crack lengths also, were mostly found to be linear even near fracture loads, because of low ductility of aluminum alloy. The principles of LEFM were therefore valid and the use of parameter K for fracture characterization was justified.

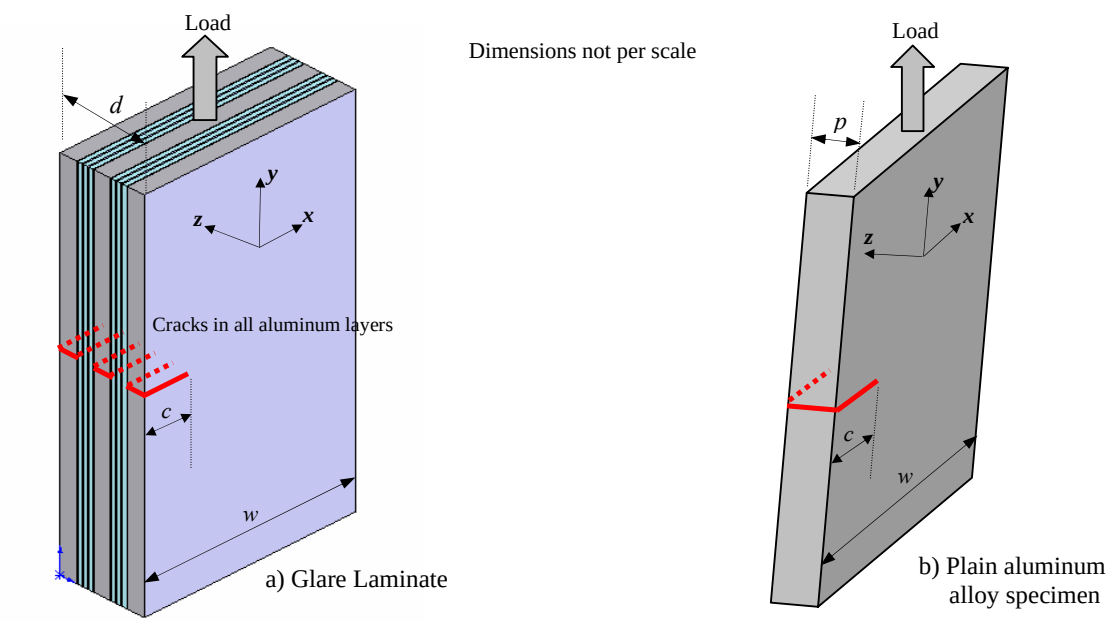

Figure 2. Crack configuration in Glare laminate and in plain aluminum alloy specimen

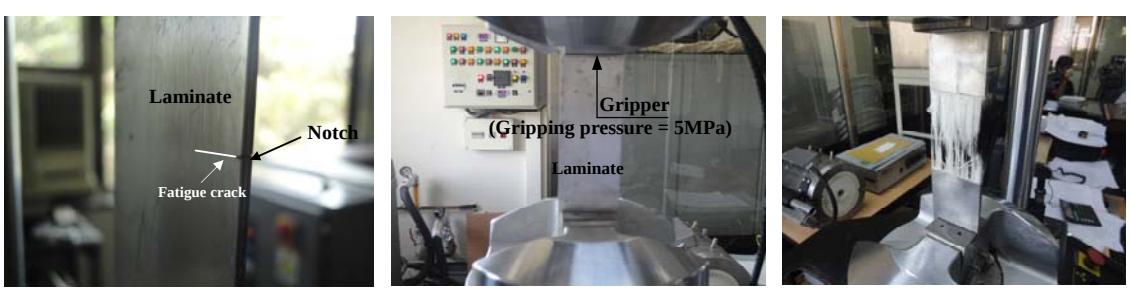

a) Cracked laminate b) Laminate on test rig c) Tested laminate

Figure 3. Fracture test arrangement

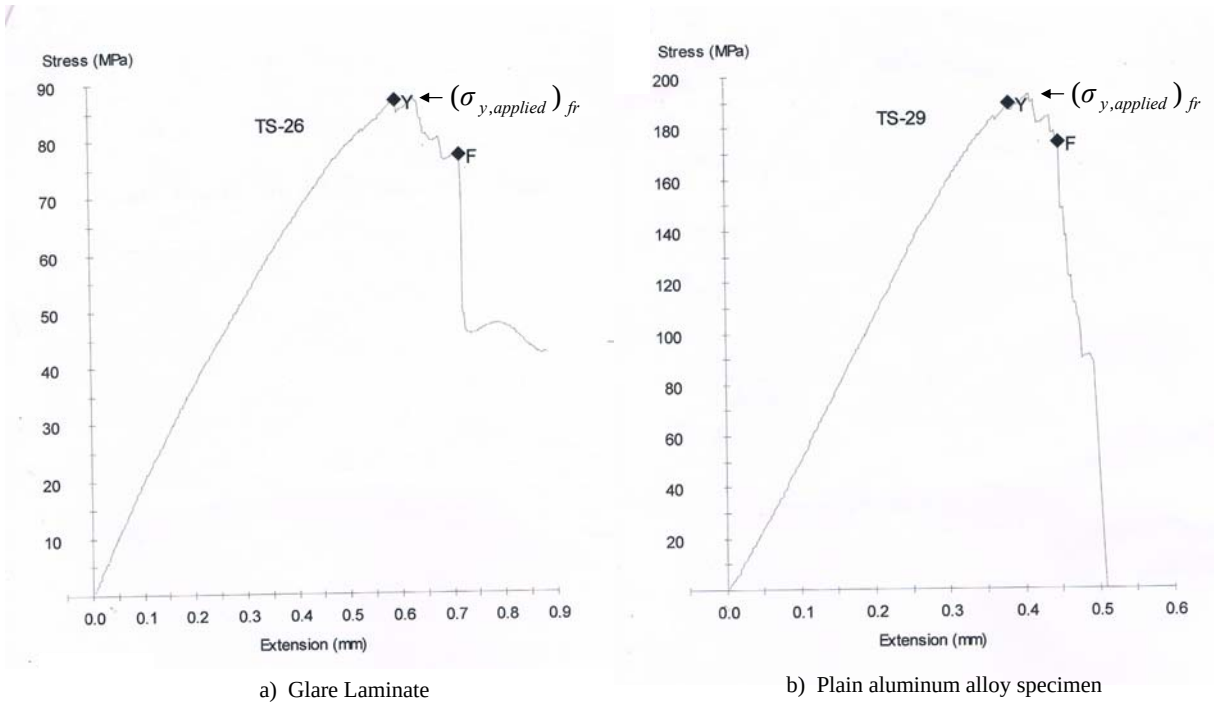

a) Glare Laminate

b) Plain aluminum alloy specimen

Figure 4. Sample load-extension plots of Glare laminate and of plain aluminum alloy specimen with 20 mm long cracks

Table 2. Critical stress and fracture toughness of Glare laminates and of plain aluminum alloy specimens

Glare laminates								
Laminate No.	d (mm), t_{al} (mm)	c (mm)	w (mm)	CF	$(\sigma_{y,applied})_{fr}$ (MPa)	$(\sigma_{y,induced,al})_{fr}$ (MPa)	$K_{C,lam}$ $(\mathrm{MPa}\sqrt{\mathrm{m}})$	$K_{C,al}{}^{d} = K_{tip}$ $(\mathrm{MPa}\sqrt{\mathrm{m}})$
1	2.39, 0.53	5.0	50.0	1.183	120.0	204.36	30.32	18.40
2	2.30, 0.5	7.0	49.6	1.248	150.0	243.27	45.05	18.67
3	2.50, 0.5	9.5	51.0	1.34	210.0	321.16	74.33	18.10
4	2.20, 0.4	14.0	50.3	1.587	120.0	204.36	68.04	19.00
5	2.50,0.4	20.0	50.7	2.07	90.0	165.36	85.96	18.10
Refer Section 3, Induced stress value in fibre at fracture is given below: - (+ve is tensile and -ve is compressive) Laminate No. 1: $(\sigma_{y,induced,f})_{fr}$ = -21.92 MPa, Laminate No. 2: $(\sigma_{y,induced,f})_{fr}$ = +15.36 MPa Laminate No. 3: $(\sigma_{y,induced,f})_{fr}$ = +89.91 MPa, Laminate No. 4: $(\sigma_{y,induced,f})_{fr}$ = -21.92 MPa Laminate No. 5: $(\sigma_{y,induced,f})_{fr}$ = -59.2 MPa								
Plain aluminum alloy specimens								
Specimen No.	p (mm)	c (mm)	w (mm)	CF	$(\sigma_{y,applied})_{fr}$ (MPa)	$K_{C,al}$ $(\mathrm{MPa}\sqrt{\mathrm{m}})$	$K_{IC,al}$ $(\mathrm{MPa}\sqrt{\mathrm{m}})$	
1	0.66	5.0	50.20	1.182	280	41.53	14.48	
2	0.65	7.0	50.45	1.244	240	44.30	14.70	
3	0.86	9.5	50.50	1.343	75	17.41	11.06	
4	0.60	14.0	50.45	1.580	210	69.80	16.81	
5	0.36	20.0	50.36	2.088	190	99.47	16.05	
Average $K_{IC,al}$ = 14.62 $\mathrm{MPa}\sqrt{\mathrm{m}}$								

5. Numerical analysis

Refer Figure 5a). 3D finite element models of all cracked Glare laminates without delaminations were created with 8 noded, solid 185 elements in aluminum and 8 noded, layered solid shell 190 elements in fibre and resin layers. Half of the laminates were only modeled due to symmetry. The bottom nodes representing cracks in all aluminum and resin layers were unconstrained while the nodes of un-cracked fibre layers were constrained in y direction (v = 0) as shown in Figure 5b). Stress-strain data of materials, available in Figure 6, were used in the material models of the software. Fracture stress values, $(\sigma_{y,applied})_{fr}$, taken from Table 2, were applied at the top edges of the laminates. Residual stress developing in materials during laminate curing at 160 deg. C, whose values were obtained using $T_{cuiring}$ = 160 deg. C and $T_{ambient}$ = 30 deg. C in Section 3, were introduced over nodes in x and y directions. The residual stress was same in all the laminates. Their values are given below (+ve is tensile and -ve is compressive):-

i) Aluminum = 46.17 MPa (+ve) in x dir., 48.36 MPa (+ve) in y dir.
ii) Resin = 25.59 MPa (+ve) in x dir., 25.73 MPa (+ve) in y dir.
iii)Fibre = 173.92 MPa (-ve) in x dir., 171.02 MPa (-ve) in y dir.

Crack energy release rate can be represented by J integral in LEFM. J in x-y plane over cyclic path, P, [4] is defined by the summation of different terms at nodes on the path as follows:-

$$J = \int_P (W_e dy - T_x \frac{\partial u}{\partial x} ds - T_y \frac{\partial v}{\partial x} ds) \tag{4}$$

where W_e is the strain energy density, $T_x = \sigma_x n_x + \tau_{xy} n_y$ and $T_y = \sigma_y n_y + \tau_{xy} n_x$ are traction terms with n_x and n_y in the expressions representing unit vectors in x and y directions and u and v are displacements in stated directions. To estimate the shielding effect at the crack tips, values of J integral, J_{tip}, were found over several paths around crack tip, as shown in Figure 5b), which were then averaged to obtain the final value. Laminates without cracks were also modeled under $(\sigma_{y,applied})_{fr}$ and residual stress stated above. Their constraints are shown in Figure 5c). Since J integral value does not critically depend upon the mesh type, a simpler mesh scheme was adopted in place of square root singularity mesh type around the crack tips.

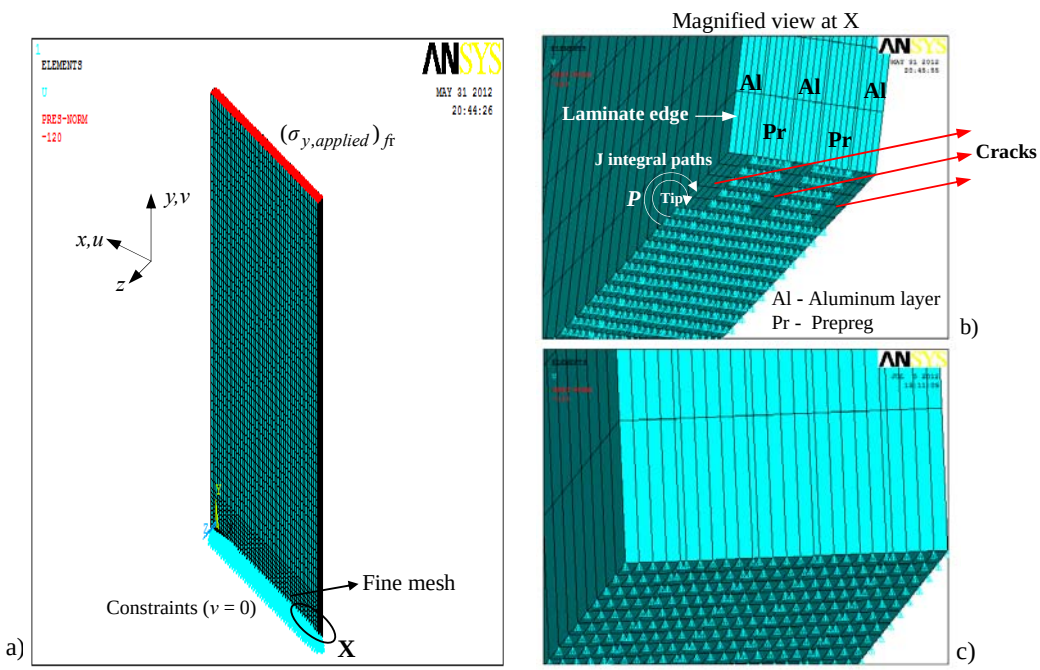

Figure 5. a) Finite element model of Glare b) Constraints in cracked Glare
c) Constraints in un-cracked Glare

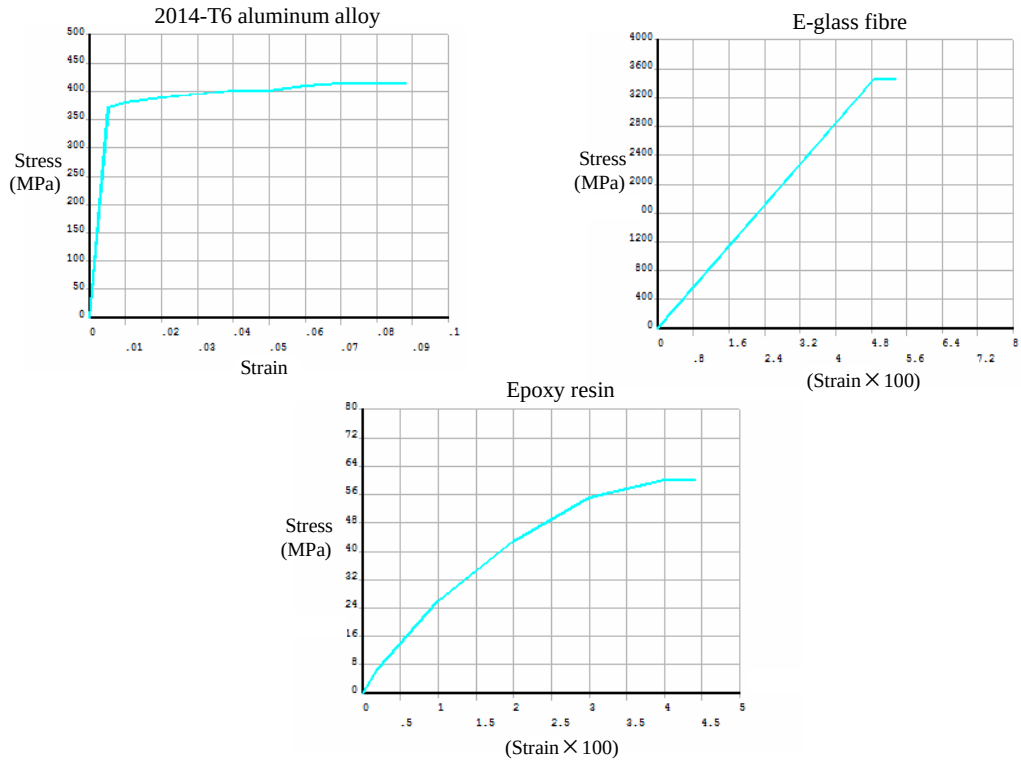

Figure 6. Stress-strain plots of materials

K_{tip} values were finally obtained from J_{tip} by LEFM relation in plane stress condition, $K_{tip} = \sqrt{E_{al} J_{tip}}$. They are presented in Table 3.

Table 3. Numerical values of stress intensity parameter at crack tips in Glare laminates

Laminate No.	J_{tip} (N/mm)	K_{tip} (MPa$\sqrt{\text{m}}$)
1	1.093	8.85
2	1.947	11.84
3	2.899	14.44
4	1.718	11.123
5	0.799	7.58

6. Observations

Refer Figure 7a) and 7b). Numerical values of, load line, induced stress in aluminum layer and in fibre layer, $(\sigma_{y,induced,al})_{fr}$ and $(\sigma_{y,induced,f})_{fr}$ respectively, of un-cracked Glare, are close to the values available in Table 2 that validates the finite element model. Sample load line stress in aluminum layer and in fibre layer, $(\sigma_{y,total,al})_{fr}$ and $(\sigma_{y,total,f})_{fr}$, of cracked Glare containing 5 mm crack are provided in Figure 7c) and 7d). Since no yielding is observed at the crack tip, LEFM regime is numerically confirmed. In addition, the values of $\frac{(\sigma_{y,total,al})_{fr}}{Y_{al}}$ are less than 0.5 that further support LEFM conditions in cracked aluminum.

a)

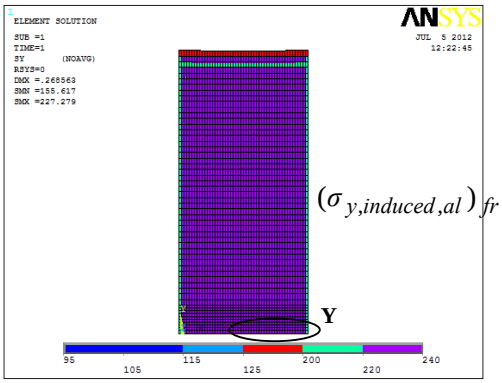

Induced stress in aluminum layer in *y* dir. of un-cracked Glare

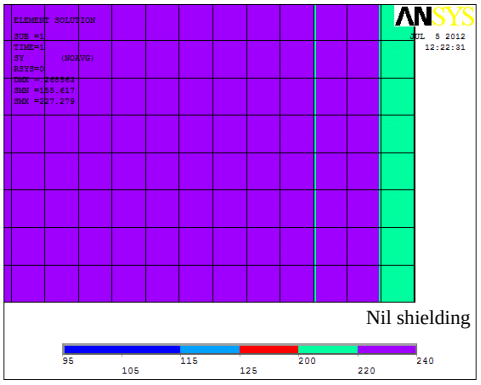

Magnified view at Y

b)

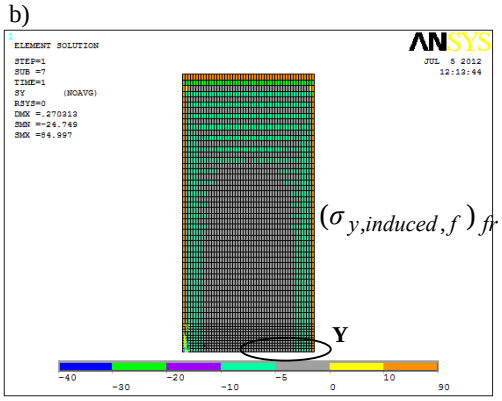

Induced stress in fibre layer in *y* dir. of un-cracked Glare

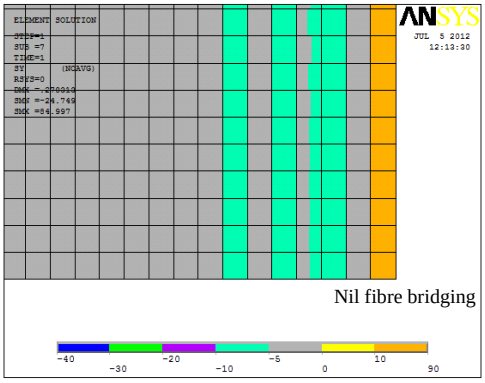

Magnified view at Y

c)

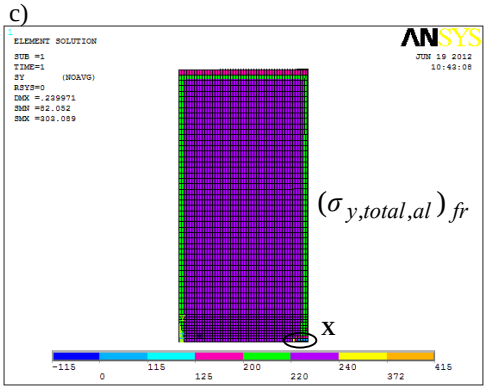

Stress in aluminum layer in *y* dir. of cracked Glare

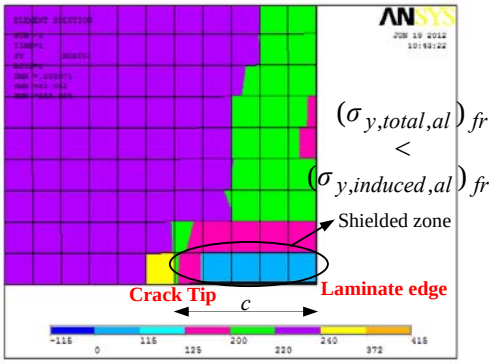

Magnified view of shielded zone in aluminum layer at X

d)

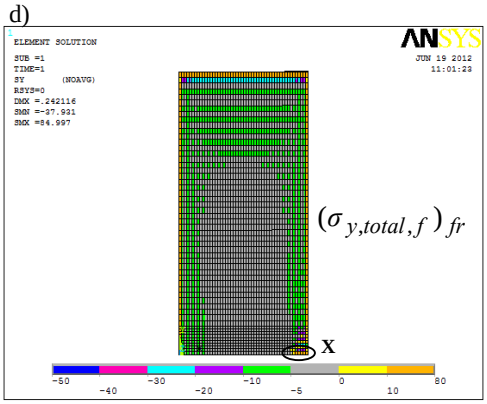

Stress in fibre layer in *y* dir. of cracked Glare

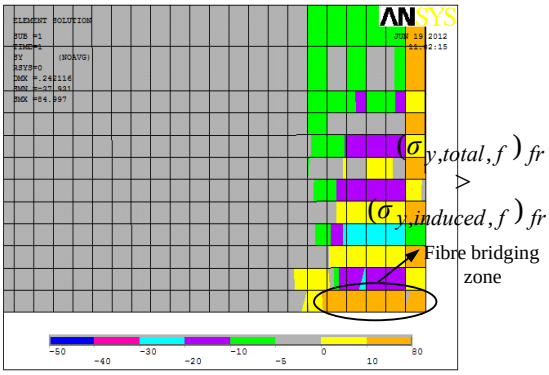

Magnified view of bridging zone in fibre layer at X

Figure 7. Load line stress plots in un-cracked and cracked Glare laminate with 5 mm crack

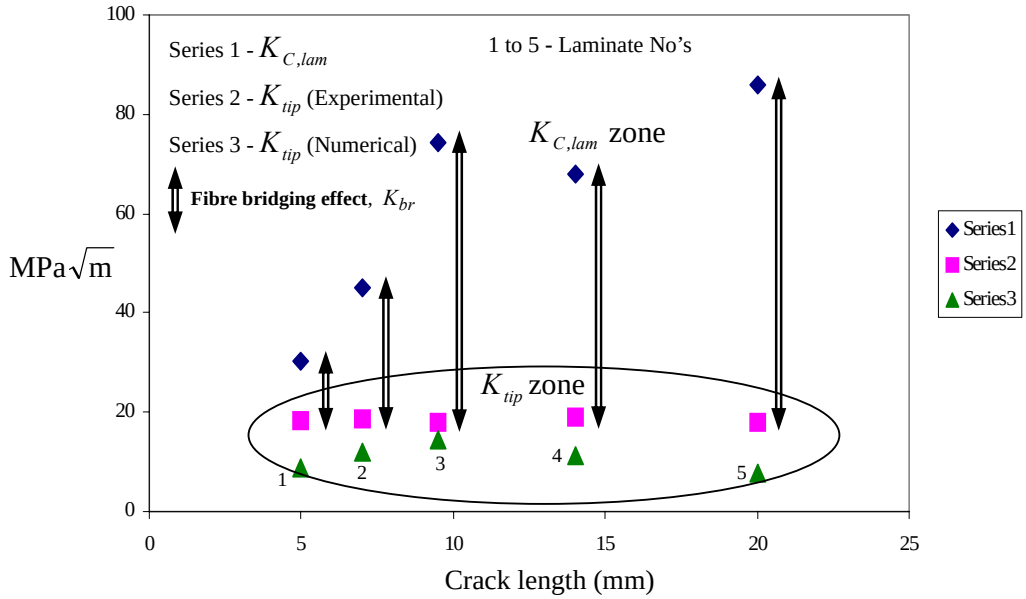

Figure 8. Comparison between experimental and numerical estimations of fibre bridging

Fulfillment of the condition, $(\sigma_{y,total,f})_{fr} > (\sigma_{y,induced,f})_{fr}$, in bridging zone of fibre layer convincingly confirms load transfer towards fibre. Also, $(\sigma_{y,total,al})_{fr} << (\sigma_{y,induced,al})_{fr}$, around cracked area of aluminum hints at the shielding effect. Although the presence of crack, as a free surface, in itself dips the load line stress field in shielded area of aluminum, the magnitude of $\{(\sigma_{y,total,al})_{fr} - (\sigma_{y,induced,al})_{fr}\}$ is found to be high enough to include both the compressive effects i.e. due to the crack and due to shielding by fibre bridging. Similar trends are observed in laminates with cracks of other sizes as well. Again from the experimental results in Table 2, the finding, $K_{C,lam} > K_{tip}$ or $K_{C,lam} > K_{C,al}{}^{d}$, adequately proves crack tip shielding and enhanced fracture toughness of the laminates vis-à-vis corresponding plain aerospace aluminum alloy specimens. Experimental and numerical results of K_{tip} are compared in Figure 8. They are close to each other. The error is attributed to slight difference between theoretical and experimental values of residual stress in aluminum layer of the laminate. The experimental values are lower than the theoretical ones. Fibre bridging effect, K_{br}, is quantified by $\{K_{C,lam} - K_{tip}\}$. The effect, in general, is found to increase with increase in crack size in aluminum layers. Absence of delaminations intensifies the effect.

Acknowledgements

The author is grateful to Science and Engineering Research Council, Department of Science and Technology, The Government of India for funding the project. Support received from the School of Mechanical and Building Sciences, VIT University, Vellore, India during the course of this work is acknowledged.

References

[1] Y.J. Guo, X.R. Wu, Bridging stress distribution in center-cracked fibre reinforced metal laminate: Modeling and Experiment. Eng Fra Mech, 63 (1999) 147-163.
[2] R.C. Alderliesten, Analytical prediction model for fatigue crack propagation and delamination growth in Glare, Int J Fat, 29 (2007) 628-646.
[3] G.R. Irwin, NRL Report 6598, 1967.
[4] J.R. Rice, A path independent integral and approximate analysis of strain concentration by notches and cracks. J App Mech, 35 (1968) 379-386.

Short/Small Crack Model Development for Aircraft Structural Life Assessment

Min Liao [1*], **Guillaume Renaud** [1], **Yan Bombardier** [1]

[1] Aerospace Structures, National Research Council Canada (NRC)
1200 Montreal Rd, Ottawa, Ontario, Canada K1A 0R6
* Corresponding author: min.liao@nrc-cnrc.gc.ca

Abstract This paper presents the testing and modeling results from an NRC project on short/small ① crack model development for aircraft structures. Fatigue tests were conducted for 7075-T73 hand forging aluminium material using precracked compact tension (C(T)) and naturally cracked single edge-notch tension (SENT) coupons, under various stress ratios. The adjusted compliance ratio (ACR) method was used for the C(T) coupon tests aiming to quantify remote closure due to plasticity and forging-induced residual stresses. For the SENT coupons, three-dimensional StressCheck finite element (FE) models were developed to accurately calculate the stress intensity factors of surface and corner cracks. Both C(T) and SENT test data were combined to develop short-long fatigue crack growth rate models. These models were then used in crack growth life analyses for coupon and component cases, taken from transport aircraft under spectrum loadings. It was shown that the newly developed models resulted in more accurate fatigue life estimations.

Keywords Short/small crack growth, 7075-T73 , Adjusted compliance ratio, Marker bands, CanGROW.

1. Introduction

Currently, the practical life prediction technologies for metallic aircraft structures are mainly safe-life (SL), damage-tolerance (DT, including fail-safe), and flaw-tolerance (including flaw-tolerance safe-life for helicopter). In addition, a combined SL and DT (two-stage) total life approach is used to overcome the limitations of these two approaches taken separately. However, the transition between SL and DT is not clearly defined and justified. One of the reasons is that the small crack region remains a "grey zone" for which a robust/practical approach and test database are still missing for many aircraft designers/manufacturers, although extensive research has been carried out in the past decades. In collaboration with other organizations, NRC is developing the Holistic Structural Integrity Process (HOLSIP) to augment the traditional SL and DT approaches with the ultimate goal to evolve HOLSIP into a new paradigm for both the design and sustainment stages. One of the current HOLSIP development efforts is to further develop the short/small crack database and the physics-based models.

Recently, an NRC project was completed with testing and modeling results for 7075-T73 aluminum forging material, which is used in Royal Canadian Air Force (RCAF) large transport aircraft [1]. A literature review revealed that short/small crack data are scarce for 7075-T73 aluminum alloys for fatigue durability analysis of aircraft structures. The short/small crack growth rate data have significant scatter due to material microstructures, specimen types and geometries, testing and measuring techniques, which lead to extensive testing time and costs. As such, some researchers perform long precrack crack tests and use the near-threshold data to represent the average small crack growth rate, which has two issues: 1) the long crack data produce overly high stress intensity threshold factor ΔK_{th} (ΔK at da/dN=3.94E-9 inch/cycle or 1E-10 m/cycle in ASTM E647) which would result in un-conservative life prediction; 2) the scatter is different from that of naturally small cracks, which are more affected by intrinsic microstructures effects.

① As per ATSM E647 (Appendix X3), a *small crack* is defined as being small when all physical dimensions (in particular, both length and depth of a surface crack) are small in comparison to a relevant microstructural scale, continuum mechanics scale, or physical size scale. While a *short crack* is defined as being short when only one physical dimension (typically, the length of a through-crack) is small according to the description of '*small crack*'.

For the long crack tests, the Adjusted Compliance Ratio (ACR) method [2] was proposed to adjust the stress intensity factor range (ΔK) by considering the remote crack closure effect, and then result in a lower threshold ΔK_{th}. Also the ACR method was able to quantify bulk residual stress in the remote closure, and then reduced the scatter and bias related to residual stress and sampling effects [3]. Efforts were also carried out on improving the ASTM E647 load reduction (LR) method, which is suspected to result in improper loading history effects on crack closure. These efforts include the compression precracking (CP) procedures [4], which also result in lower ΔK_{th} values.

For naturally nucleating small crack, the ASTM E647 (Appendix X3) introduces several experimental techniques, which are useful for measuring the growth of fatigue cracks sized on the order of 50μm or greater, and some are applicable to even smaller cracks. For small surface crack measurements, the silicon-based replication technique is at least as reliable as the traditional acetate-based replication, and it has no apparent effect on the fatigue life of the specimen. For small crack depth measurement, NRC has gained extensive experience in the use of the marker band (MB) technique to measure small crack profile on a fracture surface in a previous project.

Considering all the above factors, it was decided to test the 7075-T73 hand forging material, using both compact tension (C(T)) coupons with ACR method and single edge-notch tension (SENT) coupons with MB and replication techniques.

2. Short/small crack tests

The 7075-T73 hand forgings were made following the AMS-QQ-367 specifications. NRC received four forging blocks that were 2.0” thick, 2.5~3.5” wide, and 30”~72” long. A microstructural analysis showed that this alloy has more and larger particles than pores on the ST plane (short-transverse, the crack plane), and that the particle sizes range roughly from a few μm to 20-30μm. The grain sizes on the ST plane can reach 100μm. The tests were performed under laboratory environment; room temperature, 24 ± 3ºC and relative humidity, 30 ± 25%. The X-ray diffraction measurements, on 10 sampling spots, showed that surface residual stresses were scattered from -4 to +5 ksi (-28~34 MPa), with an average residual stress of 0.5 ksi (3.4 MPa).

2.1. Fatigue crack growth tests using C(T) coupons

A compact tension C(T) coupon was designed based on ASTM E647. The width of the coupon was 2.0” (5.08 mm) and the thickness was 0.25” (6.35mm). Each coupon was tested through precracking, K-decreasing, K-increasing, and constant loading following the E647 procedures. Six stress ratios (R=0.05, 0.33, 0.45, 0.60, and 0.80), were tested using a loading frequency of 5-10 Hz. The ACR method, developed by Fatigue Technology Associate (FTA), was used to estimate the effects of the remote crack closure, which refers to crack tip shielding as a result of contact in the crack wake behind the crack tip. This is in contrast to other shielding mechanisms near to the crack tip such as plasticity. The ACR method is based on the same measurement signals that are used for the 2% crack opening force method in E647 (Appendix X2), but it does demand high quality signals with less noise. The ACR stress intensity factor, ΔK_{ACR}, is calculated as described in Figure 1.

In addition to the ΔK_{ACR} results, the FTA software also provides two additional methods to estimate the effective stress intensity factor ranges (ΔK_{eff}) [②], i.e. the ASTM 2% opening load method ($\Delta K_{eff\text{-}OP}$) and the 2/π method ($\Delta K_{eff\text{-}2/\pi}$, partial closure correction below the opening load). Results

[②] Although the effective stress intensity factor range is a useful parameter, it should be noted that different definitions and calculations have been used in different applications. They may not be comparable to each other.

comparing these methods are provided in Figure 2 for an example coupon (No. H2, R=0.6). This figure shows large differences between the ΔK_{App} ($\Delta K_{eff\text{-}ACR}$ in the figure) and other ΔK_{eff} results at the near-threshold region. The $\Delta K_{eff\text{-}2/\pi}$ results are close to the ΔK_{ACR} whereas the $\Delta K_{eff\text{-}OP}$ results are lower than others, and the $\Delta K_{eff\text{-}OP}$ method is deemed to over-compensate the near-threshold data.

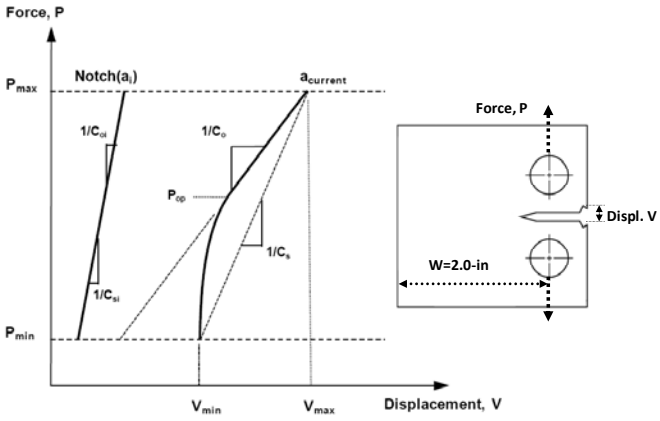

$$\Delta K_{ACR} = U_{ACR}\,\Delta K_{App}$$

$$U_{ACR} = \frac{C_{0i}}{C_{si}}\frac{C_s - C_{0i}}{C_0 - C_{0i}}$$

- ΔK_{App} is the full range, applied stress-intensity factor
- C_{oi}/C_{si} compensates for a possible bias in the secant or open-crack compliances because of signal conditioning noise or nonlinearity

Figure 1. Schematic of force-displacement curve showing critical parameters for ACR method (based on [2])

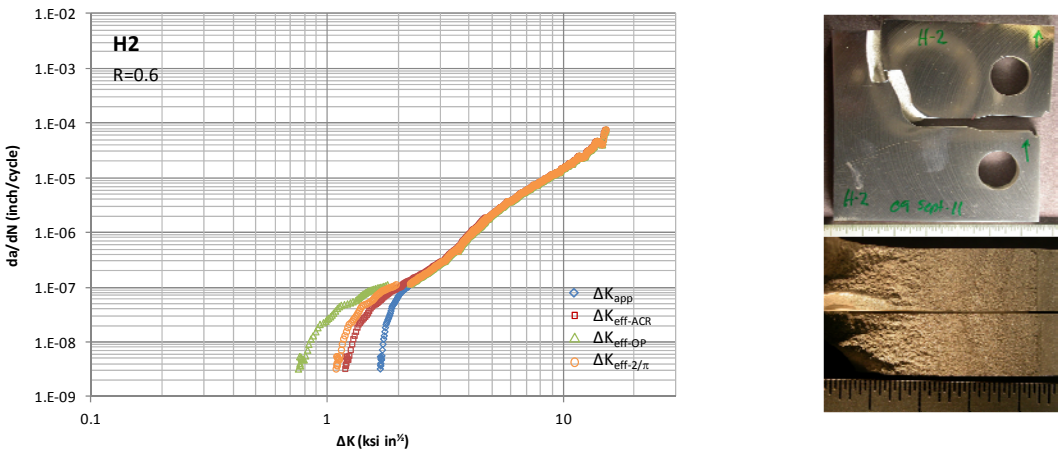

Figure 2. Typical crack growth rate results (coupon H2, R=0.60) (1-in=25.4 mm, 1.0 ksi√in=1.1 MPa√m)

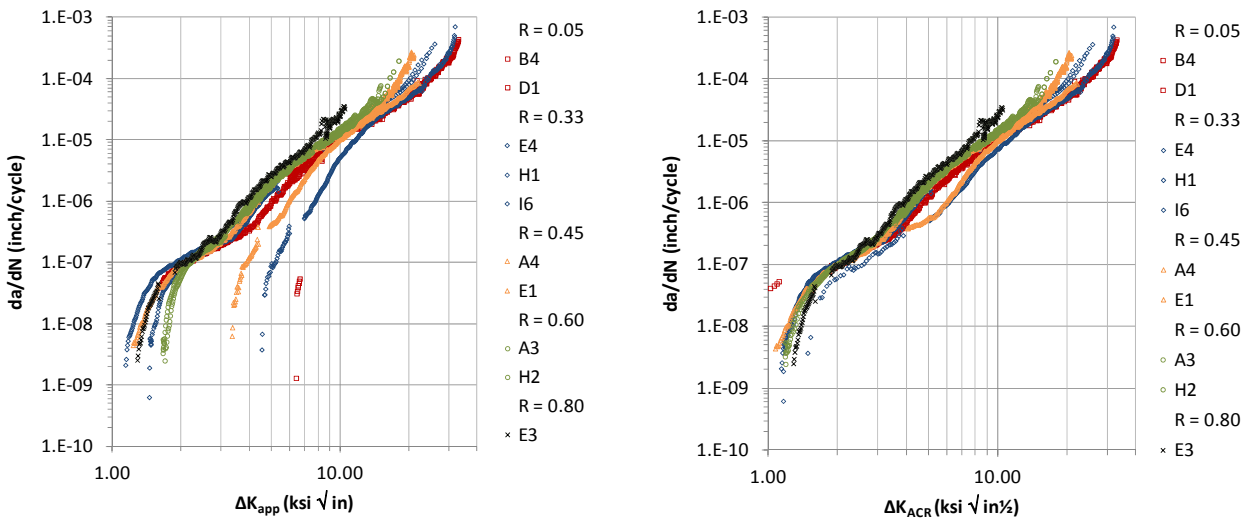

(a) da/dN-ΔK_{App} (before ACR correction) (b) da/dN-ΔK_{ACR} (after ACR correction)

Figure 3. C(T) test results at R=0.05,0.33,0.45,0.60,0.80 (1-in=25.4 mm, 1.0 ksi√in=1.1 MPa√m)

The C(T) test results for all R-ratios are presented in Figure 3: (a) da/dN-ΔK_{App} (before ACR correction); and (b) da/dN-ΔK_{ACR} (after ACR correction). The comparison shows that the ACR method reduced the data scatter especially the "fanning" effect at the near-threshold region, and gave lower ΔK_{th} values by removing the closure and residual stress effects. The scatter reduction is in the low stress ratios (R0.05-0.45) than in the high stress ratios (R0.6-0.8). It is also noted that some ACR corrections are very small possibly due to the positive residual stress effects.

2.2. Small crack tests using SENT coupons

A SENT coupon, as shown in Figure 4-(a), was used for fatigue tests with naturally nucleating small surface cracks. A test matrix, shown in Figure 4-(b), was designed using a simple center composite circumscribe (CCC) design of experiment (DOE) method aiming to provide a complete set of data under six stress ratios (R) and five stress levels. The test loading spectra were constant amplitude loading with marker band (MB) loading sequences. The silicon-based replication technique (RepliSet^{TM}) was used to measure the surface crack length, and marker bands (MB) on the fracture surfaces were reconstructed to determine the crack depth.

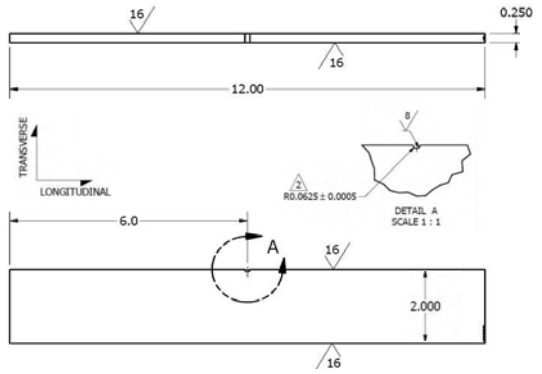

(a) SENT coupon (dimensions in inches, 1in=25.4mm)

Group No.	Replicate	Applied Max. Stress (ksi)	Applied Min. Stress (ksi)	Stress Ratio (R)
1	6	23.00	1.15	0.05
2	3	20.00	-6.00	-0.30
3	3	26.00	-7.80	-0.30
4	3	20.00	10.00	0.50
5	3	26.00	13.00	0.50
6	3	18.76	0.94	0.05
7	3	27.24	1.36	0.05
8	3	23.00	-23.00	-1.00
9	3	23.00	18.40	0.80

(b) SENT test matrix (1ksi=6.89MPa)

Figure 4. SENT coupon and test matrix

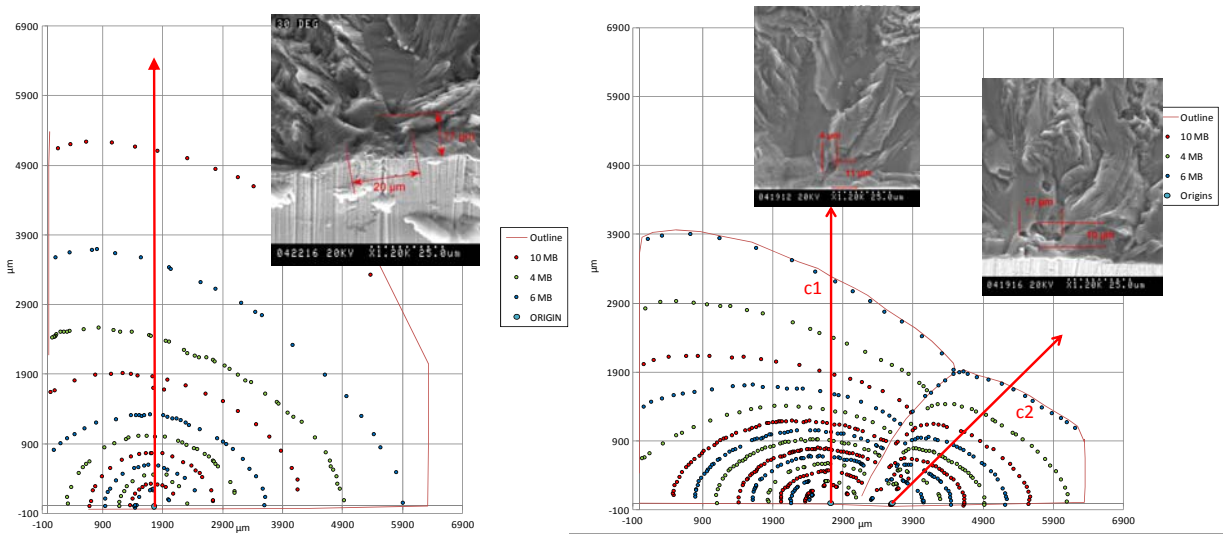

(a) single crack origin (pores)

(b) multiple crack origins (pores/particles)

Figure 5. Typical SENT coupon marker bands and nucleation sites

The smallest replica crack detection was about 12 μm, and the smallest MB measured crack was about 20 μm. The MB crack detection resolution varied with stress levels and stress ratios, but

overall the MB technique could reliably provide 100 μm crack depth measurements. Fractography showed that cracks nucleated from 1) surface scratches; 2) particles or pores; and possibly 3) intragranular cracking. Many of these naturally nucleated cracks showed fairly rough fracture surfaces. Both corner and bore surface cracks, single and multiple were observed in various SENT coupons, as shown in Figure 5-b).

In general, the small crack growth rate data showed large scatter bands and irregular 'zigzag' (acceleration/deceleration) growth. The irregular growth rate was mainly due to microstructure effects (such as grain size, orientation, and grain boundary) associated with the scattered residual stresses, and secondarily caused by the measurement resolution/accuracy. More data analysis showed that the absolute measurement error (~5 μm) of the replication technique contributed only partially to the scatter band. Overall, the irregular 'zigzag' features were largely reduced after the crack size was over ~100 μm or dc/dN was about 3.94E-7 in/cycle (1E-8 m/cycle).

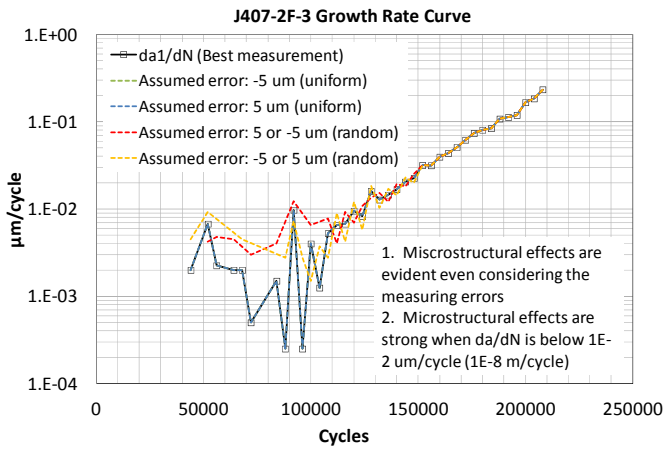

Figure 6. Typical surface small crack growth rate scatter (R= -0.3, σ_{MAX}= 20 ksi/138 MPa)

3. Small crack stress intensity factor modeling

A three-dimensional (3D) *p*-version StressCheck FE model was developed to calculate the stress intensity factors of the naturally nucleating cracks measured on the SENT test coupons [5]. The model was developed from a modified quarter-elliptical corner crack geometry at a hole. A useful feature of this model is that it was built as a parametric FE model, in which, as seen in Figure 7, various parameters can be assigned to the geometry of the crack, coupon, and mesh layers enclosing the crack front. Symmetry conditions can be assumed for surface crack modeling at a hole. The K-solutions were calculated at 96 points along the crack front, using the contour integral method with circular integration paths located between the first two concentric element layers. Eight elements were located along the crack front, with the extreme ones covering only the first and last 2 degrees to capture the peak stress intensity factor values close to the free surfaces. The analysis was performed with 8th degree polynomials. The process was automated using an Excel-based Visual Basic for Applications (VBA) program that could automatically configure the model, launch the analysis, and retrieve output results for a series of crack measurements in a specimen.

Previous verification examples have shown that the improved NRC solutions, developed from the hole geometry version of the aforementioned model, are more accurate than the classical Newman-Raju solutions, and comparable to the Fawaz-Andersson results tabulated in AFGROW, which however do not cover cracks smaller than 10% of the plate thickness and do not include the surface crack case (which are now available in the NRC solutions) [5].

The modeling of the test coupons was performed with the developed VBA program using the metrology results and crack measurements specific to each coupon. Doing so, no interpolation among crack size and crack shape values was performed. The crack growth rates were calculated using the secant method. Both the da/dN-ΔK_a (thickness direction) and dc/dN-ΔK_c (width direction) data points were calculated. The calculated crack growth rate dc/dN vs. ΔK (or $K_{\max}$ if R is negative) results of the single crack cases are illustrated in Figure 8. The ΔK_a and ΔK_c values were calculated from the StressCheck model at Φ = 85° and Φ = 0° (surface crack) or Φ = 5° (corner crack), respectively. In this paper, only single crack data were used in the K calculation.

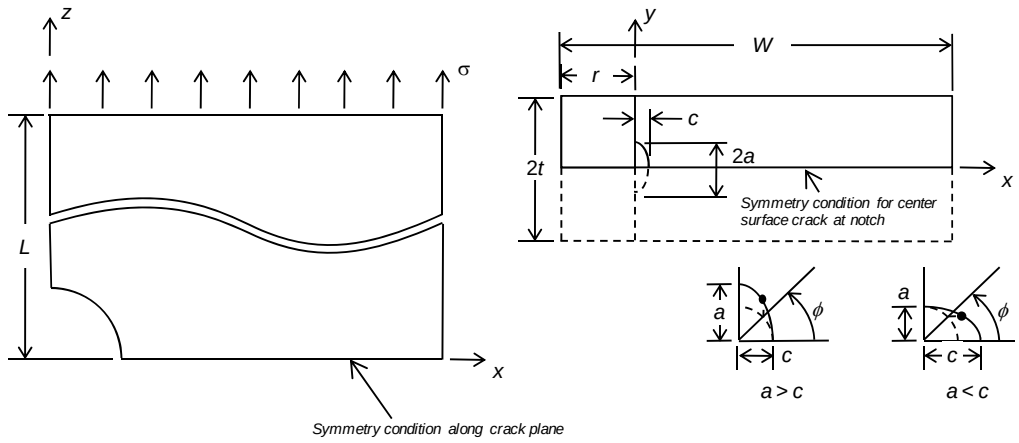

Figure 7. Definition of variables and boundary conditions

4. Comparison of precrack and natural small crack data (C(T) vs. SENT)

The crack growth rate data, generated from the C(T) tests (with and without ACR correction) and the SENT tests, are presented in Figure 8. The comparisons indicate that,

1) For long crack growth, da/dN>1E-7 in/cycle (2.54E-9 m/cycle), the C(T)-ACR and SENT test results are similar to each other, except for the R=0.05 case, which should include more crack closure than the high R-ratio cases. Without the ACR correction, some of the R=0.05 C(T) results were close to the SENT results, which had no ACR correction for the residual stress and closure effects. Meanwhile some other C(T) results showed negligible ACR correction, which involved very small residual stress, even tensile residual stress effects.
2) In the near-threshold region, da/dN<1E-7 in/cycle (2.54E-9 m/cycle), for R=0.05, the SENT results appear to give higher ΔK_{th} values than the C(T)-ACR results. The R=0.5 SENT tests did not provide enough data in the near-threshold region. But for R=0.8, the SENT results appear to give lower ΔK_{th} values than the C(T)-ACR results, for which the ACR correction is very small. Overall, the SENT results have more scatter than the C(T)-ACR results in the near-threshold region, and the SENT results should include less closure effect induced by small crack plasticity wake, but more machining-induced compressive residual stress on the surface layer (<50μm).

From the SENT and C(T) test results, a combined NRC short-long crack growth material model was developed as presented in Figure 9. The combined model is largely based on the SENT data, corrected with C(T)-ACR results to remove residual stress effect for R=0.05 and compensated with C(T)-ACR the near-threshold data for R=0.5. Note that the SENT data (ΔK) for R=-0.33 were shifted to the left using the ΔK ratio between the SENT and the C(T)-ACR long crack data for R=0.05, assuming the same residual stress effect in both tests. As a result, the NRC model is deemed to be a 'residual stress free' material model.

Some previous studies [1, 6] have indicated that, for the same 7xxx material, the plate and hand forging forms have the same composition, including particles and pores, but the grain aspect ratio and flow may be different near the surface. The hand forging shows more scatter in the crack growth rates; however, the average crack growth rates for both plate and forging are very similar to each other. Next, the developed NRC 'residual stress free' model, from the 7075-T73 forging tests, was used for fatigue life estimation of 7075-T73 plates.

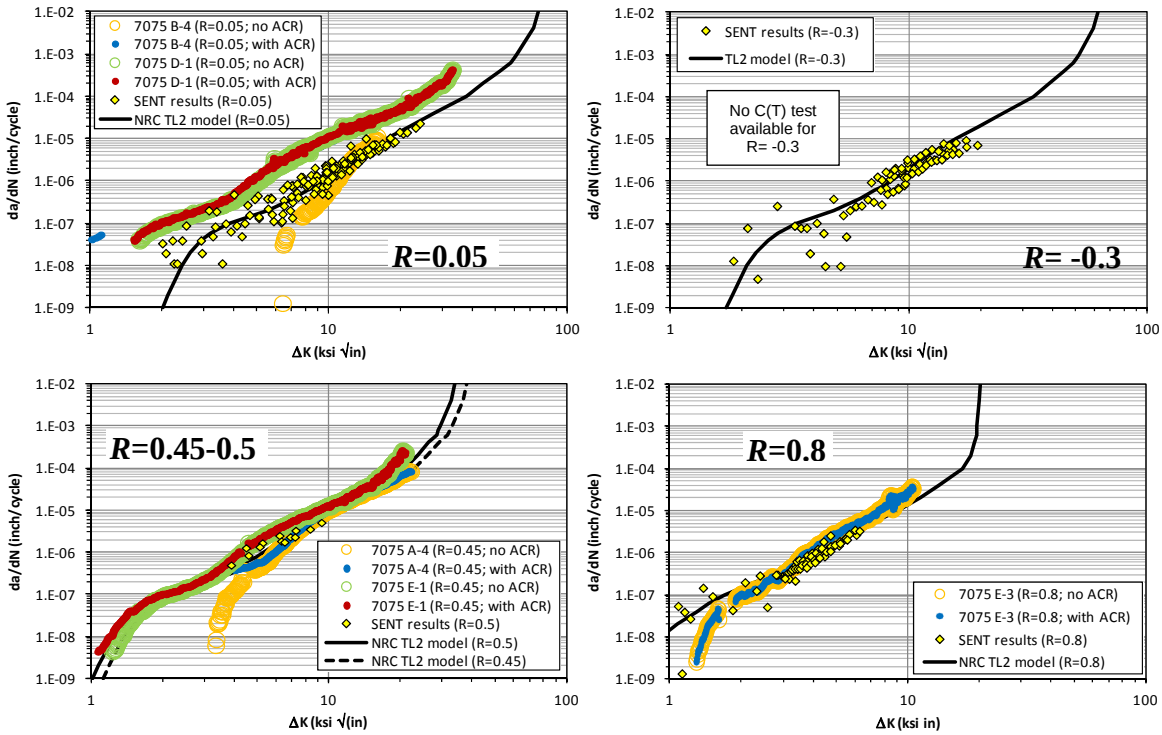

Figure 8. SENT and C(T) test results, and NRC (TL2) model for SENT (1-in=25.4 mm, 1.0 ksi√in=1.1 MPa√m)

da/dN(in/cycle)	*ΔK or K_{max}(ksi √in)*			
	***R* = 0.05**	***R* = -0.3**	***R* = 0.5**	***R* = 0.8**
1.E-09	1.42	1.20	1.01	0.71
2.E-09	1.49	1.27	1.07	0.77
1.E-08	1.69	1.46	1.25	0.92
2.E-08	1.83	1.60	1.40	1.08
4.E-08	2.04	1.79	1.61	1.30
6.E-08	2.25	1.98	1.78	1.45
1.E-07	2.66	2.33	2.09	1.69
2.E-07	3.90	3.39	2.97	2.29
4.E-07	4.98	4.37	3.92	3.16
6.E-07	5.73	5.04	4.53	3.70
8.E-07	6.31	5.56	5.02	4.13
1.E-06	6.69	5.91	5.36	4.45
2.E-06	7.93	7.01	6.40	5.36
4.E-06	9.45	8.38	7.67	6.49
1.E-05	12.28	11.00	10.29	9.12
2.E-05	15.34	13.76	12.87	11.39
4.E-05	19.38	17.23	15.84	13.52
1.E-04	26.58	23.32	20.90	16.89
2.E-04	31.27	27.15	23.81	18.38
4.E-04	36.56	31.21	26.44	18.97
6.E-04	40.52	34.23	28.38	19.45
8.E-04	41.83	35.18	28.92	19.46
1.E-03	43.14	36.18	29.55	19.61
4.E-03	50.34	41.46	32.65	20.04
1.E-02	52.96	43.39	33.80	20.28

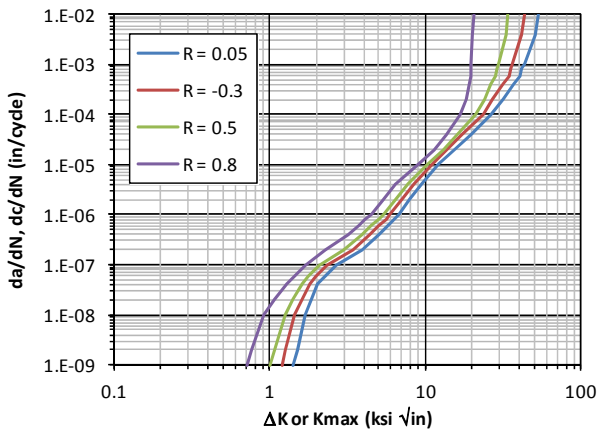

Figure 9. NRC combined material model for 7075-T73 (1-in=25.4 mm, 1.0 ksi√in=1.1 MPa√m)

5. Fatigue crack growth life estimation

5.1. Coupon life estimation

The NRC material model was used to estimate the crack growth lives of some 7075-T7351 plate

coupon tests under transport spectra [7], using the NRC in-house crack growth code CanGROW [9]. At first, a legacy material model of 7075-T7351 (Figure 10-(a)), based on the Forman equation, was used in association with the Hsu retardation model [8] using the default parameter value of $M_0 = 0.6$ and $R_{cut} = 0.3$. Both M_0 and R_{cut} are fitting parameters, and $M_0 = 1.0$, $R_{cut} = 0.0$ would create the most possible retardation and the longest life. As shown in Figure 10-(b), the fatigue life estimation using the legacy model were considered overly conservative, even when maximizing the Hsu retardation and considering that the legacy model was developed for a relative humidity of 90%. As shown in Figure 10-(b), using NRC Forman model converted from the R=0.5 curve in Figure 9, the life estimation was greatly improved, especially with the Hsu parameters calibrated at $M_0 = 0.2$ and $R_{cut} = 1.0$. Note that the spectrum was counted using the rainflow method in the above analyses.

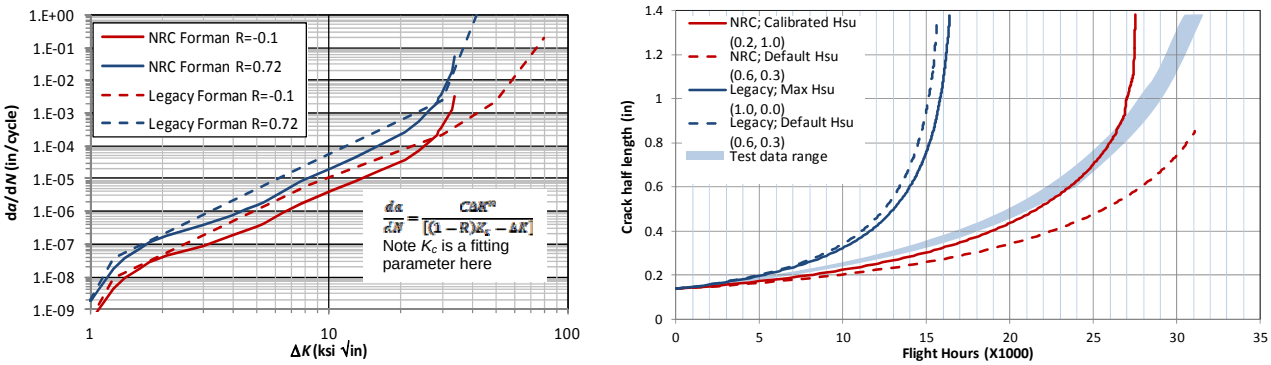

(a) 7075-T73 material model, legacy and NRC (b) Coupon life estimation using legacy and NRC models

Figure 10. Coupon life estimation using CanGROW (1-in=25.4 mm, 1.0 ksi√in=1.1 MPa√m)

It was also noted that one weakness of the Forman equation is lack of flexibility to correctly describe and shift the da/dN-ΔK curves between different stress ratios (R), because the shifting solely depends on a fitting parameter (K_C) that controls the K-factor near the fracture region. The mismatched shifting was also reported at the low-ΔK region [11]. Using the tabular data in Figure 9 should avoid this issue. In another preliminary study, the NRC model at R=0.8 was simply used as a ΔK_{eff} baseline model in FASTRAN3.8 for the coupon life estimation. As shown in Figure 11-(b), good agreement was achieved between the FASTRAN analysis and tests. Two previous 7075-T73 material models from [4,10] were also compared to the NRC model in Figure 11-(a), which resulted in one poor (blue, before calibration) and one good (yellow after calibrating) life estimations. The FASTRAN analysis used a crack closure model with more parameters (e.g. constraint factors), which calibrating details are beyond the scope of this paper. Note that the spectrum was used in the FASTRAN analysis without a cycle counting process.

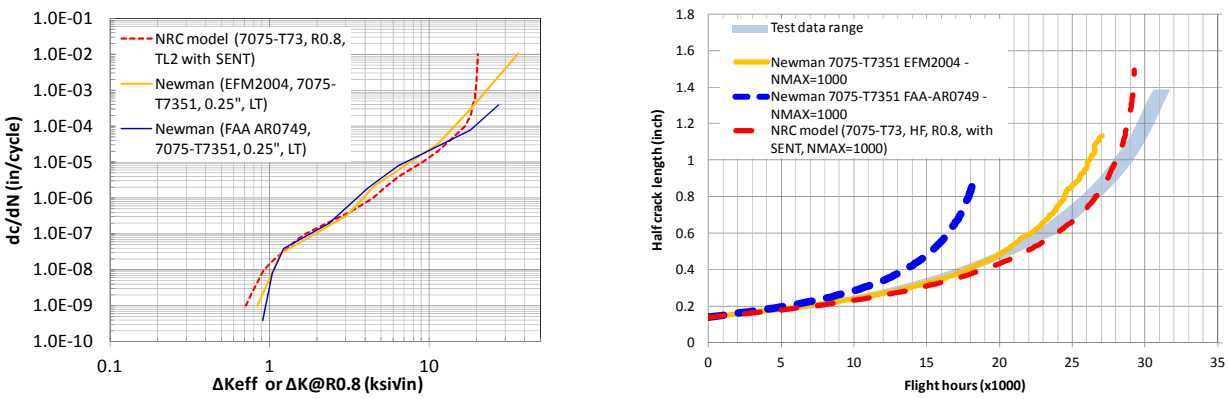

(a) 7075-T73 material models (b) Coupon life estimation

Figure 11. Coupon life estimation using FASTRAN (1-in=25.4 mm, 1.0 ksi√in=1.1 MPa√m)

5.2. Damage tolerance analysis of an aircraft component

A damage tolerance analysis (DTA) was carried out for the CW-1 critical location of the CC-130 center wing, made of 7075-T7351 plate, illustrated by the sketch in Figure 12. Since the DTA involves a multiple, phase-by-phase (PBP) crack growth analysis, the NRC in-house tool CanGROW was originally developed for such PBP analysis purpose. Prior to calibrating the CC-130 strain gauge based spectrum, the Hsu retardation model with default parameters was used in the DTA. Again, both the legacy and NRC Forman material models were used for the DTA, and the results are presented in Figure 12-(b). The legacy material model resulted in a fatigue life that was 45% shorter than that of NRC material model.

Because multiple site fatigue damage (MSD) was found in-service, the PBP analysis was updated by an MSD analysis, as shown in Figure 13. Using the unique MSD analysis module developed in CanGROW, the legacy material model provided an MSD crack growth life approximately 40% of the NRC material model. However, the MSD life to the critical crack size of 6.2 inches (157 mm) was about 17% less than the PBP life. Currently, these DTA results are considered as preliminary until a component test is available to validate these analyses.

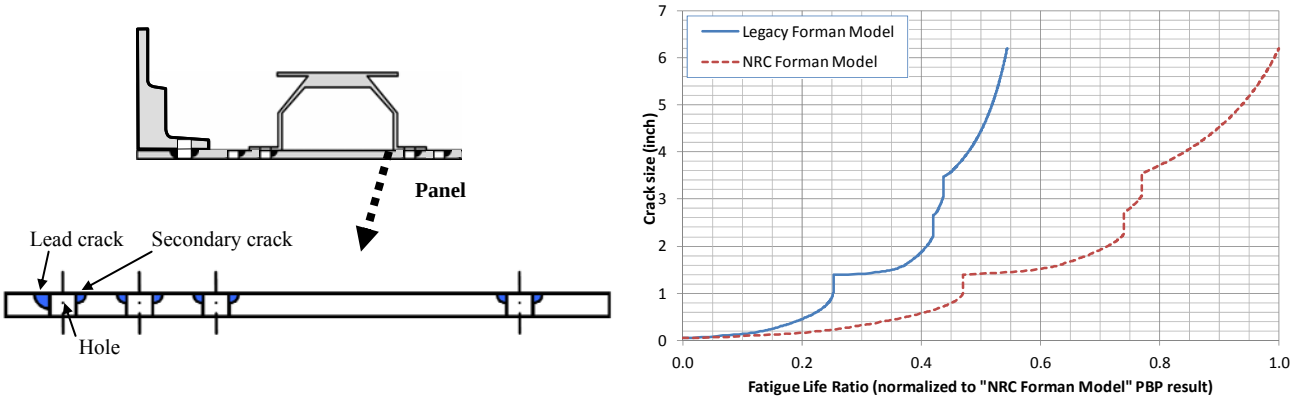

(a) PBP initial cracking model (b) Crack size vs. fatigue life

Figure 12. PBP DTA using CanGROW and CC-130 strain gauge spectrum (1-in=25.4 mm)

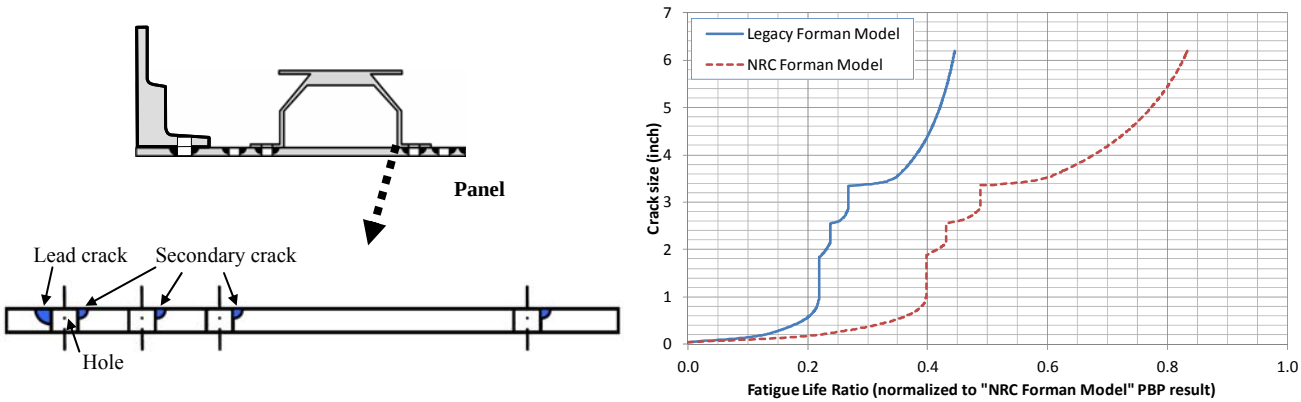

(a) MSD initial cracking model (b) Lead crack size vs. fatigue life

Figure 13. MSD DTA using CanGROW and CC-130 strain gauge spectrum (1-in=25.4 mm)

6. Conclusions

Both precracked long crack test (C(T)) and natural small crack test (SENT) have been carried out to generate short-long crack data under various stress ratios. The ACR method, coupled with the ASTM E647 load reduction method, reduced the scatter of crack growth rate data caused by the

closure and residual stress effects, especially under the low *R*-ratios but not under the high *R*-ratios. The natural small crack growth rate data showed that the "fanning" effect at the near-threshold region is mainly due to the material microstructural scatter, which cannot be determined by long crack tests. Both silicon-based replication and marker band techniques offered very good crack detection resolutions.

The C(T) and SENT data were then combined to develop an NRC material short-long crack model for 7075-T73 aluminum alloys. Using this model and the NRC in-house crack growth tool CanGROW, a good life estimation was achieved for coupon tests under transport loading spectra. Shortcomings were found for a legacy model that includes the Forman equation and Hsu retardation in the spectrum load life analysis. The CC-130 component case showed the difference in the DTA analyses using the legacy and NRC material models, for both PBP and MSD scenarios. Component test data are needed to further validate the DTA analyses and their differences. Tests cases on total fatigue life estimation are also needed to further validate the developed small crack material model.

Acknowledgements

This work was carried out with the financial support of Defence Research and Development Canada and NRC, Projects "Short Crack Model Development for Helicopter Structural Life Assessment" and "Integrated Structural Life Assessment Method for the CF Air Fleets". Thanks to Defense Science and Technology Organization (DSTO) of Australia for providing some coupon test results.

References

[1] M. Liao, G. Renaud, Y. Bombardier, R. Desnoyers, T. Benak, Short crack model development for aircraft structural life assessment – final report, LTR-SMPL-2011-0239, Sept. 2011.

[2] J.K. Donald, G.H. Bray, R.W. Bush, An Evaluation of the Adjusted Compliance Ratio Technique for Determining the Effective Stress Intensity Factor, 29th National Symposium on Fatigue and Fracture Mechanics, ASTM STP 1332, T. L. Panontin, S. D. Sheppard, Eds., American Society for Testing and Materials 1998.

[3] D.L. Ball, J.K. Donald, M.A. James, and R.J. Bucci, The relationships between crack closure, specimen compliance and 'effective' fatigue crack growth rate, Proceedings of the 2011 ICAF, Montréal, June 1-3, 2011 (pp.265-276).

[4] J.C. Newman, Jr., Analyses of Fatigue Crack Growth Databases for Use in a Damage Tolerance Approach for Aircraft Propellers and Rotorcraft, DOT/FAA/AR-07/49, 2007.

[5] G. Renaud, M. Liao, Y. Bombardier, Improved stress intensity factor solutions for surface and corner cracks at a hole, 53rd AIAA/ASME/ASCE/AHS/ASC Structures, Structural Dynamics and Materials Conference, April 2012, Honolulu, Hawaii.

[6] R.W. Bush, R.J. Bucci, P. E. Magnusen, and G.W. Kuhlman, Fatigue crack growth rate measurements in aluminum alloy forgings: effects of residual stress and grain flow, Fracture Mechanics: 23rd Symposium. ASTM STP 1189. R. Chona, Ed., ASTM, 1993, pp.568-589.

[7] R. Ogden, D. Hartley, L. Meadows, Determination of the RAAF C-130J-30 Hercules wing Structural life of type through full scale fatigue testing, 2011 ASIP Conference, San Antonio.

[8] T. Deiter, Hsu model, AFRL-RB-WP-TR-2008-3, 2004.

[9] Y. Bombardier, M. Liao, G. Renaud, A new crack growth analysis tool for the assessment of multiple site fatigue damage, Proceedings of the 2010 Aircraft Airworthiness & Sustainment Conference, Austin, USA, 2010.

[10] J.C. Newman, A. Brot, and C. Matias, Crack-growth calculations in 7075-T7351 aluminum alloy under various load spectra using an improved crack-closure model, *Engineering Fracture Mechanics*, 71 (2004) 2347–2363.

[11] R.L. Circle, F.M. Conley, A Quantitative Assessment of the Variables Involved in Crack Propagation Analysis for In-service Aircraft, *J. of Aircraft*, 18 (1980) 562-569.

Deformations and Damage Evolution of Austenitic Steel AISI304 with Martensite Phase Transformation

Gang Han[1], HuangYuan[1,2,*]

[1]School of Mechanical Engineering, Beijing Institute of Technology, 100081, China
[2]Department of Mech. Engineering,University of Wuppertal,42097, Germany
* Corresponding author: yuanhuang@bit.edu.cn

Abstract In the present paper martensite transformation in stainless steel 304 and its effects to material damage is discussed. The experiments confirm that martensite phase transformation in SS304 can be described by the Santacreu model and shows dependence on the plastic strain and stress triaxiality. The plasticity model with the martensite transformation is established based on Santacreu model and applied to describe plastic behavior of SS304 with severe plastic deformations. It is shown that the plasticity model predicts strain hardening under both compression and tension uniformly and agrees with experimental results reasonably. Although the fracture strain of SS304 can be characterized by the equivalent plastic strain precisely, fatigue tests display strong influence of the pre-strains to the fatigue life. Whereas the strain-fatigue life curve shows acceleration of fatigue damage in strain-controlled fatigue tests, the stress versus fatigue life curve reveals significantly higher bearing capacity due to pre-strains. This result implies that application of the pre-strain should only be used if the mechanical loading is applied in stress-controlled cases.

Keywords: deformation induced phase transformation, plasticity mode, fatigue damage, fatigue life

1. Introduction

It is known that severe plastic deformations influence material behavior. For instance, surface treatment of critical mechanical parts is an important step in manufacturing. The improvement of fatigue behavior of the mechanical part is realized just due to compressive residual stresses and distortions of the surface material [1-3]. Quantifying effects of surface treatment in fatigue life improvement requires detailed understanding of the mechanical behavior of the material with strong distortion and variation of the residual stresses in the surface layer material. AISI304 is a popular stainless steel and can be found in many industrial branches. On the other side, the stainless steel SS304 is meta stable austenite material, its crystallographic structures can transform to martensite phase under plastic deformations [4-6]. The deformation-induced martensite transformations have been studied for many years, especially in material science communities on kinetics of transformation [7-10].

Due to martensite phase the stainless steel behaviors significantly differently from the austenitic steel, both in plastic deformation and failure [11-15]. Using known models to establish a continuum mechanics model for quantifying effects of surface treatment needs detailed understanding of evolution of microstructure and meso-mechanical behavior of the distorted material [7-10]. Especially, phase transformation under severe compressive deformation is less investigated in the past.

The present work dedicates to identify a plasticity model for SS304 under severe plastic deformations, especially under compressive deformations, and to clarify effects of the pre-strains to material failure under monotonic and cyclic loading. Based on extensive experiments, the plasticity model under consideration of the martensite transformation should be applied to predict fatigue life of the compressive deformed specimens and to quantify effects of the compressive strains to material failure evolution.

2. Plasticity for austenitic steel with martensite phase transformation

2.1 Kinetics of Martensite Transformation

The previous experimental observations confirm that the austenitic steel AISI304 transforms to martensite phase due to plastic deformations. The volume fraction of martensite phase increases with deformations. Olson and Cohen [7] studied the phase transformation and suggested an isotropic phase transformation law that describes the martensite content evolution as a function of plastic strain and temperature. The model was extended by Stringfellow et al [8] by incorporating the dependency of the stress triaxiality. According to the Stringfellow evolution of the martensite content, χ, depends on stress triaxiality η and plastic strain $\bar{\varepsilon}^p$ which reads

$$\dot{\chi} = (1-\chi)\left(A\dot{\bar{\varepsilon}}^p + B\dot{\eta}\right) \tag{1}$$

with the stress triaxiality $\eta = \sigma_m / \sigma_e$ and the equivalent plastic strain $\dot{\bar{\varepsilon}}^p = \sqrt{\frac{2}{3}\dot{\varepsilon}_{ij}^p \dot{\varepsilon}_{ij}^p}$.σ_m and σ_e denote hydrostatic stress and Mises stress, respectively. A and B are model parameters generally depending on the temperature and the stress state. For uniaxial material testing η is constant (η=1/3 for uniaxial tension and -1/3 for uniaxial compression, respectively), so that the martensite content is a monotonic function of the plastic strain and can be expressed as

$$\chi = 1 - \exp\left(-A\bar{\varepsilon}^p\right). \tag{2}$$

The Stringfellow model predicts a monotonic relationship between the stress triaxialityrate without explicit effects of the stress triaxiality. Santacreu et al. [9] suggested an alternative evolution law reads

$$\dot{\chi} = \left(\chi_{\max} - \chi\right) mD\left(D\bar{\varepsilon}^p\right)^{m-1} \dot{\bar{\varepsilon}}^p \tag{3}$$

with

$$D = D_0 + D_1\eta. \tag{4}$$

In the expressions above $\chi_{\max}$ denotes the maximum fraction for martensite transformation, D_1 represent effects of stress triaxiality, m and D_0 denote influences of plastic strain. In the original suggestion of Santacreu et al. [9] the parameter D should further related with the Lode angle, i.e. the third deviatoric stress invariant allowing to build the surface corner in the stress space.

Since $\dot{\bar{\varepsilon}}^p$ is non-negative, the martensite transformation is a monotonic function of time. Therefore, the model only considers austenite-martensite transformation, while the reverse transformation is prohibited. The total form of the Santacreu model reads

$$\chi = \chi_{\max}\left[1 - \exp\left(-\left(D\bar{\varepsilon}^p\right)^m\right)\right] \tag{5}$$

forgiving stress triaxlity.

Both martensite transformation models predict a linear correlation between the plastic strain rate and transformation rate. Stringfellow addressed additionally that the transformation is further influenced by the stress triaxialityrate which is generally rather difficult to be identified in material testing. Furthermore, the martensite transformation may occur for varying stress triaxiality without plastic deformations, which is not confirmed in the stainless steel SS304. A major difference is the explicit expression to the stress triaxiality which allows to apply for FEM computations. In the present work the Santacreu model will be used for considering plasticity of the SS304 under consideration of the martensite transformation.

2.2 Plasticity with phase transformation

The conventional J_2 plasticity is applicable for the present stainless steel without considering

martensite transformation [12]. The potential function is defined as

$$f = \sigma_e - k = 0, \tag{6}$$

where σ_e denotes the effective Mises stress for kinematic hardening, $\sigma_{ij} = \sqrt{\frac{3}{2}\left(s_{ij} - \alpha_{ij}\right)\left(s_{ij} - \alpha_{ij}\right)}$, k is the material resistance against plastic deformation. The backstress is assumed to be

$$\dot{\alpha}_{ij} = \frac{2}{3} c_L \dot{\varepsilon}_{ij}^p - c_{NL} \alpha_{ij} \dot{\bar{\varepsilon}}^p, \tag{7}$$

in the nonlinear kinematic hardening model. According to the associated flow rule the plastic strain rate is proportional to the derivative of the potential function,

$$\dot{\varepsilon}_{ij}^p = \dot{\lambda} \frac{\partial f}{\partial \sigma_{ij}} = \frac{3}{2} \dot{\lambda} \frac{s_{ij} - \alpha_{ij}}{\sigma_e}, \tag{8}$$

where the plastic multiplier $\dot{\lambda} \geq 0$ and the deviatoric stress $s_{ij} = \sigma_{ij} - \sigma_m \delta_{ij}$. The equivalent plastic strain is defined as $\bar{\varepsilon}^p = \int \dot{\bar{\varepsilon}}^p dt = \int \dot{\lambda}\, dt$.

The plasticity model contains both kinematic hardening and isotropic hardening. Whereas the kinematic hardening takes the conventional form [11], the isotropic hardening is affected by martensite transformation and expressed by the deformation resistance,

$$\dot{k} = H_\varepsilon \dot{\bar{\varepsilon}}^p + H_\chi \dot{\chi}, \tag{9}$$

that is, the deformation resistance is linear proportional to plastic strain rate and martensite transformation rate. Both plastic strain hardening modulus, H_ε, and phase transformation hardening modulus, H_χ, are functions of stress and strain states.

Taking the combined hardening model [11] into account, the material resistance under absence of phase transformation can be written as

$$k_\varepsilon = k_0 + H_0\left[1 - \exp\left(-\beta \bar{\varepsilon}^p\right)\right], \tag{10}$$

with the model parameters k_0 as initial yield stress of the material, H_0 as plastic hardening factor and β hardening exponent. Consequently, the hardening due to plastic deformation can be expressed as

$$H_\varepsilon = \beta H_0 \exp\left(-\beta \bar{\varepsilon}^p\right), \tag{11}$$

The additional phase transformation hardening modulus, H_χ, has to be determined based on experimental observation. Investigation of Beese [10] confirmed a constant modulus H_χ provides sufficient accurate results for steels. Based on the Santacreu model the isotropic hardening can be expressed into

$$\dot{k} = \left[H_\varepsilon + H_\chi\left(\chi_{\max} - \chi\right) m D \left(D \bar{\varepsilon}^p\right)^{m-1}\right] \dot{\bar{\varepsilon}}^p, \tag{12}$$

with H_ε defined in Eq. (11).

Under uniaxial loading condition, the equations can be simplified due to $\sigma_e = |\sigma - \alpha|$ and $\bar{\varepsilon}^p = |\varepsilon^p|$ where σ and ε^p are the first principal stress/plastic strain, respectively. The stress-plastic strain curve under monotonic tensile testing can be expressed as

$$\sigma_y = \alpha + k, \tag{13}$$

where the backstress can be evaluated from

$$\alpha = \frac{2c_L}{3c_{NL}}\left[1 - \exp\left(-c_{NL}\varepsilon^p\right)\right] \tag{14}$$

and the isotropic hardening stress is expressed as

$$k = k_0 + H_0\left[1 - \exp\left(-\beta \bar{\varepsilon}^p\right)\right] + \chi_{\max} H_\chi \left[1 - \exp\left(-\left(D \bar{\varepsilon}^p\right)^m\right)\right] \tag{15}$$

with D defined in Eq. (4).In expressions above D and χ_{max} have been identified from the phase transformation curve. The plasticity behavior of the material is described by k_0, H_0, β and H_χ as well as c_L and c_{NL}. In comparing with the conventional combined hardening model [11], one more parameter H_c has to be considered from the tensile tests. Note the formulations above are only valid for monotonic loading.

3. Experiments and Results

3.1 Specimens

In the present work the austenitic stainless steel 304 is investigated, almost versatile and widely used stainless steel and available in a wider range of products. The austenitic structure gives the steel excellent toughness, even down to cryogenic temperatures. The chemical components are summarized in Table 1.

Table 1. Chemical composition of the stainless steel 304

C	Cr	Ni	Mn	Si	P	S	Fe
0.04	17.1	8.1	1.05	0.41	0.035	0.003	bal

Table 2. Mechanical property of the stainless steel 304 after solution treatment

E (GPa)	Ultimate Stress (MPa)	Yield stress (MPa)	Elongation (%)	Hardness (MPa)
200	650	240	100	100

The material used in the present work underwent solution treatment (annealing), heated to 1100°C for 1 hour and cooled down to room temperature in air, to eliminate the residual stresses and initial effects from manufacturing. The mechanical property of the heat treated SS304 is listed in Table 2.

To study effects of deformations to material property, two kinds of specimens have been tested: (1) The plate specimens were fabricated for learning development of Martensite phase in SS304 under tension and compression. The specimen geometry is given in Fig. 1(a). To study development of the martensite phase under compression, the plate specimens can be pressed in the thickness. (2) The tension specimens were taken for tension and fatigue tests, as shown in Fig. 1(b).

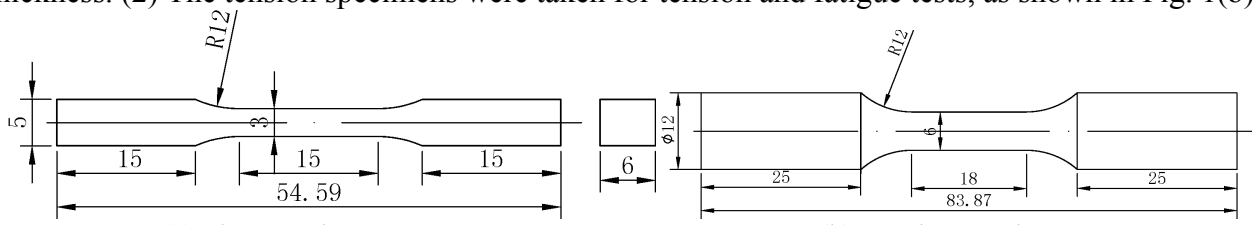

(a) Plate specimen (b) Tension specimen

Figure 1: Specimen geometries tested in the present work. The plate specimens were fabricated for studying martensite phase transformation and the tension bars for fatigue tests.

3.2 Experimental observation of Martensite phase transformation

To quantify evolutions of the martensite phase transformation under compression and it's effects to mechanical property, the plate specimens were pressed in their thickness direction. With various press forces the thickness of the final plate specimens varies between 6mm (0% deformation) and 2.8mm (-53.3% thickness reduction). Mainly ca. -10%, -20%, -30%, -40% and -50% of reduction in specimen thickness were realized. The stress triaxiality under this loading state is η=-1/3.

The tension effects were studies in uniaxial tension specimens after given tensile strains (η=1/3). Five different deformation grades were examined, 20% - 80%. Note the true strain, i.e. the

logarithmic strain, for tension is smaller than the engineering strain, whereas the value of the compressive true strain is generally larger than that of the linear strain. It results in different martensite content for the same deformation grade (engineering strain) in martensite evolution since the martensite evolution law is expressed by the true strain, Eq. (3).

Experimental observations reveal that SS304 is a metastable austenitic steel [16-18]. Figure 2 confirms development of crystallographic pictures of the SS304 after different deformations. The figure demonstrates clearly that the density of martensite needles increases with strains. In pictures dark lines denote martensite phase in the needle form. The pictures reveal that the grain size is ca. 100μm and remains constant even after severe plastic deformations. However, martensite seems proportional increasing with deformations, under both tension and compression. After -45% compression deformations, a large part of austenitic contents in material has been transformed into dark martensite phases. The phase transformation changes and disorders the microstructure of grains, thus arises resistance of the dislocation motions. The material with martensite phase obtains higher strength and less ductility. Experiments do not show significant difference in development of martensite phase under tension from that under compression.

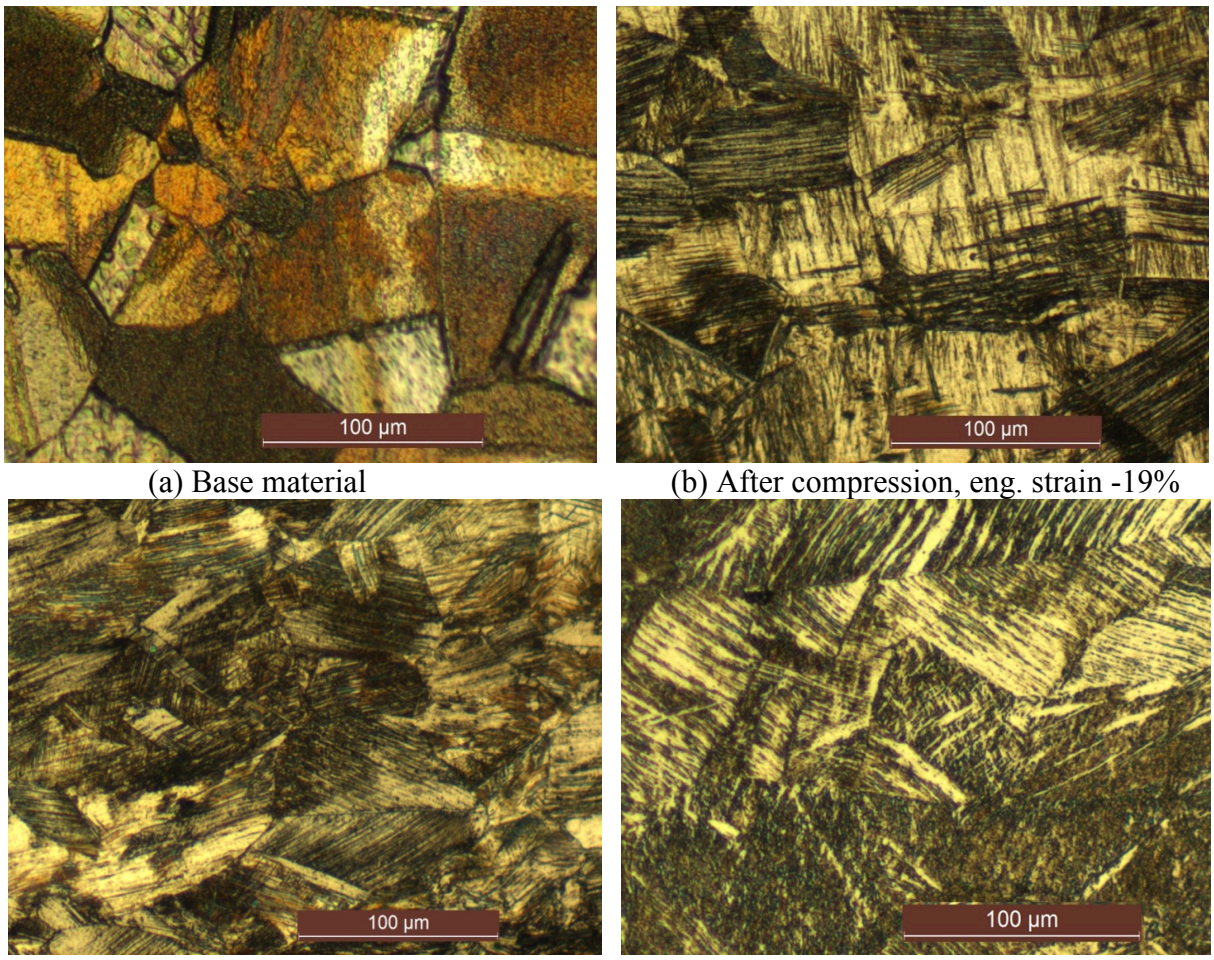

(a) Base material (b) After compression, eng. strain -19%

(c) After compession, eng. strain -45% (d) After tension, eng. strain 40%

Figure 2: Crystallographic pictures of the SS304 after different deformations. The dark phases denote the martensite content.

3.3 Experimental measurement of martensite phase evolution

A ferritescope[19-22] is used to measure the martensite content in the plate specimens. The method measure the martensite content based on changes of the linear relationship between the output

voltage and the magnetic permeability of the sample. If the sample is qualified properly, this method is easy in use and reliable [10, 22].

To study evolution of the martensite phase in SS304, the pre-strained specimens are measured using the ferritescope. The experimental data are shown in Figure 3, in which the martensite content under compressive and tensile uniaxial loading is plotted as a function of the equivalent true plastic strain. Note the true strain, i.e. logarithmic strain, is used here and deviates from the linear engineering strain significantly. The present experimental data reveal that the evolution of the martensite phase in the stainless steel SS304 is determined by the plastic deformation and affected by the stress triaxiality η, but the development seems different from the results in [23].

The solid lines denote prediction from the Santacreu model, Eq. (5), with χ_{max}=1, m=2.55, D_0=1.23 and D_1=0.907. Fig. 3 shows variations of experiments and model predictions. In the present work more general experiments under multi-axial loading condition about evolution of martensite phase are not available. It is an open issue whether or not the stress triaxiality further affects devemopment of the martensite transformation.

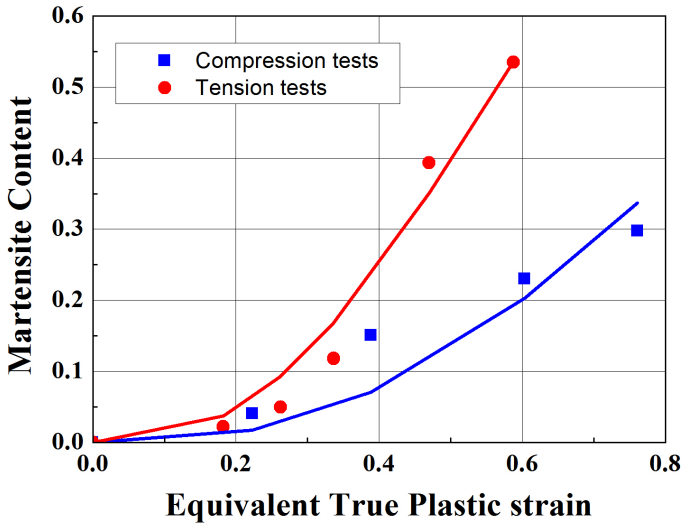

Figure 3: Evolution of the martensite phase in SS304 under both compression and tension. Symbols denote experimental data determined by the ferritescope, whereas the solid lines are predictions from the Santacreu model, Eq. (5).

3.4 Stress-strain relationships

Pre-pressed plate specimens were tested under uniaxial tensile loading condition and the results are summarized in Fig. 4(a). The reduction in the specimen thickness, i.e. pre-strain, varies from 0% (Base material without initial pressing) to 38.6%. The thickness reduction of 38.6% means -48.8% of logarithmic strain. Note that the amplitude of the logarithmic strain under compression is generally larger than the linear strain. In the figure the engineering stress is plotted as a function of the engineering strain which was measured using an extensometer from Epsilon Technology. It is trivial that the stress-strain curves depend on the initial pre-strains. Due to cold work the pressed specimens were broken with smaller strains. Interesting is that the stress increases with the pre-strain significantly.

Under uniaxial loading condition the equivalent plastic strain equals the amplitude of the plastic elongation strain, i.e.

$$\bar{\varepsilon}_{eq}^{p} = \int \sqrt{\frac{2}{3}\dot{\varepsilon}_{ij}^{p}\dot{\varepsilon}_{ij}^{p}}\,dt = \int \dot{\varepsilon}^{p}\,dt = \sum \Delta\varepsilon_{i}^{p}\ , \tag{16}$$

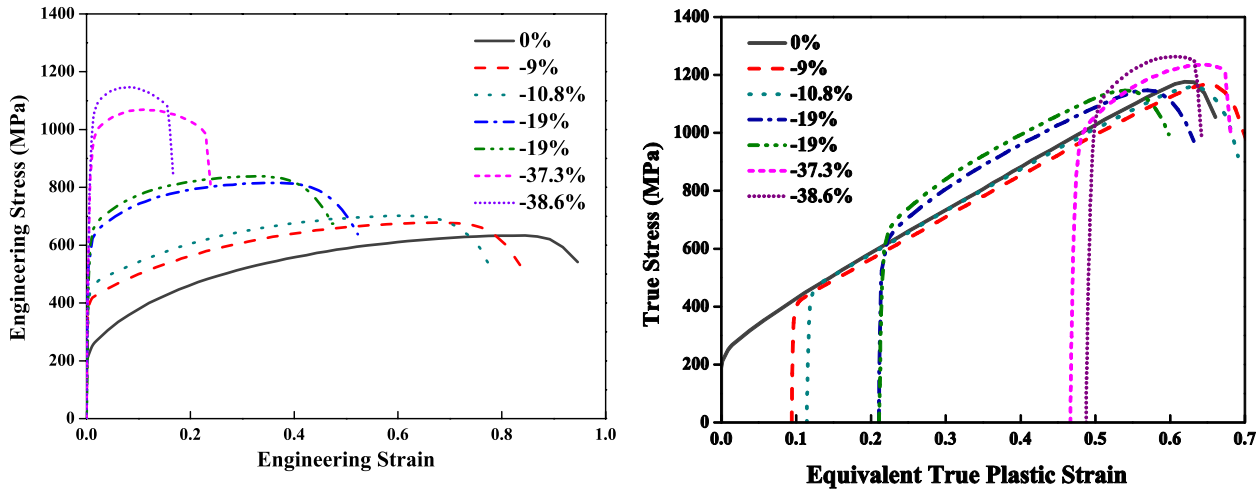

(a) Engineering stress vs. engineering strain curves (b) True stress vs. equivalent true strain curves

Figure 4: Stress-strain curves from tensile tests. The pre-strain was induced by pressing in the thickness. The legends show the reduction of the specimen thickness.

The summation of the plastic strain goes through all loading history. For the pre-strained specimens, the total equivalent plastic strain sums the initial compressive plastic strain and plastic strain under uniaxial tension. The true stress versus total equivalent true plastic strain is shown in Fig. 4(b).

The diagram reveals that the true stress of the tensile specimen is a monotonic function of the plastic strain. Before material damage dominates, the material resistance again deformation grows almost linearly with the plastic strain. The pre-strain induces more resistance than the tension, which implies effects of the anisotropy of the material due to large plastic deformations. If one assumes isotropic material behavior, the anisotropy could be caused by the martensite transformation. The fracture true strains of all specimens exceed 60% and seem less dependent on the pre-strains. The experimental results confirm that the stress-strain curve of SS304 is not so sensitive to the tension or compression, i.e. stress triaxiality.

4. Identification of the plasticity model

Based on the experimental data the plasticity model under consideration of the martensite transformation presented in the previous section can be identified using the least square fitting, Table 3 for the identified parameters. In the table the kinematical hardening in the plastic model is neglected for lacking in corresponding experimental data.

The prediction of the plasticity model under consideration of the martensite transformation is plotted in Fig. 5, together with the experimental data. Reasonable agreement between experiments and model predictions is obtained for all pre-strains, although slight deviations for high pre-strains are observed. Inelastic hardening of specimens can be described by the present plasticity model well.

Table 3.Parameters for constitutive model of the stainless steel 304

Martensite transformation parameters	Plastic isotropic hardening parameters
χ_{max}=1	k_0=220MPa
m=2.55	β=1
D_0=1.23	H_0=2000MPa
D_1=0.907	H_χ=300 MPa

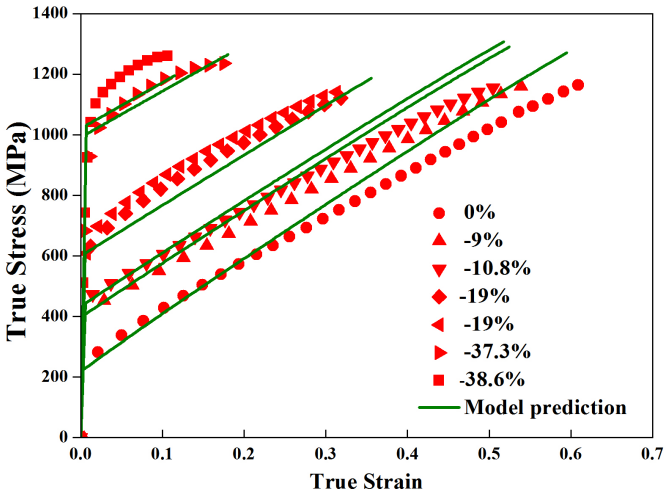

Figure 5: Comparison between experimental data and prediction of the plasticity model under consideration of the martensite transformation.

More results are summarized in Fig. 6, in which true stress at 10% plastic strain and ultimate stress of the SS304 under different pre-strains are plotted. Due to martensite transformation both stress at 10% plastic strain and ultimate stress can be different. The ultimate stress is taken from the maximum stress in the tension tests. The results show, however, that the stress monotonically grows with pre-strain, whereas the ultimate stress of the specimen is independent of initial deformations. Fig. 6(b) shows that the ultimate stress of SS304 is independent of loading history. The prediction of the plasticity model is acceptable.

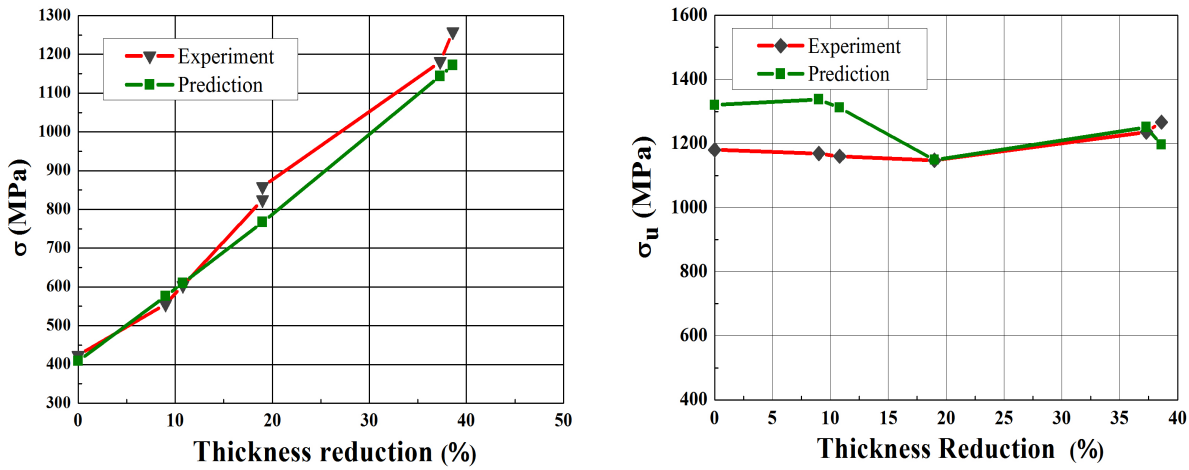

(a) True stress at 10% plastic strain (b) Ultimate stress

Figure 6: Comparison between experimental data and prediction of the plasticity model under consideration of the martensite transformation.

5. Fracture and Fatigue Behavior

Martensite phase transformation affects plastic behavior of the stainless steel SS304. Since H_χ in Eq. (15) is positive, the martensite phase will generally increase the hardening of the material. Due to enbrittlement through martensite phase, however, fracture toughness of SS304 decreases with growth of martensite content. Effects of the martensite phase to material failure have to be

considered carefully.

Figure 7 displays that the fracture strain in the plate specimens decreases with the pre-strain, which seems to be corrected by the total equivalent plastic strain. This result shows the fracture strain for the SS304 is independent of loading history. Martensite transformation seems not to change the fracture strain significantly.

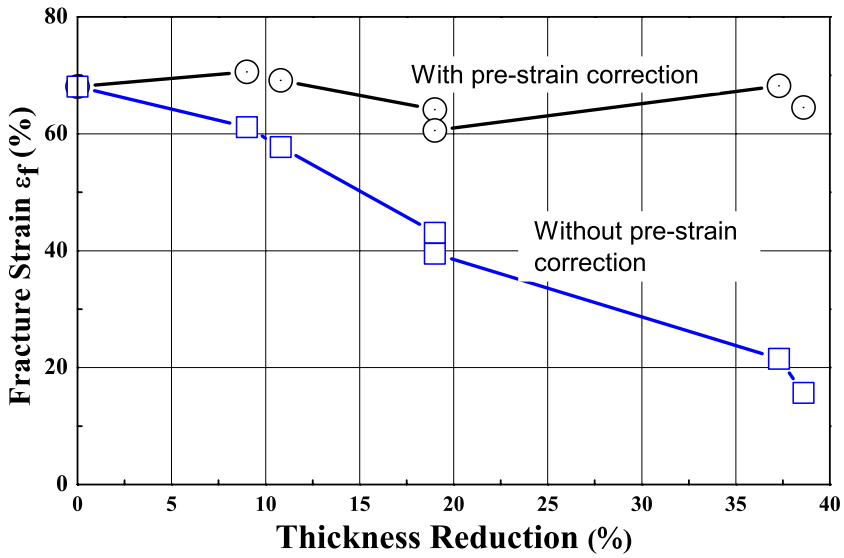

Figure 7: Fracture strains as a function of pre-strains. Fracture strain with pre-strain denotes the total equivalent strain including the initial deformations. The other curves represent fracture strain measured in specimens.

Effects of the pre-strain to fatigue life are not studied systematically. Observations of Miao et al. [14] reveal non-monotonic correlations between LCF life and initial plastic strains. By giving strain amplitudes, stress variations depend on initial treatment of the specimens significantly. In this sense, stress-controlled tests provide totally different results than the strain-controlled tests.

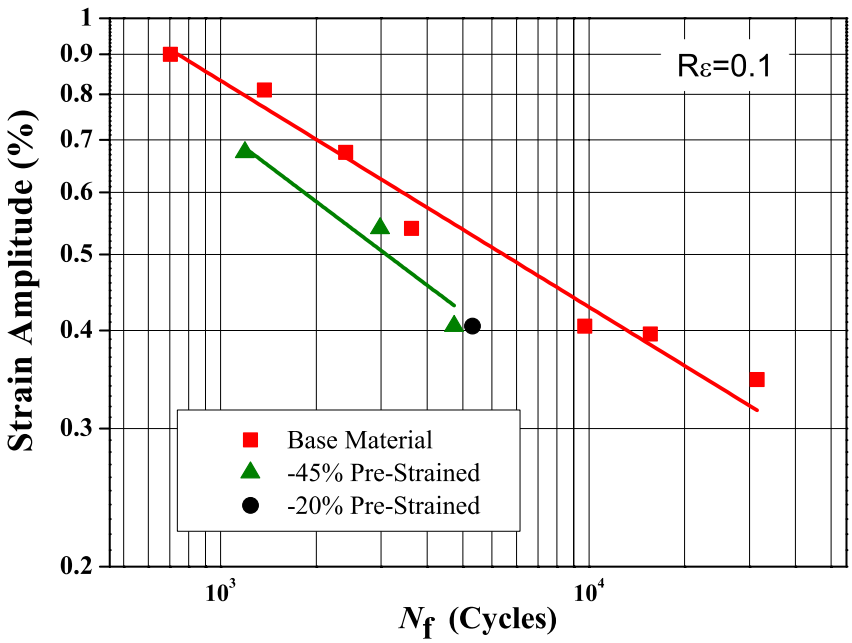

Figure 8: Strain-fatigue life curves for both base material and pressed material from strain-controlled fatigue tests.

In the present work several pre-strained tensile specimens were tested under given strain amplitude with the loading ratio 0.1. The results are shown in Fig. 8. From the diagram one sees that the pre-strain reduces LCF fatigue life of the specimen. In the figure the fatigue life is expressed in the form of Basquin model

$$\varepsilon_a = A\left(N_f\right)^m, \tag{17}$$

with A and m as material specific parameters. For the base material it was identified A=7.034 and m=-0.3083. For the pre-strained specimen A=8.322 and m=-0.35. This result implies that the pre-strained specimen loses almost 50% LCF life of the original untreated specimen. The grade of pre-strain seems to affect fatigue damage secondarily. One major for the life reduction is caused by the significant difference in applied stress amplitude. Due to huge strain hardening induced by plastic deformations and martensite phase transformation in pre-straining treatment, the pre-strained specimens are significantly high strengthed than the base material. It follows that the pre-strained specimens were under much higher stresses than the base material specimens, by giving strain amplitudes, as shown in Fig. 9. The stress amplitude in Fig. 9 is the final stabilized stress amplitude in strain-controlled fatigue tests. From the figure one learns that the pre-strained specimens are much stronger than the base material specimens, that is, by giving fatigue life, the pre-strained specimens can bear much higher mechanical loads.

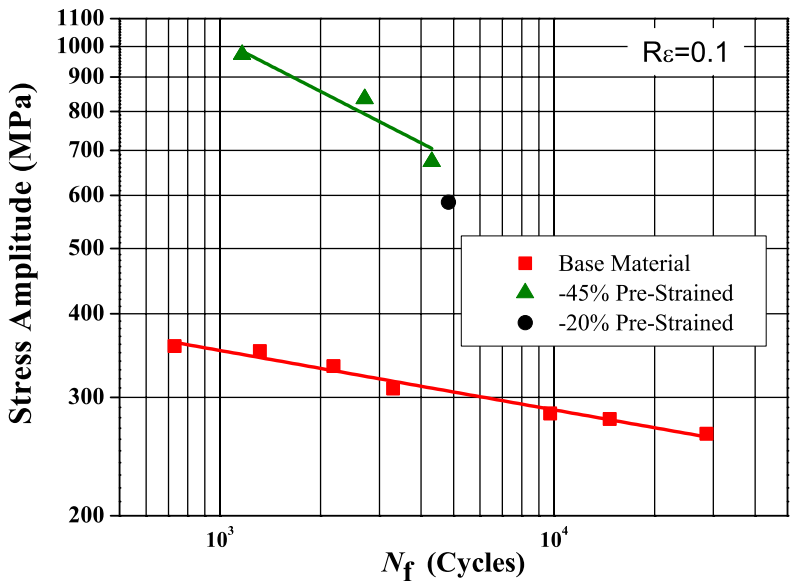

Figure 9: The stabilized stress amplitude as a function of fatigue life from strain-controlled fatigue tests.

6. Conclusions

In the present paper a systematical work on martensite transformation in stainless steel 304 and its effects to material damage is presented. The first experiments confirm that matensite phase transformation in SS304 can be described by the Santacreu model and shows significant dependence on stress triaxiality.

The plasticity model with the martensite transformation is established based on after Santacreu model and can be applied to describe plastic behavior of SS304 with severe plastic deformations. The plasticity model predicts strain hardening under both compression and tension uniformly. Computational predictions agree with experimental results reasonably.

Although the fracture strain of SS304 can be characterized by the equivalent plastic strain precisely, fatigue tests display strong influence of the pre-strains to the fatigue life. Whereas the strain-fatigue life curve shows acceleration of fatigue damage in strain-controlled fatigue tests, the stress versus fatigue life curve reveals significantly higher bearing capacity due to pre-strains. This result implies

that application of the pre-strain should only be used if the mechanical loading is applied in stress-controlled cases.

References

[1] Schulze V. Modern Mechanical Surface Treatment – States, Stability, Effects. Wiley-VCH Verlag GmbH &Co. KGaA. 2006.
[2] Altenberger I, Nalla RK, Noster U, Liu G, Scholtes B. Residual tress stability and near-surface microstructures in high temperature fatigued mechanically surface treated Ti-6Al-4V. Materialwissenschaft und Werkstofftechnik, 34 (2009) 29 – 541.
[3] Liu J, Yuan H. Prediction of residual stress relaxations in shot-peened specimens and its application for the rotor disc assessment. Materials Science and Engineering, A 527 (2010) 6690–6698.
[4] V. Mertinger, E. Nagy, F. Tranta, J. Sólyom, Strain-induced martensitic transformation in textured austenitic stainless steels. Materials Science and Engineering: A, 481–482 (2008) 718-722.
[5] S.S.M. Tavares, D. Gunderov, V. Stolyarov, J.M. Neto, Phase transformation induced by severe plastic deformation in the AISI 304L stainless steel. Materials Science and Engineering: A, 358 (2003) 32-36.
[6] S.K. Ghosh, P. Mallick, P.P. Chattopadhyay, Effect of cold deformation on phase evolution and mechanical properties in an austenitic stainless steel for structural and safety applications. Journal of Iron and Steel Research, International, 19 (2012) 63-68.
[7] G.B. Olson, M. Cohen, Kinetics of strain-induced martensitic nucleation. Metallurgical Transactions A, 6 (1975) 791-795.
[8] R.G. Stringfellow, D.M. Parks, G.B. Olson, A constitutive model for transformation plasticity accompanying strain-induced martensitic transformations in metastable austenitic steels. ActaMetallurgica et Materialia, 40 (1992) 1703-1716.
[9] PO Santacreu, JC Glez, G Chinouilh, T Frölich. Behaviour model of austenitic stainless steels for automotive structural parts. Steel Research International, 77(2006) 686-691.
[10] A.M. Beese, D. Mohr, Effect of stress triaxiality and Lode angle on the kinetics of strain-induced austenite-to-martensite transformation. Acta Materialia, 59 (2011) 2589-2600.
[11] J.L. Chaboche, A review of some plasticity and viscoplasticity constitutive theories. International Journal of Plasticity, 24 (2008) 1642-1693.
[12] J. Lublin. Plasticity theory. Pearson Educational Inc., 2006.
[13] Socie DI, Marquis GB. Multiaxial Fatigue, SAE International, Arrendale, 2000.
[14] C.J. Miao et al. Investigation of low-cycle fatigue behavior of austenitic stainless steel for cold-stretched pressure vessels. Journal of Zhejiang University- Science A (Applied Physics and Engineering), 14(2013): 31-37.
[15] Z. Mei, J.W. Morris, Influence of deformation-induced martensite on fatigue crack propagation in 304-type steels, Metallurgical Transactions A, 21 (1990) 3137-3152.
[16] A. Das, S. Sivaprasad, M. Ghosh, P.C. Chakraborti, S. Tarafder, Morphologies and characteristics of deformation induced martensite during tensile deformation of 304 LN stainless steel. Materials Science and Engineering: A, 486 (2008) 283-286.
[17] K. Mumtaz, S. Takahashi, J. Echigoya, Y. Kamada, L. F. Zhang, H. Kikuchi, K. Ara, M. Sato, Magnetic measurements of martensitic transformation in austenitic stainless steel after room temperature rolling. Journal of Materials Science, 39 (2004) 85– 97.
[18] W.S. Lee, C.F. Lin, The morphologies and characteristics of impact-induced martensite in 304L stainless steel, ScriptaMaterialia, 43 (2000) 777-782.
[19] G. Hu, C.C. Xu, J.G.Yuan, Deformation induced martensite transformation and its magnetic memory effect of austenitic 304 stainless steel. Nondestructive Testing, 30(2008)216-219.
[20] Y.X. Ren, The comparison test of α-phases of austenite and ferrite austenite double phases of stainless steel,Physical Testing and Chemical Analysis Part A:Physical Testing, 41(2005) 184-185.
[21] C.C. Xu, X.S.Zhang, G.Hu, Microstructure change of AISI304 stainless steel in the course of cold working. Journal of Beijing University of Chemical Technology (Natural Science Edition), 29(2002) 27-31.
[22] J. Talonen, P. Aspegren, H. Hanninen, Comparison of different methods for measuring strain induced alpha' -martensite content in austenitic steels, Materials Science and Technology, 20 (2004) 1506-1512.
[23] C.C Young, Transformation toughening of phosphocarbide-strengthened austenitic steels. Doctoral thesis, Massachusetts Institute of Technology, Cambridge, MA, USA, 1988.

The local concept to assess weldment with help of nano-indentation and FEM simulation

Jie Fang, Huang Yuan*

Department of Mechanical Engineering, University of Wuppertal, Germany
* Corresponding author: h.yuan@uni-wuppertal.de

Abstract In this work the local mechanical behavior and fatigue resistance of the welding material were investigated with help of nano-indentation. By assuming a power-law strain hardening, the elastoplastic properties of the welding joint material were identified from inverse nano-indentation analysis with help of finite element simulation. With the known mechanical property of the weldment the fatigue should be described by the local stresses and strains. A critical plane based Cruse-Meyer model was introduced to predict the fatigue life of weldment. The predictions agree with experiments. Combined with critical distance concept the local fatigue life model was extended to predict fatigue life of holed specimens. The present work attempted to establish more reliable and more accurate a local fatigue and damage description of the weldment for engineering structures.

Keywords Nano-indentation, Weldment, Notched Fatigue, Extended Cruse-Meyer Model, Critical Distance Method.

1. Introduction

With the development of aero engines, welding has been widely used to manufacture aircraft engine components for better performance. Many welding methods such as tungsten inert gas welding, plasma welding, electron beam welding (EBW), diffusion welding and friction welding have been developed and used for the welding of Inconel alloys. Compared with traditional fusion welding technology, the electron beam welding has a narrow heat-affected zone with little distortion and low residual stresses [1]. Very high quality welds can be made during the manufacturing of complex components. Being a fusion welding process, the weld joint of EBW has significantly different properties to the base material.

Nano-indentation is a method to extract the mechanical properties of materials from load-displacement measurements [2]. Hardness and Young's modulus can be obtained from the indentation curve based on the Oliver and Pharr method [3] to characterize micromechanical behavior of material. More depth knowledge about mechanical properties can be gained with help of finite element simulation through an inverse analysis procedure [4]. The local mechanical property of the weldment makes it possible to establish fatigue life prediction based on local stress and strain variations.

In design of a gas turbine engine, notches and holes are not avoidable, for instance, in disks and blades, which cause local stress concentrations and lead to significant reduction in fatigue life. In industrial design the stress concentration factor, K_t, is often used to characterize the stress concentration. Under cyclic loading, the fatigue notch factor, K_f, is introduced to describe the change of fatigue strength [5]. Notched fatigue strength depends not only on K_t, but also on the stress gradient which relates the material volume with the high stress. Peterson [6] and Neuber [7] try to describe the difference between K_f with K_t through empirical relations. Siebel and Stieler [8] proposed using the stress gradient at a notch root for evaluation of the notch effect. Taylor developed the former works and proposed the theory of critical distance (TCD) [9]. Susmel and Talyor [10,11,12] successfully extended the TCD to the LCF regime. By employing an elasto-plastic critical plane approach, the TCD is extended to consider multi-axial fatigue.

In this work the stress-strain relation and tensile fatigue resistance of the EB weld joints are investigated. This work aims to develop a method to determine the local elastoplastic properties of

weldment material, and to predict fatigue life of weldment with stress concentrations. The local elastoplastic properties of weldment material are derived from inverse nano-indentation analysis. From FEM simulation the nominal stress-strain curve of weld joint is obtained and compared with the monotonic tensile curve. A critical plane method based Cruse-Meyer model is applied to predict the fatigue life of weldment. Combined with critical distance method center holed specimen fatigue life was calculated and compared with the experiment.

2. Experiments

Inconel 718 is a precipitation-hardenable nickel-chromium alloy, contains large amount of iron, niobium and molybdenum. Due to the outstanding combination of tensile strength, high temperature creep strength and high resistance to fatigue, this alloy is widely used in the high pressure compressor and turbine discs of commercial and military aero engines and recommended for using up to 650°C [13]. The composition of the alloy is given in Table 1. After electron beam welding process, post-weld heat treatment was applied. Specimens were cut from the welded joint material with weldment in the center of the specimen. Surface of raw specimens was removed and machined to a thickness of 4mm, resulting weldment shape changing from bell shape to trapezoid shape. Fig. 1 shows the geometry of the holed specimen. All tests were carried out at the room temperature.

Table 1. Chemistry of Inconel 718

	Ni	Fe	Cr	Mo	Nb	Al	Ti	C
Weight%	balance	18.5	19.0	3.0	5.1	0.5	0.9	0.04

2.1 Tensile and Fatigue Test

Monotonic tensile test was conducted at strain rate 10^{-4}/s. Cracks originated from the weldment. Tensile failure occurred in the center of weldment, while shear failure occurred in the outer side. Yield stress and ultimate tensile stress of weld joint were lower than base material. Fatigue tests were performed under stress control at stress ratio, R = -1, 0.1. The fatigue life was defined as the number of cycles when a specimen was completely separated.

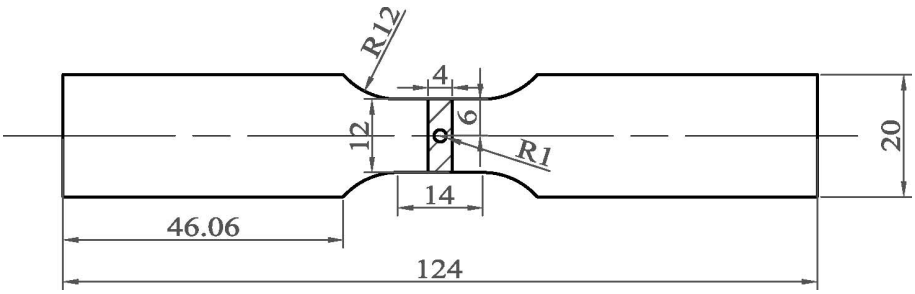

Figure 1. Geometry of center holed EB welded specimen.

2.2 Macroscopic and microscopic observation of weld joint

Fig. 2a shows the fusion region of EB welding joint by macroscopic observation. The fusion zone is quite narrow, formed in 2-4mm width. The fusion boundary is clearly evident. No significant heat affected zone can be seen. The evolution of microstructure from the base material to the fusion zone can be clearly recognized. Fig. 2b shows a microscopic observation near fusion boundary. Large

grain size gradient between the weldment (left side) and the base material (right side) is clearly seen. The average grain size of the base material is about 50μm. In the fusion zone, the microstructure is composed of columnar grains, while original grain structure no longer exits. The columnar grains orient perpendicular to the direction of the radial fusion boundary. The grain differences between fusion zone and base material would lead to different mechanical behavior.

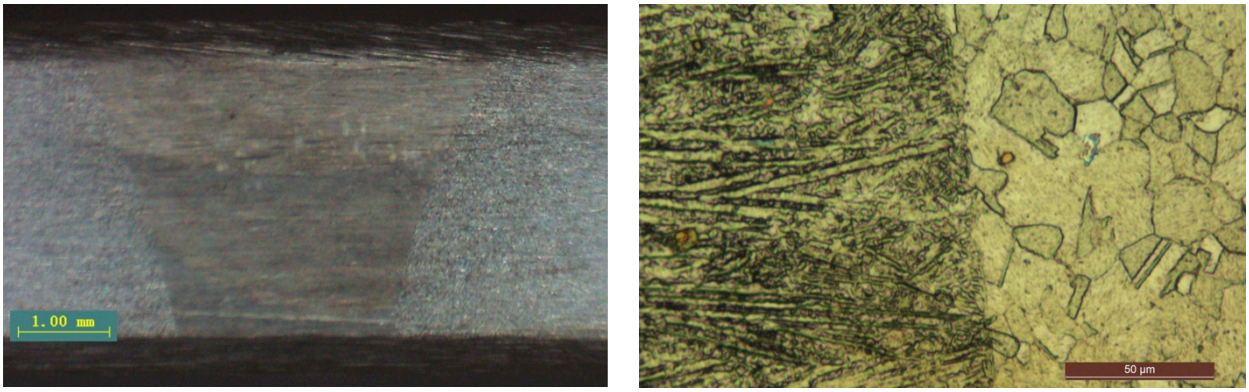

(a) (b)

Figure 2. (a) Macroscopic view of the weld joint and (b) Microstructure of the fusion boundary.

2.3 Nano-indentation test

For nano-indentation test, a nano indenter G200 from Agilent Technologies was used. The depth resolution is 0.01nm and the force resolution is 50nN. Berkovich indenter was used for the identation tests. During the test, the displacement of the indenter has been controlled. The maximum depth limit was 2μm and peak hold time was 10 s. Indentation tests were carried out in five times and on a longitudinal section of weldment. The measured hardness shows a normal distribution and listed in Table 2. Due to larger grain size in the base material compared with the indentation depth (2μm), larger scattering of measured hardness were obtained. For the weldment material, the scatter band was smaller. Generally the hardness of weldment material is higher than base material.

Table 2. Measured indentation hardness

	Mean Value (GPa)	Standard Deviation
Base Material	3.48	0.53
Weldment material	3.10	0.33

3. Nano-indentation Simulation and Results

In order to determine the local stress-strain behavior of the weldment, nano-indentation technology was used. Through inverse analysis, the nano-indentation data can help to evaluate the elastoplastic properties of weldment.

3.1 FEM modeling

The indentation process was simulated in the commercial FEM code ABAQUS. Four-node axisymmetric elements were used in the simulation. Large strain feature was considered. Due to the

indenter was much stiffer than the test material, the indenter was considered as a perfect rigid and modeled as axisymmetric analytical rigid 140.6° cone, based on the equivalent contact area to depth ratio as a perfect Berkovich indenter. A reference point was defined to manipulate the translation of the indenter. The analysis was carried out under the displacement control without friction between the contact surfaces. Fig. 3 shows the mesh used in the analysis. The length of the whole mesh square is 30 micrometer. Finer meshes near the indenter were created to be able to describe the deformation and stress gradient below the indenter with sufficiently high accuracy. The base of the square was completely constrained, and the nodes along the center line were constrained in the horizontal direction due to axi-symmetry.

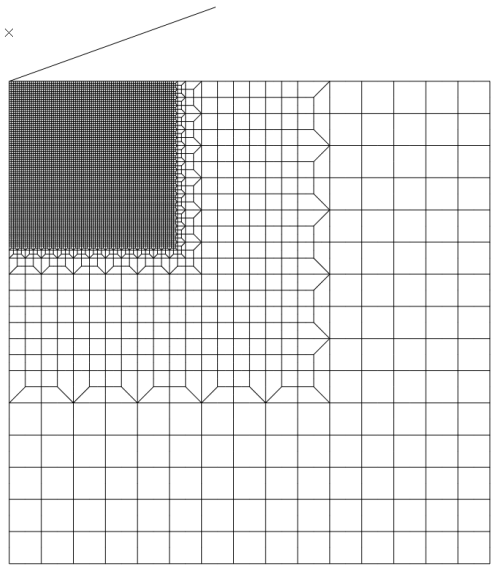

Figure 3. Mesh used in the finite element simulations

3.2 Elastoplastic material model

Due to the negligible heat affect zone, the fusion zone was assumed isotropic and homogeneous. A one-dimensional constitutive relation for the linear elastic, power law plastic material indicated in Eq. 1 was applied to describe the stress-strain relationship,

$$\sigma = \begin{cases} E\varepsilon, \sigma \le \sigma_{\mathrm{y}} \\ K\varepsilon^{n}, \sigma > \sigma_{y} \end{cases}, \tag{1}$$

where parameter σ_{y} is the initial yield stress, E represents the Young's modulus, K is the strain hardening coefficient and n is the strain hardening exponent. Young's modulus can be evaluated based on Oliver and Pharr method [3]. Through adjusting these input material parameters, different load-displacement curves can be obtained from finite element simulation. By comparing FE load-displacement curves with the experimental one, the best match should represent the correct input of material parameters, as shown in Fig. 7.

3.3 Simulation results

Fig. 4a shows the Mises stress distribution at indentation depth 1.94 μm. The stresses in the right part of the sample square are nearly zero, which means that the dimension of the sample square is enough and the boundary effect could be neglected. After unloading as shown in Fig. 4b, compression residual stresses could be found beneath the indenter tip.

As shown in Fig. 5, a load-displacement curve obtained by inverse nano-indentation analysis was compared with the measured load-displacement curves. Using the assumed linear elastic, power law plastic model, the simulated load-displacement curve cannot exactly match the shape of test curve. Simulated curve intersects with test curves, lower in small indentation depth and higher in large. The maximum load predicted matches that of experiment to within 5%.

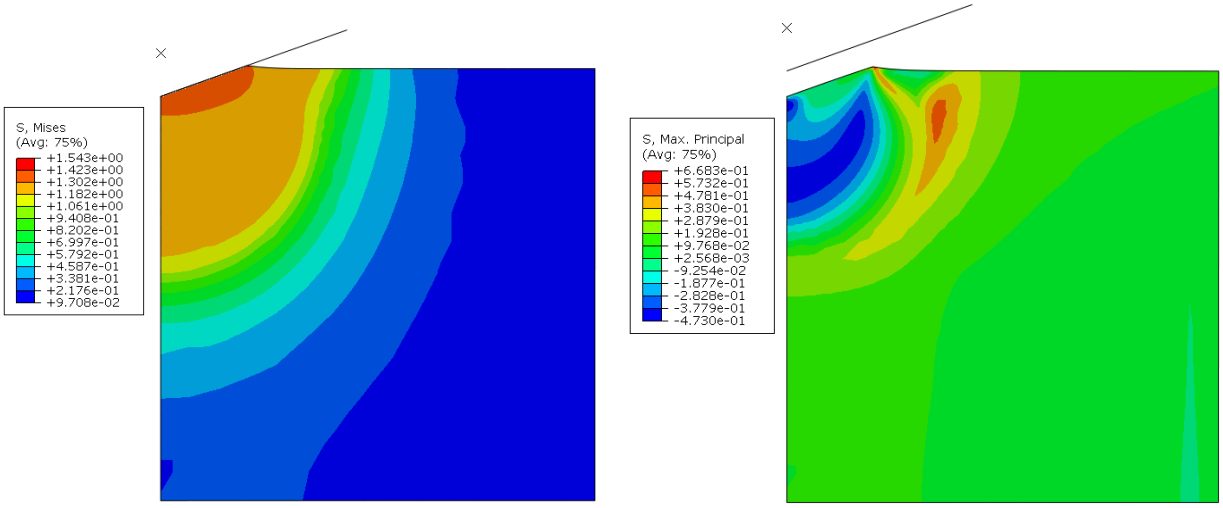

(a) (b)

Figure 4. Mises stress distribution under loading (a) and unloading (b) conditions.

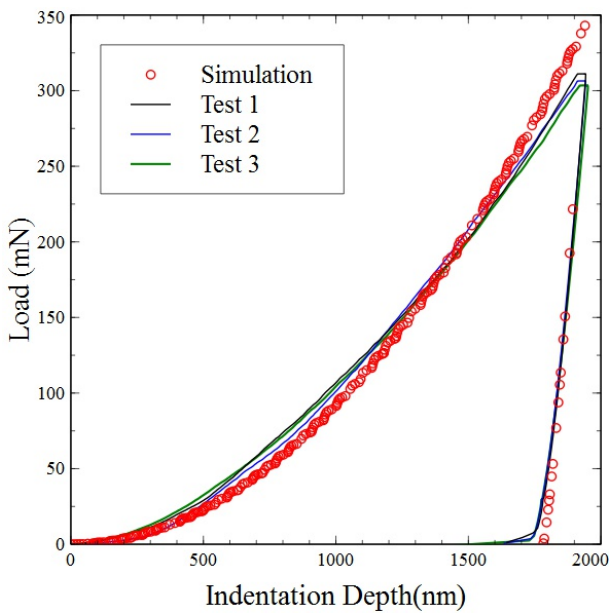

Figure 5. Comparison of load-displacement curves

3.3 Tensile test verification

Because of irregular weldment shape and narrow width, the weldment material properties cannot be obtained from a simple tension test. The nominal tensile curve of the welded specimen was determined from the uniaxial tension. The nominal strain was measured based on gauge length l_0=12mm. Using of the weldment material parameters indentified from the nano-indentation, FE simulations for the tensile test were carried. Comparison between the experiment and computation is shown in Fig. 6.

A quarter symmetry model was built for computation of local stresses and strains. Due to material difference between base metal and weldment, strains and stresses can be discontinuous on the fusion boundary. Maximum effective plastic strain at the 1250MPa nominal loading stress appears in the center of the weldment, while the maximum Mises stress on the maximal loading is localized on the fusion boundary. This coincides with the test, in which the plastic deformation occurs on the weldment. A comparison of nominal stress-strain curves between FEM simulation results with the experiment was carried out in Fig. 6. Calculated nominal strain was determined based on the initial gauge length of 12mm. A good correlation was obtained. The elastic moduli from base material, weldment material are nearly the same as the nominal behavior. Due to different yield stress of welding material, the nominal yield tensile stress is lower than base material. Yield will first occur in the weldment.

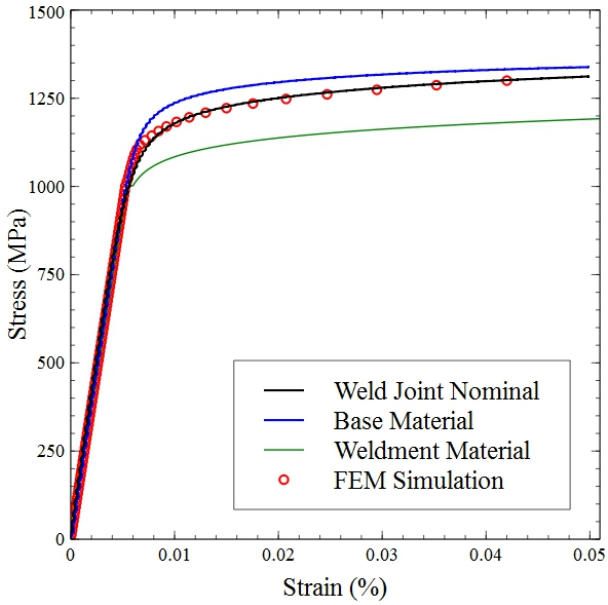

Figure 6. Comparison of tensile stress-strain curves.

4. Fatigue Life Prediction

4.1 Extended Cruse-Meyer model

The Cruse-Meyer model [15] includes both cyclic strain range $\Delta\varepsilon$ and mean stress σ_m as variable for predicting fatigue life in an explicit power law form for the uniaxial loading,

$$N_f = A\Delta\varepsilon^B 10^{C\sigma_m}, \tag{2}$$

where *A, B, C* are specific model parameters, σ_m is the mean stress, N_f is the number of cycles to failure, $\Delta\varepsilon$ is the strain amplitude. The Cruse-Meyer model is simple and practical for engineering application due to its explicit expression form.

The model can be extended to multiaxial fatigue by combining it with the critical plane concept. This critical plane concept postulates that fatigue cracks initiate and grow on certain planes where the material is mostly damaged [16]. Taking the concept of the Cruse-Meyer model, material failure under stress multiaxial state is described by the maximum normal strain range and the mean normal

stress acting on the maximum normal strain range plane. The extended Cruse-Meyer model is expressed as

$$N_f = A(\Delta\varepsilon_{\max})^B 10^{C\sigma_{n,mean}}. \tag{3}$$

Obviously, this equation is identical with the original Cruse-Meyer model.

In this work the parameters A and B are from the fitting of local strain-life curve of weldment at R = -1. And parameter C can be estimated at R = 0.1. In order to obtain the local stress and strain, FE computations were conducted for cyclic loadings with isotropic hardening assumed. Material properties were from previous analysis. Fig. *7* presents comparison between the predicted fatigue lifetime with the experimental results. All data are within the scatter band with a factor of 2.

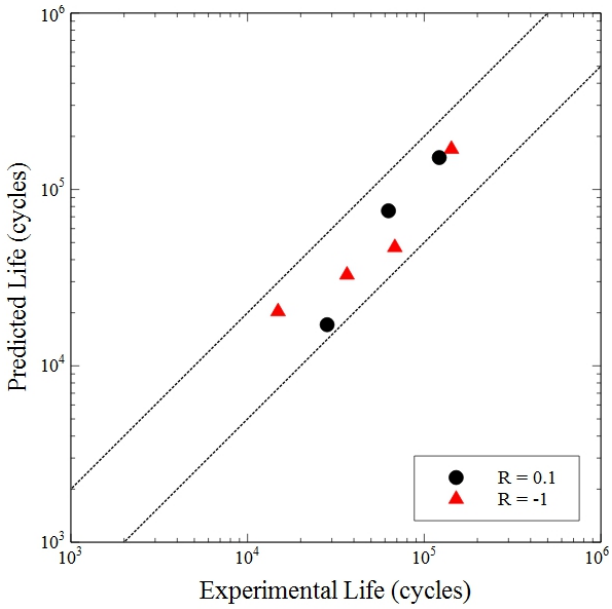

Figure 7. Fatigue life comparison results based on Cruse-Meyer model

4.2 Notched Fatigue Prediction

Even under uniaxial cyclic loading, the presence of a hole will cause a local multiaxial stress fields near the notch root, axial and circumferencial strresses. Below the root surface the stress state is general bi-axial tensile loading mode, although the axial tensile stress dominates. Additionally, the stresses and strains vary with the distance substantially. Hence, the multiaxial fatigue models find application to analyze the problem. The prediction from the extended Cruse-Meyer model is listed in Table 3, based on the local stresses and strains at the notch root surface. The parameters *ABC* are taken from the previous smooth fatigue analysis. Obviously, the prediction is too conservative in comparing with experiments.

Combining the extended Cruse-Meyer model with the critical distance method should improve the prediction. Two criteria, i.e. PM based and LM based, can be defined as

$$N_{p,d} = [A(\Delta\varepsilon_{\max})^B 10^{C\sigma_{n,mean}}]_d, \tag{4}$$

$$N_{p,l} = \frac{1}{l}\int_0^l A(\Delta\varepsilon_{\max})^B 10^{C\sigma_{n,mean}} . \quad (5)$$

One key issue in the critical distance method is determining the critical distance, *d*. Until now there is no effective method except searching to determine the critical distance for elasto-plastic problem. The most popular method is to determine the distance by minimizing the deviations between prediction and experiments. For instance, one may use the least square method to minimize $||N_{p,d}-N_f||$ or $||N_{p,l}-N_f||$ and to find the most appropriate distance. It follows that the critical distance for the PM is 0.437mm and 0.7mm for the LM. Generally, one may assume that the distance should be independent of loading ratio and temperature.

Table 3 lists the results for Cruse-Meyer PM and LM models. Results confirm significant improvement in predictions, in comparing with prediction results at root surface. The critical distance concept introduces a new variable into the model and makes it more flexible. However, applicability of it needs more detailed experimental and computational efforts. From the results we can observe LM predicted a little better than PM.

Table 3. Notched fatigue life comparison results

Notched Specimen No.	Experimental Life (cycles)	Predicted Life (cycles)		
		Root Surface	PM, d=0.437mm	LM, l=0.7mm
1	16201	923	12351	12450
2	31248	2439	44232	38132

5. Conclusions

It's been shown that the strength of Inconel 718 EB weldment is lower than that of the base metal, the weldment material properties cannot be obtained from simple tension test. Nano-indentation tests are useful to investigate the mechanical properties of weld joint. By assuming a power law plastic model, the elastoplastic properties of weldment material were derived from inverse nano-indentation analysis with help of finite element simulation. To verify the results, a comparison of nominal stress-strain curve between calculated and test results was carried out. The accuracy of the results is satisfactory.

To predict the fatigue life of weldment, the simple Cruse-Meyer model was extended to multiaxial fatigue directly and applied for this prediction. The predicted smooth fatigue lives were found to agree with the experimental data. Combining it with the critical distance concept provides a reasonable prediction for notched specimen fatigue. The basic assumption here is that the critical distance should be constant for the specific material and fatigue model which has to be verified further. Empirical determination of the critical distance needs to be refined.

References

[1] H. Schultz. Electron beam welding. Abington publishing, Cambridge, 1993.
[2] A.C. Fischer-Cripps, Nanoindentation. Vol. 1. Springer, 2011.
[3] W.C. Oliver, G.M. Pharr, An improved technique for determining hardness and elastic modulus using

load and displacement sensing indentation experiments. Journal of Materials Research, 7(1992) 1564-1583.
[4] S. Kucharski, Z. Mróz, Identification of yield stress and plastic hardening parameters from a spherical indentation test, International Journal of Mechanical Sciences, 49(2007) 1238-1250.
[5] J.A. Bannantine, J.J. Comer, J.L. Handrock, Fundamentals of metal fatigue analysis. Upper Saddle River, New Jersey: Prentice Hall, 1990.
[6] R.E. Peterson, Analytical approach to stress concentration effects in aircraft materials. In: Proceedings of the WADC Symposium on Fatigue of Metals. U.S. Air Force, Dayton, OH, USA, 1959.
[7] H. Neuber, Theoretical calculation of strength at stress concentration, Czech. J. Phys., 19(1996) 400.
[8] E. Siebel, M. Stieler, Dissimilar stress distributions and cyclic loading(in german). Z.VDI, 1997.
[9] David Taylor, The theory of critical distances, Elsevier, 2007.
[10] L. Susmel, D. Taylor, A novel formulation of the theory of critical distances to estimate lifetime of notched components in the medium-cycle fatigue regime. Fatigue Fract Eng Mater Struct 30(2007) 567–81.
[11] L. Susmel, D. Taylor, On the use of the theory of critical distances to estimate fatigue strength of notched components in the medium-cycle fatigue regime. In: Proceedings of FATIGUE 2006 Atlanta, USA.
[12] L. Susmel, Modified Wöhler curve method, theory of critical distances and Eurocode 3: A novel engineering procedure to predict the lifetime of steel welded joints subjected to both uniaxial and multiaxial fatigue loading, International Journal of Fatigue, 30(2008) 888-907.
[13] F. C. Campbell, Elements of metallurgy and engineering alloys. ASM International (OH), 2008.
[14] D.W. Worthem, D.F. Socie, Inhomogeneous deformation in INCONEL 718 during monotonic and cyclic loadings. Metallurgical and Materials Transactions A, 21 (1990) 3215–3220.
[15] T. Cruse, S. Mahadevan, R. Tryon, Fatigue reliability of gas turbine engine structures, NASA Contractor Report NASA/CR-97-206215,1997.
[16] M.W. Brown, K.J. Miller, A theory for fatigue under multiaxial stress-strain conditions. Proceeding of the Institution of Mechanical Engineers, 187(1973) 745-755.

Application of Fluid-Solid Couple on Multidisciplinary Optimization Design for Turbine Blade

JIA Zhi-gang[1,*], WANG Rong-qiao[2], HU Dian-yin[2], FAN Jiang[2], Shen Xiu-li[2]

[1] China aviation engine establishment, Beijing, 100028, China
[2] School of Jet Propulsion, Beijing University of Aeronautics and Astronautics, Beijing 100191, China
* Corresponding author: jia2001720@126.com

Abstract The multi-field coupled analysis, a higher precision, is an interaction effect among the fluid, the structure strength and the thermal on the turbine design. Considering the coupled effect in the multidisciplinary optimization design (MDO) could further excavate the design potential and improve the optimization precision on the turbine. Thus the paper firstly shows the automatic process of the fluid-solid closely coupled analysis method based on the ALE which would be the foundation of the turbine MDO. The comparison between the analysis result of the couple and the single discipline on the turbine blade proves the transdisciplinary influence each other. Based on kinds of the different precise analysis methods, this paper secondly puts forward the multiple-precision strategy in order to balance the cost and the precision on turbine MDO. This strategy studies the variable complexity method (VCM) which is improved by the two-point scale function and the periodic updating technology and three kinds of precise models including the fluid-solid closely coupled analysis, the single discipline analysis and the approximate equation. The strategy solves the difficulty of disciplinary decoupling and coordination by the collaborative optimization (CO) strategy. Finally, the new strategy could finish the turbine MDO with acceptable performance.

Keywords fluid-solid closely coupled analysis; multidisciplinary design optimization (MDO); variable complexity method (VCM); collaborative optimization (CO) strategy; turbine design;

1. Introduction

Turbine blade working in the environment of the high temperature, high pressure and high centrifugal force is a typical component involving the multidisciplinary and the multi-flied coupled design. The MDO as a new design idea could design complex structure by adequately exploring the interaction mechanism between disciplines [1]. The previous MDO established on the foundation of the discipline analysis and completed the design process through decoupling and coordination among disciplines. Thus, the accuracy of the discipline analysis is an important factor on the MDO.

The development of the fine design contributes to further excavate the design potential on the engine. A single disciplinary numerical analysis is not accurate enough to discover some exact design problem which would improve the performance. The coupled analysis [2, 3] is a main method to achieve a high precision which has been the goal pursued by engineer and academic on the turbine. The fluid-solid couple, a crossed discipline between the fluid and the solid, is particularly prominent on the turbine blade. Its feature is that the structure generates deformation under the action of the fluid load while this deformation in turn affects the flow field. Making clear the relationship of the fluid-solid couple is conducive to further excavate the design performance.

If the coupled analysis was applied on the MDO, it would provide the favorable safeguard of the numerical precision for the engine design. However, previous study has shown that the coupled analysis has a high cost and numerical noise which would be serious influence on MDO cost, even convergence. Recently, the blade has developed various precision methods, such as the approximate equation which is low precise, the single discipline analysis and the discipline coupled analysis. The characteristics of the low precision are low cost and low numerical noise. How to organize these different accuracy analytical methods and fully express their advantages is a key content on greatly increasing the efficiency and accuracy of the blade MDO. The variable complexity modeling (VCM)

[4] could manage various models so that it could balance the cost and the precision of the MDO [5], and get a feasible optimal solution and avoid numerical noise. Nevertheless, the VCM also exist some shortage in the organization, so some improving methods are required.

Recently the MDO has made a great progress in some technology, but a lot of theory and methods which still stay in academic research stage without verification on complex engineering system design could have distance with the practical application. Therefore, this paper, in view of the aero-engine turbine and the high precise coupled analysis, will fully discuss the MDO method of the complex structure, which not only has very important significance and challenging but also provides certain technical support for the development of aero-engine.

2. Turbine Fluid-Solid Coupled Analysis

2.1. ALE Problem of Fluid-Solid Couple

For the coupled problem, the most difficulty lies in the unified coordinate system and the coordination of two phases interface. The Solid habits using the Lagrange coordinate system with a view to the particle, while the fluid uses the Euler coordinate system with a view to the space point. The descriptive differences could not be distinguished on a little movement problem, but is very complicated for big movement and nonlinear problem. The ALE (Arbitrary Lgrangian-Eulerian) method which Hirt puts forward to describe the free liquid in 1974 has been widely used [6]. It provides an efficient way connecting the Laplace system in solid with the Euler system in fluid. The ALE coordinate system could move in the space motion by any speed. If its velocity is zero, that is Euler system. If the speed equals to the particle velocity, that is namely the Laplace system. Thus the ALE coordinate system provides a unified description for two kinds of coordinate system.

This paper describes the fluid field in the ALE. The spatial domain uses the finite element discrete format, while the Navier-Stokes equation adopts the substep calculation format in the time domain. The fluid-solid closely coupled based on the ALE can combine the ANSYS with the CFX to complete iterative computation. When they solve in sequence, the interface need transfer the pressure from the fluid to the solid, and then transfer the displacement to fluid. This method considers the interaction between fluid and solid, so the accuracy is relative higher.

2.2. Dynamic Grid Technology and Coupled Step Settings

Because of the moving interface, the discrete equation of the fluid field must allow the grid mobile and the grid deformation. There are two kinds of the way [7-10]. The first one is named mesh fairing method dealing with the small mobile. This operation pulls and extrudes the grid in a small range displacement. That could be realized by solving the Laplace's equation. If the grid deformation is serious, the mesh fairing method is not enough to provide the high quality grid. In other case, the new grid must be established in maybe different grid topology. The variable value will be interpolated to the new nodes next time step. Because the grid nodes are inconformity before and after remeshing, the interpolation inevitably would produce the error. The remeshing cost is huge for hundreds of thousands nodes, so the efficiency could drop. Then, if the deformation is not a lot, for example that the maximum deformation in this paper is less than 1.4 mm (analysis data), the small-scale coupled timestep could solve the dynamic grid problem with the first method. Every coupled variable transfers more smoothly by the small-scale coupled timestep.

Usually, a blade employs the corresponding period of the first order natural frequency as the total timestep. The first order natural frequency is 723.522Hz. Its corresponding period is 0.00138s. Then

this value is discrete for 10 steps as the coupled sub-timestep. The total time of the solid analysis and the fluid analysis should be same as the coupled time.

2.3. Process of Fluid-Solid Coupled Analysis Based on ALE

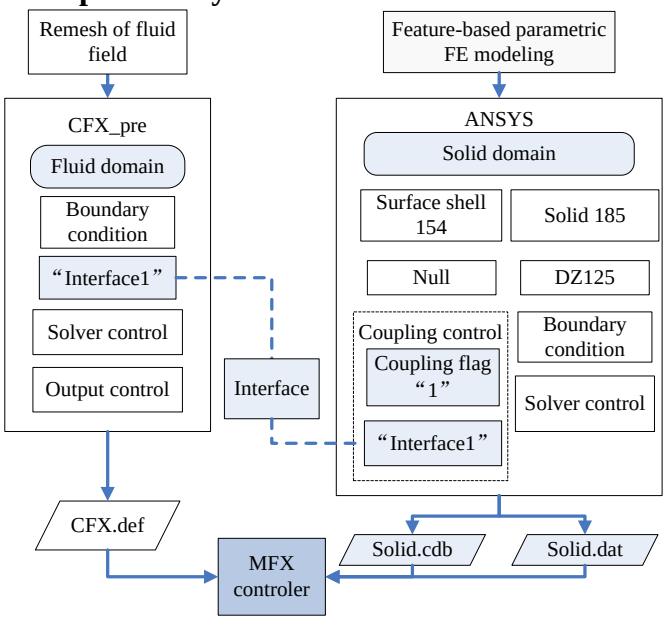

Figure.1 Process of the fluid-solid closely coupled analysis

Considering the inheritance of the analysis method, the paper establishes the flow of a fluid-solid closely coupled analysis on the turbine blade shown in figure 1, when the method of the parametric FE modeling based feature solves remeshing on the solid domain. The solid domain uses the ANSYS, while the fluid domain employs the CFX. The research process is steadily forward when every solver gets convergence. The mesh fairing method solves the mesh move. The coupled control does not only solve the conversion between the Eulerian coordinate system and the Lagrange coordinate system, but also transfers the pressure and the solid displacement. The MFX controller links solution files of two domains. The CFX.def contains fluid domain solver, while the solid domain file is divided into the model file (Solid.cdb) and the coupling file (Solid.dat). Finally, a batch is employed to call for each module of the process.

3. MDO technologies

The basic idea of the VCM [11] is: how to effectively use various precise models and bring the feasible solution based on the less cost. The traditional VCM mainly concentrated in both of the high and low precise analysis. The low precise model could improve the optimization efficiency, while the high precise analysis is responsible for introducing the correction factors which would enhance the precision of the results from the low precision during the cycle. Meanwhile, the correction factor is updated after several optimization iterations called interval method [12]. Thus it could be seen that the traditional VCM mainly includes two kinds of precision, the correction factor and the interval method. The paper will modify these three aspects so as to enhance the model management ability and adapt the higher precise method.

3.1. Various precise models

Set x as design variable. $f_{\mathrm{h}}(x)$ indicating the response of the coupled analysis in this paper is the high precise results; $f_{\mathrm{l}}(x)$ on behalf of the single discipline analysis response is the moderate

accuracy analysis results; $f_{\mathrm{r}}(x)$ is the result of the response surface method belong to the low precise model. First of all, the medium accuracy analysis $f_{\mathrm{l}}(x)$ computes design points picked out by DOE, and the initial correction factor corrects them as $\tilde{f}_{\mathrm{h}}(x)$. This group of data could construct the initial optimization object and constraints, $f_{\mathrm{r}}(x)$, which would be used in optimization cycle; a correction factor is get by contrasting the high precise analysis $f_{\mathrm{h}}(x)$ with the medium precise analysis $f_{\mathrm{l}}(x)$, and the correction factor could be updated in the optimization process.

3.2. Periodic Updating Method

The correction factor in the traditional VCM could be updated once in several times cycle on the interval method. This method reduces the calling number of the high precise model on the optimization, so it does not only ensure the accuracy and also the efficiency. However, the interval method is often lack of rationality in the search space. For example, the difference between high and low precise analysis could not be constant in design space. When the difference tends to perhaps stable, the interval should be adopted large. When the difference has great fluctuation in the certain design space, the interval may be small. Therefore, the constant interval could not meet the fact. Therefore, it is worth studying problem how to properly use the high precise model to reasonable correct the low precise model.

This paper shows a new method called the periodic updating method. When the initial approximate function achieves convergence, the variable records as x_1^*. Meanwhile, the correct factor could be computed, when $f_{\mathrm{h}}(x_1^*)$ and $f_{\mathrm{l}}(x_1^*)$ is obtained by two kinds of precise analysis. New $\tilde{f}_{\mathrm{h}}(x_1^*)$ would be get by correct factor and added to the previous database. Then the approximation function would be reframed by the least square method from the updated database. The correct function and the approximate function reframed synchronously after the inner convergence provides a relative better time calling the high precise model in the periodic updating method.

3.3. Two-Point Scale Function

The correct method of $f_l(x)$ is called the scale function. Presently, the kinds of the correct factor have the additive factor and the multiplication factor, as well as their high order form, so the scale function are often divided into the addition scale function and the multiplication scale function. The value of $f_h(x_0)$ and $f_l(x_0)$ is obtained at the initial point x_0. The formula (1) could get a constant addition factor. The subscript "0" means the initial. The multiplication factor is as formula (2):

$$\alpha(x_0) = f_h(x_0) - f_l(x_0) \qquad (1)$$

$$\beta(x_0) = \frac{f_h(x_0)}{f_l(x_0)} \qquad (2)$$

The result of the approximate function will be corrected as $\tilde{f}_h(x)$ in the loop. The approximation of the $f_h(x)$ is expressed as the formula (3) and (4) at its design point x. The $\tilde{f}_h(x)$ obviously contains the information of the high accurate analysis and simplifies calculation process by the approximation model. $\tilde{f}_h(x)$ represents the data to construct the approximation function.

$$f_h(x) \approx \tilde{f}_h(x) = f_l(x) + \alpha(x_0) \qquad (3)$$

$$f_h(x) \approx \tilde{f}_h(x) = f_l(x)\beta(x_0) \qquad (4)$$

The addition scale function and the multiplication scale function do not make the full use of the high precise numerical results in the whole optimization process. They use only the high precise analysis results of a point. The previous high precise analysis result is difficult to reflect in the subsequent scale function. This paper introduces the two point scale function which combines the multiplication factor and the additive factor. At the initial point x_0, the two-point scale function displays for the formula (5); similarly, the scale function is formula (6) at x_1^*. α_1 and β_1 is solved from the formula (5) and formula (6) simultaneous as formula (7).

$$f_h(x_0) = \beta_1 f_l(x_0) + \alpha_1 \qquad (5)$$

$$f_h(x_1^*) = \beta_1 f_l(x_1^*) + \alpha_1 \qquad (6)$$

$$\beta_1 = \frac{f_h(x_1^*) - f_h(x_0)}{f_l(x_1^*) - f_l(x_0)} \qquad (7)$$
$$\alpha_1 = f_h(x_1^*) - \beta_1 f_l(x_1^*)$$

Accordingly, when the i th approximation function achieves convergence in inner loop, the $f_h(x_i^*)$ and $f_l(x_i^*)$ is obtained by calling the high and medium accuracy analysis at the design point x_i^*. The optimal solution x_{i-1}^*, the corresponding $f_h(x_{i-1}^*)$ and $f_l(x_{i-1}^*)$ could be also gain in the $i-1$th inner loop. Therefore the α_i and β_i could be list in the formula (8) and (9) :

$$\begin{aligned} f_h(x_{i-1}^*) &= \beta_i f_l(x_{i-1}^*) + \alpha_i \\ f_h(x_i^*) &= \beta_i f_l(x_i^*) + \alpha_i \end{aligned} \qquad (8)$$

$$\beta_i = \frac{f_h(x_i^*) - f_h(x_{i-1}^*)}{f_l(x_i^*) - f_l(x_{i-1}^*)} \qquad (9)$$
$$\alpha_i = f_h(x_i^*) - \beta f_l(x_i^*)$$

Where α_i is the additive correct term, and β_i the multiplicative correct term. The two-point scale function inherits the former and later value of the high precise results, and need not calculate the additional derivative information. Thus the computational efficiency and precision are ensured simultaneously. Therefore, before the start of the $i+1$th inner loop, the original data will be corrected in accordance with the formula (10).

$$\tilde{f}_h(x_i^j) = \beta_i f_l(x_i^j) + \alpha_i \qquad (10)$$

Where i stands for the number of inner loop executed; $j = 1 \cdots n$, n is the total number of sampling point. Then the value of $\tilde{f}_h(x_i^j)$ $j = 1 \cdots n$ could construct the approximate function $f_R(x_{i+1})$ of objects and constraints in the $i+1$th inner loop by the least-squares regression method.

3.4. Multiple-Precision Optimization Strategy

The collaborative optimization (CO) strategy [13, 14] need usually call a large number of discipline analyses. That means very expensive cost. Because the extra compatible constraint is optimization target in subsystem layer, the cost further increases. The CO efficiency has been improved by the approximation method [15], which is a good solution for the interdisciplinary relatively independent. However the inherent couple of the turbine blade does not reflected in a previous study. The discipline coupled analysis stands for the development of the high precise numerical method. Compared with the single discipline analysis, the closely coupled analysis need consume more cost.

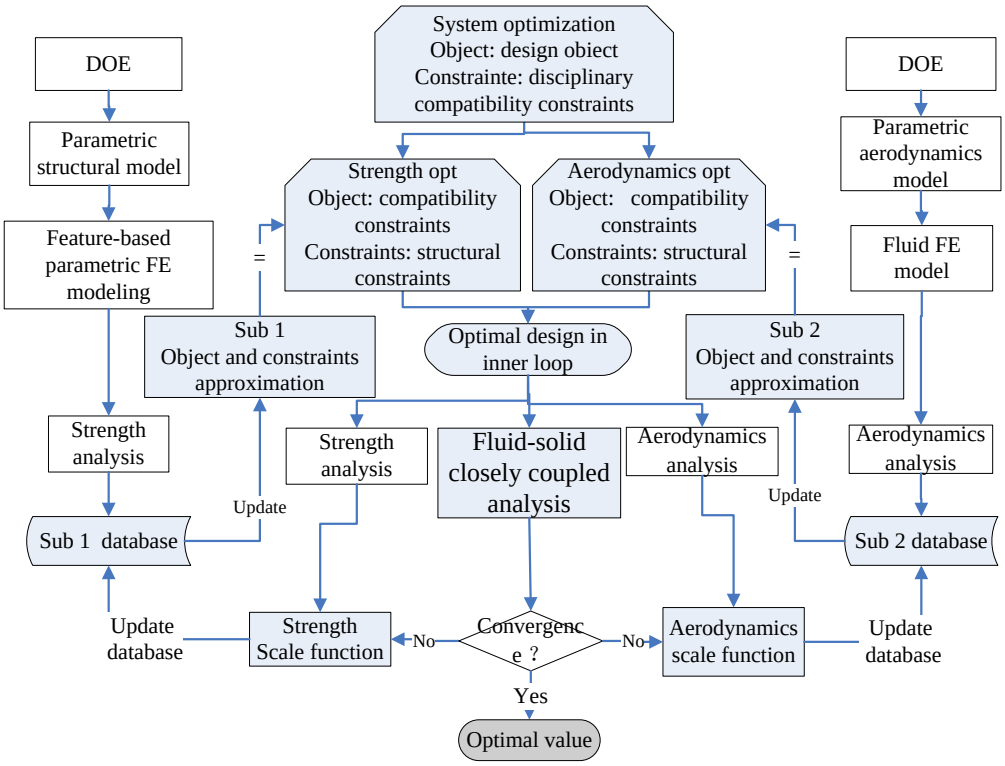

Figure.2 Multiple-precision optimization strategy

The figure 2 shows the multiple-precision optimization strategy which is the CO strategy referring the couple on the turbine blade MDO. This strategy will employ the coupled analysis into the CO strategy by using VCM technology. The way does not only improve the precision, but also makes the optimization results with the higher feasibility. The system level optimizer connects two sub-system optimizers which are used for processing the structure strength optimization and the fluid optimization. The database of the discipline 1 and discipline 2 contains their discipline analysis response and the corrected result at every DOE points. The object and constraint function in the sub-system optimizer is gain by the least square method at the database. The characteristic of fig.2 is nesting a CO strategy in the systemic loop. The optimal value of the CO will accept the aerodynamics analysis, the structure analysis and the flow-solid closely coupled analysis. The former two belong to the medium precision analysis. The latter's response data provides the scale function for the former two. Therefore the CO strategy is skeleton. The various precise methods are the core, and the VCM is the organization mode joining each element. The difference value of the high precision analysis, $f_{\mathrm{h}}(x_{i+1}^{*}) - f_{\mathrm{h}}(x_{i}^{*}) \le 10^{-3}$, is less than 10^{-3} as the convergence criterion.

4. Coupled Analysis and MDO on the turbine blade

4.1. Model Parameters

The structure includes a shroud and a blade whose parameters are shown in figure 3 [16]. The nine shroud parameters are empirically chosen in this optimization, while this paper chooses six blade parameters which are the axial length (DZ_1, DZ_2 and DZ_3) and installation angle (γ_1, γ_2 and γ_3) on three sections of the hub, middle, and tip are blade parameters, as shown in fig.4. They have more influence on the aerodynamic performance. Constructing approximation of the fluid discipline needs at least 28 DOE points for the aerodynamics analysis. The approximate equations of the structure discipline need at least 136 DOE points. Design variables are $X = \{X_1, X_2\}$, including:

$$X_1 = \{x_4, x_5, x_6, x_7, x_8, x_9, x_{10}, x_{11}, x_{12}\}$$
$$X_2 = \{D_{Z1}, D_{Z2}, D_{Z3}, \gamma_1, \gamma_2, \gamma_3\} \quad (11)$$

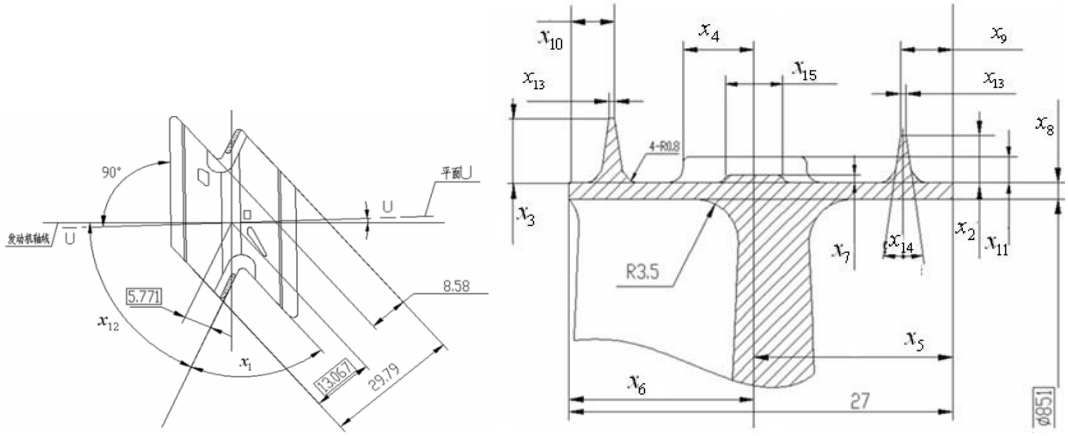

Figure.3 Parameters of shroud

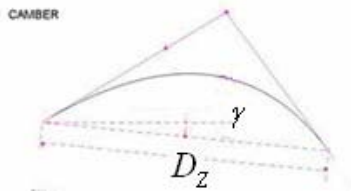

Figure.4 Parameters of a section

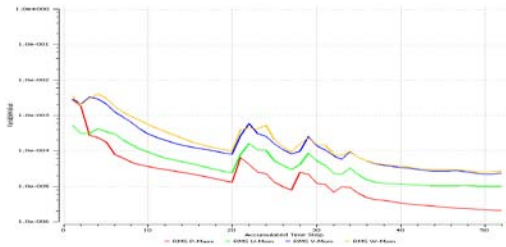

Figure.5 Convergence process of the close coupled field on the standard working speed

4.2. Result Analysis of Coupled Calculation on Turbine Blade

Fig.5 shows the convergence curve of the fluid-solid closely coupled analysis at the standard working speed on turbine blade. The result of the steady state aerodynamics calculation conducts the initial condition for the coupled analysis. This way is in favor of convergence. It could be seen that several important indexes of the fluid field has reached convergence after three big shocks which respectively represent the process transferring three times of coupled data. The three shocks also reveal that the distortion of the structure has great influence on the flow field.

Table.1 Result contrast between the closely coupled analysis and the aerodynamics analysis

	Max temperature(K)	Min temperature（K）	Max pressure（Pa）	efficiency
Aerodynamics	1332.11	853.625	603182	87.4964
Closely coupled	1339.07	889.327	599312	88.1004
Absolute error	6.96	35.702	-3870	0.604
Relative error	0.5225%	4.1824%	-0.6416%	0.6903%

Table 1 shows the calculation results of the closely coupled field and the single fluid field at the work speed. It could be found that the coupled field has the higher isentropic efficiency and the mass flow. The statistical results show the difference of minimum temperature is 35.702 °. The relative error of the maximum pressure and max temperature is respectively 0.64% and 0.5225%.

Further comparing the stress and displacement before and after couple, table 2 gives the calculation results of the maximum displacement and maximum stress under various kinds of loads. Additionally, the centrifugal load and the aerodynamic load are separately considered. The aerodynamics load (A) is from the closely coupled analysis. The maximum stress of the closely

coupled analysis is 593.548MPa located in the blade root trailing edge. In the aerodynamics load, the maximum stress is 43.016 MPa, which is much less than the value, 552.697MPa, under the centrifugal load condition. From magnitude, the displacement and the stress in the coupled calculation is equivalent to the total effect of the centrifugal load and the aerodynamics load.

Table.2 Contrast of the maximum displacement and stress under different load condition

Load type	Max Von Mises stress（MPa）		Max displacement（mm）	
	blade	shroud	blade	shroud
Centrifugal load	552.697	433.24	1.348	1.5348
Aerodynamics load（A）	43.016	——	0.09335	0.09916
Centrifugal load +（A）	593.548	435.944	1.411	1.613

4.3. Optimization Model of Turbine Blade Based on CO Strategy

The turbine blade adopts the DZ125 materials. The material requires that the equivalent stress is not more than 75%$\sigma_{0.1}$, the maximum stress of the joint is not more than 60%$\sigma_{0.1}$, and the contact stress is less than the allowable pressure stress. The temperature of the material is restricted to 1273.5K and the mass flow (mf) limited in range $[102.5,112.5](kg.s^{-1})$. Additionally the radial tip elongation is not more than 0.01m. Those are constraint condition, definited $Y=\{Y_1,Y_2\}$, where Y is the system response value, Y_1 the response value of the structure strength discipline, Y_2 the fluid discipline response value, as formula (12). The object function adopts the weighted sum of the isentropic efficiency and the total mass in the formula (13):

$$\begin{aligned} &Y_1=\{dx_{tip},\sigma_{shroud},\sigma_{chamfer},\sigma_{blade},\sigma_{contact}\} \\ &Y_2=\{mf,T\} \end{aligned} \tag{12}$$

$$\begin{cases} F(X)=W_1/\eta(X)+W_2*m(X)/m_0(X) \\ m(X)=m_1(X)+m_2(X) \\ m_0(X)=m_{10}(X)+m_{20}(X) \end{cases} \tag{13}$$

Where $\eta(X)$ is the isentropic aerodynamics efficiency function, $m(X)$ the quality function of the shrouded blade, $m_0(X)$ the initial model quality of the shrouded blade. The subscript 1 is the blade and the subscript 2 is shroud. W_1 and W_2 is the weighted factor, respectively taking 0.7 and 0.3. The MDO model of the turbine shrouded blade can be wrote as formula (14).

$$\begin{cases} find:\ X \\ \min F(X)=W_1/\eta(X)+W_2*m(X)/m_0 \\ s.t.\quad g_1=dx_{tip}-0.01\le 0 \qquad g_5=\sigma_{contact}-173.0\le 0 \\ g_2=\sigma_{shroud}-645.5\le 0 \qquad g_6=mf\in[78.5,80.5] \\ g_3=\sigma_{chamfer}-516.4\le 0 \qquad g_7=T-1273.5\le 0 \\ g_4=\sigma_{blade}-697.0\le 0 \qquad \mathrm{X}\in[X^l,X^u] \end{cases} \tag{14}$$

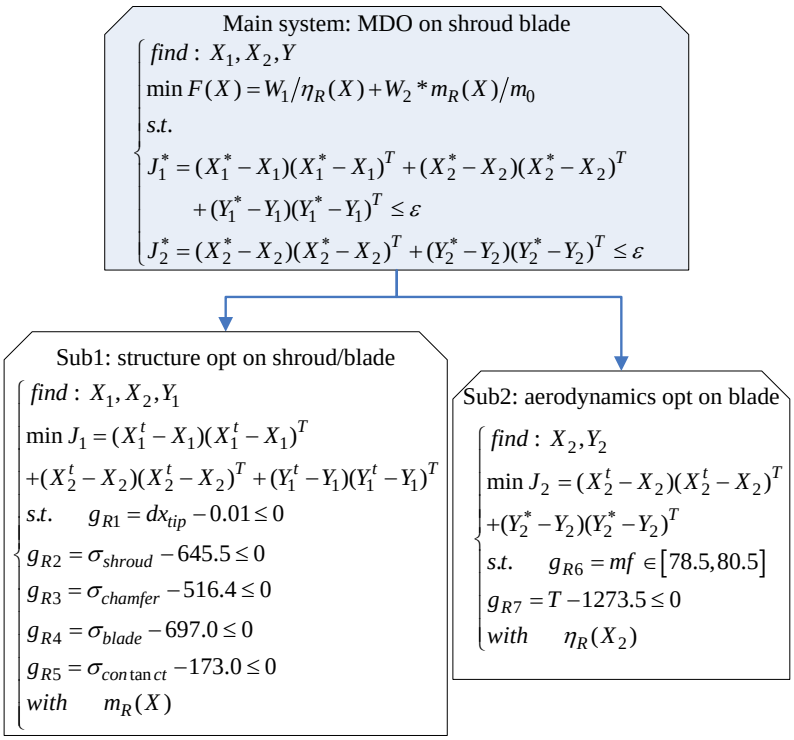

Figure.6 Optimization algorithm structure based on the CO strategy

Figure 6 shows the optimization algorithm structure of the blade MDO based on the CO strategy. $g_{Ri}, i = 1 \cdots 7$ stands for the approximate function. $m_R(X)$ and $\eta_R(X)$ respectively represent two sub-system targets. ε is the permissible error of compatible constraint taking $\varepsilon = 10^{-3}$.

4.4. Optimization Results Analysis

The paper establishes the multiple-precision optimization strategy. Present three kinds of analysis model on turbine blade have embodied in the CO framework by the VCM methods. The figure 7 describes shape changes in the blade root, middle and tip. Table 3 is the numerical response contrast. Under the constraints, the total mass drops 6.68% and the blade efficiency increases 5.55%.

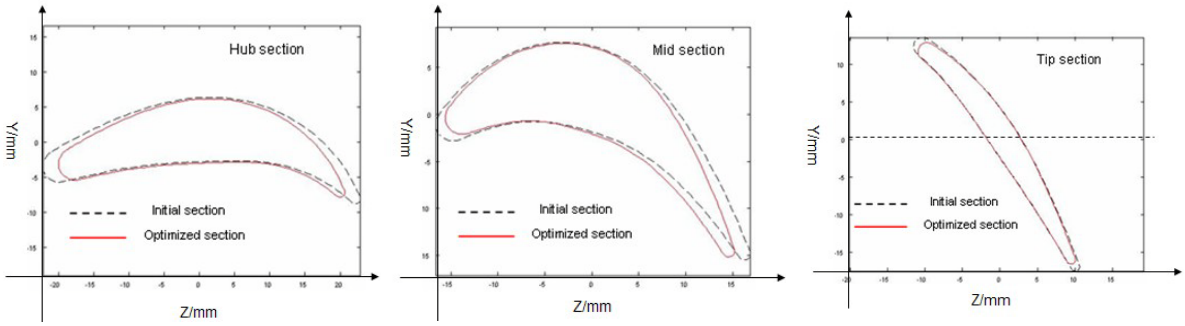

Figure.7 Compared shapes before and after optimization at the hub, mid and tip section

Table 4 shows the optimization cost of the shrouded blade. "——" represents none in the table. Because the approximate function runs quickly, the cost of the inner loop is not easy to statistics indicated with ".....". From the table, major time consumption comes from the DOE, the calling number and the number of the inner loop, total of which is 7163 minutes (518+1665+4980), while the approximation function and updating overall occupies only 38 minutes (7201-7163). It shows that the approximate function could greatly improve the efficiency in optimization process. Because the fluid-solid closely coupled analysis costs very huge, the calling number directly affects the

efficiency. The time consumption from the high precise analysis is about 4980 minutes, accounting for nearly 70% of the total time cost. The method pays some cost. However for accurate turbine blade design, the high precise numerical method is indispensable on the optimization. Considering the efficiency, the paper calculates the correction factor to correct the approximation function so that the optimal value could have the high precision and high feasibility.

Table.3 Result before and after optimization on shrouded blade

$Y=\{Y_1,Y_2\}$	Constraints	Initial value	Optimal value	Effect
Strength constraints (Y_1)	d_{xtip} /MPa	0.0035	0.00295	-15.71%
	σ_{shroud} /MPa	435.024	450.3	3.51%
	$\sigma_{chamfer}$ /MPa	270.125	295.364	9.25%
	σ_{blade} /MPa	593.141	575.364	-3.00%
	$\sigma_{contact}$ /MPa	80.1019	105.673	+31.92%
Aerodynamics constraints (Y_2)	$m_f / kg.s^{-1}$	107.363	106.825	-0.50%
	T /K	1234.86	1187.75	-1.3%
	Object	Initial value	Optimal value	Effect
Strength object	$m(X)$/g	203.27	189.7	-6.68%
Aerodynamics object	$\eta(X)$	0.874964	0.92353	5.55%
Weight object	$F(X)$	1.100	1.0379	-5.65%

Table.4 Cost of multiple precision MDO strategy on turbine

Discipline	Analysis type	Model accuracy	DOE number	Calling number	Cycling number	Cost (min)
Strength	Strength analysis	medium	136	8	——	518
	Approximation	low	——	——	9528	……
Aerodynamics	Aerodynamics analysis	medium	28	8	——	1665
	Approximation	low	——	——	6864	……
Couple	closely coupled analysis	high	——	9	——	4980
——				Total cost		7201

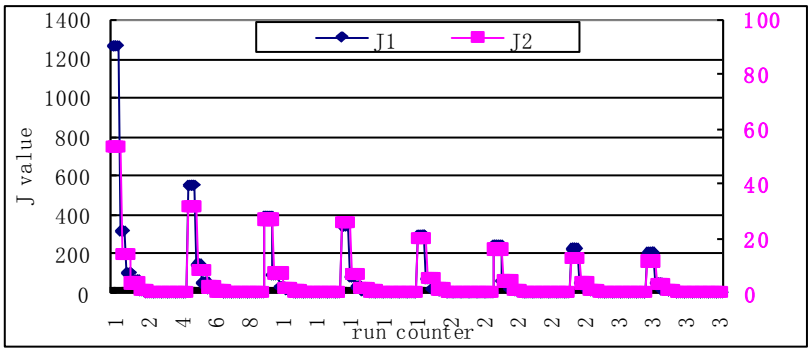

Figure.8 Convergence curve of the Compatibility constraints J_1^*, J_2^* on the system layer

The compatibility constraint is an important index measuring convergence in the CO strategy. Fig.8 shows the convergence curve of the compatibility constraint J_1^*, J_2^* during the system layer. J1 represents J_1^* and J2 represents J_2^*. Because the value has huge difference, two kinds of longitudinal axis are adopted. The eight convergence phases show that the whole process constructs and updates 8 times of the approximate function. Because the $i+1$th optimization starts with the

optimal value of the ith optimization, the J_1^* and J_2^* of the $i+1$th optimization is obviously smaller than them in the ith optimization (initial value in the $i+1$th time is much better), and converges faster. Each value in the database is revised by the high precise analysis in inner loop. Thus the approximation function has greater change (see figure 8). That is the main reason that this strategy needs more internal optimization, namely calling more number of the high precise analysis.

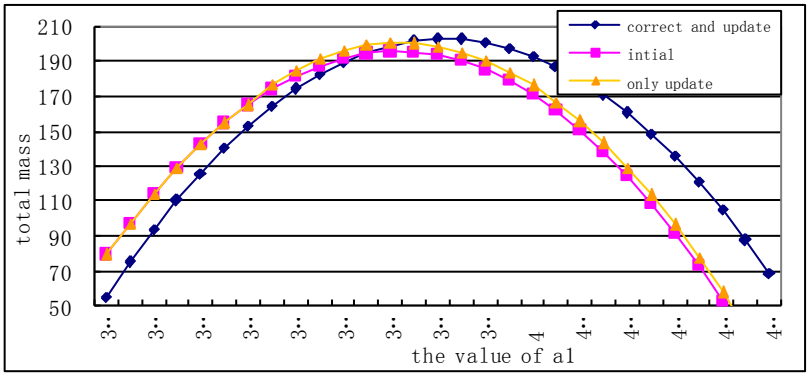

Figure.9 Initial target approximate function, the 8th corrected and updated, and only updated target approximate function at x_9

Figure 9 shows the initial target approximate function (C1), the 8th corrected and updated approximate function (C2), and 8th only updated target approximate function (C3) at x_9. The C2 parabolic axis of symmetry has obviously offset in relative to the C1 curve, while the C3 has the almost same axis with the C1, but its parabolic top is little different. The change of the parabolic axis just comes from the high precise analysis result which corrects the lower precise analysis.

Conclusion

This paper firstly explores the current fluid-solid coupled algorithm on the turbine design. According to the principle of the ALE with existing commercial software, the dynamic grid technology of the blade fluid domain is realized by the small coupled step length and the mesh fairing method. Then combining with the previous remesh technology, the paper establishes the process of the turbine blade fluid-solid closely coupled analysis based on the ALE.

Further the multiple-precision optimization strategy is established. The high precision of the fluid-solid coupled analysis should be applied to the turbine blade MDO to improve the design accuracy. Because of the huge cost of the high precise analysis, this paper studies the VCM methods from three aspects which are various precise models, the periodic update and the two point scale function in order to improve the efficiency and accuracy of the optimization. The VCM introduces the high, medium and low precise model into the MDO. The method of the periodic update properly employs the high precision model to reasonable correct the low precision model. The two point scale function adequately utilizes the high precise analysis of the optimization process to correct the result of the low precise model.

Finally, comparing the calculated results before and after coupling, the paper detailedly analyses the influence of disciplinary couple. Introducing the structural displacement, the total efficiency of the coupled field is slightly higher than single fluid analysis; the aerodynamic force is much smaller relative to the centrifugal force, the maximum equivalent stress of the closely couple is probably equivalent to the sum of individual effects of the aerodynamic force and centrifugal force. Additionally, the paper lists the optimal value on the multiple-precision optimization strategy. The result ensures the precision and efficiency of the turbine blade MDO after the optimization method

only calls nine times of the high precise analysis.

References

[1] WANG Rong-qiao, JIA Zhi-gang, FAN Jiang, HU Dian-yin，Shen Xiu-li. Hexahedral mesh regeneration method for MDO on complex aero-engine components[J]. Journal of Aerospace Power, 201109, 26(9): 2032-2038. （in Chinese）

[2] Hirt C. W., Amsden A. A., Cook J. L. An Arbitrary Lagrangian-Eulerian Computing Method for All Flow Speeds[J]. Journal of Computational Physics. 1974, 14(3): 227-253.

[3] Carstens V., Kemme R., Schmitt S. Coupled Simulation of Flow-Structure Interaction in Turbomachinery[J]. Aerospace Science and Technology. 2003, 7(4): 298-306.

[4] Singh G., Grandhi R. V. Mixed-Variable Optimization Strategy Employing Multifidelity Simulation and Surrogate Models[J]. AIAA Journal. 2010, 48(1): 215-223.

[5] Baker M. L., Munson M. J., Alston K. Y., et al. Integrated Hypersonic Aeromechanics Tool (IHAT)[R]. Norfolk, Virginia: 12th AIAA International Space Planes and Hypersonic Systems and Technologies. AIAA paper 2003-6952. 2003.

[6] Hirt C. W., Amsden A. A., Cook J. L. An Arbitrary Lagrangian-Eulerian Computing Method for All Flow Speeds[J]. Journal of Computational Physics. 1974, 14(3): 227-253.

[7] Dinh Q. V., Mantel B., He J. W. A Cartesian Grid Finite Element Method for Aerodynamics of Moving Rigid Bodies[J]. 1992, 1: 883-890.

[8] Grüber B., Carstens V. Computation of the Unsteady Transonic Flow in Harmonically Oscillating Turbine Cascades Taking into Account Viscous Effects[J]. Journal of Turbomachinery. 1998, 120(1): 104-111.

[9] Richter, Leyland R., Penelope L. Precise Pitching Airfoil Computations by Use of Dynamic Unstructured Meshes[R]. AIAA 24th fluid dynamics conference. AIAA 93-2971. 1993.

[10] Blom F. J., Leyland P. Analysis of Fluid-Structure Interaction by Means of Dynamic Unstructured Meshes[J]. Journal of Fluids Engineering. 1998, 120: 792.

[11] Kaufman M., Balabanov V., Giunta A. A., et al. Variable-Complexity Response Surface Approximations for Wing Structural Weight in HSCT Design[J]. Computational Mechanics. 1996, 18(2): 112-126.

[12] Macmillin P. E. Trim, Control, and Performance Effects in Variable-Complexity High-Speed Civil Transport Design[D]. Virginia Polytechnic Institute and State University, 1996.

[13] Shanno D. F. Conditioning of Quasi-Newton Methods for Function Minimization[J]. Mathematics of Computation. 1970, 24(111): 647-656.

[14] Goldfarb D. A Family of Variable Metric Methods Derived by Variational Means[J]. Mathematics of Computation. 1970, 24(109): 23-26.

[15] Sangook J., Young-Hee J., Rho A. J., et al. Application of Collaborative Optimization Using Response Surface Methodology to an Aircraft Wing Design[R]. Albany, New York: 10th AIAA/ISSMO Multidisciplinary Analysis and optimization conference. AIAA 2004-4442. 2004.

[16] WANG Rong-qiao, JIA Zhi-gang, Yang Jun-jie, HU Dian-yin, FAN Jiang, Shen Xiu-li. Study on disk and blade design based on multi-layer optimization strategy. Journal of Aerospace Power. 201206, 27(6): 1201-1209. （in Chinese）

Influence of high temperature ageing on the toughness of advanced heat resistant materials

Mattias Calmunger[1,*], **Guocai Chai**[1, 2], **Sten Johansson**[1], **Johan Moverare**[1]

[1] Division of Engineering Materials, Department of Management and Engineering, Linköping University, SE-58183 Linköping, Sweden
[2] AB Sandvik Material Technology R&D center, SE-81181 Sandviken, Sweden
* Corresponding author: mattias.calmunger@liu.se

Abstract Advanced biomass, biomass co-firing in coal-fired and future advanced USC coal-fired power plants with high efficiency require the materials to be used at even higher temperature under higher pressure. The reliability and integrity of the material used are therefore of concern. In this study, the influence of ageing at temperatures up to 700°C for up to 3 000 hours on the toughness of two advanced heat resistant austenitic steels and one nickel alloy are investigated. The influence on toughness due to differences in the chemical composition as well as the combined effect of precipitation and growth of the precipitates has been analysed by using SEM techniques. The fracture mechanisms that are active for the different ageing treatments are identified as a function of temperature and time. Local approach methods are used to discuss the influence of the precipitation and growth of precipitates on the toughness or fracture in the different aged materials.

Keywords High-temperature, ageing, toughness, austenitic stainless steel, nickel base alloy

1. Introduction

Renewable and more efficient energy resources such as biomass, biomass co-firing in coal-fired power plants and future advanced ultra-super critical (AUSC) coal-fired power plants for sustainable energy production are greatly desired. To increase efficiency higher temperature and pressure are used. Today austenitic stainless steels are commonly used as structural material in these power plants and they need to have good reliability and structure integrity with respect to the higher temperature and pressure [1, 2].

High-temperature long term ageing provides a range of precipitates that differ with ageing conditions and alloy composition. Precipitates from ageing of austenitic stainless steel and nickel base alloys have been studied by others [3-7]. Austenitic stainless steels are expected to provide reliable service for 30 years or more [3]. Their detailed mechanical properties are dependent on the stability of the microstructure particularly the formation, dissolution and coarsening of participates. In this study the influence of precipitation and growth of precipitates on toughness due to different compositions and high-temperature treatment are investigated.

2. Materials and experimental details

2.1. Materials

The experiments were conducted on two austenitic stainless steels (AISI 304 and Sanicro 28) and one nickel base alloy (Alloy 617), supplied by Sandvik Material Technology, see table 1 for nominal compositions in wt%. The materials are heat treated for normalizing.

Table 1. Compositions for the different materials in wt%.

Material	C	Si	Mn	Cr	Ni	W	Co	Cu	N	Mo	Fe
AISI 304	0.06	0.3	1.4	18.5	8.2	-	-	-	-	-	Bal.
Sanicro 28	0.02	0.43	1.83	27	31	0.02	0.09	0.9	0.05	3.4	Bal.
Alloy 617	0.1	-	-	22.5	53.8	-	12	-	0.5	9	1.1

2.2. Ageing and toughness tests

Standard sample with a dimension of 50x10x10mm (EN 10045-1) was used. The samples were aged at 650°C and 700°C in air-environment for 1000 and 3000 hours before the toughness testing. Impact toughness test has been performed at room temperature (RT), two to three samples at each temperature were tested.

2.3. Scanning electron microscope investigation

For the microstructural investigation of deformation and fracture behaviour scanning electron microscopy (SEM), electron channeling contrast imaging (ECCI) and an energy dispersive x-ray system (EDS) were used. An HITACHI SU-70 FEG-SEM and a Zeiss Sigma FEG-SEM were used to perform these microstructural investigations. ECCI uses the orientation dependence of the crystal lattice planes with respect to the incident electron beam to generate an image using backscattered electrons. Dislocations create small distortions in the crystal lattice which affect the backscattered electron intensity, allowing the imperfection to be imaged as a contrast change [8].

3. Results

3.1. Toughness test results

Table 2 shows the results of the impact tests, which reveals two different responses. The nickel base alloy, Alloy 617, is ductile at all ageing conditions and is more ductile than both austenitic stainless steels at all conditions. It seems that the impact toughness increases with both increasing temperature and longer times, but is affected more by temperature according to the energy differences in table 2. For the two austenitic stainless steels the impact toughness decreases with both increasing temperature and longer times. For AISI 304 the temperature has the biggest influence on the impact toughness. The material becomes brittle when the material has been aged at 700°C. Sanicro 28 has relatively high impact toughness at both 650°C and 700°C for 1000 hours, but the impact toughness decreases with increasing temperature, especially at 700°C, the material becomes brittle for about 3000 hours.

Table 2. Energy for each alloy at different ageing times and temperatures.

Material	Energy [J] 650°C & 1000h	Energy [J] 650°C & 3000h	Energy [J] 700°C & 1000h	Energy [J] 700°C & 3000h	Energy [J] Reference (RT)
AISI 304	75	31	10	6	243
Sanicro 28	100	64	50	5	>300
Alloy 617	127	137	137	151	>300

3.2. Precipitates and its influence on the toughness

The toughness is strongly influenced by the precipitates formed during the high-temperature ageing process. Table 3 shows the precipitates appearing in Sanicro 28 at the four ageing conditions. Comparing table 2 and 3 it is clear that the largest impact toughness decrease for Sanicro 28 (50 J to 5 J) is due to increasing amount of sigma phase, σ, with needle shape. The σ-phase is a brittle tetragonal phase and can differ relatively much in composition and occur at different ageing conditions depending on chemical composition of the aged material [3, 9]. This indicates that both temperature and time are important for the impact toughness of Sanicro 28. The Cr,Mo-rich carbides in Sanicro 28 is probably $M_{23}C_6$ and/or M_6C depending on ageing condition [3, 10]. Intergranular carbides can be observed in all samples of the tested materials and occur before intragranular precipitation. AISI 304 show similar precipitation progress as Sanicro 28, but the amount of σ-phase seems to be larger already from the first ageing condition and the needle shaped σ-phase appear at all ageing conditions except of 650°C and 1000 hours, AISI 304 also has a larger amount of σ-phase with needle shape at each ageing condition [3, 11, 12]. For the nickel base alloy Alloy 617, γ´ precipitate is a main precipitate which grows at higher temperature and longer times, which probably is the reason for the increase in impact toughness with both temperature and time. Compared to non-aged material ductility decreases when the material is aged due to precipitates that increases the strength. However, when the precipitates grow larger and are evenly distributed the strength decreases and the ductility increases again. Other precipitates that are common but not detected by the EDS investigation in this study due to their small size in these ageing conditions is carbides as $M_{23}C_6$ [6, 7, 13].

Table 3. Precipitates of Sanicro 28 for different ageing conditions.

Ageing condition	Precipitates	Location of precipitates	Shape/amount
650°C & 1000h	Cr,Mo-rich carbides σ	Intergranular Intergranular	Rectangular/large Round/small
650°C & 3000h	Cr,Mo-rich carbides σ	Intergranular Intergranular	Rectangular/large Round/small
700°C & 1000h	Cr,Mo-rich carbides σ	Inter- and intragranular Inter- and intragranular	Rectangular/large Round/small, needle/small
700°C & 3000h	Cr,Mo-rich carbides σ	Inter- and intragranular Inter- and intragranular	Rectangular/large Round/large, needle/large

Figure 1 illustrates how the amount of σ phase affect the impact toughness for these three materials. The amount of precipitate is given by ThermoCalc-simulations [14]. The impact toughness is decreasing when the fraction of σ phase increases. There are notable differences for the two ageing conditions. At the ageing condition, 700°C for 3000h, the impact toughness is much lower than other conditions. One of the reasons is that this figure only considers the effect of σ-phase since the other phases can also play important roles, another reason is the shape of the precipitates that changes from rectangular to needle shaped. Also the ThermoCalc-simulation is only valid for equilibrium which not necessarily the samples that have been aged and then impact tested are.

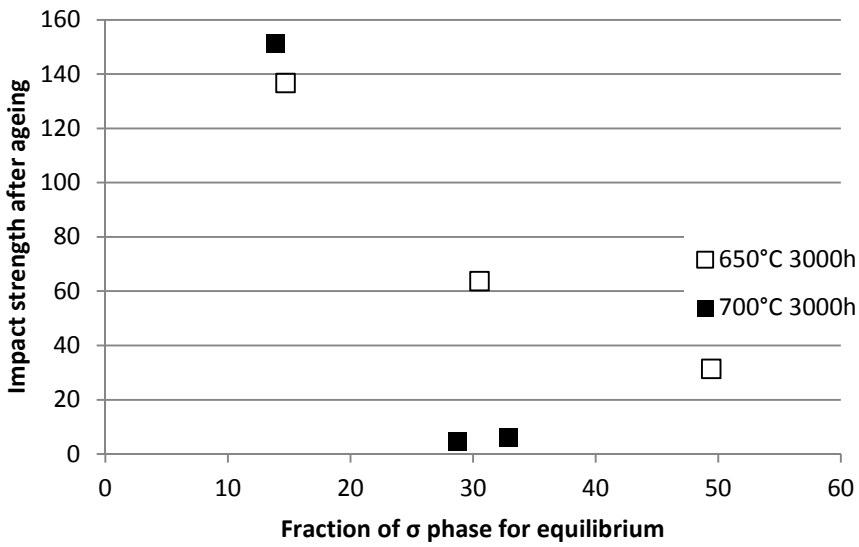

Figure 1. Show how the impact toughness is influences by the amount of σ phase at equilibrium after ageing at 650°C and 700°C for 3000 hours.

3.3. Fractures

The microstructure investigation reveals that the precipitates strongly affect the fracture behaviour. AISI 304 and Sanicro 28 show intergranular fracture after they have been aged at 650°C for 3000 hours (Fig. 2). However, the fracture morphology is different. Fracture surfaces in AISI 304 shows small and shollow dimples, while fracture surfaces in Sanicro 28 are rather smooth. Fracture surfaces in the nickel base alloy Alloy617 are still ductile and intergranular fracture is rarely seen.

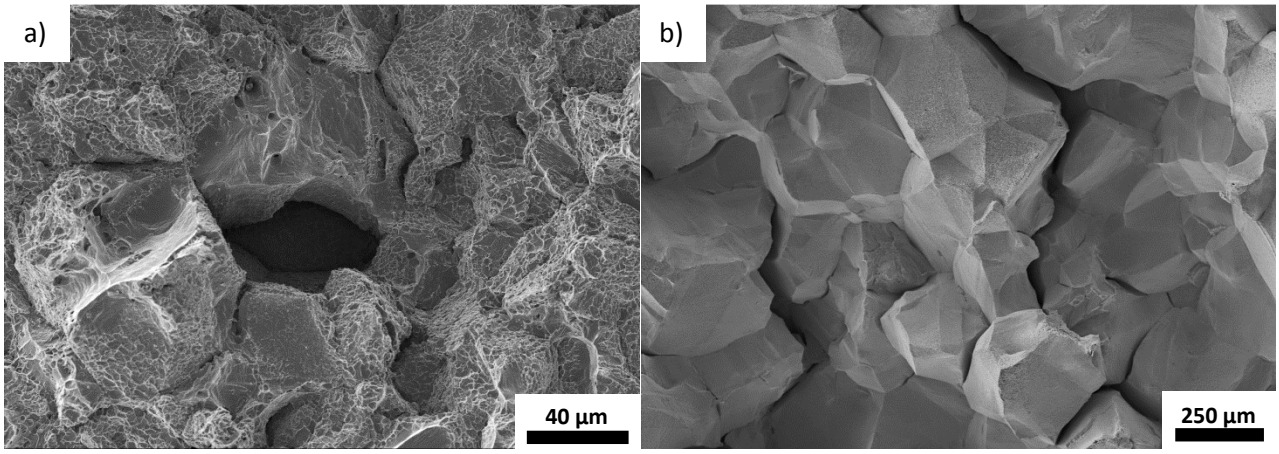

Figure 2. Pictures showing fracture surfaces from the impact tested samples, a) AISI 304 and b) Sanicro 28, both materials have been aged at 650°C for 3000h.

At 700°C, cleavage fracture can be observed in the stainless steels aged for 3000 hours (fig. 3). Typically step like or layer cleavage planes are found and some dimples can still be observed at the fracture surfaces.

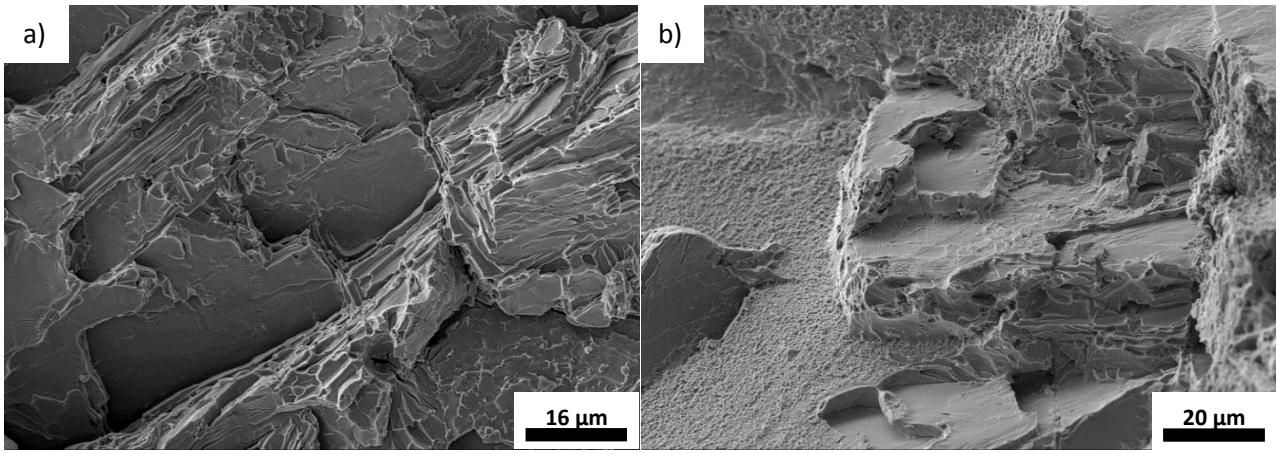

Figure 3. Cleavage fracture and elongated dimples from the impact tested samples after ageing at 700°C for 3000h, a) AISI 304 and b) Sanicro 28.

4. Discussion

As shown previously, ageing at 650°C and 700°C will lead to precipitation of different intermetallic phases with different morphologies. Since these materials are hard, stress concentration can form around the particles during creep or other deformation process, which leads the formation of local cracking or fracture [15]. Four types of cracks can be identified as shown in Fig. 4.

I. Cracks form at the particles within the grains. Due to stress concentration, this type of crack can induce cleavage fracture if the matrix is hard or brittle.
II. Cracks form at the particles at the grain boundaries. This may cause intergranular cracking if the matrix is tough or cleavage fracture if the matrix is brittle.
III. Cracks form along the needle shaped particle. This type of crack can create a high stress concentration, which can induce cleavage fracture if the matrix is not tough enough.
IV. Cracks form outside of grain boundary due to the shift of the cracking particles. This can cause both intergranular cracking and cleavage cracking.

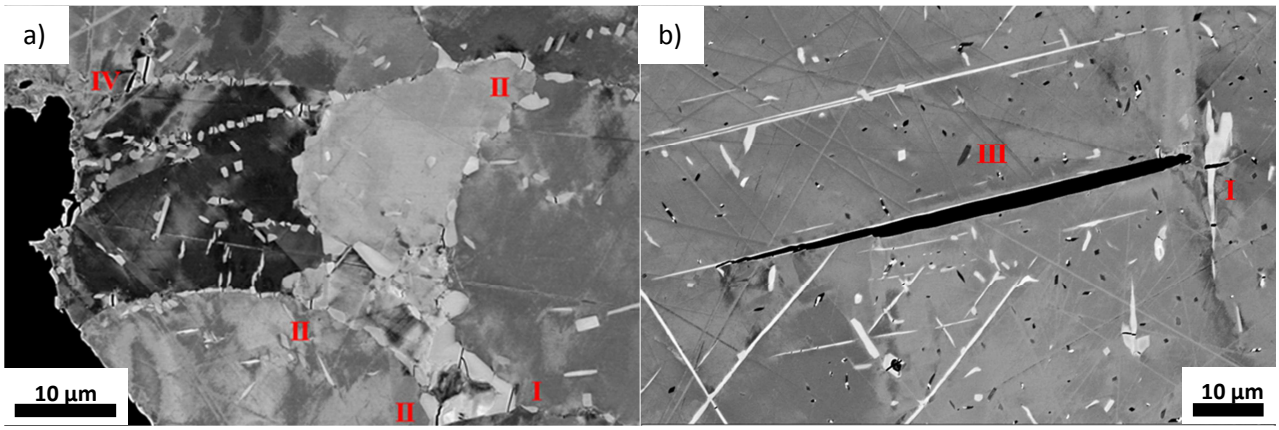

Figure 4. Precipitation induced cracks, a) AISI 304 aged at 650°C for 3000 hours and b) Sanicro 28 aged at 700°C for 3000 hours.

For the 304 material, needle shaped sigma phase can precipitate during ageing at 700°C for 3000h (Fig. 5a), which can form type III cracks during the impact toughness testing and lead to the formation of step type cleavage (Fig. 5b). This leads to low impact toughness.

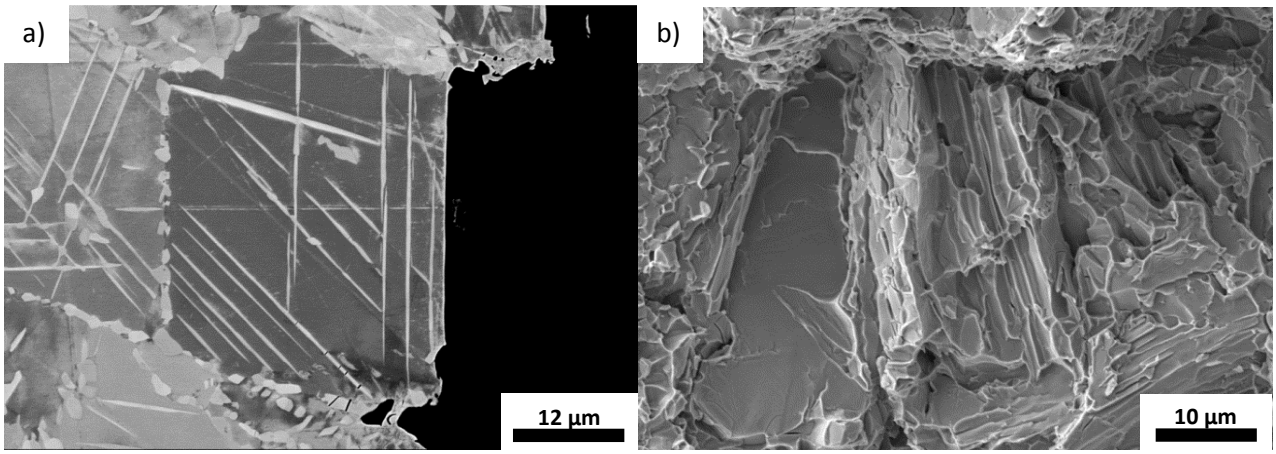

Figure 5. a) Precipitates in the aged 304 material at 700°C for 3000h and b) fracture after the impact toughness testing.

At 650°C, grain boundary carbides are the main precipitates (fig. 6a) and type II cracks can form during the impact toughness testing, which can lead to the formation of intergranular cracking (fig. 6b). Relatively low impact toughness can then be obtained.

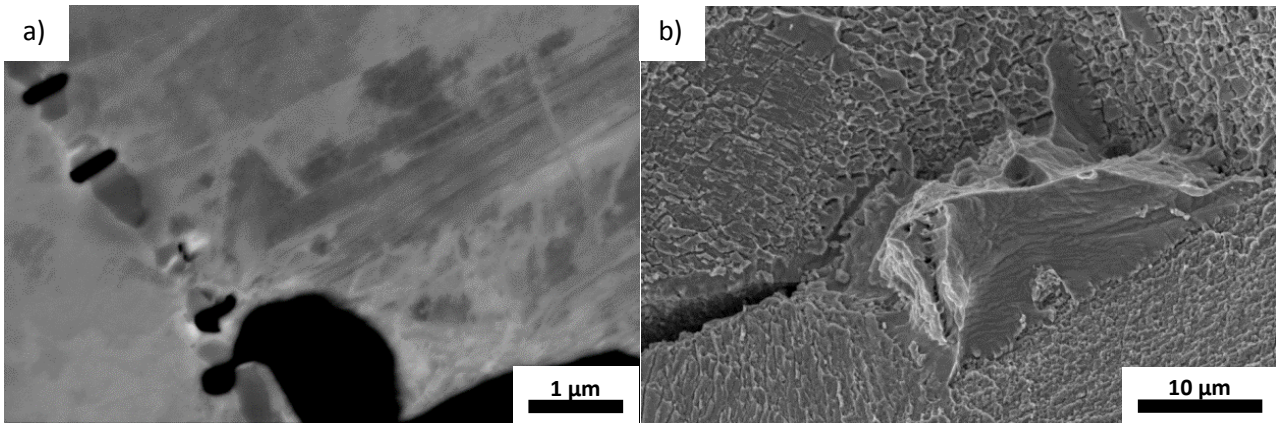

Figure 6. a) Precipitates in the aged Sanicro 28 material at 650°C for 3000h and b) fracture after the impact toughness testing.

Alloy 617 is a nickel based alloy and $Ni_3(Al,Ti)$ type of γ' is the main precipitate in the grains (Fig. 7a), but grain boundary carbides can also be observed [7]. In this case type II cracks can be observed and partial intergranular cracking can occur (Fig. 7b). Since the carbide density at the grain boundaries is relatively low, the material can still show good impact toughness.

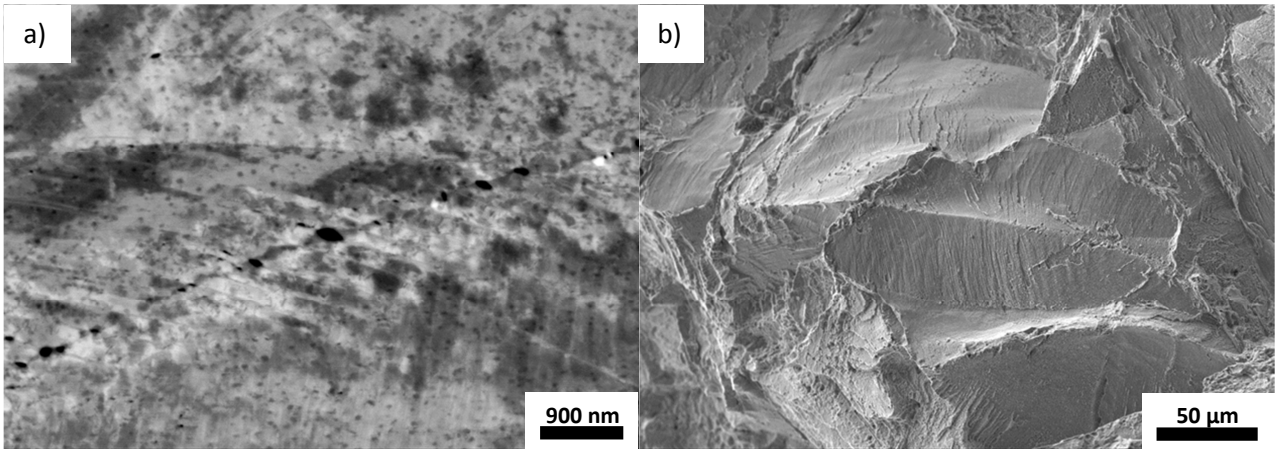

Figure 7. a) Precipitates in the aged Alloy 617 material at 700°C for 3000h and b) fracture after the impact toughness testing

The results and discussion above shows that initiation and propagation of fracture in the aged austenitic stainless steel is local. They can behave very differently in different materials, as explained by the four different crack-types. Local approach to fracture should be applied by considering the heterogeneous mechanical behaviors in these two phases.

5. Conclusions

The fracture initiation and propagation in the aged austenitic stainless steel is very local. They behave very differently in these materials at high temperature due to different chemical compositions affecting nucleation, growth and shape of precipitates. The brittle σ-phase can appear in the austenitic stainless steel after 1000 hours at 650°C and then increases in amount. The amount and shape have strong effect on the fracture behaviour, where needle shaped σ-phase which mostly appear at high temperature (700°C) after longer ageing time (3000 hours) lead to a low impact toughness and brittle fractures both locally and on a macro-level in the specimen. The nickel base alloy show higher impact toughness with increasing ageing temperature and time. Local approach to fracture should be applied by considering the heterogeneous mechanical behaviours in these two kinds of materials.

Acknowledgements

Present study was financially supported by AB Sandvik Material Technology in Sweden and the Swedish National Energy Administration through the Research Consortium of Materials Technology for Thermal Energy Processes, Grant No. KME-501. Agora Materiae and Strategic Faculty Grant AFM at Linköping University are also acknowledged.

References

[1] R. Viswanathan, K. Coleman, U. Rao, Materials for ultra-supercritical coal-fired power plant boilers, Int. J. Pressure Vessels Piping. 83 (2006) 778-783.
[2] J. Pettersson, H. Asteman, J. Svensson, L. Johansson, KCl Induced Corrosion of a 304-type Austenitic Stainless Steel at 600°C; The Role of Potassium, Oxidation of Metals. 64 (2005) 23-41.
[3] T. Sourmail, Precipitation in creep resistant austenitic stainless steels, Materials Science and Technology. 17 (2001) 1-14.
[4] M. Schwind, J. Källqvist, J.-. Nilsson, J. Ågren, H.-. Andrén, σ-PHASE PRECIPITATION IN STABILIZED AUSTENITIC STAINLESS STEELS, Acta Materialia. 48 (2000) 2473-2481.

[5] M. Farooqa, R. Sandströma, M. Lundberg, Precipitation during long time ageing in the austenitic stainless steel 310, Materials at High Temperatures. 29 (2012) 8-16.
[6] J.K. Wright, L.J. Carroll, C. Cabet, T.M. Lillo, J.K. Benz, J.A. Simpson, W.R. Lloyd, J.A. Chapman, R.N. Wright, Characterization of elevated temperature properties of heat exchanger and steam generator alloys, Nucl. Eng. Des. 251 (2012) 252-260.
[7] M. Speicher, A. Klenk, K. Maile, E. Roos, Behaviour of Ni-based alloys for fossil-fired power plant components in the long-term creep regime, Advanced Materials Research. 278 (2011) 241-246.
[8] I. Gutierrez-Urrutia, S. Zaefferer, D. Raabe, Electron channeling contrast imaging of twins and dislocations in twinning-induced plasticity steels under controlled diffraction conditions in a scanning electron microscope, Scr. Mater. 61 (2009) 737-740.
[9] L.K. Singhal, J.W. Martin, The formation of ferrite and sigma-phase in some austenitic stainless steels, Acta Metallurgica. 16 (1968) 1441-1451.
[10] K. Guan, X. Xu, H. Xu, Z. Wang, Effect of aging at 700 °C on precipitation and toughness of AISI 321 and AISI 347 austenitic stainless steel welds, Nucl. Eng. Des. 235 (2005) 2485-2494.
[11] J. Källqvist, H.-. Andrén, Microanalysis of a stabilised austenitic stainless steel after long term ageing, Materials Science and Engineering: A. 270 (1999) 27-32.
[12] I. Nikulin, A. Kipelova, R. Kaibyshev, Effect of high-temperature exposure on the mechanical properties of 18Cr–8Ni–W–Nb–V–N stainless steel, Materials Science and Engineering: A. 554 (2012) 61-66.
[13] R.C. Reed, Superalloys: Fundamentals and Applications, Cambridge University Press, Cambridge, 2006.
[14] B. Sundman, B. Jansson, J. Andersson, The Thermo-Calc databank system, Calphad. 9 (1985) 153-190.
[15] B.Z. Margolin, V.A. Shvetsova, G.P. Karzov, Brittle fracture of nuclear pressure vessel steels—I. Local criterion for cleavage fracture, Int. J. Pressure Vessels Piping. 72 (1997) 73-87.

Experimental Studies of Thermal Aging Effects on the Tensile and Tearing Fracture Behavior of Carbon Black Filled Rubbers

Xiaoling Hu, Yan Li, Xiu Liu, Wenbo Luo*

College of Civil Engineering and Mechanics, Xiangtan University, 411105, China
* Corresponding author: luowenbo@xtu.edu.cn

Abstract The effects of thermal aging on the tensile and tearing fracture behavior of carbon black filled rubbers with different filler loadings have been investigated in this paper. Thermal aging experiments were performed in a convection oven at 70°C and 120°C for various periods of aging time. Measurements of tensile strength, stretch to fracture and tearing strength were conducted with a 5943 Instron single column materials testing system as a function of aging time and aging temperature. It is found that the initial elastic modulus increases with increasing aging time, while the tensile strength decreases with the increase in aging time up to 100 hours and then increases when the material aged over 144 hours. The changes in tensile strength and stretch to fracture are found to be dependent on aging temperature, the higher the aging temperature, the more pronounced decrease in tensile strength and stretch to fracture. From the tearing fracture tests, the tearing strength generally is found to decrease with the increase in aging time.

Keywords Rubber, Thermal aging, Tensile strength, Stretch to fracture, Tearing energy

1. Introduction

Natural rubber is one of the most important elastomers, and its properties are usually reinforced by incorporation with carbon black (CB) of varying surface chemistry and aggregate size/aspect ratio to suit the application concerned [1]. CB filled rubbers are visco-hyperelastic materials, their mechanical properties are time- and temperature-dependent. Thermal aging causes both cross-linking and chain-scission. Cross-linking yields usually the increase in modulus and the decrease in extensibility of the material. Rubbers are susceptible to oxidative ageing due to their unsaturated carbon–carbon double bonds in the backbone. Elevated temperatures usually promote such an oxidative ageing [2]. The objective of this paper is to investigate the effect of thermal aging degradation upon the mechanical properties of filled rubbers with different CB loadings. The effects of aging are measured by the changes in tensile strength, stretch to fracture, initial elastic modulus and tear strength.

2. Experimental

2.1. Material and samples

The materials used for mechanical testing in this work are CB filled natural rubber vulcanizates. The formulations of the rubber compounds are listed in Table 1.Thin rectangular strips as shown in Fig.1, having the length of 100 mm and width of 10 mm, used for uniaxial tension tests are cut from a 2 mm thick vulcanized rubber sheet, which is provided by the Zhuzhou Times New Material Technology Co., Ltd. in China.

Table 1. Formulations of the rubber compounds (phr)

Compound	NR	CB (N330)	ZnO	Stearic acid	Antioxidant	Sulfur	Accelerator	Aromatic oil
A	100	11.2 *	5	3	1	2.5	0.7	3
B	100	37.6 *	5	3	1	2.5	0.7	3

* 11.2 phr CB = 5 vol% CB, 37.6 phr CB = 15 vol% CB

According to the ISO 34 standard method A, the samples used for tear fracture tests are processed into trouser test pieces. Each piece has a cut of depth 40mm, which is made with a razor blade, at the center of the width of the test piece in the direction indicated in Fig.2.

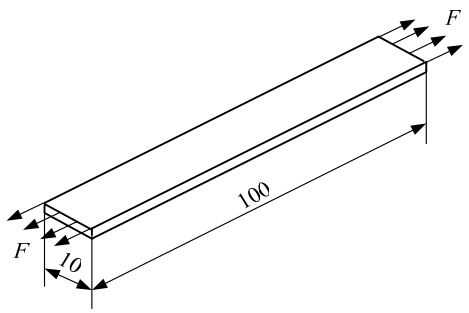

Fig.1 Test piece for uniaxial tension

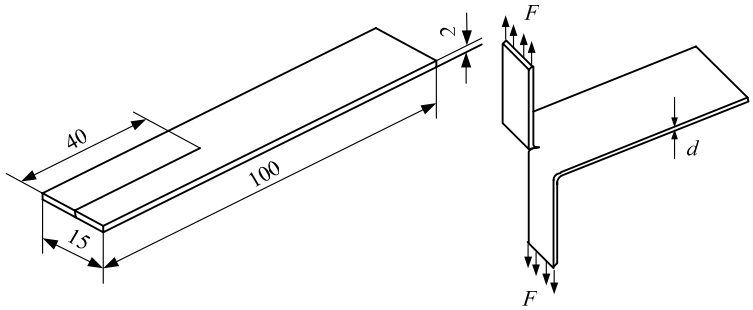

Fig.2 Trouser sample for tear fracture testing

2.2. Measurements

We examined the tensile and tear fracture properties of CB filled natural rubbers which have been subjected to isothermal aerobic aging. The thermal aging was conducted with a circulated air oven at temperatures of 70°C and 120°C for periods of time ranging from 10 hours to 144 hours. Uniaxial tension and tear fracture tests were conducted with a 5943 Instron single column materials testing system. The effects of aging were measured by the changes in tensile strength, stretch to fracture, initial elastic modulus and tear strength. The tensile strength is defined by the ratio of the peak force of the force-stretch curve to the reference cross section area. The Initial elastic modulus is the slop of the stress-stretch curve at very small stretches. The tear strength T_s is given by the formula

$$T_s = \frac{F}{d} \tag{1}$$

where F is the median force acting on the arm of the test piece, calculated in accordance with ISO 6133, d is the median thickness of the test piece.

3. Results

3.1. Tensile stress-strain properties

Uniaxial tension tests up to fracture under a constant rate of 100mm/min were conducted at 23°C. Fig.3 shows the stress-stretch curves of rubbers with 5 vol% CB and 15 vol% CB, aged at 120°C for various periods of time. It is obvious that the tensile strength, stretch to fracture and initial elastic modulus change with aging time. Figs. 4-6 show the variations of these tensile properties with aging time. It is found that the initial elastic modulus increases with increasing aging time, while the tensile strength decreases with the increase in aging time up to 100 hours and then increases when the material aged over 144 hours. Moreover, the stretch to fracture decreases with increasing aging time, this phenomenon was reported in the literature [3]. Compared to 5 vol% CB filled rubber, there are more pronounced changes in the tensile properties for 15 vol% CB filled rubber.

In vulcanizates the bond energy between the sulfur crosslink atoms and the polymer backbone greatly differ. There are three types of crosslinks in the vulcanizates: polysulfidic, disulfidic and monosulfidic [4]. The maximum service temperature of natural rubber is about 70°C, i.e., the mechanical properties of natural rubber aged at 70°C would not change significantly, however, the carbon black filled natural rubbers would experience severer thermal degradation at temperature above 70 ^{o}C [5]. As seen in Figs.7-9 the change in tensile properties are found to be dependent on aging temperature, the higher the aging temperature, the more pronounced decrease in tensile

strength and stretch to fracture, and the more pronounced increase in initial elastic modulus.

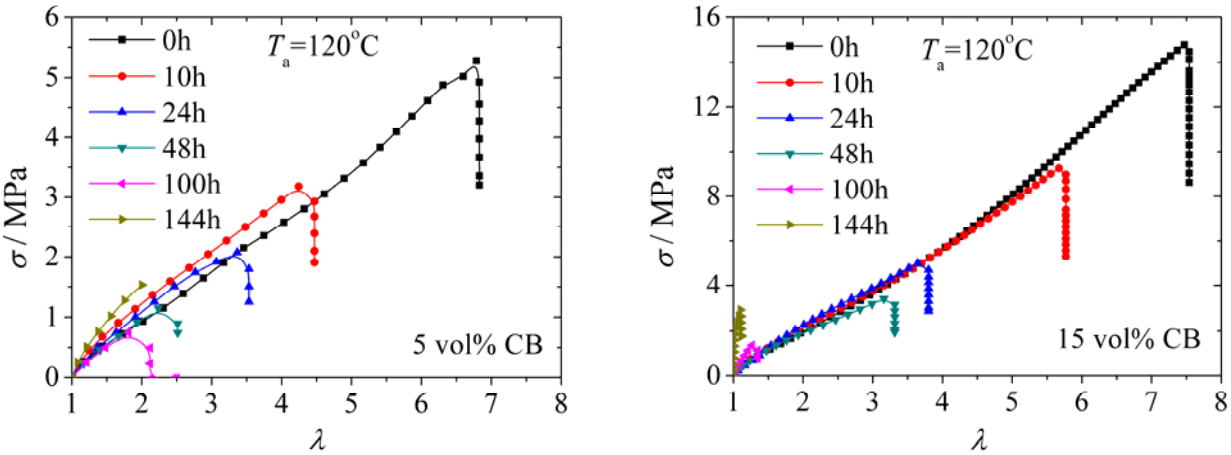

Fig.3 Tensile stress-stretch curves of filled rubber with 5 vol% and 15 vol% CB, aged at 120°C

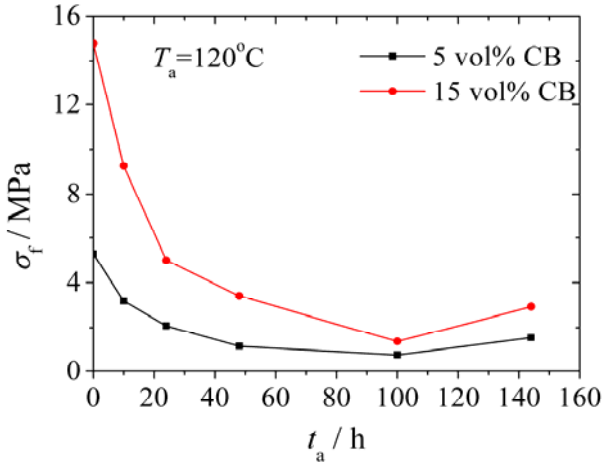

Fig.4 Variation of tensile strength with aging time for CB filled rubbers aged at 120°C

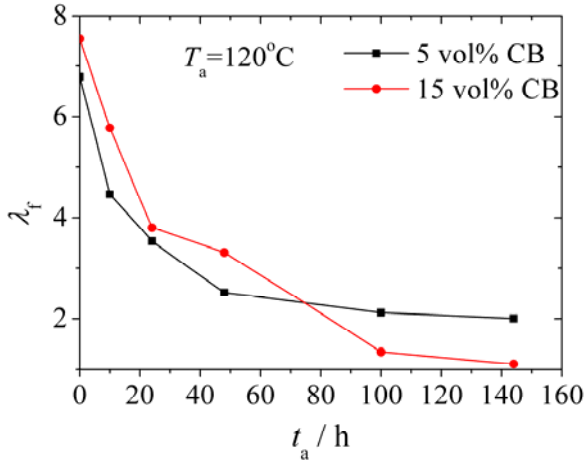

Fig.5 Variation of stretch to fracture with aging time for CB filled rubbers aged at 120°C

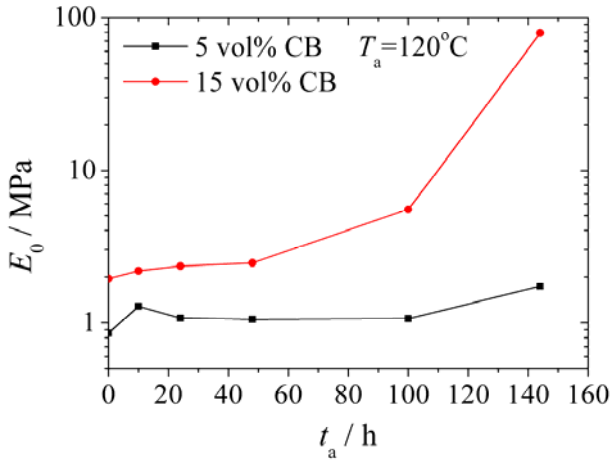

Fig.6 Variation of initial elastic modulus with aging time for CB filled rubbers aged at 120°C

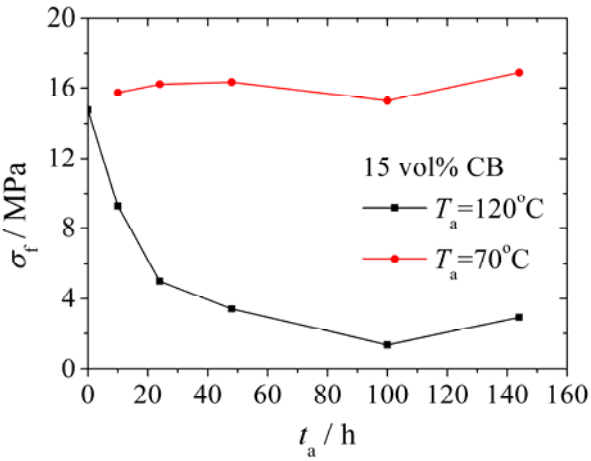

Fig.7 Variation of tensile strength with aging time for 15 vol% CB filled rubbers aged at 120°C and at 70°C

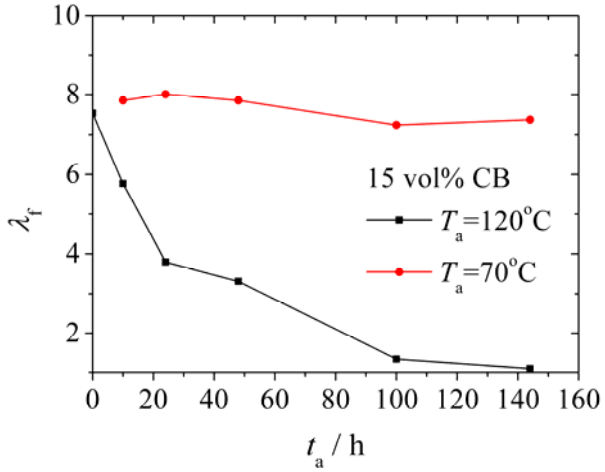

Fig.8 Variation of stretch to fracture with aging time for CB filled rubbers aged at 120°C and at 70°C

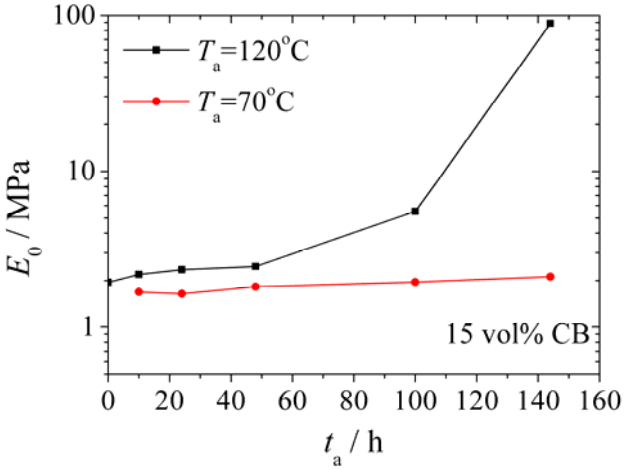

Fig.9 Variation of initial elastic modulus with aging time for CB filled rubbers aged at 120°C and at 70°C

3.2. Tear force-displacement curve and tear strength

Tear fracture tests under a constant rate of 100mm/min were conducted at 23°C. Fig.10 shows the tear force-displacement curves for 15 vol% CB filled rubbers aged for various periods of time at 120°C. The tear strength defined by Eq.(1) is plotted as a function of aging time as shown in Fig.11. It is seen that the tear strength decreases in the early aging period, and increases with aging time when the aging time extends to 48 hours. Such decrease-increase trend with respect to aging time is similar to the variation of the tensile strength with aging time.

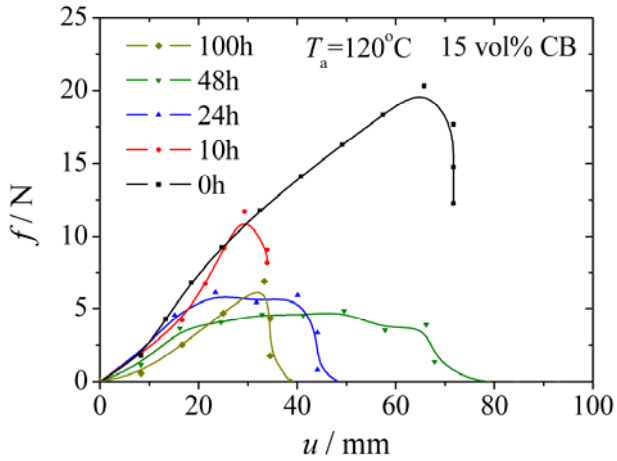

Fig.10 Tear force-displacement curve for 15 vol% CB filled rubber aged for various periods of time at 120°C

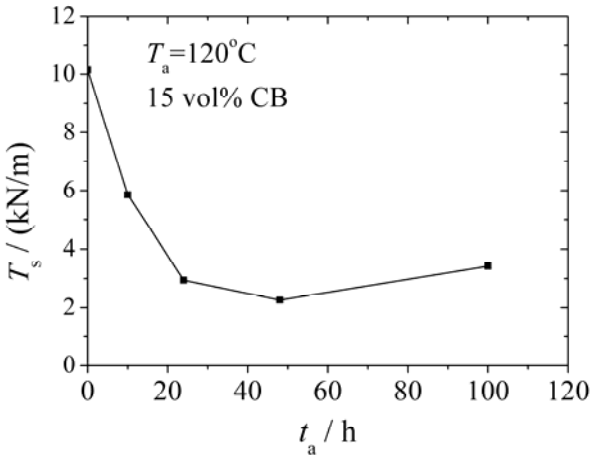

Fig.11 Variation of tear strength with aging time for 15 vol% CB filled rubber aged at 120°C

4 Conclusions

The effects of thermal aging on the tensile and tearing fracture behavior of carbon black filled rubbers with different filler loadings have been investigated in this work. It is found that the initial elastic modulus increases with increasing aging time, while the tensile strength and tear strength decrease firstly with the increase in aging time and then increase when the age proceeds. Moreover, the change in mechanical properties due to thermal aging is found to be dependent on aging temperature, the higher the aging temperature, the more pronounced deterioration in tensile strength and stretch to fracture.

Acknowledgements

This work was supported by NSFC (No.11172256), Hunan Provincial Science and Technology Program (No.2012FJ4061), Hunan Provincial Innovation Foundation for Postgraduate (No. CX2011B270, No.CX2012B258) and the Aid Program for Science and Technology Innovative Research Team in Higher Educational Institutions of Hunan Province, China.

References

[1] N. Rattanasom, T. Saowapark, C. Deeprasertkul, Reinforcement of natural rubber with silica/carbon black hybrid filler. Polymer Testing. 26(2007)369-77.

[2] H. Dal, M. Kaliske. A micro-continuum-mechanical material model for failure of rubber-like materials: Application to ageing-induced fracturing. Journal of the Mechanics and Physics of Solids, 57(2009)1340-1356.

[3] G.R.Hamed, J. Zhao, Tensile behavior after oxidative aging of gum and black-filled vulcanizates of SBR and NR. Rubber Chemistry and Technology 72(1999)721-730.

[4] K.A.J. Dijkhuis, J.W.M. Noordermeer, W.K. Dierkes, The relationship between crosslink system, network structure and material properties of carbon black reinforced EPDM. European Polymer Journal 45(2009)3302-3312.

[5] J.T. South, S.W. Case, K.L. Reifsnider. Effects of thermal aging on the mechanical properties of natural rubber. Rubber Chemistry and Technology, 76(2003) 785-802.

A fracture-based model of periodic-arrayed indentation for rock cutting

Yu Jun Xie[1,*], Bo Yang Xiang[1] and Xiao Zhi Hu[2*]

[1] Department of Mechanical Engineering, Liaoning Shihua University, Fushun, 113001, P. R. China.
[2] School of Mechanical and Chemical Engineering, The University of Western Australia, Perth, WA 6009, Australia.
* Corresponding author: yjxie@lnpu.edu.cn, xiao.zhi.hu@uwa.edu.au.

Abstract When an half-space elastic substrate is subject to indentation with rigid, flat-ended and periodic indenters, a periodic singular stress fields and K-dominant regions should arise adjacent to the indenter edges. The concept of indentation stress intensity factor K_{ind} is introduced to describe the singular indentation stress field, which mathematically is very similar to that of a mode I crack. The singular indentation stress field is sufficient to induce cracking from a smooth crack-free surface, which can potentially play a significant role in damage analysis of rock cutting. In the present article, a fracture-based model is proposed for rock breakage by using an energy-based method. The indentation stress intensity factor K_{ind} and indentation cracking equation for rock cutting model have been formulized.

Keywords Fracture, Contact mechanics, Indentation stress intensity factors, Indentation.

1. Introduction

A rock-cutting tool schematically illustrated in Fig.1 can be modeled by periodic rigid and flat-tipped indenters. It is noted from the work [1-4] that a mixed-mode singular stress field exists in an incompressible substrate at the sliding contact edge of a rigid flat-ended indenter pressing down onto the substrate. Subsequently, the damage in a form of the micro-crack initiation on the contact surface will be induced by such a singular stress field, which can contribute substantially to rock cutting. In the present work, a fracture-based method similar to the classical fracture mechanics is proposed to formularize the cracking or indentation damage induced by the singular indentation stress field next to the corners of the periodic indenters.

2. Periodic indentation configurations

The modeling of rock cutting problem to be investigated is illustrated in Fig.1. The periodic indenters is pressed on to the surface of half plane substrate, which occupies the region $0 < x_2 < h < +\infty$, $-\infty < x_1 < +\infty$ and is constrained to deform in plane strain normal to the $x_1 - x_2$ plane. The substrate is supposed to be elastically isotropic, with Young's modulus E and Poisson's ratio μ. The periodic arrayed indenters is supposed to be rigid, with contact width $2l$ and center-to-center contact spacing $2t$. The calculations for indentation stress intensity factors are carried out based on one of the periodic Cell 1 and Cell 2 that lies between $-t/2 < x_1 < t/2$. Two limiting cases of friction are considered: (i) perfect smooth sliding between the indenter and the substrate; and (ii) small frictional sliding contact between the indenter and the substrate.

3. Asymptotic stress field in sliding contact

3.1. Boundary Condition

A typical fretting contact problem of a rigid flat-ended indenter with half width a, sliding on a homogeneous, isotropic, elastic body in half plane is shown in Fig.2. The Cartesian coordinates (x_1, x_2), and the polar coordinates (r, θ), both with the origin at the left edge of the indenter, are selected. Normal force N and tangential force Q act on the indenter and the following normal and shear

tractions along interface have been solved in closed form [4],

$$p(x_1) = -\frac{N \sin \lambda\pi}{\pi}\left(2 - \frac{x_1}{a}\right)^{\lambda-1}\left(\frac{x_1}{a}\right)^{-\lambda} \tag{1}$$

and

$$q(x_1) = fp(x_1), \tag{2}$$

where f is the coefficient of friction; λ is determined by

$$\tan \lambda\pi = \frac{2(1-\mu)}{f(1-2\mu)}, \quad 0 < \lambda < 1. \tag{3}$$

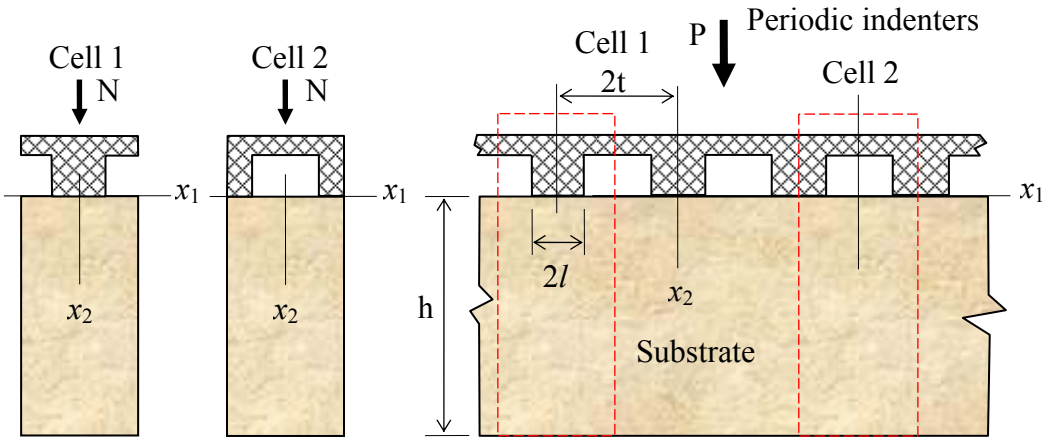

Fig.1 The two-dimensional indentation model for rock cutting with n periodic indentaters.

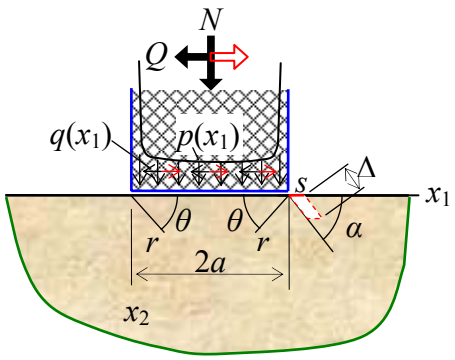

Fig.2. Indentation configuration, integral path $s \to 0$ and $\Delta \to 0$.

Eq.(1) shows that the stress state near the indenter corner may vary in the form

$$\sigma_{ij} = \begin{cases} 0\left(r^{\lambda-1}\right), & x_1 = 2a \\ 0\left(r^{-\lambda}\right), & x_1 = 0 \end{cases} \quad \text{as} \quad r \to 0. \tag{4}$$

For special cases either with $\mu = 0.5$ or $f = 0$, Eq.(3) leads to $\lambda = 0.5$, showing the same order of stress singularity as that for a sharp crack tip.

For $\mu = 0.5$, the substrate becomes incompressible. The asymptotic stress boundary conditions of the substrate in the contact area next to the left and right corners then become

$$\sigma_{22}\,|_{\theta=0} = -\frac{N}{\pi\sqrt{2ar}} \tag{5}$$

and

$$\sigma_{21}\,|_{\theta=0} = \frac{fN}{\pi\sqrt{2ar}} \tag{6}$$

for the two cases of $\mu = 0.5$ and $f = 0$.

3.2. Singular stress fields due to the normal and tangential loads

The singular stress field at the sharp edge of the contact between a rigid flat-ended indenter and substrate is known from the asymptotic contact analyses of and Nadai [4]. Using the polar coordinates (r, θ), Fig.2, the stresses at the left corner can be found as follows due to the normal load:

$$\begin{pmatrix} \sigma_{rr}^{I} \\ \sigma_{\theta\theta}^{I} \\ \sigma_{r\theta}^{I} \end{pmatrix} = -\frac{K_{I-ind}}{\sqrt{2\pi r}} \begin{pmatrix} \cos\frac{\theta}{2}\left(1+\sin^2\frac{\theta}{2}\right) \\ \cos^3\frac{\theta}{2} \\ \sin\frac{\theta}{2}\cos^2\frac{\theta}{2} \end{pmatrix}. \tag{7}$$

This expression indicates that the stress state for indentation is a “negative” Mode-I singular stress field for cracked solids, where

$$K_{I-ind} = \frac{N}{\sqrt{\pi a}}, \tag{8}$$

which defines actually an indentation stress intensity factor. The familiar Mode-I singular stress field is obtained by removing the negative sign and changing $K_{\text{I-ind}}$ into K_{I} for cracked solids with mode-I loads. Only difference between tensile mode-I stress field and indentation stress field is sign “-” in their equations.

Nadai [4] gave also the asymptotic stress field due to the tangential load as

$$\begin{pmatrix} \sigma_{rr}^{II} \\ \sigma_{\theta\theta}^{II} \\ \sigma_{r\theta}^{II} \end{pmatrix} = \frac{K_{II-ind}}{\sqrt{2\pi r}} \begin{pmatrix} \sin\frac{\theta}{2}\left(1-3\sin^2\frac{\theta}{2}\right) \\ -3\sin\frac{\theta}{2}\cos^2\frac{\theta}{2} \\ \cos\frac{\theta}{2}\left(1-3\sin^2\frac{\theta}{2}\right) \end{pmatrix}, \tag{9}$$

where

$$K_{II-ind} = fK_{I-ind}. \tag{10}$$

Actually, the Eq.(9) is identical to the classical Mode-II singular stress fields when $K_{\text{II-ind}} = K_{\text{II}}$.

3.3 Characters of the stress fields

It is clear from the above discussion that the asymptotic stress field, $\sigma_{ij} = \sigma_{ij}^{I} + \sigma_{ij}^{II}$, induced by the sliding contact is a typical mixed-Mode I-II singular stress field for incompressible substrates and friction free. This singular stress field is responsible for surface crack initiation on the crack-free surface of the substrate at the contact edge. This finding is significant as it shows that singularity and distribution of the stress field induced by surface contact of a flat-ended indenter are identical to those of a mixed-mode crack. As a result, the concepts of stress intensity factor and fracture toughness can now be introduced unambiguously into contact mechanics and associated contact damage. Therefore, Eqs.(7)-(10) represent an important advance by defining the indentation stress intensity factors, K_{I-ind} and K_{II-ind}, and the K_{ind}-dominant region at the contact edge. In other words, the fracture mechanics theory, such as the Griffith’s criterion, is applicable in the case of the boundary fracture induced by the sliding contact. It should be pointed out that for finite boundary contact problems, Eqs.(7), (9) and (10) are still effective, for which case the K_{I-ind} should be

solved by the concerned method.

4. Conservation integral

Based on the two-dimensional conservation law, for a closed integration path without any crack and cavity in it, the following integrals will vanish [5-8].

$$J_j = \int_s \left(wn_j - T_i u_{i,j}\right) ds \,. \tag{11}$$

Eq.(11) has two components, J_1 and J_2. J_1 is so-called J-integral. They can all be used to calculate the stress intensity factors for the cracked elastic bodies. In the following section some key steps to estimate the SIF for the indentation have been developed based on the J_2-integral.

5. Stress intensity factors for periodic indentations

As the definition of the half plane substrate, i.e., $0 < x_2 < h < +\infty$, $-\infty < x_1 < +\infty$, any plane $x_1 = kt,\ k = 0, 1, 2....$ is the symmetrical plane. Then, the Cell 1 shown in Fig.1 is considered for the calculation of the stress intensity factors for periodic indentations. Note that there are two singular stress fields next to the two corners of every indenter for all cells.

Select a closed integration path $s_{abcdefghija}$ as shown in Fig.3 for Cell 1. From the Eq.(11), following result can be given[5-8].

$$J_2 = \oint_{s_{abcdefghija}} \left(wn_2 - T_i u_{i,2}\right) ds = 0 \,. \tag{12}$$

For the paths s_{bc} and s_{de}, because the symmetry, $T_2 = 0$, $n_2 = 0$ and $u_{1,2} = 0$, and the following result can be found.

$$J_2 = \int_{s_{bc}} \left(wn_2 - T_i u_{i,2}\right) ds = \int_{s_{de}} \left(wn_2 - T_i u_{i,2}\right) ds = 0 \,. \tag{13}$$

Let the s_{gh} and s_{ij} be straight lines; and s_{fg} and s_{ja} a quarter of a circle. If the s_{ija} and s_{fgh} are within the K-dominant regions, we have [11-13]

$$J_2 = \int_{s_{gh}} \left(wn_2 - T_i u_{i,2}\right) ds = \int_{s_{ij}} \left(wn_2 - T_i u_{i,2}\right) ds = 0 \tag{14}$$

and

$$J_2 = \int_{s_{fg}} \left(wn_2 - T_i u_{i,2}\right) ds = \int_{s_{ja}} \left(wn_2 - T_i u_{i,2}\right) ds = \frac{\left(1-\mu^2\right) K_{I-ind}^2}{2\pi E} \quad \text{(plane strain).} \tag{15}$$

When the cross sectional area where the s_{cd} located is relatively far from the contact zone, the following expression can be given by

$$J_2 = \int_{s_{cd}} \left(wn_2 - T_i u_{i,2}\right) ds = \overline{w}^- + N\widetilde{u}_{2,2}^- \,, \tag{16}$$

where the $\widetilde{u}_i$ shows the displacement of neutral axis. This displacement can be given by elementary strength theory of materials [11-13]. $\overline{w}$ is the strain energy density per unit length of the cell. For the s_{hi}, we have

$$J_2 = \int_{s_{hi}} \left(wn_2 - T_i u_{i,2}\right) ds = -\left(\overline{w}^+ + N\widetilde{u}_{2,2}^+\right). \tag{17}$$

Then, substituting Eqs.(13)-(17) to Eq.(12), it gives

$$J_2 = \frac{\left(1-\mu^2\right) K_{I-ind}^2}{\pi E} + 2\int_{s_{ab}} w ds = \left(\overline{w}^- + N\widetilde{u}_{2,2}^-\right) - \left(\overline{w}^+ + N\widetilde{u}_{2,2}^+\right) = \frac{N}{2}\left(\widetilde{u}_{2,2}^- - \widetilde{u}_{2,2}^+\right), \tag{18}$$

which can be interpreted as the energy release per unit moving of boundary s_{iab} and s_{efh} in

x_2-direction or the crack mouth widening energy release rate for cracked solids [11-13]. The axial strain $\tilde{u}_{2,2}^{-}$, $\tilde{u}_{2,2}^{+}$ have been found[11-13]

$$\tilde{u}_{2,2}^{-} = -\frac{N}{EA} \tag{19}$$

and

$$\tilde{u}_{2,2}^{-} = -\int_0^1 \frac{N d\xi}{EA[1-(1-l/t)\sqrt{1-\xi^2}]} = -\frac{N}{EA}\left(\frac{2}{(1-l/t)\sqrt{1-(1-l/t)^2}}\arctan\sqrt{\frac{2-l/t}{l/t}} - \frac{\pi}{2(1-l/t)}\right). \tag{20}$$

Because the free action of the substrate surface and s_{ab} and s_{ef} is out of the K-dominant regions, the integral in left-hand side of Eq. (18) is a small quantity, which can be neglected. Substituting Eqs.(19) and (20) into Eq.(18), it will yield

$$K_{I-ind} = \frac{N}{\sqrt{\pi t}} f\left(\frac{l}{t}\right), \tag{21}$$

where the normalized stress intensity factor can be found as

$$f\left(\frac{l}{t}\right) = \frac{\pi}{2}\left\{\frac{1}{1-\mu^2}\left[\frac{2}{(1-l/t)\sqrt{1-(1-l/t)^2}}\arctan\sqrt{\frac{2-l/t}{l/t}} - \frac{\pi}{2(1-l/t)} - 1\right]\right\}^{1/2}. \tag{22}$$

Eq.(22) varying with perimeter l/t is given in Fig.4.

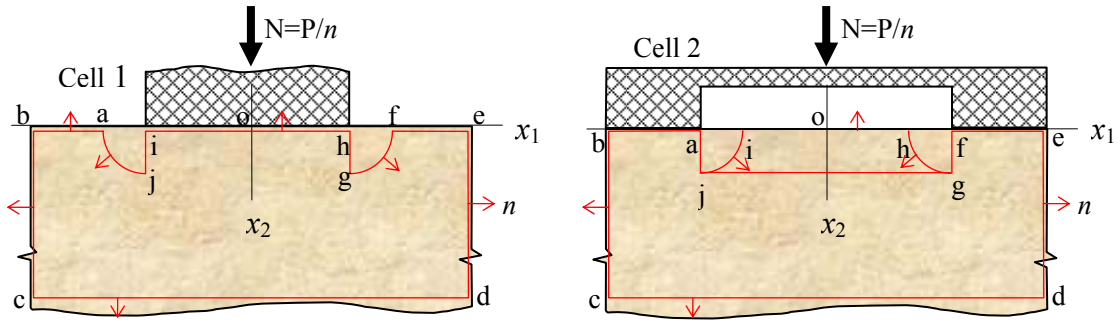

Fig.3. Contours of integration for the Cell 1 and Cell 2.

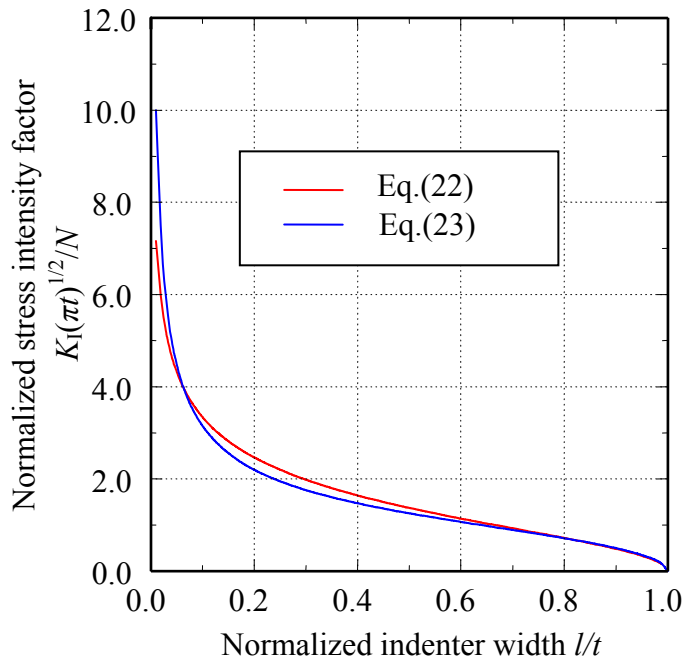

Fig.4. the scheme of the normalized stress intensity factor.

6. An indirect technique on the periodic indentation

In above sections, a simple and direct method is proposed to estimate the indentation stress intensity factor for singular stress field induced by indentation. In this section, an alternative and indirect technique is considered.

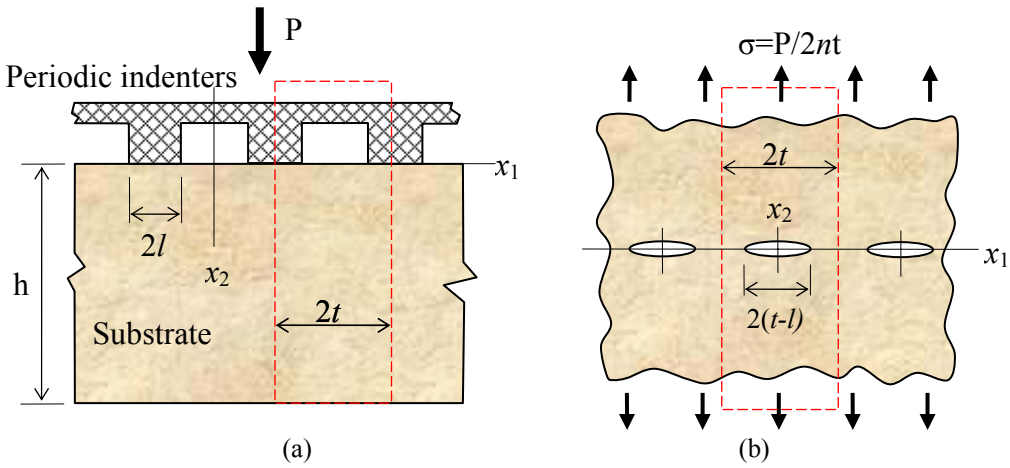

Fig.5. Periodic indentation and related periodic crack model. (a) Periodic indentation; (b) Related crack model.

For any Mode-I indentation, the related crack model can be found[9]. For various crack configurations, the stress intensity factors had been found and collected in the handbooks such as [14]. Hence, a simple and indirect technique of the crack analogue may be used to solve the indentation stress intensity factor for the Mode-I indentation based on the existing literature for the crack analysis. As a main research object in present work, i.e., periodic indentation, the related crack model can be given in Fig.5(b). For such a periodic array of collinear cracks, the exact solution of the stress intensity factor can be found [14].

$$K_{I-ind} = \frac{N}{\sqrt{\pi t}}\left\{\frac{\pi}{2}\tan\left[\frac{\pi}{2}\left(1-\frac{l}{t}\right)\right]\right\}^{1/2}. \tag{23}$$

It varying with the normalized indenter width l/t can be found in Fig.4.

7. Boundary cracking in complete sliding contact

7.1 Energy release rate for boundary cracking

From the geometrical point of view, boundary crack initiation can always be defined as a boundary movement in some direction, with the limit $s \to 0$ taken and the notch-like boundary becomes a crack, as shown in Fig.2. Then, the energy release rate of boundary cracking can be defined as[10-13]

$$G = (J_1)|_{s\to 0}\cos\alpha + (J_2)|_{s\to 0}\sin\alpha\ , \tag{24}$$

where

$$(J_1)|_{s\to 0} = \lim_{s\to 0}\int_s wn_1 ds = \int_{s_{in}}(wn_1 - T_i u_{i,1})ds \tag{25}$$

and

$$(J_2)|_{s\to 0} = \lim_{s\to 0}\int_s wn_2 ds = \int_{s_{in}}(wn_2 - T_i u_{i,2})ds\ . \tag{26}$$

The integration path s_{in} in Eqs.(25) and (26) is any integration path within the substrate, and $s_{in}+s$

form a closed integral loop. The $(J_1)|_{s\to 0}$ denotes the driving force of boundary cracking in direction x_1 when the limit taken exists, or the energy release rate with unit boundary movement s in direction x_1; $(J_2)|_{s\to 0}$ denotes the driving force in direction x_2, or the energy release rate with unit boundary movement s in direction x_2.

For a homogenous and isotropic substrate Griffith's criterion [15] states that the crack will extend when the critical value $G_{\max}$ is reached [15,16]

$$G_{\max} = G_c \,. \tag{27}$$

For a standard cracked specimen subjected to Mode-I loading, $G_{\max} = J_1$ and G_c can be calibrated as

$$G_c = J_{IC} = K_{IC}^2 \left(1-\mu^2\right)/E \,, \tag{28}$$

where K_{IC} is the Mode-I fracture toughness. However, in the present case of surface crack initiation, a mixed-mode condition is expected as the singular stress field is generated by the sliding contact with the rigid flat-ended indenter.

7.2 Critical cracking angle and critical load.

Firstly, $(J_1)\big|_{s_{ob}\to 0}$ can be found. Let $s = s_{ob}$ in Eq.(25) as shown in Figs.2 and 6 adjacent to the right corner of the indenter and s be within the K_{ind}-dominant region. Because $T_i = 0$ and $n_1 = 0$ on the integration path s_{ob}, the energy-based driving force for boundary cracking in x_1 direction in this case can be found as

$$(J_1)\big|_{s_{ob}\to 0} = \lim_{s_{ob}\to 0} \int_{s_{ob}} w n_1 ds = 0 \,. \tag{29}$$

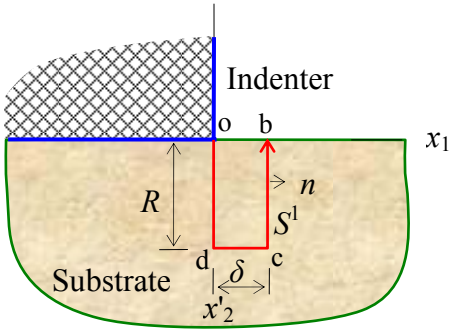

Fig.6. Integration path adjacent to punch corner within the K_{ind}-dominant region for J_2.

Next step is to calculate $J_2|_{s_{ob}\to 0}$. As shown in Figs.2 and 6, let $s = s_{ob}$, $s_{in} = S^1_{odcb}$ in Eq.(26) and take the limit $s_{ob}\to 0$, $\delta/R \to 0$ and $R\to 0$, which means that the $s_{in} = S^1_{odcb}$ is within the K_{ind}-dominant region and $S^1_{odcb}\to 0$. Then, the energy-based driving force for boundary cracking in x_2 direction becomes [10,16]

$$(J_2)|_{s_{ob}\to 0} = \lim_{s_{ob}\to 0} \int_{s_{ob}} w n_2 ds = -\frac{4\left(1-\mu^2\right)}{E} \lim_{\substack{\delta/R\to 0\\ R\to 0}} \int_{S^2_{odcb}} \mathrm{Im}\left(\Phi^2 + \Phi\overline{\Phi} - z\overline{\Phi}'\overline{\Phi} - \overline{\Phi}\,\overline{\Psi}\right) n_1 ds \,, \tag{30}$$

where

$$\Phi(z) = \frac{K_I - K_{II} i}{2\sqrt{2\pi z}} \,, \quad \Psi(z) = \frac{K_I + 3K_{II} i}{4\sqrt{2\pi z}} \,, \tag{31}$$

in which $K_I = -K_{I-ind}$ and $K_{II} = K_{II-ind}$ for indentation singular stress fields. From Eqs.(30) and (31), it can be readily obtained that

$$(J_2)|_{s\to 0}=\frac{(1-\mu^2)K_{I-ind}^2}{2\pi E}(1+\pi f-f^2),\ \text{for the plane strain condition.} \tag{32}$$

From Eqs.(24), (29) and (32), the total energy release rate of boundary cracking induced by the sliding contact at any angle α can be found as

$$G=(J_1)|_{s_{ob}\to 0}\cos\alpha+(J_2)|_{s_{ob}\to 0}\sin\alpha=\frac{(1-\mu^2)K_{I-ind}^2}{2\pi E}(1+\pi f-f^2)\sin\alpha\,. \tag{33}$$

Setting $\frac{dG}{d\alpha}=0$, i.e., $\cos\alpha_c=0$, we have

$$\alpha_c=\frac{\pi}{2}, \tag{34}$$

where α_c is the critical cracking angles, which is vertical to the contact boundary.

Cracking occurs when G reaches its critical or maximum value. The critical or maximum energy-based driving force for boundary cracking can then be solved from Eq. (33), i.e.

$$G_{\max}=\frac{(1-\mu^2)K_{I-ind}^2}{2\pi E}(1+\pi f-f^2). \tag{35}$$

From the Eqs.(27) and (35), the critical condition of substrate boundary cracking beneath the contact surface can be found as

$$G_{\max}=\frac{(1-\mu^2)K_{I-ind}^2}{2\pi E}(1+\pi f-f^2)=G_{IC}\,. \tag{36}$$

Finally, the normalized critical load P can be expressed as

$$\frac{P_c}{n\sqrt{\pi t}K_{IC}}=\frac{2}{(1+\pi f-f^2)^{1/2}\tan^{1/2}[0.5\pi(1-l/t)]} \tag{37}$$

for a given indenter size 2*l* from Eqs.(23), (28) and (36). Fig.7 shows the effect of perimeter *l/t* on the normalized critical loads.

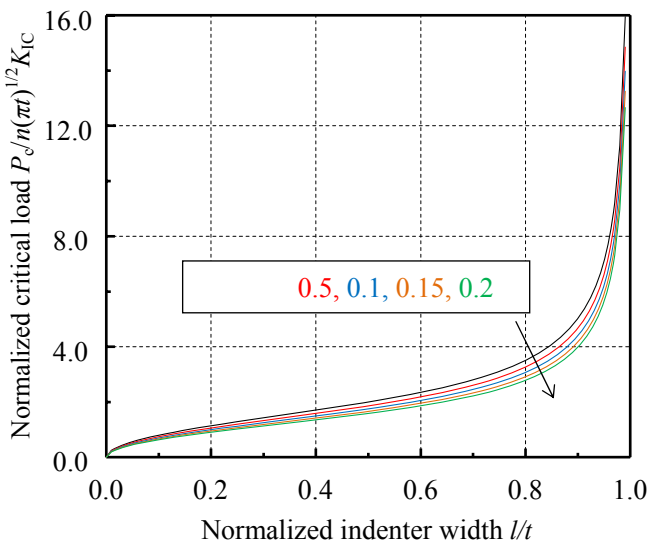

Fig.7. The effect of the normalized indenter width on the normalized critical load.

8. Conclusions

A fracture model of periodic indentation for rock cutting is proposed and formulated by using an energy-based method. The present approach specifies the contribution of indentation on the rock

cutting and provides a closed form solution for the energy release rate of mixed-mode boundary cracking as determined by the mixed mode singular stress field induced by the sliding contact. The driving forces in the form of J_i-integral for surface crack initiation at the contact boundary, the critical energy release rate and the critical load have been analytically determined. The critical cracking angles, critical loads have also been derived.

The present study shows that the frictional coefficient between the indenter and substrate uniquely characterizes the asymptotic singular stress field, and hence is considered as the primary parameter to determine the critical load of the indenter under the condition of slip near the edge of contact. The findings in this study may be helpful for establishing the damage mechanisms in the complex process of rock cutting by tools with the flat-tipped teeth.

Acknowledgement

This work was supported by National Natural Science Foundation of China (Grant Nos. 50771052 and 50971068, 11272141), Gledden Senior Fellowship from the University of Western Australia, and Natural Science Foundation of Liaoning (Grant Nos. LS2010100 and 20102129).

References

[1.] E. Giannakopoulos, T. C. Lindley, and S. Suresh, Aspects of connections and life-prediction methodology for fretting-fatigue. Acta Mater, 46 (1998) 2955-2968.
[2.] E. Giannakopoulos, T. A. Venkatesh, T. C. Lindley and S. Suresh, The role of adhesion in contact fatigue. Acta Mater, 47 (1999) 4653-4664.
[3.] B. Yang and S. Mall, On crack initiation mechanism in fretting fatigue. ASME J. Appl. Mech, 68 (2001) 76-80.
[4.] A. I. Nadai, Theory of flow and fracture of solids, McGraw-Hill, New York, 1963.
[5.] J. D. Eshelby, The force on an elastic singularity. Phil. Trans. Roy. Soc. London Ser. A, 244 (1951) 87-112.
[6.] G. C. Sih. Inelastic behaviour of solids. In: Sih GC editor. Dynamic aspects of crack aspects of crack propagation, New York: Mc-Graw-Hill Book, Co; 1969, p.607-639.
[7.] J. R. Rice, A path-independent integral and the approximate analysis of strain concentrated by notches and cracks. ASME J. Appl. Mech, 35 (1968) 379-386.
[8.] B. Budiansky and J. R. Rice, Conservation laws and energy-release rates. ASME J. Appl. Mech, 40 (1973) 201-203.
[9.] Y. J. Xie and D. A. Hills, Quasibrittle fracture beneath a flat bearing surface. Eng. Fract. Mech, 75 (2008) 1223–1230.
[10.] Y. J. Xie, X. Z. Hu, and X. H. Wang, Frictional contact induced crack initiation in incompressible substrate. Eng Fract Mech. 2011; 78: 2947–2956.
[11.] Y. J. Xie, A Theory on Cracked Pipe. Int. J. Press. Vessel. and Pip, 75 (1998) 865-869.
[12.] Y. J. Xie, X. Zhang and X. H. Wang, An exact method on penny-shaped cracked homogeneous and composite cylinders. Int. J. Solid. and Struct, 38 (2001) 6953-6963.
[13.] Y. J. Xie, An analytical method on circumferential periodic cracked pipes and shells. Int. J. Solid. and Struct, 37 (2000) 5189-5201.
[14.] H. Tada, P. C. Paris and G. R. Irwin, The stress analysis of cracks handbook (2nd Ed.), Paris Productions, Inc., St. Louis, 1985.
[15.] A. Griffith. The Phenomena of rupture and flow in solids. Phil. Trans. Roy. Soc. London Ser. A, 221 (1921) 163-198.
[16.] G. P. Cherepanov, Mechanics of brittle fracture, McGraw-Hill International Book Co, New York, 1979.

Theoretical Analysis of Effects of Confining Pressure on the Stress Intensity Factors for Cracked Brazilian Disk

Jigang Xu[1], Shiming Dong[1*], Zhenlin Wang[1]

[1]College of Architecture and Environment, Sichuan University, Chengdu 610065, China
* Corresponding author: smdong@scu.edu.cn

Abstract: In order to investigate effects of confining pressure on the stress intensity factors for a cracked Brazilian disk, the closed-form expressions of the stress intensity factors were obtained by using the weight function method in fracture mechanics for the cracked Brazilian disk loaded by the confining pressure, and then the explicit expressions of the stress intensity factors were achieved under both the confining pressure and diametrical forces loading condition. Based on the formulas of the stress intensity factors, effects of confining pressure on stress intensity factors of the cracked Brazilian disk was analyzed. The analyzed results show that the confining pressure has no effects on the mode II stress intensity factor, however, mode I stress intensity factors decrease with the increasing confining pressure. In addition, effects of confining pressure on the loading condition of pure mode II crack were also investigated. The analyzed results show that the critical loading angle for pure mode II crack decreases gradually to 0 degree with the increasing confining pressure.

Key Words: cracked Brazilian disk, stress intensity factor, confining pressure, critical loading angle

1. Introduction

Fracture toughness is an important parameter to describe the mechanical behavior of brittle materials and fracture toughness test is one of the main tasks of the fracture mechanics. How to accurately test fracture toughness of brittle materials has been studied by many researchers. It is very important to select a Suitable specimen for performing fracture toughness tests. The cracked Brazilian disk has been widely used for fracture toughness test of brittle materials as its closed-form solutions of the stress intensity factors can be achieved [1,2], and it can be easily achieved pure mode I, pure mode II and mixed-mode (I-II). Liu et al.[3] used the cracked Brazilian disk to measure the fracture toughness of fiber-reinforced composite material. Dong et al.[4,5] conducted the Brazilian disk test to investigate the static and dynamic fracture mechanical properties of PMMA. Nasseri et al.[6] conducted the Brazilian disk test to study the anisotropy of granite fracture toughness. However, most of the fracture toughness tests were conducted in a situation without confining pressure by now. This is not consistent with the actual working condition of some materials. As we know, many practical engineering structure materials serve in situation with confining pressure, such as underground rocks, structures in the deep water and so on. However, the material mechanical properties under the action of confining pressure are different from the properties under without confining pressure [7]. In order to investigate effects of confining pressure on the fracture toughness of brittle materials, many researchers have performed the fracture toughness experiments under the confining pressure loading conditions. But there were some unsolved problems in their experimental principle. For example, Al-Shayea et al.[8] have studied the effects of confining pressure on fracture toughness of a limestone rock using straight notched Brazilian disk specimens and hydraulic fracturing technique. They calculated rock mode I and mode II stress intensity factors by using the approximation formulas proposed by Atkinson et al.[1] and the variation of fracture toughness was found to be linearly

proportional to confining pressure from 0 to 28MPa. In addition, they compared their experimental results with some similar results proposed by other researchers and found that the tendency of fracture toughness increased with the increasing confining pressure was basically consistent but the corresponding relation of fracture toughness for different rocks was not the same, and some relationship were nonlinear. It is necessary to point out that this method belongs to Brazilian disk experiment under both confining pressure and diametrical forces loading condition. The validity and reliability of the results obtained by using the stress intensity factor formulas which only consider concentrated load regardless of confining pressure to calculate the stress intensity factors(or fracture toughness) under both the confining pressure and diametrical forces loading condition are debatable. And, whether or not the critical loading condition (or critical loading angle) for pure mode II crack under both the confining pressure and diametrical forces is the same with the critical loading condition (or critical loading angle) for pure mode II crack under diametrical forces has to be discussed. Lou et al.[9] designed a test system of the mode I and mode II fracture toughness for rocks using Brazilian disk specimens and hydraulic fracturing technique on MTS multifunctional material testing machine, and calculated the mode I and mode II stress intensity factors by using the approximation formulas proposed by Atkinson et al.[1]. They analyzed the effects of specimen size, confining pressure and other factors on the mode I and mode II fracture toughness of rocks according to the experimental data. The results showed that: both of the mode I and mode II fracture toughness increased with the increasing confining pressure in a certain pressure range, but the trend was not obvious under high confining pressure. Their experiment principle and calculation formula of stress intensity factors are similar to Al-Shayea's method and formula [8], and have similar problems.

Therefore, how to evaluate effects of confining pressure on the stress intensity factors and critical loading angle for pure mode II crack is an important problem, and is worth of further investigating. It will provide the theoretical foundations for conducting fracture toughness tests under confining pressure. In the present paper, based on the formula of the stress intensity factors for central cracked circular disk subjected to diametrical forces, the closed-form expressions of the stress intensity factors for central cracked circular disk subjected to confining pressure was obtained firstly and then the explicit expressions of the stress intensity factors were achieved under both the confining pressure and diametrical forces loading condition. Finally, the effects of confining pressure on the stress intensity factors and critical loading angle was analyzed.

2. Stress intensity factors for Cracked Brazilian Disk under confining pressure

2.1 Stress components for uncracked Brazilian Disk under confining pressure

The schematic diagram of an uncracked Brazilian disk under confining pressure is shown in Fig.1. The thickness of the disk is B and the radius is R .

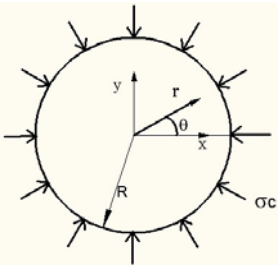

Fig.1 Uncracked Disk under confining pressure

The disk is assumed to be made of isotropic elastic material and obey the small deformation hypothesis. The stress distributions in the disk relative to a polar coordinate system can be obtained based on the elasticity theory [10] as

$$\sigma_r = -\sigma_c \ , \sigma_\theta = -\sigma_c \ , \ \tau_{r\theta} = 0 \tag{1}$$

2.2 Stress intensity factors for cracked disk under confining pressure

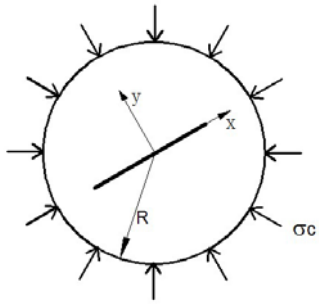

Fig.2 Cracked Brazilian Disk under confining pressure loading

The weight function method is used to calculate the stress intensity factors for the cracked disk. The cracked Brazilian disk subjected to confining pressure σ_c is shown in Fig.2. The x-axis lies in the crack plane. The coordinate origin is located at the center of the disk. a is the half length of the crack, R is the disk radius and B is the thickness. Then the $K_I^{'}$ and $K_{II}^{'}$ can be given as

$$K_{\mathrm{I}}^{'} = \int_0^a h_1(x,a)\sigma_\theta(x)dx \tag{2}$$

$$K_{\mathrm{II}}^{'} = \int_0^a h_2(x,a)\tau_{r\theta}(x)dx \tag{3}$$

where h_1 and h_2 are weight functions, $\sigma_\theta, \tau_{r\theta}$ are the stress components of the uncracked Brazilian disk under confining pressure. Specifically, h_1 and h_2 can be expressed as [11]:

$$h_1(x,a) = \frac{2}{\sqrt{\pi a}}[\frac{1}{\sqrt{1-\rho_1^2}} + c_{11}\sqrt{1-\rho_1^2} + c_{12}(1-\rho_1^2)^3] \tag{4}$$

$$h_2(x,a) = \frac{2}{\sqrt{\pi a}}[\frac{1}{\sqrt{1-\rho_1^2}} + c_{21}\sqrt{1-\rho_1^2} + c_{22}(\sqrt{1-\rho_1^2})^3] \tag{5}$$

where

$$c_{11} = \frac{8-4\alpha+3.8612\alpha^2-15.9344\alpha^3+24.6076\alpha^4-13.234\alpha^5}{\sqrt{1-\alpha}} - 8 \tag{6}$$

$$c_{12} = \frac{-8+4\alpha-0.6488\alpha^2+14.1232\alpha^3-24.2696\alpha^4+12.596\alpha^5}{\sqrt{1-\alpha}} + 8 \tag{7}$$

$$c_{21} = \frac{5-2.5\alpha+1.4882\alpha^2-2.376\alpha^3+1.1028\alpha^4}{\sqrt{1-\alpha}} - 5 \tag{8}$$

$$c_{22} = \frac{-4+2\alpha+0.4888\alpha^2+0.81112\alpha^3-0.7177\alpha^4}{\sqrt{1-\alpha}} + 4 \tag{9}$$

（$\alpha = a/R, \rho_1 = x/a$）

By substituting Eqs.(1) and (4) into Eq.(2), respectively, the following explicit formula of the stress intensity factors can be yielded as

$$K_{\mathrm{I}}^{'} = -\sigma_c \sqrt{\pi a}\, f_{11} \tag{10}$$

where $f_{11} = 1 + \frac{1}{2}c_{11} + \frac{3}{8}c_{12}$. It is clear, for $\tau_{r\theta} = 0$, $K_{\mathrm{II}}^{'} = 0$.

2.3 Stress intensity factors under both confining pressure and diametrical forces loading condition

The cracked disk subjected to a pair of diametral-compressive force P and ambient confining pressure σ_c is shown in Fig.3. a is the half length of the crack, the disk radius is R and thickness is B, θ is the loading angle (the angle of inclination of the crack relative to the line of loading). The stress intensity factors for cracked Brazilian disk subjected to a pair of diametral-compressive P have been given as [2]

$$K_{\mathrm{I}}^{''} = \sigma\sqrt{\pi a}[\, f_{11} + 2\sum_{i=1}^{n} A_{1i} f_{1i} \alpha^{2(i-1)}] \tag{11}$$

$$K_{\mathrm{II}}^{''} = 2\sigma\sqrt{\pi a}\sum_{i=1}^{n} A_{2i} f_{2i} \alpha^{2(i-1)} \tag{12}$$

where $\sigma = \frac{P}{\pi BR}$, coefficients f_{ji} and angle coefficients A_{ji} (j=1,2; i=1,2,…...n) are shown in the literature[2].

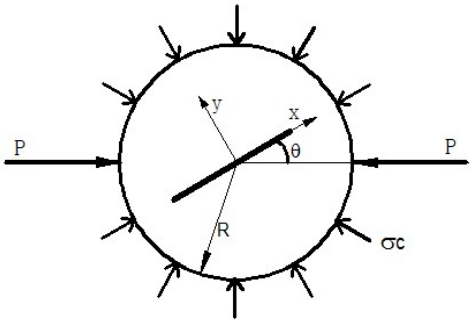

Fig.3 Cracked Brazilian Disk under both confining pressure and diametrical forces loading

Now, based on the diametral-compressive P load, the confining pressure (σ_c) was applied. By employing the superposition principle of stress intensity factors [12], the stress intensity factors for cracked Brazilian disk under both confining pressure σ_c and diametrical forces P can be obtained

$$\begin{aligned} K_{\mathrm{I}} &= K_{\mathrm{I}}^{'} + K_{\mathrm{I}}^{''} \\ &= -\sigma_c\sqrt{\pi a}\, f_{11} + \sigma\sqrt{\pi a}[\, f_{11} + 2\sum_{i=1}^{n} A_{1i} f_{1i} \alpha^{2(i-1)}] \\ &= (\sigma - \sigma_c)\sqrt{\pi a}\, f_{11} + 2\sigma\sqrt{\pi a}\sum_{i=1}^{n} A_{1i} f_{1i} \alpha^{2(i-1)} \end{aligned} \tag{13}$$

By letting $\sigma_c / \sigma = t$, then $\sigma_c = t\sigma$. Where t is a dimensionless scaling factor (simply called confining pressure coefficient) and different confining pressure coefficients are correspond to different confining pressures. Then K_I can be written as

$$K_{\mathrm{I}} = \sigma(1-t)\sqrt{\pi a}\, f_{11} + 2\sigma\sqrt{\pi a}\sum_{i=1}^{n} A_{1i} f_{1i} \alpha^{2(i-1)} \tag{14}$$

The normalized stress intensity factor, F_I may be written as

$$F_{\mathrm{I}} = \frac{K_{\mathrm{I}}}{\sigma\sqrt{\pi a}} = (1-t) f_{11} + 2\sum_{i=1}^{n} A_{1i} f_{1i} \alpha^{2(i-1)} \tag{15}$$

For $K_{II}^{'}=0$, $K_{II}=K_{II}^{'}+K_{II}^{''}=K_{II}^{''}$, which means that confining pressure σ_c has no effects on mode II stress intensity factor. Eq. (12) can still be used to calculate mode II stress intensity factors under both confining pressure and diametrical forces loading condition.

3. Effects of confining pressure on stress intensity factors

To investigate the effects of the confining pressure on the stress intensity factors, according to Eq. (15), we take t=0. 1、0. 5、1. 0, respectively, and calculate the mode I stress intensity factors F_I for different relative crack length α and loading angle θ. The calculated results are shown in Fig.4.

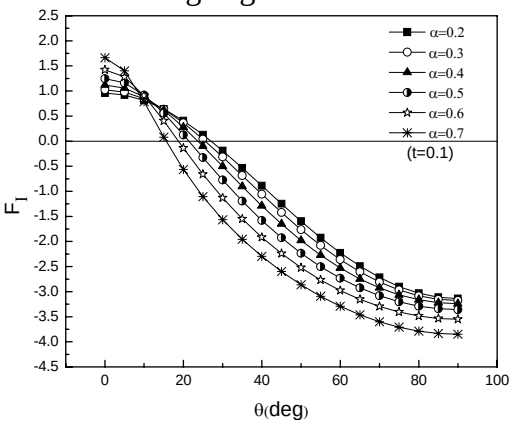

(a) t=0.1

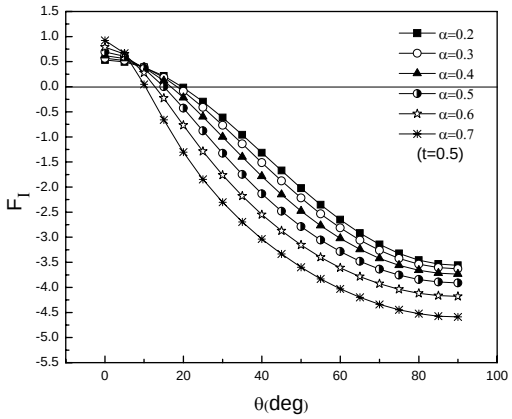

(b) t=0.5

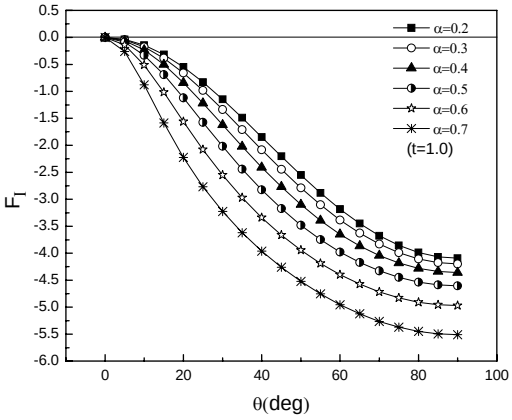

(c) t=1.0

Fig.4 Normalized stress intensity factors F_I for different confining pressures

In addition, in order to further analyze the effects of confining pressure on the stress intensity

factors, taking α =0.3、0.5、0.7 as example, we calculate the mode I stress intensity factors F_I for fixed relative crack length but different confining pressures. Results are shown in Fig.5.

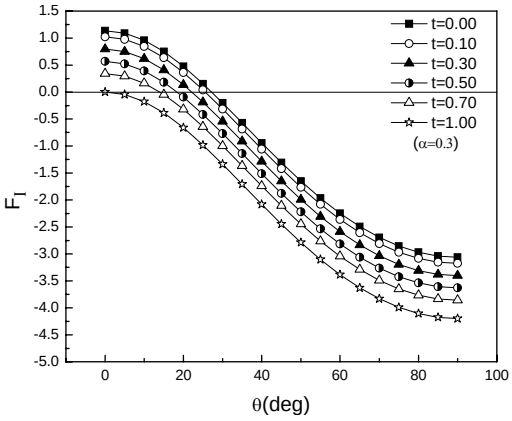

(a) $\alpha = 0.3$

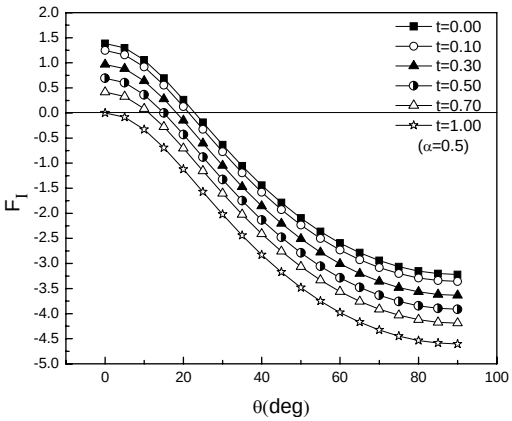

(b) $\alpha = 0.5$

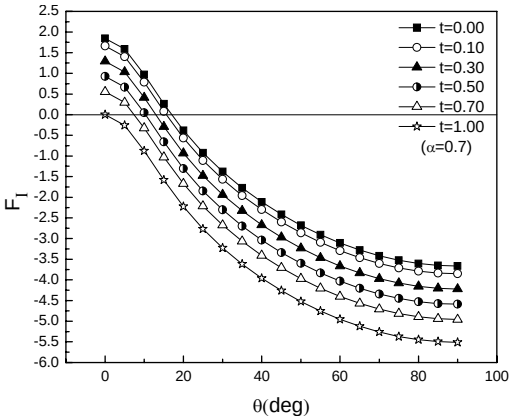

(c) $\alpha = 0.7$

Fig.5 Effects of confining pressure on stress intensity factors for a fixed relative crack length

The Fig.4 and Fig.5 show that confining pressure significantly influences the mode I stress intensity factors for cracked Brazilian disk. The mode I stress intensity factors decrease with the increasing confining pressure at any relative crack length. When the confining pressure coefficient (t) is less than 1, the mode I stress intensity factors for cracked Brazilian disk always change from positive to negative with the increasing the loading angle. However, the mode I stress intensity factors will always be negative values for any relative crack length while the confining pressure coefficient t>1. Due to the mode I stress intensity factors are negative, crack will be closed, and hence, we cannot test the pure mode I fracture toughness when the confining pressure coefficient t>1.

4. Effects of confining pressure on pure mode II crack loading condition

According to the definition of the pure mode I loading and pure mode II loading, the pure mode II crack can be determined from the conditions that $K_{\mathrm{I}}=0$, $K_{\mathrm{II}}\neq 0$. By letting $K_{\mathrm{I}}=0$ in Eq.(14), we get

$$(1-t)f_{11}+2\sum_{i=1}^{n}A_{1i}f_{1i}\alpha^{2(i-1)}=0 \qquad (16)$$

It's not easy to directly achieve the closed-form solutions from Eq. (16), but the solution is $\theta=\theta(t,\alpha)$ which means that the pure mode II loading angle is the function of α and *t*. According to Eq. (16), we develop a small program to compute the critical loading angle θ_c for various α and different coefficients t, the results are listed in Table 1.

Tab.1 the critical loading angles θ_c(°) for pure mode II crack with different confining pressures

α	θ_c(°)						
	t=0[2]	t=0.1	t=0.3	t=0.5	t=0.7	t=1.0	t>1
0	30.00	28.32	24.73	20.70	15.89	0	No real solution
0.1	29.67	28.00	24.43	20.44	15.67	0	No real solution
0.2	28.72	27.06	23.56	19.66	15.05	0	No real solution
0.3	27.23	25.60	22.20	18.45	14.07	0	No real solution
0.4	25.27	23.70	20.43	16.89	12.81	0	No real solution
0.5	22.93	21.40	18.30	15.02	11.31	0	No real solution
0.6	20.18	18.72	15.82	12.84	9.58	0	No real solution
0.7	16.96	15.57	12.92	10.33	7.60	0	No real solution
0.8	13.07	11.79	9.49	7.41	5.35	0	No real solution
0.9	8.17	7.05	5.32	3.99	2.81	0	No real solution

From Table 1 we can know that the confining pressure significantly influences the loading condition of pure mode II crack. As the confining pressure increases, the critical loading angle for pure mode II crack decreases gradually to 0 degree.

5. Discussion

5.1 Mode I fracture toughness under confining pressure

According to the experiment results in the literature [8], the fracture toughness increases with the increasing confining pressure (Fig.6). Al-Shayea et al.[8] used the five-term approximation formula proposed by Atkinson et al.[1] to calculate the mode I stress intensity factors, which is equivalently letting n=5 in Eq.(11). They ignored the effects of confining pressure on stress intensity factors; therefore, the failure load $P_{\max}$ increased with the increasing confining pressure and thus the test values of the fracture toughness increased with the confining pressure. However, according to Eq.(14) presented in this paper, mode I stress intensity factors decrease with the increasing confining pressure. Under confining pressure loading condition, though the test values of the failure load increase, but part of the load has to offset the 'negative effect' caused by confining pressure on K_I. So according to Eq.(14), though the failure load show an increase with the increasing confining pressure, the fracture toughness may be unchanged actually.

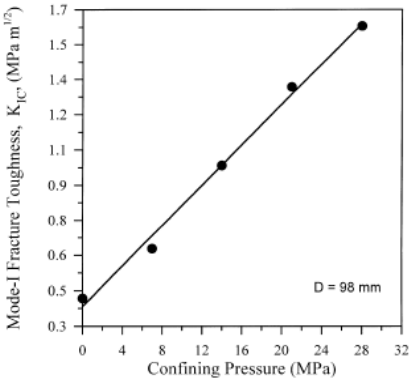

Fig. 6 Variation of mode-I fracture toughness under confining pressure **[8]**

5.2 Mode II fracture toughness under confining pressure loading

For loading angle $\theta = 0°$, we usually think that materials will produce the pure mode I fracture. Now, this viewpoint may be reasonable only under without or low confining pressure loading conditions, the fracture mode of materials may be pure mode II fracture around $0°$ loading angle under high confining pressure. On the other hand, according to the literature [2], for $\theta = 0°$, $K_{II} \equiv 0$, so the failure of the specimen is no longer pure fracture mechanics problem when the confining pressure coefficient $t \geq 1$.

In the literature [8], the critical loading angle of the pure mode II crack was calculated by using the five-term approximation formula proposed by Atkinson et al.[1] which ignored the effects of confining pressure. For example, when α=0.3, they used $\theta_c = 29°$. However, according to the present paper, the critical loading angle for pure mode II crack decreases with the increasing confining pressure.

6. Conclusion

(1) The stress intensity factors are obtained by using the weight function method in fracture mechanics for the cracked Brazilian disk loaded by the confining pressure, and then the explicit expressions of the stress intensity factors are achieved under both the confining pressure and diametrical forces loading condition, which can be used to calculate the stress intensity factors for any relative crack length and any confining pressure.

(2) Analyzed results show that confining pressure significantly influences the mode I stress intensity factors for the cracked Brazilian disk. The mode I stress intensity factors decrease with the increasing confining pressure, however, the confining pressure has no effects on the mode II stress intensity factors.

(3) Calculation results show that confining pressure significantly influences the loading condition for the pure mode II crack: as the confining pressure increases, the critical loading angle for pure mode II crack decreases gradually to 0 degree.

(4) The fracture mode of materials may be pure mode II around $0°$ loading angle under high confining pressure loading.

Acknowledgements

This work was supported by the National Natural Science Foundation of China (project no. 11172186) and the Program for Changjiang Scholars and Innovative Research Team (Project No. IRT1027)

References

[1] C Atkinson, RE Smelser, J Sanchez, Combined mode fracture via the cracked Brazilian disk test. Int J Fracture, 18(1982)279-291.

[2] SM Dong, Y Wang and YM Xia, Stress intensity factors for central cracked circular disk subjected to compression. Engng Fract Mech, 71(2004) 1135-114.

[3] C Liu, Y Huang, ML Lovato et al, Measurement of the fracture toughness of a Fiber-reinforced composite using the Brazilian disk geometry. Int J Fract, 87(1997)241-263.

[4] SM Dong, J Zhou, Y Wang et al, Experimental study on fracture behavior of PMMA under mixd-mode loading.Journal of Mechanical Strength , 28(2006) 556-561

[5] J Zhou, Y Wang, YM Xia, Mode-I fracture toughness of PMMA at high loading rates. J. Mater. Sci. 41(2006)8363-8366.

[6] MHB Nasseri, B Mohanty, Fracture toughness anisotropy in granitic rocks. Int J Rock Mech Min Sci, 45(2008)167-193.

[7] WN Chen，and Ravichandran G., Static and dynamic compressive behavior of aluminum nitride under moderate confinement. Journal of the American Ceramic Society, 79(1996)579-584.

[8] NA Al-Shayea, K Khan and SN Abduljauwad, Effects of confining pressure and temperature on mixed-mode (I-II) fracture toughness of a limestone rock. Int J Rock Mech Min Sci, 37(2000)629-643.

[9] YS Lou, M Chen, MY Shi et al, Measurement of type-I and type-II fracture toughness for rocks and its influence factors analysis. Journal of China University of Petroleum, 31(2007)85-89

[10] GQ Wang, GB Ding, CH Liu et al, Elasticity Mechanics, China Railway Publishing House, 2004

[11] T Fett, Stress intensity factors and T-stress for internally cracked circular disks under various boundary conditions. Engng Fract Mech, 68(2001)1119-1136.

[12] Anderson, TL, Fracture mechanics fundamentals and applications, CRC Press, 1991.

Separation of the Energy Release Rate of Fracture

Tianmin Guo

Siemens AG, Duisburger Straße 145, 47829 Krefeld, Germany

e-mail: tianmin.guo@gmail.com

Abstract

Formally, the Griffith's energy release rate, the Irwin's integral expression of crack closure energy and the Rice's J-integral give same results for linear elastic material. But let us ask a question: do these three approaches really give an exact mathematical equality and an identical physical meaning? For this purpose, a uniform equation was therefore introduced into our new investigation. Thus, not only the Irwin's integral expression of crack closure energy and the Rice's J-integral can be derived from this uniform equation, but a very important result has been also obtained from them: the energy release rate is separable into two parts. The first part describes the extension of the crack front surface and the second the distortion.

Keywords the Griffith's energy release rate, the Irwin's integral expression of crack closure energy, the Rice's J-Integral and the new found S_k-Integral und T_k-Integral

1. Introduction

Cracks and fractures are known natural phenomena and occur everywhere in our daily lives. They are mostly associated with catastrophic consequences. Therefore attempts have been made for a long time to understand and finally to master them.

As a pioneer, Griffith (1920) [2] has laid a foundation through examining these phenomena energetically. Based on the Inglis (1913) [1] identified stress and displacement field for an elliptical crack-like hole in an infinite plate, he has considered the energy balance and introduced a new quantity "energy release rate" into the fracture mechanics. His mind was so fundamental that it has always been of great importance for the further development of fracture mechanics. But his theory was limited only on linear elastic material behavior and mode I loading case.

Irwin (1957, 1964) [3, 4] expanded the Griffith's thought on complicated load cases and established a relationship between the energy release rate and the stress intensity factor. So the stress intensity factor for linear elastic material has been widely used.

A path-independent integral, the well-known J-integral was introduced by Cherepanov (1967) [11] and Rice (1968a) [7] into the fracture mechanics. Rice in particular has derived a connection between the Griffith's energy release rate and the J-integral and interpreted the J-integral as an extended energy release rate. Since that time, the J-integral rapidly disseminated and was used for elastic-plastic material in the fracture mechanics.

All this shows a significant development in the classical fracture mechanics and is the foundation of the fracture mechanics. The classical fracture mechanics has found variety applications for many different areas. However, it must be clearly mentioned that it can only describe the crack problem in relatively simple cases and under certain conditions. It is not yet able to handle and exactly describe complicated crack problems in both natural events as well as in everyday life and eventually to solve.

This situation can certainly not satisfy us and the problems mentioned above let us thoroughly think whether the foundation of the fracture mechanics is consistent and where and what has not

been considered.

The aim of this paper is to deal with such problems and to find a possible satisfactory solution. For this purpose it first has to deal with the existing theories systematically.

The investigation has the following assumptions: continuum mechanics of observation, stationary crack, quasi-static, small deformations, isotropic and linear elastic material behavior, elastic-plastic material behavior with power-law hardening and J_2 deformation theory.

There are other theories and attempts to deal with and to describe such problems. These are not part of this paper, and they are not discussed here.

2. The Classical Theories of Fracture Mechanics

2.1 Griffith's Theory

At first Griffith (1920) [2] published his fundamental work on the treatment of crack problems. He investigated an infinite plate with a crack-like elliptical hole under tension (Fig. 1) and gave an energy balance to this plate

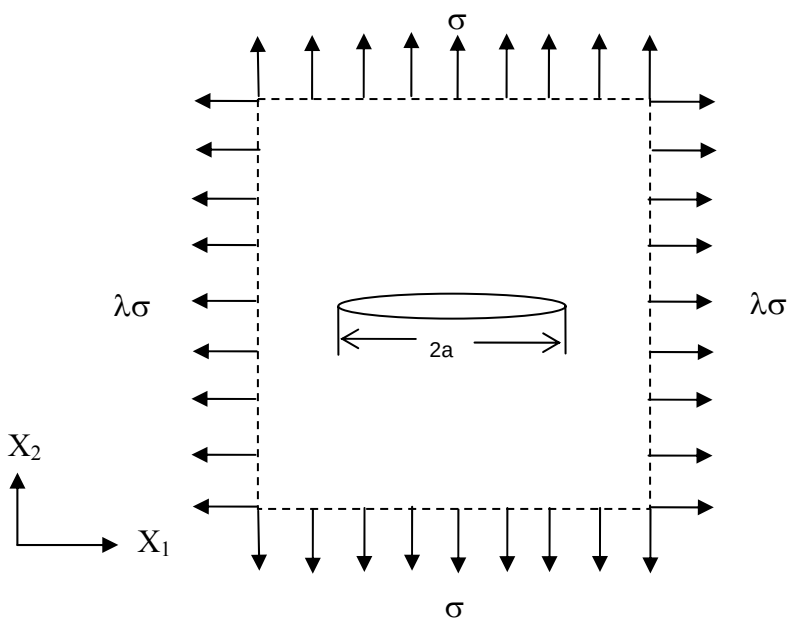

Fig. 1: an infinite plate with a crack-like elliptical hole under tension (Mode I)

$$\frac{\partial}{\partial a}(U - W - O) = \frac{\partial}{\partial a}(-\Pi - O) \geq 0\,, \tag{2.1}$$

where U is the work done by the external force, W the strain energy, $\Pi = -U + W$ the potential energy and O the surface energy.

Under consideration of the so-called “fixed-grips“ condition and with help of the stress and displacement field of Inglis (1913) [1] and by the vanish of the short axle of the ellipse he obtained following equation

$$\Pi = W = W_0 - \frac{\pi a^2 \sigma^2}{E'}\,, \tag{2.2}$$

where W_0 is the strain energy without crack, $E' = E$ for plane stress, $E' = E/(1-\nu^2)$ for plane strain, E is the elastic modulus and ν the Poisson's Ratio.

With Eq. (2.2) he got the energy release rate

$$G_I = -\frac{\partial \Pi}{\partial (2a)} = -\frac{\partial W}{\partial (2a)} = \frac{\sigma^2 a \pi}{E'} . \tag{2.3}$$

The index I denotes the mode I and the factor 2 means the whole elliptical crack length.

For the surface energy O he assumed the form

$$O = 4a\gamma , \tag{2.4}$$

where γ is the specific surface energy and should be a material constant. By substituting Eq. (2.3) and (2.4) into Eq. (2.1), the Eq. (2.1) becomes

$$G_I \geq 2\gamma . \tag{2.5}$$

With this, he predicted that the unstable crack growth occurs when the equation (2.5) is fulfilled.

From the Griffith's investigation it can be summarized:

His study is based on a two-dimensional, infinite plate with an elliptic crack-like hole under mode I loading case. He established the global energy balance for the whole body and recognized that under the fixed grips condition the strain energy change could only be considered and a residual amount of the strain energy change has to be given in order to proceed with the crack. This residual amount of energy divided by the crack change must have the same size or is larger than the surface energy, which then can create the new surface. From this energy, he has introduced a well-known fracture mechanics quantity which is referred to as "energy release rate".

It was unclear whether the Griffith's theory is applicable for general or complicated crack problems.

2.2 Irwin's Work

Irwin (1957, 1964) [3, 4] has attempted to answer the questions above. He extended Griffith's theory for mode I to mode II and III for linear elastic materials. Under consideration that the energy to close the crack (2.6)

$$I = \lim_{\Delta a \to 0} \frac{1}{\Delta a} \int_{A_1} \frac{1}{2} (\sigma_{12}^0 u_1^1 + \sigma_{22}^0 u_2^1 + \sigma_{23}^0 u_3^1) n_2^1 dA \tag{2.6}$$

has to be equal to the energy to extend the crack, he obtained a well-known equation

$$G = I = \frac{K_I^2}{E'} + \frac{K_{II}^2}{E'} + \frac{K_{III}^2}{E}(1+\nu) , \tag{2.7}$$

where σ_{ij} is the stress tensor, u_i the displacement vector and n_i the normal on the crack front surface. $(\,)^0$ refers to the state of the time t and $(\,)^1$ the state of the time $t + \Delta t$, A_1 is the crack front surface to the state of time $t + \Delta t$ and K_I, K_{II}, K_{III} are the stress intensity factors for mode I, mode II and mode III.

So, a connection between the global quantity "energy release rate" G and the crack front field "stress intensity factor" K was given. Nevertheless the problem is that the equation (2.6) includes σ_{ij}^{0}, u_i^1 und n_j^1 which refer to the different states of time. This makes the equation (2.6) difficult to use for complicated problems.

2.3 The J-Integral

The path-independent J-integral

$$J = \int_A (wn_1 - \sigma_{ij} u_{i,1} n_j) dA \tag{2.8}$$

was introduced by Cherepanov (1967) [11] und Rice (1968a) [7] into the fracture mechanics to determine some specific problems. The J-integral is not only applicable to linear elastic material but also used for hyper-elastic material. Specifically, Rice (1968b) [8] and Budiansky and Rice (1973) [9] have derived the relationship

$$-\frac{\partial \Pi}{\partial a} = \int_{A_0} wn_1 dA\,, \tag{2.9}$$

and by consideration of the traction-free crack surface the equation (2.9) is finally equal to the J-integral

$$-\frac{\partial \Pi}{\partial a} = J\,. \tag{2.10}$$

So the following Eq. (2.11)

$$J = G = \frac{K_I^2}{E'} + \frac{K_{II}^2}{E'} + \frac{K_{III}^2}{E}(1+\nu) \tag{2.11}$$

is obtained, which is valid for linear elastic material, where w is the strain energy density, A_0 the crack front surface to the state of time t, A the area refers to any path in body, σ_{ij} the stress tensor, u_i the displacement vector and n_i the normal and $(\,)_{,1} = \partial(\,)/\partial x_1$.

It is seen above that for linear elastic material, the J-integral is both equal to the Griffith's energy release rate Eq. (2.10) and supplies the same result as from the Eq. (2.7) provided by Irwin. It is also applicable to elastic-plastic material. Thus, the J-integral became important in fracture mechanics and particularly for elastic-plastic material.

However, it can be recognized from the equations (2.6) and (2.8), that on the one hand the two equations Eq. (2.6) and Eq. (2.8) seem to be quite different, although they provide identical results (Eq. (2.7) and Eq. (2.11)), and on the other hand that the two integrals refer to different crack front surfaces, whereby the equation (2.6) to the crack front surface is linked to the time $t + \Delta t$, and the equation (2.8) is linked to the time t.

Due to the different formulations of the above theories we can provide the following questions:

- Do the Griffith's energy release rate G, the Irwin's I-integral expression of the crack closure energy and the Rice's J-integral really describe the same fact?
- Is there a uniform rule from which the different equations as Eq. (2.6) and Eq. (2.8) can be derived?
- Does new knowledge hide behind this difference?

To answer these questions requires us to conduct a thorough analysis in the next chapter.

3. Uniform Formulations of the Energy Release Rate

3.1 General Formulations

Let us first consider the change of the potential energy in a cracked elastic body shown in Figure 2(a), where the deformation of the crack front surface is adopted as shown in Figure 2(b),

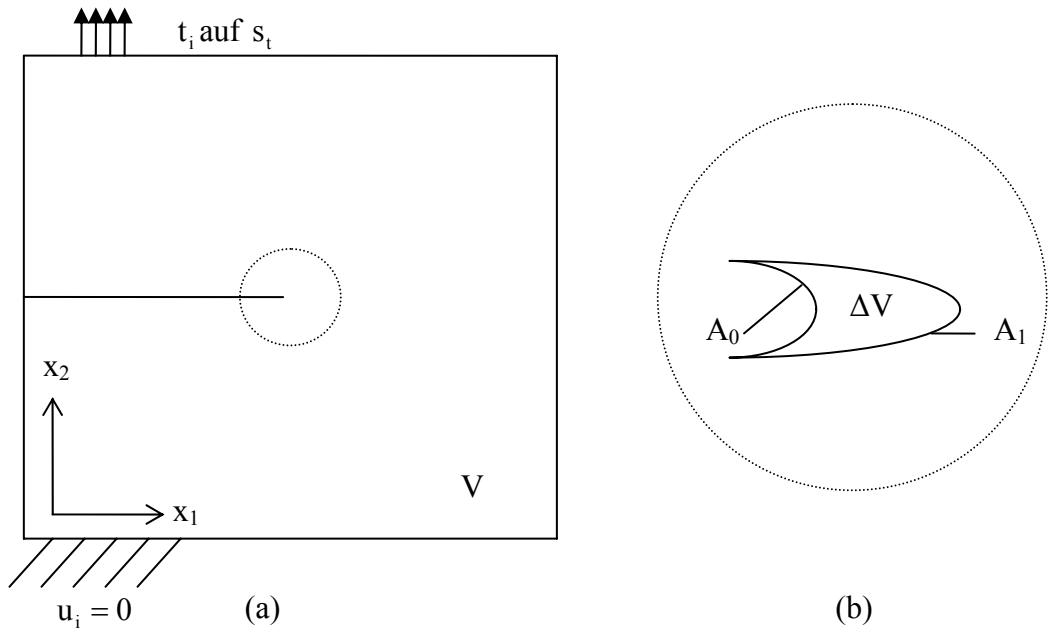

Fig. 2: (a) a cracked body, (b) the crack front field

$$\dot{\Pi} = (W - U)^{\bullet} = \frac{d}{dt}\int_{v} w dV - \frac{d}{dt}\int_{s_t} t_i u_i dA . \tag{3.1}$$

In the above equation Π is the potential energy, W is the strain energy, w is the specific strain energy, U is the work done by the external force, σ_{ij} is the stress tensor, ε_{ij} is the strain tensor, u_i is the displacement vector, t_i the force on the surface s_t and V the volume, $\dot{(\,)} = d/dt$ is the material time derivative and t the time-like parameter. It follows

$$\dot{\Pi} = \int_{V} \dot{w}\, dV - \int_{s_t} t_i \dot{u}_i\, dA + \lim_{\Delta t \to 0} \frac{1}{\Delta t} \int_{\Delta V} w(t + \Delta t) dV . \tag{3.2}$$

By looking at the first and the second term in the equation (3.2) and by the use of the Gaussian theorem, the terms cancel each other, so we get

$$\dot{\Pi} \quad = \quad \lim_{\Delta t \to 0} \frac{1}{\Delta t} \int_{\Delta V} w(t + \Delta t) dV . \tag{3.3}$$

This equation (3.3) is the basic equation from which we can derive different quantities.

3.2 Conventional Derivation

From the basic equation (3.3) Rice (1968b) [8], Eshelby (1970, 1956) [5, 6] and Budiansky & Rice received (1973) [9] a relation. For this, we give here the same formulation as by Budiansky & Rice (1973) [9] written:

$$\dot{\Pi} = \lim_{\Delta t \to 0} \frac{1}{\Delta t} \int_{\Delta V} w(t+\Delta t) dV = \int_{A_0} w\, v_i\, m_i dA\,, \tag{3.4}$$

where v_i is the velocity and m_i the normal outward. By substituting $v_i = \delta_{ik}$, $m_i = -n_i$ and $\xi_k \equiv -\dot{\Pi}$, we obtain

$$\xi_k = \int_{A_0} w\, n_k dA\,. \tag{3.5}$$

By consideration of traction-free crack surface it follows

$$\xi_k = J_k \tag{3.6}$$

and

$$J_k = \int_A (w\, n_k - \sigma_{ij} u_{i,k} n_j) dA\,, \tag{3.7}$$

where Eq. (3.6) is Eshelby's result [5] and J_k is the Integral derived by Knowles & Sternberg (1971/1972) [10] and with k = 1 J_k is the J-Integral

$$J_1 = J. \tag{3.8}$$

Thus, the connection between the J_k integral and the energy release rate has been established.

3.3 A New and Generalized Way to Derive the Irwin's I-integral

Let us now consider the specific strain energy w in Eq. (3.3) for linear elastic material

$$w(t+\Delta t) = w^1 \approx (\sigma_{ij}^0 \varepsilon_{ij}^1 + \Delta\sigma_{ij} \varepsilon_{ij}^0)/2\,. \tag{3.9}$$

The term $\Delta\sigma_{ij}\Delta\varepsilon_{ij}/2$ in the above equation has disappeared because of having an infinitesimal size of higher order. By substituting Eq. (3.9) into Eq. (3.3) and under consideration of the equilibrium condition $\sigma_{ij,j} = 0$ and the traction-free crack surface as well as with help of the Gaussian theorem, it follows

$$\dot{\Pi} = \lim_{\Delta t \to 0} \frac{1}{\Delta t} \int_{\Delta V} \frac{1}{2} \sigma_{ij}^0 \varepsilon_{ij}^1 dV = \lim_{\Delta t \to 0} \frac{1}{\Delta t} \int_{A_1} \frac{1}{2} \sigma_{ij}^0 u_i^1 m_j^1 dA\,. \tag{3.10}$$

In the Eq. (3.10) the expression $\lim_{\Delta t \to 0} \frac{1}{\Delta t} \int_{\Delta V} \frac{1}{2} \Delta\sigma_{ij} \varepsilon_{ij}^0 dV$ vanishes, which can be proved by using the mean value theorem of the integral

$$\lim_{\Delta t \to 0} \frac{1}{\Delta t} \int_{\Delta V} \frac{1}{2} \Delta\sigma_{ij} \varepsilon_{ij}^0 dV = \lim_{\Delta t \to 0} \frac{1}{\Delta t} \frac{1}{2} (\Delta\sigma_{ij} \varepsilon_{ij}^0)_M \Delta V = 0\,,$$

where M is a certain point in the volume ΔV.

By substituting $I^* = -\dot{\Pi}$ and $m_i = -n_i$ and by replacing t with the actual crack length a into (3.10), we get the generalized equation

$$I^* = \lim_{\Delta a \to 0} \frac{1}{\Delta a} \int_{A_1} \frac{1}{2} \sigma_{ij}^0 u_i^1 n_j^1 dA \,. \tag{3.11}$$

For a special case of j = 2 it follows

$$I = I^*\big|_{j=2} = \lim_{\Delta a \to 0} \frac{1}{\Delta a} \int_{A_1} \frac{1}{2} (\sigma_{12}^0 u_1^1 + \sigma_{22}^0 u_2^1 + \sigma_{32}^0 u_3^1) n_2^1 dA \,. \tag{3.12}$$

This is the Irwin's equation (2.6).

In the equation (3.11) it is seen that they have the quantities σ_{ij}^0, u_i^1 and n_j^1 which relate to the different times. As mentioned above, this leads to a difficult use of the equation (3.11) for complicated problems.

4. Separation of the Energy Release Rate and Introduction of Two New Quantities

4.1 A New Vector Quantity S_k for Describing the Crack Front Extension

The specific strain energy w in Eq. (3.3) for linear elastic material has an another form

$$w(t + \Delta t) = w^1 \approx (\sigma_{ij}^1 \varepsilon_{ij}^0 + \sigma_{ij}^0 \Delta\varepsilon_{ij}) / 2 \,. \tag{4.1}$$

The term $\Delta\sigma_{ij}\Delta\varepsilon_{ij} / 2$ in the above equation has also disappeared because of having an infinitesimal size of higher order. By substituting the Eq. (4.1) into Eq. (3.3) and by considering the equilibrium condition $\sigma_{ij,j} = 0$ and the traction-free crack surface as well as by using the Gaussian theorem, it follows

$$\dot{\Pi} = \lim_{\Delta t \to 0} \frac{1}{\Delta t} \int_{\Delta V} \frac{1}{2} \sigma_{ij}^1 \varepsilon_{ij}^0 dV = \lim_{\Delta t \to 0} \frac{1}{\Delta t} \int_{A_0} \frac{1}{2} \sigma_{ij}^1 u_i^0 m_j^0 dA \,. \tag{4.2}$$

In the Eq. (4.2) the expression $\lim_{\Delta t \to 0} \frac{1}{\Delta t} \int_{\Delta V} \frac{1}{2} \sigma_{ij}^0 \Delta\varepsilon_{ij} dV$ vanishes, which can be also proved by using the mean value theorem of the integral

$$\lim_{\Delta t \to 0} \frac{1}{\Delta t} \int_{\Delta V} \frac{1}{2} \sigma_{ij}^0 \Delta\varepsilon_{ij} dV = \lim_{\Delta t \to 0} \frac{1}{\Delta t} \frac{1}{2} (\sigma_{ij}^0 \Delta\varepsilon_{ij})_M \Delta V = 0 \,,$$

where M is a certain point in the volume ΔV.

The equation (4.2) is new and will therefore be used furthermore to derive a new quantity. Now we consider the above equation (4.2)

$$\lim_{\Delta t \to 0} \frac{1}{\Delta t} \int_{A_0} \frac{1}{2} \sigma_{ij}^1 u_i^0 m_j^0 dA = \int_{A_0} \frac{1}{2} \frac{\partial \sigma_{ij}}{\partial t} u_i m_j dA \,. \tag{4.3}$$

Since t is a time-like parameter and can be replaced by the actual crack extension a for the quasi-static problem, it follows with help of $m_i = -n_i$ and by use of the directional derivative

$$-\frac{d\Pi}{da} = l_k \int_{A_0} \frac{1}{2} \sigma_{ij,k} u_i n_j dA \,, \tag{4.4}$$

where l_k is the direction vector of the crack extension. Now we get a new quantity, which is denoted with S_k

$$S_k = \int_{A_0} \frac{1}{2} \sigma_{ij,k} u_i n_j dA . \tag{4.5}$$

Then the Eq. (4.4) can be written as follows

$$-\frac{d\Pi}{da} = l_k S_k . \tag{4.6}$$

By using the above equation (4.5) and by help of the Gaussian theorem as well as by considering $\sigma_{ij,j} = 0$ and $\varepsilon_{ij} = (u_{i,j} + u_{j,i})/2$, we can derive a path-independent integral by converting

$$\oint_B \frac{1}{2} \sigma_{ij,k} u_i n_j dA = \int_V \frac{1}{2} \sigma_{ij,k} u_{i,j} dV = \oint_B \frac{1}{2} w^c n_k dA , \tag{4.7}$$

where w^c is the complementary energy density and B is an arbitrary closed area in the body. Since $w = w^c$ for linear elastic material, it follows

$$\oint_B \frac{1}{2} \sigma_{ij} u_{i,k} n_j dA = \oint_B \frac{1}{2} w n_k dA . \tag{4.8}$$

Finally, we can form a new quantity

$$\oint_B \frac{1}{2} (\sigma_{ij,k} u_i - \sigma_{ij} u_{i,k}) n_j dA , \tag{4.9}$$

which always vanishes. By consideration of the traction-free crack surface and B=A+(-A_0) we can then write

$$S_k = \int_{A_0} \frac{1}{2} \sigma_{ij,k} u_i n_j dA = \int_A \frac{1}{2} (\sigma_{ij,k} u_i - \sigma_{ij} u_{i,k}) n_j dA . \tag{4.10}$$

Based on the Griffith's energy release rate we have derived a new vector quantity S_k from the basic equation (3.3), which has an integral form (4.5). This integral is path-independent (4.9) and describes the crack front extension.

However, it must be clearly stated that the two equations (3.11) and (4.4) are derived only under the condition that the deformation of the crack front surface is assumed as in Figure 2. Whether this assumption is true for the real deformation of the crack front surface has yet to be thoroughly analyzed and investigated. To answer this question we have to continue considering the basic equation (3.3) even more precisely.

4.2 A Second New Vector Quantity T_k for Describing the Crack Front Distortion

From the basic equation (3.3), we have handled the strain energy density and generated two important results: a) the first form (3.9) leads to a generalized Irwin's integral expression of crack closure energy, b) the second form (4.1) provides a new vector quantity S_k, which has an integral form, and this integral is path-independent.

Now the question arises whether S_k is a single quantity which can be obtained from the basic equation (3.3) and what and where has not been taken into account.

Therefore, we must again consider the basic equation (3.3) accurately. In the above consideration

we have tacitly assumed, that the volume fraction of ΔV is like in Figure 2, without analyzing it. To check whether this assumption for the deformation of the actual crack front surface is true, the deformation of the crack front surface must be again examined carefully. Let us now consider the body with cracks (Fig. 1) again. Under loading, the crack will extend and at the same time it will open, as shown below in Figure 3. As already known, only a small crack front surface will help for crack growth. Thus, the volume fraction ΔV must be included by surfaces A_0, A_1 and A_β. Especially the surface A_β describes the crack opening and this has been neglected until now.

By using the Gaussian theorem the basic equation (3.3) can be written in the new volume fraction ΔV (Fig. 3) as follows

$$\dot{\Pi} = \lim_{\Delta t \to 0} \frac{1}{\Delta t} \int_{\Delta V} \frac{1}{2} \sigma_{ij}^{1} \varepsilon_{ij}^{0} dv = \lim_{\Delta t \to 0} \frac{1}{\Delta t} \int_{A_0} \frac{1}{2} \sigma_{ij}^{1} u_i^0 m_j^0 dA + \lim_{\Delta t \to 0} \frac{1}{\Delta t} \int_{A_\beta} \frac{1}{2} \sigma_{ij}^{1} u_i^0 m_j^\beta dA . \tag{4.11}$$

The first term of equation (4.10) has already been dealt above. The second term is new and we will study it more precisely now. By replacing the time t with the crack length a and by use of the Stockes's theorem, the second term can be reformulated as follows

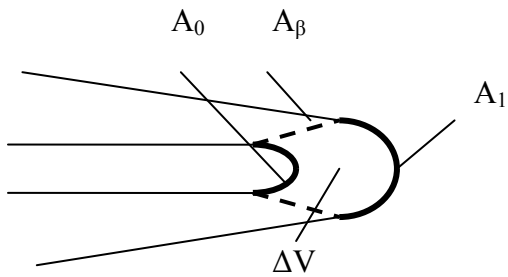

Fig. 3: real deformation of the crack front surface

$$\lim_{\Delta t \to 0} \frac{1}{\Delta t} \int_{A_\beta} \frac{1}{2} \sigma_{ij}^{1} u_i^0 m_j^\beta dA = -l_k \int_{A_0} \frac{1}{2} \varepsilon_{qml} \varepsilon_{ljk} \partial_m \sigma_{ij} u_i n_q dA , \tag{4.12}$$

where l_k is the direction vector of the crack extension, ε_{ijk} is the alternative tensor and ∂_i is the differential operator. Now we receive a second new quantity T_k

$$T_k = \int_{A_0} \frac{1}{2} \varepsilon_{qml} \varepsilon_{ljk} \partial_m \sigma_{ij} u_i n_q dA , \tag{4.13}$$

which describes the distortion of the crack front surface.

It can easily be proved that the surface integral T_k above is path-independent by using the Gaussian theorem

$$\begin{aligned} T_k = \oint_B \frac{1}{2} \varepsilon_{qml} \varepsilon_{ljk} \partial_m \sigma_{ij} u_i n_q dA &= \oint_B \frac{1}{2} (\partial_k \sigma_{ij} u_i n_j - \partial_j \sigma_{ij} u_i n_k) dA \\ &= \int_V \frac{1}{2} (\partial_j \partial_k \sigma_{ij} u_i - \partial_k \partial_j \sigma_{ij} u_i) dV \\ &= 0 \end{aligned}$$

where B is an arbitrary closed area. It can be seen above, that

- the new vector quantity T_k has an integral form,
- it is path-independent,
- it describes the distortion of the crack front surface.

5. Two New Quantities S_k and T_k for Elastic-Plastic Material Behavior

Now we will extend the new found quantities S_k and T_k for linear elastic material behavior into elastic-plastic material behavior with power law hardening. So let us write the strain energy density w for this material as follows

$$w \approx \frac{n}{n+1}\sigma_{ij}\varepsilon_{ij}\,, \tag{5.1}$$

where n is the hardening parameter of material. In the above equation the part of elastic strain energy density is neglected, since the value of this part is very small in comparison with the plastic part.

It is shown that the Eq. (5.1) is a more generalized form of the strain energy density, which is valid not only for elastic-plastic material behavior but with n=1 also valid for linear elastic material behavior. Therefore, we can derive some quantities for this material as done in the last chapter 3 and 4.

In analogy to Eq. (3.11) we get the new generalized I^*-integral for elastic-plastic material behavior

$$I^* = \lim_{\Delta a \to 0} \frac{1}{\Delta a} \int_{A_1} \frac{n}{n+1}\sigma_{ij}^0 u_i^1 n_j^1 dA\,. \tag{5.2}$$

In the same way we can still receive in analogy to Eq. (4.10)

$$S_k = \int_{A_0} \frac{n}{n+1}\sigma_{ij,k} u_i n_j dA = \int_A \left(\frac{n}{n+1}\sigma_{ij,k} u_i - \frac{1}{n+1}\sigma_{ij} u_{i,k}\right) n_j dA \tag{5.3}$$

and finally in analogy to Eq. (4.13)

$$T_k = \int_{A_0} \frac{n}{n+1}\varepsilon_{qml}\varepsilon_{ljk}\partial_m \sigma_{ij} u_i n_q dA\,. \tag{5.4}$$

The integrals of the new found quantities S_k and T_k in Eq. (5.3) and (5.4) for this material behavior are also path-independent.

6. Crack Driving Energy and Crack Force

In the above considerations, we have examined the basic equation (3.3) and could first derive the previously existing fracture mechanics parameters such as the generalized Irwin's I*-integral expression of the crack closure energy and the generalized Rice's J_k-integral. In particular we found the both new quantities S_k and T_k, where S_k describes the crack front extension and T_k the crack front distortion. Now, we can write the generalized energy release rate (4.11) as follows

$$-\frac{d\Pi}{da} = (S_k + T_k) l_k\,. \tag{6.1}$$

By substituting $P_k = S_k + T_k$ and by setting k = 1 for a special case "pure mode I", we obtain a very important result from the equation (6.1):

$$G = P_1 = S_1 + T_1, \tag{6.2}$$

where G is the Griffith's energy release rate. This means:

the energy release rate is separable and can be separated into two parts.

By introduction of $W_F = -\Pi$ the equation (6.1) finally becomes

$$dW_F = P_k da_k, \tag{6.3}$$

where W_F is the crack driving energy. The equations (6.1) and (6.3) show that the change of the crack driving energy consists of two vector quantities P_k and da_k, whereby da_k is the crack front deformation. Thus, the vector quantity P_k contains the force character and is therefore identified as the whole crack force. Since $P_k = S_k + T_k$, S_k or T_k represents a partial crack force. The energy balance of the cracked body can be reformulated as follows:

$$\frac{dU}{da} - \frac{dW}{da} - \frac{dW_F}{da} = 0, \tag{6.4}$$

where U is the work done by the external force, W is the strain energy and W_F is the crack driving energy.

5. Summary and Conclusion

The questions that we set at the beginning of the article, are already covered in detail and answered. The important results can be summarized as follows:

- We have introduced a uniform equation (3.3) and derived the previously existing fracture mechanics parameters such as the generalized Irwin's I^*-integral expression of the crack closure energy and the generalized Rice's J_k-integral from it,
- based on the uniform equation (3.3), we have also found two new vector quantities S_k und T_k, which indicate that the energy release rate can be separated into the new found vector quantities S_k und T_k, where S_k provides the crack front extension, and the other T_k describes the crack front distortion,
- the two vector quantities S_k and T_k are formulated in an integral form and are path-independent,
- it has also given that the new quantities S_k and T_k as well as the generalized Irwin's I^*-integral expression of the crack closure energy are not only valid for linear elastic material behaviour but also for elastic-plastic material behavior,
- the two vector quantities S_k und T_k have the force character. So S_k is denoted as the partial crack force for crack front extension and T_k the partial force for crack front distortion.

References

[1] Inglis, C.E. (1913): Stresses in a plate due to the presence of cracks and sharp corners. Proc. Inst. Naval Arch. 60, pp 210-230

[2] Griffith, A.A. (1920): The phenomena of rupture on flow in solids. Phil. Trans. Roy. Soc. London, vol. A221, pp 163-198

[3] Irwin, G.R. (1957): Analysis of stresses and strains near the end of a crack traversing a plate. J. Appl. Mech., vol. 24, pp 361-364

[4] Irwin, G.R. (1964): Structural aspects of brittle fracture. Appl. Materials Research, vol. 3, pp 65-81

[5] Eshelby, J. D. (1970): The Energy Momentum Tensor in Continuum Mechanics, Inelastic Behaviour of Solids, ed. Kanninen, M. F., et al., McGraw-Hill, New York

[6] Eshelby, J. D. (1956): The Continuum Theory of Lattice Defects, Solid State Physics, Vol. III, eds. Seitz, F. and Turnbull, D., Academy Press

[7] Rice, J.R. (1968a): A path independent integral and the approximate analysis of strain concentrations by notches and cracks. J. Appl. Mech., vol. 35, pp 379-386

[8] Rice. J.R. (1968b): Mathematical analysis in the mechanics of fracture. In Fracture: An Advanced Treatise, vol. 2, pp 191-193

[9] Budiansky, B. and Rice. J.R. (1973): Conservation laws and energy release rates. J. Appl. Mech., vol. 40, pp 201-203

[10] Knowles, J. K. and Sternberg, E. (1971/1972): On a Class of Corsevation Laws in Linearized and Finite Elastostatics, Archive for Rat. Mech. and Analysis, vol. 44, pp 187-211

[11] Cherepanov, C.P. (1967): Crack propogation in continuous media, Appl. Math. Mech., vol. 31, pp 476-488

Fracture Analysis of Particulate MEE Materials Using a Domain-Independent Interaction Integral Method

Hongjun Yu[1,3,*], **Linzhi Wu**[2,*]

[1] Institute of Applied Mathematics, Harbin Institute of Technology, Harbin 150001, China
[2] Center for Composite Materials, Harbin Institute of Technology, Harbin 150001, China
[3] School of Civil Engineering, Harbin Institute of Technology, Harbin 150001, China
* Corresponding author: yuhongjun@hit.edu.cn (Hongjun Yu); wlz@hit.edu.cn (Linzhi Wu)

Abstract This paper first introduces an expanded tensor notation to express the basic relations of magneto-electro-elastic (MEE) media and then, derives a domain formulation of the interaction integral on the basis of the expanded tensor notation for computing the intensity factors (IFs). The present interaction integral does not require material properties to be differentiable and moreover, it is domain-independent for material interfaces, which may make the interaction integral to become one of the most promising techniques in analyzing the crack problems of MEE composites. Then, the numerical implementation of the interaction integral combined with the extended finite element method (XFEM) is introduced. Using this method, the crack problems of a particulate MEE plate are studied.

Keywords Magneto-electro-elastic (MEE), Crack, Interaction integral, Intensity factors (IFs), Extended finite element method (XFEM)

1. Introduction

Magneto-electro-elastic (MEE) materials have drawn significant interest in several engineering fields as a class of important functional materials, such as magnetic field probes, electronic packaging, actuators, waveguides, sensors, phase investors, transducers. However, a great drawback of MEE materials is their inherent brittleness and low fracture toughness. Generally, these materials may fail prematurely in service due to some defects arising during the manufacturing process and thus, it is of practical significance to learn the fracture feature of MEE materials. Liu et al. [1] studied Green's functions for a cracked MEE body. Wang and Mai [2] obtained a general two-dimensional (2D) solution of the MEE fields around the crack tip. Gao et al. [3] derived an explicit solution in closed form for the intensity factors (IFs) and electro-magnetic fields inside a crack in MEE media. After that, considerable theoretical research works were carried out on the fracture problems of MEE materials. However, most of the theoretical research works restrict MEE media to be infinite and only a few simple configurations can be solved. Therefore, numerical techniques are usually employed in actual fracture analyses of MEE materials.

Among numerical methods, the interaction integral has generated a great interest for its convenience in decoupling mechanical stress intensity factors (SIFs), electric displacement intensity factor (EDIF) and magnetic induction intensity factor (MIIF). The interaction integral was proposed by Stern et al. [4] to decouple mechanical mode-I and mode-II SIFs on the basis of the J-integral by a superposition of two admissible states. Recently, the interaction integral was extended to solve the IFs of piezoelectric (PE) media [5] and those of MEE media [6]. For MEE materials, the interaction integral published previously has a shortcoming that is it requires the material properties to be differentiable. Generally, MEE materials are a category of composites composed of PE and PM phases, and the interfaces between constituent phases may reduce their reliability since the interfaces generally act as sources of failures in service. Therefore, the interfaces can not be ignored when the fracture behaviors of MEE composites are concerned. Fortunately, Yu et al. [7] have developed a new interaction integral for PE solids which is domain-independent for material interfaces. This point brings a great convenience to the fracture analysis of the composites with

complex interfaces. Then, this paper will derive a domain-independent interaction integral for MEE composites.

2. Basic relations and interaction integral

2.1. Basic equations for PE media

The field equations for a linear MEE medium in the absence of body forces, volume charge and concentrated magnetic source are given as follows.

2.1.1. Governing equations

- Constitutive equations

$$\begin{aligned} \sigma_{ij} &= C_{ijkl}\varepsilon_{kl} - e_{lij}E_l - h_{lij}H_l \\ D_i &= e_{ikl}\varepsilon_{kl} + \kappa_{il}E_l + \beta_{il}H_l \quad , \\ B_i &= h_{ikl}\varepsilon_{kl} + \beta_{il}E_l + \gamma_{il}H_l \end{aligned} \tag{1}$$

- Kinematic equations

$$\varepsilon_{ij} = \frac{1}{2}(u_{i,j} + u_{j,i}), \quad E_i = -\phi_{,i}, \quad H_i = -\varphi_{,i} \ . \tag{2}$$

- Equilibrium equations

$$\sigma_{ij,i} = 0, \quad D_{i,i} = 0, \quad B_{i,i} = 0 . \tag{3}$$

where u_i, σ_{ij} and ε_{ij} are the elastic displacement, stress, strain tensors, respectively; ϕ, D_i and E_i are the electric potential, electric displacement, electric field tensors, respectively; φ, B_i and H_i are magnetic potential, magnetic induction, magnetic field tensors, respectively; C_{ijkl}, κ_{il}, and γ_{il} are the elastic stiffness, dielectric permittivity and magnetic permeability tensors, respectively; e_{ikl}, h_{ikl} and β_{il} are the PE, PM and electro-magnetic tensors, respectively. The repetition of an index implies summation with respect to the index over its range.

2.1.2. Expanded tensor notation

By letting

$$\begin{aligned} & u_4 = \phi, \quad u_5 = \varphi, \\ & \sigma_{4j} = D_j, \quad \sigma_{5j} = B_j, \quad \sigma_{i'j'} = 0, \qquad , \\ & 2\varepsilon_{4j} = -E_j, \quad 2\varepsilon_{5j} = -H_j, \quad \varepsilon_{i'j'} = 0 \end{aligned} \tag{4}$$

$$\begin{aligned} & C_{4jkl} = e_{jkl}, \quad C_{5jkl} = h_{jkl}, \\ & C_{4j4l} = -\kappa_{jl}, \quad C_{5j5l} = -\gamma_{jl}, \quad C_{4j5l} = -\beta_{jl}, . \\ & C_{i'j'kl} = C_{i'j'k'l} = 0, \quad C_{i'j'k'l'} \text{ arbitrary value} \end{aligned} \tag{5}$$

we can extend the tensors u_i, σ_{ij}, ε_{ij} and C_{ijkl} $(i, j, k, l = 1,2,3)$ respectively into u_I, σ_{IJ}, ε_{IJ} and C_{IJKL} $(I, J, K, L = 1,2,...,5)$ which meet the symmetry relations $\sigma_{IJ} = \sigma_{JI}$, $\varepsilon_{IJ} = \varepsilon_{JI}$ and $C_{IJKL} = C_{JIKL} = C_{IJLK} = C_{KLIJ}$. Here, the subscripts $i', j', k', l' = 4,5$. A Cartesian coordinate system only contains x_1-axis and x_2-axis and thus,

$$n_4 = n_5 = 0, \quad (*)_{,4} = (*)_{,5} = 0 . \tag{6}$$

where $(*)$ denotes an arbitrary variable or expression. According to the above relations, Eqs. (1)

-(3) can be expressed in an expanded tensor notation respectively as

$$\sigma_{IJ} = C_{IJKL}\varepsilon_{KL}\,, \tag{7}$$

$$\varepsilon_{IJ} = \frac{1}{2}(u_{I,J} + u_{J,I})\,, \tag{8}$$

$$\sigma_{IJ,I} = 0\,. \tag{9}$$

2.2. Definition of the interaction integral

2.2.1. Interaction integral

A 2D linear MEE solid with an electrically and magnetically impermeable crack is considered. The interaction integral is the 'cross term' in the J-integral by superimposing the actual fields (u_I, σ_{IJ}, ε_{IJ}) and some known auxiliary fields (u_I^{aux}, σ_{IJ}^{aux}, ε_{IJ}^{aux}). As shown in Fig. 1, the J-integral for MEE media is [2]

$$J = \lim_{\Gamma_\varepsilon \to 0} \int_{\Gamma_\varepsilon} (F\delta_{1i} - \sigma_{ij}u_{j,1} - D_i\phi_{,1} - B_i\varphi_{,1})n_i d\Gamma\,. \tag{10}$$

where $F = (\sigma_{jk}\varepsilon_{jk} - D_jE_j - B_jH_j)/2$ is the electro-magnetic enthalpy density for linear MEE media, δ_{ij} is Kronecker delta and n_i is the unit outward normal vector to the contour Γ_ε. According to Section 2.1.2, the J-integral can also be expressed as

$$J = \lim_{\Gamma_\varepsilon \to 0} \int_{\Gamma_\varepsilon} (\frac{1}{2}\sigma_{JK}\varepsilon_{JK}\delta_{1I} - \sigma_{IJ}u_{J,1})n_I d\Gamma\,. \tag{11}$$

Superposition of an actual state and a auxiliary state leads to another equilibrium state (state S) for which the J-integral is

$$J^{(S)} = \lim_{\Gamma_\varepsilon \to 0} \int_{\Gamma_\varepsilon} [\frac{1}{2}(\sigma_{JK} + \sigma_{JK}^{aux})(\varepsilon_{JK} + \varepsilon_{JK}^{aux})\delta_{1I} - (\sigma_{IJ} + \sigma_{IJ}^{aux})(u_{J,1} + u_{J,1}^{aux})]n_I d\Gamma\,. \tag{12}$$

By expanding Eq. (12) as $J^{(S)} = J + J^{aux} + I$ where J and J^{aux} are respectively the J-integral corresponding to the actual state alone and the auxiliary state alone, one obtains the interaction integral as

$$I = \lim_{\Gamma_\varepsilon \to 0} \int_{\Gamma_\varepsilon} [\frac{1}{2}(\sigma_{JK}\varepsilon_{JK}^{aux} + \sigma_{JK}^{aux}\varepsilon_{JK})\delta_{1I} - (\sigma_{IJ}u_{J,1}^{aux} + \sigma_{IJ}^{aux}u_{J,1})]n_I d\Gamma\,. \tag{13}$$

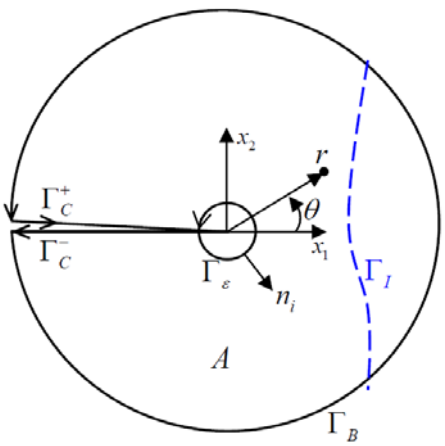

Figure 1. Integral contours around the crack tip

2.2.2. Auxiliary fields

For nonhomogeneous MEE materials, the auxiliary fields have different choices [6] and an incompatibility formulation is selected in this paper. Namely, in the polar coordinate system (r,θ) with the origin at the crack tip, the expanded auxiliary fields are defined as

$$u_J^{aux} = \sqrt{\frac{2r}{\pi}} K_N^{aux} f_J^N(\theta), \quad \sigma_{IJ}^{aux} = \frac{K_N^{aux}}{\sqrt{2\pi r}} g_{IJ}^N(\theta), \quad \varepsilon_{IJ}^{aux} = C_{IJKL}^{-1}(\mathbf{x})\sigma_{KL}^{aux} \tag{14}$$

where the index $N = \{II,\ I,\ III,\ IV,\ V\}$ denotes different crack opening modes with the value corresponding to a general subscript $I = \{1,\ 2,\ 3,\ 4,\ 5\}$; K_I^{aux}, K_{II}^{aux}, K_{III}^{aux}, K_{IV}^{aux} and K_V^{aux} denote the auxiliary mode-I, mode-II, mode-III mechanical SIFs, EDIF and MIIF, respectively. The angular functions $f_J^N(\theta)$ and $g_{IJ}^N(\theta)$ are the standard angular functions for a crack in a homogeneous MEE medium, which depend only on the material properties at the crack-tip location, and their detailed definitions can be found in Ref. [6].

2.3. Calculations of the interaction integral

The infinitesimal contour integral in Eq. (13) can not be obtained directly in numerical calculations and thus, it is usually converted into an equivalent domain integral. To begin, as shown in Fig. 1, consider a closed contour $\Gamma_0 = \Gamma_B + \Gamma_\varepsilon^- + \Gamma_C^+ + \Gamma_C^-$ where Γ_ε^- is the opposite path of the contour Γ_ε. According to the assumption that the crack faces are assumed to be mechanical traction-free, electrically impermeable and magnetically impermeable, it can be easily proved that

$$I = -\lim_{\Gamma_\varepsilon \to 0} \oint_{\Gamma_0} [\frac{1}{2}(\sigma_{JK}\varepsilon_{JK}^{aux} + \sigma_{JK}^{aux}\varepsilon_{JK})\delta_{1I} - (\sigma_{IJ}u_{J,1}^{aux} + \sigma_{IJ}^{aux}u_{J,1})]n_I q d\Gamma . \tag{15}$$

where q is an arbitrary weight function with value varying smoothly from 1 on Γ_ε to 0 on Γ_B.

When the material properties are continuously differentiable, applying divergence theorem to Eq. (15), one obtains

$$I = -\int_A \{[\frac{1}{2}(\sigma_{JK}\varepsilon_{JK}^{aux} + \sigma_{JK}^{aux}\varepsilon_{JK})\delta_{1I} - (\sigma_{IJ}u_{J,1}^{aux} + \sigma_{IJ}^{aux}u_{J,1})]q\}_{,I} dA. \tag{16}$$

where A is the domain enclosed by the contour Γ_0 for $\Gamma_\varepsilon \to 0$. According to Eqs. (7)-(9) and Eq. (14), the interaction integral in Eq. (16) can be simplified as [7]

$$I = \int_A \{(\sigma_{IJ}u_{J,1}^{aux} + \sigma_{IJ}^{aux}u_{J,1} - \sigma_{JK}^{aux}\varepsilon_{JK}\delta_{1I})q_{,I} + \sigma_{IJ,1}^{aux}[C_{IJKL}^{-1}(\mathbf{0}) - C_{IJKL}^{-1}(\mathbf{x})]\sigma_{KL}q\}dA. \tag{17}$$

Compared with the expression in Ref. [6] for nonhomogeneous MEE media, the expression in Eq. (17) does not contain any term related to the derivatives of material properties with respect to the coordinates. Therefore, the present interaction integral can facilitate the facture analysis of practical MEE materials whose derivatives of material properties are difficult to obtain.

Moreover, when the integral domain A contains an interface on which the properties are discontinuous (see the dash line Γ_I in Fig. 1), A needs to be divided into two parts for using divergence theorem. Similarly to Ref. [7], the interface has no contribution to the interaction integral and thus, the same expression in Eq. (17) can be obtained. Namely, the present interaction integral does not require the material properties to be continuous, which brings a great convenience to the fracture studies of MEE composites for the integral domain can be chosen to a region containing arbitrary material interfaces.

2.4. Extraction of the fracture parameters

This section will introduce how to solve the IFs by using the interaction integral. For linear MEE

solids, the J-integral is equal to the total potential energy release rate which is expressed as [6]

$$J = \frac{1}{2} Y_{MN} K_M K_N, \quad (M, N = II, I, IV, V) \tag{18}$$

where Y_{MN} is the generalized Irwin matrix which depends on the material constants at the crack-tip location [6]. Applying Eq. (18) to the superimposed state S gives

$$J^{(S)} = \frac{1}{2} Y_{MN} (K_M + K_M^{aux})(K_N + K_N^{aux}). \tag{19}$$

By expanding Eq. (19) as $J^{(S)} = J + J^{aux} + I$, we can obtain the interaction integral as

$$I = Y_{MN} K_M K_N^{aux}. \tag{20}$$

By taking values of the vector [K_{II}^{aux}, K_I^{aux}, K_{IV}^{aux}, K_V^{aux}] to be [1, 0, 0, 0], [0, 1, 0, 0], [0, 0, 1, 0] and [0, 0, 0, 1], sequentially, Eq. (19) reduces to

$$I^{(II)} = K_{II} Y_{11} + K_I Y_{12} + K_{IV} Y_{14} + K_V Y_{15}, \tag{21}$$

$$I^{(I)} = K_{II} Y_{21} + K_I Y_{22} + K_{IV} Y_{24} + K_V Y_{25}, \tag{22}$$

$$I^{(IV)} = K_{II} Y_{41} + K_I Y_{42} + K_{IV} Y_{44} + K_V Y_{45}, \tag{23}$$

and

$$I^{(V)} = K_{II} Y_{51} + K_I Y_{52} + K_{IV} Y_{54} + K_V Y_{55}. \tag{24}$$

By simultaneously solving Eqs. (21)-(24), the IFs K_I, K_{II}, K_{IV} and K_V can be obtained.

3. Numerical implementation

3.1. Extended finite element method

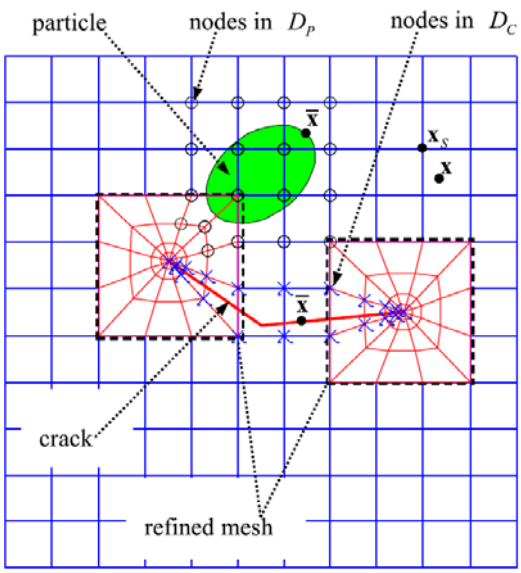

Figure 2. Finite element mesh of a plate with a crack and a particle [7]

To compute the interaction integral, the values of the actual fields u_I, σ_{IJ} and ε_{IJ} in the integral domain need to be obtained first. Generally, the numerical methods such as the finite element method (FEM), the extended finite element method (XFEM) and the element-free Galerkin method (EFGM) are adopted to compute these values. Here, the XFEM is used and the approximations of the expanded displacements are adopted as

$$u_I^h = \sum_{i\in D_S} N_{(i)} u_I^{(i)} + \sum_{i\in D_P} N_{(i)} \psi_{(i)}^b b_I^{(i)} + \sum_{i\in D_C} N_{(i)} \psi_{(i)}^c c_I^{(i)}$$
$$\psi_{(i)}^b = \left|\mathbf{x}-\bar{\mathbf{x}}\right| - \left|\mathbf{x}_{(i)}-\bar{\mathbf{x}}\right|, \quad \psi_{(i)}^c = H(\mathbf{x}-\bar{\mathbf{x}}) - H(\mathbf{x}_{(i)}-\bar{\mathbf{x}}) \quad , \tag{25}$$

where the variable marked by the index (i) denotes the value corresponding to node i; $\mathbf{x}$ is an arbitrary point; $\bar{\mathbf{x}}$ is a point on the discontinuous surface (crack or interface) which is closest to point $\mathbf{x}$; N is the standard finite element shape function; ψ^b and ψ^c are the shifted enrichment functions for material interfaces and cracks, respectively; D_S is the set of all nodes in mesh; D_P and D_C are the sets of the nodes enriched with ψ^b and ψ^c, respectively; u_I are the standard nodal displacements; b_I and c_I are additional degrees of freedom for the nodes in D_P and those in D_C, respectively; $H(\mathbf{x})$ is a Heaviside step function. In order to improve the numerical precision, the mesh around the crack tip is refined as shown in Fig. 5

In finite element computations, Eqs. (7)-(9) are usually written in the matrix form as

$$\boldsymbol{\sigma} = \mathbf{C}\boldsymbol{\varepsilon}, \quad \boldsymbol{\varepsilon} = \mathbf{L}\mathbf{u}, \quad \mathbf{L}^T\boldsymbol{\sigma} = \mathbf{0}, \tag{26}$$

where

$$\begin{aligned} \mathbf{u} &= [u_1, \quad u_2, \quad \phi, \quad \varphi]^T, \\ \boldsymbol{\sigma} &= [\sigma_{11}, \quad \sigma_{22}, \quad \sigma_{12}, \quad D_1, \quad D_2, \quad B_1, \quad B_2]^T, \\ \boldsymbol{\varepsilon} &= [\varepsilon_{11}, \quad \varepsilon_{22}, \quad 2\varepsilon_{12}, \quad -E_1, \quad -E_2, \quad -H_1, \quad -H_2]^T, \end{aligned} \tag{27}$$

$$\mathbf{L} = \begin{bmatrix} \partial/\partial x_1 & 0 & \partial/\partial x_2 & 0 & 0 & 0 & 0 \\ 0 & \partial/\partial x_2 & \partial/\partial x_1 & 0 & 0 & 0 & 0 \\ 0 & 0 & 0 & \partial/\partial x_1 & \partial/\partial x_2 & 0 & 0 \\ 0 & 0 & 0 & 0 & 0 & \partial/\partial x_1 & \partial/\partial x_2 \end{bmatrix}^T . \tag{28}$$

The material parameters in stiffness matrix $\mathbf{C}$ are given in Voigt notation. Using the relation between the indices $11\to1$, $22\to2$, $33\to3$, $23\to4$, $31\to5$ and $12\to6$, the constitutive Eq. (1) can be written in Voigt notation as:

$$\sigma_\alpha = C_{\alpha\beta}\varepsilon_\beta - e_{j\alpha}E_j - h_{j\alpha}H_j, \quad D_i = e_{i\beta}\varepsilon_\beta + \kappa_{ij}E_j + \beta_{ij}H_j, \quad B_i = h_{i\beta}\varepsilon_\beta + \beta_{ij}E_j + \gamma_{ij}H_j . \tag{29}$$

where the subscripts $\alpha, \beta = 1,2,...,6$ and $i, j = 1,2,3$. For 2D MEE media, the stiffness matrix $\mathbf{C}$ in Eq. (26) is defined as

$$\mathbf{C} = \begin{cases} \mathbf{C}_{\mathrm{I}} & \text{(plane strain)} \\ \mathbf{C}_{\mathrm{I}} - \mathbf{C}_{\mathrm{II}}\mathbf{C}_{\mathrm{II}}^T / C_{33} & \text{(plane stress)} \end{cases} \tag{30}$$

where

$$\mathbf{C}_{\mathrm{I}} = \begin{bmatrix} C_{11} & C_{12} & C_{16} & e_{11} & e_{21} & h_{11} & h_{21} \\ C_{12} & C_{22} & C_{26} & e_{12} & e_{22} & h_{12} & h_{22} \\ C_{16} & C_{26} & C_{66} & e_{16} & e_{26} & h_{16} & h_{26} \\ e_{11} & e_{12} & e_{16} & -\kappa_{11} & -\kappa_{12} & -\beta_{11} & -\beta_{12} \\ e_{21} & e_{22} & e_{26} & -\kappa_{12} & -\kappa_{22} & -\beta_{12} & -\beta_{22} \\ h_{11} & h_{12} & h_{16} & -\beta_{11} & -\beta_{12} & -\gamma_{11} & -\gamma_{12} \\ h_{21} & h_{22} & h_{26} & -\beta_{12} & -\beta_{22} & -\gamma_{12} & -\gamma_{22} \end{bmatrix}, \quad \mathbf{C}_{\mathrm{II}} = \begin{bmatrix} C_{13} \\ C_{23} \\ C_{36} \\ e_{13} \\ e_{23} \\ h_{13} \\ h_{23} \end{bmatrix} \tag{31}$$

Then, Eq. (25) can be written in the matrix form as

$$\mathbf{u}^h = \sum_{i=1}^{n} N_{(i)} \left(\mathbf{u}^{(i)} + \psi_{(i)}^b \mathbf{b}^{(i)} + \psi_{(i)}^c \mathbf{c}^{(i)} \right) \tag{32}$$

where $\mathbf{b}=[b_1,\ \ b_2,\ \ b_4,\ \ b_5]^T$, $\mathbf{c}=[c_1,\ \ c_2,\ \ c_4,\ \ c_5]^T$ and n is the node number in an element.

3.2. Numerical discretization of the interaction integral

In numerical computations, the interaction integral in Eq. (17) needs to be discretized in the crack-tip local coordinate system as

$$I=\sum_{e=1}^{e_A}\sum_{p=1}^{p_e}\left\{\begin{array}{l}\left[\dfrac{\partial q}{\partial x_1}\boldsymbol{\sigma}_{\mathrm{I}}^T+\dfrac{\partial q}{\partial x_2}\boldsymbol{\sigma}_{\mathrm{II}}^T\right]\dfrac{\partial \mathbf{u}^{aux}}{\partial x_1}+\left[\dfrac{\partial q}{\partial x_1}(\boldsymbol{\sigma}_{\mathrm{I}}^{aux})^T+\dfrac{\partial q}{\partial x_2}(\boldsymbol{\sigma}_{\mathrm{II}}^{aux})^T\right]\dfrac{\partial \mathbf{u}}{\partial x_1}\\ -\dfrac{\partial q}{\partial x_1}(\boldsymbol{\sigma}^{aux})^T\boldsymbol{\varepsilon}+\dfrac{\partial(\boldsymbol{\sigma}^{aux})^T}{\partial x_1}\left[\mathbf{C}^{-1}(\mathbf{0})-\mathbf{C}^{-1}(\mathbf{x})\right]\boldsymbol{\sigma}\end{array}\right\}_p\left|\mathbf{J}\right|_p w_p\,. \tag{33}$$

where $\boldsymbol{\sigma}_{\mathrm{I}}=[\sigma_{11}\quad \sigma_{12}\quad D_1\quad B_1]^T$ and $\boldsymbol{\sigma}_{\mathrm{II}}=[\sigma_{12}\quad \sigma_{22}\quad D_2\quad B_2]^T$; e_A is the number of elements in the integral domain A; p_e is the number of integration points in one element; $\left|\mathbf{J}\right|_p$ and w_p represent respectively the determinant of Jacobian matrix and the corresponding weight factor at the integration point p. Here, the derivative of actual displacement vector is

$$\frac{\partial \mathbf{u}}{\partial x_1}=\sum_{i=1}^{n}\left\{\frac{\partial N_{(i)}}{\partial x_1}\mathbf{u}^{(i)}+\left(\psi_{(i)}^b\frac{\partial N_{(i)}}{\partial x_1}+N_{(i)}\frac{\partial \psi_{(i)}^b}{\partial x_1}\right)\mathbf{b}^{(i)}+\psi_{(i)}^c\frac{\partial N_{(i)}}{\partial x_1}\mathbf{c}^{(i)}\right\}. \tag{34}$$

4. Numerical examples

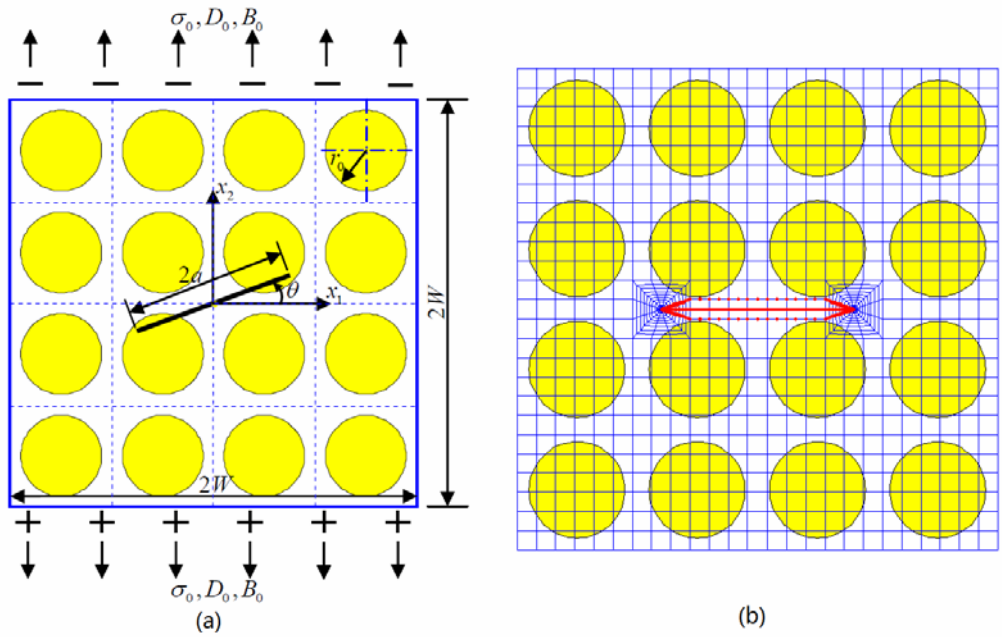

Figure 3. A 2D particulate MEE plate with a crack: (a) geometry and boundary conditions; (b) finite element mesh

As shown in Fig. 3(a), a 2D $CoFe_2O_4$ particle-reinforced $BaTiO_3$ matrix composite plate is considered. The plate of unit length ($W=0.5$) is composed of 16 square cells of length $W/2$ each of which contains a circular particle of radius r_0 at its center. Therefore, the volume fraction of the particles is $V_f=4\pi r_0^2/W^2$ and in this paper, $V_f=0.5$. In the center of the plate, there exists an inclined crack of length $2a$ and angle θ measured counterclockwise. The poling directions of both

the matrix and the particles are all assumed to be along x_2-axis. The magneto-electro-mechanical loading $\sigma_0 = 1$, $D_0 = 10^{-10}\sigma_0$ and $B_0 = 10^{-8}\sigma_0$ are applied along the top and bottom edges. Meanwhile, an equivalent homogeneous MEE plate of the same geometry and boundary conditions as that shown in Fig. 3(a) is adopted to compare the differences of the IFs. The material constants are given in Table 1, where the word "effective" denotes the properties of the equivalent homogeneous MEE plate.

First, we discuss a horizontal crack ($\theta = 0°$) with the crack length varying from $a/W = 0.2$ to $a/W = 0.8$. Fig. 3(b) shows the mesh configuration which consists of 1009 element and 3082 nodes. Eight-node quadrilateral (Q8) elements are used over most of the mesh and six-node quarter-point (T6qp) singular elements are employed around the crack tips. The region composed of four-layer elements around each crack tip is adopted to be the integral domain. The IFs are normalized by the factors $K_I^0 = K_{II}^0 = \sigma_0\sqrt{\pi a}$, $K_{IV}^0 = 10^{-10}\sigma_0\sqrt{\pi a}$ and $K_V^0 = 10^{-8}\sigma_0\sqrt{\pi a}$ in this paper.

Table 1. Material parameters

Parameters	C_{11}	C_{12}	C_{13}	C_{33}	C_{44}	e_{31}	e_{33}	e_{15}	
	(10^9 Pa)					(C/m^2)			
$BaTiO_3$ [8]	166	77	78	162	43	-4.4	18.6	11.6	
$CoFe_2O_4$ [8]	286	173	170.5	269.5	45.3	0	0	0	
Effective [9]	226	125	124	216	44	-2.2	9.3	5.8	
Parameters	h_{31}	h_{33}	h_{15}	κ_{11}	κ_{33}	β_{11}	β_{33}	γ_{11}	γ_{33}
	(N/Am)			(10^{-9} C^2/Nm^2)		(10^{-12} Ns/VC)		(10^{-6} Ns^2/C^2)	
$BaTiO_3$ [8]	0	0	0	11.2	12.6	0	0	5	10
$CoFe_2O_4$ [8]	580.3	699.7	550	0.08	0.093	0	0	590	157
Effective [9]	290.2	350	275	5.64	6.35	5.367	2737.5	297	83.5

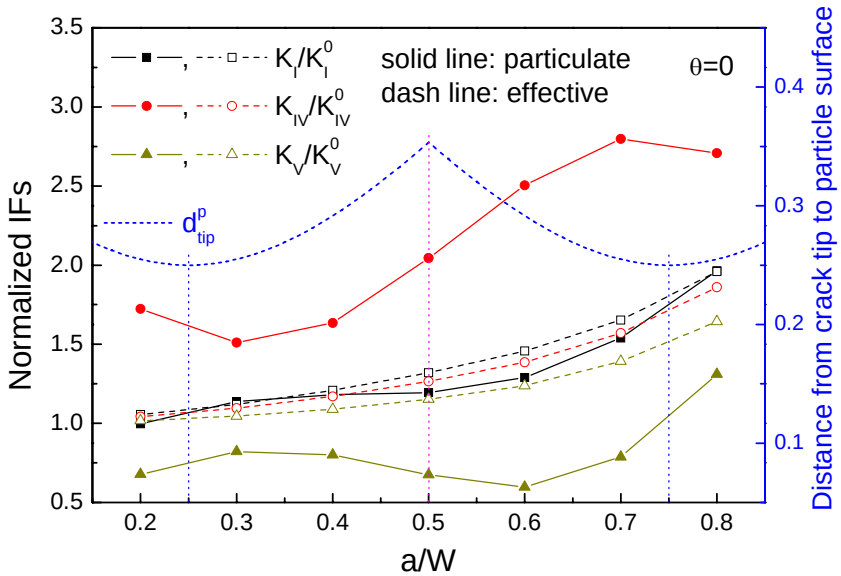

Figure 4. Normalized IFs vs crack length.

Fig. 4 shows the normalized IFs obtained at the right crack tip and the distance from the crack tip to the particle surface d_{tip}^p. The results show that with the increasing of crack length a/W, the

normalized IFs K_I / K_I^0, K_{IV} / K_{IV}^0 and K_V / K_V^0 are all increase monotonously for the crack in the equivalent homogeneous MEE plate while none of them varies monotonously for the crack in the particulate MEE plate. Besides, for the same geometry configuration, the EDIF (MIIF) for the particulate plate is quite larger (smaller) than that for the equivalent homogeneous plate. The reason may be that both of the crack tips are located in the PE phase.

Next, a crack of fixed length ($a/W = 0.4$) is considered and the angle θ varies from $0°$ to $90°$. As shown in Fig. 5, both of the crack tips are located in the matrix for $\theta = (0°, 90°)$ and in the particles for $\theta = 18° \sim 72°$. Fig. 6(a) and (b) show the normalized IFs obtained at the right crack tip varying with the crack angle. The results show that although obvious differences can be noted between the IFs for the particulate plate and those for the equivalent homogeneous plate, the varying trends of the SIFs are very similar for these two plates, while both the EDIF and MIIF vary distinctly with the increasing of the angle θ. The above phenomena imply that the actual PE/PM microstructures and the relative position between the crack and particles have great effects on the fracture performance of MEE composites.

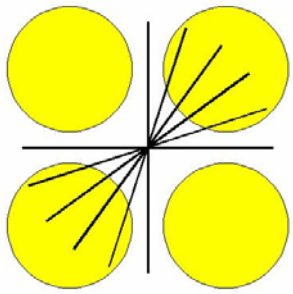

Figure 5. Crack locations for different angle θ.

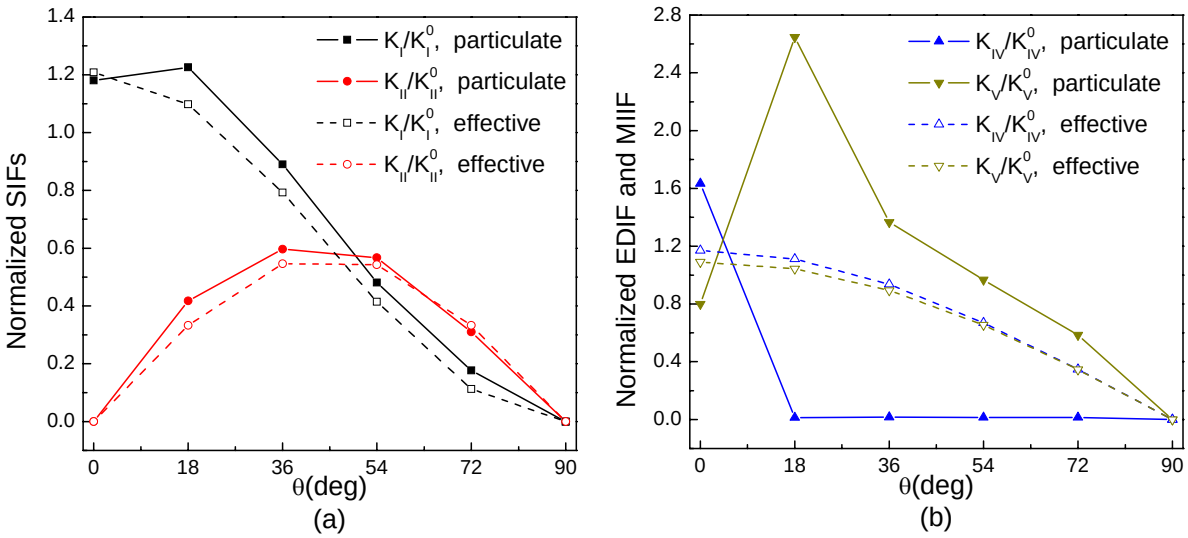

Figure 6. Normalized IFs vs angle θ for $a/W = 0.4$: (a) SIFs; (b) EDIF and MIIF.

5. Summary

MEE composites contain PE and PM phases and the interfaces between these constituent phases may reduce the reliability of MEE composites since the interfaces generally act as sources of failures in service. The complex interface environment brings a great difficulty to the fracture analysis of these MEE composites. This paper first introduces a domain form of the

interaction integral on the basis of an expanded tensor notation to solve the SIFs, EDIF and MIIF. The interaction integral does not require material properties to be differentiable and moreover, it is domain-independent for material interfaces which bring a great convenience to the fracture analysis of practical MEE composites. Using this method, the fracture problems of a particulate MEE composite are studied. The results imply that the actual microstructures of MEE composites composed of PE and PM phases have a great influence on their fracture performance.

Acknowledgements

This work is sponsored by NSFC (Grant Nos. 11072068 and 11202058), the China Postdoctoral Science Foundation (Grant Nos. 20110491071 and 2012T50338), the Fundamental Research Funds for the Central Universities (Grant No. HIT. NSRIF. 2013082).

References

[1] J.X. Liu, X.L. Liu, Y.B. Zhao, Green's functions for anisotropic magnetoelectroelastic solids with an elliptical cavity or a crack. Int J Eng Sci, 39 (2001) 1405-1418.
[2] B.L. Wang, Y.W. Mai, Crack tip field in piezoelectric/piezomagnetic media. Eur J Mech A-Solids, 22 (2003) 591-602.
[3] C.F. Gao, H. Kessler, H. Balke, Crack problems in magnetoelectroelastic solids. Part I: exact solution of a crack. Int J Eng Sci, 41 (2003) 969-981.
[4] M. Stern, E.B. Becker, R.S. Dunham, A contour integral computation of mixed-mode stress intensity factors. Int J Fract, 12 (1976) 359-368.
[5] M. Enderlein, A. Ricoeur, M. Kuna, Finite element techniques for dynamic crack analysis in piezoelectrics. Int J Fract, 134 (2005) 191-208.
[6] B.N. Rao, M. Kuna, Interaction integrals for fracture analysis of functionally graded magnetoelectroelastic materials. Int J Fract, 153 (2008) 15-37.
[7] H.J. Yu, L.Z. Wu, L.C. Guo, J.W. Ma, H. Li, A domain-independent interaction integral for fracture analysis of nonhomogeneous piezoelectric materials. Int J Solids Struct, 49 (2012) 3301-3315.
[8] L. Pasternak, Doubly periodic arrays of cracks and thin inhomogeneities in an infinite magnetoelectroelastic medium. Eng Anal Bound Elem, 36 (2012) 799-811
[9] W.J. Feng, Y.S. Li, X. Han, Z.H. Xu, Application of the extended traction boundary element-free method to the fracture of two-dimensional infinite magnetoelectroelastic solid. Sci China-Phys Mech Astron, 54 (2011) 1141-1153.

Buckling Analysis of a Nanowire Lying on Winkler-Pasternak Elastic Foundation

Tiankai Zhao[1], Jun Luo[1,*]

[1] Department of Mechanics , Huazhong University of Science and Technology, Wuhan 430074, China
* Corresponding author: luojun.l@gmail.com

Abstract The Steigmann-ogden surface elasticity model and the Timoshenko beam theory are adopted to study the axial buckling of a nanowire (NW) lying on Winkler-Pasternak substrate medium. Explicit solutions of the critical buckling force and buckling mode are obtained analytically. The influences of the surface stress effect, the geometry of the NW and the elastic foundation moduli are systematically discussed.

Keywords Surface effect, Nanowire, Timoshenko beam theory, Buckling

1. Introduction

Nanowire (NW) based devices have found important applications in various fields. Traditional beams theories failed to interpret the size dependent mechanical behavior of these devices due to their surface stress effect. The Gurtin-Murdoch model [1-2] has been widely accepted to study the mechanical behavior of nanostructures and nano defects [3-7]. Some researchers found that the effective elastic moduli of nanostructures under bending and tension are different[8-9], which could not be explained by the Gurtin-Murdoch model. Chhapadia et al.[10] pointed out that the above discrepancy could be explained with the modified framework proposed by Steigmann and Ogden [11-12]. On the other hand, buckling has long been thought as an unwanted issue and should be strictly avoided in structural designs. However, it was demonstrated by some researchers that controlled buckling of slender structures such as thin films, nanowires and nanotubes on compliant substrates could be utilized in the design of flexible electronics. This paper aims to study the axial buckling of a simply supported NW lying on Winkler-Pasternak elastic foundation with the Timoshenko beam model and Steigmann–Ogden theory. The influences of the surface stress effect, the geometry of the NW and the elastic foundation moduli are systematically discussed.

2. Solution of the Problem

Consider a NW lying on a deformable substrate, which is subjected to distributed transverse load and axial forces at both ends. We assume the NW has a circular cross section. The total energy of the axially loaded nanobeam can be written as:

$$U_{Total}(w) = U_{Bulk}(w) + U_{Surface}(w)\,, \tag{1}$$

where:

$$U_{Bulk}(w) = \int_0^L \int_A \frac{1}{2} E(y\frac{\partial \psi}{\partial x})^2 dAdx + \int_0^L \int_A \frac{\kappa}{2} G(\frac{\partial w}{\partial x} - \psi)^2 dAdx \quad , \tag{2}$$

$$U_{Surface}(w) = \int_0^L \int_S [-\tau_0 y\frac{\partial \psi}{\partial x} + \frac{1}{2}C_0(y\frac{\partial \psi}{\partial x})^2 + \frac{1}{2}C_1(\frac{\partial^2 w}{\partial x^2})^2]dSdx \quad . \tag{3}$$

Here, A denotes the area of the cross section, κ is the shear coefficient, C_0 and C_1 are the surface elastic modulus and the Steigman-Ogden constant, respectively, S denotes the circumference of the cross section. The potential energy of the lateral and axial load is given by:

$$U_f(w) = -\int_0^L f(x)w(x)dx - \frac{1}{2}\int_0^L N(\frac{\partial w}{\partial x})^2 dx\,, \tag{4}$$

where

$$f(x) = q(x) + q^s(x) + q^f(x)\,. \tag{5}$$

Here, $q^s(x)$ stands for the equivalent lateral force due to the residual surface stress and $q^f(x)$ represents the distributed force arising from the substrate medium. To minimize the total potential energy, we apply the variational theory,

$$\delta\left[U_{Total}(w) + U_f(w)\right] = 0\,. \tag{6}$$

Finally, we get:

$$\begin{cases} GA\kappa(\frac{\partial^2 w}{\partial x^2} - \frac{\partial \psi}{\partial x}) + f(x) - N\frac{\partial^2 w}{\partial x^2} = 0 \\ GA\kappa(\frac{\partial w}{\partial x} - \psi) + \frac{\partial}{\partial x}((EI + C_0 I^* + C_1 S)\frac{\partial \psi}{\partial x}) = 0 \end{cases}, \tag{7}$$

where $I = \int_A y^2 dA$, $I^* = \int_S y^2 dS$, $S^* = \int_S n_y^2 dS$. Take partial derivative of the second equation with respect to x, and substitute the first equation into the second equation, we have:

$$\left[(EI)^* + \frac{(EI)^*}{GA\kappa}(H-N) + \frac{(EI)^*}{GA\kappa}C_p\right]\frac{\partial^4 w}{\partial x^4} + \left[N - \frac{(EI)^*}{GA\kappa}C_w - H - C_p\right]\frac{\partial^2 w}{\partial x^2} + C_w w(x) = 0\,. \tag{8}$$

The general solution of Eq. (8) can be written as:

$$w(x) = Ae^{mx}\,. \tag{9}$$

Substituting Eq. (9) into Eq. (8), we can solve m.

The boundary conditions of a simply supported NW are given as follows:

$$w(0) = 0\,,\quad w''(0) = 0\,, \tag{10a}$$

$$w(L) = 0\,,\quad w''(L) = 0\,. \tag{10b}$$

Substitute Eqs.(10a,b) into Eq. (9), we can get the characteristic equation to solve the critical buckling force. The corresponding buckling mode is given by Eq. (9).

3. Results and Discussions

The buckling force of the NW is normalized with the critical buckling force of a classic simply supported Euler-Bernoulli beam. To see qualitatively how the surface stress effect and the Steigmann-Ogden correction influence the buckling behavior of the NW, we adopt the following material parameters in this study:

$$E = 76\,\text{Gpa}\,, \upsilon = 0.3\,,\ \ \tau_0 = 0.65\ \text{N/m}\,,\ \ C_0 = -1.39\,\text{N/m}\,,\ \ C_1 = \pm 153.6\,\text{eV}\,.$$

In Figure 1., we ignore the transverse shear effect of the substrate. The diameter and Steigmann-Ogden constant are chosen to be $3.5\,\text{nm}$ and $153.6\,\text{eV}$ respectively. All the results are normalized with the critical buckling force of a classic simply supported Euler-Bernoulli beam at each aspect ratio. Figure 1. shows that the surface effect has significant influences on the normalized critical buckling forces. When the Steigmann-Ogden constant is positive, the critical buckling force is greater than that predicted by the Gurtin-Murdoch theory, which implies that the NW is stiffened. It is also noted that the influence of the surface effect (predicted either by the Gurtin-Murdoch model or the Steigmann-Ogden model) on the critical buckling force decreases when the diameter of the NW increases. The difference between the result predicted by the Gurtin-Murdoch theory and that by the Steigmann-Ogden theory is also largely decreased as the diameter of the NW increases. Fig. 1 also shows that the critical buckling force for a finitely long NW is always larger than that for an infinitely long NW.

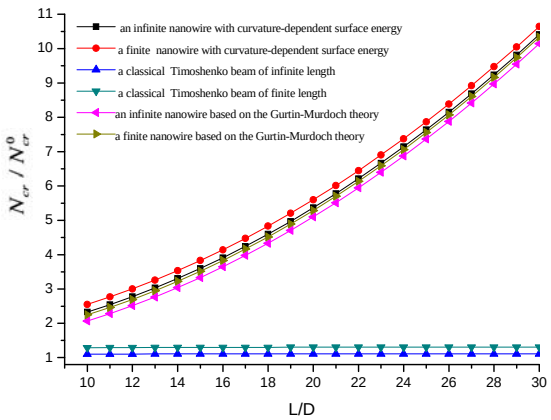

Figure 1. The normalized critical buckling force of a simply support NW lying on Winkler substrate medium.

In Figure 2., the influences of the Winkler and Pasternak moduli on the critical buckling force are studied with the Timoshenko beam model. The material parameters are the same with those in Figure 1.. The diameter of the NW is set to $3.5\,\text{nm}$. From Figure 2., we find that both the Winkler modulus and the Pasternak modulus tend to stiffen the NW. As a result, the buckling force for a NW lying on substrate medium is always larger than that of a free NW. It is also noticed that the critical buckling force is more sensitive to the Pasternak modulus.

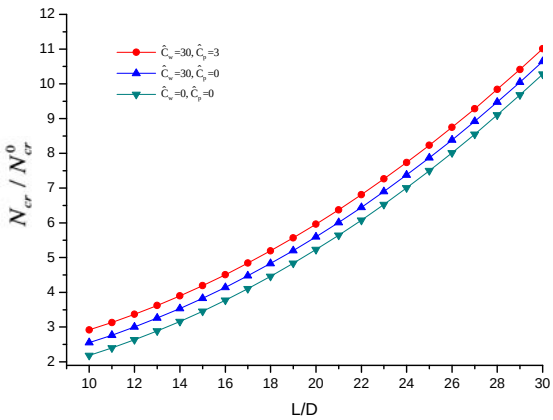

Figure 2. Variation of the normalized critical buckling force of a simply supported NW lying on Winkler-Pasternak substrate medium with respect to its aspect ratio. The diameter of the NW is $3.5\,\mathrm{nm}$.

4. Conclusions

In this paper, the Steigmann-Ogden model is adopted to characterize the surface effect of the NW. Explicit solutions are obtained for the critical buckling force and buckling mode of a simply supported NW lying on Winkler-Pasternak substrate medium with the Timoshenko beam theory. The following conclusions are drawn through this study:

(1) The shear effect, the surface stress effect and curvature dependent surface energy all have influences on the critical buckling force of the NW. The importance of these influences is highly dependent on the diameter and aspect ratio of the NW.

(2) The Steigmann-Ogden correction can stiffen or soften the NW, depending on the sign of the Steigmann-Ogden constant.

(3) Both the Winkler modulus and Pasternak modulus tend to stiffen the NW. The critical buckling force of the NW is more sensitive to the Pasternak modulus.

Acknowledgement

The support of National Natural Science Foundation of China under contract No. 10802032 is most sincerely appreciated.

References

[1] M.E. Gurtin and A.I. Murdoch, A continuum theory of elastic material surfaces. Arch Ration Mech Anal, 57 (1975) 291–323.

[2] M.E. Gurtin and A.I. Murdoch, Surface stress in solids. Int J Solids Struct., 14 (1978) 431–440.

[3] P. Sharma, S. Ganti, N. Bhate, Effect of surfaces on the size-dependent elastic state of nano-inhomogeneities. Appl Phys Lett, 82 (2003) 535–537.

[4] G.F. Wang and X.Q. Feng, Surface effects on buckling of nanowires under uniaxial compression. Appl Phys Lett, 94 (2009) 141913–1419133.

[5] H.L. Duan, J. Wang, Z.P. Huang, B.L. Karihaloo, Size-dependent effective elastic constants of solids containing nano-inhomogeneities with interface stress. J Mech Phys Solids, 53 (2005) 1574–1596.

[6] L.H. He and C.W. Lim, On the bending of unconstrained thin crystalline plates caused by the change in surface stress. Surf Sci, 478 (2001) 203-210.

[7] H. S. Park, Surface stress effects on the critical buckling strains of silicon nanowires. Comput Mater Sci, 51 (2012) 396-401.

[8] M.T. McDowell, A.M. Leach, and K. Gall, Bending and tensile deformation of metallic nanowires. Modelling Simul Mater Sci Eng, 16 (2008) 045003.

[9] G. Yun and H.S. Park, Surface Stress Effects on the bending properties of FCC metalnanowires. Phys Rev B: Condens. Matter, 79 (2009) 195421.

[10] P. Chhapadia, P. Mohammadi, and P. Sharma, Curvature-dependent surface energy and implications for nanostructures. J Mech Phys Solids, 59 (2011). 2103-2115.

[11] D.J. Steigmann and R.W. Ogden, Plane deformations of elastic solids with intrinsic boundary elasticity. Proc R. Soc London, A, 453 (1997) 853–877.

[12] D.J. Steigmann and R.W. Ogden, Elastic surface substrate interactions. Proc . R Soc London, A, 455 (1999) 437–474.

Effect of thermally activated energy on dislocation emission from a blunted crack tip

X. Zeng[1], Q.H. Fang*[1, 2], Y.W. Liu[1]

[1] College of Mechanical and Vehicle Engineering, Hunan University, Changsha, 410082 Hunan Province, PR China
[2] School of Mechanical and Manufacturing Engineering, The University of New South Wales, NSW 2052, Australia
* Corresponding author: Fangqh1327@tom.com

Abstract Thermally activated processes are of fundamental importance for the understanding and modeling of strength of structural materials. The effect of thermally activated on dislocation emission from an elliptically blunted crack tip is investigated. Critical stress intensity factors were simulated for edge dislocation emission from a blunt crack under mode I and mode II loading conditions at high temperature. The results show the impact of thermally activated processes is remarkable, which can affect the value of the critical stress intensity factors for dislocation emission, but doesn't alter the emission angle. The applied electric load will increase with decreasing temperature.

Keywords thermally activated, blunted crack, dislocation emission

1. Introduction

Dislocation emission from a crack tip is one of the most fundamental process for understanding the ductile-brittle behavior in crystalline materials [1]. Once dislocations are emitted, they move out of the crack tip area, leaving behind a dislocation-free zone. An internal back stress due to the dislocations emitted from crack tip accommodates the stress intensity due to applied load, causing an increase in fracture toughness of materials[2]. The previous formulations [3-5] assume the crack tip to be sharp, a situation that is not observed experimentally [6]. However, a real crack in a material is always of finite length and the radius of curvature of the crack tip is never small enough to be zero [7,8]. Physically, an atomically sharp crack will be blunted by one atomic plane. On the other hand, the emission of a dislocation from crack tip results in crack blunting [9,10]. Lung and Wang [11], and Lee [7] calculated the image force on the dislocation near a blunt crack tip. Critical stress intensity factors were developed for edge dislocation emission from a blunt crack [12, 13].

In this paper, we investigated the effect of thermally activated on the emission of edge dislocation from a blunted crack tip. It is also well known that plastic deformation of nanocrystalline and ultrafine-grained metals is thermally activated. Furthermore, thermal activation parameters, such as activation volume and strain-rate sensitivity exponent, strongly depend on grain size and temperature [14-17].When thermally activated deformation processes are to be discussed, the applied stress is generally considered to have two components, i.e.,

$$\tau = \tau_a + \tau^*\left(T, \dot{\gamma}\right) \tag{1}$$

where τ is the applied shear stress, τ_a is the long-range internal stress and is athermal in nature. The thermal component τ^* is often called the effective stress and depends on test temperature T and shear strain rate $\dot{\gamma}$. The shear strain rate is formally written as an Arrhenius-type rate equation

[18–21].

$$\dot{\gamma} = \dot{\gamma}_0 \exp\left[-\frac{G\left(\tau^*\right)}{kT}\right] \tag{2}$$

where $\dot{\gamma}_0$ is a pre-exponential factor, $G\left(\tau^*\right)$ the stress-dependent activation energy for the thermally activated dislocation motion, k the Boltzmann constant.

The present contribution mainly tackles the influence of thermally activated effect on the critical stress intensity factors when dislocation is assumed to be emitted under mode I and mode II loads.

2. Modeling

According to the work of Lubarda [22], the stress fields of an edge dislocation emitted from the surface of the void correspond to the imposed displacement discontinuity along the cut from the surface of the void to the center of the dislocation. As shown in Fig.1, an infinite elastic medium with the elastic properties ν and μ contains a blunted crack (an elliptically hole) of a the radius of curvature $\rho = b^2/a$, where μ is the shear modulus and ν is the Poisson's ratio. The blunted crack is straight and infinitely extended in a direction perpendicular to the xy-plane. Edge dislocation 1 with Burgers vector b_1 was emitted from the surface of the blunted crack to the point $z_0 = a - \rho/2 + r_0 e^{i\theta}$, which represent polar coordinates based on an origin behind the crack root, and edge dislocation 2 with Burgers vector b_2 is located at the surface of crack $z_d = a - \rho/2 + r_d e^{i\theta}$. They are both assumed to be straight and infinite along the direction perpendicular to the xy-plane, and $b_1 = -b_2 = b_x + ib_y = b_r e^{i\theta}$.

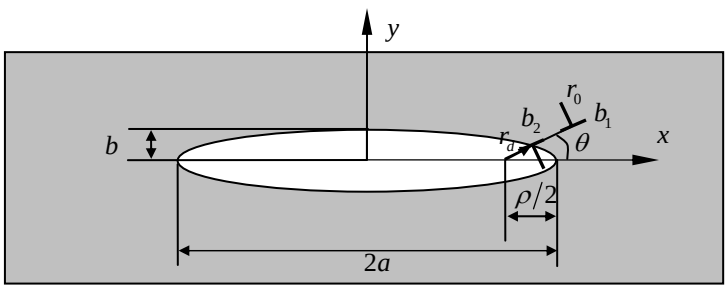

Figure 1 Dislocation emission from an elliptically blunted crack tip.

we first consider only a short range thermal barrier and the associated effective stress component τ^*. The activation energy $G(\tau^*)$ in Eq. (2) is frequently expressed as[20]

$$G(\tau^*) = G_0\left[1 - \left(\frac{\tau^*}{\tau_m}\right)^p\right]^q, \quad 0 \le p \le 1, \quad 1 \le q \le 2, \tag{3}$$

where p and q are phenomenological parameters reflecting the shape of a resistance profile,

G_0 is the activation energy and τ_m is the effective stress at 0K . From Eqs. (2) and (3), we have

$$\tau^* = \tau_m \left\{ 1 - \left[\frac{kT \ln\left(\dot{\varepsilon}_0 / \dot{\varepsilon}\right)}{G_0} \right]^{1/q} \right\}^{1/p} . \tag{4}$$

For given G_0, $\dot{\varepsilon}_0$, p and q, this equation expresses the temperature and strain-rate dependence of the effective stress τ^*.

Now we calculate the effective slip stress τ_m at 0K. According to the work of Nakatani et al.[23], the effective slip stress agrees with Rise's theoretical prediction. We proceed to map conformally the infinite region outside the elliptical hole in the $z = x + iy$ plane to the infinite region outside a circle of a radius R in the $\zeta = \xi + i\eta$ plane through a transformation function

$$z = \omega(\zeta) = \frac{c}{2}\left(\zeta + \frac{1}{\zeta} \right) \tag{5}$$

where $c = \sqrt{a^2 - b^2}$ and $R = \sqrt{(a+b)/(a-b)}$.

The stress fields can be expressed as[ ]

$$\sigma_y + \sigma_x = 2[\varphi'(z) + \overline{\varphi'(z)}] = 2[\varphi'(\zeta)/\omega'(\zeta) + \overline{\varphi'(\zeta)/\omega'(\zeta)}] \tag{6}$$

$$\sigma_y - \sigma_x + 2i\tau_{xy} = 2\left[\bar{z}\varphi''(z) + \psi'(z)\right]$$

$$= 2\left[\overline{\omega(\zeta)}\left[\varphi''(\zeta)\omega'(\zeta) - \varphi'(\zeta)\omega''(\zeta)\right] / \left[\omega'(\zeta)\right]^3 + \psi'(\zeta)/\omega'(\zeta) \right] \tag{7}$$

Using Muskhelishvili's complex potential method [24], the complex potential functions in the $\zeta = \xi + i\eta$ plane can be easily calculated as

$$\varphi(\zeta) = \gamma \ln(\zeta - \zeta_0) - \gamma \ln(\zeta - \zeta_d) - \gamma \ln(\zeta - R^2/\bar{\zeta}_0) + \gamma \ln(\zeta - R^2/\bar{\zeta}_d)$$

$$+ \frac{\bar{a}_0 \bar{\gamma} R^2}{(\zeta - R^2/\bar{\zeta}_0)\bar{\zeta}_0^2} - \frac{\bar{a}_d \bar{\gamma} R^2}{(\zeta - R^2/\bar{\zeta}_d)\bar{\zeta}_d^2} \tag{8}$$

$$\psi(\zeta) = \chi(\zeta) - \frac{\bar{\omega}(R^2/\zeta)}{\omega'(\zeta)}\varphi'(\zeta) \tag{9}$$

$$\chi(\zeta) = \bar{\gamma} \ln(\zeta - \zeta_0) - \bar{\gamma} \ln(\zeta - \zeta_d) - \bar{\gamma} \ln(\zeta - R^2/\bar{\zeta}_0) + \bar{\gamma} \ln(\zeta - R^2/\bar{\zeta}_d)$$

$$+ \frac{a_0 \gamma}{\zeta - \zeta_0} - \frac{a_d \gamma}{\zeta - \zeta_d} \tag{10}$$

where $\gamma = \dfrac{\mu b_1}{4\pi i(1-\nu)}$, $\zeta_0 = \dfrac{1}{c}\left(z_0 + \sqrt{z_0^2 - c^2}\right)$, $a_0 = \dfrac{(R^4 + \zeta_0^2)\zeta_0}{R^2(\zeta_0^2 - 1)} - \dfrac{\zeta_0^2(\bar{\zeta}_0^2 + 1)}{\bar{\zeta}_0(\zeta_0^2 - 1)}$, $\zeta_d = \dfrac{1}{c}\left(z_d + \sqrt{z_d^2 - c^2}\right)$,

$$a_d = \frac{(R^4+\zeta_d^2)\zeta_d}{R^2(\zeta_d^2-1)} - \frac{\zeta_d^2(\bar{\zeta}_d^2+1)}{\bar{\zeta}_d(\zeta_d^2-1)}.$$

According to the Peach-Koehler formula[25], and considering Eqs. (6)—(7), we obtain the image force acting on the dislocation

$$\begin{aligned} f_x - if_y &= \left[\hat{\tau}_{xy}(z_0)b_x + \hat{\sigma}_y(z_0)b_y\right] + i\left[\hat{\sigma}_x(z_0)b_x + \hat{\tau}_{xy}(z_0)b_y\right] \\ &= \left(b_y + ib_x\right)\left[\hat{\varphi}'(z_0) + \overline{\hat{\varphi}'(z_0)}\right] + \left(b_y - ib_x\right)\left[\bar{z}_0\hat{\varphi}''(z_0) + \hat{\psi}'(z_0)\right], \end{aligned} \tag{11}$$

where f_x and f_y are the force in the x and y directions, respectively, $\hat{\sigma}_x(z_0)$, $\hat{\sigma}_y(z_0)$ and $\hat{\sigma}_{xy}(z_0)$ are the components of the perturbation stress fields at the dislocation point z_0, $\hat{\varphi}'(z_0)$ and $\hat{\psi}'(z_0)$ are the perturbation complex potentials in the matrix.

According to Qaissaunee and Santare[26], the perturbation complex potentials are calculated as follows:

$$\begin{aligned} \hat{\varphi}'(z_0) = \Bigg[& -\frac{\gamma}{\zeta_0(\zeta_0^2-1)} - \frac{\gamma}{\zeta_0-\zeta_d} - \frac{\gamma}{\zeta_0 - R^2/\bar{\zeta}_0} + \frac{\gamma}{\zeta_0 - R^2/\bar{\zeta}_d} \\ & - \frac{\bar{a}_0\bar{\gamma}R^2}{(\zeta_0\bar{\zeta}_0 - R^2)^2} + \frac{\bar{a}_d\bar{\gamma}R^2}{(\zeta_0\bar{\zeta}_d - R^2)^2}\Bigg] \Big/ \omega'(\zeta_0), \end{aligned} \tag{12}$$

$$\begin{aligned} \hat{\varphi}''(z_0) = \Bigg\{ \Bigg[& \frac{\gamma(2\zeta_0^2-1)}{\zeta_0^4(\zeta_0^2-1)^2} + \frac{\gamma}{(\zeta_0-\zeta_d)^2} + \frac{\gamma}{(\zeta_0 - R^2/\bar{\zeta}_0)^2} - \frac{\gamma}{(\zeta_0 - R^2/\bar{\zeta}_d)^2} \\ & + \frac{2\bar{\zeta}_0\bar{a}_0\bar{\gamma}R^2}{(\zeta_0\bar{\zeta}_0 - R^2)^3} - \frac{2\bar{\zeta}_d\bar{a}_d\bar{\gamma}R^2}{(\zeta_0\bar{\zeta}_d - R^2)^3}\Bigg] - \frac{c}{\zeta_0^3}\hat{\varphi}'(z_0)\Bigg\} \Big/ \left[\omega'(\zeta_0)\right]^2, \end{aligned} \tag{13}$$

$$\begin{aligned} \hat{\psi}'(z_0) = \Bigg\{ & -\frac{\bar{\gamma}}{\zeta_0-\zeta_d} - \frac{\bar{\gamma}}{\zeta_0 - R^2/\bar{\zeta}_0} + \frac{\bar{\gamma}}{\zeta_0 - R^2/\bar{\zeta}_d} - \frac{\bar{\gamma}}{\zeta_0(\zeta_0^2-1)} + \frac{\gamma\zeta_0^2(\bar{\zeta}_0^2+1)}{\bar{\zeta}_0(\zeta_0^2-1)^3} \\ & + \frac{a_d\gamma}{(\zeta_0-\zeta_d)^2} - \frac{\gamma(R^4+1)(\zeta_0^3+3\zeta_0)}{R^2(\zeta_0^2-1)^3} - \frac{\zeta_0(\zeta_0^2+R^4)}{R^2(\zeta_0^2-1)}\Bigg[\frac{\gamma}{(\zeta_0-\zeta_d)^2} \\ & + \frac{\gamma}{(\zeta_0 - R^2/\bar{\zeta}_0)^2} - \frac{\gamma}{(\zeta_0 - R^2/\bar{\zeta}_d)^2} + \frac{2\bar{\zeta}_0\bar{a}_0\bar{\gamma}R^2}{(\zeta_0\bar{\zeta}_0 - R^2)^3} - \frac{2\bar{\zeta}_d\bar{a}_d\bar{\gamma}R^2}{(\zeta_0\bar{\zeta}_d - R^2)^3}\Bigg] \\ & - \frac{\zeta_0^4 - \zeta_0^2R^4 - 3\zeta_0^2 - R^4}{R^2(\zeta_0^2-1)^2}\Bigg[-\frac{\gamma}{\zeta_0-\zeta_d} - \frac{\gamma}{\zeta_0 - R^2/\bar{\zeta}_0} + \frac{\gamma}{\zeta_0 - R^2/\bar{\zeta}_d} \\ & - \frac{\bar{a}_0\bar{\gamma}R^2}{(\zeta_0\bar{\zeta}_0 - R^2)^2} + \frac{\bar{a}_d\bar{\gamma}R^2}{(\zeta_0\bar{\zeta}_d - R^2)^2}\Bigg]\Bigg\} \Big/ \omega'(\zeta_0). \end{aligned} \tag{14}$$

Based on Stagni[27], the primary physical interest lies on the effective slip stress τ_m which are given by

$$\tau_m = \mathrm{Re}\left\{ i\left[\hat{\varphi}'(z_0) + \overline{\hat{\varphi}'(z_0)} \right] - ie^{2i\theta}\left[\overline{z}_0 \hat{\varphi}''(z_0) + \hat{\psi}'(z_0) \right] \right\}. \tag{15}$$

For the linear elastic analysis of plane cases, Creager and Paris's equations [28] can be used to evaluate the stress fields for an elliptically blunted head. So from Creager and Paris's solutions, the in-plane slip stress due to the applied mode I SIF K_{I} and mode II SIF K_{II} is given by

$$\tau_a = \frac{K_{\mathrm{I}}}{2\sqrt{2\pi r_0}} \sin\frac{\theta}{2}\left(1 + \cos\theta + \frac{\rho}{r_0}\right) + \frac{K_{\mathrm{II}}}{\sqrt{2\pi r_0}}\left(\cos\frac{3\theta}{2} + \frac{1}{2}\sin\theta\sin\frac{\theta}{2} - \frac{\rho}{2r_0}\cos\frac{\theta}{2}\right). \tag{16}$$

Combining Eqs. (1), (4), (15) and (16), we obtain the slip stress acting on the dislocation. The equilibrium distance, r_0, at which the total force on the edge dislocation is zero, is given by

$$\frac{K_{\mathrm{I}}\sin\frac{\theta}{2}}{2\sqrt{2\pi r_0}}\left(1 + \cos\theta + \frac{\rho}{r_0}\right) + \frac{K_{\mathrm{II}}}{\sqrt{2\pi r_0}}\left(\cos\frac{3\theta}{2} + \frac{\sin\theta}{2}\sin\frac{\theta}{2} - \frac{\rho\cos\frac{\theta}{2}}{2r_0}\right) + \tau^* = 0 \tag{17}$$

Referencing to the work of Rice and Thomson [1], if the distance between the crack tip and the zero-slip-force position of a dislocation is less than the core radius of dislocation, a new dislocation would be emitted spontaneously from the crack tip. In the present analysis, we assume that the core radius of the dislocation is equal to Burgers vector b_r. Thus, $r_0 = r_d + b_r$, and r_d is expressed by

$$r_d = \frac{\sqrt{a^2 - 0.25a\rho(\sin\theta)^2} - (a - \rho/2)\cos\theta}{\rho(\cos\theta)^2 + a(\sin\theta)^2}\rho. \tag{18}$$

So we obtain the critical applied mode I SIF:

$$K_{\mathrm{I}}^C = -2\sqrt{2\pi r_0}\,\tau^* \Big/ \sin\frac{\theta}{2}\left(1 + \cos\theta + \frac{\rho}{r_0}\right). \tag{19}$$

Similar to the mode I crack, we have the normalized critical applied mode II SIF:

$$K_{\mathrm{II}}^C = -\sqrt{2\pi r_0}\,\tau^* \Big/ \left(\cos\frac{3\theta}{2} + \frac{1}{2}\sin\theta\sin\frac{\theta}{2} - \frac{\rho}{2r_0}\cos\frac{\theta}{2}\right). \tag{20}$$

3. Analysis

Utilizing Eqs. (19) and (20), the influence of the surface stress on the critical applied SIFs can be evaluated. Wang et al.[18] examined the temperature dependence of nanocrystalline Ni at a tensile strain rate of $1\times10^{-4}\,\mathrm{s}^{-1}$. The numerical calculations are presented for a set of thermally activated properties: $p = 0.24$, $q = 1.3$, $\dot{\varepsilon}_0 = 1\times10^{7}\,\mathrm{s}^{-1}$ and $G_0 = 3.0\mathrm{eV}$ $(4.81\times10^{-19}\mathrm{J})$ (Ni)[29].

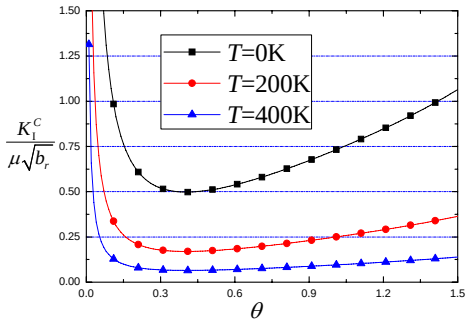

Figure 2 Critical normalized SIF $K_{\mathrm{I}}^{C}/\mu\sqrt{b_r}$ as a function of emission angle θ with different temperature T at $\rho = 0.01a$, $a = 200b_r$ for nanocrystalline Ni. $T = 0$: $K_{\mathrm{I}\min}^{C}/\mu\sqrt{b_r} = 0.498$, $\theta_{cr} = 0.404$; $T = 200$: $K_{\mathrm{I}\min}^{C}/\mu\sqrt{b_r} = 0.170$, $\theta_{cr} = 0.404$; $T = 400$: $K_{\mathrm{I}\min}^{C}/\mu\sqrt{b_r} = 0.065$, $\theta_{cr} = 0.404$.

For an elliptically blunted crack, the shape can be described by a and the ratio ρ/a. Fig. 2 show the critical normalized SIF for edge dislocation emission as a function of emission angle θ with different temperature T for mode I applied stress ($\rho = 0.01a$, $a = 200b_r$). The minimum value of $K_{\mathrm{I}}^{C}/\mu\sqrt{b_r}$ indicates the most probable angle θ_{cr} for dislocation emission, and the minimum critical stress and the relative most probable angle for dislocation emission are $K_{\mathrm{I}\min}^{C}/\mu\sqrt{b_r} = 0.498$, $\theta_{cr} = 0.404$ for $T = 0$; $K_{\mathrm{I}\min}^{C}/\mu\sqrt{b_r} = 0.170$, $\theta_{cr} = 0.404$ for $T = 200$; $K_{\mathrm{I}\min}^{C}/\mu\sqrt{b_r} = 0.065$, $\theta_{cr} = 0.404$ for $T = 400$. It is clearly found that the critical SIF decreases from infinity to a minimum and then increases with increasing emission angle θ, which is in agreement with the result in the previous papers[12, 13]. And with the increasing temperature, the minimum value of critical SIF decreases, while the most probable angle for dislocation emission does not change. It means that the high temperature make the dislocation emission take place easily.

The critical normalized SIF $K_{\mathrm{I}}^{C}/\mu\sqrt{b_r}$ as a function of emission angle θ with different crack shape at $T = 200\mathrm{K}$ are displayed in Fig. 3(a) and (b). Fig.4(a) and (b) show the critical normalized SIF $K_{\mathrm{I}}^{C}/\mu\sqrt{b_r}$ as a function of temperature T with different crack shape at $\theta = 0.5$. They are been seen that the minimum critical SIF and the relative most probable angle are increases with increasing crack length and radius of curvature. And with the increase of temperature, the critical SIF increases, and with the increase in crack length and radius of curvature, the change of the critical load increases.

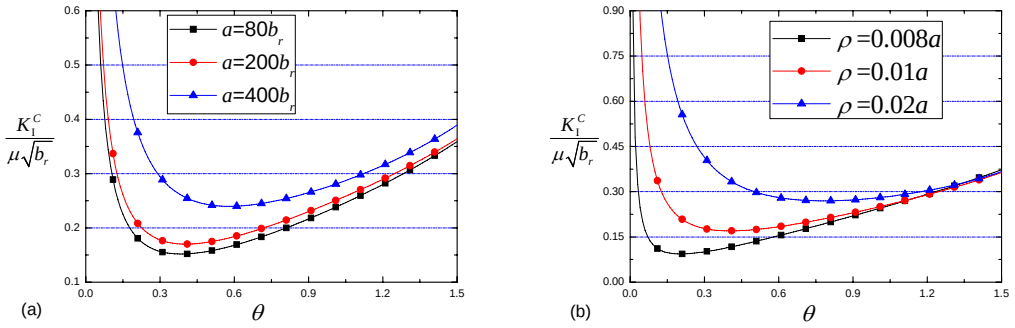

Figure 3 Critical normalized SIF $K_{\mathrm{I}}^{C}/\mu\sqrt{b_r}$ as a function of emission angle θ with different crack shape at $T=200\mathrm{K}$: (a) for $\rho=0.01a$; (b) for $a=200b_r$.

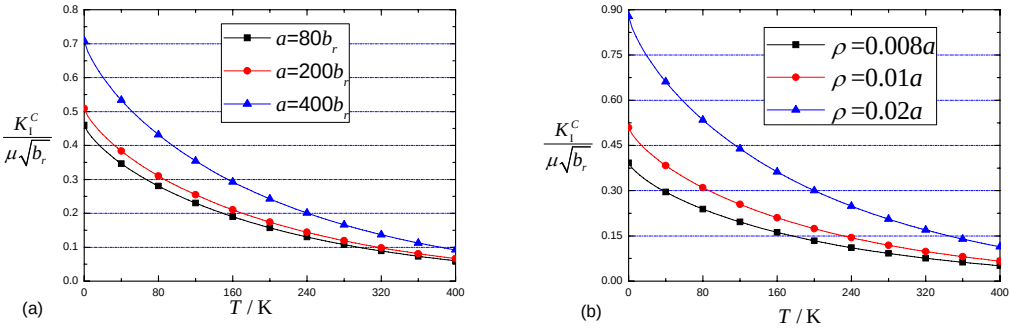

Figure 4 Critical normalized SIF $K_{\mathrm{I}}^{C}/\mu\sqrt{b_r}$ as a function of temperature T with different crack shape at $\theta=0.5$: (a) for $\rho=0.01a$; (b) for $a=200b_r$.

4. Conclusions

The effect of thermally activated on dislocation emission from an elliptically blunted crack tip is investigated. Considering the mechanism that the stress fields of an edge dislocation emitted from the surface of the void correspond to the imposed displacement discontinuity along the cut from the surface of the void to the center of the dislocation, the critical stress intensity factors for edge dislocation emission from a blunt crack under mode I and mode II loading conditions at high temperature were simulated in nanocrystalline and ultrafine-grained metals. The results show the impact of thermally activated processes is remarkable, which can affect the value of the critical stress intensity factors for dislocation emission, but does not alter the emission angle. With the increasing temperature, the minimum value of critical SIF decreases. And the high temperature make the dislocation emission take place easily.

Acknowledgements

The authors would like to deeply appreciate the support from the NNSFC (11172094 and 11172095) and the NCET-11-0122. This work was also supported by Hunan Provincial Natural Science Foundation for Creative Research Groups of China (Grant No.12JJ7001).

References

[1] J.R. Rice, R. Thomson, Ductile versus brittle behaviour of crystals. Philos Mag, 29 (1974) 73-97.

[2] I.H. Lin, R, Thomson, Cleavage, dislocation emission, and shielding for cracks under general loading. Acta Metall, 34 (1986) 187-206

[3] C.C. Huang, C.C. Yu, S. Lee, The behavior of screw dislocations dynamically emitted from the tip of a surface crack during loading and unloading. J Mater Res, 10 (1995) 183-189.

[4] T.C. Wang, Dislocation nucleation and emission from crack tip. Int J Fract, 69 (1995) 295-306.

[5] Y.Z. Tsai, S. Lee, Dynamic emission of screw dislocations from a propagating crack tip. J Appl Phys, 81 (1997) 2089-2093.

[6] J.H. Chen, Q. Wang, G.Z. Wang, Z. Li, Fracture behavior at crack tip—a new framework for cleavage mechanism of steel. Acta Mater, 51 (2003) 1841-1855.

[7] S. Lee, The image force on the screw dislocation around a crack of finite size. Eng Fract Mech, 27 (1987) 539-545.

[8] B.T. Chen, T.Y. Zhang, S. Lee, Interaction of an edge dislocation with an elliptical hole in a rectilinearly anisotropic body. Mech Mater, 31 (1999) 71-93.

[9] S.M. Ohr, An electron microscopy study of crack tip deformation and its impact on dislocation theory of fracture. Mater Sci Eng, 72 (1985) 1-35.

[10] S.J. Zhou, A.E. Carlsson, R. Thomson, Crack blunting effects on dislocation emission from cracks. Phys Rev Lett, 72 (1994) 852-855.

[11] C.W. Lung, L.Wang, The image force on the dislocation near a finite length crack tip. Philos Mag, 50 (1984) L91-L24.

[12] M. Huang, Z. Li, Dislocation emission criterion from a blunt crack tip. J Mech Phys Solids, 52 (2004) 1991-2003.

[13] Q.H. Fang, Y. Liu, Y.W. Liu, B.Y. Huang, Dislocation emission from an elliptically blunted crack tip with surface effects. Physica B 404 (2009) 3421-3424.

[14] Y.M.Wang, E. Ma, Strain hardening, strain rate sensitivity, and ductility of nanostructured metals. Mater Sci Eng A, 375 – 377 (2004) 46-52.

[15] Q.Wei, S. Cheng, K.T. Ramesh, E. Ma, Effect of nanocrystalline and ultrafine grain sizes on the strain rate sensitivity and activation volume: fcc versus bcc metals. Mater Sci Eng A, 381 (2004) 71-79.

[16] R.W. Hayes, D. Witkin, F. Zhou, E.J. Lavernia, Deformation and activation volumes of cryomilled ultrafine-grained aluminum. Acta Mater, 52 (2004) 4259-4271.

[17] Y.J. Li, X.H. Zeng,W. Blum, Transition from strengthening to softening by grain boundaries in ultrafine-grained Cu. Acta Mater, 52 (2004) 5009-5018.

[18] Y.M.Wang, A.V. Hamza, E. Ma, Temperature-dependent strain rate sensitivity and activation volume of nanocrystalline Ni. Acta Mater, 54 (2006) 2715 – 2726.

[19] H. Conrad, Thermally activated deformation of metals. J Metals, 16 (1964) 582-588.

[20] U.F. Kocks, A.S. Argon, M.F. Ashby, Thermo-dynamics and Kinetics of Slip. Prog Mater Sci, 19 (1975) 1 – 278.

[21] M. Dao, L. Lu, R.J. Asaro, J.T.M. De Hosson, E. Ma, Toward a quantitative understanding of mechanical behavior of nanocrystalline metals. Acta Mater, 55 (2007) 4041-4065.

[22] V.A. Lubarda, Image force on a straight dislocation emitted from a cylindrical void. Int J Solids

Struct, 48 (2011) 648-660.

[23] A. Nakatani, H. Kitagawa, Y. Shibutani, K. Nakatani, Molecular dynamics study on ductile crack process effect of temperature on dislocation nucleation. Mater Sci Res Int, 1 (1995) 11-16.

[24] NI. Muskhelishvili, Some basic problems of the mathematical theory of elasticity, Noordhoff International Publishing, Leyden 1975.

[25] J.P. Hirth, J. Lothe, Theory of Dislocations, 1982, 2nd edn. (John Wiley, New York).

[26] M.T. Qaissaunee, M.H. Santare, Edge dislocation interacting with an elliptical inclusion surrounded by an interfacial zone. Q J Mech Appl Math, 48 (1995) 465-482.

[27]L. Stagni, Edge dislocation near an elliptic inhomogeneity with either an adhering or a slipping interface - A comparative study. Phil Mag A, 68(1993) 49-57.

[28] M. Creager, P.C. Paris, Elastic field equations for blunt cracks with reference
to stress corrosion cracking. Int J Fract Mech, 3 (1967) 247-252.

[29] L. Hollang, E. Hieckmann, D. Brunner, C. Holste, W. Skrotzki, Scaling effects in the plasticity of nickel. Mater Sci Eng A, 424 (2006) 138 – 153.

Effect of cooperative grain boundary sliding and migration on emission of dislocations from a crack tip in nanocrystalline materials

H. Feng [1], Q.H. Fang [1, 2,*], Y.W. Liu [1]

1 State Key Laboratory of Advanced Design and Manufacturing for Vehicle Body (Hunan University), Changsha 410082, China

2 School of Mechanical and Manufacturing Engineering, The University of New South Wales, NSW 2052, Australia

* Corresponding author: fangqh1327@tom.com ; Qi-hong.fang@unsw.edu.au

Abstract Interaction of the cooperative grain boundary sliding and migration with a crack in deformed nanocrystalline materials is investigated using the complex variable method. Effects of the two disclination dipoles produced by the cooperative deformation on the emission of lattice dislocations from the crack tip are theoretically described. The complex form expressions of the stress field and the force field are divided. The critical stress intensity factors for the first dislocation emission are calculated. Influences of disclination strength, grain size, locations of the two disclination dipoles as well as crack length on the critical stress intensity factors are discussed in detail. Results show that, the cooperative deformation has great influence on dislocation emission from the crack tip. In general, the cooperative deformation can promote the lattice dislocation emission from the crack tip, thus improve the toughness of the nanocrystalline materials.

Keywords nanocrystalline materials; crack; grain boundary sliding; grain boundary migration; dislocation emission;

1. Introduction

Nanocrystalline metals and ceramics show outstanding mechanical and physical properties, which represent the subject of rapidly growing research efforts motivated by a wide range of their applications [1-8]. However, in most cases, nanocrystalline materials have superior strength, hardness and good wear resistance but at the expenses of both low tensile ductility and low fracture toughness, which considerably limit their practical utility [3-5, 9-11]. At the same time, there are several examples of nanocrystalline materials showing considerable tensile ductility at room temperatures [4, 12-14], or superplasticity at elevated temperatures [14, 15], and significant fracture toughness that can be often higher than that of their polycrystalline or singlecrystalline counterparts [4, 16-19]. The nature of the outstanding combination of good ductility and superior strength is not quite clear, which creates high interest in understanding the toughening mechanisms that specific for nanocrystalline materials. Recently, many models have been developed to explain this phenomenon. In most of them, intergrain sliding, grain boundary migration, triple junction diffusional creep, Coble creep, rotational deformation and nanoscale deformation twinning have been theoretically described as specific deformation modes in nanocrystalline materials. And the specific toughening mechanisms are attributed to specific deformation modes in nanocrystalline materials [20-25].

Recently, rapidly growing attention has been focused on a new physical mechanism or mode of plastic deformation in nanocrystalline metals and ceramics. The new specific deformation mode represents the cooperative grain boundary sliding and stress-driven grain boundary migration process near the tips of growing cracks [26]. Grain boundary sliding is an important deformation mechanism in nanocrystalline materials [3, 4, 10]. It is also one of the specific deformation modes showing superplasticity in nanocrystalline materials [4, 15]. Non-accommodated grain boundary sliding in nanocrystalline solids creates defects (dislocations and disclination dipoles) at triple junctions of grain boundaries. These defects can initiating the formation of cracks, in which case a nanocrystalline solid tends to exhibit brittle behaviour [27, 28]. In contrast, if grain boundary

sliding is effectively accommodated, nanocrystalline solids show enhanced ductility and/or superplasticity [4, 15, 29]. And it is effectively realized that accommodation of grain boundary sliding occurs through lattice dislocation emission from triple junctions, diffusion, and rotational deformation [4, 15, 29]. There has been a new way to accommodate grain boundary sliding through grain boundary migration suggested and theoretically analyzed [20, 26]. Grain boundary migration is another toughening micromechanism [30] and specific deformation mode in nanocrystalline materials [3, 22].

The new accommodation mode we discussed above involving the cooperative grain boundary sliding and stress-driven grain boundary migration, servers as a special deformation mode enhanced compared to pure grain boundary sliding in nanocrystalline materials [20]. In the cooperative process, defects created by grain boundary sliding are, in part, accommodated by defects created by grain boundary migration. The cooperative grain boundary sliding and migration has been theoretically described as a deformed mode operation in crack-free nanocrystalline materials in Bobylev et al. [20]. And it is theoretically revealed that the mode enhances the ductility of nanocrystalline solids in wide ranges of their structural parameters. In the work of Ovid'ko et al. [26], the cooperative grain boundary sliding and migration process near crack tips has been described, and its effect on the fracture toughness of nanocrystalline materials has been theoretically analyzed. The results show that the mechanism considerably enhances the fracture toughness of nanocrystalline materials.

The previous works have lots of experimental and theoretical results suggest that the cooperative grain boundary sliding and migration serving as a special deformation contributes to the toughening of nanocrystalline materials [20, 26]. But the effect of the cooperative grain boundary sliding and migration on the emission of lattice dislocations from crack tips has not been well quantitatively studied. Considering nanocrystalline solids with cracks, if the stress intensity near the crack tip is large enough, the crack can induce plastic shear through the emission of lattice dislocations from the crack tip. The emission of dislocations from cracks causes effective blunting of cracks, thus suppresses their growth, improves the toughness of nanocrystalline materials. So the crack blunting and growth processes are controlled by dislocation emission from crack tips. In the context discussed, there is large interest in the effect of the cooperative mode on lattice dislocation emission from crack tips. The main aim of the paper is to study the effect of the cooperative grain boundary sliding and migration on lattice dislocation emission from the crack tip using a theoretical mode.

2. Model and problem formulation

Let us consider a deformed nanocrystalline solid with a crack under remote mode I loadings and remote mode II loadings. The solid is supposed to be an elastically isotropic solid characterized by the shear modulus μ and Poisson's ratio ν. For definiteness, referring to the approximation in Ovid'ko et al. [26], we will focus our analysis on the situation where the crack is flat and plane, and characterized by the length L. For simplicity, we assume that the defect structure of the solid is the same along the coordinate axis z perpendicular to the xy plane. This assumption will allow us to simplify the mathematical analysis of the problem in our study, reducing it to the consideration of a two-dimensional structure. At the same time, the two-dimensional description definitely reflects the key aspects of the problem.

The applied loadings and high stress concentration near the crack tip can induce both grain boundary sliding and migration near this crack tip. And the geometry of the cooperative grain boundary sliding and migration deformation is schematically presented in Fig. 1. Fig. 1a depicts a deformed nanocrystalline solid with a flat crack. The formation of two disclination dipoles CD and BE results from the cooperative grain boundary sliding and migration process and the dislocation emission is shown in Fig. 1b [26].

Within the model, the vertical grain boundary AB is assumed to be normal to the crack growth direction and make an angle φ with the grain boundaries AA_1 and BB_2. Let the triple junction

A lie at a vertical distance p and a horizontal distance p' from the crack tip and the length of all grain boundaries in the initial state be denoted as d. The disclination dipole CD of wedge disclinations is characterized by the strength magnitude ω and the arm $|x-y|$. The disclination dipole BE is characterized by the strength magnitude ω and the arm y. And x, y denote the distances of the grain boundary sliding and migration.

Let us introduce a Cartesian system (x,y) and a polar coordinate system (r,θ) with the origins at the point O. Then, the coordinates of the disclinations located at the points D, C, E and B can be described as $z_1\left(=r_1\mathrm{e}^{\mathrm{i}\theta_1}\right)$, $z_2\left(=r_2\mathrm{e}^{\mathrm{i}\theta_2}\right)$, $z_3\left(=r_3\mathrm{e}^{\mathrm{i}\theta_3}\right)$ and $z_4\left(=r_4\mathrm{e}^{\mathrm{i}\theta_4}\right)$, respectively. And the coordinates $\left(r_j,\theta_j\right)$ are calculated as follows:

$r_1(y)=\sqrt{y^2+p^2-2yp\cos\varphi}$, $r_2(x)=\sqrt{x^2+p^2-2xp\cos\varphi}$, $r_3(y)=\sqrt{y^2+(p+d)^2-2y(p+d)\cos\varphi}$, $r_4=p+d$;
$\theta_1(y)=-\arccos(y\sin\varphi/r_1)$, $\theta_2(x)=-\arccos(x\sin\varphi/r_2)$, $\theta_3(y)=-\arccos(y\sin\varphi/r_3)$, $\theta_4=-\pi/2$.

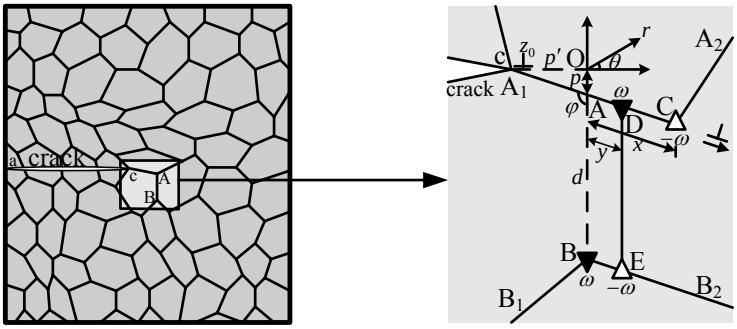

(a) (b)

Fig. 1 The cooperative grain boundary sliding and migration in a deformed nanocrystalline solid with a crack (a) General view. (b) The formation of two disclination dipoles CD and BE results from the cooperative grain boundary sliding and migration process, and the dislocation emission from the crack tip.

Now, let us calculate the stress fields produced by the cooperative grain boundary sliding and migration in the deformed nanocrystalline solid with a flat crack.

For the plane strain problem, stress fields (σ_{xx}, σ_{xy} and σ_{yy}) and displacement fields (u_x and u_y) may be expressed in terms of two Muskhelishvili's complex potentials $\Phi(z)$ and $\Psi(z)$ in the complex plane $z=x+\mathrm{i}y$: [31]

$$\sigma_{xx}+\sigma_{yy}=2\left(\Phi(z)+\overline{\Phi(z)}\right), \tag{1}$$

$$\sigma_{yy}-\mathrm{i}\sigma_{xy}=\Phi(z)+\overline{\Phi(z)}+z\overline{\Phi'(z)}+\overline{\Psi(z)}, \tag{2}$$

$$2\mu\left(u_x'+u_y'\right)=(3-4\nu)\Phi(z)-\overline{\Phi(z)}-z\overline{\Phi'(z)}-\Psi(z), \tag{3}$$

where $u_x'=\partial u_x/\partial x$, $u_y'=\partial u_y/\partial x$, $\Phi'(z)=\mathrm{d}\left[\Phi(z)\right]/\mathrm{d}z$, the over-bar represents the complex conjugate.

And the stress fields can be written as

$$\sigma_{xx}=\mathrm{Re}\left[2\Phi(z)-\bar{z}\Phi'(z)-\Psi(z)\right], \tag{4}$$

$$\sigma_{xy}=\mathrm{Im}\left[\bar{z}\Phi'(z)+\Psi(z)\right], \tag{5}$$

$$\sigma_{yy}=\mathrm{Re}\left[2\Phi(z)+\bar{z}\Phi'(z)+\Psi(z)\right]. \tag{6}$$

The boundary condition of the crack for the present problem can be expressed as

$$\sigma_{yy}(t)-\mathrm{i}\sigma_{xy}(t)=0,\quad t\in\text{crack}. \tag{7}$$

According the Romanov and Vladimirov [32], the elastic stress fields produced by a wedge disclination characterized by strength ω, located at the point z_k $(=x_k+\mathrm{i}y_k)$ in an infinite homogeneous medium may be expressed as follows:

$$\sigma_{xx}=\frac{\mu\omega}{2\pi(1-\nu)}\left(\frac{1}{2}\ln\left((x-x_k)^2+(y-y_k)^2\right)+\frac{(y-y_k)^2}{(x-x_k)^2+(y-y_k)^2}\right), \tag{8}$$

$$\sigma_{xy}=-\frac{\mu\omega}{2\pi(1-\nu)}\frac{(x-x_k)(y-y_k)}{(x-x_k)^2+(y-y_k)^2}, \tag{9}$$

$$\sigma_{yy}=\frac{\mu\omega}{2\pi(1-\nu)}\left(\frac{1}{2}\ln\left((x-x_k)^2+(y-y_k)^2\right)+\frac{(x-x_k)^2}{(x-x_k)^2+(y-y_k)^2}\right). \tag{10}$$

Assume that the elastic fields produced by the cooperative grain boundary sliding and migration in an infinite homogeneous medium can be evaluated by using two complex potentials $\Phi_{\Delta 0}(z)$ and $\Psi_{\Delta 0}(z)$.

Substituting Eqs. (8) and (9) into formula (1), Eqs. (9) and (10) into formula (2), referring to the work in Muskhelishvili [31], Fang et al. [33] and Liu et al. [34], the complex potentials $\Phi_{\Delta 0}(z)$ and $\Psi_{\Delta 0}(z)$ can be taken in the forms:

$$\Phi_{\Delta 0}(z)=\frac{\mu\omega}{4\pi(1-\nu)}\sum_{k=1}^{4}s_k\ln(z-z_k), \tag{11}$$

$$\Psi_{\Delta 0}(z)=-\frac{\mu\omega}{4\pi(1-\nu)}\sum_{k=1}^{4}s_k\frac{\overline{z}_k}{z-z_k}. \tag{12}$$

where $s_k\ (k=1,2,3,4)$ denote the sign of a specified disclination and are defined as $s_1=s_4=1$, $s_2=s_3=-1$.

From Eqs. (11) and (12) together with formulae (1) and (2), we obtain the stress fields which are identical to the results in Eqs. (8)-(10). Eqs. (11) and (12) are singularity principal parts of complex potentials on the problem of the cooperative grain boundary sliding and migration in an infinite homogeneous medium without the crack.

For the problem shown in Fig. 1, the complex potentials $\Phi_{\Delta}(z)$ and $\Psi_{\Delta}(z)$ can be written an

$$\Phi_{\Delta}(z)=\Phi_{\Delta 0}(z)+\Phi_{\Delta}^{*}(z), \tag{13}$$

$$\Psi_{\Delta}(z)=\Psi_{\Delta 0}(z)+\Psi_{\Delta}^{*}(z), \tag{14}$$

where $\Phi_{\Delta 0}(z)$ and $\Psi_{\Delta 0}(z)$ indicate the terms due to the presence of the cooperative grain boundary sliding and migration located in infinite medium, and $\Phi_{\Delta}^{*}(z)$ and $\Psi_{\Delta}^{*}(z)$ refer to the terms resulting from the interaction of the cooperative grain boundary sliding and migration with the crack, which are holomorphic in the region.

By using Riemann-Schwarz's symmetry principle, we introduce a new analytical function

$$\Omega_{\Delta}(z)=-\overline{\Phi}_{\Delta}(z)-z\overline{\Phi'}_{\Delta}(z)-\overline{\Psi}_{\Delta}(z). \tag{15}$$

The substitution of Eqs. (13) and (14) into Eq. (15) yields

$$\Omega_{\Delta}(z)=-\frac{\mu\omega}{4\pi(1-\nu)}\sum_{k=1}^{4}s_k\left(\ln(z-\overline{z}_k)+\frac{z-z_k}{z-\overline{z}_k}\right)+\Omega_{\Delta}^{*}(z), \tag{16}$$

where $\Omega_{\Delta}^{*}(z)$ is holomorphic in the region.

Considering the above complex potentials, the crack boundary condition (7) can be written an

$$\left[\Phi_{\Delta}(t)-\Omega_{\Delta}(t)\right]^{+}+\left[\Phi_{\Delta}(t)-\Omega_{\Delta}(t)\right]^{-}=0,\quad t\in\text{crack}, \tag{17}$$

$$\left[\Phi_{\Delta}(t)-\Omega_{\Delta}(t)\right]^{+}-\left[\Phi_{\Delta}(t)-\Omega_{\Delta}(t)\right]^{-}=0,\quad t\in\text{crack}, \tag{18}$$

where the superscripts "$+$" and "$-$" denote the boundary values of the physical quantity as z approached the crack from the upper half plane and the lower half plane.

Without loss in generality, we assume that two ends of the crack are located at points a and c on the x-axis. Therefore, the complex potentials $\Phi_{\Delta}(z)$ and $\Psi_{\Delta}(z)$ have the following forms:

$$\Phi_{\Delta}(z)=\frac{\mu\omega}{8\pi(1-\nu)}\sum_{k=1}^{4}s_k\left(\ln\frac{z-z_k}{z-\overline{z}_k}-\frac{z-z_k}{z-\overline{z}_k}\right)$$

$$+\frac{\mu\omega}{8\pi(1-\nu)}X_0(z)\sum_{k=1}^{4}s_k\left(\frac{1}{X_0(z_k)}\ln(z-z_k)-z_k+\overline{z}_k-\frac{1}{X_0(\overline{z}_k)}\left(\frac{z-z_k}{z-\overline{z}_k}+\ln(z-\overline{z}_k)\right)\right), \tag{19}$$

$$\Psi_{\Delta}(z)=\frac{\mu\omega}{8\pi(1-\nu)}\sum_{k=1}^{4}s_k\left(\frac{3z-z_k}{z-\overline{z}_k}-\frac{\overline{z}_k}{z-z_k}-\frac{z(z-z_k)}{(z-\overline{z}_k)^2}\right)-\frac{\mu\omega}{8\pi(1-\nu)}X_0(z)\sum_{k=1}^{4}s_k\left(\frac{1}{X_0(z_k)}\frac{\overline{z}_k}{z-z_k}+\frac{1}{X_0(\overline{z}_k)}\left(\frac{z(z-z_k)}{(z-\overline{z}_k)^2}-\frac{3z-z_k}{z-\overline{z}_k}\right)\right)$$

$$-\frac{\mu\omega}{8\pi(1-\nu)}X_0'(z)\sum_{k=1}^{4}s_k\left(\frac{1}{X_0(z_k)}z\ln(z-z_k)-z(z-\overline{z}_k)-\frac{1}{X_0(\overline{z}_k)}z\left(\frac{z-z_k}{z-\overline{z}_k}+\ln(z-\overline{z}_k)\right)\right), \tag{20}$$

where $X_0(z)=1\big/\sqrt{(z-a)(z-c)}$, $X_0'(z)=\mathrm{d}X_0(z)/\mathrm{d}z$.

Substituting Eqs. (19) and (20) into formulae (4), (5) and (6), we obtain the stress fields due to the cooperative grain boundary sliding and migration.

3. The emission force of lattice dislocations

Let us consider the emission of lattice dislocations from the crack tip. For simplicity, we focus on the situation where the dislocations are of edge character and their Burgers vectors lie along the slip plane that makes an angle θ with the x-axis.

For the first dislocation located at $z_0=r_0\mathrm{e}^{\mathrm{i}\theta_0}$ in the coordination system, the elastic fields can be evaluated by using the complex potentials $\Phi_{\perp}(z)$, $\Psi_{\perp}(z)$ and $\Omega_{\perp}(z)$.

Referring to the work in Fang et al. [35-37], the complex potentials can be expressed as:

$\Phi_{\perp}(z)=\Phi_{\perp 0}(z)+\Phi_{\perp}^{*}(z)$, $\Psi_{\perp}(z)=\Psi_{\perp 0}(z)+\Psi_{\perp}^{*}(z)$,

where $\Phi_{\perp 0}(z)=\dfrac{w}{z-z_0}$ and $\Psi_{\perp 0}(z)=\dfrac{\overline{w}}{z-z_0}+\dfrac{w\overline{z}_0}{(z-z_0)^2}$.

Using the same method in the section 2, we can obtain

$$\Phi_{\perp}(z)=\frac{1}{2}\left(\frac{w}{z-z_0}-\frac{w}{z-\overline{z}_0}-\frac{\overline{w}(z_0-\overline{z}_0)}{(z-\overline{z}_0)^2}\right)$$

$$+\frac{1}{2}X_0(z)\left(\frac{1}{X_0(z_0)}\frac{w}{z-z_0}+\frac{1}{X_0(\overline{z}_0)}\frac{w}{z-\overline{z}_0}+\frac{1}{X_0(\overline{z}_0)}\frac{\overline{w}(z_0-\overline{z}_0)}{(z-\overline{z}_0)^2}+X_0(\overline{z}_0)\frac{\overline{w}\overline{z}_0(z_0-\overline{z}_0)}{z-\overline{z}_0}\right), \tag{21}$$

$$\Omega_{\perp}(z)=\frac{1}{2}\left(\frac{w}{z-z_0}-\frac{w}{z-\overline{z}_0}-\frac{\overline{w}(z_0-\overline{z}_0)}{(z-\overline{z}_0)^2}\right)$$

$$-\frac{1}{2}X_0(z)\left(\frac{1}{X_0(z_0)}\frac{w}{z-z_0}+\frac{1}{X_0(\overline{z}_0)}\frac{w}{z-\overline{z}_0}+\frac{1}{X_0(\overline{z}_0)}\frac{\overline{w}(z_0-\overline{z}_0)}{(z-\overline{z}_0)^2}+X_0(\overline{z}_0)\frac{\overline{w}\overline{z}_0(z_0-\overline{z}_0)}{z-\overline{z}_0}\right), \tag{22}$$

$$\Psi_{\perp}(z)=-\Phi_{\perp}(z)-z\Phi_{\perp}'(z)-\overline{\Omega}_{\perp}(z), \tag{23}$$

where $w=\dfrac{\mu}{4\pi(1-\nu)}(b_y-\mathrm{i}b_x)$.

The above complex potentials $\Phi_{\perp 0}(z)$ and $\Phi_{\perp}^{*}(z)$ are consistent with the complex functions ϕ_d' and $\phi_i'(z)$ in Zhang and Li [38].

Then, the force acting on the edge dislocation consists of three parts: the image force, the force produced by the cooperative grain boundary sliding and migration and the external force.

Firstly, using the Peach-Koehler formula [39], the image force can be written as

$$f_{\perp}=f_x-\mathrm{i}f_y=\left[\overset{\curvearrowright}{\sigma}_{xy}(z_0)b_x+\overset{\curvearrowright}{\sigma}_{yy}(z_0)b_y\right]+\mathrm{i}\left[\overset{\curvearrowright}{\sigma}_{xx}(z_0)b_x+\overset{\curvearrowright}{\sigma}_{xy}(z_0)b_y\right]$$

$$=\frac{\mu b^2}{\pi(1+\kappa)}\left(\frac{\Phi_\perp^*(z_0)+\overline{\Phi_\perp^*(z_0)}}{w}+\frac{\bar{z}_0\Phi_\perp^{*\prime}(z_0)+\Psi_\perp^*(z_0)}{\bar{w}}\right) \tag{24}$$

where $\acute{\sigma}_{xx}$, $\acute{\sigma}_{xy}$ and $\acute{\sigma}_{yy}$ are the components of the perturbation stress, and

$$\Phi_\perp^*(z_0)=\lim_{z\to z_0}\left(\Phi_\perp(z)-\Phi_{\perp 0}(z)\right),\quad \Phi_\perp^{*\prime}(z_0)=\lim_{z\to z_0}\frac{\mathrm{d}\left(\Phi_\perp(z)-\Phi_{\perp 0}(z)\right)}{\mathrm{d}z},\quad \Psi_\perp^*(z_0)=\lim_{z\to z_0}\left(\Psi_\perp(z)-\Psi_{\perp 0}(z)\right).$$

Then, the force produced by the cooperative grain boundary sliding and migration can be written as [39]

$$\begin{aligned} f_\Delta &= f_x-\mathrm{i}f_y=\left[\sigma_{xy}(z_0)b_x+\sigma_{yy}(z_0)b_y\right]+\mathrm{i}\left[\sigma_{xx}(z_0)b_x+\sigma_{xy}(z_0)b_y\right] \\ &=\frac{\mu b^2}{\pi(1+\kappa)}\left(\frac{\Phi_\Delta(z_0)+\overline{\Phi_\Delta(z_0)}}{w}+\frac{\bar{z}_0\Phi_\Delta'(z_0)+\Psi_\Delta(z_0)}{\bar{w}}\right), \end{aligned} \tag{25}$$

where σ_{xx}, σ_{xy} and σ_{yy} are the components of the stress fields produced by the cooperative grain boundary sliding and migration.

Lastly, the external force acting on the edge dislocation can be written as (Fang et al., 2012)

$$f_\Gamma=b\sigma_{r\theta}=\frac{b}{\sqrt{2\pi r}}\left(\frac{1}{2}\sin\theta\cos\frac{\theta}{2}K_{\mathrm{I}}^{app}+\left(\cos\frac{3\theta}{2}+\sin^2\frac{\theta}{2}\cos\frac{\theta}{2}K_{\mathrm{II}}^{app}\right)\right), \tag{26}$$

where $\sigma_{r\theta}$ is the in-plane shear stress due to the applied model I and mode II stress intensity factors, K_{I}^{app} and K_{II}^{app} are the generalized mode I and mode II stress intensity factors produced by the remote loadings.

Then, the dislocation emission force acting on the edge dislocation can be written as

$$f_{emit}=f_x\cos\theta+f_y\sin\theta+f_\Gamma=\mathrm{Re}\left[f_\perp+f_\Delta\right]\cos\theta-\mathrm{Im}\left[f_\perp+f_\Delta\right]\sin\theta+f_\Gamma \tag{27}$$

Substituting Eqs. (24), (25) and (26) into the Eq. (27), we have the expression of the dislocation emission force.

4. The critical stress intensity factors for the dislocation emission

A commonly accepted criterion for the emission of dislocations from a crack tip is, when the force acts on them, is equal to zero. Moreover, the dislocation distance to the crack surface must be equal to, or larger than, the dislocation core radius [40]. Combining expressions (24)-(27) and $f_{emit}=0$ yields the critical stress intensity factor K_{IC}^{app} and K_{IIC}^{app} for the dislocation emission as follows. We discuss the effects of the cooperative grain boundary sliding and migration on the emission of lattice dislocations from the crack tip.

$$K_{\mathrm{II}}^{app}=0,\quad K_{\mathrm{IC}}^{app}=\frac{2\sqrt{2\pi r_0}}{b\sin\theta\cos(\theta/2)}\left(\mathrm{Im}\left[f_\perp+f_\Delta\right]\sin\theta-\mathrm{Re}\left[f_\perp+f_\Delta\right]\cos\theta\right),$$

$$K_{\mathrm{I}}^{app}=0,\quad K_{\mathrm{IIC}}^{app}=\frac{\sqrt{2\pi r_0}}{b\left(\cos(3\theta/2)+\sin^2(\theta/2)\cos(\theta/2)\right)}\left(\mathrm{Im}\left[f_\perp+f_\Delta\right]\sin\theta-\mathrm{Re}\left[f_\perp+f_\Delta\right]\cos\theta\right),$$

where $f_\perp+f_\Delta=\dfrac{\mu b^2}{\pi(1+\kappa)}\left(\dfrac{2\,\mathrm{Re}\left[\Phi_\perp^*(z_0)+\Phi_\Delta(z_0)\right]}{w}+\dfrac{\bar{z}_0\left(\Phi_\perp^{*\prime}(z_0)+\Phi_\Delta'(z_0)\right)+\Psi_\perp^*(z_0)+\Psi_\Delta(z_0)}{\bar{w}}\right)$.

Let us calculate the critical stress intensity factors K_{IC}^{app} and K_{IIC}^{app} in the situation, where the cooperative grain boundary sliding and migration forms near the crack tip, as shown in Fig. 1. We define the critical normalized stress intensity factors (SIFs) as $K_{\mathrm{IC}}^0=K_{\mathrm{IC}}^{app}/\mu\sqrt{b}$ and $K_{\mathrm{IIC}}^0=K_{\mathrm{IIC}}^{app}/\mu\sqrt{b}$.

We use the following typical values of parameters of the nanocrystalline material Ni: $\mu=73\,\mathrm{Gpa}$, $\nu=0.31$ [41]. We assume that the crack tip located at the coordinate origin, the Burgers vector of the edge dislocation $b=0.25\,\mathrm{nm}$ and the dislocation core radius $r_0=b/2$.

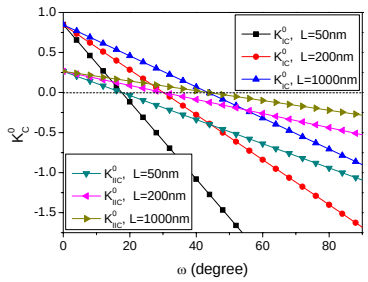

Fig. 2 Dependences of the critical normalized SIFs K_C^0 on the disclination strength ω with different crack lengths L ($\varphi = 2\pi/3$, $\theta_0 = \pi/6$, $d = 15\,\text{nm}$, $p = 0$, $x/d = 0.3$, $y/d = 0.1$)

With different crack lengths L, the variations of the critical normalized stress intensity factors (SIFs) K_{IC}^0 and K_{IIC}^0 with respect to the disclination strength ω are respectively shown in Fig. 2. We found that the critical normalized SIFs K_{IC}^0 and K_{IIC}^0 both decrease with the increment of the disclination strength ω. With the same crack length L, the critical normalized SIFs K_{IC}^0 and K_{IIC}^0 have an intersection at the critical point ω_0, where the critical normalized SIFs equal to zero. When the disclination strength is larger than the critical value ω_0, the dislocation can emit from the crack tip without any external loadings. And the critical value ω_0 will increase with increasing of the crack length L. So the cooperative grain boundary sliding and migration can promote the dislocation emission from the crack tip, thus improve the toughness of the nanocrystalline materials. We can also see that, with the same disclination strength and the same crack length, the critical normalized SIF K_{IIC}^0 is much smaller than K_{IC}^0, which means the mode II loadings are easier than the mode I loadings to make the dislocation emit form the crack tip.

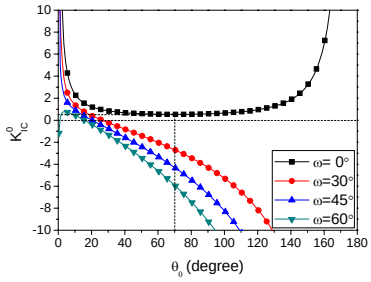

Fig. 3 Dependences of the critical normalized SIFs K_{IC}^0 on the edge dislocation emission angle θ_0 ($\varphi = 2\pi/3$, $L = 100\,\text{nm}$, $d = 15\,\text{nm}$, $p = 0$, $x/d = 0.3$, $y/d = 0.1$)

The critical normalized SIFs versus the dislocation emission angle θ_0 with different disclination strengths ω are depicted in Fig. 3 and Fig. 4. We can see that, the critical normalized SIFs have totally different variation tendency compared to the situation that the cooperative grain boundary sliding and migration is vanished ($\omega = 0°$). For the model I stress intensity factors in Fig. 3, the critical normalized SIF firs decrease then increase with increasing of the edge dislocation emission angle when the cooperative grain boundary sliding and migration does not exist ($\omega = 0°$). And in this case, the most probable angle for the edge dislocation emission is $70.53°$, which is in good agreement with the result in Huang and Li [42]. But for the disclination strength $\omega = 30°$ and $45°$, the critical normalized SIFs K_{IC}^0 sharply decrease with increasing of the dislocation emission angle, and transfer the positive dislocations emission to the negative dislocations emission. And the most probable angle for the dislocation emission is $26.25°$ for $\omega = 30°$ and 20.25 for $\omega = 45°$, respectively. For the disclination strength $\omega = 60°$, the critical normalized SIFs K_{IC}^0 first increase then decrease with the increment of the dislocation emission angle. There are two most probable angle for the positive dislocation emission, and they are $0.95°$ and $15.75°$.

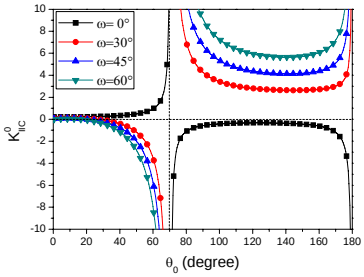

Fig. 4 Dependences of the critical normalized SIFs K^0_{IIC} on the edge dislocation emission angle θ_0 ($\varphi = 2\pi/3$, $L = 100\,\mathrm{nm}$, $d = 15\,\mathrm{nm}$, $p = 0$, $x/d = 0.3$, $y/d = 0.1$)

For the mode II stress intensity factors in Fig. 4, when the cooperative grain boundary sliding and migration does not exist ($\omega = 0°$), the critical normalized SIFs increase from a finite positive value to infinity with increasing of the edge dislocation emission angle, then switch to negative value. And the most probable angle for the positive dislocation emission is $0°$, that for the negative dislocation is $123.75°$. In other cases, the critical normalized SIFs decrease from finite negative values to infinity, then switch to positive values with the increment of the dislocation emission angle. And the most probable angle for the negative dislocation emission is always $0°$, that for the positive dislocation is $144.25°$ for $\omega = 30°$, $141.25°$ for $\omega = 45°$, and 139.75 for $\omega = 60°$.

The dependences of the critical normalized SIFs on the dislocation emission angle with different ratios x/d and y/d are shown in Figs. 5-6. We can see that, the critical normalized SIFs versus the dislocation emission angle have different variation tendency depending on the values of the ratios x/d and y/d. It is not only we described above.

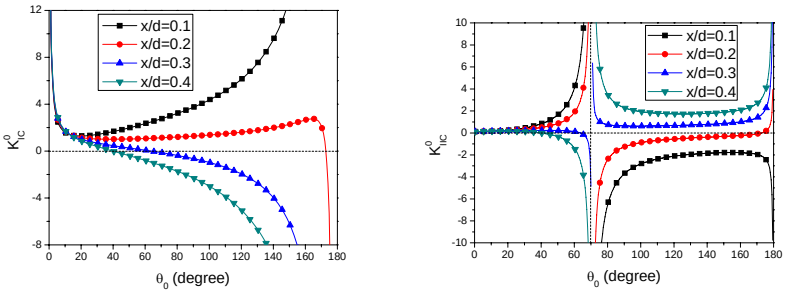

Fig. 5 Dependences of the critical normalized SIFs K^0_{C} on the dislocation emission angle θ_0 with different ratio x/d ($\omega = \pi/6$, $\varphi = 2\pi/3$, $L = 100\,\mathrm{nm}$, $d = 15\,\mathrm{nm}$, $p = 0$, $y/d = 0.3$)

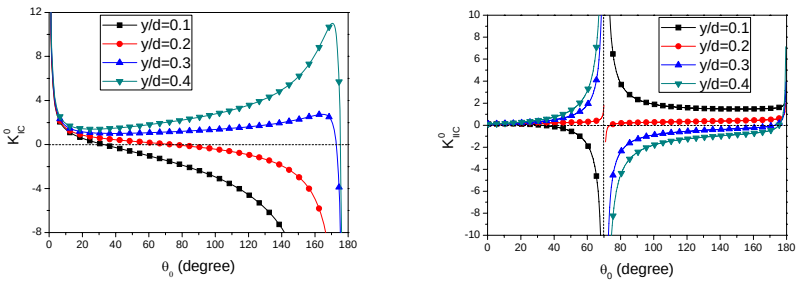

Fig. 6 Dependences of the critical normalized SIFs K^0_{C} on the dislocation emission angle θ_0 with different ratio y/d ($\omega = \pi/6$, $\varphi = 2\pi/3$, $L = 100\,\mathrm{nm}$, $d = 15\,\mathrm{nm}$, $p = 0$, $x/d = 0.2$)

The critical normalized SIFs K^0_{IC} versus the grain size d with different angles φ between grain boundaries are depicted in Fig. 7. It indicates that the critical normalized SIFs first increase then decrease with the increment of the grain size d, but decrease with increasing of the angle φ between grain boundaries. There is a critical grain size making the critical normalized SIFs equal to zero. And when the grain size d is larger than the critical value, the dislocation can emit from the crack tip without any loadings. The critical value also decreases with increasing of the angel φ between grain boundaries.

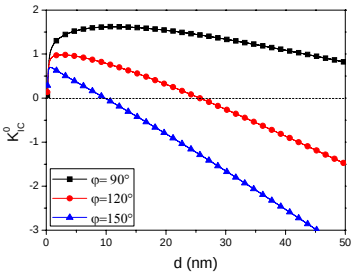

Fig. 7 Dependences of the critical normalized SIFs K_{IC}^0 on the grain size d with different angles φ ($\omega=\pi/6$, $\theta_0=\pi/6$, $L=100\,\mathrm{nm}$, $p=d$, $x/d=0.3$, $y/d=0.1$)

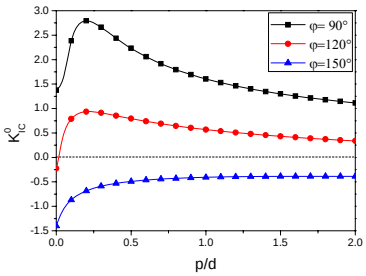

Fig. 8 Dependences of the critical normalized SIFs K_{IC}^0 on the ratio p/d with different angles φ ($\omega=\pi/6$, $\theta_0=\pi/6$, $L=100\,\mathrm{nm}$, $d=15\,\mathrm{nm}$, $x/d=0.3$, $y/d=0.1$)

Fig. 8 plots the variations of the critical normalized SIFs with respect to the ratio p/d with different angles φ between grain boundaries. We found that the critical normalized SIFs first increase then decrease to constants with the increment of the ratio p/d for $\varphi=90°$ and $120°$, but just increase to a constant for $\varphi=150°$. And in this situation, if the angle φ between the grain boundaries is large enough, the critical normalized SIF is always negative, which means the dislocation emission from the crack tip is very easy.

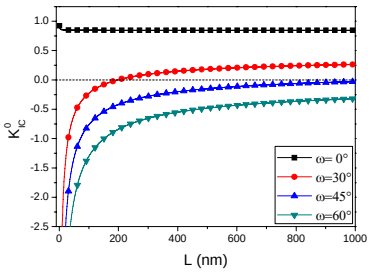

Fig. 9 Dependences of the critical normalized SIFs K_{IC}^0 on the crack length L with different strengths ω ($\theta_0=\pi/6$, $\varphi=2\pi/3$, $d=15\,\mathrm{nm}$, $p=0$, $x/d=0.3$, $y/d=0.1$)

The dependences of the critical normalized SIFs on the crack length with different disclination strengths are shown in Fig. 9. The critical normalized SIFs K_{IC}^0 increase with the increment of the crack length, and tend to constants when the crack length is large enough. So the dislocation emission from the short crack tip is much easier, and growth of the long crack is easier. We can also see that, when the cooperative grain boundary sliding and migration does not exist, the crack length just slightly affects the critical normalized SIFs. In comparison, the cooperative grain boundary sliding and migration contributes a lot to the dislocation emission and the crack blunting.

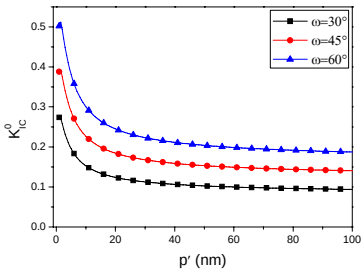

Fig. 10 Dependences of the critical normalized SIFs K_{IC}^{0} on the distance between crack tip and coordinate origin p' ($\theta_0 = \pi/6$, $\varphi = 2\pi/3$, $L = 300\,\mathrm{nm}$, $d = 15\,\mathrm{nm}$, $p = 0$, $x/d = 0.3$, $y/d = 0.1$)

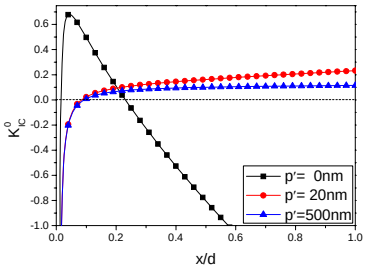

Fig. 11 Dependences of the critical normalized SIFs K_{IC}^{0} on the ratio x/d with different distances p' ($\omega = \pi/6$, $\theta_0 = \pi/6$, $\varphi = 2\pi/3$, $L = 100\,\mathrm{nm}$, $d = 15\,\mathrm{nm}$, $p = 0$, $y/d = 0.1$)

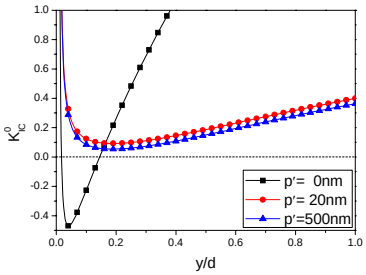

Fig. 12 Dependences of the critical normalized SIFs K_{IC}^{0} on the ratio y/d with different distances p' ($\omega = \pi/6$, $\theta_0 = \pi/6$, $\varphi = 2\pi/3$, $L = 100\,\mathrm{nm}$, $d = 15\,\mathrm{nm}$, $p = 0$, $x/d = 0.3$)

If the crack tip is not at the coordinate origin, we define the horizontal distance between the crack tip and the coordinate origin is p'. Fig. 10 plots the dependences of the critical normalized SIFs on the distance between the crack tip and the coordinate origin p' with different disclination strengths. The critical normalized SIFs decrease and tend to constants with increasing of the distance p'. The variations of the critical normalized SIFs on the ratios x/d and y/d with different distances p' are depicted in Fig. 11 and Fig. 12, respectively. Fig. 11 indicates that the critical normalized SIFs first increase then decrease with the increment of the ratio x/d when the crack tip is at the coordinate origin ($p' = 0$), and the change is remarkable. In other cases, the critical normalized SIFs just increase with increasing of the ratio, and the distances p' have slight influence on them. The variation tendency of the critical normalized with respect to the radio y/d is just opposite to that to the radio x/d.

5. Concluding remarks

Thus, the interaction of the cooperative grain boundary sliding and migration with the crack is investigated by the complex variable method. We have theoretically described the effects of the two wedge disclination dipoles produced by the cooperative grain boundary sliding and migration on the emission of edge dislocations from the crack tip in deformed nanocrystalline metals and ceramics. The critical stress intensity factors for the first dislocation emission are calculated. The influence of the disclination strength, the grain size, the location of the two disclination dipoles and the crack length on the critical stress intensity factors is discussed in detail. Some conclusions are summarized as follows.

(1) The cooperative grain boundary sliding and migration can promote the dislocation emission from the crack tip, which causes effective blunting of the crack, thus suppresses its growth, and improves the toughness of nanocrystalline materials.

(2) There is a critical disclination strength value making the critical stress intensity factor equal to zero and the dislocation can emit from the crack tip without any external loadings. And the mode II loadings are easier than the mode I loadings to make the dislocation emit form the crack tip.

(3) The critical stress intensity factor has different variation tendency depending on the disclination strength and the geometry of the two disclination dipoles. For each situation, the most probable emission angles for positive dislocation and negative dislocation are different.

(4) The grain size has great effect on the dislocation emission from the crack tip. The critical stress intensity factors first increase then decrease with increasing of the grain size. And there is a critical grain size making the dislocation can emit from the crack tip without any external loadings.

(5) The dislocation emission from the shorter crack tip is much easier. So, the shorter crack can be easily blunted, and the longer crack tends to grow.

(6) The location and geometry of the cooperative grain boundary sliding and migration have great influence on the critical stress intensity factors.

Acknowledgements

The authors would like to deeply appreciate the support from the NNSFC (11172094 and 11172095) and the NCET-11-0122. The work was also supported by the Fundamental Research Funds for the Central Universities, Hunan University.

References

[1] P. Barai, G.J. Weng, Mechanics of a nanocrystalline coating and grain-size dependence of its plastic strength. Mech Mater, 43 (2011) 496-504.

[2] S.V. Bobylev, A.K. Mukherjee, I.A. Ovid'ko, Emission of partial dislocations from amorphous intergranular boundaries in deformed nanocrystalline ceramics. Scripta Mater, 60(1) (2009) 36-39.

[3] M. Dao, L. Lu, R.J. Asaro, J.T.M. De Hosson, E. Ma, Toward a quantitative understanding of mechanical behavior of nanocrystalline metals. Acta Mater, 55(12) (2007) 4041-4065.

[4] C.C. Koch, I.A. Ovid'ko, S. Seal, S. Veprek, Structural nanocrystalline materials: Fundamentals and Applications, Cambridge University Press, Cambridge, 2007.

[5] M.A. Meyers, A. Mishra, D.J. Benson, Mechanical properties of nanocrystalline materials. Prog Mater Sci, 51 (2006) 427-556.

[6] S.H. Xia, J.T. Wang, A micromechanical model of toughening behavior in the dual-phase composite. Int J Plast, 26 (2010) 1442-1460.

[7] K. Zhou, A.A. Nazarov, M.S. Wu, Competing relaxation mechanisms in a disclinated nanowire: temperature and size effects. Phys Rev Lett, 98 (2007) 035501.

[8] K. Zhou, M.S. Wu, A.A. Nazarov, Relaxation of a disclinated tricrystalline nanowire. Acta Mater, 56 (2008) 5828-5836.

[9] C.C. Koch, Structural nanocrystalline materials: an overview. J Mater Sci, 42(5) (2007) 1403-1414.

[10] I.A. Ovid'ko, Deformation and diffusion modes in nanocrystalline materials. Int Mater Rev, 50 (2005) 65-82.

[11] R.T. Zhu, J.Q. Zhou, H. Jiang, D.S. Zhang, Evolution of shear banding in fully dense nanocrystalline Ni sheet. Mech Mater, 51 (2012) 29-42.

[12] S. Cheng, E. Ma, Y.M. Wang, L.J. Kecskes, K.M. Youssef, C.C. Koch, U.P. Trociewitz, K. Han, Tensile properties of in situ consolidated nanocrystalline Cu. Acta Mater, 53(5) (2005) 1521-1533.

[13] K.M. Youssef, R.O. Scattergood, K.L. Murty, J.A. Horton, C.C. Koch, Ultrahigh strength and high ductility of bulk nanocrystalline copper. Appl Phys Lett, 87 (2005) 091904.

[14] K.M. Youssef, R.O. Scattergood, K.L. Murty, C.C. Koch, Nanocrystalline Al-Mg alloy with ultrahigh strength and good ductility. Scripta Mater, 54(2) (2006) 251-256.

[15] A.V. Sergueeva, N.A. Mara, A.K. Mukherjee, Grain boundary sliding in nanomaterials at elevated temperatures. J Mater Sci, 42(5) (2007) 1433-1438.

[16] S. Bhaduri, S.B. Bhaduri, Enhanced low temperature toughness of Al_2O_3-ZnO_2 nano/nano composites. Nanostruct Mater, 8(6) (1997) 755-763.

[17] A.A. Kaminskii, M.S. Akchurin, R.V. Gainutdinov, K. Takaichi, A. Shirakava, H. Yagi, T. Yanagitani, K. Ueda, Microhardness and fracture toughness of Y_2O_3- and $Y_3Al_5O_{12}$- based nanocrystalline laser ceramics. Crystallogr Rep, 50(5) (2005) 569-873.

[18] R.A. Mirshams, C.H. Xiao, S.H. Whang, W.M. Yin, R-Curve characterization of the fracture toughness of nanocrystalline nickel thin sheets. Mater Sci Eng A, 315(1-2) (2001) 21-27.

[19] Y. Zhao, J. Qian, L.L. Daemen, C. Pantea, J. Zhang, G.A. Voronin, T.W. Zerda, Enhancement of fracture toughness in nanostructured diamond-SiC composites. Appl Phys Lett, 84 (2004) 1356.

[20] S.V. Bobylev, N.F. Morozov, I.A. Ovid'ko, Cooperative grain boundary sliding and migration process in nanocrystalline solids. Phys Rev Lett, 105 (2010) 055504.
[21] S.V. Bobylev, N.F. Morozov, I.A. Ovid'ko, Cooperative grain boundary sliding and nanograin nucleation process in nanocrystalline, ultrafine-grained, and polycrystalline solids. Phys Rev B, 84 (2011) 094103.
[22] M.Yu. Gutkin, I.A. Ovid'ko, Grain boundary migration and rotational deformation mode in nanocrystalline materials. Appl Phys Lett, 87 (2005) 251916.
[23] P.A. Juan, S. Berbenni, L. Capolungo, Prediction of internal stresses during growth of first- and second-generation twins in Mg and Mg alloys. Acta Mater, 60 (2012) 476-486.
[24] N.F. Morozov, I.A. Ovid'ko, A.G. Sheinerman, E.C. Aifantis, Special rotational deformation as a toughening mechanism in nanocrystalline solids. J Mech Phys Solids, 58 (2010) 1088-1099.
[25] I.A. Ovid'ko, A.G. Sheinerman, Ductile vs. brittle behavior of pre-cracked nanocrystalline and ultrafine-grained materials. Scripta Mater, 58 (2010) 5286-5294.
[26] I.A. Ovid'ko, A.G. Sheinerman, E.C. Aifantis, Effect of cooperative grain boundary sliding and migration on crack growth in nanocrystalline solids. Acta Mater, 59 (2011) 5023-5031.
[27] I.A. Ovid'ko, A.G. Sheinerman, Special strain hardening mechanism and nanocrack generation in nanocrystalline materials. Appl Phys Lett, 90(17) (2007) 171927.
[28] I.A. Ovid'ko, A.G. Sheinerman, Enhanced ductility of nanomaterials through optimization of grain boundary sliding and diffusion processes. Acta Mater, 57(7) (2009) 2217-2228.
[29] A.V. Sergueeva, N.A. Mara, N.A. Krasilnikov, R.Z. Valiev, A.K. Mukherjee, Cooperative grain boundary sliding in nanocrystalline materials. Philos Mag, 86(36) (2006) 5797-5804.
[30] I.A. Ovid'ko, A.G. Sheinerman, E.C. Aifantis, Stress-driven migration of grain boundaries and fracture processes in nanocrystalline ceramics and metals. Acta Mater, 56(12) (2008) 2718-2727.
[31] N.L. Muskhelishvili, Soma basic problems of mathematical theory of elasticity, Leyden, Noordhoff, 1975.
[32] A.E. Romanov, V.I. Vladimirov, Disclinations in crystalline solids, in: Nabarro, F.R.N., Dislocation in solids, Amsterdam, Elsevier, 1992, pp. 191-402.
[33] Q.H. Fang, Y.W. Liu, C.P. Jiang, B. Li, Interaction of a wedge disclination dipole with interfacial cracks. Eng Fract Mech, 73 (2006) 1235-1248.
[34] Y.W. Liu, Q.H. Fang, C.P. Jiang, A wedge disclination dipole interaction with a circular inclusion. Phys Stat Sol (A), 203(3) (2006) 443-458.
[35] Q.H. Fang, Y.W. Liu, C.P. Jiang, Edge dislocation interacting with an interfacial crack along a circular inhomogeneity. Int J Solids Struct, 40 (2003) 5781-5797.
[36] Q.H. Fang, Y.W. Liu, B. Jin, P.H. Wen, Effect of interface stressed on the image force and stability of an edge dislocation inside a nanoscale cylindrical inclusion. Int J Solids Struct, 46 (2009) 1413-1422.
[37] Q.H. Fang, H. Feng, Y.W. Liu, S. Lin, N. Zhang, Special rotational deformation effect on the emission of the dislocations from a crack tip in deformed nanocrystalline solids. Int J Solids Struct, 49 (2012) 1406-1412.
[38] T.Y. Zhang, J.C.M. Li, Image forces and shielding effects of an edge dislocation near a finite length crack. Acta Metall Mater, 39 (1991) 2739-2744.
[39] J.P. Hirth, J. Lothe, Theory of dislocations, second ed, John-wiley, New York, 1964.
[40] J.R. Rice, R. Thomson, Ductile versus brittle behaviour of crystals. Philos Mag, 29 (1974) 73.
[41] J.P. Hirth, J. Lothe, Tgeiry of dislocations, Wiley, New York, 1982.
[42] M.X. Huang, Z.H. Li, Dislocation emission criterion from a blunt crack tip. J Mech Phys Solids, 52 (2004) 1991-2003.

Flat-tipped Indentation Fracture Mechanics

Xiaozhi Hu[1*] and Yujun Xie[2*],

[1] School of Mechanical and Chemical Engineering, University of Western Australia, Perth, WA 6009, Australia
[2] Department of Mechanical Engineering, Liaoning Shihua University, Fushun, 113001, P. R. China
* Corresponding author: xiao.zhi.hu@uwa.edu.au, yjxie@lnpu.edu.cn

Abstract A singular stress field exists in an elastic substrate around the contact edge with a rigid flat-tipped indenter. This surface-contact-induced singular stress field can also be described by the stress intensity factor concept, if the indentation stress intensity factor K_{ind} is introduced for indentation cracking analysis. The K_{ind}–controlled singular stress field is almost identical to that of the Mode-I tensile singular stress field around the crack tip, except the negative sign due to the compressive nature of surface contact loading.

This study presents an energy-based fracture mechanics analysis for the indentation stress intensity factor (ISIF) K_{ind} and the indentation-induced boundary cracking within the K_{ind}-dominant region around the contact edge. It is found that the critical indentation stress intensity factor exists, and the relation between the indentation fracture toughness $K_{IC\text{-}ind}$ and the common Mode-I fracture toughness K_{IC} is established analytically, showing $K_{IC\text{-}ind} = 2.5K_{IC}$. The indentation-cracking angle at the contact edge is also determined.

The fracture mechanics model on surface contact cracking induced by a flat-tipped indenter provides a useful alternative for measuring the fracture toughness K_{IC}, which can be useful for characterization of surface fracture properties of bulk elastic bodies and coating fracture properties of layered structures such as MEMS.

Keywords Indentation, Indentation fracture toughness, Contact mechanics, Surface cracking

1. Introduction

Frictional sliding induced surface damage in the form of micro-crack initiation can be the precursor for potentially much severe structural damage. Fracture mechanics modeling concerning this important structural integrity issue has been an interesting topic for years [1-3]. It is noted from the work [1,2,4,5] that a mixed-mode singular stress field exists in an incompressible substrate at the sliding contact edge of a rigid flat-ended indenter pressing down onto the substrate. This study will examine closely the process of micro-crack initiation on the contact surface, which is controlled by the singular stress field at the sharp corner of the flat-ended indenter, and the cracking angle.

The familiar singular stress fields are those associated with sharp cracks in elastic solids, through which the Mode-I fracture toughness K_{IC} at the critical loads can be determined from the common stress intensity factors. Although the singular stress field in an incompressible substrate at the sliding contact edge of a rigid flat-ended indenter is not due to the presence of a sharp crack tip, this contact-induced singular stress field does share some similar features with those of a crack-induced singular stress field, which implies the well-known concepts of linear elastic and elastic-plastic fracture mechanics such as the stress intensity factor K and the J-integral [6-11] can be adopted for modeling of the crack initiation from a crack-free surface under frictional sliding wear.

The significance of fracture mechanics modeling of contact crack initiation can be seen from fretting fatigue and other engineering applications such as rock fracture mechanisms in rock cutting. This study will present a new methodology based on the aforementioned singular stress field generated at the sliding contact edge of a rigid flat-ended indenter, which will connect the contact mechanics together with the fracture mechanics by using energy-based modeling.

2. The energy release rate for boundary cracking

This section describes the method we used to derive the strain energy release rate associated with sliding contact crack initiation from the crack-free boundary. The energy release rate related to a boundary movement has been investigated by Eshelby [6], Sih [7], Budiansky and Rice [8,9]. Consider a three-dimensional (3D) elastostatic boundary problem with material contained within the surface boundary *S*+*s* (Fig. 1), where the portion *s* of the boundary is traction-free, and the external loading is imposed only on *S*. Without changing the boundary conditions on *S*, impose a continuously varying sequence of static solutions, related to the displacements *u*, given by a time-like parameter *t*. Details of the procedure can be consulted in references [9], and here, only the result of energy release rate per unit time, $\partial\Pi/\partial t$, is given, i.e.

$$\frac{\partial \Pi}{\partial t} = \int_s w v_i m_i ds \,, \tag{1}$$

where v_i denotes the '*velocity*' of the points on *s* and m_i is the current outward normal to *s*. In the case of two-dimensional deformation fields as shown in Fig. 2, relevant to the present problem, the energy release rate remains of the same form as Eq. (1).

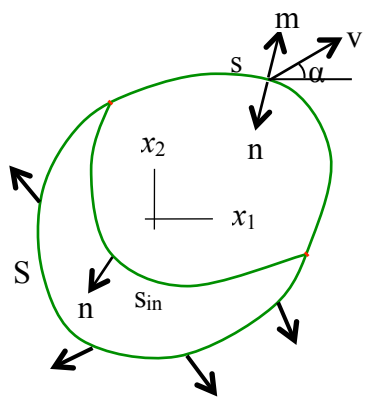

Figure 1. Two-dimensional deformation fields and integration path.

Let $v_i = e_i = \Delta_i / \Delta$, which corresponds to two components of unit boundary movement, so that $e_1 = \cos\alpha$, $e_2 = \sin\alpha$, where α is the angle between boundary movement Δ and x_1. Let $n_i = -m_i$ be the unit tensor inward normal to boundary *s*, which means that the boundary *s* moves inward, and let all points on boundary *s* move in the same direction. Thus, the energy release rate for the boundary movement is given by

$$\overline{G} = -\frac{\partial \Pi}{\partial \Delta} = \int_s w e_i n_i ds = e_i J_i = J_1 \cos\alpha + J_2 \sin\alpha \,, \tag{2}$$

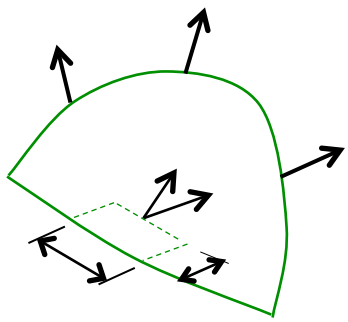

Figure 2. Boundary movement or cracking as $s \to 0$ the notch-like boundary becomes a crack.

and from the conservation law, J_i, proposed by Eshelby [6]

$$J_j = \int_s w n_j ds = \int_{s_{in}} \left(w n_j - T_i u_{i,j} \right) ds, \tag{3}$$

where s_{in} is any integration path within the area closed by boundary $S+s$, and $s_{in}+s$ form a closed integral loop.

From the geometrical point of view, boundary crack initiation, regardless whether it occurs at a crack tip, a notch corner or on a general crack-free boundary, can always be defined as a boundary movement in some direction, with the limit $s \to 0$ taken and the notch-like boundary becomes a crack, as shown in Fig. 2 and Fig. 3. Then, the energy release rate of boundary cracking can be defined as

$$G = (J_1)|_{s\to 0} \cos\alpha + (J_2)|_{s\to 0} \sin\alpha, \tag{4}$$

where $(J_1)|_{s\to 0}$ denotes the driving force of boundary cracking in direction x_1 when the limit taken exists, or the energy release rate with unit boundary movement s in direction x_1; $(J_2)|_{s\to 0}$ denotes the driving force in direction x_2, or the energy release rate with unit boundary movement s in direction x_2.

For a homogenous and isotropic substrate Griffith's criterion [9] states that the crack will extend when the critical value $G_{\max}$ is reached [10,11]

$$G_{\max} = G_c. \tag{5}$$

For a standard cracked specimen subjected to Mode I loading, $G_{\max} = J_1$ and G_c can be calibrated as

$$G_c = J_{IC} = K_{IC}^2 (1-\mu^2)/E, \tag{6}$$

where K_{IC} is the Mode-I fracture toughness.

3. Asymptotic stress field in sliding contact

3.1. Boundary Condition

A typical fretting contact problem of a rigid flat-ended indenter with half width a, sliding on a homogeneous, isotropic, elastic body in half plane is shown in Fig. 3. The Cartesian coordinates (x_1, x_2), and the polar coordinates (r, θ), both with the origin at the left edge of the indenter, are selected. Normal force P and tangential force Q act on the indenter and the following normal and shear tractions along interface have been solved in closed form [4],

$$p(x_1) = -\frac{P \sin\lambda\pi}{\pi} \left(2 - \frac{x_1}{a}\right)^{\lambda-1} \left(\frac{x_1}{a}\right)^{-\lambda} \tag{7}$$

and

$$q(x_1) = f p(x_1), \tag{8}$$

where f is the coefficient of friction; λ is determined by

$$\tan\lambda\pi = \frac{2(1-\mu)}{f(1-2\mu)}, \quad 0 < \lambda < 1 \tag{9}$$

and μ is Poisson's ratio of the substrate.

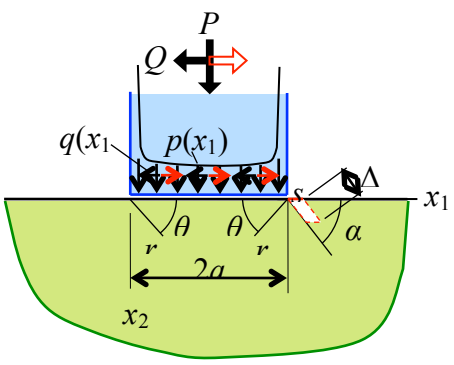

Figure 3. Indentation configuration, integral path $s \to 0$ and $\Delta \to 0$.

Eq. (7) shows that the stress state near the indenter corner may vary in the form

$$\sigma_{ij} = \begin{cases} 0\left(r^{\lambda-1}\right), & x_1 = 2a \\ 0\left(r^{-\lambda}\right), & x_1 = 0 \end{cases} \quad \text{as} \quad r \to 0. \tag{10}$$

For special cases either with $\mu = 0.5$ or $f = 0$, Eq. (9) leads to $\lambda = 0.5$, showing the same order of stress singularity as that for a sharp crack tip.

For $\mu = 0.5$, the substrate becomes incompressible. The asymptotic stress boundary conditions of the substrate in the contact area next to the left and right corners then become

$$\sigma_{22}\,|_{\theta=0} = -\frac{P}{\pi\sqrt{2ar}} \tag{11}$$

and

$$\sigma_{21}\,|_{\theta=0} = \frac{fP}{\pi\sqrt{2ar}} \tag{12}$$

for the two cases of $\mu = 0.5$ and $f = 0$.

3.2. Singular stress fields due to the normal and tangential loads

The singular stress field at the sharp edge of the contact between a rigid flat-ended indenter and substrate is known from the asymptotic contact analyses of and Nadai [4]. Using the polar coordinates (r, θ), Fig. 3, the stresses at the left corner can be found as follows due to the normal load:

$$\begin{pmatrix} \sigma_{rr}^{I} \\ \sigma_{\theta\theta}^{I} \\ \sigma_{r\theta}^{I} \end{pmatrix} = -\frac{K_{I-ind}}{\sqrt{2\pi r}} \begin{pmatrix} \cos\frac{\theta}{2}\left(1+\sin^2\frac{\theta}{2}\right) \\ \cos^3\frac{\theta}{2} \\ \sin\frac{\theta}{2}\cos^2\frac{\theta}{2} \end{pmatrix}. \tag{13}$$

This expression indicates that the stress state for indentation is a “negative” Mode I singular stress field for cracked solids, where

$$K_{I-ind} = \frac{P}{\sqrt{\pi a}}, \tag{14}$$

which defines actually an indentation stress intensity factor. The familiar Mode-I singular stress field is obtained by removing the negative sign and changing $K_{I\text{-}ind}$ into K_I. Only difference between tensile mode-I stress field and indentation stress field is sign “-” in their equations.

Nadai [4] gave also the asymptotic stress field due to the tangential load as

$$\begin{pmatrix} \sigma_{rr}^{II} \\ \sigma_{\theta\theta}^{II} \\ \sigma_{r\theta}^{II} \end{pmatrix} = \frac{K_{II-ind}}{\sqrt{2\pi r}} \begin{pmatrix} \sin\frac{\theta}{2}\left(1-3\sin^2\frac{\theta}{2}\right) \\ -3\sin\frac{\theta}{2}\cos^2\frac{\theta}{2} \\ \cos\frac{\theta}{2}\left(1-3\sin^2\frac{\theta}{2}\right) \end{pmatrix}, \tag{15}$$

where

$$K_{II-ind} = fK_{I-ind} = \frac{fP}{\sqrt{\pi a}}. \tag{16}$$

Actually, Eq. (15) is identical to the classical Mode II singular stress fields when $K_{II\text{-}ind} = K_{II}$.

3.3. Characters of the stress fields

It is clear from the above discussion that the asymptotic stress field, $\sigma_{ij} = \sigma_{ij}^{I} + \sigma_{ij}^{II}$, induced by the sliding contact is a typical mixed-mode I-II singular stress field for incompressible substrates and friction free. This singular stress field is responsible for surface crack initiation on the crack-free surface of the substrate at the contact edge. This finding is significant as it shows that singularity and distribution of the stress field induced by surface contact of a flat-ended indenter are identical to those of a mixed-mode crack. As a result, the concepts of stress intensity factor and fracture toughness can now be introduced unambiguously into contact mechanics and associated contact damage. Therefore, Eqs. (14-17) represent an important advance by defining the indentation stress intensity factors, $K_{I\text{-ind}}$ and K_{II-ind}, and the K_{ind}-dominant region at the contact edge. In other words, the fracture mechanics theory, such as the Griffith's criterion, is applicable in the case of the boundary fracture induced by the sliding contact.

4. Calculation methods on indentation stress intensity factor

4.1. Application of J_1-integral in the indentation fracture

For a closed integration path $s_{abcdefa}$ as shown in Fig.4, following J_1-integral can be gotten.

$$J_1 = \oint_{s_{abcdefa}} \left(wn_1 - T_i u_{i,1}\right) ds = 0. \tag{17}$$

If the path $s_{abcdefa}$ is divided into $s_{abcdefa} = s_{ab} + s_{bcd} + s_{de} + s_{afe}$, because of $n_1 = 0$ on surface of the substrate, $T_i = 0$ on the s_{ab}, $T_1 = 0$ and $u_{2,1} = 0$ on the s_{de}, we have

$$J_1 = \int_{s_{ab}} \left(wn_1 - T_i u_{i,1}\right) ds = 0 \tag{18}$$

and

$$J_1 = \int_{s_{de}} \left(wn_1 - T_i u_{i,1}\right) ds = 0. \tag{19}$$

Then substituting Eqs. (18) and (19) into Eq. (17), it follows that

$$J_1 = \oint_{s_{abcdefa}} \left(wn_1 - T_i u_{i,1}\right) ds = -\int_{s_{afe}} \left(wn_1 - T_i u_{i,1}\right) ds + \int_{s_{bcd}} \left(wn_1 - T_i u_{i,1}\right) ds = 0. \tag{20}$$

It can then be rearranged to give

$$J_1 = \int_{s_{afe}} \left(wn_1 - T_i u_{i,1}\right) ds = \int_{s_{bcd}} \left(wn_1 - T_i u_{i,1}\right) ds, \tag{21}$$

which means that along any two paths, s_{afe} and s_{bcd}, starting from the any point on the left free boundary to any one on the contact boundary, the J_1-integrals are identical. It shows theoretically

that this integral is path independent.

If the integration path s_{afe} is half of a circle and within the K_{ind}-dominant region, it is not difficult to get

$$J_1 = \int_{s_{afe}} (wn_1 - T_i u_{i,1}) ds = \frac{1-\mu^2}{2E} K_I^2 \quad \text{(plane strain).} \tag{22}$$

Then, Eq. (21) becomes

$$J_1 = \frac{1-\mu^2}{2E} K_I^2 = \int_{s_{bad}} (wn_1 - T_i u_{i,1}) ds \tag{23}$$

This equation is a key formula to construct a method to calculate the ISIFs induced by the indentation. Additionally, this method can be applied to the contact problems with the finite and infinite boundaries.

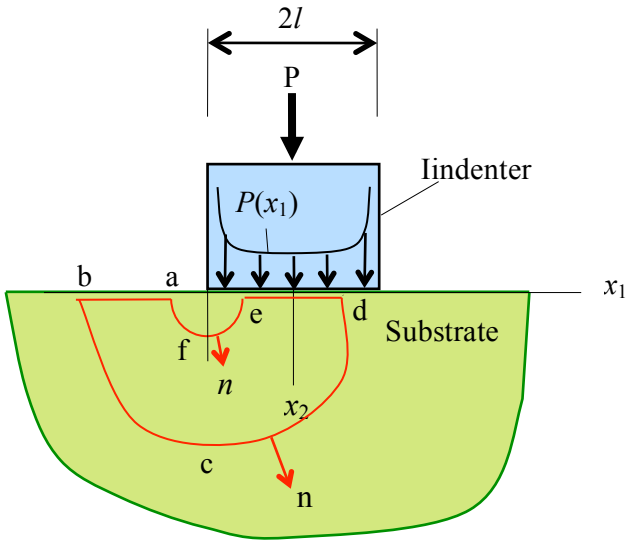

Figure 4. Integration path for Mode-I indentation.

4.2. Application of J_1-integral in the indentation fracture for layered substrate

For the layered substrate, two closed integration paths as shown in Fig. 5 will be considered in present work. One is the pant $s_1 = s_{mn} + s_{nedcbam}$ and the other $s_2 = s_{m'fn'} + s_{n'm'}$. Additionally, as $n_1 = 0$, T_i and $u_{i,1}$ are continuous on the paths s_{mn} and $s_{n'm'}$, from conservation law, we have the following contour integrals.

$$J_1 = \int_{s_{mn}} T_i u_{i,1} ds + \int_{s_{nedcbam}} (wn_1 - T_i u_{i,1}) ds = 0 \quad \text{for the closed path } s_1, \tag{24}$$

$$J_1 = \int_{s_{m'n'}} T_i u_{i,1} ds + \int_{s_{m'fn'}} (wn_1 - T_i u_{i,1}) ds = 0 \quad \text{for the closed } s_2. \tag{25}$$

$$\text{and} \quad J_1 = \int_{s_{m'n'}} T_i u_{i,1} ds = -\int_{s_{mn}} T_i u_{i,1} ds \tag{26}$$

According to Eqs. (18), (19), (24)-(26), it can be found that

$$J_1 = \int_{s_{bcd}} (wn_1 - T_i u_{i,1}) ds = \int_{s_{afe}} (wn_1 - T_i u_{i,1}) ds, \tag{27}$$

which indicates that the integral is path independent for composite substrate similar to the Eq. (21).

If the integration path s_{bcd} is half circle and within the K_{ind}-dominant region, the following equation can be found.

$$J_1 = \frac{1-\mu_c^2}{2E_c} K_I^2 = \int_{s_{afe}} \left(w n_1 - T_i u_{i,1} \right) ds \,. \tag{28}$$

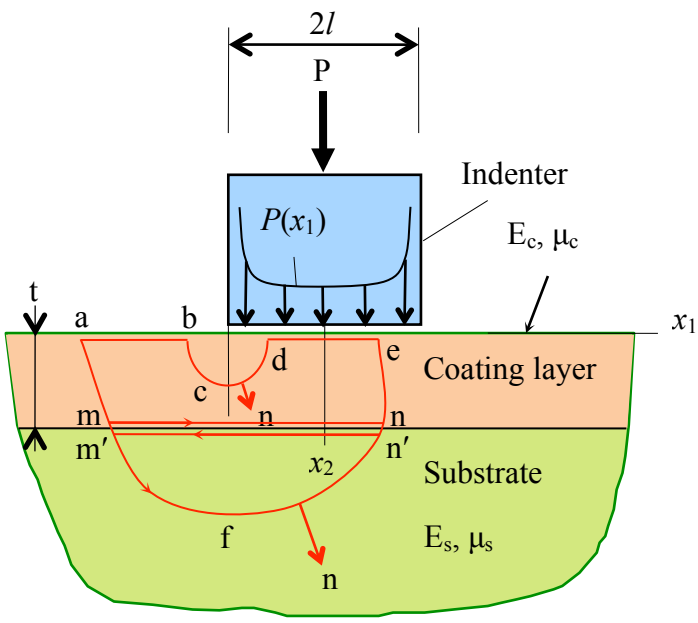

Figure 5. Integration path for the layered substrate for Mode-I indentation.

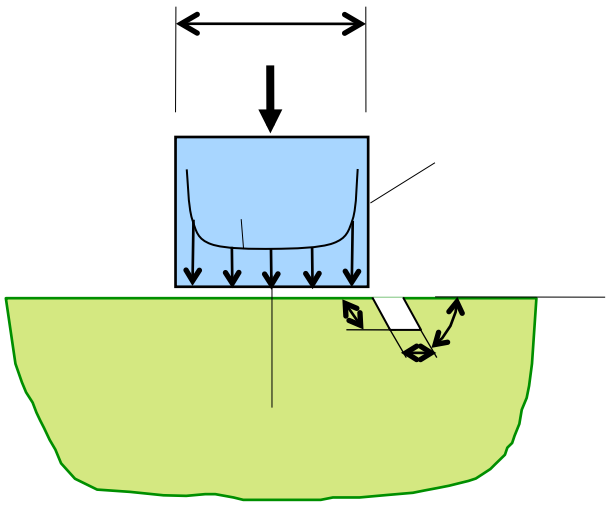

Figure 6. Boundary cracking for Mode-I indentation.

5. Boundary cracking in Mode-I indentation

In section 2, an expression describing the strain energy release rate of boundary cracking has been derived. It will be used to discuss the boundary cracking in the case of the complete sliding contact

in this section.

Let $s = s_{ob}$ in Eq. (3) as shown in Fig. 6 adjacent to the right corner of the indenter and s be within the K_{ind}-dominant region. Because $T_i = 0$ and $n_1 = 0$ on the integration path s_{ob}, the energy-based driving force for boundary cracking in x_1 and x_2 directions in this case can be found in [12-16]

$$\left(J_1\right)\Big|_{s_{ob}\to 0} = \lim_{s_{ob}\to 0}\int_{s_{ob}} w n_1 ds = 0. \tag{29}$$

and

$$J_2\,|_{s\to 0} = \frac{\left(1-\mu^2\right)K_{I-ind}^2}{2\pi E}, \text{ (plane strain).} \tag{30}$$

From Eqs. (4), (29) and (30), the total energy release rate of boundary cracking induced by the sliding contact at any angle α can be found as

$$G = \left(J_1\right)|_{s_{ob}\to 0}\cos\alpha + \left(J_2\right)|_{s_{ob}\to 0}\sin\alpha = \frac{\left(1-\mu^2\right)K_{I-ind}^2}{2\pi E}\sin\alpha. \tag{31}$$

Setting $\frac{dG}{d\alpha} = 0$, i.e., $\cos\alpha_c = 0$, we have

$$\alpha_c = \frac{\pi}{2}, \tag{32}$$

where α_c is the critical cracking angles, which is vertical to the contact boundary.

Cracking occurs when G reaches its critical or maximum value. The critical or maximum energy-based driving force for boundary cracking can then be solved from Eq. (31), i.e.

$$G_{\max} = \frac{\left(1-\mu^2\right)K_{I-ind}^2}{2\pi E}. \tag{33}$$

From the Eqs. (5), and (33), the critical condition of substrate boundary cracking beneath the contact surface can be found as

$$G_{\max} = G_C = \frac{\left(1-\mu^2\right)K_{IC-ind}^2}{2\pi E}. \tag{34}$$

for Mode-I indentation, where the K_{IC-ind} is the boundary fracture toughness for Mode-I indentation. Then, K-based fracture criterion for Mode-I indentation can be given by

$$K_{I-ind} = K_{IC-ind} \tag{35}$$

From Eqs. (34) and (6), it can be determined that

$$K_{IC-ind} = FK_{IC}, \tag{36}$$

where F is an enlarging factor, and is given by

$$F = \sqrt{2\pi} = 2.5066. \tag{37}$$

Therefore, Eq. (36) indicates that the common fracture toughness for a Mode-I tensile crack can also be determined by the indentation test method presented in this study. Recently, this indentation method has been successfully used to determine the fracture toughness of glass [16] and brittle polymers [17].

6. Conclusions

A fracture-based modelling for boundary cracking induced by indentation singular stress field has been investigated by using energy-based method. The concept of indentation stress intensity factor is introduced to descript the intensification of the indentation singular stress field. Typical calculation method on ISIFs has been given by using the partial J-integral. This study presents also an energy-based fracture mechanics analysis for the ISIF and the indentation-induced boundary

cracking within the $K_{I\text{-}ind}$-dominant region around the contact edge. It is found that the critical indentation stress intensity factor exists, and the relation between the indentation fracture toughness $K_{IC\text{-}ind}$ and the common Mode-I fracture toughness K_{IC} is established analytically, showing $K_{IC\text{-}ind} = 2.5K_{IC}$. The indentation-cracking angle at the contact edge is also determined. The present fracture mechanics model on surface contact cracking induced by a flat-tipped indenter provides a useful alternative for measuring the fracture toughness K_{IC}, which can be useful for characterization of surface fracture properties of bulk elastic bodies and coating fracture properties of layered structures.

Acknowledgements

This work was supported by National Natural Science Foundation of China (Grant Nos. 50771052 and 50971068, 11272141), Gledden Senior Fellowship from the University of Western Australia and Natural Science Foundation of Liaoning (Grant Nos. LS2010100 and 20102129).

References

[1]. A.E. Giannakopoulos, T.C. Lindley, S. Suresh, Aspects of connections and life-prediction methodology for fretting-fatigue. Acta Mater, 46 (1998) 2955-2968.

[2]. A.E. Giannakopoulos, T.A. Venkatesh, T.C. Lindley, S. Suresh, The role of adhesion in contact fatigue. Acta Mater, 47 (1999) 4653-4664.

[3]. B. Yang, S. Mall, On crack initiation mechanism in fretting fatigue. ASME J Appl Mech, 68 (2001) 76-80.

[4]. A.I. Nadai, Theory of flow and fracture of solids. New York: McGraw-Hill, 1963.

[5]. Y.J. Xie, D.A. Hills, Quasibrittle fracture beneath a flat bearing surface. Eng Fract Mech, 75 (2008) 1223–1230.

[6]. J.D. Eshelby, The force on an elastic singularity. Phil Trans Roy Soc London A 244 (1951) 87-112.

[7]. G.C. Sih, Inelastic behaviour of solids. In: Sih GC editor. Dynamic aspects of crack aspects of crack propagation, New York: Mc-Graw-Hill Book, Co, 1969, pp.607-639.

[8]. J.R. Rice, A path-independent integral and the approximate analysis of strain concentrated by notches and cracks. ASME J Appl Mech, 35 (1968) 379-386.

[9]. B. Budiansky, J.R. Rice, Conservation laws and energy-release rates. ASME J Appl Mech 40 (1973) 201-203.

[10]. A.A, Griffith, The Phenomena of rupture and flow in solids. Phil Trans Roy Soc London A 221 (1921) 163-198.

[11]. G.P Cherepanov, Mechanics of brittle fracture. New York: McGraw-Hill International Book Co, 1979.

[12]. Y.J. Xie, D.A. Hills, Quasibrittle fracture beneath a flat bearing surface. Engineering Fracture Mechanics 75 (2008) 1223–1230.

[13]. Y.J. Xie, K.Y. Lee, X.Z. Hu, Y.M. Cai, Applications of conservation integral to indentation with a rigid punch. Engineering Fracture Mechanics 76 (2009) 949–957.

[14]. Y.J. Xie, X.Z. Hu, X.H. Wang, J. Chen, K.Y. Lee, A theoretical note on mode-I crack branching and kinking. Engineering Fracture Mechanics 78 (2011) 919–929.

[15]. Y.J. Xie, X.Z. Hu, X.H. Wang, Frictional contact induced crack initiation in incompressible substrate. Engineering Fracture Mechanics, 78 (2011) 2947–2956

[16]. Y. J. Xie, X. Z. Hu, J. Chen and K.Y. Lee, Micro-indentation fracture from flat-ended cylindrical indenter. Fatigue & Fracture of Engineering Materials & Structures, 35 (2012) 45–55.

[17]. X. Zhang, X.Z. Hu, Determination of fracture toughness of brittle polymers from contact crack induced by flat-tipped cylindrical indenter. Polymer Testing, 31 (2012) 765-769.

Free edge coupling effect of piezoelectric cross-ply laminated plates

Chao Han[1,*], **Zhangjian Wu**[1]

[1] Department of MACE, The University of Manchester, M13 9PL, UK
* Corresponding author: Chao.Han-2@postgrad.manchester.ac.uk

Abstract
Free edge effect of laminated plates has been extensively investigated in the past two decades. Due to the boundary condition limitation, very limited work on piezoelectric laminated plates with free edges was carried out. In this paper, coupled and uncoupled analytical analyses on the interlaminar stresses in the vicinity of the free edges of piezoelectric laminated plates are presented on the basis of three-dimensional elasticity and piezoelectricity. The state space equations for cross-ply piezoelectric laminates subjected to uniaxial extension are obtained by considering all independent elastic and piezoelectric constants. The equations satisfy the boundary conditions at free edges and the continuity conditions across the interfaces between plies of the laminates. Three dimensional exact solution is sought and validated by comparing present numerical results with those of existing approximate analytical and finite element models. The singularity of the interlaminar stresses near the free edges is confirmed and the electromechanical coupling effects give much higher interlaminar stresses at the free edges in comparison with those of the corresponding uncoupled cases.

Keywords: piezoelectricity, laminated plate, coupling effect, interface stress, exact solution

1. Introduction

In recent decades, composite materials have extensive popularity in high-performance products that demand for high-strength, lightweight among many fields. Due to the development of multifunctional structures, smart materials and structures, which can perform sensing, controlling, actuating with distinct direct and converse piezoelectric effects, are widely used in many applications such as structural vibration control, precision positioning, aerospace and nanotechnology. Piezoelectric structures are often made from multi-layered thin films of dissimilar materials in the forms of stacks. For example, a piezoelectric laminated plate with simply-supported conditions, as a multilayer stack, was investigated by many researchers such as Heyliger [1], Lee and Jiang [2], Cheng et al. [3] and Xu et al. [4]. Sheng et al. [5] presented state space solution for laminated piezoelectric plate with clamped and electric open-circuited boundary conditions.

It is well-established that due to the discontinuity of material properties at the interfaces, a highly concentrated interlaminar stress field can occur in the vicinity of the free edges which will lead to interlaminar failures such as delamination or matrix cracking. Pipes and Pagano [6] presented a 3D elastic solution for the free-edge effect for a symmetric laminate strip under uniaxial tension. By using Lekhnitskii's [7] stress potential as well as the eigenfunction technique, Wang and Choi [8] investigated the stress singularities at the free edge of laminated plate. Becker [9] presented a closed-form solution by introducing a particular warp deformation which decays rapidly towards the laminate interior to reflect the free edge effect. Most recently, analytical solutions were developed by Tahani and Nosier [10] within Reddy's layerwise theory (LWT) to investigate the free edge effect problem of general cross-ply laminates with finite dimensions under uniform axial extension. Recently Zhang et al. [11] give the 3D analytical solution for the free edge cracking effect in composite laminates under extension and thermal loading by using state space method.

Due to the piezoelectric coupling effects in piezoelectric laminated plate, the mechanical and electrical behavior becomes more complex. Thus an accurate determination of coupling effect on free edge interlaminar stresses and deformation is essential in the design of elastic and piezoelectric

structure. By using Fourier transforms to reduce electro-elastic boundary value problem to the solutions of integral equations, Ye and He [12] solved the problem of electric field concentrations of a pair of parallel electrodes arrayed in one plane. Finite element method was chosen to show the effect of piezoelectric coupling on interlaminar stresses and electric field strengths near the free edge by Artel and Becker [13]. In addition, an analytical solution was also developed to determine the state variables of piezoelectric elasticity in the vicinity of free edges using a layerwise displacement theory by Mirzababaee and Tahani [14].

In this paper, on the basis of 3D elasticity and piezoelectricity, an exact analytical solution that satisfies both mechanical and electric boundary conditions is established by considering continuity of displacements, transverse stresses, electric potentials and vertical electric displacements across interfaces between different materials.

2. Fundamental State Space Method Formulation

2.1. State space equations for cross-ply piezoelectric plate

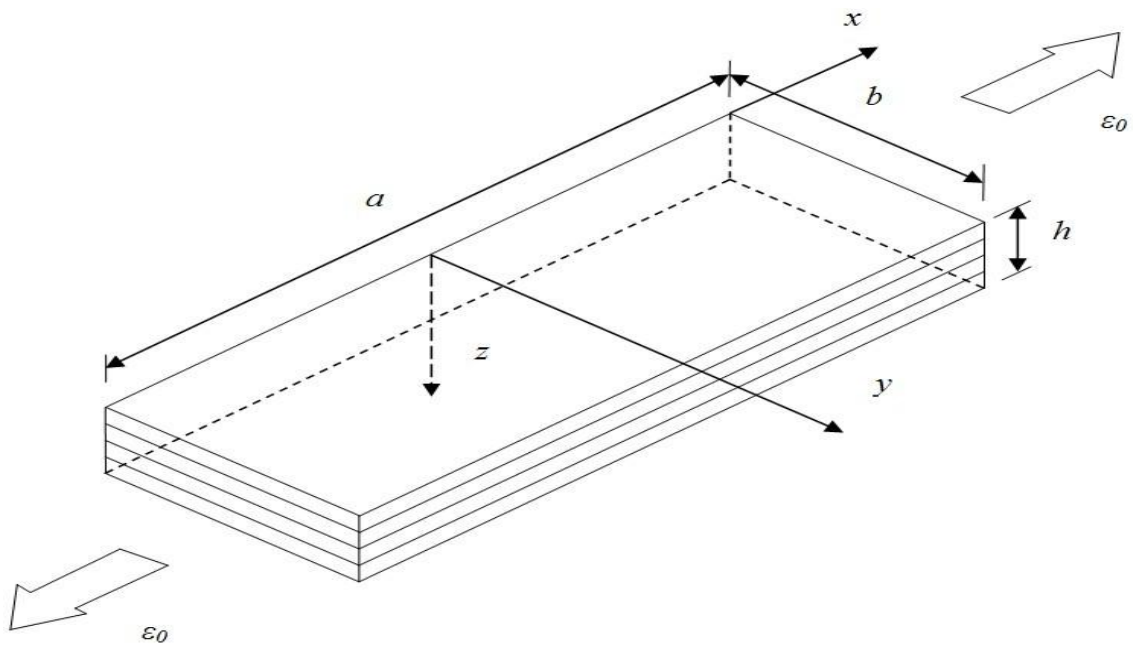

Figure 1. Geometry of a piezoelectric laminated plate

The rectangular piezoelectric laminated plate is subjected to a uniform constant axial strain ε_0 and it is assumed to have length a, width b, and uniform thickness h (Fig. 1). The principle elastic directions of plate coincide with the axes of the chosen rectangular coordinate system and full coupled three-dimensional piezoelectric-elastic constitutive relations of orthotropic piezoelectric lamina are given

$$\{\sigma\} = [C]\{\varepsilon\} - [e]^T \{E\}, \tag{1}$$

$$\{D\} = [e]\{\varepsilon\} + [\in]\{E\}, \tag{2}$$

Where $\{\sigma\}$, $\{\varepsilon\}$, $\{E\}$ and $\{D\}$ are, respectively, stress, strain, electric field, and electric displacement vectors. $[C]$, $[e]$ and $[\epsilon]$ are elastic, piezoelectric and electric permittivity constants, respectively. Explicit forms of Eqs. (1) and (2) are given as follows:

$$\begin{Bmatrix}\sigma_x\\ \sigma_y\\ \sigma_z\\ \tau_{yz}\\ \tau_{xz}\\ \tau_{xy}\end{Bmatrix}=\begin{bmatrix}C_{11} & C_{12} & C_{13} & 0 & 0 & 0\\ C_{12} & C_{22} & C_{23} & 0 & 0 & 0\\ C_{13} & C_{23} & C_{33} & 0 & 0 & 0\\ 0 & 0 & 0 & C_{44} & 0 & 0\\ 0 & 0 & 0 & 0 & C_{55} & 0\\ 0 & 0 & 0 & 0 & 0 & C_{66}\end{bmatrix}\begin{Bmatrix}\varepsilon_x\\ \varepsilon_y\\ \varepsilon_z\\ \gamma_{yz}\\ \gamma_{xz}\\ \gamma_{xy}\end{Bmatrix}-\begin{bmatrix}0 & 0 & e_{31}\\ 0 & 0 & e_{32}\\ 0 & 0 & e_{33}\\ 0 & e_{24} & 0\\ e_{15} & 0 & 0\\ 0 & 0 & 0\end{bmatrix}\begin{Bmatrix}E_x\\ E_y\\ E_z\end{Bmatrix}, \tag{3}$$

$$\begin{Bmatrix}D_x\\ D_y\\ D_z\end{Bmatrix}=\begin{bmatrix}0 & 0 & 0 & 0 & e_{15} & 0\\ 0 & 0 & 0 & e_{24} & 0 & 0\\ e_{31} & e_{32} & e_{33} & 0 & 0 & 0\end{bmatrix}\begin{Bmatrix}\varepsilon_x\\ \varepsilon_y\\ \varepsilon_z\\ \gamma_{yz}\\ \gamma_{xz}\\ \gamma_{xy}\end{Bmatrix}+\begin{bmatrix}\in_{11} & 0 & 0\\ 0 & \in_{22} & 0\\ 0 & 0 & \in_{33}\end{bmatrix}\begin{Bmatrix}E_x\\ E_y\\ E_z\end{Bmatrix}. \tag{4}$$

Due to the uniform extension ε_0 and infinite length in the x direction, the state variables are independent from the longitudinal coordinate x, therefore, the linear strain-displacement relations of elasticity and the components of electric field vector can be written as

$$\begin{gathered}\varepsilon_x=\frac{\partial u}{\partial x}=\varepsilon_0,\quad \varepsilon_y=\frac{\partial v}{\partial y},\qquad \varepsilon_z=\frac{\partial w}{\partial z},\\ \gamma_{yz}=\frac{\partial w}{\partial y}+\frac{\partial v}{\partial z},\ \gamma_{xz}=\frac{\partial u}{\partial z}+\frac{\partial w}{\partial x}=0,\ \gamma_{xy}=\frac{\partial u}{\partial y}+\frac{\partial v}{\partial x}=0,\\ E_x=-\frac{\partial \varphi}{\partial x}=0,\ E_y=-\frac{\partial \varphi}{\partial y},\qquad E_z=-\frac{\partial \varphi}{\partial z}.\end{gathered} \tag{5}$$

Where u, v and w represent displacements in the x, y and z directions, respectively.

Gaussian law and stress equilibrium equations of the elastic body are given below

$$\begin{cases}D_{x,x}+D_{y,y}+D_{z,z}-q=0\\ \sigma_{x,x}+\tau_{xy,y}+\tau_{xz,z}+f_x=0\\ \tau_{xy,x}+\sigma_{y,y}+\tau_{yz,z}+f_y=0\\ \tau_{xz,x}+\tau_{yz,y}+\sigma_{z,z}+f_z=0\end{cases}. \tag{6}$$

By considering Eqs. (3)-(6) and assuming the electrical body charge q as well as body forces f_i to be zero, we can get $\tau_{xz}=0$, $\tau_{xy}=0$, $D_x=0$ and other 9 state variables v, w, σ_x, σ_y, σ_z, τ_{yz}, D_y, D_z, φ. They are all independent of x, and can be expressed as $v(y,z)$, $w(y,z)$, $\sigma_y(y,z)$, $\sigma_z(y,z)$, $\tau_{yz}(y,z)$, $D_y(y,z)$, $D_z(y,z)$, and $\varphi(y,z)$. After a lengthy derivation process based on Eqs. (3)-(6) the following first-order partial differential equations are obtained:

$$\frac{\partial}{\partial z}\{R\}=[A]\{R\}+\{B\}, \tag{7}$$

$$\{R\}=\begin{Bmatrix} v \\ D_z \\ \sigma_z \\ \tau_{yz} \\ \phi \\ w \end{Bmatrix},[A]=\begin{bmatrix} 0 & 0 & 0 & \alpha_{19} & \alpha_{20}\beta & \alpha_{21}\beta \\ 0 & 0 & 0 & -\alpha_{17}\beta & -\alpha_{18}\beta^2 & 0 \\ 0 & 0 & 0 & -\beta & 0 & 0 \\ -\alpha_{13}\beta^2 & -\alpha_{15}\beta & -\alpha_{14}\beta & 0 & 0 & 0 \\ \alpha_5\beta & \alpha_7 & \alpha_6 & 0 & 0 & 0 \\ \alpha_1\beta & \alpha_3 & \alpha_2 & 0 & 0 & 0 \end{bmatrix},\{B\}=\begin{Bmatrix} 0 \\ 0 \\ 0 \\ 0 \\ \alpha_8 \\ \alpha_4 \end{Bmatrix}\varepsilon_0. \tag{8}$$

The following in-plane stresses and electric displacements are also obtained:

$$\begin{Bmatrix} \sigma_x \\ \sigma_y \end{Bmatrix}=\begin{bmatrix} \alpha_9\cdot\beta & \alpha_{10} & \alpha_{11} \\ \alpha_{13}\cdot\beta & \alpha_{14} & \alpha_{15} \end{bmatrix}\begin{Bmatrix} v \\ \sigma_z \\ D_z \end{Bmatrix}+\begin{Bmatrix} \alpha_{12} \\ \alpha_{16} \end{Bmatrix}\varepsilon_0,$$
$$D_y=\begin{bmatrix} \alpha_{17} & \alpha_{18}\cdot\beta \end{bmatrix}\begin{Bmatrix} \tau_{yz} \\ \phi \end{Bmatrix}. \tag{9}$$

Constants related to material property can be expressed as follows:

$$\alpha_1=\frac{-e_{32}\cdot e_{33}-C_{23}\cdot\in_{33}}{\Delta_1},\ \alpha_2=\frac{\in_{33}}{\Delta_1},\ \alpha_3=\frac{e_{33}}{\Delta_1},\ \alpha_4=\frac{-e_{31}\cdot e_{33}-C_{13}\cdot\in_{33}}{\Delta_1},\ \alpha_5=\frac{C_{33}\cdot e_{32}-C_{23}\cdot e_{33}}{\Delta_1},$$
$$\alpha_6=\frac{e_{33}}{\Delta_1},\ \alpha_7=\frac{-C_{33}}{\Delta_1},\ \alpha_8=\frac{C_{33}\cdot e_{31}-C_{13}\cdot e_{33}}{\Delta_1},\ \alpha_9=C_{12}+\alpha_1\cdot C_{13}+\alpha_5\cdot e_{31},\ \alpha_{10}=\alpha_2\cdot C_{13}+\alpha_6\cdot e_{31},$$
$$\alpha_{11}=\alpha_3\cdot C_{13}+\alpha_7\cdot e_{31},\ \alpha_{12}=C_{11}+\alpha_4\cdot C_{13}+\alpha_8\cdot e_{31},\ \alpha_{13}=C_{22}+\alpha_1\cdot C_{23}+\alpha_5\cdot e_{32}, \tag{10}$$
$$\alpha_{14}=\alpha_2\cdot C_{23}+\alpha_6\cdot e_{32},\ \alpha_{15}=\alpha_3\cdot C_{23}+\alpha_7\cdot e_{32},\ \alpha_{16}=C_{12}+\alpha_4\cdot C_{23}+\alpha_8\cdot e_{32},$$
$$\alpha_{17}=\frac{e_{24}}{C_{44}},\ \alpha_{18}=-\frac{e_{24}^2}{C_{44}}-\in_{22},\ \alpha_{19}=\frac{1}{C_{44}},\ \alpha_{20}=-\frac{e_{24}}{C_{44}},\ \alpha_{21}=-1,\ \Delta_1=e_{33}^2+C_{33}\cdot\in_{33},\ \beta=\frac{\partial}{\partial y}.$$

Assuming that the displacements v can be expressed as:

$$v(y,z)=\bar{v}(y,z)+v^{(0)}(z)\cdot(1-\frac{2y}{b}), \tag{11}$$

Where $v^{(0)}(z)$ is the unknown boundary displacement function that can be determined by imposing traction free conditions and open-circuit conditions on the free edges. The following Fourier series expansions are used:

$$\begin{cases} \bar{v}(y,z)=\sum_{n=0}^{\infty}\bar{v}_n(z)\cdot Sin(\eta\cdot y) \\ D_z(y,z)=\sum_{n=0}^{\infty}D_n(z)\cdot Cos(\eta\cdot y), \\ \sigma_z(y,z)=\sum_{n=0}^{\infty}Z_n(z)\cdot Cos(\eta\cdot y) \end{cases} \quad \begin{cases} \tau_{yz}(y,z)=\sum_{n=0}^{\infty}Y_n(z)\cdot Sin(\eta\cdot y) \\ \phi(y,z)=\sum_{n=0}^{\infty}\phi_n(z)\cdot Cos(\eta\cdot y)\ , \\ w(y,z)=\sum_{n=0}^{\infty}w_n(z)\cdot Cos(\eta\cdot y) \end{cases} \tag{12}$$

$$y=-\frac{2b}{\pi}\sum_{n=0}^{\infty}\frac{Cos(n\pi)}{n}\cdot Sin(\eta\cdot y), \tag{13}$$

Where $\eta = n\pi/b$, since a uniformly distributed extension is applied, displacement v is zero at $y = b/2$.

By introducing Eqs. (11)-(13) into Eq. (7) the following non-homogeneous state space equation for an arbitrary value of n is obtained:

$$\frac{d}{dz}\{R_n(z)\} = \left[\overline{A}_n\right]\{R_n(z)\} + \{B_n(z)\}, \tag{14a}$$

Where
$$\{R_n(z)\} = \left[\overline{v}_n(z) \quad D_n(z) \quad Z_n(z) \quad Y_n(z) \quad \phi_n(z) \quad w_n(z)\right]^T, \tag{14b}$$

$$\left[\overline{A}_n\right] = \begin{bmatrix} 0 & 0 & 0 & \alpha_{19} & -\alpha_{20}\eta & -\alpha_{21}\eta \\ 0 & 0 & 0 & -\alpha_{17}\eta & \alpha_{18}\eta^2 & 0 \\ 0 & 0 & 0 & -\eta & 0 & 0 \\ \alpha_{13}\eta^2 & \alpha_{15}\eta & \alpha_{14}\eta & 0 & 0 & 0 \\ \alpha_5\eta & \alpha_7 & \alpha_6 & 0 & 0 & 0 \\ \alpha_1\eta & \alpha_3 & \alpha_2 & 0 & 0 & 0 \end{bmatrix}, \tag{14c}$$

$$\{B_0(z)\} = \begin{Bmatrix} 0 \\ 0 \\ 0 \\ 0 \\ -\frac{2}{b}\cdot\alpha_5\cdot v^{(0)}(z) + \alpha_8\cdot\varepsilon_0 \\ -\frac{2}{b}\cdot\alpha_1\cdot v^{(0)}(z) + \alpha_4\cdot\varepsilon_0 \end{Bmatrix}, \{B_n(z)\} = \begin{Bmatrix} -\frac{2(1+Cos(n\pi))}{n\pi}\cdot\frac{dv^{(0)}(z)}{dz} \\ 0 \\ 0 \\ 0 \\ 0 \\ 0 \end{Bmatrix}. \tag{14d}$$

The solution of non-homogeneous state space equation in Eq. (14) can be obtained as

$$\{R_n(z)\} = e^{\left[\overline{A}_n\right]\cdot z}\{R_n(0)\} + \int_0^z e^{\left[\overline{A}_n\right]\cdot(z-\tau)}\{B_n(\tau)\}d\tau = \left[G_n(z)\right]\{R_n(0)\} + \{H_n(z)\},\ z\in[0,h], \tag{15}$$

Where $[G_n(z)]$ is called transfer matrix and $\{H_n(z)\}$ is non-homogeneous vector.

Consider the piezoelectric laminated plate consists of N different plies and suppose a ply is composed of K fictitious sub-layers. It is assumed that thickness of all the fictitious sub-layers approaches zero uniformly as K is sufficient large. In addition different plies may have different materials, which leads to in-plane stresses discontinuity at the interface. For an arbitrary sub-layer j in ith ply, we can establish its state equation:

$$\{R_n(z_i)\}_{i,j} = \left[G_n(z_i)\right]_{i,j}\{R_n(0)\}_{i,j} + \{H_n(z_i)\}_{i,j},\ z_i\in[0,d_i] \tag{16}$$

The non-homogeneous vector $\{H_n(z_i)\}_{i,j}$ from above equation contains unknown boundary functions and their derivatives. As discussed before, we divide ith ply into K_j thin sub-layers. The thickness of each sub-layers is $d_i = h_i/k_i$. If the fictitious sub-layer is sufficiently thin, it is reasonable to assume that the unknown functions are linearly distributed within the thin layers in the z-direction:

$$\begin{gathered} v_{i,j}^{(0)}(z) = v_{i,j}^t\cdot(1-\frac{z}{d_{i,j}}) + v_{i,j}^b\cdot(\frac{z}{d_{i,j}}), \\ z\in[0,d_i], i=1,2,\cdots N, j=1,2,\cdots K_i. \end{gathered} \tag{17}$$

Where $v_{i,j}^t$, $v_{i,j}^b$ are the end values of $v_{i,j}^{(0)}(z)$ at the top and bottom surfaces of the jth thin sub-layers, respectively.

By imposing continuity conditions at the interface of adjacent sub-layers $\{R_n(d_i)\}_{i,j} = \{R_n(0)\}_{i,j+1}$ and adjacent plies $\{R_n(h_i)\}_i = \{R_n(0)\}_{i+1}$, we can obtain the relationship between the state variables of the bottom and top surfaces of the plate as follows

$$\{R_n(h_N)\} = [\Pi]\{R_n(0)\} + \{\overline{\Pi}\}, \tag{18}$$

Where $\{R_n(0)\}$ and $\{R_n(h_N)\}$ are the state vectors of top and bottom surfaces of the plate, respectively, and $[\Pi]$ is the state transfer matrix. The non-homogeneous vector $\{\overline{\Pi}\}$ contains $K_1 + K_2 + \cdots + K_N + 1$ boundary unknown coefficients $v_{i,j}^t$, $v_{i,j}^b$ which can be determined by mechanical and electric boundary conditions at the free and electric open-circuited edges.

2.2. Boundary conditions of cross-ply piezoelectric plate

For an electric load free surface, open-circuited and traction-free conditions are considered, the top and bottom surface conditions are obtained:

$$[D_n(0) \quad Z_n(0) \quad Y_n(0) \quad \tau_{xz}(0)]^T = [0 \quad 0 \quad 0 \quad 0]^T, \tag{19a}$$

$$[D_n(h_N) \quad Z_n(h_N) \quad Y_n(h_N) \quad \tau_{xz}(h_N)]^T = [0 \quad 0 \quad 0 \quad 0]^T. \tag{19b}$$

The plate has free edges and electrical open-circuited conditions at $y = 0$, $y = b$ as follows:

$$\sigma_y = \tau_{xy} = \tau_{zy} = D_y = 0, \tag{20}$$

where $\tau_{xy} = 0$, $\tau_{zy} = 0$, $D_y = 0$ are satisfied automatically. The remaining boundary condition to be satisfied is $\sigma_y = 0$. Due to symmetry, we only impose the condition at $y = 0$, and substitute the second equation of Eq. (9) into the first expression of Eq. (20) yields

$$\sum_{n=0}^{\infty}[\alpha_{13} \cdot \eta \cdot \bar{v}_n(z) + \alpha_{14} \cdot Z_n(z) + \alpha_{15} \cdot D_n(z)] + \alpha_{16} \cdot \varepsilon_0 - \alpha_{13} \cdot \frac{2}{b} \cdot v^{(0)}(z) = 0. \tag{21}$$

The following algebra equation system can be obtained by introducing Eqs. (18) and (19) and eventually the boundary unknown constants can be determined by considering Eqs. (21) and (22).

$$\begin{Bmatrix} v_n(z) \\ D_n(z) \\ Z_n(z) \end{Bmatrix} = -\begin{bmatrix} \Pi_{11}(z) & \Pi_{15}(z) & \Pi_{16}(z) \\ \Pi_{21}(z) & \Pi_{25}(z) & \Pi_{26}(z) \\ \Pi_{31}(z) & \Pi_{35}(z) & \Pi_{36}(z) \end{bmatrix} \begin{bmatrix} \Pi_{21} & \Pi_{25} & \Pi_{26} \\ \Pi_{31} & \Pi_{35} & \Pi_{36} \\ \Pi_{41} & \Pi_{45} & \Pi_{46} \end{bmatrix}^{-1} \begin{Bmatrix} \overline{\Pi}_2 \\ \overline{\Pi}_3 \\ \overline{\Pi}_4 \end{Bmatrix} + \begin{Bmatrix} \overline{\Pi}_1(z) \\ \overline{\Pi}_2(z) \\ \overline{\Pi}_3(z) \end{Bmatrix}. \tag{22}$$

3. Numerical examples and results

To validate the present method, numerical examples are presented for symmetric cross-ply piezoelectric laminated plates and comparisons are made between the current solution and work done by Artel and Becker [13], and Mirzababaee and Tahani [14]. The free-edge effect in the laminated plate with and without electromechanical coupling is investigated and two laminated layups $[0^o / 90^o]_s$ and $[90^o / 0^o]_s$ are considered. The material properties are given in Table 1 which comprises the mechanical properties of a T300/Epoxy and the piezoelectric and electrical properties of a PZT-5A. The uniaxial extension ε_0 is 0.1% and the width b is ten times larger than the thickness h, in addition, the thickness of each ply in the laminate is identical.

Table 1. Mechanical and electrical properties of the piezoelectric plate

Elastic Stiffness (GPa)	Piezoelectric Coefficients (C/m^2)	Dielectric Properties ($C^2/(Jm)$)
$C_{11}=137$ $C_{12}=C_{13}=3.75$ $C_{22}=C_{33}=10.9$ $C_{23}=3$ $C_{44}=3.97$ $C_{55}=C_{66}=5$	$e_{31}=e_{32}=-5.4$ $e_{33}=15.8$ $e_{24}=e_{15}=12.3$	$\epsilon_{11}=\epsilon_{22}=1730\epsilon_0$ $\epsilon_{33}=1700\epsilon_0$ $\epsilon_0=8.859\times10^{-12}$

Distributions of stresses and electric field strength components at the $[0^o/90^o]$ interface in a $[0^o/90^o]_s$ laminate and at the $[90^o/0^o]$ interface in a $[90^o/0^o]_s$ laminate are presented for the electromechanical uncoupled and coupled cases. From Fig. 2 it is very clear that interlaminar normal stress σ_z shows a possible singular behavior in the vicinity of free edge and ascends to a finite value at the free edge for both cases. For the coupled electric and mechanical circumstance, there is a good agreement between present results and those of Artel and Becker [13], and Mirzababaee and Tahani [14]. In addition, the values of coupled one are approximately two times larger than those of uncoupled one in the present results.

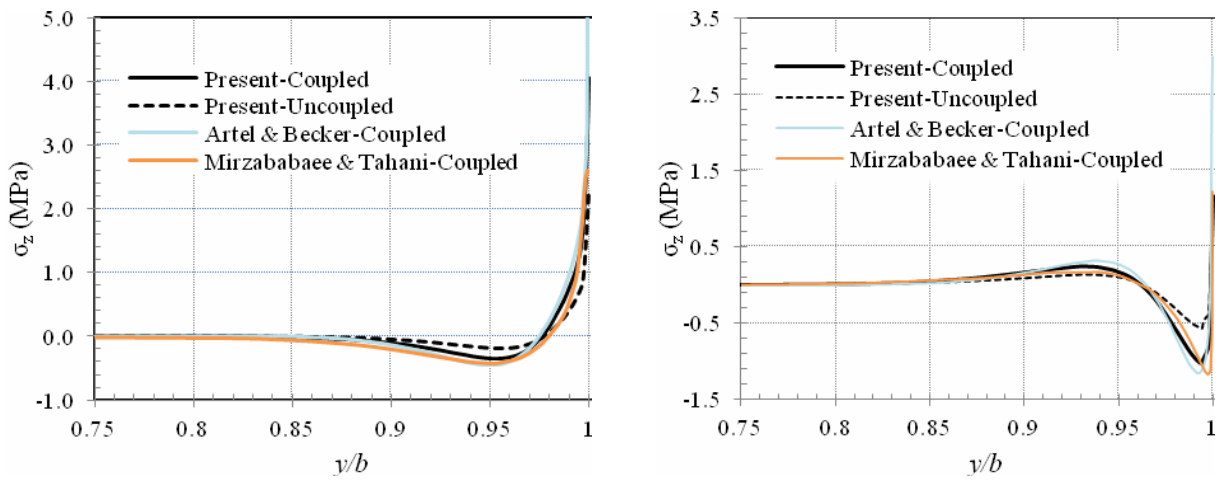

(a) $[0^o/90^o]_s$ (b) $[90^o/0^o]_s$

Figure 2. Distributions of interlaminar normal stress σ_z

The variations of interlaminar normal stress σ_z at the interfaces through thickness at the free edges are depicted in Fig. 3. It is shown that the present uncoupled results have good agreement with those of Mirzababaee and Tahani [14] and the present coupled results have decent agreement with those of Mirzababaee and Tahani [14]. However, neither of above results for uncoupled and coupled is in good agreement with those of Artel and Becker [13], especially at the interfaces between different material plies. From Fig. 3 it is seen that the values of present coupled results are also approximately two times larger than those of present uncoupled results quantitatively.

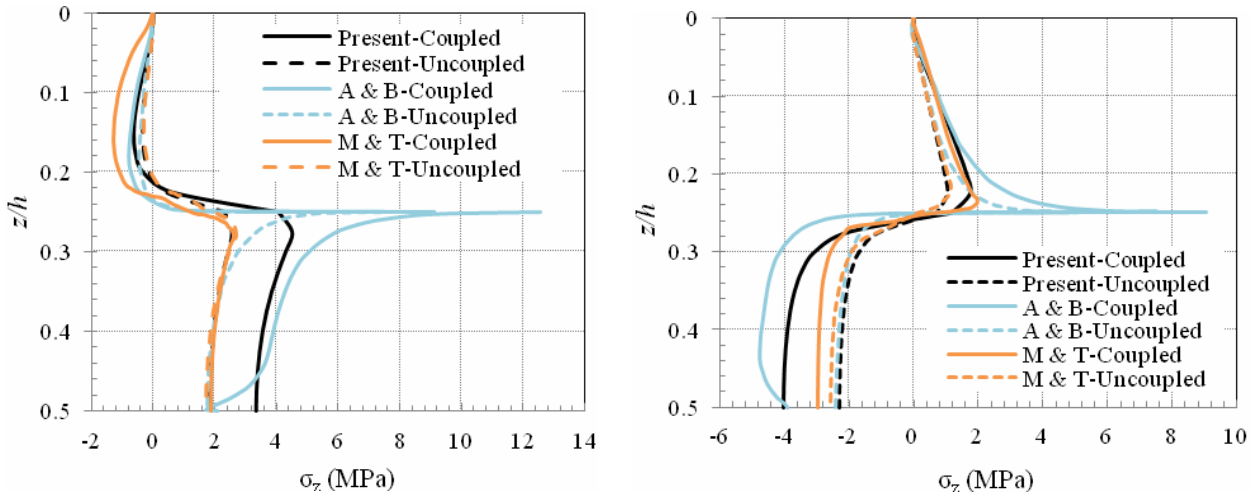

(a) $[0^o / 90^o]_s$ (b) $[90^o / 0^o]_s$

Figure 3. Through thickness variations of interlaminar normal stress σ_z

The variations of interlaminar stress τ_{yz} for uncoupled and coupled ones are shown in Fig. 4. The present results agree well with those of Artel and Becker [13], and Mirzababaee and Tahani [14] near the free edge. The value of τ_{yz} changes abruptly near the free edge at the interface and descends to zero at the free edge. In contrast to present results, those of Artel and Becker [13], and Mirzababaee and Tahani [14] cannot satisfy the traction free condition along free edges. Present results shows that interlaminar stress gradient occurs near the free edge due to the dissimilar properties of adjacent plies and coupled stresses are larger than those of uncoupled.

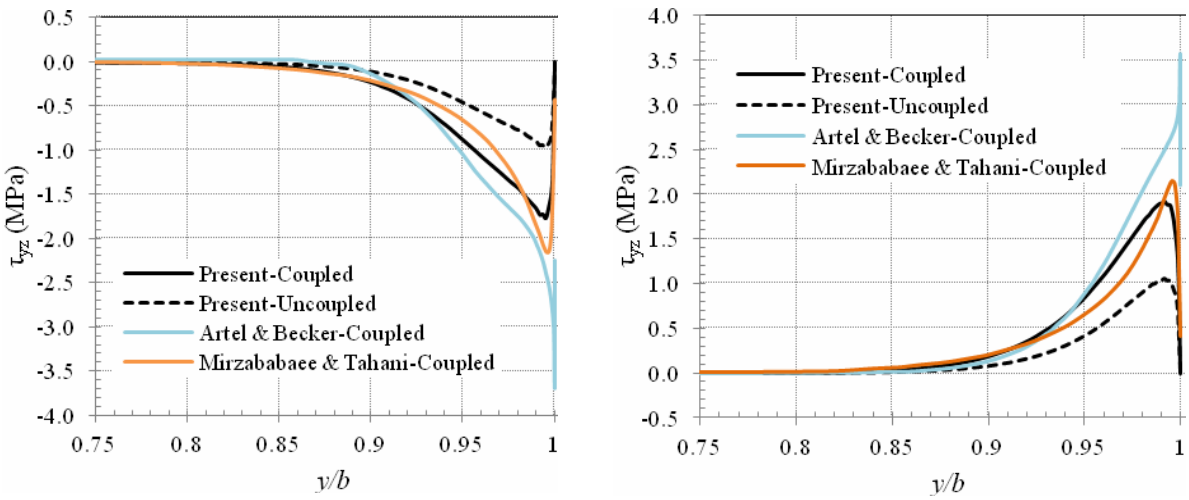

(a) $[0^o / 90^o]_s$ (b) $[90^o / 0^o]_s$

Figure 4. Distributions of interlaminar shear stress τ_{yz}

Electrical quantities gradient may also occur in the vicinity of free edge at interfaces. The electric field component E_y changes dramatically near the free edge and vanishes at the free edge. Moreover, another electric field component E_z becomes singular at the free edge. In addition, it is worth to mention that present results disagreed with those of Artel and Becker [13], and Mirzababaee and Tahani [14] in magnitude.

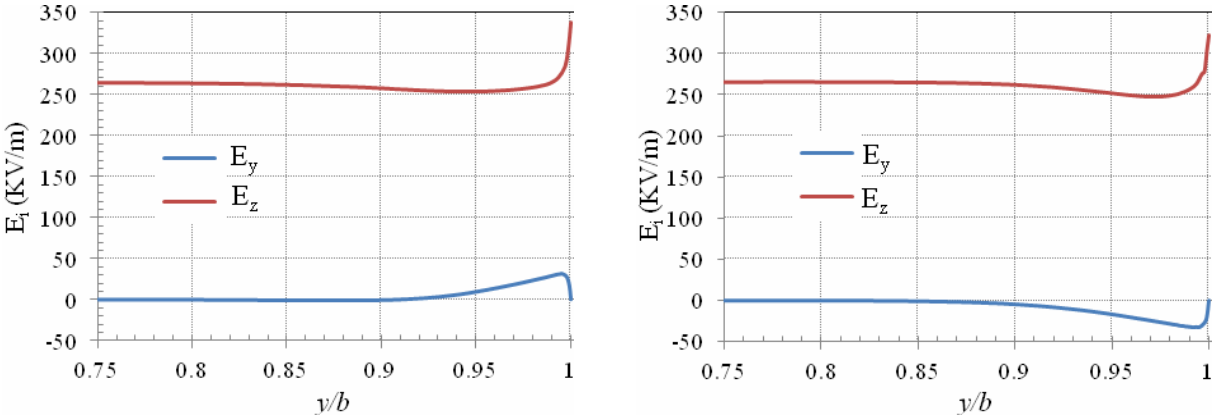

(a) $[0^o / 90^o]_s$ (b) $[90^o / 0^o]_s$

Figure 5. Distributions of electric field strength components E_i

On the basis of comparative analyses in this section, it is seen that the results of Artel and Becker [13], and Mirzababaee and Tahani [14] violate traction free boundary conditions at free edges. Furthermore, the FEM solution from Artel and Becker [13] fails to guarantee the continuity of transverse normal stress at interface of two different materials, deficiencies mentioned above were overcome by present solution. Both the stress and electric field strength singularities were observed with suitable layer refinement in *z*-direction.

4. Conclusions

State space method for an analytical solution has been developed to investigate the coupling effect on piezoelectric laminated plates and the singularities in the vicinity of free edges. Cross-ply laminated plates with and without electromechanical coupling subjected to uniform axial strain have been studied. To validate this method, comparisons were made between present results and those of other analytical and FEM solutions in the literature.

By satisfying all the mechanical and electric boundary conditions, especially tractions free conditions at free edges, and guaranteeing the continuity of transverse stresses and electric quantities across the interfaces between different material plies, the solutions show a significant piezoelectric effect on the laminated plate near the free edges and interlaminar stresses increase magnificently in coupled circumstance compared with those of uncoupled.

References

[1] P. Heyliger, Exact solution for simply supported laminated piezoelectric plates. J. Appl. Mech. Trans. ASME. 64 (1997) 299-306.
[2] J.S. Lee, L.Z. Jiang, Exact electroelastic analysis of piezoelectric laminae via state space approach. Int J. Solids Struct. 33 (1996) 977-990.
[3] Z.Q. Cheng, C.W. Lim, S. Kitpornchai, Three-dimensional exact solution for inhomogeneous and laminated piezoelectric plates. Int. J. Eng. Sci. 37 (1999) 1425-1439.
[4] K. Xu, A.K. Noor, Three-dimensional analytical solution for coupled thermoelecroelastic response of multilayered plates. Comput. Methods Appl. Mech. Eng. 126 (1995) 355-371
[5] H.Y. Sheng, H. Wang, J.Q. Ye, State space solution for thick laminated piezoelectric plates with clamped and electric open-circuited boundary conditions. International Journal of Mechanical Sciences. 49 (2007) 806-818.
[6] R.B. Pieps, N.J. Pagano, Interlaminar stresses in composite laminates under uniform axial

extension. J. Compos. Mater. 4 (1970) 538-548.
[7] S.G. Lehknitskii, Theory of elasticity of anisotropic elastic body. Holden Day, San Francisco, 1963.
[8] S.S. Wang, I. Choi, Boundary-layer effects in composite laminates. Asme J Appl Mech. 49 (1982) 541-560.
[9] W. Becker, Closed-form solution for the free-edge effect in cross-ply laminates. Compos Struct. 26 (1993) 39-45.
[10] M. Tahani, A. Nosier, free edge analysis of general cross-ply composite laminates under extension and thermal loading. Compos Struct. 60 (2003) 91-103.
[11] D. Zhang, J.Q. Ye, H.Y. Sheng, Free-edge and ply cracking effect in cross-ply laminated composites under uniform extension and thermal loading. Compos Struct. 76 (2006) 314-325.
[12] R.Q. Ye, L.H. He, Electric field and stresses concentrations at the edge of parallel electrodes in piezoelectric ceramics. International journal of solids and structures. 38 (2001) 6941-6951.
[13] J. Artel, W. Becker, Coupled and uncoupled analysis of piezoelectric free-edge effect in laminated plates. Compos Struct. 69 (2005) 329-335.
[14] M. Mirzababaee, M. Tahani, Accurate determination of coupling effects on free edge interlaminar stresses in piezoelectric laminated plates. Materials and Design. 30 (2009) 2963-2974.

Improvement of crack-tip stress series with Padé approximants

Gaëtan Hello[1,*], Mabrouk Ben-Tahar[2], Jean-Marc Roelandt[2]

[1] UFR Sciences et Technologies - LMEE, Université d'Evry Val d'Essonne, 91020, France
[2] Laboratoire Roberval, Université de Technologie de Compiègne, 60200, France
* Corresponding author: gaetan.hello@ufrst.univ-evry.fr

Abstract The most favored description of bi-dimensional crack-tip stress fields relies on Williams expansion. In this framework, each stress component is defined as a series which has a certain convergence behavior. Generally, the series is truncated after its first term since it is the most influential one at the vicinity of the crack-tip because of its well-known singularity. However, for some applications, the need for higher order terms arises and the study of truncation influence becomes important. The investigations performed by the authors for a specific fracture configuration have shown the existence of a convergence disk and of rather low convergence rates far from the crack-tip. In this communication, we propose to transform truncated stress series into Padé Approximants (PA) in order to improve both convergence domains and convergence rates. These approximants are rational functions whose coefficients are defined so as to fit the prescribed truncated series. The PA may be obtained following two different procedures. In practical tests, PA stemming from crack-tip stress series exhibit wider convergence domains and higher convergence rates.

Keywords Crack-tip, Williams series, Padé approximant

1. Introduction

The stress field at the vicinity of a crack-tip in a plane medium may be described using the so-called Williams series [1, 2]. Each term of the series is the product of three factors. Two of them concern respectively the angular and radial dependencies of the field. Their general expressions are known analytically and are the same for all fracture configurations [3, 4]. All the specific information related to the actual problem (geometry and loading conditions) is held by the third factor. Hence, to each fracture problem corresponds a specific infinite set of multi-order stress intensity factors.

Concerning the determination of these sets, research has been mainly focused on their first element (the Stress Intensity Factor "Ki" associated to the stress singularity) and on their second one (the T-stress "T" associated to a constant stress state). In [5], closed form asymptotic expansions for the problem of a finite straight crack in an infinite plane medium submitted to uniform remote loads have been proposed. Expressions are provided for the multi-order stress intensity factors in either mode I or mode II problems using both power series (Williams series) and Laurent series. Thanks to these expressions, the convergence behavior of crack-tip stress expansions may be studied. The existence of the expected radii of convergence is observed. Rates of convergence are quantified.

With the description of the crack-tip stress field by series arises the problem of truncation influence. The accuracy of the series representation improves as the number of terms increases. However, the convergence is rather slow and the summation procedure is numerically limited to a few hundreds terms. The aim of this work is then to improve the accuracy of the stress description based on the a-priori knowledge of a given number of terms in the series. A method based on Padé approximants (PA) is proposed [16-20]. These approximants are rational functions whose coefficients are defined so as to fit the prescribed truncated series.

The communication starts with the description of the procedure leading to closed-form crack-tip stress solutions, the presentation of techniques related to Padé approximation follows and the efficiency of the method is assessed for a practical fracture configuration.

2. Crack-tip stress series

The representation of crack-tip stress field at the vicinity of a crack-tip is generally performed with the so-called Williams crack-tip stress expansion [1, 2]:

$$\sigma_{ij}\left(r,\theta\right)=\sum_{m=1}^{2}\sum_{k=-\infty}^{\infty}a_k^m f_k^{m,ij}\left(\theta\right)r^{k/2-1} \tag{1}$$

This polar description establishes the separate nature of radial and angular dependencies. These dependencies also appear to be universal in the sense that they are the same for all fracture configurations. The particularity of each problem appears through an infinite set of specific coefficients – the first one of those being the Stress Intensity Factor (SIF). While SIF have been determined for numerous configurations, the evaluation of higher order coefficients has been less prolific (see [5] for a list of works on the subject). On the analytical point of view, just a few papers (for instance [6, 7]) have dealt with the subject. The authors have recently determined general closed form expressions for the following fracture configuration:

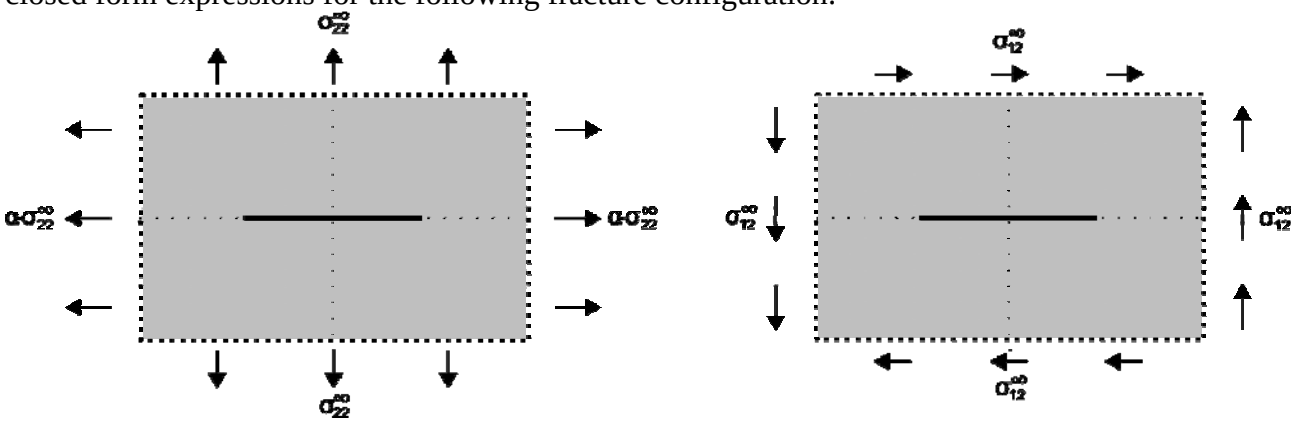

Figure 1. Fracture configuration: (left) mode-I, (right) mode-II

The procedure leading to coefficients exact definitions is described in the next subsections.

2.1. Complex solutions

Complex analysis provides a convenient way to deal with bi-dimensional elasticity. Positions are defined with a single complex number and Lamé-Navier equations may be expressed by simple "complex" operators. The formalism has largely beneficiated from the seminal works of Kolosov, Muskhelishvili and coworkers [8, 9]. A popular presentation of the method is due to Westergaard [10] who expressed the stress state in term of a complex potential ("Westergaard stress function"). Westergaard's initial work has then been improved, for instance by Sih [11]. Stress functions have been found for several fracture configurations [12, 13]. The last improvement in the domain has been provided by Sanford [14, 15]. With his "generalized Westergaard approach", he has shown that the solution should involve two complex potentials.

For mode-I, the stress state may be expressed with the potentials Z_1 and Y_1 according to:

$$\sigma_{11}^1=\operatorname{Re}Z_1-x_2\left(\operatorname{Im}Z_1'+\operatorname{Im}Y_1'\right)+2\operatorname{Re}Y_1 \tag{2}$$

$$\sigma_{22}^1=\operatorname{Re}Z_1+x_2\left(\operatorname{Im}Z_1'+\operatorname{Im}Y_1'\right) \tag{3}$$

$$\sigma_{12}^1=-\operatorname{Im}Y_1-x_2\left(\operatorname{Re}Z_1'+\operatorname{Re}Y_1'\right) \tag{4}$$

And for Mode-II with the potentials Z_2 and Y_2:

$$\sigma_{11}^2=\operatorname{Im}Y_2+x_2\left(\operatorname{Re}Y_2'+\operatorname{Re}Z_2'\right)+2\operatorname{Im}Z_2 \tag{5}$$

$$\sigma_{22}^{2} = \operatorname{Im} Y_2 - x_2 \left(\operatorname{Re} Y_2 ' + \operatorname{Re} Z_2 ' \right) \tag{6}$$

$$\sigma_{12}^{2} = -x_2 \left(\operatorname{Im} Y_2 ' + \operatorname{Im} Z_2 ' \right) + \operatorname{Re} Z_2 \tag{7}$$

The need for two complex potentials in the Westergaard approach appears coherent with the two complex potentials involved in the Kolosov-Muskhelishvili formalism.

For the fracture configuration depicted in (Fig. 1), mode-I complex potentials have the following expressions:

$$Z_1(z) = \sigma_{22}^{\infty} \frac{z}{\sqrt{z^2 - a^2}}, \quad Y_1(z) = \sigma_{22}^{\infty} \frac{(\alpha - 1)}{2} \tag{8}$$

While for mode-II:

$$Z_2(z) = \sigma_{12}^{\infty} \frac{z}{\sqrt{z^2 - a^2}}, \quad Y_2(z) = 0 \tag{9}$$

2.2. Identification of Williams series coefficients

In order to describe the stress-field in a planar cracked domain at the vicinity of the crack-tip, it is possible to use either Williams series (Eq. 1) or Sanford generalized Westergaard approach (Eq. 2-7). The stress state being unique, the two approaches must be equivalent. In [5], a procedure is described in order to transform the complex solution into the series one. Basically, complex potentials are expanded as closed-form convergent power series, these expression lead to complex stress series through (Eq. 2-7), and then, using the coordinates inter-relation $z = a + re^{i\theta}$, polar series may be retrieved.

For the configuration depicted in (Fig. 1), mode-I coefficients are then:

$$a_{2n+1}^{1} = \frac{(-1)^{n+1} (2n)!}{2^{3n+\frac{1}{2}} (n!)^2 (2n-1)} \frac{\sigma_{22}^{\infty}}{a^{n-\frac{1}{2}}}, \quad n \geq 0 \tag{10}$$

$$a_{2}^{1} = \frac{\sigma_{22}^{\infty} (\alpha - 1)}{4} \tag{11}$$

$$a_{k}^{1} = 0, \quad otherwise \tag{12}$$

And for mode-II :

$$a_{2n+1}^{2} = \frac{(-1)^{n} (2n)!}{2^{3n+\frac{1}{2}} (n!)^2 (2n-1)} \frac{\sigma_{12}^{\infty}}{a^{n-\frac{1}{2}}}, \quad n \geq 0 \tag{13}$$

$$a_{k}^{2} = 0, \quad otherwise \tag{14}$$

If one considers the stress state along the radius associated with a given angle, it may be described by two polynomial series of r :

$$\sigma_{ij}^{m}(r,\theta) = \frac{1}{\sqrt{r}} \sum_{k=0}^{\infty} a_{2k+1}^{m,ij} f_{2k+1}^{m,ij}(\theta) r^{k} + \sum_{k=1}^{\infty} a_{2k}^{m,ij} f_{2k}^{m,ij}(\theta) r^{k-1} \tag{15}$$

3. Padé Approximants

3.1. Generalities

When series are used so as to describe physical quantities, the question of the accuracy of such a

representation for practical purposes appears. Series are often truncated and in general the more terms there are, the better is the accuracy. However, sometimes it is neither possible nor accurate to include higher order terms of the expansion. In addition, the series has a radius of convergence beyond which the series diverges no matter how many terms are considered. Ideally, starting from a given truncated series, it would be interesting to devise a method that could both improve convergence rates and converge beyond the series radius of convergence. Padé approximants are known to provide such improvements [16-20]. The applicability of PA to crack-tip stress fields seems possible since (Eq. 15) holds polynomial series of the kind:

$$f\left(r,\theta\right)=\sum_{k=0}^{\infty}c_k\left(\theta\right)r^k \tag{16}$$

For the definition of PA in the general case, a function is supposed to a have a convergent polynomial expansion at the point $z=a$ where the coefficients $c_k \in \mathbb{C}$ are explicitly known:

$$f\left(z\right)=\sum_{k=0}^{\infty}c_k\cdot\left(z-a\right)^k \tag{17}$$

Associated with this function, the $\left[m,n\right]$ Padé approximant is the rational function:

$$f_{m,n}\left(z\right)=\frac{P_{m,n}\left(z\right)}{Q_{m,n}\left(z\right)} \tag{18}$$

Where the numerator and denominators are polynomials satisfying:

$$\begin{aligned}&\deg\left(P_{m,n}\left(z\right)\right)\le m,\quad \deg\left(Q_{m,n}\left(z\right)\right)\le n,\\&f_{m,n}\left(z\right)Q_{m,n}\left(z\right)-P_{m,n}\left(z\right)=O\left(z-a\right)^{m+n+1},\\&Q_{m,n}\left(0\right)\ne 0.\end{aligned} \tag{19}$$

In order to enforce the uniqueness of the approximant, the first term of the denominator is set to one:

$$Q_{m,n}\left(0\right)=1 \tag{20}$$

The numerator and denominator have then the expressions:

$$P_{m,n}\left(z\right)=\sum_{k=0}^{m}p_k\left(z-a\right)^k \tag{21}$$

$$Q_{m,n}\left(z\right)=1+\sum_{k=1}^{n}q_k\left(z-a\right)^k \tag{22}$$

The PA has $m+n+1$ unknown coefficients which requires the knowledge of the same amount of successive coefficients c_k in the initial series. The fact that coefficients p_k, q_k are not forced to be different from zero may lead to polynomials with maximum exponents lesser than the chosen ones $\left(m,n\right)$. In addition, the denominator being polynomial, it may exhibit spurious zeros that create non-physical singularities in addition to the expected ones.

3.2. Algebraic determination of Padé approximants coefficients

If the coefficients in the initial series are explicitly known, the coefficients in the $\left[m,n\right]$ Padé approximant may be determined with an algebraic process. We here suppose that $m\ge n$ without loss of generality. The enforcement of conditions (Eq. 19, 20) provides two linear systems. The first one enables to deduce $q_1,\ldots,q_n$ from $c_{m-n+1},\ldots,c_{m+n}$:

$$\begin{bmatrix} c_m & c_{m-1} & \mathrm{L} & c_{m-n+1} \\ c_{m+1} & c_m & \mathrm{L} & c_{m-n+2} \\ \mathrm{M} & \mathrm{M} & & \mathrm{M} \\ c_{m+n-1} & c_{m+n-2} & \mathrm{L} & c_m \end{bmatrix} \cdot \begin{bmatrix} q_1 \\ q_2 \\ \mathrm{M} \\ q_n \end{bmatrix} = -\begin{bmatrix} c_{m+1} \\ c_{m+2} \\ \mathrm{M} \\ c_{m+n} \end{bmatrix} \tag{23}$$

And the second one to determine $p_1,...,p_m$ from $q_1,...,q_n$ and $c_{m-n},...,c_m$

$$\begin{bmatrix} p_0 \\ p_1 \\ \mathrm{M} \\ p_m \end{bmatrix} = \begin{bmatrix} c_0 & 0 & \mathrm{L} & 0 \\ c_1 & c_0 & \mathrm{L} & 0 \\ \mathrm{M} & \mathrm{M} & & \mathrm{M} \\ c_m & c_{m-1} & \mathrm{L} & c_{m-n} \end{bmatrix} \cdot \begin{bmatrix} q_1 \\ q_2 \\ \mathrm{M} \\ q_n \end{bmatrix} \tag{24}$$

This algebraic computation of the PA may be performed either numerically or analytically. For the later, the use of a symbolic computation software like *Maple*, *Mathematica* or *Maxima* seems convenient. As an example, let's consider the following function:

$$f(x) = \frac{x}{\sqrt{x^2-1}} \tag{25}$$

A truncated series expansion at $x=1$ can be derived analytically:

$$s_f(x,n)_{x=1} = \sum_{k=0}^{n} \left[\frac{1}{\sqrt{x-1}} \frac{1}{k!} \frac{d^k}{dx^k} \left(\frac{x}{\sqrt{x+1}} \right)_{x=1} \right] \cdot (x-1)^k \tag{26}$$

Its radius of convergence is equal to 2 and convergence rates are rather low near the border of the convergence domain. Based on the knowledge of 5 coefficients in (Eq. 26), the closed-form expression of the $[2,2]$ PA can be determined, here with the help of symbolic computations:

$$f_{2,2}(x) = \frac{1}{\sqrt{x-1}} \frac{\frac{1}{\sqrt{2}} + \frac{167}{136\sqrt{2}}(x-1) + \frac{249}{1088\sqrt{2}}(x-1)^2}{1 + \frac{65}{136}(x-1) + \frac{29}{1088}(x-1)^2} \tag{27}$$

For $x = 2.9$, the truncated series $s_f(x,4)_{x=1}$ (5 coefficients) provides a result with 6.117E-2 of relative error while the associated PA $f_{2,2}(x)$ has a lower error of 7.554E-4.

3.3. Numerical evaluation of Padé approximants values with the epsilon algorithm

If the practical purpose of the PA is to compute the value of the stress field for some points of interest, the calculation of coefficients p_k, q_k is just an intermediate step and not a goal in itself. It comes out that Wynn's epsilon algorithm [21, 22] is able to calculate directly the value of the PA from successive intermediate sums of the given truncated series. It the intermediate sum with $n+1$ terms of the series expansion of f is:

$$S_n = s_f(z,n) \tag{28}$$

Then the following algorithm produces the numerical evaluation of the associated PA:

$$\begin{aligned}
&\varepsilon_{-1}^{j} = 0, \quad j = 0,1...,n \\
&\varepsilon_{0}^{j} = S_j, \quad j = 0,1,...,n \\
&\varepsilon_{k}^{j} = \varepsilon_{k-2}^{j+1} + \left(\varepsilon_{k-1}^{j+1} - \varepsilon_{k-1}^{j}\right)^{-1}, \quad k = 1,...,n \quad and \quad j = 0,...,n-k
\end{aligned} \tag{29}$$

This algorithm may be presented more conveniently using columns:

$$\begin{array}{lllll}
0 & \varepsilon_0^0 = S_0 & \varepsilon_1^0 & \mathrm{K} & \varepsilon_n^0 \\
\varepsilon_{-1}^1 = 0 & \varepsilon_0^1 = S_1 & \mathrm{M} & \mathrm{N} & \\
\mathrm{M} & \mathrm{M} & \varepsilon_1^{n-1} & & \\
\varepsilon_{-1}^n = 0 & \varepsilon_0^n = S_n & & &
\end{array} \tag{30}$$

As is appears in (Eq. 29), the evaluation of a new epsilon requires the inversion of a combination of previous epsilons. If the value of the last epsilon were to be expressed in terms of the initial partial sums, the observed expression would have the structure of a continued fraction. On the theoretical point of view, PA, the epsilon algorithm and continued fractions are deeply interrelated [18].

As an example, let's consider again the function (Eq. 25). The series representation of the function only converges within a disk of radius 2 centered at x=1. Employing the epsilon algorithm, is it possible to use the partial sums of successive truncated series in order to evaluate accurately the function for some points outside the convergence disk. For instance, even though the point x=4 lies outside the disk, a relative error of less than 10^{-6} can be achieved through the epsilon algorithm with 11 partial sums.

4. Tests

In order to assess the convergence improvement provided by PA, we consider the mode-I configuration depicted in (Fig. 1). For this problem, an exact complex solution is available with the injection of the complex potentials (Eq. 8) into Sanford's generalized Westergaard equations (Eq. 2-4). A closed-form series representation is available as well. Combining Williams general definition (Eq. 1) with the specific expressions of coefficients a_k^1 provided in (Eq. 10-12), an exact series like (Eq. 15) is defined.

From the exact series, three truncated series with respectively 5, 7 and 9 terms are considered. If the angle is fixed to zero, these truncated series may be transformed into PA using the algebraic procedure described in (Subsection 3.2). The series with 5 terms lead to the PA:

$$[2,2]_{\sigma_{22}^1(r,0)} = \frac{\sigma_{22}^{\infty}\sqrt{a}}{\sqrt{r}} \cdot \frac{\frac{1}{\sqrt{2}} + \frac{167}{136\sqrt{2}}\frac{r}{a} + \frac{249}{1088\sqrt{2}}\left(\frac{r}{a}\right)^2}{1 + \frac{65}{136}\frac{r}{a} + \frac{29}{1088}\left(\frac{r}{a}\right)^2} \tag{31}$$

The series with 7 terms provide:

$$[3,3]_{\sigma_{22}^1(r,0)} = \frac{\sigma_{22}^{\infty}\sqrt{a}}{\sqrt{r}} \cdot \frac{\frac{1}{\sqrt{2}} + \frac{1171}{792\sqrt{2}}\frac{r}{a} + \frac{1649}{3168\sqrt{2}}\left(\frac{r}{a}\right)^2 + \frac{709}{16896\sqrt{2}}\left(\frac{r}{a}\right)^3}{1 + \frac{577}{792}\frac{r}{a} + \frac{413}{3168}\left(\frac{r}{a}\right)^2 + \frac{169}{50688}\left(\frac{r}{a}\right)^3} \tag{32}$$

And the PA for the truncated series with 9 terms is:

$$[4,4]_{\sigma_{22}^{1}(r,0)} = \frac{\sigma_{22}^{\infty}\sqrt{a}}{\sqrt{r}} \cdot \frac{\frac{1}{\sqrt{2}} + \frac{7979}{4616\sqrt{2}}\frac{r}{a} + \frac{32295}{36928\sqrt{2}}\left(\frac{r}{a}\right)^2 + \frac{22585}{147712\sqrt{2}}\left(\frac{r}{a}\right)^3 + \frac{16337}{2363392\sqrt{2}}\left(\frac{r}{a}\right)^4}{1 + \frac{4517}{4616}\frac{r}{a} + \frac{19}{64}\left(\frac{r}{a}\right)^2 + \frac{4203}{147712}\left(\frac{r}{a}\right)^3 + \frac{985}{2363392}\left(\frac{r}{a}\right)^4} \quad (33)$$

In any case, the epsilon algorithm (Subsection 3.3) is able to provide the required value for the different PA at any point.

4.1. Qualitative comparison

The series expansion is performed at the crack-tip z=a. The radius of convergence is therefore equal to 2a. The series is not able to converge beyond this limit. In (Fig. 2), the exact complex solution, the truncated series representation with 9 terms, and the PA with 9 coefficients are compared. As expected, the series representation has only a good correspondence with the reference near the crack-tip and diverges beyond the radius of convergence. PA exhibits an excellent correspondence with the complex solution inside the whole convergence disk. The behavior outside the disk is also close to the reference. A spurious singular points appears at z=-2a. PA solution seems thus to have better convergence rates and a larger convergence domain.

4.2. Quantitative comparison

The approximate representations with truncated series and PA (Eq. 31-33) are now compared in (Fig. 3). Within the convergence disk, the more terms hold the series, the better is the solution. Beyond the convergence radius series diverge. PA approximations have far better convergence rates inside most of the convergence disk. PA are also able to provide accurate results far beyond the series convergence limit.

5. Conclusion

In this communication, Padé approximants have been used in order to improve the convergence behavior of crack-tip stress series. Starting from closed-form truncated series, it is possible to either determine exactly the coefficients in the PA or to estimate directly its value at any point. With the same amount of “information” (ie coefficients), the PA associated to a given truncated series provides better convergence rates inside the series convergence disk and is also able to converge outside the disk.

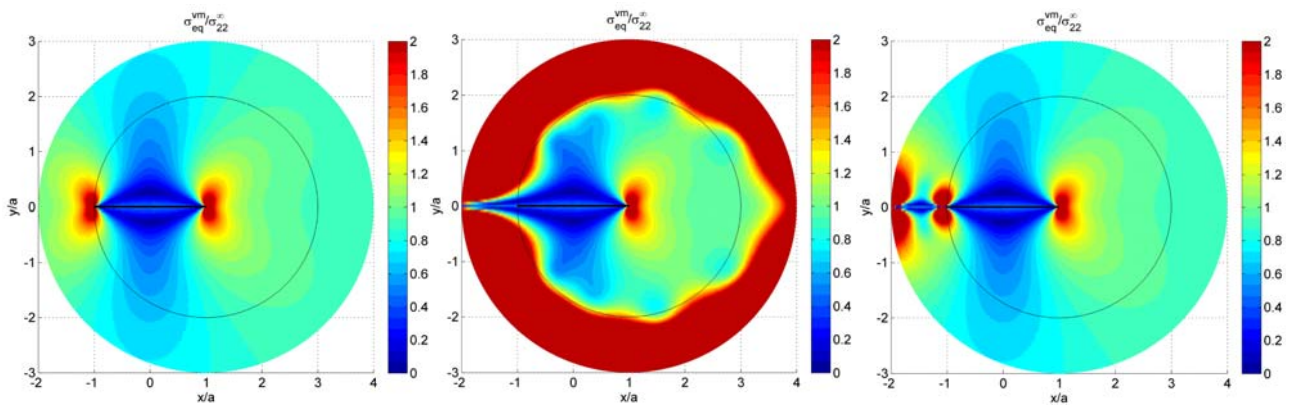

Figure 2. Stress state representation for: (left) Westergaard exact solution, (center) truncated series with 9 terms, (right) Padé approximant [4,4] with 9 coefficients.

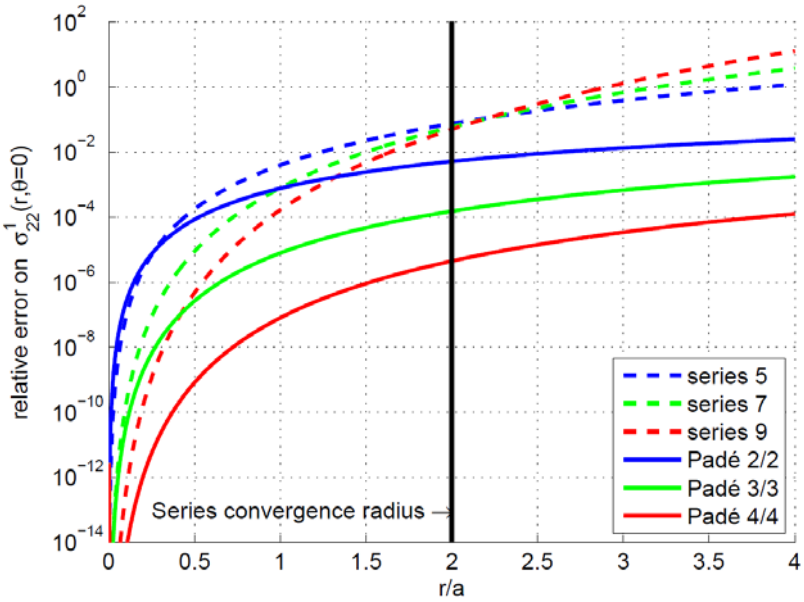

Figure 3. Relative error on $\sigma^1_{22}(r,\theta=0)$ for series representations with 5,7 and 9 terms and their associated Padé approximants $[2,2]$, $[3,3]$ and $[4,4]$.

Acknowledgements

This work was financially supported by French National Research Agency (ANR) under grant project COSINUS MACSIM.

References

[1] M. L. Williams, Stress singularities resulting from various boundary conditions in angular corners of plates in extension. J Appl Mech, 19 (1952) 526–528.
[2] M. L. Williams, On the stress distribution at the base of a stationary crack. J Appl Mech, 24 (1957) 109–114.
[3] D.R.J. Owen, A.J. Fawkes, Engineering fracture mechanics: numerical methods and applications, Pineridge Press, Swansea, 1983.
[4] B.L. Karihaloo, Q.Z. Xiao, Accurate determination of the coefficients of elastic crack tip asymptotic field by a hybrid crack element with p-adaptivity. Eng Frac Mech, 68 (2001) 1609–1630.
[5] G. Hello, M. Ben-Tahar, J.-M. Roelandt, Analytical determination of coefficients in crack-tip stress expansions for a finite crack in an infinite plane medium. Int J Solids Struct, 49 (2012) 556–566.
[6] P. Theocaris, C. Spyropoulos, Photoelastic determination of complex stress intensity factors for slant cracks under biaxial loading with higher-order term effects. Acta Mechanica, 48 (1983) 57–70.
[7] P. C. Paris, Secondary elastic crack tip stresses which may influence very slow fatigue crack growth. Fatigue Fract Eng Mater Struct, 25 (2002) 791–794.
[8] G. Kolosov, On the application of the complex function theory to a plane problem of the mathematical theory of elasticity [in russian], Dorpat University, 1909.
[9] N. Muskhelishvili, Some Basic Problems of Mathematical Theory of Elasticity, Noordhoff, Leyden, 1953.
[10] H. Westergaard, Bearing pressures and cracks. J Appl Mech, A (1939) 49–53.
[11] G. Sih, On the Westergaard method of crack analysis. Int J Fract, 2 (1966) 628–631.
[12] H. Tada, P. C. Paris, Irwin G. R., The stress analysis of cracks handbook, ASME, New York,

2000.
[13] E. Gdoutos, C. Rodopoulos, J. Yates, Problems of Fracture Mechanics and Fatigue : A Solution Guide, Academic Publishers, Dordrecht, 2003.
[14] R.J. Sanford, A critical re-examination of the westergaard method for solving opening-mode crack problems. Mech Research Comm, 6 (1979) 289–294.
[15] R.J. Sanford, Principles of Fracture Mechanics, Prentice Hall, 2003.
[16] G. Baker, Essentials of Padé approximants, Academic Press, 1975.
[17] G. Baker, P. Graves-Morris, Padé approximants basic theory, Addison-Wesley publishing company, 1981.
[18] C. Brezinski, History of Continued Fractions and Padé Approximants, Springer Verlag, 1991.
[19] C. Brezinski, M. Zaglia, Extrapolation Methods: Theory and Practice, North Holland, 1991.
[20] G. Baker, P. Graves-Morris, Padé approximants, Cambridge University Press, 1996.
[21] P. Wynn, On a device for computing the em(sn) transformation. Maths Tables and Other Aids to Computation, 10 (1965) 91–96.
[22] P. Graves-Morris, D. Roberts, A. Salam, The epsilon algorithm and related topics. J Computational Applied Maths, 122 (2000) 51–80.

On Symmetric Crack Formation in Plates under Central Bending

Ilya Nickolaevich Dashevskiy

A. Ishlinsky Institute for Problems in Mechanics, Russian Academy of Sciences, 119526, Russia
dash@ipmnet.ru

Abstract The energy approach is used to propose a model of brittle fracture of a thin plate (and a wedge) under bending by a point indenter, which permits studying some possible mechanisms determining the number of sectors into which the plate breaks. Since the energy necessary to form new cracks and the total elastic bending energy of the n triangular sectors-beams arising under bending vary in opposite directions with variation in both the crack length L and n, it follows that the total energy required to form n sectors has a minimum depending on L and n, and it is this minimum that determines the number n of the arising sectors. In the simplest scheme, the number of developing cracks turns out to be independent of the plate physical-mechanical characteristics, and its thickness and varies from 2 to 4 as the wedge opening angle varies from 0 to 2π. An analysis is performed and a qualitative interpretation of the obtained results is given. Possible refinements of the proposed model in various directions are discussed.

Keywords Crack Formation, Plate, Bending, Model

1. Introduction. Statement of the Model. Energy Relations

When studying the interaction of ice fields with icebreakers, ice-resistant structure footings, and other objects and in several other cases (fracture of glass and other brittle materials), there arise problems leading to the scheme of fracture of a plate made of a brittle material by a point indenter or by a lumped force in which several cracks begin to develop under the indenter and cut out the corresponding number of sectors in the plate [1,2], being different in different cases.

For the theoretical estimate of the number of sectors arising in crack formation in a plate under the action of an indenter, we assume that:

(1) The plate is loaded by a point indenter.
(2) As the plate strength is exhausted, fracture occurs instantaneously with the formation of a symmetric system of radial cracks.
(3) One can neglect the irreversible (nonelastic, thermal, etc.) losses (i.e., the plate behavior is quasibrittle) and the possible dynamics (vibrations and waves).
(4) The main contribution to the energy balance equation is made by the energy of formation of new surfaces (cracks) and by the elastic bending energy of the arising sectors. In this case, for simplicity, we assume that the strain of the undisturbed (and hence preserving the former rigidity) peripheral part of the plate is small and its contribution to the energy balance equation can be neglected. Thus, in fact, it becomes an unstrained foundation for the arising sectors, which are rigidly fixed to it by their bases.
(5) The minimum-energy-consuming fracture scheme is realized; i.e., the total energy is minimal in this case.

First, consider the case in which the load is applied at the plate center. Under the assumption that the arising sectors are equal to each other, we can write

$$W = nLh\gamma + nU, \tag{1}$$

where $W = W(n, L)$ is a function of the total energy expenditure in the crack formation, n is the

number of arising cracks (and sectors), L is the length of arising cracks, h is the plate thickness, γ is the effective surface energy of fracture, and U is the bending energy of each of the arising triangular sectors-beams.

Write out the expression for the elastic bending energy U of one sector

$$U = \frac{u^2}{2\Pi} \tag{2}$$

where Π is the bending compliance of the sector, u – the indenter vertical displacement (descent).

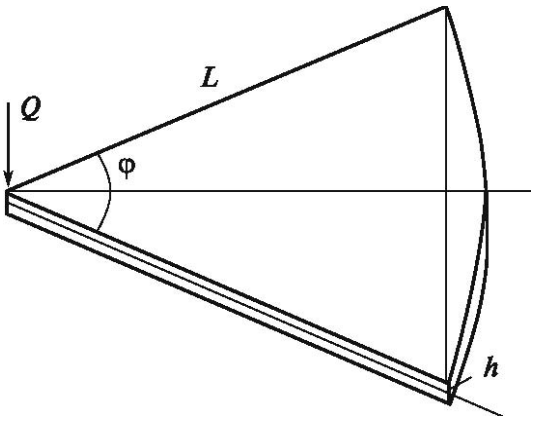

Figure 1

Treating the sector as a cantilever beam triangular in plan (i.e., a cantilever of variable width) working in bending (Fig. 1), we write out the expression for its compliance in the form ([3], Table 18)

$$\Pi = \frac{u}{Q} = \frac{3L^2 \cos^3(\varphi/2)}{Eh^3 \sin(\varphi/2)} \tag{3}$$

where Q is the force acting at the end of each beam, L is the length of the lateral surface of the sector (equal to the length of the arising cracks), E is the Young modulus, h is the plate thickness, and φ is the central angle of the sector.

In the case of formation of n equal cracks in a solid plate, $\varphi = 2\pi/n$. Taking into account this relationship and substituting successively of Eq. (3) in Eq. (2) and then in Eq. (1) we obtain for the function of total energy expenditures

$$W = n\left[Lh\gamma + \frac{Eh^3 \sin(\pi/n)}{6L^2 \cos^3(\pi/n)} u^2\right] \tag{4}$$

2. Minimization of the Expression for the Energy Expenditure. The Case of a Solid Plate

Let minimize the obtained expression for W with respect to the crack length L and their number n. We rewrite Eq. (4) as

$$W = AL\left(1 + \frac{B}{L^3}\right) \tag{5}$$

$$A = nh\gamma \tag{6}$$

$$B = \frac{Eh^2 \sin(\pi/n)}{6\gamma \cos^3(\pi/n)} u^2 \tag{7}$$

By computing the derivative $\partial W/\partial L$ and by equating it with zero, we obtain

$$\frac{B}{L^3} = \frac{1}{2} \tag{8}$$

$$L = \sqrt[3]{(2B)} = \left[\frac{Eh^2 \sin(\pi/n)}{3\gamma \cos^3(\pi/n)} u^2 \right]^{\frac{1}{3}} \tag{9}$$

Now we substitute A, L, and B/L^3 computed by Eq. (6), Eq. (9) and Eq. (8) into Eq. (5) and obtain

$$W = Cn \left[\frac{\sin(\pi/n)}{\cos^3(\pi/n)} \right]^{1/3} \tag{10}$$

$$C = \frac{3}{2} h\gamma \left(\frac{Eh^2 u^2}{3\gamma} \right)^{1/3} \tag{11}$$

Since C is independent of n, it is convenient to divide W by πC and consider the inverse function of $\pi C/W$. In Eq. (10), we pass from the discrete variable n to the continuous variable x by the formulas

$$\pi/n \to x,\ n > 2,\ 0 < x < \pi/2 \tag{12}$$

and from Eq. (10) we obtain the following expression for the cube of this new function

$$\left(\frac{\pi C}{W(n)} \right)^3 = \left(\frac{\pi}{n} \right)^3 \frac{\cos^3(\pi/n)}{\sin(\pi/n)} \to \left| \frac{\pi}{n} \to x \right| \to \frac{(x \cos x)^3}{\sin x} \equiv \Omega(x) \tag{13}$$

We replace the minimization of the function $W(n)$ by the maximization of the function $\Omega(x)$ with respect to x. One can readily show that this function has a single maximum at $x_0 \approx 0.84$. Since, according to Eq. (12), the discrete variable n and the continuous variable x are related as $x \leftrightarrow \pi/n$, it follows that the extreme value of n is one of the two integers nearest to $\pi/x_0 \approx \pi/0.84 \approx 3.74$. By checking the minimum of the function

$$w(n) \equiv \left[\frac{W(n)}{C} \right]^3 = n^3 \frac{\sin(\pi/n)}{\cos^3(\pi/n)}$$

for $n = 3, 4$, we obtain

$$w(4) < w(3), \quad n_{\min} = 4 \tag{14}$$

3. The Case of a Wedge (*n*–1 Cracks and n Sectors)

We assume that the plate has the shape of a wedge with opening angle Φ, $0 \le \Phi \le 2\pi$, and the point indenter acts at the vertex of this wedge. Then the appearance of n-1 cracks in this plate corresponds to the formation of n sectors with opening angle Φ/n. In problems on an icebreaker in ice fields, the case $\Phi = 2\pi$ corresponds to the case of an icebreaker in the mouth of the channel crushed by it ([1], p. 72), and $\Phi = \pi$ corresponds to the case of an icebreaker coming over the ice field edge or a slant smooth support. Operating similar to paragraph 2, we obtain in this case instead of Eq. (10), Eq. (13)

$$w_\Phi(n,\Phi) \equiv \left[\frac{W_\Phi(n,\Phi)}{C}\right]^3 = n^3\left(1-\frac{1}{n}\right)^2 \frac{\sin[\Phi/(2n)]}{\cos^3[\Phi/(2n)]} \tag{15}$$

$$\Omega_\Phi(x,\Phi) = \frac{(x\cos x)^3}{(\Phi/2-x)^2 \sin x} \tag{16}$$

and replace the minimization of $W_\Phi(n, \Phi)$ by the maximization of $\Omega_\Phi(x, \Phi)$ with respect to x.

Then, for the complete plane (plate) with half-infinite cut $\Phi = 2\pi$, Eq. (16) acquires the form

$$\Omega_\Phi(x,2\pi) = \frac{(x\cos x)^3}{(\pi-x)^2 \sin x} = \frac{\Omega(x)}{(\pi-x)^2} \tag{17}$$

for which the relation of the type Eq. (14) remains valid, $w_\Phi(4, 2\pi) < w_\Phi(3, 2\pi)$. Thus, for $\Phi = 2\pi$ the function $W_\Phi(n, 2\pi)$ of energy expenditures in crack formation attains its minimum for $n_{\min} = 4$ as well.

For a plate-half-plane, $\Phi = \pi$, and Eq. (16) becomes

$$\Omega_\Phi(x,\pi) = \frac{(x\cos x)^3}{(\pi/2-x)^2 \sin x} = \frac{\Omega(x)}{(\pi/2-x)^2} \tag{18}$$

Here the function $W\Phi(n,\pi)$ attains its minimum at $n_{\min} = 2$.

Thus, as the opening angle Φ of the loaded wedge decreases, the number n of sectors minimizing the total energy expenditures necessary for their formation decreases from $n = 4$ for $\Phi = 2\pi$ to $n = 2$ for $\Phi = \pi$. The natural question arises: How does $n_{\min}$ vary as Φ varies from 0 to 2π; in particular, for what values of the wedge opening angle Φ does $n_{\min}$ vary from $n = 2$ to $n = 3$ ($\Phi_{2\to3}$) and from $n = 3$ to $n = 4$ ($\Phi_{3\to4}$)? To answer this question, it suffices to compute $w_\Phi(n,\Phi)$ for Φ varying from π to 2π by Eq. (15) for $n = 2, 3, 4$. In Fig. 2, we present the graph of the dependence of $\ln[w_\Phi(n,\Phi)]$ on the wedge opening angle Φ. The points of intersection of $w_\Phi(2,\Phi)$ with $w_\Phi(3,\Phi)$ and of $w_\Phi(3,\Phi)$ with $w_\Phi(4,\Phi)$ give precisely the values of the wedge opening angles Φ at which the number $n_{\min}$ of the formed sectors (or cracks) is changed, $\Phi_{2\to3} \approx 4.43$ and $\Phi_{3\to4} \approx 5.94$. The sectors with maximum opening angle (near $\Phi_{2\to3}/2 \approx 2.21$ rad) are formed for Φ close to $\Phi_{2\to3} \approx 4.43$.

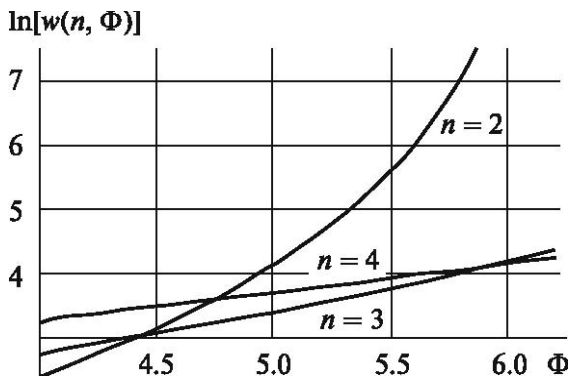

Figure 2

4. Example

After the number n of cracks formed in fracture is found, one can use the Eq. (9) to estimate the order of the lengths of these cracks L, for example, in the case of a solid plate made of window glass. But here we encounter another difficulty. By Eq. (9), the length of the formed cracks is determined by the value of the critical deflection u^*. In the framework of this model, nothing can be said about u^*, since we do not specify any local fracture criterion and do not study the stress field distribution. But if for some u^* the plate is destroyed according to the above model, then in this plate there arise four symmetric cracks of length determined by Eq. (9) with $n = 4$.

This implies an interesting observation. Suppose that an artificial stress concentrator, a conic cave (countersinking) is placed on the lower part of the plate under the indenter. Then different u^* are realized depending on the dimensions (depth and opening angle) of this cave, and, respectively, systems of cracks of different L will be formed.

In a similar way, in the case of symmetric extension of the strip edges (Fig. 3) by u under the action of loads applied on a small part of dimension $d > \delta$ (δ is the unknown dimension of the defect in the material), we assume that the plate is mechanically isotropic, in strength and in imperfection, and we do not precisely know what defects are contained in the plate. But since the crack-like defects perpendicular to the load direction are most dangerous, the fracture occurs for different displacements u^* of the force application points depending on the maximum initial dimension δ of such defects. The lengths of the arising cracks L are different and correspond to the energy U accumulated at this time.

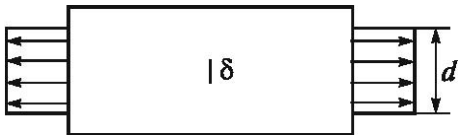

Figure 3

To obtain estimates of the length L of the arising cracks by Eq. (9) in the framework of the proposed model, it is necessary to introduce some reasonable values of the critical deflection u^* and some actual values of the glass mechanical characteristics E, h, and γ. The effective surface fracture energy γ can be expressed in terms of the crack growth resistance K_{IC} by the Irwin formula

$$\gamma = \frac{K_{IC}^2 (1-\mu^2)}{E} \tag{19}$$

where μ is the Poisson ratio. For glass, we set $E = 6\times10^{10}$ N/m^2, $\mu = 0.3$ ([4], p. 116), and $K_{IC} = 0.8$ kg/mm$^{3/2}$ $= 0.8\cdot10$ N/(10^{-3} m)$^{3/2}$ $= 8\times10^{4.5}$ N/m$^{3/2}$ ([5], p. 620); the typical values of the glass thickness h are $h \cong (1 \div 10)$ mm $= (10^{-3} \div 10^{-2})$ m; for u^*, we take several values proportional to h by the formula $u^* = \alpha h$, where $\alpha = 1$; 10^{-1}; 10^{-2}; 10^{-3} .

By substituting γ expressed by Eq. (19) into Eq. (9) and by taking $n = 4$, we see that for such parameter values the lengths of the cracks arising in glass can be of the order of several centimeters already for $\alpha = 10^{-3}$. For the thickness $h = 4\cdot10^{-3}$ m typical of window glass, the relative deflections $\alpha = 10^{-3}$, 10^{-2} imply the values $L \cong 0.1$ m and $L \cong 0.5$ m, respectively, for L.

5. A circular plate of finite dimensions

The above model can be extended to the case of a circular plate of finite dimensions. In this case the dimensionless function of the energy of crack $w(n, l)$, similar to the function Eq. (4), takes the form:

for a clamped plate

$$w(n,l) = nl + B\frac{1}{\frac{\kappa}{n}\frac{\cos^3(\pi/n)}{\sin(\pi/n)}l^2 + \left(1 - l^2 + 6l^2\ln l\right) - C_3\left(3 - 3l^2 + 2\ln l\right)}10^{-2m}$$

for a freely supported plate

$$w(n,l) = nl + B\frac{10^{-2m}}{\frac{\kappa}{n}\frac{\cos^3(\pi/n)}{\sin(\pi/n)}l^2 + \left(6l^2\ln l - 4l^2 + 2\ln l + 4\right) + C\left[3(1-\mu)l^2 - 2(1+\mu)(1+\ln l) + (1-\mu)\right]}$$

for a clamped annular plate

$$w = nl + B\frac{10^{-2m}}{\frac{\kappa}{n}\frac{\cos^3(\pi/n)}{\sin(\pi/n)}\left(2r_i l + l^2\right) + \left[1 - (r_i + l)^2 + 6(r_i + l)^2\ln(r_i + l)\right] - C_3\left[3 - 3(r_i + l)^2 + 2\ln(r_i + l)\right]}$$

where this time

$$w(n,l) = \frac{W}{R^* h\gamma}$$

$$l = L/R^*$$

$$B \equiv \frac{2\pi}{3}\frac{E^2 h^4}{(1-\mu^2)^2 R^{*3} K_{Ic}^2}$$

$$\kappa = \frac{4\pi}{1-\mu^2} \geq 13$$

$$C_3(\mu, l) = 2l^2\frac{1 - (\mu+1)\ln l}{(1-\mu) + (1+\mu)l^2}$$

$$C = \frac{(3+\mu)l^2 + (1-\mu) - 2(1+\mu)l^2\ln l}{(1-\mu^2)(1-l^2)},$$

R^* is the radius of the annular plate, $r_i = R_i/L$ – dimensionless inner radius of the annular plate, m – the parameter that determines the magnitude of the critical plate deflection or elastic energy stored in the plate at the crash moment.

6. Discussion of the Obtained Results and Accepted Assumptions

First, we note that at the first glance it seems rather strange that the obtained "optimal" values of the number of sectors (or cracks) are independent (except for the wedge opening angle Φ) of any geometrical and physical parameters of the model: the plate thickness, its rigidity, and fracture viscosity. To understand this fact, we recall that, for a given wedge (with angle Φ at the vertex), it is required to find a system of cracks of number and length such that the energy necessary to create such a system (this energy is the sum of the energies of formation of new surfaces and the energy of

bending of the arising sectors) be minimal over all n and L. This minimization with respect to L implies the condition that the energy required to form the cracks is equal to the doubled energy used to bend the arising sectors (Eq. 5, Eq. 8) and the "optimal" crack length L is expressed in terms of the thickness and the plate physical characteristics by a power law (Eq. 9). As a result, it follows from these relations that the total energy W is proportional to the crack formation energy whose expression contains all the above parameters only as factors raised to various powers and which then disappear in the process of optimization. Since we only take into account the strain of the plate central part cut by cracks, the solution does not contain the plate fixation conditions in any way.

The character of variation in the number of arising sectors n with varying wedge opening angle Φ may also be explained qualitatively. The function W of total energy expenditures is the sum of the crack formation energy $nLh\gamma$ and the energy nU of elastic bending of sectors-beams. For small $\Phi < \Phi_{2\to3}$, the arising sectors are narrow, and their total elastic energy weakly decreases as n increases, but the crack formation energy always increases linearly in n. Therefore, the minimum of W is realized for the minimum feasible value $n = 2$ at which the energy is minimal. For large Φ and small n, the elastic energy U is very sensitive to variations in n (moreover, as $\Phi \to 2\pi$, in the framework of the accepted scheme, the value $n = 2$ is associated with $U \to \infty$). As a result, the minimum point moves upwards, first, towards $n = 3$ for $\Phi = \Phi_{2\to3}$ and then towards $n = 4$ for $\Phi = \Phi_{3\to4}$. In this case, $U_{n=2,\,\Phi\to2\pi} \to \infty$, which conceptually reflects the fact of a sharp increase in the rigidity of the arising sectors and hence in the accumulated elastic energy and formally shows that the beam model cannot be used.

As follows from the results in Sec. 4, the computed length of the arising cracks can be comparable with the general dimensions of the plate L_p (for example, for typical window glass). This means that, on the one hand, there is a natural upper limit for possible values of lengths of the arising cracks, and on the other hand, it is necessary to take into account the plate dimensions and the corresponding boundary conditions.

Consider one purely kinematic consequence of the boundedness of possible crack lengths. As the crack length $L = L_p$ is attained in the energy balance Eq. (4), the further increase in W in the left-hand side can be counterbalanced in the right-hand side for fixed $L = L_p$ only by an increase in n. For a small excess over the calculated $L > L_p$, the energy excess is small and obviously can be radiated as elastic vibrations and waves (which is not detected by the proposed model). But, starting from a certain moment, the accumulated energy becomes sufficient for the formation of a picture with five rather than four symmetric cracks, and then with six, etc. Then, in general, the number n of arising cracks is always determined as the integral part of the solution of an equation of the form Eq. (4) with respect to n for L_p and given values of W (or u^*) and the other quantities contained in it. Thus, for a sufficiently small imperfection (high strength) of the plate, which permits accumulating a large amount of elastic energy, the finiteness of its dimensions may result in an increase in the number of cracks arising in it.

In the case of nonsymmetrical conditions of the plate support (when the lengths of the arising cracks are limited only in several directions), the symmetry of the crack formation picture is generally violated.

For example, consider a plate in the form of a long strip clamped along the long sides. Let us trace the evolution of the crack formation picture as the accumulated elastic energy and, respectively, the lengths of the arising cracks increase. As long as these lengths are much less than the characteristic dimensions of the plate, the picture remains symmetric (for simplicity, we assume that the cracks are oriented as in Fig. 4). But for sufficiently large cracks such that $L/2^{1/2} \cong b/2$ (where b is the plate

width), the cracks in the symmetric picture cannot grow further outside the plate boundaries. The energy expenditure of the original symmetric fracture scheme with $n = 4$ becomes exhausted. Then, we obtain the problem of minimal-power-consuming fracture scheme under the conditions that two transverse sectors are bounded in height by the plate half-width, i.e., the problem of minimization of W with respect to L and n with constraints in the form of inequalities such as $L_{i,y} \leq b/2$. The picture begins to distort. If we formally remain in the class of rectilinear solutions-cracks, then we obtain solutions-intervals with ends sliding along the long sides of the plate away from the ordinate axis (the cracks begin to bend towards the plate axis). Just as above, starting from certain values of W (or u^*), a symmetric solution with $n > 4$ may appear, etc.

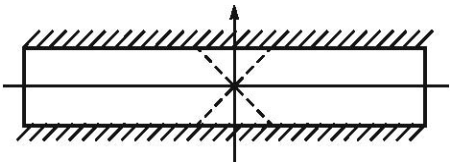

Figure 4

In practice, the arising cracks are obviously curvilinear, and this fact must be taken into account by more realistic models of crack formation.

Acknowledgements

This research was partially supported by the RFBR under project No. 11-08-01243.

References

[1] R.V. Goldstein (Ed.) *Mechanics and Physics of Ice*, Nauka, Moscow, 1983 [in Russian].

[2] S.S. Solntsev, E.M. Morozov, *Fracture of glass*, Mashinostroenie, Moscow, 1978 [in Russian].

[3] G.S. Pisarenko, A.P. Yakovlev, and V.V. Matveev, *Reference Book in Strength of Materials*, Naukova Dumka, Kiev, 1975 [in Russian].

[4] V.E. Kuz'michev, *Physics Laws and Formulas*, Reference book, Naukova Dumka, Kiev, 1989 [in Russian].

[5] G.P. Cherepanov, *Mechanics of Brittle Failure*, Nauka, Moscow, 1974 [in Russian].

Edge dislocation emission from nanovoid with the effect of neighboring nanovoids and surface stress

Yingxin Zhao[1], Qihong Fang[1,2*], Youwen Liu[1], Chunzhi Jiang[1,3]

[1] College of Mechanical and Vehicle Engineering, Hunan University, Changsha, 410082 Hunan Province, PR China
[2] School of Mechanical and Manufacturing Engineering, The University of New South Wales, NSW 2052, Australia
[3] Department of Physics and Electronic Information Engineering, Xiangnan University, Chenzhou 423000, PR China
* Corresponding author: email address Fangqh1327@tom.com

Abstract Experimental evidence, molecular dynamics simulations and theoretical analyses of nanovoid growth and coalescence in ductile materials indicate that nanovoid growth, coalescence, and stain localization depend strongly on distribution and volume fraction of the nanovoids in ductile porous materials. In the light of this mechanism, a generalized self-consistent theoretical model to describe the dislocation emitted from nanovoid accounting for the effect of neighboring nanovoids is suggested. The explicit solution to the critical stress is derived by means of the complex variable method. The influence of the nanovoid size, the surface effect, nanovoid content and uniform distribution density of neighboring nanovoids in the effective medium on the critical condition required for dislocation emission from nanovoid surface is discussed.

Keywords dislocation emission; neighboring nanovoid interactions; nanovoid volume fractions; surface stress

1. Introduction

The effect of preexisting volume defects, such as voids and cracks, is generally to lead to an increase in ductility and a reduction in the load carrying capacity of the porous material. A critical mechanism of ductile damage usually involves the nucleation, growth and coalescence of nanovoids, as a result of the applied loading conditions, in a plastically deforming porous materials. According to what we know, there is lacking study about nanovoid growth by dislocation mechanisms, which depends on the size and distribution of the nanovoids in nanoporous materials. In order to quantitatively estimate the interaction of multiple nanovoids in the particular case of porous solids, a generalized self-consistent analytical approach is utilized to study the effects of neighboring defect interactions, and void distribution and volume fractions on the dislocation emission from nanovoid surface, in which a large number nanovoids are statistically homogeneously distributed. It is also a feasible choice for two-dimensional situations in which the voids are roughly cylindrical and near uniformly distributed. The size-effect modeled here pertains to the surface elasticity theory of Gurtin-Murdoch on the nanometer scale. The explicit solution to the critical stress is derived by means of the complex variable method. The influence of the nanovoid size, the surface effect, nanovoid content and uniform distribution density of neighboring nanovoids in the effective medium on the critical condition required for dislocation emission from nanovoid surface is discussed.

2. Modeling and solution

In this section, we present a framework for a generalized self-consistent theory accounting for the effect of neighboring nanovoids in ductile nanoporous materials, based on the dynamics of void nucleation and growth. For a two-dimensional case, the constitutive model for the material is divided into three regions: the inner circular region representing the nanovoid phase, the intermediate annular region representing the matrix phase, and the infinitely extended outer region representing composite phase or effective medium. Elastic deformation under plane strain conditions is assumed and the nanovoids are assumed to be and remain cylindrical, and are statistically homogeneously distributed so that their shape is characterized by a single parameter.

Lubarda [1, 2] have modified previous analysis by using the expression for the image force on a dislocation emitted from the surface of the void. In this case, the stress fields of an edge dislocation emitted from the surface of the void correspond to the imposed displacement discontinuity along the cut from the surface of the void to the center of the dislocation. The geometrical structure is shown in Fig. 1. One edge dislocation with Burgers vector B_0 was emitted from the surface of the circular nanovoid to the point z_0 in the matrix phase, and $z_0 = \left(R_1 + \rho e^{i\theta}\right)e^{i\varphi}$. The rest edge dislocation with Burgers vector B_1 is located at the surface of the circular nanovoid, and $z_1 = R_1 e^{i\varphi}$. They are both assumed to be straight and infinite along the direction perpendicular to the xy -plane, and $B_0 = -B_1 = b_x + ib_y = b_z e^{i(\varphi+\theta)}$, $b_z = \sqrt{b_x^2 + b_y^2}$.

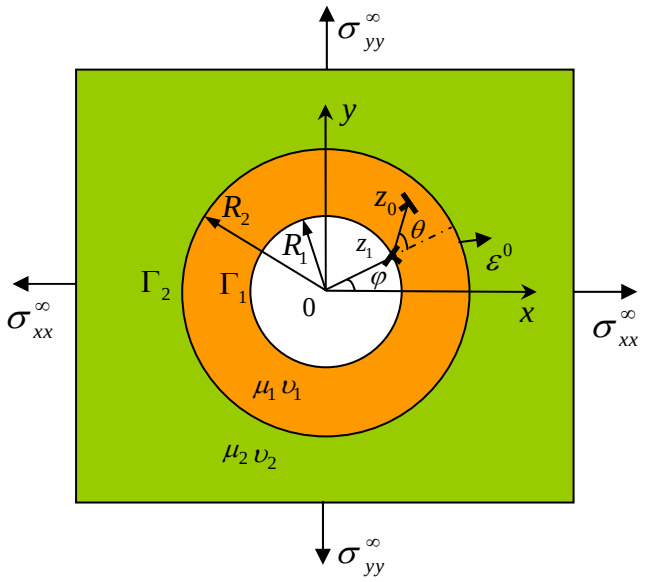

Fig.1 Dislocation emitted from the nanovoid surface in generalized self-consistent model

For the current problem, the elastic strain and stress in the two materials produced by lattice mismatch and dislocations can easily be calculated using the theory of elasticity. For nanovoid surface, surface stress resulting from a surface free energy and a constant residual stress was suggested in the Gurtin-Murdoch model [3-5]. So according to Sharma et al. [6], the equilibrium equation and the constitutive relations on the surface Γ_1 and the interface Γ_2 can be expressed as

$$\left[\sigma_{rr1}(t) + i\sigma_{r\theta 1}(t)\right]^- = \frac{1}{R_1}\left[\sigma_{\theta\theta 1}^0(t) - i\frac{\partial \sigma_{\theta\theta 1}^0(t)}{\partial \theta}\right] \tag{1}$$

$$\left[\sigma_{rr2}(\zeta) + i\sigma_{r\theta 2}(\zeta)\right]^- - \left[\sigma_{rr1}(\zeta) + i\sigma_{r\theta 1}(\zeta)\right]^+ = 0 \tag{2}$$

$$\left[u_{r1}(\zeta) + iu_{\theta 1}(\zeta)\right]^+ - \left[u_{r2}(\zeta) + iu_{\theta 2}(\zeta)\right]^- = u_r^0 + iu_\theta^0 \tag{3}$$

where u_r and u_q are the displacement components, s_{rr} and s_{rq} are the stress components in the polar coordinates, u_r^0 and u_θ^0 are the displacements induced by growth or shrink of neighboring voids. In addition, $|t| = R_1$, $|\zeta| = R_2$. The symbols R_1 and R_2 are the inner and outer radii of the intermediate annular region (the matrix phase).

For plane strain problem, stress fields and displacement fields may be expressed in terms of Muskhelishvili's complex potentials [7] $\Phi(z)$ and $\Psi(z)$

$$\sigma_{yy}+\sigma_{xx}=2\left[\Phi(z)+\overline{\Phi(z)}\right] \tag{4}$$

$$\sigma_{yy}-\sigma_{xx}+2i\sigma_{xy}=2\left[\bar{z}\Phi'(z)-\Psi(z)\right] \tag{5}$$

$$2\mu\left(u_x'+u_y'\right)=iz\left[\kappa\Phi(z)-\overline{\Phi(z)}+\bar{z}\overline{\Phi'(z)}+\frac{\bar{z}}{z}\overline{\Psi(z)}\right] \tag{6}$$

where $u_x'=\partial u_x/\partial\theta$, $u_y'=\partial u_y/\partial\theta$, $\Phi'(z)=d\left[\Phi(z)\right]/dz$, the overbar represents the complex conjugate, μ is the shear modulus of the bulk solid, υ is Poisson's ratio of the bulk solid , $\kappa=3-4\upsilon$ for plane strain state.

Under the assumption that the interface adheres to the bulk without slipping, and in the absence of body forces, according to Sharma et al. [6] based on Gurtin and Murdoch surface/interface model, the constitutive equation in the surface region is given as

$$\sigma_{\theta\theta}^0=\tau^0+\left(2\mu^0+\lambda^0-\tau^0\right)\varepsilon_{\theta\theta}^0 \tag{7}$$

where $\sigma_{\theta\theta}^0$ and $\varepsilon_{\theta\theta}^0$ denote surface stress and strain, μ^0 and λ^0 are surface Lame constants, τ^0 is the residual surface tension.

According to Gao [8], the uniform eigenstrains could be represented to express the displacements produced by the mismatch strains ε of the matrix and the effective medium.

$$u_r^0+iu_\theta^0=R_2\varepsilon \qquad |\zeta|=R_2 \tag{8}$$

where ε is dilatational or shrunk eigenstrain of neighboring voids in the matrix phase. The effective medium plasticity mismatches ε may be produced due to the yield stress and the strain hardening exponent on the nanovoid growth and coalescence. It is possible, of course, that to be attributed to mismatchs of the thermal expansion coefficient between the constituents.

According to Muskhelishvili [7], two complex potentials $\Phi_1(z)$ and $\Psi_1(z)$ in the matrix can be taken the following forms

$$\Phi_1(z)=\frac{\gamma_0}{z-z_0}+\frac{\gamma_1}{z-z_1}+\Phi_{10}(z) \tag{9}$$

$$\Psi_1(z)=\frac{\overline{\gamma_0}}{z-z_0}+\frac{\gamma_0\overline{z_0}}{(z-z_0)^2}+\frac{\overline{\gamma_1}}{z-z_1}+\frac{\gamma_1\overline{z_1}}{(z-z_1)^2}+\Psi_{10}(z) \tag{10}$$

Two complex potentials $\Phi_2(z)$ and $\Psi_2(z)$ in the effective medium can be taken the following forms

$$\Phi_2(z)=\frac{\gamma_0'+\gamma_1'}{z}+\Gamma_1+\Phi_{20}(z) \tag{11}$$

$$\Psi_2(z)=\frac{\overline{\gamma_0'}+\overline{\gamma_1'}}{z}+\Gamma_2+\Psi_{20}(z) \tag{12}$$

where $\gamma_k=-i\mu_1 B_k/\left[\pi(1+\kappa_1)\right]$, $\gamma_k'=-i\mu_2 B_k/\left[\pi(1+\kappa_2)\right]$ $(k=0,1)$, $\Gamma_1=\left(\sigma_{xx}^{\infty}+\sigma_{yy}^{\infty}\right)/4$, $\Gamma_2=\left(\sigma_{yy}^{\infty}-\sigma_{xx}^{\infty}+2i\sigma_{xy}^{\infty}\right)/2$

(σ_{xx}^{∞}, σ_{yy}^{∞} and σ_{xy}^{∞} are the remote stresses). $\Phi_{10}(z)$, $\Psi_{10}(z)$, $\Phi_{20}(z)$ and $\Psi_{20}(z)$ are holomorphic and the first two can be expanded in Laurent series

$$\Phi_{10}(z)=\sum_{k=0}^{\infty}a_k z^k+\sum_{k=1}^{\infty}b_k z^{-k} \tag{13}$$

$$\Psi_{10}(z)=\sum_{k=0}^{\infty}c_k z^{k-2}+\sum_{k=1}^{\infty}d_k z^{-k-2} \tag{14}$$

where the unknown coefficients a_k, b_k, c_k and d_k could be determined from the boundary conditions (1)-(3).

According to the work of Fang and Liu [9] and Zhao et al. [10], by a sufficient number of calculations, the explicit expressions of two complex potentials $\Phi_1(z)$ and $\Psi_1(z)$ in the matrix can be given

$$\Phi_1(z)=\frac{\gamma_0}{z-z_0}+\frac{\gamma_1}{z-z_1}+\sum_{k=0}^{\infty}a_k z^k+\sum_{k=1}^{\infty}b_k z^{-k} \tag{15}$$

$$\Psi_1(z)=\frac{\overline{\gamma_0}}{z-z_0}+\frac{\gamma_0\overline{z_0}}{(z-z_0)^2}+\frac{\overline{\gamma_1}}{z-z_1}+\frac{\gamma_1\overline{z_1}}{(z-z_1)^2}+\sum_{k=0}^{\infty}c_k z^{k-2}+\sum_{k=1}^{\infty}d_k z^{-k-2} \tag{16}$$

3. Critical stress for dislocation emission

According to Hirth and Lothe [11] and Peach-Koehler formula, the image force acting on the dislocation can be written as

$$f_x-if_y=(b_y+ib_x)\left[\Phi_0(z_0)+\overline{\Phi_0(z_0)}\right]+(b_y-ib_x)\left[\overline{z_0}\Phi_0'(z_0)+\Psi_0(z_0)\right] \tag{17}$$

where f_x and f_y are the force acting on the edge dislocation with Burgers vector B_0 in the x and y directions, respectively. $\Phi_0(z_0)$ and $\Psi_0(z_0)$ are the perturbation complex potentials in the matrix.

According to Qaissaunee and Santare [12], the perturbation complex potentials are calculated as follows:

$$\Phi_0(z_0)=\frac{\gamma_1}{z-z_1}+a_{01}+a_{02}\Gamma_1+a_1 z+(a_{21}+a_{22}\Gamma_2)z^2+\sum_{k=3}^{\infty}a_k z^k+b_1 z^{-1}+\left(b_{21}-b_{22}\overline{\Gamma_2}\right)z^{-2}+\sum_{k=3}^{\infty}b_k z^{-k} \tag{18}$$

$$\Psi_0(z_0)=\frac{\overline{\gamma_1}}{z-z_1}+\frac{\gamma_1\overline{z_1}}{(z-z_1)^2}+(c_{01}-c_{02}\Gamma_1)z^{-2}+c_1 z^{-1}+c_{21}+c_{22}\Gamma_2+\sum_{k=3}^{\infty}c_k z^{k-2}+d_1 z^{-3}+\left(d_{21}-d_{22}\overline{\Gamma_2}\right)z^{-4}+\sum_{k=3}^{\infty}d_k z^{-k-2} \tag{19}$$

Based on Stagni [13], the primary physical interest lies on the component of the force along the Burgers vector direction (glide force) which are given by

$$f_g=f_x\cos(\theta+\varphi)+f_y\sin(\theta+\varphi) \tag{20}$$

Adopting the criterion from Lubada et al. [14], it is assumed that the dislocation with Burgers

vector B_0 will be emitted from the surface of the void if its equilibrium distance ρ from the surface of the void is equal to the dislocation core cut-off radius ρ_0 (one half of the dislocation width, which represents the extent of the dislocation core spreading). In the equilibrium dislocation position, the glide force vanishes, namely $f_g = 0$. In the present study, we consider the remote applied critical stress is the stress required to keep dislocation with Burgers vector B_0 in equilibrium position. A lower stress would suffice to keep the dislocation in the equilibrium at the distance greater than ρ_0, i.e., the equilibrium position of the dislocation is unstable, and the dislocation would be driven away from the void indefinitely, or until it is blocked by an obstacle. The angle $\theta = \theta_{cr}$ at which the dislocation is emitted from nanovoid corresponds to the minimum value of the applied stress $\sigma_{cr}^{\min}$. So by letting $\rho = \rho_0$ specifies the stress required to emit the dislocation from the surface of the nanovoid.

When considering the effect of the remote axial loading, we suppose that $\sigma_{xx}^{\infty} = \sigma$, $\sigma_{yy}^{\infty} = j_1\sigma$, $\sigma_{xy}^{\infty} = j_2\sigma$, it yields $\Gamma_1 = (1+j_1)\sigma/4$, $\Gamma_2 = (j_1 - 1 + 2ij_2)\sigma/2$. The following expression for the critical stress σ_{cr} can be expressed as follows:

$$\sigma_{cr} = \frac{\mathrm{Re}\left[f_{img}\right]\cos(\theta+\varphi) - \mathrm{Im}\left[f_{img}\right]\sin(\theta+\varphi)}{\mathrm{Im}\left[M\right]\sin(\theta+\varphi) - \mathrm{Re}\left[M\right]\cos(\theta+\varphi)} \tag{21}$$

where $f_{img} = (b_y + ib_x)\left[\Phi_{0d}(z_0) + \overline{\Phi_{0d}(z_0)}\right] + (b_y - ib_x)\left[\overline{z_0}\Phi'_{0d}(z_0) + \Psi_{0d}(z_0)\right]$

$$\Phi_{0d}(z_0) = \frac{\gamma_1}{z - z_1} + a_{01} + a_1 z + a_{21}z^2 + \sum_{k=3}^{\infty} a_k z^k + b_1 z^{-1} + b_{21}z^{-2} + \sum_{k=3}^{\infty} b_k z^{-k}$$

$$\Psi_{0d}(z_0) = \frac{\overline{\gamma_1}}{z - z_1} + \frac{\gamma_1 \overline{z_1}}{(z - z_1)^2} + c_{01}z^{-2} + c_1 z^{-1} + c_{21} + \sum_{k=3}^{\infty} c_k z^{k-2} + d_1 z^{-3} + d_{21}z^{-4} + \sum_{k=3}^{\infty} d_k z^{-k-2}$$

$$M = (b_y + ib_x)\begin{bmatrix} \left(a_{02} + \overline{a_{02}}\right)(1+j_1)/4 + a_{22}(j_1 - 1 + 2ij_2)z_0^2/2 - b_{22}(j_1 - 1 - 2ij_2)z_0^{-2}/2 \\ + \overline{a_{22}}(j_1 - 1 - 2ij_2)\overline{z_0^2}/2 - \overline{b_{22}}(j_1 - 1 + 2ij_2)\overline{z_0^{-2}}/2 \end{bmatrix}$$
$$+ (b_y - ib_x)\begin{bmatrix} a_{22}z_0\overline{z_0}(j_1 - 1 + 2ij_2) + b_{22}z_0^{-3}\overline{z_0}(j_1 - 1 - 2ij_2) + c_{02}z_0^{-2}(1+j_1)/4 \\ + c_{22}(j_1 - 1 + 2ij_2)/2 - d_{22}z_0^{-4}(j_1 - 1 - 2ij_2)/2 \end{bmatrix}$$

It is found that the remote critical stress is independent of location from which the dislocation will be emitted, which is accord with the result of Zeng et al. [15].

4. Condition for dislocation emission

The critical stress required to emit the dislocation from the surface of the nanovoid can be determined accurately and explicitly given by Eq. (21). In this section considerable attention has be paid to elaborating the influence of the nanovoid size, the surface effect, nanovoid content and uniform distribution density of neighboring nanovoids in the effective medium on the critical condition required for dislocation emission from nanovoid surface. In this paper, we suppose that the normalized critical stress for the edge dislocation emitted from nanovoid surface by the shear modulus of the matrix $\sigma_{cr0} = \sigma_{cr}/\mu_1$, the intrinsic lengths of the nanovoid surface $\alpha = \mu_1^0/\mu_1$, $\beta = \lambda_1^0/\mu_1$ and $\delta = \tau_1^0/\mu_1$, the ratio of the shear modulus of the matrix and the

effective medium $a = \mu_2/\mu_1$, the radius of the nanovoid $b = R_1/b_z$, the relative uniform distribution density of neighboring nanovoids $c = R_2/R_1$. Former studies have indicated that the surface properties can be either positive or negative, depending upon the material type and the surface crystallographic orientation. According to their results, the absolute values of intrinsic lengths α, β and δ are nearly $1\mathring{A}$ [16]. In addition, let $\upsilon_1 = \upsilon_2 = 0.25$. The present study focuses exclusively on the effect of nanovoid content and uniform distribution density of neighboring nanovoids in the effective medium on the critical condition for splitting of dislocation from nanovoid surface, providing a remote equal biaxial loading.

Fig. 2 shows the critical stress to induce dislocation emission from the nanovoid surface as a function of emission angle with different ratios of the shear modulus of the matrix and the effective medium and surface elasticity. One should notice that, when nanovoid size is fixed, the smaller the chosen ratio of the shear modulus is, the larger nanovoid volume fractions the nanoporous materials contain. The figure presents the critical stress required to emit dislocation decreases, while relative most probable critical angle for dislocation emission increases as the ratio of the shear modulus decreases. That is to say, when nanovoid size is fixed, the larger nanovoid volume fractions in the nanoporous materials make the dislocation emission take place more easily, relative most probable critical emission angle more pronouncedly depart from the direction 45°. They mean that the distinct softening behavior can be happened and then significantly enhances capability of dislocation emission from nanovoid surface in the nanoporous materials. We have observed a strong influence of surface effect on critical condition for dislocation emission. The positive surface elasticity increases the critical stress and the relative most probable critical angle for dislocation emission, while the negative surface elasticity reduces them. And the larger positive value of surface elasticity makes the dislocation emission from nanovoid take place more difficultly. So it is well shown that the ductility of the material increases with increasing nanosize void volume fraction and the porosity would evidently affect the ductility of structural materials.

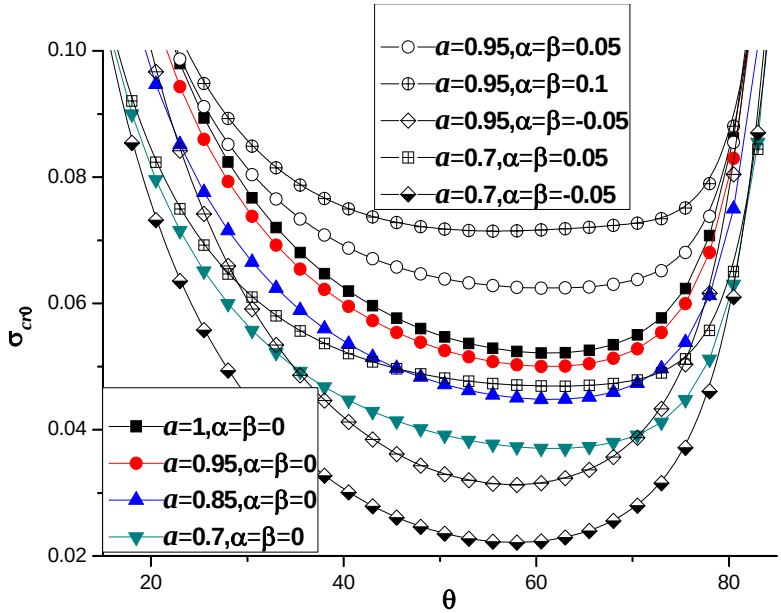

Fig. 2 Dependences of normalized critical stress σ_{cr0} on emission angle θ with different ratios of the shear modulus of the matrix and the effective medium $a = \mu_2/\mu_1$ and surface elasticity for $\rho_0 = b_z$, $\varepsilon = 0$, $j_1 = 1$, $j_2 = j_3 = 0$, $b = 8$, $c = 1.5$, $\delta = 0$.

Fig.3 shows normalized critical stress for dislocation emission to take place as a function of emission angle with different nanovoid sizes and surface residual stresses. When the nanovoid volume fraction is given, if the nanovoid size decreases, there must be larger number of same-size neighboring nanovoids. The figure shows the critical stress and relative most probable critical angle for dislocation emission decrease as the nanovoid size increases. That is, when the nanovoid volume fraction is fixed, the larger nanovoid size in the nanoporous materials makes the dislocation emission take place more easily, relative most probable critical emission angle less pronouncedly depart from the direction 45°. In other words, the dependence of critical stress on the neighboring number of nanovoids under the same void volume fraction can evidently be observed. Under the condition of constant void volume fraction, the larger the neighboring number of nanovoids is, the higher the critical stress becomes. It indicates that the load-carrying capacity and the stress resistivity of materials can be enhanced by redistributing a large void into multiple small ones at nanoscale. These results are reasonable agreement with that of molecular dynamics simulations by Mi et al. [17]. As well-evident from the Fig. 3, we know that the negative surface residual stress would increase the critical stress, while the positive one reduces it. It means that the nanovoid surface characterized by the positive surface residual stress clearly promotes dislocation emission and improves the ductility of the nanoporous materials. The larger the positive surface residual stress is, the more easily the dislocation emitted from nanovoid surface is. The larger neighboring number of nanovoids under the same void volume fraction has a greater role in the critical stress required for dislocation emission.

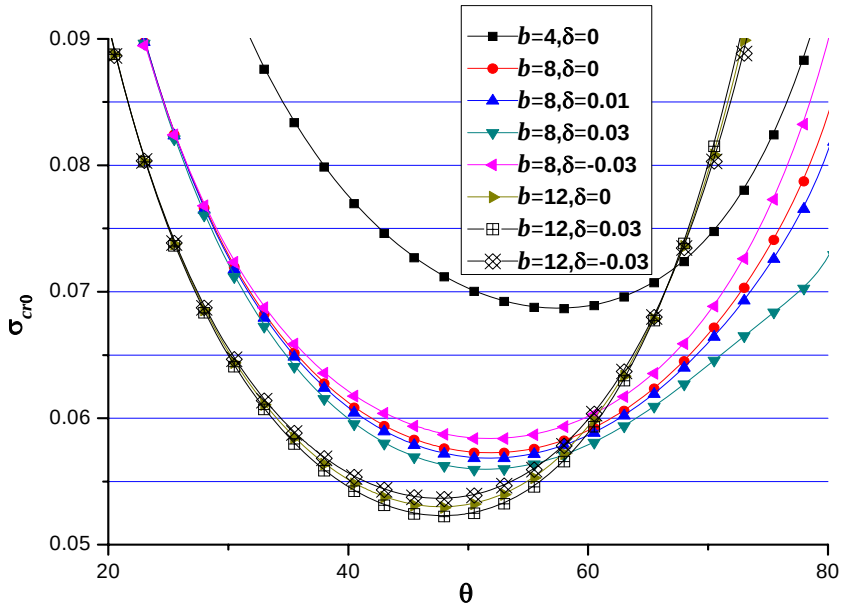

Fig. 3 Dependences of normalized critical stress σ_{cr0} on emission angle θ with different nanovoid sizes and surface residual stresses for $\rho_0 = b_z$, $\varepsilon = 0$, $j_1 = 1$, $j_2 = j_3 = 0$, $a = 0.9$, $c = 1.5$, $\alpha = \beta = 0$.

In this case in Fig. 4, namely $a = 0.9$, it means that the void volume fraction keeps the same, and c characterizes the distance of neighboring nanovoids or the uniform distribution density of the neighboring nanovoids. The larger physical quantity c, it demonstrates the larger neighboring

distance or the rougher distribution of the neighboring nanovoids under the same void volume fraction. From Fig. 4, it is found that the critical stress decreases clearly, while the relative most probable critical angle for dislocation emission increases as the physical quantity c increases. That is, with the initial void volume fraction and nanovoid size keep the same, the distinct hardening behavior can be happened and then significantly suppresses capability of dislocation emission from nanovoid surface in the nanoporous materials with improving the uniform distribution density of the neighboring nanovoids. It is also visibly indicates that the larger the negative surface residual stress is, the harder the dislocation emitted from nanovoid surface becomes. These observations demonstrate that at nanoscale void distribution plays a role in determining the deformation behavior of ductile metals.

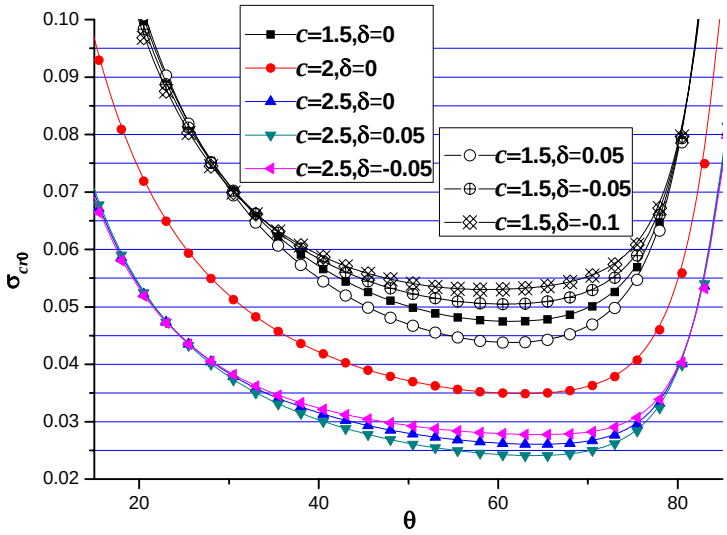

Fig. 4 Dependences of normalized critical stress σ_{cr0} on emission angle θ with different uniform distribution densities of the neighboring nanovoids and surface residual stresses for $\rho_0 = b_z$, $\varepsilon = 0$, $j_1 = 1$, $j_2 = j_3 = 0$, $a = 0.9$, $b = 8$, $\alpha = \beta = 0$.

5. Conclusions

In conclusion, when nanovoid size is fixed, the larger nanovoid volume fractions in the nanoporous materials make the dislocation emission take place more easily. Under the condition of constant void volume fraction, the larger the neighboring number of voids is, the higher the critical stress becomes. With the initial void volume fraction and nanovoid size keep the same, the distinct hardening behavior can be happened and then significantly suppresses capability of dislocation emission from nanovoid surface in the nanoporous materials with improving the uniform distribution density of the neighboring nanovoids. Softening or hardening of nanovoid surface due to surface effect has a pronounced effect on the critical condition for dislocation emission.

Acknowledgements

The authors would like to deeply appreciate the support from the NNSFC (11172094 and 11172095) and the NCET-11-0122. This work was also supported by Hunan Provincial Natural Science Foundation for Creative Research Groups of China (Grant No.12JJ7001).

References

[1] V.A. Lubarda, Emission of dislocations from nanovoids under combined loading. Int J Plast, 27 (2011) 181–200.

[2] V.A. Lubarda, Image force on a straight dislocation emitted from a cylindrical void. Int J Solids Struct, 48 (2011) 648–660.

[3] M.E. Gurtin, A.I. Murdoch, A continuum theory of elastic material surfaces. Arch Rat Mech Anal, 57 (1975) 291–323.

[4] M.E. Gurtin, A.I. Murdoch, Surface stress in solids. Int J Solids Struct, 14 (1978) 431–440.

[5] M.E. Gurtin, J. Weissmuller, F. Larche, A general theory of curved deformable interfaces in solids at equilibrium. Philos Mag A, 78 (1998) 1093–1109.

[6] P. Sharma, S. Ganti, N. Bhate, Effect of surfaces on the size-dependent elastic state of nano-inhomogeneities. Appl Phys Lett, 82 (2003) 535–537.

[7] N.L. Muskhelishvili, Some Basic Problems of Mathematical Theory of Elasticity, P. Noodhoff, Groningen, 1975.

[8] Z.J. Gao, A circular inclusion with imperfect interface: Eshelby's tensor and related problems. J Appl Mech, 62 (1995) 860–866.

[9] Q.H. Fang, Y.W. Liu, Size-dependent interaction between an edge dislocation and a nanoscale inhomogeneity with interface effects. Acta Mater, 54 (2006) 4213–4220.

[10] Y.X. Zhao, Q.H. Fang, Y.W. Liu, Edge misfit dislocation formation at the interface of a nanopore and infinite substrate with surface/interface effects. Phil Mag, 92 (2012) 4230–4249.

[11] J.P. Hirth, J. Lothe, Theory of Dislocations, McGraw-Hill, New York, 1982.

[12] M.T. Qaissaunee, M.H. Santare, Edge dislocation interaction with an elliptical inclusion surrounding by an interfacial zone. Q J Mech Appl Math, 48 (1995) 465–482.

[13] L. Stagni, Edge dislocation near an elliptic inhomogeneitywith either an adhering or a slipping interface-a comparative study. Phil Mag A, 68 (1993) 49–57.

[14] V.A. Lubarda, M.S. Schneider, D.H. Kalantar, B.R. Remington, M.A. Meyers, Void growth by dislocation emission. Acta Mater, 52 (2004) 1397–1408.

[15] X. Zeng, Y.W. Liu, P.H. Wen, Dislocation emission from nanovoid with surface effects. Int J Mech Sci, 61 (2012) 65–70.

[16] R.E. Miller, V.B. Shenoy, Size-dependent elastic properties of nanosized structural elements. Nanotechnology, 11 (2000) 139–147.

[17] C.W. Mi, D.A. Buttry, P. Sharma, D.A. Kouris, Atomistic insights into dislocation-based mechanisms of void growth and coalescence. J Mech Phys Solids, 59 (2011) 1858–1871.

Edge dislocation emission from nanovoid with the effect of neighboring nanovoids and surface stress

Yingxin Zhao[1], Qihong Fang[1,2*], Youwen Liu[1], Chunzhi Jiang[1,3]

[1] College of Mechanical and Vehicle Engineering, Hunan University, Changsha, 410082 Hunan Province, PR China
[2] School of Mechanical and Manufacturing Engineering, The University of New South Wales, NSW 2052, Australia
[3] Department of Physics and Electronic Information Engineering, Xiangnan University, Chenzhou 423000, PR China
* Corresponding author: email address Fangqh1327@tom.com

Abstract Experimental evidence, molecular dynamics simulations and theoretical analyses of nanovoid growth and coalescence in ductile materials indicate that nanovoid growth, coalescence, and stain localization depend strongly on distribution and volume fraction of the nanovoids in ductile porous materials. In the light of this mechanism, a generalized self-consistent theoretical model to describe the dislocation emitted from nanovoid accounting for the effect of neighboring nanovoids is suggested. The explicit solution to the critical stress is derived by means of the complex variable method. The influence of the nanovoid size, volume fraction and uniform distribution density of neighboring nanovoids in the effective medium as well as the surface effect on the critical condition required for dislocation emission from nanovoid surface is discussed.

Keywords dislocation emission; neighboring nanovoid interactions; nanovoid volume fractions; surface stress

1. Introduction

The effect of preexisting volume defects, such as voids and cracks, is generally to lead to an increase in ductility and a reduction in the load carrying capacity of the porous material. A critical mechanism of ductile damage usually involves the nucleation, growth and coalescence of nanovoids, as a result of the applied loading conditions, in a plastically deforming porous materials. According to what we know, there is lacking study about nanovoid growth by dislocation mechanisms, which depends on the size and distribution of the nanovoids in nanoporous materials. In order to quantitatively estimate the interaction of multiple nanovoids in the particular case of porous solids, a generalized self-consistent analytical approach is utilized to study the effects of neighboring defect interactions, and void distribution and volume fractions on the dislocation emission from nanovoid surface, in which a large number nanovoids are statistically homogeneously distributed. It is also a feasible choice for two-dimensional situations in which the voids are roughly cylindrical and near uniformly distributed. The size-effect modeled here pertains to the surface elasticity theory of Gurtin-Murdoch on the nanometer scale. The explicit solution to the critical stress is derived by means of the complex variable method. The influence of the nanovoid size, the surface effect, nanovoid content and uniform distribution density of neighboring nanovoids in the effective medium on the critical condition required for dislocation emission from nanovoid surface is discussed.

2. Modeling and solution

In this section, we present a framework for a generalized self-consistent theory accounting for the effect of neighboring nanovoids in ductile nanoporous materials, based on the dynamics of void nucleation and growth. For a two-dimensional case, the constitutive model for the material is divided into three regions: the inner circular region representing the nanovoid phase, the intermediate annular region representing the matrix phase, and the infinitely extended outer region representing composite phase or effective medium. Elastic deformation under plane strain conditions is assumed and the nanovoids are assumed to be and remain cylindrical, and are statistically homogeneously distributed so that their shape is characterized by a single parameter.

Lubarda [1, 2] have modified previous analysis by using the expression for the image force on a dislocation emitted from the surface of the void. In this case, the stress fields of an edge dislocation emitted from the surface of the void correspond to the imposed displacement discontinuity along the cut from the surface of the void to the center of the dislocation. The geometrical structure is shown in Fig. 1. One edge dislocation with Burgers vector B_0 was emitted from the surface of the circular nanovoid to the point z_0 in the matrix phase, and $z_0 = \left(R_1 + \rho e^{i\theta}\right)e^{i\varphi}$. The rest edge dislocation with Burgers vector B_1 is located at the surface of the circular nanovoid, and $z_1 = R_1 e^{i\varphi}$. They are both assumed to be straight and infinite along the direction perpendicular to the xy -plane, and $B_0 = -B_1 = b_x + ib_y = b_z e^{i(\varphi+\theta)}$, $b_z = \sqrt{b_x^2 + b_y^2}$.

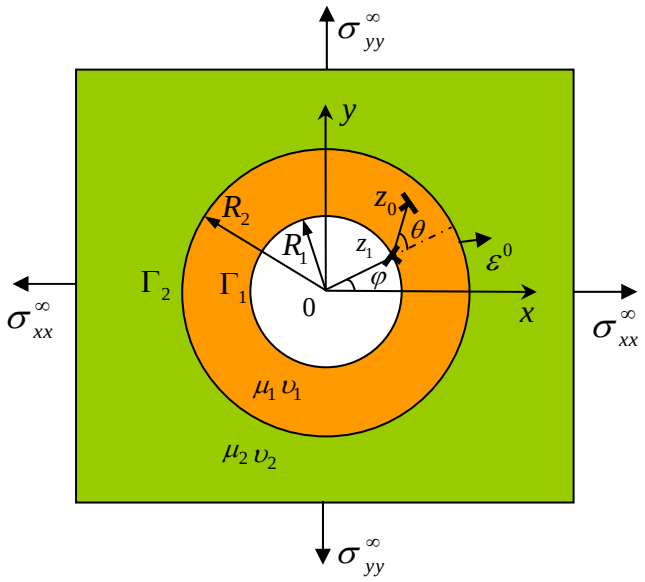

Fig.1 Dislocation emitted from the nanovoid surface in generalized self-consistent model

For the current problem, the elastic strain and stress in the two materials produced by lattice mismatch and dislocations can easily be calculated using the theory of elasticity. For nanovoid surface, surface stress resulting from a surface free energy and a constant residual stress was suggested in the Gurtin-Murdoch model [3-5]. So according to Sharma et al. [6], the equilibrium equation and the constitutive relations on the surface Γ_1 and the interface Γ_2 can be expressed as

$$\left[\sigma_{rr1}(t) + i\sigma_{r\theta 1}(t)\right]^- = \frac{1}{R_1}\left[\sigma_{\theta\theta 1}^0(t) - i\frac{\partial \sigma_{\theta\theta 1}^0(t)}{\partial \theta}\right] \tag{1}$$

$$\left[\sigma_{rr2}(\zeta) + i\sigma_{r\theta 2}(\zeta)\right]^- - \left[\sigma_{rr1}(\zeta) + i\sigma_{r\theta 1}(\zeta)\right]^+ = 0 \tag{2}$$

$$\left[u_{r1}(\zeta) + iu_{\theta 1}(\zeta)\right]^+ - \left[u_{r2}(\zeta) + iu_{\theta 2}(\zeta)\right]^- = u_r^0 + iu_\theta^0 \tag{3}$$

where u_r and u_q are the displacement components, s_{rr} and s_{rq} are the stress components in the polar coordinates, u_r^0 and u_θ^0 are the displacements induced by growth or shrink of neighboring voids. In addition, $|t| = R_1$, $|\zeta| = R_2$. The symbols R_1 and R_2 are the inner and outer radii of the intermediate annular region (the matrix phase).

For plane strain problem, stress fields and displacement fields may be expressed in terms of Muskhelishvili's complex potentials [7] $\Phi(z)$ and $\Psi(z)$

$$\sigma_{yy}+\sigma_{xx}=2\left[\Phi(z)+\overline{\Phi(z)}\right] \tag{4}$$

$$\sigma_{yy}-\sigma_{xx}+2i\sigma_{xy}=2\left[\bar{z}\Phi'(z)-\Psi(z)\right] \tag{5}$$

$$2\mu\left(u_x'+u_y'\right)=iz\left[\kappa\Phi(z)-\overline{\Phi(z)}+\bar{z}\overline{\Phi'(z)}+\frac{\bar{z}}{z}\overline{\Psi(z)}\right] \tag{6}$$

where $u_x'=\partial u_x/\partial\theta$, $u_y'=\partial u_y/\partial\theta$, $\Phi'(z)=d\left[\Phi(z)\right]/dz$, the overbar represents the complex conjugate, μ is the shear modulus of the bulk solid, υ is Poisson's ratio of the bulk solid , $\kappa=3-4\upsilon$ for plane strain state.

Under the assumption that the interface adheres to the bulk without slipping, and in the absence of body forces, according to Sharma et al. [6] based on Gurtin and Murdoch surface/interface model, the constitutive equation in the surface region is given as

$$\sigma_{\theta\theta}^0=\tau^0+\left(2\mu^0+\lambda^0-\tau^0\right)\varepsilon_{\theta\theta}^0 \tag{7}$$

where $\sigma_{\theta\theta}^0$ and $\varepsilon_{\theta\theta}^0$ denote surface stress and strain, μ^0 and λ^0 are surface Lame constants, τ^0 is the residual surface tension.

According to Gao [8], the uniform eigenstrains could be represented to express the displacements produced by the mismatch strains ε of the matrix and the effective medium.

$$u_r^0+iu_\theta^0=R_2\varepsilon \qquad |\zeta|=R_2 \tag{8}$$

where ε is dilatational or shrunk eigenstrain of neighboring voids in the matrix phase. The effective medium plasticity mismatches ε may be produced due to the yield stress and the strain hardening exponent on the nanovoid growth and coalescence. It is possible, of course, that to be attributed to mismatchs of the thermal expansion coefficient between the constituents.

According to Muskhelishvili [7], two complex potentials $\Phi_1(z)$ and $\Psi_1(z)$ in the matrix can be taken the following forms

$$\Phi_1(z)=\frac{\gamma_0}{z-z_0}+\frac{\gamma_1}{z-z_1}+\Phi_{10}(z) \tag{9}$$

$$\Psi_1(z)=\frac{\overline{\gamma_0}}{z-z_0}+\frac{\gamma_0\overline{z_0}}{(z-z_0)^2}+\frac{\overline{\gamma_1}}{z-z_1}+\frac{\gamma_1\overline{z_1}}{(z-z_1)^2}+\Psi_{10}(z) \tag{10}$$

Two complex potentials $\Phi_2(z)$ and $\Psi_2(z)$ in the effective medium can be taken the following forms

$$\Phi_2(z)=\frac{\gamma_0'+\gamma_1'}{z}+\Gamma_1+\Phi_{20}(z) \tag{11}$$

$$\Psi_2(z)=\frac{\overline{\gamma_0'}+\overline{\gamma_1'}}{z}+\Gamma_2+\Psi_{20}(z) \tag{12}$$

where $\gamma_k=-i\mu_1 B_k/\left[\pi(1+\kappa_1)\right]$, $\gamma_k'=-i\mu_2 B_k/\left[\pi(1+\kappa_2)\right]$ $(k=0,1)$, $\Gamma_1=\left(\sigma_{xx}^{\infty}+\sigma_{yy}^{\infty}\right)/4$, $\Gamma_2=\left(\sigma_{yy}^{\infty}-\sigma_{xx}^{\infty}+2i\sigma_{xy}^{\infty}\right)/2$

(σ_{xx}^{∞}, σ_{yy}^{∞} and σ_{xy}^{∞} are the remote stresses). $\Phi_{10}(z)$, $\Psi_{10}(z)$, $\Phi_{20}(z)$ and $\Psi_{20}(z)$ are holomorphic and the first two can be expanded in Laurent series

$$\Phi_{10}(z)=\sum_{k=0}^{\infty}a_k z^k+\sum_{k=1}^{\infty}b_k z^{-k} \tag{13}$$

$$\Psi_{10}(z)=\sum_{k=0}^{\infty}c_k z^{k-2}+\sum_{k=1}^{\infty}d_k z^{-k-2} \tag{14}$$

where the unknown coefficients a_k, b_k, c_k and d_k could be determined from the boundary conditions (1)-(3).

According to the work of Fang and Liu [9] and Zhao et al. [10], by a sufficient number of calculations, the explicit expressions of two complex potentials $\Phi_1(z)$ and $\Psi_1(z)$ in the matrix can be given

$$\Phi_1(z)=\frac{\gamma_0}{z-z_0}+\frac{\gamma_1}{z-z_1}+\sum_{k=0}^{\infty}a_k z^k+\sum_{k=1}^{\infty}b_k z^{-k} \tag{15}$$

$$\Psi_1(z)=\frac{\overline{\gamma_0}}{z-z_0}+\frac{\gamma_0\overline{z_0}}{(z-z_0)^2}+\frac{\overline{\gamma_1}}{z-z_1}+\frac{\gamma_1\overline{z_1}}{(z-z_1)^2}+\sum_{k=0}^{\infty}c_k z^{k-2}+\sum_{k=1}^{\infty}d_k z^{-k-2} \tag{16}$$

3. Critical stress for dislocation emission

According to Hirth and Lothe [11] and Peach-Koehler formula, the image force acting on the dislocation can be written as

$$f_x-if_y=(b_y+ib_x)\left[\Phi_0(z_0)+\overline{\Phi_0(z_0)}\right]+(b_y-ib_x)\left[\overline{z_0}\Phi_0'(z_0)+\Psi_0(z_0)\right] \tag{17}$$

where f_x and f_y are the force acting on the edge dislocation with Burgers vector B_0 in the x and y directions, respectively. $\Phi_0(z_0)$ and $\Psi_0(z_0)$ are the perturbation complex potentials in the matrix.

According to Qaissaunee and Santare [12], the perturbation complex potentials are calculated as follows:

$$\Phi_0(z_0)=\frac{\gamma_1}{z-z_1}+a_{01}+a_{02}\Gamma_1+a_1 z+(a_{21}+a_{22}\Gamma_2)z^2+\sum_{k=3}^{\infty}a_k z^k+b_1 z^{-1}+\left(b_{21}-b_{22}\overline{\Gamma_2}\right)z^{-2}+\sum_{k=3}^{\infty}b_k z^{-k} \tag{18}$$

$$\Psi_0(z_0)=\frac{\overline{\gamma_1}}{z-z_1}+\frac{\gamma_1\overline{z_1}}{(z-z_1)^2}+(c_{01}-c_{02}\Gamma_1)z^{-2}+c_1 z^{-1}+c_{21}+c_{22}\Gamma_2+\sum_{k=3}^{\infty}c_k z^{k-2}+d_1 z^{-3}+\left(d_{21}-d_{22}\overline{\Gamma_2}\right)z^{-4}+\sum_{k=3}^{\infty}d_k z^{-k-2} \tag{19}$$

Based on Stagni [13], the primary physical interest lies on the component of the force along the Burgers vector direction (glide force) which are given by

$$f_g=f_x\cos(\theta+\varphi)+f_y\sin(\theta+\varphi) \tag{20}$$

Adopting the criterion from Lubada et al. [14], it is assumed that the dislocation with Burgers

vector B_0 will be emitted from the surface of the void if its equilibrium distance ρ from the surface of the void is equal to the dislocation core cut-off radius ρ_0 (one half of the dislocation width, which represents the extent of the dislocation core spreading). In the equilibrium dislocation position, the glide force vanishes, namely $f_g = 0$. In the present study, we consider the remote applied critical stress is the stress required to keep dislocation with Burgers vector B_0 in equilibrium position. A lower stress would suffice to keep the dislocation in the equilibrium at the distance greater than ρ_0, i.e., the equilibrium position of the dislocation is unstable, and the dislocation would be driven away from the void indefinitely, or until it is blocked by an obstacle. The angle $\theta = \theta_{cr}$ at which the dislocation is emitted from nanovoid corresponds to the minimum value of the applied stress $\sigma_{cr}^{\min}$. So by letting $\rho = \rho_0$ specifies the stress required to emit the dislocation from the surface of the nanovoid.

When considering the effect of the remote axial loading, we suppose that $\sigma_{xx}^{\infty} = \sigma$, $\sigma_{yy}^{\infty} = j_1\sigma$, $\sigma_{xy}^{\infty} = j_2\sigma$, it yields $\Gamma_1 = (1+j_1)\sigma/4$, $\Gamma_2 = (j_1 - 1 + 2ij_2)\sigma/2$. The following expression for the critical stress σ_{cr} can be expressed as follows:

$$\sigma_{cr} = \frac{\mathrm{Re}\left[f_{img}\right]\cos(\theta+\varphi) - \mathrm{Im}\left[f_{img}\right]\sin(\theta+\varphi)}{\mathrm{Im}\left[M\right]\sin(\theta+\varphi) - \mathrm{Re}\left[M\right]\cos(\theta+\varphi)} \tag{21}$$

where $f_{img} = (b_y + ib_x)\left[\Phi_{0d}(z_0) + \overline{\Phi_{0d}(z_0)}\right] + (b_y - ib_x)\left[\overline{z_0}\Phi'_{0d}(z_0) + \Psi_{0d}(z_0)\right]$

$$\Phi_{0d}(z_0) = \frac{\gamma_1}{z - z_1} + a_{01} + a_1 z + a_{21}z^2 + \sum_{k=3}^{\infty} a_k z^k + b_1 z^{-1} + b_{21}z^{-2} + \sum_{k=3}^{\infty} b_k z^{-k}$$

$$\Psi_{0d}(z_0) = \frac{\overline{\gamma_1}}{z - z_1} + \frac{\gamma_1 \overline{z_1}}{(z - z_1)^2} + c_{01}z^{-2} + c_1 z^{-1} + c_{21} + \sum_{k=3}^{\infty} c_k z^{k-2} + d_1 z^{-3} + d_{21}z^{-4} + \sum_{k=3}^{\infty} d_k z^{-k-2}$$

$$M = (b_y + ib_x)\begin{bmatrix} \left(a_{02} + \overline{a_{02}}\right)(1+j_1)/4 + a_{22}(j_1 - 1 + 2ij_2)z_0^2/2 - b_{22}(j_1 - 1 - 2ij_2)z_0^{-2}/2 \\ + \overline{a_{22}}(j_1 - 1 - 2ij_2)\overline{z_0^2}/2 - \overline{b_{22}}(j_1 - 1 + 2ij_2)\overline{z_0^{-2}}/2 \end{bmatrix}$$
$$+ (b_y - ib_x)\begin{bmatrix} a_{22}z_0\overline{z_0}(j_1 - 1 + 2ij_2) + b_{22}z_0^{-3}\overline{z_0}(j_1 - 1 - 2ij_2) + c_{02}z_0^{-2}(1+j_1)/4 \\ + c_{22}(j_1 - 1 + 2ij_2)/2 - d_{22}z_0^{-4}(j_1 - 1 - 2ij_2)/2 \end{bmatrix}$$

4. Condition for dislocation emission

The critical stress required to emit the dislocation from the surface of the nanovoid can be determined accurately and explicitly given by Eq. (21). In this section considerable attention has be paid to elaborating the influence of the nanovoid size, the surface effect, nanovoid content and uniform distribution density of neighboring nanovoids in the effective medium on the critical condition required for dislocation emission from nanovoid surface. In this paper, we suppose that the normalized critical stress for the edge dislocation emitted from nanovoid surface by the shear modulus of the matrix $\sigma_{cr0} = \sigma_{cr}/\mu_1$, the intrinsic lengths of the nanovoid surface $\alpha = \mu_1^0/\mu_1$, $\beta = \lambda_1^0/\mu_1$ and $\delta = \tau_1^0/\mu_1$, the ratio of the shear modulus of the matrix and the effective medium $a = \mu_2/\mu_1$, the radius of the nanovoid $b = R_1/b_z$, the relative spacing between neighboring nanovoids or uniform

distribution density of neighboring nanovoids $c = R_2/R_1$. Former studies have indicated that the surface properties can be either positive or negative, depending upon the material type and the surface crystallographic orientation. According to their results, the absolute values of intrinsic lengths α, β and δ are nearly $1\mathring{A}$ [15]. In addition, let $\upsilon_1 = \upsilon_2 = 0.25$. The present study focuses exclusively on the effect of nanovoid content and uniform distribution density of neighboring nanovoids in the effective medium on the critical condition for splitting of dislocation from nanovoid surface, providing a remote equal biaxial loading.

Fig. 2 shows the critical stress to induce dislocation emission from the nanovoid surface as a function of emission angle θ with different ratios of the shear modulus of the matrix and the effective medium $a = \mu_2/\mu_1$ and surface elasticity. One should notice that, when nanovoid size b is fixed, the smaller the chosen ratio of the shear modulus a is, the larger nanovoid volume fraction the nanoporous materials contain. The figure presents the critical stress required to emit dislocation decreases, while relative most probable critical angle for dislocation emission increases as the ratio of the shear modulus decreases. That is to say, when nanovoid size is fixed, the larger nanovoid volume fraction in the nanoporous materials makes the dislocation emission take place more easily, and relative most probable critical emission angle more pronouncedly depart from the direction 45°. They mean that the distinct softening behavior can be happened and the interaction among neighboring nanovoids becomes important as nanovoid volume fraction increases. Therefore, it can significantly enhance capability of dislocation emission from nanovoid surface, favor the nanovoid growth, and then result in decreased ductility of the nanoporous materials. So it is well shown that the ductility of the material depresses with increasing nanosize void volume fraction and the porosity would evidently affect the ductility of structural materials, in agreement with the analysis by Tvergaard and Hutchinson [16]. We have observed a strong influence of surface effect on critical condition for dislocation emission. The positive surface elasticity increases the critical stress and the relative most probable critical angle for dislocation emission, while the negative surface elasticity reduces them. And the larger positive value of surface elasticity makes the dislocation emission from nanovoid take place more difficultly.

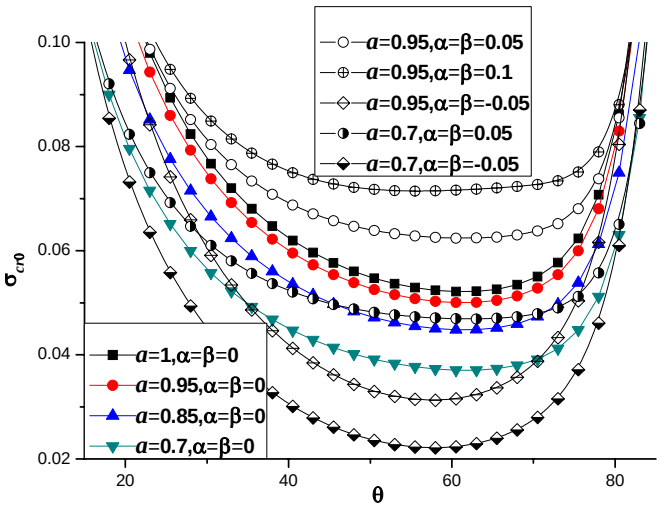

Fig. 2 Dependences of normalized critical stress σ_{cr0} on emission angle θ with different ratios of the shear modulus of the matrix and the effective medium $a = \mu_2/\mu_1$ and surface elasticity for $\rho_0 = b_z$, $\varepsilon = 0$, $j_1 = 1$, $j_2 = j_3 = 0$, $b = 8$, $c = 1.5$, $\delta = 0$.

Fig.3 shows normalized critical stress for dislocation emission to take place as a function of emission angle θ with different nanovoid sizes and surface residual stresses. When the nanovoid volume fraction is given, if the nanovoid size decreases, there must be larger number of same-size neighboring nanovoids. The figure shows the critical stress and relative most probable critical angle for dislocation emission decrease as the nanovoid size increases. That is to say, when the nanovoid volume fraction is fixed, the larger nanovoid size in the nanoporous materials makes the dislocation emission take place more easily, relative most probable critical emission angle less pronouncedly depart from the direction 45°. In other words, the dependence of critical stress on the neighboring number of nanovoids under the same void volume fraction can evidently be observed. Given the same void volume fraction, improved critical stress is accompanied with an increase in the neighboring number of nanovoids. The larger neighboring number of nanovoids under the same void volume fraction has a greater role in the critical stress required for dislocation emission. This is because the load-carrying capacity and the stress resistivity of materials can be enhanced by redistributing a large void into multiple small ones at nanoscale. These results are reasonable agreement with that of molecular dynamics simulations by Mi et al. [17]. As well-evident from the Fig. 3, we know that the negative surface residual stress would increase the critical stress, while the positive one reduces it. It means that the nanovoid surface characterized by the positive surface residual stress clearly promotes dislocation emission and lessens the ductility of the nanoporous materials. The larger the positive surface residual stress is, the more easily the dislocation emitted from nanovoid surface is.

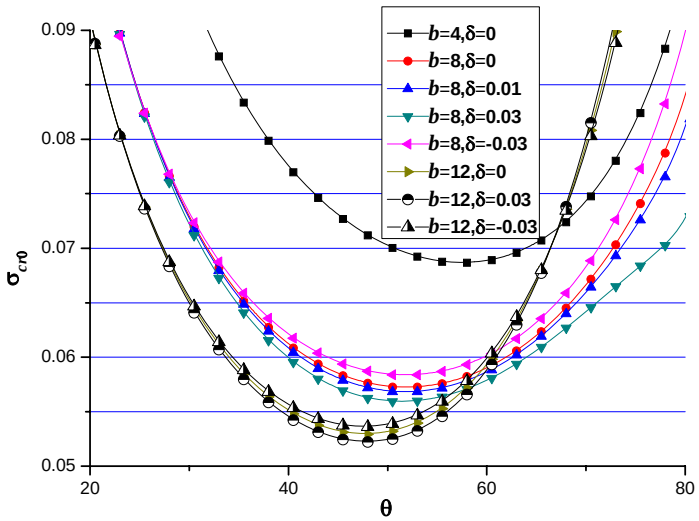

Fig. 3 Dependences of normalized critical stress σ_{cr0} on emission angle θ with different nanovoid sizes and surface residual stresses for $\rho_0 = b_z$, $\varepsilon = 0$, $j_1 = 1$, $j_2 = j_3 = 0$, $a = 0.9$, $c = 1.5$, $\alpha = \beta = 0$.

In this case in Fig. 4, namely $a = 0.9$ and $b = 8$, it means that for given void volume fraction and nanovoid size, c characterizes the spacing of neighboring nanovoids or the uniform distribution density of the nanovoids. The smaller physical quantity c defines the smaller neighboring spacing or the denser distribution of the nanovoids under the same void volume fraction and nanovoid size. As is seen from Fig. 4, the critical stress decreases clearly, while the relative most probable critical angle for dislocation emission increases as the physical quantity c decreases. That is, the initial void

volume fraction and nanovoid size remain constant, the distinct softening behavior can be happened and then significantly promotes capability of dislocation emission from nanovoid surface in the nanoporous materials with improving the uniform distribution density of the neighboring nanovoids. In other words, increasing nanovoid spacing can impede the nanovoid growth and increase ductility. These conclusions are further confirmed by the earlier experiment from Dubensky and Koss [18], and the finite element analysis from Gao et al. [19]. It is also visibly indicates that the larger the negative surface residual stress is, the harder the dislocation emitted from nanovoid surface becomes. These observations demonstrate that the density of nanovoid concentration and the surface residual stress have a significant effect on determining the deformation behavior of ductile materials.

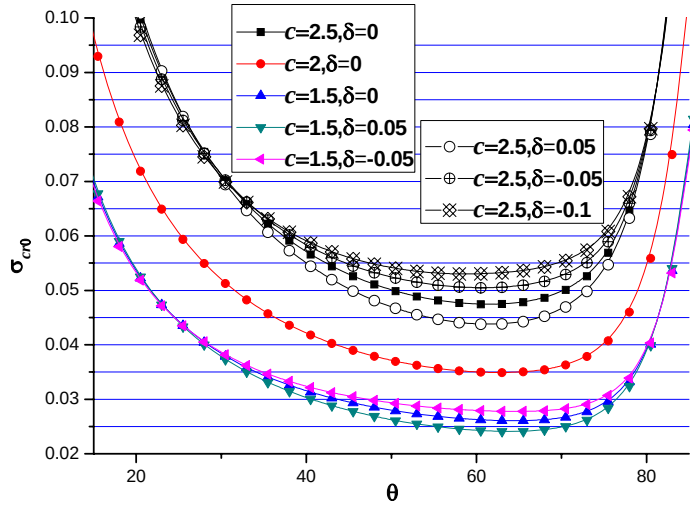

Fig. 4 Dependences of normalized critical stress σ_{cr0} on emission angle θ with different uniform distribution densities of the neighboring nanovoids and surface residual stresses for $\rho_0 = b_z$, $\varepsilon = 0$, $j_1 = 1$, $j_2 = j_3 = 0$, $a = 0.9$, $b = 8$, $\alpha = \beta = 0$.

5. Conclusions

In conclusion, when nanovoid size is fixed, the larger nanovoid volume fraction in the nanoporous materials makes the dislocation emission take place more easily, relative most probable critical emission angle more pronouncedly depart from the direction 45°. Under the condition of constant void volume fraction, the larger the neighboring number of voids is, the higher the critical stress becomes. For given void volume fraction and nanovoid size, the distinct softening behavior can be happened and then significantly promotes capability of dislocation emission from nanovoid surface in the nanoporous materials with improving the uniform distribution density of the neighboring nanovoids.

Acknowledgements

The authors would like to deeply appreciate the support from the NNSFC (11172094 and 11172095) and the NCET-11-0122. This work was also supported by Hunan Provincial Natural Science Foundation for Creative Research Groups of China (Grant No.12JJ7001).

References

[1] V.A. Lubarda, Emission of dislocations from nanovoids under combined loading. Int J Plast, 27

(2011) 181–200.
[2] V.A. Lubarda, Image force on a straight dislocation emitted from a cylindrical void. Int J Solids Struct, 48 (2011) 648–660.
[3] M.E. Gurtin, A.I. Murdoch, A continuum theory of elastic material surfaces. Arch Rat Mech Anal, 57 (1975) 291–323.
[4] M.E. Gurtin, A.I. Murdoch, Surface stress in solids. Int J Solids Struct, 14 (1978) 431–440.
[5] M.E. Gurtin, J. Weissmuller, F. Larche, A general theory of curved deformable interfaces in solids at equilibrium. Philos Mag A, 78 (1998) 1093–1109.
[6] P. Sharma, S. Ganti, N. Bhate, Effect of surfaces on the size-dependent elastic state of nano-inhomogeneities. Appl Phys Lett, 82 (2003) 535–537.
[7] N.L. Muskhelishvili, Some Basic Problems of Mathematical Theory of Elasticity, P. Noodhoff, Groningen, 1975.
[8] Z.J. Gao, A circular inclusion with imperfect interface: Eshelby's tensor and related problems. J Appl Mech, 62 (1995) 860–866.
[9] Q.H. Fang, Y.W. Liu, Size-dependent interaction between an edge dislocation and a nanoscale inhomogeneity with interface effects. Acta Mater, 54 (2006) 4213–4220.
[10] Y.X. Zhao, Q.H. Fang, Y.W. Liu, Edge misfit dislocation formation at the interface of a nanopore and infinite substrate with surface/interface effects. Phil Mag, 92 (2012) 4230–4249.
[11] J.P. Hirth, J. Lothe, Theory of Dislocations, McGraw-Hill, New York, 1982.
[12] M.T. Qaissaunee, M.H. Santare, Edge dislocation interaction with an elliptical inclusion surrounding by an interfacial zone. Q J Mech Appl Math, 48 (1995) 465–482.
[13] L. Stagni, Edge dislocation near an elliptic inhomogeneitywith either an adhering or a slipping interface-a comparative study. Phil Mag A, 68 (1993) 49–57.
[14] V.A. Lubarda, M.S. Schneider, D.H. Kalantar, B.R. Remington, M.A. Meyers, Void growth by dislocation emission. Acta Mater, 52 (2004) 1397–1408.
[15] R.E. Miller, V.B. Shenoy, Size-dependent elastic properties of nanosized structural elements. Nanotechnology, 11 (2000) 139–147.
[16] V. Tvergaard, J.W. Hutchinson, Two mechanisms of ductile fracture: void by void growth verse multiple void interaction. Int J Solids Struct, 39 (2002) 3581–3597.
[17] C.W. Mi, D.A. Buttry, P. Sharma, D.A. Kouris, Atomistic insights into dislocation-based mechanisms of void growth and coalescence. J Mech Phys Solids, 59 (2011) 1858–1871.
[18] E.M. Dubensky, D.A. Koss, Void/pore distributions and ductile fracture. Metall Trans A, 18 (1987) 1887–1895.
[19] X.S. Gao, T.H. Wang, J. Kim, On ductile fracture initiation toughness: Effects of void volume fraction, void shape and void distribution. Int J Solids Struct, 42 (2005) 5097–5117.

Multi-scale modeling and diffraction-based characterization of elastic behaviour of human enamel

Tan Sui[1,*], Michael A. Sandholzer[2], Nikolaos Baimpas[1], Igor Dolbnya[3], Gabriel Landini[2], Alexander M. Korsunsky[1]

[1] Department of Engineering Science, University of Oxford, Parks Road, Oxford OX1 3PJ, United Kingdom
[2] School of Dentistry, College of Medical and Dental Sciences, University of Birmingham, St Chad's Queensway, Birmingham B4 6NN, United Kingdom
[3] Diamond Light Source, Harwell Oxford Campus, Didcot OX11 0DE, United Kingdom

* Corresponding author: tan.sui@eng.ox.ac.uk

Abstract The relationship between the ultrastructure of human enamel and its mechanical behaviour is studied in this paper. Two synchrotron X-ray diffraction techniques, wide and small angle X-ray scattering (WAXS/SAXS) were used in combination to obtain multi-scale quantitative information about the response of human enamel to *in situ* uniaxial compressive loading. The interpretation of WAXS data gives elastic lattice strains within the hydroxyapatite (HAp) crystals, the stiff reinforcing phase in human enamel. The apparent modulus was determined linking the external load and the internal HAp strain. SAXS interpretation, allows the quantification of the nano-scale HAp crystallite distribution within human enamel. A multi-scale Eshelby equivalent inclusion model of the enamel was proposed that represents the hierarchical mineralized tissue as a two-level composite: micro-level model with rod embedded in the homogenised enamel material, and nano-level model with HAp crystallites embedded in the rod. Satisfactory agreement was achieved between model and experiment, suggesting that the new multi-scale approach accurately reflects the structure and mechanics of human enamel, and may help guide new biomimetic designs.

Keywords Enamel, WAXS/SAXS, Eshelby model, Mechanical properties

1. Introduction

Enamel, a highly mineralized substance, is a hard and brittle material that covers the crown portion of teeth. It is predominately composed of inorganic hydroxyapatite (HAp) crystals and organic collagen [1]. While at the macro-scale the enamel can be thought of as a continuum, at the microstructural level some notable features are present, in particular, aligned long prisms (or rods) with a keyhole-shaped cross-section, and with the top oriented toward the crown of the tooth [2]. Further, at the nano-scale level, needle-like HAp crystals are found with several tens of nanometers in thickness [3].

Understanding the effects of microstructural features of enamel on the performance of human teeth requires the understanding of how the mechanical properties are related to the complex hierarchical structure. Over half a century, studies have been conducted on the macro-scale mechanical properties of enamel [4]. While an increasing number of publications describe microstructural effects [5], relatively few studies have focused on the influence of the nano-scale structure [6]. There appears to be a demand for further investigation across the scales using advanced techniques and models to establish a solid basis to understand the hierarchical structure-property relationship.

One suitable method to study this is small angle X-ray scattering (SAXS), an advanced non-destructive technique used to reveal information about nano-scale structure and orientation in crystalline and amorphous materials [7]. Another X-ray technique, wide angle X-ray scattering (WAXS), is used to study crystal lattices and their deformation behaviour, e.g. the elastic properties of composites [8,9]. WAXS has been applied only recently to the study of mineralized biological composites, such as bones and bovine teeth [10-13], but few studies have been devoted to study human enamel [14]. Therefore, for the present study a combined SAXS/WAXS setup with *in situ* compressive loading of human enamel samples was selected. It is hoped that the results obtained

here will be helpful to understand the internal architecture and hierarchical properties of human dental tissues.

Quite a few models of composites have been proposed to describe the interaction of different phases, including bounding principles of Voigt and Reuss, as well as Jones and BW models [15,16]. One widely accepted model, also used in this study, is the Eshelby inclusion model, often used to describe the structure-property relationship of materials like composites [17,18]. Recently, it has been applied in the research of dentine [19,20], and has been proven to be useful to predict the elastic response of dentine. However, this Eshelby approach has not been used to describe human enamel.

In this paper, the elastic lattice strain, orientation and degree of alignment of HAp crystals within a human enamel sample under compressive loading were measured by the combined *in situ* synchrotron X-ray techniques (WAXS and SAXS). The multi-scale Eshelby model was developed to reflect the hierarchical structure of enamel, and to predict the elastic response to mechanical loading. The model was validated by comparison with experimental data.

2. Method and Materials

2.1. Sample preparation

A freshly extracted sound human third molar (ethical approval obtained from the National Research Ethics Committee; NHS-REC reference 09.H0405.33/Consortium R&D No.1465) was washed and mechanically cleaned in distilled water to eliminate residues and kept in a -20°C freezer for a maximum of 14 days before the experiment. The tooth was rehydrated using distilled water and 2mm thick enamel disks were cut just below the enamel-cement line using a low speed diamond saw (Isomet Buehler Ltd., Lake Bluff, Illinois, USA). The disks were further cut into smaller bars and polished using a series of polishing papers to produce a 2×2×2mm cube of enamel. The sample was kept for 5 days in distilled water in a commercial fridge at 4°C until the experiment was undertaken.

2.2. In-situ scattering measurements

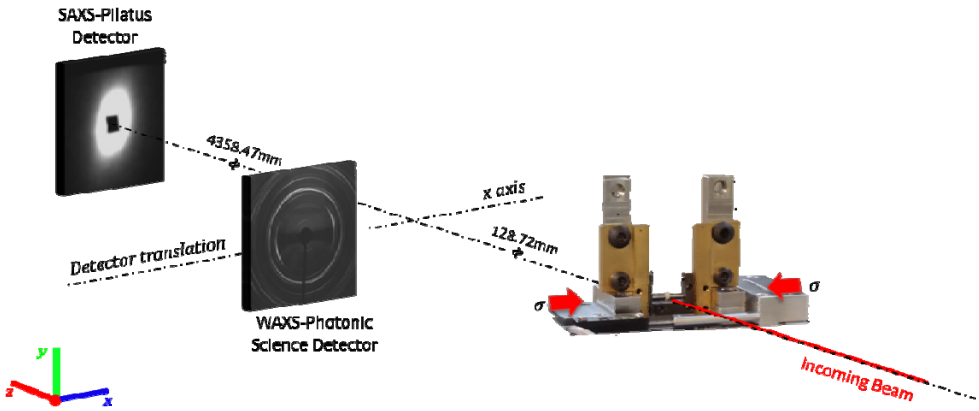

Figure 1. In situ loading of enamel under simultaneous WAXS/SAXS experimental set-up

The experiment was performed on the B16 beamline at Diamond Light Source (DLS, Oxford, UK). A schematic diagram of the experimental set-up is shown in Fig. 1. The cubic sample of human enamel was slowly deformed along x-direction in the laboratory coordinate system (Fig. 1) under compressive loading at a displacement rate of 0.2 mm/min until failure, using a remotely operated and monitored compression rig (Deben, Suffolk, UK) with a 5KN calibrated load cell.

The monochromatic X-ray beam at the photon energy of 17.99keV was used and collimated to the spot size of 0.5× 0.5mm^2. The beam was incident at the sample perpendicular to its loading direction. Two separate WAXS and SAXS detectors were alternately setup to collect the patterns at consecutive loading increments downstream of the beam. WAXS patterns were recorded using a Photonic Science Image Star 9000 detector (Photonic Science Ltd., UK) with a sample-to-camera distance of 128.72mm. Further downstream, a Pilatus 300K detector (Dectris, Baden, Switzerland) was positioned at a distance of 4358.47mm to collect SAXS patterns. In order to record both WAXS and SAXS patterns at each scanning location, the WAXS detector was translated laterally to expose the SAXS detector after each WAXS exposure. A lightly compacted disk of standard silicon powder and a dry chicken collagen sample inserted close to the sample position were used as calibration standards, and to determine the sample-to-detector distance to good precision.

2.3. Scattering data analysis

2.3.1. WAXS data analysis

WAXS data can be interpreted in terms of the shift of the diffraction peak obtained from a cluster of HAp crystals, so that the average micro-strain (lattice strain) in the crystals can be deduced [8,9]. The typical WAXS pattern of HAp is shown in Fig. 2 (only the (002) peak is selected for interpretation). The apparent elastic lattice strain of the HAp phase was computed by observing the changes in the interplanar spacing between the lattice planes [21]:

$$\varepsilon = \frac{d_{002} - d_{002}^{0}}{d_{002}^{0}} \tag{1}$$

where d_{002} is the deformed *d*-spacing and d_{002}^{0} is the reference strain-free value. In detail, 2D diffraction images were firstly pre-processed using Fit2D [22]. The (002) peak of interest from each pattern was “caked” (i.e. binned in the radial-azimuthal coordinates) within a range of 20° in the loading direction (Fig. 2a). Subsequently the 1D radial plot of intensity within each sector was fitted with Gaussian to obtain the peak centre position. As the load increase, the peak centre position shift with respect to the strain-free reference point allowed the calculation of HAp elastic lattice strain. In addition, the structural orientation angle was determined from the strain-free sample by azimuthal-radial “caking” of the (002) peak over the entire range of 360°, and fitting the azimuthal centre position of the pronounced peaks [23].

2.3.2. SAXS data analysis

For SAXS data analysis, the pattern from the strain-free sample was taken as reference. Due to the dense distribution of crystals in enamel, the electron density changes that occur in the gaps between crystalline particles gives rise to the scattering signal [24]. It is also understood that the orientation of the gaps between rods roughly coincides with the orientation of the crystals within the rod [19]. Thus, the information from gap scattering can be used to deduce the orientation and degree of alignment (percentage of aligned particles) of HAp crystals. To quantify it, the 2D SAXS patterns were processed by integrating over the entire relevant range of scattering vector *a*, resulting in a function $I(\varphi)$ of the azimuthal angle φ [25,26]. The predominant orientation φ_0 of the mineral crystals is determined by the position of the two peaks in the plot of $I(\varphi)$. Further, the degree of alignment ρ can be calculated by the ratio of the two areas under the curve of $I(\varphi)$:

$$\rho = \frac{A_{oriented}}{A_{total}} \tag{2}$$

where A_{total} is the total area below the curve, and $A_{oriented}$ refers to the area above the constant background level $A_{umoriented}$. Thus, the value of ρ ranges from 0 to 1, with $\rho = 0$ indicating no predominant orientation within the plane of the section, while $\rho = 1$ indicates a perfect alignment of all crystals [25,26].

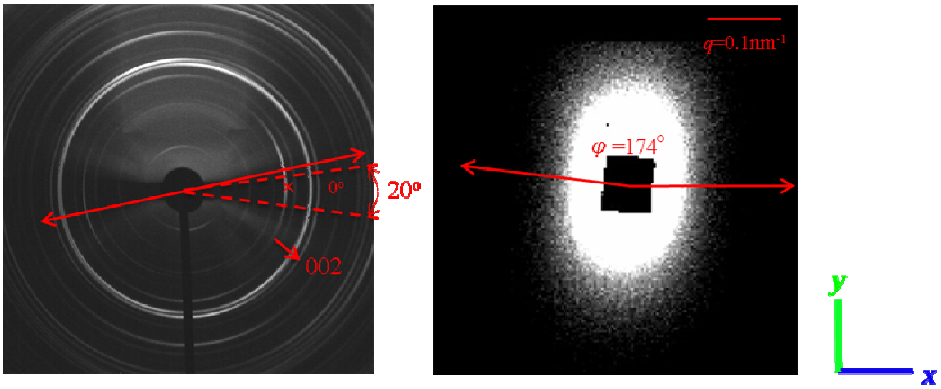

Figure 2. Representative WAXS and SAXS patterns of enamel

3. Model formulation

Human enamel has a hierarchical two-level composite structure, where the first level is represented by the keyhole-like rod and the second level by the bunch of HAp crystals within one rod [27]. Fig. 3a shows the keyhole-like microstructure of enamel, modified from Habelitz [28], and demonstrates how the HAp crystals are distributed within the rod in 3D. Fig. 3b-d provide schematic illustration of the geometric model derived from the enamel structure, where the first level regards the whole enamel sample as composed of aligned rods within a collagen matrix phase (Fig. 3b), and the second level considers the rod as a composite in detail, consisting of partially aligned HAp crystals and a collagen matrix. Both levels are non-dilute systems with a number of inhomogeneous inclusions. For simplicity, both rod and HAp crystals are assumed to be of needle shape (Fig. 3b-d).

3.1. First level model: multiple aligned rod inclusions within enamel

The purpose of the first-level model is to establish the relationship between the externally measured stress σ^A and the stress in the rod inclusions $\sigma^{inclusion} = \sigma^{rod}$. According to the Eshelby model derivation [29], the stress in the inclusion can be expressed as

$$\sigma^{inclusion1} = \left\{ T - (1 - f_1)\left\{ (C_{matrix1} - C_{rod})\left[S_1 - f_1(S_1 - I) \right] - C_{matrix1} \right\}^{-1} (C_{matrix1} - C_{rod}) T^{-T} C_{matrix1}^{-1} \right\} \sigma^A$$

$$\text{or, simplified} \quad \sigma^{inclusion1} = K_1 \sigma^A \tag{3}$$

where f_1 is the volume fraction of rod inclusion, S_1 the Eshelby tensor for a cylinder corresponding to the rod shape, $C_{matrix1}$ and C_{rod} are the stiffness of collagen matrix and rod, respectively, and T is the tensor transformation (rotation) matrix that depends on the Euler angles giving the orientation of the rods with respect to the fixed laboratory system. In the present model this was fixed, as it was

assumed that the rods were all aligned with the loading direction.

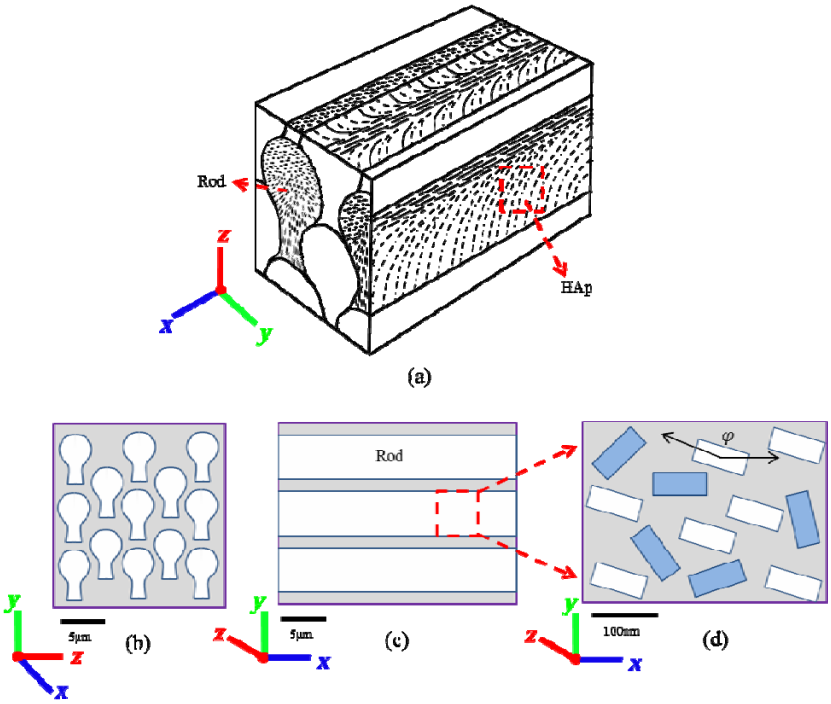

Figure 3. Schematic diagrams of hieratical enamel structure and multi-scale Eshelby model.

To determine the stress within the inclusion, knowledge of the rod stiffness matrix is required. The rod is regarded as a composite consisting of the same volume fraction of collagen and mineral crystals as the whole enamel. The stiffness of the rod C_{rod} can thus be determined and is given as:

$$C_{rod} = \left\{ C_{matrix2}^{-1} - f_2 \left\{ \left(\langle C \rangle_{HAp} - C_{matrix_2} \right) \left[\langle S_2 \rangle - f_2 \left(\langle S_2 \rangle - I \right) \right] + C_{matrix2} \right\}^{-1} \left(\langle C \rangle_{HAp} - C_{matrix2} \right) C_{matrix2}^{-1} \right\}^{-1} \quad (4)$$

3.2. Second level model: HAp inclusion within one rod

The purpose of the second-level model is to establish the relationship between the external stress and the average strain in the HAp crystals in a rod: $\langle \varepsilon \rangle^{HAp}$ ($\sigma^{inclusion1} = K \langle \varepsilon \rangle^{HAp}$). Here the stress within the rod inclusion $\sigma^{inclusion1}$ found from the first-level model serves as the external stress in the second-level model. The overall stiffness of the rod C_{rod} is required to link the average strain in the HAp crystals with the external stress obtained in the first-level model. A single HAp crystal can be regarded as a single inhomogeneity with needle-like shape, and thus the corresponding Eshelby tensor S_2 should again be that for the cylinder. The alignment of HAp crystals within the rod is also partial, so that the real value of the apparent stiffness *K* is given by a combination of the values for two separate cases, namely, that of fully random distribution, and perfect alignment.

3.2.1 Multiple perfectly aligned HAp crystals

Supposing the alignment direction of HAp crystals is described by the transformation matrix *T*, the measured crystal strain corresponds to the mean strain value for all the crystals within the considered gauge volume. The relationship between the average HAp strain and the external load (rod stress from the first-level model) can be established as follows:

$$\langle\varepsilon\rangle_{aligned}^{HAp} = \left\{\left\{\left(I - C_{matrix2}^{-1}\langle C\rangle_{HAp}\right)^{-1}\left[\langle S_2\rangle - f_2(\langle S_2\rangle - I)\right]^{-1} - I\right\}^{-1} T^{-T} + T^{-T}\right\} C_{matrix2}^{-1}\sigma^{inclusion1}$$

$$\text{or, simplified } \sigma^{inclusion1} = K_{aligned}\langle\varepsilon\rangle_{aligned}^{HAp} \tag{5}$$

where $\langle C\rangle_{HAp}$ and $\langle S_2\rangle$ are the average elastic stiffness tensor and Eshelby tensor of HAp crystals within gauge volume [30], f_2 the volume fraction of HAp with respect to the entire rod, and $C_{matrix2}$ is the stiffness tensor of collagen. Since all the crystals are perfectly aligned, the average value of $\langle C\rangle_{HAp}$ and $\langle S_2\rangle$ can be represented by the single crystal values $\langle C\rangle_{HAp} = C_{HAp}, \langle S_2\rangle = S_2$. Note that different orientation angles would lead to different values of $\langle\varepsilon\rangle_{aligned}^{HAp}$.

3.2.2 Multiple randomly distributed HAp crystals

The relationship between the average HAp lattice strain and rod stress is independent of the transformation matrix in Eq. 5 in the case of an isotropic cluster with randomly distributed crystals. The relationship becomes

$$\langle\varepsilon\rangle_{random}^{HAp} = \left\{\left\{\left(I - C_{matrix2}^{-1}\langle C\rangle_{HAp}\right)^{-1}\left[\langle S_2\rangle - f_2(\langle S_2\rangle - I)\right]^{-1} - I\right\}^{-1} + I\right\} C_{matrix2}^{-1}\sigma^{inclusion1}$$

$$\text{or, simplified } \sigma^{inclusion1} = K_{random}\langle\varepsilon\rangle_{random}^{HAp} \tag{6}$$

Note that in contrast with the case of perfectly aligned crystals, the average value of $\langle S_2\rangle$ no longer equals the single crystal value S_2. Instead, it must be obtained by the volume average over all the crystals.

3.2.3 Multiple HAp inclusions with partial orientation

For the partially aligned HAp distribution (Fig. 3d), $K_{partial_aligned}^{HAp}$ is given by the mixtures between K_{random} and $K_{aligned}$:

$$K_{partial_aligned}^{HAp} = (1 - f_{aligned})K_{random} + f_{aligned}K_{aligned} \tag{7}$$

where $f_{aligned}$ is the volume fraction of the aligned crystals with respect to all HAp crystals, i.e. the degree of alignment of crystals revealed by SAXS. Thus, the relationship between external stress (in rod) and average internal HAp lattice strain becomes

$$\sigma^{inclusion1} = K_{partial_aligned}^{HAp}\langle\varepsilon\rangle^{HAp} \tag{8}$$

Further, the relationship between HAp strain and the externally applied stress can be established by combining Eq. 3 and Eq.8.

$$\sigma^{A} = K_1^{-1}\sigma^{inclusion1} = K_1^{-1}K_{partial_aligned}^{HAp}\langle\varepsilon\rangle^{HAp} = K\langle\varepsilon\rangle^{HAp} \tag{9}$$

4. Experimental results and model evaluation

4.1. Nano-scale HAp distribution and the mechanical response of enamel

The apparent radial shifts of the (002) peak centre position obtained from the WAXS pattern (Fig. 2a) were measured under compressive loading applied on the longitudinal direction with respect to

the rods. Fig. 4a shows the experimental results of the applied stress vs. HAp lattice strain, indicating the expected linear relationship. The ratio of the stress and the average HAp lattice strain gives the apparent modulus [31]. The preferential orientation of HAp crystals obtained by WAXS pattern analysis is shown to be roughly perpendicular to the arc, while that obtained by SAXS pattern is shown to be roughly along the short axis of the elliptical SAXS pattern (Fig. 2). The detailed values from experiment and model are listed in Table 1.

4.2. Evaluation and testing of multi-scale Eshelby model

In the model, the material properties and other parameters were derived from the literature, and refined by fitting with the experimental data. The average mineral concentration (HAp volume fraction) has been reported to be ~95% in each level of enamel, so that the overall volume fraction of HAp could be close to 85%, which is consistent with [6]. In general, Young's modulus of 1GPa for collagen is found in the literature, without taking into account the viscoelasticity or viscoplasticity [19,20]. Polycrystalline HAp is considered to be transversely isotropic with five independent elastic constants [32]. To describe the shape of the rod and of the HAp crystallites for each level, the Eshelby tensor for the cylinder was used. It was assumed that the lengths of ellisptical axes a_1 and a_2 within the transverse cross-section were the same, a_1/a_2=1). The apparent modulus K was calculated based on the different preferred orientation angles of the HAp crystals obtained by both SAXS and WAXS. All the parameters refined to obtain the best fit are listed in Table 1. A comparison of the experimental results and the model evaluation is plotted in Fig. 4. Good agreement is observed.

Table 1 Experimental results from SAXS/WAXS, and the refined structural parameters of the enamel used in the two-level Eshelby model

Parameter	**Enamel**
Orientation (from SAXS)	174°
Orientation (from WAXS)	14°
Degree of alignment	0.6
K_exp.	124.3 GPa
$f_1 = f_2$	96%
C_{matix1}	E_m=1GPa, v_m=0.3
C_{matix2}	E_m=1GPa, v_m=0.3
C_{HAp}	E_{xx}=140GPa, G_{xy}= G_{xz}=39.6GPa v_{xy}= v_{xz} =0.3, v_{yz}=0.2 E_{yy}= E_{zz}=114.3GPa
$S_{cylinder1} = S_{cylinder2}$	$a_1 / a_2 = 1$
K_model (from SAXS)	122.9 GPa
K_model (from WAXS)	120.4 Gpa

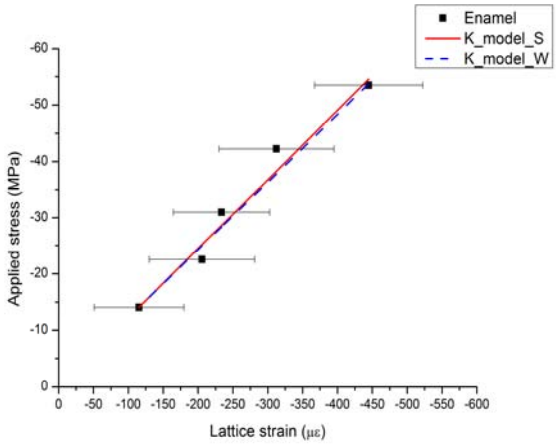

Figure 4. Comparison of the experimental data (markers) and modeling results for applied compressive stress vs. elastic lattice strain for HAp crystals.

5. Discussion & Conclusion

The agreement of the apparent modulus K results calculated using the HAp preferred orientation angles determined by SAXS and WAXS suggests that the SAXS patterns arising from gap scattering can be used to deduce the HAp orientation distribution, i.e. the gaps are almost parallel to HAp crystals inside the rod. Further validation can be demonstrated by examining in more detail the effect of crystal orientation on the apparent modulus. A 3D model of perfectly aligned crystals inside a rod is established (Fig. 5a) with the angle φ describing the rotation of the alignment direction around the global z axis. When all HAp crystals are aligned along the global x-direction, φ equals to 0°. By changing the perfect alignment direction (changing the transformation matrix in Eq. 5), the variation of $K_{aligned}$ obtained in the loading direction can be calculated (Fig. 5b). From Fig. 5b, the corresponding results using the real orientation angles found in the experiment (174° from SAXS and 14° from WAXS) are found to be $K_{aligned_SAXS}$ = 133.19GPa and $K_{aligned_WAXS}$ = 128.25 GPa, i.e. closely similar values. Meanwhile, due to the high degree of alignment of HAp crystals in the enamel, the value of the overall apparent modulus $K^{HAp}_{partial_aligned}$ lies close to the value $K_{aligned}$. The enamel displays strong microscopic elastic anisotropy. It is interesting to note that the stiffest orientation is, as expected, around 0° with respect to the loading direction. However, the most compliant orientation observed is not at 90°, i.e. perpendicular to the loading direction, but rather around 50° or 130°.

In this study, the longitudinal apparent Young's modulus of human enamel was measured during in situ elastic compression by the combination of synchrotron WAXS and SAXS for the first time. This provides access to the information on both the structural and mechanical aspects of the sample and allows us to make further progress compared to previous studies that only used WAXS [11,14]. A multi-scale Eshelby inclusion model was established to estimate the elastic material properties of the enamel in terms of its constituents, considering it as a two-level composite. Good agreement with the experimental data was obtained, indicating an improvement of the earlier proposed composite model [15,16] The model offers a powerful tool for the evaluation of the apparent modulus of enamel-like composites, and helps understand the relationship between the external load

and the internal HAp strain. It also helps understanding of the mechanical properties of hierarchical biomaterials.

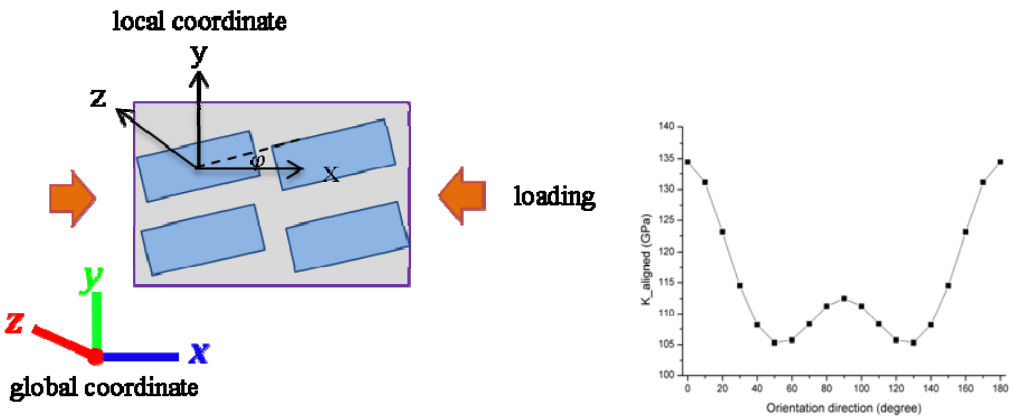

Figure 5. (a) A simple 3D example of aligned HAp crystals (alignment angle φ=0° is shown). (b) $K_{aligned}$ variation with respect to the alignment angle (0°-180°).

Acknowledgements

Diamond Light Source is acknowledged for the provision of beamtime at Test Beamline B16 under allocations MT7807 and MT7989. AMK wishes to acknowledge EPSRC support through grants EP/H003215/1 and EP/I020691/1, and the use of facilities at the Research Complex at Harwell.

References

[1] F.A. Siang, S. Mahnaz, V.S. Michael, *et al*. Comparison of mechanical behaviours of enamel rod and interrod regions in enamel. J Mater Res., 27 (2012) 448-456.
[2] G.A. Macho, Y. Jiang, I.R. Spears. Enamel microstructure—a truly three-dimensional structure. J Hum Evol., 45 (2003) 81-90.
[3] B. Kerebel, G. Daculsi, L.M. Kerebel. Ultrastructural studies of enamel crystallites. J Dent Res. 57 (1979) 306-312.
[4] L.H. He. Mechanical behavior of human enamel and the relationship to its structural and compositional characteristics. phd thesis, 2008.
[5] T. Nakamura, C. Lu, C.S. Korach, Mechanical Properties of Tooth Enamel: Microstructural Modeling and Characterization, Conference Proceedings of the Society for Experimental Mechanics Series, 2011(9999) 171-179.
[6] S. Bechtle, H. Özcoban, E.T. Lilleodden, *et al*. Hierarchical flexural strength of enamel: transition from brittle to damage-tolerant behavior. J.R. Soc. Interface, 9 (2012) 1265-1274.
[7] P. Fratzl, S. Schreiber, K. Klaushofer. Bone mineralization as studied by small-angle x-ray scattering. Connect Tissue Res., 34 (1996) 247-254.
[8] M.L. Young, J.D. Almer, M.R. Daymond, *et al*. Load partitioning between ferrite and cementite during elasto-plastic deformation of an ultrahigh-carbon steel. Acta Mater, 55 (2007) 1999–2011.
[9] M.L. Young, J. DeFouw, J.D. Almer, *et al*. Load partitioning during compressive loading of a Mg/MgB2 composite. Acta Mater, 55 (2007) 3467–3478.
[10] A.C. Deymier-Black, J.D. Almer, S.R. Stock, *et al*. Synchrotron X-ray diffraction study of load partitioning during elastic deformation of bovine dentin. Acta Biomater, 6 (2010) 2172–2180.
[11] J.D. Almer, S.R. Stock. High energy X-ray scattering quantification of in situ-loading-related strain gradients spanning the dentin enamel junction (DEJ) in bovine tooth specimens. J Biomech., 43 (2010) 2294–2300.
[12] A. Singhal, J.D. Almer, D.C. Dunand. Variability in the nanoscale deformation of

hydroxyapatite during compressive loading in bovine bone. Acta Biomater., 8 (2012) 2747–2758.
[13] J.D. Almer, S.R. Stock. Internal strains and stresses measured in cortical bone via high-energy X-ray diffraction. J Struct Biol., 152 (2005) 14–27.
[14] K. Fujisaki, M. Todoh, A. Niida, *et al*. Orientation and deformation of mineral crystals in tooth surfaces. J Mech Behav Biomed Mater, 10 (2012), 176-182.
[15] R.M. Jones. Mechanics of Composite Materials, Second edition. Taylor&Francis, Inc., Philadelphia, PA, 1999.
[16] B. Bar-On, H.D. Wagner. Elastic modulus of hard tissues. J. Biomech. 45(2012a), 672–678.
[17] P.J. Withers, W.M. Stobbs, O.B. Pedersen. The application of the Eshelby method of internal stress determination to short fibre metal matrix composites. Acta Metallurgica. 37 (1989) 3061-3084.
[18] Y. Takao, M. Taya. The effect of variable fiber aspect ratio on the stiffness and thermal-expansion coefficients of a short fiber composite. J Compos Mater., 21 (1987) 140-156.
[19] Q.H. Qin, M.V. Swain. A micro-mechanics model of dentine mechanical properties. Biomaterials, 25 (2004) 5081-5090.
[20] B. Huo. An inhomogeneous and anisotropic constitutive model of human dentin. J Biomech, 38 (2005) 587-594.
[21] A.M. Korsunsky, N. Baimpas, X. Song, *et al*. Strain tomography of polycrystalline zirconia dental prostheses by synchrotron X-ray diffraction. Acta Mater, 59 (2011) 2501-2513.
[22] A.P. Hammersley. "FIT2D: An Introduction and Overview". ESRF Internal Report1997.
[23] M. Al-Jawad, A. Steuwer, S.H. Kilcoyne, 2D mapping of texture and lattice parameters of dental enamel, Biomaterials. 28 (2007) :2908-2914.
[24] T. Tanaka, N. Yagi, T. Oht, *et al*. Evaluation of the distribution and orientation of remineralized enamel crystallites in subsurface lesions by X-Ray diffraction. Caries Res, 44 (2010) 253-259
[25] W. Tesch, T. Vandenbos, P. Roschgr, *et al*. Orientation of mineral crystallites and mineral density during skeletal development in mice deficient in tissue nonspecific alkaline phosphatase. J Bone Miner Res, 18 (2003) 117-125.
[26] W. Tesch, N. Eidelman, P. Roschger, *et al*. Graded microstructure and mechanical properties of human crown dentin. Calcified Tissue Int., 69 (2001) 147-57.
[27] A. Nanci. Ten Cate's Oral Histology: Development, Structure and Function. MosbyInc, St. Louis, Missouri, 2003.
[28] S. Habelitz, S.J. Marshall, G.W. Marshall Jr, *et al*. Mechanical properties of human dental enamel on the nanometre scale. Arch Oral Biol., 46 (2001) 173-183.
[29] T.W. Clyne, P.J. Withers. An introduction to metal matrix composites. First paperback edition 1995. ed. Cambridge: Cambridge University Press; 1993.
[30] T.W. Chou, C.T. Sun. Nanocomposites. In: Hyer M, W, editor.: DEStech Inc; 2012.
[31] J.M. Powers, J.W. Farah. Apparent Modulus of Elasticity of Dental Amalgams. J Dent Res, 54 (1975) 902.
[32] A. Öchsner, W. Ahmed, Biomechanics of Hard Tissues, John Wiley & Sons, 2011

Fracture toughness measurements on bovine enamel by indentation techniques

J. Rodríguez[1*], M.A. Garrido[1], L. Ceballos[2]

[1] Departamento de Tecnología Mecánica, Universidad Rey Juan Carlos, 28933 Madrid, Spain
[2] Departamento de Estomatología, Universidad Rey Juan Carlos, 28933 Madrid, Spain
* Corresponding author: jesus.rodriguez.perez@urjc.es

Abstract. Many works have attempted to estimate the fracture toughness of enamel by indentation techniques. Most of these works have in common the use of equations whose success in determining the actual value of fracture toughness depends on the particular three-dimensional pattern of cracks. Although microscopic techniques are usually employed, only a superficial image of the cracks is provided, and no information about the propagation within the enamel is given. Therefore, there is some uncertainty about the applicability of this type of equations. More recently, an alternative methodology based on an energetic approach has been developed to estimate the fracture toughness by depth sensing indentation that is not so affected by the cracks pattern generated.

In this work, the energetic approach to indentation fracture toughness of bovine enamel is presented and compared with those toughness values obtained using the most common expressions reported in the literature. The results showed that some modifications in the energetic methodology should be performed in order to apply it successfully.

Keywords indentation fracture toughness, enamel

1. Introduction

Enamel is the hardest and stiffest tissue of mammals. It forms the outer layer of the tooth and shows a characteristic hierarchical microstructure. At large scale, the enamel consists of rods encapsulated by thin protein rich sheaths that are arranged parallel in a direction perpendicular to the dentino-enamel junction (DEJ) from dentin to the outer enamel surface [1]. The enamel microstructure of all mammals appears to be very similar on a histochemical and anatomic basis [2].

Numerous methods have been employed to experimentally measure the fracture toughness (K_C) of the enamel. The determination of K_C by indentation technique is based on measuring the size of cracks induced in a material during indentation. Several expressions are available to determine K_C by this technique, depending on the indenter geometry and crack morphology. One of the most widely used expressions for radial cracks is the relationship proposed by Lawn, Evans and Marshall [3]:

$$K_C = k\left(\frac{E}{H}\right)^n \frac{P}{c^{3/2}} \tag{1}$$

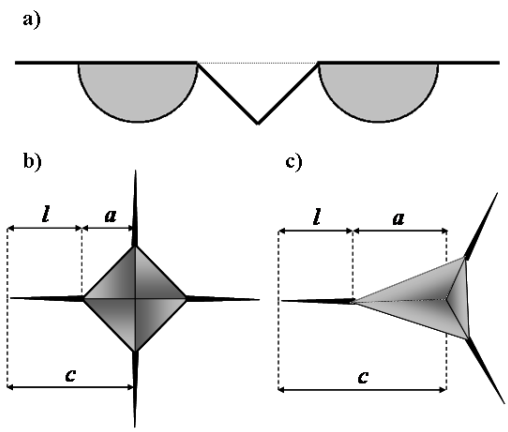

Figure 1. a) Palmqvist cracks configuration; b) crack parameters for Vickers indenter; c) crack parameters for Berkovich indenter.

where P is the maximum indentation load, c is the crack length (Fig. 1), E is the elastic modulus and H is the hardness. The parameters k and n are empirical constants equal to 0.016 ±0.004 and 0.5, respectively. Other studies [4] determined k = 0.0098 and n = 3/2.

For Palmqvist cracks configuration, where the cracked areas are represented by semicircles of diameter equal to the crack length measured from an impression corner (Fig. 1a), many expressions have been developed to calculate K_C. Niihara et al. [5] proposed the following expression:

$$K_C = k\left(\frac{E}{H}\right)^{2/5} \frac{P}{a\sqrt{l}} \tag{2}$$

where a is the half-diagonal of the indentation impression, l is the crack length and k was determined as 0.0089 (Fig. 1b).

Laugier [6] proposed an alternative expression for Palmqvist cracks:

$$K_C = x_V\left(\frac{a}{l}\right)^{1/2}\left(\frac{E}{H}\right)^{2/3} \frac{P}{c^{3/2}} \tag{3}$$

where x_V was determined as 0.015.

However, the applicability of these equations encounters three basic difficulties. First, all these equations are semi-empirical as there is no theoretical basis behind these expressions. Second, it is necessary to obtain a particular pattern of cracks (Fig. 1a) and to know the morphology of the cracks in the plane parallel to the loading direction in order to implement the Eqs. (1)-(3). Third, all these equations were developed for ceramic materials and for the symmetrical Vickers indentations (Fig. 1b). Therefore, they are not valid for the asymmetrical Berkovich indentations. Some efforts have been made to obtain similar equations to those described above but properly modified for Berkovich indentations [7] (Fig. 1c). Combining the model proposed by Laugier [6] and the Ouchterlony´s radial cracking modification factors [8], fracture toughness can be determined according to Eq. (4).

$$K_C = 1.073 \cdot x_V \left(\frac{a}{l}\right)^{1/2} \left(\frac{E}{H}\right)^{2/3} \frac{P}{c^{3/2}} \tag{4}$$

Other alternative method to determine the fracture toughness consists on calculating the energy released during cracking, as a measure of the fracture toughness (Li et al. 1997) [9]. This method is based on the formation of a constant force step during the application of indentation load. This force step is associated with the sudden formation and propagation of cracks. The step length depends on how much the indenter and cracks suddenly advance into the material. This energetic method calculates the fracture toughness comparing the area limiting by the load-displacement curve with crack generation and the hypothetical one if cracking does not occur (Fig. 2). If the Mode I fracture is assumed, the threshold stress intensity required for the fracture can be written as:

$$\mathrm{K_{IC}} = \left[\left(\frac{\mathrm{E}}{\left(1-\nu^2\right)}\right) \cdot \left(\frac{\Delta \mathrm{U}}{\mathrm{A}}\right)\right]^{1/2} \tag{5}$$

where K_{IC} is the indentation fracture toughness of the material, ΔU is the strain energy obtained from the area between extrapolated load-displacement curve and the step of experimental one (Fig. 2), E is the elastic modulus, ν is the Poisson´s ratio and A represents the cracked area.

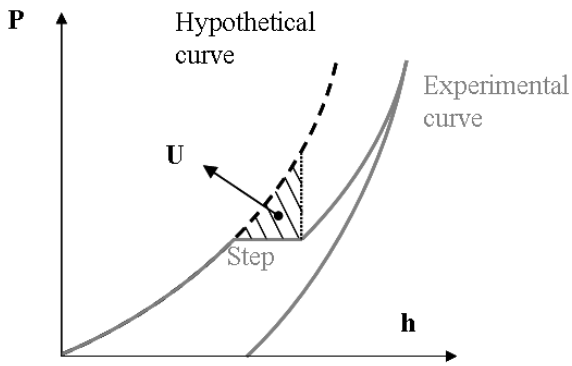

Figure 2. Strain energy obtained from the area between extrapolated load-displacement curve and the step of experimental one.

This method can be used even when a particular cracks pattern is not obtained. However, a constant load step during the loading branch is necessary in order to apply the Eq. (5). Additionally, a good estimation of cracked area is essential to obtain reliable results.

Therefore, the aim of this study was to evaluate the reliability of the energetic methodology using depth sensing indentation technique to estimate the indentation fracture toughness of bovine dental enamel. These values were compared with those traditionally obtained by applying the semi-empirical equations based in a specific pattern of cracks, Eqs. (1)-(4).

2. Experimental procedure

Eight incisors were extracted from bovines of two years old. The teeth were cleaned and stored in artificial saliva prior to the tests. The labial surfaces of the specimens were polished using a

mechanical grinder (Labopol-5, Struers, Copenhagen, Denmark) with polishing cloths with alumina suspension slurry of 3 µm and OP-A (Struers, Copenhagen, Denmark). Afterwards, the specimens were kept fully hydrated in artificial saliva at room temperature before the indentation tests.

Hardness and elastic modulus of bovine enamel surfaces were studied by nanoindentation (Nanoindenter XP-MTS System Corporation) using a Berkovich indenter with a tip radius of 100 nm. Before each batch tests, the Berkovich diamond indenter was calibrated on a standard fused silica specimen.

A Continuous Stiffness Measurement module (CSM) was chosen. This method consists of applying multiple unloading cycles of very small displacement during the loading process. The Oliver-Pharr methodology [10] was applied on each of these partial unloading cycles, providing values of elastic modulus, *E*, and hardness, *H*, as a continuous function of load or penetration depth. A maximum penetration depth of 300 nm was fixed for all indentation tests. Three rows of 20 indentations were done on each sample. Each indentation was separated 100 µm to each other. During the loading branch, continuous loading-unloading cycles with amplitude of 2 nm and a frequency of 45 Hz were superimposed.

Additionally, 5 indentations were done on each sample using the CSM module up to a maximum penetration depth of 2000 nm. This penetration depth was sufficient to generate a characteristic pattern of cracks, which extended from the corners of the Berkovich imprint and propagated along the enamel microstructure. After the indentation tests, the residual imprints were observed by Scanning Electron Microscopy (SEM) under low vacuum condition and taking care that the samples remained inside the microscope the shortest time in order to prevent an excessive dehydration and consequently, the cracks propagation due to residual stresses.

3. Results

Figure. 3 shows two SEM images of typical residual imprints from depth sensing indentations at different maximum penetration depths and their corresponding contact stiffness versus contact depth curves: 300 nm (Fig. 3a) and 2000 nm (Fig. 3b). Indentations at maximum penetration depth of 300 nm were characterized by the absence of cracks in the edges of the residual imprint (Fig. 3a). Additionally, the contact stiffness, *S*, showed a linear trend with the square root of the contact area, A, between the indenter and the material surface (Fig. 3a), as predict the theoretical relation between them [10]. By contrast, the indentations obtained for a maximum penetration depth of 2000 nm were characterized by the presence of radial cracks from the edges of the residual imprints (Fig. 3b). All residual imprints showed a similar superficial cracks pattern, consequently, the semi-empirical equations described in the introduction section could be applied. In addition, in these indentation tests, the cracks deflected during their propagation through the enamel microstructure. It was also noted that the contact stiffness lost its linear dependency with the square root of contact area (Fig. 3b), coinciding with the formation and propagation of cracks during the indentation process.

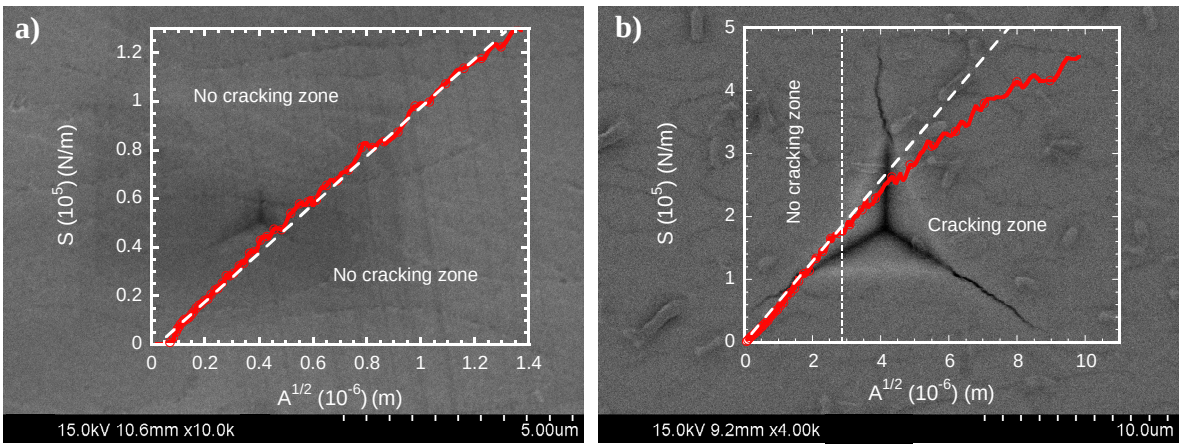

Figure 3. Typical pattern of cracks obtained from nanoindentations carried out at different maximum penetration depths: a) 300 nm; (b) 2000 nm. Their corresponding indentation contact stiffness versus squared root of the contact area plots were put over each image.

3.1. Mechanical properties: elastic modulus, hardness and fracture toughness.

Table 1 summarizes the hardness and elastic modulus of bovine enamel obtained from indentation tests at maximum penetration depth of 300 nm, where the loading did not cause the initiation of cracks. The values obtained in this study were very similar to those reported in preview works [11-13].

Data in Table 1 also include the fracture toughness of enamel according to the equations previously described (see Eqs. (1-5)).

It is noteworthy that, in all cases, there was not any constant load step. Therefore, it was not possible to apply the energetic methodology as described in the introduction section.

Elastic modulus , *E* (GPa)	92 ±6	Oliver-Pharr [10]
Hardness, *H* (GPa)	4.7 ±0.3	Oliver-Pharr [10]
Indentation fracture toughness, K_C (MPa$\sqrt{\text{m}}$)	0.39 ±0.14	Eq (1) [3]
	0.5 ±0.2	Eq (2) [5]
	0.6 ±0.2	Eq (3) [6]
	0.7 ±0.2	Eq (4) [8]
	2.5 ±0.7	Eq (9)

Table 1. Experimental results of elastic modulus, E, hardness, H and indentation fracture toughness, K_C.

4. Discussion

There is some scatter in the literature about the actual fracture toughness of enamel [13]. Table 1 shows the fracture toughness values obtained after applying the semi-empirical equations (1) to (4). These data were within the range of those reported by other authors. Hassan et al. (1981) [14] have reported values of human tooth enamel, using a Vickers indenter combined with a semi-empirical equation type 1 (Eq. (1)), in the range of 0.7 to 1.37 MPa·m$^{1/2}$. Xu et al. (1998) [12] reported fracture toughness values of 0.84 MPa·m$^{1/2}$ for labial human enamel also using a Vickers indenter with semi-empirical equation type 1 (Eq. (1)). Bajaj and Arola (2009) [15] reported fracture toughness values for human enamel that ranged from 1.79 MPa·m$^{1/2}$ to 2.37 MPa·m$^{1/2}$ obtained from R-curve analysis, and Baldassarri et al. (2008) [16] obtained values of 0.5 MPa·m$^{1/2}$ and 1.3 MPa·m$^{1/2}$ for transversal and midsagital enamel orientation, respectively, using a Vickers indenter on rat tooth. Rasmussen and Patchin (1984) [17] used SEM fractography and work-of-fracture techniques to investigate the fracture properties of human enamel and dentin as a function of the temperature of an aqueous environment. In this work, the specimens were notched in order to give controlled fracture in one of two preferred directions, either "perpendicular" or "parallel" to the rods for enamel. They reported values of work-of-fracture for human enamel that range from 0.13 J/m^2 (fracture toughness of 1.09 MPa·m$^{1/2}$) for parallel direction to 1.90-2.00 J/m^2 (fracture toughness of 4.18-4.29 MPa·m$^{1/2}$) for perpendicular orientation, at room temperature. The experimental load-displacement curves did not show, in our case, a constant load step during the loading branch (Fig. 5). In order to apply an energetic approach, an alternative methodology had to be developed.

The proposed procedure is based on the contact stiffness variation due to cracking during the indentation process. It should be noted that besides the cracking process, could also have other phenomena that may affect the contact stiffness, as quasi-plastic deformation phenomena associated with the movement of the water and protein phase due to the indentation. However, given the conditions under which the indentation tests were made, with high frequencies of the loading and unloading cycles (45 Hz), and small penetration depths in each cycle (2 nm), the contribution of these phenomena to the variation of the contact stiffness can be considered negligible.

It is well known that the area under the load-displacement curve is the work performed by the indenter during elastic-plastic deformation. However, if cracking occurs, part of the elastic energy stored will be released to create new crack surfaces. This will be reflected as a change in the contact stiffness and, consequently, the relationship between contact stiffness, *S*, and the squared root of the contact area, *A*, will not be linear as the contact theory predicts [10]:

$$S = 2 \cdot E_r \cdot \frac{\sqrt{A}}{\sqrt{\pi}} \tag{6}$$

where E_r is the reduced elastic modulus. For Berkovich indenters, the contact area is obtained from the following equation:

$$A = 24.5 \cdot h_p^2 + C_1 \cdot h_p + C_2 \cdot h_p^{1/2} + C_3 \cdot h_p^{1/4} + \ldots \tag{7}$$

where h_p is the contact depth and C_i are fitting constants obtained from calibration on fused silica.

As Fig. 3 showed, in a typical curve of contact stiffness versus squared root of the contact area, the tendency should be linear according to Eq. (6); however, the linearity only remains during the initial stage, before cracking occurs.

It is possible to identify in the S-$A^{1/2}$ curve a critical point associated with the onset of cracking (S^*, $A^{1/2\,*}$). To do this, successive linear fits were made until a minimum regression coefficient of 0.99 was reached.

According to the Oliver-Pharr methodology [10], it is possible to calculate the load and penetration depth values corresponding to the critical point associated with the cracking initiation, P^* and h^*.

For values (*P*, *h*) lower than the critical point, the indentation process took place without cracking. For higher values, the indentation process was characterized by the nucleation and propagation of cracks. The load-penetration depth curve for values lower than the critical one was extrapolated according to the Kick's law [18], $P = C \cdot h^2$, to the maximum penetration depth of 2000 nm, obtaining a hypothetical curve characteristic of a non cracking process. Fig. 4 shows a comparative example between the experimental indentation curve, with cracking and the hypothetical indentation curve without cracking.

Now, it is possible to apply the energetic methodology through Eq. (5) with the consideration that the strain energy associated to the cracking process, ΔU, could be obtained from the difference between the hypothetical and experimental indentation curves up to the maximum penetration depth, when the maximum crack length was reached. The indentation fracture toughness values so obtained are included in Table 2.

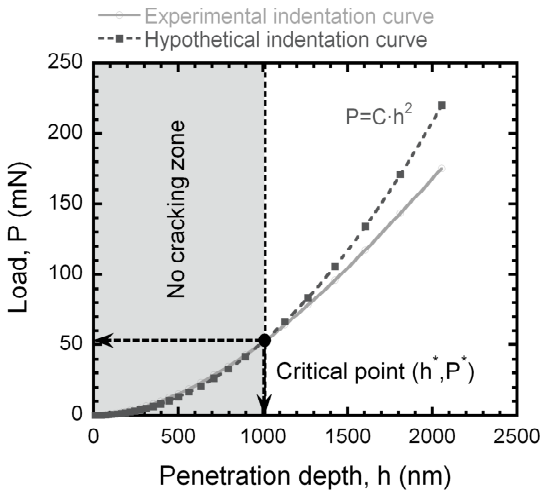

Figure 4. Indentation load versus penetration depth of experimental and hypothetical indentation curve.

5. Conclusions

In this work, an energetic methodology, adapted to depth sensing indentation, has been developed to determine the enamel fracture toughness. The method is based on the contact stiffness variation due to the cracking process. The values obtained using this methodology, were compared with those provided by traditional equations based on a particular crack pattern. The results obtained were in agreement with those reported by other authors that use traditional tests to evaluate the fracture toughness of the enamel.

References

[1] Von Koenigswald, W., Sander, P.M., 1997. Tooth Enamel Microstructure. Von Koenigswald, W., Sander, P.M., editors. Taylor & Francis publisher. 37-41 Mortimer Street, London, W1T 3JH.

[2] Eisenmann, D.R., 1998. Enamel structure. In: Oral Histology. Development, Structure and Function. AR Ten Cate editor. St. Louis, pp. 218-235.

[3] Lawn, B.R., Evans, A.G., Marshall, D.B., 1980. Elastic/plastic indentation damage in ceramics: The median/radial crack system. J. Am. Ceram. Soc. 63, 574–581.

[4] Anstis, G.R., Chantikul, P., Lawn, B.R., Marshall, D.B., 1981. A Critical Evaluation of Indentation Techniques for measuring Fracture Toughness: I, Direct Crack Measurements. J. Am. Ceram. Soc. 64, 533-538.

[5] Niihara, K., Morena, R., Hasselmann, D.P.H., 1983. A fracture mechanics analysis of indentation-induced Palmqvist crack in ceramics. J. Mater. Sci. Lett. 2, 221-223.

[6] Laugier, M.T., 1987. New formula for indentation toughness in ceramics. J. Mater. Sci. Lett. 6, 355–356.

[7] Mullins, L.P., Bruzzi, M.S., McHugh, P.E., 2007. Measurement of the microstructural fracture toughness of cortical bone using indentation fracture. J. Biomech. 40, 3285–3288.

[8] Ouchterlony, F., 1976. Stress intensity factors for the expansion loaded star crack. Eng. Fract. Mech. 8, 447-448.

[9] Li, X., Diao, D., Bhushan, B., 1997. Fracture mechanisms of thin amorphous carbon films in nanoindentation. Acta Mater. 45, 4453-4461.

[10] Oliver, W.C., Pharr, G.M., 1992. An improved technique for determining hardness and elastic modulus using load and displacement sensing indentation experiments. J. Mater. Res. 7, 1564-1583.

[11] Garrido, M.A., Giráldez, I., Ceballos, L., Gómez del Río, M.T., Rodríguez, J., 2011. Nanotribological behaviour of tooth enamel rod affected by bleaching treatment. Wear. 271, 2334– 2339.

[12] Xu, H.H.K., Smith, D.T., Jahanmir, S., Romberg, E., Kelly, J.R., Thompson, V.P., Rekow, E.D., 1998. Indentation damage and mechanical properties of human enamel and dentin. J.

Dent. Res. 77, 472–480.

[13] He, L.H., Swain, M.V., 2008. Understanding the mechanical behavior of human enamel from its structural and compositional characteristics. J. Mech. Behav. Biomed. Mater. 1, 18-29.

[14] Hassan, R., Caputo, A.A., Bunshash, R.F., 1981. Fracture toughness of human enamel. J. Dent. Res. 60, 820-827.

[15] Bajaj, D., Arola, D, 2009. On the R-curve behavior of human tooth enamel. Biomat. 30, 4037-4046.

[16] Baldassarri, M., Margolis, H.C., Beniash, E., 2008. Compositional Determinants of Mechanical Properties of Enamel. J. Dent. Res. 87, 645-649.

[17] Rasmussen, S.T., Patchin, R.E., 1984. Fracture Properties of Human Enamel and Dentin in an Aqueous Environment. J. Dent. Res. 63, 1362-1368.

[18] Kick, F., 1885. Das Gesetz der proportionalen Wiederstande und seine Anwendung, Art. Felix, Leipzig.

Study of the Mechanical Properties of Bones Under Fracture Healing Conditions with Specific Medical Treatments, Using 4 Point Bending Tests and Ultra-Micro Indentation Techniques

Soraya Diego[1], Estela Ruiz[1], José A. Casado[1], Diego Ferreño[1], Manuel Redondo[1], María I. Pérez[2], José A. Riancho[2], Isidro Carrascal[1], Claudia Demian[1], Federico Gutiérrez-Solana[1] and Christopher Vilupillai[1]

[1] Department of Materials Science University of Cantabria. 39005 Santander (Cantabria). Spain
[2] Universitary Hospital Marqués de Valdecilla. Avda. Valdecilla s/n, 39008 Santander (Cantabria), Spain
* Corresponding author: jose.casado@unican.es

Abstract This paper aims to compare the effectiveness of two medical treatments in healing an induced pseudoarthrosis (bone fracture without direct contact thus driving a callus formation) on the right femurs of Sprague Dawley laboratory rats. To further understand and quantify the mechanical effects of each treatment, the bone mechanical properties were analysed in terms of the following parameters: hardness and elastic modulus using ultra-micro indentation tests, and maximum force, energy absorbed up to maximum force and rigidity using four point bending tests.

To assess the effectiveness of the treatments in terms of mechanical performance, the results were compared against a control group and a regular bone fracture (direct contact between broken bone parts without a gap). Both treatments were successful in restoring properties similar to the control group in terms of overall hardness (in both cortical and trabecular bone tissues) and rigidity. However, one of them appears to provide higher values of maximum force, energy absorbed and bone hardness.

The results provide information that can be extrapolated to further understand the treatment of human bone fractures in terms of mechanical properties. The data enables the comparison of the outcomes that both treatments have on the biomechanical functioning of bone fractures.

Keywords pseudoarthrosis, four point bending test, ultra-micro indentation test, osseous callus

1. Introduction

Since the 1990s, several studies have been trying to transfer engineering methods to analyze biological materials [1-5]. This gave rise to one of the fundamental principles of biomechanics: the reaction of a tissue of an organism to stimuli, obeys the same laws that govern the behavior of typical “engineering” materials. Thus making applicable the methods used to measure engineering material properties to biological tissues, such as bones for example. In order to understand human bone tissues it is usual to study animal bones, as they provide an ideal biomechanical model due to their size and rudimentary functioning, simplifying the analysis of mechanical properties.

This paper compares the effectiveness of two medical treatments, “A” and “B”, on a subtraction osteotomy of Sprague Dawley rat femurs against a control group and a normal fracture. The aim of the paper is to study the effect of “A” and “B” on the healing of a subtraction osteotomy, by applying methods used for calculating engineering material properties. This investigation is complemented with other studies about biological parameters which haven´t been finished yet; for this reason it is necessary to maintain the confidentiality of the name of the treatments considered until the whole study is completed. Results were acquired through 4 point bending tests on the bone sample shafts (diaphysis) and ultra-micro indentation tests on the bone sample extremities (lower and upper extremities). The 4PBTs provided maximum force, energy absorbed up to maximum force and rigidity. The UMI tests enabled the determination of the cortical and trabecular bone hardness and elastic modulus. The data were obtained by using the left and right femurs of twelve

rats, collected in three separate occurrences once every 12 weeks. Due to the biological nature of the material, variations in the results are substantial, even between samples that have undergone identical treatments.

Assessing the effectiveness of “A” and “B” on the fracture healing of rat bones is important, as it supplies information on the viability of using such treatments for humans. Sprague Dawley rats were used because of their similarity to humans in reaction to diseases. This report provides the mechanical properties of the bones for each treatment. If a treatment is successful in providing the bone with feasible parameters, it can then be further investigated for potential human use. Although, this report is only a small step towards the process it helps to determine and document the outcomes, difficulties and considerations when using the treatments considered.

2. Methodology

2.1. Sample procurement

To acquire the data for the study, 12 female Sprague-Dawley rats were raised in identical environmental conditions (diet, temperature and humidity). The rats were randomly divided into 4 groups, to which were applied a specific medical treatment according to the weight of the animal. This study is divided into three phases, where each phase consists of 4 rats. The phases follow each other chronologically in 3-month intervals. The samples are thus harvested every 3 months. A rat provides two bone samples: its left and right femur, which is then prepared and conserved for biomechanical testing. The rats undergo a surgical procedure at approximately 6 months of age. The average age of a Sprague Dawley rat is around 2.5-3.5 years [6], at 6 months the animals have reached maturity. At the end of the 12-week treatment period, each rat was sacrificed for bone extraction. The samples of this study have been separated into four different groups: normal fracture, control group, “A” treatment and “B” treatment (Table 1).

Table 1. Sample group characterization

Sample Group Description	Label	Group Name
Normal fracture with physiological serum	F+S	Normal fracture
Subtraction osteotomy with physiological serum	OS+S	Control group
Subtraction osteotomy with “B” treatment	OS+B	“B” treatment
Subtraction osteotomy with “A” treatment	OS+A	“A” treatment

The physiological serum acts as a placebo for the normal fracture and control group, whilst providing the animals with the required nutrients. The operation procedure was the same for the OS+S, OS+A and OS+B sample groups. The surgical procedure and theoretical bone healing progression has been summarized in the sketch of Figure 1. The operation of F+S samples was similar except that there was no bone subtraction and thus no gap, as it is a simple fracture. In the operation, the rat’s skin was incised and a 2 mm section from the centre of the femur was removed, (subtraction osteotomy). Once the gap was created a stainless steel screw (2mm x 24mm) was inserted in the lower extremity of the right femur to maintain the gap. To verify that the callus was developing correctly, the animals were monitored taking x-rays of the right femurs (Figure 2: 7 days after the operation, 6 weeks after start the treatment and 12 weeks prior to the slaughter). The pictures were analized to measure the gap size (in mm) and evolution throughout the treatment. In order to conduct the biomechanical tests on the bones, they were removed from the rats by surgical procedure carried out by medical personnel. The extracted bones were conserved to avoid their deterioration through drying, in a saline solution (HBSS) at 4ºC until they were tested.

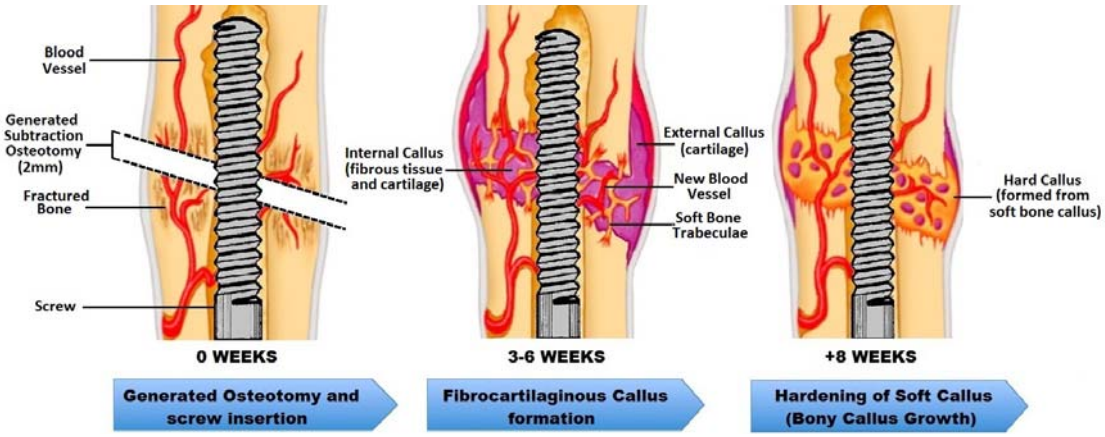

Figure 1. Sketch of the fracture healing progress throughout the study [1]

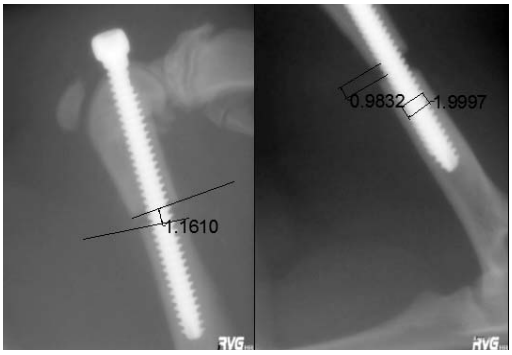

Figure 2. Gap measurement and scale verification

2.2 Four Point Bending Test (4PBT)

The bones were cleaned to remove any excess of cartilage or ligaments. Figure 3a shows the process by using a saw, a mechanical clamp and protective wrapping, to prevent any damage to the sample. Once the bone extremities had been removed (Figure 3b) they were conserved for UMI testing.

a) 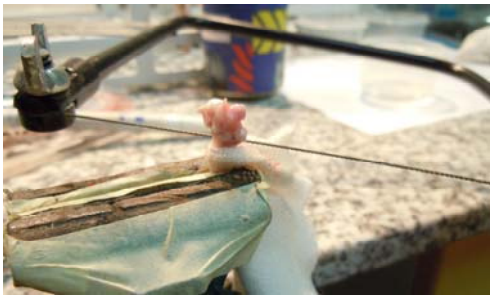 b)

Figure 3. a) Removal of bone upper extremity during sample preparation and b) final aspect

The samples were tested within 24 hours of the bone extraction to obtain the most accurate results possible. Before each test the bones were preheated to 37ºC in a saline solution to replicate the temperature in the bone's usual environment. 4PBTs were carried out on the diaphysis (shaft of the bone) using an universal testing machine (0.5 class). The sample was placed within a methacrylate container, and a water bath was set to 37°C. A pump was then positioned so that the heated serum could flow around the sample, thus recreating the in vivo conditions. Figure 4a displays the main elements of the installation.

In biomechanics, 4PBTs are important as they allow the application of a bending load to a bone shaft sample, which is generally how mid-shaft femur fractures occur [7]. During the 4PBTs the loading force was exerted by a hydraulic piston, through two points namely two cylindrical steel rods. The sample received this load whilst being laid between two cylindrical rods at 15mm apart. The load rate was 10 mm/min until the two points of the hydraulic arm reached the centre of the sample surface. Figure 4b shows the hydraulic actuator before it has reached the sample. F represents the force exerted by the hydraulic arm. In a 4PBT bone samples act as beams, the upper part of the bone being in compression and the lower part in tension. During the tests, the force-displacement graphs were obtained by collecting the numerical data obtained from the machine. These graphs enabled the determination of three mechanical properties: maximum force (F_{max}), energy absorbed up to the maximum force (E_a) and rigidity which are represented in the typical force-displacement curve obtained during a 4PBT shown in Figure 5.

a)

b) 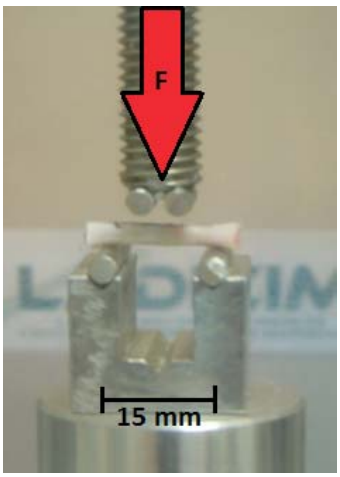

Figure 4. a) Four point bending test setup and b) Detail of bone sample about to be loaded for a 4PBT

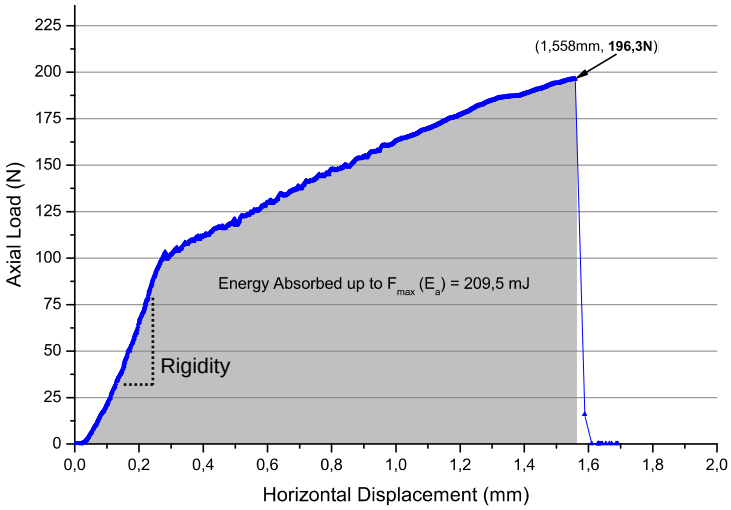

Figure 5. Typical force-displacement curve of a 4PBT

2.3 Ultra-Micro Indentation Test (UMI)

The second experiment undertaken on the samples was the UMI test, enabling the extraction of hardness [8-9] and elastic modulus parameters from the samples. The cut bone extremities were

embedded in a two-component acrylic (see Figure 6a) to provide the samples with a support that can then be used to polish the surface using an automatic grinder (see Figure 6b). The grinder holds down the sample, using suction cups, onto rotating (150 rpm) polishing plates to smooth the surface. The machine uses water as a lubricant. The polishing process is gradual being the carbide papers of the following grain sizes: 500, 1200, 2400 and 4000. Finally, a velvet disc was used to provide a smooth finish to the samples before they were tested (see Figure 6c).

a) b) c)

Figure 6. a) Embedding bone extremities in resin. b) polishing machine. c) polished bones

Once the samples were polished, they were stored in a saline solution at 5°C to avoid the exposed polished surface from deteriorating. Prior to test the samples were preheated to 37°C in a controlled saline solution bath to recreate in vivo conditions. The UMI tests were carried out using a Shimadzu DUH-211 with a pyramidal Berkovich indenter tip (see Figure 7a and 7b). The test consists of two main phases, loading up to 150 mN and then discharging. Each phase is followed by a holding period: 10 seconds for the loading and 5 seconds for the discharge. The loading and unloading rate was 2,6648 mN/sec. On each sample, both the trabecular and cortical tissues were analyzed. For each area 14 indentations were made in order to obtain the hardness and elastic modulus. The hardness calculated is defined as the ratio between the force applied by the indenter and the area left after the indentation (see Figure 7c).

a) 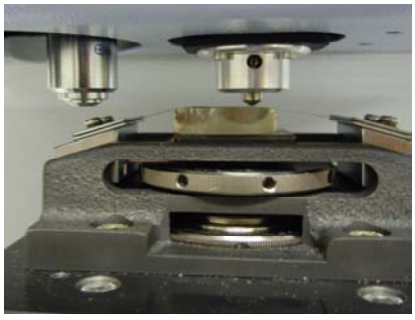 b) 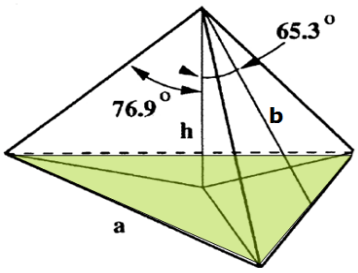

c) 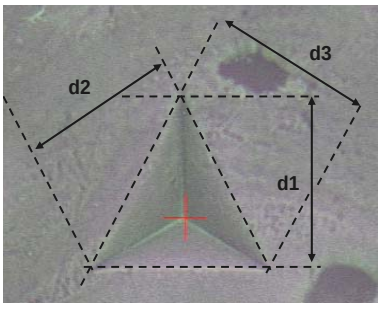

Figure 7. UMI test description. a) Machine. b) indenter tip geometry. c) projected area

A typical UMI graph is shown in Figure 8. The loading and discharge phases are clearly visible and h_f, h_r, h_s, h_c and h_m all represent specific indentation depths that occur during the test. The dashed line, with a slope S, is used to calculate the indentation elastic modulus. It intersects the x-axis at the depth h_r. Once the data was collected it was analyzed using variety of statistical tools.

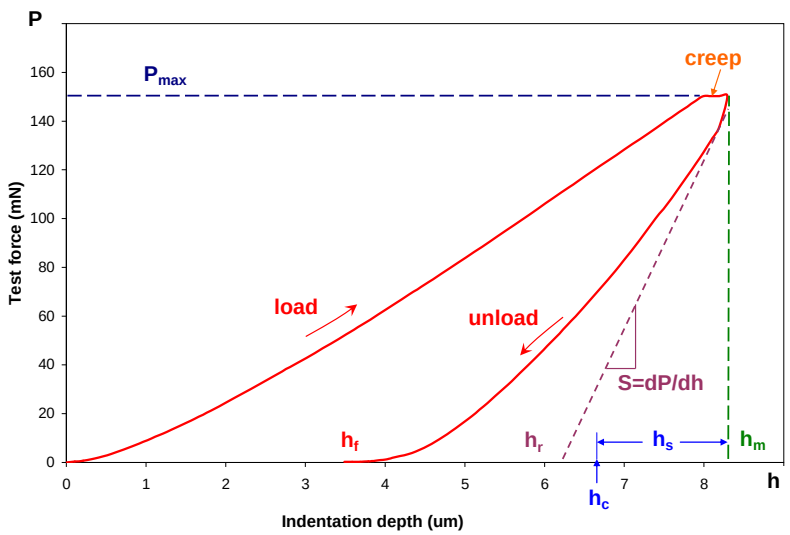

Figure 8. Typical UMI graph of force against indentation depth

3. Results and Discussion

3.1 Four Point Bending Tests

3.1.1 Maximum Force

Figure 9 shows the F_{max} values obtained. Above each sample group is the average, followed by the standard deviation and its line of proportional length. For ease of comparison, the maximum forces of both left and right femur have been included on the figure.

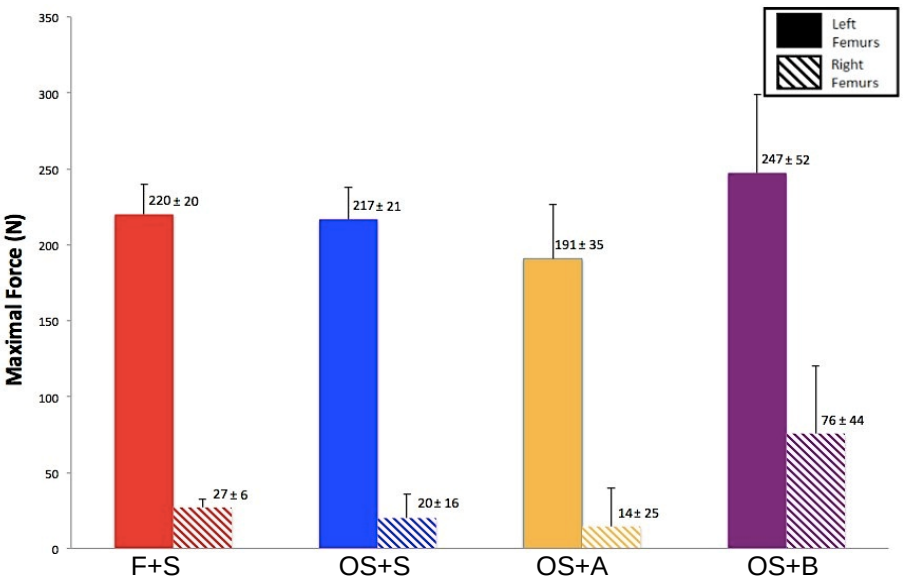

Figure 9. Bar chart displaying maximum force values and variation for each treatment

The relationship between the gap size and F_{max} confirms the effectiveness of "B" treatment over "A" treatment. Using the gap sizes (measured on the x-rays) and the F_{max} values above, the relationship between the gap size and F_{max} can be plotted using power trend lines (Figure 10).

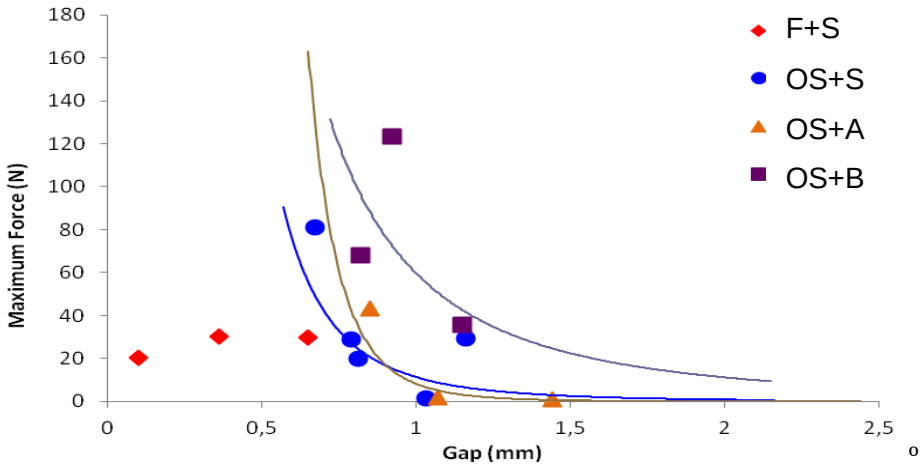

Figure 10. Relationship between F_{max} and gap size

In Figures 9 and 10, the patterns are clear in terms of the effectiveness of the treatments. Above a certain gap size (Figure 10) the "B" treatment is more effective than the "A" treatment; as for the same gap the samples require a higher F_{max}.

3.1.2 Energy Stored up to Maximum Force

The energy absorbed up to the point of maximum force (E_a) can be seen in the bar chart of Figure 11. Above each bar is the average energy absorbed and variation (standard deviation) represented numerically and by a line of proportional length.

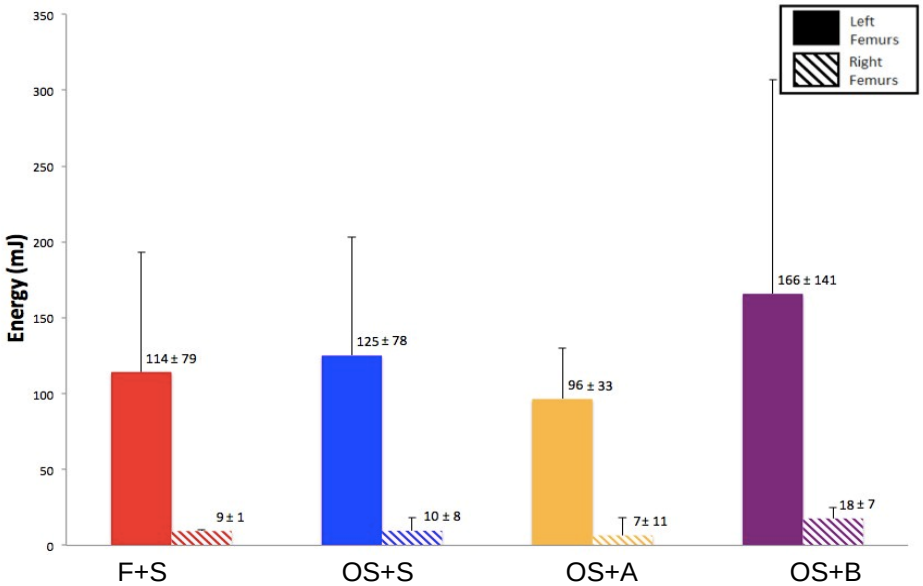

Figure 11. Energy absorbed up to maximum force

3.1.3 Rigidity

The rigidity of the samples obtained from the force-displacement curves are shown in the scatter point diagram of Figure 12. Both left and right femur data have been placed on the diagram to facilitate comparison. The average rigidity is indicated alongside the data points of each group.

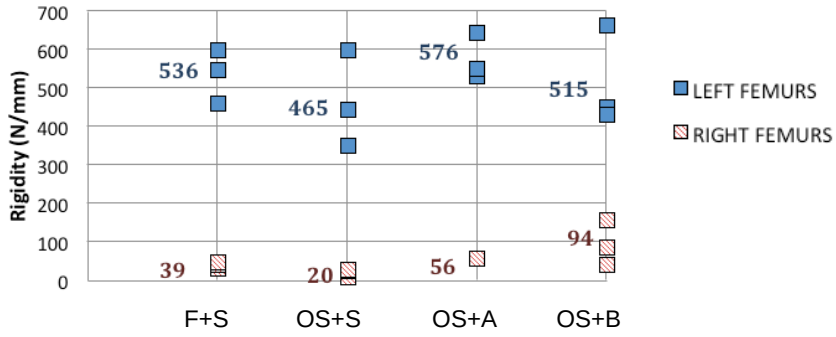

Figure 12. Scatter plot diagram of rigidity values for each sample

The values obtained for rigidity vary substantially, although there does appear to be a trend. The pattern is more evident in the right femurs, where the effect is more acute due to the subtraction osteotomy. The rigidity of the normal fracture is considerably higher than that of the subtraction osteotomy for left and right femurs. These results are expected, as a normal fracture should be more rigid than a bone that has undergone a surgical procedure (subtraction osteotomy).

3.2 Ultra-Micro Indentation Tests

3.2.1 Cortical and Trabecular Hardness

UMI tests were carried out to measure cortical and trabecular hardness. Both of the two types of tissue must be represented separately as they have different biological structure. To enable a clearer understanding Figure 13 shows the areas analyzed on the bones. There is a box plot diagram for each of the four groups, enabling a comparison of the data obtained for the same area of different samples.

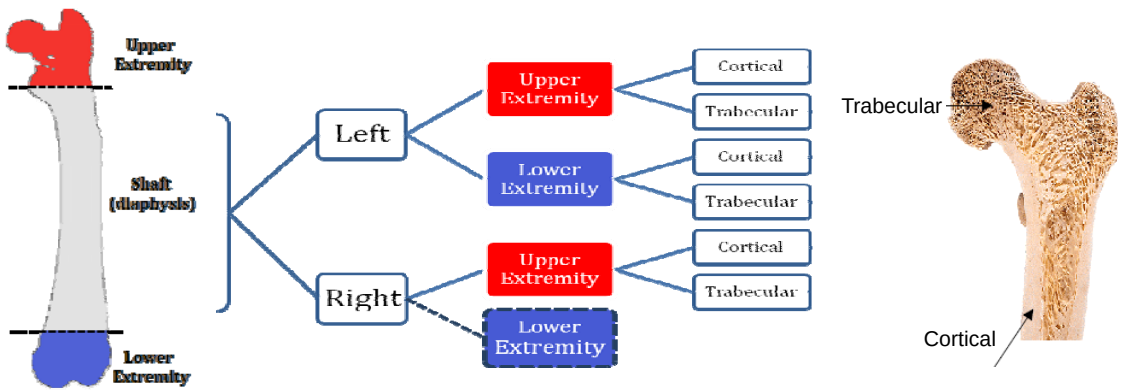

Figure 13. Diagram schematising the various areas used for hardness testing

As an example Figure 14 presents the hardness of one area depicted in Figure 13. The boxes represent the interquartile ranges (25 and 75%), the horizontal line the median and the unfilled square the mean. The whiskers are outliers. Crosses indicate the minimum and maximum points. To compare the treatments to the control group a two-sample t-test was used. The null hypothesis of this test is that the means of the two groups compared are equal. Using a level of 0.05, if the p parameter is lower than 0.05, the two sample groups compared are significantly different.

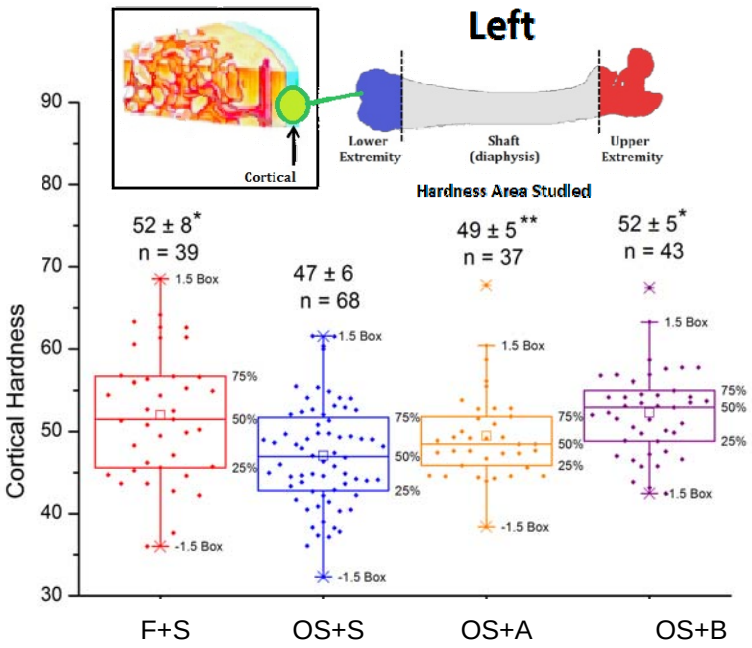

Figure 14 - Cortical hardness for the lower extremities of left femurs.
*p<0.01 for OS+S vs. F+S and OS+S vs. OS+B. **P~0.05 for OS+S vs. OS+A.

3.2.2 Elastic Modulus

The indentation elastic moduli of the left femurs are similar. Figure 15 shows the values of the right femurs and there is an obvious difference between the four groups. The cortical elastic modulus of the control group (OS+S) is lower than that of each of the treatments. In the operated bones the medical treatments increase the cortical elastic modulus to the values of a normal fracture.

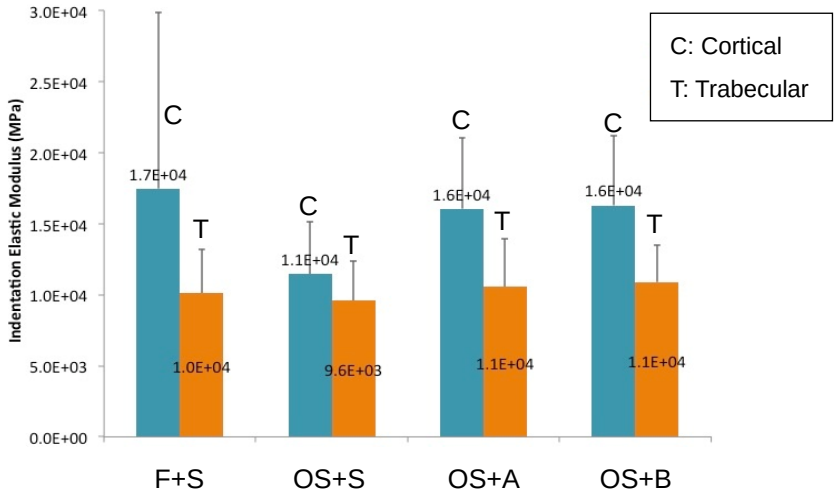

Figure 15 - Bar chart of indentation elastic modulus for right femurs

4. Conclusions

- Traditional techniques used to characterize the mechanical behavior of engineering materials can successfully be applied to biological materials. The methods used enable the comparison of the effects of the medical treatments on the mechanical properties of the material studied.

- 4PB tests results show that "B" treatment provides the highest results relating to callus resistance, toughness and rigidity. The relationship between the maximum force and the gap size for the right femurs also shows that B treatment is above that of the "A" treatment.

Treatment	F_{max} (N)	E_a (mJoule)	Rigidity ($N \cdot mm^{-1}$)
"A" (right femurs)	14	7	56
"B" (right femurs)	76	18	94

- UMI tests results show that cortical tissue is consistently harder than the trabecular bone. In both cases "B" treatment provides harder samples and is thus more effective.

Treatment	Cortical Hardness (GPa)	Trabecular Hardness (GPa)
"A" (right femurs)	0,61 ± 0,08	0,54 ± 0,05
"B" (right femurs)	0,67 ± 0,1	0,57 ± 0,06

"A" and "B" treatments provide, especially in the right operated femurs, an elastic modulus equal to that of a normal fracture.

- Examining the bone fracture healing of rat femurs in a pseudoarthrosis model, "B" treatment provides pathological bones with more suitable biomechanical properties than "A" treatment.

Acknowledgements

The authors of this work would like to express their gratitude to IFIMAV (Institute of formation and Investigation Marqués de Valdecilla) for the economical support to perform the study.

References

[1] P. Siegel. ANAT 416: Development, Disease and Regeneration, Lecture: Bone Remodelling and Fracture Repair. [Class handout]. Retrieved March 5, 2012.
[2] F. H. Netter. Musculoskeletal system: Anatomy, physiology, and metabolic disorders. Summit, New Jersey: Ciba-Geigy (1987).
[3] A. G. Robling, A. B. Castillo & C. H. Turner. Biomechanical and Molecular Regulation of Bone Remodeling. The Annual Review of Biomedical Engineering, vol. 8, (2006) 455–498.
[4] V. C. Mow & W. M. Lai. Mechanics of Animal Joints. Annual Review of Fluid Mechanics, vol. 11, p. 247. Retrieved March 28, 2012
[5] C. H. Turner & D. B. Burr. Basic biomechanical measure of a bone: a tutorial. Bone, vol. 14, (1993) 595–608.
[6] Sprague Dawley. (2001, January 31). Retrieved March 03, 2012, from http://www.sageresearchmodels.com/research-models/outbred-rats/sprague-dawley
[7] A. I. King. Fundamentals of Impact Biomechanics: Part 2. Biomechanics of the Abdomen, Pelvis, and Lower Extremities. Annual review of Biomedical Engineering, 3, (2011) 27–55.
[8] S. L., Ferreri, B. Hu & Y. Qin. Nano indentation Measurements of Viscoelastic Materials Properties are sensitive to Preparation Techniques. *Bioengineering Conference,* Proceedings of the 2010 IEEE 36th Annual Northeast. Stony Brook, New York: Stony Brook University.
[9] L. Sun et al. Evaluation of the mechanical properties of rat bone under simulated microgravity using nanoindentation. Acta Biomaterialia, vol. 5 (9) 2009.

Determination of the mechanical properties of normal and calcified human mitral chordae tendineae

José A. Casado[1], Soraya Diego[1], Diego Ferreño[1,*], Estela Ruiz[1], Isidro Carrascal[1], David Méndez[1], José M. Revuelta[2], Alejandro Pontón[2], José M. Icardo[3], and Federico Gutiérrez-Solana[1]

[1] LADICIM - University of Cantabria, E.T.S. Ingenieros de Caminos, Canales y Puertos, Spain
[2] Hospital Universitario Marqués de Valdecilla, Santander, Spain
[3] University of Cantabria, Faculty of Medicine, Spain
* Corresponding author: ferrenod@unican.es

Abstract The aim of the present research is to determine the influence of the calcification of human mitral valves on the mechanical properties of their marginal chordae tendineae. The study was performed on marginal chords obtained from thirteen human mitral valves, explanted at surgery, including six non-calcified, four moderately calcified and three strongly calcified valves. The mechanical response of the chords from the non-calcified and moderately calcified valves was determined by means of quasi-static tensile tests (the poor condition of the strongly calcified valves prevented them from being mechanically characterised). The material parameters that were obtained and analysed (the Young's modulus, the secant modulus, the proportional limit stress, the ultimate strength, the strain at fracture and the density of energy stored up to maximum load) revealed noticeable differences in mechanical behaviour between the two groups of mitral chordae tendineae. Large scatter was obtained in all cases, nevertheless, considering the mean values, it was observed that the normal chords are between three and seven times stiffer or more resistant than the moderately calcified ones. On the contrary, the results obtained for the strain at fracture showed a rather different picture as, in this case, no significant differences were observed between the two families of chords. A scanning electron microscopy study was conducted in order to find out the relevant features of the calcium deposits present in the calcified chordae tendineae. In addition, the general aspects appreciated in the stress vs. strain curves were correlated with the collagen morphological evidences determined microscopically. Finally, the calcium content present in the three groups of chords was quantitatively determined through atomic absorption spectroscopy; then, the relation between the mechanical properties of normal and moderately calcified chords as a function of its calcium content was obtained. This analysis confirmed the existence of a strong correlation between calcium content and stiffness or resistance whereas the influence on the ductility seems to be negligible.

Keywords mitral chordae tendineae, tensile test, calcium content, atomic absorption spectroscopy

1. Introduction and scope of the research

1.1. The mitral valve and the mitral chordae tendineae

The mitral valve (MV) is composed of four elements (see Fig. 1 (a)): the valve annulus, the valve leaflets (anterior and posterior), the mitral chordae tendineae (MCT) and the papillary muscles [23, 31, 13]. The MCT link the free edges and the ventricular surface of both leaflets of the MV to the papillary muscles, thus preventing the backflow of the blood into the left atrium during ventricular contraction. Several equivalent classifications for the MCT are proposed in the literature [13, 29, 12, 26, 27, 3, 20, 31, 24]. In general, the MCTs are classified according to their insertion sites on the mitral leaflets. In this sense, the anterior leaflet includes: (i) marginal chordae and (ii) strut chordae. The posterior leaflet has: (i) marginal chordae; (ii) basal chordae and (iii) commissural chordae. In Fig. 1 (b), a typical layout of MCT is shown [24, 17, 16, 13, 22, 24].

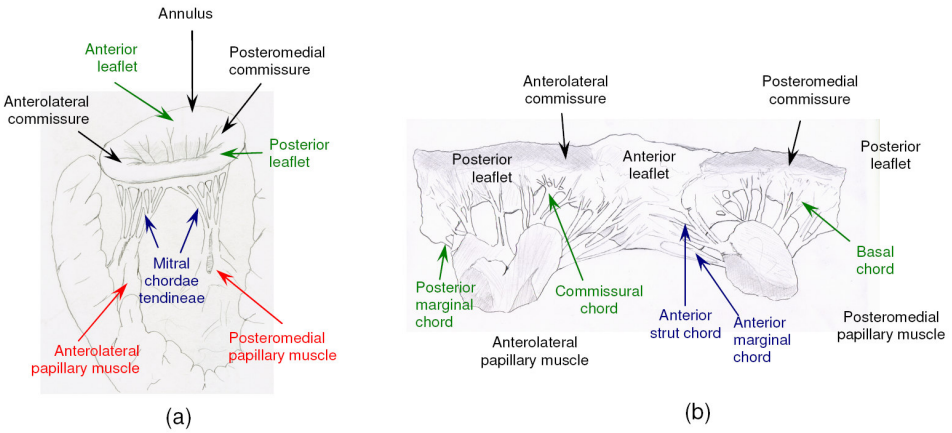

Fig. 1. Schematic drawing of the MV showing the valve leaflets, the papillary muscles and the MCT, (a), and schematic drawing of a MV as a continuous piece of tissue, (b).

1.2. Mitral valve calcification

Mitral regurgitation (MR) is the reflux of blood from the left ventricle into the left atrium during cardiac systole [4]. Carpentier et al. introduced a pathophysiologic classification of MR [2] based on the mitral leaflet motion. MR with normal motion is type I, with increased motion is type II and with restricted motion is type III. Heart valves are frequent locations of extensive calcium deposits, in particular because of rheumatic disease [19, 18, 6, 25].

1.3. Scope of the research

In this experimental study, the biomechanical properties of normal and calcified human MCT were determined. The objectives of the study are threefold: (i) to characterise (by means of quasi-static tensile tests) the mechanical behaviour of normal and calcified MCT; (ii) to quantitatively determine (through atomic absorption spectroscopy, AAS) the amount of calcium present in MCT, correlating this content with their mechanical response; (iii) to describe (through scanning electron microscopy, SEM) the relevant features associated to the fracture process and to the calcium deposits in the MCT. In the past, several studies [12, 21, 8, 16, 14, 15, 28, 10] were carried out in order to characterise the mechanical response of MCT. Nevertheless, to the knowledge of the authors, no experimental data on calcified human MCT are currently available, the present work being, therefore, the first attempt to obtain this information.

1.4. Material and methods

After receiving the approval of the Ethics Committee of the Marqués de Valdecilla University Hospital (Santander, Spain), the surgeons participating in the research provided a set of 13 human MVs. They classified the available MVs into three different groups: (i) 6 were obtained from patients (4 men and 2 women, aged between 36 and 63) who required heart transplant and whose MVs were not affected by any disease. The functional marginal MCT excised from these MVs constitute the control group of this study; (ii) 4 moderately calcified MVs and, (iii) 3 strongly calcified MVs, were obtained from patients who required valve replacement (1 man and 3 women, aged between 48 and 74 for the moderately calcified; 2 men and 1 women, aged between 54 and 79 for the strongly calcified Mvs). The overall appearance of the three kinds of mitral valves is shown in Fig. 2. The MVs provided by the surgeons were taken from the operating room to the mechanical laboratory in a portable refrigerator. The protocol proposed by Prot [22] was followed to preserve the integrity of the biological material.

(a) (b) (c)

Fig. 2. General aspect of the three kinds of MVs studied in this research: (a) a healthy MV, (b) a moderately calcified MV, (c) a strongly calcified MV

2. Experimental techniques

The MCT were excised from the MVs preserving part of the leaflets and the papillary muscle in order to facilitate the adhesion of the specimen to the set up designed to perform the tests. To avoid the slipping of the tissue from the clamps, and adequate set up was designed and fabricated. In all cases, calibrated photographs of the specimens were taken to determine the average cross-sectional area (A0) and the initial gauge length (L0) of the specimen [13]. The tensile tests were performed under displacement control conditions, applying a constant rate of 1 mm/min following the procedure described by Ritchie [24, 7]. The stress – strain curve of each test was obtained and the relevant mechanical parameters of the material were determined: the Young's modulus (E), the secant modulus (E_s), the proportional limit stress (σ_P), the ultimate strength (σ_R), the strain at fracture (ε_R) and the density of energy (energy per unit volume of the specimen) stored up to maximum load (E_a). To detect the calcium deposits in the MCT, some specimens were observed by means of SEM with a JEOL JSM 5800 scanning electron microscope. AAS technique was used to determine the concentration of calcium in some selected samples [9].

3. Experimental results

3.1. Tensile tests

The force vs. elongation curve represented in Fig. 3 (a) corresponds to a tensile test performed on one of the functional MCT analysed. The figure includes a text box with the geometric dimensions of the chord as well as some relevant points (A, B, C and D, represented as solid points). The stress vs. strain curve (engineering variables) is represented in Fig. 3 (b), where the most representative mechanical parameters are included (E, E_s, σ_P, σ_R, ε_R and E_a). This example allows the general features of the mechanical response of the MCT to be appreciated:

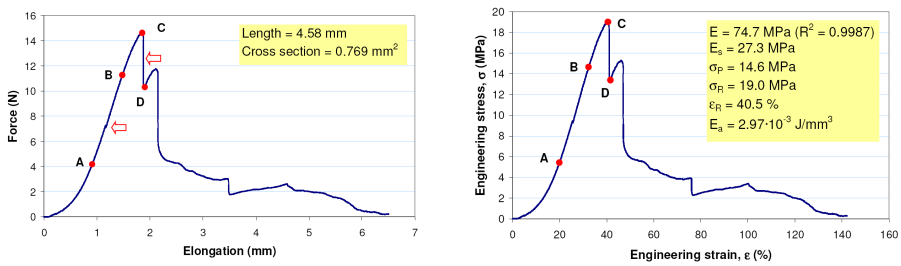

(a) (b)

Fig. 3. Typical curve of mechanical behaviour of one of the MCT, showing the relevant features: (a) force vs. elongation; (b) stress vs. strain (engineering variables)

As stated above, one of the main aims of this research consists of comparing the mechanical response of normal and moderately calcified MCT. For this purpose, in Fig. 4, the average stress-strain curves of both families are shown, including the standard deviations. Moreover, each of the datasets was represented, see Fig. 5, using a box plot.

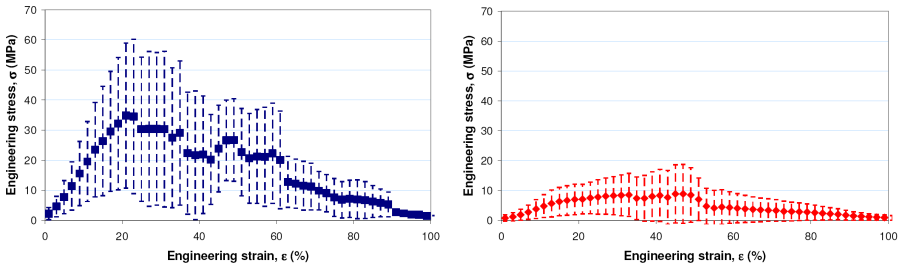

(a) (b)

Fig. 4. Average stress-strain curve for the normal, (a), and moderately calcified, (b), chordae, including the standard deviations

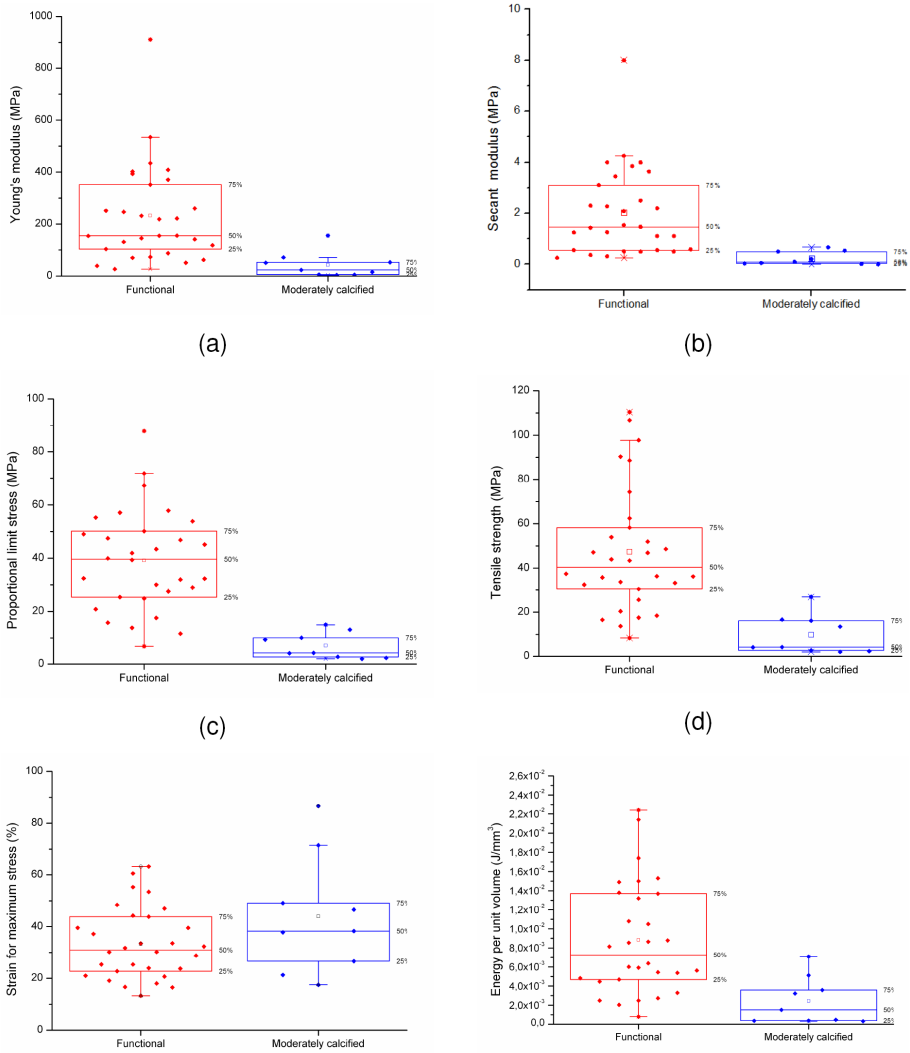

(a) (b) (c) (d) (e) (f)

Fig. 5. Box plots representing the mechanical parameters analysed for normal and moderately calcified MCT: (a) Young´s modulus; (b) secant modulus; (c) proportional limit stress; (d) tensile strength; (e) strain at fracture; (f) density of energy up to maximum load

3.2. SEM and EDS analysis

In Fig. 6, a comparison between a normal chord (a), a moderately calcified one (b) -both previously tested up to fracture- and one MCT obtained from one of the strongly calcified MVs available for the research (c), are shown.

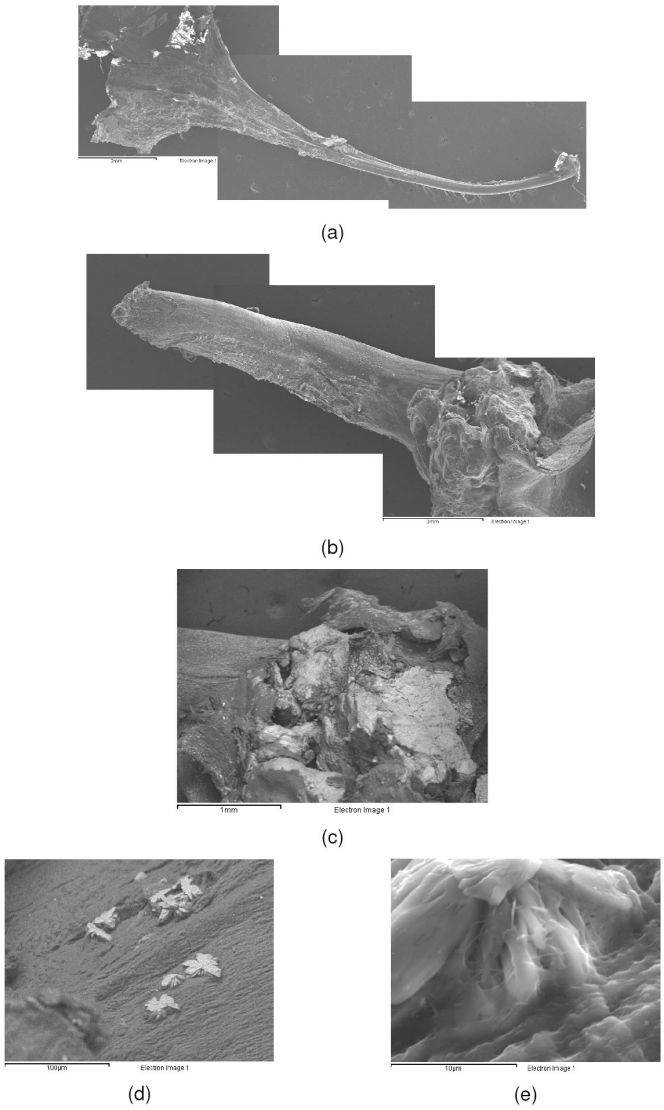

Fig. 6. Comparison through SEM between: (a) a normal, (b) a moderately calcified and (c) a strongly calcified MCT. (d) General perspective of some surface calcium deposits; (e) detail of a deposit deeply rooted in the chord.

3.3. Determination of the calcium content present in the chordae through atomic absorption spectroscopy

The calcium content of several MCT was determined through AAS. Specifically, the material analysed consisted of: (i) 15 MCT obtained from the 6 normal MVs, (ii) 8 MCT obtained from the 4 moderately calcified MVs and, (iii) 6 MCT obtained from the 3 strongly calcified MVs. The normal and moderately calcified chords were among those previously subjected to tensile tests (the two halves of each specimen were jointly analysed). The calcium content measured (expressed in terms of mg Ca / mg dry tissue) is represented in Fig. 7 (notice that a logarithm scale was used).

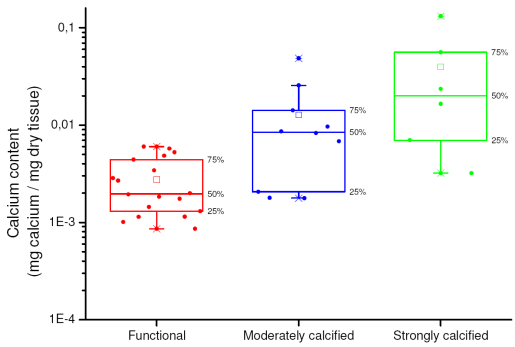

Fig. 7. Values of the calcium content measured through AAS in functional, moderately calcified and strongly calcified MCT

4. Discussion

4.1. Tensile tests

After carefully analysing the tensile curves, the following systematic characteristics were identified: i) The curves show a pronounced nonlinear behaviour in their initial region. For reduced loads, the collagen fibres are in relaxed conditions and appear wavy and crimped (Section 4.2 includes some additional microscopic information) [5, 22, 24]. ii) Next, a region of linear behaviour develops from point A to point B. The points included in this interval were used to obtain E, see Fig. 3 (b). From a microstructural point of view, the crimp patterns disappear and the collagen fibres are progressively straightened and aligned by the applied force. iii) From point B, the curve starts to bend until point C, where a sudden fracture takes place. The coordinates of point C correspond to ε_R and σ_R. iv) In general, irregularities consisting of partial unloads were observed in the experimental curves (see the arrows in Fig. 3 (a)).

Taking into consideration the information gathered in Fig. 5, the following aspects can be drawn: i) A great difference between functional and moderately calcified MCT is appreciated when the mechanical parameters related with the stiffness (E, Es) or the resistance (σ_P, σ_R or E_a) are considered. Indeed, observing the mean values of these parameters reveals that, on average, the normal MCT are between three and seven times stiffer or more resistant than the moderately calcified chords. ii) Although there is not enough information available to conduct a statistical analysis of the distribution of minimum values, the results clearly suggest that these are noticeably lower for the moderately calcified chords than for the functional ones, whenever the stiffness or resistant parameters (E, E_s, σ_P, σ_R or E_a) are being considered. iii) The results obtained for the strain at fracture, εR show a rather different picture: in this case, see Fig. 5 (e), no significant differences can be seen between normal and moderately calcified MCT.

4.2. SEM and EDS analysis

In Section 4.1, the relevant aspects of a typical stress vs. strain curve were described and explained because of the microstructural changes that take place as a MCT is stretched. In order to confirm the validity of the above mentioned explanations, several previously tested MCT were fixed in 3% glutaraldehyde, carefully opened in longitudinal direction with the help of a scalpel, and examined by SEM. In Fig. 8, a comparison between the arrangements of collagen fibres in a non-previously tested MCT (Fig. 8 (a)), and a MCT tested up to fracture (Fig. 8 (b)) is shown. In addition, several interrupted tests were conducted to examine the validity of the explanation of the sudden unloads

detected in the experimental curves. These tests consist of stretching some chords until the first unload occurs (therefore, before the final fracture); immediately after that, the test is stopped and the chord is longitudinally opened to be examined in the SEM.

4.3. Determination of the calcium content present in the chordae through atomic absorption spectroscopy

In Fig. 9, the relation between the mechanical properties of normal and moderately calcified MCT as a function of calcium content is represented (notice that a logarithm scale was used in all cases). The data included in each of the graphs were fitted through a potential law function (a linear fitting on a log-log scale) to show the trends of the different families of data. The equation of the fitting and the R-squared value are shown on a chart box. This set of figures serves to confirm some of the aspects reported previously in Section 1; thus, the influence of the calcium content is clear for the mechanical parameters E, E_s, σ_P, σ_R and E_a. In contrast, the effect of the amount of calcium on the strain at fracture, ε_R, seems to be negligible.

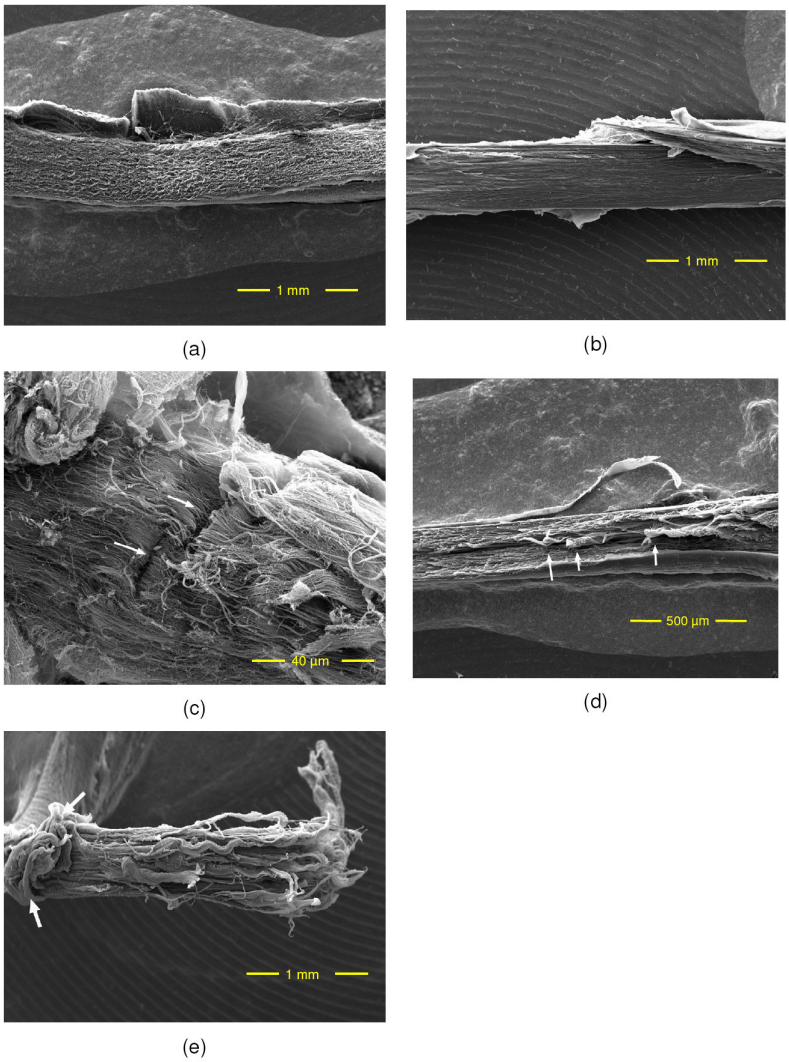

Fig. 8. SEM micrographs comparing the collagenous core of a non previously tested MCT, (a), with another chord tested up to fracture, (b). Picture (c) shows some micro-fractures detected in the collagen fibres of MCT previously subjected to interrupted tensile tests whereas in (d), the retraction of some broken fibres is appreciated (see the arrows). Micrograph (e) allows the detailed appearance of the fracture region of a MCT to be appreciated; the outer spongy layer of the chord is retracted (arrows) due to its higher elasticity.

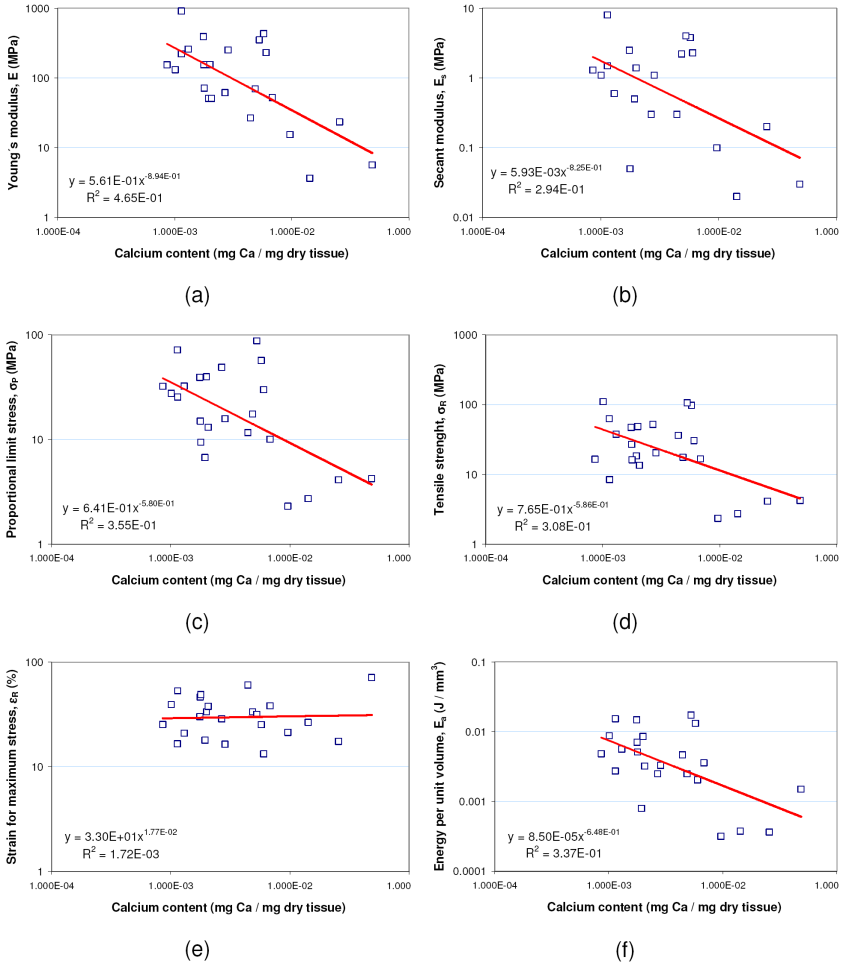

Fig. 9. Graphs representing the influence of the calcium content on the mechanical parameters analysed for normal and moderately calcified MCT: (a) Young´s modulus; (b) secant modulus, (c) proportional limit stress; (d) tensile strength; (e) strain at fracture; (f) density of energy up to maximum load.

5. Conclusions

In general, although large scatter was systematically obtained, a great difference can be observed between functional and moderately calcified MCT when the mechanical parameters related with the stiffness (Young's modulus, secant modulus) or the resistance (proportional limit stress, ultimate strength and density of energy stored up to maximum load) are considered. In contrast, no significant differences can be seen between normal and moderately calcified MCT when comparing the strain at fracture. The amount of calcium present in normal, moderately and strongly calcified chords was measured through AAS; noticeable differences in calcium content were detected between them, although large scatter was present in the results. This analysis allowed the correlation between the measured mechanical properties and the level of calcification of normal and moderately calcified chords to be established. Finally, the relevant features associated with the fracture process and the calcium deposits in the MCT were examined with the SEM. In this sense, the calcium deposits (presumably in the form of hydroxyapatite) present in the moderately and strongly calcified chords were observed; in this latter case, some deposits of deeply rooted substances were appreciated. Moreover, several previously tested MCT together with some chords subjected to interrupted tensile tests were opened and examined in the SEM. As a result, some explanatory mechanisms were proposed in order to justify the typical aspects observed in the stress vs. strain curves.

Acknowledgments

The authors wish to express their gratitude to the Instituto de Formación e Investigación Marqués de Valdecilla (IFIMAV) for their funding of the research. Moreover, the participation of J.M. Icardo was supported by grant CGL2008-04559/BOS from the Ministerio de Educación y Ciencia.

References

[1] Anyanwu, A.C., Bridgewater, B., Adams, D.H. 2010. The lottery of mitral valve repair surgery. Heart 96, 1964-1967.

[2] Carpentier, A., Chauvaud, S., Fabiani, J.N., et al., 1980. Reconstructive surgery of mitral valve incompetence: ten-year appraisal. J Thorac Cardiovasc Surg. 79, 338-348.

[3] David, T.E., Burns, R.J., Bacchus, C.M., Druck, M.N., 1984. Mitral valve replacement for mitral regurgitation with and without preservation of chordae tendineae. J Thorac Cardiovasc Surg, 88 (5 Pt 1): 718-25.

[4] Edmunds, L.H. Jr., 1997. Cardiac surgery in the adult. McGraw-Hill. New York.

[5] Fratzl, P., Misof, K., Zizak, I., Rapp, G., Amenitsch, H., Bernstorff, S.,1998. Fibrillar structure and mechanical properties of collagen. J. Struct.Biol. 122, 119-122.

[6] Fulkerson, P.K., Beaver, B.M., Auseon, J.C., Graber, H.L.,1979. Calcification of the mitral annulus: etiology, clinical associations, complications and therapy. Am J Med. 66, 967.

[7] Fung, Y.C., 1993. Biomechanics. Mechanical properties of living tissues. Springer.

[8] He, S., Weston, M.W., Lemmon, J., Jensen, M., Levine, R.A., Yoganathan, A.P., 2000. Geometric distribution of chordae tendineae: an important anatomic feature in mitral valve function. Journal of Heart Valve Disease 9. 4, 495–503.

[9] ISO 7980:1986. Water quality. Determination of calcium and magnesium. Atomic absorption spectrometric method.

[10] Jimenez, J.H., He, S., Soerensen, D.D., He, Z., Yoganathan, A.P., 2003. Effects of a Saddle Shaped Annulus on Mitral Valve Function and Chordal Force Distribution: An In Vitro Study. Annals of Biomedical Engineering. 31(10), 1171-1181.

[11] Jimenez, J.H., Soerensen, D.D., He, Z., Ritchie, J., Yoganathan, A.P, 2005. Mitral valve function and chordal force distribution using a flexible annulus model: an in vitro study. Annals of Biomedical Engineering. 33, 557-566.

[12] Kunzelman, K.S., Cochran, R.P., 1990. Mechanical properties of basal and marginal mitral valve chordae tendineae. ASAIO Transactions 36 (3), M405–408.

[13] Lam, J.H.C., Ranganathan, N., Wigle, E.D., Silver, M.D., 1970. Morphology of the human mitral valve chordae tendineae: a new classification. Circulation XLI, 449-458.

[14] Lim, K.O., Boughner, D.R., 1975. Mechanical properties of human mitral valve chordae tendineae: variation with size and strain rate. Canadian Journal of Physiology. 53, 330–339.

[15] Lim, K.O., Boughner, D.R., 1976. Morphology and relationship to extensibility curves of human mitral valve chordae tendineae. Circulation Research 39, 580–585.

[16] Lomholt, M., Nielsen, S.L., Hansen, S.B., Andersen, N.T., Hasenkam, J.M., 2002. Differential tension between secondary and primary mitral chordae in an acute in-vivo porcine model. Journal of Heart Valve Disease. 11 (3), 337–345.

[17] Millington-Sanders, C., Meir, A., Lawrence, L., Stolinski, C., 1998. Structure of chordae tendineae in the left ventricle of the human heart. Journal of Anatomy. 192, 573-581.

[18] Nair, C.K., Aronow, W.S., Stokke, K., Mohiuddin, S.M., Thomson, W., Sketch, M.H., 1984. Cardiac conduction defects in patients older than 60 years with aortic stenosis with and without mitral anular calcium. Am J Cardiol. 53, 169–172.

[19] Nair, C.K., Sketch, M.H., Ahmed, I., Thomson, W., Ryschon, K., Woodruff, M.P., et al., 1987. Calcific valvular aortic stenosis with and without mitral annular calcium. Am J Cardiol. 60,

865–870.
[20] Nielsen, S.L., Timek, T.A., Green, G.R., Dagum, P., Daughters G.T., Hasenkam, J.M., Bolger, A.F., Ingels, N.B., Miller, C., 2003. Influence of Anterior Mitral Leaflet Second-Order Chordae Tendineae on Left Ventricular Systolic Function. Circulation. 108, 486.
[21] Obadia, J.F., Casali, C., Chassignolle, J.F., Janier, M., 1997. Mitral subvalvular apparatus: different functions of primary and secondary chordae. Circulation 96 (9), 3124–3128.
[22] Prot, V. Skallerud, B., Sommer, G., Holzapfelb, G.A., 2010. On modelling and analysis of healthy and pathological human mitral valves: Two case Studies. Journal of the mechanical behaviour of biomedical Materials. 167-177.
[23] Ranganathan, N., Lam, J.H., Wigle, E.D., Silver, M.D., 1970. Morphology of the human mitral valve II—the valve leaflets. Circulation. XLI, 459–567.
[24] Ritchie, J.L., 2004. The material properties of the chordae tendineae of the mitral valve: an in vitro investigation. Ph.D. Georgia Institute of Technology.
[25] Roberts, W.C., Waller, B.F., 1981. Mitral valve "anular" calcium forming a complete circle or "O" configuration: clinical and necropsy observations. Am Heart J. 101, 619.
[26] Rodriguez, F., Langer, F., Harrington, K.B., et al. 2004. Importance of mitral valve second-order chordae for left ventricular geometry, wall thickening mechanics, and global systolic function. Circulation 14;110 (11 Suppl 1):II115-II122.
[27] Rodriguez, F., Langer, F., Harrington, K.B. et al. 2005. Effect of cutting second-order chordae on in-vivo anterior mitral leaflet compound curvature. J Heart Valve Dis 14(5), 592-601.
[28] Sedransk, K.L., Grande-Allen, K.J., Vesely, I., 2002. Failure Mechanics of Mitral Valve Chordae Tendineae. Journal of Heart Valve Disease. 11, 644-650.
[29] Virmani, R., Atkinson, J.B., Forman, M.B., Rabinowitz, A.M., 1987. Mitral valve prolapse. Hum Pathol. 18, 596–602.
[30] Votta, E., Arnoldi, A., Invernizzi, A., Ponzini, R., Veronesi, F., Tamborini, G., Pepi, M., Alamanni, F., Redaelli, A., Caiani, E.G., 2009. Mitral valve patient-specific finite element modelling from 3-D real time echocardiography: a potential new tool for surgical planning. MICCAI Workshop on Cardiovascular Interventional Imaging and Biophysical Modelling, CI2BM09.
[31] Yoganathan, A. P., Lemmon, J. D., Ellis, J. T., 2000. Hard Tissue Replacement. The Biomedical Engineering Handbook: Second Edition. Ed. Joseph D. Bronzino, Boca Raton: CRC Press LLC.

Understanding Backspatter due to Skull Fracture from a Ballistic Projectile

Raj Das[1,*], Justin Fernandez[2], Alistair Collins[1], Anurag Verma[1], Michael Taylor[3]

[1]Department of Mechanical Engineering, University of Auckland, Auckland 1010, New Zealand
[2]Auckland Bioengineering Institute, University of Auckland, Auckland 1010, New Zealand
[3]Institute of Environmental Science and Research (ESR), Christchurch 8041, New Zealand
* Corresponding author: r.das@auckland.ac.nz

Abstract In forensics, a challenge arises from relating observed evidence to the actual events. Specifically, in cranial wounds resulting from a gunshot, the study of backspatter patterns (material propagated opposite to the direction of the projectile) can provide information about the cause by linking material to the firearm, shooter or surrounding objects. Firstly, this study investigates the physics during backspatter from a high speed projectile impact by evaluating two skull simulant materials. Secondly, we evaluate the suitability of a mesh-free method called Smoothed Particle Hydrodynamics (SPH) to model the fracturing and splashing mechanism during backspatter.

The study has shown that projectile impact causes fragmentation of material at the impact site, whilst transferring momentum to fragmented particles. The particles travel along the path of least resistance, leading to partial material movement in the reverse direction of the projectile causing backspatter. The amount of backspatter depends on the strain limit of each material and how rapidly the bullet hole closes. The path of resistance is dependent on the constitutive properties of the materials. MDF was found to be a better simulant for a human skull than polycarbonate as demonstrated by the backspatter pattern. SPH was a suitable numerical method for modeling the high speed impact fracture, fragmentation during backspatter. The simulation predictions agreed well to the experimental data of medium density fiberboard (MDF).

Keywords Backspatter, cranial injury, skull simulant, impact, SPH.

1. Introduction

Wound ballistics is the study of phenomena that arises when a projectile strikes and penetrates a human or animal [1]. Due to variability in biological wounds from projectiles, computational predictions are increasingly playing a role in drawing conclusions. One important feature of wound ballistics is ‘backspatter’, a term used to describe any tissue ejected from a gunshot entrance in the opposite direction to the line of fire [2, 3]. However, while well documented, backspatter mechanics is not fully understood and involves multiple factors including transfer of kinetic energy, rapid expansion of gas, and high deformation of biological material.

Following a firearm discharge, “high velocity” blood spatter [4] is created and often characterised by a finely spattered pattern [2]. The spatter pattern is usually circular when the projectile is at right angles to the surface and a narrow elongated pattern forms when the projectile is at narrower angles [5]. These larger elongated patterns may be analysed to determine the angle of impact and origin [5, 6]. The distance travelled by backspatter is reported as highly variable in the literature. For example, close gunshots to the head of live calves produced backspatter between 0-50 cm with a maximum distance of 119 cm [6]. A case study of an atypical gunshot wound by Verhoff and Karger [7] involved a suicide where extensive backspatter was observed to travel up to 4.6 m. Physical experiments from shots to a bloodied sponge covered in a rigid material resulted in backspatter travelling 30-60 cm [2, 4].

The biological contents of backspatter include brain tissue, bone fragments, skin tissue, adipose tissues and blood. Factors affecting the pattern include muzzle to target distance, calibre of firearm [2] and anatomical location with most studies focused on the cranium.

The significance of backspatter lies in crime scene reconstruction [2]. Specifically, backspatter travels opposite to the line of fire and can therefore be deposited on the firearm, the shooter and surrounding objects. Hence, factors such as weapon type, range of shot [3], blood stain patterns on the hands of victims proving suicides [5], and homicide information may be derived [8].

A key series of experiments by German pathologist Bernd Karger stands out as the most comprehensive study of backspatter [3, 6, 9]. Nine live New Jersey calves (5-6 months old) destined for slaughter were shot in the right temple 10 cm horizontally below the right eye. Key findings included that backspatter results varied with each shot despite a controlled environment but the pattern was a consistent fine mist with every shot immediately after bullet impact. Synthetic models [2, 4] consisting of blood soaked sponges encased in outer coatings produced more reproducible baskspatter patterns, were inexpensive and avoided ethical issues. There are several case studies [7, 8, 10, 11] that describe backspatter in non-fatal human shootings, suicides, and homicides. These results can provide a specific situation to validate computational models.

The three main mechanisms that are thought to contribute to backspatter include; (i) subcutaneous gas effects; (ii) temporary cavitation related to intracranial pressure; and (iii) tail splashing. In general, a combination of all three factors may cause backspatter. Subcutaneous gas effects result from pressurized gases during the muzzle discharge [12]. During close range shots the pressurised muzzle gases enter the wound produced by the bullet and become trapped in the subcutaneous space between the skin and skull. This causes ‘starburst or stellate’ entrance wounds in what is known as a ‘blow-out’ effect where the skin mushrooms and a pocket is created under the skin [2, 9]. The hot, pressurised gases expand within this pocket space and create a backwards streaming of gas escaping ou oft the entrance wound. The accelerating force from the escaping gas drives blood and soft tissue opposite to the direction of fire [2, 4, 9].

Temporary cavitation related intracranial pressure occurs as a bullet passes through a medium creating a temporary cavity in its wake, a feature of all missile wounds [13]. In the case of a bullet wound to the head, a large temporary cavity would be created because of the low retentive forces of brain tissue [13]. The brain is contained within the rigid skull, and therefore as a temporary cavity expands a high pressure is created within the cranium. The high pressure within the cranium and the subsequent collapse of the temporary cavity creates a force to drive tissue and blood back out the entrance wound [7, 9]. Karger proposed that anatomical structures similar to liquid filled cavities provide the best conditions for temporary cavitation [14]. Fackler [15] believed that the collapse of a temporary cavity is the only mechanism that creates backspatter.

The phenomenon of ‘tail-splash’ is the backwards streaming of destroyed material or fluid along the lateral surface of a high velocity bullet as it penetrates a dense medium [9, 13, 14]. Karger [14] suggested that ‘tail-splash’ occurs when a bullet penetrates the brain and lateral streaming of brain matter and blood occurs towards the line of fire. This is most closely related to the mechanism evaluated in this study.

There have been numerous computational studies of high velocity impacts related to ballistics, but little research has been conducted related to backspatter. Finite element analysis (FEA) of ballistic helmet impacts and the effect on the human cranium [16, 17] stresses within the head and brain were used to evaluate the performance of a helmet. FEA studies have simulated particle projectiles in the opposite direction to the line of fire [18-20], which would appear to be backspatter. These are projectile impacts to human bones, namely the parietal bone of the skull [18] and the mandible (jaw) bone [19, 20]. The use of FEA provided good results when compared to experimental data with the relatively simple material models used. Backspatter or its significance was not the focus of those studies. A further FEA study to recreate the wounding that occurred in an actual death [21]

suggested that computer prediction is a useful tool for testing the physics of human ballistic wounding. Many of these studies used LS-DYNA software as the FEA solver [16, 17, 19, 20, 22], and Smooth Particle Hydrodynamics (SPH) [22, 23] was also shown to be useful.

Physical experiments can play crucial roles and are essential to understand the complex mechanisms, characterise the associated material behaviour during backspatter, and validate the computational models. For example, the constitutive relations of biological materials, specifically under high strain rates, are often not known, and need to be determined experimentally. In relation to backspatter, the scope and extent of experiments with animals or animal parts are limited because of ethical and practical reasons. Hence there is an urgent need to develop alternative (simulant) material that will enable conducting large number of experiments to understand backspatter and its relationship to the actual events. The key criterion of simulant material is their properties either individually or in combination need to be close to the biological material (skull, tissue, fluid, etc) relevant to backspatter, and thus they are expected to demonstrate similar events under backspatter conditions. This study focuses on understanding the mechanisms of backspatter and evaluates two simulant materials for human skulls to rate their usefulness as a synthetic material for forensic investigations. Secondly, we evaluate the suitability of a mesh-free method called Smoothed Particle Hydrodynamics (SPH) to model the splashing mechanism during backspatter using a medium density fiberboard (MDF) panel, which is compared to the identical experiment.

2. Approach and Methodology

Ballistic experiments were conducted at The Royal New Zealand Police College shooting range in the presence of trained firearms experts. The experimental setup is shown in Fig. 1. In the first experiment a series of 100 × 100 mm^2 panels made of Medium density fiberboard (MDF) and Polycarbonate (PC) materials were tested. MDF is made up of wood fibers combined with a resin, and made into panels by applying high pressure and temperature. Polycarbonate was also chosen as the material as it is not brittle and thus would not shatter as a result of projectile impact.

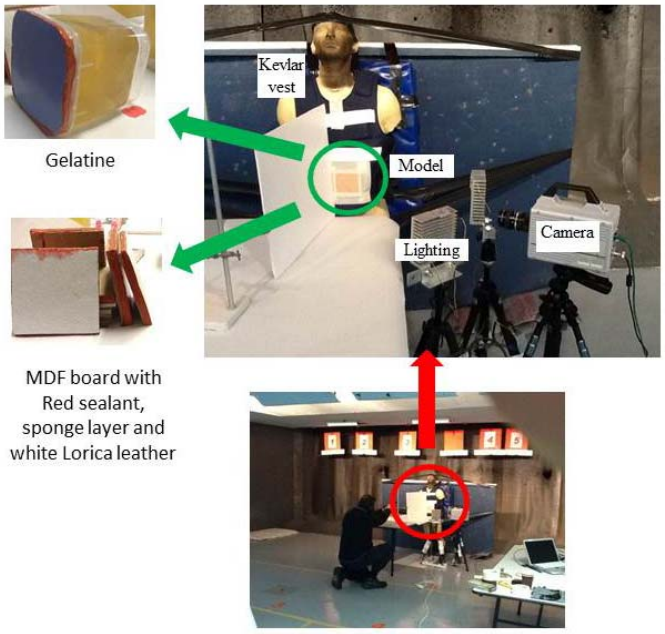

Figure 1. Experimental setup: the physical model was placed on a Kevlar vest with halogen lighting and recorder using a high speed camera.

The assembled physical models were attached to a Kevlar bullet proof vest on a dense foam testing

dummy. The vest and testing dummy was taped to a large flat board to support it and keep the midriff area of the dummy perpendicular to the ground. A table was placed in front of the dummy and the centre of the models taped to the vest 25 cm above the table surface. A 9 mm calibre handgun was used in the experiment with Magtech 9 mm luger centerfire full metal jacket ammunition. The models were shot from a distance of 1 m and fired from a position perpendicular to the model surface. The experiment was filmed with a SA1 high-speed digital video camera with a 55 mm lens and capture rate of 16000 fps. The lighting was achieved with three 1000 W quartz halogen lamps. A large white plastic board was held by clamps behind the model. This board acted as a light reflector to increase the brightness and track the backspatter from the models. Large white sheets of blotch paper were attached for each experiment to the table in front of the models, the plastic board reflector, and the ground immediately around the setup. This was so the spattered particles could be observed and recorded.

3. Computational Simulation

Conventional FEA is not suitable for high impact fracture simulations due to a number of factors including capturing the natural crack initiation and propagation, separation of failed elements, maintaining the integrity of elements in highly non-linear deformations, and capturing highly fragmented filamentary crack paths [24]. Consequently, Smooth Particle Hydrodynamics (SPH) was adopted as a suitable method due its mesh free nature. SPH solves a system of partial differential equations with the domain discretised into a series of particles that represent specific material volumes. SPH modelling has been successfully applied to fluid flow problems in the past. More recently there has been a growing interest in modelling solid deformation problems with SPH [24-29]. SPH is ideally suited to modelling the backspatter from a projectile impact due to its proven ability in modelling fractured discrete structures and damage evolution.

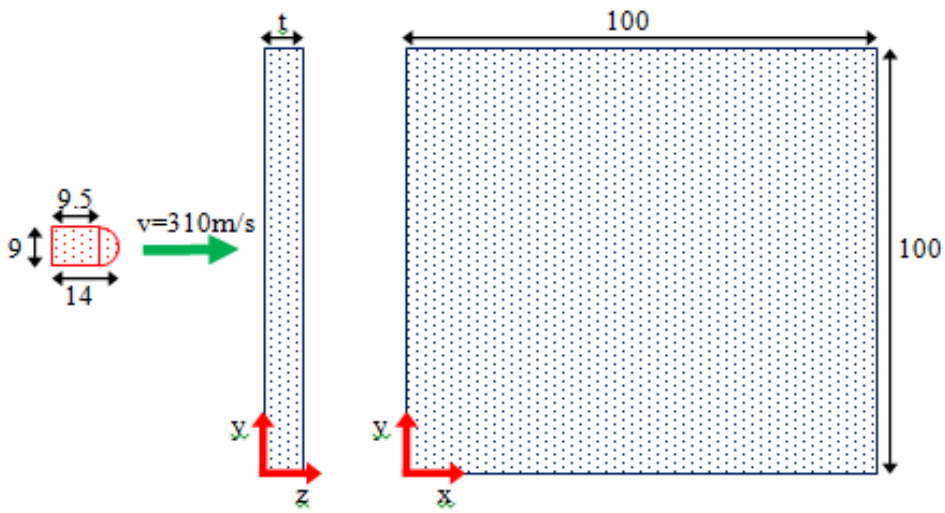

Figure 2. Computational simulation configuration (dimensions in mm, not drawn to scale)

Table 1. Material properties for MDF and polycarbonate used in the computational model

Material	Density	Shear Modulus	Yield Stress	Bulk Modulus	Failure Strain	Reference
MDF	750 kg/m^3	1357 MPa	42 MPa	2778 MPa	0.5%	[30, 31]
Polycarbonate	1190 kg/m^3	785 MPa	62 MPa	3010 MPa	100%	[32]

The computational model was setup as shown in Fig. 2. A panel of dimension 100 × 100 mm^2 was rigidly fixed at its edges and is impacted by a projectile at its centre. The projectile/bullet shape was simplified as a cylinder, 9 mm in diameter and 9.5 mm long with a semi-hemisphere of radius 4.5 mm at the end. The initial velocity of the bullet was set to 310 m/s. The computational model was simulated for 6 ms after the bullet impact. Both the panel and projectile were discretised with a particle spacing of 1 mm. A particle convergence (equivalent to mesh convergence in FEA) analysis using the von Mises stress showed that the stress varied by less than 2% with a change in model resolution from 1.25 to 1 mm particle spacing, establishing the resolution of 1 mm was sufficiently accurate. Depending on the thickness, the SPH panel was made up of between 61,206 - 71,407 particles and the projectile contained 1,246 particles. The projectile was modelled as solid copper with a Johnson Cook plasticity model [33]. MDF and polycarbonate were modelled using the material properties in Table 1. The model was solved using the LS-DYNA SPH solver.

4. Results

4.1 High speed impact tests

High speed photographs of a representative example of MDF and PC tested are given in the following section. The behaviour of the simulant materials and the associated advantages and disadvantages in relation to simulating backspatter are summarised in Table 2. For each material, two samples were tested, denoted by MDF1 and MDF2 for the Medium density fiberboard samples, and PC1 and PC2 for the Polycarbonate samples.

Fig. 3 shows the fracture pattern for MDF panels. Small particles (1-2 mm in size) were observed to travel in the direction opposite to the line of fire for both tests. Particles emerged in a radial cone shape with most debris travelling in the upwards direction (Fig. 3c-d). Smaller particles travelled away from the model, whilst larger particles and fragments remained in the region of impact (Fig. 3c). The time for the initial splashing backspatter to occur after bullet impact was 0.28 ms. The backspatter continued to expel from the hole for 6.35 ms. The size of the entrance hole was 9.0 mm with no evidence of radial cracking from the impact site. Large fragments of MDF fractured off leaving damage areas of around 15 mm in diameter at the exit site. Observation of the blotch paper revealed a majority of spattered material was located between 0.5 - 1 m from the model setup.

Two plain 4.5 mm polycarbonate panels as the skull simulant were also tested with PC1 highlighted in Fig. 4. The projectile induced a concave bend in the entire panel. A local radial wave travelled outwards to the edges of the panel 0.19 ms after impact in both cases. Following this the entire panel vibrated sending ripples through the panel. No backspatter was observed for PC panels. The entrance hole was much larger for polycarbonate compared to that observed for MDF.

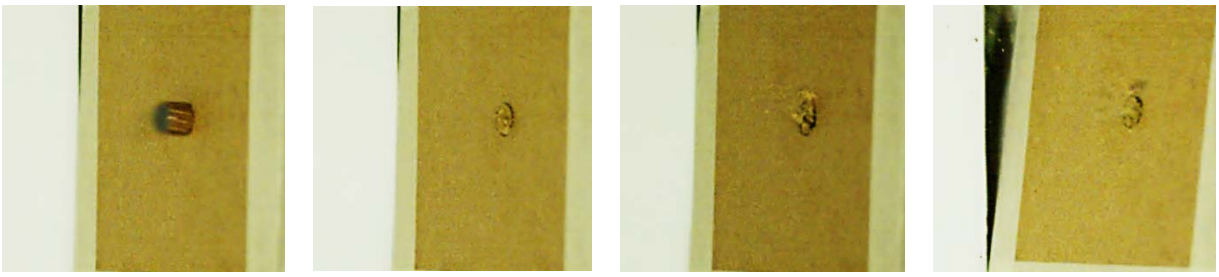

(a) 0 ms (b) 0.25 ms (c) 1 ms (d) 4 ms

Figure 3. Fracture pattern and backspatter due to projectile impact on MDF (MDF1)

Table 2. Advantages and disadvantages of materials as simulants for human skulls

Material	Advantages	Disadvantages
MDF as a skull/bone simulant	MDF behaves in a brittle manner similar to human bones. MDF produces material backspatter under a high velocity projectile impact. Bone is known to produce similar backspatter [3, 34].	There was no fracture of MDF other than in the area immediately around projectile impact. Fracture lines and cracks are often seen to radiate out from the impact site of a projectile as happens in a skull/bone [35].
Polycarbonate as a skull/bone simulant	There are limited advantages of polycarbonate as a bone simulant.	Polycarbonate did not produce any material backspatter on impact, and there was no material fracture in the form of cracking. The ductile nature of polycarbonate makes it a poor simulant for bone.

(a) 0 ms (b) 0.25 ms (c) 1 ms (d) 4 ms

Figure 4. Deformation behaviour during projectile impact on polycarbonate (PC1)

4.2 Computational SPH model of MDF panels

Next we developed a computational model to simulate backspatter using the SPH method. To evaluate the suitability of SPH as an efficient method to capture the impact fracture, fragmentation, post-impact particulate ejection, we simulated the impact of a projectile into a 6 mm MDF panel. Fig. 5 shows the evolution of von Mises stress (left column) and plastic strain (right column) of the plate at various times after the projectile impact. Particle colouring represents a range of 0-20 MPa for von Mises stress and 0-0.5 (failure strain) for plastic strain.

On impact (Fig. 5a) high impact stresses are generated around the projectile tip leading to fracture at the impact point (shown by red particle dispersion). The stressed zone expand radially but are not large enough to produce failure (only 4-12 MPa), and no plastic deformation is noticed outside the fracture site (Fig. 5b). The stress waves reach the plate boundaries, reflect and then dampen. Some fragmented particles at impact have now moved away from the impact site in the opposite direction of the projectile motion leading to backspatter (Fig. 5c-d). The majority of particles clump and fall at the impact site. Failure is only predicted at the impact site.

The SPH model prediction was then compared against the equivalent MDF experiment. Fig. 6 compares the fracture pattern and particle movements against the SPH prediction. Backspatter predictions at 1 and 4 ms show particle movement over a similar distance to the experiment. This means that the velocity of the particles would also be similar. The pattern of spray is also similar representing a 3D cone pattern. The predicted entrance site is also similar to that of the experiment and no fracture is observed away from the impact site in both modelling and experiment.

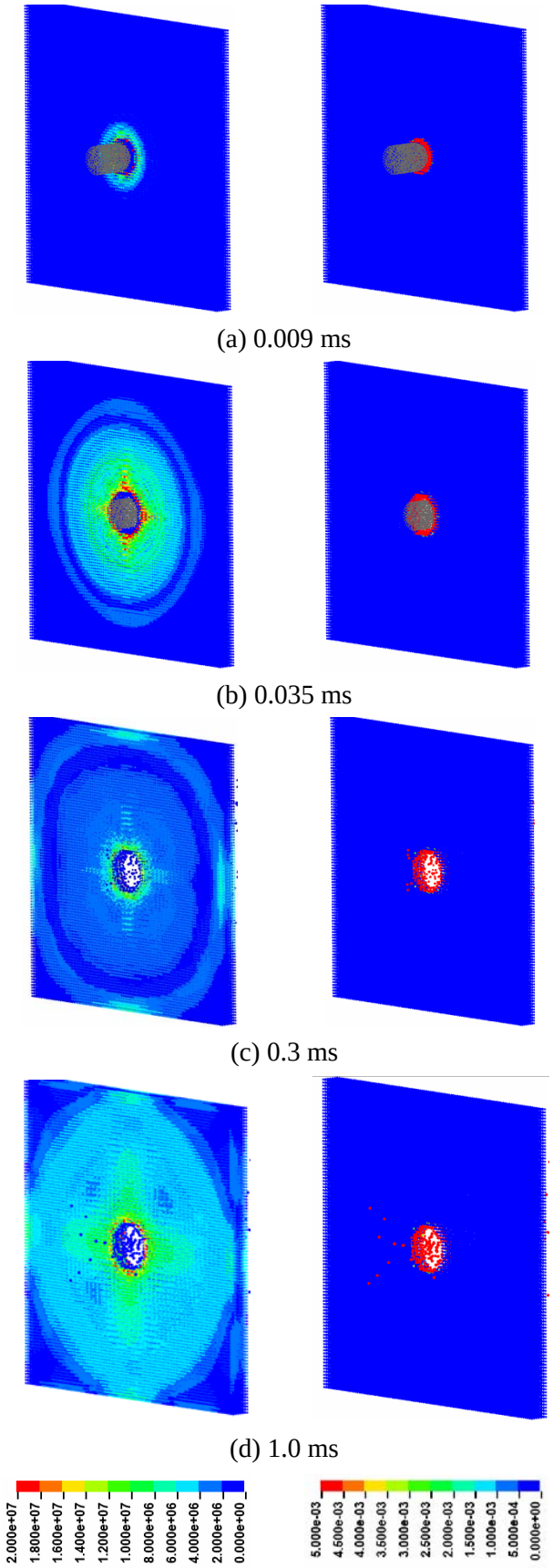

Figure 5. SPH simulation of projectile impact on MDF, left: coloured by von Mises stress (0 - 20 MPa), and right: coloured by plastic strain (0 - 0.006)

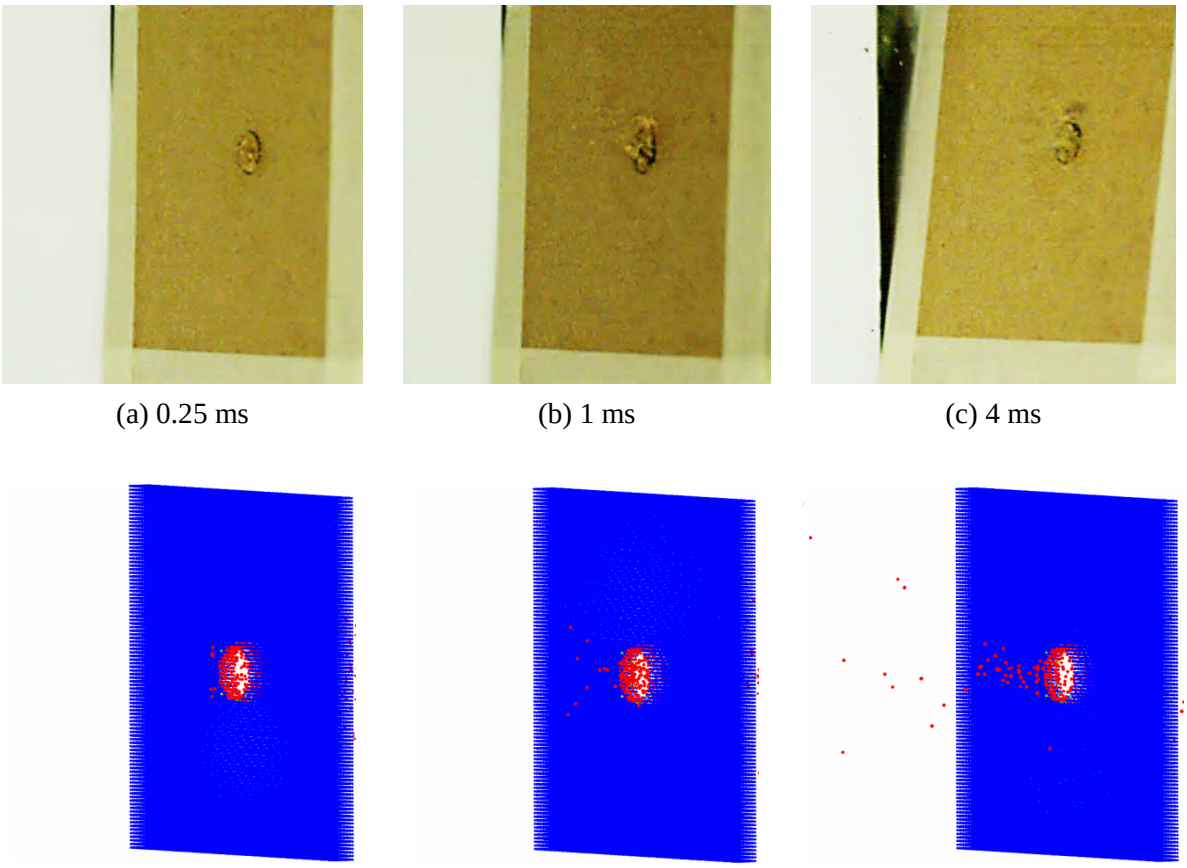

(a) 0.25 ms (b) 1 ms (c) 4 ms

(d) 0.25 ms (e) 1 ms (f) 4 ms

Figure 6. Comparison of experimental (a-c, physical model MDF-1) and computational (d-f) results of projectile impact on MDF (d-f: coloured by plastic strain, red=0.5%)

5. Discussion and Conclusions

The study has shown that projectile impact causes fragmentation of material at the impact site, whilst transferring momentum to fragmented particles. The particles travel along the path of least resistance, leading to partial material movement in the opposite direction of the projectile motion, which is known as backspatter. The amount of backspatter depends on the strain limit of each material and the closure time of the initial projectile hole.

SPH was shown to be an ideal numerical method for handling the high impact fragmenting nature of the materials, and the predictions compared well to the experimental data of medium density fiberboard (MDF). Results were also noted to be highly dependent on the constitutive laws. Specifically, the MDF impact fracture results suggest that energy from the projectile causes material at the impact site to fail in a brittle manner with fracture into small particles. Momentum is transferred from the projectile to the particles with the majority of fragments travelling in the original projectile direction. However, for a proportion of the fragments the entrance site acts as the path of least resistance causing material movement axially backwards. This is similar to the tail-splashing mechanism that is postulated as a mechanism of backspatter from a cranial gunshot [9, 13, 14]. The other potential skull simulant, polycarbonate, has a high failure strain and good impact resistance, compared to a real skull, leading to a lack of backspatter and no significant material fracture. Bullet impact in human bones is known to leave a clear hole and shows radial facture [35] suggesting that polycarbonate is not a suitable simulant for human bone or skull.

This is the first study to use SPH to study backspatter in ballistic impacts. The SPH model

simulated the backspatter particle speed, timing and spray pattern consistent with the same experiment.

Finally from the materials we tested, MDF was found to be best suited to simulating skull/bone. MDF is a better simulant material for skull than polycarbonate under high velocity projectile impact. MDF displays similar brittle properties to bone and produced backspatter. Polycarbonate was very ductile with limited material fracture thus was not a good simulant for bone.

Future work will focus on extending the model to multiple layers and ductile materials. This can be extended to include biological material with an anatomically based human or porcine model. Other mechanisms such as intracranial overpressure and the subcutaneous gas effect have also been theorised. A computational model could be further extended to simulate these mechanisms of backspatter. This would create a more complete model of what happens in reality. This research is thus an important step towards creating a tool to help forensic scientists accurately recreate crime scenes and provide evidence that leads to justice in serious crime investigations.

References

[1] R.M. Coupland, M.A. Rothschild, M.J. Thali, B.P. Kneubuehl, R.M. Coupland, M.A. Rothschild, and M.J. Thali, Introduction to Wound Ballistics. ed. B.P. Kneubuehl: Springer Berlin Heidelberg 2011, pp. 1-2.

[2] B.G. Stephens, and T.B. Allen, Back Spatter of Blood from Gunshot Wounds - Observations and Experimental Simulation. Journal of Forensic Sciences, vol. 28 (2) (1983). pp. 437-439.

[3] B. Karger, R. Nusse, and T. Bajanowski, Backspatter on the Firearm and Hand in Experimental Close-Range Gunshots to the Head. The American Journal of Forensic Medicine and Pathology, vol. 23 (3) (2002). pp. 211-213.

[4] J.O. Pex, and C.H. Vaughan, Observations of High Velocity Bloodspatter on Adjacent Objects. Journal of Forensic Sciences, vol. 32 (6) (1987). pp. 1587-1594.

[5] K. Yen, M.J. Thali, B.P. Kneubuehl, O. Peschel, U. Zollinger, and R. Dirnhofer, Blood-Spatter Patterns: Hands Hold Clues for the Forensic Reconstruction of the Sequence of Events. American Journal of Forensic Medicine and Pathology, vol. 24 (2) (2003). pp. 132-140.

[6] B. Karger, R. Nusse, H.D. Troger, and B. Brinkmann, Backspatter from Experimental Close-Range Shots to the Head II- Microbackspatter and the Morphology of Bloodstains. International Journal of Legal Medicine, vol. 110 (1997). pp. 27-30.

[7] M.A. Verhoff, and B. Karger, Atypical gunshot entrance wound and extensive backspatter. Int J. Legal Med., vol. 117 (2003). pp. 229-231.

[8] M. Kleiber, D. Stiller, and P. Wiegand, Assessment of shooting distance on the basis of bloodstain analysis and histological examinations. Forensic Science International, vol. 119 (2001). pp. 260-262.

[9] B. Karger, R. Nusse, G. Schroeder, S. Wustenbecker, and B. Brinkmann, Backspatter from Experimental Close-Range Shots to the Head I-Macrobackspatter. International Journal of Legal Medicine, vol. 109 (1996). pp. 66-74.

[10] M.J. Thali, K. Yen, P. Vock, C. Ozdoba, B.P. Kneubuehl, M. Sonnenschein, and R. Dirnhofer, Image-guided virtual autopsy findings of gunshot victims performed with multi-slice computed tomography and magnetic resonance imaging and subsequent correlation between radiology and autopsy findings. Forensic Sci Int, vol. 138 (1-3) (2003). pp. 8-16.

[11] S.A. Padosch, R.B. Dettmeyer, C.W. Schyma, P.H. Schmidt, and B. Madea, Two simultaneous suicidal gunshots to the head with robbed police guns. Forensic Science International, vol. 158 (2-3) (2006). pp. 224-228.

[12] M.C. Taylor, T.L. Laber, B.P. Epstein, D.S. Zamzow, and D.P. Baldwin, The effect of firearm muzzle gases on the backspatter of blood. International Journal of Legal Medicine, vol. (2010). pp. 1-12.

[13] J.J. Amato, L.J. Billy, N.S. Lawson, and N.M. Rich, High Velocity Missile Injury: An Experimental Study of the Retentive Forces of Tissue. The American Journal of Surgery, vol. 127 (1974). pp. 454-459.
[14] B. Karger, Forensic Ballistics. *Forensic Pathology Reviews* 5 2008 pp. 139-172.
[15] Evaluating Impact Spatter Bloodstains. In *Bloodstain Pattern Analysis with an Introduction to Crime Scene Reconstruction, Third Edition*: CRC Press 2008, pp. 199-229.
[16] M. Aare, and S. Kleiven, Evaluation of head response to ballistic helmet impacts using finite element method. International Journal of Impact Engineering, vol. 34 (2007). pp. 596-608.
[17] J. Yang, and J. Dai, Simulation-Based Assessment of Rear Effect to Ballistic Helmet Impact. Computer-Aided Design & Applications, vol. 7 (1) (2010). pp. 59-73.
[18] A. Mota, S. Klug, M. Ortiz, and A. Pandolfi, Finite-element simulation of firearm injury to the human cranium. Computational Mechanics, vol. 31 (2003). pp. 115-121.
[19] Z. Tang, W. Tu, G. Zhang, Y. Chen, T. Lei, and Y. Tan, Dynamic simulation and preliminary finite element analysis of gunshot wounds to the human mandible. Injury, Int J. Care Injured, vol. 43 (2012). pp. 660-665.
[20] Z. Tang, Z. Zhou, G. Zhang, Y. Chen, T. Lei, and Y. Tan, Establishment of a three-dimensional finite element model for gunshot wounds to the human mandible. Journal of Medical Colleges of PLA, vol. 27 (2012). pp. 87-100.
[21] J. Raul, C. Deck, F. Meyer, A. Geraut, R. Willinger, and B. Ludes, A finite element model investigation of gunshot injury. International Journal of Legal Medicine, vol. 121 (2007). pp. 143-146.
[22] N. Kilic, and B. Ekici, Ballistic resistance of high hardness armour steels against 7.62mm armor piercing ammunition. Materials and Design, vol. 44 (2013). pp. 35-48.
[23] M. Lee, and Y.H. Yoo, Analysis of ceramic/metal armour systems. International Journal of Impact Engineering, vol. 25 (2001). pp. 819-829.
[24] R. Das, and P.W. Cleary, Effect of Rock Shapes on Brittle Fracture using Smooth Particle Hydrodynamics. Theoretical and Applied Fracture Mechanics, vol. 53 (2010). pp. 47-60.
[25] L.D. Libersky, and A.G. Petschek, Smooth particle hydrodynamics with strength of materials. In *Advances in the Free-Lagrange Method*, ed. Trease and Crowley, Berlin: Springer 1990,
[26] J.P. Gray, J.J. Monaghan, and R.P. Swift, SPH elastic dynamics. Computer Methods in Applied Mechanics and Engineering, vol. 190 (49-50) (2001). pp. 6641-6662.
[27] R. Das, and P.W. Cleary, Effect of rock shapes on brittle fracture using Smoothed Particle Hydrodynamics. Theoretical and Applied Fracture Mechanics, vol. 53 (1) (2010). pp. 47-60.
[28] R. Das, and P.W. Cleary, A mesh-free approach for fracture modelling of gravity dams under earthquake. International Journal of Fracture, vol. 179 (1-2) (2013). pp. 9-33.
[29] S. Karekal, R. Das, L. Mosse, and P.W. Cleary, Application of a mesh-free continuum method for simulation of rock caving processes. International Journal of Rock Mechanics and Mining Sciences, vol. 48 (5) (2011). pp. 703-711.
[30] A.W.P.A. Incorporated, EWPAA Facts about Particleboard and MDF. 2008.
[31] H. van Dyk 2008. Development of a Wood Fiber Composite using Nonwoven Textile Technology. North Carolina State University.
[32] J.E. Mark, Polymer Data Handbook. Second. Oxford University Press, 2009.
[33] G.R. Johnson, and W.H. Cook, Fracture characteristics of three metals subjected to various strains, strain rates, temperatures and pressures. Engineering Fracture Mechanics, vol. 21 (1) (1985). pp. 31-48.
[34] B.R. Burnett, Detection of Bone and Bone-Plus-Bullet Particles in Backspatter from Close-Range Shots to Heads. Journal of Forensic Science, vol. 36 (6) (1991). pp. 1745-1752.
[35] M. Oehmichen, C. Meissner, H.G. Konig, and H.B. Gehl, Gunshot injuries to the head and brain caused by low-velocity handguns and rifles. A review. Forensic Sci Int, vol. 146 (2-3) (2004). pp. 111-20.

All-Atom CSAW: An Ab Initio Protein Folding Method

Weitao Sun[1*]

[1] Zhou Pei-Yuan Center for Applied Mathematics, Tsinghua University, Beijing, 100084, China
* Corresponding author: sunwt@tsinghua.edu.cn

Abstract Conditioned Self-Avoiding Walk (CSAW) was first developed as a tool to simulate protein folding Based on CSAW algorithm, All-atom Conditioned Self-Avoiding Walk (AA-CSAW) was developed around 2007. The polypeptide chain is simulated as effectively rigid cranks -Ca-CO-NH- units lined by covalent bonds. Bond lengths and bond angles are set as fixed optimal values. All-atom amino acid sidechain is attached to very Ca atom. The structure of polypeptide is fully described by backbone dihedral angles φ, ψ and the sidechain dihedral angles χ. A trial structure is randomly generated by pivoting the polypeptide chain and sidechains. In the pivot algorithm, the backbone dihedral angles φ, ψ for each residue are chosen according to probability distributions in Ramachandran plot. The dihedral angle distributions are improved by 3-residue fragment set investigation. The effective energy of protein structure is constructed by considering hydrophobic effect, desolvation effect and hydrogen bonding interaction. An appropriate three dimensional structure is accepted with a probability according to Metropolis scheme. In order to evaluate the accepted structures in Monte Carlo simulations, the ratio of secondary structure content to radius of gyration is introduced. CASP09 target example shows that AA-CSAW is an efficient and promising ab initio method.

Keywords protein folding simulation, self-avoiding walk, coarse-grained, sidechain atom

1. Introduction

In physiological conditions, globular protein folds from randomly coiled polypeptide chain into a characteristic three-dimensional structure in water solution. Protein folding is a stochastic process and there are huge amount of protein molecules in organism. The observable macroscopic properties have microscopic interpretations based on collective molecule behaviors. Meanwhile, individual protein molecule undergoes a Brownian motion and it's hard to describe the movements of each molecule. In addition, protein structure is at the edge of thermo-equilibrium. Delicate balance between entropy-enthalpy exist throughout the folding process. We believe that statistical thermodynamics is a prior way for protein folding problem.

Polypeptide chains in solutions incessantly change shape and position by thermal agitation. This Brownian motion can be characterized in more quantitative fashion by the use of phenomenological models. One such model is summarized by the Langevin equation of motion[1, 2]. Monte Carlo (MC) simulation samples typical configurations from a Boltzmann distribution determined by potential energy and temperature of the system. Monte Carlo method solves the stochastic models without consideration of the analytical representations of the system. It is clear that the Monte Carlo model does not represent the dynamic behavior of the real system directly. According to the ergodicity theorem, "time average" will converge to the "configuration average" in a large system. Estimations from MC simulations often correspond very well with those from MD simulations.

In All-tom CSAW method[3]., we first set up an initial unfolded structure. Then the structure is pivoted by randomly choosing backbone dihedral angles ϕ,ψ and sidechain torsion angle χ. This candidate structure is checked by self-avoiding walk criteria to make sure that there are no atom overlaps. The structure energy is calculated for the pivoted peptide chain. A Metropolis scheme is used to determine if the new structure should be accepted. If accepted, this pivoted structure is saved and used as the starting point for the next loop. Otherwise, the structure is restored to the one before pivot. Then a new pivot is carried out in the next loop.

2. “Crank” model of Amino acid

Amino acids are molecules containing an amine group, a carboxylic acid group and a side chain that varies between different amino acids. The amine and carboxylic acid groups of amino acids react to form amide bonds. One amino acid molecule can react with another and become joined through an amide linkage. This polymerization of amino acids yields the newly formed peptide bond and a molecule of water.

The protein is a linear polymer of the 20 different kinds of amino acid, which are linked by peptide bonds. All of the 20 amino acids have in common a central carbon atom (C_α) to which are attached a hydrogen atom, an amino group, and a carboxyl group (COOH). What distinguishes one amino acid from another is the side chain attached to the C_α. The main-chain atoms are a carbon atom C_α, an NH group bound to C_α, and a carbonyl group C’=O, where the carbon atom C’ is attached to C_α. The basic repeating unit along the main chain is thus (NH- C_α-C’=O), which is the residue of the common parts of amino acids after peptide bonds have been formed.

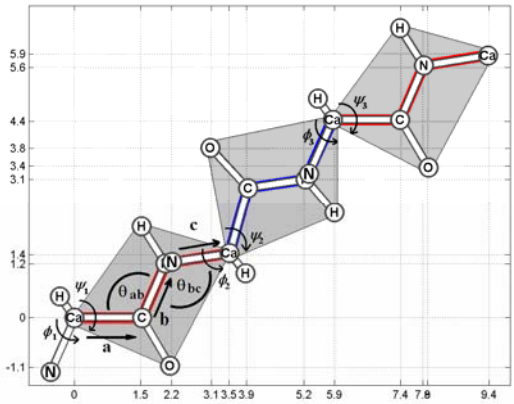

Figure 1. Crank chain model of protein backbone structure

The peptide bond tend to be planar and the rigid peptide dihedral angle (the bond between C’ and N) is always close to 180 degrees (Figure 1). Here C’ indicate the carbon atom bonded to C_α. Because of the double-bond unrotatable feature of peptide bond, the atoms C_α-C’=O-N are constrained in a rigid plane, called peptide plane. There are obvious repeating patterns -Cα-C'=N-Cα in protein backbone. The interlink within these atoms form a crank-shaped rigid body. Thus, we introduce a ‘crank’ unit –Cα-C1=N- in CSAW. Crank is a simplification of amino acid residues. The Cα atom is located at origin point.

3. Add sidechain atoms to residue

What distinguish protein from common polymers are the diversity of residue sidechains. There are 20 natural amino acid residues in protein. They can be classified into several groups, such as hydrophobic, charged, polar and so on. Some works show that hydrophobic/hydrophilic residue types are enough to create secondary structures (such as alpha helix). However, the importance of other subtle properties of amino acid sidechains are still underestimated. The delicate sidechain differences may shed light to the folding of native structure.

As for coarse-grained model, all atom sidechains are substantially important. The single sphere sidechain model is good. But sometimes spurious overlaps happen when anisotropic residue sidechains come close to each other. In single ball sidechain model, many important dense configurations will be ignored, which prevent protein structure from search correct folding path in conformation space. Protein folding simulations of real proteins make demand of an all-atom

sidechain CSAW method. We developed the all-atom self-avoiding walk method as a coarse-grained ab initio protein folding simulation method with atom details[3].

Since crank model can provide atom locations for backbone atoms, the central problem is how to determine the sidechain atom coordinates if the atom coordinates are known for a backbone structure in arbitrary orientation. Thanks for the knowledge of amino acid structure, we have the atom coordinates for sidechain in some special orientation. As a consequence, we can determine the sidechain atom coordinates by matching amino acid to the backbone of a crank.

As the structure of 20 amino acids are well determined by experiment observation, we have the atom coordinates for any type of residues, including backbone $\mathbf{X}_{BB}^{obs}$ and sidechain $\mathbf{X}_{SC}^{obs}$. The only problem is that the observed amino acid structure are usually not in the same orientation as in crank model. If the backbone parts N-C_α-C-O of observed amino acid structure overlap with crank model, it is obvious that the crank sidechain atom will be determined by $\mathbf{X}_{SC}^{crank} = \mathbf{X}_{SC}^{obs}$.

4. Pivot algorithm

The protein chain is simulated by a series of cranks connected at C_α atom. The chain conformation will change when the torsion angle φ and ψ are modified. In order to create a new conformation in AA-CSAW, we pivot the chain at certain randomly selected C_α atom by changing φ and ψ to specified values (Figure 2). The crank chain pivot procedure can be summarized as following steps.

1. Start with initial chain.
2. Choose a crank randomly as pivot point and change the torsion angles
3. Rotate end portion about pivot point.
4. Check atom overlaps. If no overlap, accept and update chain conformation.
5. If overlap, go to **2.**

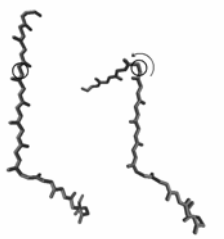

Figure 2. Pivot polypeptide chain by changing torsion angles

5. Non-covalent Interactions and structure energy

In AA-CSAW, we consider the most important non-covalent interactions in water solution, such as hydrophobic effect, hydrogen bonding.

Hydrophobic residues, such as Alanine, Valine and Phenylalanine, tend to congregate in an aqueous (i.e. water) environment. The absence of hydrogen bonding between water and non-polar groups constitutes an important source of the protein stability in aqueous solution, known as hydrophobic effect. With the help of such effect, a hydrophobic core is usually formed in globular protein. The assembly of hydrophobic residues is thus considered as the driving force of the collapse of peptide chain[4].

Hydrophobicity is usually expressed as the Gibbs energies of transfer from water into the reference state. When globular protein fold from denature to native structure, hydrophobic residues come together and free energy decrease. The transfer hydrophobic amino acid residues from cyclohexane

into water is energetically costly. Thus the burial of hydrophobic sidechains in the folding reaction is energetically favorable.

In order to model this folding process, energy decrease caused by hydrophobic residue aggregation is simulated by residue contact degree. The hydrophobicity of amino acids are represented by h. When h is positive, the residue is hydrophobic. Otherwise, it is hydrophilic. Table 1 shows the hydropobic properties of 20 amino acids. If residue m has multiple contact neighbors, the hydrophobic energy variation is the summation of residue hydrophobicities.

Table 1. Hydrophobicity of 20 amino acids

Amino acid	3-letter codes	1-letter codes	Hydrophobicity	Amino acid	3-letter codes	1-letter codes	Hydrophobicity
Alanine	Ala	A	0.05	Leucine	Leu	L	0.15
Arginine	Arg	R	-0.42	Lysine	Lys	K	-0.21
Asparagine	Asn	N	-0.28	Methionine	Met	M	0.04
Aspartic Acid	Asp	D	-0.35	Phenylalanine	Phe	F	0.06
Cysteine	Cys	C	0.01	Proline	Pro	P	
Glutamic Acid	Glu	E	-0.25	Serine	Ser	S	-0.21
Glutamine	Gln	Q	-0.21	Threonine	Thr	T	-0.15
Glycine	Gly	G	0.00	Tryptophan	Trp	W	0.03
Histidine	His	H	-0.17	Tyrosine	Tyr	Y	-0.03
Isoleucine	Ile	I	0.15	Valine	Val	V	0.13

Hydrophilicity at 25℃ is relative to glycine, and is based on the partitioning of a sidechain analogue between the two states [5-8].

Hydrogen bond (H-bond) contains both positive (H-donor) and negative (H-acceptor) partial charges. It represents a combination of covalent and electrostatic interactions, but the main component is the electrostatic attraction between hydrogen donor and acceptor. Hydrogen bonding interactions between backbone O atom and N-H atoms has different stabilities in different situations. The Gibbs energy contributions per hydrogen bond in the interior of proteins are estimated to be 10-60 kJ/mol[5, 9, 10]. While the hydrogen bond interaction in protein structure is much weaker at the surface, where the relative permittivity of water is close to 80.

6. Example of CASP09 target simulation

Here we show the CASP09 target T619 (3NRW) as an folding simulation example. T619 has 111 amino acids and is composed of five helices (Figure 3(A)). The initial structure is unfolded long chain. The final predicted 3-D structure by CSAW is shown in Figure 3(B).

In addition to the final structure, we calculate many other important parameters for the whole folding process. The hydrophobic energy and hydrogen bond energy are shown in Figure 3(A). Although the electrostatic energy is not involved in current AA-CSAW as a driving force, we do calculate it for charged residues through Coulomb's law.

The interesting features of energy curves are (1) Hydrophobic (hp) energy decreases fast within first 300 steps. Then hp curve fluctuates around a stable value. This indicates a fast structure collapse in the very early folding stage. Afterwards the hydrophobic residue clusters do not grow greatly. (2) Hydrogen bond (hb) energy curve descends continuously during the whole folding process. The

decrease trend implies a sustained hydrogen bond formation (see Figure 3(B)), which is an indicator of increasing secondary structure. (3) The cross of hp and hb energy curves show that hydrophobic effect dominate the early folding stage and the hydrogen bonding interaction controls the following stage after a transition state around step 3500.

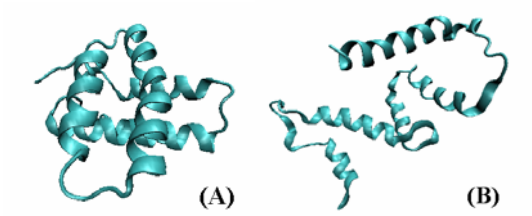

Figure 2. Native and predicted structure of target T619

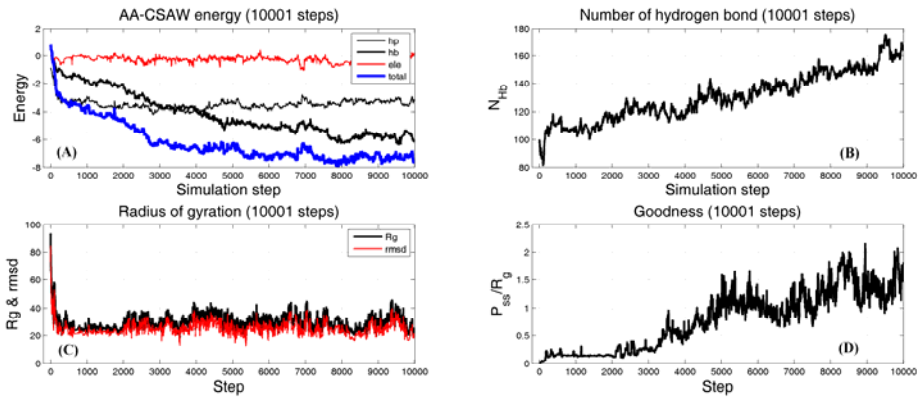

Figure 3. Simulation results for 10001 steps of target T619. (A) Hydrophobic (hp) energy, hydrogen bond (hb) energy, electrostatic (ele) energy and total energy. (B) Number of hydrogen bond. (C) Predicted structure radius of gyration and RMSD. (D)Structure evaluation parameter

The radius of gyration (Rg) and RMSD curves show obvious stages during the folding process. (1) Before update step 300, there is a fast collapse of Rg. This is a reasonable result from fast mainchain collapse driven by hydrophobic effect. In this stage, protein backbone can pivot freely because of relatively less residue repulsive forces. As residues packing to each other, the hydrophobic cores are formed and there are many hydrogen bonds appear. Hydrophobic energy and hydrogen bonding energy have a sharp decrease during the first 300 steps, so as the number of hydrogen bonds in this fast collapse stage (Figure 3(B)). Considering definition of CSAW energy, protein backbone collapse fast to a globular structure containing may hydrophobic cores. This globular shaped structure becomes more stable with the help of hydrogen bonds. (2) From update step 300 to 2000, there is a slow packing process. Protein structure Rg decrease slowly from 30 Å to 20 Å. The decrease of hydrophobic and hydrogen bonding energy also slows down. This means that it become difficult for protein to find a 'comfortable' structure with lower energy.

As the hydrophobic residue cluster grow to a certain size, the increase of hydrophobic effect will slow down. This is caused by the dewetting effect near large hydrophobic cluster surface. On the contrary, hydrogen bonding interaction keep increasing as more H-bond appear. Hydrogen bond energy take the place of hydrophobic energy. Since hydrophobic effect cannot hold the globular structure as tight as before, protein has more chance to expand in volume and accommodate more hydrogen bonds. Consequently, the radius of gyrations show large fluctuation after step 2000.

Large Rg fluctuation makes protein structure much more flexible, which provides a better way to search native structure in conformation space. Figure 3(D) shows that the structure become better and better after the turning point around step 2000. Whenever the control of hydrophobic effect relaxes, the structure optimization speeds up. Thus, a modifiable hydrophobic effect, which is the true physical picture in protein folding, is much reasonable than a constant one.

7. Conclusions

The newly developed AA-CSAW method integrates both coarse-grained crank backbone model and rotatable sidechain atoms to improve protein structure prediction. The deep physical understandings of noncovalent interactions lead to incorporation of solvent effect in hydrophobic and hydrogen bond energy calculation. To our best knowledge, this is the first time to propose such improved algorithm in coarse-grained ab initio method. The cluster-size dependent hydrophobic effect makes the structure much more flexible. Thus, the hydrophobic and hydrogen bonding interactions are well balanced as two stages in folding process. CASP09 target example shows that the AA-CSAW method is now ready to simulate some real and large structures.

Acknowledgements

I thank Professor Kerson Huang for interesting and helpful discussions. The work in this paper is sponsored Tsinghua University Initiative Scientific Research Program (20101081751). Part of this work is supported by Institute of Advanced Studies at Nanyang Technological University.

References

[1] K. Huang. PROTEIN FOLDING AS A PHYSICAL STOCHASTIC PROCESS. Biophysical Reviews and Letters, 3 (2008) 1-18.

[2] K. Huang. CONDITIONED SELF-AVOIDING WALK (CSAW): STOCHASTIC APPROACH TO PROTEIN FOLDING. Biophysical Reviews and Letters, 2 (2007) 139-54.

[3] W. Sun. Protein folding simulation by all-atom CSAW method. IEEE International Conference on Bioinformatics and Biomedicine, 2 (2007) 45 - 52.

[4] W. Kauzmann. Some Factors in the Interpretation of Protein Denaturation. Adv Protein Chem, 14 (1959) 1-63.

[5] P. Dauber, Hagler A. T. Crystal packing, hydrogen bonding, and the effect of crystal forces on molecular conformation. Accts Chem Res, 13 (1980) 105-12.

[6] P. L. Privalov, Makhatadze G. I. Contribution of hydration to protein folding thermodynamics. 2. The entropy and Gibbs energy of hydration. J Mol Biol, 232 (1993) 660-79.

[7] A. Radzicka, Wolfenden R. Comparing the polarities of the amino acids: side chain distribution coefficients between the vapor-phase, cyclohexane, 1-octanol, and neutral aqueous solution. Biochemistry 27 (1988) 1664-70.

[8] T. E. Creighton. Proteins-Structures and molecular properties. 2 ed, W. H. Freeman and Company, New York, 1993.

[9] A. T. Hagler, Dauber P., Lifson S. Consistent force field studies of intermolecular forces in hydrogen bonded crystals. III. The C=O...H-O hydrogen bond and the analysis of the energetics and packing of carboxylic acids. J Am Chem Soc, 101 (1979) 5131-41.

[10] G. I. Makhatadze, Privalov P. L. Contribution of hydration to protein folding thermodynamics. 1. The enthalpy of hydration. J Mol Biol, 232 (1993) 639-59.

Technology in Locomotion and Domotic Control for Quadriplegic

Mauricio Plaza PhD.[1,*], Oscar Avilés PhD.[2], William Aperador PhD.[3]

[1,2,3] Department of Mechatronics, Universidad Militar Nueva Granada , Bogotá, Colombia
[1,2,3] Mauricio.plaza@unimilitar.edu.co, oscar.aviles@unimilitar.edu.co, William.aperador@unimilitar.edu.co

Abstract

The electronic control technology for mobility and domotics control (home automation systems) can be a great help to people with spinal injuries who have major limitations in the mobility and in the use of devices for normal life activity. The design of different type of technologies to provide to the patient aids is able to increase his quality of life.

A spinal cord injury (SCI) is typically defined as damage or trauma to the spinal cord that in turn results in a loss or impaired function resulting in reduced mobility or feeling.

Typical common causes of damage to the spinal cord are trauma or disease. The resulting damage to the spinal cord is known as a lesion, and the paralysis is known as quadriplegia or quadraplegia / tetraplegia if the injury is in the cervical (neck) region, or as paraplegia if the injury is in the thoracic, lumbar or sacral region.

Equipment manufacturers say that designing applications for users with disabilities is not cost-effective. Most of these systems are designed for users who are not disabled; therefore, systems that address disabled users need special interfaces in order to be accessible.

In this paper we present a method for developing an electric and mechanical prototype for quadriplegic people provided that they can perform specific grade of mobility. Using an infrared technique, computer vision technology and mechanical design, users can perform some activities for improve his quality of live and give some grade of independence.

Keywords Electric chair, quadriplegic, spinal injure

1. Introduction

1.1Complete and Incomplete Spinal Cord Injury

There are typically two types of lesions associated with a spinal cord injury, these are known as a complete spinal cord injury and an incomplete spinal cord injury. Both of this level can be partial solve whit the design proposed in this research.

A complete type of injury means the person is completely paralyzed below their lesion; this type of injury is most concerned with the research. There are no possibility or therapy and it is necessary a technological solution for the patient mobility.

Whereas an incomplete injury, means only part of the spinal cord is damaged. A person with an incomplete injury may have sensation below their lesion but no movement, or vice versa. There are many types in incomplete spinal cord injuries, and no two are the same.

Incomplete spinal cord injury can be solving whit the technology used for people with complete paralyses with some simple modifications.

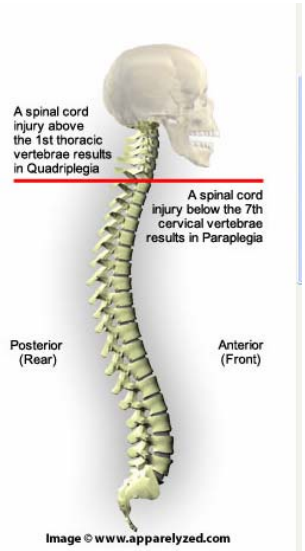

Figure 1. Spinal Cord Injury level

Quadriplegia is caused by damage to the cervical spinal cord segments at levels C1-D8. Damage to the spinal cord is usually secondary to an injury to the spinal vertebrae in the cervical section of the spinal column. The injury to the structure of the spinal cord is known as a lesion and may result in the loss of partial or total function in all four limbs, meaning the arms and the legs. Because the damage produces loss of control in four limbs, the research proposes the use of the jam and head movements to control the mobility and domotic operation (figure 1.)

Typical causes of quadriplegia from damage to the spinal cord are trauma (such as car crash, fall or sports injury), disease (such as transverse myelitis or polio) or congenital disorders, such as muscular dystrophy. It is possible to injure the spinal cord without fracturing the spine, such as when a ruptured disc or bony spur on the vertebra protrudes into the spinal column.

1.2 Symptoms of Quadriplegia

Upon visual inspection of a quadriplegic patient, the first symptom of quadriplegia is impairment to the arms and legs.

Quadriplegia is defined in different ways depending on the level of injury to the spinal cord. C1–C4 usually affects arm sensation and movement more so than a C5–C7 injury; however, all quadriplegics have or have had some kind of finger dysfunction. That kind of injure do not permit the control with the limb, but with the only move part like head and jam.

A person with damage to the spinal cord at the cervical spinal cord segment C1 (the highest cervical vertebra, at the base of the skull) will probably lose function from the neck down and require permanent assist. In order to provide some degrade of freedom, the design of control technology and special interface are the goal of the research

A person with a C8 spinal cord injury may lose function from the chest down, but still retain use of the arms and much of the hands. In this case the design of technology could be less efficient and with different interface.

The degree of the injury to the cellular structures of the spinal cord is very important. A complete severing of the spinal cord will result in complete loss of function from that spinal segment down. A partial severing or even bruising or swelling of the spinal cord results in varying degrees of mixed function and paralysis.

The prototype proposed is thinking in the high level of quadriplegia. The other type of injure can be solve whit very simple modifications.

1.3ASIA impairment scale

Spinal cord injuries are classified by the American Spinal Injury Association (ASIA) classification. The ASIA scale grades patients based on their functional impairment as a result of the injury, grading a patient from A to D

A	Complete	No motor or sensory function is preserved in the sacral segments S4–S5.
B	Incomplete	Sensory but not motor function is preserved below the neurological level and includes the sacral segments S4–S5.
C	Incomplete	Incomplete: motor function is preserved below the neurological level, and more than half of key muscles below the neurological level have a muscle grade less than 3.
D	Incomplete	Incomplete: motor function is preserved below the neurological level, and at least half of key muscles below the neurological level have a muscle grade of 3 or more.
E	Normal	

1.4 Spinal Shock Overview

Spinal shock following a spinal cord injury is a specific term that relates to the loss of all neurological activity below the level of injury. This loss of neurological activity includes loss of motor, sensory, reflex and autonomic function.[7-8].

1.5 Spinal Cord Injury Levels

Spinal cord injury levels are used to explain the different severities of paralysis, following an injury to the spinal cord. Generally, the higher the level of injury to the spinal cord, the greater the degree of paralysis will result.

1.6 Functionality of C1, C2, C3 Quadriplegic

1.6.1 Mobility & Movement

Limited head and neck movements can be done depending on muscle strength. The research prototype include an oral mouse to solve this problem

1.6.2 Complete paralysis of arms, body and legs.

Sympathetic nervous system will be compromised possibility of Autonomic Dysreflexia. Electric wheelchair may possibly be controlled by either neck an oral movement controller; this will vary depending on dexterity. Complete assistance required during mealtimes.

1.6.3 Personal Care

Complete personal assistance is required. The person will need assistance with washing, dressing, and assistance with bowel and bladder management. The prototype can free a personal care for mobility and house interface control.

1.6.4 Domestic Care

Complete domestic care is required, such as household cleaning, washing of clothes and kitchen duties, preparation of meals and general household duties. Again, the prototype can free a personal care for mobility and house interface control.

1.6.5 Communication

A computer may be operated using head movement recognition, mouth stick recognition. Telephone can be used using oral mouse recognition and headset.

1.6.6 Environmental Control

The system designed permitting remote control of electronic devices in the immediate surroundings. A person can independently turn lights, radio, and television on and off, answer or initiate phone calls, and unlock a door. Essentially any aspect of the environment can be controlled depending upon the system's complexity.

A hardware and software system, allowing the user programmed or spontaneous control over remote, electrically operated appliances.

The prototype is special technology equipment providing disabled access of the physical

environment like automatic door openers, environmental control units and modular unit for electric wheel chair control and control units for other assistive technologies [9].

2. Designing of technology and interfaces for quadriplegic people

Paralysis is broadly characterized by the loss of muscle control, power and movement to one or more parts of the body. Quadriplegic is a person with damage to the spinal cord at a high level, resulting in sensory and motor function impairment in all four limbs and the trunk. It is caused by damage to the brain or the spinal cord at a high level C1 - C8 - in particular, spinal cord injuries secondary to an injury to the cervical spine. The persons develop a dependency that limits his possibilities and his quality of life. Independence in his daily activities improves notably his autoesteem and liberates his family of an additional responsibility.

Using the knowledge and experience on rehabilitation technology, the research group began thinking of developing new products for people with quadriplegia due to spinal cord injury or other causes. The basic needs are the locomotion, activation of devices as light, television, doors remote control or communications. The present project intends to identify the basic needs of quadriplegic people and the possible solutions using technology of infrared tracking and new design of oral mouse. Diagrams of the Different path result of the jam movements, used for oral mouse design. (Figure 2-5)

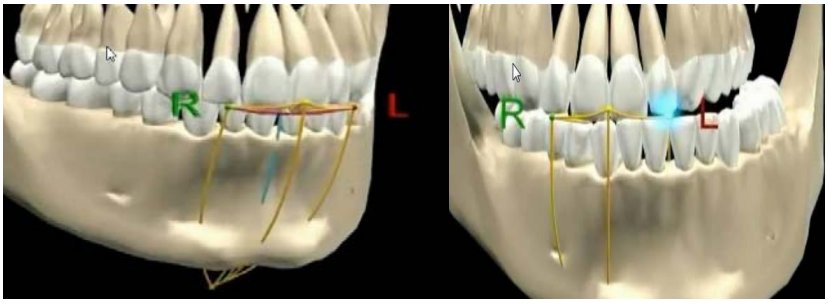

Figure 2. Fontal and lateral movements

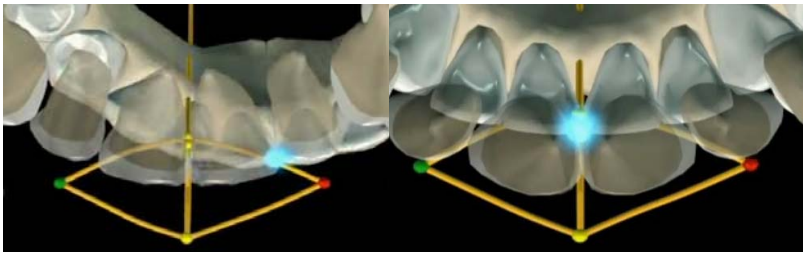

Figure 3. Upper path

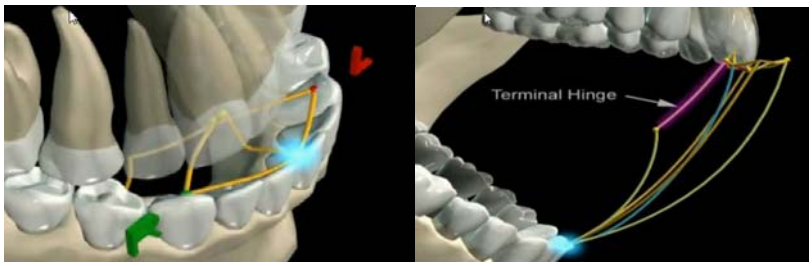

Figure 4. Lowewr path

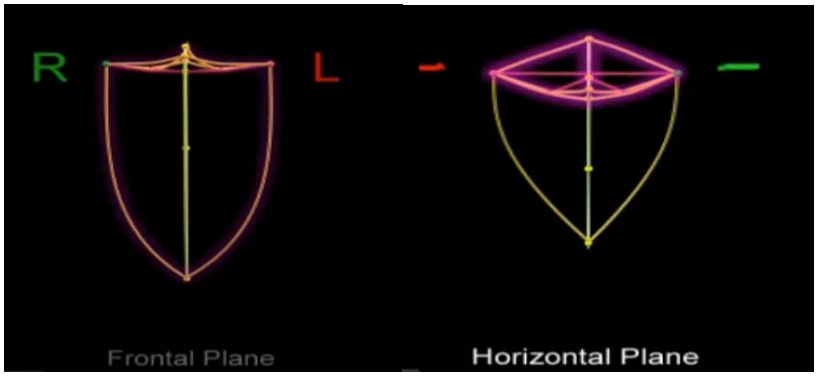

Figure 5. Fontal and horizontal plane path

Quadriplegia is a disorder where an individual loses the use of all four limbs: legs and arms, as well as other parts of their body. In some cases the individual may still have partial movement in one limb or several parts of their body. One of the aims of the project is to provide an opportunity for persons with paraplegia seeking to re-establish themselves in community living. The persons with limitations in his members develop dependency from other people, for his primary needs of movement and common and daily activities. This dependency deteriorates his life quality and of the person dedicated to his care. For this limitation, the autoesteem of the person with limitations is low, creating psychological and physical problems that can be solved partially by means of some type of technology.

Figure 6. Traditional Electric chair

Living with and managing quadriplegia is difficult, but not impossible. Those suffering from the condition need to be prepared to make changes in their life and their home. We have an opportunity to help on this process. The devices designed have to take special characteristics like low cost, control with movement of the head, in some cases with finger activation, good accuracy and easily to maneuver. The basic idea of the project consists of develop an infrared tracking device that allows the devices activation by means of the movement of the head to quadriplegic people [1].

In some cases the affected person has the possibility of basic finger movement that allows activating the devices like a switch or the activation by means of a trackball. It will be studied and will leave the use possibility of the two devices depending on the injury type and the mobility possibilities [3]. The development of this device improves the quality of life of the affected people and opens new alternatives for handling different activities in this kind of persons [2]. They hope to use these signals to guide motorized assistance mechanisms that restore mobility in a specific area. The involved costs are low, the operation capacity is simple and his development is possible. The prototype include an infrared tracking system, a computer that processes the signal from the system and a display with the chosen options, a power system for the relay control and a digital system that is the interface with the power unit [4].(figure 7.)

The main objective is to determine the needs of the people with limitations of mobility and to propose solutions with devices bases on infrared tracking and oral mouse.

Figure 7. Electronic control prototype

Technology of electric wheelchair control (figure 6.) and domotics systems can really change the life to the people with spinal injuries; especially in the cases of major limitations in the use of the upper limbs. In order to provide an electronic device or system, with the purpose to increase the quality of life and opportunities for participation and inclusion, it is necessary that this process follows a well-established methodology and a multidisciplinary approach (mechanical and electric

science). Our procedure consists of some phases: 1) Analysis of user needs. At this stage we consider the type of disability 2) Finding aid. We consider the cost, service and facilities, 3) customization of the device. 4) Design of the technology.

The specific objectives are:

- To determine the primary needs of persons with limitations of movement
- To study the possible solutions to obtain a certain percentage of independence
- To use technology of infrared tracking to supply part of the needs of mobility and devices control.
- To escalate the project to different grades of incapability (small movements of hand, total immobility of members...)
- To realize a prototype that allows a person with a certain grade of incapability, to be able to have high level of independence with the control of some devices and mobility in a specific area.
- A person using the final project to control a wheelchair, for example, only has to move your head about going straight ahead or turning left and the chair follows their command. However, they do not have to worry about colliding with obstacles because the wheelchair itself monitors and reacts to its environment.

3. Methodological Approach

- Bibliographical review. Allows knowing the current advances in the devices control for quadriplegic systems. It allows the comparison of alternative systems as control with EEG. It allows the review of current technologies in infrared systems.
- Surveys in the health sector. It allows understanding the specific needs in persons with these limitations. It allows validating the proposal and to determine if there are improves in the model.
- Prototype preparation and simulation.
- Prototype test with quadriplegic people and improvement of the model.
- Final prototype development
- Technical test and prototype improvement, we have done is combine the intelligence of the person with the artificial intelligence of the device.
- Field test
- Model improvement
- Final prototype development

4. Conclusion

The final prototype improves the quality of life of quadriplegic people. The prototype must have the possibility of allowing the control of electrical wheel chairs, of some devices connected to a wireless control system, only by means of the movement of the head.

We hope that the solution should be practical, easy use and should not generate very high costs, as well as safety and immunity to the noise. These characteristics allow that the system should be robust characteristics and easy to reproduce. The persons who have this system must have the possibility of easy movement in a specific area by means of the movement of some part of the body that still has control.

The system has the capacity to adjust itself to the characteristics of each individual driver, and thereby is able to improve the efficiency with which it senses the driver's commands.

People, for example, do not consciously send commands to every muscle in each leg in order to walk and do not think where to step to avoid an. Similarly, a wheelchair-bound user of the project simply has to send the signal to go in a certain direction and the chair figures out how to get there.

A person using the final project to control a wheelchair, for example, only has to move your head about going straight ahead or turning left and the chair follows their command. However, they do not have to worry about colliding with obstacles because the wheelchair itself monitors and reacts to its environment.[5]

The fact that is an infrared system allows being immune to electrical noise, as generated by the electric chairs and allows low costs and easy design of engineering. These characteristics are desirable to reduce costs and to make the project possible.

References

[1] A. Biocca, A survey of position trackers, Presence: Teleoperators and Virtual Environments, v.1 n.2, p.173-200, Spring 1999

[2] A. B. Zoss, H. Kazerooni, A. Chu, “Biomechanical design of the Berkeley Lower Extremity Exoskeleton (BLEEX)“, IEEE/ASME Trans. Mechatronics, vol. 11, no. 2, pp. 128-138, 2006.

[3] Adam C. Esser, MD, James G. Koshy, Ph.D, Henry W. Randle, MD, Ph.D. “Ergonomics in Office-Based Surgery: A Survey-Guided Observational Study”. American Society for Dermatologic Surgery, Inc. November 2007

[4] A. J van den Bogert, “Exotendons for assistance of human locomotion”, Biomed. Eng., Online, 2:17, 2003.

[5] A. M. Dollar, H. Herr, “Lower Extremity Exoskeletons and Active Orthoses: Challenges and State-of-the-Art”, IEEE Trans. Rob., vol. 24, no. 1, 2008.

[6] Axel Mulder. "Human movement tracking technology". Technical report, School of Kinesiology, Simon Fraser University, 2000

[7] Kenneth Meyer , Hugh L. Applewhite , Frank

[8] Olivier Faugeras, Three-dimensional computer vision: a geometric viewpoint, MIT Press, Cambridge, MA, 2001

[9] R. T. Tsai "An Efficient and Accurate Camera Calibration Technique for 3-D Machine Vision", Proceedings of the IEEE Conference on Computer Vision and Pattern Recognition, 2001.

The Crack Growth Behavior in electrolyte membrane under Mechanical-electrochemical Loading

Yun J Chen[1], Yi Sun[1,*], Yi Z Liu[1], Chen Wang[1]

[1] Department of Astronautic Science and Mechanics, Harbin Institute of Technology, Harbin 150001, PR China

[*] Corresponding author: sunyi@hit.edu.cn

Abstract As the key component of SOFC (solid oxide fuel cell), a theoretical framework has been built to illustrate the coupling effect between oxygen vacancy concentration and stress field in early works. Here, the coupling theory is expanded and more affecting factors are taken into consideration. An electrolyte membrane with a macro crack is studied by a modified multi-scale method under fully coupling effect. It can be observed that the crack propagates with the increase of remote loadings, and the fracture mode is brittle fracture. The local stress concentration at the crack tip influences significantly the electromechanical fields and the fracture toughness of the stoichiometric sample ($Ce_{0.8}Gd_{0.2}O_{1.9}$) may be reduced from 0.9493MPa•m$^{1/2}$ of uncoupled value to 0.5142MPa•m$^{1/2}$. It can be concluded that the coupling effect is important for the electrolyte in the working environment; especially in the case of the existence of a crack.

Keywords: electrolyte membrane, mechanical-electrochemical coupling, multi-scale simuation, fracture toughness

1. Introduction

As an energy conversion device, solid oxide fuel cell (SOFC) can generate high efficiency electric power without environment pollution[1], and it has attracted more and more attention for its excellent property. Meanwhile, as the core component, considerable researches have been completed to study the performance of the electrolyte[2].

The GDC (Gadolinium (Gd_2O_3) doped ceria (CeO_2)) is regarded as a promising candidate electrolyte material for its higher ionic conductivity[3]. When two cerium ions (Ce^{4+}) are replaced by gadolinium ions (Gd^{3+}), an oxygen vacancy is generated to maintain electrical neutrality. And oxygen ions can transport through the electrolyte at high temperature. In the working environment, the effects of temperature and stress are inevitable, the electrolyte actually works in a complicated coupling field[4-6].

In the present work, a modified multi-scale method is introduced and applied to simulate the electrolyte with a crack under the full coupling effect. Based on the simulation results, the reasons and the process of the electrolyte failure can be further revealed.

2. Framework of the coupling effect

2.1. The stress-induced diffusion potential

When the electrolyte (GDC) is at low oxygen partial pressure, extra oxygen vacancies are generated owing to reduction reaction, and the elastic constants of the material can be assumed a function of the vacancy concentration:

$$C_{ijkl} = C_{ijkl}^{0} + \sum_{\alpha} \left(\partial C_{ijkl} / \partial \rho_{\alpha} \right) \Big|_{\rho=\rho_{\alpha}} d\rho_{\alpha} \tag{1}$$

where, ρ_α is the molar fraction of defect α, and C_{ijkl}^0 is the elastic constant of stoichiometric material $\left(\rho_\alpha = \rho_\alpha^0\right)$. For isotropic material, there are only two independent parameters: E, v.

$$C_{ijkl} = Ev\big/\big((1+v)(1-2v)\big)\delta_{ij}\delta_{kl} + E\big/\big(2(1+v)\big)\left(\delta_{ik}\delta_{jl} + \delta_{il}\delta_{jk}\right) \tag{2}$$

Here, η_α, $\eta_{E\alpha}$ and $\eta_{v\alpha}$ are introduced for convenience:

$$\eta_\alpha = dV\big/\left(3V^0 d\rho_\alpha\right),\ \eta_{E\alpha} = dE\big/\left(E^0 d\rho_\alpha\right),\ \eta_v = dv\big/\left(v^0 d\rho_\alpha\right) \tag{3}$$

where, V^0, E^0 and v^0 are volume, Young's modulus and Poisson's ratio of the stoichiometric material. The real Young's modulus and Poisson's ratio are:

$$E = E^0\left(1 + \sum_\alpha \eta_{E\alpha}\Delta\rho_\alpha\right) \tag{4}$$

$$v = v^0\left(1 + \sum_\alpha \eta_{v\alpha}\Delta\rho_\alpha\right) \tag{5}$$

In the next, $\sum\eta$, $\sum E$ and $\sum v$ are introduced to represent $\sum_\alpha \eta_\alpha\Delta\rho_\alpha$, $\sum_\alpha \eta_{E\alpha}\Delta\rho_\alpha$ and $\sum_\alpha \eta_{v\alpha}\Delta\rho_\alpha$.

By using these symbols, formula (2) can be rewritten as:

$$C_{ijkl} = C_{ijkl}^0\left(1 + \sum E - \frac{v^0}{1+v^0}\sum v\right) + \frac{E^0 v^0}{(1+v^0)(1-2v^0)^2}\left(\sum v\right)\left(\delta_{ij}\delta_{kl}\right) \tag{6}$$

where

$$C_{ijkl}^0 = E^0 v^0\big/\left(\left(1+v^0\right)\left(1-2v^0\right)\right)\delta_{ij}\delta_{kl} + E^0\big/\left(2\left(1+v^0\right)\right)\left(\delta_{ik}\delta_{jl} + \delta_{il}\delta_{jk}\right) \tag{7}$$

Based on formula (6), the constitutive relation can be defined:

$$\begin{aligned}\sigma_{ij} &= C_{ijkl}\varepsilon_{kl}^E = C_{ijkl}\left(\varepsilon_{kl} - \varepsilon_{kl}^*\right)\\ &= K^0\left(1 + \sum E - \frac{v^0}{1+v^0}\sum v\right)\left[v^0\varepsilon_{kk}\delta_{ij} + \left(1-2v^0\right)\varepsilon_{ij} - \left(1+v^0\right)\sum\eta\delta_{ij}\right]\\ &\quad + \frac{K^0 v^0}{1-2v^0}\left(\sum v\right)\left(\varepsilon_{kk} - \sum\eta\right)\delta_{ij}\end{aligned} \tag{8}$$

where $\varepsilon_{ij}^* = \sum_\alpha \eta_\alpha\Delta\rho_\alpha\delta_{ij}$ is the eigenstrain caused by non-stoichiometry effect, η_α is called coefficient of compositional expansion (CCE), and $K^0 = E^0/\left((1+v^0)(1-2v^0)\right)$.

The full diffusion potential for isotropic material can be described[7-8]:

$$\begin{aligned}\tau_\alpha &= \frac{1+3\sum\eta}{2}\left\{\frac{v^0}{E^0}\left(\eta_{v\alpha} - \eta_{E\alpha}\right)\left(\sigma_{kk}\right)^2 + \frac{1+v^0}{E^0}\left(\eta_{E\alpha} - \frac{v^0}{1+v^0}\eta_{v\alpha}\right)\sigma_{ij}\sigma_{ij}\right\}\\ &\quad + \eta_\alpha\left\{-\frac{3v^0}{2E^0}\left(\sigma_{kk}\right)^2 + \frac{3\left(1+v^0\right)}{2E^0}\sigma_{ij}\sigma_{ij} - \sigma_{kk}\right\}\end{aligned} \tag{9}$$

Because the Poisson's ratio has less affected by oxygen vacancy, η_v can be set zero. Once τ_V is obtained, it can be plugged into diffusion and mechanical equations[8]. The distribution of oxygen vacancy and stress field under coupling effect can be calculated.

In the present work, the electrolyte is $Ce_{0.8}Gd_{0.2}O_{1.9}$ (20GDC), the corresponding non-stoichiometry chemical formula is $Ce_{0.8}Gd_{0.2}O_{1.9-\delta}$ (δ represents the $\Delta\rho_V$ in formula (8)). The parameters in the coupling theory can be calculated by molecular dynamics simulations: $E^0 = 236.036\text{GPa}$, $v^0 = 0.267$, $\eta = 0.0728$, $\eta_E = -0.9571$ [9].

2.2. The coupling effect of the planar electrolyte

In this section, a planar electrolyte is selected to study the coupling effect, as shown in Fig.1.

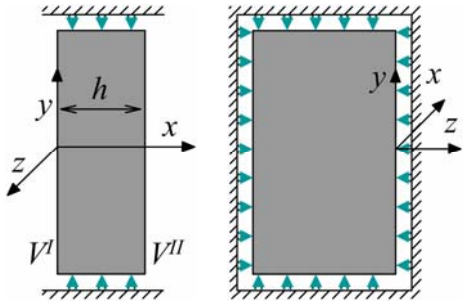

Figure 1. Schematic of electrolyte membrane

The thickness of the membrane is h, and it is completely fixed along y and z directions. The displacement boundary conditions are:

$$u_1 = u(x),\ u_2 = u_3 = 0 \tag{10}$$

where, $x = x/h$, and the range of values allowed for it is $0:1$. The strain tensors are:

$$\varepsilon_{ij}(x_1) = du(x_1)/dx_1\,\delta_{1i}\delta_{1j} \tag{11}$$

Stress tensor can be obtained:

$$\sigma_{11}(x_1) = K(1-v^0)\left(\varepsilon_{11}(x_1) - \left(1+v^0\right)/\left(1-v^0\right)\eta\Delta\rho_V(x_1) - \left(1+v^0\right)/\left(1-v^0\right)\varepsilon^c\right) \tag{12}$$

$$\sigma_{22}(x_1) = \sigma_{33}(x_1) = Kv^0\left(\varepsilon_{11}(x_1) - \left(1+v^0\right)/v^0\,\eta\Delta\rho_V(x_1) - \left(1+v^0\right)/v^0\,\varepsilon^c\right) \tag{13}$$

where $K = K_0(1+\eta_E\Delta\rho_\alpha)$, and ε^c represents constant strain. Here, pressure is low and no shearing strain exists, so σ_{11} can be assumed zero. According to formula (12), $\varepsilon_{11}(x_1)$ can be obtained:

$$\varepsilon_{11}(x_1) = \left(1+v^0\right)/\left(1-v^0\right)\varepsilon_c + \left(1+v^0\right)/\left(1-v^0\right)\eta\Delta\rho_V(x_1) \tag{14}$$

Then, the stress tensors can be rewritten as:

$$\sigma_{22} = \sigma_{33} = -\bar{E}\eta\Delta\rho_V(x_1)\left(1+\eta_E/\eta\,\varepsilon^c + \eta_E\Delta\rho_V(x_1)\right) \tag{15}$$

where $\bar{E} = E^0/(1-v^0)$. Bringing formula (15) into (9), we can obtain:

$$\tau_V(x_1) = \bar{E}\left\{P_0 + P_1\Delta\rho_V(x_1) + P_2\left(\Delta\rho_V(x_1)\right)^2 + P_3\left(\Delta\rho_V(x_1)\right)^3\right\} \tag{16}$$

where:

$$\begin{cases} P_0 = 2\eta\varepsilon^c + 3\eta(\varepsilon^c)^2 + \eta_E(\varepsilon^c)^2, \ P_1 = 2\eta^2(1+3\varepsilon^c) + \eta\eta_E\varepsilon^c(3\varepsilon^c+2) \\ P_2 = \eta^2\left(6\eta_E\varepsilon^c + 3\eta + \eta_E\right), \ P_3 = 3\eta^3\eta_E \end{cases} \tag{17}$$

Besides, the oxygen partial pressure is $\log\left(\mathrm{P}_{\mathrm{O}^2}(x=0)/\mathrm{P}_{\mathrm{O}^2}(x=1)\right) = -20$, and the chemical boundary conditions can be obtained based on experimental datas[10]: $\delta(x=0) = 0.1407$, $\delta(x=1) = 0$ .Until now, all necessary parameters are obtained: $E^0 = 236.036\mathrm{GPa}$, $\Delta\rho_V(0) = 0.1407$, $\rho_0 = 0.1$, $\eta = 0.0728$, $\eta_E = -0.9571$, $v^0 = 0.267$.

3. Description of the multi-scale method

Here, the multi-scale method is defined a combined method of MD simulation with finite element method (FEM). As illustrated in Fig.2.(1), the center-cracked specimen can be decomposed into three parts: in the far field, it is governed by the linear elastic fracture mechanics, at the crack tip, the region is modeled by MD simulation, and the between is called transition region[11].

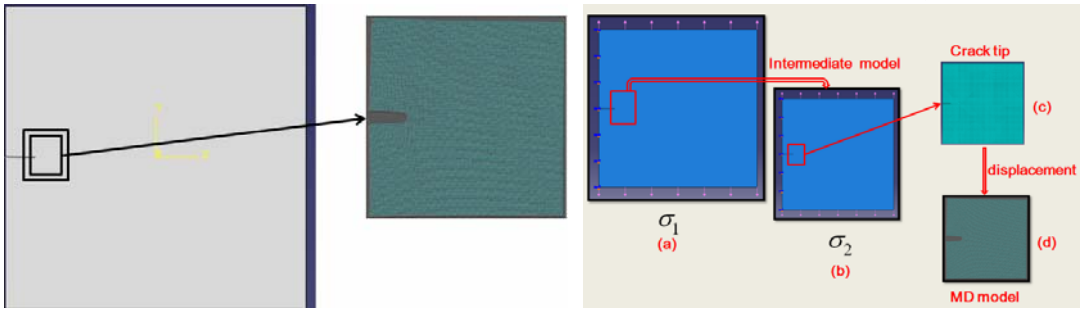

(1) (2)

Figure 2. Illustration of the multi-scale model

As seen in Fig.2.(2), an intemediate model is introduced, its size is far smaller than the initial model. During the calculation process, the stress intensity factor (SIF) K_I of the initial model is calculated firstly by FEM. Then the external load σ_2 for the intermediate model can be computed with the same K_I. For the intermediate model, the element size around crack tip is controlled as the same as the lattice constant of CeO_2, as seen in Fig.2.(2) (c). After the second FEM calculation is completed, the displacements of boundary nodes can be obtained. And then, these displacements are applied to the MD model as boundary conditions for MD simulation. In MD simulation, NPT ensemble is selected, temperature is controlled at 1100K, time step is 1fs (1e-15s), and the in-home potential is used[9].

4. Simulated results and discussion

The electrolyte membrane with a crack is presented in Fig.3.(a), the length of the crack is 0.04mm,

with the thickness of membrane is 2mm. When the model is loaded, the vacancy concentration near crack tip will be influenced significantly by the high stress field, the interesting phenomenon is called local stress effect.

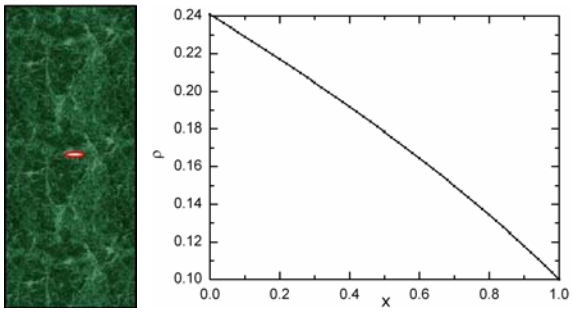

(a) (b)

Figure 3. (a) Cross-section of the electrolyte membrane with crack

(b) Distribution of concentration of oxygen vacancy when no local stress effect is considered

Because the stress field is just affected by oxygen vacancy, so only oxygen vacancy is considered here for studying the local stress effect. For comparison, the coupling field without local stress effect is investigated firstly. The diffusion equation of oxygen vacancy is[8]:

$$J = -D\nabla\rho - \left(V_m \rho D\right)/\left(RT\right)\nabla\tau \tag{18}$$

Based on the deduction in section 2.2, the diffusion potential τ can be described as:

$$\tau = 3\bar{E}\eta^3\eta_E\Delta\rho^3 + \left(\bar{E}\eta^2\eta_E + 3\eta^3\bar{E}\right)\Delta\rho^2 + 2\bar{E}\eta^2\Delta\rho \tag{19}$$

Where, $\bar{E} = E^0/\left(1-\nu^0\right)$. Equation (19) is plugged into equation (18), the diffusion equation can be obtained:

$$\begin{aligned}\hat{J} = &-\frac{d\rho}{dx} - \frac{V_m\rho}{RT}\left\{9\bar{E}\eta^3\eta_E\rho^2 + \left(2\bar{E}\eta^2\eta_E + 6\eta^3\bar{E} - 18\eta^3\eta_E\rho_0\bar{E}\right)\rho\right\}\frac{d\rho}{dx} \\ &+ \frac{2\bar{E}V_m\rho}{RT}\left[\left(\eta^2\eta_E + 3\eta^3\right)\rho_0 - \eta^2\right]\frac{d\rho}{dx}\end{aligned} \tag{20}$$

where, $\hat{J} = \left(Jh\right)/D$, $x = x/h$, h is the thickness of the membrane. The implicit solution can be given out by integrating the equation with chemical boundary conditions:

$$\rho^4 + 2.8751\rho^3 - 6.8512\rho^2 - 1.1028\rho + 0.6189 - 0.4431x = 0 \tag{21}$$

The numerical solution can be calculated by programing the equation, the result is shown in Fig.3.(b).

In order to study the local stress effect, the stress field of the crack-tip (where $\theta = 0$) is applied to the region around the crack tip directly. After the external stress (σ_c) is applied, the stress tensor near the crack tip ($\theta = 0$) can be described as:

$$\begin{aligned}\sigma_{11} &= \frac{K_I}{\sqrt{2\pi}} x^{-1/2} = \frac{K_I}{\sqrt{2\pi h}} x^{-1/2} \\ \sigma_{22} &= -\bar{E}\eta\Delta\rho + \frac{K_I}{\sqrt{2\pi}} x^{-1/2} \\ &= -\bar{E}\eta\Delta\rho + \frac{K_I}{\sqrt{2\pi h}}\left(\frac{x}{h}\right)^{-1/2} = -\bar{E}\eta\Delta\rho + \frac{K_I}{\sqrt{2\pi h}} x^{-1/2}\end{aligned} \tag{22}$$

Where, x is normalized. Similarly, τ can be deduced according to formula (9):

$$\begin{aligned}\tau &= 3\bar{E}\eta^3\eta_E\Delta\rho^3 + \left[\bar{E}\eta^2\left(\eta_E + 3\eta\right) + 3\eta^2\eta_E\sigma_c\frac{3v-1}{1-v}\right]\Delta\rho^2 \\ &+ \left[\frac{3\eta\eta_E}{\bar{E}}\sigma_c^2 + \eta\sigma_c\left(3\eta + \eta_E\right)\frac{3v-1}{1-v} + 2\bar{E}\eta^2\right]\Delta\rho \\ &+ \frac{1}{\bar{E}}\left(3\eta + \eta_E\right)\sigma_c^2 - 2\eta\sigma_c\end{aligned} \tag{23}$$

For convenience,

$$\begin{aligned}&A = 3\bar{E}\eta^3\eta_E,\ B = \bar{E}\eta^2\left(\eta_E + 3\eta\right) + 3\eta^2\eta_E\sigma_c\frac{3v-1}{1-v} \\ &C = \frac{3\eta\eta_E}{\bar{E}}\sigma_c^2 + \eta\sigma_c\left(\eta_E + 3\eta\right)\frac{3v-1}{1-v} + 2\bar{E}\eta^2 \\ &D = \frac{1}{\bar{E}}\left(3\eta + \eta_E\right)\sigma_c^2 - 2\eta\sigma_c\end{aligned} \tag{24}$$

Formula (24) is plugged into equation (18), we can obtain:

$$\begin{aligned}\hat{J} &= -\frac{d\rho}{dx} - \frac{V_m\rho}{RT}\left\{3A\rho^2 + \left(2B - 6A\rho_0\right)\rho + \left(3A\rho_0^2 - 2B\rho_0 + C\right)\right\}\frac{d\rho}{dx} \\ &= -\left\{A'\rho^3 + B'\rho^2 + C'\rho + 1\right\}\frac{d\rho}{dx}\end{aligned} \tag{25}$$

where,

$$A' = 3V_m/\left(RT\right)A,\ B' = \left(2B - 6A\rho_0\right)V_m/\left(RT\right),\ C' = \left(3A\rho_0^2 - 2B\rho_0 + C\right)V_m/\left(RT\right) \tag{26}$$

By integrating equation (25), the implicit solution can be obtained:

$$3A'\rho^4 + 4B'\rho^3 + 6C'\rho^2 + 12\rho = -12\hat{J} + \mathrm{M} \tag{27}$$

where M is a arbitrary constant generated during integration.

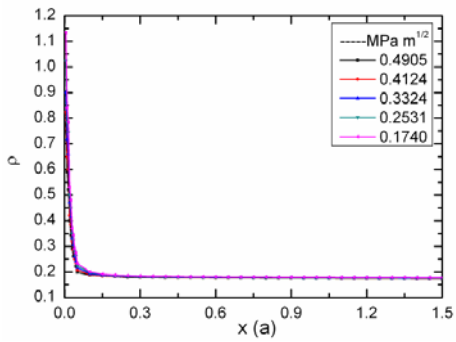

Figure 4. Distribution of concentration of oxygen vacancy near crack tip when stress field of crack tip is applied

As for $\sigma_c = K_I \big/ \sqrt{2\pi x}$, singularity exists at $x = 0$. In order to obtain vacancy concentration at crack tip, the K_I is given firstly, and the effective scope of the local stress effect is seted as $1.5a$, where $a = 0.02\text{mm}$ is half the length of the crack. Then the value at $x = 1.5a$ is calculated, as seen in Fig.4, the value is compared to the corresponding value in Fig.3, it can be found that the difference between the two results is no more than 1%. So the value at $x = 1.5a$ is selected as the initial value for the calculation. Then the value at crack tip can be calculated through multiple numerical iteration. The results are plotted in Fig.4. According to the results, it can be observed that the range of values of $\rho(x \approx 0)$ is $0.75:1.2$, the range of δ is $0.65:1.1$ ($\rho(x \approx 0) - \rho_0$). Based on the chemical formula of non-stoichiometric GDC ($Ce^{4+}_{0.8-x}Ce^{3+}_{x}Gd^{3+}_{0.2}O^{2-}_{1.9-\delta}$), it can be concluded that the value of δ at crack tip is 0.4 when the local stress effect is considered. The corresponding chemical formula of GDC is $Ce^{3+}_{0.8}Gd^{3+}_{0.2}O^{2-}_{1.5}$. After the multi-scale simulations is completed, the fracture toughness is $0.5142\text{MPa}\sqrt{\text{m}}$. Compared to the fracture toughness of $Ce_{0.8}Gd_{0.2}O_{1.9}$ (20GDC) ($0.9493\text{MPa}\sqrt{\text{m}}$), it is reduced by 45.83%. So, in the process of production and application of the material, the local stress effect should be specially focused.

5. Conclusion

In the work, the coupling theory of the electrolyte in the working environment is presented. In order to study the local stress effect, the electrolyte membrane with crack is selected, and the mechanical behavior of the membrane is studied by using a multi-scale method. According to the simulated results, it can be found that when micro crack exists in the electrolyte membrane, the stress at crack tip is much bigger, and the concentration of oxygen vacancy at crack tip is severely affected. Based on the simulated results, the fracture toughness of the model is decreased to $0.5142\text{MPa}\sqrt{\text{m}}$ when the local stress effect is considered in the working condition, it is reduced by 45.83% compared to the uncoupled value ($0.9493\text{MPa}\sqrt{\text{m}}$). So, in the process of production and application of the material, the local stress effect should be specially focused.

Acknowledgements

This work is supported by National Natural Science Foundation of China (10972066), the Foundation of Excellent Youth of Heilongjiang Province, and the Research Fund for the Doctoral Program of Higher Education of China (20122302110020).

References

[1] P. Datta, P. Majewski, F. Aldinger, Study of gadolinia-doped ceria solid electrolyte surface by XPS. Mater Charact, 60 (2009) 138-143.

[2] J Roa, E Gilioli, F Bissoli, Study of the mechanical properties of CeO_2 layers with the

nanoindentation technique. Thin Solid Films, 518 (2009) 227-232.
[3] R. Mangalaraja, S. Ananthakumar, K. Uma, Microhardness and fracture toughness of $Ce_{0.9}Gd_{0.1}O_{1.95}$ for manufacturing solid oxide electrolytes. Mat Sci Eng A-Struct, 517 (2009) 91-96.
[4] G.Y. Wang, V.L. Saraf, M.C. Wang, Microstructure and ionic conductivity of alternating multilayer structured Gd-doped ceria and zirconia thin films. J Mater Sci, 44 (2009) 2021-2026.
[5] F. Ye, T. Mori, J. Zou, A structure model of nano-sized domain in Gd-doped ceria. Solid State Ionics, 180 (2009) 1414-1420.
[6] A. Kossoy, Y. Feldman, R Korobko, Influence of Point-Defect Reaction kinetics on the Lattice Parameter of $Ce_{0.8}Gd_{0.2}O_{1.9.}$ Adv Funct Mater, 19 (2009) 634-641.
[7] C.H Wu, The role of Eshelby stress in composition-generated and stress-assisted diffusion. J Mech Phys Solids, 49 (2001) 1771-1794.
[8] N. Swaminathan, J. Qu, Y. Sun, An electrochemomechanical theory of defects in ionic solids: Theory. Philos Mag, 87 (2007) 1705-1721.
[9] Z.W. Cui, Y. Sun, Y.J. Chen, Semi-ab initio interionic potential for gadolinia-doped ceria. Solid State Ionics, 187 (2011) 8-18.
[10] P.D Coll, M.D. Lopez, P. Nunez, Reducibility of $Ce_{1-x}Gd_xO_{2-x}$ in prospective working conditions. J Power Sources, 173 (2007) 291-297.
[11] R.H. Tabar, L. Hua, M. Cross, A multi-scale atomistic-continuum modelling of crack propagation in a two-dimensional macroscopic plate. J Phys-Condens Mat, 10 (1998) 2375-2387.

Mechanisms of failure in porcelain-veneered sintered zirconia restorations

Tan Sui[1,*], Kalin Dragnevski[1], Tee K. Neo[2,3], Alexander M. Korsunsky[1]

[1] Department of Engineering Science, University of Oxford, Parks Road, Oxford OX1 3PJ, United Kingdom
[2] Specialist Dental Group, Mount Elizabeth Medical Centre, 3 Mount Elizabeth, #08-08/08-10, Singapore 228510, Singapore
[3] Faculty of Dentistry, National University of Singapore, 11 Lower Kent Ridge Road, Singapore 119083, Singapore
* Corresponding author: tan.sui@eng.ox.ac.uk

Abstract The continuous increase in the demand for highly aesthetic and natural-appearing dental restorations and the development of strong ceramic materials has led to the adoption of sintered ceramics as new load-bearing components used in dental prosthetics. Zirconia is one of the most attractive restorative materials due to its advantageous mechanical properties and biocompatibility. Veneering porcelains are used to coat the surface of zirconia to enhance the aesthetic appearance of prostheses. Nevertheless, porcelain-veneered zirconia restorations are prone to failure primarily by the fracture of the veneering layers. In this paper, the nature of the interfacial bonding and failure modes on samples of broken porcelain-veneered sintered zirconia restorations were studied using Environmental Scanning Electron Microscopy (ESEM) with Energy-Dispersive X-ray (EDX) analysis. Typical fractographic features were observed in broken porcelain-zirconia prosthesis. The chipping mode fractures in the veneering porcelain indicated the dominance of the cohesive fracture mode, in agreement with clinical experience reported in the literature. The crack initiation and propagation within the veneered porcelain layer was also observed and analyzed by a further examination of the fractographic features on both the prosthetic samples and the fractured surface of porcelain zirconia bars. The result indicates that the crack initiated at the location of maximum stress (point of occlusal contact). In addition, it is surmised that the fragility of the prosthesis may result from the high Vickers hardness and the associated low toughness of porcelain.

Keywords zirconia-based dental prosthesis, interface bonding, failure mode, mechanical properties

1. Introduction

Recent decades witnessed a continuous and considerable increase in the demand for highly aesthetic and natural-appearing dental restorations. At the same time, development of strong engineering ceramic materials took place. The above trends led to the adoption of sintered ceramics as new load-bearing components used in dental prosthetics [1]. Zirconia is one of the most attractive restorative materials due to its advantageous mechanical properties, biocompatibility and aesthetic appearance. Veneering porcelains with mechanical properties inferior to zirconia are used to coat the surface of zirconia to enhance the natural appearance of prostheses [2-4]. Nevertheless, porcelain-veneered zirconia restorations are prone to failure primarily by the fracture of the veneering layers [5]. This has been the dominant clinically observed failure mode, also called chipping mode failure [5,6]. One measure of the liability of dental ceramics to failure is fracture toughness, defined as the critical stress intensity factor at which a crack starts to propagate, and used as a measure of the resistance to catastrophic failure [7-9]. Possible procedures used to enhance the fracture toughness of veneering ceramics, without compromising their hardness, are likely to help reduce the incidence of such failures in clinical practice.

In this paper, the fractured surface of porcelain-veneered sintered zirconia prosthesis samples was examined under Environmental Scanning Electron Microscopy (ESEM) with Energy-Dispersive X-ray (EDX) analysis in order to identify the crack initiation sites and the propagation direction based on the observed fractographic features [10]. To validate further, the observed crack initiation features, some specially fabricated samples in the form of zirconia-porcelain bars were broken by three-point bending, and the fracture surfaces examined under ESEM. Vickers indentation was also

carried out in the attempt to explain the fragility of the porcelain.

2. Experimental procedure

Two samples (designated "prosthesis #1 and #2") of porcelain-veneered sintered zirconia restorations were supplied for analytical examination as examples of clinical failure. Fig.1 illustrates the failure mode primarily confined to the porcelain veneer and commonly referred to as "chipping". Fig.1(a) shows the image of prosthesis #1 taken with the fractured unit when still mounted in the oral cavity (9, left maxillary central incisor), whilst Fig.1(b) shows a similar chipping failure in the veneering porcelain on the upper 1st molar.

(a) (b)

Figure 1 Porcelain-veneered sintered zirconia restoration.
(a) fractured unit mounted in the oral cavity; (b) chipping failure on the upper 1st molar.

Energy-Dispersive X-ray (EDX) analysis is a technique for surface examination conducted within the Environmental Scanning Electron Microscopy (ESEM) vacuum chamber and allows the determination of specific elemental composition at high spatial resolution. ESEM with EDX analysis was firstly carried out on the prosthesis samples (Fig. 1) to investigate the nature of interfacial bonding and fracture features in order to identify the crack initiation sites and propagation directions. To investigate further the fracture mechanism and material properties, nine cylindrical porcelain-veneered zirconia bars were fabricated, three of which (designated "bar #1-#3") were fractured by three-point bending. The fractured surfaces were studied by ESEM, while the other six bar samples (designated "Vickers #1-#6") were indented by Vickers hardness testing machine. The corresponding Vickers hardness and toughness values were evaluated with the aid of ESEM imaging.

3. ESEM characterization of prosthesis samples

3.1. Interfacial bonding

EDX is useful in determining elemental distribution of materials, and thus the mutual elemental diffusion can be identified. In the present study, EDX analysis was conducted on the broken surfaces within the region shown in Fig. 2(a). The results indicate that the porcelain region contains a high overall concentration of O and silicon (Si), due to the high silica (SiO_2) content. Notably, there is evidence of not only Si diffusing into the Zr-rich domain (Si map), but also zirconium (Zr) diffusing into the Si-rich porcelain domain (Zr map). This evidence of mutual elemental diffusion of Zr and Si reveals the origins of the good mechanical bonding observed between zirconia ceramic copings and porcelain veneers [11-13]. It is also worth noting that the studies of fracture surfaces of the sample supplied failed to identify prominent cases of adhesive fracture localized along the

interface (that is marked with an arrow). The combination of these observations suggests that the interfacial bonding between zirconia and porcelain can be classified as strong.

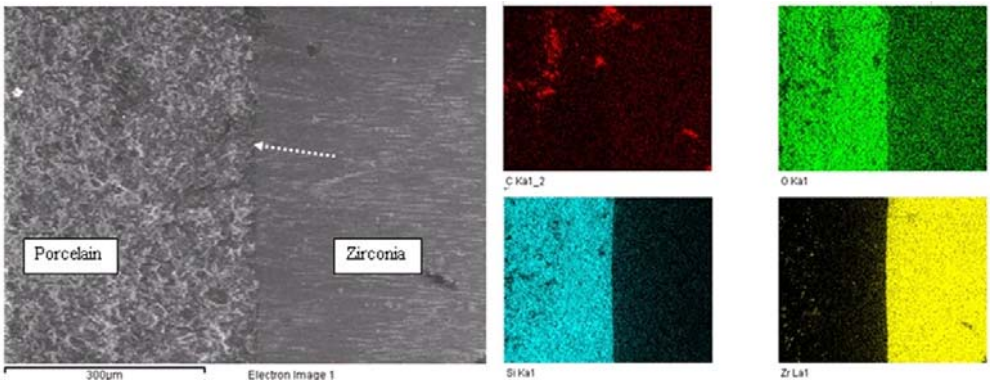

(a) (b)

Figure 2 ESEM image and corresponding elemental X-ray maps of the region of interfacial bonding

3.2 Pre-existing defects

The preparation procedure used for porcelain naturally leads to the formation of gas bubbles that persist as defects within the veneering layer. This may increase the likelihood of crack initiation at these positions under the applied mastication load, and may lead to chipping mode cracking in which the fracture propagates by connecting different defects. Fig. 3 illustrates the presence of the pre-existing pores of a range of sizes within prosthesis #1. The SEM image shown was collected from the occlusal-facing fracture surface remaining after chipping. The characteristic semi-spherical smooth dimples represent the remainder after the passage of a crack through pre-existing pores. The presence of both large pores (>20μm) and smaller pores (~10 μm) is noted. Therefore, it appears that some control over the pore size or the distribution of flaws within porcelain veneer after firing would be helpful in reducing the possibility of crack initiation. Since quality control over individual restorations appears to be prohibitively expensive, this would be probably best exercised through control of the thermal schedules and over the veneer shape and thickness.

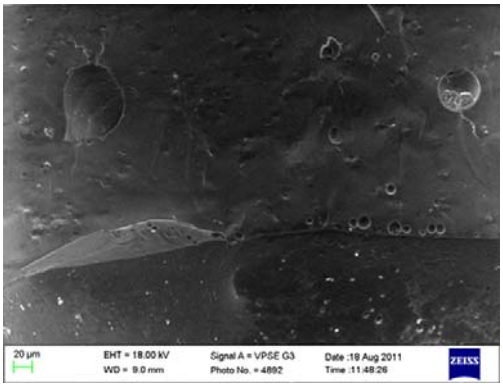

Figure 3 ESEM image of the porcelain fractured surface, showing presence of pre-existing pore defects

3.3 Chipping mode fracture

In most cases, the chippings were contained entirely within the porcelain layer and did not reach the interface with the zirconia core, i.e. the cohesive fracture mode was observed. However, it is conceivable that cracks initiated close to or at the veneering surface may propagate across the unit and through the interface to cause the final failure, in which case the adhesive mode of fracture would be observed. A micrograph of chipping mode failure observed is illustrated in Fig. 4(a). The

cohesive fracture through the porcelain layer is in agreement with literature that crack initiation within the veneered porcelain layer is the dominant failure mode for both metal coping and all-ceramic restorations [14]. Fig. 4(b) illustrates a region of oblique fracture in porcelain that propagated towards and along the interface of the underlying zirconia structure. Further confirmation was sought by EDX analysis. It is apparent that the top left region is Si-rich (porcelain), while the bottom right region is rich in zirconium (core).

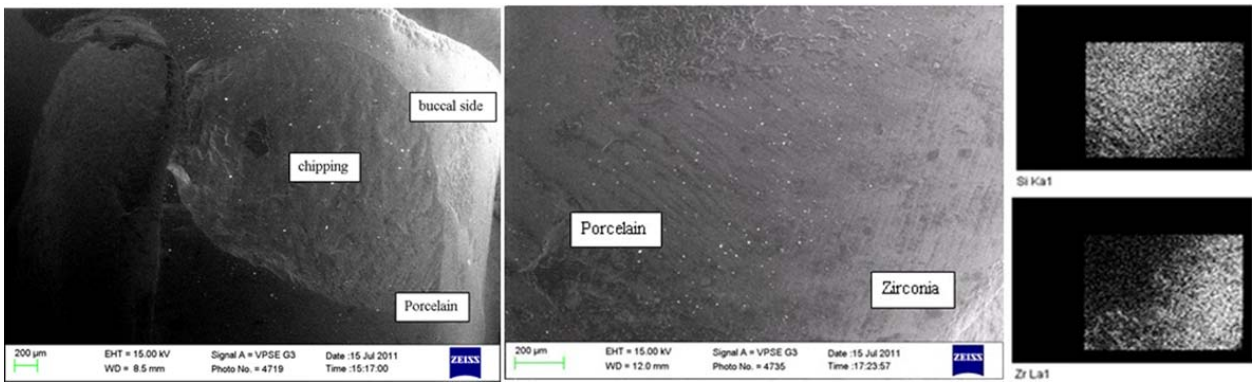

(a) (b)

Figure 4 Typical two fracture modes on the surface of restoration. (a) Overall micrograph of chipping failure; (b) An oblique fracture in porcelain that propagated towards and along the interface with the underlying zirconia core structure

3.4 Crack initiation and propagation

Fractographic analysis was used to determine the crack propagation direction and the crack initiation location by identifying certain common features, namely “wake hackle” and “arrest lines” (identified below in Fig. 5) [15,16]. These were found at the fractured surfaces within the samples investigated in this report, and were used to trace the crack propagation back to the fracture origin. Wake hackle is generally formed when a crack passes a discontinuity, e.g. void. It is associated with the high stress field experienced by the void as the crack propagates close to it. This usually causes crack re-initiation at a point that lies slightly above or below the major crack plane. However, the fastest moving major crack eventually catches up with this new propagating micro-crack, and the latter becomes incorporated in the master crack. Meanwhile, a tell-tale surface hollow or elevated region is left behind, which is referred to as the “wake hackle”, pointing in the direction of crack propagation. Arrest line is another indicator of the crack propagation direction. It is approximately perpendicular to the general direction of propagation. Since the growing crack expands in different directions during growth, the crack origin lies behind the concave side of the crack front. Hence, the fracture origin can be traced back to the approximate center of expanding arrest lines family observed at the fracture surface [17].

Fig. 5 shows the surface of a porcelain-initiated fracture in the chipping on the surface of prosthesis #2, with crack initiated at defects in the veneer located at or close to the occlusal surface. The region indicated by the rectangular white box in Fig. 5(a) is shown at higher magnification in Fig. 5(b), where the wake hackle and arrest line features are identified. Fractographic analysis shows that crack may progress from two origins (Fig. 5(a)) lying on the left of the picture, within the porcelain veneer layer and at or close to the surface. Hence we draw the conclusion that fracture initiated close or at the veneer surface, and propagated across the unit and through the interface to cause final failure. Meanwhile, material aspects (coefficients of thermal expansion, thermal conductivity mismatch, phase transformation [18,19]) of porcelain close to the surface may give rise to residual stresses throughout the restoration that likely to promote chipping.

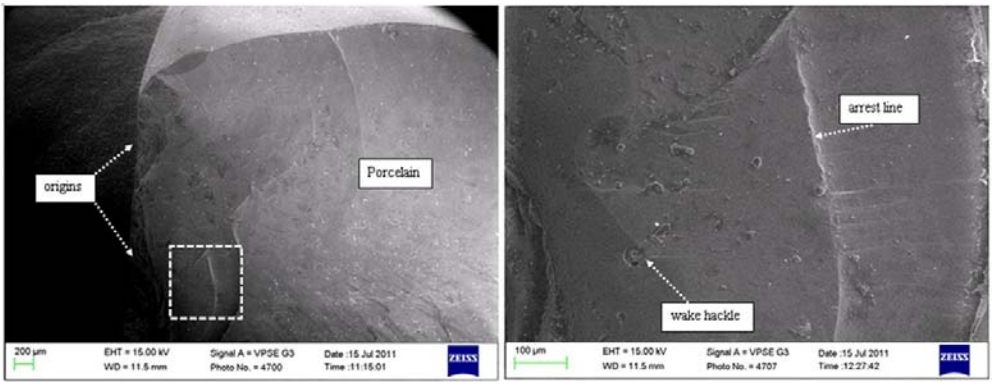

(a) (b)

Figure 5 Fractographic features in porcelain layer of prosthesis #2. (a) Surface of a porcelain-initiated fracture in the chipping on the surface; (b) Higher magnification image of the highlighted (white dashed square) region in (a)

In the case of prosthesis #1, considering the junction between the occlusal fractured surface and the lingual side of the restoration, we conclude that the crack initiation may have occurred at this junction and propagated from the junction to the occlusal surface, roughly from left to right in Fig. 6. The short dashed arrows on the lingual side are considered as the candidate sites for crack initiation, and longer dashed arrows on the occlusal side indicate the putative crack propagation direction. Thus, the crack may initiate on the lingual side with a concentrated force perpendicular to the lingual side, which leads to the crack initiation and propagation on the cross section, i.e. occlusal side, and final breakage. It is worth noting the change of direction of the crack that is seen in Fig. 6. This is likely to indicate a transition from friction-assisted cone crack induced by the grinding contact at the porcelain surface, to faster pressure-induced tensile fracture mode that leads to the subsequently observed fracture [5].

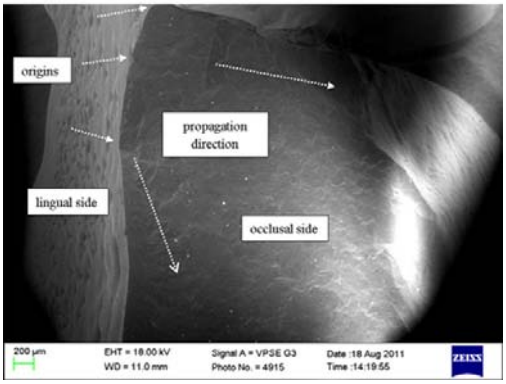

Figure 6 Fractographic features in porcelain layer of prosthesis #1

4. ESEM characterization of broken porcelain-zirconia bars

4.1 Fractured surface after three-point bending

To validate the above observations made on prostheses samples, three-point bending was carried out on three zirconia-porcelain bars and the fractured surface was examined by means of ESEM. A schematic diagram of the three-point bending experiment is shown in Fig. 7(a). As a brittle material, the porcelain fails most readily in tension. The crack is expected to initiate from the location of maximum tensile stress, i.e. the “top” position (marked with yellow circle in Fig. 7(a)). This was

verified by the detailed analysis of fractographic features shown in Figs. 7(b) and 7(c) (images of one representative sample) that indicate the crack propagation from “top” to “bottom” (marked with white dashed arrow Fig.7(b)), although the features were only visible on the “left” and “right” sides, or both sides of the cross section (marked with red circle in Fig. 7(a)) due to the breakaway of the porcelain on the “top” or “bottom” sides.

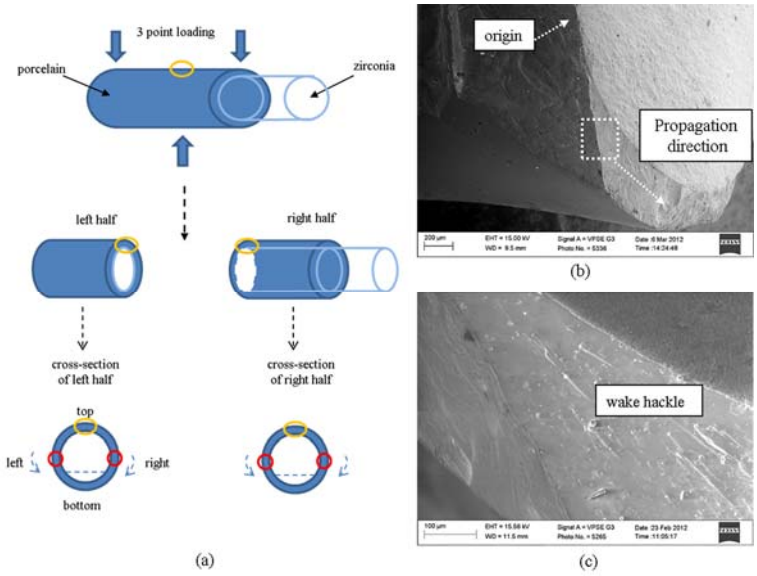

Figure 7 Schematic representation of the three-point bending test and failure of the specimens
(a) three-point bending; (b) & (c) typical ESEM images of the fractured surfaces

4.2 Vickers hardness and toughness evaluation

Further evaluation of the mechanical properties of the veneering porcelain (hardness and fracture toughness) was carried out using Vickers indentation on six zirconia porcelain bar samples (designated “Vickers #1-#6”). The formulas used for the evaluation of Vickers hardness and toughness are [8,20,21].

$$H = \frac{F}{A} = \frac{1.854F}{d^2} \tag{1}$$

$$K_{IC} = 0.016\left(\frac{E}{H}\right)^{0.5}\left(\frac{F}{c^{1.5}}\right) \tag{2}$$

where F is the applied force on the diamond indenter (unit of N), A is the surface area of the resulting indentation (unit mm^2), d the average length of the diagonal left by the indenter (the average of two diagonals d_1 and d_2) with the unit of mm, c the crack size measured from the center of the indentation (unit of mm), H is Vickers hardness (unit of GPa) and E is Young’s modulus (unit of GPa), and K_{IC} is the fracture toughness (unit of MPa/m$^{1/2}$). For illustration, the indentation impression in sample Vickers #1 is shown in Fig. 8. The results of all six indented samples with loads of 10N and 50N are listed in Table 1.

Table 1 Hardness and toughness of the indented samples

Sample	Load (N)	d_1 (μm)	d_2 (μm)	d (μm)	Vickers hardness (GPa)	c (μm)	E (GPa)	Toughness (MPa/m$^{1/2}$)
#1	10	45.96	47.35	46.66	8.516	71.88	65	0.725
#2	10	41.95	44.35	43.15	9.957	56.60	65	0.960
#3	10	39.92	44.66	42.29	10.367	49.62	65	1.146
#4	50	98.68	70.70	84.69	12.925	178.5	65	0.752
#5	50	98.31	104.5	101.405	9.015	182	65	0.875
#6	50	122.1	125.0	123.55	6.073	194.3	65	0.966

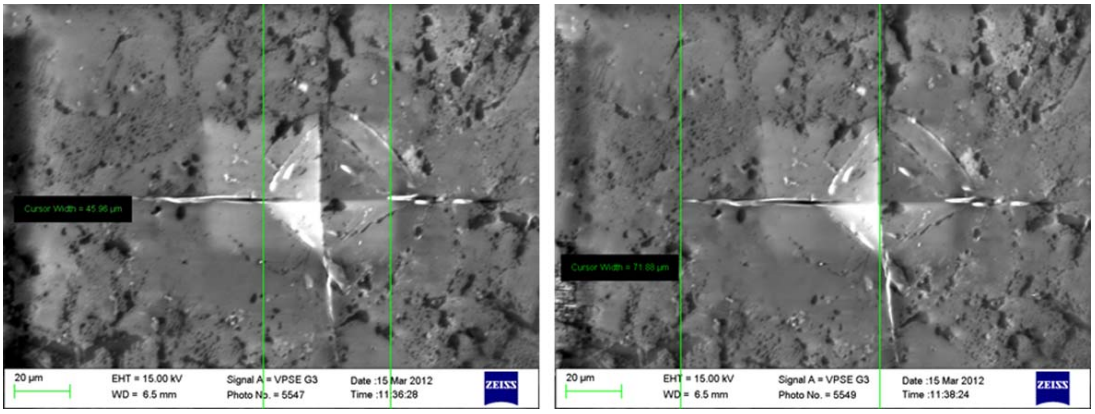

(a) (b)

Figure 8 Vickers hardness and toughness determination for specimen Vickers #1 (10N load)
(a) measurement of the diagonal length; (b) measurement of the crack length

In the results found in the literature, the average toughness of porcelain has been reported to lie in the range 1.5-2.1MPa/m$^{1/2}$, and the hardness in the range 4-8GPa [7,9,20,21], the results demonstrate that the porcelain used in this experiment has a relatively high hardness, and accordingly a reduced level of toughness. This may be due to the inherent chemical formulation of the porcelain or its processing history. Notably, merely the presence of a population of voids is likely to result in reduced toughness, but may not lead to increased hardness observed in our experiments.

5. Conclusion

Conclusions are made based on the ESEM and EDX analyses conducted for this paper. The strength of the zirconia-porcelain interface is derived from the mutual diffusion of zirconium and silicon at the interface. Chipping mode fractures observed in the veneering porcelain indicate the dominance of the cohesive fracture. Adhesive fracture may only be observed in the case of crack travelling at a very shallow angle to the interface. Failure of all-ceramic zirconia-based restorations by porcelain veneer chipping is a complex process that depends on a large number of factors. Pre-existing defects in the porcelain veneer may promote chipping mode cracking and final failure. The results from fractured surface examination of the porcelain zirconia bars further confirm that in the real prosthesis the crack is likely to initiate at the position in lingual side with maximum stress. Moreover, great Vickers hardness and low toughness suggest the weakness of porcelain. Exercising control over these fabrications appears to be a critical requirement for clinical practice.

Acknowledgements

The authors would like to thank Igor N Dyson for his great help in performing the three-point bending and Vickers indentation.

References

[1] F. Zarone, S. Russo, R. Sorrentino, From porcelain-fused-to-metal to zirconia: Clinical and experimental considerations, Dent Mater, 27 (2011) 83-96.

[2] H.M. Al-Dohan, P. Yaman, J.B. Dennison, M.E. Razzoog, B.R. Lang, Shear strength of core–veneer interface in bi-layered ceramics, J Prosthetic Dent, 91 (2004) 349-355.

[3] M. Guazzato, K. Proos, L. Quach, M.V. Swain, Strength, reliability and mode of fracture of bilayered porcelain/zirconia (Y-TZP) dental ceramics, Biomaterials, 25 (2004) 5045-5052.

[4] G. Isgro, P. Pallav, J.M. van der Zel, A.J. Feilzer, The influence of the veneering porcelain and different surface treatments on the biaxial flexural strength of a heat-pressed ceramic, J Prosthetic Dent, 90 (2003) 465-473.

[5] E.D. Rekow, N.R.F.A. Silva, P.G. Coelho, Y. Zhang, P. Guess, and V.P. Thompson, Performance of dental ceramics challenges for improvements, J Dent Res, 90 (2011) 937-952.

[6] B.E. Pjetursson, I. Sailer, M. Zwahlen, C.H. Hammerle, A systematic review of the survival and complication rates of all-ceramic and metal–ceramic reconstructions after an observation period of at least 3 years. Part I: Single crowns, Clin Oral Implants Res., 18 (2007) 86-96.

[7] H. Wang, G. Isgro, P. Pallav, A.J. Feilzer, Fracture toughness determination of two dental porcelain with the indentation strength in bending method, Dent Mater, 23(2007) 755-759.

[8] M. Taira, Y. Nomura, K. Wakasa, M. Yamaki, A. Matsui, Studies on fracture toughness of dental ceramics, J Oral Rehabil, 17(1990) 551-563

[9] S. Al-Shehri, Relative fracture toughness and hardness of dental ceramics, Saudi Dental Journal,14 (2002) 67-72.

[10] J.F. Mansfield, X-ray analysis in the ESEM a challenge or a contradiction, Mikrochimica Acta 132 (2000) 137–143.

[11] M.Yamaoka, H.Murakami, S.Miyazaki, Diffusion and incorporation of Zr into thermally grown SiO2 on Si(1 0 0), Appl Surf Sci, 216 (2003) 223-227.

[12] J.C. Durand, B. Jacquot, H. Salehi, M. Fages, J. Margerit, F.J. Cuisinier, Confocal Raman microscopic analysis of the zirconia/feldspathic ceramic interface, Dent Mater, 28 (2012) 661-671.

[13] H.J. Kim, H.P. Lim, Y.J. Park, M.S. Vang, Effect of zirconia surface treatments on the shear bond strength of veneering ceramic, J Prosthet Dent. 105 (2011) 315-322.

[14] P.G. Coelho, J.M. Granjeiro, G.E. Romanos, M. Suzuki, N.R. Silva, G. Cardaropoli, V.P. Thompson, J.E. Lemons, Basic research methods and current trends of dental implant surfaces, J Biomed Mater Res B Appl Biomater, 88 (2009) 579-596.

[15] J.B. Quinn, G.D. Quinn, J.R. Kelly, S.S. Scherrer, Fractographic analyses of three ceramic whole crown restoration failures, Dent Mater, 21 (2005) 920-929.

[16] S.S. Scherrer, J.B. Quinn, G.D. Quinn, H.W. Wiskott, Fractographic ceramic failure analysis using the replica technique, Dental Mater, 23 (2007) 1397-1404.

[17] B. Taskonak, J. Yan, J.J.Jr Mecholsky, A. Sertgozc, A. Kocak, Fractographic analyses of zirconia-based fixed partial dentures, Dental Mater, 24 (2008)1077-1082.

[18] M.J. Tholey, M.V. Swain, N. Thiel, SEM observations of porcelain Y-TZP interface, Dent Mater, 25 (2009) 857-862.

[19] M.V. Swain, Unstable cracking (chipping) of veneering porcelain on all-ceramic dental crowns and fixed partial dentures, Acta Biomater. 5 (2009) 1668-1677.

[20] J.J. Kruzic, D.K. Kim, K.J. Koester, R.O. Ritchie, Indentation techniques for evaluating the fracture toughness of biomaterials and hard tissues. J Mech Behav Biomed, 2(2009) 384-395.

[21] J.J. Kruzic, R.O. Ritchie, Determining the toughness of ceramics from Vickers indentations

using the crack-opening displacements: an experimental study. J Am Ceram Soc., 86(2003) 1433-1436.

Paper Template for 13th International Conference on Fracture

FirstName LastName[1,*], Second Author[1], Third Author[2]

Cracking simulation of ceramic materials under thermal shock by a non-local fracture model

Li Jia[1,*], Song Fan[2], Jiang Chiping[3]
[1]LSPM, CNRS UPR 3407, Université Paris XIII, Villetaneuse, France;
[2]State Key Laboratory of Nonlinear Mechanics, Institute of Mechanics, Chinese Academy of Sciences, Beijing, China;
[3]Solid Mechanics Research Center, Beijing University of Aeronautics and Astronautics, Beijing, China
[*]Corresponding author: jia.li@univ-paris13.fr

Abstract: In this work, we attempted to simulate the cracking process of ceramic beams subjected to quenching from different high temperatures to the ambient one. Based on a non-local damage theory and the linear fracture mechanics, a numerical model was established and implemented into a finite element code. This model is adjusted with two critical situations: it is equivalent to the maximum principal stress criterion when the specimen is subjected to uniform tensile stress and to the Griffith-Irwin criterion for the growth of a macro-crack. By using this numerical model, the initiation and propagation of cracks in quenched ceramic specimens were simulated. It was proved that the proposed damage model is capable to describe the detailed cracking process with high reliability comparing to the experimental results. Several typical characteristics in thermal shock failure such as the multi-cracking procedure, the hierarchical crack distribution, the distances between cracks etc. were faithfully described with high accuracy.

Key words: Thermal shock; Crack patterns; Non-local fracture model; Numerical simulations; Ceramics

1. Introduction

Ceramic materials exhibit excellent high temperature mechanical properties, corrosion resistance, wear resistance, erosion resistance, oxidation resistance etc. However, they are in general quite vulnerable to thermal shock failure. In general, crack formation is considered as the major reason of failure in thermo-structural engineering. Understanding the mechanisms of cracking process in ceramics under thermal loads has been one of the most importance tasks in the research of this field.

The earliest researches on fracture of ceramic materials underwent thermal shock by Kingery [1,2] and Hasselman [3]. Afterward, numerous theoretical and experimental studies on thermal shock failure of ceramics have been reported [4-15]. However, the crack pattern formation under thermal shock is quite a rapid and highly complicated process. This process is difficult to capture with available experimental techniques. Only final crack patterns can easily be observed. This is why direct numerical simulations are particularly interesting in reproducing the cracking process. As results, the failure mechanisms and the control parameters can be better understood. Unfortunately, the direct numerical simulations have rarely been reported in the literature so far due to the inherent complexities in multi-cracking modelling.

In this work, a non-local failure criterion was used and implemented into a finite element code and then applied to simulate the crack evolution in ceramic materials subjected to thermal shock. The proposed fracture model is equivalent to the maximum principal stress criterion for a specimen under pure tensile loading, and to the Griffith-Irwin criterion for the crack propagation. Consequently, this non-local fracture model can both predict crack initiation as well as crack

growth. The numerical simulations successfully reproduce the cracking patterns in ceramic specimens after quenching. The periodical and hierarchical characteristics of the crack patterns are predicted with satisfactory accuracy. Moreover, the direct numerical simulations faithfully describe whole the cracking process, including the crack initiation, crack growth and crack arrest during quenching tests. By comparing to the previous experimental results, the accuracy and efficiency of the proposed model are examined and discussed. Finally, we give some concluding remarks and directions to follow in future works.

2: Non-local damage model

We first outline briefly the non-local fracture model proposed in Li et al. [16-17]. The basic idea of this model consists in replacing the local damage driving force, an effective stress σ_e for example, by its weighted average over a representative volume V [18]:

$$\tilde{\sigma}_e(\mathbf{x}) = \frac{1}{\int_V \alpha(\mathbf{x}-\mathbf{y})d\mathbf{y}} \int_V \alpha(\mathbf{x}-\mathbf{y})\sigma_e(\mathbf{y})d\mathbf{y} \tag{1}$$

where α is a weighting function. In the present work, a cone-shape function is adopted for simplicity:

$$\alpha(r) = \begin{cases} 0 & r > R \\ 1 - \dfrac{r}{R} & r \le R \end{cases} \tag{2}$$

where $r = \|\mathbf{x}-\mathbf{y}\|$; R is the radius of non-local action, representing a material characteristic length which defines the size of interaction zone in failure process.

We assume reasonably that the failure in ceramic materials under uniform stress fields obeys the maximum principal stress criterion. However, it can not directly be utilized to predict crack growth due to the stress singularity near the crack tips. This shorthand can be overcome by a non-local formulation such like Eq. (1). Thus, the non-local maximum principal stress criterion can be written as follows:

$$D = \begin{cases} 0 & \tilde{\sigma}_1 < \sigma_c \\ 1 & \tilde{\sigma}_1 \ge \sigma_c \end{cases} \tag{3}$$

where D is the damage, σ_c is the ultimate stress of the material, $\tilde{\sigma}_1$ is the non-local first principal stress. We enforce the validity of criterion (3) in two special cases: First, it should be valid in the case of a uniform tensile load. It is clear that this condition is automatically satisfied since in this case, we have $\tilde{\sigma}_1 = \sigma_1$. Second, it should be valid for the growth of a mode-I crack. To this end, we assume that the near-tip stress field is governed by the Williams asymptotic expansion [19]. Therefore, for a mode-I loaded crack, the non-local first principal stress near the crack tip writes, according to (1) and (2):

$$\tilde{\sigma}_1(r,\theta)=\frac{1}{\int_0^R\int_{-\pi}^{\pi}\left(1-\frac{r'}{R}\right)r'dr'd\theta'}\int_0^R\int_{-\pi}^{\pi}\left(1-\frac{r'}{R}\right)\frac{K_I}{\sqrt{2\pi r}}\left(1+\cos\frac{\theta}{2}\right)\left|\sin\frac{\theta}{2}\right|r'dr'd\theta' \tag{4}$$

where K_I is the stress intensity factor, r and θ are the polar coordinates with the origin at the crack tip. Under mode I loading, the maximum non-local principal stress is located at a point on the crack axis near the crack tip $r=r_0,\theta=0$ due to the symmetry. We assume that r_0 is small such that the stress at its vicinity is still governed by the crack-tip asymptotic field. On the one hand, according to the damage criterion (3), the element at $(r=r_0,\theta=0)$ is broken when $\tilde{\sigma}_1\geq\sigma_c$. On the other hand, from the Griffith-Irwin criterion of fracture [20-21], the crack grows when $K_I\geq K_{Ic}$, where K_{Ic} is the critical stress intensity factor. This condition permits us to determine the non-local action radius R by resolving numerically the following equation:

$$f(R)=\sigma_c-\max_{r_0}\int_0^R\int_{-\pi}^{\pi}\frac{3}{\pi R^2}\left(1-\frac{r'}{R}\right)\frac{K_{Ic}}{\sqrt{2\pi r}}\left(1+\cos\frac{\theta}{2}\right)\left|\sin\frac{\theta}{2}\right|r'dr'd\theta'=0 \tag{5}$$

with

$$r=\sqrt{(r_0+r'\cos\theta')^2+(r'\sin\theta')^2}\qquad \tan\theta=\frac{r'\sin\theta'}{r_0+r'\cos\theta'}$$

Thus, the non-local damage criterion (3) is exactly equivalent to Griffith-Irwin criterion when the non-local action radius R is determined by (5). Consequently, we can confirm that in the cases of uniform tensile loads and mode-I cracks, the fracture can exactly be predicted by using the criterion (3). From this point of view, the proposed non-local criterion can be used to predict the crack initiation as well as the crack propagation. In practice, we just need to find the point where the non-local principal stress is maximal: this point is broken when the non-local stress attaints the material strength.

The proposed non-local fracture criterion was implemented into a finite element code. As the criterion (3) is an instantaneous damage model, an element is linearly elastic before its complete failure. Therefore, the crack propagation prediction is very similar to that adopted in the linear elastic fracture mechanics: A linear elastic calculation is first carried out for the cracked structure; then the crack propagation is determined according to a suitable criterion. This procedure is then repeated after each small crack progression in the structure. In the present work, the crack propagation is represented by successive eliminations of groups of damaged elements.

3. Thermal shock problem

The proposed non-local criterion was used to evaluate the cracking process in ceramic specimens under thermal shock.

3.1 Experiments

Jiang et al. [14] carried out quenching experiments on ceramics plates from different temperatures. This experimental study will be used in the validation of the proposed model. In Jiang et al. [14], 99% Al_2O_3 powder was thermoformed into 50mm×10mm×1mm thin specimens. They were bound up with inconel wires and heated to a temperature T_0 ranged from 300°C to 600°C. After that, the heated specimens were dropped into a water bath of T_∞=20°C by free fall. Figure 1 shows the thermal shock crack patterns. From Figure 1, we can remark the following points:

- The number of cracks increases as the initial temperature increases;
- The lengths of the cracks increase as the initial temperature increases;
- The crack spacing decreases as the initial temperature increases;
- A tendency towards equal spacing between cracks can be observed;
- The crack patterns exhibit a hierarchical structure. One can distinguish 2 classes' cracks for quenching tests with T_0=300°C, and 3 classes' cracks for quenching tests with T_0=350°C ~ 600°C. However, the frontiers of the different classes are not always clear.

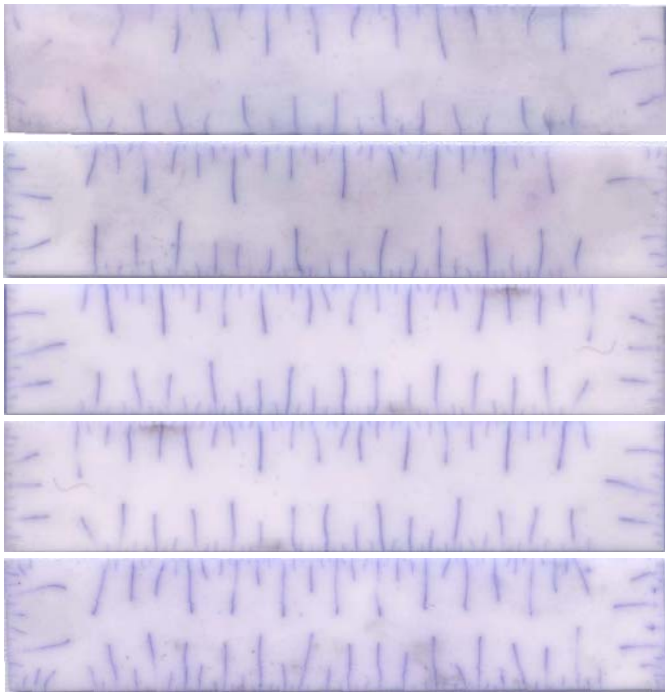

T_0=300°C

T_0=350°C

T_0=400°C

T_0=500°C

T_0=600°C

Figure 1: Crack patterns after quenching experiments

3.2 Model

By considering the symmetry of the specimen, a quart of it was meshed by using three-node plane stress elements. The side size of the elements is about d= 0.05mm, e.g. about a half of the non-local action radius R. When the failure criterion is fulfilled in an element, it will be eliminated from the model, together with its immediate neighbouring elements. The successive damaged spots form a damaged band with a width of about 0.12mm.

3.3 Temperature and thermal stress fields

The experimental conditions allow us to regard the temperature field as two-dimensional. Establish a Cartesian coordinate system Oxy with the origin at the centre of the specimen and x and y

coinciding with the specimen axes. Noting that during the process of water quenching, the water temperature holds at T_∞=20°C in the bath. According to the thermal transfer calculation, the temperature distribution at any instant in the specimen writes:

$$\frac{T}{T_0}=\left[\sum_{m=1}^{\infty}X_m\exp\left(-\alpha_m^2\frac{at}{L_1^2}\right)\cos\left(\alpha_m\frac{x}{L_1}\right)\right]\left[\sum_{m=1}^{\infty}Y_m\exp\left(-\beta_m^2\frac{at}{L_2^2}\right)\cos\left(\beta_m\frac{y}{L_2}\right)\right] \quad (6)$$

where t is the time, $a=k/\rho c$; k, ρ, c are the thermal conductivity, density and specific heat, respectively; T_0 is the initial temperature assumed to be uniform in the specimen; and

$$X_m=\frac{2\sin\alpha_m}{\alpha_m+\sin\alpha_m\cos\alpha_m} \quad Y_m=\frac{2\sin\beta_m}{\beta_m+\sin\beta_m\cos\beta_m}$$

with α_m and β_m are the roots of the following transcendent equations:

$$\tan\alpha_m=\frac{hL_1}{k\alpha_m} \quad \tan\beta_m=\frac{hL_2}{k\beta_m}$$

where L_1 and L_2 are respectively the semi-length and semi-width of the specimen; h is the convective heat transfer coefficient.

3.4: Material parameters

The ceramic specimens were assumed to be linearly elastic, homogeneous and isotropic. From available data, Young's modulus E, Poisson's ratio ν, the ultimate tensile stress σ_c, the density ρ [22], and the energy release rate G [23] of 99% Al_2O_3 ceramics are listed in Table 1. The critical stress intensity factor is deduced from $K_{Ic}=\sqrt{GE}$. The non-local action radius deduced from (5) is R=0.1176mm. Conversely, the thermal parameters such like the thermal conductivity k, the specific heat c and the thermal expansion coefficient α are temperature-dependent [24-26]. Consequently, adopting constant values in the quenching simulations is an approximate and simplified assumption. The values used in the simulations are taken from [24-26] and also listed in Table 1. The available data [27-30] on the convective heat transfer coefficient h in thermal shock give scattering estimations ($h \approx 10^4$~10^5W/(m^2·K)). In this work, a constant value for h was used in all the simulations, its value was estimated such that the numerical results on average crack spacing at each quenching temperature approximately agree with the experimental measurement. The value used in the present work is h =50000W/(m^2·K).

Table 1: Mechanical and thermal parameters used in the simulations

E(MPa)	ν	σ_c(MPa)	ρ(kg/m^3)
370000	0.3	180	3980;
G(J/m^2)	k(W/(m.K))	c(J/(kg.K))	α
24.3	31	880	7.5×10^{-6}

4. Results and discussions

4.1: Direct comparison with the experiments

Figure 2 illustrates the final crack patterns of the simulations for different initial quenching temperature. For comparison, the experimentally obtained crack patterns are also showed. Globally speaking, the simulations reproduce faithfully the crack patterns obtained from quenching tests. The resemblance between the numerical results and the real tests is obvious. Following remarks can be made:

1. As in quenching tests, multi-cracking patterns are obtained;
2. As in quenching tests, the cracks can be classified into 2 or 3 hierarchical levels;
3. As in quenching tests, the tendency towards equal crack spacing is obvious.

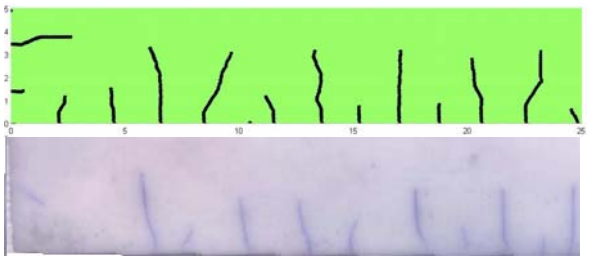

(*a*) T_0=300°C

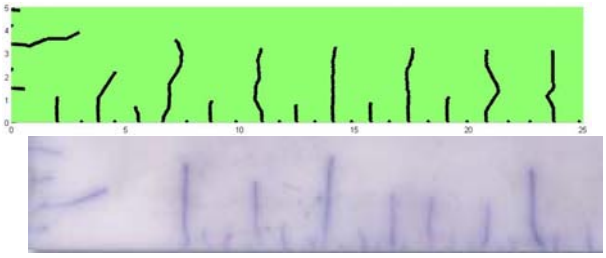

(*b*) T_0=350°C

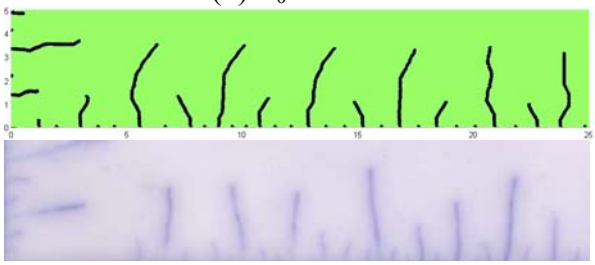

(*c*) T_0=400°C

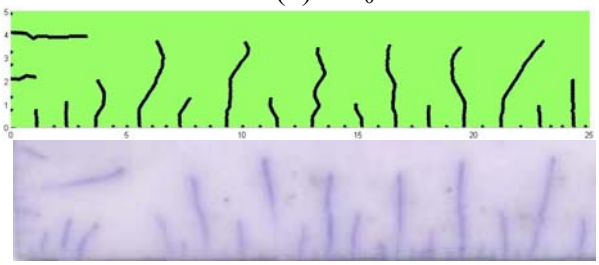

(*d*) T_0=500°C

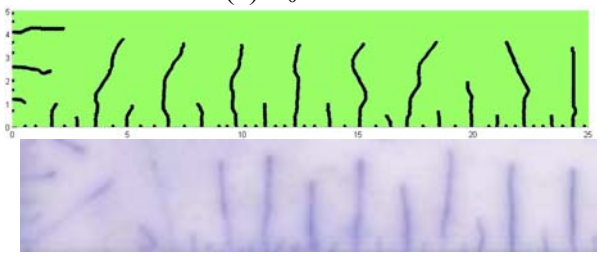

(*e*) T_0=600°C

Figure 2: Comparison between the crack patterns in numerical models and in real specimens

4.2: Characteristic values of the crack patterns

Statistically speaking, the principal features of the crack patterns can be brought out from numerical results. Table 2 shows the comparison between the experimental and numerical results on average crack spacing *s* observed at the specimen surfaces. From this comparison, we can see the numerical simulations are quite accurate, even by using constant material parameters.

Table 2: Dimensionless average crack spacing $\bar{s} = s/L_2$

T_0	300°C		350°C		400°C		500°C		600°C	
	test	simulation	test	simulation	test	Simulation	test	simulation	test	simulation
$\bar{s}$	0.32	0.333	0.184	0.181	0.16	0.158	0.142	0.133	0.12	0.105

Although the morphologies are very similar between the experimental crack patterns and the numerical ones, the quantitative comparison on crack lengths p is not evident due to the data scattering of the experimental results. By assuming that each crack level obeys a Gaussian distribution, Jiang et al. [14] described the crack length distribution by a combined Gaussian function. This analysis allowed the classification of the cracks according to their length in a statistical manner. In Table 2, we list the average lengths of the longest cracks of the experimental and numerical crack patterns. The comparison shows a good agreement, even though the numerical simulations provide smaller crack lengths comparing to the experiments.
The principal reason of this difference may be the blunt form of the crack tips in numerical models, in which the cracks were represented by damaged bands with a finite thickness.

Table 3: Dimensionless crack length $\overline{p} = p/L_2$

T_0	300°C		350°C		400°C		500°C		600°C	
	test	simulation	Test	simulation	test	simulation	Test	simulation	test	simulation
$\overline{p}$	0.72	0.64	0.74	0.65	0.72	0.68	0.78	0.73	0.8	0.75

4.3: Cracking process during the thermal shock

Figure 3 shows the first crack initiations at the specimen surface. The distribution of the first principal stresses is also shown by means of a colouring map. From this image, we can observe that, at a critical time where the temperature gradient reaches a sufficiently high level, the first crack will appear at the location where the non-local first principal stress is maximal and fulfils the failure criterion (3). After that, the stresses are relaxed at this location, and the stress redistribution furnishes another location where the first principal stress is maximal. If the fracture criterion (3) is always fulfilled, a new crack onset takes place. Since the stress distribution is nearly uniform along the specimen surface, the first crack initiations are somewhat randomly located, depending only on the scattering of the numerical results. The following cracks will appear between the most distant cracks previously formed. This procedure will repeat until the temperature gradient is no longer capable to produce sufficient stress concentration to onset new cracks.

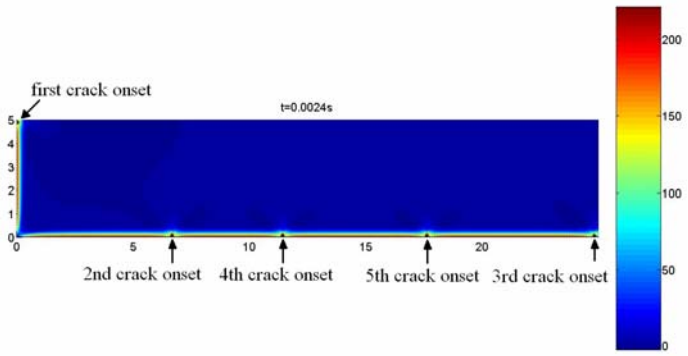

Figure 3: First crack initiations

Figure 4 shows some different steps of the cracking process. The crack growth scheme can be summarized by observing these images. At the beginning, the thermal shock cracks initiate and propagate uniformly with approximately a nearly equal spacing (Fig. 4-*a*). At this step, the thermal shock cracks propagate simultaneously and very rapidly, then the propagation speed decreases gradually with release of the thermal stresses until the strain energy cannot support simultaneous propagation of all the cracks. Consequently, only a reduced number of cracks continue to propagate, whereas the other cracks stop. The crack spacing increases until 2 or 3 times larger than the previous one (Fig. 4-*b*). In the following steps, the crack growth may deviate and attempt to form equal crack spacing (Fig. 4-*c*). This procedure may repeat several times until the strain energy induced by thermal stresses cannot support propagation of any crack. The final simulation crack patterns (Fig. 4-*d*) are very similar to those observed in experimental results. This remark supports the cracking process above described.

The colouring map represents the levels of first principal stresses (unity in MPa). From Figure 4, the locations of stress concentrations can clearly be observed. The competition amongst the stress concentrations at different locations leads to the formation of multi-crack failure patterns. The proposed damage model provides a natural manner in reproducing them. Comparing to the traditional treatment of fracture mechanics in which the crack growth conditions should be examined at each crack tip, the present method is much more simple and robust to deal with multi-cracking problems.

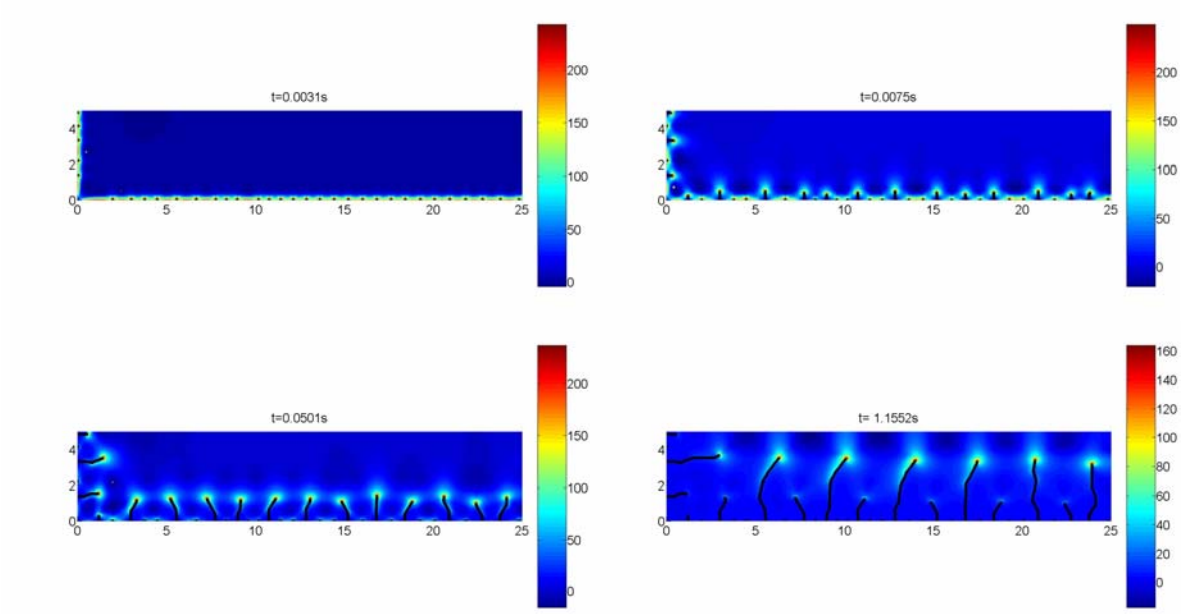

Figure 4: Crack patterns at different times, T_0=500°C

5. Conclusions and future works

In this work, a non-local failure model was described to predict crack initiation and crack growth in brittle materials and then implemented into a finite element code. This non-local fracture model was

successfully applied to simulating the crack evolution in ceramic materials subjected to thermal shock. From the results of the numerical simulations, the following conclusions can be formulated:

1. The numerical simulations reproduced faithfully the crack patterns in ceramic specimens after quenching tests. The periodical and hierarchical characteristics of the crack patterns were accurately predicted;
2. The parameters describing the crack patterns such as the average crack spacing and the crack lengths were correctly estimated from the numerical results;
3. The numerical simulations allow a direct observation on crack initiation and growth in the specimens, which is quite a difficult task in experimental studies.
4. The finite element implementation of the proposed non-local criterion allows accurate cracking simulations for real structures under thermal shock. The theoretical concept is clear and simple. The numerical model is robust, easy to apply to different engineering structures subjected to thermal shock.

Acknowledgements

This work was supported by the funding from the French ANR program T-Shock ANR-10-INTB-0915 and the National Natural Science Foundations of China (Grants Nos. 11061130550 and 11172023).

References

[1] W. D. Kingery, Metal-ceramic interaction: IV, absolute measurement of metal-ceramic interfacial energy and interfacial adsorption of silicon from iron-silicon alloys,
J. Am. Ceram. Soc., 1954, 37: 42~25.

[2] W.D. Kingery, Factors affecting thermal stress resistance of ceramic materials, J. Am. Ceram. Soc., 1955, 38: 3~15.

[3] D.P.H. Hasselman, Approximate theory of thermal stress resistance of brittle ceramics involving creep, J. Am. Ceram. Soc., 1969, 50: 454~457.

[4]. Mai, Y. W., Thermal stress resistance and fracture toughness of two tools ceramics. J. Mat. Sc., 1976, 11, 1430–1438.

[5]. Hasselman, D. P. H., Strength behaviour of polycristalline alumina subjected to thermal shock. J. Am. Ceram. Soc., 1970, 53(9), 490–495.

[6]. Ziegler, G. and Heinrich, J., Effect of porosity on the thermal shock behaviour of reaction sintered silicon nitride. Ceramurgia Inter., 1980, 6(1), 25–30.

[7] T.K. Gupta, Strength degradation and crack propagation in thermally shocked alumina, J. Am. C eram. Soc., 1972, 55(5): 249~253.

[8] J.A. Coppola, D.P.H. Hasslman, Strength loss of brittle ceramics subjected to severe thermal sho ck, J. Am. Ceram. Soc., 1972, 55(9): 481~489.

[9] T. J. LU and N. A. FLECK, THE THERMAL SHOCK RESISTANCE OF SOLIDS
, Acta mater. Vol. 46, No. 13, pp. 4755-4768, 1998

[10] Bažant ZP, Ohtsubo H, Aoh K. Stability and post-critical growth of a system of cooling or shrinkage cracks. Int J Fract 1979; 15(5): 443-456.

[11] Nemat-Nasser S, et al. Unstable growth of thermally induced interacting cracks in brittle solids.

Int J Solids Structures 1978; 14(6): 409-430.
[12] Bahr HA, Fischer G, Weiss HJ. Thermal-shock crack patterns explained by single and multiple crack propagation. J Mater Sci 1986; 21(8): 2716-2720.
[13] Hans-Achim Bahr, Hans-Jurgen Weiss, Ute Bahr, Martin Hofmann, Gottfried Fischer, Stefan Lampenscherf, Herbert Balke , Scaling behavior of thermal shock crack patterns and tunneling cracks driven by cooling or drying, Journal of the Mechanics and Physics of Solids 58 (2010) 1411–1421
[14] C.P. Jiang, X.F. Wu, J. Li , F. Song, Y.F. Shao, X.H. Xu, P. Yan, A study of the mechanism of formation and numerical simulations of crack patterns in ceramics subjected to thermal shock, Acta Materialia 60 (2012) 4540–4550
[15] B.Bourdin, J.-J. Marigo, C. Maurini, The variational approach to fracture mechanics: application to numerical simulation of thermal-shock cracks, IV European Conference on Computational Mechanics (ECCM2010), 16-21 May 2010 Paris, France.
[16] Li Jia, Tian Xiao Xiao, Abdelmoula Radhi, A damage model for crack prediction in brittle and quasi-brittle materials solved by the FFT method, International Journal of Fracture, 2012, Vol 173:135–146
[17] Li Jia, Meng Songhe, Tian Xiao Xiao, Song Fan, Jiang Chiping, A non-local fracture model for composite laminates and numerical simulations by the FFT method, Composites, Part B 43 (2012) 961–971
[18] Pijaudier-Cabot G, Bazant ZP. Nonlocal damage theory. J Engng Mechanics ASCE, 1987;113:1512-1533.
[19] Williams M.L. (1952), Stress singularities resulting from various boundary conditions in angular corners of plates in extension. ASME Journal of Applied Mechanics, 19,526-528
[20] Griffith AA. The phenomena of rupture and flow in solids. Philosophical Transactions of the Royal Society of London, 1920;221:163–198
[21] Irwin G. Linear fracture mechanics, fracture transition and fracture control, Eng. Fract. Mech., 1968;1:241-257
[22] Zhang YL, Ma JP. Applicable Ceramic Material Manual. Beijing: Chemical Industry Press; 2006. (in Chinese)
[24] Zhang QC. Mechanical Properties of Ceramics. Beijing: Science Press; 1987. (in Chinese)
[25] Touloukian YS, Ho CY. Thermophysical properties of matter. Thermal conductivity of nonmetallic solids, vol. 2. New York: Plenum Press; 1972.
[26] Touloukian YS, Ho CY. Thermophysical properties of matter. Specific heat of nonmetallic solids, vol. 5. New York: Plenum Press; 1972.
[27] Jiang DL et al. China materials engineering canon. Beijing: Chemical Industry Press; 2006 [in Chinese].
[28] Becher PF. Effect of water bath temperature on the thermal shock of Al_2O_3. J Am Ceram Soc 1981; 64(1): C-17-C-18.
[29] Kim Y, Lee WJ, Case ED. The measurement of the surface heat transfer coefficient for ceramics quenched into a water bath. Mater Sci Eng A 1991; 145(1): L7-L11.
[30] Zhou ZL, Song F, Shao YF, Meng SH, Jiang CP, Li J, Characteristics of the surface heat transfer coefficient for Al2O3 ceramic in water quench, *J Europ Ceram Soc* 2012 ; 32 : 3029–3034

Mechanical Characterization of Sisal Fiber Reinforced Cement Mortar

Roberto Fujiyama[1], Fathi Darwish[2], Marcos Pereira[3,*]

[1] Department of Mechanical Engineering, Pará Federal University, Belém PA 66075-110, Brazil
[2] Department of Civil Engineering, Fluminense Federal University, Niterói RJ 24210-240, Brazil
[2] Department of Materials Engineering, Catholic University of Rio de Janeiro, Rio de Janeiro RJ 22451-901, Brazil
* Corresponding author: marcospe@puc-rio.br

Abstract The purpose of this work is to evaluate the mechanical characteristics of sisal fiber reinforced cement mortar. The composite material was produced from a mixture of sand, cement and water in the proportions of 1:1:0.4, respectively. Sisal fibers, amounting to 3% of the weight of cement, were added to the mixture in two different lengths, namely 25 and 45 mm. Mechanical characterization of both the composite and the plain mortar was carried out by means of three point bend, compression and impact tests. Specimens containing parallel sided notches of different root radii were loaded in three point bending in an effort to determine the effect of the fibers on the fracture behavior of the material in the presence of discontinuities. The results obtained indicate that, while fiber reinforcement leads to a decrease in the ultimate compressive strength, J integral calculations at maximum load for the different notch root radii have indicated, particularly for the case of long fibers, a significant superiority of the reinforced material in comparison with the plain cement mortar, in consistence with the impact test data.

Keywords Composite material, Impact energy, Fracture initiation, J-integral

1. Introduction

It is well known that the presence of short randomly dispersed fibers in a cementitious matrix can result in an appreciable improvement in the mechanical behavior of the produced composite. This improvement is clearly manifested by the significant superiority of the composite´s toughness in comparison with that of the plain matrix. The increase in toughness, due to the incorporation of fibers, can be attributed, largely, to the fiber bridging mechanism, whereby the fibers take an active part in supporting tensile loading, in controlling matrix microcracking and in reducing the rate of crack propagation. The fiber reinforced concrete will, therefore, exhibit a pseudoductile behavior, maintaining considerable load carrying capacity after cracking of the matrix.

Starting early seventies, a number of studies [1-4] have been made regarding the use of natural fibers, such as sisal and bamboo, as reinforcing elements in cement mortars and in concretes. The focus in these works has been on the evaluation of the mechanical properties of the resulting composites as a function of the characteristics of their constituents, and the results obtained have indicated the viability of using natural fibers as reinforcing agents in cementitious matrices.

The present work was initiated with the purpose of evaluating the effect of sisal fibers on the compressive strength and fracture resistance of hardened cement mortar. Taking into account their potential use in structural applications, the evaluation of the notch sensitivity of sisal fiber reinforced mortar, in comparison with that of plain mortars, is considered to be an important undertaking. Accordingly, the J-integral approach was adopted and specimens containing deep notches of different root radii were cast in appropriate molds, cured and then loaded in three point bending. The J-integral values at maximum load were calculated and correlated with the notch root

radius, for both plain and reinforced mortars. Finally, the J-integral results are also correlated with the impact energy of unnotched prismatic bars having the Charpy dimensions.

2. Materials and Experimental Procedure

The mortar mixture used in the present study was composed of Portland cement PC 32, washed dry sand and tap water, in the proportions of 1:1: 0.4, respectively. The sand had fineness modulus of about 3.33, a maximum particle size of 2 mm and an apparent density of 1.6 g/cm^3.

As to the production of the reinforced mortar, sisal fibers, in an amount of 3% to the cement weight, were added to the mixture in two different lengths, namely 25 and 45 mm. The fibers had average mechanical properties of 670 MPa tensile strength, 4% elongation and 30 GPa elastic modulus.

Compressive strength of the materials was determined making use of cylindrical specimens (50 mm in diameter and 100 mm in length) which were cast from the plain and reinforced mortar mixtures. The specimens were loaded at room temperature (23 ºC) in a universal testing machine with a cross-head speed of 10^{-5} m/s.

In order to determine the load-displacement (P-δ) curves of the materials, notched prismatic specimens (50x50x300 mm) with 270 mm loading span were submitted to three point bending with a test speed of $2x10^{-5}$ m/s at room temperature. The specimens were cast from the plain and fiber reinforced mortar mixtures containing a 25 mm deep parallel sided notch with 0.5, 1, 1.5, 2 and 2.4 mm root radius. Unnotched specimens with identical geometry were also tested in three point bending.

Impact testing was carried out on unnotched prismatic specimens (10x10x50 mm), using a low capacity Charpy type impact machine appropriate for low toughness brittle materials.

3. Results and Discussion

3.1. Compressive Strength

The tests pointed that the plain mortar specimens loaded in compression suffered a highly unstable mode of failure, whereas the fiber-reinforced mortars exhibited a more stable behavior, characterized by larger deformations with a gradual drop in the applied load. Table 1 presents the compressive strength calculated from the ultimate load. From this table it can be verified that the presence of sisal fibers has a deleterious influence on the strength level. Moreover, this influence turns out to be more significant for the long fibers in comparison with the shorter ones. This can be attributed to a decrease in the mortar's density, associated with an increase in its porosity [5-6]. However, it should be mentioned that the specimen integrity was preserved over a wider deformation range in the presence of longer fibers.

Table 1. Compressive strength of the plain and reinforced mortars

Mortar	Compressive Strength (MPa)
plain	28 ± 1
reinforced with 25 mm sisal fibers	25 ± 1
reinforced with 45 mm sisal fibers	22 ± 1

3.2. Fracture Resistance

The values of the maximum loads obtained during the bending tests according to the notch root radius (ρ) of the specimens are presented in Tables 2, 3 and 4 for the different types of mortars. In these tables, the maximum load corresponds to the average of three tests.

Table 2. Maximum load to the notch root radius for the plain mortar

ρ (mm)	Maximum Load (N)
unnotched	1539.1 ± 17.3
0.5	359.1 ± 20.6
1.0	368.5 ± 15.3
1.5	391.9 ± 16.1
2.0	397.1 ± 6.4
2.4	437.2 ± 51.6

Table 3. Maximum load to the notch root radius for mortar reinforced with 25 mm fibers

ρ (mm)	Maximum Load (N)
unnotched	2195.2 ± 66.5
0.5	801.0 ± 60.1
1.0	845.9 ± 99.7
1.5	858.4 ± 81.1
2.0	992.1 ± 52.2
2.4	1074.0 ± 83.9

Table 4. Maximum load to the notch root radius for mortar reinforced with 45 mm fibers

ρ (mm)	Maximum Load (N)
unnotched	2453.2 ± 47.0
0.5	1014.8 ± 44.4
1.0	1127.9 ± 26.7
1.5	1190.6 ± 28.9
2.0	1225.4 ± 35.2
2.4	1494.9 ± 31.9

The load carrying capacity of all mortars considered in the present study decreased with the presence of notches in the specimens. Concerning the notched bend specimens for all mortar conditions, the ultimate load was found to decrease as the notch became sharper. However, the incorporation of sisal fibers by the mortar was associated with an appreciable increase of the ultimate load during the tests, with the long fibers being more effective in promoting mortar resistance than the 25 mm fibers.

The J-integral values at maximum load (J_m) were calculated from the integrated energy (U) under the load displacement curve, using the Rice estimation formula [7]. The variation of J_m with the notch root radius for the plain mortar is presented in Fig. 1.

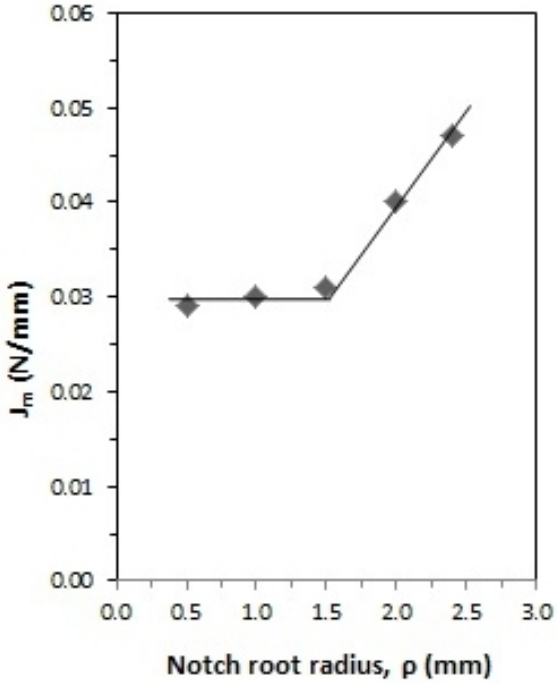

Figure 1. Variation of J-integral at maximum load with the notch root radius for the plain mortar

One may observe that the variation of J_m with ρ is in agreement with the effect normally detected for metallic and nonmetallic materials, where the J-integral value at fracture initiation varies linearly with the root radius. As fracture initiation in the plain mortar occurs essentially at the maximum load, J_m can, therefore, be considered a good estimate of the J-integral value corresponding to the event of failure initiation in the mortar. For small root radii ($\rho \leq 1.5$ mm), though, J_m becomes independent of ρ, remaining at a constant level discriminated as J_{Ic} and considered as a material characteristic. The limiting root radius, which is equivalent approximately to 1.5 mm, is also considered a material constant of microstructural significance, apparently compatible with the fact that the sand, used as a constituent of the mortar mixture, had a maximum particle size of 2 mm.

As to the reinforced mortars, the variation of J_m with the notch root radius is presented in Fig. 2, for both the 25 and 45 mm sisal fibers, in comparison with the J_m level of the plain mortar. In addition to the extremely beneficial effect of fibers on the mortar's fracture resistance, the figure also indicates that a better fracture resistance of the mortar was associated with the use of 45 mm sisal fibers.

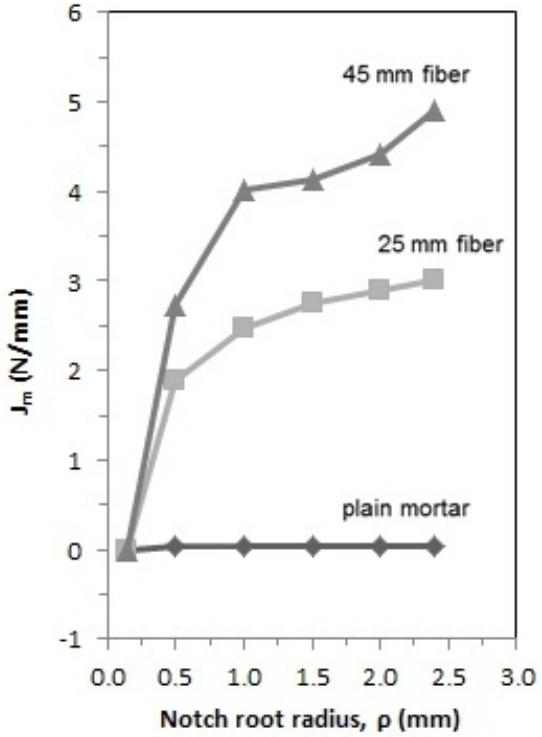

Figure 2. Variation of J-integral at maximum load with the notch root radius for the plain and reinforced mortars

The impact energy results are presented in Table 5, for the three mortars conditions. The individual energy levels shown in the table correspond to the average of five tests with a standard deviation of about 12%.

Table 5. Impact energy of the plain and reinforced mortars

Mortar	Impact Energy (J)
plain	0.45 ± 0.05
reinforced with 25 mm fibers	2.04 ± 0.22
reinforced with 45 mm fibers	3.28 ± 0.35

One can therefore conclude that the use of sisal fibers as a reinforcing element in mortar results in a considerable increase in the impact resistance and that such an increase is considerably more significant for the longer fibers. This beneficial influence is attributed to the fact that, even as the matrix cracks, the load carrying capacity is replenished by invoking fiber loading. This maintains the specimens' integrity as they continue to deform and hence to absorb more energy. The superiority of long fibers in promoting impact resistance is related to the higher load carrying capacity, as well as deformability, of the mortars reinforced with such fibers.

The correlation between the impact energy levels and J-integral results is presented in Fig. 3, whereby an essentially linear relationship is seen to exist between the two parameters.

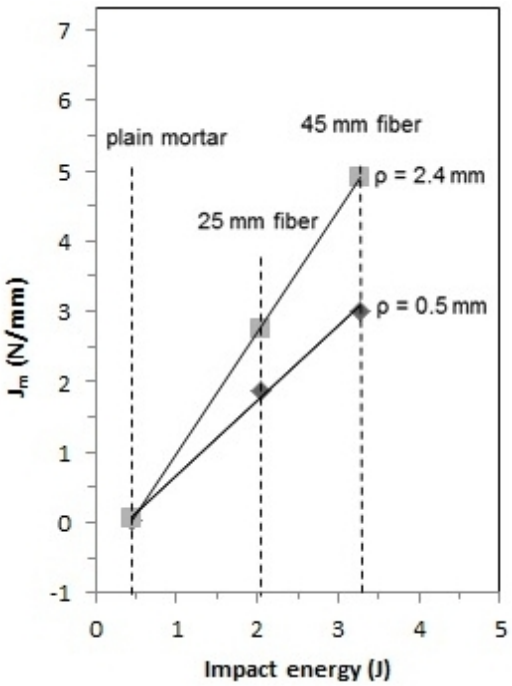

Figure 3. Correlation between J-integral at maximum load and impact energy for the reinforced mortars with notch root radius of 0.5 and 2.4 mm

4. Conclusions

Regarding the study described herein, the evaluation of the effect of sisal fibers on the compressive strength and fracture resistance of hardened cement mortar, the following conclusions can be drawn:

- The use of sisal fibers decreases the mortar's compressive strength. However, the fiber-reinforced mortars exhibit retardation during the failure process, characterized by larger deformations and gradual drop in the applied load, when compared with the plain mortar.
- The deleterious influence of sisal fibers on the compressive strength of reinforced mortar seems to be more significant for long fibers than for shorter ones.
- The presence of sisal fibers in cement mortar considerably improves its fracture resistance. This improvement is manifested by an increase in the J-Integral values determined at maximum load in the presence of deep notches with different root radii.
- Results of impact tests on unnotched specimens indicate a pronounced improvement in impact energy levels due to sisal fibers incorporated to cement mortar.
- Longer sisal fibers are seen to be more effective than shorter ones in promoting fracture resistance of reinforced mortars.

References

[1] R.T. Fujiyama, Cement Mortar Reinforced by Sisal Fibers: Microstructural and Mechanical Characterization (in Portuguese). M.Sc. Thesis, Catholic University of Rio de Janeiro, Rio de Janeiro, 1997.

[2] J. Brescansin, Fracture Behavior of Cementitious Matrix Composite Reinforced with Bamboo Pulp (in Portuguese). M.Sc. Thesis, Catholic University of Rio de Janeiro, Rio de

Janeiro, 2003.

[3] R.D. Toledo Filho, Natural Fiber Reinforced Mortar Composites: an Experimental Characterization (in Portuguese). D. Sc. Thesis, Catholic University of Rio de Janeiro, Rio de Janeiro, 1997.

[4] E.F. Campello, Fatigue Behavior of Cementitious Composites Reinforced by Bamboo Pulp (in Portuguese). M.Sc. Thesis, Catholic University of Rio de Janeiro, Rio de Janeiro, 2006.

[5] F.O. Okafor, O.J. Eze-Uzomaka, N. Egbuniwe, The structural properties and optimum mix proportions of palmnut fiber-reinforced mortar composite. Cem Concr Res, 26 (1996), 1045-1055.

[6] B.P. Hughes, N.I. Fattuhi, Stress-strain curves for fiber reinforced concrete in compression. Cem Concr Res, 7 (1977), 173-183.

[7] T.L. Anderson, Fracture Mechanics, Second Edition, CRC Press, New York, 1995.

Analysis of stress singularity field near the cross point of inclusion and free surface by 3D element free Galerkin method
（Influence of radius of curvature at vertex for stress singularity field）

Takahiko Kurahashi[1,*], **Yasuyuki Tsukada**[2], **Hideo Koguchi**[2]

[1] Department of Mechanical Engineering, Nagaoka National Courage of Technology,
888 Nishikatakai, Nagaoka, Niigata 940-8532, Japan
[2] Department of Mechanical Engineering , Nagaoka University of Technology,
1603-1 Kamitomioka, Nagaoka, Niigata 940-2188, Japan
* Corresponding author: kurahashi@nagaoka-ct.ac.jp

Abstract In this report, we investigate variation of stress distribution and intensity of stress singularity near the cross point of inclusion and free surface based on 3D element free Galerkin method (EFGM). We especially focus on influence of radius of curvature at vertex for stress singularity field. As for computational model, silicon and resin bonded structure is employed.

Keywords Stress distribution, Intensity of stress singularity, 3D EFGM, Radius of curvature at vertex

1. Introduction

Intensity of stress singularity near interface edge for bonded structures is investigated by a lot of researchers [1], [2]. Variation of intensity of stress singularity with respect to thickness of adhesive layer, interface width, slanted side surface have already investigated. As for the computational methods, the boundary element method (BEM) and the finite element method (FEM) are frequently used to compute stress distribution. In addition, the element free Galerkin method (EFGM) is also recently employed for stress analysis[3]. In this study, the EFGM is employed in stress analysis for bonded structures. In addition, eigen analysis based on the FEM is carried out to obtain order of stress singularity[4]. As the computational model, a structure made by resin with silicon plate inclusion is employed. We especially focus on influence of radius of curvature at vertex for stress singularity field in this study(See Fig.1).

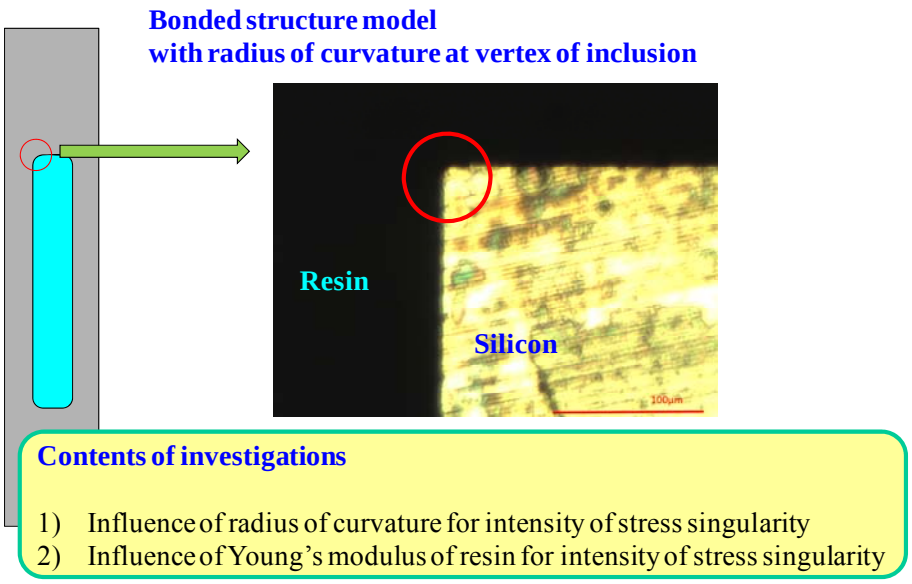

Figure 1. Image diagram of target model

2. Stress analysis by the EFGM and analysis of order of singularity by the FEM

The characteristics of the EFGM is that the interpolation function at evaluation point is given by the information in the domain influence (See Fig 2.). Example of the interpolation function is written as Eq. (1).

$$u(\mathbf{x}) = q_1(\mathbf{x})u_1 + q_2(\mathbf{x})u_2 + q_3(\mathbf{x})u_3 + \Lambda + q_n(\mathbf{x})u_n = \{q(\mathbf{x})\}^T\{u\}, \tag{1}$$

where q indicates shape function, and n indicates number of referred nodes in the domain influence. In addition, forth order spline function is employed as the weighting function in the EFGM. Procedure of discretization is same as the traditional FEM. Detail of discretization is shown in reference [3].

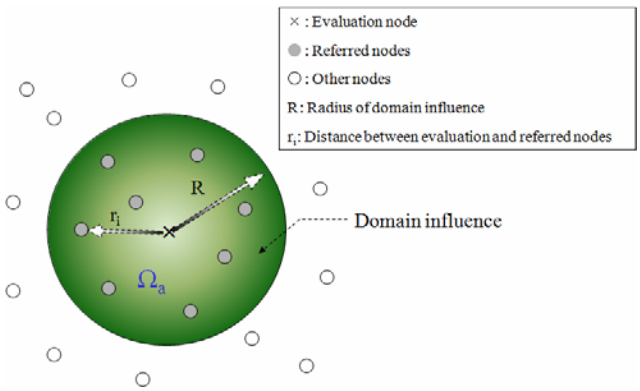

Figure 2. Domain influence

In addition, if the order of singularity is expressed by λ, the stress distribution is written as $\sigma_{ij} \propto 1/r^{\lambda} = 1/r^{1-p} = r^{p-1}$. Here, p indicates characteristic root. Because the stress is expressed as gradient of the displacements u_i, the relationship the displacements and distance r is given $u_i \propto r^p$ by the integration of $\sigma_{ij} \propto r^{p-1}$. If displacements for each element are expressed by interpolation function shown in Eq. (2) and the interpolation function is substituted to equation of the principle of virtual work, a characteristic equation is finally derived as shown in Eq. (3).

$$\bar{u}_r(r,\theta,\phi) = \left(\frac{r}{r^0}\right)^p \sum_{i=1}^{8} h_i \bar{u}_{ri}, \tag{2}$$

$$\left(p^2[\mathbf{A}] + p[\mathbf{B}] + [\mathbf{C}]\right)\{\mathbf{x}\} = \{\mathbf{0}\}, \tag{3}$$

where $\bar{u}_i$ is expressed by $u_i - u_o$, and u_i and u_o represent spherical displacements at an arbitrary point in the spherical surface. In addition, h_i indicates the shape function. In the Eq. (3), p indicates characteristic root and vector $\{\mathbf{x}\}$ denotes superposed displacement vector in entire domain, and matrices $[\mathbf{A}]$, $[\mathbf{B}]$ and $[\mathbf{C}]$ represent the coefficient matrices derived by finite element procedure. Detail of this formulation is shown in reference [4].

3. Numerical experiments

3.1. Variation of intensity of stress singularity $K_{1\varphi\varphi}$ with respect to radius of curvature R

In this study, a structure made by resin with silicon plate inclusion shown in Fig.3 is employed as a numerical model. Nodal distribution around target area and material properties are shown in Fig.4 and Tab.1. In case of computational model of R=0, order of stress singularity λ at vertex on silicon surface is obtained as 0.436. In this study, the radius of curvature R at vertex of silicon plate is changed as shown in Tab.2.

In case that tensile stress, 10MPa, is applied to top surface, stress distribution $\sigma_{\varphi\varphi}$ on surface in silicon plate with respect to angle φ is shown in Fig.5. It is seen that gradient of stress distribution $\sigma_{\varphi\varphi}$ is almost same for each angle φ. Next, comparison of stress distribution $\sigma_{\varphi\varphi}$ on silicon surface at angle direction φ=315° is carried out. The result is shown in Fig.6. It is found that stress value decreases with increasing the radius of curvature R and constant stress region of $\sigma_{\varphi\varphi}$ near point O, i.e., stress singularity disappearance region, increases with increasing the radius of curvature R. Here, in Fig. 6, solid line indicates fitting line by $\sigma_{\varphi\varphi}= K_{1\varphi\varphi}r^{-0.436}$. In addition, relationship between intensity of stress singularity $K_{1\varphi\varphi}$ and radius of curvature R is shown in Fig.7. From this result, it is found that intensity of stress singularity $K_{1\varphi\varphi}$ almost linearly decreases with increasing the radius of curvature R.

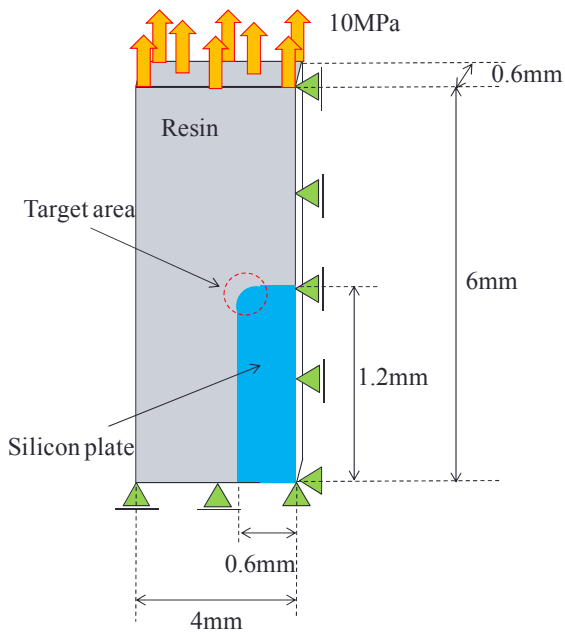

Figure 3. Computational model

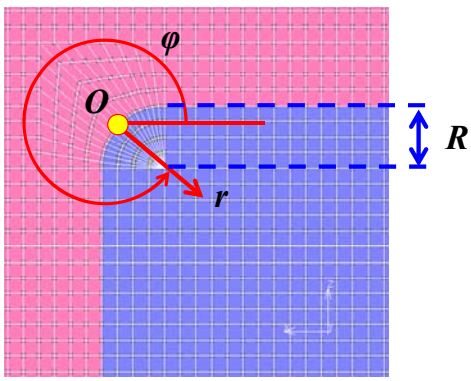

Figure 4. Nodal distribution around target area

Table 1. Material properties

	Silicon	Resin
Young's modulus (GPa)	166	5.49
Poisson's ratio	0.26	0.32

Table 2. Computational conditions

Radius of curvature R (μm)	0.000	3.125	6.250	12.500
Number of nodes	27,607	15,467	16,423	21,727

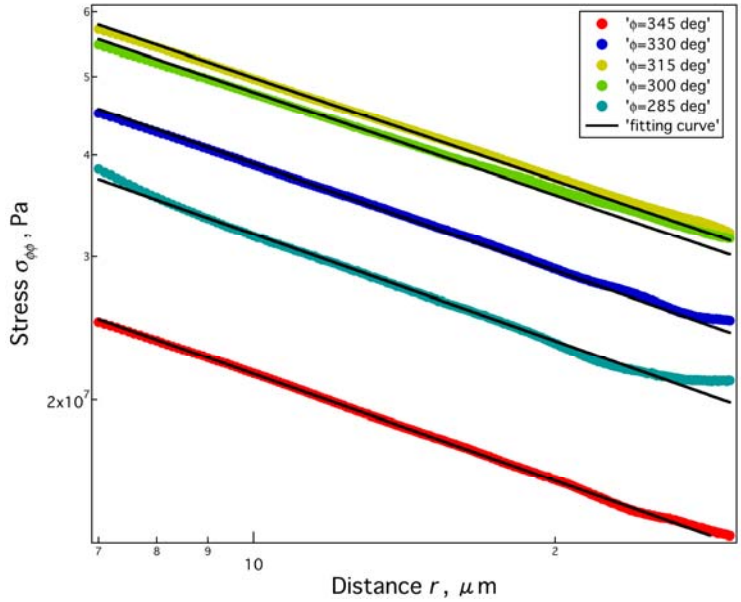

Figure 5. Variation of stress distribution $\sigma_{\varphi\varphi}$ on silicon surface with respect to angle φ (R=0mm)

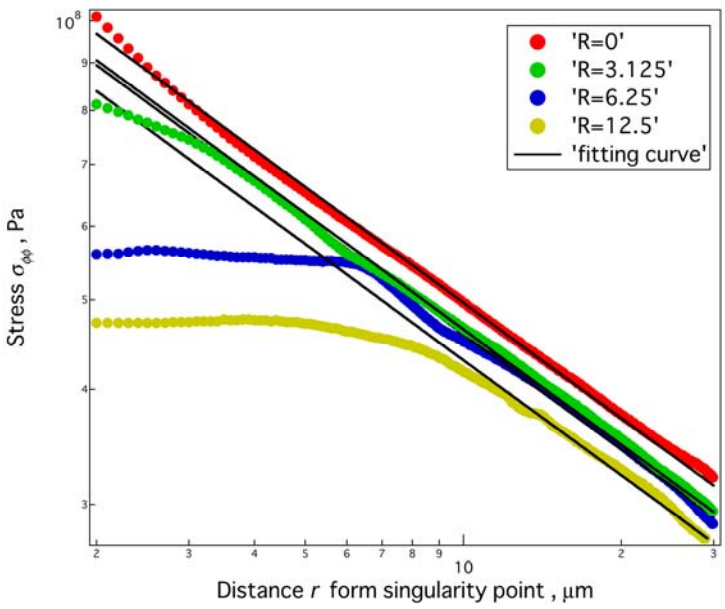

Figure 6. Variation of stress distribution $\sigma_{\varphi\varphi}$ on silicon surface at angle direction φ =315° with respect to radius of curvature R

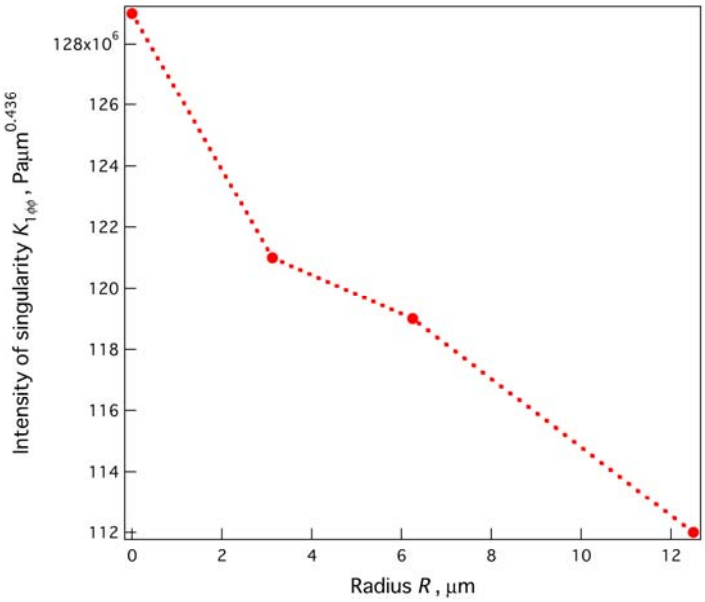

Figure 7. Relationship between intensity of stress singularity $K_{1\varphi\varphi}$ and radius of curvature R

3.2. Variation of intensity of stress singularity $K_{1\varphi\varphi}$ with respect to Young's modulus of resin

Next, in case of computational model, R=3.125μm, relationship between stress distribution and Young's modulus of resin is investigated. In this section, Young's modulus of silicon and resin are expressed by E_1 and E_2. First of all, order of singularity λ is listed in Tab.3. It is seen that order of singularity λ gradually decreases with increasing Young's modulus of resin E_2. Fig.8 shows variation of stress distribution $\sigma_{\varphi\varphi}$ on silicon surface at angle direction, φ =315°, with respect to Young's modulus of resin E_2. It is found that value of stress $\sigma_{\varphi\varphi}$ decreases with increasing Young's modulus of resin E_2. In addition, variation of intensity of stress singularity $K_{1\varphi\varphi}$ with respect to Young's modulus of resin E_2 is shown in Fig.9. It is seen that intensity of stress singularity $K_{1\varphi\varphi}$ decreases with increasing Young's modulus of resin E_2.

Table 3. Order of singularity λ (In case of R=0 model)

Young's modulus of resin E_2 (GPa)	0.10	0.50	1.00	5.49	10.00
Order of singularity λ	0.545	0.437	0.429	0.436	0.384

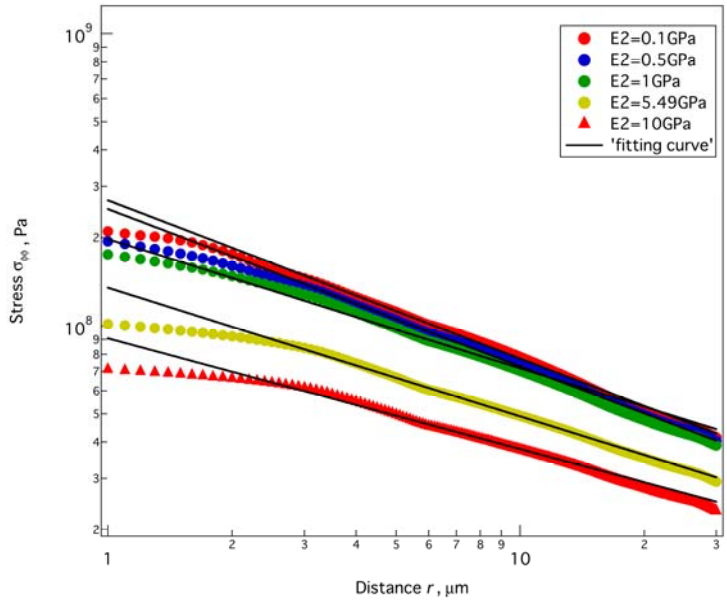

Figure 8. Variation of stress distribution $\sigma_{\varphi\varphi}$ on silicon surface at angle direction $\varphi = -45°$ with respect to Young's modulus of resin

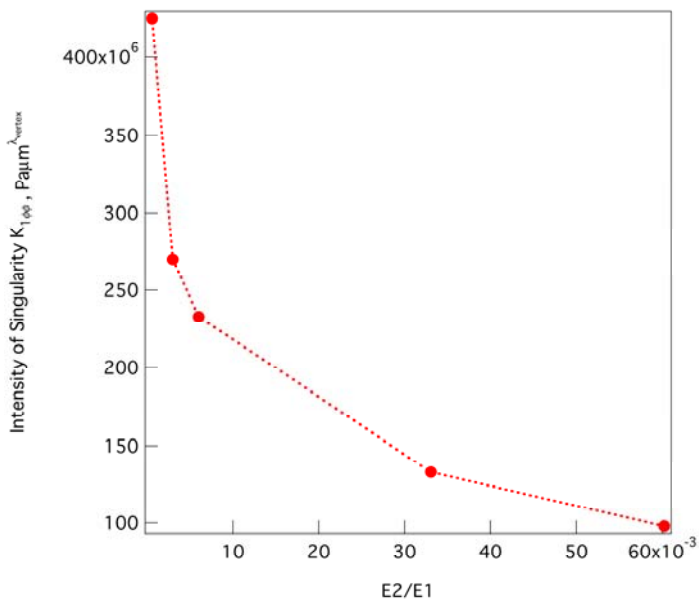

Figure 9. Variation of intensity of stress singularity $K_{1\varphi\varphi}$ with respect to Young's modulus of resin E_2

4. Conclusins

In this study, we investigated about the relationship between intensity of singularity $K_{1\theta\theta}$ and radius of curvature R for computational model of a structure made by resin with silicon plate inclusion. As numerical methods, the EFGM is applied to stress analysis, and the finite element eigen analysis is applied to obtain order of singularity at vertex on silicon surface. Conclusions in this study are shown below.

Examinations for change of radius of curvature around singularity point

- Stress value $\sigma_{\varphi\varphi}$ decreases with increasing the radius of curvature R.
- Constant stress region of $\sigma_{\varphi\varphi}$ near point O, i.e., stress singularity disappearance region, increases with increasing the radius of curvature R.
- Intensity of stress singularity $K_{1\varphi\varphi}$ almost linearly decreases with increasing the radius of curvature R.

Examinations for change of Young's modulus of resin in case of R=3.125μm model

- Value of stress $\sigma_{\varphi\varphi}$ decreases with increasing Young's modulus of resin E_2.
- Intensity of stress singularity $K_{1\varphi\varphi}$ decreases with increasing Young's modulus of resin E_2.

References

[1] T. Kurahashi, A. Ishikawa and H. Koguchi, Evaluation of Intensity of Stress Singularity for 3D Dissimilar Material Joints Based on Mesh Free Method, 11th International Conference on the Mechanical Behavior of Materials, *Procedia Engineering*, 10, (2011) 3095-3100 .

[2] Hideo Koguchi, Kazuhisa Hoshi, Evaluation of joining strength of silicon-resin interface at a vertex in 3D joint structures, *InterPACK2011*, (2011).

[3] T.Belytschko, Y.Y.Lu and L.Gu, Element-free Garerkin methods, *Int. J. Numer. Meth. Engrg.*, 37(5), (1994) 229-256.

[4] S.S.Pageau and S.B.Bigger,JR, Finite element evaluation of free - edge singular stress fields in anisotropic materials, *Int.J.Numer.in Engng.*, 38, (1995) 2225-2239.

Finite element analysis of erosive wear for offshore structure

Z.G. Liu[1*], S. Wan[1], V.B. Nguyen[1], Y.W. Zhang[1]

[1] Institute of High Performance Computing, 1 Fusionopolis Way, #16-16 Connexis, 138632, Singapore
* Corresponding author: liuzh@ihpc.a-star.edu.sg

Abstract Erosive wear, which is a complex material damage process caused by particle impacting on the surface of equipments, has been a major concern in oil & gas industry. In this work, we employ three-dimensional finite element (FE) method to investigate the erosion process under multiple particle impacts with both spherical and irregular non-spherical particles. We take into account both elastic-plastic material behaviors, which is described by Johnson-Cook visco-plastic model, and material removal, which is governed by the Johnson-Cook failure model. The relationships between the erosion rate and the particle velocity and impact angle are obtained and compared with published data. The implications of the current simulation results are also discussed.

Keywords Erosion rate, Solid particle impact, Finite element analysis (FEA), Failure

1. Introduction

Erosion wear, which arises from solid particle impacting, is one of the major failure modes that cause offshore structure damage. Erosion is found in a wide range of equipments in offshore industry, in which solid particles are entrained into fluid flow in the operating process, such as gas turbine, oil & gas pipeline, drilling platforms, etc [1]. This damage mode affects not only operating process, but also safety and economics as well. Therefore, it is necessary to find a good predictive method to accurately predict the erosion rate for offshore equipment.

The erosion mechanism is different in ductile and brittle materials. A number of studies have been performed to reveal the erosion mechanisms of ductile and brittle materials [2-6]. It is now known that brittle materials erode by cracking and chipping, while ductile materials erode by a sequence of micro-cutting, forging and fracture, etc [7]. Hence, erosion rate and mechanism are highly dependent on material types.

So far, several experimental methods have been developed to determine the eroded volume of a material. However, the experimental data found in the literature often refer to a particular material without specifying their properties and operating conditions. Therefore, the experimental erosion rate for the same material reported by different authors can differ greatly [8].

Numerical simulations, such as the Finite Element Method (FEM), have also been used to characterize erosion wear. Previously, 2D models were mainly used to investigate the influencing parameters of erosion wear. However, 2D simulation cannot correctly consider the effects of multi-particle erosion. Hence, 3D FEM models have been often used to study the erosion process. For example, Alman et al. [9] studied erosion behavior of both brittle and ductile materials, and concluded that the impact angle is important for erosion mechanism: A ductile material exhibits the maximum erosion rate at an impact angle of about 20-40°, while a brittle material shows the maximum erosion rate at an impact angle of 90°. ElTobgy et al. [6] studied erosion wear process using multiple impacts with perfect spherical particles, and pointed out that single-particle impact is insufficient, and three or more particles are needed to simulate the erosion process. Subsequently, Wang et al. [7] performed finite element simulations on erosion wear with 100 sphere particles and analyzed the erosion rate of both ductile and brittle materials, and compared their simulation results with that using other computational models.

In this study, we perform three-dimensional FEM simulations using the Johnson-Cook models to study the erosion rate for multiple impacts with both spherical and non-spherical solid particles on a deformable substrate. The main objective is to analyze the erosion rate of different particles with

different impact angles and velocities, and compare the present simulation results with that using other computational and theoretical models.

2. Modeling

2.1. Material model

2.1.1 General property

The erosion process has been studied widely using numerical approaches such as finite element method. One key point in simulation is the choice of material model considering strain, strain rate and temperature. To study erosion process, a model must have three important components: elasticity, plasticity, damage initiation and damage growth. In this study, the substrate material is Ti-6Al-4V, and elastic response of the material is assumed to be linear and defined by elastic modulus and Poisson's ratio. Thermal response is ignored because of transient process.

2.1.2. Plasticity model

The Johnson-Cook visco-plastic model (J-C) is used in this study [10, 11]. In this model, flow stress $\bar{\sigma}$ depends on equivalent plastic strain ($\bar{\varepsilon}$), equivalent plastic strain rate ($\dot{\bar{\varepsilon}}$), and temperature. The model can be expressed as follows:

$$\bar{\sigma} = (\mathrm{A} + \mathrm{B}\bar{\varepsilon}^{\mathrm{n}})\left(1 + \mathrm{C}\ln\left(\frac{\dot{\bar{\varepsilon}}}{\dot{\bar{\varepsilon}}_0}\right)\right)(1 - \mathrm{T}^{*\mathrm{m}}), \tag{1}$$

where A, B, C and m are material constants, n is strain hardening exponent, $\dot{\bar{\varepsilon}}/\dot{\bar{\varepsilon}}_0$ is the normalized equivalent plastic strain rate (typically normalized by a strain rate of 1.0 s^{-1}), and T^* is the homologous temperature which is defined as:

$$\mathrm{T}^* = \frac{\mathrm{T} - \mathrm{T_r}}{\mathrm{T_m} - \mathrm{T_r}}, \tag{2}$$

where T is the current temperature, $\mathrm{T_r}$ is the reference temperature, $\mathrm{T_m}$ is the melting temperature of material. The model assumes that strength is isotropic.

2.1.3. Failure model

Johnson-Cook failure model is applied for the ductile failure criterion [10, 11], in which the equivalent plastic strain at the onset of damage, $\bar{\varepsilon}_D^{pl}$, is assumed to be a function of stress triaxiality (η), strain rate ($\dot{\varepsilon}^*$) and temperature. Johnson-Cook damage model is expressed in term of the failure strain as follows:

$$\bar{\varepsilon}_D^{pl} = [d_1 + d_2 exp(-d_3\eta)](1 + d_4 \ln \dot{\varepsilon}^*)(1 + d_5 T^*), \qquad \eta = \frac{p}{q} \tag{3}$$

where $d_1 - d_5$ are material constants, p is the pressure stress (positive in tension), q is the von-Mises stress, and T^* is the homologous temperature.
In the explicit finite element method, the overall damage variable D captures the combined effects of all active damage mechanisms, and is computed in terms of the individual damage variables. The damage parameter D is defined as:

$$D = \frac{\sum \Delta\varepsilon^{pl}}{\bar{\varepsilon}_D^{pl}} \tag{4}$$

In each finite element, $(\sum \Delta\varepsilon^{pl})_i$ is calculated, and the damage parameter D for element i is subsequently calculated during each time step. When the damage parameter D reaches the value of

1, the element i is assumed to have failed and removed from the model instantly [7].

2.1.4. Equation of state

When a ductile material is impacted by erodent particles at a considerably high speed, the Grüneisen equation of state (EOS) [7] is used to simulate the shockwave effects for ductile material. The shockwave velocity υ_s is much higher than the elastic-plastic wave or material velocity. Across the shock wave, a discontinuity takes place in material properties. The cubic shock velocity υ_s and material particle velocity υ_p obey the following relation:

$$\upsilon_s = C_0 + S\upsilon_p \tag{5}$$

Table 1. Material constants of Ti-6Al-4V

Material properties	Symbol	Ti–6Al–4V
Density	ρ (kg/m^3)	4428
Elastic modulus	E (GPa)	113.8
Poisson's ratio	ν	0.31
J-C yield strength	A (MPa)	1098
J-C hardening coefficient	B (MPa)	1092
J-C strain hardening exponent	n	0.93
J-C strain rate constant	C	0.014
J-C softening exponent	m	1.1
Melting temperature	T_m (K)	1878
J-C damage constant	d_1	–0.09
J-C damage constant	d_2	0.27
J-C damage constant	d_3	0.48
J-C damage constant	d_4	0.014
J-C damage constant	d_5	3.87
Elastic bulk wave velocity	C_0 (km/s)	5.13
Slope in υ_s vs. υ_p diagram	S	1.028
Grüneisen coefficient	γ_0	1.23

where C_0 is the elastic bulk wave velocity. For compressed materials ($\mu > 0$), the pressure is defined as follows:

$$P = \frac{\rho_0 C_0^2 \mu[1+(1-\gamma_0/2)\mu-(a/2)\mu^2]}{[1-(S-1)\mu]^2} + \gamma_0 E, \tag{6}$$

For expanded materials ($\mu < 0$), the pressure is defined as follows:

$$P = \rho_0 C_0^2 \mu + (\gamma_0 + a\mu)E_0 \tag{7}$$

where γ_0 is the Grüneisen gamma, a is the first-order volume correction to γ_0, and $\mu = \rho/\rho_0 - 1$, ρ is for current density, and ρ_0 is initial density. The material constants for Ti-6Al-4V are listed in Table 1.~~Table 1~~ [6].

2.2. FE model

The erosion wear process is simulated using a commercial finite element solver, ABAQUS/Explicit (Version 6.11-2). The analysis is performed using Lagrangian formulation. In previous study,

ElTobgy et al. [6] reported that single particle impact is insufficient to simulate the erosion process, three and more particles are needed to analyze multiple particle interactions. In this study, 5 particles are used to ensure the accuracy of the model. In general, the erosion rate (%) is used to describe the erosion wear performance of the substrate material. Our objective is to analyze the material erosion rate under various processing conditions. The erosion rate is defined as [7]:

$$erosion\ rate = \frac{cumulative\ mass\ loss\ of\ substrate\ material}{impact\ particles\ weight} \tag{8}$$

2.2.1. Impact particle

Two kinds of impact particle are used in the present simulation study, that is, spherical and irregular non-spherical particles. The purpose is to consider the effect of particle shape on material removal mechanism. The impacting material is steel with a density of 7800 kg/m^3. In the finite element model, the impact particle material is modeled as a rigid body. The element for the impact particle is 3-node and 4-node bilinear quadrilateral rigid elements (R3D3 and R3D4).

2.2.2. Impact substrate

The substrate is modeled as a deformable elastic plastic material, and the eight-node brick hexahedral element with reduced integration and hourglass control (C3D8R) is used to mesh the substrate. The accuracy of the material removal prediction is tested with different grid sizes for convergence test. In this study, mesh size is chosen to ensure neither time-consuming nor leading to unreasonable discrepancy. Figures 1 and 2 show the FE model of spherical and irregular particles. General contact is defined between the impacting particles and substrate material. The contact property is assumed to follow coulomb friction, and the friction coefficient between impact particle and substrate is assumed to be 0.2 [12], the boundary condition is applied to ensure that the substrate is fixed for bottom plane and the particles rotation are constrained in all three directions.

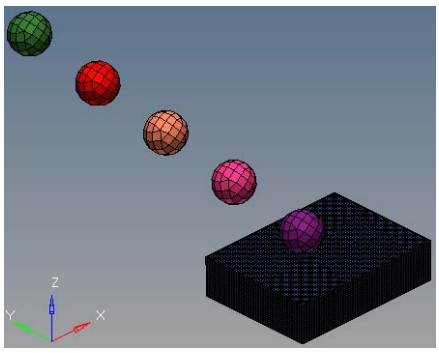

Figure 1. Spherical particle FE model

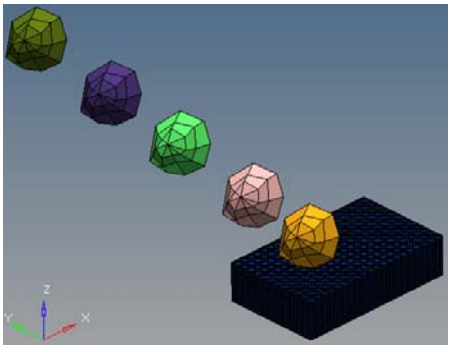

Figure 2. Irregular particle FE model

When particles impact the substrate, some of impacts, depending on the impact velocity and angle, will only deform the material surface without causing material removal, leading to the hardening of substrate material. In the previous attempts of erosion wear process simulation, most of them do not consider such hardening effect. In practice, the influence of multi-particle impacts is obvious in erosion process since the impact contact may change after multiple impacts. Therefore, although ideal cases, in which particle impacts with the same velocity and angle are employed, it is still necessary to adopt the multiple particle impact model. Figure 3 shows the material removal after each spherical particle impact. It clearly shows that the material removal increases with increasing impact times under the same impact condition.

ElTobgy et al. [6] showed that the erosion rate is affected by a number of system parameters, such

as particle velocity and impact angle, etc. Here we would like to calculate the erosion rates for various cases with a velocity range of 70-130m/s (10m/s interval) and an angle range of 20-75°. In addition, ElTobgy et al. [6] also pointed out that the sphere sizes have no obvious influence on erosion rate. Therefore in the present paper, we fix the sphere size, that is, the volume of the irregular impact particle is chosen to have the same volume as the spherical one with a diameter of 1mm. The same velocity and angle ranges for both spherical and irregular particles are used in the present study. The detailed analysis will be presented in the next section.

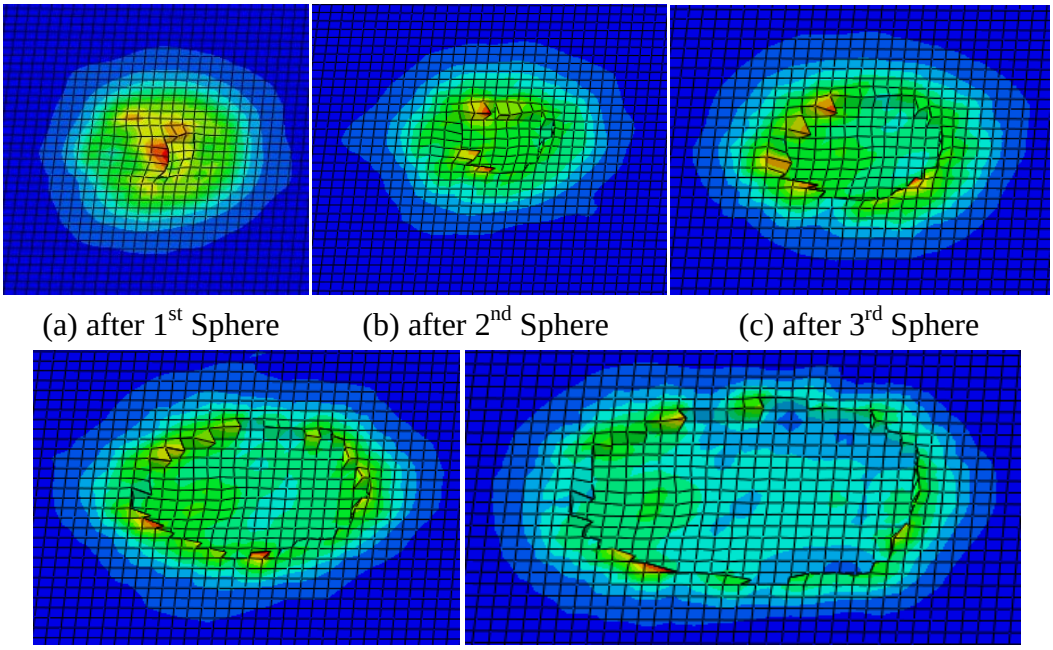

(a) after 1st Sphere (b) after 2nd Sphere (c) after 3rd Sphere

(d) after 4th Sphere (e) after 5th Sphere

Figure 3. Material removal for 5 particle impacts sequentially (velocity =100m/s, angle = 30°)

3. Results and discussion

3.1. Effect of impact velocity on erosion rate

To calculate the erosion rate, we perform FE simulations on the impact of spherical particles at an impact angle of 45° and different velocities using the same substrate and impacting material. Table 2 shows the cumulative mass loss of substrate material after each sphere impact. It is seen that when the velocity is low, no material removal occurs or mass loss is relatively small. When the impact velocity is high, however, more mass loss occurs and in some cases, the penetration occurs after several particle impacts.

Table 2. Cumulative mass loss of the substrate material (10^{-6}kg)

Angle	Velocity (m/s)	1st Sphere	2nd Sphere	3rd Sphere	4th Sphere	5th Sphere
45°	70	0	0	0	1.10E-03	6.70E-03
	80	0	0	5.60E-03	2.66E-02	5.37E-02
	90	0	3.90E-03	3.10E-02	7.20E-02	1.16E-01
	100	0	1.44E-02	6.53E-02	1.20E-01	1.78E-01
	110	5.00E-04	3.60E-02	9.96E-02	1.68E-01	penetration
	120	5.50E-03	5.86E-02	1.44E-01	penetration	
	130	1.55E-02	9.91E-02	2.08E-01	penetration	

Figure 4 shows cumulative mass loss of the substrate material after 5 sphere particle impacts. It is seen that the material removal is very small after the first impact and then increases with the number of impacts. In some cases, impact particles are able to penetrate into the substrate, which is not included in the cumulative mass loss.

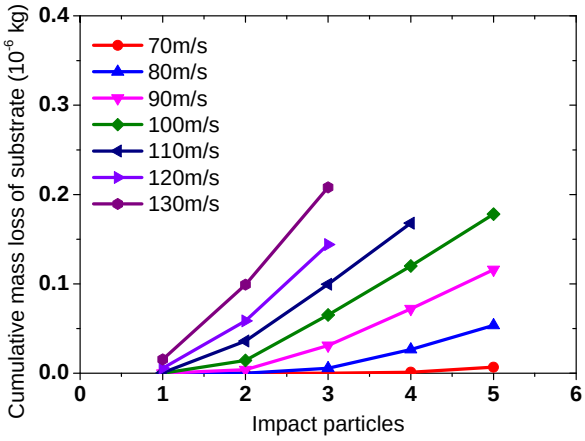

Figure 4. Variation of cumulative substrate mass loss

As defined in the above section, erosion rate is the ratio of the cumulative mass loss of the substrate and the weight of impact particles. The relationship between erosion rate and impact velocity was proposed following a power law function from publications [13 - 16], that is,

$$erosion\ rate \ \propto \ V^n \tag{9}$$

However, the exponent value n differs with different literatures. Finnie [13] proposed the exponent of 2 and Hashish [14] gave a value of 2.5, respectively. Scheldon et al. [15] experimentally obtained an exponent value in the range of 2-3, while Yerramareddy et al. [16] reported a value of 2.35 for Ti-6Al-4V. In general, the exponent value n is in the range of 2.0 - 2.7. For metallic material, the value is in the range of 2.0 - 2.5 [6, 7].

Figure 5 shows the relation of erosion rate with the impact velocities in log - log scale. The slope of linear fitting curve gives an exponent value n equal to 2.22 for Ti-6Al-4V, which is in accordance with the range reported by other researchers [13-16]. In addition, ElTobgy et al. [6] explained the reason for the relation between velocity and erosion rate in terms of energy aspect.

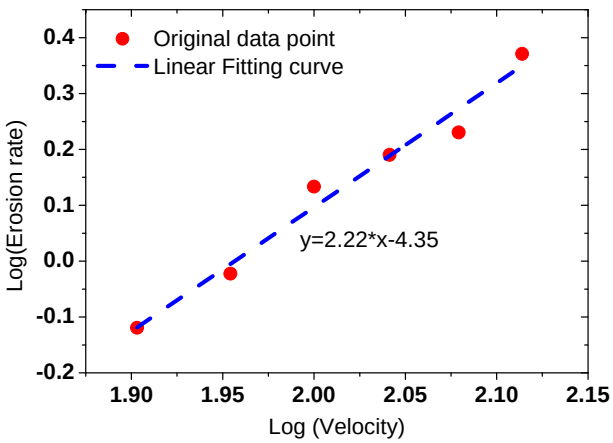

Figure 5. Erosion rate vs. velocity in log-log scale

Similarly, the relations between erosion rate and impact velocity have also been analyzed with irregular non-spherical particles. Figure 6 shows erosion rate and velocity relationship in log-log scale. The exponent value provided by the slope of linear fitting curve is 2.40, which is also in the

reported range [13-16]. However, the simulated exponent for irregular particles is higher than that for spherical particles. It can be explained from energy conversion. It is known that the kinetic energy is transformed into strain energy during impact. In this irregular non-spherical impact case, more kinetic energy is transformed into strain energy, resulting in more wear damage. Hence, at the same velocity, the erosion rate of the substrate material under irregular particle impacting is higher than that under spherical particle impacting. It will be interesting to investigate material removal with different particle geometries (cubic, tetrahedron, pentahedron, etc) in the future work, and study the relationship between erosion rate and geometry.

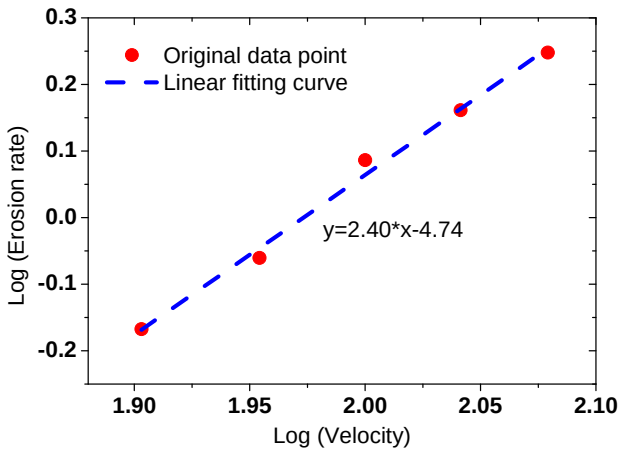

Figure 6. Erosion rate vs. velocity in Log-Log scale

3.2. Effect of impact Angle on erosion rate

Impact angle is also an important parameter influencing solid particle erosion. It was reported that the maximum erosion rate angle is a function of substrate material and is independent of erodent material properties [17]. Figures 7 and 8 show the relation between erosion rate and impact angle at velocities of 100m/s and 80m/s, respectively. Clearly, at the two different impact velocities, the two patterns are very similar, with the maximum erosion rate for both cases occurring at angle of 40-45°. ElTobgy et al. [6] obtained peak erosion rate at a 40° angle for Ti-6Al-4V, Wang et al. [7] reported maximum erosion rate at about 30° for the same substrate material, while Yerramareddy et al. [16] experimentally determined the maximum erosion rate occurs at an angle of 35-40°. Hence, the ranges of maximum erosion rate predicted from our finite element model are close to that from these literature data.

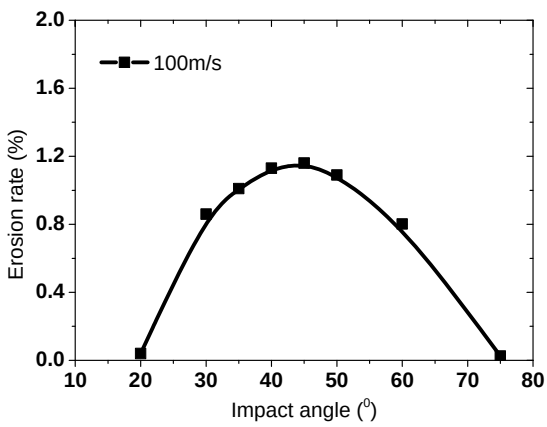

Figure 7. Erosion rate vs. velocity (v=100m/s)

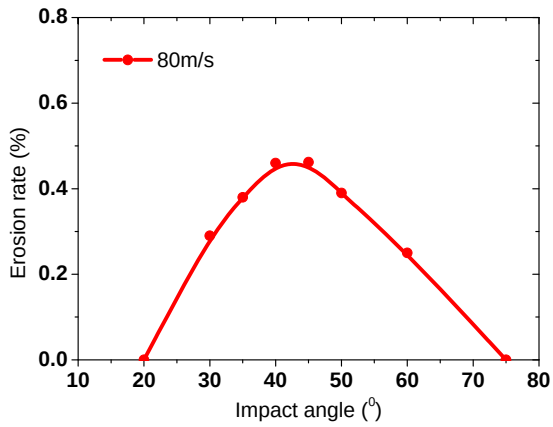

Figure 8. Erosion rate vs. velocity (v=80m/s)

4. Conclusions

We have performed FE simulations to study the erosion rate of a deformable substrate under multiple impacts using both spherical and irregular non-spherical solid particles. The material model employed is Johnson-Cook visco-plastic model for plastic deformation and Johnson-Cook material failure criterion for material removal. A five-particle impact process is employed to analyze the erosion process. The relations between the erosion rate and the impact angle and velocity have been obtained and compared with literature data. It is found that the erosion rate and velocity obey a power law relation and the exponent value obtained from our finite element simulation is in accordance with the literature ones. The exponent for irregular particles is higher than that for regular sphere particles. The impact angle for the maximum erosion rate predicted from our finite element simulation is in the range of 40-45°. This range agrees well with the published data. Interesting future research works include the establishment of the relation between material removal and particle geometry and the application of the model to study the erosion processes in complex offshore structures.

References

[1] Keles, Ozgul and Inal, O.T., A Review on Solid Particle Erosion of Ductile and Brittle Materials, Recent Res. Devel. Mat. Sci. 3, (2002) 499–528.
[2] I. Finnie, Erosion of surfaces by solid particles. Wear, 3 (1960) 87–103.
[3] J.G.A. Bitter, A study of erosion phenomena. Part I, Wear, 6 (1963) 5–21.
[4] J.G.A. Bitter, A study of erosion phenomena. Part II, Wear, 6 (1963) 169–190.
[5] I.M. Hutchings, Ductile–brittle transitions and wear maps for the erosion and abrasion of brittle materials. J. Phys. D: Appl. Phys. 25 (1992) A212–A221.
[6] M.S. ElTobgy, E. Ng, M.A. Elbestawi., Finite element modeling of erosive wear. International Journal of Machine Tools & Manufacture, 45 (2005) 1337–1346.
[7] Yu-Fei Wang, Zhen-Guo Yang., Finite element model of erosive wear on ductile and brittle materials. Wear, 265 (2008) 871–878.
[8] D. Aquaro, E. Fontani, Erosion of Ductile and Brittle Materials, Meccanica, 36 (2001) 651-661.
[9] D. Alman, J. Tylczak, J. Hawk, M. Hebsur, Solid particle erosion behavior of an Si3N4–MoSi2. Mater. Sci. Eng. A261 (1999) 245–251.
[10] G.R. Johnson, W.H. Cook, A constitutive model and data for metals subjected to large strains, high strain rates and high temperatures, in: Proceedings of the 7th International Symposium on Ballistics, The Hague, 1983, pp.541–547.
[11] G.R. Johnson, W.H. Cook, Fracture characteristics of three metals subjected to various strains, strain rates, temperatures and pressures. Eng. Fract. Mech, 21 (1) (1985) 31–48.
[12] M. Meo, R. Vignevic, Finite element analysis of residual stress induced by shot peening process. Adv. Eng. Software, 34 (2003) 569–575.
[13] I. Finnie, The mechanism of erosion of ductile metals. Proceedings of the Third National Congress on Applied Mechanics, New York, 1958, pp. 527–532.
[14] M. Hashish, Modified model for erosion, Seventh International Conference on Erosion by Liquid and Solid Impact. Cambridge, England, 1987, pp. 461–480.
[15] G.L. Scheldon, A. Kanhere, An investigation of impingement erosion using single particles. Wear, 21 (1972) 195–209.
[16] S. Yerramareddy, S. Bahadur, Effect of operational variables, microstructure and mechanical properties on the erosion of Ti–6Al–4V. Wear, 142 (1991) 253–263.
[17] G.R. Desale, B.K. Gandhi, S.C. Jain, Effect of erodent properties on erosion wear of ductile type materials. Wear, 261 (2006) 914–921.

Computational Method for Crack Layer Model

Haiying Zhang[1,*], Alexander Chudnovsky[1]

[1] Department of Civil and Materials Engineering, University of Illinois at Chicago, 60607, USA
* Corresponding author: haiyin@uic.edu

Abstract Crack layer (CL) model is applied for modeling of brittle fracture of engineering thermoplastics. It specifically used in polyethylene structures, where a process zone (PZ) formed in front of crack is a narrow wage-type layer consisting of drawn fibers and membranes. To model CL requires an evaluation of stress intensity factors (SIF) and crack opening displacements (COD) within the crack and PZ domains. This paper is aimed to construct SIF and COD formulas for three specific geometries: a semi-infinite crack in an infinite solid; a single-edge notched specimen, standard Pennsylvania notch test (PENT, ASTM F 1473) and a new stiff constant-*K* (SCK) specimen. The approximate SIF and COD formulas are expressed as superposition of two elastic solutions one due to remote load and another associated with closing forces. The paper presents the computational technique in details. The approximate expressions of SIF and COD are used to present the method of computation the shape and the size of PZ, as well as the crack and PZ driving forces. The CL parameters then are used in simulation of CL growth and prediction of the lifetime of engineering structures made of thermoplastics.

Keywords Crack layer model, slow crack growth, process zone, Green's function

1. Introduction

In continuum mechanics, a crack is conventionally considered as an ideal cut in an elastic, elasto-plastic or visco-elasto-plastic medium. The concept of surface (fracture) energy associated with crack faces introduced by Griffith [1] was the first important step in thermodynamics of brittle failure. Barenblatt [2, 3] proposed a simple model of cohesive forces acting along the crack surfaces in a vicinity of crack tip. A year later Dugdale [4] independently developed a similar model for plastic deformation along an extension of crack-cut. Mathematically the two models turn to be identical and are commonly referred to as the Dugdale-Barenblatt (D-B) Model (also known as Cohesive Zone Model). The essential assumption of D-B model is that the stress singularity at the crack tip vanishes due to cohesive forces or plastic deformation at the crack front zone. Formally it expressed as zero stress intensity factor (SIF, K), i.e., $K = 0$. However, the stress singularity results from two basic assumptions of linear elastic fracture mechanics: 1) linear elastic stress-strain relations are maintained in near crack tip region without limitation; 2) the crack is ultimately sharp with zero curvature at the tip. In real engineering materials, however, neither of these two assumptions is correct. Indeed, 1) a damage in form of crazing, micro-cracking, shear-banding, cavitation etc. is formed in response to high stresses and the crack-damage interaction limits the stress level in the damage zone region; 2) large deformation of the crack front region results in the positive crack tip curvature, even when it could be zero before loading. It implies that the crack in engineering materials is commonly surrounded by a damage zone (generally called "process zone") and the crack-damage interaction plays the major role in formation of stress field as well as in fracture propagation process.

This leads to an alternative approach to studies of SCG known as Crack Layer (CL) model [5, 6]. CL model was originally proposed more than 3 decades ago and after that was further developed and applied for modeling various aspects of brittle fracture process [7-13]. In CL model the crack and the process zone, which usually precedes and surrounds the crack during fracture propagation in plastic components, considered as one thermodynamic system, Crack Layer. In HDPE, the process zone (PZ) is a thin wedge shape layer of cold drawn fibers and membranes. The stress and strain fields in CL model can be presented as a superposition of that in the specimen with cut off CL

subjected to an external load (F_∞ or σ_∞) and a thin wedge shape PZ domain with variable width ω_0 of original material that undergoes cold drawing under a distributed closing tractions σ_{dr} as shown in Figure 1.

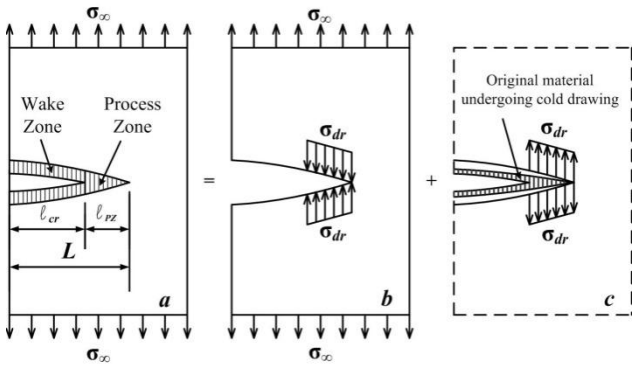

Figure 1. Decomposition of Crack Layer Model.

Accordingly, CL growth is decomposed into two closely coupled processes: 1) the PZ growth into the surrounding original material; 2) the crack penetration into the PZ [13].

The thermodynamic forces for such elementary processes are conventionally presented as the derivatives from Gibbs potential of the system with respect to the corresponding CL geometrical parameters such as the crack and the PZ lengths. Performing the calculations one can show that the thermodynamic force driving PZ growth X^{PZ} is expressed as [13]:

$$X^{PZ} = \frac{K_{tot}^2}{E'} - \gamma^{tr} \cdot \frac{\partial V^{PZ}}{\partial \ell_{PZ}}, \tag{1}$$

where K_{tot} is the total SIF presented as the sum of SIF due to remote load σ_∞ and SIF due to traction σ_{dr} along the PZ boundary; E' plane strain Young's modulus; γ^{tr} the specific energy of transformation, i.e., the work required to transform a unit mass of original material into an equal mass of oriented unstressed state plus the difference of strain energy densities in the original and drawn states; V^{PZ} PZ volume; and ℓ_{PZ} process zone size.

Similarly, the crack driving thermodynamic force X^{cr} has the following form [13],

$$X^{CR} = J_1^{cr} - 2\gamma, \tag{2}$$

where J_1^{cr} is the energy release rate due to crack extension into the PZ, when PZ is stationary, and 2γ is surface (fracture) energy per unit length.

A stationary CL configuration takes place, when the thermodynamic forces are not positive, i.e., $X^{PZ} \le 0$ and $X^{CR} \le 0$. The equilibrium is achieved, when the both forces equal zero. At a small deviation from equilibrium, a thermodynamic system has a tendency to return to the equilibrium state. However, fracture is an essentially irreversible process: there is no "healing", when the PZ fibers are broken, or PZ advances into the original material via cavitation followed by cold drawing of the material between the cavities and formation of membranes and fibers. Thus, when CL departs from one stationary state, it moves into next stationary configuration. Such process of crack layer propagation continues by crack and process zone assisting mutual growth. The described CL propagation is formalized in the following system of coupled ordinary differential equations with respect to the crack length (ℓ_{cr}) and the PZ size (ℓ_{pz}):

$$\begin{cases} \dot{\ell}_{cr} = k_1 X^{CR}, \ if \ X^{CR} \geq 0, and \ \dot{\ell}_{cr} = 0, if \ X^{CR} < 0 \\ \dot{\ell}_{pz} = k_2 X^{PZ}, \ if \ X^{PZ} \geq 0, and \ \dot{\ell}_{pz} = 0, if \ X^{PZ} < 0 \end{cases}, \tag{3}$$

where k_1, and k_2 are the kinetic coefficients, which are evaluated experimentally.

Evaluation of CL driving forces requires a computation of SIF and crack opening displacement (COD). In this paper we present a semi-analytical method of SIF and COD computations. The method is illustrated by solution for three geometries: a semi-infinite crack in an infinite solid; a single-edge notched specimen, standard PENT specimen (ASTM F 1473) and a stiff constant-*K* (SCK) specimen. The approximate formulas for SIF and COD are expressed as superposition of two elastic solutions for the listed above samples due to: 1) remote load σ_∞ or F_∞ ; and 2) closing force σ_{dr}. The close form solution for a semi-infinite crack in an infinite homogeneous and linear elastic solid is used as the basic expression. The solution for any finite specimen geometry is constructed by introducing a geometry correction factor to the basic expression. The Green's functions technique is effectively used to construct analytical expressions for SIF and COD. Then, the approximate expressions for SIF and COD are employed in computations of the CL driving forces and simulations of the slow fracture propagation process in HDPE [8, 13].

2. Semi-Infinite Crack in an Infinite Plate

2.1. SIF Formula

The decomposition shown in Fig. 1 is first applied to the semi-infinite crack in an infinite homogeneous and linear elastic solid subjected to a distributed load σ_∞ over L and a crack closing load σ_{dr} on PZ (see Figure 2 below). L is the length of CL, which is the summ of actual crack length ℓ_{cr} and PZ size ℓ_{pz}, i.e., $L = \ell_{cr} + \ell_{pz}$. The SIF Green's function for the semi-infinite crack is well known:

$$G^{SIF}(x) = \sqrt{\frac{2}{\pi x}}, \tag{4}$$

where the origin of the coordinates is placed at the crack tip.

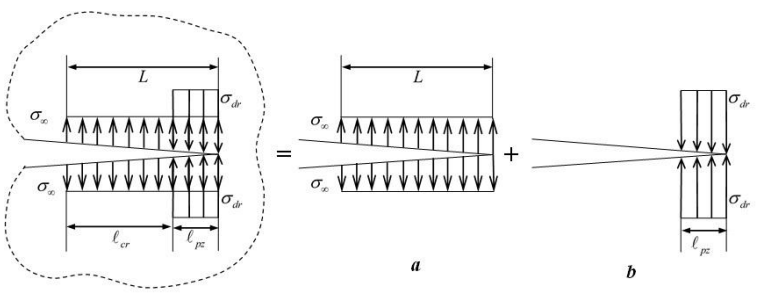

Figure 2. Decomposition of the problem of a semi-infinite crack in an infinite plate subjected to a distributed load σ_∞ and a closing force σ_{dr} on PZ.

For the boundary conditions and loading shown in Figure 2 *a* and *b*, SIFs are readily obtained by the standard application of Green's function:

Boundary Condition *a*: $$K_\infty = K_I(\sigma_\infty) = \int_0^L \sigma_\infty G^{SIF}(x)dx = \frac{2\sqrt{2}\sigma_\infty\sqrt{L}}{\sqrt{\pi}} \ ; \tag{5}$$

Boundary Condition *b*: $$K_{dr} = K_I\left(\sigma_{dr}\right) = \int_0^{\ell_{pz}} \sigma_{dr} G^{SIF}(x)dx = \frac{2\sqrt{2}\sigma_{dr}\sqrt{\ell_{pz}}}{\sqrt{\pi}} \quad . \tag{6}$$

By applying the superposition to stress filed, the total SIF for the semi-infinite crack loaded as shown on the left side of Figure 2 is:

$$K_{tot} = K_\infty - K_{dr} = \frac{2\sqrt{2}}{\sqrt{\pi}}\left(\sigma_\infty\sqrt{L} - \sigma_{dr}\sqrt{\ell_{pz}}\right) \quad . \tag{7}$$

2.2. COD Formula

The COD $\delta(x)$ is convenient to express in the following integral form using an axillary fictitious force $Q(x)$ perpendicular crack face [14]:

$$\delta(x) = \frac{2}{E'}\int_0^L K_I(\sigma_\infty,\xi)K_I(Q,\xi)\Big|_{Q=1} d\xi \quad . \tag{8}$$

We select the origin of coordinate at the beginning of distributed load σ_∞, i.e., on the distance L from the crack tip (see Figure 2a). For calculations of COD δ due to distributed load two cases should be considered: **Case I**: $0 < x \le L$, $x \le \xi \le L$ and **Case II**: $x \le 0$, $0 \le \xi \le L$.

In the Case I,

$$\delta\left(\sigma_\infty, x\right) = \frac{2}{E'}\int_x^L \left[K_I(\sigma_\infty,\xi)K_I(Q,\xi)\right]\Big|_{Q=1} d\xi \tag{9}$$

Substituting Eqs. 4 and 5 into Eq. 9, one can find the COD formula. It is noted that x in Eq. 4 should be replaced by $\xi - x$ due to the change of the origin. Finally, the COD is:

Case I: $\delta\left(\sigma_\infty, x\right) = \frac{8\sigma_\infty}{\pi E'}\int_x^L \frac{\sqrt{\xi}}{\sqrt{\xi - x}} d\xi$; and Case II: $\delta\left(\sigma_\infty, x\right) = \frac{8\sigma_\infty}{\pi E'}\int_0^L \frac{\sqrt{\xi}}{\sqrt{\xi - x}} d\xi$ (10)

Performing the integration in (10), and shifting the origin to the crack tip one finds the COD:

$$\delta_\infty = \delta\left(\sigma_\infty, x\right) = \frac{8\sigma_\infty}{\pi E'}\sqrt{Lx} + \frac{4\sigma_\infty\left(L - x\right)}{\pi E'}\ln\left|\frac{\sqrt{x} + \sqrt{L}}{\sqrt{x} - \sqrt{L}}\right|, \quad x \ge 0 . \tag{11}$$

The reduction of COD due to the closing force σ_{dr} is determined by the same procedure. It takes form:

$$\delta_{dr} = \delta\left(\sigma_{dr}, x\right) = \frac{8\sigma_{dr}}{\pi E'}\sqrt{\ell_{pz}x} + \frac{4\sigma_{dr}\left(\ell_{pz} - x\right)}{\pi E'}\ln\left|\frac{\sqrt{x} + \sqrt{\ell_{pz}}}{\sqrt{x} - \sqrt{\ell_{pz}}}\right|, \quad x \ge 0 . \tag{12}$$

The analytical expression for total COD for the semi-infinite crack loaded as shown in Fig.2 is:

$$\begin{aligned}\delta_{tot}\left(x\right) = \delta(\sigma_\infty, x) - \delta(\sigma_{dr}, x) &= \frac{8\sigma_\infty}{\pi E'}\sqrt{Lx} + \frac{4\sigma_\infty\left(L - x\right)}{\pi E'}\ln\left|\frac{\sqrt{x} + \sqrt{L}}{\sqrt{x} - \sqrt{L}}\right| \\ &- \frac{8\sigma_{dr}}{\pi E'}\sqrt{\ell_{pz}x} - \frac{4\sigma_{dr}\left(\ell_{pz} - x\right)}{\pi E'}\ln\left|\frac{\sqrt{x} + \sqrt{\ell_{pz}}}{\sqrt{x} - \sqrt{\ell_{pz}}}\right|\end{aligned} . \tag{13}$$

Figure 3 shows an example of COD profile for normalized stress $\bar{\sigma} = \sigma_\infty / \sigma_{dr} = 0.4$ and CL sizes

$\bar{\ell}_{pz} = \ell_{pz} / \ell_{cr} = 0.1$. Clearly the COD formula captures the beak-type opening at the tip of the crack.

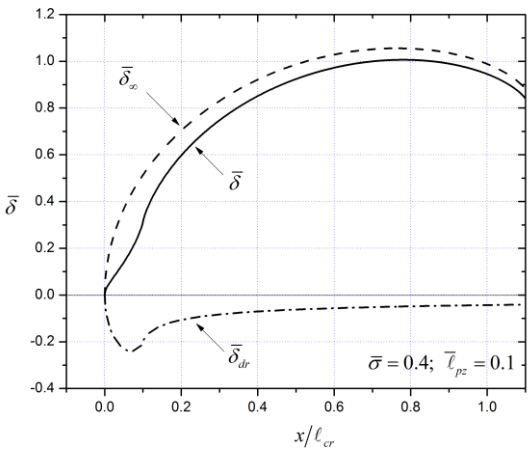

Figure 3. A COD in the crack – load configuration shown in Figure 2 left. Dashed line is COD due to $\bar{\sigma} =$ 0.4; the negative COD is the closure due to drawing stress $\bar{\ell}_{pz} = 0.1$.

3. Single Edge Notch Specimen

The PENT is a standard test widely used for evaluation of the slow crack growth (SCG) resistance of polyethylene (PE) pipes. In PENT the failure time is recorded and used to rank various PE with respect to SCG resistance.

3.1. SIF Formula

A single edge notch (SEN) specimen is used in PENT. The specimen is subjected to a constant load ($\sigma_\infty = 2.4MPa$) and undergoes creep until failure. A closing load σ_{dr} is applied on the PZ that is in front of actual crack. The SIF due to σ_∞ is determined in the following way [14]:

$$K_\infty = K_I(\sigma_\infty) = \sigma_\infty \sqrt{\pi L} \cdot F_1(L/W). \tag{14}$$

where, L is CL length ($L = \ell_{cr} + \ell_{pz}$) in mm, W the width of the specimen in mm. The correction factor $F_1(L/W)$ with better than 0.5% accuracy can be found in [14].

Similarly the SIF Green's function for SEN specimen is (x is counted from the edge) is:

$$G_{SEN}^{SIF} = \frac{2}{\sqrt{\pi L}} \cdot F_2(x/L, L/W), \tag{15}$$

with the correction factor $F_2(L/W)$ given in [14]. Thus, $K_{dr} = \int_{\ell_{cr}}^{L} \frac{2\sigma_{dr}}{\sqrt{\pi a}} \cdot F_2(x/L, L/W)\,dx$ and by superposition one readily finds the total SIF expression in terms of known correction factors:

$$K_{tot} = \sigma_\infty \sqrt{\pi L} \cdot F_1(L/W) - \int_{\ell_{cr}}^{L} \frac{2\sigma_{dr}}{\sqrt{\pi L}} \cdot F_2(x/L, L/W)\,dx. \tag{16}$$

3.2. COD Formula

The COD depends on the crack size ℓ_{cr}, the PZ size ℓ_{pz}, the width of the specimen W, and the load. It is convenient to normalize the crack size and PZ size as follows $\bar{\ell}_{cr} = \ell_{cr}/W$ and $\bar{\ell}_{pz} = \ell_{pz}/\ell_{cr}$. The COD for PENT specimen has been evaluated numerically using FRANC2D. The calculation has been carried on a series of PENT specimen configurations with $\bar{\ell}_{cr} = 0.35, 0.45, 0.55$. For each $\bar{\ell}_{cr}$, the normalized PZ size varies $\bar{\ell}_{pz} = 0.1, 0.2, 0.3, 0.4$. By comparing the numerical results with COD for the semi-infinite crack, we obtain the COD expression for the PENT. Here "comparison" means the first term on the right hand side of semi-infinite crack solution (Eq. 11) is replaced by the Williams expansion [15] $\left(ax^{1/2} + bx^{3/2} + cx^{5/2} + ...\right)$, x is the distance measured from the tip of the PZ, and the higher order term are ignored. The difference is represented by $Diff$ throughout the paper. The coefficients a, b, and c are determined for each combination of $\bar{\ell}_{cr}$ and $\bar{\ell}_{pz}$ by least squares fitting. Analytical expressions for three coefficients are provided by fitting the numerical results.

Hence, the normalized COD due to the remote load σ_∞ is the sum of $Diff$ and the second term in the right hand side of the semi-infinite crack solution (Eq. 11):

$$\delta_\infty = \delta(\sigma_\infty, \bar{x}) = \frac{8\sigma_\infty W}{\pi E'}\left[\sqrt{\bar{x}}\left(a + b\bar{x} + c\bar{x}^2\right) + \frac{1}{2}\bar{\ell}_{cr}\left(1 + \bar{\ell}_{pz} - \bar{\ell}_{pz}\bar{x}\right)\ln\left|\frac{\sqrt{\bar{\ell}_{pz}\bar{x}} + \sqrt{1+\bar{\ell}_{pz}}}{\sqrt{\bar{\ell}_{pz}\bar{x}} - \sqrt{1+\bar{\ell}_{pz}}}\right|\right]. \tag{17}$$

The same procedure is applied to the COD due to σ_{dr}, except that the second term on the right hand of Eq. 12 instead of Eq. 11 is used. It leads to the following expressed:

$$\delta_{dr} = \delta(\sigma_{dr}, \bar{x}) = \frac{8\sigma_{dr} W}{\pi E'}\left[\sqrt{\bar{x}}\left(a' + b'\,\bar{x} + c'\,\bar{x}^2\right) + \frac{1}{2}\bar{\ell}_{cr}\bar{\ell}_{pz}\left(1 - \bar{x}\right)\ln\left|\frac{\sqrt{\bar{x}}+1}{\sqrt{\bar{x}}-1}\right|\right]. \tag{18}$$

The total opening δ_{tot} is: $\delta_{tot} = \delta_\infty - \delta_{dr}$.

4. Constant-*K* Specimen

Equation of SCG is commonly formulated as a functional relation between crack growth rate and SIF that usually depends on the remote load, crack and PZ lengths (CL size) as well as specimen geometry. Thus, one needs to monitor crack and PZ lengths in real time to formulate CL growth equations. It is technically challenging to monitor CL dimensions in SCG process in not transparent materials. A specimen for which SIF does not depend on crack length allows one to reconstruct the SCG rate ~ SIF relations without monitoring the process. Tapered Double Cantilever Beam (TDCB) has long been used for crack growth studies in metals [16]. Unfortunately, in application to polymers, TDCB specimen displays a very large deformation that compromises the assumptions of linear elasticity. A stiff constant-*K* (SCK) specimen has been design for relatively soft materials [13]. It is stiffer than TDCB and a few other alternative specimen geometries examined. That was a reason for the name. The diameters and locations of holes are designed to maintain the constancy of SIF. The side grooves reduce the plane stress effect in the surface layers.

4.1. SIF Formula

In SCK specimen, SIF due to remote load F_∞ is independent on crack length in the crack size range $0.15 < \ell_{cr}/W < 0.4$ and simply related to the applied load (F_∞, B_0, B_e, and W are specified in Figure 5):

$$K_\infty \equiv K_I\left(F_\infty\right) = 6.56\frac{F_\infty}{B_{eff}\sqrt{W}}. \tag{19}$$

The Green's function for SIF due to self-equilibrated double forces applied to the crack faces in SCK specimen is obtained by introducing a correction factor to the Green's function of semi-infinite crack in an infinite solid ($G^{semi} = \sqrt{\frac{2}{\pi x}}$):

$$G^{SCK}(x,L,W) = \sqrt{\frac{2}{\pi x}} + \frac{\alpha}{L}x^{1/2} + \frac{\beta}{L^2}x^{3/2}. \tag{20}$$

where x is the distance from the tip of crack layer (CL), L is CL length ($L = \ell_{cr} + \ell_{pz}$)
Thus, the SIF due to σ_{dr} is obtained by integrating the Green's function over the PZ size and the total SIF K_{tot} is obtained by $K_{tot} = K_\infty - K_{dr}$.

4.2. COD Formula

Based on numerical analysis of SCK specimens with different geometries ($\ell_{pz}/L = 0.1$, 0.2, 0.25, 0.3; and $L/W = 0.2$, 0.25, 0.3, 0.35), the COD δ_∞ and δ_{dr} at a point x due to the remote load F_∞ and σ_{dr} respectively can be presented in the following forms:

$$\delta_\infty = \frac{8}{\pi E'}\frac{F_\infty}{\sqrt{B_0 B_e}}\sqrt{\frac{x}{L}}\left(\alpha + \beta\frac{x}{L} + \gamma\frac{x^2}{L^2}\right) \text{ and } \delta_{dr} = \frac{8\sigma_{dr}W}{\pi E'}\sqrt{\frac{x}{\ell_{pz}}}\left(\alpha' + \beta'\frac{x}{\ell_{pz}} + \gamma'\frac{x^2}{\ell_{pz}^2}\right) \tag{21}$$

The coefficients α, β, and γ are functions of only one variable L/W and the coefficients α', β', and γ' are simple functions of ℓ_{pz}, L and W. The total opening is: $\delta_{tot} = \delta_\infty - \delta_{dr}$.

The same approach is readily applicable to other specimen geometries. Thus, the evaluation of CL parameters is the building block for calculation of CL driving forces and simulation of CL growth.

5. Examples of Crack Layer Growth Simulation

The process zone driving force X^{PZ} monotonically decreases with increase of PZ size. The equilibrium PZ size ℓ_{pz}^{eq} corresponds to vanishing of the corresponding thermodynamic force:

$$\frac{K_{tot}^2}{E'} - \gamma^{tr}\cdot\left.\frac{\partial V^{PZ}}{\partial \ell_{PZ}}\right|_{x=\ell_{pz}} = 0. \tag{22}$$

The experimental determination of the equilibrium PZ size is conducted by direct observations of striations of fracture surface in discontinuous CL growth. A comparison of calculated equilibrium PZ size ℓ_{pz}^{eq} with experimental data (Figure 4 (a)) at elevated temperature is shown in Figure 4 (b).

Note the experimental equilibrium size of process zone is measured directly from the fracture surface as shown in Figure 4 (a). The CL model predictions agree very well with observations. It is also interesting to compare ℓ_{pz}^{eq} with conventional D-B model prediction. The process zone size ℓ_{pz}^{DB} in D-B model is determined by the requirement $K_{tot}=0$ with K_{tot} defined by $K_{tot}=K_{\infty}-K_{dr}$. It is also shown in Figure 4 (b) that the experimentally observed equilibrium size of process zone ℓ_{pz}^{eq} is significantly smaller than ℓ_{pz}^{DB} predicted by D-B model. In this specific example, the equilibrium size of process zone ℓ_{pz}^{eq} is within the range of 1.3~2.8mm, whereas D-B prediction ℓ_{pz}^{DB} is between 3.8~8.8mm, three times larger. This could be expected since the D-B model ignores the energy dissipation by cold drawing of original material into the oriented fibers of PZ. There are clear trends in ℓ_{pz}^{eq} dependency on load and temperature: 1) For a given temperature, the equilibrium PZ size ℓ_{pz}^{eq} linearly increases with increase of load; 2) For the same value of K_{∞}, ℓ_{pz}^{eq} increases with increase of temperature; 3) The ℓ_{pz}^{eq} in CL model is significantly smaller than the D-B zone size; 4) The difference between the equilibrium PZ in CL and D-B zone sizes increases with increasing load.

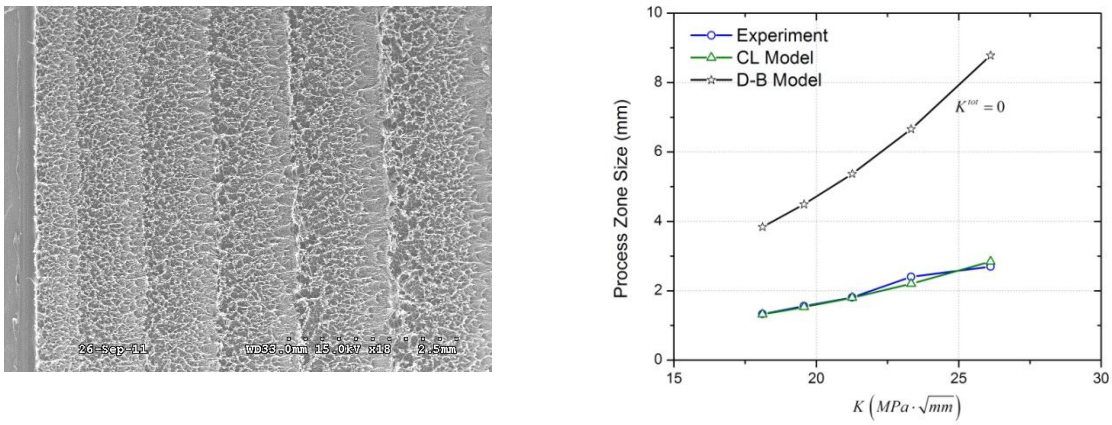

(a) (b)

Figure 4. (a). Fracture surface of a CT specimen test at 80°C (Note: the first striation is resulted from the pre load and thus ignored); (b) Comparison of predicted ℓ_{pz}^{eq} values with observations from (a).

The PZ and crack thermodynamic forces (Eqs. 1-2) are non-linear functions of crack and process zone lengths. Thus, the system of Eq. 3 despite of its simple appearance is a nonlinear system of ODE, solution of which calls for numerical methods. Below we show two examples of numerical simulation of CL growth in a compact tension (CT) specimen that has the same geometry as SCK except holes. SIF in CT specimen increases with crack length. The first example is shown in Figures 5 (a). It presents a discontinuous, stepwise crack layer growth from one stationary CL configuration to the next one.

At the beginning the crack is stationary, whereas PZ grows toward its equilibrium size $L \approx 9.5mm$. The first equilibrium size of CL L is reached in about $t=4\,hours$, and is maintained constant until the degradation of PZ material triggers the crack growth into PZ. It is depicted by the lower dash line moving up at $t\approx 28\,hours$. The crack propagates through PZ and gets arrested at the time $t\approx 33\,hours$, when it meets the original material at the tip of PZ. PZ grows accompanying the crack growth, since $X^{PZ}>0$ during this time; X^{PZ} decreases with an increase of the PZ length and CL

reaches the second stationary configuration, when X^{PZ} vanishes. A newly drawn material constitutes the new PZ. Then, the same degradation process takes over the drawn material and crack propagates through the second PZ the same way as in the first step. In CT specimen, the maximal value of X^{PZ} increases with CL length. As a result, the equilibrium PZ size increases and the duration of steps decreases with step number leading to an accelerated CL growth and final instability and transition to rapid crack propagation.

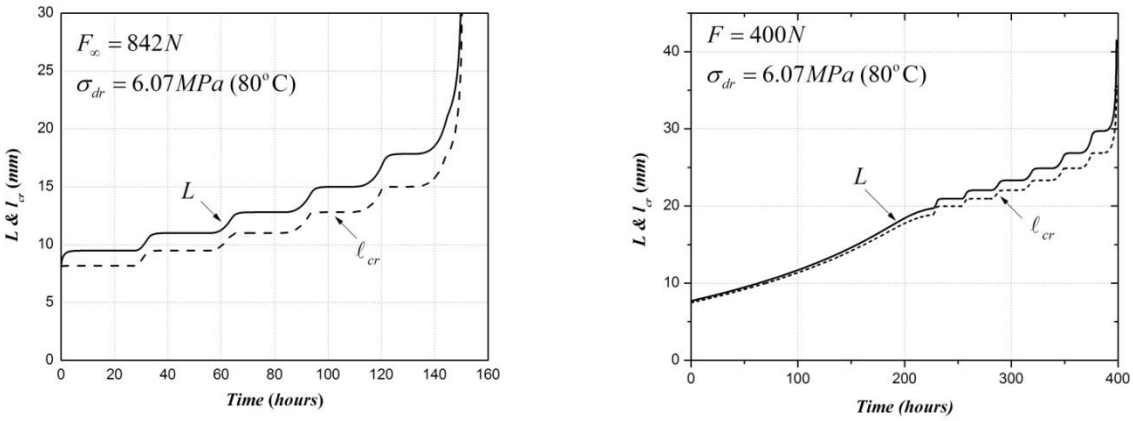

(a) (b)

Figure 5. (a) Numerical simulation of discontinuous crack layer growth for a CT specimen at 80°C; (b) Numerical simulation of transition from continuous to discontinuous CL growth.

The second example presents a different scenario of CL propagation: a transition from continuous to a discontinuous, stepwise CL growth shown in Figure 5 (b).

In this case, at the beginning, the PZ material degradation rate is comparable with the rate of PZ growth. In such case, the crack starts to grow into PZ before PZ reaches equilibrium. This process appears as continuous CL growth and the lines of $\ell_{cr}(t)$ and $L(t)$ practically coincide up to $t \approx 33\,hours$ as shown in Figure 5 (b). However, with increase of K_{tot} the PZ growth rate increases whereas the degradation rate of PZ material is the same. Thus, PZ "runs" away from the crack and PZ size becomes larger and larger and finally reaches the equilibrium size. It triggers a transition of from continuous CL growth mechanism to the discontinuous one. After such transition, the same process of discontinuous CL growth as described above (Figure 5 (a)) takes place.

For comparison with the vast literature on phenomenological crack growth studies, we introduce an average rate of crack layer growth $<\dot{L}>$ as a ratio between CL length increment in discontinuous growth and the duration of corresponding step. A correspondence between $<\dot{L}>$ and the SIF due to remote load K_∞ in double logarithmic scale represents the crack layer growth simulation in the conventional Paris-Erdogan equation form. The rate $<\dot{L}>$ depends on basic fracture parameters such as kinetic coefficients k_1 and k_2 in Eq. 3, σ_{dr}, γ^{tr} and γ as well as elastic and creep properties. It also depends on specimen shape and size, crack size as well as the magnitude and rate of applied load. The relation between the numerical simulation of $<\dot{L}>$ and the remote load SIF K_∞ allows one to establish a correspondence between empirical coefficients in Paris-Erdogan equation and basic material properties. Apparently, there are changes in the SCG pattern depending on load, CL size and temperature. It can be translated into different powers in Paris-Erdogan equation.

6. Conclusions

The focus of the paper is brittle fracture in PE structures resulting from crack growth. We outlined an alternative to the conventional approach for lifetime assessment. Our approach consists of a sound physical model of SCG and numerical simulation of the process. A combination of modeling and experimental work is required to evaluate the basic parameters employed in constitutive equations of the model. After that the numerical simulation of SCG can be readily performed. The experimental work is convenient to conduct with SCK specimen, since no in-situe observation is required and numerical tools for data analysis are developed. Note: the crack initiation time is ignored. Thus, the lifetime assessment is a conservative one: it gives the lower bound of life expectance.

References

[1] A.A. Griffith, The phenomena of rupture and flow in solids. Philos T Roy Soc A, 221 (1921) 163–198.
[2] G.I. Barenblatt, On equilibrium cracks formed in brittle fracture. General concepts and hypothesis. Axisymmetric cracks. J Appl Math Mech (PPM), 23, No. 3 (1959) 622–636.
[3] G.I. Barenblatt, Mathematical theory of equilibrium cracks in brittle fracture, Adv Appl Mech, VII (1962) 55–129.
[4] D.S. Dugdale, Yielding of steel sheets containing slits. J Mech Phys Solids, 8 (1960) 100–104.
[5] A. Chudnovsky, V.A. Dunaevsky, and V.A. Khandogin, On the Quasistatic Growth of Cracks, Arch Mech, 30, 2 (1978) 165–174.
[6] V. Khandogin, A. Chudnovsky, The Thermodynamic Analysis of Quasistatic Crack Growth, Dynamics and Strength of Aircraft Construction, 4 (1978) 148–175.
[7] J. Botsis, A. Chudnovsky, A. Moet, Fatigue Crack Layer Propagation in Polystyrene. 1. Experimental-Observations, Int J Fracture, 33 (1987) 263–276.
[8] J. Botsis, A. Chudnovsky, A. Moet, Fatigue Crack Layer Propagation in Polystyrene. 2. Analysis, Int J Fracture, 33 (1987) 277–284.
[9] K. Kadota, A. Chudnovsky, Constitutive-Equations of Crack Layer Growth, Polym Eng Sci, 32 (1992) 1097–1104.
[10] A. Stojimirovic, K. Kadota, A. Chudnovsky, An Equilibrial Process Zone in Polymeric Materials, J Appl Polym Sci, 46 (1992) 1051–1056.
[11] B. H. Choi, W. Balika, A. Chudnovsky, G. Pinter, R.W. Lang, The Use of Crack Layer Theory to Predict the Lifetime of the Fatigue Crack Growth of High Density Polyethylene, Polym Eng Sci, 49 (2009) 1421–1428.
[12] A. Chudnovsky, Y. Shulkin, Application of crack layer theory to modeling of slow crack growth in polyethylene, Int J Fracture, 97 (1999) 83–102.
[13] A. Chudnovsky, Z. Zhou, and H. Zhang, Lifetime Assessment of Engineering Thermoplastics, Int J Eng Sci, 59 (2012) 108–139.
[14] H. Tada, P. Paris, and G. Irwin, The Stress Analysis of Crack Handbook, ASME Press, New York, 2000.
[15] M.L. Williams, On the stress distribution at the base of a stationary crack, J Appl Mech, 24 (1957) 109–114.
[16] S. Mostovoy, P.B. Crosley, and E.J. Ripling, Use of crack loaded specimens for measuring plane-strain fracture toughness, J Mater, 2 (1967) 661–681.

Modelling Damage in Nuclear Graphite

Thorsten Becker [1,*], **James Marrow**[2]

[1] Department of Mechanical and Mechatronic Engineering, Stellenbosch University, Stellenbosch 7600, South Africa
[2] Department of Materials, University of Oxford, Oxford OX1 3PH, United Kingdom
* Corresponding author: tbecker@sun.ac.za

Abstract In this paper a non-local coupled plasticity and damage model for nuclear graphite is presented. The model is the adaption of an existing model for quasi-brittle materials that allows for the degradation (as a function of load) of the material properties. The model arises from the continuum-based approach and uses concepts of isotropic damaged elasticity in combination with isotropic tensile and compressive plasticity to represent inelastic behaviour. In this work fracture of Gilsocarbon polygranular graphite is simulated in the FE environment for compact tension and three point bend specimens. The model consists of a combination of non-associated multi-hardening plasticity and scalar (isotropic) damage elasticity that describe the irreversible damage that occurs during the fracturing process in graphite. The simulations exhibit the observed softening and degradation of the material and found to be size and geometry independent.

Keywords Nuclear graphite, fracture mechanics, micro-cracking, non-local damage plasticity model.

1. Introduction

Nuclear graphite, a high purity grade polygranular graphite, is used for structural components as well as neutron moderators in high temperature nuclear reactors. Functionally, graphite components are arranged in the form of keyed bricks to accommodate the thermal and radiation induced deformations throughout the life of a reactor. Potentially, these dimensional changes may lead to stresses that are sufficient for crack initiation in the brittle graphite, particularly at keyway roots and other discontinuities. The structural integrity of such components is of importance, and has been assessed historically with either probability of failure methodologies (such as the Weibull approach) [1–4] or the fracture mechanics methodology [5–12].

Weibull's weakest link theory anticipates that the larger the volume of material the greater the chance that a defect exists within the volume [13]. Simple application of this theory is inconsistent with experimental results; failure predictions of graphite components from small specimens do not agree with those of larger specimens [14]. An adaptation to the Weibull approach has been proposed by Hindley et al. [1] which incorperates a fixed volume size to ensure size independence; however, the results have shown to be conservative [1].

Recent studies have shown graphite behaviour to be non-linear [15] for non-irradiated medium grained graphites (Gilsocarbon and NBG10). Crack propagation is associated with a fracture process zone (FPZ) in which extensive micro-cracking results in irreversable energy dissipation. One of the biggest challenges in predicting component failure in graphite when using conventional fracture mechanics is that the fracture process is influenced by the graphite's micro-, meso- and macrostructures, which are characterised by the number and distribution of internal pores and cracks [15]. For example, crack propagation in Gilsocarbon is primarily linked with damage initiation and propagation from these internal features. In a notched specimen under an increasing load, isolated and randomly distributed micro-cracks develop predominantly ahead of the notch tip and propagate orthogonally to the tensile strain in the loading direction. It is during this phase that damage accumulates; ultimately the micro-cracks coalesce into a macro-crack. The propagation of the macro-crack is accompanied by bridging or branching through the maze of micro flaws and is

preceded by a fracture process zone (FPZ) ahead of the crack tip. Therefore, fracture processes in graphite may depend primarily on the stability of the interfacial cracks (micro-cracks) which is a function of the material structure [6,15,16].

Becker et al. [15] has shown, using the Double Torsion geometry [17] and an algorithm to calculate the fracture parameters from digital image correlation obtained displacement fields [18], that:

- The LEFM fracture parameters G_{Ic} or K_{Ic} are dependent on specimen geometry and size.
- The non-linear contributions to the energy dissipated during fracture seem dependent on specimen geometry and size.
- *R*-curve behaviour seems dependent on specimen geometry and size.

However

- The elastic contributions to the energy dissipated during fracture appear to be independent of specimen geometry and size.

These mechanisms of fracture are not unique. Quasi-brittle materials, like concrete, rock and many other materials including various fiber composites and particulate composites, coarse-grained or toughened ceramics, ice, cemented sands, grouted soils, bone, paper, wood, wood-particle board, etc experience similar mechanism of fracture [19]. Such materials are generally considered as brittle, yet behave in a non-linear fashion due to the development of a sizable FPZ that can occupy a large portion of the structure and is believed to be geometry and size dependent [19].

One way to model quasi-brittle fracture is the use of a non-local damage plasticity model, such as proposed by Lubliner and coauthors [20] and Lee and Fenves [21]. Here, the behavior of micro cracking is modelled on a macroscopic level by stiffness degradation combined with plasticity to provide an appropriate evolution of a yield surface during the formation of damage. The model uses a fracture energy based scalar damage variable to represent the damage state. In addition to the damage variable, the model introduces elastic and plastic degradation variables to simulate the degradation of elastic stiffness.

This paper presents the utilisation of this non-local damage-plasticity (DP) model for quasi-brittle materials to simulate graphite fracture. The framework of the non-local DP model is presented and the calibration of the model parameters with experimental data for Gilsocarbon. Finally, the model is implemented using two different test geometry examples, namely a three point bend (3PB) geometry and two compact tension (CT) geometries.

2. Framework for plastic-damage model for nuclear graphite

The model simulates failure implicitly in the Finite Element (FE) environment and consists of a combination of non-associated multi-hardening plasticity and scalar (isotropic) damaged elasticity variables to describe the irreversible damage that occurs during the fracture. This requires the definition of a yield surface and a flow rule. The degradation mechanisms of tensile cracking and compressive crushing are defined respectively as G_f, the fracture energy, and as a stress-displacement hardening relationship in compression . The degradation of the elastic stiffness in tension and compression is defined as a scalar, which is a function of the cracking displacement or strain. As static conditions are simulated, a strain rate independent model is assumed. For details regarding the model derivation, the reader is referred to the papers by Lubliner [20] and Lee and Fenves [21].

The yield function takes the form of the Drucker and Prager yield criterion to account for different evolution of strength under tension and compression. The evolution of the yield surface is controlled by the two hardening variables ε_c^{pl} and ε_t^{pl}. In terms of effective stresses, the yield function takes the form [22]:

$$F = \frac{1}{1-\alpha}\left(\bar{p} - 3\alpha\bar{q} + \beta\varepsilon_t^{pl}\langle\hat{\bar{\sigma}}_{max}\rangle - \gamma\langle\hat{\bar{\sigma}}_{max}\rangle\right) - \hat{\bar{\sigma}}_c\varepsilon_c^{pl} \leq 0 \tag{1}$$

where, α, β and γ are dimensionless constants, $\langle\hat{\bar{\sigma}}_{max}\rangle$ is the algebraic maximum principal stress, $\bar{p}$ the hydrostatic pressure, which is a function of the first stress invariant I_1 (defined as $\bar{p} = I_1/3$), and $\bar{q}$ the Von Mises equivalent stress, described as $\bar{q} = \sqrt{2J_2}$ (where J_2 is the second deviatoric stress invariant). α, β and γ are given as:

$$\alpha = \frac{f_{b0}/f_{c0} - 1}{2f_{b0}/f_{c0} - 1} \tag{2}$$

$$\beta = \frac{f_{c0}}{f_{t0}}(\alpha - 1) - (1 + \alpha) \tag{3}$$

$$\gamma = \frac{3(1-\kappa_c)}{2\kappa_c - 1} \tag{4}$$

where, f_{c0} and f_{b0} are the compressive and compressive biaxial elastic limit respectively, f_{t0} the tensile elastic limit, and κ_c is the ratio of the second stress invariant on the tensile meridian to that on the compressive meridian at the elastic limit for any given value of the pressure invariant such that the maximum principal stress is negative (the default value is 2/3) [22].

To compute the non-elastic stress-strain behaviour, the plastic-damage model assumes non-associated potential flow as [22]:

$$\dot{\varepsilon}^{pl} = \lambda\frac{\partial G(\bar{\sigma})}{\partial\bar{\sigma}} \tag{5}$$

where the flow rule G is the Drucker-Prager hyperbolic function [22]:

$$G = \sqrt{(\epsilon_{cc}f_{t0}tan\psi)^2 + (\bar{q})^2} - \bar{p}tan\psi \tag{6}$$

where ϵ_{cc} is the eccentricity, which defines the rate at which the plastic potential function approaches the asymptote. ψ is the dilation angle (measured in the $\bar{p}$ - $\bar{q}$ plane at a high confining pressure.

The post-yield behaviour in tension is defined according to the energy criterion G_f. Quasi-brittle behaviour is characterised by a stress-displacement response and the fracture energy is invoked by specifying the post-yield stress as a function of cracking displacement. The tensile damage is converted to a cracking displacement value using a relationship where the specimen length l is assumed to be one unit length in FE implementation [22]. The post-yield behaviour in compression is defined as a displacement-hardening/softening behaviour. A cracking displacement u_c^{ck} is defined as the total displacement minus the elastic displacement corresponding to the undamaged material. This requires the softening data in terms of the cracking displacement [22]:

$$u_t^{pl} = u_t^{ck} - \frac{1}{1-d_t}\frac{\sigma_t l}{E_0} \tag{7}$$

3. Identification of the model parameters

The nuclear graphite grade modelled was Gilsocarbon (GCMB grade, IG-110) graphite, a near isotropic material [23]. Typical material properties are reported as 11.9 GPa for the Young's modulus and the tensile strength of 20 MPa [23]. The Poisson's ratio was taken as 0.21 [23]. The numerical strategy for solving the non-local DP problem requires the knowledge of the constitutive material parameters of Gilsocarbon, which include the definition of the yield surface, the flow rule, the load response and the material degradation.

3.1. Yield Surface and Flow Rule

The plane stress cross section for the failure surface in the principal stress space is shown in Figure 1a. The data shown was extracted from various literature sources on the biaxial behaviour of Gislocarbon (which have been listed in the captions for convenience). The typical uniaxial compressive yield stress to biaxial yield compressive stress ratio was found to be 0.81 [24]. The dilatancy and eccentricity values, ψ and the ϵ_{cc} respectivly, were extracted from Brocklehurst [2,25] as shown in Figure 1b. The dilation angle, measured in the p - q plane at high confining pressure, was calculated as 30°. Note, similar values were found for concrete, a quasi-brittle material, where ψ is between 30° to 40° [26]. Figure 1 shows that the Ducker-Prager criterion is an excellent fit to the failure data. Since a plane stress problem is assumed the triaxial parameter λ is of little significance [21].

3.2. Stiffness Degradation

The tension softening behaviour or post-yield behaviour is defined according to the fracture energy criterion $G_{f,}$ which is approximately 250 J/m^2 [15] for Gilsocarbon. To determine the stiffness degradation behaviour requires a complex testing apparatus, such as the tests done by Gopalaratnam and Shah [27] for concrete. At point in time when this work was undertaken these data were not available and thus a linear evolution of the damage variable with efffective plastic displacement is currently assumed. This ensures that when the effective plastic displacement reaches a critical value, the material stiffness will be fully degraded. The compressive load response was defined according to Oku [28]. The stiffness degradation behaviour was also defined as a linear evolution of the damage variable with effective plastic displacement. As static conditions are simulated a strain rate independent model is assumed. The parameters are summarised in Table 1.

Table 1: Material parameters of the DP model for Gilsocarbon

Elastic Properties:	
Young's modulus E_0	11.9 GPa
Poisson's ratio ν	0.21
Yield Surface and Flow Rule:	
Dilation angle ψ	30°
Eccentricity ϵ_{cc}	4.8
Biaxiality ratio	0.81
Tension softening:	
Fracture energy	250 J/m^2
Compression hardening:	
20 MPa	0 mm
65 MPa	0.015 mm
1 MPa	0.045 mm

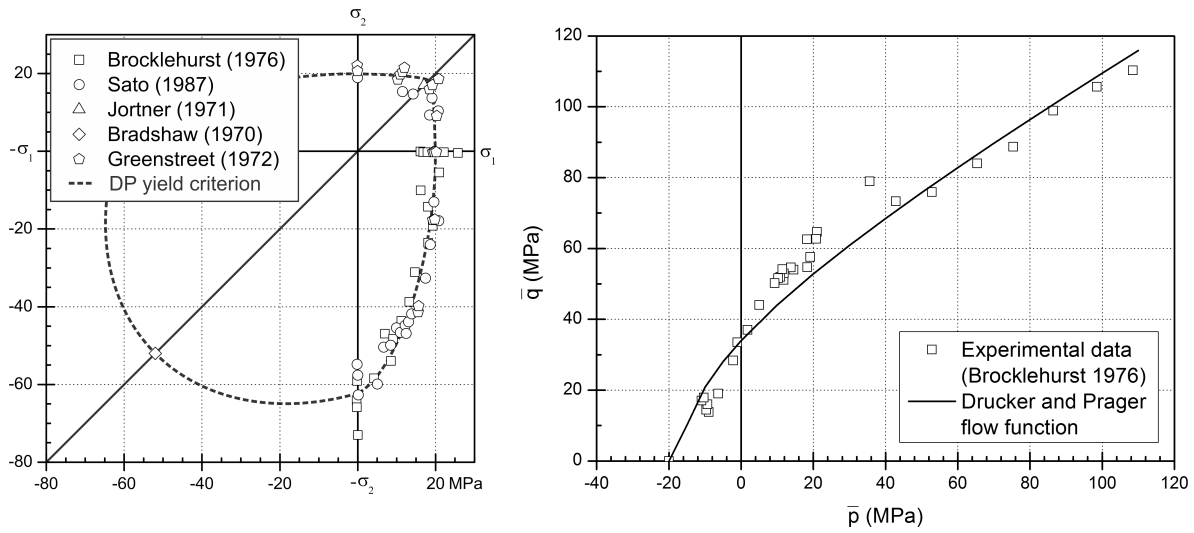

(a) (b)

Figure 1: (a) Biaxial failure data for Gislocarbon. The data was extracted from Brocklehurst [2], Sato et al. [29], Jortner [30], Bradshaw [24] and Greenstreet [31]. (b) Drucker-Prager hyperbolic plastic potential function in the meridional plane. Experimental data was extracted from Brocklehurst [2].

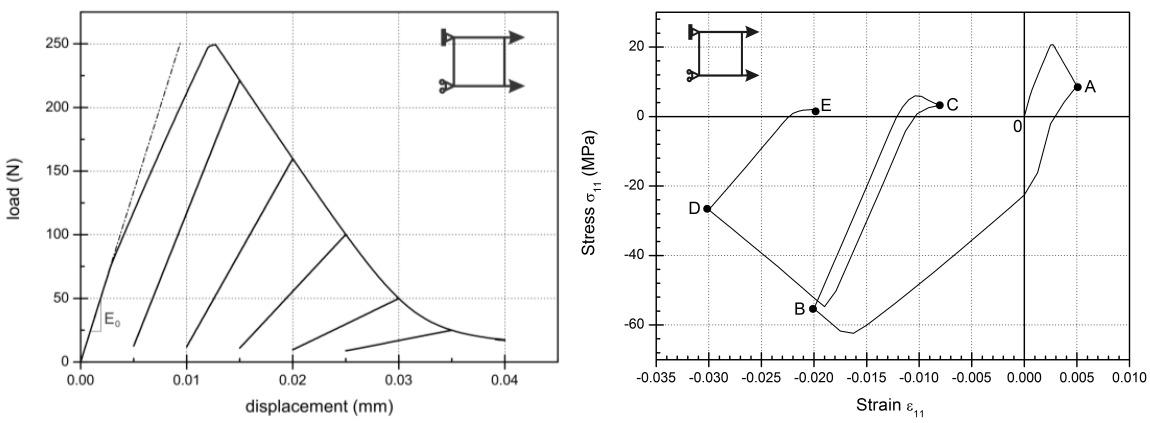

Figure 2: (a) Numerical solution of cyclic uniaxial loading in tension. (b) Numerical Solution for Full Cyclic Loading (Path: O-A-B-C-D-E).

3.3. Model Behaviour

To present the behaviour of the DP model a single monotonic uni-axial loading and full cyclic monotonic uni-axial loading element is simulated. This uses a linear elastic quadratic full integration element. The material properties used for each model are presented in Table 1. The element mesh size of 7.4 x 7.4 mm was utilised, as it represents the by Bazant et al. [32] defined characteristic length of Gislocarbon [33]. The model was implemented in the FE environment of ABAQUS/Standard (Version 6.9).

The non-local DP model monotonic uni-axial loading response, in Figure 2a, shows the softening response and the stiffness degradation (damage formation). The full cyclic (tension and compression) monotonic uni-axial loading response, in Figure 2b, resembles the hysteresis curve of

the simulation results in Figure 2a, because energy is dissipated during the tensile reloading (path B-C-D). Similar to Lee and Fenves [21], Figure 2 shows that the model can simulate quasi-brittle material behaviour subjected to cyclic loading for which the hysteresis curve in the tensile region is negligible compared with the compressive counterpart.

4. Numerical Implementation

The non-local DP model was implemented using two different Gislocarbon test geometry examples, namely a three point bend (3PB) gemetry and two compact tension (CT) geometries. Plane stress conditions were assumed to allow for short computational times and numerical convergence. The computations were implemented in ABAQUS/Standard (Version 6.9). The material properties used for each model are presented in Table 1.

The first example is the two CT specimens tested by Fazluddin [8] and Hodgkins [7]. Note, for Hodgkins' specimen configuration the width of part of the specimen was reduced in order to allow the progression of the crack to be monitored in three dimensions using X- Ray tomography [7]. The numerical models consisted of 1480 and 1320 four noded plane strain elements for Fazluddin's and Hodgkins' geometries respectively (which only represent the symmetrical half). The second example, 3PB specimen, consists of 896 four noded linear plane strain elements and similarly only represents the symmetrical half of the specimen. To avoid convergence issues, only DP elements are utilised in the region in which fracture is expected to occur (elsewhere linear elastic conditions are assumed). Some mesh refinement was performed in the vicinity of the notch-tip to achieve mesh-insensitive results. Boundary conditions are applied with an analytically rigid pin with defined hard frictionless contact in displacement control.

The failure envelope is well captured in both the CT specimens and the 3PB specimen. The tensile damage localisation at peak load, which manifests itself by a reduction of the load at fracture, shows similarities to the experimental observations reported by Becker et al. [15]. The experimental data from Hodgkins provided a load-unloading response (Figure 3b) and the non-local DP model is capable, to a certain degree, of simulating this behaviour. Discrepencies exist as some load carrying capability remains in fully degraded elements since the stress-displacement behaviour has been defined with a failure stress of 1 MPa for numerical stability [22]. The 3PB geometry exhibits a more brittle response compared to the CT geometry, which is noticeable from the more severe post peak load drop when comparing Figure 3 and Figure 4.

It is worth reiterrating that experimentally obtained R-curve data has shown a geometry dependent fracture behavior of Gilsocarbon, where the non-linearities due to the FPZ and the wake effects result in variations of the apparent fracture toughness [15]. Since the DP model is a non-local approach it is size and geometry independent. The degradation and hence softening of the material is confined to the defined yield criteria and flow rule. As damage develops ahead of the crack tip, the yield surface shrinks in the stress space leading to a softening interfacial constitutive law. Fracture has occurred when the work done by the tractions meets the fracture mechanics based criterion. The DP failure model can be viewed as an extension or generalisation of the cohesive zone model proposed by Zou et al. [34], in that it couples together the effects of stress/displacement curves to derive a combined non-local stress and fracture mechanics based failure criterion. Because the DP model is non-local it is not confined to stress singularities and is thus believed to be a more accurate representation of graphite fracture.

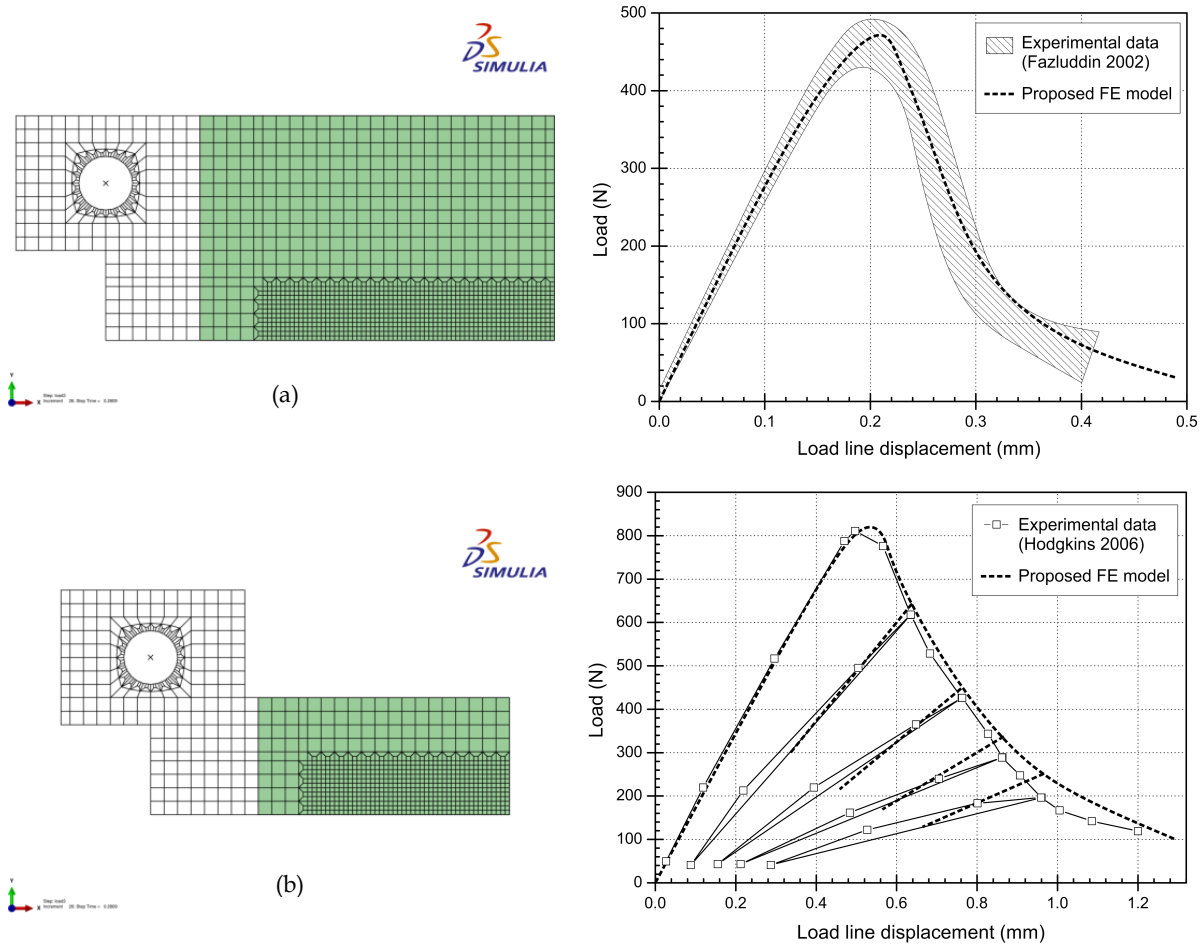

Figure 3: FE mesh of the two DP simulated CT specimens: (a) according Fazluddin's CT specimen [8] with W = 50 mm and the load displacement curves. (b) according Hodgkins' CT specimen [7] with W = 87 mm and the load displacement curves. Coloured elements indicate DP elements.

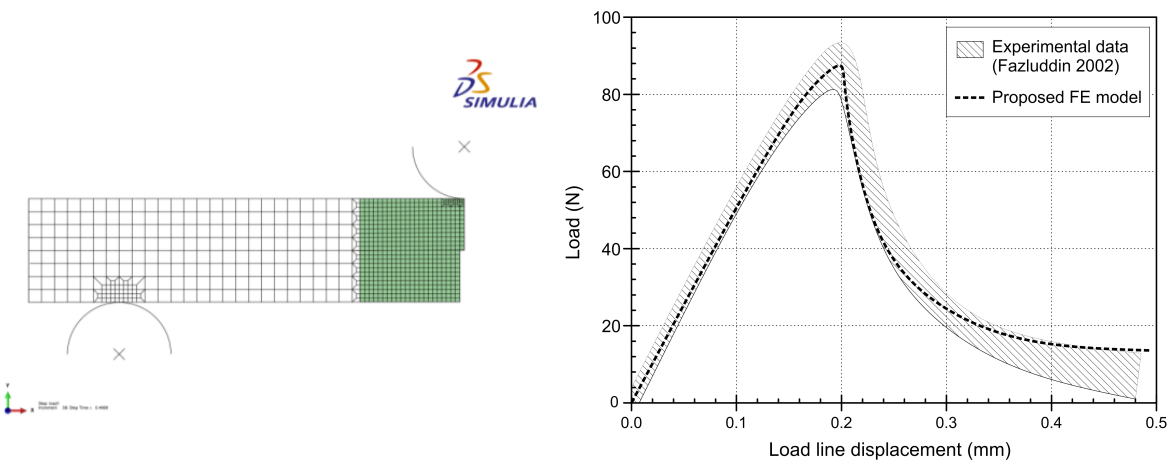

Figure 4: Fazluddin's geometry and loading setup of the three point bending simulation [8] and load-displacement curve. Coloured elements indicate DP elements.

5. Conclusion

The non-local DP model is a useful methodology in the rate-independent, non-linear modelling of fracture in Gilsocarbon. The significance of the result is both theoretical and practical: On the theoretical plane, though the conventional EPFM methodology has been shown to be limited in the application in nuclear graphite, it was demonstrated that the fracture parameters calculated using EPFM are relevant as they describe the inherent failure behviour. Since the model allows for the bulk degradation of material ahead of the crack tip, fracture is not constrained to a singularity, but is simulated as the degradation of the material ahead of the crack tip. The practical significance is that the DP model has shown excellent agreement with experimental results and hence motivates for further investigations of using non local DP models to simulate quasi-brittle fracture in nuclear graphite that has been degraded by operation in reactor environments.

Acknowledgments

TH Becker would like to express his appreciation for the University of Cape Town and the people involved in facilitating this research and to the University of Manchester for providing the required experimental equipment, such as the mechanical testing apparatuses as well as for the use of the server cluster.

References

[1] M.P. Hindley, M.N. Mitchell, C. Erasmus, R. McMurtry, T.H. Becker, D.C. Blaine, A.A. Groenwold, Journal of Nuclear Materials, Available online 30 October 2012, ISSN 0022-3115, 10.1016/j.jnucmat.2012.10.030.
[2] J. Brocklehurst, M. Darby, Materials Science and Engineering 16 (1974) 91–106.
[3] B. Mitchell, J. Smart, S. Fok, B. Marsden, Journal of Nuclear Materials 322 (2003) 126–137.
[4] J.P. Strizak, IAEA-TECDOC-690 (Ed.), 1991, p. 16.
[5] P. Ouagne, G.B. Neighbour, B. McEnaney, Journal of Physics D: Applied Physics 35 (2002) 927–934.
[6] A. Hodgkins, T. Marrow, P. Mummery, B. Marsden, A. Fok, Materials Science and Technology 22 (2006) 1051.
[7] A.D. Hodgkin, Crack Propagation in Nuclear Graphite, PhD Thesis, The University of Manchester, 2006.
[8] S. Fazluddin, Crack Growth Resistance in Nuclear Graphite, University of Sheffield, 2002.
[9] M. Sakai, K. Urashima, M. Inagaki, Journal of the American Ceramic Society 66 (1983) 868–874.
[10] M. Sakai, J. Yoshimura, Y. Goto, M. Inagaki, Journal of the American Ceramic Society 71 (1988) 609–616.
[11] M.R. Ayatollahi, a. R. Torabi, Carbon 48 (2010) 2255–2265.
[12] P.J. Heard, M.R. Wootton, R. Moskovic, P.E.J. Flewitt, Journal of Nuclear Materials 401 (2010) 71–77.
[13] W. Weibull, Roy. Swedish Ins. Eng. Res. 153 (n.d.) 1–55.
[14] M.P. Hindley, M.N. Mitchell, D.C. Blaine, A.A. Groenwold, Journal of Nuclear Materials 420 (2012) 110–115.
[15] T.H. Becker, T.J. Marrow, R.B. Tait, Journal of Nuclear Materials 414 (2011) 32–43.
[16] M. Mostafavi, T.J. Marrow, Engineering Fracture Mechanics 78 (2011) 1756–1770.
[17] T.H. Becker, T.J. Marrow, R.B. Tait, Experimental Mechanics 51 (2011) 1511–1526.

[18] T.H. Becker, M. Mostafavi, T.J. Marrow, Fatigue and Fracture of Engineering Materials and Structures 35 (2012) 971–984.
[19] Z. Bazant, Engineering Fracture Mechanics 69 (2002) 165–205.
[20] J. Lubliner, International Journal of Solids and Structures 25 (1989) 299–326.
[21] J. Lee, G.L. Fenves, Journal of Engineering Mechanics 124 (1998) 892.
[22] ABAQUS, User's Manual, Version 6.9, ABAQUS Inc., Prvidence, Rhode Island, 2010.
[23] S.D. Preston, B.J. Marsden, Carbon 44 (2006) 1250–1257.
[24] W.G. Bradshaw, Mechanical and Thermal Properties of Glass-like Carbons, Technical Report CONF-701105 (1972).
[25] C. Berre, P. Mummery, B. Marsden, T. Mori, P.J. Withers, Journal of Nuclear Materials 381 (2008) 128.
[26] R. Malm, Predicting Shear Type Crack Initiation and Growth in Concrete with Non-linear Finite Element Method, Royal Institute of Technology (KTH), Stockholm, Sweden, 2009.
[27] V. Gopalaratnam, S. Shah, Journal Proceedings 82 (1985) -323.
[28] T. Oku, M. Eto, Nuclear Engineering and Design 143 (1993) 239–243.
[29] S. Sata, Nuclear Engineering and Design 23 (1987) 62.
[30] J. Jortner, Technical Report AFML-TR-71 (1971) 253.
[31] W. Greenstreet, G. Yahr, R. Valachovic, Carbon 11 (1973) -57.
[32] Z. Bazant, Advanced Cement Based Materials 4 (1996) 128–137.
[33] T.H. Becker, Understanding and Modelling the Damage and Fracture Characteristics of Nuclear Grade Graphite, PhD Thesis, University of Cape Town, 2011.
[34] Z. Zou, Journal of Nuclear Materials 324 (2004) 116–124.

A Stabilized Sequential Coupling Algorithm for Hydro-mechanical Systems using Reproducing Kernel Particle Method

Yongning XIE[1], **Gang WANG**[1,*]

[1] Department of Civil and Environmental Engineering
The Hong Kong University of Science and Technology, Hong Kong SAR, China
* Corresponding author: gwang@ust.hk

Abstract Sequential coupling scheme is a flexible numerical scheme to solve a coupled hydro-mechanical system. However, it suffers from severe numerical instability. Stability analysis of a sequential coupling scheme is performed in this paper. It is derived that the numerical scheme can be unconditionally stable with a stabilization term introduced to the fluid equation, while it is only conditionally stable without the stabilization. Reproducing Kernel Particle Method (RKPM) is used for spatial discretization. One dimensional consolidation in an elastic medium is conducted to verify the sequential scheme, and the convergence behavior during the iterations is presented.

Keywords hydro-mechanical coupling, sequential, meshfree, stability

1. Introduction

Sequential coupling scheme has been extensively studied in the past decades to solve the coupled hydro-mechanical system (*e.g.* [1-4]). It has great advantage over the traditional fully-coupled numerical scheme due to its *modularity* such that the fluid and the mechanical solver for corresponding governing equations can be executed separately without many extra manipulations. The coupling effect is fulfilled through the information exchange between two solvers. *Modularity* is particularly advantageous in practical applications. However, the convenience does not come without any price. The numerical stability and convergence is one problem frequently encountered using the sequential scheme. As has been demonstrated in literatures, different sequential algorithms require different stability conditions [4].

One part of this work is to seek a stable sequential couplings scheme. It is worth pointing out that the current study only focuses on the stability and convergence problem in the temporal space. To achieve this goal, a stabilization term is introduced to the fluid equation. Using the conventional stability analysis, it is found that the scheme can be unconditionally stable with a suitably chosen relaxation parameter. Another part of the work is to employ one type of meshfree methods, Reproducing Kernel Particle Method (RKPM), for spatial discretization. Due to their high order interpolations and *mesh-free* nature, meshfree methods are generally considered to have advantage in handling problems with large strains or strain localization. These features are not demonstrated in this paper as the emphasis is more on the formulation and stability of the sequential scheme. However, the numerical results do suggest the applicability of RKPM to the coupling scheme developed. More interesting features of RKPM may show up if nonlinear constitutive models are used and more complicated boundary value problems considered.

This paper is arranged as follows: Governing equations for the hydro-mechanical system are presented first, followed by the spatial discretization by RKPM and algorithm of sequential scheme. Stability analysis of the numerical scheme is presented subsequently. Numerical simulations for verification of the stability conditions are then demonstrated.

Throughout the paper, letter in bold face denotes tensor or vector. $()_{,i}$ denotes partial derivative with respect to coordinate. A superscript dot over a variable $\dot{()}$ denotes the time derivative of that variable. δ_{ij} is the Kronecker delta tensor.

2. Governing Equations

The coupled formulation of fully saturated porous media used in this work is so-called $\mathbf{u}-p$ formulation, in which the displacement of solid $\mathbf{u}$ and pore fluid pressure p are treated as two primary unknown variables [5]. The governing equations are derived from the equation of momentum equilibrium of solid-fluid mixture and equation of mass conservation of fluid as follows:

$$(\sigma'_{ij} - p\delta_{ij})_{,j} - \rho\ddot{u}_i + \rho b_i = 0 \tag{1}$$

$$\left(k_{ij}(-p_{,j} + \rho_f b_j)\right)_{,i} + \dot{\varepsilon}_{ii} + \frac{n\dot{p}}{K_f} = 0 \tag{2}$$

where σ'_{ij} is the effective stress tensor, which is related to the total stress σ_{ij} and pore fluid pressure p via $\sigma'_{ij} = \sigma_{ij} + p\delta_{ij}$. The effective stress in tension and pressure in compression are assigned with positive sign. ρ and ρ_f are the mass densities of the mixture and fluid, respectively. b_i is unit body force, k_{ij} is permeability tensor, which has a dimension of $[\text{length}]^3[\text{time}]/[\text{mass}]$ and is related to the conventional permeability k'(dimension: $[\text{length}]/[\text{time}]$) by $k = k'/\rho_f g$; ε_{ij} is the strain tensor; n is the porosity; K_f is the bulk modulus of the fluid. It should be noted that the governing equations presented here are simplified from [5] with the assumption that solid grains are incompressible.

The effective stress σ'_{ij} can be calculated from the constitutive relationship in rate form as follows:

$$\dot{\sigma}'_{ij} = C_{ijkl}\dot{\varepsilon}_{kl} \tag{3}$$

where C_{ijkl} is the tangent modulus of the solid and ε_{ij} is strain tensor.

The solid-fluid behaviors are coupled in that changing pore pressure influences the mechanical equilibrium state of the mixture, and the volumetric strain rate of the mixture affects the mass balance of the fluid. While the coupling problem can be approximated and solved in a decoupled manner in some special cases, the coupling effect is an important for a strongly coupled hydro-mechanical system and it cannot be neglected.

3. Spatial Discretization with RKPM

Denote $\mathbf{N}^u$ and $\mathbf{N}^p$ as the shape functions for displacement $\mathbf{u}$ and pore water pressure p, respectively. The semi-discrete form of the governing equations (1) and (2) can be obtained by multiplying the governing equations (1) and (2) by $\left(\mathbf{N}^u\right)^T$ and $\left(\mathbf{N}^p\right)^T$ respectively, followed by integration by part:

$$\mathbf{M}\ddot{\mathbf{u}} + \mathbf{K}\mathbf{u} - \mathbf{Q}\mathbf{p} - \mathbf{f}^u = 0 \tag{4}$$

$$\mathbf{Q}^T\dot{\mathbf{u}} + \mathbf{H}\mathbf{p} + \mathbf{S}\dot{\mathbf{p}} - \mathbf{f}^p = 0 \tag{5}$$

where

$\mathbf{M} = \int_\Omega (\mathbf{N}^u)^T \rho \mathbf{N}^u d\Omega$ (mass matrix); $\mathbf{K} = \int_\Omega \mathbf{B}^T \mathbf{C} \mathbf{B} d\Omega$ (stiffness matrix)

$\mathbf{f}^u = \int_{\Gamma_t} (\mathbf{N}^u)^T \bar{\mathbf{t}} d\Gamma_t + \int_\Omega (\mathbf{N}^u)^T \rho \mathbf{b} d\Omega$ (external forces)

$\mathbf{Q} = \int_\Omega \mathbf{B}^T \mathbf{m} \mathbf{N}^p d\Omega$ (coupling matrix); $\mathbf{H} = \int_\Omega (\nabla \mathbf{N}^p)^T \mathbf{k} \nabla \mathbf{N}^p d\Omega$ (permeability matrix);

$\mathbf{S} = \int_\Omega (\mathbf{N}^p)^T \frac{n}{K_f} \mathbf{N}^p d\Omega$ (compressibility matrix); $\mathbf{f}^p = \int_\Omega (\nabla^T \mathbf{N}^p)(\mathbf{k} \rho_f \mathbf{b}) d\Omega + \int_{\Gamma_w} (\mathbf{N}^p)^T \bar{q} d\Gamma_w$

and $\mathbf{m} = [1\ 1\ 1\ 0\ 0\ 0]^T$, $\mathbf{B}$ is strain-displacement matrix (the spatial derivatives of the shape functions). The boundary conditions are $\mathbf{u} = \bar{\mathbf{u}}$ on displacement boundary $\mathbf{\Gamma}_u$ and $\mathbf{t} = \bar{\mathbf{t}}$ on traction boundary $\mathbf{\Gamma}_t$, $p = \bar{p}$ on pressure boundary $\mathbf{\Gamma}_p$ and $q = \bar{q} = -\boldsymbol{n}^T \boldsymbol{k}(-\nabla \boldsymbol{p} + \rho_f \boldsymbol{b})$ on flux boundary Γ_w. The total boundary $\mathbf{\Gamma} = \mathbf{\Gamma}_u \bigcup \mathbf{\Gamma}_t = \mathbf{\Gamma}_p \bigcup \mathbf{\Gamma}_w$. Proper initial boundary conditions should also be given for the numerical simulation to start off.

RKPM shape functions ([6,7]) are used in this study. The RKPM shape functions interpolate the solution over discrete nodes, which, unlike the conventional FEM, have no topological connectivity relationship. Here only the formulation of shape functions and essential boundary imposition are briefly introduced. Readers may refer to [6-8] for the detailed formulations and implementations.

Function $u(x)$ in the domain can be approximated by the following formulation

$$u(\boldsymbol{x}) = \int_\Omega u(\bar{\boldsymbol{x}}) K(\boldsymbol{x} - \bar{\boldsymbol{x}}; \tilde{n}) d\bar{V} \tag{6}$$

where $u(\bar{\boldsymbol{x}})$ are the values of field variables at particles. $K(\boldsymbol{x} - \bar{\boldsymbol{x}}; \tilde{n})$ is the compactly-supported kernel function formulated in RKPM as multiplication of a correction function $C(\boldsymbol{x}, \bar{\boldsymbol{x}})$ and a window function $\Phi(\boldsymbol{x} - \bar{\boldsymbol{x}})$, *i.e.*, $K(\boldsymbol{x} - \bar{\boldsymbol{x}}) = C(\boldsymbol{x}, \bar{\boldsymbol{x}}) \Phi(\boldsymbol{x} - \bar{\boldsymbol{x}})$. The correction function $C(\boldsymbol{x}, \bar{\boldsymbol{x}})$ is assumed to be linear with respect to $(\boldsymbol{x} - \bar{\boldsymbol{x}})$. The window function may take the form of a cubic spline or Gaussian function and has a rectangular or circular support in 2D case. Accordingly, the displacement can be interpolated as

$$u^h(\boldsymbol{x}) = \sum_{J=1}^{NP} N_J(\boldsymbol{x}) u_J \tag{7}$$

where the reproducing kernel approximant (shape function) $N_J(\boldsymbol{x})$ is given by

$$N_J(\boldsymbol{x}) = C(\boldsymbol{x}, \boldsymbol{x}_J) \Phi(\boldsymbol{x} - \boldsymbol{x}_J) \Delta V_J \tag{8}$$

$\boldsymbol{x}_J$ and ΔV_J are the position and contributing volume of the Jth node, respectively. The RKPM shape function does not possess Kronecker delta property, *i.e.* $u^h(\boldsymbol{x}_I) \neq u_I$. Therefore, special treatment is required to impose the essential boundary conditions. In this paper, the essential boundary condition is reinforced by transformation method ([7]).

4. Sequential Coupling Scheme

There are numerous sequential coupling schemes with varied degrees of success in stability ([4]). This study introduces a simple stabilization term by considering the difference of pore fluid pressures between successive iterations. Rewrite the mechanics solver and fluid solver as follows:

$$\text{Mechanics Solver}: \quad \mathbf{M}\ddot{\boldsymbol{u}}_{n+1}^{(i+1,k+1)} + \mathbf{C}_{n+1}^{(i+1,k)} \dot{\mathbf{u}}_{n+1}^{(i+1,k)} + \mathbf{K}_{n+1}^{(i+1,k)} \mathbf{u}_{n+1}^{(i+1,k)} - \mathbf{Q}\mathbf{p}_{n+1}^{(i+1)} - \mathbf{f}_{n+1}^{u} = 0 \tag{9}$$

$$\text{Fluid Solver:}\quad \left(\mathbf{H}\Delta t_f+\mathbf{S}\right)\mathbf{p}_{n+1}^{(i+1)}+\boxed{\tilde{\mathbf{S}}\left(\mathbf{p}_{n+1}^{(i+1)}-\mathbf{p}_{n+1}^{(i)}\right)}+\mathbf{Q}^{T}\left(\mathbf{u}_{n+1}^{(i)}-\mathbf{u}_{n}\right)-\mathbf{S}\mathbf{p}_{n}-\mathbf{f}_{n+1}^{p}\Delta t_f=0 \qquad (10)$$

In the above equations, subscripts n and $n+1$ represent the real time t_n and t_{n+1}, respectively, $\Delta t_f = t_{n+1} - t_n$ is the time increment. $\mathbf{p}_n$ and $\mathbf{u}_n$ are solutions of pressure and displacement at t_n. The displacement rate in Eq.(5) is approximated as $\dot{\mathbf{u}}_{n+1} = \dfrac{\mathbf{u}_{n+1}^{(i)} - \mathbf{u}_n}{\Delta t_f}$. During the iterations within one step, the fluid solver and mechanics solver are executed sequentially, with iteration numbers denoted by superscripts i, $i+1$ (e.g., $\mathbf{p}_{n+1}^{(i)}$, $\mathbf{p}_{n+1}^{(i+1)}, \mathbf{u}_{n+1}^{(i+1,*)}$). The flow solver solves the pressure at once implicitly, while the mechanics solver solves the displacement explicitly through iterations, denoted by superscripts k, $k+1$... (e.g. $\mathbf{u}_{n+1}^{(i+1,k)}$, $\mathbf{u}_{n+1}^{(i+1,k+1)}$).

The boxed term in the flow solver is added to stabilize the system. $\tilde{\mathbf{S}}$ is an introduced parameter which will be determined in order to satisfy the numerical stability requirement and to achieve an optimal convergence rate. The stabilization term is essentially a term related to the variation of pressure increment during successive iterations, which vanishes when $\mathbf{p}_{n+1}^{(i+1)} \to \mathbf{p}_{n+1}^{(i)}$ and a consistent solution of displacement and pore water pressure is consequently achieved. Without the stabilization term, the solution of Eq. (10) (*i.e.* $\mathbf{p}_{n+1}^{(i+1)}$) may be unstable or even unattainable, as will be demonstrated by stability analysis in Section 5.

The sequence of solver calling varies in different schemes ([4]). The sequential scheme in this study first updates the pore water pressure by calling the flow solver, and then updates the displacement using the mechanical solver. Nested numerical iterations (denoted using subscript n and superscripts i, k) are required to solve the system. The general procedure is listed as the following.

(1). Initialization at the start of time: $\mathbf{p}_0 = \mathbf{p}_{ini}$, $\mathbf{u}_0 = \mathbf{u}_{ini}$.

(2). Start time integration $n = 0$

(a) Initialization $\mathbf{p}_{n+1}^{(0)} = \mathbf{p}_n$, $\mathbf{u}_{n+1}^{(0)} = \mathbf{u}_n$, update $\mathbf{f}_{n+1}^{u}$ and $\mathbf{f}_{n+1}^{p}$.

(b) Start iteration scheme $i = 0$.

i. Call flow solver to solve for $\mathbf{p}_{n+1}^{(i+1)}$:

$$\mathbf{p}_{n+1}^{(i+1)}=\left(\mathbf{H}\Delta t_f+\mathbf{S}+\tilde{\mathbf{S}}\right)^{-1}\left[\tilde{\mathbf{S}}\mathbf{p}_{n+1}^{(i)}-\mathbf{Q}^{T}\left(\mathbf{u}_{n+1}^{(i)}-\mathbf{u}_{n}\right)+\mathbf{S}\mathbf{p}_{n}+\mathbf{f}_{n+1}^{p}\Delta t_f\right]$$

ii. Call mechanics solver using predictor-corrector integration method. k starts from 0. $\mathbf{u}_{n+1}^{(1,0)} = \mathbf{u}_n$.

A. Compute the predictors:

$$\tilde{\mathbf{u}}_{n+1}^{(i+1,k+1)} = \mathbf{u}_{n+1}^{(i+1,k)} + \Delta t\mathbf{v}_{n+1}^{(i+1,k)} + \frac{(\Delta t)^2}{2}\left(1-2\beta\right)\ddot{\mathbf{u}}_{n+1}^{(i+1,k)}$$

$$\tilde{\mathbf{v}}_{n+1}^{(i+1,k+1)} = \mathbf{v}_{n+1}^{(i+1,k)} + (1-\gamma)\Delta t\ddot{\mathbf{u}}_{n+1}^{(i+1,k)}$$

$\Delta t = 10^{-5}$ s (pseudo-time step)

B. Update $\square\mathbf{K}_{n+1}^{(i+1,k+1)} = \int_{\Omega}\mathbf{B}^{T}\mathbf{C}\left(\nabla^{s}\tilde{\mathbf{u}}_{n+1}^{(i+1,k+1)}\right)\mathbf{B}d\Omega$ for nonlinear materials.

C. Compute $\ddot{\mathbf{u}}_{n+1}^{(i+1,k+1)} = \mathbf{M}^{-1}\left(\mathbf{Q}\mathbf{p}_{n+1}^{(i+1)} + \mathbf{f}_{n+1}^{u} - \tilde{\mathbf{C}}\tilde{\mathbf{v}}_{n+1}^{(i+1,k+1)} - \square\mathbf{K}_{n+1}^{(i+1,k+1)}\tilde{\mathbf{u}}_{n+1}^{(i+1,k+1)}\right)$

D. Compute the correctors:

$$\mathbf{u}_{n+1}^{(i+1,k+1)} = \tilde{\mathbf{u}}_{n+1}^{(i+1,k+1)} + \beta(\Delta t)^2\ddot{\mathbf{u}}_{n+1}^{(i+1,k+1)}$$

$$\mathbf{v}_{n+1}^{(i+1,k+1)} = \tilde{\mathbf{v}}_{n+1}^{(i+1,k+1)} + \gamma\Delta t\ddot{\mathbf{u}}_{n+1}^{(i+1,k+1)}$$

E. Check whether $\frac{\| \mathbf{F}_{unbal} \|}{\| \mathbf{F}_{tot} \|} \le TOL_{unbal}$.

If NO, $k \Leftarrow k+1$ and go to (2)(b) iiA.

F. End mechanics solver. Commit $\mathbf{u}_{n+1}^{(i+1)} = \mathbf{u}_{n+1}^{(i+1,k+1)}$.

iii. Check whether both the solutions $\mathbf{p}_{n+1}^{(i+1)}$ and $\mathbf{u}_{n+1}^{(i+1)}$ satisfy the convergence criteria, *i.e.* $\left\| \mathbf{p}_{n+1}^{(i+1)} - \mathbf{p}_{n+1}^{(i)} \right\| / \left\| \mathbf{p}_{n+1}^{(i+1)} \right\| \le TOL_p$ and $\left\| \mathbf{u}_{n+1}^{(i+1)} - \mathbf{u}_{n+1}^{(i)} \right\| / \left\| \mathbf{u}_{n+1}^{(i+1)} \right\| \le TOL_u$. If NO, $i \Leftarrow i+1$, and go to (2)(b)i.

iv. End iteration scheme.

(c) Update $\mathbf{p}$ and $\mathbf{u}$: $\mathbf{p}_{n+1} = \mathbf{p}_{n+1}^{(i+1)}$ and $\mathbf{u}_{n+1} = \mathbf{u}_{n+1}^{(i+1)}$.

(d) If n < total time step, $n \Leftarrow n+1$, and go to (2)(a).

(3). End time integration.

where $\mathbf{v} = \dot{\mathbf{u}}$ is the velocity vector, $\mathbf{F}_{unbal}$ is the unbalanced force, $\mathbf{F}_{tot}$ is the total applied force. $TOL_{unbal}, TOL_p, TOL_u$ are tolerance for the unbalance force, pore water pressure variation and displacement variation, respectively. β and γ are the two numerical parameters for the integration method. In the simulations presented in this paper, $\beta = 0.25, \gamma = 0.5$ are used. $\mathbf{C}$ is taken as the conventional Rayleigh damping given by $\mathbf{C} = a\mathbf{M} + b\mathbf{K}$.

As mentioned before, the mechanics and fluid solvers may employ different solution schemes. In the scheme proposed, the fluid solver is formulated using implicit integration for pressure, while mechanics solver solves displacement explicitly. The reason for this is that fluid solver is generally 'more' linear and can be efficiently solved while highly nonlinear constitutive model may be used in the mechanics solver which makes the implicit method much more difficult. Besides, in the mechanics solver, the mass matrix in step (2)(b)iiC can be approximated as a diagonally-lumped mass matrix, inversion of which can be readily obtained. The computation cost would be significantly reduced, especially for large-scale boundary value problems, where a large number of degrees of freedom are inevitably involved.

5. Stability Analysis

Based on the sequential scheme described in Section 4, the stability analysis on three levels needs to be inspected, *i.e.* stability of individual solvers, stability of iterations within one step (*i.e.* $k \to k+1$, called *iteration stability* hereafter), stability during time marching (*i.e.* $n \to n+1$, called *staggered stability* hereafter). It should be noted that stability of the former is only a necessary but not sufficient condition for the stability of the latter. Stable individual solvers does not guarantee the stability of iterations between these solvers, nor does a stable pair of solutions at one step guarantee stable solutions during the time marching. A stable iterative scheme requires numerical stability on all the three levels. In this work, the stability analysis of iterations during one step is approached in two ways, one by perturbation theory [9] and the other by error propagation [10]. Detailed analysis is presented as follows.

5.1 Stability of Individual Solvers

As shown in Section 4, the equation of momentum equilibrium is solved explicitly. As proved in [16], with Rayleigh damping used and $\beta \ge \frac{\gamma}{2} \ge \frac{1}{4}$, the mechanics solver is unconditionally stable. The fluid solver with implicit time difference scheme is called once during every iteration, therefore

there is no need to test the stability of flow solver in this level.

5.2 Iteration stability

The iteration stability analysis is approached both by perturbation theory and error propagation method. The formulations with and without stabilization term are both derived to study the effect of stabilization term.

5.2.1 Perturbation theory

Assume a stable pair of solutions ($\mathbf{u}$ and p) is given during each iteration by the two solvers. The fluid equations at two successive iterations $i+1$ and i are given by

$$\left(\mathbf{H}\Delta t_f+\mathbf{S}\right)\mathbf{p}_{n+1}^{(i+1)}+\tilde{\mathbf{S}}\left(\mathbf{p}_{n+1}^{(i+1)}-\mathbf{p}_{n+1}^{(i)}\right)+\mathbf{Q}^T\left(\mathbf{u}_{n+1}^{(i)}-\mathbf{u}_n\right)-\mathbf{S}\mathbf{p}_n-\mathbf{f}_{n+1}^{p}\Delta t_f=0 \tag{11}$$

$$\left(\mathbf{H}\Delta t_f+\mathbf{S}\right)\mathbf{p}_{n+1}^{(i)}+\tilde{\mathbf{S}}\left(\mathbf{p}_{n+1}^{(i)}-\mathbf{p}_{n+1}^{(i-1)}\right)+\mathbf{Q}^T\left(\mathbf{u}_{n+1}^{(i-1)}-\mathbf{u}_n\right)-\mathbf{S}\mathbf{p}_n-\mathbf{f}_{n+1}^{p}\Delta t_f=0 \tag{12}$$

Subtracting (12) from (11), it yields

$$\left(\mathbf{H}\Delta t_f+\mathbf{S}+\tilde{\mathbf{S}}\right)\left(\mathbf{p}_{n+1}^{(i+1)}-\mathbf{p}_{n+1}^{(i)}\right)-\tilde{\mathbf{S}}\left(\mathbf{p}_{n+1}^{(i)}-\mathbf{p}_{n+1}^{(i-1)}\right)+\mathbf{Q}^T\left(\mathbf{u}_{n+1}^{(i)}-\mathbf{u}_{n+1}^{(i-1)}\right)=0 \tag{13}$$

Likewise, the following equation holds for a mechanical system with the essential boundary,

$$-\mathbf{Q}\left(\mathbf{p}_{n+1}^{(i)}-\mathbf{p}_{n+1}^{(i-1)}\right)+\mathbf{K}\left(\mathbf{u}_{n+1}^{(i)}-\mathbf{u}_{n+1}^{(i-1)}\right)=0 \tag{14}$$

Then the displacement increment during the iteration can be solved as

$$\left(\mathbf{u}_{n+1}^{(i)}-\mathbf{u}_{n+1}^{(i-1)}\right)=\mathbf{K}^{-1}\mathbf{Q}\left(\mathbf{p}_{n+1}^{(i)}-\mathbf{p}_{n+1}^{(i-1)}\right) \tag{15}$$

Inserting (15) into (13), variations of pore fluid pressure during three successive iterations can be expressed as the following,

$$\left(\mathbf{p}_{n+1}^{(i+1)}-\mathbf{p}_{n+1}^{(i)}\right)=\underbrace{\left(\mathbf{H}\Delta t_f+\mathbf{S}+\tilde{\mathbf{S}}\right)^{-1}\left(-\mathbf{Q}^T\mathbf{K}^{-1}\mathbf{Q}+\tilde{\mathbf{S}}\right)}_{\mathbf{A}}\left(\mathbf{p}_{n+1}^{(i)}-\mathbf{p}_{n+1}^{(i-1)}\right) \tag{16}$$

To get a stable and convergent solution of $\mathbf{u}$ and $\mathbf{p}$, the variation of pore fluid pressure during two successive iterations should vanish with iteration continues (while from (15), the variation of displacement also vanishes), which requires that the spectral norm of the amplification matrix $\mathbf{A}$ to be smaller than 1, viz

$$\|\mathbf{A}\|<1 \tag{17}$$

With a suitably selected stabilization term $\tilde{\mathbf{S}}$, (17) can be satisfied unconditionally with no limit imposed on the time step size. As is self-evident, the stabilization term would influence the amplification matrix, and therefore influence the convergence rate of the iterations. The closer $\|\mathbf{A}\|$ approaches zero, the faster the solution converges. Ideally, $\tilde{\mathbf{S}}=\mathbf{Q}^T\mathbf{K}^{-1}\mathbf{Q}$ provides the fastest convergence rate. In this ideal case, the iterative scheme ends after the third iteration, *i.e.*, it obtains

the required solutions in two iterations and needs a third one for tolerance checking.
If the stabilization term is not included, the stability condition requires that the amplification factor must satisfy the following condition

$$\left\| \left(\mathbf{H}\Delta t_f + \mathbf{S} \right)^{-1} \left(-\mathbf{Q}^T \mathbf{K}^{-1} \mathbf{Q} \right) \right\| < 1 \tag{18}$$

For a prescribed boundary value problem, $\mathbf{H}$, $\mathbf{S}$ and $\mathbf{K}$ usually remain unchanged, therefore the range of time step Δt_f for a stable iterative scheme is constrained by (18). The scheme is thus conditionally stable when the stabilization term is not introduced.

5.2.2 *Error propagation method*

Denote by $\left(\tilde{\mathbf{p}}, \tilde{\mathbf{u}}\right)$ the true solutions. $\mathbf{r}_{n+1}^p$ and $\mathbf{r}_{n+1}^u$ are the local truncation errors due to temporal discretization. Eq.(19) is the flow equation with true solution and truncation error implemented.

$$\left(\mathbf{H}\Delta t_f + \mathbf{S}\right)\tilde{\mathbf{p}}_{n+1} + \tilde{\mathbf{S}}\left(\tilde{\mathbf{p}}_{n+1} - \tilde{\mathbf{p}}_{n+1}\right) + \mathbf{Q}^T\left(\tilde{\mathbf{u}}_{n+1} - \tilde{\mathbf{u}}_n\right) - \mathbf{S}\tilde{\mathbf{p}}_n - \mathbf{f}_{n+1}^p \Delta t_f = \mathbf{r}_{n+1}^p \tag{19}$$

Subtracting (11) from (19) and denoting the pressure error as $\mathbf{e}_n^{p,(i)} = \tilde{\mathbf{p}}_n - \mathbf{p}_n^{(i)}$, it becomes

$$\left(\mathbf{H}\Delta t_f + \mathbf{S} + \tilde{\mathbf{S}}\right)\mathbf{e}_{n+1}^{p,(i+1)} - \tilde{\mathbf{S}}\mathbf{e}_{n+1}^{p,(i)} + \mathbf{Q}^T\left(\mathbf{e}_{n+1}^{u,(i)} - \mathbf{e}_n^u\right) - \mathbf{S}\mathbf{e}_n^p = \mathbf{r}_{n+1}^p \tag{20}$$

Similarly, the displacement error $\mathbf{e}_n^{u,(i)} = \tilde{\mathbf{u}}_n - \mathbf{u}_n^{(i)}$ is given by

$$-\mathbf{Q}\mathbf{e}_{n+1}^{p,(i)} + \mathbf{K}\mathbf{e}_{n+1}^{u,(i)} = \mathbf{r}_{n+1}^u \tag{21}$$

$$-\mathbf{Q}\mathbf{e}_n^p + \mathbf{K}\mathbf{e}_n^u = \mathbf{r}_n^u \tag{22}$$

Subtracting (22) from (21), it reads

$$\mathbf{e}_{n+1}^{u,(i)} - \mathbf{e}_n^u = \mathbf{K}^{-1}\mathbf{Q}\left(\mathbf{e}_{n+1}^{p,(i)} - \mathbf{e}_n^p\right) + \mathbf{K}^{-1}\left(\mathbf{r}_{n+1}^u - \mathbf{r}_n^u\right) \tag{23}$$

Substituting (23) into (20), it yields

$$\left(\mathbf{H}\Delta t_f + \mathbf{S} + \tilde{\mathbf{S}}\right)\mathbf{e}_{n+1}^{p,(i+1)} - \tilde{\mathbf{S}}\mathbf{e}_{n+1}^{p,(i)} + \mathbf{Q}^T\mathbf{K}^{-1}\mathbf{Q}\left(\mathbf{e}_{n+1}^{p,(i)} - \mathbf{e}_n^p\right) + \mathbf{Q}^T\mathbf{K}^{-1}\left(\mathbf{r}_{n+1}^u - \mathbf{r}_n^u\right) - \mathbf{S}\mathbf{e}_n^p = \mathbf{r}_{n+1}^p$$

$$\Rightarrow \underbrace{\left(\mathbf{H}\Delta t_f + \mathbf{S} + \tilde{\mathbf{S}}\right)}_{\mathbf{A}'}\mathbf{e}_{n+1}^{p,(i+1)} = \underbrace{\left(\tilde{\mathbf{S}} - \mathbf{Q}^T\mathbf{K}^{-1}\mathbf{Q}\right)}_{\mathbf{B}'}\mathbf{e}_{n+1}^{p,(i)} + \underbrace{\left(\mathbf{S} + \mathbf{Q}^T\mathbf{K}^{-1}\mathbf{Q}\right)}_{\mathbf{C}'}\mathbf{e}_n^p + \underbrace{\mathbf{r}_{n+1}^p - \mathbf{Q}^T\mathbf{K}^{-1}\left(\mathbf{r}_{n+1}^u - \mathbf{r}_n^u\right)}_{\mathbf{r}'_{n+1}}$$

$$\Rightarrow \mathbf{e}_{n+1}^{p,(i+1)} = \left(\mathbf{A}'\right)^{-1}\mathbf{B}'\mathbf{e}_{n+1}^{p,(i)} + \left(\mathbf{A}'\right)^{-1}\mathbf{C}'\mathbf{e}_n^p + \left(\mathbf{A}'\right)^{-1}\mathbf{r}'_{n+1}$$

$$\Rightarrow \mathbf{e}_{n+1}^{p,(i+1)} = \mathbf{G}\mathbf{e}_{n+1}^{p,(i)} + \mathbf{H}'\mathbf{e}_n^p + \left(\mathbf{A}'\right)^{-1}\mathbf{r}'_{n+1}$$

$$\Rightarrow \mathbf{e}_{n+1}^{p,(i+1)} = \mathbf{G}^{i+1}\mathbf{e}_{n+1}^{p,(0)} + \sum_{l=0}^{i}\mathbf{G}^l\mathbf{H}'\mathbf{e}_n^p + \sum_{l=0}^{i}\mathbf{G}^l\left(\mathbf{A}'\right)^{-1}\mathbf{r}'_{n+1}$$

$$\Rightarrow \mathbf{e}_{n+1}^{p,(i+1)} = \mathbf{G}^{i+1}\mathbf{e}_{n+1}^{p,(0)} + \left(\mathbf{I} - \mathbf{G}^{i+1}\right)\left(\mathbf{I} - \mathbf{G}\right)^{-1}\mathbf{H}'\mathbf{e}_n^p + \left(\mathbf{I} - \mathbf{G}^{i+1}\right)\left(\mathbf{I} - \mathbf{G}\right)^{-1}\left(\mathbf{A}'\right)^{-1}\mathbf{r}'_{n+1} \tag{24}$$

Therefore, to ensure the error does not grow during the iterations (with increasing i), the spectral norm of $\mathbf{G}$ should be

$$\|\mathbf{G}\| = \left\|\left(\mathbf{A}'\right)^{-1}\mathbf{B}'\right\| = \left\|\left(\mathbf{H}\Delta t_f + \mathbf{S} + \tilde{\mathbf{S}}\right)^{-1}\left(\tilde{\mathbf{S}} - \mathbf{Q}^T\mathbf{K}^{-1}\mathbf{Q}\right)\right\| < 1 \tag{25}$$

This stability criterion is identical to that of (17).

5.3 Staggered stability

This part is to prove that the error does not grow during the time marching (i.e. from $t_0 \to t_1 \to \cdots \to t_n$). The error in (24) can be further written as

$$\begin{aligned}
&\mathbf{e}_{n+1}^{p,(i+1)} = \mathbf{G}^{i+1}\mathbf{e}_{n+1}^{p,(0)} + \left(\mathbf{I}-\mathbf{G}^{i+1}\right)\left(\mathbf{I}-\mathbf{G}\right)^{-1}\mathbf{H}'\mathbf{e}_n^p + \left(\mathbf{I}-\mathbf{G}^{i+1}\right)\left(\mathbf{I}-\mathbf{G}\right)^{-1}\left(\mathbf{A}'\right)^{-1}\mathbf{r}'_{n+1} \\
&\Rightarrow \mathbf{e}_{n+1}^{p,(i+1)} = \mathbf{L}_{n+1}\mathbf{e}_{n+1}^{p,(0)} + \mathbf{M}_{n+1}\mathbf{e}_n^p + \mathbf{N}_{n+1}\mathbf{r}'_{n+1} \\
&\Rightarrow \mathbf{e}_{n+1}^{p,(i+1)} = \mathbf{L}_{n+1}\mathbf{e}_{n+1}^{p,(0)} + \sum_{l=0}^{n}\mathbf{M}_{n+1}\cdots\mathbf{M}_{n+1-l}\mathbf{L}_{n-l}\mathbf{e}_{n-l}^{p,(0)} \\
&\qquad + \mathbf{M}_{n+1}\cdots\mathbf{M}_0\mathbf{e}_0^p + \sum_{l=0}^{n}\mathbf{M}_{n+1}\cdots\mathbf{M}_{n+1-l}\mathbf{N}_{n-l}\mathbf{r}'_{n-l} + \mathbf{N}_{n+1}\mathbf{r}'_{n+1}
\end{aligned} \tag{26}$$

If a full iteration (*i.e.* large value of i) is adopted, $\mathbf{L} = \mathbf{G}^i \to 0$; or in the special case that $\mathbf{G} = 0$, $\mathbf{L} = 0$, then the first two terms on the right side in the last equation of (26) vanish. Also considering that the truncation error $\mathbf{r}' \propto O(\Delta t^2)$ [11], to ensure the stability of the staggered procedure, it requires that

$$\|\mathbf{M}\| = \left\|\left(\mathbf{I}-\mathbf{G}^{i+1}\right)\left(\mathbf{I}-\mathbf{G}\right)^{-1}\mathbf{H}'\right\| = \left\|\left(\mathbf{H}\Delta t_f + \mathbf{S} + \mathbf{Q}^T\mathbf{K}^{-1}\mathbf{Q}\right)^{-1}\left(\mathbf{S} + \mathbf{Q}^T\mathbf{K}^{-1}\mathbf{Q}\right)\right\| < 1. \tag{27}$$

Therefore, the staggered procedure is unconditionally stable as long as (25) is satisfied.

6. Numerical Simulations

In this section, a 1D consolidation with elastic medium is carried out to verify the iterative coupling scheme described before. The effects of support sizes on the number of iterations are also demonstrated.

6.1 1D Consolidation with stabilization term

As shown in Figure 1, a 10-m thick saturated elastic medium on an impervious base is subjected to a surface surcharge of $20\,kPa$. Impervious boundaries are assigned to two sides and the base of the domain. A free flow boundary, *i.e.* $p = 0\ kPa$, is assigned to the top surface. Young's modulus of the elastic medium is E=10*Mpa*, Poisson's ratio is $\nu = 0.2$, and the permeability is $5\times10^{-8}\,m/s$. The initial pore water pressure p_0 is 20 *kPa* and effective stress is zero. Support size of 1.5 times of the particle interval is used in the simulations. As derived before, the stabilization term $\tilde{\mathbf{S}} = \mathbf{Q}^T\mathbf{K}^{-1}\mathbf{Q}$ should be used to achieve an optimal convergence rate. However, for mathematical simplicity, $\tilde{\mathbf{S}} = \int_\Omega (\mathbf{N}^p)^T \frac{1}{K}\mathbf{N}^p d\Omega$ is used in the simulation presented here to demonstrate the convergence behavior of the iterative scheme. K is the bulk modulus. The error tolerance are set as $TOL_p = TOL_p = 10^{-3}$. The pore water pressure distribution along the mid-column nodes in the simulation is presented and compared with the analytical solution in Figure 2. The simulation and

analytical results are in good agreement, indicating that the soil-water coupled scheme is effective in solving the consolidation and dissipation problems.

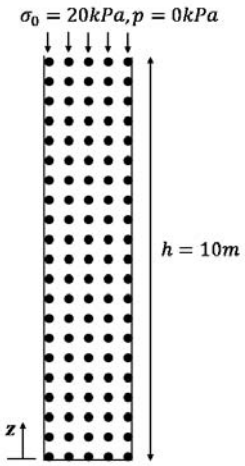

Figure 1. 1D consolidation model setup

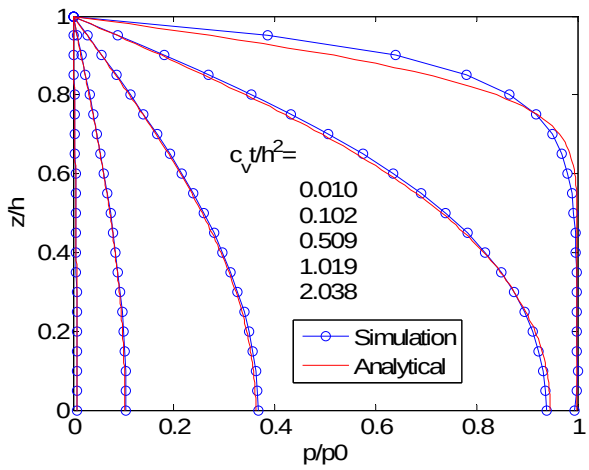

Figure 2. Normalized isochrones distribution of p

Figure 3 present the change of relative error norm during the first 100 iterations. Every line represents the convergence behavior of the relative error norms of **u** and p during one time step. The error norms decrease linearly in a log scale until the prescribed tolerances values are satisfied, i.e., $\left\|\mathbf{p}_{n+1}^{(i+1)} - \mathbf{p}_{n+1}^{(i)}\right\| / \left\|\mathbf{p}_{n+1}^{(i+1)}\right\| \le 10^{-3}$ and $\left\|\mathbf{u}_{n+1}^{(i+1)} - \mathbf{u}_{n+1}^{(i)}\right\| / \left\|\mathbf{u}_{n+1}^{(i+1)}\right\| \le 10^{-3}$. Figure 4 shows the number of iterations needed in each time step of the simulation. In general, convergence can be achieved in around 5 iterations. However, a varying number of iterations are needed in the later part of the simulation.

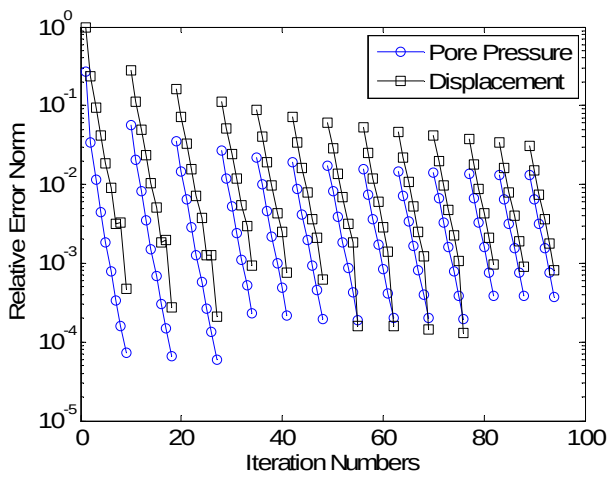

Figure 3 Relative Error Norm

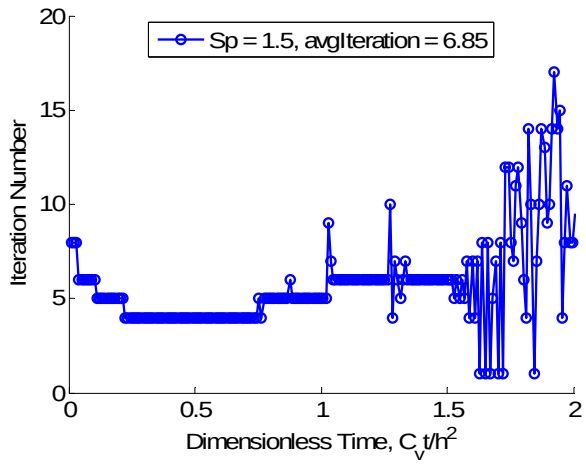

Figure 4. Comparison of iterations numbers

7. Conclusions

A sequential hydro-mechanical coupling scheme using RKPM is presented in this paper. From the stability analysis and numerical simulations, the following conclusions can be drawn

- With a suitably chosen stabilization matrix $\tilde{\mathbf{S}}$, the stabilization technique is proved to be able to effectively make the scheme unconditionally stable. Without the stabilization term, the scheme is proved to be conditionally stable.

- From 1D consolidation simulation case, the solution will effectively converge to the prescribed tolerance during the iterations.
- The effect of stabilization term on the convergence rate should be further explored. An optimal value should be pursued whenever possible.
- The applicability of the iterative scheme for nonlinear problems should be further studied.

Acknowledgements

Funding supports from Research Project Competition (UGC/HKUST) grant No. RPC11EG27 and Direct Allocation Grant DAG08/09.EG01, DGA11EG03G are gratefully acknowledged.

References

[1] C. Felippa, K. Park, Staggered transient analysis procedures for coupled mechanical systems: formulation, Comput. Meth. Appl. Mech. Eng. 24 (1) (1980), 61-111.

[2] O. Zienkiewicz, D. Paul, and A. Chan, Unconditionally stable staggered solution procedure for soil-pore fluid interaction problems, Int. J. Numer. Methods Eng. 26 (5) (1988) 1039-1055 .

[3] B. Schrefler, L. Simoni, and E. Turska, Standard staggered and staggered Newton schemes in thermo-hydro-mechanical problems, Comput. Meth. Appl. Mech. Eng. 144 (1) (1997) 93-109 .

[4] J. Kim, Sequential methods for coupled geomechanics and multiphase flow, Ph.D. thesis, Stanford University (2010).

[5] O. Zienkiewicz, A. Chan, M. Pastor, B.A. Schrefler, T. Shiomi, Computational Geomechanics with Special Reference to Earthquake Engineering: John Wiley (Chichester and New York), 1999.

[6] W. Liu, S. Jun, Y.F. Zhang, Reproducing kernel particle methods, International Journal for Numerical Methods in Fluids 20 (1995) 1081-1106.

[7] S. Li, W. Liu. Meshfree and particle methods and their applications, Applied Mechanics Reviews 55 (2002) 1-34.

[8] T. Hughes, The finite element method: linear static and dynamic finite element analysis, Englewood Cliffs, New Jersey: Prentice-Hall International , Inc., 1987.

[9] T. Belytschko, W. K. Liu, and B. Moran, Nonlinear finite elements for continua and structures. New York: John Wiley & Sons Inc., 2000.

[10] E. Turska, K. Wisniewski, and B. A. Schrefler, Error propagation of staggered solution procedures for transient problems, Computer methods in applied mechanics and engineering 114(1) (1994) 177-188.

[11] E. Turska, and B. A. Schrefler, On convergence conditions of partitioned solution procedures for consolidation problems, Computer methods in applied mechanics and engineering 106(1) (1993) 51-63.

Random elasto-plastic lattice modeling of damage in fibrous materials

Keqiang Hu[1,*], **Zengtao Chen**[1], **K. C. Li**[2], **X. Frank Xu**[3]

[1] Department of Mechanical Engineering, University of New Brunswick, Fredericton, NB, Canada E3B 5A3
[2] Department of Chemical Engineering, University of New Brunswick, Fredericton, NB, Canada E3B 5A3
[3] School of Civil Engineering, Beijing Jiaotong University, Beijing 100044, China
* Corresponding author: ckhu@unb.ca, keqianghu@163.com

Abstract A random elasto-plastic lattice network model is developed to simulate the damage behavior of fibrous materials. Elasto-plastic bar elements are used to construct a regular lattice network with the random element strength distributions to simulate the randomness of the continuum fibrous materials. The structural response of the elasto-plastic lattice network under displacement controlled loading is studied using finite element method. Small deformation theory is used and the modified Newton-Raphson algorithm is applied to solve the nonlinear finite element equations. The effects of correlation length of the strength distribution of bar elements on the global behaviors are studied.

Keywords Damage, Random elasto-plastic lattice, Nonlinear finite element method, Correlation length

1. Introduction

Complexity of failure is reflected from sensitivity of strength to small defects and wider scatter of macroscopic behaviors. The information of materials at micro-scale is random and can only be partially measurable, which leads to the complicated failure mechanisms for the random heterogeneous materials [1-3]. Various types of lattice type models such as central force model, electrical fuse model, bond-bending model, and beam-type model have been used to study progressive damage of heterogeneous materials, such as concrete, rock, ceramics and paper. It is a relatively simple but powerful technique to identify microcracking, crack branching, crack tortuosity and bridging, thus allowing the fracture process to be followed until complete failure [4-8]. A comprehensive review of the lattice models for micromechanics applications can be found in Ostoja-Starzewski [9].

The failure properties of fibrous materials have been a subject of research for the past decades [10-12]. As the structure of fibrous material is inhomogeneous, the role of disorder has great influence on the mechanical and rheological properties, and statistical growth models can simulate the heterogeneous fibrous materials well. The fibers in fibrous materials are full of imperfections and exhibit a wide variety, of natural origin, in dimensions and mechanical properties, and the mechanical properties of fibrous materials can be varied significantly by selecting different types of fibers [13]. Paper, a material known to everybody, has a fibrous network structure consisting of wood fibers. A random geometry fiber network model [14] was considered to study the special elastic orthotropy of machine-made papers, which has anisotropy in the two principal directions, the machine direction (MD) and the cross direction (CD). It was shown that the random geometry may lead to a macroscopic property of special elastic orthotropy [14]. A two-dimensional beam network model was proposed as a micromechanics model to simulate paper's failure process due to sequential breakages of fibers and/or bonds, and the numerical results showed the effects of fiber length and the ratio of fiber strength to bond strength on the failure characteristics of paper [7].

In this paper, a random elasto-plastic lattice model is proposed according to the equivalence of strain energy instead of the true network structure in fibrous materials. The concept of unit cell is

adopted to calibrate the material properties of the network based on those of the continuum paper. To characterize the heterogeneity of the microstructure of fibrous materials, the yield strength of the elasto-plastic fiber element is considered to follow a correlated random distribution. Nonlinear finite element method is utilized to study the structure response of the lattice under external tension loading. The lattice network can be considered as a stochastic representative volume element (SRVE), which transports the local effects into global solutions with uncertainty information, e.g. probability distribution. The effect of the correlation length on the strength of the SRVE is studied.

2. Random lattice model

To simulate the damage of fibrous materials, one of the most effective numerical approaches is to use the lattice model that allows disorder to be introduced naturally. Since fibrous material microstructure is extremely complicated, as shown in Figure 1, it is very hard to construct a numerical network exactly the same as the true physical one. Therefore, the idea of adopting a regular lattice equivalent to macro-level continuum in terms of strain energy [8, 9, 15, 16], is applied to study the damage of fibrous materials. For simplicity, the regular triangular network, as shown in Figure 2, is used in this work to study the failure properties of fibrous material structures. The fibers are distributed in three different directions with an increment of $\pi/3$, which leads to the isotropic properties of the structure when all fibers are assigned the uniform properties [8, 9]. In the framework of finite element method, the nodes correspond to fiber-to-fiber bonds, while two-node elements are formed by fiber segments between every two neighboring nodes.

To simulate the randomness of the microstructure of fibrous materials, we need to generate random field (RF) samples according to given probability distributions. In this study, non-Gaussian RF samples are generated from underlying Gaussian RF samples by the so-called translation method. An overview of the random field simulation is presented in [17]. For simplicity, bar-elements are used to construct the regular lattice network, and there are two translation degrees of freedom for each node. The bar elements are considered elasto-plastic and their yield strength is assumed to follow a correlated random Weibull distribution [1]. A Weibull RF sample Y can be generated from an underlying Gaussian RF sample X via [1]

$$Y = F_W^{-1}(F_g(X)) \tag{1}$$

where $F_g(\cdot)$ is the standard normal cumulative density function (cdf), and $F_W^{-1}(\cdot)$ is the inverse of the Weibull cdf. The correlation function of the underlying Gaussian RF is assumed to be

$$\rho(x, y) = \exp\left[-\left(x^2 + y^2\right)/d^2\right] \tag{2}$$

where d indicates the correlation length.

As a rule of thumb, an average tensile strength of fibrous materials can be chosen as equal to elastic modulus times $(1.0 \pm 0.1)\%$ [13]. The generated random Weibull distribution with a set mean value is mapped to the regular lattice network to characterize the heterogeneity of the microstructure. For example, two of the Weibull RF samples are shown in Figure 3 for $d = 1$ and $d = 4$, respectively. In Figure 3, the strength values are normalized by the mean value of the

samples, and $d = 1$ denotes that the correlation length is equal to the element length. It is shown that as the correlation length d increases, the points over the range d are more likely correlated.

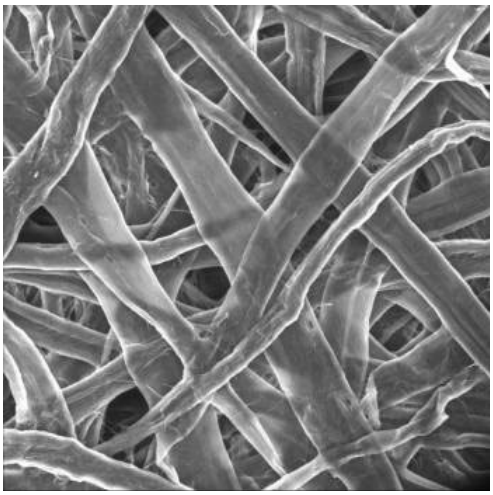

Figure 1. Scanning electron microscope image of a fibrous material structure [12].

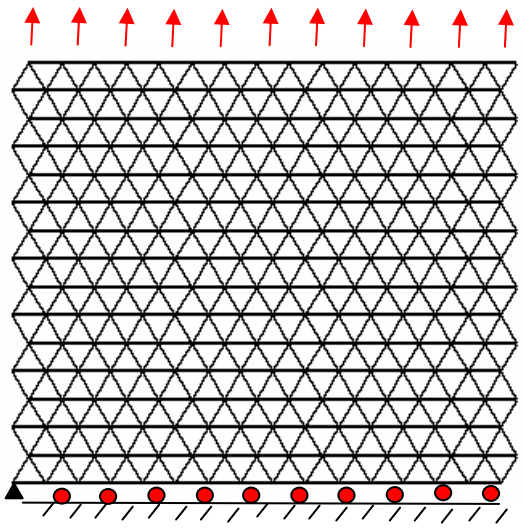

Figure 2. Geometry of the truss lattice model.

3. Lattice parameter calibration

The basic idea in setting up the elastic lattice models is based on the equivalence of strain energy stored in a unit cell (the bold-black part in Figure 4), of a volume V of a lattice with its continuum counterpart (the bold-red part in Figure 4), under uniform strain [9]

$$E_{cell} = E_{continuum} \tag{3}$$

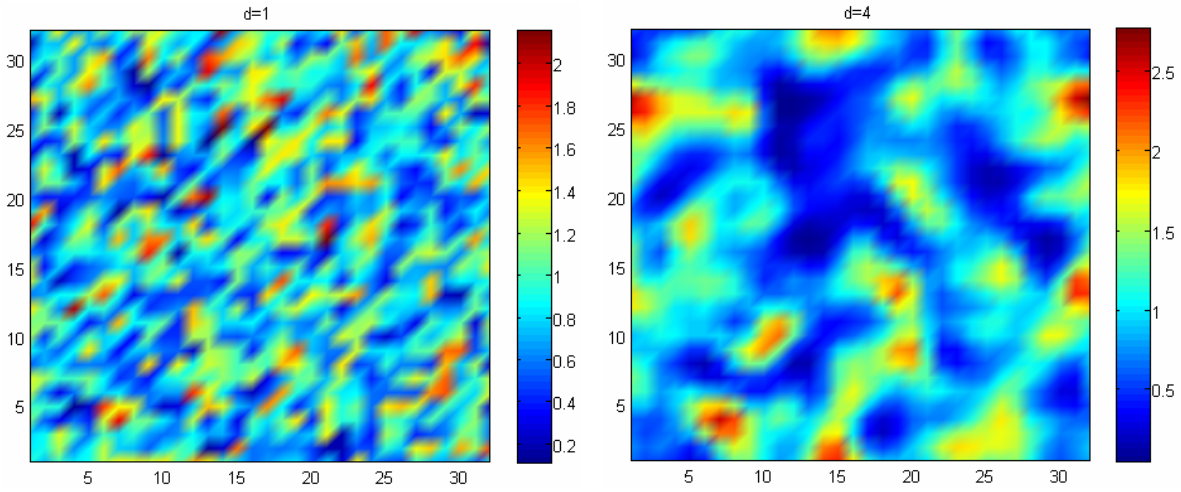

Figure 3. Correlated Weibull RF samples.

The relationship in Eq. (3) is based on the space periodicity of the current regular lattice, which is constructed by arranging the hexagonal unit cell as shown in Figure 4 periodically. The numbers in Figure 4 denote the corresponding nodes. For a regular lattice model, as shown in Figure 2 and Figure 4, the energies of the cell and its continuum equivalent, respectively, are

$$E_{cell} = \frac{1}{2}\sum_{b=1}^{6} \mathbf{F}^{(b)} \cdot \mathbf{u}^{(b)} \tag{4}$$

$$E_{continuum} = \int_V \sigma \cdot \varepsilon dV \Big/ 2 = V\, C_{ijkm}\varepsilon_{ij}\varepsilon_{km} \Big/ 2 \tag{5}$$

where, b stands for the b th spring element, C_{ijkm} are material parameters, σ is the stress tensor and ε is the strain tensor. In the two-dimensional (2D) setting, the volume of the unit cell is $V = \sqrt{3}l^2 t/2$, with t being the thickness of the continuum counterpart of the unit cell and l being the spacing of neighboring unit cells which is equal to the length of the element.

Consider the regular triangular network of Figure 2 with central force interactions only, which are described, for each element b, by

$$F_i = k_{ij}^{(b)} u_j = \alpha^{(b)} n_i^{(b)} n_j^{(b)} u_j \tag{6}$$

where $\alpha^{(b)}$ is the spring constant of half-lengths of the central interactions. The unit vectors $\mathbf{n}^{(b)}$ at respective angles $\theta^{(b)}$ of the first three α springs are

$$\begin{aligned}
&\theta^{(1)} = 0^{\circ},\ \ n_1^{(1)} = 1,\ \ n_2^{(1)} = 0 \\
&\theta^{(2)} = 60^{\circ},\ \ n_1^{(2)} = 1/2,\ \ n_2^{(2)} = \sqrt{3}/2 \\
&\theta^{(3)} = 120^{\circ},\ \ n_1^{(3)} = -1/2,\ \ n_2^{(3)} = \sqrt{3}/2
\end{aligned} \tag{7}$$

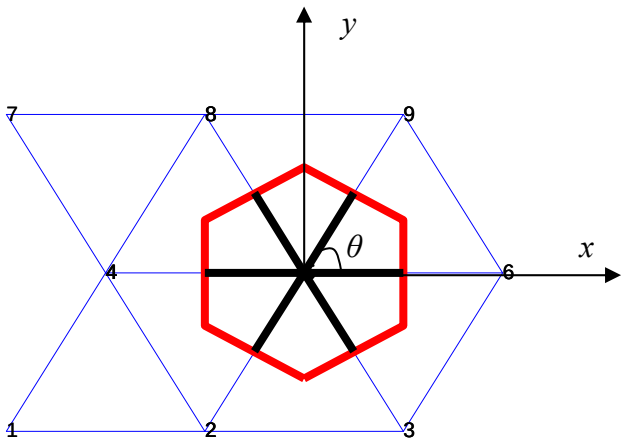

Figure 4. Unit cell of the lattice and coordinate system

Due to the requirement of symmetry with respect to the center of the unit cell, the other three springs ($b = 4,5,6$) have the same properties as $b = 1,2,3$, respectively.
Every node has two degrees of freedom, and it follows that the strain energy of a unit hexagonal cell of such a lattice, under conditions of uniform strain $\boldsymbol{\varepsilon} = (\varepsilon_{11}, \varepsilon_{22}, \varepsilon_{12})$, is

$$E_{cell} = \frac{1}{2}\sum_{b=1}^{6} \mathrm{F}^{(b)} \cdot \mathrm{u}^{(b)} = \frac{l^2}{8}\sum_{b=1}^{6} \alpha^{(b)} n_i^{(b)} n_j^{(b)} n_k^{(b)} n_m^{(b)} \varepsilon_{ij} \varepsilon_{km} \tag{8}$$

From Eqs. (3), (5), and (8), the stiffness tensor can be obtained as

$$C_{ijkm} = \frac{l^2}{4V}\sum_{b=1}^{6} \alpha^{(b)} n_i^{(b)} n_j^{(b)} n_k^{(b)} n_m^{(b)} \tag{9}$$

In particular, taking all $\alpha^{(b)}$ as the same $\alpha^{(b)} = \alpha$, and substituting the value $V = \sqrt{3} l^2 t/2$ and Eq. (7) into (9), we can get

$$C_{1111} = C_{2222} = \frac{9\alpha}{8\sqrt{3}t},\ \ C_{1122} = C_{2211} = C_{1212} = \frac{3\alpha}{8\sqrt{3}t} \tag{10}$$

It can be observed that the condition

$$C_{1212} = (C_{1111} - C_{1122})/2 \tag{11}$$

is satisfied and there are only two independent elastic moduli, which means the modeled continuum

is isotropic. The classical Lame constants can be obtained from Eq. (9) as ($\lambda = C_{1122} = C_{2211}$; $\mu = G = \frac{C_{1111} - C_{1122}}{2}$) [18]:

$$\lambda = G = 3\alpha / 8\sqrt{3}t \tag{12}$$

By using the relationship of Young's modulus and the Lame constants

$$E = G(3\lambda + 2G)/(\lambda + G) = 5G/2 \tag{13}$$

$$v = \lambda / [2(\lambda + G)] = 1/4 \tag{14}$$

The equivalent material properties of the spring elements can be expressed in terms of the continuum properties

$$\alpha = 16E\sqrt{3}t/15 \tag{15}$$

Suppose the cross section of the bar element is A, its Young's modulus is E_f and its length is l, we have

$$\alpha = \frac{E_f A}{l/2} = \frac{2E_f A}{l} \tag{16}$$

From Eqs. (15) and (16), we can get the Young's modulus of the bar-element with square cross-section as:

$$E_f = \frac{8\sqrt{3}}{15}\left(\frac{l}{t}\right)E \tag{17}$$

It can be seen from Eq. (17) that Young's modulus of longer fiber elements need to be larger to have the same strain energy as the continuum counterpart, which is in agreement with the conclusion of Liu et al. [7].

4. Numerical algorithm

In this study a random elasto-plastic model is used and the network is constructed from a lattice where all the elements between nearest-neighbor sites are bar elements with the same cross-section area. Finite element method is applied to study the structure response of the lattice network under external tensile loading, as shown in Figure 2. For simplicity, bar element with perfect-plastic properties is chosen, and the perfect plasticity of the bar elements are displayed in Figure 5. The expression of the elemental stiffness matrix is

$$k = \frac{E(\varepsilon)A}{l}\begin{bmatrix} C^2 & CS & -C^2 & -CS \\ CS & S^2 & -CS & -S^2 \\ -C^2 & -CS & C^2 & CS \\ -CS & -S^2 & CS & S^2 \end{bmatrix}, \quad C = \cos\theta, \quad S = \sin\theta \tag{18}$$

where the orientation θ denotes the angle between the axis of the bar element and the coordinate

axis, as shown in Figure 4. The Young's modulus of the perfect-plastic bar element $E(\varepsilon)$ can be given as

$$E(\varepsilon)=\begin{cases} E_0 & (0\le\varepsilon\le\varepsilon_Y) \\ \sigma_Y/\varepsilon & (\varepsilon>\varepsilon_Y) \end{cases} \tag{19}$$

where E_0 is the Young's modulus of the bar-element within the elastic limit, σ_Y is the yield stress ε_Y and is the yield strain.

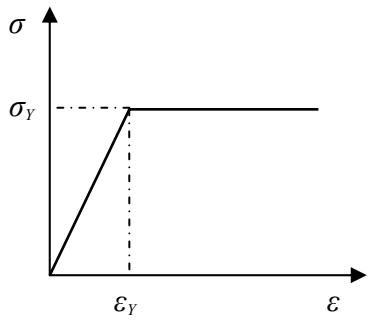

Figure 5. Bar element with perfect plasticity property.

The isotropic damage model with an equal degradation of the elastic moduli postulates the stress-strain law as following

$$\sigma=(1-\eta)E_0\varepsilon \tag{20}$$

$$\eta=1-\varepsilon_Y/\varepsilon,\ (\varepsilon>\varepsilon_Y) \tag{21}$$

where η is a scalar damage variable; for an undamaged material, η is zero and the response is linear elastic. To study the damage process of the lattice network, displacement constraints are imposed on the top and the bottom lines of the lattice system and a secant stiffness algorithm is applied.

The global stiffness of the lattice network can be obtained by assembling all the elements in the network as

$$K=\sum k \tag{22}$$

The network is applied by uniaxial tensile displacement on the top side, as shown in Figure 2, with the left-bottom end being fixed and the y-directional displacement of the nodes on the bottom line being zero. By applying the boundary conditions, we can get a system of non-linear equations to solve for all the degrees of freedom of the system:

$$[K(u)]\{u\}=\{F\} \tag{23}$$

which can be solved by using the modified Newton-Raphson method as

$$\{u_{i+1}\} = \{u_i\} - [[K(u_i)]\{u_i\} - \{F\}]/[K_0] \tag{24}$$

where $[K_0]$ is a secant stiffness matrix, which is kept unchanged within each load cycle, and the subscript i represents the equilibrium iteration. The criterion for stopping the numerical iteration is

$$\|\{u_{i+1}\} - \{u_i\}\|/\|\{u_i\}\| < \delta \tag{25}$$

where $\| \ \|$ denotes a norm and δ is a tolerance value.

5. Numerical example

As paper is a material which has a fibrous network structure consisting of wood fibers, it is convenient to apply the random lattice model to study the failure process of the fibrous structure of paper. Without loss of generality, the Young's modulus of paper can be chosen as $E_c = 2GPa$ [19], and the corresponding Young's modulus of the bar element (within the limit of elasticity) can be obtained using Eq. (17), provided by choosing the length and the cross section of the element as $l = 10mm,\ t = 0.1mm$. It is noted that fibers in paper maybe not exactly perfect-plastic as assumed in the present model, the aim of the study is to find the effect of correlation length on global strength when plasticity is considered.

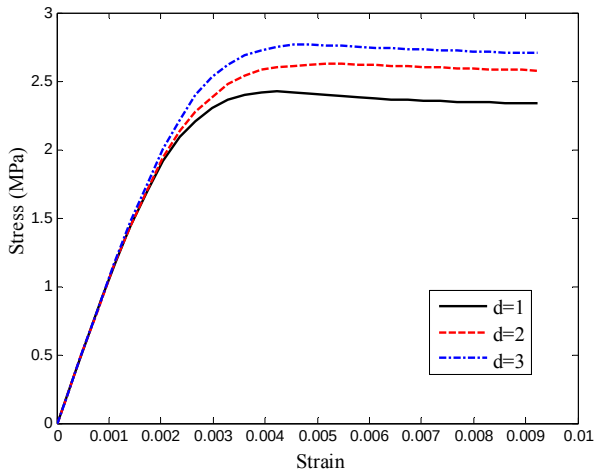

Figure 6. Stress-strain curves of the random elasto-plastic lattice.

The stress-strain curves of the lattices of size (8×8), which denotes the number of nodes of the system is 8×8, are shown in Figure 6. Each curve for a correlation length d is the mean value of stress-strain curves of 100 random lattice samples. The strength of the lattice increases as the

correlation length d increases from 1 to 3. It can be seen the phenomena of "strain softening" after the maximum stress value is reached, which corresponds to the decreasing external loads when the stiffness of the system becomes smaller after some elements become plastic. By checking the linear part of the stress-strain curve, we can get the Young's modulus of the lattice network as $E \approx 0.5E_c = 1GPa$, which indicates that the effect of the elasto-plastic properties of the elements will lead to the decrease of the Young's modulus. The macroscopic strength of the fibrous material decreases with reduction of the correlation length, which equivalent to increase of the sample size, this is consistent with the statistical size effect, even when plasticity is presented.

6. Conclusions

In this study a random lattice network model is introduced to simulate the damage behavior of heterogeneous fibrous materials. Elasto-plastic bar elements are used to construct a regular triangular lattice with the random field strength distributions to characterize the randomness of the continuum fibrous materials. The material properties and geometric size of the elements in the lattice networks are calibrated based on the equivalence of the elastic strain energy. Nonlinear finite element method has been applied to study the structural response of the lattice network under external tensile loading. The correlation length of the strength distribution of bar elements has great influence on the strength of the random lattice networks. The macroscopic strength of the fibrous material decreases with reduction of the correlation length, which is equivalent to increase of the sample size.

Acknowledgements

The present work is supported by the Atlantic Innovation Fund, and is gratefully acknowledged.

References

[1] K. Hu, X.F. Xu, Probabilistic upscaling of material failure using random field model. Algorithms, 2 (2009) 750-763.
[2] X.F. Xu, X. Chen, L.H. Shen, A Green-function-based multiscale method for uncertainty quantification of finite body random heterogeneous materials. Comput Struct, 87 (2009) 1416-1426.
[3] Z. Yang, X.F. Xu, A heterogeneous cohesive model for quasi-brittle materials considering spatially varying random fracture properties. Comput Methods Appl Mech Engrg, 197 (2008) 4027-4039.
[4] Z.P. Bazant, M.R. Tabbara, M.T. Kazemi, G. Pijaudier-Cabot, Random particle model for fracture of aggregate or fibre composites. J Eng Mech, ASCE, 116 (1990) 1686-1705.
[5] W.A. Curtin, H. Scher, Brittle fracture in disordered materials: a spring network model. J Mater Res, 5 (1990) 535-553.
[6] E. Schlangen, J.G.M. van Mier, Simple lattice model for numerical simulation of fracture of concrete materials and structures. Mater Struct, 25 (1992) 534-542.
[7] J.X. Liu, Z.T. Chen, K.C. Li, A 2-D lattice model for simulating the failure of paper. Theor Appl Fract Mech, 54 (2010) 1-10.
[8] B.L. Karihaloo, P.F. Shao, Q.Z. Xiao, Lattice modeling of the failure of particle composites.

Eng Fract Mech, 70 (2003) 2385-2406.
[9] M. Ostoja-Starzewski, Lattice models in micromechanics. Appl Mech Rev, 55 (2002) 35-60.
[10] K.J. Niskanen, Strength and Fracture of Paper, KCL Paper Science Center, Espoo, Finland, 1993.
[11] L.I. Salminen, A.I. Tolvanen, M.J. Alava, Acoustic emission from paper fracture. Phys Rev Lett, 89 (2003) 185503.
[12] P. Isaksson, R. Hagglund, Analysis of the strain field in the vicinity of a crack-tip in an in-plane isotropic paper material. Int J Solids Struct, 44 (2007) 659-671.
[13] A. Mikko, N. Kaarlo, The physics of paper. Reports on Progress in Physics, 69 (2006) 669-723.
[14] M. Ostoja-Starzewski, D.C. Stahl, Random fiber networks and special elastic orthotropy of paper. J Elasticity, 60 (2000) 131-149.
[15] H.J. Gao, P. Klein, Numerical simulation of crack growth in an isotropic solid with randomized internal cohesive bonds. J Mech Phys Solids, 46 (1998) 187-218.
[16] J.X. Liu, S.C. Swng, J. Zhang, N.G. Liang, Lattice type of fracture model for concrete. Theor Appl Fract Mech, 48 (2007) 269-284.
[17] L. Graham-Brady, X.F. Xu, Stochastic morphological modeling of random multiphase materials. J Appl Mech, 75 (2008) 061001.
[18] C.T. Wang, Applied Elasticity, McGraw-Hill Book Company, New York, 1953.
[19] S. Wlodzimierz, M. Krzysztof, T. Wiktorian, An analysis of Young's modulus distribution in the paper plane. Fibers Text East Eur, 14 (2006), 91-94.
[20] R.A. Donald, P.P. Pradeep, D.K. Bhattacharya, Essentials of Materials for Science and Engineering, Cengage Learning, 2004.

Cohesive Zone Analysis of Crack Propagation on a Hierarchical Structured Interface

Xiaoru Wang[1], **Akihiro Nakatani**[1,*]

[1] Department of Adaptive Machine Systems, Osaka University, Suita, Osaka 565-0871, Japan

[*] Corresponding author: nakatani@ams.eng.osaka-u.ac.jp

Abstract Hierarchical ramification structures are found of superior strength during fracture. Crack propagation along cohesive zone model binding with hierarchical ramification structures is simulated to analyze the fracture process. The feature of specified bonding surface results special pattern of crack propagation. Therefor, the potential that by changing the morphology of the bonding surface may control the toughness of the material is illustrated.

Keywords Computational Mechanics, Cohesive Zone Model, Hierarchical Structure, Fracture Toughness, Criterion

1. Introduction

Some biological materials have the internal structures that exhibit superior performances in mechanical properties[1]. There are quite a few studies to investigate the fundamental mechanism of the biological systems in order to develop the artificial bio inspired materials. In this study, we focus on the the hierarchical ramification structures that contribute to high fracture toughness. The hierarchical ramification structures are often observed in many biological system. The structures appear as fractal geometries which are generated naturally via quite simple rules and they contribute to redundancy for safety of their life.

In this study, the cohesive zone model is adopted to a hierarchical structured interface and the crack propagation on the interface is studied.

First, the problem of double cantilever beam problem is solved to estimate the fundamental effect of the microstructure of interface. According to the simple calculation, it is shown that the redundancy of ramification structure yields high fracture toughness.

Secondly, the quasi-static crack propagation is studied in bulk materials. The small scale yielding condition is assumed and the linear elastic solution specifies the boundary displacement component. The boundary value problem in linear elasticity is solved for increasing remote stress intensity factor by using finite element method. The displacement field and stress distribution obtained by the simulation is discussed to study the mechanism of crack propagation. The relationships between the remote stress intensity factor and representative crack length are plotted for several cases of different microstructures. The effective interface area and the effective surface energy depends on the internal microstructure of interface. The effect of geometry cause the complex pattern of bonding-debonding domain. As the result, the representative length scale of fracture process zone depends on the heterogeneity and morphology of microscopic structure. The fracture toughness which is estimated as a remote stress intensity factor changes associated with the change of the fracture process zone due to the microstructure.

2. Theory

2.1. Cohesive Zone Model

Cohesive zone model is frequently used to analyze crack propagation. In this modeling, a cohesive zone is placed between bulk elements as shown in Fig.1. Fracture can be regarded as elements separating along the cohesive surface resisted by cohesive traction[2][3]. As the separation occurs, the traction increases to a maximum and then falls back to 0. The procedure means the element separates completely, and the area under the traction-separation curve corresponds with the effective surface energy that needed for complete separation.

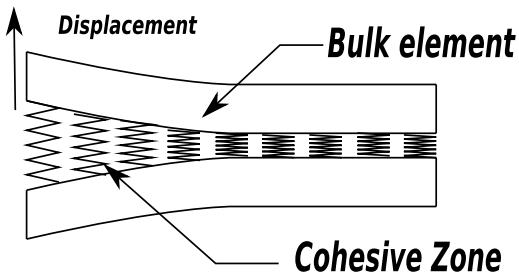

Figure 1. Cohesive zone model placed between bulk elements

2.2. Cohesive Zone Law

The traction vector $\boldsymbol{T} = (T_n, T_t)$ can be derived from the effective surface energy $\phi(\boldsymbol{\Delta})$.($E.g.$[4][5])

$$\boldsymbol{T} = -\frac{\partial\phi(\boldsymbol{\Delta})}{\partial(\boldsymbol{\Delta})} \tag{1}$$

where $\boldsymbol{\Delta} = (\Delta_n, \Delta_t)$. The components T_n, T_t and Δ_n, Δ_t are the normal and tangential components of traction vector and relative displacement vector, respectively.

The surface energy [4] can be written as:

$$\phi(\Delta_n, \Delta_t) = \phi_n + \phi_n \exp\left(-\frac{\Delta_n}{\delta_n}\right)\left(\left[1 - r + \frac{\Delta_n}{\delta_n}\right]\frac{1-q}{r-1} - \left[q + \left(\frac{r-q}{r-1}\right)\frac{\Delta_n}{\delta_n}\right]\exp\left(-\frac{\Delta_t^2}{\delta_t^2}\right)\right) \tag{2}$$

where δ_n and δ_t represent the character length that satisfy $T_n(\delta_n) = \sigma_{\max}$, $T_t(\delta_t/\sqrt{2}) = \tau_{\max}$. Stress $\sigma_{\max}$ and $\tau_{\max}$ represent the maximum of normal traction and tangential traction, respectively. Pameters are defined as $q = \phi_t/\phi_n$, $r = \Delta_n'/\delta_n$, where Δ_n' represents the value of Δ_n when $T_n = 0$. ϕ_n and ϕ_t are the areas under the normal traction-separation curve and the shear traction-separation curve representing the surface energy for complete separation respectively and can be calculated as:

$$\phi_n = \sigma_{\max}\exp(1)\delta_n, \quad \phi_t = \sqrt{\exp(1)/2}\tau_{\max}\delta_t \tag{3}$$

From Eqs.(1) and (2),the normal and shear traction can be obtained:

$$T_n = \frac{\phi_n}{\delta_n}\exp\left(-\frac{\Delta_n}{\delta_n}\right)\left(\frac{\Delta_n}{\delta_n}\exp\left(-\frac{\Delta_n^2}{\delta_n^2}\right) + \frac{1-q}{r-1}\left[1 - \exp(-\frac{\Delta_n^2}{\delta_n^2})\right]\left[r - \frac{\Delta_n}{\delta_n}\right]\right) \tag{4}$$

$$T_t = 2\left(\frac{\phi_n \Delta_t}{\delta_t^2}\right)\left[q + \left(\frac{r-q}{r-1}\right)\frac{\Delta_n}{\delta_n}\right]\exp\left(-\frac{\Delta_n}{\delta_n}\right)\exp\left(-\frac{\Delta_t^2}{\delta_t^2}\right) \tag{5}$$

2.3. Frame element

Frame element is the combination of truss element which represents axial tension and beam element that represents bending (E.g. [6]). Consider the frame element shown in Fig. 2, the element nodal

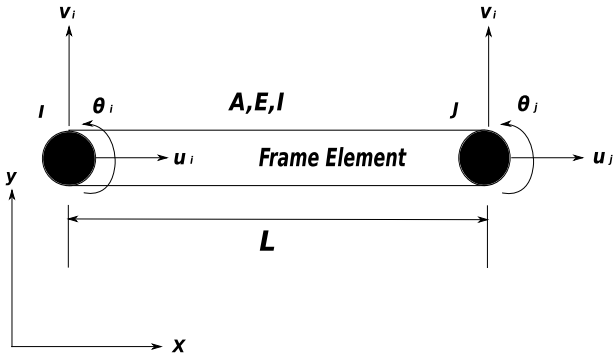

Figure 2. Image of frame element

displacement vector $\boldsymbol{d}_{\text{Frame}}$ and the vector of element nodal loads $\boldsymbol{F}_{\text{Frame}}$ are set as:

$$\left(\ \boldsymbol{d}_{\text{Frame}}\ \right)^{\text{T}} = \left(\ u_i \quad v_i \quad \theta_i \quad u_j \quad v_j \quad \theta_j\ \right)^{\text{T}} \tag{6}$$

$$\left(\ \boldsymbol{F}_{\text{Frame}}\ \right)^{\text{T}} = \left(\ P_i \quad Q_i \quad M_i \quad P_j \quad Q_j \quad M_j\ \right)^{\text{T}} \tag{7}$$

As shown in Fig. 2, u, v, and θ are the x-direction displacement, y-direction displacement and deflection angle, respectively. P, Q, and M represent the x-direction load, y-direction load and bending moment, respectively. The stiff equation of frame element can be expressed as:

$$\left(\ F_{\text{Frame}}\ \right) = \left(\ k_{\text{Frame}}\ \right)\left(\ d_{\text{Frame}}\ \right) \tag{8}$$

where $[k_{\text{Frame}}]$ represents the element stiff matrix of the frame element of x-direction. Furthermore, if we set the length, area of cross section, Young's modulus and moment of inertial of area as l, A, E, I, then consider the frame element that inclined at the degree of β to the x-direction.

By coordinate transformation, the stiff equation of the frame element of any direction can be obtained:

$$\begin{pmatrix} P_i^* \\ Q_i^* \\ M_i^* \\ P_j^* \\ Q_j^* \\ M_j^* \end{pmatrix} = \begin{bmatrix} F & G & H & -F & -G & H \\ G & U & V & -G & -U & V \\ H & V & S & -H & -V & T \\ -F & -G & -H & F & G & -H \\ -G & -U & -V & G & U & -V \\ H & V & T & -H & -V & S \end{bmatrix} \begin{pmatrix} u_i^* \\ v_i^* \\ \theta_i^* \\ u_j^* \\ v_j^* \\ \theta_j^* \end{pmatrix} \tag{9}$$

Where the components can be represented as:

$$
\begin{aligned}
S &= \frac{4EI}{l} \\
T &= \frac{2EI}{l} \\
F &= \frac{AE}{l}\cos^2\beta + \frac{12EI}{l^3}\sin^2\beta \\
G &= \frac{AE}{l}\sin\beta\cos\beta - \frac{12EI}{l^3}\sin\beta\cos\beta \\
H &= -\frac{6EI}{l^2}\sin\beta \\
U &= \frac{AE}{l}\sin^2\beta + \frac{12EI}{l^3}\cos^2\beta \\
V &= \frac{6EI}{l^2}\cos\beta
\end{aligned}
$$

2.4. Energy Release Rate

With the propagation of crack, it is found the surface energy decreases to form new crack surface. Using the stress intensity factor K_I, the potential energy release rate $\mathcal{G}$ can be calculated as:

$$\mathcal{G} = \frac{1-\nu^2}{E}K_I^2. \tag{10}$$

When considering about double cantilever beam, with the Young's modulus of E,and the moment of inertial of area as I, and the bending moment M acting on the free edge of the beam, the energy release rate can be calculated as:

$$\mathcal{G} = \frac{M^2}{2EI} \tag{11}$$

3. Analysis Model and Analysis method

3.1. Discrete Cohesive Zone Model

Consider a linear elastic solid in Fig. 3 with Young's modulus of E and Poisson's ratio of ν and established with cohesive zone model in Fig. 4(a). Fig. 4(b) shows the general continuously cohesive zone model, while Fig. 4(c) is the discrete cohesive zone model on the basis of Fig. 4(b) with periodic characteristic length of l. In the periodic structure, set the cohesive zone model with the length of b,and make the last $l-b$ of debonding area. Also in this study, we set $b = 1/2l$. The small scale yielding condition is assumed and the boundary condition is set with a displacement field of $K_\mathrm{I} = \dot{K}_\mathrm{I}t$ with $\dot{K}_\mathrm{I} = 50\mathrm{GPa}\sqrt{\mathrm{m}}/\mathrm{s}$. Using the discrete cohesive model,crack propagation is studied.

With the Griffith theory, fracture toughness K_IC can be evaluated with surface energy Γ as:

$$K_\mathrm{IC} = \sqrt{\frac{E\Gamma}{1-\nu^2}} \tag{12}$$

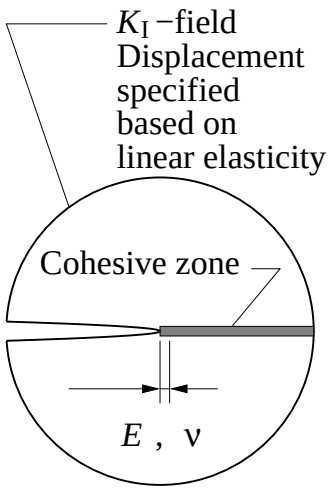

Figure 3. Schematics of problem

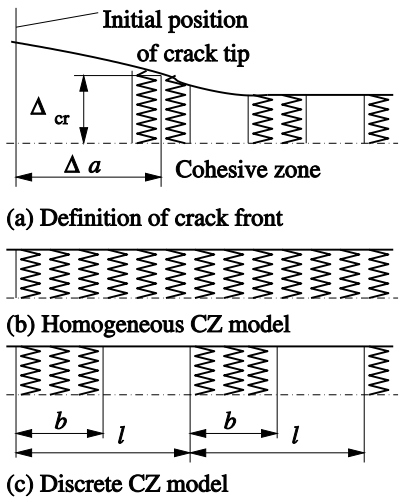

Figure 4. Detail of Cohesive zone

And here for general continuously cohesive zone model, $\Gamma = \phi_n$. So with $b = 1/2l$, the discrete cohesive zone model has the surface energy of $1/2\phi_n$ and the stress intensity factor can be obtained as $K_I = \sqrt{1/2}K_{\mathrm{IC}}$.

3.2. Microscopic Structure with Cohesive Zone Model

Microscopic structures with different mythologies show unique feature of strength. Consider two patterns of structures made of frame elements bound with cohesive zone shown in Fig.5 and Fig.6, set the y-direction displacement and simulate the separation of the element.

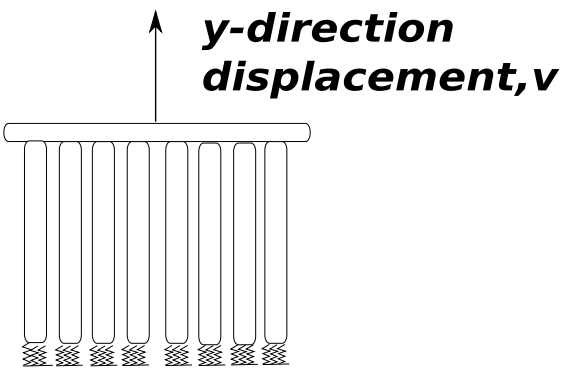

Figure 5. Unit Discrete Structure

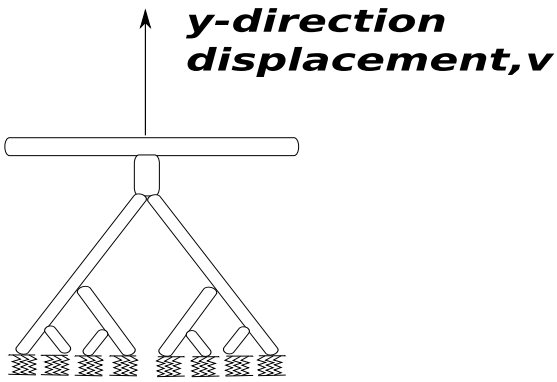

Figure 6. Unit Hierarchical Structure

The bottom of the structures are bound with cohesive zone model, when separation happens, the traction-time curve can be shown as Fig.7

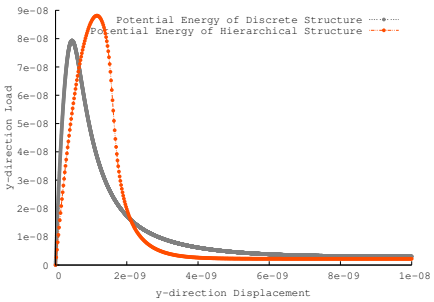

Figure 7. Force-displacement relations of microsopic structures

With the feature talked above, by using the model of continuous cohesive zone model, continuous microscopic structures can be obtained. As shown in Fig. 8, cohesive zone is replaced by structures. All the structures are binding with cohesive zone models at the end of the elements, and the angular velocity at the free edge is set as $\omega = 5 \times 10^{-7}$rads/s.

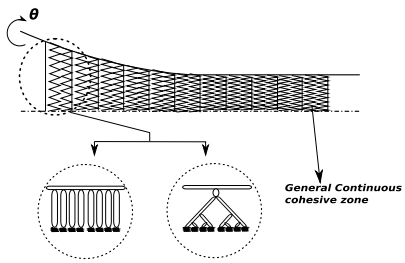

(a) Continuous Structure with cohesive zone model

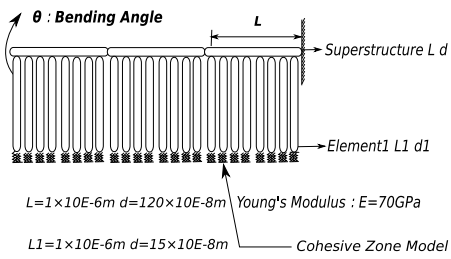

(b) Discrete Structure with cohesive zone model

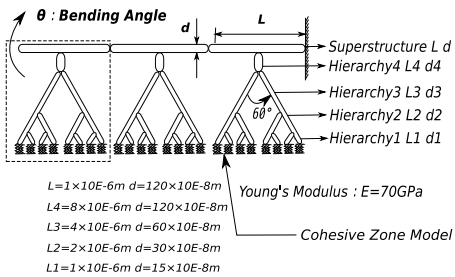

(c) Hierarchical ramification structure with cohesive zone model

Figure 8. Schematics of pealing problem of canti-lever

4. Analysis Result

4.1. Discrete Cohesive Model

The fracture toughness of the general continuously cohesive zone model can be calculated as $K^*_{\mathrm{IC}} = 0.358\mathrm{MPa}\sqrt{\mathrm{m}}$, therefor the theoretical value of the stress intensity factor will be $K_{\mathrm{IC}} = \sqrt{1/2}K^*_{\mathrm{IC}}$.

Using discrete cohesive zone model and general continuously cohesive zone model to simulate the crack propagation and comparing the stress intensity factor as shown in Fig.9

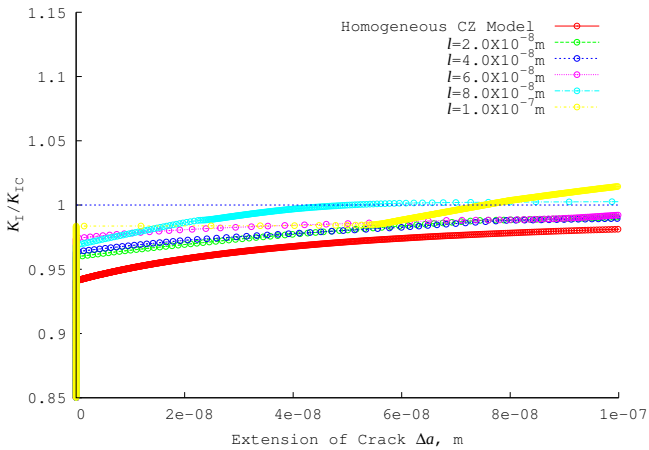

Figure 9. The stress intensity factor of discrete cohesive zone model of different characteristic lengths comparing with the theoretical value

Figure 9 shows the result of different characteristic lengths. The strength of the material increases with the characteristic length. Also, the stress intensity factors of discrete cohesive zone models are all above the one of general continuously cohesive zone model. Therefore, the possibility that the interface morphology of cohesive zone has an impact on the strength of material is illustrated.

4.2. Microscopic Structure with cohesive zone model

The average potential energy to make a new fracture surface can be calculated as $\phi_n^* = \phi_n/\Delta d = 1.28 \times 10^{-10}$J/m. Using this data, the theoretical moment in proportion to strength of the bulk material can be obtained as $K^* = \sqrt{\phi_n^* EI} = 9.55 \times 10^{-13}$Nm.

By using simulation, the simulate data of the strength of structures with cohesive zone model and the deformation can be obtained.

As shown in Fig.10, the strength of discrete structure exceeds the one of hierarchical structure at first and is reversed during the crack propagation . When crack propagates, the strength of discrete structure turns constant while the one of hierarchical structure shows several jump which represents the thorough separation of unit structures. Although theoretical result overwhelms simulation results, since the result of hierarchical structure increases during element separation, the strength of hierarchical structure shows more resistance to crack propagation.

When the strength of hierarchical structure jumps as shown in Fig.12, crack propagation occurs. From the deformed hierarchical structure graph, the details of crack propagation can be illustrated.

Figures 13(a)- (h) show the details of crack propagation and element separation. The upper graphs represent the total image of deformed structures while the lower ones represent the enlarged view

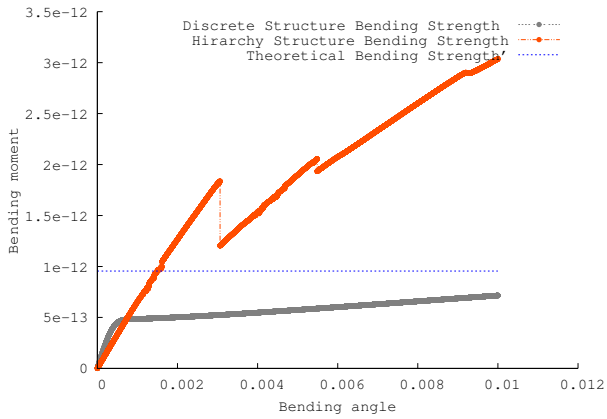

Figure 10. Strength of different models

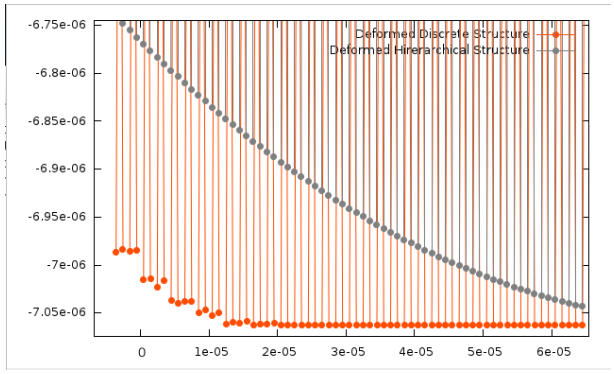

Figure 11. Deformed Microscopic Structures

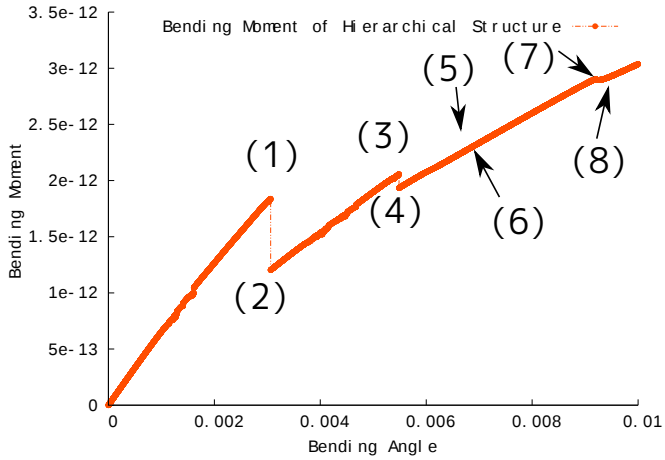

Figure 12. Separations on cohesive zone during crack propagation

of the cohesive zone. When first jump happens in Fig.12 at (1) and (2), the first unit hierarchical structure separates completely and crack propagates as in Fig. 13(a) and Fig. 13(b). The second jump at (3) and (4) corresponds to Fig. 13(c) and Fig. 13(d), half of the unit structure separates while the other half parts contains both bonding and separated elements. This half parts completely separates at (5) and (6) shows in Fig12 without jumps.After the first two unit structures separate completely, the third one begin to separates at (7) and at (8) half of the unit structure thoroughly separates.

The hierarchical structure separates at a certain distributive way. Due to the special feature of hierarchical structure, the elements do not separate in regular order. Instead, after the initial separation, the element separates next shifts in one structure.

After all the elements separate in one structure, the crack propagation happens. While for discrete structure, the elements separate in the regular order, after the first separation happens, the elements next separates sequentially. Discrete structure may be destroyed quickly after the first element separation, while hierarchical structure can suffer more due to its special separating feature.

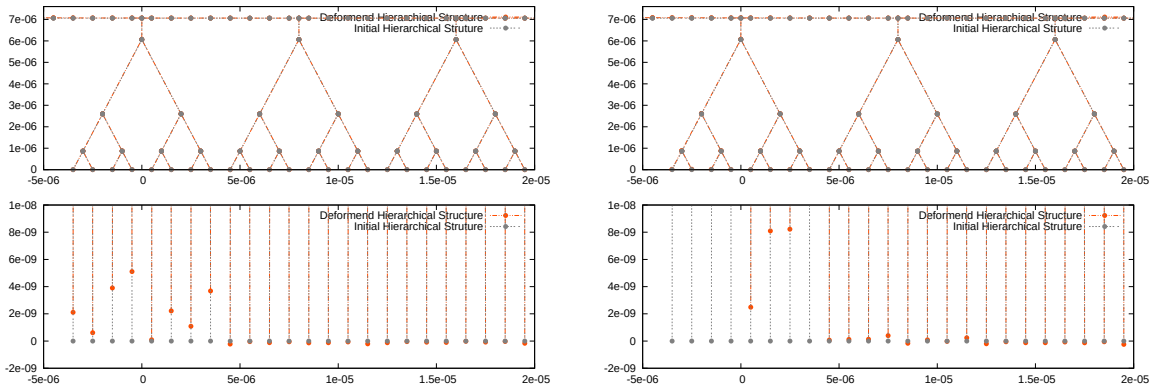

(a) at point(1)

(b) at point(2)

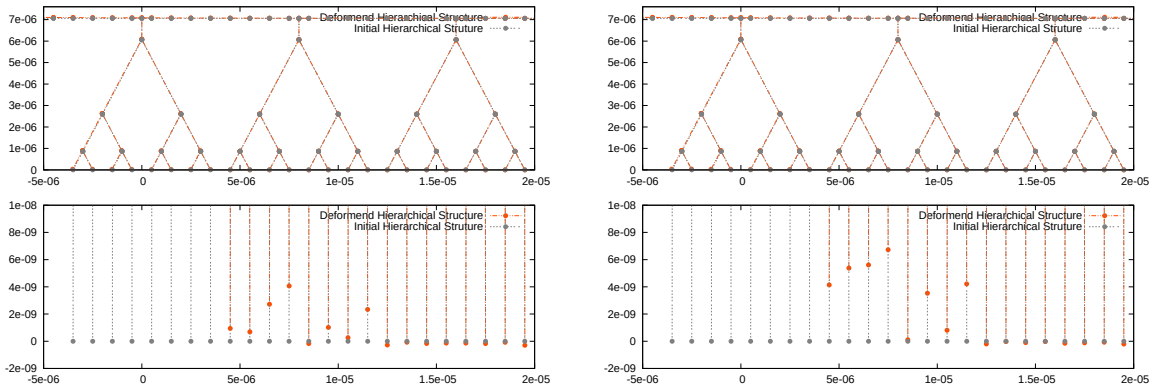

(c) at point(3)

(d) at point(4)

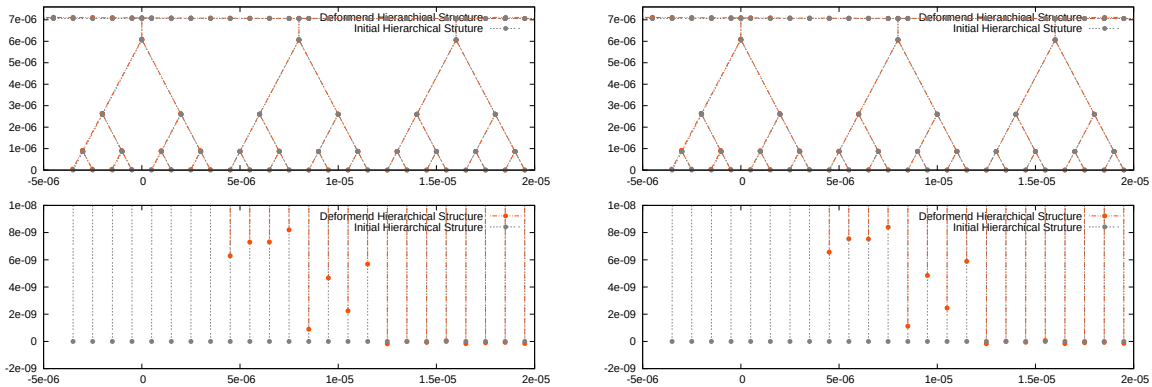

(e) at point(5)

(f) at point(6)

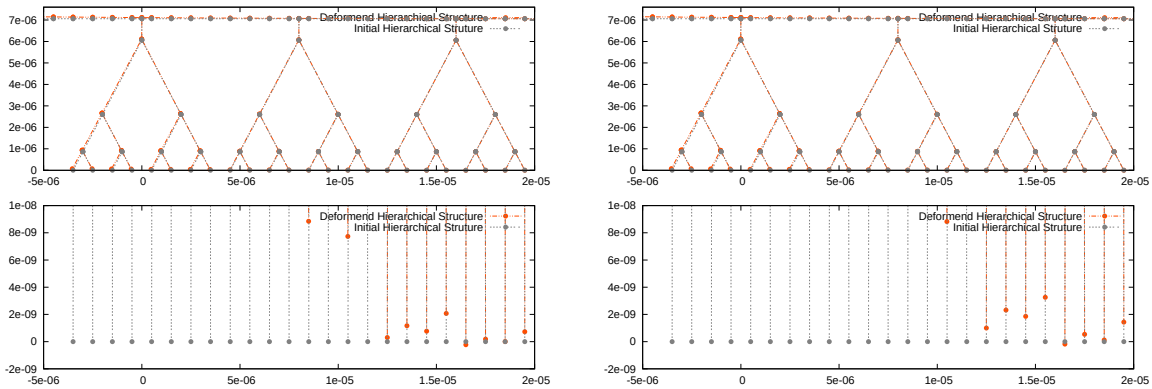

(g) at point(7)

(h) at point(8)

Figure 13. Deformed Hierarchical Structure

5. Conclusions

The strength of the material has been evaluated via simulation of discrete cohesive zone model and microscopic structures bound with cohesive zone model. By changing the morphology of the interface, sophisticated design of the strength and the properties of crack propagation of material will be possible.

Acknowledgments

This work was supported by Grants-in-Aid for Scientific Research (KAKENHI). We would also like to thank Prof. Y. Doi whose opinions have helped us very much throughout the production of this study.

References

[1] D. Xie, A.G. Salvi, A.M. Waas, A.Caliskan, Discrete Cohesive Zone Model to Simulate Static Fracture in Carbon Fiber Textile Composites, AIAA2005-2320 (2005) 1-21.
[2] René Kregting, Cohesive zone model towards a robust implementation of irreversible behaviour, MT05.11, 2005.
[3] P. D. Zavattieri, L.G. Hector Jr, A.F. Bower, Cohesive zone simulations of crack growth along a rough interface between two elastic-plastic solids, Eng Fract Mech, 75 (2008) 4309-4332.
[4] X.-P. Xu, A. Needleman, Void nucleation by inclusion debonding in a crystal matrix, Model Simul Mat Sci Eng, 1 (1992) 111-132.
[5] A. Nakatani, W.J. Drugan, E. Van der Giessen and A. Needleman,Crack tip fields at a ductile single crystal-rigid material interface, Int J Fract, 122 (2003) 131-159.
[6] R.D.Cook, Concepts and Applications of Finite Element Analysis, Wiley, 1981, pp.56-89.

Modeling of cracked structures containing voids subjected to fatigue and dynamic loads using XFEM

KIRED Mohamed Riad[1], HACHI Brahim Elkhalil[1,*], GUESMI Mohamed[1], RECHAK Said [2], BADAOUI Mohamed[1].

[1] Laboratoire de Développement en Mécanique et Matériaux, University of Djelfa, PB 3117, Djelfa, Algeria.
[2] Laboratoire de Génie Mécanique et Développement, ENP, Algiers, Algeria.

[*]br_khalil@yahoo.fr

Abstract. In this paper, we present a modeling of planar structures under dynamic loading containing stationary cracks in order to determine the dynamic stress intensity factor (DSIF). This parameter will be evaluated by using the eXtended Finite Element Method (XFEM) coupled with the interaction integral technique. Some examples of validation of the computer code developed in this work were tested. The good correlation of the obtained results in fatigue with the literature proves the effectiveness of the method as well as the developed computer code. In the dynamic case, a parametric study on the presence, position and size of the void with respect to the crack and also on the crack type (crack edge and central crack) was conducted for some practical applications.
Keywords: Stress Intensity Factor, Extended Finite Element Method, Dynamic Loads, Fatigue, Void.

1. Introduction and stat of the art

In the cracking of fragile and quasi-fragile structures containing voids (holes) and subjected to quasi-static and dynamics loadings, the characterized parameter is the Stress Intensity Factor (SIF). Many techniques have been used in literature to evaluate this parameter. Among which we mention the finite element method FEM [1], the boundary element method BEM [2], the finite difference method FDM [3], and the symmetric-Galerkin boundary element method SGBEM [4]. We note that the FEM is the most popular for its flexibility and efficiency. However, it requires a special treatment of discontinuities and singularities of fields due to the presence of the crack. For this purpose, a new FEM approach has been developed by Belytschko and Black [5] named eXtended Finite Element Method (XFEM). It consists to take into account the discontinuity at the crack edges and the singularity at the crack tip by enrichment of neighboring nodes with new degrees of freedom via the new shape functions associated with elements containing these nodes. Among the first who addressed the problem of voids by using XFEM in static are Sukumar and Chopp [9], by introducing a new enrichments for voids. Recently, J M Pais [10] has treated voids problem using XFEM but limited on static and quasi-static loadings.

In this context, this work seeks to model the behavior of structures containing simultaneously voids and stationary cracks and subjected to different types of loads (fatigue loads and dynamic Heaviside step loading). The SIF will be evaluated using a global approach; based on the J integral. Also, in this work, we will test the effect of size and position of the void. The obtained results will be compared with other works in literature.

2. XEFM formulation

The XFEM introduces in the approximation of the displacement field three types of enrichments [5]:
-A discontinuous function H (Heaviside function) that enriches the split nodes (Fig. 1):

$$H(x)=\begin{cases}+1 & if\ \ \phi(x)\geq 0\\ -1 & if\ \ \phi(x)\leq 0\end{cases}. \tag{1}$$

Where ϕ is the level set function that determines the normal position of node *(x)* from the crack.
-Four (04) singular functions for each tip node (Fig. 1):

(2)

$$F(x)=\sqrt{r}\,\{\sin(\theta/2),\ \sin(\theta/2)\sin(\theta),\ \cos(\theta/2),\cos(\theta/2)\sin(\theta)\}.$$

-For void nodes, we add the following enrichment [9]:

$$V(x)=\begin{cases}0 & if\ \ \chi(\mathrm{x})<0\ \text{(inside of the void)}\\ 1 & if\ \ \chi(x)>0\ \text{(outside of the void)}\end{cases}. \tag{3}$$

Where χ is the level set function of voids
The approximate displacement fields are as follows:

$$u(x)\approx V(x)\left[\sum N_i(x)u_i+\sum_{i\in I_H}N_i(x)H(x)a_i+\sum_{i\in I_{Br}}N_i(x)\left(\sum_{k=1}^{4}F_k(x)b_{i,k}\right)\right] \tag{4}$$

In addition to traditional unknown u_i, we consider the unknowns a_i and b_k corresponding to the enrichment functions H et F_k, respectively.

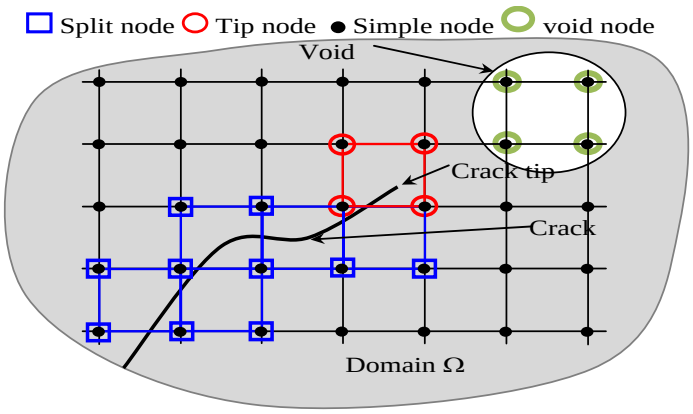

Fig. 1 Types of XFEM enrichments of the meshed domain.

3. Interaction integral method for SIF computation

There are several methods to evaluate the SIF. In this work we use the J integral method by using the interaction integral (Fig.2). Because its global character, this method is the most stable technique.

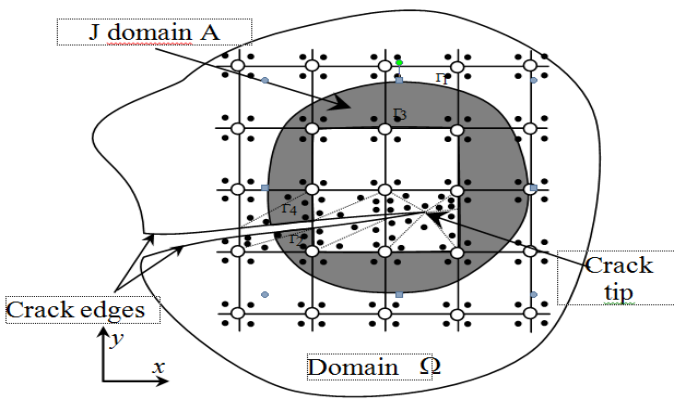

Fig.2 Method of SIF computing: interaction integral technique.

This method introduced by Sih et al [8], combines with the actual field an auxiliary field satisfying the boundary conditions of the problem. In this case, The J integral is given as follows:

$$J = J_{act} + J_{aux} + M. \tag{5}$$

Where J_{act}, J_{aux} are the J integrals in the actual and auxiliary fields, respectively, and M is the interaction integral that we are interested in, defined by :

$$M = \int_A \left[\sigma_{ij} \frac{\partial u_i^{aux}}{\partial x_1} + \sigma_{ij}^{aux} \frac{\partial u_i}{\partial x_1} - W^M \delta_{1i} \right] \frac{\partial q}{\partial x_i} d\Gamma = \frac{2}{E'} \left(K_I K_I^{aux} + K_{II} K_{II}^{aux} \right). \tag{6}$$

With $W^M = \left(\sigma_{ij} \varepsilon_{ij}^{aux} + \sigma_{ij}^{aux} \varepsilon_{ij} \right) / 2$ is the strain energy of interaction and $E' = E$ in plane stress and $E' = E/(1-\nu^2)$ in plane strain. Therefore, the stress intensity factor in mode I and II take the form:

$$K = \frac{E'}{2} M. \tag{7}$$

We take $K_I^{aux} = 1, K_{II}^{aux} = 0$ in mode I and $K_I^{aux} = 0, K_{II}^{aux} = 1$ in mode II. The computing procedure of M is based on the Gauss points within the elements of J domain area A (see Fig 2).

4. Fatigue application

We validate the computer software carried out in this study and based on the above developments, in quasi-static (fatigue) loading, we consider a plate (Fig. 3) of size $2L \times 2l = 120mm \times 65mm$ with an edge crack of length $2a$, with $a = 10mm$, and 3 holes (one is of diameter 20 *mm* and the two others for the load action are both of 13 *mm*). The material properties are $E = 71.7 \times 10^9$ Pa, $\nu = 0.3$. The stress state is plane strain with a mesh of 60x120 elements. The plate is under uniaxial fatigue load with a variation of $\Delta p = 20KN$ with 12 increments of *da=3 mm*.

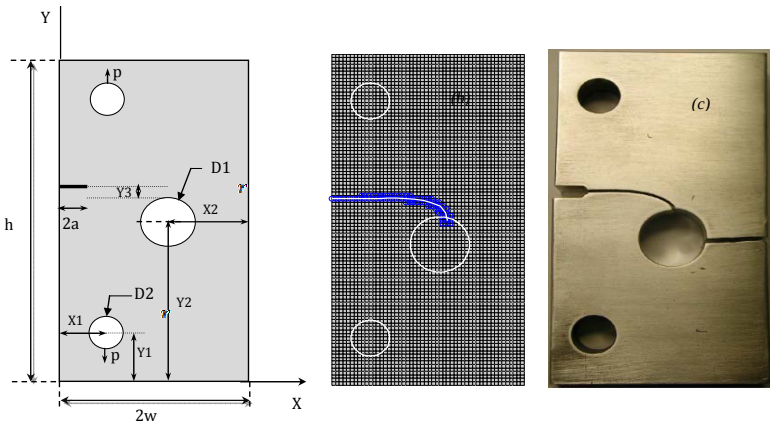

Fig.3 the considered validation: (a) Cracked plate containing voids,(b) results using XFEM, (c) experimental results [11]

In this case, the crack growth path is followed and compared with that obtained by Giner et al. [11], the results are regrouped in Fig 3. The obtained results as shown in Fig 3b are approximately close to the experimental ones Fig 3c proved so the accuracy of this approach.

5. Dynamic applications

For dynamic loads, we are limited to present our results only.

5.1. Plate with edge crack

We consider a reference problem of a plate (Fig. 5.a) of size $2L \times 2l = 400mm \times 300mm$ with an edge crack of length $2a$, with $a/l = 0.24$. The material properties are $E = 2.1\times10^{11}$ Pa, $\nu = 0.3$ and $\rho = 3220$Kg/m^3. With plane strain state and a mesh of 60x120 elements. The plate is under uniaxial dynamic tensile $\sigma_y(t,\sigma_0)$ of Heaviside step load (Fig. 4.b) with $\sigma_0 = 20\times10^6$ Pa,

We're going to evaluate the no normalised SIF $K_{I\,ad}$ at the crack tip and the maximum of y component of normalised stress σ_{ad} on A point situated at the nearest node to the crack tip defined as:

$$K_{I\,ad} = K_I / (\sigma_0\sqrt{\pi a}) \tag{8}$$

$$\sigma_{ad} = \sigma_{yy} / \sigma_0 \tag{9}$$

Curves on Fig 4.c were found with sliding the void horizontally with a step of (1/7)a. These Figures represent the variation of $K_{I\,ad}$ and σ_{ad} versus the relative position x/2w.

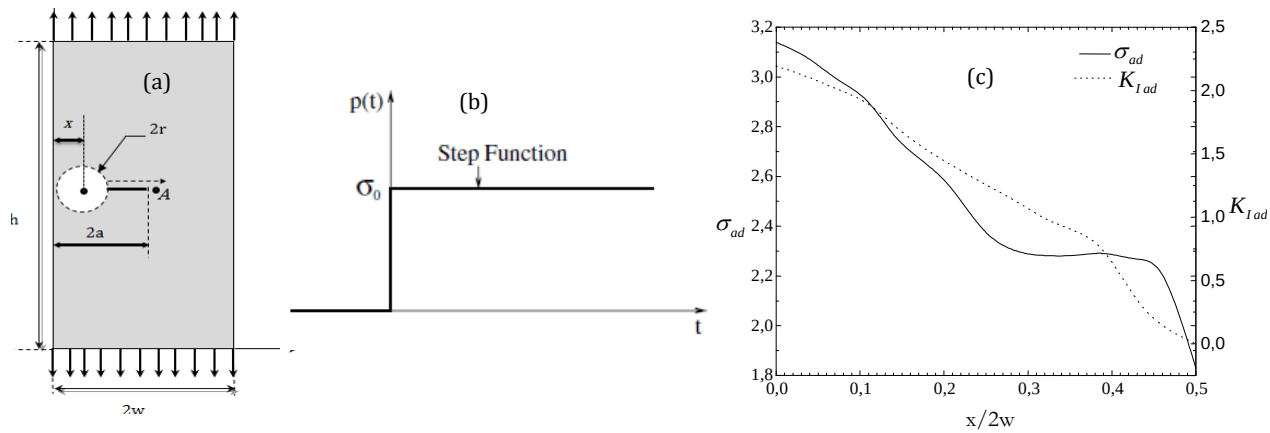

Fig.4 (a) considered geometries, (b). Dynamic load Heaviside (c) SIF and maximum stress

Fig 4c shows that both $K_{I\,ad}$ and σ_{ad} decreases with the distance of the hole to the crack tip; it is like the crack length decreases. The SIF continues to decline up then vanishes when the hole reached the crack tip. That is why holes at the crack tips are considered a very practical solution to stop their growth.

5.2. Plate with central crack

We reanalysis the precedent example but with a central crack crossed by a hole of a diameter varying from 2a/10 to 2a/1.1 as shown in Fig 4a.

In this example, we are going to evaluate the dimensionless SIF given in relation (8) for different diameters of hole to verify its role to increase the cracking plate resistance. Effectively, from the curves in Figure 5.b, the hole more and more bigger extinct more and more the SIF and therefore the risk of crack growth.

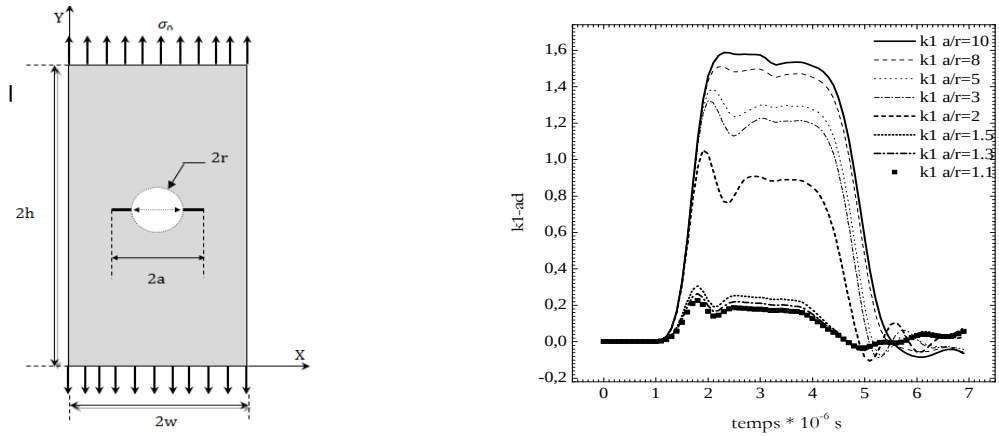

Fig.5 (a) considered geometries, (b). DSIF for different sizes of hole

6. Conclusion

This study presents a computational procedure to evaluate the SIF for cracked structures with void using XFEM. The correlation of the obtained results with the literature for the fatigue application demonstrates the effectiveness of this procedure. The obtained results of dynamic applications agree very well with the attended physical results which approve so the robustness of our approach. As perspectives of this study the present approach can be extended to problems of multi-voids and dynamic crack propagation.

References

[1] S.H. Song, G.H. Paulino, Dynamic stress intensity factors for homogeneous and smoothly heterogeneous materials using the interaction integral method, Int. J. Solids Struct. 43 4830–4866.(2006).

[2] F. Chirino, J. Dominguez, *Dynamic analysis of cracks using boundary element method*, Engrg. Fract. Mech. 34 1051–1061. (1989).

[3] Y.M. Chen, *Numerical computation of dynamic stress intensity factors by a Lagrangian finite difference method*, Engrg. Fract. Mech. 7. 653–660. (1975).

[4] A.-V. Phan, L.J. Gray, A. Salvadori, *Transient analysis of the dynamic stress intensity factors using SGBEM for frequency-domain elastodynamics*, Comput. Methods Appl. Mech. Engrg ,199. 3039-3050. (2010).

[5] T. Belytschko, T. Black, *Elastic crack growth in finite elements with minimal remeshing*, Int. J. Numer. Meth. Engng. 45,601-620. (1999).

[6] T. Belytschko, H Chen, *Singular enrichment finite element method for elastodynamic crack propagation*, International Journal of Computational Methods, 1 (1), 1–15. (2004).

[7] J. Réthoré, A.Gravouil, A. Combescure, *An energy-conserving scheme for dynamic crack growth using the extended finite element method*, Int. J. Numer. Meth. Engng. 63, 631–659. (2005).

[8] G.C. Sih, P. Paris, and G. Irwin, *On cracks in rectilinearly anisotropic bodies*, International Journal of Fracture Mechanics, 1 (3) 189–203. (1965)

[9] Sukumar .N, Chopp D. L , Möes . N , Belytschko T., Modeling holes and inclusions by level sets in the extended finite-element method. 6183-6200, s.l. : Comput. Methods Appl . Mech. Engrg., 2001, Vol. 190.

[10] Pais, M., MATLAB Extended Finite Element (MXFEM) Code v1.2, www.matthewpais.com, 2011.

[11] E. Giner ., N. Sukumar ., J. E. Tarancon ., F. J. Fuenmayor ., *An Abaqus implementation of the extended finite element method*, Departamento de Ingenierıa Mecanica y de Materiales

Mixed mode computation of the dynamic stress intensity factor for cracked 2D structures with inclusion using XFEM

HOUA Alaa Eddine [1, a], HACHI Brahim Elkhalil[1,b], GUESMI Mohamed [1,c], HABOUSSI Mohamed[2,d], BADAOUI Mohamed [1,e].

[1] Laboratoire de développement en mécanique et Matériaux, University of Djelfa, PB 3117, Djelfa, Algeria.
[2] Laboratoire des sciences des procédés et des matériaux , UPR CNRS 3407, University Paris 13, Villetaneuse, France

[a]alaahoua@gmail.com, [b]br_khalil@yahoo.fr, [c]guesmi.mohamed@yahoo.fr, [d]mohamed.haboussi@lspm.cnrs.fr, [e]badaoui.mohamed@yahoo.fr

Abstract. This work deals with dynamic modelings of cracked structures containing inclusions using the eXtended Finite Element Method (X-FEM). The proposed theoretical developments focused on the case of the dynamic analysis, which constitutes the originality of the work. A computer code has been set up based on this theoretical framework. Several applications have been treated in order to demonstrate the effectiveness and robustness of the X-FEM based code for modeling cracked structures containing inclusions subjected to dynamic loadings.

Keywords: the eXtended Finite Element Method, Stress Intensity factor, inclusion, Dynamic Loads.

1. Introduction

In linear fracture mechanics, the Dynamic Stress Intensity Factor (DSIF) is used to characterize the cracking of fragile and quasi-fragile structures under dynamic loadings. In literature, we find many techniques to evaluate this parameter, among which we mention the finite element method (FEM) [1], the finite difference method (FDM) [2], the boundary element method (BEM) [3] and the symmetric-Galerkin boundary element method (SGBEM) [4]. We note that the FEM is the most popular for its flexibility and efficiency. However, it requires a special treatment of discontinuities and singularities of the unknown fields when cracks and inclusions that are present in the material are considered in the analysis as in the present study. To overcome such issues, a new FEM approach named eXtended Finite Element Method (XFEM) has been developed by Belytschko and Black [6] in 1999. It consists in taking into account the discontinuity at the crack edges and the singularity at the crack tip by enrichment of the neighboring nodes with new degrees of freedom, via the new shape functions, associated to elements containing those nodes. In 2004, a new enrichment function for inclusions has been proposed by Sukumar and Chopp [5]. Recently, J. M. PAIS (2010) used the eXtended Finite Element Method (XFEM) to study cracks and their propagation subjected to static and fatigue loadings [7]. In the authors knowledge, the earliest published papers treating the dynamic problems by using XFEM, but without inclusion, are due to Belytschko and Chen [8], Réthoré et al. [9], and Grégoire [10]. Other work has addressed this problem with a new approach such the one of A.V. Phan et al. [4] who used the symmetric-Galerkin boundary element method SGBEM.

In the present work, a modeling approach based on the XFEM method is proposed to describe the behavior of structures containing stationary cracks and inclusions, that are subjected to different types of dynamic loads (Heaviside step loading and triangular blast loading). Hence, the Dynamic Stress Intensity Factor (DSIF) will be evaluated by XFEM using the J integral. Moreover, the effect of the relative position of the inclusion with regard to the crack will be examined. For validation purpose, the results given by our approach will be compared to those of A.V. Phan et al. [4] obtained by using the SGBEM.

2. Presentation of the XFEM method

The XFEM introduces in the approximation of the displacement field three types of enrichments [6]:
- A discontinuous function H (Heaviside function) that enriches the split nodes (Fig. 1):

$$H(x)=\begin{cases}+1 & if\ \ \phi(x)\geq 0\\ -1 & if\ \ \phi(x)\leq 0\end{cases}. \tag{1}$$

Where ϕ is the level set function that determines the normal position of node *(x)* from the crack.
- Four singular functions for each tip node (Fig. 1):

$$F(x)=\sqrt{r}\,\{\sin(\theta/2),\ \sin(\theta/2)\sin(\theta),\ \cos(\theta/2),\cos(\theta/2)\sin(\theta)\}. \tag{2}$$

- One function associated with the interface nodes of the inclusion:

$$\upsilon(x)=\begin{cases}+1 & if\ \ \zeta(x)=0\\ 0 & if\ \ not\end{cases} \tag{3}$$

Where ζ is the level set function of the inclusion.

The approximate displacement fields are as follows:

$$u(x)\approx\sum N_i(x)u_i+\sum_{i\in I_H}N_i(x)H(x)a_i+\sum_{i\in I_{Br}}N_i(x)\left(\sum_{k=1}^{4}F_k(x)b_{i,k}\right)+\upsilon(\mathrm{x})\mathrm{a_e}. \tag{4}$$

In addition to traditional unknowns u_i, we consider the unknowns a_i, b_k and a_e corresponding to the enrichment functions H, F_k and υ respectively.

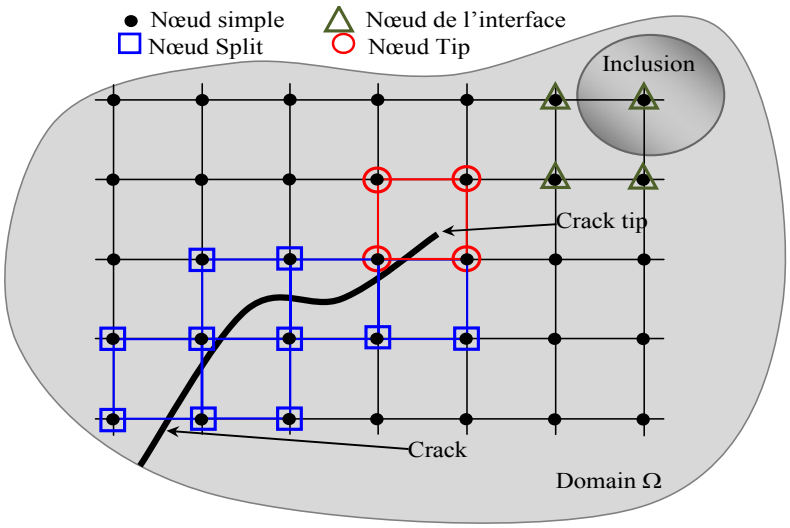

Fig. 1 Types of XFEM enrichments of the meshed domain.

3. Interaction integral method for DSIF computation

There are several methods to evaluate the DSIF. In this work, we use the method of the *J* integral by using the interaction integral (Fig.2). Because of its global character, it is the most stable technique.

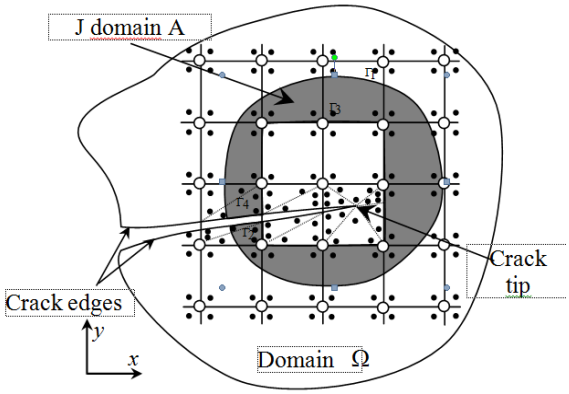

Fig. 2 Computing method of DSIF: interaction integral technique.

This method introduced by Sih et al [11], combines with the actual field an auxiliary field satisfying the boundary conditions of the problem. In this case, The *J* integral is given as follows:

$$J = J_{act} + J_{aux} + M. \tag{5}$$

Where J_{act}, J_{aux} are the J integrals in the actual and auxiliary fields, respectively, and M is the interaction integral that we are interested in, defined by :

$$M = \int_A \left[\sigma_{ij} \frac{\partial u_i^{aux}}{\partial x_1} + \sigma_{ij}^{aux} \frac{\partial u_i}{\partial x_1} - W^M \delta_{1i} \right] \frac{\partial q}{\partial x_i} d\Gamma = \frac{2}{E'} \left(K_I K_I^{aux} + K_{II} K_{II}^{aux} \right). \tag{6}$$

With $W^M = \left(\sigma_{ij} \varepsilon_{ij}^{aux} + \sigma_{ij}^{aux} \varepsilon_{ij} \right) / 2$ is the strain energy of interaction and $E' = E$ in plane stress and $E' = E/(1-\nu^2)$ in plane strain. Therefore, the stress intensity factors in mode I and II take the form:

$$K = \frac{E'}{2} M. \tag{7}$$

We take $K_I^{aux} = 1, K_{II}^{aux} = 0$ in mode I and $K_I^{aux} = 0, K_{II}^{aux} = 1$ in mode II. The computing procedure of *M* is based on the Gauss technique, the integration points are within the elements describing the area *A* of the *J* domain (see Fig 2).

4. Applications

We consider a plate of size 2w × 2h = 30mm × 40 mm containing an internal crack of initial length 2l = 4.8 mm and an inclusion of diameter d = 4 mm as shown in Fig. 3. The plate is subjected to a uniaxial Heaviside step tension loading σ(t) or a triangular blast loading with t1 = 2 μs and t2 = 8 μs. The inclusion is eccentrically positioned relatively to the crack center as shown Fig 3. The material properties for the plate and the inclusion are respectively: E = 260 GPa and 640 GPa, υ = 0.08 and 0.01, and ρ = 3.220 kg/m3 and 3.515 kg/m3. The DSIFs evaluated at crack tip *A*, and normalized with respect to the SIF of a similar situation in infinite plate under a uniaxial tension σ_0 without inclusion. The normalized DSIFs for this problem are defined as:

$$\overline{K_I} = \frac{K_I}{\sigma_0 \sqrt{\pi a}} \qquad \overline{K_{II}} = \frac{K_{II}}{\sigma_0 \sqrt{\pi a}} \tag{8}$$

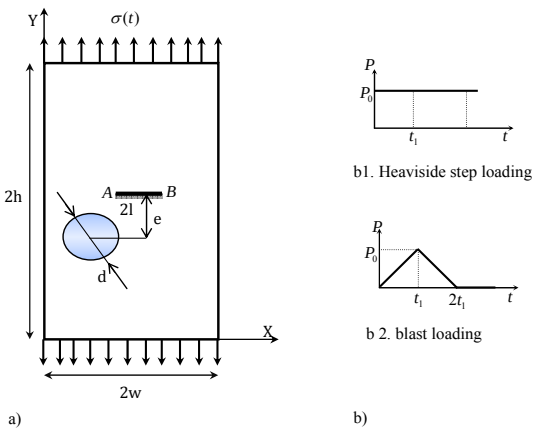

Fig.3 The validation problem: a) Cracked plate with inclusion, b) Different types of loadings.

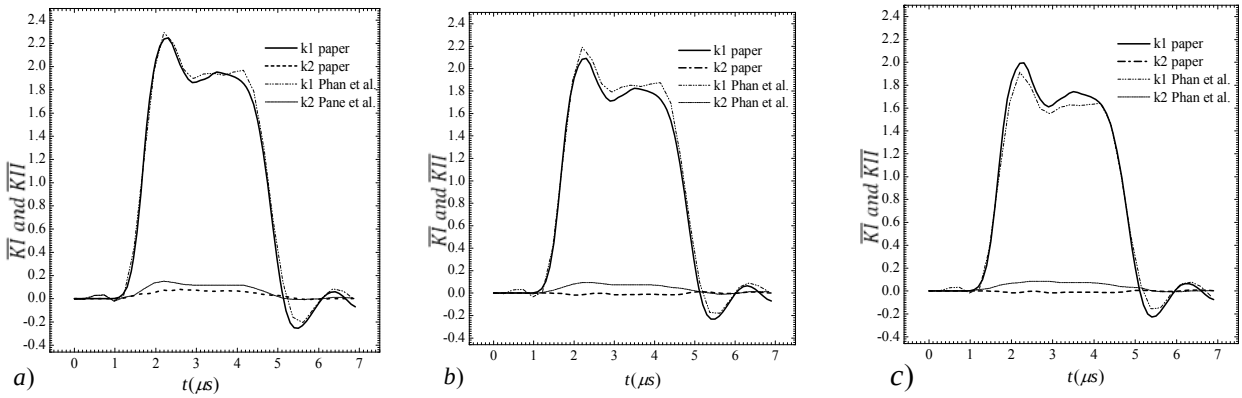

Fig.4 The plate under Heaviside step loading with different positions of the inclusion; (a) e= 3d/4 (b) e= d/2, (c) e= d/4.

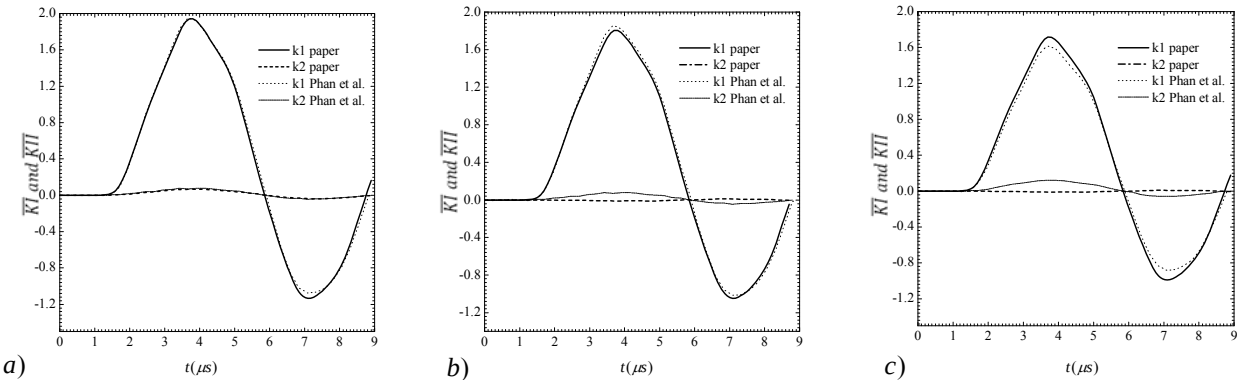

Fig.5 The plate under triangular blast loading with different positions of the inclusion; (a) e= *3d/4* (b) *e= d/2*, (c) *e= d/4*.

Figures 4 and 5 can be shown, there is an acceptable correlation between the obtained results and those of Phan et al. [4] using SGBEM, for different positions of the inclusion as well as for KI and KII.

We can note here that for DSIF KII, our results are closer to the exact solution (zero) compared to those obtained by Phan et al.[4].

Compared to the Heaviside step loading, the triangular blast loading increases more the negative value of KI and decreases more the positive peaks. This shows that the Heaviside step loading is

more dangerous than the triangular blast loading. The quality of the obtained results demonstrates well the effectiveness of the proposed approach and the resulting computer code.

5. Conclusion

This study presents a computational procedure to evaluate the DSIF for stationary cracks in plate containing inclusions using the XFEM method. The agreement of the obtained results with those found in the literature for several treated configurations demonstrates the effectiveness and the robustness of the proposed procedure. As a perspective, this work will be extended to problems of multi inclusions, multi cracks, different form of the inclusion and dynamic crack propagation.

References

[1] S.H. Song, G.H. Paulino, Dynamic stress intensity factors for homogeneous and smoothly heterogeneous materials using the interaction integral method, Int. J. Solids Struct. 43 4830–4866 (2006).

[2] F. Chirino, J. Dominguez, Dynamic analysis of cracks using boundary element method, Engrg. Fract. Mech. 34 1051–1061. (1989).

[3] Y.M. Chen, Numerical computation of dynamic stress intensity factors by a Lagrangian finite difference method, Engrg. Fract. Mech. 7. 653–660. (1975).

[4] A.-V. Phan, L.J. Gray, A. Salvadori, Transient analysis of the dynamic stress intensity factors using SGBEM for frequency-domain elastodynamics, Comput. Methods Appl. Mech. Engrg , 199. 3039-3050. (2010).

[5] Sukumar .N, Chopp D. L , Möes . N , Belytschko T.; Modeling holes and inclusions by level sets in the extended finite-element method. 6183-6200, s.l. : Comput. Methods Appl . Mech. Engrg., 2001, Vol. 190.

[6] T. Belytschko, T. Black, Elastic crack growth in finite elements with minimal remeshing, Int. J. Numer. Meth. Engng. 45,601-620. (1999).

[7] Matthew Jon Pais; Accurate integration of fatigue crack growth models through kriging and reanalysis of the extended finite element method, edité par University of FLORIDA, (2010).

[8] T. Belytschko, H Chen, Singular enrichment finite element method for elastodynamic crack propagation, International Journal of Computational Methods, 1 (1), 1–15. (2004).

[9] J. Réthoré, A.Gravouil, A. Combescure, An energy-conserving scheme for dynamic crack growth using the extended finite element method, Int. J. Numer. Meth. Engng. 63, 631–659. (2005).

[10] D. Grégoire, Initiation, propagation, arrêt et redémarrage de fissures sous impact, doctorate thesis of INSA, 2008.

[11] G.C. Sih, P. Paris, and G. Irwin, On cracks in rectilinearly anisotropic bodies, International Journal of Fracture Mechanics, 1 (3) 189–203 (1965).

Size Effect Analysis of Recycled Concrete Fracture based on Micromechanics Using the Base Force Element Method

Yijiang Peng [1,*], Nana Dang [1], Lijuan Zhang [1], Jiwei Pu [1]

[1] Department of Civil Engineering, Beijing University of Technology, Beijing 100124, China
* Corresponding author: pengyijiang@bjut.edu.cn

Abstract In this paper, the base force element method (BFEM) on damage mechanics is used to analyze the fracture properties of recycled aggregate concrete (RAC) on meso-level. The recycled aggregate concrete is taken as five-phase composites consisting of natural coarse aggregate, new mortar, new interfacial transition zone(ITZ) , old mortar and old ITZ on meso-level. The random aggregate model is used to simulate the meso-structure of recycled aggregate concrete. The size effects of mechanics properties of RAC under uniaxial tension loading are simulated using the BFEM on damage mechanics. The simulation results agree with the test results. This analysis method is the new way for investigating fracture mechanism and numerical simulation of mechanical properties for recycled aggregate concrete.

Keywords Base force element method (BFEM), Micromechanics, Fracture property, Size effect, Recycled aggregate concrete (RAC)

1. Introduction

Concrete is considered as heterogeneous composites which mechanical performance is much related with the microstructure of material. The mechanical performance is usually obtained using experimental method. However, testing usually consumes a large amount of manpower and material resources, and test results are usually more discrete. In order to overcome this defect, the concept of numerical concrete was presented by Wittanmm et al (1984) based on micro-mechanics. Subsequently, some scholars did some creative works in this field, and made a number of models. Among them, the two important models are the lattice model and the random aggregate model. For example, Schlangen et al (1992, 1997) applied the lattice model to simulate the failure mechanism of concrete. Liu et al (1996) adopted the random aggregate model to simulate cracking process of concrete using FEM. Peng et al (2001) adopted the random aggregate model to simulate the mechanics properties of rolled compacted concrete on meso-level using FEM. Du et al (2008) simulated the failure mechanism of beam under impact loading and triangular cyclic loading by using displacement-controlled FEM, stress-strain curves and dynamic bending strengths of specimens.

Recycled concrete material which is used as a green building material has attracted more and more researchers with the shortage of resources and an increasing number of construction wastes. They have carried out series of experiments and some conclusions have been reached. An overview of study on recycled aggregate concrete has been given by Xiao et al (2012). However, because of the complexity of recycled coarse aggregates, conclusions made by different researchers are usually not very accordant, even opposite sometimes. To remove effects of experimental conditions, some numerical researches on meso-level was considered. For example, numerical simulation on stress-strain curve of recycled concrete was taken by Xiao et al (2009) with Lattice Model under uniaxial compression. A method on meso-mechanics analysis was proposed by Peng et al (2011) using FEM for recycled aggregate concrete based on random aggregate model. However, the Numerical researches on the damage mechanism for recycled concrete material have just begun.

In recent years, a new type of finite element method - the Base Force Element Method (BFEM) has been developed by Peng et al (2006-2012) based on the concept of the base forces by Gao (2003). In this paper, the BFEM on potential energy principle is used to analyze recycled aggregate concrete (RAC) on meso-level. The size effects of mechanics properties of recycled aggregate

concrete in uniaxial tension test are simulated using the BFEM. The simulation result agrees with the test result. This research method is the new way for investigating fracture mechanism and numerical simulation of mechanics properties of recycled aggregate concrete.

2. Basic Equation

Consider a two-dimensional domain of solid medium, let $\boldsymbol{x}^{\alpha}(\alpha=1,2)$ denote the Lagrangian coordinate system, where $\boldsymbol{P}$ and $\boldsymbol{Q}$ the position vectors of a material point before and after deformation, respectively. Two triads for original and current configurations can be defined as:

$$\boldsymbol{P}_{\alpha}=\frac{\partial \boldsymbol{P}}{\partial x^{\alpha}}, \qquad \boldsymbol{Q}_{\alpha}=\frac{\partial \boldsymbol{Q}}{\partial x^{\alpha}}, \tag{1}$$

Let $\boldsymbol{u}$ denotes the displacement of a point, then

$$\boldsymbol{u}=\boldsymbol{Q}-\boldsymbol{P} \tag{2}$$

The gradient of displacement $\boldsymbol{u}_{\alpha}$ can be written as:

$$\boldsymbol{u}_{\alpha}=\frac{\partial \boldsymbol{u}}{\partial x^{\alpha}}=\boldsymbol{Q}_{\alpha}-\boldsymbol{P}_{\alpha} \tag{3}$$

Then, the Green strain $\boldsymbol{\varepsilon}$ can be written as

$$\boldsymbol{\varepsilon}=\frac{1}{2}(\boldsymbol{u}_i\otimes\boldsymbol{P}^i+\boldsymbol{P}^i\otimes\boldsymbol{u}_i) \tag{4}$$

In order to describe the stress state at a point $\boldsymbol{Q}$, a parallelogram with the edges $\mathrm{d}x^1\boldsymbol{Q}_1, \mathrm{d}x^2\boldsymbol{Q}_2$ is shown in Figure 1. Define,

$$\boldsymbol{T}^{\alpha}=\frac{\mathrm{d}T^{\alpha}}{\mathrm{d}x^{\alpha+1}}, \qquad \mathrm{d}x^{\alpha}\to 0 \tag{5}$$

where 3=1 for indexes. Quantities $\boldsymbol{T}^{\alpha}(\alpha=1,2)$ are called the base forces at point $\boldsymbol{Q}$ in the two-dimensional coordinate system x^{α}.

According to the definitions of various stress tensors, the relation between the base forces and various stress tensors can be given. The Cauchy stress is

$$\boldsymbol{\sigma}=\frac{1}{A_Q}\boldsymbol{T}^{\alpha}\otimes\boldsymbol{Q}_{\alpha}. \tag{6}$$

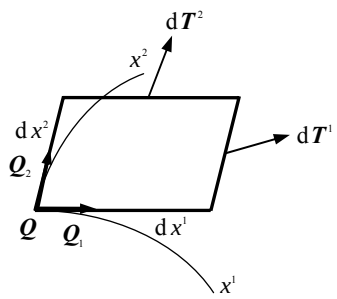

Figure 1. Base Forces on a plane element

Further, the base forces are given as follows

$$\boldsymbol{T}^{\alpha}=\rho A_Q\frac{\partial W}{\partial \boldsymbol{u}_{\alpha}}=\rho_0 A_P\frac{\partial W}{\partial \boldsymbol{u}_{\alpha}} \tag{7}$$

in which W is the strain energy density, ρ_0 is the mass density before deformation.

Equation (7) expresses the $\boldsymbol{T}^{\alpha}$ by strain energy directly. Thus, $\boldsymbol{u}_{\alpha}$ is just the conjugate variable of $\boldsymbol{T}^{\alpha}$. It can be seen that the mechanics problem can be completely established by means of $\boldsymbol{T}^{\alpha}$ and $\boldsymbol{u}_{\alpha}$.

3. Model of BFEM with Triangular Element

We will derive explicit expressions for stiffness matrices of a triangular element now, base on the concept of "base forces". Consider a triangular element with boundary S as shown in Figure 2.

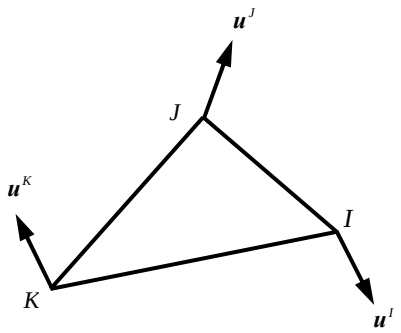

Figure 2. A triangular element

For the small displacement case, the real strain $\boldsymbol{\varepsilon}$ can be replaced by $\bar{\boldsymbol{\varepsilon}}$. We can obtain the average stress in element as

$$\bar{\boldsymbol{\varepsilon}} = \frac{1}{A}\int_A \boldsymbol{\varepsilon}\,\mathrm{d}A \tag{8}$$

in which A is the area of element.

Substituting Equation (4) into Equation (8), we have

$$\bar{\boldsymbol{\varepsilon}} = \frac{1}{2A}\int_A \left(\boldsymbol{u}_{\alpha}\otimes\boldsymbol{P}^{\alpha}+\boldsymbol{P}^{\alpha}\otimes\boldsymbol{u}_{\alpha}\right)\mathrm{d}A \tag{9}$$

Using Green' theorem, Equation (9) becomes

$$\bar{\boldsymbol{\varepsilon}} = \frac{1}{2A}\int_S \left(\boldsymbol{u}\otimes\boldsymbol{n}+\boldsymbol{n}\otimes\boldsymbol{u}\right)\mathrm{d}s \tag{10}$$

where $\boldsymbol{n}$ is the current normal of boundary S.

When the element is small enough, Equation (10) can be written as

$$\bar{\boldsymbol{\varepsilon}} = \frac{1}{2A}\sum_{i=1}^{3} L_i\left(\boldsymbol{u}_i\otimes\boldsymbol{n}_i+\boldsymbol{n}_i\otimes\boldsymbol{u}_i\right) \tag{11}$$

where L_i is the length of edge $i(i=1,2,3)$, $\boldsymbol{n}_i$ denotes the external normal of edge $i(i=1,2,3)$, $\boldsymbol{u}_i$ is the displacement of geometric center of edge $i(i=1,2,3)$.

Further, we assume that any edge of the triangular element in the deformation process keeps its edges straight lines. Then, we can obtain the following expression for $\boldsymbol{u}_i$:

$$\boldsymbol{u}_i = \frac{1}{2}\left(\boldsymbol{u}_I+\boldsymbol{u}_J\right) \tag{12}$$

where $\boldsymbol{u}_I$ and $\boldsymbol{u}_J$ denote the displacements of both ends of edge $i(i=1,2,3)$, respectively.

Substituting Equation (12) into Equation (11) yields

$$\bar{\boldsymbol{\varepsilon}} = \frac{1}{2A}\left(\boldsymbol{u}_I \otimes \boldsymbol{m}^I + \boldsymbol{m}^I \otimes \boldsymbol{u}_I\right) \tag{13}$$

The summation rule is implied in the above equation, and $\boldsymbol{m}^I$ is

$$\boldsymbol{m}^I = \frac{1}{2}\left(L_{IJ}\boldsymbol{n}^{IJ} + L_{IK}\boldsymbol{n}^{IK}\right) \tag{14}$$

where L_{IJ} and L_{IK} are the length of edges IJ and IK, $\boldsymbol{n}^{IJ}$ and $\boldsymbol{n}^{IK}$ denote the external normal of edges IJ and IK, respectively.

Then, for an isotropic material, the strain energy in the element is reduced to

$$W_D = \frac{AE}{2(1+\nu)}\left[\frac{\nu}{1-2\nu}\left(\bar{\boldsymbol{\varepsilon}} : \boldsymbol{U}\right)^2 + \bar{\boldsymbol{\varepsilon}} : \bar{\boldsymbol{\varepsilon}}\right] \tag{15}$$

in which E is Young's modulus, ν is Poisson's ratio.

Substituting (13) into (15) we have

$$W_D = \frac{E}{4A(1+\nu)}\left[\frac{2\nu}{1-2\nu}\left(\boldsymbol{u}_I \cdot \boldsymbol{m}^I\right)^2 + \left(\boldsymbol{u}_I \cdot \boldsymbol{u}_J\right)m^{IJ} + \left(\boldsymbol{u}_I \cdot \boldsymbol{m}^J\right)\left(\boldsymbol{u}_J \cdot \boldsymbol{m}^I\right)\right] \tag{16}$$

where

$$m^{IJ} = \boldsymbol{m}^I \cdot \boldsymbol{m}^J \tag{17}$$

From Equation (16), we can obtain the force acting on this element at node I

$$\boldsymbol{f}^I = \frac{\partial W_D}{\partial \boldsymbol{u}^I} = \boldsymbol{K}^{IJ} \cdot \boldsymbol{u}_J \tag{18}$$

where

$$\boldsymbol{K}^{IJ} = \frac{E}{2A(1+\nu)}\left[\frac{2\nu}{1-2\nu}\boldsymbol{m}^I \otimes \boldsymbol{m}^J + m^{IJ}\boldsymbol{U} + \boldsymbol{m}^J \otimes \boldsymbol{m}^I\right] \tag{19}$$

Here, $\boldsymbol{K}^{IJ}$ is a second-order tensor that is called the stiffness matrix.

The characteristics of the stiffness matrix $\boldsymbol{K}^{IJ}$ compared with the traditional FEM are as:

(1) This expression of stiffness matrix $\boldsymbol{K}^{IJ}$ can easily be extended to apply for arbitrary polygonal elements problem in two dimensions or arbitrary polyhedral element problem in three dimensions.

(2) The expression of the stiffness matrix $\boldsymbol{K}^{IJ}$ is a precise expression, and it is not necessary to introduce the Gauss' integral for calculating the stiffness coefficient at a point.

(3) This expression of $\boldsymbol{K}^{IJ}$ can be used for calculating the stiffness of various elements with a unified method.

(4) This expression of stiffness matrix $\boldsymbol{K}^{IJ}$ can be used in any coordinate system.

(5) The method of constructing the stiffness matrix does not regulate the introduction of interpolation.

The model of the base force element method will be used to analysis the damage problem for recycled aggregate concrete and be used to analysis the relationships of meso-structure and macroscopic mechanical performance of recycled concrete.

4. Random Aggregate Model for RAC

Based on the Fuller grading curve, Walraven J.C et al (1981) put the three dimensional grading curve into the probability of any point which located in the sectional plane of specimens, and its expression as follow:

$$P_c(D < D_0) = P_k\left(1.065\left(\frac{D_0}{D_{\max}}\right)^{\frac{1}{2}} - 0.053\left(\frac{D_0}{D_{\max}}\right)^4 - 0.012\left(\frac{D_0}{D_{\max}}\right)^6 - 0.0045\left(\frac{D_0}{D_{\max}}\right)^8 - 0.0025\left(\frac{D_0}{D_{\max}}\right)^{10}\right) \tag{20}$$

where P_k is the volume percentage of aggregate volume among the specimens, in general $P_k = 0.75$, D_0 is the diameter of sieve pore, $D_{\max}$ is the maximum aggregate size.

According to (20), the numbers of coarse aggregate particles with various sizes can be obtained. By Monte Carlo method, random to create the centroid coordinates of all kinds of coarse aggregate particles, namely to generate random aggregate model.

According to the projection method, we dissect the specimens of RAC with different phases of materials. Then, the phase of recycled coarse aggregate, the phase of new hardened cement, the phase of old hardened cement, and the phase of new and old interfacial transition zone (ITZ) can be judged by a computer code as Figure 3:

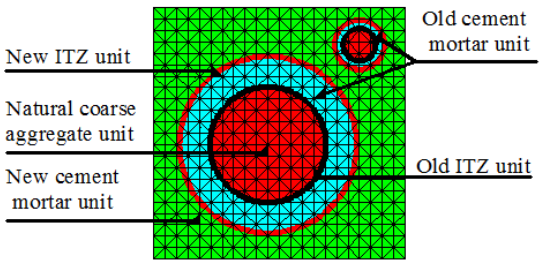

Figure 3. Attribute recognition figure

5. Damage Model of Materials

Components of RAC such as recycled coarse aggregate, new mortar, old mortar, new interfacial transition zone (New ITZ) and old interfacial transition zone (Old ITZ) are basically quasi-brittle material, whose failure patterns are mainly brittle failure.

In this paper, according to the characteristics of recycled concrete on meso-structure, the damage degradation of recycled concrete is described by the bilinear damage model, and the failure principal is the criterion of maximum tensile strain. Damage constitutive model is defined as $\widetilde{E} = E(1-D)$ as shown in Figure 4, where the damage factor D can be expressed as fallow:

$$D = \begin{cases} 0 & \varepsilon < \varepsilon_0 \\ 1 - \dfrac{\eta-\lambda}{\eta-1}\dfrac{\varepsilon_0}{\varepsilon} + \dfrac{1-\lambda}{\eta-1} & \varepsilon_0 < \varepsilon \le \varepsilon_r \\ 1 - \lambda\dfrac{\varepsilon_0}{\varepsilon} & \varepsilon_r < \varepsilon \le \varepsilon_u \\ 1 & \varepsilon > \varepsilon_u \end{cases} \tag{21}$$

where f_t is the tensile strength of material, the residual tensile strength is defined as $f_{tr} = \lambda f_t$, the residual strength coefficient λ ranges from 0 to 1, the residual strain is $\varepsilon_r = \eta\varepsilon_0$, η is the residual strain coefficient, the ultimate strain is defined as $\varepsilon_u = \xi\varepsilon_0$, where ξ is ultimate strain coefficient, ε is principal tensile strain of element.

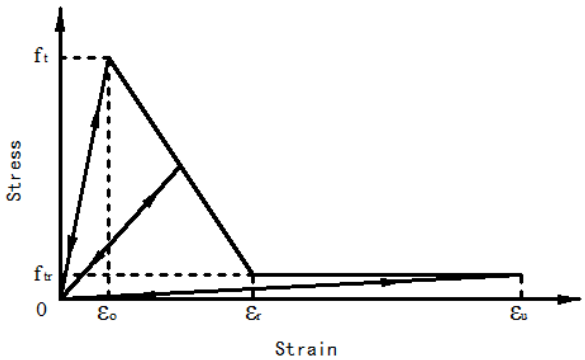

Figure 4. Bilinear damage model

6. Numerical Example

According to the test results got from the experiment, material parameters of recycled aggregate are selected, which is completely coherent with model material used in the experiment. Material parameters of numerical simulation are shown in table 1. The recycled concrete specimens were loaded by displacement steps.

Table 1. Material parameters of uniaxial tensile tests

Materials	Elastic modulus/GPa	Position ratio	Tensile strength/MPa	λ	η	ξ
Natural coarse aggregate	50	0.16	10	0.1	5	10
Old ITZ	25	0.2	2	0.1	3	10
Old cement mortar	25	0.22	2.5	0.1	4	10
New ITZ	30	0.2	2	0.1	3	10
New cement mortar	30	0.22	3	0.1	4	10

For the size 100mm×100mm×100mm of tension specimen, the numbers of coarse aggregate particles can be obtained according to Equation (20). By Monte Carlo method, random to create the centroid coordinates of all kinds of coarse aggregate particles, namely to generate random aggregate model as Figure 5:

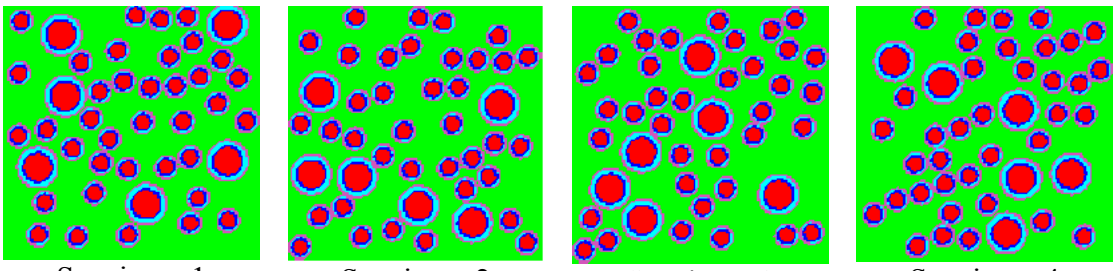

Specimen 1 Specimen 2 Specimen 3 Specimen 4

Figure 5. Random aggregate model with 100mm×100mm×100mm

The uniaxial tensile stress -strain curve of recycled concrete is getting as shown in Figure 6. The tensile strengths of the four specimens were 2.64Mpa, 2.69MPa, 2.67MPa and 2.69MPa. The uniaxial tensile strength average of the specimen group is 2.67MPa. The result BFEM on meso-damage analysis for RAC is consistent with the test results.

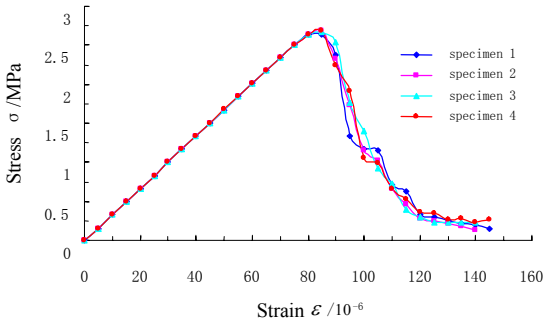

Figure 6. Stress-strain curve of RAC with 100mm×100mm×100mm

For the size 150mm×150mm×150mm of tension specimen, the numbers of coarse aggregate particles can be obtained according to Equation (20). By Monte Carlo method, random to create the centroid coordinates of all kinds of coarse aggregate particles, namely to generate random aggregate model as Figure 7:

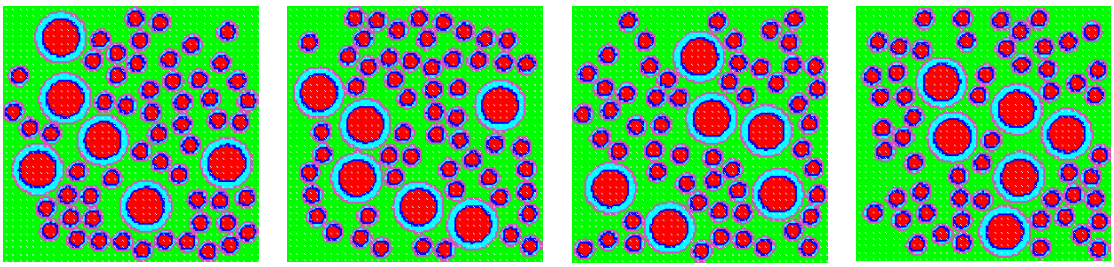

Specimen 1 Specimen 2 Specimen 3 Specimen 4

Figure 7. Random aggregate model with 150mm×150mm×150mm

The uniaxial tensile stress -strain curve of recycled concrete is getting as shown in Figure 8. The tensile strengths of the four specimens were 2.51Mpa, 2.50MPa, 2.52MPa and 2.51MPa. The uniaxial tensile strength average of the specimen group is 2.51MPa.

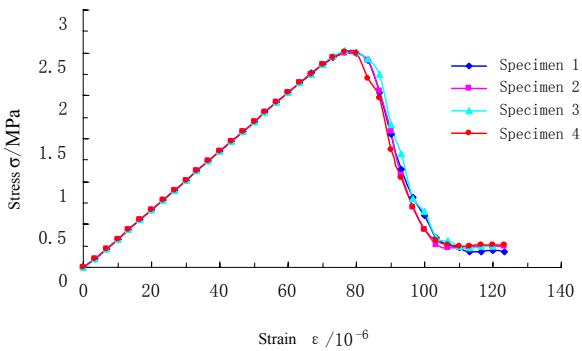

Figure 8. Stress-strain curve of RAC with 150mm×150mm×150mm

For the size 300mm×300mm×300mm of tension specimen, the numbers of coarse aggregate particles can be obtained according to Equation (20). By Monte Carlo method, random to create the centroid coordinates of all kinds of coarse aggregate particles, namely to generate random aggregate model as Figure 9:

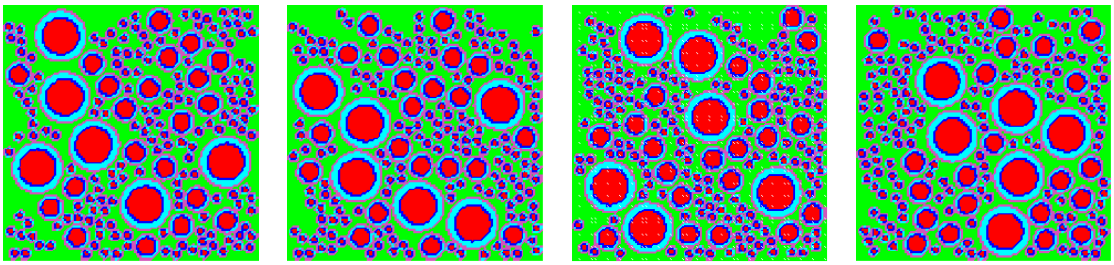

Specimen 1 Specimen 2 Specimen 3 Specimen 4

Figure 9. Random aggregate model with 300mm×300mm×300mm

The uniaxial tensile stress -strain curve of recycled concrete is getting as shown in Figure 10. The tensile strengths of the four specimens were 2.29Mpa, 2.30MPa, 2.31MPa and 2.28MPa. The uniaxial tensile strength average of the specimen group is 2.30MPa.

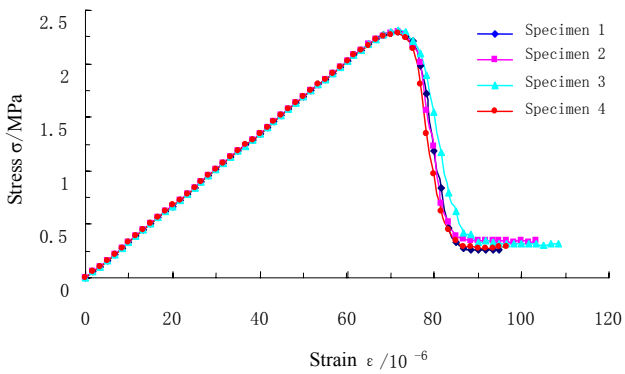

Figure 10. Stress-strain curve of RAC with 300mm×300mm×300mm

The size effects of mechanics properties of RAC under uniaxial tension loading are shown in table 2.

Table 2. Different sizes of recycled concrete compressive strength under uniaxial tension loading

Different sizes of recycled concrete	Tensile strength/MPa
100mm×100mm×100mm	2.67
150mm×150mm×150mm	2.51
300mm×300mm×300mm	2.30

7. Conclusions

(1) In this paper, a model of the base force element method (BFEM) is proposed for the damage analysis problem and is used to simulate the relations of meso-structure and macro-strength of recycled aggregate concrete (RAC). The characteristics of the BFEM are that the expression of the stiffness matrix $\boldsymbol{K}^{IJ}$ is a precise expression, and it is not necessary to introduce the Interpolation function and the Gauss' integral for calculating the stiffness coefficient at a point. The numerical results show that this method can be used for damage analysis of the RAC.

(2) In order to simulate the meso-structure of recycled concrete material, the recycled aggregate concrete is taken as five-phase composites consisting of natural coarse aggregate, new mortar, new interfacial transition zone (ITZ) , old mortar and old ITZ on meso-level in this paper. The random aggregate model is used for the numerical simulation of uniaxial tensile performance of recycled aggregate concrete. The results by the BFEM show that the uniaxial tensile strengths of specimens are approximately coincident with the experiment results, and the size effect of specimens is agree with the common rule.
(3) The numerical simulation provides a new way for research on mechanical properties of recycled aggregate concrete.

Acknowledgements

This work is supported by the National Science Foundation of China, No. 10972015, 11172015.

References

[1] Du, X. L., Tian, R. J. Peng, Y. J. and Tian, Y. D. (2008). Numerical simulation on the three-graded concrete beam under dynamic loading. *World Earthquake Engineering*, 24(1), 1-5.
[2] Gao, Y. C. (2003). A new description of the stress state at a point with applications. *Archive of Applied Mechanics* , 73(3-4): 171-183.
[3] Liu, G. T. and Wang, Z. M. (1996). Numerical simulation of fracture of concrete materials using random aggregate model. *Journal of Tsinghua University (Science and Technology)*，36(1), 84-89. (in Chinese)
[4] Peng, Y. J., LI, B. K. and Liu, B. (2001). Numerical simulation of the mechanics properties of rolled compacted concrete on meso-level. *Journal of Hydraulic Engineering*, 32(6), 19-22.
Peng, Y. J., Dang, N. N. and Cheng, J. (2011). A method on meso-mechanics analysis for recycled aggregate concrete based on random aggregate model. *Chinese Congress of Theoretical and Applied Mechanics (CCTAM2011)*, 1-6. (in Chinese)
[5] Peng, Y. J. and Jin, M. (2006). New complementary finite-element method based on base forces. *Chinese Journal of Applied Mechanics*, 23(4), 649-652. (in Chinese)
[6] Peng, Y. J. and Jin, M. (2007a). Application of the Base Forces concept in finite element method on potential energy principle. *Journal of Beijing Jiaotong University*, 31(4), 1-4. (in Chinese)
[7] Peng, Y. J. and Jin, M. (2007b). A New Finite Element Method on Potential Energy Principle by Base Forces. *Journal of Beijing University of Technology*, 33(7), 687-692. (in Chinese)
[8] Peng, Y. J. and Jin, M. (2007c). Finite element method for arbitrary meshes based on complementary energy principle using the base forces. *Engineering Mechanics*, 24(10), 41-45. (in Chinese)
[9] Peng, Y. J. and Liu, Y. H. (2009). Base force element method of complementary energy principle for large rotation problems. *Acta Mechanica Sinica*, 25(4), 507-515.
[10] Peng, Y. J., Dong, Z. L., Peng, B. And Liu, Y. H. (2011). Base force element method (BFEM) on potential energy principle for elasticity problems. *International Journal of Mechanics and Materials in Design*, **7**(3): 245-251.
[11] Peng, Y. J., Dong, Z. L., Peng, B., Zong, N. N. (2012). The application of 2D base force element method (BFEM) to geometrically nonlinear analysis. *International Journal of Non-Linear Mechanics*, 47(3), 153 – 161.
[12] Schlangen, E. and Van Mier, J. G. M. (1992). Simple lattice model for numerical simulation of fracture of concrete materials and structures. *Materials and Structures*, 25(9), 534-542
[13] Schlangen, E., and Garbocai, E. J. (1997). Fracture simulations of concrete using lattice models: computational aspects. *Engineering Fracture Mechanics*, 57(2/3), 319-322.
[14] Walraven, J. C. and Reinhardt, H. W. (1981). Theory and experiments on the mechanical behavior of cracks in plain and reinforced concrete subjected to shear loading. *HERON*, **26**(1A), 1-68.

[15] Wittmann, F. H., Roelfdtra, P. E. and Sadouki, H. (1984). Simulation and analysis of composite structures. *Material Science Engineering*, 68(1), 239-248.
[16] Xiao, J. Z., Du, J. T. and Liu, Q. (2009). Numerical Simulation on Stress-Strain Curve of Recycled Concrete under Uniaxial Compression with Lattice Model. *Journal of Building Materials*, 12(5), 511-514. (in Chinese)
[17] Xiao, J. Z., Li, W. G., Fan, Y. H. and Huang, X. (2012). An overview of study on recycled aggregate concrete in China (1996-2011). *Construction and Building Materials*, 31(1), 364-383.

Identification of fracture process under moisture variation in wood materials

Frédéric Dubois[1,*], **Rostand Moutou Pitti**[2,3,4], **Eric Fournely**[2,3], **Destrebecq JF**[2,3]

[1] Heterogeneous Material Research Group, Civil Engineering and Durability department, University of Limoges, Egletons, 19300, France
[2] Clermont Université, Université Blaise Pascal, Institut Pascal, BP 10448, F-63000 CLERMONT-FERRAND, France
[3] CNRS, UMR 6602, IP, F-6317, Aubière, France
F-63000, Clermont-Ferrand, France
[4] CENAREST, IRT, BP 14070, Libreville, Gabon
* Corresponding author: frédéric.dubois@unilim.fr

Abstract The instantaneous fracture of wood material is commonly the source of important accident in the mechanical industries and civil engineering structures. This fact proves that it is necessary to propose a model capable to identify or predict the crack initiation in such materials. In this work, an analytical and numerical model taking into account the stress relaxation coupled with hygrothermal effects and an ageing viscoelastic behavior is proposed. This approach includes shrinkage – swelling effects with orthotropy properties in the radial and transversal directions. This model is applied to a green wood slice during the natural drying process. The viscoelastic properties inducing a partial hydric stress relaxation and a finite element model is proposed based on a orthotropic generalized Kelvin Voigt model taking into account a moisture content dependence on its rheological properties as mechano-sorptive effects. The fracture criterion is introduced according to the Tsai-Wu or Hill approaches rewritten in terms of energy criterion and the numerical model allows to focusing the crack growth initiation localization. Some experimental results are compared with numerical modeling to predict the shrinkage process integrating the crack growth initiation.

Keywords Green wood drying, experimental characterization, finite element method, crack growth initiation

1. Introduction

Aided by its environmental benefits, the wood material is widely used in engineering structures and also, in civil and industrial buildings. As structure element, this material is often machined after drying but also immediately after cutting as green wood. However, the natural or artificial shrinkage due to drying process is commonly responsible of deformations and crack appears in wood pieces or timber structures [1]. Among these deformations, the cup, twist, crook and bow are defects due to the moisture variations, and are even more marked on the wood pieces cut up and stored outdoor during a long time. These behaviors are mainly reinforced by the environmental effects, but also by the orthotropic nature, the heterogeneous aspect, and the anisotropic character of the wood material. In this fact, it is essential, for the lumber, to investigate the different processes that lead to these phenomena in this shape of green wood during the drying.

After the tree felling, the wood log starts a drying phase. Initially, we note the diffusion of the free water molecules to reach the fiber saturation point. In a second step, the bound water migrates from the wood heart until the surface. During this phase, wood is subject to shrinkage swelling effect. The orthotropic properties in the radial tangential plane causes strain blockings inducing hygrothermal stresses. Moreover, in the hygroscopic domain, elastic properties are characterized by a moisture content dependence. The coupling between a tension stress increasing and the elastic property evolutions induce a mechano-sorptive process. Simultaneously, during the tree growth, it is usually observed a mechanical state distribution providing maturation stresses.

The moisture content of freshly felled timber varies enormously, so that in the literature, the deformations and the evolution of drying-induced stresses in wood are studied according numerous methods. Thus, analytical approaches have been developed by Cave [2]. Also, the theoretical expression taking into account the drying time of thin lumber has been developed by Bekhta et al. [3]. Dubois et al. [4] have proposed the analytical approach of elastic response in wood under

moisture content variations. In addition, numerical modeling has been used in order to model the alteration of mechanical properties of wood during drying phase or to study the shape of sawn timber subjected to moisture variation. Simultaneously, several authors have coupling numerical and experimental techniques to analyze the shrinkage . Among them, Kowalski et al. [6] have shown the efficiency of the analytical approach for the identification of fracture process in dried wood based on acoustic emission technique; Kowalski et al. have also presented a model of drying providing the evaluation of moisture content distribution in wood during the drying rate periods, with the moisture content at the body surface reaches the fiber saturation point (FSP). In this work, the radial and tangential strains (inducing crack process) due to the natural drying of a green wood slice are investigated by analytical, experimental and numerical methods.
The first part of the paper recalls the experimental setup composed of a green wood slice in Douglas, a high-sensitivity balance and a video camera. The device is based on the mark tracking method composed of an acquisition system date recording the displacement of targets posted on the wood slice during the drying phase. Simultaneously, the sample is placed on an electronically balance providing the weight measure versus time. The second part details the analysis of experimental results; in this case, the evolution of moisture content versus time is posted in order to obtain the PSF. The radial and transversal strains are computed according to an analytical approach based on a mathematical model coming from cylindrical strain calculations. In the last part, this analytical method is coupling with the swelling-shrinkage tensor taking into account an orthotropic configuration. The finite element calculation is limited, in this paper, at an elastic behavior integrating a mechano-sorptive effect. Also the actual numerical model predicts the cracking due to the transversal shrinkage.

2. Experimental setup

The experimental protocol is based on a green wood slice in Douglas fir with a thickness of 30mm just peeled. Sample is initially conditioned in water in order to assure its saturation. As shown in Figure 1, the preparation of the specimen consists of drawing black marks according to a polar reference centered at the sample heart. In a second step, the sample is placed in the experimental chamber in which the temperature of 22°C and a relative humidity of 33%RH are maintained constant. The sample is placed on a precision balance in order to measure the masse evolution during the drying process. In the same time, black marks allow performing a marking tracking protocol in order to record displacements of these marks using the videometric technology [18]. Versus time, sample mass, displacements and the crack evolution are simultaneously recorded until the mass stability corresponding to the moisture content balance. In order to evaluate the average value of moisture content, samples are placed in a 103°C environment by using an oven.

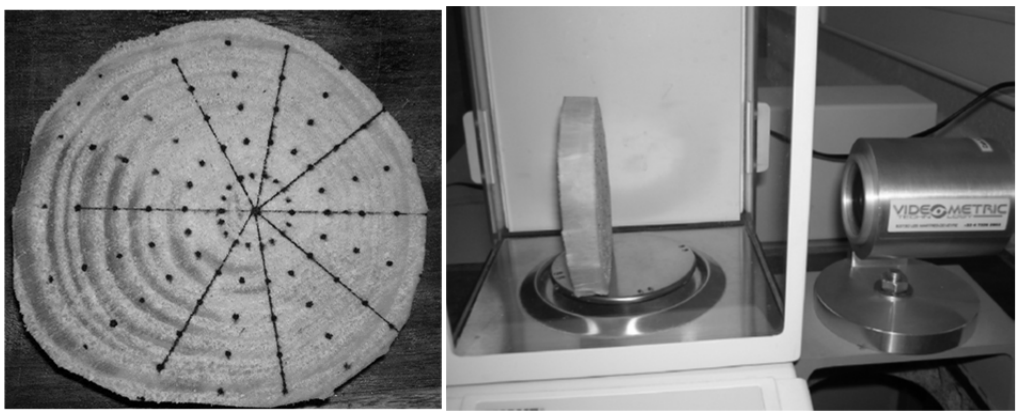

Figure 1. Experimental sample and device

3. Experimental result analysis

3.1. Moisture content evolution

The first results concern the moisture content evolution during drying tests. The graphic in Figure 1 is characterized by a first linear evolution corresponding to the free water migration. At the end of test, we can observe the moisture content equilibrium around 8%. While shrinkage swelling effect start below the fiber point saturation, it is necessary to detect this point. Assuming that the fiber point saturation gives a non linearity in the time moisture content curve, a zoom of the last graph provides an estimation of the specific moisture content value of 30% corresponding to the point saturation fiber limit. This value is further confirmed by studying strain deformations,

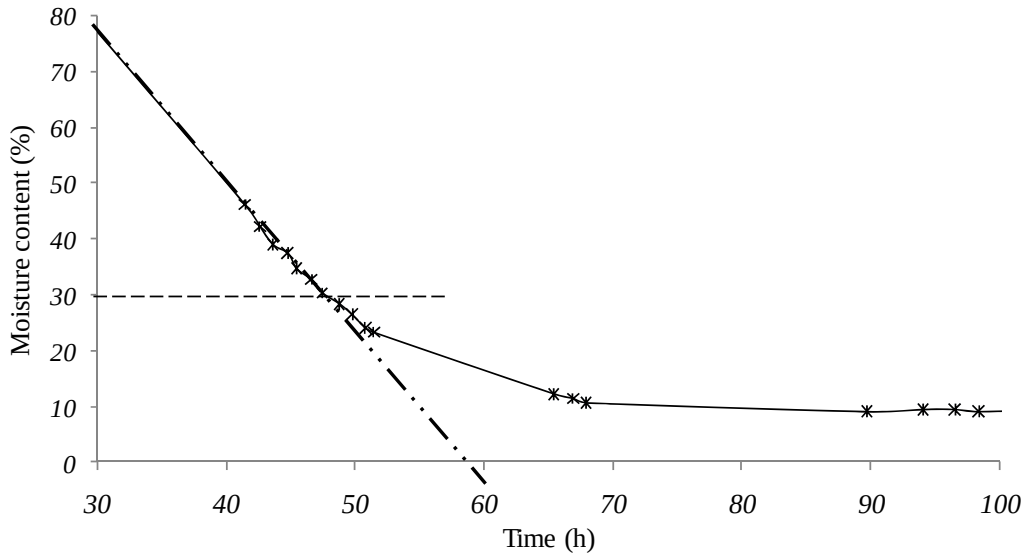

Figure 2. Moisture content evolution and fiber point saturation localization

3.2. Strain evolution

The mark tracking method allows the calculation of displacements of each black mark center. The mechanical exploration requests the definition of strains and, more precisely, radial and tangential components. With this consideration, a specific derivation of displacement fields must be operated. Let us consider a perfect circular slice with a polar referential centered at this center, Figure 3. M' is the image of the displacement of M.

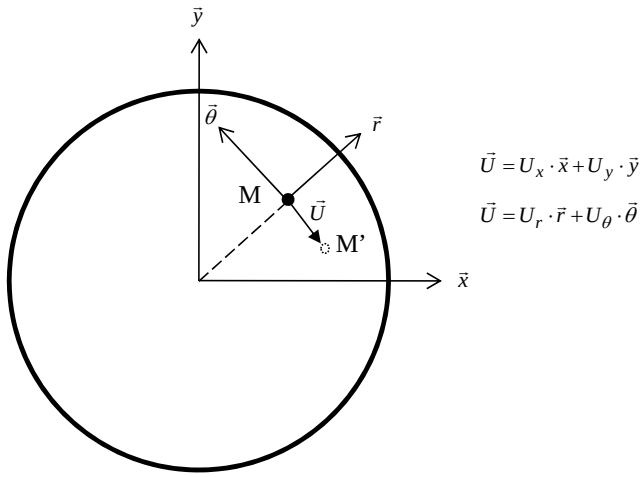

Figure 3. Polar referential in a perfect circular slice

In order to identify each black mark, Figure 4 proposes a notification by the intersection between

radiuses and rings. For example, the mark M_i^j is the point at the intersection between the radius R_i and the ring or crown C_j. Let us note that radial and tangential strains are defined at the middle point comprised between M_1 and M_2. According to this remark, the radial strain is calculated at the point M_2^{1-2} corresponding to a point placed in the radius n°2 and between rings 1 and 2.

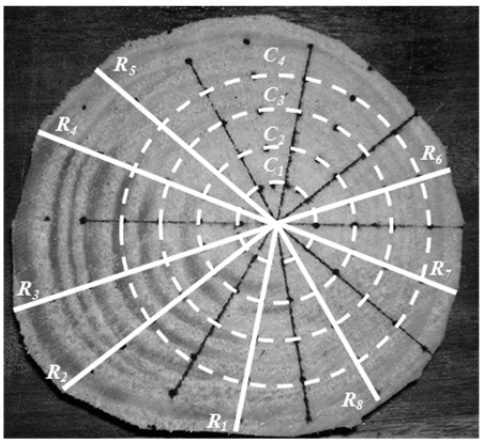

Figure 4. Notification of radius and rings

With the same way, the tangential strain is calculated at the point M_{2-3}^2 placed in the ring n°2 and between radiuses 2 and 3. Figures 5 presents radial strains along radius n°3.

show strain evolution along intermediary radius.

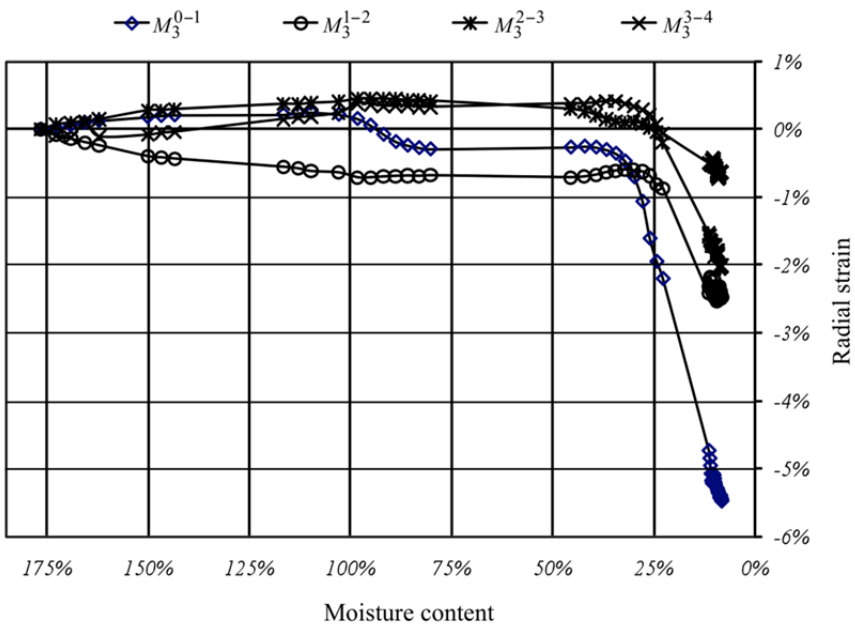

Figure 5. Radial strain along radius n°3

Experimental tangential strains are measured along crowns C_1 to C_5. Firstly, results are presented in terms of tangential strain evolution versus time for points M_{i-j}^l placed in the intersection of crown C_l and the radius comprised between radius R_i and R_j. Figure 6 and 7 show strain evolution along intermediary radius.

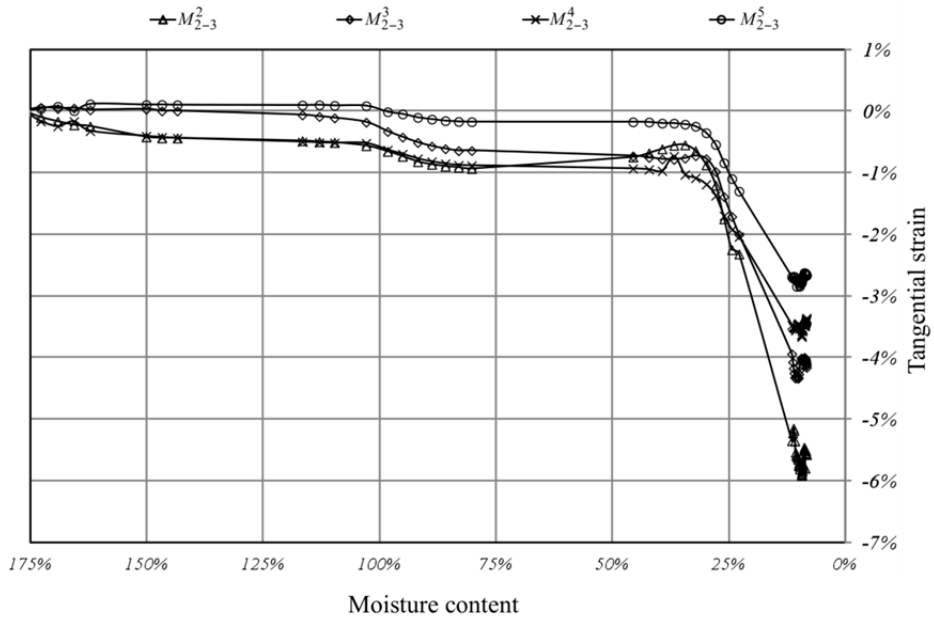

Figure 6. Tangential strains for radius comprised between R_2 and R_3

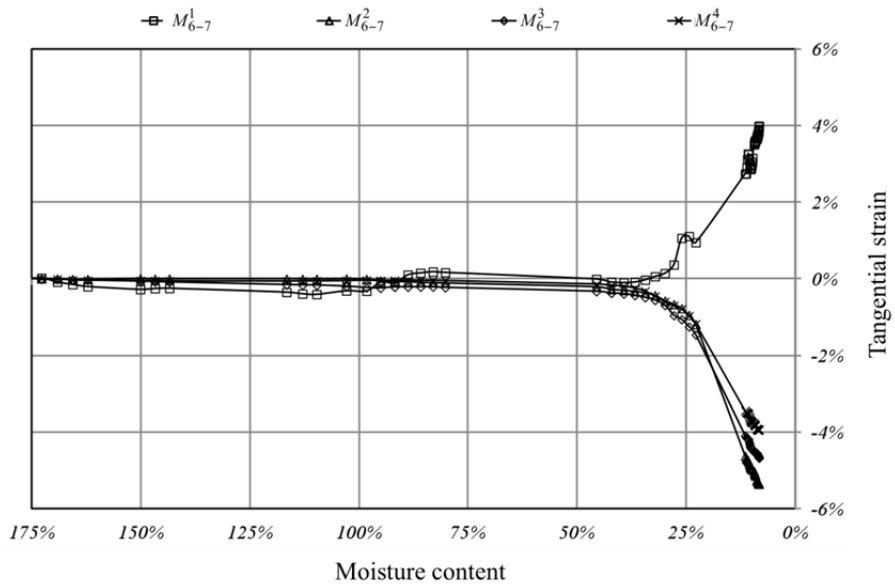

Figure 7. Tangential strains for radius comprised between R_6 and R_7

These results can highlight few points:

- The tangential strains are, in the whole, in a compression increasing during drying process.
- At a moisture content level, the tangential strain seems increasing at the sample center
- An heterogeneity can be observed around the crack initiation vicinity
- Around 18% of moisture content, we can observe a jump of tangential strain valued near the radius R_1 and R_7 near the sample edge which can be explain by the crack growth initiation.

4. Finite element approach

The simulation of the drying process in free disk requests the development of a specific model

taking into account different mechanical behavior such as shrinkage-swelling effects, the elastic property dependence on moisture content and the material orthotropy.

4.1. Mechano-sorptive model

The coupling between moisture content variations and mechanical behavior is based on the addition of shrinkage-swelling response and mechano-sorptive behavior. During drying process, Gril et al. and Husson et al. has putted in evidence one hygro-lock effect affecting elastic and viscoelastic responses [4]. According to a creep representation, the mechanical model can be assimilated by a generalized Kelvin Voigt model in which each springs accept an elastic hygro-lock behavior completed by an uncoupled shrinkage-swelling element as shown in Figure 8 in its uniaxial form.

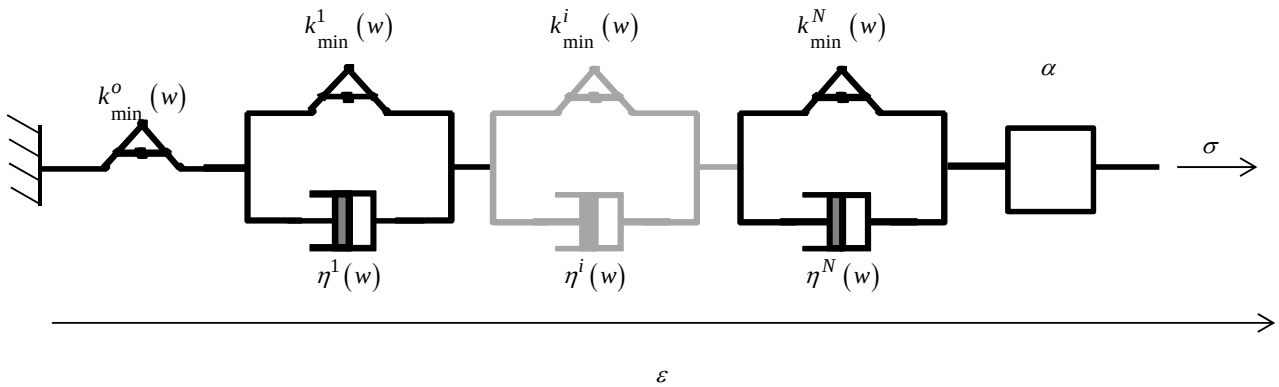

Figure 8. Generalized Kelvin Voigt model with hygro-lock properties

The generalized mechano-sorptive behavior is defined according to the following hereditary integral form:

$$\varepsilon(t)=\int_0^t \frac{1}{k^o_{\min}(\tau,t)}\cdot\frac{\partial\sigma}{\partial\tau}d\tau+\sum_{i=1}^{N}\int_0^t\left[\int_\tau^t \frac{1}{\eta^i(\vartheta)}.\exp^{-\int_\tau^\vartheta \frac{k^i_{\min}(\alpha,t)}{\eta^i(\alpha)}.d\alpha}.d\vartheta\right]\cdot\frac{\partial\sigma}{\partial\tau}.d\tau+\int_0^t \alpha\cdot\frac{\partial w}{\partial\tau}\cdot d\tau \qquad (1)$$

4.2. Incremental formulation

The finite element implementation requests a time incremental formulation allowing the integration, step by step, of the hereditary behavior induced by viscoelastic and hygro-lock effects. The incremental formulation is developed in order to simplify the integral calculus by summarizing complete past history in an additional variable. In this case, the numerical algorithm requests to update mechanical field during a time increment. Let us introduce a time discretization as follow:

$$t_n = t_{n-1} + \Delta t_n \qquad (2)$$

At the time t_n, the strain and mechanical stress can be defined from their value at the time t_{n-1} such as

$$\varepsilon(t_n)=\varepsilon(t_{n-1})+\Delta\varepsilon_n \quad \text{and} \quad \sigma(t_n)=\sigma(t_{n-1})+\Delta\sigma_n \qquad (3)$$

$\Delta\varepsilon_n$ and $\Delta\sigma_n$ are increments of strain and mechanical stress during the time step Δt_n, respectively. The incremental formulation consists on the evaluation of the strain increment according to the following constitutive equation:

$$\Delta\varepsilon_n = A_n \cdot \Delta\sigma_n + \tilde{\varepsilon}\left(t_{n-1}\right) \tag{4}$$

A_n is a pseudo compliance function which enables us to traduce the instantaneous strain response induced by the mechanical stress increment. $\tilde{\varepsilon}_{n-1}$ is the complete past history effects of moisture content and loadings on strains. Finally, the finite element structuring integrates the orthotropic properties in the radial tangential referential. In this condition, the uniaxial incremental formulation (4) can be generalized in the following finite element form:

$$\Delta\underline{\underline{\varepsilon}}_n = \mathbf{A} \cdot \Delta\underline{\underline{\sigma}}_n + \tilde{\underline{\underline{\varepsilon}}}\left(t_{n-1}\right) \tag{5}$$

$\Delta\underline{\underline{\varepsilon}}_n$ and $\Delta\underline{\underline{\sigma}}_n$ designate increments of strain and stress tensors, respectively. In order to solve this equation by a finite element algorithm, let us employ the technique proposed by Ghazlan et al. which is derived from the virtual work principle. If the nodal displacement vector increment is noted $\left\{\Delta U\left(t_n\right)\right\}$, the balance equation, in the discretized domain V, can be written as follow

$$\mathbf{K}_T \cdot \left\{\Delta U\left(t_n\right)\right\} = \left\{\Delta F^{ext}\left(t_n\right)\right\} + \left\{\Delta\tilde{F}\left(t_{n-1}\right)\right\} \tag{6}$$

$\mathbf{K}_T$ is an equivalent tangent matrix assembled from the tensor $\mathbf{A}$.

4.3. Finite element results

As shown in Figure 9, the finite element mesh is realized according to a global positioning system centered on the heart specimen allowing defining the center of the cylindrical orthotropic reference. The contact surface between specimen and balance is operated by blocking its vertical displacements. A referential point is also blocked in its vertically in order to eliminate a rigid body displacement. We assume a perfect slice of this surface according to isostatic boundary conditions. Specific lines (radius and crowns) have been integrated in mesh in order to have a concordance with experimental black mark displacements, Figure 1.

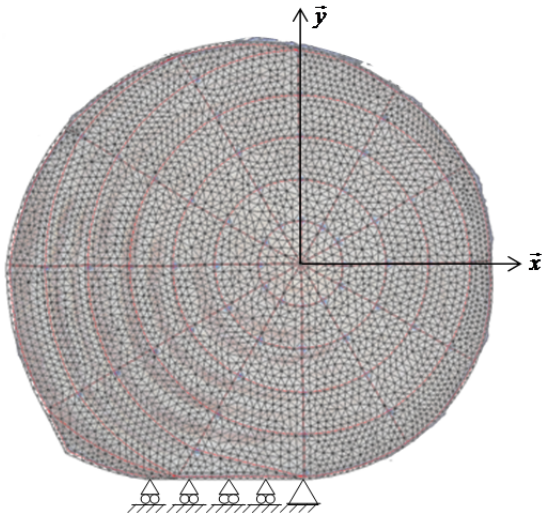

Figure 9. Finite element mesh

According to the last finite element algorithm, mechanical fields are computed versus moisture content level with an increment of 1%. In accordance with Figure 2, the fiber saturation point is assumed to be around 30% inducing representative strain evolutions. All mechanical fields are calculated in the local orthotropic system. For a final moisture content of 8% corresponding to the crack growth initiation, the numerical displacements are plotted in Figure 10 with an amplification factor of 2.

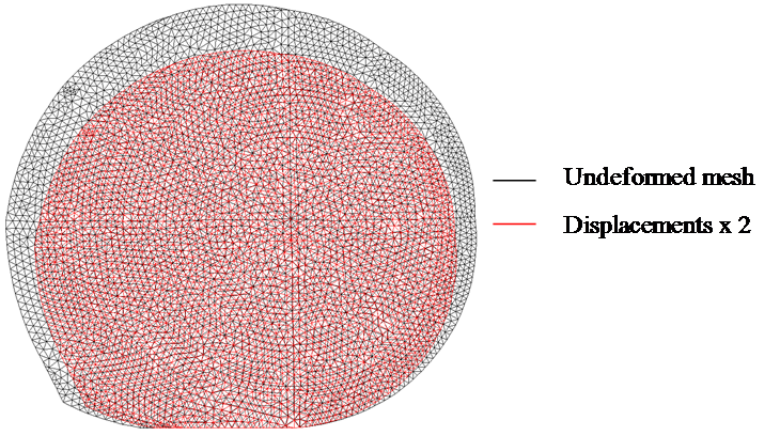

Figure 10. Finite element displacements

Figures 11 and 12 present the comparison between radial and tangential strains given by finite element approach and experimental data. In order to clarify visibility, we choose to represent experimental measurements for extreme rings for radius n°6. For radius n°6, we can observe a very good agreement between experimental and simulation results. However, the results in terms of tangential strains present differences induced by the development of a crack in the end of test. At the moisture content of 8%, mappings of σ_{RR}, σ_{TT} and σ_{RT} are posted in Figures 13 to 15. About radial stresses, we can observe an evolution of heart (compression state) toward outside (tension state) with a radial homogeneity. The combination of tangential and shear stresses illustrates that the crack growth initiation is based on a coupling between tangential tensions and shear state according to a mixed mode configuration.

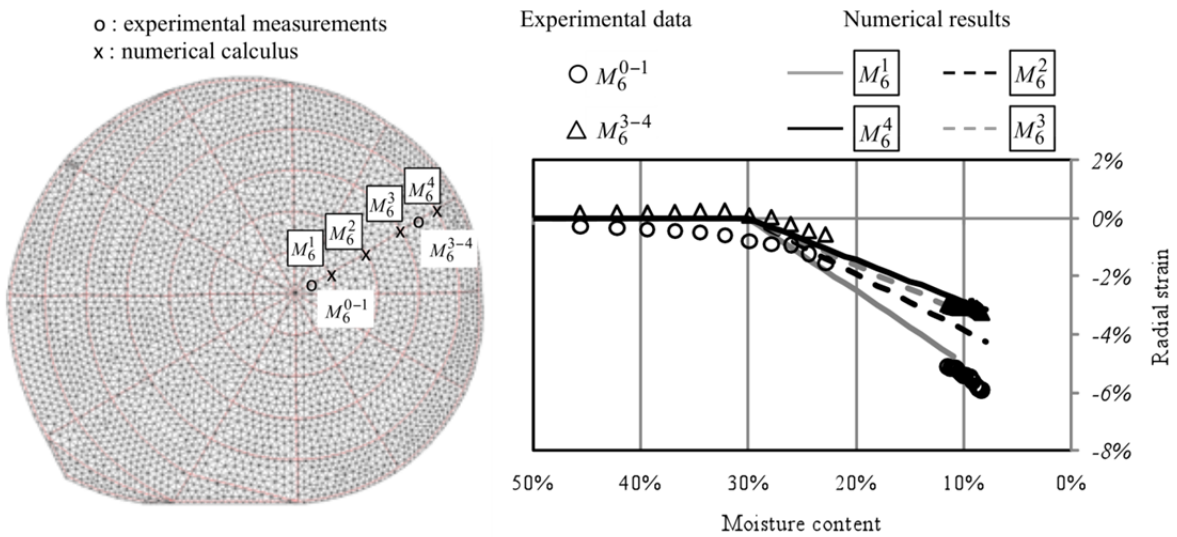

Figure 11. Comparison between experimental and numerical radial strains along radius n°6

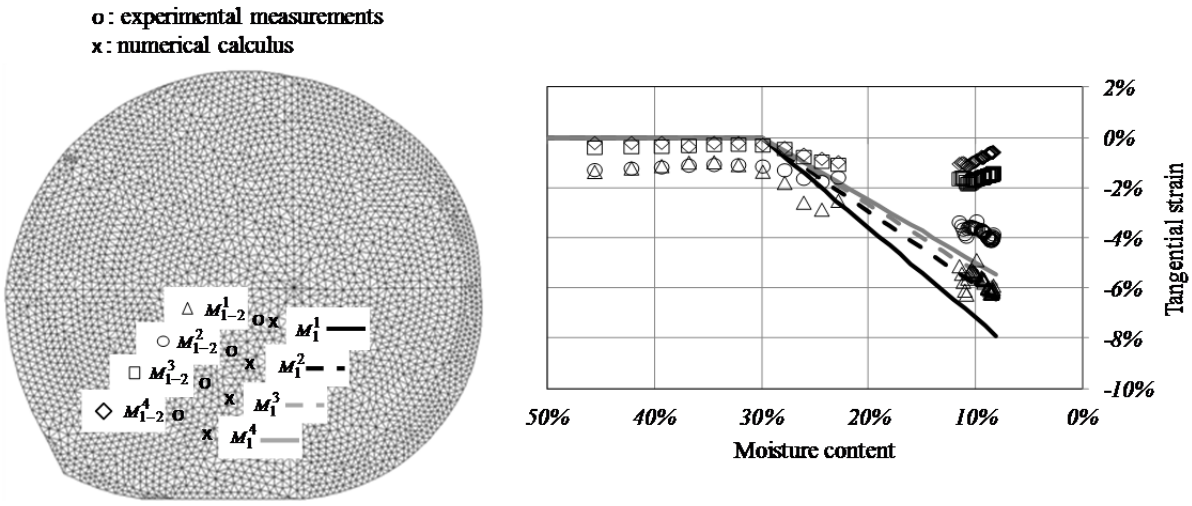

Figure 12. Comparison between experimental and numerical tangential strains along radius n°1

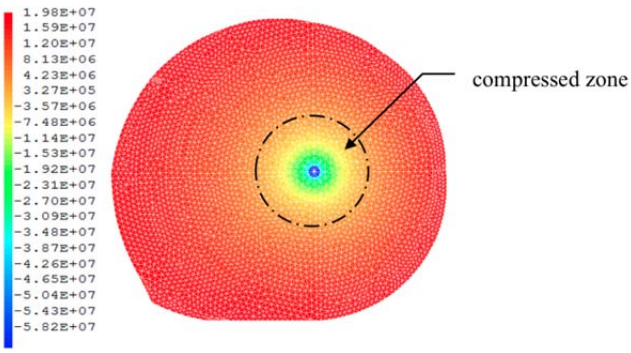

Figure 13. Radial stress mapping at 8% of moisture content

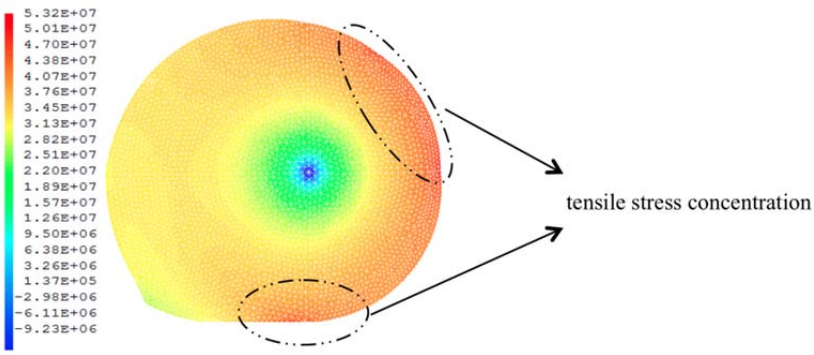

Figure 14. Tangential stress mapping at 8% of moisture content

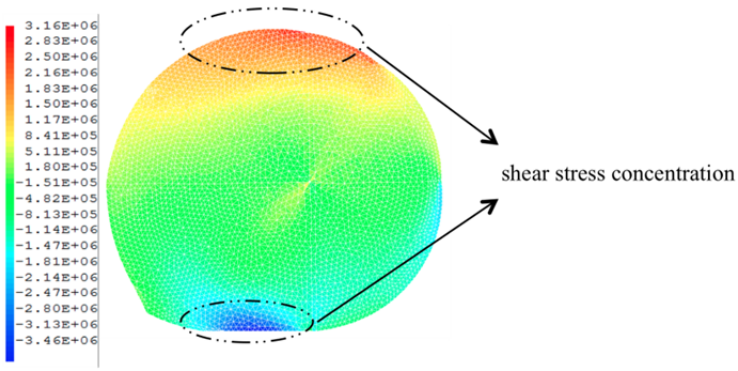

Figure 15. Shear stress mapping at 8% of moisture content

By considering a classical Tsai-Wu's criterion written in a stress form, the Figure 16 shows us the mapping of the function f by noting its concentration in the crack growth zone vicinity.

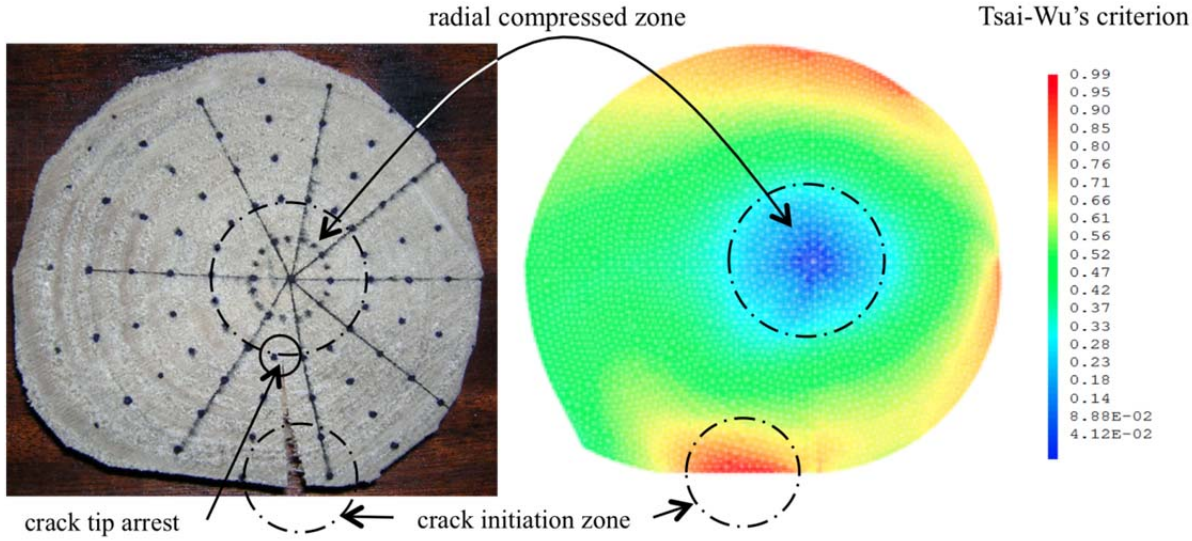

Figure 16. Shear stress mapping at 8% of moisture content

5. Conclusion

The strain and fracture process due to the natural drying of green wood slice have studied in this work. The experimental device, composed of a sensitively balance, a video camera, a slice with tracked, have provided to own the displacement in the slice axis during drying phase. The experimental protocol is completed with a numerical model integrating mechano-sorptive effect. In this context, a finite element model based on an incremental formulation is developed. By using comparisons between finite element results and experimental marker tracking data, the stress field is computed in the cylindrical orthotropic radial-transverse reference by taking into account cylindrical defects induced by conditions of the tree growth. By performing a strength criterion based on Tsai-Wu or Hill approaches, the numerical model allows to focusing the crack growth initiation localization.

References

[1] A.P. Schniewind, R.A. Pozniak, On the fracture toughness of Douglas fir wood, Engineering Fracture Mechanic, 1971, 223–230.
[2] I.D. Cave, A theory of the shrinkage of wood, Wood Science and Technoly, 1972, (6), 284-292.
[3] P. Bekhta, I. Ozarkiv, S. Alavi, S. Hiziroglu, A theoretical expression for drying time of thin lumber, Bioresource Technoly, 2006, (97), 1572–1577.
[4] F. Dubois, J. M. Husson, N. Sauvat, N., Manfoumbi Modeling of the viscoelastic, mechano-sorptive behavior in wood, Mechanics of Time Dependent Materials, doi: 10.1007/s11043-012-9171-3, 2012.
[5] S.J. Kowalski, A. Smoczkiewicz-Wojciechowska, Stresses in dried wood, Modeling and experimentation, Transp Porous Med., 2007, (66), 145-158.

T-stress evaluation in nonhomogeneous materials under thermal loading by means of interaction energy integral method

Fengnan Guo[1], Licheng Guo[1,*], Hongjun Yu[2]

[1] Department of Astronautic Science and Mechanics, Harbin Institute of Technology, Harbin, 150001,China
[2] Institute of Applied Mathematics, Harbin Institute of Technology, Harbin 150001, China
* Corresponding author: guolc@hit.edu.cn

Abstract This paper addresses finite element evaluation of the non-singular T-stress in nonhomogeneous materials under steady-state thermal loads by means of interaction energy integral method. The interaction energy integral method developed in this paper can solve the T-stress with high accuracy and efficiently in nonhomogeneous materials. The interaction energy integral method in conjunction with the extended FEM is used to solve several representative examples to show its validity. It can be found that the present method is efficiency to calculate the T-stress in nonhomogeneous materials.

Keywords Interaction energy integral, T-stress, Interface, Nonhomogeneous materials

1. Introduction

Stress intensity factors (SIFs) play a significant role in linear elastic fracture mechanics as they characterize the crack-tip stress and strain fields. Apart from the SIFs, the T-stress [1], which is the nonsingular term, has become another key parameter in fracture mechanics because it has been found the T-stress affects the crack growth direction, shape and size of the plastic zone, crack-tip constraint and fracture toughness greatly [2-4].

Many researchers evaluated T-stress when the material is subject to mechanic loading [5-8], however, there are few researches on T-stress when the material is subject to thermal loading. Sladek and Sladek [9] used the conservation integral method to evaluate the T-stress and the stress intensity factors in stationary thermoelasticity. Dag [10] used J integral to evaluate the mix-mode SIFs and the T-stress in FGMs under thermal loading. KC and Kim [11] and Kim and KC [12] have studied the SIFs and T-stress in FGMs under thermal loading using the interaction energy integral method. However, all of the above paper did not consider the situation that the materials contain interfaces.

2. Interaction energy integral formulation

The traditional J-integral given by Rice [13] is

$$J = \lim_{\Gamma_0 \to 0} \int_{\Gamma_0} (W \ \delta_{1j} - \sigma_{ij} u_{i,1}) n_j d\Gamma \tag{1}$$

where W is the strain energy density given by

$$W = \frac{1}{2}\sigma_{ij}\varepsilon_{ij}^{m} = \frac{1}{2}\sigma_{ij}(\varepsilon_{ij}^{t} - \varepsilon_{ij}^{th}) \tag{2}$$

and n_j is the outward normal vector to the contour Γ_0, as shown in Fig. 1, and δ_{ij} is the Kronecker delta. In Eq. (2), ε_{ij}^{m} is the mechanical strain, ε_{ij}^{t} denotes the total strain, $\varepsilon_{ij}^{th} = \alpha\Delta\theta\delta_{ij}$ refers to thermal strain, α represents the thermal expansion coefficient and $\Delta\theta = \theta - \theta_0$ denotes temperature change with θ_0 is the initial temperature.

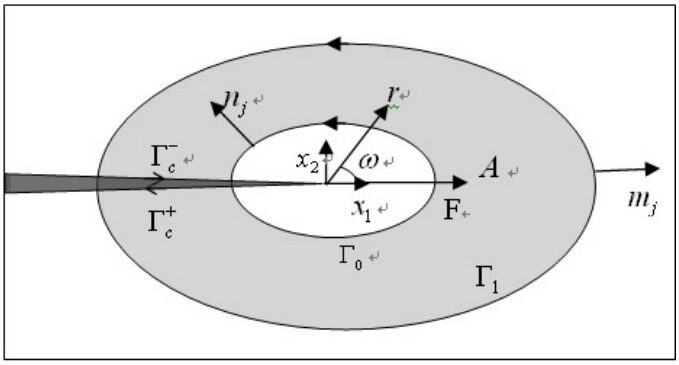

Fig. 1. Schematic illustration of the contour integrals and domain integrals.

The J-integral can be deduced to an equivalent domain integral (EDI) by using the divergence theorem, that is

$$J = \int_A (\sigma_{ij} u_{i,1} - W\ \delta_{1j})_{,j}\, q dA + \int_A (\sigma_{ij} u_{i,1} - W\ \delta_{1j}) q_{,j} dA \tag{3}$$

In the interaction energy integral method, the auxiliary fields, including displacements (u^{aux}), strains (ε^{aux}), and stresses (σ^{aux}) are used. These auxiliary fields need to be suitably defined in order to evaluate T-stress and TSIFs in nonhomogeneous materials. Here we adopt analytical fields originally developed for homogeneous materials and the "incompatible formulation" is chosen in this paper [14].

As shown in Fig.1, there is a point force F applied to the crack tip in an infinite plane. The auxiliary displacement fields and the auxiliary stress fields for T-stress are chosen as follows [11, 12],

$$\begin{aligned} u_1^{aux} &= -\frac{F(\kappa_{tip}+1)}{8\pi\mu_{tip}} \ln\frac{r}{d} - \frac{F}{4\pi\mu_{tip}} \sin^2\omega \\ u_2^{aux} &= -\frac{F(\kappa_{tip}-1)}{8\pi\mu_{tip}} \omega + \frac{F}{4\pi\mu_{tip}} \sin\omega\cos\omega \end{aligned} \tag{4}$$

$$\begin{aligned} \sigma_{11}^{aux} &= -\frac{F}{\pi r}\cos^3\omega \\ \sigma_{22}^{aux} &= -\frac{F}{\pi r}\cos\omega\sin^2\omega \\ \sigma_{12}^{aux} &= -\frac{F}{\pi r}\cos^2\omega\sin\omega \end{aligned} \tag{5}$$

where d is the coordinate of a fixed point on the x_1 axis, μ_{tip} is the shear modulus evaluated at the crack-tip, and

$$\kappa_{tip} = \begin{cases} \dfrac{3-\nu_{tip}}{1+\nu_{tip}} & \text{(plane stress)} \\ 3-4\nu_{tip} & \text{(plane strain)} \end{cases} \tag{6}$$

And the auxiliary strain fields $\varepsilon_{ij}^{aux} = S_{ijkl}(\mathbf{x})\sigma_{kl}^{aux}$, which is incompatible with the auxiliary displacement fields [15]. Since S_{ijkl} is the compliance tensor of the actual materials, not the compliance tensor of the crack tip, it can be got that: $\varepsilon_{ij}^{aux} \neq (u_{i,j} + u_{j,i})/2$.

Superposition of the actual and auxiliary fields leads to a new equilibrium state.

$$J^{1+2}=\int_A((\sigma_{ij}+\sigma_{ij}^{aux})(u_{i,1}+u_{i,1}^{aux})-\frac{1}{2}(\sigma_{ik}+\sigma_{ik}^{aux})(\varepsilon_{ik}^{m}+\varepsilon_{ik}^{aux})\delta_{1j})_{,j}qdA$$
$$+\int_A((\sigma_{ij}+\sigma_{ij}^{aux})(u_{i,1}+u_{i,1}^{aux})-\frac{1}{2}(\sigma_{ik}+\sigma_{ik}^{aux})(\varepsilon_{ik}^{m}+\varepsilon_{ik}^{aux})\delta_{1j})q_{,j}dA \tag{7}$$

The interactional part is called interaction energy integral [14]. Here, it can be derived as

$$I=\int_A(\sigma_{ij}^{aux}u_{i,1}+\sigma_{ij}u_{i,1}^{aux}-\sigma_{ik}^{aux}\varepsilon_{ik}^{m}\delta_{1j})q_{,j}dA$$
$$+\int_A(\sigma_{ij}^{aux}u_{i,j1}+\sigma_{ij}u_{i,j1}^{aux}-\sigma_{ij,1}^{aux}\varepsilon_{ij}^{m}-\sigma_{ij}^{aux}\varepsilon_{ij,1}^{m})qdA \tag{8}$$

According to the relationship of the displacement and strain in elastic mechanics, one may write

$$\sigma_{ij}^{aux}u_{i,j1}=\frac{1}{2}\sigma_{ij}^{aux}(u_{i,j1}+u_{j,i1})=\sigma_{ij}^{aux}\varepsilon_{ij,1}^{t}=\sigma_{ij}^{aux}(\varepsilon_{ij,1}^{m}+\varepsilon_{ij,1}^{th}) \tag{9}$$

The second integral can be obtained as

$$\int_A(\sigma_{ij}^{aux}u_{i,j1}+\sigma_{ij}u_{i,j1}^{aux}-\sigma_{ij,1}^{aux}\varepsilon_{ij}^{m}-\sigma_{ij}^{aux}\varepsilon_{ij,1}^{m})qdA=\int_A(\sigma_{ij}u_{i,j1}^{aux}-\sigma_{ij,1}^{aux}\varepsilon_{ij}^{m}+\sigma_{ij}^{aux}\varepsilon_{ij,1}^{th})qdA \tag{10}$$

If the extra strain field $\varepsilon_{ij}^{aux0}=S_{ijkl}^{tip}\sigma_{kl}^{aux}$ is introduced, we can get the formulation $\varepsilon_{ij}^{aux0}=\frac{1}{2}(u_{i,j}^{aux}+u_{j,i}^{aux})$, Here S_{ijkl}^{tip} is a compliance tensor at the crack tip [15]. Thus, the interaction energy integral can be written as

$$I=\int_A(\sigma_{ij}^{aux}u_{i,1}+\sigma_{ij}u_{i,1}^{aux}-\sigma_{ik}^{aux}\varepsilon_{ik}^{m}\delta_{1j})q_{,j}dA$$
$$+\int_A(\sigma_{ij}(S_{ijkl}^{tip}-S_{ijkl}(x))\sigma_{kl,1}^{aux})qdA+I^{th} \tag{11}$$

where

$$I^{th}=\int_A(\sigma_{ij}^{aux}\varepsilon_{ij,1}^{th})qdA=\int_A\sigma_{ii}^{aux}[\alpha_{,1}(\theta-\theta_0)+\alpha\theta_{,1}]qdA \tag{12}$$

In the above derivation process, the domain of the integral is chosen arbitrarily around the crack-tip, so the interaction energy integral for thermal fracture problems is domain-independent.

3. Evaluation of the T-stress from the interaction energy integral

The contour integral around the crack tip can be written as

$$I=\lim_{\Gamma_0\to 0}\oint_{\Gamma_0}(\sigma_{ik}\varepsilon_{ik}^{aux}\delta_{1j}-\sigma_{ij}u_{i,1}^{aux}-\sigma_{ij}^{aux}u_{i,1})n_j d\Gamma \tag{13}$$

Here we can consider only the stress parallel to the crack direction, i.e.

$$\sigma_{ij}=T\delta_{1i}\delta_{1j} \tag{14}$$

Where T denotes the T-stress. The force *f* is in equilibrium can be expressed as

$$f=-\lim_{\Gamma_0\to 0}\oint_{\Gamma_0}\sigma_{ij}^{aux}n_j d\Gamma \tag{15}$$

We can also obtain the following relationship from the kinematic equations

$$u_{i,1}=\varepsilon_{11}^{t}\delta_{i1}=(\varepsilon_{11}^{m}+\varepsilon_{11}^{th})\delta_{i1} \tag{16}$$

It can be rewritten as

$$u_{i,1}=(\frac{\sigma_{11}}{E}+\alpha\Delta\theta C^*)\delta_{i1} \tag{17}$$

where $C^*=1$ for generalized plane stress and $C^*=1+\nu(x)$ for plane strain. Substituting Eq. (14) and Eq.(17) into the contour integral, one obtains

$$I=-\lim_{\Gamma_0\to 0}\oint_{\Gamma_0}(\frac{T}{E}+\alpha\Delta\theta C^*)\sigma_{ij}^{aux}n_j d\Gamma=(\frac{T}{E_{tip}^*}+\alpha_{tip}\Delta\theta_{tip}C_{tip}^*)\cdot f \tag{18}$$

Then we can get

$$T = \frac{I}{f} \cdot E_{tip}^{*} - \alpha_{tip} \Delta\theta_{tip} C_{tip}^{*} E_{tip}^{*} \tag{19}$$

Where

$$E_{tip}^{*} = \begin{cases} E_{tip} & \text{(plane stress)} \\ \dfrac{E_{tip}}{1-\nu_{tip}^{2}} & \text{(plane strain)} \end{cases} \qquad C_{tip}^{*} = \begin{cases} 1 & \text{(plane stress)} \\ 1+\nu_{tip} & \text{(plane strain)} \end{cases} \tag{20}$$

So, the T-stress can be evaluated easily if we can obtain the interaction energy integral I. As Yu et al. [15] proved, the equivalent domain integral is not referred to in the above analysis and as a result, both the domain size and the material properties in the integral domain are not limited for the equivalent domain integral.

4. Numerical examples and discussions

To test the validity of the method developed in the above section, two crack problems in nonhomogeneous materials are considered.

Example 1: An edge crack in a homogeneous plate.

An edge crack of length "*a*" is located in a homogeneous plate which subjected to steady-state thermal loading. The temperature boundary of the example is assumed to be $\theta_1 = \theta_0 = 0°C$ and $\theta_2 = 1°C$. This problem have been studied by Sladek and Sladek [9] and KC and Kim [11]. The following data are used for the numerical analysis:

$$L/W = 4,\ \ a/W = 0.1 \sim 0.8,\ \ \nu = 0.3,\ \ E(x) = 1.0\times10^{5},\ \ \alpha(x) = 1.67\times10^{-5},\ \ \lambda = 1$$

Tables 1 present the mode-I TSIFs and the T-stress for various crack lengths. The T-stress obtained is in good agreement with those reported in Sladek and Sladek [9].

Table 1 Comparison of the mode-I TSIF and T-stress in homogeneous materials under thermal loading (Example 1)

a/W	Sladek and Sladek's results		Present results	
	K_1	T-stress	K_1	T-stress
0.1	0.6454	-0.4317	0.6432	-0.4198
0.2	0.776	-0.2179	0.7756	-0.2196
0.3	0.7951	-0.0314	0.7953	-0.0322
0.4	0.7527	0.1463	0.753	0.1489
0.5	0.6705	0.3258	0.6708	0.3295
0.6	0.5601	0.5075	0.5605	0.5142
0.7	0.4288	0.698	0.4291	0.7064
0.8	0.2825	0.896	0.2828	0.9095

Example 2: An edge crack in a FGMs plate.

In this example, an edge crack problem in a FGMs plate is studied. The material properties, Young's modulus and thermal expansion coefficient are exponential functions of x, while Poisson's ratio is

constant. The temperature boundary of the example is assumed to be $\theta_1 = \theta_2 = 0.5\theta_0$ and $\theta_0 = 10°C$.

The following data are used in the FEM analyses:

$$L/W = 8,\ a/W = 0.5,\ E(x) = E_1 \times e^{\frac{\delta x}{W}},\ \alpha(x) = \alpha_1 \times e^{\frac{\gamma x}{W}},\ \lambda(x) = \lambda_1 \times e^{\frac{\beta x}{W}},\ \delta = \ln(\frac{E_2}{E_1}),$$

$$\gamma = \ln(\frac{\alpha_2}{\alpha_1}),\ \beta = \ln(\frac{\lambda_2}{\lambda_1}),$$

$$E_1 = 1.0,\ E_2 = 5,\ \alpha_1 = 0.01,\ \alpha_2 = 0.02,\ \lambda_1 = 1,\ \lambda_2 = 10,\ \nu = 0.3$$

Different element numbers $N_W \times N_L$ (81×648, 101×808 and 121×968) for two different temperature conditions are chosen. The results are shown in Table 2. It can be seen that the present results agree well with the solutions provided by KC and Kim [11]. From these two examples, the convergence and the accuracy of the present method are verified.

Table 2 Comparison of the mode-I TSIF and T-stress in FGMs for different thermal loading (Example 2)

Loading condition	Element numbers	Present results		KC and Kim's results		
		K_1/K_0	T-stress	K_1/K_0	T-stress	3D T-stress
$T_1 = 0.5T_0$	81×648	0.0023	0.00589	0.0229	0.0067	0.006
	101×808	0.0023	0.00592			
	121×968	0.0023	0.00594			
$T_1 = 0.05T_0$	81×648	0.00438	0.01118	0.00437	0.0126	0.0115
	101×808	0.00438	0.01124			
	121×968	0.00438	0.01129			

5. Conclusions

In this paper, a modified interaction energy integral for thermal loading condition is derived for the T-stress computations. The interaction energy integral is proved to be domain-independent for thermal conditions. It can be found that the numerical results are in good agreement with those in published papers. The present method is effective to analyze the thermal fracture problems of nonhomogeneous materials.

Acknowledgements

This work is sponsored by NSFC(11072067), NSFC (10802056), NSFC (11202058), NCET(08-0151), Ph. D Programs Foundation of Ministry of Education of China, Science Funds for Distinguished Young Scholar of Heilongjiang Province, China, SRF for ROCS (SEM), Heilongjiang Science Fund for ROCS and China Postdoctoral Science Foundation (20110491071) and the Fundamental Research Funds for the Central Universities (Grant No. HIT. NSRIF. 2013082).

References

[1] J.R. Rice. Limitations to the small scale yielding approximation for crack tip plasticity. J Mech Phys Solids. 22 (1974) 17-26.

[2] Z.Z. Du, J.W. Hancock. The Effect of Nonsingular Stresses on Crack-Tip Constraint. J Mech

Phys Solids. 39 (1991) 555-67.
[3] S.G. Larsson, Carlson AJ. Influnece of non-singular stress terms and specimen geometry on small scale yielding at crack tips in elastic-plastic materials. . J Mech Phys Solids. 21 (1973) 263-77.
[4] N.P. O'DOWD, C. Shih, R. Dodds. The role of geometry and crack growth on constraint and implications for ductile/brittle fracture. American Society for Testing and Materials. 2 (1995) 134-59.
[5] J.H. Kim, G.H. Paulino. T-stress, mixed-mode stress intensity factors, and crack initiation angles in functionally graded materials: a unified approach using the interaction integral method. Comput Method Appl M. 192 (2003) 1463-94.
[6] C.S. Chen, R. Krause, R.G. Pettit, L. Banks-Sills, Ingraffea AR. Numerical assessment of T-stress computation using a p -version finite element method. Int J Fracture. 107 (2001) 177-99.
[7] A. Sutradhar, G.H. Paulino. Symmetric Galerkin boundary element computation of T-stress and stress intensity factors for mixed-mode cracks by the interaction integral method. Eng Anal Bound Elem. 28 (2004) 1335-50.
[8] G.H. Paulino, J.H. Kim. A new approach to compute T-stress in functionally graded materials by means of the interaction integral method. Eng Fract Mech. 71 (2004) 1907-50.
[9] J. Sladek, V. Sladek. Evaluation of T-stresses and stress intensity factors in stationary thermoelasticity by the conservation integral method. Int J Fracture. 86 (1997) 199-219.
[10] S. Dag. Mixed-mode fracture analysis of functionally graded materials under thermal stresses: A new approach using J(k)-integral. J Therm Stresses. 30 (2007) 269-96.
[11] A. KC, J.H. Kim. Interaction integrals for thermal fracture of functionally graded materials. Eng Fract Mech. 75 (2008) 2542-65.
[12] J.H. Kim, A. KC. A generalized interaction integral method for the evaluation of the T-stress in orthotropic functionally graded materials under thermal loading. J Appl Mech-T Asme. 75 (2008).
[13] J.R. Rice. A path independent integral and the approximate analysis of strain concentration by notches and cracks. J Appl Mech-T Asme. 35 (1968) 379-86.
[14] H.J. Yu, L.Z. Wu, L.C. Guo, S.Y. Du, Q.L. He. Investigation of mixed-mode stress intensity factors for nonhomogeneous materials using an interaction integral method. Int J Solids Struct. 46 (2009) 3710-24.
[15] H.J. Yu, L.Z. Wu, L.C. Guo, H. Li, S.Y. Du. T-stress evaluations for nonhomogeneous materials using an interaction integral method. Int J Numer Meth Eng. 90 (2012) 1393-413.

Torsional properties of bamboo-like structured Cu nanowires

Haifei Zhan and Yuantong Gu*

School of Chemistry, Physics and Mechanical Engineering,
Queensland University of Technology, Brisbane, QLD, 4001, Australia
* Corresponding author: yuantong.gu@qut.edu.au

Abstract Recently, researchers reported that nanowires (NWs) are often polycrystalline, which contain grain or twin boundaries that transect the whole NW normal to its axial direction into a bamboo like structure. In this work, large-scale molecular dynamics simulation is employed to investigate the torsional behaviours of bamboo-like structured Cu NWs. The existence of grain boundaries is found to induce a considerably large reduction to the critical angle, and the more of grain boundaries the less reduction appears, whereas, the presence of twin boundaries only results in a relatively smaller reduction to the critical angle. The introduction of grain boundaries reduces the torsional rigidity of the NW, whereas, the twin boundaries exert insignificant influence to the torsional rigidity. NWs with grain boundaries are inclined to produce a local HCP structure during loading, and the plastic deformation is usually evenly distributed along the axial axis of the NW. The plastic deformation of both perfect NW and NWs with twin boundaries is dominated by the nucleation and propagation of parallel intrinsic stacking faults. This study will enrich the current understanding of the mechanical properties of NWs, which will eventually shed lights on their applications.

Keywords Grain Boundary, Twin Boundary, Nanowire, Torsion, Molecular Dynamics

1. Introduction

Metal and semiconductor nanowires (NWs) have been widely utilized as active components of nanoelectromechanical systems (NEMS) due to their extraordinary mechanical, electrical, optical and thermal properties, such as high frequency resonators, field effect transistors (FETs), and other devices [1]. Hence, a comprehensive understanding of the mechanical properties of NWs is increasingly required. There have been a number of experimental, theoretical and computational studies on the properties of NWs. On the experimental front, researchers have studied the mechanical behaviours of NWs under bending, tension, compression and vibration. On the theoretical and computational front, either surface-based extensions of continuum elasticity theory [2] or multi-scale computational techniques [3] has been employed to investigate the mechanical properties of NWs. Besides, molecular dynamics (MD) simulations has also being frequently adopted to explore structure-property relationship for NWs under different loading conditions [4-7].

It is noticed that most of current studies have focused on mono-crystalline NWs due to the decreased possibility of defects and flaws in nanoscale materials. However, recent experimental studies reveal that NWs also contain certain defects. For instance, metal NWs are found usually polycrystalline, containing grain boundaries (GBs) that transect the whole NW normal to its longitudinal axis into a bamboo structure [8]. Sansoz et al. [9] revealed that, twin boundaries (TBs) are ubiquitous for both synthesis and properties in nano-enhanced FCC metals. Therefore, understanding the influence from GBs or TBs to the properties of NWs is crucial to enhance/realize their applications. There have been a number of studies on the mechanical behaviours of defected

NWs either with GBs, TBs or pre-existing defects. For example, Cao et al. [10] demonstrated that, polycrystalline Cu NWs exhibit tensile deformation behaviour distinctly different from their single crystal counterparts. A serial of investigation on the twinned Cu NWs under tensile deformation has been conducted by Cao and his group members [11]. Au and other metal NWs with twin boundaries have also been extensively studied by Sansoz and his group members [12]. The influence of different pre-existing defects on the mechanical properties of metal NWs under tension [13, 14], compression [15] have also been investigated. It is noticed that majority of current studies on polycrystalline NWs have emphasized on the mechanical properties under uniaxial loading conditions, and the study of their mechanical performance under torsion is still lack in the literature. Thus, we perform a comprehensive investigation of the influence from GBs or TBs on the torsional properties of Cu NWs using large-scale MD simulations in the present work.

2. Computational details

Large-scale MD simulations were carried out on bamboo-like polycrystalline Ag NWs with square cross-section, which were constructed either with GBs or coherent TBs. In detail, the bamboo-like NW with GBs were generated according to the work by Cao et al. [10], i.e., the <100> crystalline direction is chosen as the misorientation axis, and the GBs separating individual grains are ∑5(310)36.9° symmetric high-angle tilt GBs, which has a high density of coincident atomic sites across the interface (see Fig. 1a). This structure has also been experimentally observed [16] and studied using numerical simulations [10] by previous researchers. We considered a serial of such NWs that contain different numbers of GBs with an identical size (4.34 nm×4.57 nm×46.64 nm) and constant grain boundary spacing (GBS). Specifically, GBs numbers including 0, 1, 3, 4 and 9 were considered which leads the GBS ranging from 4.57-11.43 nm (that is comparable to the experimentally investigated grain size of 5-40 nm). Similarly, for the bamboo-like NW with (111) coherent TBs, a serial of NWs that contain different numbers of TBs (i.e., 0, 1, 3, 4 and 9) and a constant twin boundary spacing (TBS) were considered, with the TBS ranging from 6.26-15.65 nm (see Fig. 1b). The size of the NW was uniformly chosen as 5.90 nm×6.13 nm×63.87 nm. We modelled Cu using the embedded-atom-method (EAM) potential developed by Foiles et al. [17]. This potential was fitted to a group of parameters, including cohesive energy, equilibrium lattice constant, bulk modulus, and others [18].

During each simulation, the NW was first created assuming bulk lattice positions, and then relaxed to a minimum energy state using the conjugate gradient algorithm, i.e. the length of the NW was allowed to decrease in response to the tensile surface stress. We then used the Nose-Hoover thermostat [19, 20] to equilibrate the NW at a constant temperature 10 K (NVT ensemble) for 400 ps at a time step of 4 fs while holding the newly obtained length of the NW fixed. Finally, a pair of constant torsional loads was applied to the two ends of the NW as schematically shown in Fig. 1a. No periodic boundary conditions were utilized at any point during the simulation process. The overall simulation methodology to study the torsional properties of the NWs is identical to that used previously for mono-crystalline Cu NWs [21]. All simulations were performed using the open-source LAMMPS code developed at Sandia National Laboratories [22]. In order to recognize the defects in NWs, the centro-symmetry parameter (CSP) [23] is utilized, which increases from

zero for perfect FCC lattice to positive values for defects and for atoms close to free surfaces.

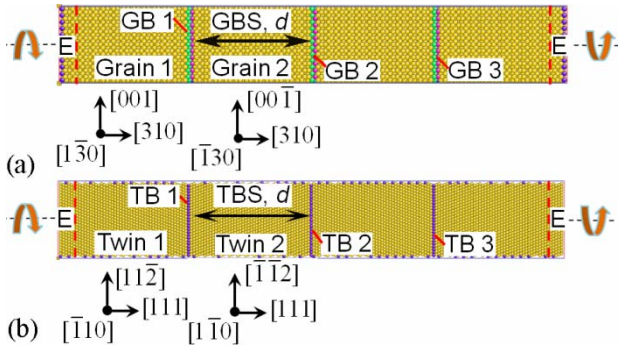

Figure 1. (a) A polycrystalline Cu NW containing three GBs with a nearly square cross-section. (b) A polycrystalline Cu NW containing three TWs with a nearly square cross-section. Both NWs were divided into three sections, including mobile region, and two rigid boundary regions 'E'.

3. Results and discussion

Following studies will focus on the impacts from GBs or TBs on the critical angle, torsional rigidity and the plastic deformation of NWs. The critical angle refers as the angle when plastic deformation or dislocations begin to emit. While the torsional rigidity (GI_p) can be obtained from the strain energy (ΔE) versus torsional angle (φ) curve through the relation of $\Delta E=(GI_p)\varphi^2/(2L)$ [21].

3.1. Polycrystalline nanowire with GBs

Mono-crystalline NW and polycrystalline NWs contain different numbers of GBs were firstly studied. Fig. 2 shows the changing trend of ΔE along with the increase of φ for these different cases. It is evident from Fig. 2 that due to the presence of GBs, the ΔE-φ curve appears a significant difference from that of the perfect NW. In detail, for the perfect NW, ΔE-φ curve exhibits a parabolic portion before yielding, after which the strain energy received an obvious reduction, and the critical angle approximates 1.627 rad. Whereas, the ΔE-φ curves for NWs with GBs show a considerably shortened parabolic portion, and this parabolic portion is apparently different from that of the perfect NW. In other words, a much smaller critical angle is observed for NWs with GBs. Particularly, ΔE-φ curves for NWs possess more than 1 GB exhibit a relatively flat fluctuation part after passing the critical angle. Selected atomic configurations are presented to investigate the deformation process of the NW.

Fig. 3 shows the atomic configurations of different NWs at different torsional angle values. Basically, for the perfect NW, the crystal structure retains its original crystal structure (see Fig. 3a1) until the torsional angle arrives 1.634 rad, which shows a relatively long elastic deformation period. After yielding, stacking faults (SFs) begin to nucleate around the centre of the NW as shown in Fig. 3a2. It is observed that, the plastic deformation has concentrated around the central area of the NW (see Fig. 3a3), which involves with the nucleation and propagation of both intrinsic and extrinsic SFs.

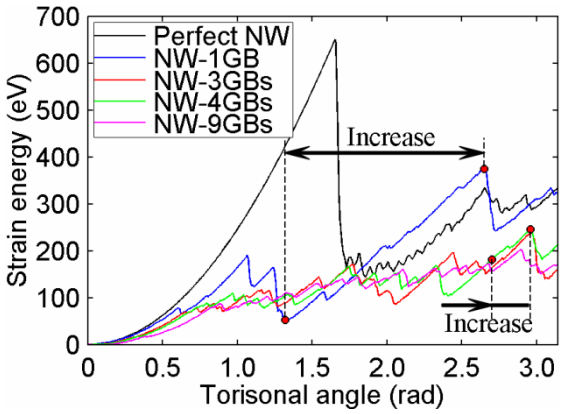

Figure 2. Strain energy versus torsional angle curves for Cu NWs with GBs.

For the NW with one GB, an extremely early yielding is observed, which only corresponds to a critical angle of 0.603 rad. The evident existence of intrinsic SF is observed at the torsional angle 0.848 rad (see Fig. 3b1), which is initiated from the location of the GB. With further loading, more SFs are generated which is associated with a sharp strain energy decrease as illustrated in Fig. 3b2. Interestingly, a local HCP structure is produced between the torsional angle around 1.319 and 2.652 rad (see Fig. 3b3), which results a considerable strain energy increase as pointed out in Fig. 2.

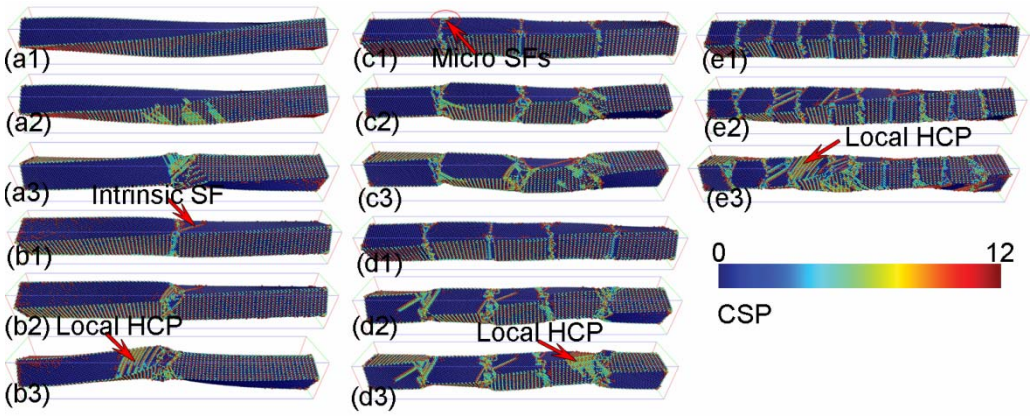

Figure 3. Atomic configurations at different torsional angles. Perfect NW: (a1) 1.634 rad, (a2) 1.665 rad, (a3) 2.482 rad; NW with one GB: (b1) 0.848 rad, (b2) 1.1 rad, (b3) 2.199 rad; NW with three GBs: (c1) 0.691 rad, (c2) 2.042 rad, (c3) 2.796 rad; NW with four GBs: (d1) 0.817 rad, (d2) 2.356 rad, (d3) 2.89 rad; NW with nine GBs: (e1) 1.759 rad, (e2) 2.733 rad, (e3) 0.911 rad.

Similar as the previous case, the NW with three GBs also exhibits a particularly early yielding (around 0.654 rad). However, in contrast to the large volume of SFs for the NW with one GB after yielding (see Fig. 3b1), only micro SFs are generated initially around the locations of GBs as shown in Fig. 3c1. Along with the increase of the torsional strain, more SFs are generated around the two outside GBs (i.e., GBs 1 and 3 in Fig. 1a) as revealed in Fig. 3c2. It is observed that, no large SFs nucleation is occurred around the middle GB (i.e., GB 2 in Fig. 1a) only until the torsional angle reaches 2.444 rad (see Fig 3c3).

For the NW with four GBs, a low critical angle around 0.798 rad is observed. After yielding, SFs

first nucleate from the two middle GBs, and their existence are found around all four GBs with further deformation, i.e., the plastic deformation is almost evenly distributed along the four GBs (see Fig. 3d2). Similar as the NW with one GB, a local HCP structure (see Fig. 3d3) is produced during the torsional angle between 2.702 and 2.959 rad, which also causes apparent strain energy resumption as highlighted Fig. 2. This structure is dissolved gradually afterwards.

The critical angle is estimated around 0.880 rad for the NW with nine GBs, after which, intrinsic SFs nucleate from the location of GBs (see Fig. 3e1). According to Fig. 3e2, the presence of SFs is found between all GBs, implying the evenly distributed plastic deformation along the NW axis. It is supposed that owing to the small GBS, further propagation of SFs is stopped by GBs, which induces a gradual increasing trend of the strain energy (refer to Fig. 2). To mention that, a local HCP structure is also generated around the middle area of the NW as illustrated in Fig. 3e3.

In short, the introduction of GBs has greatly decreased the critical angle, and led to an extremely early yielding comparing with the perfect NW. Additionally, NWs with GBs are inclined to produce a local HCP structure during loading, whose occurrence is detected for NWs with 1, 4 and 9 GBs.

3.2. Polycrystalline nanowire with TBs

We then consider polycrystalline NWs that contain different numbers of TBs. Fig. 4 illustrates the trajectory of ΔE with the increase of φ for these different cases. Different with the NWs with GBs (in Fig. 2), the elastic portion of the ΔE-φ curve for all different NWs almost overlaps with that of the perfect NW. Comparing with the critical angle of 1.703 rad, an earlier yielding is observed with the presence of TBs. Particularly, the ΔE-φ curve shows a regular reduction and resumption processes as partially shown in Fig. 4. To unveil the corresponding underlying mechanism, the atomic configurations are extensively investigated. Due to the similarity of plastic deformation, only the snapshots of the perfect NW and NWs with one, three and six TBs are presented in Fig. 5.

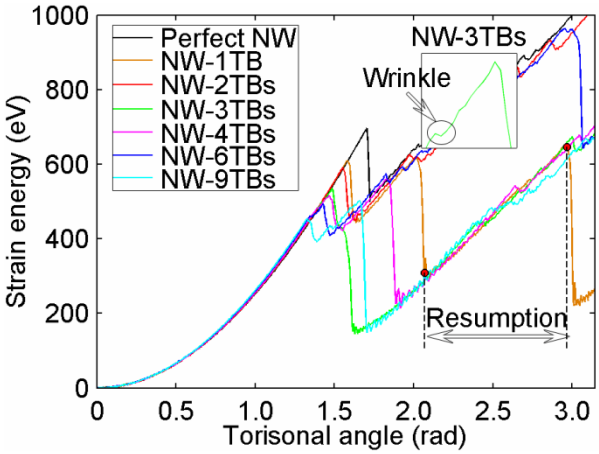

Figure 4. Strain energy versus curves for NWs with TBs.

Figure 5a1-a3 shows the atomic configurations of the perfect NW at three different torsional angles. As is seen, before yielding, the original crystal structure of the NW appears unchanged (see Fig.

5a1). Since the NW possesses a <111> axial direction, which leads to the SFs that laying on the (111) planes all perpendicular to the NW's axis. From Fig. 5a2, several parallel intrinsic SFs are observed after yielding, which initiate from the surface of the NW. With increasing loading, more parallel SFs are developed with these SFs becoming larger and larger. It is observed that, after plastic deformation, the exposure surface of the deformed area becomes {111} planes rather than the original {110} or {112} planes (see the inset of Fig. 5a3).

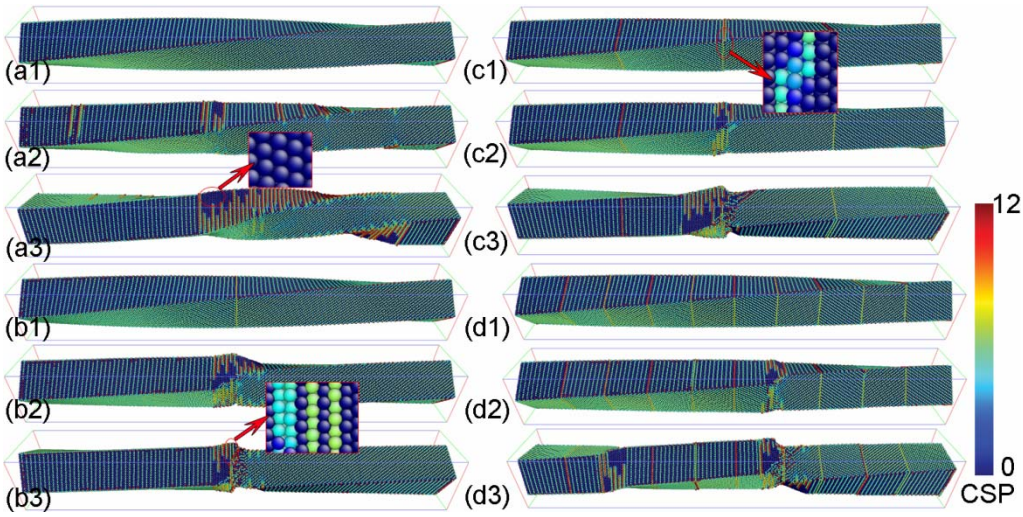

Figure 5. Atomic configurations at different torsional angles. Perfect NW: (a1) 1.696 rad, (a2) 1.728 rad, (a3) 2.827 rad; NW with one TB: (b1) 1.571 rad, (b2) 1.634 rad, (b3) 2.199 rad; NW with three TBs: (c1) 1.445 rad, (c2) 1.508 rad, (c3) 2.827 rad; NW with nine TBs: (d1) 1.382 rad, (d2) 1.319 rad, (d3) 2.827 rad.

The introduction of the TBs is found to exert obvious influence to the plastic deformation of the NW. According to Fig. 5b1, the NW with one TB also shows an intact crystal structure during elastic deformation, which however, produces less SFs than that of the perfect NW at the onset of yielding (see Fig. 5a2), and those SFs are all around the location of the TB (see Fig. 5b2). Particularly, in contrast to the pure existence of intrinsic SFs in the perfect NW, an extrinsic SF is even developed around the original twinning plane for the NW with one TB, as shown in the inset of Fig. 5b3. In addition, the deformed structure is found unchanged during several torsional angle intervals, which contributes to apparent strain energy resumptions as highlighted in Fig. 3.

NWs with three, four and six TBs show similar deformation process. Basically, for the NW with three TBs, an obvious wrinkle event is generated before the obvious strain energy decrease, as pointed out in Fig. 4, which is found to originate from the early SFs nucleation around the TB's locations (see inset of Fig. 4c1). After yielding, less SFs are usually generated around the locations of TBs comparing with the perfect NW (e.g., such as the NW with three TBs in Fig. 4c2). In particular, the plastic deformation is usually concentrated around one of the TBs, leaving the crystal structure around other TBs unchanged (see Fig. 4c3). For the NW with nine TBs, though no wrinkle event is observed, the plastic deformation is still similar as NWs with three, four and six TBs, i.e., the NW appears unchanged during the elastic deformation, and intrinsic SFs first nucleate from the locations of TBs. Specifically, most of the plastic deformation emerges in the area where SFs first nucleated. To mention that, the exposure surface of the deformed area for all defected NWs, are

uniformly found as the {111} planes.

Before concluding, we compare the critical angle among all NWs as listed in Table 1. To note that, for ΔE-φ curves that possess a wrinkle event, the torsional angle when obvious strain energy decrease occurs is taken as the critical angle. Generally, for the NW with GBs, a considerably large reduction of the critical angle is observed, e.g., for the NW with one GB, a 63.08% reduction is estimated. Furthermore, the reduction percentage is found decreased with increasing GB's number. Different from the NW with GB, the presence of TB results in a relatively smaller reduction to the critical angle, and the increase of TB's number aggravates the critical angle reduction. Additionally, from Figs. 2 and 4, the elastic portion of ΔE-φ curves appears obvious deviation and almost overlaps with that of the perfect NW for NWs with GBs and TBs, respectively. This phenomenon suggests that, the introduction of GBs will reduce the torsional rigidity, whereas, the TBs exert insignificant influence to the torsional rigidity of the NW.

Table 1. Critical angle (rad) as obtained from different tested samples.

GB/TB No.		0	1	2	3	4	6	9
NW-GB	Critical angle	1.634	0.6032	-	0.6535	0.798	-	0.8796
	Reduction (%)	-	63.08	-	60.01	51.16	-	46.17
NW-TB	Critical angle	1.696	1.577	1.552	1.483	1.464	1.426	1.382
	Reduction (%)	-	7.02	8.49	12.56	13.68	15.92	18.51

4. Conclusions

Based on the large-scale MD simulation, the torsional properties of the bamboo-like Cu NWs that contain either GBs or TBs are explored. Major conclusions are drawn as below:

- The existence of GBs induces a considerably large reduction to the critical angle, and the more of GBs the less reduction appears. On the contrary, the presence of TB results in a relatively smaller reduction to the critical angle, and the more of TBs the more severe reduction appears;
- The introduction of GBs reduces the torsional rigidity of the NW, whereas, the TBs exert insignificant influence to the torsional rigidity;
- The plastic deformation is obviously influenced by GBs. Specifically, NWs with GBs are inclined to produce a local HCP structure during loading, whose occurrence is detected for NWs with 1, 4 and 9 GBs. What's more, the plastic deformation of NWs with GBs is usually evenly distributed along the axial axis in contrast to the concentrate plastic deformation around the middle region for the perfect NW;
- A similar plastic deformation mechanism is observed for both perfect NW and NWs with TBs, i.e., dominated by the nucleation and propagation of parallel intrinsic SFs. Same as the NWs with GBs, all partial dislocations are initiated from the locations of TBs.

This study will enrich the current understanding of the mechanical properties of NWs, which will eventually shed lights on the applications of NWs.

Acknowledgements

Support from the ARC Future Fellowship grant (FT100100172) and the High Performance Computer resources provided by the Queensland University of Technology are gratefully acknowledged.

References

[1] P. Xie, Q. Xiong, Y. Fang, Q. Qing, and C. M. Lieber, Local electrical potential detection of DNA by nanowire-nanopore sensors, *Nat. Nanotechnol.,* 7 (2011), pp. 119-125.

[2] G. Wang and X. Feng, Surface effects on buckling of nanowires under uniaxial compression, *Appl. Phys. Lett.,* 94 (2009), p. 141913.

[3] H. S. Park and P. A. Klein, Surface stress effects on the resonant properties of metal nanowires: the importance of finite deformation kinematics and the impact of the residual surface stress, *J. Mech. Phys. Solids,* 56 (2008), pp. 3144-3166.

[4] H. S. Park and J. A. Zimmerman, Modeling inelasticity and failure in gold nanowires, *Phys. Rev. B,* 72 (2005), p. 54106.

[5] H. F. Zhan and Y. T. Gu, A fundamental numerical and theoretical study for the vibrational properties of nanowires, *J. Appl. Phys.,* 111 (2012), pp. 124303-9.

[6] H. F. Zhan and Y. T. Gu, Theoretical and numerical investigation of bending properties of Cu nanowires, *Comput. Mater. Sci.,* 55 (2012), pp. 73-80.

[7] H. F. Zhan and Y. T. Gu, Modified beam theories for bending properties of nanowires considering surface/intrinsic effects and axial extension effect, *J. Appl. Phys.,* 111 (2012), p. 084305.

[8] A. Bietsch and B. Michel, Size and grain-boundary effects of a gold nanowire measured by conducting atomic force microscopy, *Appl. Phys. Lett.,* 80 (2002), pp. 3346-3348.

[9] F. Sansoz, H. Huang, and D. H. Warner, An atomistic perspective on twinning phenomena in nano-enhanced fcc metals, *JOM Journal of the Minerals, Metals and Materials Society,* 60 (2008), pp. 79-84.

[10] A. Cao, Y. Wei, and E. Ma, Grain boundary effects on plastic deformation and fracture mechanisms in Cu nanowires: Molecular dynamics simulations, *Phys. Rev. B,* 77 (2008), p. 195429.

[11] A. Cao and Y. Wei, Atomistic simulations of the mechanical behavior of fivefold twinned nanowires, *Phys. Rev. B,* 74 (2006), p. 214108.

[12] C. Deng and F. Sansoz, Fundamental differences in the plasticity of periodically twinned nanowires in Au, Ag, Al, Cu, Pb and Ni, *Acta Mater.,* 57 (2009), pp. 6090-6101.

[13] H. F. Zhan and Y. T. Gu, Atomistic exploration of deformation properties of copper nanowires with pre-existing defects, *CMES: Computer Modeling in Engineering & Sciences,* 80 (2011), pp. 23-56.

[14] H. F. Zhan, Y. T. Gu, C. Yan, X. Q. Feng, and P. Yarlagadda, Numerical exploration of plastic deformation mechanisms of copper nanowires with surface defects, *Comput. Mater. Sci.,* 50 (2011), pp. 3425-3430.

[15] H. F. Zhan and Y. T. Gu, "Molecular dynamics study of dynamic buckling properties of nanowires with defects," in *14th Asia-Pacific Vibration Conference*, HongKong, 2011.

[16] K. L. Merkle, High-resolution electron microscopy of grain boundaries, *Interface Sci.(Netherlands),* 2 (1995), pp. 311-345.

[17] S. M. Foiles, M. I. Baskes, and M. S. Daw, Embedded-atom-method functions for the fcc metals Cu, Ag, Au, Ni, Pd, Pt, and their alloys, *Phys. Rev. B,* 33 (1986), pp. 7983-7991.

[18] A. Voter, Embedded atom method potentials for seven fcc metals: Ni, Pd, Pt, Cu, Ag, Au, and Al, *Los Alamos Unclassified Technical Report LA-UR,* (1993), pp. 93-3901.

[19] W. G. Hoover, Canonical dynamics: Equilibrium phase-space distributions, *Phys. Rev. A,* 31 (1985), pp. 1695-1697.

[20] S. Nosé, A unified formulation of the constant temperature molecular dynamics methods, *J. Chem. Phys.,* 81 (1984), p. 511.

[21] H. F. Zhan, Y. T. Gu, C. Yan, and P. K. D. V. Yarlagadda, Numerical exploration of the defect's effect on mechanical properties of nanowires under torsion, *Adv. Mat. Res.,* 335 (2011), pp. 498-501.

[22] S. Plimpton, Fast parallel algorithms for short-range molecular dynamics, *J. Comput. Phys.,* 117 (1995), pp. 1-19.

[23] C. L. Kelchner, S. J. Plimpton, and J. C. Hamilton, Dislocation nucleation and defect structure during surface indentation, *Phys. Rev. B,* 58 (1998), pp. 11085-11088.

Computational prediction of fracture toughness of polycrystalline metals

Yan Li, David L. McDowell and Min Zhou*

The George W. Woodruff School of Mechanical Engineering,
School of Materials Science and Engineering
Georgia Institute of Technology, Atlanta, GA 30332-0405, U.S.A.

* Corresponding author: min.zhou@me.gatech.edu

Abstract

A three-dimensional multiscale computational framework based on the cohesive finite element method (CFEM) is developed to establish relations between microstructure and the fracture toughness of ductile polycrystalline materials. This framework provides a means for evaluating fracture toughness through explicit simulation of fracture processes involving arbitrary crack paths, including crack-tip microcracking and branching. Fracture toughness is computed for heterogeneous microstructures using the *J*-integral, accounting for the effects of grain size, texture, and competing fracture mechanisms. A rate-dependent, finite strain, crystal plasticity constitutive model is used to represent the behavior of the bulk material. Cohesive elements are embedded both within the grains and along the grain boundaries to resolve material separation processes. Initial anisotropy due to crystallographic texture has a strong influence on inelastic crack tip deformation and fracture toughness. Parametric studies are performed to study the effect of different cohesive model parameters, such as interface strength and cohesive energy, on the competition between transgranular and intergranular fracture. The two primary fracture mechanisms are studied in terms of microstructure characteristics, constituent properties and deformation behaviors. The methodology is useful both for the selection of materials and the design of new materials with tailored properties.

Keywords

cohesive finite element method, crystal plasticity, microstructure-fracture toughness, multiscale framework

1. Introduction

Microstructural design is an important approach for enhancing material properties such as fracture toughness for many industries, including aerospace and automotive engineering. It is of great importance to quantify how an advancing crack interacts with the microstructure at multiple length scales and how microstructure determines a material's fracture toughness through the activation of different fracture mechanisms. A lot of efforts have been made to develop 2D simulation methods to study the crack initiation and propagation in brittle materials (cf. Xu and Needleman [1], Zhai et al. [2] and Li and Zhou [3, 4]) and metallic polycrystalline materials (cf. Guo et al. [5] and Hao et al. [6]). However, fracture is inherently a 3D problem. Most of these 2D models, which assume plane strain conditions, cannot capture the 3D morphologies and orientation of grains, nor do they track crack-material interactions due to non-planar crack extension. This paper aims at expanding the current 2D capabilities to 3D by considering realistic microstructures and incorporating crystalline plasticity in constitutive response modeling. Both intergranular and transgranular fracture modes are

considered in the cohesive finite element method (CFEM) framework developed. This framework also provides a means for evaluating fracture toughness through explicit simulation of 3D fracture processes in microstructures by calculating the *J*-integral.

2. Model structure

Our proposed framework consists of two length scales. At the microscopic scale, 3D cohesive elements with 6-node zero thickness (COH3D6) permeate the whole microstructure as an intrinsic part of material characterization. Constitutive relations for the grains and grain boundaries are specified separately. The cohesive relation allows damage and crack surface separation to be considered. Fracture emerges as a natural outcome of the deformation process without the use of any failure criterion. The macroscopic region is homogenized by using the Mori-Tanaka method. Structural response, such as fracture toughness K_{IC}, is evaluated by calculating the *J*-integral along an arbitrary contour in the homogenized region.

2.1. Generation of 3D polycrystal samples

Voronoi tessellation has been one of the most popular techniques for generating polycrystalline microstructures due to its simplicity, space-filling nature and the availability of theoretical results on the topological properties [7-8]. However, microstructures generated in this way are not always consistent with experimental results [9]. To realistically capture the topological and statistical properties of microstructures, a method for generating a 3D polycrystalline microstructure from a series of 2D images is developed. This capability extends the source of 2D images from computer generated microstructures to realistic section images obtained by Electron Back Scatter Diffraction (EBSD) or Focused Ion Beam (FIB) diffraction. In this paper, the 2D microstructure images are generated by an ellipsoidal packing algorithm [10]. Ellipsoidal grains are randomly placed with the aspect ratios and grain sizes fitted to pre-defined distributions. In order to obtain good delineation of grain boundary and potential crack trajectory, unstructured tetrahedral meshes are generated by iso2mesh [11] as illustrated in Fig. 1.

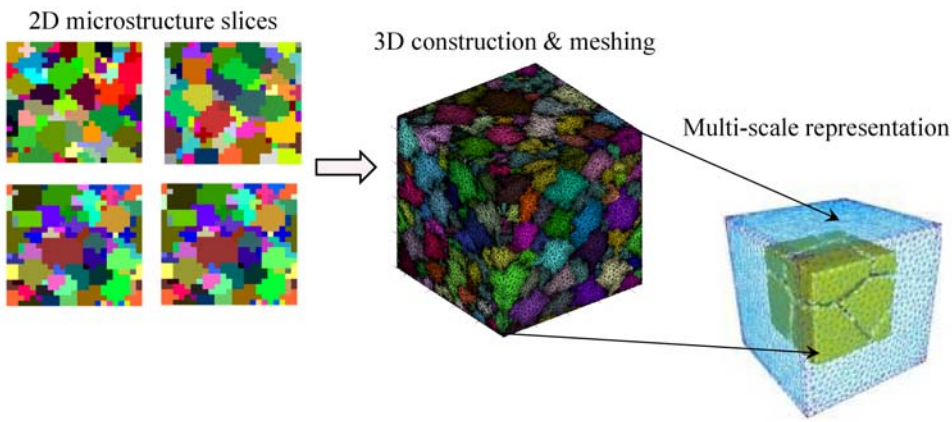

Fig.1 3D microstructure reconstruction and meshing.

2.2. 3D cohesive element insertion

Embedding cohesive surfaces into complicated 3D microstructure meshes is not a trivial task. The biggest challenge lies in how to effectively deal with the changes in the 3D nodal and elemental connectivities due to the introduction of cohesive surfaces. An algorithm has been developed to automatically insert 3D cohesive elements along grain boundaries and within individual grains. The method generally includes the following steps: (1). Find the node set which will be duplicated. The set can be defined as nodes along grain boundaries or within arbitrary grains. (2). Sort out the target elements which include the node set, then duplicate the nodes and redistribute the updated node labels to the corresponding elements. Assign the same coordinates to the duplicated nodes as the virgin nodes. (3). Generate cohesive elements with consistent nodal ordering (clockwise or counter-clockwise) in adjacent element facets. The top and bottom facets are determined by calculating the surface normal. Either top or bottom face can be defined by a positive surface normal value. The key lies in keeping the pattern consistent. (4). Create different cohesive element sets. Sort out cohesive elements that belong to grains or grain boundaries so that different cohesive laws can be correctly assigned.

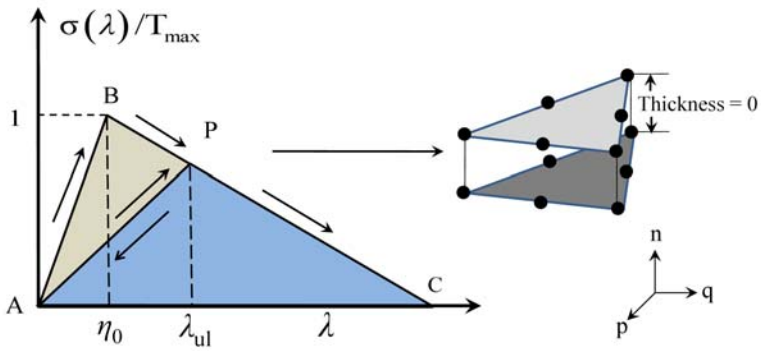

Fig.2 Bilinear traction-separation law.

Both cohesive elements along grain boundaries and within grains follow the bilinear traction-separation law as shown in Fig. 2. This law is derived from a potential Φ which is a function of separation vector Δ through a state variable defined as $\lambda = \sqrt{\left(\Delta_n/\Delta_{nc}\right)^2 + \left(\Delta_t/\Delta_{tc}\right)^2}$. This variable describes the effective instantaneous state of mixed-mode separations. Here, $\Delta_n = \mathbf{n}\cdot\mathbf{\Delta}$ and $\Delta_t = \sqrt{\left(\Delta_p\right)^2 + \left(\Delta_q\right)^2} = \sqrt{\left[\left(\mathbf{\Delta} - \left(\mathbf{\Delta}\cdot\mathbf{n}\right)\mathbf{n}\right)\cdot\mathbf{p}\right]^2 + \left[\left(\mathbf{\Delta} - \left(\mathbf{\Delta}\cdot\mathbf{n}\right)\mathbf{n}\right)\cdot\mathbf{q}\right]^2} = \left|\mathbf{\Delta} - \left(\mathbf{\Delta}\cdot\mathbf{n}\right)\mathbf{n}\right|$ denote, respectively, the normal and tangential components of $\mathbf{\Delta}$, with $\mathbf{n}$ being unit normal and $\mathbf{p}$ and $\mathbf{q}$ being two unit tangential vectors. Note that $\mathbf{n}$, $\mathbf{p}$ and $\mathbf{q}$ are mutually perpendicular to each other and form a right-handed triad. Δ_{nc} is the critical normal separation at which the cohesive strength of an interface vanishes under conditions of pure normal

deformation ($\Delta_t = 0$). Similarly, Δ_{tc} is the critical tangential separation at which the cohesive strength of an interface vanishes under conditions of pure shear deformation ($\Delta_n = 0$). $T_{\max}$ represents the maximum traction that the cohesive element can sustain before damage initiates.

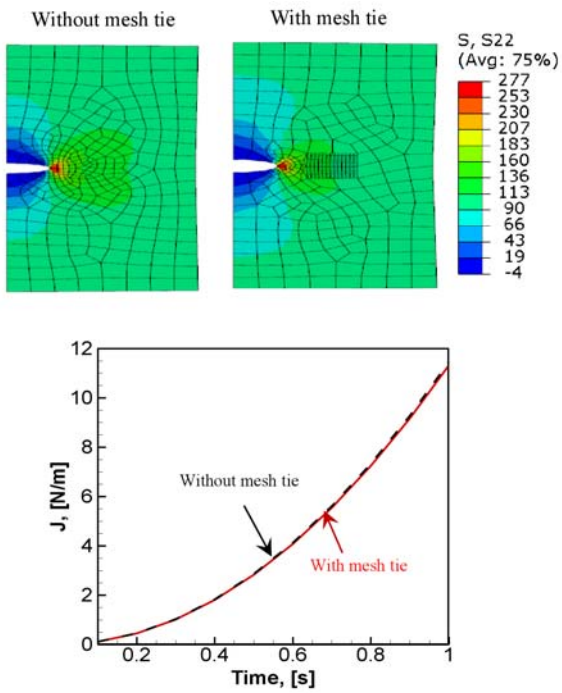

Fig.3 Effect of mesh tie constraint on the calculated J values.

2.3. Generation of mesh tie constraint

Calculation of the *J*-integral in the homogenized region requires a closed contour. It would very difficult to define contours if the homogenized region is meshed with unstructured elements. To solve the problem, two regions of mesh are used. An unstructured tetrahedral mesh is used for the microstructure region and a structured tetrahedral mesh is used for the homogenized region. It would be extremely challenging to create a transitional region that connects the two types of meshes. Instead, the mesh tie constraint in ABAQUS is used. This constraint requires no conformity of node connection between the two regions. It circumvents the problem with acceptable accuracy. As illustrated for a 2D problem in Fig. 3, there is only a very minor difference between the *J* values for cases with and without the mesh tie constraint. It should be noted that iso2mesh cannot generate perfect microstructure meshes with smooth exterior surfaces and sharp vertices as shown in Fig. 4. If the two regions cannot be seamlessly attached, the energy loss caused by the gap will significantly influence the accuracy of calculation. We innovatively develop an algorithm to generate a shell mesh which is around the unsmoothed microstructure block to ensure proper node and element connectivity. The two regions are successfully assembled using the mesh tie constraint as illustrated in Fig. 5.

2.4. Crystal plasticity formulation

Plastic deformation at the macroscopic scale in metals is a manifestation of dislocation motion and interaction at the microscopic scale. The details are intimately related to the basic crystallographic nature of the material as well as the current state of the microstructure. Macroscopic models of plasticity lack the ability to link these fundamental mechanisms to the bulk material response without very substantial experimental characterization. Furthermore, these models give relatively little physical connection between the actual deformation processes and the observed material behavior. Many formulations of constitutive laws for the elastic-plastic deformation of single and polycrystals have long been proposed (cf. Talor [12], Hill and Rice [13], Asaro and Rice [14], Peire et al. [15] and McGinty and McDowell [16]). The basic premise of these theories is that macroscopic plastic deformation is related to the cumulative process of slip (or twin) system shearing relative to the lattice. This methodology provides a physical link between the processes at radically different length scales. The two basic components of crystal plasticity model are the kinematic and kinetic relations. The kinematic relations provide the mathematical framework for describing the physical process of dislocation motion based on continuum deformation fields, whereas the kinetic relations incorporate the material and/or mechanism dependence of non-equilibrium dislocation motion and interaction.

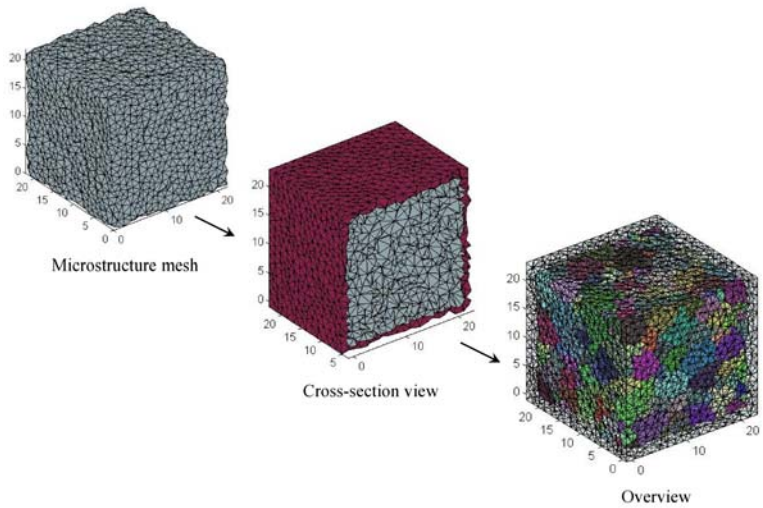

Fig. 4 Shell mesh region around the unsmoothed microstructure mesh.

The multiplicative decomposition of the total deformation gradient is given by

$$\mathbf{F} = \mathbf{F}^e \cdot \mathbf{F}^p, \tag{1}$$

where $\mathbf{F}^e$ is the elastic deformation gradient representing the elastic stretch and rotation of lattice, and $\mathbf{F}^p$ is the plastic deformation gradient describing the collective effects of dislocation motion along the active slip planes relative to a fixed lattice in the reference configuration. Unit vectors $\boldsymbol{s}_0^\alpha$

and $\boldsymbol{n}_0^\alpha$ denote the slip direction and the slip plane normal direction, respectively for the αth slip system in the undeformed configuration. The resolved shear stress on each slip system is related to the Cauchy stress tensor $\boldsymbol{\sigma}$ according to

$$\tau^\alpha = \boldsymbol{\sigma}:\left(\boldsymbol{s}^\alpha \otimes \boldsymbol{n}^\alpha\right), \tag{2}$$

where the slip vectors have been rotated into the current configuration. Under the application of the resolved shear stress, the shearing rates $\dot{\gamma}^\alpha$ on the slip systems are related to the plastic velocity gradient in the intermediate configuration according to

$$\mathbf{L}^p = \sum_\alpha \dot{\gamma}^\alpha \, \mathbf{s}_0^\alpha \otimes \mathbf{n}_0^\alpha, \tag{3}$$

with $\dot{\gamma}^\alpha$ ascribed to follow the rate-dependent flow rule as

$$\dot{\gamma}^\alpha = \dot{\gamma}_0 \left\langle \frac{\tau^\alpha - \chi^\alpha}{g^\alpha} \right\rangle^m \operatorname{sgn}\left(\tau^\alpha - \chi^\alpha\right), \tag{4}$$

where m is the reverse strain rate sensitivity exponent and g^α and χ^α are drag stress and back stress, respectively on the αth slip system. These quantities evolve according to

$$\begin{cases} \dot{g}^\alpha = H \sum_{\beta=1} q^{\alpha\beta} \left|\dot{\gamma}^\beta\right|, \text{ and} \\ \dot{\chi}^\alpha = A_{kin} \dot{\gamma}^\alpha - A_{dyn} \chi^\alpha \left|\dot{\chi}^\alpha\right|. \end{cases} \tag{5}$$

Here $q^{\alpha\beta}$ is the latent hardening coefficient, H, A_{kin} and A_{dyn} are the isotropic hardening, kinematic hardening and dynamic recovery coefficients, respectively. These non-linear coupled differential equations are solved via the fourth order Runge-Kutta integration scheme using VUMAT.

3. Conclusion

A cohesive finite element based multi-scale framework is developed to simulate crack initiation and propagation in 3D polycrystalline microstructures. Crystal plasticity is incorporated into the constitutive relations so as to capture how anisotropic deformation and texture evolution affect

crack propagation and the activation of different fracture mechanisms. The methodology is useful both for the selection of materials and the design of new materials with tailored properties.

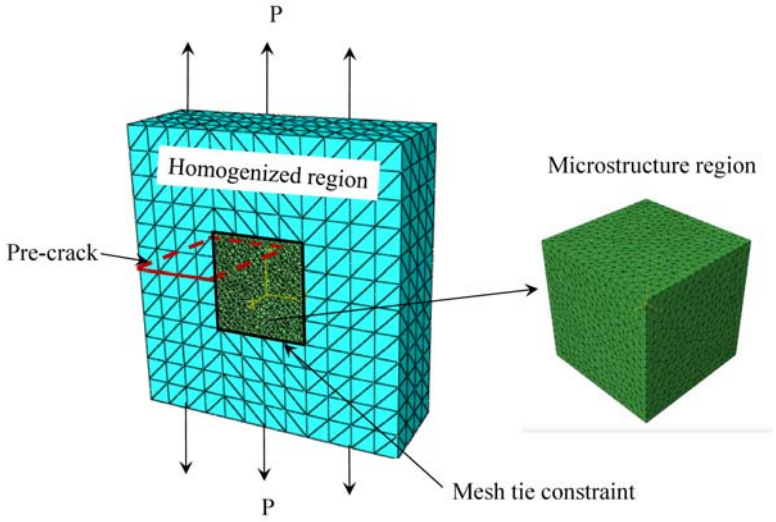

Fig. 5 Model assembly between microstructure and homogenized region by mesh tie.

Acknowledgements

This research is primarily supported by the NSF Center for Computational Materials Design (CCMD) at Georgia Institute of Technology and Pennsylvania State University. MZ also acknowledges support from the National Research Foundation of Korea through WCU Grant No. R31-2009-000-10083-0.

References

[1] X. P. Xu and A. Needleman, "Numerical Simulations of Fast Crack-Growth in Brittle Solids," *J. Mech. Phys. Solids*, vol. 42, p. 1397, Sep 1994.

[2] J. Zhai, V. Tomar, and M. Zhou, "Micromechanical simulation of dynamic fracture using the cohesive finite element method," *Journal of Engineering Materials and Technology*, vol. 126, pp. 179-191, Apr 2004.

[3] Y. Li and M. Zhou, "Prediction of fracture toughness of ceramic composites as function of microstructure: I. Numerical simulations," *Journal of the Mechanics and Physics of Solids*, vol. 61, pp. 472-488, 2013.

[4] Y. Li and M. Zhou, "Prediction of fracturess toughness of ceramic composites as function of microstructure: II. analytical model," *Journal of the Mechanics and Physics of Solids*, vol. 61, pp. 489-503, 2013.

[5] X. Guo, K. Chang, L. Q. Chen, and M. Zhou, "Determination of fracture toughness of AZ31 Mg alloy using the cohesive finite element method," *Engineering Fracture Mechanics*, vol. 96, pp. 401-415, 2012.

[6] S. Hao, H. Lin, R. R. Binomiemi, D. M. G. Combs, and G. Fett, "A multi-scale model of

intergranular fracture and computer simulation of fracture toughness of a carburized steel," *Computational Materials Science,* vol. 48, pp. 241-249, 2010.

[7] A. Leonardi, P. Scardi, and M. Leoni, "Realistic nano-polycrystalline microstructures: beyond the classical Voronoi tessellation," *Philosophical Magazine,* vol. 92, pp. 986-1005, 2012/03/11 2012.

[8] T. Luther and C. Könke, "Polycrystal models for the analysis of intergranular crack growth in metallic materials," *Engineering Fracture Mechanics,* vol. 76, pp. 2332-2343, 2009.

[9] T. Xu and M. Li, "Topological and statistical properties of a constrained Voronoi tessellation," *Philosophical Magazine,* vol. 89, pp. 349-374, 2009/02/01 2009.

[10] C. P. Przybyla and D. L. McDowell, "Simulation-based extreme value marked correlations in fatigue of advanced engineering alloys," *Procedia Engineering,* vol. 2, pp. 1045-1056, 2010.

[11] F. Qianqian and D. A. Boas, "Tetrahedral mesh generation from volumetric binary and grayscale images," in *Biomedical Imaging: From Nano to Macro, 2009. ISBI '09. IEEE International Symposium on,* 2009, pp. 1142-1145.

[12] G. I. Taylor, "Plastic strain in metals.," *Journal of the Institute of Metals,* vol. 62, pp. 307-324, 1938.

[13] R. Hill and J. R. Rice, "Constitutive analysis of elastic-plastic crystals at arbitrary strain," *Journal of the Mechanics and Physics of Solids,* vol. 20, pp. 401-413, 1972.

[14] R. J. Asaro and J. R. Rice, "Strain Localization in Ductile Single-Crystals," *Journal of the Mechanics and Physics of Solids,* vol. 25, pp. 309-338, 1977.

[15] D. Peirce, R. J. Asaro, and A. Needleman, "An Analysis of Nonuniform and Localized Deformation in Ductile Single-Crystals," *Acta Metallurgica,* vol. 30, pp. 1087-1119, 1982.

[16] R. D. McGinty and D. L. McDowell, "Application of multiscale crystal plasticity models to forming limit diagrams," *Journal of Engineering Materials and Technology-Transactions of the Asme,* vol. 126, pp. 285-291, Jul 2004.

Residual stress effects on the propagation of fatigue cracks in the weld of a CA6NM stainless steel

Alexandre Trudel[1,*], **Myriam Brochu**[1], **Martin Lévesque**[1]

[1] Department of Mechanical Engineering, École Polytechnique de Montréal, Montréal, Canada
* Corresponding author: alexandre.trudel@polymtl.ca

Abstract The fatigue crack growth behavior in an automatic flux core arc weld was investigated for stainless steel alloy CA6NM. As-welded and heat treated compact tension specimens were prepared with the crack propagation plane perpendicular to the weld. Constant stress intensity factor range tests were performed at a load ratio R = 0.1 to reveal intra-specimen fatigue crack growth rate variations and differences between the fatigue crack growth behavior of as-welded and heat treated specimens. Comparing the fatigue crack growth rate of as-welded and heat treated specimens revealed that the crack propagates at a faster rate in the as-welded specimens where indications point to the existence of tensile residual stresses acting on the crack tip by inhibiting crack closure. As for the heat treated specimens, when the crack is in the base metal, the fatigue crack growth rate decreases accompanied by an increase in crack closure levels. Tensile residual stresses that may have remained after the post-weld heat treatment and their subsequent relaxation with crack growth could explain this behavior.

Keywords Welding, Stainless Steel, Fatigue Crack Growth, Residual Stresses, Crack Closure

1. Introduction

Cast martensitic stainless steel alloy CA6NM has been used to manufacture hydraulic turbine runners for many decades. Its high strength, weldability and resistance to corrosion and cavitation damage make it a prime candidate for this application. Turbine runners are manufactured by welding cast blades to a cast core using a matching filler metal such as 410NiMo. During service, the cyclic loads acting on the runners can lead to fatigue failures [1]. A damage tolerance approach for the stress analysis of turbine runners can be an efficient strategy to account for the discontinuities, such as casting and welding defects as well as partial penetration weld joint designs, found in these components. A good knowledge of material resistance to fatigue crack growth is therefore needed.

During welding, residual stresses develop and are believed to have a significant influence on the fatigue crack growth behavior of CA6NM welds. Weld-induced residual stresses arise from the elastic interactions between the constraining base metal and the weld metal shrinkage upon solidification and cooling. In stainless steel CA6NM, the volumetric expansion resulting from the austenite to martensite transformation, in conjunction with the low transformation temperature, contributes to the buildup of residual stresses during the welding process [2]. Previous studies have shown that significant tensile and compressive residual stresses can be found in as-welded CA6NM welds [2, 3]. These studies have also shown that post-weld heat treatment (tempering) can reduce the residual stress level. Thibault and al. obtained a 75 percent reduction of the maximum tensile residual stress measured in a five beads V-preparation weld (534 MPa to 136 MPa) [2]. Moisan and al. also showed that the maximum average tensile residual stress in a multi-pass T-joint was reduced after post-weld heat treatment by an amount of 73 percent (204 MPa to 56 MPa) [3].

A fatigue crack growing in a weld can be under the influence of tensile or compressive residual stresses, depending on the geometry of the joint and the position of the crack tip. Under tensile residual stresses, the crack tip is submitted to higher maximum and minimum loads resulting in a higher effective load ratio. This can also affect the effective stress intensity factor range as it can prevent closure, often resulting in higher fatigue crack growth rates (FCGR) [4-6]. On the other hand, compressive residual stresses can accentuate crack closure and be beneficial if they reduce the effective stress intensity factor range and thus the fatigue crack growth rate [5].

The main objective of this study was to characterize the effect of residual stresses on the fatigue crack growth behavior of a flux-cored arc weld consisting of alloy CA6NM and filler metal 410NiMo. Intra-specimen fatigue crack growth rate variations between the filler metal (FM), heat affected zone (HAZ) and base metal (BM), as well as the effect of post-weld heat treatment on fatigue crack growth behavior were studied. Microhardness profiles and metallographic observations were realized on as-welded (AW) and heat treated (HT) specimens encompassing the three zones (FM, HAZ and BM) in order to position the fusion line and determine the width of the heat affected zone. Fatigue crack growth tests were carried out at constant stress intensity factor ranges in order to highlight the effect of residual stresses on the fatigue crack growth behavior. The results are discussed based on the effect of the residual stresses as well as crack closure.

2. Experimental procedure

2.1. Materials

The materials used in this study are base metal martensitic stainless steel alloy CA6NM, and the matching filler metal 410NiMo. The chemical composition and mechanical properties of the CA6NM alloy used are given in Table 1 and Table 2, respectively. Using a fully automated flux-cored arc welding (FCAW) process, 40 mm of weld was built up at the surface of a 50 mm thick CA6NM plate. The welding parameters are given in Table 3. The welded plate was cut in two parts, one of which underwent a post-weld heat treatment at 600°C for two hours. Specimens were prepared from both plates for microhardness measurements and fatigue testing.

Table 1. Chemical composition of base metal CA6NM (weight %) [7].

Material	C	Mn	Si	S	P	Cr	Ni	Mo
CA6NM	0.02	0.66	0.59	0.008	0.031	13.04	4.07	0.53

Table 2. Mechanical properties of base metal CA6NM [7].

Yield strength	Tensile strength	Young's Modulus	Elongation	Reduction Area
763 MPa	837 MPa	206 GPa	27.0 %	58.8 %

Table 3. Welding parameters.

Process	Shielding gas	Wire diameter	Voltage	Current	Speed	Heat input
FCAW	75% Ar, 25% CO_2	1.6 mm	27.5 V	260 A	5 mm/s	1.4 kJ/mm

2.2 Microhardness measurements and metallographic observations

As-welded (AW) and heat treated (HT) specimens encompassing the three zones (FM, HAZ and BM) were sampled for microhardness measurements and metallographic observations. A rough polish was performed with abrasive paper of grit sizes ranging from 240 to 800, followed by a final polish using polycrystalline diamond suspension of sizes 6 μm, 3 μm and 1 μm. Vickers microhardness profiles were taken across the as-welded and heat treated specimens using a force of 100 gf and a dwell time of 15 seconds. The indentation spacing was 100 μm and measurements were taken on a length of 12 mm starting in the filler metal up to the unaffected base metal. A modified Fry's reagent was used to chemically etch the specimens and metallographic observations were realized to position the fusion line.

2.3. Fatigue testing

Compact tension (CT) specimens having a width of 50.8 mm and a thickness of 12.7 mm were machined from heat treated and as-welded plates in accordance with ASTM E647 [8]. The notches were aligned perpendicularly to the welding direction to allow for the crack to grow through each zone of the joint (FM, HAZ and BM). As seen in Fig. 1, the crack tip was positioned in the filler metal at 7 mm from the fusion line (FL). Constant stress intensity factor range tests in river water environment were performed at a constant load ratio R = 0.1 and at a frequency of 20 Hz using a 100 kN MTS servo-hydraulic machine. As-welded and heat treated specimens were tested at stress intensity factor ranges of 8 $MPa{\cdot}m^{½}$ and 20 $MPa{\cdot}m^{½}$. The crack length was continuously monitored using the compliance method with a crack mouth clip gauge. The load and crack opening displacement (COD) were recorded for every cycle and used to determine the closure loads. The closure stress intensity factor (K_{cl}) was defined for a compliance offset of 2 percent [8]. The effective stress intensity factor range (ΔK_{eff}) was calculated by the difference between the maximum applied stress intensity factor (K_{max}) and the closure stress intensity factor (K_{cl}).

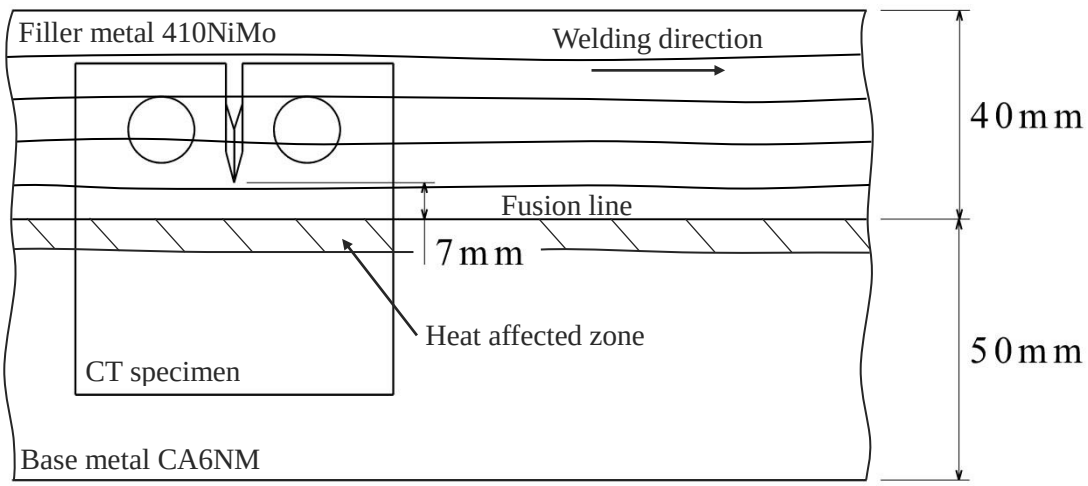

Figure 1. Compact tension specimen sampling layout. Starter notch aligned perpendicularly to the welding direction. Crack tip positioned at 7 mm from the fusion line in the FM.

3. Results

3.1. Microhardness measurements and metallographic observations

The microhardness profiles of the as-welded and heat treated specimens are shown in Fig. 2a and b, respectively. Metallographic observations were realized to identify the position of the fusion line as shown in Fig. 3 for an as-welded joint. The microstructure of the heat treated joint is visually similar and has been omitted. The heat affected zone extends from the fusion line to the microhardness plateau characterizing the base metal, as indicated in Fig. 2. The shape of the microhardness profile is similar for both specimens. The microhardness has its highest value in the filler metal and decreases from the fusion line down to characteristic values of the base metal. The heat affected zone extends up to about 5 mm from the fusion line. The main difference between the two profiles is the microhardness of the filler metal, which is 360 HV on average in the as-welded condition and 325 HV following the tempering heat treatment. These results are in good agreement with what was measured by Thibault and al. from a FCAW CA6NM joint using filler metal 410NiMo [9].

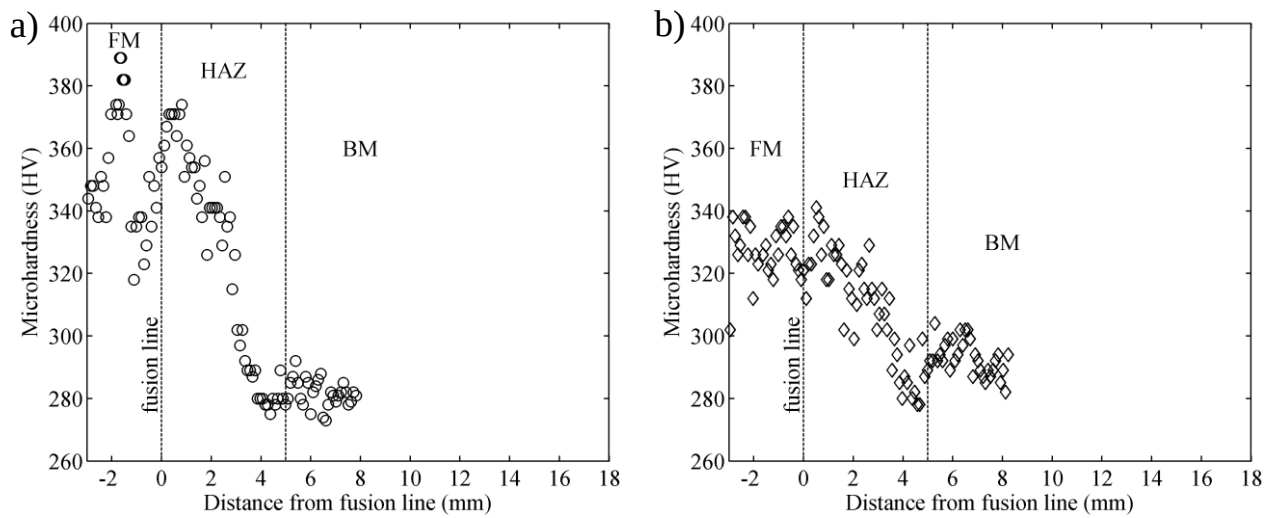

Figure 2. Microhardness profiles a) As-welded specimen b) Heat treated specimen, 2 hours at 600°C.

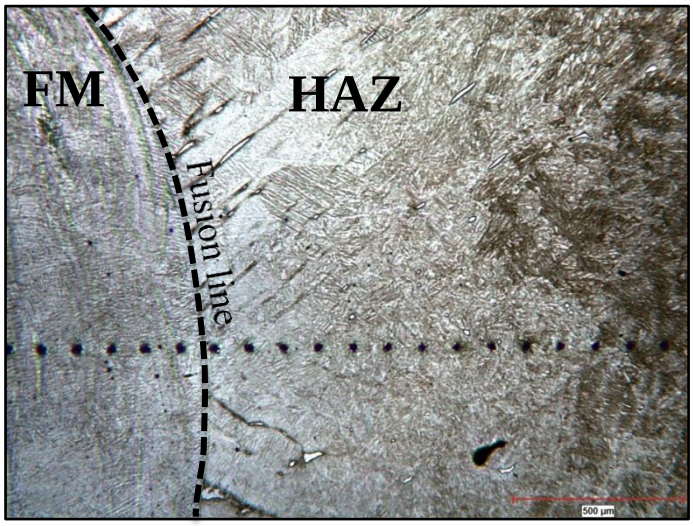

Figure 3. As-welded joint microstructure near the fusion line revealed by etching (50X).

3.2 Fatigue tests

Fig. 4 shows the results of the fatigue tests for as-welded and heat treated specimens at ΔK = 8 MPa·m^{½} and ΔK = 20 MPa·m^{½}. Table 4 shows the mean fatigue crack growth rate in the three zones (FM, HAZ and BM) of as-welded and heat treated specimens. When comparing a given zone at a given stress intensity factor range, the fatigue crack growth rate is always lower in the heat treated specimens than in the as-welded specimens, suggesting that the post-weld heat treatment improves the fatigue crack growth resistance. Pukasiewicz et al. found a similar behavior where the fatigue crack growth rate in the fusion zone of an as-welded CA6NM welded joint was considerably lowered after post-weld heat treatment [10]. In as-welded specimens, the fatigue crack growth rate decreases regularly from the filler metal and into the heat affected zone, before stabilizing in the base metal for both stress intensity factor ranges. These intra-specimen variations are believed to be attributed to microstructural effects and are the subject of an ongoing research. The gradual decrease of the fatigue crack growth rate is not observed in the heat treated specimen. At ΔK = 8 MPa·m^{½}, the fatigue crack growth rate remains fairly constant up to 9 mm from the fusion line (4 mm into the base metal), then decreases by approximately 50 percent and stabilizes at 13 mm from the fusion line. The same behavior, though less pronounced, is also observed at ΔK = 20 MPa·m^{½}, where the fatigue crack growth rate decreases by approximately 20 percent.

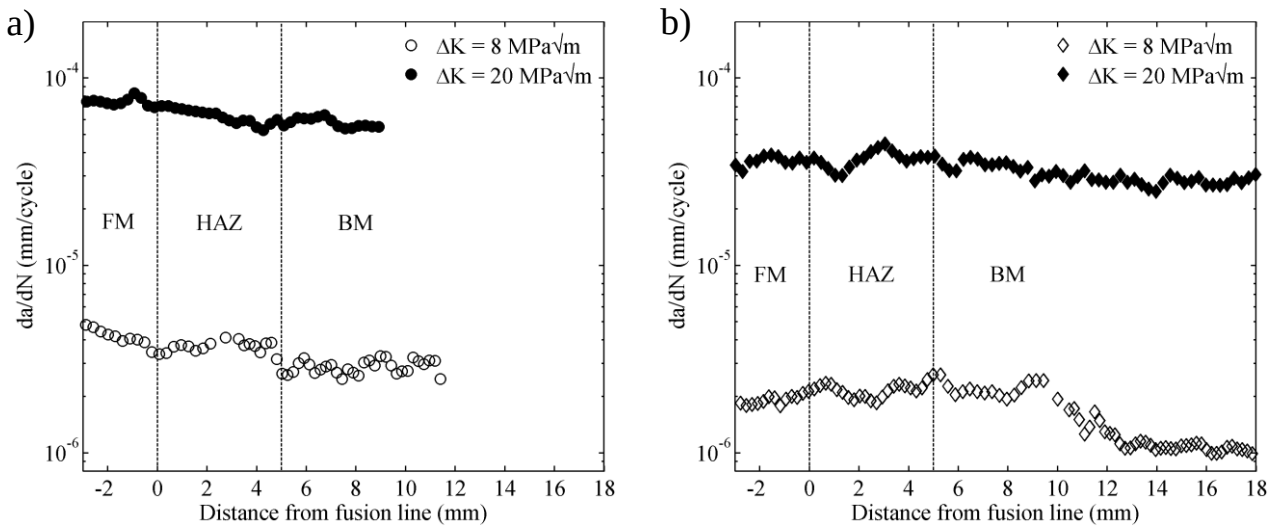

Figure 4. Constant ΔK test results a) As-welded specimens b) Heat treated specimens.

Table 4. Mean FCGR in the FM, HAZ and BM of as-welded and heat treated specimens.

ΔK (MPa·m^{½})	Fatigue crack growth rate (mm/cycle)						
	As-welded specimens			Heat treated specimens			
	FM	HAZ	BM	FM	HAZ	BM	
						Up to 9 mm from FL	After 13 mm from FL
8	$4.2\cdot10^{-6}$	$3.7\cdot10^{-6}$	$2.9\cdot10^{-6}$	$1.9\cdot10^{-6}$	$2.1\cdot10^{-6}$	$2.2\cdot10^{-6}$	$1.1\cdot10^{-6}$
20	$7.5\cdot10^{-5}$	$6.3\cdot10^{-5}$	$5.8\cdot10^{-5}$	$3.6\cdot10^{-5}$	$3.7\cdot10^{-5}$	$3.5\cdot10^{-5}$	$2.8\cdot10^{-5}$

4. Discussion

This section presents an analysis of the constant stress intensity factor range tests results. The higher fatigue crack growth rates found in the as-welded specimens are discussed in terms of tensile residual stresses causing the opening of the crack. The fatigue crack growth rate variations observed in the heat treated specimens are discussed in terms of residual stress relaxation and crack closure.
Fig. 5 shows the base metal fatigue crack growth curves obtained at load ratios R = 0.1 and R = 0.7 [1], along with the mean fatigue crack growth rate obtained in the base metal from the constant stress intensity factor range test results (Table 4). The mean fatigue crack growth rate in the base metal of the heat treated specimens was calculated from the stabilized data starting at 13 mm from the fusion line. For the heat treated specimens, a good agreement is found between the R = 0.1 base metal fatigue crack growth curve and the fatigue test results, for both stress intensity factor ranges. These results, along with the intra-specimen fatigue crack growth rate variations noted in the last section (Fig. 4b), are discussed further in terms of residual stress relaxation and crack closure. Furthermore, the fatigue crack growth rates in the as-welded specimens at $\Delta K = 8$ MPa·m^{½} (empty circles) and $\Delta K = 20$ MPa·m^{½} (filled circles) correlate well with the R = 0.7 base metal baseline. Several indications suggesting the presence of tensile residual stresses responsible for the higher effective load ratio seen by the as-welded specimens are discussed next.

4.1. Fatigue crack growth behavior of as-welded specimens

The typical load-compliance offset curve for as-welded specimens is shown in Fig. 6a. For both stress intensity factor ranges and at all crack lengths, the specimen's response does not deviate from the fully-open crack compliance. This indicates that the crack remains fully-open and that the effective stress intensity factor range is equal to the applied stress intensity factor range. This corresponds to an effective stress intensity factor range ratio ($U = \Delta K_{eff}/\Delta K$) equal to unity in Fig. 6b (circles). It is well known that, for ductile materials free of residual stresses, plasticity-induced crack closure plays a significant role in reducing the effective stress intensity factor range [11].

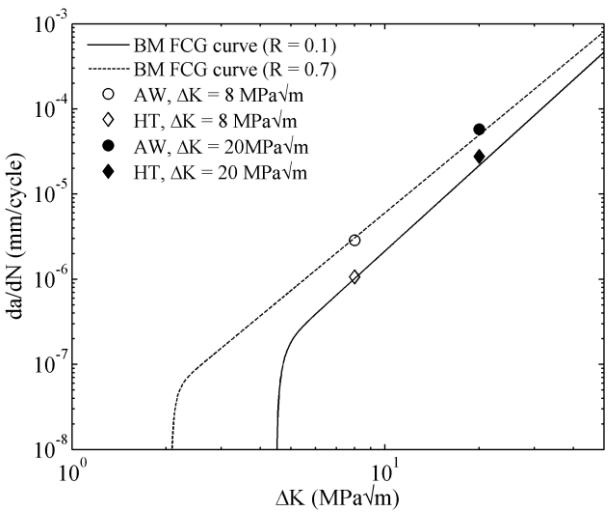

Figure 5. Comparison between the mean FCGR in the BM obtained from the constant ΔK tests and the BM fatigue crack growth curve in the Paris regime at load ratios R = 0.1 and R = 0.7 [1].

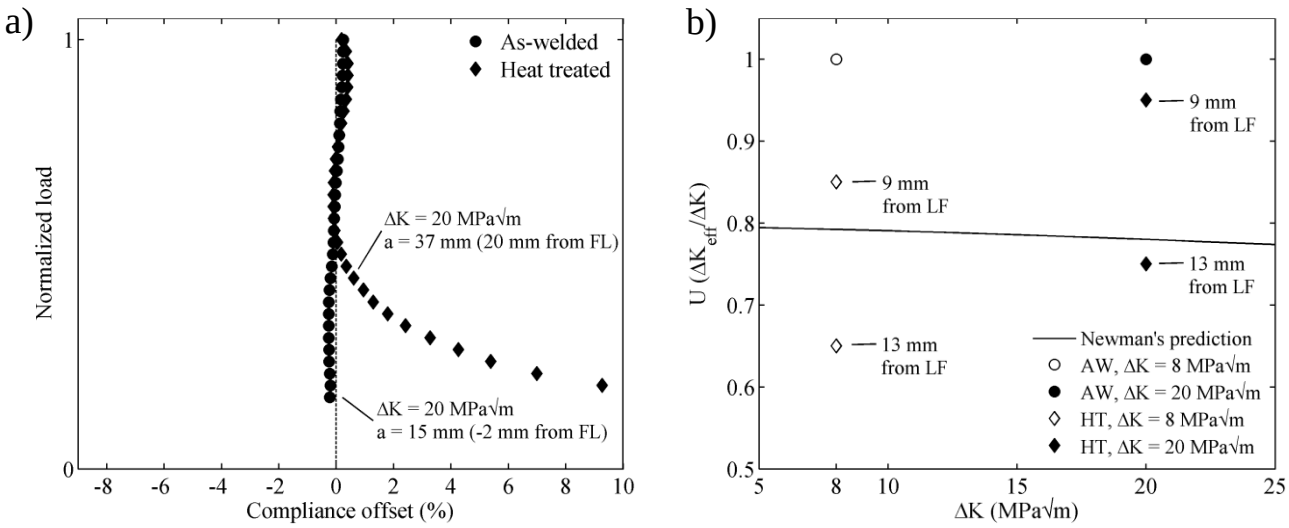

Figure 6. a) Typical load-compliance offset curves for as-welded and heat treated specimens. b) Comparison between experimental values of U and Newman's prediction.

The solid line in Fig. 6b was calculated using Newman's plasticity-induced closure stress equation [12, 13] and represents an upper bound of the effective stress intensity factor range ratio. Experimental data above this upper bound indicate the existence of a crack opening mechanism. Tensile residual stresses are believed to act as such a mechanism in the as-welded specimens, since tensile residual stresses are typically found in CA6NM welds.

To further assess the presence of tensile residual stresses, an as-welded compact tension specimen with a crack length of 20 mm was incrementally loaded from 500 N to -12000 N and the crack opening displacement was recorded (Fig. 7). A closure load of -1000 N was found with a 2 percent compliance offset criterion. The existence of a negative closure load is another strong indication that tensile residual stresses are acting on the crack by preventing it to close at positive loads. A similar behavior has been observed in the welds of three different kinds of steels where tensile residual stresses caused the crack to remain fully open at a load ratio R = 0, resulting in higher fatigue crack growth rates than that of the base metal [5].

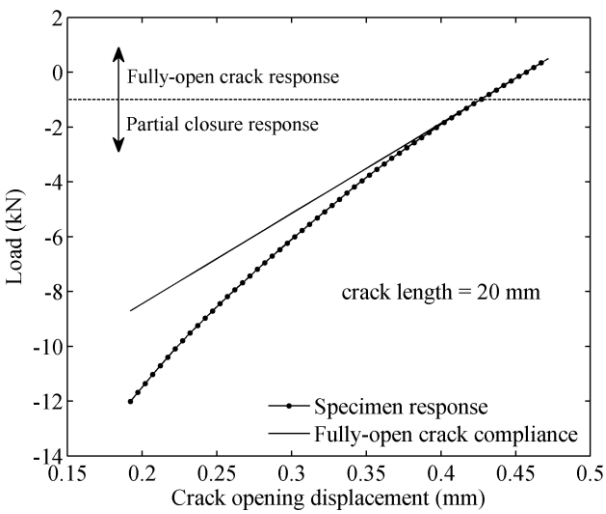

Figure 7. As-welded specimen load-COD curve from a single compression excursion (a = 20 mm).

4.2. Fatigue crack growth behavior of heat treated specimens

The crack closure behavior of the heat treated specimens is different. Crack closure was observed at both stress intensity factor ranges and for all crack lengths and the typical load-compliance offset curve is shown in Fig. 6a. Fig. 6b shows the effective stress intensity factor range ratio for the heat treated specimens when the crack is at 9 mm from the fusion line and at 13 mm from the fusion line. As a first observation, crack closure is more important at $\Delta K = 8$ MPa·m^{½} for equal crack lengths. This is expected since crack closure is more pronounced for low stress intensity factor ranges [14].
Furthermore, up to 9 mm from the fusion line, the effective stress intensity factor range ratio remains above Newman's theoretical upper bound for both stress intensity factor ranges. This is an indication that tensile residual stresses may have remained after post-weld heat treatment, partially inhibiting crack closure. These results are consistent with previous studies that showed that the post-weld heat treatment may not completely eliminate the residual stresses in CA6NM welds [2, 3].
On the other hand, the effective stress intensity factor range ratio of the crack at 13 mm from the fusion line is below the upper bound predicted by Newman for plasticity-induced crack closure for both stress intensity factor ranges. This is an indication that tensile residual stresses at the crack tip may have relaxed with crack growth and that crack closure is not inhibited. Tensile residual stresses are known to redistribute and eventually relax following the growth of a fatigue crack [15]. After complete relaxation of the tensile residual stresses, common closure mechanisms such as plasticity-induced, roughness-induced and oxide-induced crack closure become fully active and the global closure level is increased.
The evolution of the measured effective stress intensity factor range ratio against crack length is shown in Fig. 8 (triangles). Crack closure is rather constant up to 9 mm from the fusion line, than it increases as the crack grows and eventually stabilizes. A good correlation is observed between the profiles of the fatigue crack growth rate (circles) and the effective stress intensity factor range ratio (triangles). This shows that the fatigue crack growth behavior of the heat treated specimens is directly affected by the variation of crack closure.

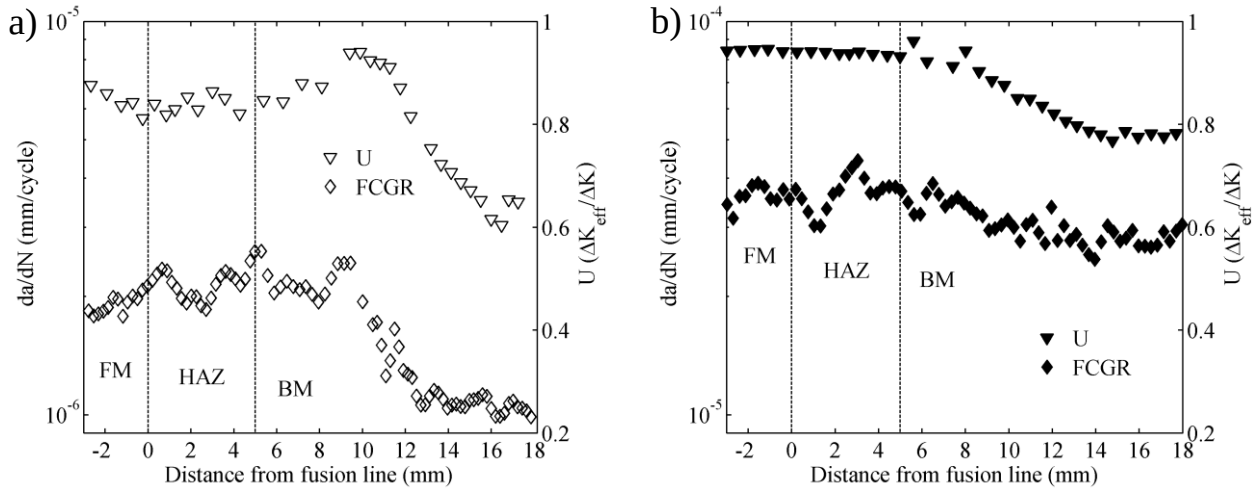

Figure 8. Relationship between U and the FCGR against the crack length for heat treated specimens a) $\Delta K = 8$ MPa·m^{½} b) $\Delta K = 20$ MPa·m^{½}.

5. Conclusion

The main objective of this study was to investigate the effect of residual stresses on the fatigue crack growth behavior of a stainless steel alloy CA6NM welded joint. From the results, the following conclusions can be drawn.

In as-welded specimens, many clues point to the fact that tensile residual stresses are present at the crack tip and are having an effect on the fatigue crack growth behavior. This hypothesis is supported by: (1) A higher effective load ratio indicated by the agreement between the mean R = 0.1 experimental base metal fatigue crack growth rate and the R = 0.7 base metal fatigue crack growth curve. (2) An effective stress intensity factor range ratio equal to unity for all crack lengths meaning that a crack opening mechanism is present. (3) A negative closure load on an as-welded specimen at a crack length of 20 mm.

It is also believed that some tensile residual stresses remain after post-weld heat treatment, as evidenced by the effective stress intensity factor range ratio being superior to Newman's prediction for plasticity-induced crack closure. In addition, an increase in crack closure when the crack is in the base metal points to the fact that the tensile residual stresses were relaxed with crack growth and that closure mechanisms become fully active.

This study showed that tensile residual stresses, which are strongly believed to be present in the as-welded specimens, caused the crack to remain fully open, this having a detrimental effect on the fatigue crack growth resistance of CA6NM welds. Moreover, the fatigue crack growth resistance was found to be improved in the heat treated specimens compared to the as-welded specimens. This is attributed to the residual stresses relaxation after tempering and with crack growth, allowing closure mechanisms to become active and reducing the fatigue crack growth rates. This shows the importance of a good residual stress level control through post-weld heat treatment.

Acknowledgements

This study was made possible by the support of Alstom Hydro, Hydro-Québec and the National Science and Engineering Research Council of Canada (NSERC). The authors wish to thank Prof. Yves Verreman for his invaluable technical insights as well as technologists Carlo Baillargeon and Benedict Besner for their help with the fatigue testing procedure.

References

[1] M. Sabourin, D. Thibault, D. A. Bouffard, and M. Levesque, "New parameters influencing hydraulic runner lifetime," presented at the 25th IAHR Symposium on Hydraulic Machinery and Systems, Timisoara, Romania, 2010.

[2] D. Thibault, P. Bocher, M. Thomas, M. Gharghouri, and M. Côté, "Residual stress characterization in low transformation temperature 13%Cr–4%Ni stainless steel weld by neutron diffraction and the contour method," *Mat Sci Eng A-Struct*, vol. 527, pp. 6205-6210, 2010.

[3] É. Moisan, M. Sabourin, M. Bernard, and T. Bui-Quoc, "Residual stress measurements in hydraulic turbine welded joints," presented at the IAHR 23rd Symposium on Hydraulic Machinery and Systems, Yokohama, Japan, 2006.

[4] Y. B. Lee, C. S. Chung, Y. K. Park, and H. K. Kim, "Effects of redistributing residual stress on the fatigue behavior of SS330 weldment," *Int J Fatigue*, vol. 20, pp. 565-573, 1998.

[5] A. Ohta, N. Suzuki, and Y. Maeda, "Unique fatigue threshold and growth properties of welded joints in a tensile residual stress field," *Int J Fatigue,* vol. 19, pp. 303-310, 1997.

[6] C. Jang, P.-Y. Cho, M. Kim, S.-J. Oh, and J.-S. Yang, "Effects of microstructure and residual stress on fatigue crack growth of stainless steel narrow gap welds," *Mater Design,* vol. 31, pp. 1862-1870, 2010.

[7] J. Lanteigne, M. Sabourin, T. Bui-Quoc, and D. Julien, "The characteristics of the steels used in hydraulic turbine runners," presented at the IAHR 24th Symposium on Hydraulic Machinery and Systems, Foz Do Iguassu, Brazil, 2008.

[8] ASTM, "E647-11e1 Standard Test Method for Measurement of Fatigue Crack Growth Rates," ed: ASTM International, 2011.

[9] D. Thibault, P. Bocher, and M. Thomas, "Residual stress and microstructure in welds of 13%Cr–4%Ni martensitic stainless steel," *J Mater Process Tech,* vol. 209, pp. 2195-2202, 2009.

[10] A. G. M. Pukasiewicz, S. L. Henke, and W. J. P. Casas, "Effect of post-weld heat treatment on fatigue crack propagation in welded joints in CA6NM martensite stainless steel," *Welding International,* vol. 20, pp. 947-952, 2006.

[11] W. Elber, "The significance of fatigue crack closure," *Damage Tolerance in Aircraft Structures, ASTM STP 486,* pp. 230-242, 1971.

[12] J. C. Newman, "A crack opening stress equation for fatigue crack growth," *Int J Fracture,* vol. 24, pp. 131-135, 1984.

[13] J. C. Newman Jr, J. H. Crews Jr, C. A. Bigelow, and D. S. Dawicke, "Variations of a global constraint factor in cracked bodies under tension and bending loads," *Constraint Effects in Fracture Theory and Applications: Second Volume, ASTM STP 1244,* pp. 21-42, 1995.

[14] S. Suresh and R. O. Ritchie, "Near-threshold fatigue crack propagation: a perspective on the role of crack closure," presented at the Symp. on Concepts of Fatigue Crack Growth Threshold, Philadelphia, USA, 1983.

[15] R. C. McClung, "A literature survey on the stability and significance of residual stresses during fatigue," *Fatigue Fract Eng M,* vol. 30, pp. 173-205, 2007.

Cutting Zone Temperature and Specific Cutting Energy Measurement and Evaluation in Machining Metals

Y. Yifrach[1], **U. Ben-Hanan**[2]
[1] Department of Mechanical Engineering, ORT Braude College, P.O. Box 78, Karmiel 21982, Israel
[2] Department of Mechanical Engineering, ORT Braude College, P.O. Box 78, Karmiel 21982, Israel
Email: yifrach@braude.ac.il

Abstract The knowledge of the temperature that develops between tools and the raw material is needed for optimizing the cutting parameters. A controlled Grinding experiment was compared with a thermo-mechanical finite elements model (FEM) simulating the temperature distributions and other effects occurring in the cutting zone. An electric Grinding was controlled by [Labview] software, keeping the torque and rotational speed constant and preventing disruption of fixed air flow.
The processed material was glass ceramics, the mechanical and thermal properties of which are known from the literature. A finite elements model was developed and its parameters determined by matching the computed Nodes with thermocouples' temperature measurements. The experiment was carried out by single slot cutting, without cooling. The value of cutting power was based on specific cutting energy (U), known from the literature and calculation of (MRR) from the cutting parameters (depth & width of cut, feed rate). The dynamic model simulated the movement of cutting tool by sampling heat sources along the path. The fit obtained between dynamic model and the measurements enables a reliable calculation of the specific cutting energy (U) for every combination of tool cut and raw material.

Keywords: cutting, specific cutting energy (U), Material removal rate (MRR), finite element method (FEM).

1. Introduction

Most of the energy of machining is transformed to heat. The heat transfer from the cutting zone depends on the heat capacity of the raw material and on its configuration. The temperature rise of the cutting zone may limit the cutting speed and cutting depth, causing tool wear and limiting its life, and creating thermal stress in the raw material and distortions of its surface.
It is therefore highly desirable to measure the cutting zone temperature and relate it to the cutting performance parameters (depth of cut, cutting velocity, feed, linear speed of cutting progress, power required, Specific Grinding Energy). Due to the nature of metal cutting, it is not possible to measure temperature directly in the cutting zone.
The main techniques used to evaluate the surface temperatures during machining are Thermocouple method and infrared photographic technique [1-4]. Two arrays of thermocouples were lined along both sides of the cutting path for measuring the temperature development throughout the working piece according to the drill's advancement in recent years; the finite element method has particularly become the main tool for simulating metal cutting processes. It is especially important that FEM analysis can help to investigate the temperature distributions and other effects occurring in the

cutting zone. A finite element (FEM) thermal analysis program (NASTRAM software) was developed and reported here, utilizing a moving heating source model [5-6]. In that model, the grinding zone is assumed as a band source of heat that moves along the upper surface of the workpiece. The heat to the Workpiece in dry grinding was calibrated by matching between experimental data using an embedded thermocouples and FEM analysis temperature response. The FEM is used for extrapolation the temperature data from the measured points to the cutting zone.

2. Data acquisition system

The data acquisition system consists of controller, amplifier, A/D convertor, and LabVIEW (Laboratory Virtual Instruments Engineering Workbench) for windows software developed by National Instruments. Once the program runs, thermocouples' temperature and normal grinding force were collected and recorded on an Excel file.

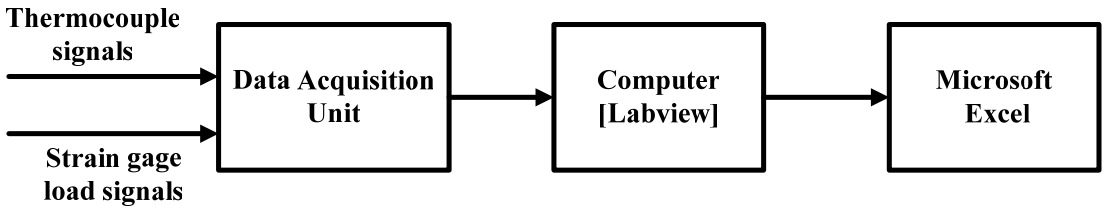

Figure 1. Schematic representation of Data acquisition system

3. Calibration experiment versus finite elements model

The thermal analysis model utilizes parameters from the literature (specific heat capacity, Thermal conductivity and Density).The objective of calibration experiment is to verify the model and calibrate the parameters by matching the results with measurements.

A solder-iron served as a heat source. It was placed at the center of the plate (x=0;y=39mm). An equally-spaced array of four thermocouples was placed in the upper surface and another two thermocouples – on the lower surface (Figure 4).

The temperature at each thermocouple was measured after they reached a steady-state, 450 seconds after the initiation of the heat source (Figure 9). Plots of y-cut temperature distribution at each thermocouple's position were calculated by the model (Figure 6). The ratio of the values at the peaks (locations of the thermocouples) matched the ratio of the measured values at the respective thermocouples. Values of (h) were then iterated in the model to reach a match with the measurements for $h_{final} = 2.0 \cdot 10^{-4} \left[W/mm^2 \cdot {}^0C \right]$. This is exhibited in Figure 6.

The temperature evolution with time (as measured and displayed Figure 8) was then compared with a time evolution run of the model (Figure 9), which shows a good match.

It is then easy to estimate the heat transfer coefficient (h) after calibrating the finite elements model, for every combination of tool cut and raw material.

3.1. Calibration model of ceramic plate mesh

The full model was built with Solid elements. The dimensions of the plate are 78x78x5 mm. The mesh of the plate model consists of identical elements, with the size of 1x1x1 mm. The total amount of elements in the plate is 30420

3.2. Experimental set-up

The experiment set up and workpiece are described in Figure 2 and Figure 3. It should be noted that this experimental setup is in use for measuring dental bur wear research [5].

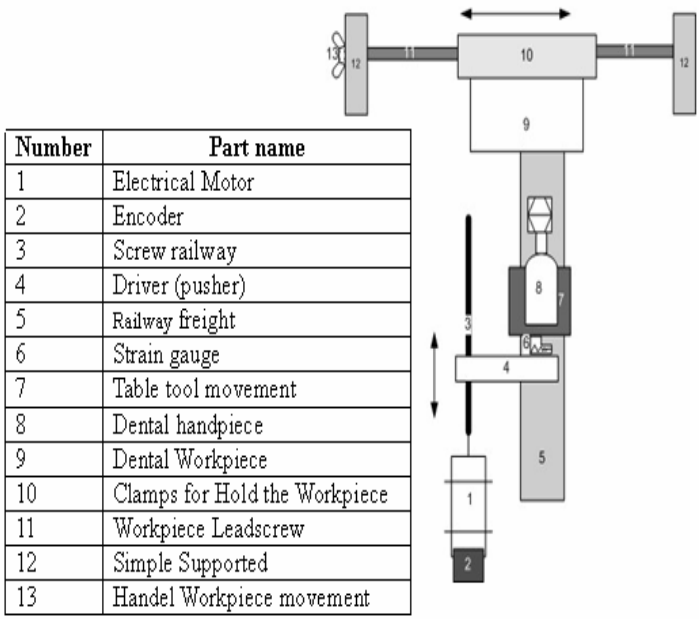

Number	Part name
1	Electrical Motor
2	Encoder
3	Screw railway
4	Driver (pusher)
5	Railway freight
6	Strain gauge
7	Table tool movement
8	Dental handpiece
9	Dental Workpiece
10	Clamps for Hold the Workpiece
11	Workpiece Leadscrew
12	Simple Supported
13	Handel Workpiece movement

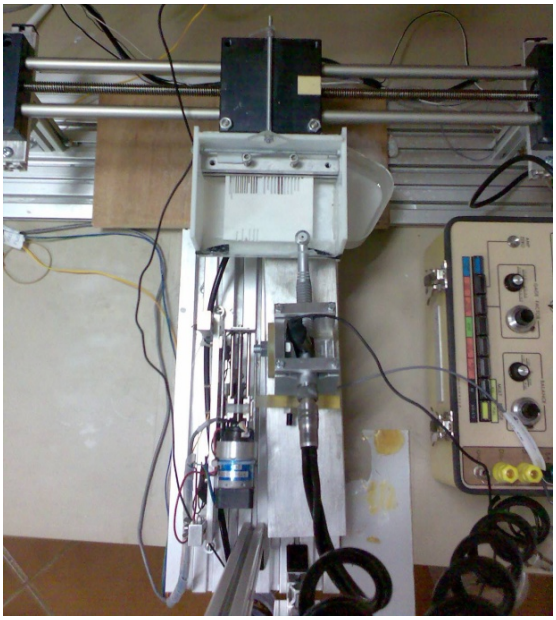

Figure 2. Schematic representation and photo of Experimental set-up

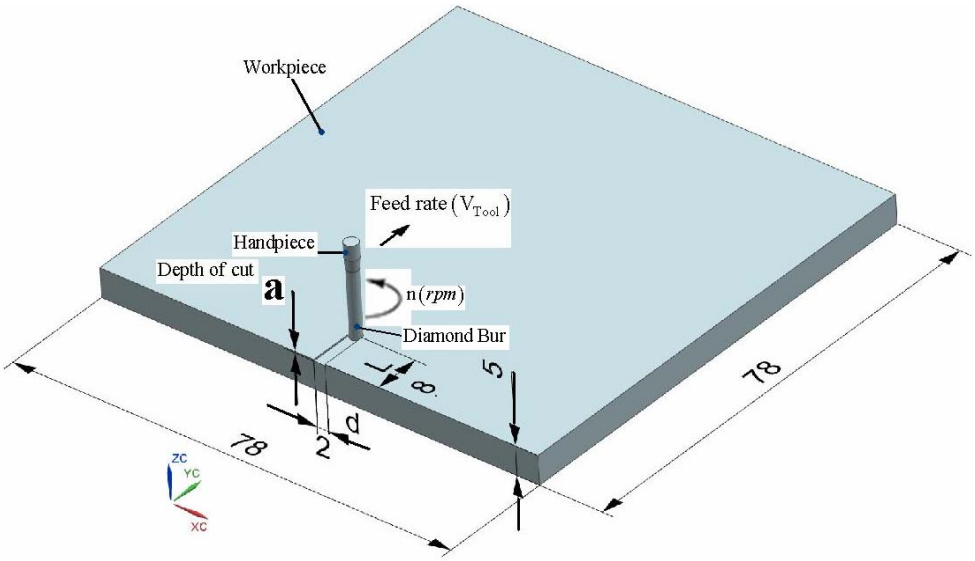

Figure 3. Detailed illustration of the bur- Dental Workpiece movement

3.3. Boundary conditions for calibration static (steady-state) model

(1) The temperature of the heat source is 330°C
(2) The other surfaces that without contact with the heat source will with Convection region.

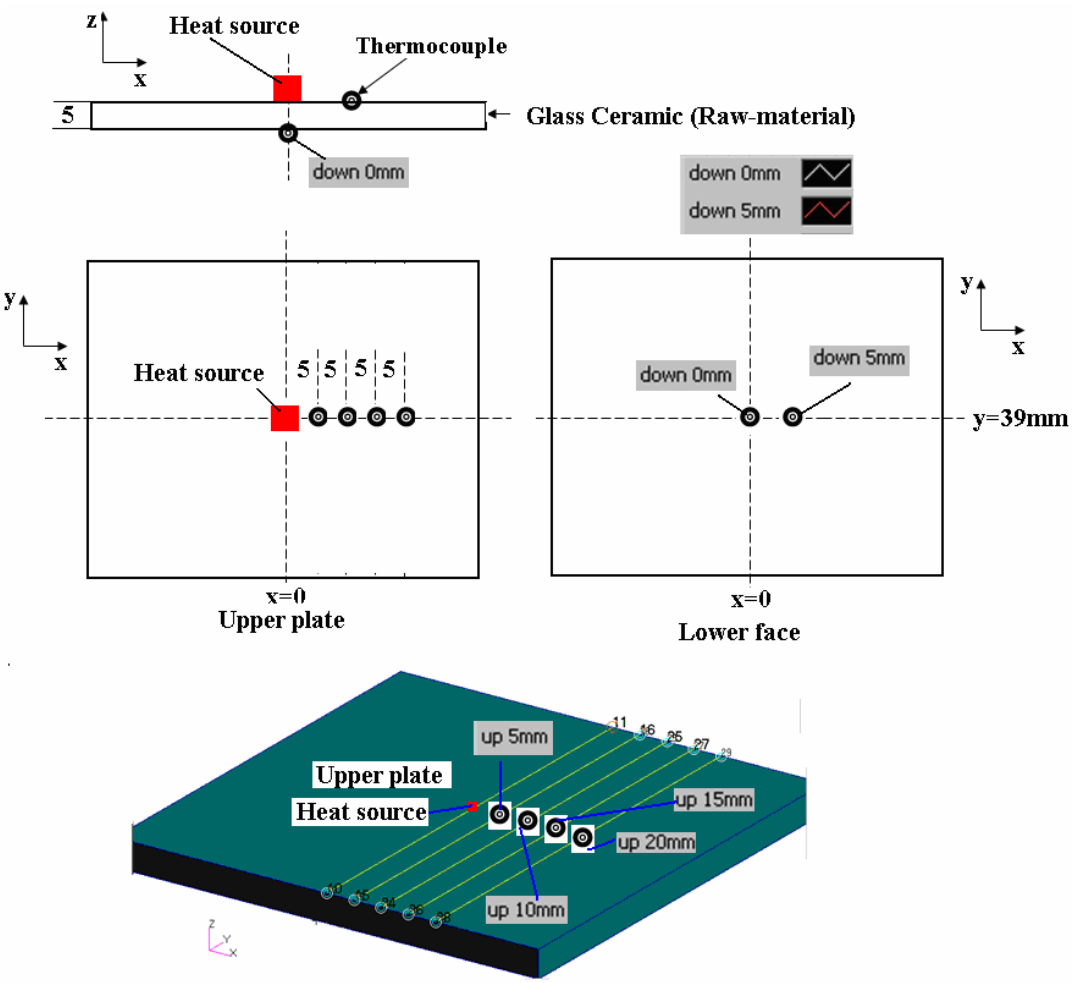

Figure 4. Experiment configuration of thermocouples for measuring the temperature

The convection is assumed to have a small impact on the heat distribution. A fixed heat transfer coefficient (h) is therefore assumed over the working piece. It was estimated (h_{final}) by varying the parameters of the analytical results to match with the measured ones at the thermocouples.
The thermal properties of the ceramic plate (Table 1) were given to the calibrate model and to the grinding model.

Table 1. Thermal properties of the ceramic plate

Material	Thermal conductivity	Specific heat	Density
Machinable Ceramic	$k = 1.46 \cdot 10^{-3} \left[{}^{w}\!/_{mm \cdot {}^{0}C} \right]$	$c_p = 790 \left[{}^{J}\!/_{Kg \cdot {}^{0}C} \right]$	$\rho = 2520 \left[{}^{Kg}\!/_{m^3} \right]$

3.4. Model calibration static results

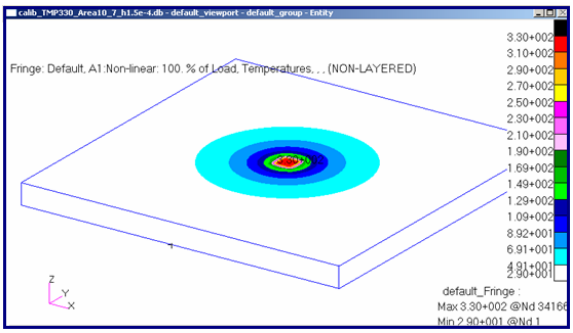

Figure 5. The temperature distribution on the upper surface

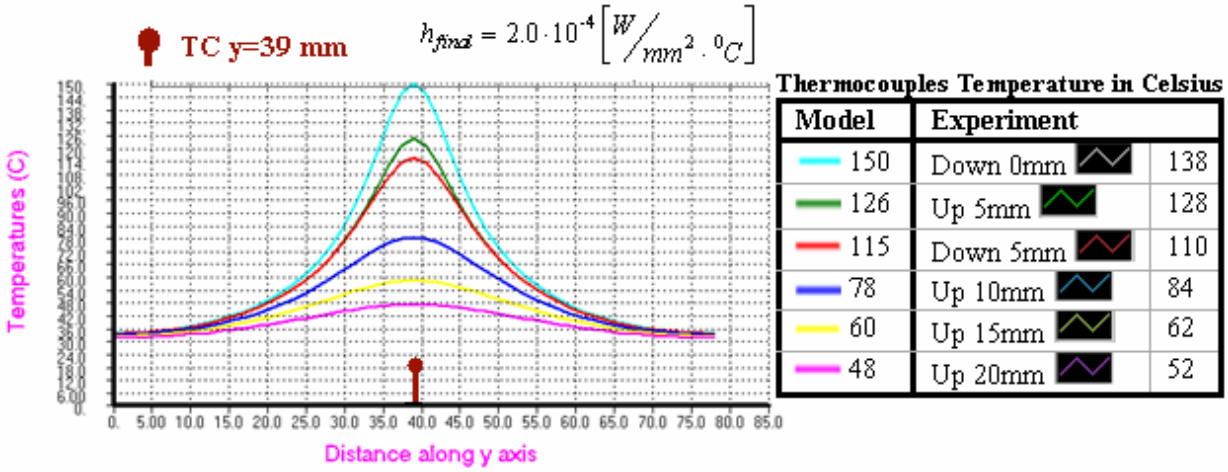

Figure 6. The temperature distribution along y axis on the lower and upper surface

Due to the symmetry of the problem in terms of geometry, loads (heat source) and boundary condition (there is no convection across symmetrical planes) we built a quarter-plate model and thereby save calculation time. A fine-mesh was built near the heat source to capture the delicate changes (Figure 7) so that the gradient temperature through the thickness of the plate is exhibited clearly. It should be noted that the quarter model results are the same as the complete model (described in Figure 5 and 6).

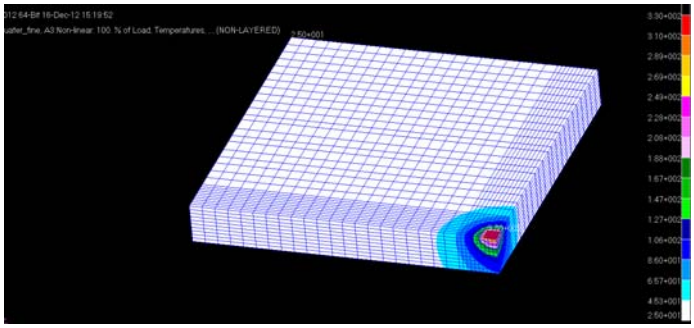

Figure 7. The distribution and size of the temperature on the quarter model, described with fine mesh near the heat source

3.5. Results and discussion from Calibration experiment versus finite elements model

(1) We can see that the temperatures distribution is identical in all curves and received an excellent match with the experiment temperature in stable condition (Figure 6) and (Figure 8).

(2) In this experiment and FEM model the thickness of the plate is relatively small, so the temperature will be higher in the lower-surface (under the heat source) and not on the upper face within 5 mm from the heat source, since the heat dispersed faster in radial direction than in the depth plate direction.

3.6. FEM dynamic model (transient) for calibration

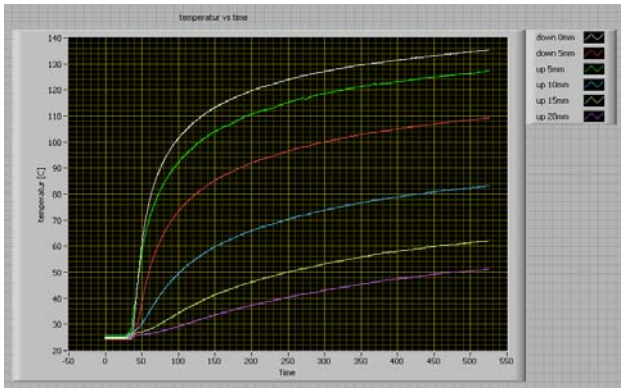

Figure 8. Experimental temperature results versus time of six thermocouples

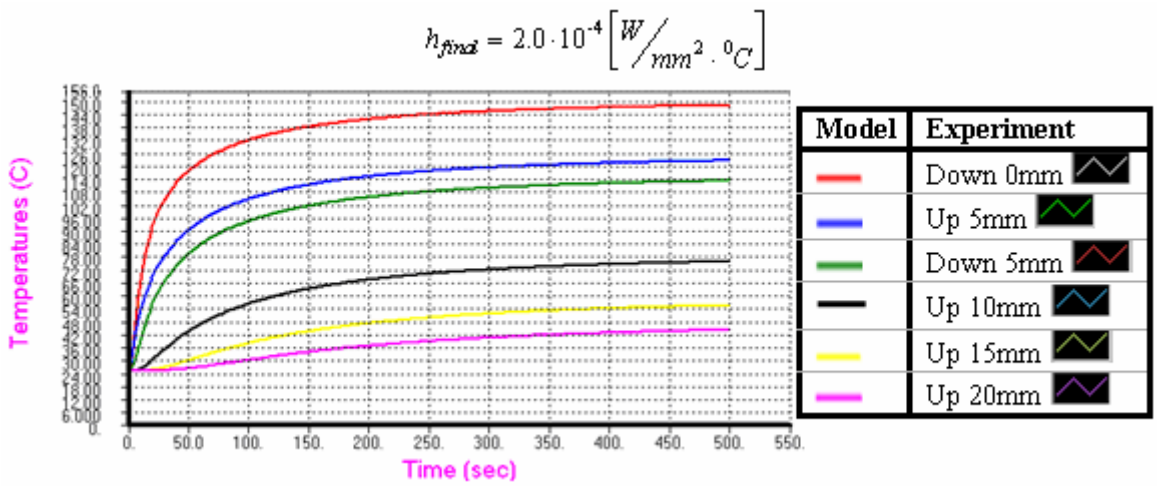

Figure 9. Transient model temperature results versus time of six thermocouples

3.7. Results and discussion of model (transient) for calibration

(1) Receiving in the model and experiment the same distribution temperature in six thermocouples.

(2) Steady state condition of the temperature in each thermocouples nodes in the model is accepted after about 500 seconds and received an excellent match with the experiment temperature in stable condition

(3) Conclusion: There is good reliability in measuring temperature with thermocouples.

4. Grinding experiment without internal or external cooling

The objectives of the experiment are: measuring the temperature of the workpiece in grinding without cooling and calibrating by matching between experimental data, using embedded thermocouples, and FEM analysis temperature response. The FEM is used for extrapolation of the temperature data from the measured node points to the cutting zone.

4.1. Experiment grinding configuration of thermocouples for measuring the temperature

An equally-spaced array of 6 thermocouples was placed in the upper surface (Figure 10), three on each side, symmetric to the cutting tool position. This positioning ensures reliable experiment results. Another two thermocouples were placed on the lower surface.

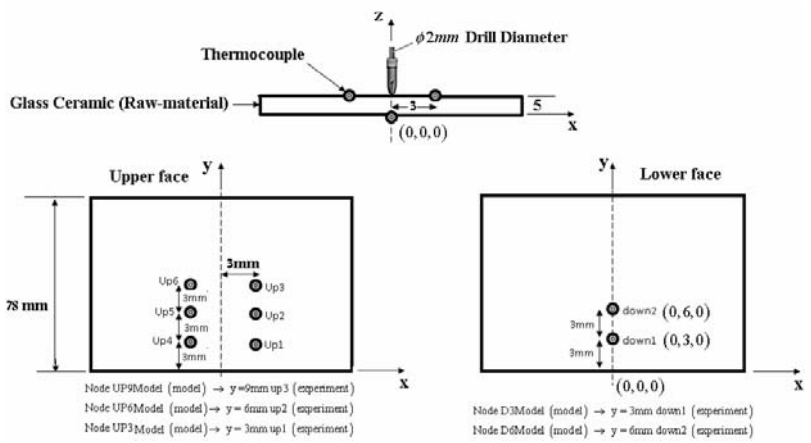

Figure 10. Experiment grinding configuration of thermocouples for measuring the temperature.

4.2. Description of the mesh and the boundary conditions in the grinding model

Due to the symmetry of the problem in terms of geometry, loads (heat moving sources) and boundary condition (there is no convection across the symmetrical plane and on the moving heating sources) we built a half-plate model and thereby save calculation time. A fine-mesh was built near the heat moving sources to capture the delicate changes (Figure 11).

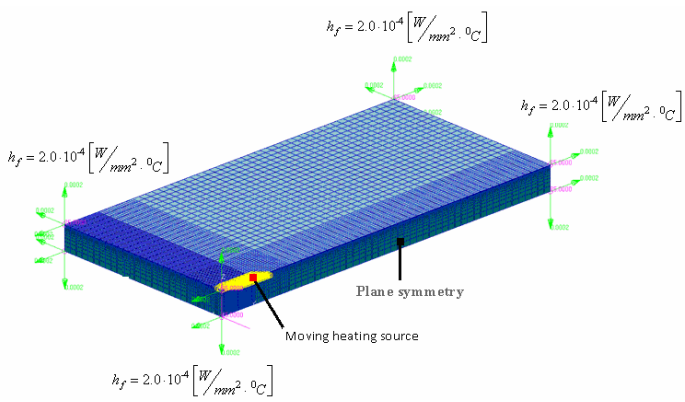

Figure 11. Boundary conditions for half a grinding model with fine mesh near the heat source

4.3. Description of the heat sources in the grinding model without cooling

The grinding area is located on the center of the upper surface of the plate. The grinding is executed from the center of the edge towards the center of the plate for a distance of 8 mm (the yellow strip in Figure 11). In the experiment the cutting movement is a continuous motion, as for the model, the simulation of the cutting movement is discrete. Along the grinding area a fine mesh was formed and 36 heat sources were placed, all with the same power and same operation time (each one starts to operate after its predecessor stops). The power of the first heat source, which is placed on the edge, increases from zero till half the diameter of the cutting tool penetrated the plate. From this point on its power equals the power of the other heat sources.

4.4. Grinding experiment conditions

The experiment was executed four times with the conditions described below (Table 2)

Table 2. Operational conditions

Parameter	$P_{Machine}\left(Watt\right)$	$n_{Tool}\left(rpm\right)$	$a_{cut}\left(mm\right)$	$V_{Tool}\left(mm/\sec\right)$	$L_{cut}\left(mm\right)$
Value	40	200,000	0.32	0.033	8

4.5. Estimation of the cutting power in the experiment

The experiment system has no power measurement system. Therefore, the value of cutting power was based on specific cutting energy (U), known from the literature and the calculation of MRR that depends on the cutting parameters (depth and width of cut, feed rate). U depends on the depth of the cut. The MRR value is calculated in Eq. (1) and the cutting power is calculated in Eq. (2).

$$MRR\left(\frac{mm^3}{\sec}\right)=V_{Tool}\left(\frac{mm}{\sec}\right)\cdot A_{cut}\left(mm^2\right)\rightarrow A_{cut}=\left(\frac{\pi\cdot d_{Tool}}{2}\right)\cdot\left(a\right)=\left(\frac{\pi\cdot 2}{2}\right)\cdot\left(0.32\right)=1.0mm^2 \tag{1}$$

$$MRR=0.033\left(\frac{mm}{\sec}\right)\cdot 1.0=0.033\left(\frac{mm^3}{\sec}\right)$$

$$P_{cut}=U\left(Watt\cdot Sec/mm^3\right)\cdot MRR\left(\frac{mm^3}{\sec}\right)=30\cdot 0.033=1.0\left(Watt\right) \tag{2}$$

The estimated value of the cutting power is 1 Watt for the full plate.
Given half a plate in the model, 0.5 Watt was entered to the grinding model as the thermal power.

4.6. Experiment results versus grinding model results

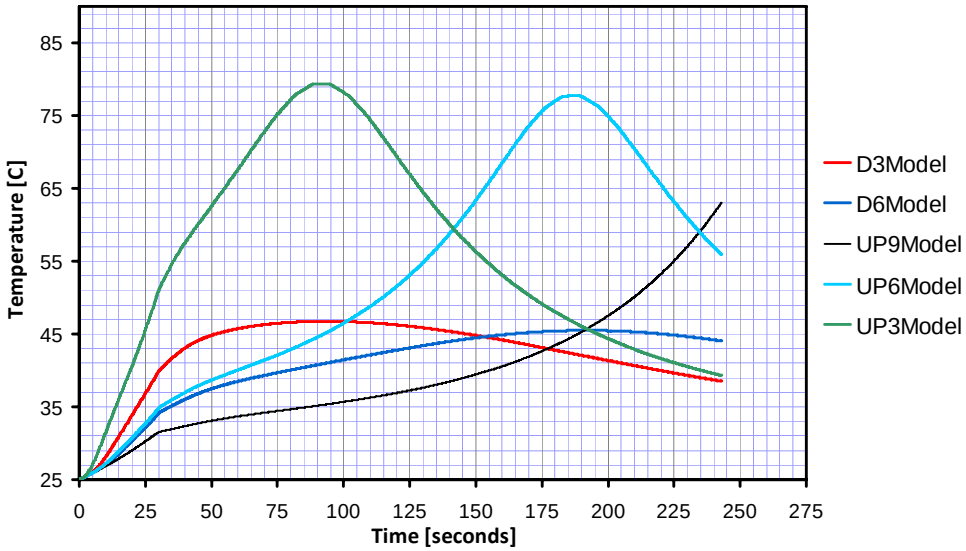

Figure 12. Half model temperature results versus time of five thermocouples

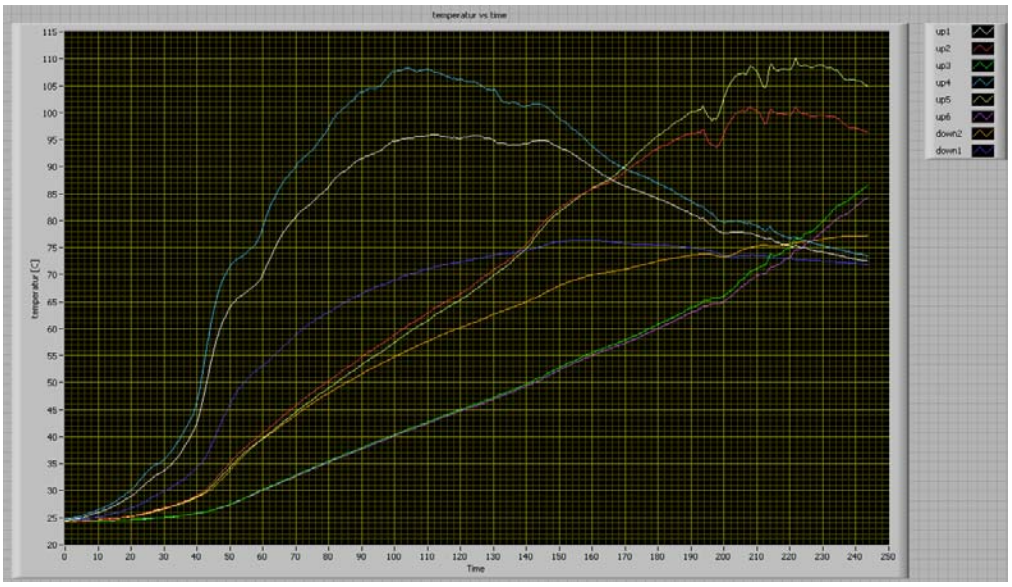

Figure 13. Experimental temperature results versus time of eight thermocouples

5. Results and discussion from Experiment results versus grinding model results

(1) There is a similarity between the graph behaviors of the model to the one of the experiment.

(2) There is a mismatch in the form of the temperature distribution between the model and the experiment, at the first 40 seconds. This is due to the following reasons:

(2.1) Perhaps there is a problem with the adhesive of the thermocouples that causes contact resistance in addition to their thermal mass.

(2.2) It should be noted that in the first 40 seconds the cutting power varies and stabilizes only after the cutting tool penetrates the plates half its diameter.

The objective of this research is to evaluate the temperature around the cutting zone. Due to the low temperatures during the first 40 seconds, the accuracy there is less important.

(3) The temperatures in the experiment are higher by 20% than those of the model. The reason for the difference is that in the model the reaction caused by the contact of the cutting tool lower edge with the plate was neglected. This difference can be solved by executing peripheral milling. Another reason for the gap is the high value of depth of cut (0.32 mm) in grinding. Using a lower value will reduce the temperature gap.

Future work will further develop power measurement in the experiment by measuring the electrical power (Volt, Ampere) or by measuring the torque and the rpm of the rotating cutting tool.
Further experiments will be held with a variety of depths of cut (25, 50, 100, and 150 μm).
The specific cutting energy (U) can by calculated by measuring the cutting power from the experiment and dividing by the calculate MRR. In this case the temperature measurement is unnecessary.

Acknowledgement:

This research was supported by a grant from the ORT Braude College research committee & The Ministry of Industry in Israel.

References

[1] D.A. Stephenson, Tool-Work Thermocouple Temperature Measurement, Trans. ASME.J. Eng. Ind. (1993) 432-437.
[2] D.A. Stephenson, Assessment of steady state metal cutting temperature models based on simultaneous infrared and Thermocouple data, Trans. ASME.J. Eng. Ind. (1991) 121-128.
[3] G..S. Reichenbach, Experimental Measurement of metal cutting temperature distributions, Trans. ASME.J. (1958) 525-546.
[4] G. Boothroyd, Photographic technique for the determination of metal cutting temperatures, Br. J. Applied Physics. 12 (1961) 238-242.
[5] M. Regev, H. Judes, U. Ben-Hanan, Wear Mechanisms of Diamond Coated Dental Burs, Tribology - Materials, Surfaces & Interfaces, (2010) 38-42
[6] N. Bianco, O. Manca, S. Nardini, Comparison between Thermal Conductive Models for Moving Heat Sources in Material Processing, ASME HTD, 369-6. (2001) 11-22.
[7] N. Bianco, O. Manca, V. Naso, Numerical analysis of transient temperature fields in solids by a moving heat source, HEFAT2004, 3rd Inte. Conf. on Heat Transfer, Fluid Mechanics and Thermodynamics, Paper n. BN2, 21 – 24 June 2004, Cape Town, South Africa. 2004.
[8] D.A. Doman, A. Warkentin, R. Bauer, Finite element modeling approaches in grinding, International Journal of machine tools and manufacturing, (2009) 109-116.
[9] J.O. Outwater, M.C. Chaw, Surface temperatures in grinding, ASME Transactions, (1952) 74(1) 73-81.
[10] X. Xu, S. Malkin, Comparison of methods to measure grinding temperatures, Journal of Manufacturing science and engineering, (2001).191-195.
[11] C. Milton Shaw, Metal cutting principle, UK Oxford University Press, London, 2005
[12] G. Bootthrody, Fundamentals of Metal Machining and Machine Tools, McGraw-Hill, New York, 1981.
[13] TW. Hwang, CJ. Evans, S. Malkin, Size effect for specific energy in grinding of silicon nitride. Wear, (1999) 225: 862–867.
[14] TW. Hwang, S. Malkin, Upper bound analysis for specific energy in grinding of ceramics. Wear, (1999) 231: 161–171.

Modeling of Damage Evolution in Particulate Reinforced Composites with VCFEM

Ran Guo[1,*], **Wenyan Zhang**[1], **Benning Qu**[1], **Yongjin Chen**[1]

[1] Department of Engineering Mechanics, Faculty of Civil Engineering and Architecture, Kunming University of Science and Technology, Kunming 650500, China
[2] Faculty of EEFF, Institute of GGHH, City Post Code, Country
* Corresponding author: prof.guo@189.cn

Abstract The modeling of fatigue crack initiation and propagation for particulate reinforced composites and the study of the behavior of a functionally graded material with interface cracks are facilitated with a new Voronoi Cell Finite Element Method (VCFEM), considering the matrix-inclusion interfacial fatigue crack and matrix fatigue crack. In the new element, all possible contacts on the crack edge are considered by contact seeking and remeshing methods, when the crack is closing under all possible changing loads. The fatigue crack initiates when the fatigue damage exceeds certain critical damage value, and fatigue crack propagation are simulated by gradual seeking crack propagating directions and new crack tips, using a remeshing method that a damaged node at the crack tip is replaced by a pair of nodes, a new crack tip node is assigned at the crack propagating directions and a more pair of nodes are needed to be added on the crack edge near the crack tip in order to better facilitate the free-traction boundary condition. The first example has been given for Particle-reinforced metal-matrix composites with 20 elliptical inclusions to simulate the fatigue crack initiation and propagation under plane stress conditions. It appears that this method is a more efficient way to deal with the interfacial damage of composite materials. In the second example, the results show that the mechanical properties of functionally gradient materials are influenced by the particles' size, topological structure, and interfacial deboning strength. With the interface cracking the overall stiffness of functionally gradient materials is gradually reduced.

Keywords VCFEM, Finite element method, Fatigue crack, Particulate reinforced composites

1. Introduction

Particulate-reinforced metal-matrix composites (MMCs) have attracted significant attention in recent times in both the academic community and in the industrial sector. Since MMC combine well-known superior properties such as low density, high strength, stiffness, creep and wear resistance, they are appropriate candidates for numerous aerospace and automotive applications. However, the differences in thermo-mechanical properties of matrix and inclusion develop stresses during fabrication and in service. This may lead to voids nucleation, cracking and decohesion at the interface, which affects seriously fracture properties.

The validity of modeling real composites practically with heterogeneities of arbitrary shapes, sizes or dispersions, depends considerably on the consideration of the irregular microstructure. The accurate micromechanical modeling of actual two-phase materials is very complicated due to the irregular microstructural configurations that exist in real materials.

A large number of models have been developed to predict the effective elastic properties of heterogeneous materials and their dependence on materials microstructure, such as homogenization theory, cell methods, traditional displacement based FEM, A hybrid finite element approach by Zhang and Katsube[1], a Voronoi Cell Finite Element Method (VCFEM) for modeling of non-uniform microstructures with heterogeneities introduced by Ghosh and co-workers in a series of papers[2~3] and a series of works on VCFEM are done[5-6].

Introduction a new Voronoi cell finite element model (VCFEM) on the base of the assumed stress hybrid variational principle to model fatigue crack initiation and propagation in a Particle-reinforced metal-matrix composites (MMCs) with heterogeneities of arbitrary shapes, sizes or dispersions is the objective of the present study. In the new element, considering the

matrix-inclusion interfacial fatigue crack, matrix fatigue crack and all possible contact on the crack edge, fatigue crack initiation and propagation is simulated by a new remeshing method. All possible contact on the crack edge when the crack closed under all possible fatigue loads are sought along every crack edge. The fatigue crack initiates when the fatigue damage exceeds certain critical damage value. The fatigue crack propagation is simulated by gradually seeking crack propagating directions and new crack tips, using a remeshing method that a damaged node at the crack tip is replaced by a pair of nodes, a new crack tip node is assigned at the crack propagating directions and a more pair of nodes are needed to be added on the crack edge near the new crack tip in order to better facilitate the free-traction boundary condition. The first example has been given for Particle-reinforced metal-matrix composites with 20 elliptical inclusions to simulate the fatigue crack initiation and propagation under plane stress conditions. It appears that this method is a more efficient way to deal with the interfacial damage of composite materials. The simulation results are compared with those of general fine finite element model and a good agreement is obtained. In the second example, the results show that the mechanical properties of functionally gradient materials are influenced by the particles' size, topological structure, and interfacial deboning strength. With the interface cracking the overall stiffness of functionally gradient materials is gradually reduced.

2. The Voronoi Cell Finite Element Model

2.1. Hybrid Element Assumptions and Weak Forms

In the Voronoi cell element method, each cell represents a basic structural element of the microstructure, which includes a particulate with its matrix neighborhood. A new cell element, including an interfacial crack and a matrix crack, is shown in Fig. 1. The matrix and inclusion phase in each Voronoi cell Ω_e are denoted by Ω_m and Ω_c, respectively, i.e., $\Omega_e = \Omega_m \cup \Omega_c$. The bonded inclusion-matrix interface is indicated by $\partial\Omega_b$ and the debonded interface is indicated by $\partial\Omega_c$ on the inclusion side and by $\partial\Omega_m$ on the matrix side. The element boundary $\partial\Omega_e$ is assumed to be composed of prescribed displacement boundary $\partial\Omega_e^d$, prescribed traction boundary $\partial\Omega_e^t$, inter-element boundary $\partial\Omega_e^i$ and free boundary $\partial\Omega_e^f$, i.e., $\partial\Omega_e = \partial\Omega_e^d \cup \partial\Omega_e^t \cup \partial\Omega_e^i \cup \partial\Omega_e^f$. The matrix crack edges $\partial\Omega_{m1}$, $\partial\Omega_{m2}$, $\partial\Omega_{m3}$ and inclusion crack edge $\partial\Omega_c$ have outward normals $\mathbf{n}^{m1}$, $\mathbf{n}^{m2}$, $\mathbf{n}^{m3}$ and $\mathbf{n}^c$, respectively, while $\mathbf{n}^e$ is the outward normal to the element boundary $\partial\Omega_e$.

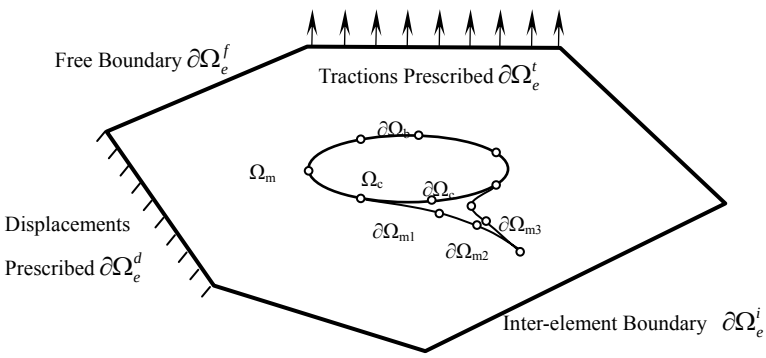

Figure 1. A Voronoi cell finite element with part interfacial crack and matrix crack

In an incremental formulation to account for the onset and growth of the fatigue crack, $\boldsymbol{\sigma}$ is an equilibrated stress field corresponding a strain field $\boldsymbol{\varepsilon}$; $\mathbf{u}$ is a compatible displacement field on the element boundary at the beginning of an increment; $\Delta\boldsymbol{\sigma}$ is the equilibrated stress increment in Ω_e;

$\Delta\mathbf{u}$ is a compatible displacement increment on $\partial\Omega_e$ and $\Delta\bar{\mathbf{f}}$ is a traction increment on the traction boundary $\partial\Omega_e^t$. An element complementary energy function can be expressed as follows:

$$\begin{aligned}
\Pi_{mc}^{e}\left(\Delta\boldsymbol{\sigma},\Delta\mathbf{u}\right) &= \int_{\Omega_e}\frac{1}{2}\left(\boldsymbol{\sigma}+\Delta\boldsymbol{\sigma}\right)\mathbf{S}\left(\boldsymbol{\sigma}+\Delta\boldsymbol{\sigma}\right)d\Omega-\int_{\partial\Omega_e}\mathbf{n}^{e}\cdot\left(\boldsymbol{\sigma}+\Delta\boldsymbol{\sigma}\right)\cdot\left(\mathbf{u}+\Delta\mathbf{u}\right)d\partial\Omega \\
&+\int_{\partial\Omega_{te}}\left(\bar{\mathbf{f}}+\Delta\bar{\mathbf{f}}\right)\cdot\left(\mathbf{u}+\Delta\mathbf{u}\right)d\partial\Omega+\int_{\partial\Omega_b}\mathbf{n}^{b}\cdot(\boldsymbol{\sigma}^{m}+\Delta\boldsymbol{\sigma}^{m}-\boldsymbol{\sigma}^{c}-\Delta\boldsymbol{\sigma}^{c})\cdot\left(\mathbf{u}^{b}+\Delta\mathbf{u}^{b}\right)d\partial\Omega \\
&-\int_{\partial\Omega_{m1}}\mathbf{n}^{m1}\cdot\left(\boldsymbol{\sigma}^{m1}+\Delta\boldsymbol{\sigma}^{m1}\right)\cdot\left(\mathbf{u}^{m1}+\Delta\mathbf{u}^{m1}\right)d\partial\Omega-\int_{\partial\Omega_c}\mathbf{n}^{c}\cdot\left(\boldsymbol{\sigma}^{c}+\Delta\boldsymbol{\sigma}^{c}\right)\cdot\left(\mathbf{u}^{c}+\Delta\mathbf{u}^{c}\right)d\partial\Omega \\
&-\int_{\partial\Omega_{m2}}\mathbf{n}^{m2}\cdot\left(\boldsymbol{\sigma}^{m2}+\Delta\boldsymbol{\sigma}^{m2}\right)\cdot\left(\mathbf{u}^{m2}+\Delta\mathbf{u}^{m2}\right)d\partial\Omega \\
&-\int_{\partial\Omega_{m3}}\mathbf{n}^{m3}\cdot\left(\boldsymbol{\sigma}^{m3}+\Delta\boldsymbol{\sigma}^{m3}\right)\cdot\left(\mathbf{u}^{m3}+\Delta\mathbf{u}^{m3}\right)d\partial\Omega
\end{aligned} \tag{1}$$

where, $\Delta\mathbf{u}^b$, $\Delta\mathbf{u}^c$, $\Delta\mathbf{u}^{m1}$, $\Delta\mathbf{u}^{m2}$ and $\Delta\mathbf{u}^{m3}$ are the displacement increments of the crack edges in an element. The total energy for an entire heterogeneous structure that contains *N* inclusions is obtained by adding the element energy functions for *N* elements:

$$\Pi_{total}^{mc}=\sum_{e=1}^{N}\Pi_{element}^{mc} \tag{2}$$

By setting the first variation of $\Pi_{element}^{mc}$ in Eq.(1) with respect to the stress increments $\Delta\boldsymbol{\sigma}$ to zero, the element displacement relations in each of the element Ω_e can be obtained. Setting the first variation of $\Pi_{element}^{mc}$ with respect to boundary displacement increments $\Delta\mathbf{u}$ to zero, obtains the traction reciprocity conditions on the inter-element boundaries and traction boundaries as shown in Fig. 1, and setting the first variation of $\Pi_{element}^{mc}$ with respect to boundary displacement increments $\Delta\mathbf{u}^b$, $\Delta\mathbf{u}^c$, $\Delta\mathbf{u}^{m1}$, $\Delta\mathbf{u}^{m2}$ and $\Delta\mathbf{u}^{m3}$ to zero, obtains the traction reciprocity conditions on the interfaces of inclusion-matrix as shown as follows:

$$\begin{aligned}
&\mathbf{n}^{b}\cdot\left(\boldsymbol{\sigma}^{c}+\Delta\boldsymbol{\sigma}^{c}\right)=\mathbf{n}^{b}\cdot\left(\boldsymbol{\sigma}^{m}+\Delta\boldsymbol{\sigma}^{m}\right) && \text{on bonded interface } \partial\Omega_b \\
&\mathbf{n}^{c}\cdot\left(\boldsymbol{\sigma}^{c}+\Delta\boldsymbol{\sigma}^{c}\right)=\mathbf{0} && \text{on debonded interface } \partial\Omega_c \\
&\mathbf{n}^{m1}\cdot\left(\boldsymbol{\sigma}^{m1}+\Delta\boldsymbol{\sigma}^{m1}\right)=\mathbf{0} && \text{on debonded interface } \partial\Omega_{m1} \\
&\mathbf{n}^{m2}\cdot\left(\boldsymbol{\sigma}^{m2}+\Delta\boldsymbol{\sigma}^{m2}\right)=\mathbf{0} && \text{on the first crack edgee } \partial\Omega_{m2} \\
&\mathbf{n}^{m3}\cdot\left(\boldsymbol{\sigma}^{m3}+\Delta\boldsymbol{\sigma}^{m3}\right)=\mathbf{0} && \text{on the second crack edge } \partial\Omega_{m3}
\end{aligned} \tag{3}$$

2.2. Method of Solution

The stresses in the matrix and inclusion phases can be individually described to accommodate stress jumps across the interface. The expressions may be assumed for stress functions $\Phi(x,y)$ in the matrix and inclusion phases in the form as

$$\Delta\boldsymbol{\sigma}^{m}=\mathbf{P}^{m}\Delta\boldsymbol{\beta}^{m} \qquad (\text{in } \Omega_m) \tag{4}$$

$$\Delta\boldsymbol{\sigma}^{c}=\mathbf{P}^{c}\Delta\boldsymbol{\beta}^{c} \qquad (\text{in } \Omega_c) \tag{5}$$

where $\Delta\boldsymbol{\beta}^m$ and $\Delta\boldsymbol{\beta}^c$ correspond to a set of undetermined stress coefficients; $\mathbf{P}^m$ and $\mathbf{P}^c$ are matrixes of interpolation functions. Compatible displacement increments on the element boundary $\partial\Omega_e$ as well as on the crack edges $\partial\Omega_b$, $\partial\Omega_c$ and $\partial\Omega_m$ are generated by interpolating in terms of generalized nodal values as:

$$\Delta\mathbf{u}=\mathbf{L}\left\{\Delta\mathbf{q}^{e}\right\},\ on\ \ \partial\Omega_e;$$

$$\Delta\mathbf{u}^b = \mathbf{L}^b\left\{\Delta\mathbf{q}^b\right\},\ on\ \ \partial\Omega_b\ ;$$

$$\Delta\mathbf{u}^c = \mathbf{L}^c\left\{\Delta\mathbf{q}^c\right\},\ on\ \ \partial\Omega_c\ ;$$

$$\Delta\mathbf{u}^{m1} = \mathbf{L}^{m1}\left\{\Delta\mathbf{q}^{m1}\right\},\ \text{on}\ \ \partial\Omega_{m1}\ ; \tag{6}$$

$$\Delta\mathbf{u}^{m2} = \mathbf{L}^{m2}\left\{\Delta\mathbf{q}^{m2}\right\},\ \text{on}\ \ \partial\Omega_{m2}\ ;$$

$$\Delta\mathbf{u}^{m3} = \mathbf{L}^{m3}\left\{\Delta\mathbf{q}^{m3}\right\},\ \text{on}\ \ \partial\Omega_{m3}$$

where $\Delta\mathbf{q}^e$, $\Delta\mathbf{q}^b$, $\Delta\mathbf{q}^{m1}$, $\Delta\mathbf{q}^{m2}$, $\Delta\mathbf{q}^{m3}$ and $\Delta\mathbf{q}^c$ are generalized displacement increment vectors, and $\mathbf{L}$, $\mathbf{L}^b$, $\mathbf{L}^{m1}$, $\mathbf{L}^{m2}$, $\mathbf{L}^{m3}$ and $\mathbf{L}^c$ are interpolation matrices. Substituting Eq. (4), (5) and (6) into the energy function (1), and setting the first variations of $\Pi^{mc}_{element}$ with respect to the stress coefficients $\Delta\boldsymbol{\beta}^m$ and $\Delta\boldsymbol{\beta}^c$, respectively to zero, yields following two weak forms of the kinematic relations. Let $\{d\beta\}^i$ corresponds to the correction to $\Delta\beta$'s in the ith iteration, the weak form of the kinematic relations may be expressed as:

$$\begin{bmatrix} \mathbf{H}^m & \mathbf{0} \\ \mathbf{0} & \mathbf{H}^c \end{bmatrix} \begin{Bmatrix} d\boldsymbol{\beta}^{m^i} \\ d\boldsymbol{\beta}^{c^i} \end{Bmatrix} = \begin{bmatrix} \mathbf{G}_e & -\mathbf{G}_{mb} & \mathbf{G}_{mm1} & \mathbf{0} & \mathbf{G}_{mm2} & \mathbf{G}_{mm3} \\ \mathbf{0} & \mathbf{G}_{cb} & \mathbf{0} & \mathbf{G}_{cc} & \mathbf{0} & \mathbf{0} \end{bmatrix} \begin{Bmatrix} d\mathbf{q}^{e^i} \\ d\mathbf{q}^{b^i} \\ d\mathbf{q}^{m1^i} \\ d\mathbf{q}^{c^i} \\ d\mathbf{q}^{m2^i} \\ d\mathbf{q}^{m3^i} \end{Bmatrix} \tag{7}$$

where

$$\mathbf{H}^m = \int_{\Omega_m} \mathbf{P}^{m^T} \mathbf{S}_m \mathbf{P}^m d\Omega \tag{8}$$

$$\mathbf{H}^c = \int_{\Omega_c} \mathbf{P}^{c^T} \mathbf{S}_c \mathbf{P}^c d\Omega \tag{9}$$

$$\mathbf{G}_e = \int_{\partial\Omega_e} \mathbf{P}^{m^T} \mathbf{n}^{e^T} \mathbf{L} d\partial\Omega \tag{10}$$

$$\mathbf{G}_{mm1} = \int_{\partial\Omega_m} \mathbf{P}^{m^T} \mathbf{n}^{m1^T} \mathbf{L}^{m1} d\partial\Omega \tag{11}$$

$$\mathbf{G}_{mm2} = \int_{\partial\Omega_m} \mathbf{P}^{m^T} \mathbf{n}^{m2^T} \mathbf{L}^{m2} d\partial\Omega \tag{12}$$

$$\mathbf{G}_{mm3} = \int_{\partial\Omega_m} \mathbf{P}^{m^T} \mathbf{n}^{m3^T} \mathbf{L}^{m3} d\partial\Omega \tag{13}$$

$$\mathbf{G}_{cc} = \int_{\partial\Omega_c} \mathbf{P}^{c^T} \mathbf{n}^{c^T} \mathbf{L}^c d\partial\Omega \tag{14}$$

$$\mathbf{G}_{mb} = \int_{\partial\Omega_b} \mathbf{P}^{m^T} \mathbf{n}^{b^T} \mathbf{L}^b d\partial\Omega \tag{15}$$

$$\mathbf{G}_{cb} = \int_{\partial\Omega_b} \mathbf{P}^{c^T} \mathbf{n}^{b^T} \mathbf{L}^b d\partial\Omega \tag{16}$$

or in a condensed form

$$d\boldsymbol{\beta}^i = \mathbf{H}^{-1}\mathbf{G}d\mathbf{q}^i \tag{17}$$

Setting the first variation of the total energy functional (1) with respect to $\Delta\mathbf{q}^e$, $\Delta\mathbf{q}^b$, $\Delta\mathbf{q}^m$ and $\Delta\mathbf{q}^c$ to zero, results in the weak form of the traction reciprocity conditions as

$$\sum_e \mathbf{G}^T d\boldsymbol{\beta}^i = \sum_e \overline{\mathbf{F}} - \sum_e \mathbf{G}^T \begin{Bmatrix} \boldsymbol{\beta}^m + \Delta\boldsymbol{\beta}^{m^i} \\ \boldsymbol{\beta}^c + \Delta\boldsymbol{\beta}^{c^i} \end{Bmatrix} \tag{18}$$

where

$$\overline{\mathbf{F}} = \begin{bmatrix} \overline{\mathbf{F}}^e \\ \mathbf{0} \\ \mathbf{0} \\ \mathbf{0} \\ \mathbf{0} \\ \mathbf{0} \end{bmatrix}; \qquad \overline{\mathbf{F}}^{eT} = \int_{\partial\Omega_{tc}} \left(\overline{\mathbf{f}} + \Delta\overline{\mathbf{f}}\right)^T \mathbf{L} d\partial\Omega \tag{19}$$

Substituting Eq. (17) into the weak form expressions of the traction reciprocity conditions Eq. (18), yields:

$$\sum_e \mathbf{K}_e d\mathbf{q}^i = \sum_e \overline{\mathbf{F}} - \sum_e \mathbf{G}^T \begin{Bmatrix} \boldsymbol{\beta}^m + \Delta\boldsymbol{\beta}^{m^i} \\ \boldsymbol{\beta}^c + \Delta\boldsymbol{\beta}^{c^i} \end{Bmatrix} \tag{20}$$

where

$$\mathbf{K}_e = \begin{bmatrix} \mathbf{G}_e^T & \mathbf{0} \\ -\mathbf{G}_{mb}^T & \mathbf{G}_{cb}^T \\ \mathbf{G}_{mm1}^T & \mathbf{0} \\ \mathbf{0} & \mathbf{G}_{cc}^T \\ \mathbf{G}_{mm2}^T & \mathbf{0} \\ \mathbf{G}_{mm3}^T & \mathbf{0} \end{bmatrix} \cdot \begin{bmatrix} \mathbf{H}^{m^{-1}} & \mathbf{0} \\ \mathbf{0} & \mathbf{H}^{c^{-1}} \end{bmatrix} \cdot \begin{bmatrix} \mathbf{G}_e & -\mathbf{G}_{mb} & \mathbf{G}_{mm1} & \mathbf{0} & \mathbf{G}_{mm2} & \mathbf{G}_{mm3} \\ \mathbf{0} & \mathbf{G}_{cb} & \mathbf{0} & \mathbf{G}_{cc} & \mathbf{0} & \mathbf{0} \end{bmatrix} = \begin{bmatrix} \mathbf{K}_1 & \mathbf{K}_2 \end{bmatrix} \tag{21}$$

$$\mathbf{K}_1 = \begin{bmatrix} \mathbf{G}_e^T\mathbf{H}^{m^{-1}}\mathbf{G}_e & -\mathbf{G}_e^T\mathbf{H}^{m^{-1}}\mathbf{G}_{mb} & \mathbf{G}_e^T\mathbf{H}^{m^{-1}}\mathbf{G}_{mm1} \\ -\mathbf{G}_{mb}^T\mathbf{H}^{m^{-1}}\mathbf{G}_e & \mathbf{G}_{mb}^T\mathbf{H}^{m^{-1}}\mathbf{G}_{mb} + \mathbf{G}_{cb}^T\mathbf{H}^{c^{-1}}\mathbf{G}_{cb} & -\mathbf{G}_{mb}^T\mathbf{H}^{m^{-1}}\mathbf{G}_{mm1} \\ \mathbf{G}_{mm1}^T\mathbf{H}^{m^{-1}}\mathbf{G}_e & -\mathbf{G}_{mm1}^T\mathbf{H}^{m^{-1}}\mathbf{G}_{mb} & \mathbf{G}_{mm1}^T\mathbf{H}^{m^{-1}}\mathbf{G}_{mm1} \\ \mathbf{0} & \mathbf{G}_{cc}^T\mathbf{H}^{c^{-1}}\mathbf{G}_{cb} & \mathbf{0} \\ \mathbf{G}_{mm2}^T\mathbf{H}^{m^{-1}}\mathbf{G}_e & -\mathbf{G}_{mm2}^T\mathbf{H}^{m^{-1}}\mathbf{G}_{mb} & \mathbf{G}_{mm2}^T\mathbf{H}^{m^{-1}}\mathbf{G}_{mm1} \\ \mathbf{G}_{mm3}^T\mathbf{H}^{m^{-1}}\mathbf{G}_e & -\mathbf{G}_{mm3}^T\mathbf{H}^{m^{-1}}\mathbf{G}_{mb} & \mathbf{G}_{mm3}^T\mathbf{H}^{m^{-1}}\mathbf{G}_{mm1} \end{bmatrix} \mathbf{K}_2 = \begin{bmatrix} \mathbf{0} & \mathbf{G}_e^T\mathbf{H}^{m^{-1}}\mathbf{G}_{mm2} & \mathbf{G}_e^T\mathbf{H}^{m^{-1}}\mathbf{G}_{mm3} \\ \mathbf{G}_{cb}^T\mathbf{H}^{c^{-1}}\mathbf{G}_{cc} & -\mathbf{G}_{mb}^T\mathbf{H}^{m^{-1}}\mathbf{G}_{mm2} & -\mathbf{G}_{mb}^T\mathbf{H}^{m^{-1}}\mathbf{G}_{mm3} \\ \mathbf{0} & \mathbf{G}_{mm1}^T\mathbf{H}^{m^{-1}}\mathbf{G}_{mm2} & \mathbf{G}_{mm1}^T\mathbf{H}^{m^{-1}}\mathbf{G}_{mm3} \\ \mathbf{G}_{cc}^T\mathbf{H}^{c^{-1}}\mathbf{G}_{cc} & \mathbf{0} & \mathbf{0} \\ \mathbf{0} & \mathbf{G}_{mm2}^T\mathbf{H}^{m^{-1}}\mathbf{G}_{mm2} & \mathbf{G}_{mm2}^T\mathbf{H}^{m^{-1}}\mathbf{G}_{mm3} \\ \mathbf{0} & \mathbf{G}_{mm3}^T\mathbf{H}^{m^{-1}}\mathbf{G}_{mm2} & \mathbf{G}_{mm3}^T\mathbf{H}^{m^{-1}}\mathbf{G}_{mm3} \end{bmatrix}$$

Eq. (21) is used to iteratively calculate for the nodal displacement increments. Then, the stress coefficients may be calculated by Eq. (17) and the stresses at any location within the element may be obtained from (4) and (5).

2.3. Simulation of Fatigue Crack Initiation and Propagation

Under the constant amplitude loadings, the fatigue damage under a non-linear fatigue damage rule evolutes as:

$$\frac{\delta\omega}{\delta N} = [\frac{\Delta\sigma}{2B(1-\omega)}]^{\beta}(1-\omega)^{-\gamma} \tag{22}$$

where B，β and γ are the material constants. Eq. (22) deduces the fatigue life:

$$N_F(\Delta\sigma, \overline{\sigma}) = \frac{1}{\beta+\gamma+1}[\frac{\Delta\sigma}{2B(\overline{\sigma})}] \tag{23}$$

For simulating fatigue damage accumulation under gradual step-by-step constant amplitude loadings, the fatigue damage accumulation at the nth step is deduced by integrating Eq. (22).

$$\omega_n = 1 - [(1-\omega_{n-1})^m - mN_n(\frac{\Delta\sigma_n}{2B})^\beta]^{\frac{1}{m}} \tag{24}$$

where where ω_{n-1} is the total fatigue damage at the end of the n-1th step; N_n is the cycle life increment at the nth step; $\Delta\sigma_n$ is the nth constant amplitude loading ; the variable $m = 1+\gamma+\beta$; the material constants $B = b_1 + b_2\overline{\sigma}_n$; b_1 and b_2 are the material constants.

3. Examples of Numerical Calculation

All analyses of numerical examples conducted with the VCFEM codes are executed under plane stress assumptions.

3.1. Simulation of the Damage in Complex Microstructure

In the first example, a structure consists of 20 elliptical inclusions with different size (see Fig. 2a). The inclusions are arranged randomly in a square matrix of 10×10 mm^2 and the matrix-inclusion interface of every inclusion is composed of 8 sides, in which no side is debonded before loading. The fatigue crack will initiate and propagate gradually where the total fatigue damage of the interfacial points is greater than the given critical fatigue damage. The vertical displacement on the top edge and the bottom edge and the horizontal displacement on the left edge are fixed, and the displacement controlled fatigue loads are applied on the right edge with the maximal displacement 7×10^{-6} mm and the minimal displacement 7×10^{-7} mm.

Figure 2. (a) The crack propagation status in a square particulate reinforced composites plate with 20 circle inclusions; (b) the horizontal stress component contours within the matrix and inclusion of VCFEM model

Material properties are as follows:
Matrix(Al2024): Young's Modulus $E_{Al} = 72\,GPa$, Poisson's Ratio $v_{Al} = 0.33$;
Inclusions(SiC): Young's Modulus $E_{SiC} = 430\,GPa$, Poisson's Ratio $v_{SiC} = 0.25$;

The given critical fatigue damage c=1 and the material constant β=6， m=1.

In every VCFEM element the stress field in the matrix is represented by a 75 terms expansion composed of 42 polynomial terms (8th order complete polynomial expansion of the Airy function) and 33 reciprocal terms (1 reciprocal terms for each exponent in the polynomial terms, from 2 to 7) While the stress field in the inclusions is modeled using only the first 63 polynomial terms. The

fatigue crack propagation status is shown in Fig. 2(a), and the distribution of the horizontal stress component σ_x calculated by the VCFEM model is showed in Fig. 2(b), when fatigue cycles are 8×10^5. It appears that the VCFEM model has considerable accuracy and high efficiency in dealing with the initiation and propagation of the fatigue crack of Particle-reinforced metal-matrix composites.

3.2. The Study of the Behaviour of a Functionally Graded Material

In the second example, the fatigue crack evolution in the SiC/Al functionally gradient material are simulated with the different volume fraction ratio of SiC of 25%, 40%, 55%, 70%, in which the specific distribution is shown in Fig. 3(a) and the specify voronoi tessellation mesh of functionally gradient materials is shown in Fig. 3(b).

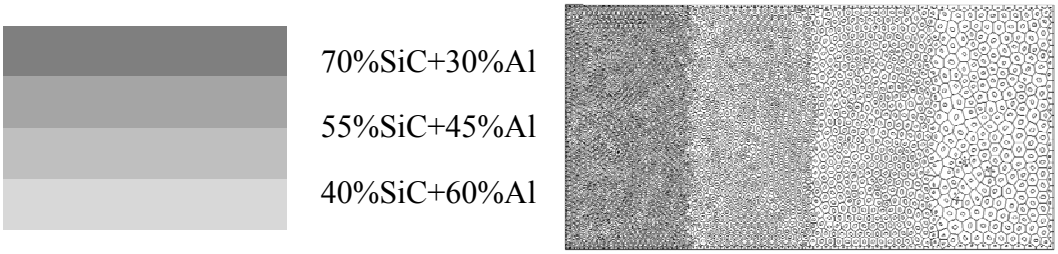

Figure 3. (a) section schematic of SiC/Al functionally gradient materials;
(b) Voronoi tessellation mesh of FGMS

In this model, the Al is Al2024-T6 with the elastic modulus E_{Al} = 72GPa; the Poisson's ratio V_{Al} = 0.33; the yield stress was 70MPa; tangent modulus E_t = 14.5GPa; followed J2 flow theory; SiC is with the elastic modulus E_{SiC} = 430GPa; Poisson's ratio V_{SiC} = 0.25; the yield stress of SiC 100MPa; tangent modulus 50GPa. The width of the specimen is 4mm; the thickness is 8mm, each gradient layer thickness is 2mm. About 4700 inclusions were modeled, the boundary conditions of the model were constrained as follows: the right hands of this specimen were constrained in Ux, Uy directions, and the left hands of the specimen were enforced 0.001 uniform displacement. The critical normal stress leading interfacial crack is 30MPa. In order to evaluate the influence of the interface cracks, a comparison with the model which does not take the interface cracks into consideration was made. The curve of displacement and reaction force was shown in Fig. 4.

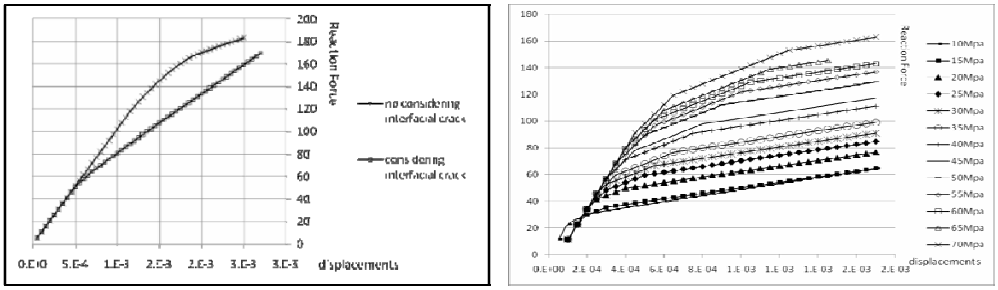

Figure 4. (a) curves of displacement and reaction force;
(b) The effect of interface bond strength

In Fig. 4(a), the results show that the overall stiffness of functionally gradient materials is gradually reduced when the interfaces are cracked. Compared with the model which does not take the interface cracks into consideration the overall stiffness is reduced largely. In Fig. 4(b), the results show that the overall stiffness of the specimen is increasing with the enhancement of interface bond strength. In this test, we can see that when the interface bond strength is between 10-35MPa the overall stiffness of the specimen is increased slowly or can't even reach the yield strength. In this case the SiC particles are a kind of damage to the Al matrixes, because they cannot work together

perfectly. With interface bond strength increasing for example between 35-70MPa, the overall stiffness of the specimen is increased obviously. And the yield strength is higher than 90MPa. So in this situation the spacemen can work very well. And the gradient performance of the functionally gradient materials is not obviously affected by the interfacial crack.

4. Conclusion

In this study, the modeling of fatigue crack initiation and propagation for particulate reinforced composites is facilitated with new Voronoi Cell Finite Element Method (VCFEM), considering the matrix-inclusion interfacial fatigue cracks, matrix fatigue cracks and crack closures. In the new element, all possible contacts on the crack edge is considered by contact seeking and remeshing methods, when the crack is closing under all possible changing loads. The fatigue crack initiates when the fatigue damage exceeds certain critical damage value, and fatigue crack propagation are simulated by gradual seeking crack propagating directions and new crack tips in a remeshing method.

The second example of Particle-reinforced metal-matrix composites with 20 elliptical inclusions shows that the VCFEM has considerable accuracy and high efficiency in dealing with the initiation and propagation of the fatigue crack. Good agreements are obtained between the results of VCFEM and the general finite element method, not given in this paper.

This kind of VCFEM method can predict functionally gradient material particles' interfacial crack accurately. The particles' size, topological structure, and interfacial deboning strength will influence FMES' mechanical behavior. With the interface cracking the overall stiffness of functionally gradient materials is gradually reduced.

Acknowledgements

The financial support by the National Natural Science Foundations of China (Nos. 11072092 and Nos. 11262007) is gratefully acknowledged.

References

[1] J. Zhang, and N. Katsube, A hybrid finite element method for heterogeneous materials with randomly dispersed rigid inclusions. Int J Numer Methods Eng, 38 (1995) 1635–1653.
[2] S. Ghosh, and S. N. Mukhopadhyay, Material based finite element analysis of heterogeneous media involving dirichlet tessellations. Comput Methods Appl Mech Eng, 104 (1993) 211–247.
[3] S. Ghosh, and S. Moorthy, Elastic-plastic analysis of arbitrary heterogeneous materials with the voronoi-cell finite-element method. Comput Methods Appl, 121 (1995) 373–409.
[4] S.Ghosh, Y. Ling, et al., Interfacial debonding analysis in multiple fiber reinforced composites. Mech mater, 32 (2000) 561–591.
[5] R. Guo, H. J. Shi and Z. H. Yao, Numerical simulation of thermo-mechanical fatigue properties for particulate reinforced composites. Acta Mechanica Sinica, 21(2) (2005) 160–168.
[6] R. Guo, H. J. Shi and Z. H. Yao, The modeling of interfacial debonding crack in particle reinforced composites using Voronoi cell finite element method. Comput Mech, 32(1-2) (2003) 52–59.

A New Interface Element for Shell Structures Delamination Analysis

Biao Li[1,*], **Yazhi Li**[1], **Jie Su**[1]

[1] School of Aeronautics, Northwestern Polytechnical University, Xi'an 710072, China
* Corresponding author: libiao@mail.nwpu.edu.cn

Abstract A combined interface element consists of eight rigid beams and a zero thickness cohesive element is presented. The type of elements are used in conjunction with shell elements to constitute the three dimensional model. In the FE model, intralaminar damage takes place within the shell elements and interlaminar damage is restricted to occur at the interface elements. The eight-node interface elements are of finite thickness, with each node possessing six DOFs. No additional DOFs are required in the FE model except those of shell elements. The translational and rotational movements of the shell nodes contribute to the deformation of the interface elements. The interfacial damage accumulation and final delamination are characterized by progressive stiffness degradation of the internal cohesive element. The crack growth in double cantilever beam (DCB) was simulated with the proposed elements and corresponding finite element model. The simulation results agree well with the experimental ones and analytical solutions.

Keywords composite laminate, cohesive zone model, interface element, delamination

1. Introduction

Fiber reinforced composites are mostly used in the form of laminates, which are susceptible to interfacial delamination due to the weak interfacial bonding strength. Several numerical tools such as fracture mechanics based virtual crack closure technique (VCCT) [1, 2] and damage mechanics based cohesive zone model (CZM) method [3, 4] have been proposed to simulate the interfacial fracture process. CZM is superior to other methods in that the initiation and growth of delamination are considered within the same analysis without previous knowledge of crack position. The conventional way of applying CZM is to embed the cohesive elements among the layers of three dimensional solid elements (Fig. 1a). A softening constitutive law described by traction-displacement jump curve is introduced for the cohesive elements. The irreversible softening process is initiated when the traction attains the maximum interfacial strength and delamination is fully developed when the local energy release rates approach their critical values. However, it has been shown that highly refined mesh is required within cohesive zone which is a softening region ahead of crack tip [5]. The length of cohesive zone is usually on the order of 1 mm for typical polymeric matrix composite, which requires that much smaller elements is unacceptable for large scale application of delamination analysis using solid elements. On the other hand, more computational efficient shell elements are suitable for modeling thin walled structures than solid elements [6].

In this paper, we present a new interface element being used in conjunction with shell elements to constitute three dimensional models for laminated structures. Double cantilever beam (DCB) test are simulated using the proposed interface elements and corresponding finite element model. The simulated results are compared with experimental results and analytical solutions.

2. Finite element model

2.1. Model description

In the finite element model, laminated structures are divided into several sublaminates through the thickness. A sublaminate is a set of adjacent physical layers among which debonding is unlikely to occur. All sublaminates are modeled with four node quadrilateral shell elements on mid-planes of

them. The finite thickness interface elements are used to connect shell elements belonging to adjacent sublaminates, see Fig. 1b. Thus the laminates could be considered as sandwich shells stacked by shell elements and the interface elements. In this way, the intralaminar and interlaminar damages could be considered separately with both kinds of elements.

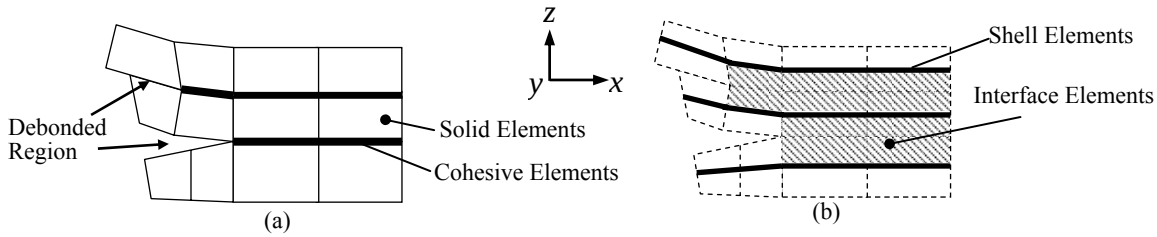

Figure 1. (a) 3D solid model (b) 3D shell model

The interface element consists of eight rigid beams and a zero thickness cohesive element. The master node of a rigid beam is used to connect external shell node, and its slave node is used to connect internal cohesive element node. The rigid beams transfer the translational and rotational movements of the shell nodes to the internal cohesive element (Fig. 2). Interlaminar fracture takes place at the internal cohesive elements. Although being composed of discrete rigid beams and cohesive element, the interface element presents itself as a solid one in which DOFs of the internal nodes have been eliminated by deduction of its kinematic formulae. There will be no additional DOFs are required in the FE models except those of shell elements. The interface element has been implemented in the commercial FE code ABAQUS [7] via its user element subroutine (UEL). Newton-Cotes full integration scheme is adopted.

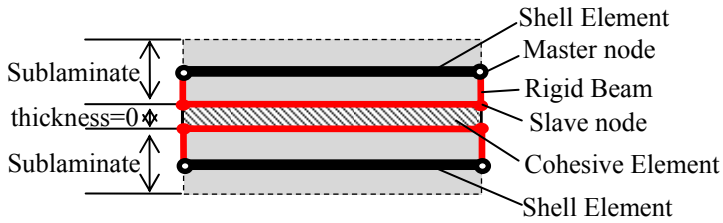

Figure 2. Schematic of the connection of shell elements and interface element

2.2. Interface element formulation

In the interface element, the relation of the nodal displacements between master and slave nodes of the *i*th (*i*=1,…,8) rigid beam can be given as:

$$\boldsymbol{u}_{\mathrm{S}}^{i} = \boldsymbol{t}_{\delta i}\boldsymbol{u}_{\mathrm{M}}^{i} \quad (\mathrm{i}=1,\ldots,8) \tag{1}$$

where $\boldsymbol{u}_{\mathrm{M}}^{i}=\left(u_{\mathrm{M}}^{i},v_{\mathrm{M}}^{i},w_{\mathrm{M}}^{i},\theta_{\mathrm{Mx}}^{i},\theta_{\mathrm{My}}^{i},\theta_{\mathrm{Mz}}^{i}\right)^{\mathrm{T}}$ and $\boldsymbol{u}_{\mathrm{S}}^{i}=\left(u_{\mathrm{S}}^{i},v_{\mathrm{S}}^{i},w_{\mathrm{S}}^{i},\theta_{\mathrm{Sx}}^{i},\theta_{\mathrm{Sy}}^{i},\theta_{\mathrm{Sz}}^{i}\right)^{\mathrm{T}}$ are the displacement vectors at master and slave nodes of *i*th rigid beam respectively. $\boldsymbol{t}_{\delta i}$ is the displacement transformation matrix of the two nodes:

$$\boldsymbol{t}_{\delta i}=\begin{bmatrix} 1 & 0 & 0 & 0 & z_S^i-z_M^i & -\left(y_S^i-y_M^i\right) \\ 0 & 1 & 0 & -\left(z_S^i-z_M^i\right) & 0 & x_S^i-x_M^i \\ 0 & 0 & 1 & y_S^i-y_M^i & -\left(x_S^i-x_M^i\right) & 0 \\ 0 & 0 & 0 & 1 & 0 & 0 \\ 0 & 0 & 0 & 0 & 1 & 0 \\ 0 & 0 & 0 & 0 & 0 & 1 \end{bmatrix} \tag{2}$$

where x, y, z are coordinates, subscript S and M denote the slave and master nodes respectively, superscript i is the number of rigid beams. Similarly, the relation of nodal forces between master and slave nodes can be expressed as:

$$\boldsymbol{F}_{\mathrm{S}}^{i} = \boldsymbol{t}_{\mathrm{Fi}} \boldsymbol{F}_{\mathrm{M}}^{i} \tag{3}$$

where $\boldsymbol{F}_{\mathrm{M}}^{i}$ and $\boldsymbol{F}_{\mathrm{S}}^{i}$ is the master and slave nodal force of ith rigid beam. $\boldsymbol{t}_{\mathrm{Fi}}$ is the nodal force transformation matrix. Furthermore, the relation of the two transformation matrices can be obtained according to the principal of virtual work:

$$\boldsymbol{t}_{\delta \mathrm{i}}^{\mathrm{T}} = -\boldsymbol{t}_{\mathrm{Fi}}^{-1} \tag{4}$$

The relations (1) and (3) for all rigid beams in an interface element are brought together as:

$$\boldsymbol{u}_{\mathrm{S}}^{\mathrm{N}} = \boldsymbol{T}_{\delta} \boldsymbol{u}_{\mathrm{M}}^{\mathrm{N}} \text{ and } \boldsymbol{F}_{\mathrm{S}}^{\mathrm{N}} = \boldsymbol{T}_{\mathrm{F}} \boldsymbol{F}_{\mathrm{M}}^{\mathrm{N}} \tag{5}$$

where

$$\boldsymbol{T}_{\delta} = \begin{bmatrix} \boldsymbol{t}_{\delta 1} & & & 0 \\ & \boldsymbol{t}_{\delta 2} & & \\ & & \cdots & \\ 0 & & & \boldsymbol{t}_{\delta 8} \end{bmatrix} \quad \text{and} \quad -\boldsymbol{T}_{\mathrm{F}}^{-1} = \boldsymbol{T}_{\delta}^{\mathrm{T}} \tag{6}$$

The displacement jumps of internal cohesive element, $\boldsymbol{\delta}$, can be obtained as:

$$\boldsymbol{\delta} = \boldsymbol{B} \boldsymbol{\psi} \boldsymbol{u}_{\mathrm{S}}^{\mathrm{N}} \tag{7}$$

where

$$\boldsymbol{\psi} = \begin{bmatrix} \boldsymbol{\gamma} & & & \\ & \boldsymbol{\gamma} & & \\ & & \cdots & \\ & & & \boldsymbol{\gamma} \end{bmatrix}_{24\times 48}, \quad \boldsymbol{\gamma} = \begin{bmatrix} 1 & 0 & 0 & 0 & 0 & 0 \\ 0 & 1 & 0 & 0 & 0 & 0 \\ 0 & 0 & 1 & 0 & 0 & 0 \end{bmatrix}$$

is used to pass translational movements of the slave nodes to cohesive element. $\boldsymbol{B}$ transforms the nodal displacements of the cohesive element to local displacement jumps.
The constitutive law for internal cohesive element can be defined as:

$$\boldsymbol{\tau} = \boldsymbol{D} \boldsymbol{\delta} \tag{8}$$

where $\boldsymbol{\tau}$ is stress vector, $\boldsymbol{D}$ is damaged elasticity matrix. With the use of virtual work principle, we get the stiffness matrix of the interface element:

$$\boldsymbol{K} = \boldsymbol{T}_{\delta}^{\mathrm{T}} \boldsymbol{\psi}^{\mathrm{T}} \int_{\Gamma} \boldsymbol{B}^{\mathrm{T}} \boldsymbol{D} \boldsymbol{B} d\Gamma \boldsymbol{\psi} \boldsymbol{T}_{\delta} \tag{9}$$

The nodal force vector of the element is:

$$\boldsymbol{F} = \boldsymbol{T}_{\delta}^{\mathrm{T}} \boldsymbol{\psi}^{\mathrm{T}} \int_{\Gamma} \boldsymbol{B}^{\mathrm{T}} \boldsymbol{\tau} d\Gamma \tag{10}$$

It is seen that the nodal force vector and stiffness matrix of the new interface element can be simply obtained from cohesive element as follows:

$$\boldsymbol{K} = (\boldsymbol{\psi} \boldsymbol{T}_{\delta})^{\mathrm{T}} \boldsymbol{K}_{\mathrm{cohesive}} (\boldsymbol{\psi} \boldsymbol{T}_{\delta}) \quad \text{and} \quad \boldsymbol{F} = (\boldsymbol{\psi} \boldsymbol{T}_{\delta})^{\mathrm{T}} \boldsymbol{F}_{\mathrm{cohesive}} \tag{11}$$

2.3. Bilinear constitutive law

A bilinear constitutive damage model under pure Mode I loading is adopted for the new interface element, see Fig.3. The interfacial damage is initiated after the normal traction attains the interfacial tensile strength. After that, the stiffness is gradually reduced to zero. The onset displacement is obtained as: $\delta_3^{\mathrm{o}} = N/K$, where N is the interfacial tensile strength and K is the interfacial stiffness. The area under the traction-displacement jump curve is the Mode I fracture toughness G_{IC}:

$$\int_0^{\delta_3^f} \tau_3 d\delta_3 = G_{\mathrm{IC}} \tag{12}$$

where τ_3 is normal traction. The final displacements δ_3^f can be obtained as: $\delta_3^f = 2G_{\mathrm{IC}} / N$.

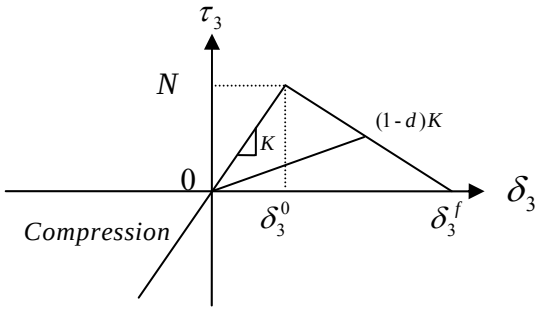

Figure 3. Pure Mode I bilinear constitutive law

3. Numerical simulation of DCB specimen

The double cantilever beam (DCB) is a standard specimen for mode I fracture and has been widely investigated. In this section, we simulated the DCB test [8] using the proposed interface element and relevant FE model. The specimen is made up of T300/977-2 unidirectional laminates $[0]_{24}$. The geometry and boundary conditions are shown in Fig. 4 and material properties are listed in Table 1.

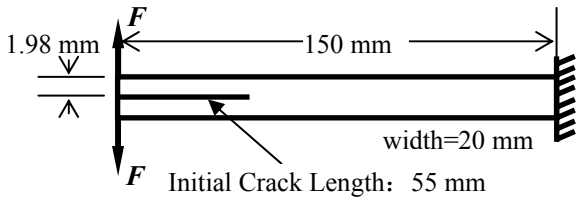

Figure 4. Geometry and boundary condition for DCB test

Table 1. Properties for T300/977-2[8]

E_{11}	E_{22}=E_{33}	G_{12}=G_{13}	G_{23}
150.0 GPa	11.0 GPa	6.0 GPa	3.7 GPa
ν_{12}=ν_{13}	ν_{23}	G_{IC}	N
0.25	0.45	0.352 kJ/m^2	60 MPa

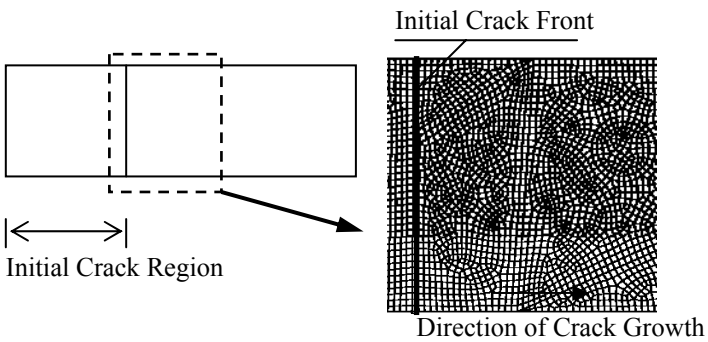

Figure 5. Irregular mesh for DCB model

The FE model for DCB specimen was built with two layers of shell elements at the mid-planes of both beam arms. The interface elements were employed to connect the upper and lower shells except where of pre-crack. The interfacial stiffness was chosen as K=10^6 N/mm^3 . To demonstrate the applicability of the interface element, we established two models with regular and irregular

meshes respectively. The regular mesh contains 24000 square shell elements, 7600 interface elements and 24682 nodes. The element size of the mesh is 0.5 mm×0.5 mm. The irregular mesh shown in Fig. 5 contains 29320 shell elements, 9296 interface elements and 30006 nodes and the nominal element size of which is 0.5 mm. The curves of load vs. deflection by FE analysis, experiment and analytical solutions were presented in Fig. 6, in which the analytical solution is obtained using a corrected beam theory for mode I case.

It can be seen that the coincidence of the simulation results between regular and irregular meshes is very well. The predicted strength is closed to the experimental one. The simulated result of load vs. deflection curve achieves good agreement with experimental and analytical results. The mesh with the new interface elements is easy to be built for the same geometric form as brick elements. The longitudinal stress contours are exhibited in Fig. 7 on the deformed meshes at different moments of loading. The scaling factor of the deformation display is 4.0.

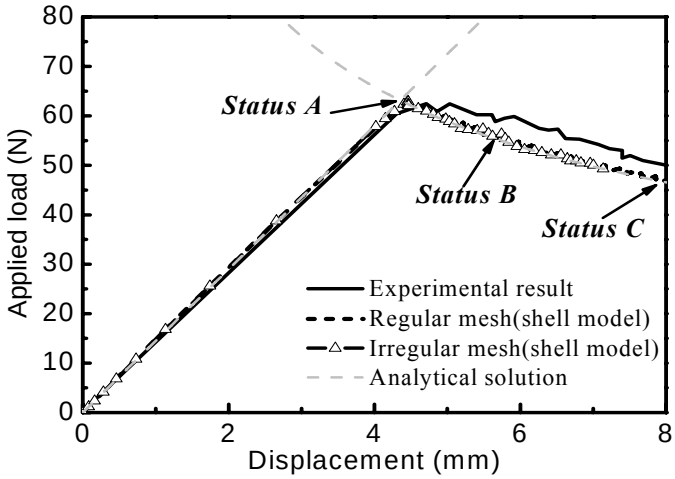

Figure 6. Results comparison for DCB

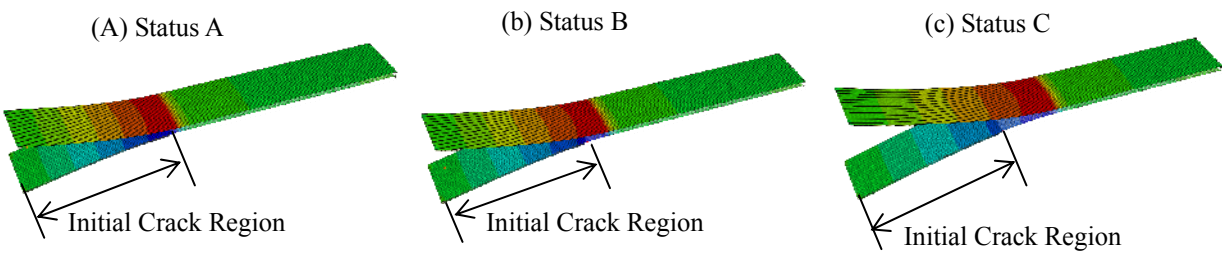

Figure 7. S_{11} stress contour of DCB specimen at different status (regular mesh)

4. Conclusions

A combined interface element is proposed to be used together with shell element to establish finite element model of the shell structures and conduct interfacial fracture analysis. The new interface element comprised of a zero-thickness cohesive zone element and a number of rigid beam elements. The shell thickness offset and nodal translational and rotational degrees of freedom are considered by the use of rigid beams. A bilinear constitutive law is applied to the new interface element. The modeling technique greatly reduces the model scale as compared with the model built with solid elements. By the simulations of double cantilever beam test, good agreements are achieved among the results of simulation, experiment and analytical solution.

References

[1] E.F. Rybicki, M.F. Kanninen. A finite element calculation of stress intensity factors by a modified crack closure integral. Engineering Fracture Mechanics, 1977, 9: 931-938.

[2] I.S. Raju. Calculation of strain-energy release rates with higher order and singular elements. Engineering Fracture Mechanics, 1987, 28:251-274.
[3] A. Hillerborg, M. Modeer, P.E. Petersson. Analysis of crack formation and crack growth in concrete by means of fracture mechanics and finite elements. Cem Concr Res, 1976,6:773-782.
[4] V.K. Goyal, E.R. Johnson, C.G. Davila. Irreversible constitutive law for modeling the delamination process using interfacial surface discontinuities. Composite Structures, 2004,65:289-305.
[5] P.W. Harper, S.R. Hallett. Cohesive zone length in numerical simulations of composite delamination. Engineering Fracture Mechanics, 2008,75:4774-4792.
[6] P.J. Gray, C.T. McCarthy. A global bolted joint model for finite element analysis of load distributions in multi-bolt composite joints. Composite: Part B, 2010, 41: 317-325.
[7] ABAQUS 6.11 User's Manual, ABAQUS Inc, Province, RI, USA, 2011.
[8] A. Turon, C.G. Davila, P.P. Camanho, et al. An engineering solution for mesh size effects in the simulation of delamination using cohesive zone models. Engineering Fracture Mechanics, 2007,74:1665-1682.

Advanced remeshing techniques for complex 3D crack propagation

Vincent Chiaruttini[1,*], **Vincent Riolo**[1,2], **Frederic Feyel**[1]

[1] Onera, DMSM/MNU, Chatillon, France
[2] LMS, Ecole polytechnique, Palaiseau, France
* Corresponding author: vincent.chiaruttini@onera.fr

Abstract This paper is related to the development of an efficient numerical technique to simulate the propagation of 3D cracks that can evolve inside complex industrial structures due to intense fatigue loading. In this prospect, an adaptive remeshing approach is presented: based on an efficient mesh intersection algorithm, and using robust automatic meshers developed at INRIA, this approach allows to insert almost any kind of cracks in very complex meshes. Associated to a fast and accurate stress intensity factor evaluation, a kinking angle criterion and a fatigue propagation law, such remeshing algorithms allow to simulate complex crack growth phenomena (with coalescing multiple cracks, crack fronts splitting, contact in small deformation, etc.) in the context of linear elastic fracture mechanics.

Keywords 3D crack growth, adaptive remeshing, conform crack remeshing, linear elastic fracture mechanics.

1. Introduction

The accurate prediction of crack propagation becomes increasingly necessary in a wide range of industrial applications (aeronautic, automotive industry, civil engineering, etc.). Mostly due to a better optimisation and a higher level of complexity, manufacturing requires ever more sophisticated design techniques and precise damage tolerance analysis in order to correctly evaluate lifetime assessment. Critical parts, such as rotors in aircraft engines, are actively investigated for cracks, using non-destructive means of detection. Such parts, if cracked, are usually replaced immediately for safety reason, However, crack detection technologies have limitations, and some very small initiated cracks might not be detected during inspections. It is thus necessary to find a way to correctly define when the next inspection should occur. Modeling how such small cracks propagate due to fatigue loading is believed to be a solution.

During the last decades, many new approaches have been developed to efficiently deal with complex 3D crack growth simulations under fatigue loading. Two main families of methods have been highly investigated by the computational mechanical community: on the one hand, PUM based methods that allows the presence of a crack inside a discretized component as a possible discontinuities of the unknown fields (like the famous X-FEM/Levelset method [1] with non-conform crack meshing), on the other hand method that describes the crack as evolving boundaries of the discrete domain (boundary elements based methods [2], finite element methods with remeshing [3], etc.).

Concerning the standard finite element approach, recent improvements of meshing and remeshing techniques allow the generation of complex 3D meshes that could be refined in local areas of interest where a crack could propagate. Thus, inserting the discontinuity surface in such meshes was one of the last drawback of those methods. Traditional approaches, usually based on a cracked CSG model, or mesh generation with boolean operations, generally lead to a lack of robustness which make them difficult to deal with complex geometries.

In order to push the lines of remeshing based techniques, a new algorithm as been developed. Our approach is mostly based on a fast and efficient crack insertion algorithm. The robustness and quickness of this method is obtained by the way the cracked mesh is represented (linked to element mesh size near the surface of discontinuity). In fact, each volumetric element of the initial mesh that crosses the crack surface is cut. An important assumption is that the generated surface can be approximated by the polygonals built on the input element edges intersection points. Some special treatments are also performed on element faces to carry out the crack front intersection and some topological difficulties that could arise for highly curved cracks. This resulting mesh is finally rebuilt using an adaptive remeshing strategy in order to eliminate bad quality elements and provide a suitable discretization for accurate finite element solution and stress intensity factors computation.

The next section is related to the description of the crack insertion algorithm that builds a refined mesh closely to the crack front. The third section presents two numerical assessments (a validation problem and a complex crack growth simulation) computed using the software Z-Cracks (within all the herein presented algorithms have been implemented). Finally some conclusion and prospects to this work will be presented.

2. Crack insertion algorithm

Usually, industrial component model for structural integrity analysis are described using constitutive solid geometry (CSG) and efficient automatic meshers are able to deliver correct input for standard finite element solvers. Thus, when cracked structure is concerned, it is necessary to be able to introduce an initial crack geometry in the corresponding model. The current approach is based on the modification of an initial uncracked finite element mesh, that will be modified due to the presence of the crack and refined in the front vicinity.

For a 3D discrete problem, such an algorithm can be separated in five main stages:

- generating an accurate initial crack geometry.
- applying an adaptive refinement operation of the initial structure volumetric mesh.
- performing the “cutting” operation that builds a boundary mesh which contains the crack.
- performing an adaptive refinement operation on the cracked mesh for accurate finite element solution computation.
- boundary regeneration to separate the crack lips.

The first stage is related to the design of a suitable geometry that represents the surface of the crack itself. Such geometry must be discretized and represented by a surface mesh made of linear triangular elements. Such elements must be small enough to represent with a good accuracy the initial crack surface geometry. The most common case is a penny shape initial crack. In this case a radial mesh is performed using a prescribe number of sectors (usually about 64, possibly more for higher values of maximal/minimal radius ratio for elliptic shapes). Then an adaptive remeshing process is always run: using the *Yams* surface remeshing software from Distene/Inria, the element size is reduced to a minimal prescribed value on the boundary of the surface (that corresponds to the crack front) and the edges element size is adapted where important local curvature has been observed, while the mesh quality is optimized.

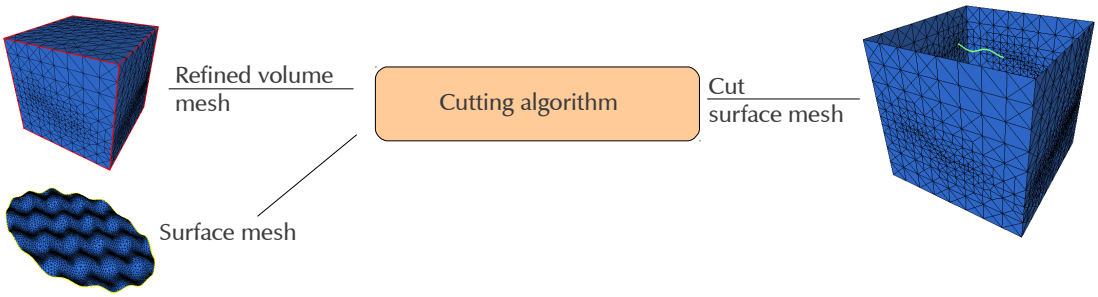

Figure 1. Cutting surface input/output.

The second stage of the a algorithm is related to a volumetric mesh adaption of the uncracked structure closely to the crack geometry. This operation is done using an iterative process. For each point of the actual volumetric mesh, the closest point of the crack surface will be searched (using a binary tree with a *log(n)* complexity for *n* points on the crack surface). Let *d* be the distance between any those two points. Thus an explicit refinement function is applied to specify the required element size on the volumetric mesh:

$$(d) = \begin{cases} h_{min}, \text{if } d < N\, h_{min} \\ \min\left(h_{min}\left(1 + \alpha_r\left(d - N\, h_{min}\right), h\right)\right) \text{ else} \end{cases} \tag{1}$$

where h_{min} is a minimal edge length, N is the number of minimal size element layers that must be imposed closely to the crack surface, α is a refinement factor (usually chosen within $0.1<\alpha<1.$) and h is the actual mesh size (meaning that only a refinement operation is done).

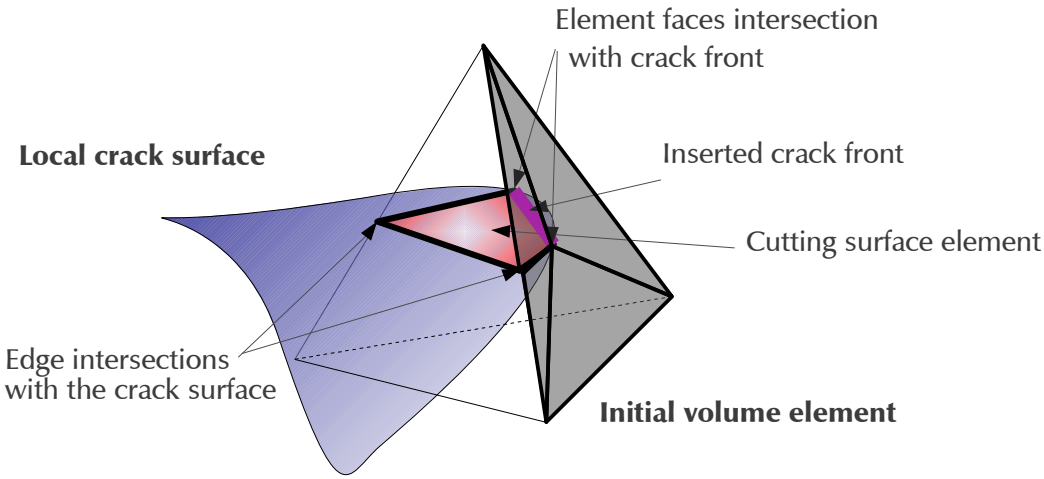

Figure 2. Operation on a near surface cut element.

The volumetric remeshing operation is then carried out on the complete mesh (or only a subdomain close enough to the crack surface - while the interface with the rest of the mesh must be exactly preserved). This stage is done using the *meshadapt* software from Distene/Inria where the imposed isotropic refinement map is imposed. Another required distance map is finally rebuilt (using the same refinement function) on the output mesh and compared to the actual edges size. If the size maps are close enough, convergence is assumed to be reached, in the other case another remeshing

iteration is done.

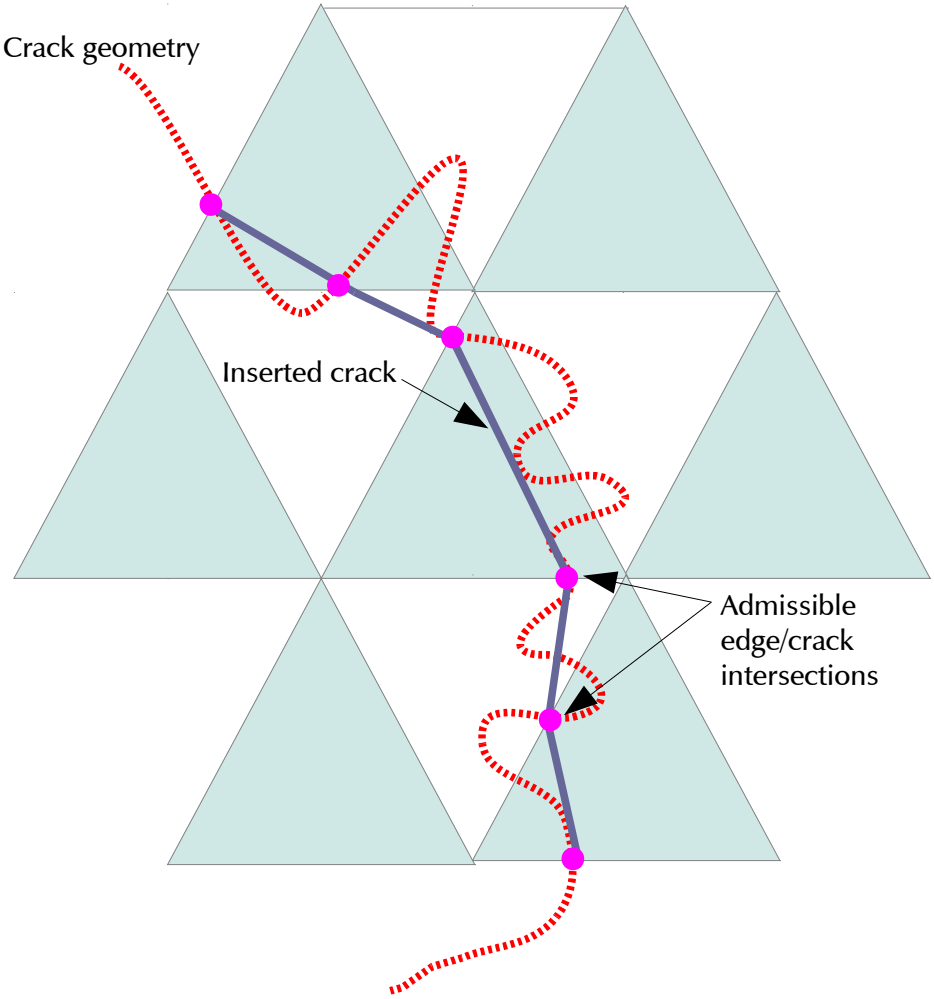

Figure 3. Simplification of a complex 2D crack geometry.

The next stage is related to the "cutting" algorithm, the aim of this stage is to generate a suitable approximation of the subtraction boolean operation between the volumetric mesh and the crack surface mesh (see figure 1). However, on complex meshes, such operation is very difficult to be operated robustly (due to the numerical errors in the numerous required operations). In order to make this operation much more robust, the approach is based on an idea out-coming from the X-FEM/levelset approach: the approximation of the crack surface will be restrained to the fine volumetric mesh topology. The algorithm 1 and the figure 2 give some details about the generation of the cracked surface mesh. In case of a very complex crack surface, an approximation will be obtained with such kind of algorithm (see figure 3), for very accurate cracked mesh generation the initial uncracked mesh must be accordingly refined near the crack surface. Since a convex surface is generated during each element splitting, the method is only valid for linear simplex elements (during the process non-convex elements will be automatically split in simplex sub-elements).

Algorithm 1 Cutting surface algorithm.

```
new_faces ← {}
for i ← 0, ··· , N_elements do
    element ← elements[i]
    if intersect_surface(bounding_box(element)) then
        {} ← inter_nodes
        for j ← 0, ··· , N_edges^element do
            edge_inter ← intersect_surface(element.edge[j])
            if edge_inter.size()%2 = 1 then
                inter_nodes.add(center(edge_inter))
            end if
        end for
        for j ← 0, ··· , N_faces^element do
            face_inter ← intersect_front(element.face[j])
            if face_inter.size()%2 = 1 then
                inter_nodes.add(center(face_inter))
                if element.face[j].unshared() then
                    new_faces.add(rebuid_cut_face(element.face[j]))
                end if
            else
                if element.face[j].unshared() then
                    new_faces.add(element.face[j])
                end if
            end if
        end for
        if inter_nodes.size() > 2 then
            new_faces.add(convex_faces(inter_nodes))
        end if
    else
        for j ← 0, ··· , N_faces^element do
            if element.face[j].unshared() then
                new_faces.add(element.face[j])
            end if
        end for
    end if
end for
```

After a cleaning operation (that delete the too bad quality simplex elements), the last adaptive remeshing operation is done using the Distene/Inria remeshing tools, another iterative algorithm is involved in order to converge to a suitable mesh for FE computation and stress intensity factor extraction. The size map will now be build using the distance from any point of the volumetric mesh to the crack front nodes (using the previously defined size function (1)). When convergence is achieved the last stage is related to the boundary regeneration in order to separate both sides of the crack surface. In this respect a global/local coloring algorithm is used. The fast global approach is used on continuous zone without branching nodes while the local approach is required to deal with branching nodes.

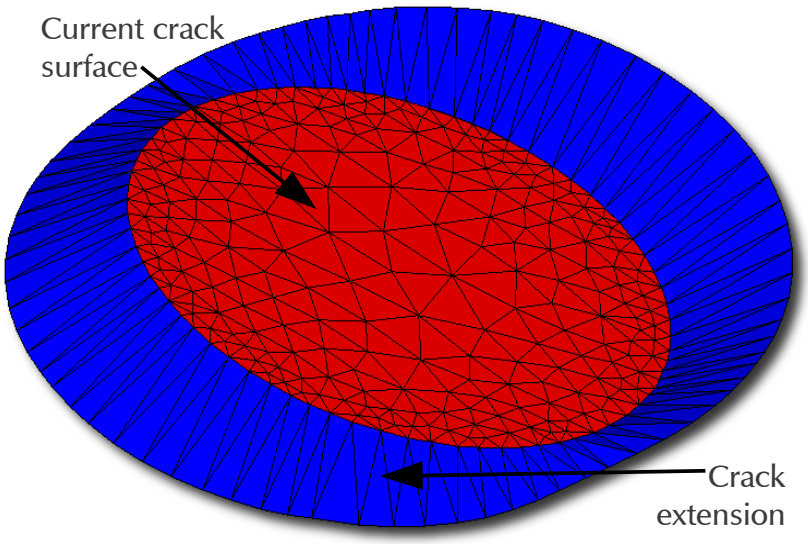

Figure 4. Crack extension during a propagation simulation.

During a crack propagation simulation, such kind of strategy will be adapted as a fewer number of operation is required. Starting from the current cracked mesh, an explicit surface will be generated as the extension of the crack front during a given time step (see figure 4). Thus, the current volumetric mesh, that is already sufficiently refined if the crack advance is small enough, will be directly cut by the crack extension surface. Then only the cleaning operations and a single adaptive remeshing step will be done, before the crack lips regeneration.

3. Numerical assessments

Such a technique for cracked structure meshing has been implemented in our finite element suite Z-Set [4]. A dedicated new module, Z-Cracks, that includes the meshing algorithms, an efficient stress intensity factor extraction post-processing [5,6] has been developed. This tool has been successfully applied to many complex simulations, and two examples will be herein presented: a validation of a crack growth experiment, and the numerical simulation of a very complex crack path will be presented.

3.1. Crack propagation on a biaxial notched specimen

This example is based on the numerical simulation of a mixed mode crack propagation experiment done on a biaxial notched specimen. This specimen has been designed to be able to apply a controlled uniform stress field in its center. The notch is oriented with a 45° angle with the loading directions (see figure 5). Two loading phases are imposed:

- to initiate the crack in the direction of the notch, the same fatigue effort level is imposed on the both directions.
- when the crack has sufficiently advanced, the loading is changed in order to impose an approximate constant vertical stress field in the center part.

The mechanical behavior is assumed to be isotropic linear elastic (E=210 000MPa as Young modulus and ν=0.3 as Poisson coefficient) under small deformations.

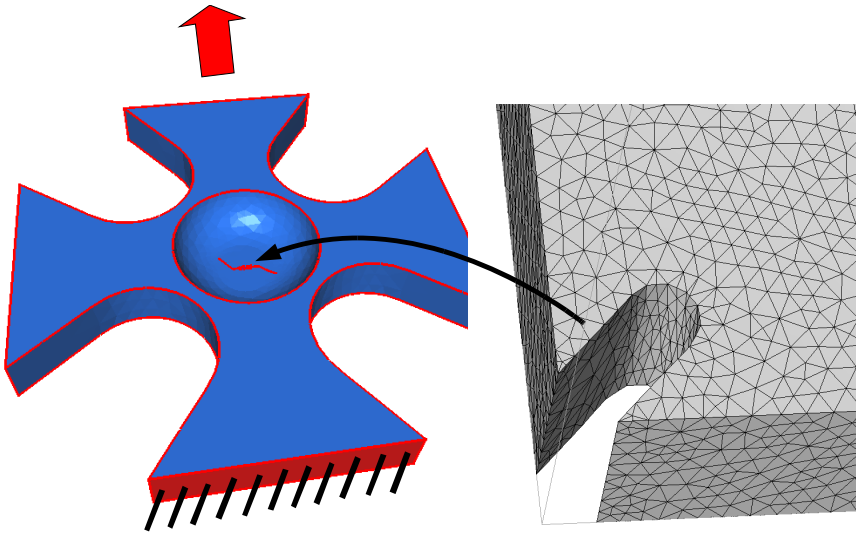

Figure 5. Biaxial notched specimen for crack propagation.

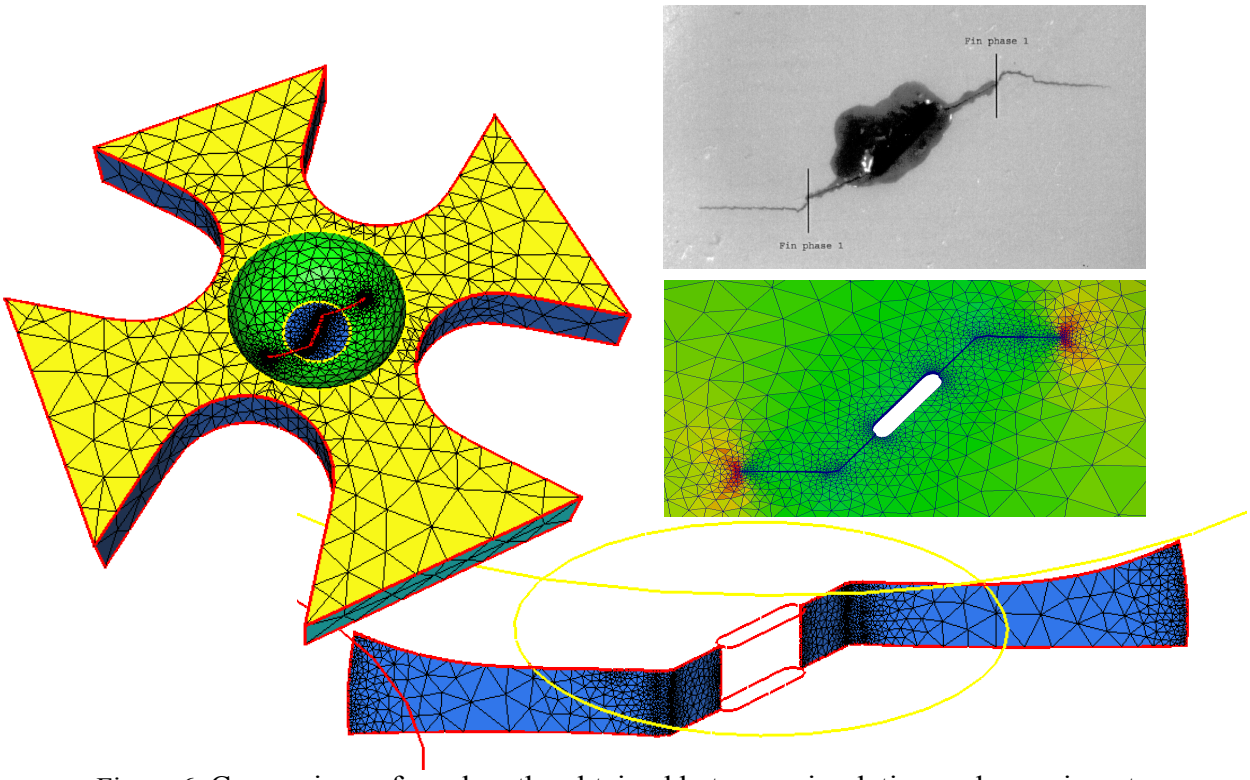

Figure 6. Comparison of crack paths obtained between simulation and experiment.

Both test observation and crack growth simulation show that when the loading is changed, the crack branches. The figure 6 shows the comparison between the experiment and the simulation crack paths.

3.2 Mixed mode crack propagation on a multi-perforated sample structure

This last example highlights the robustness of the method to deal with a very complex crack propagation simulation. The multiperforated sample geometry has been obtained from the Inria geometry database[1], the unit length size and the coordinate system used to describe boundary conditions refer to the downloaded geometry.

The mechanical behavior is assumed to be isotropic linear elastic (E=210 000MPa as Young modulus and ν=0.3 as Poisson coefficient) under small deformations. The boundary conditions are: a prescribed null displacement in all directions on the bottom face (z=-50), vertical displacement Uz=1 and sheer displacement Uy=-2 on the top face (z=50). A fatigue loading is imposed with a simple [0 → 1 → 0] loading cycle. A Paris law is used with a m=3 exponent on the ΔK equivalent mode I stress intensity factor. The initial crack is a 1. radius disc with a (50.0000 1.79113 -8.14958) center position and a vertical normal direction (0. 0. 1.).

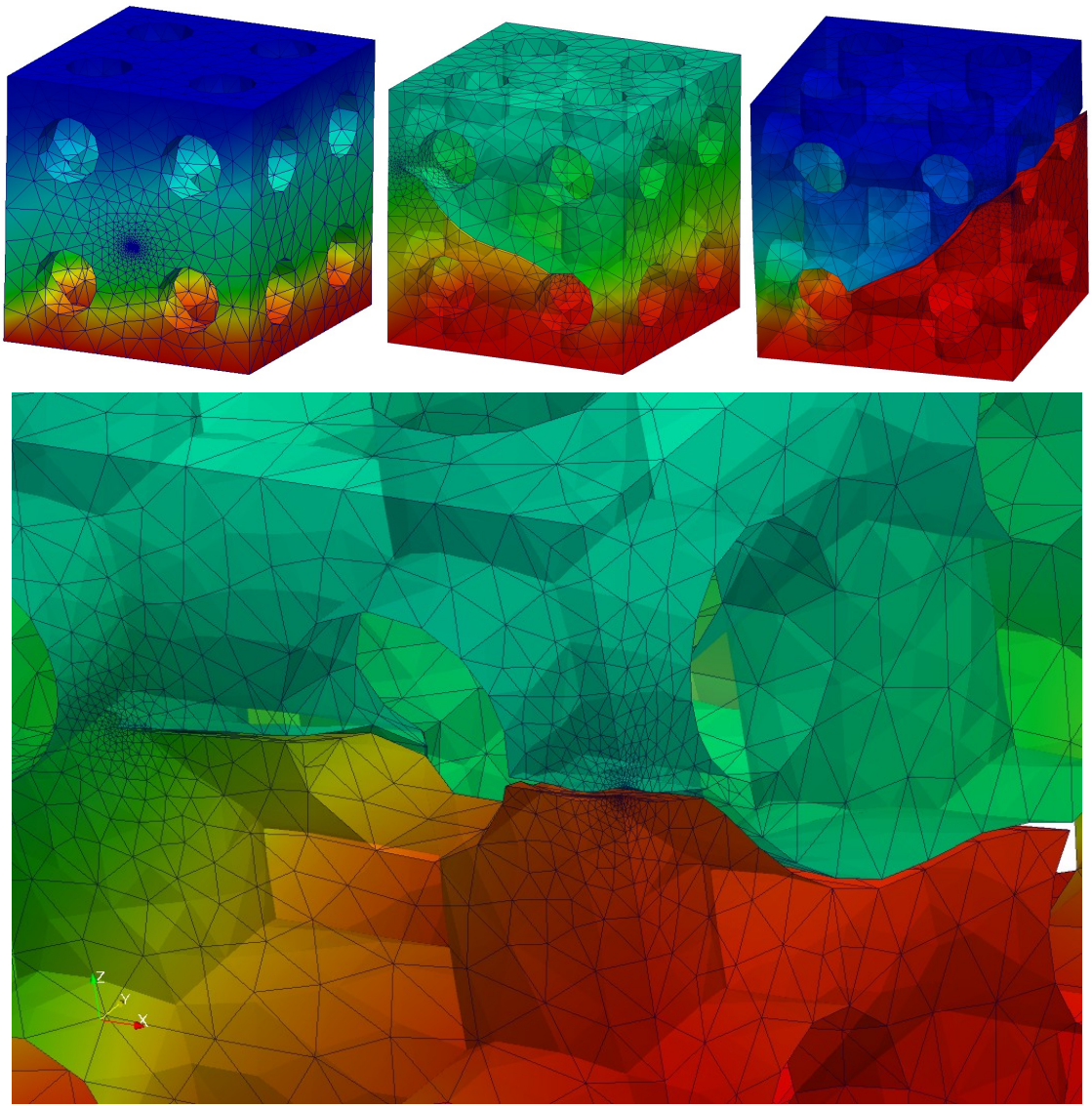

Figure 7. Crack propagation on a multiperforated structure under mixed mode fatigue loading.

1 To be downloaded at:
http://www-roc.inria.fr/gamma/download/affichage.php?dir=DREXEL\&name=drxl_cheese2\&last_page=30

The computation has been performed in 1h26mn on a dual core laptop with 110 remeshing steps. The mesh is built of linear tetrahedron, producing about 20 000 to 35 000 degrees of freedom, depending of the crack geometry complexity during the growth. Material integration, linear solver and stress intensity factors processes are multi-threaded. Some pictures of the cracked mesh are shown on figure 7, an animation can be watched on the web[2] as others example on plates, or 3D structures with coalescing cracks.

4. Conclusion

A robust meshing technique for 3D crack growth simulations has been presented. This method, based on a simplification of the usual boolean operation between meshes, has been implemented in the finite element software Z-set and allows to perform complex crack propagation computations for academic problems (adaptive cohesive zone modeling [7], for instance) as well as for industrial components.

References

[1] N. Moes, J. Dolbow, and T. Belytschko. A finite element method method for crack growth without remeshing. Int. Journal for Num. Meth. In Engrg, 46:131–150, 1999.

[2] B.J. Carter, P.A. Wawrzynek, and A.R. Ingraffea. Automated 3-d crack growth simulation. Int. J. Numer. Methods Engrg., 47:229–253, 2000.

[3] Robert W. Zimmerman Adriana Paluszny. Numerical simulation of multiple 3d fracture propagation using arbitrary meshes. Comput. Methods Appl. Mech. Engrg., 200:953–966, 2011.

[4] J. Besson and R. Foerch. Large scale object-oriented finite element code design. Comp. Meth. in Appl. Mech. and Eng., 42:165–187, 1997.

[5] M. Gosz, J. Dolbow, and B. Moran. Domain integral formulation for stress intensity factor computation along curved three-dimensional interface cracks. International Journal of Solids and Structures, 35(15):1763 – 1783, 1998.

[6] V. Chiaruttini, J. Guilie, V. Riolo, and M. Bonnet. Fast and efficient stress intensity factors computations for 3D cracked structures application to unstructured conform meshes or X-FEM discretization. *in preparation*.

[7] V. Chiaruttini, D. Geoffroy, V. Riolo, and M. Bonnet. An adaptive algorithm for cohesive zone model and arbitrary crack propagation, European Journal of Computational Mechanics, 21:208-218, 2012.

2 http://www.youtube.com/user/OneraMNU/videos

Time-Domain BEM for Dynamic Crack Problems in Thin Piezoelectric Structures

Hongjun Zhong[1], Jun Lei[1,*], Chuanzeng Zhang[2]

[1] Department of Engineering Mechanics, Beijing University of Technology, 100124, China
[2] Department of Civil Engineering, University of Siegen, D-57076 Siegen, Germany
* Corresponding author: leijun@bjut.edu.cn

Abstract A 2-D time-domain boundary element method (BEM) is developed to study the static and dynamic fracture problems in thin piezoelectric structures under electromechanical loadings. The traditional displacement boundary integral equations (BIEs) are applied on the external boundary and the hypersingular traction BIEs are applied on the crack faces. The present time-domain BEM uses a quadrature formula for the temporal discretization to approximate the convolution integrals and a collocation method for the spatial discretization. Quadratic quarter-point elements are implemented at the crack tip. The strongly singular and hypersingular integrals are evaluated by a regularization technique based on a suitable variable change. The nearly singular integrals arisen in thin structures are dealt with by two ways. The first one is based on a nonlinear coordinate transformation method for curve-quadratic elements. The second method is on an analytical integration method for straight quadratic elements to avoid the nearly singularity. A displacement extrapolation technique is used to determine the dynamic intensity factors (DIFs) including the dynamic stress intensity factors (DSIFs) and dynamic electrical displacement intensity factor (DEDIF). Some examples are presented to verify the effectiveness and stability of present BEM in thin piezoelectric structures.

Keywords thin piezoelectric structure, time-domain boundary element method, nearly singular integration, dynamic intensity factors

1. Introduction

With intrinsic electro-mechanical coupling characteristics, piezoelectric materials are widely used in smart structures. For typical engineering piezoelectric materials like PZT and PVDF, it's difficult to be applied to the complicated shape structures. Therefore, painting technology is developed, which forms piezoelectric coatings on the structures to produce electro-mechanical coupling function. But cracks may occur in the coating or between the coating and the matrix during preparation or under complex electro-mechanical loadings. So it's significant to study the fracture problems in the thin piezoelectric structure.

For general dynamic crack problems in piezoelectric materials, numerical methods are more feasible due to the mathematical complexity of the initial boundary value problems. Particularly, Boundary Element Method (BEM) has certain advantages in fracture analysis. In 2008, time-domain BEM for transient dynamic crack analysis of linear piezoelectric solids was implemented by García-Sánchez et al. [1], who used the Lubich convolution quadrature formula for the temporal discretization and a collocation method for the spatial discretization. However, its extension to dynamic cracks in thin piezoelectric structures is not straight-forward, since the corresponding dynamic Green's functions have quite complicated mathematical structures, which generate nearly singularity during integration when the field point is very close to the source point. In 2002, Liu and Fan [2] successfully applied the BEM in the static analysis of thin piezoelectric solids. The nearly singular integrals were solved by an analytical method. But they didn't take cracks into consideration.

To apply the time-domain BEM to the crack analysis of thin piezoelectric structures, two methods are developed to deal with the nearly singular integrals. The first one is based on a nonlinear coordinate transformation method for curve-quadratic elements. The second method is on an analytical integration method for straight quadratic elements. Numerical results are presented to verify the accuracy of the present integral equations and the time-domain BEM.

2. Time-domain BIEs for Piezoelectric Materials

2.1. Piezoelectric Equations

Consider a 2D homogeneous, linear cracked piezoelectric solid occupying domain Ω with boundary Γ. To describe the electric-elastic fields, the 'extended' variables u_J, f_J, σ_{iJ}, ε_{Ji} are defined:

$$u_J = \begin{cases} u_j \\ \phi \end{cases}, \quad f_J = \begin{cases} f_j & J = j = 1,2 \\ -q & J = 3 \end{cases}, \quad \sigma_{iJ} = \begin{cases} \sigma_{ij} \\ D_i \end{cases}, \quad \varepsilon_{Ji} = \begin{cases} \varepsilon_{ji} & J = j = 1,2 \\ E_i & J = 3 \end{cases}, \tag{1}$$

which combine the elastic variables involving the displacement u_j, body force f_j, stress σ_{ij}, strain ε_{ij}, and the electric ones including electric potential ϕ, charge q, electrical displacement D_j, field E_j. Without body forces and electrical charge, the governing equations and the constitutive equations under quasi-electrostatic assumption are given by

$$\sigma_{iJ,i} = \rho \delta^*_{JK} \ddot{u}_K, \quad \sigma_{iJ} = C_{iJKl} \varepsilon_{Kl}, \tag{2}$$

where ρ is the mass density, "," designates spatial derivative, while "$\cdot$" denotes temporal derivative. The capital index is from 1 to 3 while lower case letter index takes 1 or 2. The extended Kronecker delta δ^*_{JK} is defined by

$$\delta^*_{JK} = \begin{cases} \delta_{JK} & J, K = 1,2 \\ 0 & \text{otherwise} \end{cases}. \tag{3}$$

Material constants C_{iJKl} are as follows,

$$C_{iJKl} = \begin{cases} c_{ijkl}, & J = j = 1,2; \quad K = k = 1,2 \\ e_{jil}, & K = 3; \quad J = j = 1,2 \\ e_{kli}, & J = 3; \quad K = k = 1,2 \\ -\kappa_{il}, & J = K = 3 \end{cases}. \tag{4}$$

in which c_{ijkl}, e_{ijk} and κ_{ik} are the elasticity constants, piezoelectric constants and dielectric constants, respectively. The extended strain and displacement relations are given by

$$\varepsilon_{ij} = \left(u_{i,j} + u_{j,i}\right)/2, \quad E_i = -\varphi_{,i}. \tag{5}$$

2.2. Time-domain Boundary Integral Equations

On the boundary Γ, the displacement and traction BIEs are

$$c_{IJ}(\boldsymbol{x}_0) u_J(\boldsymbol{x}_0, t) = \int_\Gamma \left(u^G_{IJ} * p_J - p^G_{IJ} * u_J\right) \mathrm{d}\Gamma + \int_{\Gamma^+_C} p^G_{IJ} * \Delta u_J \mathrm{d}\Gamma, \quad \boldsymbol{x}_0 \in \Gamma, \tag{6}$$

$$p_J(\boldsymbol{x}_0, t) = \int_\Gamma \left(d^G_{IJ} * p_J - s^G_{IJ} * u_J\right) \mathrm{d}\Gamma + \int_{\Gamma^+_C} s^G_{IJ} * \Delta u_J \mathrm{d}\Gamma, \quad \boldsymbol{x}_0 \in \Gamma^+_C, \tag{7}$$

where $c_{IJ}(\boldsymbol{x})$ are free term constants, "$*$" denotes Riemann convolution, Δu_J are the extended crack-opening-displacements, u^G_{IJ} and p^G_{IJ} are 2D time-domain dynamic displacement and the

traction fundamental solutions. d_{IJ}^{G} and s_{IJ}^{G} are fundamental solutions of higher order. These fundamental solutions have been derived by Wang and Zhang [3].

2.3. Laplace-domain dynamic fundamental solutions

The traction fundamental solutions p_{IJ}^{G} and d_{IJ}^{G} have a strong singularity of Cauchy type, while the higher-order traction fundamental solution s_{IJ}^{G} has a hypersingularity. To deal with the singularity, it is advantageous to split the fundamental solutions into a singular static part and a regular dynamic part. The singular static parts are given by

$$p_{IJ}^{\mathrm{G(S)}}\left(\boldsymbol{x}_0,\boldsymbol{x}\right)=\frac{1}{\pi}\mathrm{Re}\left[\sum_{M=1}^{3}L_{JM}Q_{MI}\frac{\mu_M n_1(\boldsymbol{x})-n_2(\boldsymbol{x})}{z_M-z_M^0}\right], \tag{8}$$

$$d_{IJ}^{\mathrm{G(S)}}\left(\boldsymbol{x}_0,\boldsymbol{x}\right)=-\frac{1}{\pi}\mathrm{Re}\left[\sum_{M=1}^{3}L_{JM}Q_{MI}\frac{\mu_M n_1(\boldsymbol{x}_0)-n_2(\boldsymbol{x}_0)}{z_M-z_M^0}\right], \tag{9}$$

$$s_{IJ}^{\mathrm{G(S)}}\left(\boldsymbol{x}_0,\boldsymbol{x}\right)=\frac{1}{\pi}\mathrm{Re}\left[\sum_{M=1}^{3}T_{IJ}^{M}\frac{\mu_M n_1(\boldsymbol{x})-n_2(\boldsymbol{x})}{(z_M-z_M^0)^2}\right], \tag{10}$$

where

$$z_M=x+\mu_M y,\ \ z_M^0=x_0+\mu_M y_0,\ \ M=1,2,3. \tag{11}$$

$\boldsymbol{x}_0(x_0,y_0)$ is the source point while $\boldsymbol{x}(x,y)$ the observation point. L_{JM}, Q_{MI}, T_{IJ}^{M} and μ_M are determined by the anisotropic material constants [3].

2.4. Time-stepping scheme

To approximate the Riemann convolution integrals in BIEs, Lubich quadrature formula is used [1]

$$f\left(t\right)=g\left(t\right)*h\left(t\right)\cong\sum_{j=0}^{n}\omega_{n-j}\left(\Delta t\right)h\left(j\Delta t\right), \tag{12}$$

where time t is divided into N equal time-steps, and the weights $\omega_{n-j}\left(\Delta t\right)$ are determined by

$$\omega_{n-j}\left(\Delta t\right)=\frac{r^{-(n-j)}}{N}\sum_{m=0}^{N-1}\hat{g}\left[\delta\left(\zeta_m\right)/\Delta t\right]\mathrm{e}^{-2\pi i\cdot(n-j)m/N}, \tag{13}$$

in which $\hat{g}\left(\cdot\right)$ stands for the Laplace-transformation of the function $g(t)$. After the temporal and spatial discretization, a system of linear equations for the discrete boundary quantities can be obtained. Leaving all the unknown boundary quantities on the left-hand side, an explicit time-stepping scheme

$$\boldsymbol{x}_k^n=\left(\mathbf{A}_{kl}^0\right)^{-1}\cdot\left(\boldsymbol{y}_l^n-\sum_{j=1}^{n-1}\mathbf{A}_{kl}^{n-j}\cdot\boldsymbol{x}_l^j\right), \tag{14}$$

can be obtained for computing the unknown boundary quantities at the n-th time-step.

3. Computation of singular integrals

When a collocation point is on one element Γ_e, the BIEs possess strongly singular and hypersingular integrals. After discretization, the singular integrals correspond to the following integrals,

$$I_M=\int_{\Gamma_e}\frac{\mu_M n_1(\boldsymbol{x})-n_2(\boldsymbol{x})}{z_M-z_M^0}\phi_q d\Gamma,\ \ I_M'=\int_{\Gamma_e}\frac{\mu_M n_1(\boldsymbol{x})-n_2(\boldsymbol{x})}{(z_M-z_M^0)^2}\phi_q d\Gamma \tag{15}$$

where ϕ_q (q=1,2,3) is the quadratic shape function and $\boldsymbol{n}(\boldsymbol{x})$ donates the outward unit normal

vector to the boundary. A complex variable is introduced as

$$\chi_M = z_M - z_M^0 = x - x_0 + \mu_M (y - y_0) . \tag{16}$$

With this transformation,

$$I_M = \int_{\Gamma_e} \frac{1}{\chi_M} \phi_q d\chi_M , \quad I'_M = \int_{\Gamma_e} \frac{1}{\chi_M^2} \phi_q d\chi_M . \tag{17}$$

ϕ_q can be considered as a function of χ_M, and its first Taylor series at $\chi_M = 0$ is

$$\phi_q(\chi_M) = \phi_q(\chi_M = 0) + \mathrm{O}(\chi_M) = \phi_{q0} + \mathrm{O}(\chi_M) . \tag{18}$$

With the substitution of Eq. (18) into I_M,

$$I_M = \int_{\Gamma_e} \frac{1}{\chi_M} (\phi_q - \phi_{q0}) d\chi_M + \phi_{q0} \int_{\Gamma_e} \frac{1}{\chi_M} d\chi_M . \tag{19}$$

The first part in Eq. (19) can be calculated by Gaussian quadrature formula. The second integral is strongly singular but can be evaluated analytically as

$$\int_{\Gamma_e} \frac{1}{\chi_M} d\chi_M = \log(\chi_M)|_{\Gamma_e} . \tag{20}$$

For I'_M, the Taylor-series is expanded to two terms. Then, the integral can be transformed to

$$I'_M = \int_{\Gamma_e} \frac{\phi_q - (\phi_{q0} + \phi'_{q0} \cdot \chi_M)}{\chi_M^2} d\chi_M + \phi_{q0} \int_{\Gamma_e} \frac{1}{\chi_M^2} d\chi_M + \phi'_{q0} \int_{\Gamma_e} \frac{1}{\chi_M} d\chi_M . \tag{21}$$

The first integral can be computed by Gaussian integral quadrature. The second and third integral can be evaluated analytically as

$$\int_{\Gamma_e} \frac{1}{\chi_M^2} d\chi_M = -\frac{1}{\chi_M}\bigg|_{\Gamma_e} , \quad \int_{\Gamma_e} \frac{1}{\chi_M} d\chi_M = \log(\chi_M)|_{\Gamma_e} . \tag{22}$$

4. Computation of nearly singular integrals

When the collocation point is very close to the integration point in thin piezoelectric structures, nearly singular integrals appear. To deal with this problem, two methods are developed for curve quadratic elements and straight quadratic element. On the analogy of the solution to the singular problems in section 3, the nearly singular integrals can be classified into three kinds

$$J_M = \int_{\Gamma_e} \frac{\mu_M n_1(\boldsymbol{x}) - n_2(\boldsymbol{x})}{z_M - z_M^0} \phi_q d\Gamma , J'_M = \int_{\Gamma_e} \frac{\mu_M n_1(\boldsymbol{x}) - n_2(\boldsymbol{x})}{(z_M - z_M^0)^2} \phi_q d\Gamma , J''_M = \int_{\Gamma_e} \frac{\mu_M n_1(\boldsymbol{x}_0) - n_2(\boldsymbol{x}_0)}{z_M - z_M^0} \phi_q d\Gamma . \tag{23}$$

4.1. Curve quadratic element

For isoparametric quadratic element, similar method as the singular integrals can be applied. Local coordinate system of $\xi[-1,1]$ is introduced. When collocation point $\boldsymbol{x}_0$ is very close to Γ_e, the nearest point on Γ_e to $\boldsymbol{x}_0$ is assumed to be $\boldsymbol{Q}(x', y')$ which has the local coordinate ξ', so

$$z'_M = x' + \mu_M y' . \tag{24}$$

Let $\chi_M = z_M - z'_M$, $\chi_M^0 = z'_M - z_M^0$, so J_M can be transformed into

$$J_M = \int_{\Gamma_e} \frac{1}{\chi_M + \chi_M^0} \phi_q d\chi_M . \tag{25}$$

With the substitution of Taylor expansion of ϕ_q, J_M can be separated into two parts as follows

$$J_M = \int_{\Gamma_e} \frac{\phi_q - \phi_{q0}}{\chi_M + \chi_M^0} d\chi_M + \phi_{q0} \int_{\Gamma_e} \frac{1}{\chi_M + \chi_M^0} d\chi_M \,. \tag{26}$$

The second integral can be calculated analytically as

$$\int_{\Gamma_e} \frac{1}{\chi_M + \chi_M^0} d\chi_M = \log(\chi_M + \chi_M^0)\,|_{\Gamma_e} \,. \tag{27}$$

For the first integral in Eq.(26), with the substitution of local coordinate ξ, the detailed formulation for q=1 is

$$\int_{\Gamma_e} \frac{\phi_1 - \phi_{10}}{\chi_M + \chi_M^0} d\chi_M = \int_{\Gamma_e} \frac{[\mu_M(c\xi + d) + (a\xi + b)][(\xi - \xi')^2 + (\xi - \xi')(2\xi' - \xi_3)]}{(\xi_1 - \xi_3)\xi_1[a_M(\xi - \xi')^2 + b_M(\xi - \xi') + c_M]} d\xi \,, \tag{28}$$

where

$$a_M = \frac{a + \mu_M c}{2} \,, b_M = 2a_M \xi' + (b + \mu_M d) \,, c_M = a_M \xi'^2 + (b + \mu_M d)\xi' + (x_2 - x_0) + \mu_M (y_2 - y_0) \,. \tag{29}$$

ξ_i (i=1,2,3) are the local coordinates of the collocation points on the element. With a linear transformation $\zeta = \xi - \xi'$, Eq. (28) can be transformed into

$$\int_{\Gamma_e} \frac{\phi_1 - \phi_{10}}{\chi_M + \chi_M^0} d\chi_M = \int_{\Gamma_e} \frac{[\mu_M(c\zeta + c\xi' + d) + (a\zeta + a\xi' + b)][\zeta^2 + \zeta(2\xi' - \xi_3)]}{(\xi_1 - \xi_3)\xi_1(a_M\zeta^2 + b_M\zeta + c_M)} d\zeta \,. \tag{30}$$

Then nonlinear transformation $\zeta = \varsigma^m$ proposed by Luo et al. [4] can be added to Eq. (30), so that it can be calculated using the standard Gaussian quadrature formula.

For J'_M, second Taylor series are essential, and the equation can be separated into three parts as

$$J'_M = \int_{\Gamma_e} \frac{\phi_q - (\phi_{q0} + \phi'_{q0}\chi_M)}{(\chi_M + \chi_M^0)^2} d\chi_M + \int_{\Gamma_e} \frac{\phi_{q0} - \phi'_{q0}\chi_M^0}{(\chi_M + \chi_M^0)^2} d\chi_M + \int_{\Gamma_e} \frac{\phi'_{q0}}{\chi_M + \chi_M^0} d\chi_M \,. \tag{31}$$

The third part can be evaluated as in Eq. (27), and the second part can also be evaluated by

$$\int_{\Gamma_e} \frac{1}{(\chi_M + \chi_M^0)^2} d\chi_M = -\left. \frac{1}{\chi_M + \chi_M^0} \right|_{\Gamma_e} \,. \tag{32}$$

With linear transformation, the first part when $q = 1$ can be transformed into

$$\int_{\Gamma_e} \frac{\phi_1 - (\phi_{10} + \phi'_{10}\chi_M)}{(\chi_M + \chi_M^0)^2} d\chi_M = \int_{\Gamma_e} \frac{[\mu_M(c\xi + d) + (a\xi + b)][1 - (2\xi' - \xi_3)a_M / b_M]\zeta^2}{(\xi_1 - \xi_3)\xi_1(a_M\zeta^2 + b_M\zeta + c_M)^2} d\zeta \,, \tag{33}$$

nonlinear transformation can also be applied.

For the cases $q = 2$ and $q = 3$, the integrals J_M and J'_M can be evaluated in the same way as the case $q = 1$.

For J''_M, with the substitution of

$$\psi_q = \frac{\mu_M n_1(\mathbf{x}_0) - n_2(\mathbf{x}_0)}{\mu_M n_1(\mathbf{x}) - n_2(\mathbf{x})} \phi_q \,, \tag{34}$$

it can be changed into

$$J''_M = \int_{\Gamma_e} \frac{1}{\chi_M + \chi_M^0} \psi_q d\chi_M \,, \tag{35}$$

which has a similar form to J_M. So it can be evaluated with the advantage of the first Taylor-expansion series of ψ_q. The formulation is so complicated that it isn't listed here.

4.2. Straight element

For isoparametric quadratic element, the denominators of the nearly singular integrals possess a relative high order of ξ, which brings difficulty for the integration. So the non-isoparametric quadratic straight line element is introduced. The boundary quantities are described by the same shape functions as the isoparametric quadratic element, while the geometry quantities x and y can be described as

$$x = \frac{x_3 - x_1}{2}\xi + \frac{x_1 + x_3}{2}, \quad y = \frac{y_3 - y_1}{2}\xi + \frac{y_1 + y_3}{2}, \tag{36}$$

in which (x_1, y_1) and (x_3, y_3) are respectively the start and end point of the element. With the above expressions, $z_M - z_M^0$ can be represented by a linear function of ξ,

$$z_M - z_M^0 = (a + \mu_M c)\xi + (b + \mu_M d) - (x_0 + \mu_M y_0), \tag{37}$$

where $a = \frac{x_3 - x_1}{2}$, $b = \frac{x_1 + x_3}{2}$, $c = \frac{y_3 - y_1}{2}$, $d = \frac{y_1 + y_3}{2}$. So ξ gains the following expression,

$$\xi = \frac{z_M - z_M^0 - [b - x_0 + \mu_M (d - y_0)]}{a + \mu_M c}. \tag{38}$$

Nearly singular integrals can be expressed as

$$L_M = \int_{\Gamma_e} \frac{\phi_q}{z_M - z_M^0} dz_M, \quad L'_M = \int_{\Gamma_e} \frac{\phi_q}{(z_M - z_M^0)^2} dz_M. \tag{39}$$

$$L''_M = \frac{[\mu_M n_1(\mathbf{x}_0) - n_2(\mathbf{x}_0)]\sqrt{a^2 + c^2}}{A_M} \int_{\Gamma_e} \frac{\phi_q}{z_M - z_M^0} dz_M. \tag{40}$$

As the difference between L''_M and L_M is just a coefficient, only Eq. (39) should be evaluated.

Let $q = 1$, with the substitution of Eq. (38) into ϕ_1, the shape functions can be expressed as

$$\phi_1 = \frac{(z_M - z_M^0)^2 - [2B_M + (\xi_2 + \xi_3)A_M](z_M - z_M^0) + (B_M + \xi_2 A_M)(B_M + \xi_3 A_M)}{A_M^2 (\xi_1 - \xi_2)(\xi_1 - \xi_3)}, \tag{41}$$

where $A_M = a + \mu_M c$, $B_M = b - x_0 + \mu_M (d - y_0)$. Therefore L_M can be separated into three parts as follows,

$$\begin{aligned} \int_{\Gamma_e} \frac{\phi_1}{z_M - z_M^0} dz_M = & \frac{1}{(\xi_1 - \xi_2)(\xi_1 - \xi_3)A_M^2} \int_{\Gamma_e} (z_M - z_M^0) dz_M - \frac{2B_M + (\xi_2 + \xi_3)A_M}{(\xi_1 - \xi_2)(\xi_1 - \xi_3)A_M^2} \int_{\Gamma_e} dz_M \\ & + \frac{(B_M + \xi_2 A_M)(B_M + \xi_3 A_M)}{(\xi_1 - \xi_2)(\xi_1 - \xi_3)A_M^2} \int_{\Gamma_e} \frac{1}{z_M - z_M^0} dz_M \end{aligned}. \tag{42}$$

The three integrals can be evaluated analytically,

$$\int_{\Gamma_e} (z_M - z_M^0) dz_M = \left. \frac{(z_M - z_M^0)^2}{2} \right|_{\Gamma_e}, \tag{43}$$

$$\int_{\Gamma_e} dz_M = z_M \big|_{\Gamma_e}, \quad \int_{\Gamma_e} \frac{1}{z_M - z_M^0} dz_M = \log(z_M - z_M^0)\big|_{\Gamma_e} \tag{44}$$

With similarity of the expressions, the integrals can be evaluated in the same way when $q = 2, 3$.

Similarly, L'_M can also be divided into three parts. Two of them can be integrated by Eq. (44), the other one can be evaluated as follows,

$$\int_{\Gamma_e} \frac{1}{(z_M - z_M^0)^2} dz_M = -\left. \frac{1}{z_M - z_M^0} \right|_{\Gamma_e} . \tag{45}$$

With straight line element applied, the nearly singular integrals can be integrated analytically, and the separated parts have simple expressions.

5. Numerical examples

5.1. A central crack in finite plate

For the first example, a central crack of length 2*a* in a homogeneous and linear piezoelectric plate is considered to verify the correctness of the two methods. As shown in Fig. 1, the plate with width 2L × height 2H is under a pure uniform mechanical tensile loading of $\sigma_0 = 1\text{Mpa}$.

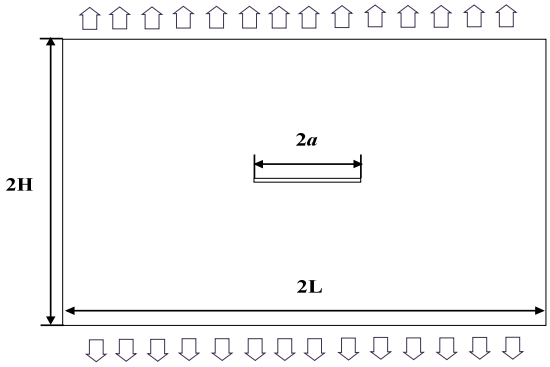

Figure 1. A central crack in a piezoelectric plate

Normalized stress intensity factor $K_I / (\sigma_0 \sqrt{\pi a})$ is presented versus L/*a* of the finite plate, the results have been plotted and compared with the corresponding FEM results presented by Cao and Kuang [5] to test the accuracy of the present integration methods. Different heights are considered with H/*a*=0.368, 0.568, 0.968 and 4.618. The two methods coincide well with each other, and they also match well with the FEM results. It should be pointed out that the FEM results are obtained for the condition that the thickness *b* of the plate is 0.01*a*. It can be found from Fig.2 that the values of SIF are approaching to the stable values when the ratio of L/*a* is larger than 2.0, which means these values reach the case of a central crack in the corresponding strips with the height 2H.

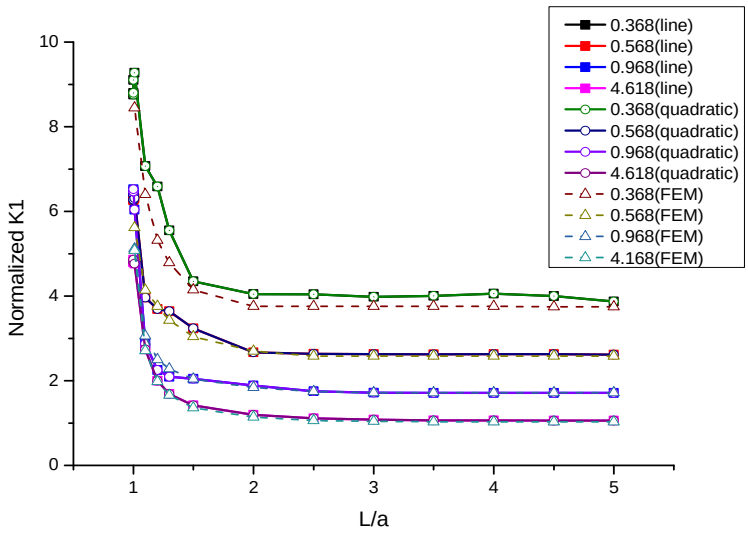

Figure 2. Normalized stress intensity factors for different dimensions

5.2. A central crack in thin piezoelectric structure

When H decreases to a very small value, the plate becomes piezoelectric film. Since the film is thin, the crack length is set to be relatively small. Let L/a=25, 50, normalized stress intensity factor $K_I/(\sigma_0\sqrt{\pi a})$ is presented versus H/*a* which is changing from 1 to 1×10^{-6}. When the ratio is as small as 10^{-6}, it is sufficient for modeling many thin piezoelectric films as used in smart materials and micro-electro-mechanical systems.

With the decrease of H, the stress intensity factor keep increasing when the strip is relatively thick, namely H/*a* is higher than 0.01. But in the interval [0, 0.01], the SIFs become stable. Since the crack is small, the value of $K_I/(\sigma_0\sqrt{\pi a})$ is not so high. For the straight line element method, the stress intensity factors at H/*a*=1×10^{-6} jump slightly.

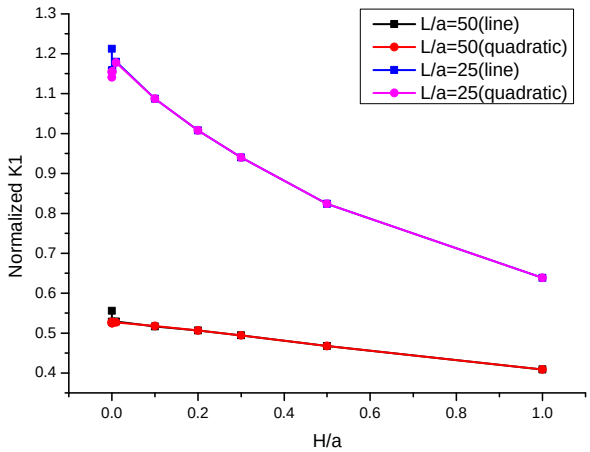

Figure 3. Normalized stress intensity factors versus H/*a*

Dynamic intensity factors are also taken into consideration. For H/*a*=0.1, L/*a*=25, Fig. 3 shows the normalized dynamic intensity factors versus dimensionless time tc_L/H, where

$$c_L = \sqrt{(C_{22} + e_{22}^2/\varepsilon_{22})/\rho}\,. \tag{46}$$

The methods of line element and quadratic element are both used and the results coincide with each other very well.

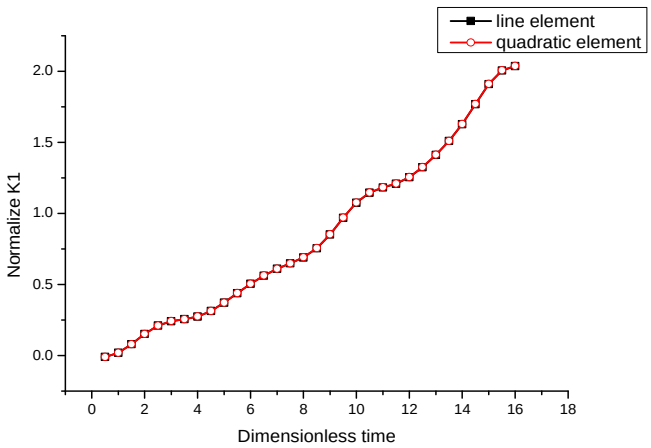

Figure 4. Normalized dynamic stress intensity factors versus dimensionless time

6. Conclusions

Transient dynamic crack problems in piezoelectric thin structures are considered. Two methods are presented to deal with the nearly singular problems in the Laplace domain fundamental solutions. The first method for quadratic element is semi-analytical and the second method for straight line element is analytical. Static stress intensity factor of a piezoelectric plate is obtained for different structural dimensions. The results have been compared with FEM results and the agreement verifies the accuracy of the present methods. Then cracks in thin structures are considered, normalized intensity factors of both static and dynamic cases are obtained. The results indicate that the two methods function well when the ratio of the film thickness to the crack length is as small as 10^{-6} which is sufficient for modeling many thin piezoelectric films and coatings.

Acknowledgements

This work is supported by the Natural Science Foundation of China under Grant No. 11002006 and the German Research Foundation (DFG) under the project number ZH 15/6-1 and ZH 15/6-3, which are gratefully acknowledged.

References

[1] F. García-Sánchez, C.H. Zhang, A. Sáez, 2-D transient dynamic analysis of cracked piezoelectric solids by a time-domain BEM. Comput. Methods Appl. Mech. Engrg., 197 (2008) 3108–3121.

[2] Y.J. Liu, H. Fan, Analysis of thin piezoelectric solids by the boundary element method. Comput. Methods Appl. Mech. Engrg., 191 (2002) 2297–2315.

[3] C.Y. Wang, C.H. Zhang, 3-D and 2-D dynamic Green's functions and time-domain BIEs for piezoelectric solid. Engineering Analysis with Boundary Elements, 29 (2005) 454–465.

[4] J.F. Luo, Y.J. Liu, E.J. Berger, Analysis of two-dimensional thin structures (from micro- to nano-scales) using the boundary element method. Computational Mechanics, 22 (1998) 404–412.

[5] Z.J. Cao, Z.B. Kuang, A finite element modeling for directly determining intensity factors of piezoelectric materials with cracks. Int J Fract, 149 (2008) 67–85.

Transient Dynamic Crack Analysis in Decagonal Quasicrystal

Jan Sladek[1,*], **Vladimir Sladek**[1], **Slavomir Krahulec**[1], **Chuanzeng Zhang**[2], **Michael Wünsche**[2]

[1] Institute of Construction and Architecture, Slovak Academy of Sciences, 84503 Bratislava, Slovakia
[2] Department of Civil Engineering, University of Siegen, D-57068 Siegen, Germany
* Corresponding author: jan.sladek@savba.sk

Abstract: A meshless method based on the local Petrov-Galerkin approach is proposed to solve initial-boundary value crack problems in decagonal quasicrystals. These quasicrystals belong to the class of two-dimensional quasicrystals, where the atomic arrangement is quasiperiodic in a plane, and periodic in the perpendicular direction. The ten-fold symmetries occur in these quasicrystals. The two-dimensional (2-d) crack problem is represented by a coupling of phonon and phason displacements. Both stationary governing equations and dynamic equations represented by the Bak model with oscillations for phason are analyzed here. Nodal points are spread on the analyzed domain, and each node is surrounded by a small circle for simplicity. The spatial variation of the phonon and phason displacements is approximated by the Moving Least-Squares (MLS) scheme. After performing the spatial integrations, one obtains a system of ordinary differential equations for certain nodal unknowns. That system is solved numerically by the Houbolt finite-difference scheme as a time-stepping method.

Keywords: Meshless local Petrov-Galerkin method (MLPG), phonon, phason, intensity factors

1. Introduction

Qusicrystals discovered in 1984 combine aperiodic long-range positional order with noncrystallographic rotational symmetry [1]. Decagonal quasicrystals (QC) belong to the class of two-dimensional quasicrystals, where the atomic arrangement is quasiperiodic in a plane, and periodic in the third direction. The problem can be decomposed into plane and anti-plane elasticity. Here, we consider only the plane elasticity, because the anti-plane elasticity is a classical one.

Experimental observations [2] have shown that quasicrystals are brittle. Therefore, to understand the effect of cracks on the mechanical behaviour of a quasicrystal, the crack analysis of quasicrystals, including the determination of the stress intensity factors, the elastic field, the strain energy release rate and so on, is a prerequisite. Many crack investigations in the QC are focused on Griffith cracks in an infinite body, where analytical solutions are available for one and two-dimensional quasicrystals [3-6]. Elastodynamics of quasicrystals brings some additional problems. A unique opinion on governing equations for the phason field is missing. According to Bak [7] the phason describes particular structure disorders in qusicrystals, and it can be formulated in a six-dimensional space. Since there are six continuous symmetries, there exist six hydrodynamic vibration modes. Then, phonons and phasons play similar roles in the dynamics and both fields should be described by similar governing equations, namely the balance of momentum. Lubensky and his students [8] were thinking that the phason field should be described by a diffusion equation with very a large diffusion time. According to them, phasons are insensitive to spatial translations and phason modes represent the relative motion of the constituent density waves. Rochal and

Lorman [9] suggested the minimal model of the phonon-phason dynamics in quasicrystals to reconcile contradictions between Bak´s and Lubensky´s arguments. In literature, analyses of dynamic crack problems are very seldom [10-12].

The purpose of this paper is to develop a reliable computational method for a general crack problem in quasicrystals with a finite size. Up to date we have practically only analytical solutions for simple boundary value problems of elasticity for quasicrystals. However, there are some limitations to apply analytical approaches for complicated boundary value problems. The finite difference method has been applied to elasto-hydrodynamics problems by Fan [12]. The basic equations for the finite element formulation can be found in the Fan`s book too. Meshless methods for solving PDE in physics and engineering sciences are a powerful new alternative to the traditional mesh-based techniques. Focusing only on nodes or points instead of elements used in the conventional FEM, meshless approaches have certain advantages. The meshless local Petrov-Galerkin (MLPG) method is a fundamental base for the derivation of many meshless formulations, since trial and test functions can be chosen from different functional spaces. The MLPG method with a Heaviside step function as the test functions has been successfully applied to multi-field coupled and crack problems [13,14].

In the present paper, the MLPG is applied to crack analysis in decagonal quasicrystals under static and transient dynamic loads. The MLPG formulation is developed for the Bak`s model. The coupled governing partial differential equations are satisfied in a weak-form on small fictitious subdomains. Nodal points are introduced and spread on the analyzed domain and each node is surrounded by a small circle for simplicity, but without loss of generality. The spatial variations of the phonon and phason displacements are approximated by the Moving Least-Squares (MLS) scheme. After performing the spatial MLS approximation, a system of ordinary differential equations for certain nodal unknowns is obtained. Then, the system of the ordinary differential equations of the second order resulting from the equations of motion is solved by the Houbolt finite-difference scheme [15] as a time-stepping method.

2. Local integral equations

Two displacement fields named phonon and phason displacements are used for the deformation theory of quasicrystals [12]. The generalized Hooke`s law for plane elasticity of decagonal QC is given as

$$\sigma_{11} = c_{11}\varepsilon_{11} + c_{12}\varepsilon_{22} + R(w_{11} + w_{22}), \qquad \sigma_{22} = c_{12}\varepsilon_{11} + c_{22}\varepsilon_{22} - R(w_{11} + w_{22}),$$

$$\sigma_{12} = \sigma_{21} = 2c_{66}\varepsilon_{12} + R(w_{21} - w_{12}),$$

$$H_{11} = K_1 w_{11} + K_2 w_{22} + R(\varepsilon_{11} - \varepsilon_{22}), \qquad H_{22} = K_1 w_{22} + K_2 w_{11} + R(\varepsilon_{11} - \varepsilon_{22}),$$

$$H_{12} = K_1 w_{12} - K_2 w_{21} - 2R\varepsilon_{12}, \qquad H_{21} = K_1 w_{21} - K_2 w_{12} + 2R\varepsilon_{12}, \tag{1}$$

where ε_{ij} and σ_{ij} correspond to the phonon strain and stress tensor, and w_{ij} and H_{ij} denote the

phason strain and stress tensor, respectively. Symbols c_{ij} , R and K_i denote phonon elastic constants, phonon-phason coupling parameter and phason elastic constants, respectively. The phonon and phason strains are defined as

$$\varepsilon_{ij}(\mathbf{x}) = \frac{1}{2}\left(u_{i,j} + u_{j,i}\right), \tag{2}$$

$$w_{ij}(\mathbf{x}) = w_{i,j}(\mathbf{x}), \tag{3}$$

where $u_i(\mathbf{x})$ and $w_i(\mathbf{x})$ are the phonon and phason displacements, respectively. The phonon field describes the mechanical displacements of the crystal system, and the phason field represents the atom arrangement along the quasiperiodic direction. The phonon strains are the same as in classical elasticity and they are symmetric. However, the phason strains are new physical quantities used only in quasi-crystal elasticity and they are asymmetric.

According to Bak`s model [7] the phason structure disorders are realized by fluctuations in quasicrystals. The balance of momentum is valid for phonon deformation and similarly for phason oscillations too. Then, the model is described by following governing equations:

$$\sigma_{ij,j}(\mathbf{x},\tau) + X_i(\mathbf{x},\tau) = \rho \ddot{u}_i(\mathbf{x},\tau), \tag{4}$$

$$H_{ij,j}(\mathbf{x},\tau) + g_i(\mathbf{x},\tau) = \rho \ddot{w}_i(\mathbf{x},\tau), \tag{5}$$

where $\ddot{u}_i$, $\ddot{w}_i$, ρ, X_i and g_i denote the acceleration of the phonon and phason displacements, the mass density, and the body force vectors, respectively. Both governing equations have mathematically a similar structure.

The MLPG method constructs a weak-form over the local fictitious subdomains such as Ω_s, which is a small region taken for each node inside the global domain [16]. The local subdomains could be of any geometrical shape and size. In the present paper, the local subdomains are taken to be of a circular shape for simplicity. The local weak-form of the governing equations (4) and (5) can be written as

$$\int_{\Omega_s} \left[\sigma_{ij,j}(\mathbf{x},\tau) - \rho \ddot{u}_i(\mathbf{x},\tau) + X_i(\mathbf{x},\tau)\right] u_{ik}^*(\mathbf{x})\, d\Omega = 0, \tag{6}$$

$$\int_{\Omega_s} \left[H_{ij,j}(\mathbf{x},\tau) - \rho \ddot{w}_i(\mathbf{x},\tau) + g_i(\mathbf{x},\tau)\right] u_{ik}^*(\mathbf{x})\, d\Omega = 0, \tag{7}$$

where $u_{ik}^*(\mathbf{x})$ is a test function. Applying the Gauss divergence theorem to the first domain integrals in both equations one gets

$$\int_{\partial\Omega_s} \sigma_{ij}(\mathbf{x},t) n_j(\mathbf{x}) u_{ik}^*(\mathbf{x}) d\Gamma - \int_{\Omega_s} \sigma_{ij}(\mathbf{x},t) u_{ik,j}^*(\mathbf{x}) d\Omega + \int_{\Omega_s} \left[-\rho \ddot{u}_i(\mathbf{x},t) + X_i(\mathbf{x},t)\right] u_{ik}^*(\mathbf{x}) d\Omega = 0, \tag{8}$$

$$\int_{\partial\Omega_s} H_{ij}(\mathbf{x},t) n_j(\mathbf{x}) u_{ik}^*(\mathbf{x}) d\Gamma - \int_{\Omega_s} H_{ij}(\mathbf{x},t) u_{ik,j}^*(\mathbf{x}) d\Omega + \int_{\Omega_s} \left[-\rho \ddot{w}_i(\mathbf{x},t) + g_i(\mathbf{x},t)\right] u_{ik}^*(\mathbf{x}) d\Omega = 0, \tag{9}$$

where $\partial\Omega_s$ is the boundary of the local subdomain which consists of three parts $\partial\Omega_s = L_s \cup \Gamma_{st} \cup \Gamma_{su}$ [16]. Here, L_s is the local boundary that is totally inside the global domain, Γ_{st} is the part of the local boundary which coincides with the global traction boundary, i.e., $\Gamma_{st} = \partial\Omega_s \cap \Gamma_t$, and similarly Γ_{su} is the part of the local boundary that coincides with the global displacement boundary, i.e., $\Gamma_{su} = \partial\Omega_s \cap \Gamma_u$.

By choosing a Heaviside step function as the test function $u_{ik}^*(\mathbf{x})$ in each subdomain the local weak-forms (6) and (7) are converted into the following local integral equations

$$\int_{L_s+\Gamma_{su}} t_i(\mathbf{x},\tau)d\Gamma - \int_{\Omega_s} \rho\ddot{u}_i(\mathbf{x},\tau)d\Omega = -\int_{\Gamma_{st}} \bar{t}_i(\mathbf{x},\tau)d\Gamma - \int_{\Omega_s} X_i(\mathbf{x},\tau)d\Omega, \tag{10}$$

$$\int_{L_s+\Gamma_{su}} h_i(\mathbf{x},\tau)d\Gamma - \int_{\Omega_s} \rho\ddot{w}_i(\mathbf{x},\tau)d\Omega = -\int_{\Gamma_{st}} \bar{h}_i(\mathbf{x},\tau)d\Gamma - \int_{\Omega_s} g_i(\mathbf{x},\tau)d\Omega. \tag{11}$$

The expressions for the traction and the generalized traction vectors result from the constitutive equations and are given as

$$t_i(\mathbf{x},\tau) = \left[c_{ijkl}(\mathbf{x})u_{k,l}(\mathbf{x},\tau) + R_{ijkl}(\mathbf{x})w_{k,l}(\mathbf{x},\tau)\right]n_j(\mathbf{x}), \tag{12}$$

$$h_i(\mathbf{x},\tau) = \left[K_{ijkl}(\mathbf{x})w_{k,l}(\mathbf{x},\tau) + R_{ijkl}(\mathbf{x})u_{k,l}(\mathbf{x},\tau)\right]n_j(\mathbf{x}), \tag{13}$$

where $n_j(\mathbf{x})$ is the unit outward normal vector to the boundary $\partial\Omega_s$.

The trial functions are chosen to be the MLS approximations by using a number of nodes spreading over the domain of influence. The approximated functions for the phonon and phason displacements can be written as [16]

$$\mathbf{u}^h(\mathbf{x},\tau) = \mathbf{\Phi}^T(\mathbf{x})\cdot\hat{\mathbf{u}}(\tau) = \sum_{a=1}^{n} \phi^a(\mathbf{x})\mathbf{u}^a(\tau), \tag{14}$$

$$\mathbf{w}^h(\mathbf{x},\tau) = \sum_{a=1}^{n} \phi^a(\mathbf{x})\hat{\mathbf{w}}^a(\tau), \tag{15}$$

where the nodal values $\hat{\mathbf{u}}(\tau) = \left(u_1^a(\tau),\, u_2^a(\tau)\right)^T$ and $\hat{\mathbf{w}}(\tau) = \left(w_1^a(\tau),\, w_2^a(\tau)\right)^T$ are fictitious parameters for the phonon and phason displacements, respectively, and $\phi^a(\mathbf{x})$ is the shape function associated with the node *a*. The number of nodes *n* used for the approximation is determined by the weight function $m^a(\mathbf{x})$. A 4th order spline-type weight function [16] is applied in the present work.

Then, the traction vector $t_i(\mathbf{x},\tau)$ at a boundary point $\mathbf{x}\in\partial\Omega_s$ is approximated in terms of the same nodal values $\hat{\mathbf{u}}^a(\tau)$ and $\hat{\mathbf{w}}^a(\tau)$ as

$$\mathbf{t}^h(\mathbf{x},\tau)=\mathbf{N}(\mathbf{x})\mathbf{C}\sum_{a=1}^{n}\mathbf{B}^a(\mathbf{x})\hat{\mathbf{u}}^a(\tau)+\mathbf{N}(\mathbf{x})\mathbf{R}\sum_{a=1}^{n}\mathbf{B}_w^a(\mathbf{x})\mathbf{w}^a(\tau)\,, \tag{16}$$

where $\mathbf{N(x)}$ is related to the normal vector $\mathbf{n(x)}$ on $\partial\Omega_s$ and the matrices $\mathbf{B}^a$ and $\mathbf{B}_w^a$ are represented by the gradients of the shape functions with

$$\mathbf{N}(\mathbf{x})=\begin{bmatrix} n_1 & 0 & n_2\\ 0 & n_2 & n_1\end{bmatrix},\qquad \mathbf{B}^a(\mathbf{x})=\begin{bmatrix}\phi^a_{,1} & 0\\ 0 & \phi^a_{,2}\\ \phi^a_{,2} & \phi^a_{,1}\end{bmatrix},\qquad \mathbf{B}_w^a(\mathbf{x})=\begin{bmatrix}\phi^a_{,1} & 0\\ 0 & \phi^a_{,2}\\ \phi^a_{,2} & -\phi^a_{,1}\end{bmatrix},$$

and the material matrices

$$\mathbf{C}=\begin{bmatrix} c_{11} & c_{12} & 0\\ c_{12} & c_{22} & 0\\ 0 & 0 & c_{66}\end{bmatrix}\quad,\qquad \mathbf{R}=\begin{bmatrix} R & R & 0\\ -R & -R & 0\\ 0 & 0 & -R\end{bmatrix}\quad.$$

Similarly the generalized traction vector $h_i(\mathbf{x},\tau)$ can be approximated by

$$\mathbf{h}^h(\mathbf{x},\tau)=\mathbf{N}_h(\mathbf{x})\mathbf{R}_h\sum_{a=1}^{n}\mathbf{B}^a(\mathbf{x})\hat{\mathbf{u}}^a(\tau)+\mathbf{N}_h(\mathbf{x})\mathbf{K}\sum_{a=1}^{n}\mathbf{B}_{hw}^a(\mathbf{x})\mathbf{w}^a(\tau)\,, \tag{17}$$

where

$$\mathbf{N}_h(\mathbf{x})=\begin{bmatrix} n_1 & 0 & n_2 & 0\\ 0 & n_2 & 0 & n_1\end{bmatrix},\qquad \mathbf{K}=\begin{bmatrix} K_1 & K_2 & 0 & 0\\ K_2 & K_1 & 0 & 0\\ 0 & 0 & K_1 & -K_2\\ 0 & 0 & -K_2 & K_1\end{bmatrix},$$

$$\mathbf{B}_{hw}^a(\mathbf{x})=\begin{bmatrix}\phi^a_{,1} & 0\\ 0 & \phi^a_{,2}\\ \phi^a_{,2} & 0\\ 0 & \phi^a_{,1}\end{bmatrix},\qquad R_h=\begin{bmatrix} R & -R & 0\\ R & -R & 0\\ 0 & 0 & -R\\ 0 & 0 & R\end{bmatrix}.$$

Satisfying the essential boundary conditions and making use of the approximation formulae (14) and (15) one obtains the discretized form of these boundary conditions as

$$\sum_{a=1}^{n}\phi^a(\zeta)\hat{\mathbf{u}}^a(\tau)=\bar{\mathbf{u}}(\zeta,\tau)\,, \tag{18}$$

$$\sum_{a=1}^{n}\phi^a(\zeta)\mathbf{w}^a(\tau)=\bar{\mathbf{w}}(\zeta,\tau)\,,\qquad \text{for}\ \ \zeta\in\Gamma_u\,. \tag{19}$$

Furthermore, in view of the MLS-approximations (16) and (17) for the unknown quantities in the local integral equations (10) and (11), we obtain their discretized forms as

$$\sum_{a=1}^{n}\left[\left(\int_{L_s+\Gamma_{st}}\mathbf{N}(\mathbf{x})\mathbf{C}\mathbf{B}^a(\mathbf{x})d\Gamma\right)\ddot{\hat{\mathbf{u}}}^a(\tau)-\left(\int_{\Omega_s}\rho(\mathbf{x})\phi^a d\Omega\right)\ddot{\hat{\mathbf{t}}}^a(\tau)\right]+$$

$$+\sum_{a=1}^{n}\left(\int_{L_s+\Gamma_{st}}\mathbf{N}(\mathbf{x})\mathbf{R}\mathbf{B}_w^a(\mathbf{x})d\Gamma\right)\hat{\mathbf{w}}^a(\tau)\;=\;-\int_{\Gamma_{st}}\bar{\mathbf{t}}(\mathbf{x},\tau)d\Gamma-\int_{\Omega_s}\mathbf{X}(\mathbf{x},\tau)d\Omega\,, \tag{20}$$

$$\sum_{a=1}^{n}\left(\int_{L_s+\Gamma_{st}}\mathbf{N}_h(\mathbf{x})\mathbf{R}_h\mathbf{B}^a(\mathbf{x})d\Gamma\right)\ddot{\hat{\mathbf{u}}}^a(\tau)\;-\sum_{a=1}^{n}\left(\int_{L_s+\Gamma_{st}}\mathbf{N}_h(\mathbf{x})\mathbf{K}\mathbf{B}_{hw}^a(\mathbf{x})d\Gamma\right)\mathbf{w}^a(\tau)-$$

$$-\sum_{a=1}^{n}\left(\int_{\Omega_s}\rho(\mathbf{x})\phi^a d\Omega\right)\ddot{\hat{\mathbf{w}}}^a(\tau)=-\int_{\Gamma_{st}}\bar{\mathbf{h}}(\mathbf{x},\tau)d\Gamma+\int_{\Omega_s}\mathbf{g}(\mathbf{x},\tau)d\Omega\,, \tag{21}$$

which are considered on the sub-domains adjacent to the interior nodes as well as to the boundary nodes on Γ_{st}.

Collecting the discretized local integral equations together with the discretized boundary conditions for the phonon and phason displacements results in a complete system of ordinary differential equations which can be rearranged in such a way that all known quantities are on the r.h.s. Thus, in matrix form the system becomes

$$\mathbf{A}\ddot{\mathbf{x}}+\mathbf{C}\mathbf{x}=\mathbf{Y}\,. \tag{22}$$

There are many time integration procedures for the solution of this system of ordinary differential equations. In the present work, the Houbolt method is applied [15].

3. Computation of stress intensity factors

It can be proved that both phonon and phason stresses exhibit the same singularity $r^{-1/2}$, where r is the radial coordinate with origin at the crack-tip [17]. Neglecting higher-order infinitesimal terms in the analytical solution, one can obtain the asymptotic expression of stresses at the crack-tip vicinity proportional to $r^{-1/2}$. For the mode-I crack under a pure phonon load we have the following asymptotic stresses in polar coordinate system [11]:

$$\sigma_{11}(r,\theta)=\frac{K_I^{\parallel}}{\sqrt{2\pi r}}\cos\frac{1}{2}\theta\left(1-\sin\frac{1}{2}\theta\sin\frac{3}{2}\theta\right),$$

$$\sigma_{22}(r,\theta)=\frac{K_I^{\parallel}}{\sqrt{2\pi r}}\cos\frac{1}{2}\theta\left(1+\sin\frac{1}{2}\theta\sin\frac{3}{2}\theta\right),$$

$$\sigma_{12}(r,\theta)=\sigma_{21}(r,\theta)=\frac{K_I^{\|}}{\sqrt{2\pi r}}\cos\frac{1}{2}\theta\cos\frac{3}{2}\theta\,, \tag{23}$$

$$H_{11}(r,\theta)=-\frac{d_{21}K_I^{\|}}{\sqrt{2\pi r}}\sin\theta\left(2\sin\frac{3}{2}\theta+\frac{3}{2}\sin\theta\cos\frac{5}{2}\theta\right),$$

$$H_{22}(r,\theta)=\frac{d_{21}K_I^{\|}}{\sqrt{2\pi r}}\frac{3}{2}\sin^2\theta\cos\frac{5}{2}\theta\,,$$

$$H_{12}(r,\theta)=-\frac{d_{21}K_I^{\|}}{\sqrt{2\pi r}}\frac{3}{2}\sin^2\theta\sin\frac{5}{2}\theta\,,$$

$$H_{21}(r,\theta)=\frac{d_{21}K_I^{\|}}{\sqrt{2\pi r}}\sin\theta\left(2\cos\frac{3}{2}\theta-\frac{3}{2}\sin\theta\sin\frac{5}{2}\theta\right), \tag{24}$$

where

$$d_{21}=\frac{R\left(K_1-K_2\right)}{4\left(MK_1-R^2\right)}\,,$$

$$K_I^{\mathrm{P}}=\lim_{r\to 0}\sqrt{2\pi r}\,\sigma_{22}(r,0)\,, \tag{25}$$

and $M=(c_{11}-c_{12})/2$.

4. Numerical examples

In the first example a straight central crack in a finite quasicrystal strip under a pure phonon load is analyzed (Fig. 1). The strip is subjected to a stationary or impact mechanical load with Heaviside time variation and the intensity $\sigma_0=1Pa$ on the top side of the strip. The material coefficients of the strip correspond to Al-Ni-Co quasicrystal and they are given by

$c_{11}=L+2M=23.43\cdot 10^{10}\,Nm^{-2}$, $c_{12}=L=5.74\cdot 10^{10}\,Nm^{-2}$, $K_1=12.2\cdot 10^{10}\,Nm^{-2}$,

$K_2=2.4\cdot 10^{10}\,Nm^{-2}$, $\rho=4180\,kg/m^3$, $\Gamma_w=4.8\cdot 10^{-19}\,m^3s/kg$.

The crack-length $2a=1.0m$, strip width ratio $a/w=0.4$, and strip-height $h=1.2w$ are considered. Due to the symmetry of the problem with respect to the crack-line as well as vertical central line, only a quarter of the specimen is numerically analyzed. Both phonon and phason displacements in the quarter of the specimen are approximated by using 930 (31x30) nodes equidistantly distributed.

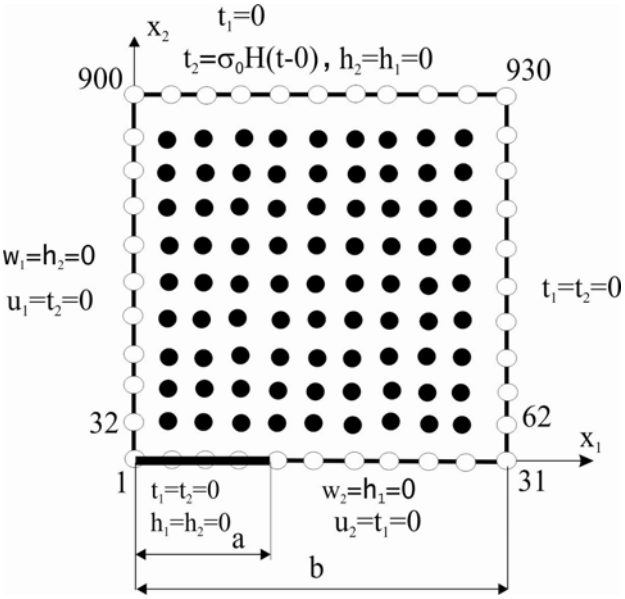

Figure 1. Central crack in a finite homogeneous strip

Numerical results for the phonon displacement u_2 along the crack-face for various coupling parameter *R* are given in Fig. 2. For a vanishing coupling parameter *R/M* = 0, we obtain phonon displacements corresponding to conventional elasticity. One can observe a good agreement between the FEM and present MLPG results. The FEM results have been obtained by the COMSOL code with 576 quadrilateral elements. One can observe that the phonon crack-opening-displacements increase with increasing value of the coupling parameter. The stress intensity factor (SIF) is computed by using equation (25) and the extrapolation technique from stresses ahead of the crack-tip with finite distances. The normalized SIF $K_I^{\mathrm{P}}/\sigma_0\sqrt{\pi a}$ is increasing from 1.139 at R/M=0 to 1.323 at R/M=0.5.

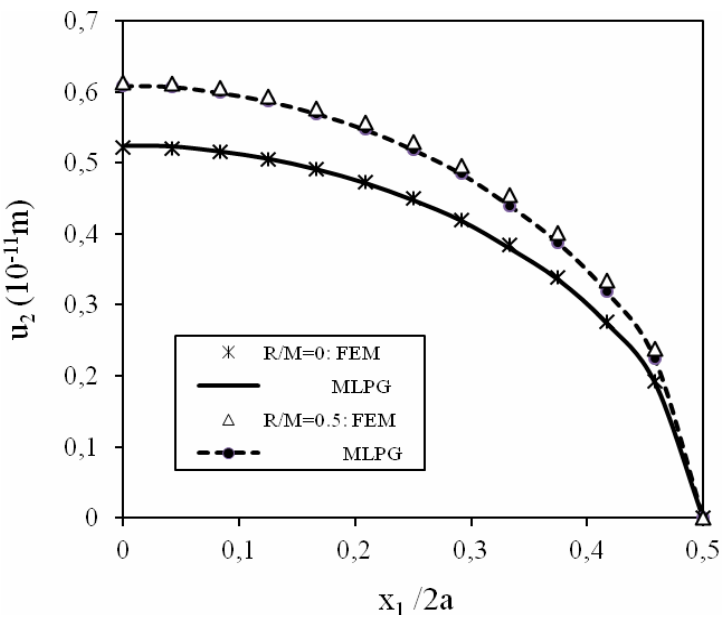

Figure 2. Variations of the phonon crack displacement with the normalized coordinate $x_1/2a$

In the next example, we analyze the same cracked strip under an impact load with Heaviside time variation $\sigma_0 H(t-0)$. The normalized SIF is compared with the FEM results in Fig. 3 for R/M=0.5 . The time variable is normalized as $c_L \tau / h$, where $c_L = \sqrt{c_{11}/\rho}$ is the velocity of longitudinal wave. One can observe again a good agreement of the FEM and MLPG results. Only some differences appear at larger time instants.

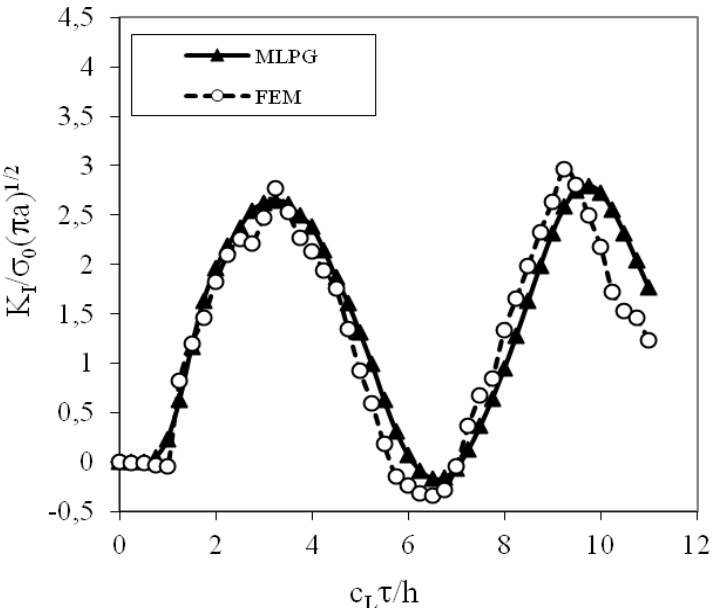

Figure 3. Temporal variation of the normalized SIF for the central crack in a strip under an impact load

Acknowledgements

The authors gratefully acknowledge the supports by the Slovak Science and Technology Assistance Agency registered under number APVV-0014-10, the Slovak Grant Agency VEGA-2/0011/13, and the German Research Foundation (DFG, Project-No. ZH 15/23-1).

References

[1] D. Shechtman, I. Blech, D. Gratias, J.W. Cahn, Metallic phase with long-range orientational order and no translational symmetry. Phys Rev Lett, 53 (1984) 1951–1953.
[2] C.Z. Hu, W.Z. Yang, R.H. Wang, Symmetry and physical properties of quasicrystals. Advanced Physics 17 (1997) 345-376.
[3] T.Y. Fan, Y.W. Mai, Elasticity theory, fracture mechanics and some relevant thermal properties of quasicrystal materials. Applied Mechanics Review 57 (2004) 325-344.
[4] W.M. Zhou, T.Y. Fan, Plane elasticity problem of two-dimensional octagonal quasicrystal and crack problem. Chinese Physics 10 (2001) 743-747.
[5] Y.C. Guo, T.Y. Fan, A mode-II Griffith crack in decagonal quasicrystals. Appl Math Mechanics 22 (2001) 1311-1317.
[6] L.H. Li, T.Y. Fan, Complex variable function method for solving Griffith crack in an icosahedral quasicrystal. Science in China G51 (2008) 773-780.

[7] P. Bak, Phenomenological theory of icosahedral incommensurate (quasiperiodic) order in Mn-Al alloys. Phys Rev Lett 54 (1985) 1517-1519.
[8] T.C. Lubensky, S. Ramaswamy, J. Joner, Hydrodynamics of icosahedral quasicrystals. Phys Rev B 32 (1985) 7444-7452.
[9] S.B. Rochal, V.L. Lorman, Minimal model of the phonon-phason dynamics on icosahedral quasicrystals and its application for the problem of internal friction in the Ni-AlPdMn alloys. Phys Rev B 66 (2002) 144204.
[10] A.Y. Zhu, T.Y. Fan, Dynamic crack propagation in a decagonal Al-Ni-Co quasicrystal. J Phys: Condens Matter 20 (2008) 295217.
[11] T.Y. Fan, Z.Y. Tang, W.Q. Chen, Theory of linear, nonlinear and dynamic fracture for quasicrystals. Engn Fracture Mech 82 (2012) 185-194.
[12] T.Y. Fan, Mathematical Theory of Elasticity of Quasicrystals and its Applications, Springer, Beijing, 2011.
[13] J. Sladek, V. Sladek, Ch. Zhang, M. Wünsche, Crack analysis in piezoelectric solids with energetically consistent boundary conditions by the MLPG. CMES-Computer Modelling in Engineering & Sciences 68 (2010) 185-220.
[14] J. Sladek, V. Sladek, S. Krahulec, E. Pan, Enhancement of the magnetoelectric coefficient in functionally graded multiferroic composites. J Intell Mat Syst Struct 23 (2012) 1644-1653.
[15] J.C. Houbolt, A recurrence matrix solution for the dynamic response of elastic aircraft. Journal of Aeronautical Sciences 17 (1950) 371-376.
[16] S.N. Atluri, The Meshless Method, (MLPG) for Domain & BIE Discretizations, Tech Science Press, Encino, 2004.
[17] X.F. Li, T.Y. Fan, Y.F. Sun, A decagonal quasicrystal with a Griffith crack. Philosophical Magazine A 79 (1999) 1943-1952.

Finite Deformation Modeling of Crystalline Defects in Hyper-elastic Material

Akihiro Nakatani[1,*], **Mitsuhiro Akita**[1]

[1] Department of Adaptive Machine Systems, Osaka University, Suita, Osaka 565-0871, Japan
[*] Corresponding author: nakatani@ams.eng.osaka-u.ac.jp

Abstract An updated Lagrangian formulation is established to deal with the finite deformation of hyper-elastic body including the discontinuous slips due to the nucleation of lattice defects. The principle of virtual power is modified to treat the discontinuous deformation measured by initial lattice and a computational model is established by a penalty method with Lagrange multiplier. A few examples are shown for the application of geometrically non-linear deformation of hyper-elastic body including some dislocation structures and they are compared with the solutions of linear elasticity. The results have showed that the proposed method can be applicable to the analysis of kink deformation which had been observed experimentally in long-period stacking ordered magnesium alloy.
Keywords Computational Mechanics, Finite Deformation, Hyper-elasticity, Driving Force

1. Introduction

Magnesium alloys containing long-period stacking order (LPSO) phase have attracted a great deal of attention. The origins of both high strength and high ductility of these alloys are thought to be related to the grain refinement of matrix phase and kink deformation band of LPSO phase. Collective behaviors of dislocations on basal slip planes are important for the formation of kink deformation which consists of unique arrangement of microscopic lattice defects.

Theoretical studies of the relationship between lattice defect theory and generalized continuum theory have been carried out since early time, but they are still developping[4, 5, 6, 7].

There are quite a few literature of the deformation analysis using discrete dislocation plasticity and some disclination dynamics; e.g. deformation mechanism and mechanical properties[1], Interface crack[2], grain boundary[3], and so on.

However, there are few studies of formulation based on finite deformation except for Refs.[8, 9, 10]

In this study, the boundary value problem based on discrete defect theory is formulated to study the kink deformation using finite deformation theory. The essential mechanism of kink deformation is related to instabilities like buckling or localization of deformation. It will be important to consider the boundary value problem including lattice defects such as dislocations and disclinations.

2. Formulation

Some relative discontinuous displacement on planes $\partial\Gamma$ is considered in a hyper-elastic body Ω. Current coordinates for deformed position $\boldsymbol{x}$ is referred to the reference coordinates $\boldsymbol{X}$ for initial position, as shown in Fig.1. The displacement $\boldsymbol{u}$ is defined by $\boldsymbol{u} = \boldsymbol{x} - \boldsymbol{X}$. The tensors $\boldsymbol{F}$, $\boldsymbol{v}$, and $\boldsymbol{L} = \partial\boldsymbol{v}/\partial\boldsymbol{X}$

($\boldsymbol{l} = \partial \boldsymbol{v}/\partial \boldsymbol{x}$) are deformation gradient, velocity of a material point, and velocity gradient tensors, respectively An updated Lagrangian formulation is established.

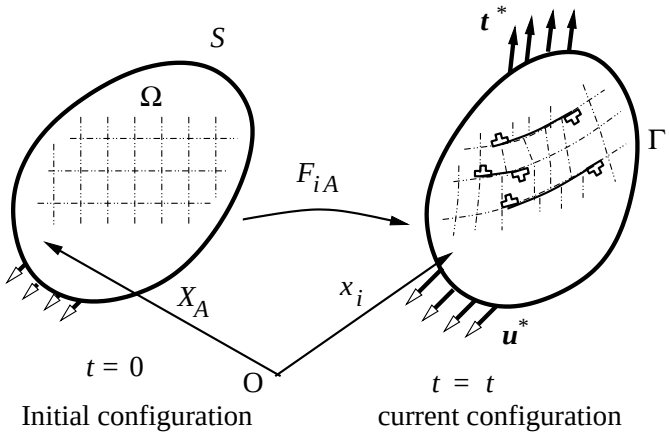

Figure 1. Boundary value problem of elastic body including discontinuous planes

2.1. Updated-Lagrangian Formulation

St.Venant-Kirchhoff material is assumed to be analyzed. The second Piola-Kirchhoff stress tensor $\boldsymbol{S}$ is expressed as a function of Green-Lagrange strain $\boldsymbol{E}$ as following:

$$S_{AB} = C^{(0)}_{ABCD} E_{CD} \tag{1}$$

where $\boldsymbol{C}^{(0)}$ is the elastic tensor. Truesdell's stress rate $\check{\boldsymbol{T}}$ is defined as follows:

$$\check{\boldsymbol{T}} = \dot{\boldsymbol{T}} - \boldsymbol{l}\boldsymbol{T} - \boldsymbol{T}\boldsymbol{l}^{\mathrm{T}} + \boldsymbol{T}\mathrm{tr}\boldsymbol{l}, \tag{2}$$

where $\boldsymbol{T}$ and $\dot{\boldsymbol{T}}$ are Cauchy stress tensor and its material derivative. Then, we assume the linearity between the Truesdell's stress rate $\check{\boldsymbol{T}}$ and strain rate tensor $\boldsymbol{d}$ with a tensor $\boldsymbol{C}$:

$$\check{T}_{ij} = C_{ijkl} d_{kl} \tag{3}$$

Using an approximation of the updated Lagrangian formulation, we obtain

$$C_{ijkl} = \frac{1}{J} F_{iA} F_{jB} F_{kC} F_{lD} C^{(0)}_{ABCD}. \tag{4}$$

where

$$J = \det|\boldsymbol{F}|. \tag{5}$$

For the UL formulation, the principle of virtual power is written as follows:

$$\int_{\Omega} \delta \boldsymbol{d}^T \mathbb{C} \boldsymbol{d} dv + \int_{\Omega} \delta \boldsymbol{l}^T \boldsymbol{T} \boldsymbol{l} dv = \int_{\Omega} \rho \dot{\boldsymbol{b}} \cdot \delta \boldsymbol{v} dv + \int_{\partial\Omega} \dot{\boldsymbol{t}}^* \cdot \delta \boldsymbol{v} da, \tag{6}$$

where ρ, $\dot{\boldsymbol{b}}$, and $\dot{\boldsymbol{t}}^*$ are mass density, body force, and surface traction, respectively.

2.2. Internal Discontinuous Deformation

The relative slip of $b\tau(t)$ on a slip plane $\partial\Gamma$ is described by

$$b\tau(t)M_A = X_A^+ - X_A^-, \qquad \text{on } \partial\Gamma, \tag{7}$$

where M_A is the tangential vector along slip direction. $\boldsymbol{X}^+$ and $\boldsymbol{X}^-$ are the upper and lower reference coordinates on the slip plane at time t, respectively. b means the amount of unit discontinuous slip such as the norm of Burgers's vector. A monotonically increasing function $\tau(t)$ is varied from 0 to 1; $\tau(0) = 0$ and $\tau(t_{\text{end}}) = 1$, where t_{end} is the finish time. A linearized assumption of slip amount from $t = t^{(i)}$ to $t = t^{(i)} + \Delta t$ gives

$$b\tau(t^{(i)} + \Delta t) = b\tau(t^{(i)}) + b\dot{\tau}\Delta t, \tag{8}$$

where $\dot{\tau}$ means the temporal rate of τ. From Eq.(7),

$$b\tau(t^{(i)})M_A = (\boldsymbol{F}^{-1})^+_{Ai}x_i^+ - (\boldsymbol{F}^{-1})^-_{Ai}x_i^-, \tag{9}$$

and

$$\begin{aligned} b\tau(t^{(i)} + \Delta t)M_A = &((\boldsymbol{F}^{-1})^+_{Ai} + (\boldsymbol{F}^{-1})^{+\bullet}_{Ai}\Delta t)(x_i^+ + \dot{x}_i^+\Delta t) \\ &- ((\boldsymbol{F}^{-1})^-_{Ai} + (\boldsymbol{F}^{-1})^{-\bullet}_{Ai}\Delta t)(x_i^- + \dot{x}_i^-\Delta t). \end{aligned} \tag{10}$$

Then, a rate type constraint condition is described by

$$b\dot{\tau}M_A - (\boldsymbol{F}^{-1})^+_{Ak}l^+_{ki}x_i^+ - (\boldsymbol{F}^{-1})^-_{Ak}l^-_{ki}x_i^- - ((\boldsymbol{F}^{-1})^+_{Ai}v_i^+ - (\boldsymbol{F}^{-1})^-_{Ai}v_i^-) = 0, \tag{11}$$

and

$$b\dot{\tau}M_A - (\boldsymbol{F}^{-1})^+_{Ak}L^+_{kB}X_B^+ - (\boldsymbol{F}^{-1})^-_{Ak}L^-_{kB}X_B^- - ((\boldsymbol{F}^{-1})^+_{Ai}v_i^+ - (\boldsymbol{F}^{-1})^-_{Ai}v_i^-) = 0, \tag{12}$$

in current coordinates system and in reference coordinates system, respectively. For the sake of simplicity in this study, we use the approximation as following

$$b\dot{\tau}\bar{F}_{iA}M_A - (v_i^+ - v_i^-) = 0, \qquad \text{where} \quad \bar{F}_{iA} = F_{iA}^+ + F_{iA}^-. \tag{13}$$

There are several approached for the computational setup. For example, the extended finite element formulation can be used as well as some cohesive zone model. In this study, we use the double nodes on the slip plane. A Lagrange multiplier λ_{L} is introduced to take into account the constraint condition (13), and the principle of virtual power (6) is modified as

$$\begin{aligned} &\int_\Omega \delta\boldsymbol{d}^T\mathbb{C}\boldsymbol{d}dv + \int_\Omega \delta\boldsymbol{l}^T\boldsymbol{T}\boldsymbol{l}dv + \int_{\partial\Gamma} \lambda_{\text{L}}\left(b\dot{\tau}\bar{\boldsymbol{F}}\boldsymbol{M} - (\boldsymbol{v}^+ - \boldsymbol{v}^-)\right)\cdot(\delta\boldsymbol{v}^+ - \delta\boldsymbol{v}^-)\,ds \\ &= \int_\Omega \rho\dot{\boldsymbol{b}}\cdot\delta\boldsymbol{v}dv + \int_{\partial\Omega} \boldsymbol{t}^*\cdot\delta\boldsymbol{v}da. \end{aligned} \tag{14}$$

3. Analysis Examples

3.1. Analysis Model

The isotropic hyper-elasticity model (St.Venant-Kirchhoff material) is used in the finite displacement assumption:

$$S_{AB} = C_{ABCD}E_{CD}, \quad C_{ABCD} = 2\mu\delta_{AC}\delta_{BD} + \lambda\delta_{AB}\delta_{CD}, \tag{15}$$

where $\boldsymbol{S}$ and $\boldsymbol{E}$ are the second Piola-Kirchhoff stress tensor and the Green-Lagrange strain. The parameter λ and μ are Lamé's constants. In this study, Poisson's ratio $\nu = \lambda/(2\lambda + 2\nu)$ is set to be 0.4.

Some results are compared with the analysis based on linear elasticity in the small displacement assumption:

$$T_{ij} = C_{ijkl}\varepsilon_{kl}, \quad C_{ijkl} = 2\mu\delta_{ik}\delta_{jl} + \lambda\delta_{ij}\delta_{kl}, \tag{16}$$

where $\boldsymbol{T}$ and ε is Cauchy stress tensor and small strain tensor, respectively.

Plane strain problems are assumed in a rectangular specimen of $100b \times 20b$, where b means the amount of unit discontinuous slip. The displacement on the left edge of the specimen is fixed and four different problems as shown in Fig. 2 are solved: Fig. 2(a) a dislocation dipole composed of two dislocations on 1-slip plane, (b) three dislocation dipoles on 3-slip planes, (c) some dislocation structures arranged on 3-slip planes, and (d) three dislocation dipoles on 3-slip planes under both compression and shear loading.

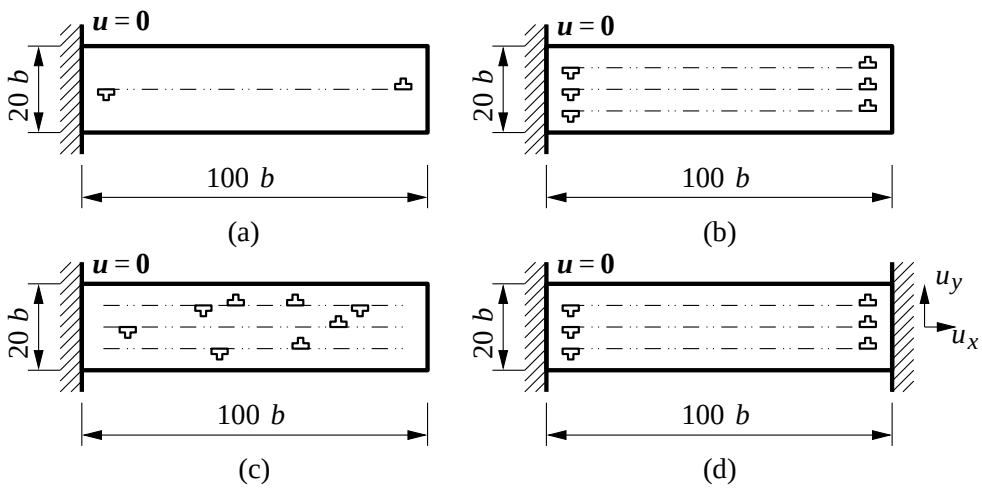

Figure 2. Schematics of model of analysis

3.2. Results of Analysis

3.2.1. Dislocation Dipoles on Slip Planes

Figure 3 shows the distribution of stress σ_{yy} on deformed body for (a) one dislocation dipole on 1-slip plane model, and for (b) three dislocation dipoles on 3-slip plane model. In Fig.3(a), the dislocation on the left affects a repulsive image force due to the fixed boundary condition. On the other hand, the

dislocation on the right affects an attractive image force due to the traction-free boundary condition. According to the comparison between linear elasticity and hyper-elasticity models, both are almost same qualitatively.

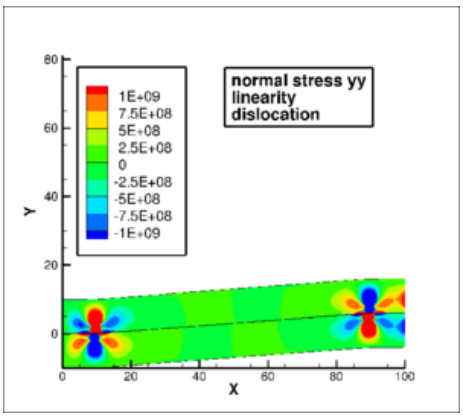

(i) linear elasticity model

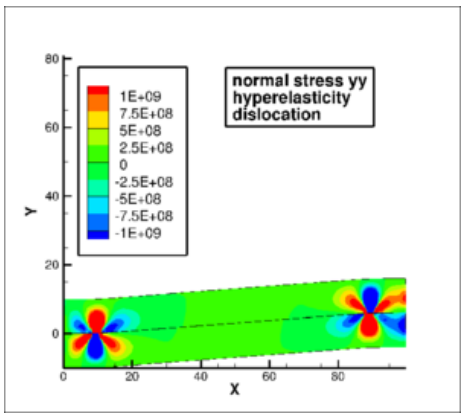

(ii) hyper-elasticity model

(a) 1-slip plane model

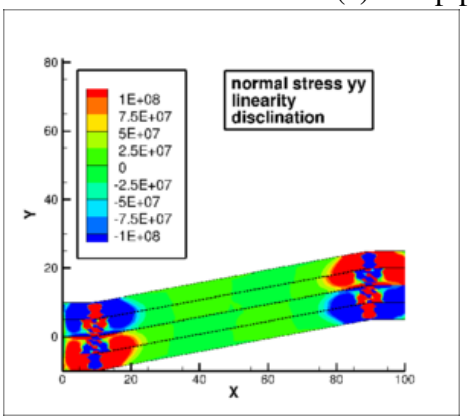

(i) linear elasticity model

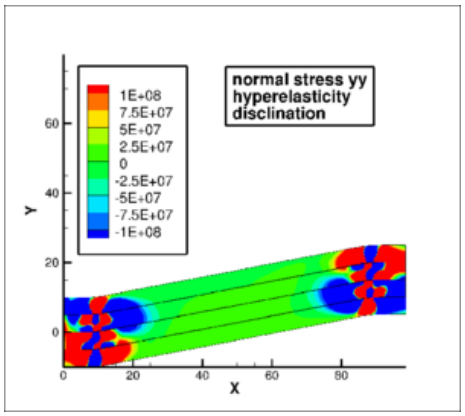

(ii) hyper-elasticity model

(b) 3-slip plane model

Figure 3. Distribution of stress σ_{yy} on deformed body

For the 3-slip plane model in Fig.3(b), the manners of image forces that act dislocations are similar to that for the 1-slip plane model in Fig.3(a). However, according to the comparison between linear elasticity and hyper-elasticity models, there appears some difference. The shape of stress contour has symmetry with respect to the neutral axis for the linear elasticity model. It is naturally understood, because the principle of superposition can be assumed in the small deformation theory. On the other hand, the shape of stress contour has non-symmetry with respect to the neutral axis for the hyper-elasticity model. This occurs due to the contribution of non-symmetric deformed shape of specimen.

3.2.2. Kink Deformation of Dislocations

The kink deformation in model 1 (Fig. 4(a)) and model 2 (Fig. 4(b)) corresponds to a wedge-type and ridge-type kink deformations, respectively. The deformation in model 3 (Fig. 4(c)) consists of two wedge-type kink deformation patterns. When the two edge dislocation array near the center of specimen merges to a dislocation wall on a single plane, model 3 is reduced to model 2. These types of kink deformation are often observed in zinc and LPSO magnesium alloy. The discrete dislocation plasticity based on finite deformation theory will be applicable to the investigation of such kink

deformation mechanism.

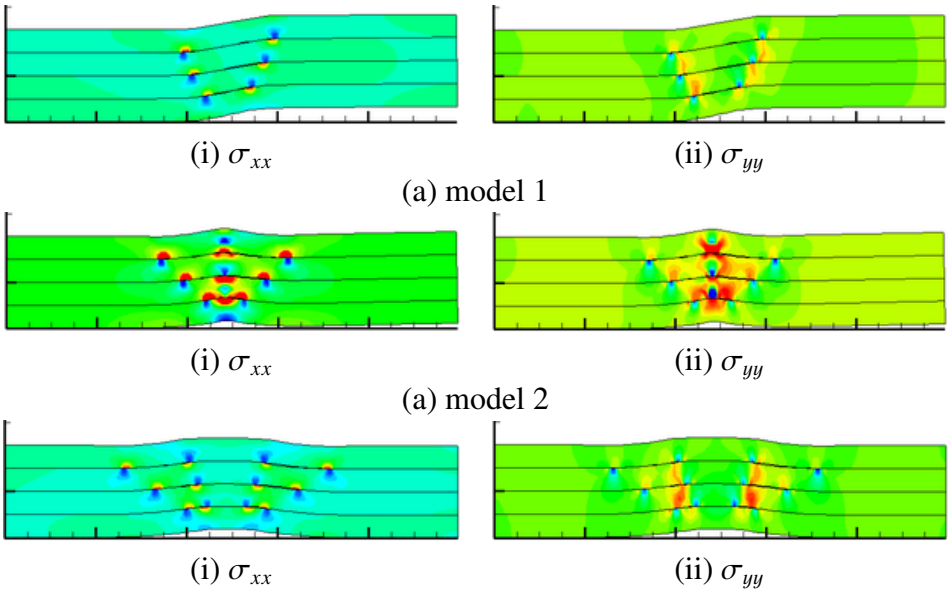

(i) σ_{xx} (ii) σ_{yy}

(a) model 1

(i) σ_{xx} (ii) σ_{yy}

(a) model 2

(i) σ_{xx} (ii) σ_{yy}

(a) model 3

Figure 4. Kink deformation expressed using discrete dislocations

3.2.3. Dislocation Dipoles on Slip Planes under Loading

Figure 5 shows the stress distribution σ_{xx} on deformed body for three dislocation dipoles on 3-slip plane model under both compression and shear loading. According to the comparison between (i) linear elasticity and (ii) hyper-elasticity models, deformed shape of specimens are similar to each other, but there appears some difference both qualitatively and quantitatively.

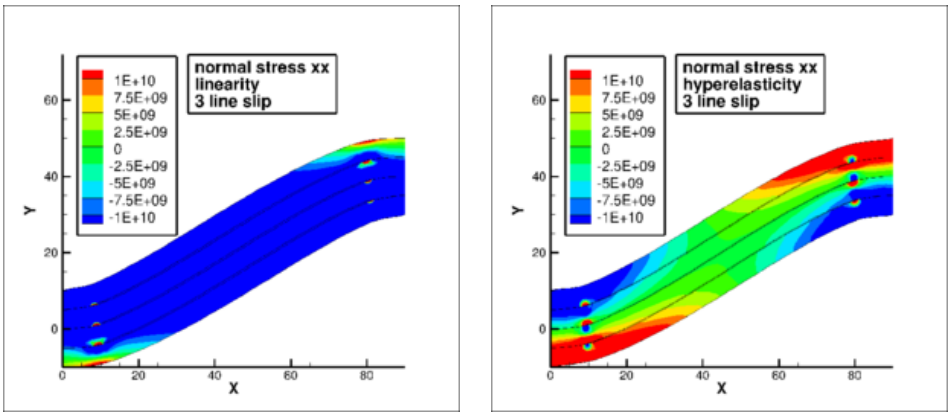

(i) linear elasticity model (ii) hyper-elasticity model

Figure 5. Distribution of stress σ_{xx} on deformed body under compression- shearing test

The stress contour for the linear elasticity model is simply recognized by the superposition of intrinsic stress field of dislocations and their image field, and external loading of compression and shearing. On the other hand, the typical bending stress due to the deformed shape of specimen can be observed in the shape of stress contour for the hyper-elasticity model.

4. Conclusions

An updated Lagrangian formulation based on finite deformation theory has been established for structural analysis of deformation of hyper-elastic body including lattice defects. A few examples have been shown for the application of the geometrically non-linear deformation of hyper-elastic body including lattice defects. The results have showed that the method can be applicable to the analysis of kink deformation which had been observed experimentally in long-period stacking ordered magnesium alloy. The criterion of dislocation nucleation, short-range interaction of lattice defects, and driving force of lattice defects should be discussed in the further study.

Acknowledgments

This work was supported by Grants-in-Aid for Scientific Research (KAKENHI).

References

[1] M. Seefeldt, Disclinations in Large-strain Plastic Deformation and Work-Hardening, Rev Adv Mat Sci 2 (2001) 44-79.
[2] A. Nakatani, W.J. Drugan, E. Van der Giessen, A. Needleman, Crack Tip Fields at a Ductile Single Crystal-Rigid Material Interface, Int J Fract 122 (2003) 131-159.
[3] V. Taupin, L. Capolungo, C. Fressengeas, A. Das, M. Upadhyay, Grain Boundary Modeling Using an Elasto-Plastic Theory of Dislocation and Disclination Fields, J Mech Phys Solids 61 (2013), 370-384.
[4] D.G.B. Edelen, A Gauge Theory of Dislocation and Disclinations, Springer-Verlag, Lecture Note in Physics, 1983.
[5] J.D. Clayton, D.L. McDowell, D.J. Bammann, Modeling dislocations and disclinations with finite micropolar elastoplasticity, Int J Plasticity 22 (2006) 210-256.
[6] M. Braun, Linear Elasticity with Couple Stresses, in: J.-F. Ganghoffer, F. Pastrone (eds.) Mech Microstru Solids 2, LNACM 50, Springer-Verlag Berlin Heidelberg 2010, pp.1-8.
[7] L. M. Zubov, Continuum Theory of Dislocations and Disclinations in Nonlinearly Elastic Micropolar Media, Mech Solids 46 (2008), 348-356.
[8] Leonid M. Zubov, Nonlinear Theory of Dislocations and Disclinations in Elastic Bodies, Springer, 1997.
[9] V.S. Deshpande, A. Needleman, E. Van der Giessen, Finite strain discrete dislocation plasticity, J Mech Phys Solids 51 (2003), 2057-2083.
[10] A. Acharya, C. Fressengeas, Coupled Phase Transformation and Plasticity as a Field Theory of Crystal Defects, Int J Fract 174, 87-94 (2012).

Investigation on 3D fatigue crack propagation in surface-cracked specimens

X. Li, H. Yuan*, J.Y. Sun

Department of Mechanical Engineering, University of Wuppertal, Germany.
* Corresponding author: h.yuan@uni-wuppertal.de

Abstract In the present work the fatigue crack growth in AISI304 specimens is investigated experimentally. In 3D finite element analysis the virtual crack closure technique is applied to calculate distributions and variations of the stress intensity factor along the surface crack front. It is confirmed that the stress intensity factor along the surface crack front non-uniformly varies with crack growth. Crack growth rate is proportional to the stress intensity factor distribution in the 3D cracked specimen. The fatigue crack growth in surface cracked specimens can be described by the Forman model identified in conventional CT specimens. For crack growth in the free specimen surface the arc length seems more suitable to quantify crack progress. Geometry and loading configuration of the surface cracked specimen seem to not affect the fatigue crack growth substantially.

Keywords: Surface crack, crack front, fatigue crack growth, 3D stress intensity factor

1. Introduction

In engineering critical cracks exist mainly on surfaces of mechanical components. To predict fatigue crack growth life, characterization and verification of a surface crack through the conventional fracture mechanics specimen, such as compact tension C(T), are of interesting. From fracture analysis it is known that the stress field in a 3D surface crack differs from the conventional plane strain tip field. The stress intensity factor (SIF) depends additionally on crack front curvature, crack edge to free surface and structure configuration. Especially, SIF may vary non-proportionally with crack growth. Predictability and accuracy of the fracture mechanics to 3D surface crack are still interesting issue for many mechanical parts under complex loading conditions.

In the present work, surface crack in circular rod of stainless steel AISI304 is studied experimentally. The crack growth rate (da/dN) versus stress intensity factor (ΔK) relation with different load ratios (R) was firstly obtained from standard CT specimens. Fatigue crack growth in the CT specimens can be described by the Forman model [1]. To investigate surface crack growth the axial tension rods are fabricated and pre-cracked. Fatigue crack growth tests on the rods were carried out at different load ratios. Backtracking method [2, 3] was attempted for monitoring crack shape evolution. To obtain more accurate SIFs, beach marks on the crack surface were represented by fitting elliptical arc curves. 3D finite element meshes are generated in compliance with the crack configurations. The SIF along the whole crack front was calculated via the virtual crack closure technique (VCCT) [4-7]. The relation of crack shape evolution with the SIF distribution along the crack front was discussed. Finally, the Forman model obtained from the standard CT specimen is used to predict the surface crack evolution in tensile rods.

2. Calculation of SIF for a surface crack

A 3D crack front can be represented by an elliptical arc crack front [8-16] as shown in Fig. 1. a denotes the depth of the surface crack. The elliptical crack can be described by the semi-axes, a and b. For a given crack depth, the crack shape can be controlled by the aspect ratio $\alpha=a/b$. For a straight line crack $\alpha=0$, whereas

α=1 represents a part-circular crack [9-10, 14-16]. Carpinteri [9] discussed the crack aspect ratio influence on the stress-intensity factor of elliptical-arc crack front. The maximum stress intensity factor is attained in correspondence to the deepest point on the crack front in the case of *a/b*=0, while it is attained near the external surface in the case of *a/b*=1. Shin and Cai [15] evaluated stress intensity factors along an elliptical surface crack front in a rod using experimental backtracking technique and finite analysis.

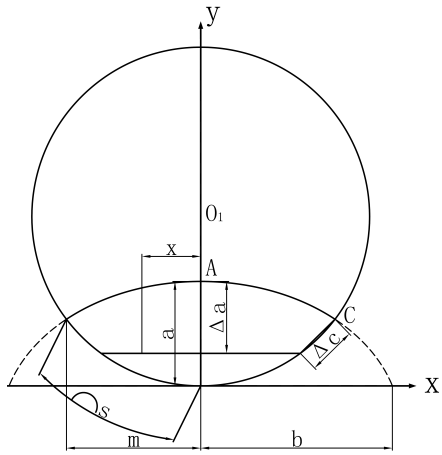

Figure 1. Sketch of surface crack geometry.

For the present specimens, the known solutions cannot directly be applied due to arbitrary crack front. The virtual crack closure technique (VCCT) is widely applied in computing energy release rates based on finite element analysis. The VCCT method provides the energy release rate G_I based on the work to be done by the nodal force $F_{y,i}(a)$ against the relative nodal point displacement $\Delta u_{y,i}(a+\Delta a)$ in order to close the crack by Δa [17]. The nodal force $F_{y,i}(a)$ can be obtained from the first step analysis where the crack is closed. The nodal point displacement can be obtained from the second step analysis where the crack has been extended to its full length $a+\Delta a$, as illustrated in Fig. 2.

$$\Delta E_y = \frac{1}{2} F_{y,i}(a) \cdot \Delta u_{y,i}(a+\Delta a) \tag{1}$$

$$\Delta G_I^{2D} = -\frac{\Delta E_y}{t \cdot \Delta a} \tag{2}$$

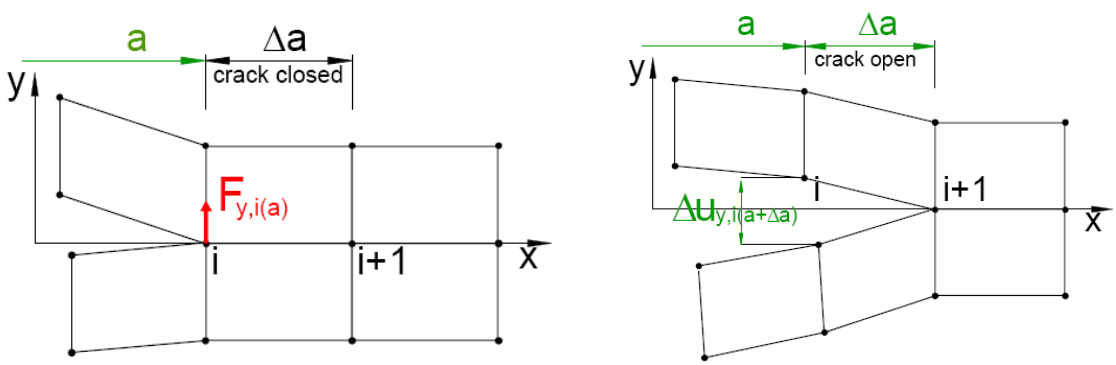

Figure 2. Illustration of VCCT.

Equation (2) is derived under assumption that the crack front is straight. For an arbitrary shaped crack front the mode definition constantly changes along the counter. A local crack tip coordinate system is

necessary to be defined at each nodal point along the front [18]. A half of element and element surface is related to the node in calculation of the energy release rate.

In linear elastic fracture mechanics (LEFM), the energy release rate G is connected to the stress intensity factor K as:

$$K = \sqrt{G \cdot E'} \quad , \quad \text{with} \quad E' = \begin{cases} E & \text{for plane stress} \\ \dfrac{E}{1-\nu^2} & \text{for plane strain} \end{cases} \tag{3}$$

In above equation, E denotes the Young's modulus and μ Poisson's ratio.

3. Experimental procedure

Standard compact tension (CT) specimens (50mm wide × 12.5mm thick) confirming to ASTM E647 and rod specimens (10mm in diameter and 138mm long) are tested. The chemical components of the tested material AISI 304 stainless steel are given in Table. 1. The heat treatment of the raw material is undertaken in vacuum with 1100 °C for one hour and followed by quick cooling in air. The straight-front initial notch was generated in the rod by wire-electrode cutting. The initial flaw depth is taken 1.5mm for all load ratios.

Table 1. Chemical composition of AISI304

Element	C	Si	Mn	P	S	Cr	Ni
(wt %)	0.040	0.41	1.05	0.035	0.003	17.1	8.1

All tests were performed on MTS 810 servo-hydraulic tension-torsion test machine at room temperature. The CT specimens were tested at the load ratios R=0.1, 0.3 and 0.5 with a loading frequency of 15 Hz. The rod specimens were tested at the load ratios R=0, 0.1 and 0.4 with a loading frequency of 10 Hz. To reduce the experimental error, two specimens were tested at a given loading condition and the test results show a good repeatability. All specimens were tested under a loading with sinusoidal waveform and in force control.

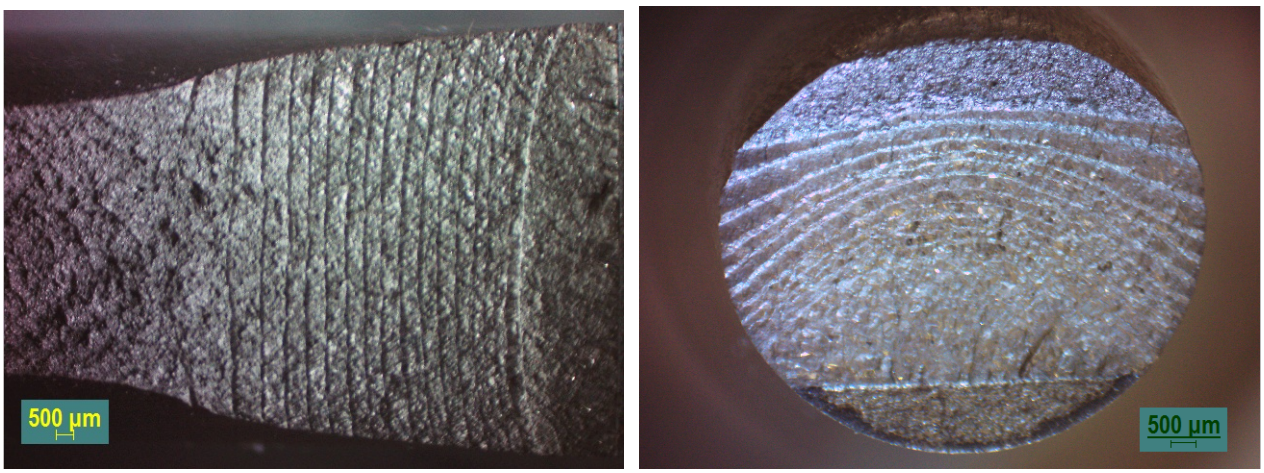

Figure 4. Typical beach marked crack surfaces of CT (left) and rod (right) specimen.

Instantaneous crack fronts were recorded by creating beach marks using a waveform that the mean load

will keep constant but the load amplitude will reduce to 50% for several cycles. By comparing successive crack profiles obtained after loading for designated cycle numbers of each interval, the crack growth rate at different points on the crack front can be evaluated. The crack growth length in CT specimens and the crack depth as well as the surface crack arc length in rod specimens will be measured under light microscope. Fig. 4 shows typical beach marked crack surfaces for CT specimen and rod specimen.

4. Crack propagation behavior of CT specimen

A simple and well known method for predicting fatigue crack propagation is a power law described by Paris and Erdogan [19], and it is also known as Paris law. Forman [20] improved the model by considering effects of K_C and stress ratio. Hartman and Schijve [21] proposed the following equations which is the continuation of Forman's work by including the threshold stress intensity factor ΔK_{th}:

$$\frac{da}{dN} = \frac{C \cdot (\Delta K - \Delta K_{th})^m}{(1-R)K_C - \Delta K} \tag{4}$$

where C is the intercept and m is the slop on the double logarithmic plot of da/dN versus ΔK. K_c is the fracture toughness for the material and ΔK_{th} is the threshold stress intensity factor value for fatigue crack growth which is sensitive to R.

For AISI304 material, the fracture toughness K_c is 133 MPa$\sqrt{\mathrm{m}}$ and the threshold value ΔK_{th} with R=0 8.053 MPa$\sqrt{\mathrm{m}}$. Fitting with the experiment data, the coefficient can be fixed as $C=10^{-5.74232}$ and $m=2.80192$. The experiment data are shown in Fig. 5 with identified Forman model curves. In the figure the loading ratio effect is clearly illustrated and experimental data agree with the Forman model.

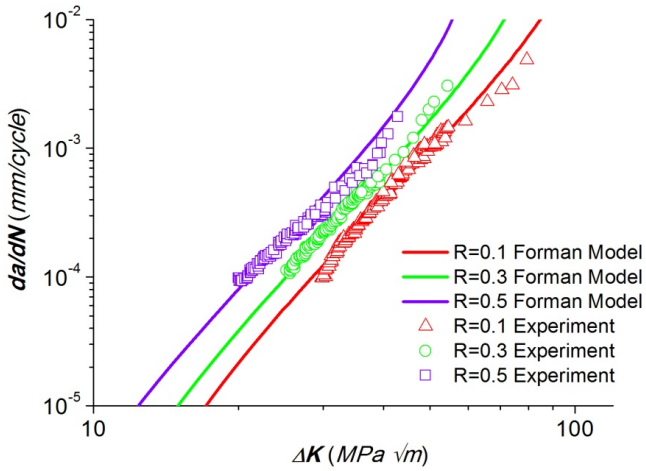

Figure 5. Crack growth curve of CT specimens.

5. Crack propagation in cracked rod specimens

The crack geometry of the rod specimen is described in Fig. 1. An equivalent elliptical arc curve is used to indicate the actual crack front after certain number loading cycles. 3D FE model is generated with symmetric boundary conditions, as shown in Fig. 6. The location of the points on the crack front can be described by the location x/h. with x=0 for the middle of the specimen and $x=h$ for the specimen surface. The crack growth of the deepest point A and the surface point C are represented as the depth length Δa and the chord length Δc,

respectively.

From fracture mechanics, the SIF K_I for small surface crack can be calculated from

$$K_I = F \cdot \sigma \sqrt{\pi a} \tag{5}$$

where σ is the nominal stress on uncracked ligament and a is the crack depth at point A. F is the geometry factor. Obviously, F is a function of the crack front geometry and the location. On the other hand, F represents the non-dimensionalized SIF

$$F = \frac{K_I}{\sigma \sqrt{\pi a}} \tag{6}$$

and can be taken as a variable to characterize distribution of the SIF in the crack front.

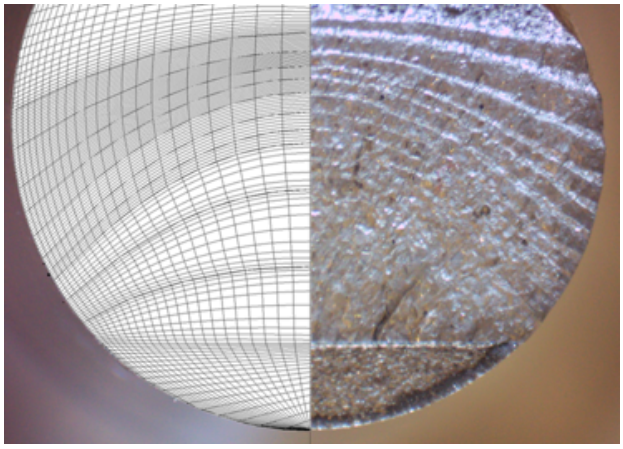

Figure 6. Element meshes of the cross section in compliance with the crack configurations.

To verify the computation of surface crack analysis, the geometry factor F is plotted as a function of the crack depth in Fig. 7(a). The result confirms that VCCT provides reliable results in comparing with other methods [9, 15]. In general, the solution by Carpinteri [9] seems higher, whereas Shin [15] agrees with VCCT.

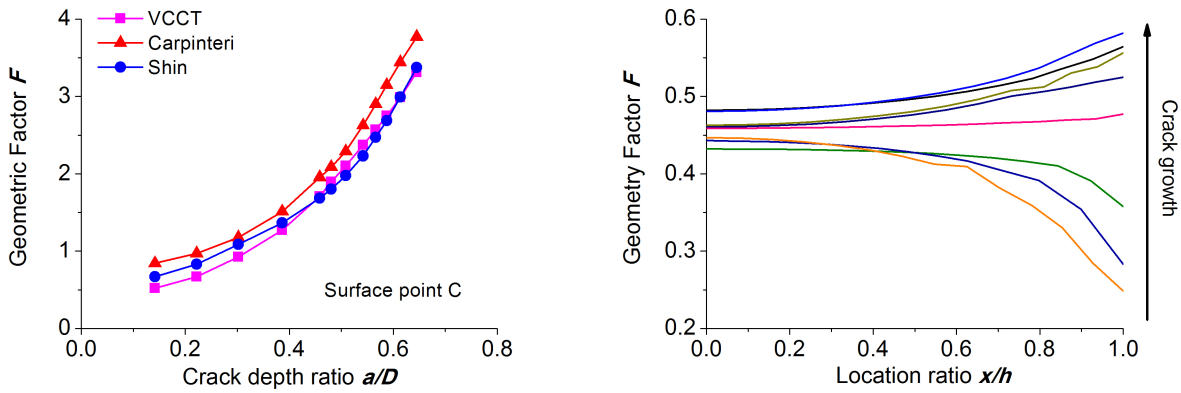

(a) F as a function of crack depth (b) F as a function of crack front

Figure 7. Variations of the geometry factor with the crack geometry

Fig. 7(b) shows variations of F along the crack front during crack shape evolution in the rod specimen, as shown in Fig. (6). For the initial notch, a straight crack front with the crack aspect ratio $\alpha=0$ reveals the maximum SIF in the specimen middle and the SIF decreases with the distance x/h. It implies that the crack propagation starts at Point A and the crack front tends to become curved. With the crack developed α increases, the distribution of SIF reaches gradually constant in the whole crack front. In this region the crack front attains a uniform growth rate. Due to varying geometry of the circular rod, the stationary crack growth cannot maintain long. The SIF at the crack front near rod surface increases and becomes maximal in the SIF distribution. It follows that the crack propagation near the rod surface is quicker than elsewhere. Variations of the geometry factor F agree with experimental observation, as shown in Fig 6.

The variations of the geometry factor F can be further found in fatigue crack growth. In Fig. 9 ΔK is plotted as a function of crack growth for Points A and C with different loading ratios. Due to transient behavior the crack growth near the initial straight notch is not included in the figure, so that the SIF at C is mainly larger than that at A in the whole crack growth process. The curvature of the crack front decreases with crack growth, that is, the crack rate in the middle of the specimen is lower than that near the specimen surface.

The difference of the crack rate can be further observed in Fig. 10, in which the crack length at A and C is plotted as functions of loading cycles. The predictions are based on the Forman model identified from the CT specimens. The figure shows that the prediction of the Forman model agrees with the experiments well for all investigated loading ratios. Note that the crack length at A is represented by the crack depth a and the surface point B is given by the arc length s respectively. Fatigue crack growth in the 3D surface cracked specimen can be described by the conventional long crack model.

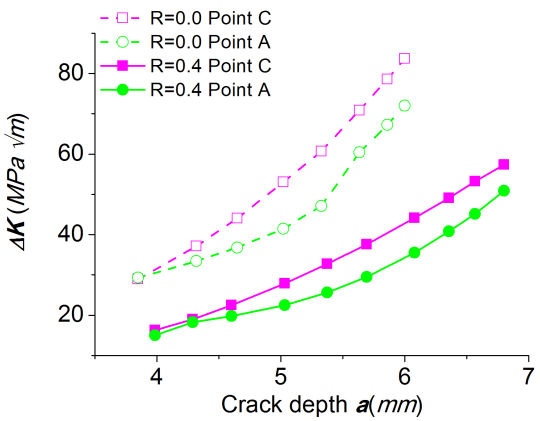

Figure 9. Development of ΔK in the crack front Point and Point C in the cracked rod

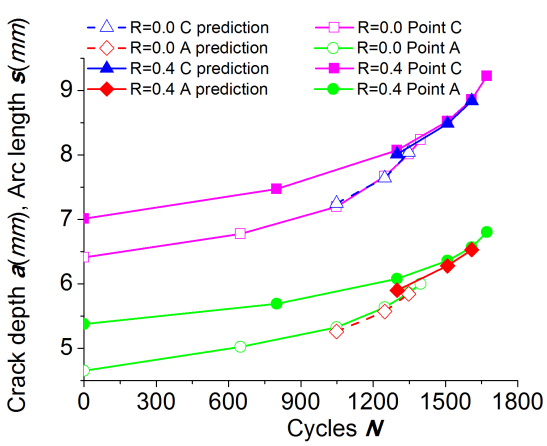

Figure 10. Crack growth in a surface cracked specimen in fatigue tests.

The crack rate curves for surface crack at Points A and C are plotted together with the experimental data for CT specimen in Fig. 11. The Forman model baselines obtained from CT specimens, Eq. (6), are illustrated in the figure. In the range with lower ΔK, the crack growth at the internal crack front is faster than that at the surface point. For high loading range, the crack growth at the surface becomes higher. This phenomenon is also reported by Shin [15]. Generally, the surface crack data agree with the Forman model.

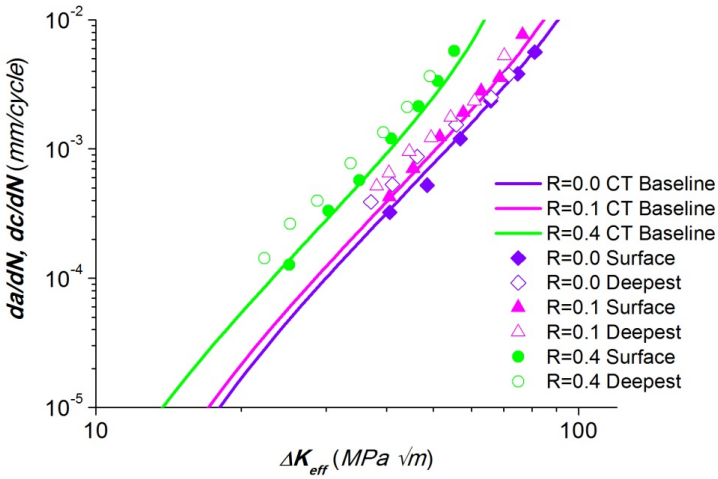

Figure 11. Crack growth behavior of rod specimen.

6. Conclusions

The fatigue crack growth in AISI304 specimens is investigated experimentally. The surface crack in 3D rod under tension is characterized by the fatigue crack data from the CT specimen. 3D finite element models are generated in compliance with the surface crack configurations and the stress intensity factor along the crack front is calculated through virtual crack closure technique. The present work confirms:

1. The stress intensity factor along the surface crack front non-uniformly varies with crack growth. Crack growth rate is proportional to the stress intensity factor distribution in the 3D cracked specimen. After crack grows up over the crack front, the maximum of the stress intensity factor appears near the free surface of the tensile rod, so that the crack front curvature becomes smaller.
2. Experiments confirm that the fatigue crack growth in surface cracked specimens can be described by the Forman model identified in conventional CT specimens. For crack growth in the free specimen surface the arc length seems more suitable to quantify crack progress.
3. Geometry and loading configuration of the surface cracked specimen seem to not affect the fatigue crack growth substantially. The Forman model can predict local crack front growth rather precisely.

Acknowledgements

The authors thank financial support of the German Science Foundation (DFG) under the contact number YU119/5-2.

References

[1] R. G. Forman, V. E. Kearney and R. M. Engle (1967). Numerical analysis of crack propagation in cyclic-loaded structures. *Journal of Basic Engineering* **89(3)**: 459-464.

[2] T. L. Mackay and B. J. Alperin (1985). Stress intensity factor for fatigue cracking in high strength bolts. *Engineering Fracture Mechanics* **21(2)**: 391-397.

[3] C. S. Shin and C. Q. Cai (2004). Experimental and finite element analyses on stress intensity factors of an elliptical surface crack in a circular shaft under tension and bending. *International Journal of Fracture* **129**: 239-246.

[4] E. F. Rybicki and M. F. Kanninen (1977). A finite element calculation of stress intensity factors by a modified crack closure integral. *Engineering Fracture Mechanics* **9**: 931-938.

[5] E. F. Rybicki, D. W. Schmueser and J. Fox (1977). An energy release rate approach for stable crack growth in the free-edge delamination problem. *Journal of Composite Materials* **11**: 470-487.

[6] I. S. Raju (1987). Calculation of strain-energy release rates with higher order and singular finite elements. *Engineering Fracture Mechanics* **28**: 251-274.

[7] F. G. Buchholz, H. Grebner, K. H. Dreyer and H. Krome (1988). 2D- and 3D-applications improved and generalized modified crack closure integral method. *In Computational Mechanics'88*, **vol. 1** (Eds. S. N. Atluri et al.), Springer Verl., New York.

[8] M. A. Astiz (1986). An incompatible singular elastic element for two- and three-dimensional crack problems. *International Journal of Fracture* **31**: 105-124.

[9] A. Carpinteri (1992). Elliptical-arc surface cracks in round bars. *Fatigue of Engineering Materials* **15(11)**: 1141-1153.

[10] A. Carpinteri and R. Brighenti (1996). Fatigue propagation of surface flaws in round bars: a three-parameter theoretical model. *Fatigue & Fracture of Engineering Materials & Structures* **19(12)**: 1471-1480.

[11] A. Levan and J. Royer (1993). Part-circular surface cracks in round bars under tension, bending and twising. *International Journal of Fracture* **61**: 71-99.

[12] K. D. Thompson and S. D. Sheppard (1992). Stress intensity factors in shafts subjected to torsion and axial loading. *Engineering Fracture Mechanics* **42(6)**: 1019-1034.

[13] K. D. Thompson and S. D. Sheppard (1992). Fatigue crack growth in notched and plain shafts subjected to torsion and axial loading. *Engineering Fracture Mechanics* **43(1)**: 55-71.

[14] N. Couroneau and J. Royer (1998). Simplified model for the fatigue growth analysis of surface crack in round bars under mode I. *International Journal of Fatigue* **20(10)**: 711-718.

[15] C. S. Shin and C. Q. Cai (2004). Experimental and finite element analyses on stress intensity factors of an elliptical surface crack in a circular shaft under tension and bending. *International Journal of Fracture* **129**: 239-246.

[16] F. P. Yang and Z. B. Kuang (2007). Stress intensity factor for surface fatigue crack in a round bar under cyclic axial loading. *Fatigue & Fracture of Engineering Materials & Structures* **30**: 621-628.

[17] F. G. Buchholz, A. Chergui and H. A. Richard (1999). Computational fracture analyses by means of virtual crack closure integral methods. *In 6th Congreso Argentino de Mecanica Computational (MECOM99)* **29**: 1-19, Argentina.

[18] R. Krueger (2004). Virtual crack closure technique: History, approach, and applications. *Applied Mechanics Reviews* **57(2)**: 109-143.

[19] PC. Paris and F. Erdogan(1963). A critical analysis of crack propagation laws. *Journal of Basic Engineering* **85**: 528-534.

[20] R. G. Forman, V. E. Kearney and R. M. Engle (1967). Numerical analysis of crack propagation in cyclic-loaded structures. *Journal of Basic Engineering* **89(3)**: 459-464.

[21] A. Hartman and J. Schijve (1970). The effects of environment and load frequency on the crack propagation law for macro fatigue crack growth in alumimum alloys. *Engineering Fracture Mechanics* **1(4)**: 615-631.

[22] A. Carpinteri and S. Vantadori (2008). Surface cracks in round bars under cyclic tension or bending. *Engineering Materials* **378**: 341-354.

[23] J. Torbio, J. C. Matos, B. Gonzalez, J. Escuadra (2009). Numerical modeling of crack shape evolution for surface flaws in round bars under tensile loading. *Engineering Failure Analysis* **16(2)**: 618-630.

[24] J. Torbio, J. C. Matos, B. Gonzalez, J. Escuadra (2011). Compliance evolution in round cracked bars under tensile fatigue. *Engineering Fracture Mechanics* **78(18)**: 3243-3252.

[25] S. Beretta and M. Carboni (2006). Experiments and stochastic model for propagation lifetime of railway axles. *Engineering Fracture Mechanics* **73(17)**: 2627-2641.

[26] P. Bortot and S. Beretta (2012). On the estimation of fatigue crack growth in a contaminated H_2S environment by interrupted cyclic tests. *In 19th European Conference on Fracture* **371**, Russia.

Wedge Splitting Test on Fracture Behaviour of Fiber Reinforced and Regular High Performance Concretes

Kamil Hodicky[*1], **Thomas Hulin**[1], **Jacob W. Schmidt**[1] **and Henrik Stang**[1]

[1]Department of Civil Engineering, Technical University of Denmark, Kongens Lyngby, DK-2800, Denmark
* Corresponding author: kamh@byg.dtu.dk

Abstract The fracture behaviour of three fiber reinforced and regular High Performance Concretes (HPC) is presented in this paper. Two mixes are based on optimization of HPC whereas the third mix was a commercial mix developed by CONTEC ApS (Denmark). The wedge splitting test setup with 48 cubical specimens was used experimentally and the cracked non-linear hinge model based on the fictitious crack model was applied for the interpretation of the results. The stress-crack opening relationships were extracted by using inverse analysis algorithm for various multi-linear softening curves. The fracture mechanics parameters such as crack opening displacement (COD), fracture energy and characteristic length were experimentally determined. Experiments were performed at 1, 3, 7 and 28 days. Fracture energy, G_f, was found to increasing with age, while the characteristic length, L_{ch}, was found to decrease.

Keywords High Performance Concrete, Wedge Splitting Test, Inverse Analysis, Fictitious crack model.

1. Introduction

Development of fiber reinforced concrete plays important role in industrialization of the building industry. The possibility of replacement of ordinary reinforcement is presently very important topic [1]. The number of practical applications of fiber-reinforced High Performance Concrete (HPC) is increasing like foundation slabs, foundations and walls. The fibres are likely to replace the ordinary reinforcement completely [2]. While the other structures like beams and slab, fibers can be used in combination with ordinary reinforcement or pre-stressed reinforcement. The both cases show improvement of working environment at the construction site and potential benefits due to economical factors. The one of main benefits of fiber reinforcement is an ability to transfer stress across a crack. However, if fiber-reinforced HPC is to be a more widely used material, general simple test method is needed for the concrete industry. This is necessary for fiber-reinforced HPC, where industry lacks such a method to verify their daily production quality control. Further, it would provide relevant material data allowing to the structural engineers design of structures that are safe and cost-efficient. As design tools seem to become more advanced and the design requirements are more complex, the need of fracture properties is required for structural analysis. Therefore there is a need of simple test method that allows determining the fracture properties of fiber-reinforced HPC with acceptable accuracy, which can be used by companies in their daily production without expensive investment to testing equipment.

In last two decades the tensile behaviour of non-fiber and fiber reinforced concretes is mostly described by the concepts of the fictitious crack model. The most often used non-linear fictitious crack model was originally developed by Hillerborg [3]. This model is able to closely describe the fracture properties of concrete. However, determination of softening curves of stress-crack opening relationships can cause particular difficulties like in case of uniaxial tensile test and three point bending [4]. Another option is the wedge splitting test setup (WST), which is made for indirect determination of the softening curve. The WST was originally proposed by Linsbauer and Tschegg [5] and later developed by Brühwiler and Wittmann [6]. The researchers have greatly used the WST-method, and recently interest in the method increased rapidly. Its main advantage lies in its simplicity and stability. Furthermore, a standard cube is used, but the test can also be performed on core-drilled samples from the existing structure. Moreover, it was proven by Østergaard et al. [4] and Hansen et al. [7] that the test is suitable for early-aged concretes because it doesn't suffer

problems cause by self-weight of the specimen. The work of Elser et al. [8] should be mentioned as well. Their work presented the fracture behaviour of polypropylene fiber-reinforced concrete.
The present paper focuses on the inverse analysis of WST approach developed by Østergaard et al. [4] for bi-linear softening curve and the approach, which comes out Skocek et al. [9] work for multi-linear softening curve. So far, Østergaard's bi-linear softening curves are mostly used to approximate the softening behaviour of concretes. It is expected that refinement of the softening curves will reflect in improved accuracy of the WST simulation. For that purpose the semi-analytical approached is used as the background for inverse analysis of the WST. The inverse analysis is capable in estimating both elastic and fracture properties from the WST. Fracture energy, G_f, was found to increasing with age, while the characteristic length, L_{ch}, was found to decrease.

2. Modelling

Loading of the specimen by wedge leads to splitting force and subsequently initiation of a crack at the bottom of the notch. Furthermore with increase of load stable crack propagation is observed. The control of the experiment may be performed by crack mouth opening displacement or by constant displacement rate of the wedge. The crack hinge model (CHM) to the WST geometry was developed by Ulfkjaer et al. [10] and later extended by Olesen [11]. The CHM simulates the area closely surrounded by propagated crack. The hinge is modelled as array of springs, which are attached to the rigid boundaries of the element. The stress transferred by the spring is assumed to be linear elastic in the pre-cracked state, whereas the cracked state is determined by the stress-crack opening relationship as shown in Eq. (1)

$$\sigma = \begin{cases} \sigma(\varepsilon) = E\varepsilon & \text{Preckracked State} \\ \sigma_w(w) = g(w) f_t & \text{Cracked State} \end{cases} \tag{1}$$

where E represent elastic modulus, ε denotes elastic strain, $\sigma_w(w)$ denotes stress-crack opening relationship with crack opening w, and f_t represents tensile strength. In Fig.1 the function $g(w)$ is for the N-linear ($N \geq 2$) softening curve is shown and is defined as :

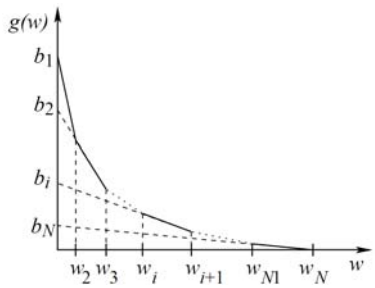

Figure 1. The scheme of multi-linear softening curve.

$$g(w) = b_i - a_i w; \quad w_{(i-1)} < w < w_i \tag{2}$$

where w_i corresponds to the intersection of i-th and i + 1th line and has the form:

$$w_i = \frac{b_i - b_{i+1}}{a_i - a_{i+1}} \text{ where } i < N \tag{3}$$

The critical crack width (width at which $g(w) = 0$) is calculated by:

$$w_N = w_c = \frac{b_N}{a_N} \tag{4}$$

with N equals to number of lines in the softening curve. Fig. 2 shows hinge model geometry, which is described by the half of the angular deformation φ and depth of the neutral axis y_0.

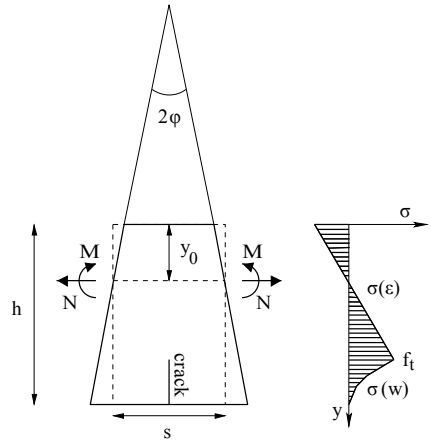

Figure 2. The hinge model and assumed stress distribution.

Olesen [11] analytically determined crack opening $w(y)$ for each point y for known stress $\sigma(y)$. The mean of longitudinal strains, $\varepsilon^*(y)$ is then calculated as:

$$\varepsilon^*(y) = (y - y_0)2\varphi / s \tag{5}$$

Then deformation of an incremental strip of the hinge is given by $u(y) = s\varepsilon^*(y)$, where s is the length of the hinge ($s = 0.5h$). Once crack occurs, $u(y)$ can be computed as the sum of the elastic deformation and the crack opening according Eq. (6).

$$u(y) = s\varepsilon^*(y) = s\frac{\sigma_w(w(y))}{E} + w(y) \tag{6}$$

The stress distribution equation can be obtained by combining Eq. (5) and (6) as follows:

$$\sigma_w(w(y)) = \frac{\varsigma_i - 2\varphi(y - y_0)\beta_i}{1 - \beta_i}\frac{E}{s} \tag{7}$$

Solving Eq. (7) by introducing cohesive law (Eq.1) with respect to $w(y)$ and $\sigma_w(w(y))$ the following solution is observed:

$$\sigma_w(w(y)) = \frac{\varsigma_i - 2\varphi(y - y_0)\beta_i}{1 - \beta_i}\frac{E}{s} \tag{8}$$

$$w(y) = \frac{2\varphi(y - y_0) - \varsigma_i}{1 - \beta_i} \tag{9}$$

where ς_i and β_i are dimensionless factors:

$$\beta_i = \frac{f_t a_i s}{E} \quad \text{and} \quad \varsigma_i = \frac{f_t b_i s}{E} \tag{10}$$

For additional information on the development and implementation of the CHM see the following references [4,9,11]. However, two equations have to be fulfilled to determine the material properties from the CHM:

$$M_{ext} - M_{hinge} = 0 \text{ and } CMOD_{obs} - CMOD_{WST} = 0 \tag{11}$$

where M_{ext} is the external bending moment and M_{hinge} stands as bending moment transferred by hinge. The $CMOD_{obs}$ represents the observed $CMOD$ and $CMOD_{WST}$ is computed $CMOD$. The external bending moment, M_{ext} can be calculated as follow:

$$M_{ext} = P_{sp}\left(d_2 - y_0\right) + \frac{1}{2}P_v d_1 + \frac{1}{2}mge \tag{12}$$

where

$$P_v = P_{sp}\frac{2\tan\alpha_w + \mu_c}{1 - \mu_c \tan\alpha_w} \tag{13}$$

refers to splitting load, P_{sp}, and vertical load P_v; α_w stands for wedge angle, μ_c for friction in the roller bearing, m denotes mass of the specimen, g is the acceleration of gravity and e represents the horizontal distance between the axis of symmetry of the specimen and the centre of gravity of one half of the specimen. The bending moment transferred by hinge, M_{hinge} is computed by:

$$M_{hinge} = \int_0^h \sigma\left(y\right)\left(y - y_0\right)dy \tag{14}$$

where σ stands for cohesive law from Eq. (1). The $CMOD_{WST}$ is defined as sum of elastic deformation of the specimen, δ_e; deformation due to presence of the crack opening, δ_w; and deformation caused by geometrical amplification, δ_g.

$$CMOD_{WST} = \delta_e + \delta_w + \delta_g \tag{15}$$

The evaluation of the elastic deformation, δ_e can be found in Tada et al. [15] as

$$\delta_e = \frac{P_{sp}}{Et}v_2 \tag{16}$$

where t = specimen thickness and v_2 is a function of the ratio between the length of the initial notch and the distance from the loading line to the bottom of the specimen.

$$v_2 = \frac{x}{\left(1-x\right)^2}\left(38.2 - 55.4x + 33.0x^2\right) \tag{17}$$

The ratio is given by $x = 1 - h/b$ (See Fig.3). The deformation due to presence of the crack opening, δ_w can be directly computed from Eq. (9) at $y = h$. Finally, deformation caused by geometrical amplification, δ_g is derived as

$$\delta_g = 2\left(b - h\right)\left(\frac{\delta_w}{2d} - \frac{\varphi^{el}}{1-\beta_i}\right) \tag{18}$$

where φ^{el} is denoted as maximum elastic angular deformation of the hinge and β_i is dimensionless factors defined in Eq. (10).

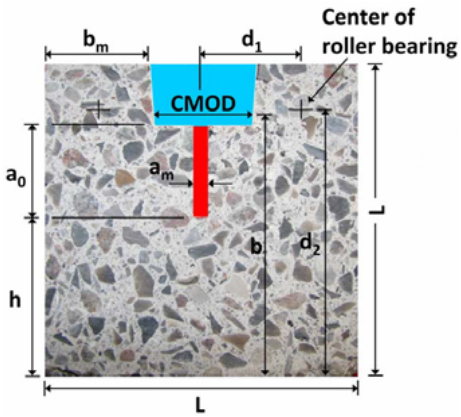

Figure 3. WST specimen geometry with the blue area indicating the groove and the red area indicating 4.5mm notch.

The computation of inverse analysis is based on three steps that are repeated until convergence criteria are obtained. The first step involves computation of elastic modulus, E. Therefore, only data corresponding to the elastic loading are considered. Determination of elastic modulus is very fast and reliable since the part of working diagram is governed by E. Once elastic modulus is found, the tensile strength ft and the first decreasing branch of softening curve a1 are searched. Furthermore, N-1 searchings are performed in order to find a_i and b_i, where $i \geq 2$. The process of inverse analysis can be written as:

$$
\begin{aligned}
&\text{while } (\text{convergence is not achived}) \\
&\min_{E} \sum_{j=1}^{K^{el}} \left\| P_{j,obs} - P_{j,hinge} \right\| \\
&\min_{f_t, a_1} \sum_{j=1}^{K} \left\| P_{j,obs} - P_{j,hinge} \right\| \\
&\text{for } i \geq 2 \\
&\min_{a_1, b_1} \sum_{j=1}^{K} \left\| P_{j,obs} - P_{j,hinge} \right\| \\
&\text{check convergence}
\end{aligned}
\tag{19}
$$

Where K is total number of recorded load-crack opening pairs in the experiment, K^{el} is number of recorded load-crack opening pairs corresponding to elastic part of loading, $P_{j,obs}$ denotes splitting force in j-th recorded load-crack opening pair, $P_{j,hinge}$ is optimized splitting force in j-th computed load-crack opening pair.

The each measurement can be influenced by errors, and it is impossible to fit the model exactly to the measurements, which means that the choice of the suitable robust form $\|P_{obs} - P_{hinge}\|$ plays important role. The iterative process minimizes the difference between observed loads applied in the experiments, P_{obs}, and the load predicted by CHM, P_{hinge} according to the error normalization function as:

$$\left\| P_{obs} - P_{hinge} \right\| = \sqrt{1 + \frac{\left(P_{obs} - P_{hinge} \right)^2}{2}} - 1 \tag{20}$$

The stopping criteria for the maximum relative difference for two subsequent sets were used fracture energy; G_f obtained from Eq. (21) and the characteristic length, L_{ch} from Eq. (22).

$$G_f = \frac{f_t}{2} \sum_{i=1}^{N} \left[\left(2b_i - a_i \left(w_{i-1} + w_i \right) \right) \left(w_i - w_{i-1} \right) \right] \tag{21}$$

$$L_{ch} = \frac{E G_f}{f_t^2} \tag{22}$$

The points obtained from the experimental load-CMOD data used by the inverse analysis program to determine the cohesive laws were selected equidistantly in regards to arch length in the normalized coordinate system. The linear interpolation is used for points selected between measured data. The arc length increment used for given analysis was 0.05.

3. Experimental procedure

The present work represents three fiber reinforced and regular HPC mixes. The first mix was a commercial mix developed by CONTEC ApS and was denoted as Contec mix. Another two HPC mix designs were based on research work of Ozbay et al. [13]. These two mixes were denoted as DTU mixes. The DTUI mix was designed to correspond to the mechanical properties of the Contec mix. The DTUII mix was adjusted by bauxite sand and fly ash to obtain better mechanical properties than Contec and DTUI. The mix designs are shown in Table 1. A 60l pan mixer was used for mixing; mixing time was 2 minutes for the dry mixing and 5 minutes with water and super-plasticizer. The vibrating time was chosen to be 30s. After casting, the specimens were left to harden in a climate chamber (22±2 °C and 65±5% RH). Specimens were demoulded after 24h and put in the water at 20 °C for curing. The experimental programme presented in this paper included 48 wedge splitting tests.

WST-specimens were casted in special PVC moulds with groove and notch made for this purpose. The geometry of the WST-specimen is shown in Fig. 3. The WST-cube has length L = 100mm and thickness t = 100mm. The height of the ligament was h = 50mm. The mean width of notch a_m = 4.5mm, however, the walls of a real notch were a little bit inclined in order to avoid demoulding problems. The length of notch was a_0 = 28mm. Position of center of roller bearing, where splitting load is applied was d_1 = 39.5mm and d_2 = 85.4mm.

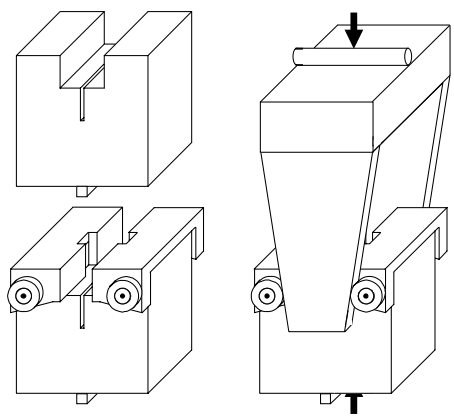

Figure 4. Schematic showing of experimental WST test setup.

Fig. 4 shows WST experimental setup, where the rotational joints are used to prevent unwanted restrained. The rotational joint (a rectangular bar) was placed below specimen combined with roller bearing above the wedge.

Loading is controlled by displacement measurements from a clip gage inserted into the groove of the WST specimen to measure the CMOD. Distance b = 83.5mm describes contact position of the clip gage. The clip gage was modified by using brass feet to contact the side of the groove. The vertical load was recorded by the testing machine, and subsequently used for calculation of the splitting load. The wedge angle from the vertical axis was used 15°. The constant displacement rate of the wedge was kept initially of 0.05 mm/s to a CMOD of 0.5mm. After reaching a CMOD of 0.5mm, the displacement rate was increased to 0.10mm/s to minimize testing time.

Table 1 – Mix designs (kg/m^3)

Mix	Contec	DTUI	DTUII	Contec-F	DTUIF	DTUIIF
Cement (CEM I 52.5 R)	/	495	460	/	495	460
Binder Contop S 105-2	582.3	/	/	582.3	/	/
CA, granite, 02-05 mm	832.3	868.4	1015.6	832.3	868.4	1015.6
FA, sea gravel, 0.1-1.5 mm	763.7	781.6	/	763.7	781.6	/
FA, bauxite sand, 0-1 mm	/	/	609.4	/	/	609.4
Silica fume	/	55	57.5	/	55	57.5
Fly ash	/	/	57.5	/	/	57.5
Superplasticizer	/	11	25.9	/	11	25.9
Glass fibers	/	/	/	4.04	4.0	3.5
Polypropylene fibers	/	/	/	2.02	2.0	1.78
Total dry mass	2178.3	2200	2200	2184.4	2206	2205.3
Water-cementitious material ratio	0.304	0.25	0.25	0.304	0.25	0.25
Water-cementitious material ratio*	/	0.27	0.295	/	0.27	0.295

* including the water content of the superplasticizer

4. Results and discussion

Fig. 5a shows the load-CMOD curves demonstrate the performance of the model and of the inverse analysis (Example for DTUIF at 28 day maturity). It is visible that computation based on softening curve for N = 3 provide better approximation compared to the bi-linear curve. The computational time was approximately 15 minutes with softening curve for N = 2 and approximately 25 minutes with softening curve for N = 3. The increase in computational time is compensated with increase in accuracy of the model.

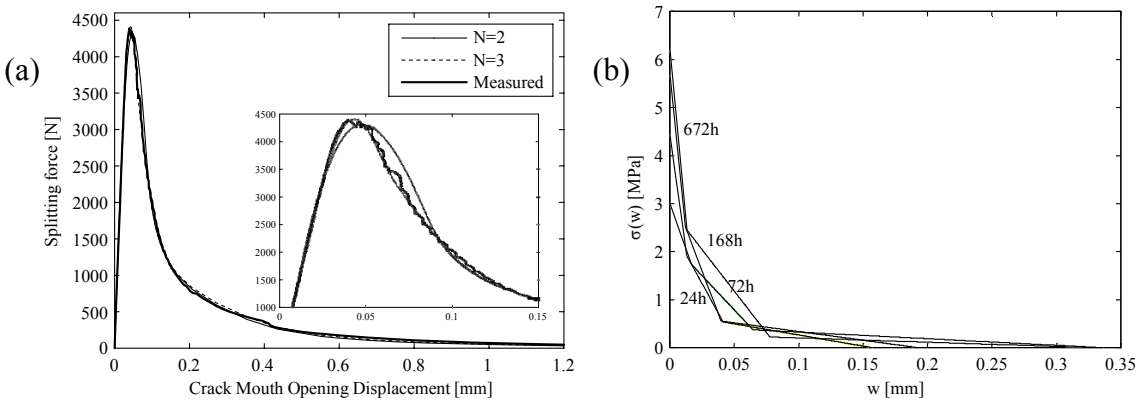

Figure 5. Example of comparison of the measured and the computed load-CMOD curves for DTUIF at 28 day maturity (a) and stress-crack opening relationships for DTUIF for different ages (b).

Fig. 5b shows an example of stress-crack opening relationships at different ages for DTUIF. Furthermore, it shows the fracture energy given by the area under the curves is increasing with age.

The development of modulus of elasticity E seen in Fig. 6 shows some scatter and furthermore, a drop in E is seen for DTUII mix. With the exception of the Contec mixes, the mean static elastic modulus of the concretes E_{cm}, reached about 60GPa after 28 days. The static elastic modulus of the Contec mixes was at 40GPa, thus significantly lower. This seems to be caused by discontinues grain size distribution curve and by a disadvantageous pore size distribution of the hardened concrete. The static elastic modulus of the DTU mixes developed significantly faster than Contec mixes.

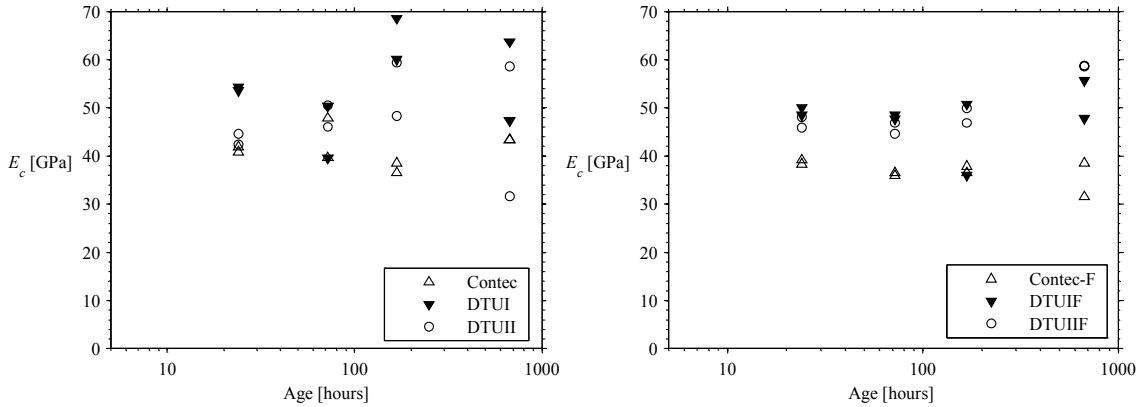

Figure 6. Development in modulus of elasticity.

Fig. 7 shows the development in the tensile strength, f_t. The 28 days tensile strength of all HPC mixes was high around 6 MPa. The tensile strength of the DTU mixes made with silica fume, fly ash and cement with rapid hardening was observed to develop faster. After three days it was at roughly 5 MPa - well above the strength of the Contec mixes, 3 MPa. Tensile strength development of Contec mixes tended to increase slower than DTU mixes. There was no obvious change of tensile strength caused by adding fibers to HPC matrix.

In general results of development of elastic modulus E and tensile strength f_t follow the literature, see e.g. [4]. Their results also indicate a drop in the modulus of elasticity at 28 days.

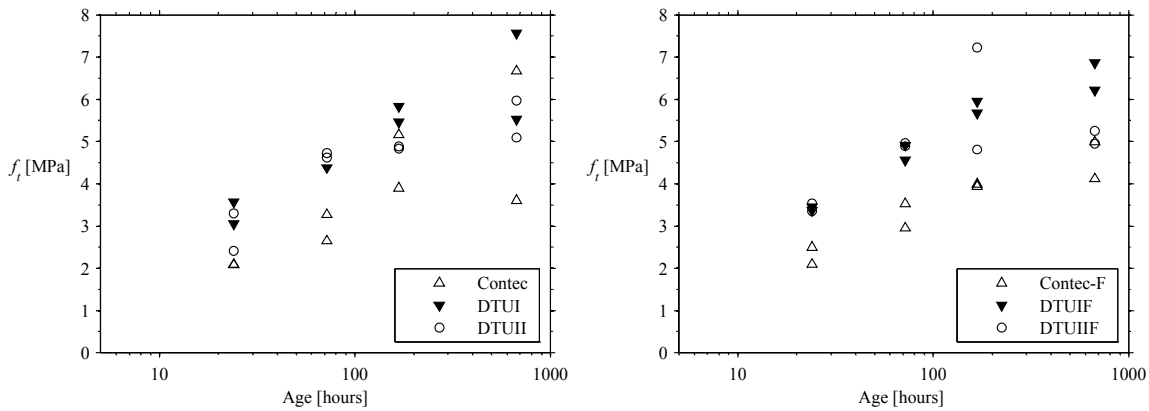

Figure 7. Development in tensile strength.

Development in fracture energy with age is shown in Fig. 8. The development of this property is in agreement with observation found in literature see e.g. [1,4]. Same as at these papers the fracture energy is found increase with age.

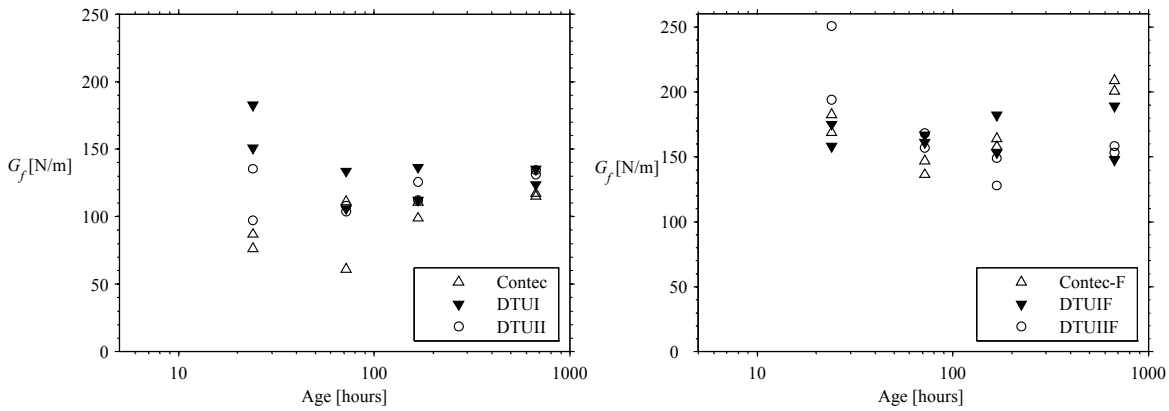

Figure 8. Development in fracture energy.

Fig. 9 shows the development in characteristic length. The general trend in the development of the characteristic length despite the scatter was observed to decrease with maturity. The same results were also found in literature, e.g. [4].

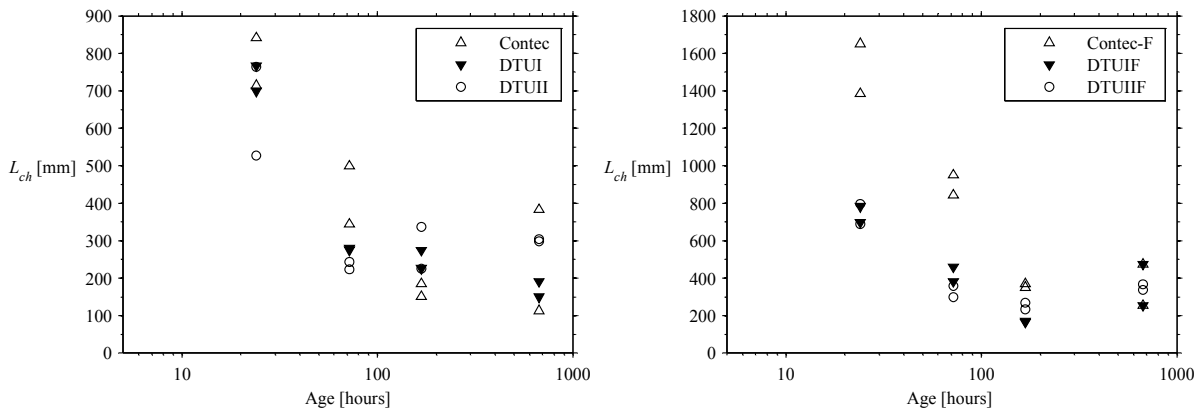

Figure 9. Development in characteristic length.

5. Conclusion

This paper presents knowledge of the inverse analysis of the WST. The fracture behaviour of three fiber reinforced and regular HPC were investigated. The wedge splitting test setup with 48 cubical specimens was used experimentally and the cracked non-linear hinge model based on the fictitious crack model was applied for the interpretation of the results. The stress-crack opening relationships were extracted by using inverse analysis algorithm for various multi-linear softening curves. The fracture mechanics parameters such as crack opening displacement (COD), fracture energy and characteristic length were experimentally determined. Experiments were performed at 1, 3, 7 and 28 days. Fracture energy, G_f, was found to increasing with age, while the characteristic length, L_{ch}, was found to decrease.

The conclusions that can be drawn from this study are that:

- The wedge splitting test is suitable test method for assessment of fracture properties of regular and glass-polypropylane fiber reinforced HPC.
- The test method is easy to handle and the execution is relatively fast.
- Using the inverse analysis, the both elastic and fracture properties may be interpreted from the test results as a bi-linear or multi-linear stress-crack opening relationship.
- The refinement of the softening curves reflects in improved accuracy of the WST simulation in comparison with bi-linear softening curves with acceptable increase of computational time.

References

[1] I. Löfgren, H. Stang, J.F. Olesen, The WST-method for fracture testing of fibre-reinforced concrete, Mater Struct 4 (2008) 197- 211.
[2] A. Jansson, I. Löfgren, K. Gylltoft, Flexural behaviour of members with a combination of steel fibres and conventional reinforcement, Nord Concr Res 2(42) (2010) 155-171.
[3] M. Hillerborg, M. Modeer, P.E. Peterson, Analysis of crack formation and crack growth in concrete by means of fracture mechanics and finite elements, Cem Concr Res 6 (1976) 773-782.
[4] L. Østergaard, D. Lange, H. Stang, Early-age stress-crack opening relationships for high performance concrete, Cem Concr Composites 26(5) (2006) 563-572.
[5] H.N. Linsbauer, E.K. Tschegg, Fracture energy determination of concrete with cube shaped specimens, Zement und Beton 31 (1986) 38-40 (in German).
[6] E. Brühwiler, F.H. Wittmann, The wedge splitting test, a new method of performing stable fracture mechanics test, Eng Fract Mech 35(1-3) (1990) 117-125.
[7] E.J. de Place Hansen, E.A. Hansen, M. Hassanzadeh, H. Stang, Determination of the Fracture energy of concrete: A comparison of the three-point bend test on notched Beam and the wedge-splitting test, Nordtest Project No 1327-97, SP Swedish National Testing and Research Institute, Building Technology, SP Report 09 (1998), Borås, Sweden, p.87.
[8] M. Elser, E.K. Tschegg, S.E. Stanzl-Tschegg, Fracture behaviour of polypropylene-fibre-reinforced concrete under biaxial loading: An experimental investigation, Composites Science and Technology 56(8) (1996) 933-945.
[9] J. Skocek, H. Stang, Inverse analysis of the wedge splitting test, Eng Fract Mech 75(10) (2008) 3173-3188.
[10] J.P Ulfkjaer, S. Krenk, R. Brincker, Analytical model for fictitious crack propagation in concrete beams. J Eng Mech 121(1) (1995) 7-15.
[11] J.F. Olesen, Fictitious crack propagation in fiber-reinforced concrete beams, J Eng Mech 127(3) (2001) 272-80.
[12] H. Tada, P. Paris, G. Irwin, The stress analysis of cracks handbook, Paris Productions Incorporated, 226 Woodbourne Dr., St. Louis, Missouri, USA, 1985.
[13] E. Ozbay, M. Gesoglu, E. Guneyisi, Transport properties based multi-objective mix proportioning optimization of high performance concretes, Mat Struc 44 (2011) 139-154.

Instability and failure of particulate materials caused by rolling of non-spherical particles

Elena Pasternak[1*], Arcady V. Dyskin[2]

[1] School of Mechanical and Chemical Engineering, University of Western Australia, 6009, Australia
[2] School of, Civil and Resource Engineering University of Western Australia, 6009, Australia
* Corresponding author: arcady@civil.uwa.edu.au

Abstract In particulate materials under compression at the peak load the accumulated damage allows particle rolling. For non-spherical particles the moment equilibrium dictates that further increase in displacement requires reduced shear stress producing an effect of apparent negative stiffness; its value depends upon the magnitude of the compressive stress. Dilatancy produced by rolling particles reduces the value negative stiffness, while the contraction phase causes immediate instability. Material with rolling particles is macroscopically modelled as a matrix containing inclusions with negative shear modulus. When the concentration of negative stiffness inclusions is low, the effective shear modulus is positive and the material is stable. When the concentration reaches a critical level the effective shear modulus abruptly becomes negative and the material loses stability. Furthermore, there exists a special value of negative shear modulus of inclusions (and hence the magnitude of compressive stress) when the critical concentration becomes zero, such that the first rolling particle induces the global instability.

Keywords Rolling particles, Negative shear modulus, Effective shear modulus, Critical concentration, Dilation

1. Introduction

The importance of particle rotations (and the associated rotational degrees of freedom) in the mechanisms of instability and failure of particulate materials has long been recognised (e.g. [1-7]). The particle rotations were observed in physical experiments (e.g. [8-10]) and discrete element simulations (e.g. [11-14]). The modelling of the effect of particle rotation was mainly based on the concept of spherical (circular in 2D) particles, which offered the maximum simplicity. The effect of particle shape was thought to be quantitative, for instance resulting in reduced velocities of particle flow and increased stresses (e.g. [15]). However, the non-spherical particles can interlock – a phenomenon that does not exist in spherical particles [16]. Furthermore, rotations of non-spherical particles cause elbowing [17] that is coupling between the rotations and normal stresses. Both these mechanisms could lead to qualitatively new phenomena, such as the apparent negative stiffness [18-23]. It was further pointed out in [24] that in producing the negative stiffness effect the role of non-spherical particles could be played by clusters of connected spherical particles. The role of non-spherical particles and clusters of spherical particles is also discussed in [25].

Dyskin and Pasternak [20-24] modelled the apparent negative stiffness associated with particle rotations without taking into account the effect elbowing has on dilation/contraction. Here we include the latter into consideration. This will be accomplished in Section 2. Section 3 models the volume elements with apparent negative stiffness as inclusions in a matrix with positive definite elastic moduli and takes into account the interaction between the inclusions. This result gives an insight into the effect of rotating particles on global stability.

2. Apparent negative stiffness caused by rotating particles. The effect of elbowing

Consider a particulate material loaded in compression to near the peak load. We assume that in the process of loading considerable amount of defects have been accumulated, mainly on the bonds (cement) between the particles such that some particles are now partially detached from the matrix, Fig. 1. The balance of moments of shear and normal forces shown in Fig. 1 about point O reads

$$T\sin\varphi + P\cos\varphi = 0, \quad \pi/2 \le \varphi \le \pi\,. \tag{1}$$

Here l is the corresponding particle diameter, T and P are the magnitudes of the shear and normal forces and angle φ is related to the position of the particle at the moment of detachment. Obviously, the moment equilibrium is only possible for the range of angles φ indicated in (1) and in Fig. 1a; when $\varphi<\pi/2$, Fig. 1b, the particle becomes unstable. It is reasonable to assume that the initial packing of particles was a stable one similar to the configuration shown in Fig. 1a. The analysis below is based in infinitesimal deformations and hence all movements considered will leave the initially stable configuration in its stable state. For that reason we will disregard the unstable configurations shown in Fig. 1b.

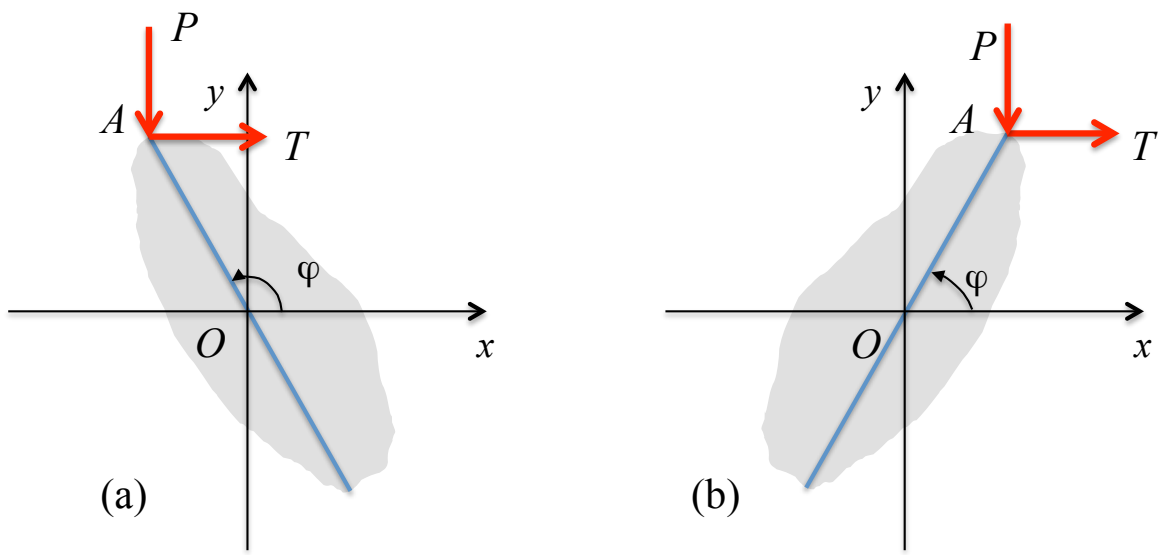

Figure 1. A moment balance of rotating (rolling) partially detached particle: (a) stable configuration, (b) unstable configuration.

Suppose the particle underwent an infinitesimal rotation $d\varphi$. This will change the coordinates (x, y) of point A, Fig. 1 by $dx=-l\sin\varphi\, d\varphi$ and $dy=l\cos\varphi\, d\varphi$. The moment equilibrium (1) imposes the following force increments:

$$dT\sin\varphi - T\frac{\cos\varphi}{\sin\varphi}\frac{dx}{l} + dP\cos\varphi - T\frac{\sin\varphi}{\cos\varphi}\frac{dy}{l} = 0\,. \tag{2}$$

We now assume that the change dP in the magnitude of compression is proportional to the vertical displacement such that

$$dP = k_m\frac{dy}{l}\,. \tag{3}$$

where k_m is the stiffness of the surrounding parts of the particulate material. Hereafter we refer to the surrounding parts of the particular material as the *matrix*.

Substituting (3) into (2), expressing T via P through the equation of moment equilibrium (1) and taking into account that dy=-dx $\cos\varphi/\sin\varphi$ we obtain

$$dT = \left\{-P\frac{1}{\sin^3\varphi} + k_m\frac{\cos^2\varphi}{\sin^2\varphi}\right\}\frac{dx}{l}\,. \tag{4}$$

It is seen that the coefficient between incremental shear force dT and incremental shear strain dx/l can assume negative values, when $P>k_m\sin\varphi\cos^2\varphi$. We call this effect the *apparent negative stiffness*.

Following [20-23] we model the collective effect of rotating particles by treating them as negative stiffness inclusions (inclusions with negative shear modulus, μ_{incl}) embedded in a matrix with positive definite elastic moduli. We then use the theory of effective characteristics in order to determine the elastic moduli of such a composite at macroscale and determine the conditions of global instability. In order to incorporate this phenomenon into a continuum description of the granulate material consider a representative volume element, that is an element of size $H>>l$. We introduce normal p and shear τ stresses acting on the faces of the element. Therefore we can treat normal and shear forces from (4) as $P\sim pl^2$ and $T\sim\tau l^2$. For the sake of simplicity we will treat the normalised matrix stiffness as the bulk modulus of the matrix, $\kappa_m\sim k_m/l^2$. Then we can express the average shear modulus, μ_{incl}, associated with the particle rotation as

$$\mu_{incl} = -\frac{p}{\sin^3\varphi} + \kappa_m\frac{\cos^2\varphi}{\sin^2\varphi}\,. \tag{5}$$

Here angle φ is interpreted as an average angle, which provides a combined description of particle shapes and initial packing.

The negative stiffness is achieved when

$$p > p_{\min}(\varphi) = \kappa_m \sin\varphi \cos^2\varphi \,. \tag{6}$$

Dependence (6) and its interpretation are shown in Fig. 2. It is seen that the dense packing produces negative stiffness at lower pressures that the loose one.

Two interim conclusions could be made here. Firstly, the compressive stress required to produce the effect of apparent negative stiffness could be of the order of the bulk modulus of the surrounding rock. That is only possible when the bulk modulus is sufficiently reduced by the damage accumulated in the preceding loading, namely near the peak load. Another conclusion is that the phenomenon of apparent negative stiffness depends upon the density of the initial packing.

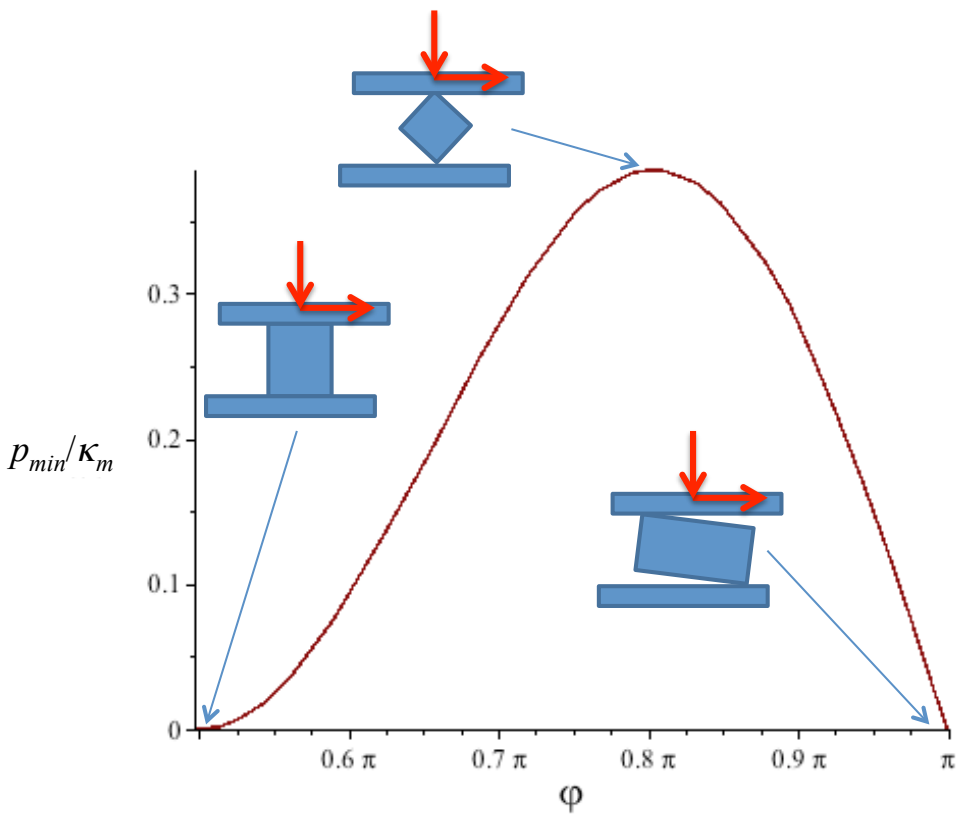

Figure 2. Dependence (6) and its interpretation: the smallest values of the minimal compressive stress magnitude p_{min} needed to ensure the negative stiffness are achieved at dense packing (angles close to $\pi/2$ and π), while the loose packing (angles close to $3\pi/4$) requires higher compressive stresses to show negative stiffness.

3. Effect of rotating particles on global stability

The presence of negative stiffness means the loss of positive definiteness of the tensor of elastic

moduli (or the quadratic form of elastic energy) and hence the loss of uniqueness of the elastic solution. The material with negative stiffness becomes intrinsically unstable; its actual stability or instability depends upon the boundary conditions, i.e. the type of loading applied. The best known example of this type of dependence upon the boundary conditions is the post-peak loading of rock or concrete sample which is only possible if the loading device is sufficiently stiff and the loading is displacement controlled.

In the case under consideration the negative stiffness associated with particle rotation/rolling is a local phenomenon. We model it as a negative stiffness (negative shear modulus) inclusion in a conventional matrix. The stability/instability of the inclusion should depend upon the deformability of the matrix. This suggests that the global stability of the material with rotating particles could be determined by considering the matrix filled with negative stiffness inclusions and determining the effective moduli of such a composite. If the tensor of effective moduli is positive definite, the particulate material is stable, otherwise it is unstable.

The theory of effective characteristics of a matrix with negative stiffness inclusions was developed in [23, 26]. Following [23] we model the negative stiffness inclusions as spherical inclusions with negative shear modulus given by (5) and the (positive) bulk modulus, κ_{incl}, equal to that of the matrix, $\kappa_{incl} = \kappa_m$. The shear modulus of the matrix, μ_m is assumed to be positive.

The simplest case usually considered in the theory of effective characteristics is the case of low concentrations (volumetric fractions) of inclusions. In this case the interaction between the inclusions can be neglected and the problem of determination of the effective moduli is reduced to the determination of the change in the average strain (volumetric averaging over representative volume element is presumed) caused by a single inclusion under uniform stress. This is so-called approximation of low concentrations. It was shown in [27] and then in [23, 26] that the application of the approximation of low concentrations to the matrix with negative stiffness inclusions leads to a singularity, which in our case happens at a certain critical value of the negative shear modulus. The singularity means that the influence of the inclusions on the effective moduli is infinite at any concentrations. The existence of the singularity can be interpreted as the increasing influence of interaction between the inclusions as the shear modulus of inclusion tends to that (negative) value. Therefore one has to use the methods of computing effective moduli that account for the interaction.

We use the differential self-consistent method, which in the case of isotropic matrix with spherical inclusions of any concentrations c leads to the following system of differential equations obtained in [28]:

$$\begin{cases} \dfrac{d\kappa_{eff}}{dc} = \dfrac{\kappa_{incl} - \kappa_{eff}}{1-c} \dfrac{\kappa_{eff} + \kappa^*}{\kappa_{incl} + \kappa^*}, \quad \kappa^* = \dfrac{4}{3}\mu_{eff} \\ \dfrac{d\mu_{eff}}{dc} = \dfrac{\mu_{incl} - \mu_{eff}}{1-c} \dfrac{\mu_{eff} + \mu^*}{\mu_{incl} + \mu^*}, \quad \mu^* = \dfrac{\mu_{eff}}{6} \dfrac{9\kappa_{eff} + 8\mu_{eff}}{\kappa_{eff} + 2\mu_{eff}} \\ \kappa_{eff}\Big|_{c=0} = \kappa_m, \quad \mu_{eff}\Big|_{c=0} = \mu_m \end{cases} . \tag{7}$$

where c is the volumetric fraction (concentration) of inclusions.

In our case, $\kappa_{incl} = \kappa_m$ and therefore $\kappa_{eff} = \kappa_m$ is an obvious solution of the first equation in (7). Due to the uniqueness of the solution of this system of differential equations, there are no other solutions.

We now normalise the moduli with κ_m by formally assuming that $\kappa_m = 1$. After introducing the notations

$$\mu_{eff} = \mu, \quad \mu_{incl} = -m\mu_m, \quad m = \frac{p}{\sin^3\varphi} - \frac{\cos^2\varphi}{\sin^2\varphi} . \tag{8}$$

system (7) is reduced to

$$\begin{cases} \dfrac{d\mu}{dc} = \dfrac{-5\mu}{1-c} \cdot \dfrac{(4\mu+3)(m\mu_m + \mu)}{8\mu^2 - 3(4m\mu_m - 3)\mu - 6m\mu_m} \\ \mu\Big|_{c=0} = \mu_m \end{cases} . \tag{9}$$

Derivative $d\mu/dc$ is discontinuous when the denominator in the right hand site of (9) vanishes. The discontinuities correspond to points μ_1 and μ_2:

$$\mu_{1,2} = \frac{\sqrt{3}}{16}\left[(4m\mu_m - 3)\sqrt{3} \pm \sqrt{48\mu_m^2 m^2 - 8m\mu_m + 27}\right]. \tag{10}$$

It can be shown that $\mu_2 < 0 < \mu_1$. Since the initial condition in (9) is $\mu(0) = \mu_m > 0$, the solution of (9) can only reach point μ_1, after which the effective shear modulus drops to a certain negative value determined by the global loading device which applies the load to the particulate material [23, 26]. We therefore treat the modulus μ_1 as a point of global intrinsic instability of the particulate material.

Solution of (9) can be obtained in the following implicit form

$$\frac{\left(\mu+m\mu_m\right)^5}{\mu^2\left(4\mu+3\right)}=\mu_m^3\frac{\left(1+m\right)^5}{4\mu_m+3}\left(1-c\right)^5. \tag{11}$$

The point of instability is reached when $\mu=\mu_1$. This happens at the concentration of negative stiffness inclusions

$$c_{cr}=1-\frac{\mu_1+m\mu_m}{1+m}\left[\frac{4\mu_m+3}{\mu_m^3\mu_1^2\left(4\mu_1+3\right)}\right]^{1/5}. \tag{12}$$

The dependencies (11) and (12) are shown in Figs. 3 and 4 respectively for different values of m and μ_m. It is seen from Fig. 3 that the effective shear modulus can both increase and decrease with concentration of the negative stiffness inclusions depending upon the values of parameters m and μ_m. The plot of critical concentration, Fig. 4a, shows that there exist combinations of parameters m and μ_m at which the critical concentration is zero. That means that at the instance when the particle rotations start and make the corresponding shear modulus negative, the particulate material loses stability. Dependence of the value of negative shear modulus of inclusions vs. the shear modulus of the matrix is shown in Fig 4b. It is seen that the dependence is relatively weak; the value of the negative shear modulus that delivers zero critical concentration is of the order of the shear modulus of the matrix.

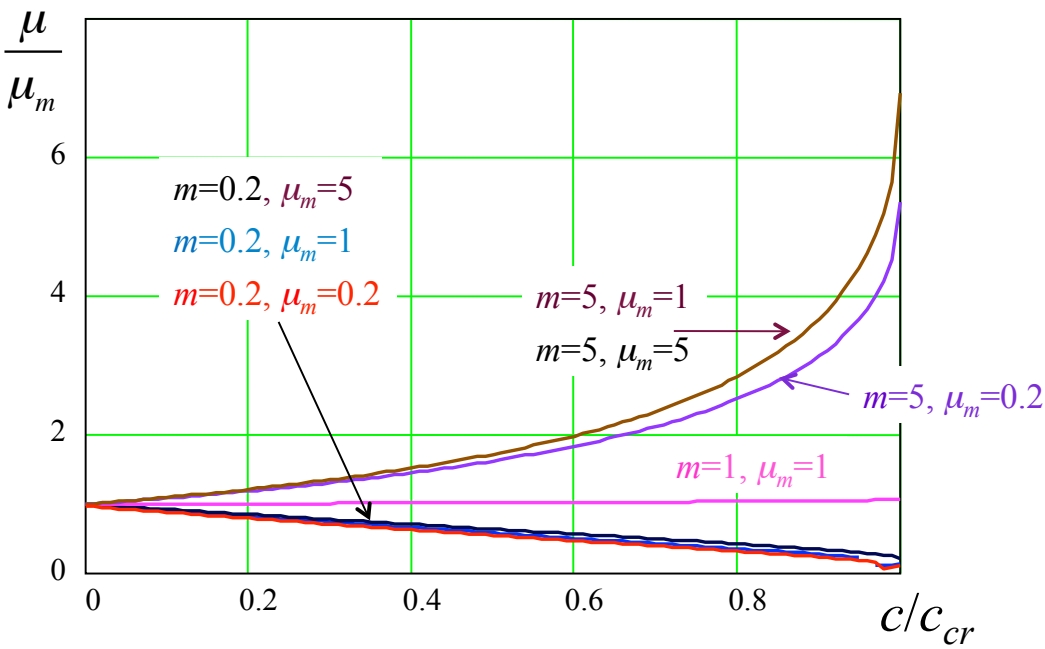

Figure 3. Effective shear modulus μ vs. volumetric fraction (concentration) of negative stiffness inclusions c. Three pairs of parameters m and μ_m on the left side of the picture refer to nearly indistinguishable dependencies in the same order from top to bottom.

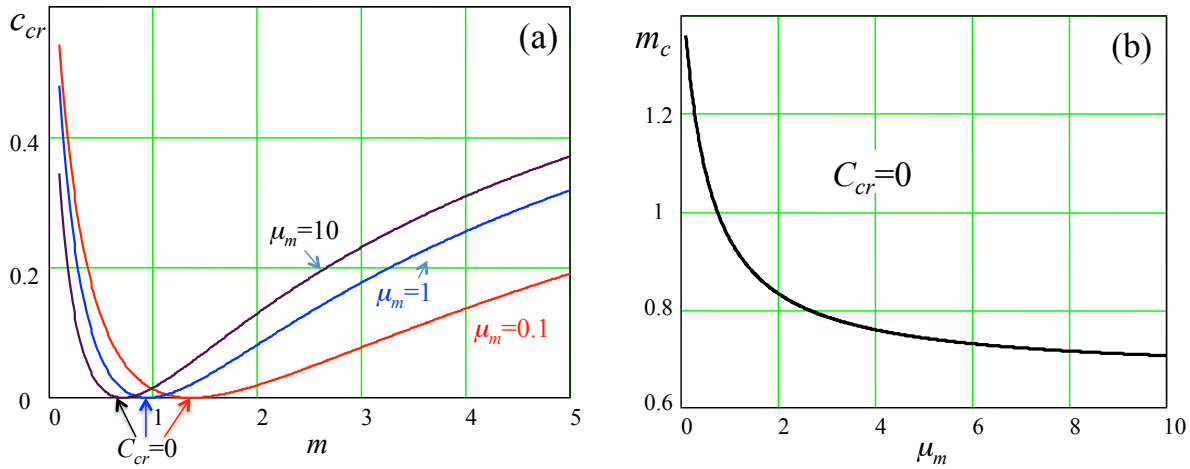

Figure 4. The critical concentration of negative stiffness inclusions c_{cr}: (a) its dependence upon the value m of negative shear modulus of inclusions; (b) the values m_{cr} of negative shear modulus of inclusions delivering zero critical concentration.

From here it is seen that the magnitude of compressive stress that produces the global instability of the particulate material is

$$p_{cr} / \kappa_m = m_c \sin^3 \varphi + \sin \varphi \cos^2 \varphi \,. \tag{13}$$

4. Conclusions and outlook

The ability of partially detached non-spherical particles to roll or rotate leads to the effect of apparent negative stiffness (negative shear modulus), whose value depends on the magnitude of the applied compressive stress. This is a property of particle non-sphericity: rotation of spherical (or circular in 2D) particles does not produce negative stiffness. Rotation of non-spherical particles also produces elbowing which results in dilation of the surrounding material. Depending of the initial packing, dilation can lead to the reduction of the value of negative shear modulus such that the magnitude of compressive stress needed to effect negative stiffness is of the order of the bulk modulus. Therefore the effect of negative stiffness is only relevant to the particulate materials loaded in compression up to the peak when the damage created in the course of loading has considerably weakened the material and made the moduli sufficiently low.

The global instability of the particulate material with rolling or rotating particles is reached when the effective shear modulus is no longer positive. This happens when the concentration (volumetric fraction) of negative stiffness areas reaches a certain critical value that depends upon the value of negative shear modulus and the shear modulus of the surrounding material. There exist a combination of these parameters which makes the critical concentration zero, meaning that the first rolling particle results in global instability.

The theory proposed casts light on the mechanics of compressive failure of particular materials such as rock and concrete as well as on the mechanism instability of granular materials. Another possible application of this theory is in the design of a special class of hybrid materials based on specially

shaped particles or blocks to ensure the desirable properties of the hybrid not achievable otherwise. In particular, according to Fig. 3 the presence of rotating non-spherical particles in a matrix can either increase or decrease the effective shear modulus depending upon the magnitude of applied compressive stress. This suggests a method of designing materials whose moduli can be controlled by applied load without the creation of additional internal damage.

Acknowledgements

The authors acknowledge the financial support through the ARC Discovery grant DP120102434.

References

[1] H-B. Mühlhaus, I. Vardoulakis, The thickness of shear bands in granular materials, Géotechnique 37 (1987) 271-283.
[2] H.-B. Mühlhaus, R. de Borst, E.C. Aifantis, Constitutive models and numerical analyses for inelastic materials with microstructure, in: G., Beer, et al (Eds.) Computing Methods and Advances in Geomechanics (1991) pp. 377-385.
[3] C.S. Chang, L. Ma, Elastic material constants for isotropic granular solids with particle rotation, Int. J. Solids Structures 29 (1992) 1001-1018.
[4] H.-B. Mühlhaus,. Continuum models for layered and blocky rock. In: Comprehensive Rock Eng., Invited Chapter for Vol. II: Analysis and Design Methods, Pergamon Press (1993) pp. 209-230.
[5] H-B. Mühlhaus, F. Oka, Dispersion and wave propagation in discrete and continuous models for granular materials, Int. J. Solids Structures 33 (1996) 2841-2858.
[6] E. Pasternak, H.-B. Mühlhaus, A.V. Dyskin, On the possibility of elastic strain localisation in a fault, Pure Appl. Geophys. 161 (2004) 2309-2326.
[7] E. Pasternak, H.-B. Mühlhaus, Generalised homogenisation procedures for granular materials. Eng Math, 52 (2005) 199-229.
[8] D.M. Mueth, G.F. Debregeas, G.S. Karczmar, P.J. Eng, S.R. Nagel, H.M. Jaeger, Signatures of granular microstructure in dense shear flows. Nature 406 (2000), 385.
[9] J. Desrues, G. Viggiani, Strain localization in sand: an overview of the experimental results obtained in Grenoble using stereophotogrammetry. Int. J. Numer. Anal. Meth. Geomech. 28 (2004) 279–321.
[10] A. Rechenmacher, S. Abedi, O. Chupin, Evolution of force chains in shear bands in sands. Geotechnique, 60 (2010) 343–351.
[11] H.J. Herrmann, Physics of granular media. Chaos, Solitons and Fractals, 6 (1995) 203-212.
[12] Y. Kishino, C. Thornton, Discrete element approaches, in: M. Oda, K. Iwashita (Eds.), Mechanics of Granular Materials. An introduction. Balkema. Rotterdam, Brookfield (1999) 147-223.
[13] K. Bagi, M.R. Kuhn, Different rolling measures for granular assemblies. In: Vermeer, Ehlers, Herrmann and Rahmm (Eds.) Modelling of Cohesive-Frictional Materials, Taylor and Francis Group, London (2004) pp. 3-12.
[14] F. Allonso-Marroquin, I. Vardoulakis, H.J. Herrmann, D. Weatherley, P. Mora, Effect of rolling on dissipation in fault gouge. Phys. Rev. E, 74 (2006).
[15] P.W. Cleary, M.L. Sawley, DEM modelling of industrial granular flows: 3D case studies and the effect of particle shape on hopper discharge. Applied Mathematical Modelling 26 (2002) 89-111.
[16] A.V. Dyskin, Y. Estrin, A.J. Kanel-Belov, E. Pasternak, Topological interlocking of platonic solids: A way to new materials and structures, Phil. Mag. Lett. 83(2003) 197-203.

[17] E. Pasternak, A.V. Dyskin, Y. Estrin, Deformations in transform faults with rotating crustal blocks. Pure Appl. Geophys. 163 (2006) 2011-2030.
[18] Y. Estrin, A.V. Dyskin, E. Pasternak, S. Schaare, S. Stanchits, A.J. Kanel-Belov, Negative stiffness of a layer with topologically interlocked elements. Scripta Materialia, 50 (2003) 291-294.
[19] S. Schaare, A.V. Dyskin, Y. Estrin, S. Arndt, E. Pasternak, A. Kanel-Belov, Point loading of assemblies of interlocked cube-shaped elements. Int. J. Engineering Sciences 46 (2008) 1228–1238.
[20] A.V. Dyskin, E. Pasternak, Friction and localisation associated with non-spherical particles, in: S. Bonelli, C. Dascalu, F. Nicot (Eds.) Advances in Bifurcation and Degradation in Geomaterials. Proceedings of the 9th International Workshop on Bifurcation and Degradation in Geomaterials, Springer (2011) pp. 53-58.
[21] A.V. Dyskin, E. Pasternak, Rock mass instability caused by incipient block rotation, in: Harmonising Rock Engineering and the Environment, in: Proc. Q. Qian, Y. Zhou (Eds.) 12th International Congress on Rock Mechanics, CRC Press / Balkema (2012) 4pp.
[22] A.V. Dyskin, E. Pasternak, Rock and rock mass instability caused by rotation of non-spherical grains or blocks, in: Rock Engineering & Technology for Sustainable Underground Construction. Proc. Eurock 2012, paper 102P.
[23] A.V. Dyskin, E. Pasternak, Mechanical effect of rotating non-spherical particles on failure in compression. Phil. Mag. 92 (2012) 3451-3473. DOI: 10.1080/14786435.2012.704421.
[24] A.V. Dyskin, E. Pasternak, Bifurcation in rolling of non-spherical grains and fluctuations in macroscopic friction, European Mechanics Society, in: G.A. Holzapfel, R.W. Ogden (Eds.), Proc. ESMC 2012, 8th European Solid Mechanics Conference, Graz, Austria, 2012, 2pp.
[25] M.Z. Miskin, H.M. Jaeger, Adapting granular materials through artificial evolution. *Nature Materials* (2013) 1–6, doi:10.1038/nmat3543.
[26] A.V. Dyskin, E. Pasternak, Elastic composite with negative stiffness inclusions in antiplane strain. Intern. J. Engin. Sci. 58 (2012) 45-56.
[27] R.S. Lakes, W.J. Drugan, Dramatically stiffer elastic composite materials due to a negative stiffness phase? J. Mech. Phys. Solids 50 (2002) 979-1009.
[28] R. McLaughlin, A Study of the Differential Scheme in Composite Materials, Intern. J. Engin. Sci. 15 (1977) 237-244.

Mechanism of in-plane fracture growth in particulate materials based on relative particle rotations

Arcady V. Dyskin [1,*], **Elena Pasternak** [2]

[1] Deep Exploration Technologies Cooperative Research Centre, School of Civil and Resource Engineering, University of Western Australia, 6009, Australia
[2] Deep Exploration Technologies Cooperative Research Centre, School of Mechanical and Chemical Engineering, University of Western Australia, 6009, Australia
* Corresponding author: arcady@civil.uwa.edu.au

Abstract In-plane fracture propagation in particulate materials (rock, concrete) under high tri-axial compression is observed in both Mode I tensile cracks (opened by additional load), Mode II shear cracks and in Mode I anti-cracks (compaction bands). This commonality suggests that when the conventional fracture mechanisms are supressed by high compression, a new universal mechanism takes over. We propose a fracture growth mechanism based on mutual rotations of the particles leading to breakage of inter-particle bonds followed by particle detachment and re-compaction. The Cosserat characteristic lengths are found to be of the order of the particle size. This allows expressing the stress concentrations as an intermediate asymptotics (between the Cosserat continuum characteristic length and the crack length). For Mode I crack and anti-crack and for Mode II crack the stress singularities are the same as for the cracks in a classical continuum, while the moment stress has a stronger singularity (3/2 power). This stress singularity leads to relative particle rotations and bending of interparticle bonds. The tensile microstress induced by the bending is an order of magnitude higher than the stress associated with conventional stress singularities.

Keywords Fracture Criterion, Grain rotation, Moment stress, Small-scale Cosserat continuum, Compaction band

1. Introduction

Fracture mechanics recognises 3 main fracture modes, one tensile (Mode I) and two shear (Modes II and III). Numerous experiments show that in brittle and quasi-brittle materials without pronounced planes of weakness, Mode I cracks are capable of in-plane growth, that is growing in their own plane, while Mode II cracks kink. In rock fracturing in compression however two more phenomena are observed. Firstly, it is in-plane propagation of shear bands; they start at near the peak load and propagate at an angle to the load direction throughout the rock sample separating it into two parts. This zone looks like shear (Mode II) crack (e.g. [1-3]) and is usually treated as such, but contrary to the behaviour of genuine Mode II crack it does not kink. Secondly, it is the existence and in-plane propagation of Mode I anti-cracks, which are the cracks that propagate under compressive load applied normally to their surface. In this case the load has the sign reverse to the conventional Mode I cracks giving the name to this type of cracks. They are observed in rocks and rock masses as compaction bands (e.g. [4-8]) and in laboratory experiments on rock samples in uniaxial compression as anti-wing cracks generated at the locations of compressive stress concentration created by pre-existing cracks [9, 10].

In-plane propagation of shear bands is usually associated with the formation of en-echelons of tensile (micro) cracks (e.g. [11-14]), however the process by which these cracks eventually merge and form the continuation of the shear band is not clear. Indeed, the tensile cracks grow parallel in the direction of maximum compressive stress. In order to merge the cracks should either start growing in a lateral direction, which is not possible, as they will be closed by the largest principal compressive stress, or to initiate shear microcracks by yet unknown mechanism. Thus even in the simple 2D case the mechanism of coalescence of en-echelon cracks is not clear. Even less clear is the mechanism of crack coalescence in 3D, when the orientation of the cracks forming en-echelon is

more complex since they can rotate out of plane still being parallel to the direction of maximum compression.

Another challenge is to understand the mechanism of in-plane propagation of compaction bands and anti-wing cracks. For instance, the criterion of compaction band propagation cannot be based on simple substitution of rock failure in tension with rock failure in compression, as proposed e.g., in [15]. Indeed, the failure in compression is preceded by the formation of multitude of parallel tensile cracks in the direction of maximum compression (e.g., wing cracks). Such wing cracks are not observed in the compaction bands. On the contrary observations of thin sections suggest random orientations of cracks and grains within the compaction bands (e.g. [6, 16, 17]). Multiple microcracks are even observed in the directions normal to the direction of compression (see for instance the thin sections presented in [16]). Obviously, such microcracks cannot be produced by compressive stresses but it is conceivable that they are produced as a result of mutual rotations of the grains.

We *hypothesise* that both the compaction band and anti-wing crack propagation involves mutual rotation of the grains followed by fragmentation of the cement connecting the grains and subsequent rearrangement and compaction of the grains. (We note that the anti-wing cracks were observed in rocks with grain structure such as granodiorite, but never in homogeneous materials such as PMMA [10].) Given that grain rotations are directly observed in the shear bands in granular materials [18-20], we assume that grain rotations can also form the mechanism of in-plane shear band propagation.

Continuum modelling of rocks with grain rotations requires the use of Cosserat or micropolar continuum (e.g. [21-23]), which additionally considers rotational degrees of freedom and introduces the moment stress. Another difference from the classical continuum is that the Cosserat continuum possesses characteristic lengths (Cosserat characteristic lengths). Extensive research was devoted to cracks in such continua based on considering stress singularities at the crack tip, e.g. [24-27]. These singularities reflect the asymptotics of stress concentration when the distance to the crack tip tends to zero. In other words the traditional approach considers the distances smaller than the Cosserat characteristic lengths.

It was however pointed out in [29-31] that when a Cosserat continuum is used to model a particulate material such as rocks with grain microstructure, the asymptotics of small distances to the crack tip is beyond the resolution of the continuum. Indeed, a continuum description of a heterogeneous material is based on the introduction of representative volume elements whose size, H, is naturally much larger than the characteristic microstructural length, l_m, which is the scale at which the material can no longer be considered smooth. Then the equivalent continuum is introduced by averaging the relevant physical fields over these volume elements (e.g. [28]). While the equivalent continuum can formally address any distances, including infinitesimal, the interpretation of the calculated physical fields in terms of the original material (needed for instance to formulate the fracture criteria) is only possible in terms of distances *larger* than l_m. This concept poses no restrictions on classical continuum modelling since the classical continua are scale independent.

The situation however is different for higher order continua, such a Cosserat continuum, since they possess internal length scales. It was shown in [29-32] that for particulate materials in which particles are cemented to each other (e.g. rocks with granular structure or concrete), the Cosserat lengths are of the order of the grain size, l_m. Therefore the only asymptotics in the Cosserat continuum that are relevant to the particulate materials are the asymptotics that concern distances

$r>>l_m$. This translates into the notion that the meaningful Cosserat solutions are those that correspond to the asymptotics $r/l_m \to \infty$. We call such a continuum the *small-scale Cosserat continuum*. In this approach the relevant stress singularities at the crack tip are given by the intermediate asymptotics, which refers to the distances infinitesimal with respect to the crack dimensions but infinitely large compared to the Cosserat lengths. It is interesting that the technique of obtaining the intermediate asymptotics simplifies the analysis since the derivation of the asymptotics is less involved than the orthodox calculation of the stress singularities in Cosserat continuum.

In this paper we use the concept of the *small-scale Cosserat continuum* and propose a universal criterion of in-plane growth of shear cracks and compaction bands in compression based on the concentration of moment stresses. In this criterion the actual failure is produced by tensile fracturing of the cement layers between the grains caused by the bending moments associated with the concentration of moment stresses. This mechanism is independent of the sense of the moment stress; the latter only controls the location and direction of the induced tensile microcracks.

2. Crack propagation caused by moment stress concentration

The classical fracture criteria are based on the notion of crack propagation by separating two surfaces by applied stresses and expressing the conditions of the separation either in terms of critical forces or critical energy. In particulate materials consisting of particles (grains) and connected by cement bonds another micro failure mechanism can be at work: bending the cement layer by mutual rotation of adjacent particles and its cracking by flexure cracks, Fig. 1. Essentially what this mechanism is doing is translating the moment stress acting at scale H into microscopic tensile stresses at scale l_m. Since scale l_m is beyond the resolution of the (Cosserat) continuum that models the particulate material at scale $H>>l_m$, the failure criterion should be formulated in terms of moment stress μ_{ij}. Given that both stress and moment stress have singularity at the crack tip, we will use the approach proposed in [33] in which the crack propagation criterion is based on comparing the stress at a certain distance from the crack tip with the local material strength. It is natural to use l_m in place of such a length (see also [29-31]). Hence, for the simple case of fracture criterion controlled by a single moment stress component one has

$$\left|\mu_{ij}(l_m)\right| = \mu_c \,. \tag{1}$$

Here μ_{ij} is the moment stress component controlling local failure and the absolute value sign indicates that the instance of local failure is independent of the sense of the moment stress; the sign only controls the side of the link between the neighbouring particles from which it starts breaking. The critical value of moment stress μ_c represents the particular mechanism of bond breakage and microscopic properties of the material of the bond. From the symmetry analysis it can be found [29-31] that the moment stresses invoke the bond bending and fracturing shown in Fig. 2. It is seen that while the flexure cracks in Mode I crack are roughly coplanar with the main crack, the flexure cracks in Mode II crack form en-echelon of microcracks normal to the main crack. Yet, it is the bond (cement) breakage associated with relative particle rotations that separate the particles from the matrix and thus effect the crack propagation. The formation of en-echelon cracks is thus an

accompanying phenomenon.

The proposed fracture criterion involves the use of the main terms of the double asymptotics $l_m/H \to 0$, $H/L \to 0$, where L is the characteristic length of the crack. The consistent application of this double asymptotics leads to the concept of small-scale Cosserat continuum.

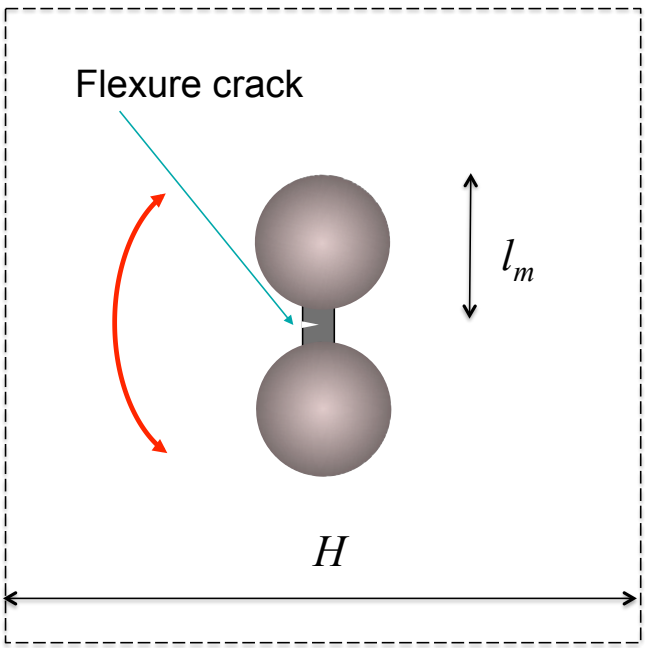

Figure 1. A volume element of size H loaded by a moment stress causing mutual rotation of neighbouring particles. The latter causes flexure (tensile) microcrack at scale $l_m \ll H$.

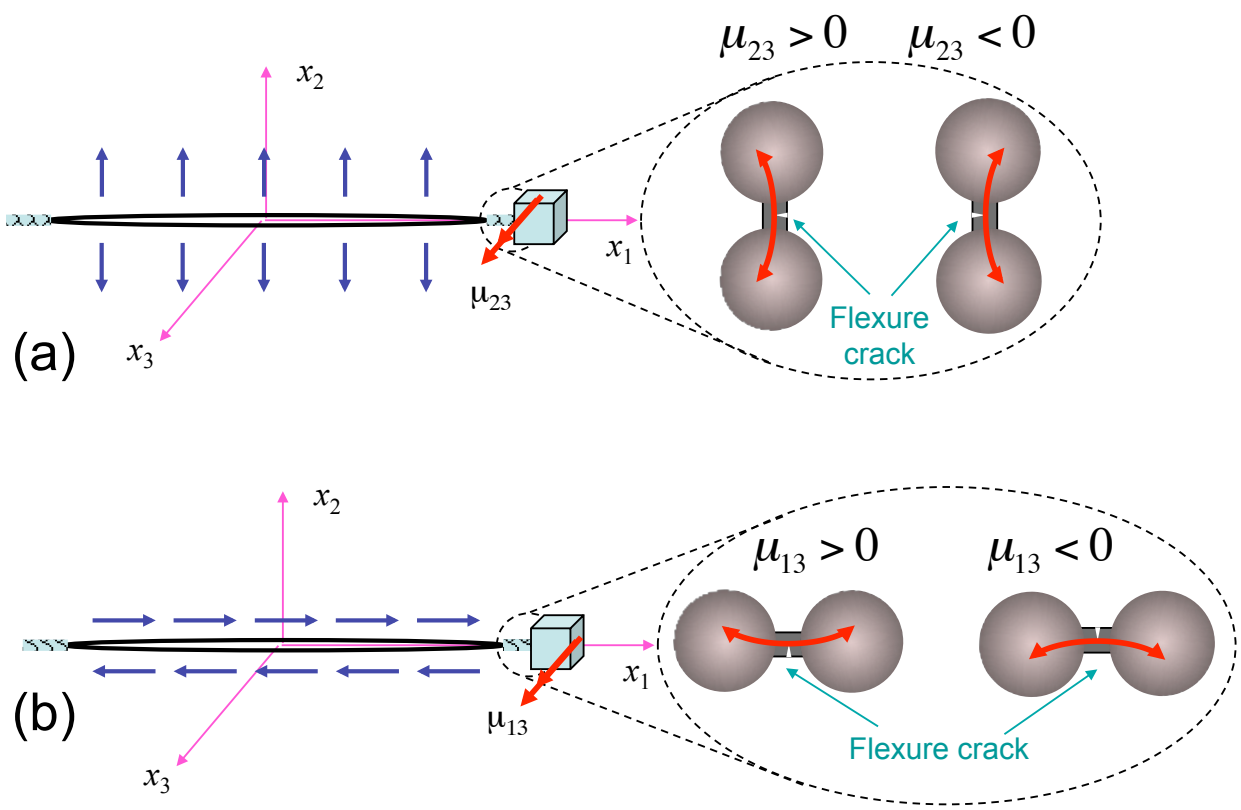

Figure 2. The direction of bending and the microcracking for (a) Mode I and (b) Mode II cracks. The corresponding bond is broken independently of the direction of microcrack (flexure crack) propagation, which is controlled by the sign of the corresponding moment stress.

3. Small-scale Cosserat continuum

We consider here the case of isotropic particulate material with internal rotations. The corresponding Cosserat continuum is defined by the following equilibrium and constitutive equations in the co-ordinate frame (x_1, x_2, x_3) (e.g. [34])

$$\sigma_{ji,j} = 0, \quad \mu_{ji,j} + \varepsilon_{ijk}\sigma_{jk} = 0, \quad i,j = 1,2,3$$
$$\sigma_{ji} = (\mu+\alpha)\gamma_{ji} + (\mu-\alpha)\gamma_{ij} + \lambda\gamma_{kk}$$
$$\mu_{ji} = (\gamma+\varepsilon)\kappa_{ji} + (\gamma-\varepsilon)\kappa_{ij} + \beta\kappa_{kk} \tag{2}$$

where σ_{ij} and μ_{ij} are stress and moment stress, ε_{ijk} is the alternating tensor. Here we use the deformation measures - the strain and curvature-twist tensors

$$\gamma_{ji} = u_{i,j} - \varepsilon_{kji}\varphi_k, \qquad \kappa_{ji} = \varphi_{i,j} \tag{3}$$

where u_i and φ_i are independent displacement and rotation vectors respectively and index $(,j)$ denotes differentiation with respect to x_j, μ, α, γ, ε, λ, β are the Cosserat elastic moduli.

According to [29-31] the main term in the asymptotics $l_m/H \to 0$ can formally be obtained from the equations of the Cosserat continuum with constrained rotations (the couple stress continuum),

where rotations are no longer independent of the displacements, but are related in the usual fashion

$$\varphi_i = \tfrac{1}{2}\varepsilon_{ijk}u_{i,k} \,. \tag{4}$$

Thus, the small scale Cosserat continuum formally involves a simpler theory – the couple stress theory. Further simplification is achieved if we recall that cracks can be represented as continuous distributions of dislocations and disclinations [35-37]. If we are interested in Modes I and II only then it can be shown that it is sufficient to consider only dislocations.

The determination of stress field produced by a dislocation involves solving the equations in displacements and rotations (with boundary conditions set in displacements) with the subsequent determination of the strain measures (3) and stress and moment stress fields using the constitutive law (2). In order to solve the equations for dislocations we use the correspondence theorem [24, 38] that states that any solution of the Navier equations (equations of equilibrium in displacements) of classical elasticity (without moment stress) is also a solution of the corresponding equations of equilibrium in displacements in the couple-stress theory, away from singular points [24]. Therefore the main asymptotic term of the stress and moment stress fields produced by dislocations can be obtained from the classical elastic solutions for the dislocations with the subsequent use of (4) for the already calculated displacement field to find the constrained rotations, the deformation measures (3) and finally the stress and moment stress using the constitutive relations (2).

Since the cracks are considered as appropriate distributions of dislocations, the above framework can be applied to determine the stress and moment stress produced by the cracks in the asymptotics of small-scale Cosserat continuum. In particular, this procedure can be used to determine stress and moment stress singularities in the intermediate asymptotics shown in Fig. 1. The resulting equations are presented in the following section.

4. Intermediate asymptotics for moment stress singularity at the crack tip

We consider a 2D crack in the plane strain approximation and find the stress singularities on the line of crack continuation using the theory outlined in the previous section. For a Mode I crack we obtain

$$\sigma_{11}(r) = \sigma_{22}(r) = \frac{K_I}{\sqrt{2\pi r}}, \quad \sigma_{12}(r) = \sigma_{21}(r) = 0, \quad \mu_{13} = 0, \quad \mu_{23} = -\frac{K_I l_m^2 \alpha}{2\mu}\frac{3-2\nu}{r^{3/2}\sqrt{2\pi}} \tag{5}$$

For a crack of Mode II we obtained the following stress singularities

$$\sigma_{11}(r) = \sigma_{22}(r) = 0, \quad \sigma_{12}(r) = \sigma_{21}(r) = \frac{K_{II}}{\sqrt{2\pi r}}, \quad \mu_{13} = \frac{K_{II} l_m^2 \alpha}{2\mu}\frac{4(1-\nu)+3}{r^{3/2}\sqrt{2\pi}}, \quad \mu_{23} = 0 \tag{6}$$

We see that the stress at the crack tip has the conventional square root singularity, while the moment stresses has stronger (power 3/2) singularity. This power of the moment stress singularity

was reported in [24, 26, 38].

It is also worth mentioning that the moment stress μ_{23} in Mode I crack has the sign opposite to the sign of K_I. Thus for the conventional Mode I crack the moment stress is negative: the flexure cracks grow in the direction of propagation of the main crack, Figs. 2a, 3a. In the case of anti-crack the direction of flexure crack growth is opposite to the direction of propagation of the main crack, Figs. 2a, 3b. We emphasise that the role of flexure cracks is to initiate the breakage of the cement bonds between the particles, while the ultimate fracture propagation is produced by further particle rotations and particle detachment form the bulk of the material.

The beginning of flexure crack propagation and the resulting bond breakage are controlled by microscopic tensile stress on the edge of the bond, which is caused by moment stress μ_{23}. The value of the microscopic tensile stress is determined by the Cosserat continuum stresses σ_{22} and μ_{23} acting at a point $r=l_m$ of the continuum. In other words this is a superposition of the tensile stress generated by bending (moment stress μ_{23}) and the normal stress σ_{22}. The latter is positive for Mode I cracks and negative for anti-cracks, Fig. 3.

It was shown in [29] for Mode II crack that the microscopic tensile stress created by bending can be an order of magnitude higher than the conventional stress applied to the bond. This makes the mechanism based on moment stress the main fracture growth mechanism.

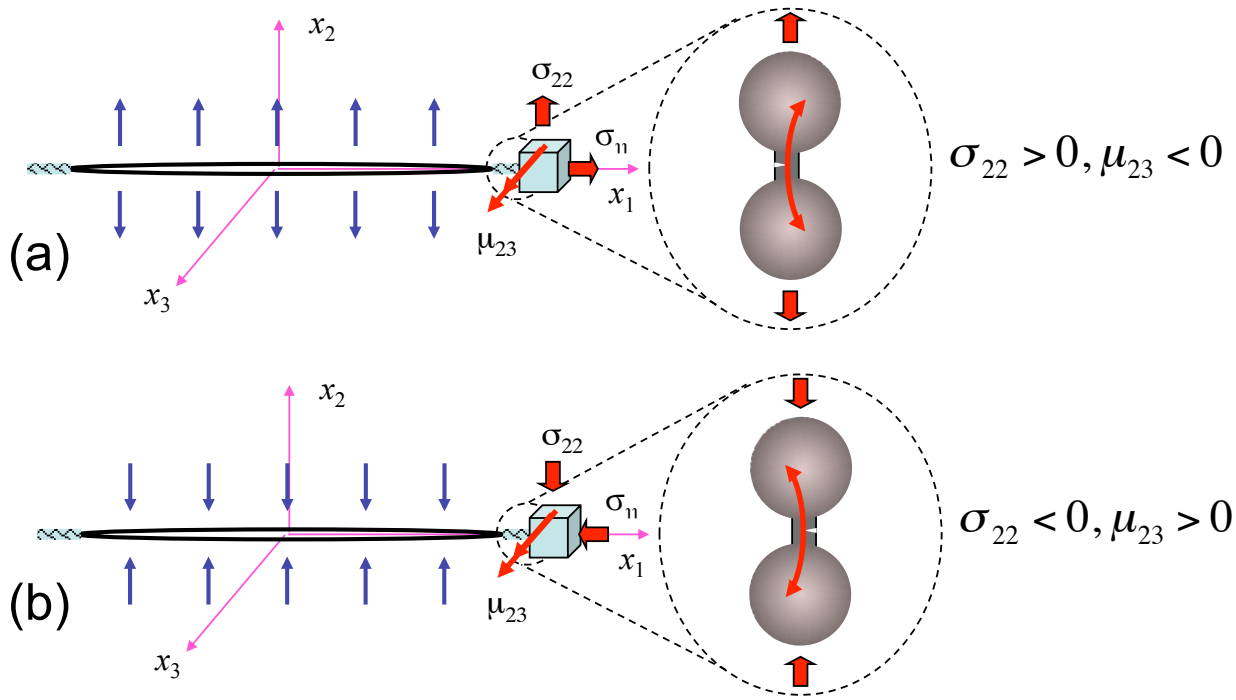

Figure 3. The directions of flexure crack propagation controlled by the sign of moment stress μ_{23}: (a) Mode I crack; (b) anti-crack.

5. Conclusions

Particulate materials such as rocks with granular microstructure and concrete permit relative rotations of the grains independent on their displacements. Therefore the criteria of crack propagation in such materials should include the grain (particle) rotations and the associated moment stresses. This is achieved by considering bending of the cement links/bonds between neighbouring particles caused by their relative rotation. The bending produces tensile stress on one side of the link, which eventually initiates a flexure crack (microcrack as seen from the scale of the propagating fracture). The initiation of the flexure crack leads to the link breakage and ultimately effects the particle detachment from the bulk of the material. The fracture mechanism based on link breakage and particle detachment is independent of the sign and source of the moment stress; only the side of the link where the flexural crack starts and the orientation/position of the link that is fractured first are affected. It is assumed that after the first link is broken the resistance to particle rotation is diminished sufficiently to permit breakage of other links and allow for the complete particle detachment. This criterion can explain the in-plane growth of Mode I and Mode II cracks as well as the anti-cracks (compaction bands).

Modelling of fracture propagation that involves moment stress requires the use of Cosserat (micropolar) continuum, which includes rotational degrees of freedom on top of the conventional translation ones. The Cosserat continuum possesses characteristic lengths that in the case of particulate materials with cement bonds/links between the particles are of the order of the particle size. Since the resolution of a continuum cannot be better than the microstructural length (the particle size in our case) the stress singularity at the crack tip only refers to the distances from the crack tip larger than the particle size and therefore larger than the Cosserat characteristic lengths. This leads to the concept of small-scale Cosserat continuum that is an asymptotics of small Cosserat lengths. This asymptotics formally leads to the Cosserat continuum with constrained rotations (the couple stress continuum). Modelling dislocations and Mode I and II cracks in such a continuum allows further simplification whereby the stress and moment stress distribution can directly be obtained from the displacement field produced by conventional dislocations and cracks by applying the relations of the couple stress theory. It was found that while the stresses have conventional square root singularity, the moment stresses have singularity of the power 3/2.

The actual fracture criterion is based on the stress and moment stress computed at a distance from the crack tip equal to the particle size (the Cosserat length). The tensile stress produced in the link/bond between particles by the moment stress is an order of magnitude higher than the one associated with the classical stress singularity. This suggests that the rotational mechanism of crack growth can actually supersede the traditionally perceived mechanism based on the tensile stress concentration only.

The flexure cracks formed in the process of particle rotations are seen at the scale of the crack as microcracks which are either coplanar to the main crack in the cases of Mode I crack or anti-crack or form en-echelon in the case of Mode II crack. The actual crack propagation is however caused by detachment (separation) of the particles from the bulk of the material and hence the appearance of en-echelon cracks is essentially a secondary effect accompanying the rotational mechanism of crack propagation.

Acknowledgements

The work has been supported by the Deep Exploration Technologies Cooperative Research Centre

whose activities are funded by the Australian Government's Cooperative Research Centre Programme. This is DET CRC Document 20**/***.

References

[1] Z. Reches, D.A. Lockner, Nucleation and growth of faults in brittle rocks. J. Geophys Res. 99B (1994) 18,159-18,173.
[2] A.M. Puzrin, L.N. Germanovich, S. Kim, Catastrophic failure of submerged slopes in normally consolidated sediments, Géotechnique, 54 (2004) 631-643.
[3] A.M. Puzrin, L.N. Germanovich, The growth of shear bands in the catastrophic failure of soils. Proceedings of the Royal Society: A - Mathematical, Physical and Engineering Sciences, 461 (2005) 1199-1228.
[4] S. Tembe, P. Baud, T.-f. Wong, Stress conditions for the propagation of discrete compaction bands in porous sandstone. J Geophys Res. 113 (2008) B09409.
[5] E. Townend, B.D Thompson, P.M Benson, P.G Meredith, P. Baud, R.P. Young, Imaging compaction band propagation in Diemelstadt sandstone using acoustic emission locations. Geophys Res Lett. 35 (2008), L15301.
[6] J. Fortin, S. Stanchits, G. Dresen and Y. Guéguen, Acoustic emission and velocities associated with the formation of compaction bands in sandstone. J Geophys Res., 111, B10 (2006) B10203.
[7] J. Fortin, S. Stanchits, G. Dresen and Y. Guéguen, Acoustic Emissions Monitoring during Inelastic Deformation of Porous Sandstone: Comparison of Three Modes of Deformation. Pure Appl. Geophys. 166 (2009) 823-841.
[8] R.A. Schultz, Scaling and paleodepth of compaction bands, Nevada and Utah. J Geophys. Res., 114, B3 (2009) B03407.
[9] R.H.C. Wong, Y.S.H. Guo, L.Y. Li, K.T. Chau, W.S. Zhu, S.C. Li, Anti-wing crack growth from surface flaw in real rock. Fracture of Nano and Engineering Materials and Structures, C8 (2006) 825-826.
[10] R.H.C. Wong, Y.S.H. Guo, L.Q. Liu, P.X. Liu, S.P. Ma, Nucleation and growth of anti-wing crack from tips of strike-slip flaw, in: Proceedings of the 42nd US Rock Mechanics Symposium (USRMS). San Francisco, Canada, 2008, pp. 221-229.
[11] A.N. Stavrogin, A.G. Protosenya, Plastichnost gornykh porod [Plasticity of rocks], Moscow, Nedra Press, 1979 (in Russian).
[12] D.A. Lockner, D.E. Moore, Z. Reches, Microcrack interaction leading to shear fracture, in: Proc. 33rd U.S. Symposium on Rock Mechanics, Rotterdam: Balkema (1992) pp. 807-816.
[13] Z. Reches, D.A. Lockner, Nucleation and growth of faults in brittle rocks. J. Geophys Res. 99B (1994) 18,159-18,173.
[14] A.V. Dyskin, L.N. Germanovich, A model of fault propagation in rocks under compression, in: Proc. *35th US Symposium on Rock Mechanics*, Balkema, Rotterdam and Brookfield (1995) pp. 731-738.
[15] J.W. Rudnicki, K.R. Sternlof, Energy release model of compaction band propagation. Geophys. Res. Let., 32 (2005) L16303.
[16] K.R. Sternlof, J.W. Rudnicki, D.D. Pollard, 2005. Anticrack inclusion model for compaction bands in sandstone. J Geophys Res., 110, B11 (2005) B11403.
[17] P. Eichhubl, J.N Hooker, S.E Laubach, Pure and shear-enhanced compaction bands in Aztec Sandstone. Journal of Structural Geology, 32 (2010) 1873-1886.
[18] Y. Kishino, C. Thornton, Discrete element approaches, in: M. Oda, K. Iwashita (Eds.), Mechanics of Granular Materials. An introduction. Balkema. Rotterdam, Brookfield (1999) 147-223.

[19] J. Desrues, G. Viggiani, Strain localization in sand: an overview of the experimental results obtained in Grenoble using stereophotogrammetry. Int. J. Numer. Anal. Meth. Geomech., 28 (2004) 279–321.
[20] A. Rechenmacher, S. Abedi, O. Chupin, Evolution of force chains in shear bands in sands. Geotechnique, 60 (2010) 343–351.
[21] R.D. Mindlin, Tiersten, H.F., Effects of couple-stresses in linear elasticity. Archive of Rational Mechanics and Analysis 11 (1962) 415–448.
[22] W.T. Koiter, Couple-stresses in the theory of elasticity. Parts I and II. Proceedings of the Koninklijke Nederlandse Akademie van Wetenschappen B67 (1964) 17–44.
[23] R.A. Toupin, Perfectly elastic materials with couple stresses. Archive of Rational Mechanics and Analysis 11 (1962) 385–414.
[24] E. Sternberg, R. Muki, The effect of couple stress on the stress concentration of a crack. Int. J. Solids Struct., 3 (1967) 69-95.
[25] C. Atkinson, F.F. Leppington, The effect of couple stresses on the tip of a crack. *Int. J. Solids Structures*, 13 (1977) 1103-1122.
[26] N.F. Morozov, Mathematical Issues of the Crack Theory, Nauka, Moscow (in Russian), 1984.
[27] P.A. Gourgiotis, H.G. Georgiadis, An approach based on distributed dislocations and disclinations for crack problems in couple-stress elasticity. Intern J Solids and Struct. 45 (2008) 5521–5539.
[28] G.K. Batchelor, Transport properties of two-phase materials with random structure. Annal. Rev. Fluid Mech., Palo Alto, California Ann. Rev., Inc., 6 (1974) 227-255.
[29] A.V. Dyskin, E. Pasternak, Rotational mechanism of in-plane shear crack growth in rocks under compression, in: Y. Potvin, J. Carter, A. Dyskin, R. Jeffrey (Eds.) Proc. 1st Southern Hemisphere International Rock Mechanics Symposium SHIRMS 2008, Australian Centre for Geomechanics, 2008, 2, pp. 111-120.
[30] E. Pasternak, A.V. Dyskin, Intermediate asymptotics for scaling of stresses at the tip of crack in Cosserat continuum, in: Proc. 12th Intern. Conf. Fracture ICF12, Ottawa, 2009. Paper T40.014.
[31] A.V. Dyskin, E. Pasternak, Cracks in Cosserat continuum – Macroscopic modelling, in: G.A. Maugin, A.V. Metrikine (Eds.) Mechanics of Generalized Continua: One hundred years after the Cosserats. Springer series "Advances in Mechanics and Mathematics", Vol. 21 (2010). Springer, New York, 35-42.
[32] E. Pasternak, H.-B. Mühlhaus, A.V. Dyskin, On the possibility of elastic strain localisation in a fault, Pure Appl. Geophys. 161 (2004) 2309-2326.
[33] A.V. Dyskin, Crack growth criteria incorporating non-singular stresses: Size effect in apparent fracture toughness. Intern. J. Fracture, 83 (1997) 191-206.
[34] W. Nowacki, The linear theory of micropolar elasticity, in: W. Nowacki and W. Olszak (Eds.), Micropolar Elasticity, 1974, Wien, New York: Springer - Verlag, 1-43.
[35] B.A. Bilby, J.D. Eshelby, Dislocation and the Theory of Fracture, in: *Fracture, An Advanced Treatise*, edited by H. Liebowitz, Vol. I, Microscopic and Macroscopic Fundamentals, 1968, Academic Press, New York and London, 99-182.
[36] P.A. Gourgiotis, H.G. Georgiadis, Distributed dislocation approach for cracks in couple-stress elasticity: shear modes. Intern. J. Fracture, 147 (2007) 83-102.
[37] P.A. Gourgiotis, H.G. Georgiadis, M.D. Sifnaiou, Couple-stress effects for the problem of a crack under concentrated shear loading. Mathematics and Mechanics of Solids, 17 (2011) 433-459.
[38] V.A. Lubarda, The effects of couple stresses on dislocation strain energy. Intern. J. Solids and Struct., 40 (2003) 3807-3826.
[39] V. Kobelev, Mircopolar model of fracture for composite material. Meccanica, 41 (2006) 653-660.

Simulation of Damage and Crack Propagation in Three-Point Bending Asphalt Concrete Beam

Guowei Zeng[1,2,*], **Xinhua Yang**[1], **Fan Bai**[1] **Anyi Yin**[1]

[1] School of Civil Engineering and Mechanics, Huazhong University of Science and Technology, 430074, China
[2] Hubei Province Key Laboratory of Systems Science in Metallurgical Process, Wuhan University of Science and Technology, 430065, China
* Corresponding author: zengguow@126.com

Abstract A brittle damage-based constitutive model is proposed to characterize the crack initiation and propagation behavior of asphalt mastic under low temperature. The fracture criterion is regarded as a dominant of damage. For asphalt concrete combining aggregate and asphalt mastic, a 2D finite element model including the aggregate generation and packing algorithm and Usermat subroutine technique is developed to perform the crack initiation and propagation. A series of FE simulations are performed to evaluate effects of crack location on crack propagation of asphalt concrete. The numerical results are validated by comparison with the corresponding experiments and other result which based on fracture criterion of maximum circumferential tensile stress. The model and method are proved to be rational and capable of describing the cracking behavior of asphalt concrete with different crack location.

Keywords Asphalt concrete, Three-Point Bending Beam, Numerical Simulation, Brittle Damage, Crack

1. Introduction

Crack is the one of most common distresses of asphalt materials and reduces the road service capacity. Furthermore it also allow for the infiltration of moisture, which result in a rapid deterioration of the pavement structure. It can be suggested that heterogeneity of composites affected its fracture behavior and leading to a significant complexity in crack propagation analysis [1]. The mechanism of crack growth and evaluation of the characterization of fractured pavement structure generally are the fundamental problems in the pavement engineering. They have been more widely focused and studied by the researchers and engineers in recently years [2-5]. The fracture resistance of asphalt concrete significantly influences the service life of asphalt pavements and consequently the maintenance of the pavement network.

Numerous researchers [6-8] proved that the mechanical properties of asphalt concrete are significantly affected by micro structural details and some material parameters, including asphalt content, aggregate type, gradation of aggregate particles, distribution and orientation of aggregates, void ratio, and so on. According to combination of the micromechanical properties of asphalt concrete and heterogeneity, the mechanism cracking behavior for asphalt concrete can be simulated more accurately by construct the micromechanical model containing information about its components and microstructures. For this aim, the current study presents an approach based on the CDM, which considers the concrete heterogeneity.

Asphalt concrete can be described as a multiphase material containing coarse aggregates, mastic cement(including asphalt binder and fine aggregates), and air voids. In this method, the numerical sample model is constructed by replacing the irregular aggregate geometry to resemble real polygon, circle, elliptical and so on. The aggregate content, gradation and some structural parameters, aggregates are generated and randomly located in a prescribed region. Then the generations are assigned to coarse aggregates and the rest region to the mastic. With this method the mechanical properties and fracture of asphalt concrete were evaluated by Xu et al. in[9], Yang et al. in[10] and Yin et al. in[11, 12]. Especially Yin et al. [11, 12] successfully applied the numerical sample model method to investigate the gestation and propagation of the crack in two-dimensional models including three-point bending asphalt mixture beam with pre-crack and uniaxial tensile

beam.

Accurate failure predictions can only be obtained if microstructural damage is taken into account in the fracture modelling. This requirement has led to the development of the so-called local or continuum approaches to fracture, in which fracture is regarded as the ultimate consequence of the material degradation process. This paper employ the user defined material technique in FEM directly, a constitute equations of damage model which cover the all potential failure area are developed. The damage model allows damage assessments at every point of a structure for any geometry or loading, as long as the damage mechanisms and stress-strain curve are known. This paper is an attempt to advance our understanding of relationship between crack path and microstructure features as they apply to damage evolution in three point bending asphalt bending beam.

The objective of this paper is to propose a fracture criteria based on damage model for investing cracking behaviors of the three point bending test of asphalt concrete beam. The proposed damage model is implemented in the commercial finite element analysis software Ansys via the user defined subroutine UPFs .The numerical simulation compared with the experimental results to validate our present criterion. The results show that the proposed criterion reasonably predicts the crack growth initiation in different pre-crack locations and aggregate distributions.

2. Random heterogeneous modeling for asphalt concrete

2.1. Brittle damage model for asphalt mastic

For the case of isotropic damage evolution，continuum damage mechanics（CDM）introduces a field variable to represent the damage in a continuum sense. In this paper, this concept has later been used to model the initiation and growth of cracks. By assuming homogeneous distribution of micro voids and the hypothesis of strain equivalence, which states that the strain behavior of a damaged material is represented by constitutive equations of the virgin material (without damage) in the potential of which the stress is simply replaced by the effective stress

$$\tilde{\sigma} = \frac{\sigma}{1-D} \tag{1}$$

where σ is the stress tensor for the undamaged material. And the corresponding scalar damage variable $D = 1 - E_D / E_0$, in which E_D is the effective elastic modulus of the damaged materials, E_0 is the elastic constant of the virgin material and D has a range from 0 to 1, D=0 means that material is intact ,while D=1 means that material is damaged completely.

The another form of the effective stress can be given by

$$\sigma = E_0(1-D)\varepsilon \tag{2}$$

Extended the model to three-dimensional form, such that:

$$\sigma_{ij} = E_{ijkl}(1-D)\varepsilon_{kl} + \frac{D}{3}\delta_{ij}E_{\rho\rho kl}\varepsilon_{kl} \tag{3}$$

Written it to the form of matrix, the constitute law is

$$\boldsymbol{\sigma} = \tilde{D}\boldsymbol{\varepsilon} \tag{4}$$

where $\tilde{D}$ is elastic damage stiffness matrix which is relative to the elastic modulus E, poisson ratio v and scalar damage variable D which is expressed as

$$\bar{\mathbf{D}}^{0}=\frac{E}{1+\mu}\begin{bmatrix} B & A & A & 0 & 0 & 0 \\ A & B & A & 0 & 0 & 0 \\ A & A & B & 0 & 0 & 0 \\ 0 & 0 & 0 & C & 0 & 0 \\ 0 & 0 & 0 & 0 & C & 0 \\ 0 & 0 & 0 & 0 & 0 & C \end{bmatrix} \tag{5}$$

where

$$A=\frac{\mu}{1-2\mu}+\frac{D}{3} \tag{6}$$

$$B=\frac{1-\mu}{1-2\mu}-\frac{2D}{3} \tag{7}$$

$$C=\frac{1-D}{2} \tag{8}$$

The Mazars and Pijaudier-cabot[13] had described the damage behavior of quasi-brittle materials like concrete and rock by equal strain, this paper follows their suggestion and the definition of equal total strain is

$$\varepsilon=\sqrt{\sum_{i}^{3}\left(\left\langle \varepsilon_i \right\rangle\right)^2} \tag{9}$$

where ε_i are the principal strains. For bituminous material the damage is only related to the tensile strain, so it is supposed that the damage is induced only by tensile strains in this paper. Then specify strain $\left\langle \varepsilon_i \right\rangle=\varepsilon_i$ if $\varepsilon_i>0$ and $\left\langle \varepsilon_i \right\rangle=0$ otherwise.

The damage parameter D starts at a damage threshold level $\varepsilon=\varepsilon_f$ and is updated during damage growth which occurs according to an evolution law such that $D=D(\varepsilon)$, which can be determined from the uniaxial tests. a linear elastic behavior has been sustained up to a peak tensile strength point $\sigma_t=E\varepsilon_f$ which is illustrated in Fig. 2(a), then the stress-strain curve followed by descending branch up to a strain ε_u at which the load-carrying capacity is exhausted(and thus $D=1$), so the proposed damage evolution law reads:

$$D(\varepsilon)=\begin{cases} 0 & 0<\varepsilon\le\varepsilon_f \\ \dfrac{\varepsilon_u(\varepsilon-\varepsilon_f)}{\varepsilon(\varepsilon_u-\varepsilon_f)} & \varepsilon_f<\varepsilon<\varepsilon_u \end{cases} \tag{10}$$

where ε_f , ε_u represent strain for threshold of damage and strain for critical of damage respectively. Fig. 2(b) illustrates the damage evolution curve.

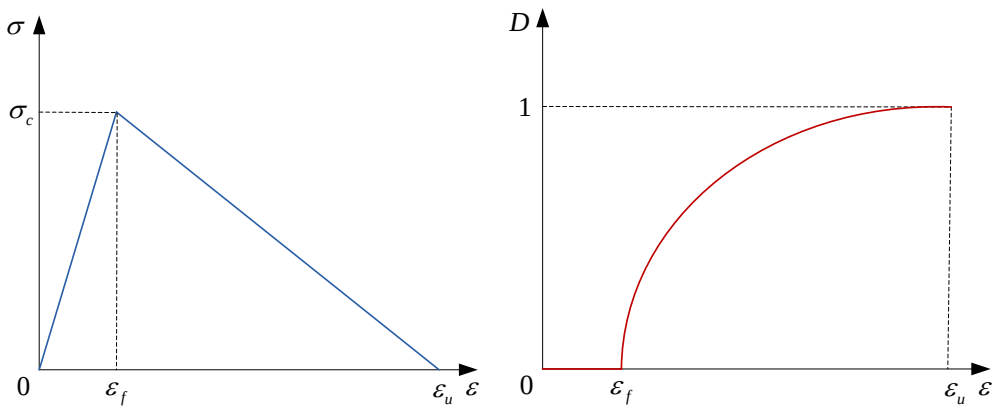

(a)curve of stress-strain (b)curve of damage evolution
Fig. 2 curves of the proposed damage model

2.2. Aggregate generation and packing algorithm

Utilizing a self-compiled algorithm, all spheric aggregates (or round aggregates for 2D) are converted into their corresponding inscribed polyhedra (or regular polygons). The detail of the algorithm was described in the work of Yin et al. [11, 12]. For convenience, the somplete aggregate gradation listed in Table 1 was treated as a simplified aggregate gradation listed Table 2.
Two 2D mesostructural asphalt concrete specimens of different coarse aggregate distributions with the gradation simplified aggregate are created by the generation and packing algorithm, shown in Fig.1 (a) and (b), respectively. In those two figures, the black region represents asphalt mastic and the white regular octagons are graded coarse aggregates.

Table 1. Complete aggregate gradation

Sieve size (mm)	16.0	13.2	9.5	4.75	2.36	1.18	0.6	0.3	0.15	0.075
Passing rate (%)	100	98.1	80.8	52.2	34.1	27.5	20.6	14.1	9.9	7.7

Table 2. Simplified aggregate gradation

Sieve size (mm)	16.0	13.2	9.5	4.75	2.36
Passing rate (%)	100	98.1	80.8	52.2	34.1

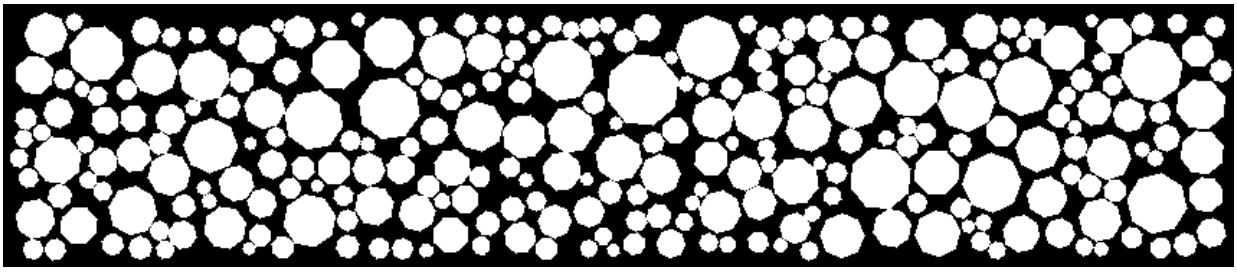

（a）

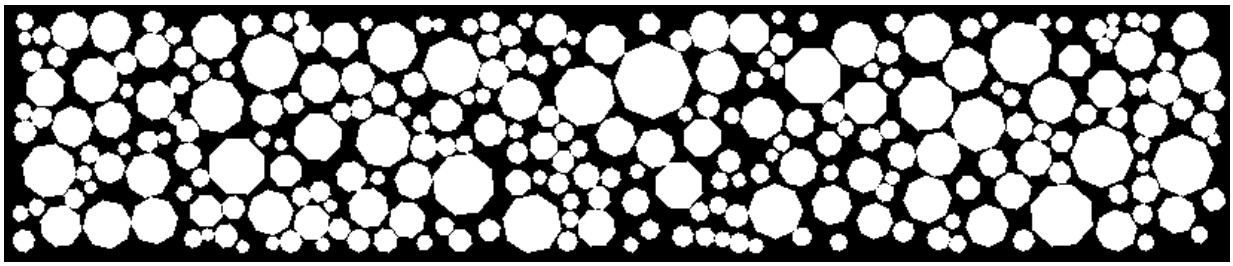

（b）
Figure. 1 Two 2D numerical specimens of asphalt concrete

2.3. The finite analysis using damage mechanics for asphalt concrete

The asphalt mastic is assigned to obey an elastic damage constitute law which implemented into the FEM software. A USERMAT subroutine defining the damage elastic material property is coded using the FORTRAN language. Then it is compiled and integrated into the main program by a user defined variable can save the value of damage.

A series of 2D asphalt concrete samples with the dimensions of 150mm×50mm and coarse aggregate gradation shown in Table 2 are modeled. The element we used is 8-node plane183 and the asphalt concretes are treated as composite materials in which component of coarse aggregates which is assigned to elastic material property and asphalt mastic which is assumed to be elastic damage material. The aggregate generation and packing algorithm is used to create its micromechanical asphalt concrete with coarse aggregate, the rest region is modeled as the asphalt mastic. Three point bending experiments are virtually performed. The material properties of coarse aggregate and asphalt mastic are needed to assign independent material parameters. In general, aggregates are linearly elastic, but asphalt mastic is effected by the temperature. In the current paper the asphalt mastic is assumed to be elastic and brittle damaged since temperature is enough low [12], although viscoelasticity in the matrix has been considered in higher temperature. Therefore the detailed parameters of asphalt mastic and coarse aggregates are listed in the Table 3.

Table 3. List of material parameters at T=5℃

Elastic damage model for asphalt mastic			
$E(GPa)$	ν	ε_f	ε_u
0.612	0.35	0.002	0.07
Elastic model for coarse aggregate			
$E(GPa)$		ν	
40		0.15	

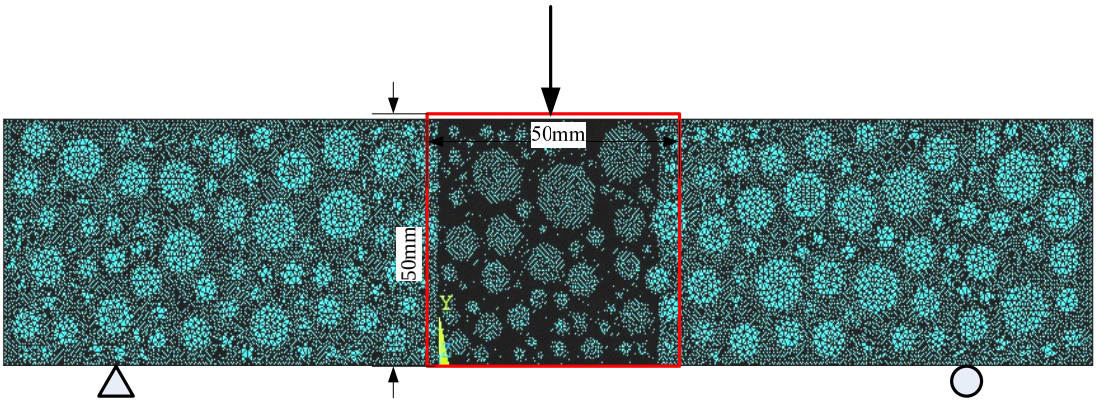

(a) Mesh configuration of the whole beam

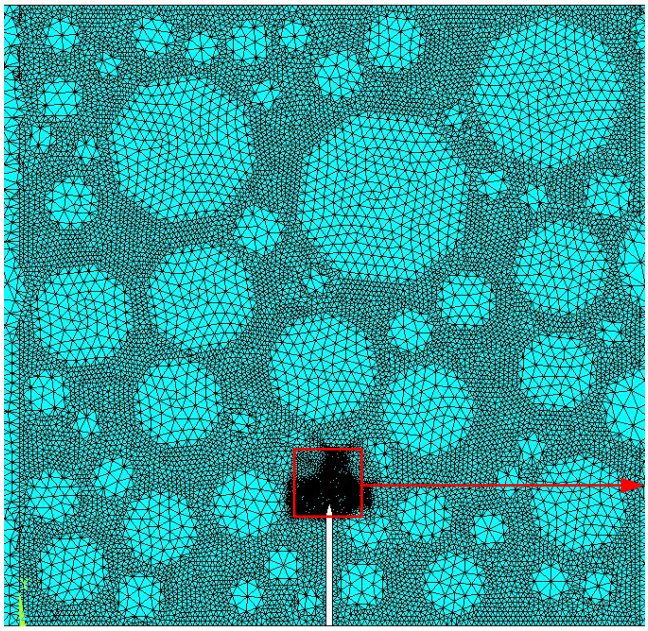

(b) Mesh in the mesoscale region

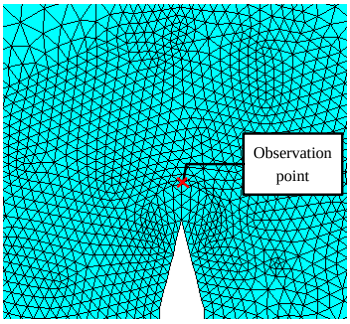

(c) Mesh near the crack tip

Figure 2. Mesh configuration of the three-point bending beam specimen with a central crack

The fracture of asphalt concrete is mainly due to accumulation and coalescence of microscopic cracks existing or induced by load. One of the features of fracture investigation is the proposed criterion for crack growth initiation. By introducing a damage variable in the constitutive relation, the element fractures and a crack occurs when the fracture threshold within the elements is reached in the numerical simulation. Namely the propagation of crack is the migration of damage zone where are equal to the critical damage value gradually for the material of around crack tip. In this paper, the crack is assumed to only grow in asphalt mastic since mastic stiffness weaker than coarse aggregates several quantities and fracture criterion is given based on damage value as follows:

$$D = D_c \tag{11}$$

Once the damage value near the crack tip reaches its critical value D_c, the fracture occurs and propagates. D_c =0.85, which is referred to the results given by Sun et al. [14].

3. Results and discussion

In order to investigate the effect of crack location, several RVEs with three different crack locations were cut from the actual size model: a center crack, a 20mm off-center crack and a 40mm off-center crack are plotted in Fig. 9. By increasing the loading step, the damage around the crack tip will grow until eventually the first element will reach to the critical damage parameter, D_c. At this stage the new crack tip coordinates will be determine by a self-compiled searching program and the crack will advance as much as the new crack tip point. This progress continues until final failure of the specimen.

The experimental [12] and numerical crack paths of three crack locations are plotted in Fig.3 and Fig. 4, the simulation results showed good agreement with the experimental paths. Due to the similar coarse aggregate distribution, the simulation results were similar to the results computed by the fracture criterion based on the maximum circumferential tensile stress especially. The damage-based fracture criterion is validated to feasible by the comparison. Furthermore, the paths of this paper predicted showed agreement with the experimental paths more closely than the curves given by Yin et al. [12] in some regions. Then it can be proved the effect of aggregate is more significant to the damage evolution. Form total comparison it can be seen the father the crack is away from the beam center, the larger its kinking angle is. But the crack trends to grow towards to the beam top midspan.

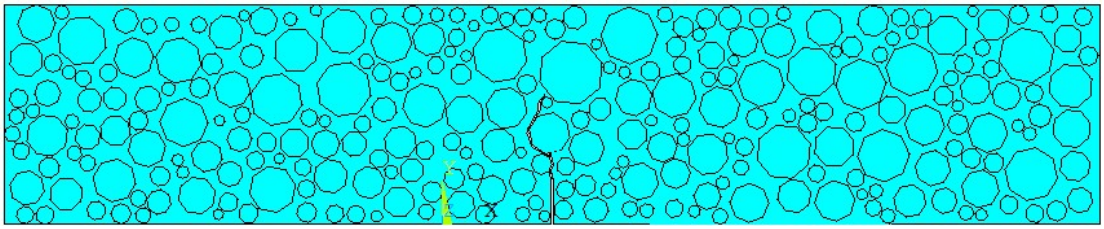

(a) Actual size FEM model for crack location 0mm

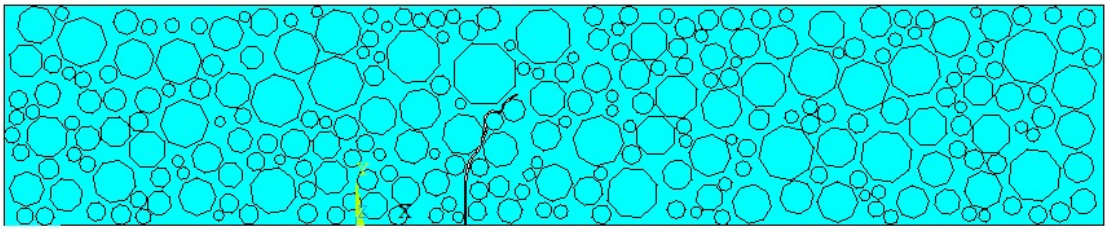

(b) Actual size FEM model for crack location 20mm

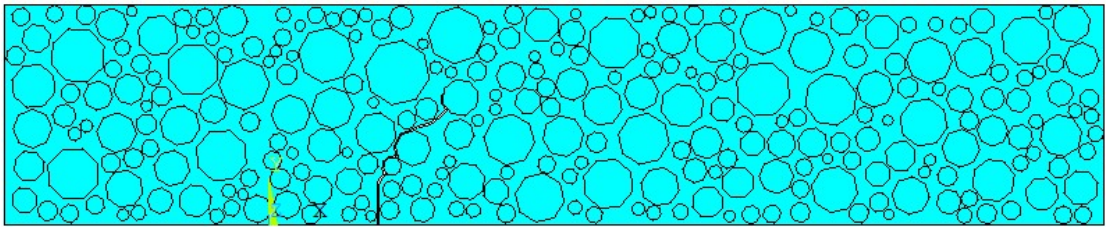

(c) Actual size FEM model for crack location 40mm

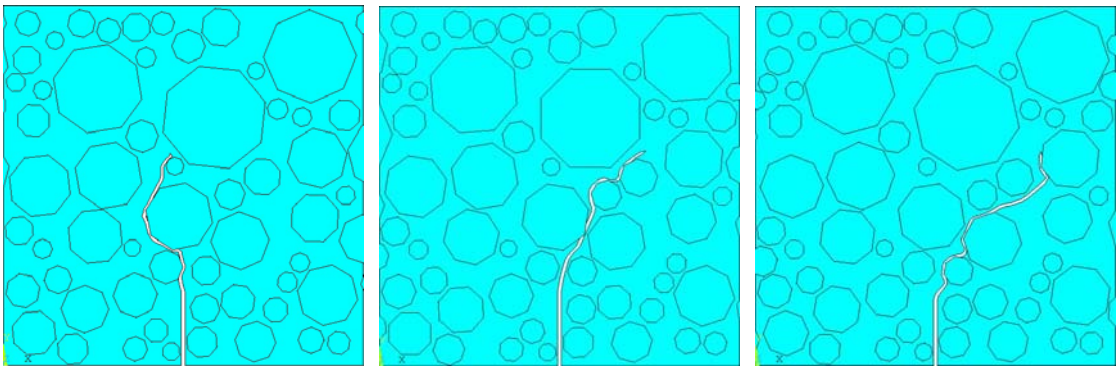

(d) RVEs for 0mm (e) RVEs for 20mm (f) RVEs for 40mm

Figure 3. Crack paths for different crack location

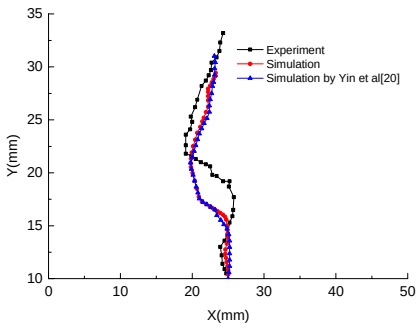

(a) 0mm off-center crack

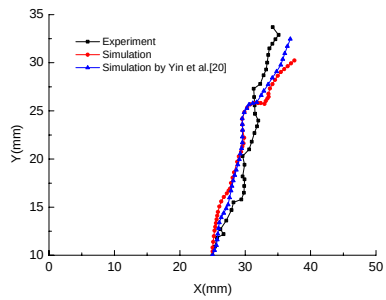

(b) 20mm off-center crack

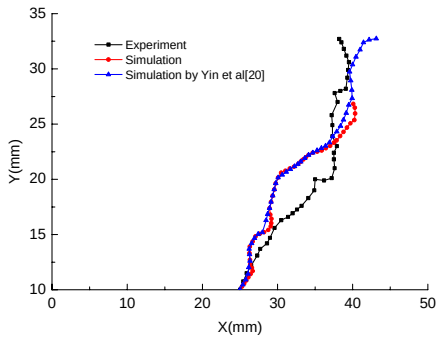

40mm off-center crack

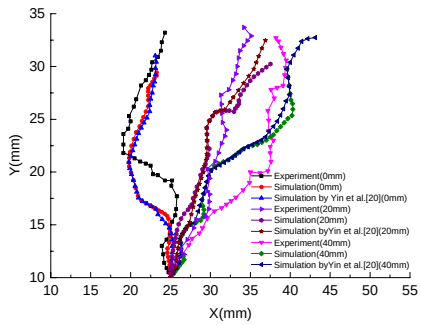

Total merged plot for three crack locations

Figure 4. Experimental and numerical crack paths of three kinds of crack

A numerical two-dimensional micromechanical modeling frame considering the heterogeneity feature has been developed to simulate the cracking behavior of asphalt concrete based on the aggregate generation and packing algorithm. Incorporating a damage mechanics approach with this solution allowed the development of a softening model capable of predicting typical global inelastic behavior found in asphalt materials, the proposed model used to compare between the computer simulated results and experimental data of the cracked three-point bending beam, the results showed that the overall agreement is satisfactory.

Acknowledgements

This work is supported by the National Natural Science Foundation of China (Grant No.

10872073 and Grant No. 51004079), National Basic Research Program of China (973 Program: 2011CB013800) and the Hubei Province Key Laboratory of Systems Science in Metallurgical Process of China (Program: Y201119).

References

[1]. Yang, Z.J., et al., Monte Carlo simulation of complex cohesive fracture in random heterogeneous quasi-brittle materials. International Journal of Solids and Structures, 2009. 46(17): p. 3222-3234.

[2]. Birgisson, B., et al., Determination and prediction of crack patterns in hot mix asphalt (HMA) mixtures. Engineering Fracture Mechanics, 2008. 75(3): p. 664--673.

[3]. Evangelista Jr, F., J.R. Roesler and S.P. Proen C C A, Three-dimensional cohesive zone model for fracture of cementitious materials based on the thermodynamics of irreversible processes. Engineering Fracture Mechanics, 2012.

[4]. Portillo, O. and D. Cebon, Experimental and Numerical Investigation of Fracture Mechanics of Bitumen Beams. Engineering Fracture Mechanics, 2012.

[5]. Tschegg, E.K., M. Jamek and R. Lugmayr, Fatigue crack growth in asphalt and asphalt-interfaces. Engineering Fracture Mechanics, 2011. 78(6): p. 1044--1054.

[6]. Airey, G.D., A.E. Hunter and A.C. Collop, The effect of asphalt mixture gradation and compaction energy on aggregate degradation. Construction and Building Materials, 2008. 22(5): p. 972-980.

[7]. Liu, Q. and D. Cao, Research on material composition and performance of porous asphalt pavement. Journal of Materials in Civil Engineering, 2009. 21(4): p. 135-140.

[8]. Shen, D., M. Kuo and J. Du, Properties of gap-aggregate gradation asphalt mixture and permanent deformation. Construction and Building Materials, 2005. 19(2): p. 147-153.

[9]. Xu, R., et al., A three-dimensional aggregate generation and packing algorithm for modeling asphalt mixture with graded aggregates. Journal of Mechanics, 2010. 26(2): p. 165-171.

[10]. Yang, S.F., et al., Three-Dimensional Numerical Evaluation of Influence Factors of Mechanical Properties of Asphalt Mixture. Journal of Mechanics, 2012. 28(03): p. 569--578.

[11].Yin, A., et al., Tensile fracture simulation of random heterogeneous asphalt mixture with cohesive crack model. Engineering Fracture Mechanics, 2012.

[12].Yin, A., et al., Multiscale fracture simulation of three-point bending asphalt mixture beam considering material heterogeneity. Engineering Fracture Mechanics, 2011. 78(12): p. 2414--2428.

[13].Mazars, J. and G. Pijaudier-Cabot, Continuum damage theory - application to concrete. Journal of Engineering Mechanics, 1989. 115(2): p. 345-365.

[14]. Sun, Y., J. Liu and T. Yu. Coupling analysis of fracture mechanics and damage mechanics for fiber-reinforced asphalt concrete pavement. in 2006 ASME International Mechanical Engineering Congress and Exposition, IMECE2006, November 5, 2006 - November 10, 2006. 2006. Chicago, IL, United states: American Society of Mechanical Engineers.

A New LEFM Based Description of Concrete Fracture and Size Effects

Kim Wallin

VTT Materials and Built Environment, P.O. Box 1000, FI-02044 VTT, Espoo, Finland
Kim.Wallin@vtt.fi

Abstract Concrete is a so called quasi-brittle material which, despite predominantly elastic material response, exhibits in tension loading a stable non-linear fracture response, when tested under displacement control. The reason for the non-linearity is the development of a fracture process zone, in front of the crack, due to micro-cracking and crack bridging. It has become increasingly popular to model the fracture process zone with different cohesive zone models. However, their use requires sophisticated finite element modeling and their success is directly related to the correctness of the assumed stress relaxation in the fracture process zone. An alternative is to use LEFM combined with an effective crack length. The effect of the fracture process zone is to make the specimen sense the crack as being longer than $a_0+\Delta a$. The fracture process zone causes thus an effective increase in the crack driving force but also the apparent fracture resistance increases since the fracture process zone effectively "blunts" the crack tip. This simple method, that does not require any finite element modeling, can be used as an aid to select the proper cohesive zone model for more sophisticated modeling.

Keywords Concrete fracture, size effect, fracture toughness, quasi-brittle materials, K-R.

1. Introduction

Concrete is a so called quasi-brittle material which, despite predominantly elastic material response, exhibits in tension loading a stable non-linear fracture response, when tested under displacement control (Fig. 1 [1]). The reason for the non-linearity is the development of a fracture process zone, in front of the crack, due to micro-cracking and crack bridging. An excellent review of the physical fracture process of concrete has been given in e.g. [2] and need not be covered here in any more detail. Here, the focus is on the fracture mechanical description of the effect of the fracture process zone on the structural behavior of the test specimen and prediction of size effects.

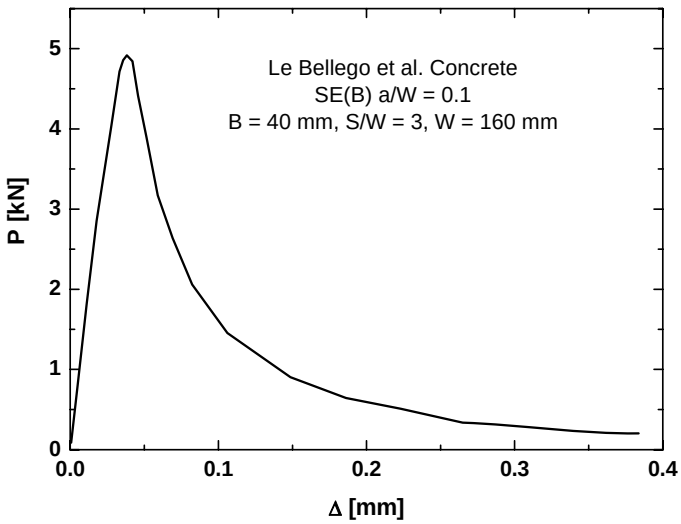

Figure 1. Example of a typical load-displacement relationship for concrete in a SE(B) fracture toughness test [1].

The cracking of concrete is schematically presented in Fig. 2. The shaded area in Fig. 2, relates to the micro-cracked material. The part of the micro-cracked material, lying in front of the macroscopic crack (including initial crack length a_0 and extended crack Δa), constitutes the active fracture process zone. In this region the material cohesion is weakened due to the micro-cracking. The effect of the fracture process zone is to make the specimen sense the crack as being longer than $a_0+\Delta a$. The fracture process zone causes thus an effective increase in the crack driving force. The effect of the fracture process zone is similar in nature to the Irwin plasticity correction [3] for metals.

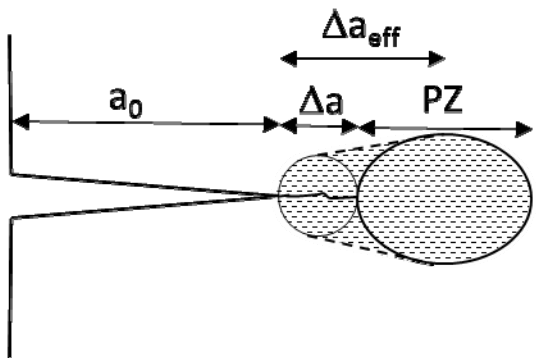

Figure 2. Schematic presentation of the fracture process of concrete. The initial crack length is a_0 and the macroscopic extended crack is Δa. PZ is the size of the active fracture process zone.

The part of the micro-cracked material that becomes engulfed in the crack wake, is no longer actively affecting the crack driving force, but it has absorbed energy related to the micro-crack surfaces. This has the effect of increasing the materials effective fracture resistance (Fig. 3).

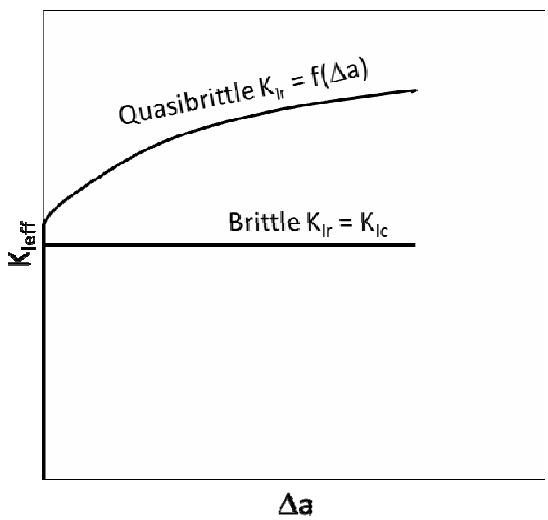

Figure 3. Schematic definition of the difference between an ideally brittle and a quasi-brittle material.

Often, fracture toughness tests of concrete are actually assessed by estimating an effective stress intensity factor and effective crack length [4], to derive an effective K-R curve in line with the ASTM E561 – 10 test standard [5]. This procedure is, however, not widely used, partly due to the question regarding the significance of the effective crack length and effective crack driving force. Another method called the double-K or double-G criterion is based on the estimate of the stress intensity at the onset of first crack extension (with a non-developed fracture process zone) and the

stress intensity corresponding to maximum load in the test [4]. This method is really an improvement of the classical tests where the maximum load has been combined with the initial crack length (a_0) to obtain a nominal fracture toughness value. The challenge with the double-K criterion lies in the reliable detection of the moment of crack initiation, which is almost invisible on the load-displacement record. Also, the estimation of the crack length at maximum load contains an experimental challenge and the necessity to combine both estimates of the crack tip displacement and load displacement. This prevents the method from becoming a simple quality assurance type of fracture toughness estimate.

As a compromise to the use of the classical nominal load maximum stress intensity factor, a special size effect expression has been proposed by Bažant. (See e.g. [6]). The Bažant size effect expression is versatile and has been shown to describe well the size effect in load maximum values of concrete and other quasi-brittle materials. The Bažant size effect expression for load maximum (P_{max}) can be expressed in the form of Eq. (1). B and W denote the fracture toughness specimen thickness and width and σ_f corresponds to the tensile stress of the material. The constant c accounts for specimen geometry and W_0 is a normalizing constant. The constants c and W_0 are determined by fitting to test results from different size specimens of identical geometry. Apparently the only weakness with the size effect expression is that a comparison between different loading geometries is not possible without the inclusion of additional fitting parameters [7].

$$\frac{P_{\max}}{B \cdot W} = \frac{c \cdot \sigma_f}{\sqrt{1 + \frac{W}{W_0}}}, \tag{1}$$

Here, a LEFM based estimate of the effective stress intensity factor and the effective crack growth at maximum load in a fracture mechanics test is used to obtain a simple power law approximation of the effective K-R curve that is applicable to the description of not only different size specimens, but also specimens with varying geometry.

2. Estimate of Maximum Load

In the case of metals, the materials tearing resistance is usually well described with a simple power law expression. Assuming, that the evolution of the fracture process zone and its effect on the effective materials fracture resistance behaves similarly to metals, also the effective stress intensity factor as a function of the effective crack growth should be possible to approximate with a power law in the form of Eq. (2).

$$K_{Ieff} \approx K_{1mm} \cdot \Delta a_{eff}^{m}, \tag{2}$$

For metals, when the tearing resistance is expressed in J-integral units, the power m is close to 0.5 or less. Thus, in K units the power should be in the vicinity of 0.25. If the fracture process zone size is very small compared to the crack growth, Δa, the power m will be small. If it is large compared to Δa, the power m should be closer to 0.25 or even above. When the relation between crack growth and fracture process zone no longer exists, the power m is expected to grow uncontrollable. This is not, however, expected to occur until well beyond the maximum load value.

The effective stress intensity factor is related to load and the effective crack length by Eq. (3).

$$K_{Ieff} = \frac{P}{B \cdot \sqrt{W}} \cdot f\left(\frac{a_0 + \Delta a_{eff}}{W}\right), \tag{3}$$

Eq. (3) differs from the classically used nominal stress intensity factor, which is calculated using only the initial crack size (a_0). The nominal stress intensity factor under-predicts the true effective crack driving force and should not be used in the assessment of quasi-brittle materials.

Combining Eqs. (2) and (3) leads to a relation between load and effective crack growth, Eq. (4).

$$P = \frac{K_{1mm} \cdot \Delta a_{eff}^{m} \cdot B \cdot \sqrt{W}}{f\left(\frac{a_0 + \Delta a_{eff}}{W}\right)}, \tag{4}$$

When the derivative of Eq. (4) (dP/da) is 0, the load and effective crack length correspond to maximum load. This leads to the relation between power m and effective crack extension in the form of Eq. (5) [8].

$$m = \frac{\Delta a_{effP\max}}{W} \cdot \frac{f'\left(\frac{a_0 + \Delta a_{effP\max}}{W}\right)}{f\left(\frac{a_0 + \Delta a_{effP\max}}{W}\right)}, \tag{5}$$

Eq. (5) is general and can be applied to any geometry for which the shape function f(a/W) is known. A numerical inversion of Eq. (5) is quite simple. One can tabulate a set of a_0, m and $\Delta a_{effPmax}$ values for a desired geometry and then a specific equation may be fitted to the data, or the information can be interpolated from the table. As an example, the solutions for the standard SE(B) and C(T) specimens are shown graphically in Figs 4a and b. An approximate solution for the standard SE(B) specimen with span width S/W = 4 is given by Eq. (6) and for the standard C(T) specimen with H/W = 0.6 is given in Eq. (7).

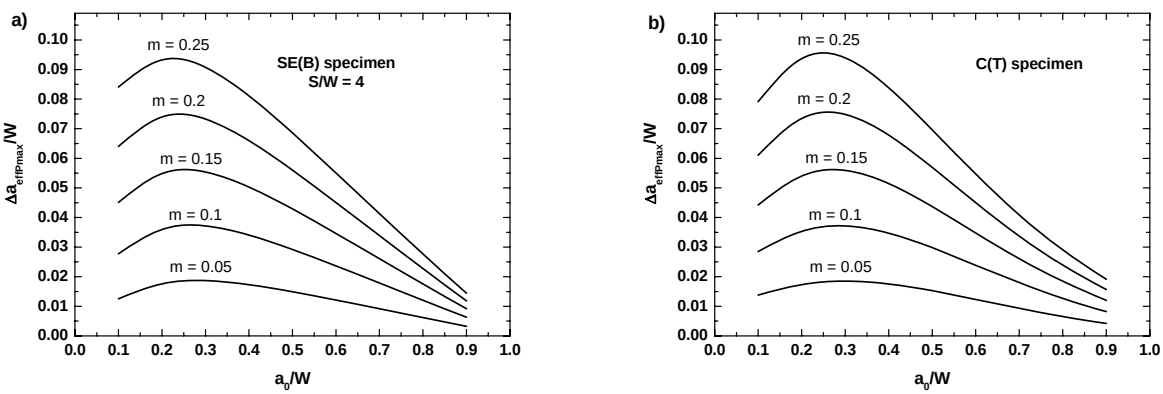

Figure 4. Effective crack growth corresponding to maximum load for standard SE(B) and C(T) specimens

$$\frac{\Delta a_{effP\max}}{W} \approx \frac{0.001118 + \left(\frac{a_0}{W}\right)^2 \cdot m - \left(\frac{a_0}{W}\right) \cdot m}{0.3886 \cdot \mathrm{m} - 0.1963 - \left(\frac{a_0}{W}\right) - 2.147 \cdot \left(\frac{a_0}{W}\right) \cdot \mathrm{m}} \qquad \left[\frac{S}{W} = 4, \frac{a_0}{W} \geq 0.1\right], \tag{6}$$

$$\frac{\Delta a_{effP\max}}{W} \approx \frac{m \cdot \sqrt{\frac{a_0}{W}}}{0.1542 + 8.063 \cdot \left(\frac{a_0}{W}\right)^2 \cdot m + exp\left\{2.94 \cdot \left(\frac{a_0}{W}\right)^2\right\} - 0.8219 \cdot m} \qquad \left[\frac{H}{W} = 0.6, \frac{a_0}{W} \geq 0.1\right], \tag{7}$$

It is important to note that Eqs. (6) and (7) are applicable only for standard specimen geometries. Especially in the case of the SE(B) specimen often different S/W ratios are used in the tests. For such tests, the standard f(a/W) expression can be adjusted e.g. by Eq. (8) [9] to be used together with its derivative in Eq. (5).

$$\mathrm{f}\left(\frac{\mathrm{a}}{\mathrm{W}}\right)_{\mathrm{S/W}} = \mathrm{f}\left(\frac{\mathrm{a}}{\mathrm{W}}\right)_{\mathrm{S/W=4}} \cdot \left\{1 + \left(1 - \frac{4\mathrm{W}}{\mathrm{S}}\right)\left(0.08\left(1 - \frac{\mathrm{a}}{\mathrm{W}}\right) + 0.24\left(1 - \frac{\mathrm{a}}{\mathrm{W}}\right)^2 - 0.28\left(1 - \frac{\mathrm{a}}{\mathrm{W}}\right)^3\right)\right\}, \tag{8}$$

The analysis consists of solving the power m and K_{1mm} iteratively by combining Eqs (4) and (5) to provide the correct maximum load values for different size and/or geometry specimens. The result is obtained in the form of the effective K-R curve in the form of Eq. (2) which then can be used for the evaluation of other geometries. For a constant geometry and fixed initial crack size ratio (a_0/W), the effective crack growth is directly related to the specimen width (W).

The proposed method relies on the assumption that the effective K-R curve up to maximum load can be approximated by a simple power law. Karihaloo and Nallathambi [10] collected a large number of SE(B) data and estimated from the experimental load-displacement traces, the relation between initial crack length and the effective (based on effective compliance) crack length corresponding to maximum load. Their results have been reproduced in Fig. 5.

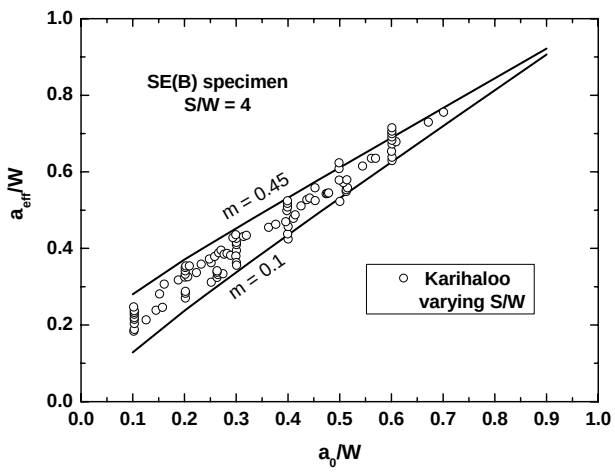

Figure 5. Estimate of effective crack length at maximum load, Eq. (6), compared to Karihaloo and Nallathambi experimental data from SE(B) specimens with varying S/W [10].

Included in the figure are theoretical estimates from Eq. (6) for the m values 0.1 and 0.45. It should be pointed out that the theoretical estimates are for a fixed span width of S/W = 4, whereas the Karihaloo and Nallathambi data contains specimens with varying span widths. A shorter span width increases the shear stresses in the specimen, having the effect of increasing the size of the fracture process zone. This translates into a larger m value. Overall, the Karihaloo and Nallathambi data provides a strong validation of Eq. (6) and the assumption that the effective K-R curve up to maximum load can be approximated by a simple power law.

3. Discussion

Fig. 6 compares the maximum load for varying crack length data from three different specimen sizes [11] are shown to be well described with a single effective K-R curve. Originally the smallest specimen size data was discarded as representing incomparable data due to a too small specimen size. Therefore the power law effective K-R curve was only fitted to the two larger specimen sizes. However, the use of the effective K-R curve describes well all three specimen sizes. Fig. 6 includes also another "small" specimen data set [12] representing the same type of concrete. The points denoted as squares with crosses lie very close to the other "small" specimen data (open squares), indicating that the fracture toughness of the concretes is similar.

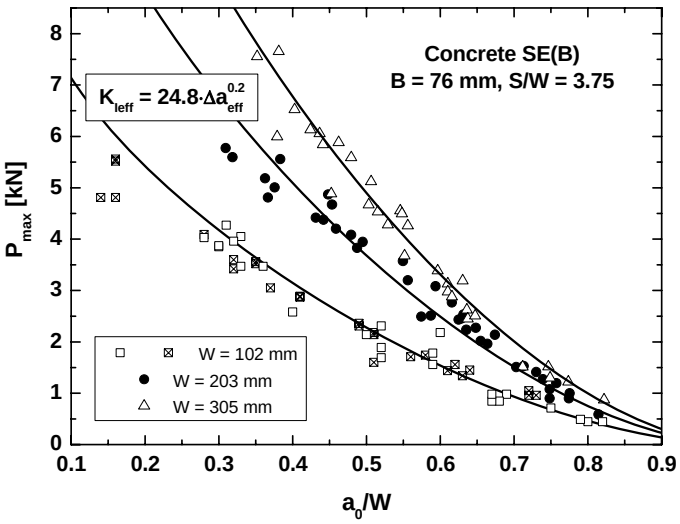

Figure 6. The maximum load for three different specimen sizes with strongly varying initial crack lengths are all described by a single K-R curve. The data has been taken from [11]. The squares marked by a cross are from [12], but their behavior is practically identical to the other specimens.

These examples show the descriptive power of the power law effective K-R curve estimated based on the maximum load values.

The effective K-R curve describes well the specimen behavior up to maximum load. This is exemplified in Fig. 7, where SE(B) data for limestone is analyzed. Fig. 7a, shows the maximum load values for self-similar specimens of different size [13]. Even though limestone differs from concrete, the fracture process is sufficiently similar to enable the use of limestone as an example. The power law K-R curve was fitted to the maximum load data in Fig. 7a. Then, the K-R curve estimate was used to predict the load displacement up to maximum load for the three different specimen sizes (Figs 7b, c, d). For the prediction, the crack is first advanced several small steps of Δa_{eff}. Next the K-R curve is used to estimate the K_{Ieff} and P corresponding to a + Δa_{eff}. Finally the

estimated load is used to calculate the displacement corresponding to a + Δa_{eff}, from the theoretical compliance. Considering the scatter of individual load-displacement traces, the prediction up to maximum load is excellent. Thus, this very simple power law K-R procedure can be used to predict the non-linearity in concrete and stone structures up to maximum load.

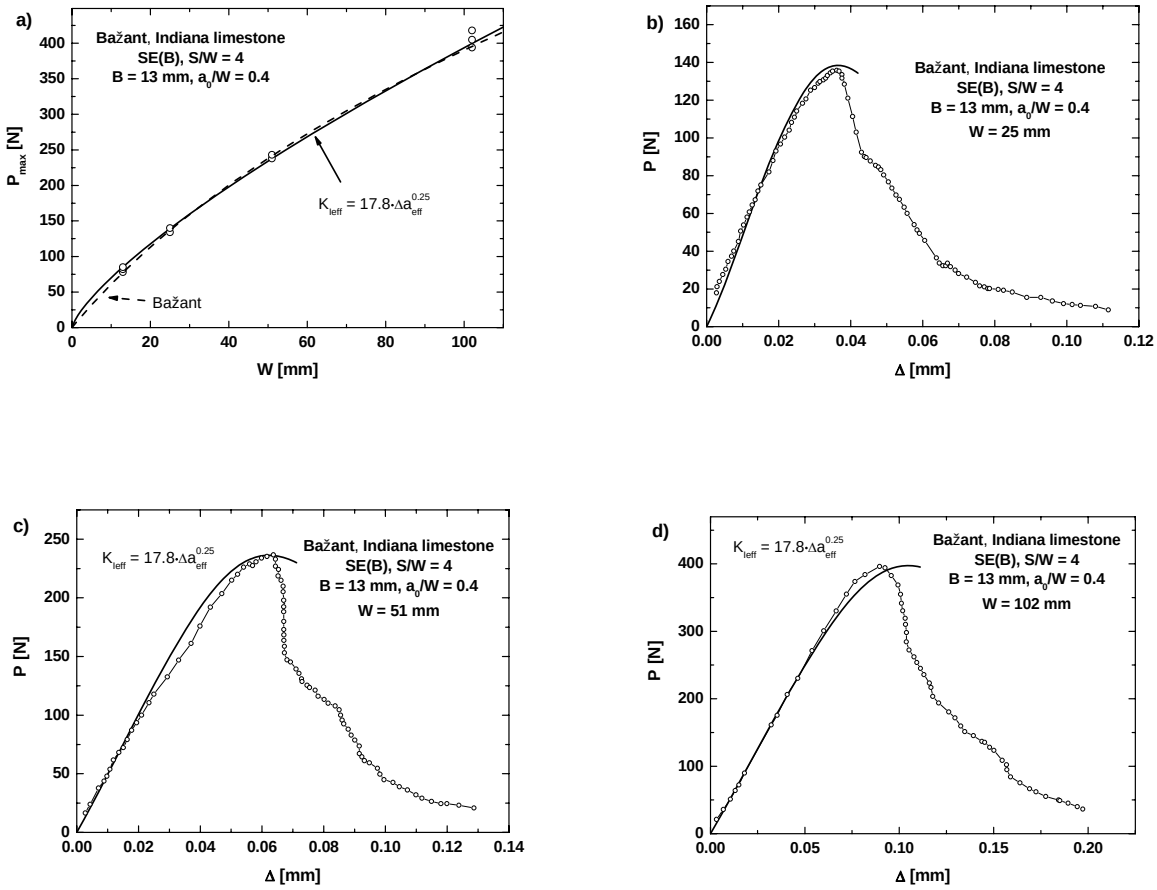

Figure 7. The prediction of load displacment dependence up to maximum load, based on simple effective K-R curve fitting to maximum load data. Data taken from [13].

Beyond maximum load, the connection between the effective crack length and the fracture process zone size breaks up. This is highlighted in Fig. 8. The load-displacement data was extracted from [1], so that for each specimen size representative upper and lower bound load-displacement traces were digitized. The effective crack length was estimated directly from the individual load-displacement data pairs, assuming that all the non-linearity is due to effective crack growth. Fig. 8a shows the effective crack driving force versus absolute effective crack growth and Fig. 8b shows the effective crack driving force versus proportional crack growth. Also included in the plots is the effective K-R curve estimated for the maximum load values. It is seen that for crack growth up to maximum load and slightly beyond, the effective K-R curve follows the absolute effective crack growth, whereas for large crack growths the effective K-R curve follows the proportional effective crack growth. This is a direct result of the fracture process zone evolution. Prior to maximum load, the fracture process zone is controlled by the fracture mechanical loading introduced by the crack. At some point, the connection between process zone size and the effective crack length breaks up. Finally, when the facture process zone has fully engulfed the crack and possibly extended to the free surface, the fracture process zone size develops as if there was no single crack in the structure.

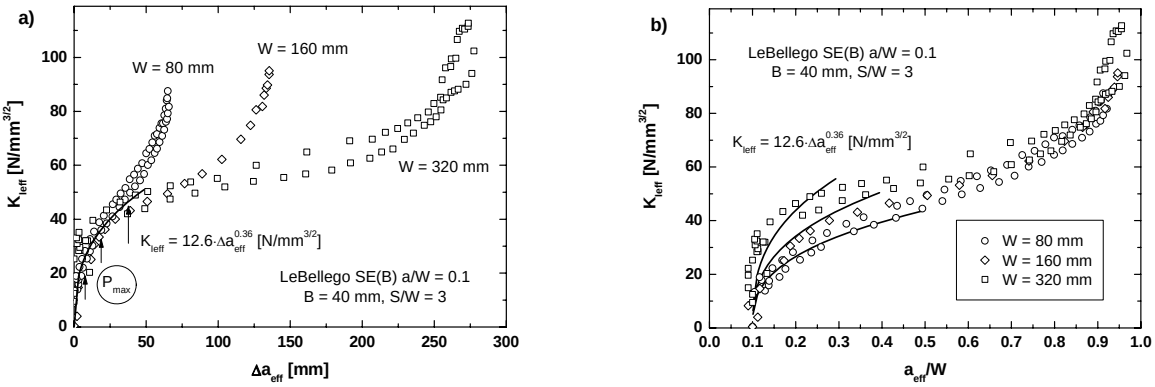

Figure 8. Normalization of effective crack driving force versus effective crack growth for self-similar SE(B) specimens of different size. Data extracted from [1]. Fig. 8a shows the effective crack driving force versus absolute effective crack growth and Fig. 8b shows the effective crack driving force versus proportional crack growth. Also included in the plots is the effective K-R curve estimated for the maximum load values.

The power law method contains similarities to an analytical cohesive zone method, which has been applied to describe the size effect in SE(B) specimens [14, 15]. The power law method is, however, much easier to use and provides an at least as good description of the size effect as can be seen by comparing Fig. (6) with Figs (4-6) in [15]. The advantage of the power law procedure lies in the very simple quantification of the fracture process zone development. A small power m indicates a brittle material, where the fracture process zone remains small throughout the fracture process. This is the case for m values of the order of 0.1 and below. The other extreme is a large m value in which case the material is crack insensitive and the damage comes mainly from the fracture process zone evolution. The method enables also the quantification of constraint in terms of the power m.

The procedure results in the estimate of the effective stress intensity factor corresponding to 1 mm effective crack growth.

4. Summary and Conclusions

Concrete is a so called quasi-brittle material which, despite predominantly elastic material response, exhibits in tension loading a stable non-linear fracture response, when tested under displacement control. The reason for the non-linearity is the development of a fracture process zone, in front of the crack, due to micro-cracking and crack bridging. The effect of the fracture process zone is to make the specimen sense the crack as being longer than $a_0+\Delta a$. The fracture process zone causes thus an effective increase in the crack driving force and apparent fracture resistance. The fracture modeling of concrete has been considered a mature theory. However, Present state of the art testing and assessment methods are somewhat cumbersome to use. Here, a LEFM based estimate of the effective stress intensity factor and the effective crack growth at maximum load in a fracture mechanics test is used to obtain a simple power law approximation of the effective K-R curve. It is shown that it is applicable to the description of not only different size specimens, but also specimens with varying geometry. The method is based on a new theoretical estimate of the effective crack growth corresponding to maximum load.

It can be concluded that:

- The presented procedure results in a simple two parameter description of the effective fracture resistance of quasibrittle materials.
- The procedure describes the effect of initial crack length on the maximum load values.
- The procedure enables the construction of the load-displacement dependence up to maximum load.
- The procedure enables a simple classification of the materials fracture process zone evolution.
- The procedure can be used in the context of the so called double-K criterion to describe the effective initiation toughness value.
- The procedure can be used to examine constraint effects on the materials fracture process zone evolution.
- In the future, the procedure may be used to assist damage mechanics type modeling of the failure of quasi-brittle materials.

Acknowledgements

This work has been part of the FAR project belonging to the SAFIR 2014 research program funded by VTT and by the State Nuclear Waste Management Fund (VYR), as well as other key organizations. The present work is connected to the quantification of constraint effects in brittle and quasi-brittle materials.

References

[1] C. Le Bellégo, J.F. Dubé, G. Pijaudier-Cabot, B. Gérard, Calibration of nonlocal damage model from size effect tests. European Journal of Mechanics A/Solids, 22 (2003) 33–46.
[2] S. Kumar, S.V. Barai, Concrete fracture models and applications, Springer-Verlag, Berlin Heidelberg, 2011.
[3] G.R. Irwin, Plastic zone near a crack and fracture toughness. Sagamore Research Conference Proceedings, Vol. 4, 1961.
[4] S. Xu, H.W. Reinhardt, Determination of double-K criterion for crack propagation in quasibrittle materials, Part II: Analytical evaluating and practical measuring methods for three-point bending notched beams. Int. J. Fract., 98 (1999) 151–77.
[5] ASTM E561–10, Standard Test Method for K-R Curve Determination. Annual book of standards, Volume 03.01. ASTM International West Conshohocken, PA, 2011.
[6] Z.P. Bažant, J. Planas, Fracture and size effect in concrete and other quasibrittle materials, CRC Press, Florida, 1998.
[7] Z.P. Bažant, P.A. Pfeiffer, Determination of fracture energy from size effect and brittleness number. ACI Materials Journal, 84 (1987) 463–80.
[8] K.R.W. Wallin, Critical assessment of the standard ASTM E 399. J. ASTM Int., 2, (2005).
[9] K.R.W. Wallin, Fracture toughness of engineering materials - estimation and application, EMAS Publishing, Warrington UK, 2011.
[10] B.L. Karihaloo, P. Nallathambi, Fracture toughness of plain concrete from three-point bend specimens. Materials and Structures/Matériaux et Constructions, 22, (1989). 85–93.
[11] T.M.E. Refai, S.E. Swartz, Fracture behavior of concrete beams in three-point bending considering the influence of size effects, Report No. 190, Engineering Experiment Station, Kansas State University; 1987.
[12] C.G. Go, S.E. Swartz, Energy methods for fracture-toughness determination in concrete. Exp. Mech., 26, (1986), 292–6.
[13] Z.P. Bažant, R. Gettu, M.T. Kazemi, Identification of nonlinear fracture properties from size effect tests and structural analysis based on geometry-dependent R-curves, Int. J. Rock Mech. Min. Sci. & Geomech. Abstr., 28, (1991) 43–51.
[14] Z. Wu, S. Yang, X. Hu, J. Zheng, An analytical model to predict the effective fracture toughness of concrete for three-point bending notched beams, Engng. Frac. Mech., 73, (2006),

2166–2191.
[15] S.T. Yang, X.Z. Hu, Z.M. Wu, Influence of local fracture energy distribution on maximum fracture load of three-point-bending notched concrete beams, Engng. Frac. Mech., 78, (2011), 3289–3299.

Effect of Characteristic Specifications on Fracture Toughness of Asphalt Concrete Materials

Hamid Behbahani[1], MohammadReza. M. Aliha[2,*], Hassan. Fazaeli[1], Mohammad.H. Rezaeifar[1]

[1] School of Civil Engineering, Iran University of Science and Technology (IUST), Narmak, 16846-13114, Tehran, Iran
[2] Welding and Joining Research Center, School of Industrial Engineering, Iran University of Science and Technology (IUST), Narmak, 16846-13114, Tehran, Iran
* Corresponding author: mrm_aliha@iust.ac.ir

Abstract In this research, the fracture toughness (K_{Ic}) of different compositions of asphalt mixtures is investigated experimentally and the effects of asphalt characteristic specifications including the aggregate size, aggregate type (i.e. limestone and siliceous), air void percentage and bitumen type on fracture toughness is studied. Several edge cracked specimens with the shape of semi-circular and subjected to symmetric three point bend loading were manufactured with different compositions and then tested at -15°c. The experimental results showed the noticeable influence of characteristic specifications of asphalt mixtures on the value of fracture toughness. Generally, the value of fracture toughness decreases for those mixtures containing smaller size of aggregates made of siliceous with higher percentages of air voids and softer binder types.

Keywords Asphalt mixture, Low temperature, Fracture toughness, Characteristic specifications

1. Introduction

Annually huge amount of money is spent for the design, construction and maintenance of asphalt pavements. Many types of cracks (e.g. top-down cracks in the surface of asphalt pavements) initiated due to daily or seasonal cyclic thermal loads or mechanical traffic loading are known as one of the main causes for the overall failure and a common mode of deterioration in asphalt pavement of roads and highways. Consequently, asphalt cracking may increase noticeably the maintenance and rehabilitation cost of pavements and hence the investigation of crack growth behavior in the asphalt pavements and overlays is an important issue for design, construction and maintenance of roads and highways in many countries. Under subzero and very low temperatures, asphalt pavements often behave as a brittle material and, hence, the risk of sudden fracture from pre-existing cracks in the pavement increases.

Some experimental studies have been done in the past for investigating the crack growth behavior of asphalt pavements, using different test specimens. From the experimental view point, a suitable test specimen for asphalt mixtures should have simple geometry and loading setup. Accordingly, a few test specimens have been used in the past by researchers to obtain the value of fracture toughness for asphalt materials. The edge cracked rectangular beam subjected to three or four point bending [1, 2], the disc shape compact-tension specimen [3-5] and the semi circular bend (SCB) specimen subjected to three point bend loading [6-9] are some of the most frequently used configurations for fracture toughness testing of asphalt materials. For example, the fracture resistance of various asphalt mixtures has been investigated experimentally using SCB, the edge cracked rectangular beam specimen subjected to four-point loading, and the center crack plate under tension specimens by Molennar and coworkers [10,11]. Chen et al. [12] also employed the SCB specimen to study the effect of temperature on the fracture toughness of asphalt mixtures. Among

the mentioned specimens, the SCB specimen can be considered as a suitable and favorite configuration for asphalt mixtures because it can be manufactured easily from standard field coring equipments or gyratory compactor machines and then it can also be tested easily by using ordinary testing apparatuses and fixtures. Moreover, in comparison with the rectangular beam specimens, the SCB samples need less asphalt mixtures for specimen preparation and consequently decrease the weight of test samples and cost of experiments. Hence, the SCB specimen has been used in the past for investigating the fracture behavior of asphalt mixtures [6-12]. Fig. 1 shows the SCB specimen schematically which is a semi-circular specimen of radius *R* and thickness *t*. When the SCB specimen is subjected to symmetric three-point bending with a loading span of 2S, the vertical edge crack of length *a* experiences pure mode I deformation (crack opening). The specimen can also be used for mixed mode I/II (tension – shear) experiments simply by inclining its direction relative to the applied load *P* direction or changing its location relative to the loading points.

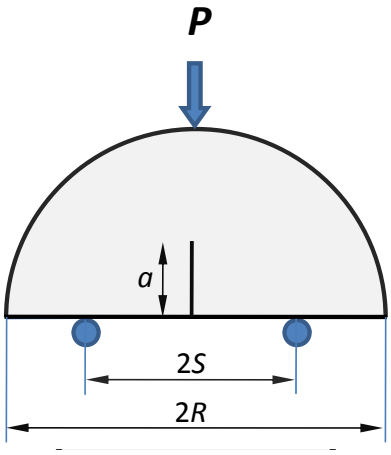

Figure 1. The edge cracked SCB specimen subjected to symmetric bend loading.

Since asphalt mixtures are complicated materials, their properties, performance, durability and mechanical strength depend strongly on the composition of the ingredients, manufacturing process, mix design, type of aggregates and binders, service and temperature conditions and etc. Therefore, in this research, fracture resistance of different compositions of asphalt mixture is investigated experimentally using SCB specimen and the effects of asphalt characteristic specifications including the aggregate size, air void percentage and bitumen type on fracture load and fracture toughness are studied.

2. Asphalt mixtures manufacturing

For preparation of asphalt mixtures, two aggregate types made of limestone and siliceous with three gradations (i.e. aggregate sizes of No. 4, 5 and 6 according to Iranian paving standard- code 234) were considered. The corresponding nominal maximum aggregate size (NMAS) for these three aggregate size numbers are 12.5 mm, 9 mm and 4.75 mm, respectively. The aggregate gradations and their percentages used for asphalt mixtures of this study have been presented in Table 1. Also, two binder penetration grade of 60/70 (the most commonly used type for paving the roads in Iran) and 85/100 (a suitable type for cold climates) were utilized for preparation of asphalt mixtures. Specifications of

each binder have been presented in Table 2. Using the Marshall Mix design method, the optimum percentages of binders were determined as presented in Table 3.

Table 1. Asphalt mixture aggregate gradation

Gradation number	NO.4	NO.5	NO.6
	NMAS: 12.5mm	NMAS: 9 mm	NMAS: 4.75 mm
Sieve size	Passing percent		
19	100	100	100
12.5	95	100	100
9	80	85	100
4.75	59	70	90
2.36	43	49.5	82.5
1.18	30	33	60
0.5	18	22	45
0.3	13	15	23.5
0.15	8	10	11.5
0.075	6	6	10

Table 2. Specifications of binders.

Test	Standard test	Unit	Binder type	
			60-70	85-100
Specific Gravity (25 °C)	ASTM D70	gr/cm3	1.03	1.01
Flash Point (Cleveland)	ASTM D92	°C	308	294
Penetration (25 °C)	ASTM D5	°C	62	94
Ductility (25 °C)	ASTM D113	cm	100	105
Softening point	ASTM D36	°C	49	42
Kinematic Viscosity @ 120 °C	ASTM D2170	mm2/s	810	512
Kinematic Viscosity @ 135 °C	ASTM D2170	mm2/s	420	221
Kinematic Viscosity @ 150 °C	ASTM D2170	mm2/s	232	120
Penetration index (PI)a	–	–	–1.12	-1.98

[a] $PI = [1952 – 500 \log (Pen_{25}) – 20SP] / [50 \log (Pen_{25}) – SP – 120]$

Table 3. Optimum percentages of binders for asphalt mixture samples

Binder type	Penetration grade 60-70			Penetration grade 85-100		
NMAS (mm)	12.5	9	4.75	12.5	9	4.75
Lime stone aggregates	4.8	5.1	5.7	4.6	-	-
Siliceous aggregates	5.2	-	-	-	-	-

3. Specimen manufacturing and testing

After mixing the aggregates (i.e. limestone and siliceous of different sizes) with binders (i.e. 60/70 and 85/100 bitumen) at 155°C, cylindrical specimens with diameter of 150 mm and height of 130

mm were manufactured using super pave gyratory compactor machine (SGC). The numbers of gyratory rotations (i.e.35, 70 and 90) were also varied that results in changing the void percentage in the prepared mixtures. The cylinder were then sliced using a rotary diamond saw machine to obtain circular discs of height approximately about 30 mm. Each disc was splited into two halves to produce two semi circles. A very narrow notch with length of 20 mm and width of 0.4 mm was then introduce at the middle of flat edge by a very thin rotary high speed diamond saw blade. Consequently, several edge cracked SCB specimens were manufactured and maintained in a freezer with temperature of -15°C for 6 hours to conduct the fracture tests. Fig. 2 shows some of the steps of specimen preparation for fracture toughness experiments.

Figure 2. Some of the steps for preparing the SCB test specimens.

After preparation of the test samples, they were tested using a compression test machine having capacity of 15kN. The tests were carried out at -15°C under displacement control conditions with a constant cross head speed of 3 mm/min. The SCB specimens were tested using a three-point bend fixture with the loading span of 2*S* = 100 mm (i.e. *S/R* = 0.67). For conducting the tests, the SCB specimens were placed carefully inside the fixtures and then were loaded until the final fracture. The complete load-displacement data were recorded during the tests using a computerized data logger. The load-displacement curves for all the samples were nearly linear, showing the brittle failure behavior of the tested asphalt mixtures at low temperature of -15°C. Others [13-15] have also mentioned that the asphalt mixtures behave as a linear elastic material at low subzero temperatures. Therefore, fracture toughness of the tested asphalt mixtures were determined from the maximum load recorded for each test. A total number of 45 specimens with different compositions were manufactured and for each mix design, three SCB specimens were tested successfully. Fig. 3 shows the test setup and a typical load-displacement curve obtained for one of the tested specimens.

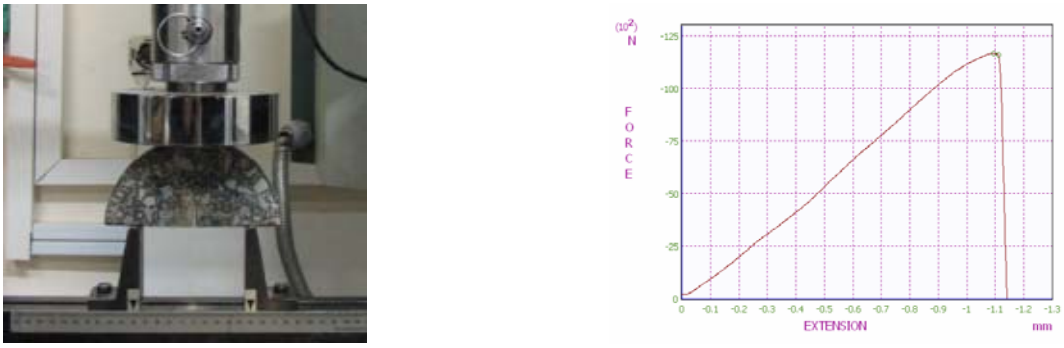

Figure 3. loading setup used for testing of SCB specimen made of asphalt mixture and a typical load-displacement curve obtained for -15°C.

4. Results and discussion

Mode-I fracture toughness (K_{Ic}) was determined for each cracked SCB specimen from following equation [16]:

$$K_{Ic} = \frac{Y_I P_f}{2Rt}\sqrt{\pi a} \tag{1}$$

where P_f and Y_I are the critical peak (or fracture) load and the geometry factor for the SCB specimen, respectively. Y_I is function of the crack length to radius ratio (a/R) and the loading span to radius ratio (S/R). Some analytical and numerical solutions are available for obtaining Y_I [e.g. 16,17]. For example, for the tested mode I samples in this research (i.e. with a/R = 0.27 and S/R = 0.67), the corresponding geometry factor has been determined by Ayatollahi and Aliha [16] using finite element analysis as: Y_I = 3.73.

By recording the final fracture loads from the experiments, the corresponding values of K_{Ic} for the tested asphalt materials were calculated from Eq. (1) for different compositions of the asphalt mixture. Details of the experimental results including critical fracture load and corresponding value of fracture toughness for each specimen have been presented in Table 4. The first column in this Table defines the mix type and for easy understating, the specimens are designated as *x-y-z*, in which *x* indicates the type of aggregate (i.e L for limestone and S for siliceous), *y* indicates the aggregate size number (i.e. 4, 5 and 6) and *z* shows the binder type (i.e. 60 for 60/70 and 85 for 85/100). According to the obtained results the average Averages value of K_{Ic} for the tested mixtures varies between 0.6 MPa.m$^{0.5}$ and 1MPa.m$^{0.5}$.

Fig. 4 compares the influence of asphalt characteristic specifications on the value of mode I fracture toughness. As seen from this figure, generally by increasing the void percentage (i.e. decreasing the number of gyratory rotations in the SGC machine) the value of K_{Ic} is reduced and this reduction is more pronounced for mixtures containing siliceous aggregates. As shown in Fig. 4a, it can be concluded that depending on the void percentage the value of fracture toughness for mixtures made of limestone is about 25 to 60% greater than the corresponding values of K_{Ic} for siliceous mixtures. A noticeable increase in the value of fracture toughness is also seen when the stiffer binder (i.e. bitumen 60/70) is used (see Fig. 4b). This is mainly because of the higher stiffness of the asphalt mixture which increases the crack growth resistance. Moreover, based on Fig. 4 (c) it is obvious that K_{Ic} increases when the size of aggregates becomes greater in the asphalt mixtutre. This can be attributed to the lesser amount of binder and greater amount of aggregates in the texture of asphalt mixture which can increase the general stiffness and strength and the required fracturing load of the material. Consequently, According to the results of this research, the risk of low temperature brittle fracture in the asphalt mixtures can be generally increased for siliceous aggregates, smaller aggregate sizes, higher percentages of voids and the higher penetration grades of the binders.

Table 4. Details of the fracture loads and fracture toughness data obtained for the tested asphalt mixtures.

specimen	Gyratory rotation numbers	Sample Number	Peak load (N)	Average of peak load (N)	Average of K_{Ic} ($MPa.m^{0.5}$)
S-4-60	90	1	4174	4732	0.87
		2	4381		
		3	5641		
	70	1	3220	3651.33	0.67
		2	3556		
		3	4178		
	35	1	3501	3603.66	0.66
		2	4100		
		3	3210		
L-4-60	90	1	5268	5713.33	1.05
		2	5583		
		3	6289		
	70	1	5343	5724.66	1.05
		2	5326		
		3	6505		
	35	1	5000	5323.33	0.98
		2	4997		
		3	5973		
L-4-85	90	1	4770	4977	0.91
		2	4579		
		3	5582		
	70	1	4937	4956	0.91
		2	4700		
		3	5231		
	35	1	5160	4947	0.91
		2	4732		
		3	4949		
L-5-60	90	1	4622	5384.33	0.99
		2	5337		
		3	6194		
	70	1	4673	5084	0.93
		2	5495		
		3	-		
	35	1	5165	5072	0.93
		2	4930		
		3	5121		
L-6-60	90	1	4803	4894.33	0.90
		2	5160		
		3	4720		
	70	1	4193	4511.66	0.83
		2	4731		
		3	4611		
	35	1	3765	3506	0.64
		2	3405		
		3	3348		

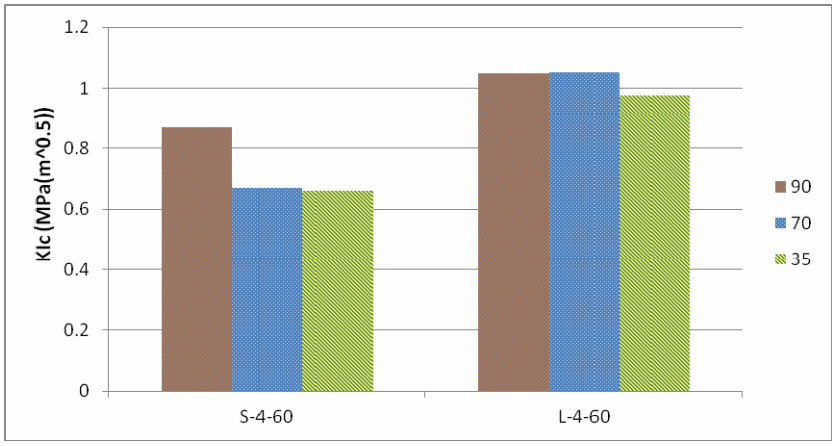

(a)

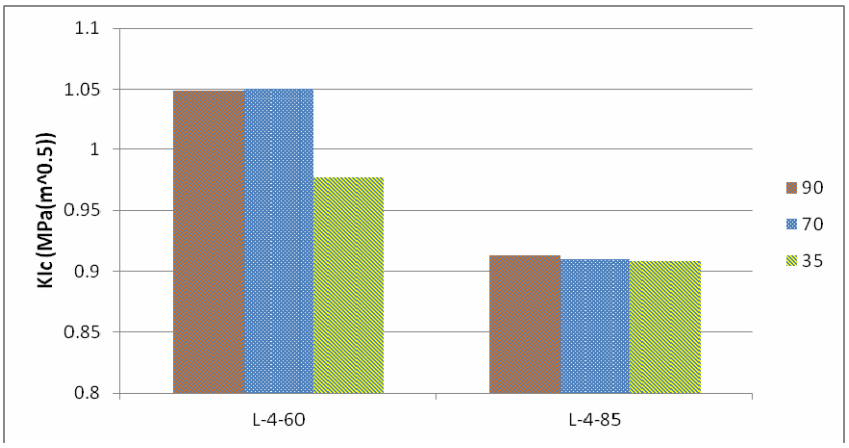

(b)

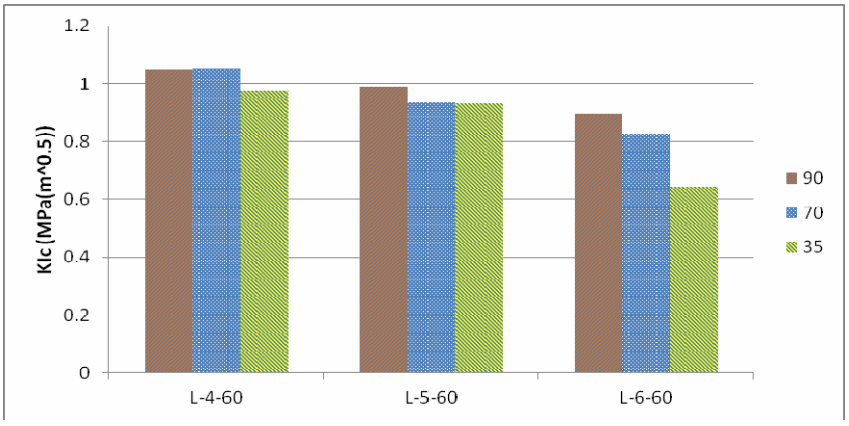

(c)

Figure 4. Comparison of asphalt characteristic specifications on the fracture toughness (K_{Ic}) of different asphalt mixtures.

5. Conclusions

- Fracture toughness of different asphalt mixtures was determined experimentally using several SCB specimens at low temperature conditions.
- The influence of asphalt characteristic specifications such as void percentage, aggregate type, aggregate size and binder type were studied on the value of mode I fracture toughness.
- It was observed that the risk of low temperature fracturing in the asphalt mixtures increases for mixtures containing siliceous aggregates, smaller aggregate sizes, greater percentages of voids and higher penetration grades of the binders.

References

[1] A. Braham, W. Buttlar, F. Ni, Laboratory Mixed-Mode Cracking of Asphalt Concrete Using the Single-Edge Notch Beam, Road Mater Pave Des, 11, (2010) 947-968.

[2] M. P. Wagoner, W. G. Buttlar, G. H. Paulino, Development of a Single-Edge Notched Beam Test for Asphalt Concrete Mixtures, Journal of Testing and Evaluation, 33, (2005), Paper ID JTE12579

[3] M. P. Wagoner, W. G. Buttlar, G. H. Paulino, P. Blankenship, Investigation of the Fracture Resistance of Hot-Mix Asphalt Concrete Using a Disk-Shaped Compact Tension Test, Transp Res Rec,1929, (2005)183-192.

[4] H. Kim, M. P. Wagoner, W. G. Buttlar, Numerical fracture analysis on the specimen size dependency of asphalt concrete using a cohesive softening model, Constr Build Mater, 23, (2009) 2112-2120.

[5] B. Behnia, E. V. Dave, S. Ahmed, W. G. Buttlar, H. Reis, Effects of Recycled Asphalt Pavement Amounts on Low-Temperature Cracking Performance of Asphalt Mixtures Using Acoustic Emissions, Transp Res Rec, 2208, (2011) 64-71.

[6] M. Ameri, A. Mansourian, S. Pirmohammad, M.R.M Aliha, M.R. Ayatollahi, Mixed mode fracture resistance of asphalt concrete mixtures, Engng Fract Mech 93, (2012), 153-167.

[7] J. H. Liu, Fatigue Life Evaluation of Asphalt Rubber Mixtures Using Semi-Circular Bending Test, Adv Mater Res, 255,(2011) , 3444-3449.

[8] X. J. Li, M.O. Marasteanu, Using Semi Circular Bending Test to Evaluate Low Temperature Fracture Resistance for Asphalt Concrete, Exp Mech, 50,(2010) 867–876.

[9] L. N. Mohammad, M. Kim, M. Elseifi, Characterization of Asphalt Mixture's Fracture Resistance Using the Semi-Circular Bending (SCB) Test, 7th RILEM International Conference on Cracking in Pavements, RILEM Bookseries 4, (2012) 1-10.

[10] A. A. A. Molenaar, A. Scarpas, X. Liu, G. Erkens, Semi-circular bending test; simple but useful. J Assoc Asphalt Tech, 71, (2002) 794–815.

[11] J. M. M. Molenaar, A.A.A. Molenaar, X. Liu, Resistance to crack-growth and fracture of asphalt mixture. In: 6th international RILEM symposium on performance testing and evaluation of bituminous materials; 2003. pp. 618–25.

[12] X. Chen, W. Li, H. Li, Evaluation of fracture properties of epoxy asphalt mixtures by SCB test. J Southeast Univ, 25, (2009) 527–530.

[13] M. Novak, B. Birgisson, R. Roque. Near-surface stress states in flexible pavements using measured radial tire contact stresses and ADINA. Comp Struct, 81, (2003), 859–870.

[14] X. J. Li, M. O. Marasteanu, The fracture process zone in asphalt mixture at low temperature. Engng Fract Mech 77, (2010) 1175–1190.

[15] M. Fakhri, M. Farokhi, P. T. Kheiry, Modeling of top-down cracking (TDC) propagation in sphalt concrete pavements using fracture mechanics theory. Adv Test Charact Bituminous Mater II, (2009) 681–692.

[16] M.R. Ayatollahi, M.R.M. Aliha, Wide range data for crack tip parameters in two disc-type specimens under mixed mode loading, Comp Mater Sci, 38, (2006) 660-670.

[17] I. Lim, I. W. Johnston, S.K. Choi, Stress intensity factors for semi-circular specimens under three-point bending, Engng Fract Mech, 3, (1993) 363–82.

A constitutive approach to fracture simulation based on augmented virtual internal bond method

Zhennan Zhang*, **Shaofeng Yao**

School of Naval Architecture, Ocean and Civil Engineering, Shanghai Jiao Tong University, Shanghai, 200240, China

* Corresponding author: zhennanzhang@sjtu.edu.cn

Abstract The K-dominant zone, which is a small area surrounding the fracture tip, has been the interesting focus of the fracture mechanics. In the traditional linear elastic fracture mechanics(LEFM), a stress intensity factor is used to characterize the stress field of the K-dominant zone and a separate fracture criterion is used to predict the fracture behaviors. However, when using LEFM to simulate fracture propagation, the computation of stress intensity factor is a tough problem. The LEFM is actually a phenomenological methodology. The fracture behaviors are determined by material microstructure. The augmented virtual internal bond(AVIB) is a constitutive model based on microstructure. Its constitutive relation is derived from the micro bond potential, which contains the micro fracture mechanism. Hence, the so-called fracture criterion is implicitly built in the constitutive relation. In this paper, the AVIB constitutive model is used in the K-dominant zone while the usual linear elastic constitutive model is used in the rest zone to simulate fracture propagation. By this method, the computation of stress intensity factor is avoided. When and how fracture propagation is completely governed by the AVIB constitutive relation. It provides an efficient approach to fracture simulation.

Keywords Fracture simulation, Augmented virtual internal bond, Constitutive model，Microstructure

1. Introduction

In the methodology of linear elastic fracture mechanics(LEFM), the singular mechanical field of crack tip is characterized by the so-called stress intensity factors (SIFs). Whether fracture propagates is governed by SIF and material fracture toughness. So, many fracture criteria in terms of SIFs have been proposed. When using FEM to simulate fracture behaviors, the SIF is a key factor that has to be calculated. However, the computation of SIF is a tough problem in computational mechanics, which requires very fine mesh scheme at vicinity of crack tip or special treatment on mesh scheme. The cohesive surface methodology pioneered by Barenblatt[1] and Dugdale[2] take a different philosophy to deal with the fracture tip problem. It is assumed that there is a cohesive zone ahead of crack tip, which is governed by a cohesive law. The cohesive law is characterized by the cohesive strength and the fracture energy. When using this method, the stress intensity problem, therefore the SIF problem, is avoided. However, in FEM simulation, a cohesive zone is usually inserted into the bulk material, which brings inconvenience to numerical procedure. In the present paper, the cohesive properties of microstructure at vicinity of crack tip are directly built in the constitutive relation through augmented virtual internal bond(AVIB)[3] model. Hence, in the present simulation strategy, only at the K-dominant zone is the AVIB constitutive model used while at the rest zone, the linear elastic constitutive model is used. The present method is suggested highly efficient, avoiding the SIF computation and fracture criteria problem.

2. Constitutive relation of material at vicinity of crack tip

Before the deformation of material reaches its linear elastic limit, the linear elastic continuum constitutive relation can well describe the behaviors of material. However, once the deformation exceeds this limit, the conventional continuum constitutive model couldn’t well describe it. In such situation, the augmented virtual internal bond(AVIB)[3] is an effective approach to address this

problem. Hence, the idea of the present method can be depicted by Fig.1. At the K-dominant zone which experience large deformation, the AVIB constitutive model is used while at the rest zone where the deformation is small, the linear elastic constitutive model is adopted.

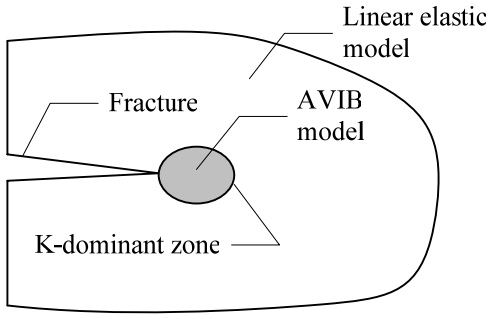

Fig.1 Depiction of the constitutive approach to fracture simulation.

In VIB theory[4], the solid is considered to consist of randomized discrete material particles on micro scale and the constitutive relation is directly derived from the interactions between material particles. The AVIB generalizes the original VIB model in that the shear deformation effect between material particles is considered via Xu-Needleman potential. Therefore, the AVIB can represent material with different Poisson ratios. The micro structure of AVIB is shown in Fig.1.

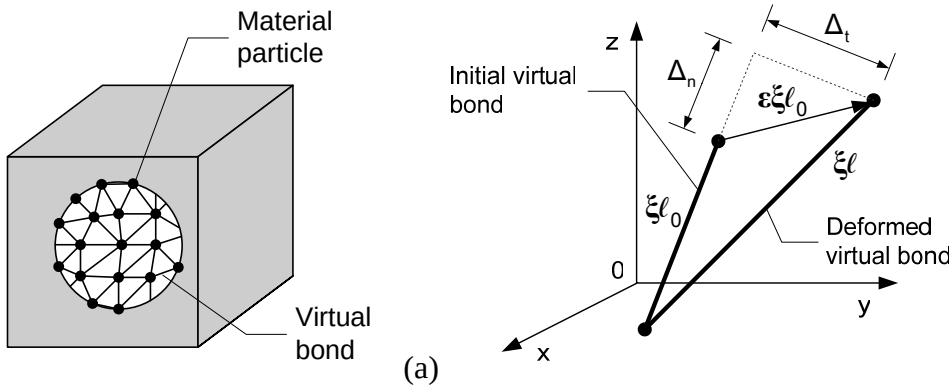

Fig.2 Micro structure of AVIB and micro bond deformation ($\boldsymbol{\varepsilon}$ denotes the strain tensor; $\boldsymbol{\xi}$ the bond orientation vector; l_0 the original bond length)

The micro bond can be described by the following simplified Xu-Needleman potential[5]

$$U(\Delta) = \phi_n - \phi_n \exp\left(-\frac{\Delta_n}{\delta_n}\right)\left(1+\frac{\Delta_n}{\delta_n}\right)\left[1-q+q\exp\left(-\frac{\Delta_t^2}{\delta_t^2}\right)\right] \tag{1}$$

where Δ_n, Δ_t are respectively the normal and shear bond deformation. In AVIB, they are calculated as

$$\begin{aligned} \Delta_n &= \boldsymbol{\xi}^T \boldsymbol{\varepsilon} \boldsymbol{\xi} l_0 \\ \Delta_t^2 &= \left[\boldsymbol{\xi}^T \boldsymbol{\varepsilon}^T \boldsymbol{\varepsilon} \boldsymbol{\xi} - \left(\boldsymbol{\xi}^T \boldsymbol{\varepsilon} \boldsymbol{\xi}\right)^2\right] l_0^2 \end{aligned} \tag{2}$$

Based on Eq.(2), define the second-order tensor $\mathbf{N}$, $\mathbf{P}$ and the forth-order tensor $\mathbf{Q}$ respectively as

$$
\begin{aligned}
N_{ij} &= \frac{1}{\mathrm{l}_0}\cdot\frac{\partial\Delta_n}{\partial\varepsilon_{ij}} = \xi_i\xi_j \\
P_{ij} &= \frac{1}{\mathrm{l}_0^2}\cdot\Delta_t\cdot\frac{\partial\Delta_t}{\partial\varepsilon_{ij}} = \varepsilon_{ip}\xi_p\xi_j - \left(\boldsymbol{\xi}^T\boldsymbol{\varepsilon}\boldsymbol{\xi}\right)\xi_i\xi_j \\
Q_{ij} &= \frac{1}{\mathrm{l}_0^2}\cdot\left(\frac{\partial\Delta_t}{\partial\varepsilon_{kl}}\cdot\frac{\partial\Delta_t}{\partial\varepsilon_{ij}} + \Delta_t\frac{\partial^2\Delta_t}{\partial\varepsilon_{ij}\partial\varepsilon_{kl}}\right) = \delta_{ik}\xi_j\xi_l - \xi_i\xi_j\xi_k\xi_l
\end{aligned}
\tag{3}
$$

where δ_{ij} being the Kronecker delta.

According to this micro structure, the strain tensor of material[3] can be derived as

$$
\sigma_{ij} = \frac{\partial\Phi}{\partial\varepsilon_{ij}} = \frac{1}{V}\left\langle\frac{\partial U}{\partial\Delta_n}\cdot\frac{\partial\Delta_n}{\partial\varepsilon_{ij}} + \frac{\partial U}{\partial\Delta_t}\cdot\frac{\partial\Delta_t}{\partial\varepsilon_{ij}}\right\rangle \tag{4}
$$

and the tangent modulus of material as

$$
\begin{aligned}
C_{ijkl} = \frac{\partial^2\Phi}{\partial\varepsilon_{ij}\partial\varepsilon_{kl}} = \frac{1}{V}\Bigg\langle &\frac{\partial^2 U}{\partial\Delta_n^2}\cdot\frac{\partial\Delta_n}{\partial\varepsilon_{kl}}\cdot\frac{\partial\Delta_n}{\partial\varepsilon_{ij}} + \frac{\partial U}{\partial\Delta_n}\cdot\frac{\partial^2\Delta_n}{\partial\varepsilon_{ij}\partial\varepsilon_{kl}} \\
&+ \frac{\partial^2 U}{\partial\Delta_t^2}\cdot\frac{\partial\Delta_t}{\partial\varepsilon_{kl}}\cdot\frac{\partial\Delta_t}{\partial\varepsilon_{ij}} + \frac{\partial U}{\partial\Delta_t}\cdot\frac{\partial^2\Delta_t}{\partial\varepsilon_{ij}\partial\varepsilon_{kl}} \\
&+ \frac{\partial^2 U}{\partial\Delta_n\partial\Delta_t}\cdot\frac{\partial\Delta_t}{\partial\varepsilon_{kl}}\cdot\frac{\partial\Delta_n}{\partial\varepsilon_{ij}} + \frac{\partial^2 U}{\partial\Delta_t\partial\Delta_n}\cdot\frac{\partial\Delta_n}{\partial\varepsilon_{kl}}\cdot\frac{\partial\Delta_t}{\partial\varepsilon_{ij}}\Bigg\rangle
\end{aligned}
\tag{5}
$$

in which Φ denotes the strain energy density of a micro element; $\boldsymbol{\varepsilon}$ the strain tensor; V the volume of the micro element and $\langle \mathrm{L} \rangle = \int_0^{2\pi}\int_0^{\pi}(\mathrm{L})D(\theta,\phi)\sin\theta d\theta d\phi$ in spherical coordinates for 3D case and $\langle \mathrm{L} \rangle = \int_0^{2\pi}(\mathrm{L})D(\theta)d\theta$ for 2D case.

Substituting Eqs.(1,2,3) into Eqs.(4,5), the stress tensor and tangent modulus tensor can be rewritten as

$$
\sigma_{ij} = \frac{1}{V}\left\langle f_n\cdot N_{ij} + f_t\cdot P_{ij}\right\rangle \tag{6}
$$

and

$$
C_{ijkl} = \frac{1}{V}\left\langle f_A\cdot N_{ij}N_{kl} + f_B\cdot Q_{ijkl} - f_C\cdot P_{ij}P_{kl} - f_D\cdot\left(P_{ij}N_{kl} + N_{ij}P_{kl}\right)\right\rangle \tag{7}
$$

in which the coefficients are respectively

$$
\begin{aligned}
&f_n = A_0 \cdot c_1 c_3 \cdot \frac{\Delta_n}{l_0}, \qquad f_t = B_0 \cdot c_1 c_2 c_4 \\
&f_A = A_0 \cdot c_1 c_3 c_5, \qquad f_B = B_0 \cdot c_1 c_2 c_4 \\
&f_C = B_0 \cdot c_1 c_2 c_4 \cdot \frac{2 l_0^2}{\delta_t^2}, \qquad f_D = B_0 \cdot c_1 c_2 \cdot \frac{l_0 \Delta_n}{\delta_n^2}
\end{aligned} \tag{8}
$$

The coefficient in Eq.(8) are respectively

$$
\begin{aligned}
&A_0 = \frac{\phi_n l_0^2}{\delta_n^2}, \quad B_0 = \frac{2q\phi_n l_0^2}{\delta_t^2}, \quad c_1 = \exp\left(-\frac{\Delta_n}{\delta_n}\right), \quad c_2 = \exp\left(-\frac{\Delta_t^2}{\delta_t^2}\right) \\
&c_3 = 1 - q + q \cdot c_2, \quad c_4 = 1 + \frac{\Delta_n}{\delta_n}, \quad c_5 = 1 - \frac{\Delta_n}{\delta_n}
\end{aligned} \tag{9}
$$

In [3], Zhang and Gao proposed a remedy method for element size sensitivity, which essentially embedded the fracture energy into the constitutive relation. By adjusting the material parameters at fracture tip, AVIB can keep the strain energy release rate constant. According to the idea of AVIB, the adjusted parameters at crack tip is

$$
\tilde{A}_0 = A_0/\lambda, \quad \tilde{B}_0 = B_0/\lambda, \quad \tilde{\delta}_n = \lambda \delta_n, \quad \tilde{\delta}_t = \lambda \delta_t \tag{10}
$$

where λ is the adjustment coefficient. The adjustment coefficient takes the following values for different cases.

$$
\lambda = \begin{cases}
\lambda = \dfrac{2J(1-2\nu)}{3\pi h E \varepsilon_t^2} & \text{for} \quad \text{3D} \\
\lambda = \dfrac{J(1-\nu)}{2hE\varepsilon_t^2} & \text{for} \quad \text{2D-stress} \\
\lambda = \dfrac{J(1+\nu)(1-2\nu)}{2hE\varepsilon_t^2} & \text{for} \quad \text{2D-strain}
\end{cases} \tag{11}
$$

in which J is the intrinsic J-integral of material; h is the element size, as

$$
h = c\sqrt{S} \tag{12}
$$

where S is the area of an element and c is a geometrical factor. In the numerical examples discussed in the next section, take $c = 4\sqrt{2}$.

3 . Criterion of crack tip element

When using the present method, it is necessary to identity the element of crack tip. Usually, the

crack tip element deformation is very large. Hence, to detect the crack tip element, the following criterion is adopted in the present paper.

$$\varepsilon_1 > \varepsilon_t \tag{13}$$

In which ε_1 is the first principle eigenstrain value of strain tensor.

4 . simulation example

To show the validation of the present method, a three-point-bending(TPB) test reported in[6] is presented simulated. The material parameterrs provided by [6] are: the Young's modulus $E = 30.5$ GPa, Poisson ratio $\nu = 0.2$; tensile strength $f_t = 3.8$ MPa and fracture energy $G_f = 62.5$ N/m. With these parameters, the calibrated parameters are $\varepsilon_t = 0.2486 \times 10^{-3}$ and $\varepsilon_c = 2.486 \times 10^{-3}$. The specimen, boundary conditions and mesh configuration are shown in Fig.3. The displacement controlling loading scheme is adopted. Each step is 0.002486 mm.

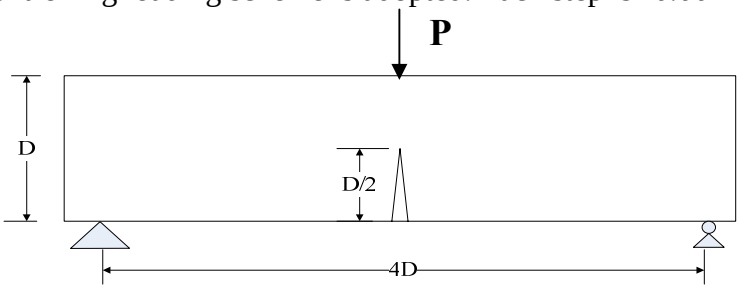

Fig.3 The specimen and boundary conditions of TPB test. $D = 0.075$ m and the sample thickness is 0.05m.

The simulation results are shown in Fig.4 and Fig.5. From Fig.4, it is seen that crack propagates gradually with loading increasing. The propagation pattern agrees with the observation in the experiment[6]. Fig.5 shows the comparison between the experimental and the simulated results. From Fig.6 it is seen that the present method can well predict the fracture propagation, free of the element size sensitivity problem.

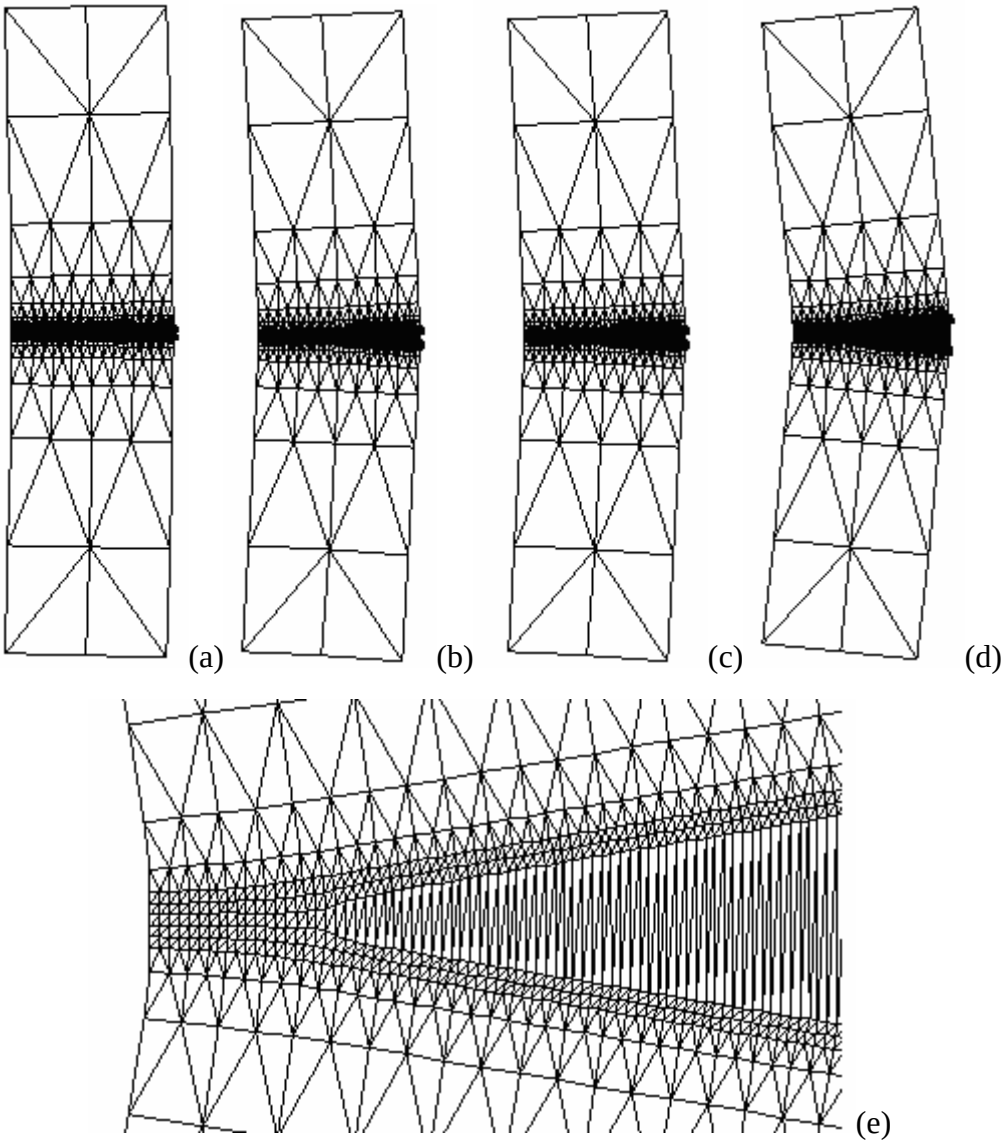

Fig.4 Crack propagation process (a) Step = 6; (b) Step = 16; (c) Step = 30; (d) Step = 50; (e) Crack tip zone zoomed in at Step =50. (Node displacement is magnified 200 times.)

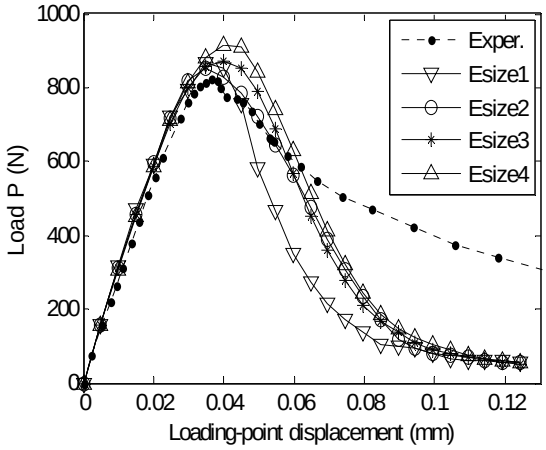

Fig.5 Comparison between the simulated load-displacement curves and the experimental results. ('Exper.' denotes the experimental results. The beam is discretized into N segments along the width in the middle cross section of beam. Esize1, Esize2 ,Esize3 and Esize4 correspond to the segment number 32, 64,128,and 256, respectively.)

5 .Conclusion remarks

At the K-dominant zone, a micro-macro cohesive constitutive model is used while at the rest zone, the linear elastic constitutive model is used. By this method, the fracture propagation can well be predicted. The simulation example suggests that the present method is validated. By the present method, the fracture criterion is directly built in the constitutive model. It avoids the choice of separate fracture criterion problem and the computation of stress intensity factor, which brings great convenience to fracture simulation.

Acknowledgement:

The present work is supported by National Natural Science Foundation of China (No. 11172172), which is gratefully acknowledged.

References

[1] Barenblatt, G.I., The formulation of equilibrium cracks during brittle fracture: General ideas and hypotheses, axially symmetric cracks. Appl. Math. Mech.(PMM), 23(1959) 622-636.

[2] Dugdale, D.S., Yielding of steel sheets containing slits. Journal of mechanics and physics of solids, 8(2)(1960) 100-104.

[3] Zhang, Z.N. and H.J. Gao, Simulating fracture propagation in rock and concrete by an augmented virtual internal bond method. International Journal for Numerical and Analytical Methods in Geomechanics, 36 (4)(2012) 459-482.

[4] Gao, H.J. and P. Klein, Numerical simulation of crack growth in an isotropic solid with randomized internal cohesive bond. Journal of the Mechanics and Physics of Solids, 46(2)(1998) 187-218.

[5] Xu, X.P. and A. Needleman, Numerical simulations of fast crack growth in brittle solids. Journal of Mechanics and Physics of Solids, 42(1994) 1397-1434.

[6] Yu, R.C., G. Ruiz, and E.W.V. Chaves, A comparative study between discrete and continuum models to simulate concrete fracture. Engineering Fracture Mechanics, 75(2008) 117-127.

Investigation on the Failure Mechanisms in Sandstones under Uniaxial Compression by Digital Image Correlation

Ganyun Huang*, Hao Zhang, Haipeng Song, Yilan Kang

Department of Mechanics, Tianjin University, Tianjin 300072, China
* Corresponding author: g.y.huang@hotmail.com

Abstract Sandstone samples have been compressed uniaxially till failure. The displacement field during the deformation process has been obtained by digital image correlation (DIC) technique. It has been observed that the rock samples ruptured through splitting parallel to the compression direction, as conventional experiments indicated. But upon analyzing the apparent strain field, no sliding cracks or shear cracks have been found that are suggested to drive the splitting failure. Instead, deformation band like structure has been detected. The splitting failure has been observed to be the direct result of the localization of the some scattered small cracks. The micromechanism underlying may be the buckling of force chains that induces delamination between them.

Keywords uniaxial compression, failure mechanism, sandstone, digital image correlation

1. Introduction

The failure of rocks under compression may hold important implications in many aspects such as geophysics, civil engineering and mining sciences. In fact, uniaxial compressive strength has even been a key parameter in estimating the performance of cutters in rock drilling. Despite the wide variety of rock types, a large body of experiments have demonstrated the rock fails under uniaxial compression via axial splitting or shear faulting [1-4]. Such macroscopic failure mode can be well explained by the nucleation and propagation of the wing cracks that is assumed to depend on the existence of sliding cracks. Experiments on samples with pre-existing cracks, or more exactly cuts inclined to the compression direction have also proved the wing crack formation and propagation that leads to axial splitting [5-7]. Model of wing crack formation and propagation has been widely applied to the damage and micromechanics of rock like brittle materials [8-11]. However, the model depends critically on the existence of sliding or shear cracks. No experiments have been reported on the nucleation of the shear cracks. Thus what the physical micromechanisms drive the axial splitting under uniaxial compression remains an open question.

In rock like brittle materials, it has been conventionally believed that microcracks with a random distribution of various orientations exist, which may make the nucleation of sliding cracks dispensable. If it is true, then analyzing the full-field deformation behavior of as-received rock samples under uniaxial compression may help to reveal splitting induced by the sliding crack or the physical micromechanisms for axial splitting. Combination of the uniaxial compression test and DIC technique may suit the purpose very well. Indeed, through DIC technique, full field displacement on the sample surface can be obtained efficiently without contact and hence damage. Applicability of the technique to the rock deformation has already been demonstrated in our previous work [12]. Thus, we will use DIC technique to study the deformation behavior of rocks under uniaxial compression so as to cast some new light on the failure mechanisms at microscopic level.

2. Experiments

Samples of dimension 25×25×50 mm were cut from a large sandstone block from Yunnan, China. All the sample surfaces were randomly painted with artificial speckles. Then the sandstone samples were uniaxially compressed along the longest sides on the electric universal machine

(CSS-44100). Compressive load was controlled by displacement mode at a speed of 0.06mm/min. During the whole loading stage, a CCD camera (1004×1003 pixels, 8bits) under the illumination of two light sources was installed perpendicularly to the samples so as to capture the images that were simultaneously stored on a computer disc for subsequent processing. The length-pixel ratio of the images is 61.7μm/pixel and recording frequency was 1frame/s. It is worth mentioning that only the images in the area as indicated by the white rectangle in Fig.1(a) will be used to obtain the displacement fields. The experimental setup is illustrated in Fig.1(b).

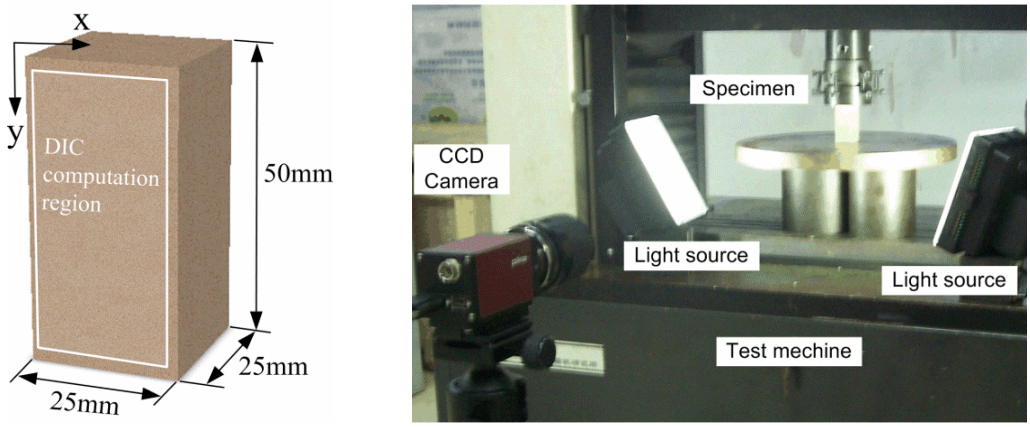

(a) (b)

Fig.1 (a) sandstone sample and (b) experimental setup

In the present work, the image was processed by our in-house DIC software. A relatively small calculation subset size (21×21 pixels) and step length (10 pixels) were chosen to increase the spatial resolution of the measurement. The displacement measurement accuracy in our test was at least 1μm based on our calibration.

3. Results and discussions

The load-displacement (at the contact interface) recorded by the electric universal machine is present in Fig. 2. It can be seen that except at the initial stage, the load is almost proportional to the displacement even till failure (with macroscopic crack). The sample fails at a load level of about 68kN via axial splitting.

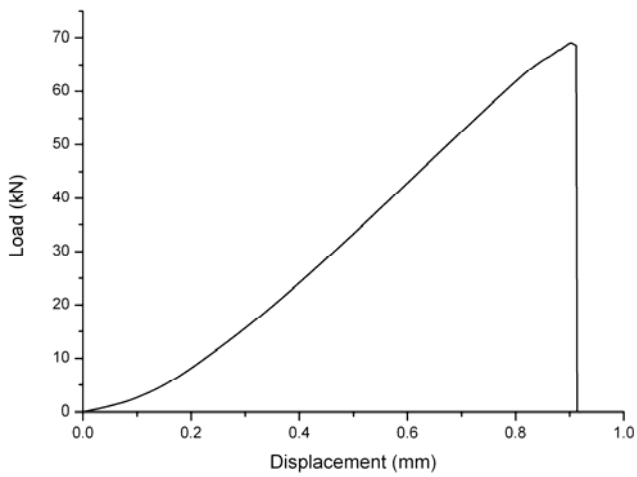

Fig.2 Load-displacement curve during the uniaxial compression of a sandstone sample

Using the DIC technique as handled in [12], we have obtained the displacement fields in the region indicated by the white rectangle in Fig. 1(a). Distributions of the displacements at load levels of 40, 55, 62, 62.7 and 64.5 kN have been presented respectively in Fig.3.

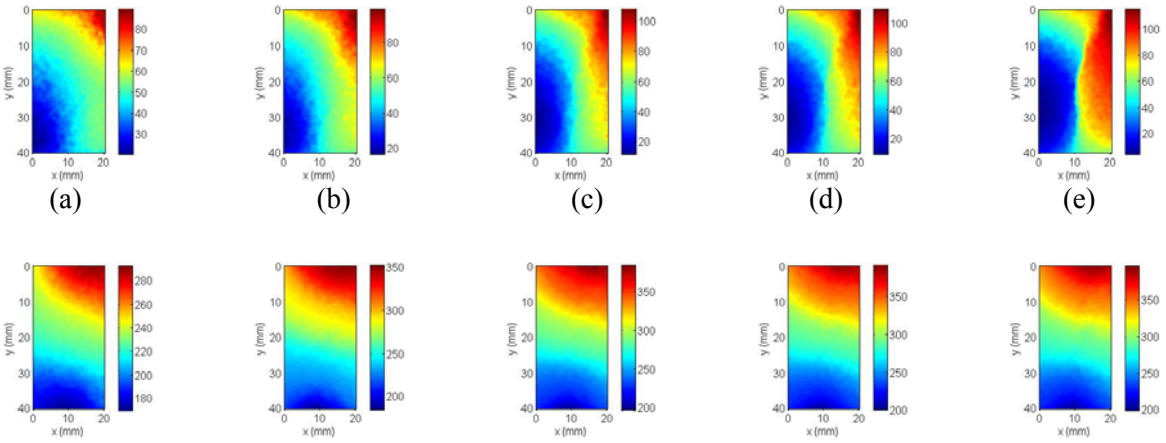

Fig.3 The horizontal (a-e) and vertical (f-j) displacements on the sample surface at load levels of 40, 55, 62, 62.7 and 64.5 kN respectively (unit in the legend is micron)

The displacement distributions clearly indicate uneven deformation has occurred especially when the applied load is close to the rupture load where the color pattern for the horizontal displacement is highly discontinuous at the middle of the sample. Partially the inhomogeneous deformation may be induced by the micro-structure in the sandstone. Observations by optical microscopy have indeed shown the sandstone is composed of grains of microns but the grain size is rather homogeneous (results not shown). It may also be the result inherent to the sandstone. To better analyze the deformation behavior, the apparent strain on the surface has been calculated since when there are cracks, displacement jumps may appear due to the crack faces sliding and opening and induce large apparent strain.

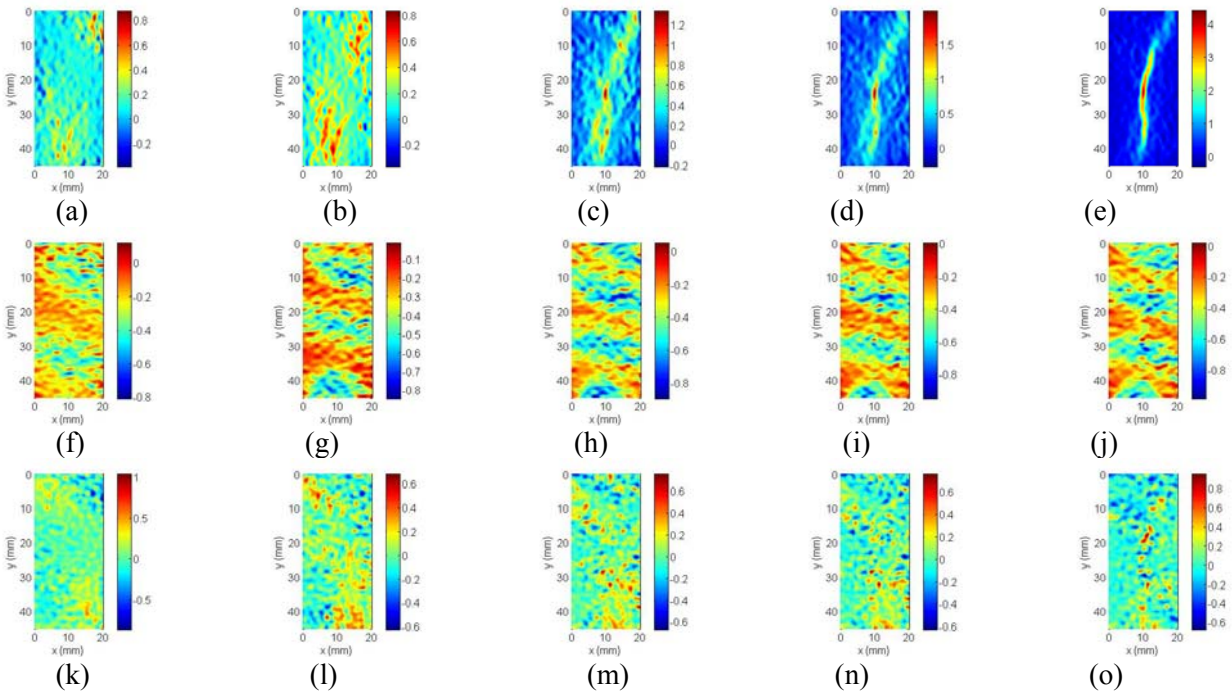

Fig. 4 apparent ε_{xx} (a-e), ε_{yy} (f-j) and γ_{xy} (k-o) on the sample surface at load levels of 40, 55, 62, 62.7 and 64.5 kN respectively (The values are in percentage)

The apparent strain distributions corresponding to load levels of 40, 55, 62, 62.7 and 64.5 kN respectively have been demonstrated respectively in Fig. 4. The apparent ε_{xx} at a given load level is inhomogeneous. The regions with apparent ε_{xx} value much larger than the average are highly localized and somewhat scattered at relatively lower load levels. For example, see Fig.4 (a) and (b). Such regions may be considered as locally split given the much larger than average values of the apparent ε_{xx}. With the increase in compressive load, the regions with apparent ε_{xx} much larger than the average become to join up and are distributed almost along a line inclined to the loading direction as shown in Fig. 4(d). Close to the rupture load, the regions with relatively large value of apparent ε_{xx} are distributed along a line and from the color pattern in Fig. 4(e) look like a macroscopic crack. The final rupture actually did propagate along that line. The apparent ε_{yy} behaves completely different. The area of interest as indicated in Fig. 1(a) is alternated with regions of small apparent ε_{yy} (nearly not deformed) and those of larger apparent ε_{yy}. Deformation band structure forms. The number of bands increases with compressive load. The bands tend to be broken at the middle along a vertical line, possibly due to the damage leading to splitting. Distribution of the apparent engineering shear strain γ_{xy} is also localized but much more scattered than that of apparent ε_{xx}. In most cases, the largest magnitude of the apparent shear strain is smaller than those of apparent ε_{xx} and apparent ε_{yy}. In fact, at relatively large compressive load, the apparent ε_{xx} has the largest magnitude among all the apparent strain components on the surface. It may be the result from the axial splitting and so the apparent strain ε_{xx} can be conveniently used for identification of cracking and damage in our experiments.

The deformation band structure in the apparent ε_{yy} appears rather unexpected although compaction bands or shear bands have been observed in rocks with high porosity and usually under confinement [13, 14]. Because the porosity in our samples is very low (about 5%), the formation of deformation band can hardly be attributed to the sandstone compaction. Moreover, the banded structure evolves with compressive load even at levels larger than 30 kN, see Fig.4 (f-j) and no hardening behavior has been found in Fig.2 at those load levels. We have also excluded the possibility of artificial factors. Other algorithm has been adopted to calculate the apparent ε_{yy} but with similar results despite the slight difference in magnitude (results now shown). Besides, the precision for displacement measurement is adequate given the high levels of loading applied in those results. The formation of band structure in ε_{yy} may affect the failure behavior of the present sandstones under uniaxial compression. Conventionally, axial splitting has been explained by formation and propagation of wing cracks that depends on the existence of a sliding crack or shear crack. However, no evidence for that has been detected. Before the final rupture via axial splitting, if there were sliding microcracks, the apparent shear strain would be very large and dominant over other apparent strain components at the crack faces. However, as mentioned above, the apparent ε_{xx} has the largest magnitude in those situations. The line along which the much-larger-than-average apparent strain ε_{xx} is distributed seems to be consistent with the shear plane predicted by Mohr-Coulomb strength criterion. But it cannot result from shear but rather from the coalescence of the relatively scattered and local splitting.

With in mind that Bazant et al has suggested that under uniaxial compression splitting crack band may form which would subsequently result in the formation of column bundles [15], we have enlarged the displacement by fifty times so as to visualize the deformed profile of the area of interest. The results are demonstrated in Fig.5. Dash blue lines are plotted only guided eyes. If the material points distributed along a line with same x can be considered a column, then one may find that the area of interest deforms by compressing the columns and some of them *buckled* locally. By scrutinizing the results in Fig. 5, one may also notice that the buckled regions are correlated with

the banded structure in the apparent ε_{yy}. Moreover, the axial splitting may be driven by the buckling induced delamination between the columns. Thus it is likely deformation of the present sandstone under compression can be described by force chain model as applied in mechanics of granular materials [16]. However, more detailed experiments are required to confirm it and whether such a failure mechanism is applicable to other brittle rocks under uniaxial compression remains for future study.

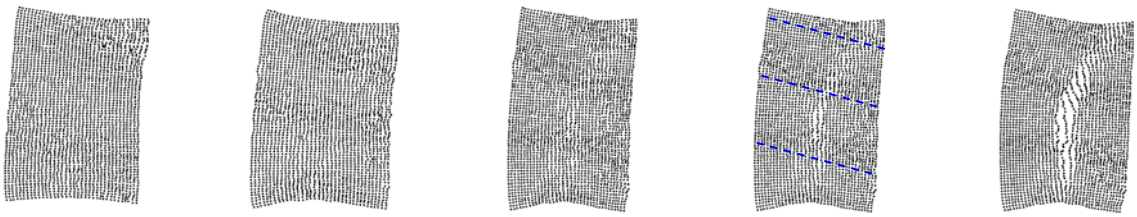

(a) (b) (c) (d) (e)

Fig. 5 Visualization of the deformed profile by zooming out displacement by 50 times at load level of 40, 55, 62, 62.7 and 64.5 kN (The difference in width and height is caused by different display ratio)

4 Concluding remarks

Samples of sandstone under uniaxial compression were studied experimentally by combing the conventional compressive test with DIC technique. Deformation field and its evolution with loading have been obtained with the aid of DIC technique. It has been found the sandstone deformed in an inhomogeneous manner and failed via axial splitting. However the failure mode cannot be attributed to the wing crack formation and nucleation. Instead, the macroscopic crack formed via coalescence of some local axial splitting microcracks and the micromechanism may be the buckling of force chains that induces delamination. Although more detailed experiments are required to verify it, the present results may cast new light on understanding the failure mechanism in brittle materials under compression.

Acknowledgements

This work was supported by the National Natural Science Foundation of China under Grant Nos.11072170 and 11127202.

References

[1] J. Gramberg, Axial cleavage fracturing, a significant process in mining and geology. Eng. Geol., 1(1965) 31-72.
[2] S. Peng, A. M. Johnson, Crack growth and faulting in cylindrical specimens of Chelmsford granite. Int J Rock Mech Min Sci., 9(1972) 37-86.
[3] M. S. Paterson, Experimental deformation and faulting in Wombeyan marble. Bull. Geol. Soc. Am. 69(1958) 465-76.
[4] B. T. Brady, Theory of earthquakes. I. A scale independent theory of rock failure. Pure Appl Geophs. Res., 112(1974) 701-25.
[5] E. Z.Lajtai, Brittle failure in compression. Int. J. Fract., 10(1971) 525 – 536.
[6] H. Horii, S. Nemat-Nasser, Brittle failure in compression: splitting, faulting and brittle-ductile transition. Phil. Trans. R. Soc. Lond. A., 319(1986) 337-374.
[7] A. Bobet, H. H. Einstein, Fracture coalescence in rocktype materials under uniaxial and biaxial compression. Int. J. Rock Mech. Min. Sci., 35(1998) 863-888.

[8] Y. Okui, H. Horii, Stress and time-dependent failure of brittle rocks under compression: A theoretical prediction. J. Geophys. Res., 102(1997) 14869-14881.
[9] H. B. Li, J. Zhao, T. J. Li, Micromechanical modeling of the mechanical properties of a granite under dynamic uniaxial compressive loads. Int. J. Rock Mech. Min. Sci., 37(2000) 923-935.
[10] B. Paliwal, K. T. Ramesh, An interacting micro-crack damage model for failure of brittle materials under compression. J. Mech. Phys. Solids., 56(2008) 896 – 923.
[11] H. S Bhat, C. G.Sammis, A. J. Rosakis, The micromechanics of Westerley granite at large compressive loads. Pure Appl. Geophys. ,168(2011) 2181–2198
[12] H. Zhang, G. Huang, H. Song, Y. Kang, Experimental investigation of deformation and failure mechanisms in rock under indentation by digital image correlation. Eng Fract Mech., 96(2012) 667-675.
[13] P. Baud, S. Vinciguerra, C. David, A. Cavallo, E. Walker, T. Reuschle, Compaction and failure in high porosity carbonates: Mechanical data and microstructural observations. Pure Appl. Geophys., 166(2009) 869-898
[14] V. Vajdova, W. Zhu, T. M. N. Chen, T. Wong, Micromechanics of brittle faulting and cataclastic flow in Tavel limestone. J.Struct. Geol., 32(2010) 1158-1169.
[15] Z. P. Bazant, Y. Xiang, Size effect in compression fracture: splitting crack band propagation. J. Eng. Mech., 123(1997) 162-172.
[16] S. Ostojic, E. Somfai, B. Nienhuis, Scale invariance and universality of force networks in static granular matter. Nature, 439(2006) 828-830.

Rock fracture toughness testing using SCB specimen

M. R. Ayatollahi[1,*], M. J. Alborzi[1]

[1] Fatigue and Fracture Lab., School of Mechanical Engineering, Iran University of Science and Technology, Narmak, 16846 Tehran, Iran

* Corresponding author: m.ayat@iust.ac.ir

Abstract There are various testing methods for measuring fracture toughness of rocks. The semi-circular bend (SCB) specimen has recently received much attention by researchers for testing mode I fracture toughness of rocks and other geo-materials. While the SCB specimen is often prepared by a straight crack, chevron notched semi-circular bend specimen (CCNSCB) has been rarely utilized. In this paper, using the analytical methods for evaluating the minimum dimensionless stress intensity factor ($Y^*_{\min}$) of chevron notched specimens, the slice synthesis method is employed to obtain the dimensionless critical stress intensity factor of the specimen. Then, fracture tests are performed on a white crystalline rock under mode I loading using the CCNSCB specimen. The experimental results show very little scatter in the measured values of fracture toughness.

Keywords Rock, CCNSCB, Experiments, Finite element modeling

1. Introduction

Fracture mechanics provides an engineering description for the transformation of an intact structural component into a broken one through crack extension [1]. Physical operations like blasting and crushing which are used in practical applications such as tunneling, drilling and mining projects are often considered as a process of formation and growth of cracks in rock masses. Fracture toughness is a major parameter in fracture mechanics which represents the energy required to initiate brittle failure around the crack tip. Fracture experiments on full scale rock masses are difficult and expensive. Thus, researchers prefer to perform their fracture analyses utilizing various laboratory-scale cracked specimens. Three testing methods have been suggested by the International Society for Rock Mechanics (ISRM) for measuring rock fracture toughness: (i) Chevron Bend specimen method (CB) (ii) Short Rod specimen method (SR) [2], and (iii) Cracked Chevron Notched Brazilian Disc (CCNBD) specimen method [3]. The semi-circular bend (SCB) specimen proposed by Chong and Kuruppu [5] has also recently received much attention by researchers. Some advantages of the SCB specimen are its simplicity, minimal requirement of machining and ability of preparation from rock cores. The SCB specimen can also be used as an alternative to the ISRM standard specimens in determining fracture toughness in orthogonal directions of transversely isotropic materials or sedimentary rock, such as sandstone or oil shale [6]. In addition to the rocks, the SCB method has been applied to other core-based brittle materials, such as concrete and asphalt. Furthermore, SCB is a suitable specimen to rock fracture toughness test at high strain rates [6].

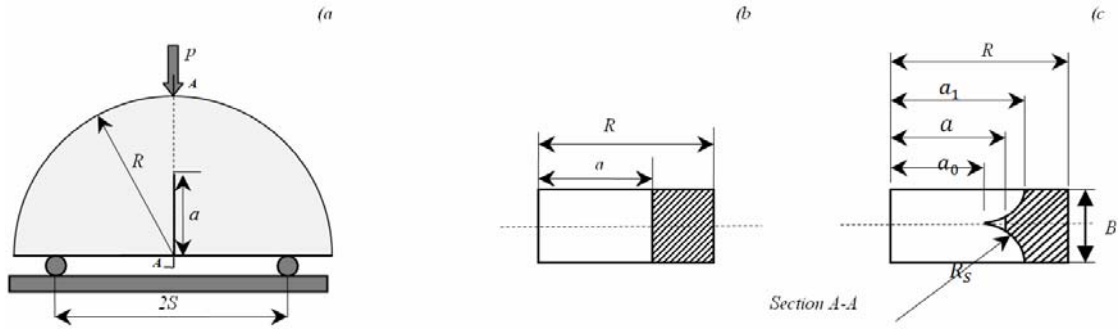

Figure 1. a) Schematic view of SCB specimen b) Straight crack c) Chevron notched

Crack in rock test specimens are usually created either with a straight front or a chevron shape, as shown in Figure 1. The chevron notched SCB specimen in the static mode has been rarely studied and only a limited SIF calibration was done by Kuruppu using a 3D finite element method [7–9].
The fracture toughness values of SCB with straight crack are calculated from [10]:

$$K_{IC} = \frac{P_f \sqrt{\pi a}}{2Rt} Y_I (a/R, S/R) \tag{1}$$

where P_f is the maximum failure load, Y_I is the dimensionless stress intensity factor, *t*, *R* and *a* are the thickness, radius of SCB specimen and crack length, respectively. Y_I, also known as geometry factor, is a function of the ratio of crack length over the semi-disc radius (a/R) and the ratio of half-distance between the two bottom supports over the semi-disc radius (S/R) [11]. Lim et al. [10] found SIFs in terms of a/R and S/R. Their results can be summarized by the following relation:

$$Y_I = S/R\left(2.91 + 54.39\alpha - 391.4\alpha^2 + 1210.6\alpha^3 - 1650\alpha^4 + 875.9\alpha^5\right) \tag{2}$$

where α is a/R.
If a standard CCNBD specimen is cut into two equal parts, two pieces of CCNSCB are obtained. Figure (1-c) shows the chevron notched SCB specimen and its geometrical coefficients. $\alpha_0 (= a_0/R)$, $\alpha_1 (= a_1/R)$ and $\alpha_m (= a/R)$ are the dimensionless initial crack length, dimensionless final crack length and dimensionless critical crack length, respectively. α_s is a coefficient obtained from dividing R_s (radius of rotary saw) by *R*. Also $\alpha_B (= B/R)$ is the normalized thickness.
Similar to the equation suggested by ISRM for the CCNBD specimen [4], the initiation fracture toughness K_{IC} of CCNSCB specimen can be determined as:

$$K_{IC} = \frac{P_{\max}}{B\sqrt{D}} Y^*_{\min} \tag{3}$$

where $P_{\max}$ is the measured maximum load, *B* and *D* are the thickness and diameter of the disc respectively, $Y^*_{\min}$ is the minimum value of Y^*, which is the dimensionless stress intensity factor (SIF). It should be noted that all the restrictions and the geometrical relationships for the CCNBD is assumed to be applicable to CCNSCB too. So far, several approximate analytical methods have been used to determine Y^*, although applicability and accuracy of any of these methods have not been evaluated in CCNSCB. In this paper a slice synthesis method (SSM) is presented to evaluate the minimum dimensionless stress intensity factor in the CCNSCB specimen. Then, its accuracy is examined using both experimental test and finite element method. Experimental results show that the CCNSCB specimen can be employed for measuring rock fracture toughness.

2. Slice synthesis method in CCNSCB specimen

Slice synthesis method, proposed first by Bluhm [12], is a semi-analytical method for solving fracture problems with curved crack fronts. Wang et al. [13] used the SSM to calculate the stress intensity factor of CCNBD. In this method, the thickness of the sample is cut into a number of slices each with a thickness Δt as shown in Fig. 2. The analysis of a single slice is easier than analyzing the whole specimen. First, analytical equations are written for each slice. Then, by combining these equations, an equation for the entire sample can be achieved according to the

equilibrium principle. Analytical relations can be extracted in specimens of complex configuration using SSM method. No analytical relationship has been reported in papers for obtaining the stress intensity factors for the CCNSCB specimen and it is rather difficult using experimental or numerical methods. Every slice in CCNSCB is considered as a SCB with the straight crack. In fact, the central portions of CCNSCB with the straight crack front width *b* need not to be cut into thin slices. Since analytical solutions exist for the calculation of the stress intensity factor in the SCB specimen with a straight crack, an equation can be written for each portion and also for the middle section and finally with combining the stress intensity factors of these two sections, the formula for calculating the dimensionless stress intensity factor of the CCNSCB is obtained. More details on the procedure can be found in [13], but the general equation is written as:

$$Y^{*}=\left[\frac{b/B}{Y(\alpha)}+\sum_{i=1}^{N}\frac{2.\Delta t/B}{\beta Y(\alpha_i)}\right]^{-1} \tag{4}$$

where Δt and N are the thickness of each slice and the number of slices, respectively. Y is the dimensionless stress intensity factor of SCB with straight crack and $\alpha_i = a_i/R$ where a_i is the crack length of *i*th slice. Parameters Δt, α_i and *b* are related to the dimensionless crack length (α).

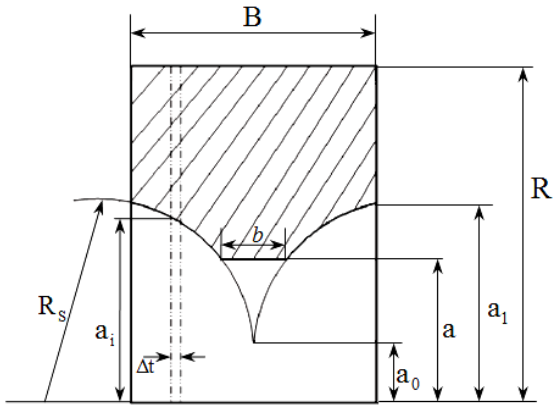

Figure 2. Slice synthesis method for CCNSCB specimen

β reflects the difference between the stress intensity factor of the central part and that of the lateral part. β can be calculated as:

$$\beta = 1+\gamma\frac{\alpha_1-\alpha}{\alpha_B} \tag{5}$$

The important and difficult part of the SSM method is the calculation of β. By comparing the results of three-dimensional finite element analysis, Wang et al. [13] predicted the coefficient γ to be 0.9 in CCNBD specimens. Here, we employed SSM method in the CCNSCB specimen used previously by Kuruppu [8] and by comparing the results of SSM with the results of kuruppu [8], γ =0.5 was found an appropriate value.

Thus, to find the minimum dimensionless stress intensity factor in CCNSCB, it is sufficient to minimize equation (4) as:

(6)

$$\frac{\partial Y^*}{\partial \alpha} = 0$$

The related numerical results will be presented and discussed later in section 4.

3. Sample preparation and fracture toughness tests

A crystalline rock was selected for fracture toughness tests. This type of rock contains very few discontinuities and can be assumed to be isotropic and homogeneous.

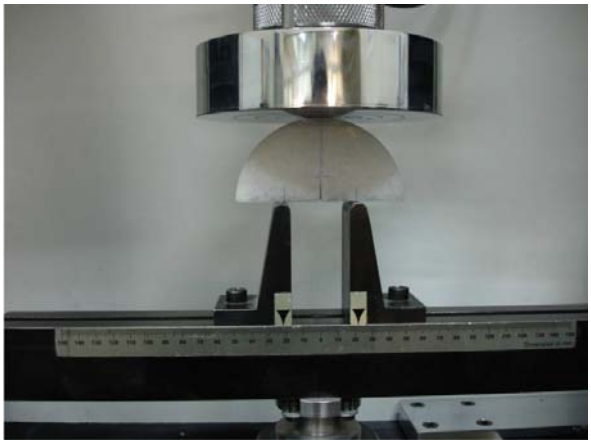

Figure 3. Loading set-up utilized for conducting fracture tests in CCNSCB specimen

The rock samples were prepared from a rock sheet of 20mm thick using water jet to form semi-circular disks of diameter 80mm. A rotary saw of radius $R_s = 50$mm and thickness 0.6mm was used to generate the chevron notch in the specimens. The penetration of rotary saw into specimens was considered 11mm. In the experiments, the half-distance between the two bottom supports (*S*) was 20mm. The standard 3-point bend loading was used for fracturing the SCB specimens (see Fig. 3). After creating the chevron notch, the specimen was placed inside the loading set-up and the failure loads were recorded. SANTAM/STM-150 machine with a capacity of 15000N was utilized for conducting the fracture tests on the CCNSCB specimens.

4. Dimensionless stress intensity factor

4.1. Numerical and experimental results

It was observed in the entire experiments that when the load reached its critical level, sudden failure took place for the test samples. The load-displacement curve was almost linear up to the maximum load. Thus, using the critical failure load in each experiment, the fracture toughness values of CCNSCB specimen can be computed from Eq. 3. The details of experimental results obtained from each test including, the fracture loads are listed in Table 1.

Using the maximum load obtained from the experiment, the corresponding fracture toughness is calculated using finite element modeling. The singular elements were considered in the first ring of elements surrounding the crack tip for producing the square root singularity of stress/strain field. A *J*-integral based method was used for obtaining the stress intensity factors. Fig. 4 shows a typical mesh pattern generated for simulating the CCNSCB specimen.

The average value of maximum load was 1.877kN and using this value in the finite element model, mode I fracture toughness K_{IC} is obtained 1.208 MPa.m$^{1/2}$ and by its substitution in Eq. (3), the dimensionless stress intensity factor in the CCNSCB specimen is found 3.64. During the simulation,

the critical crack length is derived from Eq. 6. Average K_{IC} values for 3D model of CCNSCB considered were confirmed to converge to constant values with Twenty-five concentric rings of crack front mesh elements. Here, fracture toughness is considered from the middle point of crack front.

Table 1. Summary of fracture tests conducted on CCNSCB specimens manufactured from the crystalline rock

Test No.	$p_{\max}(kN)$
1	1.914
2	1.82
3	1.8
4	1.871
5	1.876
6	1.981
Average	**1.877**

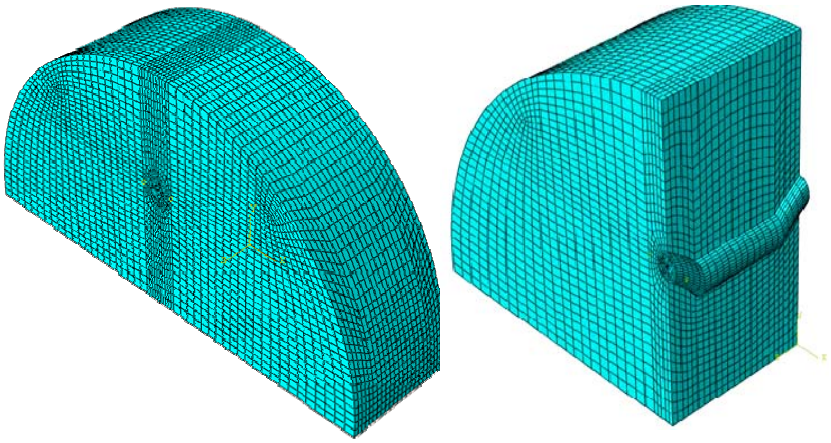

Figure 4. A typical finite element mesh used for simulating CCNSCB specimen.

The experiments conducted on CCNSCB showed that before the crack reaches its critical length, no significant resistance is observed with crack extension. Indeed, in the chevron-notched specimens, the crack is allowed to extend sub-critically, due to the high stress concentration. The chevron notch causes the crack propagation to initiate at the tip of the V alignment and to extend radially outwards in a stable fashion until the point where the fracture toughness is obtained. V or chevron shape generates a process of stable crack growth under increasing load, from the initial crack length (a_0) to its critical length (a_m). Beyond a_m, the crack extension takes place in an unstable fashion. At the critical length, the pre-crack has fully developed in the rock sample and the fracture toughness is evaluated. This procedure also provides a smaller fracture process zone (FPZ), compared to a straight crack. The experimental results also show that V-shaped grooves provide sharper critical cracks and lower scatter in fracture loads. Therefore, this specimen can be a good alternative for measuring fracture toughness of rock masses and for investigating the process of crack growth in brittle materials.

4.2. SSM method results

By using the dimensionless geometric parameter (α_S, α_0, α_1 and α_B) and substituting into equation (3), SSM model predicts the value of 3.541 for minimum dimensionless stress intensity factor, which is 2.7% lower than the value obtained from the experimental data (see Fig. 5). Also note that Y_I is the dimensionless stress intensity factor of the SCB specimen with a straight crack. Here, equation (2) was used for calculating Y_I.

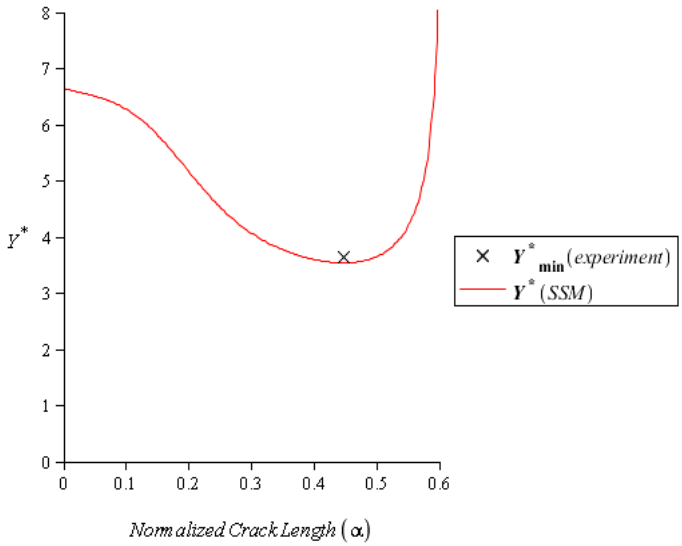

Figure 5. slice synthesis method utilized for estimating $Y^*_{\min}$ in CCNSCB specimen

Because of the convenience and accuracy of SSM, this method can be suggested as a reliable method for evaluating the minimum dimensionless stress intensity factor ($Y^*_{\min}$) in the CCNSCB specimens.

5. Conclusions

Although the SCB specimens with straight crack front have been used frequently by researchers, very few studies have been reported on the use of CCNSCB specimen in rock fracture toughness testing. The minimum dimensionless stress intensity factor of CCNSCB was calculated using SSM and its accuracy was assessed experimentally and by finite element method.

Figure 6. Fracture surface of CCNSCB specimen

Under mode I loading, a V-shaped (chevron) crack results in the automatic formation of a sharp and

natural crack in the specimen causing a lower scatter in the experimentally obtained fracture loads. Observed fracture surface shows that surface roughness of the cracked chevron notched specimens is relatively low for the tested white crystalline rock (see Fig. 6). Meanwhile, it is finally recommended that similar fracture tests are performed on the SCB specimens having straight cracks and the experimental results are compared when these two different methods are used for generating the artificial crack.

References

[1] M. F. Kanninen and C. H. Popelar C. H, Advanced Fracture Mechanics", Oxford Engineering Science Series, Vol. 15. Oxford University Press, New York, 1985.

[2] Matsuki K, Hasibuan S. S, Takahashi H, "Specimen size Requirements for determining the inherent fracture toughness of rocks according to ISRM suggested Methods", Journal of applied mechanics, Vol. 18, 1991, pp. 413-427.

[3] F. Quchterlony, ISRM Suggested methods for determining fracture toughness of rocks, Int. J. Rock. Mech. Min. Sci. & Geomech. Abstr, Vol. 25, 1988, pp. 264-294.

[4] ISRM Testing Commission (co-ordinator: RJ Fowell), Suggested method for determining mode I fracture toughness using cracked chevron notched Brazilian disc (CCNBD) specimens: Int J Rock Mech Min Sci & Geomech Abstr, 32, 1995, pp. 57–64.

[5] K.P. Chong, M.D. Kuruppu and J.S. Kuszmual, Fracture toughness determination of layered materials: Engineering Fracture Mechanics, 28(1), 1987, pp. 43-54.

[6] M.D. Kuruppu, K.P. Chong, Fracture toughness testing of brittle materials using semi-circular bend (SCB) specimen, Engineering Fracture Mechanics, 2012, pp. 1-18 .

[7] M.D. Kuruppu, Fracture toughness measurement using chevron notched semi-circular bend specimen, Int J Fract, Vol. 86(4), 1997, pp33–38 .

[8] M.D. Kuruppu, Stress intensity factors of chevron-notched semi-circular specimens, In: Basu et al., editors. Proc 3rd APCOM, the aust inst of min & met. 1998, pp. 111–112.

[9] M.D. Kuruppu, Fracture toughness testing of geomaterials using semi-circular specimen, In: Proc geo engng, Technomic Publishing Lancaster, PA; [Proc in CD], vol. 2, 2000.

[10 I.L. Lim, I.W. Johnston, S.K. Choi, J.N. Boland, Fracture testing of a soft rock with semi-circular specimens under three-point loading, Part 1 – Mode I. Int J Rock Mech Min Sci, Vol. 31, 1994, pp. 185–97.

[11] I.L. Lim, I.W. Johnston, S.K. Choi, Stress intensity factors for semi-circular specimens under three-point bending, Eng. Fract. Mech., 44, 1993, pp. 363–382.

[12] Bluhm J. I., Slice synthesis of a three dimensional Work of Fracture specimen, Engng Fracture Mech. 7, 1975, pp. 593-604.

[13] Q.Z. Wang, X.M. Jia, L.Z. Wu, Wide-range stress intensity factors for the ISRM suggested method using CCNBD specimens for rock fracture toughness tests. Int J Rock Mech Min Sci, 41, 2004, pp. 709–16.

Modeling Fracture Processes in Numerical Concrete

Zhiwei Qian[1,2,*], **Erik Schlangen**[2], **Guang Ye**[2], **Klaas van Breugel**[2]

[1] Materials innovation institute M2i, Delft, the Netherlands
[2] Delft University of Technology, Delft, the Netherlands
* Corresponding author: z.qian@tudelft.nl

Abstract Modeling the fracture processes in concrete requires a material structure of concrete to start with. The material structure of concrete can be obtained either experimentally by X-ray computed tomography, or numerically by a computer simulation. A simplified way to represent the material structure of concrete is to put multiple spheres in a matrix, where the spheres are interpreted as aggregates. This assumption of the shape of aggregates might have influences on the fracture processes in concrete, such as the microcracks propagation path. Recently the Anm material model was proposed and implemented, which can produce a material structure of concrete with irregular shape aggregates. The irregular shape is represented by a series of spherical harmonic coefficients. The further mechanical performance evaluation would benefit from this more realistic material structure. In this paper a material structure of concrete is simulated by the Anm material model. A number of irregular shape particles are planted in a matrix. This material structure is then converted into a voxelized image. Afterwards a random lattice mesh is made, and three types of lattice elements are defined, which represent aggregates, matrix and interface respectively. A uniaxial tensile test is set up and simulated by fixing all the lattice nodes at the bottom of the specimen and imposing a prescribed unit displacement onto all the nodes at the top. The lattice fracture analysis gives the stress-strain response and microcracks propagation, from which some mechanical properties such as Young's modulus, tensile strength and fracture energy can be predicted.

Keywords Lattice Fracture, Tensile Test Simulation, Irregular Shape Aggregates

1. Introduction

The material structure of concrete determines its global performance. Normal concrete is made from coarse aggregates (e.g. crushed stones, river gravels), fine aggregates (e.g. sands), cement and water. A chemical reaction starts immediately when water is mixed with cement, and reaction products are produced. The resulting cement paste keeps aggregates together and forms a system which is able to carry loads. Mortar consists of cement paste and sand, and concrete is composed of mortar and coarse aggregates.

Generally speaking there are two different approaches to obtain the material structure of concrete, which are X-ray computed tomography and computer simulations. From the modeling point of view, the material structure of concrete can be represented by particles embedded in matrix material model. The particles are interpreted as coarse aggregates, and the matrix as mortar. A simplified way to represent coarse aggregates is to use spheres. However this simplification might alter the real material structure of concrete, and thus may change the fracture processes in concrete, such as the microcracks propagation path. Recently the Anm material model was proposed and implemented, which can produce a material structure of concrete with irregular shape aggregates [1]. The irregular shape is represented by a series of spherical harmonic coefficients. The more realistic material structure would make the prediction of fracture processes more precise.

Numerical modeling of fracture processes in brittle materials, such as cement paste, mortar, concrete and rocks, started in the late 1960s with the landmark papers of Ngo and Scordelis [2] and Rashid [3], in which the discrete and smeared crack models were introduced. Especially the latter approach gained much popularity, and in the 1970s comprehensive efforts were invested in developing constitutive models in a smeared setting which could reproduce the experimentally

observed stress-strain characteristics of concrete. However neither of them could tell the fracture processes in detail. In the 1990s, Schlangen and van Mier proposed another model to compensate the drawbacks of discrete and smeared crack models, which is called lattice fracture model [4].

The concept of lattice was proposed by Hrennikoff in the 1940s to solve elasticity problems using the framework method [5]. In the 1970s and 1980s the lattice model was introduced in theoretical physics to study the fracture behavior of disordered media [6, 7]. In the field of material sciences, a model was proposed by Burt and Dougill to simulate uniaxial extension tests, which consists of a plane pin-jointed random network structure of linear elastic brittle members having a range of different strengths and stiffnesses [8].

In the lattice fracture model, the continuum is replaced by a lattice of beam elements. Subsequently, the microstructure of the material can be mapped onto these beam elements by assigning them different properties, depending on whether the beam element represents a grain or matrix. Various conventional laboratory experiments like uniaxial tensile test, compressive test, shear test, bending test and torsional test can be simulated by the lattice fracture model and the model can be applied towards a wide range of multiphase materials, such as concrete [9], cement paste [10], graphite and fiber reinforced concrete [11].

In this paper a material structure of concrete is simulated by the Anm material model. A number of irregular shape particles are planted in a matrix. This material structure is then converted into a voxelized image. Afterwards a random lattice mesh is made, and three types of lattice elements are defined, which represent aggregates, matrix and interface respectively. A uniaxial tensile test is set up and simulated by fixing all the lattice nodes at the bottom of the specimen and imposing a prescribed unit displacement onto all the nodes at the top. The lattice fracture analysis gives the stress-strain response and microcracks propagation, from which some mechanical properties such as Young's modulus, tensile strength and fracture energy can be predicted.

2. Simulation of the material structure of concrete

The concept of particles embedded in matrix is the essential of the Anm material model. An empty container is created to represent a concrete specimen at the beginning, and then all the particles representing coarse aggregates are placed one after another into this container, from the larger ones to smaller ones. It is good to start with the largest particles as it would be more difficult to place them if they were processed at a later stage. All the particles are separated into several sieve ranges according to the particle sizes indicated by the particle widths. The largest sieve range is processed first, a width within this sieve range is picked randomly and assigned to a particle which is chosen from the appropriate particle shape database. The particle shape database can be created for different classes of aggregates with the procedures proposed in [12]. An arbitrary rotation is performed on the particle to get rid of possible orientation bias, which might be introduced during the production of the particle shape database. After the rotation the particle is placed at a randomly chosen location in the specimen. The particle is checked against all the previously placed particles for overlap. If no overlap is detected, then the particle enters the simulation box successfully, otherwise it will be moved to a new randomly chosen location. The reassignment of the location is subject to a pre-defined maximum number of attempts. After the consecutive failures reach the limit, the particle will be resized to another randomly selected width within the current sieve range, and then be thrown into the specimen following the same trial-and-error procedure. The particle size rescale is also subject to a pre-defined maximum number of attempts. If the rescales do not help, then the particle will be rotated again to have another orientation. If the problem still exits, then a new shape will be chosen from the particle shape database. In case the particle cannot find its

position eventually, it may suggest there is no space available for new particles within the current sieve range. The next sieve range will be processed if no availability for the current sieve range is concluded, or all the particles within the current sieve range have already been placed. The above trial-and-error procedure is called parking procedure and it is the essential of the Anm material model.

Concrete specimen of the size 150 mm in the cubic shape is simulated by the Anm material model. The specimen has two phases, the mortar matrix and crushed stone aggregates. Non-periodic material boundary applies, which requires all the particles are inside the specimen and no part of a particle can pass through a surface. The total mass of the crushed stones is 2653 g, the corresponding volume is 1001132 mm^3, and 64% of which are in the sieve 8~16 mm, the rest 36% are in the sieve 4~8 mm. The particle size is taken as the particle width and its distribution for the coarse aggregates is given in Figure 1. The volume percentage of the crushed stones in the concrete specimen is 30%. The simulated material structure of the concrete specimen with irregular shape crushed stones is sketched in Figure 2.

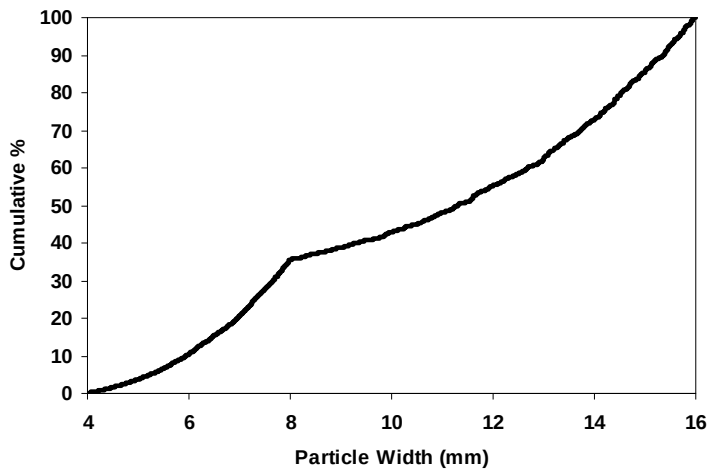

Figure 1. Particle size distribution for the coarse aggregates in concrete

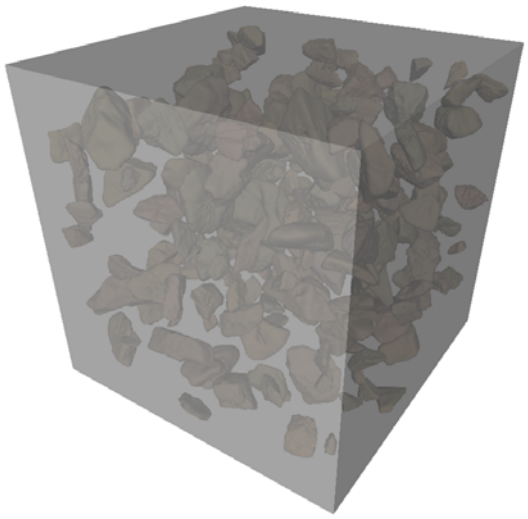

Figure 2. The material structure of the 150 mm concrete specimen with irregular shape crushed stones

3. Fracture processes in the numerical concrete

The fracture processes in concrete can be predicted by the lattice fracture model. The material structure of concrete is obtained in the previous section, and the next step is to evaluate its mechanical performance by simulating a uniaxial tensile test on it. To reduce the computational effect, a smaller specimen of the size 40 mm is cut out from the original 150 mm specimen at its center. The 40 mm concrete specimen is then digitized at the resolution of 1 mm, and consists of two solid phases namely stone and mortar. A lattice network is constructed based on the digital concrete specimen, and three types of lattice elements are identified, which represent crushed stone, mortar and interface respectively, as shown in Figure 3. The local mechanical properties are given in Table 1. The properties of the lattice elements representing mortar are varied randomly to reflect the heterogeneity of mortar phase.

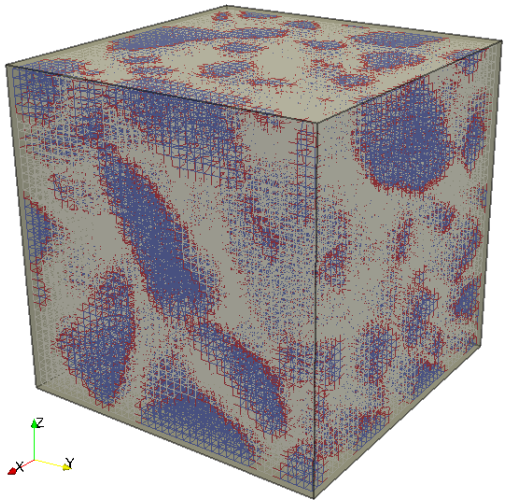

Figure 3. Lattice mesh of the 40 mm numerical concrete specimen

Table 1. Local mechanical properties of stone, mortar and interface elements in concrete

	Young's modulus (GPa)	Tensile strength (MPa)
Stone	70	24
Mortar	17~65	1.1~19.5
Interface	41	1

A uniaxial tensile test is simulated on the lattice system meshed from the 40 mm concrete specimen as shown in Figure 3, using the local mechanical properties listed in Table 1. All the lattice nodes on the bottom surface of the specimen are fixed, and a unit prescribed displacement is imposed on the nodes located on the top surface, as illustrated in Figure 4.

The lattice fracture analysis consists of multiple steps. At every analysis step it is required to determine the critical element and the corresponding system scaling factor after the calculation of comparative stress in every lattice element. The critical element is the one with highest stress/strength ratio when the system is loaded by a unit prescribed displacement. The inverse of the ratio is defined as a system scaling factor. The system scaling factor, together with the reactions on the restraint boundaries, determines one scenario of critical load-displacement pairs. The critical element is removed from the system and if the system does not fail completely yet, it is recomputed as the system is updated due to the element removal. Multiple analysis steps are carried out until the system fails. Hence a set of load-displacement pairs can be obtained and used to plot the load-displacement diagram, which can be converted to a stress-strain diagram later to represent the

constitutive relation of the material. The step-by-step removal of critical lattice elements indicates the microcracks evolution in the specimen. Thus the microcracks propagation and the cracks pattern in the final failure state can also be simulated.

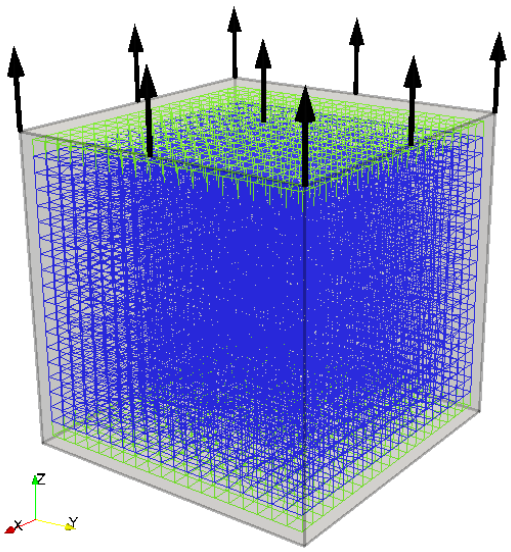

Figure 4. Uniaxial tensile test setup

For the example given in this paper, the resulting stress-strain response is presented in Figure 5, and some mechanical properties can be computed as given in Table 2.

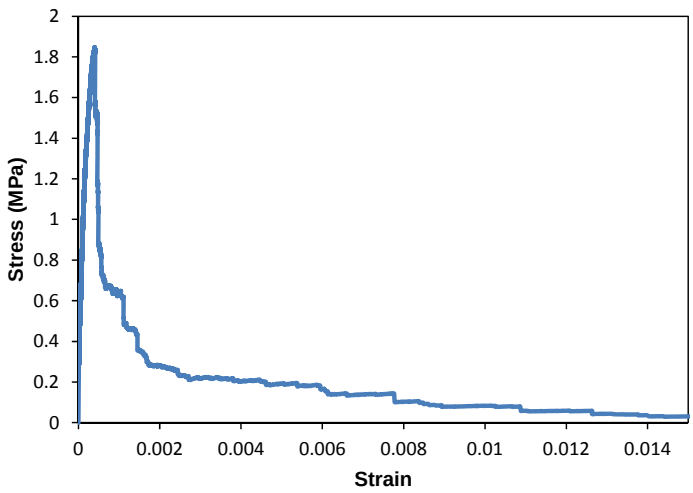

Figure 5. Simulated stress-strain response of the 40 mm concrete specimen

Table 2. Simulated mechanical properties of the 40 mm concrete specimen

Young's modulus (GPa)	Tensile strength (MPa)	Strain at peak load	Fracture energy (J/m^2)
31	1.8	0.04%	127

The pattern of the simulated stress-strain response of the 40 mm concrete specimen is similar to the one observed in laboratory, and the mechanical properties computed from the stress-strain diagram are also located within the reasonable range.

4. Summary and conclusions

In this paper a material structure of concrete is simulated by the Anm material model. A number of irregular shape particles are planted in a matrix, representing coarse aggregates in mortar. This material structure of concrete is then converted into a voxelized image. After that a random lattice mesh is made, and three types of lattice elements are identified, which represent aggregates, matrix and interface respectively. A uniaxial tensile test is set up and simulated by fixing all the lattice nodes at the bottom of the specimen and imposing a prescribed unit displacement onto all the nodes at the top. The lattice fracture analysis gives the stress-strain response and microcracks propagation, from which some mechanical properties such as Young's modulus, tensile strength and fracture energy can be predicted. The simulated mechanical properties of the numerical concrete specimen are quite reasonable, which is a positive evidence that proves the feasibility of the proposed modeling procedures.

Acknowledgements

This research was carried out under project number M83.1.12459 in the framework of the Research Program of the Materials innovation institute M2i (http://www.m2i.nl). Part of this work was sponsored by the European Union FP7 project CODICE (http://www.codice-project.eu).

References

[1] Qian, Z., Multiscale Modeling of Fracture Processes in Cementitious Materials, PhD thesis, Delft University of Technology, 2012
[2] Ngo, D. & Scordelis, A., Finite Element Analysis of Reinforced Concrete Beams, J Am Concr Inst, 1967, 64, 152-163
[3] Rashid, Y., Ultimate strength analysis of prestressed concrete pressure vessels, Nuclear Engineering and Design, 1968, 7, 334-344
[4] Schlangen, E. & van Mier, J., Experimental and numerical analysis of micromechanisms of fracture of cement-based composites, Cement and Concrete Composites, 1992, 14, 105-118
[5] Hrennikoff, A., Solution of problems of elasticity by the framework method, Journal of Applied Mechanics, 1941, 8, 169-175
[6] Ziman, J. M., Models of disorder: the theoretical physics of homogeneously disordered systems, Cambridge University Press, 1979
[7] Herrmann, H. J.; Hansen, A. & Roux, S., Fracture of disordered, elastic lattices in two dimensions, Phys. Rev. B, American Physical Society, 1989, 39, 637-648
[8] Burt, N. J. & Dougill, J. W., Progressive Failure in a Model Heterogeneous Medium, Journal of the Engineering Mechanics Division, 1977, 103, 365-376
[9] Schlangen, E., Experimental and Numerical Analysis of Fracture Processes in Concrete, PhD thesis, Delft University of Technology, 1993
[10] Qian, Z.; Schlangen, E.; Ye, G. & van Breugel, K., Prediction of Mechanical Properties of Cement Paste at Microscale, Materiales de Construccion, 2010, 60, 7-18
[11] Schlangen, E. & Qian, Z., 3D modeling of fracture in cement-based materials, Journal of Multiscale Modelling, 2009, 1, 245-261
[12] Garboczi, E., Three-dimensional mathematical analysis of particle shape using X-ray tomography and spherical harmonics: Application to aggregates used in concrete, Cement and Concrete Research, 2002, 32, 1621-1638

Stability and fracture analysis of arch dam based on deformation reinforcement theory

Yuanwei Pan[1,*], **Yaoru Liu**[1], **Qiang Yang**[1]

[1] Department of Hydraulic Engineering, Tsinghua University, 100084, China
* Corresponding author: pyw10@mails.tsinghua.edu.cn

Abstract Fracture is a common and significant failure mode of high arch dam. Current theories are still limited in fracture analysis of 3-D structure. In this paper, deformation reinforcement theory (DRT) is deduced and elaborated with a definition of stability that an elasto-plastic structure is stable if equilibrium condition, kinematical admissibility and constitutive equations can simultaneously be satisfied under given external loads. Furthermore, a global stability analysis method of elasto-plastic structure based on DRT is presented. Unbalanced forces can be used to evaluate the stability of structure and indicate fracture initiation and propagation. FEM expression of DRT is deduced and implemented in a three dimensional nonlinear FEM program, and successfully applied in dam heel cracking and multi-crack analysis of arch dam. As statically indeterminate structure, high arch dam is capable of stress redistribution to some extent while cracking occur. This process was expressed in FEM program by iteration and convergence of unbalanced forces. Both elasto-plastic FEM analysis and geo-mechanical experiments are performed on Baihetan and Xiaowan arch dams. Results show that unbalanced forces can be used as the indication of fracture initiation and propagation.

Keywords arch dam, cracks, fracture, stability, unbalanced force

1. Introduction

From the point of view of failure analysis, fracture is a common and significant failure mode of high arch dam, which may result in many problems. In fracture analysis, various factors should be taken into consideration, e.g., material properties, surface notches, cracks, shape and size of structure and working conditions. Those factors present many challenging problems of practical importance range from the micro-scale cavity of materials to macro-scale cracks in engineering structures.

Fracture mechanics has now developed many branches such as linear elastic fracture mechanics (LEFM), nonlinear fracture mechanics, fatigue analysis (e.g., lifetime prediction) and dynamic fracture mechanics. Irwin and Orowan extended Griffith's classical work on brittle materials and proposed both stress and energetic criterions to analyze cracking [1–3], i.e., the stress intensity factor (SIF) and energy release rate, which provided precise measure of fracture toughness and succeeded in predicting cracking behavior. Some significant advances were made by theoretical and experimental mechanics researchers in nonlinear fracture analysis. Wells suggested to assess ductile fracture toughness with crack opening displacement (COD) [4]. Rice proposed J-integral that characterize the intensity of near tip elastic-plastic deformation fields [5]. Besides, numerical methods have developed rapidly, including Finite Element Method (FEM), Discrete Element Method (DEM), Boundary Element Method, eXtended FEM, Numerical Manifold Method and etc.

Those theories mentioned above are based on planar analysis. There is still severe limitation on the applicability of those theories when extended to three-dimension structure. Besides, very little progress has yet been made on understanding the nucleation, growth and interaction of cracks. The description of multi-crack behavior involves complex nonlinear overall deformation, which is beyond the capacity of common numerical methods based on linear plastic.

This paper presents a new approach to deal with cracks in stability and fracture analysis of 3-D structure. Unbalanced force, derived from the Deformation Reinforcement Theory (DRT) [6, 7], could be the criterion of initiation of fracture, the distribution area and magnitude of which could indicate fracture propagation direction [8]. FEM expression of DRT was deduced and implemented

in a three dimensional nonlinear FEM program, and successfully applied in dam heel cracking and multi-crack analysis of arch dam. Both FEM analysis and geo-mechanical experiments are performed on Baihetan and Xiaowan arch dams. Results show that unbalanced forces can be used as the indication of fracture initiation and propagation.

2. Deformation Reinforcement Theory

2.1. Definition of structural stability

Geotechnical structure are characterized by magnificent scale and complicated configurations and working conditions. The classical elasto-plastic theory aims at solving the displacement and stress fields that simultaneously satisfy all the basic equations in boundary value problem, including kinematic admissibility, equilibrium condition and constitutive equations. However, the existence of such solution requires that the structure is stable, i.e., a state where no failure occurs [9]. Structural instability occurs when action is greater than resistance, and the difference between action and resistance defines the unbalanced force. Considering the arbitrary kinematical and equilibrium stress-field, $\boldsymbol{\sigma}_1$, which is termed the trial elastic stress:

$$\boldsymbol{\sigma}_1 = \boldsymbol{\sigma}_0 + \Delta\boldsymbol{\sigma}^{\mathrm{e}} = \boldsymbol{\sigma}_0 + \boldsymbol{D} : \Delta\boldsymbol{\varepsilon} . \tag{1}$$

The kinematical and stable stress-field, $\boldsymbol{\sigma}$, which is the real stress response, could be identified by the following minimization problem:

$$\begin{gathered} \min E\left(\boldsymbol{\sigma}^{yc}\right), \forall f\left(\boldsymbol{\sigma}^{yc}\right) \le 0, \\ E\left(\boldsymbol{\sigma}^{yc}\right) = \frac{1}{2}\left(\boldsymbol{\sigma}_1 - \boldsymbol{\sigma}^{yc}\right) : \boldsymbol{C} : \left(\boldsymbol{\sigma}_1 - \boldsymbol{\sigma}^{yc}\right). \end{gathered} \tag{2}$$

Eq. (2) is known as the closest-point projection method (CPPM) [10], as shown in Fig. 1.

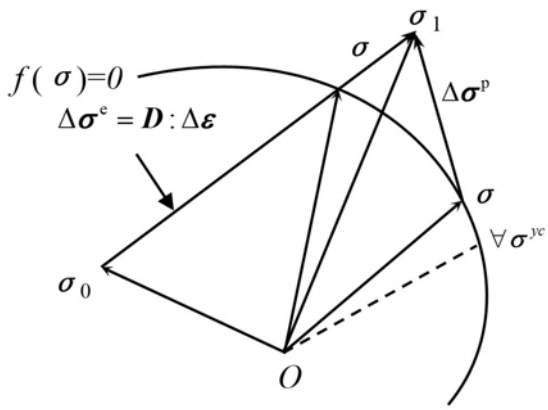

Figure 1. Diagram of elastic-plastic stress adjustment

The difference between $\boldsymbol{\sigma}_1$ and $\boldsymbol{\sigma}$ is the plastic-stress increment field $\Delta\boldsymbol{\sigma}^{\mathrm{p}}$:

$$\Delta\boldsymbol{\sigma}^{\mathrm{p}} = \boldsymbol{\sigma}_1 - \boldsymbol{\sigma} . \tag{3}$$

The plastic-stress increment field $\Delta\boldsymbol{\sigma}^{\mathrm{p}}$ leads to the plastic-strain increment field $\Delta\boldsymbol{\varepsilon}^{\mathrm{p}} = \boldsymbol{C} : \Delta\boldsymbol{\sigma}^{\mathrm{p}}$, while $\boldsymbol{C}$ is the fourth-order compliance tensors.

Clearly, the minimization variable $\boldsymbol{\sigma}$ restricted by the yield criterion can be viewed as the material resistance while the minimization objective $\boldsymbol{E}$ in Eq. (2), termed the volume density of the plastic complementary energy (PCE), represents the difference between the plastic dissipations of the stress action and the material resistance,

$$E\left(\boldsymbol{\sigma}\right) = \frac{1}{2}\left(\boldsymbol{\sigma}_1 - \boldsymbol{\sigma}\right) : \boldsymbol{C} : \left(\boldsymbol{\sigma}_1 - \boldsymbol{\sigma}\right). \tag{4}$$

Thus, stability of a material point can be interpreted as the condition that the stress action is greater

than the material resistance in the sense of plastic dissipation: $E(\boldsymbol{\sigma}) > 0$. Furthermore, stability of a structure whose volume is V can be deduced as

$$\Delta E = \frac{1}{2}\int_V \Delta\boldsymbol{\sigma}^{\mathrm{p}} : \boldsymbol{C} : \Delta\boldsymbol{\sigma}^{\mathrm{p}} \mathrm{d}V . \tag{5}$$

This equation shows that ΔE is also the norm of plastic-stress increment field $\Delta\boldsymbol{\sigma}^{\mathrm{p}}$. If $\Delta E = 0$, then $\Delta\boldsymbol{\sigma}^{\mathrm{p}}$ is always zero and the structure is stable. If $\Delta E > 0$, the structure is unstable.

2.2. Expression in FE analysis

In this section, DRT is deduced and implemented in elasto-plastic FE analysis. For simplicity, the problem is restricted in displacement method, which means the kinematic admissibility is naturally satisfied.

Since $\boldsymbol{\sigma}_1$ is a equilibrium stress-field, it satisfies equilibrium condition:

$$\boldsymbol{F} = \sum_e \int_{Ve} \boldsymbol{B}^{\mathrm{T}} \boldsymbol{\sigma}_1 \mathrm{d}V . \tag{6}$$

$\boldsymbol{F}$ is equivalent nodal force vector of external loads. $\boldsymbol{B}$ denotes the displacement gradient matrix.

Applied with Eq. (3) and after simple manipulations, Eq. (6) can be recast into the following expression:

$$\Delta\boldsymbol{U} = \sum_e \int_{Ve} \boldsymbol{B}^{\mathrm{T}} \Delta\boldsymbol{\sigma}^{\mathrm{p}} \mathrm{d}V = \sum_e \int_{Ve} \boldsymbol{B}^{\mathrm{T}} (\boldsymbol{\sigma}_1 - \boldsymbol{\sigma}) \mathrm{d}V = \boldsymbol{F} - \sum_e \int_{Ve} \boldsymbol{B}^{\mathrm{T}} \boldsymbol{\sigma} \mathrm{d}V . \tag{7}$$

$\Delta\boldsymbol{U}$ is the driving force of the deformation process that can be termed the unbalanced force. It's also referred to as the residual force in FEM, which is a set of equivalent nodal forces of the difference between the two stress fields $\boldsymbol{\sigma}_1$ and $\boldsymbol{\sigma}$.

2.3. Fracture analysis based on DRT

Liu Y. R. et al. proved both theoretically and experimentally that the unbalanced force can be used as the prediction and measurement of failure mechanism [8]. Failure occurs where there is unbalanced force subjected to prescribed loads, and the structure is unstable in the sense of PCE. So the unbalanced force can be used to evaluate fracturing of structure.

According to DRT, unbalanced forces are the driving force of structural failure, and fracture is part of the failure mechanism. Thus, unbalanced forces could be the determination of fracture location. The area where unbalanced forces occur is the location where the fracture initiates. Furthermore, the amount of unbalanced force incurred by external load represents the extent of fracture propagation. The development of unbalanced forces is the process of propagation of the fracture.

3. Application in high arch dam

In this section, unbalanced forces are applied to indicate initiation of dam heel cracking, and to verify the dominating cracks from multi-crack arch dam.

3.1. Dam heel cracking analysis of Baihetan arch dam

Baihetan arch dam, located in an asymmetrical "V"-shaped valley, is 289 m high. Both 3-D finite element numerical and geo-mechanical experiments are performed. The finite element mesh model is shown in Fig. 2(a). Various rock materials and faults are simulated. The size of FE model is as follows:

Upper stream: 1.5 times of the height of dam (500 m);

Down stream: 2.5 times of the height of dam (700 m);
Left and right banks: 3 times of the height of dam (800 m each);
Height above the dam: 50 m;
Height beneath the dam: 324 m.
Fig. 2(b) is photo of the arch dam model and distribution of devices. The geo-mechanical model is built in a steel frame whose size is 4.6 m×4.6m×2.8 m. The model scale is 1:250.

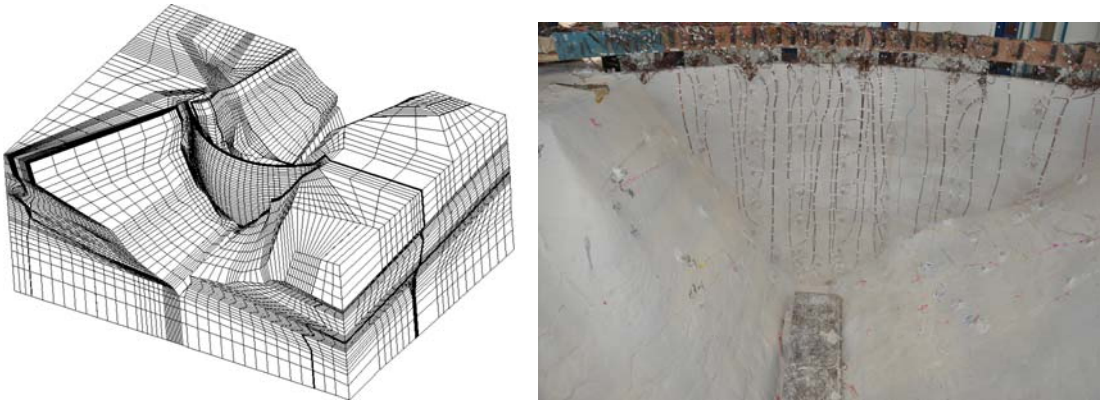

(a) Numerical mesh (b) geo-mechanical model
Figure 2. Numerical mesh and geo-mechanical model of Baihetan arch dam

Fig. 3 shows that unbalanced forces of upstream surface concentrate near the foundation plane, especially the dam heel near river bed area. Unbalanced forces distribution contour of dam heel in different work conditions are shown in Fig. 4. The unbalanced forces concentrated in the upstream river bed area near the dam heel instead of the dam itself, where there is a fault crossing. Unbalanced forces form a significant banding in this area, which is termed as the indication of cracks initiation.
Cracking status of the dam heel near river bed area during the geo-mechanical test are illustrated in Fig. 5. When work load reaches 1.5 times water pressure, micro-cracks initiate in the upstream river bed about 14.5 m away from dam heel, which agrees with the FE analysis results. Cracks propagate as work load increases to 2.0 times water pressure, and begin to penetrate through the river bed.

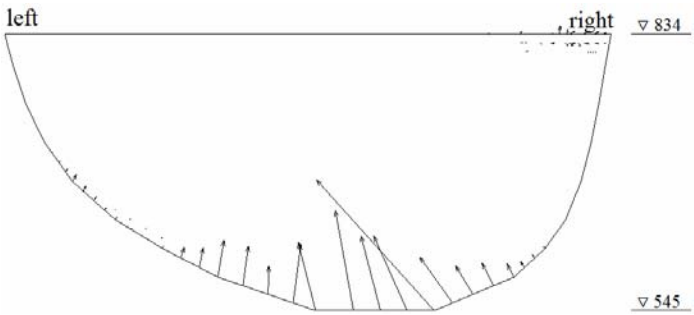

Figure 3. Unbalanced forces distribution of upstream surface

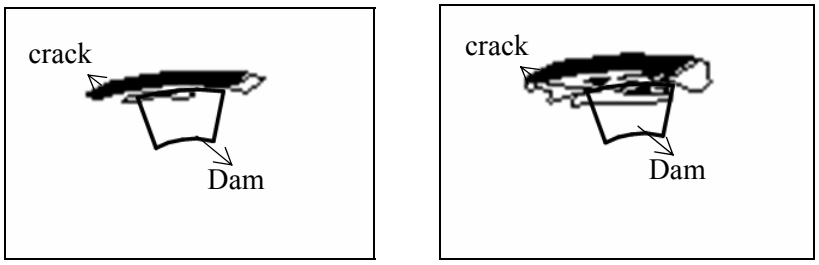

(a) 1.5 times water pressure (b) 2.0 times water pressure
Figure 4. Unbalanced forces distribution of dam heel

(a) 1.5 times water pressure (b) 2.0 times water pressure

Figure 5. Cracking status of the dam heel near river bed area

3.2. Fracture analysis of Xiaowan arch dam

Xiaowan arch dam is subjected to numerous cracks due to the temperature control program. In the following example, we simulate the major cracks in the dam and analyze parameters sensitivity with DRT method. Results and conclusions of geo-mechanical model test are also given as comparison with numerical method.

FE computation model of Xiaowan includes 58989 nodes and 53850 elements, while 11 cracks in the dam are simulated with thin layer elements, as shown in Fig. 6. Since engineering measures have been applied, the parameters of crack elements are as follows: E=5GPa, μ=0.3, γ=27.5kN/m^3, f=1.12, c=0.9MPa. Parameters E, f, c are reduced with certain percentages in five schemes, respectively 100% (scheme 1), 50% (scheme 2), 30% (scheme 3), 10% (scheme 4) and 5% (scheme 5). Both normal and overload conditions are included in each scheme. Unbalanced forces of cracks and dam heel in scheme 1 and 3 are given by Table 1 and Table 2.

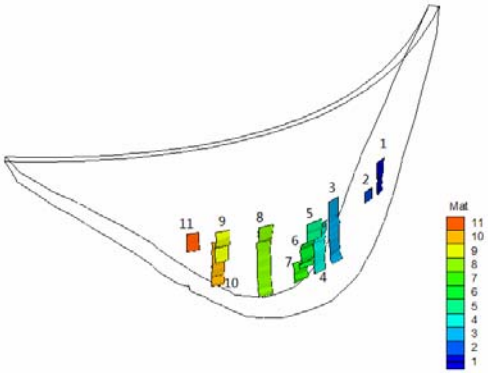

Figure 6. Distribution of cracks in Xiaowan arch dam

Table 1. Unbalanced forces of cracks and dam heel in scheme 1 (10^4 N)

No.	Crack	Dam weight	Water pressure	1.5 times water pressure	2 times water pressure	2.5 times water pressure
1	13lf-1	0.06	0.00	0.36	1.36	32.50
2	13lf-2	0.01	0.00	1.23	4.84	76.41
3	20lf-1	0.02	0.00	0.00	0.00	13.92
4	20lf-2	0.00	0.00	0.58	6.63	11.95
5	22lf-1	0.00	0.00	0.00	0.00	0.00
6	22lf-3	0.00	0.00	0.00	0.00	0.00
7	22lf-4	0.00	0.00	0.00	0.00	0.00
8	25lf-1	0.00	0.00	0.00	0.00	1.04
9	28lf-1	0.01	0.00	0.00	0.00	3.99
10	28lf-2	0.05	0.00	1.91	13.10	24.79
11	30lf-1	0.00	0.01	0.41	16.73	29.77
Dam heel		4122.63	40249.56	257289.9	415601.5	561660.5

* Crack 13lf-1 in the table means the first crack in No. 13 dam section, and so on.

Table 2. Unbalanced forces of cracks and dam heel in scheme 3 (10^4 N)

No.	Crack	Dam weight	Water pressure	1.5 times water pressure	2 times water pressure	2.5 times water pressure
1	13lf-1	0.11	0.88	1.59	3.11	38.11
2	13lf-2	0.04	1.98	25.22	67.44	92.83
3	20lf-1	0.13	0.00	0.00	0.00	14.30
4	20lf-2	0.00	18.05	597.84	1902.98	3216.86
5	22lf-1	0.00	0.00	0.00	0.00	0.00
6	22lf-3	0.06	0.00	0.00	0.00	0.00
7	22lf-4	0.00	0.00	0.00	0.00	0.00
8	25lf-1	0.25	0.00	0.00	0.00	0.47
9	28lf-1	155.71	0.00	0.95	20.05	110.01
10	28lf-2	0.65	18.39	2321.18	9522.02	18778.98
11	30lf-1	69.33	0.19	29.91	124.81	897.03
Dam heel		4005.15	40225.05	257428.3	415430.9	561604.5

Table 1 and Table 2 show that unbalanced forces of dam heel increase earlier than cracks in the dam. Dam heel contributes the major unbalanced forces in all condition. Namely, dam heel cracking occurs before any crack propagates. Among all existing cracks, 20lf-2 and 28lf-2 are the dominating cracks in the process of fracture propagation.

The final crack status of upstream dam surface in geo-mechanical model test is shown in Fig. 7. In normal working condition, dam cracks are mostly in compression-shear state, and neither yielding nor tension fracture is involved. Dam heel cracking occurs as the work load increases to 1.7~3.0 times normal pressure. There is no sign of crack propagation in the dam during the test. Instead, cracks that occur on the dam surface begin to extend after the work load reaches 4.0 times normal pressure. Experimental results indicate that dam heel cracking, compared with dam cracks, is the dominating problem of Xiaowan arch dam, which is corresponding to FEM results.

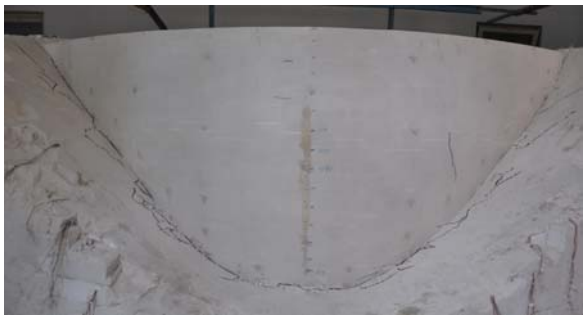

Figure 7. The final crack status of upstream dam surface

4. Conclusions

This paper presents a new approach to deal with cracks in stability and fracture analysis of 3-D structure. Unbalanced force, derived from the Deformation Reinforcement Theory (DRT), could be the criterion of initiation of fracture, the distribution area and magnitude of which could indicate fracture propagation direction. FEM expression of DRT is deduced and implemented in a three dimensional nonlinear FEM program, and successfully applied in dam heel cracking and multi-crack analysis of arch dam. Both elasto-plastic FEM analysis and geo-mechanical experiments are performed on Baihetan and Xiaowan arch dams. Dam heel cracking and multi-crack propagation analysis are presented. Results of geo-mechanical experiments show great agreement with FEM analysis. Unbalanced forces can be used as the indication of fracture initiation and propagation.

Acknowledgements

The work reported here was supported by State key Laboratory of Hydroscience and Hydraulic Engineering under grant No. 2013-KY-2 and China National Funds for Distinguished Young Scientists under grant No. 50925931.

References

[1] G. R. Irwin, Fracture dynamics, in: Fracturing of metals. Cleveland: Am. Soc. Metals, 1948. 147–166.
[2] E. Orowan, Fracture and strength of solids, in: Rep. on Progr. in Phys., 1948. 185.
[3] G. R. Irwin, Analysis of stresses and strains near the end of a crack transversing a plate. J. Appl. Mech., 24 (1957) 361–364.
[4] A. A. Wells, Application of fracture mechanics at and beyond general yielding. British Welding J, 10 (1963) 563–570.
[5] J. R. Rice, A path independent integral and the approximate analysis of strain concentration by notches and cracks, Journal of Applied Mechanics, 35 (1968) 379-386.
[6] Yang Q., Liu Y. R., Chen Y. R., Zhou W. Y., Deformation reinforcement theory and global stability and reinforcement of high arch dams. Chin J Rock Mech Eng, 6 (2008) 1121–1136.
[7] Yang Q., Chen X., Zhou W. Y., Yang R. Q., On unbalanced forces in 3D elastoplastic finite element analysis. Chin J Geotech Eng, 3 (2004) 323–326.
[8] Liu Y. R., Chang Q., Yang Q., WANG C. Q., GUAN F. H., Fracture analysis of rock mass based on 3-D nonlinear Finite Element Method. Sci China Tech Sci, 54 (2011) 556–564.
[9] Yang Q., Leng K. D., Chang Q., Liu Y. R., Failure mechanism and control of geotechnical structures. Yang Q., et al. (Eds.), Constitutive Modeling of Geomaterials, Springer Berlin Heidelberg, 2013, pp. 63-87.
[10] Simo, J. C., Kennedy, J. G., Govindjee, S., Non-smooth multisurface plasticity and viscoplasticity, Loading/unloading conditions and numerical algorithms. Int. J. Numer. Methods Engrg. 26 (1988) 2161–2185.

ACOUSTIC EMISSION DETECTION IN CONCRETE SPECIMENS: EXPERIMENTAL ANALYSIS AND SIMULATIONS BY A LATTICE MODEL

I. Iturrioz[1], G. Lacidogna[2], A. Carpinteri[2]

(1) *Federal University of Rio Grande do Sul*
Department of Mechanical Engineering
Porto Alegre, RS, Brazil

(2) *Politecnico di Torino*
Department of Structural Engineering and Geotechnics
Torino, Italy

ABSTRACT

In civil engineering, materials subjected to stress or strain states a quantitative evaluation of damage is of great importance due to the critical character of this phenomena, which at certain point suddenly turns into catastrophic failure.

An effective damage assessment criterion is represented by the statistical analysis of the Acoustic Emission (AE) amplitude distribution signals that emerges from the growing micro-cracks. The amplitudes of such signals are distributed according to the Gutenberg- Ritcher (GR) law and characterized through the *b*-value which systematically decreases with damage growth.

The *b*-value analysis was conducted on two experimental tests carried out on concrete specimens loaded up to failure. The first one is a prismatic specimen subjected to uniaxial compression load, the second one is a pre-cracked beam subjected to three point bending test.

The truss-like Discrete Element Method (DEM) was used to made numerical simulation on the experimental tests. The comparison between experimental and numerical analyses, in terms of load vs. time diagram and AE data, elaborated throughout the *b*-value and signals frequencies variations, provided results in good agreement.

Key words: Concrete; Lattice model; AE technique; *b*-value; Damage parameter.

1. INTRODUCTION

The most advanced method for a non-destructive quantitative evaluation of damage progression is the acoustic emission (AE) technique. Physically, AE is a phenomenon caused by a structural alteration in a solid material, in which transient elastic-waves due to a rapid release of strain energy are generated. AEs are also known as stress-wave emissions.

AE waves, whose frequencies typically range from kHz to MHz, propagate through the material towards the surface of the structural element, where they can be detected by sensors which turn the released strain energy packages into electrical signals Traditionally, in AE testing. a number of parameters are recorded from the signals, such as arrival time, velocity, amplitude, duration and frequency. From these parameters damage conditions and localization of AE sources in the specimens are determined, Carpinteri et. al. (2009).

Using the AE technique, an effective damage assessment criterion is provided by the statistical analysis of the amplitude distribution of the Acoustic Emission (AE) signals generated by growing microcracks. The amplitudes of such signals are distributed according to the Gutenberg-Richter (GR) law, $N(\geq A) \propto A^{-b}$, where N is the number of AE signals with amplitude $\geq A$. The exponent b of the GR law, the so-called b-value, changes with the different stages of damage growth: while the initially dominant microcracking generates a large number of low-amplitude AE signals, the subsequent macrocracking generates fewer signals of higher amplitude. On the other hand, the damage process is also characterized by a progressive localization identified through the fractal dimension D of the damaged domain. It may be proved that $2b=D$ (Aki(1967), Carpinteri 1994;

Turcotte (2003) ; Rundle *et al*. (2003); Carpinteri *et al*. (2008)). Therefore, by determining the *b*-value it becomes possible to identify the energy release modalities in a structural element during the AE monitoring process. The extreme cases envisaged are D = 3.0, which corresponds to b=1.5, a critical condition in which the energy release takes place through small defects evenly distributed throughout the volume, and D=2.0, which corresponds to b = 1.0, when energy release takes place on a fracture surface. In the former case diffused damage is observed, whereas in the latter case two dimensional cracks are formed leading to the separation of the structural element.

Moreover, in seismology, the energy released during an earthquake can be linked with seismogram amplitude thanks to the classical expression proposed by Ritcher (1958), $E_s \propto A^c$, where: A is the earthquake amplitude, and c=[1.5, 2] is an exponent obtained experimentally from earthquakes measurements. Another expression appearing in a seismological context, in Chakrabarti and Benguigui (1997), is $N(>=E_s) \propto E_s^{-d}$, where N is the cumulative distribution of released energy and d=[0.8,1.1] is an exponent obtained from earthquakes observations.

2 RELATIONSHIP BETWEEN SIGNAL AMPLITUDE AND THE NUMBER OF AE EVENTS

Magnitude (m) is a geophysical log-scale quantity which is often used to measure the amplitude of an electrical signal generated by an AE event. Magnitude is related to amplitude (A), expressed in volts (V), by the following equation:

$$m = \text{Log } A. \tag{1}$$

The widely accepted Gutenberg–Richter (GR) law, initially proposed for seismic events, describes the statistical distribution of AE signal amplitudes :

$$N(\geq \text{A}) = \zeta A^{-b}, \tag{2}$$

where ζ and exponent b are coefficients that characterize the behavior of the model. We shall focus our attention on coefficient b.

By rewriting Eq. (2.2) as a logarithmic equation:

$$\text{Log}(\, N \geq \text{A}) = \text{Log } \zeta - bm, \tag{3}$$

where N is the number of AE peaks with magnitude greater than m, and coefficient b, referred to as ‘‘*b*-value”, is the negative slope of the *Log N* vs. *m* diagram. Microcracks release low-amplitude AEs, while macrocracks release high-amplitude AEs. This intuitive relationship is confirmed by the experimental observation that the area of crack growth is proportional to the amplitude of the relative AE signal Pollock (1973).

From Eq. (2.3) we find that a regime of microcracking generates weak AEs, and therefore leads to relatively high *b*-values (raising the threshold *m*, gives rise to a fast decline in the number of surviving signals). When macrocracks start to appear, instead, lower *b*-values are observed.

Therefore the analysis of the *b*-value, which changes systematically with the different stages of fracture growth has been recognized as a useful tool for damage level assessment. In general terms, the fracture process moves from micro to macrocracking as the material approaches impending failure and the *b*-value decreases. While testing the materials undergoing brittle failure, the *b*-value is found to be around 1.5 in the initial stages. It then decreases with increasing stress level to ≈1.0 and even less as the material approaches failure:

Furthermore, as pointed out in Carpinteri et. al. (2009), the statistical analysis of *b*-values is closely correlated with the fractal geometry approach in the damage and fracture mechanics of heterogeneous materials. Fractal geometry is the natural tool to characterize self-organized processes, emphasizing their universality and the scaling laws arising at the critical points.

3. THE TRUSS-LIKE DISCRETE ELEMENT METHOD

The truss-like DEM used in this work represents the continuum by means of a periodic spacial arrangement of bars with the masses lumped at their ends. A lumped mass of ($\rho L^3/2$) corresponds to each internal node, where ρ is the density and *L* the length of a cubic module. The nodes will have a lumped mass of ($\rho L^3/16$) if they are localized in the corner, ($\rho L^3/8$) on the edges and ($\rho L^3/4$) on a free surface. The discretization uses a basic cubic module constructed using 20 bar elements and 9 nodes showed in Figure 1(a) and 1(b). Every node has three degrees of freedom, which are the three components of the displacement vector in the global reference system.

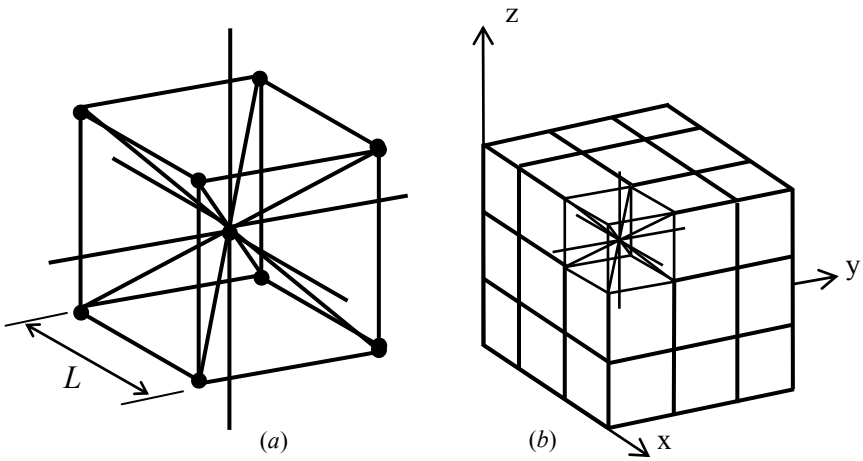

Figure 1. DEM discretization strategy: (a) basic cubic module, (b) generation of a prismatic body.

In case of an isotropic elastic material, the cross-sectional area A_l of the longitudinal elements (those defining the edges of the module and those parallel to the edges connected to the node located at the centre of the module) in the equivalent discrete model is:

$$A_l = \phi L^2 \tag{4}$$

where *L* is the length of the side of the cubic module under consideration. The function $\phi = (9+8\delta)/(18+24\delta)$, where $\delta = 9\nu/(4-8\nu)$, accounts for the effect of the Poisson's ratio *ν*. Similarly, the area A_d of the diagonal elements is:

$$A_d = \frac{2}{\sqrt{3}}\delta\phi L^2 \tag{5}$$

The coefficient $2/\sqrt{3}$ in equation (2) accounts for the difference in length between the longitudinal and the diagonal elements, this is, $L = 2/\sqrt{3} \cdot L_d$.

To arrive at expression of ϕ it is necessary to have equivalence between the isotropic elastic coefficient matrix and a computation of the equivalent directional properties of the bars as proposed by Nayfes Heftzy (1978).

It is important to point out that for $v = 0.25$, the correspondence between the equivalent discrete solid and the isotropic continuum is complete. On the other hand, discrepancies appear in the shear terms for values of $v \neq 0.25$. These discrepancies are small and may be neglected in the range $0.20 \leq v \leq 0.30$. For values outside this range, a different array of elements for the basic module should be used (see Nayfeh and Hefzy, 1978). It is interesting to note that while no lattice model can exactly represent a locally isotropic continuum, it can also be argued that no perfect locally isotropic continuum exists in practical engineering applications. Isotropy in solids is a bulk property that reflects the random distribution of the constituent elements orientation.
The equations of motion are obtained from equilibrium conditions of all forces acting on the nodal masses, resulting in a system of equations of the form:

$$\mathbf{M}\ddot{\mathbf{x}} + \mathbf{C}\dot{\mathbf{x}} + \mathbf{F}(t) - \mathbf{P}(t) = 0 \tag{6}$$

in which $\mathbf{x}$, $\dot{\mathbf{x}}$ and $\ddot{\mathbf{x}}$ denote vectors containing the nodal displacements, velocities and accelerations, respectively, while **M** and **C** are the mass and damping matrices, both are diagonals and the damping matrix is proportional only to the mass. The vectors $\mathbf{F}(t)$ and $\mathbf{P}(t)$ contain the internal and external nodal load.

Following the Courant-Friedrichs-Lewy criterion (see Bathe, 1996), the stability of the integration scheme is ensured by limiting the size of the time step. For the present implementation, the elements in the worst condition (this is, those requiring the smallest Δt) are the diagonal ones. Thus, considering the relationships in Equations (4) and (5), the limitation to the time increment is:

$$\Delta t \leq \frac{0.6L}{C_\rho} \tag{7}$$

where C_ρ is the longitudinal wave speed,

$$C_\rho = \sqrt{E/\rho} \tag{8}$$

The truss-like DEM has a natural ability to model cracks. They can be introduced into the models as pre-existent features and as the irreversible effect of crack nucleation and propagation. Pre-existent cracks are modeled using a simple strategy which consists in duplicate the nodes located on the crack surface together with the elimination of the elements connecting the material on both sides of the crack. This way, the DEM discretization is allowed to "open" along the crack locus, and pre-existent cracks are integrated seamlessly into the DEM formulation. Crack nucleation and propagation make use on non-linear constitutive models for material damage which allow the elements to break when they attain a critical condition. The details about the formulation and implementation of these non-linear constitutive models are given in the next section.

3.1 Non-linear constitutive models for material damage

Rocha *et al*. (1991) extended the lattice method here implemented (DEM) to model quasi brittle materials. To this end, they introduced the bilinear constitutive relationship illustrated in Figure 2. This constitutive law aims to capture the irreversible effects of crack nucleation and propagation by accounting for the reduction in the element load carrying capacity. The area under the force versus strain curve (the area of the triangle OAB in Figure 2) is the energy density necessary to fracture the area of influence of the element. Thus, for a given point *P* on the force vs. strain curve, the area of the triangle *OPC* represents the reversible elastic energy density stored in the element, while the area of the triangle *OAP* is the dissipated fracture energy density. Once the dissipated energy density equals the fracture energy, the element fails and loses its load carrying capacity. On the

other hand, in the case of compressive loads the material behaves as linear elastic. Thus, the failure in compression is induced by indirect traction. This assumption is reasonable for quasi-brittle materials for which the ultimate strength in compression is usually from five to ten times larger than that in tension (see Kupfer and Gerstle, 1973).

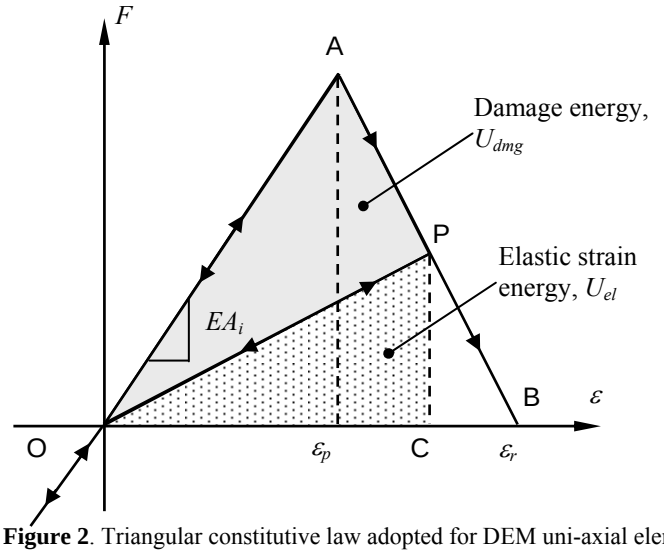

Figure 2. Triangular constitutive law adopted for DEM uni-axial elements.

Constitutive parameters and symbols in Figure 2 are (see Rocha *et al.*, 1991; and Riera and Rocha, 1991):

- *Force, F*: the element axial force as a function of the longitudinal strain ε.
- *Element area, A*: depending whether a longitudinal or a diagonal element is considered the values for A_l or A_d, see equations (4) and (5), should be adopted.
- *Element stiffness*: depending whether a longitudinal or a diagonal element is obtained multiplying the Young Modulus (E) by A_l or A_d, should be adopted.
- *Length of the DEM module, L.*
- *Specific fracture energy, G_f*: the fracture energy per unit area, which is coincident with the material fracture energy, G_c.
- *Equivalent fracture area,* A_i^f : this parameter enforces the condition that the energy dissipated by the fracture of the continuum material and its discrete representation are equivalent. With this purpose, a cubic sample with dimensions $L \times L \times L$ is considered. The energy dissipated when a continuum sample fractures into two parts due to a crack parallel to one of its faces is

$$\Gamma = G_f \Delta = G_f L^2 \tag{9}$$

where Δ is the fracture area. By contrast, the energy dissipated when the DEM module fractures in two parts has to account for the contribution of five longitudinal elements (four coincident with the module edges and one internal one) and four diagonal elements, see Figure 1(a). Then, the energy dissipated by a DEM module can be written as follows

$$\Gamma_{\text{DEM}} = G_f \left(4\ 0.25\ c_A + c_A + 4\ c_A \left(\frac{2}{\sqrt{3}} \right)^2 \right) L^2 \tag{10}$$

where the first term in the sum accounts for the four edge elements, the second term accounts for the internal longitudinal element, and the third term considers the contribution of the four diagonal elements. It is worth noting that the coefficient 0.25 in the first term accounts for the general case of an internal module with its four edge elements shared with four neighbors modules. When dealing with modules on the model surface, some of the edge elements could be shared by two elements or not shared at all. For such cases expression (10) has to be modified accordingly.

The coefficient c_A in equation (10) is a scaling parameter used to enforce the equivalence between Γ and Γ_{DEM}. Thus, equating expressions (9) and (10) results

$$G_f L^2 = G_f \left(\frac{22}{3} c_A \right) L^2 \tag{11}$$

from which it can be easily deduced that $c_A = 3/22$. Finally, the equivalent transverse fracture area of the longitudinal elements is

$$A_l^f = (3/22) L^2 \tag{12}$$

while for the diagonal elements is

$$A_d^f = (4/22) L^2 \tag{13}$$

- *Critical failure strain (ε_p)*: the maximum strain attained by the element before damage initiation (point A in Figure 2). The relationship between ε_p and the specific fracture energy, G_f, is given in terms of Linear Elastic Fracture Mechanics concepts. In this way

$$\varepsilon_p = R_f \sqrt{\frac{G_f}{E\left(1-\nu^2\right)}} \tag{14}$$

where R_f is the so-called failure factor, which accounts for the presence of an intrinsic defect of size d. R_f is defined as

$$R_f = \frac{1}{Y\sqrt{d}} \tag{15}$$

where Y is a dimensionless parameter that depends on both the specimen and the crack geometry.

It is worth noting here that the intrinsic defect size, d, is predetermined, and it could be consider as a material property.

Any disorder in the material properties is introduced to the model by specifying a random distribution in the specific fracture energy, G_f.

- *Limit strain (ε_r)*: the strain value for which the element loses its load carrying capacity (point C in Figure 2). This value must be set to satisfy the condition that, upon the failure of the element, the dissipated energy density equals the product of the element influence area, A_i^f, times the specific fracture energy, G_f, divided by the element length. This is

$$\int_0^{\varepsilon_r} F(\varepsilon) d\varepsilon = \frac{G_f \, A_i^f}{L_i} = \frac{K_r \, \varepsilon_p^2 \, E \, A_i}{2} \tag{16}$$

in which the sub indexes i have to be specialized to l or d depending whether the element under consideration is a longitudinal or diagonal one, respectively.
The coefficient K_r in equation (16) is a function of the material properties and the element length, L_i. With equation (16), the expression for K_r can be retrieved:

$$K_r = \left(\frac{G_f}{E\varepsilon_p^2}\right)\left(\frac{A_i^f}{A_i}\right)\left(\frac{2}{L_i}\right) \tag{17}$$

In order to guarantee the stability of the algorithm, the condition $K_r \geq 1$ must be accomplished (Riera and Rocha, 1991). In this sense it is interesting to define the critical element length

$$L_{cr} = 2\left(\frac{G_f}{E\varepsilon_p^2}\right)\left(\frac{A_i^f}{A_i}\right) \tag{18}$$

The coefficient $\left(\frac{A_i^f}{A_i}\right)$ in equation (18) is $\left(\frac{A_l^f}{A_l}\right) = \frac{3}{22\phi}$ and $\left(\frac{A_d^f}{A_d}\right) = \frac{\sqrt{3}}{11\,\delta\phi}$ for the longitudinal and diagonal elements respectively (see equations (4), (5), (12) and (13)). In the special case of an isotropic continuum with ν =0.25, the value of the functions δ=1.125 and ϕ=0.4, which results in $\left(\frac{A_l^f}{A_l}\right) \approx \left(\frac{A_d^f}{A_d}\right) \approx 0.34$. Thus, for practical purposes a single value of the critical element length can be used for both the longitudinal and diagonal elements. Therefore, the above stability condition can be expressed as:

$$K_r = \frac{L_{cr}}{L_i} \geq 1 \quad \Rightarrow \; L_i \leq L_{cr} \tag{19}$$

There is a maximum element length which preserves the stability of the element constitutive relationship.
Finally, the expression for the limit strain is

$$\varepsilon_r = K_r \varepsilon_p \tag{20}$$

It is interesting to note that in contrast to the usual practice in finite and boundary elements, the constitutive relationship in the DEM is not a function of the material properties only. The element constitutive relationship introduced above is defined in terms of parameters which are material properties (ε_p, E, R_{fc} and G_f), depend on model discretization (A_i^f and L) and depend on both, the material properties and the model discretization (E_i^A and ε_r). Besides, it is worth noting that although the DEM uses a scalar damage law to describe the uniaxial behavior of the elements, the global model accounts for anisotropic damage since it possesses elements orientated in different spatial directions. More sophisticated constitutive law that lets us incorporate more flexibility in the shape of the constitutive law and including plasticity discharge is published in Kosteski *et al.* (2011).

Studies about mesh convergence carried with DEM using mesh coarser that presented in the applications are shown in Kosteski *et al.* (2011), Miguel (2010). When we have interest in calibrating some problem it is necessary to adjust four parameters for a simple test that are, the global Elastic modulus (E), the density ρ, the G_f that is connected directly with the material toughness and the called critical strain ε_p connected with the strain in which the global model lives to be linear. If the model takes into account the random nature of the material, for example considering a G_f as random field, the characteristic of the distribution and its correlation length must be also furnished.

Another important feature of this approach is the assumption that G_f is a 3D random field with a Weibull probability distribution.

The local strain associated with maximum loading in each bar is called critical strain (ε_p). This value is also a random variable and its variability, which is measured using the coefficient of variation CV, is related to the G_f parameter by the following equation

$$CV(\varepsilon_p) = 0.5\ CV\ (G_f). \tag{21}$$

The minimum value of ε_p determined in all the specimen bars is associated with the global strain for which a specimen loses linearity.

More exhaustive explanations of this version of the lattice model may be found in Kostesky (2011), (2012) Applications of the DEM in studies involving non-homogeneous materials subjected to fracture, such as concrete and rock, may be found in Riera and Iturrioz (1998), Dalguer *et al*. (2003)], Miguel *et al*. (2008), Iturrioz *et al*. (2009), and Miguel *et al*. (2010).

4. NUMERICAL AND EXPERIMENTAL RESULTS RELATED TO ACOUSTIC EMISSION

In the following, illustrative experimental results as well as numerical simulations of laboratory tests aimed at the determination of the *b* value on small scale rock or concrete samples are described in detail. Updated information on the fundaments and performance of the lattice formulation of the Discrete Element Method (DEM) proposed by Riera (1984), which was employed in the numerical analyses reported below, may be found in Kosteski *et al.* (2011). The study will focus on Accoustic Emmission (AE) tests reported by Carpinteri *et al.* (2009). The first test consists of a 160×160×500mm concrete prism subjected to uniaxial compression. The laboratory specimen was modeled by means of a 27×27×86 DEM cubic modules array, with the boundary conditions shown in Figure 5b. The parameters adopted in the DEM model are: Young´s modulus of the material E=9.0 GPa, mass density ρ=2500Kg/m2, mean value of the material toughness $\mu(G_f)$=560N/m and the linear elastic limit strain $\varepsilon_p=2.4\times10^{-4}$. The random nature of the material is taken into account by assuming the toughness as a random field with a coefficient of variation CV= 0.5. The value of the concrete modulus E=9GPa was adopted on account of the fact that the test sample was subjected during 48 hours to a uniform compression load of 1300 kN, then unloaded. During the ensuing test the damaged specimen was reloaded up to its final collapse while monitored by AE sensors. Figure 5(b) shows the location of the AE sensor, at which accelerations in the direction normal to the specimen surface were computed employing the DEM.

The second example consists of a three point bending test. The concrete specimen dimensions were (80×150×700mm) with a 30mm pre-fissure length in the middle. The AE sensor was mounted as indicated by the gray box in Figure 6(b). Material properties were $E=35GPa$, ρ=2500Kg/m2, mean value of the toughness $\mu(G_f)$=130N/m and linear elastic limit strain $\varepsilon_p=6.4\times10^{-5}$. Additional details concerning the experiments are given by Carpinteri *et al.* (2009, 2009b). Again, the non-homogeneous nature of concrete is taken into account in the numerical simulations by assuming that the toughness is a 3D random field with CV= 0.25, moreover the applied displacement rates on DEM models were reduced until no inertial effects could be detected in the output.

Figure 3 shows the load vs. time diagrams measured in the experiments and determined herein by numerical simulation. The peak loads and the areas under the curves are similar in both examples, except for the loss of linearity of the experimental curve for uniaxial compression near the peak load, which suggests that large damage occurred before the peak, effect that is not observed in the numerical analysis. The load vs. time diagrams of both controlled displacement tests are quite different: in the compression test an explosive collapse occurs, while in the three point bending test a softening branch after the peak load is reached can be seen. Figure 4 shows the

normalized energy balance in both tests determined by numerical simulation. In the uniaxial compression test, 95% of the external work is available in the form of elastic energy when the final collapse occurs, resulting in an explosive failure. On the other hand, in the three point bending test the external work is smoothly dissipated during the entire process and the available potential energy at the end of the test is not sufficient to produce an explosive collapse. Note that $E_{max}=U_e+U_k+U_d$ at t^*. In both examples, due to the slow rate of loading, the kinetic energy remains low throughout most of the test, although when collapse occurs under uniaxial compression, there is a sudden shift of elastic energy to kinetic energy. The final rupture configurations observed in the experimental setup and predicted numerically can be seen for the uniaxial compression test in Figure 5 and for the Three Point Bend test in Figure 6.

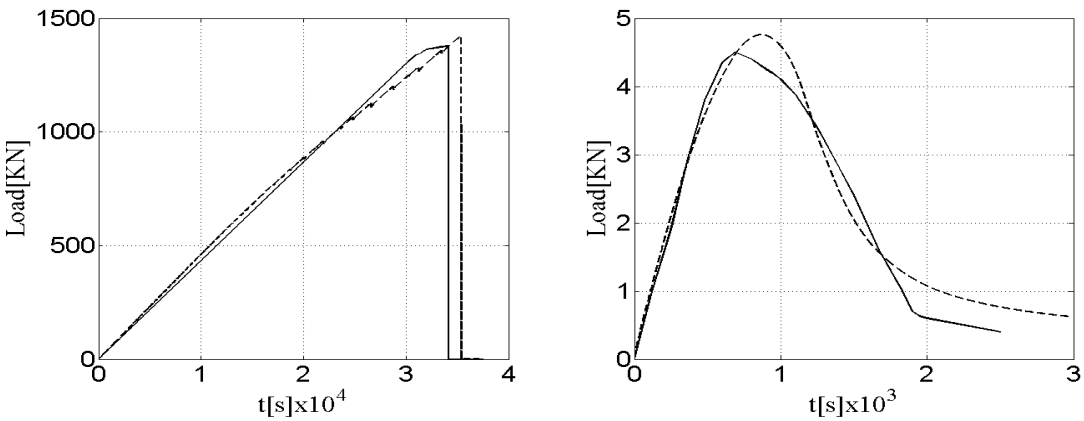

Figure 3. Load vs. time functions determined experimentally (continuous lines) and numerically (dashed lines): (a) Uniaxial compression test, (b) The three point bending test.

A summary of the numerical results concerning Acoustic Emission (AE) for both tests is presented next. They are considered as AE signal in the numerical simulation the normal surface acceleration in points localized on the specimen. Figure 7 shows the occurrence of individual AE events as vertical bars on the time axis. The height of each bar is proportional to the intensity of the event, registered on the sample surface. The figure also shows the total load vs. time curves on the samples. Histograms of the number of AE events and the evolution with time of the accumulated number of events are shown in Figure 8 for the uniaxial compression test and for the three points bending test. Finally Figure 9 shows the relations between the number of AE events and their magnitudes in logarithmic scale. Straight lines were fitted to the simulated data within selected time intervals, as indicated in the graphs. The magnitude scale was normalized. All the signals utilized for the *b*-values calculation in the numerical simulation had higher amplitudes than the fixed threshold A_{thres}. For this reason, only few events were identified in the simulation (about 200 in each example). By decreasing even further the displacement rate and adoting a lower threshold, it would be possible to identify more AE peaks, thus increasing the sample size, but the extension of the analysis was considered unnecessary. The values of *b* computed in both examples are compatible with the values determined experimentally by Carpinteri *et al.* (2009, 2009b). In addition, the numerical simulations reproduced the tendency observed in laboratory experiments, which show that *b* decreases towards values around unity as the degree of damage increases. Note that in the uniaxial compression test the *b* value was observed to decrease from 1.69 to 1.19, while according to DEM predictions it decreases from 1.47 to 1.16. In the laboratory bending test, *b* decreases from 1.49 to 1.11, while the numerical simulation predicts a decrease from 1.10 to 1.03.

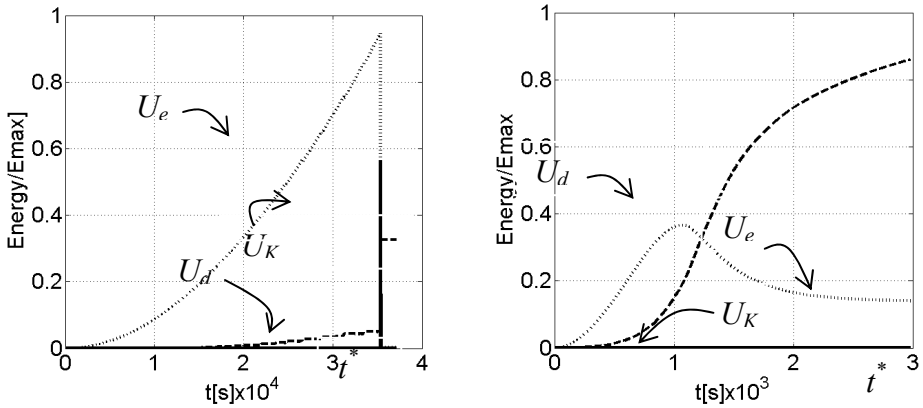

Figure 4. Energy balance vs time (U_e= elastic energy, U_k= kinetic energy, U_d= dissipated energy (a) Uniaxial compression (E_{max}=4888Nm), (b) Three point bending (E_{max}=0.65Nm).

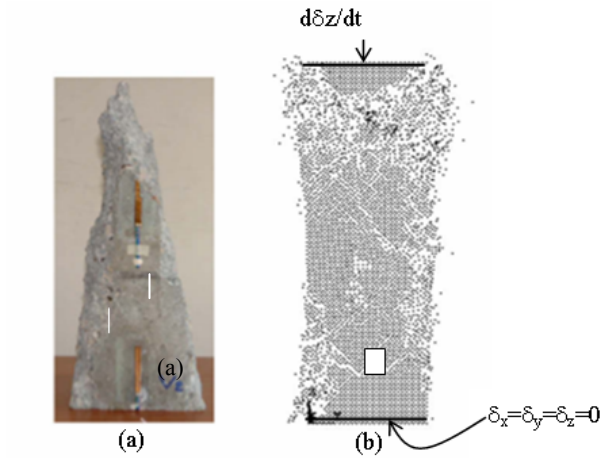

Figure 5. (a) Final rupture configuration of concrete specimen subjected to uniaxial compression (Carpinteri *et al.,* 2009) and (b) collapse configuration predicted by DEM model after peak load is reached (only nodal masses are shown). The white rectangle indicates the position of the sensor.

Finally Figure 10 presents plots of the logarithm of the number of events larger than given amplitudes vs. the logarithms of the amplitudes for the DEM simulations of the compression test (left plot) and of the three points bending test (right plot). Notice that the shape of these curves are similar to the typical curve for seismic data shown in Figure 3, which according to Scholz (2002), from the size distribution of subfaults, may be expected to present slopes given by b_1= ⅔ and b_2= 1. While similar values are usually found in actual seismic records for specific faults or seismic regions, they differ from some of the laboratory or numerical simulations results for small samples discussed herein.

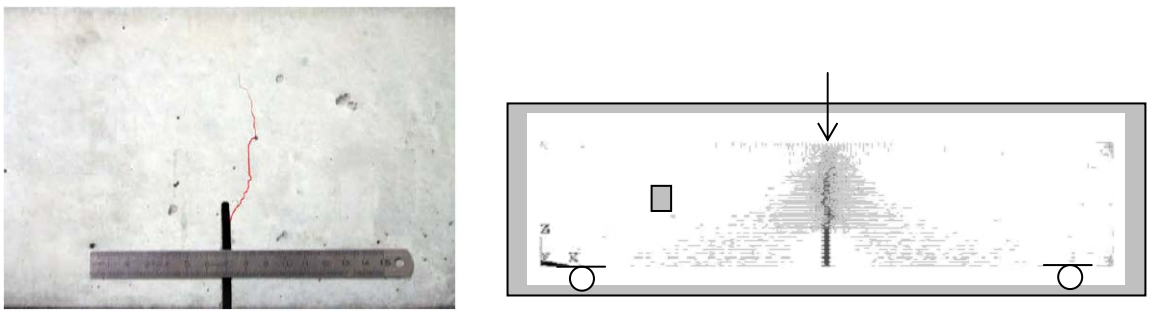

(a) (b)

Figure 6. (a) Detail of the exerimental rupture configuration of the specimen subjected to Three Point Bending (Carpinteri *et al.*, 2009a) (b) Numerical rupture configuration according to DEM (only damaged bars are plotted). The small gray rectangle indicates the position of the sensor.

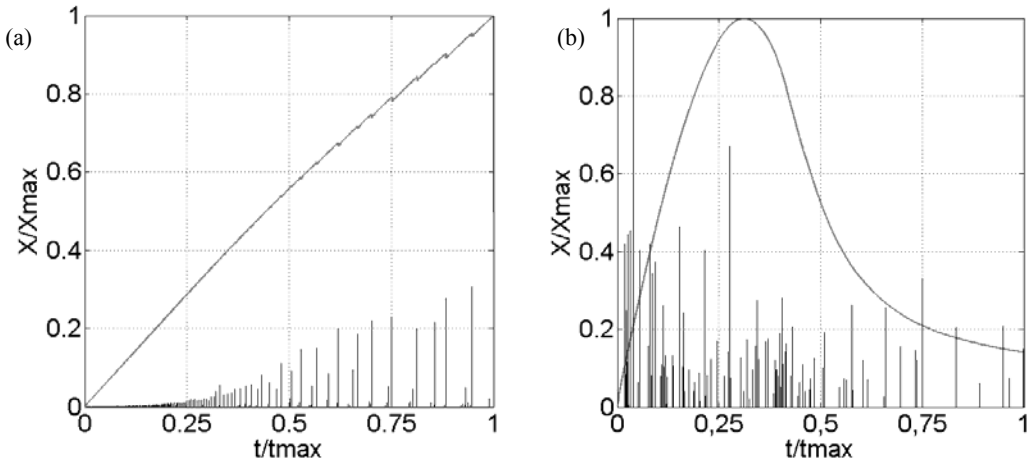

Figure 7. The continuous curves indicate the total load in the DEM models, while the bars show the amplitudes of AE events. Both axis were normalized to the maximum value. (a) Uniaxial compression test, (b) Three points bending test.

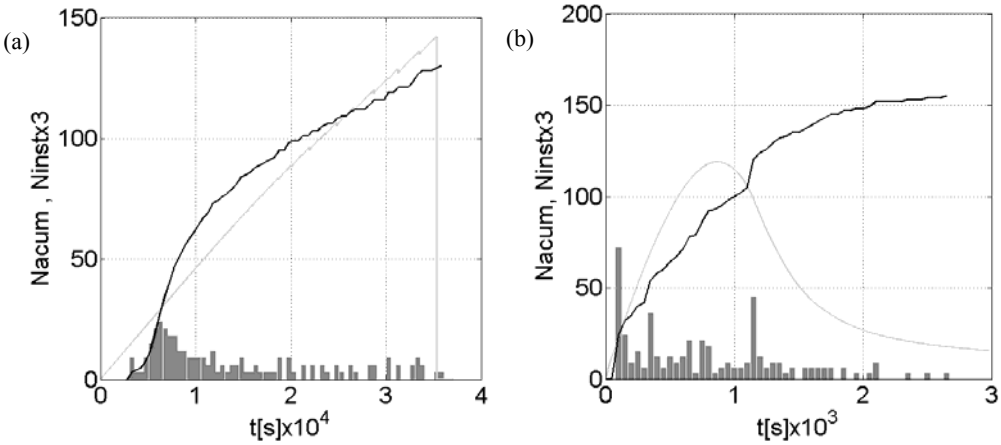

Figure 8. Histograms of the number of AE events and evolution with time of the accumulated number of AE events (thich line) and loas evolution (thin line) for: (a) Uniaxial compression test, (b) Three points bending test.

5. CONCLUSIONS

In this work, two experimental tests carried out on concrete specimens loaded up to failure are analyzed. One was a prismatic specimen subjected to uniaxial compressive loading, the other was a pre-cracked beam subjected to the three point bending test. For both examples experimental and numerical results are presented. The numerical simulations were performed using a version of the truss-like Discrete Element Method (DEM). During the tests, the Acoustic Emission (AE) technique was used to monitor the damage process taking place in the specimens. The numerical and experimental results obtained in the two examples are compared, and their intrinsic differences are identified.

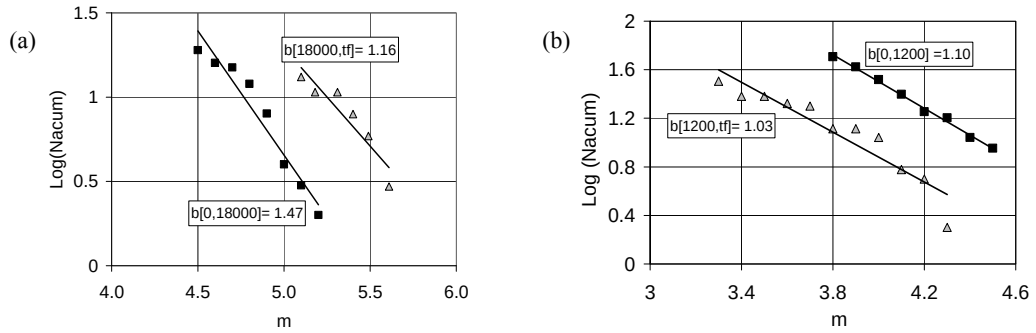

Figures 9. Determination of *b* - coefficients for simulated response in (a) uniaxial compression test and (b) three point bending test. The time intervals intervals used in the computation of *b* values are indicated between brackets.

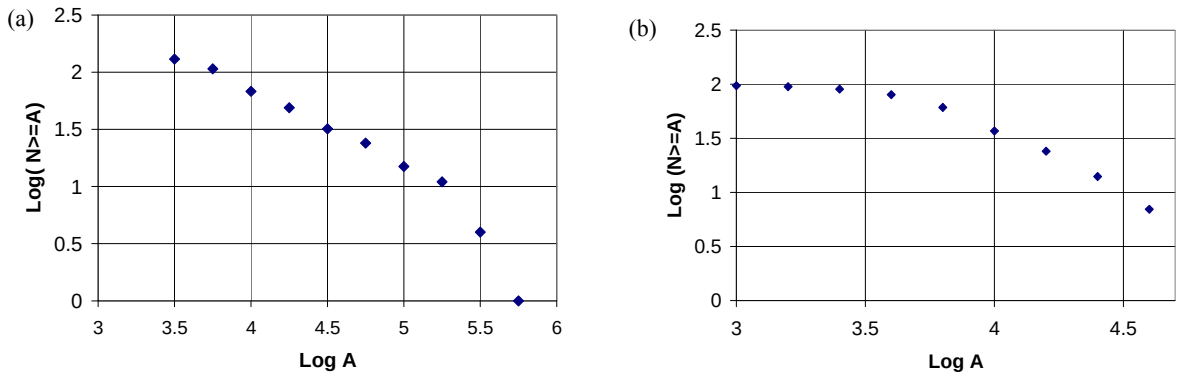

Figure 10. plots of the logarithm of the number of events with amplitudes larger than A vs. the logarithm of A for the DEM simulations of compression (left) and of three points bending (right). The *b* values in the high magnitudes regions are b_2= 2.40 (compression) and b_2= 1.16 (bending).

From these analyses, the following conclusions may be drawn.

- The comparison between the experimental and numerical results shows reasonable correlations, for both examples, in terms of conventional results, such as load vs. time and final configurations.

- In terms of the distribution of AE event amplitudes in time, the results were seen to be consistent, and any differences observed between the experimental and numerical results were accounted for. It is important to point out that the numerical *b*-values obtained are compatible with the experimental values and in good agreement with damage theories (Carpinteri et. al. (2009)), showing a tendency to decrease during the damage process.

- The low number of AE events analyzed in the numerical simulations (fewer than 200 events in both cases) compared with the number determined by AE monitoring is an issue to be discussed in detail in relation to the results obtained. However, the aim of these numerical simulations, as mentioned above, was to identify the general trends on a preliminary base. To increase the number of AE events analyzed in the numerical simulations you need a finer discretization, something we shall do after this initial exploration of the applicability of DEM simulations to this kind of process.

- This study has shown the potential applications of the truss-like Discrete Element Method (DEM) not only to simulate AE monitoring analysis, but also to provide a better understanding of the relationships between the basic AE parameters.

Acknowledgements
The financial support provided by the Regione Piemonte (Italy) through the RE-FRESCOS Project is gratefully acknowledged. The authors also wish to thank the Brazilian agency CNPq - National Council for Scientific and Technological Development for funding this research.

REFERENCES

Aki, K.: Scaling law of seismic spectrum. *J. Geophys. Res.* 1967; 72, 1217-1231.

Bathe KJ (1996) Finite element procedures. Prentice-Hall, Inc., New Jersey.

Carpinteri A.: Scaling laws and renormalization groups for strength and toughness of disordered materials. *Int J Solid Struct* 1994; 31:291–302.

Carpinteri A., Lacidogna G., Niccolini G., Puzzi S.: Critical defect size distributions in concrete structures detected by the acoustic emission technique. *Meccanica* 2008; 43: 349–63.

Carpinteri A., Lacidogna G., Niccolini G.: Fractal analysis of damage detected in concrete structural elements under loading. Chaos, *Solitons and Fractals* 2009; 42: 2047–2056.

Carpinteri A., Lacidogna G., Puzzi S.: From criticality to final collapse: evolution of the b-value from 1.5 to 1.0. *Chaos Soliton Fract* 2009; 41:843–853.

Chakrabarti B. K., Benguigui L. G.: *Statistical Physics of Fracture and Breakdown in Disordered Systems*. Clarendon Press, Oxford, 1997.

Dalguer L. A., Irikura K., Riera, J. D.: Simulation of tensile crack generation by three-dimensional dynamic shear rupture propagation during an earthquake. *J. Geophys. Res*. 2003; 108(B3): 2144.

Iturrioz I., Miguel L. F. F., Riera J. D.: Dynamic fracture analysis of concrete or rock plates by means of the Discrete Element Method. *Latin American Journal of Solids and Structures* 2009; 6: 229–245.

Kosteski L., Iturrioz I., Batista R.G., Cisilino A. P.: The truss-like discrete element method in fracture and damage mechanics. *Engineering Computations*, 2011; 6: 765–787.

Kosteski, L.E.; Barrios, R.; Iturrioz, I.: Crack propagation in elastic solids using the truss-like discrete element method. Int J Fract, 2012;DOI 10.1007/s10704-012-9684-4.

Nayfeh A.H., Hefzy M. S.: Continuum modeling of three-dimensional truss-like space structures. *AIAA Journal*, 1978; 8:779–787.

Kupfer HB, Gerstle KH (1973) Behaviour of concrete under biaxial stresses. *Journal of the Engineering Mechanics Division, American Society of Civil Engineers*, 99:853-866.

Miguel L. F. F., Iturrioz I., Riera J.D.: Size effects and mesh independence in dynamic fracture analysis of brittle materials. *Computer Methods Modeling in Engineering & Sciences*, 2010; 56:1-16.

Miguel, L. F. F., Riera, J. D., and Iturrioz, I.: Influence of size on the constitutive equations of concrete or rock dowels. *International Journal for Numerical and Analytical Methods in Geomechanics* 2008; 32: 1857–188.

Pollock A. A.: *Acoustic emission-2: acoustic emission amplitudes. Non-Destruct. Test* 1973;6: 264–9.

Richter C. F.: *Elementary Seismology*. W. H. Freeman, San Francisco and London, 1958.

Riera J. D.: Local effects in impact problems on concrete structures. Proceedings, *Conference on Structural Analysis and Design of Nuclear Power Plants*, Porto Alegre, RS, Brazil, 1984; Vol. 3, CDU 264.04:621.311.2:621.039.

Riera JD, Rocha MM (1991) A note on the velocity of crack propagation in tensile fracture. *Revista Brasileira de Ciencias Mecânicas*, 12/3:217-240.

Riera J.D., Iturrioz I: Discrete element model for evaluating impact and impulsive response of reinforced concrete plates and shells subjected to impulsive loading. *Nuclear Engineering and Design*, 1998; 179: 135-144.

Rocha MM, Riera JD, Krutzik NJ (1991) Extension of a model that aptly describes fracture of plain concrete to the impact analysis of reinforced concrete. In: *International Conference on Structural Mechanics Reactor Technology* (SMIRT 11), Tokyo, Japan.

Rundle J., Turcotte D., Shcherbakov R., Klein W., Sammis, C.: Statistical physics approach to understanding the multiscale dynamics of earthquake fault systems. *Reviews of Geophysics* 2003; 4: 8755–1209.

Scholz, C.H.: *The Mechanics of Earthquakes and Faulting*, 2002; 2nd. Edition, Cambridge University Press.

Turcotte D. L., Newman W.I., Shcherbakov R.: Micro and macroscopic models of rock fracture. *Geophys J. Int*. 2003; 152:718–28.

Particle simulation of AE statistics and fracture in concrete TPB test

Alberto Carpinteri[1], Giuseppe Lacidogna[1], Stefano Invernizzi[1,*], Amedeo Manuello[1]

[1] Department of Structural, Geotechnical and Building Engineering, Politecnico di Torino, 10129, Torino, Italy.
* Corresponding author: Stefano.invernizzi@polito.it

Abstract We present some experimental results and numerical simulations of acoustic emissions (AE) due to damage propagation in a concrete specimen subjected to the three-point bending (TPB) test. The test is performed under Crack-mouth opening displacement control. Moreover, AE are detected by an eight sensors experimental device, which allows for signal localization and complete storing of the signal wave. The AE cumulative number, the time frequency analysis and the statistical properties of AE time series will be numerically simulated adopting the so-called "particle method strategy". The method provides the velocity of particles in a set simulating the behavior of a granular system and, therefore, is suitable to model the compressive wave propagation and AE (corresponding to cracking) in a solid body. The localization of AE events is correctly reproduced. In addition, the Gutenberg-Richter statistics of AE events due to cracking, crucial for the evaluation of damage and remaining lifetime, were simulated and result in agreement with the experimental evidences.

Keywords Particle method, three-point bending test, acoustic emission, concrete.

1. Introduction

Damage and fracture characterizing the bending failure of heterogeneous materials such as concrete are complex processes involving wide ranges of time and length scales, from the micro- to the structural-scale. They are governed by the nucleation, growth and coalescence of microcracks and defects, eventually leading to the final collapse, and to the loss of the classical mechanical parameters, such as nominal strength, dissipated energy density and deformation at failure, as material properties [1]. Furthermore, the collapse mechanism is strongly related to the cracking pattern developing during the loading process. It changes from cracking and crushing, for slender beams, to shear failure characterized by the formation of inclined slip bands for deeper beams.
Instrumental and nondestructive investigation methods are currently employed to measure and check the evolution of adverse structural phenomena, such as damage and cracking, and to predict their subsequent developments. The choice of a technique for controlling and monitoring concrete or masonry structures is strictly correlated with the kind of structure to be analyzed and the data to be extracted [2–4].
This study addresses the three point bending test carried out in the laboratory in combination with acoustic emission (AE) monitoring. A similar approach has been already exploited in [5] attempting to link the amount of AE with the structural deflections.
In the assessment of structural integrity, the AE technique has proved particularly effective [5-7], in that it makes it possible to estimate the amount of energy released during the fracture process and to obtain information on the criticality of the process underway. Strictly connected to the energy detected by AE is the energy dissipated by the monitored structure. The energy dissipated during crack formation in structures made of quasi-brittle materials plays a fundamental role in the behavior throughout their entire life. Recently, according to fractal concepts, an ad hoc method has been employed to monitor structures by means of the AE technique [8]. The fractal theory takes into account the multiscale character of energy dissipation and the strong size effects associated with it. With this energetic approach, it becomes possible to introduce a useful damage parameter for structural assessment based on a correlation between AE activity in the structure and the corresponding activity recorded on specimens of different sizes, tested to failure by means of pure

compression tests.
In the following, the experimental results about the three-point bending configuration are also simulated numerically, exploiting a discrete element strategy. The main achievement of the present work consists in showing how the amount of cracking obtained from the numerical simulation and the experimentally detected AE events share the same temporal scaling laws

2. Experimental test

2.1. Acoustic Emission

The estimation of active cracks is of significant importance for any structural inspection. For an early warning of crack nucleation, the classification of active cracks is a great deal of the AE technique [9].
AE signals due to microcracks are detected by AE sensors attached on the surface of the concrete specimen. The signal waveforms are recorded by the AE measurement system. In order to classify active cracks, AE parameters such as rise time and peak amplitude of each signal are considered to calculate the rise angle (RA) value, defined as the ratio of the rise time (expressed in *ms*) to the peak amplitude (expressed in V) [9–12].

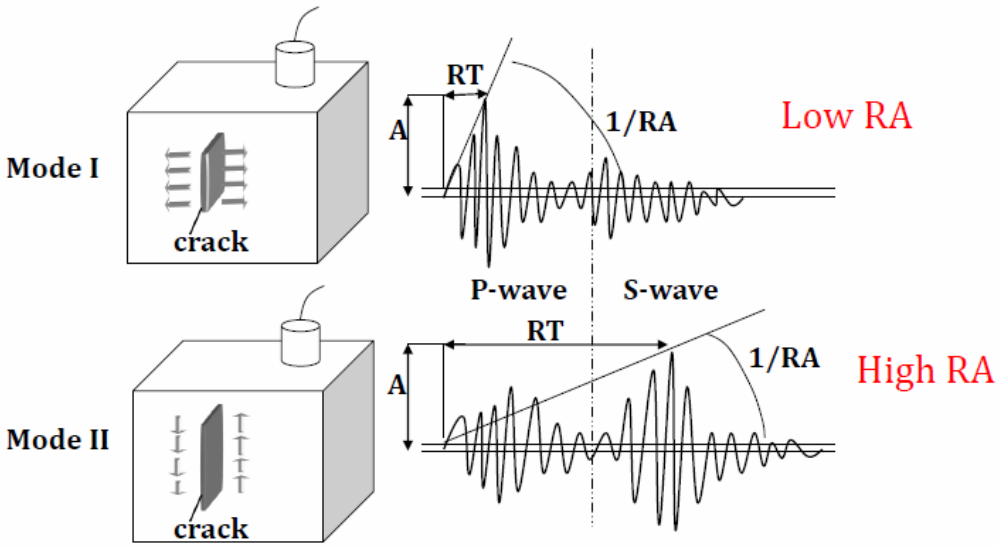

Figure 1. Typical waveforms of tensile and shear events. A is the amplitude and RT the rise time (time between the onset and the point of maximum amplitude) of the waveforms [13].

The shape of the AE waveforms is typical of the fracture mode (Fig. 1). Shear events are characterized by long rise times and usually high amplitudes, whereas low rise time values are typical of tensile crack propagations. These conditions are synthesized by the RA value.
Another parameter used to characterize the cracking mode is the Average Frequency (AF) expressed in kHz. The AF values are obtained from the AE ringdown count divided by the duration time of the signal. The AE ringdown count corresponds to the number of threshold crossings within the duration time. In general, the shift from higher to lower values of AF could indicate the shift of the cracking mode from tensile to shear [14]. Nevertheless, when a cracking process involves the opening of large cracks (Mode I), the frequency attenuation must be a function of this discontinuity. In other words, in this case the wavelength of the AE signals needs to be larger for the crack opening to be overcome, and the shift of the frequencies from higher to lower values could support

also a dominant tensile cracking mode [8].

2.2. Three-point bending test

The results of the three-point bending test performed on a beam having dimensions 100x100x840 mm (Fig. 2a) are herein reported. From the mechanical point of view, the overall behavior is characterized by a normal softening post-peak phase, as shown in Fig. 2b. The fracture energy, evaluated according to the RILEM recommendations [15], is equal to 0.124 N/mm. The corresponding total dissipated energy is equal to 0.62 J.
The evolution of the applied load, and of recorded AE with time is shown in Fig.3. The AE average frequencies range between 180 kHz and 150 kHz (Fig. 4a). A shift in frequencies from higher to lower values (Fig. 4a) and a significant decrease in RA values (Fig. 4b) after the peak load are observed (Fig. 4b). The evolution of the damage from the initial notch towards a Mode I crack is proved both by the RA and the AF decrease.

(a)

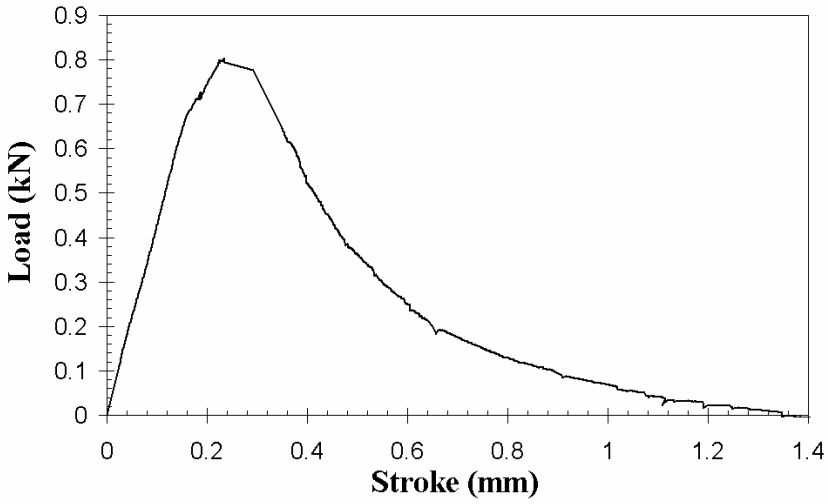

(b)

Figure 2. Three-point bending test: (a) experimental setup; (b) load vs. deflection curve.

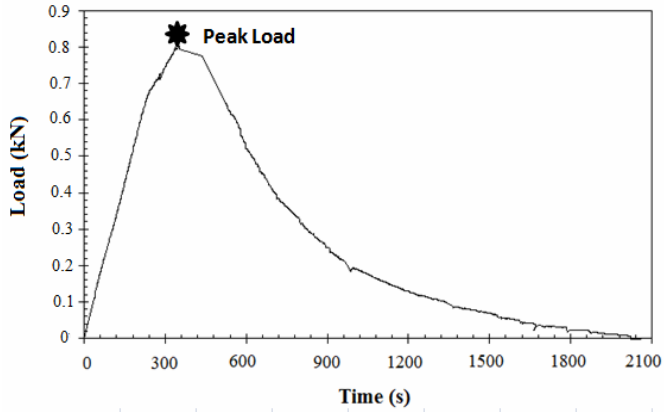

(a)

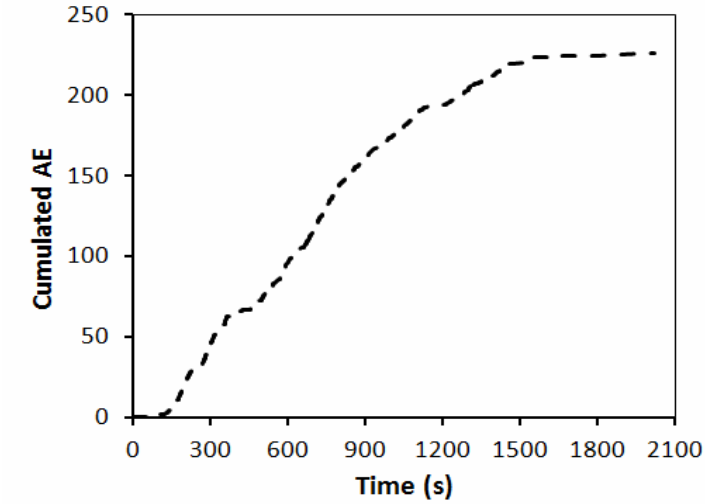

(b)

Figure 3. Three-point bending test: (a) load vs. time; (b) cumulated AE events vs. time.

The RA values obtained from the three-point bending test are considerably higher than what is obtained in case of small specimens (e.g. compression tests on cylindrical specimens [16]): as a matter of fact the additional propagation distance from AE sources to sensors, considering attenuation mechanisms, involves an increase in AE signals rise time [13]. Since the longitudinal waves are the fastest type, the delay in each AE signal between longitudinal and shear waves grows with the increasing of the propagation length, and consequently the RA rises from lower to higher values.

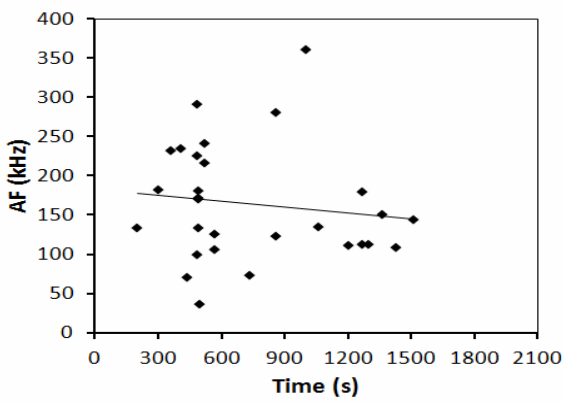

(a)

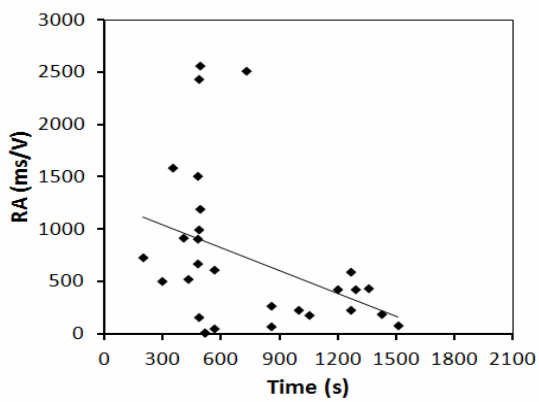

(b)

Figure 4. Three-point bending test: (a) AF values vs. time; (b) RA values vs. time;

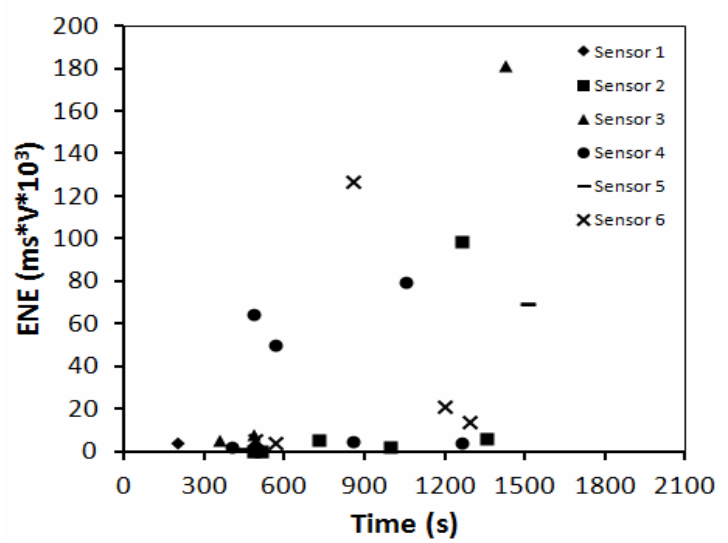

Figure 5. AE signal energy vs. time.

The signal energies of the AE events detected during the test are reported in Fig. 5, distinctly for each sensor. The average value of the total released AE signals energy is estimated as $126 \cdot 10^3$ *msV*.

3. Particle simulations

The simulations have been carried out with ESyS-Particle, an open source implementation of the Distinct Element Method [17]. ESyS-Particle has been developed in-house within the Earth Systems Science Computational Centre (ESSCC) at the University of Queensland [18] since 1994.
The simulation is based on direct integration of the Newton's motion equations with the Verlet algorithm. The normal interaction between colliding particles is linear and proportional to the particle small overlapping, whereas Coulomb friction, with both static and dynamic friction coefficients, rules the tangential interaction. In addition, bonded links are established between neighbor particles, according to the scheme in Figure 6. The bonded link is elastic perfectly brittle. The rupture of the bond is based on a fracture criterion that accounts for the axial, shear, torsion and bending behavior. The particles are filled together with the random packing algorithm LSMGenGeo [18], on the base of the maximum and minimum particle radius, which in our case correspond respectively to the maximum and minimum concrete aggregate radius (i.e. r_{max}=7.5 mm, r_{min}=1.5 mm).

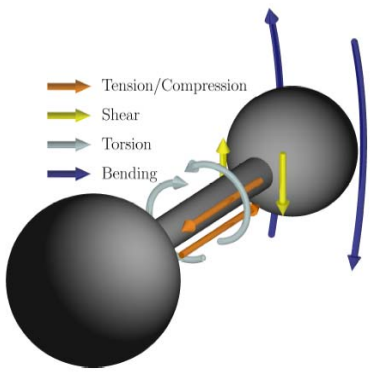

Figure 6. Scheme of the bonded interaction between two particles .

An exclusion method provides that once the bonded link is broken, the frictional interaction takes place between the neighbor particles. When the maximum and minimum radius of particles are quite different, experience shows that a power-law size distribution is obtained, providing a good approximation of the actual concrete aggregate size distribution. The bending moment is applied to the specimen by means of moving planes, provided that the particles closer to the platens were bonded to the moving planes.

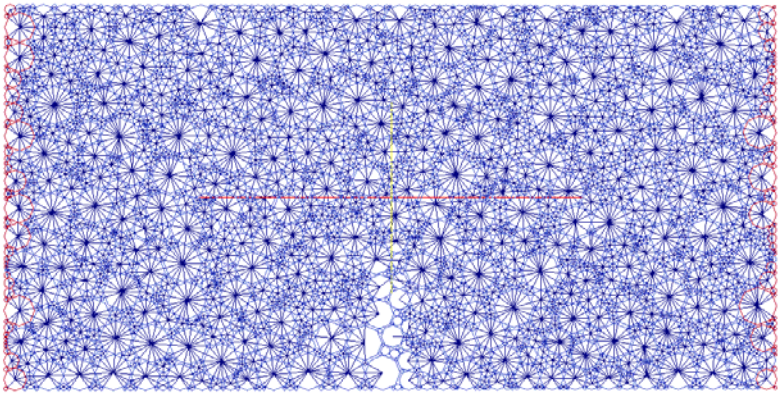

(a)

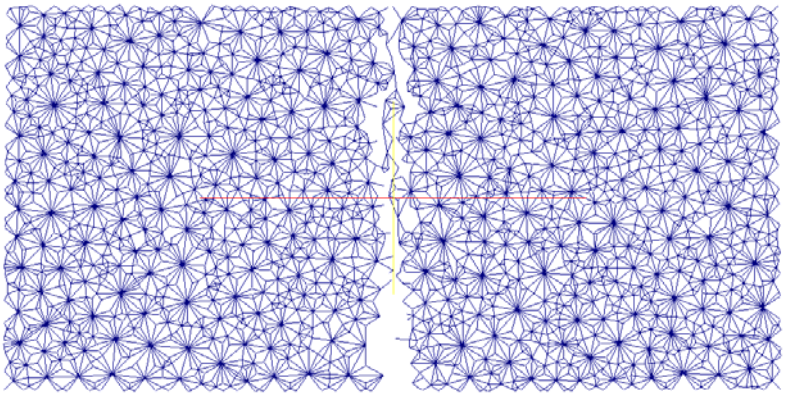

(b)

Figure 7: Three point bending test: initial configuration (a); final configuration (b).

The simulations are carried out at a fixed maximum strain velocity equal to $10^{-4}s^{-1}$. A viscous type damping, proportional to the particle velocity is introduced in the simulation. The choice of the damping coefficient (in our case equal to 0.02) is based on the minimum value that regularizes the simulation without affecting the stress-strain behavior.

The position and velocity of each particle during the simulation can be recorded at a certain integration time.

In order to limit the model complexity and the computational needs, a two-dimensional simulation of three-point bending test and AE acquisition [12] has been performed. The particle discretization was limited to the central region of the beam, where almost uniform bending was simulated imposing the rotation of the extreme sections (shown in red in Fig. 7a). The initial notch is obtained removing the corresponding bonds. As soon as the bonds between particles reach the failure limit, they are removed, and the crack proceeds to the extrados of the beam (Fig. 7b).

In the present study, special attention was paid to the simulation of the temporal scaling of the acoustic emission, rather than to provide a detailed interpretation of the experimental test. Nevertheless, the mechanical parameters adopted in the analysis were chosen to better interpolate the experimental strength in the whole dimensional range.

4. Comparison between numerical and experimental AE statistics

Since the studies of Mogi and Scholz [19,20] on AE, we know that the Gutenberg-Richter empirical law can be observed at the laboratory sample scale. They showed that a significant overlap exists between the definition of AE and earthquake. This is further reinforced by the evidence that brittle fracture obeys similar statistics from tectonic earthquakes to the dislocation movements smaller than micron size. Moreover, in recent years, experiments employing acoustic emission have established remarkable results concerning the model of process zone and the quasistatic fault growth. Such experiment-based knowledge is expected to be useful for studying the fundamental behavior of natural earthquakes, because it is widely accepted that fault systems are scale-invariant [21, 22] and there exist universal similarities between faulting behaviors, from small-scale microcracking to large-scale seismic events. For example, AE events caused by microcracking activity [19–23] and stick-slip along a crack plane [24, 25] are similar to those generated by natural earthquakes.

By analogy with seismic phenomena, in the AE technique the magnitude may be defined as follows [26, 27]:

$$m = \mathrm{Log}\, A_{\max} + f(r), \tag{4}$$

where $A_{\max}$ is the amplitude of the signal expressed in μV and $f(r)$ is a correction coefficient whereby the signal amplitude is taken to be a decreasing function of the distance r between the source and the AE sensor. In seismology, the Gutenberg-Richter empirical law [28]:

$$\mathrm{Log}\, N(\geq m) = a - bm, \tag{5}$$

expresses the relationship between magnitude and total number of earthquakes in any given region and time period, and is the most widely used statistical relation to describe the scaling properties of seismicity. In Eq. (5), N is the cumulative number of earthquakes with magnitude $\geq m$ in a given area and within a specific time range, while a and b are positive constants varying from a region to another and from a time interval to another. Eq. (5) has been used successfully in the AE field to study the scaling laws of AE wave amplitude distribution. This approach evidences the similarity between structural damage phenomena and seismic activities in a given region of the Earth, extending the applicability of the Gutenberg-Richter law to structural engineering [29].

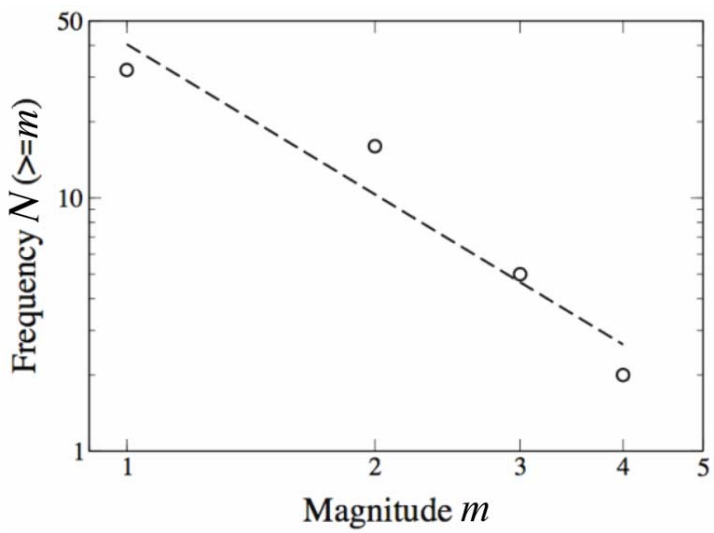

Figure 10: Frequency magnitude bilinear diagram: a=40.4, b=1.97.

The magnitude of each event is obtained summing up the number of bonds broken in each non-overlapping time window, in this case equal to 300 time steps. Finally, the frequency of the magnitude events that overcame a certain value m is reported in the classical Gutember-Richter chart (Figure 7c). It is worth noting that, in agreement with the experimental acquisition [29], the computed frequencies are aligned on a straight line. The slope of this line, which corresponds to the *b* value, is higher than the experimental value, and equal to 1.97. Further analyses are necessary to investigate the effect of the simulation dimensionality, and to obtain a better parameter calibration of the model.

5 CONCLUSIONS

The AE results obtained from the three-point bending tests, prove that the variation of the AE parameters during the loading process strictly depends on the specimen damage: a decrease in frequency may be provoked both by dominant shear cracking process and by dominant tensile cracking process. Therefore, the two different cracking modes have to be discriminated through a different AE parameter, such as the rise angle (RA), that is defined as the ratio of the rise time to the peak amplitude of each signal. Low RA values suggest a Mode I crack propagation, whereas high RA values are obtained in case of Mode II crack propagation. All the monitored damage processes display an increase in AE signal energy content approaching the final failure.
The preliminary distinct element numerical simulation of the AE statistics in the three-point bending test showed a good qualitative simulation of the Gutember-Richter law. Further analyses are necessary to investigate the effect of the simulation dimensionality, and to obtain a better parameter calibration of the model.

Acknowledgements

The financial support provided by the Regione Piemonte (Italy) RE-FRESCOS Project, is gratefully acknowledged.

References

[1] A. Carpinteri, M. Corrado and G. Lacidogna, Three different approaches for damage domain characterization in disordered materials: Fractal energy density, *b*-value statistics, renormalization group theory. Mechanics of Materials, 53 (2012) 15–28.
[2] A. Carpinteri, P. Bocca, Damage and Diagnosis of Materials and Structures, Pitagora Editrice, Bologna, Italy 1991.
[3] S. Invernizzi, G. Lacidogna, A. Manuello, A. Carpinteri. AE monitoring and numerical simulation of a two-span model masonry arch bridge subjected to pier scour. Strain, 47:2 (2011) 158–169.
[4] A. Anzani, L. Binda, A. Carpinteri, S. Invernizzi, G. Lacidogna, A multilevel approach for the damage assessment of historic masonry towers . Journal of Cultural Heritage, 11 (2010) 459–470.
[5] A. Carpinteri, S. Invernizzi, G. Lacidogna, Structural assessment of a XVIIth century masonry vault with AE and numerical techniques, International Journal of Architectural Heritage, 1(2), (2007) 214–226.
[6] A. Carpinteri, G. Lacidogna, A. Manuello, S. Invernizzi, L. Binda, Stability of the vertical bearing structures of the Syracuse Cathedral: Experimental and numerical evaluation. Materials & Structures, 42 (2009) 877–888.
[7] A. Carpinteri, S. Invernizzi, G. Lacidogna, In situ damage assessment and nonliner modelling of an historical masonry tower. Engineering Structures, 27 (2005) 387–395.
[8] A. Carpinteri, G. Lacidogna, N. Pugno, Structural damage diagnosis and life-time assessment by acoustic emission monitoring, Engineering Fractures Mechanics, 74 (2007) 273–289.

[9] C. Grosse and M. Ohtsu, Acoustic Emission Testing, Springer 2008.
[10] RILEM Technical Committee TC212-ACD, Acoustic Emission and related NDE techniques for crack detection and damage evaluation in concrete: Measurement method for acoustic emission signals in concrete. Mater. Struct., 43 (2010) 1177–81.
[11] RILEM Technical Committee TC212-ACD, Acoustic Emission and related NDE techniques for crack detection and damage evaluation in concrete: Test method for damage qualification of reinforced concrete beams by Acoustic Emission. Mater. Struct. 43 (2010) 1183–6.
[12] RILEM Technical Committee TC212-ACD, Acoustic Emission and related NDE techniques for crack detection and damage evaluation in concrete: Test method for classification of active cracks in concrete by Acoustic Emission. Mater. Struct. 43 (2010) 1187–9.
[13] D.G. Aggelis, A.C. Mpalaskas, D. Ntalakas and T.E. Matikas, Effect of wave distortion on acoustic emission characterization of cementitious materials. Construction and Building Materials, 35 (2012) 183–190.
[14] K. Ohno, M. Ohtsu, Crack classification in concrete based on Acoustic Emission. Constr. Build. Mater. 24 (2010) 2339-46.
[15] RILEM 50-FMC Committee, Determination of the fracture energy of mortar and concrete be means of three-point bend tests on notched beams. Mater. Struct. 18 (1986) 286-90.
[16] G. Lacidogna, F. Accornero, M. Corrado, and A. Carpinteri, Crushing and fracture energies in concrete specimens monitored by Acoustic Emission, VIII International Conference on Fracture Mechanics of Concrete and Concrete Structures, FraMCoS 8, Toledo, Spain, March 10-14, 2013.
[17] https://twiki.esscc.uq.edu.au/bin/view/ESSCC/ParticleSimulation
[18] https://launchpad.net/esys-particle/
[19] K. Mogi, Magnitude frequency relations for elastic shocks accompanying fractures of various materials and some related problems in earthquakes", Bull. Earthquake Res. Inst. Univ. Tokyo, 40 (1962) 831–853.
[20] C. H. Scholz, The frequency-magnitude relation of microfracturing in rock and its relation to earthquakes, Bull. Seismol. Soc. Am., 58 (1968) 399–415.
[21] T. Hirata, "Fractal dimension of fault system in Japan: fracture structure in rock fracture geometry at various scales", Pure Appl. Geophys. 131 (1989) 157–170.
[22] E. Bonnet, O. Bour, N.E. Odling, P. Davy, I. Main, P. Cowie, B. Berkowitz, "Scaling of fracture systems in geological media", Rev. Geophys. 39 (2001) 347–383.
[23] D.A. Lockner, J.D. Byerlee, V. Kuksenko, A. Ponomarev, A. Sidorin, "Quasi static fault growth and shear fracture energy in granite", Nature 350 (1991) 39–42.
[24] N. Kato, K. Yamamoto, T. Hirasawa, Microfracture processes in the break down zone during dynamic shear rupture inferred from laboratory observation of near-fault high-frequency strong motion, Pure Appl. Geophys. 142 (1994) 713–734.
[25] X.L. Lei, O. Nishizawa, K. Kusunose, A. Cho, T. Satoh, On the compressive failure of shale samples containing quartz-healed joints using rapid AE monitoring: the role of asperities, Tectonophysics 328 (2000) 329–340.
[26] S. Colombo, I.G. Main, M.C. Forde, Assessing damage of reinforced concrete beam using "*b*-value" analysis of acoustic emission signals, J. Mat. Civil Eng. (ASCE) 15 (2003) 280–286.
[27] M.V.M.S. Rao, P.K.J. Lakschmi, Analysis of *b*-value and improved b-value of acoustic emissions accompanying rock fracture, Curr. Sci. – Bangalore 89 (2005) 1577–1582.
[28] C.F. Richter, Elementary Seismology. W.H. Freeman, San Francisco 1958.
[29] S. Invernizzi, A. Carpinteri, G. Lacidogna, Particle-based numerical modeling of AE statistics in disordered materials, Meccanica, 48:1 (2013) 211–220.

Numerical Modeling on the Stress-Strain Response and Fracture of Modeled Recycled Aggregate Concrete

Wengui Li[1,2], Jianzhuang Xiao[1,*], David J. Corr[2], Surendra P. Shah[2]

[1] Department of Building Engineering, Tongji University, Shanghai 200092, China
[2] Center for Advanced Cement-Based Materials, Northwestern University, Evanston 60208, USA
* Corresponding author: jzx@tongji.edu.cn

Abstract According to the nanoindentation tests, the constitutive relationship of the Interfacial Transition Zones (ITZs) in Recycled Aggregate Concrete (RAC) is proposed with a plastic-damage constitutive model. Based on the meso/micro-scale constitutive relations of mortar matrix, numerical studies were undertaken on Modeled Recycled Aggregate Concrete (MRAC) under uniaxial loadings to predict mechanical behavior, particularly the stress-strain response. The tensile stress tends to concentrate in the ITZs region, which leads to the development of microcracks. After the calibration and validation with experimental results, the effects of the mechanical properties of ITZs and new mortar matrix on the stress-strain response and fracture of MRAC were analyzed. The FEM modeling is capable of simulating the complete stress-strain relationship of MRAC, as well as the overall fracture pattern. It reveals that the mechanical properties of new mortar matrix and the corresponding new ITZ play a significant role in the overall stress-strain response and fracture process of MRAC.

Keywords Modeled recycled aggregate concrete (MRAC), Interfacial transition zones (ITZs), Plastic-damage constitutive model, Stress-strain response, Fracture

1. Introduction

Most of cement-based materials have intrinsic heterogeneous and nonlinear mechanical behaviors due to the random distribution of multiple phases over the nano-, micro-, meso- and macro-scales [1-4]. A better understanding of mechanical properties including the failure processes by both experiments and computer modeling has become one of the most critical research topics for concrete [5-7]. Corr *et al.* predicted the mechanical properties of concrete in tension with the consideration of meso-scale randomness in the cohesive interface properties [8]. Cusatis *et al.* formulated the Lattice Discrete Particle Model (LDPM) and simulated experiments include uniaxial and multiaxial compression, tensile fracture, shear strength, and cyclic compression tests [9, 10]. Moreover, concrete was simulated with plasticity-damage constitutive model, and showed a very good correlation with the experimental results [11].

With the emergence of nanoindentation technique, it is available to experimentally measure the properties of the ITZ (Interfacial Transition Zone) between aggregate and mortar matrix [12, 13]. Due to the recent advances in understanding the microstructure, thickness, and mechanical properties of the ITZ and the developments of computational methods, the micromechanical behavior of concrete can be effectively simulated to get a deeper insight into the effect of each phase (such as aggregate size and shape, ITZ thickness and micromechanical properties, and the mortar matrix mechanical properties, etc.).

In this study, Modeled Recycled Aggregate Concrete (MRAC) is a volume element of RAC which is used to simplify the real RAC study. A plastic-damage model is adopted within FEM analysis. The mechanical properties of ITZs in MRAC are obtained by a nanoindentation technique. Two-dimensional microscale numerical modeling is conducted in order to investigate the effects of ITZs on the overall behavior and failure process of MRAC under both uniaxial loadings.

2. Modeled recycled aggregate concrete

The MRAC consists of nine recycled coarse aggregate surrounded by a mortar matrix [5, 14]. Recycled coarse aggregate is idealized to have a round shape. The MRAC used in numerical simulation is shown in Figure 1. The MRAC means the recycled coarse aggregates are embedded within new mortar matrix as a square array. This is an assumption made to simplify the real RAC and provide useful information regarding crack initiation and mechanical response of RAC under loadings. The idealization of regular distribution of recycled coarse aggregates in RAC not only simplifies the problem but also assists in studying the effect of different phases on overall failure behavior of RAC.

(a) MRAC specimen (b) MRAC schematic

Figure 1. Modeled recycled aggregate concrete (MRAC)

3. Constitutive relationships

3.1. Mortar matrix

Mortar matrix shows softening behavior after reaching its peak tensile or compressive stress, which is due to toughening mechanics within the fracture process zone. Both micro-cracking development and irreversible deformations contribute to the nonlinear response of mortar matrix. A plastic-damage constitutive model for mortar matrix is developed by former investigators [11, 15]. Anisotropic damage with a plasticity yield criterion and a damage criterion are introduced to adequately describe the plastic and damaged behavior of mortar matrix.

In order to account for different effects under tensile and compressive loadings, two damage criteria are adopted: one for compression and a second for tension such that the total stress is decomposed into tensile and compressive components. The strain equivalence hypothesis is used in deriving the constitutive equations, so that the strains in the effective (undamaged) and damaged configurations are set equal.

3.2. ITZs

With the emergence of nanoindentation techniques, it is now possible to directly measure the micromechanical properties of the ITZs. A total of 341 indents were performed in an array at each studied area (Figure 3 (a) and (b)). Microhardness testing on cement paste found that there is a linear relationship between microhardness and compressive strength. The hardness obtained from nanoindentation is assumed to provide a linear relationship between

hardness and strength [16, 17]. In this study, the distribution of indentation modulus was used as a basis for the property characteristics of old ITZ and new ITZ, such as the thickness, elastic modulus and strength related to old and new mortar matrix, respectively. Figure 3 (c) and (d) show the indentation modulus distributions with the distance across old ITZ and new ITZ. In this test, greater porosity in the ITZs caused the reduced elastic modulus and strength, relative to those of related mortar matrix.

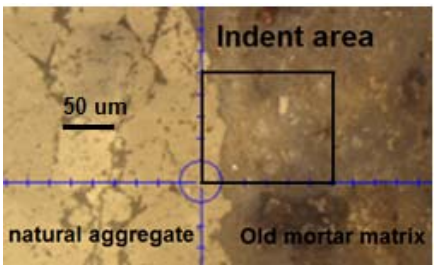

(a) Indent area in old ITZ of RAC

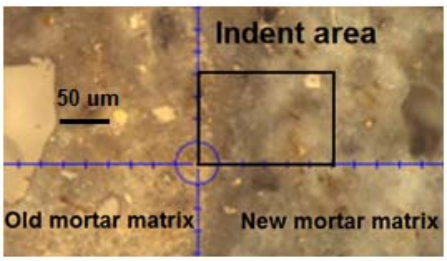

(b) Indent area in new ITZ of RAC

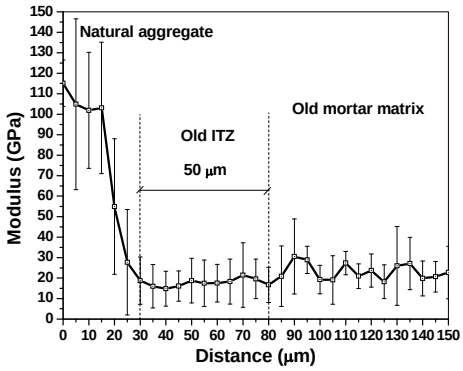

(c) Modulus distribution across old ITZ

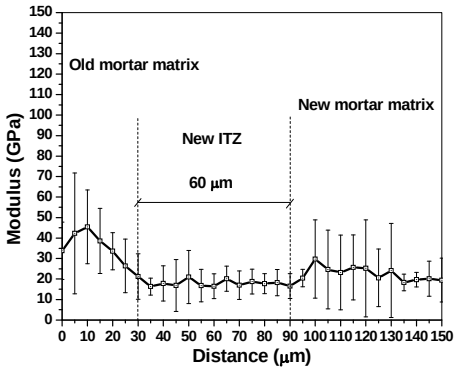

(d) Modulus distribution across new ITZ

Figure 3. Nanomechanical properties of ITZs in RAC [9, 35]

The old ITZ and new ITZ thickness was estimated by locating the places where there is slight variation in the indentation modulus with the distance from the natural aggregate or old mortar matrix surface, and the indentation modulus distribution of the ITZs seem to be close to those of corresponding old mortar matrix and new mortar matrix. Based on the nanoindentation results, the thicknesses of old ITZ and new ITZ are found to be around 50 μm and 60 μm, respectively. Moreover, the average indentation modulus of old ITZ and new ITZ were found to be approximately 80% and 85% of those of old mortar matrix and new mortar matrix, respectively. We choose a linear relationship between indentation hardness and strength. Considering the hardness has a similar distribution with the modulus in the ITZs regions, the strengths of old ITZ and new ITZ are assumed to be 80% and 85% of those of old mortar matrix and new mortar matrix, respectively. For the mortar matrix, elastic modulus, the strength (peak stress), and deformation capacity (peak strain and ultimate strain) parameters are obtained according the experimental data from Refs. [5, 14]. In case of the ITZs, the relative mechanical properties (elastic modulus and strength) to those of mortar matrix can be provided by the nanoindentation test. Combining the descriptions in this and above sections, the predicted uniaxial tensile and compressive stress-strain relationships for both ITZs and mortar matrix based on the plastic-damage constitutive model are shown in Figure. 4.

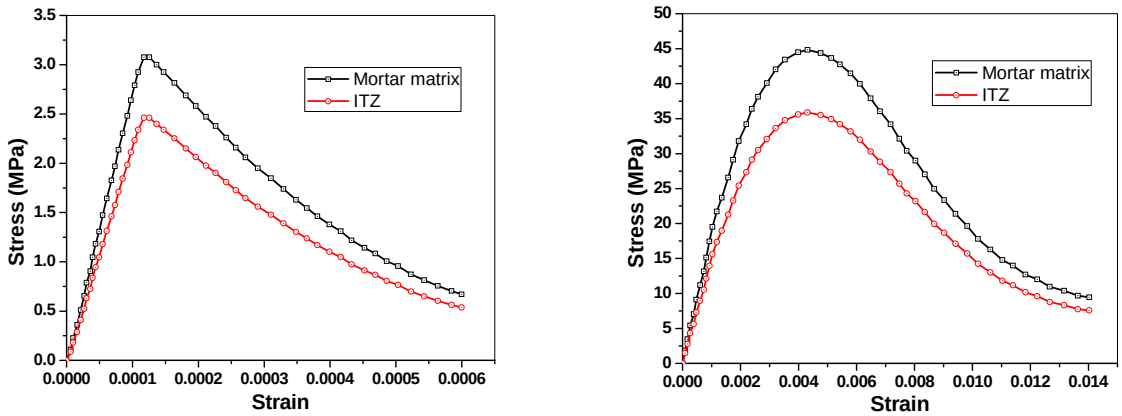

(a) Uniaxial tension (b) Uniaxial compression

Figure 4. Uniaxial stress-strain relation of ITZs and mortar matrix

3.3. Natural aggregate

Granite cylinders are used as natural aggregate in the MRAC. Based on the experiment results [5], there were not cracks or damage observed in the natural aggregates during loading. In the current study, natural aggregate is modeled as linear-isotropic material. It behaves linearly throughout the analysis. For the numerical calibration validation, the materials parameters of each phase in MRAC, which were determined according to the experimental data, are listed in Table 1. However, the Poisson's ratios of new ITZ and old ITZ were defined as 0.20 [18].

Table 1. Material properties of each phase in MRAC

MRAC	Thickness (μm)	Elastic modulus (GPa)	Poisson's ratio (ν)	Strength (MPa) Compressive (f_c)	Tensile (f_t)
Natural aggregate	—	80.0	0.16	—	—
Old mortar (OM)	—	25.0	0.22	45.0	3.00
New mortar (NM)	—	23.0	0.22	41.4	2.76
Old ITZ (OI)	50.0	20.0	0.20	36.0	2.40
New ITZ (NI)	60.0	18.0	0.20	33.1	2.21

4. FEM simulation and test verification

4.1. FEM model

The software program (ABAQUS 6.11) was used for the FEM analyses. 4-node plane stress quadrilateral (CPS4R) elements were used to mesh the MRAC. The 2D micro-scale FEM model of MRAC is shown in Figure 5. The model was subjected to a uniformly distributed displacement at the top edge, as the displacement-controlled loading scheme was used. The *Y* degrees of freedom were fixed at the bottom edge, while the *X* degrees of freedom and rotation were not constrained. The FEM model has a total of 34240 elements in this simulation.

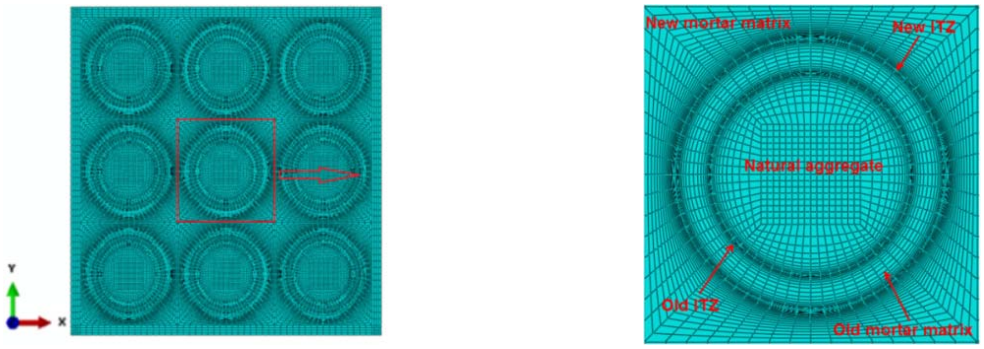

(a) Overall FEM model (b) Details of each phase

Figure 5. 2D micro-scale FEM model of MRAC

4.2. Modeling implementation

In this paper, ABAQUS/explicit quasi-static analyses were applied for the numerical simulation [19, 20, 21]. The ABAQUS/explicit quasi-static solver used an analysis time of 0.1 second (period time). A displacement-controlled loading scheme was adopted in this simulation. In order to obtain complete stress-strain curves, after trial and comparison, all the analyses for uniaxial tension and compression were ended at a displacement d=0.09 mm (ultimate strain 0.0006) and 0.9 mm (ultimate strain 0.006), respectively.

The FEM numerical response depends on two sets of parameters. The first set is relevant to the tensile and compressive stress data which are provided as a tabular function of strain, which is directly obtained from the constitutive relation of each phase in MRAC. These mechanical properties are provided by experimental study and mix design. The other one is the definition of the damage variable as a tabular function of the inelastic strain for both the tensile and compression. If the damage variable is specified, ABAQUS automatically calculates the inelastic and plastic strain values.

Generally, the maximum tensile stress (S_{11}) tends to concentrate mainly in the ITZs in Figure 6. These stress concentrations could lead to the development of microcracks along these regions, which in turn could lead to the failure of the MRAC. As the properties of the ITZs are weaker than those of other phases in the MRAC, the stress concentrations mainly occur in these regions and may lead to or promote the failure. Experimental results also proved that bond cracks firstly appeared around the weak ITZs, and then propagated into the mortar by connecting with each other [5, 14].

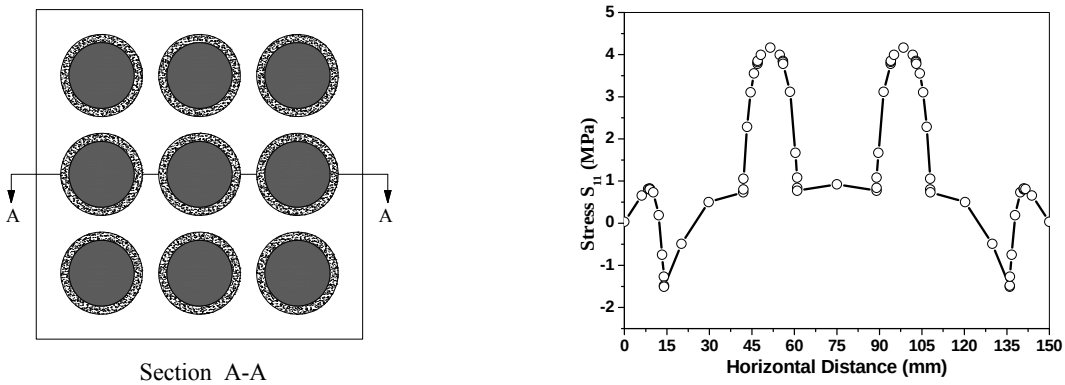

(a) Cross section in MRAC (b) Tensile stress S_{11} distribution

Figure 6. Stress distribution for section A-A

4.3. Simulation results

4.3.1. Uniaxial compression

According to the above parameters and descriptions, the complete compressive stress-strain curve and failure process of MRAC under uniaxial compression loading were calculated. In order to calibrate and validate the FEM, the MRAC was studied by compression test using Digital Image Correlation (DIC) technique [5, 14]. The experimental data are relevant to compression tests on MRAC specimens with the same old cement mortar mixture design (w/c=0.45) but three different new cement mortar mixture designs (w/c=0.36, 0.45, and 0.55). The mixture proportion details of MRAC specimens are listed in Table 2. The experimental setup and basic failure pattern are shown in Figure 7.

Table 2. Mixture proportion of cement mortar in MRAC [5]

MRAC	Old mortar (w/c ratio)	Mass, kg/m^3			New mortar (w/c ratio)	Mass, kg/m^3		
		Water	Cement	Sand		Water	Cement	Sand
MRAC-30-20	0.45	160	356	565	0.55	160	276	589
MRAC-30-30	0.45	160	356	565	0.45	160	356	565
MARC-30-40	0.45	160	356	565	0.36	160	444	539

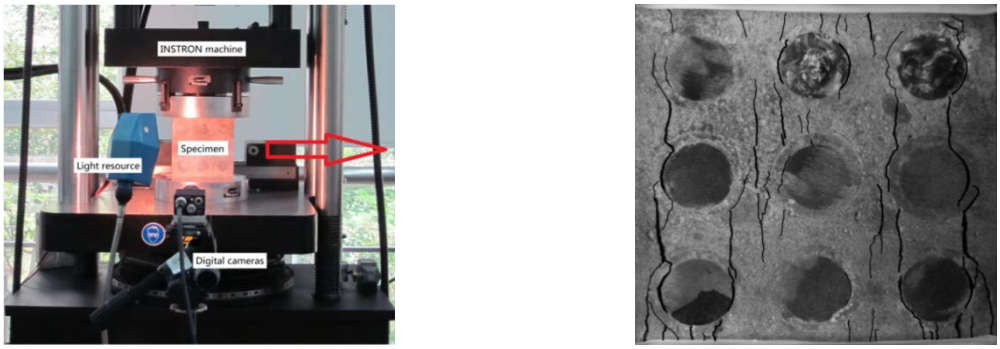

(a) Experimental and DIC setup (b) MRAC failure pattern

Figure 7. Experimental study on MRAC under uniaxial compression [5, 14]

To investigate the compressive stress-strain curve and crack propagation of MRAC, numerical simulation relevant to the mechanical behavior of MRAC with different new mortar matrix and corresponding new ITZ under uniaxial loading is considered herein. The analysis was conducted on MRAC specimens with one mixture for old cement mortar and three mixtures for new cement mortar (MRAC30-20, MRAC30-30 and MRAC30-40). For the real MRAC, the properties of old/new ITZ properties are actually somewhat related or proportional to the old/new mortar matrix properties. When varying the relative mechanical properties of new mortar matrix to old mortar matrix, the relative mechanical properties between new ITZ and new mortar matrix were kept constant with a ratio of 0.85. The different stress-strain curves of MRAC are shown and compared in Figure 8. It is also found that the peak stress and strain increase with the decrease of water-to-cement ratio of the new mortar matrix.

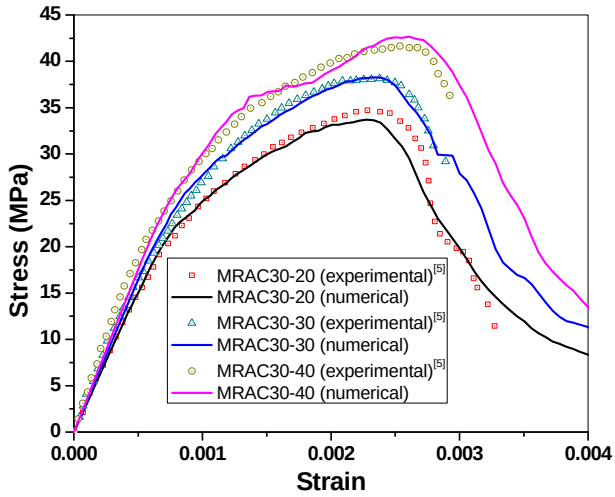

Figure 8. Compressive stress-strain curves of MRAC

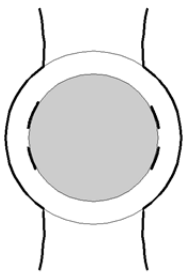

(a) MRAC30-20 (Experimental) [5]

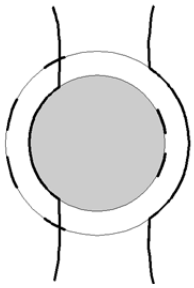

(b) MRAC30-30 (Experimental) [5]

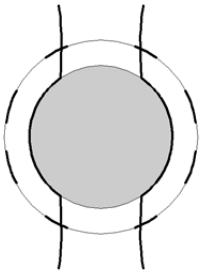

(c) MRAC30-40 (Experimental) [5]

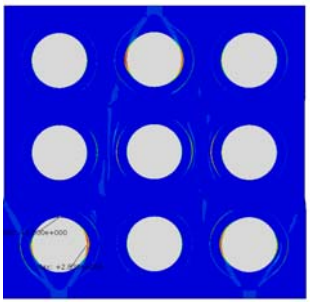

(d) MRAC30-20 (Numerical)

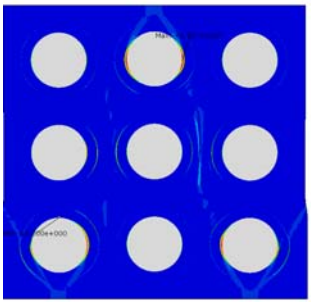

(e) MRAC30-30 (Numerical)

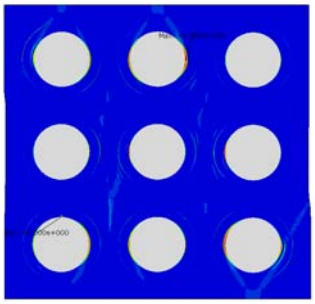

(f) MRAC30-40 (Numerical)

Figure 9. Simulated microcrack development under compression

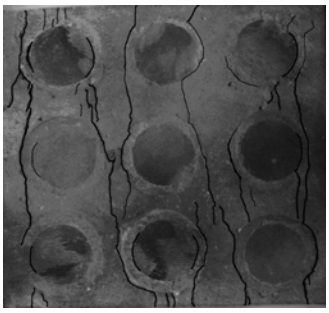

(a) MRAC30-20 (Experimental) [5]

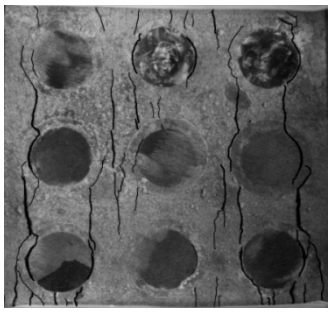

(b) MRAC30-30 (Experimental) [5]

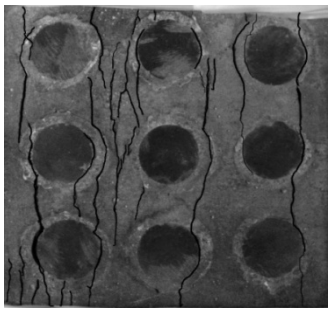

(c) MRAC30-40 (Experimental)[5]

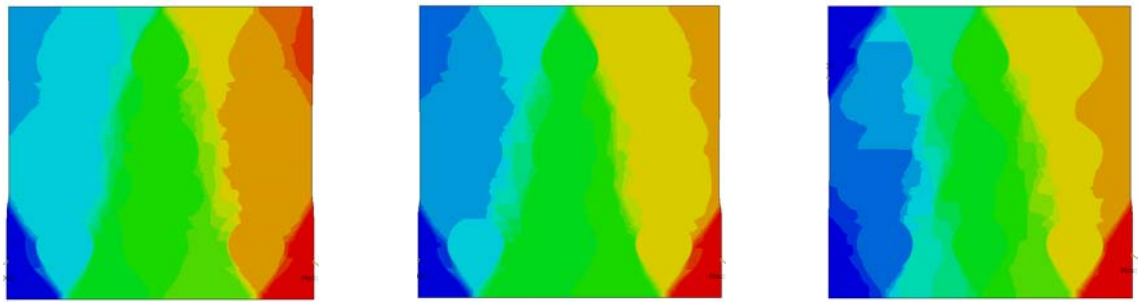

(d) MRAC30-20 (Numerical) (e) MRAC30-30 (Numerical) (f) MRAC30-40 (Numerical)

Figure 10. Simulated failure pattern of MRAC under compression

From Figure 9, it can be revealed that the micro-crack formations are quite different for the different MRAC specimens, which fits the experimental results very well [10, 49]. In the case of MRAC30-20, most of the first observable micro-cracks appeared at the new ITZ in quantity. As for the MRAC30-30, the first observable micro-cracks formed around both old and new ITZ. In the MRAC30-40, most of the first observable micro-cracks initiated at the old ITZ. With the comparison between experimental and numerical micro-cracks initiation, it can be concluded that the numerical results agree well with the experimental evidences. Figure 10 represents the numerical failure pattern for MRAC under uniaxial compression. With the load increasing, micro-cracks, which were found around the ITZs, start connecting with each other, and cross the old mortar matrix regions. Finally, the cracks propagate into new mortar parallel to the loading direction. From the view point of failure pattern of MRAC, the numerical results are also in good agreement with the experimental ones [5, 14].

4.3.2 Uniaxial tension

The numerical tensile stress-strain curves of MRAC with different new mortar matrix are presented in Figure 11. It appears that both the pre-peak load and post-peak load behavior are influenced by the mechanical properties of new mortar matrix. It can be clearly seen that the pre-peak region is nearly linear, while in the post-peak load region there is a subsequently steep drop of load and a long tail. The jumps in the post-peak load stage are due to the crack opening. The tensile strength and elastic modulus of MRAC increase with the increase of the mechanical properties of new mortar matrix. However, the model with higher mechanical properties exhibits less ductility than that with lower mechanical properties of new mortar matrix. This numerical evidence shows a good agreement with the experimental tendency of normal concrete model [8]. For the stress-strain curves, the crack localization corresponds to the steep branch after the peak stress, and mortar matrix prevails on the ITZs failure in the tail of the softening curves. However, ITZs failure still exists in the post-peak stage such as the slipping effect.

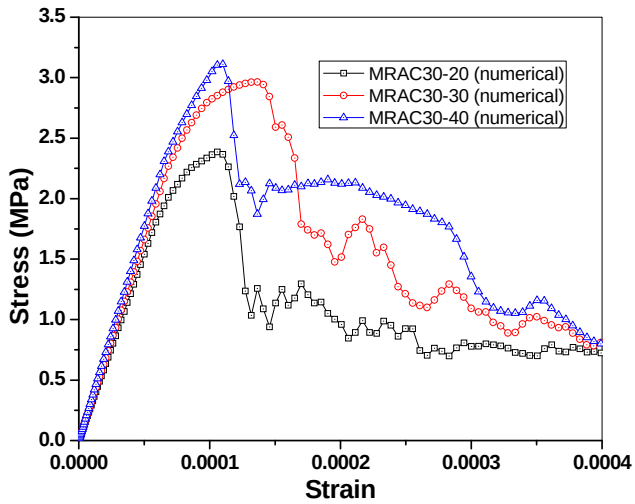

Figure 11. Tensile stress-strain curve of MRAC

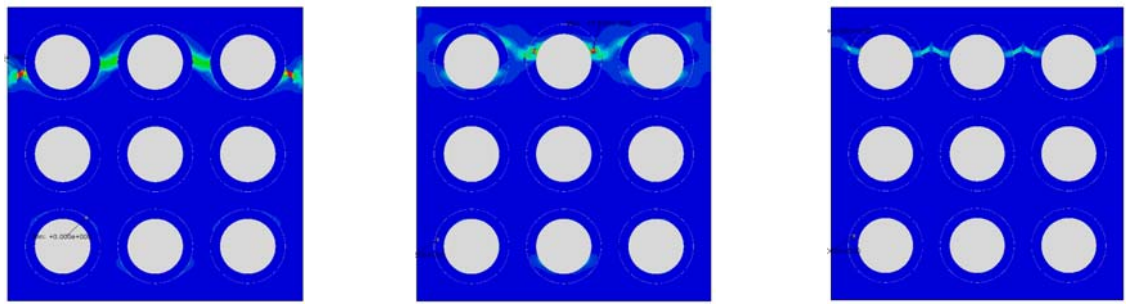

(a) MRAC30-20 (b) MRAC30-30 (c) MRAC30-40

Figure 12. Simulated microcrack development under tension

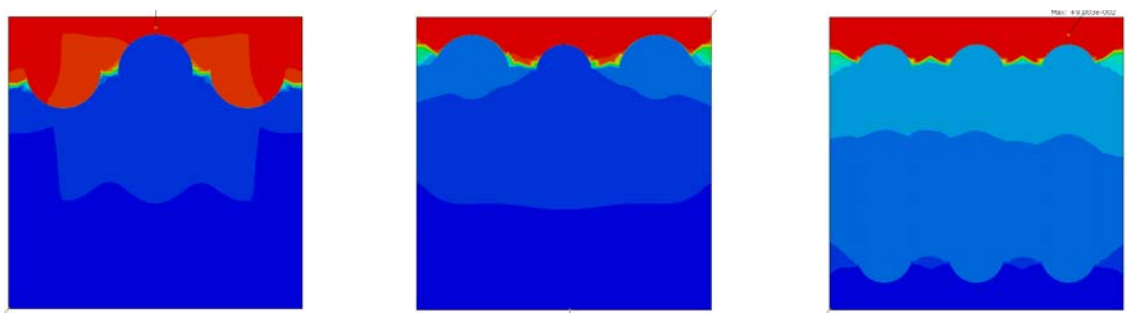

(a) MRAC30-20 (b) MRAC30-30 (c) MRAC30-40

Figure 13. Simulated failure pattern of MRAC under tension

The micro-crack propagation for the MRAC models at the peak loading level is shown Figure 12. It can be seen that strain concentrations are clear around the ITZs. It can be found that the failure cracks initiate in ITZs, and propagate laterally until the whole failure. These results show that the different new mortar matrix produces a different ITZ failure. In the case of MRAC30-20, micro-crack localization occurs around the new ITZ. For MRAC30-30, the micro-crack concentration formed at both new ITZ and old ITZ. However, for MRAC30-40, the localization process mainly forms at the old ITZ. The similar cracking localization is also observed in MRAC under compression in the experimental research [5,14]. This phenomenon is due to the competition between micro-cracks located at old ITZ and new ITZ. Moreover, the final configuration is dependent on the relative strength of new mortar matrix to old mortar matrix.

Figure 13 shows vertical displacement contour maps of MRAC at post-peak load stage. At the post-peak loading stage, with the load increasing, macro-cracks propagate across the old mortar matrix, and start to develop in both ITZs and mortar matrix regions. For MRAC30-20, the main failure macro-crack forms around the new ITZ and propagates through the new mortar matrix laterally until the whole failure. While for MRAC30-30, the main failure crack develops around both new ITZ and old ITZ, and propagates through both old and new mortar matrix. However, for the MRAC30-40, the main failure crack goes around the old ITZ and propagates across the old and new mortar matrix.

5. Conclusions

Numerical simulations of Modeled Recycled Aggregate Concrete (MRAC) under both uniaxial compression and uniaxial tension loadings have been presented. The effects of properties of new mortar matrix and ITZs on the stress-strain response and fracture process are investigated. The main conclusions can be drawn as follows:

(1) The constitutive relation of the ITZ is proposed within the framework of a plastic-damage plasticity constitutive model. The constitutive relation is similar to that of the mortar matrix, but the elastic modulus and strength are lower than those of the mortar matrix;
(2) The FEM modeling is capable of simulating the complete stress-strain curve, as well as the overall fracture patterns including localization of deformation and the micro-crack pattern. Fine agreement between experimental and numerical results is obtained in the calibration and validation;
(3) The new mortar matrix and new ITZ has a significant influence on the stress-strain responses and failure patterns of MRAC. With the increase in the mechanical properties of the new mortar matrix, the strength increases correspondingly, and the micro-crack localization mitigates from the new ITZ to the old ITZ;
(4) It can be concluded that the mechanical damage plasticity model simulations provide valuable insights into the relationship between nano/micro-scale mechanical properties and macro-scale mechanical behavior in recycled aggregate concrete.

Acknowledgements

The authors would like to acknowledge the financial support from the National Natural Science Foundation of China (51178340). The authors gratefully acknowledge Prof. John Bolander in University of California, Davis for his constructive comments and suggestions. The first author would also like to thank China Scholarship Council (CSC) for its financial support during his study at Northwestern University.

References

[1] N. Tregger, D. Corr, L. Graham-Brady, S. Shah, Modeling the effect of mesoscale randomness on concrete fracture. Probabilistic Engineering Mechanics, 21(2006) 217-225.
[2] W.G. Li, J.Z. Xiao, Z.H. Sun, S. Kawashima, S.P. Shah, Interfacial transition zones in recycled aggregate concrete with different mixing approaches. Construction and Building Materials, 35(2012) 1045-1055.
[3] M. Yip, Z. Li, B.S. Liao, J.E. Bolander, Irregular lattice models of fracture of multiphase particulate materials. International Journal of Fracture, 140(2006) 113-124.
[4] G. Lilliu, J.G.M. van Mier, On the relative use of micro-mechanical lattice analysis of 3-phase particle composites. Engineering Fracture Mechanics, 74(2007) 1174-1189.
[5] J.Z. Xiao, W.G. Li, Z.H. Sun, S.P. Shah, Crack propagation in recycled aggregate concrete under uniaxial compressive loading. ACI Materials Journal, 109(2012)

451-461.
[6] J.Z. Xiao, W.G. Li, D.J. Corr, S.P. Shah, Simulation study on the stress distribution in modeled recycled aggregate concrete under uniaxial compression. Journal of Materials in Civil Engineering, in press, 2012.
[7] D. Asahina, E.N. Landis, J.E. Bolander, Modeling of phase interfaces during pre-critical crack growth in concrete. Cement and Concrete Composites, 33(2011) 966-977.
[8] D. Corr, M. Accardi, L. Graham-Brady, S. Shah, Digital image correlation analysis of interfacial debonding properties and fracture behavior in concrete. Engineering Fracture Mechanics, 74 (2007) 109-121.
[9] G. Cusatis, D. Pelessone, A. Mencarelli, Lattice Discrete Particle Model (LDPM) for concrete failure behavior of concrete. I: Theory. Cement and Concrete Composites, 33(2011) 881-890.
[10] G. Cusatis, A. Mencarelli, D. Pelessone, Baylot J, Lattice Discrete Particle Model (LDPM) for failure behavior of concrete. II: Calibration and Validation. Cement and Concrete Composites, 33(2011) 891-905.
[11] S.M. Kim, R.K. Abu Al-Rub, Meso-scale computational modeling of the plastic-damage response of cementitious composites. Cement and Concrete Research, 41(2011) 339-358.
[12] P. Mondal, S.P. Shah, L.D. Marks, Nanoscale characterization of cementitious materials. ACI Materials Journal, 105(2008) 174-179.
[13] J.Z. Xiao, W.G. Li, Z.H. Sun, D.A. Lange, S.P. Shah, Studying interfacial transition zones in recycled aggregate concrete with nanoindentation. Cement & Concrete Composite, in press, 2012.
[14] W.G. Li, J.Z. Xiao, Z.H. Sun, P. S.P. Shah, Failure processes of modeled recycled aggregate concrete under uniaxial compression. Cement & Concrete Composites, 34 (2012)1149-1158.
[15] U. Cicekli, G.Z. Voyiadjis, R.K. Abu Al-Rub, A plasticity and anisotropic damage model for plain concrete. International Journal of Plasticity, 23(2007)1874-1900.
[16] S. Igarashi, A. Bentur, S. Mindess, Microhardness testing of cementitious materials. Advanced Cement Based Materials, 4(1996) 48-57.
[17] C. Bobko, F.-J. Ulm, The nano-mechanical morphology of shale. Mechanics of Materials, 40 (2008) 318-337.
[18] G. Ramesh, E.D. Sotelino, W.F. Chen, Effect of transition zone on elastic moduli of concrete materials. Cement and Concrete Research, 26(1996) 611-622.
[19] Z.J. Yang, X.T. Su, J.F. Chen, G.H. Liu, Monte Carlo simulation of complex cohesive fracture in random heterogeneous quasi-brittle materials. International Journal of Solids and Structures, 46 (2009) 3222-3234.
[20] H.X. Yu, I.W. Burgess, J.B. Davison, R.J. Plank, Numerical simulation of bolted steel connections in fire using explicit dynamic analysis. Journal of Constructional Steel Research, 64(2008) 515-525.
[21] Version 6.11 Theory Manual, ABAQUS, 2011.

Determination of Residual Fracture Toughness of Post-fire Concrete Using Analytical and Weight Function Method

YU Kequan[1,*], **LU Zhoudao, YU jiangtao**

[1] Department of civil engineering, Tongji University, Shanghai 200092, China
* Corresponding author: zjzjykq@163.com

Abstract: Determination of double-K fracture parameter using both analytical and weight function method is carried out in present research. In calculating the cohesive fracture toughness, two situations are divided at critical load. Wedge-splitting tests with ten temperatures varying from 20ºC to 600ºC are implemented. The complete load-crack opening displacement curves are obtained from which the initial and critical fracture toughness could be calculated experimentally. The validation of double-K fracture model to the post-fire concrete specimens is proved. Meanwhile the weight function method agrees well with the analytical method.

Keywords: double-K fracture parameter, analytical method, weight function method, post-fire concrete

1. Introduction

It was established that linear elastic fracture mechanics could be only applicable to large-mass concrete structures and could not be applicable to medium and small-scale concrete structures. Since late 1970s, many nonlinear fracture models have been proposed by various groups of researchers to study the behavior of crack propagation in quasi-brittle materials like concrete [1-6].

Experimental results show that the fracture process of concrete structures undergoes three main stages: (i) crack initiation, (ii) stable crack propagation, and (iii) unstable fracture. Accordingly, the double-K fracture criterion initially introduced by Xu and Reinhardt [6] shows the crack initiation, crack propagation and failure during a fracture process until the maximum load is reached. And the two size-independent parameters, initial cracking toughness, K_I^{ini} and unstable fracture toughness, K_I^{un} can be used to study the crack propagation of concrete.

In order to determine the double-K fracture parameters analytically [7, 8] the value of cohesion toughness, K_I^c due to cohesive stress distribution in the fictitious fracture zone is computed using method proposed by Jenq and Shah [9]. In this method, the determination of K_I^c is done using a special numerical technique because of existence of singularity problem at the integral boundary. Under such circumstances, the use of universal form of weight function will provide a closed form expression for determining the value of K_I^c. And it has proven its accuracy in determining the double-K fracture parameter compared to analytical method [10].

The influences of geometrical parameter [11], specimen geometry [12, 13] and size-effect [7, 8, and 14] on fracture toughness were studied by various researchers. It was found that the influence of a_o/D ratio and shape of test specimen are relatively less than the size- effect on the values of fracture parameters.

The influence of temperature on the fracture parameters was also considered by several researchers, but mainly on the fracture energy and material brittleness [15-19], relatively fewer discussion on the fracture toughness [20-21].s Considering there exist many structures subjected to fire or high temperatures, the influence of temperature on the fracture properties needs further studied.

The present paper is aimed at to determine the residual fracture toughness of wedge splitting specimens subjected to high temperatures and prove the validation of double-K fracture model to the post-fire concrete. The wedge-splitting experiments of totally ten temperatures varying from 20ºC to 600ºC and the specimens size 230×200×200 mm with initial-notch depth ratios 0.4 are implemented. Both analytical and weight function methods are used to calculate the residual fracture toughness parameters. Comparison between the two methods and to experimental results is carried out respectively. From the calculated values of double-K fracture parameters using experimental results the nondimensional parameter, brittleness of concrete may be conceived. Hence, the paper is structured to present the following: (i) details of softening traction-separation law of post-fire concrete, (ii) determination of double-K fracture parameters using existing analytical method, (iii) implementation of weight function method, and (v) experimental validation and comparison of results.

2. Softening traction-separation law of post-fire concrete

The softening traction-separation law is a prior to determine the double-K fracture parameters, at room temperature, many expressions have been proposed based on direct tensile tests [22-26]. Based on numerical studies, simplified bilinear expressions for the softening traction-separation law (illustrated in Fig.1) were suggested by Petersson in 1981[22], Hilsdorft and Brameshuber in 1991 [25], and Phillips and Zhang in 1993 [26]. The area under the softening curve was defined as the fracture energy G_F by Hillerborg et al in 1976 [1]. Therefore, one could get the following equation:

$$G_F = \frac{1}{2}(f_t w_s + \sigma_s w_0) \tag{1}$$

As a consequence, a general form of the simplified bilinear expression of the softening traction-separation law is given as follows:

$$\begin{cases} \sigma = f_t - (f_t - \sigma_s) w / w_0 & 0 \le w \le w_s \\ \sigma = \sigma_s (w_0 - w) / (w_0 - w_s) & w_s \le w \le w_0 \\ \sigma = 0 & w \ge w_0 \end{cases} \tag{2}$$

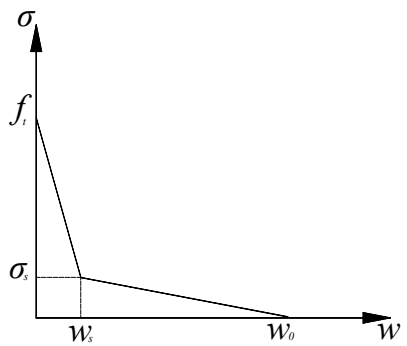

Fig. 1. The bilinear softening traction-separation law

Different values of the break point (σ_s, w_s) and the crack width w_0 at stress-free point were used for the expression proposed by different researchers. In present work, the bilinear softening function of concrete proposed by Petersson is used for post-fire specimens:

$$\begin{cases} \sigma_s = f_t / 3 \\ w_s = 0.8 G_F / f_t \\ w_0 = 3.6 G_F / f_t \end{cases} \tag{3}$$

3. Analytical determination of cohesive fracture toughness

3.1 Effective crack extension length and residual Young's modulus

The linear asymptotic superposition assumption is considered in the analytical method presented by Xu and Reinhardt [7, 8] to introduce the concept of linear elastic fracture mechanics for calculating the double-K fracture parameters. Detailed explanation of the above assumption can be found elsewhere [7].

Based on this assumption, the value of the equivalent-elastic crack length for WS specimen is expressed as:

$$a = (h + h_0)\{1 - (\frac{13.18}{E \cdot b \cdot c + 9.16})^{1/2}\} - h_0 \tag{4}$$

Where $c=CMOD/P$ is the compliance of specimens, b is specimens thickness; h is specimens height and h_0 is the thickness of the clip gauge holder. For calculation of critical value of equivalent-elastic crack length a_c, the value of crack mouth opening displacement ($CMOD$) and P is taken as $CMOD_c$ and P_u respectively.

The residual Young's modulus E is calculated using the P-$CMOD$ curve as:

$$E = \frac{1}{bc_i}[13.18 \times (1-\alpha)^2 - 9.16] \tag{5}$$

Where $c_i=CMOD_{ini}/P_{ini}$, is the initial compliance before cracking, $\alpha= (a_0+h_0)/ (h+h_0)$. The value of critical equivalent-elastic crack length a_c and residual Young's modulus E are listed in Table 2.

3.2 Crack opening displacement along the fracture process zone

Since the cohesive stress distribution along the fracture process zone depends on the crack opening displacement and the specified softening law, it is important to know the value of crack opening displacement along the fracture line. It is difficult to measure directly the value of COD along the fracture process zone, for practical purposes the value of $COD(x)$ at the crack length x is computed using the following expression [3]:

$$COD(x) = CMOD\{(1-\frac{x}{a})^2 + (1.018 - 1.149\frac{a}{h})[\frac{x}{a} - (\frac{x}{a})^2]\}^{1/2} \tag{6}$$

For calculation of critical value of crack tip opening displacement $CTOD_c$, the value of x and a (see in Fig.4) in Eq. (6) is taken to be a_o and a_c, respectively. The value of cohesive stress along the fictitious fracture zone to the corresponding crack opening displacement is evaluated using bilinear stress-displacement softening law as given in Eq. 3.

3.3 Determination of stress intensity factor caused by cohesive force

The standard Green's function [27] for the edge cracks with finite width of plate subjected to a pair of normal forces is used to evaluate the value of cohesive toughness. The general expression for the crack extension resistance for complete fracture associated with cohesive stress distribution in the fictitious fracture zone for Mode I fracture is given as below:

$$K_I^{\,c} = \int_{a_0}^{a} 2\sigma(x)F(\frac{x}{a},\frac{a}{h})/\sqrt{\pi a}dx \tag{7}$$

Where

$$F(\frac{x}{a},\frac{a}{h})=\frac{3.52(1-x/a)}{(1-a/h)^{3/2}}-\frac{4.35-5.28x/a}{(1-a/h)}+\left\{\frac{1.30-0.30(x/a)^{3/2}}{\sqrt{1-(x/a)^2}}+0.83-1.76\frac{x}{a}\right\}\left\{1-(1-\frac{x}{a})\frac{a}{h}\right\} \tag{8}$$

and $\sigma(x)$ is the cohesive force at crack length x, see in Fig.3, its expression is shown in Eqs.9 or 11. At critical condition the value of a is taken to be a_c in Eqs.7 and 8. The integration of the Eq.8 is done by using Gauss-Chebyshev quadrature method because of existence of singularity at the integral boundary.

As shown in Fig.2, two conditions at critical load, i.e., $CTOD_c \leq w_s$ and $w_s \leq CTOD_c \leq w_c$ may arise at the notch-tip while using bilinear softening function. For specimens subjected to temperatures less than 120ºC, the critical $CTOD_c$ is less than w_s; whereas, for temperatures higher than 120ºC, the critical $CTOD_c$ is wider than w_s.

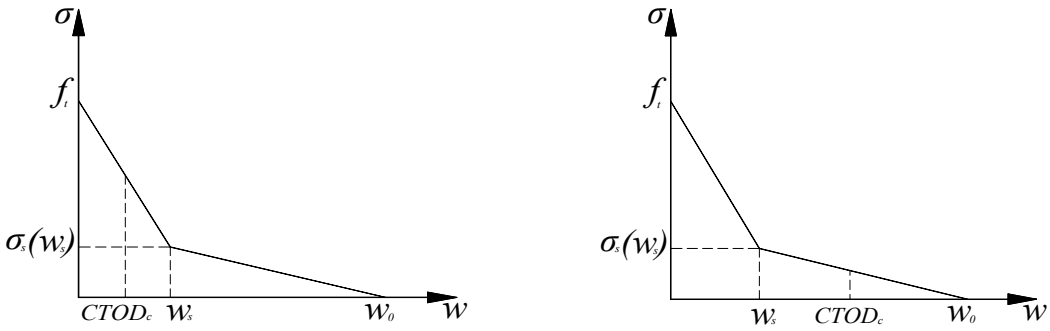

(a) When $CTOD_c \leq w_s$ (b) When $CTOD_c > w_s$

Fig.2. Two different situations for $CTOD_c$ and w_s

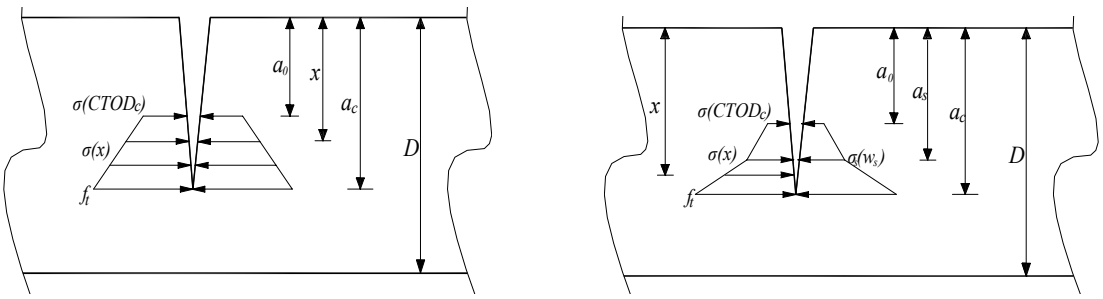

(a) The linear distribution of cohesive force (b) The bilinear distribution of cohesive force

Fig.3. Cohesive force distribution along the crack length at critical load

A. When the critical $CTOD_c$ corresponding to maximum load P_u is less than w_s as shown Fig.2a. The distribution of cohesive stress along the fictitious fracture zone is approximated to be linear as shown in Fig.3a. The variation of cohesive stress along the fictitious fracture zone for this loading condition i.e., $a_o \leq a \leq a_c$ or $0 \leq CTOD \leq CTOD_c$ is written as:

$$\sigma(x)=\sigma(CTOD_c)+(f_t-\sigma(CTOD_c))(x-a_0)/(a_c-a_0) \tag{9}$$

where, σ ($CTOD_c$) is the critical values of cohesive stress being at the tip of initial notch. The value of σ ($CTOD_c$) is determined by using bilinear softening function:

$$\sigma(CTOD_c)=\sigma_s(w_s)+\frac{w_s-CTOD_c}{w_s}(f_t-\sigma_s(w_s)) \tag{10}$$

B. When the critical $CTOD_c$ corresponding to maximum load P_u is wider than w_s as shown Fig.2b. The distribution of cohesive stress along the fictitious fracture zone is approximated to be bilinear as shown in Fig.3b. The variation of cohesive stress along the fictitious fracture zone for this loading condition, also, $a_o \leq a \leq a_c$ or $0 \leq CTOD \leq CTOD_c$ is written as:

$$\begin{cases} \sigma_1(x) = \sigma(CTOD_c) + (\sigma_s(w_s) - \sigma(w))\dfrac{(x-a_0)}{(a_s-a_0)} & a_s \le x \le a_0 \\ \sigma_2(x) = \sigma_s(w_s) + (f_t - \sigma_s(w_s))\dfrac{(x-a_s)}{(a_c-a_s)} & a_s \le x \le a_c \end{cases} \tag{11}$$

The value of σ ($CTOD_c$) is determined by using bilinear softening function:

$$\sigma(CTOD_c) = \frac{w_0 - CTOD_c}{w_0 - w_s}\sigma_s(w_s) \tag{12}$$

The limits of integration of Eq.7 should be taken in two steps: $a_o \le x \le a_s$ for cohesive stress $\sigma_1(x)$ and $a_s \le x \le a_c$ for cohesive stress $\sigma_2(x)$ respectively. The same Green's function F(x/a, a/h) for a given effective crack extension will be determined using Eq.8. The calculated formula is listed as follows:

$$K_I^{\,c} = \int_{a_0}^{a_s} 2\sigma_1(x)F(\frac{x}{a_c},\frac{a_c}{h})/\sqrt{\pi a_c}\,dx + \int_{a_s}^{a_c} 2\sigma_2(x)F(\frac{x}{a_c},\frac{a_c}{h})/\sqrt{\pi a_c}\,dx \tag{13}$$

The effective crack length at break point a_s (shown in Fig.3b), is computed from the following nonlinear expression [24] by substituting COD (a_s), $CMOD$, a_c and h:

$$COD(a_s) = CMOD\{(1-\frac{a_s}{a_c})^2 + (1.018 - 1.149\frac{a_c}{h})[\frac{a_s}{a_c} - (\frac{a_s}{a_c})^2]\}^{1/2} \tag{14}$$

Where COD (a_s) is the crack opening displacement at a_s, a_c is the effective crack length (according to Eq.4) and h is the specimen height.

4. Proposed method to determine cohesive fracture toughness using weight function

4.1. Introduction of weight function

Use of weight functions for calculation of stress intensity factors provides an efficient analytical technique for fracture mechanics applications. The method of weight function was initially proposed by Bueckner [28] and Rice [29] for determination of stress intensity factors and crack face displacements in cracked bodies under arbitrary applied stress fields. The value of cohesive fracture toughness K_s may be directly determined using weight function as below:

$$K_S = \int_0^a \sigma_s(x)m(x,a)dx_s \tag{15}$$

The term $m(x, a)$ in Eq.15 is known as weight function and expressed as:

$$m(x,a) = \frac{E'}{2K_r}\frac{\partial u_r}{\partial a} \tag{16}$$

where, a = crack length; $\sigma_s(x)$ = the stress distribution along the crack line in the uncracked body under the loading case s, which can be determined either experimentally or numerically or analytically; dx_s= the infinitesimal length along the crack surface; E'= E for plane stress and E'= $E/1-\nu^2$ for plane strain, E and ν are the Young's modulus and the Poisson's ratio respectively.

4.2. Determination of universal weight function for an edge crack in finite width plate

Several one-dimensional weight functions with various mathematical forms are available in literature [31-33] but their use is limited. Glinka and Shen [34] introduced one universal form of weight function expression having four terms, which can be used for variety of one-dimensional Mode I crack problems:

$$m(x,a)=\frac{2}{\sqrt{2\pi(a-x)}}[1+M_1(1-\frac{x}{a})^{1/2}+M_2(1-\frac{x}{a})+M_3(1-\frac{x}{a})^{3/2}] \tag{17}$$

For i=1，3 $$M_i=\frac{1}{\sqrt{(1-a/D)^3}}[a_i+b_i a/D+c_i(a/D)^2+d_i(a/D)^3+e_i(a/D)^4+f_i(a/D)^5] \tag{18}$$

For i=2 $$M_i=[a_i+b_i a/D] \tag{19}$$

The values of coefficients a_i, bi, c_i, d_i, e_i, f_i are given in Table 1. For an edge crack in the finite width of plate the accuracy of the weight function are verified with respect to Tada et al. [27] Green’s function.

Table 1 Coefficients of four terms weight function parameters M_1, M_2 and M_3

i	a_i	b_i	c_i	d_i	e_i	f_i
1	0.0572	-0.8742	4.0466	-7.8994	7.8550	-3.1883
2	0.4935	4.4365				
3	0.3404	-3.9534	16.1904	-16.0959	14.6302	-6.1307

4.3. Evaluation of cohesive fracture toughness

Once the weight function parameters are determined, Eq.15 is used to calculate the stress intensity factor at critical condition due to cohesive stress distribution as shown in Fig.3. The value of $\sigma(x)$ in Eq.15 is replaced by Eq.10, Eq.11, hence the closed form expression of K_I^c is can be obtained. The value of K_I^c using four terms weight function is expressed in the following form.

A. When the critical $CTOD_c$ corresponding to maximum load P_u is less than w_s as shown Fig.2a:

$$\begin{aligned}K_I{}^c=&\int_0^{a_c}\{\sigma(CTOD_c)+(f_t-\sigma(CTOD_c))(x-a_0)/(a_c-a_0)\}\times\\&\frac{2}{\sqrt{2\pi(a_c-x)}}[1+M_1(1-\frac{x}{a_c})^{1/2}+M_2(1-\frac{x}{a_c})+M_3(1-\frac{x}{a_c})^{3/2}]dx_s\end{aligned} \tag{20}$$

After integration of Eq.20 the closed form solution of K_I^c is determined as:

$$K_{Ic}=\frac{2}{\sqrt{2\pi a_c}}(A_1B_1a_c+A_2B_2a_c{}^2) \tag{21}$$

Where $A_1=\sigma(CTOD_c)$, $A_2=\frac{f_t-\sigma(CTOD_c)}{a_c-a_0}$, $S=(1-a_0/a_c)$,

$B_1=2S^{1/2}+M_1S+2/3M_2S^{3/2}+M_3S^2/2$, $B_2=4/3S^{3/2}+M_1S^2/2+4/15M_2S^{5/2}+M_3S^3/6$.

B. When the critical $CTOD_c$ corresponding to maximum load P_u is wider than w_s as shown Fig.2b.

$$\begin{aligned}K_I{}^c=&\int_0^{a_c}\left\{\sigma(CTOD_c)+(\sigma_s(w_s)-\sigma(w))\frac{(x-a_0)}{(a_s-a_0)}+\sigma_s(w_s)+(f_t-\sigma_s(w_s))\frac{(x-a_s)}{(a_c-a_s)}\right\}\times\\&\frac{2}{\sqrt{2\pi(a_c-x)}}[1+M_1(1-\frac{x}{a_c})^{1/2}+M_2(1-\frac{x}{a_c})+M_3(1-\frac{x}{a_c})^{3/2}]dx_s\end{aligned} \tag{22}$$

After integration of Eq.22 the closed form solution of K_I^c is determined as:

$$\begin{aligned}K_I{}^c=&\frac{2}{\sqrt{2\pi a_c}}\{A_1a_c[B_1-B_3]+A_3a_c{}^2[B_1-B_3-B_4+B_5]\}-\frac{2}{\sqrt{2\pi a_c}}\{A_3a_ca_0[B_1-B_3]\}\\&+\frac{2}{\sqrt{2\pi a_c}}\{A_4B_3a_c+A_5B_3a_c{}^2\}-\frac{2}{\sqrt{2\pi a_c}}\{A_5a_ca_sB_3\}+\frac{2}{\sqrt{2\pi a_c}}\{A_5B_5a_c{}^2\}\end{aligned} \tag{23}$$

Where $A_1 = \sigma(CTOD_c)$, $A_3 = \dfrac{\sigma_s(w_s) - \sigma(CTOD_c)}{a_c - a_0}$, $A_4 = \sigma_s(w_s)$, $A_5 = \dfrac{f_t - \sigma_s(w_s)}{a_c - a_0}$,

$B_1 = 2S_1^{1/2} + M_1 S_1 + 2/3 M_2 S_1^{3/2} + M_3 S_1^2/2$, $B_3 = 2S_2^{1/2} + M_1 S_2 + 2/3 M_2 S_2^{3/2} + M_3 S_2^2/2$,

$B_4 = 2/3 S_1^{1/2} + M_1 S_1^2/2 + 2/5 M_2 S_1^{5/2} + M_3 S_1^3/3$, $B_5 = 2/3 S_2^{3/2} + M_1 S_2^2/2 + 2/5 M_2 S_2^{5/2} + M_3 S_2^3/3$,

$S_1 = (1 - a_0/a_c)$, $s_2 = (1 - a_s/a_c)$.

5 Calculation of double-K fracture parameters

The two parameters (K_I^{ini} and K_I^{un}) of double-K fracture criterion for wedge-splitting test is determined using linear elastic fracture mechanics formula given in XU[8]:

$$K(P,a) = \frac{P \times 10^{-3}}{th^{1/2}} f(\alpha) \tag{24}$$

$$f(\alpha) = \frac{3.675 \times [1 - 0.12(\alpha - 0.45)]}{(1-\alpha)^{3/2}}, \alpha = \frac{a}{h} \tag{25}$$

The empirical expression (24) is valid within 2% accuracy for, $0.2 \le \alpha \le 0.8$.

Equations 24 and 25 can be used in calculation of unstable fracture toughness, K_I^{un} at the tip of effective crack length a_c, in which $a = a_c$ and P = maximum load, P_u for TPBT and CT test specimen geometries respectively. The initiation toughness, K_I^{ini} is calculated using Eqs.24 and 25 when the initial cracking load, P_{ini} at initial crack tip is known. In present paper, the P_{ini} is determined by graphical method using the starting point of non-linearity in *P-CMOD* curve described in the following section.

Generally, for post-fire concrete specimens the value of initial fracture toughness K_I^{ini} is far less than the value of critical fracture toughness K_I^{un}, especially for higher temperatures. So much more consideration is put to the critical fracture toughness K_I^{un}. In double-K fracture model, the following relation can be employed:

$$K_I^{un} = K_I^{ini} + K_I^{c} \tag{26}$$

Since there are two methods to determine the cohesive fracture toughness as mentioned above. Here we donate the experimental value, analytical value and weight function value of critical fracture toughness as $K_I^{un\text{-}e}$, $K_I^{un\text{-}A}$, $K_I^{un\text{-}W}$ respectively, and from which we would judge the validation of double-K fracture model and weight function method to the post-fire concrete.

6. Experimental validation and comparison of results

6.1. Experimental program and experimental phenomena

To obtain the complete *P-CMOD* curves, the wedge-splitting tests were implemented. A total of 50 concrete specimens with the same dimensions 230×200×200 mm were prepared, the geometry of the specimens is shown in Fig.4 (b=200mm, d=65mm, h=200mm, f=30mm, a_0=80mm, θ=15°). The concrete mix ratios (by weight) were Cement: Sand: Coarse aggregate: Water = 1.00:3.44:4.39:0.80, with common Portland cement-mixed medium sand and 16-mm graded coarse aggregate. All the specimens had a precast notch of 80 mm height and 3 mm thickness, achieved by placing a piece of steel plate into the molds prior to casting. Each wedge splitting specimen was embedded with a thermal couple in the center of specimen for temperature control.

Nine heating temperatures, ranging from 65ºC to 600ºC (T_m=65ºC, 120ºC, 200ºC, 300ºC, 350ºC,

400ºC, 450ºC, 500ºC, 600ºC), were adopted with the ambient temperature as a reference. Because it was recognized that the fracture behavior measurements were generally associated with significant scatter, five repetitions were performed for each temperature.

A closed-loop servo controlled hydraulic jack with a maximum capacity of 1000 kN was employed to conduct the wedge splitting tests (shown in Fig.5). Two Clip-on Extensometers were suited at the mouth and the tip of the crack to measure the crack mouth opening displacement (*CMOD*) and crack tip opening displacement (*CTOD*). To obtain the complete *P-CMOD* curves (shown in Fig.6), the test rate was fixed at 0.4 mm/min.

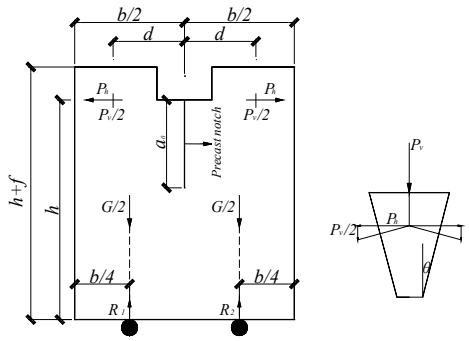

Fig. 4. The geometry of specimens

Fig. 5. The experiment set-up

For the specimens exposed to relatively lower temperatures (20ºC~200ºC), the splitting load generally reached its peak with no visible crack observed. Once the first crack initiated, the splitting load dropped dramatically. For temperatures at 20ºC~200ºC shows that the crack propagated vertically to the bottom of the specimen along with the precast notch. At temperatures above 200ºC, more than one crack branched from the tip of notch, competing to form the final fracture (shown in Fig.7).

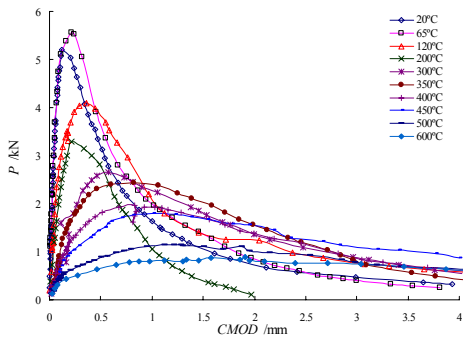

Fig.6.*P* vs *CMOD* curves of specimens with temperatures Fig. 7. Testing phenomenon of post-fire specimens

6.2. Experimental results

Fig.6 shows typical complete load-displacement curves for different heating temperatures up to 600ºC. The figure shows that the ultimate load P_u decreases significantly with increasing temperatures T_m, whereas the crack-mouth opening displacement (*CMOD*) increases with T_m. The initial slope of ascending branches decrease with heating temperatures, and the curves become gradually shorter and more extended.

The recorded maximum load P_u, the recorded crack mouth opening displacement $CMOD_c$ at P_u, the calculated crack tip opening displacement $CTOD_c$ based on Eq.14, the initial cracking load P_{ini} determined by graphical method, the calculated residual Young's modulus E based on Eq.5, the

double-K fracture parameters, i.e., K_I^{ini} and $K_I^{un\text{-}E}$ and the residual fracture energy G_F are summarized in Table 2. Here we only list part of the statistics.

Table 2 The experimental results of fracture parameters

specimen	temperature	P_{ini}/ kN	P_{max}/ kN	$CMOD_c$ /mm	$CTOD_c$ /mm	E GPa	G_F N/m	K_I^{ini} MPa·m$^{1/2}$	$K_I^{c\text{-}A}$ MPa·m$^{1/2}$	$K_I^{c\text{-}W}$ MPa·m$^{1/2}$	$K_I^{un\text{-}E}$ MPa·m$^{1/2}$	$K_I^{un\text{-}A}$ MPa·m$^{1/2}$	$K_I^{un\text{-}W}$ MPa·m$^{1/2}$
WS1	20ºC	6.19	8.33	0.174	0.065	15.30	234.15	0.505	0.666	0.691	1.061	1.171	1.196
WS2		6.28	9.81	0.120	0.039	20.51	483.66	0.523	0.571	0.608	1.070	1.094	1.131
WS3		7.26	10.40	0.210	0.079	20.66	438.22	0.610	0.968	1.002	1.497	1.578	1.612
WS4		7.02	7.92	0.152	0.060	18.88	219.39	0.357	0.799	0.818	1.091	1.156	1.175
WS5		5.65	9.39	0.237	0.096	15.45	321.05	0.503	0.715	0.742	1.213	1.218	1.245
Aver		6.55	9.17	0.178	0.068	18.16	339.30	0.498	0.744	0.772	1.186	1.243	1.271
WS11	120ºC	5.03	8.37	0.191	0.056	10.65	396.52	0.518	0.45	0.489	0.900	0.968	1.007
WS13		4.69	8.25	0.224	0.084	11.87	517.82	0.417	0.745	0.754	1.058	1.162	1.171
WS12		4.71	7.53	0.357	0.152	9.48	654.73	0.419	1.016	1.070	1.202	1.435	1.489
WS14		2.79	7.53	0.198	0.083	15.42	345.46	0.249	0.858	0.951	1.107	1.107	1.200
WS15		——	——	——	——	——	——	——	——	——	——	——	——
Aver		4.31	7.92	0.243	0.094	9.48	478.63	0.401	0.767	0.816	1.067	1.168	1.217
WS21	300ºC	1.89	3.40	0.653	0.283	2.45	437.92	0.168	0.45	0.478	0.556	0.618	0.646
WS22		3.48	5.53	0.667	0.280	3.49	611.47	0.309	0.553	0.597	0.841	0.862	0.906
WS23		1.82	3.38	0.672	0.271	1.91	341.77	0.162	0.374	0.386	0.480	0.536	0.548
WS24		2.61	4.97	0.577	0.262	1.99	564.12	0.232	0.359	0.381	0.589	0.591	0.613
WS25		2.03	4.17	0.651	0.361	4.03	549.99	0.175	0.82	0.824	0.913	0.995	0.999
Aver		2.37	4.29	0.644	0.291	2.78	501.05	0.209	0.512	0.533	0.676	0.21	0.742
Aver		2.01	3.78	0.901	0.410	1.56	490.71	0.149	0.374	0.398	0.615	0.526	0.550
WS36	450ºC	1.52	3.37	1.009	0.544	1.41	611.53	0.135	0.387	0.401	0.582	0.522	0.536
WS37		——	——	——	——	——	——	——	——	——	——	——	——
WS38		1.52	3.26	1.419	0.660	1.46	482.45	0.135	0.341	0.375	0.527	0.476	0.510
WS39		1.12	3.07	1.348	0.617	1.34	663.10	0.100	0.42	0.437	0.563	0.520	0.537
WS40		0.99	2.94	1.394	0.666	1.58	678.79	0.088	0.513	0.508	0.659	0.601	0.596
Aver		1.29	3.16	1.293	0.622	1.16	608.97	0.115	0.415	0.430	0.583	0.530	0.545
WS46	600ºC	0.76	1.13	1.482	0.684	0.47	228.23	0.067	0.174	0.188	0.221	0.231	0.245
WS47		0.53	1.48	2.082	0.684	0.48	395.06	0.063	0.209	0.216	0.277	0.284	0.291
WS48		0.81	1.65	1.908	0.813	1.14	539.22	0.072	0.478	0.512	0.550	0.550	0.584
WS49		0.58	1.14	1.687	0.973	0.38	331.99	0.052	0.188	0.198	0.225	0.225	0.235
WS50		0.62	1.48	2.082	0.727	0.38	273.07	0.068	0.155	0.161	0.213	0.213	0.219
Aver		0.62	1.38	1.848	0.799	0.57	353.51	0.064	0.241	0.255	0.297	0.301	0.315

6.3. Discussion

In order to express the influence on the residual fracture toughness in detail, Fig.8 plots the tendency of initial fracture toughness K_I^{ini} and the unstable fracture toughness K_I^{un} with heating temperatures T_m. It is concluded that the two fractures toughness decrease monotonously with T_m because of the thermal damage induced by the heating temperatures.

The initial fracture toughness continuously decreases from 0.498 kN at room temperature to 0.269 kN at 200ºC, 0.115 kN at 450ºC, and finally 0.064kN at 600ºC, with a significant loss of 0.434 kN or 96%. The unstable fracture toughness decreases from 1.186 kN at room temperature to 0.297 at 600ºC, with a significant loss of 0.889 kN or 75%.

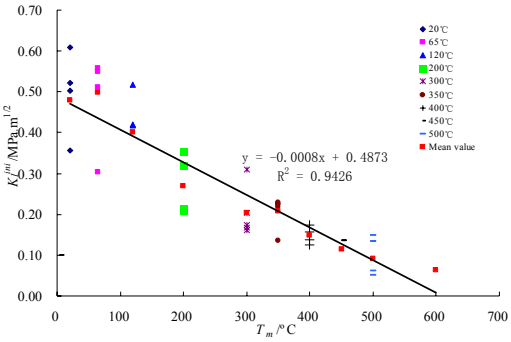

(a) The tendency of K_I^{ini} with T_m

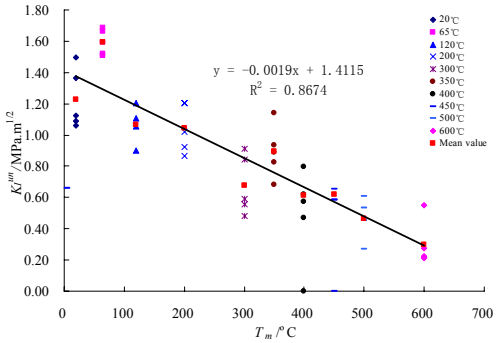

(b) The tendency of K_I^{un} with T_m

Fig.8. The tendency of residual fracture toughness with heating temperatures T_m

Comparing the result shown in Table 2, it can be known that the value of $K_I^{un\text{-}A}$ evaluated by formula (26) has a good coincidence to one calculated by inserting the values of P_{max} and a_c=D into the formula (24), i.e. the critical fracture toughness from analytical and experimental method. Fig.9 shows the relationship between the two parameters. The similar results could be concluded between the value of $K_I^{un\text{-}W}$ from formula (26) and the experimental results from formula(24).

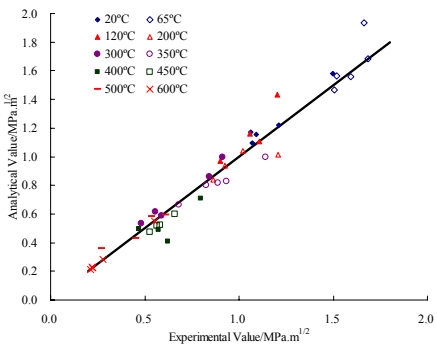

Fig.9. Comparison between analytical and experimental values of critical fracture toughness

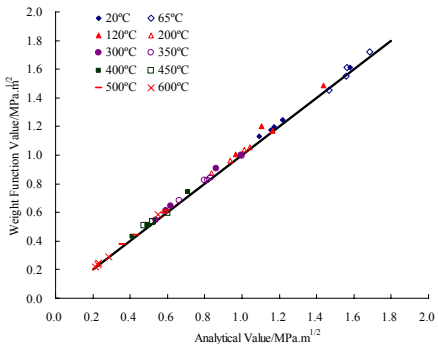

Fig.10. Comparison between analytical and weight function values of critical fracture toughness

In totally 45 effective specimens, the deviation between $K_I^{un\text{-}A}$ and $K_I^{un\text{-}E}$ of 22 specimens is below 5%, and of 40 specimens is below 15%, account for 89%of total specimens. Accordingly, the number of specimens corresponding to the same deviation between $K_I^{un\text{-}W}$ and $K_I^{un\text{-}E}$ is 20 and 42, respectively.

Fig.10shows the weight function method agrees well with the analytical method, and the deviation below 5% accounts for 65% of total specimens.

7. Conclusion

The determination of double-K fracture parameter using both analytical and weight function methods are carried out in present research. In calculating the cohesive fracture toughness, two conditions are divided at critical load: for specimens subjected to temperatures less than 120ºC, the critical $CTOD_c$ is less than w_s; whereas, for temperatures higher than 120ºC, the critical $CTOD_c$ corresponding to maximum load P_u is wider than w_s. This part of work would be a useful supplement to the existed analysis.

Wedge-splitting tests with ten temperatures varying from 20ºC to 600ºC are implemented. The complete load-crack opening displacement curves are obtained and the initial and critical fracture toughness could be calculated experimentally.

The validation of double-K fracture model to the post-fire concrete specimens is proved. In totally 45 effective specimens, the deviation between analytical value $K_I^{un\text{-}A}$ and experimental $K_I^{un\text{-}E}$ of 22 specimens is below 5%, and of 40 specimens is below 15%, account for 89% of total specimens. Accordingly, the number of specimens corresponding to the same deviation between $K_I^{un\text{-}W}$ and $K_I^{un\text{-}E}$ is 20 and 42, respectively. Meanwhile the weight function method agrees well with the analytical method, and the deviation below 5% accounts for 65% of total specimens.

Acknowledgment

The State Laboratory of Disaster Reduction in Civil Engineering (SLDRCE09-D-02) has supported this research.

.

Reference

[1] HILLERBORG A., MODEER M. and PETERSON P.E. Analysis of crack formation and crack growth in concrete by means of fracture mechanics and finite elements. Cem Concr Res, 6(6), (1976) 773-782.
[2] Bazant ZP, Oh BH. Crack band theory for fracture of concrete. Mater Struct, 16(93) (1983) 155-177.
[3] Jenq YS, Shah SP Two parameter fracture model for concrete. J Engng Mech, ASCE, 111(10) (1985) 1227-1241.
[4] Nallathambi P, Karihaloo BL. Determination of specimen-size independent fracture toughness of plain concrete. Mag Concr Res, 38(135) (1986) 67-76.
[5] Bazant ZP, Kazemi MT. Determination of fracture energy, process zone length and brittleness number from size effect, with application to rock and concrete. Int J Fract, 44 (1990) 111-131.
[6] Xu S, Reinhardt HW. Determination of double-K criterion for crack propagation in quasi-brittle materials, Part I: Experimental investigation of crack propagation. Int J Fract, 98 (1999) 111-149.
[7] Xu S, Reinhardt HW. Determination of double-K criterion for crack propagation in quasi-brittle materials, Part II: Analytical evaluating and practical measuring methods for three-point bending notched beams. Int J Fract, 98 (1999)151-177.
[8] Xu S, Reinhardt HW. Determination of double-K criterion for crack propagation in quasi-brittle materials, Part III: Compact tension specimens and wedge splitting specimens. Int J Fract, 98 (1999) 179-193.
[9] Jenq YS, Shah SP. A fracture toughness criterion for concrete. Engng Fract Mech, 21(5) (1985) 1055-1069.
[10] Kumar S, Barai SV. Determining the double-K fracture parameters for three-point bending notched concrete beams using weight function. Fatigue Fract Engng Mater Struct, 33(2010) 645-660.
[11] Murakami. Stress Intensity factors handbook. London: Pergamon Press, 1987.
[12] Shailendra Kumar, S. V. Barai. Influence of specimen geometry and size-effect on the KR-curve based on the cohesive stress in concrete. Inter J Fract, 152 (2008) 127-148.
[13] Shailendra Kumar, S. V. Barai. Influence of specimen geometry on determination of double-K fracture parameters of concrete: a comparative study. Inter J Fract, 149 (2008) 47-66.
[14] Karihaloo B L, Nallathambi P. Size effect prediction from the double-K fracture model for notched concrete. Materials and structures, 1990, 23: 178-185.
[15] Zdenek. P. Bazant and Pere C. Prat: Effect of Temperatures and Humidity on Fracture Energy of Concrete. ACI Mater J, 85(4) (1988) 262-271.

[16] Baker G: The effect of exposure to elevated temperatures on the fracture energy of plain concrete. RILEM Mater Struc, 29 (190)(1996) 383-388.
[17] Zhang B., Bicanic N., Pearce C.J. and Balabanic G.: Residual fracture properties of normal and high-strength concrete subject to elevated temperatures. Mag Concr Res, 52(2) (2000) 123-136.
[18] Nielsen C.V. and Bicanic N.: Residual fracture energy of high-performance and normal concrete subject to high temperatures. RILEM Mater Struc, 36 (262) (2003) 515-521.
[19] B. Zhang and N. Bicanic: Fracture energy of high-performance concrete at high temperatures up to 450ºC: the effects of heating temperatures and testing conditions (hot and cold). Mag Concr Res 58 (5) (2006) 277-288.
[20] G.Prokopski: Fracture toughness of concretes at high temperature. J Mater Sci, 30(1995) 1609-1612.
[21] Hisham Abdel-Fattah and Sameer A.Hamoush: Variation of the fracture toughness of concrete with temperature. Constr Build Mater, 11(2) (1997) 105-108.
[22] Petersson PE. Crack growth and development of fracture zones in plain concrete and similar materials. Division of Building Materials, Lund Institute of Technology, Report TVBM-1006, Sweden, 1981.
[23] Gopalaratnam VS, Shah SP. Softening response of plain concrete in direct tension. ACI J May-June (1985) 310-323.
[24] Reinhardt HW, Cornelissen HAW, Hordijk DA. Tensile tests and failure analysis of concrete. J Struc Engng ASCE, 112 (1986) 2462-2477.
[25] Hilsdorf HK, Brameshuber W. Code-type formulation of fracture mechanics concepts for concrete. Inter J Fract, 51 (1991) 61-72.
[26] Phillips DV, Zhang Z. Direct tension tests on notched and un-notched plain concrete specimens. Mag Concr Res, 45 (1993) 25-35.
[27] Tada H, Paris PC, Irwin G. The stress analysis of cracks handbook. Paris Productions Incorporated, St. Louis, 1985.
[27] Bueckner HF. A novel principle for the computation of stress intensity factors. Z Angew Math Mech, 50(1970) 529-546.
[28] Rice JR. Some remarks on elastic crack-tip stress fields. Int J Solid Struct, 8 (1972) 751-758
[29] Shailendra Kumar, S. V. Barai. Determining double-K fracture parameters of concrete for compact tension and wedge splitting tests using weight function. Engng Fract Mech, 76(7) (2009) 935-946.
[30] Fett T. Limitations of the Petroski – Achenbach procedure demonstrated for a simple load case. Engng Fract Mech, 29(6) (1988) 713-716.
[31] Fett T, Mattheck C, Munz D. On calculation of crack opening displacement from the stress intensity factor. Engng Fract Mech 27 (1987) 697-715.
[32] Glinka G, Shen G. Universal features of weight functions for cracks in Mode I. Engng Fract Mech, 40(6) (1991) 1135-1146.

Initiation and Propagation Behavior of a Fatigue Crack of Maraging Steel in High Humidity

Qiang Chen[1,*], **Takanori Nagano**[2], **Yuzo Nakamura**[3]
Yoshikazu Maeda[3], **Norio Kawagoishi**[4]

[1] Center for Globalization, Kumamoto University, Kumamoto 860-8555, Japan
[2] Department of Mechanical Engineering, Miyakonojo National College of Technology, Miyakonojo 885-8567, Japan
[3] Department of Mechanical Engineering, Kagoshima University, Kagoshima 890-0065, Japan
[4] Department of Mechanical System Engineering, Daiichi Institute of Technology, Kirishima 899-4395, Japan
* Corresponding author: qchen@kumamoto-u.ac.jp

Abstract The effect of humidity on the fatigue properties of 18% Ni maraging steels with different hardness and aging structure was investigated under rotating bending fatigue by varying relatively humidity from 25% to 95%. It was found that the initiation and the early propagation of a fatigue crack were accelerated in high humidity, which caused to a large decrease in fatigue strength of the alloys. In fact, the fatigue strength at 10^7 cycles obtained in RH 85% was less than a half of that in RH25%. Meanwhile, successive observation on surface fatigue progress and the fractographic analysis of fractured specimens elucidated that anodic dissolution was the main reason for promoting crack initiation whilst hydrogen embrittlement due to cathode reaction was responsible for the acceleration of crack propagation. However, the acceleration of crack propagation was suppressed by the formation of reverted austenite.

Keywords Fatigue, Maraging steel, Humidity, Ageing condition, Fatigue mechanism

1. Introduction

Maraging steel is a kind of ultrahigh strength steel that involves many strengthening mechanisms such as precipitation hardening, solid solution hardening, grain refinement and so on [1]. However, fatigue strength of maraging steel was much lower than expected on basis of its static strength, especially when compared to other steels of similar high static strength. One reason for the low resistance of the alloy to fatigue is due to its high susceptibility to humidity [2]. It is known that the effect of humidity on fatigue strength varies largely with hardness, microstructure and many other factors. However, information on the effect of humidity on the fatigue properties of maraging steel was very limited in comparison with those on its resistance to stress corrosion cracking [3].
In the present study, rotating bending fatigue tests were carried out for 18%Ni maraging steels with different hardness and aging structures in various relative humidity in order to investigate the effect of humidity on fatigue strength as well as fatigue crack initiation and crack propagation behavior.

2. Experimental procedures

The materials used were a 300-grade and 350-grade 18%Ni maraging steels. The chemical compositions in mass% of the alloys are shown in Table 1. The steels were solution treated for 5.4ks at 1123K in vacuum followed by air cooling and age hardening in a salt bath. The mean grain size of prior austenite was about 20μm in the both alloys. Table 2 shows mechanical properties of the alloys subjected to various age hardening treatments.

Table 1. Chemical composition (mass%)

Grade	C	Si	Mn	Ni	Mo	Co	Ti	Al	Fe
300G	0.005	0.05	0.01	18.47	5.14	9.09	0.89	0.11	Bal.
350G	0.001	0.01	0.01	17.89	4.27	12.36	1.3	0.08	Bal.

Table 2. Mechanical properties

Steel	Aging condition	Vickers hardness *HV*	0.2% proof stress $\sigma_{0.2}$ (MPa)	Tensile strength σ_B (MPa)	Reverted austenite γ (%)
A (300G)	753K,2.8ks	550	1730	1833	0
B (300G)	813K,150ks	550	1634	1798	10
C (350G)	753K,150ks	705	2300	2370	0

Figure 1 shows the aging curves of maraging steels. Aging conditions were determined in such a way that the 300-grade steel was either under-aged or over-aged so that it had nearly the same hardness of 550HV but different structures, while the 350-grade steel was peak-aged and had a hardness of 705HV. The above mentioned ageing conditions are indicated by circles in Fig. 1, respectively. X-ray diffraction detected that only the structure of over-aged steel featured with 10% of reverted austenite. Therefore, the effects of the hardness and the reverted austenite can be examined separately. The under-aged, over-aged and peak-aged 18%Ni maraging steels will be denoted hereafter as Steel A, Steel B and Steel C, respectively.

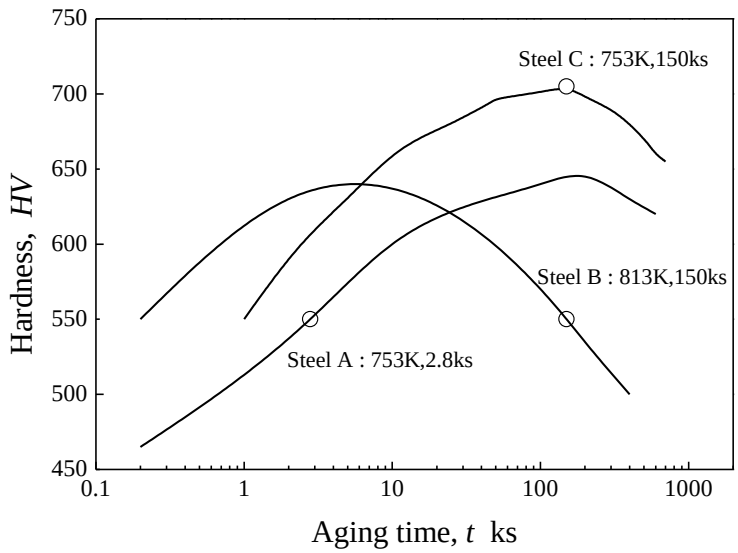

Figure 1. Aging curves of maraging steels

Figure 2 shows shape and dimensions of specimens. Fatigue strength was investigated by using plain specimens (Fig. 2a). To localize crack initiation and to better observe, partially notched specimens (Fig. 2a) were employed. Specimens were machined after solution treatment, and then aged at the different conditions displayed in Fig. 1. Prior to fatigue testing, specimens were electropolished to remove work affected layer and to better observe. Fatigue tests were carried out using a Ono-type rotating bending machine with a capacity of 15 N·m, operating at about 50Hz in the relative humidity (RH) of 25%, 45%, 65%, 85% and 95%, respectively. The humidity was controlled in the range of RH±5% while the temperature without control fell in the range of 298±3K. Surface observation and crack length measurement were conducted using plastic replication technique. Crack length, *a*, was defined along circumferential direction vertical to stress axis. Fracture morphology was analyzed under scanning electron microscope (SEM).

3. Results and discussion

3.1 Effect of humidity on fatigue properties

Figure 3 shows *S-N* curves of Steels A and C in different humidity, respectively. Fatigue strength decreases significantly with increasing humidity, irrespective of the kind of steels.

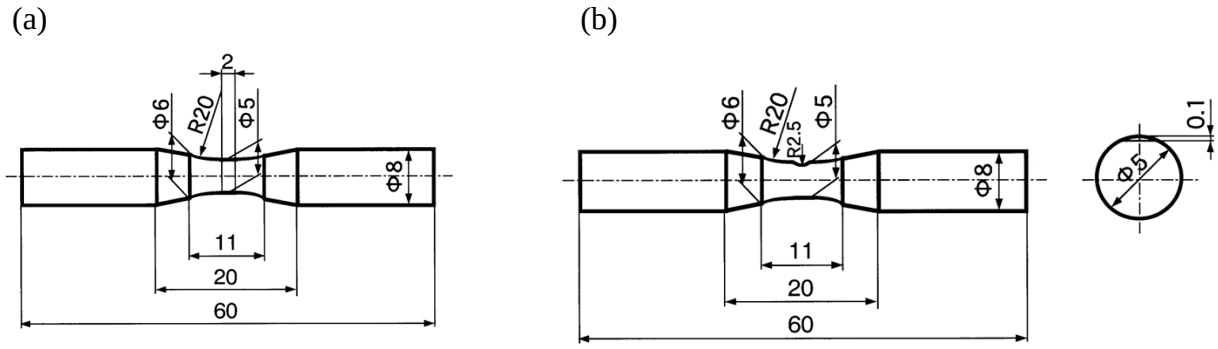

Figure 2. Shape and dimensions of (a) plain and (b) partially notched specimens

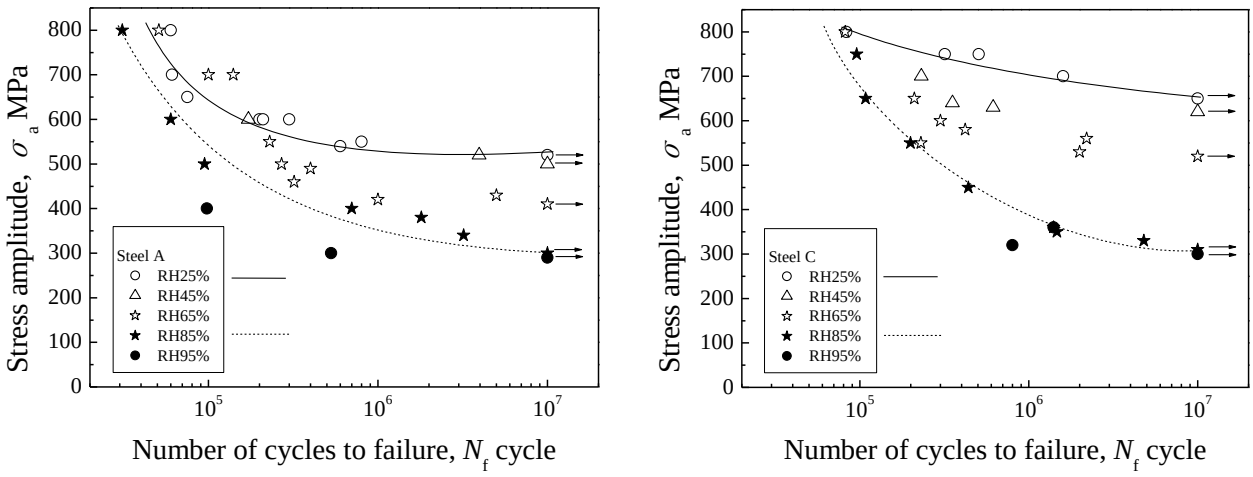

Figure 3. Variation of fatigue strength with humidity in Steels A (left) and C (right)

All of fractures originated from the surface. In low humidity, crack was not observed on the surface of non-fractured specimens tested at the stress level of fatigue limit, σ_w, which is defined as the strength for a specimen not to fail after being stressed for 10^7 cycles. In this case, it means that the fatigue limit of the alloys was determined by the resistance to crack initiation.

Figure 4 shows the humidity dependence of the fatigue limit. Effect of humidity on fatigue strength was relatively small in the range of low humidity below about RH50%. In the high humidity beyond RH50%, fatigue strength decreased largely with increasing humidity, especially the higher the static strength, the larger the decrease in fatigue strength. For example, the fatigue limit of Steel C in RH85% was less than a half of that in RH25%. The humidity examined in the current study was not particular but normal so that this marked decrease of fatigue strength in high humidity is of extremely importance in the practical applications of the alloys.

Figure 5 shows (a) crack growth curves and (b) the relation between crack length and the ratio of number of cycles to fatigue life, N/N_f, in low (RH25%) and high (RH85%) humidity, respectively.

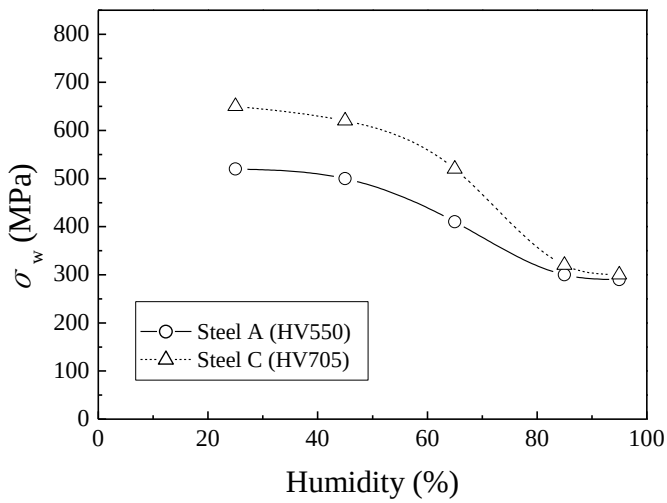

Figure 4. Humidity dependence of fatigue limit

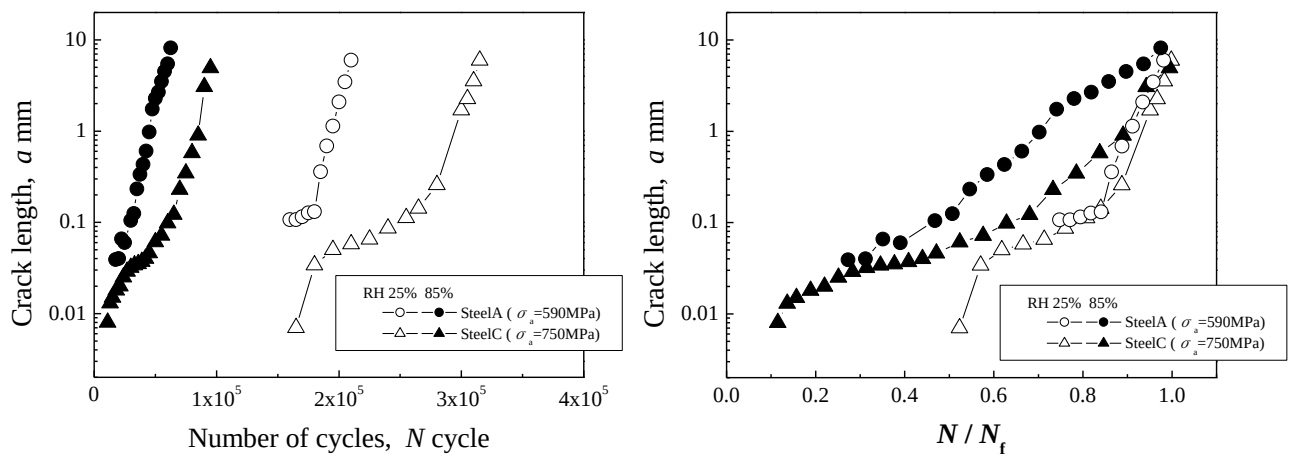

(a) *a*-*N* curves (b) *a*-N/N_f curves

Figure 5. Crack growth behavior

Both the initiation (a few grain sizes) and its early propagation (~0.16 mm) are accelerated by high humidity. Most of fatigue life (70-90%) is spent in growing a crack up to ~1 mm. On the other hand, the influence of humidity on crack growth rate is not remarkable when cracks extend to ~8 grain sizes of prior austenite, and neither is the effect of hardness, as shown in Fig. 6, indicating that the accelerations to crack initiation and early crack propagation are the main reasons for the decrease of fatigue strength in high humidity.

Figure 7 shows the effect of humidity on the feature of typical small cracks observed in Steel C. The edges of a crack corroded in RH85% look relatively wide opened in comparison with those in RH25%, suggesting the promotion of crack initiation in high humidity through anodic dissolution.

The effect of humidity on crack morphology is shown in Fig. 8. In case of Steel A, a crack that propagated in a zigzag way along grain boundaries in high humidity grew almost vertically to stress axis in low humidity. In case of Steel C, however, the influence of humidity is hardly recognized by merely optical surface observation.

Figure 9 shows morphology of fracture surfaces in Steel C. It is found that even in Steel C, brittle facets are also observed in the vicinity of crack initiation site in high humidity, arrowed in Fig. 9b, though no brittle facet is found in low humidity (Fig. 9a), which means that hydrogen embrittlement caused the acceleration of crack propagation in high humidity.

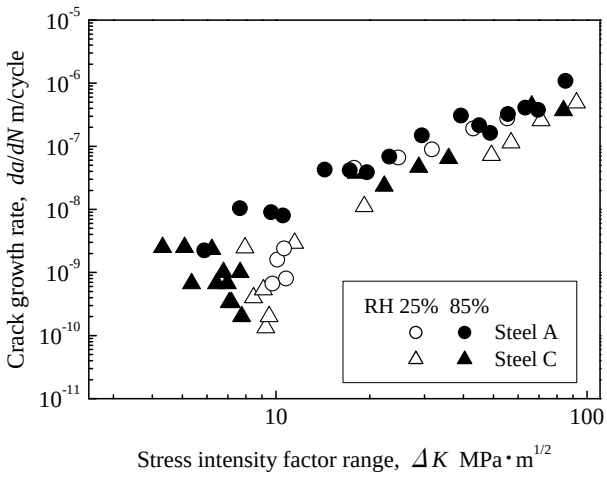

Figure 6. Crack growth rate vs. stress intensity factor range

Figure 7. Cracks observed in Steel C in low (RH25%, left) and high (RH85%, right) humidity, respectively (Axial stresses applied in the horizontal direction)

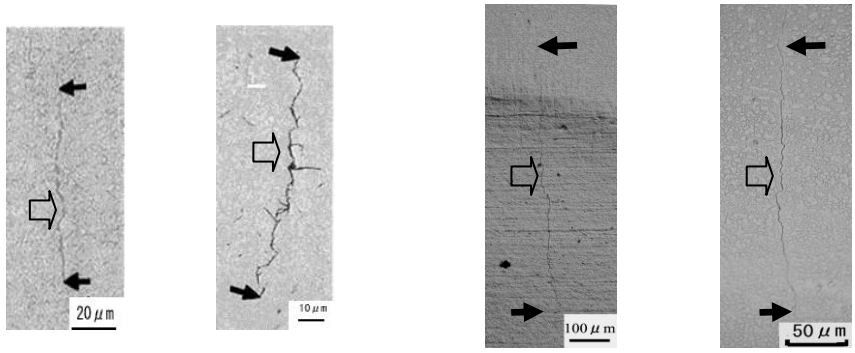

(a) Steel A: RH 25%; RH 85% (b) Steel C: RH 25%; RH 85%

Figure 8. Crack morphology observed in (a) Steel A and (b) Steel C (Blank and solid arrows indicate origin of crack initiation and crack tips, respectively. Axial stresses applied in the horizontal direction)

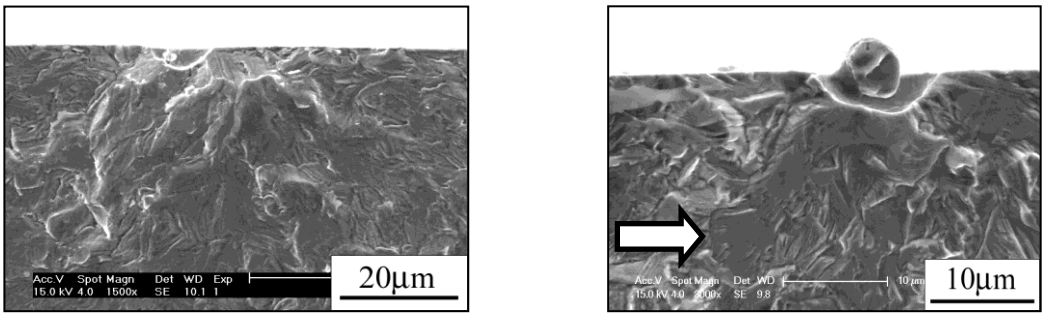

Figure 9. SEM micrographs showing fracture surfaces in RH25% (left) and RH85% (right) in Steel C

3.2 Effect of reverted austenite on fatigue properties in high humidity

Figure 10 shows the effect of reverted austenite on fatigue strength in different humidity by comparing the results of Steel B that had 10% reverted austenite with those of Steel A, which had the same hardness as Steel B but did not include any reverted austenite. Much different from that in Steel A, the fatigue strength of Steel B remains less affected by high humidity.

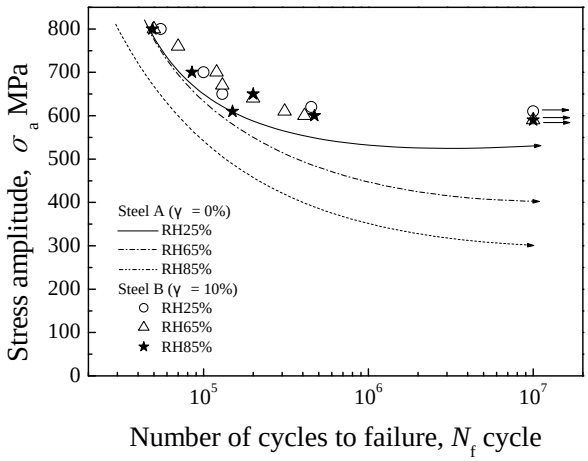

Figure 10. *S-N* curves of Steel B

The crack growth curve and the dependence of crack growth on stress intensity factor range in Steel B are shown in Figs. 11 and 12 respectively. As seen in Figs. 11 and 12, the effects of both humidity and reverted austenite on the propagation of small cracks are not distinguished in Steel B, though the crack initiation of Steel B is truly promoted by high humidity.

Further observation on crack morphology of Steel B fatigued in both low and high humidity reveals that the effect of humidity on macroscopic crack growth in Steel B is really limited, as shown in Fig. 13, implying that the reverted austenite in the matrix of Steel B does play an important role in the process of crack propagation [4], i.e. the widely distributed reverted austenite phases become trap sites of hydrogen [5, 6] and suppress the acceleration of crack propagation in high humidity due to hydrogen embrittlement.

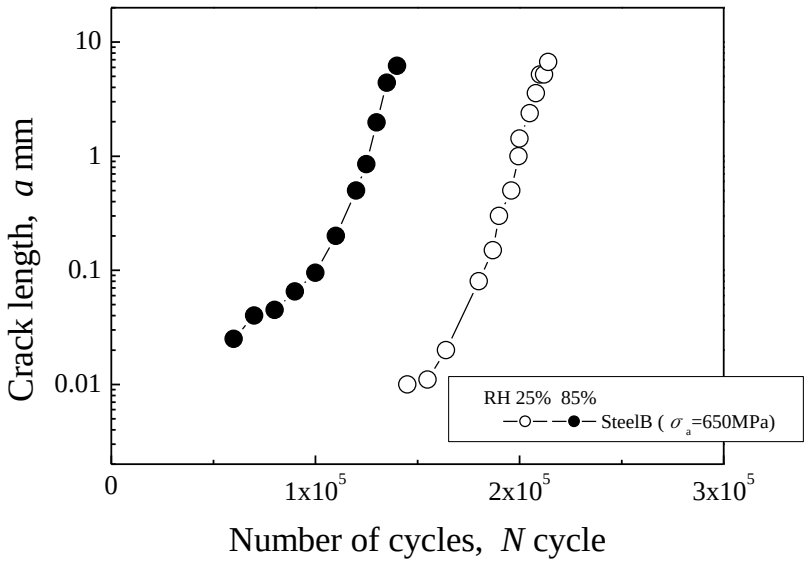

Figure 11. Crack growth curves of Steel B

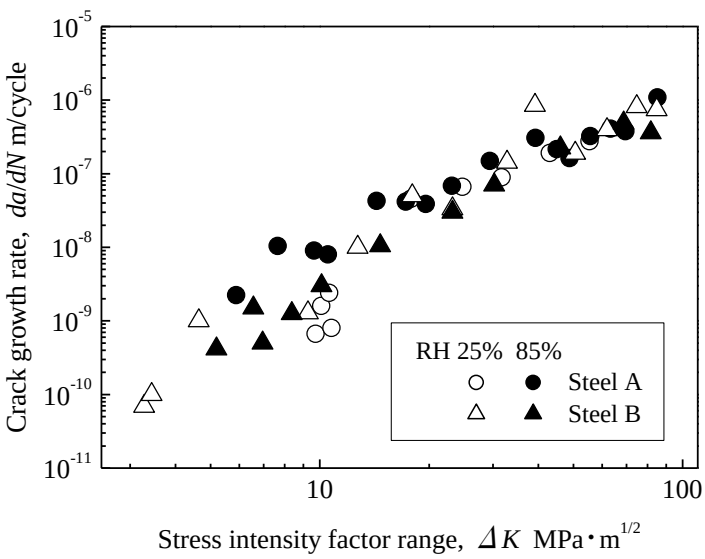

Figure 12. Crack growth rate vs. stress intensity factor range

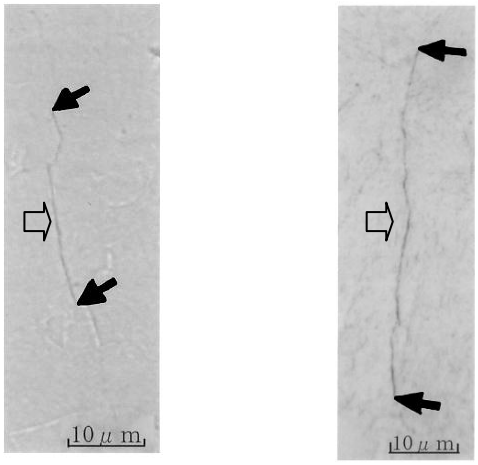

(a) RH 25% (b) RH 85%

Figure 13. Crack morphology observed in Steel B (Blank and solid arrows indicate origin of crack initiation and crack tips, respectively. Axial stresses applied in the horizontal direction)

4. Conclusions

The effects of humidity and the aging structure on the initiation and propagation of a fatigue crack of maraging steels were investigated in various relative humidity (RH). Fatigue strength was largely decreased by high humidity, though the decrease in fatigue strength was very small below the humidity of RH50%. The main reason for the decrease in fatigue strength was the acceleration of both crack initiation and small crack growth. The propagation of larger cracks was not influenced by humidity. The promotion of crack initiation was due to anodic dissolution and the acceleration of crack propagation was caused by hydrogen embrittlement in accompany with cathode reaction. The hydrogen embrittlement assisted crack propagation was suppressed by the formation of reverted austenite.

Acknowledgements

Chen is grateful to the financial supports by JSPS KAKENHI through grant number 22560097 and by JKA through grant number JS23-99.

References

[1] R.F. Decker, C.J. Novak, T.W. Londig, Developments and projected trends in maraging steels, Journal of Metals, (1967)60-66.

[2] K. Komai, S. Kita, K. Endo, Corrosion-fatigue crack growth of a high-tension steel in 1% NaCl, Transactions of the Japan Society of Mechanical Engineers, Series A, 49 (1983)1029-1035.

[3] Y. Kawabe, M. Fukamachi, S. Muneki, J. Takahashi, Increased susceptibility of 13Ni-15Co-10Mo maraging steel to hydrogen embrittlement by aging at lower temperatures, Tetsu to Hagane, 70 (1984) 896-903.

[4] M. Moriyama, S. Takaki, N. Kawagoishi, Influence of reversion austenite on fatigue property of 350 ksi grade 18% Ni maraging steel, Heat Treatment, 41(2001)266-271.

[5] P.J. Ferreira, I.M. Robertson, H.K. Birnbaum, Hydrogen effects on the interaction between dislocations, Acta Materialia, 46 (1998) 1749-1757.

[6] R.O. Ritchie, M.H. Cantro Cedemo, V. H. Zackey, E.R. Parker, Effects of Silicon additions and retained austenite on stress corrosion cracking in ultra strength steels, Metallurgical Transaction, 9A(1978) 35-40.

Crystallographic texture helps reduce HIC cracking in pipeline steels

José M. Hallen, Victoria Venegas, Francisco Caleyo*

DIM, IPN-ESIQIE, UPALM, Edif. 7, Zacatenco, México D.F., 07738, México
*Corresponding author: fcaleyo@gmail.com

Abstract The resistance of sour-service steels to hydrogen-induced cracking (HIC) has been traditionally improved through reduction in sulphur content, control of inclusion morphology, and use of low segregated, uniform microstructures. Other approaches are currently investigated; among them, the control of crystallographic texture as a mean to further reduce the susceptibility of pipeline steels to HIC. In this study, low-carbon steel samples, all within API specifications, were produce using different rolling/recrystallization schemes. These samples showed similar microstructure, but differed in their crystallographic textures. After cathodic hydrogen charging, HIC was detected in the cold- and hot-rolled/recrystallized steels, whereas the warm-rolled/recrystallized steels proved resistant to this damage. These results can be related to the differences in texture and grain boundary distribution observed in these groups of samples. It is concluded that it is feasible to improve the HIC resistance of pipeline steels through crystallography texture control and grain boundary engineering. The use of warm rolling schedules has been proven an effective solution in achieving this goal as they lead to crystallographic texture dominated by the {111}ND-fiber texture, and to a high proportion of low-angle grain boundaries. These two characteristics are necessary to further reduce, beyond traditional methods, the susceptibility of pipeline steels to HIC.

Keywords HIC, pipeline steel, crystallographic texture, warm rolling

1. Introduction

The origin, mechanisms, and consequences of Hydrogen-induced cracking (HIC) have been documented over the last several decades [1]. The strategies to reduce the incidence of this damage have not proven to be totally effective for severe operating conditions [1,2], so that the control of crystallographic texture and grain-boundary distribution of sour-service steels has recently been proposed as a means to reduce their susceptibility to HIC [3].

In recent works the authors have shown that, at a grain scale, crystallographic texture and grain-boundary character can play a significant role in HIC propagation in pipeline steels [4–6]. From the results of these studies it was postulated that the resistance of low-carbon steels to HIC could be improved by controlling their local texture and grain-boundary distribution [7]. Controlled warm-rolling, in the 600–800 °C range, was proposed as a mean to produce crystallographic textures suitable for reducing HIC because of (*i*) a reduction in the number of transgranular and intergranular cleavage paths along {001}ND-oriented[1] grains, (*ii*) a reduction in crack coalescence and stepwise HIC propagation, and (*iii*) an increase in the number of high-resistance, intergranular crack paths along coincidence site lattice and low-angle grain boundaries between {111}ND-oriented grains.

New experimental evidence is presented in this work, which supports the hypothesis that the resistance of pipeline steels to HIC can be improved at a macroscopic scale through controlled warm rolling. Several samples of pipeline steel, all within API 5L specifications [7], were obtained through different thermo-mechanical processes. These samples, all with similar microstructures, developed different crystallographic textures and grain-boundary statistics. Cathodic hydrogen charging was used to investigate their HIC behavior. The results of this study show that a strong {111}ND fiber texture, which results from warm rolling, reduces the HIC damage in sour-service pipeline steels.

[1] ND, RD, and TD refer to the pipe's Normal (radial), Rolling (axial), and Transverse (hoop) directions, respectively. {hkl}ND refers to a grain orientation for which the {hkl} plane lies parallel to the ND-TD plane.

2. Experimental details

A section of a new 610-mm (24-inch) API 5L X52 pipe was used to obtain RD-oriented strips in order to have identical starting samples of this steel (Table I). These samples were subjected to different thermomechanical treatments and a total of 5 usable samples, that is, with similar microstructures but different crystallographic textures, were selected for further testing. HIC tests were conducted by cathodic hydrogen charging for 48 hours in a hydrogen sulfide (H_2S) saturated solution under a current density of 50 mA/cm^2. The solution was selected very close to the TM 0177-B solution recommended in the NACE TM0284-96 standard [8].

Table 1. Chemical composition, in wt%, of the starting API 5L X52 steel

C	Mn	S	P	Si	Cu	Cr
0.212	1.334	0.032	0.028	0.037	0.021	0.009

Table 2 shows the thermomechanical paths followed by the investigated samples, which can be grouped into two categories: warm- rolled samples (WRA, WB), and cold- and hot-rolled samples (HRA, HRB, CRA). All samples were first austenitized at 1040°C for 1 hour, them rolled as indicated in Table 2, and finally treated at 850°C for about 100 seconds to ensure complete recrystallization with no substantial grain growth.

Table 2. Thermomechanical path followed by the investigated samples

Sample	Thickness reduction (%)	Path	Final rolling temperature (°C)
WRA	75	2 steps, 50% each	800
WRB	75	2 steps, 50% each	600
HRA	75	2 steps, 50% each	1040
HRB	50	15 steps, 5% each	1000
CRA	50	15steps, 5% each	27

The global or macrotexture X-ray texture of the samples was determined by measuring three incomplete pole figures: {110}, {200}, and {111} using a Mo texture goniometer. The orientation distribution function (ODF) of each sample was determined from the measured pole figures assuming a cubic-triclinic symmetry. The ADC method [8] was used to estimated the ODFs, which are represented here in the $\varphi_2 = 45$ deg. section of Euler space [9].
The metallographic inspection and microtexture[2] study of the samples were performed using scanning electron microscopy and automated FEG/EBSD, respectively. Orientation Imaging Microscopy (OIM) was used to analyze the EBSD measurements. Grain boundaries (GBs) were defined in the EBSD-derived orientations maps by the presence of a point-to-point misorientation greater than 3 degrees. To study the mesotexture[2] of the samples, GBs were categorized into: (*i*) low-angle (LABs, with misorientation angles less than 15 deg.), (*ii*) high-angle (HABs), and (*iii*) coincidence site lattice (CSL, Σn [9]).

3. Results

Figure 1 shows examples of typical optical micrographs taken from the studied samples. It is observed the characteristic banded pearlite/ferrite microstructure of low-strength carbon steels after

[2] The term 'microtexture' refers to individual orientation measurements that can be related to their location in the sample. 'Mesotexture' refers to the distribution, or texture, of GBs [9].

rolling and recrystallization [10]. The average grain size was found to be similar in all samples: 10 μm for the warm-rolled samples and 12 μm for the cold- and hot-rolled samples.

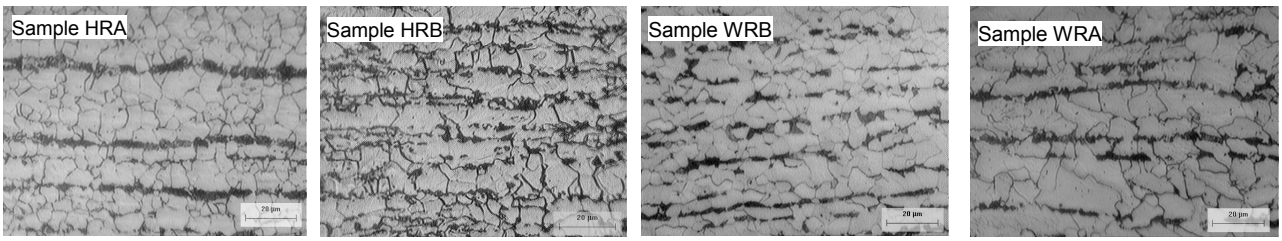

Pearlite: 10%; G.S.: 11 μm Pearlite: 15%; G.S.: 11 μm Pearlite: 12%; G.S.: 11 μm Pearlite: 14%; G.S.: 13 μm

Figure 1. Optical micrographs of some of the investigated samples (G.S.: grain size).

After cathodic hydrogen charging, the cold- and hot-rolled samples developed HIC, with cracks growing following intergranular and transgranular paths as shown in Fig. 2. In a remarkable contrast, no HIC damage was observed in any of the warm-rolled samples. It is important to stress that, given that cathodic hydrogen charging introduces more diffusible hydrogen into the steel than the standard HIC test (NACE TM0284-96, [11]), the present results are expected to be similar to those obtained had the latter method been used.

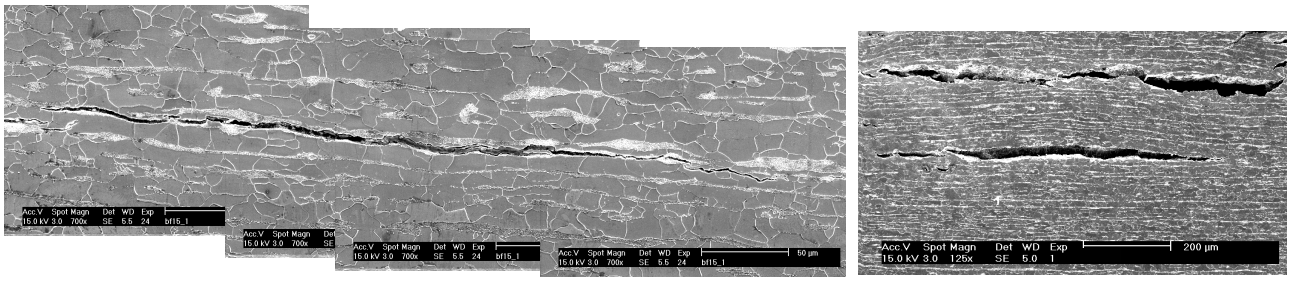

(a) (b)

Figure 2. SEM micrograph of typical HIC-damaged regions in samples CRA (a) and HRA (b).

Figure 3 shows the position of several {111}ND, {112}ND, and {001}ND orientations and fibers in the {200} and {222} pole figures, as well as the position of the α (<011>RD) and γ ({111}ND) texture fibers in the φ_2 = 45 deg. section of the ODF in Euler space. For the group of HIC-free (warm-rolled) samples, whose pole figures and ODFs are shown in Fig. 4, the crystallographic texture is far from that of a random polycrystalline sample, with a low random (phon) texture component [8]. Based on what is shown in Fig. 3, one realizes that sample WRA has a well-developed fiber texture, which is very close to {111}ND. Similarly, sample WRB shows a strong {111}ND fiber, together with a much less noticeable, yet present, {001}ND fiber.

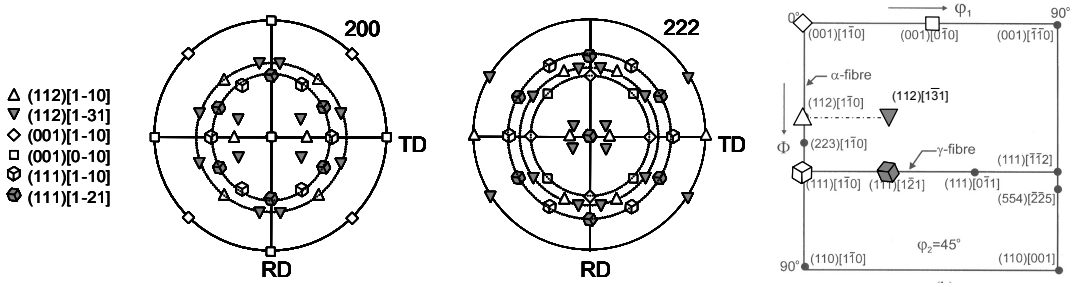

(a) (b)

Figure 3. Position of ideal orientations and texture fibers typical of rolled and recrystallized bcc steels. (a) Pole figures. (b) ODF in Euler space (φ_2 = 45 deg. section).

For the group of HIC-stricken samples, whose pole figures and ODFs are shown in Fig. 5, the crystallographic texture is markedly different from those found in the warm-rolled samples. Samples HRA and CRA show a much more isotropic texture, while sample HRB shows a very acute texture, completely dominated by the {001}<110> component. In addition, the strength of the {111}ND and {112}ND fibers in these three samples is much less sharp than in the warm-rolled ones. In sample HRA, for example, the {111}ND fiber seems to dominate the texture. However, when compared with samples WRA and WRB, the sharpness of this texture fiber is significantly less in HRA. Furthermore, the texture phon or true random component of this sample was found to be 35%, which denotes that its texture has a significant random character.

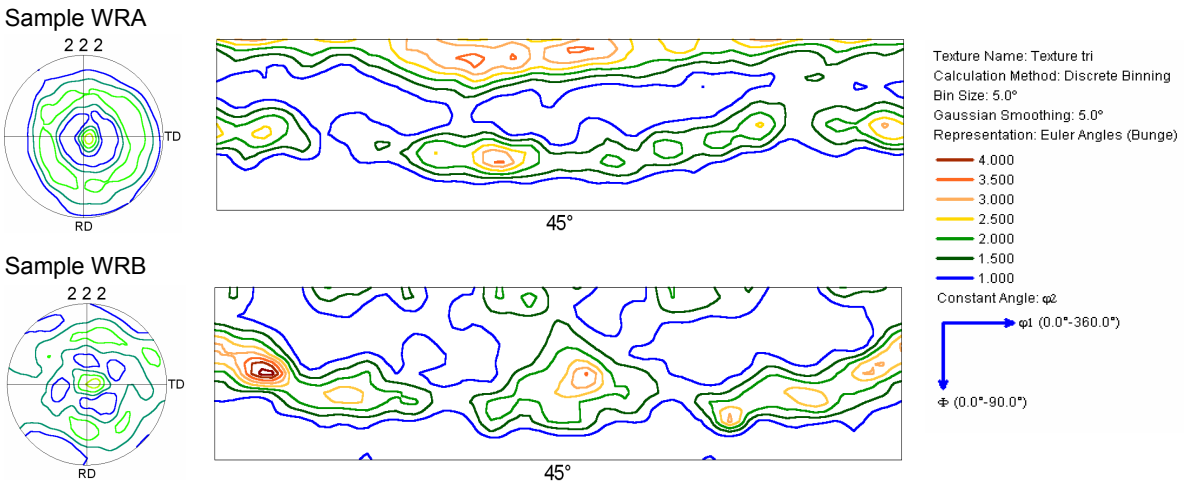

Figure 4. EBSD-derived {111} pole figure and $\varphi_2 = 45$ deg. section of the ODF in Euler space for the HIC-free group of samples.

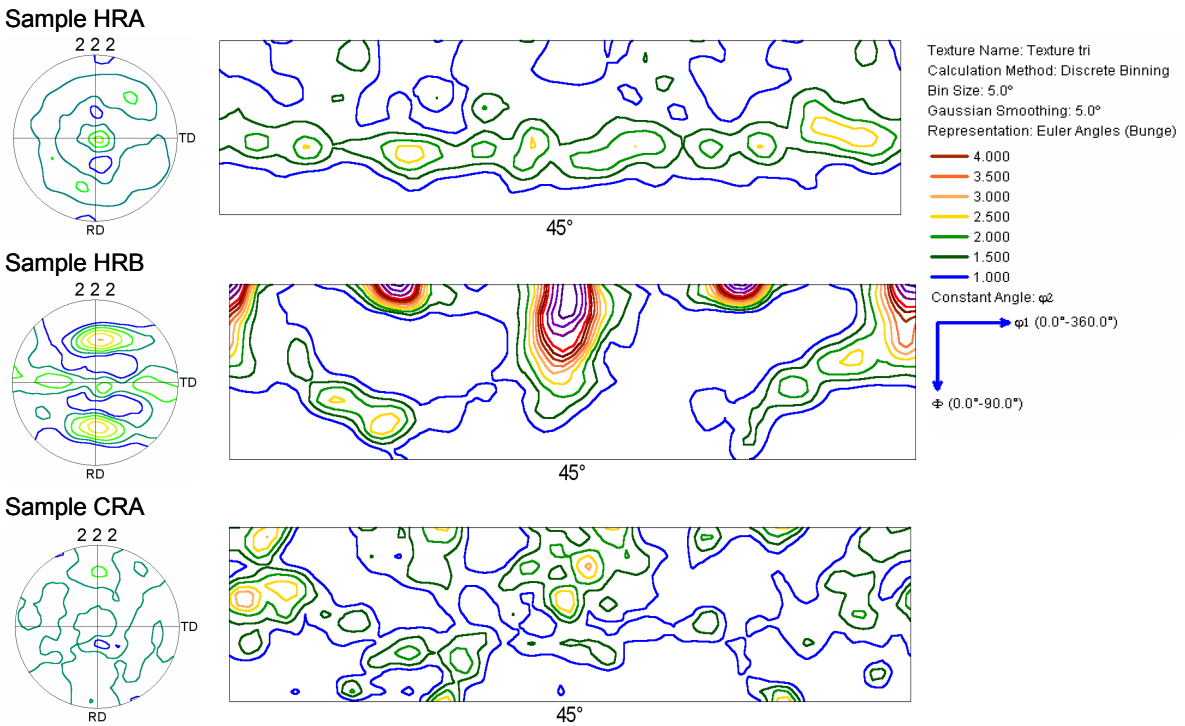

Figure 5. EBSD-derived {111} pole figure and $\varphi_2 = 45$ deg. section of the ODF in Euler space for the HIC-stricken group of samples.

The results of the metallographic inspection and crystallographic texture analysis where corroborated by the EBSD/OIM studies. The orientation (OIM) maps derived from the EBSD measurements

showed no evidence of texture heterogeneities such as orientation clustering or correlation. The microstructural and texture characteristics estimated from these maps, such as grain size and pole figures and ODFs, agree with the results previously found during the metallographic inspection and texture analysis of the studied samples.[3] Based on these findings, and on the fact that the number of grains in the orientation maps of the test samples is relatively large (of the order of, or greater than 10^4), one can be concluded that the local EBSD-derived distribution of GBs is representative of that of the bulk sample.

Figure 6 shows the grain boundary statistics or mesotexture in the HIC-free and HIC-stricken groups of samples. The first result to stress from the results in Fig. 6a is that the proportion of CSL boundaries observed for these two groups of samples is not statistically significant. Therefore, in Fig. 6b, where the average proportion of HABs and LABs are shown for both groups of samples, CSLs boundaries are accounted for as HABs.

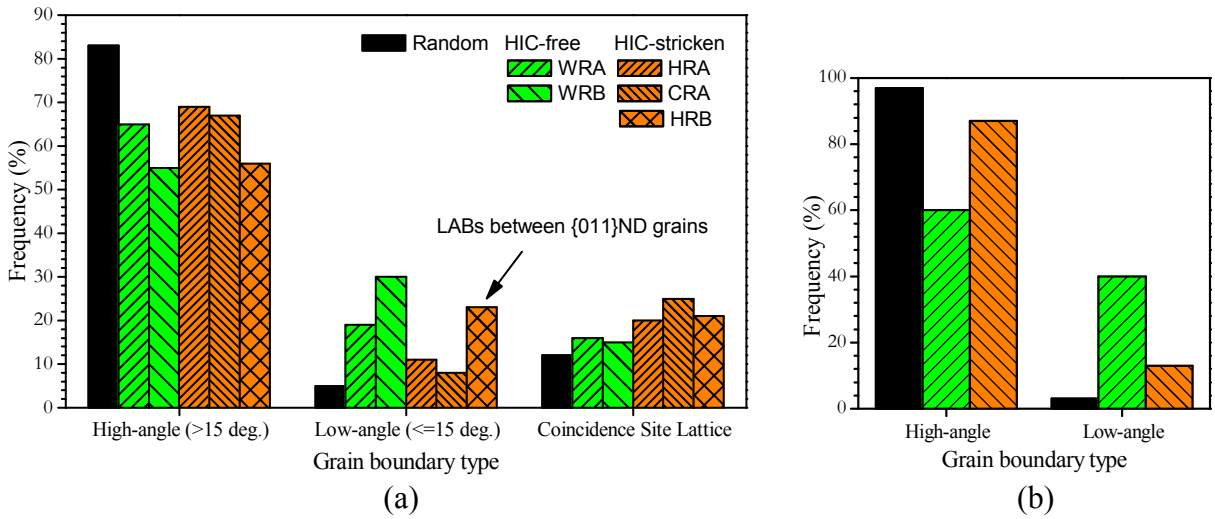

Figure 6. Mesotexture of the investigated samples. (a) By sample, considering with CSLs separately accounted for. (b) By group of samples with CSLs accounted for as high-angle boundaries.

For the group of HIC-free (warm-rolled) samples the GB statistics shows the highest proportion of low-angle boundaries and departs considerably from that of the (theoretically-deduced) random polycrystal. This result is in complete agreement with the results shown in Fig. 4 for the crystallographic texture of these samples, and is an indication that no significant orientation correlation [12] occurs in them. Similarly, orientation correlation was also neglected for the group of HIC-stricken samples. Fig. 6b also shows that, on average, the fraction of LABs in the HIC-free group of samples almost doubles that of the HIC-stricken group. In contrast, the proportion of HABs in the HIC-free group is about 45% lower than in the HIC-stricken group.

For the group of HIC-stricken samples (except for HRB) the mesotexture is the closest to that of the random polycrystal. The fraction of LABs in samples HRA and HRB, on average, close to 13%; this proportion is about half of that observed for the rest of the test samples. In a very particular case, sample HRB shows a remarkably higher fraction of LABs. However, given the results shown in Fig. 5, and under the assumption of absence of orientation correlation, it is reasonable to expect that the majority of these GBs occurs between grains with orientations close to {001}ND. The implications of this for HIC propagation is discussed later. Samples HRA and CRA show a high fraction of HABs, which, on average, is about 45% higher than the proportion observed in the HIC-free samples. Once again, sample HRB stands out as a remarkable exception, where the small fraction of HABs and CSLs can be related to the high fraction of LABs shared by {001}ND-oriented grains.

[3] Given this result, and for the sake of space economy, the pole figures and ODF presented in this paper are those obtained from the EBSD measurements

4. Discussion

In the group of samples where HIC was observed, the absence of a strong {111}ND texture fiber and the proximity of the texture to that of the random polycrystal is critical to the results of the HIC tests. In this group, HRB is the only sample whose texture significantly differs from that of the random polycrystal. The sharpness of the texture of this sample can be unambiguously related to the observed dominant proportion of {001}ND-oriented grains. The observed susceptibility of these samples to HIC can be associated with their grain mesotexture, which results from the texture that they develop during deformation and recrystallization. The relatively large proportion of high-angle GBs observed in samples HRA and CRA provide plentiful of low-resistance paths for the propagation of intergranular HIC. Sample HRB shows a significantly increased fraction of low-angle GBs, but between grains with orientations close to {001}ND (Fig. 5).

The large number of {001}ND grains observed in sample HRB reduces the resistance of this sample to HIC as it facilitates intragranular crack propagation along {001} cleavage planes oriented parallel to the pipe's rolling plane. In addition, LABs shared by {001}ND also provide low-resistance paths to intergranular, cleavage-like propagation of HIC in the same plane [5,6,12].

In a remarkable contrast, the warm-rolled, HIC-free samples show a crystallographic texture dominated by well-developed, strong {111}ND or {112}ND texture fibers. In reference [7] it was shown that, at a grain scale, these orientations impede transgranular HIC propagation on the rolling plane. One can also point out that, for a mode I loading, shear stress is null ahead of crack tips [13]; therefore, propagation of HIC in the rolling plane by shear/slip-related fracture along grains with orientation within these fibers can be predicted to be very unlikely. Another characteristic of grains with {111}ND orientations is that they can accumulate large plastic deformation when cracks are close enough to induce interaction and coalescence. This improves the resistance of the steel to HIC by reducing the driving force for growth of interacting cracks, with the consequent reduction in the probability of coalescence of closely-spaced, non-coplanar cracks [13,14].

In addition to the foregoing, the warm-rolled group of samples is particularly prone to have improved HIC resistance because it exhibits an increased number of LABs between {111}ND-oriented grains. It has been reported [7] that LABs with <111> disorientation axis have lower energies than LABs with <100> axis. As a result, a steel with a strong {111}ND texture is expected to show a reduced susceptibility to HIC due to the increased presence of low-angle boundaries with the lowest possible energy.

5. Conclusions

It has been shown that it is feasible to improve the HIC resistance of pipeline steels using crystallography texture control and grain-boundary engineering. At a macroscopic scale, this can be achieved through controlled warm (ferritic) rolling schedules. These thermomechanical processes lead to a crystallographic texture dominated by the {111}ND-fiber texture and to a mesotexture with a high proportion of low-angle, low-energy grain boundaries. These two characteristics are critical to reduce, beyond traditional practices, the susceptibility of these steels to hydrogen-induced cracking.

Acknowledgments

The comments and suggestions made by the reviewers are greatly appreciated.

References

[1] Review of Published Literature on Wet H_2S cracking of Steels Through 1989, 2003 Edition, NACE International Publication 8X294, Houston TX, 2003.

[2] C.R.F. Azevedo, Failure analysis of a crude oil pipeline. Eng. Failure Anal. 14 (2007) 978–994.

[3] M.A. Al-Anezi, S. Rao, Challenges in procurement of HIC resistant steels pipes, J. Failure Anal. Preven. 11 (2011) 385–392.
[4] V. Venegas, F. Caleyo, J.L. González, T. Baudin, J.M. Hallen, R. Penelle, EBSD study of hydrogen induced cracking in API-5L-X46 pipeline steel. Scr. Mater. 52 (2005) 147–152.
[5] V. Venegas, F. Caleyo, J.M. Hallen, T. Baudin, R. Penelle, Role of Crystallographic Texture in Hydrogen-Induced Cracking of Low Carbon Steels for Sour Service Piping, Metall. Mater. Trans. A 38 (2007) 1022–1031.
[6] V. Venegas, F. Caleyo, T. Baudin, J. M. Hallen, R. Penelle, Role of microtexture in the interaction and coalescence of hydrogen-induced cracks. Corr. Sci. 51 (2009) 1140–1145.
[7] V. Venegas, F. Caleyo, T. Baudin, J.H. Espina-Hernández, J.M. Hallen. On the role of crystallographic texture in mitigating hydrogen-induced cracking in pipeline steels. Corr. Sci. 53 (2011) 4204–4212.
[8] K. Pawlick, Determination of the orientation distribution function from pole figures in arbitrarily defined cells. Phys. Status Sol. B B134 (1986) 477–483.
[9] V. Randle and O. Engler. Introduction to Texture Analysis. Macrotexture, Microtexture and Orientation Mapping, Francis & Taylor, London, 2003.
[10] R.K. Ray, J.J. Jonas. Transformation Textures in Steel. Int. Mater. Reviews, 1990, 35, pp. 1–36.
[11] NACE Standard Test Method TM0284-96, Evaluation of Pipeline and Pressure Vessel Steels for Resistance to HIC, NACE, Houston, 1997, pp. 1–10.
[12] M.A. Arafin, J.A. Szpunar, A new understanding of intergranular stress corrosion cracking resistance of pipeline steel through grain boundary character and crystallographic texture studies. Corr. Sci. 51 (2009) 119–128.
[13] Y.Z. Wang, J.D. Atkinson, R. Akid, R.N. Parkins, Crack interaction, coalescence and mixed mode fracture mechanics. Fatigue Fract. Eng. Mater. Struct., 19 (1996) 427–439.
[14] F. Erdogan and G.C. Sih, On the crack extension in plates under plane loading and transverse shear. J. Basic Eng., 85 (1963) 519–52.

Stress Corrosion Cracking Behavior of Wrought Magnesium Alloy AZ31 and AZ61 under Controlled Cathodic Potentials

Toshifumi Kakiuchi[1,*], Yoshihiko Uematsu[1]
Masaki Nakajima[2], Yuki Nakamura[2], Kosuke Miyagi[3]

[1] Department of Mechanical and Systems Engineering, Gifu University, Gifu, 501-1193, Japan
[2] Department of Mechanical Engineering, Toyota National College of Technology, Toyota, 471-8525, Japan
[3] Howa Machinery Ltd., Kiyosu, 462-8601, Japan
* Corresponding author: kakiuchi@gifu-u.ac.jp

Abstract The stress corrosion cracking (SCC) tests were performed using the wrought magnesium alloys, AZ31, AZ61 and T5 heat treated AZ61 (AZ61-T5) in a NaCl solution under the controlled cathodic potential in order to investigate the effects of the anodic dissolution and the hydrogen embrittlement on the SCC behavior. The crack growth rate (d*a*/d*t*) of AZ31 was faster than those of AZ61 and AZ61-T5 under the same cathodic potential. The threshold stress intensity factor for SCC propagation (K_{ISCC}) of AZ31 was lower than those of AZ61 and AZ61-T5, and K_{ISCC} of AZ61-T5 was lower than that of AZ61, which is attributed to the difference of resistance to anodic dissolution. In AZ31 and AZ61, K_{ISCC} under the cathodic potential of -2.5 V was higher than those under the other cathodic potentials. In all materials, K_{ISCC} under the cathodic potential of -1.4 V was lower than those under the cathodic potentials of -3.0 V and -4.0 V. By the observations on the fracture surfaces after the SCC tests, less corrosion products were observed on the fracture surfaces under the cathodic potentials of -3.0 V and -4.0 V than on the fracture surfaces under the cathodic potential of -1.4 V.

Keywords Stress corrosion cracking, Magnesium alloy, Hydrogen embrittlement, Anodic dissolution

1. Introduction

In the recent years, light materials have been promoted to be applied in a wide variety of applications, especially in structural components of transportation machines such as airplanes and ground vehicles to reduce fuel consumption. Magnesium (Mg) alloys are the lightest among all available metals in practical use and have high specific strengths. So Mg alloys are expected as structural materials for transportation machines. However Mg alloys are sensitive to corrosion and exhibit the poor corrosion resistance compared with the other light metals such as aluminum and titanium alloys. Thus it is important to understand the corrosion properties of Mg alloys. Especially, the stress corrosion cracking (SCC) behavior is important since it could cause sudden and fatal failures.

The SCC could be attributed to the combined effects of the anodic dissolution and the hydrogen embrittlement. Especially the hydrogen embrittlement plays an important role in the SCC of Mg alloys. Previously the present authors have performed the SCC tests using the wrought Mg alloy AZ31 in a NaCl solution under the controlled cathodic potential to decouple the effects of anodic dissolution and hydrogen embrittlement and have investigated the SCC behavior [1]. In the present study, the similar SCC tests were performed using the wrought Mg alloys AZ31, AZ61 and T5 heat treated AZ61 to investigate the effects of the anodic dissolution and the hydrogen embrittlement on the SCC behavior of Mg alloys.

2. Experimental details

2.1. Material and specimen

The materials used were the wrought Mg alloys AZ31 and AZ61. The chemical compositions and

the mechanical properties of the materials are shown in Table 1 and Table 2, respectively. The β phase of Mg alloy, i.e., $Mg_{17}Al_{12}$, is more sensitive to hydrogen embrittlement than the matrix. Hence it is expected that the SCC behavior is dependent on the content of β phase. To investigate the effect of β phase on the SCC behavior, the T5 heat treated AZ61 (AZ61-T5) in which β phases were precipitated along the grain boundaries was also used. The T5 heat treatment was set to hold the material at the temperature of 170 ºC for 42 hours followed by cooling in the air. Fig. 1 shows the optical micrographs showing the microstructures of (a) AZ31, (b) AZ61 and (c) AZ61-T5. Fig. 2 shows the micrograph by a scanning electron microscope (SEM) showing the microstructure of AZ61-T5 in the high resolution. The β phase precipitates were observed along the grain boundaries.

Table 1. Chemical compositions of materials (wt%)

Material	Al	Zn	Mn	Si	Cu	Ni	Fe	Mg
AZ31	2.7	0.79	0.44	0.004	0.0011	0.0009	0.0012	Bal.
AZ61	5.8	0.65	0.29	0.01	0.002	0.002	0.002	Bal.

Table 2. Mechanical properties of materials

Material	0.2% proof stress, $\sigma_{0.2}$ (MPa)	Tensile strength, σ_B (MPa)	Elongation, δ (%)	Vickers hardness, *HV*	Elastic modulus, *E* (GPa)
AZ31	170	248	17	54	46
AZ61	192	301	19	62	44

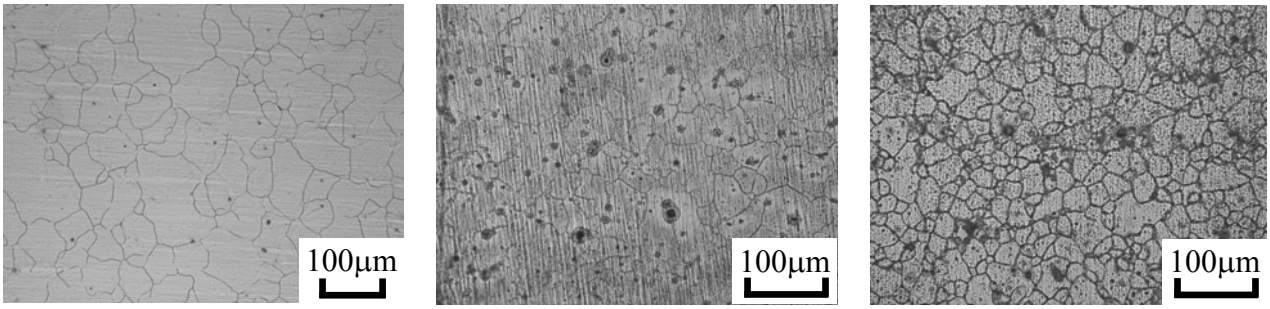

(a) AZ31 (b) AZ61 (c)AZ61-T5

Figure 1. Microstructures of materials

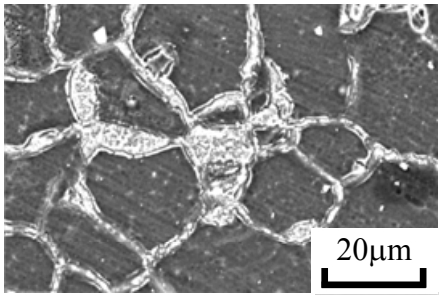

Figure 2. SEM micrograph showing β phase precipitates along grain boundaries in AZ61-T5

For the SCC tests, compact tension (CT) specimens with the configuration of a width of 50.8 mm and a thickness of 6 mm were fabricated by machining from the materials. Fig. 3 shows the configuration of a CT specimen. Prior to the SCC tests, a pre-crack with a length of 2 mm was introduced from the artificial notch root of CT specimen. Pre-cracks were introduced by a fatigue test at the frequency of 10Hz, the stress ratio of 0.1 and the initial stress intensity factor range ΔK_I of 3 MPa $m^{1/2}$.

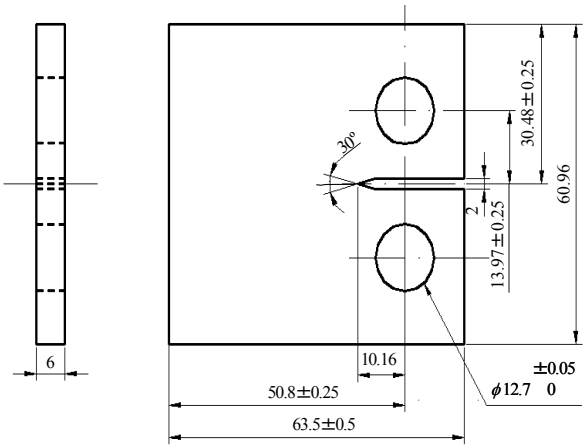

Figure 3. CT specimen configuration

2.2. Stress corrosion cracking test

Fig. 4 shows the schematic illustration of SCC test apparatus. The crack length was monitored by a crack gauge bonded to a crack-expected part of CT specimen. In the SCC tests of AZ61 and AZ61-T5, crack gauges were peeled off frequently since the crack growth rate was low and the testing time was long. So a traveling microscope was also used to monitor the crack length of AZ61 and AZ61-T5 specimens. A CT specimen with a fatigue pre-crack was attached to the creep testing machine equipped with a 3% NaCl solution tank. Prior to the loading, SCC test specimens were held in a NaCl solution at a given cathodic potential for 24 hours under no-loaded condition to charge hydrogen. After the loading, the load was gradually increased every 24 hours until a crack initiated to propagate. Once a crack initiated to propagate, the load was sustained and the crack growth was monitored by a crack gauge or a traveling microscope. In the solution tank, the Ag/AgCl and Pt electrodes were set for the reference and counter electrodes, respectively and the cathodic potential of specimen was controlled by means of a potentiostat (HA-303: HOKUTO DENKO Corp.). The cathodic potentials were controlled to be -1.4 V, -2.5 V, and -3.0 V for AZ31; 0 V, -1.4 V, -2.5 V and -4.0 V for AZ61; and -1.4 V and -4.0 V for AZ61-T5.

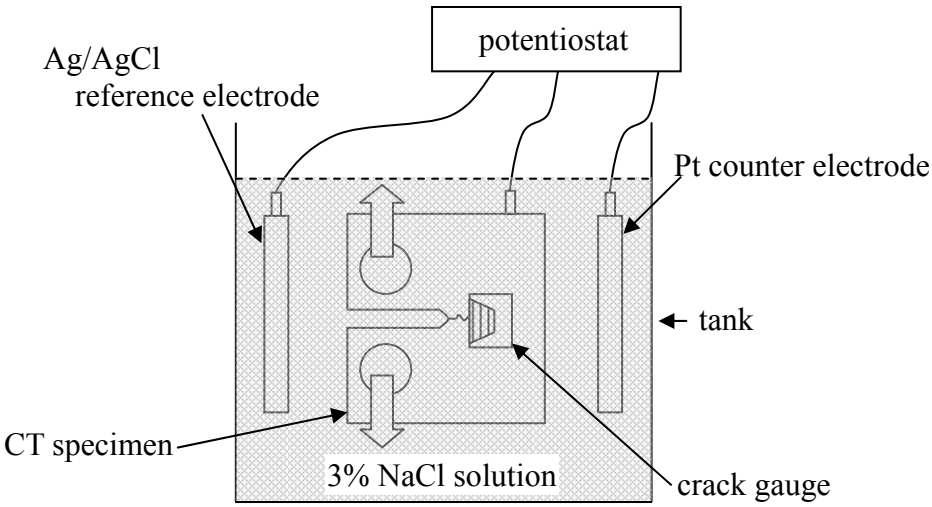

Figure 4. SCC test apparatus

The Pourbaix diagram of Mg [2], which shows the stable phase of an electrochemical system, is shown in Fig. 5. The pH of 3% NaCl solution is 7. The test conditions are also plotted in Fig. 5. It is

considered that the SCC behavior is dominated by the anodic dissolution in the corrosion region and by the hydrogen embrittlement in the immunity region. According to the Pourbaix diagram, the cathodic potential of -1.4 V corresponds to the corrosion region under which the SCC behavior is dominated by the anodic dissolution. The cathodic potentials of -3.0 V and -4.0 V correspond to the immunity region under which the SCC behavior is dominated by the hydrogen embrittlement. The cathodic potential of -2.5 V corresponds to the boundary between the corrosion and immunity regions. The SCC test conditions of cathodic potentials and electrochemical phases for each material are summarized in Table 3.

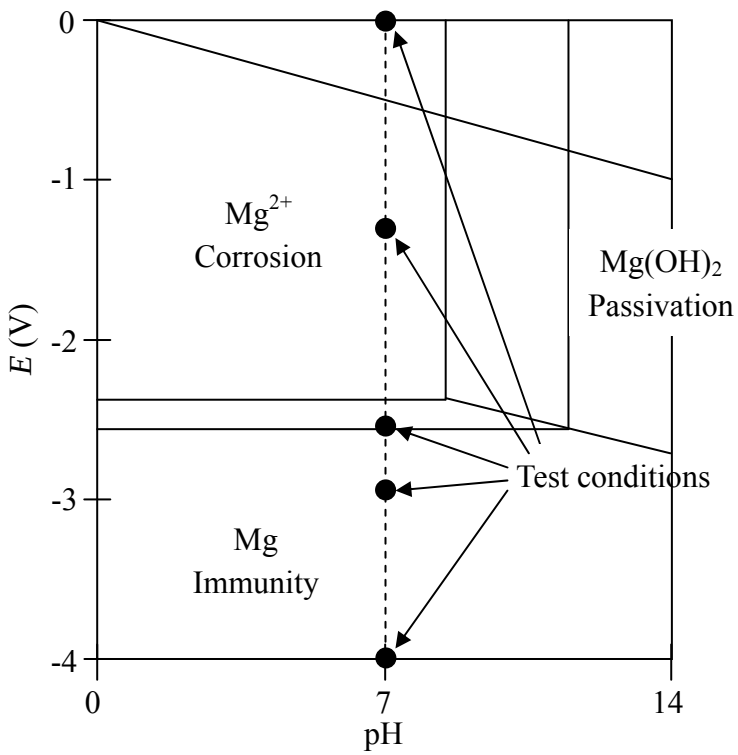

Figure 5. Pourbaix diagram for magnesium

Table 3. SCC test condition

Material	Cathodic potential				
	Corrosion region of Mg			Immunity region of Mg	
	0V	-1.4V	-2.5V	-3.0V	-4.0V
AZ31		Tested	Tested	Tested	
AZ61	Tested	Tested	Tested		Tested
AZ61-T5		Tested			Tested

3. Experimental results

3.1. Crack growth behavior

Fig. 6 shows the relationship between the crack length, *a*, and the testing time, *t*, after the crack initiated to propagate in a stable manner. The SCC behavior depends on the material, i.e., AZ31 specimens fractured more rapidly than AZ61 and AZ61-T5 specimens, and AZ61-T5 specimens fractured more rapidly than AZ61 specimens. In all materials, the final crack lengths were shorter and specimens fractured more rapidly under the cathodic potentials of -3.0 V and -4.0 V which correspond to the immunity region than under the cathodic potentials of 0 V and -1.4 V which

correspond to the corrosion region, except for the AZ61 specimen under the cathodic potential of -1.4 V. Fig. 7 shows the relationship between the crack growth rate, d*a*/d*t*, and the stress intensity factor, K_I. Crack growth rates of AZ31 are much faster than those of AZ61 and AZ61-T5, and those of AZ61-T5 are faster than those of AZ61 under the same cathodic potentials. The crack growth rate of AZ31 is not sensitive to the change of K_I values especially under the cathodic potential of -3.0 V. The relationship between the threshold stress intensity factor for the SCC propagation, K_{ISCC}, and the cathodic potential, *E*, is summarized and shown in Fig. 8. In AZ31, K_{ISCC} under the cathodic potential of -2.5 V is higher than those under the cathodic potentials of -1.4 V and -3.0 V. This tendency is the same in AZ61, i.e., K_{ISCC} of AZ61 under the cathodic potential of -2.5 V is higher than those under the other cathodic potentials. In AZ61, K_{ISCC} under the cathodic potential of 0 V is the same as that under the cathodic potential of -1.4 V. In all materials, K_{ISCC} under the cathodic potential of -1.4 V is lower than that under the cathodic potentials of -3.0 V and -4.0 V.

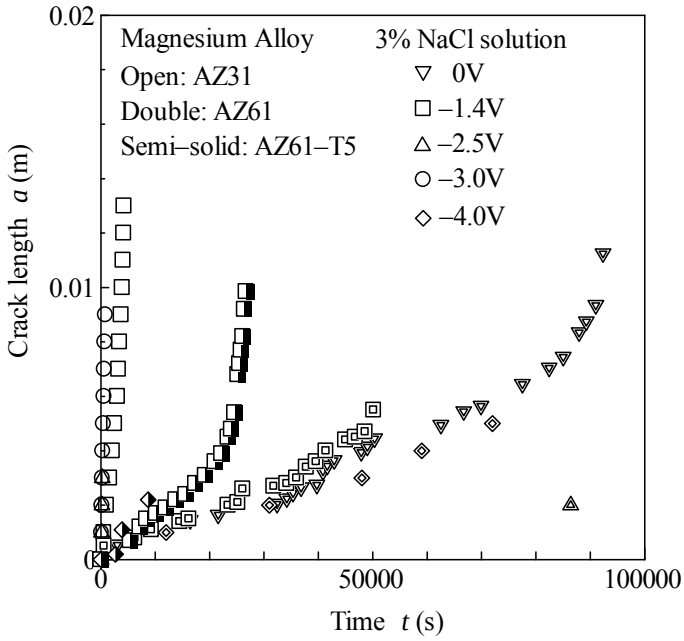

Figure 6. Relationship between crack length, *a*, and testing time, *t*

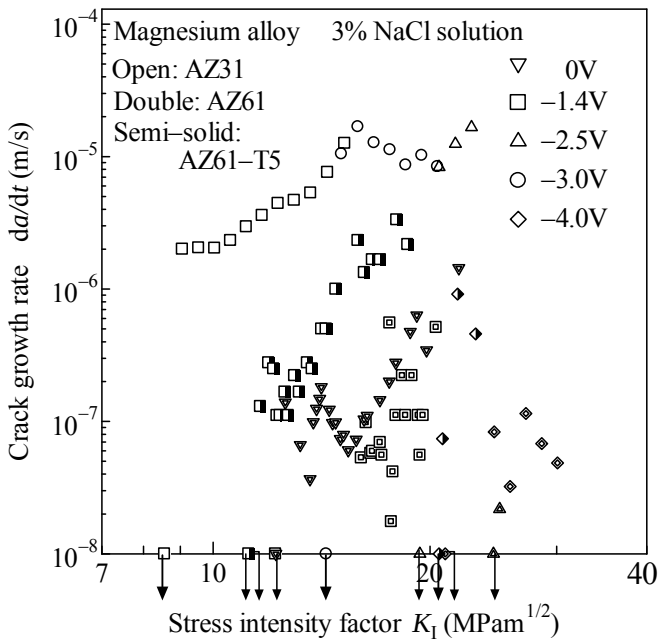

Figure 7. Relationship between crack growth rate, d*a*/d*t* and stress intensity factor, K_I

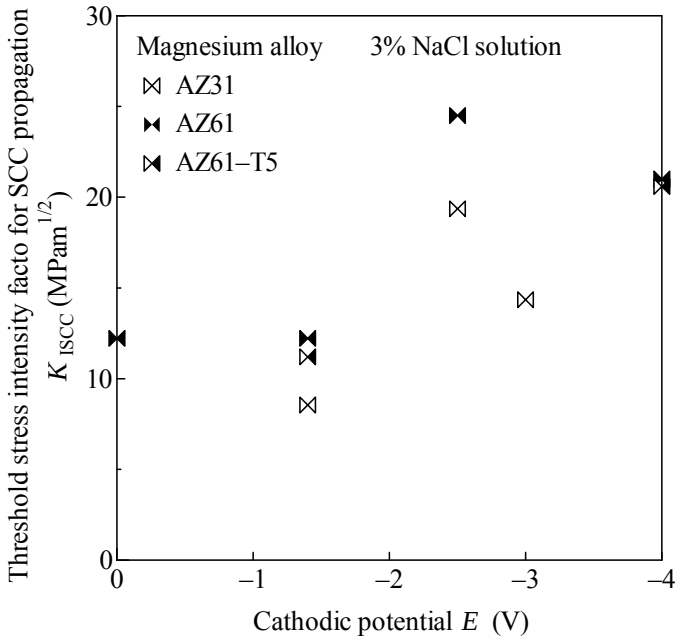

Figure 8. Relationship between threshold stress intensity factor for SCC propagation, K_{ISCC} and cathodic potential, E

3.2. Fracture surface observation

Fig. 9 shows the SEM micrographs showing the typical examples of fracture surfaces. As shown in Fig. 9 (a), the fracture surface of AZ31 under the cathodic potential of -1.4 V at K_I of 8.6 MPa m$^{1/2}$ was covered by corrosion products. However corrosion products became less on the fracture surface at K_I of 14 MPa m$^{1/2}$ as shown in Fig. 9 (b). Under the cathodic potentials of -2.5 V and -3.0 V, no corrosion products were observed as in Fig. 9 (c) and (d). In AZ61 and AZ61-T5, almost all of the fracture surfaces were covered by corrosion products and only a part of fracture surfaces were not covered as in Fig. 9 (e). As the cathodic potential became lower, corrosion products became less. Corrosion products on the fracture surfaces of AZ61 were less than those of AZ61-T5 comparatively. Some of the fracture surfaces of AZ61 remained their own morphologies under the cathodic potential of -4.0 V as in Fig. 9 (f). Except for the corrosion products, the fracture surface morphology is similar in all materials, i.e., fracture surfaces seem to be brittle covered with flat packets with fine steps without dimples as are observed in the fracture surfaces by fatigue tests [3].

4. Discussion

The crack growth rates of AZ31 specimens were much higher than those of AZ61 and AZ61-T5 specimens, which indicates the corrosion resistance of AZ31 is lower than those of AZ61 and AZ61-T5. Aluminum (Al) is added to AZ31 and AZ61 to enhance the strength and also to improve the corrosion resistance. So AZ61, which contains more Al than AZ31, exhibited better corrosion resistance. Comparing AZ61 and AZ61-T5, the crack growth rates of AZ61-T5 specimens were faster. It is attributed to the precipitated β phases which are more sensitive to corrosion than the matrix. But the β phases were precipitated along the limited region of grain boundaries so the corrosion resistance was not decreased as AZ31.

K_{ISCC} of AZ61 under the cathodic potential of -1.4 V is the same as that under the cathodic potential of 0 V, which indicates that the anodic dissolution occurred under the cathodic potential of -1.4 V as same as no cathodic potential is applied and the cathodic potential of -1.4 V did not act to decrease

the anodic dissolution. The same discussion could be made from the fracture surface observations, i.e., the fracture surface of AZ31 under the cathodic potential of -1.4 V at K_I of 8.6 MPa m$^{1/2}$ was covered with corrosion products. However, under the same cathodic potential of -1.4 V, corrosion products were less on the fracture surface at comparatively higher K_I of 14 MPa m$^{1/2}$. This is attributed to the difference of exposure time to the NaCl solution which is the corrosive environment. In the SCC tests conducted in the present study, the load was sustained once after a crack initiated to propagate. So K_I corresponds to the crack length. The fracture surface at low K_I was the area near the notch root and was exposed to the NaCl solution for longer time until a CT specimen was lead to final fracture than that at high K_I. So in the fracture surface at low K_I, the effect of the corrosive environment is large and the fracture surface became covered with corrosion products. The reason that almost all of the fracture surfaces of AZ61 and AZ61-T5, which are more insensitive to corrosion than AZ31, were covered with corrosion products is also explained by the exposure time to the corrosive environment. The crack growth rates of AZ61 and AZ61-T5 were slower and it took longer time until the final fractures than AZ31. Although AZ61 is insensitive to corrosion, the effect of longer exposure to the corrosive environment becomes large and so the fracture surfaces of AZ61 were also covered with corrosion products.

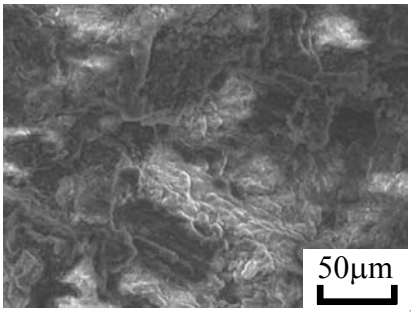

(a) AZ31, E=-1.4 V, K_I=8.6 MPa m$^{1/2}$

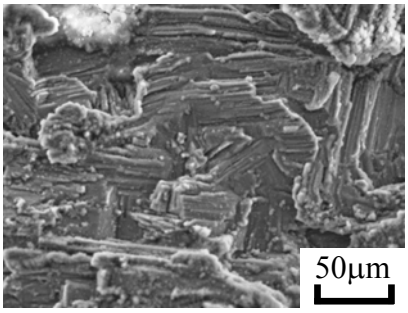

(b) AZ31, E=-1.4 V, K_I=14 MPa m$^{1/2}$

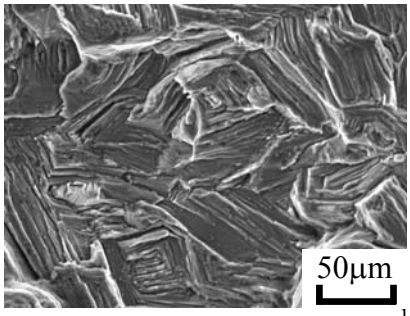

(c) AZ31, E=-2.5 V, K_I=19MPa m$^{1/2}$

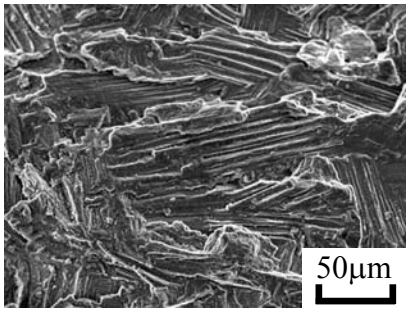

(d) AZ31, E=-3.0 V, K_I=14MPa m$^{1/2}$

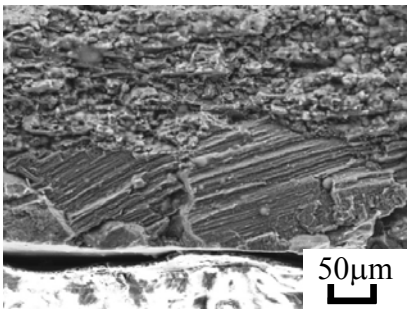

(e) AZ61, E=-1.4 V, K_I=19 MPa m$^{1/2}$

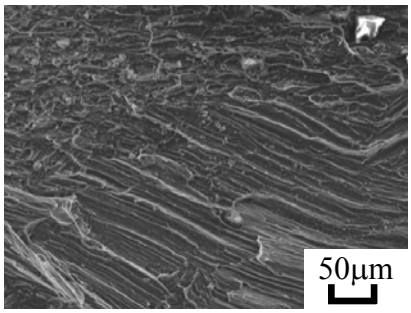

(f) AZ61, E=-4.0 V, K_I=30MPa m$^{1/2}$

Figure 9. SEM micrographs showing fracture surfaces

In AZ31 and AZ61, K_{ISCC} is the highest under the cathodic potential of -2.5 V in the boundary between the corrosion and immunity regions compared with those under higher and lower cathodic potentials. It is considered that under the higher cathodic potential, the corrosion is dominant and under the lower cathodic potential, the hydrogen embrittlement is dominant. The anodic dissolution is dependent on the cathodic potential, i.e., as the cathodic potential becomes lower, the anodic dissolution becomes decreased since the Mg phase becomes more stable than the Mg^{2+} phase as shown in Fig. 5 of the Pourbaix diagram, which is the reason that K_{ISCC} under the cathodic potential of -2.5 V is higher than that under the cathodic potential of -1.4 V. The generation of hydrogen molecules, H_2, should be also dependent on the cathodic potential, i.e., as the cathodic potential becomes lower, more H_2 are generated. Thus the lower cathodic potentials accelerated the hydrogen charging and K_{ISCC} becomes lower as the cathodic potential is lower than -2.5 V.

5. Conclusions

In the present study, the SCC tests were performed using the wrought magnesium alloys, AZ31, AZ61 and AZ61-T5 under the controlled cathodic potential and the effects of the anodic dissolution and the hydrogen embrittlement on the SCC behavior of Mg alloys were investigated. From the experimental results and the discussion, the following conclusions could be made:

(1) The crack growth rate of AZ31 was faster and K_{ISCC} of AZ31 was lower than those of AZ61 and AZ61-T5 under the same cathodic potential since the added Al acts to enhance the strength and to decrease the anodic dissolution.

(2) The crack growth rate of AZ61-T5 was faster and K_{ISCC} of AZ61-T5 was lower than those of AZ61 under the same cathodic potential since the precipitated β phases in AZ61-T5 are sensitive to hydrogen embrittlement.

(3) The crack growth rate depends on K_I. However in AZ31 the crack growth rate is not so sensitive to K_I. Especially the crack growth rate is insensitive to K_I under the cathodic potential of -3.0 V.

(4) In AZ31 and AZ61, K_{ISCC} under the cathodic potential of -2.5 V where the boundary between the corrosion and immunity regions is higher than K_{ISCC} under the higher cathodic potentials in the corrosion region where the anodic dissolution is dominant and K_{ISCC} under the lower cathodic potentials in the immunity region where the hydrogen embrittlement is dominant.

(5) In all materials, K_{ISCC} under the cathodic potential of -1.4 V was lower than that under the cathodic potentials of -3.0 V and -4.0 V.

(6) The amount of corrosion products depends on the cathodic potential and the exposure time to corrosive environment. Less corrosion products were observed on the fracture surfaces under the cathodic potentials of -3.0 V and -4.0 V than on the fracture surfaces under the cathodic potentials of 0 V and -1.4 V. A part of the fracture surfaces of AZ31 and almost all of the fracture surfaces of AZ61 and AZ61-T5 were covered with corrosion products where the exposure time was long.

References

[1] Y. Uematsu, T. Kakiuchi, M. Nakajima, Stress corrosion cracking of the wrouthg magnesium alloy AZ31 under controlled cathodic potentials, Materials Science and Engineering A, 531 (2012) 171–177.

[2] M. Pourbaix, Atlas of Electrochemical Equilibria in Aqueous Solutions, Pergamon Press, London, 1966.

[3] K. Tokaji, M. Nakajima, Y. Uematsu, Fatigue crack propagation and fracture mechanisms of wrought magnesium alloys in differenct environment, International Journal of Fatigue, 31 (2009) 1137–1143.

The influence of sea water corrosion on the resistance cracking performance of carbon steel

Wang Limin[1,*)], Han Daoping[1)], Zhang Donghuan[2)] , Li Dunyi[3)], Geng Hui[1)]

1) Department of Science, Qingdao Technological University, Qingdao 266033, China;
2) School of Transportation and Vehicle Engineering, Shandong University of Technology, 255049
3) Institute of Mechanics，Chinese Academy of Sciences，Beijing 100190 China;
* Corresponding author: wanglimin@qtech.edu.cn

Abstract As carbon steel immersed in seawater with loading, particularly with defect, its performance lead degradation and reduction in bear capacity. For the specimen of carbon steel immersed in seawater with notch and defects, its macro-mechanical properties was tested and also analyzed with electron microscopy equipment. The fracture behavior of specimen was analyzed in different test conditions, and their bearing capacity was contrast each other for loading before and after soaking. Some relation curves are gotten as the curve of crack tip opening displacement and loading, or relation between loading and the displacement of loading point for specimen before or after soaking in seawater. The specimen with plastic zone of crack-tip was soaked in seawater for short-term, according to the analysis of experimental results, the length of plastic curve between reloading and displacement is become shorter, and the material is more brittle. In the area of meso-analysis, fracture performance of seawater corrosion steel were investigated by electron microscopic observation, and checked the difference of characteristics parameters and meso-morphologies of material specimen. As to plastic, the effect of seawater on carbon steel dislocation and slip were also researched in the paper.

Key Words Carbon steel；seawater corrosion；elasto-plastic fracture；microscopic analysis；bearing capacity of structure with crack

1. Introduction

Seawater corrosion affects the mechanical properties of steel, and complex water environment is a source of metal corrosion[1-3]. For the complex corrosion process of Q235 steel in seawater, its behavior shows that the factors of affecting corrosion is including not only the voltage and pH value of them, but also microbial perturbation on the metal surface near[4-5]. The magnetic detection is also effective means to analyze the corrosion. The consequences of corrosion of metallic materials is not only reflected its weight reduction, but also it is the deterioration of bearing capacity and mechanical properties of its structure. So, the stress corrosion and fracture properties of steel is an important investigate field for anti-corrosion and material scientists.

2. Influence of seawater immersion on steel fracture process curve

The steel material were made into the test specimen of beam with prefabricated crack, and it were placed on an experiment equipment for the loading of three point bending. As shown in Figure 1, the curve of loading and the displacement of load point are expressed by series of point. For the point of square or triangle, the size of its specimen is that high

60mm, thickness 60mm, the length of prefabricated crack 18mm, the loading span 240mm and so on. The square point indicates the data of specimen without seawater immersion, and the triangle is for the specimen in seawater 60d. The hollow dots is for the specimen (H60B40A18) of dimension high 60mm, thickness 40mm, prefabricated crack length 18mm, and it is a load-displacement curve of initial loading, unloading and reloading continuously. Obviously, unloading and reloading curves are basically coincident. But the slope of curve is larger compare to the curve slope from zero load, and the results shows the material having harden characteristics. The solid circular point indicates the load-displacement curve of specimen that the 'H60B40A18' were loaded into the plastic phase, and unloaded to zero, then it immersed in seawater for 30d, and reloading on the same equipment. However, the displacement had been added the original plastic residual displacement after unloading. It can be seen that the curve slope of plastic seawater loading is lower than the unloading curve. And the curve segment become shorter over linear loading part. It shows the material performance having deterioration. For two kinds of thickness of specimen, the thicker specimen is increased significantly for the bearing capacity and deformation resistance ability of it

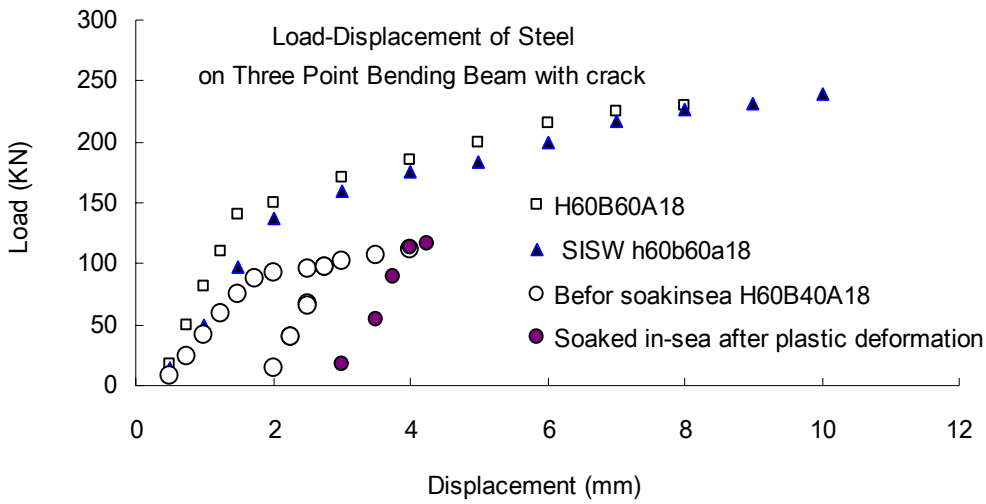

Fig 1. The curve of load-displacement for three point bending steel beam with crack

3. The influence of seawater immersion on specimen toughness

For the specimen of three point bending beam with incision, its stress intensity factor near incision root can be expressed as follows[6]

$$K_I = 1.5PS\sqrt{a}\,\frac{1.99-\frac{a}{h}\left(1-\frac{a}{h}\right)\left(2.15-3.93\frac{a}{h}+2.7\left(\frac{a}{h}\right)^2\right)}{bh^2\left(1+\frac{2a}{h}\right)\left(1-\frac{a}{h}\right)^{3/2}} \qquad (1)$$

Here, the symbol h, b, a and s are respectively represent the height, thickness, crack length and loading span. The fracture toughness of many specimens with different thickness or different prefabricated crack length, are shown in Figure 2 (a, b). Among them, the solid symbol indicates the fracture toughness of specimen without seawater immersion. And, the hollow symbols or vertical line is for the toughness value of specimen soaked in seawater for short-term that were unloading to zero after loaded firstly into the plastic stage. Figure 2(a) shows the variation of specimen fracture toughness with crack length. And Fig 2 (b) express the variation of toughness with specimen thickness. It can be seen that the toughness of seawater immersion specimen after plastic deformation is smaller than that of specimen without seawater immersion. The fracture toughness increases of specimen with the increasing of its thickness, and its toughness decreases with the increase of prefabricated crack length.

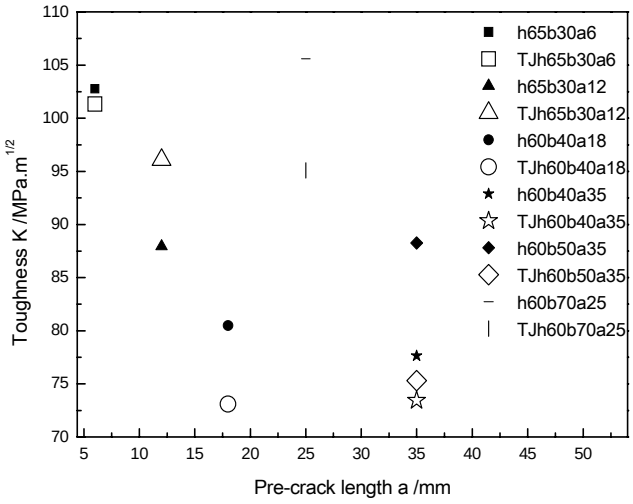

a）

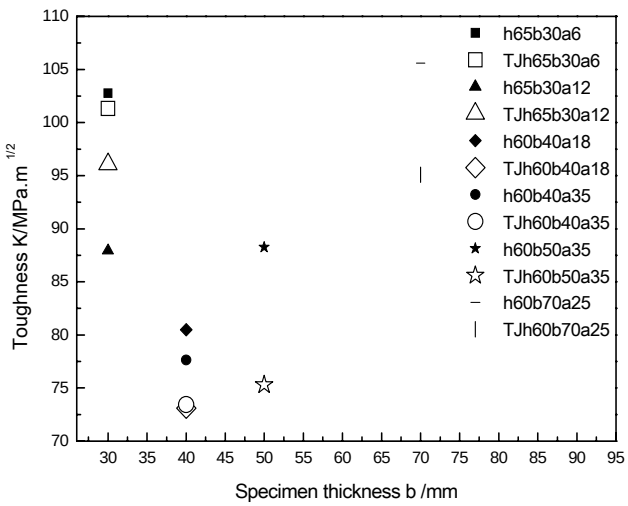

b）

Fig 2 The toughness of steel soaked in seawater or not for different pre-crack (a) or thickness (b)

4.The SEM morphology of specimen in seawater immersion

As shown in Figure 3 (i,ii)， they are the SEM photos of the location of carbon steel specimen in uniaxial tension, and its appearance size is about long 20mm, wide 4mm, thickness 0.6mm. Fig3. (i) is about the specimen soaked in seawater for 90 days, and Figure (ii) is the photo of specimen without seawater. The size and crack length of both specimen is the same about 1.5mm. The specimen shown in Fig 3. (i) is loaded for tension 1240N, and that in Fig 3(ii) is for 1656N. As to the specimen immersed in seawater, it has the phenomena of cracking and slip twinning in disorder. The images show that the steel of soaked in seawater becoming deterioration in the mechanical properties of material, and its performance of resistance damage ability is also reducing obviously.

（i） 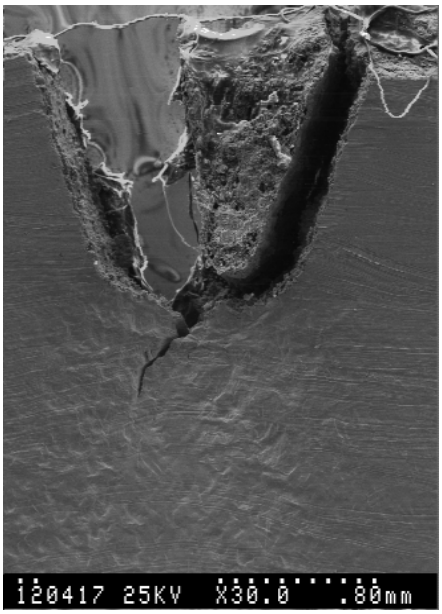

（ii） 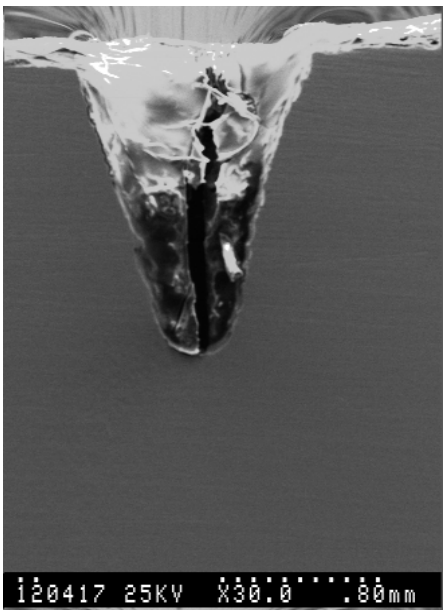

Fig 3 SEM Photos of Steel specimen （i）after soaked in seawater at load 1240 N;
（ii） not in seawater at load 1656N

The SEM photos of specimen on local corrosion part in seawater are shown in Fig 4. Here, figure (1) is for conditions without load, and figure (2) for loading 1850N. The corrosion defects and corrosion surface shedding can be seen after loading on specimen in the right picture.

5. Conclusion

1) For the steel specimen of three point bending beam with crack, its seawater immersion of short time is not significant influence on the curve of loading and displacement of experiment. But, the specimen fracture toughness slightly reduced, deformation curve become shorter or becoming brittle, when it were reloaded after loaded to plastic stage

and immersion in seawater for a period time.

2）It is found by scanning electron microscopy that the specimens of short-term sea immersion exists obvious corrosion defects, disorder slip twinning and its capacity of resistance cracking was lower than the specimen without seawater.

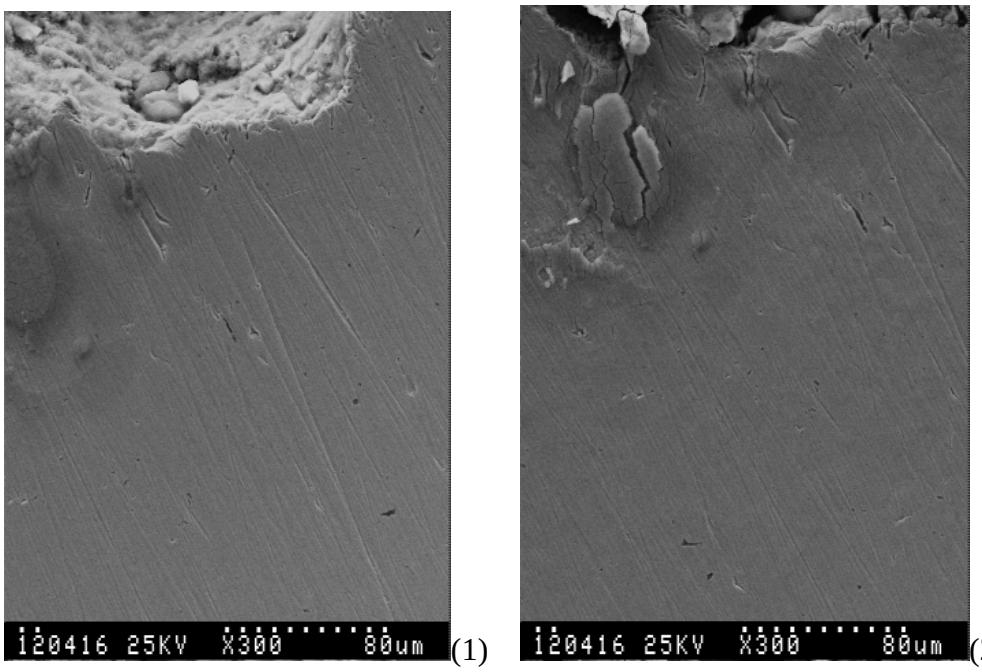

(1) (2)

Fig 4 The photos of steel local part corroded in seawater at different load （1）after soaked in seawater at load 0 N, （2） not in seawater at load 1850N

Reference

[1] Huang G Q. Corrosion behavior of carbon steels immersed in sea areas of China. Corros. Sci. Prot. Technol, 2001, 13 (2): 81-88

[2] Melchers R E, Jeffrey R. Early corrosion of mild steel in seawater. Corrosion Science, 2005, 47(7): 1678-1693

[3] Jia Yizheng, Wang Jianqiu, Han En-Hou, Ke Wei. Stress corrosion cracking behavior of X100 pipline steel in NS4 solution under constant loading test. Journal of Chinese Society for Corrosion and Protection.2011,31(3): 184-189

[4] Fragiel A, Serna S, P´erez R. Electrochemical study of two microalloyed pipeline steels in H_2S environments [J]. Int. J. Hydrogen Energy, 2005, 30: 1303-1309

[5] Zheng Y Y, Wang J, ZOU Y. Research progress on corrosion of carbon steels under rust layer in marine environment. Corrosion Science Protection Technolgy. 2011,23(1): 93-98.

[6] Hiroshi Tada, Paul C Paris, George R Irwin. The stress analysis of cracks handbook (3rd ed).New York: American Society of mechanical Engineers(ASME), 2000

Cohesive Zone Model for Intergranular Slow Crack Growth in Zirconia and Ceramic: Influence of the water concentration and Microstructure

Bassem El Zoghbi[1,*], **Rafael Estevez**[1], **Christian Olagnon**[2]

[1] Laboratoire SIMAP, UMR CNRS 5266, Grenoble-INP, UJF, Université de Grenoble, 38402, France

[2] Laboratoire MATEIS, UMR CNRS 5510, INSA Lyon, Université de Lyon, 69621, France

* Bassem.El-Zoghbi@simap.grenoble-inp.fr

Abstract We describe intergranular *slow crack growth* (SCG) in Zirconia within a cohesive zone methodology. Stress corrosion being thermally activated, a rate and temperature dependent cohesive zone formulation is proposed and shown able to capture SCG. In the present study, the influence of microstructure in terms of anisotropic properties, the grain to grain disorientation, and the initial thermal stress state that originates from the ceramic processing are shown to determine the kinetics of SCG and the level of the load threshold below which no slow crack growth is observed. The influence of the water concentration (R.H.) on the magnitude of the minimum load threshold and on the kinetics of SCG is investigated. Ultimately, this work aims at providing reliable predictions in long lasting applications of ceramics.

Keywords Zirconia, Ceramic, Slow crack growth, Cohesive Zone, Humidity

1. Introduction

Zirconia has been one of the most important ceramics and one of the prominent mechanical properties used in various domains as thermal barriers, coatings, and in medical applications. Their intrinsic advantages are wear chemical resistance and inertness. When subjected to subcritical mechanical loads in presence of water, Zirconia is prone to a delayed damage mechanism called *slow crack growth* (SCG). This damage process is environmentally assisted by the diffusion and adsorption of water molecules in the crack tip or along the grain boundaries, which will reduced the energy required for failure. SCG is characterized by the variation of the crack velocity with load level. It is show experimentally [1, 2, 7] that beyond a load threshold K_0, SCG takes place at a velocity that increases with load (regime *I*). Regime *I* depends strongly on the load level, temperature and water concentration. This process is influenced by the environment. Chevalier et al. [2] showed experimentally the influence of water concentration and temperature on SCG and on the threshold K_0 in Zirconia polycrystals (see Fig. 1). Increasing the water concentration (cf. air 25°C vs water 25°C) induced a shift in the V-K_I curve with an increase in the crack velocity and a decrease in the magnitude of K_0. The same trend is observed with increasing temperature (cf. water 25°C vs water 75°C) with an additional decreasing of the threshold K_0. The slope of regime *I* of the V-K_I curve is not affected by the environment but the kinetics of SCG (velocity, K_0) are strongly dependent on the magnitude of the mechanical load, water concentration and temperature. In the present study, we aim at predicting the load threshold K_0, the regime *I* of the V-K_I curve and at providing insight of the origin of their variation with the water concentration.

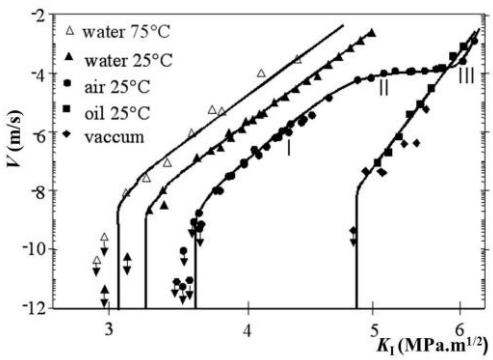

Figure 1. Slow crack growth in ceramics (Zirconia) velocity V versus the stress intensity factor K_I. The regime I shows a marked dependence with the relative humidity and temperature (data from [2]).

The mechanism underlying failure is described with a cohesive model that represents the reaction rupture process for SCG. Thus, a thermally activated formulation is adopted for the cohesive model (see Romero de la Oso et al. [2]). The formulation is shown in Romero de la Osa et al. [2-4] able to capture the regime I, the load threshold being related to the presence of initial stress (Romero de la Osa et al. [4]). We also investigate the influence of residual thermal stresses originating from the sintering process on the kinetics of SCG and on K_0. The influence of the water concentration on the kinetics of SCG and on the minimum threshold K_0 is also investigated.

2. Cohesive zone model for the reaction-rupture mechanism in ceramic

In this section, we present a cohesive zone model for the reaction-rupture mechanism underlying SCG in single and polycrystals ceramics. Michalske and Freiman [5] proposed an atomistic description accepted in the ceramic communities as a responsible for the process of SCG. They considered a bond of scilica in tension in presence of molecule of water that assists the breakdown of the bond to create two molecules of silanol. This model is reconsidered recently by Zhu et al. [6] by performing atomistic calculations. They observed that the reaction rupture is energetically favorable once a stress threshold is reached locally, with an activation energy that decrease with the applied stress. These observations are formulated with a cohesive zone methodology as Romero de la Osa et al. [3-4]. A thermally activated cohesive model is proposed where the damage opening rate for the description of the damage kinetics as

$$\dot{\Delta}_n^c = \dot{\Delta}_0 \exp\left(\frac{-U_0 + \beta\sigma_n}{k_B T}\right), \tag{1}$$

where $\dot{\Delta}_n^c$ is the opening rate between two surfaces in which damage occurs, U_0 is an activation energy, β has the dimension of a volume and σ_n is the traction normal to the cohesive surface. The pre-exponential term $\dot{\Delta}_0$ has the dimension of a velocity; k_B is the Boltzmann gas constant and T the absolute temperature.

Damage is triggered when $\sigma_n \geq \sigma_n^0$, σ_n^0 being a local load threshold. When the cumulated opening reaches a critical thickness Δ_n^{cr}, a crack is nucleated locally. The critical thickness Δ_n^{cr} is a material parameter, which is assumed to be about 1nm in crystalline material. According to Zhu et al. [6], the threshold stress σ_n^0 for the process to be energetically favorable ranging from 0 to 25% of the

athermal stress $\sigma_c = U_0/\beta$. For a traction smaller than threshold stress σ_n^0 neither damage nor reaction-rupture takes place. If the initial traction is higher than the threshold σ_n^0, the process will take place until a crack nucleates. For a traction smaller than the threshold stress σ_n^0 before the crack nucleation, the reaction-rupture stops.
In a finite element analysis, the related traction-opening is taken as

$$\dot{\sigma}_n = k_n(\dot{\Delta}_n - \dot{\Delta}_n^c), \tag{2}$$

where $\dot{\sigma}_n$ is the normal traction increment, $\dot{\Delta}_n$ is the prescribed opening rate, $\dot{\Delta}_n^c$ the damage opening rate, k_n is a stiffness that is taken large enough to ensure $\dot{\Delta}_n \approx \dot{\Delta}_n^c$ during the reaction rupture process. In this cohesive model formulation, we do not account for a contribution of the tangential mode in the reaction-rupture process. A simple elastic response is considered as

$$\dot{\sigma}_t = k_t\dot{\Delta}_t, \tag{3}$$

with $\dot{\sigma}_t$ is the tangential traction increment, $\dot{\Delta}_t$ the prescribed shear rate along the cohesive surface and k_t the tangential stiffness.
A quasi-static finite analysis is considered which uses a total Lagrangian description, the incremental shape of virtual work for this problem as (Romero de la Osa et al. [3,4])

$$\int_V \tau.\delta\dot{\eta}\, dV + \int_{Scz} \sigma_\alpha.\delta\dot{\Delta}_\alpha\, dS = \int_{\partial V} T.\delta\dot{u}\, dS, \tag{4}$$

where V and ∂V respectively represent the volume of the region in the initial configuration and its boundary, and S_{CZ} is the cohesive surface considered. The index α corresponds to the normal and tangential components in the cohesive formulation. In (Eq. 4), τ is the second Piola-Kirchhoff stress tensor, T the corresponding traction vector; $\dot{\eta}$ and ν are the conjugate Lagrangian strain rate and velocity. The governing equations are solved in a linear incremental fashion based on the rate form of (Eq. 4).

2.1. Calibration of cohesive zone parameters for Zirconia

We define a case study with an elastic bulk representing a single crystal (see Fig. 2a) under a static load. A linear elastic isotropic bulk is considered with an initial crack that is subjected to mode *I* and constant prescribed stress intensity K_I. Cohesive zone is inserted along the crack symmetry plane, where the principal stress is maximum. Small scale damage confined around the crack tip is assumed and the boundary layer approach is used to investigate mode *I* plane strain conditions. The mesh is refined around the crack propagation path (see Fig. 2b) and cohesive element of 1nm long is used. We prescribe a constant load in terms of stress intensity factor K_I as record the crack advance with time. We extract the velocity in the steady state regime and get one point in the V-K_I curve. By repeating this procedure, we are able to adjust the prediction with available experimental data [8]. The values of the Young modulus E^{iso} = 315 GPa and Poisson ratio ν^{iso} = 0.24 are derived from the cubic elastic constants of zirconia single crystals (see (Table 1). We adopt Δ_n^{cr} = 1nm, and based on Zhurkov [8] the energy barrier U_0 is of the order of the sublimation energy, with U_0 = 160kJ/mol. We still have to identify β and $\dot{\Delta}_0$, β controlling the slope of V-K_I and $\dot{\Delta}_0$ its position

(see Romero de la Osa et al. [3]). The identification of the parameters reported in Table 2, the predicted curve V-K_I being in agreement with the experimental data (see Fig. 3).

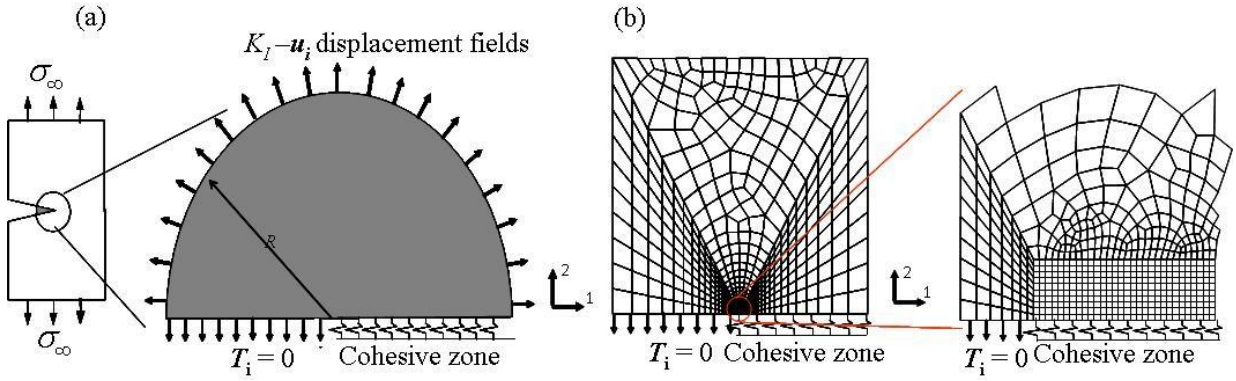

Figure 2. (a) Schematic description to model the zirconia SCG subjected to mode *I*, plain strain loading, (b) General view and zoom around the crack tip of the mesh used for the finite element analysis.

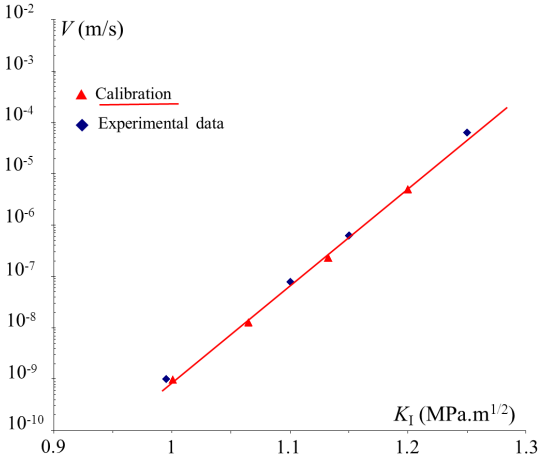

Figure 3. Calibration of cohesive zone parameters for zirconia based on experimental data [7] of SCG of zirconia single crystals

Table 1. Cubic elastic constants of zirconia single crystals (data from [9])

C_{11} (GPa)	C_{22} (GPa)	C_{33}(GPa)
430	94	64

Table 2. Parameters for the cohesive zone model for SCG in a zirconia single crystal

U_0 (kJ/mol)	Δ_n^{cr} (nm)	β (nm^3)	$\dot{\Delta}_0$ (mm/s)
160	1	0.027	3.2×10^{11}

3. Simulation and prediction of SCG in 2D zirconia polycrystal

We use the cohesive parameters indentified in the foregoing section to describe intergranular fracture under SCG in a polycrystal. We consider a granular zone composed by anisotropic hexagonal grains with random direction and with cohesive surfaces inserted along the grain boundaries. The problem formulation is depicted in Fig. 4. The polycrystalline zone is embedded in a continuum, homogeneous equivalent medium. An initial crack emerges in the granular zone. Along the remote boundary, the mode *I K*-fields are prescribed. Intergranular failure is allowed. The cubic elastic constants of zirconia grains are reported in Table 1 and the coefficients of thermal expansion are ($\alpha_1 = \alpha_3 = 10 \times 10^{-6}$ K^{-1}, $\alpha_2 = 11 \times 10^{-6}$ K^{-1}). The surrounding homogenous linear

isotropic bulk has a Young's modulus E = 315 GPa and Poisson's coefficient ν = 0.24, its isotropic coefficient of thermal expansion is taken as $\alpha = (2\alpha_1 + \alpha_2)/3$. In all cases, the polycrystal consists in a 8 × 8 grains with a grain diameter Φ_G = 0.8 μm. Two types of loading can be considered, a thermal and mechanical one. Firstly, we do not account to the initial thermal stresses originating during the cooling after sintering. We apply an instantaneous load in terms of K_I which is kept constant in time. The load is relaxed by intergranular failure. We consider a threshold stress σ_n^0 = 400 MPa corresponding to 4% of the athermal stress σ_c. In Fig. 5a, we have reported the distribution of the stress component σ_{yy} for various stages of the crack advance. The crack tip can be identified as the region with the highest stress concentration. We report the crack velocity for different load levels in Fig. 5b, that are compared with the experimental data of SCG in polycrystals for sintered Yttrium Stabilized Zirconia conducted by Chevalier et al. [7], for comparable grain sizes. We also report the curve V-K_I corresponding to the calibration of the cohesive zone for the zirconia single crystal. We observe that the predicted V-K_I curve is shifted toward larger load values for the polycrystal compared to the case of a single crystal. The slope of the V-K_I curve is comparable to the experimental data, but the predicted kinetics of SCG by simulation are faster than the experimental one. This difference may originate from 2D configuration in our simulation that promotes the crack advance in comparison with 3D configuration. Also, the initial thermal stress state is not considered here. Therefore, we now investigate their effect on SCG.

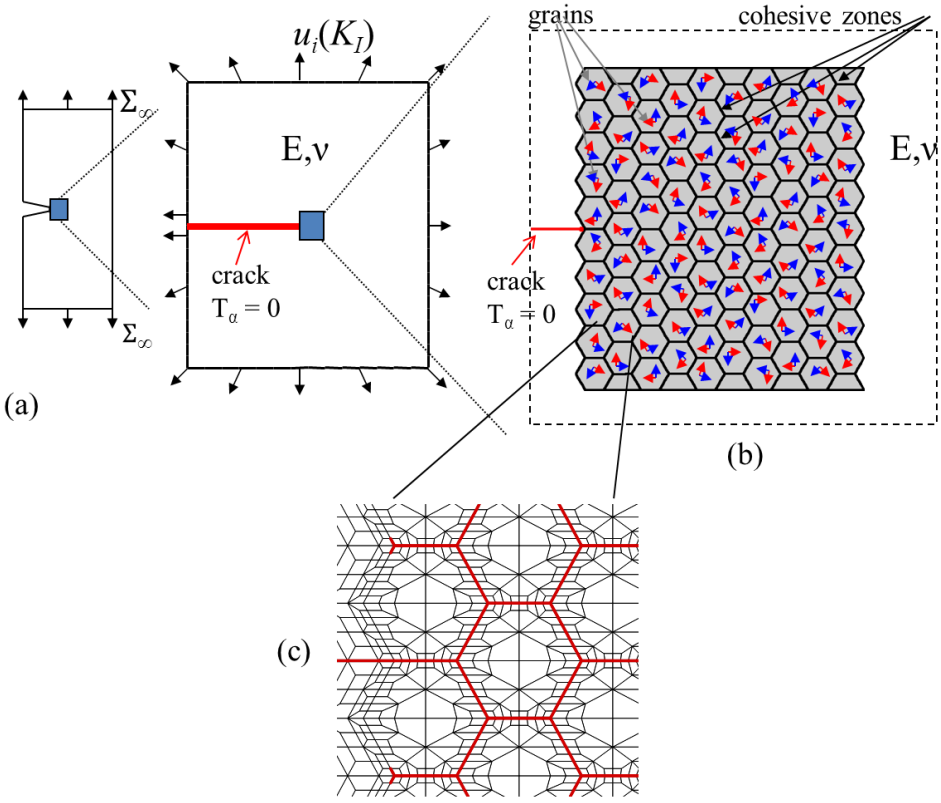

Figure 4. Small scale damage configuration used for the analysis of SCG in a 2D polycrystal

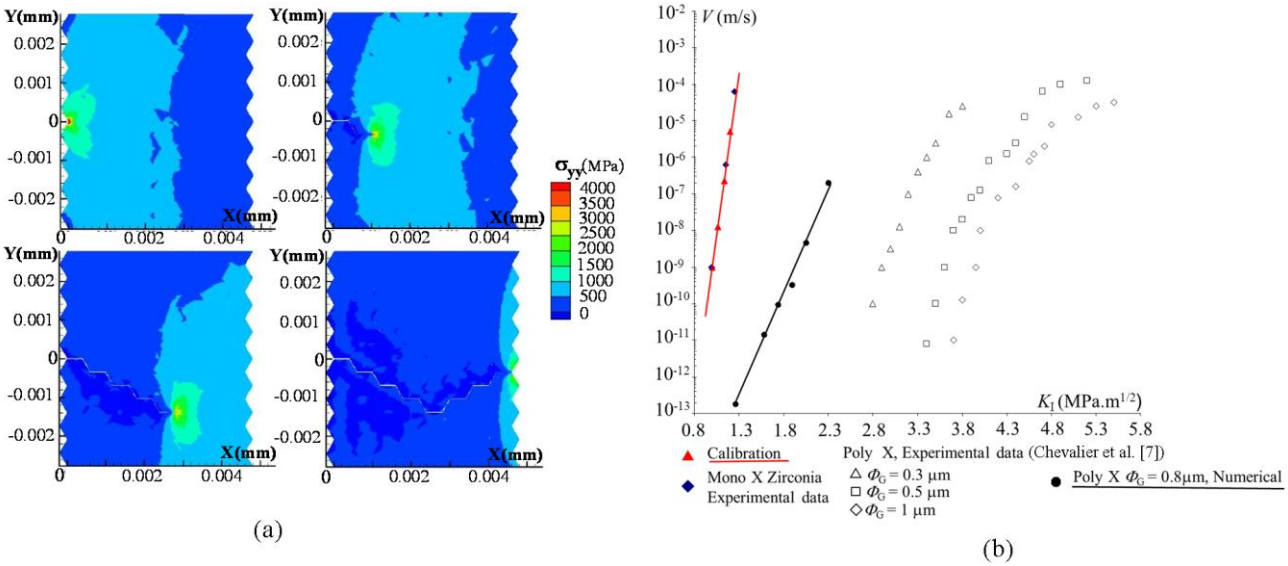

Figure 5. (a) Distribution of the stress σ_{yy} during crack propagation for a 2D polycrystal, (b) Comparison of the SCG plots V-K_I between the single crystal, the 2D polycrystal and Experimental data from [7]

3.1. Influence of the threshold stress σ_n^0 on the prediction of SCG

We now investigate the influence of threshold stress σ_n^0 corresponding to the initiation of the reaction-rupture mechanism on the SCG. Zhu et al [6] revealed the existence of a stress threshold σ_n^0 for the reaction-rupture process to be energetically favorable. The magnitude of σ_n^0 ranges is up to 25% the magnitude of the athermal stress σ_c. Therefore, we report in Fig. 6a the V-K_I curve for different values of σ_n^0 = 400, 900 and 1150 MPa corresponding to 4%, 9% and 12% of the athermal stress σ_c. We observe that the V-K_I curve is not affected by the variation of σ_n^0. However, σ_n^0 is particularly important in determining the threshold load K_0 below which no crack growth occurs. For the case with σ_n^0 = 400MPa, we do not observe a load threshold for SCG even for values as small as $K_I \approx 0.6$ MPa and $V \approx 10^{-16}$ m/s. For higher value of σ_n^0, a crack arrest is observed for K_0 = 0.9 MPa.mm$^{1/2}$ and σ_n^0 = 900 MPa. We observe that increasing the value of σ_n^0 increases the magnitude of K_0. The value of K_0 = 1.1 MPa.mm$^{1/2}$ is observed for σ_n^0 = 1150 MPa. During the relaxation if the normal traction becomes smaller than σ_n^0 before the crack nucleation, the reaction rupture stops. We report in Fig. 6b the cracks paths for arrested cracks corresponding to the threshold load K_0 below which no SCG occurs. These results show that with increasing the threshold stress σ_n^0, a threshold load of SCG can appear. It is related to the disorientation grain to grain that induce a reduction of the normal stress along the grain boundaries large enough for the normal traction σ_n becoming smaller than σ_n^0. In considering only these ingredients, we predict a threshold load of SCG in zirconia around 1MPa.m$^{1/2}$ for $\sigma_n^0 \approx 10\% \times \sigma_c$. We now investigate the influence of the thermal initial stress state on the magnitude of the threshold load K_0.

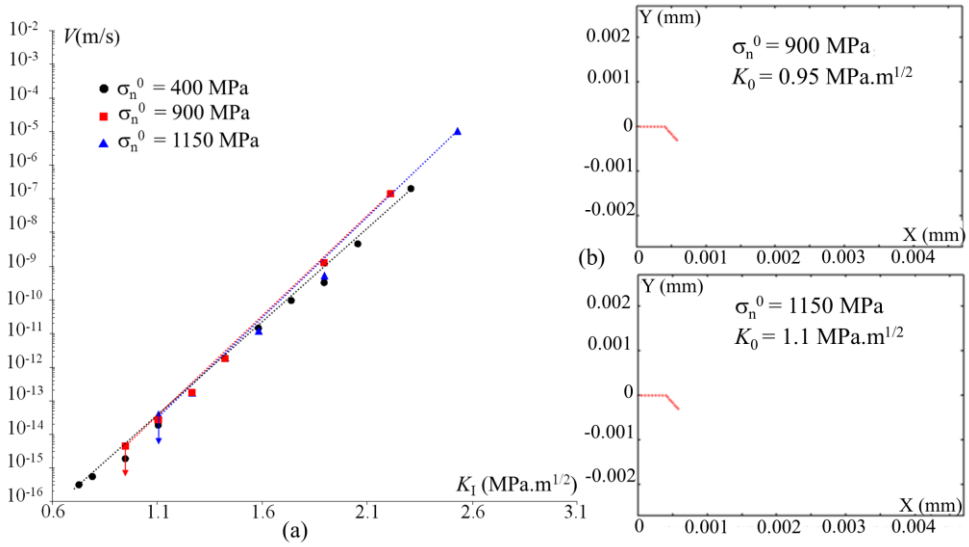

Figure 6. (a) Influence on the threshold stress of cohesive zone σ_n^0 and prediction of the V-K_I curve for Polycrystal of Zirconia with Φ_G = 0.8 μm, (b) Cracks paths for stopped cracks corresponding to the threshold load K_0 for σ_n^0 = 900 MPa and 1150 MPa.

3.2. Influence of thermal initial stresses on the prediction of SCG

During the sintering process, the material is cooled down from a temperature at approximately 1500 °C to the room temperature. This process will induce thermal stresses that originate from both the anisotropic coefficients of thermal expansion and anisotropic elastic constants of the grains. We consider the case with 8 × 8 grains, a grain size Φ_G of 0.8 μm for a uniform temperature cooling ΔT = -1500 K. The corresponding boundary conditions are presented in Fig. 7a, and the distributions of the stress component σ_{yy} reported in Fig. 7b, region under traction and compression are observed. From this initial state, we apply an external load K_I and we allow intergranular failure. For σ_n^0 = 400 MPa, 900 MPa and 1150 MPa, we report the corresponding V-K_I curves represented in Fig. 8a, 8b and 8c. For the three cases investigated, we observe that the presence of initial thermal stresses lead to a reduction of the crack kinetics. The curves V-K_I are shifted towards higher K_I values, preserving the slope of the curves corresponding to the polycrystals that are initially stress free. For the case with σ_n^0 = 400 MPa (see Fig. 8a) we observe that a threshold load K_0 now appears when we consider the initial thermal stresses. For σ_n^0 = 900 MPa and 1150 MPa, the magnitude of the threshold load of SCG increases when initial stresses are accounted for. We report in Fig. 9a, 9b and 9c the cracks paths for arrested cracks corresponding to the threshold load K_0 below which the crack is stopped for σ_n^0 = 400 MPa, 900 MPa and 1150 MPa respectively. The crack arrest is observed when the crack reaches a region where the compression is initially high enough with a locally stress level lower than threshold stress σ_n^0 of cohesive zone. The account of thermal initial stress contributes to a reduction of SCG kinetics. The magnitude of K_0 is also increased with initial thermal stress are accounted for. In the next section, we examine the influence of the water concentration on the predicted regime I and load threshold of SCG K_0.

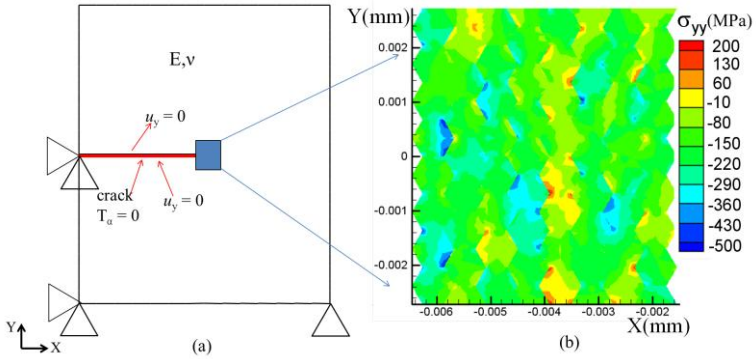

Figure 7. (a) Boundary conditions for thermal load, (b) Distribution of the stress component σ_{yy} in the polycrystal of zirconia with Φ_G = 0.8μm after a thermal cooling ΔT = -1500 K.

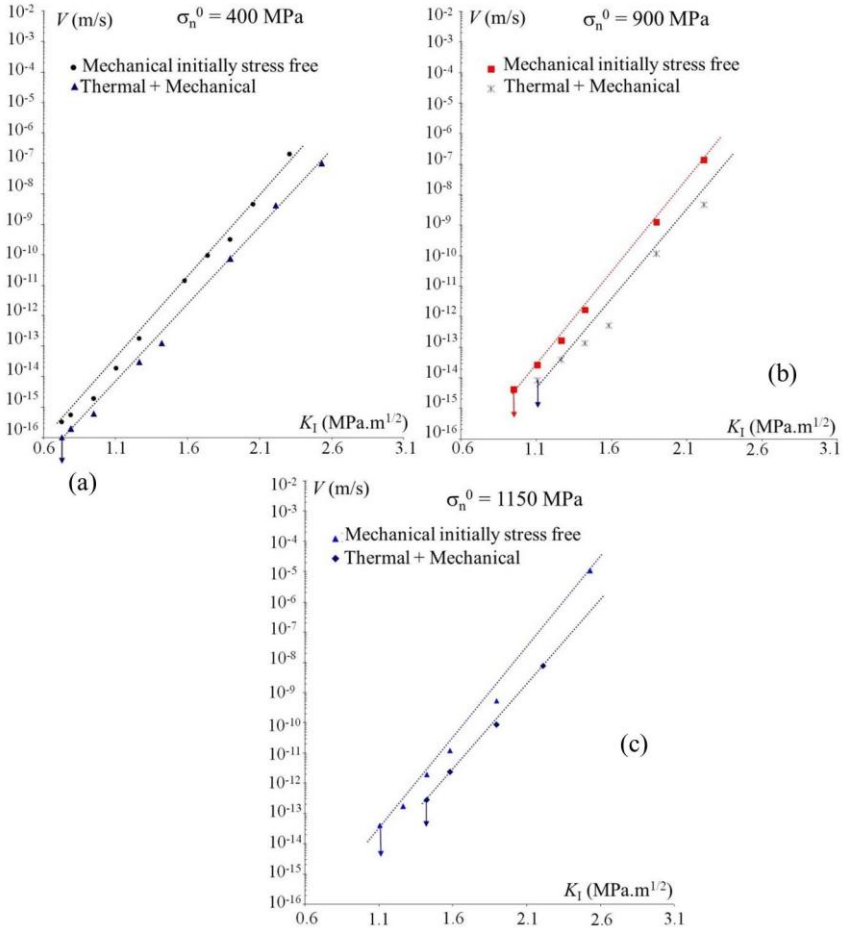

Figure 8. Influence of thermal initial stresses on the prediction of the V-K_I curves and K_0 for Polycrystals of Zirconia with Φ_G = 0.8 μm, (a) σ_n^0 = 400 MPa, (b) σ_n^0 =900 MPa and (c) σ_n^0 =1150 MPa.

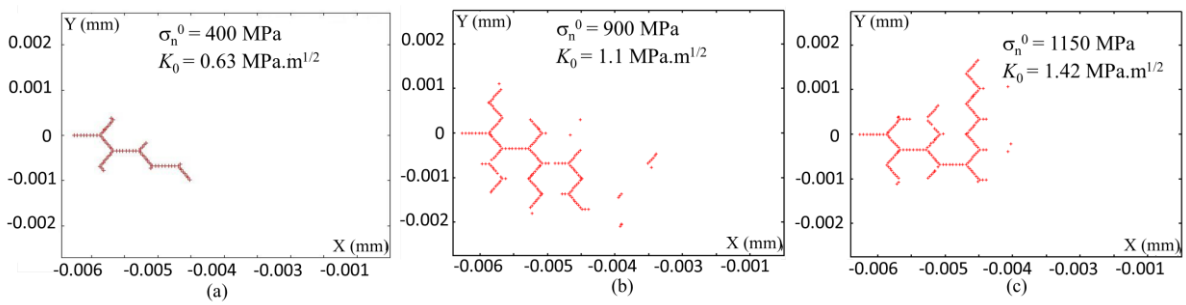

Figure 9. Cracks paths for stopped cracks, (a) σ_n^0 = 400 MPa , K_0 = 0.063 MPa.m$^{1/2}$, (b) σ_n^0 =900 MPa, K_0 = 1.1 MPa.m$^{1/2}$ and (c) σ_n^0 =1150 MPa, K_0 = 1.42 MPa.m$^{1/2}$.

3.3. Influence of water concentration on SCG

We investigate the influence of the water concentration (R.H.) on SCG in the zirconia polycrystal. We propose to account for the influence of R.H. by invoking a dependence of the energy barrier U_0 with the concentration of water molecules. By considering that an increase of R.H. results in decreasing the activation energy U_0(R.H.) that will facilitate the cracking. We consider an activation energy U_0 = 160 kJ/mol of the ambient air. We reduce this value by 10 % for an environment with more water and increase the reference value of U_0 by 10 % for a drier environment.

For each values of σ_n^0 = 900 MPa and 1150 MPa, we report the prediction in terms of V-K_I in Fig. 10a and Fig. 10b respectively. We observe that reducing the value of U_0 increases the value of the crack velocity for a given load K_I, while preserving the slope of the curve V-K_I. However, the dependence of threshold load K_0 in the water concentration is not affected by the variation of U_0(R.H.). This prediction is not in agreement with the experimental observations by Chevalier et al. [2] (see Fig. 1). We now examine the dependence of the threshold stress σ_n^0 of cohesive zone with the concentration of water molecules. When the water concentration increases, we now reduce U_0 by 10% (U_0 is increased by 10% for a drier environment). Therefore, we consider σ_n^0 = 900 MPa and U_0 = 160 kJ/mol as reference values in ambient air. The results in terms of V-K_I curves are reported in Fig. 11a. In Fig. 11b, we reported the results of the case with the references values of ambient air σ_n^0 = 1150 MPa and U_0 = 160kJ/mol. We observe that reducing the water concentration increases the threshold load K_0. These predictions are in agreement with the experimental observations in the influence of R.H on SCG by increasing the crack growth kinetics and reducing of threshold load of SCG K_0 with increasing R.H. In order to account to the first effect, we show that the dependence of energy barrier U_0 with R.H. takes account the variation of SCG kinetics with R.H. Nevertheless, it is important to take account the dependence of the threshold of activation of reaction-rupture mechanism σ_n^0 with R.H. At least this holds for the zirconia.

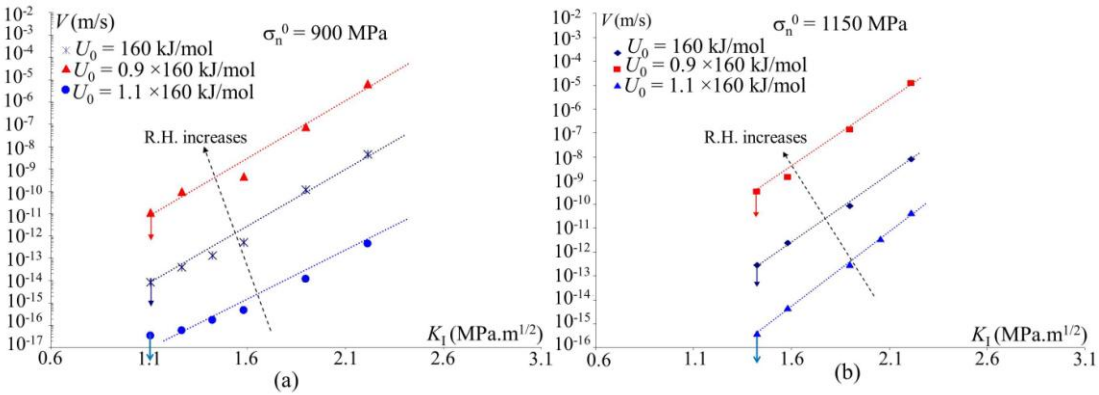

Figure 10. Influence of water concentration R.H. by its dependence with U_0 (R.H.) on the prediction of the V-K_I curves and K_0 for Polycrystals of Zirconia with Φ_G = 0.8 μm, (a) σ_n^0 = 900 MPa, (b) σ_n^0 =1150 MPa.

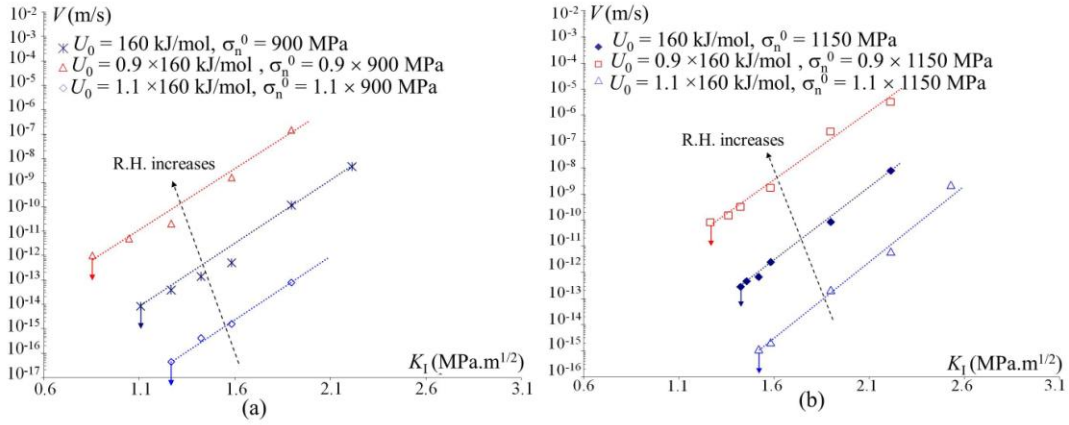

Figure 11. Influence of water concentration R.H. by its dependence with σ_n^0 (R.H.) and U_0 (R.H.) on the prediction of the V-K_I curves and K_0 for Polycrystals of Zirconia with Φ_G = 0.8 μm.

3. Conclusion

We have presented a calibration of the cohesive zone parameters for zirconia single crystal based on the cohesive zone description of Romero de la Osa et al. [3-4] for SCG in ceramics. The cohesive model is shown able to capture realistic experimental data of SCG in a single crystal. This calibration is then used to simulate intergranular failure in a 2D polycrystal. We have pointed on the influence of the stress threshold σ_n^0 for the reaction-rupture to be triggered on the prediction of the threshold load of SCG in a polycrystal. We have shown the influence of the initial thermal stresses related to processing on the kinetics of SCG and the magnitude of K_0. We also examined the influence of the water concentration on the prediction of the regime I and K_0 of SCG and showed that the water concentration can be accounted for with a dependence of the activation energy and traction threshold with the amount of water.

References

[1] K. Wan, S. Lathabai and B. Lawn, Crack velocity functions and thresholds in brittle solids in J. Am. Ceram.Soc., 1990, 6 259-68.
[2] J. Chevalier, C. Olagnon and G. Fantozzi, Subcritical crack propagation in 3y-tzp ceramics : static and cyclic fatigue, J. Am. Ceram. Soc., 1999, 82(11) :3129-3138.
[3] M. Romero de la Osa, R. Estevez, J. Chevalier, C. Olagnon, Y. Charles, L. Vignoud ,C. Tallaron, Cohesive zone model and slow crack growth in ceramic polycrystals, Int. J. Fract, 2009, 158(2) 157-167.
[4] M. Romero de la Osa, R. Estevez, J. Chevalier, C. Olagnon, Y. Charles, L. Vignoud ,C. Tallaron, Cohesive zone model for intergranular slow crack growth in ceramics : influence of the process and microstructure, Modell. Simul. Mat. Sci. Engng., 2011, 19:074009.
[5] T. A. Mischalske and S. W. Freiman, A molecular Mechanism for Stress Corrosion in Vitreous Silica, J. Am. Ceram. Soc., 66 284-8.
[6] T. Zhu and J. Li, X. Lin, S. Yip, Stress-Dependent Molecular Pathways of Silica-Water Reaction. J. Mech. Phys. Slolids, 2005, 53 1597-623.
[7] J. Chevalier and G. Fantozzi, Slow crack propagation in ceramics at the nano- and microscale : effect of the microstructure, Proceedings of the 8th Internaional Symposium on Fracture Mechanics of ceramics, held February 25 28, 2003, at the University of Houston, Texas.
[8] S. N. Zhurkov, Kinetics Concept of the Strength of Solids, J. Fract. Mech., 1965, 1 311-23.
[9] R. P. Ingel, D. Lewis, Elastic Anisotropy in Zirconia Single Crystals, J. Am. Soc., 1988, 74(4) 265-71.

Performance Deregulation Rule of Aircraft Fatigue Critical Components in Consideration of Calendar Environment

Chao Gao[1,] , Yuting He[1*], Haiwei Zhang[1], Bo Hou[1], Teng Zhang[1]

[1]Aeronautics and Astronautics Engineering College, Air Force Engineering University, Xi'an 710038, China
* Corresponding author: hyt666@tom.com

Abstract The 2A12-T4 aluminum alloy specimens were studied with accelerated environment test to simulate different parking calendar years. Afterwards, these specimens were implemented with fatigue test to fracture. Through analyzing the test data, the relationship between S-N shape parameter and parking calendar years was caculated with dynamic S-N curve method. Then, the performance deregulation rule of aircraft fatigue critical components in consideration of calendar environment was established. In addition, the rule between Detail Fatigue Rating (DFR) and parking time was also set up. Compared with the similar specimens' life from retired aircraft, the life with S-N curve and DRF method was in good agreement with actual value. The result shows that aircraft fatigue cirtical components' performance declines with the prolonging parking calendar time.

Keywords 2A12-T4 aluminum alloy, fatigue critical component, calendar environment, dynamic S-N curve, Detail Fatigue Rating

1. Introduction

Currently, the service life index of aircraft component in China includes fatigue life denoted by flight hours and calendar life denoted by calendar life. The first repair, major repair and total life are controlled according to the principle of first reach of service life index [1]. The calendar life mainly aims at the corrosive critical component and the degree of corrosive damage is the basic premise whether the component is in good working order [2]. The fatigue life mainly aims at the fatigue critical component and the remaining life depends on the degree of fatigue damage and the number of repair. Aimed at the corrosive fatigue critical component, the method of corrosive influence coefficient is usually used for the general engineering purpose to revise the attenuation of fatigue life because of the corrosive effect during service life [1,3,4]. Generally speaking, the corrosive effect of componen is mainly considered for the calendar life, however, the remaining fatigue life of component is that the design target subtracts the consumed fatigue life and don't take the effect of environment into account. Because the calendar life of aircraft at present are over 20 years [4], the representative aircraft—B-52, the calendar life are over 50 years. The effect of environment for a long time can result in the corrosion of component and reduce the anti- fatigue performance of material [1-10]. The fatigue critical component is exposed to the parking environment for a long time, which can't result in the obvious corrosion of component but can cause the microscopic damage. However, the instance that the performance is degrading for the fatigue critical component of parking aircraft because of environmental effect is never reported at home and abroad.

Aimed at the problem of performance decline for the fatigue critical component in parking environment, the accelerated environment test of different parking calendar time was carried out by using the 2A12-T4 aluminum alloy standard specimen until the specimen fracture, then the relation was calculated between the shape parameters and the parking calendar time, the model for life decline was established about the fatigue critical component under the parking condition. The model for Detail Fatigue Rating (DFR) and accelerated time were calculated and compared with the fatigue life of the same material from the retired aircraft. The result shows that the model is reliable. The result indicates that the parking environment can cause the fatigue performance decline for the fatigue critical component, and more attention should be paid to the usage and life-saving for the

old aircraft.

2. The test method and result

2.1. Manufacture of the specimen

The material of specimen is 2A12-T4 aluminum alloy with the thickness of 4 mm and the size is shown in Fig.1. The tensile strength σ_b is 450 MPa, the yield strength σ_s is 325 MPa, the extensibility δ is 15%.

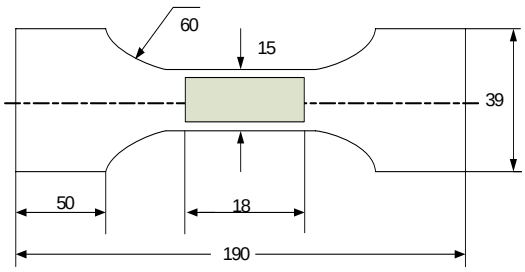

Figure 1. Specimen size

The old specimen came from fuselage slab component of some no- corrosive retired aircraft (2A12-T4 aluminum) and was machined as picture 1 according to the loading direction.

2.2. The test method

The accelerated environment test was processed in the environment box and the environment spectrum as shown in Fig.2, was used to simulate the natural environment. At present, a mount of tests on the accelerated corrosion in laboratory were aimed at the corrosive fatigue critical component and the effect of environment on the no- corrosive fatigue critical component didn't be considered [5]. Consequently, on the basis of accelerated environment spectrum of the metallic material and organic material in laboratory, the accelerated corrosive environment spectrum used on engineering at present was modified in this paper and then was applied to the accelerated test of the fatigue critical component. The fatigue critical component would suffer the environment of high temperature and humidity as the corrosive fatigue critical component was suffered, the corrosive factor could weaken as far as possible.

The accelerated environment spectrum:

①Temperature:(40±2) ℃;
②Humidity: 90%~95%RH;
③Corrosive liquor: 5%NaCl liquor;
④The time for soak every period: 7.5min, the time for exterior: 22.5min;
⑤Under the glare of the far infrared lamp, keep the surface of specimen dry.

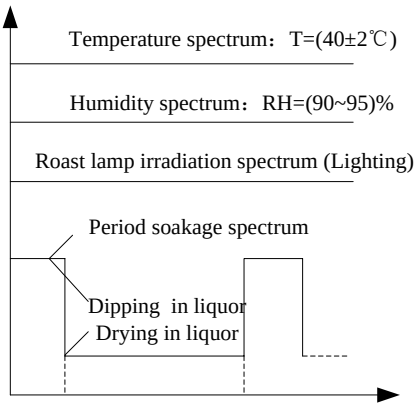

Figure 2. Accelerated environment spectrum

The surface of specimen was airproofed by the aviation silica gel.

One hour in the environment box was equal to 0.135 years in the natural environment [5], the 4 years、12 years and 20 years were simulated separately in the natural parking environment. After the accelerated environment test, the specimen of no- corrosion surface was chose to test.

The fatigue test was carried out by the MTS810 500KN fatigue test machine at room temperature with sine wave, the frequency was 20Hz, the stress ratio R was 0.06, every group would be picked up 4 valid data and the stress level had 3 groups.

2.3. The result of test

Provided that the result of test obeyed the lognormal distribution [7], the median-fatigue life could be calculated by the formula (1).

$$N_{50}(\mathrm{t}) = 10^{\frac{1}{n_t}\sum_{i=1}^{n_t}\lg N_i(t)} \tag{1}$$

Where, n_t is the number of accelerated specimen, $N_{50}(\mathrm{t})$ is the median-fatigue life, $N_I(\mathrm{t})$ is the fatigue life for the i specimen.

Table 1. Specimens' median-fatigue life

		Stress/MPa	$N_{50}(\mathrm{t})$ /10,000 cycle
Accelerated environment test	4	250	26.68
		310	12.93
		372	6.48
	12	240	26.54
		310	12.22
		372	5.97
	20	265	20.73
		310	11.83
		372	4.60
The specimen of retired aircraft		250	14.28
		290	7.83
		320	6.53

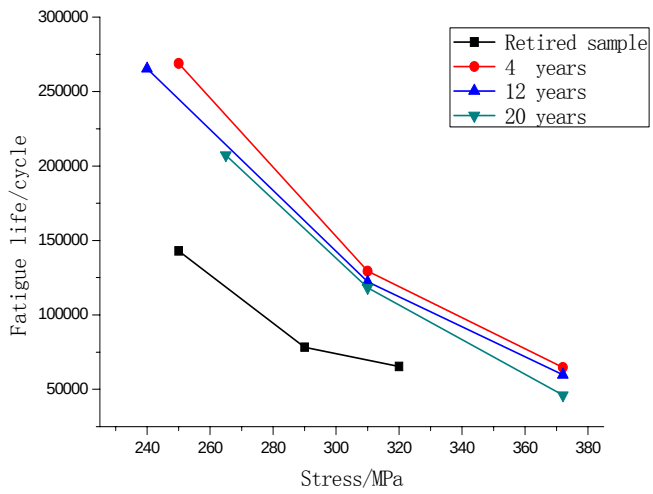

Figure 3. Specimens' stress-life curve

The Fig.3 indicated that the S-N curve moved down along with the increase of parking time, and the fatigue life declined.

3. The life analysis model for the fatigue critical component

3.1. The life model based on the dynamic S-N curve

Using the S-N curve:

$$SN^{\alpha} = C \tag{2}$$

Where, C and α are the shape parameters of material. With the service time prolonging, if the loading was not changed, the effect of environment could result in the performance decline of component. That is to say, C and α could alter with the change of time, as the formula (3) and Fig. 4 shown [10].

$$\begin{cases} C = C(\text{Parking Time}, T) \\ \alpha = \alpha(\text{Parking Time}, T) \end{cases} \tag{3}$$

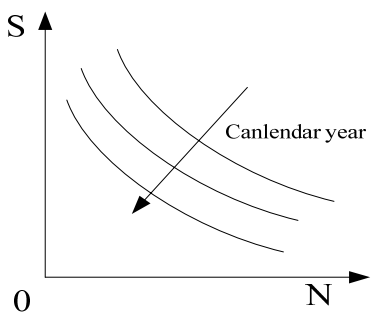

Figure 4. Dynamic S-N curve

Assuming the stress level for component was n at some loading spectrum, according to the linear accumulated damage theory, the fatigue life N could be shown as followed:

$$N = \frac{1}{\sum_{i=1}^{n} D_i} = \frac{1}{\sum_{i=1}^{n} N_i} = \frac{1}{\sum_{i=1}^{n} (\frac{C}{S_i})^{\frac{1}{\alpha}}} = \sum_{i=1}^{n} (\frac{C}{S_i})^{-\frac{1}{\alpha}} \tag{4}$$

Where, N_0 is the initial life of component and N_1 is the remaining life after parking for certain time, according to the formula (4), the formula (5) could be gotten:

$$\begin{cases} N_0 = \sum_{i=1}^{n} (\frac{C_0}{S_{0i}})^{-\frac{1}{\alpha_0}} \\ N_1 = \sum_{i=1}^{n} (\frac{C_1}{S_{1i}})^{-\frac{1}{\alpha_1}} \end{cases} \tag{5}$$

Where, S_0 and S_1 respectively is the loading level. And more:

$$\frac{N_1}{N_0} = \frac{\sum_{i=1}^{n} (\frac{C_1}{S_{1i}})^{-\frac{1}{\alpha_1}}}{\sum_{i=1}^{n} (\frac{C_0}{S_{0i}})^{-\frac{1}{\alpha_0}}} = (\frac{C_1}{C_0} \cdot \frac{S_{0i}}{S_{1i}})^{\frac{\alpha_0}{\alpha_1}} = (\frac{C_1}{C_0})^{\frac{\alpha_0}{\alpha_1}} \tag{6}$$

Where, $\mathbf{C_0}$ and α_0 respectively means the shape parameter of S-N curve for the intact component, $\mathbf{C_1}$ and α_1 respectively is the shape parameter of S-N curve after parking for some time, other parameters are the same as above.

Therefore, the model for the remaining life was set up for the component that had parked for different T years.

$$N(T+1) = \frac{N(T)}{[\frac{C(T)}{C(T+1)}]^{\frac{\alpha(T+1)}{\alpha(T)}}} \quad (T = 0, 1, 2, \ldots\ldots) \tag{7}$$

The deregulation rule for fatigue life of component at different parking time was set up in the formula (7).

The environment influence for the performance of fatigue critical component was only considered. After considering the condition of service, the formula (7) could be revised as followed:

$$N(T+1) = \frac{[N(T) - G(T)]}{[\frac{C(T)}{C(T+1)}]^{\frac{\alpha(T+1)}{\alpha(T)}}} \quad (T = 0, 1, 2, \ldots\ldots) \tag{8}$$

Where, G(T) is the flight frequency for every year.

Aiming at the current usgue situation of aircraft, the two-aparameter life prediction model could be set up based on the local environment and the test data, which considered the influence of environment for fatigue critical component.

3.2. The way of Detail Fatigue Rating

The Detail Fatigue Rating (DFR) is usually used to analyze the fatigue quality for detail component. It is the inherent fatigue performance and is the measurement for component quality and ability of enduring repeating load. That is to say, the Detail Fatigue Rating (DFR) is the max stress at the constant loads for R=0.06, the cycles are for 10^5 cycles, the confidence level is 0.95 and the

reliability ratio is 0.95 [11].

$$\sigma_{DFR} = \frac{\sigma_{m0}(1-R)}{0.94\frac{\sigma_{m0}}{\sigma_{\max}}X - 0.47(1+R)X + 0.53(1-R)} \tag{9}$$

Where, σ_{DFR} is the Detail Fatigue Rating; $\sigma_{m0} = 310$ MPa; R is the stress ratio; S is the pitch coefficient, $S = 2$; $X = S^{5-\lg N}$; N is the safe life $N_{95/95}$ for the confidence level 0.95 and the reliability ratio 0.95. If three parameters are known, then the other can be calculated among the other parameters.

First, the character life β for test data of every group should be calculated according to the Weibull distribution:

$$\beta = \left[\frac{1}{n}\sum_{i=1}^{n} N_i^{\alpha}\right]^{1/\alpha} \tag{10}$$

Where, $\alpha = 4$.

Then, the life should be calculated for the confidence level 0.95 and the reliability ratio 0.95:

$$N_{95/95} = \frac{\beta}{S_\tau S_R S_C} \tag{11}$$

Where, the specimen coefficient $S_\tau = 1$, the reliability coefficient $S_R = 2.1$ for the aluminium alloys, the confidence level coefficient S_C =1.175 for the confidence coefficient 0.95 and n=4.

4. Analysis and validation

4.1. The confirmation of model parameters

The standard S-N curve was fitted based on the test data from table 1 after accelerated environment test as Table 2 shown.

Table 2. S-N curve under different accelerated time

accelerated time /a	S-N curve	confidence level /%
4	$SN^{0.2796} = 8.2725\times10^3$	0.998
12	$SN^{0.296} = 9.7538\times10^3$	0.992
20	$SN^{0.2243} = 4.1727\times10^3$	0.986

The change rule of the shape parameters C and α was gained along with time according toTable 2, as the formula (12) shown.

$$\begin{cases} \alpha(T) = 0.238 + 0.01317\times T - 0.000695\times T^2 \\ C(\mathrm{T}) = 4883 + 1067.96\times \mathrm{T} - 55.175\times T^2 \end{cases} \tag{12}$$

The change rule of the shape parameters of S-N curve was established in the formula (12) for different parking calendar year. Therefore, the declining degree of S-N curve could be calculated at different parking time according to formula (12), and then the life of fatigue critical component could be reasonablly analysed and forecasted.

In the same way, the S-N curve was fitted according to the fatigue life of retired aircraft.

$$SN^{0.2698} = 6.1298 \times 10^3 \tag{13}$$

The specimen value of DFR was calculated based on the fatigue life corresponding with a group data from the table 1, the result was shown in Table 3.

Table 3. Detail Fatigue Rating/MPa

	Stress/MPa	Life/10,000 cycle		DFR/MPa
Accelerated 4a	310	12.004 11.860	15.187 13.580	214.1635
Accelerated 12a	310	11.613 12.454	12.616 13.286	210.8297
Accelerated 20a	310	12.280 10.654	12.642 11.802	209.8210
Retired specimen	320	7.025 5.969	5.501 7.906	187.5407

The DFR in Table 3 was fitted by the exponential form and the change rule of DFR along with the calendar year was gained.

$$\sigma_{DFR}(T) = 207.937 + 8.479 \times e^{-0.07477T} \tag{14}$$

4.2. The example

Accoding to the actual service condition, the fatigue life was only consumed about 10% when the aircraft was retired.

Aimed at the status of consumed life and combined the formula (8) with (12), the theoretical calendar life was calculated by the dynamic S-N curve as the shape parameters were same as the formula (13); The calendar life was calculated by using the DFR method according to the formula (14) as the DFR value was same as Table 3. Compared with the actual fatigue life of retired aircraft, the result was shown in Table 4.

Table 4. Comparison of theoretical value and actual calendar life

	Theoretical value /a	Actual calendar life /a	Error /%
Dynamic S-N curve method	23.17	25	-7.32
DFR method	26.009	25	4.04

The results gained from Table 4: the error was not large between the calendar life calculated by the two models and the actual life, the two models could be used to predict the rule of life deregulation for the fatigue critical component at the parking environment.

5. The result

(1) The accelerated environment test for the 2A12-T4 aluminum alloy is carried out. though comparing the fatigue life after environment test with the fatigue life of retired aircraft, the rule

of life deregulation for the fatigue critical component is analysed with the calendar parking time prolonging.

(2) According to the test results, the change rule that the shape parameter changed with the parking time is calculated by the dynamic S-N curve; the calculating model for deregulation rule of the fatigue life has been established for the fatigue critical component. The error between the predicted calendar life and the actual value is about 7.32%.

(3) The rule that the DFR changes with the parking time is gained and the error between the theoretical calendar life and the actual value is about 4.04%.

References

[1] Liu Wenting, Li Yuhai. Aircraft Component Calendar Life Evolution Technology. Beijing: Aeronautic Industry Press, 2004 (in Chinese).

[2] Zhang Dong. Accelerated Corrosive Test of the Aircraft Component Under Equivalent Environment Spectrum and the Computing Method for the Calendar Life[J]. ACTA AERONAUTICA ET ASTRONAUTICA SINCA, 2000，21(3): 196-201 (in Chinese).

[3] Yang Xiaohua, Yao Weixing, Chen Yueliang. Research calendar life of aircraft component considering the effects of calendar environment[J]. Chinese Journal of Applied Mechanics, 2002,19（3）：157-159 (in Chinese).

[4] Wang Bintuan, Yang Qingxiong. S-N Curves for LC4CS Aluminum Alloy and 30CrMnSiNi2A Steel Pre-corroded in Atmospheric Environment[J]. Journal of Mechanical Strength, 2000, 22 (3): 222-227 (in Chinese).

[5] Cui Changjing, Chen Qunzhi, Wang Yuya. Corrosive Behavior of LY12CZ Aluminum Alloy in a Laboratory Simulated Atmospheric Environment of One Airport[J]. Corrosive Science and Projection Technology, 2009, 21（3）: 291-294 (in Chinese).

[6] M.R.Sriaman, R.M.Pidapati. Life Prediction of Aircraft Aluminum Subjected to Pitting Corrosive under Fatigue Condition[J]. Journal of Aircraft，2009，46(4)：1253-1259.

[7] S.Ishihara, S.Saka, Z.Y.Nan et al. Prediction of corrosive fatigue lives of aluminium alloy on the basis of corrosive pit growth law[J]. Fatigue Fracture Engineering Materials Component，2006，29：472-480.

[8] Frederic Menan, Gilbert Henaff. Synergistic Action of Fatigue and Corrosive during Crack Growth in the 2024 Aluminium Alloy[J]. Procedia Engineering, 2010,2: 1441-1450.

[9] He Xiaofan, Liu Wenting, Jiang Dongbin. Method for Fatigue Test of Aircraft Components Considering Corrosive Influence. Journal of Beijing University of Aeronautics and Astronautics, 2003,1(29): 20-22 (in Chinese).

[10] Yang Xiao-hua, Yao Wei-xing, Chen Yue-liang. Research on Mechanical Properties of LY12CZ Aluminum Alloy under Calendar Corrosive Environment[J]. Journal of Mechanical Strength，2003，25（2）：227-228 (in Chinese).

[11] Wu Xueren. Handbook of aircraft structural metal material mechanics performance. Beijing: Aeronautic Industry Press, 1996.

Developing New Innovative Descaling and Corrosion Inhibiting Solutions to Protect Steel Equipment in the Oil and Gas Industry

Abdulghani A. Jaralla[1], Muhannad M. Al-Darbi[2,*]

[1] GLS Limited, 31 Malabar Crescent, Broomfield, Christchurch, New Zealand

[2] Department of Chemical and Biological Engineering, University of British Columbia
2360 East Mall, Vancouver, B.C. V6T 1Z3, Canada

* Corresponding author: aldarbi@interchange.ubc.ca

Abstract

Previous studies have shown that corrosion is very costly and has a major impact on the economies of industrial nations. It is estimated that the annual cost of corrosion worldwide is over 3% of the world's GDP. In the oil and gas industry alone, corrosion costs billions of dollars a year. For that, corrosion control and mitigation technologies are of great importance. It is also our duty to protect the environment, preserve resources, and protect our fellow human beings. Descaling and corrosion inhibiting methods are widely used in many industries, like in the oil and gas industry. It is very important for any industry to clean the fire tube boilers, heat exchangers, and before commissioning to clean the pipes. For the oil and gas industry, in particular, it is extremely important to acidize the wells while keeping the downhole pipe safe. In this study, a new highly effective industrial cleaning solution which is effective in descaling without causing corrosion was found which comprises a mixture of hydrochloric acid, hydrofluoric acid, one or more chelating agents, a surfactant, a copper complexing agent, and a nontoxic acridine orange inhibitor, which serves to block the anodic and cathodic sites on the steel surfaces of the process equipment.

Keywords Corrosion, Descaling Solution, Oil and Gas Industry, Inhibiting Solution, Steel

1. Background

Corrosion has a huge economic and environmental impact on virtually all facets of the world's infrastructure, from highways, bridges, and buildings to oil and gas, chemical processing, and water and wastewater systems [1].

Equipment used in power plants, chemical and petrochemical plants, paper mills, sugar mills, pipelines, air conditioners in large buildings, and many other industrial environments are subject to the formation of scale, either by circulating water or by process compounds. This includes all types of heat exchangers, boilers, vessels, piping and other equipment [2].

Precipitated solids reduce the heat transfer efficiency and oftentimes cause tube failure due to overheating which may result in plugging or fouling of the equipment [3]. To prevent interference with industrial processes, cleaning of the metal surfaces of the equipment employed therein is required. The water-formed precipitates are generally inorganic in nature, especially precipitates formed in hot closed systems, for example, in steam generators or heat exchangers [4]. Common deposits which are found

include iron oxides (magnetite and hematite), sulfides, alkaline earth carbonates, sulfates, and silicates [5].

Hydrochloric acid is widely used for the chemical cleaning of structural steel from which heat transfer and piping systems are fabricated. Hydrochloric acid forms soluble products which serve to dissolve calcium or magnesium carbonates [6]. Hydrochloric acid, does not, however, dissolve sulfates or silicates. Therefore, other chemicals must be mixed or incorporated with the hydrochloric acid. It is also well known that hydrochloric acid is highly corrosive [7]. In addition, if copper salts are present in the scale, they will dissolve and reprecipitate on iron surfaces causing severe localized corrosion [8].

It is an object of the present invention to provide a nontoxic, industrial descaling and cleaning composition which is effective in removing scales and oxides from the surfaces of the process equipment used in various industries while avoiding corrosion to the equipment.

2. Detailed description of the descaling and corrosion inhibiting Solution

The composition of the present invention includes as the non-toxic inhibitor from 40 to 200 parts per million, preferably from 60 to 100 parts per million (and most preferably 80 parts per million) of acridine orange. The chemical formula for acridine orange is: N,N,N'N'-tetramethyl-3,6 acridinediamine monohydrochloride. The use of this compound has been found to inhibit or block the anodic and cathodic sites in structural steel of the type that is commonly used in the fabrication of a variety of pieces of process equipment [9].

The benefits of using acridine orange (AO) are multifaceted and are as follows [10]:

1. AO has fast and direct protonation when added to acidic solutions. The protonation process is a charge transfer process, viz., flow independent.
2. The AO inhibitor molecules bind strongly to metal surfaces.
3. The free flat aromatic rings having a surface area of 38 A°, are bound in a plane which is parallel to the metal surface, such that the position of the positively charged hydrogen ring in AO is close to the predominant negatively charged electric layer on the metal surface.

The composition includes from about 5% to about 15%, by weight, hydrochloric acid, preferably from 5% to 10%, and most preferably 8% acid, which serves to remove most calcium, magnesium and iron oxides.

The composition also preferably includes 1% to 5%, by weight, preferably 1.5% of hydrofluoric acid, which aids in the removal of silicate containing scales [11]. The conjoint use of hydrochloric acid and hydrofluoric acid serves to accelerate the dissolution of many very hard and complex scale formations.

While various chelating agents can be employed in the composition and process of the present invention, such as EDTA, citric acid, HEDTA, etc., it has been found that a mixture of 2% citric acid and 2% EDTA is preferred since it is extremely effective in dissolving iron oxide deposits and also deposits containing copper oxides [12]. In point of fact, even sulfate-containing deposits will be dissolved when this mixture of chelating agents is employed.

The inclusion of from about 50 to about 200 parts per million (ppm), preferably 100 ppm of thiourea, will insure the maintenance of any dissolved copper in a soluble state. In the absence of such a copper complexing agent, copper oxides which are present in any scale, will dissolve and then plate out as metallic copper causing severe pitting of the industrial process equipment and the piping systems [13].

In addition, while it is optional, it has been found to be beneficial if the descaling composition includes about 0.1 grams/liter of a neutral emulsifying agent, such as alkyl benzene sulfonate to make it easier to penetrate in small cracks [14].

It has also been found that the benefits of the process of the present invention can best be achieved by employing a temperature of about 300 K or above for a period of about one (1) to about ten (10) hours, with eight (8) hours being preferred.

3. Procedure and Results

For a fuller understanding of the nature and objects of this invention, the following specific examples are given. These examples, however, are not to be construed as limiting the invention in any manner.

Example 1

A series of 5.0 cm x 2.5 cm mild steel specimens were prepared by cutting them from a single sheet of cold-rolled 1020 steel. The specimens were then polished under running tap water using a series of silicon carbide emery paper of 100, 400 and 600 grit, respectively, and then washed with distilled water and thereafter degreased with benzene and weighed on a Mettler AJ 100 electronic balance. One group of prepared steel specimens were fully immersed in 500 cc of a cleaning and descaling solution containing 8% hydrochloric acid, 1.5% hydrofluoric acid, 80 ppm of acridine orange, 2% citric acid, 2% EDTA, 0.1 g/1 of alkyl benzene sulfonate, and 100 ppm thiourea. This is referred to herein as the "inhibited solution".

Another group of steel specimens were also immersed in the foregoing cleaning and descaling solution except for the fact that the composition did not contain any acridine orange. This is referred to herein as the "uninhibited solution".

Potentiostatic polarization studies were carried out for both inhibited and uninhibited solutions under isothermal conditions at 303, 313, and 323 K and under controlled conditions of flow at 600, 1000, and 1400 rpm employing a potentiostat (Model 553-AMEL-Italy). The iron electrode was polarized from -900 mV to -100 mV (vs. saturated calomel electrode) at a sweep rate of 20 mV/min [15].

Another series of potentiostatic polarization studies were conducted for the heat transfer set of conditions, with a potential of -1000 mV being applied until a steady state heat flux was attained as indicated by the constant temperature reading from the thermocouples. Then the full polarization was carried out under isothermal conditions.

The duration of each of the weight loss experiments was eight (8) hours. At the conclusion of the test, the specimens were withdrawn, rinsed with water, then dried and reweighed. The percentage inhibitor efficiency (I%) was calculated by the following equation [16]:

$$I\% = W_u - \frac{W_I}{W_u} x100$$

Where: W_I is the weight of the inhibited sample, and W_u is the weight of the uninhibited sample.

Example 2

Performance of the Inhibitor (AO) under Controlled Conditions of Heat and Mass Transfer (Cathodic Region):

The effect of fluid flow, bulk temperature and heat transfer on the cathodic current density at a given cathodic potential of 0.1V below the corrosion potential are shown in Tables 1, 2, and 3 (Appendix I).

It can be seen from Tables 1, 2 and 3 that the cathodic current density values are independent of the flow rate, while the increase in temperature (bulk or interfacial) has a significant effect in stimulating the cathodic process [17]. This confirms the activation energy control of the cathodic reaction of hydrogen as the predominant reaction, as well as the lack of mass transfer effect on the adsorption processes of the inhibitor [18].

The increase in temperature (bulk or interfacial) has no significant effect on the inhibition efficiency, viz. the increase in temperature has no effect on the orientation of the adsorbed molecules or their geometry [19].

The high efficiency values are attributed to the ability of the inhibitor, acridine orange, to block the cathodic areas on the metal surface, leading to a significant reduction in hydrogen evolution [18].

Example 3

Acridine orange (AO) also showed high performance in blocking the anodic sites, as shown in the data presented in Tables 4, 5 and 6 (Appendix I). for both isothermal and heat transfer conditions [20].

The inhibition of the anodic sites (Tables 4-6) and cathodic sites (Tables 1-3) confirm the mixed effect of the inhibitor [15, 20].

The invention is not limited to the embodiments described above. The details involved in the description of these embodiments are for illustrative purposes only. Reasonable variations and modifications of this invention will be apparent to those skilled in the art without departing from the spirit and scope thereof.

4. Conclusion

What is claimed is:

1. A process for cleaning and inhibiting scale formation on the surfaces of process equipment which contacts circulating water and/or chemicals, which consists of: contacting the process equipment surfaces for a period of about 8 hours and at a temperature of about 300 °C and higher, which is effective to effect cleaning and/or scale inhibition with a aqueous composition consisting of:

a) About 8%, by weight, of hydrochloric acid.

b) About 1.5%, by weight, of hydrofluoric acid.

c) A chelating agent which is a mixture of about 2%, by weight, of EDTA and about 2%, by weight, of citric acid.

d) About 100 ppm of thiourea as a copper complexing agent.

e) About 40 to about 200 ppm of acridine orange.

f) Optionally a neutral emulsifying agent.

2. The process of claim 1, wherein the neutral emulsifying agent is present in the composition in an amount of 0.1 g/l.

Summary of the Invention

A highly effective industrial cleaning composition which is effective in descaling without causing corrosion has now been found which comprises a mixture of hydrochloric acid, hydrofluoric acid, one or more chelating agents, a surfactant, a copper complexing agent, and a nontoxic inhibitor, which serves to block the anodic and cathodic sites on the steel surfaces of the process equipment.

5. References

[1] Schmitt G., *et al*. (2009). Global Needs for Knowledge Dissemination, Research, and Development in Materials Deterioration and Corrosion Control. *World Corrosion Organization*. (http://www.corrosion.org/images_index/whitepaper.pdf).

[2] Li H., *et al*. (2011). Control of mineral scale deposition in cooling systems using secondary treated municipal wastewater. *Water Research* 45(2): 748–760.

[3] Vessakosol P., Charoensuk J. (2010). Numerical analysis of heat transfer and flow field around cross-flow heat exchanger tube with fouling. *Applied Thermal Engineering* 30(10): 1170–1178.

[4] Waly T. (2012). The role of inorganic ions in the calcium carbonate scaling of seawater reverse osmosis systems. *Desalination* 284: 279–287.

[5] Swietlika J. (2012). Corrosion in drinking water pipes: The importance of green rusts. *Water Research* 46(1): 1–10.

[6] Dolez P. I., Love B. J. (2002). Acid cleaning solutions for barnacle-covered surfaces. *International Journal of Adhesion and Adhesives* 22(4): 297–301.

[7] Wexler P. and Anderson B. (2005). *Encyclopedia of Toxicology* (2nd Edition): Hydrochloric Acid: 538–540 (by: Holstege C. P.). Academic Press, USA.

[8] Saremi M. and Yeganeh M. (2010). Corrosion behavior of copper thin films deposited by EB-PVD technique on thermally grown silicon dioxide and glass in hydrochloric acid media. *Materials Chemistry and Physics* 123(2–3): 456–462.

[9] Fink J. K. (2012). *Petroleum Engineer's Guide to Oil Field Chemicals and Fluids*: Chapter 6 Corrosion Inhibitors: 217–252. Elsevier, US.

[10] Sun L. *et al*. (2012). Graphene oxide adsorption enhanced by in situ reduction with sodium hydrosulfite to remove acridine orange from aqueous solution. *Journal of Hazardous Materials* 203: 101–110.

[11] Genuino H. C., *et al*. (2012). A review of hydrofluoric acid and its use in the car wash industry. *Journal of Industrial and Engineering Chemistry* 18(5): 1529–1539.

[12] Palma L. D. and Mecozzi R. (2007). Heavy metals mobilization from harbour sediments using EDTA and citric acid as chelating agents. *Journal of Hazardous Materials* 147(3): 768–775.

[13] Argañaraz M. B. Q., *et al*. (2010). Copper electrodeposition onto hydrogenated Si(1 1 1) surfaces: Influence of thiourea. *Journal of Electroanalytical Chemistry* 639 (1–2): 95–101.

[14] Song X-W., *et al*. (2012). Surface dilational rheological and lamella properties of branched alkyl benzene sulfonate solutions. *Colloids and Surfaces A: Physicochemical and Engineering Aspects* 412: 64–71.

[15] Al-Darbi M. M., *et al*. (2002). Protection of Mild Steel against Corrosion using Mixed Inhibitor Combinations. *NACE CORROSION-2002 Conference*. Denver, CO, USA. Paper No. 02013.

[16] Hegazy M.A. (2012). Evaluating four synthesized Schiff bases as corrosion inhibitors on the carbon steel in 1 M hydrochloric acid. Corrosion Science 65: 67–76.

[17] Parshin A. G., *et al*. (1982). The Influence of Heat Transfer on the Kinetics of Cathode Processes with Limiting Diffusion Stages. *Corrosion Science* 22(9): 845-855.

[18] Rozenfield I. L. (1981). *Corrosion Inhibitors*. New York: McGraw-Hill.

[19] Moccari A. A. (1999). Corrosion Inhibitor Evaluation for Materials used in Closed Cooling Water Systems. *Materials Performance* 38(9): 54-59.

[20] Singh P., *et al*. (2008). Adsorption and kinetic studies of L-leucine as an inhibitor on mild steel in acidic media. Applied Surface Science 254(18): 5927–5935.

6. Appendix I – Tables

TABLE 1

The Cathodic Current Density (mA/cm^2) for Uninhibited Chemical Cleaning Solution $\mathbf{I}_{c,u}$ and Inhibited Solution $\mathbf{I}_{c,I}$ and the Inhibition Efficiency **I%** under Isothermal Conditions. (Inhibitor Concentration 60 PPM)

	Temperature (K)								
	303			313			323		
RPM	$I_{c,u}$	$I_{c,I}$	I%	$I_{c,u}$	$I_{c,I}$	I%	$I_{c,u}$	$I_{c,I}$	I%
0	15	1.6	89	39	5.5	86	57	8.8	85
600	4.6	0.5	89	14	1.6	88.6	36	3.3	90.8
1000	4.6	0.46	90	14	1.6	88.6	34	3.0	91
1400	4.8	0.51	89.4	15	1.7	88.7	34	3.5	89.7

TABLE 2

The Cathodic Current Density (mA/cm^2) for Uninhibited Chemical Cleaning Solution under 60 kW/m^2 Heat Transfer Rate.
(The Interfacial Temperatures are Bracketed).

	Bulk Temperature (K)		
RPM	303	313	323
600	8 (322.7)	19 (330.5)	40 (339.9)
1000	7.3 (315.9)	17 (324.3)	39 (333.7)
1400	6.5 (312.3)	16 (321.6)	37 (331.4)

TABLE 3

The Cathodic Current Density $I_{c,I}$ (mA/cm^2) for Inhibited Chemical Cleaning Solution, under Heat Flux of 60 kW/m^2. I% is the Inhibitor Efficiency. Interfacial Temperature values are the same as in Table 2.

	Bulk Temperature (K)					
	303		313		323	
RPM	$I_{c,I}$	I%	$I_{c,I}$	I%	$I_{c,I}$	I%
600	0.65	92	2.3	88	4.2	89.5
1000	0.60	92	1.9	89	3.2	91.8
1400	0.58	91.1	1.7	89.4	2.8	92.4

TABLE 4

The anodic Current Density (mA/cm^2) for uninhibited Chemical Cleaning Solution $I_{a,u}$, Inhibited Solution $I_{a,I}$, and the Inhibitor Efficiency I% Under Isothermal Conditions.

	Temperature (K)								
	303			313			323		
RPM	$I_{a,u}$	$I_{a,I}$	I%	$I_{a,u}$	$I_{a,I}$	I%	$I_{a,u}$	$I_{a,I}$	I%
0	29	1.8	94	46	2.5	97	97	16	83.5
600	7	1.3	81	14	2.3	93.6	40	5.7	86
1000	6.8	1.3	81	15	2.0	86.7	36	4.8	87
1400	7.1	1.3	81.7	15	2.7	82	38	3.5	91

TABLE 5

The Anodic Current Density (mA/cm^2) for Uninhibited Chemical Cleaning Solution under 60 kW/m^2 Heat Transfer Rate (The Interfacial Temperatures are Bracketed).

	Bulk Temperature (K)		
RPM	303	313	323
600	13 (322.7)	23 (330.5)	63 (339.9)
1000	12 (315.9)	23 (324.3)	58 (333.7)
1400	11 (312.3)	20 (321.6)	48 (331.4)

TABLE 6

The Anodic Current Density $I_{a,I}$ (mA/cm^2) and the Inhibitor Efficiency I% for Inhibited Chemical Cleaning Solution, under 60 kW/m^2 Heat Transfer Rate.
(The Interfacial Temperature Values are the same as in Table 2)

	Bulk Temperature (K)					
	303		313		323	
RPM	$I_{a,I}$	I%	$I_{a,I}$	I%	$I_{a,I}$	I%
600	1.8	86	4.1	82	12	81
1000	1.6	87	3.7	84	7.8	87
1400	1.4	87	3.3	83	6.0	87

CRACK INITIATION: STRESS-CORROSION CRACK IN X-52 PIPELINE STEEL IN NEAR-NEUTRAL pH ENVIRONMENT

Mimoun Elboujdaini[1,*]; Bingyan Fang[2]; and Rrg Eadie[3]

1- CANMET Materials, Natural Resources Canada, 3303 - 33rd Street NW, Calgary, AB, Canada T2L 2A7

2- G.E. Oil & Gas PII Pipiline Solution, 4908 – 52nd Street SE, Calgary, AB, Canada, T2B-3R2

3- Dept. of Chemical and Materials Engineering, University of Alberta, Edmonton, Alberta, Canada, T6G 2G6

* {Corresponding author: **melboujd@nrcan.gc.ca**}

ABSTRACT

Specimens from a failure X-52 pipeline that had been in-service for 34 years were pitted using passivation/immersion method developed by the authors to simulate pitted pipelines observed in service. The resulting pitted samples were then cyclically loaded in near-neutral pH environment sparged with 5% CO_2 / balance N_2 gas mixture at high stress ratios (minimum stress/maximum stress), low strain rates and low frequencies which are close to those experienced in active flowing service. It was found that the majority of cracks initiated from the corrosion pits and were less than 0.5 to 0.6 mm deep, which were generally quite blunt. These cracks were transgranular in nature and designated as Stage I cracks and were typical of cracks found in most crack colonies. However, the further growth of these short blunt cracks was significantly influenced by the distribution of the nearby non-metallic inclusions. Inclusions enhanced the stress-facilitated dissolution crack growth, which is the crack growth method proposed by the authors in a related paper. When the orientation of the inclusions was at an acute angle to the orientation of the pits or cracks, and the inclusions were in the same plane as crack initiation or advance, these inclusions would enhance crack growth, or even trap hydrogen which further resulted in the formation of clusters of tiny cracks, which appeared to be caused by hydrogen. The hydrogen produced cracks could be eaten away later by the stress-facilitated further dissolution of the blunt cracks. If these cracks can grow sufficiently however they pose an integrity risk as they can initiate long cracks (near-neutral pH SCC). These hydrogen caused cracks in Stage I were rare. It was nevertheless suggested that cracks deeper than 0.5 to 0.6 mm in the field should be removed to reduce or avoid the threat of rupture. If active corrosion can be prevented such as by cathodic protection then smaller cracks are innocuous.

1. INTRODUCTION

Near-neutral pH stress corrosion cracking (NNpHSCC) has been a significant integrity issue for gas and oil pipelines for over two decades since it was first documented in 1985 [1], and it has been investigated extensively. More than 18,000 colonies of NNpH SCC had been reported on Canadian pipelines up to August 2000 [2], and more than 95% of these colonies became dormant. A small percentage, however, which might grow until failure if not detected and removed, would cause a considerable risk to pipeline integrity management. Pipeline failures have been reported to decrease recently, possibly because more rigorous pipeline integrity management programs have been in place. However, there still have been one or two ruptures a year in Canada since 1995 and numerous cracking discovered through ILI (in-line inspection) or hydrotesting. Although soil models and simulations have been developed to help assess risk [3], these are rather imprecise, and

can only predict the occurrence of minor SCC rather than significant SCC. The mechanisms for NNpHSCC are not yet understood, and further research in this area is needed.

Generally, the main part of pipeline life is consumed in the crack initiation process. Evidence from field failures suggests that corrosion pits might be a common site for crack initiation [3]. In laboratory investigation, it has been found that the earliest cracks appeared to initiate at corrosion pits [4-7] that formed around non-metallic inclusions and later cracks grew from corrosion pits that formed randomly on the surface [8-11], and some cracks induced by corrosion pits were related to stress cells caused by the difference of residual stress level over a much large area [12]. These pits may act as stress raisers to initiate cracks. Cracks can also be nucleated around other types of pits associated with metallurgical discontinuities. Wang *et. al.[13]* indicated that some corrosion pits can be formed preferentially along the heavily deformed metal in scratches on the surface. It was also reported that preferential corrosion occurs at the boundaries of pearlite colonies, and transgranular crack-like features can grow from such surface attack [14]. So NNpHSCC most commonly originates from corrosion pits.

For pipelines in the field, it generally takes years for pits to grow and initiate cracks, and the pit growth may proceed under intermittent exposure conditions. Thus, it would be difficult to study NNpHSCC processes under the conditions close to those in the field. So an accelerating technique to generate pits was employed in this study, the details of which have been reported in another paper [15]. Basically it consists of an acid-immersion treatment to passivate the surface and then a second immersion in dilute hydrochloric acid, which leads to rapid pitting growth at sites where the passive layer is either removed with a needle or at innate weaknesses in the film where pits grow spontaneously.

After the transition from pits to cracks has occurred in the field, tiny, elongated blunt cracks, frequently in crack colonies, are often seen in very large numbers [16]. The vast majority of these small cracks are found to become dormant and hence tend to be innocuous. However, if the small cracks can surpass a threshold depth, around 0.5 to 0.6 mm [17], these cracks can be activated and begin to propagate and may eventually lead to pipeline rupture if not detected and removed. So studies concerning the growth of these small cracks and how potential growth can be identified and avoided will contribute significantly to an understanding of NNpHSCC initiation and help in pipeline integrity management.

2. EXPERIMENTAL

2.1. SPECIMENTS

X-52 line pipe steel from Enbridge Pipelines Inc. that had exhibited NNpHSCC crack colonies after thirty-four years of service was used in this project. The pipe was 34” (864 mm) in external diameter and 7.9 mm in measured wall thickness. The chemical composition can be seen in Table 1. The microstructure consisted of pearlite and ferrite. It was found that there were very few, if any, inclusions on the axial transverse (A-T) surface, while there were a lot of inclusions on the radial transverse (R-T) and the axial radial (A-R) surfaces [18]. In addition, the inclusions on the R-T surface were relatively smaller than those on the A-R surface. These non-metallic inclusions (MnS) were more abundant on the axial-radial section at mid-wall [18]. Hence, it was likely that the inclusions were elongated along the axial direction during the rolling processes.

Table 1. Chemical composition of X-52 pipeline steel (wt. %)

Elements	**X-52**	**Elements**	**X-52**
C (Carbon)	0.261	Cr (Chromium)	0.027
Mn (Manganese)	1.150	Mo (Molybdenum)	0.013
P (Phosphorus)	0.008	Al (Aluminum)	0.002
S (Sulfur)	0.019	V (Vanadium)	0.003
Si (Silicon)	0.036	Nb (Niobium)	0.003
Cu (Copper)	0.033	Ti (Titanium)	0.002
Sn (Tin)	0.002	Co (Cobalt)	0.006
Ni (Nickel)	0.032	Fe (Iron)	Balance

Dog-bone specimens with dimension of 36×7×3.5 mm in reduced section were machined from pipe with the length of the specimens along the transverse direction of the pipe so that the crack-advance plane (radial-axial) was the same as for NNpHSCC in the field (see Figure 1 for a schematic of the orientations). After the sample surfaces had been ground to 1200 grit in accordance with the standard metallographic procedure, they were degreased and cleaned using acetone and ethanol.

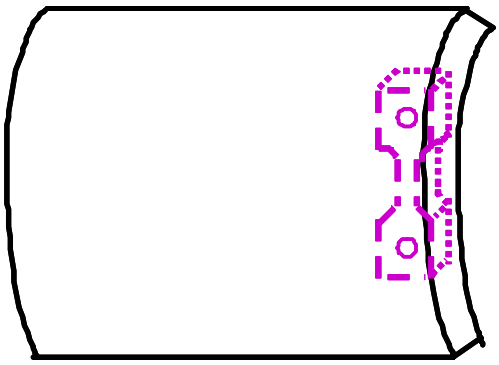

Figure 1. Schematic of the sample with orientations in the pipe.

2.2. PITTING THE SURFACES

After the surfaces were masked using PTFE tape leaving the gauge section exposed, the samples were put in concentrated H_2SO_4 solution to passivate the surfaces and then exposed to dilute HCl solution (the ratio of HCl to distilled water was 1:10) to grow pits, as reported by *Fang et al. [15]*. After 135 hours, the pitted samples were taken out and washed using tap water. Then they were cleaned using EDTA and then ethanol in an ultrasonic cleaner to ensure that the passive films on the surfaces had been almost removed.

2.3. SCC TESTS

The pitted specimens were cyclically loaded under a balanced triangular waveform as shown in Table 2 in a soil solution (ratio of soil to water is 1:5) and a NNpH inorganic test solution identified as C2 solution, both sparged with 5% CO_2 /balance N_2 gas mixture. C2 solution is made with the following ingredients 0.0274 g/L $MgSO_4 \bullet 7H_2O$, 0.0255 g/L $CaCl_2$, 0.0035 g/L KCl, 0.0195 g/L $NaHCO_3$, and 0.0606 g/L $CaCO_3$ dissolved in high purity water. The pH after sparging was close to 6.2 for the C2 solution and near 7.0 in the soil solution.

Table 2 Loading Conditions in NNpH Solutions (All were sparged with 5% CO_2)

Condition	Peak Stress	Stress ratio	Frequency	No. of cycles
A	100% SMYS	0.8	1×10^{-4} Hz	1,345
B-1	100% SMYS	0.63	7.6×10^{-5} Hz	1,394
B-2	106% SMYS	0.63	7.6×10^{-5} Hz	1,394

After testing in the solution for the desired number of cycles, the tests were stopped and the samples were taken out. After cleaning using EDTA and ethanol in the ultrasonic cleaner, the samples were rinsed and dried with warm air and the sample surface observations were made using optical microscopy (OM) and scanning electron microscope (SEM). Thereafter, the sample surfaces were sectioned step by step to examine crack and pit depths, and crack and pit shapes. The sectioning was perpendicular to the cracked and pitted surfaces, and the sectioning progressed perpendicular to the loading direction. After each grinding and polishing step, measurements were made using OM and SEM to reveal the crack and pit dimensions.

3. RESULTS AND DISCUSSION

3.1. BLUNT CRACK INITIATION AND CRACKS DISTRIBUTION

When pitted specimens were cyclically loaded in NNpH solutions, many blunt cracks were seen to initiate from the bottom of the pits (Figure 2). These pits acted as stress concentrators (micro-notches) and were the principal sites for crack initiation. The pits would locally raise the stresses near the pits. Thus, plastic deformation would occur locally, and there would be plastic zones near the corrosion pits. The iron atoms in the plastically deformed zones would have enhanced energy because of the increased dislocation density and increased stress, and would behave as anodes in the solutions relative to the less deformed and lower stressed nearby regions. Thus, stress cells would form leading to localized corrosion. So a preferential electrochemical attack occurred in the regions where plastic deformation was localized. Thus, dissolution in the plastic zones around the corrosion pits was accelerated. This, in turn, would further enhance the stress concentrations so that each cycle would create more deformed material to be removed by further corrosion. In the end, blunt cracks were initiated. These cracks were very wide, especially at the crack mouth, as shown in Figure 2. Hence, they were designated as blunt cracks or Stage I cracks. At the same time, in contrast to the fatigue cracks in air, the crack advance direction was perpendicular to the applied load direction.

After cyclic loading in NNpH environment, it was clearly seen that most of cracks were distributed between 50 and 450 μm in depth, as shown in Figure 3a, and the most probable crack depth was around 150 to 250 μm. Figure 3b shows that the median of crack depth was at 221 μm, and the lower and upper box values (quartiles) were 156 and 351 μm, respectively. The whisker was from 61 to 633 μm with a few outliers shown with asterisks. All the evidence once again reflected that the majority of crack depths were below approximately 0.5 to 0.6mm, consistent with the field observations.

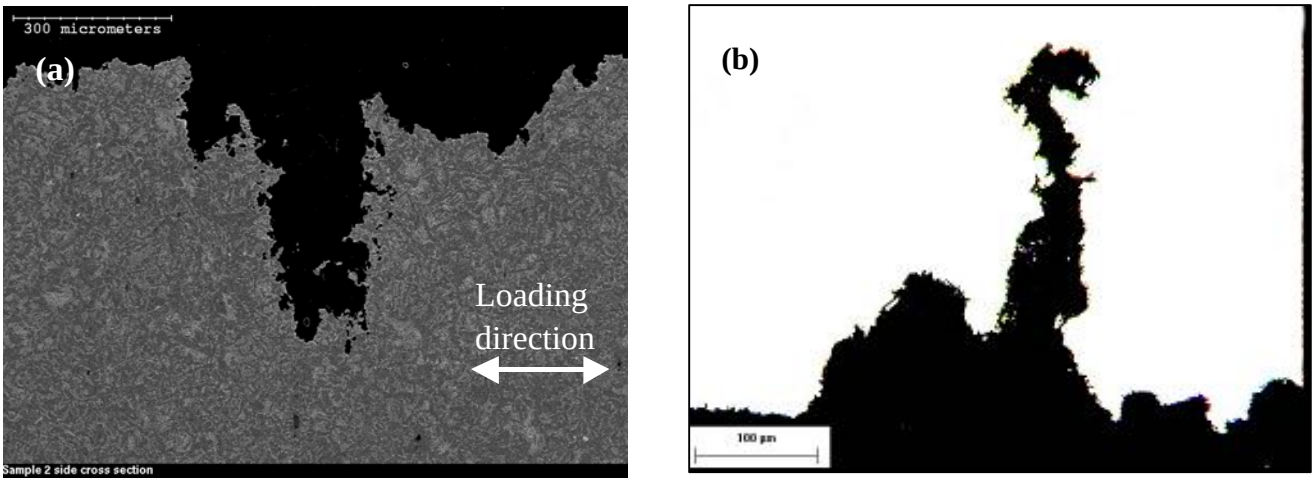

Figure 2. Photomicrographs of NNpHSCC crack cross-section features on the R-T surface cycled in NNpH solution sparged with 5% CO_2/ balance N_2 gas mixture (a) in soil solution under load condition A [19]; (b) in C2 solution under load condition A [20].

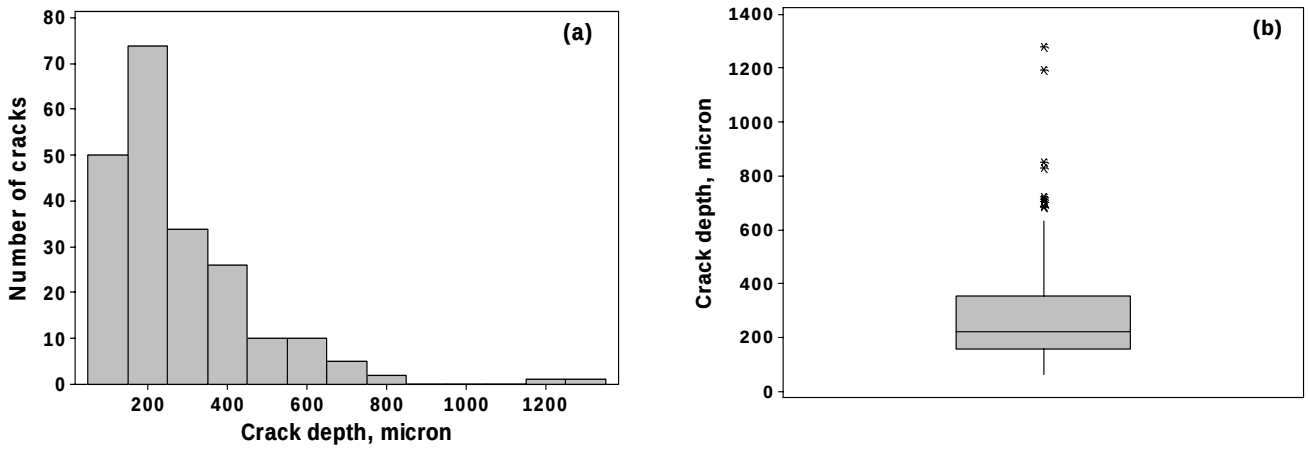

Figure 3. Distribution of crack depth on the sample cyclically loaded at condition B1 in C2 solution; (a) number of cracks versus crack depth; (b) box plot of crack depth.

3.2. BLUNT CRACK GROWTH

After blunt cracks had initiated, they might grow under benign conditions. However, the majority of the cracks would not grow to the critical depth size of 0.5 to 0.6 mm. Once the blunt crack growth rate was higher than the pit growth rate, the stress facilitated corrosion dissolution rate would be dominant and thus, dissolution would be localized and localized corrosion around the corrosion pits would be accelerated and blunt cracks would grow. In the end, dissolution formed blunt crack would survive and might grow under intermittent conditions.

It was sometimes seen that non-metallic inclusions (mainly MnS as revealed by EDS) were located ahead of the cracks on the crack advancement plane, as shown in Figure 4. When the blunt cracks grew and reached these non-metallic inclusions, the solution in the blunt crack enclaves could get to these inclusions and electrochemically react with the inclusions [5-11]. The inclusions would then

be corroded and eaten away since the non-metallic inclusions (MnS) acted as an anode and the base steel nearby acted a cathode. The relative area ratio of the base steel to the non-metallic inclusion was huge, thus, galvanic corrosion would be accelerated and corrosion attack would be localized on the inclusions, which, in return, increased stress concentrations and plastic deformation. Thus, blunt crack growth because of inclusions enhancing stress facilitated dissolution would be maintained, as reported previously [18]. When the inclusions were completely eaten away, the blunt crack would advance as stress facilitated dissolution reported previous. In addition, at this time, the stress concentration would be much higher, which might further enhance the stress riser and plastic deformation. All of these, in turn, would contribute to the blunt crack growth.

Still in Figure 4, there were few non-metallic inclusions ahead of the blunt crack tip and these aligned inclusions could contribute to significant crack growth.

Considering the microstructure differences on the different surfaces as reported in a previous paper [18], the nonmetallic inclusions were elongated along the longitudinal direction, and some inclusions were about 0.5 mm long, which would have facilitated pit nucleation, if the R-T surface was exposed to the NNpH solution, and promoted pit-to-crack transition and blunt crack growth. As the crack growth direction in depth was the same as the elongated inclusions, the latter would also have assisted crack growth, as clearly shown in Figure 5. So it was seen that the blunt cracks had grown easily when they encountered non-metallic inclusions.

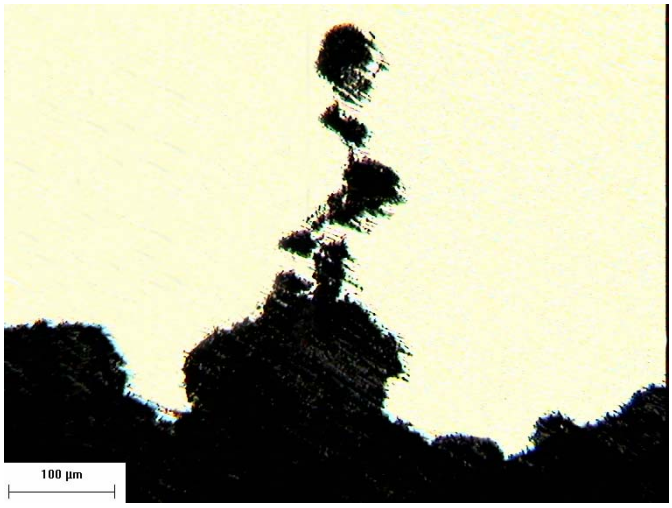

Figure 4. Photograph of a crack initiation from a corrosion pit and non-metallic inclusions located ahead of the crack tip.

(a)

Figure 5. Photographs of; (a) Stage I crack emanating from a corrosion pit and blunt crack growth associated with inclusions for the sample in NNpH environment under Condition

3.3. ORIENTATION OF INCLUSIONS AND BLUNT CRACKS

As discussed in previous section, non-metallic inclusions significantly influenced blunt crack growth. However, how they affected blunt crack growth would need to be addressed further, especially the orientation of inclusions with regard to blunt cracks.

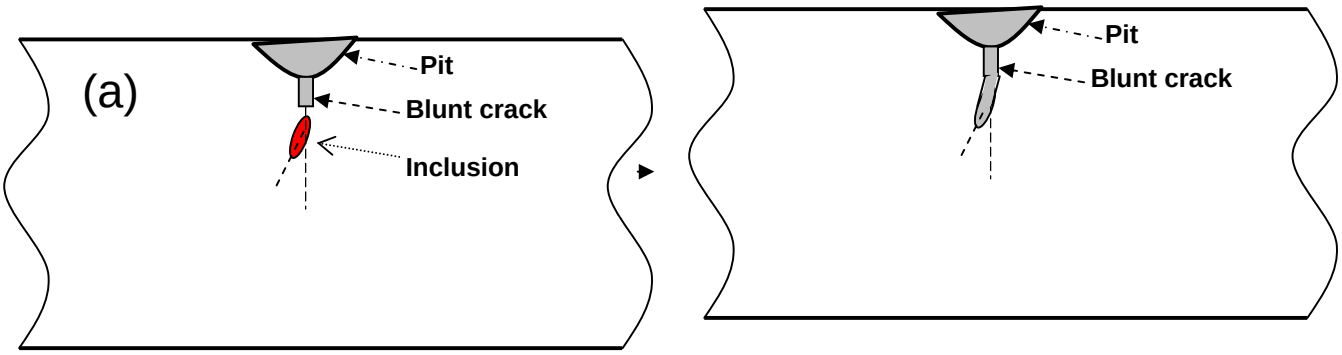

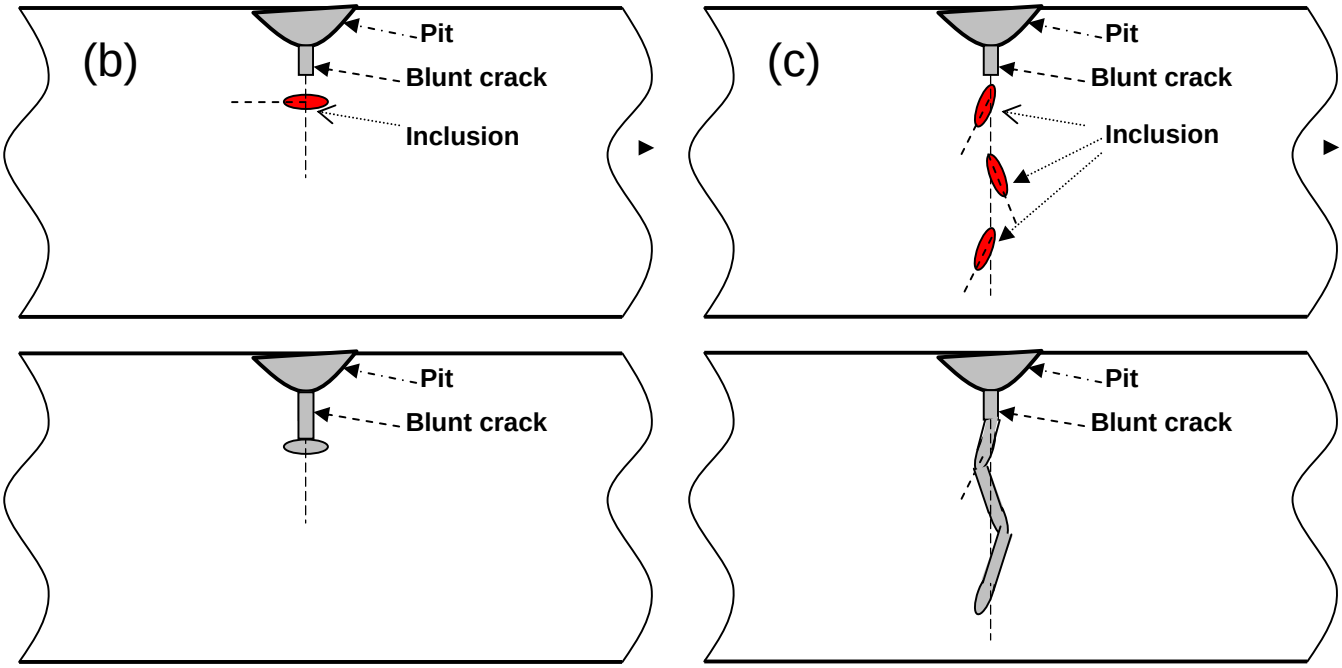

Figure 6. Schematic illustration on orientation of inclusions and blunt cracks.

When the inclusions were in the same plane as crack initiation and growth, generally, there were three types of the orientation of inclusions and blunt cracks, as shown in Figure 6.

1. The orientation of the inclusions was at a small acute angle to the orientation of the pit growth direction or blunt cracks (Figure 6a). The pits or blunt cracks would grow and encounter the inclusions, after which the blunt crack growth would be localized along the inclusions until the inclusions were eaten away completely due to accelerated galvanic corrosion. Thereafter, blunt cracks might keep growing, depending on driving forces (stress concentrations and stress intensity factors) and local environment at the crack tip.

2. The orientation of the inclusions was approximately perpendicular to the pit growth direction or blunt cracks, as shown in Figure 6b. In this case, the blunt cracks might grow and touch the inclusions under appropriate conditions. Also once the blunt cracks encountered the inclusions, the dissolution and growth would be localized on the inclusions. However, since the inclusions were approximately perpendicular to the blunt cracks, when the inclusions were corroded completely, the blunt crack tips would become much blunter, which therefore reduced stress concentrations and stress intensity factors, and hence lowered the crack growth driving forces. Thus, the cracks might stop growing and became dormant. This type of crack was also observed in this report, as shown in Figure 7 where a balloon-like morphology was seen. The cracks observed in this case might not threaten pipeline integrity from a management point of view.

3. A bunch of inclusions were aligned with the blunt cracks at small acute angles, as presented in Figure 6c. This case could be considered as repeated steps of the case 1. When the first inclusion was eaten away, the blunt crack growth might slow down and grow under intermittent conditions. However, once this blunt crack grew to the second inclusion, the latter would be dissolved by

accelerated galvanic corrosion. Thereafter, the accelerated growth and slow growth might be repeated again and again until a critical depth was exceeded when Stage II (sharp) cracks would have initiated and grew [20]. This case was also seen in this project, as shown in Figures 4 and 5, where the blunt cracks grew along the inclusions.

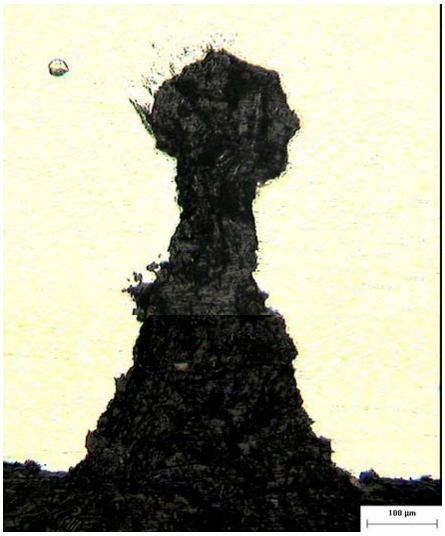

Figure 7. Photograph of a blunt crack and the blunt crack tip on R-T surface for a specimen cyclically loaded in C2 solution under condition B-1.

Since inclusions were elongated in the longitudinal direction, especially in the mid-wall, the crack growth in the longitudinal direction would be significantly influenced by the coalescence with inclusions. These cracks, if not detected and removed, might put a pipeline at a risk to cracking or failure. The case in Figure 6c was much more dangerous for pipeline integrity management. It would be helpful and important if some tools could be employed to monitor the existence of this type of crack and inclusion, and some measures could be taken to prevent the cracks from growing.

3.4. HYDROGEN EFFECT

In near-neutral pH environment, the metal in the crack tip is dissolved, assisted by stress concentration associated galvanic corrosion cells. Some of the generated hydrogen atoms outside the blunt crack enclaves, *i.e.*, specimen surfaces, and the crack walls by water reduction could entre and diffuse into the steel. The lattice (interstitial) hydrogen solubility was elevated ahead of stressed blunt cracks or pits, and these sites could accumulate higher hydrogen concentrations. The same hydrostatic stresses that increased the hydrogen solubility in the lattice also enhanced the amounts of hydrogen trapped in deep traps, such as large defects (inclusions and phase boundaries) ahead of the crack tips. When some nearby non-metallic inclusions ahead of the crack tips that were perpendicular to the applied stress had the orientation of a small acute angle to the orientation of the pits or the blunt cracks, and the nearby non-metallic inclusions ahead of the blunt cracks or pits were on the same plane as the pits or the cracks, the trapped hydrogen on these nearby non-metallic inclusions might weaken the bond strength. The interactions between the trapped hydrogen and the inclusions might occur at some regions on the inclusions in advance of the crack tips where the stress and / or strain conditions were particularly appropriate for the nucleation of clusters of tiny cracks, as

shown in Figure 8. The elongated inclusions not only influenced pit nucleation and pit growth [18], but also affected pit-to-crack

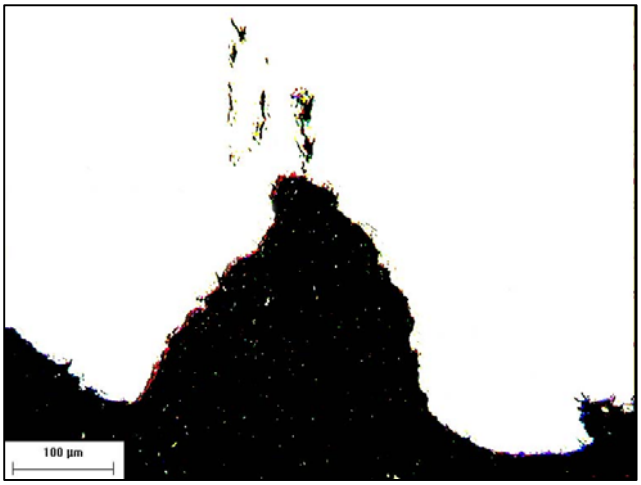

Figure 8. Tiny cracks in the inclusion ahead of the blunt crack.

transition and crack propagation, if the elongated inclusions were parallel to crack growth direction. However, if the inclusions were almost hemispherical, they would only affect the pit formation and growth, even tiny hydrogen induced cracks but these were very rare. If input fugacity of hydrogen was high enough, recombination at internal sites such as non-metallic inclusions would be prevailing, causing blistering or cracking (hydrogen-induced cracking), but this case could not happen in near-neutral pH condition. The hydrogen that diffused into the steel could also be trapped on some phase interfaces ahead of the blunt cracks, such as Figure 9, and caused tiny hydrogen related cracks to initiate. These hydrogen trapped phase interfaces were also perpendicular to the external stress applied. These hydrogen induced cracks were also rare, but they contributed to the blunt crack growth.

Under appropriate conditions, the blunt cracks or pits would continue to grow and link to the nucleated hydrogen induced tiny cracks. In the end, these hydrogen produced clusters of tiny cracks would have been eaten away by the further growth of the mother blunt cracks or pits by further strain deformation facilitated dissolution. Therefore, the overall apparent crack growth process seemed that there was only stress assisted dissolution growth, engendered by galvanic stress corrosion cells, which concealed hydrogen related tiny crack initiation, although the latter was rare and only could occur under very stringent conditions.

It could be considered that the blunt crack growth was associated with the bursts of dissolution of aligned non-metallic inclusions with the same orientation as the blunt cracks, and rare hydrogen induced tiny cracks while the rate-controlling periods seemed “non-propagation” which were concerned with the stress facilitated dissolution to form blunt cracks again that established the conditions for further crack bursts, probably because of dissolution of further non-metallic inclusions or even more rare hydrogen caused clusters of tiny cracks, or severe stress facilitated dissolution with higher stress concentrations. The crucial role of stress or strain was continued, resulting in much further dissolution, and when the total blunt cracks reached a critical size, approximately around 0.5 to 0.6 mm deep, the stress integrity factors could be sufficient, and the plastic zones ahead of the blunt

cracks tips were large enough to trap more hydrogen, leading to hydrogen related growth. At this time, the crack shape became sharp [18], and was significantly different from Stage I cracks. Thus, the cracks in this period were named Stage II cracks. Stage II cracks would grow intermittently, and in the end, they could surpass the critical threshold for long cracks, after which the cracks would grow in a typical corrosion fatigue model. This implied that for pipeline steel in near-neutral pH environment, these different mechanisms of stress corrosion cracking could have occurred within a continuous spectrum, with a gradual transition from one to another as the dominance of corrosive processes was replaced by stress or strain, led readily to the notion that steel microstructure, electrochemistry and stress or strain might interact in a variety of ways, and that the transformation from one mechanism to another might result from complex relation between stress risers, dissolution driven by stress concentrations, inclusions, and trapped hydrogen.

This is the first time that different crack types and mechanisms have been observed and reproduced in the laboratory. These different mechanisms are necessary for NNpHSCC crack initiation and early growth. These are quite consistent with the observations in the field. The sharp cracks in Stage II can create a significant risk to pipeline integrity. If they can't be detected and removed, they will likely keep growing and eventually once the long crack corrosion fatigue threshold is exceeded, cracks will grow much faster, even leading to pipeline rupture or leakage. Compared to the long crack growth stage, the blunt crack growth in Stage I and the sharp crack growth in Stage II consume a majority of pipeline life. So Stages I and II cracks are very important for pipeline integrity management and should be addressed intensively. Unfortunately, so far no research has touched Stage I blunt cracks and little has paid attention to Stage II sharp cracks, while most has focused on long crack growth.

For in-service pipelines, removing Stage II cracks that are deeper than 0.5 to 0.6 mm would benefit the pipeline integrity and enhance the remaining life. If Stage I crack growth can be impaired, that would significantly extend the remaining life. If active corrosion can be prevented such as by cathodic protection then smaller cracks are innocuous.

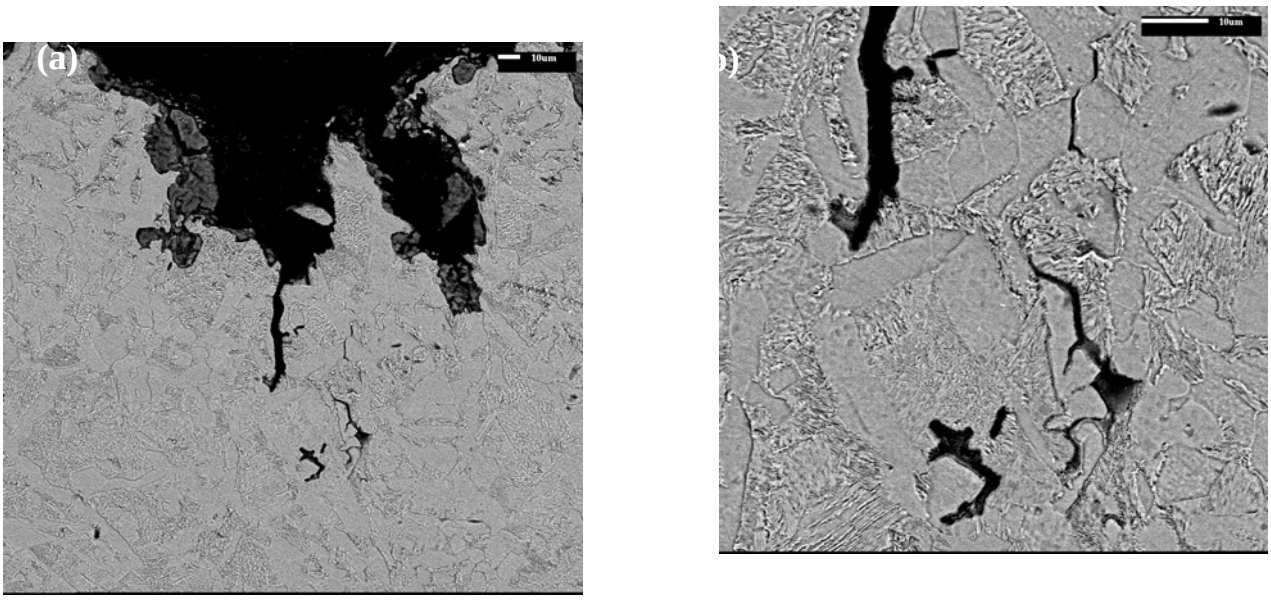

Figure 9. Tiny hydrogen produced cracks along the phase boundary between pearlite and ferrite ahead of the main crack.

4. CONCLUSIONS

Based on the results and discussion above, the following conclusions were made.

1. Blunt cracks were seen to have initiated from the corrosion pits on the pitted samples cyclically loaded in near-neutral pH environment and these blunt cracks were generally less than 0.5 to 0.6 mm deep, consistent with the observations from the field. These blunt cracks were transgranular and believed not to put pipelines at a risk from integrity management point of view.
2. The distribution of the nearby non-metallic inclusions significantly influenced the blunt crack growth by enhancing the stress-facilitated dissolution of the blunt cracks.
3. The orientation of the nearby non-metallic inclusions with regard to the blunt cracks was crucial for the blunt cracks to continue growing or keep dormant. Only when the orientation of the nearby inclusions was at a small acute angle to that of the pits or cracks, and the inclusions were in the same plane as crack initiation or extension, these inclusions would contribute to further crack growth. Thereafter, the inclusions would be eaten away by further growth of the blunt cracks.
4. When the inclusions were approximately perpendicular to the blunt crack growth, the cracks would become blunter and dormant.
5. The hydrogen trapped in the nearby inclusions and phase interface would cause clusters of tiny cracks to form, which appeared to be produced by hydrogen. These hydrogen generated cracks could be eaten away later by the stress-facilitated further dissolution of the blunt cracks.
6. When the blunt cracks reached a critical size, *i.e.*, 0.5 to 0.6 mm deep, sharp cracks would be formed, engendered by hydrogen.
7. Different mechanisms could occur in pipeline steel in near-neutral pH environment. The transformation from one mechanism to another might result from complex relation between stress risers, dissolution driven by stress concentrations, inclusions, and trapped hydrogen

ACKNOWLEDGMENTS

The authors would like to acknowledge an NSERC Strategic Grant and Enbridge Pipelines Inc. for financial support, and an NSERC/AUAF facility access grant at CANMET Materials Technology Laboratory. The authors thank Scott Ironside of Enbridge for the experimental pipeline material. One of the authors also acknowledges helpful discussions with Dr. Roger Staehle.

REFERENCES

1. NEB. Stress Corrosion Cracking on Canadian Oil and Gas Pipelines. Report of the Inquiry, National Energy Board. MH-2-95. December 1996.
2. CEPA, *CEPA* Stress Corrosion Cracking Database: Second Trending Report, August 17, 2000
3. Michael Baker Jr., Inc., Stress Corrosion Cracking Study, TTO Number 8, Integrity Management Program Delivery Order DTRS56-020D-70036, Final Report, January 2005.
4. B. Fang, R.L. Eadie, W. Chen, M. Elboujdaini, “Electrochemical Method Pits Generation and Its Application in Crack Initiation in Pipeline Steel in Near-Neutral pH Environment”, NACE International

Northern Area Western Conference "Gateway to the Oil Sands", Edmonton, Alberta, Canada, Feb. 11-14 2008.
5. B. Fang, E.-H. Han, J. Wang, W. Ke, "Mechanical and Environmental Influences on Stress Corrosion Cracking of an X-70 Pipeline Steel in Dilute Near-Neutral pH Solutions", Corrosion 63(2007), 419-432.
6. B. Fang, E-H Han, J.Q. Wang, W. Ke, "Influence of Strain Rate on Near-Neutral pH Environmentally Assisted Cracking of Pipeline Steels", Acta Metallurgica Sinica, 41 (2005), 1174-1182.
7. B. Fang, E. H. Han, J.Q. Wang, W. Ke, "Stress Corrosion Cracking of X-70 Pipeline Steel in Near-Neutral pH Solution Subjected to Constant Load and Cyclic Load Testing", Corrosion Engineering, Science and Technology, 42 (2), 123-129 (2007).
8. Y.Z. Wang, R.W. Revie, M.R. Shehata, R.N. Parkins, and K. Krist., "Initiation of Environment Induced Cracking in Pipeline Steel: Microstructural Correlations", in Proceedings of International Pipeline Conference/1998, Vol. 1, Calgary, Canada, ASTM 1998, pp.529-542.
9. M. Elboujdaini, Y.Z. Wang, and R.W. Revie, "Initiation of Stress Corrosion Cracking on X-65 Linepipe Steels in Near-Neutral pH Environment", in Proceedings of International Pipeline Conference/2000, Vol.2, Calgary, Canada, ASTM, 2000, pp.967-978.
10. M. Elboujdaini, Y.Z. Wang, R.W. Revie, R.N. Parkins, and M.T. Shehata, "Stress Corrosion Crack Initiation Processes: Pitting and Microcrack Coalescence", Corrosion/2000, (Houston, TX: NACE International), 2000, Paper No.00379.
11. Y.Z. Wang, R.W. Revie, R.N. Parkins, "Mechanistic aspects of stress corrosion crack initiation and early propagation", Corrosion/99, (Houston, TX: NACE International), 1999, Paper No.143.
12. G. Van Boven, W. Chen, R. Rogge and R. L. Sutherby, "The Effect of Residual Stress on Pitting and Stress Corrosion Cracking of High Pressure Natural Gas Pipelines", Acta mater., **55**, pp. 29-43 (2007).
13. S. H. Wang, W. Chen, T. Jack, F. King, R. R. Fessler, and K. Krist, "Role of Prior Cyclic Loading in the Initiation of Stress-Corrosion Cracks in Pipeline Steels Exposed to Near-Neutral pH Environment", in 2000 IPC, p.1005-1009.
14. R. Chu, W. Chen, S. H. Wang, F. King, and R. R. Fessler, "Microstructure Dependence of Stress Corrosion Cracking Initiation in X-65 Pipeline Steel Exposed to a Near-Neutral pH Soil Environment", Corrosion, 60, p.275-283.
15. B. Fang, R. Eadie, M. Elboujdaini, and W. Chen, , "Passivation/Immersion Method to Grow Pits in Pipeline Steel and a Study of Pit Nucleation and Growth Resulting from the Method", Corrosion Engineering, Science and Technology, 44(1), p.32-42 (2009).
16. W. Chen, F. King, and E. Vokes, Characteristics of Near-Neutral pH Stress Corrosion Cracks in an X-65 Pipeline, Corrosion, **58**, pp. 267-275 (2002).
17. W. Bouaeshi, S. Ironside, and R. Eadie, "Research and Cracking Implications from an Assessment of Two Variants of Near-Neutral pH Crack Colonies in Liquid Pipelines", Corrosion, **63**(7), pp 648-660 (2007)
18. B. Fang, R. Eadie, M. Elboujdaini, W. Chen, and E-H Han, "The Effect of Microstructure on Pit-To-Crack Transition and Crack Growth in an X-52 Pipeline Steel in Near-Neutral pH Environment", International Pipeline Conference, IPC 2008-64112, Calgary, Alberta, Canada, Sep. 29-Oct. 3, 2008.
19. B. Fang, R.L. Eadie, M. Elboujdaini, and W. Chen, "Pit-To-Crack Transition in an X-52 Pipeline Steel in Near-Neutral pH Environment: I. Formation of Blunt Cracks from Pits under Cyclic Loading", Corrosion Engineering, Science and Technology, in print.
20. B. Fang, R.L. Eadie, M. Elboujdaini, and W. Chen, "Transition from Pits to Cracks in Pipeline Steel in Near-Neutral pH Solution", Paper No. ICF2009-290, 12th International Conference on Fracture, July 12-17, 2009, Ottawa, Ontario, Canada.

Recent developments in brittle and quasi-brittle failure assessment of graphite by means of SED approach

Filippo Berto[1,*], **Paolo Lazzarin**[1], **M.R. Ayatollahi**[2]

[1]Department of Management and Engineering, University of Padua, Stradella San Nicola 3 , 36100, Vicenza, Italy
[2]Fatigue and Fracture Research Laboratory, Center of Excellence in Experimental Solid Mechanics and Dynamics, School of Mechanical Engineering, Iran University of Science and Technology, Narmak 16846, Tehran, Iran.
* Corresponding author: berto@gest.unipd.it

Abstract
Brittle fracture of isostatic graphite is studied experimentally and theoretically using plates containing key-hole notches subjected to different degrees of loading mixity. The main purpose of this paper is twofold. First, to provide a new set of experimental results on fracture of notched graphite samples, with different values of loading mixity and notch radii, which may be helpful for researchers because enlarges the very scarce available data; and second, to provide a fracture criterion for polycrystalline graphite under the above mentioned conditions. The averaged value of the strain energy density over a well-defined volume is used to predict the static strength of the considered specimens. Good agreement is found between the experimental data for the critical loads to failure and the theoretical predictions based on the constancy of the mean strain energy density over the material volume. Some preliminary tests from compression tests on the same material are summarized in the paper as well.

Keywords Brittle failure, Notches, Strain Energy Density (SED)

1. Introduction

Several researchers have studied in the past fracture resistance of polycrystalline graphite either under mode I (crack opening) or under mixed mode I/II (crack opening-sliding) loading conditions. For example, Awaji and Sato [1] were among the earliest researchers who used the cracked Brazilian disk (CBD) specimen to study mixed mode I/II fracture toughness of two polycrystalline graphite materials experimentally. CBD is a test specimen of circular shape in which a centre crack is generated in order to measure fracture toughness of brittle materials. Yamauchi et al. [2, 3] also made use of disk type specimens (i.e. CBD specimen and semi circular bend (SCB) specimen subjected to three point bend loading) and investigated the mixed mode I/II fracture toughness of graphite. Other test specimens have also been used for exploring the fracture behavior of polycrystalline graphite materials. For instance, the single-edge notch bend specimen [4] and the three-point bend sandwiched specimen [5] are two other types of specimens used in the past for fracture testing on graphite. In another attempt, Etter et al. [6] investigated the mode I fracture toughness K_{Ic} of isotropic polycrystalline porous graphite in addition to graphite/aluminum composite by means of the single-edge notched beam specimen. The extensive applications of graphite fibers in the composite materials (such as graphite/epoxy composites) have also prompted some researchers to study the fracture behavior of these materials under pure mode I and mixed mode I/II loading conditions [7-10].
Lomakin et al [11] made use of an energy release rate criterion for analyzing the fracture initiation in cracked graphite specimens under pure mode I loading. There are also several fracture criteria in literature for predicting the onset of mixed mode I/II brittle fracture in various engineering materials

like graphite. The maximum tangential stress (MTS) criterion [12], the minimum strain energy density (SED) criterion [13] and the maximum energy release rate or G criterion [14] have been used more frequently by the researchers. Using a modified MTS criterion, Ayatollahi and Aliha [15] presented good estimates for the onset of mixed mode fracture in two grades of polycrystalline graphite containing sharp cracks.

Cracks are generated in graphite mainly because of the manufacturing faults or due to the coalescence of the micro-structural pores or defects that are inherently embedded in graphite. Whereas cracks are viewed as unpleasant entities in most engineering materials, nevertheless, notches of U or V-shape are sometimes desired in design and manufacturing of products made from graphite. Graphite moulds, graphite heating elements and graphite chucks are only some examples for industrial components that contain U or V-shape notches. A review of literature shows that in spite of extensive studies on mode I and mixed fracture in cracked graphite specimens, very few papers have dealt with brittle fracture in V-notched graphite components. Ayatollahi and Torabi [16] recently conducted a series of fracture tests on three different V-notched test specimens made of a polycrystalline graphite material. They also proposed a mean stress criterion and estimated their experimental results with very good accuracy. However, the results presented by Ayatollahi and Torabi [16] are confined only to pure mode I loading conditions. There are various practical conditions where the notches in graphite components are subjected a combination of tensile and shear deformation (or mixed mode I/II loading). In a recent paper, the present authors investigated mixed mode brittle fracture in polycrystalline graphite both experimentally and theoretically [17]. First a series of fracture experiments were conducted on centrally notched Brazilian disk specimens made of graphite to determine the fracture loads under different combinations of mode I and mode II loading. Then a theory based on the SED criterion [18-22] was employed to estimate the experimentally obtained fracture loads.

The main purpose of the present paper is to provide a new set of experimental results (70 new data) on fracture of graphite samples weakened by key-holes, with different values of loading mixity, inclination angles and notch radii, which may be helpful because enlarges the very scarce available data. By using the averaged value of the strain energy density over a well-defined volume, a fracture criterion for polycrystalline graphite under the above mentioned conditions is proposed to predict the static strength of the considered specimens. The third part of the paper deals with the analysis of fracture initiation direction and crack early propagation.

2. Fracture experiments

The details of the graphite material, the test specimen and the fracture experiments are presented in this section.

2.1 Material

The fracture tests were conducted on a commercial isostatic polycrystalline graphite. The mean grain size was measured by using the SEM technique and the density was determined from the buoyancy method. The basic material properties of the tested graphite are listed in Table 1: mean

grain size is 2 μm, porosity 7%, bulk density of 1850 kg/m^3, mean tensile strength of 28.5 MPa, Young's modulus of 8.05 GPa and shear modulus of 3.350 GPa. The compressive strength is equal to 110 MPa, whereas the flexural strength is 49 MPa.

All tests were performed under load control on a servocontrolled MTS axial testing device (±100 kN/± 110 Nm, ± 75mm/± 55°). The load was measured by a MTS cell with ± 0.5 % error at full scale.

Table 1. Mechanical properties

Material Property	Value
Elastic Modulus E [MPa]	8050
Shear Modulus G [MPa]	3354
Poisson's Ratio ν	0.2
Ultimate Torsion Strength [MPa]	30
Ultimate Compression Strength [MPa]	110
Ultimate Tensile Strength [MPa]	46
Fracture toughness [MPa m$^{0.5}$]	1.06
Hardness [Shore]	58
Density [Kg/dm^3]	1.85
Porosity [%]	7
Resistivity [μohm·m]	11
Thermal Conductivity [W/(m·K)]	110

2.2 Geometry of the specimens

As shown schematically in Fig. 1, the specimen used in the present investigation is a plate containing a central key-hole crack with a notch radius ρ and the distance between the hole centres a. The specimen is subjected to tensile loading. By changing the angle β, different combinations of mode I and mode II (or tension and shear deformation) can be produced for key-holes. When the load is applied along the notch bisector (i.e. β= 0), the key-holes are subjected to pure mode I deformation. By increasing the angle β from zero, the loading condition changes from pure mode I towards mixed mode I+II. For all the tested graphite specimens, the width (W), the notch depth (a) and the thickness t were 50 mm, 10 mm and 10 mm, respectively.

Five values of notch radius ρ=0.25, 0.5, 1, 2, 4 mm were considered for manufacturing the test specimens so that the effects of the notch tip radius on mixed mode fracture of the graphite specimens are studied. With the aim to obtain different mode mixities, four values of the angle β were considered (β=0, β=30°, β=45° and β=60°).

In order to prepare the graphite test specimens, first several plates of 10 mm thick were cut from a graphite block. Then, the specimens were precisely fabricated by using a 2-D CNC water-jet cutting machine. Before conducting the experiments, the cut surfaces of the graphite specimens were polished by using a fine abrasive paper to remove any possible local stress concentrations due to surface roughness. A total number of 70 mixed mode I/II fracture tests were performed for various notch geometry parameters. For each geometry shape and loading angle, three separate fracture

tests were performed by using a universal tension-compression test machine under displacement-control condition with a loading rate of 0.05 mm/min. The load-displacement curves recorded during the fracture tests were all linear and the specimens fractured suddenly. Therefore, the use of a brittle fracture criterion based on the linear elastic fracture mechanics (LEFM) is permissible. The mean values of fracture loads (F) recorded by the test machine are presented in Table 2, for each specimen.

A review of Table 2 shows that the fracture load increases when the loading conditions change from pure mode I (β=0) towards mixed mode I+II. Furthermore the fracture load enhances for larger notch tip radii, regardless of the mode mixity.

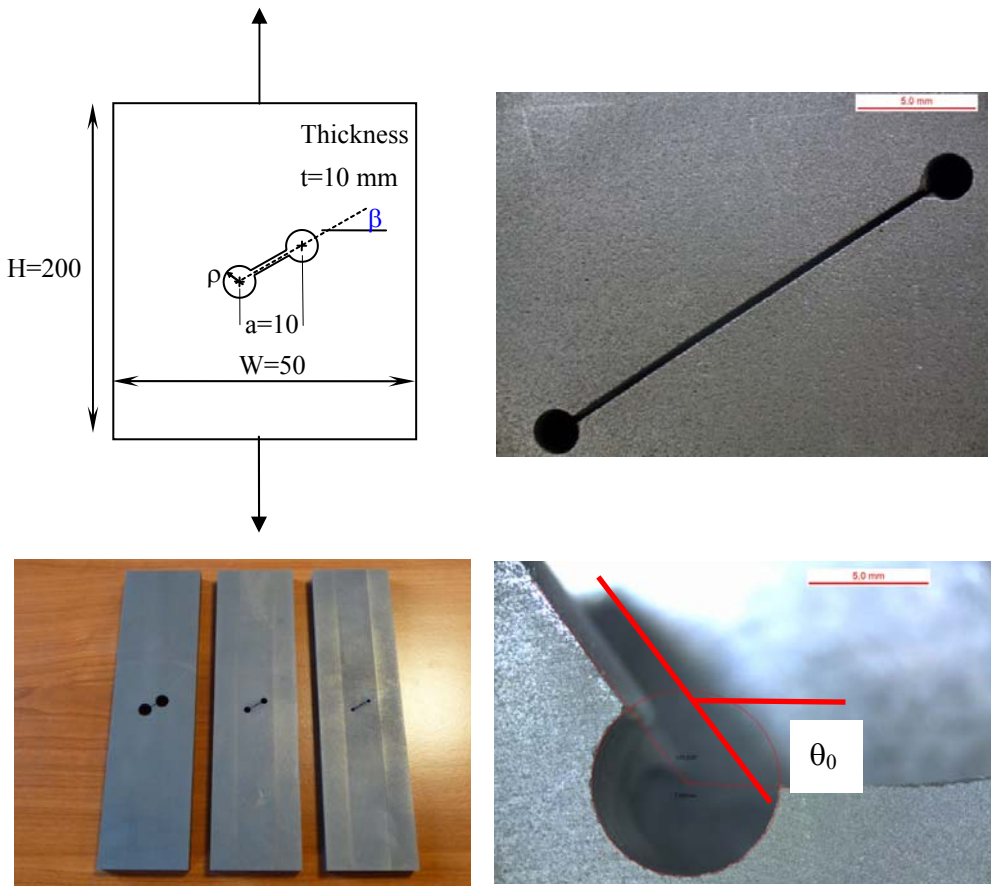

Figure 1. Geometry of the specimens (all dimensions in mm)

3. SED criterion

In order to estimate the fracture load in notched graphite components, engineers need an appropriate fracture criterion developed based on the mechanical behaviour of material around the notch tip. In this section, a strain-energy-density based criterion is described by which the fracture loads obtained from the experiments can be estimated very well.

Table 2. Outline of theoretical and numerical parameters for the strain energy density evaluation for the tested graphite specimens

ρ [mm]	β [°]	a [mm]	F [N]	F_{th} [N]	Δ [%]	σ_{max} [MPa]	SED [MJ/m^3]
0.25	0	10	3967	4146	4.31	87.0	0.1201
0.5	0	10	4060	4200	3.35	67.0	0.1225
1	0	10	3998	4483	10.82	51.8	0.1044
2	0	10	4967	5089	4.96	51.1	0.1251
4	0	10	4910	5434	9.64	45.1	0.1070
0.25	30	10	3991	3981	2.54	90.4	0.1317
0.5	30	10	4022	4030	4.41	67.7	0.1308
1	30	10	4125	4479	7.90	52.9	0.1111
2	30	10	4609	5080	9.26	47.8	0.1079
4	30	10	4775	5501	13.18	42.8	0.0991
0.25	45	10	3786	3857	2.98	89.4	0.1264
0.5	45	10	3893	4062	4.29	66.2	0.1205
1	45	10	4121	4309	4.36	56.5	0.1200
2	45	10	4972	5006	1.18	53.8	0.1293
4	45	10	4777	5243	8.90	45.6	0.1090
0.25	60	10	3995	4027	3.31	94.3	0.1291
0.5	60	10	3856	4066	5.18	68.1	0.1179
1	60	10	4114	4160	3.03	57.3	0.1283
2	60	10	4496	4669	3.71	50.7	0.1215
4	60	10	4553	5078	10.34	45.5	0.1055

The averaged strain energy density criterion (SED) as presented in Refs. [18-22] states that brittle failure occurs when the mean value of the strain energy density over a given control volume, $\overline{W}$, is equal to a critical value W_c. This critical value varies from material to material but is not dependent on the notch geometry and sharpness. The control volume is considered to be dependent on the ultimate tensile strength and the fracture toughness K_{Ic} in the case of brittle or quasi-brittle materials subjected to static loads.

Under plane strain conditions the critical length, R_c, can be evaluated according to the following expression [20]:

$$R_c = \frac{(1+\nu)(5-8\nu)}{4\pi}\left(\frac{K_{Ic}}{\sigma_t}\right)^2 \qquad (1)$$

where K_{Ic} is the fracture toughness, ν the Poisson's ratio and σ_t the ultimate tensile stress of a plain specimen that obeys a linear elastic behavior.

This critical value can be determined from the ultimate tensile stress σ_t according to Beltrami's expression

$$W_c = \frac{\sigma_t^2}{2E} \qquad (2)$$

In parallel, the control volume definition *via* the control radius R_c needs the knowledge of the fracture toughness K_{Ic} and the Poisson's ratio ν, see Eq. (1). The critical load that is sustainable by a notched component can be estimated by imposing $\overline{W}$ equal to the critical value W_c which is considered here constant under mode I, mode II and in plane mixed-mode conditions. This assumption has been extensively verified for a number of different brittle and quasi-brittle materials [20-22].

As mentioned earlier, the properties of the graphite material used in the present investigation are: σ_t= 46 MPa, K_{Ic} = 1.0 MPa.m$^{0.5}$, Poisson's ratio ν=0.2. As a result, the critical SED for the tested graphite is W_c=0.13 MJ/m^3 whereas the radius of the control volume is $R_c \cong 0.17$ mm considering realistic plane strain conditions.

Dealing with blunt notches under mixed mode loading, the problem becomes more complex than under mode I loading, mainly because the maximum elastic stress is out of the notch bisector line and its position varies as a function of mode I and mode II

stress distributions. The maximum stress occurring along the edge of circular holes has been calculated numerically by using the FE code ANSYS 12.0®. For each geometry, two models were created. The first model was mainly oriented to the determination of the point where the maximum principal stress and the maximum SED were located; the second model was more refined, with an accurate definition of the control volume where the strain energy density should be averaged. All the analyses have been carried out by using eight-node elements under the hypothesis of plane strain conditions.

Table 2 summarizes the outlines of the experimental, numerical and theoretical findings for the tested graphite specimens with four different inclination angles (β=0°, 30°, 45°, 60°), investigated in the present research. In particular, the table summarizes the theoretical (F_{th}) and the mean experimental load to failure (<*F*>) for every loading angle β and notch radius ρ. The Table also gives the maximum value of the principal stress (σ_{max}) and the SED value as obtained from the FE models of the graphite specimens by applying to the model the mean value of the critical loads. It is interesting to observe that the maximum principal stress along the notch edge is much greater (about two times) than the ultimate tensile stress of the material justifying the approach based on the average value of the SED over a control volume.

As can be noted, the agreement between the experimental results obtained for the notched graphite specimens and the theoretical predictions based on a constant value of the local strain energy is satisfactory with a maximum relative deviation equal to 12%.

4. Crack initiation angles

Dealing with crack initiation angles, they have been measured experimentally by using an optical microscope and a dedicate software called Las Leica Application Suite. The averaged value of the measured angles are compared in Table 3 with those obtained by numerical analyses identifying the point along edge where the SED and then the maximum stress reaches its critical value.

Table 3. Experimentally observed angles compared with numerical values

ρ [mm]	β [°]	$\theta_{0,\ FEM}$ [°]	$\theta_{0,\ EXP.}$ [°]	ρ [mm]	β [°]	$\theta_{0,\ FEM}$ [°]	$\theta_{0,\ EXP.}$ [°]
0.25	30	37.1	36.5	0.25	60	67.3	64.3
0.5	30	32.7	32.1	0.5	60	63.3	60.1
1	30	30.9	36.1	1	60	61.6	63.7
2	30	30.0	33.6	2	60	61.6	64.0
4	30	30.0	31.2	4	60	60.0	58.0
0.25	45	52.5	50.3				
0.5	45	50.0	54.9				
1	45	47.5	49.6				
2	45	46.2	49.1				
4	45	45.0	48.5				

5. Conclusions

The SED criterion was extended to rounded-tip notched domains in order to estimate the fracture load of notched graphite components. It was shown that the proposed method is suitable for the isostatic graphite stressed under mixed mode loading conditions, being the experimental results in good agreement with the results estimated by the SED approach. From the sound agreement between the theoretical and experimental results, it can be directly deduced that for the isostatic graphite the critical energy and the radius of the control volume are both constant material properties and independent of the loading mode, and can be simply evaluated from a pure mode I test.

References

[1] H. Awaji, S. Sato Combined mode fracture toughness measurement by the disc test. J. Eng. Mater. Technol., 100 (1978) 175-2.

[2] Y. Yamauchi, M. Nakano, K. Kishida, T. Okabe. Measurement of fracture toughness for brittle materials under mixed mode impact loading using center-notched disk specimen. Zairyo /J. Soc. Mater. Sci. Japan, 49(12) (2000) 1324-9.

[3] Y. Yamauchi, M. Nakano, K. Kishida, T. Okabe Measurement of mixed-mode fracture toughness for brittle materials using edge-notched half-disk specimen. Zairyo /J. Soc. Mater. Sci. Japan, 50(3) (2001) 229- 4.

[4] M. Li, M. Tsujimura, M. Sakai Crack-face grain interlocking/bridging of a polycrystalline graphite: The role in mixed mode fracture. Carbon, 37(10) (1999) 1633-9.

[5] L Shi, L Haiyan, Z Zhenmin, ASL Fok, BJ Marsden, A Hodgkins, PM. Mummery, J. Marrow. Analysis of crack propagation in nuclear graphite using three-point bending of sandwiched specimens. J. Nucl. Mater., 372 (2008) 141-51.

[6] Etter T, Kuebler J, Frey T, Schulz P, L¨offler JF, Uggowitzer PJ. Strength and fracture toughness of interpenetrating graphite/aluminum composites produced by the indirect squeeze casting process. Mater. Sci. Eng. A, 386 (2004) 61–7.

[7] Y.J. Yum , H. You Pure mode I, II and mixed mode interlaminar fracture of graphite/epoxy composite materials. J. Reinf. Plast. Compos., 20 (9) (2001) 794-08.

[8] C. Sukjoo, V.S. Bhavani. Fracture toughness of transverse cracks in graphite/epoxy laminates at cryogenic conditions. Composites Part B, 38 (2007) 193–0.

[9] S.N. Wosu, D. Hui, P.K. Dutta Dynamic mixed-mode I/II delamination fracture and energy release rate of unidirectional graphite/epoxy composites. Eng. Fract. Mech., 72 (2005) 1531–58.

[10] R.A. Jurf, R.B. Pipes Interlaminar fracture of composite materials. J. Compos. Mater. 16, (1982) 386-4.

[11] E.V. Lomakin, A.I. Zobnin, A.V. Berezin. Finding the fracture toughness characteristics of graphite materials in plane strain. Strength. Mater., 7(4) (1975) 484-7.

[12] F. Erdogan, G.C. Sih. On the crack extension in plates under plane loading and transverse shear. J. Basic Eng. T ASME, 85 (1963) 519-5.

[13] G.C. Sih Strain-energy-density factor applied to mixed mode crack problems. Int. J. Fract., 10 (1974) 305-21.

[14] M.A. Hussain, S.L. Pu, J. Underwood. Strain energy release rate for a crack under combined mode I and Mode II. Fracture Analysis, ASTM STP 560. (Philadelphia): American Society for Testing and Materials, 1974; 2-28.

[15] M.R. Ayatollahi, M.R.M. Aliha. Mixed mode fracture analysis of polycrystalline graphite – A modified MTS criterion. Carbon, 46 (2008) 1302-8.

[16] M.R. Ayatollahi, A.R. Torabi. Tensile fracture in notched polycrystalline graphite specimens. Carbon, 48 (2010) 2255-65.

[17] M.R. Ayatollahi, F. Berto, P. Lazzarin. Mixed Mode Brittle Fracture of Sharp and Blunt V-notches in Polycrystalline Graphite .Carbon, 49(7) (2011) 2465-74.

[18] P. Lazzarin, R. Zambardi. A finite-volume-energy based approach to predict the static and fatigue behaviour of components with sharp V-shaped notches. Int. J. Fract. 112, (2001) 275–298.

[19] P. Lazzarin, F. Berto. Some expressions for the strain energy in a finite volume surrounding the root of blunt V-notches. Int. J. Fract., 135 (2005) 161–185.

[20] F. Berto, P. Lazzarin. A Review of the volume-based strain energy density approach applied to V-Notches and Welded Structures, Theor. Appli. Fract. Mech., 52 (2009) 183-194.

[21] F. Berto, P. Lazzarin, F.J. Gómez, M. Elices. Fracture assessment of U-notches under mixed mode loading: two procedures based on the equivalent local mode I concept. Int. J. Fract., 148 (2007) 415-433.

[22] F.J. Gómez, M. Elices, F. Berto, P. Lazzarin . Local strain energy to asses the static failure of U-notches in plates under mixed mode loading. Int. J. Fract., 145 (2007) 29–45.

Stress State Dependent Failure Loci of a Talc-filled Polypropylene Material under Static Loading and Dynamic Loading

Shaoting Lin[1,*], Yong Xia[1], Chin-Hsu Lin[2], Jingyi Wang[1], Gongyao Gu[1]

[1] Department of Automotive Engineering, Tsinghua University, Beijing 100084, China
[2] Vehicle Systems Research Laboratory, GM R&D, Michigan, USA
* Corresponding author: linst06@gmail.com

Abstract A set of stress state dependent failure loci of a talc-filled Polypropylene material under static loading and dynamic loading was obtained by using a combined experimental-numerical approach. Uniaxial tension, simple shear, notched tension and punching tests were carried out to identify fracture locus under nonnegative stress triaxiality. Corresponding finite element analysis was performed to obtain the evolution of stress triaxiality of each failure element in each type of test. Different fracture prediction techniques were applied in static loading and dynamic loading, respectively. Under dynamic loading, an average value of the stress triaxiality was identified to determine stress triaxiality of critical point during the whole loading process in each type of test. By comparing force-displacement curves from both test and modeling, equivalent plastic strain in identified stress triaxiality can be obtained. Under static loading, damage evolution rule was utilized to optimize failure locus, and quadratic function was selected to optimize fracture locus. Significant difference of fracture locus between static loading and dynamic loading was observed.

Keywords Failure locus, Stress triaxiality

1. Introduction

With the rising requirements for energy saving and environment protection, thermoplastics, as one of the lightweight materials, have been widely employed in many thin-walled components of intricate shape in the automotive industry such as in interior and exterior trims. This on the other hand drives the demand for the accurate characterization of mechanical properties like yielding criteria and failure locus for thermoplastics. Particularly, fracture of thermoplastic material is commonly observed in occupant and pedestrian impacts, and some of the purposely intended fractures are crucial for absorbing impact energy and reducing occupant injury. However, the fracture behavior of thermoplastics is multifaceted, and it is sensitive to loading speed, loading mode, temperature, etc. A number of commonly-used numerical ductile fracture models such as the constant equivalent strain criterion, the Johnson-Cook (J-C) fracture model, and the Wilkinson (W) failure mode [1] have been implemented in commercial codes such as ABAQUS, LS-DYNA and PAM-CRASH. The main drawback of these fracture models is that accurate predictions of failure can only be achieved for limited stress state and strain rate, which cannot be applied for thermoplastics. New failure model developed by Y. Bai [2] extends the Mohr-Coulomb (MC) criterion from 2D shell to 3D solid such that failure strain is a function of both stress triaxiality and Lode angle parameter. But none of these models consider the influence of strain rate on failure strain, which is crucial for capturing the fracture behavior of a thermoplastic.

A general form of the strain based facture loci [3] can be written as follows.

$$\bar{\varepsilon}_f = f(\eta) = f\left(\frac{\sigma_h}{\bar{\sigma}}\right) \tag{1}$$

where $\bar{\varepsilon}_f$ is effective plastic strain to fracture, η is stress triaxiality defined by the ratio of hydrostatic stress σ_h to equivalent stress $\bar{\sigma}$. Considering the different failure behavior under static and dynamic loading for polymeric materials, we modify the Eq. (1) to the following equations.

$$\bar{\varepsilon}_f = f(\eta) = \begin{cases} f_1(\eta), \ \eta > 0, \text{static loading} \\ f_2(\eta), \ \eta > 0, \text{dynamic loading} \end{cases} \tag{2}$$

In this paper, the main task is to give the explicit Eq. (2) of a talc-filled impact modified polypropylene (PP). An empirical fracture locus depending on the parameters of stress state under both quasi static and dynamic loading was obtained using a combined experimental-numerical identification method. Different specimen geometries were designed to carry out tests of various loading conditions including uniaxial tension, simple shear, notched tension, and punching. The stress state parameters were stress triaxiality.

The material model SAMP-1 [4] (a Semi-Analytical Model for Polymers) in LS-DYNA was utilized to obtain stress triaxiality evolution of failure element during the process of loading. Two different fracture predictive techniques were applied to obtain fracture locus under static loading and dynamic loading. Under dynamic loading, stress triaxiality during the loading process in each test was stable. Therefore, an average value of stress triaxiality was accurate enough to identify stress triaxiality of critical failure point during the whole loading process in each type of test. By comparing force-displacement curves from both test and modeling, the equivalent plastic failure strain in the identified stress triaxiality was obtained. While under static loading, stress triaxiality varied greatly during the whole loading process. Damage evolution rule was utilized to optimize failure locus. Quadratic function was selected to optimize fracture locus under static loading.

2. Methodology

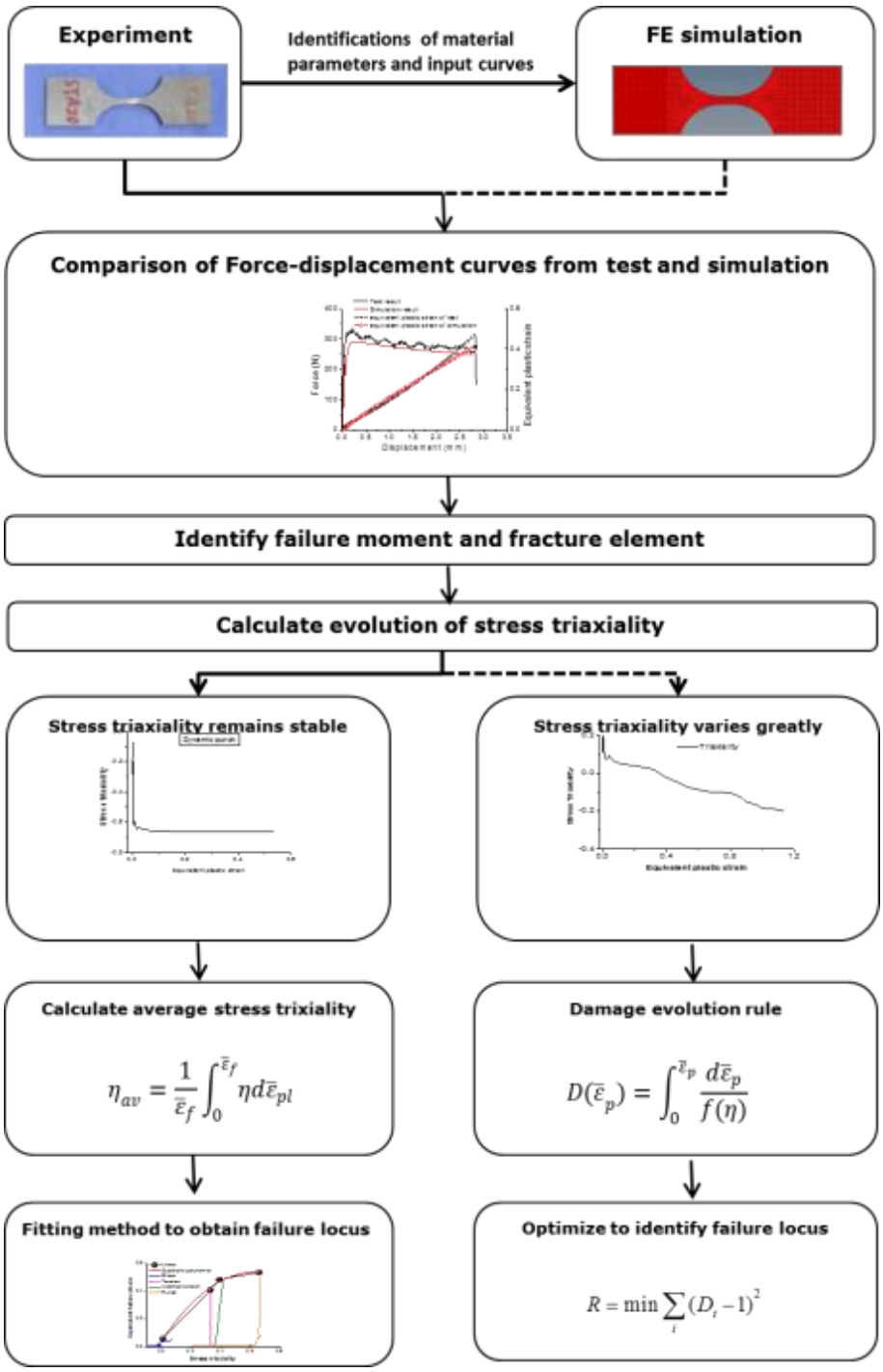

Figure 1. Procedure of identifying failure locus under static loading and dynamic loading

Bao and Wierzbicki [1, 2, 3, 5] contributed a lot on ductile failure criteria for metallic materials such as high strength steel and aluminum. Inversing engineering method was utilized to identify effective failure strain under certain stress triaxiality. Fig. 1 shows the procedure of identification of failure locus. The first step is to carry out material tests such as uniaxial tension, biaxial tension, simple shear, compression, notched-tension and punching. Basic material tests such as uniaxial tension, biaxial tension, simple shear and compression are critical for identification of material parameters and input curves, which is required in material model SAMP-1. Corresponding modeling of these tests are run to validate the material model. Also, simulations of uniaxial tension, simple shear,

notched tension and punching are run to identify equivalent failure strain under positive stress trixiality. Force-displacement curves from both test and simulation are compared to determine failure moment and extract evolution of stress triaxiality of failure element in each test. To determine stress triaxiality of critical failure point during the whole loading process, an average value of the stress triaxiality of each type of test was defined in the range from 0 to $\bar{\varepsilon}_f$

$$\eta_{av} = \frac{1}{\bar{\varepsilon}_f}\int_0^{\bar{\varepsilon}_f} \eta d\bar{\varepsilon}_{pl} \tag{3}$$

Mae [6] studied the ductile fracture locus of PP/EPR/talc Blend, using this kind of stress triaxiality approximation method as well. However, this approximation of stress triaxiality is reasonable only when stress triaxiality varies a little during the whole loading process. For polymeric materials, strain concentration is common, which leads to greatly varied stress triaxiality during the loading process especially for static loading. Y. Bai and T. Wierzbicki [2] used damage evolution rule as new popular fracture predictive technique. A linear incremental relationship was assumed here between damage indicator D and equivalent plastic strain $\bar{\varepsilon}_p$

$$D(\bar{\varepsilon}_p) = \int_0^{\bar{\varepsilon}_p} \frac{d\bar{\varepsilon}_p}{f(\eta,\bar{\theta})} \tag{4}$$

where η is stress triaxiality, $\bar{\theta}$ is lode angle parameter, and f is equivalent failure strain function. Both of the two stress direction parameters are unique functions of the equivalent plastic failure strain. A material element is considered to fail when the limit of ductility is reached, $\bar{\varepsilon}_p = \bar{\varepsilon}_f$, so that, $D(\bar{\varepsilon}_f) = 1$. In this paper, we only consider 2D fracture locus in positive stress triaxiality, thus supposing that failure strain is only dependent of stress triaxiality.

$$D(\bar{\varepsilon}_p) = \int_0^{\bar{\varepsilon}_p} \frac{d\bar{\varepsilon}_p}{f(\eta)} \ (\eta \geq 0) \tag{5}$$

To determine the explicit expression of function *f*, optimization method is required. The optimization objective function is as follows.

$$\min\{(D_T - 1)^2 + (D_S - 1)^2 + (D_N - 1)^2 + (D_P - 1)^2\} \tag{6}$$

where D_T, D_S, D_N and D_P are respectively damage indicator from tension, shear, notch tension and punch test.

Quite a few literatures show that ductile polymeric materials turn to be brittle with the increase of strain rate. Hence, in this paper, function $f(\eta)$ is studied under static loading and dynamic loading respectively. Table 1 is the test matrix for calibrating failure parameters.

Table 1. Test matrix for calibrating failure parameters

Test No.	Loading speed (m/s)	Strain rate (/s)	Stress Triaxiality range
Uniaxial tension	0.0002	0.01/s	1/3
	0.2	10/s	
Simple shear	0.0001	0.01/s	0
	0.1	10/s	
Notch tension	0.0001	0.01/s	1/3-2/3
	0.1	10/s	
Punch	0.001	/	2/3
	3.5	/	

3. Material constitutive law

A talc-filled and impact-modified polypropylene was chosen for the experimental and simulation study in this paper. All the test coupons in this paper were milled from an injecting molding plate with thickness of 3.4mm.

The material model SAMP-1 [4] in LS-DYNA developed for polymers was utilized to construct material constitutive. A quadratic form in the stress tensor is used to describe the yield surface and SAMP-1 model is restricted to isotropic formulations. The expression for the yield surface is as follows:

$$f = \sigma_{\mathrm{vm}}^2 - \mathrm{A}_0 - \mathrm{A}_1 p - \mathrm{A}_2 p^2 \leq 0 \tag{6}$$

Uniaxial tension, shear, compression and biaxial tension are four basic tests for construction of the yielding surface. Hence, all the above four tests at approximate strain rate of 0.01/s were carried out to obtain plastic true stress-strain curve as input. Fig. 2 shows equivalent stress-strain curves of four types of tests. Based on the four basic stress-strain curves, quadratic fitting formulation was selected to fit yielding surface, which is plotted in Fig. 3.

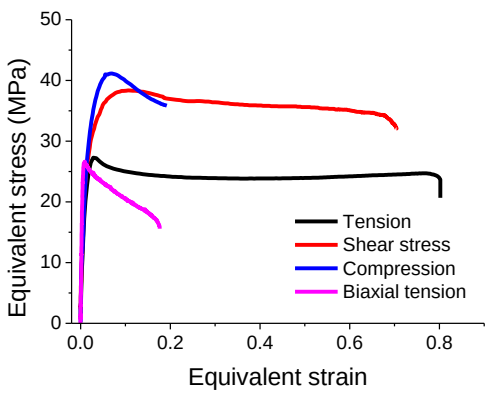

Figure 2. Input curves of SAMP-1 model

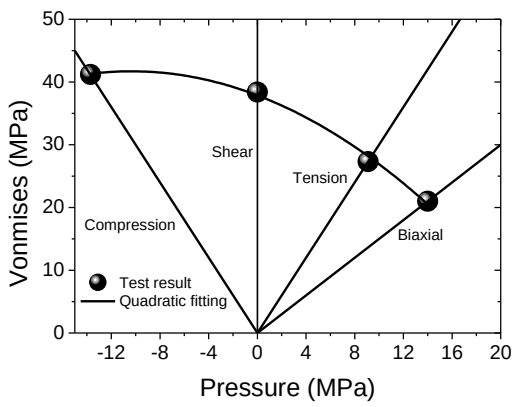

Figure 3. Yielding surface

A proper visco-plastic consideration of the rate effects is included in SAMP-1 model. In order to

characterize property of strain rate dependence of polymeric materials, multiple load curves of tension tests corresponding to different values of the plastic strain rate are input in material model. It is assumed in SAMP-1 model that strain rate effect in compression and shear is the same as the rate effect in tensile loading. However, it should be noted that this assumption may be questionable since rate effects may depend on stress state. Fig. 4 shows uniaxial tension tests at 6 strain rate of 0.01/s, 0.1/s, 1/s, 10/s, 100/s and 200/s, which were carried out in respectively at universal material test machine for quasi static test and intermediate strain rate test machine for dynamic test.

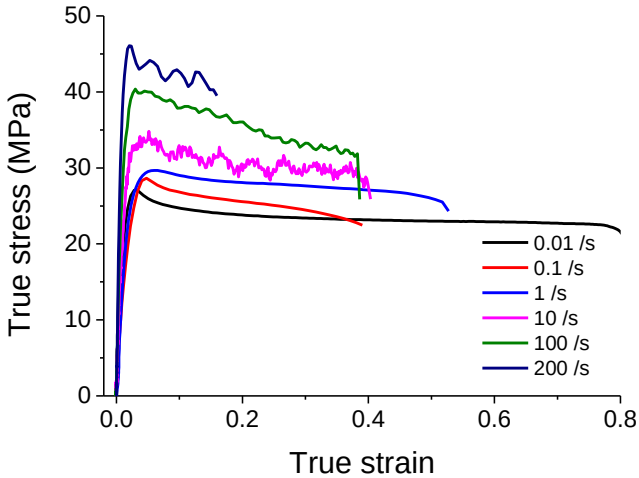

Figure 4. Uniaxial tension tests at each strain rate

4. Uniaxial tension

Fig. 5 shows specimen geometry of uniaxial tension, which was modified from the standard ASTM D638 [7]. In this paper, tension tests at strain rate of 0.01/s, 0.1/s and 1/s were carried out at universal test machine Zwick 020 and tests at strain rate of 10/s, 100/s and 200/s were conducted at intermediate strain rate hydraulic test machine. Static test set up is shown in Fig. 7 and dynamic test set up is shown in Fig. 8.

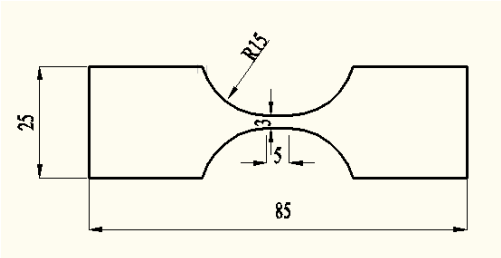

Figure 5. Schematic of tension specimen

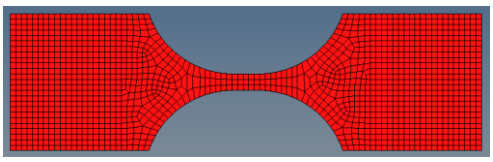

Figure 6. FEM of tension specimen

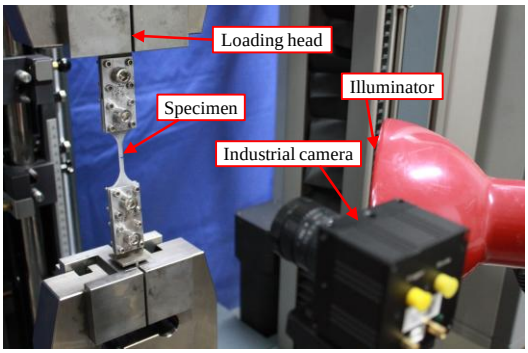

Figure 7. Test setup of quasi static test

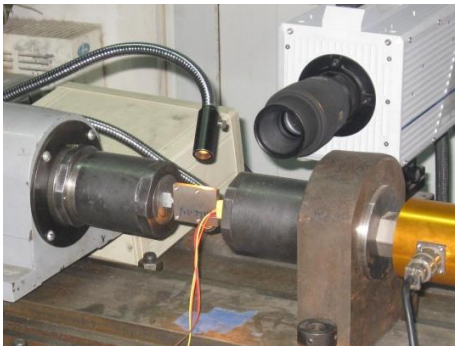

Figure 8. Test setup of dynamic test

Digital image correlation method was applied to measure the strain and displacement in gage length of tensile specimen. For force measurement, self-developed load cell (Fig. 10) was developed to measure the force signal in dynamic test. Self-developed load cell was carefully designed to avoid ringing effect which is a common problem in dynamic tests. Table 2 shows the calibration result that the linear fitting coefficient R is more than 0.9997, which indicates good consistency. In order to validate the reliability of the self-development load cell, tensile tests of LY12CZ, a commonly-known material with little strain rate effect were performed respectively at 0.5 mm/min, 5 mm/min, 1.1 m/s and 2.2 m/s and force measurements of these tests were acquired from self-developed load cell. Fig. 9 indicates no significant strain rate effect, which conforms to commonly-known mechanical property of LY12CZ. This result validates the reliability of our self-developed load cell.

Table 2. Calibration factors and correlation coefficients based on the calibration test results

Test No.	Loading speed (mm/min)	Factor (N/mV)	Correlation coefficient
1	0.2	0.539	0.9998
2	0.2	0.540	0.9998
3	0.2	0.537	0.9998
4	0.5	0.537	0.9998
5	0.5	0.533	0.9997
6	0.5	0.538	0.9998
Average value	/	0.537	/

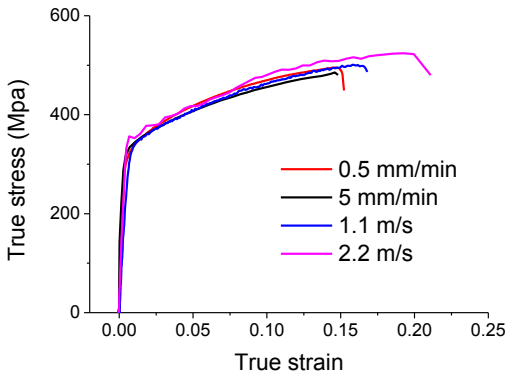

Figure 9. Tension curves at different loading speeds of LY12CZ

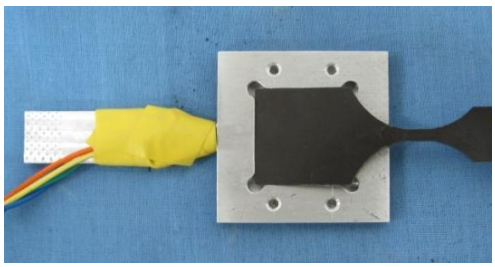

Figure 10. Self-developed load cell

In order to evaluate failure strain under tensile test, we closely investigated the tensile tests at strain rate of 0.01/s and strain rate of 10/s. For tensile test at 0.01/s, we directly obtained equivalent failure strain from test. Fig. 11 plots the force level, equivalent plastic strain and gamma (stands for the principal strain angle in radians, measure counterclockwise from the positive X-axis). Since gamma was quite close to 0, we assumed that the tensile test at 0.01/s was close to uniaxial tension stress state even though strain localization occurs after large deformation. Fig. 12 is image of specimen right before fracture and color distribution shows effective strain distribution in gage length. Via DIC method, we can acquire equivalent plastic failure strain as 0.76. Consequently, we safely identified one initial value of function $f(\eta)$ at static loading, $f(1/3) = 0.76$.

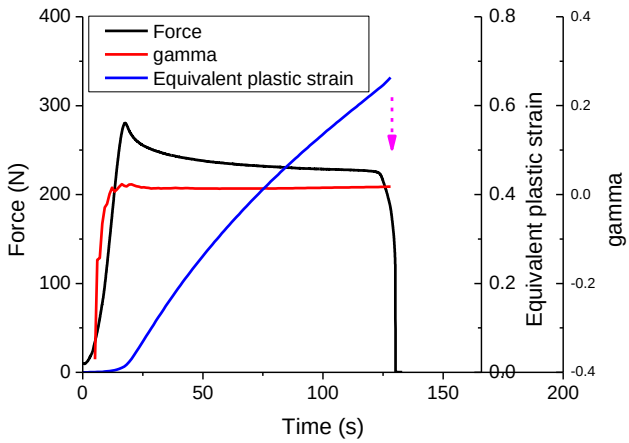

Figure 11. Equivalent strain, force and gamma coefficient, tensile test, 0.01/s

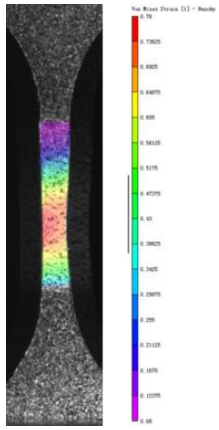

Figure 12. Strain distribution right before fracture, tension, 0.01/s

For tensile tests at 10/s, similar method can be utilized to determine fracture strain at strain rate of 10/s. Meanwhile, corresponding simulation can also help us to find the equivalent plastic failure strain and validate our test result. Simulation model was with 1mm shell element which is shown in Fig. 6. All the tensile curves under 6 strain rates, compression, shear and biaxial curves at lowest strain rate of 0.01/s were input in SAMP-1. Fig. 13 shows good correlation between simulation and test. By comparing force-displacement curves from both test and simulation, stress triaxiality evolution curve of failure element was obtained, which is shown in Fig. 14. From Fig.14, we can observe that stress triaxiality is close to 0.33, which indicates an ideal uniaxial tensile state. Since stress triaxiality at 10/s was stable, average value of stress triaxiality was calculated according to Eq. (3), $f(0.33) = 0.41$.

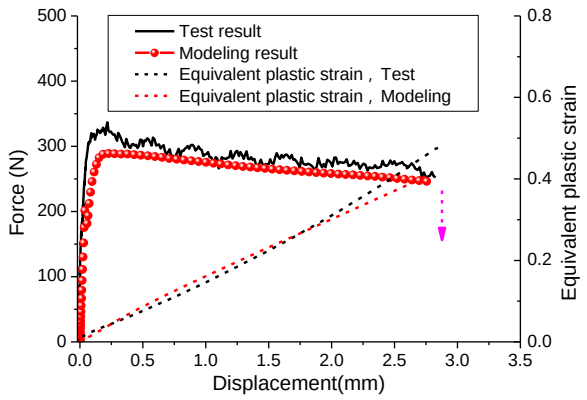

Figure 13. Comparison curves between simulation and test, tension, 10/s

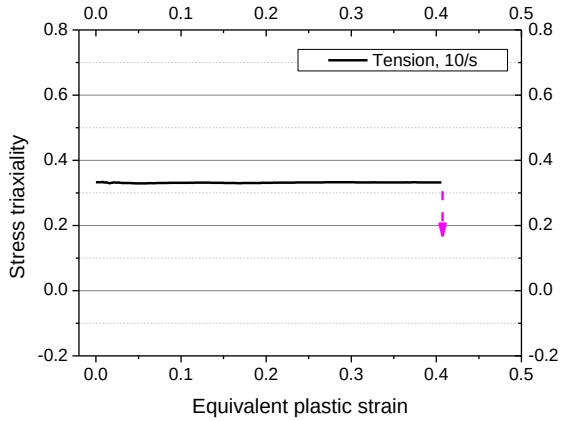

Figure 14. Stress triaxiality evolution curve, tension, 10/s

5. Simple shear

Figure 15 shows the specimen geometry of shear tests, which was similar to the design in H. Daiyan's paper [8] based on V-notched Beam standard (ASTM D 5379 [9]). Similar to tensile tests, static shear test was conducted in universal test machine with self-developed test fixture. While for dynamic shear test, similar self-developed load cell was designed to obtain force signal. Fig. 17 and Fig.18 respectively show test setup of quasi static test and dynamic test.

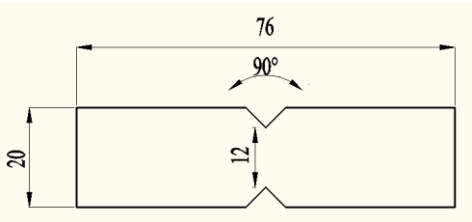

Figure 15. Schematic of shear specimen

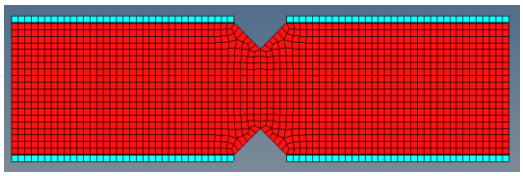

Figure 16. FEM of shear specimen

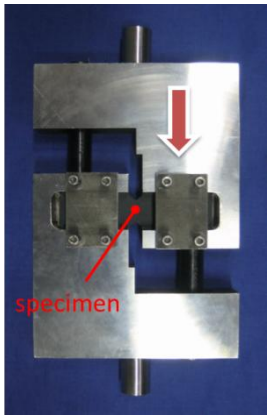

Figure 17. Test setup of quasi static test

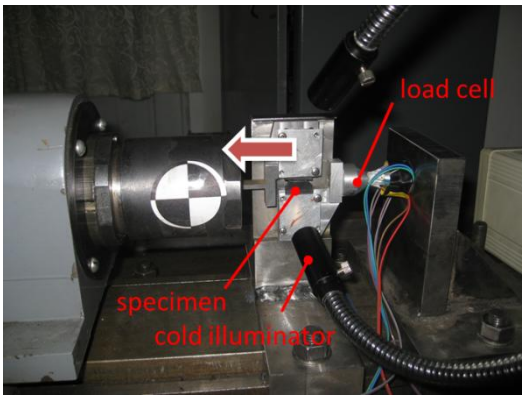

Figure 18. Test setup of dynamic test

Corresponding simulations of shear test were conducted to obtain the stress triaxiality evolution curve of failure element. Fig. 16 is the corresponding finite element model of shear specimen with 1 mm solid element. Fig. 19 and Fig. 21 shows the comparison results between simulation result and test

result respectively at 0.01/s and 10/s. By comparing the force-displacement curves of test and simulation, we identified the failure moment and obtained the stress triaxiality evolution curve of failure element. Fig. 20 and Fig.22 shows the stress triaxiality evolution curves respectively at 0.01/s and at 10/s.

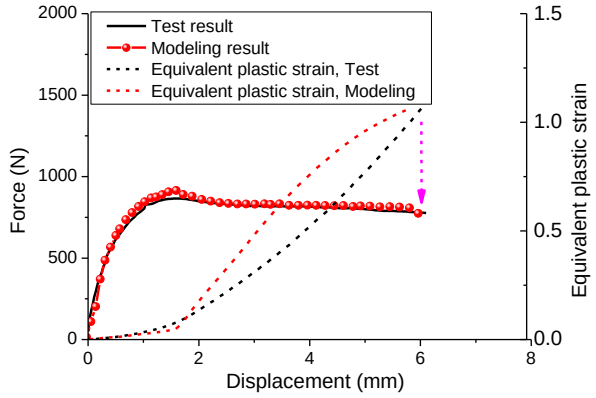

Figure 19. Comparison curves between simulation and test, shear, 0.01/s

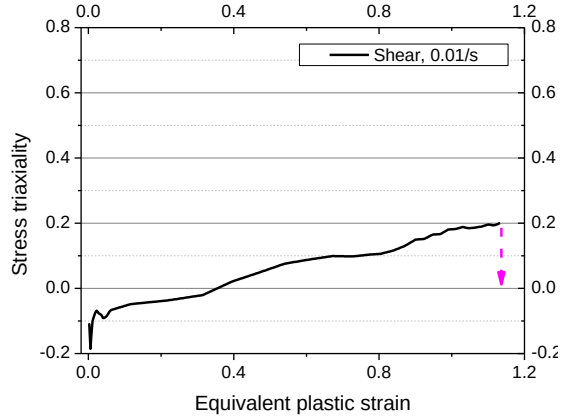

Figure 20. Stress triaxiality evolution curve, shear, 0.01/s

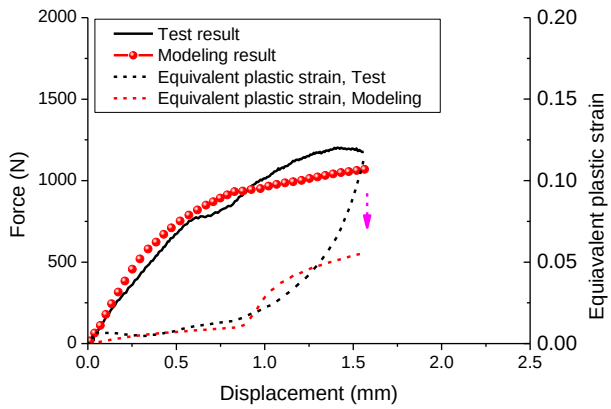

Figure 21. Comparison curves between simulation and test, shear, 10/s

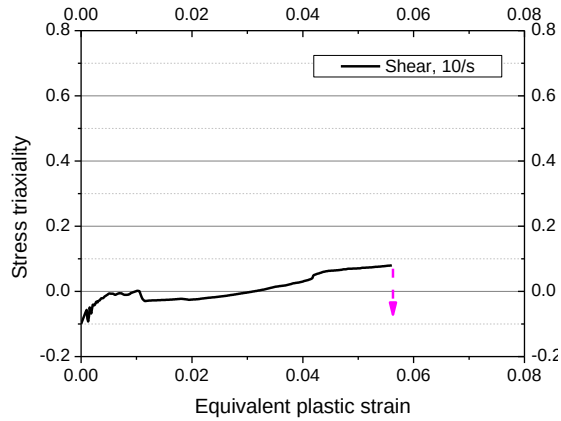

Figure 22. Stress triaxiality evolution curve, shear, 10/s

6. Notched tension

Notched tension tests were carried out to determine failure strain in stress state between uniaxial tension and biaxial tension. Fig. 23 shows schematic of notched tension specimen. Corresponding finite element model was constructed with 0.4 mm solid element, which is shown in Fig. 24. To save computation time, only half of the model was constructed.

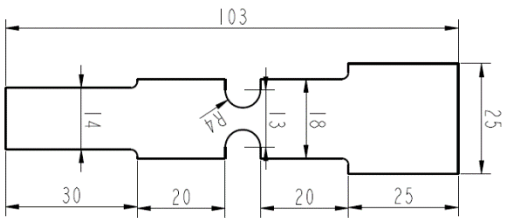

Figure 23. Schematic of notched tension specimen

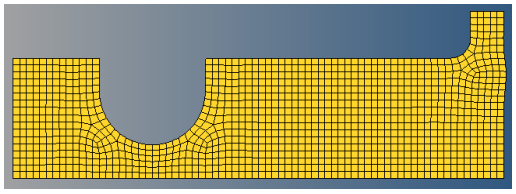

Figure 24. FEM of notched tension

Both test method and modeling technique were similar to tensile and shear test. Fig. 25 and Fig. 27 shows the comparison results between simulation result and test result respectively at 0.01/s and 10/s. Fig. 26 and Fig.28 shows the stress triaxiality evolution curves of failure element respectively at 0.01/s and at 10/s.

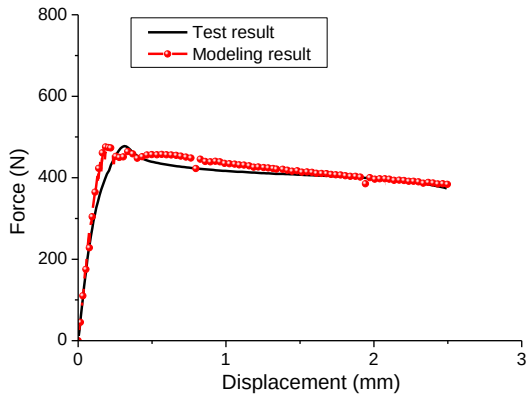

Figure 25. Comparison curves between simulation and test, notched tension, 0.01/s

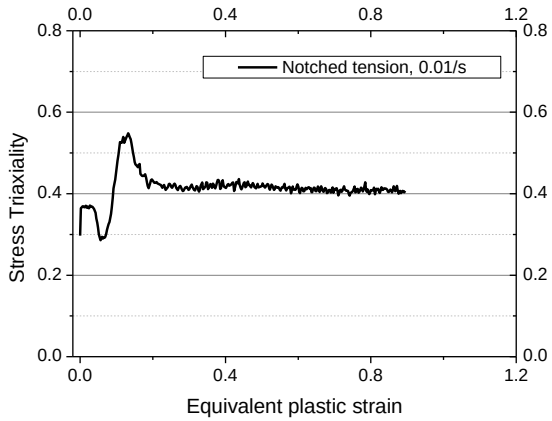

Figure 26. Stress triaxiality evolution curve, notched tension, 0.01/s

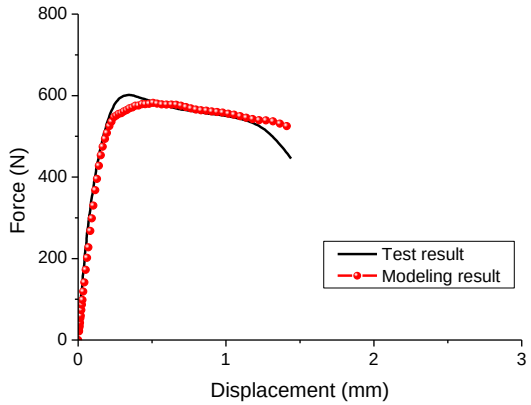

Figure 27. Comparison curves between simulation and test, notched tension, 10/s

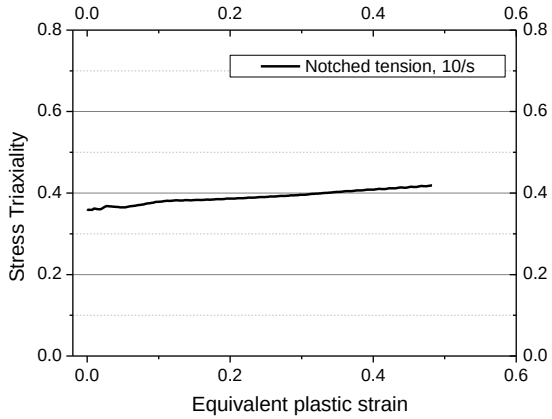

Figure 28. Stress triaxiality evolution curve, notched tension, 10/s

7. Punch

Since dominate stress triaxiality during punching loading is approximately around 0.67, punching test is used to calibrate failure locus at large stress triaxiality. The schematic of specimen for punching

tests shown in Fig. 29 mainly follows the standard of ASTM D3763 [10]. There are eight holes uniformly distributing around the outer edges of each specimen, which are used to constrain the specimen to the fixtures. Fig. 30 shows the finite element model of punch. Similarly, only quarter of the whole coupon was constructed to save computational time. Since large deformation occurred in the center region, we used fine shell element of 0.1 mm to mesh the center region.

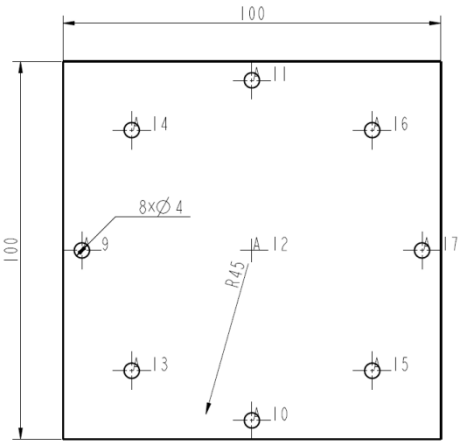

Figure 29. Schematic of punching specimen

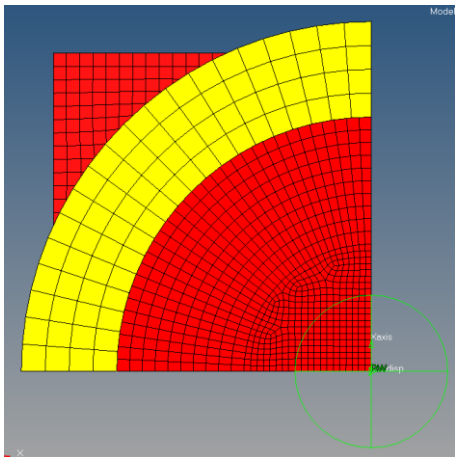

Figure 30. FEM of punch

Fig. 31 and Fig. 33 shows the comparison results between simulation result and test result respectively at 0.01/s and 10/s. Fig. 32 and Fig.34 shows the stress triaxiality evolution curves of failure element respectively at 0.01/s and at 10/s.

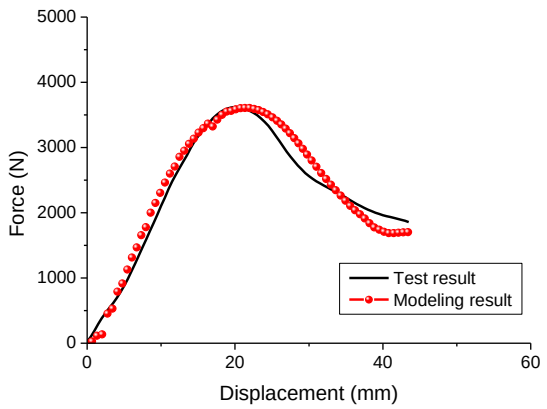

Figure 31. Comparison curves between simulation and test, punch, 0.001 m/s

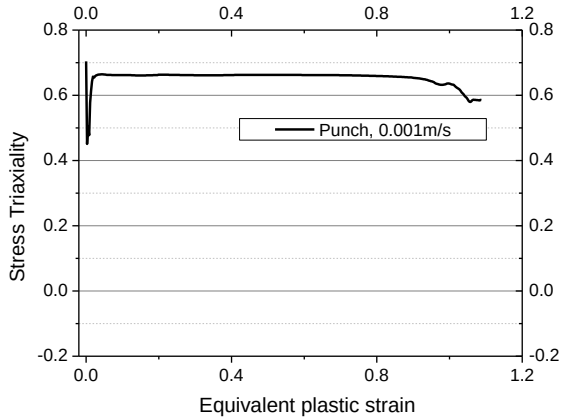

Figure 32. Stress triaxiality evolution curve, punch, 0.001 m/s

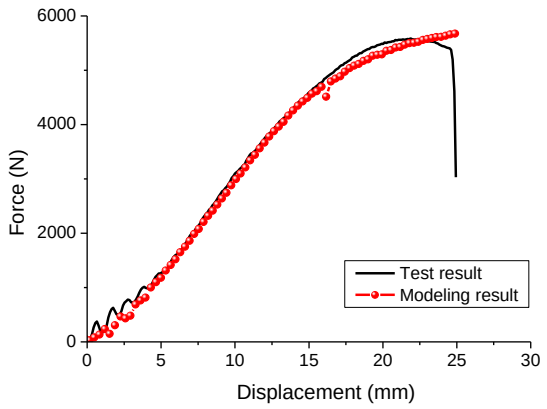

Figure 33. Comparison curves between simulation and test, punch, 3.5 m/s

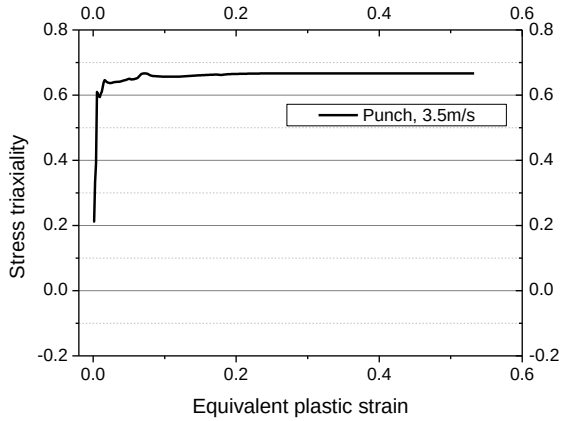

Figure 34. Stress triaxiality evolution curve, punch, 3.5 m/s

8. Construction of ductile failure criteria

8.1. Failure locus under static loading

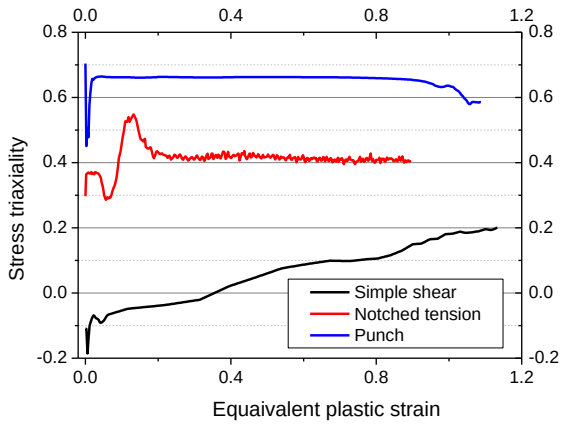

Figure 35. Stress triaxiality evolution at 0.01/s

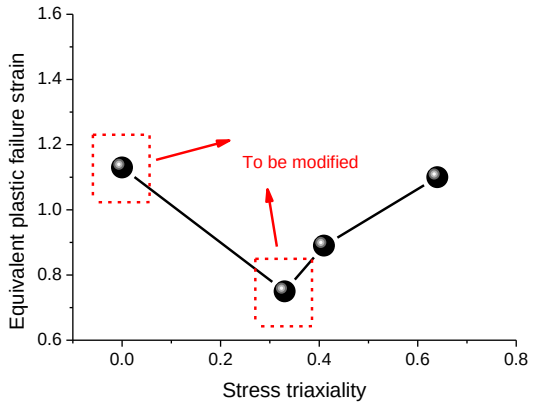

Figure 36. Failure locus from average stress triaxiality at 0.01/s

Figure 35 shows stress triaxiality evolution curves of shear, notched tension and punch under static loading. Using average stress triaxiality, we can obtain failure locus at 0.01/s shown in Fig. 36. However, since stress triaxiality varies greatly during the whole loading process in shear test, equivalent failure strain at stress triaxiality of 0 is not accurate enough. Besides, since we directly obtained equivalent failure from test via digital image correlation method in tensile test, equivalent failure strain at stress triaxiality of 0.33 is questionable as well. Therefore, damage evolution rule was used to optimize failure locus under static loading. We selected quadratic function (Eq. (7)) as optimization function. The reason we selected quadratic function partly referred to acquired four failure points in Fig. 36. Table 2 summarizes existing functions used to fitting failure locus in the equivalent strain and stress triaxiality space. And most of them are for metallic materials [3].

$$f(\eta) = B_0 + B_1\eta + B_2\eta^2 \tag{7}$$

Table 2. Equivalent failure strain, Average stress triaxiality

	Function of $f(\eta)$
Linear function	$f(\eta) = C_1\eta + C_2$

Rice-Tracey failure criteria	$f(\eta) = C_1 e^{C_2 \eta} + C_3$
Hydrostatic Stress failure criteria	$f(\eta) = \frac{C_4}{\eta}$
Power function	$f(\eta) = \eta^{C_5}$

Initial values of B_0, B_1 and B_2 were determined from acquired four points in Fig. 36. The final values of B_0, B_1 and B_2 were determined by minimizing residue R defined by Eq. (8).

$$R = (D_s - 1)^2 + (D_n - 1)^2 + (D_p - 1)^2 \tag{8}$$

Where D_s, D_n, D_p respectively stand for damage indicator in shear, notch tension and punch. Table 3 summarizes initial values and final values of coefficients B_0, B_1 and B_2. Table 4 gives values of each coefficient after optimization. Fig. 37 plots the two failure locus respectively from average stress triaxiality and from damage evolution rule. From these two comparative curves, failure strains under shear and uniaxial tension are increased after modification with optimization method.

Table 3. Initial values and final values of coefficients B_0, B_1 and B_2

	B_0	B_1	B_2
initial values	1.12	-1.97	3.04
final values	1.22	-2.05	2.96

Table 4. Coefficients after optimization

R	D_s	D_n	D_p
0.0019	1.0192	1.0083	0.9614

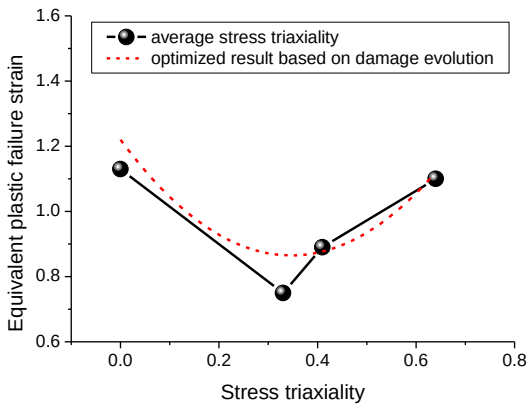

Figure 37. Failure locus from average stress triaxiality and from damage evolution rule

8.2. Failure locus under dynamic loading

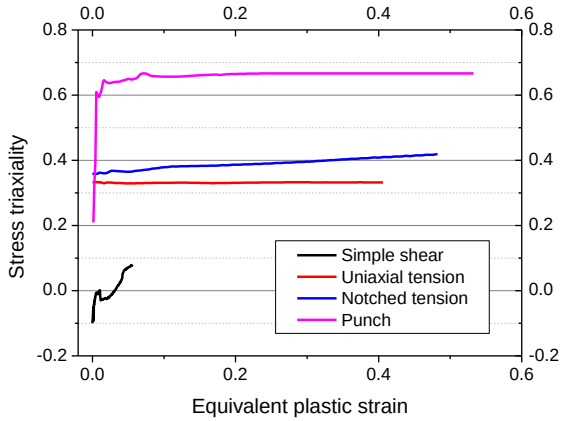

Figure 38. Stress triaxiality evolution at 10/s

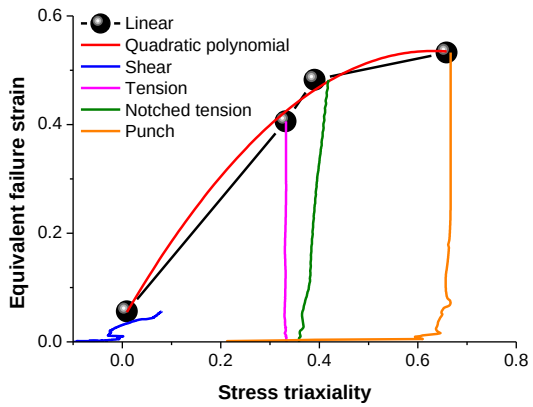

Figure 39. Failure locus at 10/s

Figure 38 shows stress triaxiality evolution curves of shear, tension, notched tension and punch under dynamic loading. We can observe that stress triaxiality of each test remains stable during loading process. Thus we can directly use the average value of stress triaxiality of each type of test. Calculation of stress triaxiality is referred to average stress triaxiality formulation Eq. (3). Table 5 summarizes the result of each test.

Table 5. Equivalent failure strain, Average stress triaxiality

Test type	Shear	Tension	Notched-tension	Punch
Average stress triaxiality	0.01	0.33	0.39	0.66
Equivalent failure strain	0.056	0.406	0.482	0.532

Quadratic polynomial fitting of four base points is plotted in Fig. 39.

9. Conclusions and Discussions

Consequently, we obtained failure locus in the space of equivalent plastic failure strain and stress triaxiality under static loading and dynamic loading. From Fig. 40, we can observe significant different failure locus between static loading and dynamic loading.

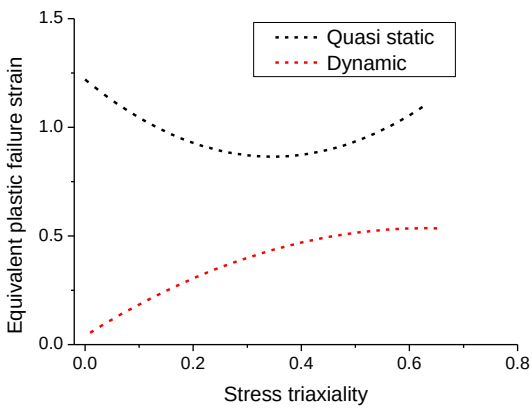

Figure 40. Failure locus under static loading and dynamic loading

We used combined experiment-numerical method to obtain failure locus in the equivalent failure strain and stress triaxiality space respectively under static loading and dynamic loading. There is significant difference between static loading and dynamic loading, which indicates strain rate impacts greatly on failure locus of the polymeric materials we studied. We utilized two failure predictive techniques to identify failure locus, trying to obtain accurate result. Under dynamic loading, average stress triaxiality method is enough determine failure locus in each type of test. While under static loading, damage evolution rule should be used to optimize the fracture locus since stress triaxiality varies greatly during the loading process especially for shear test.

10. References

[1] T. Wierzbicki, Y. Bao, Y. W. Lee, Y. Bai, Calibration and evaluation of seven fracture models. International Journal of Mechanical Sciences, 2005, 47: 719-743.
[2] Y. Bai, T. Wierzbicki, Application of extended Mohr-Coulomb criterion to ductile fracture. International Journal of Fracture, 2010, 161: 1-20.
[3] Y. Bao, T. Wierzbicki, On fracture locus in the equivalent strain and stress triaxiality space. International Journal of Mechanical Sciences, 2004, 46: 81-98.
[4] S. Kolling, A. Haufe, M. Feucht & P.A. Du Bois, SAMP-1: A Semi-Analytical Model for the Simulation of Polymers, Anwenderforum, Bamberg 2005.
[5] Y. Bao, Prediction of Ductile Crack Formulation in Uncracked Bodies. MIT PHD thesis, 2003.
[6] H. Mae, Characterization of Material Ductility of PP/EPR/talc Blend under Wide Range of Stress Triaxiality at Intermediate and High strain Rates. Journal of Applied Polymer Science, 2009, 111: 854-868.
[7] ASTM D638M, Standard test method for tensile properties of plastics, 1993.
[8] H. Daiyan, E. Andreassen, F. Grytten, H. Osnes, R.H. Gaarder, Shear testing of polypropylene materials analysed by digital image correlation and numerical simulations. Experimental Mechanics, 2012, DOI 10.1007/s11340-012-9591-7.
[9] ASTM D5379, Standard Test Method for Shear Properties of Composite Materials by the V-Notched Beam Method, 1993.
[10] ASTM D3763-95a, Standard Test Method for High Speed Puncture Properties of Plastics Using Load and Displacement Sensors, 1993.

Acknowledgements

The authors would like to thank General Motor R&D for the support on Project *Testing and Modeling of Polymeric Materials for Crash Safety CAE*. Thanks also to Foundation of Zhejiang Province Automobile Safety Technology Laboratory.

Molecular Dynamics Simulation of Fracture of Graphene

Dewapriya M. A. N.[1], Rajapakse R. K. N. D.[1,*], Srikantha Phani A.[2]

[1] School of Engineering Science, Simon Fraser University, Burnaby, BC, Canada
[2] Department of Mechanical Engineering, The University of British Columbia, Vancouver, BC, Canada
* Corresponding author: rajapaks@sfu.ca

Abstract A molecular dynamics (MD) simulation to assess the effect of crack length on the ultimate tensile strength of infinitely large armchair and zigzag graphene sheets is presented. The strength of graphene is inversely proportional to the square-root of crack length as in continuum fracture theories. Further comparison of the strength given by MD simulations with Griffith's energy balance criterion demonstrates a reasonable agreement. Armchair and zigzag graphene sheets with 2.5 nm long crack exhibit around 55% of the strength of pristine sheets. Investigation of the influence of temperature on the strength of graphene indicates that sheets at higher temperatures fail at lower strengths, due to high kinetic energy of atoms. We also observe out-of-plane deformations of the crack tip at equilibrium configuration of both types of sheets due to compressive forces acting on the crack surface. This deformation propagates with applied strain in the direction normal to the crack and eventually generates ripples in the entire sheet.

Keywords Graphene, Fracture, Molecular Dynamics, Vacancy Defects

1. Introduction

Experimental investigations with atomic force microscope (AFM) have revealed that the ultimate tensile strength and Young's modulus of graphene are around 130 GPa and 1 TPa, respectively [1]. Researchers have found experimental evidence for the existence of defects such as the absence of carbon atoms in graphene sheets [2]. The absence of carbon atoms in graphene is known as vacancy defects. The influence of vacancy defects on the strength of graphene has not been studied experimentally. However, a number of theoretical studies have been conducted, and it has been found that vacancy defects could reduce the strength of graphene by around 50% [3-9].

Khare *et al.* [4] studied the effects of large defects and cracks on the mechanical properties of carbon nanotubes and graphene using a coupled quantum mechanical/molecular mechanical method. They found that the weakening effects of holes, slits, and cracks vary only moderately with the shape of the defect, and instead depend primarily on the cross section of the defect perpendicular to the loading direction. Ansari *et al.* [5], using MD simulations, showed that the presence of vacancy defects significantly reduces the ultimate strength and strain of graphene, while it has a minor effect on Young's modulus. They also showed that defects have a lower effect in armchair direction compared to zigzag direction. Wang *et al.* [6] studied the effect of vacancy defects on the fracture strength of graphene sheets using MD. They found that vacancies can cause significant strength loss in graphene and also concluded that temperature and loading directions affect the fracture strength. Omeltchenko *et al.* [7] estimated the fracture toughness of armchair graphene from Griffith analysis and local-stress distributions, and the toughness values are 4.7 MPa $m^{1/2}$ and 6 MPa $m^{1/2}$, respectively. The study was conducted using MD simulations. A recent work from Xu *et al.* [8] revealed that the critical stress intensity factors of graphene are 4.21 MPa $m^{1/2}$ and 3.71 MPa $m^{1/2}$ for armchair and zigzag directions, respectively. They used a coupled quantum/continuum mechanics model for the study.

Coupled quantum mechanics models are generally computationally expensive and those models cannot incorporate temperature effects. Therefore, it is useful to have a simple MD model, which can be used to investigate the fracture of nanoscale systems such as graphene. This paper presents a MD simulation of fracture of armchair and zigzag graphene at temperatures of 1 K and 300 K.

2. Molecular Dynamics Simulations

Adaptive intermolecular reactive empirical bond order (AIREBO) potential [10], implemented in LAMMPS MD simulation package [11] is used in this study. Cut-off radius of AIREBO potential is set to be 2 Å to eliminate the non-physical strain hardening of the stress-strain curve [12]. Length and width of the simulation box are selected to be greater than 10 times of the crack length in order to avoid finite-size effects [13]. Strain rate and time step are 0.001 ps^{-1} and 0.5 fs, respectively. MD simulations are performed at 1K and 300K on armchair and zigzag sheets with crack lengths ranging from 4 Å to 29 Å to investigate the effect of crack length and temperature on the tensile strength (σ_{ult}). The crack lengths are defined as shown in Fig. 1.

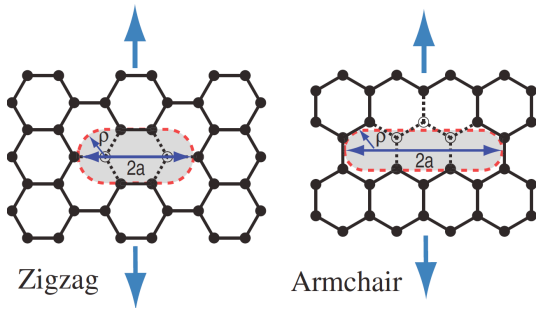

Figure 1: Crack length (2a) and crack tip radius (ρ) of armchair and zigzag graphene sheets. Arrows indicate the straining direction.

It is noticed during MD simulations that crack tips come out of the plane of graphene sheet at unstrained state. The crack tips are free edges. Deformation of free edges of graphene could be explained by considering an edge force, which arises from the difference in the energy stored in edge atoms and interior atoms [14]. As shown in Fig. 2, the out-of-plane deformation of a crack tip at equilibrium configuration is localized around the tip. However, as strain increases up to 0.018, the shape of the crack tip changes, and it acts as a localized ripple. As strain further increases up to 0.0235, this localized ripple spreads throughout the sheet.

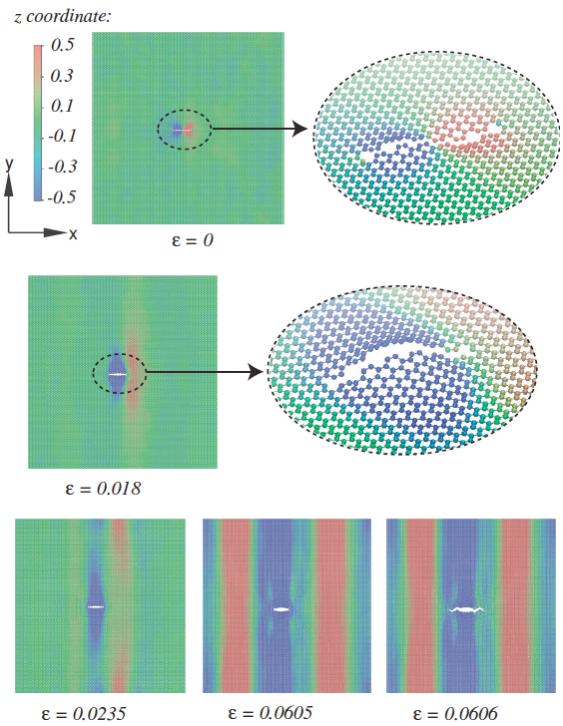

Figure 2: Ripples in 27 nm x 27 nm sheet with central crack. Strain is applied along y-direction.

3. Strength of Graphene

Stress of a graphene sheet (σ) is obtained from the gradient of the strain energy (U) - strain (ε) curve as,

$$\sigma = \frac{1}{V}\frac{\partial U}{\partial \varepsilon} \tag{1}$$

where, V is the volume of graphene sheet and the thickness of graphene is taken as 0.34 nm.

The stress-strain curves of sheets for different crack lengths at 300 K are shown in Fig. 3. The results reveal that a single vacancy (one missing atom) reduces σ_{ult} in armchair sheets by 15.7% and in zigzag sheets by 23.3%, which indicates that graphene is very sensitive to vacancy defects. It can also be noticed in Fig. 3 that Young's modulus does not change with crack length.

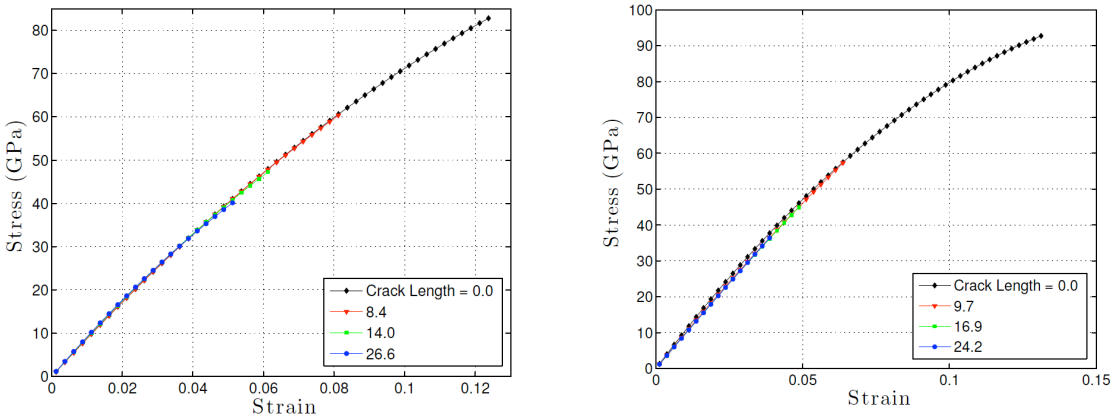

(a) (b)

Figure 3. Stress - strain curve of graphene with crack length; (a) armchair and (b) zigzag at 300 K.

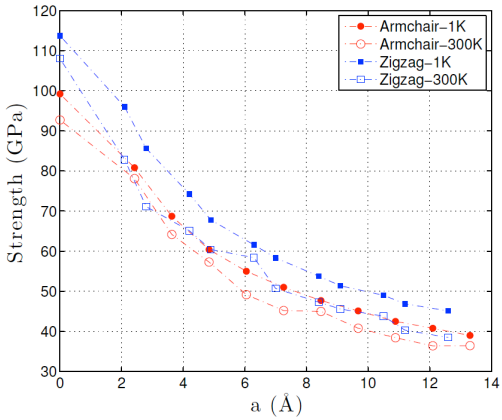

Figure 4. Effect of temperature on strength of graphene for various crack lengths.

Figure 5 shows a plot of $1/\sqrt{a}$ vs. σ_{ult}, and it clearly shows proportionality at 1 K. This indicates a formal similarity with continuum fracture mechanics. The stress intensity factor of graphene (K_I^g) can therefore be approximated as

$$K_I^g = (\sigma_f - c)\sqrt{2\pi a}, \tag{2}$$

where c is a constant (c is zero for a continuum) and a is the crack length. The values of K_I^g and c are given in Table 1 based on MD simulations. K_I^g decreases as temperature increases from 1 K to 300 K, which reflects the reduction of σ_{ult} as shown in Fig. 4. The reduction of K_I^g in zigzag sheets is greater than that of armchair. The general agreement of MD simulation results with continuum

fracture mechanics motivates further investigation of fracture of graphene using continuum concepts.

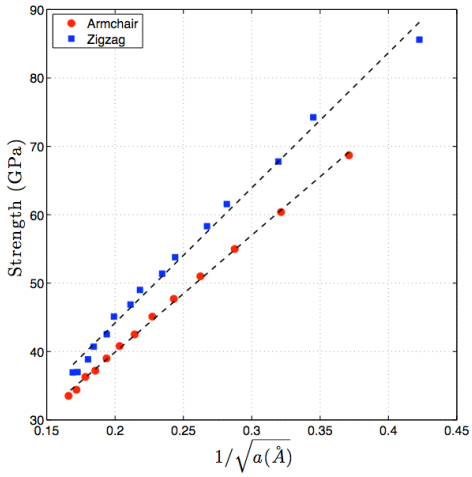

Figure 5. Variation of ultimate strength with crack length at 1 K; σ_{ult} = 120.9*(1/√a) + 5.7 and σ_{ult} = 139.7*(1/√a) + 4.7 for armchair and zigzag sheets, respectively.

Table 1: Variation of K_I^g and c with temperature.

	Temp (K)	K_I^g (MPa m$^{1/2}$)	c (GPa)
Armchair	1	4.8	5.7
	300	4.2	11
Zigzag	1	5.6	4.7
	300	4.6	4

4. Continuum Fracture Mechanics

Inglis [15] and Griffith [16] proposed two fundamental theories in fracture mechanics. Inglis derived the stress concentration due to an elliptical hole in a linearly elastic material [15]. Considering the nonlinear σ-ε relation of graphene, the remote stress at failure (σ_f) can be written as

$$\sigma_f = \sqrt{\frac{E_f \gamma_s}{4a}}, \tag{3}$$

where E_f is the tangent modulus at failure; γ_s is the surface energy and a is the crack length.

Inglis' theory was followed by Griffith's work on the fracture of brittle solids [16]. Griffith's energy balance says that failure occurs when the energy stored in the structure is sufficient to overcome the surface energy of the material. Failure stress of Griffith's model is expressed as

$$\sigma_f = \sqrt{\frac{2E_f \gamma_s}{\pi a}}. \tag{4}$$

The value of γ_s is calculated by dividing the difference in energy of a graphene sheet before and after fracture by the area of newly created surface. The value of γ_s is 5.02 J/m^2 for both armchair and zigzag graphene since the distance between two broken carbon-carbon bonds is similar in both sheets. The tangent modulus at failure is obtained from the σ-ε curves of pristine graphene sheets, and it can be expressed of as $E(\varepsilon)$ = -5.89ε + 1.08 TPa and $E(\varepsilon)$ = -3.50ε + 0.89 TPa for armchair

and zigzag sheets, respectively. The value of E_f is given by $E(\varepsilon_f)$, where ε_f is the failure strain of a sheet with a particular crack length.

A comparison of strength of graphene sheets with various crack lengths is given in Fig. 6. The strength of graphene sheets obtained from MD is between the values given by Inglis' and Griffith's approaches. The strength at 300 K shows slight fluctuations due to kinetic energy of atoms. The strength of zigzag graphene sheets given by Griffith and MD simulations agrees quite well with each other. However, both Inglis' and Griffith's theories have been derived for a flat structure, whereas graphene with a crack does not remain flat as shown in Fig. 2. The continuum theories also assume the continuity of material, which is not the case in graphene. Therefore, a perfect agreement between continuum theories and MD simulations cannot be expected.

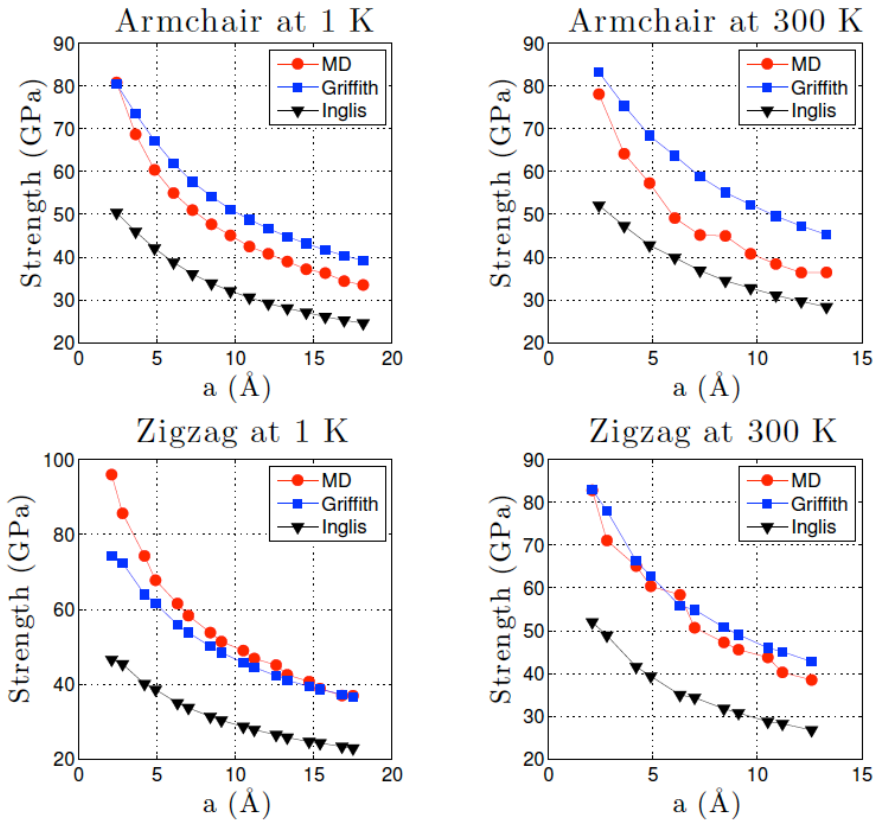

Figure 6. Comparison of Griffith's and Inglis' theories with MD simulations.

5. Conclusions

The crack tips of graphene show out-of-plane deformations at equilibrium configuration. These deformations propagate with the applied strain and eventually generate ripples in the sheet. A crack with the length of 2.5 nm reduces the strength of both armchair and zigzag graphene sheet by around 55%. Strength obtained from molecular dynamics simulations shows inverse square-root proportionality with crack length as in continuum fracture mechanics theories. Strength of graphene sheet given by Griffith's theory reasonably agrees with strength obtained from molecular dynamics simulations.

Acknowledgements

This research was supported by Natural Sciences and Engineering Research Council (NSERC) of Canada.

References

[1] C. Lee, X. Wei, J. W. Kysar, and J. Hone, Measurement of the elastic properties, intrinsic strength of monolayer graphene. Science, 321 (2008) 385-388.

[2] Hashimoto, K. Suenaga, A. Gloter, K. Urita, S. Iijima, Direct evidence for atomic defects in graphene layers. Nature, 430 (2004), 870-873.

[3] F. Banhart, J. Kotakoski, A. V. Krasheninnikov, Structural defects in graphene. ACS Nano, 5 (2011) 26-41.

[4] R. Khare, S. L. Mielke, J. T. Paci, S. Zhang, R. Ballarini, G. C. Schatz, T. Belytschko, Coupled quantum mechanical/molecular mechanical modeling of the fracture of defective carbon nanotubes and graphene sheets. Phys Rev B, 75 (2007) 075412.

[5] R. Ansari, S. Ajori, B. Motevalli, Mechanical properties of defective single-layered graphene sheets via molecular dynamics simulation. Superlattices and Microstructures, 51 (2012) 274-289.

[6] M. Wang, C. Yan, L. Ma, N. Hu, M. Chen, Effect of defects on fracture strength of graphene sheets. Computational Materials Science, 54 (2012) 236-239.

[7] Omeltchenko, J. Yu, R. K. Kalia, P. Vashishta, Crack front propagation and fracture in a graphite sheet: A molecular-dynamics study on parallel computers. Phys Rev Lett, 78 (1997) 2148-2151.

[8] M. Xu, A. Tabarraei, J. Paci, J. Oswald, T. Belytschko, A coupled quantum/continuum mechanics study of graphene fracture. Int J Fract, 173 (2012) 163-173.

[9] K. Kim, V. I. Artyukhov, W. Regan, Y. Liu, M. F. Crommie, B. I. Yakobson, A. Zettl, Ripping graphene: Preferred directions. Nano Letters, 12 (2012) 293-297.

[10] S. J. Stuart, A. B. Tutein, J. A. Harrison, A reactive potential for hydrocarbons with intermolecular interactions. J Chem Phys, 112 (2000) 6472-6486.

[11] S. Plimpton, Fast parallel algorithms for short-range molecular dynamics. J Comput Phys, 117 (1995), 1-19.

[12] O. A. Shenderova, D. W. Brenner, A. Omeltchenko, X. Su, L. H. Yang, Atomistic modeling of the fracture of polycrystalline diamond. Phys Rev B, 61(2000) 3877-3888.

[13] A. Mattoni, L. Colombo, F. Cleri, Atomic scale origin of crack resistance in brittle fracture, Phys Rev Lett, 95 (2005) 115501.

[14] Q. Lu, R. Huang, Excess energy and deformation along free edges of graphene nanoribbons. Phys Rev B, 81(2010) 155410.

[15] C. Inglis, Stress in a plate due to the presence of cracks and sharp corners. Trans R Inst Naval Architects, 60 (1913) 219–241.

[16] A. A. Griffith, The phenomena of rupture and flow in solids. Phil. Trans R Soc Lond A, 221(1921) 163-198.

Experimental study of heat dissipation process into fatigue crack tip in titanium alloys.

M.V. Bannikov[1*], **A.I. Terekhina**[1], **A.Y. Fedorova**[1], **O.A. Plekhov**[1], **O.B. Naimark**[1]

[1]Institute of continuous media mechanics Russian academy of science, 614013, Perm, Russia
*mbannikov@icmm.ru

Abstract. Paper is devoted to investigation of initiation and propagation of cracks in titanium alloys by infrared thermography study of heat generation under cyclic loading and fractography analyses of fracture surface. Two series of experiments on cylindrical specimens and flat specimens with preliminary grown fatigue crack are carried out. Spatial and time temperature evolution into crack tip is investigated, the shape and dissipative intensity at crack process zone are estimated. Based on a result of comparative analysis of the experimental data and the linear fracture mechanics equations it is shown that the spatial distribution and character of heat dissipation zone into the crack tip doesn't correspond to the conventional models. High-speed shooting (at a frequency of 1 kHz) allowed us to determine the intensity and shape of zone of energy dissipation caused by plastic deformation at the crack tip, as well as to compare the rate of energy dissipation for different stress levels. Fractured specimens were analyzed by interferometer microscope and SEM to verify the existing models of inelastic deformation at the crack tip and to improve methods of monitoring of damage accumulation during fatigue test.

Keywords fatigue, energy dissipation, thermo elasticity effect, infrared thermography, fractography

1. Introduction

The heat Dissipation caused by the evolution of the structure of the material under cyclic deformation, is the subject of intense research over recent decades. At present it is known that under cyclic deformation processes of strain localization are accompanied by intense heat generation, which makes possible early detection by infrared thermography [1].

Due to its versatility, method of infrared thermography recently been actively used at carrying out mechanical tests as to obtain detailed information about the process of nucleation and propagation of fatigue cracks [2-3] and for studying laws of conversion and energy storage during deformation [4-5]. The possibilities of the method of infrared thermography allows real-time to explore the processes of change temperature caused by thermoelasticity and localization of deformation at the crack tip, as well as the effects of friction on the crack faces during its propagation.

This paper is devoted to researching thermoelastic and thermoplastic effects in the crack tip propagating under the cyclic tensile stress applied normal to the plane of the crack. Experimentally obtained cooling effects caused by the elastic deformation of the material at the crack tip, and investigate the features of the distribution of stresses at the crack tip. High-speed photography allowed us to determine the intensity and shape of the zone of energy dissipation caused by localized plastic deformation at the crack tip, and compares the rate of energy dissipation for different stress levels.

2. Experimental conditions and materials

Experimental study of temperature evolution at the fatigue crack tip was carried out on the plane specimens of titanium alloy Ti-4.2Al-1.6Mn with frequencies ranging from 1 to 20 Hz in low-cycle

fatigue regime were investigated. Test samples were prepared from sheet with thickness 3 mm.
Geometry of specimens shown in Figure 1. In order to study thermal effects at the crack tip, specimen was pre-weakened by holes (Fig. 1a).At the initial stage of the experiment with the increased load was created fatigue crack with size of about 10 mm. Initiation of the cracks was carried out at an average load of 215 MPa, load amplitude 238 MPa and loading frequency 20 Hz. Then load was decreased for slow down crack propagation rate and for detailed study of heat generation processes in the crack tip.
Mechanical testing were carried out at 100 KN servo-hydraulic machine Bi-00-100. Analysis of the results of quasi-static testing of investigated material determine following mechanical properties of the material: Young's modulus of 64 GPa $\sigma_{0.2}$ = 683 MPa $\sigma_{в}$ = 790 MPa.

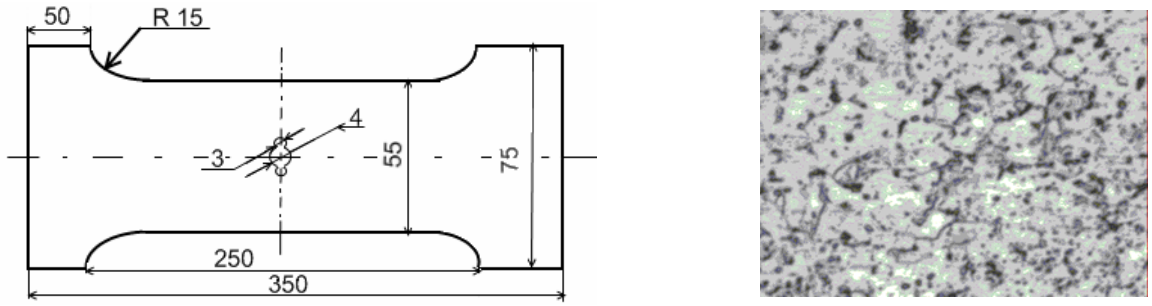

a) b)

Fig. 1. Geometry a) and structure b) of the Ti4AlMn samples to study the thermal effects in the crack tip.

During investigation the process of thermoelasticity, samples was loaded in the elastic range at frequencies 0.5, 1, 5, 10, 20 Hz and different amplitudes ranging from 100 to 350 MPa with the coefficient of asymmetry of the cycle, R = 0. To determine the strain during the experiment used an axial extensometer - Bi-06-304 with an accuracy of ± 1,5 mm.
The temperature field study was carried out by infrared camera FLIR SC 5000. Recording of the temperature field was carried out at frequencies from 350 to 950 Hz and a minimum spatial resolution from $2{\cdot}10^{-4}$ m. For the calibration of camera used standard calibration table.
During the experiment grips and specimen was shielded from external heat sources by special screen. Surface of the specimen was polished in several stages by abrasive paper (final stage of polishing grit size does not exceed 3 μm); before start of the experiment, polished surface was covered by thin layer of amorphous carbon.

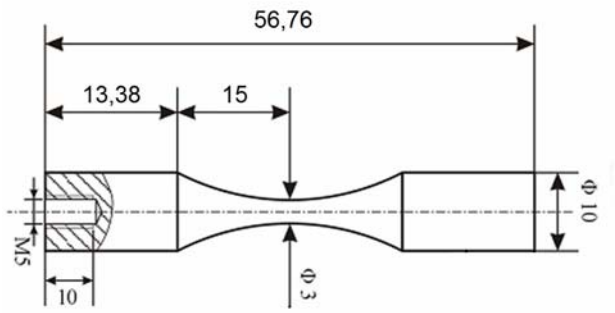

Fig.2 Typical geometry of cylindrical specimens

The second kind of experiments was carried out with cylindrical specimens (fig. 2) of pure titanium Grade 4 with different grain sizes (~25 μm and ~ 500 nm Fig. 3) to evaluate influence of grain size on fatigue strength and its dissipation properties. Structure was studied in optical microscope by chemical etching of prepared surface by sanding disc from 160 to 4000 grains per sq. cm. and

diamond suspension from 3 to 1 microns sizes.

Table 1. Chemical compound of the etching:

HNO_3	2%,
HF	2%
H_2O	96%

After polishing materials was etching by compound with shown in table 1, time of etching – 10 seconds.

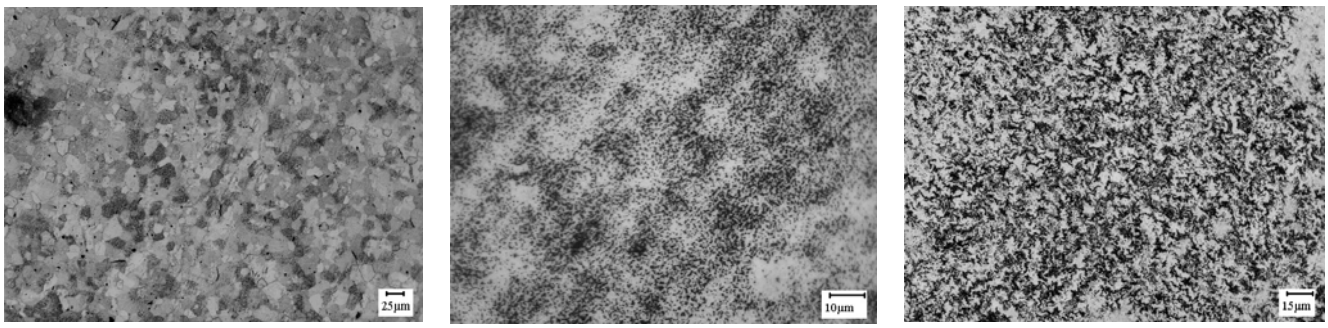

a) b) c)

Fig. 3.Structure of the Ti Grade 4 samples to study influence of grain size on fatigue strength and its dissipation properties a) initial stage with grain size ~25 μm b) Stage under Equichannel angular extrusion in condition 1 c) Stage under Equichannel angular extrusion in condition 2

High cycle testing was carried out on BOSE testing machine in laboratory of Bordeaux with frequencies 50 Hz and 10 Hz with symmetric conditions (R=-1). Test was started from stress 200 MPa. During fatigue processing, the temperature of specimen was measured by infrared camera CEDIP. When the temperature of specimen surface is reach stable value, test stopped and stress increased on 20 MPa until we get sharp rise in temperature which means reaching fatigue limit

3. Theoretical description of changes in temperature of the metal during cyclic deformation

Evolution of temperature during cyclic deformation $\sigma = \sigma_A + \Delta\sigma \sin(\omega t)$ under the assumption of homogeneity of its distribution, the absence of structural transitions and plastic deformation can be described by the Kelvin equation:

$$\mathrm{Log}\, T_t = -\frac{\beta(1-2\nu)\omega}{\rho c}\Delta\sigma \cos\omega t\,, \qquad (1)$$

where β - coefficient of thermal expansion, ρ - density, c – specific heat capacity, ν - Poisson's ratio, ω - the angular frequency of loading, $(.)_t$ - time derivative.

The solution of equation (1) has the form:

$$T = T_0 \exp[-\frac{\beta(1-2\nu)}{\rho c}\Delta\sigma \sin\omega t]\,, \qquad (2)$$

series expansion of (2) taking into account the smallness of the ratio, which stands in the exponent, gives the following relations for the first and second harmonic:

$$A_1 = T_0 \frac{\beta(1-2\nu)}{\rho c}\Delta\sigma, \qquad A_2 = \frac{T_0}{4}\left(\frac{\beta(1-2\nu)}{\rho c}\right)^2 \Delta\sigma^2, \tag{3}$$

Analysis of the relations (2), (3) leads to the conclusion that in the classical case amplitude of the first and second harmonics does not depend on frequency and are linear functions of stress amplitude and the square of the stress amplitude, respectively.

At the present time been suggested that the effect of thermoelasticity is strongly nonlinear [6]. Significant contribution to the temperature dependence of the time makes the process of changing the elastic properties of the material on temperature. Assuming the dependence of the elastic modules of the material on the temperature (λ_T, μ_T), the temperature change is described by the equation:

$$\begin{aligned} \mathrm{Log}\, T_t = &\left(-\frac{\beta(1-2\nu)}{\rho c} + \lambda_T \frac{\sigma_0}{(3\lambda+2\mu)^2 \rho c} + 2\mu_T \frac{\sigma_0(1.5\lambda^2+2\lambda\mu+\mu^2)}{\mu^2(3\lambda+2\mu)^2 \rho c}\right)\Delta\sigma\omega\cos\omega t + \\ &+\left(\frac{\lambda_T}{2(3\lambda+2\mu)^2 \rho c} + \mu_T \frac{(1.5\lambda^2+2\lambda\mu+\mu^2)}{\mu^2(3\lambda+2\mu)^2 \rho c}\right)\Delta\sigma^2\omega\sin 2\omega t \end{aligned} \tag{4}$$

At the tip of fatigue crack occurs intensive energy dissipation due to the localization of plastic deformation. The characteristic size of the zone of energy dissipation in framework of linear fracture mechanics, determined by the value of stress intensity factor. The magnitude of the stress intensity factor taking into account geometry of the sample can be estimated using the expression:

$$K = \sigma\sqrt{\pi a}\, Sec\left(\frac{\pi a}{W}\right)^{1/2}, \tag{5}$$

where W – wide of specimen, a– half-length of crack.The radius of the zone of plastic deformation on the surface of the plate is:

$$r_p = k\frac{K^2}{\sigma_y^2}, \tag{6}$$

where k – coefficient depending on the type of stress state and accepted model of plastic deformation, σ_y – flow stress. The form of the zone of plastic deformation at the crack tip under quasi-static tension can be described by the relations:
taking into account Mises criterion

$$r_p(\theta) = \frac{1}{4\pi}\frac{K^2}{\sigma_y^2}\left(1+\cos(\theta)+3\sin^2(\theta)\right), \tag{7}$$

taking into account Tresca Saint Venant criterion

$$r_p(\theta) = \frac{1}{2\pi}\frac{K^2}{\sigma_y^2}\cos^2\left(\frac{\theta}{2}\right)\left(1+\sin\left(\frac{\theta}{2}\right)\right)^2. \tag{8}$$

4. Experimental study changes in temperature during elastic deformation.

Analysis of thermal effects at the crack tip is complicated by the fact that during normal loading to the plane of the crack propagation, its trajectory is not always strictly linear. The appearance of an inflection point on the trajectory of crack leads to a significant heat release on its banks (Fig. 4).Apparently, the edges of the crack are shifted relative to each other and cause the appearance of zones of friction and/or plastic deformation, which corresponds to the hypothesis of crack closure, is used in some models of linear fracture mechanics.

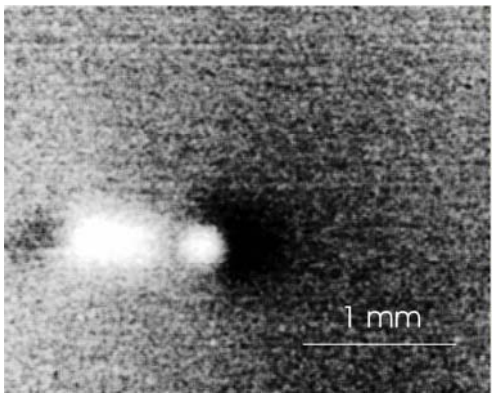

Fig. 4 The temperature distribution at the top and on the banks of the fatigue crack propagation under cyclic deformation

Figure 5 shows the change in the maximum temperature at the crack tip, stress and crack opening during loading with the stress amplitude 212 MPa, average stress 212 MPa and frequency of 5 Hz. Data from displacement sensor mounted on the crack faces, allows to suggest that the disclosure of the crack varies in phase with the applied stress.

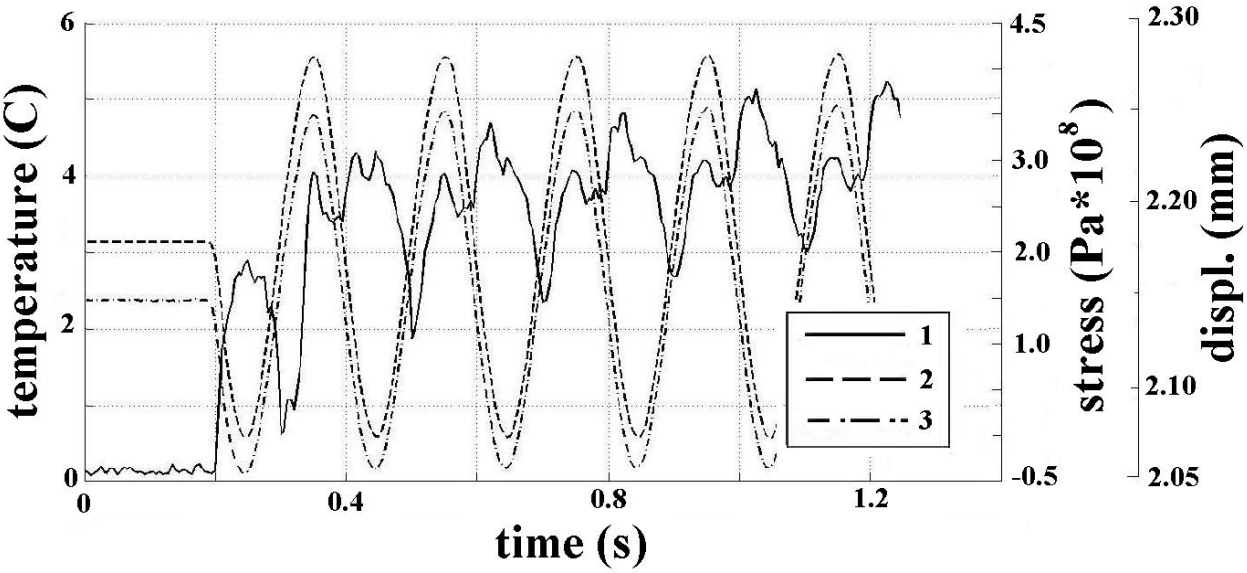

Fig.5. Changing the maximum temperature at the crack tip (1), stress (2), and the crack opening (3) in the process of cyclic loading with the amplitude of stress 212 MPa, average stress 212 MPa and frequency of 5 Hz.

Analysis of temperature data allows asserting, that the maximum of applied stress and the maximum of intensity of heat in the top of the fatigue crack does not match in time. At the beginning of the experiment the sample is loaded by middle stress and in a state of thermodynamic

equilibrium. At each loading cycle is observed area of temperature drop caused by the thermoelastic effect, which goes to the site of temperature increase caused by the local transition through the proportional limit and the formation of zones of plastic deformation. During decrease stress in the crack tip heat generation are continues. The geometry of the zones of plastic deformation is shown in Figure 6. With decreasing stress at the crack tip heat increases and the temperature reaches its maximum at practically zero stress value. Then, at the beginning of the next cycle, the temperature drops due to thermoelastic effect and the process repeats.

The main goal in investigation of cylindrical specimens was to understand principles of crack initiation and propagation inside of specimen i.e. Fish eye. For achieve this goal specimens were tested in 2 regimes – multi-cycle fatigue with using infrared camera and giga-cycle fatigue. In giga-cycle fatigue regime rise of temperature was very high and not able to control without cooling – such way infrared camera was helpless in analyzing of structure parameters. During multi-cycle fatigue was determine fatigue strength of titanium specimens by Luong method [1]. For materials with usual structure it is work well, but for nano-grain structures it is not so accurate, because damage accumulated during the formation of such a structure start to heat much earlier than usual structure, but we still can to evaluate fatigue strength limit on sharp rise temperature point (fig. 6)

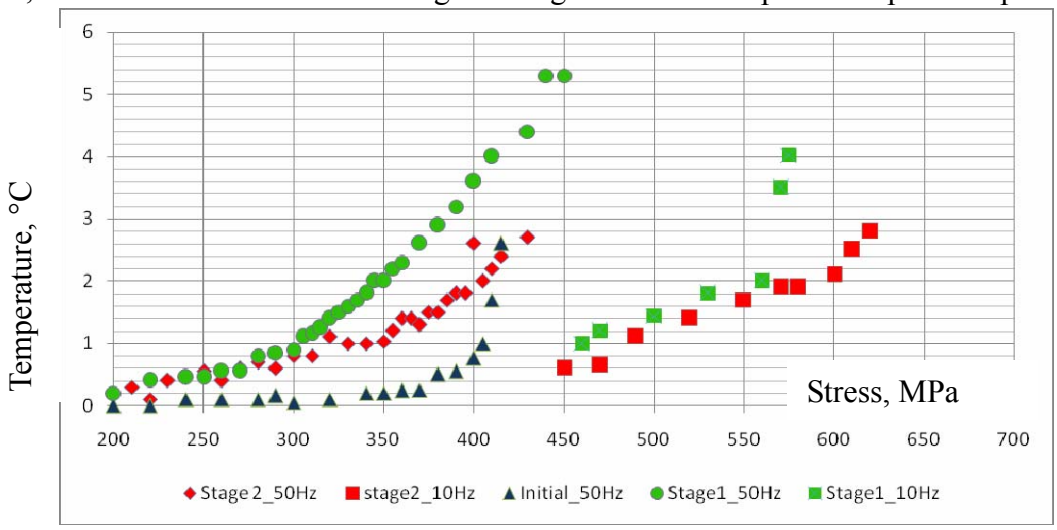

Fig6. The dependence of the surface temperature of the sample from the applied stress

Summarizing results of high cycling test and infrared camera, using Resitano-Luong technic, we can conclude that fatigue limit of Ti Grade 4 in initial stage is approximately 375 Mpa, in “Stage 1” 575 MPa, in “Stage 2” 600 MPa.

Infrared thermography methodic can high accuracy visualize zone of intense energy dissipation in the tip of fatigue crack (Fig. 7). The distribution of temperature in the crack tip during deformation may differ from the form of zones of plastic deformation due to the processes of heat conduction, so to analyze the geometry of the intense heat caused by plastic deformation, it is logical to use only the first cycle of deformation. Figure 7 shows a comparison of the observed shape of zones of intense energy dissipation in the first cycle of deformation and classical solutions of (3.4) to form zones of plastic deformation in the crack tip (in the calculations we used the following data: half crack length 4 mm, the applied stress 300 MPa). Analysis of the results suggests only a qualitative agreement forms zones of plastic deformation in the tip of fatigue crack propagation to models Mises and Tresca-Saint Venant.

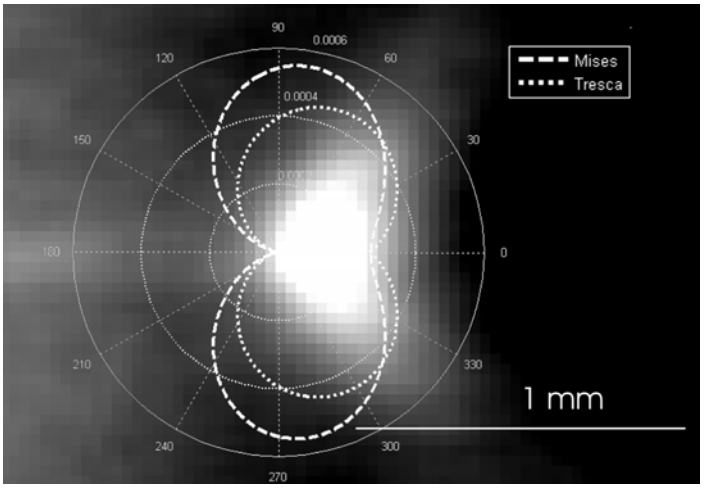

Fig.7. The form of zones of intense energy dissipation in the crack tip on the first cycle of deformation and plastic deformation zone, built on the criteria of von Mises and Tresca-Saint Venant.

5. Fractography analysis of fractured specimens.

Fractured specimens were investigated by optical and scanning electronic microscopes for qualitative analysis of fracture surface. Specimens with inside and surface crack initiation were observed. For quantitative analysis was used interferometer profiler New View 5010 which can get 3D image of investigated surface with digital data. Relief of fractured surface close to crack initiation and its propagation was analyzed.

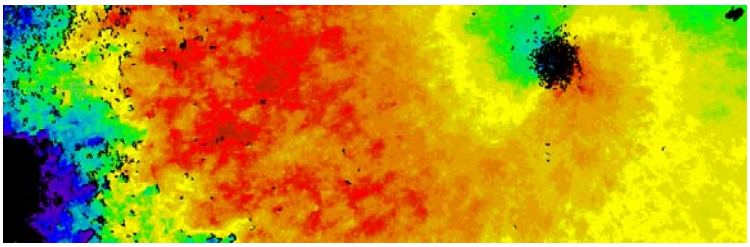

Fig 8. Typical relief of fractured specimen with inside crack initiation obtained on interferometer profiler New View.

In the study, one-dimensional image of the of the relief in certain selected sections, were analyzed by the method of Hurst in terms of the Hurst exponent, measured by the correlation function:

$$K(r) = \left\langle \underset{\{x,x+r\}}{Max}(z(x)) - \underset{\{x,x+r\}}{Min}(z(x)) \right\rangle_x \propto r^H \quad , \tag{9}$$

where z (x) - the height of the relief, depending on the coordinates, the angle brackets denote averaging over x, H - Hurst exponent.

In terms of Hurst exponent fractured relief had 2 zones with significant difference of H. First zone has circle geometry and its position around crack initiation with diameter ~ 300 μm. We assume that inside this zone was defect accumulation during fatigue loading. When this zone reach 300 μm diameter crack became instability and start propagate and we can see it on increasing of H. Second zone size reach cross section of specimen.

6 Summary.

Relations are obtained which describe change in temperature at the sample surface and the tip of fatigue crack during a uniaxial cyclic deformation taking into account the linear and nonlinear thermoelastic effects. Shown that the process of heat generation is essentially nonlinear. Using of infrared thermography methodic can effectively investigate the processes associated with both the localization of plastic deformation in the crack tip and the friction on its banks. At this stage, studies have shown experimentally that the zone of plastic deformation does not coincide with the predictions of the linear fracture mechanics, and the maximum heat is reached on the descending branch of the loading. Fracture surface has 2 zones with significant difference of Hurst exponent which correspond damage accumulation and crack propagation.

Acknowledgements

The study was supported by The Ministry of education and science of Russia, project N8753 and grant RFBR 12-01-31145 mol_a,

References

[1] M.P. Luong, Infrared thermographics scanning of fatigue in metals, Nuclear Engineering and Design. №158 (1995).

[2] O. Plekhov, N. Saintier, T. Palin-Luc, S. Uvarov, O. Naimark, Theoretical analysis, infrared and structural investigation of energy dissipation in metals under quasi-static and cyclic loading , Material Science and Engineering V. 462. N.1 (2007)

[3] O. Plekhov, T. Palin-Luc, O. Naimark, S. Uvarov, N. Saintier, Fatigue crack initiation and growth in a 35CrMo4 steel investigated by infrared thermography, Fatigue and fracture of engineering materials and structures V. 28, I. 1, (2005)

[4] W. Oliferuk, M. Maj, B. Raniecki, Experimental analysis of energy storage rate components during tensile deformation of polycrystals, Materials Science and Engineering v. 374 (2004)

[5] P. Rosakis, A.J. Rosakis, G. Ravichandran, J. Hodowany, A thermodynamic internal variable model for the partition of plastic work into heat and stored energy in metals, J. Mech. and Phys. Solids, №48 (2000)

[6] R. Jones, M. Krishnapillai, K. Cairns, N. Matthews, Application of infrared thermography to study crack growth and fatigue life extension procedures, Fatigue & Fracture of Engineering Materials & Structure, v.33 (2010)

CTOD fracture toughness assessment method of High-strength steel based on BS7910

Ziyu Xia[1, a]，**Zhangmu Miao**[1, b]，**Tao Ma**[2, a]，**Gang Chen**[2, b]，**Sheng Peng**[1, a]

1.School of Transportation, Wuhan University of Technology，Wuhan 430000

2 .Shanghai Waigaoqiao Shipbuilding Company Limited，Shanghai 200137

[a]whut_xzy@126.com, [b]zmmiao1957@yahoo.com.cn

Abstract As one of the essential criteria of assessment to welding toughness, CTOD(Crack tip opening displacement) is widely applied in engineering. The research on allowable values of the CTOD of high strength and thickness steel has been a hot issue, therefore the theoretical research in China lags behind its overseas. The present paper takes the single edge fatigue precrack of CTOD specimen as a flaw with the technical route of the British Standard 7910-2005, that is "Guide to methods for assessing the acceptability of flaws in metallic structures". In the meanwhile, make the grading assessments of the welding seam center of the EQ70/56 joints, combining the results of the CTOD tests. The assessments on welded joints of EQ70/56 show that the CTOD values are in the acceptable range. This method provides some useful guidance in researches of allowable CTOD values.

Key Word Welded joint of High strength steel，CTOD，BS7910，FAD ,EQ70/56

1 Introduction

With the development of the ocean engineering, the high-strength steel and ultra-high-strength steel are widely applied in the Deep-water Semi-Submersible Drilling Platform. As the complicated welding joints, high-strength and big thickness, the welding procedure of the marine structure becomes the key to the construction of the platform. The specification and classification societies around the world, including the CCS (China Classification Societies), are beginning to take the CTOD tests as a means to assess the toughness of the welded joints and the high-strength and heavy steel plates. However, there is much difference on the allowance value of CTOD with different societies, especially for the new high-strength and heavy steel plates.

As the development of the methods for assessing the acceptability of flaws of the welded metallic structures, the British Standard 7910:1999, called "Guide to methods for assessing the acceptability of flaws in metallic structures", replaced the old standard PD 6493:1991[1] and was being widely applied in the engineering[2]. Basing on the fracture mechanics, the stand BS7910 fulfills the assessments with the FAD (failure assessment diagram) and takes the compare between the crack resistance of the structure and the actual ability to crack loading as its main idea.

When majority standards of flaw assessment of metal structure were applied on the issue of 'Fitness for Purpose', the BS7910:1999 was amended and extended to an update version BS7910:2005[3], which has three levels of fracture assessment for the flaws in metallic structures. The choice of level depends on the materials involved, the input data available and the conservatism required.

In the standard BS7910, flaws include Planar flaws, Non-planar flaws and Shape imperfections. In the assessment of high-strength and heavy steel plates, the specimen of the CTOD test was pre-carved with crack throughout the thickness. The welding seam center of the specimen was determined by the Level 2B. In the FAD of Level 2B, the axis is assessment index of fracture toughness, appears as Kr which is the ratio of the stress intensity factor, or $\sqrt{\delta_r}$, the square root of CTOD fracture ratio. In the CTOD tests, the single edge running through crack [4] could be taken as the flaws assessed by FAD with the fracture ratio as ordinates against load ratio (Sr) as abscissa. The applied Level 2 assessment has an assessment curve given by the equation of a curve and a cut-off. If the assessment point lies within the area bounded by the axes and the assessment curve, the flaw is acceptable; if it lies on or outside the curve, the flaw is unacceptable.

The CTOD toughness assessment of the heat affected zone and welding seam center of

high-strength and thickness steel with the FAD method are summarized as follow:
1) Measure the CTOD values of the welding joints of the high-strength steel at a specific temperature;
2) Plot the stress-strain curve of the welding joints of the high-strength steel through an uniaxial tensile test, and then transfer it to a true stress-strain curve with related equations;
3) Plot the Level 2B FAD with the true stress-strain curve, make the failure assessments of the joint and the welding seam center of the high-strength steel plates;
4) Calculate the load ratio and fracture ratio (coordinates of the assessment points) with the CTOD values and stress-strain curve, and then plot the FADs with the ratios. The toughness assessments of the welding joint would be completed with the FADs.

2 CTOD experiment and results

The present paper mainly research on the FADs of the welding seam center of butt-weld joint between EQ70 and EQ56 high-strength steel plates(Level-AB) with 38 mm thickness. The CTOD test is carried out according toBS7448[5] and Offshore Standard DNV-OS-C401[6]The chemical composition of the EQ70 and EQ56 steel plates are shown in the table 1 and table 2, while the different welding technologies are shown in table 3.
The EQ 56 and EQ 70 were butt welded with equiangular welding groove (45°K style groove), by multi-layer and multi-pass manual arc welding. While it should preheat temperature to70 ℃, kept the groove straight edge perpendicular to the specimen plane, with 210 to 230 ℃thermal insulation per hour after welding. To the specimen of EQ56/70, the K type groove straight edge should perpendicular to the side of EQ70[7].
Three-point bending specimens, with single side fatigue precrack, were applied in the CTOD test and processed into 26 mm thickness(B) and 52 mm width(W). The results and effectiveness of the CTOD test were list in the table 4.

Table 1 The chemical compositions of EQ 70 specimen with 38 mm thickness (%)

C	Si	Mn	P	S	Cu	Ni	Cr	Mo
0.14	0.08	0.86	0.011	0.002	0.26	0.49	0.76	0.32
V	ZR	Ti	Nb	Sol Al	N	B	Ceq	PCM
0.04	0.005	0.013	0.016	0.064	0.0023	0.0010	0.56	—

Table 2 The chemical compositions of EQ56 specimen with 38 mm thickness (%)

C	Si	Mn	P	S	Al	Ni
0.05	0.41	1.51	0.009	0.001	0.033	0,73
Cr	Cu	Nb	V	Ti	Mo	w(C)eq
0.33	0.71	0.04	0.04	0.009	0.22	0.51

Table 3 Welding technologies of the joints of EQ70/56

Technical parameter Type	No.of welding bead	Diameter (mm)	Electricity (A)	Voltage (V)	Welding speed (mm/min)	Maximum Energy Input (kJ/mm)	Average Energy Input (kJ/mm)
A	1	3.2	130~160	20~25	69	3.62	2.85
	others	4.0	170~195	22~27	77	4.10	3.51

B	1	3.2	120~145	23~30	104	2.88	2.02
	others	4.0	180~196	25~35	112	3.68	3.02

Table 4 The CTOD experimental results of EQ70/56 specimen with 38 mm thickness

Technical parameter	Crack Position	NO.of specimens	B / mm	W / mm	a_0 / mm	δ_u / mm	Available Test
A	Welding seam center	1	26.03	52.03	26.364	0.099	Available
		2	25.99	52.02	27.026	0.137	Available
		3	26.04	52.04	26.360	0.122	Available
B	Welding seam center	1	29.99	59.96	30.156	0.243	Available
		2	30.09	60.01	29.823	0.222	Available
		3	30.09	59.90	29.990	0.192	Available

3 Uniaxial tensile test and results

Take an uniaxial tensile test on the EQ7/56 specimen with the Electric Servo-hydraulic Material Test system, under the guidance of the Standard, “Metallic materials Tensile testing at ambient temperature”[8]. The present paper take a butt-welding joint of EQ70/56 as an specimen(d_0=4mm), and get its stress-strain curve, some basic outputs were list in the table 7.

Table 7 Basic data of the uniaxial tensile test

NO.of Specimens	EQ70/56	EQ70-HAZd6
Shape of Specimen	Circular cross section	Circular cross section
Diameter(mm)	4.01	3
S_o(mm^2)	12.63	7.069
L_o(mm)	19.9	15.4
Extensometer gauge length(mm)	50	50
F_m(kN)	10.46	5.65
Tensile Strength R_m(MPa)	830	800
F_{eH}(kN)	/	5.42
Upper Yield Strength R_{eH}(MPa)	/	765
F_{eL}(kN)	/	5.24
Lower Yield Strength R_{eL}(MPa)	/	740
F_p(kN)	9.25	5.36
Proof Strength Non-proportional Extension	730	760

R_p(MPa)		
F_t(kN)	1.2	0.67
Proof total Extension R_t(MPa)	95	95
The ratio of Yield strength	0.88	0.95
The ratio of tensile strength to Yield Strength	1.14	1.05

The yield strength σ_s and ultimate strength σ_b were calculated according the equation (1) as follow:

$$\sigma_s = \frac{F_s}{A_0}, \quad \sigma_b = \frac{F_b}{A_0} \quad (1)$$

in which, F_s means the yield load, F_b means the maximum load and the A_0 original cross section area of specimen.

As the yield stress of the EQ70/56 has no yield step, it is very difficult to accurately determine its yield stress(which means it is difficult to determine the stress at the beginning of its yield step). Generally, It takes the stress, when it generate a specific permanent strain (usually 0.2%), as the yield stress [9].

At the beginning of the stress-strain curve, the stress proportionally rises against the strain, while its ratio is the elastic modulus. While the strain increased to 0.2%, plotted a straight line with a slope equaling to elastic modulus. The corresponding value to the intersection between the plotted line and the stress-strain curve was the equivalent yield stress.

The outputs of the test were forces and deformations, which should be calculated to the inputs of the stress-strain curve. In the present test, the stress $\boldsymbol{\sigma}$ and strain $\boldsymbol{\varepsilon}$ were determined by the equation (2) as follow:

$$\sigma = P/S_0, \quad \varepsilon = \delta/L_0 \quad (2)$$

According to the results of the test and calculated date, the stress-strain curve could be plotted as figure 1.

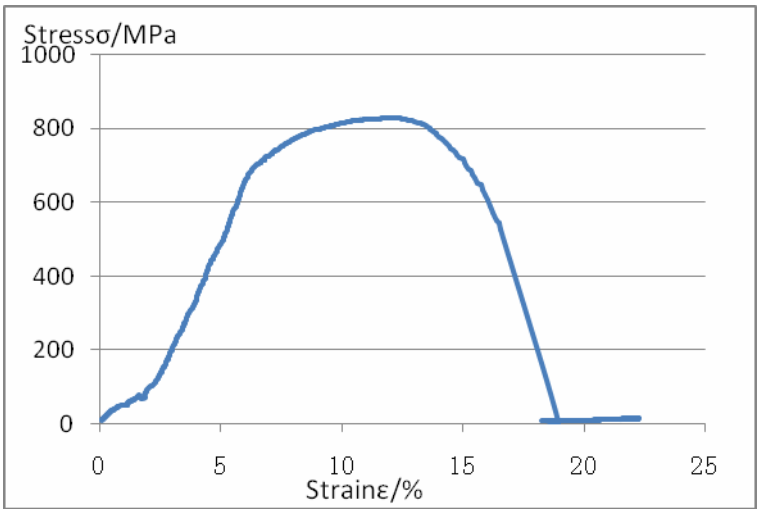

Figure 1 The stress-strain Curve of EQ70/56

The maximum load could be calculated from the displacements and forces of the test, the results

were listed in the table 8.

Table 8 The uniaxial tensile experimental results of the Welding seam center

The type of the steel	The position of the specimen	Yield Stress (Mpa)	Tensile Stress (Mpa)
EQ70/56	Welding seam center	728.8	828.2

According to the uniaxial tensile stress-strain curve, the true stress expression was as follow:

$$\sigma_t = (1 + \varepsilon)\sigma \quad (3)$$

while the true strain expression was as follow:

$$\varepsilon_t = \ln(1+\varepsilon) \quad (4)$$

Plot the true stress-strain curve from the equations (3) and (4), and then the true stress-strain curve of the welding seam center could be plotted as figure 2.

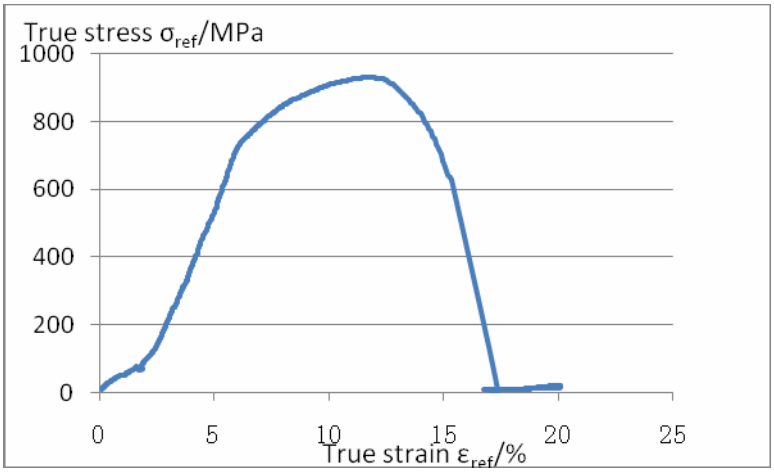

Figure 2 True stress-strain curve of EQ70/56

Under the guidance of the Standard <Metallic materials Tensile testing at ambient temperature>, it measured the elastic modulus with electrometric method. As the elastic modulus was independent of the thickness of the specimens, there was no elastic modulus distinction in the same position of the specimen. The elastic modulus E was determined by the equation (5) as follow:

$$E = \frac{F}{S_0 \varepsilon} \quad (5)$$

Here, F denotes the load increment, while the S_0 denotes the cross section area.

Table 9 The results of Elastic modulus test

Position	E （Gpa）
Welding seam center	215.5

4 The FADs of welding seam center of EQ70/56

With the Guidance of Level-2B assessment in Standard BS7910 and the true stress-strain curve from the uniaxial tensile test, it could comes to the FAD basing on the CTOD test. The boundary values of FAD(L_{rmax}) were determined by the equation (6):

$$L_{rmax}=\frac{\sigma_Y+\sigma_u}{2\sigma_Y} \quad (6)$$

The tensile strength of the EQ70/56, as well as the yield strength and the ultimate strength, could be got from the tests. Then the boundary value could be calculated by the strength as L_{rmax} = 1.06.
Stress-strain data are required at the appropriate temperature for parent material and/or weld metal. The lower yield or 0.2% proof strength, tensile strength, and modulus of elasticity should be determined together sufficient co-ordinate stress/strain points to define the curve. Particular attention should be paid to defining the shape of the stress/strain curve for strains below 1%. It is recommended that the engineering stress/strain curve should be accurately defined at the following ratios of applied stress, σ, to yield strength, σ_y: σ / σ_y =0.7,0.9, 0.98,1.0,1.02,1.1, 1. 2 and intervals of 0.1 up to σ_u.
The equations describing the assessment line are the following:
a) for Lr ≤ Lrmax

$$\sqrt{\delta_r} \text{ or } K_r=\left(\frac{E\varepsilon_{ref}}{L_r\sigma_Y}+\frac{L_r^{\,3}\sigma_Y}{2E\varepsilon_{ref}}\right)^{-0.5} \quad (6a)$$

b) for $L_r > L_{rmax}$

$$\sqrt{\delta_r} \text{ or } K_r=0 \quad (6b)$$

Where
the εref is the true strain obtained from the uniaxial tensile stress-strain curve at a true stress,LrσY.

$$L_r=\frac{\sigma_{ref}}{\sigma_Y} \quad (7)$$

According to the equations (6) and (7), the horizontal axis Lr and the vertical axis √δr could be calculated to plot the FADs of EQ70/56 and EQ70, as shown in figure 3.

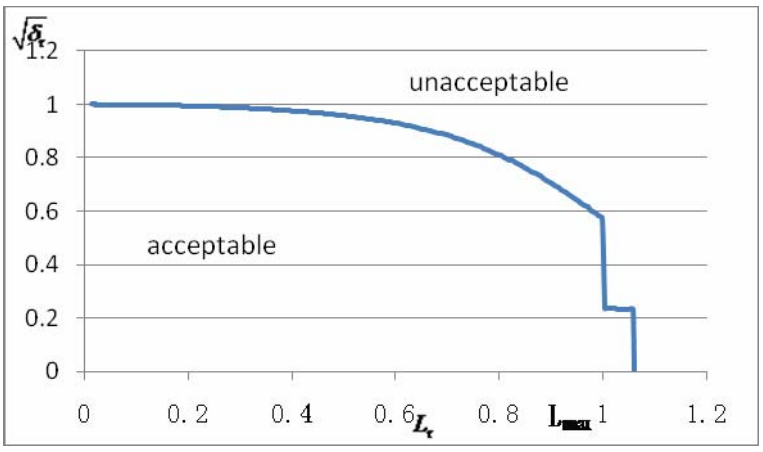

Figure 3 FAD of the welding seam center of EQ70/56

5Calculation of The CTOD test assessment point

5.1Abscissa of the assessment points

In the Level-2B assessment, the horizontal axis is L_r, which could be calculated with the the equation (7) as mentioned above in section 4 with the Standard BS7910:

While the CTOD theory was put forward initially, it was recognized that, for the elastic-perfectly plastic material, there was a plasticity area in the crack tip. Which means that the stress of the ligament area in the crack tip would not increase, after the crack tip fracture stress under general yielding. The stress of the plastic yielding area was equal to the yield strength σ_y. Therefore, while assessed the CTOD values with the Level-2B method, the value of Lr should be taken as 1.0 [10]and the abscissa of the assessment point should be 1.0 as well.

5.2 Ordinates of the assessment points

In the FAD, the vertical coordinate was fracture ratio δ_r, determined by the following equation:

$$\sqrt{\delta_r} = \sqrt{\delta_I / \delta_{mat}} \quad (8)$$

Where δ_{mat} is the fracture ratio of the material obtained by CTOD test, and the δ_I are calculated by K_I as the following equation:

$$\delta_r = \frac{K}{Xo}\delta_I = \frac{K_I^{\,2}}{X\sigma_Y E'} \quad (9)$$

X is the factor(generally of value between 1 and 2) influenced by crack tip and geometric constraint and the work hardening capability of the material. Appropriate values of X may be determined from elastic analyses which model structural constraint. If values of X are not quantified by structural analyses, use X =1.0. E' is the elastic modulus considering restrain. In the plane stress condition, $E'=E$, while $E'=1-\mu^2$, the in the plane strain condition. The applied stress intensity factor of the I-type crack, K_I, has the following general form in the three bending condition:

$$K_I = \frac{FS}{BW^{3/2}} \cdot f\left(\frac{a_0}{W}\right) \quad (10)$$

$$f\left(\frac{a_0}{W}\right) = \frac{3\left(\frac{a_0}{W}\right)^{1/2}\left[1.99 - \left(\frac{a_0}{W}\right)\left(1-\frac{a_0}{W}\right)\left(2.15 - 3.93\frac{a_0}{W} + 2.7\left(\frac{a_0}{W}\right)^2\right)\right]}{2\left(1+2\frac{a_0}{W}\right)\left(1-\frac{a_0}{W}\right)^{3/2}} \quad (11)$$

where, S denotes the distance between specimens, W denotes the width and S =4W, B denotes the thickness, F denotes the loads.

5.3 Toughness assessment of CTOD

According the method in section 5.1and 5.2, the toughness assessment of CTOD could be transferred to the assessment points in the FAD of EQ70/56, the results shown in the table 10.

Table 10 The assessment points in the FAD of EQ70/56

Technical parameters	Crack position	NO. of specimen	B/mm	δ_I /mm	δ_{mat} /mm	Lr	$\sqrt{\delta_I/\delta_{mat}}$
A	welding	1	26.03	0.012	0.099	1	0.353
	seam	2	25.99	0.014	0.137	1	0.315
	center	3	26.04	0.010	0.122	1	0.284
B	welding	1	29.99	0.017	0.243	1	0.265
	seam	2	30.09	0.016	0.222	1	0.278
	center	3	30.09	0.015	0.192	1	0.281

Note：In the present CTOD test, the elastic modulus applied in the calculation was measured in the uniaxial tensile test, instead of the parameters given by the manufacturer. The elastic modulus was $E'= \frac{E}{1-\mu^2} =$ 234.5 Gpa, which conduct the yield strength as 729 Mpa.

Then mark the coordinates of the assessment points into the PAD of the EQ70/56, as shown in figure 6.

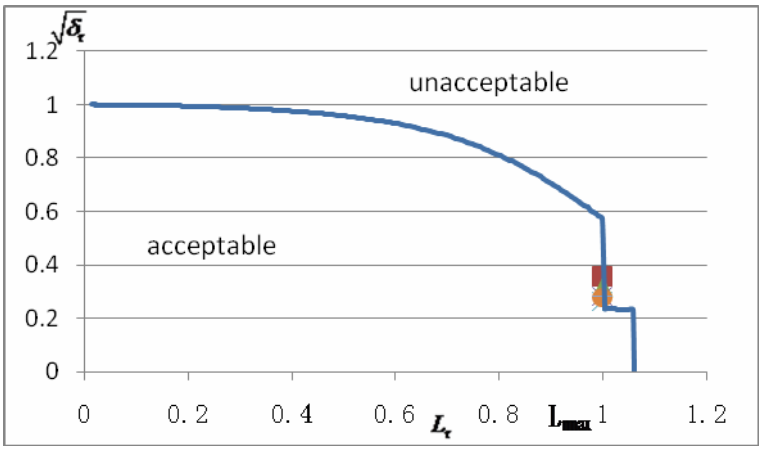

Figure 6 FAD of the EQ70/56 with the assessment points

5.4 Error analysis

It could get the stress-strain curve through the tensile test while making the toughness assessment of the CTOD of the welding joints. In the meanwhile, the Level-2B assessment required the true stress-strain curve, it should transferred the test data to the true stress-strain curve. The present

paper took the transformation as follow:
True stress

True Stress $\sigma_t=(1+\varepsilon$ (12)

True strain

True Strain $\varepsilon_t=\ln(1+$ (13)

The above equations could directly measure the responses in the range of plastic-flow, the true stress and strain could be calculated by the equations before the strain developing to necking. However, after necking, the material exceeded the elastic limit, which caused the geometric size was great different from the initial condition. The plane of the specimen was in a complicated three dimensional stress states, and the strains were nonuniform in the gauge length of the specimen. In this situation , it would bring some errors to calculate the true stress-strain.
To get more accurate true stress-strain curve, it generally used the semi-empirical and semi-analytical Bridgman formula, which was deduced to average longitudinal stress correction formula as follows:

$$\sigma=\frac{\sigma_{\text{average}}}{(1+\frac{2R}{a})\ \ln\ (1+\frac{a}{2R})} \quad (14)$$

where, R denotes the radius of the necking surface, a denotes the minimum radius after necking and σ_{average} denotes the average longitudinal stress of the minimum cross section.
The present paper provided the CTOD toughness assessment for the high strength steel plate, the more accurate results need more accurate true stress and strain while there are several method to get the true stress-strain curve after necking as Photographs method[11], FEM[[12], etc.

6 Conclusions

As the steel plates applied in the ocean engineering structure becomes more and more thicker, the acceptable CTOD value of different Standards are applied to prevent the structural safety and stability. Such as the minimum acceptable value is 0.15 mm in the DNV-OS-C401-2008, while it is 0.13 mm in the API RP2Z standard. This paper takes the single edge fatigue precrack of CTOD specimen as a flaw under the guidance of BS7910 Standard, plots the FADs of the the welding seam center. The failure boundary value is 0.576, which are applied in the acceptable value of CTOD. The average critical CTOD value is 0.06 mm, which is calculated by $\sqrt{\delta_r}=\sqrt{\delta_I}/\sqrt{\delta_{mat}}$ and far lower than the value specified by the Standards. As the true stress-strain curve is calculated within the elastic stage, which would cause the errors. If the true stress and strain are measure by photography with single specimen, the true stress and strain values would larger than the values obtained by the equations. It would caused the critical value of CTOD would larger than 0.06 mm, the results should be corrected.
In the meanwhile, the present CTOD test ensures the straightness of the front crack with the partial compression method, which would cause the results of test much more conservative[13]. According to the critical CTOD value calculated above, it suggests that the CTOD acceptable value of heavy plates could be modified lower appropriately based on value specified by Standards.

Acknowledgements

This work is an extension of Ministry of Industry and Information Technology Project, and the study is supported by the program "Research of Key Points of Whole Fabrication and Installation of Deep-Sea Semisubmersible Drilling Platform" ([2009]No382). The authors would like to thank ShiboYang, Zhangmu Miao, Sheng Peng for their prayer.

References

[1] PD6493:1991.Guidance on some methods for the derivation of acceptance levels for defects in fusion welded joints[s].British Standards Institution,1991.8

[2] Ainsworth，R.A.Developments in the flaw assessment procedures of R6 revision 4 and BS7910,American Society of Mechanical Engineers,Pressure Vessels and Piping Divison(Publication)PVP,V463,2003,P19-25

[3]BS 7910: Guide on Methods for Assessing the Acceptability of Flaws in Metallic Structures[S]. London: British Standard Institution, 2005.

[4]Yue Tian. The Fracture Toughness Assessment Method of Bridge Steel with CTOD and BS 7910 [J]. CHINA RAILWAY SCIENCE, 2010,31(2):40~44.

[5] BS7448:Part2.Method for determination of K_{IC} ,critical CTOD and critical J values of welds in metallic materials[S].British Standards Institution ,london,1997.

[6]Offshore Standard DNV-OS-C401：Fabrication and Testing of Offshore Structures[S]．DET NORSKE VERITAS．Norway,2008.

[7]Zhanguo Liu The Study on CTOD Temper of Welded Joint in Offshore Platform [D]. Wuhan：Wuhan University of Technology ,2010.

[8]Metallic materials Tensile testing at ambient temperature[S].Beijing：Chinese Carbide State Bureau of Technical Supervision，2002.

[9]David Roylance. STRESS-STRAIN CURVES[S.1] .Department of Materials Science and Engineering，Massachusetts Institute of Technology，Cambridge, MA 02139, 2001.

[10]Zhangmu Miao,Dexing Tao. EXPLORATION ON APPLICABILITY AND ACCEPTABLE VALUES IN CTOD TOUGHNESS EVALUATION FOR WELDED JOINTS [J]. Journal of Mechanical Strength,2006,28(1) : 150~ 154

[11] Guoan Li,Yanliang Lou,Yizeng Zhang. MEASUREMENT OF TRUE STRESS — STRAIN BY PHOTOGRAPHY WITH SINGLE SAMPLE [J]. Physical Test,1992,（2）:52~53.

[12] Yunpeng Jiang,Fengzhu Yue,XiaopingHan. DETERMINATION OF THE MATERIALS STRESS AND STRAIN RELA-
TIONSHIP FROM THE TENSILE SMOOTH AND NOTCHED BARS [J]. Journal of Mechanical Strength, 2003,25(2):151~15.

[13] Towers ,O.L. and Dawes, M.G.. Welding Institute Research on the Fatigue Precracking of Fracture Toughness Specimens[J]. Elastic-Plastic Fracture Test Methods. 1985.

Crack Nucleation in Phase Field Fracture Models

Charlotte Kuhn[1,*], **Ralf Müller**[1]

[1] Institute of Applied Mechanics, TU Kaiserslautern, P.O.B. 3049, 67653 Kaiserslautern, Germany
* Corresponding author: chakuhn@rhrk.uni-kl.de

Abstract Phase field fracture models are able to reproduce a wide range of phenomena, which are observed in fracture experiments. These phenomena include the nucleation of new cracks in initially undamaged material. However, none of the material parameters of a phase field fracture model is directly connected to the fracture strength of the material. Thus, the critical stress for the nucleation of new cracks is not a priori clear. Crack nucleation in a phase field fracture model is preceded by a localization of the initially homogeneous crack field in an area surrounding the nucleating crack. For homogeneous problems, it can be shown analytically that the onset of the localization is caused by the loss of stability of the crack-free homogeneous solution of the phase field equations at a certain load level. This critical stability load provides a definition of the fracture stress in the phase field model depending on the stiffness of the material, the cracking resistance and the internal length of the phase field model. The analytical findings are illustrated in finite element simulations of the phase field fracture model. Further numerical investigations analyze the crack nucleation behavior of the phase field model in more complicated scenarios, where analytical stability results are not available.

Keywords Phase field model, Fracture, Finite element method, Crack nucleation, Stability

1. Introduction

Conclusions drawn from numerical simulations often play a crucial role in the design process of structural components. In order to obtain a reliable prediction of the integrity of a structure, a fracture model must be able to reproduce a wide range of phenomena which are observed at fracture events. On the one hand, this requires criteria for the stability of pre-existing cracks as well as criteria for the nucleation of new cracks in originally undamaged material. On the other hand, the fracture model must also predict the geometry of the crack path, including possible kinking of a crack or bifurcation into several crack branches. Unlike many other continuum fracture models, which are equipped with a whole toolbox of different criteria in order to meet these requirements, the phase field approach provides a unified framework for the simulation of the entire fracture process. Different phase field fracture models have been introduced and discussed e.g. in references [1–6]. More recently, phase field fracture models based on Bourdin's regularization of the variational formulation of brittle fracture [7] have been formulated in [8–10]. All these models differ in detail, but in all formulations cracks are represented by a scalar phase field order parameter, which indicates the condition of the material and interpolates smoothly between broken and undamaged material. Cracking is addressed as a phase transition problem, and the crack evolution, obtained implicitly through the solution of the coupled field equations, covers the whole range of phenomena which need to be considered. Concerning a finite element implementation of the fracture model, the phase field approach is advantageous because the diffuse phase field cracks do not lead to discontinuous jumps in the displacement field. Thus, the discretization can be done with standard finite element shape functions, and no remeshing is required in order to simulate crack propagation.

The fracture behavior of phase field fracture models is mainly adjusted by two parameters. The cracking resistance $\mathcal{G}_c$ is a material parameter, which is a measure for the surface or fracture energy, needed to create new fracture surfaces. By means of configurational forces, it can be illustrated, that the propagation of pre-existing cracks in the phase field model agrees with the energetic considerations of classical Griffith theory, see e.g. [8, 11, 12]. The second parameter is a length

scale ξ, which primarily controls the width of the transition zone of the order parameter between broken and undamaged material. From this point of view, the length scale is merely an auxiliary numerical quantity, which recovers the sharp interface limit for $\xi \to 0$. However, some recent publications [13–16] find that, in a one dimensional setting, the length scale ξ is also crucial for the stability of crack-free, spatially homogeneous phase field solutions. At the critical load level, the crack-free solution becomes unstable and the phase field order parameter localizes until finally a crack forms. Particularly interesting is the fact, that this stability point is also related to the maximal stress response of the crack-free phase field solution. This observation allows for the definition of a fracture strength in the phase field model, which – at first sight – does not feature a material parameter, that is directly connected to the strength of the material, but is able to reproduce crack nucleation.

In this work, the crack nucleation behavior of the phase field fracture model introduced in [8] is investigated. In a first step, only the one dimensional case is considered. A stability analysis of the spatially homogeneous, crack-free solution is outlined, which yields the definition of an effective fracture strength in the one dimensional phase field model. In a second step, the problem of crack nucleation is considered in the two dimensional setting. However, a rigorous analytical stability analysis is generally not possible in the case of arbitrary inhomogeneous stress states. Therefore, based on the findings from the one dimensional case, strength estimates are derived for the two dimensional setting. These estimates are then compared to the computed stress states at crack nucleation in a finite element simulation of the phase field model.

2. Phase field formulation

In phase field fracture models, cracks are approximated by the zero set of the phase field order parameter s. This order parameter is a continuous scalar field quantity which resembles a damage variable and is often referred to as crack field in this context. It interpolates smoothly between cracks, where the order parameter takes the value zero, and undamaged material, where the value of the order parameter is one. By means of a degradation function, the crack field is coupled to the elastic stiffness tensor $\mathbb{C}$ of the material in order to model the change in stiffness between broken and undamaged material. The core of the phase field model considered in this work is the energy density functional

$$\psi(\varepsilon, s) = \frac{1}{2}(s^2 + \eta)\varepsilon : \mathbb{C}\varepsilon + \mathcal{G}_c \left(\frac{(1-s)^2}{4\xi} + \xi |\nabla s|^2 \right), \tag{1}$$

which was introduced by Bourdin [7] as a regularized approximation of the energy density of a linear elastic fractured body. The first part, which is a function of the linearized strain tensor ε and the crack field s, is the elastic stored energy. The small positive parameter $\eta \ll 1$ in the degradation function is a residual stiffness, which is introduced in order to avoid numerical difficulties, where s equals zero. The second part depends only on the crack field s and its gradient ∇s. An integration of the second bracketed term over the entire domain yields an approximation of the surface measure of the crack set, when the regularization length ξ is sufficiently small. Multiplied with the cracking resistance $\mathcal{G}_c$ it approximates the Griffith type surface energy of the crack set. By virtue of thermodynamic reasoning, the definition of the energy density functional ψ yields the material law

$$\sigma = \frac{\partial \psi}{\partial \varepsilon} = (s^2 + \eta)\mathbb{C}\varepsilon \tag{2}$$

for the stress tensor σ which, together with the equilibrium condition

$$\operatorname{div} \sigma = 0 \tag{3}$$

and the respective boundary conditions, forms the mechanical part of the problem. The evolution of the crack field is assumed to follow a Ginzburg-Landau type evolution equation, where the rate $\dot{s}$ is proportional to the negative variational derivative of the energy density functional with respect to s, i.e.

$$\dot{s} = -M\frac{\delta\psi}{\delta s} = -M\left(s\varepsilon:\mathbb{C}\varepsilon - \mathcal{G}_c\left(2\xi\Delta s + \frac{1-s}{2\xi}\right)\right). \tag{4}$$

The symbol Δ denotes the Laplace operator. The positive scalar kinetic coefficient M describes the mobility of the process. In the format of Eq. (4), the evolution equation may be regarded as a viscous approximation of the quasi-static case, which is recovered for $M \to \infty$. In order to model the irreversibility of the fracture process, Dirichlet boundary conditions $s = 0$ are applied to the crack field in the subsequent load steps, wherever a crack forms, i.e. the crack field becomes zero. At crack free boundaries with outer normal vector n, homogeneous Neumann boundary conditions $\nabla s \cdot n = 0$ apply. The coupling of the field equations (Eqs. 2-4) implicitly models the mutual interaction between the elastic stress and strain fields and the crack field s. Given a prescribed loading history, the successive solution of the coupled system of equations formed by Eqs. (2-4) yields the evolution of the mechanical stress and strain fields as well as the evolution of the crack field. Note, that no further criteria are required in order to capture even complex crack evolutions, such as the coalescence of different cracks, crack branching or the nucleation of new cracks.

3. Crack nucleation

The nucleation of new cracks in an originally undamaged structure is a somewhat delicate topic in the context of a phase field formulation. On the one hand, crack nucleation can be observed in numerical simulations of the phase field model. On the other hand, none of the parameters of the phase field fracture model is directly connected to the fracture strength σ_c of the material. In the following, the influences of the different phase field parameters on the effective fracture strength of the phase field model are investigated by means of an analytical stability analysis and numerical simulations.

3.1. The one dimensional case

3.1.1. Homogeneous solution

In a first step, a one dimensional problem is considered. A homogeneous bar of length $2L$ and Young's modulus E is strained by an increasing displacement load of $u(\pm L) = \pm u_0$ at both ends. Before any load is applied, the bar is modeled as undamaged, i.e. $s \equiv 1$. In the one dimensional setting, the equilibrium condition (Eq. 3) immediately implies that the stress σ must be constant along the entire bar. Under the assumption that the crack field remains spatially constant upon loading, it follows from the material law (Eq. 2, where Young's modulus E replaces the stiffness tensor $\mathbb{C}$) that the strain ε must be constant, too. The kinematic relation $\varepsilon = u'$ yields the strain value $\varepsilon_h = u_0/L$ prescribed by the boundary displacement. The corresponding static solution for the crack field

$$s(x) \equiv s_h = \frac{\mathcal{G}_c}{2\xi E\varepsilon_h^2 + \mathcal{G}_c} \tag{5}$$

is obtained from the one dimensional evolution equation. Accordingly, the constant stress in the bar is

$$\sigma_h = \frac{\mathcal{G}_c{}^2 E \varepsilon_h}{\left(2\xi E \varepsilon_h^2 + \mathcal{G}_c\right)^2}\,, \tag{6}$$

where the contribution of the remaining stiffness η has been neglected for the sake of algebraic simplicity. While the homogeneous crack field (Eq. 5) decreases monotonically with the increasing strain ε_h, the stress response (Eq. 6) attains a maximal value

$$\sigma_h^* = \frac{9}{16}\sqrt{\frac{\mathcal{G}_c E}{6\xi}}\,, \tag{7}$$

at a displacement load of

$$u_0^* = \sqrt{\frac{\mathcal{G}_c}{6\xi E}}\,L\,. \tag{8}$$

Interestingly, the value of the homogeneous crack field at the maximal stress load is *0.75*, independent of all of the phase field parameters, see also [10]. This is illustrated in the plots of Fig. 1, which show the evolution of the stress response and the crack field with respect to the displacement loading for different values of ξ.

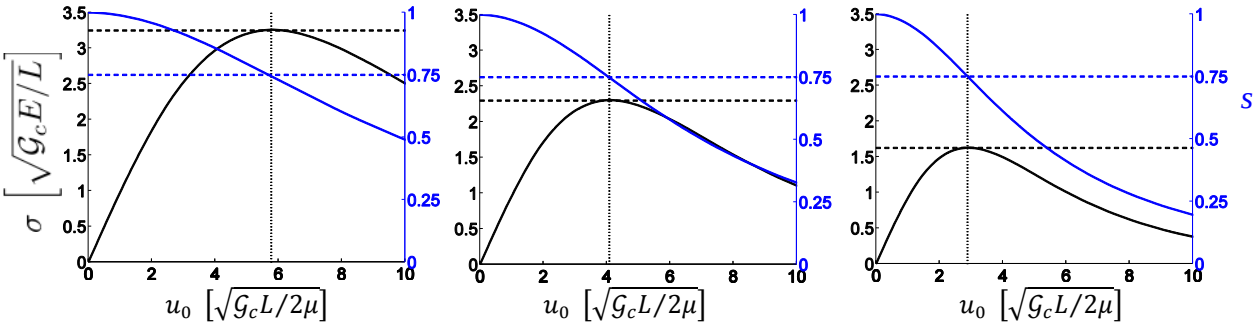

Figure 1. Stress response (black) and crack field (blue) under increasing displacement load for $\xi = 0.005L$ (left), $\xi = 0.01L$ (center) and $\xi = 0.02L$ (right)

3.1.2. Stability analysis

In order to analyze the stability of the homogeneous solution (Eq. 5), a family of symmetric test functions $s_\alpha(x) = s_\alpha(-x)$ with $s'_\alpha(\pm L) = s'_\alpha(0) = 0$ and $s_0(x) \equiv s_h$ is introduced. Symmetry is postulated for the sake of simplicity, and the restriction $s'_\alpha(0) = 0$ ensures differentiability at $x = 0$. Boundary conditions $u_\alpha(\pm L) = \pm u_0$, kinematic relations, the material law and the fact that the stress is constant yield the corresponding strain field ε_α. It can be shown that the first variation of the potential

$$\Pi(\varepsilon, s) = \int_{-L}^{L} \psi(\varepsilon, s)\,\mathrm{d}x = 2\int_0^L \psi(\varepsilon, s)\,\mathrm{d}x \tag{9}$$

vanishes for the homogeneous static solution, i.e.

$$\delta_\alpha \Pi(\varepsilon_\alpha, s_\alpha) = \frac{\mathrm{d}\Pi(\varepsilon_\alpha, s_\alpha)}{\mathrm{d}\alpha}\Big|_{\alpha=0} = 0\,. \tag{10}$$

Thus, the homogeneous solution is always a local extremum or a saddle point of the energy functional (Eq. 9). The second variation of the potential Π with respect to α is given by the expression

$$\delta_\alpha^2 \Pi = 2\left[4\frac{E}{L^3}u_0^2\left(\int_0^L \partial_\alpha s_\alpha \,\mathrm{d}x\right)^2 + 2\mathcal{G}_c\xi\int_0^L(\partial_\alpha s'_\alpha)^2\mathrm{d}x + \left(\frac{\mathcal{G}_c}{2\xi} - \frac{3E}{L^2}u_0^2\right)\int_0^L(\partial_\alpha s_\alpha)^2\mathrm{d}x\right], \quad (11)$$

where $\partial_\alpha(\cdot)$ denotes the partial derivative with respect to α. Clearly, the second variation can only become negative if the factor in front of the last integral in Eq. (11) becomes negative. If the displacement load u_0 is smaller than the load u_0^* (Eq. 8) with the maximal stress response, the second variation (Eq. 11) is positive. Thus, the homogeneous solution is a local minimizer of the total energy and therefore is considered as stable. If the displacement load u_0 becomes larger than the load u_0^*, the factor in front of the last integral becomes negative and thus, the second variation can become negative, too. The homogeneous solution is then no longer a local minimizer and becomes unstable. Consequently, the load with the maximal stress response represents a lower bound for the stability of the homogeneous solution. A further analysis of the stability of homogeneous solutions of different gradient damage formulations, is carried out in [16] and, for a broader class of gradient damage models, in [13–15]. Concerning the specific phase field fracture model under consideration, the main conclusion from these publications is, that for small values of ξ, the actual stability load lies slightly above the lower bound u_0^*. Only for rather large ξ, the actual stability load is significantly larger than u_0^*. However, regarding the regularizing character of ξ, this case is of minor interest.

3.1.3 Non-homogeneous solution

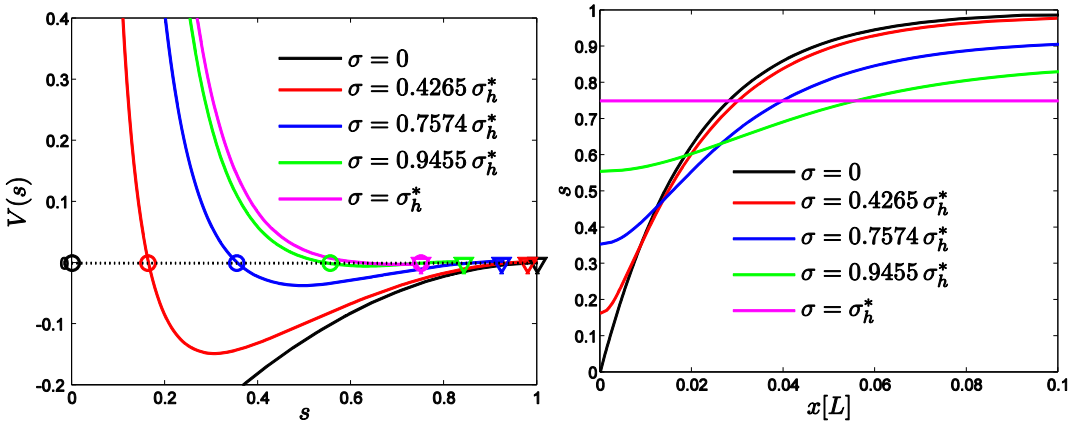

Figure 2. Function $V(s)$ and roots s_m (circles) and s_h (triangles) for different values of σ (left) and the respective inhomogeneous crack fields (right)

In this section, a semi-analytical approach to the computation of the non-homogeneous crack field at supercritical loading is outlined. More details are reported in [10, 11] for similar phase field models. A finite element study of the non-homogeneous solution stages can be found in [12]. The static one dimensional evolution equation (Eq. 4) and the material law (Eq. 2) can be recast in the format

$$\frac{2\xi\sigma^2 s}{\mathcal{G}_c E(s^2+\eta)^2} + s - 4\xi^2 s'' - 1 = 0\,. \quad (12)$$

Assuming a differentiable, symmetric solution $s(x)$ with a minimum value s_m at $x = 0$, an integration of Eq. (12) with respect to s over the interval $[s_m, s(x)]$ yields

$$\underbrace{2\xi^2(s')^2}_{V_{\mathrm{kin}}(s')} + \underbrace{\frac{\xi\sigma^2}{\mathcal{G}_c E(s^2+\eta)} - \frac{s^2}{2} + s}_{V_{\mathrm{pot}}(s)} = \underbrace{\frac{\xi\sigma^2}{\mathcal{G}_c E(s_m^2+\eta)} - \frac{s_m^2}{2} + s_m}_{V_{\mathrm{pot}}(s)}\,, \quad (13)$$

which can be interpreted as a balance law for the phase field variable s with the potential V_{pot} and

the kinetic energy V_{kin}, see [11]. With the far field boundary conditions $s'(\pm L) = 0$ and $s(\pm L) = s_h(\sigma)$, the minimum value s_m can be computed from Eq. (13) as a root of the function $V(s) = V_{\text{pot}}(s) - V_{\text{pot}}(s_h)$. The left plot in Fig. 2 shows the function $V(s)$ for different values of σ and $\xi = 0.01L$. The roots referring to $s = s_h$ are marked by triangles, and the roots referring to $s = s_m$ are marked by cycles. The extreme cases $\sigma = 0$ (black) and $\sigma = \sigma_h^*$ (magenta) require special consideration. For $\sigma = 0$ and the respective homogeneous crack field value $s_h = 1$, the function $V(s)$ is non-positive in the entire interval $[0, 1]$, and the root defining s_m vanishes. However, for $\sigma \to 0$, the root s_m of $V(s)$ approaches zero. Together with the fact that $\sigma = 0$ represents the cracked state, this consideration legitimates to set $s_m = 0$ in this case. If σ approaches the maximal value σ_h^*, the roots defining s_m and s_h collapse in a single point at $s = 0.75$.

Once the minimum value s_m has been determined, the balance law (Eq. 13) can be exploited to compute the solution $s(x)$ of Eq. (12), or rather the inverse

$$x(s) = \operatorname{sgn}(x) \int_{s_m}^{s(x)} \sqrt{\frac{2\xi^2}{V_{\text{pot}}(s_m) - V_{\text{pot}}(s)}}\, \mathrm{d}s \tag{14}$$

of the solution. The right plot of Fig. 2 shows the results of a numerical evaluation of Eq. (14) at different stress levels σ. The fully cracked solution (black) is virtually identical to the function

$$s(x) = 1 - \exp\left(\frac{-|x|}{2\xi}\right), \tag{15}$$

which is an approximation of the piecewise defined static solution of the stress free evolution equation with boundary conditions $s(0) = 0$ and $s'(\pm L) = 0$. The limit case with maximal stress response $\sigma = \sigma_h^*$ (magenta) yields the homogeneous solution $s \equiv 0.75$.

3.2. The two dimensional setting

3.2.1 Strength estimates from homogeneous test problems

As in the one dimensional setting, the length parameter ξ has a crucial impact on the fracture strength σ_c of the two dimensional phase field model. However, analytical solutions of non-homogeneous two dimensional problems are generally not available, and thus, a rigorous mathematical stability analysis cannot be carried out. In order to determine the fracture strength of the two dimensional model, relations between ξ and σ_c are derived on the basis of the two homogeneous problems depicted in Fig. 3.

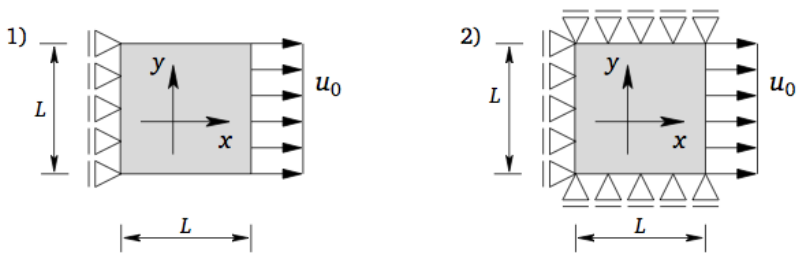

Figure 3. Homogeneous two dimensional problems for the derivation of strength estimates

For both cases, the stationary, homogeneous solution of the evolution equation is given by

$$s(x, y) \equiv s_h = \frac{\mathcal{G}_c}{2\xi\varepsilon:\mathbb{C}\varepsilon + \mathcal{G}_c}. \tag{16}$$

Due to the different boundary conditions, the elastic contribution differs slightly, depending on the ratio of the Lamé constants.

$$\varepsilon : \mathbb{C}\varepsilon = \kappa_i u_0^2 \qquad \text{with} \qquad \kappa_i = \begin{cases} \frac{2\lambda+2\mu}{\lambda+2\mu}, & \text{for } i = 1 \\ \frac{\lambda+2\mu}{2\mu}, & \text{for } i = 2 \end{cases} \tag{17}$$

The indices $i = 1, 2$ in Eq. (17) refer to the left and right setting depicted in Fig. 3. Neglecting η for algebraic simplicity, the corresponding stress in x-direction is

$$\sigma_x = \frac{2\mu\kappa_i \mathcal{G}_c{}^2 \varepsilon_x}{\left(4\mu\kappa_i \xi \varepsilon_x^2 + \mathcal{G}_c\right)^2} \tag{18}$$

with $\varepsilon_x = u_0/L$. The maximal value

$$\sigma_x^* = \frac{9}{16}\sqrt{\frac{2\mu\kappa_i \mathcal{G}_c}{6\xi}} \tag{19}$$

is attained at the displacement load

$$u_0^* = \sqrt{\frac{\mathcal{G}_c}{12\mu\kappa_i\xi}}\, L\,. \tag{20}$$

The maximal stress response (Eq. 19) and the corresponding displacement load (Eq. 20) exhibit the same asymptotic behavior with respect to ξ as in the one dimensional setting. For $\xi \to 0$ both quantities become infinitely large, while for $\xi \to \infty$ their value approaches zero. However, in the two dimensional setting, both quantities additionally depend on the factor κ_i defined in Eq. (17). As in the one dimensional case, the value of the homogeneous crack field at the maximal stress response is *0.75*, independent of all of the phase field model's parameters.

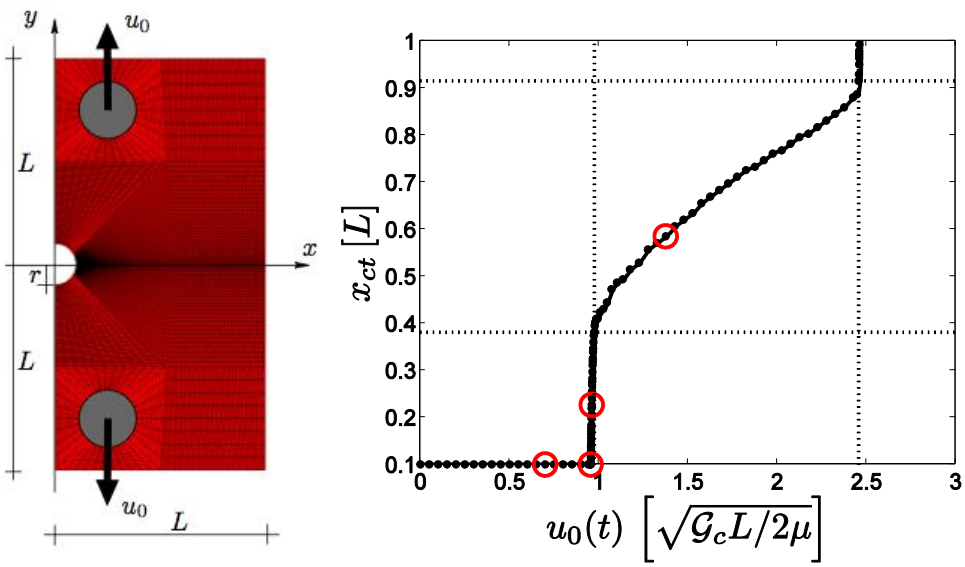

Figure 4. Simulation setup (left) and crack tip position with respect to the loading (right)

3.2.2 Numerical evaluation

In the following, the maximal stress values from Eq. (19) are compared to the actually computed stress states at crack nucleation in the phase field model, in order to evaluate the effective fracture strength σ_c of the phase field model. In the finite element simulation, the notched structure, depicted in the left plot of Fig. 4, is loaded by a linearly increasing displacement load $u_0(t)$ acting in y-

direction. The radius of the circular notch is $r = 0.1L$. The initial crack field is set to one in the entire domain in order to model the undamaged initial state. The material is assumed to be isotropic with Lamé constants $\lambda = \mu$, which is equivalent to a Poisson ratio of $\nu = 0.25$. The circular areas of diameter $d = 0.28L$ around the load application points (gray) are modeled as stiff by increasing the stiffness and the cracking resistance by a factor of *100*. The length parameter is $\xi = 0.01L$, the artificial residual stiffness in broken areas is set to $\eta = 10^{-5}$, and the kinetic coefficient is set to $M = 10\,L/\mathcal{G}_c T$, where the time scale T refers to the load factor t/T of the displacement load $u_0(t) = u_0(t/T)$. The size of the time steps is controlled by an adaptive time stepping procedure. More details on the finite element implementation of the phase field fracture model can be found in [8]. The right plot of Fig. 4 shows the position x_{ct} of the crack tip on the x-axis with respect to the displacement load (black solid line). For the evaluation the node with the largest x-coordinate where s equals zero is defined as the crack tip position. Before the onset of fracture, the crack tip position is replaced by the position of the notch ground located at $x = 0.1L$. After the critical load level is reached, an initial crack of finite length starting at the notch ground forms brutally along the x-axis at a quasi constant load level. The formation of the initial crack is followed by a phase of stable crack extension along the x-axis, where the crack grows progressively with the loading. A second phase of brutal crack extension is observed when total rupture occurs after the crack tip passes $x \approx 0.9L$. The dotted lines indicate the beginning and ending of the phase of stable crack growth. Remarkably, the crack nucleation at the non-singular stress concentration at the notch as well as the transition from brutal to stable crack extension and vice versa are mastered without any technical difficulties.

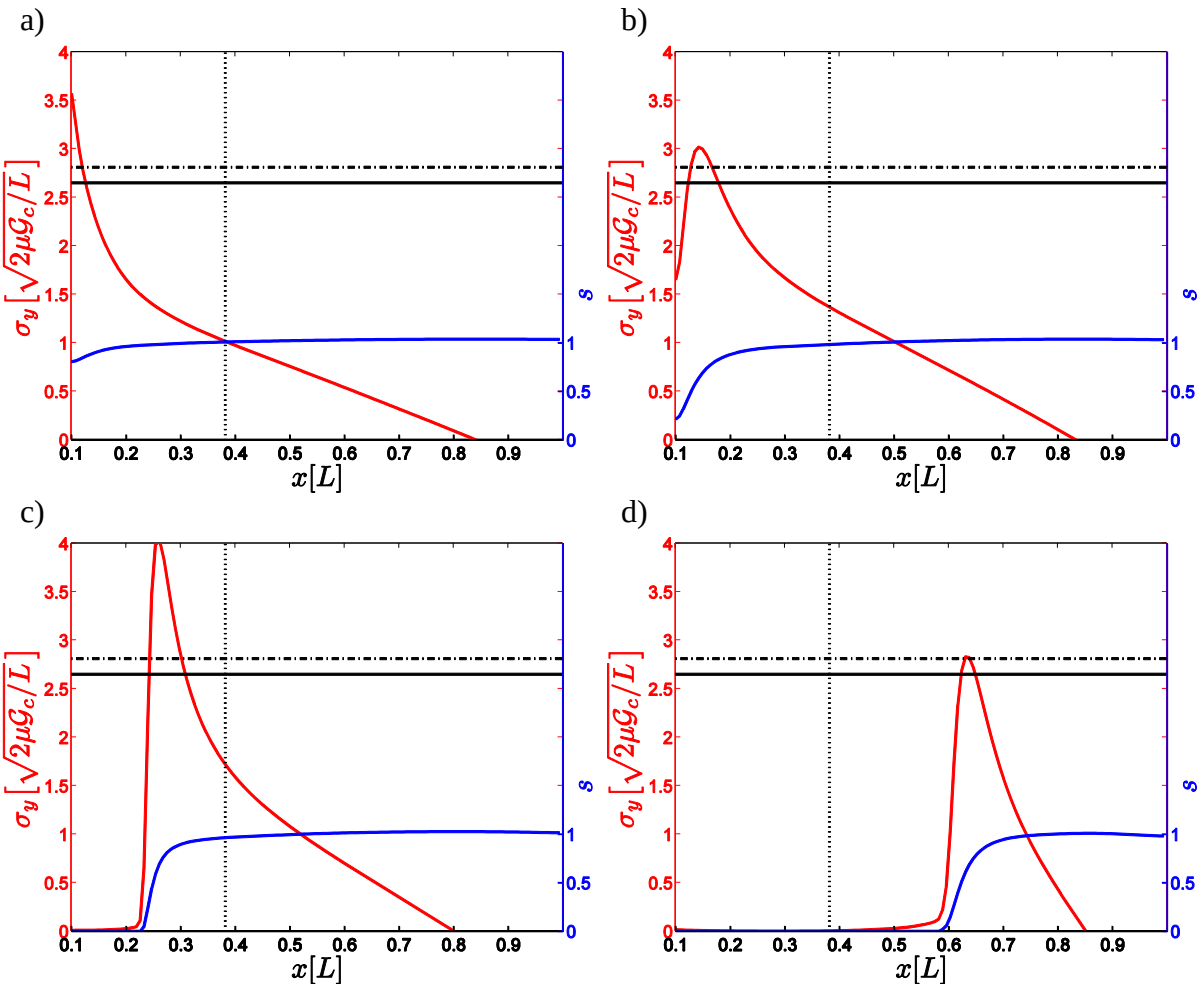

Figure 5. Stress in y-direction (red) and crack field (blue) along the x-axis at different load levels

The plots of Fig. 5 show the stress component σ_y (red) and the crack field s (blue) along the x-axis at the four load stages marked by the red circles in the right plot of Fig. 4. The vertical black dotted line marks the position of the crack tip after the formation of the initial crack. The horizontal black solid and dash-dotted lines indicate the strength estimates from Eq. (19) for the cases $i = 1$ and $i = 2$, respectively. At the load level of $u_0(t) = 0.7\sqrt{\mathcal{G}_c L/2\mu}$ (Fig. 5a), no crack nucleation is observed yet, and the numerical solution is stationary and stable. However, very close to the notch ground located at $x = 0.1L$, the stress component σ_y already exceeds the strength estimates. The value of the crack field at the notch ground is approximately $s \approx 0.80$, which is higher than the assumed critical value $s^* = 0.75$. Figure 5b) shows the y-stress and the crack field at the beginning of the phase of brutal crack nucleation at the load level $u_0(t) = 0.955\sqrt{\mathcal{G}_c L/2\mu}$. At this stage, the numerical solution becomes unstable and can no longer be considered as stationary. The crack field immediately at the notch ground is decreased to $s \approx 0.22$. Due to the loss of stiffness caused by the decreasing crack field, the stress at the notch ground decreases, too, and a stress peak develops in front of the notch. Figure 5c) shows the y-stress and crack field at $u_0(t) = 0.961\sqrt{\mathcal{G}_c L/2\mu}$, during the phase of brutal crack extension. The crack field has developed its characteristic exponential shape (cf. Eq. 15), where the material is not yet broken and is constantly zero in the fractured area. During this phase, the peak stress in y-direction significantly exceeds the maximal stress response (Eq. 19) of the homogeneous test problems. The last plot, Fig. 5d), shows the stress component σ_y and the crack field at $u_0(t) = 1.38\sqrt{\mathcal{G}_c L/2\mu}$, during the phase of stable crack extension. The peak stress is now in good agreement with the strength estimates. The crack field maintains its exponential shape and is only shifted in x-direction.

As similar results are obtained in simulations with different values of the length parameter ξ, the simulation results yield the following conclusions. For inhomogeneous stress states with maximum stresses below the derived strength estimates, no crack nucleation is observed in the phase field model. Also the exceedance of the assumed strength in a small area does not immediately lead to crack nucleation. Instead, an initial crack forms, if the stress becomes supercritical in a sufficiently large area and the crack field drops below the critical value of *0.75*. Thus, the derived strength estimates permit to judge the criticality of a computed stress state prior to crack nucleation and may therefore be interpreted as the effective fracture strength of the phase field model.

4. Conclusion and outlook

Despite the regularizing character of the length scale ξ, the stability analysis of the one dimensional model and the numerical results obtained for the two dimensional case, yield a more mechanically motivated interpretation of the parameter ξ. The stability analysis, as well as the numerical simulations, legitimate to interpret the maximal stress response obtained in homogeneous loading scenarios as the effective fracture strength σ_c of the phase field model. As a consequence of this interpretation, the length scale ξ is no longer just an arbitrary regularization length, but can be derived according to Eq. (19) from experimentally measurable data, i.e. from the cracking resistance $\mathcal{G}_c$, the fracture strength σ_c, and the Lamé constants λ and μ of isotropic materials. Thus, in conjunction with the other material parameters of the phase field model, the parameter ξ may be regarded as a material parameter itself. For the phase field formulation, the definition of the fracture strength, together with the ability to master the transition from a crack free initial state into a cracked configuration, justifies the conclusion, that the model naturally combines a strength criterion for the nucleation of new cracks with an energetically motivated Griffith type evolution law for stable crack growth.

The brutal formation of cracks of finite length at crack nucleation, observed in the simulations, challenges the limits of the quasi static formulation. Therefore, a dynamic version of the phase field model, where dynamic equations of motion replace the static equilibrium condition (Eq. 3), is currently being worked on. Within the context of the present work, especially the impact of the dynamic effects on the crack nucleation behavior of the phase field model is of interest. Another open task for future work is the influence of material inhomogeneities, such as inclusions or pores, on the effective fracture strength of the phase field model.

References

[1] I.S. Aranson, V.A. Kalatsky, V.M. Vinokur, Continuum field description of crack propagation. Phys Rev Let, 85/1 (2000) 118–121.

[2] L.O. Eastgate, J.P. Sethna, M. Rauscher, T. Cretegny, C.-S. Chen, C.R. Myers, Fracture in mode I using a conserved phase-field model. Phys Rev E, 65/3 (2002) 036117.

[3] A. Karma, A.E. Lobkovsky, Unsteady crack motion and branching in a phase-field model of brittle fracture. Phys Rev Let, 92/24 (2004) 245510.

[4] H. Henry, H. Levine, Dynamic instabilities of fracture under biaxial strain using a phase field model. Phys Rev Let, 93/10 (2004) 105504.

[5] V. Hakim, A. Karma, Crack path prediction in anisotropic brittle materials. Phys Rev Let, 95/23 (2005) 235501.

[6] F. Corson, M. Adda-Bedia, H. Henry, E. Katzav, Thermal fracture as a framework for quasi-static crack propagation. Int J Fract, 158 (2009) 1–14.

[7] B. Bourdin, G.A. Francfort, J.-J. Marigo, Numerical experiments in revisited brittle fracture. J Mech Phys Solid, 48/4 (2000) 797–826.

[8] C. Kuhn, R. Müller, A continuum phase field model for fracture. Eng Fract Mech, 77/18 (2010) 3625–3634.

[9] C. Miehe, F. Welschinger, M. Hofacker, Thermodynamically consistent phasefield models for fracture: Variational principles and multi-field FE implementations. Int J Numer Meth Eng, 83/10 (2010) 1273–1311.

[10] M.J. Borden, C.V. Verhoosel, M.A. Scott, T.J.R. Hughes, C.M. Landis, A phase-field description of dynamic brittle fracture. Comput Meth Appl Mech Eng, 217–220 (2012) 77–95.

[11] V. Hakim, A. Karma, Laws of crack motion and phase-field models of fracture. J Mech Phys Solid, 57/2 (2009) 342–368.

[12] C. Kuhn, R. Müller. On an energetic interpretation of a phase field model for fracture. PAMM, 11/1 (2011) 159–160.

[13] H. Amor, J.-J. Marigo, C. Maurini, N.K. Pham, Stability analysis and numerical implementation of non-local damage models via a global variational approach, in: WCCM8 - ECCOMAS 2008, 2008.

[14] K. Pham, H. Amor, J.-J. Marigo, C. Maurini, Gradient damage models and their use to approximate brittle fracture. Int J Damage Mech, 20/4 (2011) 618–652.

[15] K. Pham, J.-J. Marigo, and C. Maurini, The issues of the uniqueness and the stability of the homogeneous response in uniaxial tests with gradient damage models. J Mech Phys Solid, 59/6 (2011) 1163–1190.

[16] A. Benallal, J.-J. Marigo, Bifurcation and stability issues in gradient theories with softening. Modell Simul Mater Sci Eng, 15/1 (2007) 283–295.

DESIGN BASED ON DUCTILE-BRITTLE TRANSITION TEMPERATURE FOR API 5L X65 STEEL USED FOR DENSE CO_2 TRANSPORT

G Pluvinage*[1],J. Capelle[2] and Z. Azari

1.Fiabilité Mécanique. Conseils Silly sur Nied France
2. LABPS. ENIM Metz France

* Corresponding author : pluvinage@cegetel.net

Abstract. Safe and reliable transport of dense CO_2 by pipes needs a careful choice of the constitutive pipe materials to prevent brittle crack propagation after ductile or brittle failure initiation. This unexpected phenomenon can occur after failure or leak promoted by external interferences. In this case, the rapid decompression of dense CO_2 into gas leads to a very low local temperature of about -80°C.
To prevent risk of brittle fracture initiation and propagation, the material must remain ductile at this temperature. In other terms, its ductile-brittle transition temperature (DBTT) has to be lower than -80°C minus a margin.
It is admitted that the DBTT is not a material characteristic but depends on specimen geometry, loading rate and loading mode, i.e. on constraints. A loss in constraint leads to a lower brittle-ductile transition temperature.
In order to select a steel for transportation of dense CO_2, transition temperatures T_t (from tensile test), T_{K27} and T_{K50} (from Charpy test) and T_{K100} (from fracture mechanics test) have been determined on an API 5L X65 pipeline steel. These transition temperatures have been reported versus a constraint parameter, e.g. T-stress, in a master curve. Differences between different brittle-ductile transition temperatures and temperature corresponding to T-stress acting in a pipe submitted to internal pressure on the master curve, give an estimation of the conservatism of the chosen reference transition temperature.

Key words: transition temperature, pipe steel API 5L X65, constraint, T-stress, CO_2 transportation

1. INTRODUCTION

According to temperature and pressure, CO_2 is present in 3 distinct states. CO_2 is in a supercritical phase with temperatures higher than 31.1°C and pressures higher than 7.38 MPa (values of the critical point). For conditions of temperature and pressure lower than these values, CO_2 will be in a gas, liquid or solid state. Beyond its critical point, carbon dioxide enters a phase called supercritical. Dense CO_2 transport is mainly performed by pipeline. Only in the United States, the existing national CO_2 pipeline infrastructure dedicated primarily to deliver CO_2 for enhanced oil recovery (EOR) comprises 3900 miles, and an extended national CO_2 pipeline system is forecasted with the implementation of carbon dioxide capture and storage (CCS)-derived emission reductions. The entire system could be comprised between 11,000 and 23,000 additional miles dedicated CO_2 pipeline before 2050 and dependent upon the hypothetical climate stabilization policies adopted [1].
Transport of CO_2 in dense state presents a high potential for auto-refrigeration due to depressurisation, either during operations or due to equipment failure.

The ductile-brittle transition temperature (DBTT), nil ductility temperature (NDT), or nil ductility transition temperature (NDTT) of a metal represents the point at which the fracture energy passes below a pre-determined value [2].
Design against brittle fracture considers that the material exhibits at service temperature, a sufficient ductility to prevent cleavage initiation and sudden fracture with an important elastic energy release. Concretely, this means that service temperature T_s is higher than transition temperature T_t:

$$T_s \geq T_t \quad (1)$$

Service temperature is conventionally defined by codes or laws according to the country where the structure or the component is built or installed.
A Fracture Mechanics based design ensures that stress intensity factor for design is lower than admissible fracture toughness and fracture toughness is greater than 100 MPa√m (i.e. the reglementary service temperature defined is above the reference temperature). This additional criterion is expressed by:

$$T_s \geq RT_t + \Delta T \quad (2)$$

where ΔT is the uncertainty on reference temperature. This reference temperature RT_i varies according to codes (RT_{NDT} or RT_{T100}).
In this paper, a selected pipeline steel API 5L X65 is controlled by several mechanical tests in order to check if the material is eligible for dense CO_2 transportation. The material has to satisfy a design based on transition temperature with a service temperature T_s equal to -80°C minus a ΔT, where ΔT is a safety margin estimated to 8°C [3]. Due to the fact that different fracture tests give different transition temperatures, the choice of the most adequate test to provide a value close to the "structure or component" transition temperature T_{struct} is an open question. In addition, traditional design is based on transition temperature given by Charpy tests. Thus, it is necessary to know the degree of conservatism of this approach. For this purpose, three transition temperatures have been determined:

- transition temperature for elastic to elastoplastic behaviour in tension T_t,
- brittle to ductile transition temperature for Charpy V test T_{K27},
- fracture toughness transition temperature T_{100}.

It is generally admitted that fracture resistance is sensitive to constraint. Consequently transition temperatures are affected as well. In order to evaluate the sensitivity to constraint of the abovementioned transition temperature, each transition temperature has been expressed as a function of T-stress [4], which is often used as a constraint parameter and determined by a master curve. This master curve allows determining the structure transition temperature (T_{struct}) and consequently the degree of conservatism of each abovementioned transition temperature.

2. MATERIAL AND METHODS

The investigated material is a pipeline steel API 5L X65 grade supplied as seamless tube with wall thickness equal to 19 mm and external diameter of 355 mm. The typical chemical composition is given in Table 1, mechanical properties at room temperature are given in Table 2.

Table 1. Typical chemical composition of pipe steel API 5L X65 (wt %) [6].

	C	Si	Mn	P	S	Mo	Ni	Al	Cu	V	Nb
min.	0.05	0.15	1.00	-	-	-	-	0.01	-	-	-
max.	0.14	0.35	1.50	0.020	0.005	0.25	0.25	0.04	0.080	0.080	0.040

Table 2. Mechanical properties of pipe steel API 5L X65 at 20°C.

Yield stress R_e (MPa)	Ultimate strength R_m(MPa)	Elongation at failure A %	Charpy Energy K_{CV} (J)	Fracture Toughness K_{Jc} (MP√am)	Hardness HV
465.5	558.6	10.94	285.2	280	205

2.1. Transition temperature for elastic to elastoplastic behaviour in tension T_t

Tensile tests at very low temperature exhibits brittle fracture and ductile failure at high temperature. At very low temperature, fracture always occurs at yield stress. This phenomenon was proven by compressive tests where no failure occurs, but yield stress is easily determined. When test temperature reaches transition temperature, failure occurs with plasticity at ultimate stress. In other words, transition temperature is defined when ultimate strength is equal to yield stress. Plasticity is a thermal activated process and yield stress decreases exponentially with temperature according to the following relationship:

$$R_e = R_e^{\mu} + AExp(-BT) \tag{3}$$

where R_e^{μ} is a threshold, A and B are constants and T is temperature in Kelvin.
Similarly the ultimate strength decreases to temperature according to:

$$R_m = R_m^{\mu} + CExp(-DT) \tag{4}$$

where R_m^{μ} is a threshold, C and D are constants. Tensile tests have been performed on standard specimens in a temperature range [120 - 293 K] with a strain rate of about $10^{-3}s^{-1}$ [6]. Stress-strain diagrams have been recorded and the (static) yield stress and ultimate strength determined. Values of yield stress R_e, and ultimate strength R_m are reported on Figure 1. Data are fitted with equation (3) and (4). Values of R_e^{μ}, R_m^{μ} and constants A, B, C, D are reported in Table 3. Yield stress value at 0K is independent of loading rate and equal to 2320 MPa. This value is generally considered as equal to cleavage stress. Transition temperature is determined as the intersection of two curves at temperature 123 K.

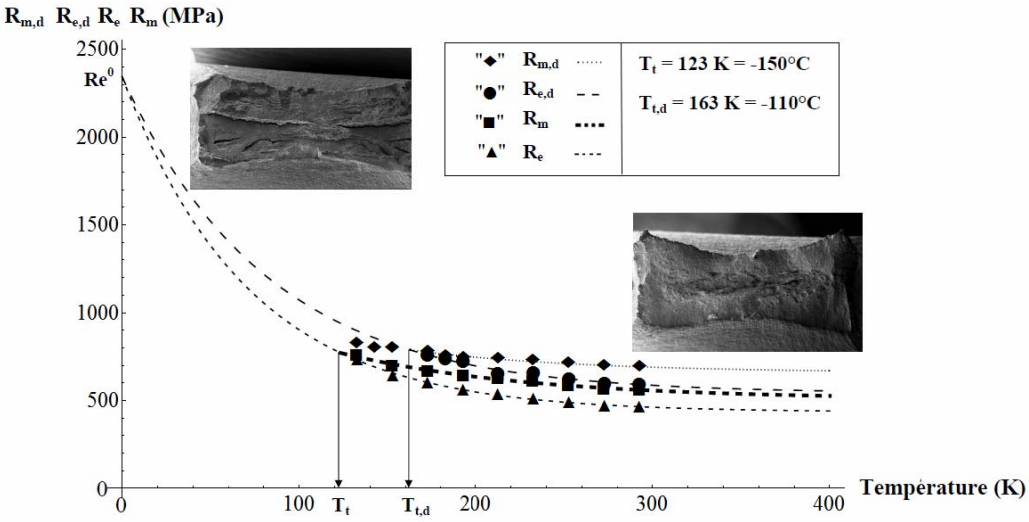

Figure 1. Evolution of static and dynamic yield stress and ultimate strength versus temperature for API 5L X65 pipeline steel.

Table 3. Values of constants of equation (3) and (4) for API 5L X65 pipeline steel for static loading.

R_e^{μ}(MPa)	A(MPa)	B (T^{-1})	R_m^{μ}(MPa)	C(MPa)	D (T^{-1})
434	1910	-0.01405	507	843	-0.0094

Dynamic yield stress (strain rate $10^2\ s^{-1}$) is determined by the method of instrumented Charpy impact test [7]. The load versus time diagram is recorded and the load at general yielding P_{GY} is evaluated. Fracture energy is defined on load displacement diagram until load at initiation, which is different from maximum load. Dynamic yield stress is then obtained using the Green and Hundy solution [8].

$$P_{GY} = L\frac{R_e(W-a)^2 B}{4W} \tag{5}$$

where W is specimen's width, B thickness, a is notch depth, and L is the constraint factor with a value of L=1.31.
Results are fitted with Equations (3) and (4) and values of constants are reported in Table 4. One notes that higher loading rate leads to higher yield stress and transition temperature.

Table 4. Values of constants of Equations (3) and (4) for API 5L X65 pipe steel for dynamic loading.

$Re^{\mu,d}$ (MPa)	A_d(MPa)	B_d (T^{-1})	$Rm^{\mu,d}$(MPa)	C_d (MPa)	D_d (T^{-1})
541	1802	-0.0012226	658	691	0.010276

2.2. Brittle to ductile transition temperature for Charpy V test T_{K27}

However, despite the introduction during the 1960's of Fracture Mechanics tests to measure fracture resistance of materials, the practice of the Charpy impact test remains. It always gives a simple and inexpensive method to classify materials by their resistance to brittle fracture. The current trend is also to use these tests to measure fracture toughness and ductile tearing strength. The comparison of the two methods requires taking into account two major differences:

- Charpy test uses a notched sample, and fracture mechanics tests use a pre-cracked specimen (but a pre-cracked Charpy specimens may also be used).
- Charpy tests are dynamic tests, although the conventional fracture mechanics tests are static ones.

Charpy energy versus temperature curve is fitted with the following relationship:

$$K_{CV} = A_{CV} + B_{CV}\tanh\left[\frac{(T-D_{CV})}{C_{CV}}\right] \tag{6}$$

where A_{CV}, B_{CV}, C_{CV}, and D_{CV} are constants. A_{CV} represents Charpy energy at transition temperature D_{cv}, B_{CV} is the energy jump between brittle and ductile plateaus and $2C_{CV}$ is the temperature range of the Charpy energy transition. Transition temperature has been determined at conventional level of 27 joules and called T_{K27} and also at half the jump between brittle and ductile plateau ($T_{K50} = D_{CV}$). Charpy impact tests have been performed on

API 5L X65 pipe steel with standard Charpy specimens at temperature range [-196°C up to 20 °C].
Experimental data are reported on Figure 2. Charpy energy and fracture aspects reveal the two failure modes below and above the transition temperature. Data are fitted according to Equation (6). Values of the four constants A_{CV}, B_{CV}, C_{CV} and D_{CV} are reported in Table 5 as well as the transition temperatures T_{K27} and T_{K50}.

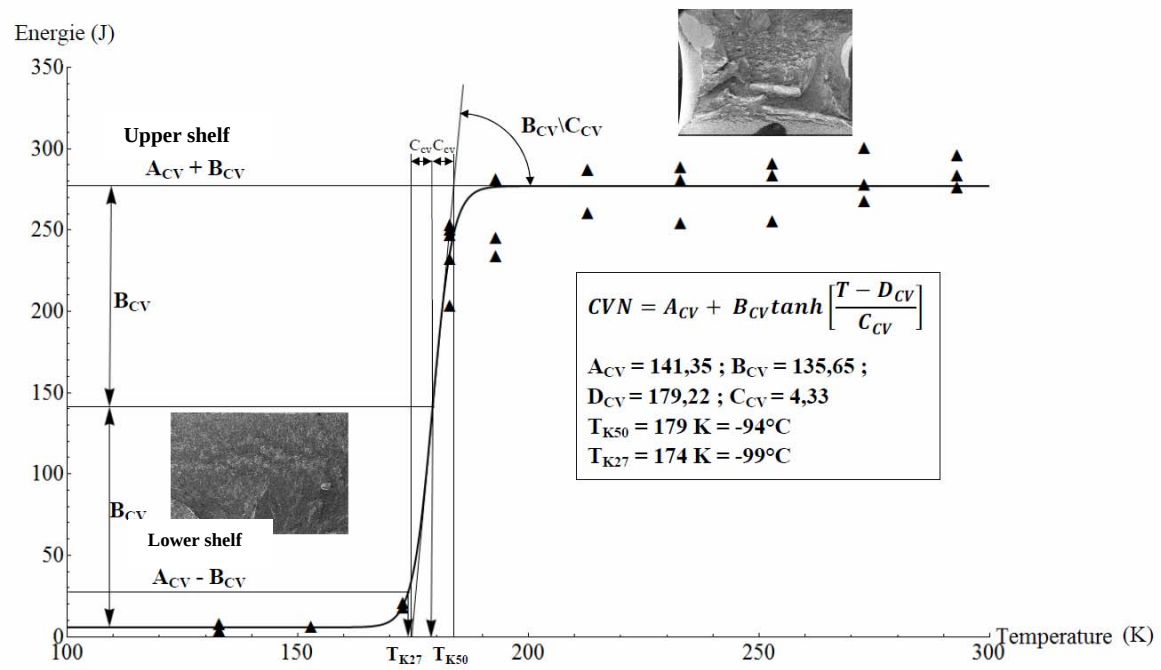

Figure 2. Charpy energy versus temperature curve for API 5L X65 pipe steel and values of parameters of Equation (6).

Table 5. Values of constants of Equation (6) for API 5L X65 pipeline steel

A_{CV} (J)	B_{CV} (J)	C_{CV} (K)	D_{CV} (K)	$T_{K\,27}$(K)	$T_{K\,50}$ (K)
141.35	135.65	4.33	179.22	174	179

2.3. Fracture toughness transition temperature T_0

Fracture toughness K_{IC} evolution versus temperature for brittle and quasi-brittle fracture can be modelled through plasticity-temperature relationship since the fracture process needs a preliminary yielding. Plasticity is a thermally activated phenomenon which follows Arrhenius law. Fracture toughness versus temperature from brittle plateau to transition foot is given by the following Equation 7:

$$K_{IC} = K_{\min} + E\exp(FT) \qquad (7)$$

K_{min} is the fracture toughness threshold, E and F are constants and T is the temperature in Kelvin. Transition temperature called T_0 is defined conventionally for a fracture toughness of 100 MPa√m.

Statistical methods are used to predict the transition toughness curve and specified tolerance limits for 1T specimens of the tested material. The standard deviation of the data distribution is a function of Weibull slope and median K_{Jc} [9]:

$$K_{Jc(median)} = 30 + 70\exp[0.019(T - T_0)] \quad (8)$$

in which T_0 is the temperature associated with the fracture toughness value of 100 MPa√m. T_0 is a characteristic parameter of the material which depends on loading rate. If fracture toughness is plotted versus the reduced temperature ($T-T_0$), the material curve is then independent of the loading rate.
Fracture toughness tests have been performed according to standard with CT specimens in the temperature range [128 – 293 K]. Fracture toughness data are plotted versus temperature in K and fitted according to Equation 7 from the brittle plateau to transition regime in Figure 3.

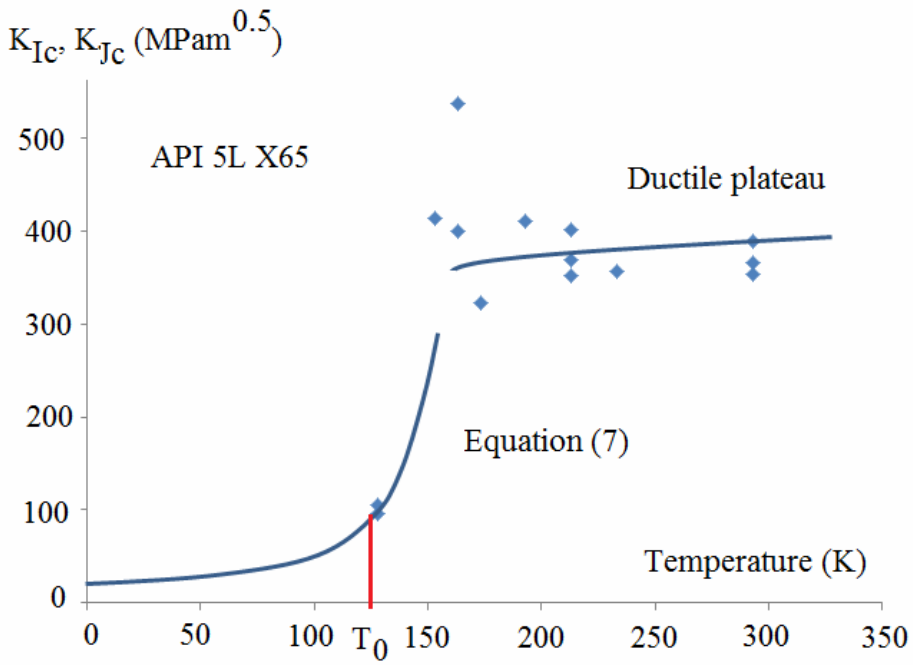

Figure 3. Evolution of fracture toughness versus temperature for API 5L X65 pipeline steel.

Transition temperature T_0 is obtained according to two methods, which are reported in Table 6:

- $T_{0.1}$ after fitting experimental data and determining the corresponding temperature to K_{Jc} = 100 MPa√m,
- $T_{0.2}$ using the following empirical relationship in Equation 9 between transition temperatures T_{K27} and T_0

$$T_{0,2} = T_{K27} - 18°C \quad (9)$$

Table 6. Different values of transition temperature T_0.

$T_{0.1}$(°C)	$T_{0.2}$(°C)
-128	-117

3. DISCUSSION

A pragmatic, engineering approach to assess the fracture integrity of cracked or notched structures requires that constraints in the test specimen approximate that of the structure to provide an "effective" toughness for use in a structural integrity assessment. Constraint effect can be represented by stress triaxiality, Q parameter [10, 11] or T-stress [12]. Here constraint is measured by T-stress which is defined by:

$$T = \left(\sigma_{xx} - \sigma_{yy}\right)_{y=0,\theta=0} \tag{10}$$

Term T represents a tension (or compression) stress. Positive T-stress strengthens the level of crack tip stress triaxiality and leads to high crack tip constraint while negative T-stress leads to a loss of constraint.

The volumetric method [2] is employed to calculate the notch fracture toughness and to estimate the effective T-stress ahead of the notch tip. It is assumed, according to the meso-fracture principle, that the fracture process requires a physical volume. This assumption is supported by the fact that fracture resistance is affected by the loading mode, specimen geometry and scale effect. To explain these effects, it is necessary to take into account the stress value and the stress gradient in all neighbouring points within the fracture process volume. This volume is assumed to be quasi-cylindrical with a fracture process zone of similar shape. The diameter of this cylinder is called the "effective distance". This procedure leads to a local fracture criterion based on two parameters, namely, the effective distance X_{ef} and the effective stress σ_{ef}.

Due to the fact that T-stress in the fracture process zone is not constant, it is also assumed to be determined by averaging the T-stress distribution over the effective distance according to a line method (Eq. 11):

$$T_{ef} = \frac{1}{X_{ef}} \int_0^{X_{ef}} T_{xx}(r)\Phi(r).dr \tag{11}$$

where $T_{xx}(r) = \left(\sigma_{xx}(r) - \sigma_{yy}(r)\right)_{\theta=0}$

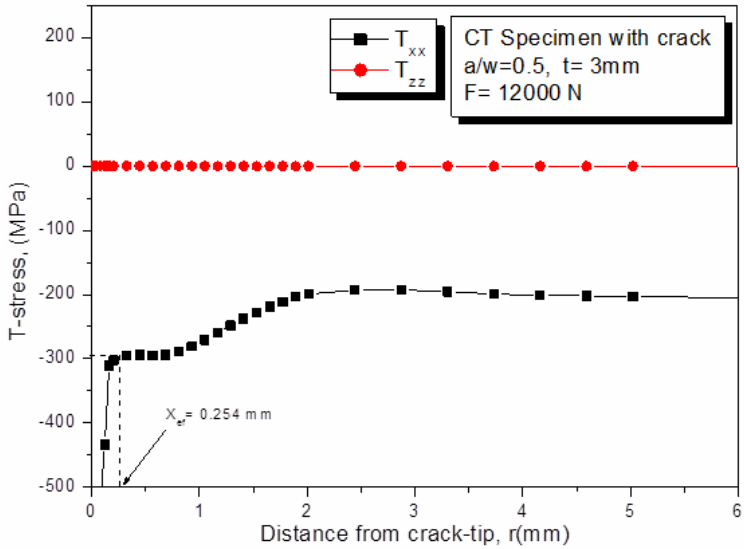

Figure 4. T_{xx} and T_{zz} distributions ahead crack tip ; CT specimen.

Stress distribution ahead of crack tip has been computed for CT specimens by finite element method using ABAQUS code. In addition, T-stress is determined by the stress difference

method i.e. the difference between the opening stress and the stress acting parallel to the crack plane. σ_{xx} was calculated in the direction θ = 180 ° (i.e., in the crack rear back direction), and the T-stress was defined as the value of σ_{xx} in region where this value is constant see fig 4. Stress distribution is computed with stress strain behaviour at transition temperature where material is quasi elastic. Therefore T stress is not sensitive to temperature.
For each test, critical load has been chosen at transition temperature at which brittle fracture is assumed under linear elastic behaviour. The considered T-stress value is the effective value given by Equation (11) for CT and Charpy specimens. For tensile specimen, T-stress is simply the stress difference (σ_{xx}- σ_{yy}) using a Poisson ratio equal to ν = 0.3. Table 7 summarizes values of T-stress and associated transition temperature.
Transition temperatures obtained with the 3 different specimens are plotted against temperature and reported in Figure 5. One notes a linear increase of transition temperature with T-stress according to the following relationship:

$$T_t = 0.0607 T_{ef} + 182 \qquad (12)$$

where T_t is the transition temperature in Kelvin and T_{ef} the effective T-stress in MPa. Transition temperature is not intrinsic to material. It decreases with loss of constraint and one notes that the choice of T_{K27} as reference temperature in Equation (2) is the most conservative.

Table 7. Specimen geometry T-stress and associated transition temperature.

Specimen	Charpy	CT	Tensile
T_{ef} (MPa)	-220	-330	-998
Transition Temperature (K)	174	156	123

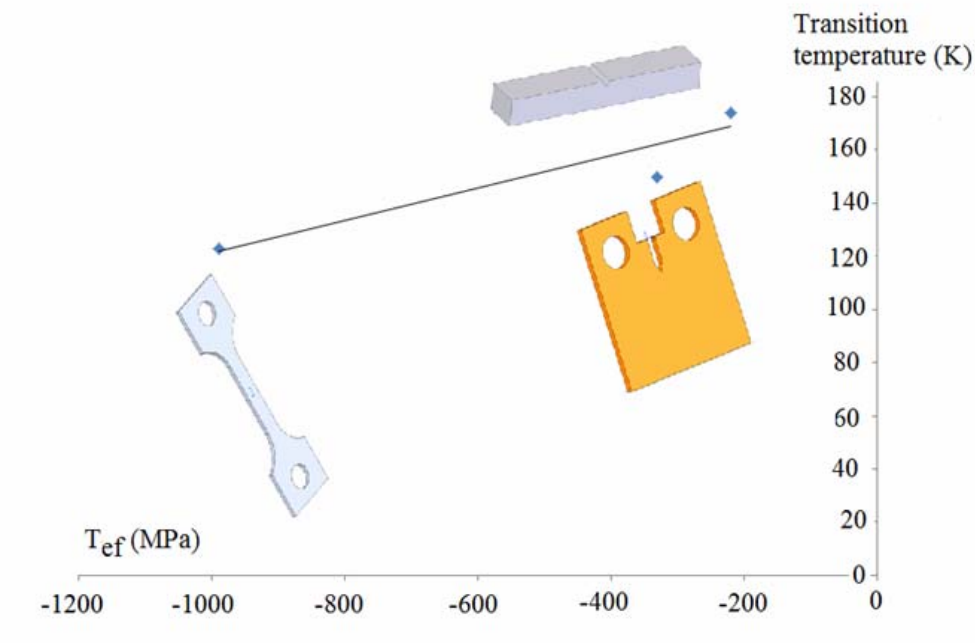

Figure 5. Evolution of transition temperature with effective T-stress (T_{ef}).

Figure 8 allowed to determine a transition temperature relative to the investigated component, i.e., a transition temperature corresponding to the same constraint as the component at failure. For that purpose, it is necessary to obtain the "material master curve" which is the relationship between fracture toughness and constraint and effective T-stress (T_{ef}) at critical pressure for a test according to the procedure described in [13].
Unfortunately, these data are not yet available for X 65 and an estimation has been evaluated on the basis of the API 5L X52 pipe steel and a pipe diameter of 610 mm and thickness equal to 5.8 mm. The pipe exhibits a surface notch with a notch angle $\varphi = 0$, a notch radius $\rho = 0.25$ mm and a notch depth (a) to thickness (t) ratio equal to a/t = 0.5. From that, the constraint range is estimated between -450 MPa and -550 MPa.
The average component transition temperature T_{comp} is deduced from the master curve and evaluated to 150 K (see Figure 6). This temperature is lower than T_{K27} transition temperature of 24 K; this value represents the degree of conservatism of using transition temperature deduced from Charpy specimens. The safety temperature range between the depressurisation temperature plus a temperature allowance and the component temperature is 35 K, which is enough, allowing to consider that API 5L X65 could be used for dense CO_2 transportation.

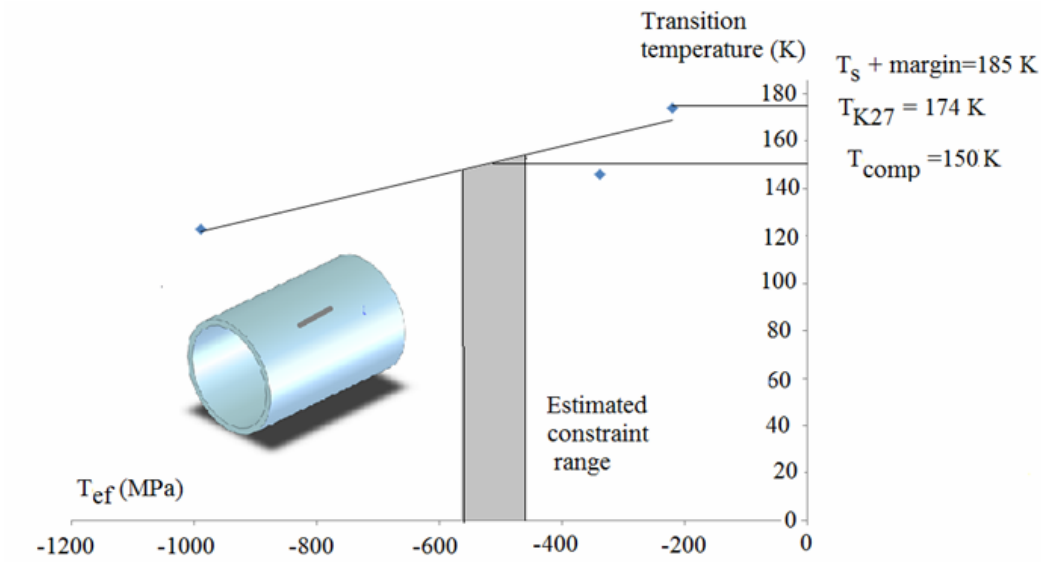

Figure 6. Estimation of component transition temperature from the master curve (T_t = f (constraint)).

4. CONCLUSION

In order to select a steel for transportation of dense CO_2, transition temperatures T_t (from tensile test), T_{K27} and T_{K50} (from Charpy test)and T_{K100} (from fracture mechanics test) have been determined on an API 5L X65 steel. These transition temperatures have been reported versus a constraint parameter, e.g. T-stress, in a master curve. Differences between different brittle-ductile transition temperatures and temperature corresponding to T-stress acting in a pipe submitted to internal pressure on the master curve, give an estimation of the conservatism of the chosen transition temperature.
Based on this methodology the selected API 5L X65 pipeline steel could be used for dense CO_2 transportation since the experimental and calculated transition temperatures are lower than the expected -80 °C following a rapid decompression of dense CO_2 pipeline rupture. The most conservative transition temperature was obtained by Charpy impact test $T_{K27,}$ which is lower than depressurisation temperature plus a temperature allowance.

References

[1] Dooley, J. J., Dahowski, R. T., Davidson, C. L. (2009). Comparing existing pipeline networks with the potential scale of future U.S. CO_2 pipeline networks, *Energy Procedia*, ***1***, 1595-1602.

[2] Pluvinage, G. (2007). General approaches of pipeline defect assessment in *Safety, Reliability and Risks associated with water, oil and Gas pipelines*, Edited by Pluvinage, G. and Elwany, M., Springer, 1-22.

[3] API 579-1/ASME FFS-1 (2007). *Fitness for Service*, American Society of Mechanical Engineers, Houston.

[4] Hadj Meliani, M., Matvienko, Y.G., and Pluvinage, G. (2011). Corrosion defect assessment on pipes using limit analysis and notch fracture mechanics, *Engineering Failure Analysis*, **18**, 271-283.

[5] Kloster, G., Probst-Hein, M. (2012). *X65 steel for seamless line pipe and risers for on- and offshore projects*, Vallourec and Mannesmann Tubes, Düsseldorf, Accessed on June 8, 2012 at www.vmtubes.com.

[6] AFNOR standard: NF EN 10002-1 (1990). *Matériaux métalliques. Essai de traction*, Association Française de Normalisation, Saint Denis La Pleine.

[7] AFNOR standard: NF EN ISO 14556 (2001). *Acier. Essai de flexion par choc sur éprouvette Charpy à entaille en V. Méthode d'essai instrumentée*, Association Française de Normalisation, Saint Denis La Pleine.

[8] Green, A. P., and Hundy, B. B. (1956). Initial plastic yielding in notch bend tests, *Journal of Mechanics and Physics of Solids*, **4,** 128-144.

[9] ASTM E1921-11a, (2003). *Standard Test Method for Determination of Reference Temperature, T_0 for Ferritic Steels in the Transition Range*, American Society for Testing and Materials, Philadelphia.

[10] Ruggieri, C., Gao, X., and Dodds, R. H., (2000). Transferability of elastic-plastic fracture toughness using the Weibull stress approach: significance of parameter calibration; *Engineering Fracture Mechanics*, **67**, 101-117.

[11] Henry, B. S., Luxmore, A. R. (1997). The stress triaxiality constraint and the Q-value as a ductile fracture parameter, *Engineering Fracture Mechanics*, **57**, pp. 375-390.

[12] Betegon, C., and Hancock, J. W. (1991). Two parameter characteristics of elastic– plastic crack-tip fields, *Journal of Applied Mechanics*, **58**, 104–101.

[13] Hadj Meliani, M., Matvienko, Y. G., Pluvinage, G. (2011). Two-parameter fracture criterion ($K_{\rho,\chi}$-$T_{ef,c}$) based on notch fracture mechanics, *International Journal of Fracture*, **167**, 173-182.

FRACTURE TOUGHNESS CRITERIA OF SMALL-SIZE SPECIMENS WITH ULTRAFINE-GRAINED STRUCTURE

Yevgeny Deryugin

Institute of Strength Physics and Materials Science of the Siberian Branch of the Russian Academy of Sciences
Russia, 634021, Tomsk, 2/4, Academichesky prospect, dee@ispms.tsc.ru

Abstract A new method for determining crack toughness of materials is described based on test data of small-size chevron-notched specimens in terms of commercial titanium VT1-0 and titanium alloy VT6 with ultrafine-grained (UFG) structure, obtained by methods of severe plastic deformation (SPD). A problem of separating a part, connected with variations in specimen ductility under crack propagation, of the total displacement of load application point, is solved. Equations to calculate specific fracture energy are obtained. The calculated values of stress intensity factor K_{Ic} are in good agreement with known test data of standard specimens.

Keywords ultrafine-grained (UFG) structure, strain localization, fracture specific fracture energy

1. Introduction

Standard crack toughness tests of materials are generally conducted using the bulk specimens not less than 10 mm in thickness. Although in many cases it is more convenient to use specimens of essentially smaller thickness for this purpose. These specimens do not require a large amount of material and high-power testing machines. Due to this, there is an issue in assessing crack toughness of ultrafine-grained (UFG) and nanostructured materials. The production of these materials in bulk specimens is connected with a series of technical problems. When testing the fracture toughness (crack toughness) of small-size specimens, the chevron-notched specimens are generally used [1-5]. Moreover, specimens with configuration of this type are not required to be fatigue pre-cracked.

In the given paper, a new method for determining crack toughness of materials is described based on test data of small-size chevron-notched specimens in terms of commercial titanium VT1-0 and titanium alloy VT6 with ultrafine-grained (UFG) structure, obtained by methods of severe plastic deformation (SPD).

In course of this study, important computational works, connected with using of chevron-notched specimens, were performed:

- Calculation of the Young 's modulus of the material E;
- Definition of specific fracture energy (crack-driving force [6]) under crack propagation G_s.

2. Determination of Young's modulus when testing chevron-notched specimens

The data on Young's modulus value for the materials with UFG structure is limited. It is known that SPD strongly affects the E value [7, 8]. A method of Young's modulus determination by test data of the chevron-notched specimens is described below.

A scheme of the chevron-notched specimen is presented in Fig. 1. This configuration of the specimen can be considered as a double-cantilever design.

A single cantilever was presented as a beam of elementary cantilevers (mini-cantilevers) of infinitesimal thickness *dx*. As seen from Fig. 1, length of the elementary cantilever at a distance of *x* from the specimen axis is equal to $l(x) = l_0 + x\cdot\mathrm{ctg}(\alpha/2)$, where l_0 is the minimum distance from the load application point to the chevron notch boundary, α is the angle at the end of the chevron notch (Fig. 1). The known formula from the elasticity theory is valid for each cantilever in the beam [9-11]:

$$E = \frac{4dP(x)}{\lambda' dx}\left(\frac{l(x)}{b}\right)^3, \tag{1}$$

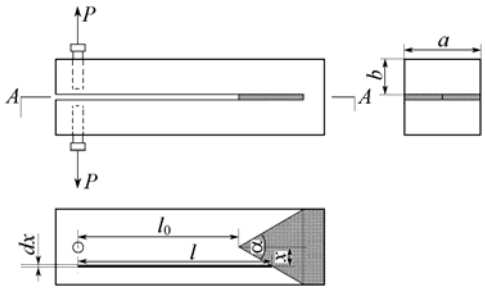

Fig. 1. Scheme of the chevron-notched specimen.

where *b* is the cantilever thickness, *dP* is the load that provides cantilever deflection in width of *dx* by the value of λ'. Displacement of load application points λ for a double-cantilever design exceeds λ' twice, i.e. $\lambda = 2\lambda'$. Accordingly, from the equation (1) we derive the dependence of elementary load *dP*, applied to the mini-cantilever's end on the variable *x*:

$$dP(x) = \frac{E\lambda}{8}\left(\frac{b}{l(x)}\right)^3 dx. \tag{2}$$

Integration of elementary forces (2) affecting each mini-cantilever along the full width of the specimen *a*, determines the actual load *P*, to which the displacement of load application points by the value of λ corresponds:

$$P = \frac{E\lambda b^3}{8}\int_{-\frac{a}{2}}^{\frac{a}{2}}\left(l_0 + x\cdot\mathrm{ctg}\left(\frac{\alpha}{2}\right)\right)^{-3} dx = \frac{E\lambda a}{4}\left(\frac{b}{l_0}\right)^3\left[4+\frac{a}{l_0}\mathrm{ctg}\left(\frac{\alpha}{2}\right)\right]\left[2+\frac{a}{l_0}\mathrm{ctg}\left(\frac{\alpha}{2}\right)\right]^{-2},$$

where *a* is the specimen width (Fig. 1).
Hence we derive the working formula to determine the Young's modulus:

$$E = \frac{8M}{a}\left(\frac{l_0}{b}\right)^3\left[2+\frac{a}{l_0}\mathrm{ctg}\left(\frac{\alpha}{2}\right)\right]^2\left[4+\frac{a}{l_0}\mathrm{ctg}\left(\frac{\alpha}{2}\right)\right]^{-1}. \tag{3}$$

The value of $M = P/\lambda$ characterizes the specimen rigidity at the initial stage of elastic loading.
According to the formula (3), the Young's modulus calculations for commercial titanium VT1-0 and titanium alloy VT6 were conducted. For the VT6-alloy with coarse-grained (CG) structure (grain size

d ranges from 7 to 10 μm), the value of *E* equal to 110±8 GPa was obtained. For the same material with UFG structure, the value of *E* is equal to 114±8 GPa. These values agree with reference data [7]. The Young's moduli of commercial titanium VT1-0 in CG and UFG states appeared equal to 111±8 GPa and 113±8 GPa, respectively, that slightly differs from the value of *E* equal to 110 GPa for commercial titanium by reference data [12, 13]. Thus, the conducted calculations with use of experimental data have shown the following:

- equation (3) can be used for approximate Young's modulus calculation for materials by test data of the chevron-notched specimens;
- grain structure refinement by SPD methods does not lead to essential change in elastic behavior of the studied specimens.

3. Definition of specific fracture energy under crack propagation G_s

Energy approach is reasonable when determining condition of unstable crack propagation. The gist of energy fracture criterion can be defined as follows: crack growth takes place if system can release energy to start crack propagation at elementary distance *dl*. Energy necessary for crack growth appears entirely due to elastic strain energy occurring in bulk of the material under the action of external applied force.

Let us consider a double-cantilever beam specimen with a narrow straight-through notch (Fig. 2) to begin with. Distance from load application points to the notch boundary is a crack in length of l_0. It was shown in the papers [6, 14] for this case that a necessary condition for crack propagation obeys the equation

$$G = \frac{P^2 d\eta}{dS}, \tag{4}$$

where P is the load applied to the specimen, $dS = 2a \cdot dl$ is the doubled area swept by the crack when propagating to the short distance dl (Fig. 2), $\eta = \lambda_e/P$ is the specimen ductility (value reverse to rigidity $M = \lambda_e/P$). The value of G determines elastic energy release rate under crack propagation. Further we shall call the characteristics of G a specific fracture energy.

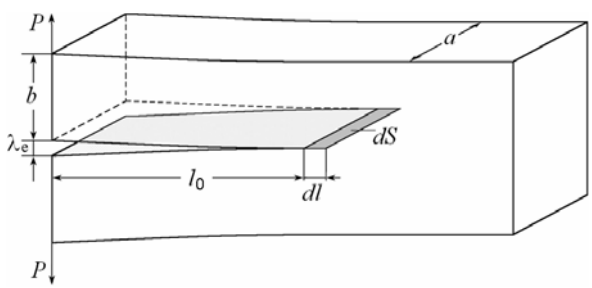

Fig. 2. Straight-through notched specimen.

According to [6], displacement of load application points λ_e for the specimen in width of a with crack length l is provided by load:

$$P = \frac{E\lambda_e a}{8}\left(\frac{b}{l}\right)^3. \tag{5}$$

Ductility of such specimen is equal to:

$$\eta = \frac{\lambda_e}{P} = \frac{8}{Ea}\left(\frac{l}{b}\right)^3.$$

Considering that dS is equal to $2a \cdot dl$, we shall find the derivative $d\eta/dS$ in the equation (4):

$$\frac{d\eta}{dS} = \frac{d\eta}{2adl} = \frac{12l^2}{Ea^2b^3}.$$

Substituting the given expression into (4), we shall obtain:

$$G = P^2\frac{d\eta}{dS} = \frac{12P^2l^2}{Ea^2b^3}. \tag{6}$$

Equation (6) determines specific fracture energy along the crack length l and external load value P, wherein the crack starts to propagate.
Substituting expression (5) into this equation, we shall derive an equation for G_s, which allow us to calculate specific fracture energy based on crack length l and the value of λ_e:

$$G = \frac{3E}{16}\frac{\lambda_e^2 b^3}{l^4}. \tag{7}$$

It is seen that in the given presentation the value of G does not depend on the specimen width a.
Let us apply these considerations to the chevron-notched specimen. Assume that in the process of loading of the given specimen, the material lost discontinuity in segment of Δl (Fig. 3). Crack front is presented as a straight line. It is easy to find from geometrical constructions that length of this line is equal to $x = 2\Delta l \cdot \mathrm{tg}(\alpha/2)$. An equation (7) can be applied to the middle part of the specimen in width of x , wherein crack length l makes $l_0 + \Delta l$. Using the equation (7), a specific fracture energy G can be found, if increment Δl is known. Moreover, it is necessary to know displacement of force application point λ_e, caused by enhancement in specimen ductility when increasing the crack length by Δl.

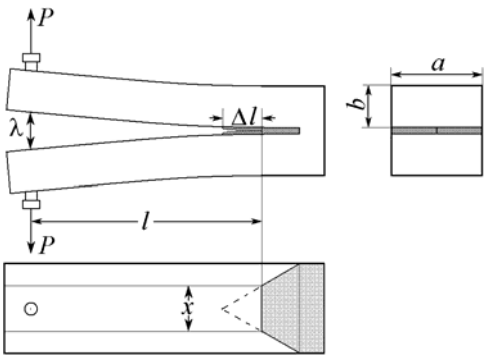

Fig. 3. Determination of the specific fracture energy G_s.

It should be noted that the experimentally measured value of λ (Fig. 3), in addition λ_e, includes the contribution due to plastic deformation of the material at the mouth of the crack, and in the volume of sample as a whole.

The value of λ_e can be determined if its dependence from the external force P is found. To determine P, let us present a specimen with a crack as a set of double-cantilever beams: with straight-through notch in width of x and with chevron notch in width of $a - x$ (Fig. 4). We shall find forces P_1 and P_2 for each part, determining equal displacement λ_e of these force application points. Using equation (5), it is easy to derive expression for the force P_1 affecting the specimen in width of $x = 2\Delta l \cdot \mathrm{tg}(\alpha/2)$, which provides displacement of load application points P_1 to the specified value of λ_e:

$$P_1 = \frac{E\lambda_e \Delta l}{4} \mathrm{tg}\left(\frac{\alpha}{2}\right)\left(\frac{b}{l}\right)^3 . \tag{8}$$

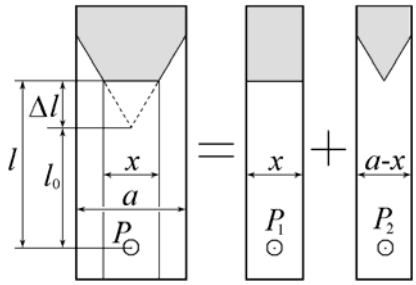

Fig. 4. Presentation of the double-cantilever beam specimen.

When applying equation (3), with regard for the width of the chevron-notched specimen equal to a-x, we shall derive an expression for the force P_2, which provides displacement of load application points to the same value of λ_e:

$$P_2 = \frac{E\lambda_e a}{8}\left[1 - \frac{2\Delta l}{a}\mathrm{tg}\left(\frac{\alpha}{2}\right)\right]\left(\frac{b}{l}\right)^3 \frac{l}{l_0}\left[4 + \frac{a}{l_0}\mathrm{ctg}\left(\frac{\alpha}{2}\right) + \frac{2\Delta l}{l_0}\right]\left[2 + \frac{a}{l_0}\mathrm{ctg}\left(\frac{\alpha}{2}\right)\right]^{-2}, \tag{9}$$

where $l = l_0 + \Delta l$.

From equations (8) and (9), an expression for λe is determined:

$$\lambda_e = \frac{8Pl^3}{Eab^3}\left[\frac{2\Delta l}{a}\mathrm{tg}\left(\frac{\alpha}{2}\right) + \left(1 - \frac{2\Delta l}{a}\mathrm{tg}\left(\frac{\alpha}{2}\right)\right)\frac{l}{l_0}\left[4 + \frac{a}{l_0}\mathrm{ctg}\left(\frac{\alpha}{2}\right) + \frac{2\Delta l}{l_0}\right]\left[2 + \frac{a}{l_0}\mathrm{ctg}\left(\frac{\alpha}{2}\right)\right]^{-2}\right]^{-1}, \tag{10}$$

where $P = P_1 + P_2$.

Equations (7) and (10) were used to calculate fracture energy determining the necessary condition for spontaneous crack propagation in studied materials.

Figure 5 presents typical loading diagrams for titanium alloy VT6 and commercial titanium VT1-0 with UFG structure obtained under testing of small-size chevron-notched specimens. Both diagrams correspond to loading rate v = 2,0 μm/s. Specimens in length of 18 mm were made of bars in section of 6x6 mm^2.

Calculations have shown that the value of G_s is maximal at the peak of loading and therefore, can serve as a crack resistance criterion of studied materials at specified geometrical parameters and loading conditions of the specimen.

Stress intensity factor is generally used as a crack resistance criterion in engineering fracture mechanics for a cleavage crack:

$$K_{Ic} = \sqrt{\frac{EG_s}{1-\nu^2}}, \tag{11}$$

where G_s is the threshold fracture energy. Formula (11) allows determining the value of K_{1c} by means of critical specific fracture energy G_s.

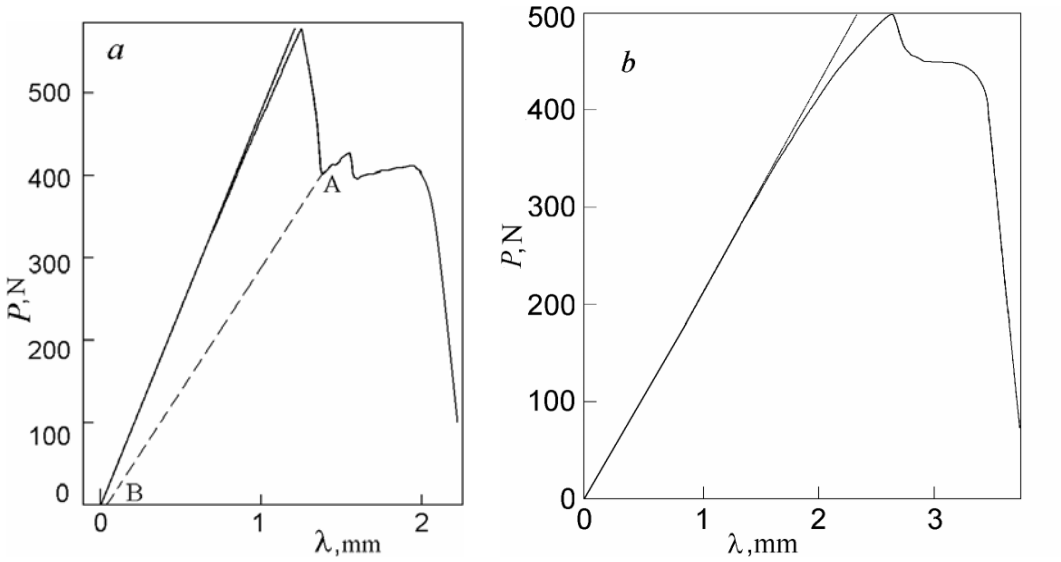

Fig. 5. Loading diagrams of the VT6-alloy (*a*) and commercial titanium VT1-0 (*b*) with UFG structure.

Values of crack resistance characteristics for the studied materials are presented in Tab. 1. It is seen that specific fracture energies of the VT6-alloy in CG and UFG states differ significantly.

Dimension of the G_s characteristics is energy per unit area. However, this value is not a surface energy of the material. The last one is several orders of magnitude smaller than fracture energy G_s. Thus, surface energy of titanium is equal to 1.7 J/m^2 [12], at the same time, energy fracture value of commercial titanium, according to our calculations, is G_s = 27.82 kJ/m^2. Agreement in values of G_s and surface energy will be observed only in case of totally brittle fracture. A colossal difference is caused by plastic strain processes intensively developing in metals and alloys that lead to essential change in shape and strain-stress state locally at the crack tip.

Table 1. Mechanical characteristics of commercial titanium VT1-0 and VT6

Material	λ_p/λ_e	G_s, kJ/m^2	K_{Ic}, MPa/m$^{1/2}$	E, GPa
VT1-0 UFG	0.11	27.82	56.37	113
VT1-0 CG				111
VT6 UFG	0.11	31.48	63.2	114
VT6 CG	0.37	53.00	90.8	110

According to equation (10), the values of λ_e are equal to 1.07 and 1.914 mm for VT6 and VT1-0, respectively. These values appeared smaller than experimentally measured displacement values of load application points λ, i.e. λ is equal to 1.21 mm for VT6 and λ makes 2.12 mm for VT1-0. Difference between measured and calculated values is caused by additional contribution of λ_p plastic strain into displacement of load application points, i.e. λ_p is equal to 0.14 mm for VT6 and λ_p is equal

to 0.28 mm for VT1-0. The relation λ_p/λ_e, apparently, can serve as mechanical characteristics determining a relative contribution of the specimen plastic distortion into displacement caused by change in specimen ductility.

4. Conclusion

A new method for determining crack toughness of materials is described based on test data of small-size chevron-notched specimens in terms of commercial titanium VT1-0 and titanium alloy VT6 with ultrafine-grained (UFG) structure, obtained by methods of severe plastic deformation (SPD). A problem of separating a part, connected with variations in specimen ductility under crack propagation, of the total displacement of load application point, is solved. A series of important computational problems connected with testing of chevron-notched specimens is solved in the study. Analytical expressions are obtained to calculate the Young's modulus of the material and to determine specific fracture energy.

The calculated values of the Young's modulus *E* and stress intensity factor K_{Ic} agree with known test data of standard specimens made of commercial titanium VT1-0 and titanium alloy VT6.

The work was supported by Russian Foundation for Basic Research. Project № 08-10-01182-a.

References

1. L.M. Barker, Theory for determining K_{Ic} from small, non-LEFM specimens, supported by experiments on aluminum. Int. J. of Fracture, 16, No. 6 (1979) 515-536.
2. C.T. Wang, R.M. Pillar, Short-rod elastic-plastic fracture toughness test using miniature specimens. J. Mater. Sci. 24 (1989) 2391-2400.
3. T.J. Grant, L. Weber, A. Mortensen, Plasticity in Chevron-notch fracture toughness testing. Engineering Fracture Mechanics, 67 (2000) 263-276.
4. B.A. Drozdovsky, T.V. Polischuk, V.P. Volkov, Chevron notch as a method of thickness decrease of the specimen at determining of K_{Ic}. Zavodskaya Laboratoriya, 6 (1987) 74-76.
5. R.R. Rakhimkulov, Matching of fracture toughness values of K_{1c}, obtained in chevron-notched specimens and based on standard technique for the steel St3sp. Neftegazovoe Delo, 2 (2010) 1-10. http://www.ogbus.ru/authors/Rakhimkulov/Rakhimkulov_1.pdf
6. D. Broek, Fundamental concepts of fracture mechanics, Vysshaya shkola, Moskow, 1980.
7. G.A. Salischev, R.M. Galeev, S.P. Malysheva et al., Change in elasticity modulus at annealing of submicrocrystalline titanium, The Physics of Metals and Metallography (FMM), V. 85. No. 3 (1998) 178-181.
8. V.I. Betekhtin, O.R. Kolobov, M.V. Narykova et al., Mechanical properties, density and defect structure of submicrocrystalline titanium VT1-0, obtained after severe plastic deformation at screw and lengthwise rolling. Journal of Technical Physics, 81, Iss. 11 (2011) 58-63.
9. M.D. Podscrebko, Resistance of materials, Vyseishaya shkola, Minsk, 2007.
10. S.P. Timoshenko, J. Gud'er. The theory of elasticity, Nauka, Moskow, 1975.
11. GOST 16483.9-73. Drevesina. Methods of elasticity modulus determination under static bending, Moskow, 1973.

12. I.S. Grigor'ev, B.Z. Meilikhova (Eds), Physical quantities, Handbook, Energoatomizdat, Moscow, 1991.
13. A.A. Il'in, B.A. Kolachev, I.S. Pol'kin, Titanium alloys. Composition, structure, properties: Handbook, VILS – MATI, Moskow, 2009.
14. R.W. Hernzberg, Deformation and Fracture Mechanics of Engineering materials, John Wiley and Sons, Toronto, New York, 1983.

A coupled stress and energy model for mixed-mode cracking of adhesive joints

Philipp Weißgraeber[1,*], Wilfried Becker[1]

[1] FG Strukturmechanik, TU Darmstadt, Germany
* Corresponding author: weissgraeber@fsm.tu-darmstadt.de

Abstract This work is concerned with the analysis of failure of adhesive joints. Typically adhesive joints fail due to cracking of the adhesive with cracks originating from the reentrant corner of the adherend and the adhesive. A failure model based on a coupled stress and energy criterion settled in the framework of Finite Fracture Mechanics (FFM) is proposed in this work. The main idea of coupled criteria in FFM is that cracks of finite size are predicted when a stress criterion is fulfilled on all points of the considered crack and simultaneously an energy criterion is fulfilled.
A failure model for adhesively bonded single lap joints is worked out that makes use of an extended weak interface model. Its closed-form analytical nature allows for an efficient formulation of the non-linear failure criterion. The effects of the involved geometric parameters are examined in detail. A comparison of the failure load predictions to experimental results is given and shows a good agreement. It is shown that the effect of the adhesive layer thickness is incorporated correctly. The failure model and its implications on the understanding of failure of adhesive joints are discussed in detail.

Keywords Brittle fracture, Finite Fracture Mechanics, adhesive joints

1. Introduction

Adhesive joints can be an interesting alternative joining method. They have several distinctive advantages over other joining techniques as e.g. welding or bolting. Adhesive bonding allows for large surface joining of thin-walled structures that can have dissimilar materials. The resulting joint has a smooth surface and a sealing function is given. But uncertain failure load predictions and lacking knowledge of failure mechanisms still hinder the widespread use of adhesive joints. To make use of their advantageous features a better understanding of this joining method must be achieved. In the last decades many researchers have worked on an improved understanding of adhesive joints. An overview on the performed research can be found in the comprehensive textbooks of this field, e.g. [1,5].
Failure models for adhesive joints mainly make use of three different approaches, namely strength of materials, fracture mechanics and damage mechanics. Most of the works given in literature focus on strength of material approaches as it has the longest history and it is well known. Unfortunately these approaches lack in the correct description of some important features. Various effects of the involved geometric parameters of a simple joint configuration cannot be fully described by these approaches. A typical outcome is for example that the strength of the adhesive seems to depend on certain geometric parameters. No solid physical explanation can be given for such a relation. The aim of the present work is to present a new failure model for adhesive joints that correctly describes the effect of the geometrical parameters and makes accurate predictions for the failure load.

2. Theoretical background

2.1. Coupled stress and energy criterion

In this work a coupled stress and energy criterion [11] is used to predict crack initiation. The criterion requires two basic material parameters: the strength of the material and the fracture toughness. The criterion is settled in the framework of Finite Fracture Mechanics (FFM) [9] that

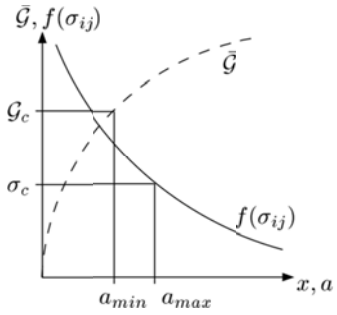

Figure 1. The stress distribution at a stress concentration and incremental energy release rate as a function of the crack length given for a general situation. The upper and lower bounds for the crack length that result from the stress and energy criterion are shown as well.

considers cracks of finite length. This allows for the assessment of crack initiation of uncracked structure, which is a remarkable advantage over classical linear elastic fracture mechanics approaches. Finite cracks have been addressed by several researchers in literature, e.g. [10,12,13,15]. The basic idea of the coupled stress and energy criterion is that the instantaneous formation of a finite crack is predicted when a stress criterion is fulfilled over the full length of the considered crack and the energy balance is fulfilled. The energy balance requires in the style of Griffith's criterion that the energy that is released in the formation of the crack is equal or exceeds the energy that is required to form the crack. Considering a crack of length a and width b with its surface Ω_c the whole coupled criterion can be written as:

$$f(\sigma_{ij}(x_i)) \geq \sigma_c \quad \forall x_i \in \Omega_c \quad \wedge \quad \bar{\mathcal{G}}(a) \geq \mathcal{G}_c \tag{1}$$

The stress criterion f is a function of the stress tensor σ_{ij} and must be chosen appropriately. σ_c is the strength and $\mathcal{G}_c$ is the fracture toughness of the considered material. The quantity $\bar{\mathcal{G}}$ is the so-called incremental energy release rate, which is the averaged energy release rate over the finite crack length:

$$\bar{\mathcal{G}}(a) = \frac{1}{a}\int_0^a \mathcal{G}(\tilde{a})\mathrm{d}\tilde{a}. \tag{2}$$

To assess the minimal load F_f, hence the effective strength, both variables of the criterion have to be identified. Both inequalities are required to identify the finite crack length a and the failure load F_f. In certain cases the stresses and the incremental energy release rate show a monotonic dependence on the crack length and the two inequalities revert to equalities. Such geometries are called positive geometries. In such cases sometimes closed-form solutions for the failure load and the crack length can be given. In the general case of inequalities an optimization problem has to be solved. The lowest load has to be found that satisfies both inequalities for any admissible crack length.

$$F_f = \min_{F,a}\left\{F \,|\, f(\sigma_{ij}(x_i)) \geq \sigma_c \quad \forall x_i \in \Omega_c \quad \wedge \quad \bar{\mathcal{G}}(a) \geq \mathcal{G}_c\right\} \tag{3}$$

The ingredients for the optimization problem are illustrated in Fig. 1. In this illustration $a_{\min}$ is the lower bound for the crack length that originates from the energetic condition. The incremental energy release typically increases for larger crack length and this leads to the lower bound for the crack length as function of the given load. The stresses are concentrated, possibly even in form of a stress singularity, and show a declining behavior. Thus, the stress criterion leads to an upper bound $a_{\max}$ for the crack length.

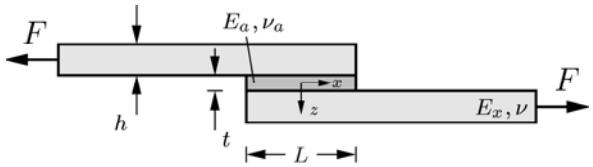

Figure 2. The considered single lap joint configuration

2.2. Linear elasticity solution for the single lap joint

To obtain an efficient failure model a closed-form solution of the mechanical behavior of the single lap joint has been chosen in this work. Since the pioneering works by Volkersen [17] and the work by Goland and Reissner [8] many linear-elasticity solutions for the single lap joint have been developed and proposed in literature. Previous works by the authors [18,19] have shown that the simplified models by Volkersen and Goland-Reissner can be used to study the failure behavior of single lap joints but not all effects are covered to the full extent. In this work an extended weak interface model is used to model the adhesive joint, the model proposed by Ojalvo and Eidinoff [14]. The distinctive feature of this model is an extended consideration of the adhesive layer thickness effect and a linear distribution of the shear stresses in the adhesive layer.
Let us consider a single lap joint under axial loading F as shown in Fig. 2.. The height of the adherends shall be h, the thickness of the adhesive layer t and the length of the overlap shall be L. The width of the joint is denoted as b. Young's modulus of the adherend ist denoted as E_x and Young's modulus of the adhesive as E_a. The respective Poisson's ratios are denoted as ν and ν_a. The shear modulus of the adhesive layer is denoted by G_a.The axial coordinate x runs from the middle of the adhesive layer. Due to the large deformations of the adherends due to bending a non-linear dependence of the bending moment at the end of the overlap to the axial force F is used:

$$M = k(F)\frac{h+t}{2}F \tag{4}$$

with $k(F)$ being the non-linear moment factor. In literature many approaches can be found for defining this moment factor. In this work the moment factor given by Tsai and Morton [16] is used:

$$k = \frac{1}{1+2\sqrt{2}\tanh\left(\sqrt{\frac{3\left(1-\nu^2\right)}{2}}\frac{L}{2h}\sqrt{\frac{F}{E_x hb}}\right)} \tag{5}$$

The peel stress in the midplane (index 0) of the adhesive layer is obtained as follows [14]:

$$\sigma_0 = \frac{F}{bL}\left(A_1\sinh\left(\alpha_1\frac{2x}{L}\right)\sin\left(\alpha_2\frac{2x}{L}\right)+A_2\cosh\left(\alpha_1\frac{2x}{L}\right)\cos\left(\alpha_2\frac{2x}{L}\right)\right) \tag{6}$$

with

$$\alpha_{1,2} = \sqrt{\pm\frac{3t\lambda^2}{2h}+\frac{1}{2}\sqrt{\frac{3E_aL^4}{2E_xth^3}}} \quad , \quad \lambda = \sqrt{\frac{G_aL^2}{4E_xth}}. \tag{7}$$

The constants A_1 and A_2 have to be obtained from the following boundary conditions.

$$\frac{L^2}{4}\frac{\partial^3\sigma_0}{\partial x^3}\bigg|_{x=\frac{L}{2}} - 3\frac{\lambda^2 t}{h}\frac{\partial\sigma_0}{\partial x}\bigg|_{x=\frac{L}{2}} = -k\frac{3E_aFL}{E_xth^2b}\left(1+\frac{t}{h}\right) \tag{8}$$

$$\left.\frac{\partial^2\sigma_0}{\partial x^2}\right|_{x=\frac{L}{2}} = k\frac{6E_aF}{E_x th^2 b}\left(1+\frac{t}{h}\right) \tag{9}$$

The shear stress in the adhesive layer can be given as

$$\tau = \tau_0 + \frac{G_a}{E_a}.\frac{\partial\sigma_0}{\partial x}z \tag{10}$$

with

$$\tau_0 = \frac{F}{bL\Omega^2}\left(\Omega\zeta\frac{\cosh\left(\Omega\frac{2x}{L}\right)}{\sinh(\Omega)} + \Omega^2 - \zeta\right), \tag{11}$$

$$\zeta = 2\lambda^2\left(1+3\left(1+\frac{t}{h}\right)^2 k\right) \quad , \quad \Omega = \lambda\sqrt{2\left(1+3\left(1+\frac{t}{h}\right)^2\right)}. \tag{12}$$

As typical for weak interface models, it is assumed that crack advancement corresponds to a shortening of the overlap length. For the case of cracks emerging from one reentrant corner of the adherends and the adhesive layer the following relationship of the differential energy release rate to the peak stresses at the end of the overlap can be derived from the energy stored in the adhesive layer at the end of the overlap:

$$\mathcal{G} = \frac{1}{2}\frac{t}{G_a}\left(\tau_{0,\max}^2 + \left(\frac{G_a}{E_a}\left.\frac{\partial\sigma_0}{\partial x}\right|_{x=-L/2}\right)^2\frac{t^2}{12}\right) + \frac{1}{2}\frac{t}{E_a}\sigma_{0,\max}^2 \tag{13}$$

As outlined previously the incremental energy release rate is to be obtained from the differential energy release rate by integration. Of course, it must be considered that the peak stresses change when the overlap length decreases with higher crack lengths.

$$\overline{\mathcal{G}} = \frac{1}{a}\int_0^a \left(\mathcal{G}(L = L_0 - \tilde{a}\right)\mathrm{d}\tilde{a} \tag{14}$$

This integral cannot be solved in closed-form analytical manner but must be solved with a numerical integration scheme.

3. The optimization problem

As discussed previously it is necessary to solve the optimization problem (3) posed by the coupled stress and energy criterion (1) to identify the failure load of the joint. For the stress function f the maximum principal stress criterion is used in this work. In the case of the presently used simplified model of the single lap joint it reads:

$$f(\sigma_{ij}) = \frac{\sigma_0}{2} + \sqrt{\left(\frac{\sigma_0}{2}\right)^2 + \left(\tau(z=-t/2\right)^2} \geq \sigma_c \tag{15}$$

As the incremental energy release rate has to be obtained by numerical integration and the stresses exhibit a non-linear dependence on the acting forces the coupled criterion cannot be solved analytically. The more general approach of solving the optimization problem with the two variables

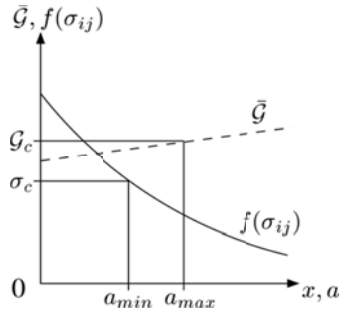

Figure 3. The stress distribution at a stress concentration and incremental energy release rate as a function of the crack length given for the case of the considered weak interface model

failure load and crack length must be followed. The optimization problem can be solved by standard method for restricted optimization. Due to the closed-form nature of the underlying equations an efficient solution is obtained using the Computer Algebra System Mathematica in Version 8.

A closer look at the optimization problem reveals interesting details of the present modeling approach. In Figure 3 the optimization problem is illustrated for the present case of a weak interface model. The most remarkable characteristics are that the stresses and hence the stress criterion do not show a singular behavior, as it is known from linear-elasticity theory and that the incremental energy release rate does not start at zero for vanishing crack lengths as it is expected for the weak singularity of the reentrant corner. The singularity order of the reentrant corner is lower than the well-known crack tip singularity. These deficiencies of the presently used model for the single lap joint concerning the stresses and the energy release rate are well-known and a typical outcome of weak interface models. It will be seen in the following that in the framework of FFM they do not have a strong effect on the results. Figure 3 shows the stress distribution and the incremental energy release rate for a loading that is lower than the failure load. The upper bound for the crack length predicted by the stress criterion is lower than the lower bound for the crack length as predicted by the energy criterion. If the loading is now increased the incremental energy release rate and the stresses will increase as well. With increased energy release and stresses now the upper and lower bound for the finite crack length are approaching each other until they will eventually coincide. Then the lowest load satisfying both conditions of the coupled criterion is found. It is the failure load of the considered joint. It can be seen, that the stress and energy criteria are not evaluated directly at position 0, which is the tip of the reentrant corner. Hence, the previously described deficiencies of the weak interface model do not play a role in the evaluation of the failure load.

4. Results

In this section results of the outlined coupled stress and energy model are presented. The effect of the geometrical parameters of the considered single lap joint on the failure load are pointed out and discussed. Furthermore a comparison to experimental results from literature is shown. In this comparison only material parameters provided from standard tests are used if available to predict the failure load.

4.1. Parameter study

For the parameter study a typical symmetric steel-epoxy joint is considered. Young's moduli of the adherend and the epoxy are: E_x=210GPa, E_a=3GPa. The corresponding Poisson's ratios are

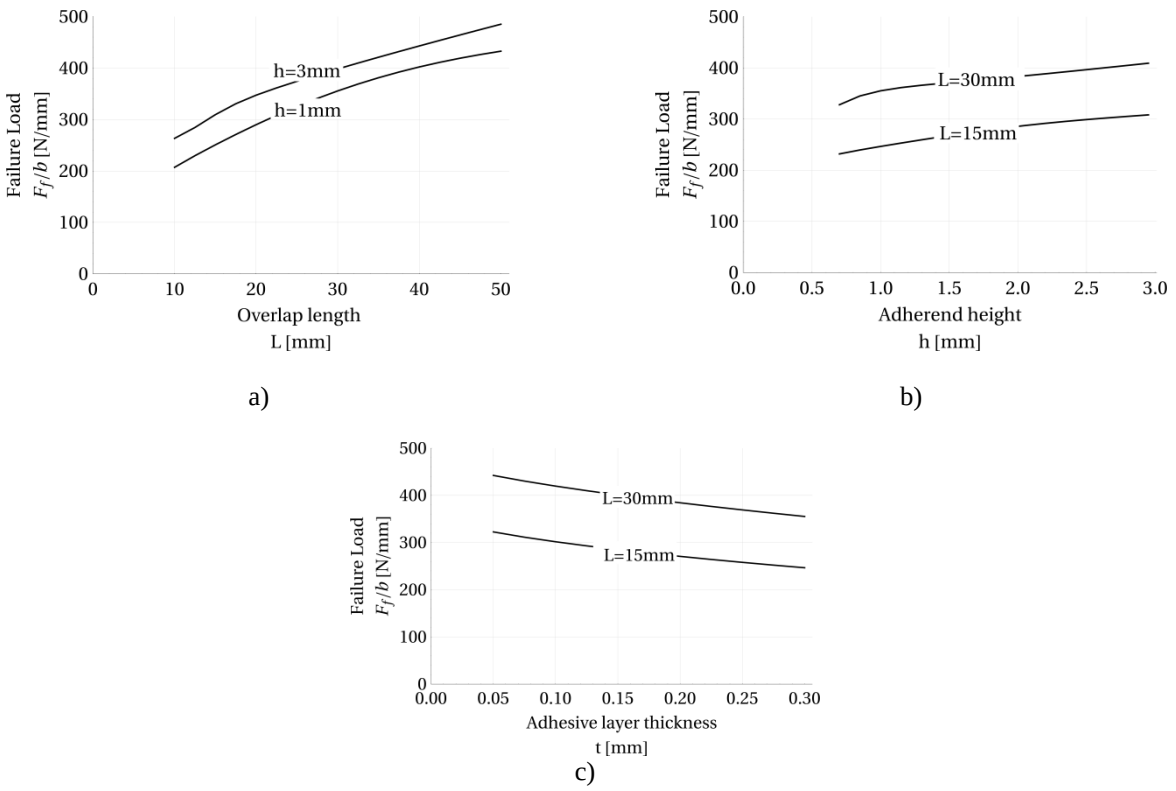

Figure 4. Effect of the geometrical parameters on the failure load of the joint

ν =0.3 and ν_a =0.4. The strength and the fracture toughness are: $\sigma_c = 45\text{MPa}$, $\mathcal{G}_c = .45\text{N/mm}$.
In Fig. 4a the effect of the overlap length L on the failure load is shown. It can be seen, that the failure load increases with higher overlap lengths. As it is well known from experiments a less pronounced increase of the failure load is observed for larger overlap lengths. The basic mechanism is the increased bondline area with more equally distributed stresses. But as the peak stresses at the end of the overlap do not become arbitrarily smaller with larger overlap lengths, the increase is less pronounced for higher overlap lengths. The effect of the adherend height on the failure load is shown in Fig. 4b. An increase of the failure loads is observed with higher adherend heights as it is for larger overlap lengths. The basic mechanism behind this effect is the improved bending stiffness of the adherends. As the bending stiffness increases the peel stresses are distributed more equally. Fig. 4c shows the dependence of the failure load on the adhesive layer thickness. A decrease of the bearable loads is predicted for thicker adhesive layers. This is in very good accordance with knowledge on adhesive joints obtained from practice and experimental results. But it is likewise contrary to failure load predictions from failure models that base on strength of material approaches [6]. The key point is the consideration of energetic criteria. The adhesive layer stores, due its relatively low stiffness, the main part of the elastic strain energy. Hence, it gives the largest contribution to the energy release rate. If now the adhesive layer is increased, the incremental energy release rate increases as well. In this model both criteria, the stress criterion and the energy criterion must be fulfilled simultaneously and hence an increased energy release rate leads to reduced failure loads. This work shows that it is possible to explain the effect of adhesive layer thickness on the failure load by means of a simple linear elastic analysis by consideration of the energy release.

Table 1. Material properties of the adhesives

	E_a [MPa]	ν_a [-]	σ_c [MPa]	$\overline{\mathcal{G}}$ [N/mm]	Ref.
AV138/HV998	4890	0.35	39.5	0.38	[2]
Hysol EA 9321	3870	0.36	46.0	0.45	[7]
Redux 326	4440	0.35	50.9	(0.3)	[6]

4.2. Comparison to experimental results

Several experimental studies have been selected for comparison to the failure load predictions. The experimental studies where chosen such that only well documented and repeated studies are used. Only adhesives with substantially brittle behavior were used for the comparison.

The effect of the adhesive layer thickness was studied experimentally by Castagnetti et al. [3] for steel adherends with two different adhesives. The results of the sufficiently brittle adhesive Hysol EA 9514 are used for comparison. In the work by da Silva et al. from 2004 [4] the effect of the overlap length on the failure load of the steel joints with a bismaleimide adhesive Redux 326 was studied. In the study by da Silva et al. from 2006 [7] three different adhesives were tested with steel adherends. From these adhesives two adhesives, AV138 and Hysol EA 9321, were sufficiently brittle. The material data that were used are summarized in Table 1. The strength and the fracture toughness are not identified by means of the used experimental results. Material parameters from standard tests that are given in literature [2,6,7] are used. No specific value for the fracture toughness could be found in literature for the bismaleimide adhesive Redux 326. It is assumed that the fracture toughness attains values around 0.3 N/mm.

The comparisons of the present failure model to the experimental results are shown in Fig. 5a-5c. Obviously, the failure load predictions agree well with the experimental results. Especially when the scattering of the experimental results is considered it becomes clear that the failure load prediction by the present model is of good quality. Another important feature is that the effects of the geometrical parameters are covered correctly by the present model. Especially the adhesive layer thickness effect has been subject to many studies that try to explain the effect on the failure load. If only stress criteria are used it appears that the strength of the adhesive reduces if thinner bondlines are considered. No physically sound explanation can be given for such a change of the adhesive strength. The present model can correctly predict the effect of the adhesive layer thickness by an additional energetic condition that must be satisfied simultaneously.

5. Summary

A new failure model for adhesive joints has been given. It bases on a coupled stress and energy criterion in the framework of FFM. A closed-form analytical model for the mechanical behavior of a single lap joint is used to set up the failure model. The failure model requires two basic failure parameters, the strength and the fracture toughness of the adhesive. A study of the effect of the geometrical parameters on the failure load on adhesive joints is shown and discussed. The predicted effects are in good accordance to general knowledge on adhesive joints. Furthermore a comparison to experimental results is shown. In general it shows a good accordance of the prediction and the experimental results. All trends are covered very well. Only failure parameters as given in published results from standard tests are used in the comparison and no fitting of the input parameters needs to be performed. A remarkable outcome is the fact that the effect of the adhesive layer thickness is covered correctly.

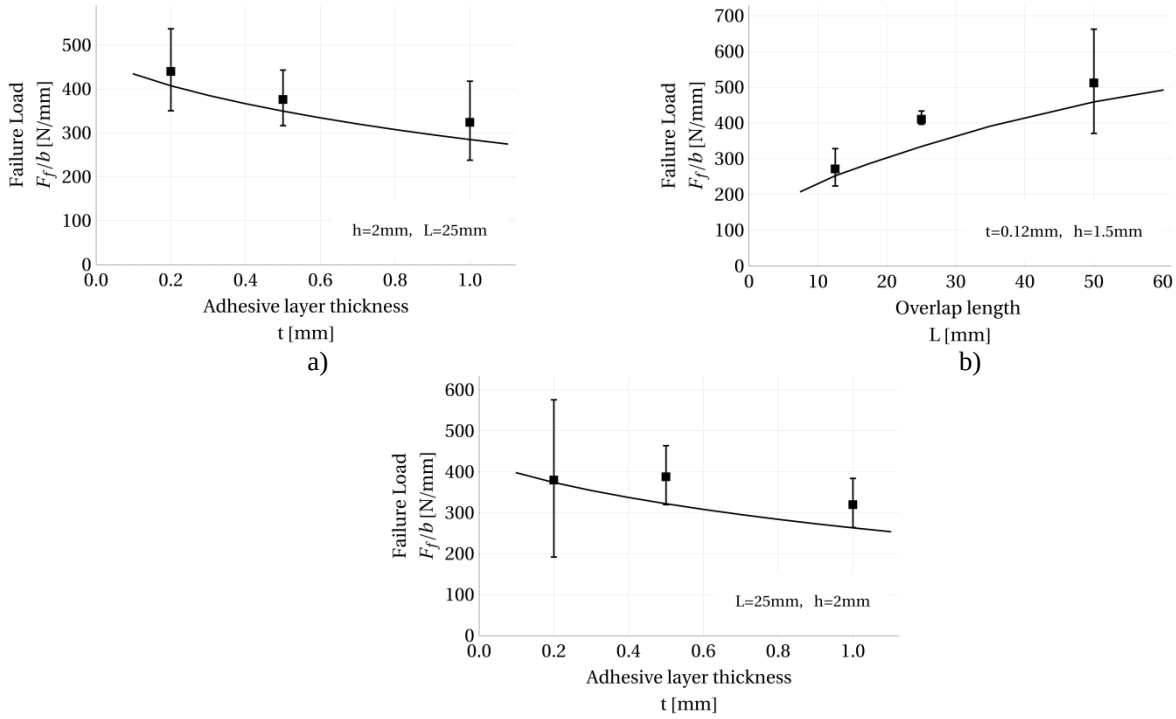

Figure 5. Comparison to experimental results

References

[1] Adams R, Comyn J, and Wake W. Structural adhesive joints in engineering. Springer, 1997.
[2] Campilho R, Banea M, Pinto A, da Silva L, and De Jesus A. Int J Adhes Adhes, 2011.
[3] Castagnetti D, Spaggiari A, and Dragoni E. J Adhes, 87(7-8):780, 2011.
[4] da Silva L, Adams R, and Gibbs M. Int J Adhes Adhes, 24(1):69, 2004.
[5] da Silva L and Campilho R. Advances in Numerical Modeling of Adhesive Joints. Springer, 2011.
[6] da Silva L, das Neves P, Adams R, Wang A, and Spelt J. Int J Adhes Adhes, 29(3):331, 2009.
[7] da Silva L, Rodrigues T, Figueiredo M, Moura MD, and Chousal J. J Adhes, 82(11):1091, 2006.
[8] Goland M and Reissner E. J Appl Mech, 11(1):A17, 1944.
[9] Hashin Z. J Mech Phys Solids, 44(7):1129, 1996.
[10] Hebel J, Dieringer R, and Becker W. Eng Fract Mech, 77(18):3558, 2010.
[11] Leguillon D. Eur J Mech A-solid, 21(1):61, 2002.
[12] Mantiˇc V. Internat J Solids Structures, 46(6):1287, 2009.
[13] Martin E, Leguillon D, and Carrère N. Internat J Solids Structures, 47(9):1297, 2010.
[14] Ojalvo I and Eidinoff H. Aiaa J, 16(3):204, 1978.
[15] Tran V, Leguillon D, Krishnan A, and Xu L. Int J Fracture, 35(1):1, 2012.
[16] Tsai M and Morton J. J Appl Mech, 61(3):712, 1994.
[17] Volkersen O. Luftfahrtforschung, 15(1/2):41, 1938.
[18] Weißgraeber P and Becker W. Key Eng Mater, 471:1075, 2011.
[19] Weißgraeber P and Becker W. In Proceedings of the 32nd Risø International Symposium in Materials Science, 479–486, 2011.

Plastic factor of front face compact tension specimens

KAIKAI SHI[1,*], LIXUN CAI[1], CHEN BAO[1]

[1] School of Mechanics and Engineering, Southwest Jiaotong University, Chengdu, Sichuan 610031, China
* Corresponding author: lix_cai@263.net

Abstract To estimate fracture toughness of irradiated material in nuclear engineering, the testing specimens with half thickness of a standard compact tension specimen are used to get the *J* resistance curve of materials according to Standard Test Method for Measured of Fracture Toughness (ASTM E1820). The normalization method recommended by ASTM E1820 is not directly applied in obtaining the fracture toughness of metallic materials because it does not provide the plastic factor of Front Face Compact Tension specimen with 12.5mm thickness and 25mm width (1/2 FFCT specimen). Based on the energy of *J* integral and the detailed finite element analysis, the plastic factor of a 1/2 FFCT specimen is presented. With the plastic factor of 1/2 FFCT, the *J* resistance curve of a 1/2 FFCT specimen and its fracture toughness can be obtained by Using the normalization method.

Keywords Front face compact tension, Load line compact tension, Plastic factor, Finite element, normalization method

1. Introduction

Structural materials, A508-Ⅲ steel which long-term service in the radiation environment , must have material damage and material aging in nuclear engineering. Long-term, department of design and operations has focused on the nuclear reactor material damage by surveillance and prevention. The problem that measuring the fracture behavior of irradiated material A508-Ⅲ steel is need to be solved as quickly as possible. The fracture behaviors of material include the fracture toughness and crack growth rate of material and so on. Based on single specimen method, the 1/2FFCT specimen is selected to estimate the fracture toughness. Because the test material is irradiated, all operations are completed by the mechanical arm. The unload compliance method require the high of neutral and test accuracy, so applying of unload compliance is restricted in fracture mechanics automatic test technology. The unload compliance method does not good coordinate with the mechanics arm. It is recommended that the normalization data reduction technology be used to in ASTM E1820-11 to determine *J* resistance curve and reduced test costs as well. The normalization data reduction technology involves the plastic factor of test bending specimen, so the plastic factor of 1/2FFCT specimen is quickly studied.

There are two ways to obtain the plastic factor which are SLF (Slip Line Field) theory [1-4] and FEA (Finite Element Analysis) [5-10]. The SLF theory assume that material behavior is perfectly elastic-plastic. It establishes the contact the plastic factor with the limit load. The FEA studies the plastic factor which considering the different stain hardening, so the FEA can more accurate analysis the plastic factor. Based on the *J* integral energy theory [11] and the detailed finite element, the plastic factor of compact tension specimen is researched.

2. Plastic Factor

2.1. Plastic Factor of Load Line Compact Tension Specimen

Rice [11] proposed the parameter *J*-integral for nonlinear elastic material as a measure of crack-tip

singularity intensity of HRR field [12-13]. Begley and Landes [14-15] first recognized that the *J* integral and its critical value can be evaluated experimentally from the interpretation of *J* as the energy release rate. A method for estimating the *J* from a single load-displacement record was proposed first by Rice et al. [16]. For a bending specimen with different sized cracks, Sumpter and Tuner [17] proposed a general expression of *J* integral. A total Δ can be separated into an elastic component Δ_{el} and a plastic component Δ_{pl}, so the *J* integral would be expressed as

$$J = J_{el} + J_{pl} \tag{1}$$

where J_{el} is the elastic component of *J* integral, J_{pl} is the plastic component of *J* integral. The elastic component of *J* can be directly calculated from the stress intensity factor *K*, as used in ASTM E1820-11 for a plane strain crack

$$J_{el} = \frac{K^2\left(1-\nu^2\right)}{E} \tag{2}$$

in which *E* is the Young's modulus and ν is the Poisson ratio. The plastic component of *J* is determined as

$$\begin{aligned} J_{pl} &= \frac{1}{B}\int_0^P \frac{\partial \Delta_{pl}}{\partial a} dP = -\frac{1}{B}\int_0^\Delta \frac{\partial P}{\partial a} d\Delta_{pl} \\ &= \frac{\eta_\Delta A_\Delta^{pl}}{Bb} \end{aligned} \tag{3}$$

where *P* is the total generalized load or force of the component, *B* is the thickness, *b* is the remaining ligament, *a* is the crack size, Δ_{pl} is a plastic component of load-point or load line displacement, η_Δ is the plastic factor of load line compact tension specimen, A_Δ^{pl} is the plastic component of area under the measured $P-\Delta$ curve.

All expressions introduced above are valid only for stationary cracks. For a growing crack, the *J* integral should consider the crack growth correction. *J* integral is independent of the loading path, so *J* value is a function of two independent variables: Δ and *a* according the deformation theory. From Eq 3, Ernst et al. [18] derived the complete differential of J_{pl} as

$$dJ_{pl} = \frac{\eta_\Delta P}{Bb} d\Delta_{pl} - \frac{\gamma_\Delta}{b} J_{pl} da \tag{4}$$

In which γ_Δ is the geometry factor of load line compact tension specimen. The γ_Δ as follows

$$\gamma_\Delta = \eta_\Delta - 1 - \frac{b}{W}\frac{\eta_\Delta^{'}}{\eta_\Delta} \tag{5}$$

Where the prime denotes the partial differential with respect to *a/W,* i.e. $\eta_\Delta^{'} = \partial \eta_\Delta / \partial\left(a/W\right)$.

Integrating Eq 4, one has

$$J_{pl} = \int_0^{\Delta_{pl}} \frac{\eta_\Delta P}{Bb} d\Delta_{pl} - \int_{a_0}^{a} \frac{\gamma_\Delta}{b} J_{pl} da \tag{6}$$

In which a_0 is the initial crack size.

Figure 1 illustrates a typical $P-\Delta_{pl}$ curve for a growing crack. This figure includes the deformation paths for an original crack length a_0 and also for two arbitrarily fixed crack lengths a_i and a_{i+1}. Since the J_{pl} in Eq 6 is valid for any loading path leading to the current values of a_i and Δ_{pl}^i, its value at point A(or B) can be determined by following path OA (or OB) for the fixed crack length a_i to the corresponding Δ_{pl}^i (or Δ_{pl}^{i+1}) in the actual $P-\Delta$ curve. Because da=0 on this loading path, from Eq 6, one has

$$J_{pl}^A = \frac{\eta_\Delta^i}{Bb_i} \int_0^{\Delta_{pl}^i} P d\Delta_{pl} \tag{7}$$

and

$$J_{pl}^B = J_{pl}^A + \frac{\eta_\Delta^i}{Bb_i} A_{\Delta_{pl}}^{i+1,i} \tag{8}$$

where $A_{\Delta_{pl}}^{i+1,i}$ represents the area under the $P-\Delta_{pl}$ curve between Δ_{pl}^i and Δ_{pl}^{i+1} with an error of the area of triangle ΔABC. Integration of Eq 6 along BC obtains an approximate result

$$J_{pl}^C = J_{pl}^B \left(1 - \frac{\gamma_\Delta^i}{b_i}\left(a_{i+1} - a_i\right)\right) \tag{9}$$

From Eqs 7 to 9, one obtains

$$\begin{aligned} &J_{pl(i+1)} \\ &= \left(J_{pl(i)} + \frac{\eta_\Delta^i}{Bb_i} A_{\Delta pl}^{i+1,i}\right)\left(1 - \frac{\gamma_\Delta^i}{b_i}\left(a_{i+1} - a_i\right)\right) \end{aligned} \tag{10}$$

This incremental expression is the LLD-based (Load Line Displacement) J estimation equation that was adopted in ASTM E1820-11and all its predecessors, where the specimen thickness B is replaced by the net thickness B_N for specimens with side grooves.

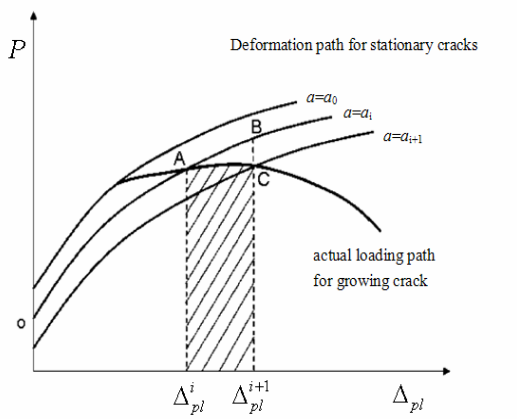

Figure1. Typical load versus plastic displacement curves for static and growing cracks

2.2. Plastic factor of front face compact tension

Following the similar route for deriving the LLD-based *J* equation, this section formulates an incremental CMOD-based (Crack Mouth Open Displacement) *J* estimation. A total CMOD, *V*, is separated into an elastic component V_{el} and a plastic component V_{pl}. As such, the total *J* can be decomposed into an elastic component J_{el} and a plastic component J_{pl}, as show in Eq 1. The J_{el} is defined in Eq 2, whereas the J_{pl} is determined by

$$J_{pl} = \frac{\eta_V A_V^{pl}}{Bb} = \frac{\eta_V}{Bb}\int_0^{V_{pl}} P dV_{pl} \tag{11}$$

where η_V is the plastic factor of front face compact tension, A_V^{pl} is the area under the measured $P-V_{pl}$ curve. Without loss of generality, it is assumed the ratio of V_{pl} and Δ_{pl} is a function of *a/W* [19]

$$\frac{V_{pl}}{\Delta_{pl}} = \lambda\left(a/W\right) \tag{12}$$

Substitution Eq 12 into Eq 11 gives

$$J_{\mathrm{pl}} = \frac{\eta_V}{Bb}\int_0^{\Delta_{pl}} Pd\left(\lambda\Delta_{\mathrm{pl}}\right) = \frac{\eta_V}{Bb}\lambda\int_0^{\Delta_{pl}} Pd\Delta_{\mathrm{pl}} \tag{13}$$

From Eqs 3, 11, 12 and 13, three equivalent expressions for this new plastic factor are obtained

$$\lambda\left(a/W\right) = \frac{V_{\mathrm{pl}}}{\Delta_{\mathrm{pl}}} = \frac{\eta_\Delta}{\eta_V} = \frac{A_V^{pl}}{A_\Delta^{pl}} \tag{14}$$

Since J_{pl} is now the function of V_{pl} and *a*, its complete differential is obtained as

$$dJ_{pl} = \frac{\eta_V P}{Bb} dV_{pl} - \frac{\gamma_V}{b} J_{pl} da \tag{15}$$

where γ_V is the geometry factor of front face compact tension specimen. The γ_V as follows

$$\gamma_V = \lambda \eta_\Delta - 1 - \frac{b}{W}\left(\frac{\lambda'}{\lambda} + \frac{\eta_V'}{\eta_V}\right) \tag{16}$$

Substituting Eq 14 into Eq 16, it is interesting to find that $\gamma_V = \gamma_\Delta$.

Integrating Eq 15 gives the plastic component of *J* in reference to the CMOD-based plastic factor and geometry factor

$$J_{pl} = \int_0^{V_{pl}} \frac{\eta_V P}{Bb} dV_{pl} - \int_{a_0}^{a} \frac{\gamma_V}{b} J_{pl} da \tag{17}$$

As similar to the load line compact tension specimen, we obtain the following CMOD-based *J* estimation equation for a growing crack

$$\begin{aligned} &J_{pl(i+1)} \\ &= \left(J_{pl(i)} + \frac{\eta_V^i}{Bb_i} A_{Vpl}^{i+1,i}\right)\left(1 - \frac{\gamma_V^i}{b_i}\left(a_{i+1} - a_i\right)\right) \end{aligned} \tag{18}$$

The CMOD-based *J* formulation is the other way to determine *J* resistance curves for 1/2FFCT specimens.

Based on the detailed FEA, the plastic factor of front face compact tension specimen is investigated. The function, $\lambda(a/W)$, is obtained by linear fitting of the least squares method, considering the difference strain hardening of material mechanical behavior. The $\lambda(a/W)$ is expressed as (be shown as in Fig. 2)

$$\begin{aligned} &\lambda(a/W) \\ &= -0.3412\left(a/W\right) + 1.5356 \end{aligned} \tag{19}$$

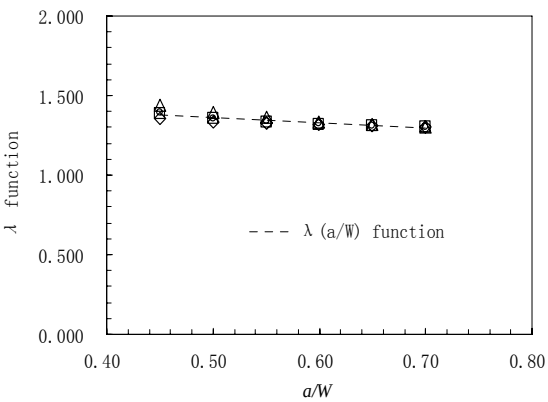

Figure 2. The function λ versus a/W curve

From Eqs 12, 14, the plastic factor of front face compact tension specimen is fitted by the following curve

$$\begin{aligned}\eta_V &= \eta_\Delta / \lambda(a/W) \\ &= 1.6729 - 0.0329\left(1 - a/W\right)\end{aligned} \tag{20}$$

3 Conclusions

1> Based on the FEA, the function λ (*a/W*) is got.

2> Connecting FEA and function λ (*a/W*), the plastic factor formulation of front face compact tension is obtained.

3> Using the plastic factor of front face compact tension specimen, the *J* resistance curve would be perfectly solved by the normalization data reduction technology in ASTM E1820-11.

Based on the plastic hinge theory of bending specimen and the plastic factor of load line compact tension, the unified plastic factor calculation is investigated in future. From the unified plastic factor, considering the normalization data reduction in ASTM E1820-11, the *J* resistance curve would be perfectly solved.

Acknowledgements

The financial support of the National Nature Science Foundation of China, Grant NO.11072205, is gratefully acknowledged. We are also grateful for the valuable assistance of Key Laboratory of Strength and Vibration, the SWJTU Laboratory.

References

[1] MERKLE J G, CORTEN H T. A J integral analysis for the compact specimen considering axial force as well as bending effects[J]. Journal of Pressure Vessel Technology, 1974, Vol. 96.

[2] EWING D J F, RICHARDS C E. The yield-point loads of singly-notched pin-loaded tensile trips[J]. Journal of the Mechanics and Physics of Solids, 1974, 22(1): 27-36.

[3] Turner C E. in Post-Yield Fracture Mechanics, LATZKO D G H (ed.), Applied Science Publishers, London, 1979: 23-211.

[4] WU S X, MAI Y W, COTTERELL B. Plastic η-factor (ηp) of fracture specimens with deep and shallow cracks[J]. International Journal of Fracture, 1990, Vol. 45: 1-18

[5] DAVIES C M, KOURMPETIS M, DOWD N P O et al. Experimental evaluation of the J or C* parameter for a range of crack geometries[J]. Journal of ASTM International, 2006, 3(4): 1-20.

[6] KIRK M T, DOIDDS R H. J and CTOD estimation equations for shallow cracks in single edge notch bend specimens[J]. Journal of Testing and Evaluation, 1993, Vol. 21: 228-238.

[7] NEVALAINEN M, DODDS R H. Numerical investigation of 3-D constraint effects on brittle fracture in SE(B) and C(T) specimens[J]. International Journal of Fracture, 1990, 74(2): 131-161.

[8] KIM Y J, KIM J S, CHO S M. 3-D constrain on J testing and crack tip constraint in M(T), SE(B) and C(T) specimens: numerical study[J]. Engineering Fracture Mechanics, 2004, 71(9-10): 1203-1218.

[9] DONATO G H B, RUGGIERI C. Estimation procedure for J and CTOD fracture parameters using three-point bend specimens[C]. Proceedings of the 6th International Pipeline Conference, 2006, Calgary, Canada, Paper Number: IPC2006-10165.

[10] KIM Y J, SCHWALBE K H. On experimental J estimation equations based on CMOD for SE(B) specimen[J]. Journal of Testing and Evaluation, 2001, 29(1): 67-71.

[11] RICE J R. A path independent integral and the approximate analysis of strain concentration by notches and cracks[J]. Journal of Applied Mechanics, 1968, Vol. 35: 379-386.

[12] HUTCHINSON J W. Singular behavior at the end of a tensile crack in a hardening material[J]. Journal of the Mechanics and Physics of Solids, 1968, Vol. 16: 13-31.
[13] RICE J R, ROSENGREN G F. Plane strain deformation near a crack tip in a power law hardening material[J]. Journal of the Mechanics and Physics of Solids, 1968, Vol. 16: 1-12.
[14] BEGLEY J A, LANDES J D. The J-integral as a fracture criterion[C]. Fracture Mechanics, ASTM STP 515, ASTM International, West Conshohocken, PA, 1972: 1-23.
[15] LANDES J D, BEGLEY J A. The effect of specimen geometry on JIC[C]. Fracture Mechanics, ASTM STP 515, ASTM International, West Conshohocken, PA, 1972: 24-39.
[16] RICE J R, PARIS P C, MERKLE J G. Some further results of J-integral analysis and estimates[C]. Progress in Flaw Growth and Fracture Toughness Testing, ASTM STP 536, ASTM International, West Conshohocken, PA, 1973: 231-245.
[17] SUMPTER J D, TURNER C E. Method for laboratory determination of JC (contour integral for fracture analysis)[C]. Cracks and Fracture, ASTM STP 61, ASTM International, West Conshohocken, PA, 1976: 3-18.
[18] ERNST H A, PARIS P C, LANDES J D. Estimations on J-integral and tearing modulus T from a single specimen test record[C]. Fracture Mechanics: 13th Conference, ASTM STP 743, ASTM International, West Conshohocken, PA, 1981: 476-502.
[19] ZHU X K, LEIS B N, JOYCE J A. Experimental estimation of J-R curves from load-CMOD record for SE(B) specimens[J]. ASTM Special Technical Publication, 2008, 5(5): 66-75.

Continuous vs. Discontinuous Crack Extension: Characterization of Ductile Tearing in Thin Plates

Volodymyr P. Naumenko*

Department of Structural Integrity, G. S. Pisarenko Institute for Problems of Strength, Kyiv 01014, Ukraine;
E-mail: v.p.naumenko@ipp.kiev.ua

Abstract There are two alternative trends of thought concerning the mechanism of crack extension in an elastic-plastic material subjected to monotonically and slowly increasing tensile (Mode I) loading. The crack advances continuously, by infinitesimal growth steps, or discontinuously in finite growth steps. In this experimental study, slant cracks were extended in thin aluminium plates, depending on theirs geometry, with or without an intermittent attainment of the local instabilities displayed in test records. It means that the mechanism of ductile tearing in the test material may be changed simply by changing the specimen geometry. This observation is not in accord with the well-known energetic considerations that a mechanism of crack extension in a non-hardening or low-hardening elastic-plastic material must be only discontinuous. A wide consensus exists that a single-parameter characterization of crack extension is conceptually possible when fracture resistance is quantified by a critical, lower-limiting value ψ_c of the Crack Tip Opening Angle (CTOA-ψ). It is of scientific and practical interest to measure CTOA-ψ for slant cracks growing at different in-plane constraint states and in this way to clear up the above contradiction. In our specimens that were fractured under the highly constrained conditions of transverse plane strain, cracks were advancing in well-defined steps.The CTOA- ψ values related to different pairs of distinct fracture events strongly depend upon the choosing the neighboring pair. They were compared with the critical angles ψ_c determined with the use of ASTM/ ISO Standard test method and also with the CTOA-ψ_n values established from profiles of fully-developed cracks.

Keywords Crack extension, Thin plates, Thin-sheet aluminium, Crack tip opening angle, In-plane constraint

1. Introduction

There is an increasing interest in the development of valid fracture criteria and standard test methods for unified assessment of ductile tearing in thin-wall components. This paper deals with the characterisation of plane stress tearing under uncontained yielding in rectangular plates (Fig. 1) made from thin sheets of a high-strength low-hardening aluminium alloy. The principal obstacle to the development of an easy-to-use procedure for assessing the resistance to stable crack extension is placed by the need to correlate too many variables governing the fracture behaviour in ductile materials. These are the parameters of elasticity, including those of out-of-plane deformation (buckling); plasticity, including those of residual stress effects and anisotropy; diffused and localised necking; damage and cracking. It seems highly improbable to predict fracture using only the near crack-tip parameters in isolation from the global deformation pattern.

Therefore, in collecting test data a purely mechanistic approach based on the minimum of assumptions was adopted. In this way, our concept of through-life fracture assessment [1-7] attempts to formalize the characterization of crack extension using only the interrelations between directly measurable quantities without taking into account the physical damage mechanisms in vicinity of a fracture process zone. Here, the term *through-life assessment* means that all measures of tear resistance can be determined continuously (from the nucleation of a tear crack and up to the complete separation) or in a point-by-point manner for test events of practical importance.

We suggest that the global fracture behavior expressed in terms of averaged quantities might be assessed immediately from diagrams of loads vs. displacements vs. distances between the extreme

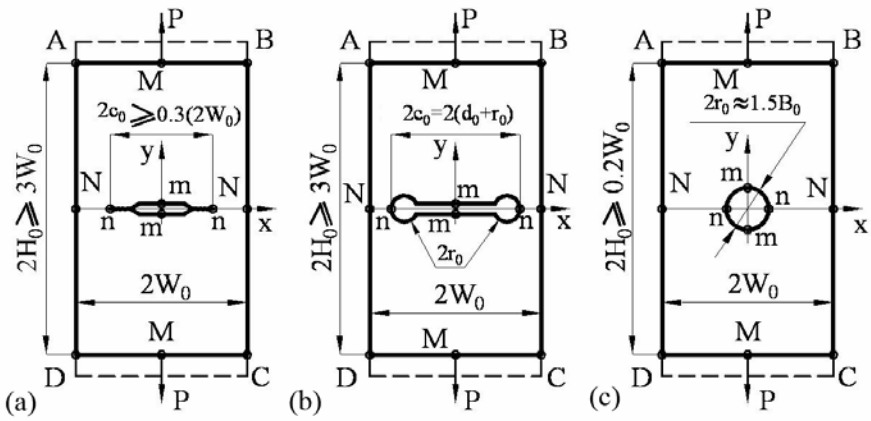

Figure 1. Geometry of the standard M(T) specimen containing initial fatigue pre-cracks at a slot tips (a) and MDR(T) (b) and MR(T) (c) specimens with simple and well-defined geometry of an original stress raiser.

points on a specimen surfaces. These are (Fig. 1) the points *m* and *n* on the inner and *M* and *N* on the outer boundaries of a specimen Problem Domain (PD). The emphasis is on experimental investigation into the effects of such constraint-related issues as geometry and size of the PD containing an original stress raiser of a relatively small size (Fig 1c).

To trigger the progressive process of single-site necking followed by single-site cracking in a predetermined location and direction, a variety of imperfections are employed in plane-stress fracture studies. According to the standard test methods [8-10], the specimen should contain initial fatigue precracks at the tips of a starting stress raiser (Fig. 1a). However, it is common knowledge that the crack extension resistance in metallic materials may be influenced significantly by the preloading history. At present, there is no possibility to establish a one-to-one correspondence between the initial fatigue damages near the crack tips in different specimens whose geometry, loading and boundary restraints vary over wide ranges.

That is why in the specimen preparation, special care must be taken to prevent the introduction of uncontrollable initial damages and residual stresses into the material to be tested. In our approach [1-7], tests are carried out on specimens with an original stress raiser having relatively simple geometry and a well-defined form of its tips (points *n* in Figs 1b and 1c). By convention, the specified open hole is taken as a damage-free defect. Its diameter $2r_0$ should be sufficiently small in comparison with the PD dimensions $2W_0$ and $2H_0$. It means that at the instant of fracture initiation the tensile stress σ averaged across the specimen ligament depends only slightly on the variation in the hole radius r_0. At the same time, the original stress raiser should be sufficiently large to concentrate all thinning and structural damage inside a single localised neck.

Constraint-related issues such as original geometry and size of the outer and inner boundaries of a MDR(T) and MR(T) specimens (Fig. 1) are investigated experimentally. The focus is on revealing the distinctions between the characteristic values of the CTOA-ψ associated with the fully-controllable pop-in fracture behaviour and those determined with the use of ASTM/ ISO Standard test method [9, 10]. This method applies specifically to fatigue pre-cracked M(T) and C(T) specimens that exhibit low constraint and are tested under slowly increasing displacement. Here and then, we deal only with the M(T) geometry (Fig. 1a) originally introduced in standard [8]. The angle ψ_c generated following the procedure and a guideline contained in standards [9, 10] is treated as insensitive to in-plane dimensions and specimen type, but is dependent upon specimen thickness. In other word, the lower-limiting value ψ_c of CTOA-ψ can be used in analyses of stable crack extension as a quantity that is independent on a level of the global in-plane constraint.

The problem under consideration is addressed in two parts. We start with comparing the profiles of fully-developed tear cracks in broken-down MR(T) and MDR(T) specimens of different geometries and size. The intent is to demonstrate a need for incorporating in current practice of testing and analysis the notion *reference level of resistance to stable crack extension*. In the second part of this work, test records with orderly dips on theirs softening branches are presented and discussed. The objective is to contrast the concepts of continuous and continuous crack extension by comparing the crack profiles generated in a course of actual and virtual enlargements of a crack cavity volume.

2. Material and Tests

The test material is aircraft-skin aluminium alloy D16AT in as-received condition, having the form of 1.4-1.5mm thick sheets. Its chemical composition and mechanical properties are close to those of AL 2024-T3. Two sets of standard tensile test specimens of width $2W_0$ = 12mm were loaded under quasi-fixed grip conditions in tension across and along the rolling direction of the sheets. The elastic and anisotropic plastic behaviour f the material was characterized by the following parameters: the elastic modulus E = 68 and 67GPa, Poisson's ratio ν = 0.32, the 0.2% offset yield strength σ_{02} = 299.4 and 338MPa, and the ultimate tensile strength σ_{UTS} = 446 and 467MPa, respectively.

The uniaxial crack extension tests were performed on MDR(T) and MR(T) specimens of large and small width $2W_0$ with stress raisers of various shapes and sizes given in Table 1. The horizontal boundaries of each PD were rigidly clamped. In the tests to separation failure, they were moving with a sufficiently small rate 0.001mm/s, i.e., under the quasi-fixed grip condition. At this rate tear crack extension in the MR(T)-1.0-1.0 specimens with square PD of width $2W_0^{BS}$ =120 mm reproducibly occurs by an intermittent attainment of the local instabilities [4].

Table 1. Principal dimensions of specimens.

Specimen code [a]	$2W_0$ (mm)	$2H_0$ (mm)	$2r_0$ (mm)	$2d_0$ (mm)	$2s(m)_0$ (mm)	$2c_0$ (mm)
1. Small width specimens						
MR(T)-0.5-10.0	1200	600	2	0	2	2
MDR(T)-0.5-10.0	1200	600	2	10	0.12	12
MDR(T)-0.5-10.0	1200	600	2	20	0.12	22
MDR(T)-0.5-10.0	1200	600	2	38	0.12	40
MDR(T)-0.5-10.0	1200	600	2	58	0.12	60
2. Large width specimens						
MR(T)-5.0-1.0	120	600	2	0	2	2
MR(T)-1.5-1.0	120	180	2	0	2	2
MR(T)-1.0-1.0	120	120	2	0	2	2
MDR(T)-1.0-1.0	120	120	2	3	0,12	5
MDR(T)-1.0-1.0	120	120	2	8	0,12	10
MDR(T)-1.0-1.0	120	120	2	18	0,12	20
MDR(T)-1.0-1.0	120	120	2	38	0,12	40
MR(T)-0.1-1.0	120	12	2	0	2	2

[a] The numerical values in the specimen code denote the shape ratio (H_0 / W_0) and the scale ratio (W_0 / W_0^{BS}). In this work we take $2W_0^{BS}$ = 120mm for the MR(T)-0.1-1.0 specimen treated as the basic geometry.

It should be emphasized that in all specimens under consideration tearing occurred by cracking parallel to the rolling direction in the plane inclined at 45° to the specimen surfaces. The regime of slant tearing starts from the very instant *i*0 of crack nucleation and continued up to the complete separation of a specimen by a growing crack at the instant *f* (Figs 2 and 3). Note that sudden formation of two short cracks near the points *n* (Fig. 1) was always preceded by a clearly distinct drop in test records at the attaining the state *t*0 (see Fig. 3b). As can be seen from Fig. 2, the decrease of PD height $2H_0$, when accompanied by the decrease of stress raiser length $2c_0$, ensure realization of the fully-controllable discontinuity of the slant crack extension process [7].

Very orderly dips on the softening branch of the diagram reflect a cyclic variation in the crack profile geometry. Each cycle consists of five test events (Figs 3a and 4). Here. 2*v*(L) is the displacement of a grips fixture that was measured in a synchronized manner with the crack extension, displacement 2*v*(m) of the points *m* (Fig 1) and force *P* (frequency 5 Hz). The diagrams in Figs (2a, 3 and 4) were obtained on the MR(T) specimens tested without the use of anti-buckling guide plates. Buckling of thin plates is a competitive failure mechanism resulting from the elastic compressive stress acting parallel to the crack growth line. Before tests of the MDR(T) specimens (Table 1) they were lightly clamped between two anti-buckling guide plates.

3. Fully-developed crack profiles

Generally, stable crack extension can be seen as interplay of concurrent processes jointly represented by seven through-life fracture curves on the so-called Integrated Fracture Diagram (IFD) [6, 7]. Of these curves, we consider in some detail only a curve describing the geometry of a fully-developed crack in a broken-down specimen. In fact this is one branch (lower-right) out of four branches of a centre crack profile (see Fig 5a). Further on, this branch of a crack, having the key importance for our approach, will be designated as *n*-relationship of the IFD.

The input data for determination of *n*-relationship are distances $2s(x)_n$ between the lower and upper borders of a fully-developed crack (Fig 5a). Of course, at points $x = \pm c_f$ this distances is taken to be zero. By comparing data presented in Figs 6a and 7a, one can find that crack profiles in the specimens of the small and large width are qualitatively similar. An unexpected result is a significant drop in $s(x)_n$ values for the MR(T)-0.5-10.0 specimen containing the shortest stress raiser. This is the single open hole of diameter $2r_0$ = 2mm.

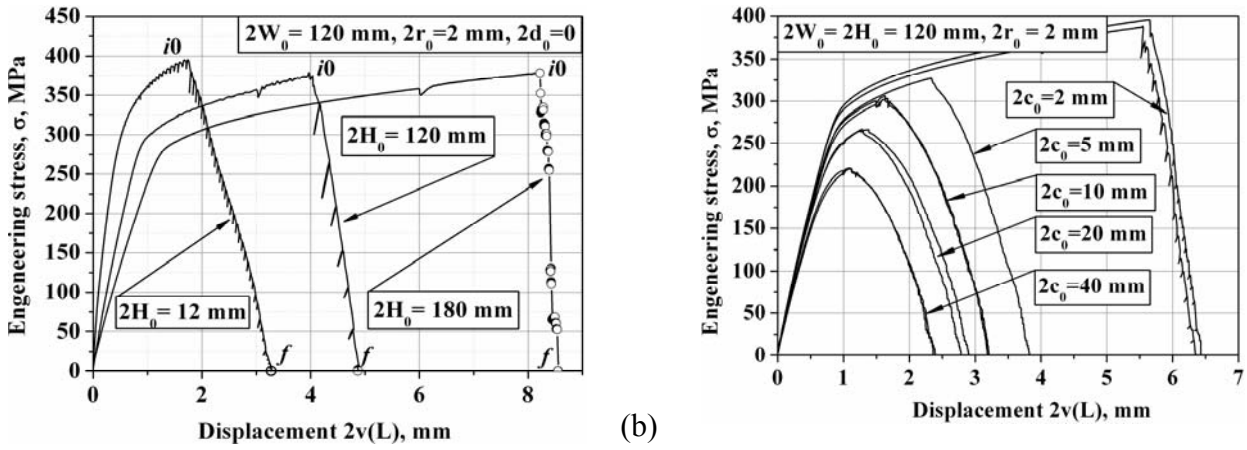

(a) (b)

Figure 2. Comparison of test records for the MR(T) specimens of width $2W_0$ = 120mm and different height $2H_0$ (a) shown together with test records for the MDR(T)-1.0-1.0 specimens having the similar PD geometry, but different length $2c_0$ of the original stress raisers with the identical curvature of theirs tips s(b).

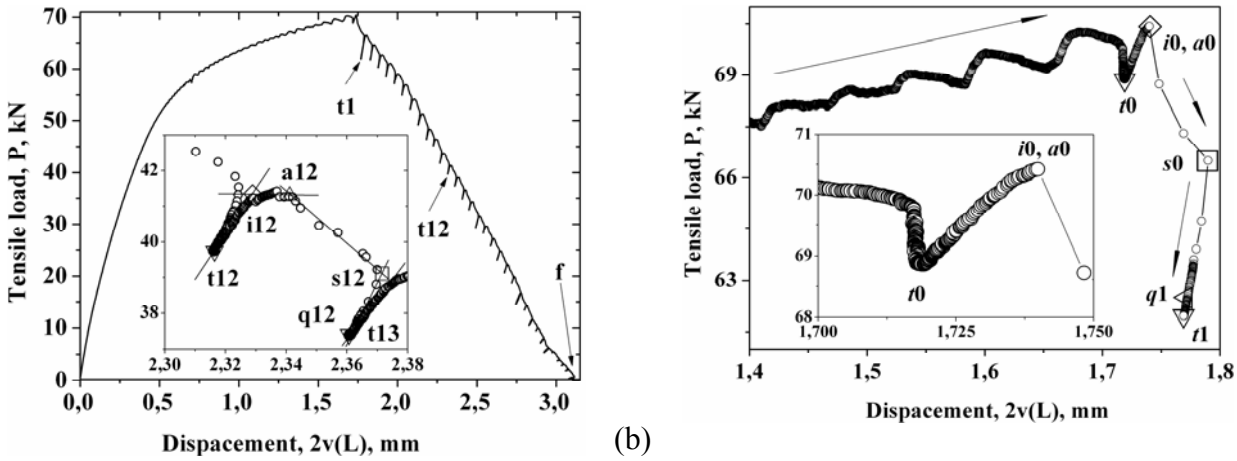

(a) (b)

Figure 3. The enlarged test record that is displayed in Fig. 2a for the MR(T)-0.1-1.0 specimen (a) and its fragment (b) demonstrating that plastic deformation before nucleation of tear cracks and during theirs extension are intrinsically unstable and develops in small temporally confined discontinuous jumps.

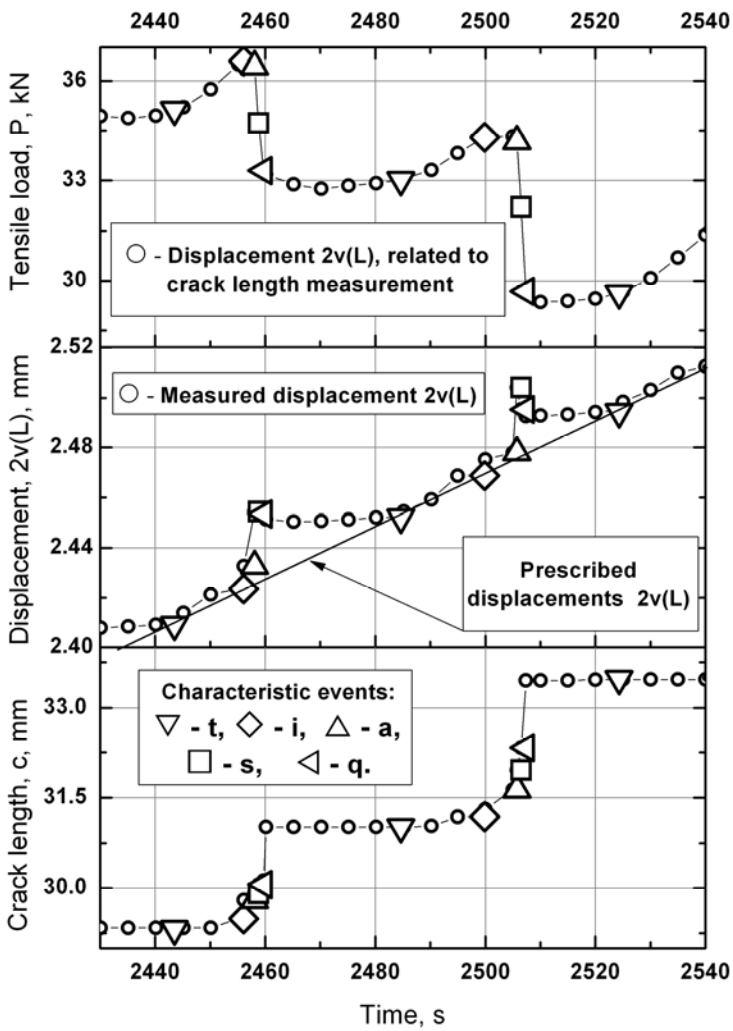

(a)

(b)

(c)

Figure 4. The timebase fragment of the test-record displayed in Fig. 3a. It is shown together with the related fragment for a synchronized dependence of increments in half-crack length *c* on time.

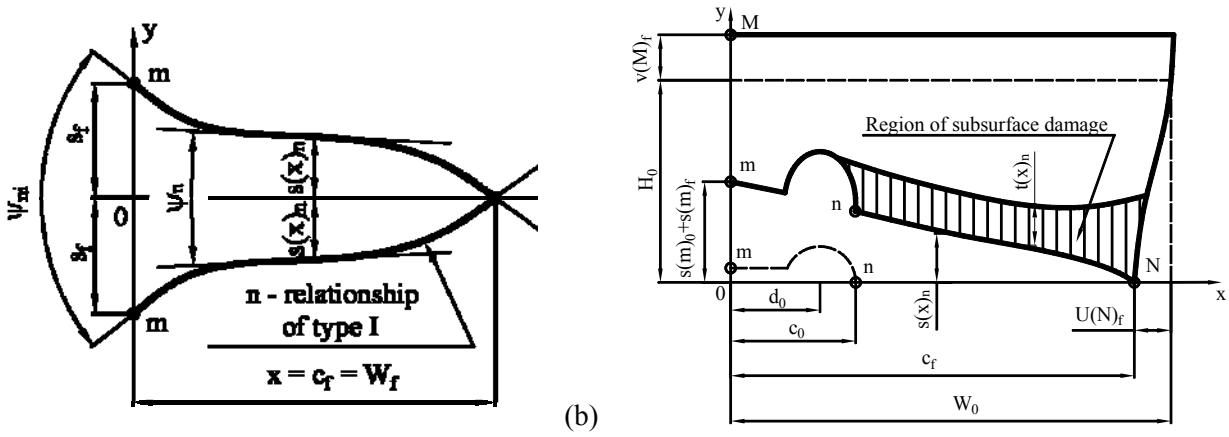

Figure 5. One-half of an idealized profile for a through-the-thickness crack formed near a point wise imperfection at the centre of a rectangular plate (a) and one-quarter of the MDR(T) problem domain in its initial and broken-down states.

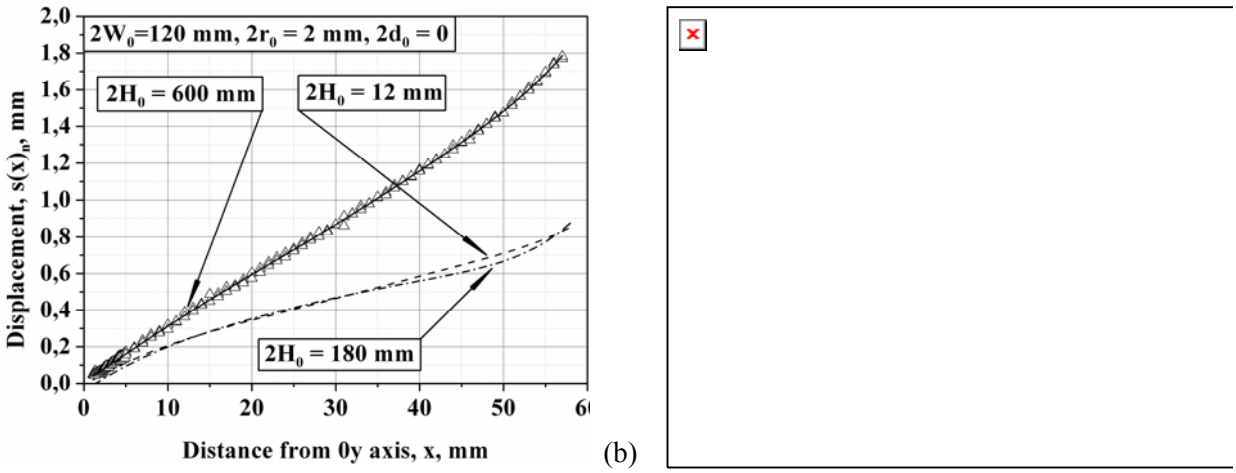

Figure 6. Through-life fracture curves expressed in terms of the post-test displacements $s(x)_n$ (a) and the post-test values $\psi(x)_n$ of the CTOA-ψ (b) for a set of the MR(T) specimens of the same width with the same hole. These tests were conducted without the use of antibuckling guide plates and without forced unloading.

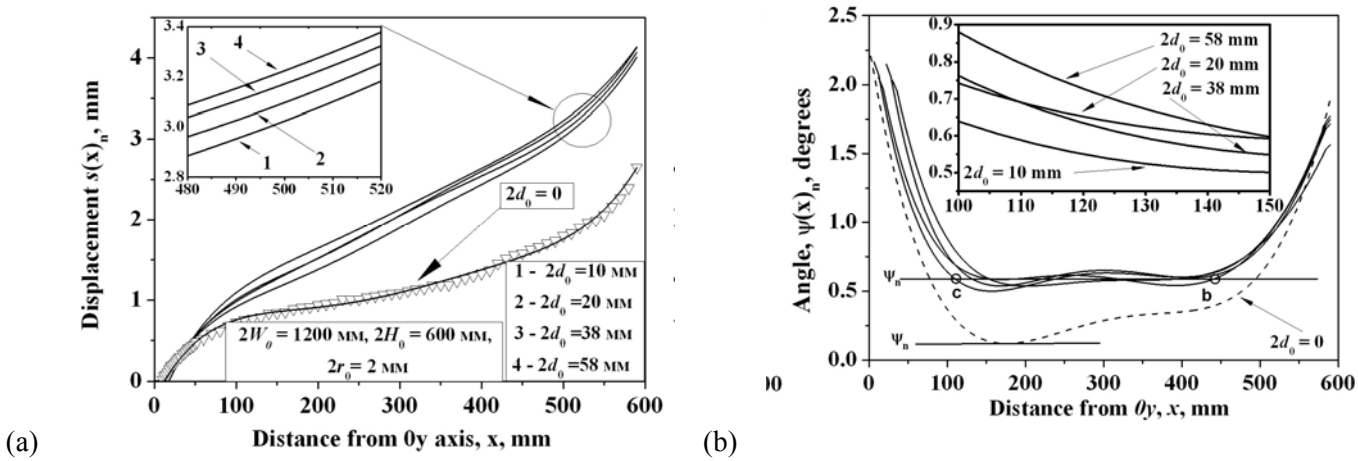

Figure 7. Through-life fracture curves expressed in terms of the post-test displacements $s(x)_n$ (a) and the post-test values $\psi(x)_n$ of the CTOA-ψ (b) for a set of specimens of the same PD size, but with different stress raisers. These tests were conducted with the use of antibuckling guide plates and without forced unloading.

4. Characterization of ductile tearing resistance

Our displacement-based approach focuses on changes in geometry of the whole crack border, instead of considering mainly the near crack-tip displacements, which are given much attention in the current test procedures [9, 10]. Generally, ductile tearing is seen as interplay of seven processes of continuous (virtual) fracture that are represented by the through-life fracture curves. These latter relate to each other on the IFD by imaginary (instantaneous) unloading-reloading cycles. Such cycles are shown as the straight-vertical lines in Fig. 8 passing through the points *c* and *b* on the *n*-relationship. They bounds the Steady State Tearing (SST) stage, when the plastic component $s(x)_n$ of the virtual crack opening displacement $s(x)$ is in direct proportion to the extension of the virtual crack tips along the $0x$ axis (Fig 1). The virtual crack extension is modelled by continuous moving the upper half of a broken-down specimen towards its lower counterpart, as a rigid body.

Plane stress tearing is considered from the viewpoint of a "moving crack tip" embedded into a fully-developed "moving neck". We assume that the crack surfaces, in their final shape, contain the entire history of accumulating the plastic deformations within the regions of subsurface damage (Fig. 5b). So, there are good reasons for quantifying the resistance to stable crack extension by the plastic component $\psi(x)_n$ of the CTOA-ψ [1-7]. Variations in the value of this angle during the virtual fracture process are determined by the following expression:

$$\psi(x)_n = 2d(s(x)_n)/dx,. \tag{1}$$

Consequently, the simplified assessment of ductile tearing can be performed using only post-test measurements of the virtual crack opening displacement $2s(x)_n$. The tensile testing of the MR(T) specimens (Fig. 1c) is the most promising and practical route to assess effects of constraint on ductile tearing in thin sheets of metallic materials. In this case, the global in-plane constraint can be varied merely by changing the distance $2H_0$ between the rigidly clamped boundaries of a specimen.

Experimental results of this and previous studies [1-7] are contradictory to the commonly accepted statement that the constraint effect in plane stress specimens is negligible. A decrease in the specimen aspect ratio H_0 / W_0 taken together with an increase in the PD width $2W_0$ elevates

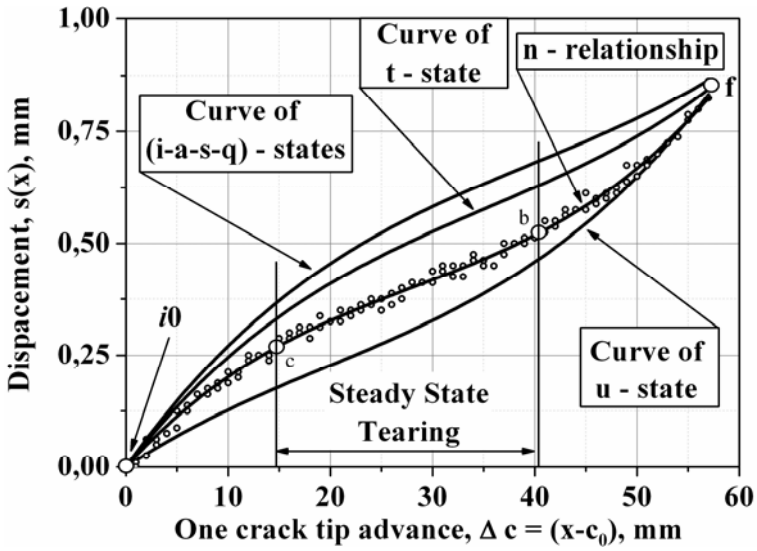

Figure 8. The Integrated Fracture Diagram (IFD) derived from test data for three identical MR(T)-1.0-1.0 specimens of the following dimensions: $2W_0 = 2H_0 = 120$mm, $2r_0 = 2$mm and $2d_0 = 0$. These tests were conducted without the use of antibuckling guide plates and with forced unloading-reloading cycles.

the in-plane constraint (Figs 6b and 7b). These changes are accompanied by the wide variations of the buckling behaviour and crack extension rate [6, 7]. An extremely high level of the global in-plane constraint corresponds to the conditions of transverse plane strain, when in the course of crack extension the outer specimen boundaries $x = \pm W_0$ are straight and fixed ($u(\mathrm{N})_f = 0$ in Fig 5b).

A sufficient level of the proximity to this conditions is achieved in testing the specimens of the basic geometry ($H_0 = 0.1W_0$). In this case, the SST resistance for the Al-alloy D16AT is presented by the angle ψ_n = (1.38 ± 0.1) degrees. This reference value is about half of the lower-limiting value ψ_c = (3.0 ± 1.5) degrees determined for the material in question in [3] with the use of ASTM/ ISO Standard test method [9, 10]. In comparison with the critical angle ψ_c, the novel characteristic of ductile tearing ψ_n is much more consistent and reproducible quantity.

Figures 6b and 7b show that the SST resistance, as measured by the angle ψ_n, contrary to fracture initiation resistance ψ_{ni}, is very sensitive to changing the specimen geometry and size. In the whole, our results [1-7] demonstrate that the CTOA-ψ depends on the combined effects of many variables, namely, PD geometry and its size, geometry and type of an original stress raiser, boundary restraints, buckling behaviour, crack extension rate, as well as technique used for evaluating this fracture parameter. In particular, one can see (Fig. 9) that the angle β associated with the different pairs of distinct fracture events strongly depends upon the choosing a neighboring pair. For the MR(T)-0.1-1.0 specimen of the basic geometry this angle closely correlates with the CTOA- ψ.

Test data for MR(T) specimens give a simple, inexpensive and yet accurate estimations of fracture initiation stress σ_{Ni} for shallow cracks originating from a typical stress raiser. The large distinctions between the lower-limiting values of this stress for the PD of different size observed in Fig. 10 call into question the very meaning of the commonly used characterisation of the net-section stresses in terms of the flow stress $\sigma_f = 0.5(\sigma_{02} + \sigma_{UTS})$. The characteristic values σ_{Nt}, σ_{Ni} and σ_{Ns} of the stress σ_N have the advantage of relating directly to the actual state and position of advancing crack tips. Besides, they relate closely to such customarily quantities as the yield strength σ_{02} and ultimate tensile strength σ_{UTS} obtained under uniform straining of the standard smooth specimens.

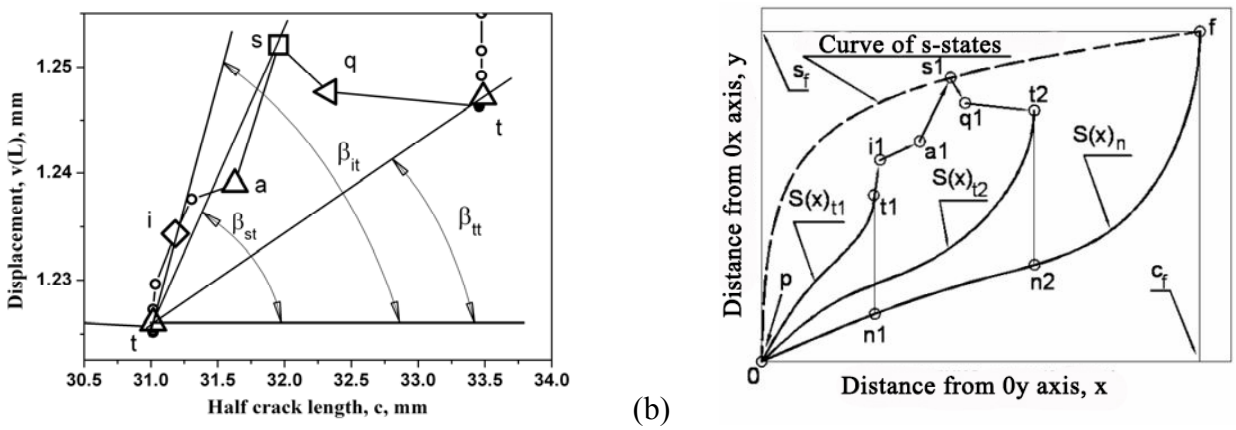

(a) (b)

Figure 9. A fragment of the test record (a) displayed earlier in Fig. 4 and schematic presentation of a transition from the one-quarter crack profile $s(x)_{t1}$ to the next profile $s(x)_{t2}$ for the spontaneously arrested crack that are shown together with two through-life fracture curves $s(x)_s$ and $s(x)_n$ related to states s and n (b).

5. General remarks

Our experimental results demonstrate that there is not worth striving for longer use of the M(T) specimen (Fig. 1a) at least in standard crack extension tests. This geometry reflects

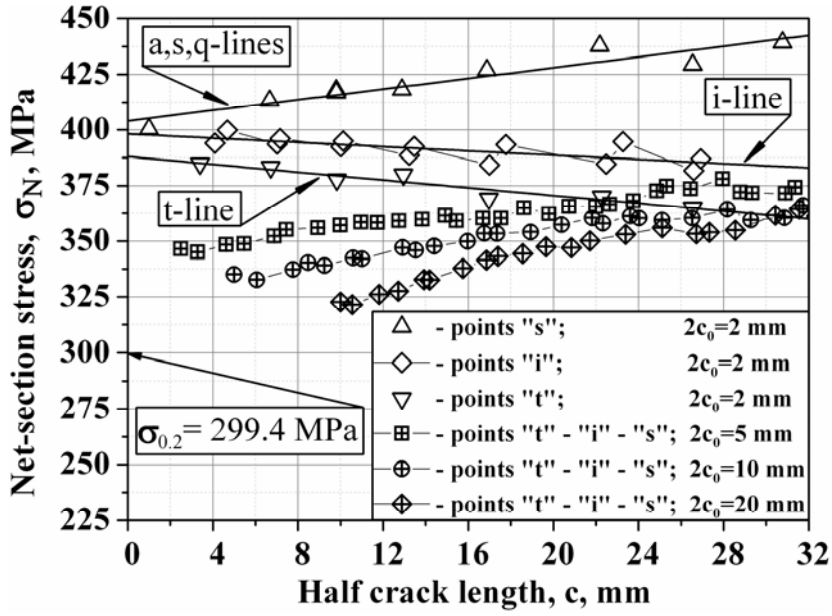

(a)

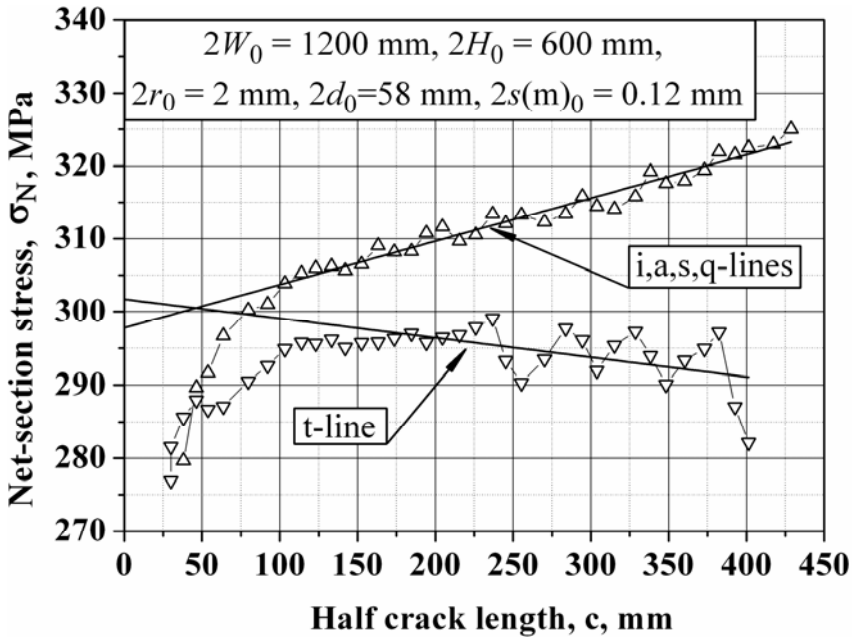

(b)

Figure 10. Experimental data for the MR(T) and MDR(T) specimens with the square PD of size $2W_0 = 2H_0 = 120$mm (a) shown together with data obtained on the MDR(T)-0.5-10.0 specimen containing the elongated stress raiser in size: $2d_0 = 58$mm, $2r_0 = 2$mm and $2s(m)_0 = 0.12$mm (b).

the out-dated incentive to apply at the horizontal PD boundaries the uniformly distributed tensile stresses. This is usually done by increasing the ratio H_0/W_0, but a price is paid in the loss of possibility to ensure realization of the fully-controllable discontinuity of the slant crack extension process. The critically important advantages of the basic MR(T) specimen result from a geometry of its PD. The smaller is the ratio H_0/W_0, the less are effects of buckling and crack extension rate on the characteristic values of the CTOA-ψ [6, 7].

As can be seen from Figs 2b and 7, the similar impact has the requirement to test the MR(T) specimens with an original stress raiser of relatively small length $2c_0 = 2r_0$. It is well known that a fatigue precrack in the M(T) specimens starts to grow by the opening mechanism and only after some advancement, comparable with the specimen thickness B_0, it propagates in the mechanism of

slanted fracture. In the MR(T) specimens, as well as in smooth tensile test specimens, nucleation of cracks and their extension both occur by one and the same mechanics of shear localisation.

Although this study is still in progress, the experimental results appear to be sufficiently significant to make the following general conclusions. It seems likely that the CTOA-ψ_c concept needs to be modified with the aim of developing the more pragmatic approach to characterization of ductile tearing resistance. In the context of this problem, the MR(T) specimen of basic geometry might be sought as an attractive alternative to geometry of the standard M(T) specimen [8-10].

Acknowledgements

I am deeply grateful to Mr. Limansky I.V. and Mr. Kravchuk, R.V. for kindly placing at my disposal the test data that were obtained in our jointly performed experimental investigation.

References

[1] V.P. Naumenko and G.S. Volkov, Assessment of plane stress tearing in terms of various crack-driving parameters, in: Fatigue and Fracture Mechanics, ASTM STP1461, S. R. Daniewicz, J. C.Newman, Jr., and K.-H. Schwalbe (Eds), West Conshohocken, PA: ASTM International, 34 (2003) 182-202.

[2] V.P. Naumenko, A.G. Atkins, Engineering assessment of ductile tearing in uniaxial and biaxial tension. Int. J. Fatique, 28 (2006) No. 5-6, 494-503.

[3] V.P Naumenko, S.V. Lenzion, I.V. Limansky, Displacement-based assessment of ductile tearing under low-constraint conditions. The Open Mechanical Engineering Journal, 2 (2008) 40-59.

[4] V.P. Naumenko, Through-life assessment of ductile tearing under low-constraint conditions, in: Proc. of 12th Int. Conf. On Fracture, Elboujdaini M., (Ed.), Ottawa, 2009, 10 pages.

[5] V.P. Naumenko, I.V Limansky, (2009), Energy-based assessment of ductile tearing in a thin-sheet aluminium alloy. Procedia Engineering, 1 (2009) issue 1, 63-66.

[6] V.P Naumenko, I.V Limansky, R.V Kravchuk, Elastic-plastic fracture under low-constraint conditions: Part I, Characteristic states of a cracked specimen. (2013), to be published in the journal Strength of Materials.

[7] V.P Naumenko, I.V Limansky, R.V Kravchuk, Elastic-plastic fracture under low-constraint conditions: Part II, Fully developed crack. (2013), to be published in the journal Strength of Materials.

[8] *E561-74*, Recommended practice for *R*-curve determination. ASTM Standard, 1974.

[9] *E2472-06*. Standard test method for determination of resistance to stable crack extension under low-constraint conditions, ASTM Standard, 2007.

[10] *ISO 22889,* Metallic materials - Method of test for the determination of resistance to stable crack extension using specimens of low constraint, International Standard, 2007.

Influence of the residual stresses on the crack deflection in ceramic laminates

Oldrich Sevecek[1,*], Michal Kotoul[1], Tomas Profant[1], Raul Bermejo[2]

[1] Institute of SMMB, Brno University of Technology, Brno 616 69, Czech Republic
[2] ISFK, Montanuniversitaet Leoben, Leoben 8700, Austria
* Corresponding author: sevecek@fme.vutbr.cz

Abstract The main goal of ceramic laminates designed with residual stresses is to increase the fracture energy of the system during fracture through energy dissipating mechanisms such as crack deflection or crack bifurcation. A computational tool based on Finite Fracture Mechanics (FFM) is implemented in this work to predict the propagation of cracks in ceramic laminates. The crack path is defined by the direction where maximum rate of the potential energy is released during fracture. Laminates studied here consist of two materials alternated in a layered structure designed with high compressive residual stresses, which are developed during cooling phase after sintering process. Different volume ratios of the material components are chosen in order to demonstrate the influence of the level of compressive residual stresses on the type of propagation (single crack deflection / crack bifurcation) and direction of the crack advance. Using the model a single crack deflection or crack bifurcation can be predicted for a given laminate. According to the calculations, the higher compressive stress in the layer is, the more the crack deflects from the straight direction and the more prone to the bifurcation. Results are in good agreement with experimental observations.

Keywords Ceramic laminates, Finite Fracture Mechanics, Crack propagation, Fracture criterion

1. Introduction

Ceramic laminates have become an alternative choice for the design of structural ceramics with improved fracture toughness and mechanical reliability. The brittle fracture of monolithic ceramics has been overcome by introducing layered architectures of different kind, i.e. geometry, composition of layers, weak interfaces, strong interfaces with residual stresses, etc. The main goal of such layered ceramics has been to increase the fracture energy of the system through energy dissipating mechanisms such as crack deflection, crack bifurcation, interface delamination, or crack shielding. Among the various laminate designs reported in literature, two main approaches regarding the fracture energy of the interfaces must be highlighted. On the one hand, laminates designed with weak interfaces have been reported to yield significant enhanced failure resistance through interface delamination [1-5]; the fracture of the first layer is followed by crack propagation along the interface, the so-called “graceful failure”, preventing the material from catastrophic failure. On the other hand, laminates designed with strong interfaces have shown significant crack growth resistance (R-curve) behavior through microstructural design (e.g. grain size, layer composition) [6-8] and/or due to the presence of compressive residual stresses, acting as a barrier (“*flaw tolerant*”) to crack propagation [2, 9-14].

The increase in fracture energy in these laminates is associated with energy dissipating mechanisms such as crack deflection/bifurcation phenomena, which act during crack propagation. The optimization of the layered design is based on the capability of the layers to deviate the crack from straight propagation. Experimental observations have shown the tendency of a crack to propagate with an angle through the compressive layer and even cause delamination of the interface [15] (see Fig. 1). It seems that the magnitude of compressive stresses may influence the angle of propagation

and subsequent delamination of the interface.

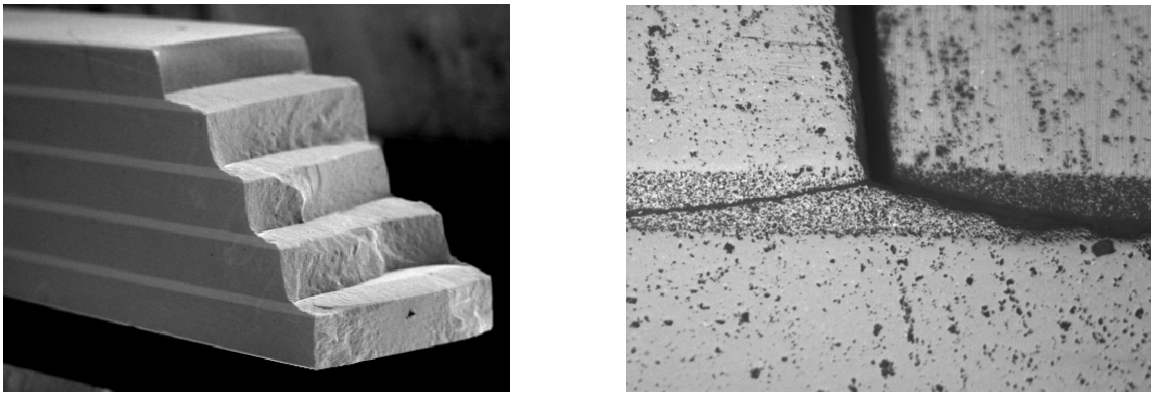

a) b)

Figure 1. a) Fracture of a ceramic laminate under flexural bending; bright layers have compressive residual stresses. b) Bifurcation of a crack entering the compressive layer of the laminate.

The prediction of the crack path upon loading in such layered systems should help in tailoring the design with maximal fracture energy. Methods based on energetic considerations are available which attempt to predict the behavior of a crack approaching the interface of dissimilar materials (see for instance Ref. [16]). However, the modeling of the propagation of an interface crack through layered architectures with residual stresses is still missing. A method which can be used to predict the conditions under which the crack deflects or bifurcates within the compressive layer is sought. In this work, a model based on the finite fracture mechanics approach is developed to interpret and predict the direction of propagation of a crack impinging an interface of a ceramic laminate designed with internal compressive residual stresses. The thermal strains in the layers occurring during sintering, which are responsible for the mechanical behavior of the laminate, are taken into account.

2. Model for crack path prediction in laminates

2.1. Material of study: loading configuration

A Finite Element analysis of a pre-cracked ceramic laminate specimen mechanically loaded in four-point bending was carried out. The thermal loading resulting from cooling down after sintering was also considered. The multilayer consists of a symmetric and periodic architecture with nine alternating layers of different thickness. In the initial state, a crack is introduced only in the first ATZ layer and impinges the first interface between ATZ and AMZ layer as depicted in Figure 2. Such laminate is subsequently subjected to the mechanical loading (4-point bend test). All the layers made of the same material, ATZ (alumina with 5% tetragonal zirconia), or AMZ (alumina with 30% monoclinic zirconia) have the same thickness, t_{ATZ} and t_{AMZ}, respectively. Table 1 gives the values of the constituent material properties employed in the calculations.

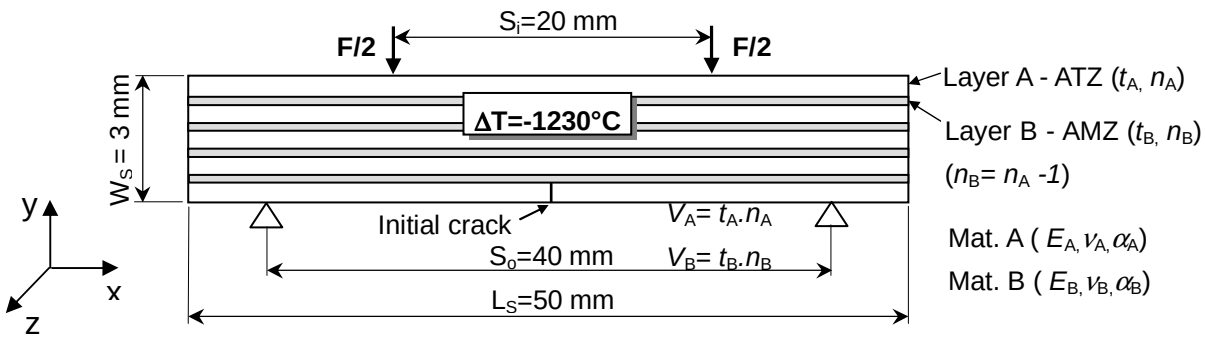

Figure 2. Schematic of the laminate of study with the applied boundary conditions (combined loading in 4-point bending flexure and residual stresses from sintering process). An initial crack is introduced in the first layer

Table 1. Young's modulus (E), Poisson's ratio (ν), Coefficient of Thermal Expansion (α), Flexural Strength (σ_f), Fracture Toughness (K_{Ic}) and Fracture Energy (G_c) of the layer materials

Material	E [GPa]	ν [-]	α x10^{-6} [K^{-1}]	σ_f [MPa]	K_{Ic} [MPa.m$^{1/2}$]	G_c [J/m^2]
ATZ	390±10	0.22	9.8±0.2	422±30	3.2±0.1	25±2
AMZ	280±10	0.22	8±0.2	90±20	2.6±0.1	23±2

In order to show the influence of the level of residual stresses on the propagation of the crack (i.e. deflection or bifurcation), three configurations with different volume ratio of the material components were considered and calculated. The total height of the laminate W_S was kept constant W_S =3mm and the thicknesses of the layers (t_{ATZ} and t_{AMZ}) were thus given by the chosen volume ratio – see (Table 2). The residual stresses corresponding to the chosen volume ratio configuration were calculated using the classical laminate theory by considering of $\Delta T = -1230°C$ (temperature between sintering and room temperature) and material properties given in the Table 1. The calculated residual stresses are listed in Table 2 as well.

Table 2. Layer thicknesses and corresponding residual stresses in the ATZ and AMZ layer for three different volume ratios of ATZ and AMZ material (W_S=const.=3mm)

V_{ATZ}/V_{AMZ} (t_{ATZ}/t_{AMZ})	t_{ATZ} [mm]	t_{AMZ} [mm]	$\sigma_{res,ATZ}$ [MPa]	$\sigma_{res,AMZ}$ [MPa]
2 (1.6)	0.400	0.250	+292	–585
5 (4.0)	0.500	0.125	+140	–695
8 (6.4)	0.533	0.083	+90	–730

2.2 Description of computational approach

In order to decide about the type of further crack propagation (single or double crack penetration) and/or about further crack propagation direction, a change of the potential energy $-\delta\Pi$ for the crack increments in all possible propagation directions has to be calculated. Direction and/or type of propagation is selected such that $\delta\Pi$ attains a maximum value (where maximum of energy is released by the fracture process). However one should note that the energy release rate (ERR) for

the crack terminating at the interface of two different materials is, for infinitesimally small crack increment, zero or infinite (depending on the singularity type). Thus the classical Griffith approach cannot be used. To bypass this problem, a theory of Finite Fracture Mechanics (FFM) can be employed – see e.g. references [20,21]. Infinitesimal crack increment is replaced by a finite crack increment for which the change of the potential energy can be calculated.

The essence of the FFM consists in the key assumption that crack propagation is a discontinuous process occurring in finite steps, rather than continuously and smoothly as in the traditional LEFM theory [20,22-24]. Mathematically, instead of using the differential form of the Griffith energy balance, the integral formulation of the Griffith criterion is applied. Such approach is of particular importance, for instance, in the case of a crack crossing thermo-elastically mismatched interfaces, where the energy release rate is either zero or infinite and, as a consequence, the differential approach fails. For example, if the crack penetrates from material layer 1 to layer 2, the concept of FFM states that the crack will follow the path which maximizes the additional energy ΔW_p released in the fracture process [24], as given by:

$$\Delta W_p = \delta\Pi_p - G_c^{(2)} a_p \,. \tag{1}$$

Here, $G_c^{(2)}$ is the toughness of the next layer to which crack penetrates, $\delta\Pi_p$ is a change of the potential energy between the original and new crack position, and a_p stands for an increment of the new crack.

Hereafter the concept of the Finite fracture mechanics is applied. Matched asymptotic expansions procedure, see e.g. [17-21], is used to derive the change of potential energy due to the perturbation caused by a single or branched crack extension of total length $a_p = a_b$ or a straight penetrating crack extension of length a_p (in several possible crack propagation directions φ_p – see Figure 3).

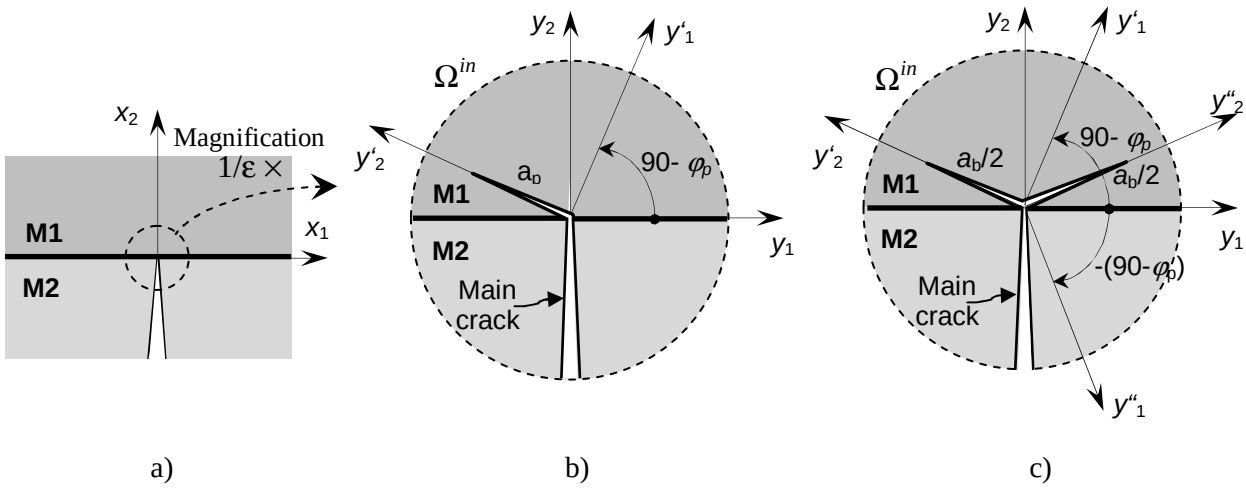

a) b) c)

Figure 3. Scheme of the a) crack terminating at the interface of M1 and M2, b) single crack deflection and c) crack bifurcation (branching) and local coordinate systems in the inner domain, where the crack extension length $a_p = a_b/2 + a_b/2 = 1$

The small perturbation parameter ε is defined as $\varepsilon = a_p/W_S << 1$, where W_S is the characteristic size of the specimen (e.g. specimen height). A second scale to the problem can be introduced, represented by the scaled-up coordinates $(y_1^\varepsilon, y_2^\varepsilon) = (x_1/\varepsilon, x_2/\varepsilon)$ which provide a zoomed-in view into the region surrounding the crack, so-called inner domain Ω^{in} (see Figure 3).

The energy release rate is defined by:

$$G\left(a_{p(b)}\right) = \frac{1}{W_S} \lim_{\delta\varepsilon \to 0} \frac{\delta\Pi_\varepsilon - \delta\Pi_{\varepsilon+\delta\varepsilon}}{\delta\varepsilon}. \tag{2}$$

Assuming that the loading is constant during crack extension, the change of the potential energy $\delta\Pi_\varepsilon$ between the unperturbed state $\mathbf{U}^0$ (without the crack extension) and perturbed state $\mathbf{U}^\varepsilon$ (with the small finite crack extension) can be obtained from the asymptotic expansion with respect to a small parameter ε as:

$$\delta\Pi_\varepsilon = \Pi^0 - \Pi^\varepsilon = \delta\Pi_\varepsilon^{(1)} + \delta\Pi_\varepsilon^{(2)} + ..., \frac{\delta\Pi_\varepsilon^{(2)}}{\delta\Pi_\varepsilon^{(1)}} \to 0 \text{ for } \varepsilon \to 0 \text{ and } \delta_2 < 1, \tag{3}$$

where

$$\delta\Pi_\varepsilon^{(1)} = \frac{W_S^{2\delta_1}}{2} H_1^2 K_{1p(b)}\left(\varphi_p\right)\varepsilon^{2\delta_1} + \frac{W_S^{\delta_1+\delta_2}}{2} H_1 H_2 \varepsilon^{\delta_1+\delta_2} \cdot \left(K'_{1p(b)}\left(\varphi_p\right) + K_{2p(b)}\left(\varphi_p\right)\right) + \frac{W_S^{2\delta_1}}{2} H_2^2 K'_{2p(b)}\left(\varphi_p\right)\varepsilon^{2\delta_2}. \tag{4}$$

Where H_1 and H_2 are generalized stress intensity factors (GSIF) and δ_1, δ_2 are the corresponding singularity exponents ($\delta_1 < \delta_2$) in the stress asymptotic expansion (see [20,21]). The coefficients $K_{1d(p)}$ and $K_{2d(p)}$ are computed in the inner domain Ω^{in}, which is unbounded for $\varepsilon \to 0$ but in the model employed in the finite element calculation, Ω^{in} is approximated by a circular region with radius R much larger than the crack extension length $a_{d(p)}$. On the circle boundary, the condition of the type $\mathbf{U}\big|_{\partial\Omega^{in}} = \rho^{\delta_1}\mathbf{u}_1(\theta)$ is prescribed. $K_{id(p)}, i = 1,2$ are calculated using the path independent integral:

$$K_{ip(b)} = \int_\Gamma \left(\sigma_{kl}^h\left(\mathcal{V}_1^h(\rho,\theta)\right) n_l \rho^{\delta_i} u_{ik}(\theta) - \sigma_{kl}^s\left(\rho^{\delta_i}\mathbf{u}_i(\theta)\right) n_l \mathcal{V}_{1k}^h(\rho,\theta)\right) ds, \quad i = 1,2 \tag{5}$$

Similarly, the coefficients $K'_{1d(p)}$, $K'_{2d(p)}$ are calculated in the inner domain whose remote boundary $\partial\Omega^{in}$ is subjected to the boundary condition $\mathbf{U}\big|_{\partial\Omega^{in}} = \rho^{\delta_2}\mathbf{u}_2(\theta)$

$$K'_{ip(b)} = \int_\Gamma \left(\sigma_{kl}^h\left(\mathcal{V}_2^h(\rho,\theta)\right) n_l \rho^{\delta_i} u_{ik}(\theta) - \sigma_{kl}^s\left(\rho^{\delta_i}\mathbf{u}_i(\theta)\right) n_l \mathcal{V}_{2k}^h(\rho,\theta)\right) ds, \quad i = 1,2 \tag{6}$$

where $\sigma_{kl}^h, \mathcal{V}_i^h, \ i = 1,2$ denotes FE approximation to the functions $\sigma_{kl}, \mathcal{V}_i$.

The second term of the change of the potential energy $\delta\Pi_\varepsilon^{(2)}$ depends on crack extension geometry. Two specific crack extension patterns are considered – crack bifurcation and crack deflection. For the case of the crack bifurcation $\delta\Pi_\varepsilon^{(2)}$ is given by:

$$\begin{aligned}\delta\Pi_{\varepsilon}^{(2)} = &-W_S^{1+\delta_1} H_1 \sigma_{xx}^{(M1)} \varepsilon^{\delta_1+1} \cos^2\varphi_p \left(\int_0^{1/2} \mathcal{V}_{1y_1'}(y')\,dy_2' + \int_0^{1/2} \mathcal{V}_{1y_1''}(y'')\,dy_2'' \right) + \\ &+ W_S^{1+\delta_1} H_1 \sigma_{xx}^{(M1)} \varepsilon^{\delta_1+1} \sin\varphi_p \cos\varphi_p \left(\int_0^{1/2} \mathcal{V}_{1y_2'}(y')\,dy_2' - \int_0^{1/2} \mathcal{V}_{1y_2''}(y'')\,dy_2'' \right) - \\ &- W_S^{1+\delta_2} H_2 \sigma_{xx}^{(M1)} \varepsilon^{\delta_2+1} \cos^2\varphi_p \left(\int_0^{1/2} \mathcal{V}_{2y_1'}(y')\,dy_2' + \int_0^{1/2} \mathcal{V}_{2y_1''}(y'')\,dy_2'' \right) + \\ &+ W_S^{1+\delta_2} H_2 \sigma_{xx}^{(M1)} \varepsilon^{\delta_2+1} \sin\varphi_p \cos\varphi_p \left(\int_0^{1/2} \mathcal{V}_{2y_2'}(y')\,dy_2' - \int_0^{1/2} \mathcal{V}_{2y_2''}(y'')\,dy_2'' \right) \gtreqless 0,\end{aligned} \tag{7}$$

while for the case of single crack deflection $\delta\Pi_{\varepsilon}^{(2)}$ reads:

$$\begin{aligned}\delta\Pi_{\varepsilon}^{(2)} = &-W_S^{1+\delta_1} H_1 \sigma_{xx}^{(M1)} \varepsilon^{\delta_1+1} \cos^2\varphi_p \int_0^1 \mathcal{V}_{1y_1'}(y')\,dy_2' + W_S^{1+\delta_1} H_1 \sigma_{xx}^{(M1)} \varepsilon^{\delta_1+1} \sin\varphi_p \cos\varphi_p \int_0^1 \mathcal{V}_{1y_2'}(y')\,dy_2' - \\ &- W_S^{1+\delta_2} H_2 \sigma_{xx}^{(M1)} \varepsilon^{\delta_2+1} \cos^2\varphi_p \int_0^1 \mathcal{V}_{2y_1'}(y')\,dy_2' + W_S^{1+\delta_2} H_2 \sigma_{xx}^{(M1)} \varepsilon^{\delta_2+1} \sin\varphi_p \cos\varphi_p \int_0^1 \mathcal{V}_{2y_2'}(y')\,dy_2' \gtreqless 0.\end{aligned} \tag{8}$$

The factors $K_{ip(b)}$ and the opening of the crack extension $\mathcal{V}_{1y_1'}, \mathcal{V}_{2y_1'}$ etc., are calculated by FEM on the inner domain – for methodology see e.g. references [20,21].
Note that GSIFs in Eqs. (4), (7) and (8) respectively are generally the sums of two contributions

$$H_1 = H_1^m + H_1^r, \quad H_2 = H_2^m + H_2^r, , \tag{9}$$

where H_i^m are due to pure flexural loading and H_i^r are due to pure thermal loading respectively. For calculation of GSIFs a two-state integral with FEM is employed - see [20,21].
Remark: If some of the GSIF H_1 or H_2 are close (or equal) to 0 (e.g. case of the crack perpendicular to the interface), then Eqs. (4), (7) and (8) will simplify significantly.

3. Results

The experimental observations (made by authors of [15]) shows that in case of laminates with higher volume ratios (V_{ATZ}/V_{AMZ}>4), the crack originated in the first ATZ layer does not stop at the interface, but arrests close behind the interface at a distance Δa (the distance Δa depends on the level of residual stresses). To explain this behavior, the thermal stress intensity factor for a wide range of crack lengths in ATZ layer and AMZ layer was calculated - see Figure 4. In terms of ERR the results are displayed in Figure 5. One can see that, for higher volume ratios, the crack has to be arrested close behind the interface since the SIF decreases rapidly by propagation in the compressive layer. At the distance of $\Delta a \cong 7\mu$m (for V_{ATZ}/V_{AMZ} =8) and distance $\Delta a \cong 27\mu$m (for V_{ATZ}/V_{AMZ} =5) the energy accumulated in the system is released and thus the crack is arrested. For subsequent propagation an additional mechanical loading is required. For the ratio V_{ATZ}/V_{AMZ} =2 the crack either arrests in much higher distance behind the interface or it propagates straight through the whole laminate (due to high tensile stresses in the first ATZ layer).

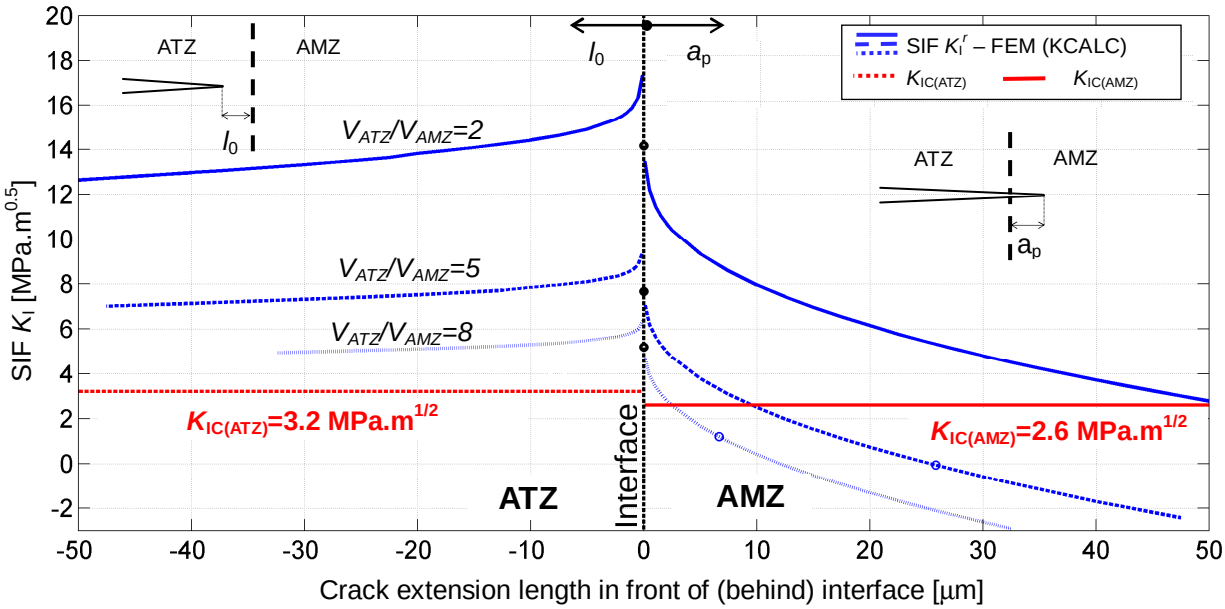

Figure 4. SIF K_I calculated for crack approaching interface and SIF K_I calculated for crack propagating straight in the second material. Laminate body was subjected to the thermal load ΔT=-1230°C. SIF K_I evaluated using ANSYS function KCALC.

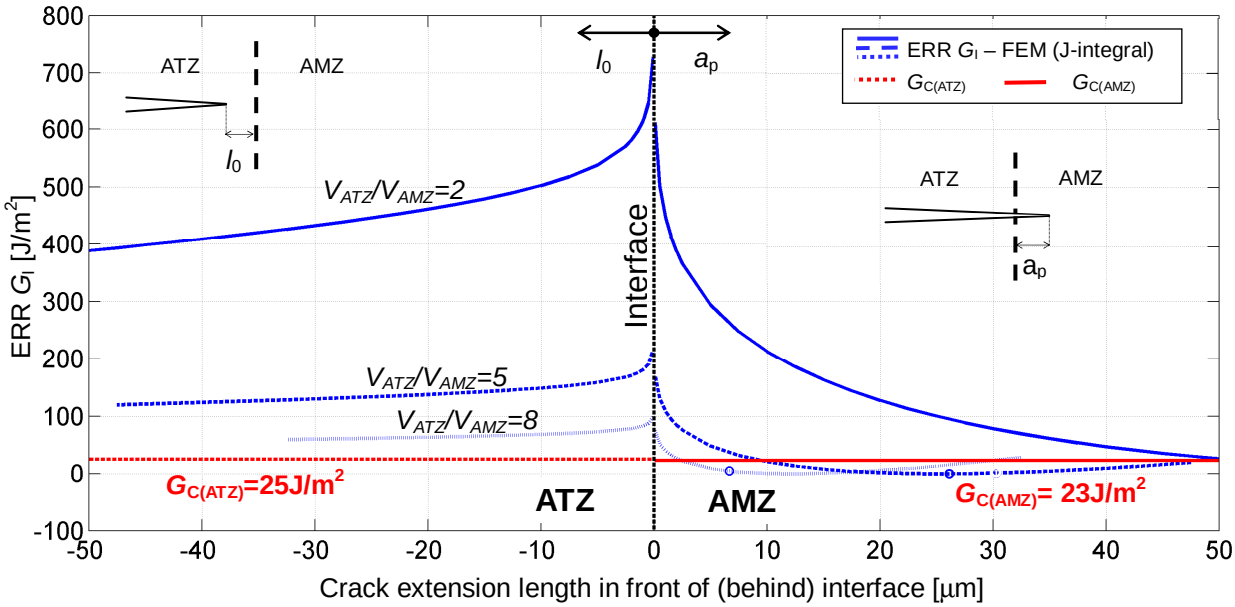

Figure 5. ERR G_I calculated for crack approaching interface and ERR G_I calculated for crack propagating straight in the second material. Laminate body was subjected to the thermal load ΔT=-1230°C. ERR G^r evaluated using the ANSYS function CINT (J-integral).

The values of the GSIFs characterizing the stress state at the crack tip for crack terminating at the interface of ATZ and AMZ layer are listed in Table 3. The GSIF for mechanical loading is calculated for a loading force of 10N. For higher forces it can be easily recalculated (due to its linear dependence on the applied load).

Table 3. Values of the GSIFs (crack terminating at the interface) for δ=0.46391, F=10N/mm, ΔT=-1230°C.

V_{ATZ}/V_{AMZ}	H^m [MPa.m$^{1-\delta}$]	H^r (ΔT) [MPa.m$^{1-\delta}$]	$\sigma_{xx}^{(AMZ)}$ (ΔT) [MPa]	$H=H^m+H^r$
2/1	0.10	2.92	-795	3.02
5/1	0.11	1.58	-795	1.69
8/1	0.11	1.07	-795	1.18

For the calculation of δΠ (Eqs. (2), (4), (7), (8)) for different propagation directions (including single penetration and bifurcation type of propagation) values of SIFs, corresponding to the state, when the crack is arrested behind the interface, were used – see Figure 5. Observe that SIF decreases rapidly with increasing length of crack extension behind the interface. In Figure 6 a), b) a ceramic laminate with volume ratio of laminate components V_{ATZ}/V_{AMZ}=8 is studied. Energetic condition for crack propagation (the additional energy ΔW≥0 - see Eq. (1)) is satisfied for the loading force F≅100N. The referred figure shows a change in potential energy for case of single penetration and crack bifurcation (for a_p=a_b=25μm). One can see that crack bifurcation is a preferred propagation type in this case (due to higher change in potential energy).

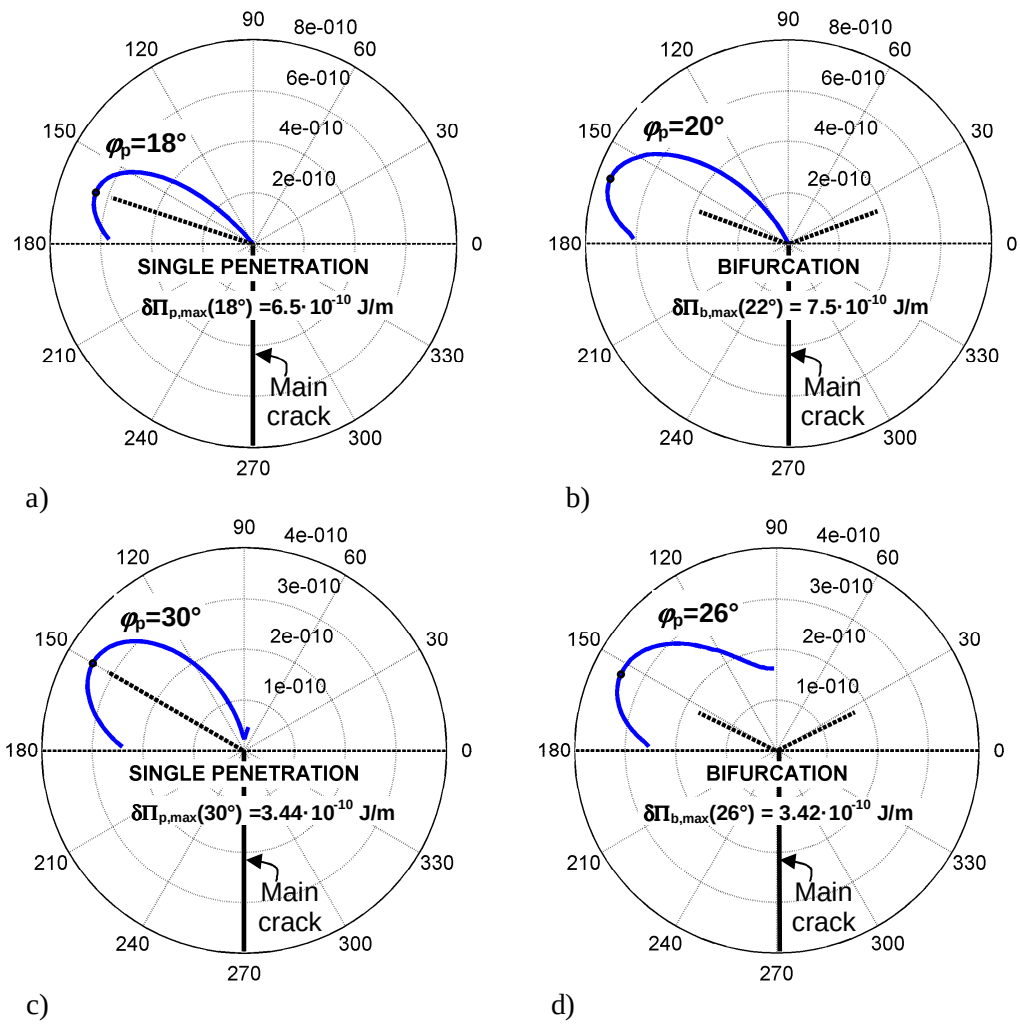

Figure 6. Variation of the change of the potential energy δΠ with the angle of the crack extension for a), b) volume ratio V_{ATZ}/V_{AMZ}=8 and c), d) V_{ATZ}/V_{AMZ}=5. For each volume ratio a case of single crack deflection - a), c) and case of the crack bifurcation - b), d) is calculated.

The same study was also made for ceramic laminate with V_{ATZ}/V_{AMZ}=5 - Figure 6 c), d) and here the critical loading force was estimated as F≅115N. In this case, a preferred propagation direction is starting to be a single deflection. For ratios V_{ATZ}/V_{AMZ}<5 only a single crack deflection is predicted as preferred propagation direction. In case of volume ratio V_{ATZ}/V_{AMZ}=2, the crack propagates almost straight, maximally with a slight deflection from the original direction (with no bifurcation phenomena).

4. Conclusions

The crack path in laminates is influenced by the magnitude and location of the compressive stresses in the internal layers. A semi-analytical model based on Finite Fracture Mechanics (FFM) theory was here developed to describe and predict the crack propagation in symmetric laminates consisting of alternated tensile–compressive layers built–up in a periodic architecture. In addition to the mechanical loading under flexural bending, a thermal loading associated with the thermal mismatch of the layers during sintering was also taken into account in the model. The fracture criterion was based on the calculation of the change of the potential energy $\delta\Pi$ for a finite crack increment length, starting from the tip of the original crack and advancing in several possible propagation directions (angle of crack propagation). From all theoretically possible crack paths, the change of the potential energy between unperturbed and perturbed state was evaluated. Direction and/or type of propagation were selected such that the change of $\delta\Pi$ would attain a maximum value.

In case of the low volume ratios (i.e. V_1/V_2= 1/1 – 4/1) single crack deflection (and in some cases straight crack propagation) is preferred with an angle lower than 20° (measured from the straight propagation). On the other hand, for relative high volume ratios, (i.e. V_1/V_2= 6/1 – 8/1), corresponding to high compressive residual stresses, crack bifurcation (i.e crack propagating simultaneously in two directions) is predicted by the model. Such behaviour is also in correspondence with the experimental observations.

Acknowledgements

The authors gratefully acknowledge a financial support through the project CZ.1.07/2.3.00/30.0005 of Brno University of Technology.

A financial support by the Austrian Federal Government (in particular from the Bundesministerium für Verkehr, Innovation und Technologie and the Bundesministerium für Wirtschaft und Arbeit) and the Styrian Provincial Government, represented by Österreichische Forschungsförderungs-gesellschaft mbH and by Steirische Wirtschaftsförderungsgesellschaft mbH, within the research activities of the K2 Competence Centre on “Integrated Research in Materials, Processing and Product Engineering”, operated by the Materials Center Leoben Forschung GmbH in the framework of the Austrian COMET Competence Centre Programme, is gratefully acknowledged as well.

References

[1] W.J. Clegg, K. Kendall, N.M. Alford, T.W. Button, J.D. Birchall, A Simple Way to Make Tough Ceramics. Nature, 347 (1990) 455-457.

[2] O. Prakash, P. Sarkar, P.S. Nicholson, Crack Deflection in Ceramic/Ceramic Laminates with Strong Interfaces. Journal of the American Ceramic Society, 78 (1995) 1125-1127.

[3] D.B. Marshall, P.E.D. Morgan, R.M. Housley, Debonding in multilayered composites of zirconia and $LaPO_4$. Journal of the american ceramic society, 80 (1997) 1677-1683.

[4] W.J. Clegg, Design of Ceramic Laminates for Strucutral Applications. Materials Science and Technology, 14 (1998) 486-495.

[5] H. Tomaszewski, H. Weglarz, A. Wajler, M. Boniecki, D. Kalinski, Multilayer ceramic composites with high failure resistance. J. of the Eur. Ceramic Society, 27 (2007) 1373-1377.

[6] D.B. Marshall, J.J. Ratto, F. Lange, Enhanced fracture toughness in layered microcomposites of Ce-ZrO_2 and Al_2O_3. J. Am. Ceram. Soc., 74 (1991) 2979-2987.

[7] J. Sanchez-Herencia, J. Moya, A. Tomsia, Microstructural design in alumina-alumina/zirconia layered composites. Scripta Materialia, 38 (1998) 1-5.

[8] R.J. Moon, K.J. Bowman, K.P. Trumble, J. Rödel, Fracture resistance curve behavior of multilayered alumina-zirconia composites produced by centrifugation. Acta Materialia, 49 (2001) 995-1003.

[9] R. Lakshminarayanan, D.K. Shetty, R.A. Cutler, Toughening of Layered Ceramic Composites with Residual Surface Compression. J. of the American Ceramic Society, 79 (1996) 79-87.

[10] M. Rao, J. Sanchez-Herencia, G. Beltz, R.M. McMeeking, F. Lange, Laminar ceramics that exhibit a threshold strength. Science, 286 (1999) 102-105.

[11] V.M. Sglavo, M. Paternoster, M. Bertoldi, Tailored Residual Stresses in High Reliability Alumina-Mullite Ceramic Laminates. J. of the Amer. Ceramic Society, 88 (2005) 2826-2832.

[12] M. Lugovy, V. Slyunyayev, N. Orlovskaya, G. Blugan, J. Kübler, M.H. Lewis, Apparent Fracture Toughness of Si_3N_4-Based Laminates with Residual Compressive or Tensile Stress in Surface Layers. Acta Materialia, 53 (2005) 289-296.

[13] R. Bermejo, Y. Torres, A.J. Sánchez-Herencia, C. Baudín, M. Anglada, L. Llanes, Residual stresses, strength and toughness of laminates with different layer thickness ratios. Acta Materialia, 54 (2006) 4745-4757.

[14] R. Bermejo, Y. Torres, C. Baudin, A.J. Sánchez-Herencia, J. Pascual, et al., Threshold strength evaluation on an Al_2O_3–ZrO_2 multilayered system. J Eur Ceram Soc, 27 (2007) 1443-1448.

[15] R. Bermejo, R. Danzer, High failure resistance layered ceramics using crack bifurcation and interface delamination as reinforcement mechanisms. Eng. Fract. Mech., 77 (2010) 2126-2135.

[16] M. He, J.W. Hutchinson, Crack Deflection at an Interface Between Dissimilar Elastic Materials. International Journal of Solids and Structures, 25 (1989) 1053-1067.

[17] E. Martin, D. Leguillon, C. Lacroix, A revisited criterion for crack deflection at an interface in a brittle bimaterial. Composites Sci. Technol., 61 (2001) 1671-1679.

[18] D. Leguillon, Strength or toughness? A criterion for crack onset at a notch. European Journal of Mechanics, A/Solids, 21 (2002) 61-72.

[19] L. Vu-Quoc, V. Tran, Singularity analysis and fracture energy-release rate for composites: Piecewise homogeneous-anisotropic materials. Comput. Methods Appl. Mech. Eng., 195 (2006) 5162-5197.

[20] M. Kotoul, O. Ševeček, T. Profant, Analysis of multiple cracks in thin coating on orthotropic substrate under mechanical and residual stresses. Eng. Fract. Mech., 77 (2010) 229-248.

[21] O. Ševeček, M. Kotoul, T. Profant, Effect of higher order asymptotic terms on the competition between crack penetration and debond at a bimaterial interface between aligned orthotropic materials. Eng. Fract. Mech., 80 (2012) 28-51.

Application of a novel finite element method to design of splices in a fiber metal subjected to coupled thermo-mechanical loading

XueCheng Ping[1,*], MengCheng Chen[2], BingBing Zheng[1], YiHua Xiao[1]

[1] School of Mechanical and Electronical Engineering, East China JiaoTong University, 330013, China
[2] School of Civil Engineering, East China JiaoTong University, 330013, China
* Corresponding author: xuecheng_ping@yahoo.com.cn

Abstract The splice concept has been developed in fiber metal laminates (FMLs) due to the limited dimensions of pretreatment facility, the autoclave curing facility and C-scan facility. Failure always initiates in the splice opening between the metal splice edges before delamination occurs in the loading direction. In this paper, a novel finite element method for obtaining stress intensities is introduced in the estimation of the failure strength of splices in FMLs. A super wedge tip element for application to bi-material wedge is developed utilizing the numerical stress and displacement field solutions based on an ad hoc finite element eigenanalysis method, from which singular stress fields near apex of arbitrary bi-material wedges under coupled thermo-mechanical loading can be obtained. Failure of double spliced FMLs with varying spliced width and fiber-layer thickness were investigated, and fracture criterion based on stress intensity factors are presented to predict splice failure.

Keywords Thermo-mechanical loading, Fracture criterion, fiber metal laminate, Splice, Super wedge tip element

1. Introduction

Fiber metal laminates, such as Arall (Aramid reinforced aluminum laminates) and Glare (S2-glass fiber reinforced aluminum laminates), were developed at Delft University of Technology as a family of structural aerospace sheet materials. They take the advantages of metal alloys and fiber-reinforced composites providing superior mechanical properties [1], and have been applied to fuselage and leading edges in aircraft structures as a replacement of high-strength aluminum alloys due to their light weight, high strength, and excellent fatigue resistance. The dimensions of a FML are only limited by the width of the aluminum layers and not by their length. The available prepreg dimensions are also not limited. The maximum dimensions of a Glare skin panel are further limited by the dimensions of the pretreatment facility, the autoclave curing facility and C-scan facility. Also the handling and transportation of the panel may be a limiting factor. Currently only aluminium sheet with widths up to 1524 mm (60 inch) can be manufactured to the required accuracy with the necessary nominal thicknesses between 0.3 and 0.5 mm. This limitation would imply the necessity of applying many costly mechanical longitudinal or circumferential joints (at a maximum distance of 1524 mm) in an aircraft fuselage. To avoid this disadvantage, the internal splicing concept has been developed to increase the maximum available sheet size [2-4].

Due to the difference in elastic properties and thermal expansion coefficients of the components joined and discontinuity of junction geometry, residual stresses exist in each layer of the FML, and most importantly, high stress concentrations occur at the aluminum splice edges under thermal environment during manufacturing and coupled thermo-mechanical loading. As a result, the structural efficiency of bonded structures depends not on the structure itself but on splice strength. Generally, the failure behavior of the spliced FML always includes two steps, i.e., the onset of

failure in the splice opening between the aluminum splice edges filled with resin during production of the material and the delamination extension in the loading direction.

Several researchers have developed theoretical concepts to describe the observed crack growth behaviour in fiber metal laminates [5-10]. These concepts start from the available methods for crack growth in monolithic aluminium sheets with additional parameters describing the bridging effect. In general, fatigue crack growth in a fiber metal laminate such as Glare is accompanied by delamination growth at the interface between the aluminium and glass fiber/adhesive layers. To incorporate this delamination growth in crack growth prediction methods, the energy release rate approach is applied to describe the delamination growth rate [7-10]. Few researchers have investigated the delamination behavior for different splicing geometries and layer thicknesses. Vries et al. [11] applied Griffith's energy criterion to calculate a delamination resistance, and Hashagen et al. [12] described the delamination in the interface by a plasticity based material model derived from a Hoffman-like yield function which bounds all states of stress in the interface. However, it is noticed that Vries et al. [11] and Hashagen et al. [12] only paid attention to the second falure processes, i.e., delamination between the prepeg layer and the aluminum layer, and the failure criterion for the splice opening between the aluminum splice edges has not been established. On the other hand, only the mechanical loading is considered in above researches, so that the established theories are not suitable for the bonded structures subjected to coupled thermo-mechanical loading.

In this paper, attempt is made to predict splice failures in fiber metal laminate subjected to coupled thermo-mechanical loading using stress singularity theory. In order to solve stress fields near the apex of bonded dissimilar materials as shown in Fig. 1, a super wedge tip element with numerical asymptotic solutions developed by Sze et al. [13] is firstly established and used for thermo-mechanical finite element analysis. Critical stress intensity factors are used as control parameters for fracture initiating at the bimaterial interface edge, and to predict fracture load for varying splice width and fiber layer thickness. The theoretical results are compared with experimental results for verification purposes.

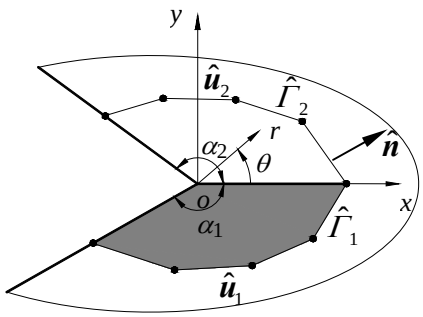

Fig. 1 Description of a bi-material wedge containing a super wedge tip element

2. Element stiffness matrix of the super wedge tip element

As shown in Fig. 1, a domain composed of bi-material sectors can be partitioned into inner and outer regions. The accurate solution to the entire domain requires coupling of the numerical solution in the inner region with that of the approximate solution through the finite element in the outer region. The coupling can be achieved by developing a super wedge tip element (as shown in Fig. 1) whose interpolation functions satisfy the governing equations exactly near the apex enforcing the inter-element displacement continuity along the common boundary and the nodes between the super

and conventional elements. The stiffness matrix for the super wedge tip element of bi-material wedge under mechanical and thermal loading is obtained by considering the total potential expressed in the following form[15]

$$\begin{aligned}\Pi = &\sum_{k=1}^{2}\left\{-\frac{1}{2}\int_{\hat{\Gamma}_k} {}^{m}_{\lambda}\boldsymbol{\sigma}^{(k)T}\boldsymbol{n}^T\, {}^{m}_{\lambda}\boldsymbol{u}^{(k)} d\Gamma - \int_{\hat{\Gamma}_k} {}^{m}_{\lambda}\boldsymbol{\sigma}^{(k)T}\boldsymbol{n}^T\, {}^{t}_{\lambda+c}\boldsymbol{u}^{(k)} d\Gamma\right\} \\ &+\sum_{k=1}^{2}\left\{\int_{\hat{\Gamma}_k} {}^{m}_{\lambda}\boldsymbol{\sigma}^{(k)T}\boldsymbol{n}^T\hat{\boldsymbol{u}}^{(k)} d\Gamma - \int_{\hat{\Gamma}_k} {}^{*}\boldsymbol{t}^{(k)T}\hat{\boldsymbol{u}}^{(k)} d\Gamma\right\} + \Pi_0\end{aligned} \tag{1}$$

The terms ${}^{m}_{\lambda}\boldsymbol{\sigma}_p^{(k)}$, ${}^{m}_{\lambda}\boldsymbol{u}_p^{(k)}$ and ${}^{t}_{\lambda}\boldsymbol{\sigma}_p^{(k)}$, ${}^{t}_{\lambda}\boldsymbol{u}_p^{(k)}$ associated with the homogeneous solutions of mechanical and thermal loadings, respectively, and in the case of thermal loading, ${}^{t}_{c}\boldsymbol{\sigma}_p^{(k)}$ and ${}^{t}_{c}\boldsymbol{u}_p^{(k)}$ represent the known complementary solutions for non-singular stress and displacement fields. These vectors can be defined as

$${}^{m}_{\lambda}\boldsymbol{\sigma}_p^{(k)} = \boldsymbol{\Sigma}^{(k)}\, {}^{m}\boldsymbol{K}\,,\quad {}^{m}_{\lambda}\boldsymbol{u}_p^{(k)} = \boldsymbol{U}^{(k)}\, {}^{m}\boldsymbol{K} \tag{2, 3}$$

$${}^{t}_{\lambda}\boldsymbol{\sigma}_p^{(k)} = \boldsymbol{\Sigma}^{(k)}\, {}^{t}\boldsymbol{K}\,,\quad {}^{t}_{\lambda}\boldsymbol{u}_p^{(k)} = \boldsymbol{U}^{(k)}\, {}^{t}\boldsymbol{K} \tag{4, 5}$$

$${}^{t}_{c}\boldsymbol{\sigma}_p^{(k)} = \boldsymbol{F}_c^{(k)}(r,\theta)\boldsymbol{q}_c^{(k)}\,,\quad {}^{t}_{c}\boldsymbol{u}_p^{(k)} = \boldsymbol{G}_c^{(k)}(r,\theta)\boldsymbol{q}_c^{(k)} + r\alpha_k\Delta T\boldsymbol{e}_r \tag{6, 7}$$

The details of $\boldsymbol{\Sigma}^{(k)}$ and $\boldsymbol{U}^{(k)}$ refer to Chen and Sze [14], and the definition of $\boldsymbol{F}_c^{(k)}$, $\boldsymbol{G}_c^{(k)}$, $\boldsymbol{q}_c^{(k)}$, $\boldsymbol{e}_r^T$ and ${}^{t}\boldsymbol{K}$ are listed in Barut et al. [15]. ΔT denotes the uniform temperature change. The unknown components of displacement vector along the common boundary segments, $\hat{\Gamma}_k$ (shown in Fig. 1), are denoted by $\hat{\boldsymbol{u}}^{(k)}$. ${}^{*}\boldsymbol{t}^{(k)}$ is the known applied traction components along the common boundary segments. $\boldsymbol{n}$ contains the components of the unite normal along $\hat{\Gamma}_k$. Π_0 represents the total potential associated with the known initial strain and stress components arising from thermal loading only. The vector of displacement components, $\hat{\boldsymbol{u}}^{(k)}$, along the common boundary between the global element and the conventional elements can be expressed in terms of the nodal displacement of the conventional elements as

$$\hat{\boldsymbol{u}}^{(k)} = \boldsymbol{L}\boldsymbol{v} \tag{8}$$

in which the matrix $\boldsymbol{L}$ contains the linear interpolation function compatible with those of the conventional elements. The vector $\boldsymbol{v}$ contains the nodal degrees of freedom associated with the conventional elements located on the boundary segment $\hat{\Gamma}_k$ of the super notch tip element.

Substituting for ${}^{m}_{\lambda}\boldsymbol{\sigma}_p^{(k)}$, ${}^{m}_{\lambda}\boldsymbol{u}_p^{(k)}$ and $\hat{\boldsymbol{u}}^{(k)}$ from Eqs. (2)-(8) into the expression for the total potential leads to

$$\Pi = -\frac{1}{2}\, {}^{m}\boldsymbol{K}^T\boldsymbol{H}\, {}^{m}\boldsymbol{K} - {}^{m}\boldsymbol{K}^T\, {}^{t}\boldsymbol{f} + {}^{m}\boldsymbol{K}^T\boldsymbol{G}\hat{\boldsymbol{v}} - \boldsymbol{v}^T\, {}^{*}\boldsymbol{f} + \Pi_0 \tag{9}$$

in which

$$\boldsymbol{H} = \sum_{k=1}^{2}\frac{1}{2}\int_{\hat{\Gamma}_k}\left[\boldsymbol{\Sigma}^{(k)T}\boldsymbol{Z}_\sigma^{(k)T}\boldsymbol{n}^{\mathrm{T}}\boldsymbol{Z}_u^{(k)}\boldsymbol{U}^{(k)} + \boldsymbol{U}^{(k)\mathrm{T}}\boldsymbol{Z}_u^{(k)T}\boldsymbol{n}\boldsymbol{Z}_\sigma^{(k)}\boldsymbol{\Sigma}^{(k)}\right]\mathrm{d}S\,,\quad \boldsymbol{G} = \sum_{k=1}^{2}\int_{\Gamma_{\mathrm{w}}}\boldsymbol{\Sigma}^{(k)T}\boldsymbol{Z}_\sigma^{(k)T}\boldsymbol{n}\boldsymbol{L}\,\mathrm{d}S$$

$${}^{t}\boldsymbol{f}^{(k)} = \sum_{k=1}^{2}\int_{\hat{\Gamma}_k}\boldsymbol{\Sigma}^{(k)T}\boldsymbol{Z}_\sigma^{(k)T}\boldsymbol{n}^{\mathrm{T}}\boldsymbol{Z}_u^{(k)}\, {}^{t}_{\lambda+c}\boldsymbol{u}_p^{(k)} d\Gamma\,,\quad {}^{*}\boldsymbol{f}^{(k)} = \sum_{k=1}^{2}\int_{\hat{\Gamma}_k}\boldsymbol{L}^{(k)}\, {}^{*}\boldsymbol{t}^{(k)} d\Gamma\,,\quad {}^{t}_{\lambda+c}\boldsymbol{u}_p^{(k)} = {}^{t}_{\lambda}\boldsymbol{u}_p^{(k)} + {}^{t}_{c}\boldsymbol{u}_p^{(k)}$$

$\boldsymbol{Z}_\sigma^{(k)}$ and $\boldsymbol{Z}_u^{(k)}$ are the coordinate systerm transformation matrices. In order to express the total potential in terms of one unknown vector, $\boldsymbol{v}$, the first variation of the total potential with respect to

${}^{m}\boldsymbol{K}$ is taken. While noting that $\delta\Pi_0 = 0$, enforcing the first variation with respect to ${}^{m}\boldsymbol{K}$ to vanish results in

$$ {}^{m}\boldsymbol{K} = H^{-1}\left\{\boldsymbol{R}\boldsymbol{v} - {}^{t}\boldsymbol{f}\right\} \tag{10} $$

Substituting for ${}^{m}\boldsymbol{K}$ in the expression for the total potential, and enforcing the first variation of the total potential to vanish results in the nodal equations of equilibrium for the global element as

$$ \delta\Pi = \boldsymbol{v}^T\left\{\boldsymbol{K}_s\boldsymbol{v} - {}^{t}\boldsymbol{F} - {}^{*}\boldsymbol{f}\right\} = 0 \tag{11} $$

leading to

$$ \boldsymbol{K}_s\boldsymbol{v} = {}^{t}\boldsymbol{F} + {}^{*}\boldsymbol{f} \tag{12} $$

in which $\boldsymbol{K}_s$ and ${}^{t}\boldsymbol{F}$ are defined as $\boldsymbol{K}_s = \boldsymbol{G}^T\boldsymbol{H}^{-1}\boldsymbol{G}$ and ${}^{t}\boldsymbol{F} = \boldsymbol{G}^T\boldsymbol{H}^{-1}\,{}^{t}\boldsymbol{f}$. The vector ${}^{*}\boldsymbol{f}$ represents the internal loading vector at a node common to both the global and conventional elements. If a node is free of conventional elements, the components of the load vector represent the external force components. The vector ${}^{t}\boldsymbol{F}$ represents the reaction force that suppresses the deformation, resulting from thermal loading only, at the common nodes of global and conventional elements.

3. Experiment results

Fig. 2 shows a fiber metal laminate specimen with splices in interrupted aluminum layer edges. The materials comprising the specimen are aluminum, woven glass fiber reinforced composite and epoxy resin. Their elastic properties and coefficients of thermal expansion are listed in Tables 1 and 2. The thicknesses of aluminum layer and epoxy resin are all 1mm, the thickness of woven glass fiber reinforced composite varies as H=1, 2, 3, the width of splices vary as w=0.5, 1, 2, 3, 4, 5, 6, and the width of all layers are 20mm. Co-cured fiber metal laminate specimens were fabricated under the manufacture's recommended cure cycle for the composite material, and Fig. 3 illustrates the fabrication process.

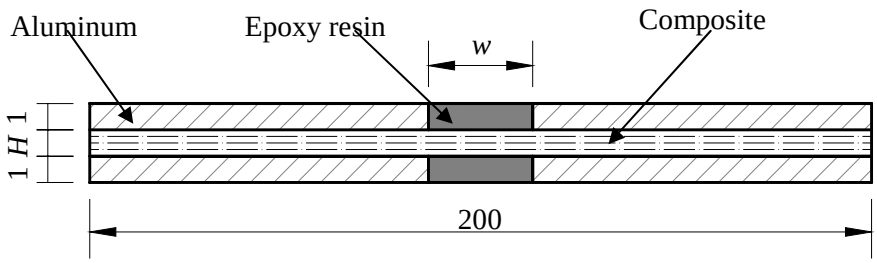

Figure 2. Dimensions of the spliced fiber metal laminate

Shimadzu EHF-EM electric-fluid serving tensile testing machine are used to test tension force, and Fig. 4 shows the tensile test apparatus. The load-displacement response curve obtained from the tensile test is linear until crack initiates at the splice, as shown in Fig. 5. Typical fractured fiber metal laminate specimens are shown in Fig. 6,by inspecting the fracture process, it is found that interface cracks initiate at the interface edge of the epoxy resin and the aluminum and propagate along the interface. Load bearing capacities F_c of the spliced fiber metal laminate specimens with varying splice width and fiber layer thickness are listed in Table 3. Experiment results show that, critical fracture load F_c increases with decreasing of splice width w, and decreases with increasing

of fiber layer thickness *H*.

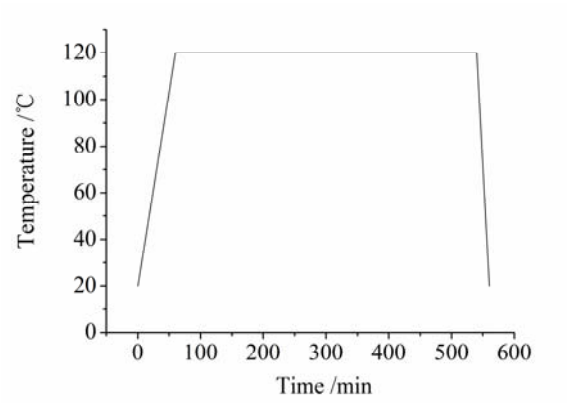

Figure 3. Cure cycle of the splices in a fiber metal laminate

Table 1. Material properties of the materials in the spliced fiber metal laminate

Materials	E_1	E_2	E_3	ν_{12}	ν_{13}	ν_{23}	G_{12}
Aluminum	72000	72000	72000	0.33	0.33	0.33	27067.67
Epoxy Resin	3200	3200	3200	0.49	0.49	0.49	1073.83
Composite	24600	24600	24600	0.025	0.363	0.025	1145

Table 2. Thermal expansion coefficients of the materials in the spliced fiber metal laminate

Materials	α_1(/°C)	α_2(/°C)	α_3(/°C)
Aluminum	1.881×10^{-5}	1.881×10^{-5}	1.881×10^{-5}
Epoxy Resin	5×10^{5}	5×10^{5}	5×10^{5}
Composite	6.443×10^{-6}	41.482×10^{-6}	6.443×10^{-6}

4. Fracture criterion of splices in a fiber metal laminate

Due to the symmetric feature of the structure, only one fourth of the structure is considered in the analysis. Fig. 7 illustrates the structure for FEM analysis and its boundary conditions. To solve the stress fields at the interface edge *o*, a 5-node super wedge tip element is used at this point, around which two-dimensional four-node element elements are used. Plane strain assumption is used in all numerical calculations.

Figure 4. Tensile test apparatus of the spliced fiber metal laminate

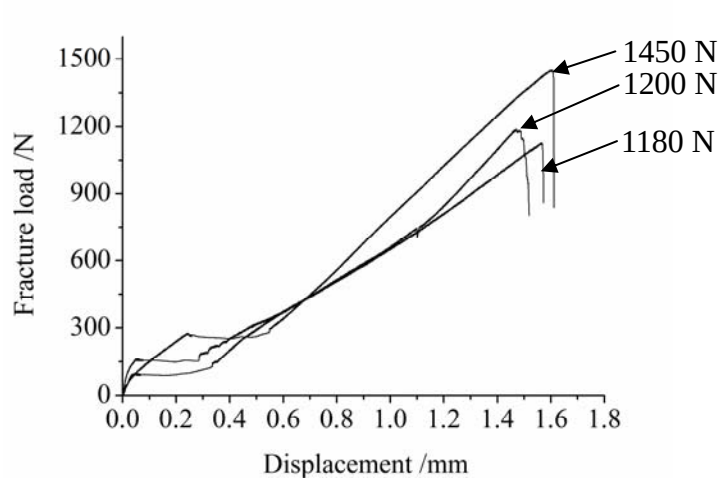

Figure 5. Load-displacement curves for *w*=4mm and *H*=1mm

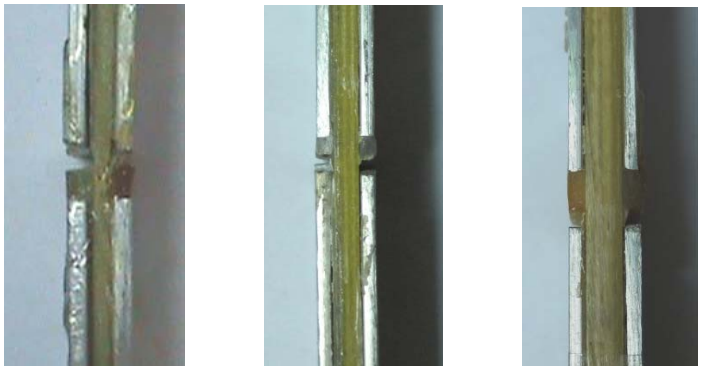

(a) (b) (c)

Figure 6. Specimens after fracture at the splices for: (a) *H*=1mm; (b) *H*=2mm; *H*=3mm;

Residual thermal stresses exist in specimens because a heat cure cycle is used, so during tensile test experiment, the specimens are actually subjected to thermo-mechanical coupled loading. If crack initiation load at the splices is determined by the stress intensity at the interface edge *o*, a suitable stress intensity parameter should be established, and the critical value of this parameter should be a constant. In other word, under coupled thermo-mechanical loading, crack will initiate when the stress intensity parameter at the interface edge reaches its critical value.

For the interface edge configuration at point *o* shown in Fig. 7, the method presented in Section 2 is applied to solve the intensity of stress fields. The singularity exponent can be obtained as λ=-0.34768 by using the finite element eigenanalysis method [13, 14]. Its corresponding angular variation of stress $\bar{\sigma}_{ij}(\theta)$ is plotted in Fig. 8. After the coefficient $\boldsymbol{q}_c^{(k)}$ is solved based on the continuity conditions across the interfaces and the traction-free conditions across the free edges, the regular stress terms near the interface edge can be obtained by Eq. (7). Fig. 9 illustrates the regular stress terms. Because there is only one singularity exponent, the stress field near interface edge *o* can be expressed as:

$$\sigma_{ij}(r,\theta) = K \cdot r^{\lambda} \cdot \bar{\sigma}_{ij}(\theta) + {}_c^t\sigma_{ij}(\theta) \tag{13}$$

where $\sigma_{ij}^{FE}(r,\theta)$ is the stress field near interface edge calculated from the present FEM analysis. If the stress intensity factor K, a summation of ${}^mK$ and ${}^tK$, can be used as interface edge fracture

cretirion, the local falure condition will be

$$K \geq K_c \tag{14}$$

Table 3. The Fracture loading of specimens with various splice width and fiber layer thickness

Splice width w (mm)	Fracture load F_c (N)		
	H=1 mm	H=2 mm	H=3 mm
0.5	2096.67	2041.38	1684.29
1	1706.67	1169.30	451.20
2	1456.67	1025.40	357.40
3	1320.00	1016.62	685.08
4	1276.67	1005.02	859.29
5	1343.33	996.10	861.48
6	1306.67	1002.40	912.00

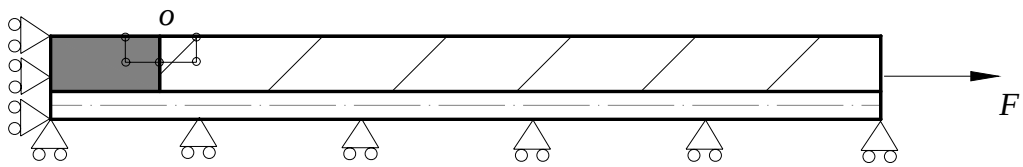

Figure 7. One quarter of a specimen and its boundary conditions

Fig. 10 shows the calculated critical stress intensity factor under coupled thermo-mechanical loading. The thermal loading is ΔT=-100°C, and the critical mechanical loadings corresponding to differenent splice width and fiber layer thickness are listed in Table 3. From Fig. 10, it can be seen that, K_c varies in a little range, which is about from 26.6 to 29.6MPa·mm$^{0.34768}$. The above results indicates that K_c nearly keeps unchanged regardless of the change of local structure, and can be used as the fracture control parameter.

The stress intensity factor at interface edges is closely related to the external thermo-mechanical loads. It is necessary to find the relationship between them. As seen from Table 3, critical load varies monotonously as the splice width and fiberlayer thickness change, and K_c, which is a constant value, can't be used directly to predict critical load. Obviously, the stress intensity factor ${}^mK_c$ caused by mechanical loading should be proportional to the mechanical loading imposed. According to this principle, the critical tensile load F_c can be predicted as

$$F_c = {}^mK_c \times F_c\big|_{w=6,H=1} / {}^mK_c\big|_{w=6,H=1} \times S / S\big|_{H=1} \tag{15}$$

where ${}^mK_c = K_c - {}^tK$, K_c is critical stress intensity factor when w is taken as 6 mm and H is taken as 1 mm, ${}^tK$ is the critical stress intensity factor under thermal loading of ΔT=-100°C, S is the cross section area of specimens. Figs. 11 and 12 show the critical stress intensity factor and critical tensile load, respectively. The experimental values of stress intensity factors shown in Fig. 11 are obtained by using critical tensile loads tested from experiments. From Fig. 12, it can be seen that the predicted critical mechanical loads are in good agreement with experimental values. Based on the predicted values of stress intensity factors, the relationship between external loads and local stresses

at interface edges of the splices is established. For various kinds of structures, Eq. (15) can predict the critical mechanical load, and it is not neccesary to experimentally determine them one by one.

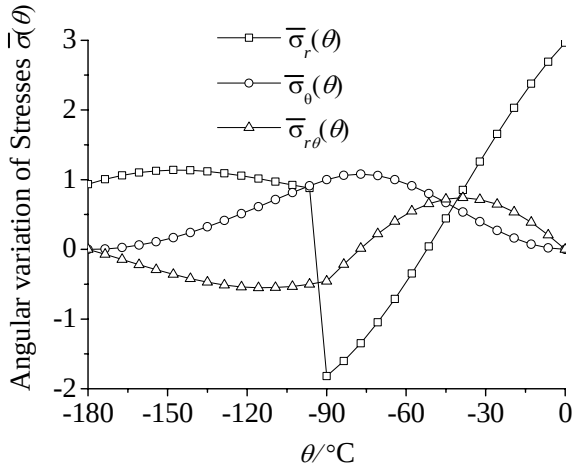

Figure 8. Angular variation of tresses around the interface edge *o*

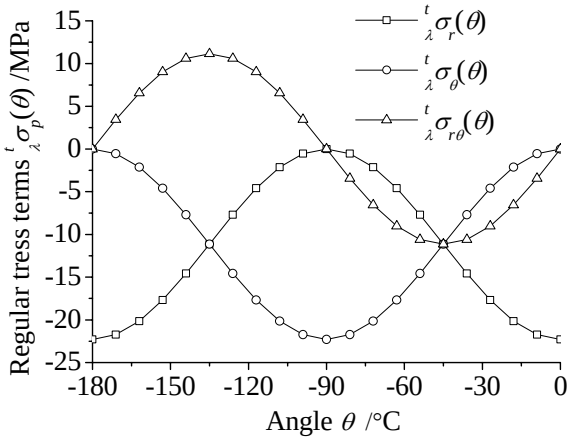

Figure 9. Regular stress terms around the interface edge *o*

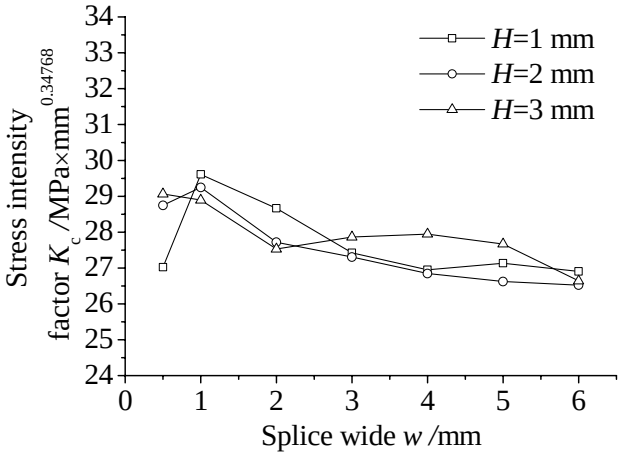

Figure 10. Critical stress intensity factor K_c of the interface edge *o*

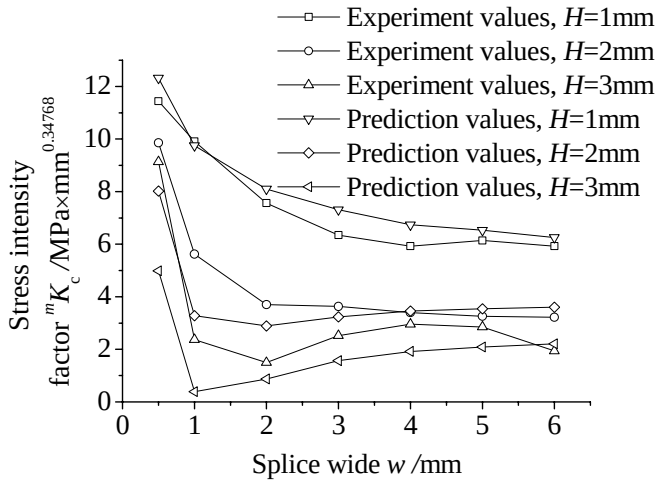

Figure 11. Critical stress intensity factor ${}^{m}K_{c}$ of the interface edge *o*

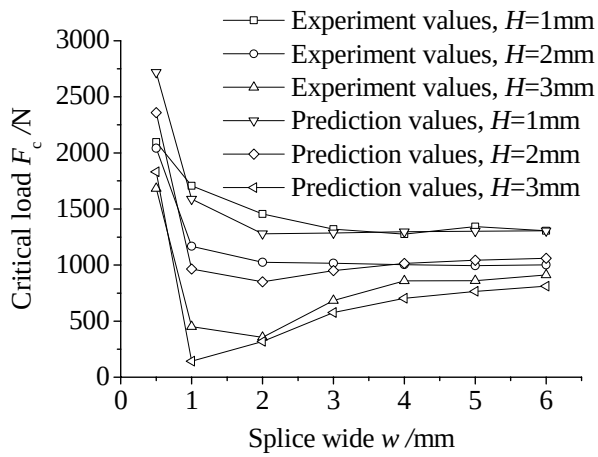

Figure 12. Critical load F_{c} of the interface edge *o*

5. Conclusions

The fracture behaviors of the splices in fiber metal laminates are investigated. The states of stresses at the interface edges of splices are analyzed based on a novel finite element method. A stress intensity factor based fracture criterion for the splice failure is established to predict critical tensile load. Through the results in this study, the following conclusions are drawn:

1) The critical stress intensity factor K_c under coupled thermo-mechanical loading can be used as local fracture criterion for the interface edges of the splices.
2) The critical stress intensity factor ${}^{m}K_c$ under mechanical loading can be used to predict the critical mechanical loading F_c.
3) Because the decrease of the splice width *w* will lead to the reduction of the stress intensity factor ${}^{t}K$ induced by residual thermal stresses, so it will make ${}^{m}K_c$ increase. Consequently, the critical mechanical loading F_c will increases.
4) Because the increase of the fiber-layer thickness *H* will lead to the increase of the stress intensity factor ${}^{t}K$ induced by residual thermal stresses, so it will cause ${}^{m}K_c$ to reduce. Consequently, the critical mechanical loading will decrease.

Acknowledgements

This study was sponsored by the National Natural Science Foundation of China under Grant No.51065008 and No.10662004, the Natural Science Foundation of Jiangxi Province under Grant No.2010GZW0013 and the Jinggang-Star training Plan for Young Scientists of Jiangxi Province under Grant No. 20112BCB23013.

References

[1] A. Vlot, J.W. Gunnink, Fiber metal laminates-an introduction. USA: Kluwer Academic Publisher, 2001.

[2] C.A.J.R. Vermeeren, T.H. Beumler, J.L.C.G. De Kanter, O.C. Van Der Jagt, B.C.L. Out, Glare design aspects and philosophies. Appl Comp Mat, 10(2003) 257-276.

[3] T.J. de Vries, A. Vlot, F. Hashagen, Delamination behavior of spliced Fiber Metal Laminates. Part 1. Experimental reslts. Comp Struct, 46(1999)131-145.

[4] F. Hashagen, R. de Borst, T. de Vries, Delamination behavior of spliced Fiber Metal Laminates. Part 2. Numerical investigation. Comp Struct, 46(1999) 147-162.

[5] T. Takamatsu, T. Shimokawa, T. Matsumura, Y. Miyoshi, Y. Tanabe, Evaluation of fatigue crack growth behaviour of Glare3 fiber/metal laminates using compliance method. Eng Fract Mech, 70(2003)2603-2616.

[6] Y.J. Guo, X.R. Wu, A phenomenological model for predicting crack growth in fiber-reinforced metal laminates under constant amplitude loading. Comput Sci Technol, 59(1999)1825-1831.

[7] R.C. Alderliesten, J. Schijve, S. van der Zwaag, Application of the energy release rate approach for delamination growth in Glare. Eng Fract Mech, 73 (2006) 697-709.

[8] R.C. Alderliesten, Analytical prediction model for fatigue crack propagation and delamination growth in Glare. Int J Fatigue, 29(2007) 628-646.

[9] P.Y. Chang, J.M. Yang, Modeling of fatigue crack growth in notched fiber metal laminates. Int J Fatigue, 30(2008)2165-2174.

[10] Marcela V. Cid Alfaro, Akke S.J. Suiker, Rene de Borst, Joris J.C. Remmers, Analysis of fracture and delamination in laminates using 3D numerical modeling. Eng Fract Mech, 76(6)(2009) 761-780.

[11] T.J. de Vries, A. Vlot, F. Hashagen, Delamination behavior of spliced Fiber Metal Laminates. Part 1. Experimental results. Comp Struct 46 (1999) 131-145.

[12] F. Hashagen, R. de Borst, T. de Vries, Delamination behavior of spliced Fiber Metal Laminates. Part 2. Numerical investigation. Comp Struct 46 (1999) 147-162.

[13] K.Y. Sze, H.T. Wang, H. Fan, A finite element approach for computing edge singularities in piezoelectric materials. Int J Solids Struct, 38(2001) 9233-9252.

[14] M.C. Chen, K.Y. Sze, A novel hybrid finite element analysis of bimaterial wedge problems. Eng Fract Mech, 68(2001)1463-1476.

[15] A. Barut, I. Guven, E. Madenci. Analysis of singular stress fields at junctions of multiple dissimilar materials under mechanical and thermal loading. Int J Solids Struct, 38(2001) 9077-9109.

Examination on a Criterion for a Debonding Fracture of Single Lap Joints from the Intensity of Singular Stress Field

Tatsujiro Miyazaki[1,*], **Nao-Aki Noda**[2], **Rong Li**[3], **Takumi Uchikoba**[3] **and Yoshikazu Sano**[2]

[1] Department of Mechanical Engineering Systems, University of the Ryukyus,
1 Senbaru, Nishihara-cho, Nakagami-gun, Okinawa 903-0213, Japan
[2] Department of Mechanical Engineering, Kyushu Institute of Technology,
1-1 Sensui-cho, Tobata-ku, Kitakyushu-shi, Fukuoka, 804-8550, Japan
[3] Department of Mechanical and Control Engineering, Graduate School of Engineering, Kyushu Institute of Technology,
1-1 Sensui-cho, Tobata-ku, Kitakyushu-shi, Fukuoka, 804-8550, Japan

* Corresponding author: t-miya@tec.u-ryukyu.ac.jp

Abstract In this study, the experimental adhesive strength is newly considered in terms of the singular stress appearing at the end of interface between the adhesive and adherent. Here the critical intensity of singular stress field is examined as the debonding criterion for all types of single lap joints under different adhesive thickness and overlap length. The intensity of singular stress can be evaluated by the application of the finite element method focusing on the stress value at the end element of the interface. It should be noted that except for the case of small overlap length the separation always occurs at the edge of the interface causing unstable growth and final brittle fracture. In this type of fracture it is found that the critical intensity of the stress singular field is constant independent of the adhesive thickness and overlap length.

Keywords Adhesion, Interface, Intensity of Singular Stress, Finite Element Method

1. Introduction

The requirements to packaging technology of semiconductors diversify with the miniaturization and high-performance of the electronics [1, 2]. The packages of semiconductors contain many various interfaces. For example, the connection of the semiconductor to the substrate, resin seal of semiconductor, multilayer structures composed of the dissimilar semiconductor materials. In order to ensure the reliability of the packages of semiconductors, the method for evaluating the debonding fracture strength properly is required [3 - 5]. Generally, the debonding strength of the dissimilar material joints depends on the material combination, load condition, adhesive condition and so on. Because the experimental evaluation of the adhesive strength is time-consuming job, the practical and convenient debonding fracture criterion and evaluation method are asked for.

Recently, the authors examined the experimental data for the butt joints of medium carbon steel bonded by epoxy resin under various adhesive thicknesses [6]. The debonding fracture criterion can be described by the constant value of the critical intensity of the singular stress field at the fracture, $K_{\sigma c}$, independent of the adhesive thickness [7]. When the joint is satisfied with the small scale yielding condition, the adhesive strength is predicted accurately by the debonding fracture criterion based on the intensity of the singular stress field [8, 9]. In this study, the debonding criterion for all types of single lap joints (SLJs) will be discussed under various adhesive thickness and overlap length in terms of the critical intensity of singular stress field as $K_{\sigma c}$ = constant. The recent experimental results performed on SLJs by Park *et al* [10] will be used. In this experiment, Park *et al* evaluated the damage zone size at fracture while considering the non-linear deformation behavior of the adhesive and adherent. Although the various methods were examined, the debonding fracture criterion cannot be expressed simply and conveniently [11, 12].

2. Experimental results of single lap joint

In this study, the experimental results obtained by Park *et al* [10] will be used in order to examine the validation of evaluation method of the adhesive strength. In the experiments, Aluminum alloy 6061-T6 and epoxy resin were used as adherent and adhesive, respectively. Table 1 shows the mechanical properties of the adherent and adhesive. Figure 1 shows the specimen configuration. Table 2 and Figure 2 show the experimental tensile adhesive strength P_{af}. As for all specimens except for specimen A10, the relation between the load and displacement is almost linear. Therefore, it can be considered that the fractures were caused by the unstable growth of the interfacial debonding crack which was initiated from the corner edge. The results bring the validation of the evaluation based on the intensity of the singular stress field. When the overlap length becomes long under constant adhesive thickness condition, the adhesive strength tends to increase; when the adhesive layer becomes thick under constant overlap length, the adhesive strength does not change remarkablely. Figure 3 shows the average shear stress at the fracture, τ_c. When l_2 is smaller than about 15mm, the τ_c becomes constant at about 28.3MPa. However, when l_2 is larger than about 15mm, the τ_c tends to decrease. The fracture is caused by the general yielding of the adhesive layer when the overlap length is small enough; in this case, the τ_c becomes constant. In this study, it is supposed that the cohesive fracture occurs when l_2 < 15mm and the adhesive fracture occurs when l_2 > 15mm. Therefore, although the fracture criterion for SLJ having small overlap length can be described by the average shear stress at the fracture, that for SLJ having long overlap length cannot be described by the stress.

Table 1 Material properties [10)]

Material	E [GPa]	ν
Adherent 6061-T6	68.9	0.30
Adhesive Epoxy resin	4.2	0.45

E : Young's modulus, ν : Poisson ratio

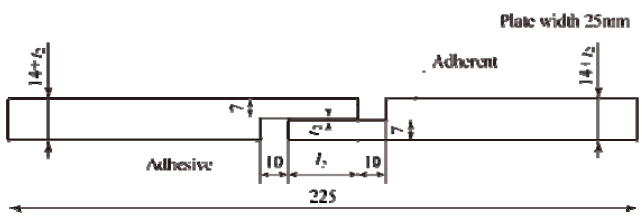

Figure 1 Specimen configurations [10)]

Table 2 Experimental tensile adhesive strength by Park *et al* [10)]

(a) t_2 = constant condition

Specimen	l_2 [mm]	t_2 [mm]	P_{af} [kN]
A10	10	0.15	6.87
A15	15	0.15	10.57
A20	20	0.15	12.41
A25	25	0.15	14.17
A30	30	0.15	14.56
A35	35	0.15	16.41
A40	40	0.15	18.09
A50	50	0.15	18.22

(b) l_2 = constant condition

Specimen	l_2 [mm]	t_2 [mm]	P_{af} [kN]
A25	25	0.15	14.17
A25-30	25	0.30	14.32
A25-45	25	0.45	14.26
A25-90	25	0.90	14.19
A30	30	0.15	14.56
A30-30	30	0.30	16.91
A30-45	30	0.45	16.12
A30-90	30	0.90	15.37

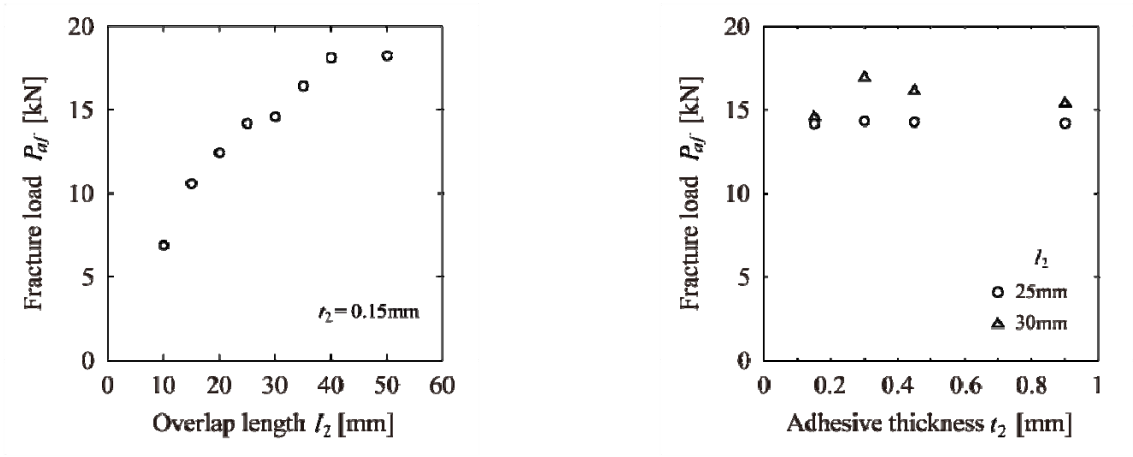

(a) $t_2 = \text{constant condition}$ (b) $l_2 = \text{constant condition}$

Figure 2 Experimental adhesive strength P_{af} [10)]

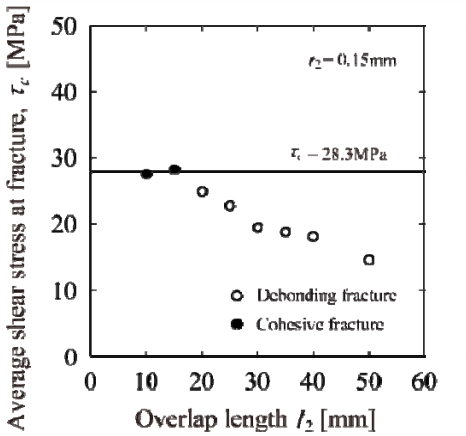

Figure 3 Average shear stress at fracture of specimens with t_2 = 0.15 mm [10)]

3. Analysis

3.1. Analysis model and method

Figure 4 shows the schematic illustration of the analysis model. Dundurs' parameters at point O are α = -0.8699 and β = -0.06642. The order of stress singularity is two different real values λ_1 = 0.6062 and λ_2 = 0.9989. When the eigenvalue equation has two different real roots, the stresses at a distance r on the interface from the corner edge O can be expressed as follows.

$$\sigma_y = \frac{K_{\sigma 1}}{r^{1-\lambda_1}} + \frac{K_{\sigma 2}}{r^{1-\lambda_2}}, \quad \tau_{xy} = \frac{K_{\tau 1}}{r^{1-\lambda_1}} + \frac{K_{\tau 2}}{r^{1-\lambda_2}} \tag{1}$$

Here, σ_y is the stress in the y direction, τ_{xy} is the shear stress.

In this analysis, the method proposed by Noda *et al* [13] is used. In this analysis, the elements near the edge corners of all models were set so as to be same size and shape. And then, minimum size of the element at the edge corner, $e_{\min}$, is changed, the influence of the mesh pattern on the stress distribution is investigated. The $e_{\min}$ value is set to 3^{-8}, 3^{-9}, 3^{-10} and 3^{-11}.

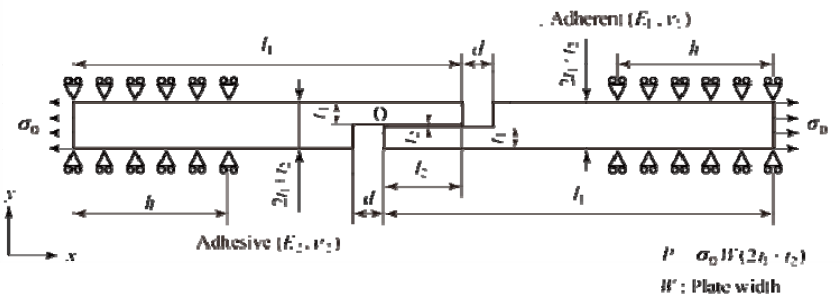

Figure 4 Analysis model and boundary condition

3.2. Characteristics of singular stress field at the edge corner

The characteristics of the singular stress field at the corner edge are mentioned using the analysis results of the specimens A25, A50 and A25-90. Figure 5 shows the relationship between the $\sigma_{y,FEM}^{\mathrm{A50}}/\sigma_{y,FEM}^{\mathrm{A25}}$, $\tau_{xy,FEM}^{\mathrm{A50}}/\tau_{xy,FEM}^{\mathrm{A25}}$ and r under the applied stress σ_0 = 1MPa. Then, Figure 6 shows the relationship between the $\sigma_{y0,FEM}^{\mathrm{A50}}/\sigma_{y0,FEM}^{\mathrm{A25}}$, $\tau_{xy0,FEM}^{\mathrm{A50}}/\tau_{xy0,FEM}^{\mathrm{A25}}$ and $e_{\min}$. When t_2 are set constant, the stress ratios almost become constant independent of $e_{\min}$. Figure 7 shows the relationship between the $\sigma_{y,FEM}^{\mathrm{A25-90}}/\sigma_{y,FEM}^{\mathrm{A25}}$, $\tau_{xy,FEM}^{\mathrm{A25-90}}/\tau_{xy,FEM}^{\mathrm{A25}}$ and r under the applied stress σ_0 = 1MPa. Then, Figure 8 shows the relationship between the $\sigma_{y0,FEM}^{\mathrm{A25-90}}/\sigma_{y0,FEM}^{\mathrm{A25}}$, $\tau_{xy0,FEM}^{\mathrm{A25-90}}/\tau_{xy0,FEM}^{\mathrm{A25}}$ and $e_{\min}$. The stress distributions of the specimen A25-90 are different from those of the specimen A50. That is because the moment which is applied to the adhesive layer changes depending on the adhesive thickness. However, when the r is smaller than about 10^{-4} mm, the $\sigma_{y0,FEM}^{\mathrm{A25-90}}/\sigma_{y0,FEM}^{\mathrm{A25}}$ and $\tau_{xy,FEM}^{\mathrm{A25-90}}/\tau_{xy,FEM}^{\mathrm{A25}}$ almost become constant. Then, the stress ratios at the edge corner, $\sigma_{y,FEM}^{\mathrm{A25-90}}/\sigma_{y,FEM}^{\mathrm{A25}}$ and $\tau_{xy0,FEM}^{\mathrm{A25-90}}/\tau_{xy0,FEM}^{\mathrm{A25}}$, become constant independent of the $e_{\min}$. From the results, the stresses on the interface near the corner edge are expressed with as follows independent of the t_2 and l_2.

$$\sigma_y = \frac{K_{\sigma 1}}{r^{1-\lambda_1}} + \frac{K_{\sigma 2}}{r^{1-\lambda_2}} \cong K_\sigma \left(\frac{1}{r^{1-\lambda_1}} + \frac{C_\sigma}{r^{1-\lambda_2}} \right), \tag{2}$$

$$\tau_{xy} = \frac{K_{\tau 1}}{r^{1-\lambda_1}} + \frac{K_{\tau 2}}{r^{1-\lambda_2}} \cong K_\tau \left(\frac{1}{r^{1-\lambda_1}} + \frac{C_\tau}{r^{1-\lambda_2}} \right) \tag{3}$$

Here, C_σ and C_τ are constant. The intensities of singular stress field of the reference problem and the unknown problem are denoted with K_σ and K_σ^*, respectively. Then, the stresses in the y direction at the edge corner of the unknown problem and the reference problem, which are obtained from the FEM analysis, are denoted with $\sigma_{y0,FEM}$ and $\sigma_{y0,FEM}^*$, respectively. From Equation (2), the relation between K_σ / K_σ^* and $\sigma_{y0,FEM} / \sigma_{y0,FEM}^*$ can be expressed as follows.

$$\frac{K_\sigma}{K_\sigma^*} = \frac{\sigma_{y0,FEM}}{\sigma_{y0,FEM}^*} \tag{4}$$

If the K_σ^* has been solved, the $\sigma_{y0,FEM}$ is equivalent with the K_σ because the $\sigma_{y0,FEM}^*$ can be obtained from the FEM analysis of the reference problem. The $\tau_{xy0,FEM}$ is also equivalent with the K_τ.

As shown in Figure 6, it is found that the different between $\sigma_{y0,FEM}^{\mathrm{A50}}/\sigma_{y0,FEM}^{\mathrm{A25}}$ and $\tau_{xy0,FEM}^{\mathrm{A50}}/\tau_{xy0,FEM}^{\mathrm{A25}}$ tends to become small with the r decreasing. Then, from Figure 8, the different between $\sigma_{y0,FEM}^{\mathrm{A25-90}}/\sigma_{y0,FEM}^{\mathrm{A25}}$ and $\tau_{xy0,FEM}^{\mathrm{A25-90}}/\tau_{xy0,FEM}^{\mathrm{A25}}$ tends to become small with the r decreasing. From Figures 6 and 8, the relations of $\sigma_{y0,FEM}^{\mathrm{A50}}/\sigma_{y0,FEM}^{\mathrm{A25}} = \tau_{xy0,FEM}^{\mathrm{A50}}/\tau_{xy0,FEM}^{\mathrm{A25}}$ and $\sigma_{y0,FEM}^{\mathrm{A25-90}}/\sigma_{y0,FEM}^{\mathrm{A25}} = \tau_{xy0,FEM}^{\mathrm{A25-90}}/\tau_{xy0,FEM}^{\mathrm{A25}}$ can be confirmed. This means $\sigma_{y0,FEM}/\sigma_{y0,FEM}^* = \tau_{xy0,FEM}/\tau_{xy0,FEM}^*$, that is, following equation.

$$\frac{K_\sigma}{K_\sigma^*} = \frac{K_\tau}{K_\tau^*} \tag{5}$$

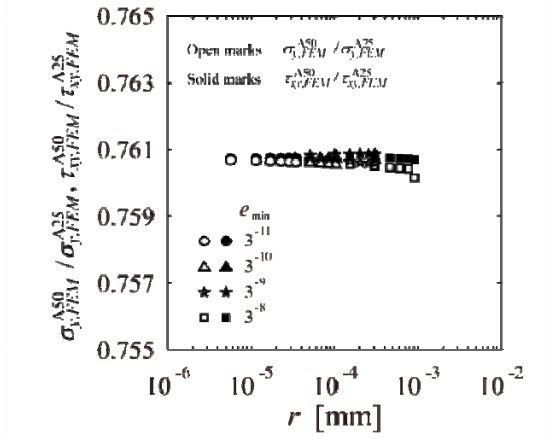

Figure 5 Relationship between $\sigma_{y,FEM}^{A50} / \sigma_{y,FEM}^{A25}$, $\tau_{xy,FEM}^{A50} / \tau_{xy,FEM}^{A25}$ and r when σ_0 = 1MPa

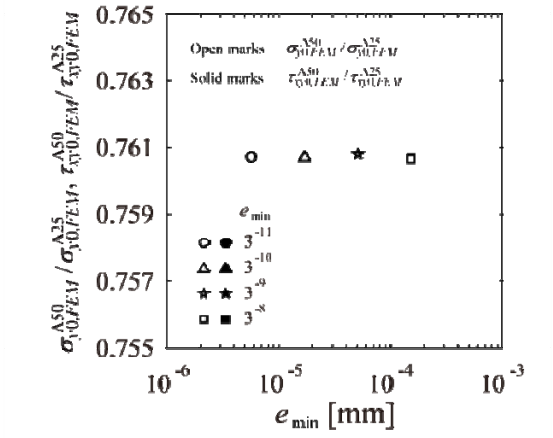

Figure 6 Relationship between $\sigma_{y0,FEM}^{A50} / \sigma_{y0,FEM}^{A25}$, $\tau_{xy0,FEM}^{A50} / \tau_{xy0,FEM}^{A25}$ and e_{min} when σ_0 = 1MPa

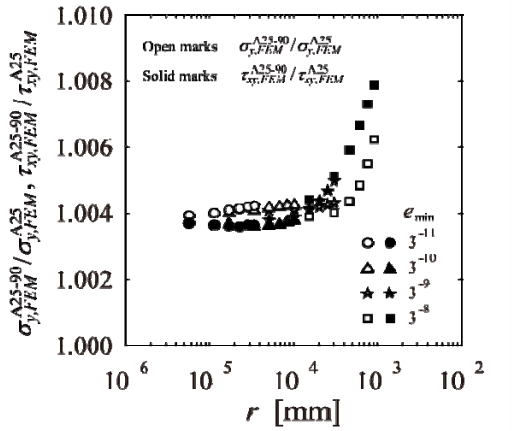

Figure 7 Relationship between $\sigma_{y,FEM}^{A25-90} / \sigma_{y,FEM}^{A25}$, $\tau_{xy,FEM}^{A25-90} / \tau_{xy,FEM}^{A25}$ and r when σ_0 = 1MPa

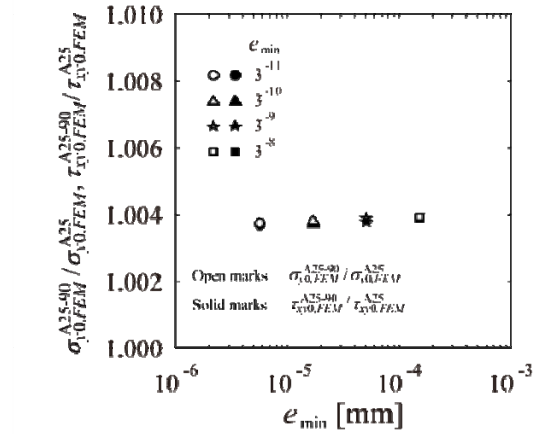

Figure 8 Relationship between $\sigma_{y0,FEM}^{A25-90} / \sigma_{y0,FEM}^{A25}$, $\tau_{xy0,FEM}^{A25-90} / \tau_{xy0,FEM}^{A25}$ and e_{min} when σ_0 = 1MPa

4. Debonding fracture criterion based on the intensity of singular stress field

Figure 9 shows the relation between $K_\sigma|_{P=1} / K_\sigma^{A25}|_{P=1}$ and l_2, where $K_\sigma|_{P=1}$ is the intensity of the singular stress field under P = 1N, and $K_\sigma^{A25}|_{P=1}$ is the $K_\sigma|_{P=1}$ of the specimen A25. When the l_2 is larger than 15mm, the $K_\sigma|_{P=1}$ tends to decrease. Figure 10 shows the relation between $K_{\sigma c} / K_{\sigma c}^{A25}$ and l_2, where $K_{\sigma c}$ is the intensity of the singular stress field under $P = P_{af}$, and $K_{\sigma c}^{A25}$ is the $K_{\sigma c}$ of the specimen A25. When the l_2 is smaller than 15mm, the $K_{\sigma c} / K_{\sigma c}^{A25}$ tends to increase. However, when the l_2 is larger than 15mm, the $K_{\sigma c} / K_{\sigma c}^{A25}$ becomes constant irrelevant to the l_2. That is because the fracture mode changed from the cohesive fracture to the adhesive fracture. It is confirmed that the solid line is the average of $K_{\sigma c} / K_{\sigma c}^{A25}$ of all specimens except for specimens A10 and A15. The open circle marks are distributed near the solid line within about 10% error.

Figure 11 shows the relation between $K_\sigma|_{P=1} / K_\sigma^{A25}|_{P=1}$ and t_2. When the t_2 is larger than 45mm, the $K_\sigma|_{P=1} / K_\sigma^{A25}|_{P=1}$ almost becomes constant. Figure 12 shows the relation between

$K_{\sigma c}/K_{\sigma c}^{\mathrm{A25}}$ and t_2. The $K_{\sigma c}/K_{\sigma c}^{\mathrm{A25}}$ values are distributed near the solid line within about 10% error.

Figure 13 shows the $K_{\sigma c}/K_{\sigma c}^{\mathrm{A25}}$ values. The average of $K_{\sigma c}/K_{\sigma c}^{\mathrm{A25}}$ values was about 0.997. The $K_{\sigma c}/K_{\sigma c}^{\mathrm{A25}}$ values are distributed near the solid line within about 10% error independent of the l_2 and t_2. It is concluded that the debonding criterion for all types of SLJs having different adhesive thickness and overlap length can be described by the critical intensity of singular stress field $K_{\sigma c}$ = constant.

5. Conclusion

In this study, the debonding fracture criterion for the SLJ having various adhesive length and overlap length was examined. It is found that the singular stress field at the edge corner can be expressed with the same formula even if the adhesive length and overlap length are different. Then when the overlap length is short enough, the fracture criterion can be expressed with the average shear stress at the fracture; when the overlap length is longer than a certain length, the criterion can be expressed with the critical intensity of the singular stress field.

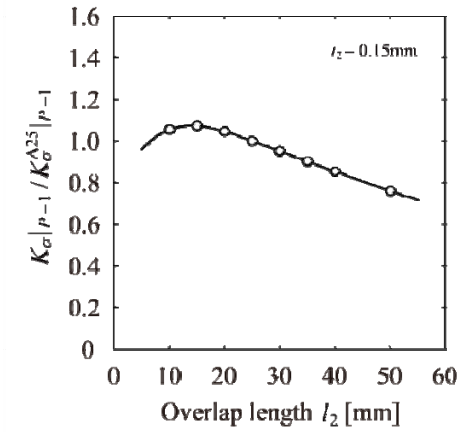

Figure 9 Relationship between $K_\sigma|_{P=1}/K_\sigma^{\mathrm{A25}}|_{P=1}$ and l_2 when P = 1N

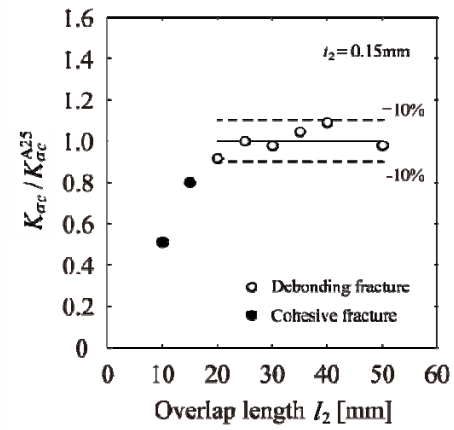

Figure 10 Relationship between $K_{\sigma c}/K_{\sigma c}^{\mathrm{A25}}$ and l_2

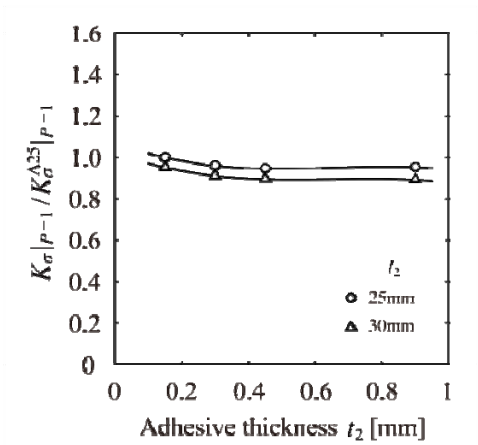

Figure 11 Relationship between $K_\sigma|_{P=1}/K_\sigma^{\mathrm{A25}}|_{P=1}$ and t_2 when P = 1N

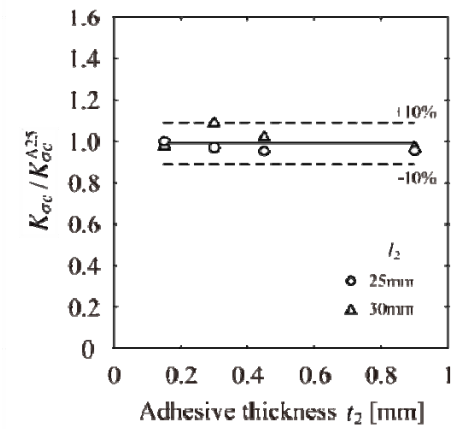

Figure 12 Relationship between $K_{\sigma c}/K_{\sigma c}^{\mathrm{A25}}$ and t_2

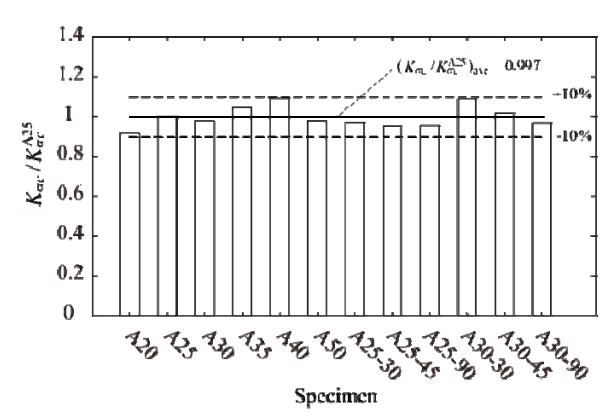

Figure 13 Comparison between $K_{\sigma c}\big/K_{\sigma c}^{\mathrm{A25}}$ values

References

[1] M. Yasuda, *Hitachi Chemical Technical Report*, No. 40 (2003), pp. 7-12 (in Japanese).
[2] M. Nakamura, *Panasonic Technical Journal*, Vol. 56, No. 4 (2008), pp. 9-16 (in Japanese).
[3] T. Shibuya, *Journal of Japan Institute of Electronics Packaging*, Vol. 7, No. 7 (2008), pp. 9-16 (in Japanese).
[4] M. Shiratori, *Trans. JSME*, Vol. 60, No. 577, Series A (1994), pp. 1905-1912 (in Japanese).
[5] R. Yuuki, *Mechanics of Interface*, Baifukan, (1993) , Tokyo.
[6] Y. Suzuki, *JSME International Journal*, Vol. 30， No. 265 (1987), pp. 1042-1051.
[7] N. -A. Noda, T. Miyazaki, K. Oda, *Proceedings of 3rd ACMFMS*, (2012), pp. 813.
[8] Z. Qian, A. R. Akisanya, *Acta Materialia*, Vol. 46, No. 14 (1998), pp. 4895 – 4904.
[9] A. Mintzas, D. Nowell, *Eng. Fract. Mech.*, 80 (2012), pp. 13 – 27.
[10] J. -H. Park, J. -H. Choi, J. -H. Kweon, *Composite Structures*, Vol. 92 (2010), pp. 2226-2235.
[11] H. Kyogoku, T. Sugibayashi, K. Ikegami, *Trans. JSME*, Vol. 52, No. 476, Series A (1986), pp. 1050-1057 (in Japanese).
[12] K. Nono, T. Nagahiro, *Trans. JSME*, Vol. 52, No. 479, Series A (1986), pp. 1698-1707 (in Japanese).
[13] N.-A. Noda, Y. Zhang, K. -T. Takaishi, X. Lan, *Trans. JSME*, Vol. 78, No. 789, Series A (2011), pp. 651-655 (in Japanese).

Fatigue delamination growth of composite laminates with fiber bridging: Theory and simulation

Lei Peng[1], Jifeng Xu[1,*]

[1] Beijing Aeronautical Science and Technology Research Institute, Beijing 102211, China
* Corresponding author: xujifeng@comac.cc

Abstract Mode I fatigue delamination growth rates and thresholds of composite laminates have been experimentally studied. Due to the fiber bridging generated across fracture interface, additional fracture resistance was found rising with crack growth, which make the traditional Paris law and threshold model unsuitable. Therefore, novel models taking the normalized strain energy release rate as fracture governing parameter were developed. The delamination resistance during fatigue crack growth caused by interface fracture and fiber bridging was totally evaluated by a new parameter namely fatigue delamination resistance G_{cf}. Excellent agreement with the experimental data was achieved by the normalized fatigue delamination growth rate and threshold models. Numerical simulation method for fatigue delamination was subsequently investigated. The fracture constitutive behavior with fiber bridging was defined by a tri-linear cohesive zone law, in which fatigue damage was introduced by a parameter available for both fracture and bridging zones. Development of the degradation law of the damage parameter is based on the normalized fatigue delamination models, enabling a direct link with experimental data. The simulation was implemented using user defined interface elements within finite element software ABAQUS.

Keywords Delamination, Fatigue crack growth, Cohesive zone, Damage degradation law, Composites

1. Introduction

Carbon fiber reinforced polymer composites are widely used in aircraft structures due to property advantages. Meanwhile, it brings design and analysis challenges caused by the ply-by-ply formulation of composites which is totally different from the traditional metal structures [1]. The failures in composite structures are mainly due to the defect, environment and out-of-plane sensitivities of the materials.

Delamination is one of the key factors for composites from damage initiation to final failures. The delamination growth behaviors have gained significant attention in the research communities in the past decade [2-7]. However, the delamination behavior of composites has not been completely understood under complex conditions, such as multidirectional interfaces, fatigue loading and fiber bridging case [8].

Linear elastic fracture mechanics is commonly utilized to study the interlaminar fracture of composites. Strain energy release rate (SERR) is accepted as the fracture governing parameter to evaluate interlaminar fracture toughness for composites rather than the stress intensity factor (SIF) for metals due to the simplicity of the calculation. Experimental studies and test methods for delamination resistance have been reviewed by Davies et al. [9] and Brunner et al. [10], numerical studies reviewed by Tay [11], respectively.

Multidirectional interface and fiber bridging are two important factors in real engineering applications, which bring significant influence on the interlaminar fracture of composite structures. As a summarized result from reports in literature [6, 12-14], multidirectional laminates always exhibit higher interlaminar fracture toughness, which is assumed to be caused by extrinsic toughening mechanisms such as blunted crack tips or deviation of the crack from the main crack plane to the adjacent layers and some in-ply energy absorption [15]. Fiber bridging could also bring considerable delamination resistance due to the energy absorbed in the bridging zone behind the

crack tip. For certain composite material systems, fiber bridging was found unavoidable and can be enhanced by multidirectional ply orientations [16]. Several laws [2, 17, 18] have been developed based on bridging zone model to evaluate the relationship between the fiber bridging stress and the crack tip opening displacement (CTOD). FEM cohesive element considering the fiber bridging effect was developed based on the bridging zone laws [19, 20].

For fatigue delamination propagation studies on composites, a Paris Law analogous linear log-log relationship between the fatigue crack growth rate and the SERR has been established by some significant fundamental works [21-26]. Fatigue degradation laws [27-30] based on cohesive interface elements and the Paris Law are developed to perform a numerical study and predict the fatigue crack growth by FEM programs. However, the Paris Law will become unsuitable for fiber bridging cases as the fatigue crack growth rate and threshold significantly affected by the additional delamination resistance. Remarkable R-curve effects on the fatigue delamination have been observed and analyzed by Hojo et al. [5] for Zanchor-reinforced laminates, Argülles et al. [31] for unidirectional laminates with fiber bridging and Shivakumar et al. [32] for woven/braided fiber composites. A bridging model was developed specially for fatigue delamination by Gregory and Spearing [33], finding that the scatter of crack propagation data was significantly reduced by applying the model.

A novel fatigue delamination resistance parameter was introduced by Peng et al. [8, 34, 35] to quantitatively evaluate the effect of R-curves on the fatigue delamination growth. Normalized fatigue crack growth rate and threshold model taking the ratio of SERR to the fatigue delamination resistance as the governing fracture parameter were subsequently developed. Excellent agreement with experiments was obtained by applying the models on experimental data from carbon/bismaleimide composite laminates.

Based on the normalized fatigue delamination model, the study presented here attempt to develop a numerical model to predict the fatigue delamination by interface elements. A tri-linear bridging zone model is adopted to simulate the fiber bridging effect. The normalized SERR is taken as the damage parameter to introduce fatigue damage by a degradation law. Numerical validation is performed by UMAT subroutine in commercial FEM software ABAQUS to show the ability of the model.

2. Model Description

2.1. Fatigue delamination growth model

A simple form of Paris Law for composites has developed by Wikins [36] and Singh and Greenhalgh [24], shown as:

$$\frac{\mathrm{d}a}{\mathrm{d}N} = A(\Delta G)^p \tag{1}$$

where da/dN is the propagation rate of delamination, ΔG the total SERR range in a fatigue cycle, A and p material constants.

For fiber bridging laminates, a normalized SERR was proposed instead to evaluate the effect of R-curve on the fatigue crack growth, express as:

$$g_{\max}(a) = \frac{G_{\max}(a)}{G_{\mathrm{cf}}(a)} \tag{2}$$

where $G_{cf}(a)$ is the fatigue delamination resistance, defined as the critical energy release rate during fatigue crack growth. The normalized Paris Law was thus reformed as:

$$\left(\frac{\mathrm{d}a}{\mathrm{d}N}\right)_a = C'(g_{\max}(a))^r \tag{3}$$

where C' and r are the new fatigue constants.

A normalized fatigue threshold parameter could also be proposed based on the fatigue delamination resistance, shown as:

$$g_{\mathrm{th}} = \frac{G_{\mathrm{th}}(a)}{G_{\mathrm{cf}}(a)} \tag{4}$$

2.2. Calculation of fatigue delamination resistance

The "compliance approach" [35] to obtain the fatigue delamination resistance, G_{cf}, is briefly introduced here. The approach is developed for fiber bridging cases and based on the following hypothesis: the delamination resistance of fatigue specimen is equal to the value of corresponding static specimen which exhibits the same force–displacement behavior. According to "compliance approach", the fatigue delamination resistance at certain crack length, a_1, could be determined by comparing the normalized compliance of fatigue and static specimens. The procedure was summarized in the following equation:

$$\begin{aligned} &\text{if } \frac{\bar{C}_{\mathrm{f}}(a_1)}{\bar{C}_{\mathrm{s}}(a_1)} - 1 < -\varepsilon_0 \\ &\qquad G_{\mathrm{cf}}(a_1) = G_{\mathrm{c}}(a\big|_{\bar{C}_{\mathrm{s}}(a)=\bar{C}_{\mathrm{f}}(a_1)}) \\ &\text{else} \\ &\qquad G_{\mathrm{cf}}(a_1) = G_{\mathrm{c}}(a_1) \end{aligned} \tag{5}$$

where $\bar{C}$ is the normalized compliance of specimen, calculated by Eq. (6). ε_0 is the critical tolerance to consider experimental scatters of the compliance. The subscript "f" and "s" indicate the fatigue and static specimens, respectively.

$$\bar{C} = \frac{1}{m} bh^3 \tag{6}$$

where m is the slope of force-displacement curve of the specimen, b and h the width and half thickness, respectively.

2.3. Fiber bridging zone model

The mode I fiber bridging zone model is discussed here, as illustrated in Fig. 1. The SERR for double cantilever beam (DCB) specimen could be calculated using the equation below [37]:

$$G_{\mathrm{I}} = \frac{3Pd}{2b(a+\chi h)} \frac{F}{N'} \tag{7}$$

where F and N' are correction factor for large displacements and load-block effect, respectively. χ is a correction for crack tip displacement and rotation, which allows for the beam not being perfectly built in. Generally, χh value can be obtained experimentally by plotting the cubic root of compliance as a function of crack length and determining the intercept on the x-axies [38]. For fiber

bridging cases, however, the compliance could be reduced by the bridging fibers, which results in a larger wrong value of χ. According to [8], experimental data for the crack length within significant bridging zone should be excluded during the fitting procedure to get the correct χ value.

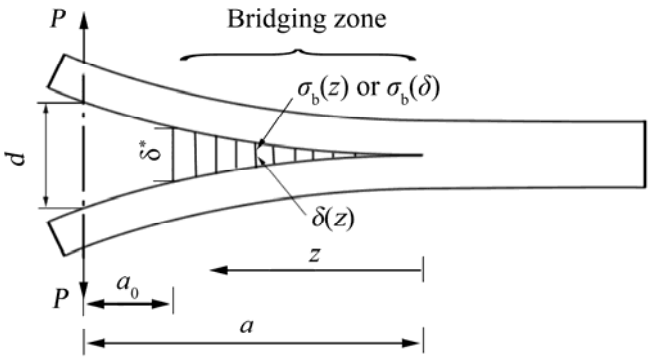

Figure 1. Illustration of fiber bridging zone for DCB specimen

A bridging zone model to calculate the bridging stress σ_b versus the CTOD δ was derived by Tamuzs et al. [18]:

$$G_c = \int_0^{\delta^*} \sigma_b(\delta)\mathrm{d}\delta + G_0 \tag{8}$$

where G_0 and G_c indicate the initial and total SERR, respectively. δ^* is the crack opening displacement at the pre-crack tip. The distribution of bridging stress could thus be experimentally determined by differentiating Eq. (8) with respect to δ^*.

2.4. Tri-linear interface element model

To simplify the numerical model, the fiber bridging behavior is described by a tri-linear constitutive law shown in Fig. 2, although the real function of bridging stress is nonlinear.

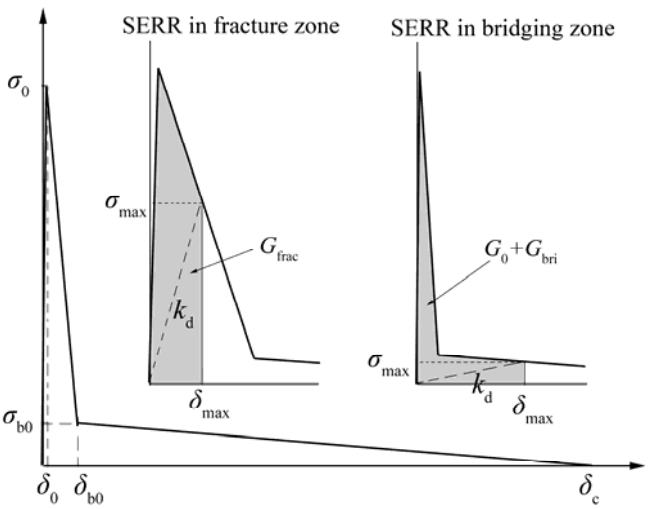

Figure 2. Illustration of the tri-linear cohesive constitutive law

The σ_0 and σ_{b0} in Fig. 2 indicate the strength at the start of fracture zone and bridging zone, respectively, while δ_0 and δ_{b0} indicate the corresponding displacement values. δ_c is the critical displacement for the final failure of the element. δ_{max} is the maximum displacement for the element being loaded and σ_{max} is the corresponding stress value. The constitutive relationship could thus be expressed as:

$$\sigma_{max} = \begin{cases} k_0\delta_{max} & \text{for } \delta_{max} \le \delta_0 \\ \sigma_0 + \dfrac{\sigma_{b0}-\sigma_0}{\delta_{b0}-\delta_0}\left(\delta_{max}-\delta_0\right) & \text{for } \delta_0 < \delta_{max} \le \delta_{b0} \\ \sigma_{b0} - \dfrac{\sigma_{b0}}{\delta_c-\delta_{b0}}\left(\delta_{max}-\delta_{b0}\right) & \text{for } \delta_{b0} < \delta_{max} \le \delta_c \\ 0 & \text{for } \delta_{max} > \delta_c \end{cases} \tag{9}$$

where $k_0 = \sigma_0/\delta_0$, presents the initial stiffness. The stiffness of damaged element could thus be expressed as:

$$k_d = \frac{\sigma_{max}}{\delta_{max}} \tag{10}$$

The calculation of SERR is summarized as follows:

$$G_{max} = \begin{cases} \dfrac{1}{2}\sigma_{max}\delta_{max} & \text{for } \delta_{max} \le \delta_0 \\ \dfrac{1}{2}\left((\sigma_0+\sigma_{max})\delta_{max} - \sigma_0\delta_0\right) & \text{for } \delta_0 < \delta_{max} \le \delta_{b0} \\ G_0 + \dfrac{1}{2}(\sigma_{max}+\sigma_{b0})(\delta_{max}-\delta_{b0}) & \text{for } \delta_{b0} < \delta_{max} \le \delta_c \\ G_T & \text{for } \delta_{max} > \delta_c \end{cases} \tag{11}$$

where the initial and total critical SERR (G_0 and G_T) have the expression shown as:

$$G_0 = \frac{1}{2}\left((\sigma_0+\sigma_{b0})\delta_{b0} - \sigma_0\delta_0\right) \tag{12}$$

$$G_T = G_0 + \frac{1}{2}\left(\sigma_{b0}(\delta_c-\delta_{b0})\right) \tag{13}$$

2.5. Fatigue degradation law

The damage parameter of tri-linear cohesive element is defined by displacement as follows:

$$d = \frac{\delta_{max}-\delta_0}{\delta_{b0}-\delta_0} \tag{14}$$

From the expression, d has a value from 0 to 1 while the element in fracture zone has a value from 1 to $(\delta_c-\delta_0)/(\delta_{b0}-\delta_0)$ in bridging zone. This definition implies that the crack tip is at the end of fracture zone where d equal to 1, which is in accordance with the linear elastic fracture mechanics. For a tri-linear cohesive element, the damage is the sum of three parts:

$$d = d_s + d_f + d_b \tag{15}$$

where the subscript “s”, “f” and “b” indicate quasi-static, fatigue and bridging damage, respectively.

Fig. 3 presents the illustration of the fatigue damage model of the tri-linear cohesive element to

simulate fatigue crack growth of DCB specimen. The fatigue damage is activated only in the fracture zone, which means the elements in bridging zone will not be degraded under cyclic loading. This hypothesis is supported by the experiment which shows that the damage in bridging zone under fatigue and static loading is equivalent for mode I delamination.

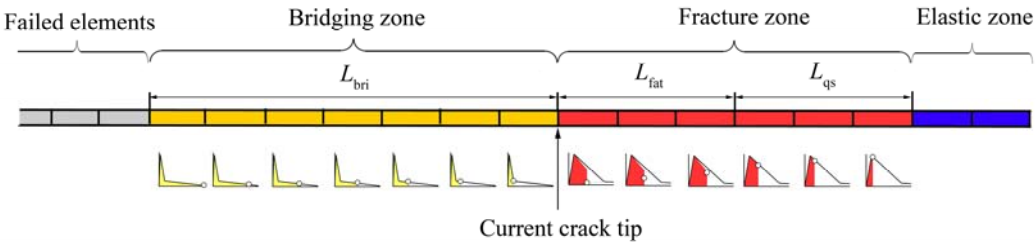

Figure 3. Damage of elements in fracture and bridging zones

A fatigue damage algorithm developed by Harper and Hallett [27] is used to link the fatigue crack growth law with the damage of cohesive elements, shown as:

$$\frac{\partial d_{\mathrm{f}}}{\partial N}=\frac{1-d_{\mathrm{s}}-d_{\mathrm{f,u}}}{L_{\mathrm{fat}}}\frac{\partial a}{\partial N} \tag{16}$$

where d_{f} and d_{s} are the fatigue and static damage, respectively. $d_{\mathrm{f,u}}$ is the unwanted fatigue damage defined by an equivalent σ-δ response under fatigue loading. By estimating the fracture zone using the normalized SERR and assuming the fatigue damage length occupy half of fracture zone, the fatigue damage law is given:

$$\frac{\partial d_{\mathrm{f}}}{\partial N}=\frac{1-d_{\mathrm{s}}-d_{\mathrm{f,u}}}{0.5\left(\dfrac{G_{\max}}{G_0}\right)L_{\mathrm{cz,f}}}\frac{\partial a}{\partial N} \tag{17}$$

where $L_{\mathrm{cz,f}}$ is the fully developed numerical fracture zone length determined by a quasi-static analysis [27].

Once the total damage d reaches the value of 1, the fatigue degradation law is suppressed and the element enters the bridging zone.

3. Results

3.1. Bridging stress

The quasi-static and fatigue delamination growth law were determined by T700/QY811 carbon/bismaleimade unidirectional laminates. Details of the specimens and experiments could be found in the authors' previously published papers [1, 8, 35].

The bridging stress calculated from experimental data by Eq. (8) is presented in Fig. 4. The actual nonlinear σ_{b}-δ response is translated to the numerical response in dotted line, which ensures the total bridging energy are equivalent by making $G_{\mathrm{A}} = G_{\mathrm{B}}$.

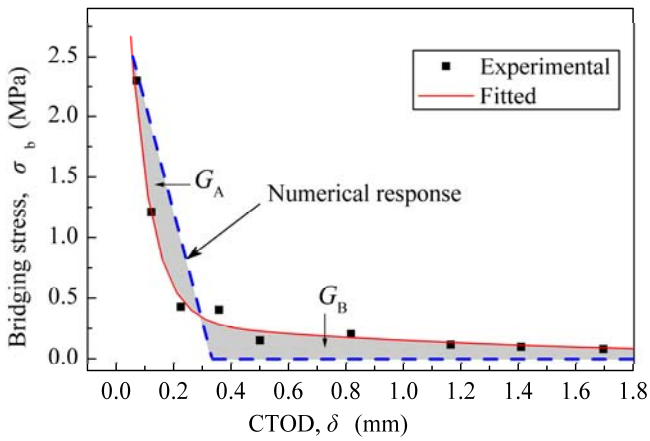

Figure 4. The experimental and numerical response between bridging stress and displacement

3.2. Fatigue crack growth rates and thresholds

The data reduction process of fatigue crack growth rates and thresholds could be found in [8]. The results are given in Fig. 5 here by applying the normalized law expressed in Eq. (2) to (4).

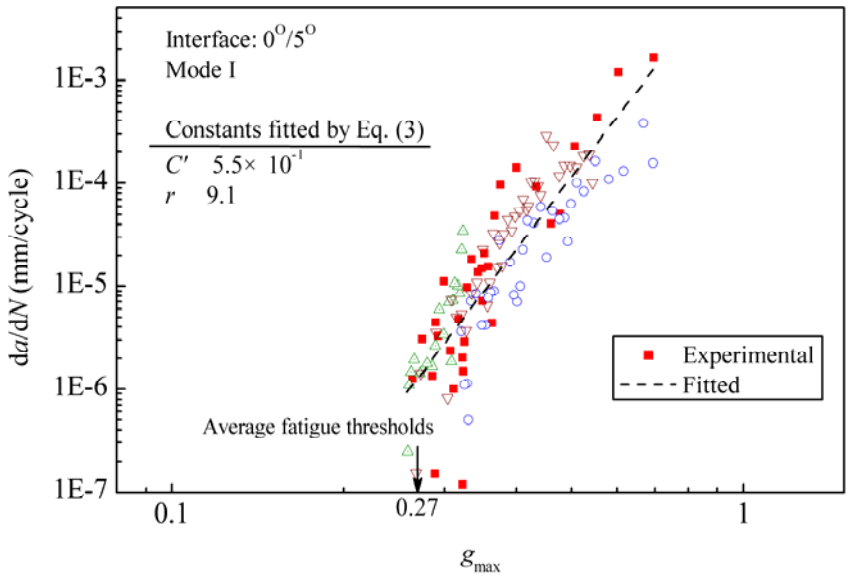

Figure 5. Experimentally obtained fatigue crack growth rates and thresholds

3.3. Numerical verification of tri-linear element

The UMAT subroutine in ABAQUS (v6.10) is used to verify the numerical model of tri-linear constitutive law. The laminate elastic properties from the tested specimens are as follows: E_{11} = 130 GPa, $E_{22} = E_{33}$ = 10.4 GPa, $G_{12} = G_{13}$ = 6.36 GPa, $\nu_{12} = \nu_{13}$ = 0.3. Interfacial properties to be input for the cohesive elements are: G_0 = 0.14 N/mm, G_c = 0.82 N/mm, σ_0 = 30 MPa, $k_0 = 1\times10^5$ N/mm^3. Varied bridging stress values from 0.5 to 2.5 are used following the rule in Section 3.1 to see the dependence of the model on bridging stresses.

The verification is performed on DCB specimen under quasi-static loading. The result of displacement-force relationship is presented in Fig. 6. The oscillations of numerical curves are caused by the large element size which was selected considering the computing size.

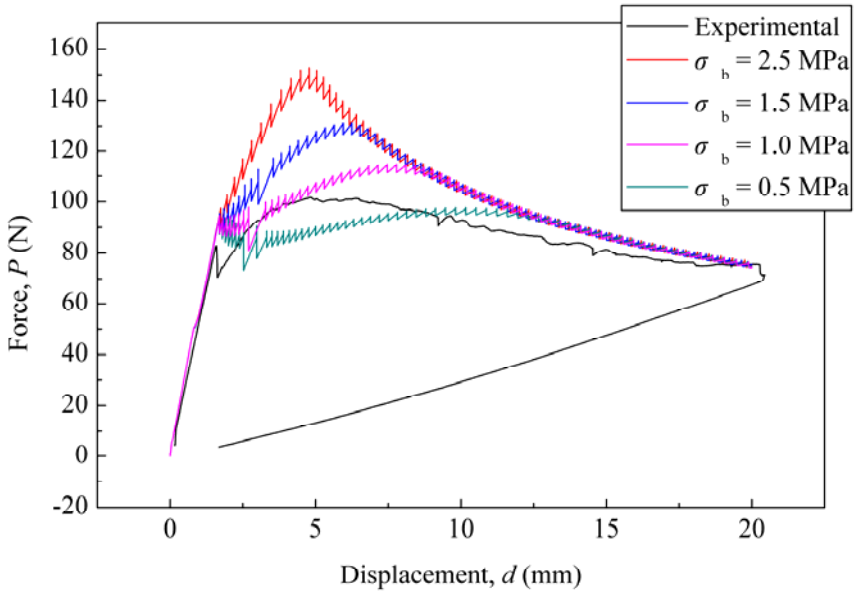

Figure 6. Force displacement response of DCB specimen from experiment and simulation

It is found that the value of bridging stress significantly affects the response of the specimen. Fig. 6 also implies that the linear law of σ_b-δ response doesn't fit the experiments very well. By making $G_A = G_B$ in Fig. 4, the determined σ_b distribution degrade the cohesive element too fast such as σ_b = 2.5 MPa in Fig. 6, or too slow as σ_b = 0.5 MPa in the figure.

4. Conclusion

The delamination growth behavior of composite laminates with fiber bridging is experimentally and numerically studied. A normalized fatigue crack growth rates law and thresholds model is presented to introduce the R-curve effect caused by fiber bridging. The cohesive element approach is also extended from bilinear constitutive response to a tri-linear response to simulate the delamination both in fracture and bridging zone.

The normalized fatigue law is found in accordance with experiments in high degree. The numerical model, however, degrades the cohesive element too fast or too slow due to the linear bridging stress law adopted. A nonlinear bridging law should be developed to fit the experiment better and a numerical verification for fatigue delamination growth will be conducted based on the new bridging law.

Acknowledgement

Financial support provided by the National High Technology Research and Development Program of China (863 Program) through grant number 2012AA040209, and by the National Natural Science Foundation of China through grant number 11202243 is gratefully acknowledged.

References

[1] L. Peng, J. Xu, J. Zhang and L. Zhao, Mixed mode delamination growth of multidirectional composite laminates under fatigue loading. Eng Fract Mech, 96 (2012) 676.
[2] L. Sorensen, J. Botsis, T. Gmür and L. Humbert, Bridging tractions in mode I delamination: Measurements and simulations. Compos Sci Technol, 68 (2008) 2350.
[3] A. J. Brunner, S. Stelzer, G. Pinter and G. P. Terrasi, Mode II fatigue delamination resistance of advanced fiber-reinforced polymer-matrix laminates: Towards the development of a standardized test procedure. Int J Fatigue, (2012).
[4] A. J. Brunner, N. Murphy and G. Pinter, Development of a standardized procedure for the characterization of interlaminar delamination propagation in advanced composites under fatigue mode I loading conditions. Eng Fract Mech, 76 (2009) 2678.
[5] M. Hojo, K. Nakashima, T. Kusaka, M. Tanaka, T. Adachi, T. Fukuoka and M. Ishibashi, Mode I fatigue delamination of Zanchor-reinforced CF/epoxy laminates. Int J Fatigue, 32 (2010) 37.
[6] J. Andersons and M. Köig, Dependence of fracture toughness of composite laminates on interface ply orientations and delamination growth direction. 64 (2004) 2139.
[7] B. D. Davidson, M. Kumar and M. A. Soffa, Influence of mode ratio and hygrothermal condition on the delamination toughness of a thermoplastic particulate interlayered carbon/epoxy composite. Composites Part A: Applied Science and Manufacturing, 40 (2009) 67.
[8] L. Peng, J. Zhang, L. Zhao, R. Bao, H. Yang and B. Fei, Mode I delamination growth of multidirectional composite laminates under fatigue loading. J Compos Mater, 45 (2011) 1077.
[9] P. Davies, B. R. K. Blackman and A. J. Brunner, Standard test methods for delamination resistance of composite materials: current status. Appl Compos Mater, 5 (1998) 345.
[10] A. J. Brunner, B. R. K. Blackman and P. Davies, A status report on delamination resistance testing of polymer-matrix composites. Eng Fract Mech, 75 (2008) 2779.
[11] T. E. Tay, Characterization and analysis of delamination fracture in composites - a review of developments from 1990 to 2001. Applied Mechanics Reviews, 56 (2003) 1.
[12] B. D. Davidson, R. D. Bialaszewski and S. S. Sainath, A non-classical, energy release rate based approach for predicting delamination growth in graphite reinforced laminated polymeric composites. Compos Sci Technol, 66 (2006) 1479.
[13] A. Quispitupa, C. Berggreen and L. A. Carlsson, On the analysis of a mixed mode bending sandwich specimen for debond fracture characterization. Eng Fract Mech, 76 (2009) 594.
[14] A. B. Pereira and A. B. de Morais, Mixed mode I + II interlaminar fracture of carbon/epoxy laminates. Composites Part A: Applied Science and Manufacturing, 39 (2008) 322.
[15] P. Naghipour, M. Bartsch, L. Chernova, J. Hausmann and H. Voggenreiter, Effect of fiber angle orientation and stacking sequence on mixed mode fracture toughness of carbon fiber reinforced plastics: Numerical and experimental investigations. Materials Science and Engineering: A, 527 (2010) 509.
[16] N. S. Choi, A. J. Kinloch and J. G. Williams, Delamination fracture of multidirectional carbon-fiber/epoxy composites under mode I, mode II and mixed-mode I/II loading. J Compos Mater, 33 (1999) 73.
[17] A. Szekrényes and J. Uj, Advanced beam model for fiber-bridging in unidirectional composite double-cantilever beam specimens. Engneering Fracture Mechanics, 72 (2005) 2686.
[18] V. Tamuzs, S. Tarasovs and U. Vilks, Progressive delamination and fiber bridging modeling in double cantilever beam composite specimens. Eng Fract Mech, 68 (2001) 513.
[19] J. Wang, Cohesive-bridging zone model of FRP-concrete interface debonding. Eng Fract Mech, 74 (2007) 2643.
[20] B. F. Søensen and T. K. Jacobsen, Characterizing delamination of fibre composites by mixed mode cohesive laws. Compos Sci Technol, 69 (2009) 445.

[21] M. Hojo, C. Gustafson, K. Tanaka and R. Hayashi, in Advanced Materials for Severe Service Applications (Tokyo, Japan, 1987) p. 353.
[22] N. Blanco, E. K. Gamstedt, L. E. Asp and J. Costa, Mixed-mode delamination growth in carbon-fibre composite laminates under cyclic loading. Int J Solids Struct, 41 (2004) 4219.
[23] L. E. Asp, A. Sjogren and E. S. Greenhalgh, Delamination growth and thresholds in a carbon/epoxy composite under fatigue loading. Journal of Composites Technology and Research, 23 (2001) 55.
[24] S. Singh and E. Greenhalgh, Mixed-mode delamination growth in carbon-fiber composites under fatigue loading, (Report DRA/SMC/CR961052/1.0 Defence Research Agency, 1996).
[25] A. Argüelles, J. Viña, A. Fernandez-Canteli, I. Viña and J. Bonhomme, Influence of the matrix constituent on mode I and mode II delamination toughness in fiber-reinforced polymer composites under cyclic fatigue. Mech Mater, 43 (2011) 62.
[26] M. Kenane, Z. Azari, S. Benmedakhene and M. L. Benzeggagh, Experimental development of fatigue delamination threshold criterion. Composites Part B: Engineering, 42 (2011) 367.
[27] P. W. Harper and S. R. Hallett, A fatigue degradation law for cohesive interface elements - Development and application to composite materials. Int J Fatigue, 32 (2010) 1774.
[28] S. Maiti and P. H. Geubelle, Cohesive modeling of fatigue crack retardation in polymers: Crack closure effect. Eng Fract Mech, 73 (2006) 22.
[29] P. Naghipour, M. Bartsch and H. Voggenreiter, Simulation and experimental validation of mixed mode delamination in multidirectional CF/PEEK laminates under fatigue loading. Int J Solids Struct, 48 (2011) 1070.
[30] A. Turon, J. Costa, P. P. Camanho and C. G. Davila, Simulation of delamination in composites under high-cycle fatigue. Compos Part A-Appl S, 38 (2007) 2270.
[31] A. Argüelles, J. Viña, A. F. Canteli, M. A. Castrillo and J. Bonhomme, Interlaminar crack initiation and growth rate in a carbon-fibre epoxy composite under mode-I fatigue loading. Compos Sci Technol, 68 (2008) 2325.
[32] K. N. Shivakumar, H. Chen, F. Abali, D. Le and C. Davis, A total fatigue life model for mode I delaminated composite laminates. International Journal of Fatigue, 28 (2006) 33.
[33] J. R. Gregory and S. M. Spearing, A fiber bridging model for fatigue delamination in composite materials. Acta Mater, 52 (2004) 5493.
[34] L. Peng, J. Zhang, R. Bao, H. Yang and B. Fei, Effect of ply orientation on the delamination growth in a laminated composite under cyclic loading: mode I, in "ICCS15" (Porto, Portugal, 2009).
[35] J. Zhang, L. Peng, L. Zhao and B. Fei, Fatigue Delamination Growth Rates and Thresholds of Composite Laminates under Mixed Mode Loading. Int J Fatigue, (2012).
[36] D. J. Wilkins, J. R. Eisenmann, R. A. Camin, W. S. Margolis and R. A. Benson, in Damage in Composite Materials, ASTM STP 775, edited by K. L. Reifsnider (American Society for Testing and Materials, 1982) p. 168.
[37] S. Hashemi, A. J. Kinloch and J. G. Williams, Mechanics and mechanisms of delamination in a poly(ether sulphone)--Fibre composite. Compos Sci Technol, 37 (1990) 429.
[38] S. Hashemi, A. J. Kinloch and J. G. Williams, Corrections needed in double-cantilever beam tests for assessing the interlaminar failure of fibre-composites. J Mater Sci Lett, 8 (1989) 125.

Microstructure and properties of welding joint of 8%Ni high strength steel

R. Cao[1], J. H. Chen[1], Y. Peng[2]
1.State Key Laboratory of Gansu Advanced Non-ferrous Metallic Materials and Key Laboratory of Non-ferrous Metal Alloys of the Ministry of Education, Lanzhou University of Technology，Lanzhou 730050, China
2. Central Iron and Steel Research Institute, Beijing 100081, China
* Corresponding author: zchen@lut.cn(J.H.Chen), caorui@lut.cn(R.Cao)

Abstract: This paper analyzes the mechanism of unmoral phenomena that in the HAZ of 8% Ni high strength steel, the charpy V toughness at -50℃ in the coarse grain HAZ is higher than that of fine grain HAZ. It is caused of different fracture. The former fracture is induced by void growing until impingement-resulting coalescence in the CG-specimen, and the latter fracture is caused by forming shear sheets of the secondary voids to connect the neighboring primary voids before their impingement. This paper reveals that the critical event for cleavage fracture in this high strength steel and weld metals is the propagation of a bainite packet-sized crack across the packet boundary into contiguous packets and the bainitic packet sizes control the impact toughness. The high-angle misorientation boundaries detected in a bainite packet by EBSD form fine tear ridges on fracture surfaces. However, they are not the decisive factors controlling the cleavage fracture. The effects of Ni content are essential factors for improving the toughness. The extra large cleavage facets seriously deteriorate the toughness, which are formed on the interfaces of large columnar crystals growing in welding pools with high heat input.
Keywords 980MPa 8%Ni high strength steel, weld metal, impact toughness, fracture, high-angle misorientation boundaries

1. Introduction

Due to its coarse grains and high hardenability, the CGHAZ(CG), which is overheated to a high temperature (up to 1350℃) shows a lowest ductility and toughness and limits the performance of welding structure [1]. On the contrary the FGHAZ (FG), which is heated to the normalization temperature (850-930℃) and has much finer grains, always shows the mechanical properties (including strength, ductitlity and toughness) superior than other regions within the HAZ. In the our paper, the abnormal phenomena that the Charpy V toughness in simulated CG are higher than those in the simulated FG are investigated with analyzing the different ductile fracture micromechanisms in associated microstructures formed by heating to 1320℃ and 900℃ [2]. With sustained improvement of the properties of high strength steels, the impact toughness has reached around 200J at lower temperatures of -50°C for 980MPa grade steels[2]. However the toughness of the weld metals with matching strength is appreciably lower than this value. How to increase the toughness of weld metal through the modification of the microstructure has been attracting a great attention of welding metallurgists.

The microstructural parameter, which controls the toughness of weld metal may be the grain size, martensite or bainite packet size, the size of area with misorientation angle larger than 15° and the brittle second phase particle size[3-8]. In this work, we use instrumented Charpy V tester, OM, SEM, TEM, EBSD and FEM calculation to identify which one in above microstructural parameters really controls the fracture and the toughness of impact Charpy V specimens. In addition, the effects of nickel addition are investigated.

2. Materials and procedures

Compositions of an 8% Ni 980MPa grade steel and various weld metals in Table 1 were used. Specimens cut in the rolling direction were heated by a heat simulating machine Thermorestor W to preset temperatures: FG (900℃), CG (1320℃), 730℃ and 600℃. The simulated heating procedures were designed as those shown in Table 2.Double heating simulations were carried out for temperatures (1320℃+1320℃, 1320℃+900℃, 1320℃+730℃, 900℃+1320℃, 900℃+900℃, and 900℃+730℃). Welding parameters of various welded joints are presented in Table 3.

The microstructures were observed by optical microscope (OP), scanning electron microscope (SEM 6700F) and transmission electron microscope (TEM JEOL2001). The grain sizes were measured by linear section method. ZEISS ULTRA 55 Field-Emission Scanning Electron Microscope was used to collect EBSD grain boundary maps and to define the orientations of microstructural features. Retained austenite films were

observed by TEM and identified by selected area diffraction pattern (SADP). Tests were carried out at -50 ℃ and room temperature (RT) by universal test machine SHIMACZU AG-10 TA for tensile tests and by instrumented impact machine CIEM-30CPC for Charpy V impact tests. The average of toughness values measured in three specimens is taken as the test result. Metallographic sections are prepared by griming, polishing fracture surface of charpy specimens at -50oC to characterize the microstructural constituents and measure the grain and packet sizes just under the fracture surface. General feature and the details of fracture facets were observed on the fracture surfaces. The distances X_f from the plastic crack tip to the site of cleavage cracking initiation was measured on the fracture surfaces of specimens which were fractured o lower temperatures with short fibrous crack extension. The distances X_f is a very important parameter by which the local fracture stress σ_f, fracture strain ε_{pc} and the critical stress triaxiality T_c are calculated. The nature of crack-initiating particles was characterized.

Critical event, which controls cleavage fracture, is defined as the stage offering the most difficulty during the crack initiation and propagation. The critical event can be revealed by the cracks which retained in the fractured specimen. Metallographic sections were prepared by cutting the specimen perpendicularly to the notch root for observation of retained cracks in fractured specimens. The lengths of retained cracks are also measured by Image software.

Table 1 Compositions of experimental metals (wt%)

Sample	C	S	P	Cr	Ni	Si+Mn+Mo+Cu+Nb+V
BM	0.08	0.002	0.008	0.60	7.58	1.77
T5-21	0.07	0.005	0.005	0.71	5.74	2.71
DM4-1	0.07	0.005	0.008	0.70	3.79	2.46
M100	0.09	0.010	0.006	0.65	6.18	2.82
T100	0.07	0.004	0.008	0.63	6.36	2.7

Table 2 Parameters of simulated heat-treat procedures

E ($kJ.cm^{-1}$)	t_p(s)	T_p(℃)	t_h(s)	$t_{8/5}$(s)	$t_{5/3}$(s)
20	15	1320	2	10	24
20	11	900	1	10	24
20	8	730	1	10	24
20	7	600	1	10	24

E:Heat-input, t_p:heating time, T_p:peak temperature, t_h: holding time, $t_{8/5}$: the cooling time from 800℃ to 300℃,

Table 3 Welding method and working condition.

Welding Method	No.	Heat Input(KJ/mm)	Shielding Gas	Arc Current(A)
TIG	T5-21	2.1KJ/mm	Ar	300A
MAG	DM4-1	1.6KJ/mm	Ar+5%CO2	280A
MAG	M100	1.6KJ/mm	Ar+5%CO2	280A
TIG	T100	2.1KJ/mm	Ar	300A

3. Mechanisms of abnormal high impact toughness in simulated welding CGHAZ of an 8%Ni high strength steel

3.1 Comparison of experimental results measured in CG-specimen and FG-specimen

As seen in Fig. 1, the strengths σ_y and σ_b at -50℃ and RT measured in tensile tests of CG-specimen are lower than those measured in FG-specimen. The plasticity in terms of ψ is also higher for FG-specimen. These results consist with the microstructures shown in Fig. 2 which show the extreme larger grains in CG-specimen and middle size grains in FG. This result can be fairly inferred from the Hall-Petch rule. However as shown in Fig. 3, the values of impact toughness measured in CG-specimen at RT and -50℃ are surprisedly higher than those measured in FG-specimen. Although from Fig. 3 and Fig. 4(a), the maximum loads of Charpy V tests measured in FG-specimen are appreciably higher than those that measured in CG-specimen, yet the load drops much faster with the crack propagation. It means that in the FG-specimen the resistance to the crack propagation is lower and at same applied load the deformation then the associated strain is lower than that of CG-specimen. These phenomena make the impact toughness, particularly the crack propagation energy E_p in Fig.3 being higher for the extreme coarse grain specimen. The reason, why

with lower strength and plasticity in tensile test, the CG-specimen exhibits a high resistance to crack extension in Charpy V test, is analyzed in following two paragraphs.

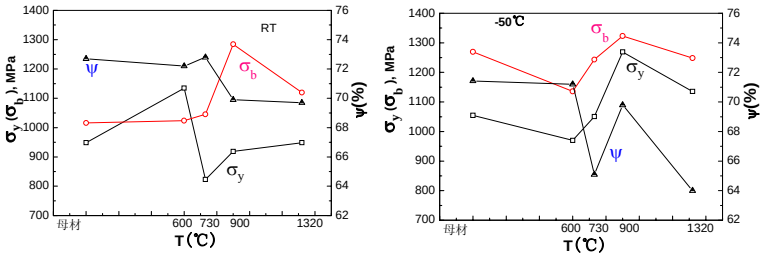

(a) (b)

Fig. 1 Results of tensile tests at RT and at -50℃

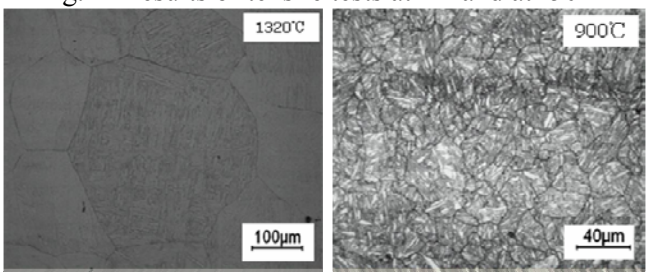

(a) Specimen ,1320℃ (b) Specimen, 900℃

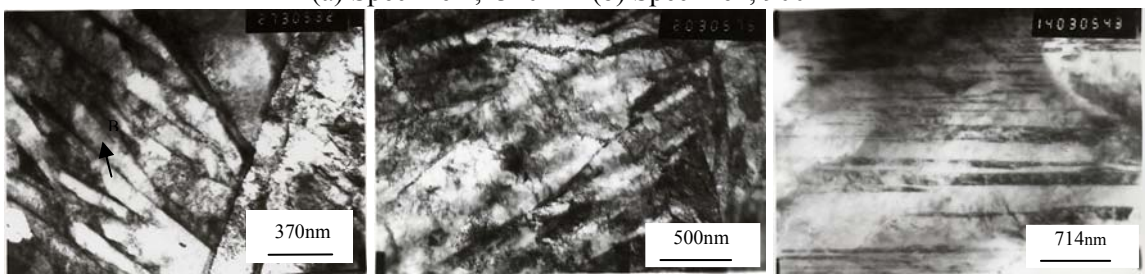

(c) Specimen ,1320℃ (d) Specimen, 900℃ (e) Specimen, 900℃

Fig. 2 Microstructures of simulated CGHAZ and FGHAZ specimen

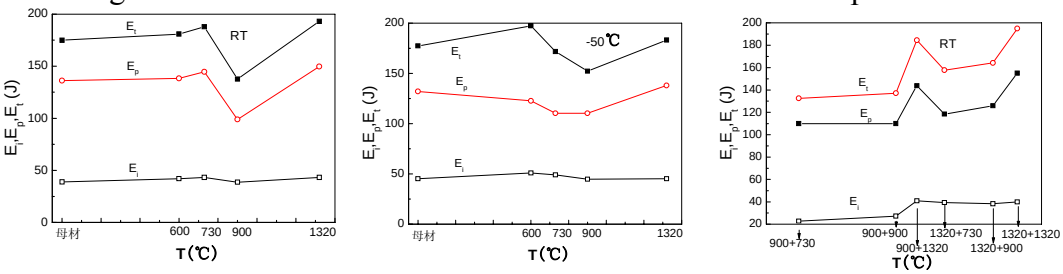

Fig. 3 The results of Charpy V tests at RT and at -50℃

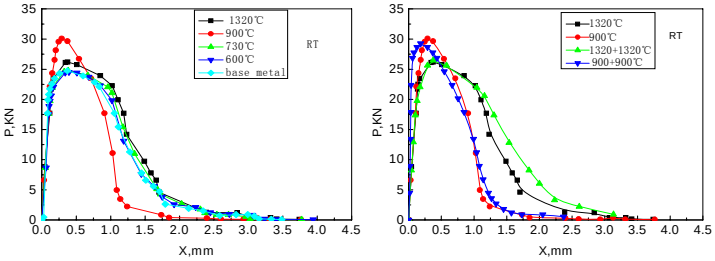

Fig. 4 Load-displacement plots measured by the instrumented impact machine(a) specimens by single heating (b) Comparison of effects of single and double heating

3.2 Different micro-mechanisms of rupture for CG-specimen and FG-specimen.

Fig. 5(a) shows the fracture surfaces of Charpy V specimen of CG. It is apparent that the ductile rupture is caused by the primary voids, which nucleate, grow until impingement-resulting coalescence and final rupture. In this case the rupture obeys the criterion of critical void growth. According to the void growth model of Rice and Tracey [7]:

$$\frac{dR}{R} = A \cdot e^{(\frac{3\sigma_m}{2\sigma_{eq}})} d\varepsilon_{eq} \qquad (1)$$

the critical radius R_c can be expressed [7] as

$$Ln(\frac{R_c}{R_0}) = 0.283\varepsilon_f^{(\frac{3\sigma_m}{2\sigma_{eq}})} \qquad (2)$$

The fracture strain ε_f increases with increasing the critical radius R_c at same stress triaxiality σ_m/σ_{eq}. As shown in Fig. 5(a) the critical radius R_c of the primary voids grow to as large as 100μm, close to the size of the lath bainite packets. Thus the corresponding fracture strain ε_f should reach a higher level and provides a higher resistance to crack propagation. However for FG-specimen, as shown in Fig. 5(b), the final rupture is caused by the shear sheets formed by numerous secondary voids, which connect the primary voids long before their impingement. Thus in FG-specimen the final rupture happens at less ε_f, once it can produce the secondary voids to connect the primary voids before they reach to impinge. Thus the primary voids in FG grow to much smaller size (Fig.5(b)) than those growing in specimen-CG(Fig. 5(a)). The total plastic strain, then the energy spent in fracture is less for the FG-specimen than for the CG-specimen. From Fig. 5, it is found that for both CG-specimen and FG-specimen, the primary voids are nucleated by inclusions, which leave black holes at the centers of the primary voids. But the original phase, which nucleates numerous small secondary voids in FG specimens cannot be identified in the fracture surfaces. Fig. 6 show fracture surfaces in same magnification, one for FG specimen (a) and the other for CG specimen (b). In Fig. 6(a) two primary voids (1 and 2) of 20-40 μm are connected by small secondary voids and numerous small secondary voids distribute on the fracture surface. In Fig. 6(b), two large primary voids (100μm in sizes) coalesce directly. Apparent plastic striations are present on void surfaces however on whole vision field no secondary void is produced.

From above analyses, the key point is the production of numerous secondary voids in the FG-specimen at a lower plastic strain, while in the CG-specimen only a few of second voids are produced even at the fracture strain. By comparing the fracture surfaces (Fig. 5(b) and the microstructures (Fig. 2(a), it is found that the sizes of primary voids correspond to the bainite packets (20-30μm) and the secondary voids correspond to the bainitic laths. Fig.2 (d) and (e) shows the transmission electron micrographs of FG-specimens. Fig.2 (d) shows the lath bainitic without carbide precipitation. The martensite laths with the width in the range of 0.2-0.4μm is consider to be much more brittle than the bainite laths. It is then inferred that the laths of the martensite are broken and nucleate the second voids at a lower level of plastic strain, before the primary voids grow to impingement and coalescence.

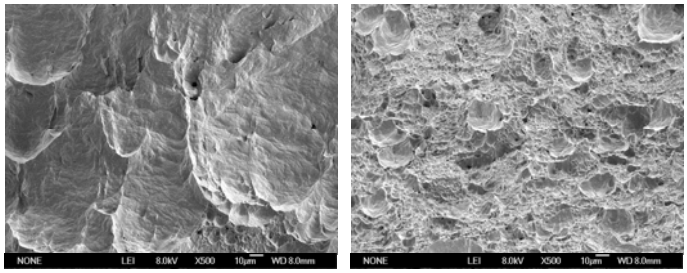

(a) Specimen ,1320℃ 198J, RT (b) Specimen, 900℃, 142J, RT

Fig. 5 Fracture surfaces of Charpy V tested specimen (a) heated to 1320(b) heated to 900 ℃

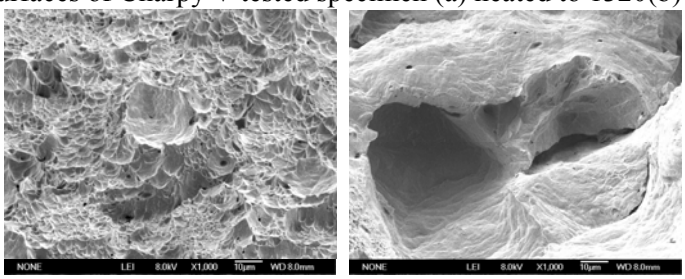

(a) (b)

Fig. 6 Fracture surfaces showing the details of rupture (a) by connection of numerous secondary voids in FG and (b) by coalescence of large primary voids in CG

By comparing the fracture surface (Fig. 5 (a) and the microstructure (Fig. 2(a)) of CG specimens, the

primary voids correspond to the large bainitic packets. The tiny carbide plates (only 0.01*0.04μm in size) precipitated inside the bainite are considered being not able to nucleate small voids. It can be concluded that although the grain sizes of CG specimens are extreme large, yet due to the high temperature (1320℃) heating, the carbon content is unified in the original austenite grain. After fast cooling the lath bainite microstructure keeps uniform in carbon content without local accumulation. The sizes of the carbide precipitation plates inside the bainitic lath are very small (only 0.01*0.04μm in size). The carbide plates with such tiny size can only be broken and nucleate the voids at a high level of plastic strain, however this high plastic strain cannot be reached before the coalescence of the primary voids in a notched Charpy V specimen with high stress triaxiality. And just this high stress triaxiality increases the rate of primary void growth.

3.3 Effects of stress triaxiality on the nucleation and growth of the voids

Fig. 1 show that both the strengths at -50℃ and RT measured in tensile tests of specimen CG are lower than those measured in specimen FG, while the Charpy V toughness is higher. The reason is analyzed as follows

Fig.7 shows fracture surfaces of CG-specimen (a) and (b) and that of FG-specimen (c) fractured by tensile tests at RT. Comparing Fig.5(a) and Fig. 7(a) for CG-specimen, it can be found that: in the impact test, the fracture is dominated by primary voids, which grow until impingement-resulting coalescence and final rupture, while in the tensile test the final rupture is caused by the secondary voids which connect the neighboring primary voids before their impingement. In FG-specimen, the fracture surfaces for both impact test (Fig. 5(b)) and tensile test (Fig. 7(b)) show rupture being caused by the shear sheets formed by numerous secondary voids which connect the neighboring primary voids long before their impingement. Therefore, the phenomena, that the CG-specimen shows the abnormal superior impact toughness, but the inferior tensile properties, can be attributed to the change of fracture mechanisms from the primary void-coalescence in the notch impact test to the secondary void-connection in the tensile test. In Charpy V tests, the energy, which is spent on the fracture by void growing until impingement-resulting coalescence in the CG-specimen is higher than that spent in the FG-specimen where the fracture is caused by forming shear sheets of the secondary voids to connect the neighboring primary voids before their impingement. However, in tensile tests, both CG-specimen and FG-specimen are fractured with the similar mechanism of connection of the primary voids by the secondary voids. The tensile properties of the CG-specimen are inferior due to its intrinsic inferiority such as large grain size.

Then the question is why for the CG-specimen, the fracture mechanism is changed from primary void coalescence in the Charpy V test to the secondary void connection in the tensile test. It is attributed to the difference of the stress triaxialities between these two types of tests. In the Charpy V impact test, because the stress triaxiality at the the notch is high, up to 1.6 by FEM calculation, while in the tensile test it varies from 0.33 to approximate 1.0 from a smooth specimen to a necking one at area reduction of 65 -70%. According to formula (2) $Ln(R_c/R_o) = 0.283\varepsilon_f(3\sigma_m/2\ \sigma_{eq})$, for the Charpy V specimen with a high stress triaxiality σ_m/σ_{eq}, the critical void radius R_c is reached at a lower fracture strain ε_f, which cannot cause the breaking of the tiny carbide plates precipitated inside the bainite laths or cause the breaking of the bainite laths in the CG-specimen. Therefore no (or only a few) secondary voids are produced in the fracture process (Fig. 6(b)). However, in the FG-specimen, the brittle martensite laths are broken at a less strain level and form numerous second voids, which connect the insufficiently growing primary voids and make an early fracture and lower toughness. In the tensile tests, the stress triaxiality is low and the plastic strain, which can reach is high. Even, in the CG-specimen, the secondary voids can be nucleated by the breaking bainitic laths (Fig.2(d)) before the impingement of the primary voids. The final fracture is caused also by the connection of insufficiently growing primary voids by the second voids (As shown in Fig. 7(a)).

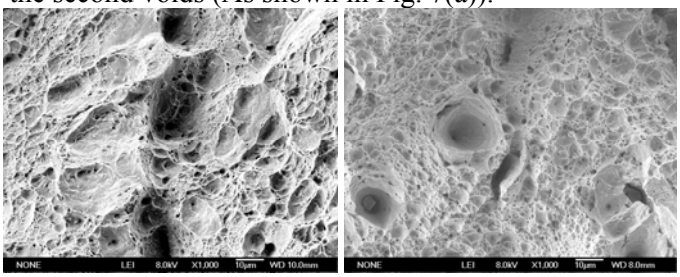

(a)1320℃ heating specimen (b) 900℃ heating specimen

Fig. 7 Fracture surfaces of specimens fractured at RT by tensile tests (a) 1320℃, (b) 900℃

4. Relationships between the microstructures and properties

The values of impact toughness measured by the instrumented Charpy V tester at temperature range from -196°C to 20°C are plotted in Fig. 8. Corresponded welding parameters and compositions are presented in Table 3.The effects on charpy toughness will be analyzed from followed aspects.

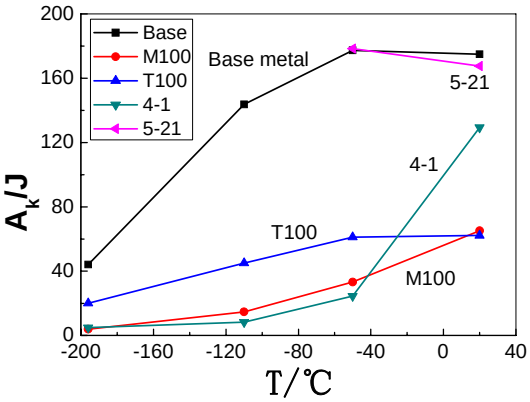

Fig 8. Charpy V values measured at various temperatures

From Fig. 8 it is found that the base metal and weld metal can be divided to two group according to the toughness measured at -50°C. The first group includes the base metal, T5-21 weld metals which present much higher impact toughness at -50°C. The second group includes DM4-1, M100 and T100, which show appreciable lower impact toughness. In following, the experimental results are focused to find the factors determining the difference of the cryogenic low temperature impact toughness between these two groups in the high strength steel and weld metals.

Fig. 9 displays the general microstructures of base metal and all weld metals. As seen in Fig. 9, the microstructure of base metal is the typical tempered lath bainite. The weld metals of T5-21 exhibit a little coarser lath bainite, and those of DM4-1 show somewhat appearance of globular bainite with some acicular ferrite. The distinct characteristics of weld metals of M100 and T100 are the black trips which are considered to be traces of segregation on the boundaries of columnar crystals growing in the weld pools. However, the remarked difference in impact toughness of metals cannot be simply attributed to the difference of these microstructures. Followed several aspects will be analyzed.

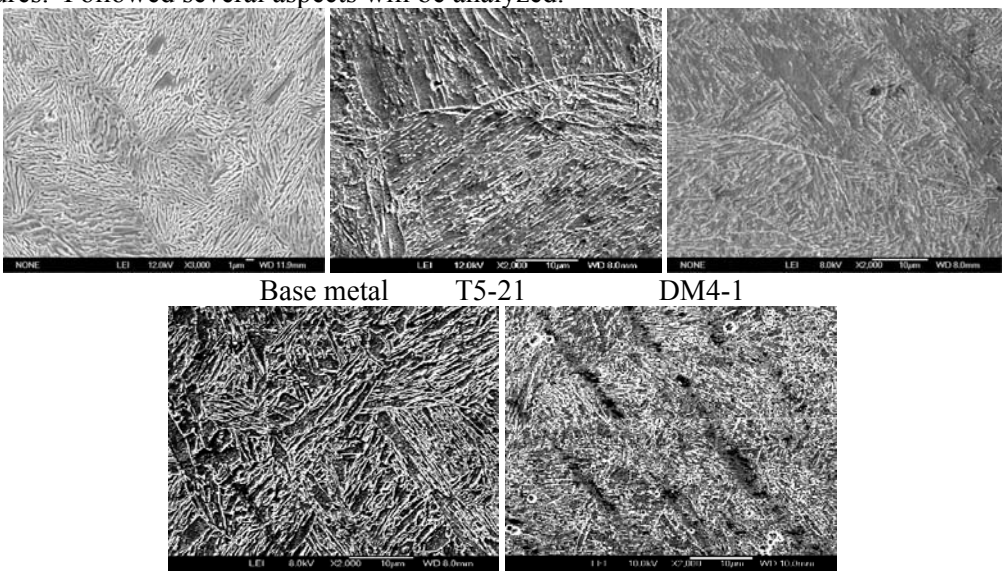

Fig 9. The microstructures of base metal and all weld metals

4.1 critical event

The critical event is the most difficult step in the crack nucleation and propagation process, which controls the cleavage fracture. The main methodology for identifying the critical event was suggested by the present author [9]. Fig. 10 shows the cracks retained in base metal and weld metal in Charpy V specimens fractured at -196°C. The lengths of retained cracks and the lengths of packets measured by random events are plotted

in right side figures. From Fig.10 in the metallographic sections of the fractured specimens, the cracks stopped at the packet boundaries, thus retained cracks were constrained in the bainitic packets in the Base metal, DM4-1, M100 and T100. And there is a consistent relationship between the lengths of the retained cracks and the sizes of the bainitic packets. Based on these experimental observations, the critical events for cleavage fracture in base metal and the weld metals are identified as the propagation of a packet-sized crack across the packet boundary into contiguous packets.

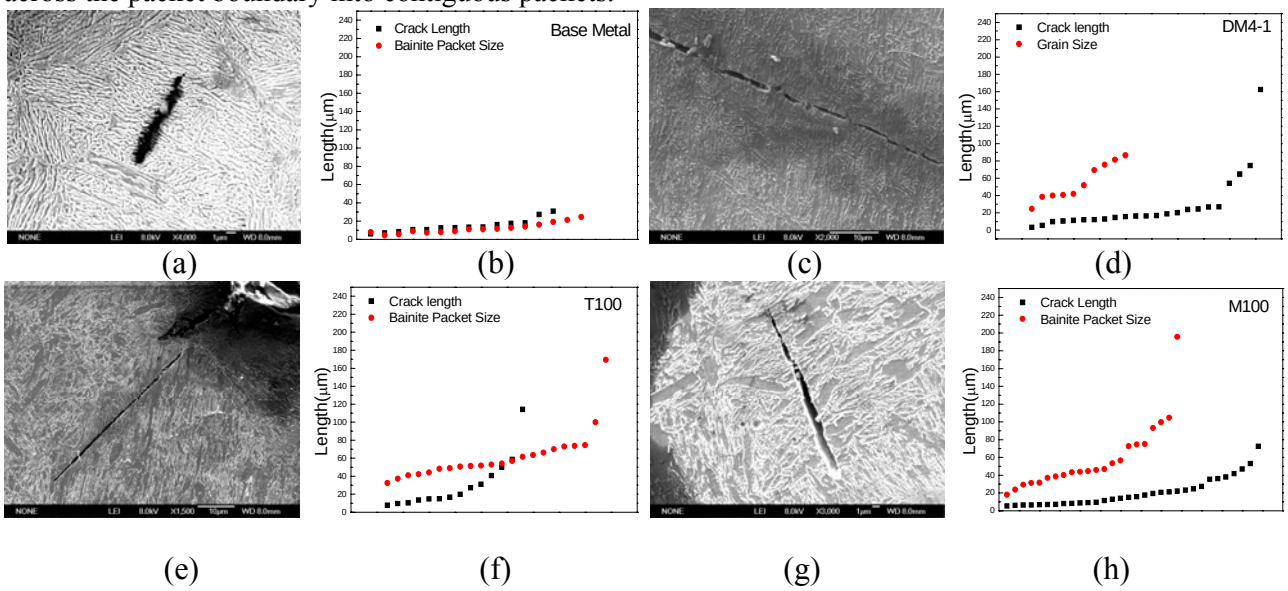

Fig 10. The cracks retained in base metal and weld metal in Charpy V specimens fractured at -196°C and the lengths of retained cracks and bainitic packets randomly measured by random event in (a) (b) base metal (c) (d) DM4-1(e) (f) T100 (g) (h) M100

4.2 Critical micro-parameters

Through the FEM calculation, the values of σ_f, ε_{pc} and T_c for base metal and weld metal DM4-1, T100 and M100 are obtained and listed in Table 3. The corresponding impact toughness measured at -196°C are listed in the Table 4. As seen in the Table 3 the local fracture stress σ_f measured in base metal are much higher than those measured in the weld metal DM4-1, T100 and M100. This is corresponded with the values of impact toughness listed in the Table 3. Table 4 lists the effective surface energy γ_p calculated from the σ_f and the area of the cleavage facet observed in front of the crack initiation site by equation. The areas of the cleavage facets observed in front of the crack initiation sites listed in Table 4 are in the order consistent with the order of packets' sizes in Fig. 12 and the calculated values of γ_p are reasonable.

Table 3 Results of calculation of σ_f, ε_{pc}, T_c

	T (℃)	P_y (KN)	P_m (KN)	σ_{yd} (MPa)	E_{-196}(J)	SCL (μm)	X_f (μm)	σ_f (MPa)	ε_{pc}	Tc
MC	-196	26.476	31.521	1236.93	44.2	600	251	2705	0.0242	1.33
DM4-1	-196	26.47	10	1236.80	5.9	0	289	1591	0	0.95
T100	-196	24.03	16.975	1158.19	20.0	275	469	1988	0.00137	1.045
M100	-196	24.79	6.57	1122.73	3.9	10	110	1581	0.00148	0.75

T ;test temperature，P_y: impact yield load，P_m: impact maximum load，σ_{yd}: impact yield strength，SZW: width of stretch zone， X_f: distance from the crack initiation site to the plastic crack tip，σ_f: local fracture stress，ε_{pc}: fracture strain，T_C: critical stress triaxiality

$$\sigma_f = \sqrt{\pi E \gamma p / (1-\upsilon^2) a} \quad \text{(for a penny-shaped crack)}$$

Table 4 Effective surface energy calculated from σ_f and the cleavage facet area

	σ_f	E	ν	a	C_0	γ_p
MC	2705	200000	0.3	22	0.43	233.26
DM4-1	1591	200000	0.3	39.7	0.73	145.62
T100	1988	200000	0.3	40	0.33	229.07
M100	1581	200000	0.3	37.7	0.45	136.55

σ_f: Local fracture stress, E: Young's modulus, ν: Poisson's ratio, a: cleavage facet area, C_o: size of second phase particle, γ_p: effective surface energy

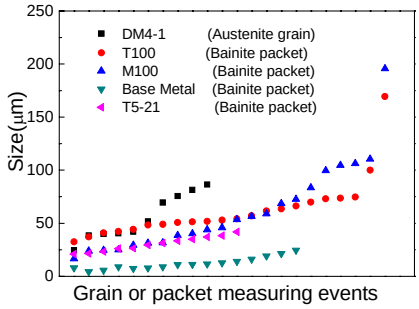

Fig 12. The grain and packet sizes measured in successive events

4.3 Effects of high degree misorientation boundaries

As stated in the introduction, Ref. [7] revealed that bainitic packet size measured by EBSD is identified as the microstructural unit controlling crack propagation in a cleavage fracture. Fig. 13 displays the higher degree misorientation boundaries depicted by EBSD for base metal and weld metals. From Fig.13, the fraction of area contained by the higher degree misorientation boundaries for the base metal is the smallest among all microstructures. Fig. 14 exhibits the histograms of the degrees of grain or packet boundaries.

In this study, as seen in Fig. 13, the sizes of the areas contained by the high misorientation degree boundaries are appreciably smaller than the sizes of the bainitic packets, however, in Fig. 10, the retained cracks are stopped by the packet boundaries, rather than by the high misorientation degree boundaries in a packet. Thus, the cleavage fracture is controlled by the bainitic packet rather than by the area contained by the high misorientation degree boundaries. In addition as shown in Fig. 13 and Fig. 14, there are not appreciable differences of the densities of high degree misorientation boundaries revealed by EBSD for T5-21and DM4-1 metals. To be surprised, the density of high degree misorientation boundaries in base metal is appreciably lower than that of weld metals. Therefore the superior impact toughness of base metal and T5-21 at -50°C cannot be attributed to the difference of the density of high degree misorientation boundaries.

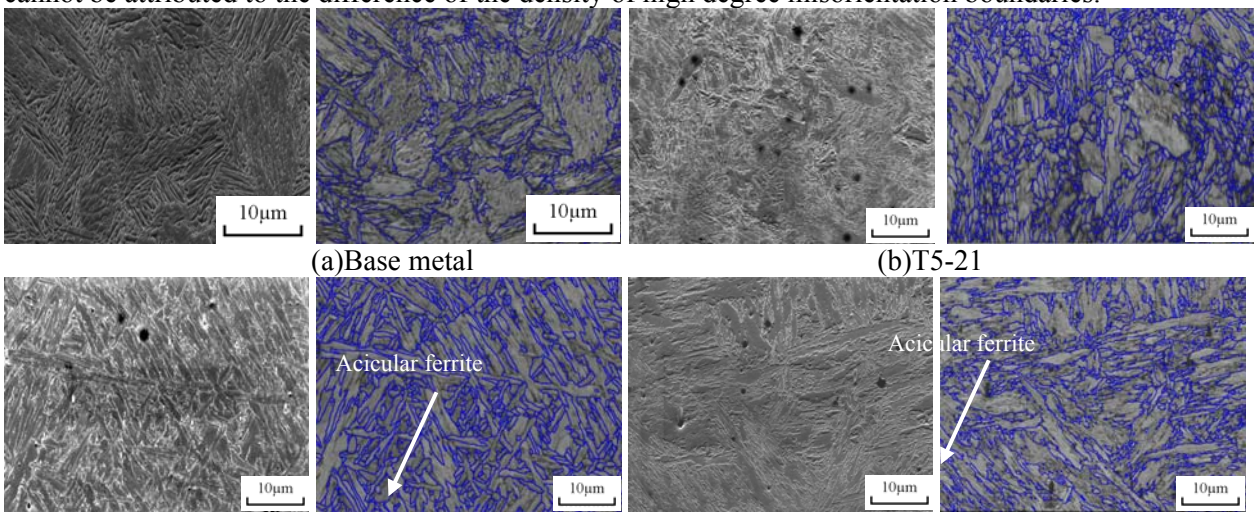

Fig 13. The higher degree misorientation boundaries depicted by EBSD for (a) base metal and weld metals (b) T5-21 (c) DM4-1 (d) M100 weld metals

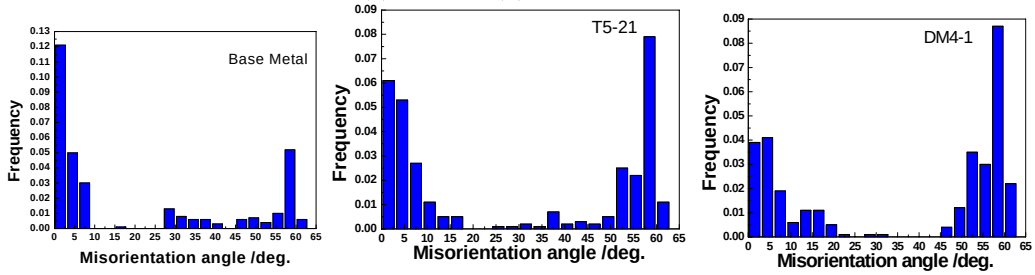

Fig 14. Histograms of the degrees of grain or packet boundaries of (a)base metal (b) T5-21 (c) DM4-1

As shown in Fig. 13 there is not appreciate differences of the densities of high degree misorientation boundaries revealed by EBSD for T5-21 and DM4-1 metals. To be surprised, the density of high degree misorientation boundaries in base metal is appreciably lower than those of weld metals.

In followed Fig. 15, by comparing the high misorientation degree boundaries and the fine tear ridges in the cleavage facets, it seems that the latter is produced by the former. Thus, in this study, the resistance to the cleavage cracking is mainly provided by the packet boundary, and the high misorientation degree boundaries offers some resistance and produce the fine tear ridges in the cleavage facets.

4.4 Decisive microstructural constituents

Based on the above discussions, it is concluded that the decisive microstructural feature which determines the impact toughness in the notched bar is the bainite packet rather than the region contained by the high misorientation degree boundaries. The bainite boundary provides the main resistance and makes the propagation of a packet-sized crack across the boundary the critical event for the cleavage fracture. The packet size specifies the critical cleavage facet and the local fracture stress σ_f. The reason why the values of impact toughness measured at -50°C for base metal, and T5-21 are generally higher than those measured for DM4-1, T100 and M100 is attributed to that the size of the bainitic packet of the former group is finer than that of the latter group. Fig. 16 shows a typical comparison between the packet sizes of the DM4-1 weld metal and the T5-21 weld metal. It is apparently that the sizes of packets in T5-21 are appreciably smaller than that in DM4-1 weld metal. The general comparison of the grain or the packet sizes is summarized in Fig. 12. As the lengths of the critical events corresponding to the sizes of packets of the first group of the base metal and T5-21 are smaller than that of the second group of DM4-1, T100 and M100. This is the reason why the impact toughness of the metals of the first group is superior to that of the metals of the second group.

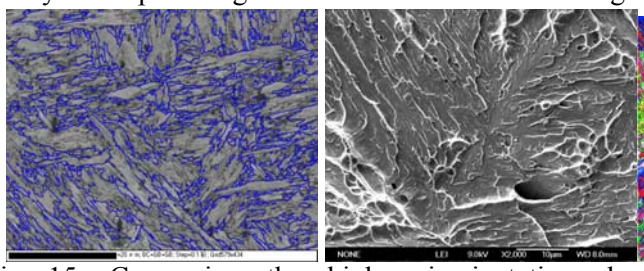

Fig 15. Comparing the high misorientation degree boundaries and the fine tear ridges on the fracture surface

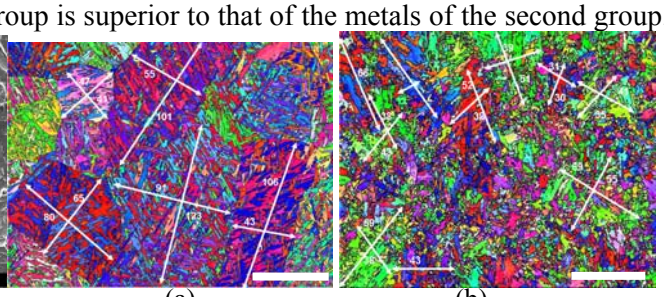

(a) (b)

Fig 16. Sizes of packets in (a)DM4-1 (b) T5-21

4.5 Effects of nickel addition

As indicated in the introduction, Ref.[8] revealed that regardless of packet size and yield strength, the addition of nickel gave rise to a decrease in Charpy V impact transition temperature of about 20°C per percent nickel. He attributed this effect to increasing the cleavage fracture resistance [8]. In this work at first the metals were divided to two groups: the first group including MC and T5-21 which presents superior impact toughness and the second group including DM4-1 which presents inferior toughness. From the composition point of view, the only appreciable distinction in alloy content is the difference in Ni contents: around 6-7% Ni for the first group and lower than 4%Ni for the second group. The effects of Ni addition were focused. Table 5 compares the relative parameters between the two groups. As seen in Table 5, the grain sizes of weld metals with higher Ni contents are finer. Besides the fine grain/packet sizes in the metals of the higher Ni content group, the fine bainitic laths and the higher fractions of the M-A constituent were observed. Because in steels with higher Ni content the flaks of the M-A constituent were found to be rich of austenite and have high plasticity[10], both fine bainitic laths and Ni-rich M-A flakes causes denser higher misorientation boundaries and higher resistance by the appearance of fine tear ridges on the fracture surface. The effect of Ni addition is considered to be decisive in the difference of impact toughness between these two groups. The mechanism of the improvement needs to be investigated in future.

Table 5 Parameters relevant to Ni content and toughness (drawn from Table 5)

No.	E_{-50^oC} (J)	Nickel (%)	Average grain size(μm)	Width of Bainite lath(nm)	Average width of Bainite lath (nm)	Area fraction of M-A(%)
MC	177	7.58	20	20-80	34	58
T5-21	163	5.74	30	65-186	113	39
DM4-1	24.5	3.79	60	180-850	428	26

4.6 Effect of welding process

Table 6 lists the values of Charpy V impact toughness and relevant parameters measured at -50°C for weld metals of T100 and T5-21.

Table 6 Parameters relevant to Ni content and toughness

No.	E_{-50^oC} (J)	Nickel (%)	Average grain size(μm)	Width of Bainite lath(nm)	Average value (nm)	Area fraction of M-A(%)
T5-21	163	5.74	30	65-186	113	39
T100	61.2	6.36	60	59-578	151	26

As listed in Table 6, while the Ni content of 6.36% in T100 weld metal is comparable with that of 5.74% in T5-21. However, the impact toughness of 61.2J of the former is much less than that of 163J in the latter. In addition, the grain sizes and the width of bainitic laths of T100 are larger than that of T5-21, the area fraction of M-A flakes is less for T100 than for T5-21. The reason which causes the inferior toughness and the factors deteriorating the toughness is attributed to the welding process. Fig. 17 displays the fracture surface (a) and the macrostructure (b and c) of the weld metal T100. From Fig. 17 it is evident that the coarse directional columnar grains exhibited in Fig. 17 (c) produce the coarse embossing fracture strips shown in Fig.17 (a) which cause the inferior toughness of weld metal T100. Table 7 lists the metallographic parameters measured in T100 and T5-21 weld metal which shows that the width of the weld of T100 is appreciably larger than that of T5-21. It is considered to be welded by horizontal weaving of the welding torch. This procedure produces high heat input at same welding current and causes larger columnar grains and segregation of impurities on the boundaries of the crystalline cells as shown in Fig. 17(b) and (c). Therefore, regardless of the higher nickel content the large columnar grains with impurity segregating boundaries make the impact toughness of the T100 weld metal inferior. The similar phenomenon was observed in the case of M100.

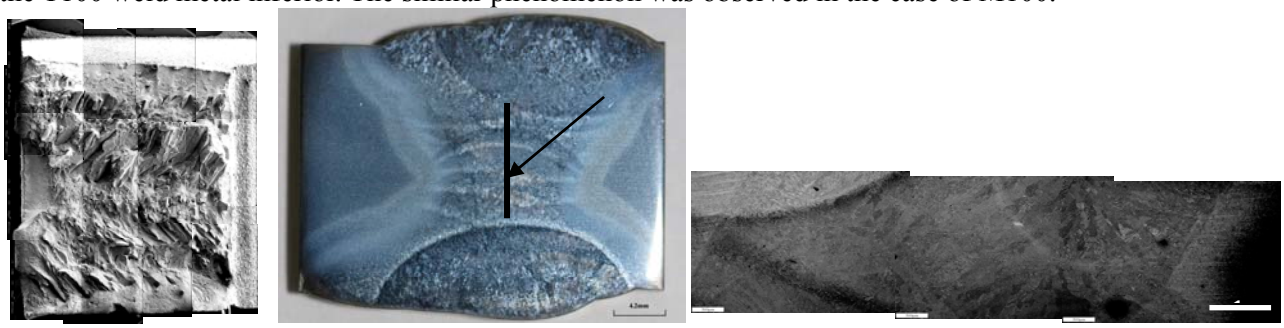

(a) (b) (c)

Fig 17. The fracture surface (a) and the macrostructure (b and c) of the weld metal T100

Table 11 Metallographic parameters measured in T100 and T5-21 weld metal

Weld metal	Weld Width (mm)	Weld depth (mm)	Columnar grain width (mm)	Sizes of fine grain (mm)
T5-21	15.9	7.4	0.29	0.11
T100	20	7.6	0.41	0.45
M100	14.3	8.5	0.47	0.16

Acknowledgements

This work was financially supported by National Nature Science Foundation of China (No. 51035004 and 51265028).

References

[1] D. Chae, C. J. YoungD. M. Goto and D. A. Koss, Metall. Mater. Trans. A, 32A(2001)2229-2237
[2] R. Cao, W.Feng, Y. Peng, W. S. Du, Z. L. Tian, J. H. Chen, Mater.Sci.Eng A. 528(2010) 631-642.
[3] J. R. Low, Deformation and fracture in solids, Springer-Verlag, Berlin, (1956) 163-176.
[4] Kamada, N. Koshizuka, T.Funakoshi, Transaction ISIJ, 16(1976)407-416.
[5] G. T. Hahn, Metall. Trans. A. 15(1984)947–959.
[6] A.Echeverria, J. M. Rodriques-Ibabe, Mater.Sci.Eng A. 346(2003)149-158.
[7] L.Rancel, M. Gomez, S. F. Medina, I. Gutierrez, Mater.Sci.Eng A. 530(2011) 21-27.
[8] R. Cao, Y. J. Yan, W. S. Du, Z. L. Tian, Y. Peng, J. H. Chen, 2011, Mater.Sc.Techno, 27(2011)145-155.
[9] J. H. Chen, G. Z. Wang, C. Yan, H. Ma, and L. Zhu, Inter. J. Fract. 83(1997)105-120.

A fracture-mechanics-based non-local damage model for crack prediction in brittle materials

Zhang Xiao-Bing[1], Li Jia[2*]

[1]LAMI, Université Blaise Pascal de Clermont, Montluçon, France;

[2]LSPM, CNRS UPR 3407, Université Paris XIII, Villetaneuse, France;

* Corresponding author: jia.li@univ-paris13.fr

Abstract: Description of crack initiation and crack growth is a principal aim of numerical simulations in fracture mechanics. In this work, we have established a non-local damage model based on the fracture mechanics for brittle materials. This non-local model associates the classical failure criteria for non-cracked materials and the Griffith criterion for cracked materials throughout a non-local approach. Consequently, this model can be used to predict the crack initiation as well as the crack growth. The maximal principal stress criterion was considered in the proposed non-local framework. It was shown that after the non-local treatment, the classical failure criteria can be used in the prediction of crack initiation and crack growth with different failure mechanisms. By using the proposed model, we carried out several numerical simulations on different specimens in order to assess the fracture process in brittle materials. From these studies, we can conclude that the present model can be used to deal with crack initiation and crack growth in brittle materials with high accuracy and efficiency.

Keywords: fracture, crack, damage, non-local model

1. Introduction

The fracture prediction of structures made of brittle materials is an important issue in engineering designs. In real structures, the failures are often initiated from a few geometrical weaknesses near which stress concentrations are formed. The stress concentrations are of many types and different levels. The failure prediction for all these stress concentrations is an essential research topic for scientists and engineers. However, it seems that fractures can be accurately predicted only for few types of stress states as so far. For brittle materials, failure criteria for two simple situations are commonly accepted:

1: Under uniform uniaxial tension, fracture occurs when the maximum tensile stress reaches the ultimate stress of the material:

$$\sigma \geq \sigma_c \tag{1}$$

2: For solids including a macrocrack, the crack grows when the Griffith criterion is fulfilled:

$$G \geq G_c \tag{2}$$

where G and G_c are respectively the energy release rate and its critical fracture value.

Unfortunately, these criteria have to be used separately: one for damage initiation and another for crack growth. In the cases when the stress distribution is not uniform but does not present a crack singularity, these criteria are no longer sufficient to describe accurate fracture conditions. Many factors such like stress gradient, multi-axial stress state or structure size may influence the material strength. With the aim of unifying these criteria in a single damage model and extending them to

more general cases, numerous fracture and damage models were proposed in the literature.

When the stress concentration presents a singularity weaker than the crack one, such a singularity can be found in the cases of sharp notches, interface cracking or cracks in ductile materials, criteria based on finite fracture mechanics were developed and reported in the literature. In simple words, these criteria are kinds of combinations of (1) and (2). [1-5]. Another class of fracture criteria was issued from the so-called cohesive models [6-10]. In all these criteria and models, one can distinguish a length scale parameter, such as the critical distance from the crack tip in finite fracture mechanics or the maximum separation distance in cohesive models.

The finite fracture concept can also be found in damage analyses. A wide variety of damage models have been proposed on the basis of continuum damage mechanics by introducing a length parameter [11-15]. The nonlocal models in a continuum damage setting, the gradient theory based damage models, the damage gradient models are some of the principal advances in this direction.

In this work, we have constructed a damage model by associating the maximal stress criterion with a non-local formalism. Moreover, equivalence has been illustrated between this non-local model and the Griffith-Irwin fracture criterion for crack propagation. Using the established non-local damage model, we carried out detailed numerical simulations on different specimens in order to study the efficiency and accuracy of the present approach. The numerical results show that the proposed damage model is capable to simulate the crack initiation as well as the crack growth in brittle composites with highly realistic description.

2: Non-local damage model

Numerous continuous damage models exist in the literature. In this work, we will use a simple failure criterion for brittle materials, i.e. the instantaneous damage model on the basis of the maximum stress criterion, namely:

$$D = \begin{cases} 0 & \sigma_1 < \sigma_c \\ 1 & \sigma_1 \geq \sigma_c \end{cases} \tag{3}$$

where σ_1 is the maximal principal stress and σ_c is the ultimate tensile stress of the material. It is clear that other more elaborate damage evolution laws exist and may be more efficient and physically more realistic for this class of materials. In the present work, (3) is adopted for simplicity.

Even though this strength criterion is commonly used in failure assessment of a non-cracked structure, however, it is not suitable to describe fracture due to cracks because of the stress singularity near the crack tips. In order to overcome this shortcoming, various methods have been proposed. Among these, the so-called non-local approaches are widely used. The basic idea of this approach consists in replacing the local damage driving force, i.e. σ_1 in the present case, by its

weighted average over a representative volume V [11]:

$$\tilde{\sigma}_1(\mathbf{x}) = \frac{1}{\int_V \alpha(\mathbf{x}-\mathbf{y})d\mathbf{y}} \int_V \alpha(\mathbf{x}-\mathbf{y})\sigma_1(\mathbf{y})d\mathbf{y} \tag{4}$$

In Equation (4), $\alpha(\mathbf{x}-\mathbf{y})$ is a space weighting function which describes the mutual non-local interactions and depends only on the distance between the source point $\mathbf{x}$ and the receiver point $\mathbf{y}$. By simplicity, we write:

$$\alpha(r) = \begin{cases} 0 & r > R \\ 1 - \dfrac{r}{R} & r \le R \end{cases} \tag{5}$$

where $r = \|\mathbf{x}-\mathbf{y}\|$; R is the radius of non-local action which defines the size of interaction zone for failure processes.

By means of the non-local principal stress, the damage model (3) can be rewritten as follows:

$$D = \begin{cases} 0 & \tilde{\sigma}_1 < \sigma_c \\ 1 & \tilde{\sigma}_1 \ge \sigma_c \end{cases} \tag{6}$$

3: Connection to the Griffith-Irwin criterion

In this section, we will prove that the non-local damage model (6) can be connected to the Griffith-Irwin criterion and therefore, can be used to predict crack growth. Consider a mode-I loaded macro-crack. According to the Williams asymptotic solution [16], the near-tip first principal stress is modulated by the stress intensity factor K_I as follows:

$$\sigma_1(r,\theta) = \frac{K_I}{\sqrt{2\pi r}}\left(1+\cos\frac{\theta}{2}\right)\left|\sin\frac{\theta}{2}\right| \tag{7}$$

Due to the symmetry, the maximal non-local principal stress is located at a point on the crack axis near the crack tip: $r = r_0, \theta = 0$. Therefore, from (4), (5), and (7):

$$\tilde{\sigma}_1(r_0) = \max_{r_0} \int_0^R \int_{-\pi}^{\pi} \frac{3}{\pi R^2}\left(1-\frac{r'}{R}\right)\frac{K_I}{\sqrt{2\pi r}}\left(1+\cos\frac{\theta}{2}\right)\left|\sin\frac{\theta}{2}\right| r' dr' d\theta' = 0 \tag{8}$$

On the one hand, if we assume that $\tilde{\sigma}_1(r_0)$ is the maximal value of $\tilde{\sigma}_1(r,\theta)$ near the crack tip, the element at the crack-tip is damaged when $\tilde{\sigma}_1(r_0) = \sigma_c$ according to the damage criterion (6). On the other hand, from the Griffith criterion of fracture, the crack grows when the energy release rate G attains its critical value G_c. For mode-I cracks, this criterion is equivalent to the Irwin criterion $K_I \ge K_{Ic}$, where K_{Ic} is the critical stress intensity factor. Therefore, the parameters R and r_0

can be found by resolving the following equation:

$$f(R) = \sigma_c - \max_{r_0} \int_0^R \int_{-\pi}^{\pi} \frac{3}{\pi R^2}\left(1 - \frac{r'}{R}\right) \frac{K_{Ic}}{\sqrt{2\pi r}}\left(1 + \cos\frac{\theta}{2}\right)\left|\sin\frac{\theta}{2}\right| r' dr' d\theta' = 0 \qquad (9)$$

with

$$r = \sqrt{\left(r_0 + r'\cos\theta'\right)^2 + \left(r'\sin\theta'\right)^2} \qquad \tan\theta = \frac{r'\sin\theta'}{r_0 + r'\cos\theta'}$$

By using the non-local scheme (4) and with R calculated from Equation (9), the damage model (6) can directly be used to predict the crack growth. To this end, we just need to find the point (r_0, θ_0) near the crack tip where the non-local principal stress is maximal: when the non-local stress attaints the material strength, the crack grows to the point (r_0, θ_0) according to the Griffith-Irwin criterion.

The above-mentioned damage model was implemented into a Fast Fourier Transfer (FFT) code. The iterative method on the basis of FFT was originally proposed by for homogenizing linear and nonlinear composites [17]. The FFT-based formulation for a periodic heterogeneous cell with damage was developed according to the original FFT scheme [18]. Since an element in a structure is linearly elastic before its complete damage, the method of crack propagation evaluation used in this work is very similar to that adopted in linear fracture mechanics: An elastic calculation is first carried out for a cracked structure, and then crack progression and the corresponding remote load are determined according to the damage criterion (6). This procedure is then repeated after each small crack progression in the structure

4: Numerical examples and discussion

In this section, we will carry out a series of numerical calculations in order to assess the performance of the present fracture model in predicting the crack evolution in brittle and quasi-brittle materials. First, we will verify its accuracy in predicting crack growth with a cell containing a central crack under pure mode-I loading. Then cells with more complicated microstructure will be considered in order to evaluate its efficiency and potentiality.

4.1: Cells with a central crack

The first numerical example is a plane stress plate containing a central crack. In the numerical simulations, the dimension of the plate is $2h \times 2h = 10 \times 10\text{mm}^2$ with a central crack of different sizes, namely a = 0, 0.1, 0.3, 0.5, 1, 2, 3 and 4mm, here a = 0 represents a non-cracked plate. The stress intensity factors of such cracks can be found in any handbook of stress intensity factors. The mechanical properties of the material are: Young's modulus E = 3000 MPa, Poisson's ratio ν = 0.3, the ultimate stress σ_c = 72MPa, the critical stress intensity factor $K_{Ic} = 36\text{MPa}\sqrt{\text{mm}}$, the non-local action radius R=0.105mm and the radius of the damaged zone r_d=0.05mm. In order to investigate

the influence of the resolution finesse on the numerical results, the cell was discretized using different grids of regularly spaced Fourier points. The resolutions used for discretization are 100×100, 200×200, 400×400 and 600×600 pixels. The pure mode-I load is prescribed by imposing an average strain $\overline{\mathbf{E}} = \{\overline{E}_{11} \quad \overline{E}_{22} \quad \overline{E}_{12}\} = \overline{E}_{11}\{1 \quad -0.3 \quad 0\}$.

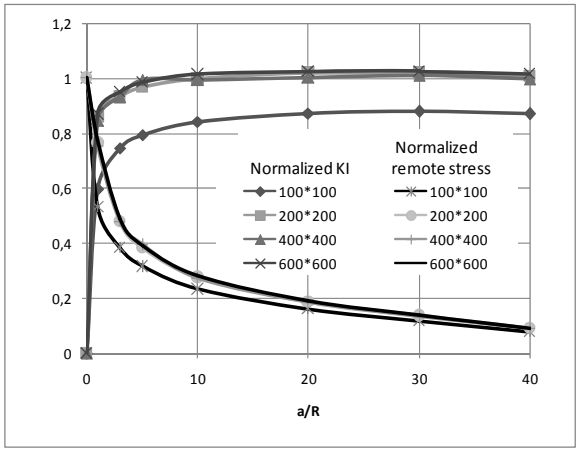

Figure 1: Normalized stress intensity factor K_I/K_{Ic} and normalized remote stresses σ^{∞}/σ_c as function of normalized semi-crack length a/R for mode-I loaded cracks at fracture

We first calculated the remote tensile loads σ^{∞} for crack growth according to the damage criterion (7). The calculations were carried out for different crack length and with different discretization resolutions. The results of these calculations are reported in Figure 1. In this figure, the stress intensity factors are normalized by the critical value K_{Ic} ; the remote stresses are normalized by the ultimate stress σ_c of the material and the crack length is normalized by the non-local action radius *R*. From this figure, several remarks can be made:

1. When the crack is sufficiently long with respect to the non-local radius *R* ($a > 3R$), the stress intensity factors evaluated from the present non-local damage model for crack growth equal correctly the critical stress intensity factor of the material. This result confirms that the proposed damage model is equivalent to the criterion $K_I \geq K_{Ic}$ for mode-I cracks;
2. When the FFT discretization is sufficiently fine, the proposed damage model is independent of the FFT grid resolution.
3. The remote stress at fracture tends to the ultimate stress of material as the crack length tends to zero. In this case, the proposed crack growth criterion degenerates to the maximum stress criterion for non-singular stresses.

4.2: Cracking in concrete

The second example deals with a recurrent problem in concrete mechanics. The concrete is often modeled by a 3-phase particle composite where stiff and strong aggregate particles are embedded in a weaker and softer cement matrix. A third phase exists between these two phases, namely a thin

zone enveloping the aggregate particles. This thin zone of extremely weak material is the interfacial transition zone (ITZ). In the composite either the ITZ phase or the matrix phase may percolate. In the literature, the fracture of such a system is usually studied by means of lattice models constructed of bar or beam network [19-21].

In this example, a basic cell of 90×90mm² was discretized by a 600×600 FTT grid. The circular particles of diameters varying from 2 to 12mm were arbitrarily distributed in the cell. The thickness of the ITZ was chosen as 0.3mm. This thickness includes at least 2 pixels with the used grid. The density of the particles and ITZ attains 20% in volume. Following material constants were used in the simulations: $\sigma_c^{(matrix)}$ = 10MPa; $\sigma_c^{(ITZ)}$ = 5MPa; $\sigma_c^{(particle)} = \infty$ for ultimate stresses; $E^{(matrix)}$ = 20000MPa; $E^{(ITZ)}$ = 30000MPa; $E^{(particle)}$ = 40000MPa for Young's moduli and $K_{Ic}^{(matrix)} = 20\text{MPa}\sqrt{mm}$, $K_{Ic}^{(ITZ)} = 10\text{MPa}\sqrt{mm}$ and $K_{Ic}^{(particle)} = \infty$ for critical stress intensity factors. A traction load $\overline{\mathbf{E}} = \overline{E}_{11}\{1 \quad -0.3 \quad 0\}$ is prescribed on the cell. By resolving Equation (9), we obtained the non-local action radius R=1.5mm. The radius of the damaged spot is taken as r_d=0.5mm. As this spot can cover both matrix and ITZ, in practice, we take precautions such that the broken zone contains only points in the matrix or only points in the ITZ according to the location of the maximal non-local principal stress.

The results of the numerical simulations are presented in Figures 2. Figure 2a shows a basic cell with matrix in gray, particles in black and ITZ in white. Global response on average stress-strain is plotted in Figure 2d. Here the average stresses are normalized by the ultimate stress of the matrix. The average stress-strain curve of the cell clearly shows a quasi-brittle behavior that is inherent to concrete. The crack growth pattern at load peak is illustrated in Figure 2b. From this figure, we can observe that the pre-peak micro-cracking essentially occurs in the ITZ, which are the weakest phase confined to the outer rim of the stiff aggregates. This damage stage constitutes the entire hardening phase of the global response. After the peak, the cracks enter into the matrix. The crack growth pattern at the end of load is shown in Figure 2c. At this stage, the bridging between different damaged ITZs leads to rapid stiffness decrease of the cell. These results agree with those obtained in the literature using lattice analysis [19-21].

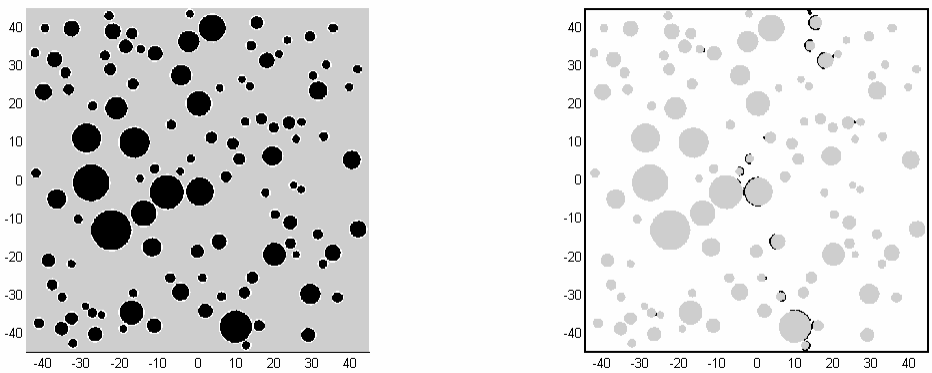

(a) (b)

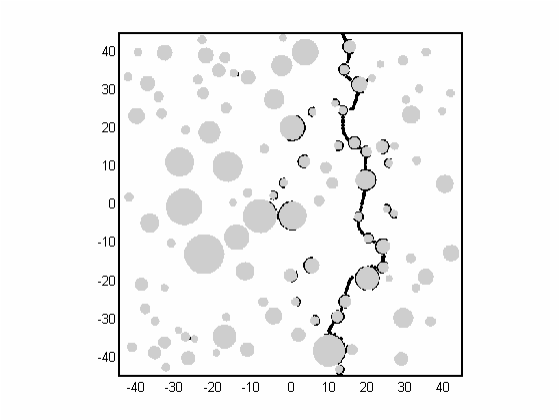

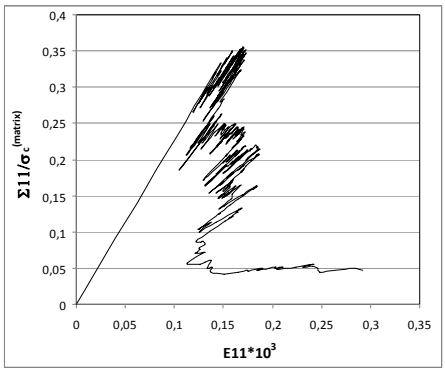

(c) (d)

Figure 2: Concrete plate containing unbreakable particles enveloped by ITZ (a), crack patterns at peak of the loading (b), at the end of the loading and global response (d) of the concrete plate

4.3: Fracture in laminate composites

Let's consider a plane strain composite laminate cell of dimension 20×18.2 mm² formed by 3 phases: matrix, fibres and interfaces. The thicknesses of these layers are: 0.625mm for matrix, 0.625mm for fibres and 0.025mm for interphases. The entire cell was divided into pixels by a 400×728 Fourier grid. Each layer of the composite is assumed to be linearly elastic and isotropic. The material parameters of each component are listed in Table 1:

Table 1: Material constants of the components

	E (MPa)	ν	σ_c (MPa)	K_{Ic} (MPa√mm)	R (mm)
Matrix (epoxy)	5100	0.35	100	50 or 200	0.105 or 1.486
Fibre (carbon)	210000	0.27	1400	700	0.105
Interphase	10451	0.3483	40 or 60	20 or 30	0.2906

The external loads can be applied by imposing average stresses $\Sigma_{11} > 0$, $\Sigma_{22} = \Sigma_{12} = 0$ or average strains $E_{11} > 0$, $E_{22} = E_{12} = 0$. The FFT simulations were carried out step by step with small crack growth (about 0.1mm) at each step until the full failure of the cell. We present hereafter a FFT simulation with a reference configuration, i.e., the basic cell subjected to a uniaxial tension by imposing average stresses $\Sigma_{11} > 0$ and $\Sigma_{22} = \Sigma_{12} = 0$ as remote loads.

Figure 3a illustrates the global response, i.e., the E_{11}–Σ_{11} curve of the cell during the loading. Figures 3b, shows the fracture patterns of the cell at the end of the failure process. With the aid of these figures, we can describe the fracture process of the composite as follows:

1. Under uniaxial tension, the global response of the composite laminate presents a saw-tooth snap-back feature. Each tooth represents the crack growth though a fibre layer;

2. When a short crack grows in a layer of matrix and meets a fibre, a high level load is needed to overcome this energy barrier. It first deviates a little into the interface or in the matrix before entering in the fibre;
3. When the crack grows in a layer of fibre and meets the matrix, it deviates slightly in the matrix before penetrating into the matrix. As the matrix strength is much lower than that of the fibre, the remote load drops significantly;
4. As the transversal main crack grows and becomes longer, the length of its deviations into the interfaces increases when it meets a fibre;
5. We can remark that the interface debonding acts as a crack arrestor as described in previous studies [3]. When the crack propagates in an interface, the crack tip mode mixity varies from mode I toward mode II. Its growth requires more and more energy according to the interface fracture criterion (Equation 15);

As a result of the interface debonding, the final fracture surfaces take a stair form as observed in previous experimental studies [22-23].

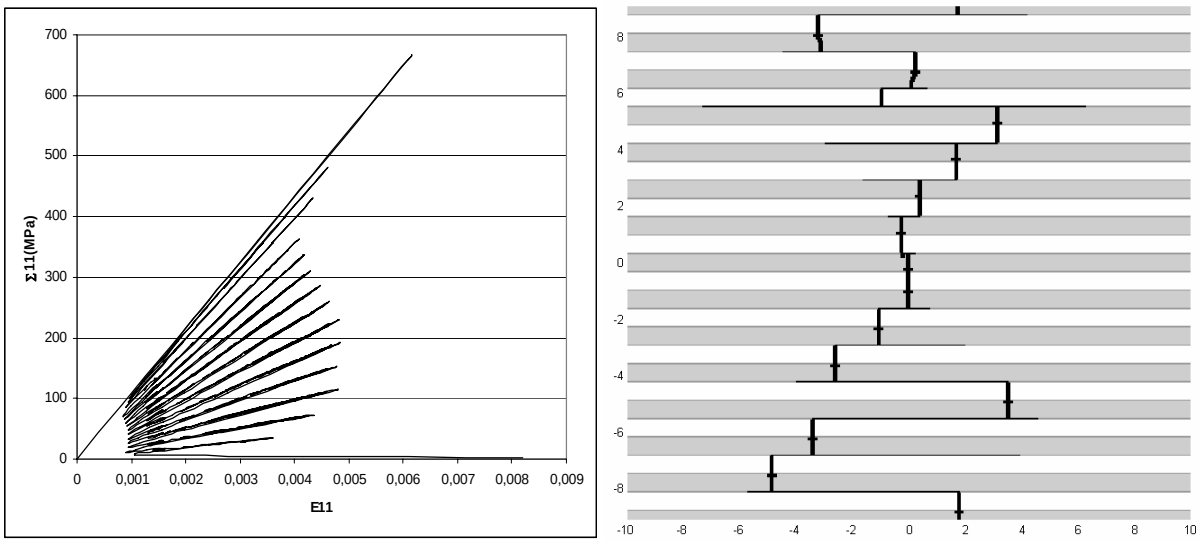

(c) (d)

Figure 3: Global response (a) and fracture patterns at the beginning (b), the middle (c) and the end (d) of the failure process of the basic cell under uniaxial tension

5: Discussions and concluding remarks

In this work, we have established a non-local fracture model and resolved it by using the Fast Fourier Transforms (FFT). The maximal stress criterion was adapted by means of the non-local concept in order to describe the fracture in brittle and quasi-brittle materials. The non-local model enables the predicted damage to be independent of the grid size. Moreover, the proposed model is equivalent to the Griffith-Irwin criterion when a macro-crack is formed. Consequently, the proposed fracture model is capable to predict crack initiation as well as crack growth. Comparisons with analytical results on pure mode-I cracks show that the proposed approach is highly efficient and accurate.

Through the examples above-presented, we can confirm that the proposed non-local crack growth models are highly accurate and efficient for the prediction of crack onset and crack propagation. Fracture in complicated microstructures can easily be simulated. Another notable advantage of the present method is its capacity to evaluate multiple crack growth as it doesn't require the calculation of the energy release rate at each crack tip. The theoretical concept of the proposed non-local fracture criterion is clear and simple. The numerical model is robust, easy to apply to different engineering structures subjected to thermal shock.

References

[1] McClintock, F. A., 1958. Ductile Fracture Instability in Shear. J. Appl. Mech., 10, 582-588
[2] Irwin G, (1968), Linear fracture mechanics, fracture transition and fracture control, Eng. Fract. Mech., 1:241-257
[3] Ritchie, R., Knott, J., and Rice, J., 1973. On the Relation between Critical Tensile Stress and Fracture Toughness in Mild Steel. J. Mech. Phys. Solids, 21, 395-410
[4] Seweryn, A., Lukaszewicz, A., 2002. Verification of Brittle Fracture Criteria for Elements with V-shaped Notches. Eng. Fract. Mech., 69, 1487-1510
[5] Leguillon, D., 2002. Strength or Toughness? A Criterion for Crack Onset at a Notch, Eur. J. Mech. A/Solids, 21, 61-72
[6] Barenblatt, G., 1959. The Formation of Equilibrium Cracks During Brittle Fracture, J. Appl. Math. Mech., 23, 434-444.
[7] Dugdale, D., 1960. Yielding of Steel Sheets Containing Slits. J. Mech. Phys. Solids, 8, 100–104.
[8] Xu, X. P., and Needleman, A., 1994. Numerical Simulation of Fast Crack Growth in Brittle Solids. J. Mech. Phy. Solids, 42, pp. 1397-1434
[9] Camacho, G.T., and Ortiz M., 1996. Computational Modelling of Impact Damage in Brittle Materials, Int. J. Solids Struct., 33, 2899–938.
[10] Mohammed, I., and Liechti, K.M., 2000. Cohesive Zone Modelling of Crack Nucleation at Bimaterial Corners. J. Mech. Phys. Solids, 48, 735–64.
[11] Pijaudier-Cabot, G., Bazant, Z.P., 1987. Nonlocal damage theory. J. of Engng. Mechanics, ASCE, 113, 1512-1533.
[12] Peerlings, R., de Borst, R., Brekelmans, W., De Vree, J., Spee, I., 1996. Some observations on localisation in non-local and gradient damage models. Eur. J. Mech. A/Solid, 15(6), 937-953
[13] Frémond, M., Nedjar, B., 1996. Damage, gradient of damage and principle of virtual power. Int. J. Solids Struct. 33, 1083-1103
[14] Francfort, G., Marigo, J-J., 1998. Revisiting brittle fracture as an energy minimization problem, J. Mech. Phys. Solids, 46, 1319-1342.
[15] Bourdin, B., Francfort, G., Marigo, J-J., 2000. Numerical experiments in revisited brittle fracture, J. Mech. Phys. Solids, 48, 797-826.
[16] Williams ML, (1961), The bending stress distribution at the base of a stationary crack. J. of Appl. Mech., 28:78–82
[17] Moulinec H, Suquet P (1998), A numerical method for computing the overall response of nonlinear composites with complex microstructure. Comput. Methods Appl. Mech. Engrg.; 157:69–94

[18] Li Jia, Tian Xiao Xiao, Abdelmoula Radhi, A damage model for crack prediction in brittle and quasi-brittle materials solved by the FFT method, International Journal of Fracture, 2012, Vol 173:135–146

[19] Ostoja-Starzewski M, Sheng PY, Alzebdeh K, (1996), Spring network models in elasticity and fracture of composites and polycrystals. Comput. Mater Sci., 7: 82–93

[20] Karihaloo BL, Shao PF, Xiao QZ, (2003), Lattice modelling of the failure of particle composites. Engng. Fract. Mech., 70-2385–2406

[21] Lilliu G, van Mier JGM., (2003), 3D lattice type fracture model for concrete, Engng. Fract. Mech., 70:927–941

[22] Raynaud C. Céramique lamellaires monolithiques en carbure de silicium, PhD Thesis, Ecole Nationale des Mines de St Etienne and Institut National Polytechnique de Grenoble, 2002.

[23] Tariolle S. Carbure de bore monolithique poreux et composites laminaires. PhD Thesis, Ecole Nationale des Mines de St Etienne and Institut National Polytechnique de Grenoble, 2003.

Ferritic-pearlitic ductile cast irons: is ΔK a useful parameter?

Francesco Iacoviello[1,*], **Vittorio Di Cocco**[1], **Alessandra Rossi**[1], **Mauro Cavallini**[2]

[1] Università di Cassino e del Lazio Meridionale, DICeM, via G. Di Biasio 43, 03043, Cassino (FR), Italy
[2] Università di Roma "La Sapienza", DICMA, via Eudossiana 18, Roma, Italy
* Corresponding author: iacoviello@unicas.it

Abstract In the last years, the role played by graphite nodules was deeply investigated by means of tensile and fatigue tests, performing scanning electron microscope (SEM) observations of specimens lateral surfaces during the tests ("in situ" tests). According to the experimental results, it is evident that graphite nodules damaging micromechanisms can't be merely classified as matrix nodule debonding, but depend on different parameters (e.g., loading conditions and matrix microstructure). In this work, the influence of microstructure and loading conditions on fatigue crack propagation resistance in DCIs is discussed. On the basis of experimental results, the applicability of ASTM E399 standard on the characterization of fatigue crack propagation resistance in ferritic-pearlitic DCIs is critically analyzed, mainly focusing the stress intensity factor amplitude role.

Keywords Fatigue crack propagation; Ductile cast irons; Damaging micromechanism; Stress intensity factor.

1. Introduction

In 1943, during the American Foundry Society (AFS) convention, J. W. Bolton made the following statements: *Your indulgence is requested to permit the posing of one question. Will real control of graphite shape be realized in gray iron? Visualize a material, possessing (as-cast) graphite flakes or groupings resembling those of malleable iron instead of elongated flakes* [1]. A few weeks later, in the International Nickel Company Research Laboratory, an addition of magnesium (as a copper-magnesium alloy) allowed to obtain nearly perfect spheres of graphite and, consequently, the first *ductile cast iron* (DCI), also known as nodular cast iron [2]. In 1948, always in the AFS Convention, the production of spherical graphite in iron by the addition of small amounts of cerium was announced by Henton Morrogh of the British Cast Iron Research Association. The first advantage of this production technique is evident: no high temperature/long duration heat treatments are necessary to obtain the desired shape of graphite elements (nodules), with a consequent strong cost reduction and really interesting mechanical properties: DCIs are able to combine the good castability of gray irons and the toughness of steels! In the last decades, different chemical compositions and heat treatments have been optimized in order to control the matrix microstructure and obtain different combinations of mechanical properties. Nowadays, DCIs are mainly used in the form of ductile iron pipes (for transportation of raw and tap water, sewage, slurries and process chemicals), but they are also widely used in safety related components for automotive applications (gears, bushings, suspension, brakes, steering, crankshafts) and in more critical applications as containers for storage and transportation of nuclear wastes. Matrix controls mechanical properties and matrix names are used to designate spheroidal cast iron types [3-5]. Ferritic DCI are characterized by good ductility and a tensile strength that is equivalent to a low carbon steel. Pearlitic DCIs show high strength, good wear resistance and moderate ductility. Ferritic–pearlitic grades properties are intermediate between ferritic and pearlitic ones. Martensitic ductile irons show very high strength, but low levels of toughness and ductility. Bainitic grades are characterized by a high hardness. Austenitic ductile irons show good corrosion resistance, good strength and dimensional stability at high temperature. Austempered grades show a very high wear resistance and fatigue strength.

Focusing the graphite nodules, Magnesium is the most common spheroidizing element used in the DCIs production: other elements like Si, Ca and rare earths are commonly added to reduce the

reaction violence and to promote graphite nodulizing, controlling the effect of impurities on nodules morphology and the matrix microstructure [6]. Different graphite elements nucleation theories are proposed in literature, mainly based on “heterogeneous mechanisms” (e.g. gas bubble theory, graphite theory, silicon carbide theory etc.) [7], and also different graphite nodules growth mechanisms are proposed [8]. The results obtained by other authors [9-11] by means of nanoindentation tests and by means of Micro Raman Spectroscopy and Electron Probe Microanalysis confirms the presence of a substructure in graphite nodules and of a gradient of mechanical properties, with cementite plates/particles that are trapped in and around the spherulite and multicomponent particles of Mg, Fe, S, C, etc. that are trapped in the spherulite or accumulate on the edges of the spherulite upon solidification. It is worth to note that, although the graphite tensile resistance is not negligible if compared to ferrite, it is its compression strength is absolutely not negligible, with compression resistance values that can be even 200 MPa [12, 13].
Fatigue crack propagation resistance in DCI is usually investigated according to ASTM E647 [14], analyzing the evolution of the crack growth rate (da/dN) with the increase of the stress intensity factor amplitude (ΔK), [15-19]. Considering that DCIs are characterized by a substantially composite microstructure, with graphite nodules that are a consistent volume fraction (usually about 10-15 %), the material homogeneity condition can be considered as critical in order to apply Linear Elastic Fracture Mechanics principles, and use the stress intensity factor range (ΔK) in order to characterize the stress conditions at the crack tip. In this work the fatigue crack propagation resistance of a three different ferritic-pearlitic DCI has been re-analyzed [19, 20].

2. DCIs fatigue crack propagation: Materials and tests results analysis

The investigated ferritic-pearlitic DCIs were obtained by means of chemical composition control: as a results, investigated matrix microstructures ranged from a completely ferritic DCI up to a completely pearlitic one (Figures 1-3). Chemical compositions and phases volume fractions are in Tab. 1-3.

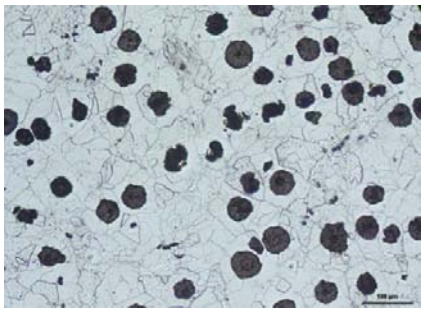

Figure 1. DCI EN GJS350-22 microstructure (100% ferrite).

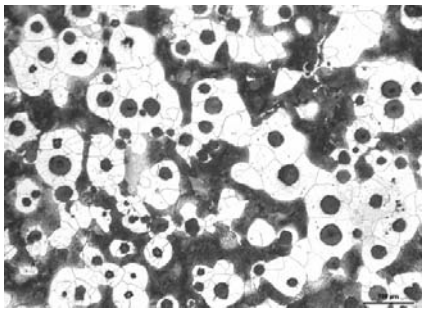

Figure 2. DCI EN GJS500-7 microstructure (50% ferrite – 50% pearlite).

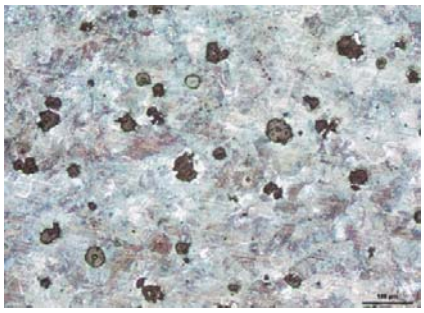

Figure 3. DCI EN GJS700-2 microstructure (100% pearlite).

Table 1. DCI EN GJS350-22 chemical composition (100% ferrite).

C	Si	Mn	S	P	Cu	Cr	Mg	Sn
3.66	2.72	0.18	0.013	0.021	0.022	0.028	0.043	0.010

Table 2. DCI EN GJS500-7 chemical composition (50% ferrite – 50% pearlite).

C	Si	Mn	S	P	Cu	Cr	Mg	Sn
3.65	2.72	0.18	0.010	0.03	-	0.05	0.055	0.035

Table 3. DCI EN GJS700-2 chemical composition (100% pearlite).

C	Si	Mn	S	P	Cu	Mo	Ni	Cr	Mg	Sn
3.59	2.65	0.19	0.012	0.028	0.04	0.004	0.029	0.061	0.060	0.098

Fatigue crack propagation tests were performed in laboratory conditions according to ASTM E647 standard [14], using 10 mm thick CT (Compact Type) specimens and considering three different stress ratio values (e.g. $R=P_{min}/P_{max}$ = 0.1; 0.5; 0.75). Tests were performed using a computer controlled servohydraulic machine in constant load amplitude conditions, considering a 20 Hz loading frequency, a sinusoidal loading waveform. Crack length measurements were performed by means of a compliance method using a double cantilever mouth gage and controlled using an optical microscope (x40).

In order to investigate the fatigue crack propagation micromechanisms, in [19, 20] the following procedures were applied:

- Scanning electron microscope (SEM) observations of the crack path during fatigue crack propagation test (cracks propagate from left to right);
- "Traditional" SEM fracture surface analysis (cracks propagate from left to right);
- 3D fracture surface reconstruction performed after SEM analysis;
- Light optical microscope (LOM) transversal crack paths analysis.

Microstructure and stress ratio influence on fatigue crack propagation resistance in ferritic-pearlitic DCIs is summarized in Figure 4.

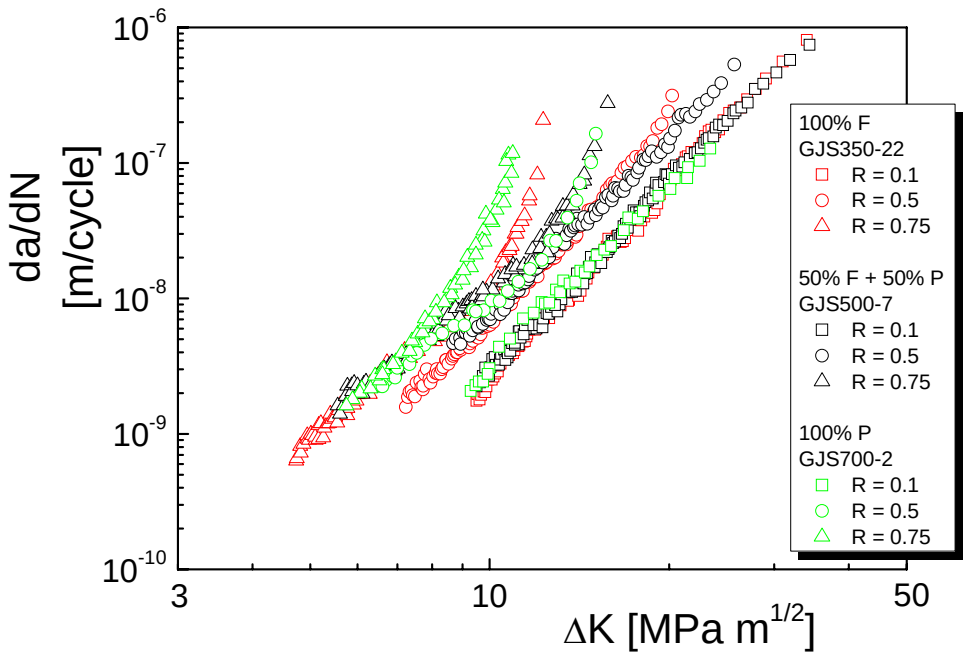

Figure 4. Loading conditions influence on fatigue crack propagation in ferritic-pearlitic DCIs.

3. LEFM considerations

Considering the linear elastic fracture mechanics principles, stress intensity factor "K" is used to quantify the stress state ("stress intensity") near the crack tip caused by a remote load or residual

stresses and, considering fatigue crack propagation, stress intensity factor range (e.g. $\Delta K = K_{max}-K_{min}$) is the main parameter used to characterize the stress conditions at the crack tip. Both K and ΔK usefulness is confirmed only considering an homogeneous and linear-elastic body: obviously, a crack tip plastic zone is always present, but, if its radius is negligible, the K parameter is still valid. Under monotonic loading, plastic zone size is usually estimated as follows:

$$r_y = \frac{1}{2\pi}\left(\frac{K}{\sigma_y}\right)^2 \quad \text{(plane stress conditions)} \tag{1}$$

$$r_y = \frac{1}{6\pi}\left(\frac{K}{\sigma_y}\right)^2 \quad \text{(plane strain conditions)} \tag{2}$$

Considering, as a first approximation, the investigated DCIs as homogeneous materials, the plastic zones size corresponding to the K_{max} value under plane strain conditions ($r_{pzK_{max}}$), calculated for the first and the last measured ΔK values (ΔK_1 and ΔK_2 respectively], can be summarized in Table 4, 5 and 6 (σ_y are considered equal to 220, 320 and 430 MPa, for the ferritic, ferritic-pearlitic and pearlitic investigated DCIs respectively). It is necessary to underline that the considered ΔK_1 and ΔK_2 are not the ΔK values corresponding respectively to the threshold and final fracture conditions, but they only can be considered as a first evaluation.

Table 4. DCI EN GJS350-22: evaluation of the plastic zone size (plane strain conditions).

R (K_{min}/K_{max})	ΔK_1 [MPa√m]	$r_{pzK_{max}}$ [mm]	ΔK_2 [MPa√m]	$r_{pzK_{max}}$ [mm]
0.1	9	0.109	32	1.368
0.5	7	0.214	20	1.754
0.75	4.5	0.355	11	2.120

Table 5. DCI EN GJS500-7: evaluation of the plastic zone size (plane strain conditions).

R (K_{min}/K_{max})	ΔK_1 [MPa√m]	$r_{pzK_{max}}$ [mm]	ΔK_2 [MPa√m]	$r_{pzK_{max}}$ [mm]
0.1	9	0.052	32	0.655
0.5	8	0.133	27	1.511
0.75	5	0.207	14	1.625

Table 6. DCI EN GJS700-2: evaluation of the plastic zone size (plane strain conditions).

R (K_{min}/K_{max})	ΔK_1 [MPa√m]	$r_{pzK_{max}}$ [mm]	ΔK_2 [MPa√m]	$r_{pzK_{max}}$ [mm]
0.1	9	0.030	22	0.179
0.5	6	0.040	13	0.203
0.75	5.5	0.145	10	0.481

Considering Figures 1-3, graphite nodules maximum diameters (d_{max}) in the investigated DCIs are respectively equal to:

- about 60-70 μm for DCI EN GJS350-22;
- about 40-50 μm for DCI EN GJS500-7 (but it is necessary to remember that nodules are surrounded by ferritic shields that are sometimes interconnected, up to 300 μm of diameter, Figure 2);
- about 45-55 μm for DCI EN GJS700-2.

Comparing d_{max} and $r_{pzK_{max}}$ values, considering that the graphite volume fraction is not negligible

(usually about 10-15%) and considering that fatigue crack propagation is characterized by the presence of a "reversed" or "cyclic" plastic zone, r_{rpz} (four times lower than the monotonic value corresponding to K_{max}) and that the tensile load reduction from the σ_{max}, and the presence of the surrounding elastic body, implies a compression condition at the crack tip, it is evident that for lower applied ΔK and/or R values:

- it is quite difficult to consider ferritic-pearlitic DCIs as homogeneous material;
- compression stress conditions are completely developed in the graphite elements at the crack tip.

Furthermore, it is necessary to remember that ferritic-pearlitic DCIs microstructure components are characterized by different mechanical properties:

- σ_Y of ferrite depends on the grain diameter, but can be assumed between 180 and 320 MPa [21].
- σ_Y of pearlite depends on the lamellae spacing, but can be assumed between to 400 and 800 MPa [21].
- graphite tensile strength is quite low (25 – 30 MPa, max [22]), but it's compression resistance is higher (even 200 MPa [23]).

On the basis of these considerations, the influence of the graphite nodules on the fatigue crack propagation should be dependent on the microstructure:

- ferritic matrix: for lower R and ΔK values the homogeneity condition is not respected; considering the r_{rpz}, it is evident that for all the investigated R values, for lower nominal ΔK values, the compression stress state is almost completely developed in the graphite nodules. Corresponding to higher ΔK values the homogeneity condition can be considered as respected, but the crack tip plastic zone can't be considered negligible (especially in plane stress conditions).
- pearlitic matrix: for all the investigated loading conditions the homogeneity condition is not respected, with d_{max} values comparable with $r_{pzK_{max}}$ values (with the exception of the higher nominal ΔK and R values); furthermore, for almost all the investigated loading conditions, the compression stress state in the reversed plastic zone is completely developed in the graphite nodules.
- ferritic-pearlitic matrix: considering the bulls eye structure of ferrite around the nodules, and the different mechanical behaviour of ferrite and pearlite, corresponding to lower nominal ΔK values, the homogeneity condition is not respected. Focusing the reversed plastic zone, corresponding to the lower ΔK values, r_{rpz} values are comparable to d_{max} values, with the compression state that is developed inside the graphite nodules. Considering the ferritic grains around the graphite nodules, the problem of the material homogeneity is evident also for ΔK values in the Paris stage.

4. Fatigue crack propagation micromechanisms

In this section, on the basis of the considerations of Section 3, and considering results already published in [19, 20], fatigue crack propagation micromechanisms in ferritic-pearlitic DCIs are re-analyzed.

Considering the ferritic DCI, the main interactions between the fatigue crack and the graphite nodule are shown in Figure 5 and 6. For lower nominal ΔK values ($r_{pzK_{max}}$ and r_{rpz} values are comparable to d_{max} values) the compression state is completely developed in the graphite nodules and secondary cracks initiate and propagate inside the nodules, with a sort of "onion-like" morphology (Figure 5). The increase of the applied ΔK implies a modification of the interaction

between graphite nodules and ferritic matrix, with the graphite nodule - ferritic matrix debonding as the main damaging micromechanism.

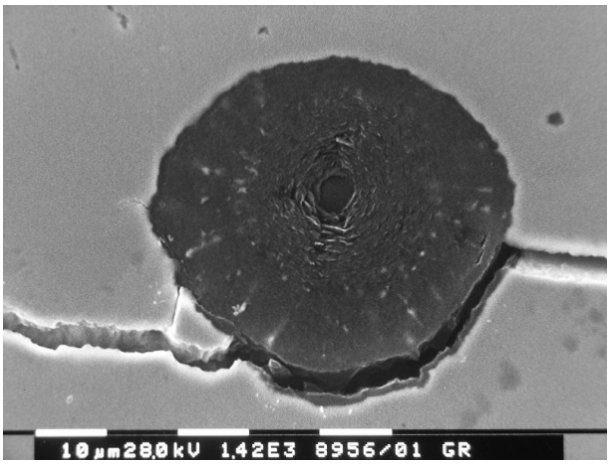

Figure 5. DCI EN GJS350-22 fatigue crack path. SEM observation of the specimen lateral surface (R = 0.1, ΔK = 10 MPa√m).

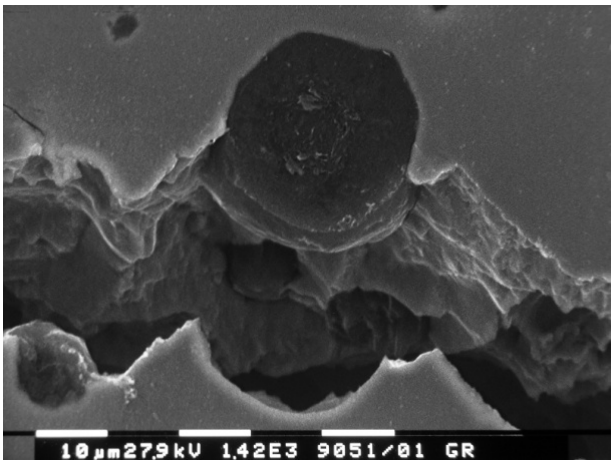

Figure 6. DCI EN GJS350-22 fatigue crack path. SEM observation of the specimen lateral surface (R = 0.1, ΔK = 22 MPa√m).

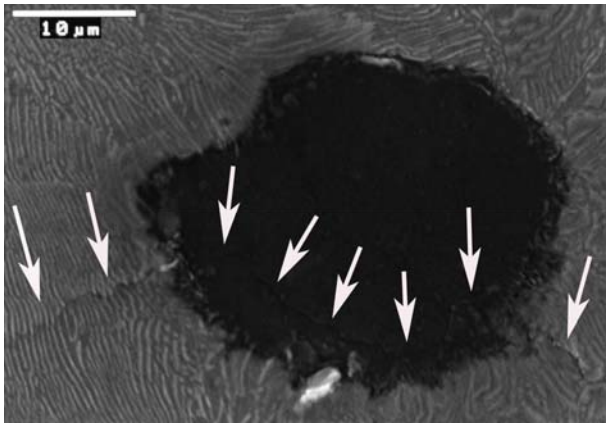

Figure 7. DCI EN GJS700-2 fatigue crack path. SEM observation of the specimen lateral surface (R = 0.1, ΔK = 22 MPa√m).

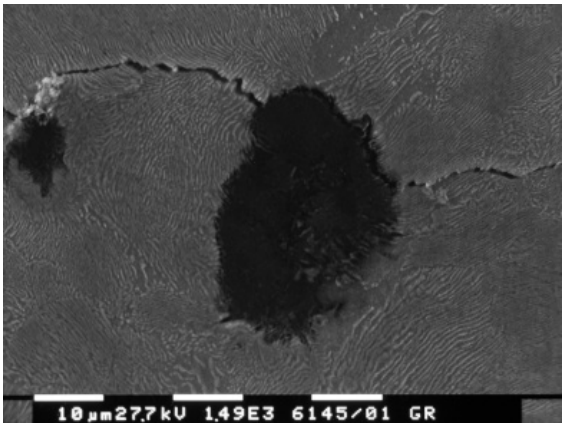

Figure 8. DCI EN GJS700-2 fatigue crack path. SEM observation of the specimen lateral surface (R = 0.5, ΔK = 10 MPa√m).

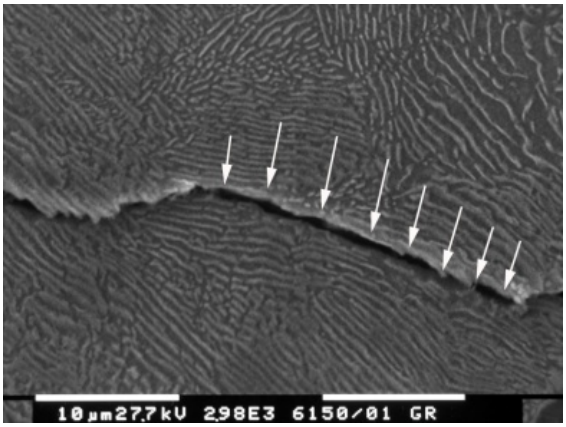

Figure 9. DCI EN GJS700-2 fatigue crack path. SEM observation of the specimen lateral surface (R = 0.75, ΔK = 7 MPa√m).

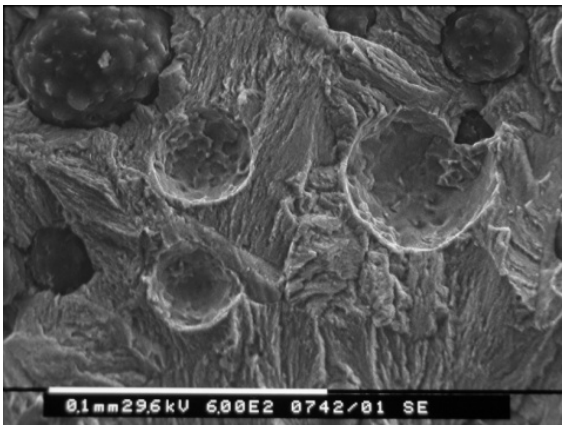

Figure 10. DCI EN GJS700-2, SEM fracture surface analysis (R = 0.1, ΔK = 16 MPa√m).

Focusing on the pearlitic DCI, the "onion like" mechanism is observed often also for higher ΔK values (Figure 7; arrows inside the graphite nodule). If the crack meets the nodule "tangentially", matrix – graphite debonding is also observed (Figure 8).
It is worth to note that the interaction between the pearlite lamellae and the fatigue crack depends on their reciprocal orientation: in fact, in Figure 7 (arrows in the matrix) the pearlitic lamellae are almost orthogonal to the crack path, with a consequent "transgranular" crack: performing a traditional SEM observation of the crack surface, these cracked lamellae have a morphology that is analogous to fatigue striations (Figure 10). If pearlitic lamellae are almost parallel to the crack path, ferrite is the preferential propagation path (arrows in Figure 7), and a traditional SEM observation of the crack surface shows a sort of cleavage.
The analysis of the microstructure influence on fatigue crack propagation in a ferritic-pearlitic DCI (with "bulls eye" microstructure morphology) is complicated by the phases distribution in the metal matrix. For all the investigated R values, considering lower ΔK values, r_{rpz} values (always calculated considering the investigated DCI as a homogeneous material) are always comparable to d_{max} values. For higher ΔK values, the graphite nodules presence is less critical. Ferritic zones around the graphite nodules are comparable to the r_{rpz} values also for the higher ΔK values. Considering the different tensile mechanical behavior of ferrite and pearlite, during fatigue loading, with K that ranges between K_{max} and K_{min}, deformation level in the involved microstructure components (ferrite and pearlite) is quite different:

- For higher K values (nearby K_{max}), plastic deformation level in ferritic shields is higher than in pearlitic matrix, due to the higher ferrite ductility;
- For lower K values (nearby K_{min}), pearlitic matrix induces a compression stress state on ferritic shields and, consequently, on graphite nodules, with an increase of crack closure effect importance. The superposition of this mechanism to the compression stress state due to the reversed plastic zone is more and more evident with the increase of ΔK and R values, with a consequent increase of the fatigue crack propagation resistance (as observed in Figure 4).

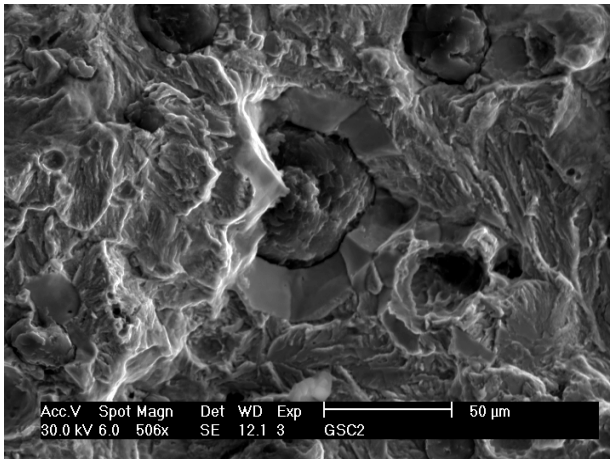

Figure 10. DCI EN GJS500-7, SEM fracture surface analysis (R = 0.1, ΔK = 15 MPa√m).

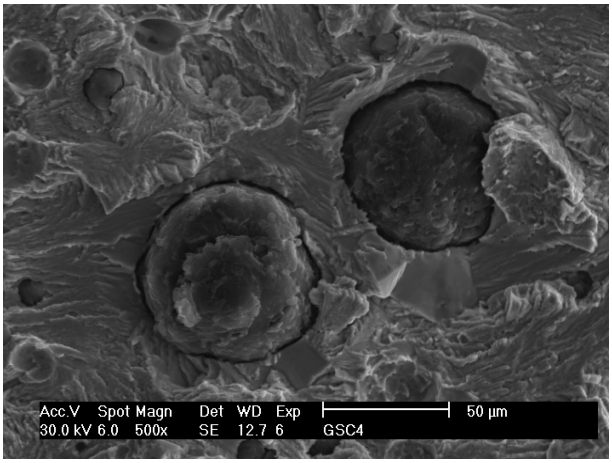

Figure 11. DCI EN GJS500-7, SEM fracture surface analysis (R = 0.75, ΔK = 8 MPa√m).

Ferritic-pearlitic DCI fracture surfaces are characterized by the presence of cleavage in ferritic shields around the graphite nodules (Figures 10 and 11) and, analogously to the pearlitic, "striations" are manly due to a "transgranular" damaging mechanism of pearlitic lamellae. All the

possible interactions between fatigue crack and graphite nodules are observed, probably due to the crack propagation direction with respect to the nodule position and to the graphite element nodularity:

- graphite nodule – matrix debonding (probably more frequent);
- onion like mechanism;
- fracture inside the graphite nodules.

5. Conclusions

Fatigue crack propagation resistance in DCI is usually investigated according to ASTM E647, investigating the evolution of the crack growth rate (da/dN) with the increase of the stress intensity factor amplitude (ΔK). Considering that DCIs are characterized by a substantially composite microstructure, with graphite nodules that are a consistent volume fraction (usually about 10-15 %), and considering the different mechanical behavior of the microstructure components, the material homogeneity condition can be considered as critical in order to apply Linear Elastic Fracture Mechanics principles.

In this work, the fatigue crack propagation resistance of a three different ferritic-pearlitic DCI has been re-analyzed, investigating the crack propagation micromechanisms and reconsidering the stress intensity factor range (ΔK) ability to characterize the stress conditions at the crack tip.

According to the observed crack propagation micromechanisms and to LEFM considerations it is possible to summarize as follows:

- Ferritic DCI: considering lower nominal ΔK and R values, $r_{pzK_{\max}}$ and r_{rpz} values that are comparable to maximum values of the graphite elements diameter; as a consequence the material homogeneity condition is not respected.
- Pearlitic DCI: $r_{pzK_{\max}}$ and r_{rpz} values that are comparable to maximum values of the graphite elements diameter for almost all the investigated loading conditions; as a consequence the material homogeneity condition is not confirmed.
- Ferritic-pearlitic DCI (with “bulls eye” microstructure morphology): for all the investigated R values, considering lower ΔK values, r_{rpz} values are always comparable to the graphite elements diameter. Corresponding to higher ΔK values, the graphite nodules presence is less critical; however, ferritic zones around the graphite nodules comparable to the r_{rpz} values also for the higher ΔK values.

As a consequence of this analysis, it is possible to conclude that, in order to analyze the fatigue crack propagation resistance of ferritic-pearlitic DCIs, stress intensity factor range ΔK is not able to describe the effective stress state at the crack tip for all the investigated conditions and it should be considered only a first approximation of the stress state based on the wrong hypothesis of a homogenous material.

6. References

[1] http://www.ductile.org/didata/Section2/2intro.htm
[2] D. K. Millis, P. A. Gagnebin, B. N. Pilling, Cast Ferrous Alloy, US patent 2485760, issued 1949-10-25.
[3] L.R. Jeckins, R.D. Forrest, Properties and selection: iron, steels and high performance alloys. ASM Handbook Ductile Iron, Metal Park (OH) ASM International, 1 (1993) 35-55.
[4] R.G. Ward, An Introduction to the Physical Chemistry of Iron and Steel Making. Arnold, London, 1962.

[5] C. Labrecque, M. Gagne. Review ductile iron: fifty years of continuous development. Can. Metall. Quart., 37 (1998) 343-378.
[6] T. Skaland, Ø. Grong, T. Grong. A model for the graphite formation in Ductile Cast Iron: Part I. Inoculation Mechanisms. Metallurgical Transactions A. 24A (1993) 2321-2345
[7] T. Skaland, Nucleation mechanisms in ductile iron (2005). Proceedings of the AFS Cast Iron Inoculation Conference, Schaumburg, Illinois, USA.
[8] D. M. Stefanescu. Solidification and modeling of cast iron—A short history of the defining moments, Materials Science and Engineering A, 413–414 (2005) 322–333.
[9] S. K.Pradhan, B. B.Nayak, B. K. Mohapatra, B. K. Mishra. Micro Raman spectroscopy and Electron Probe Microanalysis of graphite spherulites and flakes in cast irons. Metallurgical and materials transactions A. 38A (2007) 2363-2370.
[10] S. K. Pradhan, B. B. Nayak, S. S. Sahay, B. K. Mishra. Mechanical properties of graphite flakes and spherulites measured by nanoindentation. Carbon. 47 (2009) 2290-2299.
[11] N. X. Randall, M. Vandamme, F.-J. Ulm. Nanoindentation analysis as a two-dimensional tool for mapping the mechanical properties of complex surfaces. J. Mater. Res.. 24(3) (2009) 679-690.
[12] Union Carbide Corporation. Research and Development on Advanced Graphite Materials - Process development for graphite materials (1964). Technical Report No. WADD TR 61-72, - Air Force Materials Laboratory, Union Carbide Corporation, 35.
[13] http://www.azom.com, The A to Z of Materials.
[14] ASTM E647 – 11, Standard Test Method for Measurement of Fatigue Crack Growth Rates.
[15] K. Tokaji, T. Ogawa, K. Shamoto, Fatigue crack propagation in spheroidal graphite cast irons with different microstructure, Fatigue, 16 (1994) 344-350.
[16] G.L. Greno, J.L. Otegui, R.E. Boeri, Mechanisms of fatigue crack growth in Austempered Ductile Iron, Int. J. fo Fatigue, 21 (1999) 35-43.
[17] J. Yang, S.K. Putatunda, Near threshold fatigue crack growth behaviou of austempered ductile cast iron (ADI) processed by a novel two-step austempering process, Material Science and Engineering A, 393 (2005) 254-268.
[18] T. Mottitschka, G. Pusch, H. Biermann, L. Zybell, M. Kuna, Fatigue crack growth in nodular cast iron - Influences of graphite spherical size and variable amplitude loading, Journal of Physics: Conference Series 240 (2010) 012060.
[19] M. Cavallini, O. Di Bartolomeo, F. Iacoviello. Fatigue crack propagation damaging micromechanisms in ductile cast irons. Engineering Fracture Mechanics, 75 (2008) 694-704.
[20] F. Iacoviello, V. Di Cocco, M. Cavallini, Ductile cast irons: microstructure influence on fatigue crack propagation resistance. Frattura ed Integrità Strutturale, 13 (2010), 3-16.
[21] Metals Handbook Desk Edition, Second Edition, J.R. Davis, Editor, (1998) 153-173.
[22] Union Carbide Corporation. Research and Development on Advanced Graphite Materials - Process development for graphite materials. Technical Report No. WADD TR 61-72, - Air Force Materials Laboratory, Union Carbide Corporation, 35 (1964).
[23] http://www.azom.com, The A to Z of Materials.

Modeling of Strain Localization and Failure in Vanadium under Quasistatic Loading

Anastasia Kostina*, Yuriy Bayandin, Oleg Plekhov, Oleg Naimark

Institute of continuous media mechanics UB RAS, Perm, 614013, Russia
* Corresponding author: kostina@icmm.ru

Abstract The process of plastic deformation and failure of metals is accompanied by set of phenomena which cannot be easily modeled in the framework of classical models. The effects of strain localization and energy dissipation under deformation and failure require an adequate description of structure evolution at different stages of deformation process. This description can be developed based on the results of statistical model of typical mesodefect ensemble proposed in the Institute of continuous media mechanics UB RAS. The model takes into account bulk and shear parts of defect density tensor. Defect evolution is described by kinetic equations for two structural parameters: second order defect density tensor and scalar parameter, depending on the ratio of two characteristic scales (the mean size of defects and mean distance between them). The numerical simulation of strain localization and crack propagation were carried out in the finite-element package Simulia Abaqus Student Edition using procedure UMAT and XFEM.

Keywords defect evolution, energy dissipation, numerical simulation

1. Introduction

Nowadays investigation of metal fracture and knowledge of its laws have great importance in the developments of various designs and constructions. To create new technologies and improve existing ones one has to reach a more deep understanding of physical nature of failure. This understanding is needed in order to describe such phenomena, accompanying failure, as energy dissipation and strain localization.

Most existing models assume that the material failure takes place at the final stage of plastic deformation. However, the data obtained from systematic studies of defects evolution, carried out at Physical-technical institute named after A.F. Ioffe RAS [1] shows that the defects play the important role in deformation process at every stage of plastic deformation. These defects emergence at the early stage of deformation and effect on the microplasticity and failure processes. The models described the interaction between damage accumulation and plasticity processes were developed in [2-3] In this paper, the metal deformation behavior under quasi-static loading is described by one of such models, developed at the Institute of continuous media mechanics UB RAS.

The description of damage accumulation includes a consideration of the mesodefect ensemble evolution, their coherent development and interaction, the effect on the relaxation properties of materials and merging into the main crack.

The practical application of developed model requires both the verification of materials functions and generalization of the model for three dimension case. The most effective way for modeling of complex deformation phenomena is incorporation of this model for the standard finite - element packages.

This work is devoted to the generalization of developed earlier statistical based phenomenological elasto-visco-plastic model of defect evolution under deformation and failure in metals. The model takes into account defect density tensor separation bulk and shear parts. Defect evolution is described based on the kinetics of two parameters: the first parameter is second order defect density tensor, the second one - scalar parameter, depending on the ratio of two characteristic scales (the mean size of defects and mean distance between them).

The numerical simulation of strain localization on (plastic wave propagation) and crack propagation

in plate vanadium specimen under quasi-static tension, compression of inclined cylindrical specimen were carried out in the finite-element package Simulia Abaqus using procedure UMAT. The big attention was paid on the calculation of plastic work and heat dissipation under investigated process. The results were compared with original experimental data, and with the results obtained using standard (incorporated in Abaqus) elasto–plastic model.

2. Mathematical model

Mesoscopic defects (mesoshears) can be described by the following tensor [3]

$$\mathbf{s} = \frac{1}{2} S \ \ \mathbf{lb} + \mathbf{bl} \ \ , \tag{1}$$

where $\mathbf{l}$ - a unit normal to the shear plane, $\mathbf{b}$ - unit vector in the shear direction, S - shift intensity.

Averaging $\mathbf{s}$ over an elementary volume allows us to introduce the tensor parameter $\mathbf{p}$, which can be considered as a deformation caused by the defects:

$$\mathbf{p} = n\langle \mathbf{s} \rangle, \tag{2}$$

where n - defect density.

Application of dimension analysis allowed us to allocate the scale invariant structural parameter δ as

$$\delta = \left(\frac{L_n}{L_c} \right)^3, \tag{3}$$

where L_n - the mean size of the defect, L_c - the mean distance between the defects.

Solution of the self-consistency equation between the tensor micro- and macroparameters $\mathbf{s}$ and $\mathbf{p}$ allows us to establish three characteristic mode of δ [2,3]. For values of $\delta > \delta_* = 1.3$, dependence of $p(\sigma)$ (the case of uniaxial loading) is monotone and the reaction of defect formation is reversible (Fig.1). There is a metastability respect to the parameter p, associated with the orientational degrees of mesoshears freedom in the range of $1 \approx \delta_c < \delta < \delta_*$. For $\delta < \delta_c$ the jump of p becomes infinite; this characterizes unstable reaction of solid on the microshear formation.

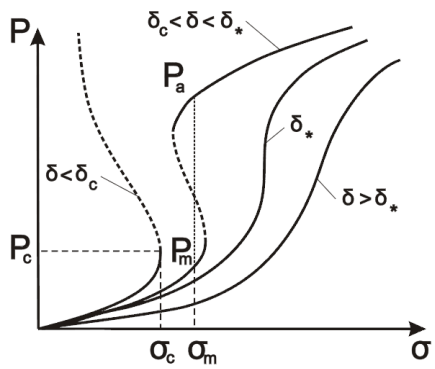

Figure 1. Typical response of a material on the defect growth

Material susceptibility to the defect growth in the deformation process in terms of δ should be determined by the current values of the structural scale i.e. the values of δ. It is also shown that these scales are determined by non-linear kinetics of $\mathbf{p}$ and thus, the defect density distribution determines the structural sensitivity to its further growth. The growth of the scales L_c, L_n means

original structure "coarsening" and the general trend is decrease of δ, this allows to assume that plasticity mechanisms and the transition to failure are the sequential structure-scaling transitions in ensembles developing substructure defects.

Full strain rate can be represented as the sum of three components: elastic strain rate $\dot{\boldsymbol{\varepsilon}}^e$, plastic strain rate $\dot{\boldsymbol{\varepsilon}}^p$ and strain rate caused by defects:

$$\dot{\boldsymbol{\varepsilon}} = \dot{\boldsymbol{\varepsilon}}^e + \dot{\boldsymbol{\varepsilon}}^p + \dot{\mathbf{p}}\,. \tag{4}$$

Elastic strains defined by linear Hooke's law:

$$\dot{\sigma}_0 = K\dot{\varepsilon}_0^e\,, \tag{5}$$

$$\dot{\boldsymbol{\sigma}}' = 2G\dot{\boldsymbol{\varepsilon}}'^e\,, \tag{6}$$

where K - isotropic elastic modulus, G - elastic shear modulus, σ_0 - spherical stress tensor, $\boldsymbol{\sigma}'$ - deviator of stress, ε_0 - spherical elastic strain tensor, $\boldsymbol{\varepsilon}'$ - deviator of elastic strain.

According to thermodynamic laws we can write dissipation inequality:

$$\boldsymbol{\sigma}' : \dot{\boldsymbol{\varepsilon}}^p - \frac{\partial F}{\partial \mathbf{p}} : \dot{\mathbf{p}} - \rho \mathbf{q} \cdot \frac{\nabla T}{T} \geq 0\,, \tag{7}$$

where F is a part of the free energy, which is responsible for the energy defect subsystem, ρ - density, $\mathbf{q}$ - heat flux vector, T - temperature.

Assuming a qusilinear relationship between the thermodynamic forces and flows, there were obtained constitutive equations for calculating kinetics of plastic and structural strains:

$$\dot{\boldsymbol{\varepsilon}}^p = A_\sigma \boldsymbol{\sigma}'\,, \tag{8}$$

$$\dot{\mathbf{p}} = A_p \left(-\frac{\partial F}{\partial \mathbf{p}} \right), \tag{9}$$

Parameters A_p, A_σ are kinetic coefficients having following form

$$A_\sigma = \exp\left(\frac{|\sigma|}{2G} \right) \frac{1}{2G\tau_\sigma}\,, \tag{10}$$

$$A_p = \exp\left(\frac{|\sigma|}{2G} \right) \frac{1}{2G\tau_p}\,. \tag{11}$$

These coefficients determine material relaxation properties due to the characteristic times of orientational transitions τ_p and relaxation transitions activated by stress τ_σ respectively. This form allows us to describe the aggregate of load curves at different strain rates.

Based on the received earlier the approximation of the non-equilibrium free energy (F) derivative of the $\mathbf{p}$ in one-dimensional case and on the assumption of coaxiality $\mathbf{p}$ and $\boldsymbol{\sigma}$, we can write

$$-\frac{\partial F}{\partial \mathbf{p}} = \frac{F_m}{p_c} \left[\frac{\boldsymbol{\Sigma}'}{\delta} + \frac{\boldsymbol{\gamma}}{\delta} - f(|\gamma|) \frac{\boldsymbol{\gamma}}{|\gamma|} - \boldsymbol{\gamma} \right], \tag{12}$$

$$f(|\gamma|) = 0.0054 + \frac{0.5192(-0.0061 + 2|\gamma|)}{0.5814 - 0.0061|\gamma| + |\gamma|^2}\,, \tag{13}$$

where $\boldsymbol{\Sigma}' = \boldsymbol{\sigma}' / 2G$ - dimensionless stress deviator tensor, $\boldsymbol{\gamma} = \mathbf{p} / p_c$ - dimensionless deformation caused by defects, $p_c = \sqrt{\theta / \alpha}$, $F_m = \lambda\theta / \alpha^2$, θ - effective temperature factor responsible for the susceptibility of the system, $\alpha \sim G / V_0$, $V_0 \sim r_0^3$ - characteristic volume of the defect nucleus with radius r_0.

The system of equations (4)-(12) can be considered as a closed system of equation for modeling of damage accumulation and plasticity process in metals.

3. Numerical simulation

Numerical simulation was carried out using the finite element package Abaqus. Material behavior is described by a statistical – thermodynamic model introducing above using the procedure UMAT. Arrays of material constants, strain, strain increments and the time step passed as input data to the procedure. Increment of stress tensor components and increment of defect density tensor components are determined from the system of constitutive equations. Values of these components at the next time step are defined as the sum of values on the previous step and the appropriate increment.

There were considered numerical experiments on the quasi-static tensile of vanadium paddle, containing a central crack, compression of an oblique cylindrical vanadium sample and fracture of an oblique cylindrical titanium sample.

Quasi-static tensile experiment was carried out on the sample, the geometry of which is shown in Fig. 2. The specimen contains a central crack; its length is 3 mm.

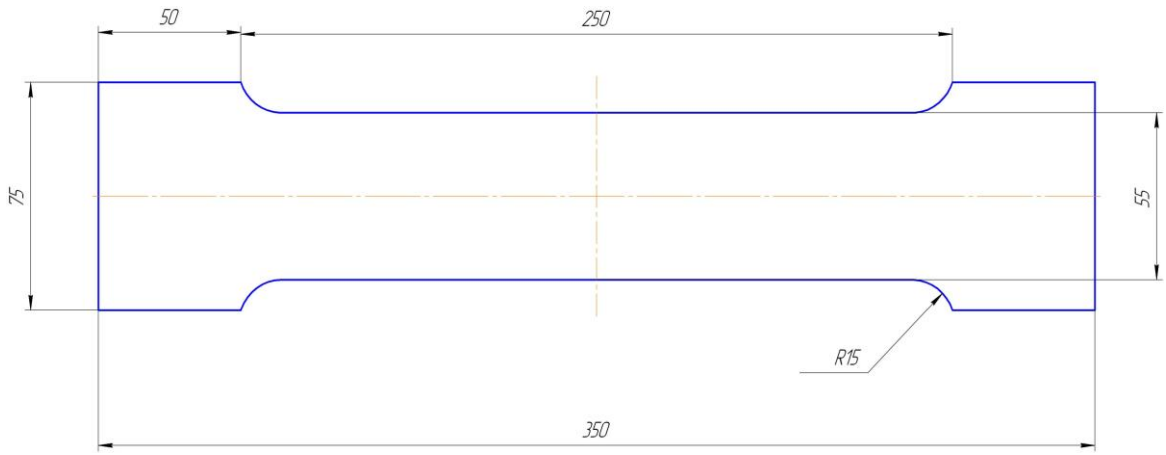

Figure 2. Geometry of specimen. All sizes are in millimeters.

The extended finite element method (XFEM) capability in Abaqus was used to model crack propagation. XFEM models a crack as an enriched feature by adding degrees of freedom in elements with special displacement functions. XFEM does not require the mesh to match the geometry of the discontinuities. It can be used to simulate initiation and propagation of a discrete crack along an arbitrary, solution – dependent path without the requirement of remeshing [5].

A maximum principal stress criterion was used to model the damage initiation. Stress state of the sample with a central crack after deformation is shown in Fig 3. Figure 4 displays the zoomed stress field near crack tip. The stress increases near the crack tip.

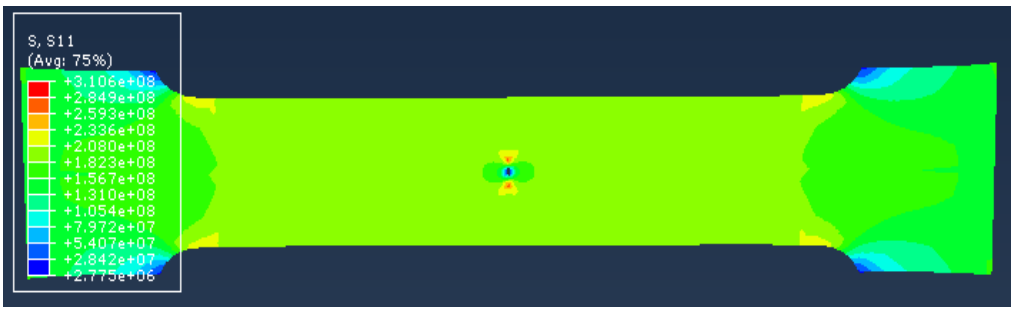

Figure 3. Component σ_{xx} (in the tension direction) of the stress tensor

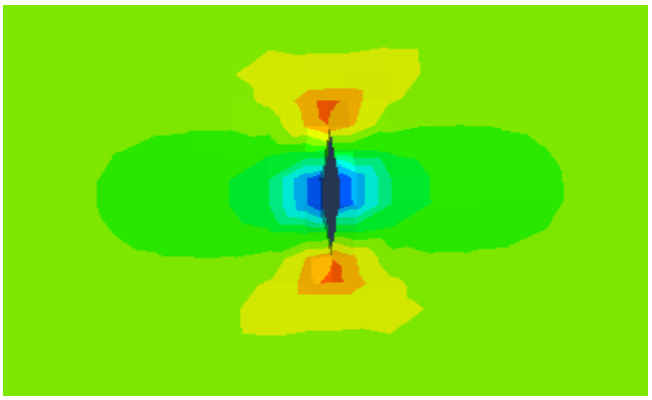

Figure 4. Stress distribution in the vicinity of the crack tip

Figures 5 shows deformation caused by defects area and figure 6 shows the shape of plastic zone. It can be seen that maximum strain localizes at the crack tip and gradually decreases with the distance from it. The magnitude of deformation, caused by defects is greater than the magnitude of plastic strain.

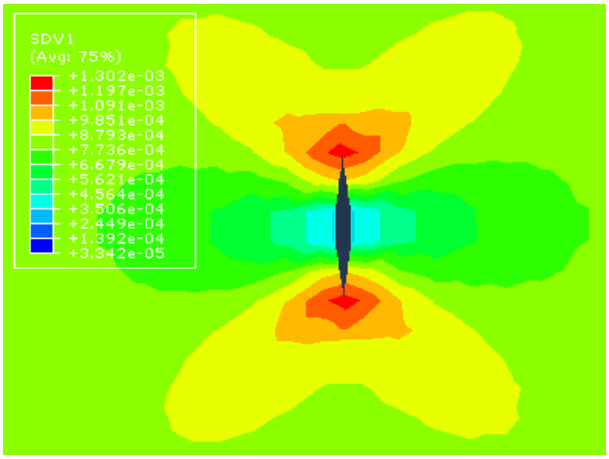

Figure 5. Component p_{xx} of the deformation tensor caused by defects near crack tip

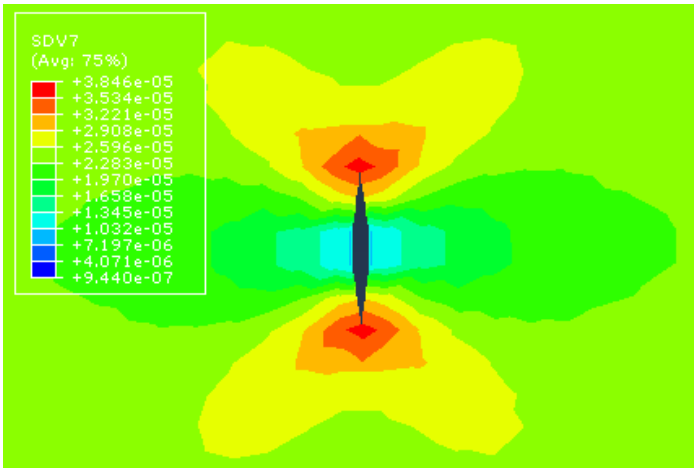

Figure 6. Component ε^{p}_{xx} of the plastic strain tensor near crack tip

Figures 7, 8 present the experimental temperature field on the specimen surface near crack tip and experimental obtained neat power near crack tip, respectively.

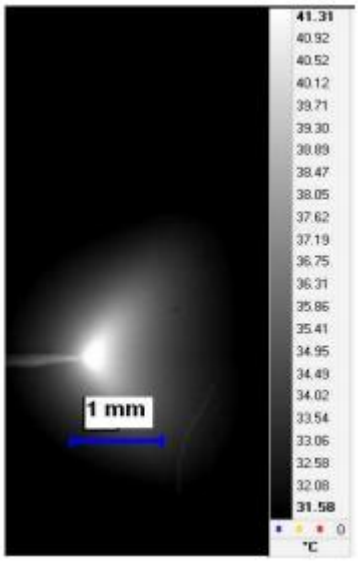

Figure 7. Experimental temperature field at the crack tip.

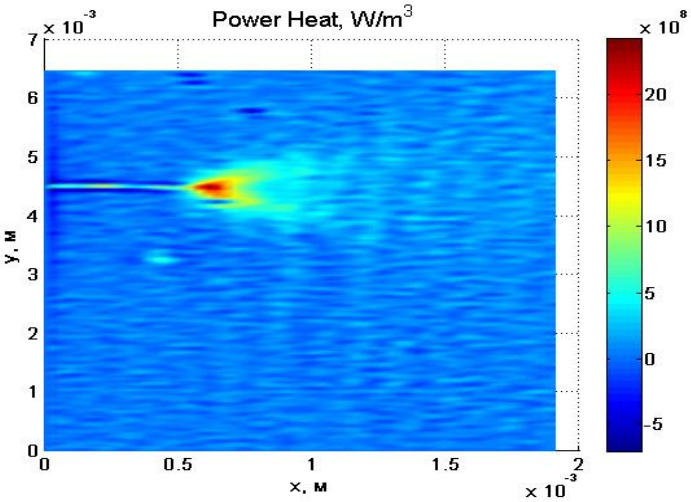

Figure 8. Experimental power of heat sources at the crack tip

Figure 9 demonstrates the strain energy distribution near crack tip. We can see several areas with the center at the crack tip and increasing radius, that is confirms the experimental data given above.

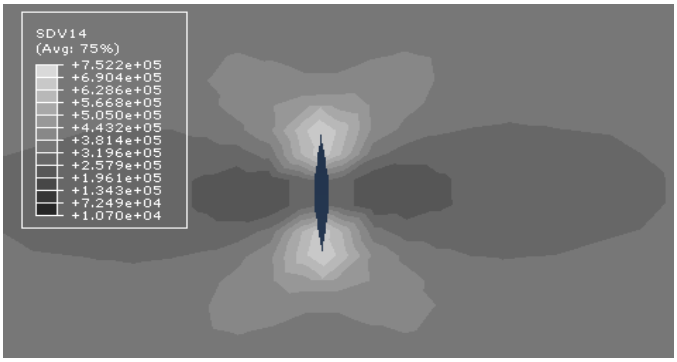

Figure 9. Numerical strain energy distribution near crack tip

Experiment on compression (Fig.10) was carried out with the vanadium samples. The specimen is an inclined cylinder; its diameter is 8 millimeters and its height is 4 millimeters. The cylinder was placed between the compressive planes; there was allowed its slip.

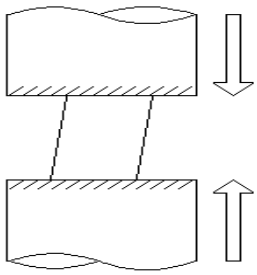

Figure 10. Experimental scheme on the quasi-static compression of vanadium

Figure 11 presents the stress-strain curves obtained experimentally (dashed line) and numerically (solid line). Results calculated by the described above model agree with experimental results.

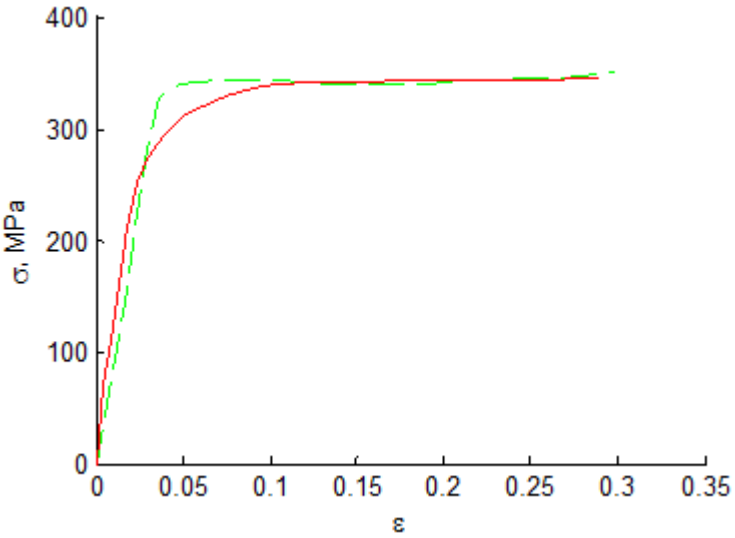

Figure 11. The simulation results of a cylindrical sample compression (dashed curve – the experimental results, the solid - numerical)

Figures 12 and 13 demonstrate various components of the plastic strain, and figures 14, 15 display the components of the deformation caused by defects. Red areas are zones where defect concentration is maximum. The experiment on the oblique sample compression was carried out to detect the shear bands in the sample, this can be seen in the simulation results. Figures 13 and 15 in cross section area show localization of these bands.

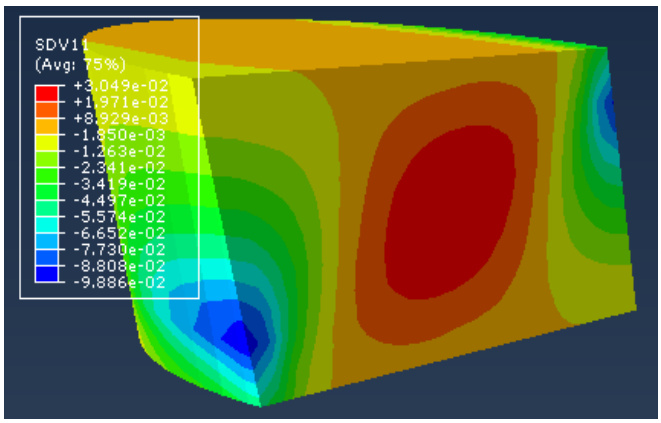

Figure 12. Component ε^{p}_{xz} of plastic strain tensor (cross section by the Oy plane)

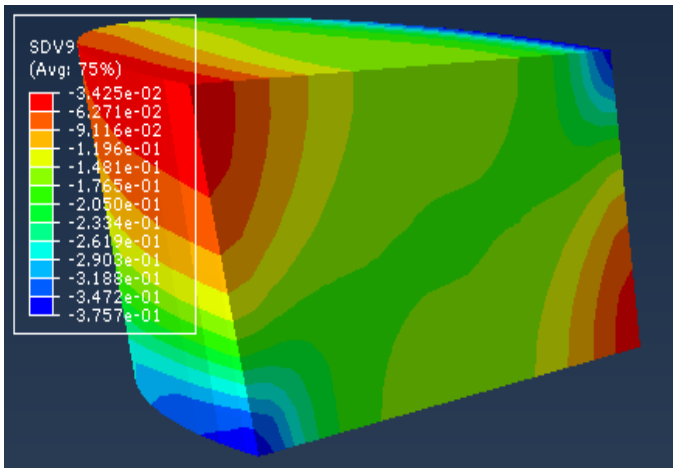

Figure 13. Component ε^{p}_{zz} of plastic strain tensor (cross section by the Oy plane)

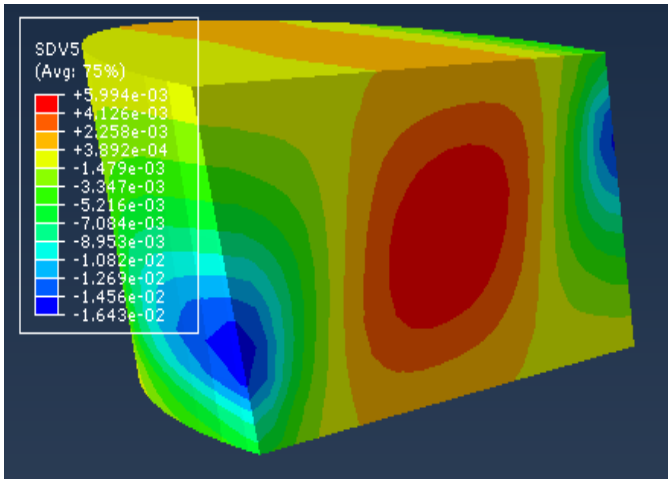

Figure 14. Component p_{xz} of the deformation tensor caused by defects

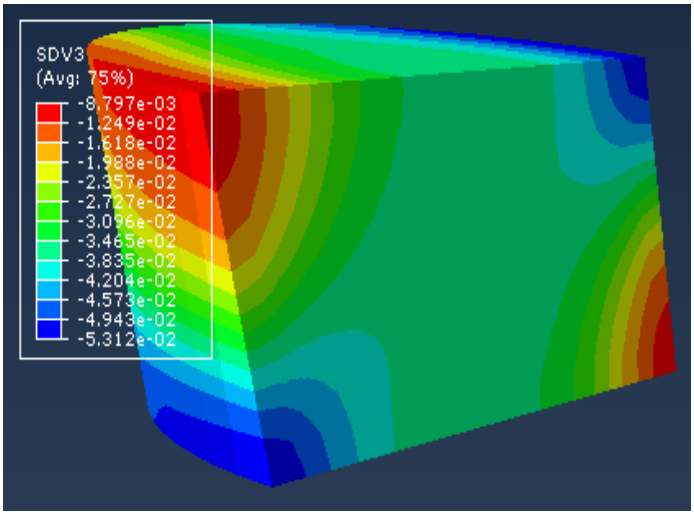

Figure 15. Component p_{zz} of the deformation tensor caused by defects

Also, there was carried out an experiment on the compression of titanium specimen of the same shape and the same sizes. The titanium with small grain size (about 0.3 mkm) is more brittle material then vanadium. The compression of this material is accompanied by crack initiation. Figure 16 presents a temperature distribution of the cracked specimen surface.

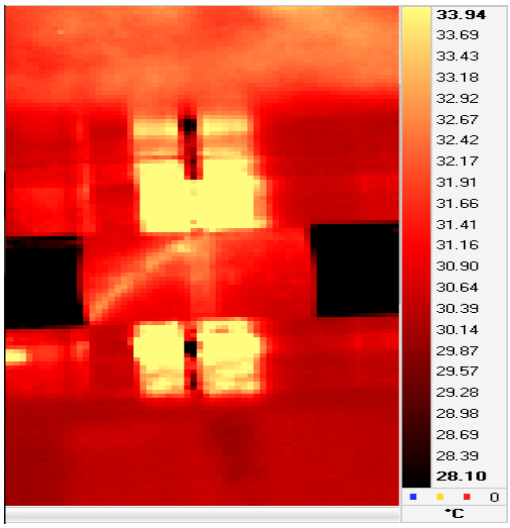

Figure 16. Cylindrical specimen after compression

Results of numerical modeling are shown in Figure 17. Maximum nominal shear stress criterion was used to initiate damage in cylinder sample. Crack location obtained by simulation is consistent with experimental data.

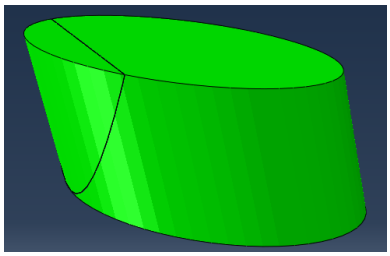

Figure 17. Numerical simulation results on the titanium specimen compression

3. Conclusion

The paper is devoted to the study of metal fracture processes under quasi-static loading. There were formulated constitutive equations for elasto-plastic medium with mesodefects. These equations were used for three-dimensional modeling of quasi-static vanadium paddle tension, compression of vanadium oblique cylinder and failure of titanium oblique cylinder sample. Numerical simulation was performed using finite-element package Abaqus by subroutine UMAT which allows user to implement his own constitutive equations. Fracture modeling was carried out using XFEM capability in Abaqus. Simulation results are in a good agreement with experimental data.

Acknowledgements

This work was supported by grant of President of the Russian Federation for support of young Russian scientists and leading scientific schools (MD-2684.2012.1) and RFBR (grant N 12-01-33072).

References

[1] V.I. Betekhtin, O.B. Naimark, A.G. Kadomzev, S.N. Grishaev, Experimental and theoretical investigation of defect structure evolution, plastic deformation and fracture, preprint ICMM UB RAS, Perm, 1997. (In Russian)
[2] Yu.V. Bayandin, Investigation of self-similar regularities of plastic front formations in metals under intense impact, PhD thesis, ICMM UB RAS, Perm, 2007. (In Russian)
[3] O.B. Naimark, Collective properties of defects ensemble and some nonlinear problems of

plasticity and failure. Physical mesomechanics, 4 (2003), pp.45-72.

[4] Naimark O.B., Bayandin Yu.V., Leontiev V.A., Panteleev I.A., Plekhov O.A. Structural-scaling transitions and thermodynamic and kinetic effects in submicro-(nano-)crystalline bulk materials Physical Mesomechanics, Volume 12, Issues 5-6, (2009), pp. 239-248.

[5] Dissault Systemes, Abaqus 6.11 Online Documentation, Dissault Systemes, Providence, Rhode Island, 2011.

Electrification of Glass by Fracture

Li Xie*, Dewen Sun, Jun Zhou

Key Laboratory of Mechanics on Western Disaster and Environment, Ministry of Education, PRC, College of Civil Engineering and Mechanics, Lanzhou University, Lanzhou, Gansu
* Corresponding author: xieli@lzu.edu.cn

Abstract In 1883, Faraday found that some crystals can be electrified by deformation and cleavage and many researchers reported that the brittle materials such as rock can also be electrified. Nowadays, a new technology was developed to forecast earthquake and collapse of mine well by detecting the electrification of rock. In the paper, we set up an instrument to measure the electrification of the broken glass. We observed the electrification of glass by fracture and the charges carried by the broken glass were measured. It was found that the amount of charges was directly proportional to the broken area of glass and the maximum surface charge density can be reached up to 0.5 $\mu C/m^2$. By SEM observation of broken surface, we can infer the charges distribute near initial nick.

Keywords Electrification of fracture; Glass slab; Surface charge density

1. Introduction

The study on electrification of fracture is not only to develop a new technology to ensure the security of mine wells [1-2], but also to be inferred an electrification mechanism of sand particles in wind-blown sand flux [3].

The fist study on the charge fracture date back to 1883, and Faraday found that some crystals can be electrified due to cleavage and deformation [4]. From then on, many researchers found that the rock can be electrified during the deformation and break. Kornfeld measured the charges and the electric field of the lithium fluoride crystal cleft by a sapphire chisel. He found that in the vast majority of cases, the field of one part of a specimen was positive over the entire extension of the cleavage, whereas the field of the other part of the specimen was negative. He thought the electrification of cleft lithium fluoride resulted from the presence of an intrinsic charge. Many researchers measured the electrification of broken rock, and inferred the charging mechanism, such as triboelectrification, electrification of electron escaping of broken surface [5-12].

Triboelectrification has been known for millennia[13] which means two materials surfaces are contacted (especially rubbed) and separated and the electrical charges can be transferred [13]. Nowadays, researchers like use the term contact electrification to name the charge transfer phenomena after two materials surfaces contact, because subsequent studies found that the contacted surfaces can be electrified if they are contacted and then separated, not necessarily rubbed. The current researches of contact electrification focus on electrification mechanism, that is what kind of charge is transferred, how to transfer charge and what is the drive force to transfer charge [14], which involve physics, chemistry and so on and interests many researchers on the electrification mechanism of chemically identical material.

However, the electrification of fracture may be different from the contact electrification, because the electrification of fracture results from the break of material, which means that the part

of the broken material can be electrified, whereas the contact electrification means the two materials surfaces can be electrified after they contacted with each other. Therefore we infer that the electrification mechanisms are different. Recent studies on the contact electrification indicate that the charges transferred are electron, iron and material sites [15-18]. Though some researchers think that the electrification of fracture results from the electrons escaping during the break of the material, the fracture of material is always accompanied with the chemical bonds breaking in microscope [19]. Therefore the asymmetrical break of the chemical bonds may be one of main reasons leading to the electrification of fracture.

In this paper we set up a instrument to measure the charges carried by a part of glass slab broken by a glass sphere. The calculated surface charge density indicates that the amount of charges carried by the broken part of the glass slab is proportion to the broken area, and we infer the mechanism of electrification of fracture by scanning the broken surface.

2 Experiment setup and measurement

We set up an instrument to measure the charges carried by the broken part of the glass slab shown as Fig.1. Main part of the instrument was put into a closed glass container with a wire netting fixed on its inside wall to shield the electric field. We also can observe the experimental procedure through the glass wall. One end of a glass slab was fixed on a moveable slideway which can be controlled outside the glass container. When the glass slab moves above the Faraday's cup, it will stop. A metal sphere falls and impacts with the glass slab which will be broken into two parts, and one part will fall into Faraday's cup. Faraday' cup induces the charge carried by the part of glass slab, which was named charge of fracture or broken charge, and the electric signal is displayed by electrometer (Type: Keighley 6517A; Precision: 100pC; Rang: 0~20nC).

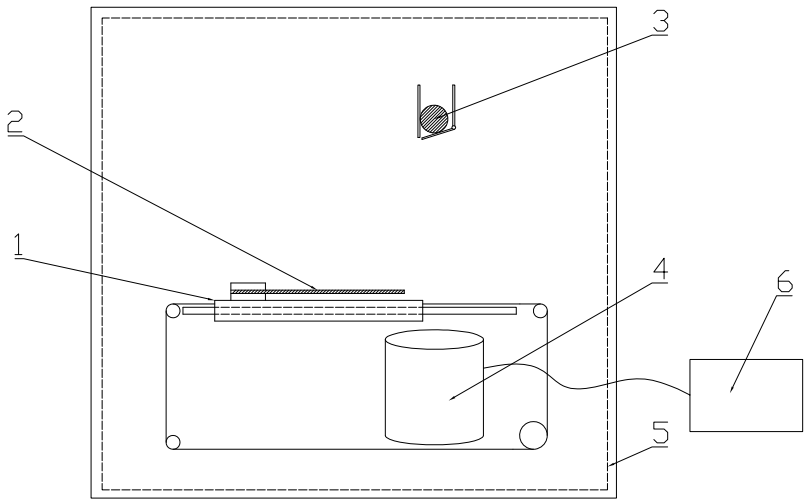

Fig.1 A sketch of instrument of electrification of fraction, in which 1 is slideway, 2 is specimen, 3 is metal sphere, 4 is Faraday cup, 5 is wire netting and 6 is electrometer

Before the experiment, we firstly mad a linear nick on the glass slab to ensure that the glass slab can be easily broken and also just broken into only two parts, by which we can easily calculate the broken area. If the linear nick is made in the middle of the glass slab, the glass slab can be symmetrically broken but otherwise asymmetrically broken, and in this paper the linear nick was made in one third of glass slabs. Then all glass slabs and glass spheres were cleaned by water and alcohol to eliminate the impurity of glass's surface and the net surface charges. The glass slabs used in our experiment were 3mm and 4mm in thickness, and 15mm and 20mm in breadth, and 150mm and 200mm in length. Given a size of the glass slab, we measured 30 results at least, that means we measured charges of 30 specimens.

3 Results and discussions

For all data we collected, we firstly eliminate the abnormal data by using Grubbs method and then classified the data by positive and negative signs. Fig. 2(a) and Fig. 2(b) show the amount of charge carried by parts of broken glass slabs, 4mm×20mm×200mm in size. The charges carried by the symmetrically broken parts shown in Fig. 2(a) and the ones carried by the asymmetrically broken parts shown in Fig. 2(b). It can be found that two parts of the glass slab broken by a metal sphere can be electrified, and the one part carried positive charge, whereas the other carried identically negative charge. The probability of presence of positive charge of negative charge is equal. For the asymmetrical case, mean amount of positive charges carried by the part is $+0.032059nC$ and mean amount of negative charges carried by the other part is $-0.03062nC$. By comparison Fig. 2(a) with Fig. 2(b), both the polarity and amount of charges carried by the broken glass slab are not related to the broken position, which is accordant with the results observed by Kornfeld [1]. We also measured the charges carried by broken parts of glass slabs with different length, and the results showed that the charge of fracture is not related to length of specimen. Therefore we only introduce the measurement results of symmetrical broken glass slabs with 200mm in length.

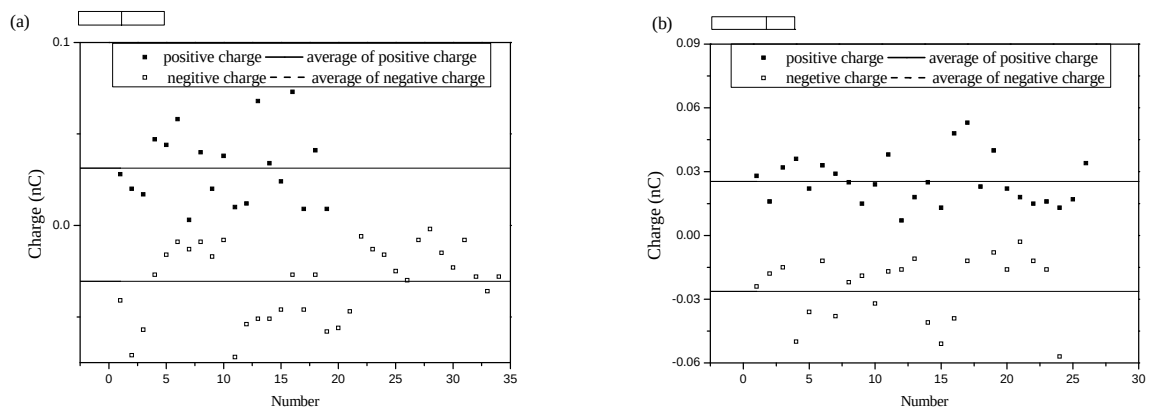

Fig.2 Charges carried by the broken part of glass slab, 4×20×200mm in size, (a) symmetric break and (b) asymmetric break

We also measured the charge of fracture of specimens in other thickness and breadth to know the effect of sizes of slabs on the amount of broken charge. Fig. 3(a) showed charges carried by broken slabs, 3mm×20mm×200mm in size. By comparing Fig. 2(a) and Fig.3(a), we found that they have a same charging law but the amount of charges shown in Fig. 2(a) is significantly lower than the one shown in Fig. 3(a), which shows that the thickness of glass slabs have an effect on the amount of broken charges. With increase of the thickness of the glass slab, the amount of charges also increases. Fig. 3(b) and Fig. 3(c) showed the charges carried by the broken parts of the glass slabs, 4mm×15mm×200mm and 3mm×15mm×200mm in sizes, respectively. We found that the breadth also has an effect on the charge of fracture, which increases with the increase of the breadth of glass slab. As mentioned above, the charge of fracture increases with the both the breadth and thickness. As well as we known, with the increase of both the breadth and thickness broken area increases, that means the increase of the broken area will lead to the increase of the charge of fracture. Therefore we calculated the mean values and standard variances of the surface charge density shown in Fig.4. From Fig.4, it can be found that the breadth has a significant effect on the charge of fracture. Especially, for the amounts of charges carried by the broken part of glass slabs, 4mm×15mm×200 and 3mm×20mm×200mm in sizes, the areas of these two cases are equal, but the surface charge densities are different and the amount of charges carried by the former is higher than the latter. The surface charge density can reach up to 0.5μC/m^2.

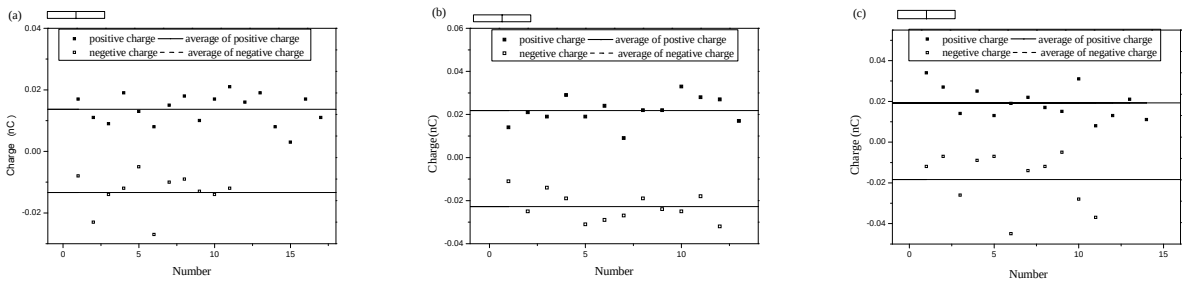

Fig. 3 Charges carried by the broken glass slab, (a) 3mm×20mm×200mm, (b) 4mm ×15mm ×200mm and (c) 3mm×15 mm×200mm in sizes

Although the charge of fracture increases with the thickness increasing when the broken areas of the specimen are given, it is still difficult to infer that the charge of fracture increases with the thickness. Because we make the linear nick on the specimen, it also has the effect on the real broken thickness. For given the deepness of nick, it has a significant effect on the broken thickness of glass slab with thinner thickness. But it is difficult to carry out the experiments to measure the charge of fracture with thickness more than 4mm, so if the surface charge density is related to the thickness is still open.

It is interesting that how to explain the electrification of fracture, which may be related to the glass network structure. We scanned the broken surface of glass by using SEM (Type: JSM-5600LV. Precision for SEM: 3.5nm. Precision for DES: 131.7eV) shown in Fig. 5(a). From the Fig. 5(a), it can be found that the broken surface is smooth but a few black spots (I), and white spots (II), which indicates it is a brittle fracture. Because the grayscale of the image is related to the atomic number to some extent, we analyzed the energy dispersive spectrum of black spots, I of Fig. 5a and white spots, II of Fig. 5(a), shown as in Figs. 5(b)-5(c), respectively. The chemical formula of glass used

in our experiment is $Na_2O{\cdot}CaO{\cdot}6SiO_2$, in which Na_2O and CaO are about 15% and 16%. Our DES is not sensitive to the elements with smaller atomic number such as H, C, O and Na, so the energy spectrums of these elements cannot be displayed in Figs. 5(b)-5(c). Comparing the Fig.5(b) with Fig.5(c), the content of element of Si is highest than the ones of others, which has not large difference in quantity of different position. It is difficult to correlate it to electrification of facture.

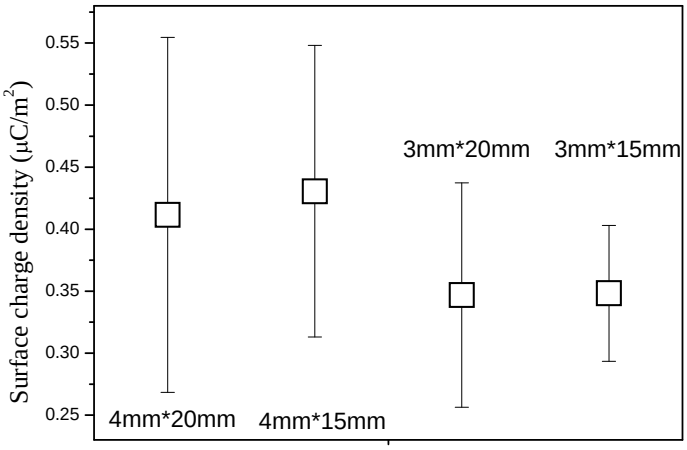

Fig. 4 Surface charge density of broken surface for different cross section

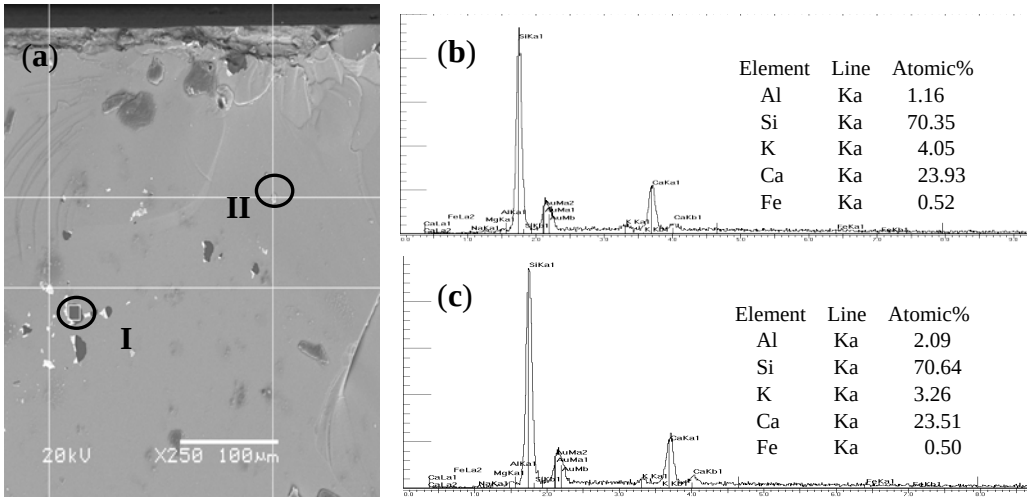

Fig. 5 SEM observation result for fractography of broken glass slab (a), in which I is a black spot and II is a white spot. (b) DES of I in (a), and (d) DES of II in (a).

It is worthy to point that, when we scanned the broken surface by SEM, we found an interesting phenomenon that is there are many white spots distributed in the broken surface and the number of white spots decrease with the distance away from the nick increasing shown as in Fig.6(a). A white spot is about 10μm in size (see Fig. 6(b)). And when we continually bombard the white spot by electrons, the white spot will disappear after several seconds. That means that the white spot is comprised by the elements with smaller atomic number. The scanned specimen has

been neutralized when we scanned it, so we infer that when the specimen was broken, the positions occupied by the white spots are the charged ones, which absorbed the charged ions such as H^+ when the broken surface put in the air. It means that the positions occupied by white spots are the charged positions when the specimen is broken. As mentioned above, the main charged positions are distributed near the prefabricated nick, therefore we can easily explain why the surface charge density is related to the thickness of glass slab but it is not linearly relationship.

However, so far we cannot know the electrification mechanism of fracture. We cannot know what results in the broken part of glass charged and why the charges distribute near the nick when the glass slab is broken. Although some reports indicate that the existing Na^+ ions make some of the $[SiO_4]$ three dimension network structures broken [20] and number of non-bridged oxygen significantly increases. Na^+ ions occurred near the center of the non-bridged oxygen hole neutralize the net charges. When the glass is broken, the Na^+ ions are free, therefore it may result in the broken glass charged. But the non-bridged oxygen should uniformly distribute in the glass, so if the inference mentioned is true, the charges also uniformly distribute in the broken surface and not near nick shown in Fig. 6(b). Unfortunately, we cannot know how to correlate the electrification mechanism with them and expect further studies.

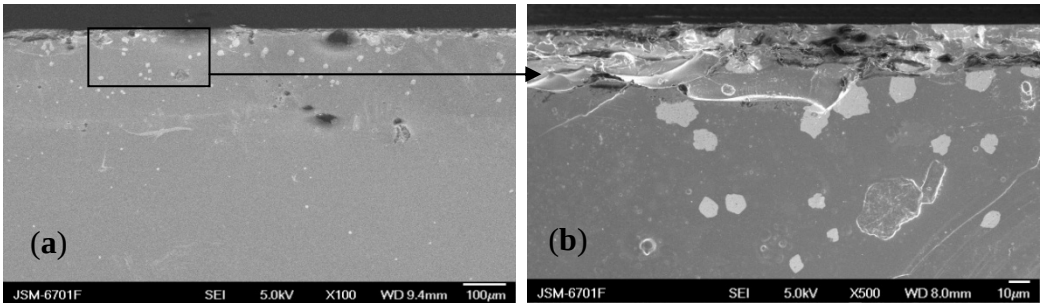

Fig. 6 SEM observation results of fratographies of broken surface of glass slab, in which many white spots distribute, (a) result magnified by 100 times and (b) result magnified by 500 times

Acknowledgements

This work is supported by the grants of National Natural Science Foundation of China (No.1121202, No.11072096 and No.11272139), and authors express their sincere appreciation to those supports.

References

[1] V. Frid. Calculation of electromagnetic radiation criterion for rockburst hazard forecast in coal mines. Pure Appl Geophys, 158 (2001) 931-944.

[2] V. Frid. Electromagnetic radiation method water-infusion control in rockburst prone strata. J Appl Geophys, 43 (2000) 5-13.

[3] S. P. Kanagy II, C. J. Mann, Electrical properties of eolian sand and silt. Earth Sci Rev, 36 (1994) 181-204.

[4] M. I. Kornfeld, Electrification of crystals by cleavage, J Phys D: Appl Phys, 11 (1978) 1295-1301.

[5] X. Wu, X. Shi, Z. Guo, Study of the electrification of granite samples under compression. Chinese Journal of Geophysics, 33 (1990) 208-211, (In Chinese).

[6] Y. Zhao, Y. Pan, G. Li, W. Ren, J. Luo, Measuring of the Charge-induced Signal of Rock during the Deformation and Fracture Process. Journal of Disaster Prevention and Mitigation Engineering, 3 (2010) 252-256, (In Chinese).

[7] A. Takeuchi, H. Nagahama, Interpretation of charging on fracture or frictional slip surface of rocks. Physics of the Earth and Planetary Interiors, 130 (2002) 285–291.

[8] T. Freund, Rocks That Crackle and Sparkle and Glow: Strange Pre-Earthquake Phenomena. J Scientific Exploration, 17 (2003) 37–71.

[9] F. St-Laurent, J. S. Derr, Earthquake lights and the stress-activation of positive hole charge carriers in rocks. Phys and Chem Earth, 31 (2006) 305–312.

[10] A. Takeuchi, N. Shirai, Electromagnetic signals associated with stick–slip of quartz-free rocks. Tectonophysics, 450 (2008) 79–84.

[11] Z. Li, E. Wang, X. He, Research on surface electric anomaly of concrete in fracture. Journal of China Coal Society, 35 (2010) 910-914, (In Chinese).

[12] Z. Li, E. Wang, Z. Liu, X. Song, Y. Li, Study on Characteristics and Rules of Surface Potential During Coal Fracture. Journal of China University of Mining & Technology, 38 (2009) 187-192, (In Chinese).

[13] M. Sow, D. J. Lacks, R. M. Sankaran, Effects of material strain on triboelectric charging: Influence of material properties. J Electrostat 2012 (In Press).

[14] D. J. Lacks, R. M. Sankaran, Contact electrification of insulating materials. J Phys D: Appl Phys, 44 (2011) 453001.

[15] J. Lowell, W. S. Truscott, Triboelectrification of identical insulators: II. Theory and further experiments. J Phys D: Appl Phys, 19 (1986) 1281-1298.

[16] L. S. McCarty, G. M. Whitesides, Electrostatic Charging Due to Separation of Ions at Interfaces: Contact Electrification of Ionic Electrets. Angew Chem Int Ed, 47 (2008) 2188–2207.

[17] J. F. Kok, D. J. Lacks. Electrification of granular systems of identical insulators. Phys Rev E, 79 (2009) 051304.

[18] M. M. Apodaca, P. J. Wesson, Contact Electrification between Identical Materials. Angew Chem, 122 (2010) 958–961.

[19] M. M. Caruso, D. A. Davis, Q. Shen, Mechanically-Induced Chemical Changes in Polymeric Materials. Chem Rev, 109 (2009) 5755–5798.

[20] S. Sunio, Glass Handbook, China Architecture & Building Press, Beijing, 1985, (In Chinese).

Influence of Microstructure on Fatigue Crack Propagation and Fracture Toughness of Large Ti-6Al-4V Cast Structure

Xin Feng[1,*], Anqi Wang[2], Yingjie Ma[1], Xinhua Wu[3], Jiafeng Lei[1], Yuyou Cui[1], Rui Yang[1]

1. Institute of Metal Research, Chinese Academy of Sciences, 72 Wenhua Road, Shenyang 110016, China
2. FalconTech, 99 Hongshan Street, The New District, Wuxi 214145, China
3. Department of Materials Engineering, Monash University, Wellington Road, Clayton, Victoria 3800, Australia

* Corresponding author: xfeng12b@imr.ac.cn

Abstract The study is part of research activities for EU-China FP7 collaborative project **(FP7-AAT-2010-RTD-CHINA)**: Casting of Large Ti Structures (COLTS) and has been carried out in order to investigate the influence of microstructure of cast Ti-6Al-4V large thin wall structure on fatigue crack propagation and fracture toughness. Some samples were post HIPped (hot isostatic pressed). The effects of grain morphology on fracture and fatigue crack propagation mechanism have also been studied. The fracture surface has been examined using scanning electron microscopy (SEM). The relationships between microstructure and fatigue crack propagation rate and fracture toughness were established and comparison has been made between the as-cast and post HIPped conditions.

Keywords Ti-6Al-4V alloy, Hot isostatic pressing, Fracture toughness, Fatigue crack growth

1. Introduction

Ti-6Al-4V alloy has been widely used in aerospace industry due to its low density, high specific strength, excellent combination of strength and toughness, and resistance to creep up to moderately high temperature. While Ti-6Al-4V alloy is mostly wrought processed, near-net-shape methods such as centrifugal investment casting are increasingly used, because the desired castings require no machining except the removal of flash around edges and possible drilling and tapping holes, which shortens the process and reduces the cost. The key issues associated with centrifugal investment casting are poor reliability and reduction in mechanical properties due to the formation of cavity and porosity during casting. These defects control the mechanical properties such as fatigue and fracture because of large stress concentration. The probability of failure due to stress concentration has been modeled by the Weibull distribution [1]. In an attempt to improve the fatigue life, the cast components usually were hot isostatically pressed (HIPped) [2], which is an effective compaction technique for the removal of internal defects such as porosity, shrinkage, and inter-dendritic cracks.

Fatigue crack growth resistance and fracture toughness are important properties for aerospace applications and have been studied extensively [3]. Since HIPing plays a noticeable role in the improvement of fatigue properties, in the current study fatigue crack growth resistance and fracture toughness were investigated on both the as-cast and post-HIPped Ti-6Al-4V alloy. The obtained results were compared and the effect of post-HIPping was discussed to gain a better understanding of the influence of post-HIPping on fatigue crack growth resistance and fracture toughness of this alloy.

2. Materials and experimental methods

The material examined in this study was Ti-6Al-4V and the cast cylinders were as shown in Figure 1, including one as-cast cylinder and the other which was post HIPped. The as-cast material have a yield stress averaged at 750MPa， the ultimate tensile stress is about 840 MPa and the elongation is about 4%. After HIPping, the yield stress is increased to 735MPa，the ultimate tensile stress is about 870MPa and the elongation is up to 8%. The Microstructures in thin sections before and after HIPping were examined by optical microscopy after polishing and etching with 1% HF + 3%HNO_3+ H_2O solution.

The fracture toughness tests using compact tension were carried out on a MTS servo-hydraulic testing system in accordance with ASTM standard E399 [4] for damage tolerance testing. Samples with the dimension of 36 mm ×37.5 mm × 15 mm were cut by electrodischarge machining (EDM) and all surfaces of each slice were ground and polished. In this testing method, a fatigue pre-cracked sample was loaded to induce crack extension while continuously measuring force versus displacement. A 3D image of the fracture surface was obtained by VHX-1000. The fracture surfaces of specific samples were examined using SEM.

The fatigue crack-growth (FCG) experiments were performed using the compact-tension samples prepared according to ASTM Standard E647-99 [5]. Fatigue crack growth testing was carried out using a RUMUL fatigue machine. Samples were cut from the thin section of the structure for FCG examination. A fatigue pre-crack was first introduced at the root of the centre notch of the sample. The crack length was measured using a crack-opening-displacement (COD) gauge using the compliance method. The fatigue crack growth tests were performed in laboratory air at a stress ratio, $R=K_{min}:K_{max}$, of 0.5. Optical microscope was used to observe the relationships between the crack path and the microstructure. Fatigue surfaces of specific samples after failure were examined by scanning electron microscopy (SEM).

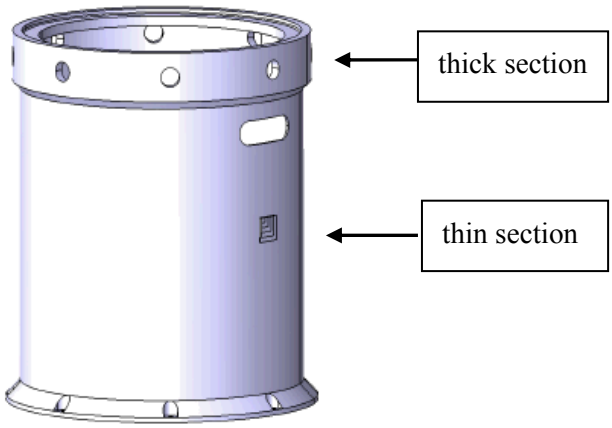

Figure 1. Ti64 component for COLTS project.

3. Results and Discussion

3.1. Microstructure

Analysis on microstructures of as-cast and post-HIPped Ti-6Al-4V showed that both samples have the lamellar colony structure and alpha film was found along beta grain boundaries. The microstructure of as-cast samples is characterized by grain size of about 2-3 mm, alpha platelet thickness of about 1.5 μ m while post-HIPped samples by grain size of about 2-3 mm, alpha platelet thickness of about 4.5 μ m. The grain size and the alpha platelet thickness increased after post-HIPping due to heating for a long time during HIPping.

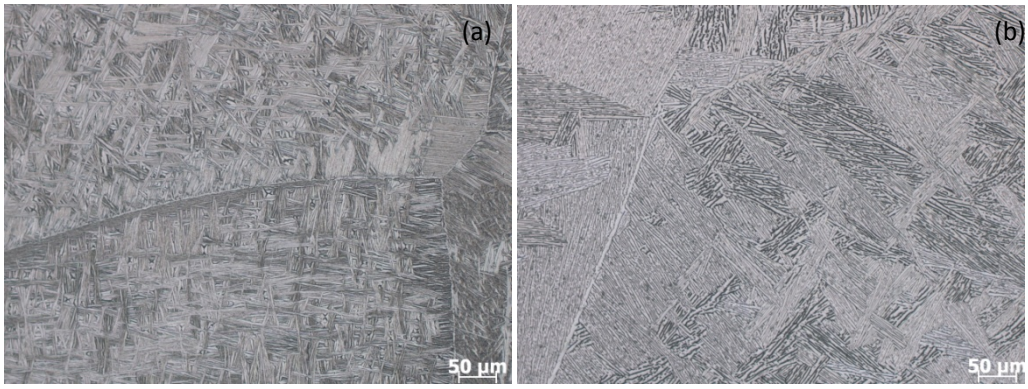

Figure 2. Optical images of microstructures in thin sections: (a) as-cast, (b) post-HIPped.

3.2. Fracture toughness

The fracture toughness sample conditions do not meet all the validity requirements ($B \geq 2.5(K_{IC}/\sigma_y)^2$), thus the testing results are considered to be an estimate of the fracture toughness. The measured fracture toughness values are 86, 83, 85 MPa $m^{1/2}$ for as-cast samples which are lower than that of post-HIPped samples (95, 97, 93 MPa $m^{1/2}$)which means the toughness was increased with increasing alpha platelet thickness. N.L. Richards also reported that the toughness obey straight-line relationships against the distance between the platelets i.e., the thickness of the alpha platelets[6].

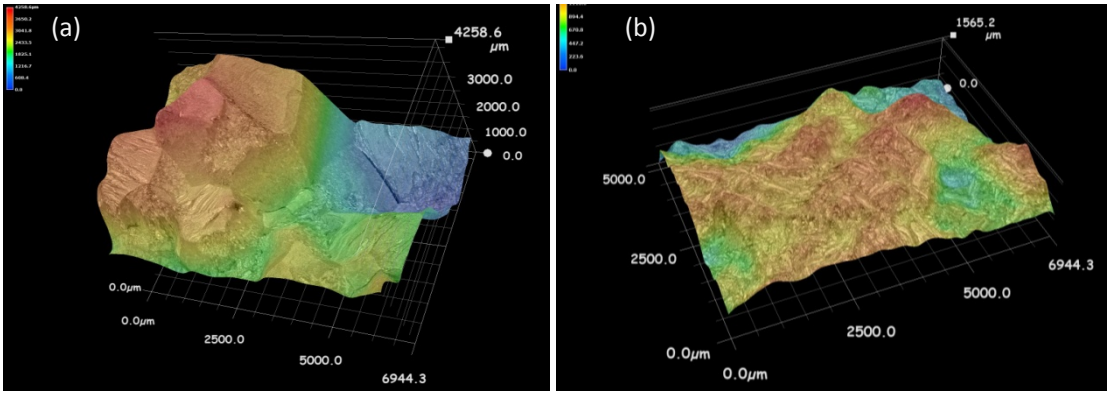

Figure 3. 3D fracture surface of Ti64 fracture toughness samples: (a) as-cast, (b) post-HIPped.

SEM fractographs for the fracture surfaces of the as-cast and post-HIPped samples are shown in

Figures 3 and 4, respectively. The fractographs show that the fracture surface changes from the intergranular-dominated fracture mode in Figure 4(a) to the transgranular fracture as shown in Figure 4(b). Figure 4(a) shows the straight edges of the grains and shiny surfaces, which indicates that the grain boundary strength is weak in some areas in the as-cast materials. The fracture surface of the post-HIPped sample is mainly transgranular, indicating improved ductility.

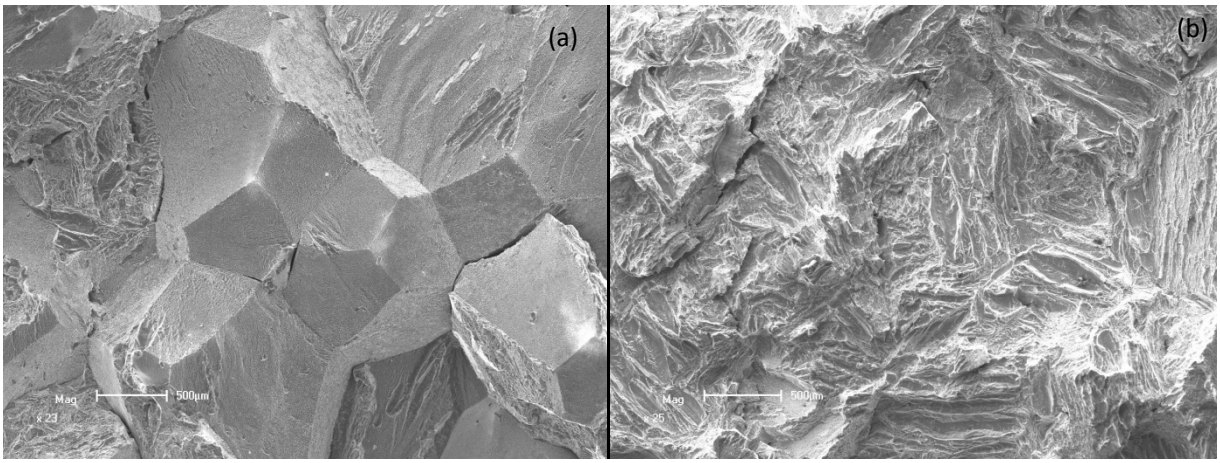

Figure 4. SEM fractographs of Ti64 fracture toughness samples: (a) as-cast, (b) post-HIPped.

3.3. Fatigue crack growth

The fatigue crack growth curves obtained for these two conditions are presented in Figure 5, which plots the fatigue crack growth rate, da/dN, against the applied stress intensity factor range. As shown in Figure 5, the rate of fatigue crack growth in the as-cast condition is faster than that after post-HIPping.

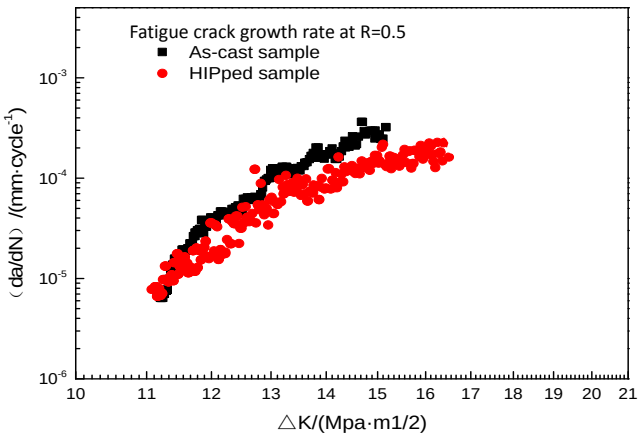

Figure 5. Fatigue crack growth resistance curves of Ti64 in both as-cast and post-HIPped state.

The crack paths in the two tested samples are shown in Figure 6. Crack deflection and branching were also found in these samples illustrated in Figure 7. The crack deflection at colony boundaries shows a zigzag path. When the crack propagated through lamellae of unfavorable orientations, it consumes more energy than a straight path, leading to a higher fatigue crack propagation resistance

[7]. The difference between the actual crack path direction and the direction of the maximal energy release varies between 2 to 15 degrees, which has been verified by Rubinstein [8]. The high magnification graphs in Figure 7(a) and (b) show that the crack deflection and branching in both samples are severe. This means that it needs more energy to proceed and enables a larger fraction of volume to contribute to stress relief by plastic deformation [9].

Fatigue fracture surface features (Figure 8) on FCG samples show a correlation to the underlying microstructure, where microstructural parameters such as the lamellar spacing and lamellar colony size appear to affect the crack propagation resistance. Chan and Kim [10] have suggested a relatively complex dependence of fatigue fracture toughness on the colony size. The thickening of alpha platelets can increase fatigue fracture toughness by contributing to crack deviation. Such improvement by alpha plate coarsening has been observed in many previous investigations [11]. It is important when the crack tip lies in a colony or the plastic zone size is similar to the thickness of platelets. The colony size can also affect the fatigue crack growth when crack propagates across colony boundaries [12]. In terms of grain boundary α, the increase in thickness of α at β grain boundary is helpful for frequent crack deviations when cracks go through the grain boundaries [13].

Fatigue striations and secondary cracks were found on fatigue fracture surfaces (Figure 8) of both samples, which indictate some ductillity of the materials. However the fatigue fracture surfaces also show that both sample conditions have similar fatigue fracture mechanisms, although, more secondary cracks were found in the as-cast Ti-6Al-4V.

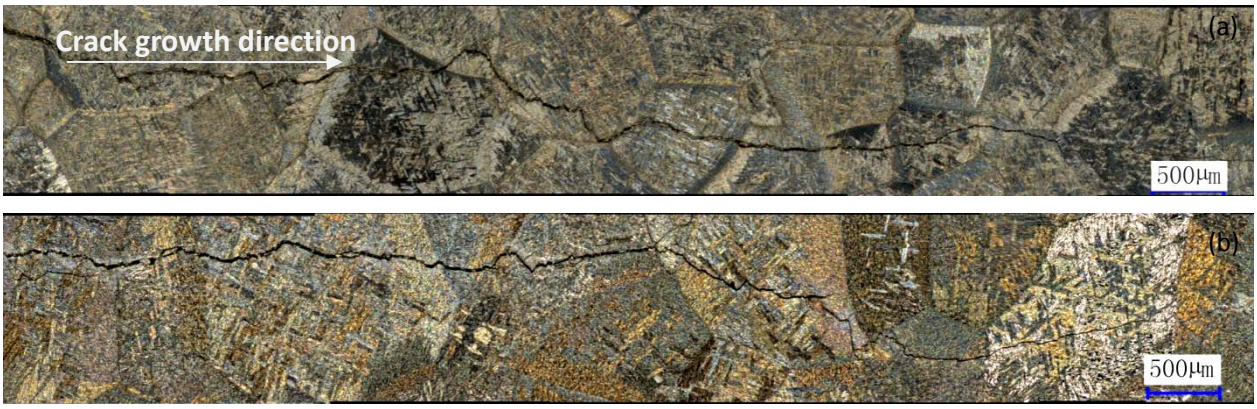

Figure 6. Crack profile of Ti64: (a) as-cast, (b) post-HIPped.

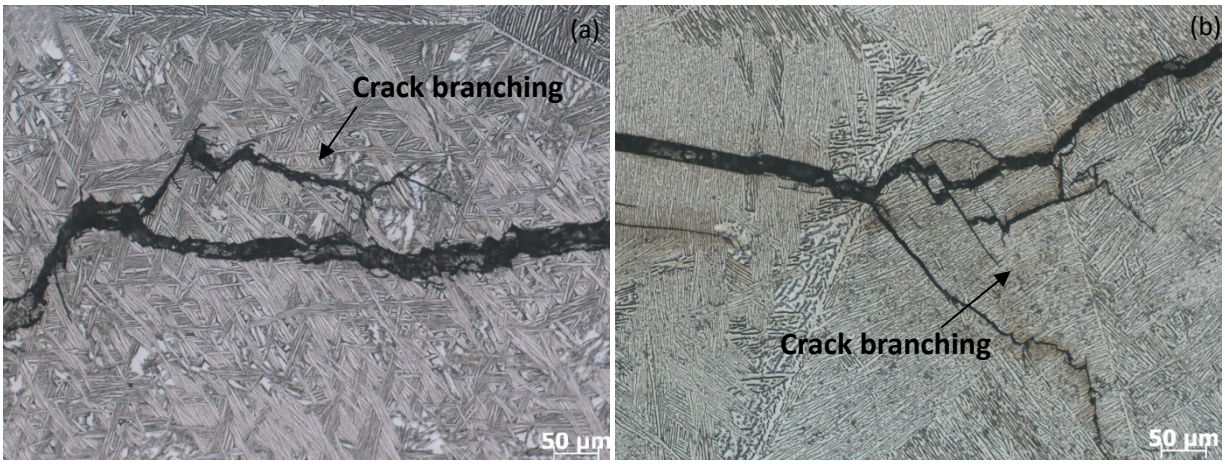

Figure 7. Crack path morphologies of Ti64: (a) as-cast, (b) post-HIPped.

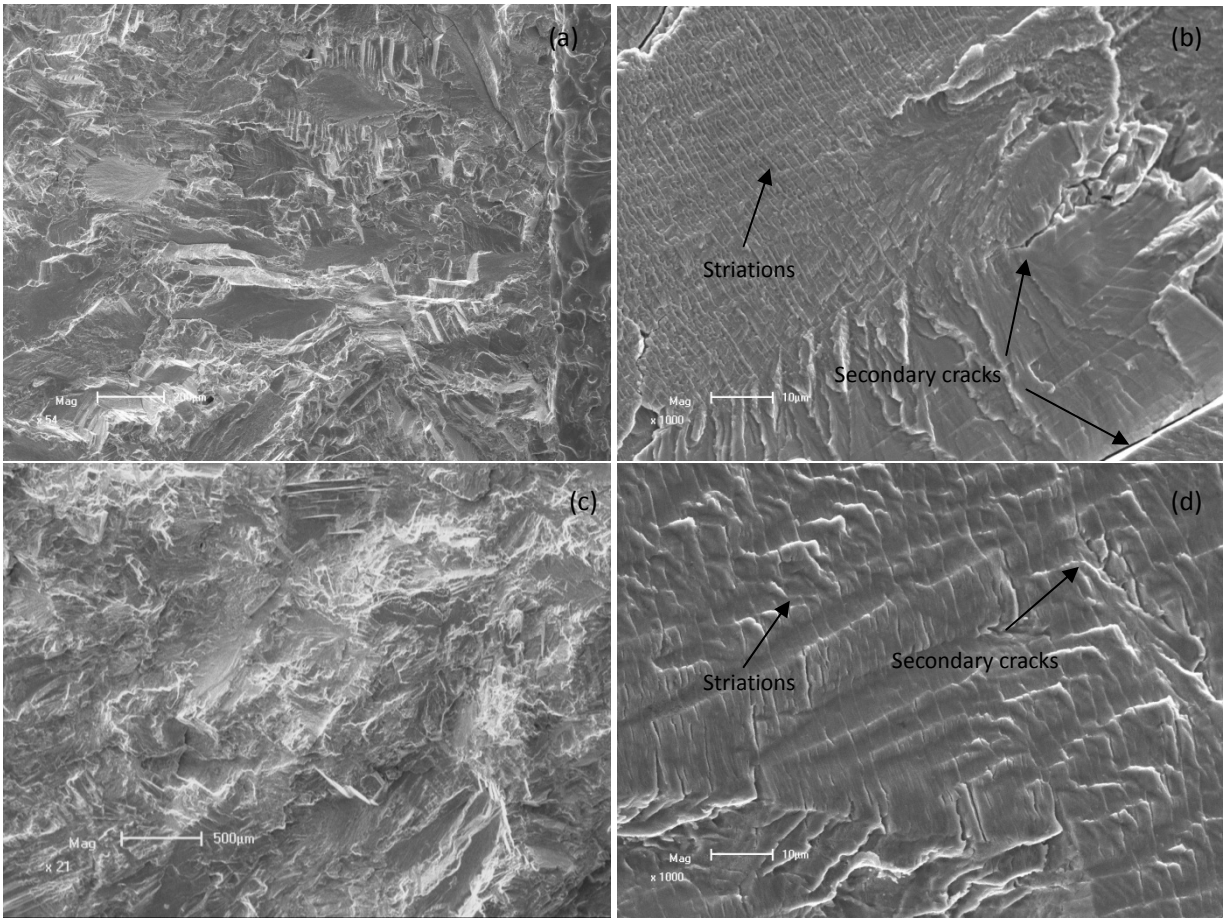

Figure 8. Scanning electron micrographs of Ti64 alloy fatigue fracture surfaces: (a) (b)as-cast, (c) (d) post-HIPped.

4. Conclusions

(1) Microstructures of Ti-6Al-4V alloy in the as-cast and post-HIPped condition were both lamellar colony structures. Following HIPping of the alloy, the thicknesses of lamellar plate and the alpha colony size both increased.
Fracture toughness of the post-HIPped samples is higher than that of the as-cast samples. This was associated with the significant reduction in the volume fraction of pores by HIPping. The fracture mode changed from the intergranular fracture into transgranular fracture.

(2) The fatigue crack growth rate of the post-HIPped sample with larger lamellar spacings was lower than that of the as-cast samples with smaller lamellar spacings. More crack deflections and branchings were found in the post-HIPped samples than in the as-cast samples, which indicates more energy was consumed in the fatigue crack propagation of the post-HIPped samples.

Acknowledgements

This work was partly sponsored by EU-China FP7 collaborative project (FP7-AAT-2010-RTD-CHINA). The authors also would like to acknowledge FalconTech, Wuxi, China for providing fatigue test machine and support during the experiments.

References

[1] W.Weibull, A Statistical distribution function of wide applicability. J. Appl. Mech. 18 (1951), pp. 293-297.

[2] C. Lei, W. Frazier, E. Lee, The effect of hot isostatic pressing on cast aluminum, JOM 49 (1997) , pp. 38-39.

[3] G. Lütjering ,A. Gysler, in Titanium Science and Technology, vol. 4, DGM, 1985, p.2068.

[4] ASTM E-399. Test methods for plane-strain fracture toughness of metallic materials. Annual Book of ASTM Standards, 1978, American Society of Testing and Materials, West Conshohoken, Pa.

[5] ASTM E-647. Measurements of fatigue crack growth rate. Annual Book of ASTM Standards. American Society of Testing and Materials, 1978, West Conshohoken, Pa.

[6] N. L. Richards,Quantitative evaluation of fracture toughness – microstructural relationships in alpha-beta titanium alloys . JMEPEG,13 (2004),pp. 218–225.

[7] K. K. Murthy, S. Sundaresan, Eng. Fract. Mech. 58 (1997), pp.29-41.

[8] A.A. Rubinstein, Mechanics of the crack path formation. Int. J. Fracture 47(1991), pp.291-305.

[9] K.S. Chan, Y-W. Kim, Effects of lamellae spacing and colony size on the fracture resistance of a fully-lamellar TiAl alloy, Acta Metall. Mater. 43 (1995), pp. 439-451.

[10] H. Margolin, Metall. Mater. Trans. 13 (1982), pp 269-274.

[11] M. Niinomi, T. Kobayashi, Fracture characteristics analysis related to the microstructures in titanium alloys, Mater. Sci. Eng A 213 (1996), pp.16-24.

[12] J.E. Campbell et al., Application of Fracture Mechanics for Selection of Metallic Structural Materials, Translated by Wang Yilin, Beijing: Metallurgical Industry Press, 1992.

[13] M.A. Langøy, S.R. Stock, Metall. Mater. Trans. A 32 (2001), pp.2297-2314.

A New Damage Identification Strategy for SHM based on FBGs and Bayesian Model Updating Method

Yanhui Zhang[1], **Wenyu Yang**[1,*]

[1] State Key Lab of Digital Manufacturing Equipment and Technology, Huazhong University of Science and Technology, Wuhan, Hubei, 430074, China
* Corresponding author: mewyang@mail.hust.edu.cn

Abstract One of the difficulties of the vibration-based damage identification methods is the nonuniqueness of the results of damage identification. The different damage locations and severity may cause the identical response signal, which is even more severe for detection of the multiple damage. This paper proposes a new strategy for damage detection to avoid this nonuniqueness. This strategy firstly determines the approximates damage area based on the statistical pattern recognition method using the dynamic strain signal measured by the distributed fiber Bragg grating, and then accurately evaluates the damage information based on the Bayesian model updating method using the experimental modal data. The stochastic simulation method is then used to compute the high-dimensional integral in the Bayesian problem. Finally, an experiment of the plate structure, simulating one part of mechanical structure, is used to verify the effectiveness of this approach.

Keywords structural health monitoring, damage detection, fiber Bragg grating, Bayesian model updating, stochastic simulation

1. Introduction

The nonuniqueness of the results of damage identification is the one of the difficulties of the vibration-based damage identification methods. The different damage locations and severity may cause identical response signal. This problem is even more severe for the detection of the multiple damage. The reason is that, the number of the measured points in real application is limited and only the limited modes could be estimated. Furthermore, the modelling error and the measurement noise is usually inevitable, some erroneous modes could have modal parameters closer to the estimated modal parameters than the model with the correct damage locations and amount [1].

By explicitly considering the modelling error and the measurement noise, Bayesian model updating approach is an excellent way to model prediction error and provide the uncertainty information of the damage identification results [2]. Based on the Bayesian formula, Bayesian model updating approach could incorporate the engineering judgments, the mathematical models and the measured data together to make robust identification for damage. The results of damage identification are expressed though the post probability density function (PDF), rather than pinpointing a single solution in the traditional deterministic approach. The post PDF quantifies the confidence level of the identified results, which usually provides an important reference for maintenance decision.

The fiber Bragg grating (FBG), considered to be a promising technology, has been increasingly applied to the SHM process. FBG has several advantages, such as immunity to electromagnetic interference, high sensitivity, light weight, and so on. The excellent multiplexing capability of the FBG facilitates its use as a distributed sensor system, which not only monitors the local key parts of the structure but also captures the overall dynamic information. Panopoulou et al. [3] developed a complete damage detection system using FBGs. The dynamic strain response data from the FBG is first measured, then the feature indices are extracted by various signal processing methods, and finally an artificial neural network is utilized to detect and locate damage. This system has been demonstrated by a thin composite panel and a honeycomb structure and is planned for use in a future application of an antenna reflector.

This paper uses the distributed FBG as the sensor network and proposes a new strategy for damage detection though two steps, which firstly estimate the approximate damage area from the dynamic strain signal using the statistical pattern recognition method, and then accurately evaluates the

damage based on Bayesian model updating method using experimental modal data. Lastly, the stochastic simulation method is used to solve the Bayesian computation issue and generate the samples of the damage parameters identified.
The following paper is organized as follows. Section 2 summaries the new damage detection strategy. Section 3 is the experimental verification section: firstly describes the experimental apparatus and procedures, and then presents the detection results of Step 1 and Step 2, respectively. A few conclusions are discussed in Section 4.

2. Theoretical Background

2.1. New Damage Identification Strategy

The traditional damage detection methods for SHM can be classified into model-based method and non-model-based method [4]. Here, the "model" refers as the physical model of the real mechanical or civil structure. The non-model method usually directly uses the signal processing or statistical method to determine whether the damage occurs. This method is simple and straightforward, but helpless for quantifying the damage, such as the size, orientation and trends of the crack. Alternatively, the model-based method requires an accurate physical model and could quantify the damage but on the cost of intensive computation.
Absorbing both advantages of the non-model method and the model-based method, a new damage detection strategy is proposed based on FBG and Bayesian model updating method. This process consists of the following two phases. (1) Roughly estimate damage area based on the distributed dynamic strain signal with the recognition accuracy of the gage lengths of FBG without a detailed analytical model. (2) Accurately identify the size, direction and depth of the damage with the recognition accuracy of the accuracy of the physical model based on Bayesian model updating method. The details of the process are showed in Fig. 1.

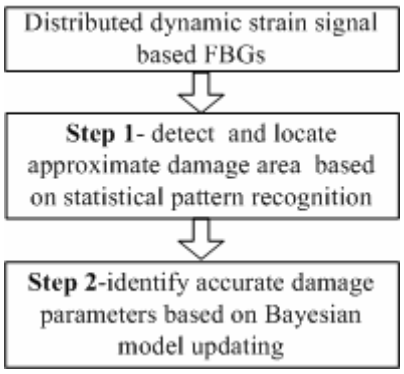

Figure 1. Detailed process of the new damage detection strategy

Based on the strain measurement, the dynamic strain response of FBG is more sensitive to the local small damage than the traditional displacement or acceleration measurements. But the environmental and operational variations, such as the change of temperature, usually disguise the signal variation induced by damage and cause the false-positive indication. So in Step 1, the dynamic strain signal is decomposed into the damage-sensitive signal component using the Hilbert-Huang Transform (HHT) method, the autoregressive (AR) model is then used to exact damage sensitive features, and lastly the Mahalanobos distance-based method is used to determine the approximate damage area, named as the damage suspicious region. But the identification accuracy of this region is low, because that is mainly affected by the grating length of FBG and the layout density of the sensor network.

In Step 2, the Bayesian model updating method is further used to identify the detailed damage parameters. The damage parameters are identified only from the damage suspicious region of Step 1.

There are several advantages for this new damage identification strategy. First, the number of the parameters to be identified has been reduced, which make the cost of the computation greatly drop. Second, the search targets of the damage identification only focus to the damage suspicious area, rather other the entire structure. The "output-equivalent" issue in the damage mechanism modelling can be effectively relieved, which refer to the problem that different damage assumes may produce identical out parameters [1].

2.2. Bayesian Model Updating Framework

Assume the damage could be expressed by the reduction of the element stiffness, but independent from the element mass. Therefore, introducing the parameter vector $\boldsymbol{\theta} = [\theta_1, ..., \theta_i, ..., \theta_N]$, which represents the contribution of the element stiffness to the system stiffness matrix, the system stiffness matrix $\mathbf{K}$ can be written as:

$$\mathbf{K}(\boldsymbol{\theta}) = \mathbf{K}_0 + \sum_{i=1}^{N} \theta_i K_i \tag{1}$$

where N is the degrees of freedom (DOFs) of the linear discrete system, θ_i ($0 < \theta_i < 1$) is non-dimensional, and the smaller the size of θ_i , the more serious the damage of element, other words, deeper the crack. The combination of adjacent damage element constitutes the shape and direction of the crack. Obviously, the accuracy of crack identification depends on the sizes of finite elements which can be controlled artificially but usually at the cost of the computation effort [5].

Based on Bayesian theorem, when given the measured data $\mathbf{D}$ and the probabilistic models M, the post PDF of $\boldsymbol{\theta}$ can be expressed as:

$$p(\boldsymbol{\theta} \mid \mathbf{D}, M) = cp(\mathbf{D} \mid \boldsymbol{\theta}, M)\, p(\boldsymbol{\theta} \mid M) \tag{2}$$

where c is a normalizing constant, $p(\boldsymbol{\theta} \mid M)$ is the prior PDF of $\boldsymbol{\theta}$, and $p(\mathbf{D} \mid \boldsymbol{\theta}, M)$ is the likehood function. Because that the measured modal frequency usually has the more precision than the other modal parameters. Moreover, the most algorithms including the mode shapes have to deal with the problems of the finite element (FE) model reduction or mode shape expansion to bridge the gap between the real structure and the simulated model. So the modal frequencies are used to construct the likelihood function, assume the N_m ($\leq N$) modes of natural frequency are considered here:

$$p(\mathbf{D} \mid M) = \frac{1}{(2\pi)^{N_s N_m/2}} \frac{1}{\Sigma^{1/2}} \exp \left\{ -\frac{1}{2} \sum_{n=1}^{N_s} \left[\boldsymbol{\psi}(n) - \psi(\boldsymbol{\theta}) \right]^T \Sigma^{-1} \left[\boldsymbol{\psi}(n) - \psi(\boldsymbol{\theta}) \right] \right\} \tag{3}$$

where $\sum$ is the variance matrix of the measured modal frequency, N_s is the number of the measured modal frequency sets, $\boldsymbol{\psi}$ is the measured modal frequency of the monitoring structure under unknown health status, and the $\psi(\boldsymbol{\theta})$ is computed modal frequency of the FE model.

The computation of the high-dimensional integral in the Bayesian method is difficult and has attracted the attention of many researchers over the decades. Several improved stochastic simulation methods have been developed to solve the high-dimensional and complex posterior PDF, such as the adaptive Metropolis-Hastings (AMH) [6], the transitional Markov chain Monte Carlo (TMCMC) [7], the Hybrid Monte Carlo (HMC) [8], and so on. Inherited from the AMH that introduced a series of intermediate PDFs, the TMCMC can not only automatically select the intermediate PDFs but

also conveniently evaluate the evidence in the Bayesian model class selection. However, the proposal distribution of the TMCMC is the random walk of Gaussian distribution, which cannot explore the local properties of the posterior PDF well. So the slice sampling is used as the algorithm of the candidate value for TMCMC, which is named as TMCMC-slice.

The improved TMCMC-slice algorithm, which has integrated the advantages of the TMCMC and slice sampling method, is used to generate the sample of the unknown parameters. Based on slice sampling, the generation of the candidate value can automatically adapt to the local features of the post PDF with fewer user-adjusted parameters. Though the gradually transitioning from the prior PDF to the post PDF, TMCMC can easier sample from the intermediate PDFs than other methods. And the ratio of Metropolis-Hasting in each iteration step could make the sample concentrate the region of high probability, which improves the convergence properties of the TMCMC-slice algorithm.

3. Experimental verification

3.1. Experimental apparatus and procedure

A 304 stainless steel plate, which is attached by four bolts on a support, was used to simulate one part of the mechanical structure. The geometric parameters of the plate are 500 mm by 500 mm and 3 mm thick. Twenty-nine gratings were bonded on the surface of the plate according to the symmetry of the structure. These gratings were assigned to four individual fibers in order to facilitate wiring, and then connected with the four channels of the optical demodulator produced by the Micron Optics Inc. The sampling rate of the FBGs was set to 2 kHz. There were also 15 accelerometers to monitor the modal parameters of the structure. The sampling rate of the accelerometer was also set to 2 kHz. The arrangement of the FBGs and accelerometers sensor network is shown in Fig. 2.

Providing the excitation for the plate structure, a vibration exciter was attached to the center of the plate using a screw with a 3mm diameter. This vibration exciter was controlled by the LMS modal testing system, which produced the 0~8 kHz broad-band stochastic excitation.

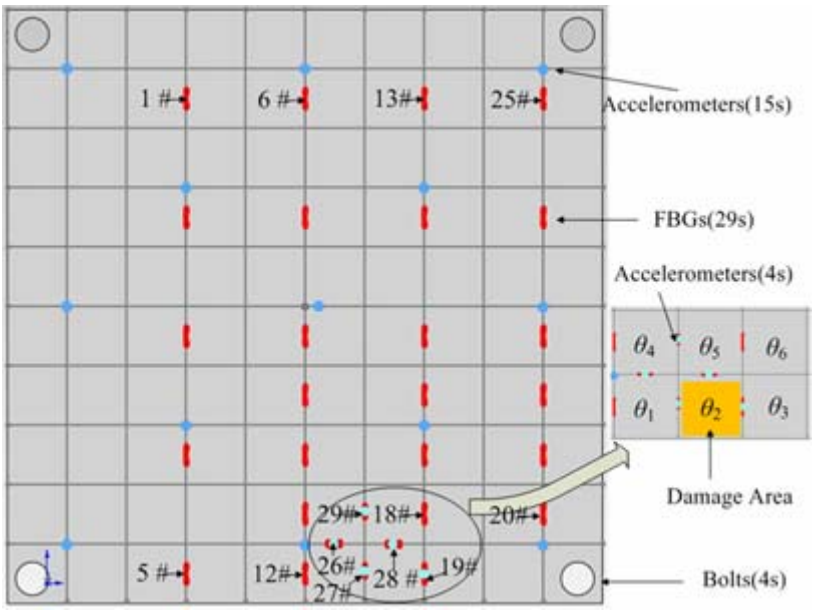

Figure 2. Layout of the FBG and accelerometer sensor network

The structural defect usually appears in most mechanical structures because of stress concentration,

fatigue, or corrosion. Therefore, the experiment here was mainly designed to identify this form of damage. The structural defect was simulated by a notch at different depths, which was directly machined on a milling machine, as shown in the upper left corner of Fig. 3. Based on the severity of the damage, there were four groups. The first group represents the baseline health state without any defect; the second group induces a defect whose size is 46 mm by 48 mm with a depth of 1.5 mm (50% thickness), as shown in the yellow region of Fig. 2. In the third group, the size of the defect remains the same, but the depth is increased to 2.4 mm (80% thickness). Finally, in the fourth group, the defect is completely though the plate (3 mm depth). The torque of the four bolts connecting the plate and the support was 80 Nm, which was strictly controlled by the torque wrench in each experimental group. The image of the experimental real objects can be observed in Fig. 3, and the details of the different health states simulated are summarized in Table 1.

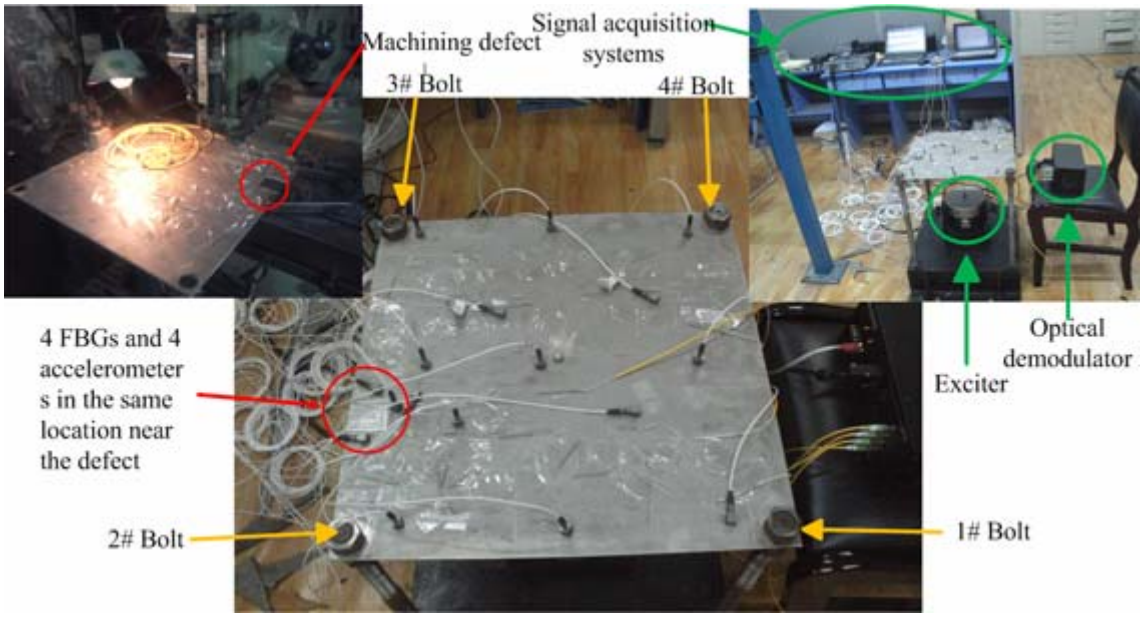

Figure 3. Picture of the experiment

Table 1. Details of different health conditions

State	Label	Description
Health state	State 1	Baseline state, no defects
Damage state 1	State 2	Defect size: 46mm × 48mm × 1.5mm
Damage state 2	State 3	Defect size: 46mm × 48mm × 2.4mm
Damage state 3	State 4	Defect size: 46mm × 48mm × 3mm

3.2. Detection Results of Step 1

For each damage state, 50 sample records are collected as damage identification according to the periodicity characteristics of the response signal. In Step 1, the dynamic strain signal from FBG is first decomposed into several intrinsic mode functions (IMFs), then the AR-based model is applied on the second level IMF component to extract the damage sensitive features and Mahalanobis distance-based pattern classification method are used to detect and locate damage. Here the sample sets from State 1 (health state), State 2 (damage state 1), State 3 (damage state 2), and State 4 (damage state 3), totally 200 samples, are used for damage identification. These samples are divided into two parts. One is the first 25 samples of State 1 as the training sample set. Another is the test sample set composed of the later 25 samples of State 1 and the remaining three damage states, totally 175 samples. The identification results of the channel 19, 26, 27, and 28 are shown in Fig. 4,

in which the blue bar indicates that no damage occurred, the red bar means the damage, and the green horizontal line is the threshold which is calculated assuming that the distribution of the square of the Mahalanobis distance is chi-square distribution with the DOFs equal to the AR model order.

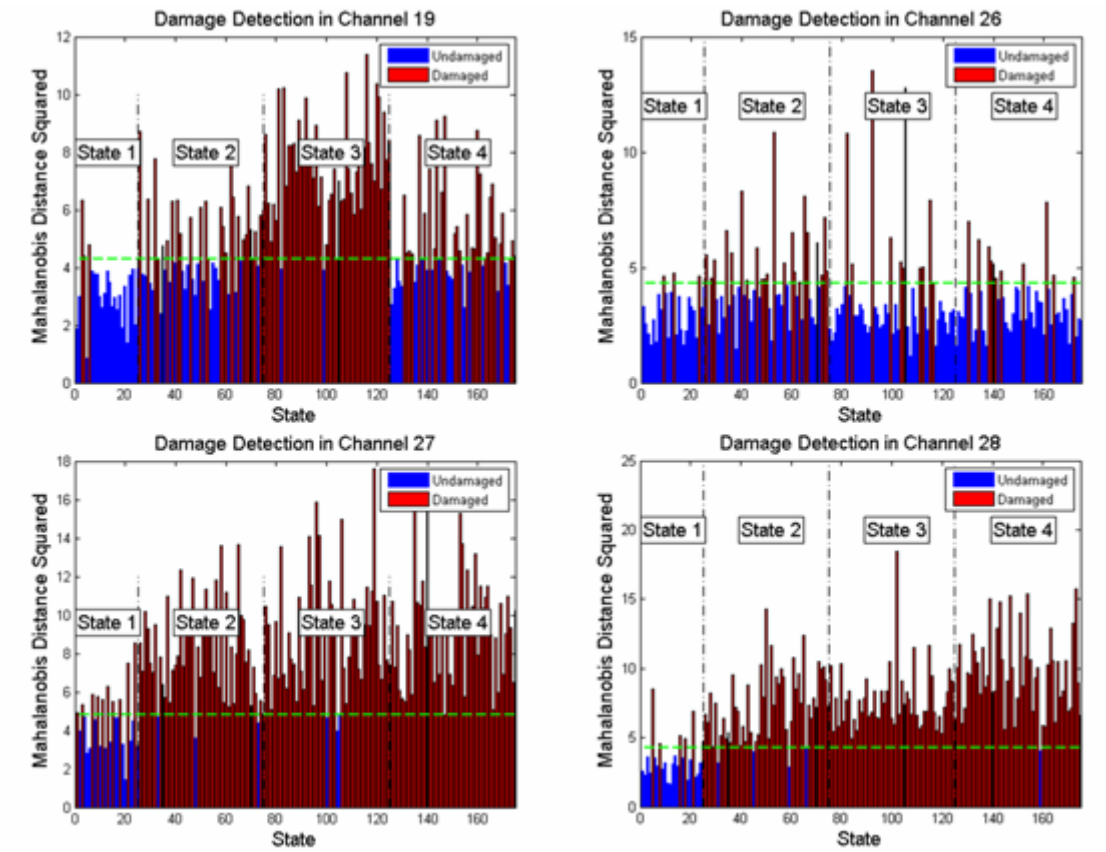

Figure 4. Results of damage detection and location in channel 19, 26, 27 and 28

There is no damage occurred when the number of blue-bar is larger than the red-bar in each state, otherwise, the damage appears. Observing the amount of the red bars, the number of the red bars in the channel 19, 27, and 28 is large, so the conclusion is that the approximate location of the damage is near the position of the channel 19, 27, and 28, but lacking more detailed information, such as the direction, size and severity about the damage. So next the Bayesian model updating method is used to identify the specific parameters of the damage.

3.3. Detection Results of Step 2

In order to identify the damage parameters, the plate structure is divided into the 100 rectangular elements of 10 by 10. Then the non-dimensional parameter, representing the contributions of the element stiffness to the system stiffness matrix, is introduced to model the damage. Based on the detection results of Step 1, only the six parameters near the damage approximate area, θ_i (i = 1, 2, …, 6), are updated in Bayesian model updating method of Step 2.

3.3.1. FE Model Refinement

A precise model is required before applying Bayesian model updating method for damage identification, so the FE model is refined to minimize the model error by conducting a series of parametric analysis.

The experimental modal frequency is firstly identified by the LMS modal analysis software using the acceleration signal. Here the results of State 1 (health state), State 2 (damage state 1), State 3 (damage state 2), and State 4 (damage state 3) are shown in Table 2.

Table 2. Modal frequency of the healthy and damage states

Mode	State 1 (Hz)	State 2 (Hz)	State 3 (Hz)	State 4 (Hz)
1	40.9330	42.4120	42.3030	41.9960
2	137.4630	135.9660	135.6860	134.9330
3	307.7550	304.8220	305.3790	301.6580
4	436.2560	436.2100	432.7160	430.4220
5	690.2900	683.8950	674.1470	679.2060
6	806.7520	803.8900	802.2440	808.0970

The geometric parameters of the plate are accurately measured as 515 mm by 515 mm and 2.95 mm thick. The density of the 304 stainless steel is 8150 kg/m^3, the Modulus of Elasticity is 189 GPa, and the Poissons ratio is 0.285. The four-node rectangular element is used in the FE model, and the size of the grid element is 51.5 mm by 51.5 mm. The nodes of the elements located in four corners are fully constrained to simulate the bolt constraint. The comparison of the modal frequency between the FE model and the actual undamaged plate is shown in Table 3.

Table 3. Comparison of the modal frequency between FE model and actual plate

Mode	Test(Hz)	FEM(Hz)	Diff(%)
1	40.9330	40.9361	0.0076
2	137.4630	140.5776	2.2658
3	307.7550	315.8144	2.6188
4	436.2560	427.5859	-1.9874
5	690.2900	703.1238	1.8592
6	806.7520	809.1443	0.2965

Although the refined FE model is close to the actual structure, the model error is modelled a Gaussian process. Then the post PDF is constructed according to the Bayesian theorem. The posterior samples of the damage parameters θ_i are generated using the stochastic simulation method based on TMCMC-slice sampling.

3.3.2. Damage Identification

The damage identification results of the TMCMC-slice algorithm are checked. The statistics of the sample are shown in Table 4, where column 1 is the actual values of the parameters, column 2 shows the identified sample mean, column 3 shows the sample standard deviation (s.d.), and column 4 displays the coefficient of variance (c.o.v.).

Table 4. Results of damage identification for plate structure based on TMCMC-slice

	Actual	Identified	s.d.	c.o.v.
θ_1	1.0000	0.9950	0.7742	0.7781
θ_2	0.5000	0.5181	0.2100	0.4053
θ_3	1.0000	2.6051	1.5647	0.6006

θ_4	1.0000	0.9500	0.8905	0.9374
θ_5	1.0000	0.6889	1.4918	2.1655
θ_6	1.0000	0.9771	0.9996	1.0231

The result of the TMCMC-slice method is satisfactory, only the identified values of θ_3 and θ_5 are deviate from the actual values, but the corresponding standard deviation (s.d.) and coefficient of variance (c.o.v.) are also large, which denote that the results have lower credibility.
Then the sample updated trajectory and probability density distribution are respectively used to further analysis the performance of TMCMC-slice, as shown in Fig. 5 and Fig. 6.

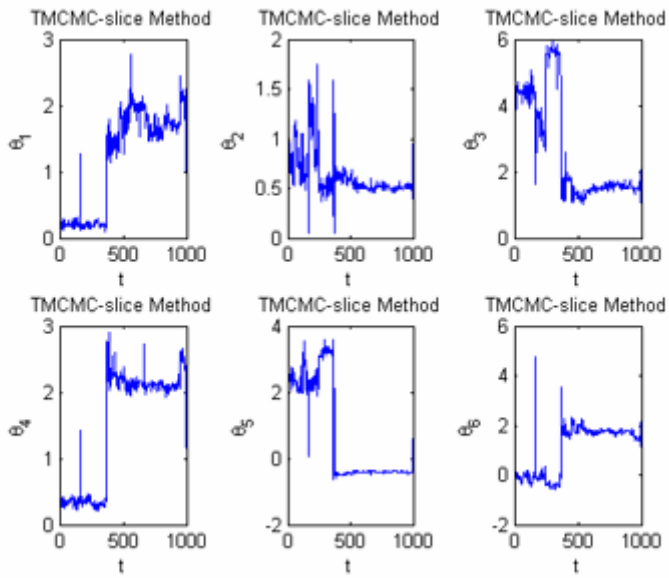

Figure 5. Sample path of the damage identification results based on TMCMC-slice

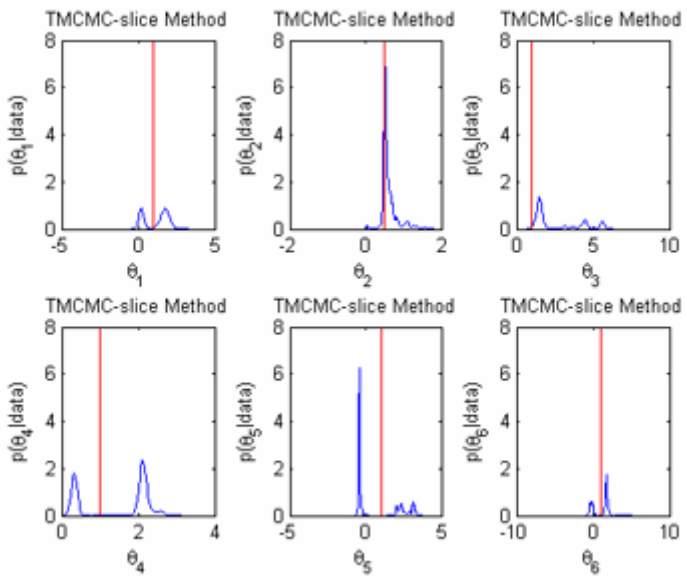

Figure 6. Probability density of the damage identification results based on TMCM-slice

4. Conclusions

This paper proposes a new damage detection strategy which can successfully identify the damage of the plate structure. Inheriting the results of Step 1, the non-dimensional stiffness parameters, only from the suspicious damage region, are updated using the Bayesian model updating method in Step 2. The significances of the method are that: when the identification of the detailed damage parameters focuses on the suspicious damage area, the number of the parameters needs to be identified has been greatly reduced, which can improve the convergence performance of the stochastic simulation method. The uncertainty of identification parameters will be reduced. More important, the nonuniqueness issue of the results of damage identification could be effectively relieved.

The finite element model which introduces local stiffness reductions representing damage may be the simplest method among these damage modelling methods for SHM. But different from the traditional usage way as [1, 9, 10] in which a damage threshold must be pre-assumed, this paper uses the stochastic simulation method to obtain the samples of the stiffness parameters. The sample means are the identified values of the parameters, which represent actual severity of damage. The value of the θ_i is closer to 1, the more health structure; closer to 0, the more serious structure damage. The sample variance gives the credibility of the recognition results. The size and orientation of the damage can be observed by the combination of the different damage elements. The accuracy of damage identification depends on the sizes of the finite elements, which can be controlled artificially but usually on the cost of the computation effort.

Although the experiment result has obtained encouraging results, how to improve the accuracy of the damage identification is the focus of the future work.

Acknowledgements

The first author would like to sincerely thank Professor Jianye Ching and Dr. Yi-Chu Chen in Taiwan for their selfless help of the TMCMC algorithm.

This work was supported by the National Natural Science Foundation of China (No. 50935005) and the Major State Basic Research Development Program of China (973 Program) (No. 2009CB724306). Authors express the most sincere thanks to these organizations.

References

[1] Sohn H, Law KH, A Bayesian probabilistic approach for structure damage detection, Earthquake Engineering & Structural Dynamics, 26 (1997) 1259-1281.

[2] Cheung SH, Beck JL, Calculation of Posterior Probabilities for Bayesian Model Class Assessment and Averaging from Posterior Samples Based on Dynamic System Data, Computer-Aided Civil and Infrastructure Engineering, 25 (2010) 304-321.

[3] Panopoulou A, Loutas T, Roulias D, Fransen S, Kostopoulos V, Dynamic fiber Bragg gratings based health monitoring system of composite aerospace structures, Acta Astronautica, In Press, Corrected Proof (2011).

[4] Doebling SW, Farrar CR, Prime MB, A summary review of vibration-based damage identification methods, Shock and Vibration Digest, 30 (1998) 91-105.

[5] Wu ZS, Li SZ, Two-level damage detection strategy based on modal parameters from distributed dynamic macro-strain measurements, Journal of Intelligent Material Systems and Structures, 18 (2007) 667-676.

[6] Beck JL, Au SK, Bayesian updating of structural models and reliability using Markov chain Monte Carlo simulation, Journal of Engineering Mechanics-Asce, 128 (2002) 380-391.

[7] Ching JY, Chen YC, Transitional markov chain monte carlo method for Bayesian model updating, model class selection, and model averaging, Journal of Engineering Mechanics-Asce, 133 (2007) 816-832.

[8] Cheung SH, Beck JL, Bayesian Model Updating Using Hybrid Monte Carlo Simulation with Application to Structural Dynamic Models with Many Uncertain Parameters, Journal of

Engineering Mechanics, 135 (2009) 243-255.
[9] Kurata M, Kim JH, Lynch JP, Law KH, Salvino LW, Asme, A PROBABILISTIC MODEL UPDATING ALGORITHM FOR FATIGUE DAMAGE DETECTION IN ALUMINUM HULL STRUCTURES, Proceedings of Proceedings of the Asme Conference on Smart Materials, Adaptive Structures and Intelligent Systems2010.
[10] Vanik MW, Beck JL, Au SK, Bayesian probabilistic approach to structural health monitoring, Journal of Engineering Mechanics-Asce, 126 (2000) 738-745.

Criticality of Damage-Failure Transitions under Dynamic and Fatigue Loading

Oleg Naimark

Institute of Continuous Media Mechanics UB RAS, 614013 Perm, Russia
Corresponding author: naimark@icmm.ru

Abstract Statistical theory of evolution of typical mesoscopic defects (microcracks, microshears) revealed specific type of criticality–structural-scaling transitions and allowed the development of phenomenology of damage-failure transition in solids with defects. The key results of statistically based phenomenology are the establishment of characteristic multiscale collective modes of defects responsible for damage-failure transitions under dynamic and fatigue loading. High resolution experiments and structural (SWFM and AFM) study in terms of scaling invariance supported the linkage of the evolution of these modes with material responses in large range of load intensity (dynamic crack propagation, fragmentation statistics, crack path under high cycle (HCF) and very high cycle (VHCF) fatigue)

Keywords multiscale damage kinetics, collective modes of defects

1. Introduction

The problem of fracture treated as a critical phenomenon represents one of the key problems of fundamental and applied physics of materials science. Experimental studies of material responses in a large range of loading rates show that the behavior of solids is intimately linked with the evolution of typical mesoscopic defects (microcracks, microshears). This characterizes generically solids under dynamic and fatigue loading, when the internal times of the evolution of ensemble of defects for different structural levels are approaching the characteristic loading times. Statistical theory of typical mesoscopic defects (microcracks, microshears) revealed specific type of criticality – the structural-scaling transitions and allowed the development of phenomenology of damage-failure transition based on the definition of non-equilibrium free energy of solid with defects. Multiscale aspects of damage-failure transition are analyzed to consider recent experiments on dynamic crack propagation, fragmentation statistics, scaling laws of fatigue.

1. Structural-scaling transitions in solid with defects

Statistical theory of the evolution of typical mesoscopic defects (microcracks, microshears) allowed us to establish specific type of critical phenomena in solid with defects – structural-scaling transitions and to propose the phenomenology of damage-failure transition [1]. The key results of the statistical theory and statistically based phenomenology are the establishment of two order parameters responsible for the structure evolution – the defect density tensor p_{ik} and the structural scaling parameter $\delta = (R/r_0)^3$, which represents the ratio of the spacing between defects and characteristic size of defects. Non-equilibrium free energy F represents generalization of the Ginzburg-Landau expansion in terms of mentioned order parameters – the defect density tensor (defect induced deformation $p = p_{zz}$ in uni-axial case) and structural scaling parameter δ:

$$F = \tfrac{1}{2} A(\delta,\delta_*)p^2 - \tfrac{1}{4} Bp^4 - \tfrac{1}{6} C(\delta,\delta_c)p^6 - D\sigma\, p + \chi(\nabla_l p)^2, \tag{1}$$

where $\sigma = \sigma_{zz}$ is the stress, χ is the non-locality parameter, A, B, C, D are the material parameters, δ_* and δ_c are characteristic values of structural-scaling parameter (bifurcation points) that define the areas of typical nonlinear material responses on the defect growth (quasi-brittle, ductile and fine-grain state) in corresponding δ–ranges: $\delta < \delta_c \approx 1$, $\delta_c < \delta < \delta_*$, $\delta > \delta_* \approx 1.3$. The damage kinetics is determined by the kinetic equations for the defect density p and scaling parameter δ

$$\dot{p} = -\Gamma_p \frac{\Delta F}{\Delta p}, \quad \dot{\delta} = -\Gamma_\delta \frac{\partial F}{\partial \delta}, \tag{2}$$

where Γ_p, Γ_δ are the kinetic coefficients, $\Delta(...)/\Delta t$ is the variation derivative. Kinetic equations Eq.2 and the equation for the total deformation $\varepsilon = \hat{C}\,\sigma + p$ ($\hat{C}$ is the component of the elastic compliance tensor) represent the constitutive equations of materials with mesodefects. Material responses on the loading realize as the generation of characteristic collective modes – the solitary waves in the range of $\delta_c < \delta < \delta_*$ and the "blow-up" dissipative structure in the range $\delta < \delta_c \approx 1$. The generation of these collective modes under the loading provides the change of the system symmetry and initiates specific mechanisms of the momentum transfer (plastic relaxation) and damage-failure transition on the scales of damage localization with the blow-up kinetics.
The damage-failure scenario includes the "blow-up" kinetics of damage localization as the precursor of crack nucleation according to the self-similar solution:

$$p = g(t)f(\xi), \xi = x/L_H, \quad g(t) = G(1 - t/\tau_c)^{-m}, \tag{3}$$

where τ_c is the so-called "peak time" ($p \to \infty$ at $t \to \tau_c$ for the self-similar profile $f(\xi)$ localized on the scale L_H, $G > 0, m > 0$ are the parameters of non-linearity, which characterise the free energy release rate for $\delta < \delta_c$. The self-similar solution Eq.3 describes the blow-up damage kinetics for $t \to \tau_c$ on the set of spatial scales $L_H = kL_c$, $k = 1,2,...K$, where L_c and L_H corresponds to the so-called "simple" and "complex" blow-up dissipative structures. Generation of the complex blow-up dissipative structures appears when the distance L_S between simple

structures approaches to the scale L_c. Similar scenario of the "scaling transition" proceeds for the blow-up structures of different complexity to involve in the process of the final stage of damage localization the larger scales of material.

The description of damage kinetics as the structural-scaling transition allowed the consideration of solid with defects as a dynamical system with spatial degrees of freedom (corresponding to the set of blow-up dissipative structures of different complexity). Stochastic behavior in this case can be linked with the dynamics of the critical state with the features of flicker noise, or $1/f$ - statistics. The systems reveal the so-called self-organized criticality (SOC) with universal behavior that is typical for the late state evolution of dynamic systems when the correlation will appear on all length of scales. The self-similar nature of mentioned collective modes associated with damage localization zones has the great importance in the case of dynamic loading, when the "excitation" of these modes can lead to the subjection of relaxation and failure to the dynamics of these modes. The examples for this situation are the transition from the steady-state to the branching regimes of crack propagation, qualitative change of the fragmentation statistics with the increase of the energy density imposed into the material.

2. Nonlinear crack dynamics. Crack branching

The understanding of self-similar scenario of damage-failure transition stimulated our experimental study of crack dynamics for the explanation of mechanisms of transition from the steady-state to the branching regime, fragmentation statistics and failure wave phenomenon [2]. The stress field in the area of crack tip in the preloaded (by external stress σ) PMMA plate and the diagram "crack velocity V versus applied stress σ" are presented in Fig.1 according to the data of high speed framing with the usage REMIX REM 10-8 camera (time lag between pictures $10\,\mu s$). Three characteristic regimes of crack dynamics were established in the different ranges of crack velocity: steady-state $V < V_C$, branching $V > V_C$ and fragmenting $V > V_B$, when the multiply branches of main crack have the autonomous behavior (Fig.1, 2). Steady-state regime of crack dynamics is the consequence of the subjection of damage kinetics to the self-similar solution of the stress distribution at the crack tip (mechanically speaking to the stress intensity factor). Bifurcation point V_C ($V_C \approx 0.4 V_R$ where V_R is the Rayleigh wave speed) corresponds to the transition to the regime, when the "second attractor" (with the symmetry properties related to the number of the blow-up dissipative structures) disturbs the steady-state regime due to the excitation of numerous new failure hotspots (the daughter cracks having the image of mirror zones on the fracture surface). The change of the symmetry properties of nonlinear system were studied under the recording of dynamic stress signal (polarization of laser beam) at the front of propagating crack in the point deviated on 4 mm from the main crack path. The corresponding phase portraits $\dot{\sigma} \sim \sigma$ for steady-state and branching regimes of crack dynamics are presented in Fig. 3 and confirmed the existence of two "attractors", which subject the crack dynamics. The first attractor is related to the intermediate asymptotic solution for the stress distribution at the crack tip. The second attractor has

degrees of freedom corresponding to the set of blow-up dissipative structures of different complexity that can be responsible for different scenario of fragmentation statistics and failure under dynamic and shock wave loading.

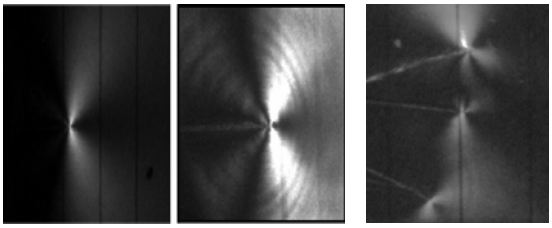

Figure 1: Stress pattern for steady-state $V < V_C$, branching $V > V_C$ and fragmenting $V > V_B$ scenario of crack dynamics.

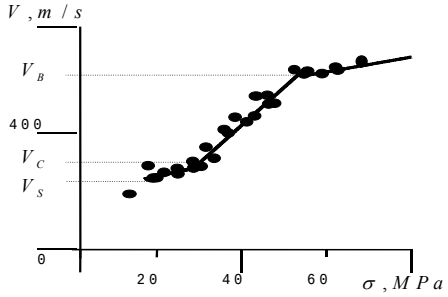

Figure 2: Crack velocity V versus stress σ.

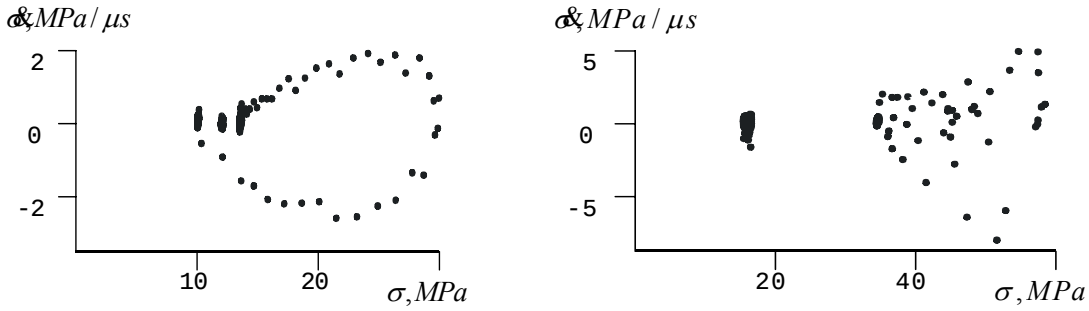

a b

Figure 3: Stress phase portraits: $\dot{\sigma} \sim \sigma$: a - $V = 200\,m/s$, b - $V = 615\,m/s$

3. $1/f$ -fragmentation statistics

Fundamental properties of failure are central in determining the temporal scenario of fragmentation statistics and fragment size distribution. Fragment size distributions can range from the relatively tight exponential functions to power-law relations spanning a number of decades in fragment size. Onset of fracture asymptotes to a range of length scales in which fragmentation is self-similar requiring that failure temporal sequences and the fragment size distributions exhibit a power-law dependence [3]. The linkage of scenario of crack propagation and symmetry properties of dynamic system “solid with defects” allowed us to propose the interpretation of temporal and spatial fragmentation statistics depending on the energy density imposed. A large number of the fragmentation statistics were proposed: log-normal, power-law, exponential, combination of exponential and power laws. These theories have focused on the prediction of mean fragment size

through energy and momentum balance principles, and on statistical issues of fragment size distribution. The energy density $E < E_C$ (E_C corresponds to the critical velocity V_C of the steady state – branching transition) provides the stress intensity controlled failure scenario. The transient densities $E_B > E > E_C$ $(V_C < V < V_B)$ lead to the exponential fragmentation statistics that is sensitive to both self-similar solutions: the self-similar stress distribution at the crack tip and collective blow-up modes of damage localization. "In-situ" fracture-luminescence sequences in dynamically loaded fused quartz rods and fragmentation statistics in recovered samples were analyzed. The power law of fracture luminescence sequences and the fragment size distribution was observed [4,5] under the increase of the energy density $E > E_B$ (Fig.4) when the multiscale damage localization occurs according to the set of blow-up dissipative structures that have the image of the stochastic "cloud" on the phase portrait (Fig. 3b). It was shown that the fragmentation time exceeds at least in two orders of magnitude the characteristic acoustic time on the sample length (100mm). The fracture luminescence signals represent the wave envelopes with the amplitudes revealing non-monotonic decay.

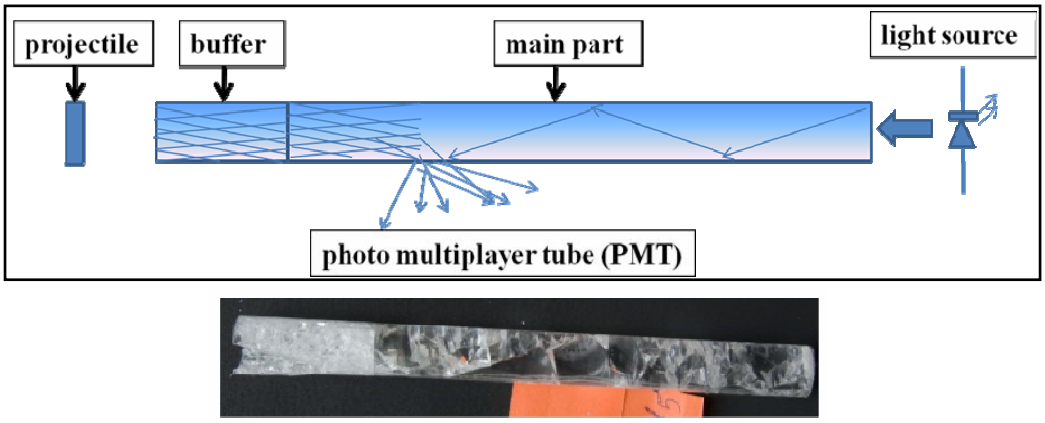

Figure 4. Fracture luminescence and fragmentation experiments

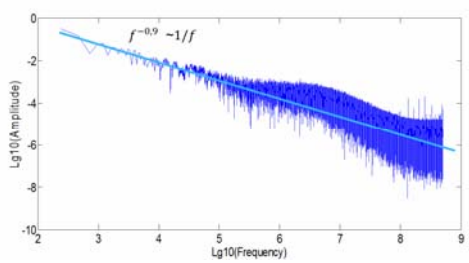

Figure 5. *1/f* fracture luminescence spectrum in dynamically loaded fused quartz rod

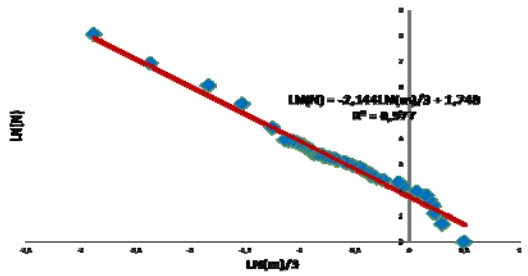

Figure 6. Fragment size cumulative distribution

Analysis of «in-situ» fracture luminescence sequences and fragmentation size statistics in dynamically loaded fused quartz established the power laws for the temporal (*1/f* spectrum) and

spatial failure scenario that are characteristic for the multiscale collective modes (blow-up dissipative structures) associated with collective behavior of the set of damage localization hotspots.

4. Resonance excitation of damage localization

The solution (3) allowed us to link the self-similar features of damage localization kinetics and generation of blow-up dissipative structures. It was established the correspondence of failure hotspots nucleation having the image of mirror zones in experiments with numerous spall failure in shocked cylindrical rods of PMMA and ultraporcelain [5,6]. The multiple mirror zones with an equal size were excited on different spall cross sections in the shocked rod when the stress wave amplitude exceeded some critical value corresponding to the transition to the so-called "dynamic branch" under spalling (Fig. 7). Theoretically predicted low limit of damage localization scale L_C shows the existence of critical energy density, which provides the limit size of fragmented structure close to L_C and the degeneration of the power low statistics into the mono-disperse distribution. Such fragmentation dynamics can be linked to the failure wave phenomenon [8]. The important feature of failure wave phenomenon is that the velocity of failure wave doesn't depend on the velocity of propagation of the single crack. The stored elastic energy in material is the main factor, which provides the ability of brittle solid to the generation of failure wave. The failure waves represent the specific dissipative structures (the "blow-up" dissipative structures) in the microshear ensemble that could be excited due to the shock wave pass [9]. Experimental study of failure wave generation and propagation was realized for the symmetric Taylor test on fused-quartz rods [10]. Fig. 8a shows the processing of a high-speed photography (upper picture) for the flyer rod traveling at 534 m/s at impact.

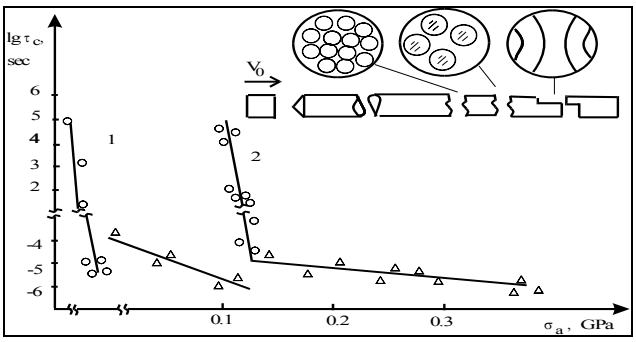

Figure 7: Fracture time t_c for shocked rod of PMMA (1) and ultraporcelain (2) versus stress amplitude σ_a.

Insert: surface pattern with mirror zones in different spall cross sections [6].

Three dark zones correspond to the image of impact surface (green triangle), failure wave (red square) and (blue diamond) the shock wave. The initial slope for the failure wave gives the front velocity $V_{fw} \approx 1.57\, km/s$ that is close to traditionally measured in the plate impact test [10]. However, the experiment revealed the increase of failure front velocity up to the value

$V_{fw} \approx 4\,km/s$. Approaching of failure wave front velocity to the shock front velocity supports theoretically based result concerning the failure wave nature as "delayed failure" with the limit of "delay time" corresponding to the "peak time" in the self-similar solution [10].

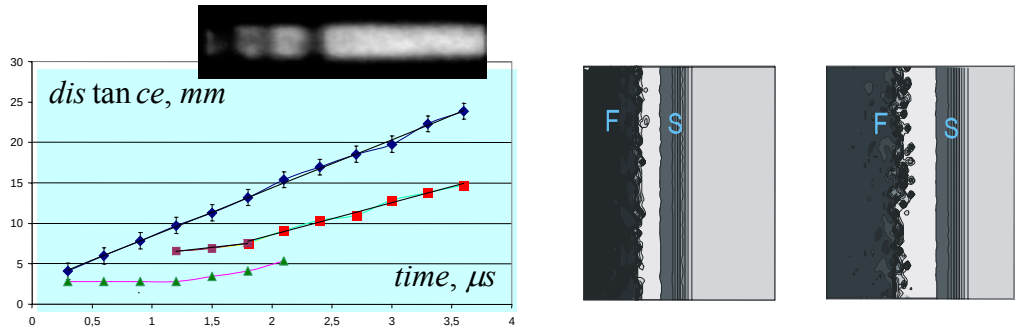

a b

Figure 8. a – The Taylor test data; b - Simulation of shock wave (S) and failure wave (F) propagation for different time [10].

Numerical simulation (Fig.8b) of damage kinetics describes the self-similar "blow-up" dynamics of damage-failure transition, supports the assumption concerning the failure wave mechanism as delayed failure with the delay time of the development of "peak regime" of "blow-up" dissipative structure. Time of the delay τ_D represents generally the sum of the induction time τ_I, that is the time of the formation of damage spatial distribution close to the self-similar profile, and the "peak time" τ_C, that is the time of "blow-up" damage kinetics. Steady-state regime of failure wave front propagation can be linked to the successive „resonance" activation of "blow-up" dissipative structures with characteristic "delay time" that is close to the "peak time" τ_C.

5. Scaling transitions and fatigue crack kinetics

Damage kinetics according to Eq. 2 reveals the specific system behavior in the ranges of scaling parameter $\delta_C < \delta < \delta_*$ and $\delta < \delta_C$ when the defect density tensor p_{ik}, influences on the correlation properties of defects on different spatial scales. The existence of two ranges of δ characterizes qualitative difference in relaxation mechanisms, which provide different dissipation ways: the orientation ordering and the formation of PSBs structures and the blow-up dissipative structures as the final stage of damage localization. The scenario of defect evolution in the range $\delta_C < \delta < \delta_*$ leads to the anomaly of the relaxation properties and, as the consequence, the energy absorbing. The high level of the structural relaxation time in the orientation metastability area in respect of the loading time $\tau_l \approx (\dot{\varepsilon})^{-1}$ coupled with the self-similar features of structure rearrangement in the scaling transition regime explains the anomaly of the energy absorbing under cycle load starting from some characteristic level of strain. This stain corresponds to the saturation

stress σ_S providing the start of the scaling transition and the saturation effect as the anomaly of energy absorbing. The microscopic mode of fatigue crack growth is strongly affected by the multiscale slip arrangement, applied stress level and the extent of near tip plasticity. In ductile solids, cyclic crack growth is observed as a process of intense localized deformation in slip bands near the crack tip which leads to the creating of new crack surfaces by shear decohesion. The important feature of cyclic loading conditions, when the onset of crack growth from pre-existing defects can occur, at stress intensity values that are well below the quasi-static fracture toughness. This observation was used as a physical basis for the Paris model, when small scale yielding assumption allowed the formulation of the crack kinetics as

$$\frac{da}{dN} = C\,\Delta K^{m}, \tag{4}$$

in the term of the stress intensity factor range defined as $\Delta K = K_{\max} - K_{\min}$, where $K_{\max}$ and $K_{\min}$ respectively are the maximum and minimum stress intensity factors, C and m are empirical constants which a functions of material properties and microstructure. This formula predicted the Paris exponent of $m \approx 4$ in agreement with experiments for most metals [11]. Since the crack growth kinetics is linked to the temporal ability of material to the energy absorbing at the crack tip area the understanding of the saturation nature can be the key factor for the explanation of the 4th power universality. It was shown that the saturation nature can be considered as a consequence of the anomaly energy absorbing in the course of structural-scaling transition in dislocation system with the creation of PSBs and long-range interaction of dislocation substructures. Taking into account that the p- kinetics is given by the 4th order difference in the power in the metastability area the qualitative dependence of the damage rate reads $\dot{p} \sim A\sigma_S^4$, where σ_S is the saturation stress in the metastability area for $\delta_C < \delta < \delta_*$. This result supports the phenomenological law proposed by Paris [11] for the HCF crack growth kinetics. It is interested to note that this channel is very powerful in the sense of the energy absorbing. For instance, similar to the Paris law, the 4th power law $\dot{\varepsilon} \approx A\sigma_A^4$ of the linkage of plastic strain rate $\dot{\varepsilon}_p$ on the stress amplitude σ_A was established at the steady-state plastic wave front for several materials experienced shock loading [9, 12].

6. Defect induced scaling and scaling laws for fatigue crack path

With the purpose of understanding of crack behavior near the fatigue crack threshold the replica technique was used to study the correlation between the scaling properties of defect induced roughness and scaling laws of fatigue crack. 3D New View high resolution data of defect induced roughness in the crack process zone (Fig.9a) under fatigue crack path revealed the existence of two

characteristic scales: the scale of the process zone L_{Pz} and the correlation length l_{sc} that is the scale when the correlated behavior of defect induced roughness has started [13].

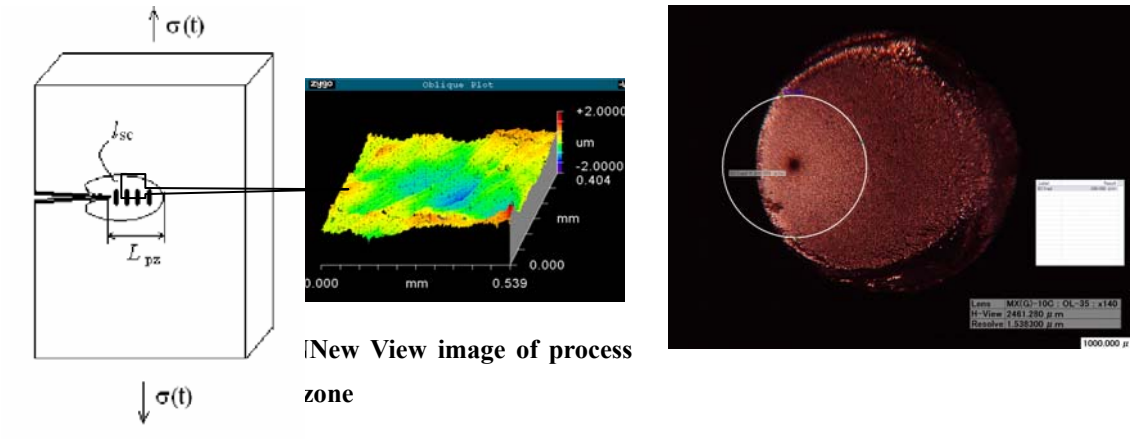

a b

Figure 9: a –roughness scaling in the process zone; b – "fish eye" area of damage localization under VHCF (fine grain titanium)

Assuming incomplete self-similarity in the variables $\Delta K/\left(E\sqrt{l_{sc}}\right)\to 0$, $l_{sc}/L_{Pz}\to 0$ and the definition of the effective stress intensity factor $\Delta K_{eff}=\Delta K\left(l_{sc}/L_{PZ}\right)^{\beta/\alpha}$ the kinetics of fatigue crack path reads

$$dl/dN=l_{sc}\left(\Delta K_{eff}/\left(E\sqrt{l_{sc}}\right)\right)^{\alpha}, \tag{5}$$

where the exponent α and β are the parameters related to the intermediate asymptotic dependence of crack rate on the stress intensity range. There is important case of the fatigue crack advance near-fatigue threshold when the scale of the process zone has the limit $L_{Pz}\to l_{sc}$, the effective stress intensity factor range ΔK_{eff} is approaching to the value ΔK and Eq.5 has the form $dl/dN=l_{sc}\left(\Delta K/\left(E\sqrt{l_{sc}}\right)\right)^{\alpha}$ This form is similar to the equation proposed by Hertzberg [14] for $l_{sc}\to b$, where b is the Burgers vector. Generally, in the limit of small scales $l_{sc}\approx b$ the application of stress intensity factor conception is problematic and numerous multiscale mesodefects interaction and corresponding scaling laws must be introduced [15]. This situation is characteristic for the fatigue of fine grain materials and especially for Very High Cycle Fatigue, when the stage of crack nucleation is dominated in the life time. The image of fracture surface of fine grain titanium (grain size ~300nm) in the condition of VHCF (number of cycles ~10^{10}) is shown in Fig.9b and revealed the "fish eye" image and the large "process zone" occupying fracture surface area in the bulk of specimen.

The research was supported by grants within the programs of the Presidium of RAS (09-П-1-1011) and by the RFBR grants (11-01-00712_a, 12-01-92002-HHC_a).

References

[1] O.B.Naimark, Defect Induced Transitions as Mechanisms of Plasticity and Failure in Multifield Continua, in: Advances in Multifield Theories of Continua with Substructure, G. Capriz and P. Mariano (eds.), Birkhäuser, Boston, 2004, p. 75-114.

[2] Naimark O.B., Uvarov S.V. Nonlinear crack dynamics and scaling aspects of fracture (experimental and theoretical study). International Journal of Fracture, 128 (2004), 285-292.

[3] D.E.Grady, Length Scales and Size Distributions in Dynamic Fragmentation Int. J.Fracture 163 (2010), 85-113.

[4] M.M. Davydova, O.B. Naimark, V.V.Leontiev and S.V. Uvarov, Scaling properties of crack branching and brittle fragmentation, European Physical Journal, Web of Conferences, 10 (2010), 00037.

[5] M.M.Davydova, O.B. Naimark and S.V. Uvarov Scaling of spatial and temporal variables in dynamic fragmentation of quartz, 9th Meeting New Models and Hydrocodes for Shock Wave processes in Condensed Matter, April 23-27, 2012, London, UK., 2012, 62-63.

[6] V.V. Belyaev and O.B. Naimark, Kinetics of multicenter falure under shock wave loading, Sov. Phys. Dokl. 312(1990), 312-318.

[7] E. N. Bellendir, V. V. Belyaev, and O. B. Naimark, Kinetics of numerous hotspot spall failure, Sov. Tech.Phys. Lett., 15 (1989), 90-94.

[8] S. V. Rasorenov, G. I. Kanel, V. E. Fortov and M. M. Abasenov, The fracture of glass under high pressure impulse loading, High Press. Res., **6** (1991), 225-241.

[9] O.B. Naimark, Structural-scaling transitions in mesodefect ensembles as mechanisms of relaxation and failure in shocked and dynamically loaded materials (experimental and theoretical study), J. Phys. IV, 134 (2006), 3-21.

[10] O.B. Naimark, S.V. Uvarov, D.D. Radford, W.G.. Proud, J.E. Field, P.D. Church, I. Cullis, T.D. Andrews, The failure front in silica glasses, in: Behavior of Dense Media under High Dynamic Pressures, A.Delpuech (ed.), 2(2003), 65-74.

[11] J-L Lataillade and O.B.Naimark, Physical Mesomechanics, Mesoscopic and nonlinear aspects od dynamic and fatigue failure (experimental and theoretical results), 7 (2004), 55-66.

[12] O.B.Naimark, Structural-scale transitions in solids with defects and symmetry aspects of field theory, Physical Mesomechanics, 13(2010), 306-317.

[13] C.Froustey, O. Naimark , M. Bannikov , V. Oborin, Microstructure scaling properties and fatigue resistance of pre-strained aluminium alloys (part 1: AleCu alloy), European Journal of Mechanics A/Solids, 29 (2010), 1008-1014.

[14] P.Paris, D.Lados, H.Tad, Reflections on identifying the real $K_{effective}$ in the threshold region and beyond, Engineering Fracture Mechanics, 75(2008), 299–305.

[15] V.A.Oborin, M.V.Bannikov, O.B.Naimark and T.Palin-Luc, Scale invariance of fatigue crack growth under giga-cycle regime of loading, Technical Physics Letters, 36(2010), 76-82.

Dynamic fracture of metals in wide range of strain rates

Alexander E. Mayer[1,*]

[1] Department of Physics, Chelyabinsk State University, Chelyabinsk, 454001, Russia
* Corresponding author: mayer.al.evg@gmail.com, mayer@csu.ru

Abstract A model of dynamic tensile fracture is constructed, which is applicable for many metals in wide range of strain rate. It considers a stage of thermofluctuation nucleation of voids and stages of voids growth and aggregation. The model contains two fitted parameter for each substance: the first parameter is a specific free energy of metal surface; the second one is a distribution parameter for weakened zones of material. These parameters are found for copper, aluminum, iron, titanium, nickel and molybdenum by fitting with the experimental data and molecular-dynamics simulations. Calculations show that there are two regions with different slope in the strain rate dependence of strength: in the first one (at strain rate < 10^8 s^{-1}) voids are nucleated in weakened zones, and strength grows up relatively fast with strain rate; in the second one (at strain rate > 10^8 s^{-1}) number of weakened zones becomes insufficient, voids are nucleated predominantly in perfect material, and the strength growth is decelerated. Plasticity is not effect on voids nucleation and on the material strength at the strain rate > 10^7 s^{-1}, but it becomes a dominant factor at the strain rate < 10^4 s^{-1}.

Keywords Fracture, High-rate tension, Metal, Micro-cracks, Two-level approach

1. Introduction

Dynamical tensile strength is an important property of materials. A number of experimental works is devoted to its determination: a plate impact [1,2], a short-pulse laser irradiation [3-5] and a powerful ion irradiation [1] can be used to produce conditions of metal rupture. Very high strain rates (above 10^9 s^{-1}) are available now in experiments on irradiation of thin foils by short laser pulses [3,5]. Molecular dynamics (MD) is also a useful method for the investigation of fracture at ultra-high strain rates [6-10]. The dynamical strength value substantially depends on the strain rate. Experiments and MD simulations can not cover all possible ranges of this parameter. Therefore, their data have to be supplemented by some approximation for using in simulations of dynamical processes in materials. For example, the strain rate dependence of the dynamic strength is commonly approximated by a simple power law [3,10]).

Various physical models of fracture typically separate the stages of the voids nucleation and of the voids growth [11]. Nucleation of voids is strongly effected by the presence of inclusions, grain boundaries and other defects of the crystal structure [12].

A modification of the model [13] is presented here, which considers weakened zones of material with reduced threshold of the micro-voids generation. It allows describing the strain rate dependence of strength in the range of strain rates from 10^3 s^{-1} up to 10^{11} s^{-1}. Kinetics of the dynamic fracture of metals is numerically investigated basing on the proposed model.

2. Model of fracture

The model uses two-level approach for fracture description. Micro-level of modeling deals with individual micro-cracks in crystalline material and describes their thermo-fluctuation nucleation, growth and aggregation. Macro-level deals with averaged values through a length scale much large the distance between the cracks. Micro-cracks growth is described with use of simplified dynamics

equation for its radius. Macro-level is described by continuum mechanics equations with additional terms, which takes the micro-cracks ensemble into account.

2.1. Voids growth equation

Let $\vec{\beta}$ to be a unit vector directed along the maximal tensile stress. Tensile stress $\sigma_\beta = \sigma_{ik}\beta_i\beta_k$ can initiate formation and growth of the opening mode cracks perpendicular to $\vec{\beta}$ (see Fig. 1). Let us consider such a micro-crack, which is supposed to be isolated and axially-symmetrical. Radius of crack is R and its half-thickness is h; its volume V_f can be estimated as a volume of cylinder $V_\mathrm{f} = \pi R^2 \cdot 2h$. Opening of crack creates non-uniform field of displacements in its vicinity. Created by a localized disturbance, the displacements have to decay with distance with on the scale R. Maximal displacements in $\vec{\beta}$ direction corresponds to the crack faces, and it is $+h$ and $-h$ for opposite faces. Therefore, the ratio h/R can be used as an estimation of the strain value in the crack vicinity. Corresponding stress can be estimated as $G(h/R)$. In the loaded medium this internal stress is superposed on the external macroscopic tensile stress σ_β. And the total stress has zero normal components on the crack faces to maintain the constant form at the fixed radius R. Hence, we obtain an estimation $h = R\sigma_\beta / G$ for the crack half-thickness; than the crack volume is $V_\mathrm{f} = 2\pi R^3 \sigma_\beta / G$. Usage of the last two formulas assumes that the crack thickness instantly adapts to variations of R or σ_β (a quasi-static approximation), it is valid when the typical time of variations τ ($\tau \approx R/\dot{R}$ or $\tau \approx 1/\dot{\varepsilon}$, where $\dot{\varepsilon}$ is the strain rate) is much longer than the transient period R/c_t. Therefore, conditions for the quasi-static approximation are the next: $\dot{R} << c_t$ and $\dot{\varepsilon} << c_t / R$; these inequalities usually take place.

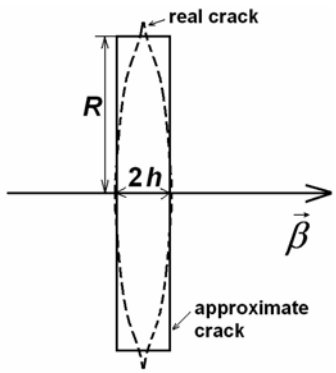

Figure 1. A separate micro-crack; the real crack shape is approximated by cylinder.

The crack grows due to separation of atoms along the plane of crack. The growth rate is restricted by inertia of the surrounding material. It is possible to formulate a Lagrange equation [14] for the micro-crack growth, using the radius R as a generalized coordinate. In this approach system is characterized by the Lagrange function $L = K - U_S - U_V$, where K is the kinetic energy of the substance movement due to the growth of micro-crack; U_S is the surface energy of the crack faces; U_V is the potential energy of crack in the field of external stresses σ_β, and by the dissipative function F, which is equal to the one half of the mechanical energy decrease rate due to plastic deformation in the micro-crack vicinity. Expression $K = \rho V_\mathrm{f} \dot{R}^2$ is used as an estimation of the

kinetic energy, where ρ is the density of substance. Work of the external stresses σ_β at the crack opening is equal to the work on the crack faces; its work on the bulk is zero because of symmetry. One can integrate the elementary work along faces and obtain the value $\sigma_\beta \cdot \delta V_{\mathrm{f}}$, where δV_{f} is an increment of the crack volume. Therefore, the potential energy of crack in the external stress field σ_β can be written as $U_V = -\sigma_\beta V_{\mathrm{f}} = -2\pi R^3 \sigma_\beta^2 / G$; negative sign here indicates that the micro-crack growth is energy-wise efficient in the tensile stress. Potential surface energy connected with two crack faces is equal to $U_S = 2\pi R^2 \gamma$.

Estimation of the dissipative function is more complex. The crack size changing is accompanied by generation of non-uniform fields of deformations and stresses in the crack vicinity, and the shear part of these stresses undergoes plastic relaxation. Due to the plastic strain the mechanical energy of the growing or collapsing crack is conversed in heat. On the base of the Orowan equation for dislocation plasticity, one can write the maximal plastic strain rate $\dot{w} = b\,\rho_D\, c_t$, where ρ_D is the scalar density of dislocations in the substance, b is the modulus of the Burgers vector of dislocations, c_t is the limiting speed of the dislocations movement. Using the ratio $h/R = \sigma_\beta / G$ as a characteristic value of deformation in the crack vicinity, we obtain a characteristic time of the plastic relaxation $\tau_D = (h/R)/\dot{w} = \sigma_\beta / (G\, b\, \rho_D\, c_t)$. This is a time interval sufficiently large for the plastic relaxation of excess shear stress in the crack vicinity if the form of crack is artificially frozen. Then the mechanical energy decrease rate can be estimated as K/τ_D (external stresses and, respectively, U_V are supposed to be fixed). Than the dissipative function is equal to $F = (1/2) K/\tau_D = \pi\rho (b\rho_D c_t) R^3 (\dot{R})^2$.

Substituting all obtained elements in the Lagrange equation, one can obtain the next equation for the crack radius:

$$\rho \frac{\sigma_\beta}{G}\left(R^2 \ddot{R} + \frac{3}{2} R (\dot{R})^2 \right) = -4(\gamma + \gamma') + 6R\frac{\sigma_\beta^2}{G}, \tag{1}$$

where $\gamma' = (\rho/2)(b\rho_D c_t) R^2 \dot{R}$ is irreversible energy (per unit area of crack faces) spending on plastic deformations; this energy dissipates both at the growth and at the collapse of the crack. It follows from the Eq. (1), that the crack grows when its radius exceeds a critical value $R_{\mathrm{cr}} = (2/3) G \sigma_\beta^{-2} (\gamma + \gamma')$. Calculations show, that at high-rate deformation the value of γ' is negligible with respect to γ for just formed cracks with critical radius. Therefore, initial crack growth occurs in a brittle mode, practically without energy dissipation on the plastic deformations. In particular, the next relation is valid with good accuracy $R_{\mathrm{cr}} = (2/3)\gamma G \sigma_\beta^{-2}$. But at the micro-crack growth, the irreversible energy γ' increases and it can reach the value of the order of : $1000\ \mathrm{J/cm^2}$ for large cracks, which exceeds the value of γ on the three orders of magnitude.

2.2. Nucleation of cracks. Weakened zones of the material

Let us consider a micro-cracks ensemble. We denote the number of micro-cracks in unit volume of substance as n. To find the micro-cracks production rate we assume, that all they are generated due to thermal fluctuations. We assume that main contribution in dn/dt is provided by cracks with critical radius R_{cr}, because cracks with $R < R_{\mathrm{cr}}$ are being healed, and generation of cracks with

$R > R_{\text{cr}}$ is the low-probability process. Formation work for critical crack is $A_{\text{cr}} = U_V\left(R_{\text{cr}}\right) + U_S\left(R_{\text{cr}}\right)$ (it is reversible process without plastic dissipation), and we obtain $A_{\text{cr}} = \left(2/3\right)\pi \cdot \gamma \cdot R_{\text{cr}}^2$. The probability of such fluctuations is $P = \exp\left(-A_{\text{cr}}/\left(k_B T\right)\right)$ [16], where T is the substance temperature, k_B is the Boltzmann constant.

Concentration of the fluctuating centers can be estimated as $n_{\text{g}} = 1/\left(8R_{\text{cr}}^3\right)$. Fluctuation frequency f can be estimated as the frequency of transverse phonon with wavelength equal to the critical crack diameter $f = c_t/\left(2R_{\text{cr}}\right)$. As a result, the cracks nucleation rate is

$$\frac{dn}{dt} = P \cdot n_{\text{g}} \cdot f = \frac{c_t}{16R_{\text{cr}}^4}\exp\left(-\frac{2\pi \cdot \gamma \cdot R_{\text{cr}}^2}{3k_B T}\right). \tag{2}$$

The Eq. (2) determines the nucleation rate in the pure, defect-free material. In the real solids there are structural defects, such as dislocations, grain boundaries in polycrystals, inclusions in alloys etc. Micro-crack formation in the defective (weakened) regions requires smaller work in comparison with the undefective one, since these regions already possess raised energy relative to the defect-free crystal material (atoms in it are weaker bounded with each other). Primary origination of voids near the defects is observed in MD simulations [7,10]. We have to consider an influence of defects on the micro-cracks formation. Faultiness of current region of the material can be characterized by a parameter γ^* in such a way, that difference $\left(\gamma - \gamma^*\right)$ defines the crack surface formation energy per unit area in this defective region, $\gamma^* < \gamma$. Then the formation work of the critical crack is equal to $A_{\text{cr}}\left(\gamma^*\right) = \left(2/3\right)\pi\left(\gamma - \gamma^*\right)R_{\text{cr}}^2$, where R_{cr} is determined by γ because the crack must grow further in the defect-free regions of crystal, hence, it should be stable at this value of surface tension. We suppose that the weakened zones are exponentially distributed on γ^*: $n\left(\gamma^*\right) = n_0 \cdot \exp\left(-\gamma^*/\Delta\gamma\right)$ where $\Delta\gamma$ is a distribution parameter. The product $n\left(\gamma^*\right)d\gamma^*$ is the number of micro-cracks nucleation centers in unit volume of substance with the faultiness parameter belonging to $d\gamma^*$ interval near the γ^*. The constant n_0 is determined by the normalization condition: $n_g = \int_0^{\gamma} n\left(\gamma^*\right)d\gamma^* = n_0 \cdot \Delta\gamma \cdot \left(1 - \exp\left(-\gamma/\Delta\gamma\right)\right)$. Than the crack generation rate is defined by the following expression:

$$\frac{dn}{dt} = \frac{c_t}{16R_{\text{cr}}^4}\frac{\left[\exp\left(-\left(2\pi\gamma R_{\text{cr}}^2\right)/\left(3k_B T\right)\right) - \exp\left(-\gamma/\Delta\gamma\right)\right]}{\left[1 - \left(2\pi\Delta\gamma R_{\text{cr}}^2\right)/\left(3k_B T\right)\right] \cdot \left[1 - \exp\left(-\gamma/\Delta\gamma\right)\right]}. \tag{3}$$

At $\Delta\gamma = 0$ (homogeneous material) this equation turns back to the Eq. (2). Thus, the proposed model of fracture contains two empirical parameters: γ and $\Delta\gamma$. The first of them, γ, is of the order of surface tension, and the second one, $\Delta\gamma$, is defined by the degree of material faultiness.

2.3. Continuous formulation

Here and further we operate with macroscopic length scale, which is much larger than the micro-crack size and the distance between the micro-cracks. It means that each physically small volume of substance contains a set of micro-cracks. Therefore, we use macroscopic fields of substance density, velocity, stresses, deformations, et alia, which are averaged over such physically small volumes. Let us assume that in considered substance element all micro-cracks have identical

spatial orientation $\vec{\beta}$. For volume element V it is possible to write: $V = V_c + V_{Sf}$, where V_c is a part of volume occupied by solid, not cracked, material, and V_{Sf} is a total volume of all micro-cracks in V. Let us introduce $\eta = V_{Sf}/V$ – the fraction of volume which is occupied by cracks. Growth of the total micro-cracks volume with rate $\dot{V}_{Sf}$ at the fixed total element volume V leads to decrease of the solid material volume with the rate $\dot{V}_c = -\dot{V}_{Sf} = -V \cdot \dot{\eta}$. If $h << R$, than this change of solid material volume occurs predominantly due to solid material deformation in the $\vec{\beta}$ direction. Corresponding deformation of substance in auxiliary coordinate system is characterized by a sole strain component:

$$\frac{dW_{\beta\beta}}{dt} = \left.\frac{\dot{V}_c}{V_c}\right|_{V=const} = -\frac{1}{1-\eta}\frac{d\eta}{dt},$$

Transformation of this strain tensor into lab coordinates is the next:

$$\frac{dW_{ik}}{dt} = -\beta_i \beta_k \left(\frac{1}{1-\eta}\frac{d\eta}{dt} \right), \tag{4}$$

where W_{ik} is symmetrical strain tensor. The use of W_{ik} as an additional strain of solid material allows considering of the tensile stresses relaxation caused by cracks nucleation and growth. Assuming that all micro-cracks in volume element have the same size, it is possible to write for the micro-cracks volume fraction $\eta = n \cdot V_f$.

The adjacent micro-cracks can coalesce forming a main crack or fractionized zone of material. We suppose that separate micro-cracks develop solitary until their diameter $2R$ reaches the value of an average distance between the cracks, which is equal to $n^{-1/3}$. If the relation $2R \geq n^{-1/3}$ is satisfied in any volume element, then material of this element is assumed to be completely fractured, and all stress components are set equal to zero in it.

In the present report a uniaxial deformation of substance along *Oz*-axis is considered with the constant macroscopic strain rate $d\varepsilon_{zz}/dt = \text{const}$. The maximal tensile stress operates along *Oz*-axis: $\vec{\beta} = \vec{e}_z$, $\sigma_\beta = \sigma_{zz}$. The continuum mechanics equations in this case are reduced to the next set:

$$\frac{d\rho}{dt} = -\rho\left(\frac{d\varepsilon_{zz}}{dt} + \frac{dW_{zz}}{dt} \right), \tag{5}$$

$$\rho\frac{dU}{dt} = \sigma_{zz}\left(\frac{d\varepsilon_{zz}}{dt} + \frac{dW_{zz}}{dt} \right) + S_{zz}\frac{dw_{zz}}{dt}, \tag{6}$$

$$\sigma_{zz} = -P(\rho, U) + S_{zz}, \tag{7}$$

$$\frac{dS_{zz}}{dt} = \frac{4}{3}G\left(\frac{d\varepsilon_{zz}}{dt} + \frac{dW_{zz}}{dt} \right) - 2G\frac{dw_{zz}}{dt}, \tag{8}$$

$$\frac{dW_{zz}}{dt} = -\frac{1}{(1-\eta)}\frac{d\eta}{dt}, \tag{9}$$

$$\eta = n \cdot \left(2\pi R^3 \frac{\sigma_{zz}}{G} \right), \tag{10}$$

where w_{zz} is the plastic distortion due to the dislocations movement; U is the specific internal energy, P is the pressure; S_{zz} is deviator of stresses. All variables here are averaged over physically small volumes. The Eqs (5)-(10) have to be completed by the Eq. (1) and Eq. (3) for the

micro-cracks nucleation and growth and by the equations for determination of the plastic distortion w_{ik} through the dislocations movement (see, for example, [17]). For determination of the pressure and temperature, the wide-range equations of state [18,19] were used in the forms of dependences $P = P(\rho, U)$ and $T = T(\rho, U)$. All equations have been integrated in time by the explicit Euler scheme with variable time step, which has been selected from the stability condition $\Delta t \leq \min\{0.1R/\dot{R}, 0.001/\dot{\varepsilon}_{zz}\}$. Parameters γ and $\Delta\gamma$ had been chosen by fitting with the experimental data [1-4,20-26] and with the of molecular-dynamics (MD) simulation results [7,9,10] for the strain rate dependences of the material strength; the obtained values of these parameters are summarized in the Table 1.

Table 1. Parameters of the fracture model. Abbreviations: m/c – monocrystalline, p/c – polycrystalline.

Substance	Cu		Al		Ti	Fe	Zn	Mo	
	m/c	p/c	m/c	p/c	p/c	p/c	m/c	m/c	p/c
γ, J/m^2	0.95	0.60	0.57	0.47	1	1	0.8	1.1	0.7
$\Delta\gamma$, J/m^2	0.029	0.029	0.016	0.016	0.027	0.036	0.029	0.034	0.034

3. Results and discussion

Strain dependences of tensile stress have been obtained in calculations; the typical dependences are shown in Fig. 2(a). Stress grows up with strain at the initial stage. Then the tension reaches some critical level, an intensive nucleation and growth of the cracks begins. It leads to relaxation of tensile stresses; the increase of stresses is changed on the decrease. Non-zero level of tensile stresses is held till the complete destruction of substance. The moment of complete destruction corresponds to the slump of stresses down to zero. The maximal obtained value of tensile stresses has to be treated as the dynamic (spall) strength of the material σ_{sp}. Dynamic strength increases with the strain rate, because the growth rate of the total volume of cracks has to be proportional to the strain rate for effective relaxation of the tensile stresses. This total volume is determined by the number and size of cracks; therefore, nucleation and growth rates have to be increased for relaxation at the increased strain rate, these rates are obtained at higher level of the tensile stresses.

Fig. 2(b) shows the strain dependences of the average radius R, the critical radius R_{cr} and the concentration n of the micro-cracks. Nucleation of cracks starts at the earliest stages of deformation, but its concentration is insignificant initially. At the low acting stresses, voids are nucleated only in weakened zones with a very high value of faultiness $\gamma^* \approx \gamma$, concentration of which is negligibly small. The critical radius decreases with the increase of strains and of the tensile stresses; zones with lower faultiness begin to contribute in nucleation of cracks, and the concentration of cracks grows fast. When the concentration reaches some value, the relaxation on micro-cracks becomes a dominant process, and the tensile stresses begin to decrease (see Fig. 2 (a)). It initiates an increase of the critical radius and slump of the nucleation rate of new cracks, only the growth of the existing micro-cracks takes place. This growth continues up to the reaching of the complete destruction, after than, R means a typical size of fragments in the destructed material. It is 30 μm and 7 μm for the strain rates 10^6 s^{-1} and 10^7 s^{-1} correspondently.

The calculated strain rate dependencies of the dynamic strength for monocrystalline and polycrystalline copper and aluminum are presented in Fig. 3 in comparison with the experimental data and MD simulation results. The model parameters γ and $\Delta\gamma$ (Table 1) have been chosen for

fitting our results with experiments and MD modeling. At the same time, the fracture model gives correct slopes of the curve $\sigma_{sp}\left(d\varepsilon/dt\right)$ in the both regimes of nucleation, and these slopes are not regulated by the model parameters. For unequivocal selecting of the parameters a simultaneous comparison with experimental data at the moderate strain rates (heterogeneous nucleation) and with results of MD simulations at very high strain rates (homogeneous nucleation) is optimal.

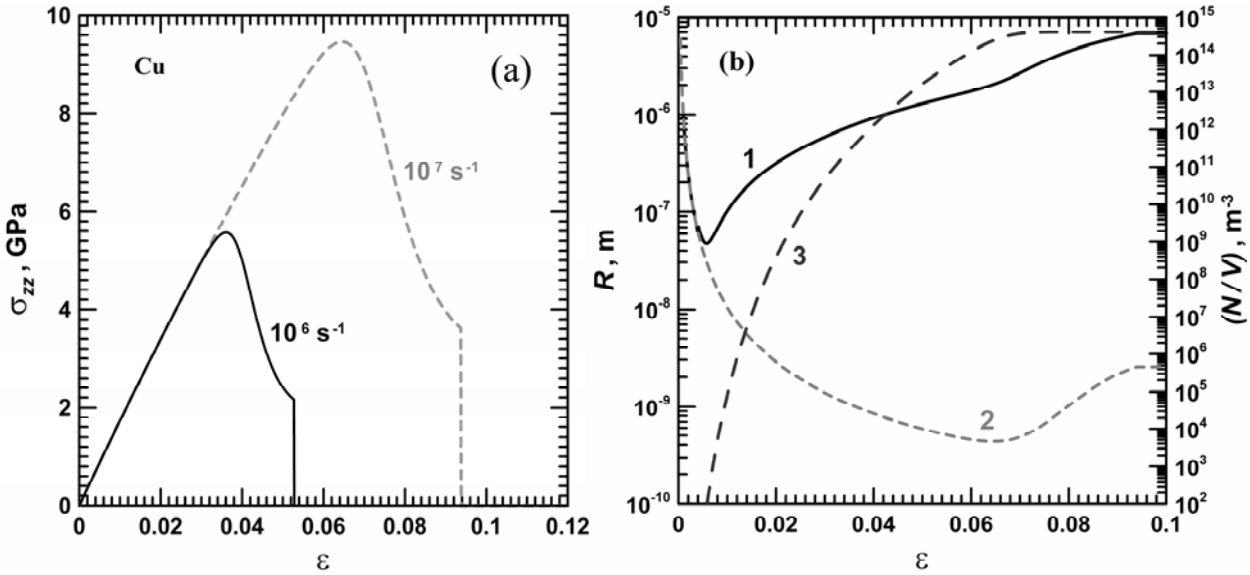

Figure 2. The strain dependence of stresses at two constant strain rates in the monocrystalline copper (a). Strain dependences of the average micro-cracks radius (1), the critical radius (2) and the concentration of micro-cracks (3) at the constant strain rate и 10^7 s^{-1} (b).

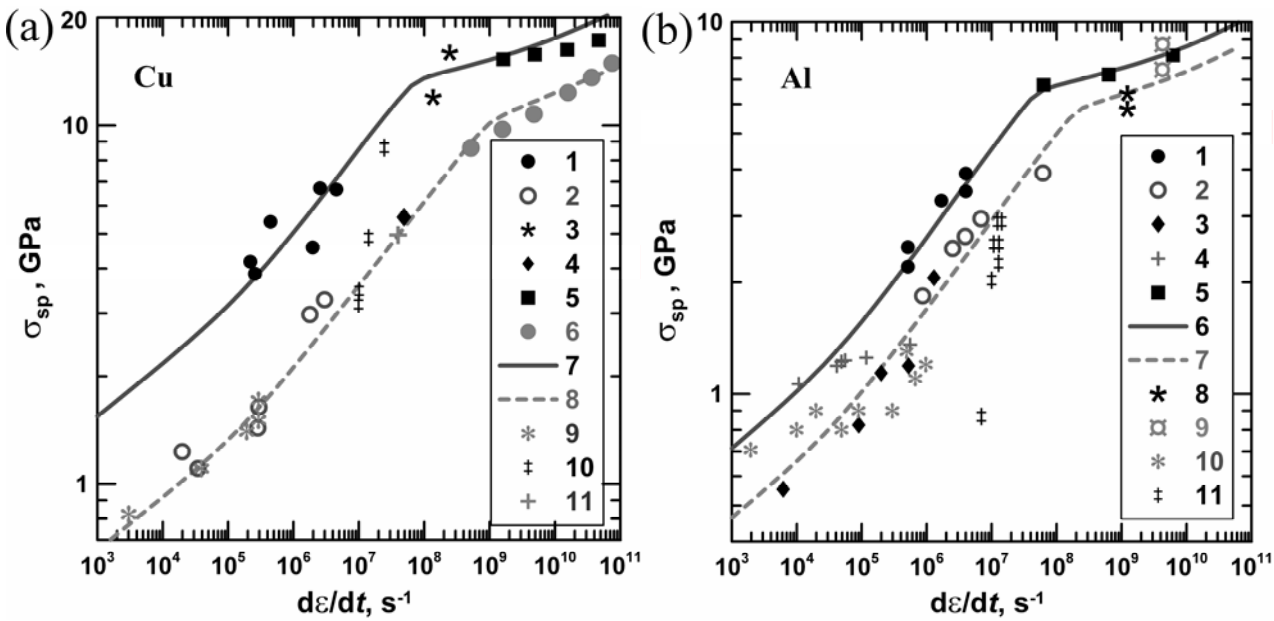

Figure 3. The strain rate dependences of the dynamic strength of copper (a) and aluminum (b). For copper (a): experimental data for monocrystals 1 – [2] and 3 – [20]; experimental data for polycrystals 2 – [2], 4 – [21], 9 – [22], 10 – [4], 11 – [23]; markers 5 for monocrystal and 6 for polycrystal are the results of MD [7]; lines are predictions of the model for monocrystals 7 and polycrystals 8. For aluminum (b): experimental data, 1 - monocrystal [1], 2 - polycrystal of 99.9% purity [24], 3 – alloy AlMg6 [25], 4 - commercially pure aluminum AD1 [26], 8 – polycristals [3], 10 – [22], 11 – [4]; results of MD for monocrystals (5) - [10] and 9 - [9]; lines are predictions of the model for monocrystals 6 and polycrystals 7.

Experimental results at the strain rates $\leq 10^8$ s^{-1} correspond to the regime of heterogeneous nucleation then the formation of micro-cracks occurs on inhomogeneities (defects of the exponential spectrum). MD results and experiments [3,20] for the strain rates $> 10^8$ s^{-1} correspond to the mode of homogeneous nucleation when the micro-cracks are typically formed in homogeneous parts of material (zones of perfect crystal or zones with a bundle of identical defects). The term «homogeneous nucleation» is conditional for polycrystals because in this case the fracture begins in the grain boundaries [7]. Therefore, we use here this term in the sense of presence of a quantity of identical uniformly distributed defects, for example, grain boundaries (in contrast with the defects of exponential spectrum).

Calculations show, that plasticity is a dominant factor influencing on the voids growth and on the dynamic strength at the strain rates $\leq 10^4$ s^{-1}. On the contrary, at the strain rates $\geq 10^7$ s^{-1}, the plasticity is negligible in the dynamic strength calculations, but it can influences on the resulting form of voids and on the picture of destructed material.

4. Conclusions

The micro-cracks nucleation and growth have been analyzed for the purpose of the dynamical fracture description. The model was formulated, which agrees well with experimental and MD data on the strain rate dependence of the dynamic strength for a number of metals. This model can be practically used in the material dynamics simulations. The strain rate dependence of the dynamic strength has two different regions corresponding to regimes of the heterogeneous nucleation (at the strain rates $< 10^8$ s^{-1}) and the homogeneous nucleation (at the strain rates $> 10^8$ s^{-1}). In the first case, the weakened zones of the material play an important role in fracture. In the second mode, the number of weakened zones is insufficient, voids are nucleated in undefected material, and the strength growth is decelerated. It contradicts with the commonly used uniform power dependence of σ_{sp} on $d\varepsilon/dt$ [3,10] in the whole region of the strain rate, therefore, the ideal strength [3] can be achieved at the higher strain rates (above 10^{11}–10^{12} s^{-1}), than it follows from the power dependence.

Acknowledgements

The study was supported by The Ministry of education and science of Russian Federation, projects 14.B37.21.0384 and 2.2320.2011.

References

[1] G.I. Kanel', S.V. Razorenov, K. Baumung, J. Singer, Dynamic yield and tensile strength of aluminum single crystals at temperatures up to the melting point. J Appl Phys, 90 (2001) 136-143.

[2] G.I. Kanel', V.E. Fortov, S.V. Razorenov, Shock waves in condensed-state physics. Phys Usp, 50 (2007) 771-791.

[3] S.I. Ashitkov, M.B. Agranat, G.I. Kanel, P.S. Komarov, V.E.Fortov, Behavior of aluminum near an ultimate theoretical strength in experiments with femtosecond laser pulses. JETP Letters, 92 (2010) 516-520.

[4] E. Moshe, S. Eliezer, E. Dekel, A. Ludmirsky, Z. Henis, M. Werdiger, I.B. Goldberg, An increase of the spall strength in aluminum, copper, and Metglas at strain rates larger than 10^7 s^{-1}. J Appl Phys, 83 (1998) 4004–4011.

[5] V.H. Whitley, S.D. McGrane, D.E. Eakins, C.A. Bolme, D.S. Moore, J.F. Bingert, The elastic-plastic response of aluminum films to ultrafast laser-generated shocks. J Appl Phys, 109 (2011) 013505.

[6] V. Dremov, A. Petrovtsev, Ph. Sapozhnikov, M. Smirnova, Molecular dynamics simulations of

the initial stages of spall in nanocrystalline copper. Phys Rev B, 74 (2006) 144110.
[7] A.Yu. Kuksin, V.V. Stegailov, A.V. Yanilkin, Atomistic simulation of plasticity and fracture of nanocrystalline copper under high-rate tension. Phys Solid State, 50 (2008) 2069–2075.
[8] Sh.N. Luo, T.C. Germann, D.L. Tonks, Spall damage of copper under supported and decaying shock loading. J Appl Phys, 106 (2009) 123518.
[9] V.V. Zhakhovskii, N.A. Inogamov, Yu.V. Petrov, S.I. Ashitkov, K. Nishihara, Molecular dynamics simulation of femtosecond ablation and spallation with different interatomic potentials. Appl Surf Sci, 255 (2009) 9592–2596.
[10] P.A. Zhilyaev, A.Yu. Kuksin, V.V. Stegailov, A.V. Yanilkin, Influence of plastic deformation on fracture of an aluminum single crystal under shock-wave loading. Phys Solid State, 52 (2010) 1619–1624.
[11] L. Campagne, L. Daridon, S. Ahzi, A physically based model for dynamic failure in ductile metals. Mech Mater, 37 (2005) 869-886.
[12] A. Molinari, T.W. Wright, A physical model for nucleation and early growth of voids in ductile materials under dynamic loading. J Mech Phys Solids, 53 (2005) 1476-1504.
[13] A.E. Mayer, V.S. Krasnikov, Copper spall fracture under sub-nanosecond electron irradiation. Engng Fract Mech, 78 (2011) 1306-1316.
[14] L.D. Landau, E.M. Lifshitz, Course of Theoretical Physics, Vol. 1, Mechanics, Butterworth-Heinemann, Oxford, 1976.
[15] A.M. Kosevich, Dynamical Theory of Dislocations, Sov Phys Uspekhi, 7 (1965) 837-854.
[16] L.D. Landau, E.M. Lifshitz, Course of Theoretical Physics, Vol. 1, Statistical physics, Part 1, Butterworth-Heinemann, Oxford, 1980.
[17] V.S. Krasnikov, A.E. Mayer, A.P. Yalovets, Dislocation based high-rate plasticity model and its application to plate-impact and ultra short electron irradiation simulations, Int J Plast, 27 (2011) 1294-1308.
[18] J. Johnson, S. Lyon, Sesame equation of state, 1986.
[19] S.N. Kolgatin, A.V. Khachatur'yants, Interpolation equations of state of metals, Teplofiz Vys Temp, 20 (1982) 90-94.
[20] E. Moshe, S. Eliezer, Z. Henis, M. Werdiger, E. Dekel, Y. Horovitz, S. Maman, I.B. Goldberg, D. Eliezer, Experimental measurements of the strength of metals approaching the theoretical limit predicted by the equation of state. Appl Phys Lett, 76 (2000) 1555–1557.
[21] D. Paisley, R. Warnes, R. Kopp, in: S.C. Schmidt, R.D. Dick, J. Forbes, D.G. Tasker (Eds.), Progress in shock compression of condensed matter-1991, Elsevier, New York, 1992.
[22] K.S. Holian (Ed.), T-4 Handbook of Material Properties Data Bases, LA-10160-MS, Los Alamos, UC-34, 1984.
[23] Z. Kaczkowski, H.S.Nam, in: A. Hernando, V. Madurga, M.C. Sanchez-Trulillo, M. Vazquez (Eds.), Magnetic Properties of Amorphous Metals, Elsevier Science, Amsterdam, 1987.
[24] G.I. Kanel, S.V. Razorenov, A.V. Utkin, K. Baumung, H.U. Karov, V. Licht, Spallations near the ultimate strength of solids, AIP Conf Proc (High-pressure science and technology–1993), 309 (1994)1043–1046.
[25] G.I. Kanel, S.V. Razorenov, V.E. Fortov, Kinetics of spallation rupture in the aluminum alloy AMg6M. J Appl Mech Tech Phys, 25 (1984) 707–711.
[26] G.I. Kanel, S.V. Razorenov, A.A. Bogatch, A.V. Utkin, V.E. Fortov, D.E. Grady, Spall Fracture Properties of Aluminium and Magnesium at High Temperatures. J Appl Phys. 79 (1996) 8310–8317.

An Equivalent Strain Gradient Theory for Evolvement of Damage in void Material

Hong Zuo*, Fangwen Wang* &Teng Hou

State Key Laboratory of Mechanical Structure Strength and Vibration, School of Aerospace, Xi'an Jiaotong Univ. Xi'an, PR. China
* Corresponding author: Email: zuohong@mail.xjtu.edu.cn; fwwang@mail.xjtu.edu.cn

Abstract In this article, the onset conditions and evolvement path of the crack initiated from void edge in void material are investigated. For this end, the plane stress numerical simulation is implemented for a series of void embedded strip samples in Al-alloy. The stress and strain distribution for the whole plane sample is analyzed by elastic-plastic FEM. Based on the correspondence between equivalent strain distributions, the trend of equivalent strain gradient and the connected style of voids in experiment, a damage evolvement theory for the crack initiation and extension from vole edge is suggested. According to the suggested theory, as the loading increased, the crack is initiated from the edge of the void where the equivalent strain around the edge of the void reached its maximum; next, the initiated crack will propagated along the direction where the absolute gradient value of equivalent strain reached its maximum. It is indicated from the related experiments that the theory can reasonably explain the phenomena of the different linkage style of two holes.

Keywords void material; path of the crack extension; equivalent strain grade; voids converge.

1. Introduction

In practical structure, the damage or degradation of material is usually the fatal factor influencing the reliability of mechanical engineering structure. However, from microscopic view, the damage in macroscopic is always induced by the accumulation of a series of voids converge, i.e., the voids nucleation, expansion and convergence under loading.

Although the crack problem has been paid great attention by mechanical scientists in fracture mechanics field near a century, a lot of fracture theory and criteria had been proposed to describe the mechanisms of crack initiation and extension. However, the void convergence problem has received fewer attentions relatively till today. Especially in the problem of convergence process of voids, much less for the theory. Only fewer studies related to the void convergence can be retrieved from the open literatures. Most of them are concentrated to the numerically simulation for the void expension and convergence and other factors such as size and direction of grain [1-4].

Thereby, thoroughly understanding the mechanism of the linkage of voids is the precondition for the processing of material and the reliability of structure during its operation. However, the process of the voids linkage under practical stress state is rather complicated considering the relation between relative location of voids and the stress direction. In this article, the problem is simplified to study the void linkage mechanism and control parameter for a multi-hole embedded plate under single loading condition.

2. Experiment

2.1. Sample

In order to investigate the damage and its evolution of the voids, a group of two-hole stripe sample is selected for the uniaxial tension fatigue test. The sample size is cut to 125mm length, 27mm width and 3mm thickness (Fig.1). The hole pair with the diameter 1mm and the hole center distance 1.5mm are embedded in the center zone around the center point of the plate, and the holes are machined to through the whole thickness, i.e., through hole. The angle of the center line of two holes with the cross section α is selected as 0 and 15 degree. Considering the sample thickness is rather small contrasted to the other sizes, the plain stress condition is applied in this test. The material of specimen is selected as Al-alloy, with the Young's module 56.36GPa, Poisson's ratio 0.33, Yield stress 308.6MPa and Ultimate strength 450.8MPa.

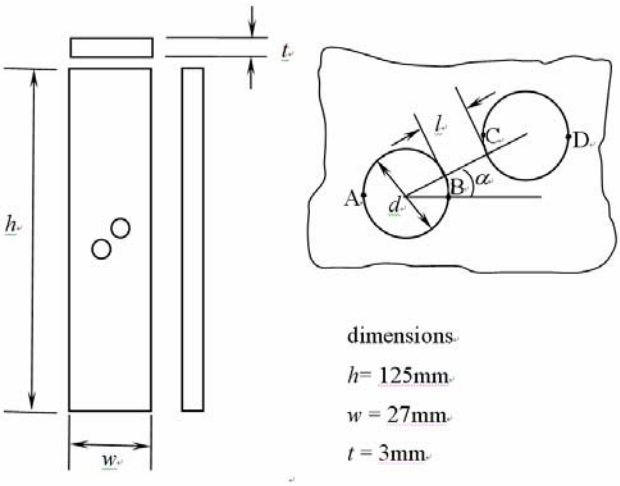

Fig.1, The sample of the fatigue test

2.2. Test

The fatigue test is implemented using a testing machine MTS-858, with the loading amplitude 0-16KN and loading frequency 1Hz (Fig.2). As the loading circle increased, the cracks will initiate from the edge of some hole early or late. Simultaneously, a CCD camera is used to record the process of the crack initiation and extension.

2.3. Result

It is widely believed that the first initiated crack should start from the inner edge of two holes, such as points B and C; owing to the circle stress in these points is larger than that in the outer points A and D. It is surprised that, for α equals 0, the first crack occurs from one point of the outer edge, the point A, see Fig.3. As the loading circle increases, the crack initiation has a little complicated. For example, in one sample, the second crack starts from the inner point of the other hole edge, the point C (see Fig.4), whereas, in another sample, we also find that the second crack starts form the

outer edge of the other hole, the point D. As the cracks started from the outer side of the hole pair

Fig.2, The fatigue test using MTS

propagate to a distance, such as 0.8mm in our experiment, the first two crack stop, meanwhile, the new crack initiated from the inner edge of the holes. It is the inner edge cracks link each other, the two holes connected (see Fig.5). Thus, as the loading circle increases continually, the outer edge cracks restart propagate till arrive to the edge of the sample.

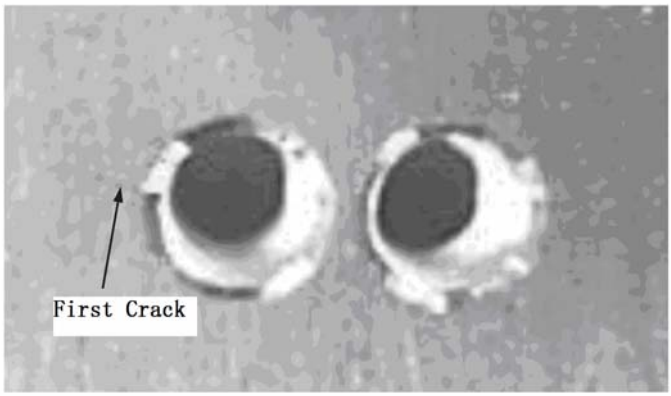

Fig.3, The first crack initiated from the outer edge of the hole

This phenomenon also occurs in the test of the sample with α equals 15 degree. As the loading circle increases, the first crack initiates from the outer edge of two holes, i.e., the point A or D. As the first two cracks propagate to some length, the crack driving force disappears, thus the cracks stop (Fig.6). Next, the inner edge cracks initiate (Fig.7) and propagate to each other till two holes connecte (Fig.8).

It is obvious that this phenomenon (the crack initiates from the outer edge firstly and after it propagates to some length, the inner crack initiates and propagates.) cannot be explained by the theories proposed till today, such as the maximum tangential stress theory, the maximum tension stress theory, and so on. Thus, in the next section, the crack initiated feature and the stress field around the holes will be investigated in detail to describe the phenomena, and a new theory based on the equivalent plastic strain field will be proposed.

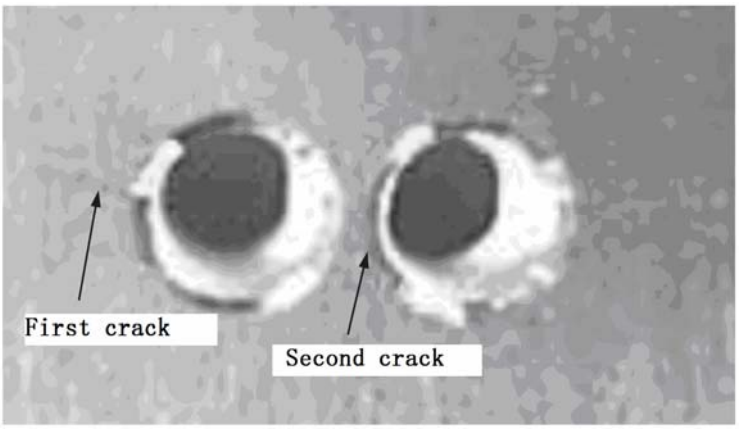

Fig.4, the second crack initiates from the inner edge of the hole in one sample

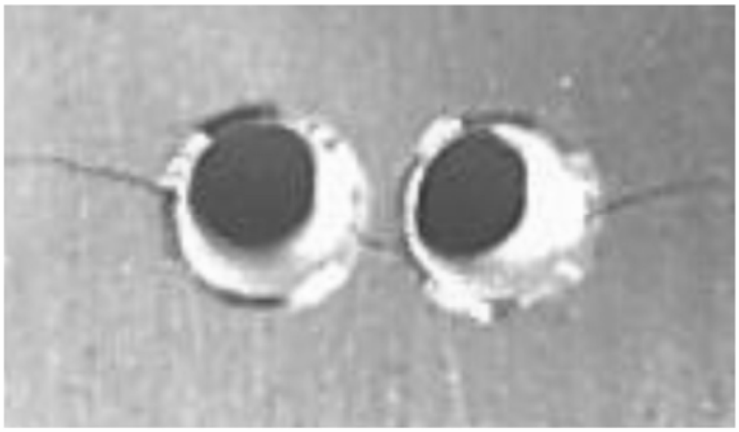

Fig.5, the inner edge cracks link each other and induce the two holes connected

3. Numerical analysis

3.1. The model of the numerical simulation

The stress strain field around the holes in the test sample is obtained by means of the elastic plastic finite element analysis. In this simulation, the numerical modal is the same as that in the fatigue test in shape and size. The mechanical properties of the material are the same as in the test. The stress strain curve of the material is shown in Figure 9. Different in the fatigue loading in the test, during the numerical simulation, a constant value of load is applied as the boundary condition for the numerical model. Thus the stress strain field obtained from the numerical simulation is the peak value stress strain field of the fatigue loading.

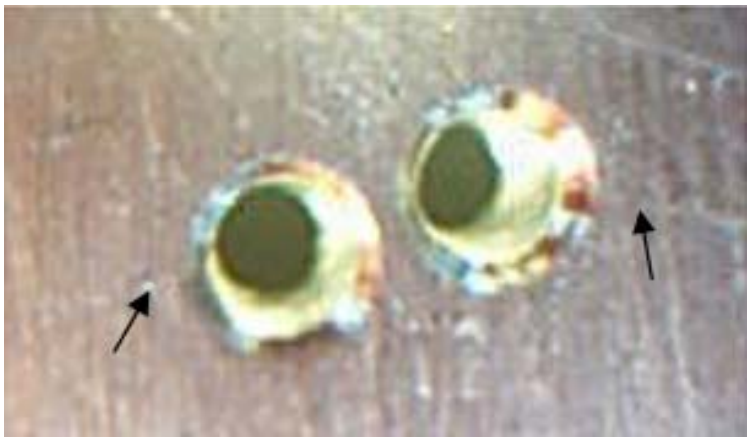

Fig.6, the first crack initiates from the outer edge of the hole

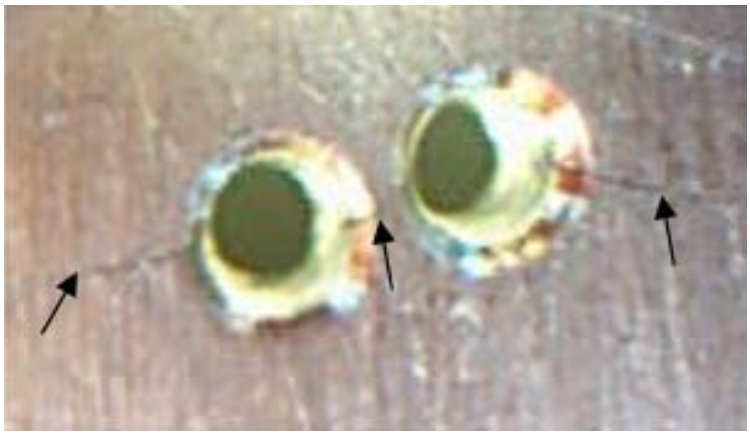

Fig.7, the inner crack initiates after the first crack stop to propagate.

Fig.8, the first crack initiates from the outer edge of the hole

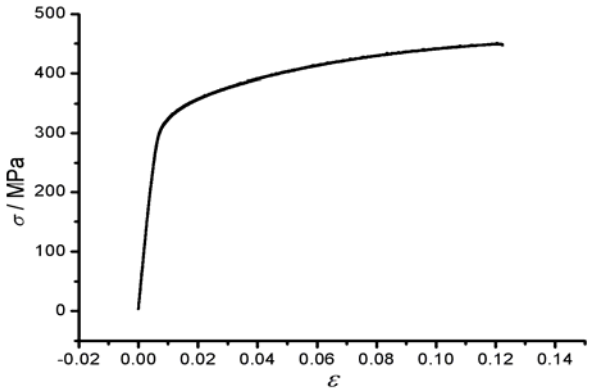

Fig.9, the stress strain curve of the material.

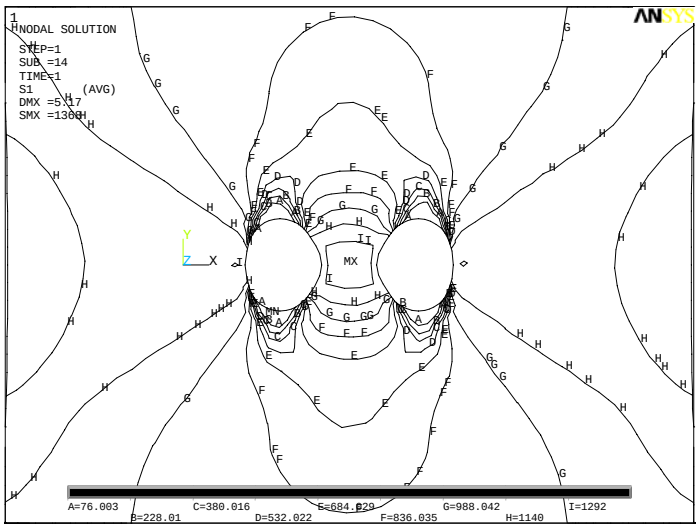

Fig.10, the principal stress distribution around the hole for α=0.

3.2. Stress strain field

For α equals 0, the property of contour line of the principal stress and the equivalent stress around the holes are shown in Figure 10 and 11 respectively. It is found from the figures that the principal stress and the equivalent stress in the first crack initiated point and the extended line is reached its maximum, However, if we compare the stress value of the initiated point with the adjacent point on the edge of the hole, we can find that there does not exist an obvious up rush for these stress compared to the surrounding edge point.

For α equals 15 degree, the contour line of the principal stress and the equivalent stress around the holes are shown in Figure 12 and 13 respectively. From these figures, we also find that there does not exist an obvious up rush for the principal stress and the equivalent stress in the initiated point from the fatigue test in the previous section compared with the surrounding edge point. Thus, it seems that the stress parameter is unsuitable to describe the crack initiation and propagation in this condition.

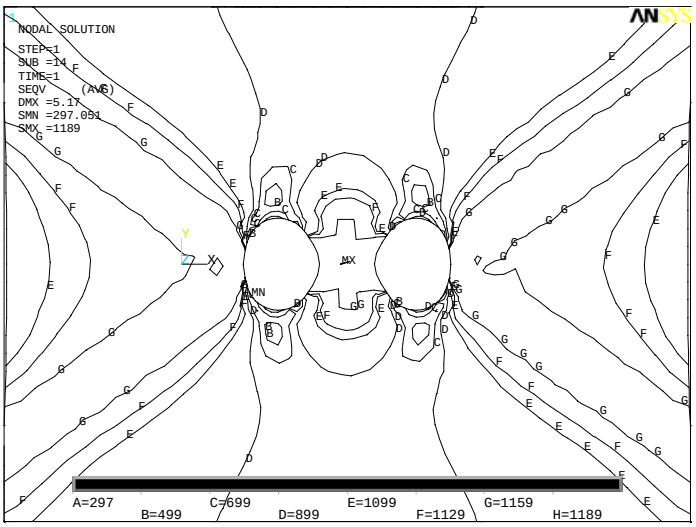

Fig.11, the equivalent stress distribution around the hole for α=0.

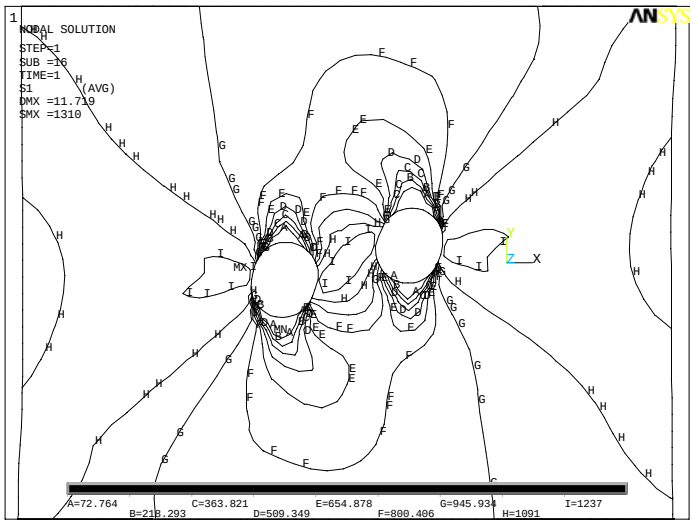

Fig.12, the principal stress distribution around the hole for α=15.

On the other hand, if we compare the equivalent strain distribution in the outer point, inner point and the adjacent point along the edge of the holes for the two sample (see Fig.14 and 15), we can find that there does exist an obvious up rush for the equivalent strain in the initiated point from the fatigue test in the previous section compared to the surrounding edge point. Thus, it seems that the parameter, equivalent strain, can be considered to describe the new phenomena we found in the test. Furthermore, comparing the first crack propagated direction with the equivalent strain field in the outer edge of the hole; it can be found that on this direction, the equivalent strain has a maximum decrease started from the outer edge point along the direction of the crack propagation, comparing with other direction.

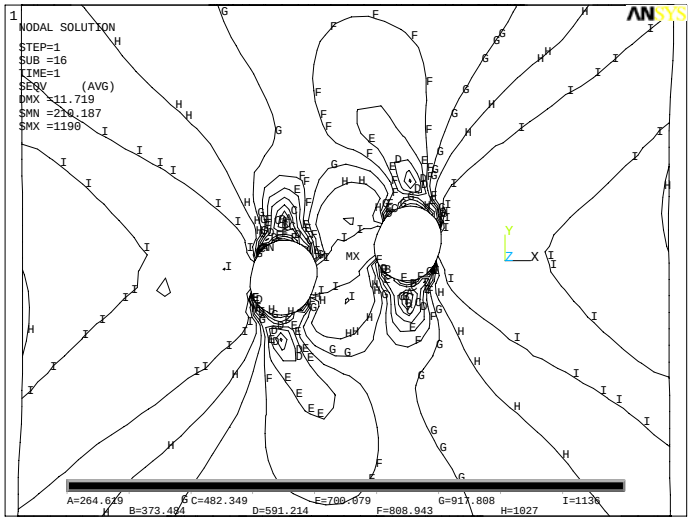

Fig.13, the equivalent stress distribution around the hole for α=15.

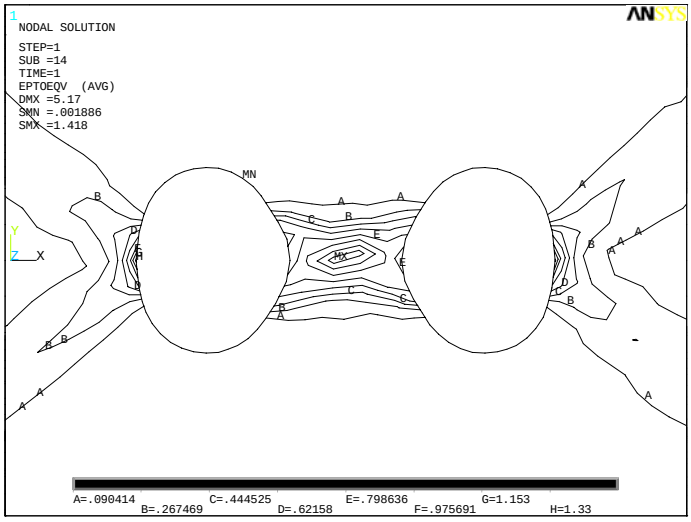

Fig.14, the equivalent strain distribution around the hole for α=0.

4. The theory of equivalent strain gradient

Based on the analysis in the previous section, a damage evolution theory based on the equivalent strain gradient is suggested in this article. The suggested criterion states that: the initiation of the crack is occurred when the equivalent strain reaches its critical value. The propagation direction of the initiated crack is coincided with the direction where the equivalent strain decrease gradient reaches its maximum.

The gradient of equivalent strain decrease with respect to the radial coordinate originating from the center point of the hole can be expressed as:

$$E_r = -\frac{\partial \varepsilon_{eq}}{\partial r}, \tag{1}$$

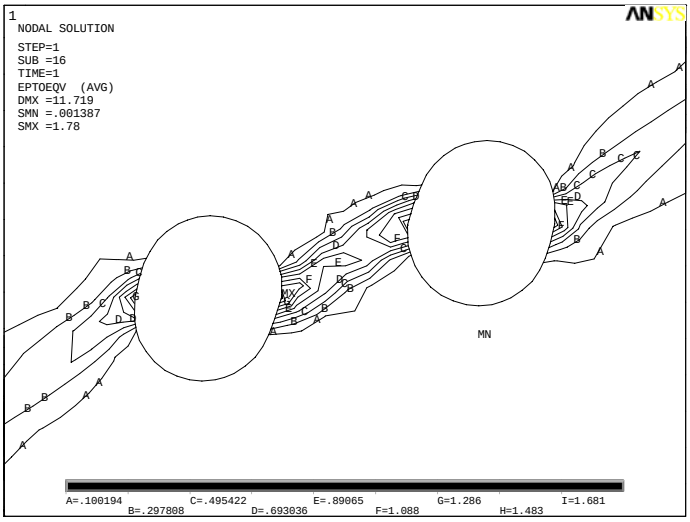

Fig.15, the equivalent strain distribution around the hole for α=15.

Thus, the maximum gradient is determined by:

$$\frac{\partial E_r}{\partial \theta} = 0 \quad \text{and} \quad \frac{\partial^2 E_r}{\partial \theta^2} \le 0, \tag{2}$$

According to this theory, the crack initiated and propagated process on the void material can be described correctly.

5. Discussion

By means of the proposed theory, we can explain the new feature of the crack initiated and propagated in the fatigue test. Analyzing the equivalent strain decreasing from the outer edge point and the inner edge point in one hole (such as the left hole in the Fig.14 and 15) and along the path on the radial direction, it is obvious that the gradient of the equivalent strain decrease in the outer point is larger than that in the inner point, although the absolutely equivalent strain value in this two point is almost the same. It can be found that the inner part material between two holes has a larger elastic or plastic deformation than the other part of material. Here, the larger plastic deformation releases large part of the peak stress near the inner point, and postpones the crack initiated in this point. As the first initiated crack startes from the outer point and propagates to some length, the gradient of the equivalent strain decreased, while the deformation around the inner edge point increased to induce the gradient of the equivalent strain decreased in this point increased till larger than that in the outer propagated crack tip. Thus the outer propagated crack stops, and the inner edge crack initiates and propagates. Thereby, the two inner cracks links and the sample separates.

6. Conclusions

According to the experimental and numerical research, it is concluded that:
(1), the stress parameter, such as the principal stress or equivalent stress, can not appropriately describe the crack initiateand propagate from the edge of a void in porous material. Whereas, the strain parameter, such as the equivalent strain, can be used to describe this phenomena.
(2), based on the detailed analysis, a theory of gradient ot the equivalent strain is suggested. According to this theory, the crack initiated point and the path of the crack from the void edge can be predicted appropriately.

Acknowledgments

This work was supported by the National Natural Science Foundation of China（10932007, 11172228）

References

[1]V. C. Orsini, M. A. Zikry, Void growth and interaction in crystalline ma-terials. Int J Plasticity, 17 (2001) 1393-1417.
[2]T. L. O'Regan, D. F. Quinn, et al. Void growth simulations in single crystals. Comput Mech, 20(1997) 115-121.
[3]M. Yang, X.H. Dong, Simulation of lattice orientation effects on void growth and coalescence by crystal plasticity. Acta Metall Sin, 22(2009) 40-50.
[4]W. H. Liu, X. M. Zhang, et al. Simulation of void growth and coalescence behavior with 3D crystal plasticity theory. Comput Mater Sci, 40(2007)130-139.

Singular Thermo-Elastic Stress Analysis of An Irregular Shaped Inclusion

MengCheng Chen[1,*], **XueCheng Pin**[2]

[1]School of Civil Engineering, East China Jiaotong University, 330013, Nanchang, P. R. China
[2] School of Mechatronics Engineering, East China Jiaotong University, 330013, Nanchang, P. R. China
* Corresponding author: *mengchengchen2012@yahoo.com.cn*

Abstract This paper develops a super element that simulates the elastic behavior around an inclusion corner. The super inclusion corner element is finally incorporated with standard four-node hybrid-stress elements to constitute an *ad hoc* hybrid-stress finite element method for thermo-elastic stress analysis of an irregular inclusion in isotropic materials under thermal and mechanical loadings. In the numerical analysis, generalized stress intensity factors at the inclusion corner are systematically calculated for various material stiffness ratio and dimensions of the inclusion in a plate subjected to thermo-mechanical loadings.

Keywords Thermo-mechanical stress, Hybrid finite element, Inclusion, Super inclusion corner element, Stress intensity factor

1. Introduction

Much attention has been paid to inclusion problems by many researchers since Eshelby's first solution to the ellipsoidal inclusion problems. The application background is found in microstructures, composite material structures and others.

As the stress intensity at an inclusion corner is governed by the corner surrounding material properties, the corner geometry conditions and loading situations, great mathematical difficulties are usually encountered in analytical solutions. Therefore, most complicated engineering problems of inclusions have to resort to numerical methods such as the finite element method (FEM) and others. Chen [1] used the body force method to calculate stress intensity factors (SIFs). The SIFs for a dissimilar material wedge under mechanical and thermal loads were determined by using the least square method [2-4]. Path-independent conservative line integrals derived from Betti's reciprocal principle were utilized to evaluate stress intensities at the interface [5-7]. The solutions from the aforementioned methods are strongly dependent on the number of element meshes. Furthermore, it is very difficult to obtain accurate numerical results for singular stress states near the apex in dissimilar materials using the conventional finite element method, even with the help of many finite elements.

To improve the accuracy of numerical results for wedge or interface problems in the traditional finite element analysis, the analytical asymptotic solutions near the apex can be used as interpolation functions to construct a stiffness matrix for special elements containing a part or interface of a wedge. Chen [8] developed an enriched element with appropriate interpolation functions to account for the singular behavior at the junction of dissimilar materials subjected to mechanical load. Similar to Chen [8]'s work, enriched finite elements were further developed by Gadi et al. [9] and Pageau and Biggers [10]. However, numerical results with enriched finite elements are still dependent on the special element size, and the convergence of the results is not guaranteed. Therefore, more accurate numerical results require a lot of refined element meshes between the special element and standard elements. For a crack that either follows or is perpendicular to the interface, Tong et al. [11] constructed a special super element for the analysis of plane crack problems. Similarly, Tan and Meguid [12] developed a singular inclusion corner

element for dissimilar material wedge problems. Mote [13], Bradford et al. [14] and Madenci et al. [15] established a special global element based on asymptotical solutions around a dissimilar material junction edge. By using the eigenfunction expansion method, Barut et al. [16] derived a special hybrid global element on the basis of exact analytical solutions of stress displacement fields under mechanical and thermal loads. In addition to the leading singular order term, a few other higher order terms were also used in constructing the special elements in Ref. [11-13, 16], which leads to more accurate numerical results

The hybrid-stress finite element method developed more than 40 years ago by Pian is now well recognized as a powerful and easy-to-use tool for solving a variety of two-dimensional linear elasticity problems containing a single or multiple singular points. To the best of the author's knowledge, the studies related to singular thermo-mechanical fields of inclusions by the hybrid-stress finite element method are absent. Moreover, a numerical solution of even a single irregular inclusion by the method could not be found in the literature, either. To predict singular stress fields around an inclusion corner under thermo-mechanical loads, a new *ad hoc* super inclusion corner element based on the numerical asymptotic solutions developed is proposed in this paper to study inclusion problems shown in Fig. 1. The validity and applicability of present approach are established through available solutions

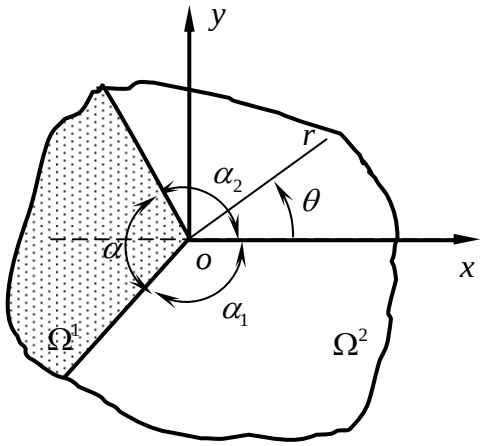

Figure 1 Local coordinate system near the inclusion corner-tip

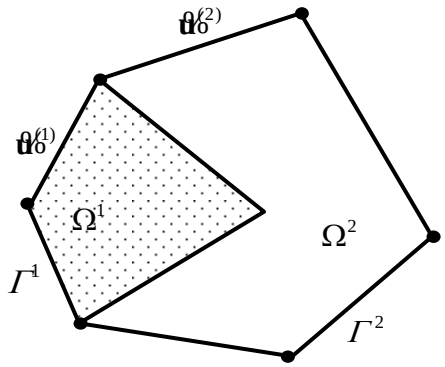

Figure 2 A super *n*-sided polygonal inclusion corner element

2. The hybrid variational functionals for thermo-elasticity involving an inclusion

Let a super *n*-sided polygonal element centered at the inclusion corner is taken as the complementary region (C-region) which contains inclusion domain Ω^2 with outer boundary Γ^2 and its surrounding matrix domain Ω^1 with outer boundary Γ^1, as shown in Fig.2.

Under appropriate continuity conditions, the stiffness matrix for a super inclusion element of dissimilar material wedge subjected to thermo-mechanical loads is written as [16]:

$$\Pi = \sum_{k=1}^{2}\left\{-\frac{1}{2}\int_{\Gamma^k} {}^{m}_{\lambda}\boldsymbol{\sigma}^{(k)T}\boldsymbol{n}^T\, {}^{m}_{\lambda}\boldsymbol{u}^{(k)}dS - \int_{\Gamma^k} {}^{m}_{\lambda}\boldsymbol{\sigma}^{(k)T}\boldsymbol{n}^T\, {}^{t}_{\lambda+c}\boldsymbol{u}^{(k)}dS\right\} + \sum_{k=1}^{2}\left\{\int_{\Gamma^k} {}^{m}_{\lambda}\boldsymbol{\sigma}^{(k)T}\boldsymbol{n}^T\boldsymbol{u}_0^{(k)}dS\right\} + \Pi_0 \tag{1}$$

in which ${}^{m}_{\lambda}(\mathrm{g}^{(k)})$ represent the unknown stress and displacement fields due to the mechanical load and ${}^{t}_{\lambda+c}\boldsymbol{u}^{(k)}$ are the known initial displacement components from the uniform temperature variation ΔT. The left subscripts $\lambda+c$ represent the summation of singular and non-singular components of the variables. Π_0 represents the total potential, given as an initial value, associated with the displacements and stresses under thermal load. Matrix $\boldsymbol{n}$ contains 3×2 components of the unit outward normal to boundary Γ^k. $\boldsymbol{u}^{(k)}$ are displacements under thermo-mechanical loads.

Introducing the coordinate system transformation matrices $(\mathrm{g}) = \boldsymbol{Z}_{\mathrm{g}}(\mathrm{g})$ and $\boldsymbol{u} = \boldsymbol{U\beta}$, $\boldsymbol{\sigma} = \boldsymbol{P\beta}$, $\boldsymbol{u}_0^{(k)} = \boldsymbol{Lq}_{\mathrm{s}}$, where matrix $\boldsymbol{L}$ is the linear interpolation function, and vector $\boldsymbol{q}_{\mathrm{s}}$ is the nodal displacement on the boundary segment Γ^k of the super corner element, then we have

$$\Pi = -\frac{1}{2}\,{}^{m}\boldsymbol{\beta}^T\boldsymbol{H}\,{}^{m}\boldsymbol{\beta} - {}^{m}\boldsymbol{\beta}^T\,{}^{t}\boldsymbol{f} + {}^{m}\boldsymbol{\beta}^T\boldsymbol{Gq}_{\mathrm{s}} + \Pi_0 \tag{2}$$

where

$$\boldsymbol{H} = \sum_{k=1}^{2}\frac{1}{2}\int_{\Gamma^k}\left[\boldsymbol{P}^{(k)T}\boldsymbol{Z}_{\sigma}^{(k)T}\boldsymbol{n}^{\mathrm{T}}\boldsymbol{Z}_{u}^{(k)}\boldsymbol{U}^{(k)} + \boldsymbol{U}^{(k)\mathrm{T}}\boldsymbol{Z}_{u}^{(k)T}\boldsymbol{nZ}_{\sigma}^{(k)}\boldsymbol{P}^{(k)}\right]\mathrm{d}S\,,\quad \boldsymbol{G} = \sum_{k=1}^{2}\int_{\Gamma^k}\boldsymbol{P}^{(k)T}\boldsymbol{Z}_{\sigma}^{(k)T}\boldsymbol{nL}\,\mathrm{d}S$$

$${}^{t}\boldsymbol{f}^{(k)} = \sum_{k=1}^{2}\int_{\Gamma^k}\boldsymbol{P}^{(k)T}\boldsymbol{Z}_{\sigma}^{(k)T}\boldsymbol{n}^{\mathrm{T}}\boldsymbol{Z}_{u}^{(k)}\,{}^{t}_{\lambda+c}\boldsymbol{u}_{p}^{(k)}dS$$

Setting $\delta\Pi = 0$ and noting that $\delta\Pi_0 = 0$, we determine that:

$${}^{m}\boldsymbol{\beta} = \boldsymbol{H}^{-1}\left\{\boldsymbol{Rq}_{\mathrm{s}} - {}^{t}\boldsymbol{f}\right\} \tag{3}$$

and thus

$$\Pi = \frac{1}{2}\boldsymbol{q}_{\mathrm{s}}^T\boldsymbol{G}^T\boldsymbol{H}^{-1}\boldsymbol{Gq}_{\mathrm{s}} - \boldsymbol{q}_{\mathrm{s}}^T\boldsymbol{G}^T\boldsymbol{H}^{-1}\,{}^{t}\boldsymbol{f} + \frac{1}{2}\,{}^{t}\boldsymbol{f}^T\boldsymbol{H}^{-1}\,{}^{t}\boldsymbol{f} + \Pi_0 \tag{4}$$

From Eq.(4), we have the following matrices:

$$\boldsymbol{K}_s = \boldsymbol{G}^T\boldsymbol{H}^{-1}\boldsymbol{G}\,,\quad {}^{t}\boldsymbol{F} = \boldsymbol{G}^T\boldsymbol{H}^{-1}\,{}^{t}\boldsymbol{f} \tag{5}$$

where $\boldsymbol{K}_s$ is the stiffness matrix of the super corner element and ${}^{t}\boldsymbol{F}$ represents the nodal force due to thermal load on the boundary segment Γ^k. This *ad hoc* element is used to model the near-field region and is combined with the conventional standard four-node hybrid-stress elements in the far-field region.

3. Definition of the stress intensity factor (SIF)

The singular stress field around the inclusion corner apex under thermo-mechanical loads can usually be expressed in a form of singular terms as:

$$\sigma_{\theta\theta} = \sum_{n=1}^{N+M} K_n r^{\lambda_n} f_{\theta\theta}^{n}(\theta) + {}_{\mathrm{c}}^{\mathrm{t}}\sigma_{\theta\theta} \tag{6}$$

$$\sigma_{r\theta} = \sum_{n=1}^{N+M} K_n r^{\lambda_n} f_{r\theta}^{n}(\theta) + {}_{\mathrm{c}}^{\mathrm{t}}\sigma_{r\theta} \tag{7}$$

where (r,θ) is a local polar coordinate system centered at the inclusion corner apex, and the axis of $\theta = 0$ is the bisector of the two wedge apexes shown in Fig.1; N represents the total number of complex singularity orders λ_n between -1 and 0, and M is the number of real singularity orders λ_n; $f_{\theta\theta}^{n}(\theta)$ and $f_{r\theta}^{n}(\theta)$ are the notch angular variation of normal stress fields and shear angular variations associated with λ_n, respectively; ${}_{\mathrm{c}}^{\mathrm{t}}\sigma_{\theta\theta}$ and ${}_{\mathrm{c}}^{\mathrm{t}}\sigma_{r\theta}$ are regular stresses caused by a thermal load.

According to Chen's work [17], the singularity orders λ_n have only two roots, i.e., λ_1 and λ_2; When Dundur's composite parameters α and β [18] meet the condition $\beta(\alpha-\beta)>0$, λ_1 and λ_2 are always real within the range of $-1<\mathrm{Re}(\lambda_1,\lambda_2)<0$. On the moment, expressions (6) and (7) can be rewritten as:

$$\sigma_{\theta\theta} = K_1 r^{\lambda_1} f_{\theta\theta}^{1}(\theta) + K_2 r^{\lambda_2} f_{\theta\theta}^{2}(\theta) + {}_{\mathrm{c}}^{\mathrm{t}}\sigma_{\theta\theta} \tag{8}$$

$$\sigma_{r\theta} = K_1 r^{\lambda_1} f_{r\theta}^{1}(\theta) + K_2 r^{\lambda_2} f_{r\theta}^{2}(\theta) + {}_{\mathrm{c}}^{\mathrm{t}}\sigma_{r\theta} \tag{9}$$

Defining $f_{\theta\theta}^{1}(\theta)$ and $f_{r\theta}^{2}(\theta)$ in such a way that $f_{\theta\theta}^{1}(\theta_0)=1$ and $f_{r\theta}^{2}(\theta_0)=1$, where θ_0 can be chosen arbitrarily, then we have

$$K_1 = \frac{1}{[1-f_{r\theta}^{1}(\theta_0)\cdot f_{\theta\theta}^{2}(\theta_0)]} \lim_{r\to 0} r^{-\lambda_1} [\sigma_{\theta\theta} - {}_{\mathrm{c}}^{\mathrm{t}}\sigma_{\theta\theta} - f_{\theta\theta}^{2}(\theta_0)\cdot(\sigma_{r\theta} - {}_{\mathrm{c}}^{\mathrm{t}}\sigma_{r\theta})]\Big|_{\theta=\theta_0} \tag{10}$$

$$K_2 = \frac{1}{[1-f_{r\theta}^{1}(\theta_0)\cdot f_{\theta\theta}^{2}(\theta_0)]} \lim_{r\to 0} r^{-\lambda_2} [\sigma_{r\theta} - {}_{\mathrm{c}}^{\mathrm{t}}\sigma_{r\theta} - f_{r\theta}^{1}(\theta_0)\cdot(\sigma_{\theta\theta} - {}_{\mathrm{c}}^{\mathrm{t}}\sigma_{\theta\theta})]\Big|_{\theta=\theta_0} \tag{11}$$

Once the values of K_1 and K_2 are obtained, the singular stress fields at every θ can be solved from Eqs.(8) and (9).

4. Numerical results and discussions

The present method is used to analyze the singular stresses around the corner apex A of a rectangular inclusion subjected to uniform temperature change ΔT as shown in Fig.Fig.3. Fig.4 shows a configuration for a super 8-node quadrilateral inclusion corner element. For the solution of the singular stress fields, around the square inclusion corner apex A, defined in Eqs.(8) and(9), the stress intensity factors K_1 and K_2 should be first determined. Generally speaking, any component of the stresses at any angle θ may be used as the compared object to determine the stress intensity factors. However, for simplicity, herein we only use the stresses at $\theta = 0^{\circ}$ and $\theta = 180^{\circ}$, that is, the stresses at points on the bisector of the vertex angle in region Ω^2 (for $\theta = 0^{\circ}$) and Ω^1 (for $\theta = 180^{\circ}$).

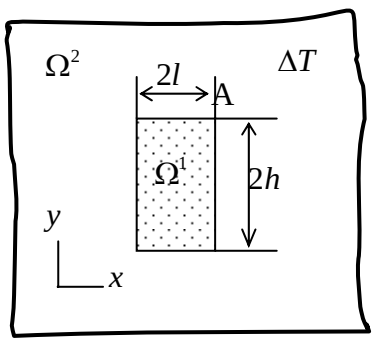

Fig.3 A rectangular inclusion in a infinite matrix under thermal loading

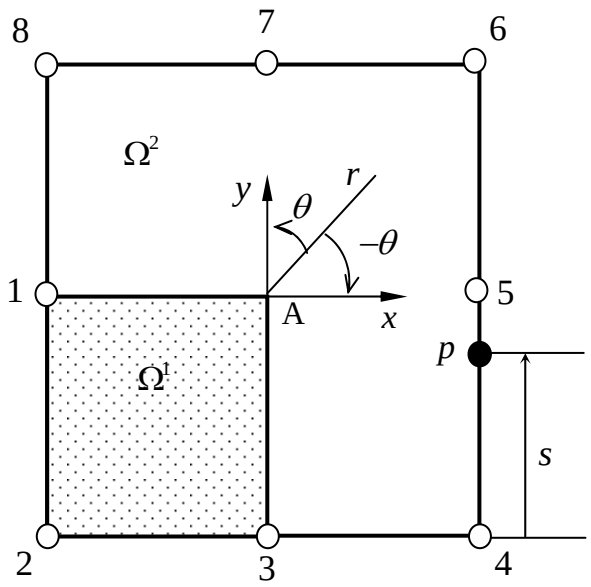

Fig.4 Configuration of a super 8-node quadrilateral inclusion corner element

An example for a square inclusion ($l = h$) is given herein. In the numerical analysis, To model the infinite plate, its width and height are all set to be$10l$; a quarter of plate is used for element divisions due to the symmetry of its geometry and loading, and 332 4-noded stress-based element and one 8-noded super elements are utilized. The material parameters of elastic modulus $E_1 : E_2 = 100$ and Poisson ratio $\nu_1 = \nu_2 = 0.3$ are employed. The singular stresses away from the apex A along the boundaries of the inclusion are analyzed with different the unknown parameters $\boldsymbol{\beta} s$. They are plotted in Fig. 5. In the Figures, for the sake of comparison, the numerical results from the commercial software ANSYS package are also shown. It is shown that the singular stresses $\sigma_{\theta\theta}$ and $\sigma_{r\theta}$ rapidly increase with the decrease of the distance away from the inclusion corner apex A along the boundary ($\theta = -135^{\circ}$) of the square inclusion, which is well recognized; When the number of $\boldsymbol{\beta} s$ meets the LBB condition: greater than equal to the number of freedom degrees of nodes in the super element minus the rigid modes (=3 in plane deformation), the present numerical results are in good agreement with the solutions of the ANSYS. Fig.6 tells us a fact that the influence of thermal expansion coefficient α_2 on the dimensionless stress factor F_1 is limited to very small the range of $\alpha_2 < 20 \times 10^{-6}$. Figs.7 and 8 give the relationships between the dimensionless stress factor F_1 and material parameters. From Fig.7, it can be seen that F_1

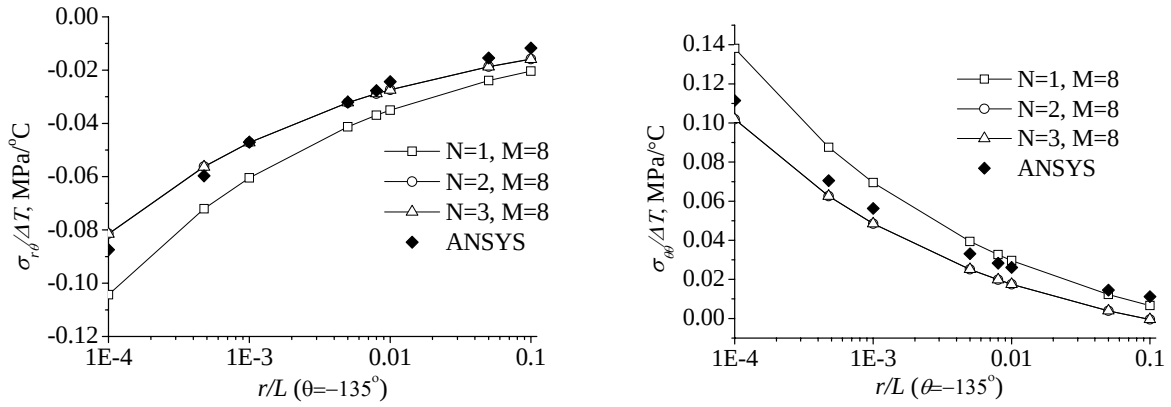

(*a*) (*b*)

Fig.5 The singular stresses away from the apex A (r/L) along the boundary ($\theta=-135^{\circ}$) of a square inclusion: (*a*) $\sigma_{\theta}/\Delta T$; (*b*) $\sigma_{r\theta}/\Delta T$

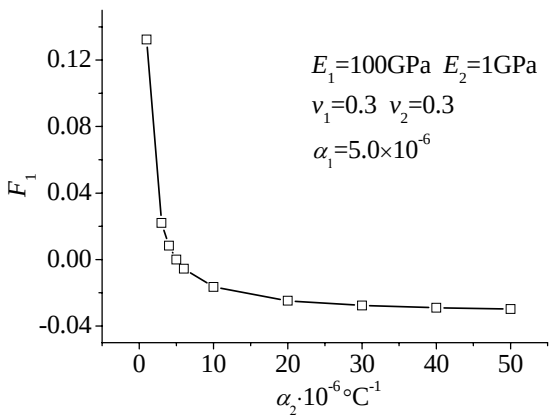

Fig.6 The effect of the thermal expansion coefficient α_2 on F_1 around the inclusion apex A

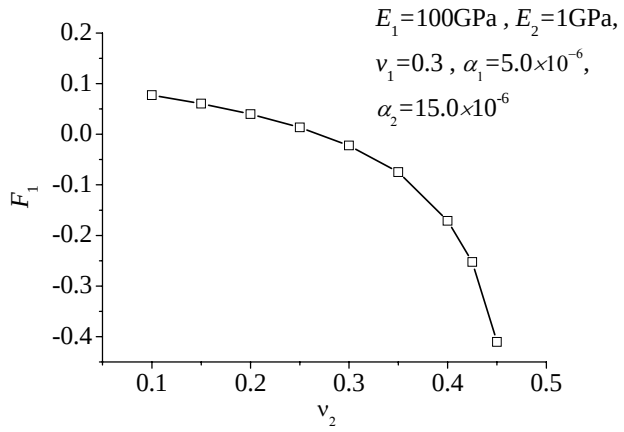

Fig.7 F_1 vs ν_2

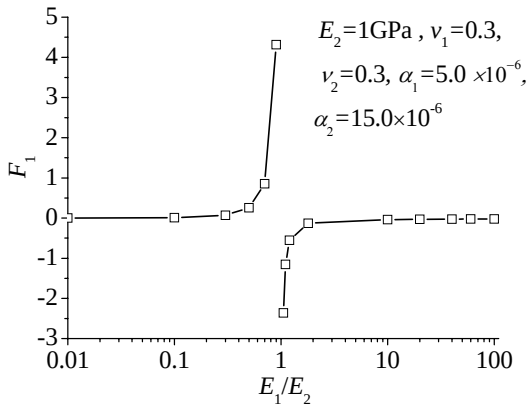

Fig.8 F_1 vs E_1/E_2

decreases more and more rapidly with increasing Poisson ratio ν_2. However, it is shown in Fig.8 that the influence of modulus ratio out of range of $-10 < |E_1 / E_2| < 10$ on the dimensionless stress factor F_1 is so small that it can be neglected. In Figs.6-8, the dimensionless expression of F_1 is defined as

$$F_1 = \frac{K_1}{\alpha_2 E_2 \Delta T \sqrt{\pi} l^{-\lambda_1}} \tag{9}$$

5. Concluding remarks

A new finite element method was developed to analyze irregular-shaped inclusion problems under thermo-mechanical loads. The method consists of a super polygonal inclusion corner element in conjunction with standard four-node hybrid-stress elements. A benchmark example of a square inclusion problem was discussed. The present results is validated by comparison with the numerical results obtained using the conventional finite element commercial software ANSYS package. The present numerical solutions show that our method provides satisfactory results with coarse meshes and is effective and applicable to thermo-mechanical problems with multiple singular points. In addition, for square inclusion problems, the following useful conclusions are drawn:

(1) The dimensionless stress intensity factor F_1 decreases more and more rapidly with increasing Poisson ratio ν_2;

(2) The influence of modulus ratio out of range of $-10 < |E_1 / E_2| < 10$ on the dimensionless stress factor F_1 is so small that it can be neglected.

Acknowledgements

This project is supported by the National Natural Science Foundation of China under Grants 10662004 and 51065008 and also in part sponsored by the Major State Basic Research Program of China (973 Program) (Grants No. 2009CB623203-3 and 2011CB612210)

References

[1] Chen DH. Stress intensity factors for V-notched strip under tension or in-plane bending. Int J Fract, 70(1995) 81-97.

[2] Munz D, Yang YY. Stress singularities at the interface in bonded dissimilar materials under mechanical and thermal loads. J Appl Mech, 59(1992) 857-881.

[3] Chen CD, Chue CH. Singular stresses near apex of wedge by finite element analysis. J Chinese Inst Eng, 26(2003) 423-434.

[4] Lu NS, Zhang Z, Yoon J, Suo ZG. Singular stress fields at corners in flip-chip packages. Eng Fract Mech, 86(2012) 38-47.

[5] Banks-Sills L, Ishbir C. A conservative integral for bimaterial notches subjected to thermal stresses. Int J Num Meth Eng, 60(2004) 1075-1102.

[6] Shin KC, Kim WS, Lee JJ. Application of stress intensity to design of anisotropic/isotropic bi-materials with a wedge. Int J Solids Struct, 44(2007) 7748-7766.

[7] Nomura Y, Ikeda T, Miyazaki N. Stress intensity factor analysis at an interfacial corner between anisotropic bimaterials under thermal stresses. Eng Fract Mech, 76(2009) 221-235.

[8] Chen EP. Finite element analysis of a bimaterial interface crack. Theo Appl Fract Mech, 3(1985) 257-262.

[9] Gadi KS, Joseph PF, Kaya AC, Enriched finite elements for a crack tip touching an interface. in: Proceedings of the ASME Materials Division, Volume 1, MD –Vol. 69-1 IMEC&E, Los Angeles, 1995, pp. 257-263.

[10] Pageau SS, Biggers SB Jr. Engriched finite elements with numerical solutions for singular stress fields. Int J Num Meth Eng 40(1997) 2693-2713.

[11] Tong P, Pian THH, Lasry SJ. A hybrid element approach to crack problems in plane elasticity. Int J Num Meth Eng, 7(1973) 297-308.

[12] Tan MA, Meguid SA. Analysis of bimaterial wedges using a new singular finite element. Int J Fract, 88(1997) 373-391.

[13] Mote CD. Global-local finite element. Int J Num Meth Eng, 3(1971) 565-574.

[14] Bradford LG, Dong SB, Nicol DAC, Westmann RA. A central crack element in fracture mechanics. Int J Fract, 24(1984) 197-207.

[15] Madenci E, Shkarayev S, Sergeev B. Thermo-mechanical stresses for a triple junction of dissimilar materials: Global-local finite element analysis. Theo Appl Fract Mech, 30(1998) 103-117.

[16] Barut A, Guven I, Madenci E. Analysis of singular stress fields at junctions of multiple dissimilar materials under mechanical and thermal loading. Int J Solids Struct, 38(2001) 9077-9109.

[17] Chen DH, Nisitani H. Singular stress field near the corner of jointed dissimilar materials. J Appl Mech, 60(1993) 607-613.

[18] Dundurs J. Effect of elastic constants on stress in a composite under plane deformation. J Compos Mater, 1(1967) 31-322.

A Mechanism-Based Approach for Predicting Ductile Fracture of Metallic Alloys

Xiaosheng Gao

Department of Mechanical Engineering, The University of Akron, Akron, OH 44325, USA
xgao@uakron.edu

Abstract Ductile fracture in metallic alloys often follows a multi-step failure process involving void nucleation, growth and coalescence. Because of the difference in orders of magnitude between the size of the finite element needed to resolve the microscopic details and the size of the engineering structures, homogenized material models, which exhibits strain softening, are often used to simulate the crack propagation process. Various forms of porous plasticity models have been developed for this purpose. Calibration of these models requires the predicted macroscopic stress-strain response and void growth behavior of the representative material volume to match the results obtained from detailed finite element models with explicit void representation. A series of carefully designed experiments combined with finite element analyses of these specimens can also be used to calibrate the model parameters. As an example, a numerical procedure is proposed to predict ductile crack growth in thin panels of a 2024-T3 aluminum alloy. The calibrated computational model is applied to simulate crack extension in specimens having various initial crack configurations and the numerical predictions agree very well with experimental measurements.

Keywords Ductile fracture, Unit cell analysis, Porous plasticity model, Stress triaxiality, Lode angle

1. Introduction

It is well-known that ductile fracture in metallic alloys is a process of void nucleation, growth and coalescence and this process is strongly affected by the stress state imposed on the material. Based on the fracture mechanism, a straight-forward approach to simulate ductile failure process is to model individual voids explicitly using refined finite elements [1-3]. A distinct advantage of this approach is the exact implementation of void growth behavior. It provides an effective method to study the mechanisms of ductile fracture and to analyze the trend of fracture toughness. However, due to sizeable difference between the characteristic length scales involved in the material failure process and the dimensions of the actual structural component, it is impractical to model every void in detail in structure failure analysis, especially for situations involving extensive crack propagation. For this reason, various forms of porous material models have been developed to describe void growth and the associated macroscopic softening during the fracture process. The Gurson-Tvergaard-Needleman porous plasticity model [4-6], which assumes voids are spherical in materials and remain spherical in the growth process, has been widely used in modeling ductile failure process and ductile crack extension. Gologanu, Leblond and Devaux [7, 8] extended the GTN model and derived a yield function for materials containing non-spherical voids. The GLD model can be applied to predict crack propagation in many processed materials, such as rolled plates.

In literature, the stress triaxiality ratio, defined as the ratio of the mean stress to the equivalent stress, is often used as the sole parameter to characterize the effect of the triaxial stress state on ductile fracture. However, recent studies show that the Lode parameter must be introduced to distinguish the stress states having the same triaxiality ratio [3, 9-11]. In this study, we describe a procedure to calibrate the material specific porous plasticity model so that it can accurately capture the material behavior in the fracture process zone with the influence of the stress state. A numerical approach is proposed to predict ductile crack growth in thin panels of a 2024-T3 aluminum alloy, where the GLD model is used to describe the void growth process and the material failure criterion is calibrated using experimental data. Model predictions are compared with experimental data for fracture specimens having various initial crack configurations.

2. Modeling the Material Behavior in the Fracture Process Zone

Ductile alloys used in engineering structures often contain impurities such as second-phase particles. Cavities often nucleate at relatively low stress levels due to fracture or decohesion of the large inclusions. For the purpose of analysis, voids are assumed to be present in the material at the outset of loading. These voids enlarge with increased plastic deformation and eventually coalesce with the assistance of the nucleation and growth of secondary microscopic voids. Therefore, material in the fracture process zone can be considered as an array of unit cells. Each cell is a representative material volume (RMV) containing a void nucleated from the inclusion.

2.1. Unit Cell Analysis

A straight-forward approach to study the ductile fracture mechanism as well as the effects of material properties and stress state on the material failure process is to conduct the unit cell analysis of a representative material volume (RMV). As an example, Figure 1(a) shows a 1/8-symmetric finite element model for a cubic RMV containing a spherical void and Fig. 1(b) shows the three-dimensional stress state applied on the RMV. The material is assumed to obey a power-law hardening, true stress-strain relation with Young's modulus E=70.4 GPa, Poisson's ratio ν=0.3, yield stress σ_0=345 MPa and strain hardening exponent N=0.14. The initial void volume fraction (volume of the spherical void / volume of the RMV) is taken as f_0 = 0.02. The initial size of the RMV is defined as $X_0 \times X_0 \times X_0$ and the deformed lengths in the x-, y- and z-directions are represented by X, Y and Z respectively.

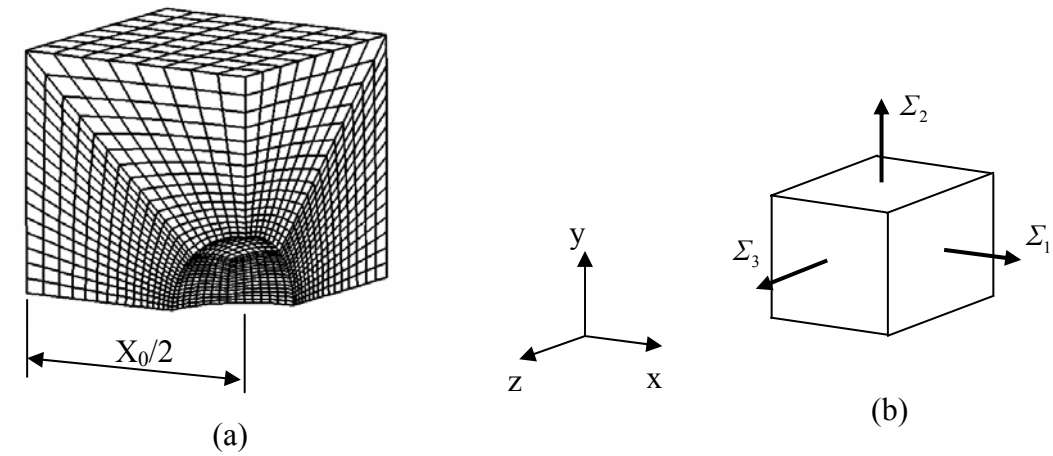

Figure 1. (a) A one-eighth symmetric finite element mesh for the RMV containing a centered, spherical void. (b) The stress state applied on the RMV.

The stress state subjected by the RMV is characterized by two parameters, the stress triaxiality ratio (T) and the Lode angle (θ)

$$T = \frac{\Sigma_1 + \Sigma_2 + \Sigma_3}{3\Sigma_e}, \quad \tan\theta = \frac{2\Sigma_3 - \Sigma_2 - \Sigma_1}{\sqrt{3}\left(\Sigma_2 - \Sigma_1\right)} \tag{1}$$

where Σ_e represents the von Mises equivalent stress. Here the numerical analyses are carried out

using the finite element program ABAQUS [12], which employs a finite strain, J_2 plasticity theory within an updated Lagrangian formulation. The displacement boundary conditions on the outer surfaces of the RMV are prescribed such that the macroscopic parameters T and θ are kept constant during the entire deformation history. Faleskog et al. [13] and Kim et al. [9] provide the details of how to prescribe the boundary conditions.

A case of axisymmetric loading is considered first, where $\Sigma_2 \geq \Sigma_1 = \Sigma_3$ ($\theta = -30^{\circ}$). Figure 2(a) shows the variation of X with the macroscopic effective strain (E_e) of the RMV. As loading continues, X gradually decreases. But when the deformation reaches a certain level, X stops decreasing and remains at a constant value. This implies that further deformation takes place in a uniaxial straining mode, which corresponds to flow localization in the ligament between adjacent voids. The shift to a macroscopic uniaxial strain state indicates the onset of void coalescence. Detailed explanation of the uniaxial straining mode can be found in references Koplik and Needleman [14] and Kim et al. [9]. Here we use E_c to denote the macroscopic effective strain at the onset of void coalescence.

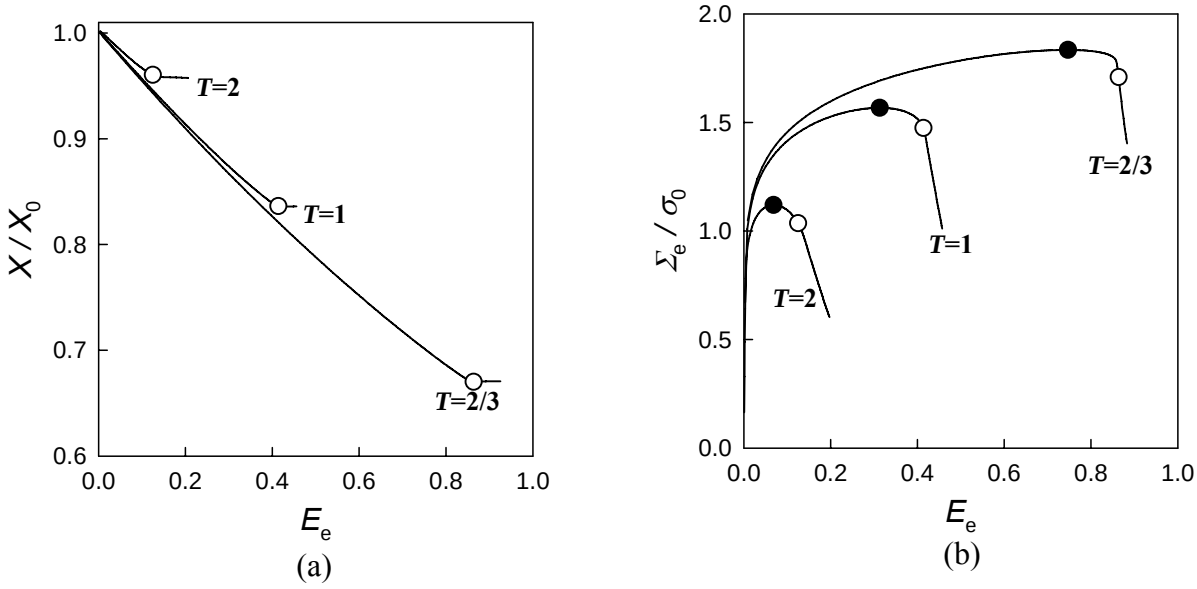

Figure 2. (a) Variation of the deformed cell width in x-direction with the macroscopic true effective strain of the cell revealing the shift to uniaxial straining. (b) Macroscopic true effective stress versus true effective strain of the void-containing RMV displaying the macroscopic softening.

The macroscopic effective stress versus effective strain curve, Figure 2(b), provides an overview of the competition between matrix material strain hardening and porosity induced softening. As deformation progresses, a maximum effective stress is reached (indicated by the filled circle), and then Σ_e decreases as strain-hardening of matrix material is insufficient to compensate for the reduction in ligament area caused by void growth. As the macroscopic effective strain reaches E_c (indicated by the open circle), a rapid drop in macroscopic effective stress occurs. As expected, both the peak stress value and the value of E_c decrease with the stress triaxiality ratio T, reflecting the decease of ductility.

In the later stage of the material failure process, secondary voids often nucleate in the ligament between enlarged primary voids and rapid growth and coalescence of these secondary voids accelerates the final ligament separation. In our analyses, it is assumed that void nucleation is plastic strain controlled and follows a normal distribution proposed by Chu and Needleman [15]. The nucleated voids are regarded to be smeared in the material and the material behavior is governed by the GTN model. Figure 3(a) compares the macroscopic effective stress versus effective strain curves between models including and not including the secondary voids. Here several values of stress triaxiality ratio, $T = 1/3$, 2/3, 1, 1.5 and 2, are considered. The open circles denote the onset of coalescence for models where secondary voids are not taken into account. The filled circles represent the onset of coalescence for models where nucleation, growth and coalescence of secondary voids are accounted for. It is clear that secondary voids significantly accelerate the void coalescence process.

To demonstrate the Lode angle effect on ductile failure, let the stress triaxiality ratio T be fixed and consider a series of stress states corresponding to different θ-values. Figure 3(b) shows the variation of E_c with θ as T taking a fixed value of 2/3. Clearly the Lode angle has an important effect on E_c.

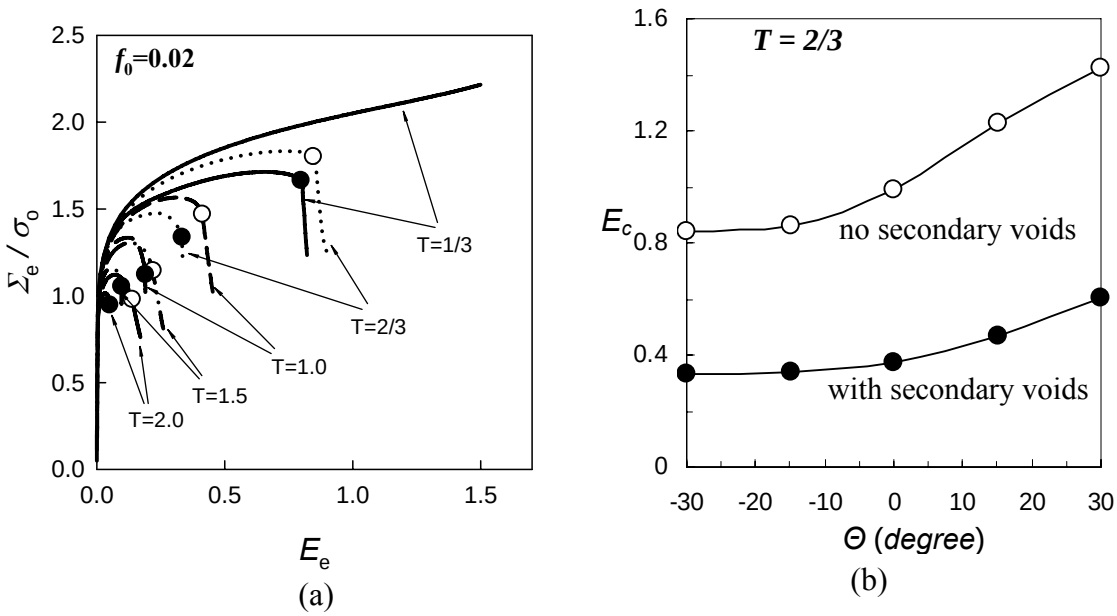

Figure 3. (a) Comparison of the macroscopic effective stress versus effective strain curves between models including and not including secondary voids. The parameters for nucleation of secondary voids are $f_N = 0.04$, $\varepsilon_N = 0.1$ and $s_N = 0.05$ [15]. (b) Variation of E_c with θ as T taking a fixed value of 2/3.

Now consider an array of T and θ values and perform unit cell analysis for each case. The variation of E_c with T and θ can be expressed by a function $E_c(T,\theta)$. Therefore, a ductile failure criterion for a given material can be established as

$$E_e = E_c(T,\theta) \tag{2}$$

where E_e denote the macroscopic effective strain of the RMV. The RMV fails when E_e reaches a critical value dependent of its stress state characterized by T and θ.

Using explicit void representation, the void growth and coalescence mechanisms and the effects of the initial relative void spacing, void pattern, void shape and void volume fraction on ductile fracture toughness can also be studied directly [16].

2.2. Porous Plasticity Models

Various forms of porous plasticity models have been developed to describe void growth in ductile solids and the associated macroscopic softening, among which the most famous model is due to Gurson [4] with the modification by Tvergaard and Needleman [5, 6]. The yield function of the GTN model has the form

$$\Phi = \frac{\Sigma_e^2}{\bar{\sigma}^2} + 2q_1 f \cosh\left(q_2 \frac{3\Sigma_h}{2\bar{\sigma}}\right) - 1 - q_1^2 f^2 = 0 \tag{3}$$

where Σ_e denotes the macroscopic Mises effective stress, Σ_h represents the macroscopic hydrostatic stress, $\bar{\sigma}$ is the current flow stress of the matrix material, and f defines the current void volume fraction. The evolution law for void volume fraction is determined by requiring the matrix material to be plastically incompressible

$$\dot{f} = (1 - f)\dot{E}_{kk}^{p} \tag{4}$$

where $\dot{E}_{kk}^{p}$ is the trace of the macroscopic plastic strain rate tensor.

The GTN model was derived for growth of spherical voids, but voids are often non-spherical in actual materials. The GLD model [7, 8], with the yield function given by Eq. (5), was derived to describe the macroscopic plastic response of ductile solids containing spheroidal voids

$$\Phi = \frac{C}{\bar{\sigma}^2}\left\|\mathbf{\Sigma}' + \eta\Sigma_h\mathbf{X}\right\|^2 + 2q(g+1)(g+f)\cosh\left(\kappa\frac{\Sigma_h}{\bar{\sigma}}\right) - (g+1)^2 - q^2(g+f) = 0 \tag{5}$$

where S is the shape parameter, $\| \ \|$ denotes the von Mises norm, $\mathbf{\Sigma}'$ is the deviatoric stress tensor, Σ_h is the generalized hydrostatic stress defined by $\Sigma_h = \alpha_2(\Sigma_{xx} + \Sigma_{zz}) + (1-\alpha_2)\Sigma_{yy}$, $\mathbf{X}$ is a tensor defined as $\mathbf{X} = (2/3)\boldsymbol{e}_y \otimes \boldsymbol{e}_y - (1/3)\boldsymbol{e}_x \otimes \boldsymbol{e}_x - (1/3)\boldsymbol{e}_z \otimes \boldsymbol{e}_z$, and ($\boldsymbol{e}_x$, $\boldsymbol{e}_y$, $\boldsymbol{e}_z$) is an orthogonal basis with $\boldsymbol{e}_y$ parallel to the axisymmetric axis of the void, and $\otimes$ denotes tensor product. The evolution equation for f is the same as Eq. (4) and derivations of the evolution equation for S can be found in Gologanu et al. [7, 8].

In order to simulate ductile fracture process, these porous plasticity models must be calibrated such that the material behavior in the fracture process zone is accurately captured. Calibration of these models requires the predicted macroscopic stress-strain response and void growth behavior of the representative material volume to match the results obtained from detailed finite element models with explicit void representation obtained from the unit cell analysis outlined in Section 2.1. Faleskog et al. [13], Kim et al. [9] and Pardoen and Hutchinson [17] describe the procedures to

determine the heuristic parameters in the GTN and GLD models as functions of material flow properties, void parameters and the stress triaxiality.

The porous plasticity models described above governs the behavior of the RMV during the void growth process. As the macroscopic effective strain (E_e) reaches E_c, void coalescence occurs and the RMV quickly loses its stress carrying capacity. We adopt the f^* function, introduced by Tvergaard and Needleman [6], to account for the effects of rapid void coalescence at failure. After E_e reaches E_c, f is replaced by f^* in the GLD model, where

$$f^* = \begin{cases} f, & f \le f_c \\ f_c + K(f - f_c), & f > f_c \end{cases} \tag{6}$$

In Eq. (6), f_c is the void volume fraction at $E_e = E_c$, $K = (f_u - f_c)/f_c$, and f_u is the f^* value at zero stress. Since AQAQUS/Standard does not provide an element removal procedure, Eq. (6) is employed until $f^* = 0.99 f_u$, after which an exponential function is used such that f^* gradually approaches to f_u (but can never reach f_u) to improve numerical stability.

3. Simulation of Crack Growth in Thin Panels of a 2024-T3 Aluminum Alloy

Dawicke and Newman performed extensive fracture tests on thin panels of a 2024-T3 aluminum alloy, including tests of C(T), M(T), and multi-site damage (MSD) specimens [18, 19]. Figure 4 show the sketches of the fracture specimens. The test data of our interest are from LT specimens with a sheet thickness of 2.3 mm. The specimens have very stiff guide plates (coated with Teflon tape) to constrain out-of-plane (buckling) displacements. In the L orientation, the 2024-T3 sheet material used in the experiments has a yield stress of 345 MPa, Young's Modulus of 71.3 GPa, and Poisson's ratio of 0.3. Quantitative metallographic analyses were performed to determine the inclusion volume fraction, shape and average spacing. It is found that the inclusion volume fraction (f_0) is approximately 0.002, the average spacing between inclusions in the LT plane is about 50 μm, and in LT specimens, the inclusions can be approximated as prolate spheroids with the aspect ratio ≈ 4.

To predict crack growth, the function $E_c(T,\theta)$ needs to be determined. The results presented in Section 2.1 suggest that E_c is not sensitive to θ when θ is in the range $-30^\circ \le \theta \le 0^\circ$. We perform finite element analyses of the fracture specimens considered in this study and find the θ-values of the representative material volumes ahead of the crack front are in the range of $-15^\circ \le \theta \le 0^\circ$. Therefore, we neglect the θ-dependence for these specimens and assume E_c has the following function form

$$E_c = \alpha e^{\beta T} \tag{7}$$

where α and β are two parameters need to be calibrated using experimental data. Two data points are needed to determine α and β. The tensile test provides one point. Figure 5(a) shows the 1/4 model for the tensile specimen and Figure 5(b) shows its experimental load-displacement curve. A sudden drop of the load-displacement curve suggests the onset of crack initiation. The stress and strain states for the critical element (at the geometry center of the specimen) at crack initiation are obtained through finite element analysis. The triaxiality T and strain ε_f are calculated as 0.45 and 0.5 respectively. Substitution of these values into Eq. (7) yields a relationship between α and β, $0.45=\alpha e^{0.5\beta}$. The next step of the calibration process seeks to match the model predicted load versus crack propagation curve with the experimental measurements for the C(T) specimen. This step entails several finite element crack growth analyses of the C(T) specimen using different values of β.

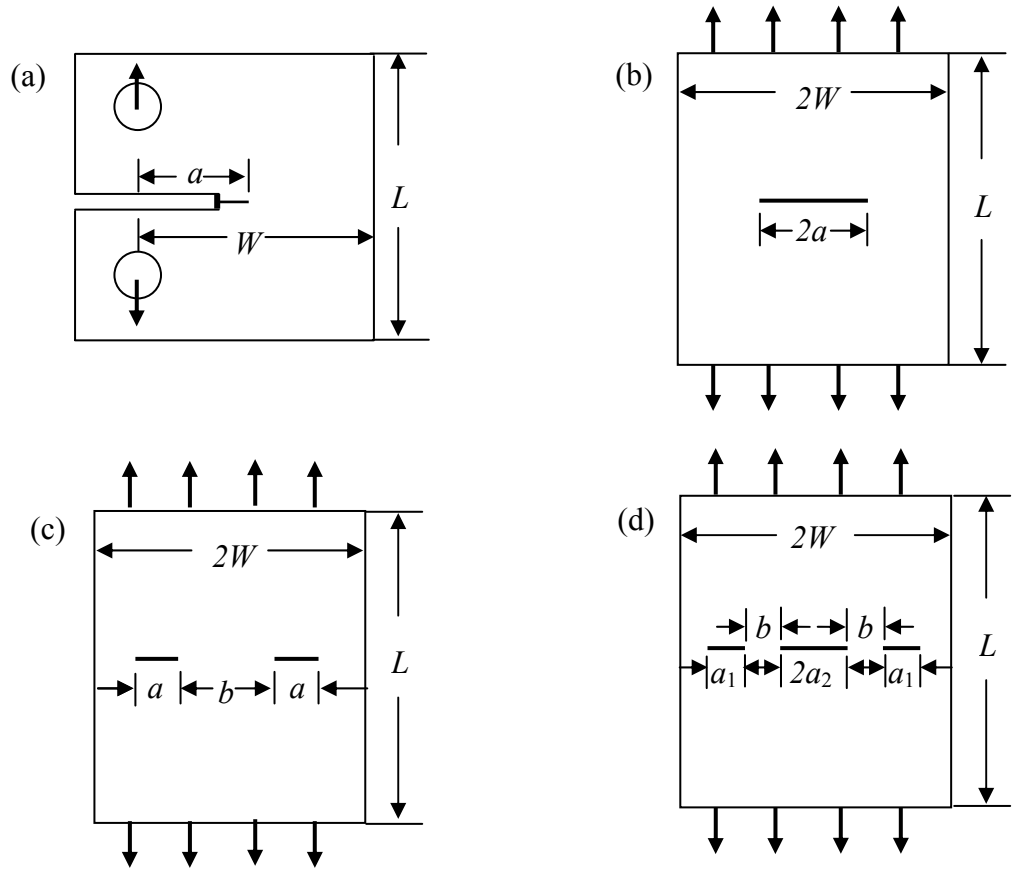

Figure 4. Fracture specimens: (a) C(T) specimen, (b) M(T) specimen, (c) MSD specimen containing two cracks, (d) MSD specimen containing three cracks.

The C(T) specimen has a width of 150 mm with a/W = 0.33, where a represents the initial crack length and W represents the specimen width. The quarter-symmetric finite element mesh has 27,400 eight-node, isoparametric solid elements (with reduced integration). The mesh near the crack front has six layers with varying thickness to capture the stress gradient in the thickness direction, where the thickest elements are at the symmetry plane. The elements directly ahead of the crack front have uniform in-plane dimensions (L_e = 50 μm) and are governed by the GLD model. All other elements follow J_2 flow plasticity. Loading of the C(T) specimen is controlled by prescribing a displacement

on a rigid pin through the hole.

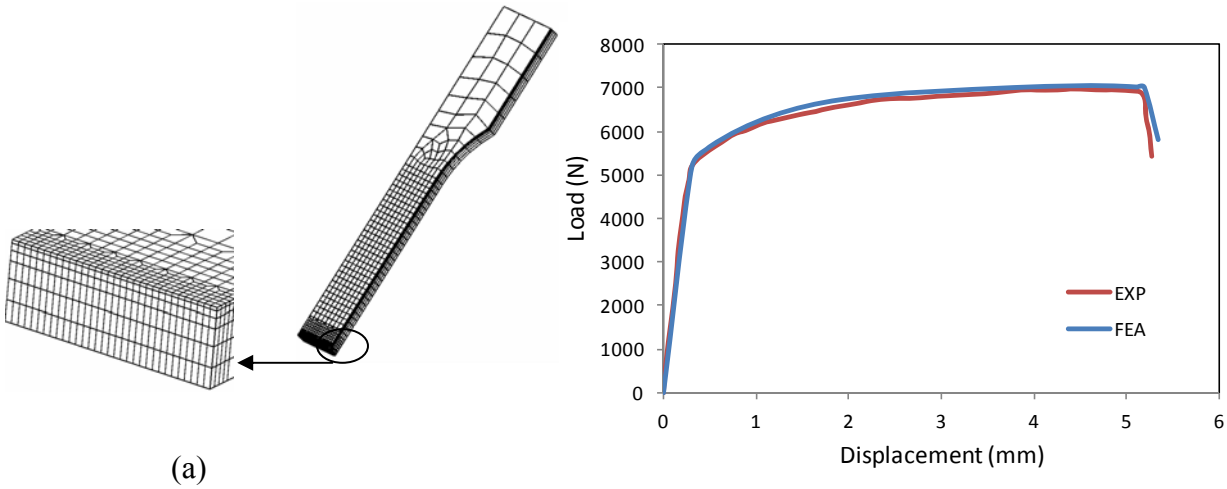

(a) (b)

Figure 5. (a) Finite element mesh for the tensile specimen. (b) Comparison of the predicted and experimental load-displacement curves.

Figure 6 shows the comparison between the model predicted load versus crack growth curve with the experimental measurements (two sets of experimental data) for different choices of α and β, where the lines represent model predictions and the symbols denote experimental measurements. Here Δa represent the amount of crack growth measured at the free surface. In the numerical model, the propagating crack front is defined by the elements which have reached the failure strain E_c. From Figure 6, it can be seen that the choice of $\alpha = 0.93$ and $\beta = -1.45$ (solid line) results in a best fit to the experimental data. Therefore, these values are the calibrated values for α and β and will be used to predict crack growth in other fracture specimens.

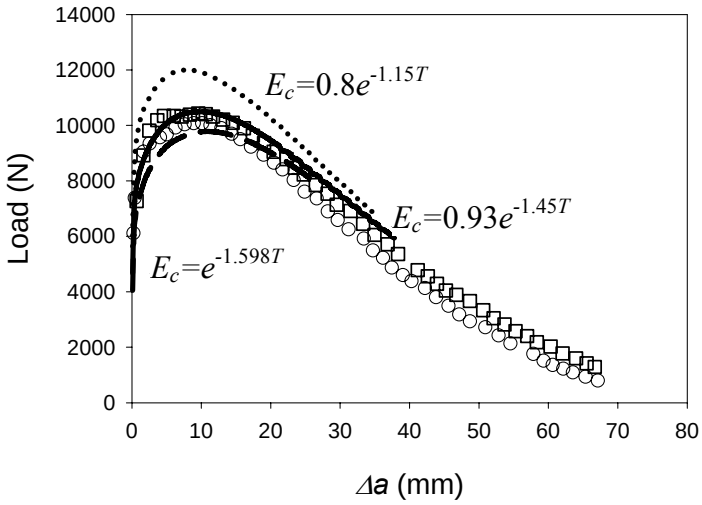

Figure 6. Comparison of the model predicted load versus crack growth curve with the experimental measured data (symbols) showing the choice of $\alpha = 0.93$ and $\beta = -1.45$ (solid line) results in a best fit to the experimental data.

The calibrated computational model is now employed to predict the crack extension behavior of M(T) and MSD specimens. Three M(T) specimens with W = 300 mm and a/W ratios of 0.33, 0.42 and 0.5 are analyzed. The element size and arrangement in the region near the crack front are kept the same as used in the C(T) specimen. The nominal remote stress, σ_R , characterizes the loading for these specimens. Figure 7(a) compares the computed load versus crack extension responses with experimental measurements, showing very good agreement for all three cases. Figure 7(b) compares the computed load versus crack extension responses with experimental measurements for a MSD specimen containing three cracks as shown in Figure 4(d). This specimen has the same width as the M(T) specimens. The center-crack length is $2a_2$ = 100 mm. The two lead cracks have the same length of a_1 = 12.5 mm. The tip-to-tip distance between the lead crack and the center crack is b = 12.5 mm. The model prediction captures accurately the load versus crack extension curve. The cusp on the predicted load versus crack extension curve corresponds to the point when the lead crack and the center crack link up.

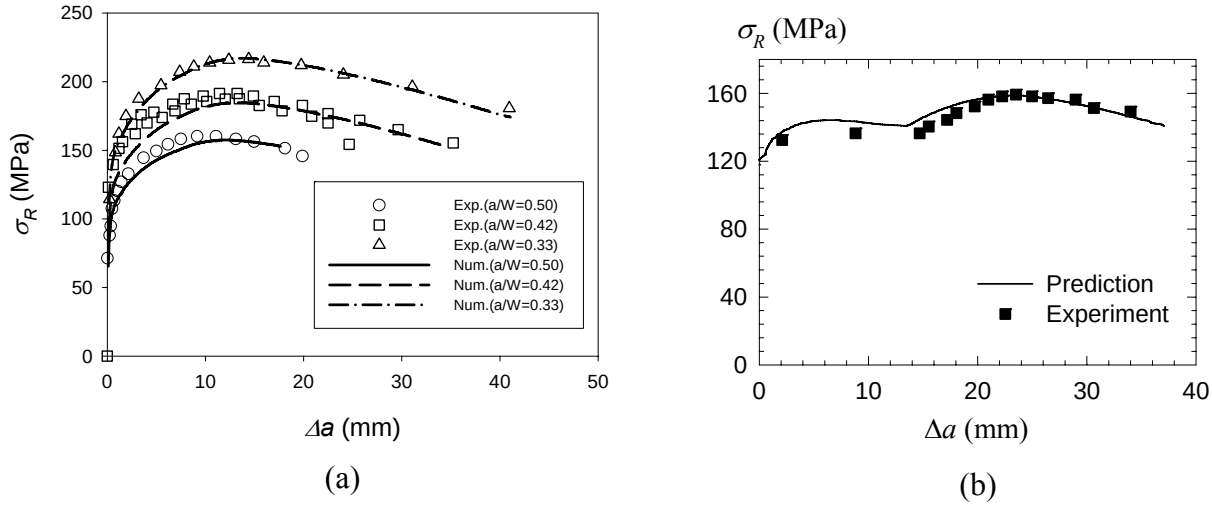

Figure 7. Comparison of the model predicted load versus crack extension responses (lines) with experimental measurements (symbols): (a) M(T) specimens, (b) MSD specimen containing three cracks.

4. Concluding Remarks

Based on the mechanism of ductile fracture in metallic alloys, this paper describes a method to predict crack growth in engineering structures. To model extensive crack extension, homogenized porous plasticity models need to be adopted to describe the material behavior in the fracture process zone and these models must be calibrated such that the material behavior is accurately captured. Unit cell analysis of the representative material volume reveals the strong effect of the stress state on the void growth and coalescence. Calibration of the porous plasticity models requires the predicted macroscopic stress-strain response and void growth behavior of the representative material volume to match the results obtained from detailed unit cell analysis. As an application, a numerical procedure is proposed to predict ductile crack growth in thin panels of a 2024-T3 aluminum alloy. The material specific GLD porous plasticity model is used to describe the void growth process and the failure criterion is calibrated using experimental data. The calibrated computational model is then applied to predict crack extension in fracture specimens having various initial crack configurations. The numerical predictions show good agreement with experimental

measurements.

References

[1] V. Tvergaard, J.W. Hutchinson, Two mechanisms of ductile fracture: void by void growth versus multiple void interaction. Int J Solids Struct 39 (2002) 3581-3597.
[2] J. Kim, X. Gao, T.S. Srivatsan, Modeling of crack growth in ductile solids: a three-dimensional analysis. Int J Solids Struct 40(2003) 7357-7374.
[3] J. Kim, G. Zhang, X. Gao, Modeling of ductile fracture: application of the mechanism-based concepts. Int J Solids Struct 44 (2007) 1844–62.
[4] A.L. Gurson, Continuum of ductile rupture by void nucleation and growth: Part I-Yield criteria and flow rules for porous ductile media. J Eng Mater Tech 99(1977) 2-55.
[5] V. Tvergaard, On Localization in ductile materials containing spherical voids. Int J Fract 18(1982) 237-252.
[6] V. Tvergaard, A. Needleman, Analysis of the cup-cone fracture in a round tensile bar. Acta Metall 32(1984) 157-169.
[7] M. Gologanu, J.B. Leblond, J. Devaux, Approximate models for ductile metals containing nonspherical voids – Case of axisymmetric prolate ellipsoidal cavities. J Mech Phys Solids 41(1993) 1723-1754.
[8] M. Gologanu, J.B. Leblond, J. Devaux, J., Approximate models for ductile metals containing nonspherical voids – Case of axisymmetric oblate ellipsoidal cavities. J Eng Mater Tech 116(1994) 290-297.
[9] J. Kim, X. Gao, T.S. Srivatsan, Modeling of void growth in ductile solids: effects of stress triaxiality and initial porosity. Eng Frac Mech71(2004) 379-400.
[10] L. Xue, T. Wierzbicki, Ductile fracture initiation and propagation modeling using damage plasticity theory. Eng Fract Mech 75 (2008)3276–93.
[11] K. Nahshon, J.W. Hutchinson, Modification of the Gurson model for shear failure. Eur J Mech A/Solids 27(2008) 1-17.
[12] SIMULIA, ABAQUS User's Manual (version 6.9), Providence, RI, 2008.
[13] J. Faleskog, X. Gao, C.F. Shih, Cell model for nonlinear fracture analysis-I. Micromechanics calibration. Int J Fract 89(1998) 355-373.
[14] J. Koplik, A. Needleman, Void growth and coalescence in porous plastic solids. Int J Solids Struct 24(1988) 835-853.
[15] C. Chu, A. Needleman, Void nucleation effects in biaxially stretched sheets. J Eng Mater Technol 102(1980) 249–256.
[16] X. Gao, T. Wang, J. Kim, On ductile fracture initiation toughness: Effects of void volume fraction, void shape and void distribution. Int J Solids Struct 42(2005) 5097-5117.
[17] T. Pardoen, J.W. Hutchinson, An extended model for void growth and coalescence. J Mech Phys Solids 48(2000) 2467-2512.
[18] D.S. Dawicke, J.C. Newman, Evaluation of fracture parameters for prediction residual strength of multi-site damage cracking, in: Proceedings from the First Joint NASA/FAA/DoD Conference on Aging Aircraft, 1997, pp. 1307–1326.
[19] D.S. Dawicke, J.C. Newman, J.C., Residual strength predictions for multiple site damage cracking using a three-dimensional finite element analysis and a CTOA criterion, in: T.L. Panontin, S.D. Sheppard (Eds), Fracture Mechanics: 29th Volume. ASTM STP 1321, Philadelphia, PA, 1998, pp. 815–829.

Effect of pre-existing microcrack on the cyclic displacement instability in thermal barrier coating systems

Luochuan Su, Weixu Zhang, T.J. Wang*

State Key Laboratory for Strength and Vibration of Mechanical Structures, School of Aerospace Engineering, Xi'an Jiaotong University, Xi'an 710049, China
* Corresponding author: wangtj@mail.xjtu.edu.cn

Abstract The displacement instability of the thermally grown oxide (TGO) layer in thermal barrier coating systems is a critical factor inducing the failure of the system by causing large scale delamination and spallation. In this paper, the effect of pre-existing microcracks within the ceramic top-coat (TC) on the cyclic displacement instability under thermal cycling is investigated by a finite element analysis. Stress and the interface morphology are obtained after thermal cycling when the microcracks pre-exist within the TC. The influence of various parameters including crack location, crack length and crack direction on the interface morphology are discussed in detail. It is demonstrated that the existing of microcracks within TC can aggravate the displacement instability and affect the stress state in TC significantly. However, when the crack is perpendicular to the flat interface, the aggravation of it on the instability is weakest.

Keywords Microcracks, Displacement instability, Thermal cycling , Thermal barrier coating

1. Introduction

Thermal barrier coating (TBC) system is widely used in the blades of gas turbines or aircraft engines as the thermal insulation component, which can protect the base material against the extreme temperature due to its low heat conductivity. Usually, a typical TBC system consists of the following multilayer (Fig. 1a): (i) a thick superalloy substrate, (ii) a bond-coat (BC) next to the substrate protecting the substrate from oxidation, (iii) a ceramic top-coat (TC) for providing thermal insulation, and (iv) a thermally grown oxide (TGO) layer forming between TC and BC due to the high temperature oxidation[1-4].

The durability of TBC focuses world attentions in recent years. The coating performance usually begins to degrade associated with the large scale delamination and spallation of TC. Studies have confirmed that the displacement instability of TGO (Fig. 1) under cyclic oxidation is a critical factor inducing the fracture and delamination in TBC made by electron bean-physical vapor deposition (EB-PVD) [2, 5-9]. The most vivid manifestation of the instability is the downward displacement of TGO into soft BC (Fig. 1a), which is motivated by the large residual compressive stress caused by thermal expansion misfit and the thermal growth of TGO [6, 10, 11]. The instability usually initiates at the region near the imperfection of BC-TGO interface and the amplitude of it extends as the extensive thermal cycling. Following factors have confirmed to have a strong influence on the instability [2, 3, 5, 6, 12-19]. (i) The thermal cycling: It is a necessary condition to cause large instability; (ii) The growth strain resulting from the volume increase in the process of BC transforming to new TGO by high temperature oxidation; (iii) The initial morphology imperfection in the BC-TGO interface; (iv) The accumulation of plastic strain in BC near the initial imperfection, which is the most relevant factor controlling the evolution of displacement instability, and (v) The creep behavior of component materials.

Due to the need of enhancing the strain tolerance of the ceramic coating, the microcracks are widely introduced in the process of coating deposition [20, 21]. Many experimental and analytical results have confirmed that pre-existing vertical surface cracks in TC can enhance the resistance to the initiation of interface crack [22-26]. Therefore, when these cracks exist at the surface of the TC, they can provide an additional capability to prevent the interface cracks developing besides enhancing the coating strain tolerance. However, as shown in Fig. 1a, these introduced microcracks

also widely exist within the TC. Experimental investigations have shown that when these microcracks appear in the region near the site of displacement instability, they would nucleate and extend as thermal cycling under the large tensile stress [5], and finally cause large scale delamination and spallation at the interface of TC-TGO [3, 4]. Based on Mumm's experiment results, Karlsson [14] modeled these cracks as traction-free internal planes and found that these cracks also can significantly promote the extending of the instability. Therefore, the existing of microcracks near the instability site would affect the durability of the system. Similarly to the surface cracks, there would be an optimal direction for the internal cracks, in which the effect of these cracks on the instability extending is weakest.

However, in all of the previous studies focusing on the displacement instability, the effect of the geometric parameters of pre-existing cracks within the TC on the instability was not considered [2, 5-7, 13-15, 19, 27] and the optimal direction is still not obtained. Hence, the objective of this paper is to explore the effect of pre-existing cracks within TC of varying length, location and direction on the displacement instability of TGO under thermal cycling and try to obtain the optimal crack direction, in which the instability development is weakest. The results may be helpful in controlling the instability and providing the probability to design a longer life TBC.

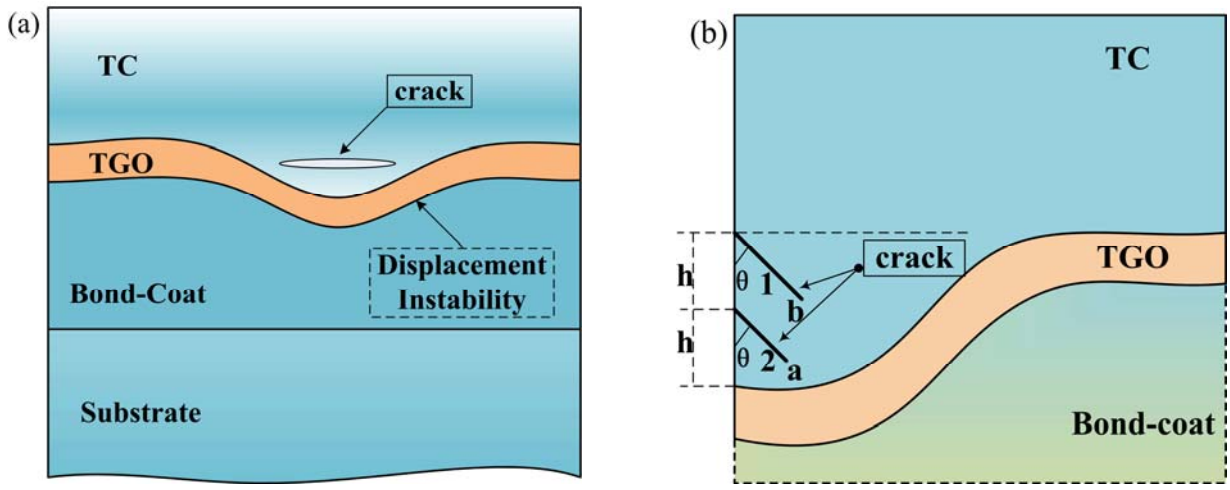

Figure 1. Schematic for (a) the multi-layer TBC system with TGO displacement instability, and (b) the microcracks within TC above the instability site.

2. Statement of the problem

Due to the microcracks appearing in the region near the site of TGO displacement instability can significantly promote the extending of instability and induce the final failure of TBC system, we only consider the case where the initial crack exists above the instability site in this problem. As shown in Fig. 1b, two different cracks are introduced in this problem: crack “a”, which is at a distance h away from the base of instability region extending from the symmetry axis to the inward of TC, and crack “b”, which is at a distance $2h$ from the base with the same morphology as crack a. Each of these two cracks is defined by the included angle θ_1 and θ_2 (Fig. 1b), respectively. It must be noted that these two cracks are not considered in this problem together and only a single static crack problem is solved. In this problem, all materials are assumed to be isotropic (the detailed material properties are described below) and the plane strain condition exists.

In order to investigate the extending of instability zone under thermal cycling when the crack exists above the instability site, cyclic thermal load is applied. In each thermal cycle, the system is cooled to ambient temperature from an initial peak temperature firstly and a thermal stress analysis is carried out associated with this temperature change. Then, the temperature rises to the initial state

with a new stress state being obtained, and this peak temperature would hold a long time, where the thermal growth of TGO layer would occur. After that, the system is cooled to ambient again. The cyclic thermal load is obtained by repeating this sequence many times.

3. The simulation scheme

3.1. Description of model

Due to the complexity of the morphology of interface and crack, the finite element method (FEM) is used to solve the problem. A conventional FEM model for the displacement instability is adapted in the calculations (Fig. 2) [13, 14]. The analysis is carried out by employing the computer program ABAQUS with the four-node, bi-liner plane strain elements. Geometric dimension of each layer is shown in the model and an initial instability zone with a depth $2h = 7.5\mu m$ and radii of curvature $R_1 = R_2 = 11.25\mu m$ is introduced. All the nodes at the right sides of the model are allowed to move with a limit of keeping an equal displacement in the X direction for them and a symmetric boundary condition is applied to the left side. The nodes on the bottom side are fixed in the Y direction to avoid rigid body motion.

In the analysis, the initial static crack is not allowed to propagate, and the length L and the angle θ for both cracks are changed as variables. The crack behavior is achieved by using the extended finite element method (XFEM) [28-31], which can simulate the crack behavior without the crack tip conforming to any node point of the finite element mesh. In addition, in all calculations, only the case of single crack within the TC is simulated and the case of multi-crack is not considered in this paper.

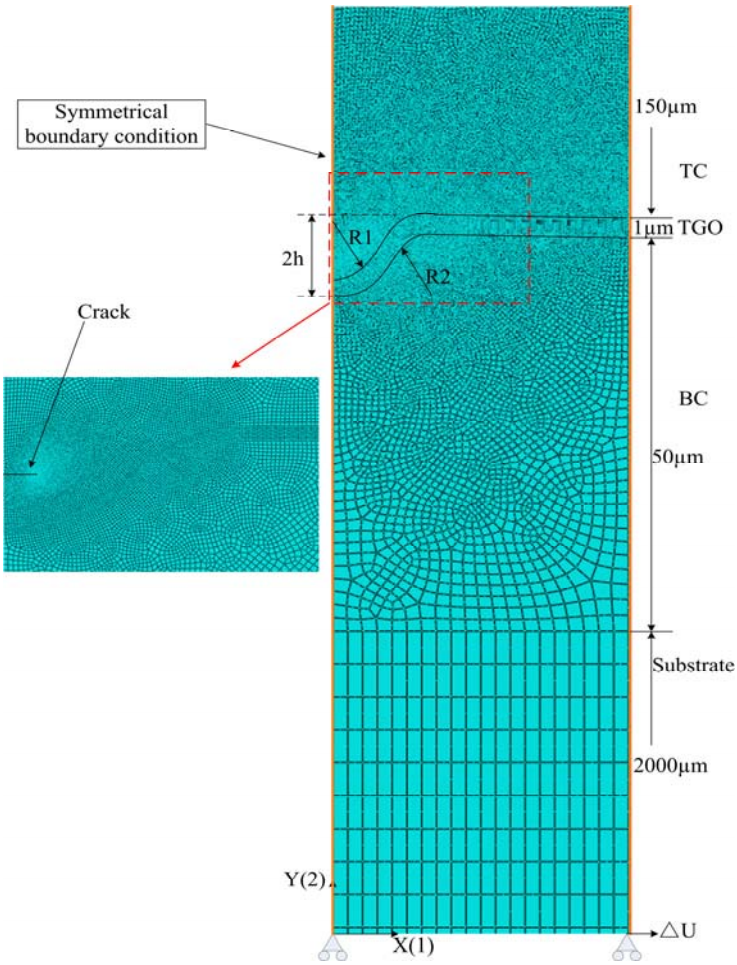

Figure 2. Finite element method model for the crack within the TC above the instability site.

3.2. Material properties

All materials used in the calculations are assumed to be isotropic and all material properties are temperature-dependent, which are summarized in [32]. Both TC and substrate are linear elastic and BC is considered as elastic-perfectly plastic with a temperature-dependent yield strength. The user subroutine, uexpan, in ABAQUS is employed to simulate the thermal growth of TGO, which was introduced by Karlsson and Evans in [13]. The growth behavior is achieved by imposing a thermal strain at the holding time of high temperature. The thermal strain consists of two components: ε_g, which is a lateral growth strain parallel to the TGO-BC interface, and ε_t, which is a thickening strain. In this paper, a ratio of lateral growth strain to thickening strain, $\varepsilon_g / \varepsilon_t = 0.5$, is used with $\varepsilon_g = 1\times10^{-3}$. Also, the TGO is allowed to yield at the peak temperature with a yield strength σ_Y^{tgo} =1 GPa and it is elastic in other temperature [13]. The sequence of thermal load is repeated 24 times with 3 hours hold time at peak temperature (1100℃) for each sequence [6, 13, 14].

4. Results and discussions

4.1. General response

Initial results are generated for an intact TC, a TC within a crack at location "a" and a TC within a crack at location "b" (Fig. 1b), respectively. Cracks in both cases have an initial length, $L = 4\mu m$ and $\theta_1 = \theta_2$ =90° in this section. A synopsis of the major findings is presented in Figs. 3-5.

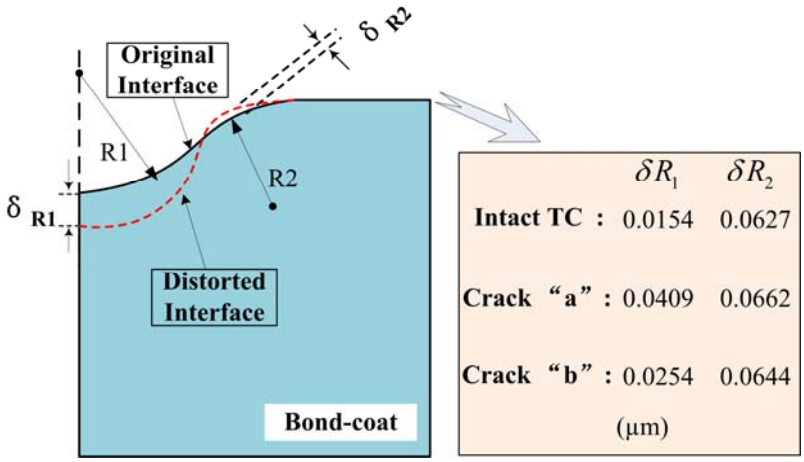

Figure 3. The distortions of BC interface after 24 thermal cycles.

Fig. 3 shows the morphology of BC-TGO interface after 24 thermal cycles. It can be seen that the interface is distorted significantly with large upward displacements around the periphery of the instability zone and large downward displacements at the base. This phenomenon is in accordance with the previous results found by experiments and simulations [5, 6]. The shape distortions at the interface are induced by the plastic deformation in BC directly, and thermal misfit stresses and thermal growth stresses are two main resources to cause the plastic deformation. From Fig. 3, we can see that all these distortions at BC-TGO interface can be represented by the change of R_1 (δR_1) and R_2 (δR_2). Therefore, in following discussions, we mainly focus on the parameters δR_1 and δR_2. Fig. 3 also presents the change of R1 (δR_1) and R2 (δR_2) when an initial crack exists within TC. It clearly shows that the distortion of the interface is more significant when the microcrack exists within TC, especially the downward displacement δR_1. In addition, the crack location also

can affect the interface distortions. Compared to the crack “b”, the crack “a”, which is more close to the base of the instability zone, results in a more significant distortion. Therefore, the existing of crack, especially the crack close to the base of instability site, can induce larger "up" and "down" displacements.

The distribution of out-of-plane stress (σ_{22}) in the intact TC presents in Fig. 4b. The tensile stresses mainly concentrate on the region above the instability site. When the tensile stress develop to a sufficient level, it can induce the cracks within the TC above the instability site and the delamination at the interface[5, 16]. The compressive stresses mainly appear in a relatively small zone near the periphery of instability zone and this compressed zone can prevent the crack initiation. Fig. 5A demonstrates the distribution of out-of-plane stress in TC along TC-TGO interface when a crack exists within TC. It can be seen clearly that the tensile stress level near the instability region would increase when the crack exists at location “a” and this increase recedes when the crack is far away from the instability region (location “b”). In other regions, the effect of crack on σ_{22} is small and can be ignored.

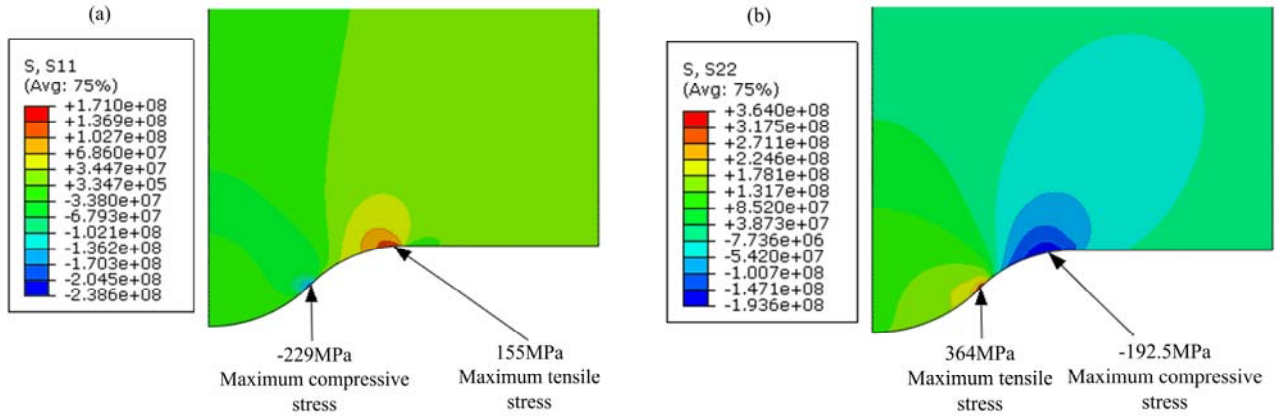

Figure 4. Stress distribution within TC when the TC is intact. (a) in-plane stress (σ_{11}) and (b) out-of-plane stress (σ_{22}).

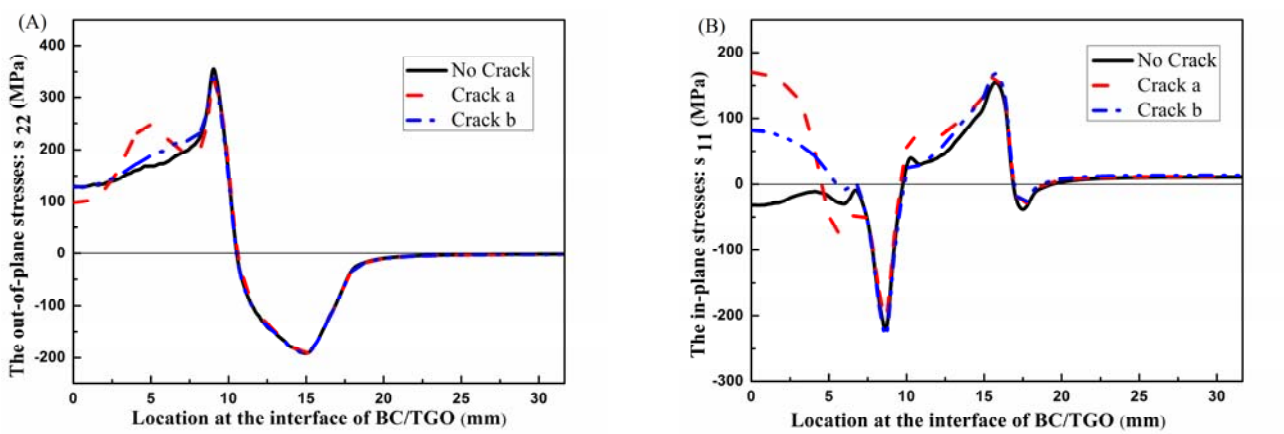

Figure 5. Stress distribution in TC along TC-TGO interface. (A) The out-of-plane stress (σ_{22}). (B) The in-plane stress (σ_{11}).

The distribution of in-plane stress (σ_{11}) in the intact TC is depicted in Fig. 4a. The compressive in-plane stress can induce the failure of the system by resulting in large-scale buckling [14]. Fig. 4a shows that the compressive σ_{11} mainly occurs in the zones above the instability site and the tensile part distributes around the periphery of the instability zone. Fig. 5B presents the distribution of in-plane stress in TC along the TC-TGO interface under the case a crack existing within TC. The existing of crack within TC makes the stress state in the region above the instability site become tensile from compressive. Especially, when the crack is close to the base of instability site (crack "a"), the tensile stress is significant. Compared to the compressive state of in-plane stress, this tensile state may reduce the probability of buckling occurring. Therefore, the existing of the crack can partly prevent the failure mode caused by buckling.

4.2. The effect of crack length

The influence of the normalized crack length $L/L_{\max}$ on the instability amplitude defined by $\delta R_1/\delta R_1^0$ and $\delta R_2/\delta R_2^0$ is shown in Fig. 6, where $L_{\max}$ is the maximum crack length used in the calculations, and δR_1^0 and δR_2^0 are the instability amplitudes when there is no crack within TC. It can be seen that both the magnitudes of the downward displacement δR_1 and the upward displacement δR_2 increase as the increase of crack length under both cracks case, and the increase rate also increase as the increase of crack length. It indicates that the crack extending would aggravate the instability and make the interface distortion be more significant. Inversely, the large interface distortion also can enhance the capacity of crack extending [3] and finally induce the failure of system. Note that the amplitude change of the displacement instability for the crack "a", which is more close to the base of instability site, is always greater than that for crack "b". This result shows that the crack close to the base of instability site has a greater enhancement on the instability. In addition, as the increase of crack length, the amplification of downward displacement δR_1 is always greater than that of upward displacement δR_2. From $L/L_{\max}=0.5$ to $L/L_{\max}=1.0$, the normalized amplification of $\delta R_1/\delta R_1^0$ is increased by more than 5 times, which can result in a markedly distortion at the interface. Therefore, the propagation of crack can significantly enhance the interface distortions as thermal cycling, especially that of the crack close to the base of instability site.

4.3. The effect of crack angle

The effect of the crack angle (θ_1 and θ_2) on the normalized instability amplitude $\delta R_1/\delta R_1^0$ and $\delta R_2/\delta R_2^0$ is shown in Fig. 7. Six different crack angles of 15°, 30°, 45°, 60°, 75° and 90° are used in the calculations for both θ_1 and θ_2. It is demonstrated that the upward displacement δR_2 is insensitive to the crack angle. However, the crack angle has a great influence on the downward displacement δR_1. When the angle is relatively small, the δR_1 increases as the increase of the crack angle. But when the crack angle makes the crack trend to be parallel the flat interface, δR_1 begins to decrease as the increase of the crack angle. From the previous analysis we can see that the propagation of crack within TC is preferential along the direction which is parallel to flat interface [33]. Therefore, when the crack direction is close to the preferential propagation direction, the crack propagation would play a dominant role and the instability of TGO can be restrained.
However, even the extending of displacement amplitude begins to slow down when the crack trends to parallel to flat interface, the effect of the crack in this direction on the displacement instability is much greater than that of the crack in the direction which is perpendicular to the flat interface.

Therefore, when the pre-existing crack is introduced within TC, the crack in the direction which is perpendicular to the flat interface is the optimal choice for preventing the large instability.

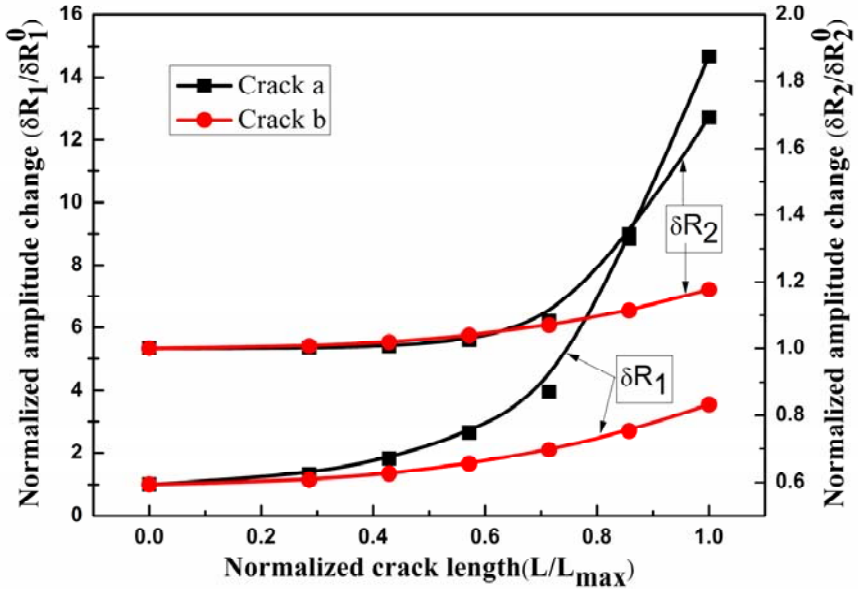

Figure 6. Normalized δR_1 and δR_2 vs. normalized crack length (L/Lmax).

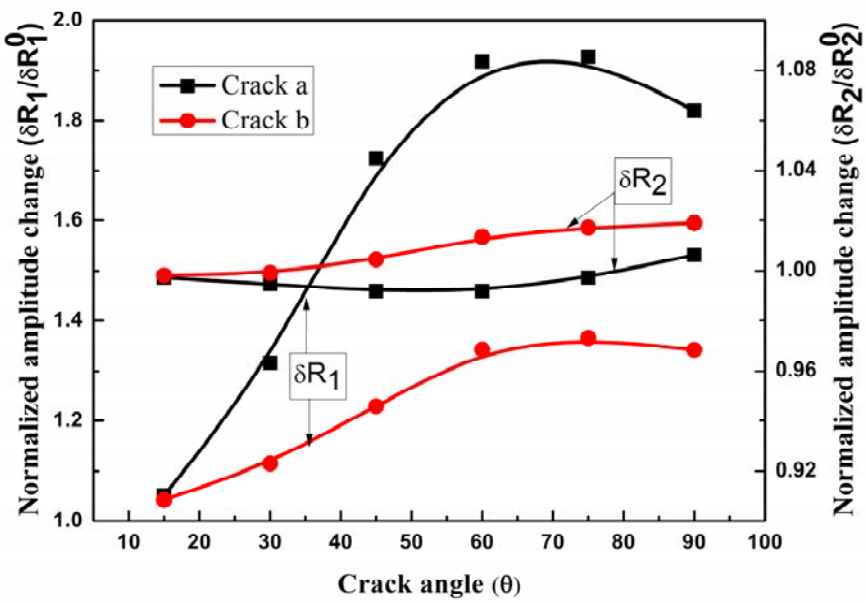

Figure 7. Normalized δR_1 and δR_2 vs. the crack angle (θ).

5. conclusions

The effect of pre-existing microcrack within TC on the displacement instability of TGO in thermal barrier systems is studied by a finite element model with the thermal growth behavior of TGO layer.

The influence of variational crack locations, length and direction on the development of stress and the instability amplitude is discussed. The main results from the calculations suggest:
(1) The crack within TC would promote the TGO displacement instability significantly, especially the crack close to the instability site.
(2) The tensile part of the out-of-plane stress, which is responsible for the delamination, mainly concentrates on the zone near the instability site and it can be promoted by the crack existing within TC. However, the compressed part of in-plane stress, which is responsible for the buckling, is restrained by this crack.
(3) The crack length and direction are two key factors affecting the displacement instability, especially the crack length. As the increase of the crack length, the amplitude of displacement instability increases significantly, which results in a serious interface distortion. The effect of crack direction mainly focuses on the downward displacement instability. The crack in the direction perpendicular to the flat interface is the optimal choice for prevent the large instability.

Acknowledgements

The work is supported by the National Natural Science Foundation of China (11021202 and 11172227) and National 973 Program (2013CB035701).

References

[1] Padture, N.P., M. Gell, and E.H. Jordan, Materials science - Thermal barrier coatings for gas-turbine engine apptications. Science, 296(2002) 280-284.
[2] Karlsson, A.M., J.W. Hutchinson, and A.G. Evans, A fundamental model of cyclic instabilities in thermal barrier systems. Journal of the Mechanics and Physics of Solids, 50(2002) 1565-1589.
[3] Evans, A.G., et al., Mechanisms controlling the durability of thermal barrier coatings. Progress in Materials Science, 46(2001) 505-553.
[4] Evans, A.G., M.Y. He, and J.W. Hutchinson, Mechanics-based scaling laws for the durability of thermal barrier coatings. Progress in Materials Science, 46(2001) 249-271.
[5] Mumm, D.R., A.G. Evans, and I.T. Spitsberg, Characterization of a cyclic displacement instability for a thermally grown oxide in a thermal barrier system. Acta Materialia, 49(2001) 2329-2340.
[6] Karlsson, A.M., C.G. Levi, and A.G. Evans, A model study of displacement instabilities during cyclic oxidation. Acta Materialia, 50(2002) 1263-1273.
[7] Ambrico, J.M., M.R. Begley, and E.H. Jordan, Stress and shape evolution of irregularities in oxide films on elastic-plastic substrates due to thermal cycling and film growth. Acta Materialia, 49(2001) 1577-1588.
[8] He, M.Y., A.G. Evans, and J.W. Hutchinson, The ratcheting of compressed thermally grown thin films on ductile substrates. Acta Materialia, 48(2000) 2593-2601.
[9] Karlsson, A.M. and A.G. Evans, A numerical model for the cyclic instability of thermally grown oxides in thermal barrier systems. Acta Materialia, 49(2001) 1793-1804.
[10] Karlsson, A.M., J.W. Hutchinson, and A.G. Evans, The displacement of the thermally grown oxide in thermal barrier systems upon temperature cycling. Materials Science and Engineering A, 351(2003) 244-257.
[11] Karlsson, A.M., J.W. Hutchinson, and A.G. Evans, A fundamental model of cyclic instabilities in thermal barrier systems. Journal of the Mechanics and Physics of Solids, 50(2002) 1565-1589.
[12] He, M.Y., A.G. Evans, and J.W. Hutchinson, The ratcheting of compressed thermally grown thin films on ductile substrates. Acta Materialia, 48(2000) 2593-2601.
[13] Karlsson, A.M. and G. Evans, A numerical model for the cyclic instability of thermally grown oxides in thermal barrier systems. Acta Materialia, 49(2001) 1793-1804.

[14] Karlsson, A.M., T. Xu, and A.G. Evans, The effect of the thermal barrier coating on the displacement instability in thermal barrier systems. Acta Materialia, 50(2002) 1211-1218.
[15] Mumm, D.R. and A.G. Evans, On the role of imperfections in the failure of a thermal barrier coating made by electron beam deposition. Acta Materialia, 48(2000) 1815-1827.
[16] Ruud, J.A., et al., Strength Degradation and Failure Mechanisms of Electron‐Beam Physical‐Vapor‐Deposited Thermal Barrier Coatings. Journal of the American Ceramic Society, 84(2001) 1545-1552.
[17] Spitsberg, I.T., D.R. Mumm, and A.G. Evans, On the failure mechanisms of thermal barrier coatings with diffusion aluminide bond coatings. Materials Science and Engineering a-Structural Materials Properties Microstructure and Processing, 394(2005) 176-191.
[18] Wright, P. and A. Evans, Mechanisms governing the performance of thermal barrier coatings. Current Opinion in Solid State and Materials Science, 4(1999) 255-265.
[19] Ding, J., F.X. Li, and K.J. Kang, Effects of material creep on displacement instability in a surface groove under thermo-mechanical cycling. Surface & Coatings Technology, 204(2009) 157-164.
[20] Ruckle, D.L., Plasma-sprayed ceramic thermal barrier coatings for turbine vane platforms. Thin Solid Films, 73(1980) 455-461.
[21] Taylor, T., D. ApplebyA E, and J. Griffiths, Plasma-sprayed yttria-stabilized zirconia coatings: structure-property relationships. Surface and Coatings Technology, 43(1990) 470-480.
[22] Zhou, B. and K. Kokini, Effect of pre-existing surface crack morphology on the interfacial thermal fracture of thermal barrier coatings: a numerical study. Materials Science and Engineering: A, 348(2003) 271-279.
[23] Fan, X., Zhang, W., T.J. Wang, Investigation on periodic cracking of elastic film/substrate system by the extended finite element method. Applied Surface Science, 257(2011) 6718-6724.
[24] Zhang, W., X. Fan, and T. Wang, The surface cracking behavior in air plasma sprayed thermal barrier coating system incorporating interface roughness effect. Applied Surface Science, 258(2011) 811-817.
[25] Kokini, K. and Y. Takeuchi, Multiple surface thermal fracture of graded ceramic coatings. Journal of thermal stresses, 21(1998) 715-725.
[26] Kokini, K., A. Banerjee, and T.A. Taylor, Thermal fracture of interfaces in precracked thermal barrier coatings. Materials Science and Engineering A, 323(2002) 70-82.
[27] He, M.Y., J.W. Hutchinson, and A.G. Evans, Large deformation simulations of cyclic displacement instabilities in thermal barrier systems. Acta Materialia, 50(2002) 1063-1073.
[28] Belytschko, T. and T. Black, Elastic crack growth in finite elements with minimal remeshing. International Journal for Numerical Methods in Engineering, 45(1999) 601-620.
[29] ES, N.M.O., J. Dolbow, and T. Belytschko, A finite element method for crack growth without remeshing. Int. J. Numer. Meth. Engng, 46(1999) 131-150.
[30] Melenk, J.M. and I. Babuska, The partition of unity finite element method: basic theory and applications. Computer Methods in Applied Mechanics and Engineering, 139(1996) 289-314.
[31] Sukumar, N., et al., Extended finite element method for three‐dimensional crack modelling. International Journal for Numerical Methods in Engineering, 48(2000) 1549-1570.
[32] Cheng, J., et al., Thermal/residual stress in an electron beam physical vapor deposited thermal barrier coating system. Acta Materialia,46(1998) 5839-5850.
[33] Bhatnagar, H., S. Ghosh, and M.E. Walter, A parametric study of damage initiation and propagation in EB-PVD thermal barrier coatings. Mechanics of Materials, 42(2010) 96-107.